



AFRL-RZ-WP-TR-2011-2064

**APPLICATION OF ADVANCED LASER DIAGNOSTICS
TO HIGH IMPACT TECHNOLOGIES**

Delivery Order 0001: Laser Diagnostics Applications

Larry P. Goss

Innovative Scientific Solutions, Inc.

FEBRUARY 2011

Final Report

Approved for public release; distribution unlimited.

See additional restrictions described on inside pages

STINFO COPY

**AIR FORCE RESEARCH LABORATORY
PROPULSION DIRECTORATE
WRIGHT-PATTERSON AIR FORCE BASE, OH 45433-7251
AIR FORCE MATERIEL COMMAND
UNITED STATES AIR FORCE**

NOTICE AND SIGNATURE PAGE

Using Government drawings, specifications, or other data included in this document for any purpose other than Government procurement does not in any way obligate the U.S. Government. The fact that the Government formulated or supplied the drawings, specifications, or other data does not license the holder or any other person or corporation; or convey any rights or permission to manufacture, use, or sell any patented invention that may relate to them.

This report was cleared for public release by the USAF 88th Air Base Wing (88 ABW) Public Affairs (AFRL/PA) Office and is available to the general public, including foreign nationals. Copies may be obtained from the Defense Technical Information Center (DTIC) (<http://www.dtic.mil>).

AFRL-RZ-WP-TR-2011-2064 HAS BEEN REVIEWED AND IS APPROVED FOR PUBLICATION IN ACCORDANCE WITH THE ASSIGNED DISTRIBUTION STATEMENT.

*//Signature//

CHARLES W. FRAYNE, Project Engineer
Combustion Branch
Turbine Engine Division
Propulsion Directorate

//Signature//

JOSEPH ZELINA, PhD
Combustion Branch
Turbine Engine Division
Propulsion Directorate

//Signature//

JEFFREY M. STRICKER
Chief Engineer
Turbine Engine Division
Propulsion Directorate

This report is published in the interest of scientific and technical information exchange, and its publication does not constitute the Government's approval or disapproval of its ideas or findings.

*Disseminated copies will show “//Signature//” stamped or typed above the signature blocks.

REPORT DOCUMENTATION PAGE				Form Approved OMB No. 0704-0188	
<p>The public reporting burden for this collection of information is estimated to average 1 hour per response, including the time for reviewing instructions, searching existing data sources, gathering and maintaining the data needed, and completing and reviewing the collection of information. Send comments regarding this burden estimate or any other aspect of this collection of information, including suggestions for reducing this burden, to Department of Defense, Washington Headquarters Services, Directorate for Information Operations and Reports (0704-0188), 1215 Jefferson Davis Highway, Suite 1204, Arlington, VA 22202-4302. Respondents should be aware that notwithstanding any other provision of law, no person shall be subject to any penalty for failing to comply with a collection of information if it does not display a currently valid OMB control number. PLEASE DO NOT RETURN YOUR FORM TO THE ABOVE ADDRESS.</p>					
1. REPORT DATE (DD-MM-YY) February 2011		2. REPORT TYPE Final		3. DATES COVERED (From - To) 13 June 2003 – 16 February 2011	
4. TITLE AND SUBTITLE APPLICATION OF ADVANCED LASER DIAGNOSTICS TO HIGH IMPACT TECHNOLOGIES Delivery Order 0001: Laser Diagnostics Applications				5a. CONTRACT NUMBER F33615-03-D-2329-0001	
				5b. GRANT NUMBER	
				5c. PROGRAM ELEMENT NUMBER 62203F	
6. AUTHOR(S) Larry P. Goss				5d. PROJECT NUMBER 3048	
				5e. TASK NUMBER 04	
				5f. WORK UNIT NUMBER 304804LD	
7. PERFORMING ORGANIZATION NAME(S) AND ADDRESS(ES) Innovative Scientific Solutions, Inc. 2766 Indian Ripple Road Dayton, OH 45440-3638				8. PERFORMING ORGANIZATION REPORT NUMBER 2829, DO 0001 Final	
9. SPONSORING/MONITORING AGENCY NAME(S) AND ADDRESS(ES) Air Force Research Laboratory Propulsion Directorate Wright-Patterson Air Force Base, OH 45433-7251 Air Force Materiel Command United States Air Force				10. SPONSORING/MONITORING AGENCY ACRONYM(S) AFRL/RZTC	
				11. SPONSORING/MONITORING AGENCY REPORT NUMBER(S) AFRL-RZ-WP-TR-2011-2064	
12. DISTRIBUTION/AVAILABILITY STATEMENT Approved for public release; distribution unlimited.					
13. SUPPLEMENTARY NOTES Report contains color. PA Case Number: 88ABW-2011-2373; Clearance Date: 27 Apr 2011. In addition to the primary research summary, this report also contains over 320 papers that were published in professional journals.					
14. ABSTRACT The technical effort for this program was divided into six major tasks, covering advanced diagnostic techniques, modeling and simulations, fundamental combustion research, high-impact-technology component studies, advanced-propulsion-system concept studies, and advanced-concept high-impact-technology demonstrations. The objectives of this ambitious program were to: <ul style="list-style-type: none"> Develop and apply advanced diagnostic techniques to the investigation of advanced-concept technologies for future-generation propulsion systems. Develop and apply advanced computational-fluid-dynamics (CFD)-based simulations and models to the investigation of advanced-concept technologies for future-generation propulsion systems. Utilize advanced diagnostics and models to design and conduct fundamental experiments that will provide a database for evaluation and application of advanced-concept technologies for future-generation propulsion systems. Identify, evaluate, and apply high-impact technologies that have the potential to reduce cost, improve performance, and reduce emissions in future-generation propulsion systems. Identify, evaluate, and apply advanced-propulsion-system cycles that will result in high-impact, revolutionary technologies for future-generation propulsion systems. Demonstrate the advanced technologies in small-engine tests and innovative low-cost flight tests. The research conducted during the program resulted in more than 325 publications and presentations.					
15. SUBJECT TERMS optical diagnostics, computational fluid dynamics, combustion, propulsion, pulsed detonation engine, flight testing, advanced combustor concepts					
16. SECURITY CLASSIFICATION OF:			17. LIMITATION OF ABSTRACT: SAR	18. NUMBER OF PAGES 1534	19a. NAME OF RESPONSIBLE PERSON (Monitor) Charles W. Frayne 19b. TELEPHONE NUMBER (Include Area Code) N/A
a. REPORT Unclassified	b. ABSTRACT Unclassified	c. THIS PAGE Unclassified			

TABLE OF CONTENTS

Section	Page
1.0 INTRODUCTION.....	1
2.0 ADVANCED-DIAGNOSTIC-TECHNIQUE DEVELOPMENT AND EVALUATION.....	2
2.1 General Overview.....	2
2.1.1 Triple-Pump Coherent Anti-Stokes Raman Spectroscopy (CARS): Temperature and Multiple-Species Concentration Measurements in Reacting Flows.....	2
2.1.2 Single-Shot Thermometry and Multiple-Species Measurements Using Dual-Pump, Dual-Broadband (DPDB) CARS in Liquid-Fueled CFM56 Combustor.....	2
2.1.3 Two-Color, Two-Photon Laser-Induced Polarization Spectroscopy (LIPS) Measurements of Atomic Hydrogen in Near-Adiabatic, Atmospheric-Pressure Hydrogen/Air Flames.....	3
2.1.4 DPDB CARS in Reacting Flows.....	3
2.1.5 Non-perturbative Modeling of Two-Photon Absorption in Three-State System.....	4
2.1.6 Multiple-Pump CARS for Quantitative Measurement of Temperature and Flame Species in Model Gas-Turbine Combustor.....	4
2.1.7 State-of-the-Art Fuel-Acidity Monitoring.....	4
2.1.8 Kinetic Behavior of Polymer-Coated Long-Period-Grating Fiber-Optic Sensors.....	5
2.1.9 Combustion Exhaust Measurements of Nitric Oxide (NO) with Ultraviolet (UV) Diode-Laser-Based Absorption Sensor.....	5
2.1.10 Optical Turbine-Engine Diagnostics for Ground-Test and On-Board Applications.....	6
2.1.11 Diode-Laser-Based UV-Absorption Sensor for High-Speed Detection of Hydroxyl Radical (OH).....	6
2.1.12 Advanced CARS Techniques for Simultaneous Species and Temperature Measurements.....	7
2.1.13 Ballistic Imaging of Liquid Core for Steady Jet in Cross Flow.....	7
2.1.14 10-kHz Detection of CO ₂ at 4.5 μ m Using Tunable Diode-Laser Difference-Frequency Generation.....	7
2.1.15 Broadband CARS Spectroscopy of Nitrogen Using ps Modeless Dye laser.....	8
2.1.16 Time-Resolved Dynamics of Resonant and Non-resonant Broadband ps CARS Signals.....	8
2.1.17 Injection-Seeded Megahertz (MHz)-Repetition-Rate Optical-Parametric-Oscillator (OPO) System.....	8
2.1.18 Water-Vapor Detection Using Asynchronous Terahertz (THz) Sampling.....	9

TABLE OF CONTENTS (Continued)

Section	Page
2.1.19 Velocity Imaging for Liquid-Gas Interface in Near Field of Atomizing Spray: Proof of Concept.....	9
2.1.20 RELIEF Velocimetry Using ps Tagging and Nd:YAG-Based Interrogation.....	10
2.1.21 Effects of Quenching on ERE-CARS of NO.....	10
2.1.22 Application of Difference-Frequency-Mixing-Based Diode Diode-Laser Sensor for Carbon-Monoxide (CO) Detection in 4.4 - 4.8 μm Spectral Region.....	10
2.1.23 Measurement of NO Concentrations in Flames Using ERE-CARS.....	11
2.1.24 Femtosecond (fs)-CARS Measurement of Gas Temperatures from Frequency-Spread Dephasing of Raman Coherence.....	11
2.1.25 Measurements of NO and OH Concentrations in Vitiated Air Using Diode-Laser-Based UV Absorption Sensors.....	11
2.1.26 Robust Procedure for Analysis of Non-Evenly Spaced Velocity Time-Series Data.....	12
2.1.27 Detection of Acetylene by ERE-CARS.....	12
2.1.28 Effects of Pressure Variations on ERE-CARS of NO.....	13
2.1.29 Detection of Atomic Hydrogen in Flames Using ps, Two-Color, Two-Photon Resonance Six-Wave-Mixing Spectroscopy.....	13
2.1.30 Theory of fs-CARS Spectroscopy of Gas-Phase Transitions.....	13
2.1.31 Improving Signal-to-Interference Ratio in Rich Hydrocarbon-Air Flames Using ps-CARS.....	14
2.1.32 Effect of Collisions on Time-Delayed ps-CARS Spectroscopy.....	15
2.1.33 Fs-CARS for High-Bandwidth, Collision-Free Temperature Measurements.....	15
2.1.34 Insensitivity of ERE-CARS to Electronic Quenching.....	15
2.1.35 Fs-CARS Measurement of Gas-Phase Species and Temperature.....	15
2.1.36 Perturbative Theory and Modeling of ERE-CARS Spectroscopy of NO.....	15
2.1.37 Applications of Ultrafast Lasers for Optical Measurements in Combusting Flows.....	16
2.1.38 Measurements of NO Concentration in Flames Using Broadband Stokes ERE-CARS.....	16
2.1.39 Theory of fs-CARS Spectroscopy for Gas-Phase Transitions.....	17
2.1.40 Single-Laser-Shot Detection of NO in Reacting Flows Using ERE-CARS.....	18
2.1.41 Collisional Effects on Molecular Dynamics in ERE-CARS.....	18
2.1.42 Development of Nearly Transform-Limited, Low-Repetition-Rate ps OPO.....	19

TABLE OF CONTENTS (Continued)

Section	Page
3.0 SIMULATION AND MODEL DEVELOPMENT AND EVALUATION.....	20
3.1 General Overview.....	20
3.1.1 CFD-Based Global Chemistry Predictions for Normal and Inverse Laminar Ethane Jet Diffusion Flames under Oxygen Enhancement and Gravity Variation.....	20
3.1.2 Macro- vs. Micro-Vortex/Flame Interactions in Hydrogen Diffusion Flames.....	20
3.1.3 Simulation of Polycyclic Aromatic Hydrocarbons (PAHs) in Trapped-Vortex Combustor (TVC).....	21
3.1.4 Gravity, Radiation, and Coflow Effects on Partially Premixed Flame.....	21
3.1.5 Effect of Diluents on Lifted Partially Premixed Flames in Normal and Microgravity: Numerical Investigation.....	22
3.1.6 Numerical Studies on Ultra-Lean Methane Premixed Flames.....	22
3.1.7 Effect of Nitromethane on Soot Formation in Heptane Jet Diffusion Flames.....	23
3.1.8 CFD-Based Global- and Detailed-Chemistry Predictions for Inverse, Laminar, Ethane Jet Diffusion Flames Under Oxygen Enhancement and Gravity Variation.....	23
3.1.9 Studies on Soot Formation in Model Gas-Turbine Combustor.....	23
3.1.10 Micro-Vortex/Flame Interactions and Their Implications in Turbulent-Flame Modeling.....	24
3.1.11 Numerical Investigation of Flame Liftoff, Stabilization, and Blowout.....	24
3.1.12 Trimethylphosphate (TMP) as Soot-Reducing Additive - Numerical Study of Jet Flames.....	25
3.1.13 Effects of H ₂ -Enrichment on Flame-Propagation Characteristics of Methane-Air Flames.....	26
3.1.14 Hysteresis in Counterflow Premixed Flame System.....	26
3.1.15 Comparison of Chemical-Kinetics Models for JP-8 Fuel in Predicting Premixed and Non-premixed Flames.....	27
3.1.16 Numerical Studies on Soot Mitigation in Model Gas-Turbine Combustor.....	28
3.1.17 Numerical Study of Evolution of Strongly Forced, Axisymmetric, Laminar Cold-Flow Jets.....	28
3.1.18 Characteristics of Propagating H ₂ -Enriched CH ₄ -Air Flames.....	29
3.1.19 Investigations on Double-State Behavior of Counterflow Premixed Flame System.....	29
3.1.20 Predictions on Sooting Behavior of Recirculation-Zone-Supported Flames.....	30
3.1.21 Experimental and Numerical Studies of Centerbody Flames.....	30

TABLE OF CONTENTS (Continued)

Section	Page
3.1.22 Can Non-premixed Stretched Flames Become Infinitely Thin?.....	31
3.1.23 Evaluation of Chemical-Kinetics Models for Heptane Combustion.....	31
3.1.24 Comparison of Chemical-Kinetics Mechanisms through Predicting Non-premixed Ethylene Jet Flame.....	32
3.1.25 Effects of H ₂ Enrichment on Propagation Characteristics of CH ₄ -Air Triple Flames.....	32
3.1.26 Numerical Studies on Cavity-Inside-Cavity-Supported Flames In Ultra-Compact Combustors.....	33
3.1.27 Stability of Lifted Flames in Centerbody Burner.....	33
3.1.28 Calculation of Multi-dimensional Flames Using Large Chemical Kinetics.....	34
3.1.29 Asymmetric Expansion of Detonation Wave in an Array of Tubes.....	34
4.0 FUNDAMENTAL EXPERIMENTS.....	36
4.1 General Overview.....	36
4.1.1 Dynamics of Vortex-Flame Interactions and Implications for Turbulent Combustion.....	36
4.1.2 Vortex-Induced Extinction of Non-Premixed Counterflow Flames.....	36
4.1.3 PIV/PLIF Investigation of Two-Phase Vortex-Flame Interactions: Effects of Vortex Size and Strength.....	37
4.1.4 Simultaneous PLIF/PIV Investigation of Vortex-Induced Annular Extinction in H ₂ -Air Counterflow Diffusion Flames.....	37
4.1.5 Influence of Spray-Flame Structure on Soot Formation in Gas-Turbine Combustors.....	37
4.1.6 Extinction Criterion for Unsteady, Opposing-Jet Diffusion Flames.....	38
4.1.7 OH PLIF and Soot-Volume-Fraction Imaging in Reaction Zone of Liquid-Fueled, Model Gas-Turbine Combustor.....	38
4.1.8 Temperature and CO ₂ Concentration Measurements in Exhaust Stream of Liquid-Fueled Combustor Using Dual- Pump CARS Spectroscopy.....	39
4.1.9 Studies of Hydroxyl Distribution and Soot Formation in in Turbulent Spray Flames.....	39
4.1.10 Influence of Fuel Type and Operating Conditions on Particulates in Gas-Turbine Combustors.....	40
4.1.11 Application of Laser Imaging Studies of Particle Formation in Gas-Turbine Combustion.....	40

TABLE OF CONTENTS (Continued)

Section	Page
4.1.12 Investigation of Dynamic Diffusion Flame of H ₂ in Air with Laser Diagnostics and Numerical Modeling.....	41
4.1.13 Unsteady Effects on Flame-Extinction Limits during Gaseous and Two-Phase Flame/Vortex Interactions.....	41
4.1.14 Simultaneous PLII, OH PLIF, and Droplet Mie Scattering in Swirl-Stabilized Spray Flames.....	42
4.1.15 DPDB CARS for Exhaust-Gas Temperature and CO ₂ O ₂ -N ₂ Mole-Fraction Measurements in Model Gas-Turbine Combustors.....	42
4.1.16 Dynamics of Inverse Diffusion Flame and Its Role in Polycyclic-Aromatic-Hydrocarbon and Soot Formation.....	43
4.1.17 Measurements of OH Mole Fraction and Temperature up to 20 kHz Using Diode-Laser-Based UV Absorption Sensor.....	43
4.1.18 Planar Imaging of Soot, Droplets, and Fluorescence for Studies of Alternative Fuel Blends in Gas-Turbine Combustion.....	44
4.1.19 Coherent Structures and Turbulent Molecular Mixing in Gaseous Planar Shear Layers.....	44
4.1.20 Non-reacting and Combusting Flow Investigation of Bluff Bodies in Cross Flow.....	44
4.1.21 Understanding Turbulent Flames through Vortex/Flame-Interaction Studies.....	45
4.1.22 NO-Concentration Profiles in Atmospheric-Pressure Flames Using ERE-CARS.....	45
4.1.23 NO-Concentration Measurements in Atmospheric-Pressure Flames Using ERE-CARS.....	46
4.1.24 Effects of Oxygenated Compounds on PAH and Soot across a Suite of Laboratory Devices.....	47
4.1.25 Effects of Nitrogen-Containing Compounds on PAH and Soot across a Suite of Laboratory Devices.....	47
4.1.26 Effects of Phosphorus Compounds on PAH and Soot across a Suite of Laboratory Devices.....	48
4.1.27 Temperature Measurements in Reacting Flows by Time-Resolved fs-CARS Spectroscopy.....	48
5.0 HIGH-IMPACT-TECHNOLOGY COMPONENT STUDIES.....	49
5.1 General Overview.....	49
5.1.1 Stator-Cascade-Flow Vectoring through Counter-Flow Blowing (CFB).....	49
5.1.2 Digital-Particle-Imaging-Velocimetry (DPIV) Measurements of Flow Field between Transonic Rotor and Upstream Stator.....	49
5.1.3 Investigation on Vortex Shedding of Jet-in-a-Cross Flow.....	50

TABLE OF CONTENTS (Continued)

Section	Page
5.1.4 Stator Cascade Flow Vectoring through Counter-Flow Blowing.....	50
5.1.5 PIV with Light-Emitting Diode: Particle Shadow Velocimetry.....	50
5.1.6 Development of Fiber-Optic PIV System for Turbomachinery Applications.....	51
5.1.7 Investigation of PSV for Transonic-Flow Applications.....	51
5.1.8 Fluidic-Control Studies for Diffusion Enhancement in Axial Compression Systems.....	52
5.1.9 PIV Study of Wake-Rotor Interactions in a Transonic Compressor at Various Operating Conditions.....	52
5.1.10 PIV Investigation of Flow Field in Transonic Compressor Cascade with Moving Shock Wave.....	53
5.1.11 PIV Study of Blade-Row Interactions in Transonic Compressor.....	53
5.1.12 Investigation of Blade-Row Interactions in Transonic Compressor Using PIV.....	54
5.1.13 PIV Measurements of Blade-Row Interactions in a Transonic Compressor for Various Operating Conditions.....	54
6.0 ADVANCED-PROPULSION-SYSTEM CONCEPT STUDIES.....	56
6.1 General Overview.....	56
6.1.1 Initiation of Detonation in a Large Tube.....	56
6.1.2 Use of Flash-Vaporization System with Liquid-Hydrocarbon Fuels in a PDE.....	56
6.1.3 Assessment of Performance of Pulsejet and Comparison with a PDE.....	57
6.1.4 Detonation Initiation of Hydrocarbon-Air Mixtures in a PDE.....	57
6.1.5 Impact of DDT Mechanism, Combustion Wave Speed, Temperature, and Charge Quality on PDE Performance.....	58
6.1.6 Performance Measurements of PDE Engine Ejectors.....	58
6.1.7 Performance Measurements of Multi-cycle PDE Exhaust Nozzle.....	59
6.1.8 Emissions-Reduction Technology for Military Gas-Turbine Engines.....	59
6.1.9 Acoustic Measurements for PDE.....	60
6.1.10 Performance Assessment of Large-Scale Pulsejet-Driven Ejector System.....	60
6.1.11 Performance Measurements of Straight and Diverging Ejectors Integrated with a PDE.....	61
6.1.12 Impact of Detonation-Initiation Techniques on Thrust in a PDE.....	61
6.1.13 Performance Measurements of Multi-cycle PDE Exhaust Nozzles.....	62

TABLE OF CONTENTS (Continued)

Section	Page
6.1.14 Effects of Tube and Ejector Geometry on Performance of PDE-Driven Ejectors.....	62
6.1.15 Effect of Supercritical Fuel Injection on Cycle Performance of a PDE.....	62
6.1.16 Experimental Study of Ejectors Driven by a PDE.....	63
6.1.17 Ignition and Detonation-Initiation Characteristics of Hydrogen and Hydrocarbon Fuels in a PDE.....	63
6.1.18 Transient Plasma Ignition (TPI) for Delay Reduction in a PDE.....	64
6.1.19 Effects of Corona, Spark, and Surface Discharges on Ignition Delay and DDT in a PDE.....	64
6.1.20 Evaluation of Catalytic and Thermal Cracking in a JP-8 Fueled PDE.....	64
6.1.21 Detonation Propagation across Asymmetric Step Expansion.....	65
6.1.22 Effect of Supercritical Fuel Injection on Cycle Performance of a PDE.....	65
6.1.23 Fuel-Composition Analysis of Endothermically Heated JP-8 Fuel for Use in a PDE.....	66
6.1.24 Direct Initiation by Detonation Branching in a PDE.....	66
6.1.25 Development of Continuous Branching PDE.....	66
6.1.26 Single-Ejector Augmentation of Multi-tube PDE.....	67
6.1.27 Investigation of Fundamental Processes Leading to PDE/Ejector Thrust Augmentation.....	67
6.1.28 Performance Studies of PDE Ejectors.....	68
6.1.29 Study on Operation of PDE-Driven Ejectors.....	68
 7.0 DEMONSTRATION OF ADVANCED-CONCEPT HIGH-IMPACT TECHNOLOGIES.....	 69
7.1 General Overview.....	69
7.1.1 A Flight-Ready PDE.....	69
7.1.2 Manned Demonstration Flight of a PDE.....	69
 8.0 REFERENCES.....	 71
 9.0 PUBLICATIONS, PRESENTATIONS, PATENTS, AND SIGNIFICANT ACCOMPLISHMENTS.....	 72
9.1 Publications, Presentations, and Patents.....	72
9.2 Significant Accomplishments.....	103
 APPENDIX - Publications and Presentations.....	 114

PREFACE

This report was prepared by Dr. Larry P. Goss of Innovative Scientific Solutions, Inc. (ISSI), and covers work performed during the period 14 June 2003 through 16 February 2011 under Air Force Contract F33615-03-C-2829, Delivery Order 0001. The contract was administered under the direction of the Air Force Research Laboratory (AFRL), Wright-Patterson Air Force Base, Ohio, with Dr. Vincent Belovich and Mr. Charles Frayne as Government Project Monitors.

GLOSSARY

ADPAC	advanced directed profan analysis code
AFRL	Air Force Research Laboratory
ASOPS	asynchronous optical sampling
BBO	barium borate
BRI	blade-row interaction
C ₂ H ₂	acetylene
CARL	Compressor Aero Research Laboratory
CARS	coherent anti-Stokes Raman spectroscopy
CARSFT	Sandia computer code that calculates theoretical spectra for coherent anti-Stokes Raman spectroscopy
CCD	charge-coupled device
CFB	counter-flow blowing
CFD	computational fluid dynamics
CFDC	computational fluid dynamics with chemistry
CIC	cavity inside cavity
CJ	Chapman-Jouget
CNC	condensation nuclei counter
CO	carbon monoxide
cw	continuous wave
2D	two dimensional
DDT	deflagration-to-detonation transition
DFFT	discrete fast Fourier transform
DNI	direct numerical integration
DPDB	dual pump dual broadband
DR	diameter ratio
DTBP	di-tertiary-butyl-peroxide
ECDL	external cavity diode laser
ERE	electronic-resonance enhanced
FOPIV	fiber-optic particle-imaging velocimetry
fs	femtosecond
H	atomic hydrogen

H ₂	molecular hydrogen
IDF	inverse diffusion flame
ISSI	Innovative Scientific Solutions, Inc.
JP-8	Jet Propellant-8 (kerosene-blend fuel refined from petroleum)
LDV	laser Doppler velocimetry
LED	light-emitting diode
LIF	laser-induced fluorescence
LII	laser-induced incandescence
LIPS	laser-induced polarization spectroscopy
LLNL	Lawrence Livermore National Laboratory
LPG	long-period grating
MATLAB	MA TRix LAB oratory - programming language for technical computing
MHz	megahertz
MIR	mid-infrared
N ₂	nitrogen
Nd:YAG	neodymium-doped yttrium aluminum garnet
Nd:YVO ₄	neodymium-doped yttrium orthovanadate
NIST	National Institute of Standards and Technology
NO	nitric oxide
NPF	non-premixed flame
NRB	non-resonant background
O	atomic oxygen
OH	hydroxyl radical
ON	octane number
OPO	optical parametric oscillator
PAH	polycyclic aromatic hydrocarbon
PDE	pulse detonation engine
PIV	particle-imaging velocimetry
PLIF	planar laser-induced fluorescence
pm	particulate matter
ppm	parts per million
PPF	partially premixed flame
PPLN	periodically poled lithium niobate

ps	picosecond
PSP	pressure-sensitive paint
RELIEF	Raman excitation and laser-induced electronic fluorescence
S-8	Fischer-Tropsch JP-8
SD	San Diego
SMI	stage-matching investigation
SMPS	scanning mobility particle sizer
THz	terahertz
TMP	trimethylphosphate
TPI	transient plasma ignition
TVC	trapped-vortex combustor
UCC	ultra-compact combustor
UNICORN	UNsteady Ignition and COmbustion with ReactionNs
UV	ultraviolet
WG	wake generator
WSR	well-stirred reactor

1.0 INTRODUCTION

This report describes the results of experimental and numerical investigations on combustion and fuel processes. The purpose of this program was to investigate and demonstrate revolutionary concepts that may make a significant contribution to the affordability and performance goals of the Versatile Affordable Advanced Turbine Engine (VAATE) program.

The objectives of this research program were to:

- 1) Develop and apply advanced diagnostic techniques to the investigation of advanced-concept technologies for future-generation propulsion systems.
- 2) Develop and apply advanced computational-fluid-dynamics (CFD)-based simulations and models to the investigation of advanced-concept technologies for future-generation propulsion systems.
- 3) Utilize advanced diagnostics and models to design and conduct fundamental experiments that will provide a database for evaluation and application of advanced-concept technologies for future-generation propulsion systems.
- 4) Identify, evaluate, and apply high-impact technologies that have the potential to reduce cost, improve performance, and reduce emissions in future-generation propulsion systems.
- 5) Identify, evaluate, and apply advanced-propulsion-system cycles that will result in high-impact revolutionary technologies for future-generation propulsion systems.
- 6) Demonstrate the advanced technologies in small-engine tests and innovative low-cost flight tests.

The research conducted during this program resulted in more than 325 publications, presentations, and patents, a complete list of which can be found in Section 9 along with brief descriptions of significant accomplishments of the ISSI staff. Complete copies of 144 of these presentations and publications are included in the Appendix. In this report the research efforts are summarized in Sections 2-7. Section 2 details the advanced-diagnostic-technique development and evaluation. Section 3 describes the effort in simulation and model development and evaluation. Section 4 documents the fundamental experiments. Section 5 details the high-impact-technology component studies. Section 6 documents the advanced-propulsion-system concept studies. Section 7 describes the demonstration of advanced-concept high-impact technologies.

2.0 ADVANCED-DIAGNOSTIC-TECHNIQUE DEVELOPMENT AND EVALUATION

2.1 General Overview

The objective of this portion of the program was to develop and apply advanced diagnostic techniques for both fundamental experiments and advanced component concept studies. The diagnostic techniques developed under this task were used to support directly the other major program tasks. A wide variety of point-wise, imaging, picosecond (ps), and fuels-specific techniques were developed and evaluated. A summary of the work accomplished on this task during the program follows.

2.1.1 Triple-Pump Coherent Anti-Stokes Raman Spectroscopy (CARS): Temperature and Multiple-Species Concentration Measurements in Reacting Flows.

Two types of triple-pump CARS systems were employed for the simultaneous measurement of temperature and multiple-species concentrations. In the first system the ro-vibrational transitions of N_2 , O_2 , and H_2 were probed using three narrowband pump beams and a broadband Stokes beam. In the second system pure rotational transitions of N_2/O_2 and the ro-vibrational transitions of N_2/CO_2 were probed using two narrowband pump beams, a broadband pump beam, and a broadband Stokes beam. The use of a broadband pump source in the second CARS system allowed rotational and ro-vibrational transitions of different molecules to be probed simultaneously. For both CARS systems the signals appeared at two distinct wavelengths. The CARS signals at the two wavelengths were separated by dichroic mirrors before being detected by two spectrometer-CCD detection systems. For proof-of-concept demonstrations, single-shot and averaged measurements were performed in an atmospheric-pressure hydrogen-air diffusion flame and in a carbon-dioxide-seeded, near-adiabatic hydrogen-air flame stabilized over a Hencken burner. To the investigators' knowledge, these represent the first reported experiments of triple-pump CARS for the simultaneous measurement of temperature and multiple-species concentrations. The results of this study were documented by S. Roy, T. R. Meyer, M. S. Brown (all of ISSI), V. N. Velur (California Institute of Technology), R. P. Lucht (Purdue University), and J. R. Gord (AFRL) in a paper that was published in *Optics Communications* [Vol. 224, Nos. 1-3, pp. 131-137 (August 15, 2003)]. The paper is included in the Appendix.

2.1.2 Single-Shot Thermometry and Multiple-Species Measurements Using Dual-Pump, Dual-Broadband (DPDB) CARS in Liquid-Fueled CFM56 Combustor.

A DPDB CARS system for the simultaneous measurement of temperature and multiple-species concentrations was demonstrated in the exhaust stream of a liquid-fueled CFM56 model gas-turbine combustor. The DPDB CARS approach employs four laser beams that generate CARS signals near two distinct wavelengths, enabling highly accurate, spatially resolved single-shot measurements within the full range of combustor operating conditions. For the proof-of-concept experiments, CARS signals from N_2-O_2 and N_2-CO_2 pairings were collected. Single-shot measurements were made for different jet fuels, fuel additives, and equivalence ratios to document correlations among particulate-size distribution, concentrations of carbon dioxide and oxygen, temperature, and fuel composition. The results of this investigation were documented by S. Roy, T. R. Meyer (both of ISSI), R. P. Lucht (Purdue University), V. M. Belovich, E.

Corporan, and J. R. Gord (all of AFRL) in three presentations at: 1) the 42nd AIAA Aerospace Sciences Meeting and Exhibit, which was held 5-8 January 2004 in Reno, NV, 2) the ACS/SAS Poster Session and Patterson College Awards, which was held 2 March 2004 in Dayton, OH, and 3) the 29th Annual Dayton-Cincinnati Aerospace Science Symposium, which was held 9 March 2004 in Dayton, OH. AIAA Paper No. 2004-0711, the publication that resulted from the first presentation, is included in the Appendix.

2.1.3 Two-Color, Two-Photon Laser-Induced Polarization Spectroscopy (LIPS) Measurements of Atomic Hydrogen in Near-Adiabatic, Atmospheric-Pressure Hydrogen/Air Flames.

Two-color, two-photon laser-induced polarization spectroscopy (LIPS) of atomic hydrogen was demonstrated and applied in atmospheric-pressure hydrogen/air flames. Fundamental and frequency-doubled beams from a single 486-nm dye laser were used in the experiments. The 243-nm pump beam in the measurements was tuned to the two-photon $n = 1 \rightarrow n = 2$ resonance of the hydrogen atom. The 486-nm probe beam was tuned to the single-photon $n = 2 \rightarrow n = 4$ resonance of the hydrogen atom. Measurements were performed in an atmospheric-pressure H₂/air flame stabilized on a near-adiabatic, flat-flame calibration burner (the Hencken burner). For the range of pump-beam intensities used, the LIPS signal was found to be nearly proportional to the square of the pump-beam intensity over a wide range of flame equivalence ratios. Spectral line shapes were recorded at flame equivalence ratios ranging from 0.85 to 2.10. Vertical H-atom number-density distribution profiles were measured in the Hencken burner. The vertical H-atom number-density profiles measured along the burner centerline for various flame equivalence ratios were compared with the results of a numerical flame calculation using the UNICORN (UNsteady Ignition and COMbustion with ReactionNs) code. Good agreement between theory and experiment was obtained for stoichiometric and rich flame conditions. For flames with equivalence ratios greater than 1.5, the H-atom concentration was substantially above the adiabatic equilibrium value--even at 50 mm above the burner surface. The slow approach to the adiabatic equilibrium H-atom concentration value can be explained by assuming partial equilibrium in the post-flame gases; the H-atom concentration is proportional to the O₂ concentration, which requires significant residence time to decrease to its very low equilibrium concentration. These results suggest that the use of the Hencken burner as a radical-measurement-technique calibration source may be of questionable value for equivalence ratios greater than 1.5 and less than 0.8. The results of this investigation were documented by W. D. Kulatilaka, R. P. Lucht (both of Purdue University), S. F. Hanna (Texas A&M University), and V. R. Katta (ISSI) in a paper that was published in *Combustion and Flame* [Vol. 137, pp. 523-537 (June 2004)]. The paper is included in the Appendix.

2.1.4 DPDB CARS in Reacting Flows.

A DPDB CARS system for making simultaneous measurements of temperature and concentrations of N₂, O₂, and CO₂ in reacting flows was demonstrated. In this system pure rotational transitions of N₂-O₂ and ro-vibrational transitions of N₂-CO₂ were probed simultaneously with two narrowband pump beams, a broadband pump beam, and a broadband Stokes beam. The main advantage of this technique is that it permits accurate temperature measurements at both low and high temperatures as well as concentration measurements of three

molecules. The results of this investigation were documented by S. Roy, T. R. Meyer (both of ISSI), R. P. Lucht (Purdue University), M. Afzelius, P.-E. Bengtsson (both of Lund Institute of Technology), and J. R. Gord (AFRL) in a paper that was published in *Optics Letters* [29(16), 1843-1845 (August 15, 2004)]. The paper is included in the Appendix.

2.1.5 Non-perturbative Modeling of Two-Photon Absorption in Three-State System.

The physics of the two-photon absorption process was investigated for a three-state system. The density-matrix equations for the two-photon interaction were solved in the steady-state limit, assuming that the pump-laser radiation was monochromatic. Collisional broadening, saturation, and Stark shifting of the two-photon resonance were investigated in detail by numerical solution of the steady-state density-matrix equations. Analytical expressions for the saturation intensity and the Stark shift were derived for the case where the single-photon transitions between the intermediate state and the initial and final states are far from resonance with the pump laser. For this case it was found that the direction of the Stark shift is dependent on the relative magnitudes of the dipole-measurement matrix elements for the single-photon transitions that couple the intermediate state with the initial and final states. Saturation and Stark shifting were also investigated for the case where the single-photon transitions between the intermediate state and the initial and final states are close to resonance with the pump laser. The results of this investigation were documented by R. P. Lucht (Purdue University), S. Roy (ISSI), and J. R. Gord (AFRL) in a paper that was published in the *Journal of Chemical Physics* [121(20), 9820-9829 (22 November 2004)]. The paper is included in the Appendix.

2.1.6 Multiple-Pump CARS for Quantitative Measurement of Temperature and Flame Species in Model Gas-Turbine Combustor.

DPDB CARS was applied for the simultaneous measurement of temperature and multiple-species concentrations in a liquid-fueled, model gas-turbine combustor. In this system pure rotational transitions of N_2-O_2 and the ro-vibrational transitions of N_2-CO_2 were probed using two narrowband pump beams, a broadband pump beam, and a broadband Stoke beam. The main advantage of this technique is that it permits very accurate temperature measurements at both low and high temperatures as well as concentration measurements of three molecules from each laser shot. Single-shot measurements of temperature and concentrations ratios of N_2-CO_2 and N_2-O_2 in the exhaust stream of a liquid-fueled, CFM56, swirl-stabilized gas-turbine combustor were made for equivalence ratios ranging from 0.4 to 1.1. The results of this study were documented by S. Roy, T. R. Meyer (both of ISSI), R. P. Lucht (Purdue University), and J. R. Gord (AFRL) in Paper No. V0034 that was presented at the International Conference on Advanced Optical Diagnostics in Fluids, Solids, and Combustion (Visualization Society of Japan/SPIE), which was held 4-6 December 2004 in Tokyo, Japan. The paper is included in the Appendix.

2.1.7 State-of-the-Art Fuel-Acidity Monitoring.

A novel iridium-oxide-based acidity sensor was developed for off-line monitoring of the acidity of fuel. The sensor works in the potentiometric mode using an IrO_x electrode as an indicating electrode and a Ag/Ag^+ electrode as a reference electrode. The data show that the IrO_x sensor responds to compounds present in fuel that have acid-base character. An off-line IrO_x sensor

would allow determination of the acidity of different fuels and discrimination between neat and thermally stressed fuels. Experimental results also indicate that the low conductance of fuel and/or the material used for sensor encapsulation may influence the response time of the IrO_x sensor. The results of this investigation were documented by J. Widera (ISSI) and J. M. Johnson (University of Dayton Research Institute) in a paper that was presented at the 226th Electrochemical Society Meeting, which was held 3-8 October 2004 in Honolulu, HI. The paper was published in the Electrochemical Society Proceedings, Vol. PV 2004-08, entitled, *Chemical Sensors VI: Chemical and Biological Sensors and Analytical Methods* [(C. Bruckner-Lea, P. Vanysek, G. Hunter, M. Egashira, N. Miura, and F. Mizutani, Eds.) (Electrochemical Society, Pennington, NJ, Fall 2004), pp. 208-214]. The paper is included in the Appendix to this report.

2.1.8 Kinetic Behavior of Polymer-Coated Long-Period-Grating Fiber-Optic Sensors.

A new method of analysis employing the time-dependent response of long-period-grating (LPG) fiber-optic sensors was introduced. The current kinetic approach allows analysis of the time-dependent wavelength shift of the sensor, in contrast to previous studies in which the LPG sensing element has been operated in an equilibrium mode and modeled with Langmuir adsorption behavior. A detailed kinetic model was presented that is based on diffusion of the analyte through the outer protective membrane coating into the affinity coating, which is bound to the fiber cladding. A simpler phenomenological approach was presented that is based on measurement of the slope of the time-dependent response of the LPG sensor. The principles of the kinetic methods were demonstrated employing a commercial Cu^{+2} sensor with a carboxymethylcellulose-sensing element. The detailed mathematical model fit the time-dependent behavior well and provided a means of calibrating the concentration-dependent time response. In the current approach copper concentrations below parts per 10^6 were reliably analyzed. The kinetic model allows early-time measurement for low concentrations of analyte, where equilibration times are long. This kinetic model should be generally applicable to other affinity-coated LPG fiber-optic sensors. The results of this study were documented by J. Widera (ISSI), C. E. Bunker (AFRL), G. E. Pacey (Miami University), V. R. Katta, M. S. Brown (both of ISSI), J. L. Elster, M. E. Jones (both of Luna Innovations), J. R. Gord (AFRL), and S. W. Buckner (St. Louis University) in a paper that was published in *Applied Optics* [Vol. 44, No. 6, pp. 1011-1017 (20 February 2005)]. The paper is included in the Appendix.

2.1.9 Combustion Exhaust Measurements of Nitric Oxide (NO) with Ultraviolet (UV) Diode-Laser-Based Absorption Sensor.

A diode-laser-based sensor was developed for UV absorption measurements of the NO molecule. The sensor is based on the sum-frequency mixing (SFM) of the output of a tunable, 395-nm, external-cavity diode laser and a 532-nm, diode-pumped, frequency-doubled Nd:YAG laser in a beta-barium-borate (β -BBO) crystal. The SFM process generates 325 ± 75 nW of UV radiation at 226.8 nm, corresponding to the ($n'=0$, $n''=0$) band of the $\text{A}^2\Sigma^+-\text{X}^2\Pi$ electronic transition of NO. Results were obtained from initial laboratory experiments in a gas cell as well as from field demonstrations of the sensor for measurements in the exhaust streams of a gas-turbine engine and a well-stirred reactor. It was demonstrated that the sensor is capable of fully resolving the absorption spectrum and accurately measuring the NO concentration in actual combustion environments. Absorption was clearly visible in the gas-turbine exhaust--even for the lowest

concentrations of 9 parts per million (ppm) for idle conditions and for a path length of 0.51 m. The sensitivity of the current system is estimated at 0.23%, which corresponds to a detection limit of 0.8 ppm in 1 m for 1000-K gas. The estimated uncertainty in the absolute concentrations that we obtained using the sensor is 10%. The results of this study were documented by T. N. Anderson, R. P. Lucht (both of Purdue University), R. Barron-Jimenez, S. F. Hanna, J. A. Caton (all of Texas A&M University), T. Walther (Darmstadt University of Technology), S. Roy, M. S. Brown (both of ISSI), J. R. Gord (AFRL), I. Critchley, and L. Flamand (both of Honeywell Engines Systems and Services) in a paper that was published in *Applied Optics* [Vol. 44, No. 8, pp. 1491-1502 (10 March 2005)]. The paper is included in the Appendix.

2.1.10 Optical Turbine-Engine Diagnostics for Ground-Test and On-Board Applications.

While optical-diagnostic techniques have been applied with great success to the fundamental study of combustion chemistry and physics in the laboratory, the challenges afforded by real-world propulsion systems demand continuing innovation if such techniques are to be adapted and transitioned for use in engineering tests and on-board monitoring and control applications. Efforts continue on transitioning aerodynamic measurement technologies from diagnostics-development laboratories to combustor test-and-evaluation facilities in the Propulsion Directorate's Combustion Branch (Turbine Engine Division). Various optical-diagnostic techniques have been applied for visualizing flow fields and quantifying temperatures and key species concentrations in several advanced combustors. The results of this investigation were documented by J. R. Gord (AFRL), T. R. Meyer, S. Roy, M. S. Brown, and S. P. Gogineni (all of ISSI) in an invited paper that was presented at NATO Conference RTO-MP-AVT-124, which was held 25-28 April 2005 in Budapest, Hungary. The paper is included in the Appendix to this report.

2.1.11 Diode-Laser-Based UV-Absorption Sensor for High-Speed Detection of Hydroxyl Radical (OH).

A new diode-laser-based UV-absorption sensor for high-speed detection of OH was developed. The sensor is based on sum-frequency generation of UV radiation at 313.5 nm by mixing the output of a 763-nm distributed-feedback diode laser with that of a 532-nm high-power, diode-pumped, frequency-doubled Nd:YVO₄ laser in a β -BBO crystal. Approximately 25 μ W of UV radiation was generated and used to probe rotational transitions in the $A^2\Sigma^+ - X^2\Pi$ ($v'=0, v''=0$) electronic transition of OH. Single-sweep, single-pass measurements of temperature and OH concentration in a stoichiometric C₂H₄-air flame were demonstrated at rates up to 20 kHz. The results of this investigation were documented by T. N. Anderson, R. P. Lucht (both of Purdue University), T. R. Meyer, S. Roy (both of ISSI), and J. R. Gord (AFRL) in two papers. The first was presented at the 4th Joint Meeting of the U. S. Sections of the Combustion Institute, which was held 20-23 March 2005 in Philadelphia, PA. The second was published in *Optics Letters* [Vol. 30, No. 11, pp. 1321-1323 (June 1, 2005)]. The second paper is included in the Appendix.

2.1.12 Advanced CARS Techniques for Simultaneous Species and Temperature Measurements.

The use of CARS spectroscopy for temperature measurements in combustion systems ranging from laboratory flames to practical combustors is well established. In the great majority of these temperature-measurement experiments, the two pump beams are obtained from the same laser source and, thus, have the same frequency. In the CARS process, the coherent Raman polarization in the medium is established by the interaction of one pump beam with the Stokes beam. The other pump beam is scattered from this induced polarization to produce the CARS signal, and there is no inherent requirement that the two pump beams have the same frequency. The measurement capabilities of the CARS technique can be greatly extended by the use of different frequencies for each of the pump beams. In dual-pump CARS, the frequencies of the two pump beams are selected so that the frequency differences between the Stokes beam and the pump beams correspond to the Raman resonances for two different species. Concentrations can be determined very accurately from the ratios of the two CARS signals. Dual-pump CARS has been used in a wide variety of experiments for accurate species-concentration measurements. Other techniques of interest include triple-pump CARS, DPDB CARS, and electronic-resonance-enhanced (ERE) CARS. High-resolution single-pulse CARS has been employed for temperature and pressure measurements in supersonic flows. The development of these nanosecond-laser-based techniques has been enabled by continuing improvements in the pulse energy, beam quality, and injection seeding of Q-switched Nd:YAG lasers. Femtosecond CARS has potential applications for high-data-rate measurements of temperature and species in reacting flows. These advanced CARS techniques were discussed by R. P. Lucht (Purdue University), S. Roy, T. R. Meyer (both of ISSI), and J. R. Gord (AFRL) in a paper that was presented at the Joint Army-Navy-NASA-Air Force (JANNAF) 40th Combustion, 28th Airbreathing Propulsion Meeting, which was held 13-16 June 2005 in Charleston, SC. The presentation is included in the Appendix to this report.

2.1.13 Ballistic Imaging of Liquid Core for Steady Jet in Cross Flow.

A time-gated ballistic-imaging instrument was used to obtain high-spatial-resolution, single-shot images of the liquid core in a water spray issuing into a gaseous cross flow. The diagnostic technique was developed further to improve the spatial resolution. Images and statistics for various jets under cross flow experimental conditions (different Weber numbers) were obtained. Series of these images reveal a near-nozzle flow field that is undergoing breakup and subsequent droplet formation by stripping. Signatures of spatially periodic behavior in the liquid core and formation of small voids during breakup were also detected. The results of this investigation were documented by M. A. Linne, M. Paciaroni, J. R. Gord (AFRL), and T. R. Meyer (ISSI) in a paper that was published in *Applied Optics* [Vol. 44, pp. 6627-6634 (November 2005)]. The paper is included in the Appendix.

2.1.14 10-kHz Detection of CO₂ at 4.5 μ m Using Tunable Diode-Laser-Based Difference-Frequency Generation.

A compact, high-speed tunable, diode-laser-based mid-infrared (MIR) laser source was developed for absorption spectroscopy of CO₂ at rates up to 10 kHz. Radiation at 4.5 μ m with a mode-hop-free tuning range of 80 GHz was generated by difference-frequency mixing the 860-nm output of a distributed-feedback diode laser with the 1064-nm output of a diode-pumped

Nd:YAG laser in a periodically poled lithium-niobate crystal. MIR absorption spectroscopy of CO₂ with a detection limit of 44 ppm m at 10 kHz was demonstrated in a C₂H₄-air laminar diffusion flame and in the exhaust of a liquid-fueled model gas-turbine combustor. The results of this investigation were documented by T. R. Meyer, S. Roy (both of ISSI), T. N. Anderson, R. P. Lucht (both of Purdue University), R. Barron-Jimenez (Texas A&M University), and J. R. Gord (AFRL) in a paper that was published in *Optics Letters* [Vol. 30, No. 22, pp. 3087-3089 (November 15, 2005)]. The paper is included in the Appendix.

2.1.15 Broadband CARS Spectroscopy of Nitrogen Using ps Modeless Dye Laser.

Broadband ps-CARS spectroscopy of nitrogen was demonstrated using 145-ps pump and probe beams and a 115-ps Stokes beam with a spectral bandwidth of 5 nm. This is, to the authors' knowledge, the first demonstration of broadband CARS using subnanosecond lasers. The short temporal envelope of the laser pulses and the broadband spectral nature of the Stokes beam will enable non-resonant-background-free, single-shot, or time-dependent spectroscopy in high-pressure or hydrocarbon-rich environments. Correlation of room-temperature, broadband, ps N₂ CARS with a theoretical spectrum was successful. The results of this study were documented by S. Roy, T. R. Meyer (both of ISSI), and J. R. Gord (AFRL) in a paper that was published in *Optics Letters* [Vol. 30, No. 23, pp. 3222-3224 (December 1, 2005)]. The paper is included in the Appendix.

2.1.16 Time-Resolved Dynamics of Resonant and Non-resonant Broadband ps CARS Signals.

The time-resolved dynamics of resonant and non-resonant broadband ps CARS signals in gas-phase media were investigated. For ~ 135-ps pump and probe beams and ~ 106-ps Stokes beams, the magnitude of the non-resonant signals was decreased by more than three orders of magnitude when the probe beam was delayed by ~110 ps, whereas the resonant nitrogen CARS signal was reduced only by a factor of three. Investigation of these time dynamics is important for understanding the optimal time delay for non-resonant background suppression as well as for understanding the collisional and Doppler dependence of the resonant CARS signals. The results of this study were documented by S. Roy, T. R. Meyer (both of ISSI), and J. R. Gord (AFRL) in a paper that was published in *Applied Physics Letters* [Vol. 87, pp. 264103-1 - 264103-3 (26 December 2005)]. The paper is included in the Appendix to this report.

2.1.17 Injection-Seeded Megahertz (MHz)-Repetition-Rate Optical-Parametric-Oscillator (OPO) System.

The ability to generate ultra-high-frequency sequences of broadly wavelength-tunable, high-intensity laser pulses was demonstrated using a custom-built OPO pumped by the third-harmonic output of a "burst"-mode Nd:YAG laser. Burst sequences consisting of six to ten pulses separated in time by between 7 and 10 ms were obtained, with average total conversion efficiency as high as ~ 35%. External-cavity diode lasers at 786 and 827 nm were used to injection seed the OPO cavity, resulting in time-averaged linewidth of ~ 200 – 300 MHz, for both the signal and idler waves. By mixing the OPO signal output (622 nm) with the residual third harmonic at 355 nm, burst sequences at 226 nm were produced, from which some

preliminary NO Planar Laser Induced Fluorescence (PLIF) image sequences were obtained. The results of this investigation were documented by N. Jiang, M. Uddi, M. Samimy, W. R. Lempert (all of The Ohio State University), G. Switzer, T. R. Meyer (both of ISSI), and J. R. Gord (AFRL) in AIAA Paper 2006-838 that was presented at the 44th AIAA Aerospace Sciences Meeting and Exhibit, which was held 9-12 January 2006 in Reno, NV. A paper was also submitted in March 2006 to *Optics Express*. The AIAA paper is included in the Appendix.

2.1.18 Water-Vapor Detection Using Asynchronous Terahertz (THz) Sampling.

The use of a fiber-coupled THz transmitter/receiver pair for spectroscopic detection of water vapor was investigated. Transmission signals of an alumina cylinder demonstrated that the measurement approach could be applied in a windowless ceramic combustor. First, a conventional commercial transmitter/receiver pair was used to make measurements for frequencies to 1.25 THz. Water-vapor absorption was clearly evident within the alumina transparency window and was readily modeled using existing databases. A variety of data-acquisition schemes was possible using THz instrumentation. To assess signal-collection techniques, a prototype THz transmitter/receiver pair was then used with the asynchronous optical-sampling (ASOPS) technique to obtain asynchronous THz-sampling signals to 1 THz without the need for an optomechanical delay line. Two mode-locked Ti:sapphire lasers operating at slightly different repetition rates were used for pumping the transmitter and receiver independently to permit a complete time-domain THz signal to be recorded. The resulting repetitive phase walkout was demonstrated by collecting power spectra of room air that exhibited water-vapor absorption. The results of this investigation were documented by M. S. Brown (ISSI), G. J. Fiechtner (Sandia National Laboratories), J. V. Rudd, D. A. Zimdars, M. Warmuth (all of Picometrix, Inc.), and J. R. Gord (AFRL) in a paper that was published in *Applied Spectroscopy* [Vol. 60, No. 3, pp. 261-265 (March 2006)]. The paper is included in the Appendix.

2.1.19 Velocity Imaging for Liquid-Gas Interface in Near Field of Atomizing Spray: Proof of Concept.

Ballistic imaging was adapted for the liquid core of an atomizing spray. An unambiguous description of the forces that act to break apart the liquid core in a spray can be provided only through direct measurement of the force vectors themselves. Therefore, it would be invaluable to obtain velocity and acceleration data at the liquid-gas interface. Double-image ballistic imaging was employed to extract velocity information through the application of image-analysis algorithms. This method was shown to be effective for liquid-phase droplet features within the resolution limit of the imaging system. In view of these results, it is clear that a three- or four-image implementation of this technique would allow the determination of acceleration and, by extension, information concerning the forces active in spray breakup. The results of this study were documented by D. L. Sedarsky, M. E. Paciaroni, M. A. Linne (all of the Lund Institute of Technology), J. R. Gord (AFRL), and T. R. Meyer (ISSI) in a paper that was published in *Optics Letters* [Vol. 31, No. 7, pp. 906-908 (1 April 2006)]. The paper is included in the Appendix.

2.1.20 RELIEF Velocimetry Using ps Tagging and Nd:YAG-Based Interrogation.

The ability to perform O₂-based RELIEF flow-tagging velocimetry in which the O₂ $v''=1$ level is initially excited and the $v''=3 \rightarrow v''=0$ transition of the Schumann-Runge system at 223.4 nm is employed for interrogation, was demonstrated experimentally. Such a strategy mitigated the requirement to use an ArF excimer laser for flow interrogation. Single-shot imaging demonstrated a potential spatially resolved velocity accuracy of ~ 2 m/s, which could be increased to better than 1 m/s with time averaging. Preliminary measurements employing a 100-ps pump laser for the stimulated Raman tagging step showed that vibrational excitation comparable to that obtained using Q-switched laser sources can be realized with pulse energies that are lower by at least one order of magnitude. The results of this investigation were documented by W. Lempert, Y. Zuzeeck, M. Uddi, K. Frederickson, N. Jiang (all of The Ohio State University), S. Roy, T. Meyer, and S. Gogineni (all of ISSI), and J. Gord (AFRL) in AIAA Paper No. 2006-2970 that was presented at the 25th AIAA Aerodynamic Measurement Technology and Ground Testing Conference, which was held 5-8 June 2006 in San Francisco, CA. The paper is included in the Appendix.

2.1.21 Effects of Quenching on ERE-CARS of NO.

The effects of gas-mixture composition on the ERE-CARS signals of NO were investigated. From previous LIF studies, quenching rates are known to change drastically, by factors of 400 - 800, in mixtures of CO₂/O₂/N₂. The observed ERE-CARS signal remained constant to within 30%, whereas LIF signals from NO were predicted to decrease by more than two orders of magnitude in the same environments. These findings are very significant for the use of NO ERE-CARS in high-pressure combustion environments where the electronic quenching rate can vary rapidly as a function of both space and time. The results of this investigation were documented by S. Roy (ISSI), W. D. Kulatilaka, S. V. Naik, N. M. Laurendeau, R. P. Lucht (all of Purdue University), and J. R. Gord (AFRL) in a paper that was published in *Applied Physics Letters* [Vol. 89, pp. 104105-1 - 104105-3 (4 September 2006)]. The paper is included in the Appendix to this report.

2.1.22 Application of Difference-Frequency-Mixing-Based Diode-Laser Sensor for Carbon-Monoxide (CO) Detection in 4.4 - 4.8 μ m Spectral Region.

An all-solid-state continuous-wave (cw) laser system for mid-infrared absorption measurements of the CO molecule has been developed and demonstrated. The single-mode, tunable output of an external-cavity diode laser (ECDL) was difference-frequency mixed with the output of a 550-mW diode-pumped cw Nd:YAG laser in a periodically poled lithium-niobate (PPLN) crystal to generate tunable cw radiation in the mid-infrared region. The wavelength of the 860-nm ECDL can be coarse tuned from 860.782 to 872.826 nm, allowing the sensor to be operated in the spectral region 4.4 - 4.8 μ m. CO-concentration measurements were performed in CO/CO₂/N₂ mixtures in a room-temperature gas cell, in the exhaust stream of a well-stirred reactor (WSR) at Wright-Patterson Air Force Base, and in a near-adiabatic hydrogen/air CO₂-doped flame. The noise-equivalent detection limits were estimated to be 1.1 and 2.5 ppm per meter for the gas-cell and flame experiments, respectively. These limits were computed for combustion gas at 1000 K and atmospheric pressure, assuming a signal-to-noise ratio of one. The sensor uncertainty was estimated to be 2% for the gas-cell measurements and 10% for the flame measurements, based on the repeatability of the peak absorption. The results of this investigation were documented by

R. Barron-Jimenez, J. A. Caton (both of Texas A&M University), T. N. Anderson, R. P. Lucht (both of Purdue University), T. Walther (TU Darmstadt), S. Roy, M. S. Brown (both of ISSI), and J. R. Gord (AFRL) in a paper that was published in *Applied Physics B* [Vol. 85, pp. 185-197 (November 2006)]. The paper is included in the Appendix.

2.1.23 Measurement of NO Concentrations in Flames Using ERE-CARS.

NO concentrations in flames were measured using ERE-CARS. Visible pump and Stokes beams were tuned to a Q-branch vibrational Raman resonance of NO. A UV probe beam was tuned into resonance with specific rotational transitions in the ($v''=1$, $v'=0$) vibrational band in the $A^2\Sigma^+ - X^2\Pi$ electronic transition, thus providing a substantial electronic-resonance enhancement of the resulting CARS signal. NO concentrations were measured at levels down to 50 parts in 10^6 in H_2 /air flames at atmospheric pressure. NO was also detected in heavily sooting C_2H_2 /air flames at atmospheric pressure with minimal background interference. The results of this study were documented by W. D. Kulatilaka, N. Chai, S. V. Naik, N. M. Laurendeau, R. P. Lucht (all of Purdue University), J. P. Kuehner (Washington and Lee University), S. Roy (ISSI), and J. R. Gord (AFRL) in a paper that was published in *Optics Letters* [Vol. 31, No. 22, pp. 3357-3359 (November 15, 2006)]. The paper is included in the Appendix.

2.1.24 Femtosecond (fs)-CARS Measurement of Gas Temperatures from Frequency-Spread Dephasing of Raman Coherence.

Gas-phase temperatures and concentrations were measured from the magnitude and decay of the initial Raman coherence in fs-CARS. A time-delayed probe beam was scattered from the Raman polarization that was induced by pump and Stokes beams to generate the CARS signal; the dephasing rate of this initial coherence was determined by the temperature-sensitive frequency spread of the Raman transitions. Temperature was measured from the CARS-signal decrease with increasing probe delay. Concentration was obtained from the ratio of the CARS and non-resonant background signals. Collision rates did not affect the determination of these quantities. The results of this investigation were documented by R. P. Lucht (Purdue University), S. Roy, T. R. Meyer (both of ISSI), and J. R. Gord (AFRL) in a paper that was published in *Applied Physics Letters* [Vol. 89, pp. 251112-1 – 251112-3 (18 December 2006)]. The paper is included in the Appendix to this report.

2.1.25 Measurements of NO and OH Concentrations in Vitiated Air Using Diode-Laser-Based UV Absorption Sensors.

Diode-laser-based sensors were implemented to measure the concentrations of NO and OH radicals in the vitiated inlet airflow of a model scramjet combustor. The sensors utilized sum-frequency-mixed sources consisting of a fixed-frequency 532-nm laser and a tunable diode laser to generate ultraviolet radiation for absorption spectroscopy with electronic transitions of OH and NO. Sensitive, interference-free absolute measurements were possible, enabling the first measurements of both species in a model scramjet combustor using diode-laser-based sensors. With wavelength-modulation spectroscopy, no absorption by OH was evident in the vitiated airflow, verifying that the OH concentration was below the 0.2-ppm detection limit of the sensor. Concentrations of NO were measured to be 200 – 1100 ppm for the vitiator conditions tested.

The results of this study were documented by T. N. Anderson, R. P. Lucht (both of Purdue University), T. R. Meyer, T. Mathur, K. D. Grinstead, Jr. (all of ISSI), J. R. Gord, M. Gruber, and C. D. Carter (all of AFRL) in AIAA Paper 2007-467 that was presented at the 45th AIAA Aerospace Sciences Meeting and Exhibit, which was held 8-11 January 2006 in Reno, NV. The paper is included in the Appendix.

2.1.26 Robust Procedure for Analysis of Non-Evenly Spaced Velocity Time-Series Data.

Laser Doppler Velocimetry (LDV) is an important tool for validation of computational fluid-dynamics (CFD) models in high-enthalpy bluff-body flows. However, in high-speed LDV, as opposed to hotwire anemometry, data must be unevenly sampled in time and cannot be analyzed using a standard Discrete Fast Fourier Transform (DFFT). Data from LDV have traditionally been processed with the Lomb Algorithm, which is a normalized periodogram representing a linear least-squares approximation of the linear regression of periodic functions. This algorithm can be computationally inefficient because a sufficiently large number of frequencies must be chosen to produce accurate results. In the present effort, spectral analysis with the Lomb Algorithm is compared with the processing of data employing a piecewise interpolation scheme developed through the use of MATLAB[®]. A series of known input signals is generated to provide a baseline for this comparison. Successful implementation in the wake of a bluff-body was achieved. Such alternative schemes are straightforward to implement, can be easily tailored for each flow application to extract the relevant low- and high-frequency modes, and may be more attractive for applications such as real-time spectral analysis of combustion control. The results of this investigation were documented by K. B. Garwick, A. Lynch, J. R. Gord, B. V. Kiel (all of AFRL) and T. R. Meyer (ISSI) in AIAA Paper 2007-1301 that was presented at the AIAA Meeting in Reno. The paper is included in the Appendix.

2.1.27 Detection of Acetylene by ERE-CARS.

Acetylene (C_2H_2) was detected at low concentrations by ERE-CARS. Visible pump and Stokes beams were tuned into resonance with Q-branch transitions in the ν_2 Raman band of acetylene. An ultraviolet probe beam was tuned into resonance with the $\tilde{A} - \tilde{X}$ electronic transition of C_2H_2 , resulting in significant electronic-resonance enhancement of the CARS signal. The signal was found to increase significantly with rising pressure for the pressure range 0.1 - 8 bar at 300 K. Collisional narrowing of the spectra appeared to be important at 2 bar and above. A detection limit of ~ 25 ppm at 300 K and 1 bar was achieved for the experimental conditions. The signal magnitudes and the shape of the C_2H_2 spectrum were essentially constant for UV probe wavelengths from 233.0 to 238.5 nm, indicating that significant resonant enhancement was achieved--even without tuning the probe beam into resonance with a specific electronic-resonance transition. The results of this study were documented by N. Chai, S. V. Naik, W. D. Kulatilaka, N. M. Laurendeau, R. P. Lucht (all of Purdue University), S. Roy (ISSI), and J. R. Gord (AFRL) in a paper that was published in *Applied Physics B Lasers and Optics* [Vol. 87, pp. 731-737 (June 2007)]. The paper is included in the Appendix.

2.1.28 Effects of Pressure Variations on ERE-CARS of NO.

The effects of pressure variations on the ERE-CARS signal of NO were studied at pressures ranging from 0.1 to 8 bar. ERE-CARS signals were recorded in a gas cell that was filled with a mixture of 300 ppm NO in N₂ buffer gas at room temperature. The ERE-CARS signal was found to increase with rising pressure up to 2 bar and to remain nearly constant thereafter. The spectra recorded at different cell pressures were modeled using a modified version of the Sandia CARSFT code. Laser-saturation effects were accounted for by systematically varying the theoretical ultraviolet probe-laser linewidth. Excellent agreement was obtained between theory and experiment for the pressure-scaling behavior of the ERE-CARS signal of NO. This finding, along with a negligible influence of electronic quenching on the ERE-CARS signal, provides strong incentive for the application of ERE-CARS to measurements of NO concentrations in high-pressure combustion environments. The results of this investigation were documented by W. D. Kulatilaka, N. Chai, S. V. Naik (all of Purdue University), S. Roy (ISSI), N. M. Laurendeau, R. P. Lucht (both of Purdue University), J. P. Kuehner (Washington and Lee University), and J. R. Gord (AFRL) in a paper that was published in *Optics Communications* [Vol. 274, pp. 441-446 (June 15, 2007)]; the paper is included in the Appendix to this report.

2.1.29 Detection of Atomic Hydrogen in Flames Using ps, Two-Color, Two-Photon-Resonance Six-Wave-Mixing Spectroscopy.

Two-color, six-wave-mixing spectroscopy techniques were investigated using ps lasers for the detection of atomic hydrogen in an atmospheric-pressure hydrogen-air flame. An ultraviolet laser at 243 nm was two-photon resonant with the $2S_{1/2} \leftarrow 1S_{1/2}$ transition, and a visible probe laser at 656 nm was resonant with H α transitions ($n = 3 \leftarrow n = 2$). The signal dependence on the polarization of the pump laser was investigated for a two-beam polarization-spectroscopy experimental configuration and for a four-beam grating configuration. A direct comparison of the absolute signal and background levels in the two experimental geometries demonstrated a significant advantage to using the four-beam grating geometry rather than the simpler two-beam configuration. The ps laser pulses provided sufficient time resolution to investigate hydrogen collisions in the atmospheric-pressure flame. Time-resolved, two-color laser-induced fluorescence (LIF) was used to measure an $n = 2$ population lifetime of 110 ps, and time-resolved, two-color six-wave-mixing spectroscopy was used to measure a coherence lifetime of 76 ps. Based on the collisional time scale, it is expected that the six-wave-mixing signal dependence on collisions is significantly reduced with ps laser pulses when compared to laser-pulse durations on the nanosecond time scale. The results of this investigation were documented by W. D. Kulatilaka, R. P. Lucht (both of Purdue University), S. Roy (ISSI), J. R. Gord (AFRL), and T. B. Settersten (Sandia National Laboratories) in a paper that was published in *Applied Optics* [Vol. 46, No. 19, pp. 3921-3927 (1 July 2007)]. The paper is included in the Appendix.

2.1.30 Theory of fs-CARS Spectroscopy of Gas-Phase Transitions.

A theoretical analysis of CARS spectroscopy of gas-phase resonances using fs lasers was performed. The time-dependent density matrix equations for the fs-CARS process were formulated and manipulated into a form that was suitable for solution by direct numerical integration (DNI). The temporal shapes of the pump, Stokes, and probe laser pulses were specified as an input to the DNI calculations. It was assumed that the laser pulse shapes were 70-fs Gaussians and that the pulses were Fourier-transform limited. A single excited electronic

level was defined as an effective intermediate level in the Raman process, and transition strengths were adjusted to match the experimental Raman polarizability. The excitation of the Raman coherence was investigated for different Q-branch rotational transitions in the fundamental 2330 cm^{-1} band of diatomic nitrogen, assuming that the pump and Stokes pulses were temporally overlapped. The excitation process was shown to be virtually identical for transitions ranging from Q(2) to Q(20). The excitation of the Raman coherences was also very efficient: for laser irradiances of $5 \times 10^{17}\text{ W/m}^2$ (corresponding approximately to a 100- μJ , 70-fs pulse focused to 50 μm), approximately 10% of the population of the ground Raman level was pumped to the excited Raman level during the impulsive pump-Stokes excitation, and the magnitude of the induced Raman coherence reached 40% of its maximum possible value. The theoretical results were compared with the results of experiments where the fs-CARS signal was recorded as a function of probe delay with respect to the impulsive pump-Stokes excitation. The results of this study were documented by R. P. Lucht, P. J. Kinnius (both of Purdue University), S. Roy (ISSI), and J. R. Gord (AFRL) in a paper that was published in the *Journal of Chemical Physics* [Vol. 127, pp. 044316-1 - 044316-17 (July 28, 2007)]. The paper is included in the Appendix.

2.1.31 Improving Signal-to-Interference Ratio in Rich Hydrocarbon-Air Flames Using ps-CARS

Interest is growing in the use of short-pulse lasers for CARS to minimize non-resonant background (NRB) contributions in a variety of applications. Using time-coincident ps pump and Stokes beams and a time-delayed ps probe beam, we achieved a three-orders-of-magnitude reduction in NRB interference can be achieved in rich hydrocarbon-air flames while preserving 60 - 80% of the CARS signal. This represents a significant improvement in signal-to-interference ratio compared with that from previous measurements in room-temperature air and is attributed to reduced rates of collisional dephasing and relaxation at flame temperatures. Measurements within the flame zone of a laminar flat-flame burner were used to investigate the characteristics of time-coincident and probe-delayed broadband ps N_2 -CARS spectra for C_2H_4 -air equivalence ratios of 0.5 - 1.2. Up to three ro-vibrational bands of N_2 were excited with each laser shot using 13-ps pump and 106-ps Stokes beams, and the CARS signal was generated using a 135-ps probe beam delayed by 165 ps. The enhanced signal-to-interference ratio achieved in the current work was one to two orders of magnitude higher than that previously obtained using polarization-selection techniques without sensitivity to the effects of birefringence caused by density gradients or test-cell windows. Moreover, the use of a 135-ps laser source in this study enabled frequency-domain “broadband” CARS with sufficient resolution to extract ro-vibrational spectral features under various flame conditions. The effect of probe delay and NRB suppression on the characteristics of these broadband CARS spectra was investigated, and evidence of preferential collision dephasing and relaxation of different ro-vibrational transitions was not detected. This promising but preliminary result must be investigated further in future work. The results of this investigation were documented by T. R. Meyer (Iowa State University), S. Roy (ISSI), and J. R. Gord (AFRL) in a paper that was published in *Applied Spectroscopy* [Vol. 61, No. 11, pp. 1135-1140 (November 2007)]. The paper was featured on the cover of the November issue of the journal and is included in the Appendix to this report.

2.1.32 Effect of Collisions on Time-Delayed ps-CARS Spectroscopy.

The effect of collisions on measured temperatures using time-delayed ps-CARS was investigated. In ps-CARS the probe beam is delayed with respect to the pump and Stokes beams to suppress the non-resonant background. The results of this study were documented by J. R. Gord (AFRL), P. Hsu, and S. Roy (both of ISSI) in a paper that was presented at the Laser Applications to Chemical, Security, and Environmental Analysis (LACSEA) Meeting, which was held 17-20 March 2008 in St. Petersburg, FL. The paper is included in the Appendix.

2.1.33 Fs-CARS for High-Bandwidth, Collision-Free Temperature Measurements.

Fs-laser-based time-resolved CARS spectroscopy of nitrogen was used to measure temperature at 1 kHz. The first few picoseconds of the time-resolved CARS signal were free of collisions for pressures up to 20 bar. The results of this investigation were documented by S. Roy (ISSI), P. J. Kinnius, R. P. Lucht (both of Purdue University), and J. R. Gord (AFRL) in an invited paper that was presented at the Laser Applications to Chemical, Security, and Environmental Analysis (LACSEA) Meeting, which was held 17-20 March 2008 in St. Petersburg, FL. The paper is included in the Appendix.

2.1.34 Insensitivity of ERE-CARS to Electronic Quenching.

Fs-laser-based time-resolved CARS spectroscopy of nitrogen was used to measure temperature at 1 kHz. It was observed that the strong laser pulse helps in keeping both the excited-state population and the ground-state coherence reasonably high, even with significant quenching. The results of this study were documented by A. K. Patnaik, S. Roy (both of ISSI), R. P. Lucht (Purdue University), and J. R. Gord (AFRL) in a paper that was presented at the Laser Applications to Chemical, Security, and Environmental Analysis (LACSEA) Meeting, which was held 17-20 March 2008 in St. Petersburg, FL. The paper is included in the Appendix.

2.1.35 Fs-CARS Measurement of Gas-Phase Species and Temperature.

The use of fs lasers for CARS measurements in gases was reviewed, and coupling of fs laser radiation with gas-phase resonances, determination of temperatures from frequency-spread dephasing, and single-shot measurements were discussed in a presentation co-authored by R. P. Lucht, R. J. Kinnius (both of Purdue University), S. Roy (ISSI), and J. R. Gord (AFRL) that was made at the Conference on Lasers and Electro-Optics/Quantum Electronics and Laser Science Conference (CLEO/QELS 08), which was held 4-9 May 2008 in San Jose, CA. The paper was published in the conference proceedings and is included in the Appendix.

2.1.36 Perturbative Theory and Modeling of ERE-CARS Spectroscopy of NO.

A theory was developed for three-laser ERE-CARS spectroscopy of NO. A vibrational Q-branch Raman polarization was excited in the NO molecule by the frequency difference between the visible Raman pump and Stokes beams. An ultraviolet probe beam was scattered from the induced Raman polarization to produce an ultraviolet ERE-CARS signal. The frequency of the ultraviolet probe beam was selected to be in electronic resonance with rotational transitions in the $A^2\Sigma^+ \leftarrow X^2\Pi$ (1,0) band of NO. This choice resulted in a resonance between the frequency of the ERE-CARS signal and transitions in the (0,0) band. The theoretical model for ERE-

CARS NO spectra was developed in the perturbative limit. Comparisons to experimental spectra were made where either the probe laser was scanned with a fixed Stokes frequency or the Stokes laser was scanned with a fixed probe frequency. At atmospheric pressure and an NO concentration of 100 ppm, good agreement was found between theoretical and experimental spectral peak locations and relative intensities for both types of spectra. Factors relating to saturation in the experiments were considered, including implications for the theoretical predictions. The results of this investigation were documented by J. P. Kuehner (Washington and Lee University), S. V. Naik, W. D. Kulatilaka, N. Chi, N. M. Laurendeau (all of Purdue University), R. P. Lucht (Purdue University and Texas A&M University), S. Roy, A. K. Patnaik (both of ISSI), and J. R. Gord (AFRL) in a paper that was published in the *Journal of Chemical Physics* [Vol. 128, pp. 174308-1 – 174308-12 (May 7, 2008)]. The paper is included in the Appendix.

2.1.37 Applications of Ultrafast Lasers for Optical Measurements in Combusting Flows.

Optical measurement techniques are powerful tools for the detailed study of combustion chemistry and physics. Although traditional combustion diagnostics based on continuous-wave and nanosecond-pulsed lasers continue to dominate fundamental combustion studies and applications in reacting flows, revolutionary advances in the science and engineering of ultrafast [picosecond- and femtosecond-pulsed] lasers are driving the enhancement of existing diagnostic techniques and enabling the development of new measurement approaches. The ultra-short pulses afforded by these new laser systems provide unprecedented temporal resolution for studies of chemical kinetics and dynamics, freedom from collisional-quenching effects, and tremendous peak powers for broad spectral coverage and non-linear signal generation. The high pulse-repetition rates of ultrafast oscillators and amplifiers allow previously unachievable data-acquisition bandwidths for the study of turbulence and combustion instabilities. The applications of ultrafast lasers for optical measurements in combustions flows and sprays, with emphasis on recent achievements and future opportunities, were reviewed by J. R. Gord (AFRL), T. R. Meyer (Iowa State University), and S. Roy (ISSI) in an invited book chapter, which appeared in the first volume of the American Chemical Society Series entitled, *Annual Review of Analytical Chemistry* [Vol. 1, pp. 663-687 (July 2008)]. The book chapter is included in the Appendix.

2.1.38 Measurements of NO Concentration in Flames Using Broadband Stokes ERE-CARS.

The CARS technique has been applied successfully in a number of applications for species-concentration and temperature measurements. These measurements were usually conducted for major species with concentration larger than 0.1%. The ERE-CARS technique can enhance the signal significantly by tuning one or more laser beams involved in the CARS process into resonance with suitable electronic transitions. Recently, visible narrowband pump and Stokes beam were utilized with a narrowband ultraviolet probe beam for measurements of NO concentrations in flames. The frequency of the probe beam was tuned into resonance with a suitable electronic transition. In previous narrowband ERE-CARS measurements, the frequency of the Stokes beam was scanned over Raman signatures of NO to acquire the ERE-CARS spectra. Single-shot, broadband ERE-CARS measurements were made. The narrowband Stokes laser was replaced by a broadband dye laser.

In the broadband ERE-CARS measurements of NO, a visible pump beam at 532 nm and broadband Stokes beam centered at 591 nm were used to excite numerous Raman resonances in the ground electronic state of NO. A third ultraviolet probe beam at 236 nm was used to enhance selectively one or two of the induced Raman resonances. Single-shot spectra were acquired using a 1-m spectrometer to disperse the signal and a back-illuminated charge-coupled-device (CCD) camera to detect the signal. A polarization method was used to suppress the non-resonant background. Single-shot measurements were performed both with the non-resonant background completely suppressed and with some of the non-resonant background transmitted in the signal channel.

ERE-CARS spectra of NO were acquired in an atmospheric-pressure hydrogen/air counter-flow diffusion flame. The single-shot detection limit in this flame was found to be ~ 10 ppm. A standard deviation of $\sim 20\%$ of the mean was found by analyzing 1000 single-laser-shot spectra at different flame locations. In measurements where some of the non-resonant background was transmitted, the standard deviation of the ratio of the resonant to non-resonant signal was found to be 15%. NO concentration profiles were obtained in a series of non-premixed hydrogen and methane flames stabilized within a counter-flow burner with a total strain rate of 20 s^{-1} . The NO concentration profiles were compared with the results of OPPDIF calculations. The results of this research were documented by N. Chai, A. Satija, S. V. Naik, R. P. Lucht, N. M. Laurendeau (all of Purdue University), S. Roy (ISSI), and J. R. Gord (AFRL) in a poster that was presented at the Work-in-Progress Poster Sessions at the 32nd International Symposium on Combustion, which was held 3-8 August 2008 in Montreal, Canada. The poster is included in the Appendix.

2.1.39 Theory of fs-CARS Spectroscopy for Gas-Phase Transitions.

The use of fs lasers for CARS spectroscopy of molecules in the gas phase offers some significant potential advantages compared with nanosecond (ns) CARS; i.e., CARS as usually performed with ns pump and Stokes lasers. These potential advantages include 1) the capability of performing real-time temperature and species measurements at data rates significantly $> 1 \text{ kHz}$, and 2) the absence of any effect of collisions in the determination of temperature and concentration from the fs-CARS signal. However, the broad spectral bandwidth of the fs laser pulses would seem to preclude the acquisition of strong CARS signals from gas-phase species. For room-air conditions, typical Raman linewidths are 0.1 cm^{-1} , while the frequency bandwidth of a Fourier-transform-limited 100-fs laser pulse is 150 cm^{-1} . However, numerous frequency pairs exist within the spectral envelopes of the pump and Stokes lasers that can contribute to the excitation of the two-photon Raman resonance. Consequently, the excitation of gas-phase Raman resonances is quite efficient, as shown in a time-dependent density matrix analysis of the interaction of 100-fs pump and Stokes pulses with gas-phase N_2 Raman resonances.

In the present scanned-probe-beam experiments, temperature and species concentration were determined from the decay of the CARS signal in the first few picoseconds (ps) after the impulsive pump-Stokes Raman pumping. The CARS signal in these initial few ps is much stronger because the numerous Raman transitions contribute coherently to the signal since they are excited with the same phase by the impulsive pump-Stokes excitation. After a few ps they begin to oscillate out of phase because of the differences in the transition frequencies of the

various Raman resonances; we refer to this phenomenon as frequency-spread dephasing. The frequency-spread dephasing time decreases with temperature because the frequency spread of transitions that contribute to the Raman coherence increases with temperature.

The potential for real-time measurements at frequencies of interest in turbulent flames is the result of the recent commercial availability of fs laser systems with pulse energies of up to a few millijoules and repetition rates of up to 20 kHz and the expected availability of commercial systems in the near future with repetition rates approaching 100 kHz. We have performed some initial single-pulse fs-CARS experiments with a 2-ps chirped probe beam. The chirped-probe-pulse fs-CARS signal beam was directed into a spectrometer, and the spectrum was recorded for each laser shot on a charge-coupled-device (CCD) camera. The temporal behavior of the Raman coherence could then be determined from the spectrum of the fs-CARS signal. Chirped-probe-pulse experiments were performed for atmospheric-pressure nitrogen in a heated gas cell and for mixtures of nitrogen and carbon monoxide. Single-pulse spectra with very high signal-to-noise ratios were acquired from atmospheric-pressure flames. A computer code for fitting the chirped-probe-pulse spectra and determining temperature and species concentrations as fitting parameters is in the early stages of development. The results of this investigation were documented by R. P. Lucht, P. J. Kinnius (both of Purdue University), S. Roy (ISSI), and J. R. Gord (AFRL) in a poster that was presented at the Work-in-Progress Poster Sessions at the 32nd International Symposium on Combustion, which was held 3-8 August 2008 in Montreal, Canada. The poster is included in the Appendix.

2.1.40 Single-Laser-Shot Detection of NO in Reacting Flows Using ERE-CARS.

Single-laser shot ERE-CARS spectra of NO were generated using the 532-nm output of an injection-seeded Nd:YAG (yttrium aluminum garnet) laser as the pump beam, a broadband dye laser at ~ 591 nm as the Stokes beam, and a 236-nm narrowband ultraviolet probe beam. Single-laser-shot ERE-CARS spectra of NO were acquired in an atmospheric-pressure hydrogen/air counterflow diffusion flame. The single-shot detection limit in this flame was found to be ~ 30 ppm, and the standard deviation of the measured NO concentration was found to be ~ 20% of the mean. The results of this study were documented by N. Chai, S. V. Naik, N. M. Laurendeau, R. P. Lucht (all of Purdue University), S. Roy (ISSI), and J. R. Gord (AFRL) in a paper that was published in *Applied Physics Letters* [Vol. 93, pp. 091115-1 – 091115-3 (September 1, 2008)]. The paper is included in the Appendix.

2.1.41 Collisional Effects on Molecular Dynamics in ERE-CARS.

The role of collisional decay in the evolution of molecular coherence and excited-state population in an ERE-CARS configuration was studied. A four-level model scheme was proposed, and a density-matrix equation was derived to determine the system evolution. It was shown that even for significantly large collisional decays, a suitable (rather strong) probe-laser intensity prevents significant depletion of the excited-state population and enhances the ground-state coherence. A physical understanding was developed for the reported insensitivity [Roy, et al., *App. Phys. Lett.* **89**, 104105 (2006)] of the ERE-CARS signal to the rate of collisional decay at the excited electronic level. The results of this investigation were documented by A. K. Patnaik, S. Roy, (both of ISSI), R. P. Lucht (Purdue University), and J. R. Gord (AFRL) in a

paper that was published in *Journal of Modern Optics* [Vol. 55, Nos. 19-20, pp. 3263-3272 (10-20 November 2008)]. The paper is included in the Appendix

2.1.42 Development of Nearly Transform-Limited, Low-Repetition-Rate, ps OPO.

A low-repetition-rate (10-Hz), ps OPG seeded at the idler wavelength with a high-power diode laser was demonstrated. The output of the OPG at ~ 566 nm was amplified in dye cells, resulting in signal enhancement by more than three orders of magnitude. The nearly transform-limited beam at ~ 566 nm had a pulsewidth of ~ 170 ps, with an overall output of ~ 2.3 mJ/pulse. The laser was tuned either by tuning the non-linear crystal or the seed-laser current. Such a simple, compact, high-performance, tunable ps laser system has a number of applications for linear and non-linear spectroscopy. The results of this study were documented by P. S. Hsu, S. Roy (both of ISSI), and J. R. Gord (AFRL) in a paper that was published in *Optics Letters* [Vol. 281, No. 24, pp. 6068-6071 (December 15, 2008)]. The paper is included in the Appendix.

3.0 SIMULATION AND MODEL DEVELOPMENT AND EVALUATION

3.1 General Overview

The objective of this portion of the program was to develop and apply simulations and models for the investigation of advanced-concept technologies for future propulsion systems. The models and simulations were used to support all the major tasks of this program. A summary of the work accomplished on this task during the program follows.

3.1.1 CFD-Based Global Chemistry Predictions for Normal and Inverse Laminar Ethane Jet Diffusion Flames under Oxygen Enhancement and Gravity Variation.

Global calculations involving five species at four different fuel compositions for ethane-jet-diffusion and inverse-diffusion flames under earth gravity and microgravity conditions were made using an axisymmetric, time-dependent CFD code. Computations were compared with experimental data obtained from NASA Glenn Research Center. Enhancement in oxygen resulted in increased flame temperatures. No significant change was observed in inverse-diffusion-flame lengths (based on maximum temperature) with oxygen enhancement and gravity variation. The results of this investigation were documented by P. Bhatia (Purdue University), V. R. Katta (ISSI), P. B. Sunderland (National Center for Microgravity Research), S. S. Krishnan (Purdue School of Engineering and Technology), and J. P. Gore (Purdue University) in a paper that was presented at the 2004 Technical Meeting of the Central States Section of the Combustion Institute, which was held 21-23 March 2004 in Austin, TX. The paper is included in the Appendix.

3.1.2 Macro- vs. Micro-Vortex/Flame Interactions in Hydrogen Diffusion Flames.

The validity of the flamelet theory was examined by studying vortex/flame interactions in a hydrogen/air opposing-jet diffusion flame. The dynamic changes to the flame structure during the interaction process were investigated. Vortices were injected toward the flame surface from the air side. A centimeter-size vortex was made to interact with a 7.0-mm-thick flame, and a micron-size vortex was made to interact with a 2.4-mm-thick flame. High vortex-propagation velocities were used for creating rapid flame extinction in both cases. While the larger vortex, regardless of the vortex-propagation velocity, tends to create a wrinkled, strained flame before causing extinction--representing a laminar flamelet--the smaller vortex tends to replace the local fluid in the flame zone with the constituent fluid and destroys the flame structure--representing a distributed reaction zone. Since the micron-size vortex is larger than the Kolmogorov length scale, a portion of the possible turbulent processes (events) in a hydrogen diffusion flame must be viewed as distributed reaction zones. The results of this investigation were documented by V. R. Katta, T. R. Meyer (both of ISSI), J. R. Gord, and W. M. Roquemore (both of AFRL) in a paper that was presented at the 2004 Technical Meeting of the Central States Section of the Combustion Institute, which was held 21-23 March 2004 in Austin, TX. The paper is included in the Appendix.

3.1.3 Simulation of Polycyclic Aromatic Hydrocarbons (PAHs) in Trapped-Vortex Combustor (TVC).

Residence time and thermo-chemical environment are important factors in determining the soot-formation characteristics of jet-engine combustors. For understanding the chemical and physical structure of the soot formed in these combustors, knowledge of flow dynamics and formation of polycyclic aromatic hydrocarbons (PAHs) is required. A time-dependent detailed-chemistry computational-fluid-dynamics (CFD) model was developed for simulation of reacting flows in a TVC. The axisymmetric TVC of Hsu et al. [*J. Propul. Power* **14**(1) (1998)] was modeled by replacing injection holes with injection slots. Ethylene-air mixtures were used as fuel. Several calculations were made by varying the equivalence ratio and velocity of the main flow. Unsteady simulations revealed that the shear-layer vortices established outside the cavity flow enhance mixing of benzene in the wake region of the afterbody. However, in all the cases considered here, most of the PAH species are produced in the cavity region. While the fuel-rich condition results in lower amounts of PAHs in the cavity region, soot is produced in more abundance in this region. The results of this investigation were documented by V. R. Katta (ISSI), and W. M. Roquemore (AFRL) in ASME Paper No. GT2004-54165 that was presented at the ASME Turbo Expo 2004: Power for Land, Sea, and Air, which was held 14-17 June 2004 in Vienna, Austria. The paper, which was published in the Conference Proceedings, is included in the Appendix.

3.1.4 Gravity, Radiation, and Coflow Effects on Partially Premixed Flames.

The objective of this investigation was to characterize gravity effects on the structure of laminar methane-air partially premixed flames through detailed simulations. The heat loss due to radiation from similar flames that were established at various gravitational accelerations and coflow velocities was examined. Radiation was modeled using the optically thin assumption that provides a limited value for the radiation heat transfer. The simulations were validated with measurements in a representative 1-g flame. The predictions were in good agreement with the measured reaction-zone topologies and temperature distributions. The simulations show that when the gravitational acceleration for a representative 1-g partially premixed double flame is instantaneously decreased to zero, it is possible to establish a nearly steady 0-g flame in roughly 2.2 s. The overall effect of radiation on the structure of the 1-g flame is relatively insignificant compared with that of the corresponding 0-g flame. As a result of radiation effects, the heights of both the inner premixed and the outer non-premixed reaction zones in the 0-g double flame increase, and the heat-release-rate intensity near the premixed reaction-zone tip decreases. When radiation effects are not included in the simulations, the peak temperatures are nearly the same for the 1-g and 0-g flames. However, with radiation the difference in these temperatures is significant. The decrease in the peak temperature due to radiation for the 0-g flame is nearly five times larger than for the 1-g flame. The value of the radiation fraction for 0-g flames without coflow can be as large as 50%, although it drops significantly in the presence of a coflow. While the flow fields upstream of the inner premixed reaction zone are nearly identical for 1-g and 0-g double flames, they are markedly different in the regions between the two reaction zones as well as downstream of the outer non-premixed reaction zone. The maximum flame temperatures and local heat-release rates increase as the gravitational acceleration increases, while the radiation fractions and inner flame heights decrease. The flickering frequency also increases from 14.7 Hz

at 1-g to 41.4 Hz at 10-g and follows the correlation $St \propto Fr^{-0.57}$ that is in accord with a previous compilation of normal gravity data. The radiation Damköhler number is inversely proportional to the Froude number. The radiation fraction decreases with increasing coflow, and the differences between the maximum flame temperatures and heat-release rates for 1-g and 0-g flames become less pronounced. Results for triple flames are in accord with those for double flames. The results of this study were documented by X. Qin (Princeton University), I. K. Puri, S. K. Aggarwal (both of the University of Illinois at Chicago), and V. R. Katta (ISSI) in a paper that was published in *Physics of Fluids* [16(8), 2963-2974 (August 2004)]. The paper is included in the Appendix.

3.1.5 Effect of Diluents on Lifted Partially Premixed Flames in Normal and Microgravity: Numerical Investigation.

The effect of fuel-stream dilution on the liftoff characteristics of partially premixed flames (PPFs) under 1- and 0-g conditions was investigated. Lifted methane-air PPFs were established in axisymmetric coflowing jets using different diluents and dilution levels. A time-accurate, implicit algorithm that employs a detailed description of the chemistry and includes radiation effects was used for the simulations. The predictions were validated through a comparison of the flame-reaction-zone topologies and liftoff heights. The effects of diluents and gravity on the flame liftoff height, topology, and base structure were characterized. The predominantly inert agents CO₂ and N₂ were considered because of their flame-suppressant characteristics. Results indicated that under identical conditions a lifted 0-g PPF is stabilized closer to the burner than a 1-g flame, and the CO₂ dilution is more effective in detaching the flame from the burner than the N₂ dilution. Additionally, the 1-g lifted flames exhibit well-organized oscillations due to buoyancy-induced instability, while the corresponding 0-g flames exhibit steady-state behavior. The results of this study were documented by A. M. Briones, S. K. Aggarwal (both of the University of Illinois at Chicago) and V. R. Katta (ISSI) in a paper that was presented at the 4th Joint Meeting of the U. S. Sections of the Combustion Institute, which was held 20-23 March 2005 in Philadelphia, PA. The paper is included in the Appendix.

3.1.6 Numerical Studies on Ultra-Lean Methane Premixed Flames.

Lean combustion has potential advantages in limiting NO_x and particulate emissions and in improving fuel-consumption efficiency. The major difficulty in achieving and sustaining lean combustion in aircraft engines is associated with the flame-stability problem. A numerical study was performed on a counterflow-premixed-flame system in an attempt to understand the stability of the ultra-lean methane/air mixture. A time-dependent, axisymmetric mathematical model known as UNICORN was used for the two-dimensional simulation of premixed flames associated with this opposing-jet burner. Sub-limit lean methane/air flames were supported in this burner by the products generated by a lean hydrogen/air premixed flame. A detailed chemical-kinetics model GRI-V1.2 (developed by the Gas Research Institute) was used for simulating the double-flame structure formed between the methane/air and hydrogen/air mixtures. Extinction of the methane flame was obtained by increasing the applied stretch rate on both of the flames. Numerical results were compared with experimental data. The role of radicals diffusing from the stable hydrogen flame in stabilizing the unstable lean methane flame was studied. The results of this investigation were documented by V. R. Katta (ISSI), Z. Cheng,

and R. W. Pitz (both of Vanderbilt University) in a paper that was presented at the 4th Joint Meeting of the U. S. Sections of the Combustion Institute, which was held 20-23 March 2005 in Philadelphia, PA. The paper is included in the Appendix.

3.1.7 Effect of Nitromethane on Soot Formation in Heptane Jet Diffusion Flame.

Residence time and thermo-chemical environment are important factors in the soot-formation processes of jet diffusion flames. For understanding the chemical and physical structure of the soot formed in jet flames, knowledge of the flow dynamics of diffusion flames is required. The UNICORN model was used for the simulation of heptane/air unsteady jet diffusion flames. A detailed chemical-kinetics model consisting of up to 197 species and 2800 elementary-reaction steps was incorporated into UNICORN for the investigation of PAH formation in heptane flames. A simple soot model based on two conservation equations and acetylene concentration was used for estimating soot production in these flames. The effect of nitromethane on the PAH species and soot formed in these flames was investigated by incorporating nitromethane chemistry. Small amounts of nitromethane were added to the fuel jet. The results of this study were documented by V. R. Katta (ISSI) and W. M. Roquemore (AFRL) in a paper that was presented at the 4th Joint Meeting of the U. S. Sections of the Combustion Institute, which was held 20-23 March 2005 in Philadelphia, PA. The paper is included in the Appendix.

3.1.8 CFD-Based Global- and Detailed-Chemistry Predictions for Inverse, Laminar, Ethane Jet Diffusion Flames Under Oxygen Enhancement and Gravity Variation.

Global-chemistry calculations (involving five species) and detailed-chemistry calculations (involving 99 species, including PAH and 1066 reactions) at four oxidizer compositions (21, 30, 50, and 100% O₂ mole fraction in N₂) were made for ethane inverse jet diffusion flames in earth gravity and in microgravity conditions using an axisymmetric, time-dependent computational-fluid-dynamics code. Computations were compared with experimental photographs of microgravity and 1-g flames. Enhancement in oxygen resulted in increased flame temperatures. Calculations reveal that oxygen enhancement causes an increase in PAH CO, and C₂H₂ emission for earth-gravity inverse diffusion flames and a decrease for microgravity inverse diffusion flames. However, the maximum parts per million (PPM) (by mass) and the flame width, in general, increase with oxygen enhancement and gravity reduction. The results of this investigation were documented by P. Bhatia (Purdue University), V. R. Katta (ISSI), S. S. Krishnan (Purdue University), P. B. Sunderland (University of Maryland), and J. P. Gore (Purdue University) in a paper that was presented at the 4th Joint Meeting of the U. S. Sections of the Combustion Institute, which was held 20-23 March 2005 in Philadelphia, PA. The paper is included in the Appendix.

3.1.9 Studies on Soot Formation in Model Gas-Turbine Combustor.

Residence time and thermo-chemical environment are important factors in the soot-formation process in combustors, especially those that employ swirl for flame stabilization. For understanding the chemical and physical structure of the soot formed in these combustors, knowledge on flow dynamics and formation of polycyclic aromatic hydrocarbons (PAHs) is required. A time-dependent, detailed-chemistry CFD model was developed for the simulation of

the reacting flows in a model swirl-stabilized combustor. While commercial JP-8 fuel was employed in the experiments, a six-component surrogate mixture was used in the calculations for mimicking the JP-8-fuel combustion. Detailed chemical kinetics were used for simulation of combustion as well as formation of PAH species. Several calculations were made for different equivalence ratios that were obtained by varying the fuel jet velocity and by maintaining the airflow unaltered. Turbulent-flow simulations revealed that two recirculation zones that are separated by the air jet establish in the swirl-stabilized combustor. Stabilization of flames between the air jets and the recirculation zones depends on the equivalence ratio. For the highly fuel-lean cases ($\phi = 0.65$), the flame is stabilized between the air jet and the central recirculation zone; for the fuel-rich cases, the flame is stabilized between the air jets and the corner recirculation zone. However, these two flames appear to coexist for slightly fuel-lean cases ($\phi = 0.85$). The predicted OH-concentration fields were compared with the OH images obtained using the PLIF technique. The results of probe measurements made in the exhaust products were also compared. The results of this study were documented by V. R. Katta, T. R. Meyer (both of ISSI), C. Montgomery (Reaction Engineering International), and W. M. Roquemore (AFRL) in AIAA Paper 2005-3777 that was presented at the 41st AIAA/ASME/SAE/ASEE Joint Propulsion Conference and Exhibit, which was held 10-13 July 2005 in Tucson, AZ. The paper is included in the Appendix.

3.1.10 Micro-Vortex/Flame Interactions and Their Implications in Turbulent-Flame Modeling.

Laminar flamelet theory is often used for representing the structure of a turbulent diffusion flame. The limitations of such representation were examined by studying various vortex/flame interactions in a hydrogen/air opposing-jet diffusion flame. Vortices were injected from the air side toward the flat flame that formed between the fuel and air jets. A centimeter-size vortex was made to interact with a 7.0-mm-thick flame, and a micron-size vortex was made to interact with a 2.4-mm-thick flame. Sufficiently high vortex-propagation velocities were used for creating flame extinction in both cases. While the larger vortices, irrespective of their propagation velocity, tend to create a wrinkled, strained flame before causing extinction--representing a laminar flamelet--the small vortices tend to replace the local fluid in the flame zone with the constituent fluid and destroy the flame structure--representing a distributed reaction zone. Since the micron-size vortex is larger than the Kolmogorov length scale, a portion of the possible turbulent processes (events) in a hydrogen diffusion flame must be viewed as distributed reaction zones. The results of this investigation were documented by V. R. Katta, T. R. Meyer (both of ISSI), J. R. Gord, and W. M. Roquemore (both of AFRL) in a paper that was presented at the 2005 Technical Meeting of the Eastern States Section of the Combustion Institute, which was held 13-15 November 2005 in Orlando, FL. The paper was published in the conference proceedings and is included in the Appendix.

3.1.11 Numerical Investigation of Flame Liftoff, Stabilization, and Blowout.

The effects of fuel-stream dilution on the liftoff, stabilization, and blowout characteristics of laminar non-premixed flames (NPFs) and partially premixed flames (PPFs) were investigated. Lifted methane-air flames were established in axisymmetric coflowing jets. Because of their flame-suppression characteristics, two predominantly inert agents, CO₂ and N₂, were used as

diluent. A time-accurate implicit algorithm that employs a detailed description of the chemistry and includes radiation effects was used for the simulations. The predictions were validated using measurements of the reaction-zone topologies and liftoff heights of both NPF and PPF. While an undiluted PPF was stabilized at the burner rim, characterized by significant radical destruction and heat loss to the burner, the corresponding undiluted NPF was lifted and stabilized in a low-velocity region extending from the wake of the burner. Detailed comparison of diluted NPF and PPF revealed that the base structures of the two flames are similar and exhibit a double-flame structure in the near-field region, where the flame stabilization depends on a balance between the reaction rate and the scalar dissipation rate; this could also be interpreted as a balance between the edge-flame speed undergoing its local scalar dissipation rate and the local flow velocity. As diluent concentration was increased, the flames became weaker, moved downstream along the stoichiometric mixture-fraction line, and stabilized at a location where they could find a local flow field that had a lower scalar dissipation rate. Further increase of the diluent concentration moved the flames farther downstream into the far-field region, where both the NPF and PPF exhibited a triple-flame structure and the flame stabilization mechanism also involved a balance between the triple-flame speed and local flow velocity. The PPFs, however, shifted to a higher liftoff height and blew out at a lower diluent concentration than the NPF, which can withstand larger amounts of dilution. In addition, both NPF and PPF were stabilized at lower liftoff heights and blew out at a lower diluent concentration when diluted with N_2 as opposed to CO_2 . The observed effects of fuel-stream dilution and partial premixing of flame liftoff and blowout can be explained using existing flame-stabilization theories. The results of this investigation were documented by A. M. Briones, S. K. Aggarwal (both of the University of Illinois at Chicago), and V. R. Katta (ISSI) in a paper that was published in *Physics of Fluids* [Vol. 18, pp. 043603-1 – 043603-13 (April 2006)]. The paper is included in the Appendix.

3.1.12 Trimethylphosphate (TMP) as Soot-Reducing Additive - Numerical Study of Jet Flames.

Doping of organophosphorus compound into flames produces phosphor-bearing species, which are known to recombine radicals such as H, O, and OH catalytically and, thereby, reduce the chemical activity in the flame zone. While such a scenario for decreasing chemical activity is being used for inhibiting flames, the possibility of its application for reducing soot in flames must be explored. A time-dependent, axisymmetric mathematical model known as UNICORN was used for studying the effects of TMP on soot production in various flames. A detailed chemical-kinetics model consisting of 238 species and 3178 elementary reaction steps was incorporated into UNICORN for the simulation of heptane flames doped with TMP. Using the same code TMP-doped ethane and propane flames were also simulated. The effects of TMP in coaxial diffusion and premixed jet flames were investigated by varying the amount of additive in the fuel jet. Premixed flames were found to be more sensitive to the presence of TMP. As expected, the burning velocity of the fuel was significantly reduced. However, an increase in soot production was also observed. In contrast, TMP was less effective in diffusion flames but decreased soot when a sufficient amount was added. The stability of the diffusion flame was not affected significantly by the presence of TMP in the fuel jet. The contrasting behavior of TMP in premixed and diffusion flames was similar in methane, propane, and heptane flames. The results of this investigation were documented by V. R. Katta (ISSI) and W. M. Roquemore (AFRL) in a paper that was presented at the 2006 Technical Meeting of the Central States

Section of the Combustion Institute, which was held 21-23 May 2006 in Cleveland, OH. The paper was published in the Conference Proceedings and is included in the Appendix.

3.1.13 Effects of H₂-Enrichment on Flame-Propagation Characteristics of Methane-Air Flames.

Lean burning of hydrocarbon yields exceptionally low pollutant emissions and superior combustion characteristics. For most hydrocarbon fuels, however, burning in the lean regime results in stability problems because of lean flammability limits. Hydrogen is an alternative fuel. The use of pure hydrogen, however, in a practical combustor is limited because of problems related to storage, low volumetric-heating value, and flashback that make the use of pure hydrogen very difficult and dangerous. For this reason, a hydrogen-hydrocarbon fuel blend may be a practical solution. Previous investigations have focused mainly on studying the effects of adding hydrogen to hydrocarbon flames using simplified configurations (e.g., counterflow one-dimensional flames and freely propagating flames). However, for most combustors, flames are exposed to both hydrodynamic and curvature-induced stretch and oscillations that drastically affect their flammability and emission characteristics. In the present investigation methane-air flames were established on axisymmetric coflowing jets, with the fuel-air mixture introduced through the inner burner and air introduced through the coannular burner. The effect of H₂-enrichment on flame propagation was investigated for a wide range of conditions. A time-accurate, implicit algorithm that employs a detailed description of the flame chemistry (GRI-Mech 1.2) and includes radiation effects was utilized for the simulations. The addition of hydrogen affected both the flame-propagation characteristics through preferential-diffusion instability and the inherent high flame speed. The results of this study were documented by A. M. Briones, S. K. Aggarwal (University of Illinois at Chicago), and V. R. Katta (ISSI) in a paper that was presented at the 2006 Technical Meeting of the Central States Section of the Combustion Institute, which was held 21-23 May 2006 in Cleveland, OH. The paper was published in the Conference Proceedings and is included in the Appendix.

3.1.14 Hysteresis in Counterflow Premixed Flame System.

The response to stretch of the counterflow flame system that is established between lean-methane-air and lean-hydrogen-air streams was investigated. The two-dimensional model known as UNICORN was used. Detailed measurements for temperature and species concentrations were made along the centerline. Numerical simulations have identified the hysteresis property of this flame system; this was later confirmed by experiments. For the given flow conditions, the flame system can have more than one stable operating mode; however, the actual operating mode depends on the manner in which the flow conditions were obtained. In an attempt to understand such hysteresis behavior of counterflow flames, simulations were performed by increasing and decreasing the stretch rates. When the stretch rate on the flame system was increased, the flame transitioned from a double-flame to a single-flame structure because of the aerodynamic-cooling process. When the stretch rate was decreased, the flame did not transition back to its double-flame structure because of stretch effects on molecular diffusion--leading to hysteresis. Flames established with various lean-methane-air mixtures were studied for determining the range for possessing hysteresis. It was found that the flame system exhibits hysteresis only for methane-air mixtures leaner than $\phi = 0.811$. However, for

$0.811 > \phi > 0.74$, a decrease in stretch increases the flame temperature because of a decrease in stretch-induced cooling and eventually returns the flame structure to a double-flame one. In this narrow range of ϕ (0.74 - 0.811), hysteresis in counterflow premixed flames is temporary, which establishes a hysteresis loop with respect to stretch rate. The results of this investigation were documented by V. R. Katta (ISSI), S. Hu, P. Wang, R. W. Pitz (all of Vanderbilt University), W. M. Roquemore, and J. Gord (both of AFRL) in a paper that was presented at the 2006 Technical Meeting of the Central States Section of the Combustion Institute, which was held 21-23 May 2006 in Cleveland, OH. The paper was published in the Conference Proceedings and is included in the Appendix.

3.1.15 Comparison of Chemical-Kinetics Models for JP-8 Fuel in Predicting Premixed and Non-premixed Flames.

CFD-based predictions were made for an opposed-jet non-premixed flame and laminar non-premixed and premixed coaxial jet flames that burn vaporized JP-8 fuel. Results were obtained for four published chemical-kinetic mechanisms for JP-8. The first is identified as the Violi-Small Mechanism (161 species and 1538 reactions); the second is the Violi-Large Mechanism (216 species and 9654 reactions); the third is the Zhang Mechanism (208 species and 2186 reactions); and the fourth is the Mawid Mechanism (226 species and 3230 reactions). Three surrogate fuels are associated with the Mawid Mechanism. Differences and similarities in laminar flame structure and stability, resulting from calculations using the four JP-8 mechanisms, were found. Calculations with the Violi-Small and Violi-Large Mechanisms predicted extinction strain rates that were within 90% of published measurement results. The flames obtained with the Zhang Mechanism were found to be the most difficult to extinguish and those obtained with the Mawid Mechanism to be the easiest to extinguish. Calculations with the Zhang Mechanism yielded the highest stability for the non-premixed jet flame and the highest flame velocity for the stoichiometric mixture of JP-8 and air in the premixed jet flame. The Mawid Mechanism resulted in coaxial non-premixed jet flames that were more stable than those obtained with the Violi Mechanisms, and yet the flame velocities predicted by the Mawid Mechanism for the premixed jet flame were lower than those predicted by the Violi Mechanisms. Calculations with the Mawid Mechanism using surrogate mixtures one and three resulted in very different limiting strain rates for the opposed-jet flame; however, for the premixed jet flame, the computed flame velocities were nearly the same for these mixtures. Numerical experiments were also performed in an attempt to understand the sensitivity of the parent compounds used in the Mawid Mechanism for possible changes in their concentrations. Direct comparisons of calculations and experimental results were very limited because published data on these simple laboratory flames that burn JP-8 are almost non-existent. Indeed, the hope is that these predictions will stimulate experiments to aid in obtaining suitable kinetic mechanisms for JP-8 flames. The results of this investigation were documented by V. R. Katta (ISSI), M. Mawid (Engineering Research and Analysis Corporation), B. Sekar, E. Corporan, J. Zelina, W. M. Roquemore (all of AFRL), and C. J. Montgomery (Reaction Engineering International) in a AIAA Paper 2006-4745 that was presented at the 42nd AIAA/ASME/SAE/ASEE Joint Propulsion Conference and Exhibit, which was held 9-12 July 2006 in Sacramento, CA. The paper is included in the Appendix.

3.1.16 Numerical Studies on Soot Mitigation in Model Gas-Turbine Combustor.

A time-dependent, detailed-chemistry CFD model was developed for evaluation of the performance of a soot-reducing additive in a model swirl-stabilized combustor. While commercial JP-8 fuel was used in the experiments, a six-component surrogate mixture was used in the calculations for mimicking the JP-8-fuel combustion. Di-tertiary-butyl-peroxide (DTBP) additive, which is known for improving the ignition characteristics of hydrocarbon fuels, was tested for its ability to reduce soot. Detailed chemical kinetics were used for simulation of JP-8+DTBP combustion and the consequent formation of PAH species. Calculations were made for different equivalence ratios that were obtained through varying the fuel jet velocity while maintaining the airflow unaltered. Turbulent-flow simulations with the base JP-8 fuel revealed that a significant amount of soot was formed for fuel-rich conditions, while negligible or no soot was formed for equivalence ratios > 0.8 . Addition of DTBP for the fuel-rich operating conditions resulted in only a marginal decrease in the amount of soot formed. Its effect on fuel-lean operation of the combustor was also found to be negligible. However, DTBP appeared to be more effective in reducing soot when the combustor was operating in the neighborhood of stoichiometric conditions. Consistent with these results, calculations made for a simple jet diffusion flame also revealed that DTBP had no effect on soot formation when it was added to the fuel jet. The results of this study were documented by V. R. Katta, T. R. Meyer (both of ISSI), C. J. Montgomery (Reaction Engineering International), and W. M. Roquemore (AFRL) in AIAA Paper 2006-5095 that was presented at the 42nd AIAA/ASME/SAE/ASEE Joint Propulsion Conference and Exhibit, which was held 9-12 July 2006 in Sacramento, CA. The paper is included in the Appendix.

3.1.17 Numerical Study of Evolution of Strongly Forced, Axisymmetric, Laminar Cold-Flow Jets.

Periodic jet forcing presents interesting opportunities for jet mixing in a variety of applications. In this study simulations were performed to study the effect of high-amplitude forcing on laminar jets ($Re = 100$) with net mass flux. For the cases presented, the effects of simulating the internal nozzle were examined, and assumptions about the nozzle flow were shown to have a significant effect on the downstream flow evolution. Studies were performed on strongly forced axisymmetric jets in two geometries: 1) jets issuing perpendicularly from a flat wall and 2) jets issuing from a straight tube (nozzle). The amplitude and frequency of the forcing function were varied to study vortex creation and the subsequent evolution downstream of the jet. For example, cases in which the peak jet velocity was three to four times the mean jet velocity were examined. The near-nozzle region was of particular interest because of the strong mixing processes that occur there. Modification of the creation of downstream large-scale vertical structures by nozzle flow processes was examined. An interesting result of this study was the fact that the strongest forcing cases possess some striking similarities to synthetic jets. For such cases the flow-reversal processes at the jet exit plane were investigated. The results of this study were documented by V. V. Barve, O. A. Ezekoye, N. T. Clemens (University of Texas at Austin), and V. R. Katta (ISSI) in a paper that was published in the *AIAA Journal* [Vol. 44, No. 8, pp. 1742-1752 (August 2006)]. The paper is included in the Appendix.

3.1.18 Characteristics of Propagating H₂-Enriched CH₄-Air Flames.

The effects of H₂ enrichment on the propagation of laminar CH₄-air triple flames in axisymmetric coflowing jets were investigated numerically. A comprehensive, time-dependent computational model that employs a detailed description of chemistry and transport was used to simulate the transient-ignition and flame-propagation phenomena. Flames were ignited in a jet-mixing layer far downstream of the burner. Following ignition, a well-defined triple flame was formed that propagated upstream with nearly constant flame-displacement speed toward the burner along the stoichiometric-mixture fraction line. As the flame approached the burner, it transitioned to a double flame and, subsequently, to a burner-stabilized non-premixed flame. Predictions were validated using measurements of the flame-displacement speed. Detailed simulations were used to examine the effects of H₂ enrichment on the propagation characteristics of CH₄-air triple flames. As H₂ concentration in the fuel blend was increased, the flame displacement and propagation speeds increased progressively as a result of the enhanced chemical reactivity, diffusivity, and preferential diffusion caused by H₂ addition. Also the flammability limits associated with the triple flames were progressively extended with the increase in H₂ concentration. The flame structure and flame dynamics were also markedly modified by H₂ enrichment, which substantially increases the flame curvature and mixture-fraction gradient as well as the hydrodynamic and curvature-induced stretch near the triple point. For all of the H₂-enriched methane-air flames investigated, a negative correlation was found between flame speed and stretch, with the flame speed decreasing almost linearly with stretch; this is consistent with the findings of previous studies. The effect of H₂ addition is a modification of the flame sensitivity to stretch since it decreases the Markstein number (Ma) and increases the flame tendency toward diffusive thermal instability (i.e., $Ma \rightarrow 0$). These results are consistent with previously reported experimental results for outwardly propagating spherical flames that are burning a mixture of natural gas and hydrogen. The results of this study were documented by A. M. Briones, S. K. Aggarwal (both of the University of Illinois at Chicago), and V. R. Katta (ISSI) in AIAA Paper 2007-180 that was presented at the AIAA Meeting in Reno. The paper is included in the Appendix.

3.1.19 Investigations on Double-State Behavior of Counterflow Premixed Flame System.

The counterflow flame system established between lean-methane-air and lean-hydrogen-air streams was investigated experimentally and numerically. A two-dimensional model known as UNICORN was used for the simulation. Detailed measurements of temperature and species concentrations were made along the centerline using Raman spectroscopy. A double-state behavior for this flame system was identified in the numerical simulations and later confirmed through experiments. For the given flow conditions, the flame system can have either a single-flame or a double-flame structure, depending on the manner in which those conditions were achieved. Detailed comparisons of the measurement results and calculations for the two flame structures were made. Calculations for various lean methane-air mixtures and stretch rates were performed in an attempt to understand the double-state behavior of counterflow premixed flames. It was found that the flame system exhibits double-state behavior only for leaner ($\phi_{\text{CH}_4} < 0.74$) methane-air mixtures. The aerodynamic and chemical structures of the flames in different stretch-rate regimes were analyzed. When the stretch rate on the flame system was increased, the flame transitioned from a double-flame to a single-flame structure as a result of the

aerodynamic-cooling process. When the stretch rate was decreased, the flame did not transition back to the double-flame structure as a result of the effects of stretch on molecular diffusion. However, for ($\phi_{\text{CH}_4} < 0.81$), a decrease in stretch rate increased the flame temperature because of a lack of stretch-induced cooling and returned the flame structure to a double-flame one. For a narrow range of equivalence ratios (0.74 - 0.81), counterflow premixed flames exhibit a hysteresis property. The results of this investigation were documented by V. R. Katta (ISSI), S. Hu, P. Wang, R. W. Pitz (all of Vanderbilt University), W. M. Roquemore, and J. R. Gord (both of AFRL) in a paper that was published in *Proceedings of the Combustion Institute* [Vol. 31, pp. 1055-1066 (January 2007)]. The paper is included in the Appendix.

3.1.20 Predictions on Sooting Behavior of Recirculation-Zone-Supported Flames.

The primary and secondary recirculation zones, which are formed between the fuel and oxidizer jets of a centerbody burner, transport fuel across the centerbody to the oxidizer jet and establish a flame that is anchored to the rim of the centerbody. Experimentally it was found that the sooting characteristics of a centerbody burner change dramatically when the operating conditions are altered systematically. A time-dependent, axisymmetric, detailed-chemistry CFD model was developed for studies of soot in a 46-mm-diameter centerbody burner. Combustion and PAH formation were simulated using Wang-Frenklach (99 species and 1066 reactions) and NIST (197 species and 2800 reactions) mechanisms. Soot was simulated using a two-equation model of Linstedt. Calculations were performed for different flow conditions under which the concentration of ethylene was reduced gradually without altering the fuel and oxidizer flow rates. Numerical experiments were performed for determining the effect of soot radiation on flame structure. Flame weakening in the transition region of the leading and trailing flame sections was found to result from soot radiation. Amazingly similar flame and soot structures were obtained with the two chemical-kinetics mechanisms considered. The results of this investigation were documented by V. R. Katta (ISSI) and W. M. Roquemore (AFRL) in Paper No. D37 that was presented at the 5th U. S. Combustion Meeting, which was held 25-28 March 2007 in San Diego, CA. The paper is included in the Appendix.

3.1.21 Experimental and Numerical Studies of Centerbody Flames.

A preliminary evaluation was conducted of a centerbody burner as a tool for developing and evaluating soot models. The burner consists of a 46-mm-diameter disk symmetrically located in an 80-mm-diameter annular quartz duct. A 7.6-mm-diameter fuel jet is located at the center of the disk. A mixture of air and excess nitrogen is supplied to the annular duct at a flow rate of 250 SLPM. Ethylene fuel, mixed with nitrogen, is supplied to the central fuel jet at a flow rate of 3.4 SLPM. The three flames studied had the same air and fuel velocity (1.2 m/s) and similar vortex characteristics. Different sooting-flame characteristics were achieved by varying the N₂ dilution in the fuel and air. For example, with no N₂ dilution almost the entire surface of the flame was sooting. The two flames with N₂ dilution had donut- and ring-shaped sooting structures. All three of the flames had the interesting characteristic that the soot path lines had spiraling trajectories that terminated at the center of the recirculation zone. Simulations, using a two-dimensional, CFD-based code (UNICORN), correctly estimated the structures of the recirculation and flame zones. Also, reasonable estimates were obtained for the global structure of the unusual sooting surfaces of the three flames, which is somewhat surprising considering the rudimentary soot

model used in UNICORN. However, the soot model was not sufficiently developed to capture the spiral trajectories of the soot particles. The spiraling path lines were correctly estimated using a particle-tracing program and flow-field data from UNICORN. Other computational experiments were conducted that provided insight into the interesting sooting characteristics of these flames. The results of this study were documented by M. Roquemore (AFRL), V. Katta (ISSI), V. Belovich, R. Pawlik, A. Lynch, J. Miller (all of AFRL), S. Stouffer, G. Justinger (both of UDRI), J. Zelina (AFRL), S. Roy (ISSI), and J. Gord (AFRL) in Paper No. D36 that was presented at the 5th U. S. Combustion Meeting, which was held 25-28 March 2007 in San Diego, CA. The paper is included in the Appendix.

3.1.22 Can Non-premixed Stretched Flames Become Infinitely Thin?

A numerical study was performed for determining the minimum possible thickness for a non-premixed hydrogen-air flame. The flat flame formed between the counterflowing fuel and the air jets was stretched through increasing jet velocities. A time-dependent model, known as UNICORN, that incorporates 13 species and 74 reactions among the constituent species was used for the simulation of the opposed-jet hydrogen-air non-premixed flame. Numerical experiments were conducted through changing the reaction rates. It was found that a non-premixed flame can only be stretched to a minimum thickness prior to its extinction. Contrary to the flamelet description for laminar stretched flames, the reaction-zone thickness for a hydrogen-air non-premixed flame can asymptotically reach a value in the range 0.5 - 1.0 mm, depending on the radical species used for measuring the thickness. This finding has an important bearing on turbulence modeling based on flamelet theory. The results of this study were documented by V. R. Katta (ISSI), W. M. Roquemore, and J. R. Gord (both of AFRL) in a paper that was presented at the 21st International Colloquium on the Dynamics of Explosions and Reactive Systems (ICDERS), which was held 23-27 July 2007 in Poitiers, France. The paper was published in the Conference Proceedings and is included in the Appendix.

3.1.23 Evaluation of Chemical-Kinetics Models for Heptane Combustion.

CFD-based predictions were obtained for non-premixed and premixed flames burning vaporized heptane fuel. Three chemical-kinetics models were incorporated into a time-dependent, two-dimensional, detailed-chemistry CFD model known as UNICORN. The first mechanism was the San Diego (SD) mechanism (52 species and 544 reactions); the second was the Lawrence Livermore National Laboratory (LLNL) mechanism (160 species and 1540 reactions); and the third was the National Institute of Standards and Technology (NIST) mechanism (197 species and 2926 reactions). Numerical models were validated through simulating an opposing-jet non-premixed flame that had been previously studied experimentally. Models were also tested for their accuracies in predicting strain-induced extinction and autoignition. Compared to traditional one-dimensional models for opposing-jet flames, two-dimensional simulations were found to yield results closer to the experimental values. All three mechanisms were reasonably close in predicting co-axial jet non-premixed and premixed flames. The SD mechanism was found to be slightly stiffer than the other two, especially in solving for premixed combustion. While LLNL kinetics resulted in a steady Bunsen-type premixed flame, SD and NIST mechanisms yielded cellular-type flame structures for the same flow conditions. The results of this investigation were documented by V. R. Katta (ISSI) and W. M. Roquemore (AFRL) in AIAA Paper 2008-1015 for

presentation at the 46th AIAA Aerospace Sciences Meeting and Exhibit, which will be held 7-10 January 2008 in Reno, NV. The paper is included in the Appendix.

3.1.24 Comparison of Chemical-Kinetics Mechanisms through Predicting Non-premixed Ethylene Jet Flame.

Since detailed chemical-kinetics mechanisms are usually developed and validated through simulation of zero- and one-dimensional flames, their performance in predicting a multi-dimensional flame must be tested prior to their use in a combustor design. The predictive capabilities of various detailed chemical-kinetics mechanisms for ethylene-air combustion were investigated through simulation of a non-premixed jet flame. A time-dependent, axisymmetric mathematical model was used for flame simulation. Five detailed chemical-kinetics models, namely, 1) the Wang-Frenklach Mechanism (99 species and 1066 reactions), 2) the Wang-Colket Mechanism (171 species and 2002 reactions), 3) the San Diego (SD) Mechanism (52 species and 544 reactions), 4) the NIST Mechanism (197 species and 2926 reactions), and 5) the LLNL Mechanism (160 species and 1540 reactions) were considered. A two-equation soot model was used in conjunction with the detailed-chemistry models for simulation of sooty ethylene flames. Calculations were made with and without soot for identifying the impact of the soot model on the chemistry models and vice versa. It was found that all of the five chemistry models predicted a non-premixed jet flame equally well when soot was not considered. However, when soot was included, the predictions diverged, with the San Diego Mechanism yielding results that were closest to those of the experiment. The results of this investigation were documented by V. R. Katta (ISSI), W. M. Roquemore (AFRL), and R. J. Santoro (Pennsylvania State University) in a paper that was presented at the 2008 Technical Meeting of the Central States Section of the Combustion Institute, which was held 20-23 April 2008 in Tuscaloosa, AL. The paper was published in the Conference Proceedings and is included in the Appendix.

3.1.25 Effects of H₂ Enrichment on Propagation Characteristics of CH₄-Air Triple Flames.

The effects of H₂ enrichment on the propagation of laminar CH₄-air triple flames in axisymmetric coflowing jets were investigated numerically. A comprehensive, time-dependent computational model that employs a detailed description of chemistry and transport was used to simulate the transient ignition and flame propagation phenomena. Flames were ignited in a jet-mixing layer far downstream of the burner. Following ignition, a well-defined triple flame was formed that propagated upstream along the stoichiometric mixture-fraction line with a nearly constant displacement velocity. As the flame approached the burner, it transitioned to a double flame and, subsequently, to a burner-stabilized non-premixed flame. Predictions were validated using measurements of the displacement flame velocity. As the H₂ concentration in the fuel blend was increased, the displacement flame velocity and local triple-flame speed increased progressively because of the enhanced chemical reactivity, diffusivity, and preferential diffusion caused by H₂ addition. Furthermore, the flammability limits associated with the triple flames were progressively extended with the increase in H₂ concentration. The flame structure and flame dynamics were also markedly modified by H₂ enrichment, which substantially increased the flame curvature and mixture-fraction gradient as well as the hydrodynamic and curvature-induced stretch near the triple point. For all of the H₂-enriched methane-air flames investigated in this study, a negative correlation was found between flame speed and stretch, with the flame

speed decreasing almost linearly with stretch, which is consistent with the results of previous studies. The H_2 addition also modified the flame sensitivity to stretch, as it decreased the Markstein number (Ma), implying an increased tendency toward diffusive-thermal instability (i.e., $Ma \rightarrow 0$). These results are consistent with the previously reported experimental results for outwardly propagating spherical flames that burn a mixture of natural gas and hydrogen. The results of this study were documented by A. M. Briones, S. K. Aggarwal (both of the University of Illinois at Chicago), and V. R. Katta (ISSI) in a paper that was published in *Combustion and Flame* [Vol. 153, pp. 367-383 (May 2008)]. The paper is included in the Appendix.

3.1.26 Numerical Studies on Cavity-Inside-Cavity-Supported Flames in Ultra-Compact Combustors.

Cavities are incorporated in the designs of future gas-turbine combustors to provide flame stability and, thereby, improve the lean-blowout characteristics. Recently, a Cavity-Inside-Cavity (CIC) design was proposed for the Air Force Research Laboratory's Ultra Compact Combustor (UCC). Numerical studies were performed to aid the understanding of the dynamics of CIC-supported flames. The complex CIC that was used in the actual hardware was simplified to make it amenable to two-dimensional models. Calculations were performed for the modified CIC using a two-dimensional, unsteady reacting-flow code known as UNICORN. Direct numerical simulations and calculations using the k - ϵ turbulence model were performed. A fast, global-chemistry model was used for studying the flame dynamics inside and in the wake region of the CIC. Calculations were performed for several CIC geometries that were generated through variation of the width of the cavity. The design CIC was found to be oversized for the secondary (circumferential) airflow used in UCCs. A detailed-chemistry model was also used to aid the understanding of the blowout characteristics of the CIC-supported flames. The results of this investigation were documented by V. R. Katta (ISSI), J. Zelina, and W. M. Roquemore (both of AFRL) in a paper that was presented at the 53rd ASME International Gas Turbine and Aeroengine Congress and Exposition, which was held 9-13 June 2008 in Berlin, Germany. The paper was published in *Proceedings of ASME Turbo Expo '08: Power for Land, Sea and Air* and is included in the Appendix.

3.1.27 Stability of Lifted Flames in Centerbody Burner.

The centerbody burner was designed with the objective of understanding the coupled processes of soot formation, growth, and burn-off through decoupling them using recirculation zones. Experimentally it was found that the sooting characteristics of the centerbody burner could change dramatically with changes in operating conditions. One of the interesting operating regimes in which the flame lifts off and forms a column of soot was identified when oxygen in the oxidizer stream was sufficiently reduced. Numerical studies were performed to aid the understanding of the lifted flames of the centerbody burner. A time-dependent, axisymmetric, detailed-chemistry CFD model (UNICORN) was used. Combustion and PHA formation were modeled using the Wang-Frenklach (99 species and 1066 reactions) Mechanism, and soot was simulated using a two-equation model of Lindstedt. Calculations reasonably predicted the structure of the lifted flame. The predicted flame lift-off height matched well with that of the experiment. Recirculation zones were formed between the flame base and the centerbody transport fuel, and its lighter fragments formed in the lifted-flame region toward the face of the

centerbody. Mixing of oxygen and fuel and its fragments between the flame base and centerbody established a premixed flame in the flame-base region. Numerical studies were conducted by increasing and decreasing the coannular flow velocity to determine the stability of the lifted flames. The results of this study were documented by V. R. Katta (ISSI) and W. M. Roquemore (AFRL) in a paper that was presented at the 2008 Technical Meeting of the Central States Section of the Combustion Institute, which was held 20-23 April 2008 in Tuscaloosa, AL. The paper was published in the Conference Proceedings and is included in the Appendix.

3.1.28 Calculation of Multi-dimensional Flames Using Large Chemical Kinetics.

A time-dependent, two-dimensional, detailed-chemistry CFD model known as UNICORN is used for solving complex flame problems. Unique features were incorporated into UNICORN for handling extremely large chemical kinetics with ease and efficiency. A sub-mixture concept was used for evaluating transport properties. This concept increased the computational speed by a factor of five for a 208-species mechanism and is expected to have even higher efficiency with larger mechanisms. An implicit treatment for certain reaction-rate terms was applied during the solution of species-conservation equations. Moving the reaction-rate source terms to the left-hand side of the partial differential equations eased the stiffness problem that is typically associated with combustion chemical kinetics. Computational speeds were further improved in UNICORN by completely integrating the chemical-kinetics mechanisms with the solution algorithm. A software-generated CFD approach was used to avoid the tedious and near-impossible task of manually integrating a large chemical-kinetics mechanism into a CFD code. Several calculations were performed to demonstrate the abilities of the UNICORN code. Chemical-kinetics mechanisms up to 366 species and 3700 reaction steps were incorporated, and simulations for unsteady multi-dimensional flames were performed on personal computers. Making use of the robustness and efficiency of the UNICORN code, detailed chemical mechanisms developed for JP-8 fuel were tested for their accuracy, and a parametric study on the role of parent species of a surrogate mixture in predicting flame extinguishment was performed. Ease of changing chemical kinetics in the UNICORN code was demonstrated through investigation of the effects of additives in JP-8 fuel. The results of this study were documented by V. R. Katta (ISSI) and W. M. Roquemore (AFRL) in a paper that was published in the AIAA Journal [Vol. 46, No. 7, pp. 1640-1650 (July 2008)]. The paper is included in the Appendix.

3.1.29 Asymmetric Expansion of Detonation Wave in an Array of Tubes.

In the development of Pulse Detonation Engines, one of the important design criteria is reliable transition of detonation generated in the ignition tube into a larger main tube in the shortest possible distance. It was thought that asymmetrically aligning the ignition and main tubes would enhance detonation transition. An exploratory numerical study was conducted to aid the understanding of detonation expansion in asymmetrically joined tube assemblies. A CFD code based on flux-corrected transport was used for the simulation of a two-dimensional detonation wave formed from a pair of ignition sources in a smaller ignition tube and expanded into a larger main tube. Numerous geometries obtained by varying the tube size and offset (asymmetry) were investigated. It was found that expansion of detonation destroys its cellular structure and generates strong triple-shock points near the walls. Asymmetric expansion creates triple-shock points that are stronger than those generated in symmetric expansion. Interaction of strong

triple-shock points with walls often leads to galloping detonations. For severe expansion ratios, a symmetric configuration resulted in a deflagration wave (failed detonation), while asymmetric configurations yielded successful detonation transition from ignition tube to main tube. The results of this investigation were documented by V. R. Katta (ISSI) in a paper that was presented at the 44th AIAA/ASME/SAE/ ASEE Joint Propulsion Conference and Exhibit, which was held 21-23 July 2008 in Hartford, CT. The paper is included in the Appendix.

4.0 FUNDAMENTAL EXPERIMENTS

4.1 General Overview

The objective of this portion of the program was to design and conduct fundamental experiments that would aid the understanding of all processes required for advanced propulsion systems. This effort required a close coupling of numerical and experimental studies and was, thus, performed by a multi-disciplinary team. A summary of the work accomplished on this task during the program follows.

4.1.1 Dynamics of Vortex-Flame Interactions and Implications for Turbulent Combustion.

Vortex-flame interactions are used to study the dynamics of unsteady laminar flamelet burning in non-premixed gaseous and two-phase flows. Such interactions provide a tractable numerical and experimental regime in which turbulent-like phenomena can be evaluated. A number of fundamental parameters were explored that have implications for the study of turbulent combustion, including scalar dissipation, unsteady flame thickness, unsteady strain rate, and a new parameter recently proposed to characterize local extinction. Particular attention was paid to time-dependent (dynamic) phenomena such as unsteadiness and flame movement that may play a significant role in turbulent-combustion modeling and validation. Results indicated that a variety of features can result in non-idealized flamelet behavior in near-unity Lewis-number flames. The sensitivity of mixture-fraction-state relationships to vortex-flame effects was analyzed and discussed. The results of this study were documented by T. R. Meyer, V. R. Katta, M. S. Brown (all of ISSI), J. R. Gord, W. M. Roquemore (both of AFRL), A. Lemaire, K. Zahring, and J. C. Rolon (all of Ecole Centrale Paris) in AIAA Paper 2003-4633 that was presented at the 39th AIAA/ASME/SAE/ASEE Joint Propulsion Conference and Exhibit, which was held 20-23 July 2003 in Huntsville, AL. The paper is included in the Appendix.

4.1.2 Vortex-Induced Extinction of Non-Premixed Counterflow Flames.

In an experimental study, unsteady-strain-rate effects on the extinction process of a laminar strained two-phase flame during the flame/vortex interaction were examined through simultaneous investigation of the flow field by Particle Imaging Velocimetry (PIV) and the reaction zone by PLIF of the CH radical. The influence on the aerodynamic extinction limits for various vortex parameters and different single- and two-phase flames was examined. The effect of different flames on the vortex flow was also investigated. The results of this study were documented by A. Lemaire, K. Zahring (both of Ecole Centrale Paris), T. Meyer (ISSI), J. Gord (AFRL), and J. C. Rolon (Ecole Centrale Paris) in a paper that was presented at the European Combustion Meeting, which was held 18-21 October 2003 in Orleans, France. The paper is included in the Appendix.

4.1.3 PIV/ PLIF Investigation of Two-Phase Vortex-Flame Interactions: Effects of Vortex Size and Strength.

The evolution of flame-surface area and the rate of CH-layer extinction were measured during the interaction of a two-phase counterflow diffusion flame with fuel-side vortices of varying size and strength. PLIF of CH was used to mark the flame front, and PIV was used to measure the strain-rate field at various phases of the interaction process. Vortices of similar initial circulation but differing in size showed widely disparate peak strain rates and CH decay rates because of varying levels of flame-induced vortex dissipation. Vortex size was also found to have a significant effect on flame-surface-area evolution during and after extinction, with the presence of droplets playing a major role in the latter. Implications of these results for the fundamental understanding of vortex-flame interactions were considered. The results of this investigation were documented by A. Lemaire (Ecole Centrale Paris), T. R. Meyer (ISSI), K. Zahringer (Ecole Centrale Paris), J. R. Gord [Air Force Research Laboratory (AFRL)], and J. C. Rolon (Ecole Centrale Paris) in a paper that was published in *Experiments in Fluids* [Vol. 36, pp. 36-42 (January 2004)]. The paper is included in the Appendix to this report.

4.1.4 Simultaneous PLIF/PIV Investigation of Vortex-Induced Annular Extinction in H₂-Air Counterflow Diffusion Flames.

High-temporal-resolution measurements of scalars and velocity were used to study vortex-induced annular (off-centerline) flame extinction during the interaction of a propagating vortex with an initially stationary counterflow hydrogen-air diffusion flame. Such an extinction process differs from classical one-dimensional descriptions of strained flamelets in that it captures the effects of flame curvature as well as dynamic strain. PLIF measurements of the hydroxyl radical (OH) were used to track flame development, and simultaneous PIV was used to characterize the two-dimensional flow field. Measurements revealed differences in local and normal strain-rate profiles along and across the reaction zone and indicated that vortex-induced curvature in the annular region may initiate the extinction process. In addition, the effect of local flame extinction on vortex evolution and dissipation was determined from measured vorticity data. The results of this study were documented by T. R. Meyer (ISSI), G. J. Fiechtner (Sandia National Laboratories), S. P. Gogineni (ISSI), J. C. Rolon (Ecole Central Paris), C. D. Carter, and J. R. Gord (both of AFRL) in a paper that was published in *Experiments in Fluids* [Vol. 36, pp. 259-267 (February 2004)]. This paper is included in the Appendix.

4.1.5 Influence of Spray-Flame Structure on Soot Formation in Gas-Turbine Combustors.

Simultaneous measurements of OH PLIF and laser-induced incandescence (LII) were used to characterize the flame structure and soot-formation process in the reaction zone of a swirl-stabilized, liquid-fueled gas-turbine combustor. Studies were performed at atmospheric pressure with heated inlet air and overall equivalence ratios ranging from 0.5 to 1.15. At low equivalence ratios ($\phi < 0.8$), large-scale structures entrain rich pockets of fuel and air deep into the flame layer; at higher equivalence ratios, these pockets grow in size and prominence, escape the OH-oxidation zone, and serve as sites for soot inception. The results of this investigation were documented by T. R. Meyer, S. Roy, S. P. Gogineni (all of ISSI), and J. R. Gord (AFRL) in a

paper that was presented at the 2004 Technical Meeting of the Central States Section of the Combustion Institute, which was held 21-23 March 2004 in Austin, TX. The paper is included in the Appendix.

4.1.6 Extinction Criterion for Unsteady, Opposing-Jet Diffusion Flames.

Dynamic flames are known to survive at strain rates that are much higher than those associated with steady-state flames. A numerical and experimental investigation was performed to aid the understanding of the extinction process associated with unsteady flames. Spatially locked unsteady flames in an opposing-jet-flow burner were established and stretched by simultaneously driving one vortex from the air side and another from the fuel side. Changes in the structure of the flame during its interaction with the incoming vortices and with the instability-generated secondary vortices were investigated using a time-dependent Computational-Fluid-Dynamics-with-Chemistry (CFDC) code known as UNICORN. The combustion process was simulated using a detailed-chemical-kinetics model that incorporates 13 species and 74 reactions. Slow-moving vortices produce a wrinkled but continuous flame, while fast-moving vortices create a locally quenched flame with its edge wrapped around the merged vortical structures. In an attempt to characterize the observed quenching process, five variables--namely, air-side, fuel-side, and stoichiometric strain rates and maximum and stoichiometric scalar dissipation rates--were investigated. It was found that these characteristic parameters cannot be used to describe the quenching process associated with unsteady flames. The flow and chemical non-equilibrium states associated with the unsteady flames are responsible for changes in the extinction values of these traditional characteristic variables. However, even though the quenching values of the scalar dissipation rates increase with the velocity of the incoming vortices, the variations are much smaller than those observed in the strain rates. It is proposed that a variable that is proportional to the air-side strain rate and inversely proportional to the rate of change in the flame temperature can be used to characterize the unsteady quenching process uniquely. The results of this study were documented by V. R. Katta, T. R. Meyer, M. S. Brown (all of ISSI), J. R. Gord, and W. M. Roquemore (both of AFRL) in a paper that was published in *Combustion and Flame* [Vol. 137, pp. 198-221 (April 2004)]. The paper is included in the Appendix.

4.1.7 OH PLIF and Soot-Volume-Fraction Imaging in Reaction Zone of Liquid-Fueled, Model Gas-Turbine Combustor.

Simultaneous measurements of OH PLIF and laser-induced incandescence (LII) were used to characterize the flame structure and soot-formation process in the reaction zone of a swirl-stabilized, JP-8-fueled, model gas-turbine combustor. Studies were performed at atmospheric pressure with heated inlet air and primary-zone equivalence ratios from 0.55 to 1.3. At low equivalence ratios ($\phi < 0.9$), large-scale structures entrained rich pockets of fuel and air deep into the flame layer; at higher equivalence ratios, these pockets grew in size and prominence, escaped the OH-oxidation zone, and served as sites for soot inception. Data were used for visualizing soot development as well as for qualitative tracking of changes in overall soot volume fraction as a function of fuel-air ratio and fuel composition. The utility of the OH-PLIF and LII measurement system for test-rig diagnostics was further demonstrated for the study of soot-mitigating additives. The results of this investigation were documented by T. R. Meyer, S. Roy, S. P. Gogineni (all of ISSI), V. M. Belovich, E. Corporan, and J. R. Gord (all of AFRL) in

ASME Paper No. GT2004-54318 that was presented at the ASME Turbo Expo 2004: Power for Land, Sea, and Air, which was held 14-17 June 2004 in Vienna, Austria. The paper was published in the conference proceedings and is included in the Appendix. Dr. Gogineni served as Session Co-organizer and Session Chair for this meeting.

4.1.8 Temperature and CO₂ Concentration Measurements in Exhaust Stream of Liquid-Fueled Combustor Using Dual-Pump CARS Spectroscopy.

Single-shot, dual-pump CARS measurements of N₂ and CO₂ were performed in the exhaust stream of a swirl-stabilized JP-8-fueled combustor under sooting conditions. The combustor was designed to study particulate formation and particle-size distributions for different flame conditions and, therefore, was operated at near-stoichiometric overall fuel-air ratios. Various jet fuels and additive concentrations were studied. These conditions pose a significant challenge for temperature measurements using standard N₂ CARS because of strong flame emission and absorption of the CARS signal by the C₂ Swan band. With the dual-pump CARS technique employed in this study, the N₂ CARS signal is generated at a wavelength (496 nm) that is not absorbed by C₂, and concentration measurements of CO₂ can be performed. The standard deviations of the single-shot temperature measurements were ~ 3-4% of the mean values for equivalence ratios ranging from 0.4 to 1.1, whereas those of the single-shot CO₂-concentration measurements were between 9 and 20% of the mean values. Previous single-shot temperature and CO₂-concentration measurements using dual-pump CARS in this liquid-fueled combustor were limited to an equivalence range of 0.45, with standard deviations in temperature of about 5-6% of the mean value of 1143 K [Lucht, et al, *AIAA J.* **41**(4), 679-686 (2003)]. The current study demonstrated a significant improvement in the applicability of single-shot CARS temperature and CO₂-concentration measurements to practical swirl-stabilized combustors under soot conditions. The results of this study were documented by S. Roy, T. R. Meyer (both of ISSI), R. P. Lucht (Purdue University), V. M. Belovich, E. Corporan, and J. R. Gord (all of AFRL) in a paper that was published in *Combustion and Flame* [**138**, 273-284 (August 2004)]. The paper is included in the Appendix.

4.1.9 Studies of Hydroxyl Distribution and Soot Formation in Turbulent Spray Flames.

A measurement system that combines several laser-based imaging techniques was developed for characterizing the instantaneous flame structure and soot-formation mechanisms in an atmospheric-pressure, swirl-stabilized, liquid-fueled, model gas-turbine combustor. Planar LII was used to map the soot volume fraction, and OH-PLIF was used to image the flame zone. Mie scattering, which appears as an interference in the OH PLIF signal, was used to a limited extent as a spray diagnostics. Optimal excitation and detection parameters to enable the simultaneous use of these techniques in turbulent spray flames were considered, along with analyses of potential sources of error. The data indicate that the flame in the near field of the swirl-stabilized injector is highly perturbed by large-scale structures and that the fluid-flame interactions have a significant impact on soot formation. Rich pockets of fuel and air along the interface between the spray flame and recirculation zone serve as locations for soot inception. The effect of local equivalence ratio was determined from qualitative analysis of the OH-PLIF data and comparison with equilibrium calculations in the recirculation region. Spatially averaged LII measurements demonstrated that soot volume fraction in the primary flame zone increases exponentially with

equivalence ratio. Preliminary results suggest that soot formation in the primary zone is strongly dependent on fuel aromatic content. The results of this investigation were documented by J. R. Gord (AFRL), T. R. Meyer, S. Roy, and S. P. Gogineni (all of ISSI) in a paper that was presented at the 12th International Symposium on Applications of Laser Techniques to Fluid Mechanics, which was held 12-15 July 2004 in Lisbon, Portugal. The paper is included in the Appendix. Dr. Gogineni served on the Advisory Committee for this conference.

4.1.10 Influence of Fuel Type and Operating Conditions on Particulates in Gas-Turbine Combustors.

A study to characterize the production of particulate-matter (PM) emissions was performed in a liquid-fueled, model gas-turbine combustor while varying fuel type and operating conditions. Laser-induced incandescence (LII), OH planar laser-induced fluorescence (PLIF), and laser Mie scattering were used, respectively, to track soot volume fraction, measure local equivalence ratio, and visualize droplet scattering in the reaction zone. A condensation nuclei counter (CNC) was employed to provide particle number density in the exhaust stream of the combustor, and a scanning mobility particle sizer (SMPS) was used to obtain particle size distribution. In-situ and ex-situ PM emissions were measured for fuel aromatic content that varied from 0% to 45% by volume as well as for paraffinic fuels that were low in aromatic and heteroatomic content. Consistent with the results of previous studies, fuels containing aromatics, which have been shown to promote PM production, were found to produce higher quantities of soot than straight-chain hydrocarbons. Laser-based measurements showed a significant correlation among physical flame structure, fuel type, and particle number density. The results of this study were documented by S. K. Chelgren, V. M. Belovich, E. Corporan, J. R. Gord (all of AFRL), M. J. DeWitt (University of Dayton Research Institute), T. R. Meyer, and S. Roy (both of ISSI) in a paper that was presented at the AFRC-JFRC 2004 Joint International Combustion Symposium that was held 10-13 October 2004 in Maui, HI. The paper is included in the Appendix.

4.1.11 Application of Laser Imaging Studies of Particle Formation in Gas-Turbine Combustion.

The goal of the current investigation was to study soot formation in the highly dynamic environment of a swirl-stabilized liquid-fueled combustor. This was accomplished through simultaneous imaging of the soot volume fraction and OH distribution in the primary reaction zone using LII and OH PLIF, respectively. Residual droplet Mie scattering was also detected in the OH PLIF diagnostic system and was used to a limited extent as a spray diagnostic. The performance and accuracy of the planar LII and OH PLIF systems were characterized in this investigation and demonstrated in studies of jet fuels and soot-mitigating additives. Preliminary analyses of the data indicate that the flame in the near field of the injector is highly perturbed by large-scale structures and that fluid-flame interactions have a significant impact on local equivalence ratio and soot formation. Rich pockets of fuel and air along the interface between the spray flame and recirculation zone serve as locations for soot inception. The effect of local equivalence ratio was determined from semi-quantitative analysis of the OH PLIF data, and good agreement was found with equilibrium calculations in the recirculation region. Spatially averaged LII measurements demonstrated that soot volume fraction in the primary flame zone increases exponentially with equivalence ratio, and these results were compared with particle-

sampling data collected in the exhaust stream. The results of this investigation were documented by A. C. Lynch, J. R. Gord, E. Corporan, V. M. Belovich (all of AFRL), T. R. Meyer, and S. Roy (both of ISSI) in a paper that was presented at the AFRC-JFRC 2004 Joint International Combustion Symposium that was held 10-13 October 2004 in Maui, HI. The paper is included in the Appendix.

4.1.12 Investigation of Dynamic Diffusion Flame of H₂ in Air with Laser Diagnostics and Numerical Modeling.

Detailed studies of flame-vortex interactions play a vital role in improving the understanding of turbulent combustion. A combined experimental and numerical study was conducted on a low-speed, buoyant, jet diffusion flame of hydrogen in air to investigate the vortex-flame interaction and the effects of preferential diffusion on the flame structure. A time-dependent, axisymmetric mathematical model with detailed transport processes and a chemical-kinetics mechanism was used to simulate the dynamics of the flame. Single-shot measurements of temperature and the concentrations of molecular hydrogen (H₂), the pollutant NO, atomic oxygen (O), atomic hydrogen (H), and OH were made using optical techniques such as CARS, degenerate four-wave mixing, and PLIF. Temperature and mole fractions of different species were presented in two-dimensional contour maps and compared with the numerical predictions. The model predicted the behavior of the experimentally observed dynamic flame quite well, including variations in temperature and molar concentrations of fuel and tracer species such as H, OH, and NO. Discrepancies in the concentration of O atoms were also noted. The results of this investigation were documented by F. Grisch, B. Attal-Tretout, A. Bresson, P. Bouchardy (all of the Office National d'Etudes et de Recherches Aeronautiques), V. R. Katta (ISSI), and W. M. Roquemore (AFRL) in a paper that was published in *Combustion and Flame* [139, 28-38 (October 2004)]. The paper is included in the Appendix.

4.1.13 Unsteady Effects on Flame-Extinction Limits during Gaseous and Two-Phase Flame/Vortex Interactions.

In highly fluctuating flows, high values of strain rate do not induce extinction of the flame front. Unsteady effects minimize the flame response to rapidly varying strain fields. In the present study the effects of time-dependent flows on non-premixed flames were investigated during flame/vortex interactions. Gaseous flames and spray flames in the external-sheath combustion regime were considered. For analyzing the flame/vortex interaction process, the velocity field and the flame geometry were simultaneously determined using PIV and LIF of the CH radical. The influence of vortex flows on the extinction limits for different vortex parameters and for different gaseous and two-phase flames was examined. If the external perturbation is applied over an extended period of time, the extinction strain rate is that corresponding to the steady-state flame, and this critical value depends mainly on the fuel and oxidizer compositions and the injection temperature. If the external perturbation is applied during a short period of time, extinction occurs at strain rates above the steady-state extinction strain rate. This deviation appears for flow-fluctuation timescales below steady-flame-diffusion timescales. This behavior is induced by diffusive processes, limiting the ability of the flame to respond to highly fluctuating flows. With respect to unsteady effects, the spray flames investigated here behave essentially like gaseous flames because evaporation takes place in a thin layer ahead of the flame

front. Extinction limits are only slightly modified by the spray, the controlling process being the competition between aerodynamic and diffusive timescales. The results of this study were documented by A. Lemaire (Ecole Centrale Paris and CNRS and University of Magdeburg), K. Zahringer (University of Magdeburg), T. R. Meyer (ISSI), and J. C. Rolon (Ecole Centrale Paris and CNRS) in a paper that was presented at the Thirtieth Symposium (International) on Combustion, which was held 25-30 July 2004 in Chicago, IL. The paper was published in the *Proceedings of the Combustion Institute* [Vol. 30, pp. 475-483 (January 2005)] and is included in the Appendix.

4.1.14 Simultaneous PLII, OH PLIF, and Droplet Mie Scattering in Swirl-Stabilized Spray Flames.

Simultaneous LII, OH PLIF, and droplet Mie scattering were used to study the instantaneous flame structure and soot-formation process in an atmospheric-pressure, swirl-stabilized, liquid-fueled model-gas-turbine combustor. Optimal excitation and detection schemes to maximize single-shot signals and avoid interferences from soot-laden flame emission were considered. The data indicate that rich pockets of premixed fuel and air along the interface between the spray flame and the recirculation zone serve as primary sites for soot inception. Intermittent large-scale structures and local equivalence ratio were also found to play an important role in soot formation. The results of this study were documented by T. R. Meyer, S. Roy (both of ISSI), V. M. Belovich, E. Corporan, and J. R. Gord (all of AFRL) in a paper that was published in *Applied Optics* [Vol. 44, No. 3, pp. 445-454 (20 January 2005)]. The paper is included in the Appendix.

4.1.15 DPDB CARS for Exhaust-Gas Temperature and CO₂-O₂-N₂ Mole-Fraction Measurements in Model Gas-Turbine Combustors.

DPDB CARS was applied for the first time to the measurement of temperature and multiple-species mole fractions in a liquid-fueled combustor of practical interest. In this system pure rotational transitions of O₂-N₂ and the ro-vibrational transitions of CO₂-N₂ were probed using two narrowband pump beams, a broadband pump beam, and a broadband Stokes beam. This technique permits highly accurate temperature measurements at both low and high temperatures as well as mole-fraction measurements of two molecules with respect to N₂ from each laser shot. Single-shot measurements of temperature and mole-fraction ratios of CO₂/N₂ and O₂/N₂ in the exhaust stream of a swirl-stabilized, JP-8-fueled, model gas-turbine combustor were made for equivalence ratios ranging from 0.45 to 1.0. Agreement between mean rotational and ro-vibrational temperatures was within ~ 3%, and mean measurements of CO₂/N₂ and O₂/N₂ mole-fraction ratios were within ~ 15% of equilibrium theory. For illustrating the ability of the current measurement system to track multiple scalar statistics in turbulent reacting flows, histograms and scatter plots of temperature and species mole fractions were made within the potential-core and turbulent-shear-layer regions of the exhaust system. The results of this investigation were documented by T. R. Meyer, S. Roy (both of ISSI), R. P. Lucht (Purdue University), and J. R. Gord (AFRL) in a paper that was published in *Combustion and Flame* [Vol. 142, pp. 52-61 (July 2005)]. The paper is included in the Appendix.

4.1.16 Dynamics of Inverse Diffusion Flame and Its Role in Polycyclic-Aromatic-Hydrocarbon and Soot Formation.

Residence time and thermo-chemical environment are important factors in the soot-formation process in flames. Recent studies have revealed that the soot generated in an inverse diffusion flame (IDF) is not fully carbonized as it is in a normal diffusion flame. For understanding the chemical and physical structure of the partially carbonized soot formed in inverse diffusion flames, knowledge of the flow dynamics of these flames is required. A time-dependent, detailed-chemistry CFD model was developed for simulation of an ethylene-air inverse jet-diffusion flame that had been studied experimentally. Steady-state simulations showed that all of the PAH species are produced outside the flame surface on the fuel side. Unsteady simulations revealed that buoyancy-induced vortices establish outside the flame because of the low fuel jet velocity (~ 40 cm/s) employed. These vortices in inverse diffusion flames, as opposed to those in normal diffusion flames, appear primarily in the exhaust jet. The advection of these vortices at 17.2 Hz increases mixing and causes PAH species to be more uniformly distributed in downstream locations. While the concentrations of rapidly formed radical and product species are not altered appreciably by the flame oscillation, concentrations of certain slowly formed PAH species are significantly changed. The dynamics of 20-nm tracer particles injected from the 1200-K fuel-side contour line suggest that soot particles are reheated and cooled alternately while being entrained into and advected by the buoyancy-induced vortices. This flow pattern could explain the experimentally observed large size and slight carbonization of IDF soot particles. The results of this study were documented by V. R. Katta (ISSI), L. G. Blevins (Sandia National Laboratories) and W. M. Roquemore (AFRL) in a paper that was published in *Combustion and Flame* [Vol. 142, pp. 33-51 (July 2005)]. The paper is included in the Appendix.

4.1.17 Measurements of OH Mole Fraction and Temperature up to 20 kHz Using Diode-Laser-Based UV Absorption Sensor.

Diode-laser-based sum-frequency generation of UV radiation at 313.5 nm was utilized for high-speed absorption measurements of OH mole fraction and temperature at rates up to 20 kHz. Sensor performance was characterized over a wide range of operating conditions in a 25.4-mm-path-length, steady, C_2H_4 -air diffusion flame through comparisons with CARS, PLIF, and a two-dimensional numerical simulation with detailed chemical kinetics. Experimental uncertainties of 5% and 11% were achieved for measured temperatures and OH mole fractions, respectively, with standard deviations of $< 3\%$ at 20 kHz and an OH detection limit of < 1 ppm in a 1-m path length. After validation in a steady flame, high-speed diode-laser-based measurements of OH mole fraction and temperature were demonstrated for the first time in the unsteady exhaust of a liquid-fueled, swirl-stabilized combustor. Typical agreement of $\sim 5\%$ was achieved with CARS temperature measurements at various fuel/air ratios, and sensor precision was sufficient to capture oscillations of temperature and OH mole fraction for potential use with multi-parameter control strategies in combustors of practical interest. The results of this study were documented by T. R. Meyer, S. Roy (both of ISSI), T. N. Anderson (Purdue University), J. D. Miller, V. R. Katta (both of ISSI), R. P. Lucht (Purdue University), and J. R. Gord (AFRL) in a paper that was published in *Applied Optics* [Vol. 44, No. 31, pp. 6729-6740 (1 November 2005)]. The paper is included in the Appendix.

4.1.18 Planar Imaging of Soot, Droplets, and Fluorescence for Studies of Alternative Fuel Blends in Gas-Turbine Combustion.

A study to characterize the production of particulate-matter emissions was performed in a liquid-fueled model gas-turbine combustor while varying fuel blends and operating conditions. The techniques of LII, OH PLIF, and laser Mie scattering were used to track soot volume fraction, measure flame products, and visualize droplet scattering in the reaction zone, respectively. Studies were performed on varying fuel blends comprised of kerosene-based jet fuel and synthetic fuel in varying concentrations over a range of equivalence ratios. Consistent with results of previous studies, fuels containing aromatics, which have been shown to promote PM production, produced higher quantities of soot than straight-chain hydrocarbons. Laser-based measurements showed a significant correlation among physical flame structure, fuel type, and particle number density. The results of this study were documented by A. C. Lynch, J. R. Gord (both of AFRL), T. R. Meyer, and S. Roy (both of ISSI) in a paper that was presented at the OSA Laser Applications to Chemical, Security, and Environmental Analysis Topical Meeting and Tabletop Exhibit, which was held 5-9 February 2006 in Incline Village, NV. The paper is included in the Appendix.

4.1.19 Coherent Structures and Turbulent Molecular Mixing in Gaseous Planar Shear Layers.

Quantitative planar visualization of molecular mixing dynamics in large- and intermediate-scale coherent structures was achieved for the first time in the developing and far-field regions of gaseous planar shear layers. A dual-tracer (NO and acetone) PLIF technique was implemented as the gaseous analogue to acid/base chemical reactions that have previously been used to study molecular mixing in liquid shear layers. Data on low-speed, high-speed, and total molecularly mixed fluid fractions were collected for low- to high-speed velocity ratios from 0.25 to 0.44 and Reynolds numbers, Re_δ , from 18 600 to 103 000. Within this range of conditions, mixed-fluid probability density functions and ensemble-averaged statistics are highly influenced by the homogenizing effect of large-scale Kelvin-Helmholtz rollers and the competing action of intermediate-scale secondary instabilities. Small-scale turbulence leads to near-unity mixing efficiencies and mixed-fluid probabilities within the shear layer, with subresolution stirring being detected primarily along the interface with free-stream fluid. Current molecular-mixing data compared favorably with previous time-averaged probe-based measurement results and provided new insight on the effects of coherent structures, velocity ratio, downstream distance, and differences between low- and high-speed fluid entrainment. The results of this investigation were documented by T. R. Meyer (ISSI), J. C. Dutton (University of Texas at Arlington), and R. P. Lucht (Purdue University) in a paper that was published in the *Journal of Fluid Mechanics* [Vol. 558, pp. 179-205 (July 2006)]. The paper is included in the Appendix.

4.1.20 Non-reacting and Combusting Flow Investigation of Bluff Bodies in Cross Flow.

A combination of Laser Doppler Velocimetry (LDV) and high-speed imaging was used to investigate bluff-body-stabilized flames. LDV data taken over several non-combusting operating conditions detailed the recirculation zone behind the bluff body as well as the effect of inlet conditions on the Karman Street vortex shedding that occurs. High-speed images of combustion

and equivalence ratio taken at blow out agreed with assertions made by Ozawa [1] and Zukoski [2] on the transitional nature of the flame from “laminar” to “turbulent” at a Reynolds number of $\sim 15,000$. The fuel-air ratio at lean blow out also correlated very well with the correlation parameter of DeZubay [3]. Finally, high-speed images supported assertions by Mehta and Soteriou [4] and by Erickson et al. [5] that under certain conditions, Karman Street vortex shedding is not suppressed by momentum and baroclinic effects and Karman Street vortices are present in the flame near lean blowout. The results of this study were documented by B. Kiel, K. Garwich, A. Lynch, J. R. Gord (all of AFRL), and T. Meyer (ISSI) in AIAA Paper 2006-5234 that was presented at the 42nd AIAA/ASME/SAE/ASEE Joint Propulsion Conference and Exhibit, which was held 9-12 July 2006 in Sacramento, CA. The paper is included in the Appendix.

4.1.21 Understanding Turbulent Flames through Vortex/Flame-Interaction Studies.

Various concepts for modeling the turbulence-chemistry interaction in non-premixed combustion were examined by studying vortex/flame interactions in a hydrogen/air, opposed-jet non-premixed flame. Unsteady flat flames were obtained by injecting vortices from the fuel and air sides of the flame surface simultaneously. Conventional characteristic parameters such as stretch rate and scalar dissipation rate cannot be used for describing the quenching process in unsteady flames. The flow and chemical non-equilibrium states of unsteady flames are responsible for variations in extinction values of these traditional characteristic variables. It was suggested that a variable that is proportional to the air-side stretch rate and inversely proportional to the rate of change in the flame temperature could be used uniquely for characterizing the unsteady quenching process. Unsteady curved flames were obtained by injecting vortices from the air side. Vortex size was varied from centimeter to sub-millimeter. The dynamic changes to the flame structure that occurred during these interaction processes were mapped onto a scalar-dissipation-rate scale. The large centimeter-size vortices, irrespective of the propagation velocity, wrinkled and stretched the flame before causing local extinction--representing typical laminar-flamelet behavior. On the other hand, the small sub-millimeter-size vortices replaced the local fluid in the flame zone with fresh air and destroyed the flame structure without causing any wrinkle or stretch on the reaction zone--representing non-flamelet behavior. Depending on vortex size, interactions between flame and millimeter-range vortices gradually deviated from the flamelet description. The results of this study were documented by V. R. Katta, S. Gogineni, T. R. Meyer (all of ISSI), J. R. Gord, and W. M. Roquemore (both of AFRL) in a paper that was presented at the 41st Combustion (CS)/29th Airbreathing Propulsion (APS)/23rd Propulsion Systems Hazards (PSHS) Joint Subcommittee Meeting, which was held 4-8 December 2006, in San Diego, CA. The paper is included in the Appendix.

4.1.22 NO-Concentration Profiles in Atmospheric-Pressure Flames Using ERE-CARS.

Measurements were made of NO in atmospheric-pressure flames using visible pump (532-nm) and Stokes (591-nm) beams with an ultraviolet probe beam (236 nm) near an electronic resonance, yielding a significantly enhanced CARS signal at 226 nm. For a hydrogen-air flame stabilized over a Hencken burner, good agreement was obtained between ERE-CARS measurements and flame computations using UNICORN, a two-dimensional flame code. Excellent agreement between measured and calculated NO spectra was obtained for heavily

sooting acetylene-air flames on the same Hencken burner. The measured shapes of NO concentration profiles determined from ERE-CARS spectra without correction for collisional effects were in excellent agreement with the shapes predicted using the OPPDIF code in conjunction with GRI 3.0 kinetics for a laminar, counterflow, non-premixed hydrogen-air flame. Effects of fuel-stream dilution (nitrogen and carbon dioxide) on measured NO concentrations were also studied in the counterflow configuration. For diluted flames, comparisons between measured ERE-CARS signals and computed number densities show good spatial agreement, and their relative magnitudes match well. Counterflow flames with various hydrogen levels in the fuel stream (pure oxygen in the oxidizer stream) and various oxygen levels in the oxidizer stream (pure hydrogen in the fuel stream) were investigated to simulate fuel-rich and oxygen-rich flames, and an optimum NO level was found. Pathway and sensitivity analyses were implemented to gain an understanding of NO formation under these conditions. The current results establish the utility of ERE-CARS for detection of NO in flames with large temperature and concentration gradients as well as in sooting environments. The results of this investigation were documented by N. Chai, S. V. Naik, W. D. Kulatilaka, R. P. Lucht, N. M. Laurendeau (all of Purdue University), S. Roy, V. R. Katta (both of ISSI), J. P. Kuehner (Washington and Lee University), and J. R. Gord (AFRL) in Paper No. G04 that was presented at the 5th U. S. Combustion Meeting, which was held 25-28 March 2007 in San Diego, CA. The paper is included in the Appendix.

4.1.23 NO-Concentration Measurements in Atmospheric-Pressure Flames Using ERE-CARS.

The ERE-CARS technique was used for measurement of NO concentration in three atmospheric-pressure flames. Visible pump (532-nm) and Stokes (591-nm) beams were used to probe the Q-branch of the Raman transition. A significant resonance enhancement was obtained by tuning an ultraviolet probe beam (236 nm) into resonance with specific rotational transitions in the ($v' = 0$, $v'' = 1$) vibrational band of the $A^2\Sigma^+ - X^2\Pi$ electronic system of NO. ERE-CARS spectra were recorded at various heights within a hydrogen-air flame, producing relatively low concentrations of NO over a Hencken burner. Good agreement was obtained between NO ERE-CARS data and the results of flame computations using UNICORN, a two-dimensional flame code. Excellent agreement between measured and calculated NO spectra was also obtained when a modified version of the Sandia CARSFT code for heavily sooting acetylene-air flames ($\phi = 0.8$ to $\phi = 1.6$) was used on the same Hencken burner. Finally, NO-concentration profiles were obtained using ERE-CARS in a laminar, counterflow, non-premixed hydrogen-air flame. Spectral scans were recorded by probing the Q_1 (9.5), Q_1 (13.5), and Q_1 (17.5) Raman transitions. The measured shape of the NO profile was in good agreement with the shape predicted using the OPPDIF code, even without correction for collisional effects. These comparisons between NO measurements and predictions established the utility of ERE-CARS for detection of NO in flames with large temperature and concentration gradients as well as in sooting environments. The results of this investigation were documented by N. Chai, W. D. Kulatilaka, S. V. Naik, N. M. Laurendeau, R. P. Lucht (all of Purdue University), J. P. Kuehner (Washington and Lee University), S. Roy, V. R. Katta (both of ISSI), and J. R. Gord (AFRL) in a paper that was published in *Applied Physics B Lasers and Optics* [Vol. 88, pp. 141-150 (June 2007)]. The paper is included in the Appendix.

4.1.24 Effects of Oxygenated Compounds on PAH and Soot across a Suite of Laboratory Devices.

The impact of oxygenated fuel additives on soot emissions was investigated in a collaborative university, industry, and government effort. The main objective of this program was to obtain a fundamental understanding of how changes in fuel composition can reduce soot and PAH emissions from military-aircraft combustors. The research team used a suite of laboratory devices that included a shock tube, a well-stirred reactor, a premixed flat flame, an opposed-flow diffusion flame, and a high-pressure turbulent reactor. The two primary additives investigated were ethanol and cyclohexanone. Fuels included ethylene, heptane, a heptane/toluene blend, and JP8. With one exception--an ethylene opposed-flow diffusion flame--the addition of an oxygenated compound led to substantial reductions in soot. Modeling of the premixed flame and opposed-jet diffusion flame was used to obtain insight into the mechanism behind the observed soot reductions. The results of this investigation were documented by T. Litzinger (Pennsylvania State University), M. Colket [United Technologies Research Center (UTRC)], M. Kahandawala [University of Dayton (UD)], V. Katta (ISSI), S.-Y. Lee (Pennsylvania State University), D. Liscinsk (UTRC), K. McNesby [Army Research Laboratory (ARO)], R. Pawlik, M. Roquemore (both of AFRL), R. Santoro (Pennsylvania State University), S. Sidhu (UD), S. Stouffer (UDRI), and J. Wu (Pennsylvania State University) in Paper No. F03 that was presented at the 5th U. S. Combustion Meeting, which was held 25-28 March 2007 in San Diego, CA. The paper is included in the Appendix.

4.1.25 Effects of Nitrogen-Containing Compounds on PAH and Soot across a Suite of Laboratory Devices.

The effect of nitrogen-bearing fuel additives on soot and PAH-emissions formation was investigated in a collaborative university, industry, and government effort. The overall objective of this program was to obtain a fundamental understanding of how changes in fuel composition can affect soot and PAH emissions from military-aircraft combustors. Six laboratory burners--including a premixed flat flame, an opposed-flow diffusion flame, a well-stirred reactor, a turbulent spray flame, a shock tube, and a high-pressure turbulent combustor--were used to investigate the impact of additives under a wide range of combustion conditions. The additives included various nitroalkanes (nitromethane, nitroethane, and nitropropane), i-propylnitrate, nitrogen dioxide, pyridine, and quinoline. Fuels included ethylene, a heptane/toluene blend, and JP8. The effects of many of the additives were examined in most experimental facilities, and the results were contrasted and compared. The experimental results were also modeled using a variety of modeling packages and mechanisms. Reductions in soot were as large as 70%, although in some cases no change was detected; in others, increases were observed. Modeling failed to offer explanations for all of the experimental observations. The results of this study were documented by M. Colket (UTRC), T. Litzinger (Pennsylvania State University), M. Kahandawala (UD), V. Katta (ISSI), S.-L. Lee (Pennsylvania State University), D. Liscinsky (UTRC), K. McNesby (ARO), A. Menon (Pennsylvania State University), M. Roquemore (AFRL), R. Santoro (Pennsylvania State University), S. Sidhu (UD), and S. Stouffer (UDRI) in Paper No. F04 that was presented at the 5th U. S. Combustion Meeting, which was held 25-28 March 2007 in San Diego, CA. The paper is included in the Appendix.

4.1.26 Effects of Phosphorus Compounds on PAH and Soot across a Suite of Laboratory Devices.

Recently researchers from universities, industry, and governmental laboratories completed a collaborative study on the impact of different types of organic fuel additives on soot and PAH emissions from military gas-turbine engines. The main objective of this program was to obtain a fundamental understanding of how even small changes in fuel composition affect soot and PAH emissions. Six different combustors--namely, a premixed flame, a co-flow diffusion flame, an opposed-flow diffusion flame, a well-stirred reactor, a shock tube, and a swirl-stabilized combustor--were used to investigate the impact of additives under a wide range of combustion conditions. The experimental results were then modeled using a variety of modeling packages and mechanisms. Results were obtained on the effects of phosphorus additives, trimethyl phosphite, trimethyl phosphate, diethyl allyl phosphate, and dimethyl methyl phosphonate on soot and PAH for several gaseous fuels and a simple JP8 surrogate, heptane/toluene. The results of this investigation were documented by S. Sidhu (UDRI), V. Belovich (AFRL), M. Colket (UTRC), M. Kahandawala (UDRI), V. Katta (ISSI), D. Liscinsky (UTRC), T. Litzinger (Pennsylvania State University), K. McNesby (ARO), R. Pawlik, M. Roquemore (both of AFRL), R. Santoro (Pennsylvania State University), and S. Stouffer (UDRI) in Paper No. F17 that was presented at the 5th U. S. Combustion Meeting, which was held 25-28 March 2007 in San Diego, CA. The paper is included in the Appendix.

4.1.27 Temperature Measurements in Reacting Flows by Time-Resolved fs-CARS Spectroscopy.

Time-resolved fs-CARS spectroscopy of the nitrogen molecule was used for the measurement of temperature in atmospheric-pressure, near-adiabatic, hydrogen-air diffusion flames. The initial frequency-spread dephasing rate of the Raman coherence induced by the ultrafast (~ 85 fs) Stokes and pump beams was used as a measure of the gas-phase temperature. This initial frequency-spread dephasing rate is completely independent of collisions and dependent only on the frequency spread of the Raman transitions at different temperatures. A simple theoretical model based on the assumption of impulsive excitation of Raman coherence was used to extract temperatures from time-resolved fs-CARS experimental signals. These extracted temperatures were in excellent agreement with the theoretical temperatures calculated from an adiabatic-equilibrium calculation. The estimated absolute accuracy and precision of the measurement technique were found to be ± 40 K and ± 50 K, respectively, over the temperature range 1500 - 2500 K. The results of this investigation were documented by S. Roy (ISSI), P. J. Kinnius, R. P. Lucht (both of Purdue University), and J. R. Gord (AFRL) in a paper that was published in *Optics Communications* [Vol. 281, No. 2, pp. 319-325 (January 15, 2008)]. The paper is included in the Appendix to this report.

5.0 HIGH-IMPACT-TECHNOLOGY COMPONENT STUDIES

5.1 General Overview

The objective of this portion of the program was to identify high-impact technologies that could lead to reduced component and operating costs for future propulsion systems. A summary of the work accomplished on this task during the program follows.

5.1.1 Stator-Cascade-Flow Vectoring through Counter-Flow Blowing (CFB).

Preliminary-design computational results showed that a significant amount of increased flow turning (12 degrees) can be achieved in a high-turning-stator example with only 0.5% core-flow CFB. The loading is held nearly constant over the entire blade with CFB, thereby turning the flow over the entire chord. To explore this approach, an existing cascade section was modified to implement a “proof-of-concept” design. Experimental data from PIV showed that an increase of 8 degrees in turning was achieved through CFB of 1%. Furthermore, an optimum amount of blowing exists to minimize wake increase and maximize flow vectoring. For this investigation the Advanced Ducted Propfan Analysis Code (ADPAC) 2-D model was calibrated by comparison to the experimental results for a range of 0.15 - 0.38% core-flow CFB. This study has shown ADPAC to be a viable design tool for CFB applications. The results of this investigation were documented by M. R. Harff, J. M. Wolff (both of Wright State University), W. W. Copenhaver, D. Car (both of AFRL), and J. Estevadeordal (ISSI) in AIAA Paper No. 2003-3408 that was presented at the 33rd AIAA Fluid Dynamics Conference and Exhibit, which was held 23 - 26 June 2003 in Orlando, FL. The paper is included in the Appendix.

5.1.2 Digital-Particle-Imaging-Velocimetry (DPIV) Measurements of Flow Field between Transonic Rotor and Upstream Stator.

The use of a planar non-intrusive measurement technique such as DPIV has made it possible to investigate many aspects of unsteady flow that were previously considered difficult because of the effect of a measurement probe on the flow field or excessively time-consuming because of the pointwise nature of LDV or Laser Transit Anemometry. Furthermore, time-accurate CFD codes are being developed and are now commonly used to simulate compressors and investigate complex unsteady-flow phenomena. DPIV measurements were made in a transonic compressor stage and used to investigate interactions between an upstream stator and a downstream transonic rotor. In particular, the interaction between the rotor bow shock and the wake shed from the upstream stator was explored and offered as a test case for unsteady CFD comparison. Results from an experiment conducted in the U. S. Air Force’s Stage-Matching-Investigation (SMI) rig showed that the complex flow field is associated with the interaction of a downstream transonic rotor with an upstream stator. The effect of changing the axial gap between blade rows was studied and DPIV plots made as an experimental data set for time-accurate CFD validation. At close spacing the wake shedding is synchronized with the rotor blade-pass frequency. The interaction of the rotor bow shock and wake generator (WG) causes the wake to expand downstream of the shock. The shock is split into two regions above and below the wake. As the shock approaches the wake-generator trailing edge, the velocity increases and causes the shock to turn more normal to the freestream flow. At far spacing the wake convects downstream in a

chaotic fashion. Bands of high and low velocity are evident from the rotor bow shock and expansion waves downstream of the shock. The interaction between the rotor bow shock and WG is much weaker than the close-spacing interaction. The wake has mixed out more at the location where it interacts with the shock and neither splits the shock in two nor turns it normal to the freestream flow. The results of this study were documented by S. E. Gorrell, W. W. Copenhaver (both of AFRL) and J. Estevadeordal (ISSI) in a paper that was presented at the ISUAAAT 03 International Symposium on Unsteady Aerodynamics, Aeroacoustics, and Aeroelasticity of Turbomachines, which was held 7-11 September 2003 in Durham, NC, and published in the Conference Proceedings. The paper is included in the Appendix.

5.1.3 Investigation on Vortex Shedding of Jet-in-a-Cross Flow.

An experimental investigation of a circular jet issuing from a wall normal to a cross flow was conducted over a momentum-ratio range of 2.0 - 15 for various jet and cross-flow Reynolds numbers. The flow field was interrogated using split-film and DPIV techniques to characterize the various regimes of the flow. The analyzed data revealed the three classic vortices that are present in a jet-in-cross-flow environment: the leading-edge horseshoe vortex, Karman-Street vortices, and the combined Kelvin-Helmholtz/Counter-Rotating Vortex Pair. It was observed that the penetration is a function not only of momentum ratio and axial location but also of both jet and cross-flow Reynolds numbers. The DPIV data qualitatively indicated an increase in the Kelvin-Helmholtz vortex-shedding frequency with cross-flow Reynolds number. The results of this investigation were documented by B. Kiel, A. Cox (both of AFRL), J. Estevadeordal, and S. Gogineni (both of ISSI) in PIV'03 Paper 3133 that was presented at the 5th International Symposium on Particle Image Velocimetry, which was held 22-24 September 2003 in Busan, Korea. The paper is included in the Appendix.

5.1.4 Stator Cascade Flow Vectoring through Counter-Flow Blowing.

Preliminary-design computational results showed that a significant amount of increased flow turning (12 degrees) can be achieved in a high turning stator example with only 0.5% core-flow CFB. To explore this approach an existing cascade section was modified to implement a “proof-of-concept” design. Experimental data from Particle Image Velocimetry (PIV) showed that an increase of 8 degrees in turning was achieved through counter-flow blowing of 0.28% of the core flow. For this investigation a simplified 2-D model was run by the ADPAC and the results compared to those from experiments for a range of 0.0% to 0.30% core flow counter-flow blowing. Based on this study, ADPAC has been shown to be a viable design tool for CFB applications. The results of this study were documented by M. R. Harff, J. M. Wolff (both of Wright State University), W. W. Copenhaver, D. Car (both of AFRL), and J. Estevadeordal (ISSI) in a paper that was published in the *International Journal of Turbo and Jet Engines* [21, 155-168 (October 2004)]. The paper is included in the Appendix.

5.1.5 PIV with Light-Emitting Diode: Particle Shadow Velocimetry.

A particle-shadow-velocimetry (PSV) technique that employs light sources with significantly lower power than lasers was developed as a variant of PIV. The PSV technique uses a non-scattering approach that relies on direct in-line illumination by a pulsed source such as a light-

emitting diode (LED) onto the camera imaging system. Narrow-depth-of-field optical setups are employed for imaging a two-dimensional plane within a flow volume, and images that resemble a “negative” or “inverse” of the standard PIV scattering mode are produced by casting particle shadows on a bright background. In this technique the amount of light reaching the image plane and the contrast of the seeding particles are significantly increased, while much lower power is required than with scattering approaches. The results of this investigation were documented by J. Estevadeordal and L. Goss (both of ISSI) in AIAA Paper No. 2005-37 that was presented at the 43rd AIAA Aerospace Sciences Meeting and Exhibit, which was held 10-13 January 2005 in Reno, NV; these authors have also submitted a provisional patent on this technique. A paper by J. Estevadeordal, L. P. Goss (both of ISSI), D. Car, and T. Bailie (both of AFRL) on this subject was presented at the 30th Annual AIAA Dayton-Cincinnati Aerospace Science Symposium (DCASS05), which was held on 8 March 2005 in Dayton, OH; these authors also submitted a paper in March 2005 for publication in Measurement Science and Technology. The AIAA paper is included in the Appendix.

5.1.6 Development of Fiber-Optic PIV System for Turbomachinery Applications.

A fiber-optic PIV (FOPIV) system was developed that is capable of delivering short, high-power laser pulses and of acquiring double-exposure images in flows without direct optical access. The system is capable of delivering Nd:YAG laser pulses of 5-ns duration and up to 50 mJ/pulse at 15-Hz rates through a single multi-mode silica fiber of 1000- to 1500-micron diameter. The tip of the laser fiber is terminated into a housing block that contains the laser-sheet-forming optics. Image transmission to the PIV camera is accomplished through a high-density 1.4-mm-diameter flexible fiber bundle composed of 100,000 quartz microfibers. A lens system is attached to the end of the imaging fiber and is designed for optimal flatness of the object plane with minimal distortion; for the current turbomachinery application, it produces a flat image of a 25-mm-diameter viewing area that is 50 mm from the object plane. This distance to the object plane is selected to maximize both viewing area and light-scattering intensity from the micron-sized seeding particles. Preliminary data were obtained from a short-test-duration turbine-engine facility without direct optical access. This application required that the PIV hardware be mounted through an interior instrumentation ring that rotates during the experiment. The results of this investigation were documented by J. Estevadeordal, T. R. Meyer, S. P. Gogineni (all of ISSI), M. D. Polanka, and J. R. Gord (both of AFRL) in AIAA Paper No. 2005-38 that was presented at the 43rd AIAA Aerospace Sciences Meeting and Exhibit, which was held 10-13 January 2005 in Reno, NV. The paper is included in the Appendix.

5.1.7 Investigation of PSV for Transonic-Flow Applications.

The PSV technique that employs light sources with significantly lower power than lasers was investigated as a variant of PIV for high-speed flow applications. The PSV technique uses a non-scattering approach that relies on direct in-line illumination by a pulsed source such as an LED onto the camera imaging system. Narrow-depth-of-field optical setups are employed for imaging a two-dimensional plane within a flow volume, and images that resemble a “negative” or “inverse” of the standard PIV scattering mode are produced by casting particle shadows on a bright background. In this technique the amount of light reaching the image plane and the contrast of the seeding particles are significantly increased, while the power required is markedly

lower than that demanded by scattering approaches. The technique was investigated for transonic-flow applications. The results of this study were documented by J. Estevadeordal and L. Goss (both of ISSI) in AIAA Paper 2005-5009 that was presented at the 35th AIAA Fluid Dynamics Conference and Exhibit, which was held 6-9 June 2005 in Toronto, Canada. The paper is included in the Appendix.

5.1.8 Fluidic-Control Studies for Diffusion Enhancement in Axial Compression Systems.

An experimental research rig was designed for evaluating candidate flow-control concepts for diffusion enhancement in axial compression systems. The rig is modular in design and capable of continuous flow in a Mach-0.7 environment with both diffusion and curvature. Candidate concepts can be evaluated inexpensively in a realistic axial-compression-system flow environment. Baseline results were obtained. Three preliminary flow-control modules were tested; all were variations on a theme of blowing-only flow control using a slot jet behind a backward-facing step. Two of the variations were preliminary investigations into the effect of the lip thickness of the backward-facing step and its impact on flow-control effectiveness. The third introduced streamwise vorticity as a means of enhancing the interaction between the blowing jet and the core stream in an effort to reduce the secondary-flow-control flow-fraction requirements. Detailed PIV, pressure-sensitive-paint (PSP), and exit total-pressure traverse measurements were performed. The results of this investigation were documented by D. Car. S. T. Bailie, C. Baudendistel, D. Gebbie (all of AFRL), and J. Estevadeordal (ISSI) in AIAA Paper 2006-417 that was presented at the 44th AIAA Aerospace Sciences Meeting and Exhibit, which was held 9-12 January 2006 in Reno, NV. The paper is included in the Appendix.

5.1.9 PIV Study of Wake-Rotor Interactions in Transonic Compressor at Various Operating Conditions.

Details of the unsteady flow field between an upstream WG and a downstream rotor closely spaced in a transonic compressor were studied at various operating conditions using PIV. Flow-visualization images and PIV data facilitated analysis of the details of shed vortices, wake motion, and wake-shock interaction phenomena. Such analysis not only aids the understanding of the effect of blade-row interactions on compressor performance but also allows verification of time-accurate CFD codes that are used to characterize transonic compressors. As the operating point changed from choked to stall and the rotor-bow shock moved upstream, distinct vortex-shedding patterns were observed that affected the wake deviation and rotor incidence. With close spacing between the WG and the rotor, vortex shedding from the WG and the passage of the rotor-bow shock were strongly synchronized, and blade-passage “phase-locked” measurements were possible. The resulting multiple images of the flow corresponding to any blade position were averaged to yield vortex and rotor-bow-shock locations at several back pressures. Using various post-processing methods, specific shed vortices and wake topological features were isolated, and details of the shock-wake interaction were captured. The results of this investigation were documented by J. Estevadeordal (ISSI), S. Gorrell, and W. Copenhaver (both of AFRL) in a paper that was published in *Journal of Propulsion and Power* [Vol. 23, No. 1, pp. 235-242 (January-February 2007)]. The paper is included in the Appendix.

5.1.10 PIV Investigation of Flow Field in Transonic Compressor Cascade with Moving Shock Wave.

The unsteady flow field produced during the interaction of a shock wave with stator blades was studied in a linear cascade using PIV. When shock waves traveling with the rotor blades in axial transonic compressors interact with upstream stator blades, unsteady phenomena are produced such as vortices and separation that induce blockage and losses. Flow visualization and PIV data, synchronized with shock-wave-passage locations, provide details of the flow field in various areas of the cascade passage. The experiments were conducted in a transonic blow-down wind tunnel with a nominal inlet Mach number of 0.65. A single moving normal shock was generated using a shock tube that was external to the wind tunnel, and this shock was introduced at the exit of the stator cascade to simulate the bow shock from a downstream rotor. PIV instantaneous measurements were made for three different shock strengths at various regions of interest and were synchronized with various instants of the shock passage. In each case, the passing shock induced a vortex of varying size and strength around the trailing edge of the stator. The flow pattern included the disruption and recovery of the transonic free stream, shock waves, vortex flow, vortex blockage, suction-side separation, spiraling arms, secondary vortices, and endwall clearance flows. The results of this study were documented by J. Estevadeordal (ISSI), M. D. Langford (Techsburg, Inc.), A. Breeze-Stringfellow (GE Aircraft Engines), S. A. Guillot (Techsburg, Inc.), and W. F. Ng (Virginia Tech) in AIAA Paper 2007-5064 that was presented at the 43rd AIAA/ASME/SAE/ASEE Joint Propulsion Conference and Exhibit, which was held 8-11 July 2007 in Cincinnati, OH. The paper is included in the Appendix.

5.1.11 PIV Study of Blade-Row Interactions in Transonic Compressor.

Details of the unsteady flow field between an upstream stator and a downstream rotor in a transonic compressor were obtained using PIV. Flow-visualization images and PIV data that facilitate analysis of vortex shedding, wake motion, wave deviation, rotor incidence, and wake-shock-interaction phenomena were acquired. Such analysis not only aids the understanding of the effect of blade-row interactions on compressor performance but also allows verification of time-accurate CFD codes that are used to characterize transonic compressors. The present investigation introduced new methods for PIV implementation in complex turbomachinery environments. The PIV measurements were synchronized with various rotor-blade locations, and the instantaneous and averaged velocity fields of the flow were calculated. Stator-wake and rotor-bow-shock flow interactions in the blade row were identified for various stator/rotor axial spacings and operating conditions. Using various post-processing methods, specific shed vortices and wake topological features were isolated and details of the shock-wake interaction captured. At far spacing, the vortices shed from the stator were phase-locked and shed as counter-rotating pairs in the wake. Rotor-bow-shock strength varied, depending on the axial gap between the stator and rotor and the operating condition. The results showed that as the rotor-bow-shock is chopped by the stator trailing edge, it turns more normal to the stator pressure surface and propagates upstream, validating a prior significant observation made with time-accurate CFD. The results of this investigation were documented by J. Estevadeordal (ISSI), S. Gorrell, D. Gebbie, and S. Puterbaugh (all of AFRL) in AIAA Paper 2007-5017 that was presented at the Joint Propulsion Conference in Cincinnati. The paper is included in the Appendix.

5.1.12 Investigation of Blade-Row Interactions in Transonic Compressor Using PIV.

The unsteady flow field between an upstream stator and a downstream rotor in a transonic compressor was investigated using PIV. For this investigation a system was developed for obtaining high-resolution velocity data from a new swirler/deswirler stator configuration in an axial-flow transonic compressor at CARL at Wright-Patterson AFB; this system was used to study blade-row interactions at various parametric and operating-point conditions. PIV data provided details of unsteady phenomena such as vortex shedding, wake motion, rotor incidence, bow-shock interactions, and stator pressure- and suction-side properties and blockage. The PIV measurements were synchronized with various rotor-blade positions, and the instantaneous and averaged velocity fields and other statistical properties of the flow were calculated for various stator/rotor axial spacings and operating conditions. Using various post-processing methods, specific shed vortices and wake topological features were isolated, and details of the shock-wake interaction were captured. Results showed the rotor-bow-shock strength and the relative position to the vortices for each condition, the relative phase-locking of the vortices to the blade position as they shed as counter-rotating pairs in the wake, and the turning of the shock to more normal to the stator pressure surface as it propagates upstream, validating a prior significant observation made with time-accurate CFD. Such details aid the understanding of the effect of blade-row interactions on compressor performance, the identification of loss-producing mechanisms, the establishment of comparisons with other wake-generator (WG) wakes such as those of the blade row of the Stage Matching Investigation (SMI) of CARL, and the verification of time-accurate CFD codes that are used to characterize transonic compressors. The results of this study were documented by J. Estevadeordal (ISSI), S. Gorrell (Brigham Young University), and S. L. Puterbaugh (AFRL) in a presentation that was made at the DCASS08. The visual materials for this presentation are included in the Appendix.

5.1.13 PIV Measurements of Blade-Row Interactions in a Transonic Compressor for Various Operating Conditions.

Detailed PIV measurements of the unsteady flow field between an upstream swirler/deswirler stator configuration and a downstream rotor in a transonic compressor were made. Flow-visualization images and PIV data provide details of vortex shedding, wake motion, and shock interaction phenomena for various operating conditions. The observations and analysis aid the understanding of the effects of blade-row interactions on compressor performance and allow verification of time-accurate CFD codes that are used to analyze transonic compressors. Synchronized measurements with various rotor-blade locations allow calculation of phase-averaged velocity fields of the flow and comparison with instantaneous realizations. Vortex shedding and wake topological features were isolated and details of the shock interactions captured. The results revealed details of the vortex-shedding phenomena in the new configurations. Data were obtained in the suction side of the deswirler using special optical-probe approaches, and comparisons with a previous SMI stator configuration were made. Various vortex shapes were produced as a result of different bow-shock strengths at near-stall and peak efficiency. At close-spacing peak efficiency, it was observed that the wake was flatter than at far spacing. Reducing the loading on the BRI stator also produced thinner wakes. The results of this study were documented by J. Estevadeordal (ISSI), S. Gorrell (Brigham Young University), and S. Puterbaugh (AFRL) in AIAA Paper 2008-4700 that was presented at the 44th

AIAA/ASME/SAE/ASEE Joint Propulsion Conference and Exhibit, which was held 21-23 July 2008 in Hartford, CT. The paper is included in the Appendix.

6.0 ADVANCED-PROPULSION-SYSTEM CONCEPT STUDIES

6.1 General Overview

The objective of this portion of the program was to identify critical propulsion-component technologies that must be addressed for advanced propulsion systems. A summary of the work accomplished on this task during the program follows.

6.1.1 Initiation of Detonation in a Large Tube.

One of the important design criteria in the development of Pulse Detonation Engines (PDEs) is to stabilize detonation in a large-diameter tube in the shortest possible distance. The initial shock train emanating from the ignition source plays an important role in transitioning the deflagration wave into a detonation. To sustain such transition in a large-diameter tube, innovative methods and strategies are required. An experimental-numerical investigation was conducted to understand the role of a contoured body suspended within the tube for enhancing the detonation transition. A CFD code based on flux-corrected transport was used for the simulation of the fate of the two-dimensional detonation wave formed from the ignition source and expanded through the gap between the centerbody and the channel walls. It was found that the reflection of transverse waves at the walls and their collision near the leading shock front are critical in sustaining a detonation wave during expansion. The shock-wall and shock-shock interactions are enhanced by the centerbody. Simulations further suggested that the effectiveness of the inserted centerbody depends strongly on its length. The results of this investigation were documented by V. Katta (ISSI), C. Tucker [Air Force Institute of Technology (AFIT)], J. Hoke (ISSI), and F. Schauer (AFRL) in a paper that was presented at the 19th International Colloquium on the Dynamics of Explosions and Reactive System, which was held 27 July - 1 August 2003 in Hakone, Japan. The paper is included in the Appendix.

6.1.2 Use of Flash-Vaporization System with Liquid-Hydrocarbon Fuels in a PDE.

In recent studies [6-7] liquid-fuel droplets were found to hinder the detonation process in a PDE. In the current study, multi-phase effects were eliminated with a flash-vaporization system that vaporizes the liquid fuels prior to mixing with air. Previously, hydrocarbon and air mixtures were transitioned from deflagration to detonations [6] but exhibited long ignition and deflagration-to-detonation transition (DDT) times. In the present study, two liquid-hydrocarbon fuels, with different octane numbers (ON), were detonated with air in a PDE to determine the effect of octane number on ignition time and DDT time. The premixed, combustible mixture filled the PDE tubes via an automotive valve and cam system, which is described in detail elsewhere [8]. N-heptane (ON-0) and isooctane (ON-100) were evaluated individually to determine the effects of automotive octane number on PDE combustion performance. The ON has been considered previously [9] as an acceptable criterion in determining the detonability for PDEs, and it is derived based on the tendency to “knock” or detonate relative to isooctane in an automotive-engine application. The goal of the present research was to show that a flash-vaporized liquid-hydrocarbon fuel system can provide the fuel and air homogeneity required to achieve detonations. The octane number was studied to determine its influence on the ignition and DDT time for hydrocarbon fuels. The flash-vaporization system provided an outstanding

method for achieving the desired mixing and vaporization, and the system operating points matched well with the liquid-vapor equilibrium-model results. The ignition times showed little dependence on fuel-injection temperatures or octane number, and no droplet effects were noted. The DDT trends were ON-dependent, and the isooctane was difficult to detonate with wave speeds below the stable Chapman-Jouget (CJ) wave speeds. The heptane detonated readily and produced wave speeds at or above CJ. The results of this investigation were documented by K. C. Tucker, P. I. King (both of the Air Force Institute of Technology), R. P. Bradley (ISSI), and F. R. Schauer (AFRL) in AIAA Paper No. 2004-0868 that was presented at the 42nd AIAA Aerospace Sciences Meeting and Exhibit, which was held 5-8 January 2004 in Reno, NV. The paper is included in the Appendix.

6.1.3 Assessment of Performance of Pulsejet and Comparison with a PDE.

The performance of a Solar PJ32 pulsejet engine, which is a 1/5-scale model of the Argus V-1 pulsejet engine developed for the Navy in 1951, was evaluated under static conditions and compared with that of a PDE firing at similar inlet and operating conditions. The pulsejet has a fuel-flow operating range of 2.5-4.5 lbm/min, which corresponds to a thrust range of 40 lbf (at lean out) to 102 lbf (at flood out). Thrust was calculated from combustion-chamber pressure histories and agreed with measured thrust within 5-10%. Peak combustion-chamber head pressures range from 8 to 20 psig, while significantly higher pressures (80-120 psig) are attained in PDEs. Airflow at the inlet of the pulsejet was measured and used to calculate specific thrust and equivalence ratio. Specific thrust ranged from 40 to 100 lbf-s/lbm over the range of fuel flows from lean to rich conditions. A similarly operating PDE has a specific thrust around 120 lbf-s/lbm, making the PDE more efficient in terms of air flow. The pulsejet equivalence ratio ranged from 0.6 to 1.0, with rated/peak thrust occurring at rich conditions. Typical fuel-specific impulse (Isp) for the pulsejet was 1400-1500 s for rated thrust conditions, whereas PDE performance (with a fill fraction of 1) was around 1800 s. For the PDE operating in the same fill-fraction range as the pulsejet (~ 0.1), PDE Isp was estimated to be 6000-8000 s, making the PDE cycle far more efficient and desirable at comparable conditions. The results of this study were documented by P. J. Litke, F. R. Schauer (both of AFRL), D. E. Paxson (NASA Glenn Research Center), R. P. Bradley, and J. L. Hoke (both of ISSI) in AIAA Paper No. 2005-228 that was presented at the 43rd AIAA Aerospace Sciences Meeting and Exhibit, which was held 10-13 January 2005 in Reno, NV. The paper is included in the Appendix.

6.1.4 Detonation Initiation of Hydrocarbon-Air Mixtures in a PDE.

Detonation initiation of hydrocarbon-air mixtures is critical to the development of the PDE. Conventionally, oxygen enrichment (such as a predetonator) or explosives are utilized to initiate detonations in hydrocarbon/air mixtures. While often effective, such approaches have performance and infrastructure issues associated with carrying and utilizing the reactive components. An alternative approach is to accelerate conventional deflagration-to-detonation speeds via DDT. Analysis of hydrocarbon-air detonability indicates that mixing and stoichiometry are crucial to successful DDT. A conventional Schelkin spiral was used to obtain DDT in hydrocarbon-air mixtures with no excess oxidizer. This spiral was observed to increase deflagrative flame speeds (through increased turbulence and flame mixing) and produce "hot-spots" that are thought to be compression-wave reflections. These hot spots resulted in micro-

explosions that, in turn, gave rise to DDT. Time-of-flight analysis of high-frequency pressure-transducer traces indicated that the wavespeeds typically accelerate to over-driven detonation during DDT before stabilizing at Chapman-Jouget levels as the combustion front propagates down the detonation tube. Results obtained for a variety of fuels indicate that DDT of hydrocarbon-air mixtures is possible in a PDE. Successful DDT in air with no oxygen enrichment was achieved with propane, 100-octane low-lead aviation gasoline, kerosene-based military jet fuel JP8, and the high-energy-density military jet fuel JP10. The results of this investigation were documented by F. R. Schauer, C. L. Miser, K. C. Tucker (all of AFRL), R. P. Bradley, and J. L. Hoke (both of ISSI) in AIAA Paper No. 2005-1343 that was presented at the 43rd AIAA Aerospace Sciences Meeting and Exhibit, which was held 10-13 January 2005 in Reno, NV. The paper is included in the Appendix.

6.1.5 Impact of DDT Mechanism, Combustion Wave Speed, Temperature, and Charge Quality on PDE Performance.

A number of factors can affect the performance of a PDE--detonation initiation, combustion wave speed, detonator wall temperature, and the homogeneity of the fuel-air charge. These factors were evaluated using a single-tube hydrogen-air PDE operating between 10 and 29 Hz. Geometries employed for DDT degrade PDE performance during the exhausting process. This effect is insignificant for hydrogen-air mixtures because the DDT mechanism can be unobtrusive, but the effect can be significant for less reactive mixtures. Typical DDT geometries used for hydrocarbon-air mixtures resulted in a degradation of 35% for the hydrogen-air mixture. The drag on the DDT mechanism was also found to increase with distance from the thrust wall. In an effort to evaluate the effect of combustion wave speed on thrust, the ignition location was varied. For choked flames the performance difference from detonation was unmeasurable; but as the maximum flame velocity decreased from the choked-flame velocity, the performance decreased. At 800 m/s the thrust was 16% below that of a detonation, and at 400 m/s the thrust degradation was between 17 and 34%. High tube-wall temperatures reduced the losses in heat during the blow-down process but increased the temperature and decreased the density of the fresh charge, resulting in lower peak pressures and charge spillage. As the tube temperature increased, PDE performance decreased by 20% at 10 Hz and by ~ 10% at 15 and 20 Hz. The axial homogeneity of the fuel-air charge was decreased by changing the location of the fuel injection. Decreases in performance of 14% were recorded at 10 Hz, even though detonation was achieved in both cases. The results of this study were documented by J. L. Hoke, R. P. Bradley (both of ISSI), and F. R. Schauer (AFRL) in AIAA Paper No. 2005-1342 that was presented at the 43rd AIAA Aerospace Sciences Meeting and Exhibit, which was held 10-13 January 2005 in Reno, NV. The paper is included in the Appendix.

6.1.6 Performance Measurements of PDE Engine Ejectors.

An experimental study on the performance of PDE ejectors was conducted. Time-averaged thrust augmentation produced by straight and diverging PDE ejectors was measured using a damped thrust stand. The ejector length-to-diameter ratio was varied from 1.25 to 5.62 by changing the length of the ejector and maintaining a nominal ejector diameter ratio of 2.75. In general, the level of thrust augmentation was found to increase with ejector length. Also, ejector performance was observed to be strongly dependent on the operating fill fraction. A new non-dimensional parameter incorporating the fill fraction was proposed. When the PDE-ejector data were represented as a function of this new parameter,

ejector data were reduced to one representative thrust-augmentation curve for ejectors of similar internal geometry. Data on straight PDE ejectors compared well with those available on straight steady-flow ejectors. Diverging PDE ejectors produced nearly twice the thrust augmentation of their straight ejector counterparts because of the additional thrust surface area that the divergence provided. All PDE ejectors tested were observed to be sensitive to the axial position of the ejector also. The optimum ejector axial placement was found to be a function of fill fraction resulting from a trade-off between the detonation-wave drag and increased mass entrainment. Downstream ejector placements performed best at low-fill-fraction operating conditions. The results of this investigation were documented by D. Allgood, E. Gutmark (both of the University of Cincinnati), J. L. Hoke, R. P. Bradley (both of ISSI), and F. R. Schauer (AFRL) in AIAA Paper No. 2005-223 that was presented at the 43rd AIAA Aerospace Sciences Meeting and Exhibit, which was held 10-13 January 2005 in Reno, NV. The paper is included in the Appendix.

6.1.7 Performance Measurements of Multi-cycle PDE Exhaust Nozzles.

Performance measurements of multi-cycle PDE exhaust nozzles were conducted using a damped thrust stand. A PDE of 1.88-m length was operated on a cycle frequency of 30 Hz at stoichiometric conditions. Both converging and diverging bell-shaped exhaust nozzles were tested for fill fractions ranging from 0.4 to 1.1. The area ratios of the nozzles were varied from 0.25 converging to 4.00 diverging. The nozzle length was negligible compared to the overall length of the PDE. Successful normalization of PDE-nozzle thrust data was obtained based on nozzle area ratio for two PDE diameters tested (2.54 cm and 5.08 cm). The optimum nozzle area ratio was found to be a function of the PDE fill fraction. For fill fractions at or below 0.5, the optimum configuration was a PDE without an exhaust nozzle. However, as the operating fill fraction was increased to values close to or above one, thrust enhancement was obtained with a converging nozzle. The diverging nozzles also showed a relative increase in their performance with increased fill fraction. However, unlike the converging nozzles, the diverging nozzles and baseline configuration were observed to be sensitive to the ignition delay. The results of this investigation were documented by D. Allgood, E. Gutmark (both of the University of Cincinnati), J. Hoke, R. Bradley (both of ISSI), and F. Schauer (AFRL) in AIAA Paper No. 2005-222 that was presented at the 43rd AIAA Aerospace Sciences Meeting and Exhibit, which was held 10-13 January 2005 in Reno, NV. The paper is included in the Appendix.

6.1.8 Emissions-Reduction Technology for Military Gas-Turbine Engines.

Future military gas-turbine engines will have higher performance than current engines, resulting in increased compressor and combustor exit temperatures, combustor pressures, and fuel-air ratios with wider operating limits. These combustor characteristics suggest undesirable exhaust emission levels of nitrogen oxides and smoke at maximum power and higher carbon monoxide and unburned hydrocarbons at low power. Major advances in combustor technology will be required to control emission levels while improving performance, durability, and cost. Current emissions-control approaches as applied to conventional swirl-stabilized combustors include rich- and lean-burn strategies, together with staged combustion. These approaches, even in fully developed form, may not be sufficient to satisfy the projected design requirements. Unconventional combustor configurations may become necessary. Engine cycles other than the standard Brayton cycle may also be employed for special applications in attempts to avoid the use of excessive combustion temperatures. Currently utilized emissions-control approaches were

considered, and a comparison was made with regard to their performance and likely potential for meeting future requirements. Experimental results were obtained for two non-conventional combustor configurations that have shown promise for advanced-engine applications. Considered were cycle changes that could result in lower peak temperatures while maintaining advanced performance. The results of this investigation were documented by G. J. Sturgess (ISSI), J. Zelina, D. T. Shouse, and W. M. Roquemore (all of AFRL) in a paper that was published in the *Journal of Propulsion and Power* [Vol. 21, No. 2, pp. 193-217 (March-April 2005)]. The paper is included in the Appendix.

6.1.9 Acoustic Measurements for PDE.

The acoustic environment of a PDE was measured. The engine consisted of one to four detonation tubes that were detonated at 20 and 40 Hz. Fill fractions and equivalence ratios of 1 and 0.5 were tested. All tests were conducted in a test cell that was not acoustically treated. Measurements were made near the exit of the tubes and up to a distance of 12 ft. Time histories and narrow-band spectral analysis were generated. A comparison of sampling frequencies of 200 K and 20 K was made. Numerous potential noise-suppression approaches were evaluated. The results indicate that a very high level pulse is generated near the exit of the tubes but tends to decrease in amplitude fairly rapidly with distance since the higher frequency energy dissipates in the atmosphere. The results of this investigation were documented by L. Shaw, K. Harris, F. Schauer (all of AFRL) and J. Hoke (ISSI) in AIAA Paper No. 2005-2952 that was presented at the 11th AIAA/CEAS Aeroacoustics Conference (26th AIAA Aeroacoustics Conference), which was held 23-25 May 2005 in Monterey, CA. The paper is included in the Appendix.

6.1.10 Performance Assessment of Large-Scale Pulsejet-Driven Ejector System.

Unsteady thrust augmentation was measured on a large-scale driver/ejector system. A 72-in.-long, 6.5-in.-diameter, 100-lb_f pulsejet was tested with a series of straight cylindrical ejectors of varying length and diameter. A tapered-ejector configuration of varying length was also tested. The objectives of the testing were to determine those dimensions of the ejectors that maximize thrust augmentation and to compare the dimensions and augmentation levels thus obtained with those of other similarly maximized but smaller scale systems on which most of the recent unsteady ejector-thrust augmentation studies have been performed. An augmentation level of 1.71 was achieved with the cylindrical-ejector configuration, and a level of 1.81 was achieved with the tapered-ejector configuration. These levels are consistent with--but slightly lower than--the highest levels achieved with the smaller systems. The ejector diameter that yielded maximum augmentation was 2.46 times the diameter of the pulsejet. This ratio closely matches those of the small-scale experiments. For the straight ejector, the length yielding maximum augmentation was ten times the diameter of the pulsejet, which was nearly the same as in the small-scale experiments. Implications for general scaling of pulsed thrust ejector systems were considered. The results of this study were documented by D. E. Paxon (NASA Glenn Research Center), P. J. Litke, F. R. Schauer (both of AFRL), R. P. Bradley, and J. L. Hoke (both of ISSI) in AIAA Paper 2006-1021 that was presented at the 44th AIAA Aerospace Sciences Meeting and Exhibit, which was held 9-12 January 2006 in Reno, NV. The paper is included in the Appendix.

6.1.11 Performance Measurements of Straight and Diverging Ejectors Integrated with a PDE.

Experimental studies were performed on a set of PDE-driven straight and diverging ejectors to determine system performance. Ejector performance was quantified by thrust measurements. The effects of PDE operating parameters and ejector geometric parameters on thrust augmentation were investigated. PDE operating parameters of fill fraction and operating frequency were varied. Augmentation was observed to decrease with increasing PDE frequency. Axial placement of the ejector was varied over a broad range, covering both upstream and downstream positions. It was found that for all cases tested, the maximum thrust augmentation occurred at a downstream ejector placement. Ejector geometries tested covered five lengths, in the range $L_{\text{EJECT}}/D_{\text{EJECT}} = 2.61 - 6.61$. The exhaust sections tested had half-angles of 0, 4, 8, and 12 degrees. It was found that the exhaust section with half-angle of 4 degrees performed best. The optimum ejector geometry was determined to have an overall length of $L_{\text{EJECT}}/D_{\text{EJECT}} = 5.61$. A maximum thrust augmentation of 85% was observed with the optimized ejector configuration at a fill fraction of 0.6 and an operating frequency of 30 Hz. The results of this investigation were documented by A. J. Glaser, N. Caldwell, E. Gutmark (all of the University of Cincinnati), J. Hoke, R. Bradley (both of ISSI), and F. Schauer (AFRL) in AIAA Paper 2006-1022 that was presented at the 44th AIAA Aerospace Sciences Meeting and Exhibit, which was held 9-12 January 2006 in Reno, NV. The paper is included in the Appendix.

6.1.12 Impact of Detonation-Initiation Techniques on Thrust in a PDE.

Detonation initiation remains an impediment to pulsed-detonation-technology efficacy. Practical fuels can now be detonated regularly in the laboratory using conventional oxygen-rich predetonators or extended DDT geometries; however, these systems are not suited for field use because of the excess oxygen required for the predetonator and the reduced performance due to drag of DDT mechanisms. The performance of a hydrogen-air multi-cycle PDE was examined using two initiation schemes--a predetonator and a DDT device--to determine a suitable initiation mechanism. DDT mechanisms typical for initiation of hydrogen and those typical for insensitive hydrocarbon fuels were examined. Because of the relative ease of detonation initiation, hydrogen was the fuel used in the main detonator tube, even with the longer DDT mechanisms employed for insensitive fuels. The predetonator employed aviation gasoline and nitrous oxide in a small (1 - 3% of the volume of the main tube) chamber to initiate a detonation and generate an upper limit on the expected performance of DDT initiators. A fuel-specific impulse value of ~ 3900 sec was achieved with the predetonator at 10 Hz and an equivalence ratio and fill fraction of unity. For DDT initiation a Schelkin-like spiral located in 10 - 70% of the main detonation tube volume was used. Below 10% of the main tube volume, DDT was found to generate identical impulse to the predetonator initiation; while for the longest DDT mechanism, located throughout 70% of the main-tube volume, a reduction in fuel-specific impulse of 44% was measured. Head-pressure measurements showed a reduced-thrust wall pressure for the DDT initiation, probably owing to the drag and dissipation of the detonation wave traveling upstream through the DDT mechanism. The results of this study were documented by J. L. Hoke, R. P. Bradley (both of ISSI), J. R. Gallia, and F. R. Schauer (both of AFRL) in AIAA Paper 2006-1023 that was presented at the 44th AIAA Aerospace Sciences Meeting and Exhibit, which was held 9-12 January 2006 in Reno, NV. The paper is included in the Appendix.

6.1.13 Performance Measurements of Multi-cycle PDE Exhaust Nozzles.

Performance measurements of multi-cycle PDE exhaust nozzles were made using a damped thrust stand. A PDE of 1.88-m length was operated on a cycle frequency of 30 Hz at stoichiometric conditions. Both converging and diverging bell-shaped exhaust nozzles were tested for PDE fill fractions ranging from 0.4 to 1.1. The area ratios of the nozzles were varied from 0.25 converging to 4.00 diverging. The nozzle length was negligible compared to the overall length of the PDE. The feasibility of normalizing the PDE-nozzle thrust data was investigated by testing two PDE combustion-chamber diameters (2.54 and 5.08 cm) with the same nozzle-area ratios. The optimum nozzle-area ratio was found to be a function of the PDE fill fraction. For fill fractions at or below 0.5, the optimum configuration was a PDE without an exhaust nozzle. However, as the operating fill fraction was increased to values near or above one, thrust enhancement was obtained with a converging nozzle. The diverging nozzles also showed a relative increase in their performance with increased fill fraction. Unlike the converging nozzles, the diverging nozzles and baseline configuration were observed to be sensitive to the ignition delay. The results of this investigation were documented by D. Allgood, E. Gutmark (both of the University of Cincinnati), J. Hoke, R. Bradley (both of ISSI), and F. Schauer (AFRL) in a paper that was published in the *Journal of Propulsion and Power* [Vol. 22, No. 1, pp. 70-77 (January-February 2006)]. The paper is included in the Appendix.

6.1.14 Effects of Tube and Ejector Geometry on Performance of PDE-Driven Ejectors.

Experimental studies were carried out to investigate the performance of various PDE-driven ejector configurations. In particular, the effects of detonation tube length and ejector-to-PDE diameter ratio (DR) were studied. This research employed a H₂-air PDE at 25-Hz operating frequency. Performance was quantified by thrust measurements. It was found that decreasing the detonation tube length increases the ejector thrust augmentation. An optimum ejector-to-PDE diameter ratio was found to exist in the range DR=3 to DR=3.67. The specific impulse of the PDE increased from the baseline no-ejector value of 3400 s to ~ 6080 s with an ejector installed. The results of this investigation were documented by A. J. Glaser, N. Caldwell, E. Gutmark (all of the University of Cincinnati), J. Hoke, R. Bradley (both of ISSI), and F. Schauer (AFRL) in AIAA Paper 2006-4790 that was presented at the 42nd AIAA/ASME/SAE/ASEE Joint Propulsion Conference and Exhibit, which was held 9-12 July 2006 in Sacramento, CA. The paper is included in the Appendix.

6.1.5 Effect of Supercritical Fuel Injection on Cycle Performance of a PDE.

The PDE relies on rapid ignition and formation of detonation waves. Significant reduction in the time that elapses during the formation of detonation waves with low-vapor-pressure liquid hydrocarbons is still required to transition the PDE from experimentation to operational use. This study was focused on PDE-operation enhancements using dual-detonation-tube, concentric-counterflow heat exchangers to elevate the fuel temperature to supercritical levels. Several operating parameters were varied, including fuel type (JP-8, JP-7, JP-10, RP-1, JP-900, and S-8), spark delay, and firing frequency. To quantify the performance, four key parameters were examined: ignition time, DDT time, detonation distance, and percent of ignitions resulting in a detonation (detonation percentage). In general, for all fuels except JP-10, increasing the fuel-

injection temperature decreased DDT time by 15% and detonation distance by up to 30%, increased the detonation percentage by up to 180%, and had minimal impact on ignition time. JP-10 was difficult to detonate, resulting in poor performance. For all fuels an increase in firing frequency resulted in a 5% decrease in DDT time at high fuel-injection temperatures but had little effect on ignition time and detonation distance. Analysis of spark delay showed that 4 ms is the best spark delay at supercritical fuel-injection temperatures, based on total time to detonation and detonation percentage. The results of this study were documented by T. M. Helfrich, P. I. King (both of the Air Force Institute of Technology), J. L. Hoke (ISSI), and F. R. Schauer (AFRL) in AIAA Paper 2006-5133 that was presented at the 42nd AIAA/ASME/SAE/ASEE Joint Propulsion Conference and Exhibit, which was held 9-12 July 2006 in Sacramento, CA. The paper is included in the Appendix.

6.1.6 Experimental Study of Ejectors Driven by a PDE.

Experimental studies were performed to gain a better understanding of the operation of ejector augmentors driven by a PDE. This research employed a H₂-air PDE at 30-Hz operating frequency. Static pressure was measured along the interior surface of the ejector, including the inlet and exhaust sections. Thrust augmentation provided by the ejector was calculated by integration of the static pressure measured along the ejector geometry. The calculated thrust augmentation was in good agreement with the augmentation found from direct thrust measurements. Both straight and diverging ejectors were investigated. The diverging-ejector pressure distribution showed that the role of the diverging section was to act as a subsonic diffuser. Ejector axial position was also studied. The ejector pressure data followed the same trend as the results of the direct thrust measurements. The optimum axial placement was found to be downstream of the PDE near $x/D_{PDE} = +2$, while upstream placements tended toward a decreasing thrust augmentation. To gain a better understanding of the observed performance trends, shadowgraph images of the detonation wave and trailing vortex interacting with the ejector inlet were obtained. The results of this investigation were documented by A. J. Glaser, N. Caldwell, E. Gutmark [all of the University of Cincinnati (UC)], J. Hoke, R. Bradley (both of ISSI), and F. Schauer (AFRL) in AIAA Paper 2007-447 that was presented at the AIAA Meeting in Reno and in a paper that was presented at DCASS07. The AIAA paper is included in the Appendix.

6.1.17 Ignition and Detonation-Initiation Characteristics of Hydrogen and Hydrocarbon Fuels in a PDE.

Over the past two decades, several fuels have been tested throughout the world in PDEs. The present research focused on developing a baseline set of ignition and detonation-initiation performance measures for six fuels in air: hydrogen, ethylene, propane, aviation gasoline (avgas), JP-8, and Fischer-Tropsch JP-8 (S-8). To quantify the ignition and detonation-initiation performance, four parameters were examined: ignition time, DDT time, DDT distance, and upper CJ wavespeed. These four parameters were presented as a function of equivalence ratio from lean-to-rich ignition limits for the six fuels of interest. Hydrogen was found to have the best ignition and detonation-initiation characteristics, followed by ethylene. Propane, avgas, JP-8, and S-8 exhibited similar ignition and detonation-initiation characteristics, as expected based on cell size. Minimum ignition times for all fuels occurred near an equivalence ratio of 1.3,

whereas the minimum DDT times and distances occurred between equivalence ratios of 1.1 and 1.2. All experimental CJ wavespeeds were within 5% of the theoretical value, with the exception of hydrogen which has an experimental CJ wavespeed that is systematically between 6% and 8% lower than the theoretical value. The results of this investigation were documented by T. M. Helfrich, F. R. Schauer (both of AFRL), R. P. Bradley, and J. L. Hoke (both of ISSI) in AIAA Paper 2007-234 that was presented at the AIAA Meeting in Reno. The paper is included in the Appendix.

6.1.18 Transient Plasma Ignition (TPI) for Delay Reduction in a PDE.

Five laboratories conducted testing and evaluation of transient plasma for PDE ignition under various conditions. The results showed significant reductions in the times required for detonation. Critical to the achievement of functional levels of thrust is increased repetition rate; thus, minimal delay to detonation times is an important parameter. Experiments were conducted at the University of Southern California and in collaboration with researchers at the Naval Postgraduate School, the Air Force Research Laboratory, Stanford University, The Ohio State University, and the University of Cincinnati. In these studies it was observed that TPI significantly reduces delay times (by a factor of two to nine) in both static and flowing systems. The results of this effort were documented by C. Cathey, F. Wang, T. Tang, A. Kuthi, M. Gundersen [all of the University of Southern California (USC)], J. O. Sinibaldi, C. Brophy (both of the Naval Postgraduate School), E. Barbour, R. K. Hanson (both of Stanford University), J. Hoke (ISSI), F. Schauer (AFRL), J. Corrigan, and J. Yu (both of The Ohio State University) in AIAA Paper 2007-443 that was presented at the AIAA Meeting in Reno. The paper is included in the Appendix.

6.1.19 Effects of Corona, Spark, and Surface Discharges on Ignition Delay and DDT in a PDE.

The ignition delays in an experimental PDE produced by thermal and non-thermal ignitions were compared. The commercial thermal ignition has a pulse duration of about 1 μ s, whereas the non-thermal ignitions have pulse durations of 100 ns. Ignition delay is an important factor, along with fill and purge times, that limits the maximum repetition rate and thrust of PDEs. For stoichiometric fuel-air mixtures with aviation gasoline at 1 atm and 360 - 480 K, an ignition delay of 6 ms was observed with a non-thermal ignition, whereas the ignition delay was 11 ms with an aftermarket automotive ignition. By replacing the resistive cable and resistor of the aftermarket ignition with a non-resistive cable and surface discharge igniter, the ignition delay was reduced to 7 ms, which is comparable to that produced by the non-thermal ignitions. The results of this study were documented by K. Busby (National Research Council), J. Corrigan, S.-T. Yu (both of The Ohio State University), S. Williams, C. Carter, F. Schauer (all of AFRL), J. Hoke (ISSI), C. Cathey, and M. Gundersen (both of USC) in AIAA Paper 2007-1028 that was presented at the AIAA Meeting in Reno. The paper is included in the Appendix.

6.1.20 Evaluation of Catalytic and Thermal Cracking in a JP-8-Fueled PDE.

PDEs depend on rapid ignition and transition from deflagration to detonation. Converting the PDE from experimental to operational use will necessitate a considerable reduction in the time

required to ignite and detonate a liquid hydrocarbon fuel, such as JP-8, in air. This research effort was focused on PDE operation enhancements using dual-detonation-tube, concentric-counterflow heat exchangers to elevate the fuel temperature levels sufficiently to induce thermal cracking. Additionally, a zeolite catalytic coating was applied to the heat-exchanger surfaces to stimulate further cracking of the fuel and reduce coke deposition. To quantify the PDE performance, three parameters were examined--ignition time, DDT time, and DDT distance. As compared with flash-vaporized JP-8/air mixtures, the cracked JP-8/air mixture produced a shorter ignition time, DDT time, and DDT distance for the majority of equivalence ratios, with a reduction in ignition time of up to 60% at 908 K. Furthermore, both the ignition and the detonability limits were expanded by cracking the fuel, with lean limits at an equivalence ratio of 0.75. Coke depositions found in the fuel filter consisted of carbon as well as substantial concentrations of silicon and aluminum, resulting from deterioration of the silica-alumina zeolite structure. Additionally, the catalyst was coated in coke deposition after 5 hr of operation, although no degradation in performance was observed. The results of this study were documented by T. M. Helfrich, F. R. Schauer (both of AFRL), R. P. Bradley, and J. L. Hoke (both of ISSI) in AIAA Paper 2007-235 that was presented at the AIAA Meeting in Reno. The paper is included in the Appendix.

6.1.21 Detonation Propagation across Asymmetric Step Expansion.

A study of confined detonation transmission across a step expansion was conducted using experimental and computational techniques. Transmission success of ethylene/air detonations at various equivalence ratios was compared with the transmission of hydrogen/air detonations. The highest rate of transmission success in the experimental results for ethylene was noted at equivalence ratios richer than the conditions of minimum cell size, indicating the presence of effects other than cell size and expansion ratio. Hydrogen proved to have better transmission success than ethylene, even when normalized to the cell size upstream of the expansion. The difference was theorized to result from the disparity in critical initiation energy of the two fuels. Computational results showed the presence of a relationship between the number of transverse waves upstream of the expansion and the degree of expansion that correlates to success or failure of a confined detonation transmission. Detonation transmissions were also observed to fail when a single transverse wave in the upstream channel was partially reflected at the step expansion. The results of this study were documented by D. R. Hopper, P. I. King [both of the Air Force Institute of Technology (AFIT)], F. R. Schauer (AFRL), V. R. Katta, and J. L. Hoke (both of ISSI) in AIAA Paper 2007-5078 that was presented at the Joint Propulsion Conference in Cincinnati. The paper is included in the Appendix.

6.1.22 Effect of Supercritical Fuel Injection on Cycle Performance of a PDE.

PDE engines produce impulsive thrust through rapid ignition and formation of detonation waves. An operational goal is a reduction in time for the formation of detonation waves in conjunction with low-vapor-pressure liquid hydrocarbons. This study focused on PDE operation enhancements using dual-detonation-tube, concentric-counterflow heat exchangers to elevate liquid-hydrocarbon fuel temperatures to supercritical levels. Variation of operating parameters included fuel type (JP-8, JP-7, JP-10, RP-1, JP-900, and S-8) and firing frequency. Of interest is the effect on ignition time, deflagration-to-detonation transition time, detonation distance, and

the percent of ignitions resulting in a detonation (detonation percentage). Except for JP-10, results for all fuels with increasing fuel-injection temperatures indicated decreases in deflagration-to-detonation transition time by up to 15%, a decrease in detonation distance by up to 30%, increases in the detonation percentage by up to 180%, and minimal impact on ignition time. JP-10 is difficult to detonate, and results were inconsistent. An increase in firing frequency resulted in a 5% decrease in deflagration-to-detonation transition time at high fuel-injection temperatures but had little effect on ignition time and detonation distance. The results of this investigation were documented by T. M. Helfrich, P. I. King (both of AFIT), J. L. Hoke (ISSI), and F. R. Schauer (AFRL) in a paper that was published in the *Journal of Propulsion and Power* [Vol. 23, No. 4, pp. 748-755 (July-August 2007)]. The paper is included in the Appendix.

6.1.23 Fuel-Composition Analysis of Endothermically Heated JP-8 Fuel for Use in a PDE.

Waste heat from a PDE was extracted via concentric tube-counterflow heat exchangers to produce supercritical pyrolytic conditions for JP-8 fuel. Offline analysis of liquid and vapor fuel samples obtained during steady-state operation indicated fuel decomposition via typical pyrolytic reaction pathways. The liquid analysis showed conversion of parent fuel components with formation of unsaturates (aromatics and alkenes) and smaller alkanes. The gaseous products consisted of predominantly C₁-C₃ alkanes and alkenes (> 50% of total vapor yield), with moderate amounts of hydrogen and C₄-C₆ alkanes and alkenes. The components that were present in the stressed fuel samples were more detonable and could be linked to improved PDE performance--specifically, shorter ignition time, shorter DDT time, and shorter DDT distance. The results of this investigation were documented by E. A. Nagley, P. I. King [both of the Air Force Institute of Technology (AFIT)], F. R. Schauer (AFRL), M. J. DeWitt [University of Dayton Research Institute (UDRI)], and J. L. Hoke (ISSI) in AIAA Paper 2008-109 for presentation at the AIAA Meeting in Reno. The paper is included in the Appendix.

6.1.24 Direct Initiation by Detonation Branching in a PDE.

An experimental study was conducted to determine the requirements necessary for successful branching of a detonation initiated in a primary detonation tube, through a crossover tube, and into a second detonation tube without the use of internal deflagration-to-detonation transition hardware. Tail-to-head branching was conducted, and a hydrogen-sourced detonation was observed to sustain a diameter expansion ratio of 1:2. The head pressure trace of a successful detonation transfer resulting in Chapman-Jouget wave speeds in the branch ignited tube was also observed. The results of this study were documented by A. R. Hausman, P. I. King, and D. R. Hopper (all of AFIT), J. L. Hoke (ISSI), and F. R. Schauer (AFRL) in AIAA Paper No. 2008-108 for presentation at the AIAA Meeting in Reno. The paper is included in the Appendix.

6.1.25 Development of Continuous Branching PDE.

A one-dimensional analysis was developed for the sizing of a continuous branching PDE. The length of the crossover tubes was found to depend on the number of thrust tubes in the engine and total engine cycle time for a given fuel/air mixture. The natural engine operating frequency was then inversely proportional to the thrust tube length. Minimal crossover tube length was desirable to reduce difficulties with detonation transmission and other inefficiencies associated

with long crossover tubes. Proof-of-concept experimentation was performed on a pair of thrust tubes connected at the tail end of a perpendicular crossover tube. Transient variations in wavespeed were observed as the engine temperature increased; but under the right conditions, consistent detonation transmission was observed. A continuous branching PDE design was demonstrated, with short crossover tubes and alternating tail-tail and head-head detonation transmission. The results of this study were documented by D. R. Hopper, P. I. King (both of AFIT), J. L. Hoke (ISSI), and F. R. Schauer (AFRL) in AIAA Paper 2008-112 for presentation at the AIAA Meeting in Reno. The paper is included in the Appendix.

6.1.26 Single-Ejector Augmentation of Multi-tube PDE.

Multiple detonation tubes were directed into a single ejector in an effort to reduce the added hardware required while maintaining the level of augmentation. By moving a single driver off axis, it was found that the augmentation level could be maintained for x/d less than 4 and y/d up to at least 1.14 for a round ejector. The ejector augmentation, however, was found to decrease by about 25% during multi-tube operation, being approximately 1.3 ejector-to-baseline augmentation ratio. A linear arrangement of detonation tubes was constructed, extrapolating typical unsteady ejector parameters. Four linear detonation tubes were directed at the linear ejector, and the highest ejector augmentation ratio was 1.25, even with reduced fill fraction. With single-tube operation, the performance of the linear ejector was at best 1.15, indicating that multi-tube effects were significant. The results of this investigation were documented by J. Hoke, R. Bradley (both of ISSI), and F. Schauer (AFRL) in AIAA Paper No. 2008-115 for presentation at the AIAA Meeting in Reno. The paper is included in the Appendix.

6.1.27 Investigation of Fundamental Processes Leading to PDE/Ejector Thrust Augmentation.

A series of shadowgraph flow visualizations was obtained in an effort to increase the understanding of the fundamental flow characteristics occurring inside an ejector that is driven by a PDE. As a supplement to the theories that have been developed through indirect thrust and static pressure measurements, these internal flow visualizations provided a uniquely direct insight into the fluid dynamics caused by the passage of the detached leading shock separated from the detonation wave and the subsequent blowdown cycle. Using a two-dimensional (2D) ejector model, flow visualizations of various ejector-PDE separation distances and ejector divergence angles were obtained. Additionally, the flow exhausting from the rear of an axisymmetric ejector was captured. A new 2D ejector model design is being developed for visualizing this type of flow while accessing more geometric parameters of interest. Furthermore, this new design allows the measurement of dynamic and static pressure along the length of the internal surface of the ejector and can simulate forward flight effects up to Mach 0.3. The results of this study were documented by N. Caldwell, E. Gutmark [both of the University of Cincinnati (UC)], J. Hoke, R. Bradley (both of ISSI), and F. Schauer (AFRL) in AIAA Paper 200-116 for presentation at the AIAA Meeting in Reno. The paper is included in the Appendix.

6.1.28 Performance Studies of PDE Ejectors.

An experimental study on the performance of PDE ejectors was conducted. Time-averaged thrust augmentation produced by straight and diverging PDE ejectors was measured using a damped thrust stand. The ejector length-to-diameter ratio was varied from 1.25 to 5.62 by changing the length of the ejector and maintaining a nominal ejector diameter ratio of 2.75. In general, the level of thrust augmentation was found to increase with ejector length. Also, the ejector performance was observed to be strongly dependent on the operating fill fraction. A new non-dimensional parameter incorporating the fill fraction was proposed. When the PDE-ejector data were represented as a function of this new parameter, the ejector data were reduced to one representative thrust-augmentation curve for ejectors of similar internal geometry. Straight PDE ejector results compared well with the available data on straight, steady-flow ejectors. Diverging PDE ejectors produced nearly twice the thrust augmentation of their straight-ejector counterparts because of the additional thrust surface area that the divergence provided. All PDE ejectors tested were observed to be sensitive to the axial position of the ejector as well. The optimum ejector axial placement was found to be a function of fill fraction resulting from a trade-off between the detonation-wave induced drag and increased mass entrainment. Downstream ejector placements performed best at low-fill-fraction operating conditions. The results of this investigation were documented by D. Allgood, E. Gutmark [both of the University of Cincinnati (UC)], J. L. Hoke, R. P. Bradley (both of ISSI), and F. R. Schauer (AFRL) in a paper that was published in *Journal of Propulsion and Power* [Vol. 24, No. 6, pp. 1317-1323 (November-December 2008)]. The paper is included in the Appendix.

6.1.29 Study on Operation of PDE-Driven Ejectors.

Experimental studies were performed to improve the understanding of the operation of ejector augmentors driven by a PDE. The research employed a H₂-air PDE at an operating frequency of 30 Hz. Static pressure was measured along the interior surface of the ejector, including the inlet and exhaust sections. Thrust augmentation provided by the ejector was calculated by integration of the static pressure measured along the ejector geometry. The calculated thrust augmentation was in good agreement with that obtained from direct thrust measurements. Both straight and diverging ejectors were investigated. The diverging-ejector pressure distribution showed that the diverging section acts as a subsonic diffuser and has a tremendous impact on the behavior of the inlet entrainment flow. Static pressure data were also collected for various ejector axial positions. These data supported the thrust-augmentation trends found through direct thrust measurements. Specifically, the optimum axial placement was found to be downstream of the PDE near $x/D_{\text{PDE}} = +2$, whereas upstream placements tended to result in decreasing thrust augmentation. To provide a better explanation of the observed performance trends, shadowgraph images of the detonation wave and trailing vortex interacting with the ejector inlet were obtained. The results of this investigation were documented by A. J. Glaser, N. Caldwell, E. Gutmark [all of UC], J. Hoke, R. Bradley (both of ISSI), and F. Schauer (AFRL) in a paper that was published in *Journal of Propulsion and Power* [Vol. 24, No. 6, pp. 1324-1321 (November-December 2008)]. The paper is included in the Appendix.

7.0 DEMONSTRATION OF ADVANCED-CONCEPT HIGH-IMPACT TECHNOLOGIES

7.1 General Overview

The objective of this portion of the program was to take high-impact technologies that show promise in the laboratory to a higher level of technology demonstration by both small-engine and in-flight demonstration. A summary of the work accomplished on this task during the program follows.

7.1.1 A Flight-Ready PDE.

Design and development efforts continue with a view toward achieving a flight-ready PDE, and testing and development are in progress in preparation for the first PDE powered flight. A PDE is a high-performance cycle that is highly scalable and efficient across a broad operating range (Mach 0-4+). The PDE being developed here utilizes off-the-shelf automotive parts to permit a quick demonstration of the first PDE flight and ascertain the viability of PDE propulsion technology. Future PDE designs will take advantage of the unique characteristics of the PDE cycle such as the possibility of self-actuation and self-aspiration that have already been demonstrated at the Pulsed Detonation Research Facility at Wright-Patterson AFB (WPAFB). The four-tube PDE employs a GM Quad-4 valve train to control the operation and timing and a standard automotive-spark-ignition system to initiate combustion within the tubes. The PDE operates on a premixed mixture of aviation-grade gasoline and air that is supplied by a standard automotive supercharger. Fuel is injected upstream of the PDE via an injection manifold that was designed and fabricated in-house and uses conventional fuel injectors. The air-fuel charge, initially ignited at atmospheric pressure, is transitioned from a deflagration to a detonation within 6-ft-long tubes using Schelkin-like spirals to achieve detonation without the use of excess oxygen. An aviation two-stroke engine is incorporated to provide the mechanical power to the PDE and all of its sub-components, including supercharger, lubrication, electrical power, and fuel systems. A Rutan-designed aircraft, the LongEZ, was selected as the test bed for the first PDE flight. The LongEZ is powered solely by the PDE, which has replaced the conventional pusher/prop system on this experimental aircraft. Final shakedown and endurance testing is in progress at WPAFB in preparation for the flight demonstration to take place at the Civilian Test Pilot Range in Mojave, CA. The results of this study were documented by P. J. Litke (AFRL), R. P. Bradley, J. L. Hoke (both of ISSI), and F. Schauer (AFRL) in a paper that was presented at the 29th Annual Dayton-Cincinnati Aerospace Science Symposium, which was held 9 March 2004 in Dayton, OH. The visual materials for this presentation are included in the Appendix.

7.1.2 Manned Demonstration Flight of a PDE.

The first-ever manned demonstration flight of an aircraft powered by a PDE was accomplished on 31 January 2008 at Mojave, California. The project for development of the engine that powered this aircraft was conceived by Dr. Fred Schauer of AFRL, and the engine was developed jointly by AFRL and ISSI. The ISSI team is under the direction of Dr. John Hoke. A Long-EZ, heavily modified by Scaled Composites and powered solely by the PDE, was flown by a test pilot from above the main runway in straight-and-level flight at altitudes up to 100 ft. At

peak thrust at the start of the run, the PDE was producing more than 200 lb. thrust. The prime objectives of the AFRL/ISSI demonstration were to show that the PDE could be used to power an aircraft, that the aircraft structure could survive the acoustic pressure of the Mach-5 shock waves exiting the detonation tubes, and that the noise level would not be prohibitive for a manned flight. The test also sought to assess the durability of the engine, which had already undergone more than 100 hr. of ground testing plus an additional 30 hr. on the integrated systems. Interest has been growing in the potential of PDEs for a range of simple, cost-effective missile propulsion systems as well as in the possible development of combustion sources for commercial and military gas turbines. Researchers hope that the first flight of an aircraft powered by a PDE will accelerate the development of a propulsion concept that promises greater simplicity, lighter weight, and a wider operating range than turbomachinery. An article entitled, "Pulse Power – Pulse Detonation Engine-Powered Flight Demonstration Marks Milestone in Mojave," by Guy Morris appeared in the February 18, 2008, issue of *Aviation Week and Space Technology*. Two articles by Graham Warwick entitled, "First Flight for PDE = Pretty Darned Extraordinary" and "US AFRL Proves Pulse-Detonation Engine Can Power Aircraft," were published in *Flight International Magazine* on 29 February 2008 and 5 March 2008, respectively. A fourth article entitled, "AFRL Tests Pulse Detonation Propulsion," appeared in the *AIAA Daily Launch* on 6 March 2008. The first three articles are included in the Appendix.

8.0 REFERENCES

1. Ozowa, R. I., *Survey of Basic Data on Flame Stabilization and Propagation for High Speed Combustion Systems*, AFAPL-TR-70-81, Air Force Aero Propulsion Laboratory, Wright-Patterson Air Force Base, OH, 1971.
2. Zukoski, E., *Experiments Concerning the Mechanism of Flame Blowoff from Bluff Bodies*, Thesis, California Institute of Technology, 1954.
3. DeZubay, E. A., "Characteristics of Disk-Controlled Flame," *Aero Digest*, 1950, pp. 54-57.
4. Mehta, P. G., and Soteriou, M. C., "Combustion Heat Release Effects on the Dynamics of Bluff Body Stabilized Premixed Reacting Flows," AIAA Paper No. 2003-0835, 41st AIAA Aerospace Sciences Meeting and Exhibit, Reno, NV, 6-9 January 2003.
5. Erickson, R., Soteriou, M. and Prashant, M., "The Influence of Temperature Ratio on the Dynamics of Bluff Body Stabilized Flames," AIAA Paper No. 2006-753, 2006, 44th AIAA Aerospace Sciences Meeting and Exhibit, Reno, NV, 9-12 January 2008.
6. Schauer, F., Stutrud, J., Bradley, R., Katta, V., and Hoke, J., "Detonation Studies and Performance Results for a Pulse Detonation Engine," International Colloquium on Advances in Confined Detonations (ICCD), Moscow, Russia, 25 July 2002.
7. Brophy, C., Sinibaldi, D., Netzer, D., and Johnson, R., "Operation of a JP-10/Air Pulse Detonation Engine," AIAA Paper No. 2000-3591, 36th AIAA/ASME/SAE/ASEE Joint Propulsion Conference, Huntsville, AL, 16-19 July 2000.
8. Schauer, F. R., Stutrud, J. S., and Bradley, R. P., "Detonation Initiation Studies and Performance Results for Pulse Detonation Engine Applications," AIAA Paper No. 2001-1129, 39th AIAA Aerospace Sciences Meeting and Exhibit, Reno, NV, 8-11 January 2001.
9. Frolov, S. M., Basevich, V. Ya., and Belyaev, A. A., "The Use of Fuel Blends and Distributed Injection for Active Detonability Control in a PDE," Paper No. 99-252, 17th International Colloquium on the Dynamics of Explosions and Reactive Systems (ICDERS), Heidelberg, Germany, 25-30 July 1999.

9.0 PUBLICATIONS, PRESENTATIONS, PATENTS, AND SIGNIFICANT ACCOMPLISHMENTS

9.1 Publications, Presentations, and Patents

“Stator Cascade Flow Vectoring through Counter Flow Blowing,” M. Harff, M. Wolff, W. Copenhaver, D. Car, and J. Estevadeordal, AIAA Paper No. 2003-3408 presented at the 33rd AIAA Fluid Dynamics Conference and Exhibit, 23-26 June 2003, Orlando, FL.

“Crystallographic and Spectroscopic Investigations of the Effect of Preparation Procedure on CdS Nanoparticles Made in Reverse Micelles,” C. E. Bunker, P. Pathak, B. A. Harruff, Y. Lin, J. Widera, J. R. Gord, and Y.-P. Sun, Presented at the AIAA/ICAS International Air and Space Symposium and Exposition, 14-17 July 2003, Dayton, OH.

“Dynamics of Vortex-Flame Interactions and Implications for Turbulent Combustion,” T. R. Meyer, V. R. Katta, M. S. Brown, J. R. Gord, W. M. Roquemore, A. Lemaire, K. Zahringer, and J. C. Rolon, AIAA Paper No. 2003-4633, Invited paper presented at the 39th AIAA/ASME/SAE/ASEE Joint Propulsion Conference and Exhibit, 20-23 July 2003, Huntsville, AL.

“Optical Sensor Platforms for Quantifying Pollutant Emissions in Combustion Exhausts,” J. R. Gord, R. Barron-Jimenez, T. N. Anderson, R. P. Lucht, S. Roy, M. S. Brown, and S. Stouffer, Presented at the 45th Rocky Mountain Conference on Applied Spectroscopy, 27-31 July 2003, Denver, CO.

“Quenching Studies of Highly Luminescent CdS Nanoparticles in the Presence of Sulfur Containing Compounds,” J. Widera, J. R. Gord, and C. E. Bunker, Presented at the 45th Rocky Mountain Conference on Analytical Chemistry, 27-31 July 2003, Denver, CO.

“Dual-Pump, Dual-Broadband Coherent Anti-Stokes Raman Scattering for Characterization of Liquid-Fueled Combustors,” S. Roy, T. R. Meyer, R. P. Lucht, V. M. Belovich, E. Corporan, and J. R. Gord, Presented at the 45th Rocky Mountain Conference on Applied Spectroscopy, 27-31 July 2003, Denver, CO.

“Effects of Dynamic Strain on OH* and CH* Luminescence in Counterflow Diffusion Flames,” J. Miller, A. Lynch, J. R. Gord, T. R. Meyer, M. S. Brown, and V. Katta, Presented at the 45th Rocky Mountain Conference on Applied Spectroscopy, 27-31 July 2003, Denver, CO.

“Initiation of Detonation in a Large Tube,” V. Katta, C. Tucker, J. Hoke, and F. Schauer, Presented at the 19th International Colloquium on the Dynamics of Explosions and Reactive Systems, 27 July – 1 August 2003, Hakone, Japan.

“Application of Advanced Optical Diagnostics for Combustion and Fluid Flows,” S. P. Gogineni and J. R. Gord, Invited Seminar, University of Texas at Austin, 12 August 2003, Austin, TX.
“Triple-Pump Coherent Anti-Stokes Raman Scattering (CARS): Temperature and Multiple-Species Concentration Measurements in Reacting Flows,” S. Roy, T. R. Meyer, M. S. Brown, V. N. Velur, R. P. Lucht, and J. R. Gord, Opt. Commun. 224(1-3), 131 (15 August 2003).

“Modeling of Two-Photon Absorption Processes: Direct Numerical Integration of the Time-Dependent Density Matrix Equations,” R. P. Lucht, S. Roy, J. R. Gord, and T. B. Settersten, Poster presented at the Gordon Research Conference on Laser Diagnostics in Combustion, 17-22 August 2003, Oxford, England.

“Triple-Pump CARS Techniques: From Laboratory Flames to JP-8-Fueled Combustors,” T. R. Meyer, S. Roy, M. S. Brown, R. P., and J. R. Gord, Poster presented at the Gordon Research Conference on Laser Diagnostics in Combustion, 17-22 August 2003, Oxford, England.

“Simultaneous CH PLIF and PIV for the Investigation of Two-Phase Vortex-Flame Interactions,” A. Lemaire, K. Zahringer, T. Meyer, J. Gord, and J. C. Rolon, Poster presented at the Gordon Research Conference on Laser Diagnostics in Combustion, 17-22 August 2003, Oxford, England.

“DPIV Measurements of the Flow Field between a Transonic Rotor and an Upstream Stator,” S. Gorrell, W. Copenhaver, and J. Estevadeordal, Presented at the ISUAAAT 03 International Symposium on Unsteady Aerodynamics, Aeroacoustics, and Aeroelasticity of Turbomachines, 7-11 September 2003, Durham, NC, and published in Conference Proceedings.

“Experimental Investigation of Two-Phase Vortex-Flame Interactions by PIV and PLIF,” K. Zahringer, A. Lemaire, T. R. Meyer, J. R. Gord, and J. C. Rolon, Presented at the German Association of Engineers Society of Energy Technology (VDI) 21st German Flame Day Meeting (21 Deutscher Flammentag), 9-10 September 2003, Cottbus, Germany.

“PIV Investigation on the Vortex Shedding of a Jet-in-a-Cross Flow,” B. Kiel, A. Cox, J. Estevadeordal, and S. Gogineni, Presented at the 5th International Symposium on PIV, 22-24 September 2003, Busan, Korea.

“Current and Future Applications of Ultrafast Lasers for Propulsion Diagnostics,” J. R. Gord, W. M. Roquemore, M. S. Brown, and J. L. Blackshire, Presented at the Directed Energy Professional Society (DEPS) Ultrashort Pulse Laser Materials Interaction Workshop, 25 September 2003, Boulder, CO.

“Vortex Induced Extinction of Non-Premixed Counterflow Flames,” A. Lemaire, K. Zahringer, T. Meyer, J. Gord, and J. C. Rolon, Presented at the European Combustion Meeting, 18-21 October 2003, Orleans, France.

“Exploring Reacting Flows Using Coherent Light,” S. Roy, Invited Presentation at Washington State University, 5 November 2003, Pullman, WA.

“Picosecond Laser-Induced Polarization Spectroscopy,” S. Roy, Invited Presentation at the Materials Directorate, 18 November 2003, Wright-Patterson Air Force Base, OH.

“Simultaneous OH PLIF and Planar LII in the Reaction Zone of a Swirl-Stabilized Combustor,” T. R. Meyer, S. Roy, S. Gogineni, E. Corporan, V. M. Belovich, and J. R. Gord, Presented at the 56th Annual Meeting of the American Physical Society, Division of Fluid Dynamics, 23-25

November 2003, East Rutherford, NJ. Dr. Gogineni was Chair of the High Speed Flows Session at this meeting.

“PIV/PLIF Investigation of Two-Phase Vortex-Flame Interactions: Effects of Vortex Size and Strength,” A. Lemaire, T. R. Meyer, K. Zahringer, J. R. Gord, and J. C. Rolon, *Exp. Fluids* 36, 36 (January 2004).

“Single-Shot Thermometry and Multiple-Species Measurements Using Dual-Pump, Dual-Broadband CARS in a Liquid-Fueled CFM56 Combustor,” S. Roy, T. R. Meyer, R. P. Lucht, V. M. Belovich, E. Corporan, and J. R. Gord, AIAA Paper No. 2004-0711, Presented at the 42nd AIAA Aerospace Sciences Meeting and Exhibit, 5-8 January 2004, Reno, NV.

“The Use of a Flash Vaporization System with Liquid Hydrocarbon Fuels in a Pulse Detonation Engine,” K. C. Tucker, P. I. King, R. P. Bradley, and F. R. Schauer, AIAA Paper No. 2004-0868, Presented at the 42nd AIAA Aerospace Sciences Meeting and Exhibit, 5-8 January 2004, Reno, NV.

“Modeling Soot in a Swirl Combustor,” V. R. Katta and W. M. Roquemore, AIAA Paper No. 2004-0645, Presented at the 42nd AIAA Aerospace Sciences Meeting and Exhibit, 5-8 January 2004, Reno, NV.

“Simultaneous PLIF/PIV Investigation of Vortex-Induced Annular Extinction in H₂-Air Counterflow Diffusion Flames,” T. R. Meyer, G. J. Fiechtner, S. P. Gogineni, J. C. Rolon, C. D. Carter, and J. R. Gord, *Exp. Fluids* 36, 259 (February 2004).

“Detection of Atomic Hydrogen Using Picosecond Laser-Induced Polarization Spectroscopy,” S. Roy, T. B. Settersten, B. D. Patterson, R. P. Lucht, and J. R. Gord, Presented at the Optical Society of America Meeting on Laser Applications to Chemical and Environmental Analysis, 9-11 February 2004, Annapolis, MD.

“OH Ground-State Energy Transfer Investigated Using Picosecond IR-UV Polarization Spectroscopy,” T. B. Settersten, X. Chen, B. D. Patterson, S. Roy, R. P. Lucht, and J. R. Gord, Presented at the Optical Society of America Meeting on Laser Applications to Chemical and Environmental Analysis, 9-11 February 2004, Annapolis, MD.

“Measurement of Nitric Oxide in Gas Turbine and Coal Combustor Exhaust Using a Diode-Lased-Based Ultraviolet Absorption Sensor,” T. N. Anderson, R. P. Lucht, R. B. Jimenez, S. Hanna, J. A. Caton, T. Walther, M. S. Brown, S. Roy, J. R. Gord, I. Critchley, and L. Flamand, Presented at the Optical Society of America Meeting on Laser Applications to Chemical and Environmental Analysis, 9-11 February 2004, Annapolis, MD.

“Measurements of Population and Orientation Relaxation Rates for Atomic Hydrogen Using Picosecond Laser-Induced Polarization Spectroscopy,” S. Roy, T. B. Settersten, R. P. Lucht, and J. R. Gord, Presented at the Annual American Chemical Society/Ohio Valley Section of the Society for Applied Spectroscopy Poster Session and Patterson College Awards, 2 March 2004, Dayton, OH.

“Calibration of Flame Chemiluminescence in Adiabatic Hydrocarbon-Air Flames,” A. C. Lynch, J. D. Miller, J. R. Gord, T. R. Meyer, and M. S. Brown, Presented at the Annual American Chemical Society/Ohio Valley Section of the Society for Applied Spectroscopy Poster Session and Patterson College Awards, 2 March 2004, Dayton, OH.

“Investigation of Flame Radicals and Particulate Distributions in Two-Phase Reacting Flow,” T. R. Meyer, S. Roy, S. P. Gogineni, J. R. Gord, V. M. Belovich, and E. Corporan, Presented at the Annual American Chemical Society/Ohio Valley Section of the Society for Applied Spectroscopy Poster Session and Patterson College Awards, 2 March 2004, Dayton, OH.

“Gas-Phase Spectroscopy Using Four-Wave Mixing Techniques,” J. R. Gord, V. M. Belovich, E. Corporan, S. Roy, T. R. Meyer, and R. P. Lucht, Presented at the Annual American Chemical Society/Ohio Valley Section of the Society for Applied Spectroscopy Poster Session and Patterson College Awards, 2 March 2004, Dayton, OH.

“Dual-Pump Dual-Broadband CARS for Fuel and Additive Studies,” J. R. Gord, V. M. Belovich, E. Corporan, S. Roy, T. R. Meyer, and R. P. Lucht, Presented at the Annual American Chemical Society/Ohio Valley Section of the Society for Applied Spectroscopy Poster Session and Patterson College Awards, 2 March 2004, Dayton, OH.

“Laser-Based Visualization of Flame Structure and Soot Inception in Highly Turbulent Spray Flames,” T. R. Meyer, S. Roy, S. P. Gogineni, J. R. Gord, V. M. Belovich, and E. Corporan, Presented at the 29th Annual AIAA Dayton-Cincinnati Aerospace Science Symposium, 9 March 2004, Dayton, OH.

“DPIV with LED Illumination: Application to Turbomachinery and Flow Control,” J. Estevadeordal, D. Car, S. Gorrell, and S. Puterbaugh, Presented at the 29th Annual AIAA Dayton-Cincinnati Aerospace Science Symposium, 9 March 2004, Dayton, OH.

“State-of-the-Art pH Monitoring of Fuel,” J. Widera and J. M. Johnson, Presented at the 29th Annual AIAA Dayton-Cincinnati Aerospace Science Symposium, 9 March 2004, Dayton, OH.

“Studies of OH*, CH*, and C2* in Methane-Air and Propane-Air Flames,” A. C. Lynch, J. D. Miller, J. R. Gord, T. R. Meyer, and M. S. Brown, Presented at the 29th Annual AIAA Dayton-Cincinnati Aerospace Science Symposium, 9 March 2004, Dayton, OH.

“In-Situ Measurements of Local Equivalence Ratio Using Chemiluminescence in an Ultra Compact Combustor,” J. Armstrong, R. Anthenien, J. Zelina, and M. Brown, Presented at the 29th Annual AIAA Dayton-Cincinnati Aerospace Science Symposium, 9 March 2004, Dayton, OH.

“Dual-Pump Dual-Broadband CARS for Fuel and Additive Studies,” J. R. Gord, V. M. Belovich, E. Corporan, S. Roy, T. R. Meyer, and R. P. Lucht, Presented at the 29th Annual AIAA Dayton-Cincinnati Aerospace Science Symposium, 9 March 2004, Dayton, OH.

“Parallel Computing for Linux Clusters – Application to Particle Image Velocimetry,” T. McCray, J. Estevadeordal, and S. Puterbaugh, Presented at the 29th Annual AIAA Dayton-Cincinnati Aerospace Science Symposium, 9 March 2004, Dayton, OH.

“Two-Color Two-Photon Laser-Induced Polarization Spectroscopy of Atomic Hydrogen in Reacting Flows,” S. Roy, T. Settersten, R. Lucht, and J. Gord, Presented at the 29th Annual AIAA Dayton-Cincinnati Aerospace Science Symposium, 9 March 2004, Dayton, OH.

“PIV and CFD Studies of Rotor Bow-Shock Strength in a Transonic Compressor,” N. Woods, S. Gorrell, and J. Estevadeordal, Presented at the 29th Annual AIAA Dayton-Cincinnati Aerospace Science Symposium, 9 March 2004, Dayton, OH.

“A Flight Ready Pulsed Detonation Engine,” P. J. Litke, R. P. Bradley, J. L. Hoke, and F. Schauer, Presented at the 29th Annual AIAA Dayton-Cincinnati Aerospace Science Symposium, 9 March 2004, Dayton, OH.

“Influence of Spray-Flame Structure on Soot Formation in Gas-Turbine Combustors,” T. R. Meyer, S. Roy, S. Gogineni, E. Corporan, V. Belovich, and J. R. Gord, Presented at the Spring Technical Meeting of the Central States Section of the Combustion Institute, 21-23 March 2004, Austin, TX.

“CFD Based Global Chemistry Predictions for Normal and Inverse Laminar Ethane Jet Diffusion Flames under Oxygen Enhancement and Gravity-Variation,” P. Bhatia, V. R. Katta, P. B. Sunderland, S. S. Krishnan, and J. P. Gore, Presented at the 2004 Technical Meeting of the Central States Section of the Combustion Institute, 21-23 March 2004, Austin, TX.

“Macro- vs. Micro-Vortex/Flame Interactions in Hydrogen Diffusion Flames,” V. R. Katta, T. R. Meyer, J. R. Gord, and W. M. Roquemore, Presented at the 2004 Technical Meeting of the Central States Section of the Combustion Institute, 21-23 March 2004, Austin, TX.

“Triple-Flame Propagation and Stabilization in a Laminar Axisymmetric Jet,” X. Qin, C. W. Choi, A. Mukhopadhyay, I. K. Puri, S. K. Aggarwal, and V. R. Katta, *Combust. Theory Modelling* 8, 293 (26 March 2004).

“Extinction Criterion for Unsteady Opposing-Jet Diffusion Flames,” V. R. Katta, T. R. Meyer, M. S. Brown, J. R. Gord, and W. M. Roquemore, *Comb. Flame* 137, 198 (April 2004).

“Interaction of Micro-Scale Vortices with Diffusion Flames,” V. R. Katta, J. R. Gord, and W. M. Roquemore, Presented at the 2004 International Conference on Numerical Combustion, 9-12 May 2004, Sedona, AZ.

“Two-Color, Two-Photon Laser-Induced Polarization Spectroscopy (LIPS) Measurements of Atomic Hydrogen in Near-Adiabatic, Atmospheric Pressure Hydrogen/Air Flames,” W. D. Kulatilaka, R. P. Lucht, S. F. Hanna, and V. R. Katta, *Combust. Flame* 137, 523 (June 2004).

“Simultaneous Laser-Induced Incandescence and OH Planar Laser-Induced Fluorescence for Studies of Soot Formation in Liquid-Fueled Gas-Turbine Combustors,” T. R. Meyer, S. Roy, S. P. Gogineni, V. M. Belovich, E. Corporan, and J. R. Gord, Presented at the Great Lakes Photonics Symposium, 7-11 June 2004, Cleveland, OH.

“Experimental and Theoretical Investigation of Two-Color, Two-Photon Laser-Induced Polarization Spectroscopy of Atomic Hydrogen,” S. Roy, Presented at the Great Lakes Photonics Symposium, 7-11 June 2004, Cleveland, OH.

“Simulation of PAHs in Trapped-Vortex Combustor,” V. R. Katta and W. M. Roquemore, ASME Paper No. GT2004-54165, Presented at the ASME Turbo Expo 2004: Power for Land, Sea, and Air, 14-17 June 2004, Vienna, Austria; published in Conference Proceedings.

“OH-PLIF and Soot Volume Fraction Imaging in the Reaction Zone of a Liquid-Fueled Gas-Turbine Combustor,” T. R. Meyer, S. Roy, S. Gogineni, E. Corporan, V. Belovich, and J. R. Gord, ASME Paper No. GT2004-54318, Presented at the ASME Turbo Expo 2004: Power for Land, Sea, and Air, 14-17 June 2004, Vienna, Austria, and published in Conference Proceedings.

“Development and Application of State-of-the-Art Advanced Diagnostics and CFD for Combustion and Fluid Flows,” S. P. Gogineni and J. R. Gord, Invited Seminar at the Technical University of Darmstadt, 18 June 2004, Darmstadt, Germany.

“Role of Advanced Diagnostics in the Development of Gas Turbine Engines,” S. P. Gogineni and J. R. Gord, Invited Seminar at the GE Jack Welsh Research Center, 21 June 2004, Bangalore, India.

“Benefits of Suction-Surface Blowing in a Transonic Compressor Stator Vane,” J. Estevadeordal, P. Koch, S. Guillot, W. Ng, and D. Car, AIAA Paper No. 2004-2207 presented at the 2nd AIAA Flow Control Conference, 28 June – 1 July 2004, Portland, OR.

“Studies of Hydroxyl Distribution and Soot Formation in Turbulent Spray Flames,” J. R. Gord, T. R. Meyer, S. Roy, and S. Gogineni, Presented at the 12th International Symposium on Applications of Laser Techniques to Fluid Mechanics, 12-15 July 2004, Lisbon, Portugal.

“Glimpse of Turbulence,” V. R. Katta, T. R. Meyer, J. R. Gord, and W. M. Roquemore Poster presented at the Thirtieth Symposium (International) on Combustion, 25-30 July 2004, Chicago, IL. This poster received First Prize in the Combustion Art Competition that was held in conjunction with this meeting.

“Unsteady Effects on Flame Extinction Limits During Gaseous and Two-Phase Flame/Vortex Interactions,” A. Lemaire, K. Zahring, T. R. Meyer, and J. C. Rolon, Presented at the Thirtieth Symposium (International) on Combustion, 25-30 July 2004, Chicago, IL. The paper will be published in Proceedings of the Combustion Institute.

“Gravity, Radiation, and Coflow Effects on Partially Premixed Flames,” X. Qin, I. K. Puri, S. K. Aggarwal, and V. R. Katta, Phys. Fluids 16(8), 2963 (August 2004).

“Temperature and CO₂ Concentration Measurements in the Exhaust Stream of a Liquid-Fueled Combustor Using Dual-Pump Coherent Anti-Stokes Raman Scattering (CARS) Spectroscopy,” S. Roy, T. R. Meyer, R. P. Lucht, V. M. Belovich, E. Corporan, and J. R. Gord, *Combust. Flame* 138(3), 273 (August 2004).

“Laser Incandescence, Fluorescence, and Mie-Scattering Images of Particulate Formation in Gas-Turbine Combustion,” A. C. Lynch, J. R. Gord, E. Corporan, V. M. Belovich, T. R. Meyer, and S. Roy, Presented at the 46th Rocky Mountain Conference on Applied Spectroscopy, 1-5 August 2004, Denver, CO.

“Measurement of Flame Temperature and Water Concentration Using Structured Emission Spectroscopy,” J. D. Miller, S. K. Chelgren, A. C. Lynch, J. R. Gord, T. R. Meyer, and M. S. Brown, Presented at the 46th Rocky Mountain Conference on Applied Spectroscopy, 1-5 August 2004, Denver, CO.

“Laser-Based Parametric Study of Particulate Formation in Gas-Turbine Combustors,” S. K. Chelgren, V. M. Belovich, E. Corporan, J. R. Gord, S. Roy, and T. R. Meyer, Presented at the 46th Rocky Mountain Conference on Applied Spectroscopy, 1-5 August 2004, Denver, CO.

“Dual-Pump, Dual-Broadband, Coherent Anti-Stokes Raman Spectroscopy in Reacting Flows,” S. Roy, T. R. Meyer, R. P. Lucht, M. Afzelius, P.-E. Bengtsson, and J. R. Gord, *Opt. Lett.* 29(16), 1843 (15 August 2004).

“State-of-the-Art Monitoring of Fuel Acidity,” J. Widera and J. M. Johnson, Presented at the 228th American Chemical Society National Meeting, 22-26 August 2004, Philadelphia, PA, and published in *Petrol. Chem. Div. Prepr.* 49(4), 473 (2004).

“Stator Cascade Flow Vectoring through Counter Flow Blowing,” M. R. Harff, J. M. Wolff, W. W. Copenhaver, D. Car, and J. Estevadeordal, *Int. J. Turbo Jet Engines* 21(3), 155 (October 2004).

“Investigation of a Dynamic Diffusion Flame of H₂ in Air with Laser Diagnostics and Numerical Modeling,” F. Grisch, B. Attal-Tretout, A. Bresson, P. Bouchardy, V. R. Katta, and W. M. Roquemore, *Combust. Flame* 139, 28 (October 2004).

“State-of-the-Art Fuel Acidity Monitoring,” J. Widera and J. M. Johnson, Presented at the 226th Electrochemical Society Meeting, 3-8 October 2004, Honolulu, HI, and published in “Sensors VI: Chemical and Biological Sensors and Analytical Methods,” Vol. PV 2004-08 (The Electrochemical Society, Pennington, NJ, Fall 2004), pp. 208-214.

“Influence of Fuel Type and Operating Conditions on Particulates in Gas-Turbine Combustors,” S. K. Chelgren, V. M. Belovich, E. Corporan, J. R. Gord, M. J. DeWitt, T. R. Meyer, and S. Roy, Presented at the AFRC-JFRC Joint International Combustion Symposium, 10-13 October 2004, Maui, HI.

“Application of Laser Imaging for Studies of Particulate Formation in Gas-Turbine Combustion,” A. C. Lynch, J. R. Gord, E. Corporan, V. M. Belovich, T. R. Meyer, and S. Roy, Presented at the AFRC-JFRC 2004 Joint International Combustion Symposium, 10-13 October 2004, Maui, HI.

“Development of a Fiber-Optic-Based PIV System for Turbomachinery Applications,” J. Estevadeordal, T. Meyer, S. Gogineni, M. Polanka, and J. Gord, Presented at the 57th Annual Meeting of the American Physical Society, Division of Fluid Dynamics, 21-23 November 2004, Seattle, WA.

“Nonperturbative Modeling of Two-Photon Absorption in a Three-State System,” R. P. Lucht, S. Roy, and J. R. Gord, J. Chem. Phys. 121(20), 9820 (22 November 2004).

“Multiple-Pump Coherent Anti-Stokes Raman Scattering for Quantitative Measurement of Temperature and Flame Species in a Model Gas-Turbine Combustor,” S. Roy, T. R. Meyer, R. P. Lucht, and J. R. Gord, Paper No. V0034 presented at the International Conference on Advanced Optical Diagnostics in Fluids, Solids, and Combustion, Visualization Society of Japan/SPIE, 4-6 December 2004, Tokyo, Japan.

“Role of Lasers in Understanding Combustion and Improving Performance of Gas Turbine Engines,” S. Roy, T. R. Meyer and J. R. Gord, Invited presentation at the Bangladesh University of Engineering and Technology, 21 December 2004, Dhaka, Bangladesh.

“Unsteady Effects on Flame Extinction Limits During Gaseous and Two-Phase Flame/Vortex Interactions,” A. Lemaire, K. Zahringer, T. R. Meyer, and J. C. Rolon, Proc. Comb. Inst. 30, 475 (January 2005).

“Performance Measurements of Multi-Cycle Pulse Detonation Engine Exhaust Nozzles,” D. Allgood, E. Gutmark, J. Hoke, R. Bradley, and F. Schauer, AIAA Paper No. 2005-222 presented at the 43rd AIAA Aerospace Sciences Meeting and Exhibit, 10-13 January 2005, Reno, NV.

“Performance Measurements of Pulse Detonation Engine Ejectors,” D. Allgood, E. Gutmark, J. Hoke, R. Bradley, and F. Schauer, AIAA Paper No. 2005-223 presented at the 43rd AIAA Aerospace Sciences Meeting and Exhibit, 10-13 January 2005, Reno, NV.

“Development of a Fiber-Optic PIV System for Turbomachinery Applications,” J. Estevadeordal, T. Meyer, S. Gogineni, M. Polanka, and J. Gord, AIAA Paper No. 2005-38 presented at the 43rd AIAA Aerospace Sciences Meeting and Exhibit, 10-13 January 2005, Reno, NV.

“PIV with LED: Particle Shadow Velocimetry (PSV),” J. Estevadeordal and L. P. Goss, AIAA Paper No. 2005-37 presented at the 43rd AIAA Aerospace Sciences Meeting and Exhibit, 10-13 January 2005, Reno, NV.

“Detonation Initiation of Hydrocarbon-Air Mixtures in a Pulsed Detonation Engine,” F. R. Schauer, C. L. Miser, K. C. Tucker, R. P. Bradley, and J. L. Hoke, AIAA Paper No. 2005-1343

presented at the 43rd AIAA Aerospace Sciences Meeting and Exhibit, 10-13 January 2005, Reno, NV.

“A MHz Repetition Rate OPO System for Ultra-High-Frame Rate PLIF Imaging,” W. R. Lempert, N. Jiang, M. Blohm, M. Samimy, G. Switzer, T. R. Meyer, and J. R. Gord, AIAA Paper No. 2005-826 presented at the 43rd AIAA Aerospace Sciences Meeting and Exhibit, 10-13 January 2005, Reno, NV.

“Assessment of the Performance of a Pulsejet and Comparison with a Pulsed-Detonation Engine,” P. J. Litke, F. R. Schauer, D. E. Paxson, R. P. Bradley, and J. L. Hoke, AIAA Paper No. 2005-228 presented at the 43rd AIAA Aerospace Sciences Meeting and Exhibit, 10-13 January 2005, Reno, NV.

“Impact of DDT Mechanism, Combustion Wave Speed, Temperature, and Charge Quality on Pulsed-Detonation-Engine Performance,” J. L. Hoke, R. P. Bradley, and F. R. Schauer, AIAA Paper No. 2005-1342 presented at the 43rd AIAA Aerospace Sciences Meeting and Exhibit, 10-13 January 2005, Reno, NV.

“Parallel Computing for Linux Clusters,” T. McCray and J. Estevadeordal, AIAA Paper No. 2005-1385 presented at the 43rd AIAA Aerospace Sciences Meeting and Exhibit, 10-13 January 2005, Reno, NV.

“Simultaneous Planar Laser-Induced Incandescence, OH Planar Laser-Induced Fluorescence, and Droplet Mie Scattering in Swirl-Stabilized Spray Flames,” T. R. Meyer, S. Roy, V. M. Belovich, E. Corporan, and J. R. Gord, Appl. Opt. 44(3), 445 (20 January 2005).

“Kinetic Behavior of Polymer-Coated Long-Period-Grating Fiber-Optic Sensors,” J. Widera, C. E. Bunker, G. E. Pacey, V. R. Katta, M. S. Brown, J. L. Elster, M. E. Jones, J. R. Gord, and S. W. Buckner, Appl. Opt. 44(6), 1011 (February 2005).

“Structured-Emission Thermometry in Hydrogen Diffusion Flames,” A. C. Lynch, S. K. Chelgren, J. D. Miller, J. R. Gord, T. R. Meyer, S. Roy, and N. Goldstein, Poster presented at the Annual Poster Session sponsored jointly by the Dayton Section of the American Chemical Society and the Society for Applied Spectroscopy, 1 March 2005, Dayton, OH.

“Real-Time Absorption Spectroscopy of the Hydroxyl Radical with Sum Frequency Generation of UV Radiation,” T. R. Meyer, S. Roy, J. R. Gord, T. N. Anderson, and R. P. Lucht, Poster presented at the Annual Poster Session sponsored jointly by the Dayton Section of the American Chemical Society and the Society for Applied Spectroscopy, 1 March 2005, Dayton, OH.

“Real-Time Absorption Spectroscopy of Carbon Monoxide and Carbon Dioxide with Difference-Frequency Generation of Mid-IR Radiation,” S. Roy, T. R. Meyer, T. N. Anderson, R. P. Lucht, and J. R. Gord, Poster presented at the Annual Poster Session sponsored jointly by the Dayton Section of the American Chemical Society and the Society for Applied Spectroscopy, 1 March 2005, Dayton, OH.

“Acquiring and Analyzing THz Spectra for Air Force Applications,” M. S. Brown, G. J. Fiechtner, J. van Rudd, D. Zimdars, and J. R. Gord, Poster presented at the Annual Poster Session sponsored jointly by the Dayton Section of the American Chemical Society and the Society for Applied Spectroscopy, 1 March 2005, Dayton, OH.

“Detecting Ballistic Photons through Dense Media Using the Optical Kerr Effect,” J. R. Gord, T. R. Meyer, M. Paciaroni, and M. A. Linne, Poster presented at the Annual Poster Session sponsored jointly by the Dayton Section of the American Chemical Society and the Society for Applied Spectroscopy, 1 March 2005, Dayton, OH.

“Comparison of Emission-Based Thermometry with Laser-Spectroscopic Methods,” A. C. Lynch, S. K. Chelgren, J. R. Gord, T. R. Meyer, S. Roy, J. D. Miller, and N. Goldstein, Presented at the 30th Annual AIAA Dayton-Cincinnati Aerospace Science Symposium, 8 March 2005, Dayton, OH.

“High-Speed Ultraviolet-Laser Sensor for Detection of the Hydroxyl Radical,” T. R. Meyer, S. Roy, J. R. Gord, T. N. Anderson, and R. P. Lucht, Presented at the 30th Annual AIAA Dayton-Cincinnati Aerospace Science Symposium, 8 March 2005, Dayton, OH.

“High-Speed Mid-Infrared-Laser Sensor for Detection of Carbon Monoxide and Carbon Dioxide,” S. Roy, T. R. Meyer, T. N. Anderson, R. P. Lucht, and J. R. Gord, Presented at the 30th Annual AIAA Dayton-Cincinnati Aerospace Science Symposium, 8 March 2005, Dayton, OH.

“Modeling of THz Spectra for Air Force Applications,” M. S. Brown, G. J. Fiechtner, J. van Rudd, D. Zimdars, and J. R. Gord, Presented at the 30th Annual AIAA Dayton-Cincinnati Aerospace Science Symposium, 8 March 2005, Dayton, OH.

“Ballistic Imaging of Liquid Column Break-Up in Dense Sprays Using Femtosecond Lasers,” J. R. Gord, B. V. Kiel, T. R. Meyer, M. Paciaroni, and M. A. Linne, Presented at the 30th Annual AIAA Dayton-Cincinnati Aerospace Science Symposium, 8 March 2005, Dayton, OH.

“Particle Shadow Velocimetry (PSV),” J. Estevadeordal, L. P. Goss, D. Carr, and T. Bailie, Presented at the 30th Annual AIAA Dayton-Cincinnati Aerospace Science Symposium, 8 March 2005, Dayton, OH.

“Heat Exchanger Design for Flash Vaporization of Liquid Hydrocarbon Fuels in a Pulsed Detonation Engine,” C. L. Miser, P. I. King, F. H. Schauer, and J. L. Hoke, Presented at the 30th Annual AIAA Dayton-Cincinnati Aerospace Science Symposium, 8 March 2005, Dayton, OH.

“Studies on Soot Formation in JP-8 Jet Diffusion Flames,” V. R. Katta and C. Montgomery, Presented at the Sixth International Symposium on Special Topics in Chemical Propulsion – Advancements in Engineering Materials and Chemical Propulsion, 8-11 March 2005, Santiago, Chile, and published in Conference Proceedings (pp. 159-160).

“Combustion Exhaust Measurements of Nitric Oxide with an Ultraviolet Diode-Laser-Based Absorption Sensor,” T. N. Anderson, R. P. Lucht, R. Barron-Jimenez, S. F. Hanna, J. A. Caton, T. Walther, S. Roy, M. S. Brown, J. R. Gord, I. Critchley, and L. Flamand, Appl. Opt. 44(8),1491-1502 (10 March 2005).

“THz Asynchronous Optical Sampling for Spectroscopic Applications,” M. S. Brown, G. J. Fiechtner, J. N. Rudd, D. Zimdars, and J. R. Gord, Presented at Optical Terahertz Science and Technology (OSA), 14-16 March 2005, Orlando, FL.

“High-Speed Measurements of OH Concentration and Temperature Using a Diode-Laser-Based Ultraviolet Absorption Sensor,” T. N. Anderson, R. P. Lucht, S. Roy, T. R. Meyer, and J. R. Gord, Presented at the 4th Joint Meeting of the U.S. Sections of the Combustion Institute, 20-23 March 2005, Philadelphia, PA.

“Effect of Nitromethane on Soot Formation in Heptane Jet Diffusion Flames,” V. R. Katta and W. M. Roquemore, Presented at the 4th Joint Meeting of the U. S. Sections of the Combustion Institute, 20-23 March 2005, Philadelphia, PA.

“CFD Based Global and Detailed Chemistry Predictions for Inverse Laminar Ethane Jet Diffusion Flames under Oxygen Enhancement and Gravity Variation,” P. Bhatia, V. R. Katta, S. S. Krishnan, P. B. Sunderland, and J. P. Gore, Presented at the 4th Joint Meeting of the U.S. Sections of the Combustion Institute, 20-23 March 2005, Philadelphia, PA.

“Numerical Studies on Ultra-Lean Methane Premixed Flames,” V. R. Katta, Z. Cheng, and R. W. Pitz, Presented at the 4th Joint Meeting of the U. S. Sections of the Combustion Institute, 20-23 March 2005, Philadelphia, PA.

“Effect of Diluents on Lifted Partially Premixed Flames in Normal and Microgravity: A numerical Investigation,” A. M. Briones, S. K. Aggarwal, and V. R. Katta, Presented at the 4th Joint Meeting of the U. S. Sections of the Combustion Institute, 20-23 March 2005, Philadelphia, PA.

“Emissions Reduction Technologies for Military Gas Turbine Engines,” G. J. Sturgess, J. Zelina, D. T. Shouse, and W. M. Roquemore, J. Gas Turb. Power 21(2), 193-217 (March/April 2005).

“Optical Turbine-Engine Diagnostics for Ground-Test and On-Board Applications,” J. R. Gord, T. R. Meyer, S. Roy, M. S. Brown, and S. Gogineni, Invited Paper presented at NATO RTO-MP-AVT-124, 25-28 April 2005, Budapest, Hungary.

“Development of Simulations/Diagnostics and Their use as a Combustor Design Tool,” W. M. Roquemore, C. A. Arana, J. R. Gord, V. R. Katta, T. R. Meyer, and M. S. Brown, Invited paper presented at the Computational Engineering and Science Conference (CESC), 26-28 April 2005, Washington, D. C.

“Acoustic Measurements for a Pulse Detonation Engine,” L. Shaw, K. Harris, F. Schauer, and J. Hoke, AIAA Paper No. 2005-2952 presented at the 11th AIAA/CEAS Aeroacoustics Conference, 23-25 May 2005, Monterey, CA.

“Diode-Laser-Based Ultraviolet Absorption Sensor for High-Speed Detection of the Hydroxyl Radical,” T. Anderson, R. P. Lucht, T. R. Meyer, S. Roy, and J. R. Gord, Opt. Lett. 30(11), 1321-1323 (1 June 2005).

“An Investigation of Particle-Shadow Velocimetry (PSV) for Transonic-Flow Applications,” J. Estevadeordal and L. Goss, AIAA Paper No. 2005-5009 presented at the 35th AIAA Fluid Dynamics Conference and Exhibit, 6-9 June 2005, Toronto, Canada.

“Advanced Coherent Anti-Stokes Raman Scattering (CARS) Techniques for Simultaneous Species and Temperature Measurements,” R. P. Lucht, S. Roy, T. R. Meyer, and J. R. Gord, Presented at the Joint Army-Navy-NASA-Air Force (JANNAF) 40th Combustion, 28th Airbreathing Propulsion Meeting, 13-16 June 2005, Charleston, SC.

“Dual-Pump Dual-Broadband CARS for Exhaust-Gas Temperature and CO₂/O₂/N₂ Mole-Fraction Measurements in Model Gas-Turbine Combustors,” T. R. Meyer, S. Roy, R. P. Lucht, and J. R. Gord, Comb. Flame 142, 52-61 (July 2005).

“Dynamics of an Inverse Diffusion Flame and Its Role in Polycyclic-Aromatic-Hydrocarbon and Soot Formation,” V. R. Katta, L. G. Blevins, and W. M. Roquemore, Comb. Flame 142, 33-51 (July 2005).

“Studies on Soot Formation in a Model Gas-Turbine Combustor,” V. R. Katta, T. R. Meyer, C. Montgomery, W. M. Roquemore, AIAA Paper No. 2005-3777 presented at the 41st AIAA/ASME/ASEE Joint Propulsion Conference and Exhibit, 10-13 July 2005, Tucson, AZ.

“Thermometry in Hydrocarbon Diffusion Flames Using Structured-Emission and Laser-Based Spectroscopy,” S. K. Chelgren, A. C. Lynch, J. D. Miller, J. R. Gord, T. R. Meyer, S. Roy, and N. Goldstein, Presented at the 47th Rocky Mountain Conference on Applied Spectroscopy, 31 July - 4 August 2005, Denver, CO.

“High-Speed Mid-Infrared Absorption Spectroscopy of CO, CO₂, and H₂O for Unsteady Reacting Flows,” J. D. Miller, T. R. Meyer, S. Roy, R. Pawlik, J. R. Gord, T. N. Anderson, and R. P. Lucht, Presented at the 47th Rocky Mountain Conference on Applied Spectroscopy, 31 July – 4 August 2005, Denver, CO.

“Broadband Picosecond Coherent Anti-Stokes Raman Scattering Spectroscopy of Nitrogen,” A. C. Lynch, J. R. Gord, S. Roy, T. R. Meyer, Presented at the 47th Rocky Mountain Conference on Applied Spectroscopy, 31 July – 4 August 2005, Denver, CO.

“Role of Soot in the Transient-Grating Signal Observed in Liquid-Fueled Combustor,” M. S. Brown, T. R. Meyer, D. T. Shouse, and J. R. Gord, Poster presented at the Gordon Research Conference on Laser Diagnostics in Combustion, 31 July – 5 August 2005, South Hadley, MA.

This poster was selected as a “Hot Topic,” and the lead author was invited to speak in a “Hot-Topics” Section.

“New Developments in Ballistic Imaging for Dense-Spray Diagnostics,” J. R. Gord, T. R. Meyer, M. Paciaroni, D. Sedarsky, and M. A. Linne, Poster presented at the Gordon Research Conference on Laser Diagnostics in Combustion, 31 July – 5 August 2005, South Hadley, MA. This poster was selected as a “Hot Topic,” and the lead author was invited to speak in a “Hot-Topics” Section.

“Development of MHz Frame Rate Optical Parametric Oscillator for PLIF Imaging,” N. Jiang, M. Blohm, W. R. Lempert, J. R. Gord, G. L. Switzer, and T. R. Meyer, Poster presented at the Gordon Research Conference on Laser Diagnostics in Combustion, 31 July – 5 August 2005, South Hadley, MA.

“Development of a High-Speed Tunable Laser Source for MIR Absorption Spectroscopy of CO, CO₂, and H₂O,” T. R. Meyer, S. Roy, J. R. Gord, T. N. Anderson, and R. P. Lucht, Poster presented at the Gordon Research Conference on Laser Diagnostics in Combustion, 31 July – 5 August 2005, South Hadley, MA. This poster was selected as a “Hot Topic,” and the lead author was invited to speak in a “Hot-Topics” Section.

“Diode-Laser-Based Ultraviolet-Absorption Sensor for High-Speed Measurements of Temperature and OH Concentration,” T. N. Anderson, R. P. Lucht, T. R. Meyer, S. Roy, and J. R. Gord, Poster presented at the Gordon Research Conference on Laser Diagnostics in Combustion, 31 July – 5 August 2005, South Hadley, MA.

“Time History of Flame Front/Vortex Interactions in a Counterflow Jet Burner,” G. B. King, T. R. Meyer, and J. R. Gord, Poster presented at the Gordon Research Conference on Laser Diagnostics in Combustion, 31 July – 5 August 2005, South Hadley, MA.

“Broadband Picosecond Coherent Anti-Stokes Raman Scattering Spectroscopy of Nitrogen Using a 100-ps Modeless Dye Laser,” S. Roy, T. R. Meyer, and J. R. Gord, Poster presented at the Gordon Research Conference on Laser Diagnostics in Combustion, 31 July – 5 August 2005, South Hadley, MA. This poster was selected as a “Hot Topic,” and the lead author was invited to speak in a “Hot-Topics” Section.

“Terahertz Propulsion Applications,” T. R. Meyer, S. Roy, M. S. Brown, J. R. Gord, G. J. Fiechtner, J. V. Rudd, and D. Zimdars, Invited Presentation at the Terahertz Ohio Workshop, 23 September 2005, Dayton, OH.

“Simulation of Dynamic Flames and Understanding Their Role in Combustion Devices,” V. R. Katta, Presented at the Modeling and Simulations Seminar, 28 September 2005, AFRL/PRTC, Wright-Patterson Air Force Base, OH.

“Tunable Diode-Laser Absorption Spectroscopy for High-Speed Combustion Monitoring,” J. D. Miller, T. R. Meyer, S. Roy, J. R. Gord, T. N. Anderson, and R. P. Lucht, Presented at the 1st Dayton Engineering Sciences Symposium, 31 October 2005, Dayton, OH.

“Role of Soot in Transient-Grating Signal Observed in Liquid-Fueled Combustor,” M. S. Brown, T. R. Meyer, D. T. Shouse, and J. R. Gord, Presented at the 1st Dayton Engineering Sciences Symposium, 31 October 2005, Dayton, OH.

“Advances in Dense-Spray Imaging Using Ultrafast Lasers,” T. R. Meyer, J. R. Gord, B. V. Kiel, M. Paciaroni, D. Sedarsky, and M. A. Linne, Presented at the 1st Dayton Engineering Sciences Symposium, 31 October 2005, Dayton, OH.

“Picosecond Coherent Anti-Stokes Raman Scattering Thermometry in Fuel-Rich Hydrocarbon-Air Diffusion Flames,” A. C. Lynch, J. R. Gord, S. Roy, and T. R. Meyer, Presented at the 1st Dayton Engineering Sciences Symposium, 31 October 2005, Dayton, OH.

“Laser Diagnostics for Particulate Mitigation Studies in Gas-Turbine Combustors,” A. C. Lynch, J. R. Gord, E. Corporan, V. M. Belovich, T. R. Meyer, S. Roy, and M. J. DeWitt, Presented at the 1st Dayton Engineering Sciences Symposium, 31 October 2005, Dayton, OH.

“Ballistic Imaging of the Liquid Core for a Steady Jet in Crossflow,” M. A. Linne, M. Paciaroni, J. R. Gord, and T. R. Meyer, Appl. Opt. 44(31), 6627-6634 (November 2005).

“Measurements of OH Mole Fraction and Temperature Up to 20 kHz by Using a Diode-Laser-Based UV Absorption Sensor,” T. R. Meyer, S. Roy, T. N. Anderson, J. D. Miller, V. R. Katta, R. P. Lucht, and J. R. Gord, Appl. Opt. 44(31), 6729-6740 (1 November 2005).

“Micro-Vortex/Flame Interactions and Their Implications in Turbulent-Flame Modeling,” V. R. Katta, T. R. Meyer, J. R. Gord, and W. M. Roquemore, Presented at the 2005 Technical Meeting of the Eastern States Section of the Combustion Institute, 13-15 November 2005, Orlando, FL, and published in Conference Proceedings.

“10-kHz Detection of CO₂ at 4.5 μ m by Using Tunable Diode-Laser-Based Difference-Frequency Generation,” T. R. Meyer, S. Roy, T. N. Anderson, R. P. Lucht, R. Barron-Jimenez, and J. R. Gord, Opt. Lett. 30(22), 3087-3089 (15 November 2005).

“High Speed Measurement of Temperature and Lifetime-Corrected Laser-Induced Fluorescence of Minor Species in Unsteady Flows,” T. R. Meyer, J. R. Gord, T. N. Anderson, and G. B. King, Provisional Patent Application submitted in December 2005.

“High-Speed Mid-Infrared Absorption Sensor Using Diode-Laser-Based Difference-Frequency Generation,” T. R. Meyer, S. Roy, J. R. Gord, R. Barron-Jimenez, T. N. Anderson, and R. P. Lucht, Provisional Patent Application submitted in December 2005.

“High-Speed Ultraviolet Absorption Sensor Using Diode-Laser-Based Sum-Frequency Generation,” T. R. Meyer, S. Roy, J. R. Gord, T. N. Anderson, and R. P. Lucht, Provisional Patent Application submitted in December 2005.

“Dual-Pump, Dual-Broadband Coherent Anti-Stokes Raman Scattering Method,” S. Roy, T. R. Meyer, R. P. Lucht, and J. R. Gord, U. S. Patent Application submitted December 2005.

“Dual-Pump, Dual-Broadband Coherent Anti-Stokes Raman Scattering Apparatus,” S. Roy, T. R. Meyer, R. P. Lucht, and J. R. Gord, U. S. Patent Application submitted December 2005.

“Broadband Coherent Anti-Stokes Raman Scattering Spectroscopy of Nitrogen Using a Picosecond Modeless Dye Laser,” S. Roy, T. R. Meyer, and J. R. Gord, Opt. Lett. 30(23), 3222-3224 (1 December 2005).

“Time-Resolved Dynamics of Resonant and Nonresonant Broadband Picosecond Coherent Anti-Stokes Raman Scattering Signals,” S. Roy, T. R. Meyer, and J. R. Gord, Appl. Phys. Lett. 87, 264103 (26 December 2005).

“Imaging System for Liquid-Surface Velocity and Acceleration Measurements in Atomizing Sprays,” T. R. Meyer, J. R. Gord, B. V. Kiel, M. E. Paciaroni, M. A. Linne, and D. L. Sedarsky, Provisional Patent Application submitted in January 2006.

“Nitric Oxide Sensor and Method,” R. P. Lucht, T. N. Anderson, S. F. Hanna, R. Barron-Jimenez, T. Walther, S. Roy, M. S. Brown, J. R. Gord, and J. A. Caton, U. S. Patent No. 6,982,426 issued 3 January 2006.

“Fluidic Control Studies for Diffusion Enhancement in Axial Compression System,” D. Car, S. Bailie, C. Baudendistal, D. Gebbie, and J. Estevadeordal, AIAA Paper No. 2006-417 presented at the 44th AIAA Aerospace Sciences Meeting and Exhibit, 9-12 January 2006, Reno, NV.

“An Injection-Seeded MHz Repetition Rate OPO System,” N. Jiang, M. Samimy, W. Lempert, G. Switzer, T. Meyer, and J. R. Gord, AIAA Paper No. 2006-838, presented at the 44th AIAA Aerospace Sciences Meeting and Exhibit, 9-12 January 2006, Reno, NV.

“The Impact of Detonation Initiation Techniques on Thrust in a Pulse Detonation Engine,” J. Hoke, R. Bradley, J. Gallia, and F. Schauer, AIAA Paper No. 2006-1023 presented at the 44th AIAA Aerospace Sciences Meeting and Exhibit, 9-12 January 2006, Reno, NV.

“Performance Measurements of Straight and Diverging Ejectors Integrated with a Pulse Detonation Engine,” A. Glaser, N. Caldwell, and E. Gutmark, J. Hoke, and R. Bradley, AIAA Paper No. 2006-1022 presented at the 44th AIAA Aerospace Sciences Meeting and Exhibit, 9-12 January 2006, Reno, NV.

“Performance Assessment of a Large Scale Pulsejet-Driven Ejector System,” D. Paxson, P. Litke, F. Schauer, R. Bradley, and J. Hoke, AIAA Paper No. 2006-1021 presented at the 44th AIAA Aerospace Sciences Meeting and Exhibit, 9-12 January 2006, Reno, NV.

“Performance Measurements of Multicycle Pulse-Detonation-Engine Exhaust Nozzles,” D. Allgood, E. Gutmark, J. Hoke, R. Bradley, and F. Schauer, J. Propul. Power 22(1), 70-77 (January-February 2006).

“Diode-Laser-Based Sum and Difference Frequency Generation for High-Speed UV and MIR Absorption Spectroscopy,” T. R. Meyer, S. Roy, T. N. Anderson, R. Barron-Jimenez, R. P. Lucht, and J. R. Gord, Presented at the OSA Laser Applications to Chemical, Security, and

Environmental Analysis Topical Meeting and Tabletop Exhibit, 5-9 February 2006, Incline Village, NV.

“Nonresonant-Background-Free Broadband Coherent Anti-Stokes Raman Spectroscopy Using Picosecond Lasers,” S. Roy, T. R. Meyer, and J. R. Gord, Presented at the OSA Laser Applications to Chemical, Security, and Environmental Analysis Topical Meeting and Tabletop Exhibit, 5-9 February 2006, Incline Village, NV.

“Planar Imaging of Soot, Droplets, and Fluorescence for Studies of Alternative Fuel Blends in Gas-Turbine Combustion,” A. C. Lynch, J. R. Gord, T. R. Meyer and S. Roy, Presented at the OSA Laser Applications to Chemical, Security, and Environmental Analysis Topical Meeting and Tabletop Exhibit, 5-9 February 2006, Incline Village, NV.

“Water-Vapor Detection Using Asynchronous THz Sampling,” M. S. Brown, G. J. Fiechtner, J. V. Rudd, D. Zimdars, M. Warmuth, and J. R. Gord, *Appl. Spectrosc.* 60(3), 261-265 (March 2006).

“An Injection-Seeded MHz Repetition Rate Optical Parametric Oscillator,” N. Jiang, M. Blohm, W. R. Lempert, G. L. Switzer, T. R. Meyer, and J. R. Gord, Submitted to *Optics Express* in March 2006.

“Plasma Ignition Systems in Pulse Detonation Engines,” J. Corrigan, F. Schauer, S.-T. Yu, J. Hoke, S. Williams, K. Busby, and C. Cathey, Presented at the 31st Annual AIAA Dayton-Cincinnati Aerospace Science Symposium, 7 March 2006, Dayton, OH.

“The Impact of Detonation Initiation Techniques on Thrust in a Pulsed Detonation Engine,” J. R. Gallia, F. R. Schauer, J. L. Hoke, and R. P. Bradley, Presented at the 31st Annual AIAA Dayton-Cincinnati Aerospace Science Symposium, 7 March 2006, Dayton, OH.

“Performance Measurements of Diverging Ejectors Driven by a Pulse Detonation Engine,” A. J. Glaser, N. Caldwell, E. Gutmark, J. Hoke, R. Bradley, and F. Schauer, Presented at the 31st Annual AIAA Dayton-Cincinnati Aerospace Science Symposium, 7 March 2006, Dayton, OH.

“Parametric Characterization for Particle-Shadow Velocimetry (PSV),” J. Estevadeordal and L. P. Goss, Presented at the 31st Annual AIAA Dayton-Cincinnati Aerospace Science Symposium, 7 March 2006, Dayton, OH.

“Temperature Measurements in Combusting Environments by Picosecond Coherent Anti-Stokes Raman Scattering,” J. R. Gord, S. Roy, and T. R. Meyer, Presented at the 31st Annual AIAA Dayton-Cincinnati Aerospace Science Symposium, 7 March 2006, Dayton, OH.

“Laser Imaging for Studies of Alternative Fuels in Gas-Turbine Engines,” A. C. Lynch, J. R. Gord, V. M. Belovich, E. Corporan, M. J. DeWitt, and T. R. Meyer, Presented at the 31st Annual AIAA Dayton-Cincinnati Aerospace Science Symposium, 7 March 2006, Dayton, OH.

“New Developments in Diode-Laser Spectroscopy for Combustion,” T. R. Meyer, S. Roy, J. R. Gord, T. N. Anderson, and R. P. Lucht, Presented at the 31st Annual AIAA Dayton-Cincinnati Aerospace Science Symposium, 7 March 2006, Dayton, OH.

“Quenching-Free Detection of Nitric Oxide Using Electronic-Resonance-Enhanced Coherent Anti-Stokes Raman Scattering Spectroscopy,” S. Roy, W. D. Kulatilaka, S. V. Naik, N. M. Laurendeau, R. P. Lucht, and J. R. Gord, Presented at the 31st Annual AIAA Dayton-Cincinnati Aerospace Science Symposium, 7 March 2006, Dayton, OH.

“RELIEF Velocimetry for Large-Scale Wind-Tunnel Facilities,” W. R. Lempert, Y. Zuzeek, M. Uddi, S. Roy, T. R. Meyer, S. P. Gogineni, and J. R. Gord, Presented at the 31st Annual AIAA Dayton-Cincinnati Aerospace Science Symposium, 7 March 2006, Dayton, OH.

“Picosecond-Time-Resolved CARS Studies of Nitrogen Collision Dynamics,” J. R. Gord, S. Roy, and T. R. Meyer, Poster presented at the Annual Poster Session sponsored jointly by the Dayton Section of the American Chemical Society and the Society for Applied Spectroscopy, 7 March 2006, Dayton, OH.

“Tunable Diode-Laser Absorption Spectroscopy for UV and Mid-IR Combustion Sensing,” T. R. Meyer, S. Roy, J. R. Gord, T. N. Anderson, and R. P. Lucht, Poster presented at the Annual Poster Session sponsored jointly by the Dayton Section of the American Chemical Society and the Society for Applied Spectroscopy, 7 March 2006, Dayton, OH.

“Effects of Alternative-Fuel Chemistry and Atomization on Soot Formation,” A. C. Lynch, J. R. Gord, V. M. Belovich, E. Corporan, M. J. DeWitt, and T. R. Meyer, Poster presented at the Annual Poster Session sponsored jointly by the Dayton Section of the American Chemical Society and the Society for Applied Spectroscopy, 7 March 2006, Dayton, OH.

“Electronic-Resonance-Enhanced CARS for Minor Species Detection,” S. Roy, W. D. Kulatilaka, S. V. Naik, N. M. Laurendeau, R. P. Lucht, and J. R. Gord, Poster presented at the Annual Poster Session sponsored jointly by the Dayton Section of the American Chemical Society and the Society for Applied Spectroscopy, 7 March 2006, Dayton, OH.

“A Numerical Investigation of Flame Liftoff, Stabilization, and Blowout,” A. Briones, S. K. Aggarwal, and V. R. Katta, *Phys. Fluids* 18, 043603 (April 2006).

“Velocity Imaging for the Liquid-Gas Interface in the Near Field of an Atomizing Spray: Proof of Concept,” D. Sedarsky, M. Paciaroni, M. A. Linne, J. R. Gord, and T. R. Meyer, *Opt. Lett.* 31(7), 906-908 (1 April 2006).

“Effect of P-Additive on Soot Formation in Jet Diffusion and Premixed Flames,” V. R. Katta and W. M. Roquemore, Presented at the 11th International Conference on Numerical Combustion, 23-26 April 2006, Granada, Spain.

“Trimethylphosphate as Soot Reducing Agent—A Numerical Study on Jet Flames,” V. R. Katta and W. M. Roquemore, Presented at the 2006 Technical Meeting of the Central States Section of

the Combustion Institute, 21-23 May 2006, Cleveland, OH, and published in Conference Proceedings.

“Hysteresis in a Counterflow Premixed Flame System,” V. R. Katta, S. Hu, P. Wang, R. W. Pitz, W. M. Roquemore, and J. R. Gord, Presented at the 2006 Technical Meeting of the Central States Section of the Combustion Institute, 21-23 May 2006, Cleveland, OH, and published in Conference Proceedings.

“Effects of H₂-Enrichment on Flame Propagation Characteristics of Methane-Air Flames,” A. M. Briones, S. K. Aggarwal, and V. R. Katta, Presented at the 2006 Technical Meeting of the Central States Section of the Combustion Institute, 21-23 May 2006, Cleveland, OH, and published in Conference Proceedings.

“Electronic-Resonance-Enhanced CARS Detection of Nitric Oxide,” W. D. Kulatilaka, S. V. Naik, N. M. Laurendeau, R. P. Lucht, S. Roy, and J. R. Gord, Presented at the 2006 Technical Meeting of the Central States Section of the Combustion Institute, 21-23 May 2006, Cleveland, OH, and published in Conference Proceedings.

“RELIEF Velocimetry Using Picosecond Tagging and Nd:YAG-Based Interrogation,” W. Lempert, Y. Zuzek, M. Uddi, K. Frederickson, N. Jiang, S. Roy, T. R. Meyer, S. Gogineni, and J. R. Gord, AIAA Paper No. 2006-2970 presented at the 25th AIAA Aerodynamic Measurement Technology and Ground Testing Conference, 5-8 June 2006, San Francisco, CA.

“Soot Production Rates in Strongly Forced Methane-Air Laminar Diffusion Flames,” V. V. Barve, N. T. Clement, O. A. Ezekoye, and V. R. Katta, AIAA Paper No. 2006-3286 presented at the 25th AIAA Aerodynamic Measurement Technology and Ground Testing Conference, 5-8 June 2006, San Francisco, CA.

“Slot Jet Flow Control for Diffusion Enhancement: Endwall Observations and Improvements,” D. Car, S. T. Bailie, and J. Estevadeordal, AIAA Paper No. 2006-3496 presented at the 25th AIAA Aerodynamic Measurement Technology and Ground Testing Conference, 5-8 June 2006, San Francisco, CA.

“Streamwise Vorticity Effects in a Curved Diffuser with Slot Jet Flow Control,” S. T. Bailie, D. Car, and J. Estevadeordal, AIAA Paper No. 2006-3497 presented at the 25th AIAA Aerodynamic Measurement Technology and Ground Testing Conference, 5-8 June 2006, San Francisco, CA.

“Investigation of Temperature Dependent Collisional Dynamics of Gaseous Molecules Using Time-Resolved Ultrafast CARS,” J. R. Gord, S. Roy, T. R. Meyer, and R. P. Lucht, Presented at the 61st International Symposium on Molecular Spectroscopy, 19-23 June 2006, Columbus, OH.

“Pressure-Scaling Behavior of Quenching-Free NO Electronic-Resonance-Enhanced CARS Signal,” S. Roy, W. D. Kulatilaka, S. V. Naik, N. M. Laurendeau, R. P. Lucht, and J. R. Gord, Presented at the 61st International Symposium on Molecular Spectroscopy, 19-23 June 2006, Columbus, OH.

“Coherent Structures and Turbulent Molecular Mixing in Gaseous Planar Shear Layers,” T. R. Meyer, J. C. Dutton, and R. P. Lucht, *J. Fluid Mech.* 558, 179-205 (July 2006).

“Effects of Tube and Ejector Geometry on the Performance of Pulse Detonation Engine Driven Ejectors,” A. J. Glaser, N. Caldwell, E. Gutmark, J. Hoke, R. Bradley, and F. Schauer, AIAA Paper No. 2006-4790 presented at the 42nd AIAA/ASME/SAE/ASEE Joint Propulsion Conference and Exhibit, 9-12 July 2006, Sacramento, CA.

“Effect of Supercritical Fuel Injection on the Cycle Performance of a Pulsed Detonation Engine,” T. Helfrich, P. King, F. Schauer, and J. Hoke, AIAA Paper No. 2006-5133 presented at the 42nd AIAA/ASME/SAE/ASEE Joint Propulsion Conference and Exhibit, 9-12 July 2006, Sacramento, CA.

“Numerical Studies on Soot Mitigation in a Model Gas-Turbine Combustor,” V. R. Katta, T. R. Meyer, C. J. Montgomery, and W. M. Roquemore, AIAA Paper No. 2006-5095 presented at the 42nd AIAA/ASME/SAE/ASEE Joint Propulsion Conference and Exhibit, 9-12 July 2006, Sacramento, CA.

“Comparison of Chemical-Kinetics Models for JP-8 Fuel in Predicting Premixed and Nonpremixed Flames,” V. R. Katta, M. Mawid, B. Sekar, E. Corporan, J. Zelina, W. M. Roquemore, and C. J. Montgomery, AIAA Paper No. 2006-4745 presented at the 42nd AIAA/ASME/SAE/ASEE Joint Propulsion Conference and Exhibit, 9-12 July 2006, Sacramento, CA.

“Non-reacting and Combusting Flow Investigation of Bluff Bodies in Cross Flow,” B. Kiel, K. Garwick, A. Lynch, J. Gord, F. Ladeinde, C. Safta, and T. Meyer, AIAA Paper No. 2006-5234 presented at the 42nd AIAA/ASME/SAE/ASEE Joint Propulsion Conference and Exhibit, 9-12 July 2006, Sacramento, CA.

“Raman-Induced Electronic-Resonance-Enhanced CARS for Minor-Species Detection in Reacting Flows,” S. Roy, W. D. Kulatilaka, S. V. Naik, N. M. Laurendeau, R. P. Lucht, and J. R. Gord, Poster presented at the 48th Rocky Mountain Conference on Analytical Chemistry, 23-27 July 2006, Breckenridge, CO.

“Temperature Measurement Using the Coherence Dephasing Rate in FAST CARS,” S. Roy, T. R. Meyer, K. D. Grinstead, Jr., R. P. Lucht, and J. R. Gord, Poster presented at the 48th Rocky Mountain Conference on Analytical Chemistry, 23-27 July 2006, Breckenridge, CO.

“Two-Line Thermometry of OH at 313 nm in Combusting Environments,” S. Roy, T. R. Meyer, J. D. Miller, J. R. Gord, T. N. Anderson, and R. P. Lucht, Poster presented at the 48th Rocky Mountain Conference on Analytical Chemistry, 23-27 July 2006, Breckenridge, CO.

“Numerical Study of Evolution of Strongly Forced Axisymmetric Laminar Cold-Flow Jets,” V. V. Barve, O. A. Ezekoye, N. T. Clemens, and V. R. Katta, *AIAA J.* 44(8), 1742-1752 (August 2006).

“Investigations on Double-State Behavior of the Counterflow Premixed Flame System,” V. R. Katta, S. Hu, P. Wang, R. W. Pitz, W. M. Roquemore, and J. R. Gord, Presented at the 31st

Symposium (International) on Combustion, 6-11 August 2006, Heidelberg, Germany, and published in Conference Proceedings.

“Ballistic Imaging of the Near Field for Jets in Gaseous Crossflow,” D. Sedarsky, M. Paciaroni, M. Linne, T. Meyer, J. Gord, and B. Kiel, Paper No. ID ICLASS06-131 presented at the 10th International Congress on Liquid Atomization and Spray Systems (ICLASS), 27 August - 1 September 2006, Kyoto, Japan.

“Effects of Quenching on Electronic-Resonance-Enhanced Coherent Anti-Stokes Raman Scattering of Nitric Oxide,” S. Roy, W. D. Kulatilaka, S. V. Naik, N. M. Laurendeau, R. P. Lucht, and J. R. Gord, Appl. Phys. Lett. 89(10), 104105 (4 September 2006).

“Triple-Pump Coherent Anti-Stokes Raman Scattering System,” J. R. Gord, S. Roy, R. P. Lucht, M. S. Brown, and G. J. Fiechtner, U. S. Patent No. 7,106,436 issued 12 September 2006.

“H₂O and CO₂ Concentration Measurements Using a Diode-Laser-Based Optical Parametric Oscillator at 2.7 μm ,” K. D. Grinstead, Jr., S. Roy, T. R. Meyer, and J. R. Gord, Presented at the 2nd Dayton Engineering Sciences Symposium, 30 October 2006, Dayton, OH.

“Application of Electronic-Resonance-Enhanced Coherent Anti-Stokes Raman Scattering Spectroscopy for Minor Species Detection in Reacting Flows,” J. R. Gord, W. D. Kulatilaka, R. P. Lucht, and S. Roy, Presented at the 2nd Dayton Engineering Sciences Symposium, 30 October 2006, Dayton, OH.

“Femtosecond CARS Measurement of Gas-Phase Temperatures from Frequency-Spread Dephasing of the Raman Coherence,” S. Roy, R. P. Lucht, and J. R. Gord, Presented at the 2nd Dayton Engineering Sciences Symposium, 30 October 2006, Dayton, OH.

“Application of a Difference-Frequency-Mixing Based Diode-Laser Sensor for Carbon Monoxide Detection in the 4.4 – 4.8 μm Spectral Region,” R. B. Jimenez, J. A. Caton, T. N. Anderson, R. P. Lucht, T. Walther, S. Roy, M. S. Brown, and J. R. Gord, Appl. Phys. B: Lasers and Optics 85(2-3), 185-197 (November 2006).

“Measurement of Nitric Oxide Concentrations in Flames using Electronic-Resonance-Enhanced Coherent Anti-Stokes Raman Scattering,” W. D. Kulatilaka, N. Chai, S. V. Naik, N. M. Laurendeau, R. P. Lucht, J. P. Kuehner, S. Roy, and J. R. Gord, Opt. Lett. 31(22), 3357 (November 15, 2006).

“RELIEF Velocimetry for Large-Scale Wind Tunnel Facilities,” S. P. Gogineni, W. Lempert, J. Gord, and R. Schmit, Presented at the 59th Annual Meeting of the American Physical Society, Division of Fluid Dynamics, 19-21 November 2006, Tampa, FL.

“Development and Application of Improved PIV System for Turbomachinery Applications,” D. Gebbie, S. Gorrell, and J. Estevadeordal, Presented at the 59th Annual Meeting of the American Physical Society, Division of Fluid Dynamics, 19-21 November 2006, Tampa, FL.

“Understanding of Turbulent Flames from Vortex/Flame-Interaction Studies,” V. R. Katta, S. P. Gogineni, T. R. Meyer, J. R. Gord, and W. M. Roquemore, Presented at the JANNAF 41st Combustion (CS)/29th Airbreathing Propulsion (APS), 23rd Propulsion Systems Hazards (PSHS) Joint Subcommittee Meeting, 4-8 December 2006, San Diego, CA.

“Femtosecond Coherent Anti-Stokes Raman Scattering Measurement of Gas Temperatures from Frequency-Spread Dephasing of the Raman Coherence,” R. P. Lucht, S. Roy, T. R. Meyer, and J. R. Gord, Appl. Phys. Lett. 89(25), 251112 (18 December 2006).

“Investigations on Double-State Behavior of the Counterflow Premixed Flame System,” V R. Katta, S. Hu, P. Wang, R. W. Pitz, W. M. Roquemore, and J. R. Gord, Proc. Comb. Inst. 31, 1055-1066 (January 2007).

“High-Repetition Rate Gas-Phase Temperature Measurements in Reacting Flows Using fs-CARS,” S. Roy, Invited paper presented at the 37th Winter Colloquium on the Physics of Quantum Electronics, 5 January 2007, Snowbird, UT.

“Ignition and Detonation-Initiation Characteristics of Hydrogen and Hydrocarbon Fuels in a PDE,” T. M. Helfrich, F. R. Schauer, R. P. Bradley, and J. L. Hoke, AIAA Paper No. 2007-234 presented at the 45th AIAA Aerospace Sciences Meeting and Exhibit, 8-11 January 2007, Reno, NV.

“Electronic-Resonance-Enhanced (ERE) Coherent Anti-Stokes Raman Scattering (CARS) Detection of Minor Species in Reacting Flows,” S. V. Naik, N. Chai, W. D. Kulatilaka, N. M. Laurendeau, R. P. Lucht, S. Roy, and J. R. Gord. AIAA Paper No. 2007-472, presented at the 45th AIAA Aerospace Sciences Meeting and Exhibit, 8-11 January 2007, Reno, NV.

“Evaluation of Catalytic and Thermal Cracking in a JP-8 Fueled Pulsed Detonation Engine,” T. M. Helfrich, F. R. Schauer, R. P. Bradley, and J. L. Hoke, AIAA Paper No. 2007-235 presented at the 45th AIAA Aerospace Sciences Meeting and Exhibit, 8-11 January 2007, Reno, NV.

“Experimental Study of Ejectors Driven by a Pulse Detonation Engine,” A Glaser, N. Caldwell, E. Gutmark, J. Hoke, R. Bradley, and F. Schauer, AIAA Paper No. 2007-447 presented at the 45th AIAA Aerospace Sciences Meeting and Exhibit, 8-11 January 2007, Reno, NV.

“Transient Plasma Ignition for Delay Reduction in Pulse Detonation Engines,” C. Cathey, F. Wang, T. Tang, A. Kuthi, M. Gundersen, J. O. Sinibaldi, C. Brophy, E. Barbour, R. K. Hanson, J. Hoke, F. Schauer, J. Corrigan, and J. Yu, AIAA Paper No. 2007-443 presented at the 45th AIAA Aerospace Sciences Meeting and Exhibit, 8-11 January 2007, Reno, NV.

“Effects of Corona, Spark and Surface Discharges on Ignition Delay and Deflagration-to-Detonation Times in Pulsed Detonation Engines,” K. Busby, J. Corrigan, S.-T. Yu, S. Williams, C. Carter, F. Schauer, J. Hoke, C. Cathey, and M. Gundersen, AIAA Paper No. 2007-1028 presented at the 45th AIAA Aerospace Sciences Meeting and Exhibit, 8-11 January 2007, Reno, NV.

“Characteristics of Propagating H₂-Enriched CH₄-Air Flames,” A. Briones, S. K. Aggarwal, and V. R. Katta, AIAA Paper No. 2007-180 presented at the 45th AIAA Aerospace Sciences Meeting and Exhibit, 8-11 January 2007, Reno, NV.

“A Robust Procedure for the Analysis of Non-Evenly Spaced Velocity Time-Series Data,” K. B. Garwick, A. Lynch, J. R. Gord, B. V. Kiel, and T. R. Meyer, AIAA Paper No. 2007-1301 presented at the 45th AIAA Aerospace Sciences Meeting and Exhibit, 8-11 January 2007, Reno, NV.

“Measurement of NO and OH Concentrations in Vitiated Air Using Diode-Laser-Based Ultraviolet Absorption Sensors,” T. N. Anderson, R. P. Lucht, T. R. Meyer, T. Mathur, K. D. Grinstead, Jr., J. R. Gord, M. Gruber, and C. D. Carter, AIAA Paper No. 2007-467 presented at the 45th AIAA Aerospace Sciences Meeting and Exhibit, 8-11 January 2007, Reno, NV.

“PIV Study of Wake-Rotor-Stage Phenomena in Transonic Compressor at Various Operating Conditions,” J. Estevadeordal, S. Gorrell, and W. Copenhaver, J. Propul. Power 23(1) 235-242 (January-February 2007).

“Interferometry of Laser-Generated Micro-Plasmas,” M. S. Brown, C. L. Rettig, K. D. Frische, J. A. Nees, J. R. Gord, and W. M. Roquemore, Poster presented at the Annual Poster Session sponsored jointly by the Dayton Section of the American Chemical Society and the Ohio Valley Section of the Society for Applied Spectroscopy, 1 March 2007, Dayton, OH.

“Minor-Species Concentration Measurements in Counterflow Diffusion Flames Using Electronic-Resonance-Enhanced CARS Spectroscopy,” S. Roy, S. V. Naik, N. Chai, W. D. Kulatilaka, R. P. Lucht, and J. R. Gord, Poster presented at the Annual Poster Session sponsored jointly by the Dayton Section of the American Chemical Society and the Ohio Valley Section of the Society for Applied Spectroscopy, 1 March 2007, Dayton, OH.

“High-Speed Thermometry Using Femtosecond CARS Spectroscopy,” J. R. Gord, S. Roy, and R. P. Lucht, Poster presented at the Annual Poster Session sponsored jointly by the Dayton Section of the American Chemical Society and the Ohio Valley Section of the Society for Applied Spectroscopy, 1 March 2007, Dayton, OH.

“Transient Temperature Measurements in a Shock Tube Using a High-Repetition-Rate Diode-Laser-Based Absorption Sensor,” K. D. Grinstead, S. Roy, T. R. Meyer, M. Kahandawala, S. S. Sidhu, C. D. Carter, and J. R. Gord, Poster presented at the Annual Poster Session sponsored jointly by the Dayton Section of the American Chemical Society and the Ohio Valley Section of the Society for Applied Spectroscopy, 1 March 2007, Dayton, OH.

“Measurements of NO in Counter-Flow Diffusion Flames Using Electronic-Resonance-Enhanced CARS Spectroscopy,” S. Roy, W. D. Kulatilaka, S. V. Naik, N. Chai, R. P. Lucht, and J. R. Gord, Presented at the 32nd AIAA Dayton-Cincinnati Aerospace Science Symposium, 6 March 2007, Dayton, OH.

“Imaging of Laser-Generated Micro-Plasmas,” M. S. Brown, C. L. Rettig, K. D. Frische, J. R. Gord, W. M. Roquemore, and J. A. Nees, Presented at the 32nd AIAA Dayton-Cincinnati Aerospace Science Symposium, 6 March 2007, Dayton, OH. Dr. Brown received the Best-Presentation Award in the Combustion Category for this paper.

“Temperature Measurements in Hydrogen-Air Diffusion Flames Using Time-Resolved Femtosecond CARS Spectroscopy,” J. R. Gord, S. Roy, and R. P. Lucht, Presented at the 32nd AIAA Dayton-Cincinnati Aerospace Science Symposium, 6 March 2007, Dayton, OH.

“Measurements of Temperature and OH Concentration in a Shock Tube Using TDLAS,” K. D. Grinstead, S. Roy, T. R. Meyer, M. Kahandawala, S. S. Sidhu, C. D. Carter, and J. R. Gord, Presented at the 32nd AIAA Dayton-Cincinnati Aerospace Science Symposium, 6 March 2007, Dayton, OH.

“PIV Study of Stator Loading Effects on Vortex Shedding in Transonic Compressor,” D. Gebbie, S. Gorrell, and J. Estevadeordal, Presented at the 32nd AIAA Dayton-Cincinnati Aerospace Science Symposium, 6 March 2007, Dayton, OH.

“Static Pressure Measurements of Pulse Detonation Engine Driven Ejectors,” A. J. Glaser, N. Caldwell, E. J. Gutmark, J. Hoke, R. Bradley, and F. Schauer, Presented at the 32nd AIAA Dayton-Cincinnati Aerospace Science Symposium, 6 March 2007, Dayton, OH.

“Soot Spirals,” S. Stouffer, G. Justinger, A. Lynch, J. Miller, M. Roquemore, V. Belovich, R. Pawlik, J. Gord, J. Zelina, V. Katta, S. Roy, and K. Grinstead, Poster presented at the Art-in-the-Science Competition that was held in conjunction with the 32nd AIAA Dayton-Cincinnati Aerospace Science Symposium, 6 March 2007, Dayton, OH. Of the 15 entries in the competition, this poster received the Second-Place Award.

“Predictions on Sooting Behavior of Recirculation-Zone-Supported Flames,” V. R. Katta and W. M. Roquemore, Paper No. D37 presented at the 5th U. S. Combustion Meeting, 25-28 March 2007, San Diego, CA.

“Femtosecond Coherent Anti-Stokes Raman Scattering Measurement of Gas Temperatures from Frequency-Spread Dephasing of the Raman Coherence,” S. Roy, R. P. Lucht, P. J. Kinnius, T. R. Meyer, and J. R. Gord, Presented at the 5th U. S. Combustion Meeting, 25-28 March 2007, San Diego, CA.

“Experimental/Numerical Visualizations of Sooting Centerbody Flames,” M. Roquemore, V. Katta, V. Belovich, R. Pawlik, A. Lynch, J. Miller, S. Stouffer, G. Justinger, J. Zelina, S. Roy, and J. Gord, Paper No. P44 presented at the 5th U. S. Combustion Meeting, 25-28 March 2007, San Diego, CA.

“Experimental and Numerical Studies of Centerbody Flames,” M. Roquemore, V. Katta, V. Belovich, R. Pawlik, A. Lynch, J. Miller, S. Stouffer, G. Justinger, J. Zelina, S. Roy, and J. Gord, Paper No. D36 presented at the 5th U. S. Combustion Meeting, 25-28 March 2007, San Diego, CA.

“Effects of Oxygenated Compounds on PAH and Soot across a Suite of Laboratory Devices,” T. Litzinger, M. Colket, M. Kahandawala, V. Katta, S.-Y. Lee, D. Liscinsk, K. McNesby, R. Pawlik, M. Roquemore, R. Santoro, S. Sidhu, S. Stouffer, and J. Wu, Paper No. F03 presented at the 5th U. S. Combustion Meeting, 25-28 March 2007, San Diego, CA.

“The Effects of Nitrogen-Containing Compounds on PAH and Soot across a Suite of Laboratory Devices,” M. Colket, T. Litzinger, M. Kahandawala, V. Katta, S.-L. Lee, D. Liscinsky, K. McNesby, A. Menon, M. Roquemore, R. Santoro, S. Sidhu, and S. Stouffer, Paper No. F04 presented at the 5th U. S. Combustion Meeting, 25-28 March 2007, San Diego, CA.

“Femtosecond Coherent Anti-Stokes Raman Scattering Measurement of Gas Temperatures from Frequency-Spread Dephasing of the Raman Coherence,” S. Roy, R. P. Lucht, P. J. Kinnius, T. R. Meyer, and J. R. Gord, Presented at the 5th U. S. Combustion Meeting, 25-28 March 2007, San Diego, CA.

“Effects of Phosphorus Compounds on PAH and Soot across a Suite of Laboratory Devices,” S. Sidhu, V. Belovich, M. Colket, M. Kahandawala, V. Katta, D. Liscinsky, T. Litzinger, K. McNesby, R. Pawlik, M. Roquemore, R. Santoro, and S. Stouffer, Paper No. F17 presented at the 5th U. S. Combustion Meeting, 25-28 March 2007, San Diego, CA.

“Nitric-Oxide Concentration Profiles in Atmospheric-Pressure Flames Using Electronic-Resonance-Enhanced Coherent Anti-Stokes Raman Scattering (ERE-CARS),” N. Chai, S. V. Naik, W. D. Kulatilaka, R. P. Lucht, N. M. Laurendeau, S. Roy, V. R. Katta, J. P. Kuehner, and J. R. Gord, Paper No. G04 presented at the 5th U. S. Combustion Meeting, 25-28 March 2007, San Diego, CA.

“Soot Spirals in Laminar Flames,” S. Stouffer, V. Katta, W. Roquemore, G. Justinger, V. Belovich, A. Lynch, J. Miller, R. Pawlik, J. Zelina, S. Roy, K. Grinstead, and J. Gord, Poster presented at the 5th U. S. Combustion Meeting, 25-28 March 2007, San Diego, CA. Of the 15 entries in the Art Exhibition that was held in conjunction with this meeting, this poster received the First-Place Award.

“Time Domain and Level-Specific Investigations of Collisions Using Picosecond Two-Color Wave-Mixing Spectroscopy,” T. B. Settersten, X. Chen, W. D. Kulatilaka, R. P. Lucht, S. Roy, and J. R. Gord, Presented at the 6th European Conference on Nonlinear Optical Spectroscopy, 12-15 May 2007, St. Petersburg, Russia.

“Ultrafast Coherent Anti-Stokes Raman Scattering Spectroscopy: Application to Reacting Flows and Plasmas,” S. Roy, Invited paper presented at the Central Regional Meeting of the American Chemical Society, 22 May 2007, Covington, KY.

“Nitric Oxide Concentration Measurements in Atmospheric-Pressure Flames Using Electronic Resonance-Enhanced Coherent Anti-Stokes Raman Scattering,” N. Chai, W. D. Kulatilaka, S. V. Naik, N. M. Laurendeau, R. P. Lucht, J. P. Kuehner, S. Roy, V. R. Katta, and J. R. Gord, Appl. Phys. B 88, 141-150 (June 2007).

“Detection of Acetylene by Electronic Resonance-Enhanced Coherent Anti-Stokes Raman Scattering,” N. Chai, S. V. Naik, W. D. Kulatilaka, N. M. Laurendeau, R. P. Lucht, S. Roy, and J. R. Gord, *Appl. Phys. B* 87, 731-737 (June 2007).

“Effects of Pressure Variations on the Electronic-Resonance-Enhanced Coherent Anti-Stokes Raman Scattering of Nitric Oxide,” W. D. Kulatilaka, N. Chai, S. V. Naik, N. M. Laurendeau, R. P. Lucht, J. P. Kuehner, S. Roy, and J. R. Gord, *Opt. Commun.* 274, 441-446 (June 15, 2007).

“Detection of Atomic Hydrogen in Flames Using Picosecond Two-Color Two-Photon-Resonant Six-Wave-Mixing Spectroscopy,” W. D. Kulatilaka, R. P. Lucht, S. Roy, J. R. Gord, and T. B. Settersten, *Appl. Opt.* 46, 3921-3927 (1 July 2007).

“Detonation Propagation across an Axisymmetric Step Expansion,” D. R. Hopper, P. I. King, F. R. Schauer, V. R. Katta, and J. L. Hoke, AIAA Paper No. 2007-5078 presented at the 43rd AIAA/ASME/SAE/ASEE Joint Propulsion Conference and Exhibit, 8-11 July 2007, Cincinnati, OH.

“PIV Investigation of the Flow Field in a Transonic Compressor Cascade with Moving Shock Waves,” J. Estevadeordal, M. D. Langford, A. Breeze-Stringfellow, S. A. Guillot, W. Solomon, and W. F. Ng, AIAA Paper No. 2007-5064 presented at the 43rd AIAA/ASME/SAE/ASEE Joint Propulsion Conference and Exhibit, 8-11 July 2007, Cincinnati, OH.

“PIV Study of Blade-Row Interactions in a Transonic Compressor,” J. Estevadeordal, S. Gorrell, D. Gebbie, and S. Puterbaugh, AIAA Paper No. 2007-5017 presented at the 43rd AIAA/ASME/SAE/ASEE Joint Propulsion Conference and Exhibit, 8-11 July 2007, Cincinnati, OH.

“Can Nonpremixed Stretched Flames Become Infinitely Thin?” V. R. Katta, W. M. Roquemore, and J. R. Gord, Presented at the 21st International Colloquium on the Dynamics of Explosions and Reactive Systems (ICDERS), 23-27 July 2007, Poitiers, France, and published in the Conference Proceedings.

“Theory of Femtosecond Coherent Anti-Stokes Raman Scattering Spectroscopy of Gas-Phase Resonant Transitions,” R. P. Lucht, P. J. Kinnius, S. Roy, and J. R. Gord, *J. Chem. Phys.* 127, 044316 (July 28, 2007).

“Effect of Supercritical Fuel Injection on Cycle Performance of Pulsed Detonation Engine,” T. M. Helfrich, P. I. King, J. L. Hoke, and F. R. Schauer, *J. Propul. Power* 23(4), 748-755 (July-August 2007).

“Ultrafast Coherent Anti-Stokes Raman Scattering Spectroscopy: Prospects and Challenges,” S. Roy, Invited paper presented at the Gordon Research Conference on Laser Diagnostics in Combustion, 12-17 August 2007, Oxford, England.

“Gas-Phase Temperature Measurements from Frequency-Spread Dephasing Rate of the Coherence Induced by Femtosecond Laser Pulses,” S. Roy, P. J. Kinnius, R. P. Lucht, and J. R.

Gord, Presented at the Gordon Research Conference on Laser Diagnostics in Combustion, 12-17 August 2007, Oxford, England.

“Do Collisions Significantly Distort Time-Delayed Picosecond Coherent Anti-Stokes Raman Scattering Signal?” S. Roy, K. D. Grinstead, and J. R. Gord, Presented at the Gordon Research Conference on Laser Diagnostics in Combustion, 12-17 August 2007, Oxford, England.

“Measurements of Nitric Oxide in Flames Using Electronic-Resonance-Enhanced (ERE) Coherent Anti-Stokes Raman Scattering (CARS) Spectroscopy,” N. Chai, W. D. Kulatilaka, S. V. Naik, N. M. Laurendeau, R. P. Lucht, J. P. Kuehner, J. R. Gord, and S. Roy, Presented at the Gordon Research Conference on Laser Diagnostics in Combustion, 12-17 August 2007, Oxford, England.

“Comparison of Time-Gated Ballistic-Photon Imaging and Shadowgraphy in Rocket Sprays,” J. Schmidt, T. R. Meyer, S. Roy, K. D. Grinstead, Jr., S. A. Danczyk, and J. R. Gord, Poster presented at the Gordon Research Conference on Laser Diagnostics in Combustion, 12-17 August 2007, Oxford, England.

“Two-Point Space/Time Correlations of Flame-Front/Vortex Interactions in a Counterflow Jet Burner,” G. B. King, K. D. Grinstead, Jr., T. R. Meyer, and J. R. Gord, Poster presented at the Gordon Research Conference on Laser Diagnostics in Combustion, 12-17 August 2007, Oxford, England.

“Improving Signal-to-Interference Ratio in Rich Hydrocarbon-Air Flames Using Picosecond Coherent Anti-Stokes Raman Scattering,” T. R. Meyer, S. Roy, and J. R. Gord, Appl. Spectrosc. 61(11), 1135-1140 (November 2007). This article was featured on the cover of this issue.

“Coherent-Repumping-Assisted Immunity of Raman Coherence to Rapid Collisional Decays,” A. K. Patnaik, S. Roy, R. P. Lucht, and J. R. Gord, Invited presentation at the XXXVIII Winter Colloquium on the Physics of Quantum Electronics, 6-10 January 2008, Snowbird, UT.

“Insensitivity of Electronic-Resonance-Enhanced Coherent Anti-Stokes Raman Scattering to Collisions,” A. K. Patnaik, S. Roy, R. P. Lucht, and J. R. Gord, Poster presented at the XXXVIII Winter Colloquium on the Physics of Quantum Electronics, 6-10 January 2008, Snowbird, UT.

“Direct Initiation by Detonation Branching in a Pulsed Detonation Engine,” A. R. Hausman, P. I. King, D. R. Hopper, J. L. Hoke, and F. R. Schauer, AIAA Paper No. 2008-108 presented at the 46th AIAA Aerospace Sciences Meeting and Exhibit, 7-10 January 2008, Reno, NV.

“Fuel Composition Analysis of Endothermically Heated JP-8 Fuel for Use in a Pulsed Detonation Engine,” E. A. Nagley, P. I. King, F. R. Schauer, M. J. DeWitt, and J. L. Hoke, AIAA Paper No. 2008-109 presented at the 46th AIAA Aerospace Sciences Meeting and Exhibit, 7-10 January 2008, Reno, NV.

“Development of a Continuous Branching Pulsed Detonation Engine,” D. R. Hopper, P. I. King, J. L. Hoke, and F. R. Schauer, AIAA Paper No. 2008-112 presented at the 46th AIAA Aerospace Sciences Meeting and Exhibit, 7-10 January 2008, Reno, NV.

“Single-Ejector Augmentation of a Multi-Tube Pulsed Detonation Engine,” J. Hoke, R. Bradley, and F. Schauer, AIAA Paper No. 2008-115 presented at the 46th AIAA Aerospace Sciences Meeting and Exhibit, 7-10 January 2008, Reno, NV.

“Investigation of Fundamental Processes Leading to Pulse Detonation Engine/Ejector Thrust Augmentation,” N. Caldwell, E. Gutmark, J. Hoke, R. Bradley, and F. Schauer, AIAA Paper No. 2008-116 presented at the 46th AIAA Aerospace Sciences Meeting and Exhibit, 7-10 January 2008, Reno, NV.

“Evaluation of Chemical Kinetics Models for Heptane Combustion,” V. R. Katta and W. M. Roquemore, AIAA Paper 2008-1015 presented at the 46th AIAA Aerospace Sciences Meeting and Exhibit, 7-10 January 2008, Reno, NV.

“Temperature Measurements in Reacting Flows by Time-Resolved Femtosecond Coherent Anti-Stokes Raman Scattering (fs-CARS) Spectroscopy,” S. Roy, P. J. Kinnius, R. P. Lucht, and J. R. Gord, Opt. Commun. 281(2), 319-325 (January 15, 2008).

“Temperature Measurements Using Time-Delayed Picosecond CARS,” S. Roy, P. Hsu, and J. R. Gord, Presented at the 33rd Annual AIAA Dayton-Cincinnati Aerospace Science Symposium, 4 March 2008, Dayton, OH.

“Slowing Down Light to Biking Speed through Resonant Laser-Matter Interactions,” A. K. Patnaik, P. S. Hsu, S. Roy, and J. R. Gord, Presented at the 33rd Annual AIAA Dayton-Cincinnati Aerospace Science Symposium, 4 March 2008, Dayton, OH.

“Transient Optical Pump/Probe Spectroscopy for Thermal-Conductivity Measurements,” J. J. Gengler, S. Roy, S. Ganguli, A. Roy, and J. R. Gord, Presented at the 33rd Annual AIAA Dayton-Cincinnati Aerospace Science Symposium, 4 March 2008, Dayton, OH.

“Low-Repetition-Rate Picosecond Optical Parametric Generator for Laser Diagnostics in Reacting Flows,” P. Hsu, S. Roy, and J. R. Gord, Presented at the 33rd Annual AIAA Dayton-Cincinnati Aerospace Science Symposium, 4 March 2008, Dayton, OH.

“Characterization of Dense Liquid Sprays with Ultrafast Ballistic Imaging,” K. D. Grinstead, Jr., J. Schmidt, T. R. Meyer, S. Roy, S. A. Danczyk, and J. R. Gord, Presented at the 33rd Annual AIAA Dayton-Cincinnati Aerospace Science Symposium, 4 March 2008, Dayton, OH.

“Ultrafast CARS for High-Speed Temperature Measurements in Reacting Flows,” J. R. Gord, P. J. Kinnius, R. P. Lucht, K. D. Frische, and S. Roy, Presented at the 33rd Annual AIAA Dayton-Cincinnati Aerospace Science Symposium, 4 March 2008, Dayton, OH.

“Laser-Induced Breakdown Spectroscopy for Detection of Volatile Aerosols,” M. S. Brown, K. D. Frische, T. G. Erickson, J. R. Gord, and W. M. Roquemore, Presented at the 33rd Annual AIAA Dayton-Cincinnati Aerospace Science Symposium, 4 March 2008, Dayton, OH.

“Investigation of Blade-Row Interactions in a Transonic Compressor Using PIV,” J. Estevadeordal, S. Gorrell, and S. L. Puterbaugh, Presented at the 33rd Annual AIAA Dayton-Cincinnati Aerospace Science Symposium, 4 March 2008, Dayton, OH.

“Development of a Continuous Branching Pulsed Detonation Engine,” D. R. Hopper, P. I. King, J. L. Hoke, and F. Schauer, Presented at the 33rd Annual AIAA Dayton-Cincinnati Aerospace Science Symposium, 4 March 2008, Dayton, OH.

“Centerbody Flame with Tight Spirals,” S. Stouffer, G. Justinger, M. Roquemore, A. Lynch, V. Belovich, J. Gord, K. Grinstead, V. Katta, and K. Frische, Poster presented at the Art-in-the-Science Competition that was held in conjunction with the 33rd AIAA Dayton-Cincinnati Aerospace Science Symposium, 4 March 2008, Dayton, OH. Of the eight entries in the competition, this poster received the Second-Place Award.

“Time-Delayed Picosecond CARS for Combustion Thermometry,” S. Roy, P. Hsu, and J. R. Gord, Poster presented at the Annual Poster Session sponsored jointly by the Dayton Section of the American Chemical Society and the Ohio Valley Section of the Society for Applied Spectroscopy, 4 March 2008, Dayton, OH.

“Slowing/Stopping Light in Coherently Prepared Media,” A. K. Patnaik, P. S. Hsu, S. Roy, and J. R. Gord, Poster presented at the Annual Poster Session sponsored jointly by the Dayton Section of the American Chemical Society and the Ohio Valley Section of the Society for Applied Spectroscopy, 4 March 2008, Dayton, OH.

“Femtosecond Pump/Probe Measurements of Thermal Conductivity,” J. J. Gengler, S. Roy, S. Ganguli, A. Roy, and J. R. Gord, Poster presented at the Annual Poster Session sponsored jointly by the Dayton Section of the American Chemical Society and the Ohio Valley Section of the Society for Applied Spectroscopy, 4 March 2008, Dayton, OH.

“Picosecond Optical Parametric Generator for Combustion Measurements,” P. Hsu, S. Roy, and J. R. Gord, Poster presented at the Annual Poster Session sponsored jointly by the Dayton Section of the American Chemical Society and the Ohio Valley Section of the Society for Applied Spectroscopy, 4 March 2008, Dayton, OH.

“Ultrafast Ballistic-Photon Imaging for Visualizing Dense Liquid Sprays,” K. D. Grinstead, Jr., J. Schmidt, T. R. Meyer, S. Roy, S. A. Danczyk, and J. R. Gord, Poster presented at the Annual Poster Session sponsored jointly by the Dayton Section of the American Chemical Society and the Ohio Valley Section of the Society for Applied Spectroscopy, 4 March 2008, Dayton, OH.

“Single-Shot Time-Resolved Femtosecond CARS for High-Bandwidth Combustion Thermometry,” J. R. Gord, P. J. Kinnius, R. P. Lucht, K. D. Frische, and S. Roy, Poster presented at the Annual Poster Session sponsored jointly by the Dayton Section of the American

Chemical Society and the Ohio Valley Section of the Society for Applied Spectroscopy, 4 March 2008, Dayton, OH.

“Laser-Induced Breakdown Spectroscopy for Detection of Volatile Aerosols,” M. S. Brown, K. D. Frische, T. G. Erickson, J. R. Gord, and W. M. Roquemore, Poster presented at the Annual Poster Session sponsored jointly by the Dayton Section of the American Chemical Society and the Ohio Valley Section of the Society for Applied Spectroscopy, 4 March 2008, Dayton, OH.

“Fs-CARS for High-Bandwidth, Collision-Free Temperature Measurements,” S. Roy, P. J. Kinnius, R. P. Lucht, and J. R. Gord. Invited paper presented at the Laser Applications to Chemical, Security, and Environmental Analysis (LACSEA) Meeting, 17-20 March 2008, St. Petersburg, FL.

“Theory of Single-Pulse Femtosecond Coherent Anti-Stokes Raman Scattering Using a Chirped Probe Beam,” A. K. Patnaik, P. J. Kinnius, R. P. Lucht, S. Roy, and J. R. Gord, Presented at the Laser Applications to Chemical, Security, and Environmental Analysis (LACSEA) Meeting, 17-20 March 2008, St. Petersburg, FL.

“Measurements of Nitric Oxide Using Single-Shot, Midband Electronic-Resonance-Enhanced Coherent Anti-Stokes Raman Scattering (ERE-CARS) Vibrational Spectroscopy,” N. Chai, S. V. Naik, R. P. Lucht, M. N. Laurendeau, S. Roy, and J. R. Gord, Presented at the Laser Applications to Chemical, Security, and Environmental Analysis (LACSEA) Meeting, 17-20 March 2008, St. Petersburg, FL.

“Effect of Collisions on Time-Delayed Picosecond Coherent Anti-Stokes Raman Scattering (ps-CARS) Spectroscopy,” J. R. Gord, P. Hsu, and S. Roy, Presented at the Laser Applications to Chemical, Security, and Environmental Analysis (LACSEA) Meeting, 17-20 March 2008, St. Petersburg, FL.

“Insensitivity of Electronic-Resonance-Enhanced Coherent Anti-Stokes Raman Scattering (ERE-CARS) to Electronic Quenching,” A. K. Patnaik, S. Roy, R. P. Lucht, and J. R. Gord, Presented at the Laser Applications to Chemical, Security, and Environmental Analysis (LACSEA) Meeting, 17-20 March 2008, St. Petersburg, FL.

“Stability of Lifted Flames in Centerbody Burner,” V. R. Katta and W. M. Roquemore, Presented at the 2008 Technical Meeting of the Central States Section of the Combustion Institute, 20-23 April 2008, Tuscaloosa, AL, and published in the Conference Proceedings.

“Comparison of Chemical-Kinetics Mechanisms Through Predicting a Nonpremixed Ethylene Jet Flame,” V. R. Katta, W. M. Roquemore, and R. J. Santoro, Presented at the 2008 Technical Meeting of the Central States Section of the Combustion Institute, 20-23 April 2008, Tuscaloosa, AL, and published in the Conference Proceedings.

“Controlling Speed of Light by Light: Slow and Stopped Light,” A. K. Patnaik, P. S. Hsu, S. Roy, and J. R. Gord, Invited presentation at the Physics Seminar at Wright State University, 25 April 2008, Dayton, OH.

“Effects of H₂ Enrichment on the Propagation Characteristics of CH₄-Air Triple Flames,” A. M. Briones, S. K. Aggarwal, and V. R. Katta, Comb. Flame 153, 367-383 (May 2008).

“Femtosecond Coherent Anti-Stokes Raman Scattering Measurement of Gas-Phase Species and Temperature,” R. P. Lucht, P. J. Kinnius, S. Roy, and J. R. Gord, Presented at the Conference on Lasers and Electro-Optics/Quantum Electronics and Laser Science Conference (CLEO/QELS), 5-9 May 2008, San Jose, CA.

“Perturbative Theory and Modeling of Electronic-Resonance-Enhanced Coherent Anti-Stokes Raman Scattering Spectroscopy of Nitric Oxide,” J. P. Kuehner, S. V. Naik, W. D. Kulatilaka, N. Chai, N. M. Laurendeau, R. P. Lucht, A. Patnaik, M. O. Scully, S. Roy, and J. R. Gord, J. Chem. Phys. 128, 174308 (May 7, 2008).

“Numerical Studies on Cavity-Inside-Cavity-Supported Flames in Ultra Compact Combustors,” V. R. Katta, J. Zelina, and W. M. Roquemore, Paper No. GT2008-50853 presented at the 53rd ASME International Gas Turbine and Aeroengine Congress and Exposition, 9-13 June 2008, Berlin, Germany, and published in Proceedings of ASME Turbo Expo '08: Power for Land, Sea, and Air.

“Applications of Ultrafast Lasers for Optical Measurements in Combusting Flows,” J. R. Gord, T. R. Meyer, and S. Roy, Invited book chapter, Annual Review of Analytical Chemistry, Vol. 1 (Eds. E. S. Yeung and R. N. Zare) (Annual Reviews, Palo Alto, CA, July 2008), pp. 663-687.

“Calculation of Multidimensional Flames Using Large Chemical Kinetics,” V. R. Katta and W. M. Roquemore, AIAA J. 46(7), 1640-1650 (July 2008).

“Asymmetric Expansion of Detonation Wave in an Array of Tubes,” V. R. Katta, AIAA Paper No. 2008-4778 presented at the 44th AIAA/ASME/SAE/ASEE Joint Propulsion Conference and Exhibit, 21-23 July 2008, Hartford, CT.

“PIV Measurements of Blade-Row Interactions in a Transonic Compressor for Various Operating Conditions,” J. Estevadeordal, S. Gorrell, and S. Puterbaugh, AIAA Paper No. 2008-4700 presented at the 44th AIAA/ASME/SAE/ASEE Joint Propulsion Conference and Exhibit, 21-23 July 2008, Hartford, CT.

“Theory of Femtosecond Coherent Anti-Stokes Raman Scattering (CARS) Spectroscopy for Gas-Phase Transitions,” R. P. Lucht, S. Roy, and J. R. Gord, Poster presented at the Work-in-Progress Poster Sessions at the 32nd International Symposium on Combustion, 3-8 August 2008, Montreal, Canada.

“Measurements of Nitric Oxide Concentration in Flames Using Broadband Stokes Electron-Resonance-Enhanced Coherent Anti-Stokes Raman Scattering,” N. Chai, A. Satija, S. V. Naik, R. P. Lucht, N. M. Laurendeau, S. Roy, and J. R. Gord, Poster presented at the Work-in-Progress Poster Sessions at the 32nd International Symposium on Combustion, 3-8 August 2008, Montreal, Canada.

“Single-Laser-Shot Detection of Nitric Oxide in Reacting Flows Using Electronic Resonance Enhanced Coherent Anti-Stokes Raman Scattering,” N. Chai, S. V. Naik, N. M. Laurendeau, R. P. Lucht, S. Roy, and J. R. Gord, *Appl. Phys. Lett.* 93(9) 091115-1 – 091115-3 (September 1, 2008).

“Collisional Effects on Molecular Dynamics in Electronic-Resonance-Enhanced CARS,” A. Patnaik, S. Roy, R. P. Lucht, and J. R. Gord, *J. Mod. Opt.* 55(19-20), 3263-3272 (10-20 November 2008).

“Efficiency and Scaling of an Ultrashort-Pulse High-Repetition-Rate Laser-Driven X-Ray Source,” C. L. Rettig, W. M. Roquemore, and J. R. Gord, *Appl. Phys. B* 93(2-3), 365-372 (November 2008).

“Performance Studies of Pulse Detonation Engine Ejectors,” D. Allgood, E. Gutmark, J. Hoke, R. Bradley, and F. Schauer, *J. Propul. Power* 24(6), 1317-1323 (November-December 2008).

“Study on the Operation of Pulse-Detonation-Engine-Driven Ejectors,” A. J. Glaser, N. Caldwell, E. Gutmark, J. Hoke, R. Bradley, and F. Schauer, *J. Propul. Power* 24(6), 1324-1331 (November-December 2008).

“Development of Nearly Transform-Limited, Low-Repetition-Rate, Picosecond Optical Parametric Generator,” P. S. Hsu, S. Roy, and J. R. Gord, *Opt. Commun.* 281(24), 6068-6071 (December 15, 2008).

“PIV Investigation of a Highly Loaded LPT Blade Using a Curved Laser Sheet,” C. Marks, R. Sondergaard, M. Wolff, and J. Estevadeordal, AIAA Paper No. 2009-0301 presented at the 47th AIAA Aerospace Sciences Meeting Including the New Horizons Forum and Aerospace Exposition, 5-8 January 2009, Orlando, FL.

“Gas Phase Temperature Measurements in Reacting Flows Using Fiber-Coupled Picosecond CARS,” J. R. Gord, P. S. Hsu, A. K. Patnaik, T. R. Meyer, and S. Roy, AIAA Paper No. 2009-1444 presented at the 47th AIAA Aerospace Sciences Meeting Including the New Horizons Forum and Aerospace Exposition, 5-8 January 2009, Orlando, FL.

“Emissions in a Pulsed Detonation Engine,” J. L. Hoke, R. P. Bradley, V. R. Katta, and F. R. Schauer, AIAA Paper No. 2009-505 presented at the 47th AIAA Aerospace Sciences Meeting Including the New Horizons Forum and Aerospace Exposition, 5-8 January 2009, Orlando, FL.

“Pressure Scaling Effects on Ignition and Detonation Initiation in a Pulsed Detonation Engine,” A. Naples, S.-T. J. Yu, J. Hoke, K. Busby, and F. Schauer, AIAA Paper No. 2009-1062 presented at the 47th AIAA Aerospace Sciences Meeting Including the New Horizons Forum and Aerospace Exposition, 5-8 January 2009, Orlando, FL.

“Schlieren Imaging of a Single-Ejector Multi-Tube Pulse Detonation Engine,” J. L. Hoke, A. G. Naples, L. P. Goss, and F. R. Schauer, AIAA Paper No. 2009-1065 presented at the 47th AIAA

Aerospace Sciences Meeting Including the New Horizons Forum and Aerospace Exposition, 5-8 January 2009, Orlando, FL.

“Soot Studies of Laminar Diffusion Flames with Recirculation Zones,” W. M. Roquemore, V. Katta, S. Stouffer, V. Belovich, R. Pawlik, M. Arstingstall, G. Justinger, J. Gord, A. Lynch, J. Zelina, and S. Roy, Presented at the 32nd International Symposium on Combustion, 3-8 August 2008, Montreal, Canada; Proc. Combust. Inst. 32(1), 729-736 (23 January 2009).

“Examination of Laminar-Flamelet Concept Using Vortex/Flame Interactions,” V. R. Katta, W. M. Roquemore, and J. R. Gord, Presented at the 32nd International Symposium on Combustion, 3-8 August 2008, Montreal, Canada; Proc. Comb. Inst. 32(1), 1019-1026 (23 January 2009).

“Impact of Soot on Flame Flicker,” V. R. Katta, W. M. Roquemore, A. Menon, S-Y Lee, R. J. Santoro, and T. A. Litzinger, Presented at the 32nd International Symposium on Combustion, 3-8 August 2008, Montreal, Canada; Proc. Combust. Inst. 32(1), 1343-1350 (23 January 2009).

“Simultaneous Water Vapor Concentration and Temperature Measurements in Unsteady Hydrogen Flames,” D. Blunck, S. Basu, Y. Zheng, V. Katta, and J. Gore, Presented at the 32nd International Symposium on Combustion, 3-8 August 2008, Montreal, Canada; Proc. Combust. Inst. 32(2), 2527-2534 (2009).

“Extinguishment of Diffusion Flames around a Cylinder in a Coaxial Air Stream with Dilution or Water Mist,” F. Takahashi and V. R. Katta, Presented at the 32nd International Symposium on Combustion, 3-8 August 2008, Montreal, Canada; Proc. Combust. Inst. 32(2), 2615-2623 (2009).

“Magneto-Optical Control of Speed of Light,” A. K. Patnaik, P. S. Hsu, S. Roy, and J. R. Gord, To be presented at the 40th Annual Meeting of the American Physical Society, Division of Atomic, Molecular, and Optical Physics, 19-23 May 2009, Charlottesville, VA.

“Effect of Orientation and Alignment Dynamics of the Angular-Momentum Distribution on the Generation of Short-Pulse, Laser-Induced Polarization-Spectroscopy (LIPS) Signals,” S. Roy, R. P. Lucht, and J. R. Gord, To be submitted to the Journal of Chemical Physics.

“Effects of Collisions on Electronic-Resonance-Enhanced Coherent Anti-Stokes Raman Scattering of Nitric Oxide,” A. K. Patnaik, S. Roy, J. R. Gord, R. P. Lucht, and T. B. Settersten, To be submitted to the Journal of Chemical Physics.

9.2 Significant Accomplishments

Dr. Sivaram Gogineni (ISSI) is a member of the ASME/IGTI Technical Committees for Fuels and Combustion, Turbomachinery, and Education.

In 2003 photographs from the following six previously published articles were selected for inclusion in “A Gallery of Fluid Motion,” a book published by the American Physical Society/Division of Fluid Dynamics (APS/DFD) (M. Samimy, K. S. Breur, L. G. Leal, and P. H.

Steen, Eds., Cambridge University Press, 2003). This book contains photographs from award-winning posters submitted over the past 18 years at the APS/DFD Annual Meetings.

1. "High Free-Stream Turbulence Influence on Turbine Film Cooling Flows," by S. Gogineni (ISSI), R. Rivir, D. Pestian (both of AFRL), and L. Goss (ISSI).
2. "Interaction of 2D Wake and Jet Plume," by W. M. Roquemore (AFRL), R. L. Britton (ISSI), R. S. Tankin (Northwestern University), C. A. Boedicker (AFIT), M. M. Whitaker, and D. D. Trump (both of ISSI).
3. "Flame-Vortex Interactions in a Driven Diffusion Flame," by K. Y. Hsu, V. R. Katta, L. P. Goss, D. D. Trump (all of ISSI), L. D. Chen (University of Iowa), and W. M. Roquemore (AFRL).
4. "Jet Diffusion Flame Transition to Turbulence," by W. M. Roquemore (AFRL), L. D. Chen, J. P. Seaba, P. S. Tschen (all of the University of Iowa), L. P. Goss, and D. D. Trump (both of ISSI).
5. "Comparison of Transitional Free Jet and Wall Jet," by S. Gogineni (ISSI), C. Shih, and A. Krothapalli (both of Florida State University).
6. "Dynamics of Jet in Cross Flow," by S. P. Gogineni, M. M. Whitaker, L. P. Goss (all of ISSI), and W. M. Roquemore (AFRL).

In 2003 Dr. W. M. Roquemore (AFRL) received the Propellants and Combustion Award. He was nominated by Dr. Sivaram Gogineni (ISSI).

The December 2003 issue of Aerospace America contains an annual review article entitled, "Fluid Dynamics," which was co-authored by Dr. Sivaram Gogineni (ISSI).

In 2003 and 2004 Dr. Sivaram Gogineni (ISSI) successfully nominated 19 AIAA members for Senior Member Upgrades, 24 members for Associate Fellow Upgrades, and two members for Fellow Upgrades (one of which was Maj. Gen. Paul Nielsen, AFRL Commander). Dr. Gogineni is Deputy Director (Honors and Awards) for Region III.

Dr. Sivaram Gogineni (ISSI) is a member of the AIAA Aerodynamics Measurement Technology Committee and the Fluid Dynamics Technical Committee; on the latter, he served as Chair of the Information and Publications Subcommittee in 2003 and 2004. He served as Chair of the Corporate Sponsorship and Keynote Address Committees for the 29th Annual AIAA Dayton-Cincinnati Aerospace Science Symposium, which was held 9 March 2004 in Dayton, OH. He is Deputy Director (Technical Activities) for Region III.

Dr. Sivaram Gogineni (ISSI) will be serving as Chair of the AIAA Web Development Team from 2003 to 2005. He was appointed by the President of AIAA from a field of 12 distinguished members to revamp the national AIAA website and lead a team of 20 AIAA members who are nationally recognized in diverse fields.

Dr. Sivaram Gogineni (ISSI) served as Session Organizer and Session Chair for the ASME/IGTI Turbo Expo, which was held 16-19 June 2003 in Atlanta, GA.

Dr. Sivaram Gogineni (ISSI) served as a Session Organizer and Session Chair at the 33rd AIAA Fluid Dynamics Conference and Exhibit, 23-26 June 2003, Orlando, FL.

An invited paper entitled, "Dynamics of Vortex-Flame Interactions and Implications for Turbulent Combustion," by T. R. Meyer V. R. Katta, M. S. Brown (all of ISSI), J. R. Gord, W. M. Roquemore (both of AFRL), A. Lemaire, K. Zahringer, and J. C. Rolon (all of Ecole Centrale Paris) was presented at the 39th AIAA/ASME/SAE/ASEE Joint Propulsion Conference and Exhibit, 20-23 July 2003, Huntsville, AL. The paper was published as AIAA Paper No. 2003-4633.

An invited seminar entitled, "Application of Optical Diagnostics to Combustion and Fluid Flows," by S. P. Gogineni (ISSI) and J. R. Gord (AFRL) was presented at the University of Texas at Austin, 12 August 2003, Austin, TX.

An invited paper entitled, "Exploring Reacting Flows Using Coherent Light," was presented by Dr. Sukesh Roy (ISSI) at Washington State University, 5 November 2003, Pullman, WA.

An invited paper entitled, "Picosecond Laser-Induced Polarization Spectroscopy," was presented by Dr. Sukesh Roy (ISSI) at the Materials Directorate, 18 November 2003, Wright-Patterson Air Force Base, OH.

Dr. Sivaram Gogineni (ISSI) served as Chair of the High Speed Flows Session at the 56th Annual Meeting of the American Physical Society, Division of Fluid Dynamics, 23-25 November 2003, East Rutherford, NJ.

Dr. Sivaram Gogineni (ISSI) served as Vice Chair of the Dayton Section of ASME during 2003 and 2004 and as Chair during 2004 and 2005.

In January 2004, Dr. Michael Brown (ISSI) became an AIAA Associate Fellow.

Dr. Sivaram Gogineni (ISSI) successfully nominated Dr. Biswa Ganguly (AFRL) to serve on the AIAA Plasma Dynamics and Lasers Technical Committee. He was selected to serve on the committee in January 2004.

Dr. Sivaram Gogineni (ISSI) served as Session Reviewer and Session Chair for the 42nd AIAA Aerospace Sciences Meeting and Exhibit, which was held 5 - 8 January 2004 in Reno, NV.

In 2004 Dr. Sivaram Gogineni (ISSI) successfully nominated Drs. Ron Hanson (Stanford University), Vince Miller (AFRL/VA), M. S. Chandra (Naval Post-Graduate School), R. Kimmel (AFRL/VA), and R. Bowersox (Texas A&M University) for ASME Fellow.

A photograph by Dr. Jordi Esteveordal (ISSI) entitled, "Wind Caprices," received the Third-Place Award in the Art in Science competition, which was held in conjunction with the 29th Annual AIAA Dayton-Cincinnati Aerospace Science Symposium, 9 March 2004, Dayton, OH.

Dr. Sivaram Gogineni (ISSI) participated in the DARPA Workshop on Ultra-Short Pulse Lasers as Next Generation Hyperspectral Radiography Sources, which was held 30-31 March 2004 in Arlington, VA.

Dr. Sivaram Gogineni (ISSI) will be serving as Associate Editor of the ASME Journal of Fluids Engineering from 2004 to 2006. He also serves as a reviewer for Experiments in Fluids, for AIAA and ASME journals, and for grants and proposals for NSF and AFOSR.

Dr. Sivaram Gogineni (ISSI) successfully nominated Dr. James Gord and Dr. Robert Hancock (both of AFRL) for the Superachiever 40 under 40 Award sponsored by the Dayton Business Journal. They received this award on 22 April 2004.

Dr. Sivaram Gogineni (ISSI) took part in the AIAA-Sponsored Congressional Visits Day, which was held 20-22 April 2004 in Washington, D. C., and in the 20th Annual Community Leader Visit to Washington, D. C. on 2-6 May 2004.

Dr. Geoffrey Sturgess (ISSI) taught a course entitled, "Basic Combustion," at Honeywell, 9-14 May 2004, Phoenix, AZ.

Dr. Sivaram Gogineni (ISSI) served as Session Co-Organizer and Session Chair for the ASME/IGTI Turbo Expo 2004: Power for Land, Sea, and Air, which was held 14-17 June 2004 in Vienna, Austria.

Dr. Sivaram Gogineni (ISSI) was invited to present two seminars: 1) "Development and Application of State-of-the-Art Advanced Diagnostics for Combustion and Fluid Flows," at the Technical University of Darmstadt on 18 June 2004 in Darmstadt, Germany, and 2) "Role of Advanced Diagnostics in the Development of Gas Turbine Engines," at the Jack Welch Research Center on 21 June 2004 in Bangalore, India.

Dr. Sivaram Gogineni (ISSI) served as Session Reviewer for the 34th AIAA Fluid Dynamics Conference and Exhibit, which was held 28 June - 1 July 2004 in Portland, OR.

Dr. Geoffrey Sturgess (ISSI) taught a one-day course entitled, "Combustor Lean Blowout and Relight," at Pratt & Whitney, 7 July 2004, Hartford, CT.

A poster entitled, "Glimpse of Turbulence," by V. R. Katta, T. R. Meyer (both of ISSI), J. R. Gord, and W. M. Roquemore (both of AFRL) received the First-Place Award in the Combustion Art Competition that was held in conjunction with the Thirtieth Symposium (International) on Combustion, 25-30 July 2004, Chicago, IL.

Dr. Sivaram Gogineni (ISSI) will serve for the period 2004 - 2006 on the Advisory Committee for the biennial International Symposium on Applications of Laser Techniques to Fluid Mechanics, which is held in Lisbon, Portugal.

Dr. Viswanath Katta (ISSI) became an ASME Fellow in August 2004.

Dr. Sukesh Roy (ISSI) was one of 86 innovative young engineers from the U. S. selected to participate in the National Academy of Engineer's 10th Annual Frontiers of Engineering Symposium, which was held 9-11 September 2004 in Irvine, CA.

Dr. Sivaram Gogineni (ISSI) became an ASME Fellow in November 2004.

Dr. Sivaram Gogineni (ISSI) was one of eight speakers at a celebration on 17 December 2004 to honor TAM Emeritus Professor Ronald J. Adrian of the University of Illinois for his 32 years of service. Other presentations were made by scientists from Princeton University, the University of California, the Illinois Institute of Technology, and TSI.

An invited paper entitled, "Role of Lasers in Understanding Combustion and Improving Performance of Gas Turbine Engines," by S. Roy, T. R. Meyer (both of ISSI) and J. R. Gord (AFRL), was presented at the Bangladesh University of Engineering and Technology, 21 December 2004, Dhaka, Bangladesh.

Dr. Sukesh Roy (ISSI) was President of the Ohio Valley Section of the Society for Applied Spectroscopy during 2004-2005.

Dr. Terrence Meyer (ISSI) was Secretary-Treasurer of the Ohio Valley Section of the Society for Applied Spectroscopy during 2004-2005.

Dr. Terrence Meyer (ISSI) was upgraded to Senior Member of AIAA in 2005.

Dr. Jordi Estevadeordal (ISSI) became an AIAA Associate Fellow in January 2005.

Dr. Terrence Meyer (ISSI) became Secretary of the Dayton Section of ASME in January 2005.

Dr. Geoffrey Sturgess (ISSI) taught two courses entitled, "Basic Combustion" and "Combustor Design," at Pratt & Whitney (through Rensselaer Polytechnic Institute), 17 - 26 January 2005 in Hartford, CT.

Dr. Sivaram Gogineni (ISSI) was notified in February 2005 that he had received the AIAA Sustained Service Award in recognition of sustained, significant service to the aerospace profession and to the AIAA and outstanding leadership in the Dayton-Cincinnati Section in Region III, and in technical activities. Dr. Gogineni was nominated by Dr. John Blanton of GEAC. Dr. Gogineni received a letter of endorsement for his outstanding efforts from Maj. Gen. Paul D. Nielsen, USAF Retired, the former Commander of WPAFB.

Dr. Geoffrey Sturgess (ISSI) taught a course entitled, "Combustor Design," at Honeywell on 12-17 February 2005 in Phoenix, AZ.

Dr. Terrence Meyer (ISSI) received the Superachiever 40 under 40 Award from the Dayton Business Journal in March 2005. He was nominated by Dr. Sivaram Gogineni (ISSI).

Dr. Sivaram Gogineni (ISSI) organized the highly successful Keynote Session for the 30th Annual AIAA Dayton-Cincinnati Aerospace Science Symposium, which was held 8 March 2005 in Dayton, OH. The keynote speaker was Dr. Peter Diamandis, founder of the \$10M X Prize (Burt Rutan's SpaceShipOne was flown to 100 kilometers twice to win this prize). In the lead article in the Business Section of the Dayton Daily News, his keynote address and the conference were highlighted.

Dr. Jordi Estevadeordal (ISSI) served as Registration Chair for the 30th Annual AIAA Dayton-Cincinnati Aerospace Science Symposium, which was held 8 March 2005 in Dayton, OH.

ISSI was a corporate sponsor again this year for the 30th Annual AIAA Dayton-Cincinnati Aerospace Science Symposium, which was held 8 March 2005 in Dayton, OH. ISSI scientists presented 16 papers at this meeting.

A photograph by Dr. Jordi Estevadeordal (ISSI) entitled, "Color Falls," received the Second-Place Award in the Art-in-Science Competition that was held in conjunction with the 30th Annual AIAA Dayton-Cincinnati Aerospace Science Symposium, 8 March 2005, Dayton, OH.

An invited paper entitled, "Optical Turbine-Engine Diagnostics for Ground-Test and On-Board Applications," by J. R. Gord (AFRL), T. R. Meyer, S. Roy, M. S. Brown, and S. Gogineni (all of ISSI) was presented at NATO RTO-MP-AVT-124, 25-28 April 2005, Budapest, Hungary.

An invited paper entitled, "Development of Simulations/Diagnostics and Their Use as a Combustor Design Tool," by W. M. Roquemore, C. A. Arana, J. R. Gord (all of AFRL), V. R. Katta, T. R. Meyer, and M. S. Brown (all of ISSI), was presented at the Computational Engineering and Science Conference (CESC), 26-28 April 2005, Washington, D. C.

At the AIAA Dayton-Cincinnati/ASME Dayton Annual Honors and Awards Program on 16 May 2005 at the University of Dayton, Dr. Sivaram Gogineni (ISSI) received the Special Service to the Dayton-Cincinnati Section Award for his contributions during Congressional Visit Day, as the Keynote Speaker Chair for the 30th Annual AIAA Dayton-Cincinnati Aerospace Science Symposium, and as Region III Representative.

Dr. Sivaram Gogineni (ISSI) served as Session Chair at the Laser Anemometry Conference, which was held in June 2005 in Lisbon, Portugal.

Dr. Sivaram Gogineni (ISSI), Deputy Director of AIAA Technical Region III, led a discussion group on program ideas at the 2005 AIAA Regional Leadership Conference, which was held 14-15 July 2005 in Tucson, AZ.

A poster entitled, "Influence of Soot on Transient-Grating Measurements in a Liquid-Fueled, Pressurized Combustor," by M. S. Brown, T. R. Meyer (both of ISSI), D. T. Shouse, and J. R. Gord (both of AFRL), which was presented at the Gordon Research Conference on Laser Diagnostics in Combustion, 31 July - 5 August 2005, South Hadley, MA, was selected as a "Hot Topic." The lead author was invited to speak in a "Hot-Topics" Section.

A poster entitled, “New Developments in Ballistic Imaging for Dense-Spray Diagnostics,” by J. R. Gord (AFRL), T. R. Meyer (ISSI), M. Paciaroni, D. Sedarsky, and M. A. Linne (all of Lund Institute of Technology), which was presented at the Gordon Research Conference on Laser Diagnostics in Combustion, 31 July - 5 August 2005, South Hadley, MA, was selected as a “Hot Topic.” The lead author was invited to speak in a “Hot-Topics” Section.

A poster entitled, “Development of a High-Speed Tunable Laser Source for MIR Absorption Spectroscopy of CO, CO₂, and H₂O,” by T. R. Meyer, S. Roy (both of ISSI), J. R. Gord (AFRL), T. N. Anderson, and R. P. Lucht (both of Purdue University), which was presented at the Gordon Research Conference on Laser Diagnostics in Combustion, 31 July - 5 August 2005, South Hadley, MA, was selected as a “Hot Topic.” The lead author was invited to speak in a “Hot-Topics” Section.

A poster entitled, “Broadband Picosecond Coherent Anti-Stokes Raman Scattering Spectroscopy of Nitrogen Using a 100-ps Modeless Dye Laser,” by S. Roy, T. R. Meyer (both of ISSI), and J. R. Gord (AFRL), which was presented at the Gordon Research Conference on Laser Diagnostics in Combustion, 31 July – 5 August 2005, South Hadley, MA, was selected as a “Hot Topic.” The lead author was invited to speak in a “Hot-Topics” Section.

Dr. Sivaram Gogineni (ISSI) was invited to participate in Executive Independent Review Team briefings on augmentors, which was held 21 September 2005 in Manchester, CT, and in the Augmentor Review Meeting at Arnold Engineering and Development Center, which was held 17-18 May 2006 at Arnold Air Force Base, TN.

An invited paper entitled, “Terahertz Propulsion Applications,” by T. R. Meyer, S. Roy, M. S. Brown (all of ISSI), J. R. Gord (AFRL), G. J. Fiechtner (Sandia National Laboratories), J. V. Rudd, and D. Zimdars (both of Picometrix, Inc.), was presented at the Terahertz Ohio Workshop, 23 September 2005, Dayton, OH. Dr. Roy was Co-Organizer of this workshop.

Dr. Sivaram Gogineni (ISSI) was instrumental in organizing, chairing, and obtaining corporate sponsorships for the 1st ASME Dayton Engineering Sciences Symposium, which was held 31 October 2005 in Dayton, OH, to celebrate the Dayton Region’s strong tradition of engineering innovation, to help commemorate ASME’s 125th anniversary in Dayton, to facilitate communication between members of the local technical community, and to provide a forum for sharpening technical-presentation skills among students, engineers, and scientists. The event was organized and sponsored by the Executive Committee of the Dayton Section of ASME, Wright State University, ISSI, and the Ohio Aerospace Institute. Dr. Terry Meyer (ISSI) served as Communications and Publications Co-Chair, and Dr. Jordi Estevadeordal (ISSI) served as Registrations Co-Chair. Dr. Gogineni will serve as a committee member to help organize the second symposium.

Dr. Sivaram Gogineni (ISSI) was informed in November of 2005 that he has been elected to the grade of Fellow of the AIAA. He received the award in April 2006 at the Annual Fellows Dinner in Washington, D. C., in conjunction with “Inside Aerospace – An International Perspective.”

Dr. Sivaram Gogineni (ISSI) served as Organizer of the Flow Control Symposium at the International Conference on Computational and Experimental Engineering and Sciences, which was held 1-6 December 2005 in Chennai, India.

Dr. Larry Goss (ISSI) received the AIAA Aerodynamic Measurement Technology Award in February 2006. He was nominated by Dr. Sivaram Gogineni.

Dr. Sivaram Gogineni (ISSI) was a member of the Program Committee for the NASA Advanced Sensors for Propulsion Conference.

Dr. Terrence Meyer (ISSI) was Presider of the Combustion-I Session at the OSA Laser Applications to Chemical, Security, and Environmental Analysis Topical Meeting and Tabletop Exhibit, 5-9 February 2006, Incline Village, NV.

Dr. Sivaram Gogineni (ISSI) is a member of the AIAA Management Technical Committee. He is Chair of the Membership Sub-Committee and is a member of the Honors and Awards Sub-Committee.

Dr. Sukesh Roy (ISSI) received the Superachiever 40 Under 40 Award from the Dayton Business Journal in March of 2006. He was nominated by Dr. Sivaram Gogineni.

Dr. Sivaram Gogineni (ISSI) was informed in January of 2006 that he had been selected to receive the 2006 Outstanding Engineers and Scientists Award, which is sponsored by the Affiliate Societies Council of Dayton. He was recognized in the Research Category and received the award at the 47th Annual Awards Ceremony, 2 March 2006, at Sinclair Community College.

Dr. Michael Brown (ISSI) was Chair of the Session on Fluid Dynamics III: High-Speed Flow Plasmas at the 31st Annual AIAA Dayton-Cincinnati Aerospace Science Symposium, which was held 7 March 2006 in Dayton, OH.

Dr. Sivaram Gogineni (ISSI) is a member of the Executive Committee of the American Physical Society, Division of Fluid Dynamics.

Dr. Sivaram Gogineni (ISSI) organized the Keynote Session for the 31st Annual AIAA Dayton-Cincinnati Aerospace Science Symposium, which was held 7 March 2006 in Dayton. The keynote speaker was Roger Launius who is Chairman of Space History at the Smithsonian Institute's National Air and Space Museum in Washington, D. C. His presentation on humans and robots in space was appropriate because of local work in aerospace and robotics. Dr. Gogineni also served as Corporate Sponsorship Co-Chair for this symposium.

Dr. Sivaram Gogineni (ISSI) took part in the AIAA-Sponsored Congressional Visits Day, which was held 4-6 April 2006 in Washington, D. C. He also participated in the Washington, D. C. Community Fly-In to advocate for funding for local projects from the U. S. Congress.

Dr. Sivaram Gogineni (ISSI) was a member of the Program Committee for the Sensors for Propulsion Measurement Applications Conference, which is a part of the SPIE Defense and Security Symposium 2006; the conference was held 17-21 April 2006 in Orlando, FL.

Dr. Viswanath Katta (ISSI) was invited to participate in the Fire Model Validation and Heat Transfer in Fires Workshops, which were held 7-9 May 2006 in Albuquerque, NM.

At the Honors and Awards Banquet of the AIAA Dayton-Cincinnati Section on 25 May 2006, Dr. Sivaram Gogineni (ISSI) received the Chairman's Award for his contributions to the Section during the past year.

Dr. Sukesh Roy (ISSI) served as a Session Chair at the 2nd Dayton Engineering Sciences Symposium, which was held 30 October 2006 in Dayton, OH.

In October 2006 Dr. Fred Schauer (AFRL) and his AFOSR-sponsored team were selected to receive the AFOSR Star Team Award for their role in pulse-detonation technology research and development. Team members from AFRL are Dr. Fred Schauer, Dr. Jeff Stutrud, Capt. Timothy Helfrich, and Capt. Paul Litke. Team members from ISSI are Dr. John Hoke, Mr. Royce Bradley, and Mr. Curt Rice.

In November 2006 Dr. Gogineni was recommended by the faculty of Wright State University and appointed by George Huang, Chair of the Department of Mechanical and Materials Engineering, to serve a three-year term on the External Advisory Board for this department. The board is composed of 12 experts from Government, industry, and academia having diverse backgrounds and interests who will review the programs and operations of the department.

Dr. Sukesh Roy (ISSI) was invited to present a paper entitled, "High-Repetition Rate Gas-Phase Temperature Measurements in Reacting Flows Using fs-CARS," at the 37th Winter Colloquium on the Physics of Quantum Electronics, 5 January 2007, Snowbird, UT.

Dr. Michael Brown (ISSI) was Chair of Session 16: Jet Flow at the 32nd Annual Dayton-Cincinnati Aerospace Science Symposium, which was held 6 March 2007 in Dayton. At this conference, a paper presented by Dr. Brown entitled, "Imaging of Laser-Generated Micro-Plasmas" [with C. L. Rettig, K. D. Frische (both of ISSI), J. Nees (University of Michigan), J. R. Gord, and W. M. Roquemore (both of AFRL)], received the Best-Presentation Award in the Combustion Category.

A poster entitled, "Soot Spirals," by S. Stouffer, G. Justinger (both of UDRI), A. Lynch, J. Miller, M. Roquemore, V. Belovich, R. Pawlik, J. Gord, J. Zelina (all of AFRL), V. Katta, S. Roy, and K. Grinstead (all of ISSI) was displayed at the Art-in-the-Science Competition that was held in conjunction with the 32nd AIAA Dayton-Cincinnati Aerospace Science Symposium, 6 March 2007, Dayton, OH. Of the 15 entries in the competition, this poster received the Second-Place Award.

Dr. Sivaram Gogineni (ISSI) was Affiliate Societies Delegate and Regional Representative and served as Organizing-Committee Chair for securing the keynote speaker at the 32nd Annual Dayton-Cincinnati Aerospace Science Symposium, which was held 6 March 2007 in Dayton.

A poster entitled, “Soot Spirals in Laminar Flames,” by S. Stouffer (UDRI), V. Katta (ISSI), W. Roquemore (AFRL), G. Justinger (UDRI), V. Belovich, A. Lynch, J. Miller, R. Pawlik, J. Zelina (all of AFRL), S. Roy, K. Grinstead (both of ISSI), and J. Gord (AFRL) was displayed at the Art Exhibition during the 5th U. S. National Combustion Meeting, which was held 25-28 March 2007 in San Diego. This poster was the result of a collaborative effort conducted by ISSI, UDRI, and AFRL/PRTC. Of the 15 entries in this competition, this poster received the First-Place Award.

Dr. Sukesh Roy (ISSI) was Vice-Chairman of the Active Optical Sensing Subcommittee for the Conference on Lasers and Electro-Optics/Quantum Electronics and Laser Science Conference (CLEO/QELS), which was held 6-11 May 2007 in Baltimore, MD.

Dr. Sivaram Gogineni (ISSI) received the ASME Dayton Section Outstanding Member Contribution Award at the ASME/AIAA Awards Banquet on 21 May 2007.

Dr. Sukesh Roy (ISSI) was invited to present a paper entitled, “Ultrafast Coherent Anti-Stokes Raman Scattering Spectroscopy: Application to Reacting Flows and Plasmas,” at the Central Regional Meeting of the American Chemical Society, 22 May 2007, Covington, KY.

Dr. Sivaram Gogineni (ISSI) served as Technical Chair at the AIAA Joint Propulsion Conference, which was held 8-11 July 2007 in Cincinnati, OH.

Dr. Sukesh Roy (ISSI) was invited to present a paper entitled, “Ultrafast Coherent Anti-Stokes Raman Scattering Spectroscopy: Prospects and Challenges,” at the Gordon Research Conference on Laser Diagnostics in Combustion, 14 August 2007, Oxford, UK

An article entitled “Improving Signal-to-Interference Ratio in Rich Hydrocarbon-Air Flames Using Picosecond Coherent Anti-Stokes Raman Scattering,” by T. R. Meyer (Iowa State University), S. Roy (ISSI), and J. R. Gord (AFRL), which was published in the November 2007 issue of Applied Spectroscopy [Vol. 61, No. 11, pp. 1135-1140], was featured on the cover of this issue.

Dr. Sukesh Roy (ISSI) became an AIAA Associate Fellow in January 2008.

Dr. Anil Patnaik (ISSI) was invited to present a paper entitled, “Coherent-Repumping-Assisted Immunity of Raman Coherence to Rapid Collisional Decays,” [co-authored by S. Roy (ISSI), R. P. Lucht (Purdue University), and J. R. Gord (AFRL)] at the XXXVIII Winter Colloquium on the Physics of Quantum Electronics, 6-10 January 2008, Snowbird, UT.

The first-ever manned demonstration flight of an aircraft powered by the pulsed detonation engine (PDE) was accomplished on 31 January 2008 at Mojave, California. The project for development of the engine that powered this aircraft was conceived by Dr. Fred Schauer of AFRL, and the engine was developed jointly by AFRL and ISSI. The ISSI team, under the

direction of Dr. John Hoke, includes Royce Bradley, Curtis Rice, and Adam Brown. The plane is now located in the Research Hangar of the Air Force Museum at Wright-Patterson AFB, OH.

ISSI was a corporate sponsor for the 33rd Annual AIAA Dayton-Cincinnati Aerospace Science Symposium, 4 March 2008, Dayton, OH. ISSI scientists were co-authors of nine presentations at this meeting.

Dr. Michael Brown (ISSI) was a member of the Organizing Committee (Corporate Sponsors Chair) and Chair of Session 38 – Innovations in Aircraft Design for the 33rd Annual AIAA Dayton-Cincinnati Aerospace Science Symposium, 4 March 2008, Dayton, OH.

A poster entitled, “Centerbody Flame with Tight Spirals,” by S. Stouffer, G. Justinger (UDRI), M. Roquemore, A. Lynch, V. Belovich, J. Gord (all of AFRL), K. Grinstead, V. Katta, and K. Frische (all of ISSI), Poster presented at the Art-in-the-Science Competition that was held in conjunction with the 33rd AIAA Dayton-Cincinnati Aerospace Science Symposium, 4 March 2008, Dayton, OH. Of the eight entries in the competition, this poster received the Second-Place Award.

Dr. Sukesh Roy (ISSI) was invited to present a paper entitled, “Fs-CARS for High-Bandwidth, Collision-Free Temperature Measurements” [coauthored by P. J. Kinnius, R. P. Lucht (both of Purdue University), and J. R. Gord (AFRL)] at the Laser Applications to Chemistry, Security, and Environmental Analysis (LACSEA) Meeting, 17-20 March 2008, St. Petersburg, FL.

Dr. Anil Patnaik (ISSI) was invited to present a paper entitled, “Controlling Speed of Light by Light: Slow and Stopped Light” [coauthored by P. S. Hsu, S. Roy (both of ISSI), and J. R. Gord (AFRL)] at the Physics Seminar at Wright State University, 25 April 2008, Dayton, OH.

Dr. Sukesh Roy (ISSI) was Presider of the Remote Sensing Session at the Conference on Lasers and Electro-Optics/Quantum Electronics and Laser Science Conference (CLEO/QELS), 5-9 May 2008, San Jose, CA.

Dr. Sukesh Roy (ISSI) and Dr. James Gord (AFRL) received in May 2008 the AIAA Dayton-Cincinnati Section Award for Outstanding Technical Contribution for the development and demonstration of ultrafast coherent anti-Stokes Raman scattering (CARS) based on state-of-the-art amplified picosecond and femtosecond lasers for ultra-high-speed thermometry and measurements of critical combustion species.

Dr. James Gord (AFRL), Dr. Terrence Meyer (Iowa State University), and Dr. Sukesh Roy (ISSI) were invited to write a chapter entitled, “Applications of Ultrafast Lasers for Optical Measurements in Reacting and Non-reacting Flows,” which was published in the American Chemical Society Series entitled Annual Review of Analytical Chemistry, Vol. 1 (Eds. E. S. Yeung and R. N. Zare) (Annual Reviews, Palo Alto, CA, July 2008), pp. 663-687.

APPENDIX - Publications and Presentations



ELSEVIER

Available online at www.sciencedirect.com

SCIENCE @ DIRECT®

Optics Communications 224 (2003) 131–137

OPTICS
COMMUNICATIONS

www.elsevier.com/locate/optcom

Triple-pump coherent anti-Stokes Raman scattering (CARS): temperature and multiple-species concentration measurements in reacting flows

Sukesh Roy^{a,*}, Terrence R. Meyer^a, Michael S. Brown^a,
Viswanathan N. Velur^b, Robert P. Lucht^c, James R. Gord^d

^a Innovative Scientific Solutions Inc., 2766 Indian Ripple Road, Dayton, OH 45440, USA

^b California Institute of Technology, Mail Code: 105-24, Pasadena, CA 91125, USA

^c Department of Mechanical Engineering, Purdue University, West Lafayette, IN 47907, USA

^d Air Force Research Laboratory, Propulsion Directorate, Wright-Patterson Air Force Base, OH 45433, USA

Received 19 May 2003; accepted 17 June 2003

Abstract

Two types of triple-pump coherent anti-Stokes Raman scattering (CARS) systems for the simultaneous measurement of temperature and multiple-species concentrations are presented. In the first system, the ro-vibrational transitions of N₂, O₂, and H₂ are probed using three narrowband pump beams and a broadband Stokes beam. In the second system, pure rotational transitions of N₂/O₂ and the ro-vibrational transitions of N₂/CO₂ are probed using two narrowband pump beams, a broadband pump beam, and a broadband Stokes beam. The use of a broadband pump source in the second CARS system allows rotational and ro-vibrational transitions of different molecules to be probed simultaneously. For both CARS systems, the signals appear at two distinct wavelengths. The CARS signals at the two wavelengths are separated by dichroic mirrors before being detected by two spectrometer-CCD detection systems. For proof-of-concept demonstrations, single-shot and averaged measurements are performed in an atmospheric-pressure hydrogen–air diffusion flame and in a carbon dioxide-seeded, near-adiabatic hydrogen–air flame stabilized over a Hencken burner. These are, to our knowledge, the first reported experiments of triple-pump coherent anti-Stokes Raman scattering for the simultaneous measurement of temperature and multiple-species concentrations.

© 2003 Elsevier B.V. All rights reserved.

PACS: 52.35.Mw; 07.57.-c; 07.60.-j

1. Introduction

Characterizing the performance and chemical efficiency of advanced reacting flow systems requires the determination of temperature and species concentrations both in the reaction zone and in the exhaust stream. Typically, these kinds of

* Corresponding author. Tel.: +1-937-255-3115; fax: +1-937-255-3139.

E-mail address: sroy@woh.rr.com (S. Roy).

data are acquired by implementing several independent techniques that are often executed serially. Ideally, these measurements would be accomplished simultaneously to minimize test-cell operation time and to enable the correlation of high-order time-varying statistics. Triple-pump coherent anti-Stokes Raman scattering (CARS) offers the possibility of monitoring the local temperature and concentrations of two target species with respect to a reference species (generally nitrogen) using a single hardware platform with high spatial and temporal resolution.

The first proof-of-concept measurements of two triple-pump CARS systems for temperature and multiple-species concentration measurements in reacting flows are discussed in this paper. These works extend the previous successful demonstration of temperature and concentration measure-

ments in laboratory flames and combustor test facilities using dual-pump CARS by Lucht et al. [1]. The dual-pump CARS technique, first demonstrated by Lucht [2], has been used for the simultaneous measurement of N_2/O_2 [2,3], N_2/H_2 [4], N_2/CH_4 [5], and N_2/CO_2 [6]. In dual-pump CARS, the wavelength of the second pump beam is selected such that the CARS spectra for the two species under study are observed at nearly the same frequency, enabling detection with a single spectrometer and charge-coupled-device (CCD) camera and eliminating systematic errors due to wavelength dependence of the detection system efficiency.

Several other CARS techniques such as dual broadband rotational CARS [7–10] and simultaneous vibrational and rotational CARS [11–14] have been used as tools for temperature and multiple-species concentration measurements.

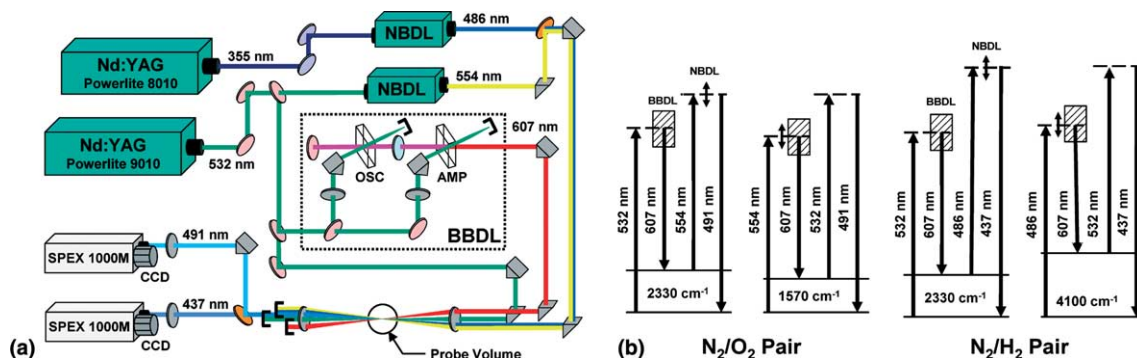


Fig. 1. (a) Schematic diagram of the first triple-pump CARS system for detecting N_2 , O_2 , and H_2 molecules. NBDL, tunable narrowband dye laser; BBDL, broadband dye laser; OSC, oscillator; AMP, amplifier. (b) Energy-level diagram of the first triple-pump CARS system for detecting N_2 , O_2 , and H_2 molecules.

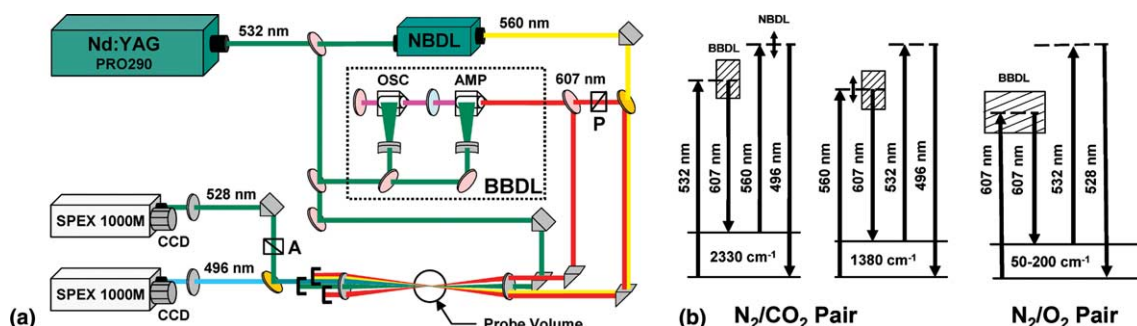


Fig. 2. (a) Schematic diagram of the second triple-pump CARS system for detecting N_2 , O_2 , and CO_2 molecules. (b) Energy-level diagram of the second triple-pump CARS system for detecting N_2 , O_2 , and CO_2 molecules.

The triple-pump CARS techniques described here allow concentration measurements of three species as well as simultaneous, accurate temperature measurements at both low and high temperature. The first triple-pump CARS system, depicted schematically in Fig. 1, is used to probe the ro-vibrational transitions of the N_2 , H_2 , and O_2 molecules. This system is essentially a combination of two dual-pump CARS systems using four laser beams to generate CARS signals near two distinct wavelengths. Both wavelength regions exhibit an N_2 CARS signal along with the CARS signal from another target molecule. Each pair of CARS signals is generated over a relatively narrow wavelength region and can be captured with fixed-wavelength detection. For proof-of-concept experiments, CARS measurements were performed in an atmospheric-pressure laminar H_2 –air diffusion flame.

In the second triple-pump CARS system, the pure rotational transitions of N_2 and O_2 molecules and the ro-vibrational transitions of N_2 and CO_2 molecules are probed. The system is shown in Fig. 2. In this system a dual-broadband rotational CARS system is combined with a dual-pump CARS system, and four laser beams are used to generate CARS signals near two distinct wavelengths. One of the pump beams in this system is broadband, allowing us to probe rotational and ro-vibrational transitions simultaneously, unlike the first triple-pump CARS system which employs either single-longitudinal-mode or narrowband pump beams. One of the main advantages of this technique is that very accurate temperature measurements can be acquired at both low and high temperatures. In the combustion zone or the exhaust of a real combustor, there is a wide spatial and temporal variation of temperature due to the inherent turbulent nature of the flow field. Under these circumstances, the rotational spectra of N_2/O_2 will provide better temperature accuracy at lower temperatures, generally below 1500 K [15]; whereas the ro-vibrational spectra of N_2/CO_2 will provide improved temperature accuracy at higher temperatures as population is transferred to higher energy levels. The proof-of-concept measurements using the second triple-pump CARS experiment were performed in an atmospheric-pressure near-

adiabatic hydrogen–air flame seeded with CO_2 and stabilized on a Hencken burner.

Detailed measurements of temperature and multiple-species concentrations using triple-pump CARS systems in laboratory flames and also in the exhaust stream of a liquid-fueled swirl-stabilized combustor are in progress at the US Air Force Research Laboratory at Wright-Patterson Air Force Base.

2. Experimental setup

The experimental schematic and energy-level diagrams of the first triple-pump CARS system are shown in Figs. 1(a) and (b), respectively. In this system the wavelengths of the laser beams were chosen to simultaneously probe the ro-vibrational transitions of N_2 , O_2 , and H_2 molecules. As evident in Fig. 1, this technique is essentially a combination of two dual-pump CARS systems, one generating a CARS signal from the N_2/O_2 pair and the other generating a CARS signal from the N_2/H_2 pair. Two injection-seeded Nd:YAG lasers operating at 10 Hz (Continuum: Powerlite Precision 8010 and Powerlite 9010) were used to pump two narrowband dye lasers and a broadband dye laser while also providing a 532-nm CARS pump beam. The broadband dye laser was used to generate a Stokes beam for each of the four CARS signals, with a frequency spectrum centered near 607 nm. The two narrowband dye lasers were used to provide the pump beams for O_2 and H_2 . The first narrowband dye laser (pumped with the 532-nm laser) provides light at 554 nm. The interaction of the 532-nm pump beam with the 607-nm Stokes beam produces an N_2 Raman polarization that coherently scatters the 554-nm pump beam, yielding an N_2 CARS signal near 491 nm. At the same time, interaction of the 554-nm pump beam with the 607-nm Stokes beam produces an O_2 Raman polarization that scatters the 532-nm pump beam, yielding an O_2 CARS signal that also appears near 491 nm. The second narrowband dye laser is pumped with the 355-nm laser beam and generates light at 486 nm. An N_2 CARS signal appearing near 437 nm is produced as the 486-nm beam is scattered by the N_2 Raman polarization. An H_2

polarization arising from the combination of the 486 and 607-nm beams scatters the 532-nm beam, producing an H_2 signal that is also near 437 nm. The incident beams are phase-matched using folded BOXCARS geometry [7], with the 554 and 486-nm beams arranged co-linearly.

For the proof-of-concept measurements, a two-channel system consisting of two spectrometers and two CCD cameras is used. The CARS signals at 437 and 491 nm are isolated using a dichroic mirror which transmits the 437-nm signal and reflects the 491-nm signal. The CARS signals are dispersed using a 1.0-m spectrometer (SPEX 1000M), equipped with a 2400-grooves/mm grating. At each spectrometer exit, a pair of lenses is used to focus the CARS spectra onto a CCD chip. The magnifications of the relay lens systems were approximately unity. For the N_2/H_2 detection system, a Pixelvision UV-enhanced, back-illuminated, unintensified CCD camera with an 1150×350 -pixel array is used. For the O_2/N_2 detection system, a back-illuminated interline-transfer CCD camera with a 1300×1110 -pixel array is used. Both cameras and the second Nd:YAG laser were synchronized with respect to one of the Nd:YAG lasers (Powerlite 8010). This experiment was performed at Texas A&M University.

The experimental schematic and energy-level diagrams of the second triple-pump CARS system are shown in Figs. 2(a) and (b), respectively. This experiment was performed at Wright-Patterson Air Force Base. This second triple-pump CARS system differs from the first in that one of the pump beams is of the broadband nature. As evident in Fig. 2, this technique is essentially a dual-pump CARS system combined with a dual-broadband CARS system, generating ro-vibrational CARS spectra from the N_2/CO_2 pair and rotational CARS signal from the N_2/O_2 pair.

An injection-seeded Nd:YAG laser (Spectra Physics Pro 290) was used to pump one narrowband dye laser and a broadband dye laser while providing a 532-nm CARS pump beam. The broadband dye laser is pumped by the 532-nm beam, and the broadband dye output, centered about 607 nm, serves as the Stokes beam for each of the CARS signals generated as well as the pump beam for the dual-broadband rotational CARS

system. The narrowband dye laser is also pumped by the 532-nm beam and provides laser radiation at approximately 560 nm. The combination of the 532-nm pump beam with the 607-nm Stokes beam produces a ro-vibrational N_2 Raman polarization that coherently scatters the 560-nm pump beam, yielding an N_2 CARS signal near 496 nm. At the same time, the 560-nm pump and the 607-nm Stokes beam produce a CO_2 Raman polarization that scatters the 532-nm pump beam, yielding a CO_2 CARS signal that also appears near 496-nm.

The spectral width of the broadband dye laser is approximately 200 cm^{-1} . This spectral width is large enough to excite the pure rotational transitions of N_2 and O_2 molecules at the ground vibrational state up to J values of approximately 30. The broadband pump beam and the broadband Stokes beam produce rotational Raman polarizations for both N_2 and O_2 molecules, which then scatter the 532-nm pump beam. The pure rotational CARS spectra appear at a wavelength of approximately 528 nm. The incident beams are again phase-matched using the folded BOXCARS geometry, with the 560 and 607-nm pump beams arranged co-linearly. The frequency of the rotational CARS signal is very close to the pump beam at 532 nm. This poses the significant challenge of discriminating the scattered light at 532 nm from the CARS signal at 528 nm. To minimize the scattered light at 532 nm, the polarization of one of the broadband pump beams at 607 nm was oriented to be orthogonal to that of the 532-nm beam. The polarization of the broadband dye beam that serves as the Stokes beam for the N_2/CO_2 CARS was not rotated. With this configuration the polarization of the pure rotational CARS signal was orthogonal to that of the 532-nm pump beam. The CARS signal at 528-nm was isolated from the background 532-nm scattered light by placing an analyzer in the detection channel with a transmission axis perpendicular to the 532-nm pump beam, as shown in Fig. 2(a). The CARS signals at 496 and 528-nm were separated using a dichroic mirror before being simultaneously detected by two 1.0-m spectrometers and two interline-transfer CCD cameras with 1300×1110 pixel arrays. The advantage of using the interline-transfer CCD camera for the acquisition of

broadband CARS spectra has been described in detail by Roy et al. [16].

The spectra acquired from both triple-pump CARS systems are normalized using a non-resonant spectrum to account for the effects of laser power drift and spectral variations in dye power [7]. The non-resonant spectrum is recorded by placing the beam-overlap region within an open argon flow tube.

3. Results and discussion

The proof-of-concept demonstration measurements for the $\text{N}_2/\text{O}_2/\text{H}_2$ triple-pump CARS system described in Fig. 1 were performed in an atmospheric-pressure, laminar, hydrogen–air diffusion flame. The exit diameter of the nozzle exit was 10 mm. The ro-vibrational N_2/O_2 and N_2/H_2 spectra shown in Figs. 3(a) and (b), respectively, were acquired at approximately 2 mm from the center of the nozzle and 0.5 mm above the nozzle lip. The spectra presented in Fig. 3 were acquired simultaneously at 2 Hz and averaged over 100 laser shots. The wavelengths of the tunable narrowband dye lasers were tuned such that the O_2 and H_2 spectra were separated from the N_2 spectrum on the CCD chips. For the spectra shown in Fig. 3,

the temperature and relative concentration are evaluated by fitting the experimental CARS spectra with the theoretical spectrum generated by the Sandia CARSFT code [17]. The temperature evaluated from the N_2/O_2 spectrum is within approximately 4% of that evaluated from the N_2/H_2 spectrum. The oxygen-to-nitrogen ratio was found to be 0.2 and the hydrogen-to-nitrogen ratio was found to be 0.58. The evaluated oxygen-to-nitrogen and the hydrogen-to-nitrogen ratios are consistent with the results of a previous dual-pump CARS experiments in this flame [3,4].

The proof-of-concept measurements using the $\text{N}_2/\text{O}_2/\text{CO}_2$ triple-pump CARS system described in Fig. 2 were performed in atmospheric-pressure, near-adiabatic hydrogen–air flames seeded with CO_2 and stabilized on a Hencken burner. The ro-vibrational spectra of N_2/CO_2 and the pure rotational spectra of N_2/O_2 were acquired simultaneously at 10 Hz. Typical single-shot ro-vibrational spectra of N_2/CO_2 and single-shot rotational spectra of N_2/O_2 are shown in Figs. 4(a) and (b), respectively, for an equivalence ratio of 0.25. The measured temperature from the ro-vibrational spectra of N_2/CO_2 is within 4–5% of the temperature evaluated from the rotational spectra of N_2/O_2 . From Fig. 4(b) it is evident that the agreement between the theoretical and experimental oxygen

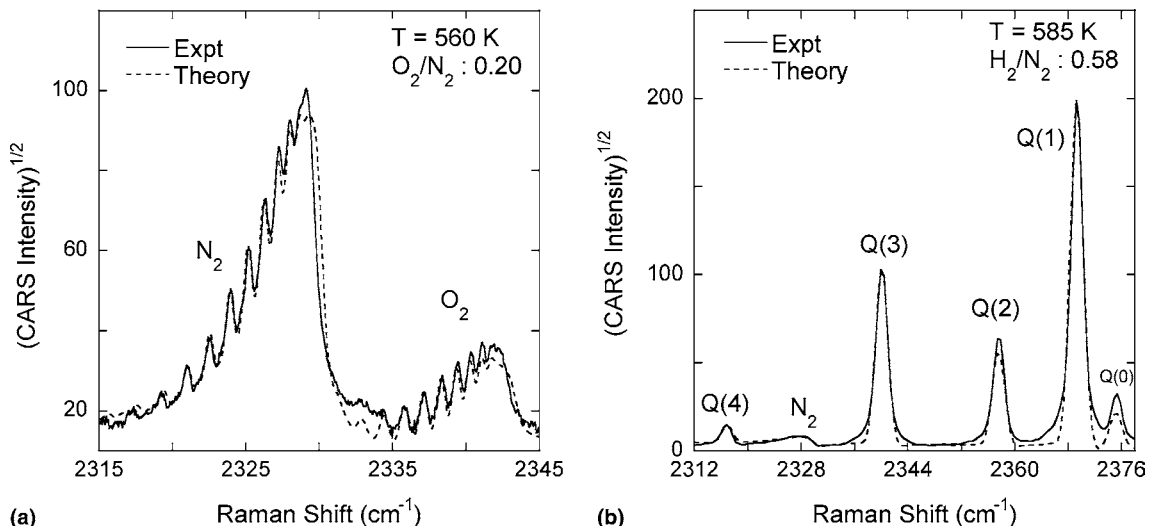


Fig. 3. (a) N_2/O_2 and (b) N_2/H_2 CARS spectra in atmospheric-pressure hydrogen–air diffusion flame. Each spectrum shown above is averaged over 100 laser shots.

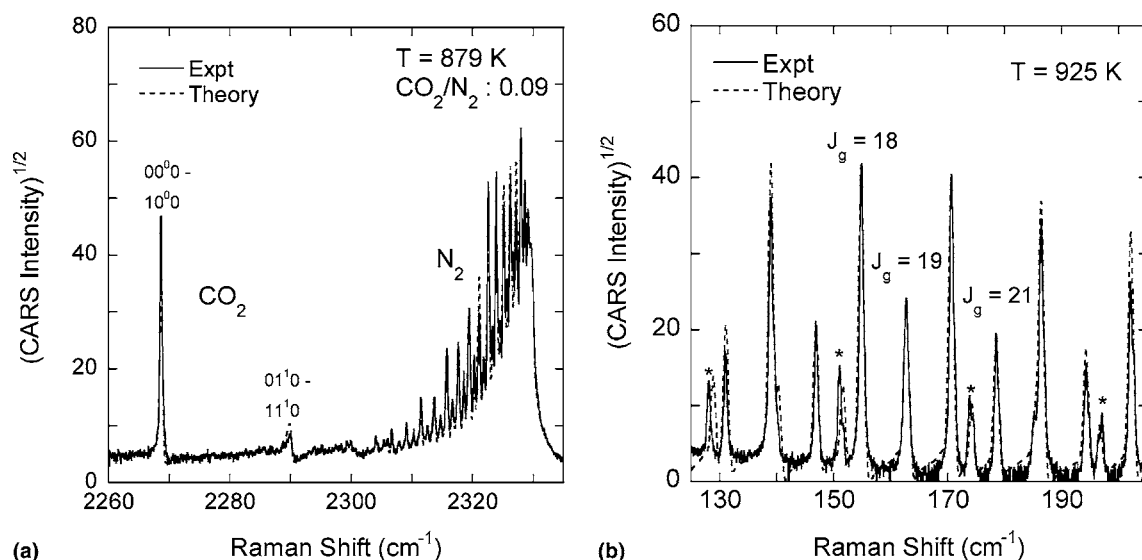


Fig. 4. Single-laser-shot (a) N_2/CO_2 and (b) N_2/O_2 spectra acquired from near-adiabatic, hydrogen–air– CO_2 flame stabilized on a Hencken burner at $\phi = 0.25$. * represents the O_2 spectral lines and J_g denotes the ground-level rotational quantum number.

lines is not as good as for the nitrogen lines. We are currently working on addressing some of the issues related to the modeling of the pure rotational spectra of the oxygen molecule in the CARSFT code. Probability density functions (PDF) of

temperature and the carbon dioxide-to-nitrogen ratio evaluated from 650 single-shot spectra are shown in Figs. 5 and 6, respectively. The mean temperature and the carbon dioxide-to-nitrogen ratio are 888 K and 0.09, respectively. The

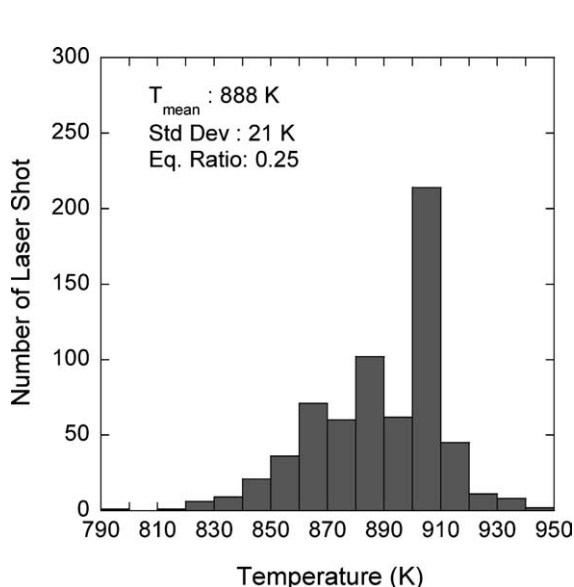


Fig. 5. PDF of temperature determined from single-laser-shot N_2/CO_2 spectra acquired from near-adiabatic hydrogen–air flame seeded with CO_2 .

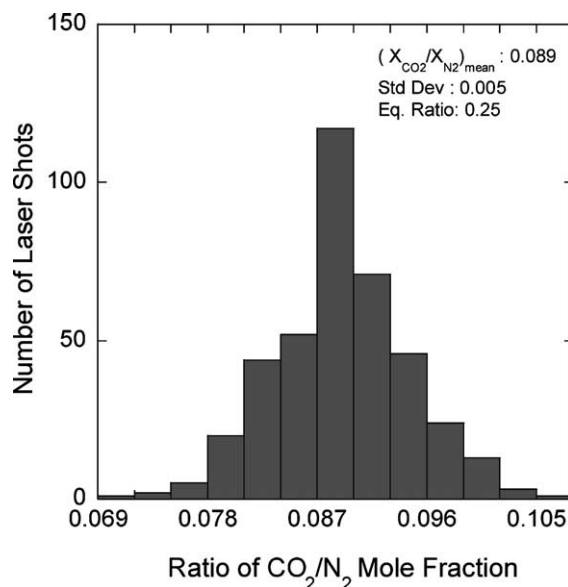


Fig. 6. PDF of carbon dioxide-to-nitrogen ratio determined from single-laser-shot N_2/CO_2 spectra acquired from near-adiabatic hydrogen–air flame seeded with CO_2 .

standard deviation of the temperature measurements is approximately 2.3% of the mean value and that of the carbon dioxide-to-nitrogen ratio is approximately 6% of the mean value. These standard deviations are a significant improvement upon previous measurements carried out in the same flame using the dual-pump CARS technique [1]. The mean carbon dioxide-to-nitrogen ratio is approximately 25% higher than the expected equilibrium value. Similar discrepancies between the measured and expected equilibrium value of CO_2 were reported by Lucht et al. [1]. A series of experiments is currently being planned to address a number of issues related to the modeling of CO_2 spectra.

4. Conclusions

Two different types of triple-pump coherent anti-Stokes Raman scattering systems for the simultaneous measurements of temperature and multiple-species concentrations were demonstrated. To our knowledge, these are the first reported experiments demonstrating the triple-pump CARS technique for the simultaneous detection of temperature and multiple-species concentrations in reacting flows. The first triple-pump CARS system is used to probe the ro-vibrational transitions of N_2 , O_2 , and H_2 , whereas the second system is used to probe the pure rotational transitions of N_2/O_2 and the ro-vibrational transitions of N_2/CO_2 . For both systems, the CARS spectra of each molecule pair occur within a distinct wavelength band, allowing two molecular spectral pairs to be acquired simultaneously using a detection system composed of two spectrometers and two cameras. Since nitrogen is a common species for each molecule pair, it can be used as a common reference for normalizing species concentrations and for improving the accuracy and dynamic range of the temperature measurement. Proof-of-concept measurements were performed in a hydrogen–air diffusion flame and a CO_2 -seeded hydrogen–air Hencken-burner flame. Simultaneous single-shot measurements of temperature and multiple-species concentrations in the exhaust stream of a liquid-

fueled swirl-stabilized combustor are in progress at the US Air Force Research Laboratory, Wright-Patterson Air Force Base.

Acknowledgements

Funding for this research was provided by the Air Force Research Laboratory, Propulsion Directorate, Wright-Patterson AFB, under Contract No. F33615-00-C-3020 and F33615-00-C-2068, and by the Air Force Office of Scientific Research [Program Monitor: Dr. Julian Tishkoff].

References

- [1] R.P. Lucht, V.N. Velur, G.J. Fiechtner, C.D. Carter, K.D. Grinstead Jr., J.R. Gord, P.M. Danehy, R.L. Farrow, *AIAA J.* 41 (3) (2003) 679.
- [2] R.P. Lucht, *Opt. Lett.* 12 (1987) 78.
- [3] R.D. Hancock, F.R. Schauer, R.P. Lucht, R.L. Farrow, *Appl. Opt.* 36 (1997) 3217.
- [4] F.R. Schauer, Ph.D. Thesis, University of Illinois at Urbana-Champaign, Urbana, IL, 1998.
- [5] S.M. Green, P.J. Rubas, M.A. Paul, J.E. Peters, R.P. Lucht, *Appl. Opt.* 37 (1998) 1690.
- [6] D. Brüggemann, B. Wies, X.X. Zhang, T. Heinze, K.F. Knoche, in: D.F.G. Durão, M.V. Heitor, J.H. Whitelaw, P.O. Witze (Eds.), *Combustion Flow Diagnostics*, Kluwer Academic, Dordrecht, 1992, p. 495.
- [7] A.C. Eckbreth, *Laser Diagnostics for Combustion Temperature and Species*, Gordon and Breach Publishers, Amsterdam, 1988.
- [8] L. Martinsson, P.-E. Bengtsson, M. Aldén, *Appl. Phys. B* 62 (1996) 29.
- [9] A. Thumann, M. Schenk, J. Jonuscheit, T. Seeger, A. Leipertz, *Appl. Opt.* 36 (1997) 3500.
- [10] J. Bood, P.-E. Bengtsson, M. Aldén, *Appl. Phys. B* 70 (2000) 607.
- [11] F.Y. Yueh, E.J. Beiting, *Appl. Opt.* 27 (1988) 3233.
- [12] P.-E. Bengtsson, L. Martinsson, M. Aldén, *Appl. Spectrosc.* 49 (1995) 188.
- [13] T. Seeger, A. Leipertz, *Appl. Opt.* 35 (1996) 2665.
- [14] C. Brackmann, J. Bood, P.-E. Bengtsson, T. Seeger, M. Schenk, A. Leipertz, *Appl. Opt.* 41 (2002) 564.
- [15] M. Aldén, J. Bengtsson, H. Edner, S. Kröll, D. Nilsson, *Appl. Opt.* 28 (1989) 3206.
- [16] S. Roy, G. Ray, R.P. Lucht, *Appl. Opt.* 40 (2001) 6005.
- [17] R.E. Palmer, *The CARSFT Computer Code for Calculating Coherent Anti-Stokes Raman Spectra: User and Programmer Information*, Sandia National Laboratories, Livermore, CA, Report No. SAND89-8206, 1989.

Single-Shot Thermometry and Multiple-Species Measurements Using Dual-Pump, Dual-Broadband CARS in a Liquid-Fueled CFM56 Combustor

Sukesh Roy* and Terrence R. Meyer*
Innovative Scientific Solutions, Inc.
2766 Indian Ripple Road, Dayton, OH 45440-3638

Robert P. Lucht†
Purdue University, Department of Mechanical Engineering
West Lafayette, IN 47907-1337

Vincent M. Belovich**, Edwin Corporan††, and James R. Gord‡
Air Force Research Laboratory, Propulsion Directorate
Wright-Patterson Air Force Base, OH 45433-7103

A dual-pump, dual-broadband (DPDB) CARS system for the simultaneous measurement of temperature and multiple-species concentrations is demonstrated in the exhaust stream of a liquid-fueled, CFM56, model gas-turbine combustor. The DPDB CARS approach employs four laser beams generating CARS signals near two distinct wavelengths, enabling highly accurate, spatially resolved, single-shot measurements within the full range of combustor operating conditions. For the proof-of-concept experiments, CARS signals from N₂-O₂ and N₂-CO₂ pairings were collected. Single-shot measurements were carried out for different jet fuels, fuel additives, and equivalence ratios to document correlations between particulate size distribution, concentrations of carbon dioxide and oxygen, temperature, and fuel composition.

Introduction

Characterization of advanced propulsion systems requires the determination of performance and combustion efficiency through measurements of temperature and species concentrations in the exhaust stream. Typically these kinds of data are acquired by implementing several independent techniques, which are often executed serially. Ideally these measurements would be accomplished simultaneously with a minimum number of diagnostics. Dual-pump, dual-broadband (DPDB) coherent anti-Stokes Raman scattering (CARS) offers the possibility of monitoring the local temperature and concentrations of two target species with respect to a reference species (usually nitrogen) using a single hardware platform that provides high spatial and temporal resolution.

We present here the demonstration of a dual-pump, dual-broadband CARS system for temperature and concentration measurements in reacting flows of practical interest. This work extends our previous demonstrations of temperature and concentration measurements in laboratory flames and combustor test facilities using dual-pump and triple-pump CARS.¹⁻² This technique is unique in that it allows for accurate temperature measurements both at low and high temperatures. In the combustion zone or the exhaust of a real combustor, there is a wide spatial and temporal variation of temperature due to the inherent turbulent nature of the flow field. In the current system, the rotational transitions of N₂-O₂ and the ro-vibrational transitions of N₂-CO₂ are probed. The rotational spectra of N₂-O₂ provide better temperature accuracy at lower temperatures, generally below 1500 K,³ whereas the ro-vibrational spectra of N₂-CO₂ provide improved temperature accuracy at higher temperatures. To our knowledge, this is the first CARS technique that uses three pump beams to simultaneously excite the transitions of three different molecules to achieve two rotational spectra (e.g., N₂ and O₂) and two ro-vibrational spectra (N₂ and CO₂). The rotational spectra provide better accuracy at low temperature because most of the population resides at lower energy levels. At higher temperatures population is transferred to

* Research Scientist, Member, AIAA

† Professor, Associate Fellow, AIAA

** R&D Engineer, Member, AIAA

†† R&D Engineer, Senior Member, AIAA

‡ Principal Research Chemist, Associate Fellow, AIAA

higher energy levels, which is reflected in more accurate ro-vibrational spectra.

The DPDB CARS system is essentially a special triple-pump CARS system where one of the pump beams is of broadband nature whereas in traditional triple-pump CARS technique the bandwidth of all the pump beams are either single-longitudinal mode or very narrow.¹ The dual-pump CARS technique, which was first demonstrated by Lucht,⁴ has been used for the simultaneous measurement of nitrogen and oxygen,^{4,5} nitrogen and hydrogen,⁶ nitrogen and methane,⁷ and nitrogen and carbon-dioxide.⁸ In dual-pump CARS, the wavelengths of the input beams are adjusted such that the CARS spectra for the two species under study are observed at nearly the same frequency. This arrangement largely eliminates potential errors arising from wavelength-dependent variations in signal transmission or detector efficiency that can complicate other multi-species CARS techniques such as dual-Stokes and dual-broadband CARS.⁹

The dual-pump CARS technique was applied by Lucht et al.² in the exhaust stream of a practical combustor for measuring temperature and CO₂ concentration from a single laser shot. However, those measurements were limited to an overall equivalence ratio (ϕ) of less than 0.5. Several other CARS techniques such as dual-broadband rotational CARS,¹⁰ and simultaneous vibrational and rotational CARS¹¹ have also been used for temperature and multiple-species concentration measurements.

In the DPDB CARS system a dual-broadband CARS system is superimposed on a dual-pump CARS system. Four laser beams are used to generate CARS signals near two distinct wavelengths. Both wavelength regions exhibit an N₂ CARS signal along with the CARS signal from another target molecule. Each pair of CARS signals is generated over a relatively narrow wavelength region and can be captured with fixed wavelength detection. Temperature and relative concentrations of the target species (with respect to N₂) are extracted either by fitting the measured CARS spectrum with a theoretical spectrum or through a Boltzmann plot. Temperatures from the N₂-CO₂ and N₂-O₂ pairs were evaluated by fitting the CARS spectra with the theoretical spectra.

Since the N₂ concentration is typically known, the amplitude of the target-species signal relative to that of the paired N₂ signal provides an absolute measure of the target-species concentration. Measurements were carried out in the exhaust stream of a liquid-fueled, swirl-stabilized CFM56 combustor. The objectives of this investigation were to perform single-laser-shot temperature and O₂ and CO₂ concentration measurements in the exhaust

stream of a liquid-fueled practical combustor under sooting conditions. Measurements were performed for a number of different jet fuels and additive concentrations over a wide range of equivalence ratios ($\phi = 0.4$ to $\phi = 1.1$). These measurements are used to provide benchmark statistical distributions of temperature and concentrations of CO₂ and O₂ in the exit plane of the combustor and to evaluate the effects of particulate mitigating additives on flame chemistry. These measurements are also used to assess the viability of future dual-pump CARS measurements in the reaction zone of the combustor under sooting conditions. These data complement laser-induced incandescent (LII) and planar laser-induced fluorescence (PLIF) measurements of soot volume fraction and OH radical concentrations, respectively, which are ongoing in the current combustor.

Experimental Setup

The schematic and the energy level diagrams of the dual-pump, dual-broadband CARS system are shown in Figs. 1 and 2, respectively. In the DPDB CARS technique a dual-pump CARS system is superimposed on a dual-broadband CARS system which is generated with a single pump-laser system.

An injection seeded Nd:YAG laser (Quanta Ray, Pro 290, Spectra Physics) is used to pump one narrowband dye laser and a broadband dye laser while providing a 532-nm CARS pump beam. In the current configuration, the broadband dye laser (pumped by 532 nm) provides an output beam centered about 607 nm that serves as the Stokes laser

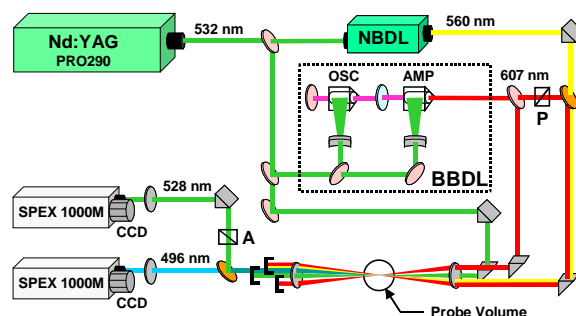


Figure 1. Schematic diagram of the dual-pump, dual-broadband CARS system. A: Analyzer, P: Polarizer, BBDL: Broadband Dye Laser, NBDL: Tunable Narrowband Dye Laser.

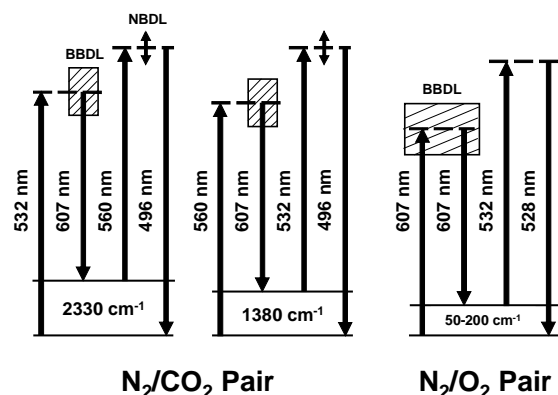


Figure 2. Energy-level diagram of the dual-pump, dual-broadband CARS system. NBDL: Tunable Narrowband Dye Laser, BBDL: Broadband Dye Laser.

for each of the four generated CARS signals. The broadband output at 607 nm also provides the pump beam for the dual-broadband rotational CARS system. The narrowband dye laser is also pumped by the 532-nm beam and provides laser radiation at approximately 560 nm. The combination of the 532-nm pump beam with the 607-nm Stokes beam produces a ro-vibrational N_2 Raman polarization that coherently scatters the 560-nm pump beam, yielding an N_2 CARS signal near 496 nm. At the same time, the 560-nm pump and the 607-nm Stokes beam produce a CO_2 Raman polarization that scatters the 532-nm pump beam, yielding a CO_2 CARS signal that also appears near 496 nm.

The spectral width of the broadband dye laser is approximately 200 cm^{-1} . This spectral width is large enough to excite the pure rotational transitions of N_2 and O_2 molecules at the ground and excited vibrational state up to J values of approximately 30. The broadband pump beam and the broadband Stokes beam produce rotational Raman polarizations for both N_2 and O_2 molecules, which then scatter the 532-nm pump beam. The pure rotational CARS spectra appear at a wavelength of approximately 528 nm. The incident beams are phase matched using the folded BOXCARS geometry, with the 560-nm and 607-nm pump beams arranged co-linearly. The frequency of the rotational CARS signal is very close to the pump beam at 532 nm. This poses the significant challenge of discriminating the scattered light at 532 nm from the CARS signal at 528 nm. To minimize the scattered light at 532 nm, the polarization of one of the broadband pump beams at 607 nm was oriented to be orthogonal to that of the 532-nm beam. The polarization of the broadband dye beam that serves as the Stokes beam for the N_2 - CO_2

CARS was not rotated. With this configuration the polarization of the pure rotational CARS signal was orthogonal to that of the 532-nm pump beam. The CARS signal at 528-nm was isolated from the background 532-nm scattered light by placing an analyzer in the detection channel with a transmission axis perpendicular to the 532-nm pump beam, as shown in Fig. 1. The CARS signals at 496-nm and 528-nm were separated using a dichroic mirror before being simultaneously detected by two 1.0-m spectrometers and two back-illuminated CCD cameras with 2000×512 -pixel arrays.

The CARS spectra are normalized using a non-resonant spectrum to account for the effects of pulse-to-pulse laser power fluctuations, long-term power drifts, and spectral variations in dye power.⁹ The non-resonant spectrum is recorded by flowing argon through a flow tube into the beam overlap region.

The combustor facility is described in detail by Roy *et al.*¹²

Results and Discussion

Temperature and CO_2 concentration measurements were performed in the exhaust stream of the liquid-fuel, swirl-stabilized combustor over a wide range of equivalence ratios for three jet fuels using the dual-pump, dual-broadband CARS technique. This CARS system exhibited excellent accuracy, as determined from temperature and CO_2 concentration measurements in a calibrated, laminar flame.¹ The standard deviations of the measured single-shot temperatures and CO_2 concentrations evaluated from the N_2 - CO_2 spectra in the calibrated flame were 2.3% and 6% of the mean values, respectively, for a wide range of equivalence ratios.¹ The jet fuels used for the current experiment were JP-8, JP-8X45, and semi-synthetic fuel. JP-8 is the standard jet fuel, which consists of commercial jet-A fuel with additives. JP-8X45 is a high energy-density fuel high in aromatics and cycloparaffins. The semi-synthetic fuel consists of 50% JET-A and 50% coal-derived compounds. The carbon-to-hydrogen ratios for the JP-8, JP-8X45, and semi-synthetic fuels are 0.52, 0.6, and 0.5, respectively. The aromatic content of the JP-8, JP-8X45, and semi-synthetic fuels are 15.9%, 40.8%, and 10.0%, respectively, measured using a standard ASTM method. The objectives of this study were to measure single-shot temperature and concentrations of CO_2 and O_2 at high equivalence ratios under sooting conditions.

Typical single-shot N_2 - CO_2 and N_2 - O_2 spectra of the DPDB CARS system acquired in the exhaust stream of the JP-8-fueled combustor for an equivalence ratio of 0.45 are shown in Figs. 3a and

3b, respectively. The solid line represents the experimental CARS signal, and the dotted line represents the theoretical CARS spectrum. The N_2 - CO_2 CARS spectrum was fitted using Sandia CARSFT code¹³ and the N_2 - O_2 rotational spectrum was fitted using the code described by Bood *et al.*¹⁰ The temperature and relative CO_2 and O_2 concentrations were evaluated by comparing the experimental spectrum with that of a theoretical one.

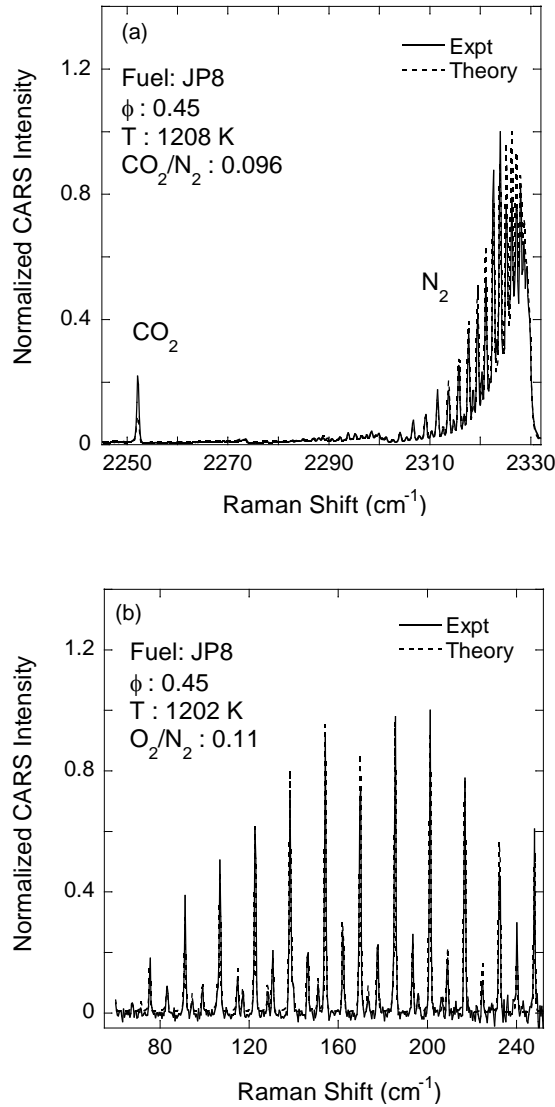


Figure 3: Single-shot (a) ro-vibrational spectrum of N_2 - CO_2 and (b) rotational spectrum of N_2 - O_2 acquired in the exhaust stream of the JP-8-fueled combustor for an equivalence ratio of 0.45. Both spectra were acquired simultaneously.

spectrums agree to within experimental uncertainty

as shown in Fig. 3. Probability density functions (PDF's) of temperatures evaluated from the single-shot N_2 - O_2 rotational spectra and the N_2 - CO_2 ro-vibrational spectra are shown in Figs. 4a and 4b, respectively. The difference in standard deviations of the rotational and ro-vibrational spectra may be due to the difference in the signal-to-noise ratio and the quality of the least-square-fitting of the experimental spectra. Two different theoretical codes were used to

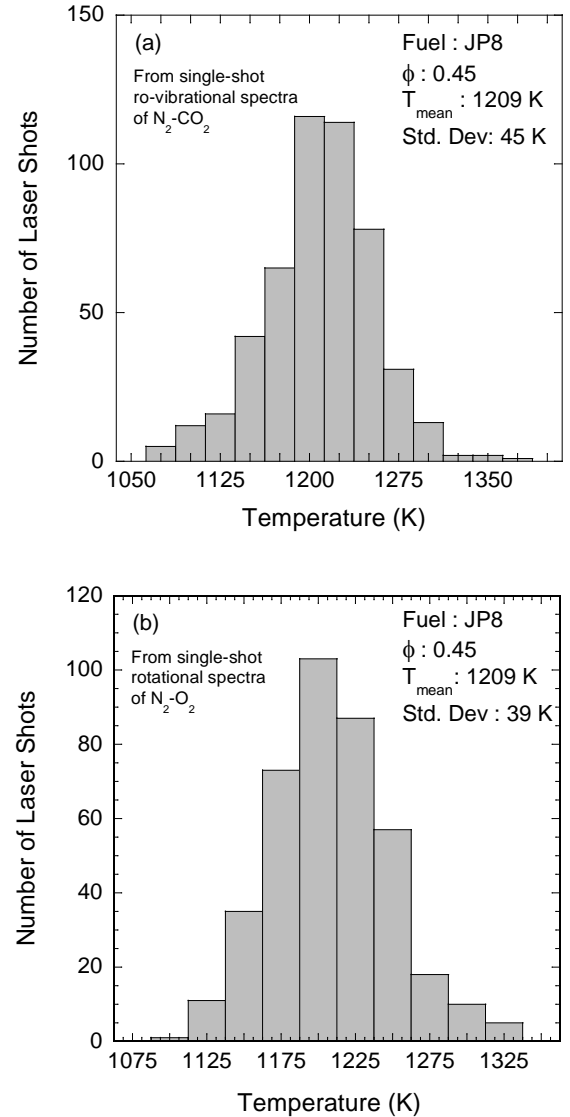


Figure 4: Single-shot temperature PDF's evaluated from the (a) ro-vibrational spectrum of N_2 - CO_2 and (b) rotational spectrum of N_2 - O_2 acquired in the exhaust stream of the JP-8-fueled combustor for an equivalence ratio of 0.45.

fit the single-shot ro-vibrational spectra and the

single-shot rotational spectra. The standard deviations of the temperature evaluated from the N_2 - CO_2 spectra and N_2 - O_2 spectra are approximately 3.75% and 3.25% of the mean value, respectively; the mean temperature is approximately 1209 K. The PDF's of the ratio of CO_2 and N_2 mole fractions and the ratio of O_2 and N_2 mole fractions are shown in Figs. 5a and 5b, respectively.

PDF's of single-shot temperature and CO_2 mole fraction for an equivalence ratio of 1.0 are shown in

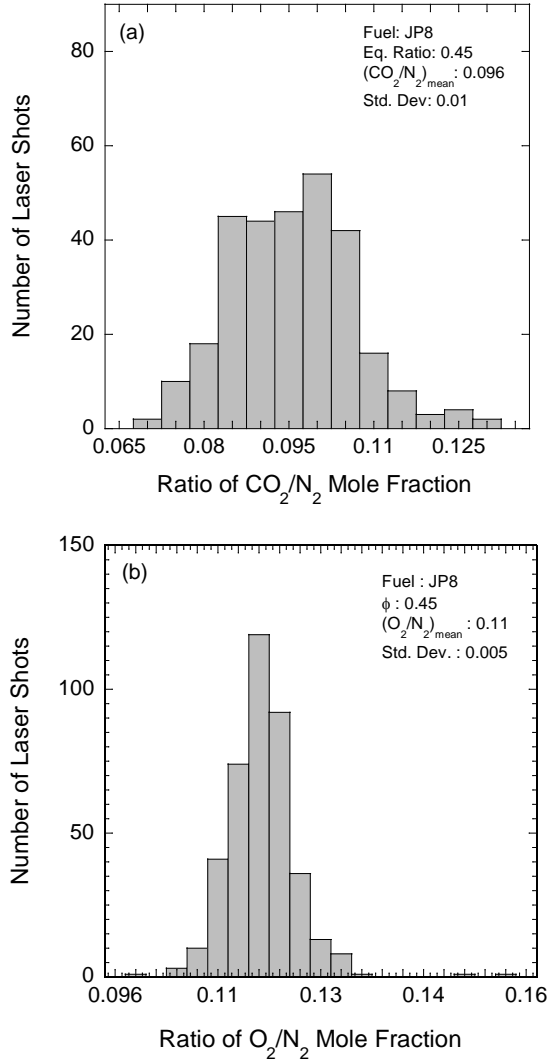


Figure 5: PDF's of the ratio of (a) CO_2 and N_2 and (b) O_2 and N_2 evaluated from the single-shot CARS spectra as discussed in Figs. 3 and 4.

stoichiometric equivalence ratios are significantly higher than the equivalence ratios of previous measurements performed in this combustor, single-shot or time-averaged.^{2,14} These show that the current setup is suitable to acquire flow-field statistics at high equivalence ratios under steady and unsteady sooting conditions. The data for the determination of oxygen concentration have not yet been analyzed. The standard deviations for the measured temperatures

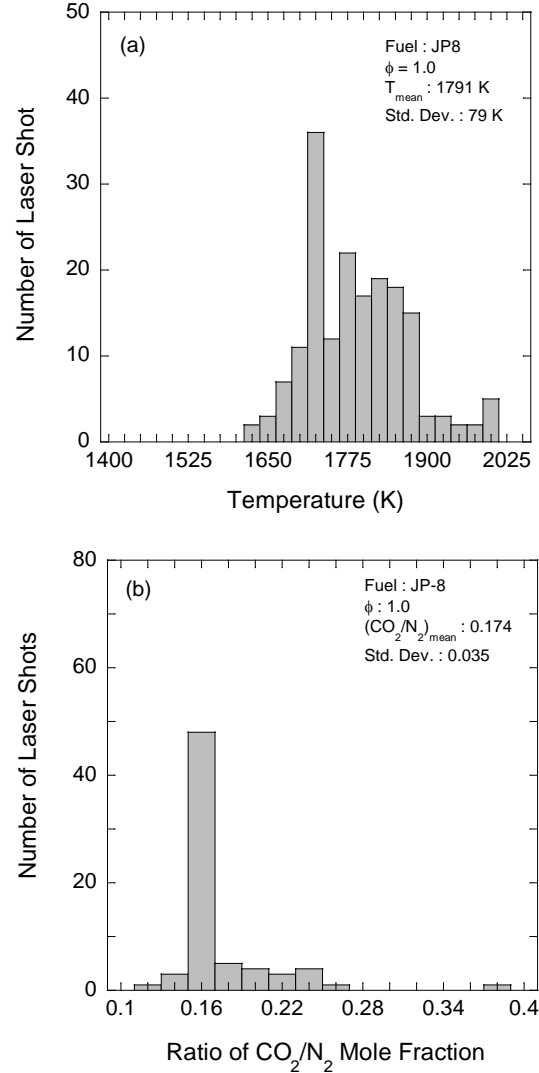


Figure 6: PDF's of (a) temperature and (b) CO_2 mole fraction determined from single-laser-shot, dual-pump N_2 - CO_2 spectra acquired at the exhaust of the JP-8-fueled combustor for an equivalence ratio of 1.0.

Figs. 6a and 6b, respectively. These near-

and CO_2 mole fractions as determined from single-

laser-shot, dual-pump N_2 - CO_2 CARS spectra are approximately 4% and 20% of the mean values, respectively. These standard deviations are larger than those measured in the calibration flame (2.3% and 6%, respectively) due in part to reduced signal-to-noise ratios, as well as to increased unsteadiness in the swirl-stabilized combustor. The increase in combustor unsteadiness is verified in Fig. 7, which shows correlation diagrams for the measured CO_2 concentrations and gas-phase temperatures determined from the single-shot, dual-pump N_2 - CO_2 spectra. A least-square fit through the data points shows a correlated increase in CO_2 concentration with temperature, indicating that temperature fluctuations are accompanied by shot-to-shot fluctuations in equivalence ratio.

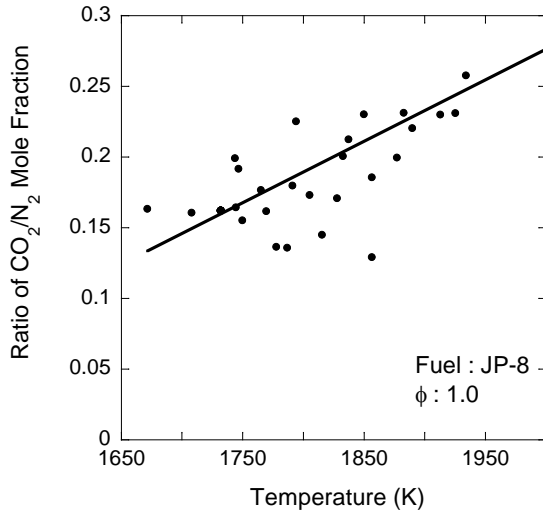


Figure 7: Temperature - CO_2 mole-fraction correlations for the single-shot CARS data for an equivalence ratio of 1.0 in the exhaust stream of the JP-8-fueled combustor.

The temperature and the CO_2 concentration measurements for all three fuels are shown in Figs. 8a and 8b, respectively. The increase in the standard deviation of the CO_2 mole fraction with equivalence ratio could be attributed to combustor unsteadiness or CARS system uncertainty, as discussed above. Both the temperature and the CO_2 concentration increase monotonically with equivalence ratio (ϕ) before reaching a maximum near an equivalence ratio of 1.0, as expected. The temperature and CO_2 concentrations begin to decrease beyond $\phi = 1.0$. As

evident from Fig. 8a, JP-8X45 produces the highest temperature due to the fuel's high aromatic/carbon content. Semi-synthetic fuel, which consists of 50% coal-derived compounds and 50% JP-8 fuel, is the least sooting among the three (due to its lower aromatic content) and displays the lowest temperature. Based on the C/H ratio, CO_2 concentrations for JP-8X should be higher than JP-8 or the semi-synthetic fuel, as confirmed in Fig. 8b,

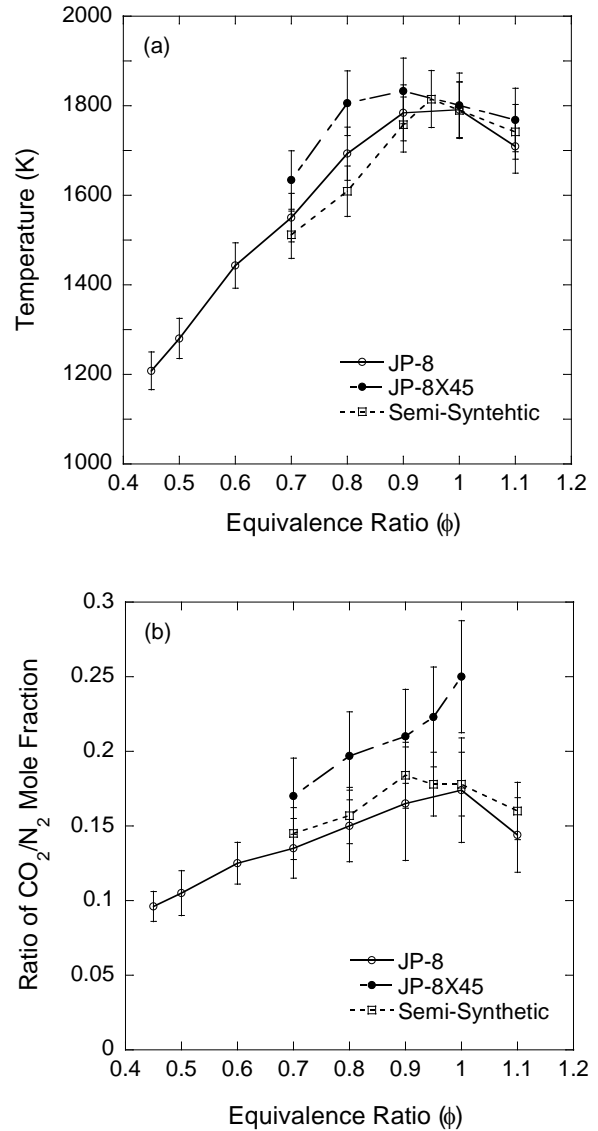


Figure 8: (a) Temperature profiles and (b) CO_2 concentration profiles in the exhaust stream of a liquid-fueled swirl-stabilized combustor for different jet fuels. The uncertainties were calculated based on the analysis of single-laser-shot, dual-pump N_2 - CO_2 CARS spectra.

while the semi-synthetic fuel should be slightly lower than JP-8, contrary to the results shown in Fig. 8b. The CO_2 concentrations were evaluated by fitting the experimental N_2 - CO_2 dual-pump spectra with that of the theoretical ones. The fitting results depend on the quality of the acquired spectra. The baselines of the spectra acquired for the semi-synthetic fuel were very noisy due to strong background scattered light. Because of the limited stock of the semi-synthetic fuel, we were unable to repeat the experiments with this fuel. However, we were able to reduce the background scattered light and the flame luminosity at high equivalence ratios significantly by placing apertures at strategic locations during the experiments with JP-8 fuel. Due to this added spatial filtering, the quality of the spectra acquired for the JP-8 fuel was higher than that of the other fuels.

A comparison with theoretical JP-8 temperature and CO_2/N_2 data from an equilibrium combustion code¹⁵ is shown in Figs. 9a and 9b, respectively. The molecular formula of JP-8 fuel is $\text{C}_{10.9}\text{H}_{20.9}$ and the heat of formation is equal to -2.48×10^5 kJ/K [private communication, T. Edwards, U.S. Air Force Research Laboratory, Wright-Patterson Air Force Base, 2001]. The measured temperatures are lower than the adiabatic flame temperatures by 21% during lean combustor operation and by 28% at the richest condition ($\phi = 1.1$). The increase in this discrepancy at higher equivalence ratios is expected due to increased heat losses at higher temperatures via heat conduction and soot radiation. The measured CO_2/N_2 mole fractions follow the correct trend with equivalence ratio, but are about 15% too high in the lean condition. Under stoichiometric to rich conditions, the difference between measured and theoretical CO_2/N_2 mole fractions decreases to about 7-9%. These discrepancies are mostly due to issues related to the spectral modeling of the CO_2 CARS spectra.¹⁻² These modeling issues are the subject of ongoing investigation and are beyond the scope of the current work.

As stated earlier, the effects of particulate-mitigating additives on temperature and CO_2 concentrations were also studied. It was hypothesized that these additives may alter the flame temperature via soot reduction or changes in flame chemistry. The additive used with JP-8 fuel is known as "KLEEN". The results of the additive study with JP-8 fuel using dual-pump N_2 - CO_2 CARS are summarized in Table 1. The current dual-pump CARS data showed no significant change in the exhaust temperature or CO_2 concentration, however, for various levels of additive concentrations with JP-8 fuel. These additives affect the particle count significantly, but seem to do so through a mechanism that does not alter the final state of the combustion products (i.e., temperature

and CO_2). This infers that other parameters, such as combustion efficiency and CO emissions, may also remain relatively unchanged with additive concentration. A more careful study in the primary flame zone where soot production takes place is necessary for more definitive conclusions regarding the effects of additives on flame chemistry, and is the subject of ongoing study. These measurements show

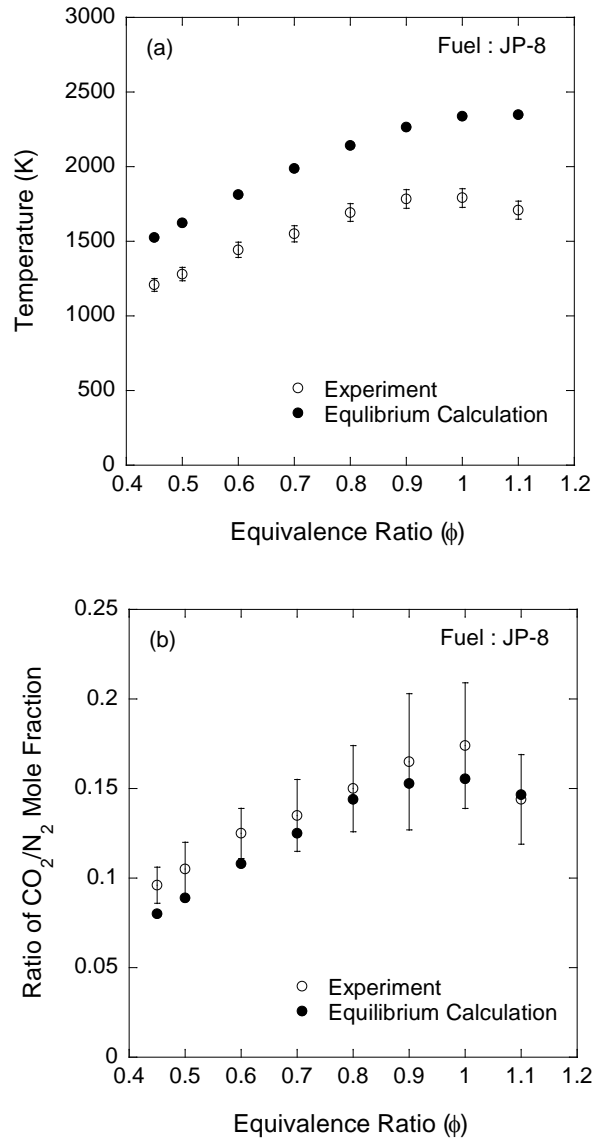


Figure 9: Comparison of the experimental results with that of the equilibrium calculations for JP-8 fuel (a) temperature profiles and (b) CO_2 concentration profiles.

that the precision of the current CARS system is ideally suited, however, for fuel and additive studies in the exhaust stream (as in the current work) or in the primary flame zone (for future work).

Conclusions and Future Direction

The application of dual-pump, dual-broadband CARS to characterize the exit conditions in a swirl-stabilized CFM56 combustor has been demonstrated. This technique is capable of providing measurements of temperature along with concentrations of two target species. Simultaneous, single-shot data acquisition enhances the precision and accuracy of the temperature measurements due to the correlation afforded by the common presence of N_2 in each of the two spectral windows. Experiments were carried out to measure the temperature and the concentrations of carbon-dioxide and oxygen at the exhaust stream of the combustor for different operating conditions. Moreover the effect of additives on the temperature and the carbon-dioxide concentration in the exhaust stream of the combustor were also investigated. Experiments were performed for three different jet fuels for equivalence ratios ranging from 0.4 to 1.1 under low-to-high sooting conditions. The standard deviations of the measured temperature and CO_2 mole fraction as determined from single-laser-shot, dual-pump N_2 - CO_2 CARS spectra were approximately 3-4% and 9-20% of the mean values, respectively, for the full range of equivalence ratios. The wide variation in the single-shot CO_2 concentration was due, in part, to the variation in temperature, as shown in Fig. 7. For a fixed equivalence ratio, the CO_2 mole fraction clearly showed an upward trend with temperature, indicating a positive correlation between temperature and equivalence ratio fluctuations. Both the temperature and the CO_2 concentration peak near an equivalence ratio of 1.0, as expected. Measurements of temperature and CO_2 concentration for a variety of particulate-mitigating additives did not show changes greater than the experimental uncertainty of the current CARS system. These measurements will allow us to pursue future CARS measurements in the reaction zone of the combustor under sooting conditions to complement laser-induced incandescence (LII) and planar laser-induced fluorescence (PLIF) measurements.

Acknowledgments

Funding for this research was provided by the Air Force Research Laboratory, Propulsion Directorate, Wright-Patterson AFB, under Contract Nos. F33615-

00-C-2068, and F33615-00-C-3020, and by the Air Force Office of Scientific Research [Program Monitor: Dr. Julian Tishkoff]. The authors also gratefully acknowledge the assistance of Mikael Afzelius of the Lund Institute of Technology, Sweden for his assistance with the rotational CARS spectral simulation code.

References

- ¹ Roy, S., Meyer, T. R., Brown, M. S., Velur, V.N., Lucht, R. P., and Gord, J. R. (2003), "Triple-Pump Coherent Anti-Stokes Raman Scattering (CARS): Temperature and Multiple-Species Concentration Measurements in Reacting Flows," *Opt. Comm.* **224**, 131-137.
- ² Lucht R. P., Velur, V. N., Fiechtner, G. J., Carter, C.D., Grinstead, Jr., K. D., Gord, J. R., Danehy, P. M., and Farrow, R. L. (2003), *AIAA Journal* **41**:679-686.
- ³ Aldén, M., J., Bengtsson, Edner, H., Kröll, S., and Nilsson, D. (1989), *Applied Optics* **28**, 3206-3219.
- ⁴ Lucht, R. P. (1987), "Three-Laser Coherent Anti-Stokes Raman Scattering Measurements of Two Species," *Optics Letters* **12**, 78-80.
- ⁵ Hancock, R. D., Schauer, F. R., Lucht, R. P., and Farrow, R. L. (1997), "Dual-Pump Coherent Anti-Stokes Raman Scattering Measurements of Hydrogen and Oxygen in a Laminar Jet Diffusion Flame," *Applied Optics* **36**, 3217-3226.
- ⁶ Schauer, F. R. (1998), "Investigation of Flame Structure and Thermal Diffusion Effects in Hydrogen Jet Diffusion Flames," Ph.D. Thesis, University of Illinois at Urbana-Champaign, Urbana, Illinois.
- ⁷ Green, S. M., Rubas, P. J., Paul M. A., Peters, J. E., and Lucht, R. P. (1998), "An Annular Phase-Matched Dual-Pump CARS System for the Simultaneous Detection of Nitrogen and Methane," *Applied Optics* **37**, 1690-1701.
- ⁸ Brüggemann, D., Wies, B., Zhang, X. X., Heinze, T., and Knoche, K. F. (1992), "CARS Spectroscopy for Temperature and Concentration Measurements in a Spark Ignition Engine," in *Combustion Flow Diagnostics*, D. F. G. Durão, M. V. Heitor, J. H. Whitelaw, and P. O. Witze, eds., Kluwer Academic, Dordrecht, The Netherlands, 495-511.
- ⁹ Eckbreth, A. C. (1988), *Laser Diagnostics for Combustion Temperature and Species*, Gordon and Breach Publishers, Amsterdam, The Netherlands.
- ¹⁰ Bood, J., Bengtsson, P.-E., and Aldén, M. (2000), *Applied Physics B* **70**, 607-620.
- ¹¹ Brackmann, C., Bood, J., Bengtsson, P.-E., Seeger, T., Schenk, M., and Leipertz, A. (2002), *Applied Optics* **41**, 564-572.

¹² Roy, S., Meyer, T. R., Lucht, R. P., Belovich, V. M., Corporan, E., and Gord, J. R. (2003), "Temperature and CO₂ Concentration Measurements in the Exhaust Stream of Liquid-Fueled Combustor Using Dual-Pump Coherent Anti-Stokes Raman Scattering (CARS) Spectroscopy," submitted to *Combustion and Flame*.

¹³ Palmer, R. E. (1989), "The CARSFT Computer Code for Calculating Coherent Anti-Stokes Raman Spectra: User and Programmer Information," Report No. SAND89-8206 Sandia National Laboratories, Livermore, California.

¹⁴ Takahashi, F., Schmoll, J. W., Switzer, G. L., and Shouse, D. T. (1994), *Twenty-Fifth Symposium (International) on Combustion*, The Combustion Institute, Pittsburgh, PA, pp. 183-191.

¹⁵ Turns, S. R. (1996), *An Introduction to Combustion*, McGraw-Hill, New York.

Table 1. Summary of additive study results with JP-8 fuel at two different equivalence ratios.

Additive Conc. (mg/L)	$\phi = 0.7$ Fuel: JP-8, Additive: KLEEN			$\phi = 1.1$ Fuel: JP-8, Additive: KLEEN		
	Exhaust Temp. (K)	Product Moles CO ₂ /N ₂	Particle Count Change	Exhaust Temp. (K)	Product Moles CO ₂ /N ₂	Particle Count Change
0	1540 ± 49	0.135 ± 0.02	-	1699 ± 64	0.144 ± 0.025	-
7800	1549 ± 51	0.142 ± 0.022	+ 11.1%	1709 ± 62	0.130 ± 0.028	-
15600	1560 ± 48	0.128 ± 0.02	+ 28.3%	1708 ± 72	0.150 ± 0.022	- 19.1%
31200	1558 ± 51	0.144 ± 0.018	+ 44.0%	1724 ± 70	0.134 ± 0.032	- 31.3%



ELSEVIER

Available online at www.sciencedirect.com

SCIENCE @ DIRECT®

Combustion and Flame 137 (2004) 523–537

Combustion
and Flame

www.elsevier.com/locate/jnlabr/cnf

Two-color, two-photon laser-induced polarization spectroscopy (LIPS) measurements of atomic hydrogen in near-adiabatic, atmospheric pressure hydrogen/air flames

Waruna D. Kulatilaka,^a Robert P. Lucht,^{a,*} Sherif F. Hanna,^b and
Viswanath R. Katta^c

^a School of Mechanical Engineering, Purdue University, West Lafayette, IN 47907-2088, USA

^b Department of Mechanical Engineering, Texas A&M University, College Station, TX 77843-3123, USA

^c Innovative Scientific Solutions, Inc., 2766 Indian Ripple Road, Dayton, OH 45440-3638, USA

Received 14 May 2003; received in revised form 11 March 2004; accepted 17 March 2004

Available online 9 April 2004

Abstract

Two-color, two-photon laser-induced polarization spectroscopy (LIPS) of atomic hydrogen has been demonstrated and applied in atmospheric pressure hydrogen/air flames. Fundamental and frequency-doubled beams from a single 486-nm dye laser were used in the experiments. The 243-nm pump beam in the measurements was tuned to the two-photon $n = 1 \rightarrow n = 2$ resonance of the hydrogen atom. The 486-nm probe beam was tuned to the single-photon $n = 2 \rightarrow n = 4$ resonance of the hydrogen atom. Measurements were performed in an atmospheric pressure H_2 /air flame stabilized on a near-adiabatic, flat-flame calibration burner (the Hencken burner). For the range of pump beam intensities used, the LIPS signal was found to be nearly proportional to the square of the pump beam intensity over a wide range of flame equivalence ratios. Spectral lineshapes were recorded at flame equivalence ratios ranging from 0.85 to 2.10. Vertical H-atom number density distribution profiles were measured in the Hencken burner. The vertical H-atom number density profiles measured along the burner centerline for various flame equivalence ratios were compared with the results of a numerical flame calculation using the UNICORN (Unsteady Ignition and Combustion with Reactions) code. Good agreement between theory and experiment was obtained for stoichiometric and rich flame conditions. For flames with equivalence ratios greater than 1.5, the H-atom concentration was substantially above the adiabatic equilibrium value, even at 50 mm above the burner surface. The slow approach to the adiabatic equilibrium H-atom concentration value can be explained by assuming partial equilibrium in the postflame gases; the H-atom concentration is proportional to the O_2 concentration which requires significant residence time to decrease to its very low equilibrium concentration. These results suggest that the use of the Hencken burner as a radical measurement technique calibration source may be of questionable value for equivalence ratios greater than 1.5 and less than 0.8.

© 2004 The Combustion Institute. Published by Elsevier Inc. All rights reserved.

Keywords: Hydrogen atom; Laser diagnostics; Laser spectroscopy; Polarization spectroscopy; Two-photon absorption; Calibration burner

1. Introduction

Atomic hydrogen is a key species in the chain-branching reactions for hydrocarbon combustion that are responsible for flame ignition, propagation, and

* Corresponding author. Fax: (765)-494-0539.

E-mail address: lucht@purdue.edu (R.P. Lucht).

stability. A reliable, proven technique for measuring atomic hydrogen will have a large impact on studies of fundamental flame structure. We introduce here the technique of two-color, two-photon laser-induced polarization spectroscopy (LIPS), which has the major advantages of high sensitivity and ease of optical alignment. LIPS is an optical diagnostic technique that is essentially a spatially resolved absorption measurement [1–3]. The LIPS signal is a coherent laser-like beam and the optical alignment is fairly simple because the signal beam is collinear with the probe beam [4]. In most LIPS experiments, both pump beam and the probe beam are of the same frequency, and a single-photon resonance is probed [5–10].

Two-photon LIPS has been demonstrated for both atomic and molecular species such as nitrogen (N_2) [11], ammonia (NH_3) [12], carbon monoxide (CO) [12], and monatomic hydrogen (H) [13–15]. However, in these studies the pump and probe beam frequencies were the same. Use of a two-photon absorption process for these species is required for the pump process, but not for the probe process. For atomic species such as the H atom, selection of a single-photon probe step enhances detection sensitivity significantly because of the high oscillator strengths of the single-photon transitions. For the H atom, a single dye laser can be used with the fundamental beam used for the probe step and the frequency-doubled beam used for the pump process; this would not be the case for other atomic species such as monatomic oxygen.

Theoretical studies of LIPS have focused almost exclusively on the investigation of single-photon resonances [1–3]. Theoretical LIPS lineshapes have been calculated and saturation effects have been investigated theoretically for the case where the pump and probe beam are at the same frequency and tuned to a single-photon resonance [16]. The pressure dependence of LIPS signals has also been studied [17]. A theoretical treatment of LIPS in cases where the pump and probe have been tuned to the $1S$ – $2S$ two-photon resonance of the H atom has been reported by Dux et al. [13], although the hyperfine structure of the transition was not included in this treatment.

The energy level structure and spectroscopy of the hydrogen atom have of course been studied extensively [18,19]. As is the case for many atomic species in flames, the first few accessible electronic energy levels for the H atom lie in the vacuum ultraviolet (VUV) spectral region. Excitation of the ground level ($n = 1$) to the lowest excited level ($n = 2$) of atomic hydrogen requires vacuum ultraviolet (UV) radiation at 121.6 nm. Aside from the difficulty of applying nonlinear optical methods such as frequency tripling to the generation of laser radiation at VUV frequencies, the laser radiation and resulting fluores-

cent radiation would be strongly absorbed in the flame medium. Thus, the technique of single-photon LIF using excitation of the $n = 2$ level in atomic hydrogen cannot be used in flame media [20].

Multiphoton excitation schemes can be used to overcome these difficulties. Various schemes of multiphoton excitation to the excited $n = 2$, $n = 3$, and $n = 4$ levels of atomic hydrogen are possible with UV excitation wavelengths. Lucht et al. [21] demonstrated two-photon laser-induced fluorescence (LIF) measurements of atomic hydrogen in flames for the first time. Since then, Aldén et al. [22], Goldsmith and co-workers [23–27], and Salmon and Laurendeau [28] have applied different multiphoton fluorescence schemes for detection of atomic hydrogen in flames. Czarnetzki et al. [20] present a comprehensive comparison of the advantages and disadvantages of various possible excitation schemes in exciting $n = 3$ and $n = 4$ levels. In the single-laser two-step (SLATS) fluorescence detection technique for atomic hydrogen demonstrated by Goldsmith and Laurendeau [23], there is the additional advantage of experimental simplicity, as a single laser source is used to generate the required excitation wavelengths for the two atomic transitions. The fundamental 486-nm beam and the frequency-doubled 243-nm beam from an Nd:YAG pumped dye laser were in simultaneous resonance with the single-photon $n = 2 \rightarrow n = 4$ transition and the two-photon $n = 1 \rightarrow n = 2$ transition, respectively. Bertagnolli et al. [29] and Löwe et al. [30] applied three-photon LIF to measure H-atom profiles in stagnation-flow and low-pressure diamond forming flames, respectively. Photochemical effects of multiphoton excitation LIF detection of H atoms have been studied extensively by Goldsmith and co-workers [31–33]. Several other laser spectroscopic techniques have also been demonstrated for detecting atomic hydrogen in flames. Laser-induced grating spectroscopy [34], two-photon-excited stimulated emission [35], photoionization controlled-loss spectroscopy [36], and two-photon-resonant four-wave-mixing spectroscopy [37] are among them.

Two-color, two-photon, LIPS for detecting atomic hydrogen in flames has been demonstrated for the first time, to our knowledge, in our laboratory. The LIPS technique described in this work is based on an excitation technique for atomic hydrogen similar to that used by Goldsmith and Laurendeau [23] for LIF measurements and by Gray et al. [34] for laser-induced grating spectroscopy. In our measurements, the circularly polarized pump beam was tuned to the two-photon 243-nm $n = 1 \rightarrow n = 2$ resonance of the hydrogen atom, and the linearly polarized probe beam was tuned to the single-photon 486-nm $n = 2 \rightarrow n = 4$ resonance of the hydrogen atom. Fundamental

and frequency-doubled beams from a single 486-nm dye laser were used. This new technique was successfully demonstrated in atmospheric-pressure hydrogen/air flames and has also been applied for measurements of H-atom profiles near the deposition substrate in low-pressure diamond forming flames [38]. The focus of this article is the experimental measurements that have been performed in near-adiabatic atmospheric-pressure hydrogen/air flames.

2. Two-color pump/probe LIPS scheme

The two-color pump/probe scheme for LIPS detection of atomic hydrogen is shown in Fig. 1. The hyperfine structure of the $1S_{1/2}$, $2S_{1/2}$, and $4P_{1/2}$ levels is depicted schematically. As indicated in Fig. 1, the pump beam is circularly polarized and two-photon absorption occurs between the lower ($F = 1$, $M_F = -1$) state and the upper ($F = 1$, $M_F = +1$) state. (Note: In the absence of hyperfine splitting of the $1S$ and $2S$ levels two-photon absorption of the circularly polarized radiation would not be allowed.) The two-photon absorption process results in an anisotropic distribution of population in the Zeeman states in the upper $2S_{1/2}$ level. This anisotropic distribution is probed using a linearly polarized 486-nm beam tuned to the single-photon $2S_{1/2}$ – $4P_{1/2}$ transition (the $2S_{1/2}$ – $4P_{3/2}$ transition is not shown for reasons of clarity). The linearly polarized 486-nm beam can be regarded as a superposition of left- and right-circularly polarized laser radiation. In the absence of the pump beam,

the two components will be unaffected by passage through the flame medium and the probe beam polarization will remain linear. After passing through the flame, the probe beam is blocked by a Glan-laser polarizer, termed the analyzer, oriented with its transmission axis normal to the direction of the linear polarization of the probe beam. However, as the probe beam traverses the medium containing the two-photon-pumped H atoms, one of the components is absorbed to a greater extent than the other component, resulting in a slight elliptical polarization for the probe beam. The increased leakage through the analyzer due to the elliptical polarization of the probe beam is the LIPS signal.

3. Experimental apparatus and procedure

A schematic diagram of the experimental system for the two-color, two-photon LIPS experiment is shown in Fig. 2. The 355-nm third harmonic of a Nd:YAG laser (Continuum Model Powerlite Precision 8010) is used to pump a dye laser (Continuum Model ND 6000). The Q-switched Nd:YAG laser has a repetition rate of 10 Hz and a maximum pulse energy of 350 mJ at 355 nm. The dye laser was operated using LD 490 laser dye. The lasing maximum of this dye was at 489 nm and the tunable range was 466–518 nm [39]. The dye was dissolved in methanol and concentrations of 560 mg/L for the oscillator and 80 mg/L for the amplifier, determined by experiment

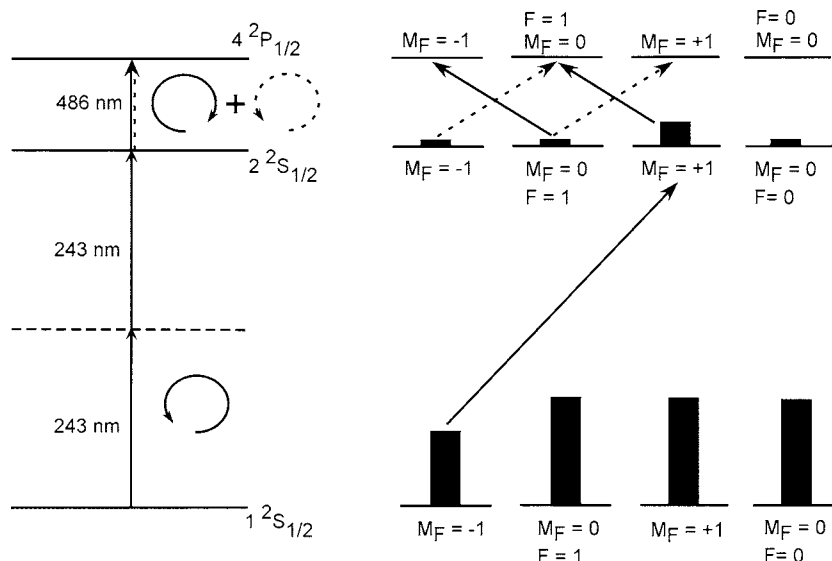


Fig. 1. Schematic diagram of the two-color, two-photon LIPS technique for the measurement of atomic hydrogen. Two-photon excitation of the $n = 2$ level with a circularly polarized pump beam at 243 nm is followed by single-photon absorption of the linearly polarized probe beam at 486 nm. The linearly polarized pump beam can be considered as a superposition of left-circularly and right-circularly polarized beams of equal magnitude.

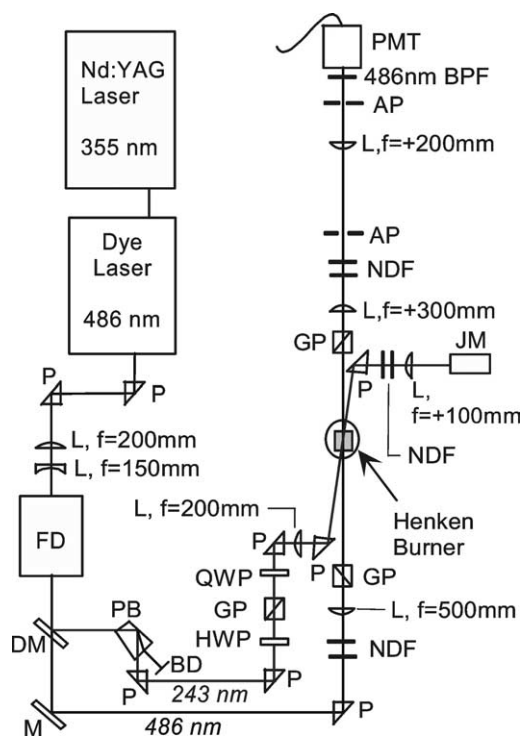


Fig. 2. Schematic diagram of the two-color, two-photon laser-induced polarization spectroscopy (LIPS) experimental apparatus. P, prism; L, lens; FD, frequency doubler/auto tracker; DM, dichroic mirror; M, mirror; PB, Pellin–Broca; BD, beam dump; HWP, half-wave plate; GP, Glan polarizer; QWP, quarter-wave plate; NDF, neutral density filters; JM, Joule meter; AP, aperture; BPF, band-pass filter; PMT, photomultiplier tube.

for our laser system, were used to obtain pulse energies of 25–35 mJ. According to the manufacturer's specifications the dye laser pulse has a linewidth of 0.07 cm^{-1} at 515 nm when using a UV grating. The minimum tunable step size is 0.001 nm, set by the dye laser control computer program. The specified re-settability of the tunable grating in the dye laser is $\pm 0.05 \text{ nm}$.

The 486-nm output beam of the dye laser was passed through a telescope having a positive lens and a negative lens with focal lengths of +200 and –150 mm, respectively. The distance between two lenses was set at 50 mm to produce a nearly collimated beam directed into the frequency-doubling apparatus (Inrad Model Autotracker III). The 243-nm output beam had a maximum pulse energy of 1.5 mJ when the input laser power was 35 mJ. The incoming 486-nm beam was vertically polarized and the frequency doubled 243-nm beam was horizontally polarized.

The ultraviolet output beam from the Autotracker III was then reflected once from a 243-nm mirror and

directed to a Pellin–Broca prism. The Pellin–Broca prism was used to disperse the 243-nm beam and the residual 486-nm beam. The residual 486-nm beam from the Pellin–Broca prism was carefully dumped with minimal scatter. The 243-nm beam was reflected from a 90° prism and then transmitted through a high-quality α -BBO (beta barium borate) polarizer with a horizontal transmission axis. This polarizer was set with its transmission axis in a vertical orientation. A zero-order 248-nm UV-grade half-wave plate was inserted before the polarizer and rotated until power was maximized through the α -BBO polarizer. The pump beam was then directed through a zero-order, anti-reflection-coated, UV-grade fused silica quarter-wave plate (QWP) centered at 248 nm. The QWP axis was set at an angle of 45° to the polarization direction of the incoming beam to obtain circular polarization of the pump beam. The circularly polarized pump beam was then directed through a 90° prism and focused by a +200-mm plano-concave lens. The focusing lens was mounted on a translation stage with its translation axis parallel to the direction of the beam propagation. The pump beam was then reflected using another 90° prism across the middle of the burner. The pump beam was placed as close as possible to the edge of the final prism to obtain the minimum crossing angle with the probe beam. All prisms and the focusing lens were UV-grade fused silica and were AR-coated for the range 225–308 nm. After passing through the flame, the 243-nm beam was reflected from another fused silica prism, directed through two 50% transmission neutral density filters, and then focused onto a Joulemeter (Molelectron Model J3-05) using a +50-mm fused-silica plano-convex lens. The Joulemeter was used to record the pump-beam pulse energy.

The 486-nm beam was transmitted through the 243-nm mirror placed after the Autotracker III and then reflected using a glass window. The front reflection from the glass window, with an intensity of approximately 4% of the total beam, was used as the probe beam for LIPS. It was directed through the center of the burner in such a way that it just cleared the vertical edge of the fused silica prism, which directed the pump beam onto the burner to achieve the minimum crossing angle of 1.8° . The probe beam was passed through a set of neutral density (ND) filters mounted on two filter wheels to control its intensity before entering the flame. A +500-mm, plano-convex BK7 lens mounted on a translation stage was used to focus the probe beam at the center of the burner. Immediately after the focusing lens, the probe beam was directed through a calcite Glan-laser polarizer with a vertical transmission axis. Another calcite Glan-laser polarizer, termed the analyzer, was placed after the burner in the probe beam path. This second polarizer

was mounted on a high-precision rotary mount having an angular resolution of 15 arcsec. The transmission axis of the analyzer was horizontal and was adjusted such that two polarizers were crossed. The rejection ratio of the crossed polarizers was measured to be $(4.2 \pm 0.2) \times 10^{-5}$. The rejection ratio is the ratio of the probe intensity transmitted through crossed polarizers to the probe intensity transmitted through uncrossed polarizers. The probe intensity when the polarizers were crossed was measured by adjusting the analyzer until the photomultiplier tube (PMT) signal was minimized. To measure the intensity transmitted when the polarizers were uncrossed, the analyzer was turned until the PMT signal became maximum. However, in this case additional ND filters with known optical density were placed in front of the PMT to maintain the signal level below the saturation limit for the PMT. This signal reading was then divided by the transmittance of ND filters to obtain the probe beam intensity when the polarizers were uncrossed. To ensure that the probe and pump beams focused and crossed exactly over the center of the burner, a 100- μm pinhole was mounted on the centerline of the burner. The probe and the pump beams were adjusted so that they were focused as close as possible to the pinhole and so that each of them passed through the pinhole.

To align the optics in the signal channel, the second Glan polarizer was slightly uncrossed and the 486-nm beam that leaked through was collimated using a +300-mm-focal-length BK7, plano-convex lens. The collimated beam was passed through an aperture and focused onto another aperture using a +200-mm BK7, plano-convex lens. The second aperture was placed 65 mm in front of a Hamamatsu R212 PMT. The PMT was approximately 2.5 m from the burner. The PMT was powered by a regulated high-voltage power supply (Stanford Research Systems, Inc., Model PS 325/2500V-25W). A 486-nm band-pass filter (Thermo Corron Model P10-486-F) was placed in front of the PMT to block scattered ultraviolet light and flame emission. A set of ND filters was placed in the beam path to control the intensity of the signal directed onto the PMT. In addition, a series of black extension beam tubes were inserted around the beam from the first aperture all the way to the PMT, and the whole system was covered by a thick black cloth. By doing this, the level of scattered light incident on the PMT was reduced to a negligible level compared with the probe leakage through the analyzer. The outputs of the PMT and the Joulemeter were connected to two separate gated integrator modules (Stanford Research Systems Model SR 250). When needed, the PMT signal output was amplified using a fast preamplifier (Stanford Research Systems Model SR 240). A digital oscillo-

scope (Hewlett Packard Model Infinium, 500 MHz) was used for real-time monitoring of the averaged signal output and the gate pulse from each gated integrator. The digital outputs of the gated integrators were recorded using a custom virtual instrument (VI) program in LabVIEW 6.1.

The non-premixed, two-dimensional, near-adiabatic, flat-flame Hencken calibration burner from Research Technologies (Model RD15X15) was used to produce atmospheric pressure H_2/air flames. The geometry of the Hencken burner and the arrangement of fuel and oxidizer channels are illustrated in Fig. 3. This burner is designed such that rapid mixing of fuel and the oxidizer takes place immediately above the burner surface. The burner incorporates a 36.5-mm square hastalloy honeycomb on the top, supporting stainless-steel fuel tubes in every fourth hon-

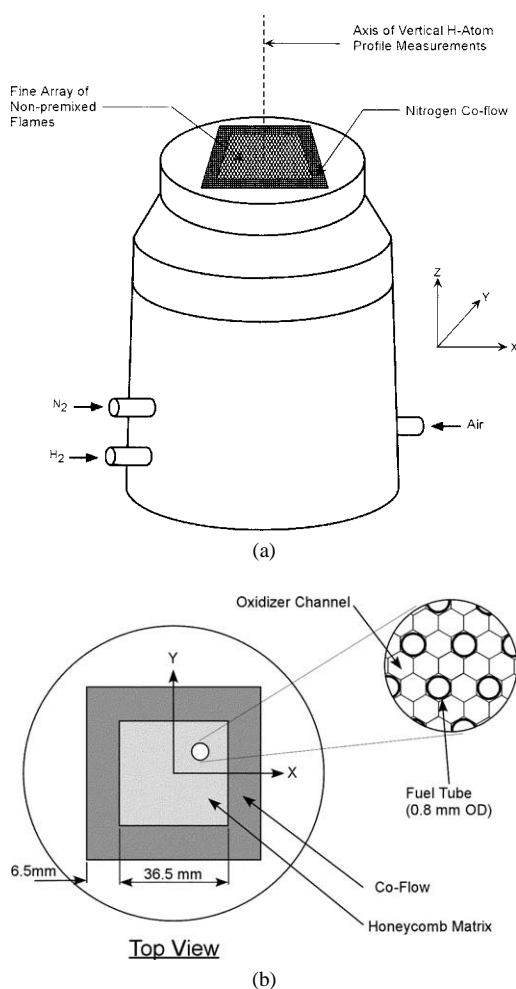


Fig. 3. (a) Hencken calibration burner used to generate hydrogen/air flames. (b) Top view of the burner showing the arrangement of fuel tubes and oxidizer channels.

eycomb cell. The fuel tubes are of 0.508-mm inside diameter and 0.813-mm outside diameter. The tubes are uniformly distributed. The honeycomb cells are 0.813 mm in diameter and have a 0.051-mm wall thickness. The fuel tubes are well sealed from the oxidizing gas. The oxidizer flows around the fuel tubes and through the honeycomb to mix with the fuel above the burner surface and, hence, a combustible mixture occurs only above the burner surface. The 36.5-mm inner square region is surrounded by a 6.5-mm-wide area which can be used to flow an inert gas co-flow around the main flame, thus creating a shroud for the flame.

The burner assembly was mounted on a platform that can be moved horizontally on slide rails. The burner assembly can be moved vertically using a step-per motor drive system. The smallest step size of the vertical motion was 0.013 mm. A linear dial gauge having a resolution of 0.025 mm was fixed between the burner assembly and the floor. It was used to measure the vertical movement of the burner.

The air and nitrogen flows were regulated using 0–4 standard-cubic-foot-per-minute (scfm) rotameters (King Instrument Co.) with needle control valves. The hydrogen was made to flow at a regulated pressure of 40 psig and the hydrogen flow was controlled by another rotameter (Gilmont Instruments, Model GF-5321-1502-65 mm) with a needle control valve. All rotameters were calibrated using a BIOS International, DryCal DC-1 primary airflow meter with DC-1HC interchangeable flow cell. The accuracy of calibration was $\pm 1\%$ in 10-sample averaged readings. According to our experience, to obtain a stable hydrogen/air flame in the equivalence ratio range $\Phi = 0.75$ to $\Phi = 2.00$, the airflow rate was fixed at 53.5 slpm and the hydrogen flow rate was varied from 15 to 50 slpm. Although the airflow rate was held constant, the rotameter used in the air line had to be adjusted from time to time to account for the pressure variations in the supply line. It was found that this rotameter had an uncertainty as high as 5.5 slpm. Thus the uncertainty of the calculated equivalence ratio values using the flow rate readings from the above flowmeters is between 13 and 17% for equivalence ratio variation between 0.75 and 2.00. For lean flames, the uncertainty increases because the hydrogen flow rates are lower.

4. Experimental results

4.1. Single-laser, two-step excitation LIF measurements

Initially, single-laser, two-step (SLATS) LIF detection of the H atom was performed. As the laser

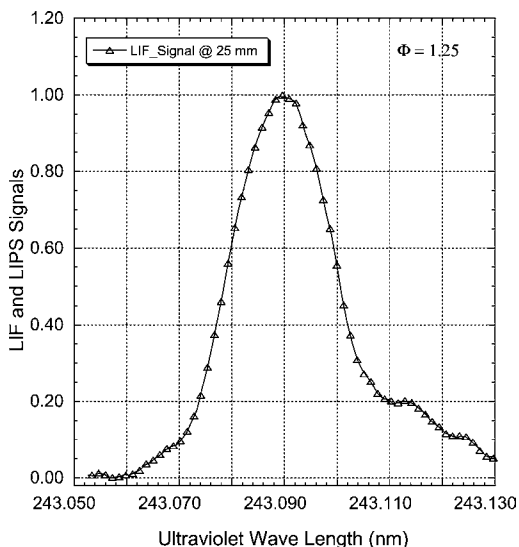


Fig. 4. Single-laser, two-step laser-induced fluorescence (LIF) signal of $4P-2S$ radiative decay of atomic hydrogen. This spectrum was recorded in the H_2 /air flame stabilized at atmospheric pressure on the Hencken calibration burner.

excitation schemes of SLATS and LIPS are similar, the SLATS measurements were performed to calibrate the dye laser wavelength. Fluorescence was collected at right angles to the laser beams using a +150-mm-focal-length, 50-mm-diameter lens. The fluorescence collected was then focused using another +300-mm-focal-length, 50-mm-diameter lens onto the R212 PMT. A 486-nm bandpass filter was used to block the ultraviolet scattered light and flame emission. Although a mechanical shutter synchronized with the laser was incorporated in front of the PMT to block background flame emission, no significant amount of emission was observed from the H_2 /air flame. The dye laser was scanned from 243.050 to 243.150 nm at a rate of 0.001 nm/s and the signal was averaged for 30 laser shots. The recorded SLATS LIF signal is shown in Fig. 4.

4.2. Laser-induced polarization spectroscopy measurements

Based on calibration results from the LIF experiment, the LIPS signal was obtained for the first time in the H_2 /air flame. To obtain the spectral lineshape of the hydrogen transition using LIPS, the 243-nm UV beam was scanned across the peak transition wavelength determined previously. The peak signal was observed at 243.090 nm and hence the UV pump beam was scanned from 243.050 to 243.150 nm. The signal was recorded in one data file for 300–500 laser shots, at one particular setting of the pump beam wavelength. Then the pump beam was blocked and

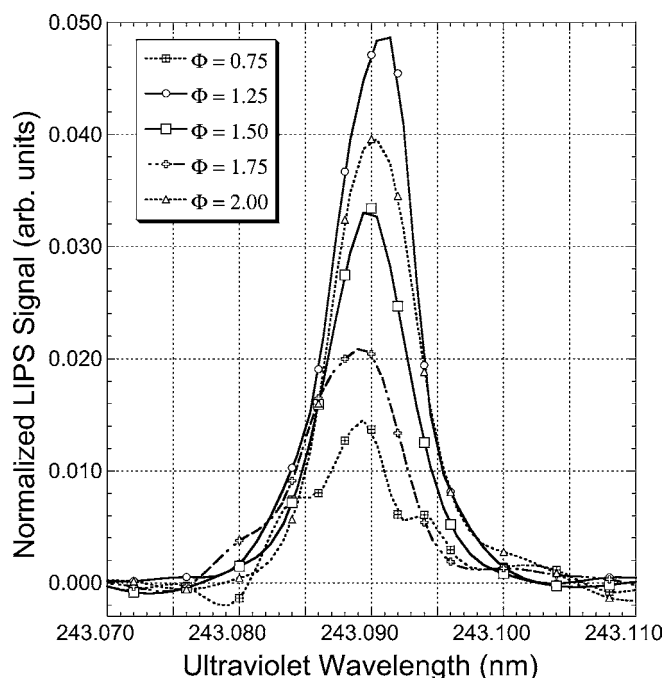


Fig. 5. LIPS lineshapes recorded for different flame equivalence ratios at 25 mm above burner surface in H_2/air flame stabilized on the Hencken burner with 64-slm nitrogen shroud flow. The absolute signal is normalized by dividing by the pump laser intensity raised to the power 2.50.

the background was recorded for the same number of laser shots as a separate data file. The quantities were averaged and the absolute LIPS signal was obtained by subtracting the background from the signal. The pump beam was scanned in larger steps of about 0.006 nm when the pump beam wavelength was far from the resonance and when the wavelength was near the resonance the step size was reduced to 0.002 nm. By these means the data acquisition process was expedited, hence minimizing the decay of the dye laser power during a scan. A set of spectral lines were obtained 3 and 25 mm above the burner surface while operating the Hencken burner with an H_2/air mixture for different equivalence ratios. The results are shown in Fig. 5. The LIPS signals obtained were very strong, and care was required to operate the signal PMT in the linear regime. The LIPS signals were clearly visible on the digital oscilloscope on single laser shots for all equivalence ratios. Initially, we recorded lineshapes that were quite broad due to PMT saturation. Subsequent to our initial measurements, neutral density filters were inserted in the signal channel to ensure that the PMT did not saturate for the acquisition of the spectra shown in Fig. 5.

The spectral lineshapes shown in Fig. 5 are plotted with peak amplitudes normalized to a value of 1.0 in Fig. 6 for equivalence ratios ranging from 0.75 to 2.00. The spectral lines are plotted versus twice the

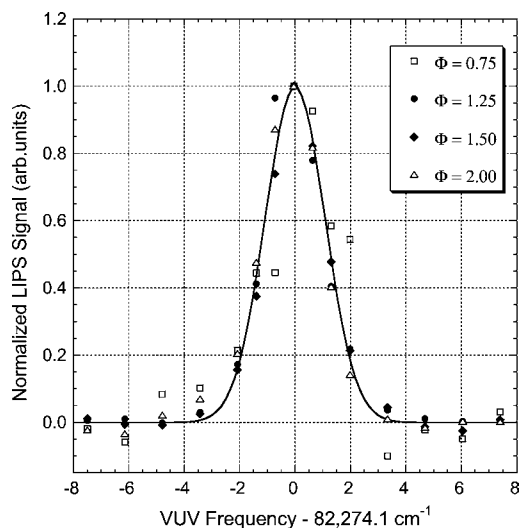


Fig. 6. LIPS lineshapes for flame equivalence ratios of 0.75, 1.25, 1.50, and 2.00 recorded at a height of 25 mm above the burner surface as shown in Fig. 5, normalized to a peak at 1.0. The solid line is a gaussian profile with a full width at half-maximum of 2.55 cm^{-1} .

frequency of the 243-nm pump beam. A gaussian profile with a full width at half-maximum of 2.55 cm^{-1} is also plotted in Fig. 6; this corresponds to the Doppler profile for the $1S-2S$ H-atom transition for

a flame temperature of 2000 K. To within the experimental scatter, the measured lineshapes are in very good agreement with this calculated Doppler profile at each equivalence ratio. This is an indication that the both the collisional linewidth and the laser spectral widths at 243 and 486 nm are much less than the Doppler width for these flame conditions. The estimated laser spectral width is approximately 0.2 cm^{-1} .

The pump laser power dependence of the LIPS signal was investigated for different flame equivalence ratios. To vary the pump power, a half-wave plate was placed in front of the first polarizer in the pump beam path and gradually rotated. When both the pump and probe laser intensities are low enough that no resonance saturation occurs, the LIPS signal will be given by

$$S_{\text{LIPS}} \propto n_{\text{H}}^2 I_{\text{pump}}^4 I_{\text{probe}}, \quad (1)$$

where S_{LIPS} is the LIPS signal (arbitrary units), n_{H} is the number density (m^{-3}) of H atoms in the ground 1S level, and I_{pump} and I_{probe} are the pump and probe laser intensities (W/m^2), respectively. The results of the investigation of the dependence of the LIPS signal on pump laser power are shown in Fig. 7. For each of the equivalence ratios, the signal is approximately proportional to the square of the pump

laser power, indicating that the 243-nm 1S–2S two-photon transition is saturated to a significant extent.

For all measurements subsequent to the initial lineshape measurements we were careful to operate the PMT in the linear response region because the LIPS signal was very strong. The PMT saturation characteristics were investigated separately. To operate in the linear region of the PMT, it was found that it is necessary to operate with a peak PMT signal level below 60 mV as observed on the digital oscilloscope with a $50\text{-}\Omega$ input impedance and a PMT voltage of 800 V. The maximum signal level for each case was observed using the digital oscilloscope prior to data acquisition, and additional neutral density filters were placed in the signal channel when needed. The pulse energy of the probe beam was not monitored during these experiments. The probe intensity should be approximately proportional to the square root of the pump intensity as they originated from the same dye laser. Also for sufficiently low probe intensities, the absolute LIPS signal will have a linear dependence on the probe intensity. The absolute LIPS signal was normalized by dividing by the pump intensity raised to the power 2.50 for all cases; we used a value for pump power dependence that was approximately the average of the measurements at different equivalence ratios. For analysis of the experimental data, therefore, we used the follow-

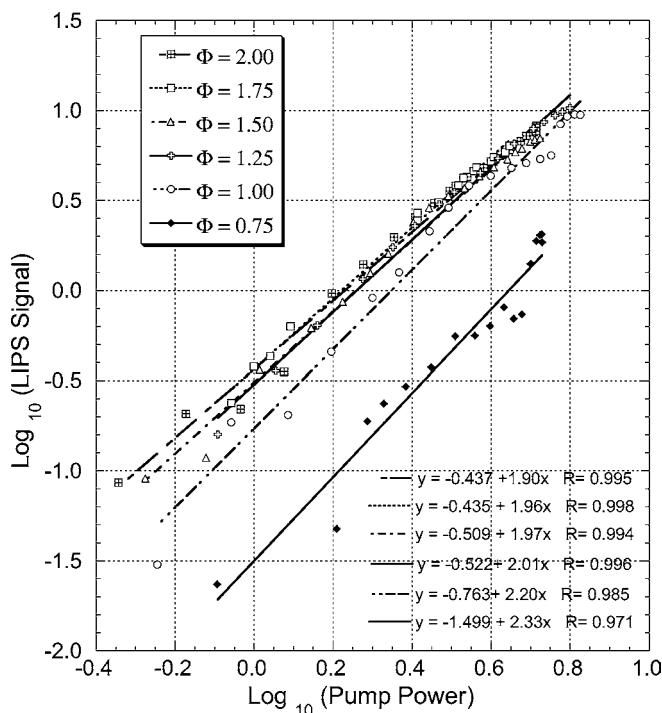


Fig. 7. Saturation profiles of the LIPS signal for different flame equivalence ratios. The H_2/air flame was operated with an N_2 shroud flow of 64 slpm in each case. Careful attention was given to avoid any possible detector saturation at high signal levels.

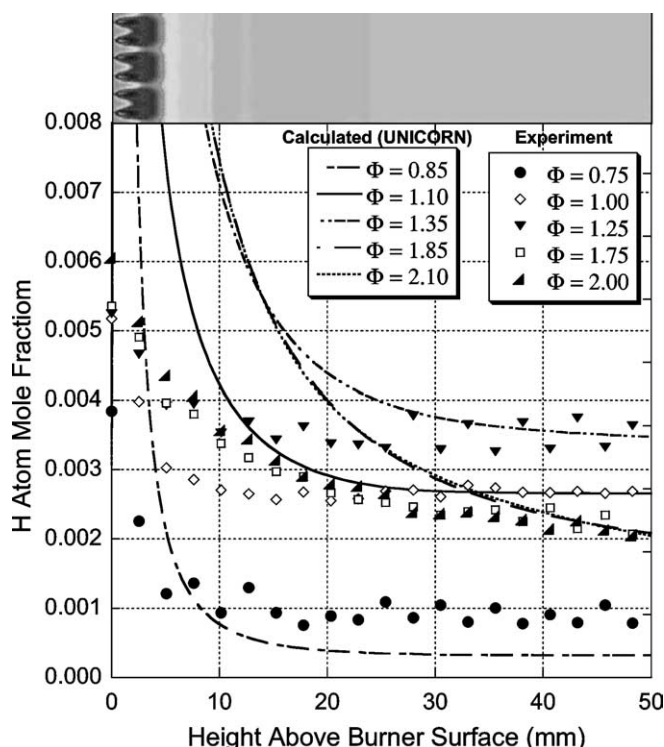


Fig. 8. Vertical profiles of the H-atom LIPS signal along the flame centerline for varying equivalence ratios. All Hencken burner flames were operated with an airflow rate of 53.5 slpm and with a nitrogen co-flow of 64 slpm. The H_2 flow rate was varied from 16.8 to 44.7 slpm and with nitrogen co-flow of 64 slpm. The LIPS signal was normalized by dividing the pump intensity to the power 2.50. The H-atom distribution profile calculated using the UNICORN code is shown above the plot for the equivalence ratio 1.75 case.

ing formula:

$$S_{LIPS} \propto n_H^2 I_{pump}^{2.00} I_{probe} \propto n_H^2 I_{pump}^{2.50} \quad (2)$$

The region just above the surface of the Hencken burner is a complex region where mixing between the fuel and air occurs and hundreds of millimeter-scale diffusion flames are established. The products from these millimeter-scale diffusion flamelets mix and continue to react until chemical equilibrium is established in the postflame gases. The mixing/reaction processes were investigated by performing vertical H-atom profile measurements along the centerline of the burner for different equivalence ratios. This measurement is of particular interest for identifying regions where chemical equilibrium is established because the Hencken burner is frequently used as a calibration burner. Vertical scans were performed for different equivalence ratios. To compensate for the variation in pump beam power due to loss of dye power in 486-nm dye laser, the burner was first moved downward in steps of 5 mm, and then moved upward in steps of 5 mm, covering the intermediate 2.5-mm intervals. The recorded vertical LIPS signal profiles for five different equivalence ratios are compared with

numerical calculations of the H-atom mole fraction profiles in Fig. 8.

The numerical calculations were performed using the UNICORN (Unsteady Ignition and Combustion with Reactions) code that was developed for Navier–Stokes simulations. More details concerning this code can be found in Refs. [40–43]. The flame formed over the Hencken burner can be viewed as the combination of several diffusion flamelets. Each of the diffusion flamelets is independently supported with a separate fuel tube (Fig. 3). The exact nature of the flamelet, such as, diffusion, premixed, or partially premixed type, depends on the flow conditions. The finite-rate-chemistry code, UNICORN, can be used to predict this flame type through detailed simulation. The flamelet established over the fuel tube of 0.81-mm outer diameter and 0.15-mm-thick wall is modeled as an axisymmetric flame. The hexagonal opening around the fuel tube through which air flows is modeled as a 1.83-mm-diameter co-annular tube. Axisymmetric calculations are performed for a physical domain of 0.915×50 mm using a 31×151 grid system. While symmetric conditions are forced at the axis as well as at the outer boundary in the radial direction,

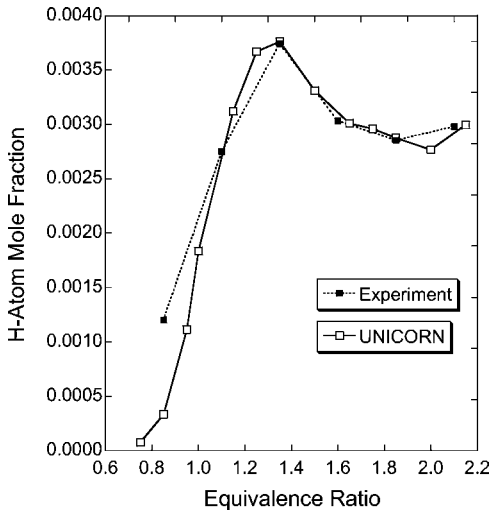


Fig. 10. Comparison of measured and calculated H-atom mole fractions versus equivalence ratio at a height 30 mm above the burner surface. The equivalence ratio for the measured H-atom mole fractions has been increased by 0.1 for each data point for best agreement with the calculated values. The measured H-atom mole fraction is normalized to the calculated value for an equivalence ratio of 1.35.

5. Discussion of results

The H-atom distributions shown in Figs. 8 and 9 for H_2 /air flames reveal some important characteristics that may have a significant influence on the measurements made using the multiflamelet Hencken burner. First, the hydrogen atom seems to reach an equilibrium state fairly rapidly (approx 20 mm high) for the near-stoichiometric flames while a considerable delay is evident in the fuel-rich flames. Second, the equilibrium concentration of H atom decreased significantly when the equivalence ratio was reduced to 0.75 from the stoichiometric value. In addition, the simulations also revealed that the peak concentration of the H atom is nearly independent of equivalence ratio. To understand these characteristics the numerical solutions obtained for various equivalence ratios are analyzed.

The calculated concentration profiles for the H and OH radicals and the O_2 molecule are shown in Fig. 11 for several equivalence ratios. A logarithmic scale was chosen for magnifying the variations in the species concentrations. The dramatic decrease in H-atom concentration for the $\Phi = 0.75$ flame compared with the other flames is clearly shown in Fig. 11a. Moreover, the H-atom concentration for the $\Phi = 2.0$ case did not reach an equilibrium value even at 50 mm above the burner surface. The OH-radical concentration (Fig. 11b), on the other hand, decreases gradually with decreasing equivalence ratio and the

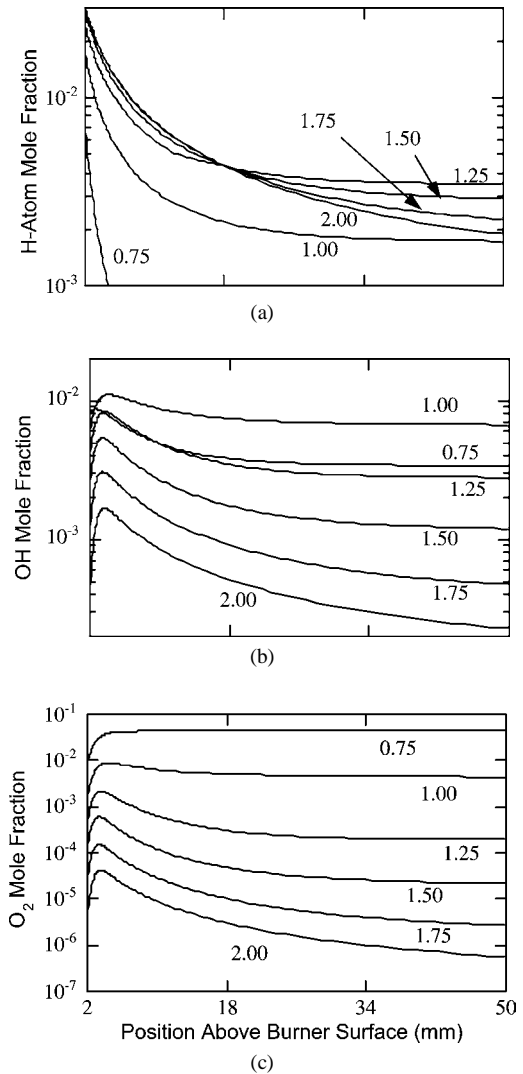


Fig. 11. Mole fraction profiles for (a) H atom, (b) OH, and (c) O_2 versus height above the burner surface for various equivalence ratios, calculated using the UNICORN code.

value at $\Phi = 0.75$ is only slightly lower than that obtained for the stoichiometric condition. The extension of the nonequilibrium regime beyond the 50-mm height for the $\Phi = 2.0$ flame is also evident in the OH and O_2 plots (Figs. 11b and 11c).

Calculations and experiments for the data presented in Fig. 8 were performed in such a way that the flow rate of air was kept constant and the flow rate of fuel was varied to obtain the desired equivalence ratio. As a result, at a given location in the burner the fluid velocity increases and, hence, the residence time decreases when equivalence ratio is increased. For example, the velocity at the 50-mm location increases from 14 m/s for the $\Phi = 1.0$ flame to 16.8 m/s for

the $\Phi = 2.0$ flame. This corresponds to a decrease of almost 20% in residence time for the $\Phi = 2.0$ flame compared with the $\Phi = 1.0$ flame.

The results of perfectly stirred reactor (PSR) calculations [44] for H_2 -air flames at various equivalence ratios are shown in Figs. 12a and 12b. The H-atom mole fraction at the exit of the PSR is plotted as a function of residence time for equivalence ratios from 0.5 to 2.0. Note that the H-atom mole fraction reaches its equilibrium value [45] at residence times on the order of 100 ms for the $\Phi = 1.0$ flame. For the $\Phi = 2.0$ flame, on the other hand, the H-atom mole fraction is still about four times its equilibrium value at a residence time of 100 ms. The slow approach to equilibrium for the $\Phi = 0.75$ flame is also evident from Figs. 12a and 12b.

The slow approach to the equilibrium concentration for the H-atom profile for the rich flames can be understood by assuming that the following bimolecular reactions are in partial equilibrium in the postflame region:



As discussed by Warnatz [46] the mole fractions of the radical species H, O, and OH can be expressed in terms of the “stable” species H_2 , O_2 , and H_2O if reactions (R1)–(R3) and are assumed to be in partial equilibrium. These relations are [47]

$$x_{\text{H}} = \left(\frac{k_{1f}^2 k_{2f} k_{3f} x_{\text{O}_2} x_{\text{H}_2}^3}{k_{1r}^2 k_{2r} k_{3r} x_{\text{H}_2\text{O}}^2} \right)^{1/2}, \quad (3)$$

$$x_{\text{O}} = \frac{k_{1f} k_{2f} x_{\text{O}_2} x_{\text{H}_2}}{k_{1r} k_{2r} x_{\text{H}_2\text{O}}}, \quad (4)$$

$$x_{\text{OH}} = \left(\frac{k_{2f} k_{3f} x_{\text{O}_2} x_{\text{H}_2}}{k_{2r} k_{3r}} \right)^{1/2}, \quad (5)$$

where k_{if} and k_{ir} are the rate coefficients ($\text{cm}^3/\text{g mol}$) for reactions R_i , $i = 1, 2, 3$, listed in Eqs. (R1)–(R3). For the flame with an equivalence ratio of 2.0, the slow approach to the equilibrium value of the H atom as a function of PSR residence time is a result of the slow approach of the O_2 concentration to equilibrium. The slow approach of the O_2 mole fraction profile to its very low equilibrium value of 2.05×10^{-7} is also evident in Fig. 11. Assuming partial equilibrium in the postflame zone of the H_2 -air flames, the H-atom mole fraction will be proportional to the square root of the O_2 mole fraction and will approach equilibrium on the same time scale as the O_2 mole fraction. A comparison of the H-atom mole fraction at the exit of the PSR and that calculated assuming partial equilibrium at the exit of the PSR is shown in Fig. 13; for

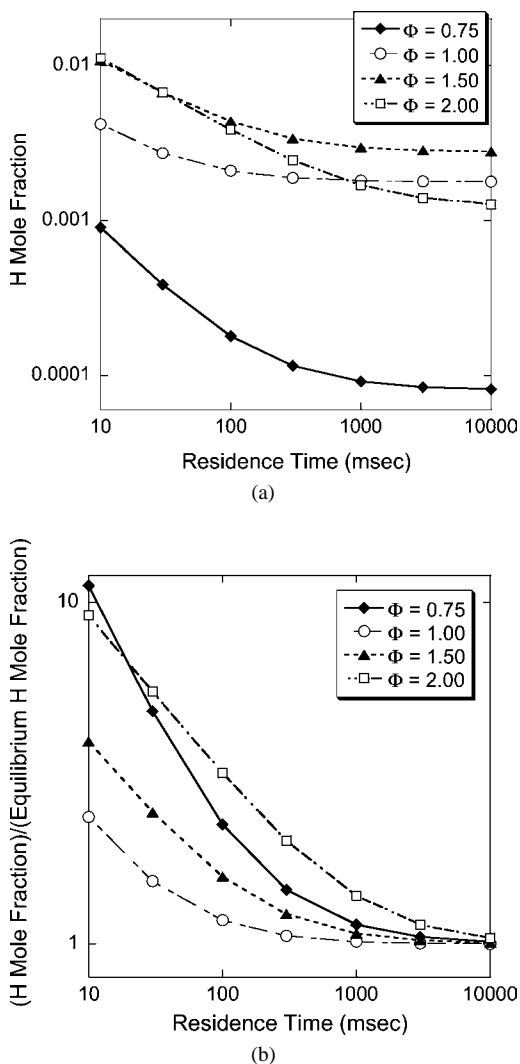


Fig. 12. Results of PSR calculations of H-atom mole fractions as a function of residence time for H_2 -air flames at various equivalence ratios. (a) Plot of H-atom mole fraction. (b) Ratio of the H-atom mole fraction to its adiabatic equilibrium value.

the partial equilibrium calculations shown in Fig. 13 the values of the rate constants were evaluated from data given in Turns [47]. As is evident from Fig. 13, the H-atom mole fraction at the PSR exit is within a factor of 2 of the partial equilibrium value for all residence times. The H-atom mole fraction cannot reach its equilibrium value until the O_2 mole fraction reaches its very low equilibrium value due to the partial equilibrium established by the fast bimolecular reactions (R1)–(R3).

Similar reasoning would explain the slow approach to equilibrium for the lean $\Phi = 0.75$ flame, except that in this case it would be the H_2 mole frac-

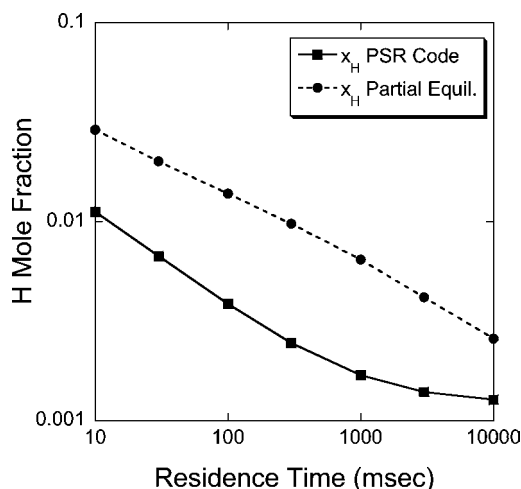


Fig. 13. H-atom mole fraction as calculated from the PSR code versus residence time, compared with the H-atom mole fraction calculated from Eq. (3) assuming the reactions (R1)–(R3) are in partial equilibrium. For the partial equilibrium calculations, the values of x_{H_2} , x_{O_2} , and x_{H_2O} and T were taken from the PSR code at the given residence time.

tion that would have to decrease to its very low equilibrium value for the H-atom mole fraction to reach its equilibrium value. For the $\Phi = 1.0$ flame, the equilibrium mole fractions for H_2 and O_2 are 0.0153 and 0.00481, respectively, and these equilibrium values are reached quickly. Thus in the $\Phi = 1.0$ flame equilibrium values of radical concentrations are reached at residence times much shorter than for the $\Phi = 2.0$ and $\Phi = 0.75$ flames. A comparison between H-atom mole fractions and temperatures calculated at a height of 50 mm above the burner surface using the UNICORN code with the adiabatic equilibrium values are shown in Fig. 14. As is evident from Fig. 14, the H-atom mole fractions are significantly higher than the adiabatic equilibrium values for equivalence ratios of 1.5 or greater, but the calculated temperature is very close to the adiabatic equilibrium value at all equivalence ratios.

Near the burner surface, the UNICORN H-atom mole fraction is much higher than that evident from the experimental measurements. This can be understood by comparing the UNICORN profile shown in Fig. 9 with the Hencken burner geometry shown in Fig. 3. The H-atom mole fraction profiles shown in Fig. 8 are calculated along a vertical line centered on a fuel tube. Our experimental probe volume is approximately 3 mm in length in the direction of propagation of the laser. Thus, for the experimental measurements, the H-atom distribution is averaged over several fuel tubes, resulting in lower H-atom mole fractions near the burner surface as compared with the numerical calculations.

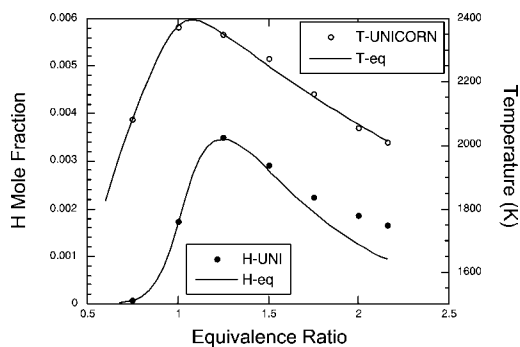


Fig. 14. H-atom mole fraction and flame temperatures as calculated from the UNICORN code at 50 mm above the burner surface for the Hencken burner compared with adiabatic equilibrium values.

For the lean flame conditions, specifically for the $\Phi = 0.75$ flame, the H-atom concentration values calculated using the UNICORN code are less than experimentally observed values, as is evident from Fig. 8. For lean conditions the LIPS signal is comparatively low and the uncertainty in determining the equivalence ratio is also high as the gas flow rates are small. In this region the H-atom mole fraction is very dependent on the equivalence ratio. Therefore it is believed that this deviation is partly due to uncertainty in experimental measurements of gas flow rates. Because of the low value of the H-atom mole fraction, there is also more uncertainty associated with the subtraction of the LIPS background signal. It is also possible that photochemical production of H atoms from water vapor is more significant under these lean conditions. Goldsmith [31] observed a high degree of photochemical production of H-atoms from the 243-nm 1S–2S step for lean flames. This behavior will be further investigated in our future experiments. By incorporating mass flow controllers to control gas flow rates, we will be able to significantly reduce the uncertainty in the measurement of the equivalence ratio. We also plan to use α -BBO polarizers in future experiments; crossed α -BBO polarizers will have rejection ratios of 10^{-7} or better [48], significantly enhancing our detection sensitivity and reducing uncertainty associated with background subtraction.

6. Conclusions and future efforts

Two-color, two-photon, laser-induced polarization spectroscopy of atomic hydrogen was demonstrated in atmospheric pressure hydrogen/air flame operated on the Hencken burner. Spectral lineshapes were recorded at different flame equivalence ratios. Saturation characteristics of the 243-nm 1S–2S two-photon excitation step were investigated. For all equivalence

ratios, the LIPS signal was approximately proportional to the square of the pump power, although the power dependence did tend to increase as the equivalence ratio decreased. In the unsaturated regime, the LIPS signal is proportional to the pump power raised to the fourth power, so the 243-nm $1S$ – $2S$ two-photon excitation step was significantly saturated for these measurements.

Measured H-atom mole fraction vertical profiles in hydrogen/air flames for flame equivalence ratios of 1.10–2.10 show good agreement with theoretical profiles for heights greater than 20 mm above the burner surface, although the collisional environments in these cases are quite different. The spectral line-shape for the LIPS measurements was very similar for the different flame equivalence ratios investigated. These results indicate that the two-color, two-photon LIPS process is fairly insensitive to the collisional quenching environment. The slower approach to the equilibrium H-atom mole fraction for the rich flames that is evident in both experiment and theory is a result of the slow approach to equilibrium of the O_2 molecule. The slow approach of the H-atom mole fraction to its equilibrium value can be explained by assuming that the fast bimolecular reactions in the H_2/O_2 system are in partial equilibrium in the post-flame region.

The development and testing of a numerical model for the Hencken burner are of great significance because of the widespread use of this burner as a calibration burner for laser diagnostics of combustion systems [29,49–51]. The results of a comparison of experiment and numerical calculations presented in this article indicate that care must be exercised in using this burner as a calibration standard for minor species measurements for very fuel-rich or very fuel-lean flames. Decreasing the flow rate of the gases to increase the residence time is one option for obtaining postflame radical concentrations that are closer to adiabatic equilibrium values, but decreasing the flow rate will also increase the heat loss to the burner. If significant heat transfer to the burner occurs, the flame conditions will of course depart from the adiabatic equilibrium condition.

The LIPS technique demonstrated in this work has the advantages of high signal levels and experimental simplicity. Future efforts will be directed at improving theoretical and numerical models of the LIPS process and at developing a tunable, high-resolution, solid-state laser source to increase the accuracy and precision of the measurements. However, one of the major difficulties with performing the H-atom measurements discussed in this article was the limited lifetime of the laser dyes used to produce the 486-nm laser radiation. The rapid degradation of the dye laser power complicated the measurements and made it dif-

ficult to normalize for laser power fluctuations. We are currently developing an injection-seeded optical parametric generator system [52] based on 355-nm pumping of solid-state β -BBO crystals for generation of single-mode, tunable 486-nm laser radiation. This system will be used in future experiments and will eliminate problems associated with laser dye degradation. Theoretical and numerical modeling analysis of the LIPS process will also continue and will be the subject of forthcoming publications.

Acknowledgments

This work was supported by the U.S. Department of Energy, Office of Basic Energy Sciences, Division of Chemical Sciences, Geosciences, and Biosciences, under Grant DE-FG03-99ER14997. The numerical flame modeling work was supported, in part, by the Air Force Office of Scientific Research (Dr. Julian Tishkoff, Technical Monitor).

References

- [1] R.E. Teets, F.V. Kowalski, W.T. Hill, N. Carlson, T.W. Hänsch, *SPIE* 113 (1977) 80–87.
- [2] C. Weiman, T.W. Hänsch, *Phys. Rev. Lett.* 36 (1976) 1170–1173.
- [3] H.H. Ritze, V. Stert, E. Meisel, *Opt. Commun.* 29 (1979) 51–56.
- [4] T.A. Reichardt, W.C. Giancola, R.P. Lucht, *Appl. Opt.* 39 (2000) 2002–2008.
- [5] W. Ernst, *Opt. Commun.* 44 (1983) 159–164.
- [6] G. Zizak, J. Lanauze, J.D. Winefordner, *Appl. Opt.* 25 (1986) 3242–3246.
- [7] K. Nyholm, R. Maier, C.G. Aminoff, M. Kaivola, *Appl. Opt.* 32 (1993) 919–924.
- [8] K. Nyholm, R. Fritzton, M. Aldén, *Appl. Phys. B* 59 (1994) 37–43.
- [9] K. Nyholm, *Opt. Commun.* 111 (1994) 66–70.
- [10] M.J. New, P. Ewart, A. Dreizler, T. Dreier, *Appl. Phys. B* 65 (1997) 633–637.
- [11] C.F. Kaminski, B. Löfstedt, R. Fritzton, M. Aldén, *Opt. Commun.* 129 (1996) 38–43.
- [12] K. Nyholm, R. Fritzton, N. Georgiev, M. Aldén, *Opt. Commun.* 114 (1995) 76–82.
- [13] R. Dux, K. Grützmacher, M.I. de la Rosa, B. Wende, *Phys. Rev. E* 51 (1995) 1416–1427.
- [14] K. Danzmann, K. Grützmacher, B. Wende, *Phys. Rev. Lett.* 57 (1986) 2151–2153.
- [15] K. Grützmacher, M.I. De La Rosa, A.B. Gonzalo, M. Steiger, A. Steiger, *Appl. Phys. B* 76 (2003) 775–785.
- [16] T.A. Reichardt, R.P. Lucht, *J. Chem. Phys.* 109 (1998) 5830–5843.
- [17] J. Walewski, C.F. Kaminski, S.F. Hanna, R.P. Lucht, *Phys. Rev. A* 64 (2001) 3816–3827.
- [18] K. Pachucki, D. Leibfried, M. Weitz, A. Huber, W. König, T.W. Hänsch, *J. Phys. B* 29 (1996) 177–195.

- [19] A.I. Ferguson, J.M. Tolchard, *Contemp. Phys.* 28 (1987) 383–405.
- [20] U. Czarnetzki, K. Miyazaki, T. Kajiwara, K. Muraoka, M. Maeda, H.F. Döbele, *J. Opt. Soc. Am. B* 11 (1994) 2155–2162.
- [21] R.P. Lucht, J.T. Salmon, G.B. King, D.W. Sweeney, N.M. Laurendeau, *Opt. Lett.* 8 (1983) 365–367.
- [22] M. Aldén, A.L. Schawlow, S. Svanberg, W. Wendt, P.L. Zhang, *Opt. Lett.* 9 (1984) 211–213.
- [23] J.E.M. Goldsmith, N.M. Laurendeau, *Opt. Lett.* 15 (1990) 576–578.
- [24] J.E.M. Goldsmith, R.J.M. Anderson, L.R. Williams, *Opt. Lett.* 15 (1990) 78–80.
- [25] J.E.M. Goldsmith, *Opt. Lett.* 10 (1985) 116–118.
- [26] J.E.M. Goldsmith, L.A. Rahn, *Opt. Lett.* 15 (1990) 814–816.
- [27] J.E.M. Goldsmith, *Appl. Opt.* 29 (1990) 4841–4842.
- [28] J.T. Salmon, N.M. Laurendeau, *Combust. Flame* 74 (1988) 221–231.
- [29] K.E. Bertagnolli, R.P. Lucht, M.N. Bui-Pham, *J. Appl. Phys.* 83 (1998) 2315–2326.
- [30] A.G. Löwe, A.T. Hartlieb, J. Brand, B. Atakan, K. Kohse-Höinghaus, *Combust. Flame* 118 (1999) 37–50.
- [31] J.E.M. Goldsmith, *Appl. Opt.* 28 (1989) 1206–1213.
- [32] J.E.M. Goldsmith, M. Aldén, U. Westblom, *Appl. Opt.* 29 (1990) 4852–4859.
- [33] J.E.M. Goldsmith, *Opt. Lett.* 11 (1986) 416–418.
- [34] J.A. Gray, J.E.M. Goldsmith, R. Trebino, *Opt. Lett.* 18 (1993) 444–446.
- [35] J.E.M. Goldsmith, *J. Opt. Soc. Am. B* 6 (1989) 1979–1985.
- [36] J.T. Salmon, N.M. Laurendeau, *Appl. Opt.* 26 (1987) 2881–2891.
- [37] J.A. Gray, R. Trebino, *Chem. Phys. Lett.* 216 (1993) 519–524.
- [38] W.D. Kulatilaka, S.F. Hanna, R.P. Lucht, in: *Proceedings, Third Joint Meeting of the U.S. Sections of the Combustion Institute*, 2003.
- [39] *Laser Dye Catalogue*, Exciton Inc., 1999.
- [40] W.M. Roquemore, V.R. Katta, in: *Proceedings, VSJ-SPIE98*, 1998.
- [41] V.R. Katta, L.P. Goss, W.M. Roquemore, *Combust. Flame* 96 (1994) 60–74.
- [42] V.R. Katta, L.P. Goss, W.M. Roquemore, *AIAA J.* 32 (1994) 84–94.
- [43] V.R. Katta, L.P. Goss, W.M. Roquemore, *Int. J. Numer. Methods Heat Fluids Flow* 4 (1994) 413–424.
- [44] F. Glarborg, R.J. Kee, J.F. Grcar, J.A. Miller, Report No. SAND86-8209, Sandia National Laboratories, 1986.
- [45] W.C. Reynolds, *The Element Potential Method for Chemical Equilibrium Analysis: Implementation in the Interactive Program STANJAN*, Department of Mechanical Engineering, Stanford Univ., 1986.
- [46] J. Warnatz, *Combust. Sci. Technol.* 26 (1981) 203–213.
- [47] S.R. Turns, *An Introduction to Combustion: Concepts and Applications*, McGraw–Hill, Boston, 2000, p. 117.
- [48] T.A. Reichardt, F. Di Teodoro, R.L. Farrow, S. Roy, R.P. Lucht, *J. Chem. Phys.* 113 (2000) 2263–2269.
- [49] R.D. Hancock, K.E. Bertagnolli, R.P. Lucht, *Combust. Flame* 109 (1997) 323–331.
- [50] Q.V. Nguyen, R.W. Dibble, C.D. Carter, G.J. Feichtner, R.S. Barlow, *Combust. Flame* 105 (1996) 499–510.
- [51] P.A. Nooren, M. Versluis, T.H. van der Meer, R.S. Barlow, J.H. Frank, *Appl. Phys. B* 71 (2000) 95–111.
- [52] W.D. Kulatilaka, T.N. Anderson, T.L. Bougher, R.P. Lucht, *Appl. Phys. B* (2004), submitted for publication.

Dual-pump dual-broadband coherent anti-Stokes Raman scattering in reacting flows

Sukesh Roy and Terrence R. Meyer

Innovative Scientific Solutions, Inc., 2766 Indian Ripple Road, Dayton, Ohio 45440

Robert P. Lucht

Department of Mechanical Engineering, Purdue University, West Lafayette, Indiana 47907

Mikael Afzelius and Per-Erik Bengtsson

Division of Combustion Physics, Lund Institute of Technology, Lund S-22100, Sweden

James R. Gord

Air Force Research Laboratory, Propulsion Directorate, Wright-Patterson Air Force Base, Ohio 45433

Received March 25, 2004

A dual-pump, dual-broadband coherent anti-Stokes Raman scattering system for simultaneous measurements of temperature and concentrations of N_2 , O_2 , and CO_2 in reacting flows is demonstrated. In this system pure rotational transitions of N_2 - O_2 and rovibrational transitions of N_2 - CO_2 are probed simultaneously with two narrowband pump beams, a broadband pump beam, and a broadband Stokes beam. The main advantage of this technique is that it permits accurate temperature measurements at both low and high temperatures as well as concentration measurements of three molecules. © 2004 Optical Society of America

OCIS codes: 120.1740, 300.6230.

A dual-pump, dual-broadband coherent anti-Stokes Raman scattering (CARS) system for simultaneous temperature and multiple-species concentration measurements in reacting flows is demonstrated. This work extends our previous demonstrations of temperature and multiple-species concentration measurements in laboratory flames and combustor test facilities using dual- and triple-pump CARS.^{1,2} Several other CARS techniques, such as dual-broadband rotational CARS^{3,4} and simultaneous vibrational and rotational CARS⁵ that employ a single-pump laser, have also been used as tools for simultaneous temperature and multiple-species concentration measurements.

The current technique allows accurate temperature measurements at both low and high temperatures. In the combustion zone or the exhaust of a real combustor there are wide spatial and temporal variations of temperature as a result of the inherently turbulent nature of the flow field. In the current system the rotational transitions of N_2 - O_2 and the rovibrational transitions of N_2 - CO_2 are probed. The rotational spectra of N_2 - O_2 provide improved temperature accuracy at lower temperatures, generally below 1500 K,⁶ whereas the rovibrational spectra of N_2 - CO_2 provide improved temperature accuracy at higher temperatures. To our knowledge this is the first CARS technique that employs two narrowband pump beams and a broadband pump beam to excite the transitions of three different molecules simultaneously to achieve two rotational spectra (e.g., N_2 and O_2) and two rovibrational spectra (N_2 and CO_2).

The experimental schematic and energy-level diagrams of the dual-pump, dual-broadband CARS system are shown in Figs. 1(a) and 1(b), respectively. As is evident from Fig. 1, this technique is essentially a combination of a dual-pump and a dual-broadband

CARS system, the former generating a rovibrational CARS signal from the N_2 - CO_2 pair and the latter generating a pure rotational CARS signal from the N_2 - O_2 pair. An injection-seeded Nd:YAG laser is used to pump one narrowband dye laser and one broadband dye laser while providing a 532-nm CARS

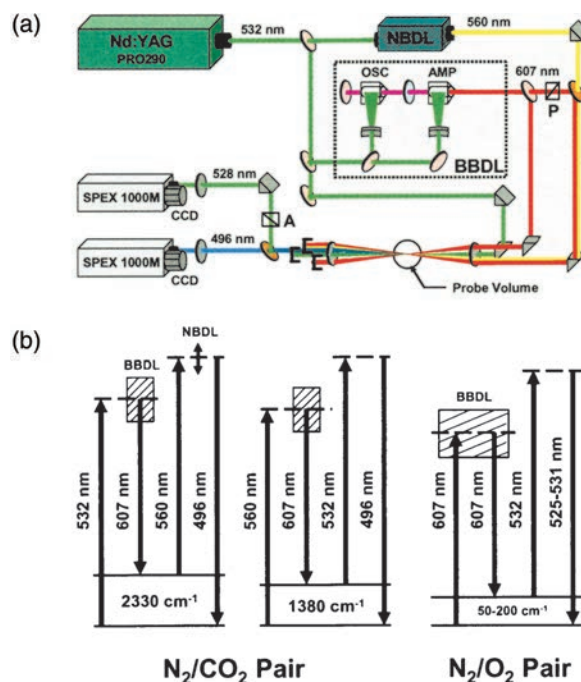


Fig. 1. (a) Schematic of the dual-pump, dual-broadband CARS system for detecting temperature and concentrations of N_2 , O_2 , and CO_2 . NBDL, narrowband dye laser; BBDL, broadband dye laser; P, polarizer; A, analyzer. (b) Energy-level diagram of the dual-pump, dual-broadband CARS system.

pump beam. The broadband dye output, centered about 607 nm, serves as the Stokes beam for each of the CARS signals generated as well as the pump beam for the dual-broadband rotational CARS system. The narrowband dye laser provides laser radiation at ~ 560 nm. The combination of the 532-nm pump beam with the 607-nm Stokes beam produces a rovibrational N_2 Raman polarization that coherently scatters the 560-nm pump beam, yielding an N_2 CARS signal near 496 nm. At the same time the 560-nm pump beam and the 607-nm Stokes beam produce a CO_2 Raman polarization that scatters the 532-nm pump beam, yielding a CO_2 CARS signal that also appears near 496 nm. The polarization of the broadband pump beams at 607 nm is oriented to be orthogonal to that of the 532-nm beam.

The broadband pump beam and the broadband Stokes beam produce rotational Raman polarizations for both N_2 and O_2 molecules, which then scatter the 532-nm pump beam. The pure rotational CARS spectra appear mainly in the 525–531-nm range. The incident beams are phase matched using the folded BOXCARS geometry, with the 560- and 607-nm pump beams arranged collinearly. The CARS signals at 496 and 528 nm are separated using a dichroic mirror before being simultaneously detected by two 1.0-m spectrometers and two nonintensified, back-illuminated CCD cameras. The CARS spectra are normalized using a nonresonant spectrum to account for the finite bandwidth of the dye-laser spectral profiles and the spectral variations in dye power. The nonresonant spectrum is recorded by placing the beam-overlap region within an open argon flow tube.

Measurements were performed in an atmospheric-pressure, near-adiabatic, hydrogen–air flame seeded with CO_2 and stabilized on a Hencken burner. The rovibrational spectra of N_2 – CO_2 and the pure rotational spectra of N_2 – O_2 were acquired simultaneously at 10 Hz. Typical 100-shot-average rotational spectra of N_2 – O_2 and rovibrational spectra of N_2 – CO_2 are shown in Fig. 2. An inherent consequence of setting up a simultaneous vibrational and rotational CARS system is that an additional broadband vibrational CARS signal will contribute to the background of the rotational spectra of N_2 – O_2 .⁵ This background contribution is subtracted by fitting a smooth curve through the base of the rotational CARS spectra. The temperature and the relative CO_2 and O_2 concentrations are evaluated by comparison of the experimental spectra with theoretical ones. As expected, the temperatures evaluated from both spectra agree to within experimental uncertainty, as shown in Fig. 2. Probability density functions of temperatures evaluated from the single-shot N_2 – CO_2 rovibrational spectra and from the N_2 – O_2 rotational spectra are shown in Figs. 3(a) and 3(b), respectively. Two different theoretical codes were used to fit the single-shot rovibrational spectra and the single-shot rotational spectra. The standard deviations of the temperature evaluated from the N_2 – CO_2 spectra and from the N_2 – O_2 spectra are $\sim 2\%$ and $\sim 2.5\%$ of the mean values, respectively. The standard deviations of the rotational and the rovibrational spectra are related

mainly to laser-mode fluctuations, as discussed in Ref. 7 and the references therein. The probability density functions of the ratio of CO_2 and N_2 mole fractions and the ratio of O_2 and N_2 mole fractions are shown in Figs. 3(c) and 3(d), respectively.

A comparison of the experimental results with an equilibrium calculation is shown in Fig. 4. As is evident from Fig. 4(a), the measured temperatures from the rovibrational spectra are approximately 20–50 K lower than those from the equilibrium calculations. The temperatures evaluated from the rotational spectra are ~ 40 K lower at low equivalence ratios, and the difference between the experimental and theoretical temperatures increases at higher temperatures. The discrepancy between the measured and the calculated temperatures may be due to the following three reasons: (1) uncertainty with the mass-flow controller, (2) radiation heat loss to the burner (~ 5 K for the equivalence ratios reported here), and (3) the signal-to-noise ratio of the experimental spectra that affects the least-squares fitting with the theoretical spectra. At higher temperatures the rotational spectra of O_2 – N_2 underpredict the equilibrium temperatures by ~ 150 K, possibly as the result of a low signal-to-noise ratio of the spectra and the fact that the subtraction of the broadband vibrational CARS signal affects the evaluated temperature to a large extent under those conditions.⁵ The measured ratios of O_2 – N_2 and CO_2 – N_2 mole fractions show reasonably good agreement with the equilibrium calculations, as shown in Fig. 4(b). There are still some issues related to the modeling of the CO_2 spectra that are

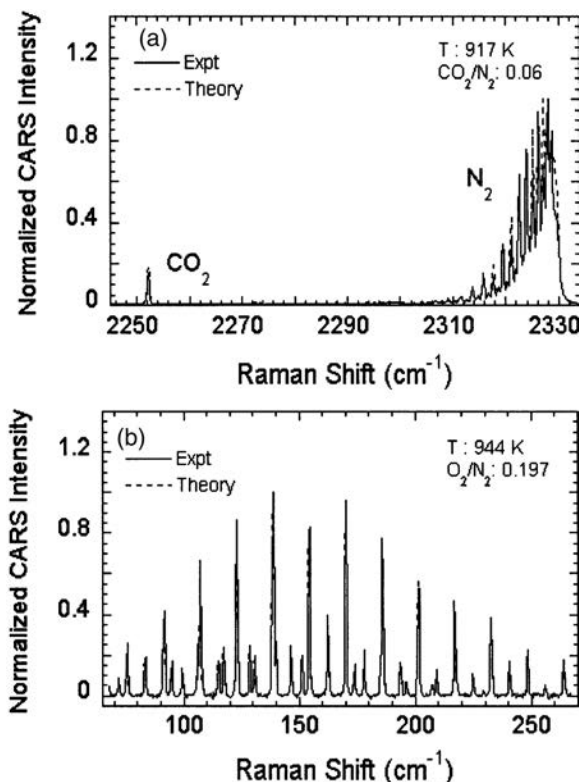


Fig. 2. Typical (a) N_2 – CO_2 and (b) N_2 – O_2 spectra acquired simultaneously in a near-adiabatic, hydrogen–air– CO_2 flame stabilized on a Hencken burner at $\phi = 0.25$.

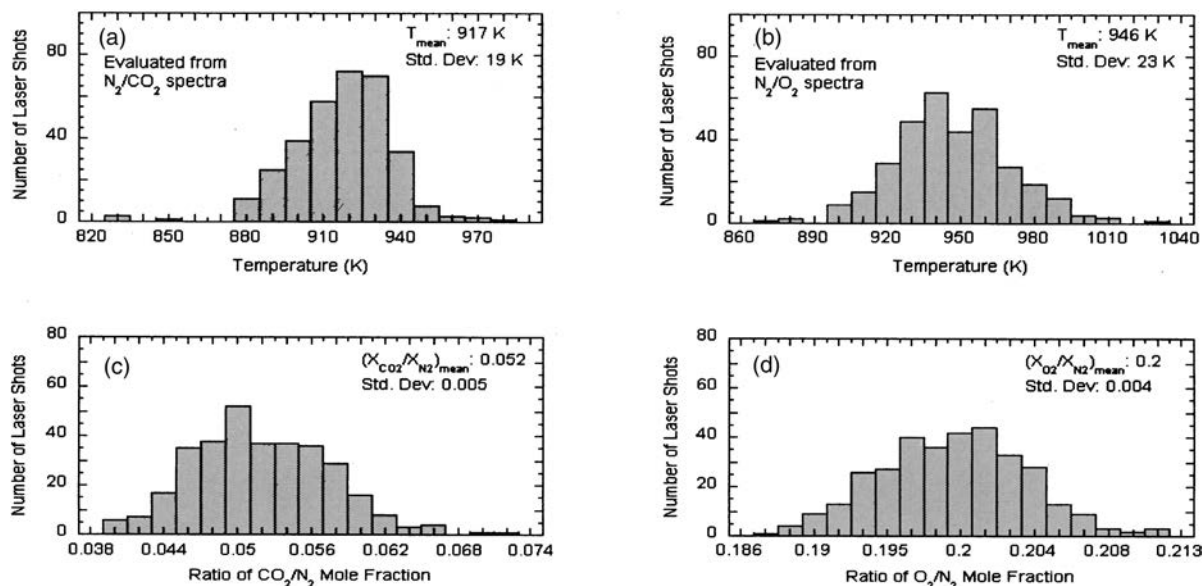


Fig. 3. Single-shot probability density functions acquired in a near-adiabatic, hydrogen–air–CO₂ flame stabilized on a Hencken burner at $\phi = 0.25$ for (a) temperature evaluated from rovibrational spectra of N₂–CO₂, (b) temperature evaluated from rotational spectra of N₂–O₂, and the ratios of (c) CO₂/N₂ and (d) O₂/N₂.

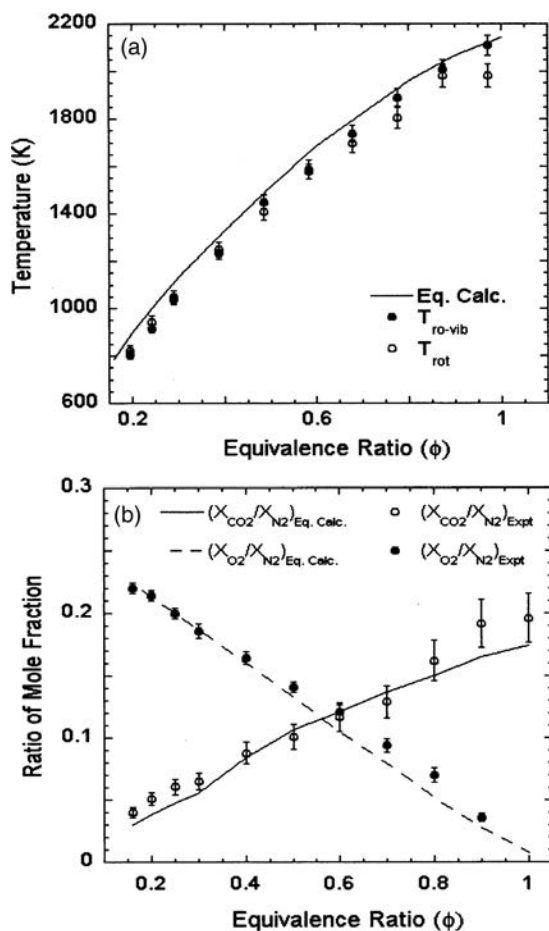


Fig. 4. Comparison of experimental results and equilibrium calculations: (a) temperature profiles and (b) profiles of the ratios of CO₂/N₂ and O₂/N₂.

beyond the scope of this work.² At high equivalence ratios the O₂/N₂ concentrations are higher than ex-

pected, which may be because of problems associated with the subtraction of the undesired background contribution. At higher temperatures the coupling between nonresonant susceptibility and concentration is higher, especially since the O₂ concentration is lower at high temperature.

In summary, a dual-pump, dual-broadband CARS system for simultaneous measurements of temperature and multiple-species concentrations in reacting flows was demonstrated. This system will allow temperature measurement in both low- and high-temperature regions in dynamically reacting flows along with the concentration of multiple species.

Funding for this research was provided by the Air Force Research Laboratory, Propulsion Directorate, Wright-Patterson Air Force Base, under contracts F33615-03-D-M2329 and F33615-00-C-2020 and by the U.S. Air Force Office of Scientific Research (Julian Tishkoff, Program Manager). S. Roy's e-mail address is suresh@innssi.com.

References

1. S. Roy, T. R. Meyer, M. S. Brown, V. N. Velur, R. P. Lucht, and J. R. Gord, *Opt. Commun.* **224**, 131 (2003).
2. R. P. Lucht, V. N. Velur, G. J. Fiechtner, C. D. Carter, K. D. Grinstead, Jr., J. R. Gord, P. M. Danehy, and R. L. Farrow, *AIAA J.* **41**, 679 (2003).
3. A. Thumann, M. Schenk, J. Jonscheit, T. Seeger, and A. Leipertz, *Appl. Opt.* **36**, 3500 (1997).
4. J. Bood, P.-E. Bengtsson, and M. Aldén, *Appl. Phys. B* **70**, 607 (2000).
5. C. Brackmann, J. Bood, P.-E. Bengtsson, T. Seeger, M. Schenk, and A. Leipertz, *Appl. Opt.* **41**, 564 (2002).
6. M. Aldén, P.-E. Bengtsson, H. Edner, S. Kröll, and D. Nilsson, *Appl. Opt.* **28**, 3206 (1989).
7. M. Afzelius and P.-E. Bengtsson, *J. Raman Spectrosc.* **34**, 940 (2003).

Nonperturbative modeling of two-photon absorption in a three-state system

Robert P. Lucht^{a)}

School of Mechanical Engineering, Purdue University, West Lafayette, Indiana 47907-2088

Sukesh Roy

Innovative Scientific Solutions, Inc., Dayton, Ohio 45440

James R. Gord

Air Force Research Laboratory, Propulsion Directorate, Wright-Patterson Air Force Base, Ohio 45433-7251

(Received 8 July 2004; accepted 2 September 2004)

The physics of the two-photon absorption process is investigated for a three-state system. The density-matrix equations for the two-photon interaction are solved in the steady-state limit assuming that the pump laser radiation is monochromatic. Collisional broadening, saturation, and Stark shifting of the two-photon resonance are investigated in detail by numerical solution of the steady-state density-matrix equations. Analytical expressions for the saturation intensity and the Stark shift are derived for the case where the single-photon transitions between the intermediate state and the initial and final states are far from resonance with the pump laser. For this case, it is found that the direction of the Stark shift is dependent on the relative magnitudes of the dipole-moment matrix elements for the single-photon transitions that couple the intermediate state with the initial and final states. Saturation and Stark shifting are also investigated for the case where the single-photon transitions between the intermediate state and the initial and final states are close to resonance with the pump laser. © 2004 American Institute of Physics.

[DOI: 10.1063/1.1809572]

I. INTRODUCTION AND MOTIVATION

Two-photon absorption was first discussed by Göppert-Mayer,¹ but it was not until the development of the laser that the technique of fluorescence detection following two-photon absorption became useful as a spectroscopic probe.^{2–4} Over the last two decades, spectroscopic techniques based on the interaction of laser radiation with two-photon-absorption resonances have emerged as powerful techniques for probing flames and plasmas. Following the initial demonstration of the technique of two-photon-absorption laser-induced fluorescence (TPA-LIF) for detection of the species O and N in a flow discharge by Bischel, Perry, and Crosley,⁵ TPA-LIF detection of H,⁶ O,⁷ CO,⁸ C,⁹ and N (Ref. 10) in flames was demonstrated. Aldén *et al.*,¹¹ Goldsmith and co-workers,^{12–16} and Salmon and Laurendeau¹⁷ have applied different multi-photon-excited fluorescence detection schemes for atomic hydrogen in flames. Czarnetzki *et al.*¹⁸ present a comprehensive comparison of the advantages and disadvantages of various possible TPA-LIF excitation schemes for the detection of the hydrogen atom.

Other diagnostic techniques based on the TPA process were developed following the demonstration of TPA-LIF. The phenomenon of amplified stimulated emission (ASE) following TPA was first observed for O-atom spectroscopy in flames.¹⁹ ASE was then detected following TPA in H,²⁰ C,²¹ and N.²² Two-wavelength TPA-induced ASE was demonstrated by Georgiev *et al.*,²³ and a TPA-pump, single-photon-

probe technique was developed by Brown and Jeffries.²⁴ TPA-based laser-induced-grating spectroscopy (TPA-LIGS) detection of atomic hydrogen was demonstrated by Gray, Goldsmith, and Trebino²⁵ and Gray and Trebino.²⁶ Two-photon laser-induced polarization spectroscopy (LIPS) has been demonstrated for both atomic and molecular species such as nitrogen (N₂),²⁷ ammonia (NH₃),²⁸ carbon monoxide (CO),²⁸ and atomic hydrogen.^{29–31,32}

Despite the numerous diagnostic applications of TPA-LIF, TPA-LIGS, and more recently TPA-LIPS, theoretical analysis of the TPA process for these diagnostic techniques has in general been limited to the results of second-order perturbation theory.^{1,33,34} The effects of collisions and Doppler broadening on the TPA line shape are discussed by Cagnac, Grynberg, and Biraben,³⁵ Bischel, Kelly, and Rhodes,³⁶ Dux *et al.*,³⁷ and Fiechtner and Gord.³⁸

In this paper we extend the previous second-order perturbative theoretical treatments with a nonperturbative analysis, allowing us to include in a rigorous manner the effects of saturation and Stark shifting on the two-photon resonance transition. The density-matrix equations for the two-photon absorption process are solved in the limit of steady state and assuming that both the two-photon transition and the single-photon resonances with the intermediate state are homogeneously broadened. Analytical expressions for the saturation intensity and the Stark shift are derived for the case where the incident laser radiation is far from resonance with the single-photon resonances between the initial state and the intermediate state, and between the final state and the inter-

^{a)} Author to whom correspondence should be addressed. Fax: 765-494-0539. Electronic mail: Lucht@purdue.edu

mediate state. The steady-state equations are also solved numerically to investigate the effects of collisions, saturation, and Stark shifting on the TPA line shape.

II. DENSITY MATRIX ANALYSIS FOR THE INTERACTION OF A TWO-STATE RESONANCE WITH MONOCHROMATIC LASER RADIATION

The time-dependent density-matrix equations for a multistate system irradiated by laser radiation are given by^{33,39–41}

$$\frac{\partial \rho_{jj}}{\partial t} = -\frac{i}{\hbar} \sum_m (V_{jm} \rho_{mj} - \rho_{jm} V_{mj}) - \Gamma_j \rho_{jj} + \sum_{m \neq j} \Gamma_{mj} \rho_{mm}, \quad (1)$$

$$\frac{\partial \rho_{\ell j}(y, t)}{\partial t} = -\rho_{\ell j}(i\omega_{\ell j} + \gamma_{\ell j}) - \frac{i}{\hbar} \sum_m (V_{\ell m} \rho_{mj} - \rho_{\ell m} V_{mj}), \quad (2)$$

where the diagonal matrix element ρ_{jj} is the occupation probability for state j , proportional to the population of state j , and the off-diagonal matrix element $\rho_{\ell j}$ is a measure of the coherence between states ℓ and j . In Eqs. (1) and (2), \hbar is Planck's constant (Js), Γ_j is the rate coefficient (s^{-1}) for population transfer from state j to all other states, Γ_{mj} is the rate coefficient (s^{-1}) for population transfer from state m to state j , $\omega_{\ell j}$ is the resonance frequency (s^{-1}) between states ℓ and j , and $\gamma_{\ell j}$ is the rate coefficient (s^{-1}) for coherence-dephasing collisions. The interaction term V_{mj} (J) is given by

$$V_{mj} = \tau \vec{\mu}_{mj} \cdot \vec{E}(\vec{r}, t), \quad (3)$$

where $\vec{\mu}_{mj} = \langle \psi_m | \vec{\mu} | \psi_j \rangle$ is the electric dipole matrix element (C m) and $\vec{E}(\vec{r}, t)$ is the laser electric field (J/C m). The laser field is given by

$$\vec{E}(\vec{r}, t) = \frac{1}{2} \hat{e} A(\vec{r}, t) \exp[+i(\vec{k} \cdot \vec{r} - \omega t)] + \text{c.c.}, \quad (4)$$

where \hat{e} is the complex unit vector for the laser field ($\hat{e} \cdot \hat{e}^* = 1$), \vec{r} is the position vector (m), $A(\vec{r}, t)$ is the slowly varying amplitude function (J/C m) for the electric field, \vec{k}_L is the propagation vector (m^{-1}), and ω_L is the angular frequency (s^{-1}). For the analysis of two-photon absorption in this paper we will assume that $\vec{r} = 0$ and that the electric-field amplitude is constant, and thus Eq. (4) reduces to

$$\vec{E}(t) = \frac{1}{2} \hat{e} A \exp(-i\omega t) + \frac{1}{2} \hat{e}^* A^* \exp(+i\omega t). \quad (5)$$

A. Density-matrix elements for transition between ground state a and excited state c

The three-state system that will be analyzed in this paper is illustrated in Fig. 1. The initial and final states, a and b , respectively, of the two-photon transition are coupled through the intermediate state c . Assuming that $V_{aa} = V_{bb} = V_{cc} = 0$ and that states a and b are not coupled by a single-

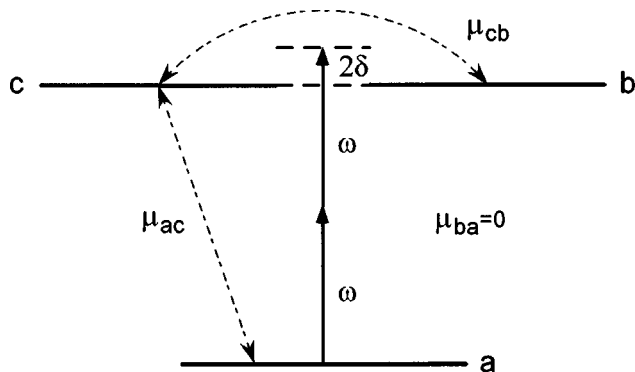


FIG. 1. Schematic diagram of the three-state system and the two-photon absorption process for the case $\omega_{cb} = 0$.

photon electric-dipole resonance ($V_{ab} = V_{ba} = 0$), the density-matrix equations for the three-state system are given by

$$\dot{\rho}_{ca} = -\rho_{ca}(i\omega_{ca} + \gamma_{ca}) - \frac{i}{\hbar} V_{ca}(\rho_{aa} - \rho_{cc}) - \frac{i}{\hbar} V_{cb} \rho_{ba}, \quad (6)$$

$$\dot{\rho}_{cb} = -\rho_{cb}(i\omega_{cb} + \gamma_{cb}) - \frac{i}{\hbar} V_{ca} \rho_{ab} - \frac{i}{\hbar} V_{cb}(\rho_{bb} - \rho_{cc}), \quad (7)$$

$$\dot{\rho}_{ba} = -\rho_{ba}(i\omega_{ba} + \gamma_{ba}) - \frac{i}{\hbar} (V_{bc} \rho_{ca} - \rho_{bc} V_{ca}), \quad (8)$$

$$\dot{\rho}_{aa} = -\Gamma_a \rho_{aa} + \Gamma_{ba} \rho_{bb} + \Gamma_{ca} \rho_{cc} - \frac{i}{\hbar} (V_{ac} \rho_{ca} - \rho_{ac} V_{ca}), \quad (9)$$

$$\dot{\rho}_{bb} = -\Gamma_b \rho_{bb} + \Gamma_{cb} \rho_{cc} + \Gamma_{ab} \rho_{aa} - \frac{i}{\hbar} (V_{bc} \rho_{cb} - \rho_{bc} V_{cb}), \quad (10)$$

$$\dot{\rho}_{cc} = -\Gamma_c \rho_{cc} + \Gamma_{ac} \rho_{aa} + \Gamma_{bc} \rho_{bb} - \frac{i}{\hbar} (V_{ca} \rho_{ac} - \rho_{ca} V_{ac}) - \frac{i}{\hbar} (V_{cb} \rho_{bc} - \rho_{cb} V_{bc}). \quad (11)$$

The angular frequencies are given by

$$\omega_{ca} = (\epsilon_c - \epsilon_a)/\hbar, \quad (12)$$

$$\omega_{cb} = (\epsilon_c - \epsilon_b)/\hbar, \quad (13)$$

$$\omega_{ba} = (\epsilon_b - \epsilon_a)/\hbar. \quad (14)$$

The following slowly varying density-matrix elements are defined at this point:

$$\rho_{ca} = \sigma_{ca} \exp(-i\omega t), \quad (15)$$

$$\rho_{cb} = \sigma_{cb} \exp(+i\omega t), \quad (16)$$

$$\rho_{ba} = \sigma_{ba} \exp(-i2\omega t). \quad (17)$$

Substituting Eq. (17) and the time derivative of Eq. (15) into Eq. (6) we obtain

$$\begin{aligned}
& \dot{\sigma}_{ca} \exp(-i\omega t) - i\omega \sigma_{ca} \exp(-i\omega t) \\
&= -\sigma_{ca} \exp(-i\omega t)(i\omega_{ca} + \gamma_{ca}) - \frac{i}{\hbar} V_{ca}(\sigma_{aa} - \sigma_{cc}) \\
&\quad - \frac{i}{\hbar} V_{cb} \sigma_{ba} \exp(-i2\omega t). \quad (18)
\end{aligned}$$

At this point let us define the radiative interaction terms,

$$V_{cb} = \tilde{V}_{cb}^+ \exp(+i\omega t) + \tilde{V}_{cb}^- \exp(-i\omega t), \quad (19)$$

$$V_{ca} = \tilde{V}_{ca}^+ \exp(+i\omega t) + \tilde{V}_{ca}^- \exp(-i\omega t). \quad (20)$$

Similar relations apply for V_{ac} and V_{bc} . Substituting Eqs. (19) and (20) into Eq. (18) and rearranging we obtain

$$\begin{aligned}
& \dot{\sigma}_{ca} \exp(-i\omega t) \\
&= -\sigma_{ca} \exp(-i\omega t)[i(\omega_{ca} - \omega) + \gamma_{ca}] \\
&\quad - \frac{i}{\hbar} [\tilde{V}_{ca}^+ \exp(+i\omega t) + \tilde{V}_{ca}^- \exp(-i\omega t)](\rho_{aa} - \rho_{cc}) \\
&\quad - \frac{i}{\hbar} [\tilde{V}_{cb}^+ \exp(+i\omega t) + \tilde{V}_{cb}^- \exp(-i\omega t)] \\
&\quad \times \sigma_{ba} \exp(-i2\omega t). \quad (21)
\end{aligned}$$

Equating terms in Eq. (21) that have the time dependence $\exp(-i\omega t)$ and neglecting terms that oscillate at $\exp(-i3\omega t)$ and $\exp(+i\omega t)$, we obtain

$$\begin{aligned}
\dot{\sigma}_{ca} &= -\sigma_{ca}[i(\omega_{ca} - \omega) + \gamma_{ca}] \\
&\quad - \frac{i}{\hbar} [\tilde{V}_{ca}^-(\rho_{aa} - \rho_{cc}) + \tilde{V}_{cb}^+ \sigma_{ba}]. \quad (22)
\end{aligned}$$

Writing the real and imaginary components of the density-matrix elements and the radiative interaction terms we obtain the following equation:

$$\begin{aligned}
\dot{\sigma}_{ca}^r + i\dot{\sigma}_{ca}^i &= -(\sigma_{ca}^r + i\sigma_{ca}^i)[i(\omega_{ca} - \omega) + \gamma_{ca}] \\
&\quad - \frac{i}{\hbar} (\tilde{V}_{ca}^{-r} + i\tilde{V}_{ca}^{-i})(\rho_{aa} - \rho_{cc}) \\
&\quad - \frac{i}{\hbar} (\tilde{V}_{cb}^{+r} + i\tilde{V}_{cb}^{+i})(\sigma_{ba}^r + i\sigma_{ba}^i). \quad (23)
\end{aligned}$$

Writing separate equations for the real and imaginary terms we obtain

$$\begin{aligned}
\dot{\sigma}_{ca}^r &= -\sigma_{ca}^r \gamma_{ca} + \sigma_{ca}^i(\omega_{ca} - \omega) + \frac{1}{\hbar} \tilde{V}_{ca}^{-i}(\rho_{aa} - \rho_{cc}) \\
&\quad + \frac{1}{\hbar} (\tilde{V}_{cb}^{+r} \sigma_{ba}^i + \tilde{V}_{cb}^{+i} \sigma_{ba}^r), \quad (24)
\end{aligned}$$

$$\begin{aligned}
\dot{\sigma}_{ca}^i &= -\sigma_{ca}^i \gamma_{ca} - \sigma_{ca}^r(\omega_{ca} - \omega) - \frac{1}{\hbar} \tilde{V}_{ca}^{-r}(\rho_{aa} - \rho_{cc}) \\
&\quad + \frac{1}{\hbar} (-\tilde{V}_{cb}^{+r} \sigma_{ba}^r + \tilde{V}_{cb}^{+i} \sigma_{ba}^i). \quad (25)
\end{aligned}$$

Repeating a similar process for Eq. (7) we obtain

$$\begin{aligned}
\dot{\sigma}_{cb} \exp(+i\omega t) &= -\sigma_{cb} \exp(+i\omega t)[i(\omega_{cb} + \omega) + \gamma_{cb}] \\
&\quad - \frac{i}{\hbar} V_{ca} \sigma_{ab} \exp(+i2\omega t) \\
&\quad - \frac{i}{\hbar} V_{cb}(\rho_{bb} - \rho_{cc}). \quad (26)
\end{aligned}$$

Substituting Eq. (20) into Eq. (26) and equating terms that oscillate at $\exp(+i\omega t)$ we obtain

$$\begin{aligned}
\dot{\sigma}_{cb} &= -\sigma_{cb}[i(\omega_{cb} + \omega) + \gamma_{cb}] \\
&\quad - \frac{i}{\hbar} [\tilde{V}_{cb}^+(\rho_{bb} - \rho_{cc}) + \tilde{V}_{ca}^- \sigma_{ab}]. \quad (27)
\end{aligned}$$

Writing the real and imaginary components of the density-matrix elements and the radiative interaction terms we obtain the following equation:

$$\begin{aligned}
\dot{\sigma}_{cb}^r + i\dot{\sigma}_{cb}^i &= -(\sigma_{cb}^r + i\sigma_{cb}^i)[i(\omega_{cb} + \omega) + \gamma_{cb}] \\
&\quad - \frac{i}{\hbar} (\tilde{V}_{cb}^{+r} + i\tilde{V}_{cb}^{+i})(\rho_{bb} - \rho_{cc}) \\
&\quad - \frac{i}{\hbar} (\tilde{V}_{ca}^{-r} + i\tilde{V}_{ca}^{-i})(\sigma_{ab}^r + i\sigma_{ab}^i). \quad (28)
\end{aligned}$$

Writing separate equations for the real and imaginary terms we obtain

$$\begin{aligned}
\dot{\sigma}_{cb}^r &= -\sigma_{cb}^r \gamma_{cb} + \sigma_{cb}^i(\omega_{cb} + \omega) + \frac{1}{\hbar} \tilde{V}_{cb}^{+i}(\rho_{bb} - \rho_{cc}) \\
&\quad + \frac{1}{\hbar} (\tilde{V}_{ca}^{-r} \sigma_{ab}^i + \tilde{V}_{ca}^{-i} \sigma_{ab}^r), \quad (29)
\end{aligned}$$

$$\begin{aligned}
\dot{\sigma}_{cb}^i &= -\sigma_{cb}^i \gamma_{cb} - \sigma_{cb}^r(\omega_{cb} + \omega) - \frac{1}{\hbar} \tilde{V}_{cb}^{+r}(\rho_{bb} - \rho_{cc}) \\
&\quad + \frac{1}{\hbar} (-\tilde{V}_{ca}^{-r} \sigma_{ab}^r + \tilde{V}_{ca}^{-i} \sigma_{ab}^i). \quad (30)
\end{aligned}$$

Repeating a similar process for Eq. (8) we obtain

$$\begin{aligned}
\dot{\sigma}_{ba} \exp(-i2\omega t) &= -\sigma_{ba} \exp(-i2\omega t)[i(\omega_{ba} - 2\omega) + \gamma_{ba}] \\
&\quad - \frac{i}{\hbar} [V_{bc} \sigma_{ca} \exp(-i\omega t) \\
&\quad - \sigma_{bc} \exp(-i\omega t) V_{ca}]. \quad (31)
\end{aligned}$$

Substituting for the radiative interaction terms and solving for terms that oscillate at $\exp(-i2\omega t)$ we obtain

$$\begin{aligned}
\dot{\sigma}_{ba} &= -\sigma_{ba}[i(\omega_{ba} - 2\omega) + \gamma_{ba}] - \frac{i}{\hbar} (\tilde{V}_{bc}^- \sigma_{ca} - \sigma_{bc} \tilde{V}_{ca}^-). \quad (32)
\end{aligned}$$

Writing the real and imaginary components of the density-matrix elements and the radiative interaction terms we obtain the following equation:

$$\begin{aligned}\dot{\sigma}_{ba}^r + i\dot{\sigma}_{ba}^i = & -(\sigma_{ba}^r + i\sigma_{ba}^i)[i(\omega_{ba} - 2\omega) + \gamma_{ba}] \\ & - \frac{i}{\hbar}(\tilde{V}_{bc}^{-r} + i\tilde{V}_{bc}^{-i})(\sigma_{ca}^r + i\sigma_{ca}^i) \\ & + \frac{i}{\hbar}(\sigma_{bc}^r + i\sigma_{bc}^i)(\tilde{V}_{ca}^{-r} + i\tilde{V}_{ca}^{-i}).\end{aligned}\quad (33)$$

Writing separate equations for the real and imaginary terms we obtain

$$\begin{aligned}\dot{\sigma}_{ba}^r = & -\sigma_{ba}^r\gamma_{ba} + \sigma_{ba}^i(\omega_{ba} - 2\omega) + \frac{1}{\hbar}(\tilde{V}_{bc}^{-r}\sigma_{ca}^i + \tilde{V}_{bc}^{-i}\sigma_{ca}^r) \\ & + \frac{1}{\hbar}(-\sigma_{bc}^r\tilde{V}_{ca}^{-i} - \sigma_{bc}^i\tilde{V}_{ca}^{-r}),\end{aligned}\quad (34)$$

$$\begin{aligned}\dot{\sigma}_{ba}^i = & -\sigma_{ba}^i\gamma_{ba} - \sigma_{ba}^r(\omega_{ba} - 2\omega) + \frac{1}{\hbar}(-\tilde{V}_{bc}^{-r}\sigma_{ca}^r + \tilde{V}_{bc}^{-i}\sigma_{ca}^i) \\ & + \frac{1}{\hbar}(\sigma_{bc}^r\tilde{V}_{ca}^{-r} - \sigma_{bc}^i\tilde{V}_{ca}^{-i}).\end{aligned}\quad (35)$$

The equations for the slowly varying population terms become

$$\begin{aligned}\dot{\rho}_{aa} = & \Gamma_{ba}\rho_{bb} + \Gamma_{ca}\rho_{cc} - \frac{i}{\hbar}(\tilde{V}_{ac}^+\sigma_{ca} - \sigma_{ac}\tilde{V}_{ca}^-) \\ = & \Gamma_{ba}\rho_{bb} + \Gamma_{ca}\rho_{cc} + \frac{1}{\hbar}(\tilde{V}_{ac}^{+r}\sigma_{ca}^i + \tilde{V}_{ac}^{+i}\sigma_{ca}^r) \\ & + \frac{1}{\hbar}(-\sigma_{ac}^r\tilde{V}_{ca}^{-i} - \sigma_{ac}^i\tilde{V}_{ca}^{-r}) + \frac{i}{\hbar}(-\tilde{V}_{ac}^{+r}\sigma_{ca}^r \\ & + i\tilde{V}_{ac}^{+i}\sigma_{ca}^i) + \frac{i}{\hbar}(\sigma_{ac}^r\tilde{V}_{ca}^{-r} - i\sigma_{ac}^i\tilde{V}_{ca}^{-i}).\end{aligned}\quad (36)$$

It is not immediately obvious that the imaginary terms in Eq. (36) are zero. However, using the relations

$$\tilde{V}_{ac}^+ = -\frac{1}{2}\bar{\mu}_{ac} \cdot (\hat{e}^* A^*) = -\frac{1}{2}(\bar{\mu}_{ca})^* \cdot (\hat{e} A)^* = (\tilde{V}_{ca}^-)^* \quad (37)$$

and

$$\sigma_{ac} = \sigma_{ca}^* \quad (38)$$

we can simplify Eq. (36) to obtain

$$\dot{\rho}_{aa} = \Gamma_{ba}\rho_{bb} + \Gamma_{ca}\rho_{cc} + \frac{2}{\hbar}(\tilde{V}_{ac}^{+r}\sigma_{ca}^i + \tilde{V}_{ac}^{+i}\sigma_{ca}^r). \quad (39)$$

In a similar fashion we obtain

$$\dot{\rho}_{bb} = -\Gamma_{b}\rho_{bb} + \Gamma_{cb}\rho_{cc} + \frac{2}{\hbar}(\tilde{V}_{bc}^{-r}\sigma_{cb}^i + \tilde{V}_{bc}^{-i}\sigma_{cb}^r) \quad (40)$$

and

$$\begin{aligned}\dot{\rho}_{cc} = & -\Gamma_c\rho_{cc} + \Gamma_{bc}\rho_{bb} - \frac{2}{\hbar}(\sigma_{ca}^r\tilde{V}_{ac}^{+i} + \sigma_{ca}^i\tilde{V}_{ac}^{+r}) \\ & - \frac{2}{\hbar}(\sigma_{cb}^r\tilde{V}_{bc}^{-i} + \sigma_{cb}^i\tilde{V}_{bc}^{-r}).\end{aligned}\quad (41)$$

III. STARK SHIFTING AND SATURATION INTENSITY FOR THE TWO-PHOTON RESONANCE TRANSITION

Analytical expressions for the Stark shift and saturation intensity of the two-photon resonance transition are derived in this section. The Stark shift is determined from an expression for the real part of the coherence density-matrix element σ_{ba} between the final and initial states for the two-photon transition. The steady-state solution for σ_{ba} is found by setting $\dot{\sigma}_{ba} = 0$ in Eq. (32) and is given by

$$\sigma_{ba} = -\frac{i(\tilde{V}_{bc}^-\sigma_{ca} - \sigma_{bc}\tilde{V}_{ca}^-)}{\hbar[i(\omega_{ba} - 2\omega) + \gamma_{ba}]}. \quad (42)$$

The steady-state solutions for the density-matrix elements σ_{ca} and σ_{bc} are found from Eqs. (22) and (27), respectively, and are given by

$$\sigma_{ca} = -\frac{i[\tilde{V}_{ca}^-(\rho_{aa} - \rho_{cc}) + \tilde{V}_{cb}^+\sigma_{ba}]}{\hbar[i(\omega_{ca} - \omega) + \gamma_{ca}]} \quad (43)$$

and

$$\sigma_{bc} = +\frac{i[\tilde{V}_{bc}^-(\rho_{bb} - \rho_{cc}) + \sigma_{ba}\tilde{V}_{ac}^+]}{[-i(\omega_{cb} + \omega) + \gamma_{cb}]}, \quad (44)$$

where we have used the relation $\sigma_{bc} = \sigma_{cb}^*$ in deriving Eq. (43). Assuming that the laser frequency is far from resonance with the single-photon resonances ca and cb , $|\omega_{ca} - \omega| \gg \gamma_{ca}$ and $|\omega_{cb} + \omega| \gg \gamma_{cb}$, we obtain

$$\sigma_{ca} = -\frac{[\tilde{V}_{ca}^-(\rho_{aa} - \rho_{cc}) + \tilde{V}_{cb}^+\sigma_{ba}]}{\hbar(\omega_{ca} - \omega)} \quad (45)$$

and

$$\sigma_{bc} = -\frac{[\tilde{V}_{bc}^-(\rho_{bb} - \rho_{cc}) + \sigma_{ba}\tilde{V}_{ac}^+]}{\hbar(\omega_{cb} + \omega)}. \quad (46)$$

Substituting Eqs. (45) and (46) into Eq. (42) we obtain

$$\begin{aligned}\sigma_{ba}[i(\omega_{ba} - 2\omega) + \gamma_{ba}] = & + \frac{i}{\hbar} \left\{ \tilde{V}_{bc}^- \frac{[\tilde{V}_{ca}^-(\rho_{aa} - \rho_{cc}) + \tilde{V}_{cb}^+\sigma_{ba}]}{\hbar(\omega_{ca} - \omega)} \right. \\ & \left. - \frac{[\tilde{V}_{bc}^-(\rho_{bb} - \rho_{cc}) + \sigma_{ba}\tilde{V}_{ac}^+]}{\hbar(\omega_{cb} + \omega)} \tilde{V}_{ca}^- \right\}.\end{aligned}\quad (47)$$

Rearranging collecting terms that involve σ_{ba} on the left-hand side of the equation we obtain

$$\begin{aligned}\sigma_{ba} \left\{ i \left[(\omega_{ba} - 2\omega) - \frac{|\tilde{V}_{cb}|^2}{\hbar^2(\omega_{ca} - \omega)} + \frac{|\tilde{V}_{ac}|^2}{\hbar^2(\omega_{cb} + \omega)} \right] + \gamma_{ba} \right\} = & \frac{i\tilde{V}_{bc}^-\tilde{V}_{ca}^-(\rho_{aa} - \rho_{cc})}{\hbar^2(\omega_{ca} - \omega)} - \frac{i\tilde{V}_{bc}^-\tilde{V}_{ca}^-(\rho_{bb} - \rho_{cc})}{\hbar^2(\omega_{cb} + \omega)}.\end{aligned}\quad (48)$$

Rewriting Eq. (48) we obtain

$$\sigma_{ba} = \frac{\frac{i\tilde{V}_{bc}^-\tilde{V}_{ca}^-(\rho_{aa}-\rho_{cc})}{\hbar^2(\omega_{ca}-\omega)} - \frac{i\tilde{V}_{bc}^-\tilde{V}_{ca}^-(\rho_{bb}-\rho_{cc})}{\hbar^2(\omega_{cb}+\omega)}}{i\left[(\omega_{ba}-2\omega) - \frac{|\tilde{V}_{cb}|^2}{\hbar^2(\omega_{ca}-\omega)} + \frac{|\tilde{V}_{ac}|^2}{\hbar^2(\omega_{cb}+\omega)}\right] + \gamma_{ba}} \\ = \frac{i\tilde{V}_{bc}^-\tilde{V}_{ca}^-[(\omega_{cb}+\omega)(\rho_{aa}-\rho_{cc}) - (\omega_{ca}-\omega)(\rho_{bb}-\rho_{cc})]}{\hbar^2(\omega_{ca}-\omega)(\omega_{cb}+\omega)(i\Delta_{ba} + \gamma_{ba})}, \quad (49)$$

where

$$\Delta_{ba} = (\omega_{ba} - 2\omega) - \frac{|\tilde{V}_{cb}|^2}{\hbar^2(\omega_{ca}-\omega)} + \frac{|\tilde{V}_{ac}|^2}{\hbar^2(\omega_{cb}+\omega)}. \quad (50)$$

The real part of σ_{ba} will go to zero at two-photon resonance, i.e., when the resonance denominator in Eq. (49) is real. The resonance denominator in Eq. (49) will be real when $\Delta_{ba} = 0$, resulting in the following expression for the two-photon resonance frequency:

$$\omega_{\text{tp, res}} = \frac{\omega_{ba}}{2} - \frac{|\tilde{V}_{cb}|^2}{2\hbar^2(\omega_{ca}-\omega)} + \frac{|\tilde{V}_{ac}|^2}{2\hbar^2(\omega_{cb}+\omega)} \\ = \frac{1}{2}[\omega_{ba} - \Delta\omega_{S,cb} + \Delta\omega_{S,ac}], \quad (51)$$

where

$$\Delta\omega_{S,cb} = \frac{|\tilde{V}_{cb}|^2}{\hbar^2(\omega_{ca}-\omega)} \\ = \frac{|\vec{\mu}_{cb} \cdot \hat{e}|^2 AA^*}{4\hbar^2(\omega_{ca}-\omega)} = \frac{|\vec{\mu}_{cb} \cdot \hat{e}|^2 I}{2c\epsilon_0\hbar^2(\omega_{ca}-\omega)}, \quad (52)$$

where c is the speed of light (m/s), ϵ_0 is the dielectric permittivity (C²/J m), and the laser intensity I (W/m²) is given by

$$I = \frac{1}{2} c \epsilon_0 A A^*. \quad (53)$$

Similarly, the magnitude of the Stark shift due to the single-photon ac resonance is given by

$$\Delta\omega_{S,ac} = \frac{|\tilde{V}_{ac}|^2}{\hbar^2(\omega_{cb}+\omega)} = \frac{|\vec{\mu}_{ac} \cdot \hat{e}|^2 I}{2c\epsilon_0\hbar^2(\omega_{cb}+\omega)}. \quad (54)$$

The sign of the overall Stark shift $-\Delta\omega_{S,cb} + \Delta\omega_{S,ac}$ depends on the relative strengths of the single-photon resonances. The Stark shift also depends on the polarization of the pump beam and the polarization properties of the single-photon resonances through the terms $|\vec{\mu}_{ac} \cdot \hat{e}|^2$ and $|\vec{\mu}_{cb} \cdot \hat{e}|^2$.

The saturation intensity for the two-photon resonance can be determined from the steady-state expression for the population ρ_{bb} of the final state. The steady-state solution for ρ_{bb} can be found from Eq. (40) and is given by

$$\rho_{bb} = -\frac{i(\tilde{V}_{bc}^-\sigma_{cb} - \sigma_{bc}\tilde{V}_{cb}^+)}{\hbar\Gamma_b}, \quad (55)$$

where we have neglected collisional transfer from state c to state b in deriving Eq. (55). Substituting into Eq. (55) using Eq. (46) we obtain

$$\rho_{bb} = +\frac{i}{\hbar\Gamma_b} \left\{ \tilde{V}_{bc}^- \frac{[\tilde{V}_{cb}^+(\rho_{bb}-\rho_{cc}) + \tilde{V}_{ca}^-\sigma_{ab}]}{\hbar(\omega_{cb}+\omega)} - \frac{[\tilde{V}_{bc}^-(\rho_{bb}-\rho_{cc}) + \sigma_{ba}\tilde{V}_{ac}^+]}{\hbar(\omega_{cb}+\omega)} \tilde{V}_{cb}^+ \right\}. \quad (56)$$

Rearranging Eq. (56) and simplifying we obtain

$$\rho_{bb} = +\frac{i(\tilde{V}_{bc}^-\tilde{V}_{ca}^-\sigma_{ab} - \sigma_{ba}\tilde{V}_{ac}^+\tilde{V}_{cb}^+)}{\hbar^2(\omega_{cb}+\omega)\Gamma_b}. \quad (57)$$

Substituting for σ_{ba} and σ_{ab} in Eq. (57) using Eq. (48) we obtain

$$\rho_{bb} = +\frac{\tilde{V}_{bc}^-\tilde{V}_{ca}^-\tilde{V}_{cb}^+\tilde{V}_{ac}^+[(\omega_{cb}+\omega)(\rho_{aa}-\rho_{cc}) - (\omega_{ca}-\omega)(\rho_{bb}-\rho_{cc})]}{\hbar^4(\omega_{cb}+\omega)^2(\omega_{ca}-\omega)(-i\Delta_{ba} + \gamma_{ba})\Gamma_b} \\ + \frac{\tilde{V}_{ac}^+\tilde{V}_{cb}^+\tilde{V}_{bc}^-\tilde{V}_{ca}^-[(\omega_{cb}+\omega)(\rho_{aa}-\rho_{cc}) - (\omega_{ca}-\omega)(\rho_{bb}-\rho_{cc})]}{\hbar^4(\omega_{cb}+\omega)^2(\omega_{ca}-\omega)(i\Delta_{ba} + \gamma_{ba})\Gamma_b}. \quad (58)$$

Simplifying Eq. (58) we obtain

$$\rho_{bb} = +\Lambda \frac{[(\omega_{cb}+\omega)(\rho_{aa}-\rho_{cc}) - (\omega_{ca}-\omega)(\rho_{bb}-\rho_{cc})]}{\Delta_{ba}^2 + \gamma_{ba}^2}, \quad (59)$$

where

$$\Lambda = \frac{2|\tilde{V}_{cb}|^2|\tilde{V}_{ac}|^2\gamma_{ba}}{\hbar^4(\omega_{cb}+\omega)^2(\omega_{ca}-\omega)\Gamma_b} \\ = \frac{|\vec{\mu}_{cb} \cdot \hat{e}|^2|\vec{\mu}_{ac} \cdot \hat{e}|^2 I^2 \gamma_{ba}}{2c^2\epsilon_0^2\hbar^4(\omega_{cb}+\omega)^2(\omega_{ca}-\omega)\Gamma_b}. \quad (60)$$

Rearranging Eq. (59) and solving for ρ_{bb} we obtain¹⁵³

$$\begin{aligned}\rho_{bb} &= \frac{\Lambda \{[(\omega_{cb} + \omega)\rho_{aa} - (\omega_{ca} - \omega_{cb} - 2\omega)\rho_{cc}]/(\Delta_{ba}^2 + \gamma_{ba}^2)\}}{1 + [\Lambda(\omega_{ca} - \omega)/(\Delta_{ba}^2 + \gamma_{ba}^2)]} \\ &= \frac{\Lambda[(\omega_{cb} + \omega)\rho_{aa} - (\omega_{ca} - \omega_{cb} - 2\omega)\rho_{cc}]}{\Delta_{ba}^2 + \gamma_{ba}^2 + \Lambda(\omega_{ca} - \omega)}.\end{aligned}\quad (61)$$

Defining the two-photon saturation intensity I_{sat} ,

$$I_{\text{sat}} = c\epsilon_0\hbar^2 \sqrt{\frac{2\Gamma_b\gamma_{ba}(\omega_{cb} + \omega)^2}{|\vec{\mu}_{cb} \cdot \hat{e}|^2 |\vec{\mu}_{ac} \cdot \hat{e}|^2}}, \quad (62)$$

and using the relation $\omega_{ba} = \omega_{ca} - \omega_{cb}$ we can rewrite Eq. (61) as

$$\rho_{bb} = \frac{\gamma_{ba}^2(I^2/I_{\text{sat}}^2)[(\omega_{cb} + \omega)\rho_{aa} - (\omega_{ba} - 2\omega)\rho_{cc}]}{(\omega_{cb} + \omega_{ba} - \omega)\{\Delta_{ba}^2 + \gamma_{ba}^2[1 + (I^2/I_{\text{sat}}^2)]\}}. \quad (63)$$

Note that I_{sat} is proportional to the square root of the product of the dephasing-collision rate coefficient γ_{ba} and the population-transfer rate coefficient Γ_b , and inversely proportional to the product of the magnitudes of the electric-dipole-moment density-matrix elements for the single-photon transitions ac and cb . Again, the dependence of the saturation intensity on the polarization of the pump beam and the polarization properties of the single-photon resonances is contained in the terms $|\vec{\mu}_{ac} \cdot \hat{e}|^2$ and $|\vec{\mu}_{cb} \cdot \hat{e}|^2$.

Taking the high-intensity limit $I^2 \gg I_{\text{sat}}^2$ for the on-resonance condition $\Delta_{ba} = 0$, and assuming that the Stark-shifting terms are small compared to ω , so that $\omega_{ba} \approx 2\omega$, we obtain

$$\begin{aligned}\rho_{bb} &= \frac{\gamma_{ba}^2(I^2/I_{\text{sat}}^2)[(\omega_{cb} + \omega)\rho_{aa} - (\omega_{ba} - 2\omega)\rho_{cc}]}{(\omega_{cb} + \omega_{ba} - \omega)\{\Delta_{ba}^2 + \gamma_{ba}^2[1 + (I^2/I_{\text{sat}}^2)]\}} \\ &\approx \rho_{aa}.\end{aligned}\quad (64)$$

In the low-intensity limit, $I^2 \ll I_{\text{sat}}^2$, and assuming that $\omega_{ba} \approx 2\omega$, Eq. (63) reduces to

$$\rho_{bb} \approx \frac{\gamma_{ba}^2(I^2/I_{\text{sat}}^2)\rho_{aa}}{\Delta_{ba}^2 + \gamma_{ba}^2}. \quad (65)$$

The low-laser-intensity spectral profile is Lorentzian with a full width at half maximum of $2\gamma_{ba}$. Assuming that $\Delta_{ba} = 0$ we obtain

$$\rho_{bb} \approx (I^2/I_{\text{sat}}^2)\rho_{aa}. \quad (66)$$

IV. NUMERICAL SOLUTION OF THE DENSITY-MATRIX EQUATIONS

The results of numerical solution of the steady-state density-matrix equations for the TPA process are presented and discussed in this section. Equations (24), (25), (29), (30), (34), (35), (39), (40), and (41) form a set of nine equations in nine unknowns; the unknowns are the real and imaginary components of the coherence density-matrix elements and the population density-matrix element for each of the three states. These equations, with the time derivatives set equal to zero, were solved using the Engineering Equation Solver

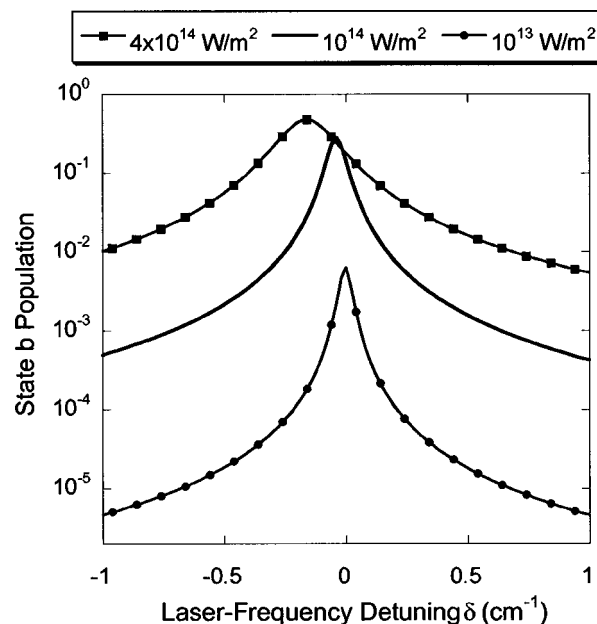


FIG. 2. Final state population ρ_{bb} vs laser-frequency detuning δ for $\omega_{ba}/2\pi c = 80\,000\text{ cm}^{-1}$, $\omega_{cb}/2\pi c = 0\text{ cm}^{-1}$, $\mu_{ac} = ea_0/4$, $\mu_{cb} = ea_0$, $\gamma_{cb} = \gamma_{ba} = 10^{10}\text{ s}^{-1}$, and $\Gamma_{ca} = \Gamma_{ba} = 5 \times 10^9\text{ s}^{-1}$. Line shapes are shown for three different laser intensities.

(Academic Version 6.867-3D). It was found that it was necessary to replace Eq. (41) with the population conservation equation

$$1 = \rho_{aa} + \rho_{bb} + \rho_{cc} \quad (67)$$

in order to obtain a converged solution to the set of equations.

A. Effect of the relative magnitudes of the electric-dipole-moment density-matrix elements

The equations were solved for the three-state system with $\omega_{bc} = 0$ as shown in Fig. 1. This case corresponds to the $1S$ - $2S$ two-photon transition in atomic hydrogen, for which the most important intermediate level is the $2P$ level. The $2P$ and $2S$ levels are nearly degenerate. Figure 2 shows the population ρ_{bb} of the final state of the two-photon transition as a function of laser detuning for three different values of the laser intensity. For the calculations shown in Fig. 2, the magnitudes of the electric-dipole-moment matrix elements $\mu_{ac} = |\vec{\mu}_{ac} \cdot \hat{e}|$ and $\mu_{cb} = |\vec{\mu}_{cb} \cdot \hat{e}|$ for the single-photon resonances are $ea_0/4$ and ea_0 , respectively, where e is the electronic charge (C) and a_0 is the Bohr radius (m). The ratio of electric-dipole-moment matrix elements for the $1S$ - $2P$ and $2P$ - $2S$ single-photon transitions is also ≈ 1.4 .⁴² For the calculations shown in Fig. 2, the dephasing-collision rate coefficients for the coherences, γ_{ba} , γ_{ac} , and γ_{cb} , were set to a value of $1.0 \times 10^{10}\text{ s}^{-1}$, and the population-transfer rate coefficients Γ_{ba} and Γ_{ca} were set to $5 \times 10^9\text{ s}^{-1}$. The frequency difference between states a and b was set to $80\,000\text{ cm}^{-1}$, and the energies of states b and c were set equal. The population-transfer rate coefficient between states b and c was set to zero, however, so that the collisional transfer between these states did not obscure the different behavior of the two states during the TPA process. The saturation inten-

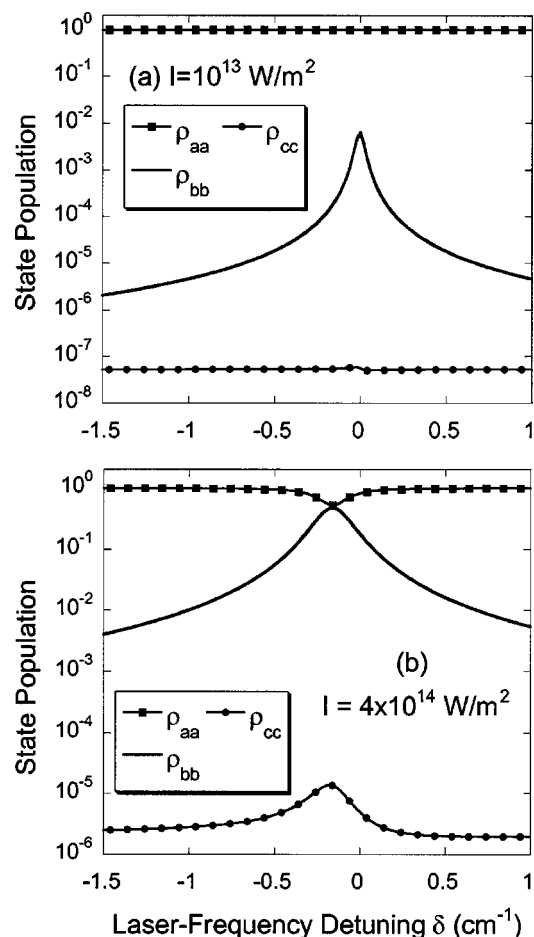


FIG. 3. State populations vs laser-frequency detuning δ for (a) nonsaturating laser intensity $I = 10^{13} \text{ W/m}^2$ and (b) saturating laser intensity $I = 4 \times 10^{14} \text{ W/m}^2$. For these calculations, $\omega_{ba}/2\pi c = 80\,000 \text{ cm}^{-1}$, $\omega_{cb}/2\pi c = 0 \text{ cm}^{-1}$, $\mu_{ac} = ea_0/4$, $\mu_{cb} = ea_0$, $\gamma_{cb} = \gamma_{ac} = \gamma_{ba} = 10^{10} \text{ s}^{-1}$, and $\Gamma_{ca} = \Gamma_{ba} = 5 \times 10^9 \text{ s}^{-1}$.

sity for this case is $1.239 \times 10^{14} \text{ W/m}^2$. As is evident from Fig. 2, the TPA line broadens and shifts significantly as the laser intensity increases from 10^{13} to $4 \times 10^{14} \text{ W/m}^2$. The population for all three states as a function of laser-frequency detuning is shown in Figs. 3(a) and 3(b) for laser intensities of 10^{13} and $4 \times 10^{14} \text{ W/m}^2$, respectively. Note that for a laser intensity of 10^{13} W/m^2 , the population of the intermediate state c is relatively insensitive to the laser-frequency detuning δ . For a laser intensity of $4 \times 10^{14} \text{ W/m}^2$, however, the population state c increases significantly near the condition of two-photon resonance, even though it is still far less than the population of either state a or state b . The dispersive character of ρ_{cc} due to the coupling of this state with both states a and b is clearly evident in Fig. 3(b).

The effect of changing the relative magnitudes of the electric-dipole-moment density-matrix elements μ_{ac} and μ_{cb} is shown in Fig. 4. For the calculations shown in Fig. 4(b), the magnitudes of the electric-dipole density-matrix elements for the two single-photon resonances are equal. The magnitudes are set to the value $\mu_{ac} = \mu_{cb} = ea_0/2$, so that the saturation intensity I_{sat} is the same as for the calculations shown in Fig. 2 [Fig. 4(a) is the same as Fig. 2, repeated for ease of comparison with Figs. 4(b) and 4(c)]. However, there is no

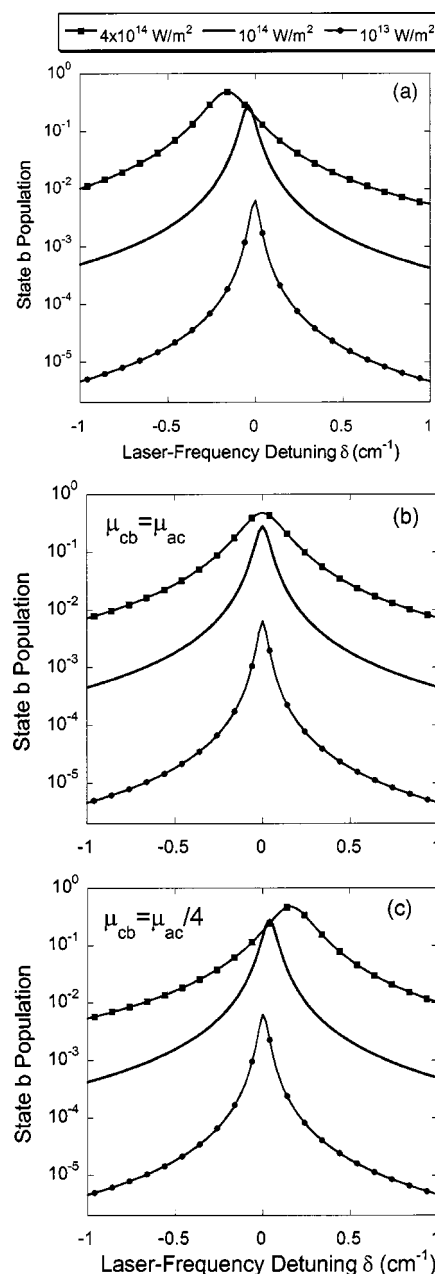


FIG. 4. Final state population ρ_{bb} vs laser-frequency detuning δ for (a) $\mu_{ac} = ea_0/4$ and $\mu_{cb} = ea_0$, (b) $\mu_{ac} = ea_0/2$ and $\mu_{cb} = ea_0/2$, (c) $\mu_{ac} = ea_0$ and $\mu_{cb} = ea_0/4$. Line shapes are shown for three different laser intensities for each case. For all three cases the following parameters were the same: $\omega_{ba}/2\pi c = 80\,000 \text{ cm}^{-1}$, $\omega_{cb} = 0 \text{ cm}^{-1}$, $\gamma_{cb} = \gamma_{ac} = \gamma_{ba} = 10^{10} \text{ s}^{-1}$, and $\Gamma_{ca} = \Gamma_{ba} = 5 \times 10^9 \text{ s}^{-1}$.

Stark shift evident in Fig. 4(b), because the electric-dipole-moment density-matrix elements μ_{ac} and μ_{cb} are equal, the Stark shifts $\Delta\omega_{S,ac}$ and $-\Delta\omega_{S,cb}$ cancel. For the calculations shown in Fig. 4(c), $\mu_{ac} = ea_0$ and $\mu_{cb} = ea_0/4$, and the Stark shift is in the opposite direction of that shown in Fig. 4(a). The saturation intensity was the same for all the calculations shown in Figs. 2–4.

B. Effect of the energy of the intermediate state c

The effect of the energy of the intermediate state c on the TPA process is examined in this section. The TPA process is

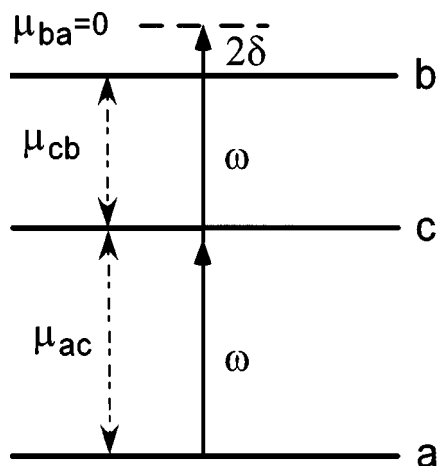


FIG. 5. Schematic diagram of the three-state system and the two-photon absorption process for the case $\omega \cong -\omega_{cb}$, $\omega \cong \omega_{ca}$.

strongly affected by the value of the frequencies ω_{ca} and ω_{cb} when the intermediate state c is midway between states a and b and thus transitions ac and cb are near single-photon resonance. This situation is illustrated schematically in Fig. 5. The results of calculations for $\omega_{ca}/2\pi c = 40\,010\text{ cm}^{-1}$ are shown in Fig. 6(a), and for $\omega_{ca}/2\pi c = 39\,990\text{ cm}^{-1}$ in Fig. 6(b). For these calculations, the collisional rate coefficients are the same as for Figs. 2–4, $\mu_{ac} = ea_0/4$ and $\mu_{cb} = ea_0$, and $\omega_{ba}/2\pi c = 80\,000\text{ cm}^{-1}$. For both Figs. 6(a) and 6(b),

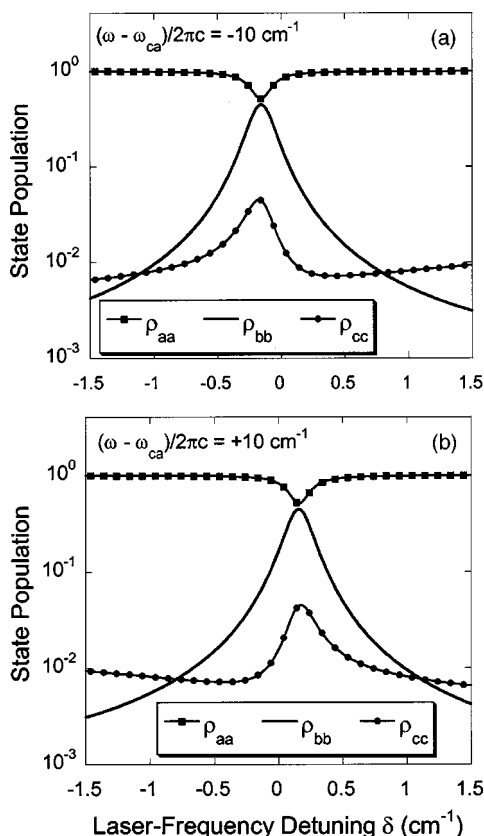


FIG. 6. State populations vs laser-frequency detuning δ for (a) $(\omega - \omega_{ca})/2\pi c = -10\text{ cm}^{-1}$ and (b) $(\omega - \omega_{ca})/2\pi c = +10\text{ cm}^{-1}$. For both cases the following parameters were the same: $\mu_{ac} = ea_0/4$, $\mu_{cb} = ea_0$, $I = 10^{11}\text{ W/m}^2$, $\gamma_{cb} = \gamma_{ac} = \gamma_{ba} = 10^{10}\text{ s}^{-1}$, and $\Gamma_{ca} = \Gamma_{ba} = 5 \times 10^9\text{ s}^{-1}$.

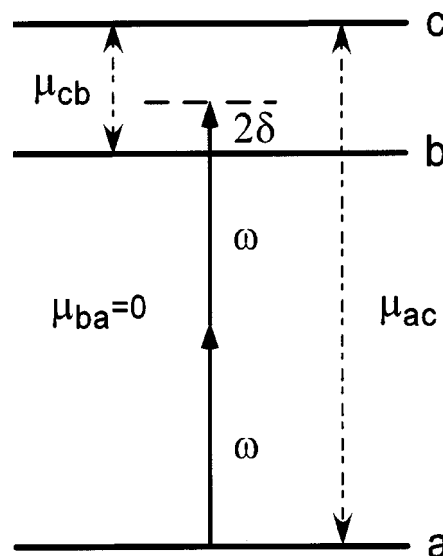


FIG. 7. Schematic diagram of the three-state system and the two-photon absorption process for the case where the energy of state c is much higher than the energy of state b .

the laser intensity for the calculations is 10^{11} W/m^2 , and the calculated saturation intensity is $3.098 \times 10^{10}\text{ W/m}^2$ for $\omega = \omega_{ba}/2$; the saturation intensity varies by $\approx 10\%$ over the laser-frequency-detuning range shown (note that it is four orders of magnitude smaller than for the calculations shown in Figs. 2–4, where the laser frequency is $40\,000\text{ cm}^{-1}$ away from single-photon resonance). The saturation behavior shown in Figs. 6(a) and 6(b) is very similar, but the Stark shift is in the opposite direction depending on whether the energy ϵ_c of the intermediate state c is less than or greater than $\epsilon_b/2$. The Stark-shifting behavior of a TPA resonance in sodium vapor using two different lasers tuned near an intermediate level was investigated by Liao and Bjorkholm.⁴³ Although our theoretical results are not directly comparable because we assume that the two-photon absorption is induced by a single laser, the qualitative nature of the Stark shift is similar in the two studies. For example, Liao and Bjorkholm⁴³ demonstrated that the sign of the Stark shift changed as one of the lasers was tuned through single-photon resonance with the intermediate level.

Figure 7 illustrates a case where $\epsilon_c \gg \epsilon_b$. A comparison of the saturation and Stark-shifting behavior of the two-photon resonance for $\omega_{cb}/2\pi c = 0\text{ cm}^{-1}$, corresponding to the calculations shown in Figs. 2–4, and $\omega_{cb}/2\pi c = 20\,000\text{ cm}^{-1}$, is shown in Fig. 8. The magnitude of the Stark shift and the degree of saturation is less for the $\omega_{cb}/2\pi c = 20\,000\text{ cm}^{-1}$ case because of the greater detuning from single-photon resonance.

V. CONCLUSIONS AND FUTURE WORK

A nonperturbative density-matrix analysis of the TPA process has been performed, and analytical expressions for the Stark shift and saturation intensity of the two-photon resonance have been derived. The saturation and Stark-shifting behavior of the TPA resonance transition has been

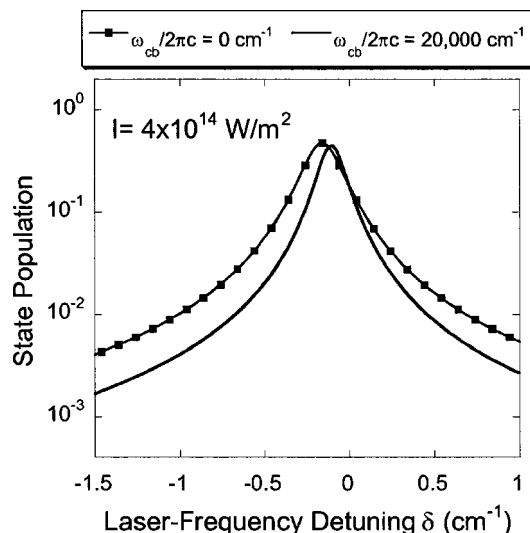


FIG. 8. Final state population ρ_{bb} vs laser-frequency detuning δ for $\omega_{ba}/2\pi c = 80\,000\text{ cm}^{-1}$, $I = 4 \times 10^{14}\text{ W/m}^2$, $\mu_{ac} = ea_0/4$, $\mu_{cb} = ea_0$, $\gamma_{cb} = \gamma_{ac} = \gamma_{ba} = 10^{10}\text{ s}^{-1}$, and $\Gamma_{ca} = \Gamma_{ba} = 5 \times 10^9\text{ s}^{-1}$. Line shapes are shown for $\omega_{cb}/2\pi c = 0\text{ cm}^{-1}$ and $\omega_{cb}/2\pi c = 20\,000\text{ cm}^{-1}$.

investigated numerically for different values of the electric-dipole-moment density-matrix elements μ_{ac} and μ_{cb} and of the energy of the intermediate state c .

The analysis and computations were performed assuming (1) that only three states participate in the TPA process, (2) that the three-state system is in steady state, (3) that only a single, monochromatic laser beam interacts with the TPA resonance, and (4) that the TPA resonance and the single-photon resonances are homogeneously broadened. The analysis presented in this paper can be extended to remove these restrictions. In the case of the fourth assumption, for example, Doppler broadening of the transition can be accounted for by dividing the atomic or molecular population into velocity groups characterized by a different resonance frequency in the laboratory frame of reference. The coherence- or population-density-matrix elements can then be determined by solving the density-matrix equations for each velocity group and then summing or integrating the coherence and population density-matrix element over all velocity groups.

The three-state assumption was imposed to simplify the physics, but for an actual atom or molecule in general one must consider the level structure in detail to describe the Stark shifting and saturation properties of the two-photon resonance. A two-photon absorption process from level A ($J_A = 2$) to level B ($J_B = 2$) is depicted schematically in Fig. 9. The two-photon process can proceed through either intermediate level C ($J_C = 1$) or intermediate level D ($J_D = 2$). The two-photon transition induced by a circularly polarized laser beam from state a ($M_J = -1$) to state b ($M_J = +1$) through state c ($M_J = 0$) is highlighted, although numerous other transition pathways with $\Delta M_J = +2$ are also coupled by the circularly polarized laser beam. The expressions for the Stark shift and saturation intensity, Eqs. (51) and (62), for the two-photon transition from state a to state b can be modified simply by summing these expressions over all possible intermediate states. In Fig. 9, the two-photon

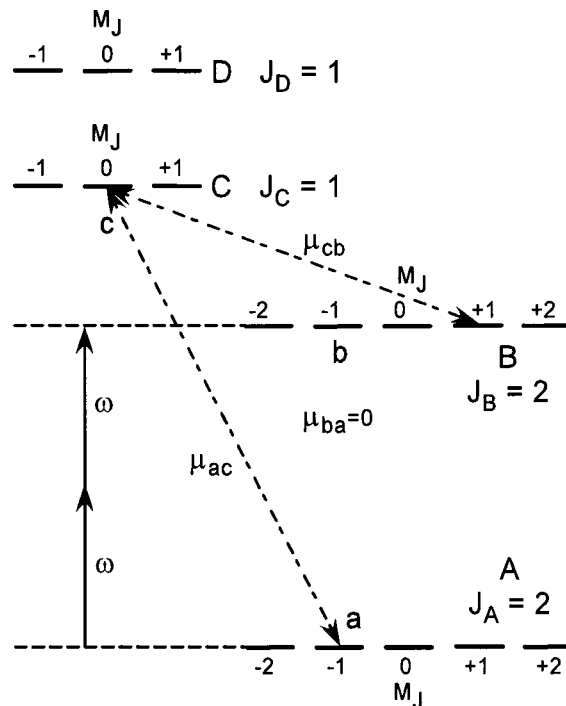


FIG. 9. Schematic diagram of the two-photon absorption process in a four-level system. The Zeeman structure of each level is depicted and a two-photon absorption process with initial state a , final state b , and intermediate state c is highlighted. The two-photon-absorption pathway that is shown is induced by circularly polarized laser radiation. Several other two-photon absorption pathways that are induced by circularly polarized laser radiation are not shown for reasons of clarity.

transition from state a to state b can also proceed through the $M_J = 0$ state in level D , but in general there will be numerous possible intermediate states. The saturation and Stark-shifting behavior of the two-photon transition from level A to level B , however, will be determined by the collective behavior of all possible two-photon-transition pathways between the Zeeman states in these levels. In general, the saturation intensities and the Stark shifts for each of these state-to-state transition pathways will be very different, resulting in asymmetric line shapes at high intensities as is shown in the work by Liao and Bjorkholm⁴³ and in the work by Huo, Gross, and McKenzie.⁴⁴

We are presently modeling the LIPS process in atomic hydrogen using direct numerical integration of the time-dependent density-matrix equations. This time-dependent numerical model includes 92 states and takes into account Doppler broadening and hyperfine splitting of the energy levels. The steady-state analysis of the three-state system presented in this paper was undertaken primarily to attain a fundamental understanding of the TPA process in a simpler system, and the analytical results that we have obtained will be quite valuable for interpreting the results of our time-dependent, 92-state model.

The equations developed in this paper are directly applicable for experiments performed with single-frequency-mode laser radiation when the laser pulse length is significantly greater than the characteristic collisional time in the medium of interest. The restriction that the laser radiation be monochromatic is becoming less of an issue with the devel-

opment of single-mode optical parametric laser systems^{45–47} and the increasing use of near-Fourier transform-limited tunable picosecond lasers⁴⁸ for TPA-based measurements in reacting flows.

It is important to understand the saturation of the TPA resonance for application of TPA-based techniques for diagnostic purposes. The dependence of the TPA laser-induced-fluorescence signal on laser intensity is frequently measured to check for the occurrence of photochemical effects.⁴⁹ In the absence of photochemical effects or saturation, the TPA-LIF signal will increase in proportion to the square of the laser intensity. If photochemical effects are significant and the species of interest is being created by laser-induced dissociation of larger molecules such as H₂O, the TPA-LIF signal will increase faster than the square of the laser intensity. If the TPA resonance is saturated, the TPA-LIF signal will increase more slowly than the square of the laser intensity. The effects of photochemistry and saturation on the laser-intensity dependence of the signal are in opposite directions. Being able to calculate the saturation intensity as discussed in this paper will at least allow researchers to determine if the TPA resonance is saturated or not, and this will help to interpret the possible effects of photochemistry on the power-dependence measurements.

ACKNOWLEDGMENTS

Funding for this research was provided by the U.S. Department of Energy, Office of Basic Energy Sciences, Division of Chemical Sciences, Geosciences, and Biosciences, under Grant No. DE-FG03-99ER14997, and by the Air Force Research Laboratory, Propulsion Directorate, Wright-Patterson AFB, under Contract No. F33615-03-D-M2329, and by the Air Force Office of Scientific Research (Dr. Julian Tishkoff, Program Manager).

- ¹M. Göppert-Mayer, *Ann. Phys. (Leipzig)* **9**, 273 (1931).
- ²W. Kaiser and C. G. B. Garrett, *Phys. Rev. Lett.* **7**, 229 (1961).
- ³E. V. Baklanov and V. P. Chebotayev, *Opt. Commun.* **12**, 312 (1974).
- ⁴T. W. Hänsch, S. A. Lee, R. Wallenstein, and C. Wieman, *Phys. Rev. Lett.* **34**, 307 (1975).
- ⁵W. K. Bischel, B. E. Perry, and D. R. Crosley, *Appl. Opt.* **21**, 1419 (1982).
- ⁶R. P. Lucht, J. T. Salmon, G. B. King, D. W. Sweeney, and N. M. Laurendeau, *Opt. Lett.* **8**, 365 (1983).
- ⁷M. Aldén, H. M. Hertz, S. Svanberg, and S. Wallin, *Appl. Opt.* **23**, 3255 (1984).
- ⁸M. Aldén, S. Wallin, and W. Wendt, *Appl. Phys. B: Photophys. Laser Chem.* **33**, 205 (1984).
- ⁹U. Westblom, P.-E. Bengtsson, and M. Aldén, *Appl. Phys. B: Photophys. Laser Chem.* **52**, 371 (1991).
- ¹⁰A. Lawitzki, J. Bittner, and K. Kohse-Höinghaus, *Chem. Phys. Lett.* **175**, 429 (1990).
- ¹¹M. Aldén, A. L. Schawlow, S. Svanberg, W. Wendt, and P. L. Zhang, *Opt. Lett.* **9**, 211 (1984).
- ¹²J. E. M. Goldsmith and N. M. Laurendeau, *Opt. Lett.* **15**, 576 (1990).
- ¹³J. E. M. Goldsmith, R. J. M. Anderson, and L. R. Williams, *Opt. Lett.* **15**, 78 (1990).
- ¹⁴J. E. M. Goldsmith, *Opt. Lett.* **10**, 116 (1985).
- ¹⁵J. E. M. Goldsmith and L. A. Rahn, *Opt. Lett.* **15**, 814 (1990).
- ¹⁶J. E. M. Goldsmith, *Appl. Opt.* **29**, 4841 (1990).
- ¹⁷J. T. Salmon and N. M. Laurendeau, *Combust. Flame* **74**, 221 (1988).
- ¹⁸U. Czarnetzki, K. Miyazaki, T. Kajiwara, K. Muraoka, M. Maeda, and H. F. Döbele, *J. Opt. Soc. Am. B* **11**, 2155 (1994).
- ¹⁹M. Aldén, U. Westblom, and J. E. M. Goldsmith, *Opt. Lett.* **14**, 305 (1989).
- ²⁰J. E. M. Goldsmith, *J. Opt. Soc. Am. B* **6**, 1979 (1989).
- ²¹M. Aldén, P.-E. Bengtsson, and U. Westblom, *Opt. Commun.* **71**, 263 (1989).
- ²²S. Agrup, U. Westblom, and M. Aldén, *Chem. Phys. Lett.* **170**, 406 (1990).
- ²³N. Georgiev, K. Nyholm, R. Fritzton, and M. Aldén, *Opt. Commun.* **108**, 71 (1994).
- ²⁴M. S. Brown and J. B. Jeffries, *Appl. Opt.* **34**, 1127 (1995).
- ²⁵J. A. Gray, J. E. M. Goldsmith, and R. Trebino, *Opt. Lett.* **18**, 444 (1993).
- ²⁶J. A. Gray and R. Trebino, *Chem. Phys. Lett.* **216**, 519 (1993).
- ²⁷C. F. Kaminski, B. Löfstedt, R. Fritzton, and M. Aldén, *Opt. Commun.* **129**, 38 (1996).
- ²⁸K. Nyholm, R. Fritzton, N. Georgiev, and M. Aldén, *Opt. Commun.* **114**, 76 (1995).
- ²⁹R. Dux, K. Grützmacher, M. I. de la Rosa, and B. Wende, *Phys. Rev. E* **51**, 1416 (1995).
- ³⁰K. Danzmann, K. Grützmacher, and B. Wende, *Phys. Rev. Lett.* **57**, 2151 (1986).
- ³¹J. Seidel, *Phys. Rev. Lett.* **57**, 2154 (1986).
- ³²K. Grützmacher, M. I. De La Rosa, A. B. Gonzalo, M. Steiger, and A. Steiger, *Appl. Phys. B: Lasers Opt.* **76**, 775 (2003).
- ³³R. H. Pantell and H. E. Puthoff, *Fundamentals of Quantum Electronics* (Wiley, New York, 1969).
- ³⁴Y. R. Shen, *The Principles of Nonlinear Optics* (Wiley, New York, 1984).
- ³⁵B. Cagnac, G. Grynberg, and F. Biraben, *J. Phys. (Paris)* **34**, 845 (1973).
- ³⁶W. K. Bischel, P. J. Kelly, and C. K. Rhodes, *Phys. Rev. A* **13**, 1817 (1976).
- ³⁷R. Dux, K. Grützmacher, M. I. de la Rosa, and B. Wende, *Phys. Rev. E* **51**, 1416 (1995).
- ³⁸G. J. Fiechtner and J. R. Gord, *J. Quant. Spectrosc. Radiat. Transf.* **68**, 543 (2001).
- ³⁹M. Sargent III, M. O. Scully, and W. E. Lamb, Jr., *Laser Physics* (Addison-Wesley, Reading, MA, 1974).
- ⁴⁰D. Marcuse, *Principles of Quantum Electronics* (Academic, New York, 1980).
- ⁴¹R. W. Boyd, *Nonlinear Optics*, 2nd ed. (Academic, New York, 2003).
- ⁴²H. A. Bethe and E. E. Saltpeter, *Quantum Mechanics of One- and Two-Electron Atoms* (Springer, Berlin, 1957).
- ⁴³P. F. Liao and J. E. Bjorkholm, *Phys. Rev. Lett.* **34**, 1 (1975).
- ⁴⁴W. M. Huo, K. P. Gross, and R. L. McKenzie, *Phys. Rev. Lett.* **54**, 1012 (1985).
- ⁴⁵Y. He, P. Wang, R. T. White, and B. J. Orr, *Opt. Photonics News* **12**, 56 (2002).
- ⁴⁶K. Bultitude, R. Stevens, and P. Ewart, *Appl. Phys. B* (to be published).
- ⁴⁷W. D. Kulatilaka, T. N. Anderson, T. L. Bougher, and R. P. Lucht, *Appl. Phys. B* (submitted).
- ⁴⁸J. H. Frank, B. D. Patterson, X. Chen, and T. B. Settersten, *Appl. Opt.* **43**, 2588 (2004).
- ⁴⁹J. E. M. Goldsmith, *Appl. Opt.* **28**, 1206 (1989).

Multiple-Pump Coherent Anti-Stokes Raman Scattering for Quantitative Measurement of Temperature and Flame Species in a Model Gas-Turbine Combustor

Sukesh Roy,^{*1} Terrence R. Meyer,^{*1} Robert P. Lucht,^{*2} and James R. Gord^{*3}

^{*1} Innovative Scientific Solutions, Inc., 2766 Indian Ripple Road, Dayton, OH 45440, USA

Tel: (937)-255-3115/Fax: (937)-656-4110

E-mail: suresh@innssi.com, sroy@woh.rr.com

^{*2} Department of Mechanical Engineering, Purdue University, West Lafayette, IN 47907, USA

^{*3} Air Force Research Laboratory, Propulsion Directorate, Wright-Patterson AFB, OH 45433, USA

Abstract: Application of dual-pump, dual-broadband (DPDB) coherent anti-Stokes Raman scattering (CARS) for the simultaneous measurement of temperature and multiple-species concentrations in a liquid-fueled model gas-turbine combustor is presented. In this system, pure rotational transitions of N_2-O_2 and the ro-vibrational transitions of N_2-CO_2 are probed using two narrowband pump beams, a broadband pump beam, and a broadband Stokes beam. The main advantage of this technique is that it permits very accurate temperature measurements at both low and high temperatures as well as concentration measurements of three molecules from each laser shot. Single-shot measurements of temperature and concentrations ratios of N_2-CO_2 and N_2-O_2 in the exhaust stream of a liquid-fueled, CFM56, swirl-stabilized gas-turbine combustor are presented for equivalence ratios ranging from 0.4-1.1.

Key words: CARS, Raman Scattering, Reacting Flows,
Gas-Turbine Combustor

1. Introduction

Characterization of advanced propulsion systems requires the determination of performance and combustion efficiency through measurements of temperature and species concentrations in the exhaust stream. Typically these kinds of data are acquired using physical probes for thermometry or extractive sampling and involve several independent techniques. Diode-laser-based absorption is a non-intrusive

alternative to extractive sampling, but it is a path-averaged approach and has limited spatial resolution. For species such as O_2 , low sensitivity also limits the temporal resolution of diode-laser-based techniques. Ideally measurements of temperature and multiple species would be accomplished simultaneously with high spatial and temporal resolution and with a minimum number of diagnostics. Dual-pump, dual-broadband (DPDB) coherent anti-Stokes Raman scattering (CARS) offers the possibility of monitoring the local temperature and concentrations of two target species with respect to a reference species (usually N_2) using a single hardware platform. Spatial resolution ranges from 50 microns to 2 mm and temporal resolution is on the order of 10 ns.

We present here the application of a DPDB-CARS system for temperature and concentration measurements in reacting flows of practical interest. This work extends our previous demonstrations of temperature and concentration measurements in laboratory flames and combustor test facilities using dual-pump and triple-pump CARS (Roy et al. 2003 and Lucht et al. 2003). The DPDB CARS technique is unique in that it allows for accurate temperature measurements both at low and high temperatures. In the combustion zone or the exhaust of a real combustor, there is a wide spatial and temporal variation of temperature due to the inherent turbulent nature of the flow field. In the current system, the rotational transitions of N_2-O_2 and the ro-vibrational transitions of N_2-CO_2 are probed. The rotational spectra of N_2-O_2 provide better temperature accuracy at lower temperatures, generally below 1500 K (Aldén et al. 1989), whereas the ro-vibrational spectra of N_2-CO_2 provide improved temperature accuracy at higher temperatures. To our knowledge, this is the first CARS technique that uses three pump beams to excite the transitions of three different molecules simultaneously to achieve two rotational spectra (e.g., N_2 and O_2) and two ro-vibrational spectra (N_2 and CO_2). The rotational spectra provide better accuracy at low temperature because most of the population resides at lower energy levels. At higher temperatures population is transferred to higher energy levels which is reflected in more accurate ro-vibrational spectra.

The DPDB CARS system is essentially a special triple-pump CARS system where one of the pump beams is of broadband nature, whereas in the traditional triple-pump CARS technique the bandwidth of all the pump beams are either single-longitudinal mode or very narrow (Roy et al. 2003). The DPDB CARS system may also be viewed as the combination of the dual-pump and dual-broadband approaches. The dual-pump CARS technique, which was first demonstrated by Lucht (1987), has been used for the simultaneous measurement of N_2 and O_2 (Lucht 1987 and Hancock et al. 1997), N_2 and H_2 (Schauer 1998), N_2 and CH_4 (Green et al. 1998), and N_2 and CO_2 (Brüggemann et al. 1992). In dual-pump CARS, the wavelengths of the input beams are adjusted such that the CARS spectra for the two species under study are observed at nearly the same frequency. This arrangement largely eliminates potential errors arising from wavelength-dependent variations in signal transmission or detector efficiency that can complicate other multiple-species CARS techniques such as dual-Stokes and dual-broadband CARS (Eckbreth 1988). Several other CARS techniques, such as dual-broadband rotational CARS (Bood et al. 2000) and simultaneous vibrational and

rotational CARS (Brackmann et al. 2002), have also been used for temperature and multiple-species concentration measurements.

In the DPDB CARS technique, a dual-broadband CARS system is superimposed on a dual-pump CARS system. Four laser beams are used to generate CARS signals near two distinct wavelengths. Both wavelength regions exhibit an N_2 CARS signal along with the CARS signal from another target molecule. Each pair of CARS signals is generated over a relatively narrow wavelength region and can be captured with fixed-wavelength detection. Temperature and relative concentrations of the target species (with respect to N_2) are extracted either by fitting the measured CARS spectrum with a theoretical spectrum or through a Boltzmann plot. Temperatures from the N_2 - CO_2 and N_2 - O_2 pairs were evaluated by fitting the CARS spectra with the theoretical spectra. Since the N_2 concentration is typically known, the amplitude of the target-species signal relative to that of the paired N_2 signal provides an absolute measure of the target-species concentration.

Measurements were carried out in the exhaust stream of a liquid-fueled, swirl-stabilized CFM56 combustor. The objectives of this investigation were to perform single-laser-shot temperature and O_2 and CO_2 concentration measurements in the exhaust stream of a liquid-fueled practical combustor under non-sooting and sooting conditions. Measurements were performed for a wide range of equivalence ratios ($\phi = 0.4$ to 1.1). The current work provides benchmark statistical distributions of temperature and concentrations of CO_2 and O_2 in the exit plane of the combustor and is used to evaluate the effects of particulate-mitigating additives on flame chemistry. These measurements complement laser-induced incandescence (LII) and planar laser-induced fluorescence (PLIF) measurements of soot volume fraction and OH radical concentrations, respectively, which are ongoing in the current combustor.

2. Experimental Setup

The schematic and the energy-level diagrams of the DPDB CARS system are

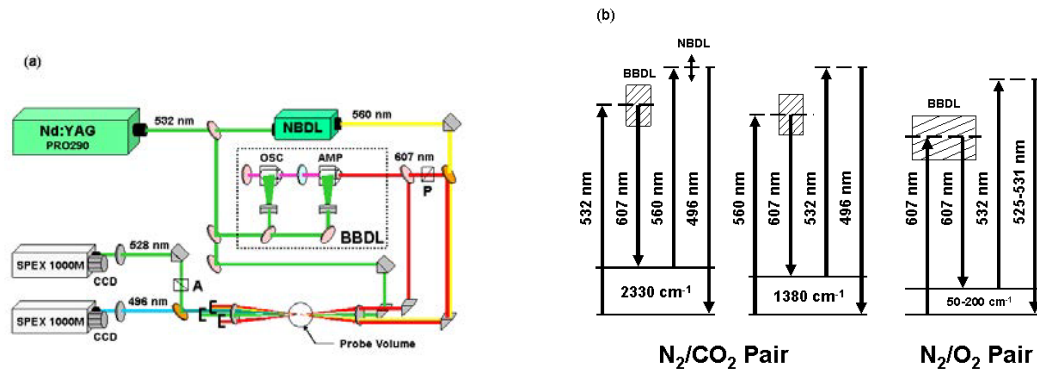


Fig. 1(a): Schematic diagram of DPDB CARS system for detecting temperature and concentrations of N_2 , O_2 , and CO_2 . (b) Energy-level diagram of DPDB CARS system.

shown in Figs. 1a and 1b, respectively. As stated previously, a dual-pump CARS system is superimposed on a dual-broadband CARS system with this approach. An injection-seeded Nd:YAG laser (Quanta Ray, Pro 290, Spectra Physics) is used to pump a narrowband dye laser and a broadband dye laser while providing a 532-nm CARS pump beam. In the current configuration, the broadband dye laser (pumped at 532 nm) provides an output beam centered at ~607 nm that serves as the Stokes laser for each of the four generated CARS signals. The broadband output at 607 nm also provides the pump beam for the dual-broadband rotational CARS system. The narrowband dye laser is also pumped by the 532-nm beam and provides laser radiation at ~560 nm. The combination of the 532-nm pump beam with the 607-nm Stokes beam produces a ro-vibrational N₂ Raman polarization that coherently scatters the 560-nm pump beam, yielding an N₂ CARS signal near 496 nm. At the same time, the 560-nm pump beam and the 607-nm Stokes beam produce a CO₂ Raman polarization that scatters the 532-nm pump beam, yielding a CO₂ CARS signal that also appears near 496 nm.

The spectral width of the broadband dye laser is ~200 cm⁻¹. This spectral width is large enough to excite the pure rotational transitions of N₂ and O₂ molecules at the ground and excited vibrational state up to rotational levels of $J \sim 30$. The broadband pump beam and the broadband Stokes beam produce rotational Raman polarizations for both N₂ and O₂ molecules, which then scatter the 532-nm pump beam. The pure rotational CARS spectra appear at a wavelength of ~528 nm. The incident beams are phase matched using the folded BOXCAR geometry, with the 560-nm and 607-nm pump beams arranged co-linearly. The frequency of the rotational CARS signal is very close to the pump beam at 532 nm. This poses the significant challenge of discriminating the scattered light at 532 nm from the CARS signal at 528 nm. To minimize the scattered light at 532 nm, the polarization of one of the broadband pump beams at 607 nm was oriented to be orthogonal to that of the 532-nm beam. The polarization of the broadband dye beam that serves as the Stokes beam for the N₂-CO₂ CARS was not rotated. With this configuration the polarization of the pure rotational CARS signal was orthogonal to that of the 532-nm pump beam. The CARS signal at 528 nm was isolated from the background 532-nm scattered light by placing a polarizer in the detection channel with a transmission axis perpendicular to the 532-nm pump beam, as shown in Fig. 1. The CARS signals at 496 nm and 528 nm were separated using a dichroic mirror and then simultaneously detected using two 1.0-m spectrometers and two back-illuminated CCD cameras with 2000×512-pixel arrays.

The CARS spectra are normalized using a non-resonant spectrum to account for the effects of pulse-to-pulse laser-power fluctuations, long-term power drifts, and spectral variations in dye power (Eckbreth 1988). The non-resonant spectrum is recorded by flowing argon through a flow tube into the beam-overlap region. The combustor facility is described in detail by Roy et al. (2004a).

3. Results and Discussion

Temperature, CO₂, O₂, and N₂ concentration measurements were performed in the exhaust stream of the JP8-fueled, swirl-stabilized combustor over a wide range of equivalence ratios using the DPDB CARS technique. This CARS system exhibited excellent accuracy, as determined from temperature and CO₂ concentration measurements in a calibrated, laminar flame (Roy et al. 2003). The standard deviations of the measured single-shot temperatures and CO₂ concentrations evaluated from the N₂-CO₂ spectra in the calibrated flame were 2.3% and 6% of the mean values, respectively, for a wide range of equivalence ratios. The objectives of this study were to measure single-shot temperature and concentrations of CO₂ and O₂ at high equivalence ratios in the exhaust of a practical combustor.

Typical single-shot N₂-CO₂ and N₂-O₂ spectra acquired using the DPDB CARS system in the exhaust stream of the JP-8-fueled combustor at an equivalence ratio of 0.45 are shown in Figs. 2a and 2b, respectively. The solid line represents the experimental CARS signal, and the dotted line represents the theoretical CARS spectrum. The N₂-CO₂ CARS spectrum was fitted using the Sandia CARSFT code (Palmer 1989), and the N₂-O₂ rotational spectrum was fitted using the code described by Bood et al. (2000). The broad vibrational-signal contribution to the rotational spectrum was subtracted by fitting a smooth profile through the baseline (Bood et al. 2000). The temperature and relative CO₂ and O₂ concentrations were evaluated by comparing the experimental spectrum with that of a theoretical one. As expected the temperatures evaluated from both spectra agree to within experimental uncertainty as shown in Fig. 2.

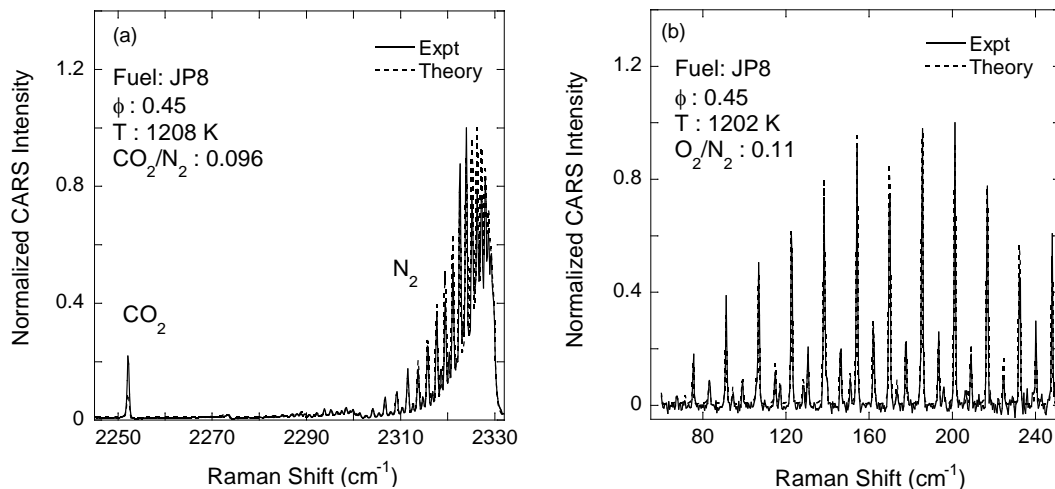


Figure 2. Single-shot (a) ro-vibrational spectrum of N₂-CO₂ and (b) rotational spectrum of N₂-O₂ acquired in exhaust stream of JP-8-fueled combustor for equivalence ratio of 0.45. Both spectra were acquired simultaneously.

Probability density functions (PDF's) of temperatures evaluated from the single-shot $\text{N}_2\text{-O}_2$ rotational spectra and the $\text{N}_2\text{-CO}_2$ ro-vibrational spectra are shown in Figs. 3a and 3b, respectively. The difference in standard deviations of the rotational and ro-vibrational spectra may be due to the difference in the signal-to-noise ratio and the quality of the least-square-fitting of the experimental spectra. Two different theoretical codes were used to fit the single-shot ro-vibrational spectra and the single-shot rotational spectra. The standard deviations of the temperature evaluated

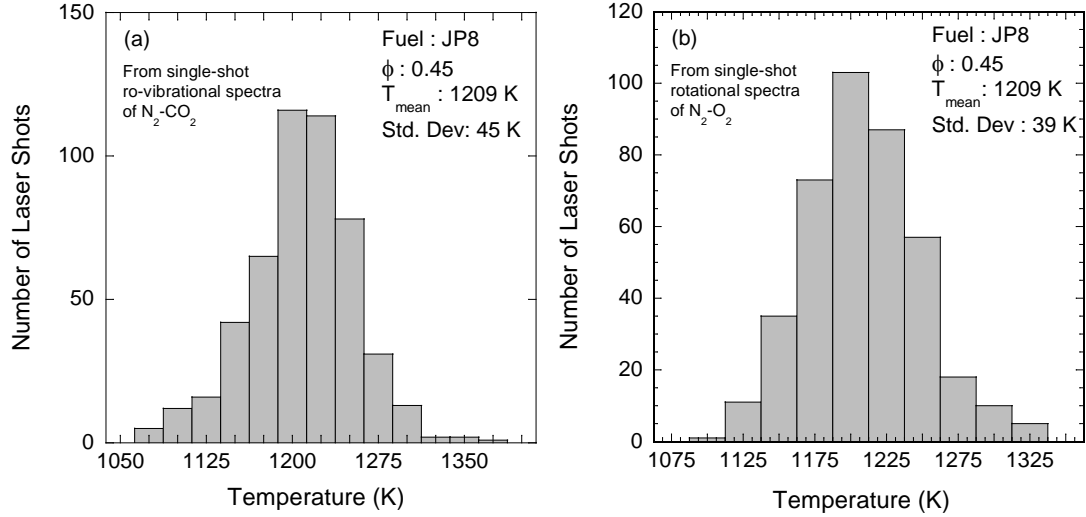


Figure 3. Single-shot temperature PDF's evaluated from the (a) ro-vibrational spectrum of $\text{N}_2\text{-CO}_2$ and (b) rotational spectrum of $\text{N}_2\text{-O}_2$ acquired in the exhaust stream of the JP-8-fueled combustor for an equivalence ratio of 0.45.

from the $\text{N}_2\text{-CO}_2$ spectra and $\text{N}_2\text{-O}_2$ spectra are $\sim 3.75\%$ and $\sim 3.25\%$ of the mean values, respectively; the mean temperature is ~ 1209 K. The PDF's of the $\text{N}_2\text{-CO}_2$ and $\text{N}_2\text{-O}_2$ ratios are shown in Figs. 4a and 4b, respectively. PDF's of single-shot

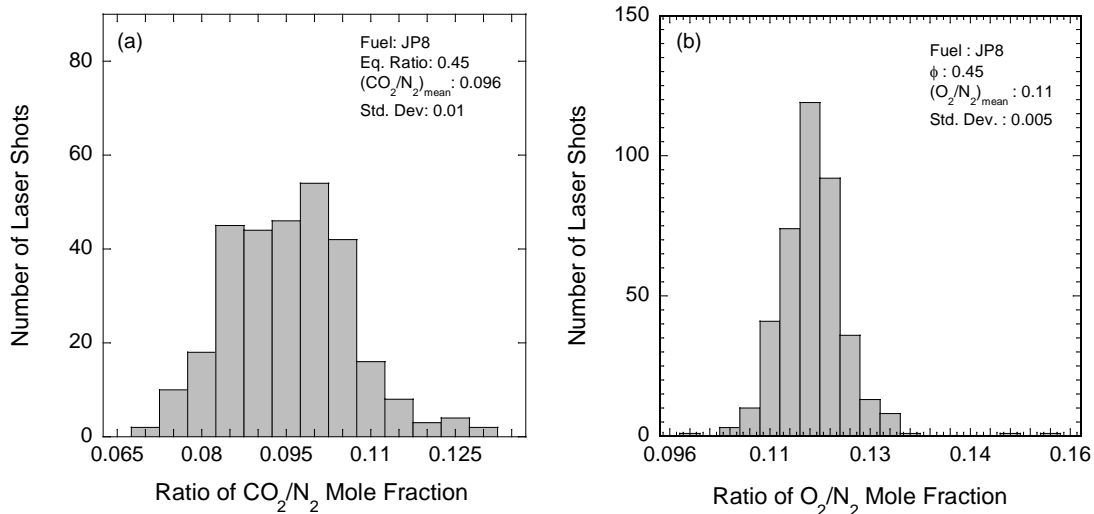


Figure 4. PDF's of the ratio of (a) CO_2 and N_2 and (b) O_2 and N_2 evaluated from the single-shot CARS spectra as discussed in Figs. 2 and 3.

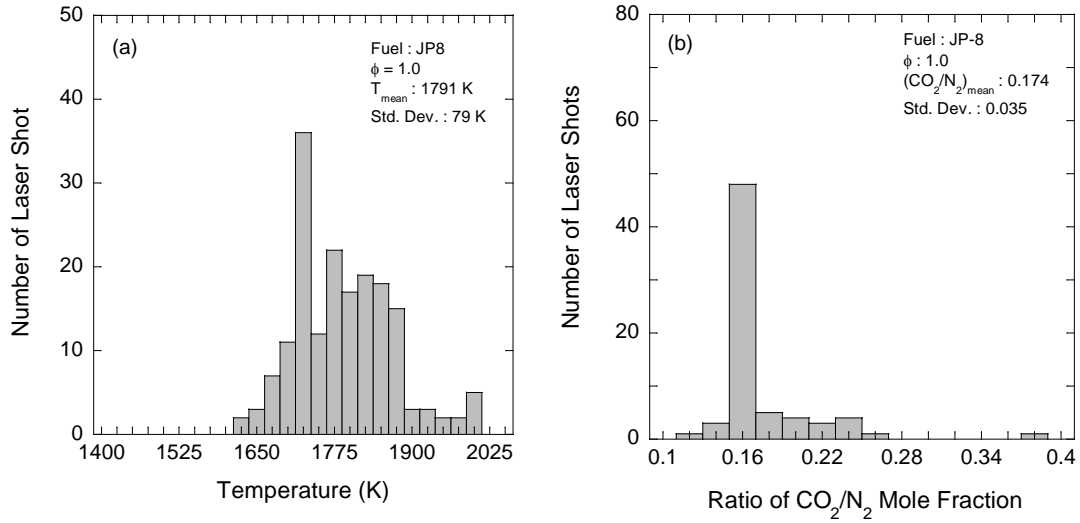


Figure 5. PDF's of (a) temperature and (b) CO₂ mole fraction determined from single-laser-shot, N₂-CO₂ ro-vibrational spectra acquired at the exhaust of the JP-8-fueled combustor for an equivalence ratio of 1.0.

temperature and CO₂ mole fraction at an equivalence ratio of 1.0 are shown in Figs. 5a and 5b, respectively. These near-stoichiometric equivalence ratios are significantly higher than the previous measurements performed in this combustor, single-shot or time-averaged (Lucht et al. 2003 and Takahashi et al. 1994). At an equivalence ratio of 1.0 where the temperature is significantly higher than 1500 K, it was very difficult to extract single-shot PDFs of oxygen concentration due to the following two reasons: (1) lower signal-to-noise ratio of the single-shot rotational spectra (<5) at these conditions in a practical combustor and (2) higher level of coupling between the nonresonant susceptibility and concentration, especially since the O₂ concentration is lower at higher equivalence ratio. In a laboratory flame, the high SNR of the rotational spectra allowed us to extract single-shot PDF's of oxygen concentration (Roy et al. 2004b).

A comparison of the experimental results with an equilibrium calculation is shown in Fig. 6. The equilibrium calculations were performed using the code provided by Turns (1996). The molecular formula of JP-8 fuel is C_{10.9}H_{20.9}, and the heat of formation is equal to $-2.48 \times 10^5 \text{ kJ/K}$ [private communication, T. Edwards, U.S. Air Force Research Laboratory, Wright-Patterson Air Force Base, 2001]. As is evident in Fig. 6a, the measured temperatures (evaluated from the ro-vibrational spectra) are lower than the adiabatic flame temperatures by 21% during lean combustor operation and by 25% at the richest condition. The temperatures evaluated from the rotational spectra are $\sim 40\text{-}50\text{K}$ lower than the temperatures evaluated from the ro-vibrational spectra. The accuracy of the temperature evaluated from the rotational spectra will be somewhat affected by the way broad vibrational-signal contribution to the rotational spectrum was subtracted (Bood et al. 2000).

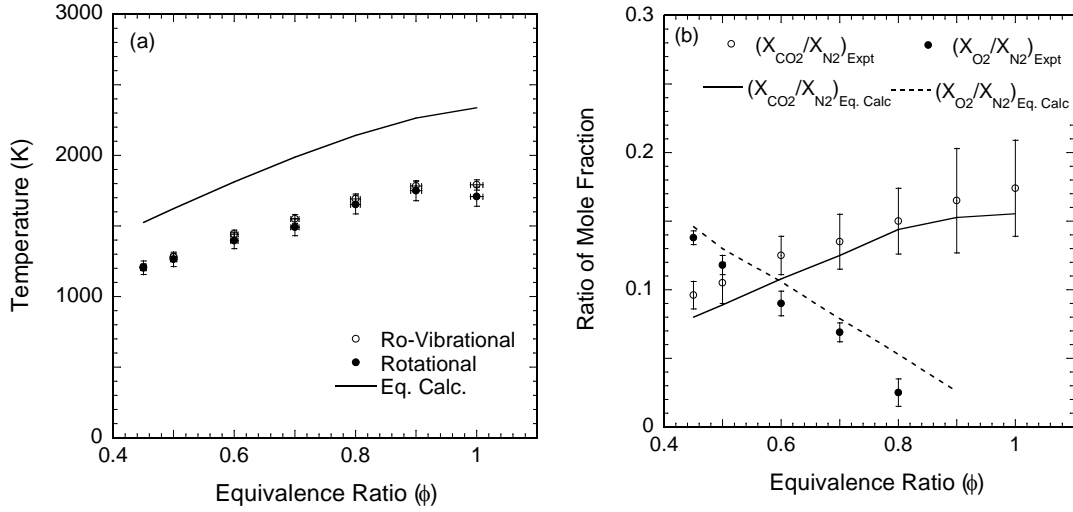


Fig. 6: Comparison of experimental results and equilibrium calculations: (a) temperature profiles and (b) profiles of ratio of CO_2/N_2 and O_2/N_2 .

The discrepancy between the measured and calculated temperatures may be due to the following four reasons: (1) heat loss due to radiation and conduction; the measurements were taken $\sim 1m$ from the nozzle and the primary flame zone is located within $\sim 0.08m$ from the nozzle, (2) flame unsteadiness and spatial averaging during the measurements, (3) uncertainty with the mass-flow controller, (4) the signal-to-noise ratio of the experimental spectra that affects the least-squares fitting with the theoretical spectra, and (5) uncertainties with the composition of JP8 fuel and subsequent equilibrium calculations. The increase in this discrepancy at higher equivalence ratios is expected, due to increased heat losses via heat conduction and soot radiation. Moreover, the temperature and the oxygen concentration will be somewhat affected by the way the broad vibrational signal contribution was subtracted from the rotational spectrum.

The measured CO_2/N_2 mole fractions follow the correct trend with equivalence ratio but are about 15% higher than the equilibrium code results for the lean condition. Under stoichiometric to rich conditions, the difference between measured and theoretical CO_2/N_2 mole fractions decreases to about 7-9%. These discrepancies are mostly due to issues related to the spectral modeling of the CO_2 CARS spectra in the CARSFT code. These modeling issues are the subject of ongoing investigation and are beyond the scope of the current work. The measured oxygen concentration at higher temperatures will be affected by the higher coupling between nonresonant susceptibility and the concentration, especially since the O_2 concentration is lower at high equivalence ratio. It was not possible to extract the concentration of oxygen beyond an equivalence ratio of 0.8. This is not surprising because the equilibrium calculation also showed the oxygen concentration in the exhaust approaching zero at an equivalence ratio of 0.9.

4. Conclusions

The application of dual-pump, dual-broadband (DPDB) CARS to characterize the exit conditions in a swirl-stabilized CFM56 combustor has been demonstrated. This technique is capable of providing measurements of temperature along with concentrations of two target species. Simultaneous, single-shot data acquisition enhances the precision and accuracy of the temperature measurements due to the correlation afforded by the common presence of N_2 in each of the two spectral windows. Experiments were carried out to measure the temperature and the concentrations of carbon-dioxide and oxygen at the exhaust stream of the combustor for different operating conditions. Experiments were performed using JP-8 fuel for equivalence ratios ranging from 0.4 to 1.1 under low to high sooting conditions, respectively. The standard deviations of the measured temperature and CO_2 mole fraction as determined from single-laser-shot, dual-pump N_2 - CO_2 CARS spectra were ~3-4% and ~9-20% of the mean values, respectively, for the full range of equivalence ratios. The standard deviations of the measured O_2 mole fractions as determined from the rotational spectra were ~5-20% of the mean values for equivalence ratios ranging from 0.45 to 0.8. This system should enable CARS measurements in the primary reaction zone of the combustor under sooting conditions to complement laser-induced incandescence (LII) and planar laser-induced fluorescence (PLIF) measurements.

Acknowledgements

Funding was provided by the Air Force Research Laboratory, Propulsion Directorate, Wright-Patterson AFB, under Contract Nos. F33615-D-03-M2829 and F33615-00-C-3020, and by the Air Force Office of Scientific Research (Dr. Julian Tishkoff, Program Monitor). The authors also gratefully acknowledge the assistance of Dr. Mikael Afzelius and Prof. Per-Erik Bengtsson of the Lund Institute of Technology, Sweden for their assistance with the rotational CARS spectral simulation code.

References

- Aldén, M., Bengtsson, P.-E., Edner, H., Kröll, S., and Nilsson, D. (1989), *Appl. Opt.* 28, 3206-3219.
- Bood, J., Bengtsson, P.-E., and Aldén, M. (2000), *Appl. Phys. B* 70, 607-620.
- Brackmann, C., Bood, J., Bengtsson, P.-E., Seeger, T., Schenk, M., and Leipertz, A. (2002), *Appl. Opt.* 41, 564-572.
- Brüggemann, D., Wies, B., Zhang, X. X., Heinze, T., and Knoche, K. F. (1992), "CARS Spectroscopy for Temperature and Concentration Measurements in a Spark Ignition Engine," in *Combustion Flow Diagnostics*, D. F. G. Durão, M. V. Heitor, J. H. Whitelaw, and P. O. Witze, eds., Kluwer Academic, Dordrecht, The Netherlands, 495-511.

- Eckbreth, A. C. (1988), *Laser Diagnostics for Combustion Temperature and Species*, Gordon and Breach Publishers, Amsterdam, The Netherlands.
- Green, S. M., Rubas, P. J., Paul M. A., Peters, J. E., and Lucht, R. P. (1998), "An Annular Phase-Matched Dual-Pump CARS System for the Simultaneous Detection of Nitrogen and Methane," *Appl. Opt.* 37, 1690-1701.
- Hancock, R. D., Schauer, F. R., Lucht, R. P., and Farrow, R. L. (1997), "Dual-Pump Coherent Anti-Stokes Raman Scattering Measurements of Hydrogen and Oxygen in a Laminar Jet Diffusion Flame," *Appl. Opt.* 36, 3217-3226.
- Lucht, R. P. (1987), "Three-Laser Coherent Anti-Stokes Raman Scattering Measurements of Two Species," *Opt. Lett.* 12, 78-80.
- Lucht R. P., Velur, V. N., Fiechtner, G. J., Carter, C.D., Grinstead, Jr., K. D., Gord, J. R., Danehy, P. M., and Farrow, R. L. (2003), *AIAA J.* 41, 679-686.
- Palmer, R. E. (1989), "The CARSFT Computer Code for Calculating Coherent Anti-Stokes Raman Spectra: User and Programmer Information," Report No. SAND89-8206 Sandia National Laboratories, Livermore, California.
- Roy, S., Meyer, T. R., Brown, M. S., Velur, V.N., Lucht, R. P., and Gord, J. R. (2003), "Triple-Pump Coherent Anti-Stokes Raman Scattering (CARS): Temperature and Multiple-Species Concentration Measurements in Reacting Flows," *Opt. Comm.* 224, 131-137.
- Roy, S., Meyer, T. R., Lucht, R. P., Belovich, V. M., Corporan, E., and Gord, J. R. (2004a), "Temperature and CO₂ Concentration Measurements in the Exhaust Stream of a Liquid-Fueled Combustor Using Dual-Pump Coherent Anti-Stokes Raman Scattering (CARS) Spectroscopy," *Combust. Flame.* 138, 273-284.
- Roy, S., Meyer, T. R., Lucht, R. P., Afzelius, M., Bengtsson, P-E., and Gord, J. R., (2004b) "Dual-pump Dual-broadband Coherent Anti-Stokes Raman Scattering in Reacting Flows," *Opt. Lett.* 29 (16), 1843-1845.
- Schauer, F. R. (1998), "Investigation of Flame Structure and Thermal Diffusion Effects in Hydrogen Jet Diffusion Flames," Ph.D. Thesis, University of Illinois at Urbana-Champaign, Urbana, Illinois.
- Takahashi, F., Schmoll, J. W., Switzer, G. L., and Shouse, D. T. (1994), *Twenty-Fifth Symposium (International) on Combustion*, The Combustion Institute, Pittsburgh, PA, pp. 183-191.
- Turns, S. R. (1996), *An Introduction to Combustion*, McGraw-Hill, New York.

STATE-OF-THE-ART FUEL ACIDITY MONITORING

Justyna Widera[†], Jay M. Johnson[‡]

[†]Innovative Scientific Solutions Inc. (ISSI)

2766 Indian Ripple Road, Dayton, OH 45440 (USA)

[‡]University of Dayton Research Institute (UDRI)

300 College Park, Dayton, OH 45469 (USA)

Development of a novel Iridium oxide based acidity sensor for off-line monitoring of the acidity of fuel is described. The sensor works in the potentiometric mode using an IrO_x electrode as an indicating electrode and a Ag/Ag⁺ electrode as a reference electrode. The data show that the IrO_x sensor responds to compounds present in fuel that have acid-base character. An off-line IrO_x sensor would allow the determination of the acidity of different fuels and the discrimination between neat and thermally stressed fuels. Experimental results also indicate that the low conductance of fuel and / or the material used for sensor encapsulation may influence the response time of the IrO_x sensor.

INTRODUCTION

Some acids can be present in aviation turbine fuels due to: naturally occurring organic acids, the presence of some fuel additives, acid treatment during the refining process and/or degradation/oxidation products of the fuel formed during service and thermal stressing. In fuel, the constituents considered to have acidic characteristics include organic and inorganic acids, esters, phenolic compounds, lactones, resins, salts of heavy metals and additives such as inhibitors and detergents. Significant acid contamination is not likely to be present because of the many check tests made during the various stages of refining. However, trace amounts of acid can be present and are undesirable because of the consequent tendencies of the fuel to corrode metals and allow higher levels of dispersed water within the fuel.

The measurement of acidity in organic liquids is a difficult, but important technique to ascertain the acidity of petroleum products. Information about acid content in fuel or lubricants is crucial, because it is an indicator of the quality of these products. An acidic reading may suggest for example, that an aircraft fuel has undergone thermal oxidation or that a lubricant has completely lost added antioxidants and needs to be replaced. The ability to continuously monitor these systems would provide an early warning for failure of these fluids. Perhaps more important than "user-level" specification testing is the fact that the fuels processing industry must deliver, worldwide, neutral products compatible with fuel systems. In this regard, the process industry must create a product and then perform acid number testing. If in-line monitoring could be performed more quickly and accurately, process changes could be affected more readily, reducing waste and reprocessing.

Commercially available pH sensors are designed to conduct measurements in the aqueous phase. The measurement of acidity in organic solvent based matrices like petroleum products is much more difficult due to their complexity and the fact that they are extremely non-conducting. Currently, the measurement of "Total Acid Number" (TAN) in non-conducting fluids is performed by tedious, time consuming and solvent intensive methods (ASTM D 3242 or D 664) based on titration (1,2). In these methods, the tested fuel sample is dissolved in 1:1 mixture of toluene/isopropanol containing a small amount of water and titrated with standard alcoholic potassium hydroxide. In the D 3242 method, the end point is indicated by the color change of the added p-naphtholbenzein solution. In the D 664 method, the inflection point during the titration is indicated potentiometrically using a glass indicating electrode and a calomel reference electrode. Clearly, a chemical sensor that could rapidly and reliably measure TAN in fuels and oils would be of tremendous use in specification testing, for monitoring / process control, as an R&D tool for additive development, and for the "Smart Nozzle" application.

In this paper we will describe our efforts to develop an iridium oxide based acidity sensor suitable for work in low conducting media like Jet fuel in these applications. We have conducted preliminary studies using the IrO_x sensing system and have obtained data showing the detection range in aqueous (pH) and non-aqueous (acidity) solutions. We will demonstrate the preliminary feasibility of the IrO_x sensor as a fast, accurate, real time acidity sensor for the testing of fuels and oils. In future work, these results will be correlated with TAN.

EXPERIMENTAL

Materials

All chemicals were obtained from Aldrich (Milwaukee, WI) and used without further purification. Water was deionized and purified using a Synergy Millipore water purification system. The IrO_x electrodes were obtained from SensIrOx (Columbus, OH). They were manufactured by a process in which an iridium wire is thermally oxidized in a lithium carbonate melt at 850 degrees C. In this process a unique iridium oxide layer (20 μm thick) containing lithium is created on the iridium wire. A small 1 mm section at the end of the Ir wire was polished and a gold lead was attached. In order to protect this contact area and provide both a solvent tight seal and electrical insulation various encapsulating materials were evaluated including: epoxy resin, polyimide resin, glass powder and ester cyanate. Eccobond 55 epoxy was obtained from Emerson & Cuming (Billerica, MA). Polyimide resin was obtained from Restek (Bellefonte, PA), glass powder 7556 was purchased from Corning (Corning, NY) and ester cyanate RS-14A; ML-2-100-1 was obtained from YLA Inc. (Benicia, CA). All of the parts necessary to build the reference electrode were purchased as follows: silver wire 0.25 mm dia, 99.9985% purity Premion[®] from Alfa Aesar (Ward Hill, MA), flexible Teflon tube with ceramic or fiber junction frit from Cypress Systems, Inc. (Lawrence, KS).

Measurements

The experimental setup consists of electrochemical cell and the electrochemical workstation Model 650B from CH Instruments (Austin, TX). The hardware is controlled and data acquisition achieved using an external PC under Windows environment. The

sensing probe is potentiometric and basically consists of two (IE, RE) electrodes, where IE refers to the indicating electrode and RE to the reference electrode. A novel, iridium oxide electrode is utilized as the indicating electrode. After exposing the sensing probe to the solution containing the analyte of interest, the signal is observed as a change in potential relative to the reference electrode. The test solution was stirred during the measurements. The reference electrode (single junction) consists of a short piece of glass or Teflon tubing filled with non-aqueous solvent (with or without salt), a Ag wire immersed in the filling solution and a porous frit separating the measurement solution from the electrode filling solution. The electrical connection between the Ag wire and the test solution is established by a very slow process of ion diffusion from the wire to the filling solution and through the frit. In some cases, the reference electrode (double junction) might have a second electrolytic bridge consisting of a second (external) filling solution, into which the single junction structure is immersed, and a second frit, which is in direct contact with the sample. In double junction structures the internal and external filling solutions can be the same or similar in composition.

RESULTS AND DISCUSSION

IrO_x demonstrates superior long-term stability when compared to commercially available (glass electrode) and other experimental pH sensors (Ion Selective Field Effect Transistor and other metal oxides electrode-based sensors) described in the literature (3-5). Metal oxide electrodes (MOEs), in general, are inherently durable and suitable for miniaturization, but MOEs made by processes other than the SensIrOx process are less stable. IrO_x has many advantages over other pH sensors including: greater accuracy, lower drift, faster response, better long-term stability, robustness and much lower cost. IrO_x based sensors do not require frequent calibration and can potentially be miniaturized.

There were some experiments performed using IrO_x sensors in aqueous solution to verify pH response across the entire pH scale, the long-term stability, sensitivity, sensor reproducibility and response time (6). All of the tests were done using a Ag/AgCl single junction reference electrode in commercially available pH buffer solutions or using acid-base titration. The IrO_x sensor showed excellent performance in aqueous solutions. The electrode exhibits excellent reversibility independent of the direction of the pH change or whether the pH was changed in small or large steps. It also shows ideal Nernstian sensitivity, a response slope of 59.0 mV/pH, excellent reproducibility and a response time on the order of seconds. These excellent results motivated us to explore the use of the IrO_x electrode for determining acidity in non-aqueous solvents.

The measurement of pH conducted in the aqueous phase has been simplified and improved to provide a wide range of products, both durable and accurate. The measurement of acidity in certain organic based liquids such as petroleum products is a difficult application due to the complex and non-polar (non-conducting) matrix. Accordingly, acetonitrile was used as a solvent into which all the fuel samples studied were diluted. The mixing ratio of all of the aliquots was 1:10 (fuel: acetonitrile). Acetonitrile was chosen as the solvent because it is partially miscible with fuel, acidic species present in fuel are soluble in it and last but not least, it is a "differentiating" solvent. The term "differentiating" means that it is a solvent that can differentiate the strengths of acids (or bases) that are equivalent in water. The solvation of H⁺ differs from one solvent to another and, even in a solution of 1M hydrogen ion, the activity of H⁺

differs drastically by solvent. In order to compare the acid-base properties in different solvents, it is convenient to define a theoretical pH scale that is common to various solvents. The pH scale in water is used as a reference to define the theoretical pH windows in various solvents in such a common pH scale (7). If the solvent is of weaker basicity than water, the pH window expands below pH=0 (more acidic than water). On the other hand, if the solvent is of weaker acidity than water, the pH window expands above pH=14 (more basic than water). These expanded pH windows open up various chemical possibilities:

- 1) In solvents with an expanded pH region below pH=0, the solvated protons (SH_2^+) have a very strong acidity and some acids, which behave as strong acids in water, tend to behave as weak acids of different strengths. Thus they can be determined separately by titration. Moreover, in such a solvent, some bases, which are too weak to titrate in water, can be titrated and their strengths can be determined.
- 2) In solvents with an expanded pH region above pH=14, the lyate ion (S^-) has very strong basicity and some bases, which behave as strong bases in water, tend to behave as weak bases of different strengths. They can be determined separately by titration. Moreover, in such a solvent, some acids, which are too weak to titrate in water, can be titrated and their strengths can be determined. Thus, acetonitrile seems to be a good choice for a solvent.

Various electrically insulating materials for encapsulation of the contact region of the iridium oxide sensor were explored. Encapsulation of this interface ideally provides a solution tight seal and electrical insulation. Encapsulation materials such as: different epoxy resins, polyimide resin, melted glass powder or ester cyanate were tested and preliminarily found to be acceptable for this purpose.

It is very important to develop and test the reference electrode for the non-aqueous application in parallel with the indicator electrode in order to get acceptable results. Because the potential of the indicator electrode will be measured with respect to it, the reference electrode has to be very stable. Electrolytic or salt bridges are used to diminish and stabilize the junction potential between solutions of different composition and to minimize cross-contamination between solutions. Double junction structures generally provide more protection from these artifacts and display slower potential drift than do single junction structures. Various reference electrodes for the non-aqueous application were built and tested. All of them contained acetonitrile as a filling solution, however various electrode designs (single and dual junction), different frits and various salts and salt combinations were tested. In our experience the most stable reference electrode (smallest drift) was a single junction design consisting of a silver wire immersed in acetonitrile filling solution containing silver perchlorate: $\text{Ag}/\text{AgClO}_4 + \text{ACN}$. The reference electrode body consisted of flexible Teflon tube with fiber frit. The reproducibility and long-term stability of this reference electrode were also tested and found to be acceptable. The responses across four electrodes were within 20 mV of each other when all were immersed in acetonitrile. All further measurements were done using this type of reference electrode.

IrO_x electrodes were tested in acetonitrile against the reference electrode and displayed good reproducibility of response. The potential difference across three different IrO_x sensors was around 15 mV. After establishing a stable background for IrO_x in acetonitrile, 1 mL of 1M acetonitrile solution of phenol was added. Exposure of the IrO_x

sensor to acetonitrile solution containing 0.1M phenol results in a potential shift to more positive potential values. This suggests that the IrO_x sensor responds to compounds having weak acid-base character like phenol. Phenols are a representative group of compounds that are known to be present in fuel. The response of the IrO_x sensor to the fuel was investigated using two aliquots, A and B, containing 10 mL of acetonitrile and 1 mL of fuel type 2747, neat or thermally stressed, respectively. The measurement was repeated three times on each aliquot. The sensor was immersed in pure acetonitrile solution between consecutive runs in order to clean it. (Fig. 1) It is clear that the sensor shows reproducible results for the same type of fuel and also that it is able to differentiate between the neat and stressed fuel. The potential shift for the aliquot containing stressed fuel is larger, as expected, consistent with the fact that stressed fuel contains more acidic species. However, the background continued to rise throughout this experiment probably because the sensor had not been given time to equilibrate between solution changes. In order to verify this, measurements of IrO_x sensor response were performed over a longer time frame in 6 different fuel cocktails: 2747, 3166 and 3804 both neat and stressed fuels, respectively. (Fig. 2) These results suggest once again, that using an off-line IrO_x sensor, it is possible to measure the acidity of different fuels and distinguish between neat and stressed fuels. The neat fuels show very similar responses. This is expected, because the TANs for these fuels as determined by the ASTM method were all very close (around 0.001, 0.002, and 0.003). On the other hand, the stressed fuels would be expected to give higher responses, consistent with their having higher TANs due to the increase in acidic species caused by the stressing process. Unfortunately, the TAN's for the stressed fuels are not routinely performed and therefore these number were not available. Our future work plans include performing the ASTM tests to determine the TAN's for stressed fuel samples.

The response times calculated for 90% of maximum response are presented in Table 1 and are in the range from 1 hour to 5 hours. All experiments to this point were done with the IrO_x sensor encapsulated in epoxy resin. From our previous studies and from the literature it is known that the response time of the IrO_x sensor in aqueous solution is on the order of seconds. This suggests that the long response time of the IrO_x sensor in non-aqueous solution may not be inherent to the sensor. The encapsulation material could be responsible for the slow response. The epoxy may adsorb some species from fuel and release them slowly with time. In order to verify this, the behavior of a bare IrO_x sensor in the cocktail containing acetonitrile and 3166 stressed fuel was checked. The response time of the bare IrO_x sensor was reduced 10 times compared to the epoxy encapsulated sensor. Therefore, the epoxy seems not to be a good encapsulation material for the application in organic solvents / jet fuel. Future work will be focused on trying different encapsulation materials for sensor protection and different sensor designs for miniaturization, with an emphasis on decreasing the response time.

CONCLUSIONS

A novel IrO_x electrode has been used to develop an off-line sensor for monitoring the acidity of fuel. The data obtained show that IrO_x sensor responds to compounds having acid-base character like phenol, for example. Using an off-line IrO_x sensor it is possible to determine the acidity of different fuels and distinguish between neat and thermally stressed fuels. It was also demonstrated that many factors influence the IrO_x

sensor response time including the encapsulation material and the conductance of the test solution. Future efforts will focus on experiments aimed at decreasing the response time.

ACKNOWLEDGMENTS

The authors gratefully thank SenIrOx for providing the IrO_x samples for our studies. This work is supported through funding from the Air Force Research Laboratory, PRTG (Mr. William E. Harrison III).

REFERENCES

1. *Annual Book of ASTM Standards, American Society for Testing and Materials* (ASTM), D3242 (2001)
2. *Annual Book of ASTM Standards, American Society for Testing and Materials* (ASTM), D664 (2001)
3. Galster H., *pH Measurements- Fundamentals, Methods, Applications, Instruments*, VCH Publishers, New York (1991)
4. Izutsu K., Yamamoto H., *Anal. Sci.*, **12**, 905-909 (1996)
5. Liu C., Bocchicchio B., Overmeyer P., Neuman M., *Science*, **207**, 188-189 (1980)
6. Yao S.; Wang M., Madou M. *J. Electrochem. Soc.*, **148**, 4, H29-H36 (2001)
7. Izutsu K., *Electrochemistry in Nonaqueous Solutions*, p. 59-83, Wiley-VCH Verlag GmbH, Weinheim (2002).

FIGURES

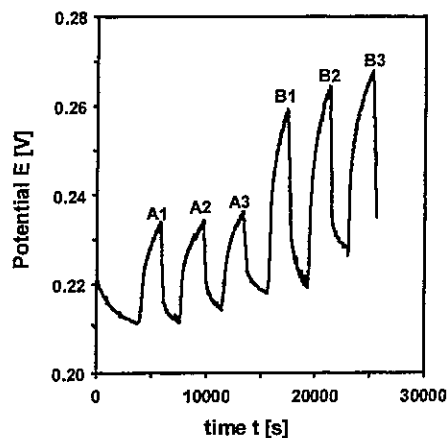


Figure 1. IrO_x sensor response to two aliquots A and B containing 10 mL of acetonitrile and 1 mL of fuel type 2747 neat or stressed, respectively. A1, A2, A3, B1, B2, B3 – consecutive runs in aliquot A and B, respectively.

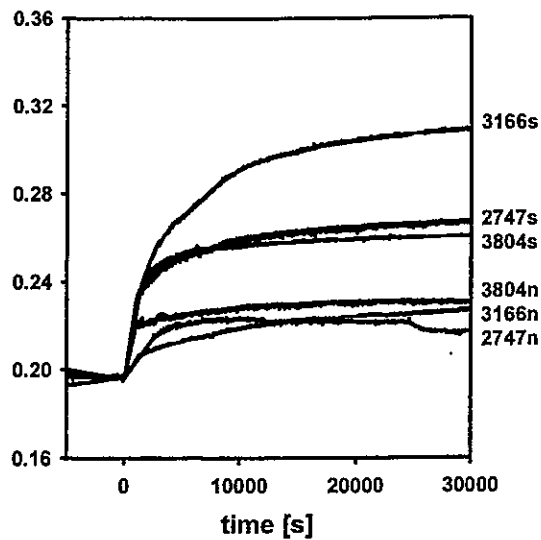


Figure 2. The potential vs. time response of epoxy encapsulated IrO_x sensor in the presence of different fuels (n –neat fuel; s – stressed fuel).

Table 1. The Response Times of IrO_x Sensor Encapsulated by Epoxy Immersed in Neat or Thermally Stressed Fuel

	$\Delta t @ 90\%$	$\Delta E @ 90\%$
3166n	5.8 h	0.02871 V
2747n	1.1 h	0.023706 V
3804n	2.3 h	0.031302 V
3166s	5.5 h	0.108054 V
2747s	3.5 h	0.064368 V
3804s	1.8 h	0.058077 V

Table 2. Comparison of Response Time of Bare and Epoxy Encapsulated IrO_x Sensor

3166s	$\Delta E_{\text{max}} @ 90\%$	$\Delta t @ 90\%$
IrO_x w/epoxy	0.108	5.50 h
Bare IrO_x	0.168	0.50 h

Kinetic behavior of polymer-coated long-period-grating fiber-optic sensors

Justyna Widera, Christopher E. Bunker, Gilbert E. Pacey, Viswanath R. Katta, Michael S. Brown, Jennifer L. Elster, Mark E. Jones, James R. Gord, and Steven W. Buckner

A new method of analysis employing the time-dependent response of long-period-grating (LPG) fiber-optic sensors is introduced. The current kinetic approach allows analysis of the time-dependent wavelength shift of the sensor, in contrast to previous studies, in which the LPG sensing element has been operated in an equilibrium mode and modeled with Langmuir adsorption behavior. A detailed kinetic model presented is based on diffusion of the analyte through the outer protective membrane coating into the affinity coating, which is bound to the fiber cladding. A simpler phenomenological approach presented is based on measurement of the slope of the time-dependent response of the LPG sensor. We demonstrate the principles of the kinetic methods by employing a commercial Cu^{+2} sensor with a carboxymethylcellulose sensing element. The detailed mathematical model fits the time-dependent behavior well and provides a means of calibrating the concentration-dependent time response. In the current approach, copper concentrations below parts per 10^6 are reliably analyzed. The kinetic model allows early-time measurement for low concentrations of the analyte, where equilibration times are long. This kinetic model should be generally applicable to other affinity-coated LPG fiber-optic sensors. © 2005 Optical Society of America

OCIS codes: 060.2370, 000.1570.

1. Introduction

The Air Force Research Laboratory is actively involved in investigating technologies with potential as fuel-quality diagnostics. The long-term goal of this program is to develop a state-of-the-art diagnostics package attached to a single-point refueling nozzle to assess key fuel properties as the fuel is dispensed. The short-term goal is to explore and develop novel technologies capable of providing in-the-field, real-time fuel analysis.^{1,2} Among the challenges associ-

ated with developing these technologies is identifying those analytes or properties that are most important for fuel characterization. A sensing platform that is independent of the analyte of interest would be an ideal starting point for fuel-quality-diagnostics development. Long-period-grating (LPG) fiber-optic sensors^{3–14} have excellent potential in this regard.

Figure 1 is a representation of a working LPG fiber-optic sensor. The important elements identified are the fiber core into which the grating is written, the fiber cladding that surrounds the core, and the affinity coating that is bonded to the cladding surface. An LPG fiber-optic sensor operates as a spectral-loss element. When broadband light is coupled through the fiber core, selected wavelengths are diffracted by the LPG from the fiber-core modes to the fiber-cladding modes. The selected wavelengths that are coupled to the latter are lost when the light exiting the fiber core is analyzed. The result is an attenuation band in the spectral profile of the light that passes through the fiber core. The position and shape of the attenuation band is dependent on the grating period of the LPG, the refractive indices of the fiber core, the fiber cladding, and the surrounding environment (or an affinity coating), the local temperature, and strain–bending and geometry of the optical fiber.

J. Widera, V. R. Katta, and M. S. Brown are with Contribution from Innovative Scientific Solutions, Inc., Dayton, Ohio 45440. C. E. Bunker (christopher.bunker@wpafb.af.mil) and J. R. Gord (james.gord@wpafb.af.mil) are with the Air Force Research Laboratory, Propulsion Directorate, Wright-Patterson Air Force Base, Ohio 45433. G. E. Pacey is with the Department of Chemistry and Biochemistry, Miami University, Oxford, Ohio 45056. J. L. Elster and M. E. Jones are with Luna Innovations, Blacksburg, Va. 24060. S. W. Buckner (buckners@slu.edu) is with the Department of Chemistry, St. Louis University, St. Louis, Mo. 63103. Address correspondence to C. E. Bunker, J. R. Gord, or S. W. Buckner.

Received 8 December 2003; revised manuscript received 4 June 2004; accepted 24 June 2004.

0003-6935/05/061011-07\$15.00/0

© 2005 Optical Society of America

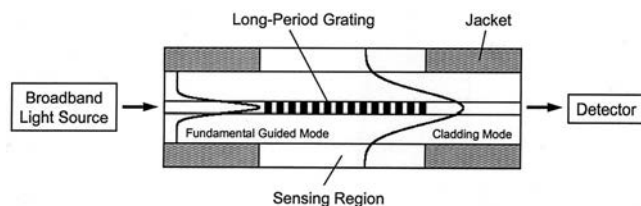


Fig. 1. Schematic representation of the LPG fiber-optic sensor. The affinity coating on the cladding collapses on exposure to Cu^{+2} solution.

Measurement of a chemical concentration by use of LPGs is predicated on local changes in the density around the sensor.¹⁵ These changes result in a change in the refractive index, which induces a change in the spectral profile of the attenuation band. Analyses have been performed heretofore in an equilibrium mode in which the fiber is allowed to equilibrate with the surroundings prior to measurement of the spectral profile change. This approach to quantification of chemicals has been used for antifreeze,¹⁶ volatile organic compounds,¹⁷ corrosion products,^{18,19} aqueous sugar solutions,²⁰ aromatic compounds dissolved in alkanes,²¹ and biological compounds.^{22,23} In previous studies the analytical measurements have shown relatively high limits of detection. The lowest limits of detection reported to date with the use of an LPG are $\sim 3 \times 10^{-4}$ M obtained in solutions of cane sugar and 90 parts per 10^6 (ppm) for trichloroethylene and toluene in air. The solution measurements were made with a novel scheme based on the separation of two adjacent spectral-loss elements, and the volatile organic compound measurements used an affinity-coated system. Although these limits of detection are useful for some remote-sensing applications, they are too large for many trace analysis applications.²⁴

Here we present an alternative method of analysis by using LPG fiber-optic sensors to monitor the time dependence of the wavelength shift on diffusion of the analyte into a selective membrane coating on the fiber surface. Diffusion into the membrane is concentration dependent, and the calibration scheme involves measurement of rate constants for this process. The kinetic model developed is general for any membrane-coated sensor.

2. Experiment

A. Materials

All chemicals were obtained from Aldrich and used without further purification. We deionized and purified water by employing a Barnstead Nanopure water-purification system.

B. Measurements

The LPG instrument (Lunascan 3000, Luna Innovations, Inc.) includes a light source, an LPG fiber-optic sensing element, and a Fabry–Perot interferometer for monitoring the attenuation band. The hardware is

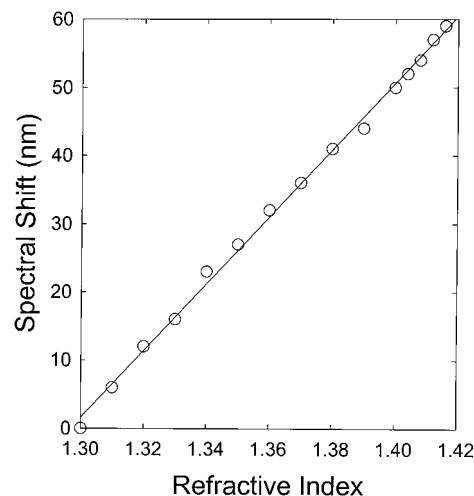


Fig. 2. Wavelength shift of the spectral-loss element versus the local refractive index for a bare LPG. Line, linear least-squares fit.

controlled and data acquisition is achieved with a laptop personal computer interfaced to the instrument. The light source is an LED with 1530-nm output. The fiber is a single-mode step-index fiber with a germanosilicate core and fused-silica cladding. The LPG is 2 cm long with a 10–15-dB isolation depth in the attenuation band. The $\text{LP}_{0,14}$ cladding mode is monitored in the current experiment. The LPG was held vertically by a stand to prevent strain and bending. Analyte solutions were raised up to the LPG to immerse the fiber in the Cu^{+2} solution. All experiments were carried out at 22 ± 2 °C. The LPG was coated with a 0.1- μm thick layer of carboxymethylcellulose as the active layer with a 1-mm-thick polysulfone-membrane protective layer. The wavelength shift of the LPG was monitored as the active layer was added to the LPG. Further addition of carboxymethylcellulose was ceased when the wavelength shift ceased. Carboxymethylcellulose has a refractive index of >1.45 when dry and 1.33 when wet. The instrument includes a Queensgate 1618 scanning Fabry–Perot interferometer. Power spectral densities were measured for the analytical signal.

To make a Cu^{+2} measurement in aqueous solution, we first immerse the fiber sensor in deionized water until a stable response is achieved. The fiber is immersed thereafter in an aqueous solution containing the Cu^{+2} analyte, and the sensor response is recorded. The time dependence of the wavelength shift of the spectral-loss element is the measured signal. Following exposure to the analyte, the fiber sensor is immersed in an aqueous solution of ethylenediaminetetraacetic acid (a copper binding agent) to aid removal of Cu^{+2} from the affinity coating and membrane. This process is followed by a second immersion in deionized water.

3. Results and Discussion

An LPG fiber sensor can be used to quantify changes in the local solvent environment surrounding the sen-

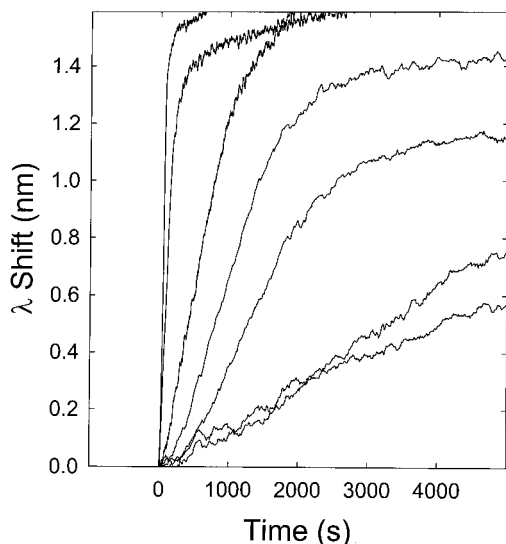


Fig. 3. Fiber-sensor responses versus time for a series of different Cu^{+2} concentrations in aqueous solution.

sor. Figure 2 shows the effect of the solvent refractive index on the position of the spectral-loss region for a bare fiber (i.e., a fiber with no affinity coating). Over the refractive-index range of 1.3–1.42, the spectral-loss region shifts ~ 60 nm in a nearly linear fashion. With the ability to detect wavelength shifts as small as 0.2 nm, the LPG system can resolve changes in the local refractive index of the order of 4×10^{-4} .

To quantify a particular analyte, we prepare the LPG fiber sensor with an affinity coating that incorporates chemically specific components for that analyte. The commercially prepared Cu^{+2} fiber sensor employed in this study is equipped with an affinity coating of carboxymethylcellulose that is bonded to the active region of the fiber and protected by a semi-permeable polysulfone membrane. The concentration dependence of this sensor was investigated over the formal copper-concentration range of 10 mM–10 μM . The response from the fiber sensor is shown in Figure 3 as spectral shift as a function of response time. The shape of the curves clearly indicates the kinetic behavior of the investigated sensor. The plateau response for the 10.0-mM solution is achieved within seconds, that of the 0.10-mM solution is achieved within minutes, and that of the 0.010-mM solution is achieved within hours. Equilibration times comparable with these have also been reported for a polymer-coated LPG sensor used to detect volatile organic compounds.¹⁷ Two different kinetic approaches are considered for analyzing the time-dependent results and preparing a calibration scheme for the LPG. The first is a detailed kinetic model that includes diffusion of the analyte into the affinity coating. The second is a simple phenomenological model that utilizes a single parameter as a measure of concentration.

To demonstrate the uniform kinetic behavior of the sensor over the concentration range of interest, we applied a normalization procedure to the curves in Figure 3. The normalized curves are plotted as λ_n

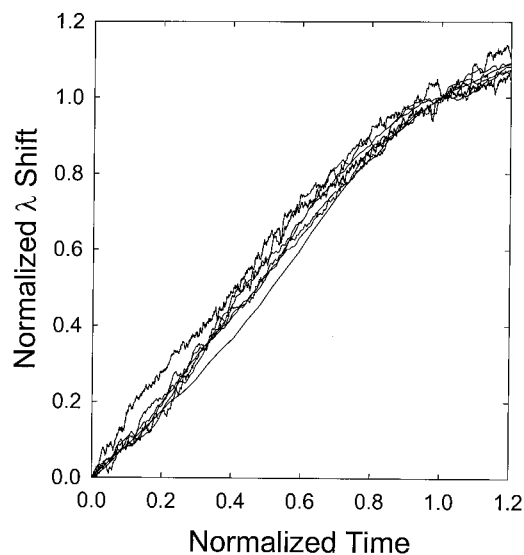


Fig. 4. Fiber-sensor responses plotted as normalized wavelength shift versus normalized time for concentrations depicted in Fig. 3.

versus t_n , with

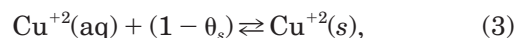
$$t_n = t/t_{\text{linear}}, \quad (1)$$

$$\lambda_n = \lambda/\lambda_{\text{linear}}. \quad (2)$$

Here the parameters t_{linear} and λ_{linear} are the long time values at which the wavelength shift begins to level off. The relationships between the normalized wavelength λ_n and the normalized time t_n for different concentrations of Cu^{+2} are shown in Figure 4. The normalized responses of the LPG sensor generally have the same shape and exhibit the same trend, indicating similar kinetic behavior for the LPG across this copper-concentration range.

Because the analytical signal is time dependent, a mathematical model describing the kinetics of Cu^{+2} migration through the polysulfone membrane and into the affinity coating was developed. The basic model for LPG behavior can be visualized as follows. The fiber optic has an outer polymer membrane and an inner affinity coating. The LPG response is induced by Cu^{+2} incorporation into the affinity coating. As Cu^{+2} diffuses into the affinity coating, the wavelength minimum and profile of the attenuation band shifts.

In the affinity coating, sites are available for Cu^{+2} adsorption. The movement of Cu^{+2} from solution into this sensing region can be described by the following reactions. First, Cu^{+2} diffuses into the outer membrane region:

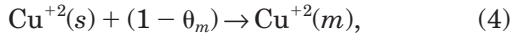


with $1 - \theta_s$ = concentration of open binding sites in the outer membrane, $\theta_s = [\text{Cu}^{+2}(\text{s})]$ = concentration of Cu^{+2} in the outer membrane, k_{f1} = rate constant for the forward reaction [Eq. (3)], and k_r = rate

constant for the reverse reaction [Eq. (3)].

If we treat the number of binding sites as a mole fraction, then $0 < \theta_s < 1$. This reaction is treated as reversible.

Penetration to the affinity coating is described in the reaction



with $1 - \theta_m$ = concentration of open binding sites in the affinity coating, $\theta_m = [\text{Cu}^{+2}(\text{m})]$ = concentration of Cu^{+2} in the affinity coating, and k_{p2} = rate constant for reaction (4).

Again, the number of binding sites is treated as a mole fraction such that $0 < \theta_m < 1$. The second reaction is treated as irreversible. This approach is mathematically tractable, whereas the system of equations is not readily solved analytically if the second reaction is treated as reversible. As will be seen below, this approximation is validated in the low-concentration regime. Deviations are observed at higher concentrations; however, the kinetic method is most important in the low-concentration regime. These reactions give rise to the following rate equations:

$$d[\text{Cu}^{+2}(\text{aq})]/dt = 0 \quad (5)$$

$$([\text{Cu}^{+2}(\text{aq})] = \text{large, constant value}),$$

$$d\theta_s/dt = k_{f1}[\text{Cu}^{+2}(\text{aq})](1 - \theta_s) - k_r\theta_s - k_{p2}\theta_s(1 - \theta_m). \quad (6a)$$

In that $[\text{Cu}^{+2}(\text{aq})] = \text{constant value}$, Eq. (6a) can be simplified to

$$d\theta_s/dt = k_{f1}'(1 - \theta_s) - k_r\theta_s - k_{p2}\theta_s(1 - \theta_m), \quad (6b)$$

$$k_{f1}' = k_{f1}[\text{Cu}^{+2}(\text{aq})]. \quad (6c)$$

For the calibration scheme (see below), the pseudo-first-order rate constant k_{f1}' is plotted as a function of $[\text{Cu}^{+2}(\text{aq})]$. To facilitate the mathematics that follows, we rearrange Eq. (6c) to

$$d\theta_s/dt = k_t(k^* - \theta_s) - k_{p2}\theta_s(1 - \theta_m), \quad (6d)$$

where $k_t = k_{f1}' + k_{r1}$ and $k^* = k_{f1}'/k_t$.

The rate equation for reaction (4) is

$$d\theta_m/dt = k_{p2}\theta_s(1 - \theta_m). \quad (7)$$

Combining Eqs. (6d) and (7) yields

$$d\theta_s/dt = k_t(k^* - \theta_s) - d\theta_m/dt. \quad (6e)$$

The relevant equations for describing the LPG data originate primarily from Eq. (7). To obtain these, however, we must solve Eqs. (6e) and (7) simulta-

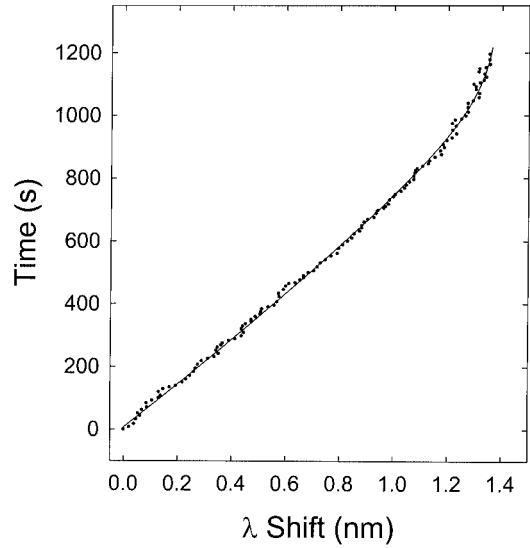


Fig. 5. Fit of kinetic model (solid curve) to fiber-sensor response (dotted curve) for 100- μM Cu^{+2} solution.

neously. After several mathematical transformations [see Appendix A, Eqs. (A1a)–(A13)], we obtain

$$d\theta_m/dt = k_{p2}(1 - \theta_m)\{k^{*'}[\ln(1 - \theta_m)] + k_{f1}'t - \theta_m\}. \quad (8)$$

Because the monitored signal is a spectral shift λ ,

$$d\lambda/dt = \lambda_{\text{max}}(k_{p2}(1 - \lambda/\lambda_{\text{max}})\{k^{*'}[\ln(1 - \lambda/\lambda_{\text{max}})] + k_{f1}'t - \lambda/\lambda_{\text{max}}\}), \quad (9)$$

where $\lambda = z\theta_m$ and $z = \lambda_{\text{max}}$, when $\theta_m = 1$. Thus

$$\theta_m = \lambda/\lambda_{\text{max}}.$$

Equation (9) relates θ_m , the concentration of Cu^{+2} in the active region, and λ , the spectral shift, to the time via the fundamental rate constants for the system. After appropriate rearrangements described in Appendix B, we obtain

$$t = (1/k_{f1}')\{L/[k_{p2}(1 - \lambda/\lambda_{\text{max}})]\} + \lambda/\lambda_{\text{max}} - k^{*'}[\ln(1 - \lambda/\lambda_{\text{max}})]. \quad (10)$$

To process the data, we invert the original LPG data, fit them to a polynomial, take the derivative of the fit, and substitute the constants into Eq. (10). This equation is then used to fit the inverted data and return the fundamental constants for the system by use of Eq. (10). Figure 5 shows a fit for the 100- μM sample. The equation fits the data and describes both the early induction period and the later rapid rise in the LPG time response. Table 1 contains the relevant rate constants obtained from the fit for the 100- μM sample. The value of $1.124 \times 10^{-3} \text{ s}^{-1}$ for the pseudo-first-order rate constant k_{f1}' implies a diffusion coefficient of $5.6 \times 10^{-6} \text{ cm}^2/\text{s}$ for diffusion of Cu^{+2} through the outer membrane. This is consistent with

Table 1. Measured Rate Constants for the Coated Fiber

Rate Constant	Result from 100- μ M Fit
$k_{f1}' (=k_{f1}[\text{Cu}^{+2}(\text{aq})])$	$1.124 \times 10^{-3} \text{ s}^{-1}$
k_{p2}	$2.769 \times 10^{-1} (\text{L/mol})/\text{s}$
$k^{*'} (= \{k_{f1}[\text{Cu}^{+2}(\text{aq})] + k_{r1}\}/k_{p2})$	$8.754 \times 10^{-2} \text{ s}^{-1}$

typical values for metal-ion migration through bulk polymers.

As is evident in Eq. (6c), k_{f1}' is a linear function of $[\text{Cu}^{+2}(\text{aq})]$. This should provide a convenient method for calibrating the LPG sensor for analysis of Cu^{+2} in solution. One can generate a calibration curve by measuring the time-dependent LPG response, fitting the data, and obtaining the rate constants. Then k_{f1}' is plotted as a function of $[\text{Cu}^{+2}(\text{aq})]$. For unknown samples the fit provides k_{f1}' , which yields the copper concentration from the calibration curve. A calibration curve for this approach is shown in Fig. 6. It is clear that two regions exist. At concentrations in the tenths of millimolar down to the micromolar range, the function is well behaved. k_{f1}' is a linear function of $[\text{Cu}^{+2}(\text{aq})]$. At higher concentrations, however, significant curvature is observed in the calibration plot. This may arise from some reversibility in the $[\text{Cu}^{+2}(\text{s})]$ -to- $[\text{Cu}^{+2}(\text{m})]$ process [see Eq. (4) above]. This reversibility causes an apparent decrease in the rate for the reaction. Physically, the kinetic model breaks down at high concentrations.

Alternatively, one can achieve calibration for this type of LPG sensor by taking the slope of the LPG response curve at short times and plotting this as a function of $[\text{Cu}^{+2}]$. Figure 7 presents the results of this approach. The behavior of the calibration scheme

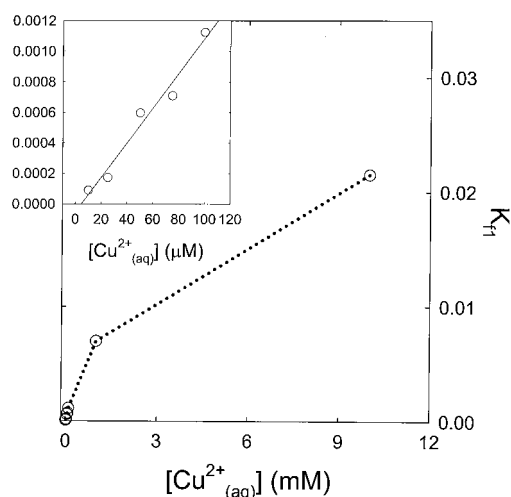


Fig. 6. LPG calibration curve with k_{f1}' plotted as a function of formal Cu^{+2} concentration in aqueous solution. The main figure covers the entire concentration range used in this study. The dotted curve is arbitrary and serves only to highlight the position of k_{f1}' values. The inset figure is an expansion of the lower concentration range in which linear behavior is observed. Solid line is obtained from a linear least-squares fit of low-concentration data.

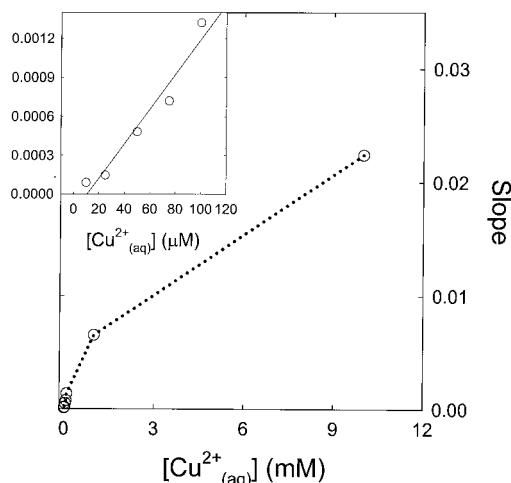


Fig. 7. LPG calibration curve with the initial slope of the spectral-loss-element response plotted as a function of Cu^{+2} concentration in aqueous solution. Dotted curve is arbitrary and used to highlight the position of slope values. Solid line is obtained from a linear least-squares fit of low-concentration data.

is similar to that for the more complex kinetic scheme demonstrated above. The method does not return any fundamental rate constants for the system, but it does provide an equally effective means for determining $[\text{Cu}^{+2}]$. Many kinetic analyses are based on measuring initial slopes of curves of concentration as a function of time.²⁵

The more detailed kinetic method may provide a new and more broadly applicable means of measuring ion diffusion in polymers, particularly for redox-inactive metals. Current approaches generally center on electrochemical methods, including thin-layer electrochemistry and cyclic voltammetry coupled with a rotating-disk electrode. The electrochemical methods are effective only for redox-active ions.²⁶ Time-resolved measurements of the LPG response can produce diffusion data for redox-active and redox-inactive ions. Careful calibration based on the current kinetic model should provide a complement to the electrochemical methods.

4. Conclusion

A new method of analysis using LPG fiber-optic sensors is introduced. The kinetic model allows early-time analysis of the response of affinity-coated LPG sensors when the analyte is concentrating into the binding membrane. This should be useful in future trace-analysis applications in which the low analyte concentrations make equilibration times long. The method has been demonstrated for calibration of a commercial Cu^{+2} sensor to sub-ppm levels. The derived kinetic model should be easily extended to other affinity-coated LPG sensors.

Appendix A

To solve Eqs. (6e) and (7) simultaneously, we make the following substitutions:

$$\theta_s^* = k^* - \theta_s, \quad (\text{A1a})$$

$$\theta_m^* = 1 - \theta_m, \quad (\text{A1b})$$

so that

$$d\theta_s^*/dt = -d\theta_s/dt, \quad (\text{A1c})$$

$$d\theta_m^*/dt = -d\theta_m/dt. \quad (\text{A1d})$$

For Eq. (7) we obtain

$$-d\theta_m^*/dt = d\theta_m/dt = k_{f2}(k^* - \theta_s^*)\theta_m^*, \quad (\text{A2a})$$

$$(-d\theta_m^*/dt)(1/k_{f2}\theta_m^*) = k^* - \theta_s^*, \quad (\text{A2b})$$

$$\begin{aligned} \theta_s^* &= k^* + (1/k_{f2}\theta_m^*)(d\theta_m^*/dt) \\ &= k^* + (1/k_{f2})[d(\ln \theta_m^*)/dt]. \end{aligned} \quad (\text{A3})$$

For Eq. (6e), substitution yields

$$\begin{aligned} d\theta_s/dt &= -d\theta_s^*/dt \\ &= k_t\theta_s^* + d\theta_m^*/dt \\ &= k_t[k^* + (1/k_{f2}\theta_m^*)(d\theta_m^*/dt)] + d\theta_m^*/dt \\ &= k_{f1}' + [(k_t/k_{f2}\theta_m^*) + 1]d\theta_m^*/dt \end{aligned} \quad (\text{A4a})$$

because

$$k_t k^* = (k_{f1}'/k_t)k_t = k_{f1}'. \quad (\text{A4b})$$

We define the following substitution:

$$a = k_t/k_{f2}, \quad (\text{A5})$$

such that

$$-d\theta_s^*/dt = k_{f1}' + [(a + \theta_m^*)/\theta_m^*]d\theta_m^*/dt. \quad (\text{A6})$$

Let

$$\theta_m^* = e^p. \quad (\text{A7a})$$

Then

$$\ln \theta_m^* = p, \quad \ln(1 - \theta_m) = p, \quad d\theta_m^*/dt = e^p dp/dt. \quad (\text{A7b})$$

This yields

$$\begin{aligned} [(a + \theta_m^*)/\theta_m^*]d\theta_m^*/dt &= [(a + e^p)/e^p]e^p dp/dt \\ &= (a + e^p)dp/dt \\ &= d(ap + e^p)/dt. \end{aligned} \quad (\text{A8})$$

Substitution of Eq. (A8) into Eq. (A6) yields

$$-d\theta_s^*/dt = k_{f1}' + d(ap + e^p)/dt, \quad (\text{A9a})$$

$$d\theta_s^*/dt + d(ap + e^p)/dt = -k_{f1}', \quad (\text{A9b})$$

$$d(\theta_s^* + ap + e^p)/dt = -k_{f1}'. \quad (\text{A9c})$$

Variable separation and integration provides

$$\theta_s^* + ap + e^p = -k_{f1}'t + Q, \quad (\text{A10})$$

with Q = constant of integration.

Substitution to achieve an expression in terms of the original variables yields

$$k^* - \theta_s + (k_t/k_{f2})[\ln(1 - \theta_m)] + (1 - \theta_m) = -k_{f1}'t - Q. \quad (\text{A11})$$

The boundary condition that θ_m and θ_s are 0 at time $t = 0$ yields

$$\theta_s = (k_t/k_{f2})[\ln(1 - \theta_m)] + k_{f1}'t - \theta_m. \quad (\text{A12a})$$

This can be written as

$$\theta_s = k^*[\ln(1 - \theta_m)] + k_{f1}'t - \theta_m, \quad (\text{A12b})$$

with

$$k^* = k_t/k_{f2}. \quad (\text{A12c})$$

Finally, substituting Eq. (A12b) into Eq. (7) yields

$$d\theta_m/dt = k_{f2}(1 - \theta_m)\{k^*[\ln(1 - \theta_m)] + k_{f1}'t - \theta_m\}. \quad (\text{A13})$$

Appendix B

The relationship of θ_m , the concentration of Cu^{+2} in the active region, and λ , the spectral shift, to the time through the fundamental rate constants of the system is given by

$$d\lambda/dt = \lambda_{\max}(k_{f2}(1 - \lambda/\lambda_{\max})\{k^*[\ln(1 - \lambda/\lambda_{\max})] + k_{f1}'t - \lambda/\lambda_{\max}\}). \quad (\text{B1})$$

This relationship is necessary to fit the LPG data. However, the differential can be solved only numerically. To obtain the constants, we take the approach of fitting the data with a fourth-order polynomial:

$$t = f(\theta_m) = k_a + k_b\theta_m + k_c\theta_m^2 + k_d\theta_m^3 + k_e\theta_m^4, \quad (\text{B2a})$$

$$t = f(\lambda/\lambda_{\max}) = k_a + k_b(\lambda/\lambda_{\max}) + k_c(\lambda/\lambda_{\max})^2 + k_d(\lambda/\lambda_{\max})^3 + k_e(\lambda/\lambda_{\max})^4. \quad (\text{B2b})$$

We plot t as a function of λ rather than the reverse because Eq. (B2b) is not separable in terms of λ . This

requires that we invert the data from the LPG and fit t versus λ . Once a fit to the data is obtained by use of Eq. (B2b), then

$$\frac{dt}{d(\lambda/\lambda_{\max})} = k_b + 2k_c(\lambda/\lambda_{\max}) + 3k_d(\lambda/\lambda_{\max})^2 + 4k_e(\lambda/\lambda_{\max})^3 = 1/L, \quad (\text{B3a})$$

where

$$d(\lambda/\lambda_{\max})/dt = L. \quad (\text{B3b})$$

Substitution into Eq. (B1) yields

$$L/[k_{f2}(1 - \lambda/\lambda_{\max})] = k^*[\ln(1 - \lambda/\lambda_{\max})] + k_{f1}'t - \lambda/\lambda_{\max}. \quad (\text{B4})$$

Appropriate rearrangement yields

$$t = (1/k_{f1}')(L/[k_{f2}(1 - \lambda/\lambda_{\max})]) + \lambda/\lambda_{\max} - k^*[\ln(1 - \lambda/\lambda_{\max})]. \quad (\text{B5})$$

The authors acknowledge M. M. Whitaker for editorial support. We acknowledge Julian Tishkoff and the Air Force Office of Scientific Research for continuing support of fuels and combustion research and acknowledge the Dayton Area Graduate Studies Institute (meow PR-MU-01-16).

References

1. L. W. Qu, R. B. Martin, W. J. Huang, K. F. Fu, D. Zweifel, Y. Lin, Y. P. Sun, C. E. Bunker, B. A. Harruff, J. R. Gord, and L. F. Allard, "Interactions of functionalized carbon nanotubes with tethered pyrenes in solution," *J. Chem. Phys.* **117**, 8089–8094 (2002).
2. B. A. Harruff and C. E. Bunker, "Spectral properties of AOT-protected CdS nanoparticles: quantum yield enhancement by photolysis," *Langmuir* **19**, 893–897 (2003).
3. K. T. V. Grattan and T. Sun, "Fiber optic sensor technology: an overview," *Sens. Actuators* **82**, 40–61 (2000).
4. A. M. Vengsarkar, P. J. Lemaire, J. B. Judkins, V. Bhatia, T. Erdogan, and J. E. Sipe, "Long-period fiber gratings as band-rejection filters," *J. Lightwave Technol.* **14**, 58–65 (1996).
5. V. Bhatia and A. M. Vengsarkar, "Optical fiber long-period grating sensors," *Opt. Lett.* **21**, 692–694 (1996).
6. B. A. L. Gwandu, X. Shu, and T. P. D. Allsop, "Simultaneous refractive index and temperature measurement using cascaded long-period grating in double-cladding fibre," *Electron. Lett.* **38**, 695–696 (2002).
7. C. C. Ye, S. W. James, and R. P. Tatam, "Simultaneous temperature and bend sensing with long-period fiber gratings," *Opt. Lett.* **25**, 1007–1009 (2000).
8. H. J. Patrick, "Self-aligning, bipolar bend transducer based on long period grating written in eccentric core fibre," *Electron. Lett.* **36**, 1763–1764 (2000).
9. Y. Liu, L. Zhang, J. A. R. Williams, and I. Bennion, "Optical bend sensor based on measurement of resonance mode splitting of long-period fiber grating," *IEEE Photon. Technol. Lett.* **12**, 531–533 (2000).
10. H. J. Patrick, S. T. Vohra, and C. C. Chang, "Long period fibre gratings for structural bend sensing," *Electron. Lett.* **34**, 1773–1775 (1998).
11. S. R. M. Kueh, R. S. Parnas, and S. G. Advani, "A methodology for using long-period gratings and mold-filling simulations to minimize the intrusiveness of flow sensors in liquid composite molding," *Compos. Sci. Technol.* **62**, 311–327 (2002).
12. Y. Liu, L. Zhang, J. A. R. Williams, and I. Bennion, "Bend sensing by measuring the resonance splitting of long-period fiber gratings," *Opt. Commun.* **193**, 69–72 (2001).
13. Y.-G. Han, B. H. Lee, W.-T. Han, U.-C. Paek, and Y. Chung, "Fibre-optic sensing applications of a pair of long-period fibre gratings," *Meas. Sci. Technol.* **12**, 778–781 (2001).
14. L. A. Wang, C. Y. Lin, and G. W. Chern, "A torsion sensor made of a corrugated long period fibre grating," *Meas. Sci. Technol.* **12**, 793–799 (2001).
15. R. Falciai, A. G. Mignani, and A. Vannini, "Long period gratings as solution concentration sensors," *Sens. Actuators B* **74**, 74–77 (2001).
16. H. J. Patrick, A. D. Kersey, and F. Bucholtz, "Analysis of the response of long period fiber gratings to external index of refraction," *J. Lightwave Technol.* **16**, 1606–1612 (1998).
17. K. Goswami, J. Prohaska, A. Menon, E. Mendoza, and R. Lieberman, "Evanescent wave sensor for detecting volatile organic compounds," in *Chemical, Biochemical, and Environmental Fiber Sensors X*, Proc. SPIE **3540**, 115–122 (1998).
18. J. A. Greene, M. E. Jones, T. A. Tran, K. A. Murphy, P. M. Schindler, V. Bhatia, R. G. May, D. Sherrer, and R. O. Claus, "Grating-based optical fiber-based corrosion sensors," in *Smart Sensing Processing and Instrumentation*, Proc. SPIE **2718**, 170–174 (1996).
19. J. Elster, J. Greene, M. Jones, T. Bailey, S. Lenahan, W. Vellander, R. Van Tassel, and W. Hodges, "Optical fiber-based chemical sensors for detection of corrosion precursors and by-products," in *Chemical, Biochemical, and Environmental Fiber Sensors X*, Proc. SPIE **3540**, 251–257 (1998).
20. X. Shu and D. Huang, "Highly sensitive chemical sensor based on the measurement of the separation of dual resonant peaks in a 100- μm -period fiber grating," *Opt. Commun.* **171**, 65–69 (1999).
21. T. Allsop, L. Zhang, and I. Bennion, "Detection of organic aromatic compounds in paraffin by a long-period fiber grating optical sensor with optimized sensitivity," *Opt. Commun.* **191**, 181–190 (2001).
22. T. A. Tran, V. Bhatia, T. D'Alberto, K. A. Murphy, and R. O. Claus, "Real-time immunoassays using fiber-optic long-period grating sensors," in *Biomedical Sensing, Imaging, and Tracking Technologies I*, Proc. SPIE **2676**, 165–170 (1996).
23. D. Appell, "Fiber sensing—clad fiber detects biological agents fast," *Laser Focus World* **34**, 26–27 (1998).
24. D. C. Harris, *Quantitative Chemical Analysis*, 6th ed. (Freeman, San Francisco, Calif., 2003).
25. J. H. Espenson, *Chemical Kinetics and Reaction Mechanisms*, 2nd ed. (McGraw-Hill, New York, 1995).
26. J. Bard and L. R. Faulkner, *Electrochemical Methods: Fundamentals and Applications* (Wiley, New York, 2001).

Combustion exhaust measurements of nitric oxide with an ultraviolet diode-laser-based absorption sensor

Thomas N. Anderson, Robert P. Lucht, Rodolfo Barron-Jimenez, Sherif F. Hanna, Jerald A. Caton, Thomas Walther, Sukesh Roy, Michael S. Brown, James R. Gord, Ian Critchley, and Luis Flamand

A diode-laser-based sensor has been developed for ultraviolet absorption measurements of the nitric oxide (NO) molecule. The sensor is based on the sum-frequency mixing (SFM) of the output of a tunable, 395-nm external-cavity diode laser and a 532-nm diode-pumped, frequency-doubled Nd:YAG laser in a β -barium borate crystal. The SFM process generates 325 ± 75 nW of ultraviolet radiation at 226.8 nm, corresponding to the ($v' = 0$, $v'' = 0$) band of the $A^2\Sigma^+ - X^2\Pi$ electronic transition of NO. Results from initial laboratory experiments in a gas cell are briefly discussed, followed by results from field demonstrations of the sensor for measurements in the exhaust streams of a gas turbine engine and a well-stirred reactor. It is demonstrated that the sensor is capable of fully resolving the absorption spectrum and accurately measuring the NO concentration in actual combustion environments. Absorption is clearly visible in the gas turbine exhaust even for the lowest concentrations of 9 parts per million (ppm) for idle conditions and for a path length of 0.51 m. The sensitivity of the current system is estimated at 0.23%, which corresponds to a detection limit of 0.8 ppm in 1 m for 1000 K gas. The estimated uncertainty in the absolute concentrations that we obtained using the sensor is 10%. © 2005 Optical Society of America

OCIS codes: 300.1030, 300.6260, 300.6540, 010.1120, 280.1740, 280.3420.

1. Introduction

Tunable diode-laser absorption sensors (TDLASs) have been widely applied to a variety of species in reacting and nonreacting flows.¹ Optical absorption sensors provide sensitive, rapid, nonintrusive, species-specific measurements of combustion product concentrations. These features of optical absorption

measurements are well suited for combustion control applications to optimize combustion efficiency and minimize pollutant emissions. In fact, a closed-loop control system based on a TDLAS for water vapor has already been demonstrated in a pulsed dump combustor.² With the complexity of the combustion process, however, direct measurement of the parameter to be controlled is desirable.³ Therefore the reduction of pollutant emissions will require specific diode-laser-based absorption sensors for each target species.

Advances in laser technology have recently led to the development of a diode-laser-based sensor for measurements of nitric oxide (NO) concentrations by use of ultraviolet (UV) absorption spectroscopy.⁴ NO is an important pollutant because of its serious environmental effects. In the atmosphere, NO reacts with sunlight to form other nitrogen oxides (NO_x) that ultimately play a role in ground-level smog, acid rain, stratospheric ozone depletion, and global warming. Since more than 95% of NO_x in the atmosphere originates from combustion processes and over 95% of this combustion-formed NO_x is in the form of NO,⁵ a great deal of attention has been devoted to developing TDLASs for characterization and reduction of NO emission from combustion equipment. However, little

T. N. Anderson (tanderson@purdue.edu) and R. P. Lucht are with the School of Mechanical Engineering, Purdue University, 585 Purdue Mall, West Lafayette, Indiana 47907-2088. R. Barron-Jimenez, S. F. Hanna, and J. A. Caton are with the Department of Mechanical Engineering, Texas A&M University, College Station, Texas 77843-3123. T. Walther is with the Institute for Applied Physics, Darmstadt University of Technology, Schlossgartenstrasse 7, Darmstadt 64289, Germany. S. Roy and M. S. Brown are with Innovative Scientific Solutions, Incorporated, 2766 Indian Ripple Road, Dayton, Ohio 45440-3638. J. R. Gord is with the U.S. Air Force Research Laboratory, Propulsion Directorate, Wright-Patterson Air Force Base, Ohio 45433. I. Critchley and L. Flamand are with the Department of Combustion and Emissions, Honeywell Engines Systems and Services, 111 South 34th Street, Phoenix, Arizona 85034.

Received 5 April 2004; accepted 9 September 2004.

0003-6935/05/081491-12\$15.00/0

© 2005 Optical Society of America

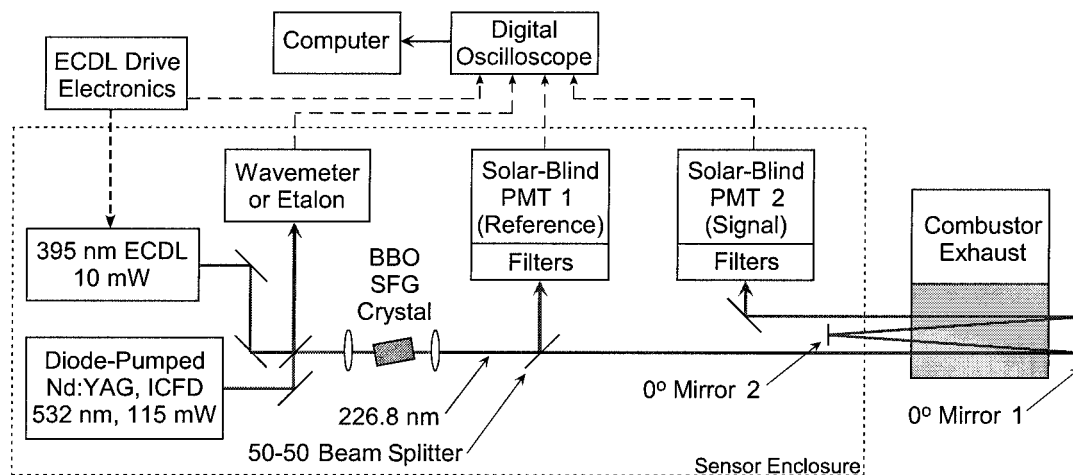


Fig. 1. Schematic diagram of the diode-laser-based NO sensor system for combustion exhaust measurements. SFG, sum-frequency generation; ICFD, intracavity frequency doubled.

progress has been made toward demonstrating these sensors in the harsh environments they will undoubtedly encounter in realistic combustion applications. In this paper we present successful TDLAS measurements of NO in the exhaust streams of a gas-turbine engine and a well-stirred reactor (WSR) to demonstrate the potential of such a system for measurements in actual combustion systems.

With one exception, all previous TDLASs for NO were based on commercially available near- and mid-infrared (IR) diode lasers^{6–13} and recently developed quantum-cascade (QC) lasers in the mid-IR.^{14–16} Near-IR absorption spectroscopy suffers potentially from severe interference by other combustion products (H_2O , CO , CO_2) as well as the weak absorption cross sections of the near-IR NO overtone transitions. These limitations have reduced the sensitivity and practicality of the sensors since many have required extractive sampling into a gas cell to reduce interference and increase sensitivity by an increase in the path length. The mid-IR measurements, although more promising, are complicated by the expense and limited availability of QC lasers and by the requirement of cryogenic cooling for the detectors and lasers.

In contrast, UV absorption measurements of NO offer fewer interferences and significantly greater absorption cross sections because of excitation of electronic transitions. The increased sensitivity and lack of CO_2 and H_2O interferences makes UV absorption ideal for practical combustion measurements. Unfortunately, no diode-laser sources are commercially available in the UV to probe these transitions. However, nonlinear optical techniques provide a relatively simple means of UV generation with commercially available diode lasers. Second-harmonic generation and sum-frequency generation have both been used to generate UV radiation for absorption spectroscopy for various species including NO.^{17–24}

We have developed a diode-laser-based UV absorption sensor based on sum-frequency mixing (SFM) for

NO.⁴ Laser radiation from a 395-nm external-cavity diode laser (ECDL) and a 532-nm ultracompact diode-pumped Nd:YAG is mixed to produce laser radiation at 226.8 nm tuned to the ($v' = 0$, $v'' = 0$) band of the $A^2\Sigma^+ - X^2\Pi$ electronic transition of NO. In this paper we first describe initial tests of the NO sensor in a laboratory gas cell. We then present results from field tests in a gas turbine auxiliary power unit (APU) and a WSR to demonstrate the practicality of this sensor in realistic combustion environments.

2. Experimental System and Procedures

The sensor is based on the SFM of 395- and 532-nm laser radiation in a β -barium borate (BBO) crystal to produce UV radiation at 226.8 nm. The laser system is described in detail in Hanna *et al.*⁴ The fundamentals of the system are discussed below. The sensor layout is illustrated schematically in Fig. 1. Approximately 10 mW of laser radiation from a tunable ECDL at 395 nm was mixed with 115 mW of radiation from a diode-pumped, intracavity frequency-doubled Nd:YAG laser at 532.299 nm (vacuum). The 395-nm beam was passed through the second green mirror to overlap the two beams. A small reflection from the back of this mirror was directed to a wavemeter or a spectrum analyzer to characterize the operation of the 395-nm ECDL during the experiment. Once overlapped, both beams were focused into a 4 mm \times 4 mm \times 8 mm long BBO crystal where approximately 325 ± 75 nW of UV radiation at 226.8 nm was produced in the SFM process. We estimated the UV power from the photomultiplier tube (PMT) output currents using the cathode radiant sensitivities and gains of the PMTs as specified by Hamamatsu. The uncertainty is due to the uncertainty in both the cathode radiant sensitivity and the gain of each PMT. This significant increase in generated UV power from our previous report⁴ is due to improvements in the alignment of the overlap of the 395- and 532-nm beams and to finer angle tuning of

the BBO crystal with the addition of a motorized rotation stage with 0.2-mrad angular resolution. The theoretical power is estimated to be 270 nW as discussed in our previous paper.⁴ The fact that the observed power is greater than the theoretical power is surprising. However, the exact values of some of the theoretical parameters such as fundamental beam powers and diameters and beam overlap at the focus are not well known, so the uncertainty of the calculated theoretical power is probably of the order of 30%. Nonetheless, the generated power was quite high and was more than sufficient for high-resolution spectroscopic measurements of NO.

After the UV radiation was generated in the BBO crystal, another lens was used to collimate the beam. We directed half of the resulting UV radiation onto a solar-blind PMT using a 50–50 beam splitter. This beam served as the reference beam, primarily to account for UV beam amplitude variations as the blue ECDL was tuned. The radiation transmitted through the beam splitter was used as the signal beam. Investigation of the UV signal beam at various locations along the path revealed substantial divergence in the horizontal direction. At a distance of 3 m from the BBO crystal, the beam height was approximately 2 mm and the beam width was over 25 mm. To correct for this horizontal beam divergence, a convex cylindrical lens with a focal length of 200 mm was placed after the beam splitter to collimate the signal beam in the horizontal direction. After we added the lens, the resulting beam width was approximately 3–5 mm at 3 m, but the beam height was still 2 mm. The reference beam did not require a similar lens since the distance to the reference PMT was too short for the beam to significantly diverge.

For all experiments, filters were used on both PMTs. Interference filters centered at 228 nm with bandwidths of 25 nm (FWHM) and peak transmissions of 22% were mounted to each PMT to block the 532- and 395-nm beams as well as any flame emission. Metallic neutral-density filters were used to attenuate both beams to keep the PMTs from saturating and to maintain the linearity of the detectors. The combination of the neutral-density filters and interference filters attenuated the 325-nW UV output by a factor of 700.

The experimental procedure and data collection process were identical for all experiments. Before we aligned the system, the center wavelength of the 395-nm ECDL was tuned coarsely so that the resulting UV wavelength was in resonance with the desired transition. During the experiment, we tuned the UV wavelength across the transition by tuning the ECDL with an internal ramp function at 5 Hz. A mode-hop-free tuning range of 24 GHz was observed for the ECDL output and thus for the UV radiation as well. The ramp voltage and the etalon fringes for the 395-nm ECDL output were recorded for each trace along with the signals from both PMTs. Data were collected with a personal computer through a four-channel digital oscilloscope by a general-purpose interface bus port and LabVIEW software. We obtained

a single spectral scan by averaging the data with the oscilloscope over 32 laser sweeps. For a 5-Hz laser scan rate, the acquisition time for the 32 laser sweeps was 6.4 s. Transfer of the 10,000 oscilloscope data points required an additional 5 s. To reduce high-frequency noise in the signal caused by beam steering in the hot exhaust, multiple spectral scans were averaged with the LabVIEW software. An equivalent of 224 laser sweeps were averaged over approximately 45 s for all the data reported in this paper. No attempt was made to reduce acquisition and processing time for these preliminary experiments.

After verifying the operation of the sensor in the laboratory,⁴ we performed field tests at two locations to test the sensor in real combustion environments. The first tests were performed on a Honeywell 131-9B gas turbine APU located at Honeywell's Engines Systems and Services facility in Phoenix, Arizona. The 90-kW APU is used to provide electrical power and cabin air in commercial aircraft when the main engines are off. Subsequent tests were performed on a WSR facility at Wright-Patterson Air Force Base in Dayton, Ohio. The WSR is a laboratory model of the compact primary zone of a gas-turbine combustor used to study emission and combustion characteristics for various fuel types. A detailed description of the WSR facility can be found in Blust *et al.* and references therein.²⁵

The optics were moved to a 0.61-m by 1.22-m optical breadboard to transport the sensor. An aluminum enclosure was also built to shield the optical system from the high temperatures of the combustors. The aluminum was not anodized, and this helped to reduce radiative heating near high-temperature flames. Dry air or nitrogen was forced through the enclosure at low flow rates to maintain stable temperatures within the enclosure during the course of the experiments. Vibrations were also expected to be a significant problem at both facilities, and the breadboards were mounted on optical benches and vibration isolation pads to reduce the vibrations transmitted to the optical components. At the Honeywell facility, the noise and vibrations were in fact so severe that the sensor had to be operated remotely from outside of the test cell. All controllers were located inside the control room and connected to the sensor with 15-m-long cables. Figure 2 shows the setup of the sensor for remote operation during measurements in the APU exhaust. A photograph of the sensor in the APU test cell is shown in Fig. 3.

In both facilities, the sensor was installed such that the signal beam passed through the combustion products approximately 5 mm from the edge of the exhaust tube along the diameter. The path length of the beam was assumed to be equal to the diameter of the exhaust tube. Multipass arrangements were used to increase the path length. This also allowed us to keep the signal PMT in the sensor enclosure for thermal stability and vibration isolation. Measurements performed in the exhaust of the Honeywell gas turbine APU required only a two-pass arrangement, and mirror 2 in Fig. 1 was not used. The total path length was

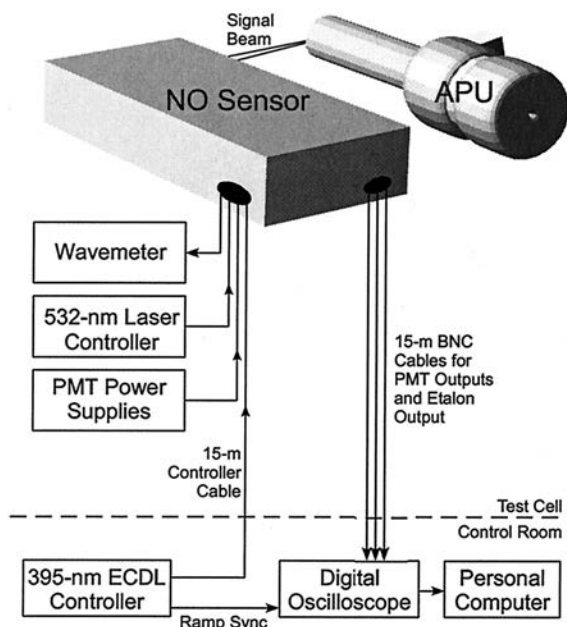


Fig. 2. Experimental layout for remote operation of the NO sensor for measurements in the exhaust of the Honeywell gas turbine APU.

0.51 m. In the WSR, the small diameter (5 cm) of the exhaust tube required four passes, as shown in Fig. 1. Since the exhaust tube was circular, the passes were arranged vertically such that each pass traversed the diameter of the exhaust progressively further downstream of the exit. The first pass was approximately 5 mm from the tube exit, and the final pass was approximately 5 cm from the exit. This maximized the path length while avoiding potential complications due to radial concentration and temperature gradients. The resulting path length was 0.2 m. For both experiments, a lens with a focal length of 100 mm

was placed approximately 75 mm in front of the signal PMT to reduce the beam size striking the PMT and to reduce the effects of the steering of the beam onto the detector.

To aid in processing the data, we measured the temperature of the exhaust gases at the location of the beam using thermocouples. Temperatures at several radial locations were recorded to determine the variation across the large exhaust tube on the Honeywell gas turbine APU. Only one thermocouple was used on the small exhaust tube of the WSR. We also sampled the exhaust gases using physical probes, and the NO concentration was measured with chemiluminescent analyzers to compare with the absorption concentration measurements. For the APU, samples at four radial locations were taken approximately 90 cm upstream from the location where the absorption measurements were performed. Since the NO was essentially frozen after exiting the engine, this was not expected to affect the comparison of the two techniques. For the WSR, the extractive probe was located in the center of the exhaust tube approximately 1 cm downstream of the absorption measurement location. Analyzers at both facilities were spanned and calibrated with analyzed calibration gases immediately before use.

3. Absorption Theory and Data Reduction

The transmission of radiation of frequency ν (cm^{-1}) through a distance L (cm) of an absorbing medium is given by Beer's law:

$$T_\nu = \frac{I}{I_0} = \exp(-k_\nu L), \quad (1)$$

where T_ν is the spectral transmission, I_0 is the incident spectral intensity, I is the transmitted radiation

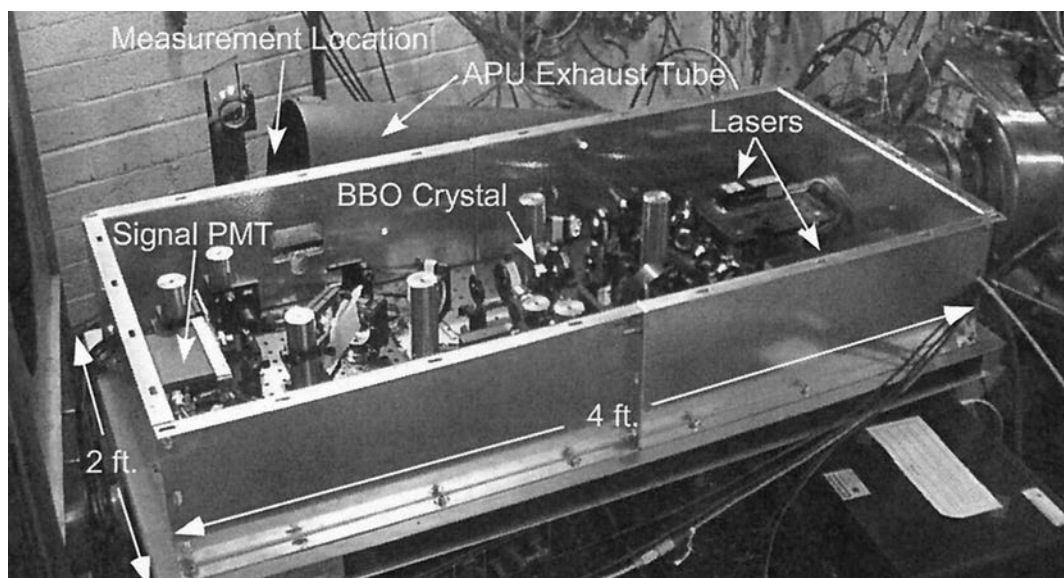


Fig. 3. Photograph of the NO sensor in the Honeywell gas turbine APU test cell. 4 ft (1.2192 m), 2 ft (0.6096 m).

intensity, and k_ν (cm^{-1}) is the spectral absorption coefficient. The spectral absorptivity A_ν is then

$$A_\nu = 1 - T_\nu = 1 - \exp(-k_\nu L). \quad (2)$$

The spectral absorption coefficient is proportional to the line strength K_{ji} and the line-shape function $G(\nu)$, or

$$k_\nu = K_{ji} G(\nu). \quad (3)$$

The line strength K_{ji} (cm^{-2}) for a transition from level i to level j is related to the Einstein spontaneous emission coefficient A_{ji} (s^{-1}) by²⁶

$$K_{ji} = \frac{\lambda_{ji}^2 A_{ji}}{8\pi c} \left(\frac{g_j}{g_i} n_i - n_j \right), \quad (4)$$

where g_i and g_j are the degeneracies of each level, n_i and n_j are the number densities of each level (cm^{-3}), c is the speed of light (cm/s), and λ_{ji} is the wavelength of the transition (cm). Einstein spontaneous emission coefficients and transition frequencies for the ($v' = 0, v'' = 0$) band of the $A^2\Sigma^+ - X^2\Pi$ electronic transition are found in Luque and Crosley.²⁷ The degeneracies for rotational energy levels J_i and J_j are $g_i = 2J_i + 1$ and $g_j = 2J_j + 1$, respectively. At thermodynamic equilibrium, the population of energy level i is related to the total number of particles N by the Maxwell-Boltzmann distribution:

$$\frac{n_i}{N} = \frac{g_i \exp(-E_i/k_B T)}{Z}, \quad (5)$$

where E_i is the total energy of level i , k_B is the Boltzmann constant, T is the gas temperature, and Z is the molecular partition function. Accurate expressions for rotational and vibrational term energies are found in Reisel *et al.* along with the molecular constants required for the calculations.²⁸ The molecular partition function Z is the sum over all possible energy levels.

For the line-shape function, a Voigt profile is assumed and the line-shape function (cm) is given by

$$G(\nu) = 2\sqrt{\frac{\ln 2}{\pi}} \frac{V(x, a)}{\Delta\nu_D}, \quad (6)$$

where $\Delta\nu_D$ is the Doppler width (FWHM, cm^{-1}) and $V(x, a)$ is the Voigt function found from

$$V(x, a) = \frac{a}{\pi} \int_{-\infty}^{\infty} \frac{\exp(-y^2)}{a^2 + (x - y)^2} dy. \quad (7)$$

The Voigt profile can be efficiently calculated with the algorithm developed by Humlíček.²⁹ Parameters for

the Voigt function are the nondimensionalized frequency

$$x = 2\sqrt{\ln 2}(\nu - \nu_{ji})/\Delta\nu_D \quad (8)$$

and the Voigt a parameter

$$a = \sqrt{\ln 2} \Delta\nu_c / \Delta\nu_D, \quad (9)$$

where ν_{ji} (cm^{-1}) is the line-center frequency of the transition and $\Delta\nu_c$ is the collision width (FWHM, cm^{-1}). The collision width is dependent on the species present in the absorbing medium and is one of the parameters that is varied to fit the theoretical absorption spectrum to the experimental spectrum. The Doppler width can be directly calculated from the gas temperature T (K), the molecular weight of the absorbing species M_{NO} (a.m.u.), and the frequency of the transition ν_{ji} (cm^{-1}) by

$$\Delta\nu_D = 7.1623 \times 10^{-7} \sqrt{\frac{T}{M_{\text{NO}}}} \nu_{ji}. \quad (10)$$

The Doppler width and the temperature are assumed to be well known and are not varied during the fitting process. Furthermore, the linewidth of the laser radiation is so narrow that it is assumed to be a delta function in the molecular line-shape modeling.

We developed a computer program to calculate the theoretical absorption as a function of wavelength for NO using the equations described above. We related the experimental results to theory by calculating the transmission through the medium using Eq. (1), where I is the signal PMT output and I_0 is the reference PMT output. After analyzing the initial results from the gas cell experiments, we observed substantial structure in the baseline due to the different responses of the signal and reference PMTs. To correct this, the transmission of the signal beam through a sample of NO was normalized by the transmission through a sample without NO. In other words, the transmission used for data analysis was

$$T_\nu = \frac{(S/R)_{\text{with NO}}}{(S/R)_{\text{without NO}}}, \quad (11)$$

where S and R refer to signal and reference PMT outputs, respectively. This corrected for the different PMT responses and flattened the baseline to 100% transmission far away from the line center as expected.

We converted the experimental absorption spectra from a time base to a frequency base using the etalon output. The time value of each etalon peak was determined and then plotted against frequency, since the spacing between each peak corresponds to the free spectral range of the etalon, or 2 GHz. The frequency-time relationship was derived by a quadratic least-squares fit. We also further processed the

experimental absorption scans to reduce oscilloscope read noise by binning 20 neighboring oscilloscope channels, reducing the number of spectral data points to 500. It was verified that the NO line shape was unaffected by the binning process. Finally, we fit the theoretical absorption spectra to the converted experimental absorption spectra by varying both the NO concentrations and collision widths manually until a best fit was achieved. The path length, pressure, and temperature were taken as measured during the experiments.

For the field demonstration experiments, several factors complicated the analysis of the absorption data. Before the experiments began, the signal and reference PMT outputs were adjusted to the same level. Broadband absorption by soot and other particulates resulted in a decrease in the signal PMT output compared with the reference PMT. This resulted in a lower S/R ratio for the signal channel, introducing error into the normalized transmission found from Eq. (11). If a clear off-resonant baseline was available in the signal channel, the transmission could be rescaled until the baseline corresponded to 100% transmission, correcting the error caused by mismatched signal and reference PMT outputs. However, the mode-hop-free tuning range of the laser system was not large enough to scan the entire width of the atmospheric-pressure-broadened NO lines, so no absorption-free baseline region was available. Nevertheless, the NO spectral line shapes are well known so that broadband attenuation in the signal channel was accounted for quite accurately by means of rescaling the NO spectrum as described below.

The modified data processing routine for the field demonstrations was an iterative procedure in which rescaling was used to shift the entire experimental absorption line shape vertically to match the theoretical absorption line shape across the entire spectrum. Typically, the experimental transmission from Eq. (11) was scaled by a factor of 0.96–1.04 in several increments. For each scaling factor, the collision width and NO concentration were varied to find the best fit. From these fits, the scaling factor that provided the best agreement between theoretical and experimental absorption line shapes across the entire spectrum was selected as the starting point for further iterations. These scaling-fitting iterations were then continued around this point until a global best fit was reached in which the difference between theory and experiment was minimized over the entire spectrum.

This routine was used to fit all the data for low NO concentrations where the absorption was of the order of several percent. For these concentrations, the structure of the baseline due to the different PMT responses (of the order of 0.5%) significantly obscured the absorption spectra. For higher concentrations, the baseline structure became negligible and the experimental absorption could be fit only with the S/R trace for the NO scan. This simplified both the processing and the data collection procedures since no air scans were necessary. However, all the results

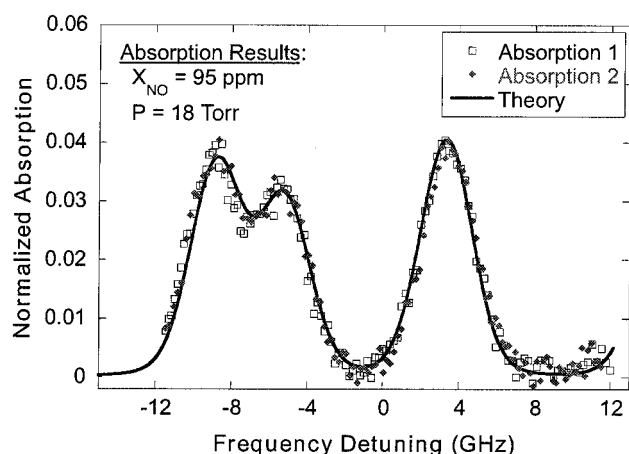


Fig. 4. Comparison of measured and calculated NO absorption line shapes for room-temperature gas cell measurement of 100 ppm NO (nominal) at 20 Torr. The Doppler width is $\Delta\nu_D = 0.099 \text{ cm}^{-1}$, and the collision-broadening coefficient is $2\gamma = 0.585 \text{ cm}^{-1}/\text{atm}$. The transitions shown are three sets of overlapped transitions (from left to right): $P_2(4)$ and $^PQ_{12}(4)$ at 44077.30 and 44077.30 cm^{-1} , $P_2(3)$ and $^PQ_{12}(3)$ at 44077.42 and 44077.42 cm^{-1} , and $P_2(5)$ and $^PQ_{12}(5)$ at 44077.71 and 44077.70 cm^{-1} .

presented in this paper were processed with both procedures to verify the accuracy of the fits.

4. Experimental Results

A. Gas Cell Measurements

A representative absorption scan for the room-temperature gas cell measurements is shown in Fig. 4. The two experimental absorption spectra (absorption 1 and 2) were recorded in a single scan as the frequency was tuned up and back down across the absorption line. The theoretical spectrum calculated with the computer code is also shown in Fig. 4. For the gas cell data, the pressure was also slightly varied around the measured value to optimize the fit. The absorption spectrum in Fig. 4 was recorded at a pressure of $2.67 \pm 0.27 \text{ kPa}$ ($20 \pm 2 \text{ Torr}$), and the best fit gave a pressure of 2.40 kPa (18 Torr), which is within the uncertainty of the gauge. The best-fit collision-broadening coefficient (FWHM) for all gas cell measurements was found to be $0.585 \text{ cm}^{-1}/\text{atm}$ (0.174 GHz/kPa), which agrees well with measurements of $0.583 \pm 0.03 \text{ cm}^{-1}/\text{atm}$ by Chang *et al.*³⁰ and $0.586 \pm 0.04 \text{ cm}^{-1}/\text{atm}$ by Danehy *et al.*³¹ for collisions of NO with N_2 at room temperature. The concentration that gave the best fit for the spectrum in Fig. 4 was 95 parts per million (ppm), which is in good agreement with the labeled concentration of $100 \pm 10 \text{ ppm}$ for the NO- N_2 gas mixture from Matheson.

The transitions shown in Fig. 4 were selected to verify the accuracy of the wavemeter and the theoretical line positions. The ECDL was tuned to 395.40 nm (vacuum) to produce UV at 226.87 nm . The transitions in Fig. 4 are three sets of overlapped transitions of the ($v' = 0, v'' = 0$) band of the

$A^2\Sigma^+-X^2\Pi$ electronic transition of NO: $P_2(4)$ and $^PQ_{12}(4)$, $P_2(3)$ and $^PQ_{12}(3)$, and $P_2(5)$ and $^PQ_{12}(5)$. The respective line centers are 44077.30 and 44077.30 cm^{-1} , 44077.42 and cm^{-1} , and 44077.71 and 44077.70 cm^{-1} , and 44077.42 cm^{-1} .²⁷ As evident from Fig. 4, the theoretical line positions as well as the line shapes agree very well with the experimental line positions and shapes.

Notation for all the transitions discussed in this paper follow the convention in Ref. 26, where a rotational transition is denoted by $\Delta^N\Delta J_{\alpha\beta}(N'')$. The change in the nuclear rotation quantum number N is denoted by S, R, Q, P, O for $\Delta N = N' - N'' = +2, +1, 0, -1, -2$, respectively. Similarly, the change in the rotational quantum number J is denoted by R, Q, P for $\Delta J = J' - J'' = +1, 0, -1$, respectively. When $\Delta J = \Delta N$, the superscript ΔN is omitted. The subscripts α and β indicate the spin-orbit coupling, where $\alpha = 1$ indicates $J' = N' + 1/2$, $\alpha = 2$ indicates $J' = N' - 1/2$, $\beta = 1$ indicates $J'' = N'' + 1/2$, and $\beta = 2$ indicates $J'' = N'' - 1/2$. When $\alpha = \beta$, only one number is given in the subscript to designate the value of both α and β .

From the initial laboratory experiments, the uncertainty in the concentration measurements by the sensor is estimated to be 10%. This value was derived from the range of concentrations measured over many experiments in the gas cell. After the field demonstrations, similar variations in concentrations confirm this estimated uncertainty. Sources of error include baseline drifts; nonlinear PMT response; and uncertainties in the path length, temperature, and pressure values. Some error could also be attributed to uncertainties in the spectral model, such as uncertainties in the molecular constants, Einstein coefficients, and line positions. Furthermore, the assumption of an infinitely narrow laser linewidth could introduce some error since the laser linewidth is only a factor of 37 narrower than the absorption linewidth in the Doppler-limited case in the gas cell experiments. The complexity of these uncertainties precludes a more rigorous calculation of the experimental uncertainty.

B. Combustion Exhaust Measurements

For the field demonstrations, the center frequency of the ECDL was tuned to 395.237 nm (vacuum) to produce UV radiation at 226.82 nm, in resonance with the $P_2(10)$ and $^PQ_{12}(10)$ overlapped transitions at 44087.79 and 44087.77 cm^{-1} , respectively.²⁷ This overlapped line pair was chosen because it is less sensitive to temperature and is well isolated at atmospheric pressure.

The results from the field tests on the APU fueled with Jet-A are shown in Figs. 5–9. The APU was run at several load conditions to produce varying levels of NO. The best-fit theoretical spectrum for each condition is also shown in Figs. 5–9. Table 1 gives the NO concentrations measured by optical absorption and by probe sampling and chemiluminescent analysis for each of the tests.

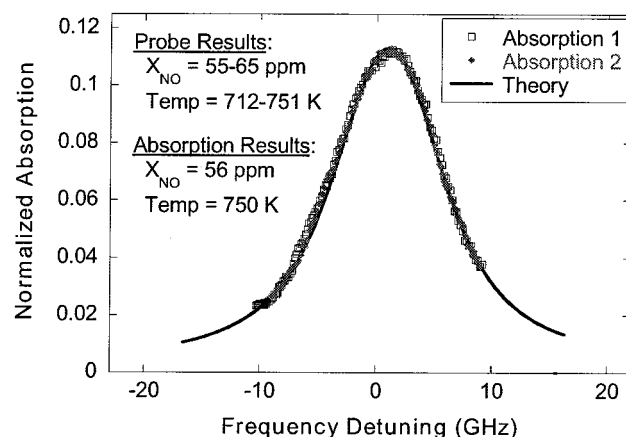


Fig. 5. Comparison of measured and calculated NO absorption line shapes for the gas turbine APU running at full load. The calculated Doppler width is $\Delta\nu_D = 0.158 \text{ cm}^{-1}$ and the collision width is $\Delta\nu_c = 0.297 \text{ cm}^{-1}$. All measurements in the APU probed the $P_2(10)$ and $^PQ_{12}(10)$ overlapped transitions at 44087.79 and 44087.77 cm^{-1} , respectively.

The temperature for the fitting routine was fixed at the average exhaust temperature as measured by the thermocouples. The resulting concentration and collision width measurements for the optical absorption measurements are insensitive to variations of 50 K or so in temperature because the population fraction of the $J = 9.5$ level is insensitive to temperature in this temperature range and the Doppler width is proportional to the square root of the temperature. Selection of a temperature-insensitive transition is also an advantage because it minimizes the effects of any inhomogeneities in the combustion exhaust along the path length of the laser beam. The Doppler broadening is much less than the collision broadening in all field demonstration experiments. Ignoring the radiation correction of the thermocouple is also justifiable since the error is small for these temperatures.

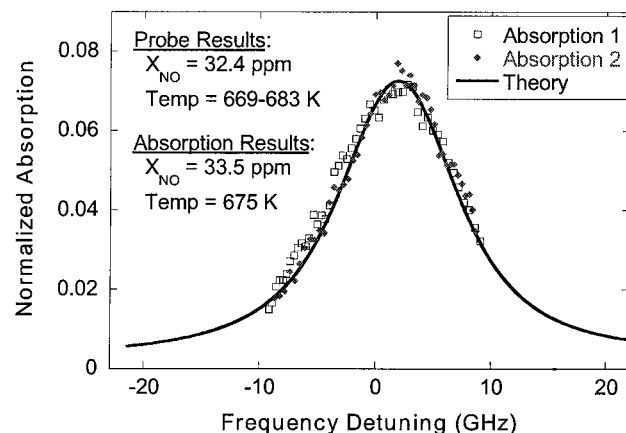


Fig. 6. Comparison of measured and calculated NO absorption line shapes for the gas turbine APU running at half of a full load. The calculated Doppler width is $\Delta\nu_D = 0.150 \text{ cm}^{-1}$ and the collision width is $\Delta\nu_c = 0.344 \text{ cm}^{-1}$.

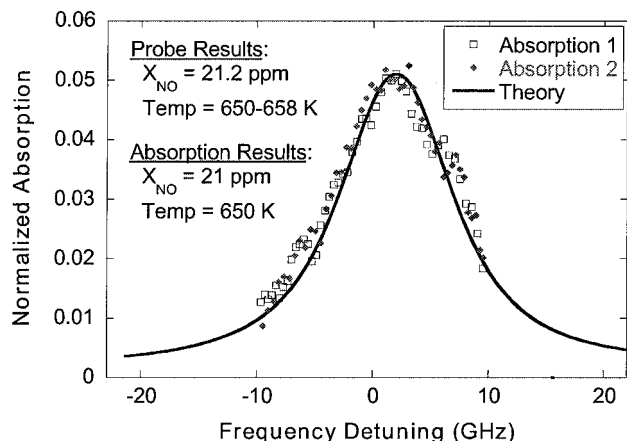


Fig. 7. Comparison of measured and calculated NO absorption line shapes for the gas turbine APU running at one third of a full load. The calculated Doppler width is $\Delta\nu_D = 0.147 \text{ cm}^{-1}$ and the collision width is $\Delta\nu_c = 0.344 \text{ cm}^{-1}$.

The concentrations listed in Table 1 indicate good agreement between measurements with the sensor and measurements with the chemiluminescent analyzer. Claimed uncertainty in the chemiluminescent analyzer readings is approximately 1% for the APU tests and approximately 3.6% in the WSR tests. As mentioned above, the experimental uncertainty of the sensor is estimated to be 10%. Thus all conditions lie within the experimental uncertainty except for low load conditions with NO concentrations near 10 ppm, as in Figs. 8 and 9. Since the line shapes and other parameters of the absorption spectra in Figs. 5–9 are consistent with other results, the anomalous results are probably due to errors in the probe measurements. The chemiluminescent analyzer was calibrated with gases near 100 ppm, so a baseline shift of a few ppm is possible and would account for the disagreement between probe and absorption measurements at low NO concentrations. Overall, however, the optical absorption measurements agree well

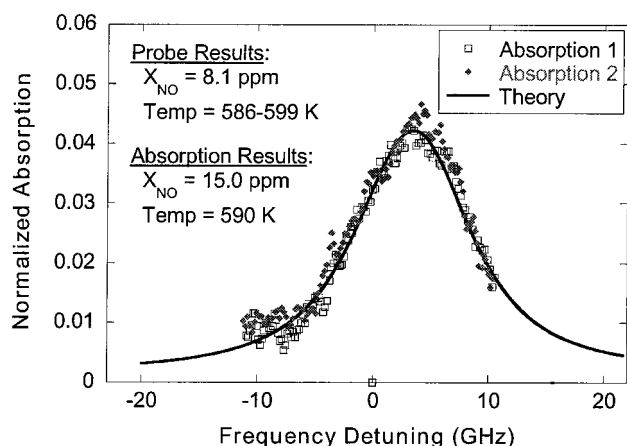


Fig. 8. Comparison of measured and calculated NO absorption line shapes for the gas turbine APU running at a low load condition. The calculated Doppler width is $\Delta\nu_D = 0.140 \text{ cm}^{-1}$ and the collision width is $\Delta\nu_c = 0.339 \text{ cm}^{-1}$.

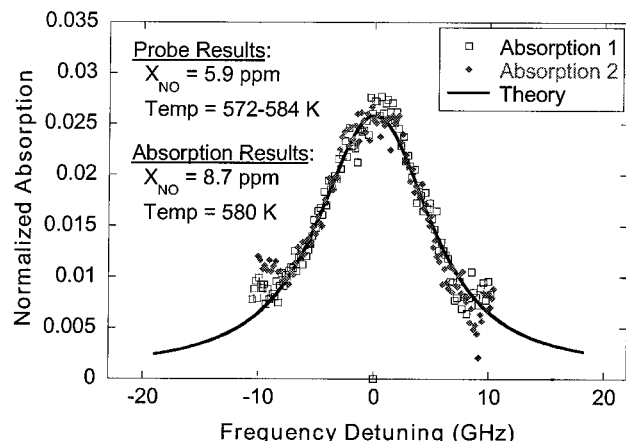


Fig. 9. Comparison of measured and calculated NO absorption line shapes for the gas turbine APU running at idle. The calculated Doppler width is $\Delta\nu_D = 0.139 \text{ cm}^{-1}$ and the collision width is $\Delta\nu_c = 0.331 \text{ cm}^{-1}$.

with the probe measurements of NO in the combustion exhaust. This level of agreement is similar to that previously demonstrated by other groups.^{11,32}

Comparison of collision widths with previous measurements requires a more detailed evaluation. Collision-broadening coefficients, 2γ , are found in the literature for NO broadened by a single species at a time.^{30,33,34} We can calculate the total collision width for a gas mixture by summing over all species, or

$$\Delta\nu_c = \sum_i 2\gamma_i P_i, \quad (12)$$

where $\Delta\nu_c$ is the collision width (FWHM, cm^{-1}), $2\gamma_i$ ($\text{cm}^{-1}/\text{atm}$) is the collision-broadening coefficient of NO by species i , and P_i (atm) is the partial pressure of species i . The collision-broadening coefficients for the broadening of NO by N_2 , H_2O , and O_2 are found by use of the relations suggested by Chang *et al.*,³⁰

$$2\gamma_{\text{N}_2} = 0.583(295 \text{ K}/T)^{0.75}, \quad (13)$$

and by Di Rosa and Hanson,³³

$$2\gamma_{\text{H}_2\text{O}} = 0.79(295 \text{ K}/T)^{0.79}, \quad (14)$$

$$2\gamma_{\text{O}_2} = 0.53(295 \text{ K}/T)^{0.66}, \quad (15)$$

where T (K) is the gas temperature. Using values of O_2 and CO_2 concentration measured during the experiments and values of H_2O and N_2 concentrations estimated for complete combustion, we calculated the predicted collision widths for each test. No broadening data are available for collisions of NO with CO_2 , so it was assumed that the CO_2 broadening coefficient was equal to the H_2O broadening coefficient. The results are shown in Table 2 along with values of collision width derived from the best-fit routine for each condition. All values agree within experimental un-

Table 1. Summary of Probe and Absorption Measurements of NO Concentration and Temperature for the Field Demonstrations^a

Test	Temperature (K)		Concentration (ppm)	
	Thermocouple	Absorption	Probe and CL	Absorption
APU full load	712–751	750	55–65	56
APU half load	669–683	675	32.4	33.5
APU one-third load	650–658	650	21.2	21
APU low load	586–599	590	8.1	15.0
APU idle	572–584	580	5.9	8.7
WSR $\Phi = 0.4$ with seeding	845	845	241.4	240
WSR $\Phi = 0.75$	1477	1477	140	130

^aProbe and CL concentration measurements indicate the measurements we obtained by probe sampling the exhaust and measuring the NO concentration with a chemiluminescent (CL) analyzer.

certainty, again confirming the accuracy of the sensor measurements even in these harsh environments.

Representative best-fit spectra for the experiments on the WSR are shown in Figs. 10–12. The probe measurements and absorption measurements for concentration and temperature are listed in Table 1. The absorption scan in Fig. 10 was taken for combustion of ethylene fuel with an equivalence ratio of $\Phi = 0.4$. This scan was taken during a preliminary experiment in the WSR with a slightly different setup

Table 2. Comparison of Measured Collision Widths to Predictions from Eqs. (12)–(15) for the Field Demonstrations

Test	Predicted (cm^{-1})	Measured (cm^{-1})
APU full load	0.306 ± 0.021	0.297
APU half load	0.319 ± 0.022	0.344
APU one-third load	0.326 ± 0.023	0.326
APU low load	0.346 ± 0.024	0.339
APU idle	0.349 ± 0.025	0.331
WSR $\Phi = 0.4$ with seeding	0.274 ± 0.019	0.282
WSR $\Phi = 0.75$	0.185 ± 0.013	0.191

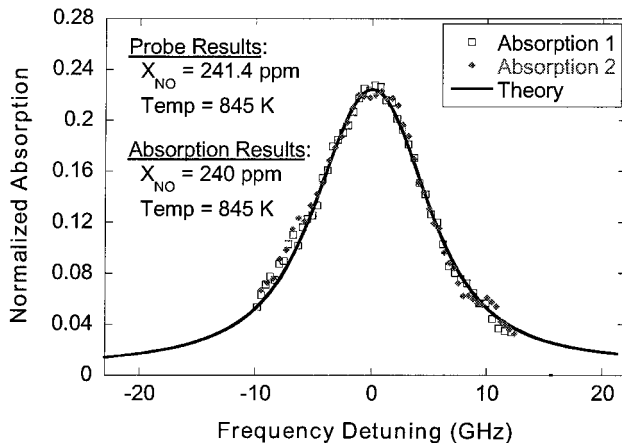


Fig. 10. Comparison of measured and calculated NO absorption line shapes for the WSR at $\Phi = 0.4$ with 3000 ppm of NO in N_2 seeded into the reactor. The calculated Doppler width is $\Delta\nu_D = 0.168 \text{ cm}^{-1}$ and the collision width is $\Delta\nu_c = 0.282 \text{ cm}^{-1}$. All measurements in the WSR probed the $P_2(10)$ and $P_{Q_{12}}(10)$ overlapped transitions at 44087.79 and 44087.77 cm^{-1} , respectively.

and operating condition from those of the primary experiments that were described above. A six-pass arrangement was used, and 3000 ppm of NO in N_2 was seeded into the reactor to find the absorption line initially. The excellent agreement among line shapes,

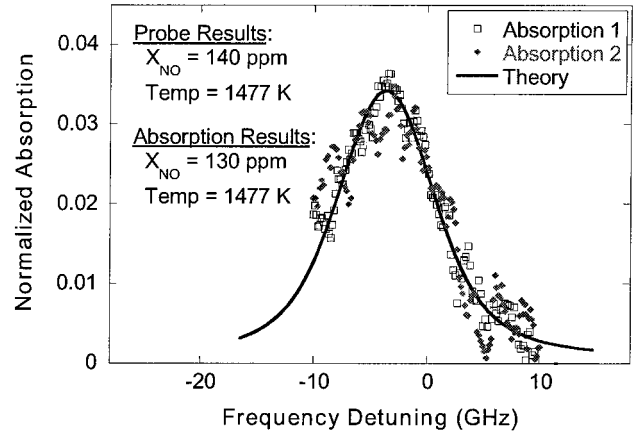


Fig. 11. Comparison of measured and calculated NO absorption line shapes for the WSR at $\Phi = 0.75$. The calculated Doppler width is $\Delta\nu_D = 0.222 \text{ cm}^{-1}$ and the collision width is $\Delta\nu_c = 0.191 \text{ cm}^{-1}$.

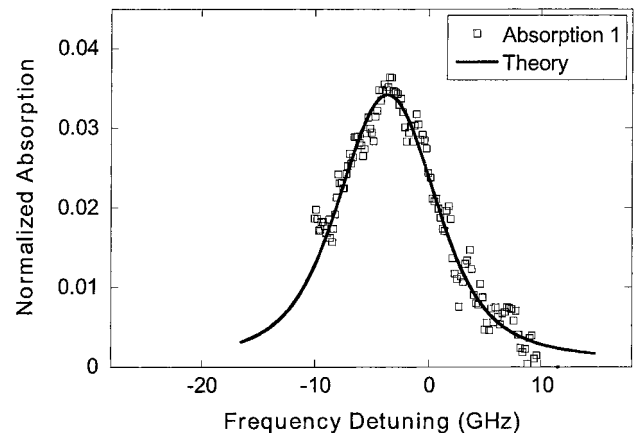


Fig. 12. Measured and calculated NO absorption spectra from Fig. 11 with the first half of the scan only. The reduction of noise without absorption 2 demonstrates the poor operation of the ECDL during the second half of the scan.

concentrations, and collisional widths encouraged further tests in the WSR to measure lower levels of NO.

Figure 11 represents the results from a second set of experiments in the WSR. Unfortunately, significantly more noise was observed in these WSR experiments because of poor operation of the ECDL. The ECDL was single mode for the portion of the scan where the frequency was increasing but exhibited mode hops for the portion of the scan where the frequency was decreasing. The effect of the multimode behavior is observed in Fig. 11 for the second half of the scan, absorption 2. The same scan is shown in Fig. 12 without the data points from the second half of the scan to demonstrate the excellent fit between theory and experiment when the laser is operating single mode.

The configuration for the tests in the WSR was more sensitive to beam steering by the hot exhaust gases because of the four-pass arrangement. Small deflections in beam direction propagated through the multiple reflections and were quite significant at the PMT. Despite the large detector area compared to the beam size, fluctuations were still observed because of the different sensitivities of different areas of the PMT photocathode. Thus slightly more noise was observed in these experiments. Nevertheless, the line shapes in Figs. 10–12 agree fairly well, and the concentrations given in Table 1 agree within the 10% experimental uncertainty of the sensor. Collision widths calculated from the best-fit spectra also agree well with the predictions from the literature, as can be seen in Table 2.

The detection limit of the sensor was estimated from the root-mean-square (rms) standard deviation of the noise in the baseline. For the gas cell experiments, the rms standard deviation was 0.17%. Assuming a signal-to-noise (S/N) ratio of 1 at the detection limit, this corresponds to a detection limit of 0.2 ppm-m (ppm in a 1-m path length) at 300 K, or 0.6 ppm-m at 1000 K. In the field demonstrations, slightly more noise was introduced into the signal from vibrations, temperature fluctuations, and beam steering because of hot exhaust gases. The rms standard deviation in the detection noise was measured from scans in hot air taken immediately after extinction of the flame in the combustors. For these scans, the rms noise increased to 0.23%, corresponding to a sensitivity of 0.3 ppm-m for 300 K gas or 0.8 ppm-m for 1000 K gas. The relatively small increase in noise from the gas cell experiments indicates that the sensor is not significantly affected by the noise and vibrations during the field demonstrations.

The low detection limit for this sensor demonstrates the advantages of UV absorption over IR absorption. In the current configuration of the sensor, only direct absorption spectroscopy and a two- or four-pass arrangement was required to achieve a sub-ppm-m detection limit in combustion exhaust. Previous sensors based on near- and mid-IR absorption generally required more complicated means to achieve detection limits of this order. The simplest

configuration used near-IR diode lasers at 1.8 μm to probe the second overtone band of NO and achieved noise-equivalent detection limits of 140 ppm-m down to several tens of ppm-m in combustion exhaust.^{6–8} These sensors relied on either balanced ratiometric detection^{6,7} or probe sampling of the exhaust and use of an external long-pass cell⁸ to reach these detection limits. Another group probed the stronger first overtone band of NO with a 2.65- μm diode laser and demonstrated a detection limit of 8 ppm-m (at 58 Torr) in a room-temperature gas cell using wavelength modulation spectroscopy.¹⁰ The measurements in both of these spectral regions were plagued by interferences from water vapor, which ultimately limits the sensitivity of these sensors.

To improve detection limits in the IR, a number of groups have probed the fundamental vibrational band of NO at 5.2–5.4 μm using cryogenically cooled IV–VI (lead salt) diode lasers or recently developed QC lasers. Sub-ppm-m detection limits were achieved with both types of laser in low-pressure, room-temperature, long-pass gas cells.^{13–15} Wehe *et al.* have performed measurements in combustion exhaust with a room-temperature QC laser and balanced ratiometric detection to reach a detection limit of 0.66 ppm-m of NO at 800 K.¹⁶ However, these sensors required cryogenically cooled detectors, and some interference with H₂O and CO₂ was still an issue for low NO concentrations. Also, analysis of the absorption line shapes was more complicated because the linewidths of the QC lasers were over 1 GHz because of frequency chirp.

Although the UV laser source for this sensor is more complicated than the lasers in the near- and mid-IR sensors, the UV sensor has nearly the same detection limit and offers significantly simpler detection schemes (no wavelength modulation spectroscopy or balanced ratiometric detection), room-temperature detectors, and straightforward spectroscopic analysis. Furthermore, the detection limits of this sensor can be improved down to quantum limits in the detectors, whereas detection limits in near- and mid-IR sensors are limited by the lowest fractional absorption by H₂O, CO, and CO₂ coinciding with the NO line of interest. For practical *in situ* measurements in combustion exhaust, this interference imposes a severe limit on the minimum-detectable NO levels, especially in higher-pressure combustors (pressure broadening) and higher-temperature gases (hot-band lines).

With UV detection of NO, the sensitivity of this sensor is ultimately limited by the shot noise in the PMTs. The S/N ratio at the shot-noise limit for PMTs is the square root of the number of photoelectrons created during the data collection process.³⁵ For an average power of roughly 0.5 nW reaching the PMTs, a cathode radiant sensitivity of 51.4 mA/W, and a measurement time of 45 s, the total number of photoelectrons created is 7.22×10^9 . The photoelectrons are distributed over 500 channels after processing, so there are only 1.44×10^7 photoelectrons per channel.

Thus the S/N ratio at the shot-noise limit is 3800. The relative error is given by the inverse of the S/N ratio, which is 0.026%. The baseline noise observed during the experiments was 0.23%, which is roughly a factor of 9 higher than the shot-noise limit. For the gas cell experiments, the noise was approximately a factor of 8 higher than the shot-noise limit.⁴ In combustion exhaust, the corresponding shot-noise-limited detection limit is 90 parts per 10⁹ of NO at 1000 K in a 1-m path assuming a S/N ratio of 1.

For these proof-of-concept experiments, no attempt was made to reduce the noise in the detection electronics, but several changes could be made to improve the sensitivity closer to the shot-noise limit. Faster modulation of the laser would reduce the flicker (or 1/f) noise and would allow more averaging to achieve the same time resolution. Electronic filtering of the signal would reduce the detection bandwidth and therefore reduce the overall detection noise. To utilize more of the generated UV, a parallel system of detectors could be used. Although this complicates the system, the S/N ratio is directly proportional to laser power and could provide significant improvements in detection limits. Finally, the more complicated scheme of wavelength modulation spectroscopy could be implemented to achieve sensitivities near the shot-noise limit.³⁶

Even at the current detection limit of the sensor, however, the sensor could be applied to combustion control applications with some improvement in data collection and processing procedures. The current demonstrations prove that the sensor can withstand the harsh environments around a gas turbine with acoustic noise up to levels of 120–125-dB overall sound pressure level and temperatures up to nearly 800 K. Furthermore, the sensor can accurately measure NO down to single-digit ppm levels at a rate of 10 Hz (twice the ramp frequency) in the exhaust. The path-averaged NO concentration measured by the sensor would provide a convenient input for operating point control of the gas turbine to maintain the NO level in the exhaust below mandated limits of 9 ppm for ground-based gas turbines.³

5. Summary and Conclusions

A diode-laser-based UV absorption sensor for NO has been developed and successfully demonstrated. The sensor is based on the sum-frequency generation of UV radiation at 226.8 nm by mixing the output of a 395-nm ECDL and a 532-nm intracavity frequency-doubled Nd:YAG laser in a BBO crystal. Approximately 325 ± 75 nW of UV is produced and used to probe several transitions in the ($v' = 0$, $v'' = 0$) band of the $A^2\Sigma^+ - X^2\Pi$ electronic transition of NO. Initial laboratory measurements in a gas cell showed excellent agreement between theoretical and experimental line shapes and between measured and actual concentrations. Experiments were then performed on a gas turbine APU and a WSR to test the operation of the sensor in the field. At the Honeywell facility, noise levels in the test cell were 120–125-dB overall

sound pressure level. In addition, the sensors operated for exhaust temperatures as high as 1500 K near the WSR. Nonetheless, the results from the field demonstrations were excellent. Good agreement was observed between the experimental and the theoretical line shapes, measured and predicted collision widths, and probe-measured and absorption-measured NO concentrations in all the combustion exhaust measurements. No evidence of interfering absorption from species other than NO was observed in either sensor test. Signal beam attenuation from broadband absorption was accounted for in the data analysis procedure. NO levels down to 9 ppm were measured in the exhaust of the gas turbine operating at idle conditions and with a path length of 0.51 m. A detection limit of 0.23% was estimated, corresponding to a sensitivity of 0.8 ppm-m of NO for 1000 K gas. The uncertainty of the sensor is estimated to be 10%. The results from these experiments indicate that this sensor can be used to accurately measure the NO emissions from real combustion systems.

The authors thank Scott Stouffer and Mike Arstingstall at Wright-Patterson Air Force Base for their help in performing these experiments.

This research was supported by the U.S. Air Force Research Laboratory, Propulsion Directorate, Wright-Patterson Air Force Base through Innovative Scientific Solutions, Inc. under contract F33615-00-C-2020, by the U.S. Environmental Protection Agency under project R-82818001, and by the U.S. Department of Energy through Honeywell Power Systems under contract DE-FC02-00-CH11053. This material is based on research supported under a National Science Foundation Graduate Research Fellowship.

References

1. M. G. Allen, "Diode laser absorption sensors for gas-dynamic and combustion flows," *Meas. Sci. Technol.* **9**, 545–562 (1998).
2. E. R. Furlong, R. M. Mihalcea, M. E. Webber, D. S. Baer, and R. K. Hanson, "Diode-laser sensors for real-time control of pulsed combustion systems," *AIAA J.* **37**, 732–737 (1999).
3. N. Docquier and S. Candel, "Combustion control and sensors: a review," *Prog. Energy Combust. Sci.* **28**, 107–150 (2002).
4. S. F. Hanna, R. Barron-Jimenez, T. N. Anderson, R. P. Lucht, J. A. Caton, and T. Walther, "Diode-laser-based ultraviolet absorption sensor for nitric oxide," *Appl. Phys. B* **75**, 113–117 (2002).
5. U.S. Environmental Protection Agency, "National air quality and emission trends report, 1998," EPA 454/R-01-004 (U.S. Environmental Protection Agency, Office of Air Quality Planning and Standards, Research Triangle Park, N.C., 2001).
6. W. J. Kessler, D. M. Sonnenfroh, B. L. Upschulte, and M. G. Allen, "Near-IR diode lasers for *in-situ* measurements of combustor and aeroengine emissions," paper AIAA-97-2706, presented at the 33rd AIAA/ASME/SAE/ASEE Joint Propulsion Conference, Seattle, Wash., 6–9 July 1997 (American Institute of Aeronautics and Astronautics, Reston, Va., 1997).
7. D. M. Sonnenfroh and M. G. Allen, "Absorption measurements of the second overtone band of NO in ambient and combustion gases with a 1.8- μ m room-temperature diode laser," *Appl. Opt.* **36**, 7970–7977 (1997).
8. R. M. Mihalcea, D. S. Baer, and R. K. Hanson, "A diode-laser

- absorption sensor system for combustion emission measurements," *Meas. Sci. Technol.* **9**, 327–338 (1998).
9. M. Snels, C. Corsi, F. D'Amato, M. De Rosa, and G. Modugno, "Pressure broadening in the second overtone of NO, measured with a near infrared DFB laser," *Opt. Commun.* **159**, 80–83 (1999).
10. D. B. Oh and A. C. Stanton, "Measurement of nitric oxide with an antimonide diode laser," *Appl. Opt.* **36**, 3294–3297 (1997).
11. P. K. Falcone, R. K. Hanson, and C. H. Kruger, "Tunable diode laser absorption measurements of nitric oxide in combustion gases," *Combust. Sci. Technol.* **35**, 81–99 (1983).
12. D. D. Nelson, M. S. Zahniser, J. B. McManus, C. E. Kolb, and J. L. Jimenez, "A tunable diode laser system for the remote sensing of on-road vehicle emissions," *Appl. Phys. B* **67**, 433–441 (1998).
13. C. Roller, K. Namjou, J. D. Jeffers, M. Camp, A. Mock, P. J. McCann, and J. Grego, "Nitric oxide breath testing by tunable-diode laser absorption spectroscopy: application in monitoring respiratory inflammation," *Appl. Opt.* **41**, 6018–6029 (2002).
14. D. M. Sonnenfroh, W. T. Rawlins, M. G. Allen, C. Gmachl, F. Capasso, A. L. Hutchinson, D. L. Sivco, J. N. Baillargeon, and A. Y. Cho, "Application of balanced detection to absorption measurements of trace gases with room-temperature, quasi-cw quantum-cascade lasers," *Appl. Opt.* **40**, 812–820 (2001).
15. D. D. Nelson, J. H. Shorter, J. B. McManus, and M. S. Zahniser, "Sub-part-per-billion detection of nitric oxide in air using a thermoelectrically cooled mid-infrared quantum cascade laser spectrometer," *Appl. Phys. B* **75**, 343–350 (2002).
16. S. Wehe, M. Allen, L. Xiang, J. Jeffries, and R. Hanson, "NO and CO absorption measurements with a mid-IR quantum cascade laser for engine exhaust applications," paper AIAA-03-0588, presented at the 41st AIAA Aerospace Sciences Meeting and Exhibit, Reno, Nev., 6–9 January 2003 (American Institute of Aeronautics and Astronautics, Reston, Va., 2003).
17. G. Hancock, V. L. Kasyutich, and G. A. D. Ritchie, "Wavelength-modulation spectroscopy using a frequency-doubled current-modulated diode laser," *Appl. Phys. B* **74**, 569–575 (2002).
18. K. A. Peterson and D. B. Oh, "High-sensitivity detection of CH radicals in flames by use of a diode-laser-based near-ultraviolet light source," *Opt. Lett.* **24**, 667–669 (1999).
19. H. R. Barry, B. Bakowski, L. Corner, T. Freearge, O. T. W. Hawkins, G. Hancock, R. M. J. Jacobs, R. Peverall, and G. A. D. Ritchie, "OH detection by absorption of frequency-doubled diode laser radiation at 308 nm," *Chem. Phys. Lett.* **319**, 125–130 (2000).
20. G. J. Ray, T. N. Anderson, J. A. Caton, R. P. Lucht, and T. Walther, "OH sensor based on ultraviolet, continuous-wave absorption spectroscopy utilizing a frequency-quadrupled, fiber-amplified external-cavity diode laser," *Opt. Lett.* **26**, 1870–1872 (2001).
21. L. Corner, J. S. Gibb, G. Hancock, A. Hutchinson, V. L. Kasyutich, R. Peverall, and G. A. D. Ritchie, "Sum frequency generation at 309 nm using a violet and a near-IR DFB laser for detection of OH," *Appl. Phys. B* **74**, 441–444 (2002).
22. D. B. Oh, "Diode-laser-based sum-frequency generation of tunable wavelength-modulated UV light for OH radical detection," *Opt. Lett.* **20**, 100–102 (1995).
23. J. Alnis, U. Gustafsson, G. Somesfalean, and S. Svanberg, "Sum-frequency generation with a blue diode laser for mercury spectroscopy at 254 nm," *Appl. Phys. Lett.* **76**, 1234–1236 (2000).
24. J. P. Koplow, D. A. V. Kliner, and L. Goldberg, "Development of a narrow-band, tunable, frequency-quadrupled diode laser for UV absorption spectroscopy," *Appl. Opt.* **37**, 3954–3960 (1998).
25. J. W. Blust, D. R. Ballal, and G. J. Sturgess, "Fuel effects on lean blowout and emissions from a well-stirred reactor," *J. Propul. Power* **15**, 216–223 (1999).
26. R. P. Lucht, S. Roy, and T. A. Reichardt, "Calculation of radiative transition rates for polarized laser radiation," *Prog. Energy Combust. Sci.* **29**, 115–137 (2003).
27. J. Luque and D. R. Crosley, "LIFBASE: Database and Spectral Simulation Program (Version 1.5)," SRI International Report MP 99-009 (SRI International, Menlo Park, Calif., 1999), www.sri.com/psd/lifbase.
28. J. R. Reisel, C. D. Carter, and N. M. Laurendeau, "Einstein coefficients for rotational lines of the (0, 0) band of the NO A²Σ⁺–X²Π system," *J. Quant. Spectrosc. Radiat. Transfer* **47**, 43–54 (1992).
29. J. Humlíček, "An efficient method for evaluation of the complex probability function: the Voigt function and its derivatives," *J. Quant. Spectrosc. Radiat. Transfer* **21**, 309–313 (1979).
30. A. Y. Chang, M. D. DiRosa, and R. K. Hanson, "Temperature dependence of collision broadening and shift in the NO A–X (0, 0) band in the presence of argon and nitrogen," *J. Quant. Spectrosc. Radiat. Transfer* **47**, 375–390 (1992).
31. P. M. Danehy, E. J. Friedman-Hill, R. P. Lucht, and R. L. Farrow, "The effects of collisional quenching on degenerate four-wave mixing," *Appl. Phys. B* **57**, 243–248 (1993).
32. M. F. Zabielski, L. G. Dodge, M. B. Colket III, and D. J. Seery, "The optical and probe measurement of NO: a comparative study," in *Eighteenth Symposium (International) on Combustion* (Combustion Institute, Pittsburgh, Pa., 1981) pp. 1591–1598.
33. M. D. Di Rosa and R. K. Hanson, "Collision broadening and shift of NO γ(0, 0) absorption lines by O₂ and H₂O at high temperatures," *J. Quant. Spectrosc. Radiat. Transfer* **52**, 515–529 (1994).
34. M. D. Di Rosa and R. K. Hanson, "Collision-broadening and -shift of NO γ(0, 0) absorption lines by H₂O, O₂, and NO at 295 K," *J. Mol. Spectrosc.* **164**, 97–117 (1994).
35. A. C. Eckbreth, *Laser Diagnostics for Combustion Temperature and Species*, 2nd ed. (Gordon & Breach, Amsterdam, The Netherlands, 1996).
36. J. A. Silver, "Frequency-modulation spectroscopy for trace species detection: theory and comparison among experimental methods," *Appl. Opt.* **31**, 707–717 (1992).

Optical Turbine-Engine Diagnostics for Ground-Test and On-Board Applications

James R. Gord

Combustion & Laser Diagnostics Research Complex
Air Force Research Laboratory, Propulsion Directorate
Wright-Patterson AFB OH 45433-7251, USA

james.gord@wpafb.af.mil

Terrence R. Meyer

Innovative Scientific Solutions, Inc.
Dayton OH 45440-3638

terrence.meyer@wpafb.af.mil

Sukesh Roy

Innovative Scientific Solutions, Inc.
Dayton OH 45440-3638

sroy@woh.rr.com

Michael S. Brown

Innovative Scientific Solutions, Inc.
Dayton OH 45440-3638

michael.brown@wpafb.af.mil

Sivaram P. Gogineni

Innovative Scientific Solutions, Inc.
Dayton OH 45440-3638

sivaram.gogineni@wpafb.af.mil

ABSTRACT

While optical diagnostic techniques have been applied with great success to the fundamental study of combustion chemistry and physics in the laboratory, the challenges afforded by real-world propulsion systems demand continuing innovation if such techniques are to be adapted and transitioned for use in engineering tests and on-board monitoring and control applications. This paper documents continuing efforts to transition aerodynamic measurement technologies from diagnostics-development laboratories to combustor test-and-evaluation facilities in the Propulsion Directorate's Combustion Branch (Turbine Engine Division). Applications of various optical diagnostic techniques for visualizing flowfields and quantifying temperatures and key species concentrations in several advanced combustors are described.

OPTICAL TURBINE-ENGINE DIAGNOSTICS

1.0 INTRODUCTION

Propulsion systems represent a substantial fraction of the cost, weight, and complexity of Air Force aircraft, spacecraft, and other weapon-system platforms. The vast majority of these propulsion systems are powered through combustion of fuel; therefore, the detailed study of combustion has emerged as a highly relevant and important field of endeavor. Much of the work performed by today's combustion scientists and engineers is devoted to the tasks of improving propulsion-system performance while simultaneously reducing pollutant emissions. Increasing the affordability, maintainability, and reliability of these systems is also a major driver.

While improved performance can be described quantitatively in many terms (*e.g.*, specific fuel consumption, thrust-to-weight ratio, etc.), it often involves efforts to increase heat release during the combustion process. Improvements may be achieved as well by reducing the length and/or weight of the combustor through informed design decisions. Engine emissions that might adversely impact the environment and the military signature of Air Force systems must be reduced while striving to improve performance. Judicious design and control of the combustor can significantly impact the affordability, maintainability, and reliability of the propulsion system by extending the useful life of engine components or by permitting the incorporation of less-expensive materials in combustor construction, for example. Pursuing these goals requires a thorough understanding of the fundamental physics and chemistry of combustion processes.

The Combustion Branch of the Air Force Research Laboratory's Propulsion Directorate (Turbine Engine Division) has adopted a philosophy for combustor-technology development aimed at achieving these goals. At the basic-research level, new diagnostic approaches are developed and tested in conjunction with extensive modeling-and-simulation efforts. Techniques are "cross-validated" through studies of fundamental combustion processes in laboratory rigs that provide favorable optical conditions while remaining computationally tractable. Axisymmetric burners with ample optical access and well-defined boundary conditions represent such test articles. The measurement and computational tools designed, tested, and matured through this basic research are applied subsequently to hardware testing and evaluation. Ultimately, sensor platforms based on these diagnostic approaches and algorithms derived in part from the combustion models are incorporated for on-board propulsion-system monitoring and control.

Development, demonstration, and application of laser-based and other optical diagnostic techniques are integral elements of that research plan. Advanced measurement techniques that exploit lasers and optics have become well-established tools for characterizing combustion.¹ Non-invasive measurement approaches are often ideally suited for visualizing complex reacting flowfields and quantifying key chemical-species concentrations and fluid-dynamic parameters. The fundamental information these techniques provide is essential for achieving a detailed understanding of the chemistry and physics of combustion processes. Furthermore, these data are critical for validating combustion models and combustor-design codes with tremendous potential for propulsion-system development. At a more applied level, hardened diagnostics provide the designer with performance data for the systems-engineering process. Diagnostics also promise to play an important role in fielded propulsion systems as elements in control and optimization schemes.

These characteristics of optical diagnostic techniques suggest a three-phased evolutionary process for their development and application. In the first phase, emphasis is placed on the diagnostic technique itself—on the chemistry and physics that define the measurement and the hardware (sources, optics, detectors, etc.) and software necessary to accomplish that measurement. During this phase of the process, a research-grade instrument is typically employed to study a well-characterized flowfield in a laboratory environment. While this phase of the diagnostics-development process is certainly essential and exciting, the ultimate utility of a diagnostic technique is significantly limited if it never sees application beyond the laboratory.

During the second phase of the process, a hardened version of the research-grade instrument is applied to achieving measurements in an engineering facility. The emphasis in this phase shifts from the diagnostic technique to the engineering application. In the third phase, a miniaturized and robust diagnostic device is incorporated into the final product, such as an actual gas turbine engine, for on-board sensing and control.

The transitions from laboratory to facility to fielded systems are fraught with significant challenges that must be addressed. During the laboratory phase of diagnostics development, conditions are typically ideal and well controlled. They might involve vibrationally isolated laser tables, humidity- and temperature-controlled environments, and sufficient space to accommodate sources, optics, mounts, and detectors required to achieve the desired measurement. Test articles often feature ample optical access and support clean-burning, gas-fueled, laminar flames operating under atmospheric or sub-atmospheric conditions. In contrast, facilities applications involve conditions characteristic of actual engine hardware. Challenges include extreme environmental conditions (heat, vibration, acoustics, etc.), limited optical access, tight geometric constraints, little operational space, fully developed turbulence, two-phase flows, soot formation, high pressure, collisional quenching, energy redistribution, optical thickness, beam steering, high background luminosity, and scattering and spectral interferences. These challenges are amplified on moving from the facility to the on-board environment. Successful transitions, first from the laboratory to the facility and then from the facility to the field, require thoughtful attention to these issues.

This paper continues with descriptions of three specific scenarios in which optical diagnostics have been applied to assess the performance and impact the design of next-generation combustors and fuels through ground testing. These applications and other opportunities for ground-test and on-board applications will be discussed in the briefing that accompanies this paper.

2.0 FLOW VISUALIZATION IN THE TRAPPED-VORTEX COMBUSTOR (TVC)

Experimental and computational techniques for the visualization of fluid flows have emerged as essential tools for increasing our understanding of the physics and chemistry of these flows. Indeed, many—if not most—of the breakthroughs in fluid mechanics and dynamics can be attributed to the understanding achieved through imaging of the various multidimensional structures in fluid flow. High-speed digital imaging, planar laser-induced fluorescence (PLIF), particle-image velocimetry (PIV), coherent-structure velocimetry (CSV), and laser-induced incandescence (LII) are amongst the diagnostic tools routinely employed for two-dimensional flow visualization in the test facilities of the Combustion Branch.

The unique geometry of the TVC has been designed to bring improved overall performance, enhanced stability, and reduced pollutant emissions to current and next-generation propulsion systems.^{2,3} It also promises benefits in terms of combustor length and pressure drop. The key features of the TVC design are evident in Fig. 1, which depicts a natural-gas-fueled TVC sector operating at atmospheric pressure. Cavities at the top and bottom of the sector promote aerodynamic trapping of a combusting vortex. Injection of fuel and air into these cavities maintains continuous pilot flames therein, enhancing fuel-air mixing and flame stability. These trapped pilot flames interact with the main fuel/air flow situated between the two cavities.

Ongoing testing of various TVC sectors is aimed at establishing design rules and assessing the performance impacts of such drivers as cavity and main geometry, fuel-injector design and placement, and air flow. Enhanced mixing techniques aimed at reducing pollutant emissions and combustor size are also under study. These efforts are supported by flow visualization achieved through high-speed digital imaging, PLIF, PIV, and CSV.

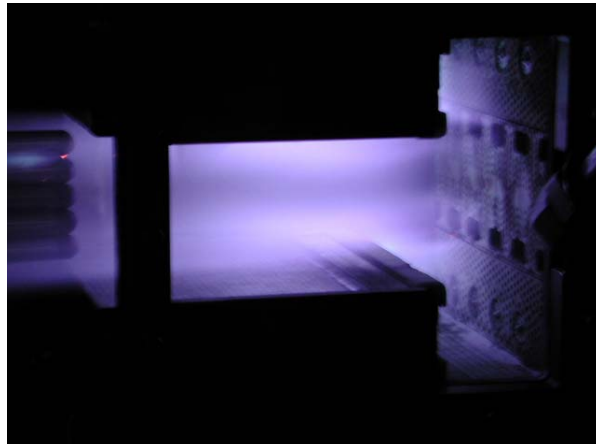
OPTICAL TURBINE-ENGINE DIAGNOSTICS

Figure 1. Natural-gas-fueled TVC sector operating at atmospheric pressure. Flow is from right to left.

High-speed digital images of the TVC have been acquired using a Phantom v5.0 CMOS-based high-framing-rate digital camera provided by Photo-Sonics International Ltd. During this study, the camera was operated at 11,200 frames per second (fps) with a resolution of 256×256 pixels and an exposure time of 10 μ s. Frame captures of the normalized flame luminosity in a JP-8-fueled TVC sector operating at pressures of 8.5 and 12 atm are depicted in Fig. 2. These high-speed visualizations provide real-time feedback during TVC testing regarding the flow pattern and flame distribution within the cavities and main sections of the combustors. Exposure times as low as 10 μ s enable flow freezing not achievable through conventional videography.

When viewed in a time-correlated sequence, such images clearly show vortical flame structures in the upper and lower cavities. These vortices act as flame holders that promote flame stability and enhance fuel-air mixing by increasing the turbulence level and the residence time.

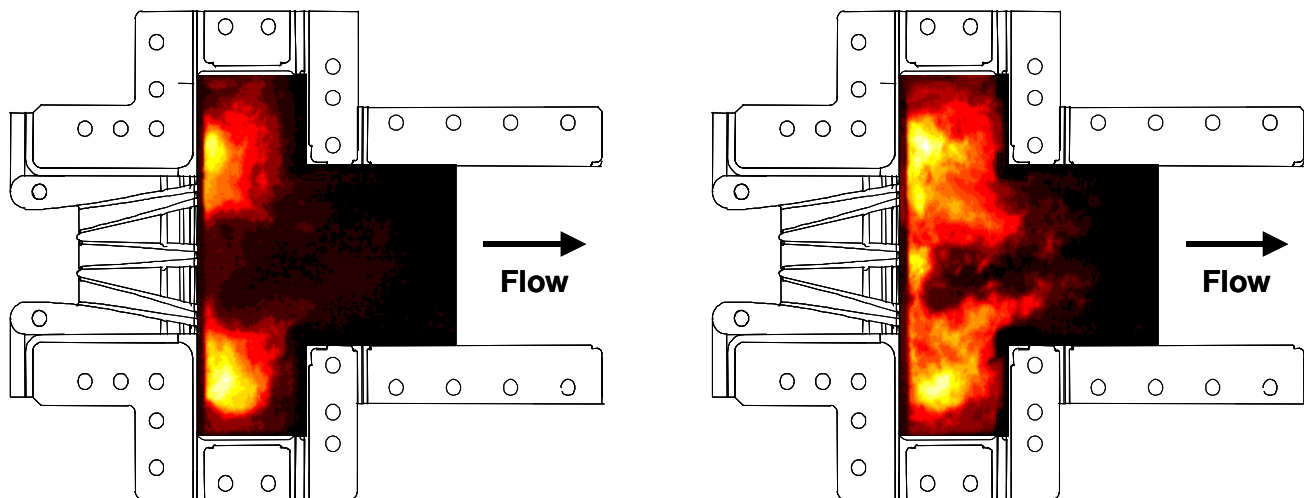


Figure 2. Flame luminosity captured with a high-speed digital camera from a JP-8-fueled TVC sector operating at 8.5 atm (left) and 12 atm (right).

While high-speed digital imaging provides a qualitative description of flame location and dynamics, PLIF can be used to visualize specific flame species. This yields a more accurate measurement of flame location and eliminates the spatial ambiguity associated with line-of-sight averaging. In the current work, PLIF of the hydroxyl radical (OH) was accomplished by exciting the $R_1(8)$ transition of the (1,0) band in the A-X system. The requisite 281.3414-nm laser sheet was generated using the frequency-doubled output of a Nd:YAG-pumped dye laser, and fluorescence from the A-X (1,1) and (0,0) bands was detected using an intensified charge-coupled device (ICCD) camera equipped with a UG-11 and two WG-295 colored glass filters to reduce visible and laser-scattered light, respectively.

OH-PLIF images were acquired in a natural-gas-fueled TVC sector for a number of fuel-injection configurations. Injection in the cavity and main sections produces the flame pattern in Fig. 3. The flame pattern obtained in the lower cavity through fuel injection in the cavity alone is depicted in Fig. 4. These data are employed to verify calculations using a conventional k- ϵ -based CFD code with chemistry.

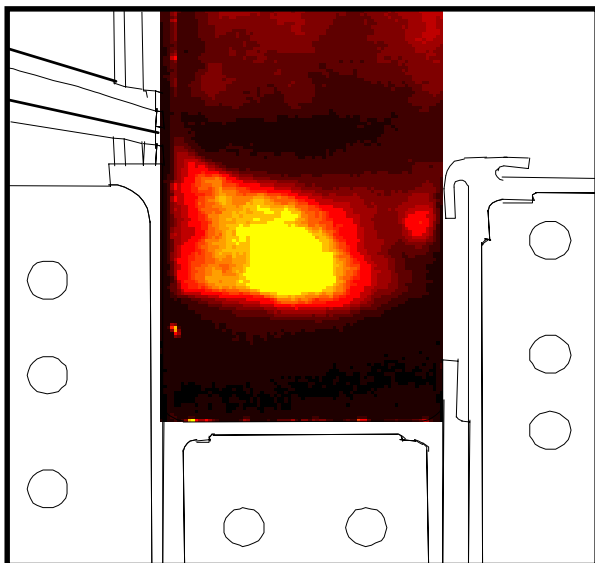


Figure 3. OH-PLIF signal obtained in the lower cavity of a natural-gas-fueled TVC with fuel injection in the cavity and main sections.

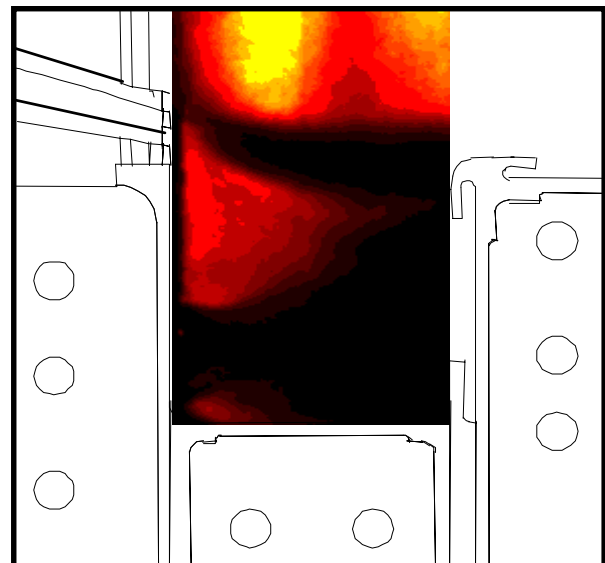


Figure 4. OH-PLIF signal obtained in the lower cavity of a natural-gas-fueled TVC with fuel injection in the cavity alone.

Velocimetry data have been acquired to complement these flame visualizations. PIV was achieved using a dual-image, digital cross-correlation configuration with two Nd:YAG lasers and a dual-frame Kodak ES4 2000×2000 pixel CCD camera. Vectors were computed using a dPIV code developed by AFRL and Innovative Scientific Solutions, Inc., using 16×16 pixel interrogation regions and 75% overlap. An average of five image pairs was employed to generate the data in Fig. 5, which compare the velocities determined by PIV in the lower cavity of the TVC sector with those computed using a commercial CFD package.

The short-exposure images acquired with the high-speed digital camera can also be used to estimate flow velocities subject to certain assumptions using CSV. This involves several image-processing steps, including the generation of isoline contours to define structure boundaries, the selection of an optimal interrogation window and overlap parameter, and cross-correlation between image pairs for determination of the local

OPTICAL TURBINE-ENGINE DIAGNOSTICS

displacement vectors. It must be stressed that CSV in combustor flows cannot provide a true measure of convective velocity due to inherent non-convective flame-intensity variations. Nonetheless, slowly varying flame structures can provide a qualitative picture of the flow structure. Such a technique can be highly valuable for flow analysis on-demand and can supplement more difficult, laser-based methods such as PIV. The latter is valuable for quantitative velocimetry and code validation, but it is not conducive to continuous operation due to window fouling and seed build-up in small passages.

The CSV image in Fig. 6 depicts the combustor flow pattern with a cavity geometry very similar to that in which the PIV data of Fig. 5 were acquired. Qualitative agreement between the two velocity fields is quite good.

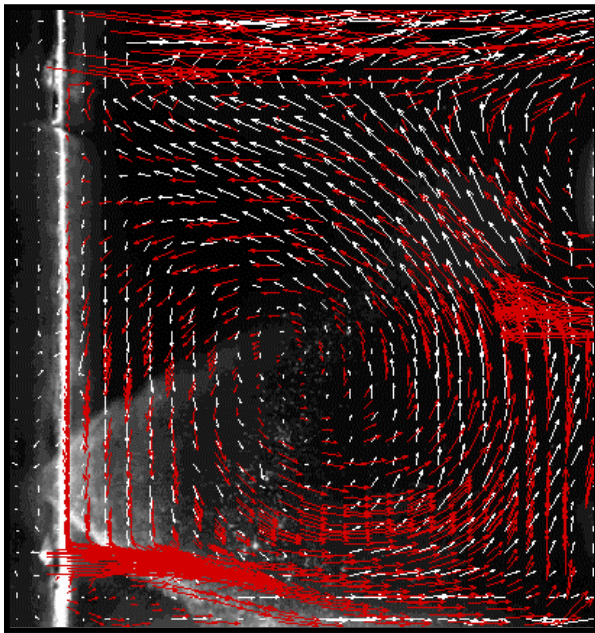


Figure 5. Comparison of PIV data (white vectors) and CFD data (red vectors) acquired in the lower cavity of a TVC sector under non-combusting

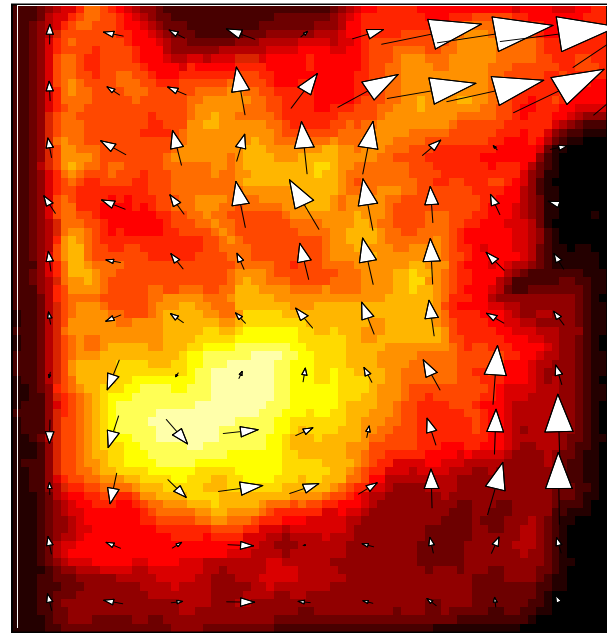


Figure 6. CSV data overlaid on a high-speed digital image of combustion in the lower cavity of a TVC sector.

3.0 SIMULTANEOUS PLANAR LII, OH PLIF, AND DROPLET MIE SCATTERING IN A CFM56-BASED MODEL COMBUSTOR

Swirl-stabilized liquid-spray injectors are commonly used in gas-turbine engines to achieve compact, stable, and efficient combustion. The flowfield in the primary zone of such a spray flame is characterized by high shear stresses and turbulent intensities that result in vortex breakdown and large-scale unsteady motions.^{4,5} These unsteady motions are known to play a key role in the formation of pollutant emissions such as carbon monoxide (CO), nitric oxide (NO), and unburned hydrocarbons (UHC).⁶⁻⁸ Considerably less is known, however, about the mechanisms that lead to soot formation in swirl-stabilized, liquid-fueled combustors. Previous investigations have relied on exhaust-gas measurements and parametric studies to gain insight into

the effects of various input conditions on soot loading.⁹⁻¹² Much of the fundamental knowledge concerning soot formation is derived from investigations of laminar diffusion flames,¹³⁻¹⁵ with only a limited number of studies having focused on unsteady effects.^{16,17} The importance of considering unsteadiness and fluid-flame interactions was demonstrated by Shaddix et al.,¹⁷ who found that a forced methane/air diffusion flame produced a four-fold increase in soot volume fraction (as a result of increased particle size) as compared with a steady flame having the same mean fuel-flow velocity.

The goal of the current investigation is to study soot formation in the highly dynamic environment of a swirl-stabilized, liquid-fueled combustor. This is accomplished using simultaneous imaging of the soot volume fraction, hydroxyl-radical (OH) distribution, and droplet pattern in the primary reaction zone using laser-induced incandescence (LII), OH planar laser-induced fluorescence (PLIF), and droplet Mie scattering, respectively. The utility of LII for two-dimensional imaging of soot volume fraction has been demonstrated in laboratory investigations^{18,19} as well as in aircraft engine exhausts.^{12,13} Brown et al.²⁰ performed planar LII for soot-volume-fraction imaging in the reaction zone of a gas-turbine combustor; their preliminary measurements employed LII alone for demonstration purposes and did not image the turbulent flame structure near the exit of the swirl cup. In the current work, we extend the work of Brown et al.²⁰ by performing LII at the exit of the swirl cup and by adding OH PLIF and Mie scattering diagnostics.

The use of OH as a flame marker is typical in studies of soot formation in diffusion flames because of its close correlation with flame temperature.^{21,22} It has also been employed in a number of investigations of swirl-stabilized combustors.^{23,24} The use of laser-saturated OH LIF for *quantitative* measurements has also been demonstrated,^{25,26} although saturation is quite difficult in the case of planar measurements. In the current investigation, we demonstrate qualitative measurements in the recirculation region using excitation levels well below saturation. OH-PLIF measurements in the liquid-spray region are more uncertain because of simultaneous droplet scattering and non-equilibrium conditions, although meaningful measurements are possible with careful consideration of potential errors. Mie scattering from large droplets, which appears in the OH images but does not preclude signal interpretation, is used to a limited extent as a spray diagnostic. As shown in Fig. 7, the experimental set-up includes an Nd:YAG for saturated LII at 532 nm and a narrowband dye laser for OH PLIF using the Q₁(9) line in the 1-0 band of the A-X system.

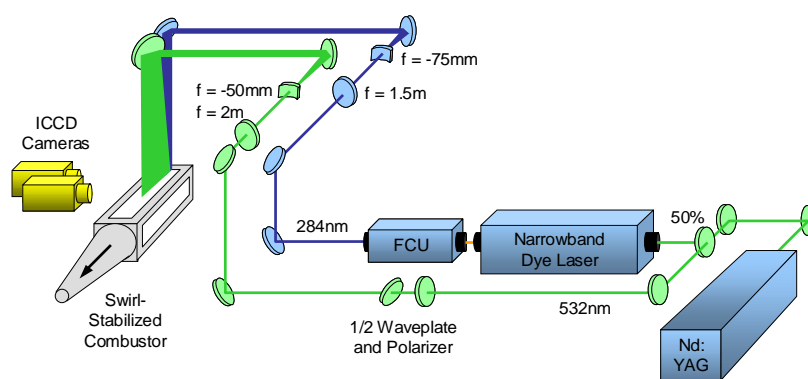


Figure 7. Simultaneous OH PLIF and LII in atmospheric-pressure, swirl-stabilized, JP8-fueled, model gas-turbine combustor.

The injector geometry and sample instantaneous OH-PLIF images for JP-8 and a non-aromatic liquid fuel are shown in Fig. 8 at an equivalence ratio of 0.8. Such images provide a clear indication of the intermittency

OPTICAL TURBINE-ENGINE DIAGNOSTICS

within the primary flame zone and are useful for characterizing the statistical behavior in terms of probability density functions. It is found, for example, that large-scale structures play a key role in the soot formation process. Intermittent regions of rich premixed fuel and air develop between the primary flame layer and recirculation zone that serve as sites for soot inception. The rate of soot production is dependent upon the frequency and spatial extent of these regions, while the rate of soot oxidation is dependent upon the availability of oxygen and OH in the primary zone and recirculation region. Hence, the overall soot volume fraction is highly sensitive to the dynamics of the injection process as well as to the local, unsteady equivalence ratio. The importance of the former is highlighted by differences in the vaporization and soot formation characteristics of JP-8 versus non-aromatic fuels, as shown in Figs. 8(b) and 2(c).

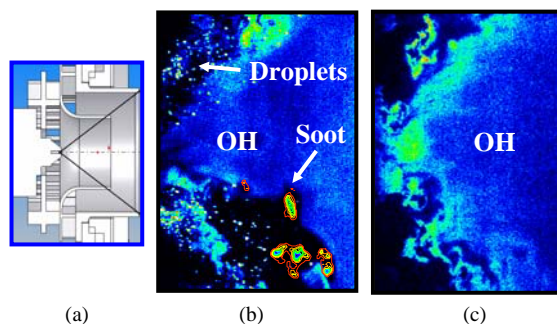


Figure 8. (a) Dual-radial swirl cup with center-mounted pressure-swirl injector, (b) primary zone with JP-8 at $\phi = 0.8$, and (c) primary zone with non-aromatic fuel at $\phi = 0.8$.

In studies of soot-mitigating additives, performed in collaboration with the Fuels Branch of ARFL, the simultaneous OH-PLIF and LII measurements were used to determine whether changes in soot production result from changes in the chemical or physical properties of the fuel. Figures 9(a) and 9(b) demonstrate the ability of the current measurement system to track local equivalence ratio and soot production, respectively. Using a droplet-free region in the recirculation zone, the time- and spatially averaged OH-PLIF signal is plotted with respect to equivalence ratio and compared with an equilibrium calculation. This provides a calibration for JP-8 that can be used qualitatively to track changes in equivalence ratio. The data in Fig. 9(a) include corrections for the effects of collisional quenching and Boltzmann-fraction variations on the OH-PLIF signal. The LII data in Fig. 9(b) show an exponential increase of the soot volume fraction in the primary zone with respect to equivalence ratio. A subsequent test using an increased LII-gate period demonstrates minimal particle-size bias and measurement repeatability. Note that the exhaust-gas sampling probe displays a threshold effect at about $\phi = 1.0$ below which soot in the exhaust is effectively oxidized by OH and O_2 due to long residence times.

Since the dependence of soot on equivalence ratio is exponential, slight changes in equivalence ratio could easily be mistaken for changes in soot particle counts in the exhaust stream. This highlights the importance of tracking equivalence ratio while performing studies of soot-mitigating additives. An example is shown in Fig. 10 where methyl acetate is added to the fuel during a test. Note the large decrease in soot volume fraction during methyl-acetate addition, as measured by LII; this corresponds to a large decrease in particle counts from the sampling probe. Note also the increase in OH-PLIF signal that, according to the results of Fig. 9(a), indicates that the fuel mixture is becoming leaner. A certain ambiguity exists, however, because the final equivalence ratio could lie on either side of the peak OH signal. Using the exponential fit to the data in Fig. 9(b), however, the change in LII signal corresponds to an equivalence ratio that is slightly on the rich side of

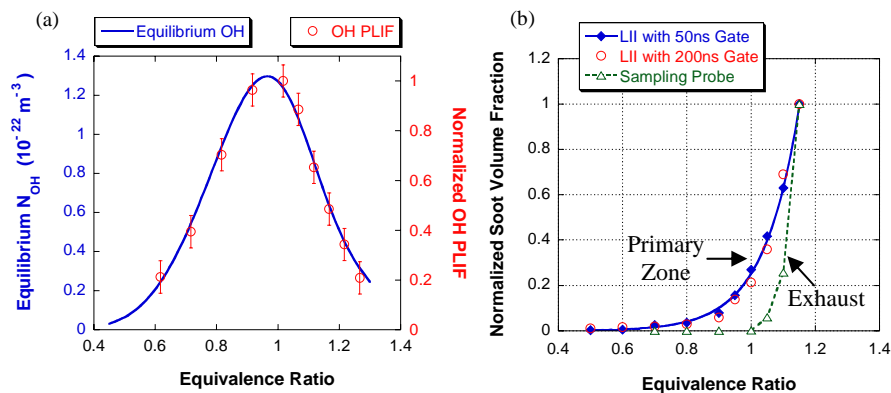


Figure 9. (a) Fit of OH data in recirculation region with equilibrium calculations and (b) comparison of normalized soot volume fraction in primary zone with particle counts in the exhaust stream.

the OH peak. An overall equivalence-ratio decrease of 0.123 due to methyl-acetate addition is measured to within 1% for both the OH-PLIF and LII data and to within 10% of flow calculations. The agreement between OH-PLIF and LII data indicates that methyl acetate in the current study did not have an effect on soot production, except for its effect on equivalence ratio. One can envision, therefore, the use of a combined LIF and LII system to track the performance of soot-mitigating additives without uncertainties in equivalence ratio.

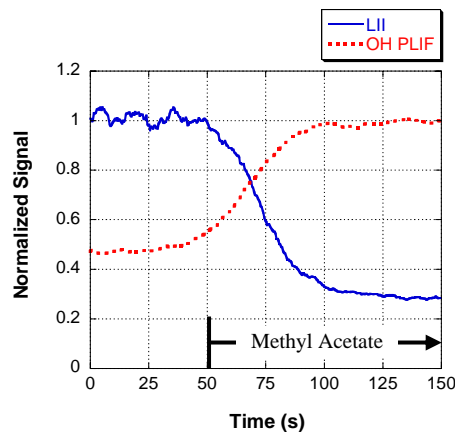


Figure 10. Drop in soot due to methyl acetate addition corresponds to decrease in ϕ as verified by OH PLIF.

4.0 TRANSIENT-GRATING THERMOMETRY IN THE TVC

Laser-induced transient or dynamic gratings have an established diagnostic history for measurement of a wide range of physical properties, including fast-carrier lifetimes, diffusion rates, and temperature. Transient-grating spectroscopy (TGS) has been repeatedly demonstrated as a technique that is suitable for application in

OPTICAL TURBINE-ENGINE DIAGNOSTICS

hydrocarbon-air flames.^{27,28} In particular, single-shot thermometry has been demonstrated under various combustion conditions.²⁸ The coherent signal is generated by Bragg scattering a continuous-wave probe beam from a laser-induced refractive-index grating that is established through the spatial and temporal overlap of two pump beams derived from the same pulsed laser.²⁹ The index grating is established through electrostriction or optical absorption and subsequent molecular collisions that transfer the absorbed energy to translational motion. The time-resolved signal appears as a damped sinusoidal oscillation. The oscillation frequency is determined by the grating spacing and the local speed of sound, which, in turn, is a function of temperature. Extraction of the temperature from the measured sound speed requires some knowledge of the ratio of the molecular mass to the specific heat ratio. For hydrocarbon-air combustion, this ratio is a very weak function of the exact mixture fraction and temperature.²⁸ Consequently, a reasonable estimate of the value of the ratio leads to accurate temperature measurements, which are easily accomplished and render the technique applicable under a wide range of combustion conditions.

Execution of the transient-grating technique requires three incident beams from two laser sources—a pulsed pump laser and a continuous-wave probe laser. The output of the pump laser is split into two beams of equal intensity that are crossed at a small angle. The spatial and temporal overlap of the pump beams creates an optical-intensity pattern that couples a very small amount of energy via electrostriction or absorption into the test region, thereby modifying the local index of refraction. The probe laser beam—incident at the Bragg scattering angle—is reflected by the spatially modulated index grating and detects the time evolution of the grating. (A schematic of the incident-beam arrangement is shown in Figure 11.) The grating structure in the fluid returns to local equilibrium through acoustic and thermal modes. The counter-propagating acoustic modes alternately interfere constructively and destructively. This imposes a temporal modulation on the signal, the period of which is determined by the local speed of sound and the grating spacing. Since the speed of sound is a function of temperature, the technique provides thermometry with high spatial resolution.

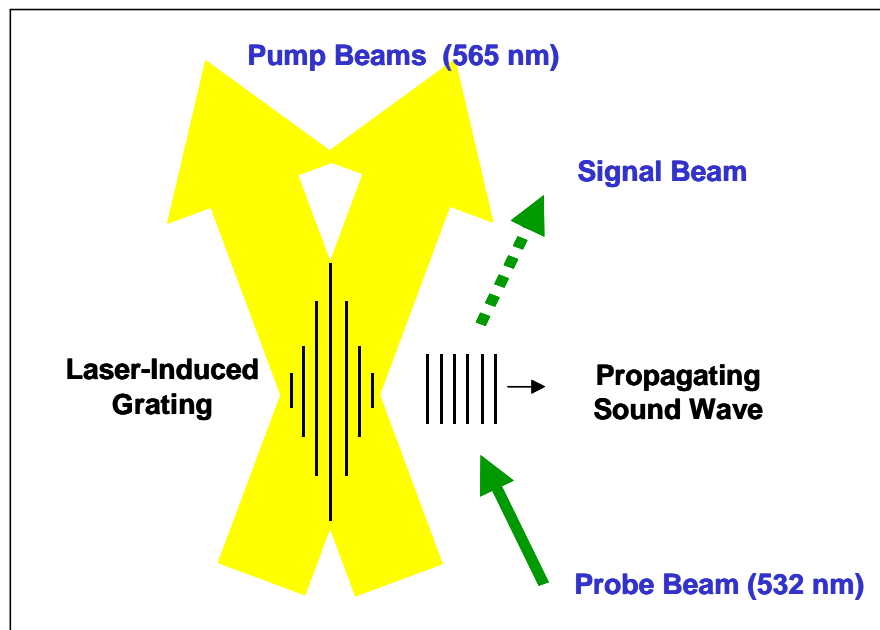


Figure 11. Schematic of incident-beam arrangement for TVC measurements. Note probe and signal beams were slightly out-of-plane with respect to pump beams.

As part of our continuing effort to develop and apply this technique, transient grating thermometry has been performed in the rich flame zone of a TVC operating under turbulent, pressurized, JP-8-fueled conditions. Measurements were accomplished at pressures of 50, 75, and 100 psi with local equivalence ratios in the range 1–1.25. The pump beams were derived from the 565-nm output of a Nd:YAG-pumped dye laser. The cw output of a vanadate laser (532 nm) provided the probe beam. While the pump lasers were not tuned to a particular molecular resonance, the detected signals showed clear signs of thermalization and the absence of nonresonant electrostriction. Soot particles and soot precursors are the likely absorbers responsible for signal generation. Beam steering was clearly evident in the form of variable pointing and random spatial modulation of the exiting beams. Due to such adverse affects, signal was not obtained on all laser shots; however, useful signals were generated with sufficient frequency to permit meaningful temperature measurements.

A typical single-shot signal is depicted in Fig. 12. Four oscillations are clearly seen. (We have found in practice that only three rings are needed for precise temperature determination.) The power spectrum corresponding to this signal is shown in Fig. 13. It is dominated by two features: a) the Rayleigh peak centered at zero frequency associated with the non-propagating thermal mode and b) the Brillouin feature associated with the counter-propagating acoustic modes. Temperature is extracted from each analyzed single-shot signal through numerical determination of the peak of the Brillouin feature in the power spectrum.

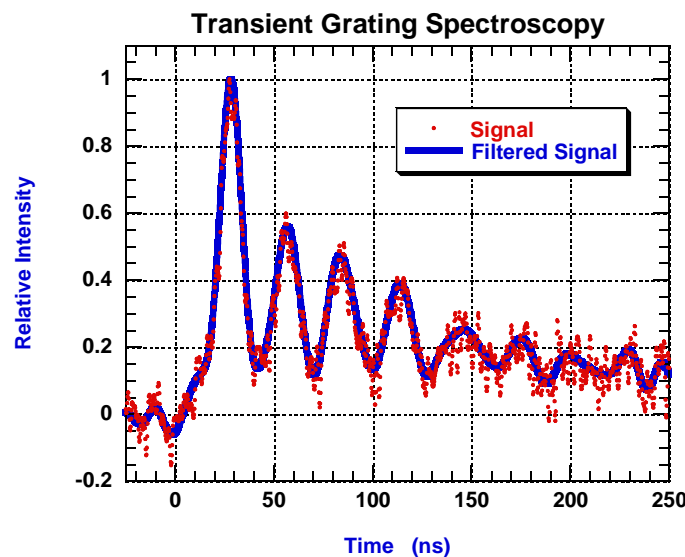


Figure 12. Single-shot TGS signal acquired in the rich flame zone of a TVC operating under turbulent, pressurized (75 psi), JP-8-fueled conditions.

In one particular data-collection run, the TVC was operated with the cavity slightly rich (equivalence ratio of ~ 1.1) at 100 psi. Signal from 1300 sequential laser shots was recorded at this condition. Roughly one-third of the single-shot signals were found to be legitimate analyzable TGS signals; the remainder were found to be compromised by electronic noise (low S/N) or beam steering. Down-selection of signals to be analyzed was performed in a two-step process. Each time-domain signal was first examined to ensure that the peak signal location fell within a meaningful delay with respect to the arrival of the pump beams. (The delay is associated with the dynamics of the grating formation.) After zero padding, each power spectrum was constructed using standard FFT routines, and the ratio of the amplitude of the Brillouin peak to that of the Rayleigh peak was

OPTICAL TURBINE-ENGINE DIAGNOSTICS

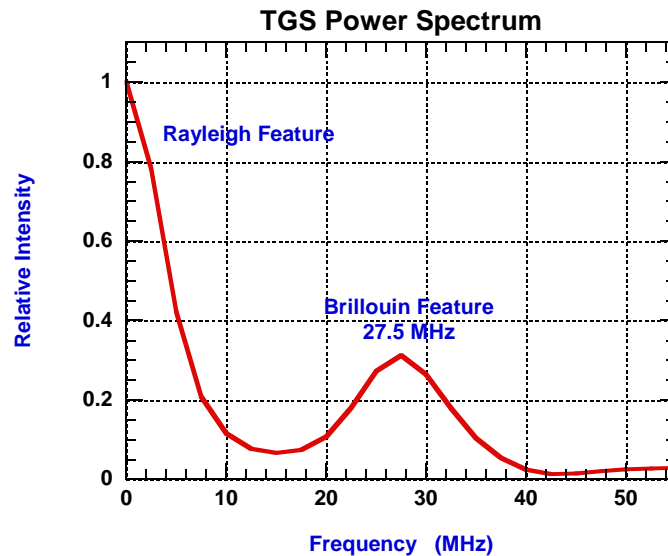


Figure 13. Power spectrum of signal shown in Fig. 12.

then determined. Spectra that exhibited ratios >0.005 were then analyzed in detail. The Brillouin feature of the down-selected set of 456 power spectra was fit using a fourth-order polynomial to find the peak. The corresponding temperatures are presented as a histogram in Fig. 14. The mean value of the temperature is 2260 K and is quite comparable to the adiabatic-flame-temperature values for decane and dodecane (sometimes considered to be single-component surrogates for JP-8) of 2200 and 2300 K, respectively. The breadth of the histogram largely reflects the local dynamic nature of the reaction zone as pockets of fluid in different relative states of combustion maturity pass through the probe volume.

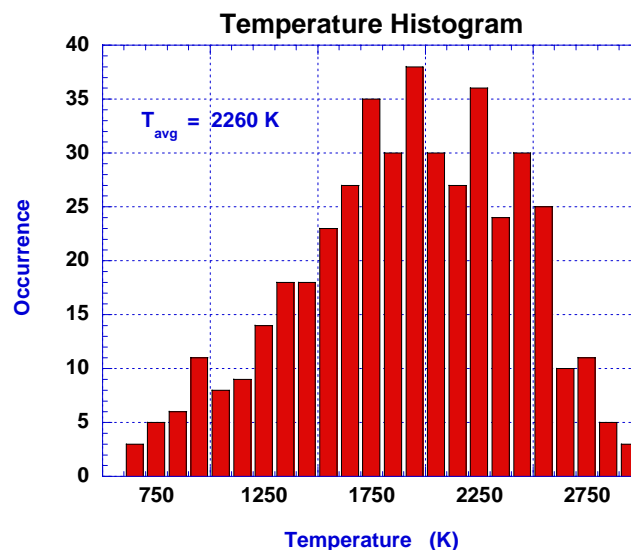


Figure 14. Temperature histogram constructed through analysis of 456 single-shot signals acquired in a TVC operating at a pressure of 100 psi.

The width of the Rayleigh feature is determined by the local thermal diffusivity and the width of the Brillouin feature is proportional to the acoustic damping coefficient that has contributions from thermal and mass diffusion, sheer and bulk viscosity. The width of these features is easily determined via fitting with power spectral functions found in the literature, permitting extraction of values for the thermal diffusivity and acoustic damping coefficient. For power spectra that exhibit temperatures near the peak of the temperature histogram ($\sim 2200 \pm 300$ K), the extracted thermal diffusivity is found to vary by $\sim 18\%$ shot-to-shot while the acoustic damping coefficient varies by $\sim 70\%$. Both the measured thermal diffusivity and acoustic damping coefficient are larger than the corresponding values calculated using the output of an equilibrium flame code that accounts only for the gas species present and not for soot. The difference between the measured and calculated values probably reflects the soot loading in the rich reaction zone.³⁰ Our current efforts are aimed at quantifying the contribution of soot to these transport properties.

5.0 CONCLUSION

Tremendous time and energy have been invested throughout the research community in the development of advanced optical diagnostics for the fundamental study of combustion chemistry and physics. The techniques developed for these important basic-research activities also have enormous potential for impacting the design, development, test, evaluation, operation, and maintenance of current and next-generation propulsion systems when those techniques are transitioned from the laboratory to the test facility and ultimately to the field.

This paper summarizes some recent efforts to transition diagnostics for use in the combustor-test facilities of the Combustion Branch at Wright-Patterson Air Force Base. Various techniques for flow visualization, including high-speed digital imaging, PLIF, PIV, CSV, and LII, as well as methods for measuring temperatures, species, and equivalence ratio have been applied in these facilities.

6.0 ACKNOWLEDGMENTS

The authors gratefully acknowledge myriad technical contributions from the members of the Combustion Branch of the Air Force Research Laboratory's Propulsion Directorate (Turbine Engine Division) and the contractors supporting that branch, especially Innovative Scientific Solutions, Inc. Financial support from the Air Force Office of Scientific Research (Dr. Julian Tishkoff, Program Manager) is gratefully acknowledged as well.

7.0 REFERENCES

- [1] A. C. Eckbreth, *Laser Diagnostics for Combustion, Temperature, and Species*, 2nd Edition, Gordon & Breach, 1996.
- [2] W. M. Roquemore, D. Shouse, D. Burrus, A. Johnson, C. Cooper, B. Duncan, K.-Y. Hsu, V. R. Katta, G. J. Sturgess, and I. Vihinen, "Trapped Vortex Combustor Concept for Gas Turbine Engines," AIAA 2001-0483 (2001).
- [3] T. R. Meyer, M. S. Brown, S. Fonov, L. P. Goss, J. R. Gord, D. T. Shouse, V. M. Belovich, W. M. Roquemore, C. S. Cooper, E. S. Kim, and J. Haynes, "Optical Diagnostics and Numerical Characterization of a Trapped-Vortex Combustor," AIAA 2002-3863 (2002).

OPTICAL TURBINE-ENGINE DIAGNOSTICS

- [4] W.-W. Kim, S. Menon, and H. Mongia, "Large-Eddy Simulation of a Gas Turbine Combustor Flow," *Combust. Sci. Technol.* **143**, 25-62 (1999).
- [5] S. Wang, S.-Y. Hsieh, and V. Yang, "Numerical Simulation of Gas Turbine Swirl-Stabilized Injector Dynamics," AIAA 2001-0334 (2001).
- [6] M. V. Heitor and J. H. Whitelaw, "Velocity, Temperature, and Species Characteristics of the Flow in a Gas-Turbine Combustor," *Combust. Flame* **64**, 1-32 (1986).
- [7] A. F. Bicen, D. G. N. Tse, and J. H. Whitelaw, "Combustion Characteristics of a Model Can-Type Combustor," *Combust. Flame* **80**, 111-125 (1990).
- [8] T. J. Held, M. A. Mueller, S.-C. Li, and H. Mongia, "Data-Driven Model for NO_x, CO and UHC Emissions for a Dry Low Emissions Gas Turbine Combustor," AIAA 2001-3425 ((2001).
- [9] W. A. Eckerle, "Soot Loading in a Generic Gas Turbine Combustor," AIAA 87-0297 (1987).
- [10] T. C. Fang, C. M. Megaridis, W. A. Sowa, and G. S. Samuelsen, "Soot Morphology in a Liquid-Fueled Swirl-Stabilized Combustor," *Combust. Flame* **112**, 312-328 (1998).
- [11] J. D. Black, "Laser Induced Incandescence Measurements of Particles in Aero-Engine Exhausts," SPIE Vol. 3821, EUROPTO Conference on Environmental Sensing and Applications, Munich, Germany (1999).
- [12] D. R. Snelling, K. A. Thomson, G. J. Smallwood, and O. L. Gulder, "Two-Dimensional Imaging of Soot Volume Fraction in Laminar Diffusion Flames," *Appl. Opt.* **38**, 2478-1485 (1999).
- [13] T. P. Jenkins, J. L. Bartholomew, P. A. DeBarber, P. Yang, J. M. Seitzman, and R. P. Howard, "A Laser-Induced Incandescence System for Measuring Soot Flux in Aircraft Engine Exhausts," AIAA 2002-3736 (2002).
- [14] R. J. Santoro, T. T. Yeh, J. J. Horvath, and H. G. Semerjian, "The Transport and Growth of Soot Particles in Laminar Diffusion Flames," *Combust. Sci. Technol.* **53**, 89-115 (1987).
- [15] D. L. Urban and G. M. Faeth, "Soot Research in Combustion Science: Introduction and Review of Current Work," AIAA 2001-0322 (2001).
- [16] Y.-H. Won, T. Kamimoto, H. Kobayashi, and H. Kosaka, "2-D Soot Visualization in Unsteady Spray Flame by Means of Laser Sheet Scattering Technique," SAE Tech. Paper 910223 (1991).
- [17] C. R. Shaddix, J. E. Harrington, and K. C. Smyth, "Quantitative Measurements of Enhanced Soot Production in a Flickering Methane / Air Diffusion Flame," *Combust. Flame* **99**, 723-732 (1994).
- [18] B. Quay, T.-W. Lee, T. Ni, and R. J. Santoro, "Spatially Resolved Measurements of Soot Volume Fraction Using Laser-Induced Incandescence," *Combust. Flame* **97**, 384-392 (1994).
- [19] R. L. Vander Wal and K. J. Weiland, "Laser-Induced Incandescence: Development and Characterization Towards a Measurement of Soot-Volume Fraction," *Appl. Phys. B* **59**, 445-452 (1994).

- [20] M. S. Brown, T. R. Meyer, J. R. Gord, V. M. Belovich, and W. M. Roquemore, "Laser-Induced Incandescence Measurements in the Reaction Zone of a Model Gas Turbine Combustor," AIAA 2002-0393 (2002).
- [21] K. C. Smyth, J. H. Miller, R. C. Dorfman, W. G. Mallard, and R. J. Santoro, "Soot Inception in a Methane/Air Diffusion Flame as Characterized by Detailed Species Profiles," *Combust. Flame* **62**, 157-181 (1985).
- [22] F. Cignoli, S. Benecchi, and Z. Giorgio, "Simultaneous One-Dimensional Visualization of OH, Polycyclic Aromatic Hydrocarbons, and Soot, in a Laminar Diffusion Flame," *Opt. Lett.* **17**, 229-231 (1992).
- [23] W.-P. Shih, J. G. Lee, and D. A. Santavicca, "Stability and Emissions Characteristics of a Lean Premixed Gas Turbine Combustor," in the Twenty-Sixth Symposium (International) on Combustion (The Combustion Institute, Pittsburg, PA, 1996).
- [24] R. E. Foglesong, T. R. Frazier, L. M. Flamand, J. E. Peters, and R. P. Lucht, "Flame Structure and Emissions Characteristics of a Lean Premixed Gas Turbine Combustor," AIAA 99-2399 (1999).
- [25] R. P. Lucht, D. W. Sweeney, and N. M. Laurendeau, "Laser-Saturated Fluorescence Measurements of OH Concentration in Flames," *Combust. Flame* **50**, 189-205 (1983).
- [26] C. D. Carter, G. B. King, and N. M. Laurendeau, "Saturated Fluorescence Measurements of the Hydroxyl Radical in Laminar High-Pressure $C_2H_6/O_2/N_2$ Flames," *Appl. Opt.* **31**, 1511-1522 (1992).
- [27] M.S. Brown and W.L. Roberts, "Single-Point Thermometry in High Pressure, Sooting, Combustion Environments," *J. Prop. Power* **15**, 119-127 (1999).
- [28] M. S. Brown, Y. Li, W. Roberts, and J. R. Gord, "Analysis of Transient-Grating Signals for Reacting-Flow Applications," *Appl. Opt.* **42**, 566-578 (2003).
- [29] H. J. Eichler, P. Gunter, and D. W. Pohl, *Laser-Induced Dynamic Gratings*, Springer-Verlag, 1986.
- [30] N.E. Molevich and V.E. Nenashev, "Effect of the Bulk Viscosity on the Sound Propagation in Nonequilibrium Suspensions of Microparticles in Gas," *Acoust. Phys.* **46**, 450-455 (2000).

Diode-laser-based ultraviolet-absorption sensor for high-speed detection of the hydroxyl radical

Thomas N. Anderson and Robert P. Lucht

School of Mechanical Engineering, Purdue University, 585 Purdue Mall, West Lafayette, Indiana 47907

Terrence R. Meyer and Sukesh Roy

Innovative Scientific Solutions, Inc., 2766 Indian Ripple Road, Dayton, Ohio 45440

James R. Gord

Air Force Research Laboratory, Propulsion Directorate, Wright-Patterson Air Force Base, Ohio 45433

Received December 2, 2004

A new diode-laser-based UV-absorption sensor for high-speed detection of the hydroxyl radical (OH) is described. The sensor is based on sum-frequency generation of UV radiation at 313.5 nm by mixing the output of a 763-nm distributed-feedback diode laser with that of a 532-nm high-power, diode-pumped, frequency-doubled Nd:YVO₄ laser in a β -barium borate crystal. Approximately 25 μ W of UV radiation is generated and used to probe rotational transitions in the $A^2\Sigma^+ - X^2\Pi$ ($v'=0, v''=0$) electronic transition of OH. Single-sweep, single-pass measurements of temperature and OH concentration in a stoichiometric C₂H₄-air flame are demonstrated at rates up to 20 kHz. © 2005 Optical Society of America
OCIS codes: 120.1740, 190.1900, 300.1030, 300.6260, 300.6540.

A number of tunable diode-laser absorption spectroscopy systems developed for detection of the hydroxyl radical (OH) have amply demonstrated the utility of these compact, rugged sensors for combustion diagnostics.^{1–7} Previous OH sensors have focused on rovibrational transitions in the near-IR^{1–3} and mid-IR⁴ or on electronic transitions in the UV.^{5–7} UV detection of flame radicals is optimal because of the large absorption cross sections of the electronic transitions and because interference from other major combustion products (e.g., H₂O, CO₂) is eliminated. In recent work, nonlinear optics techniques for generating UV radiation have been demonstrated in realistic combustion environments.⁸ However, previous UV and IR tunable diode-laser absorption spectroscopy measurements of OH have been limited to slow speeds (0.05–1 Hz) because of time averaging or lock-in detection. For high-speed measurements in unsteady flames, previous investigations required the use of picosecond time-resolved laser-induced fluorescence.⁹ By implementing a sum-frequency-mixing scheme with a newly available distributed-feedback (DFB) diode laser, we are able to generate UV radiation with tuning rates up to 20 kHz. We describe in this Letter the development of a compact diode-laser-based UV-absorption sensor for high-speed, quantitative, *in situ* measurements of OH concentration and temperature in flames.

The experimental layout of the OH sensor is shown in Fig. 1. The entire optical system was mounted on a 61 cm × 61 cm optical breadboard. We generated UV laser radiation near 313.5 nm by sum-frequency mixing the output of a high-power, diode-pumped, frequency-doubled Nd:YVO₄ laser at 532 nm with the output of a tunable DFB diode laser at 763 nm in a β -barium borate crystal. A half-wave plate and polarizer combination was used to attenuate the high-

power 532-nm beam during alignment, and half-wave plates in both beam paths allowed rotation of the polarization to vertical, as required for type I phase matching. After passing through a Faraday isolator, the 763-nm beam was upcollimated with a telescope ($f=-100$ mm and $f=200$ mm) to match the spot size and focal point of the 532-nm beam in the 5 mm × 7 mm × 6 mm crystal. The two beams were overlapped and focused into the crystal with an $f=50$ mm BK7 lens, and the UV output was recollimated with an $f=50$ mm fused-silica lens. Typically, an estimated 25 μ W of UV radiation was generated in the crystal with powers of 10 W and 35 mW for the 532- and 763-nm lasers, respectively. The UV output was then separated from the fundamental beams with two dichroic mirrors, and the residual 763- and 532-nm laser radiation was eliminated by narrow-band interference filters centered at 313 nm. The alignment procedure for a similar system is described by Hanna *et al.*¹⁰

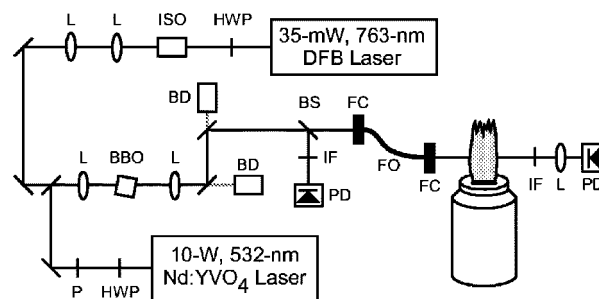


Fig. 1. Optical layout for the OH sensor system: BBO, β -barium borate crystal; BD, beam dump; BS, beam splitter; FC, fiber collimator; FO, fiber-optic cable; HWP, half-wave plate; IF, interference filter; ISO, isolator; L, lens; P, polarizer; PD, photodiode.

A beam splitter was used to reflect 30% of the UV output into a reference detector. The remaining 70% was coupled into a 2-m-long, 0.6-mm-core fused-silica fiber, pitched across the flame, sent through an interference filter, and focused onto a second detector with an $f=75$ mm fused-silica lens. Both detectors were UV-enhanced silicon p-i-n photodiodes built into a transimpedance amplifier circuit. The voltage output from each detector was filtered and amplified with a low-pass electronic preamplifier-filter before being acquired on a personal computer with a 10-MHz analog input-output card and LabVIEW software. An etalon with a free spectral range of 2 GHz was employed to monitor the frequency of the DFB laser during scanning.

Raw data were processed in a manner similar to that employed in Ref. 8, in which the ratio of the voltages from the signal and reference detectors during a scan in the flame was normalized by the ratio of the voltages from the signal and reference detectors during air scans acquired immediately after the flame was extinguished. We accounted for photodiode-bias and flame-emission offsets by subtracting the baseline voltage of each detector from the raw signals before processing. The etalon output was used to convert the processed data from time to frequency domain for spectral fitting.

Measurements of OH were performed in a steady, flat, uniform, near-adiabatic C_2H_4 -air flame stabilized on a Hencken burner. The DFB laser was tuned to 762.96 nm to produce UV radiation in resonance with the $P_2(10)$ line in the $(v'=0, v''=0)$ band of the $A^2\Sigma^+ - X^2\Pi$ electronic transition of OH at 313.526 nm ($31\,895.31\text{ cm}^{-1}$). We scanned the wavelength across the transition at rates of 2–20 kHz by modulating the injection current of the DFB laser with a triangle-wave function at frequencies of 1–10 kHz. Typical 2-kHz average and 20-kHz single-sweep absorption spectra of OH in the flame are shown in Figs. 2 and 3, respectively, for an equivalence ratio of $\Phi=1.0$ and a

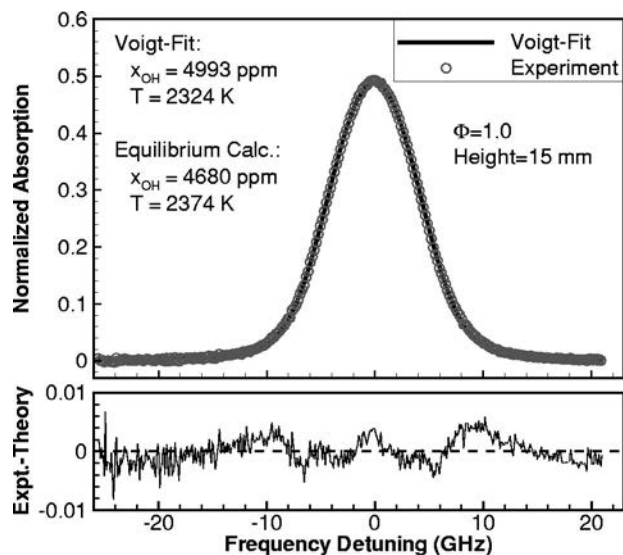


Fig. 2. Comparison of a 38-sweep average OH absorption spectrum acquired at 2 kHz in a C_2H_4 -air flame and the best-fit theoretical absorption spectrum.

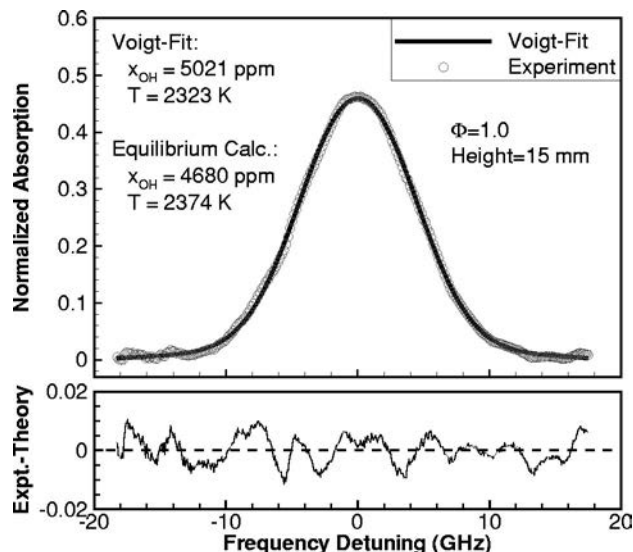


Fig. 3. Single-sweep OH absorption spectrum acquired at 20 kHz in a C_2H_4 -air flame. The theoretical spectrum is convolved with a Gaussian instrument function.

height of 15 mm above the burner. Figures 2 and 3 also show OH concentrations and temperatures from best-fit theoretical spectra.

The numerical algorithm used to calculate the theoretical spectra is described in detail in Ref. 8. The measured path length, pressure, and calculated collision width were fixed, whereas the temperature and OH-concentration values were determined using a least-squares fit of a Voigt profile to the data. This approach is accurate for demonstration purposes since the composition of the flame is close to equilibrium and the collision width can be calculated accurately with known collision-broadening coefficients for the major species.^{11–13} As shown in Fig. 2, excellent agreement is achieved between the experimental and theoretical spectra. The slight gull-wing-shaped residual is expected because the Voigt profile does not account for collisional-narrowing effects.^{11–13} When the major species and hence the collision width are unknown, a more accurate model, such as the Galatry profile, must be used to account for these effects.

To fit data acquired at 20 kHz, as in Fig. 3, the theoretical absorption line shape was convolved with a Gaussian instrument function with a FWHM of 0.127 cm^{-1} . This accounted for the slight artificial broadening introduced into the 20-kHz data by the low cutoff frequency of the electronic filter, which was required to reduce high-frequency electromagnetic interference in the photodiode circuit. No differences in linewidth were detected between unfiltered spectra at 2 and 20 kHz, indicating that the broadening was due solely to electronic filtering. We determined the Gaussian instrument function by comparing averaged filtered and unfiltered spectra.

Measurements with the sensor were found to be accurate when compared with equilibrium calculations. The average and single-sweep best-fit temperatures of 2324 and 2323 K, respectively, agree well with the equilibrium flame temperature of 2374 K. A similar 20–50-K temperature difference below equilibrium

was previously observed in coherent anti-Stokes Raman scattering measurements reported by Roy *et al.*¹⁴ for H₂-air-CO₂ flames in the same burner. The average and single-sweep OH concentrations were found to be 4993 and 5021 parts in 10⁶ (ppm), respectively, which are 7% higher than the equilibrium value of 4680 ppm. These values are also reasonable, given the proximity of the measurement location to the burner surface.

To assess random error in the sensor measurements, the time series of OH concentration and temperature shown in Fig. 4 was assembled from four separate, consecutive scans in the flame (indicated by vertical dashed lines). Assuming that the flame stabilized on the Hencken burner is steady and laminar, the fluctuations observed in the time series can be attributed to random error in the fitting process. Averaging two consecutive laser sweeps was found to reduce this random noise and also accounted for alternating asymmetries in the experimental absorption line shapes that were introduced by the electronic filter. The rms standard deviations in the 10-kHz temperature and OH-concentration measurements were 42 K and 119 ppm, respectively.

The overall uncertainty in the time-resolved measurements is a combination of random and systematic errors. Systematic propagation of measurement errors was calculated to be 45 K and 150 ppm, assuming uncertainties of 2.5%, 0.67 kPa, and 10% in the path length, pressure, and collision width, respectively. If the systematic and random errors are uncorrelated, they add in quadrature, yielding an

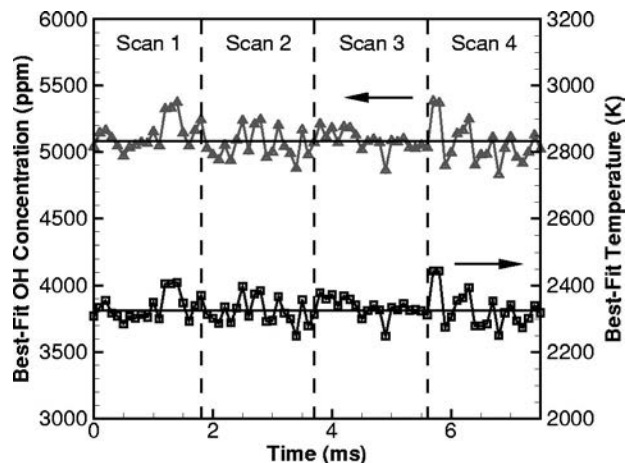


Fig. 4. 10-kHz time series of OH concentration and temperature assembled from four consecutive scans in a steady C₂H₄-air flame at $\Phi=1.0$ and a height of 15 mm.

overall uncertainty in the time-resolved measurements of temperature and OH concentration of 62 K (2.7%) and 191 ppm (3.8%), respectively.

In summary, we have successfully developed a new diode-laser-based UV-absorption DFB laser. Single-laser-sweep absorption spectra of OH were recorded at rates up to 20 kHz, demonstrating the potential of this sensor for making accurate, time-resolved measurements of OH concentration and temperature in unsteady flames.

The authors are grateful to Ralph Swaine at Coherent, Inc., for providing the Verdi laser system. Funding for this work was provided by the Air Force Research Laboratory, Propulsion Directorate, under contract F33615-00-C-2020, by the Air Force Office of Scientific Research (Julian Tishkoff, Program Monitor), and by a National Science Foundation Graduate Research Fellowship. T. N. Anderson's email address is tanderson@purdue.edu.

References

1. B. L. Upschulte, D. M. Sonnenfroh, and M. G. Allen, *Appl. Opt.* **38**, 1506 (1999).
2. T. Aizawa, T. Kamimoto, and T. Tamaru, *Appl. Opt.* **38**, 1733 (1999).
3. T. Aizawa, *Appl. Opt.* **40**, 4894 (2001).
4. G. Pesce, G. Rusciano, and A. Sasso, *Chem. Phys. Lett.* **374**, 425 (2003).
5. D. B. Oh, *Opt. Lett.* **20**, 100 (1995).
6. H. R. Barry, B. Bakowski, L. Corner, T. Freegarde, O. T. W. Hawkins, G. Hancock, R. M. J. Jacobs, R. Peverall, and G. A. D. Ritchie, *Chem. Phys. Lett.* **319**, 125 (2000).
7. G. J. Ray, T. N. Anderson, J. A. Caton, R. P. Lucht, and T. Walther, *Opt. Lett.* **26**, 1870 (2001).
8. T. N. Anderson, R. P. Lucht, R. Barron-Jimenez, S. F. Hanna, J. A. Caton, T. Walther, S. Roy, M. S. Brown, J. R. Gord, I. Critchley, and L. Flamand, *Appl. Opt.* **44**, 1491 (2005).
9. M. W. Renfro, S. D. Pack, G. B. King, and N. M. Laurendeau, *Combust. Flame* **115**, 443 (1998).
10. S. F. Hanna, R. Barron-Jimenez, T. N. Anderson, R. P. Lucht, J. A. Caton, and T. Walther, *Appl. Phys. B: Lasers Opt.* **75**, 113 (2002).
11. E. C. Rea, Jr., A. Y. Chang, and R. K. Hanson, *J. Quant. Spectrosc. Radiat. Transf.* **37**, 117 (1987).
12. E. C. Rea, Jr., A. Y. Chang, and R. K. Hanson, *J. Quant. Spectrosc. Radiat. Transf.* **41**, 29 (1989).
13. W. J. Kessler, M. G. Allen, and S. J. Davis, *J. Quant. Spectrosc. Radiat. Transf.* **49**, 107 (1993).
14. S. Roy, T. R. Meyer, R. P. Lucht, M. Afzelius, P. Bengtsson, and J. R. Gord, *Opt. Lett.* **29**, 1843 (2004).

ADVANCED COHERENT ANTI-STOKES RAMAN SCATTERING (CARS) TECHNIQUES FOR SIMULTANEOUS SPECIES AND TEMPERATURE MEASUREMENTS

R.P. Lucht

School of Mechanical Engineering, Purdue University
West Lafayette, IN 47907

S. Roy and T. R. Meyer

Innovative Scientific Solutions, Inc., 2766 Indian Ripple Road
Dayton, OH 45440

J. R. Gord

Air Force Research Laboratory, Propulsion Directorate
Wright-Patterson Air Force Base, OH 45433, USA

ABSTRACT

The use of coherent anti-Stokes Raman scattering (CARS) spectroscopy for temperature measurements in combustion systems ranging from laboratory flames to practical combustors is well-established. In the great majority of these temperature measurement experiments, the two pump beams are obtained from the same laser source and thus have the same frequency. In the CARS process, the coherent Raman polarization in the medium is established by the interaction of one pump beam with the Stokes beam. The other pump beam is scattered from this induced polarization to produce the CARS signal, and there is no inherent requirement that the two pump beams have the same frequency. The measurement capabilities of the CARS technique can be greatly extended by using different frequencies for each of the pump beams. In dual-pump CARS, the frequencies of the two pump beams are selected so that the frequency differences between the Stokes beam and the pump beams correspond to the Raman resonances for two different species. Concentrations can be determined very accurately from the ratios of the two CARS signals. Dual-pump CARS has been used in a wide variety of experiments for accurate species concentration measurements. Other techniques that will be discussed include triple-pump CARS, dual-pump, dual-broadband CARS, and electronic-resonance-enhanced CARS. The use of high-resolution single-pulse CARS for temperature and pressure measurements in supersonic flows will be briefly discussed. The development of these nanosecond-laser-based techniques has been enabled by the continuing improvements in the pulse energy, beam quality, and injection-seeding of Q-switched Nd:YAG lasers. Finally, the potential application of femtosecond CARS for high-data-rate measurements of temperature and species in reacting flows is discussed.

INTRODUCTION

Coherent anti-Stokes Raman scattering (CARS) spectroscopy has been widely used for measuring temperature and the concentration of major species in reacting flows [1]. Measurements have also been performed using CARS to determine the temperature in practical combustors and internal combustion engines [2-8]. In practical combustors, measurements of temperature using N₂ CARS are common due to its abundance everywhere in the combustor. However, applying the N₂ CARS technique for the measurement of temperature in practical combustors is always challenging mainly due to the following three reasons: (1) highly luminous environments, (2) steering of the laser beams due to density gradients, and (3) absorption of the CARS signal by the strong C₂ SWAN bands [1, 9]. Interference from flame luminosity can be minimized either by using a mechanical shutter in front of the spectrometer [10] or by using an

interline-transfer charge-coupled device (CCD) camera for the data acquisition [11]. In practical combustors with highly sooting environments, the effect of beam steering could be greatly reduced by arranging the CARS beams in a collinear fashion rather than in a folded BOXCAR geometry [1]. The absorption of the CARS signal by the strong C_2 Swan band could be avoided by shifting the CARS signal generation to a different wavelength region rather than near 473 nm.

Dual-pump CARS, first proposed by Lucht [12], allows a shift in the CARS signal output away from 473 nm by shifting one of the pump frequencies away from 532 nm. This technique also allows simultaneous concentration measurements of a second species such as O_2 , CO_2 , H_2 and CO in addition to the temperature measurements either using the nitrogen part of the CARS spectrum or using the full spectrum. The wavelength of the second pump beam is selected such that the CARS spectra for the two species under study are observed at nearly the same frequency, enabling detection with a single spectrometer and charge-coupled-device (CCD) camera and eliminating systematic errors due to wavelength dependence of the detection system efficiency. The dual-pump CARS technique has been applied for the simultaneous measurement of N_2/O_2 [12-13], N_2/H_2 [14], N_2/CH_4 [15], and N_2/CO_2 [16].

The dual-pump CARS technique was applied by Lucht et al. [17] and Roy et al. [18] in the exhaust stream of a practical combustor for measuring temperature and CO_2 concentration from a single-laser-shot. Several other CARS techniques such as triple-pump CARS [19], dual broadband rotational CARS [20-22], and simultaneous vibrational and rotational CARS [23-26] have also been used as tools for temperature and multiple-species concentration measurements. High-resolution CARS has been used for simultaneous measurement of density, temperature, and flow speed in underexpanded supersonic jet flows [27].

SURVEY OF ADVANCED CARS TECHNIQUES

DUAL-PUMP CARS

The dual-pump CARS technique allows for concentration measurements of two species as well as for simultaneous, accurate temperature measurements at both low and high temperature. Two examples of dual-pump CARS measurements are discussed here. Lucht et al. [17] and Roy et al. [18] used dual-pump CARS to perform simultaneous N_2/CO_2 measurements in a variety of laboratory flames and in a JP-8 fueled combustor. The experimental apparatus for the dual-pump CARS measurements of CO_2 and N_2 is shown in Fig. 1.

The pump source for the measurements was a Spectra-Physics GCR 5 injection-seeded,

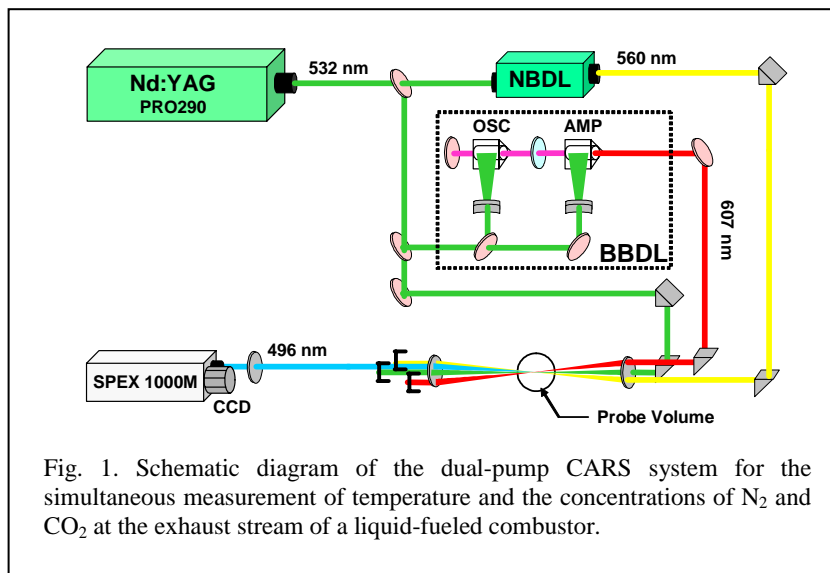


Fig. 1. Schematic diagram of the dual-pump CARS system for the simultaneous measurement of temperature and the concentrations of N_2 and CO_2 at the exhaust stream of a liquid-fueled combustor.

Q-switched Nd:YAG laser with a repetition rate of 10 Hz. The pulse energy of the 532-nm second-harmonic output of the Nd:YAG laser was approximately 600 mJ. A narrowband dye laser and a broadband dye laser were pumped using approximately 200 mJ and 300 mJ, respectively, of the 532-nm radiation from the Nd:YAG laser. The narrowband dye laser was a Continuum ND6000, which has a

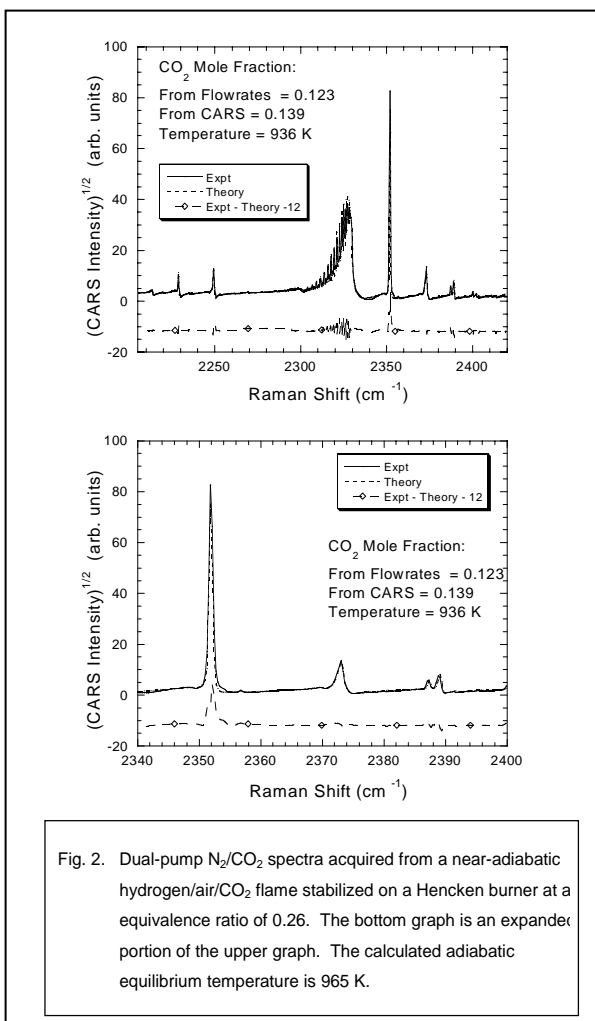


Fig. 2. Dual-pump N₂/CO₂ spectra acquired from a near-adiabatic hydrogen/air/CO₂ flame stabilized on a Hencken burner at a equivalence ratio of 0.26. The bottom graph is an expanded portion of the upper graph. The calculated adiabatic equilibrium temperature is 965 K.

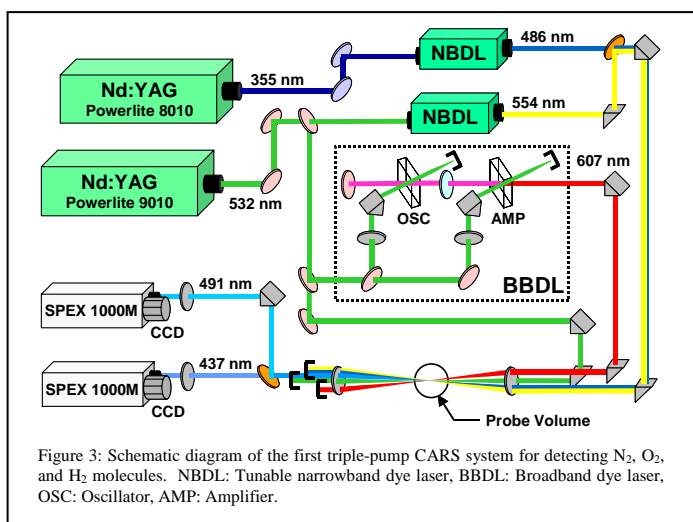
spectrometer equipped with a 2400-line-per-mm holographic grating. The wavelength of the N₂ and CO₂ CARS signals was approximately 496 nm. The wavelength of the N₂ CARS signal was adjusted by tuning the wavelength of the narrowband dye laser. The wavelength of the CO₂ CARS signal did not vary as the narrowband dye laser wavelength was tuned, however. Therefore, the frequency separation of the N₂ and CO₂ CARS signals could be adjusted and optimized so that the main features for the two molecules did not overlap.

The CARS signal was detected using a 16-bit back-illuminated PixelVision SpectraVideo CCD camera with a 165 × 1100 array of pixels (each pixel 24-μm square) at the exit plane of the spectrometer. To acquire single-laser-shot spectra at the laser repetition rate of 10 Hz, charge within each of the 1100 columns of the CCD array was accumulated in the serial register before readout; the collected charge was then digitized at a rate of 50 kpix/s. This thermo-electrically cooled CCD camera exhibited very low read noise (approximately 1.5 counts out of 65,536) and dark current (approximately 2 counts/sec), while exhibiting a quantum efficiency of approximately 80% at 500 nm.

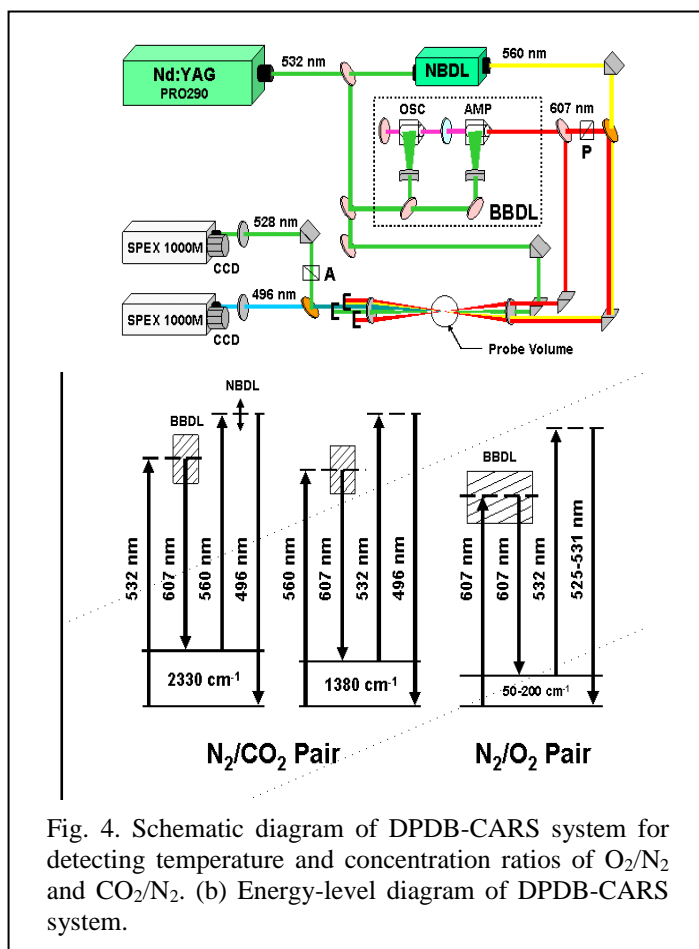
Measurements were performed in near-adiabatic hydrogen/air/CO₂ flames stabilized on a Hencken burner to obtain dual-pump CO₂/N₂ CARS spectra over a wide range of temperatures. The flowrate of the CO₂ was held constant while the hydrogen flowrate and, consequently, the temperature was varied over a wide range. Because of the near-adiabatic nature of the Hencken burner, the measured CARS temperatures can be compared with calculated adiabatic equilibrium temperatures. As shown in Fig. 2, the spectra were acquired with very good signal-to-noise ratios, and the agreement between theory and experiment is excellent.

bandwidth of 0.08 cm⁻¹. The wavelength of the narrowband dye laser was 560 nm. The broadband dye laser was a modeless design with side-pumped Bethune cells for both the "oscillator" and amplifier [20]. The spectral output of the broadband dye laser was centered at 607 nm, and the bandwidth was approximately 150 cm⁻¹ full-width-at-half-maximum (FWHM).

The CARS signal was generated using the three-dimensionally phase-matched arrangement shown in Fig. 1 (folded BOXCARS). The pulse energies for the 532-nm, 560-nm, and 607-nm beams at the CARS probe volume were typically 30 mJ, 30 mJ, and 15 mJ, respectively. The CARS focusing lens had a focal length of 400 mm. At the probe volume the measured diameter of the 532-nm beam was approximately 90±10 μm, while the 560-nm and 607-nm beam focal diameters were approximately 130±15 μm. The spatial resolution of the CARS measurements is estimated to be approximately 2 mm, the interaction length over which approximately 80% of the CARS signal is generated. After passing through the CARS probe volume, the pump, Stokes, and CARS signal beams were recollimated using a 400-mm-focal-length lens. The pump and Stokes beams were directed into beam dumps and the CARS signal beam was then focused onto the entrance slit of a SPEX 1-m



vibrational transitions of N_2 , H_2 and O_2 molecules. This system is essentially a superposition of two dual-pump CARS systems using four laser beams to generate CARS signals near two distinct wavelengths. Both wavelength regions exhibit an N_2 CARS signal along with the CARS signal from another target molecule. Each pair of CARS signals is generated over a relatively narrow wavelength region and can be captured with fixed wavelength detection. For the proof-of-concept measurements, experiments were carried out in an atmospheric-pressure laminar H_2 -air diffusion flame.



TRIPLE-PUMP CARS

Triple-pump CARS is a combination of two dual-pump CARS systems. Techniques such as triple-pump CARS are feasible for laboratories with two Q-switched Nd:YAG lasers; only one of these lasers need be injection-seeded. The triple-pump CARS technique allows for concentration measurements of three species as well as for simultaneous, accurate temperature measurements at both low and high temperature. The first triple-pump CARS system, shown in Fig. 3, was used to probe the ro-

In the second triple-pump CARS system the rotational transitions of N_2 and O_2 molecules and the ro-vibrational transitions of the N_2 and CO_2 molecules were probed. In this system a dual-broadband rotational CARS system is superimposed on a dual-pump CARS system that uses four laser beams to generate CARS signals near two distinct wavelengths. One of the pump beams in this system is obtained from a broadband dye laser, allowing us to probe rotational and ro-vibrational transitions simultaneously. This technique can be used to obtain very accurate temperature measurements both at low and high temperatures. In the combustion zone or the exhaust of a real combustor, there is a wide spatial and temporal variation of temperature due to the inherent turbulent nature of the flow field. Under these circumstances, the rotational spectra of N_2/O_2 will provide better temperature accuracy at lower temperatures, generally below 1500K [15]; whereas the ro-vibrational spectra

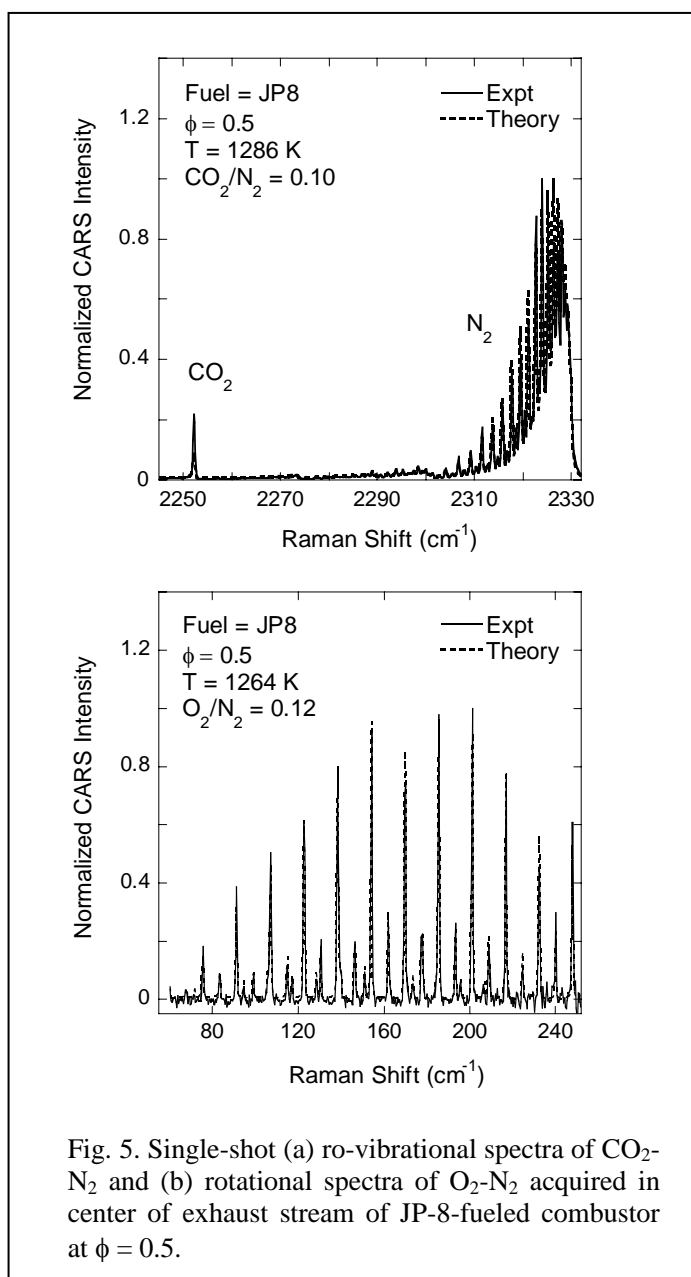


Fig. 5. Single-shot (a) ro-vibrational spectra of CO_2 - N_2 and (b) rotational spectra of O_2 - N_2 acquired in center of exhaust stream of JP-8-fueled combustor at $\phi = 0.5$.

of N_2/CO_2 will provide improved temperature accuracy at higher temperatures as population is transferred to higher energy levels. The proof-of-concept measurements using this second triple-pump CARS experiment were carried out in an atmospheric-pressure near-adiabatic hydrogen-air flame seeded with CO_2 and stabilized on a Hencken burner. Single-shot spectra recorded in the exhaust stream of a JP-8-fueled atmospheric pressure combustor are shown in Fig. 5.

HIGH-RESOLUTION CARS

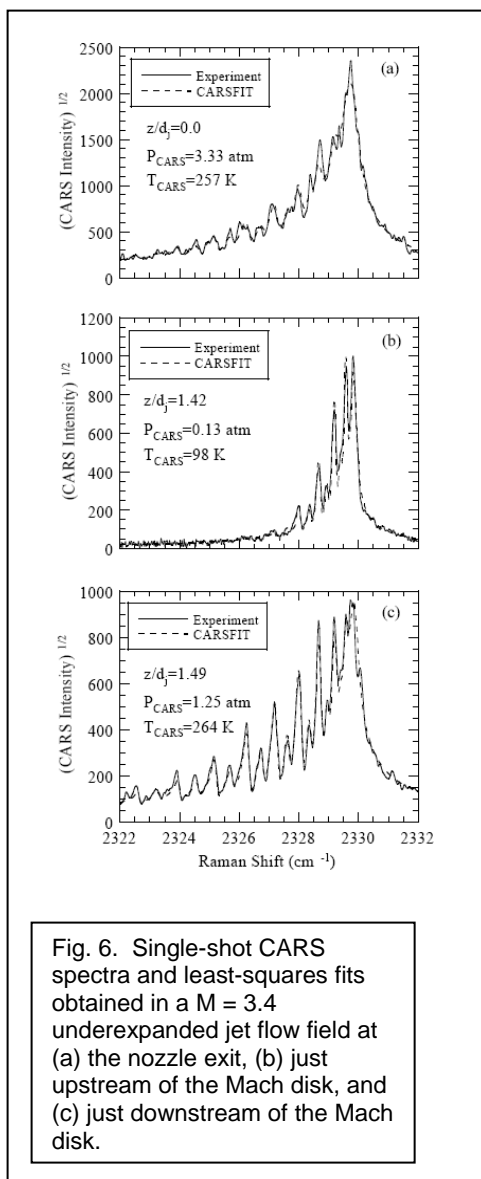
MEASUREMENTS IN

SUPERSONIC FLOWS

Mean and instantaneous measurements of pressure, temperature, and density were acquired in the flowfield of an underexpanded sonic jet using the high-resolution N_2 coherent anti-Stokes Raman scattering (CARS) technique. This non-intrusive method resolves the pressure- and temperature-sensitive rotational transitions of the $v=0 \rightarrow 1$ N_2 Q-branch to within $\Delta\omega = 0.10 \text{ cm}^{-1}$. This high-resolution for broadband CARS was achieved by using an injection-seeded, Q-switched Md:YAG laser as the pump laser, and by using a 1.25-m spectrometer and a relay lens with a magnification factor of seven to

image the spectrometer exit slit onto an unintensified CCD detector. To extract thermodynamic information from the experimental spectra, theoretical spectra, generated by an N_2 spectral modeling program, were fit to the experimental spectra in a least-squares manner. The precision and accuracy of the single-shot CARS pressure measurements increase at sub-atmospheric conditions. Typical single-shot CARS spectra from the underexpanded jet flow field are shown in Fig. 6. The pressure and temperature change drastically as the flow accelerates after leaving the nozzle exit. The expansion is nearly isentropic, and the thermodynamic conditions of $T = 98 \text{ K}$ and $P = 0.13 \text{ atm}$ just upstream of the Mach disk correspond to a Mach number of approximately 3.4.

The high-resolution CARS measurements were compared with the results of a Reynolds-averaged Navier Stokes Computational Fluid Dynamic (RANS CFD) simulation. Along the centerline of the underexpanded jet, the agreement between the mean CARS $P/T/\rho$ measurements and similar quantities extracted from the RANS CFD simulation is generally



excellent. This CARS technique is able to capture the low-pressure and low-temperature conditions of the $M=3.4$ flow entering the Mach disk, as well as the subsonic conditions immediately downstream of this normal shock.

ELECTRONIC-RESONANCE-ENHANCED CARS

MEASUREMENTS OF MINOR SPECIES

We have also investigated the application of electronic-resonance-enhanced (ERE) CARS for the measurement of minor species [29]. A dual-pump ERE CARS technique for the measurement of minor species concentrations was demonstrated. The frequency difference between a visible Raman pump beam and Stokes beam was tuned to a vibrational Q-branch Raman resonance of nitric oxide (NO) to create a Raman polarization in the medium. An ultraviolet probe beam (the second pump beam in the CARS process) was tuned into resonance with rotational transitions in the $(1,0)$ band of the $A^2\Sigma^+ - X^2\Pi$ electronic transition at 236 nm, and the CARS signal is thus resonant with transitions in the $(0,0)$ band. The energy level schematic for the ERE CARS process in NO is shown in Fig. 7.

The ERE CARS experimental system is shown in Fig. 8. We have demonstrated the detection of ERE CARS signals from NO in concentrations as low as 100 ppm, as shown in Fig. 9. Spectral scans were obtained with a fixed Stokes frequency as the ultraviolet pump frequency was varied, and with a fixed ultraviolet pump frequency as the Stokes frequency was varied. Good agreement between theory and experiment was obtained for both these cases. A spectrum obtained by scanning the ultraviolet probe beam is shown in Fig. 10. The use of the dual-pump ERE CARS technique allows us to

separate clearly the process by which the Raman coherence is induced in the medium from the ERE process where the Raman coherence is probed with a second pump beam. This separation simplifies considerably the theoretical modeling of the ERE CARS process, and may enable sensitive, selective detection of small polyatomic molecules in flames and plasmas.

SUMMARY AND CONCLUSIONS

We have reviewed several CARS techniques developed to measure species concentrations or other thermodynamic parameters such as pressure in addition to temperature. Dual-pump and triple-pump CARS systems have been used to measure species concentrations for a number of different species as well as temperature. Single-shot measurements of species concentrations and temperature have been demonstrated for the species pairs CO_2/N_2 , H_2/N_2 , O_2/N_2 in a wide range of combustion systems ranging from laboratory flames to JP8-fueled combustion test stands. The development of dual- and triple-pump CARS systems has been enabled by a number of developments. The pulse energies available from commercial Q-

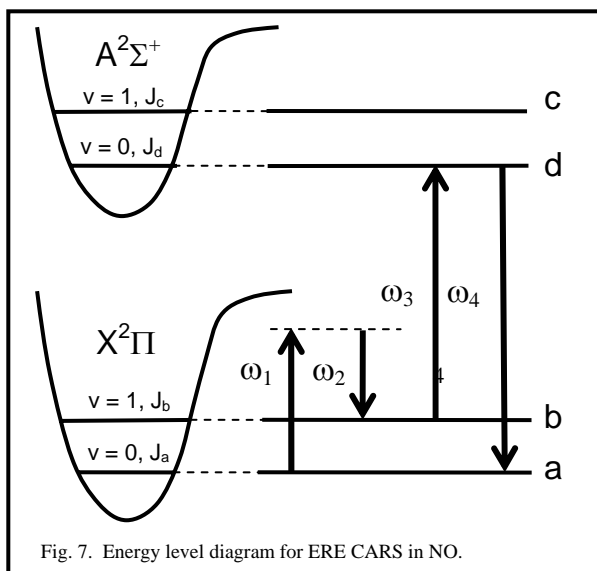


Fig. 7. Energy level diagram for ERE CARS in NO.

switched Nd:YAG laser systems has increased steadily to the point where systems with more than 1 J of pulse energy at 532 nm are now routinely available. With such high pulse energies it is easy to pump both a broadband and narrowband dye laser and obtain pulse energies that are more than sufficient for dual-pump CARS measurements, and it is feasible to perform triple-pump CARS using a single Nd:YAG laser to pump three dye lasers. In addition, reliable injection seeding systems are now available for these Nd:YAG laser systems; injection seeding ensures that the Nd:YAG laser radiation is single-longitudinal mode and results in a significant decrease in CARS noise. The development of CCD camera systems with excellent dynamic range and sensitivity has also increased the

accuracy and precision of CARS systems.

Our first NO ERE CARS measurements were performed with two narrowband dye lasers. These measurements were complicated considerably by the rapid degradation of the LD 490 laser dye used to produce the 472-nm beam. We are currently developing injection-seeded optical parametric generators (OPG) to produce tunable, single-longitudinal-mode pulsed laser radiation [30]. We anticipate that the use of these OPG systems will result in a significant decrease in the noise and therefore the detection limits for our ERE CARS measurements.

ACKNOWLEDGMENTS

Funding was provided by the Air Force Research Laboratory, Propulsion Directorate, Wright-Patterson AFB, under Contract Nos. F33615-D-03-M2829 and F33615-00-C-3020, and by the Air Force Office of Scientific Research (Dr. Julian Tishkoff, Program Monitor), Defense Advanced Research Project Agency (DARPA), by the U.S. Dept. of Energy, Office of Basic Energy Sciences, Division of Chemical Sciences, Geosciences, and Biosciences, and by the U. S. Army Research Office.

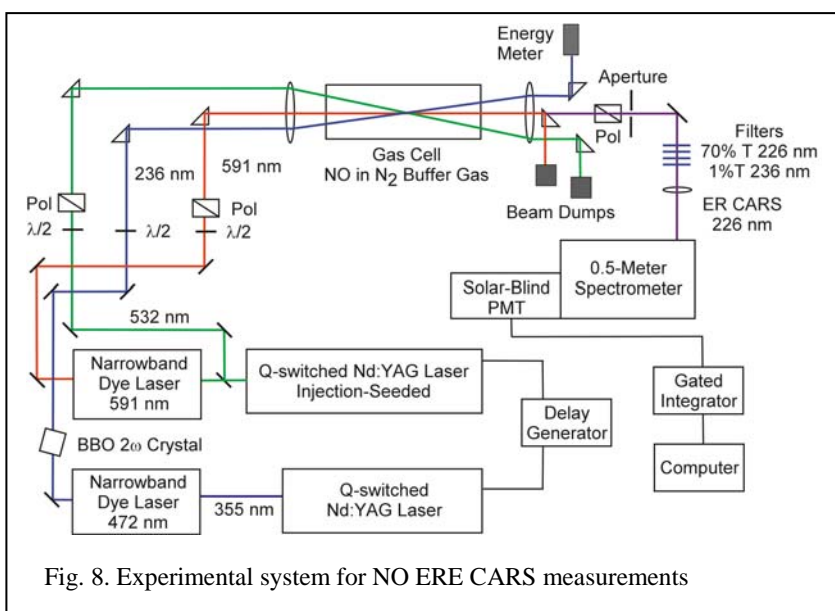
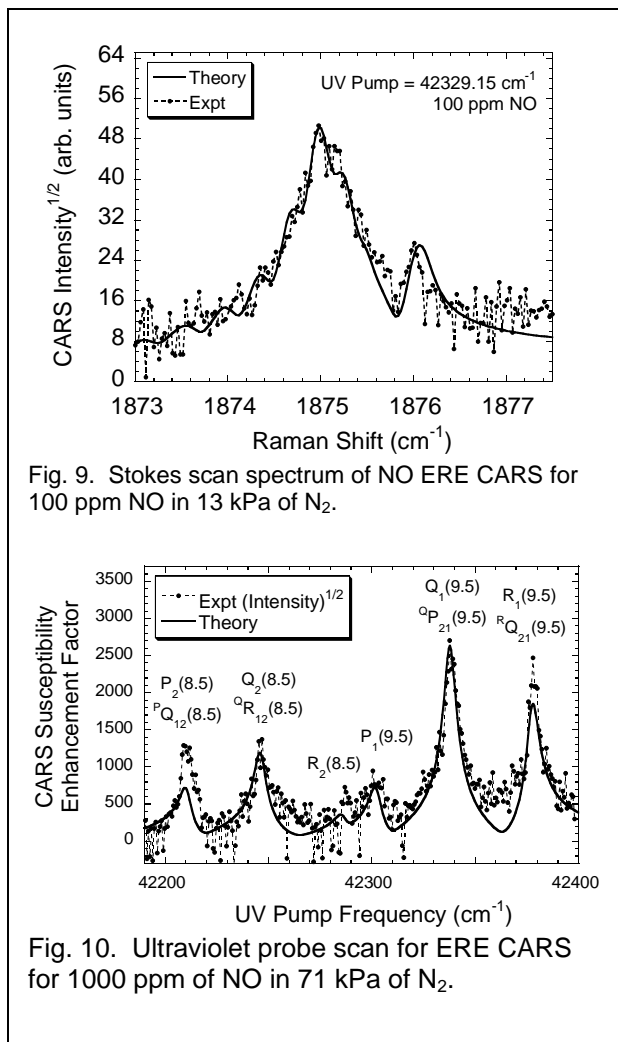


Fig. 8. Experimental system for NO ERE CARS measurements

REFERENCES

1. Fry, R. S. and Peters, S. T., **Burning Rates of Standard Solid Propellants for Gun Applications**, CPTR 99-69, CPIA/JHU, Columbia, MD (Sep 1999).
1. Eckbreth, A. C., **Laser Diagnostics for Combustion Temperature and Species**, Gordon and Breach Publishers, Amsterdam, The



- Netherlands (1988).
2. Takahashi, F., Schmoll, J. W., Switzer, G. L., and Shouse, D. T., *Twenty-Fifth Symposium (International) on Combustion*, The Combustion Institute, 1994, pp. 183-191.
3. Bood, J., Bengtsson, P.E., Mauss, F., Burgdorf, K., and Denbratt, I., *SAE Paper No: 971669*, 1997, pp. 1-12.
4. Goss, L. P., Trump, D. D., MacDonald, B. G., and Switzer, G. L., *Rev. Sci. Instrum.* 54:563-571 (1983).
5. Heneghan, S. P. and Vangsness, M. D., *Rev. Sci. Instrum.* 62(9):2093-2099 (1991).
6. Ball, D., Driver, H. S., Hutcheon, R. J., Lockett, R. D., and Robertson, G. N., *Optical Engineering* 33(9):2870-2874 (1994).
7. Hughes, P. M. J., Lacelle, R. J., and Parameswaran, T., *Combust. Sci. and Tech.* 105:131-145 (1995).
8. Klimenko, D. N., Clauss, W., Oswald, M., Smith, J., and Mayer, W., *Journal of Raman Spectroscopy* 33:900-905 (2002).
9. Dobbs, G. M., Boedeker, L. R., and Eckbreth, A. C., "Interference to CARS in highly sooting flames from C₂ absorption", *Eastern States Section of the Combustion Institute Technical Meeting*, Philadelphia, PA, 1985.
10. Roy, S., Kulatilaka, W. D., Lucht, R. P., Glumac, N. G., and Hu, T., *Combustion and Flame* 130:261-276 (2002).
11. Roy, S., Ray, G., and Lucht, R. P., *Applied Optics* 40:6005-6011 (2001).
12. Lucht, R. P., *Optics Letters* 12:78-80 (1987).
13. Hancock, R. D., Schauer, F. R., Lucht, R. P., and Farrow, R. L., *Applied Optics* 36:3217-3226 (1997).
14. Schauer, F. R., Ph.D. Thesis, University of Illinois at Urbana-Champaign, Urbana, Illinois, 1998.
15. Green, S. M., Rubas, P. J., Paul, M. A., Peters, J. E., and Lucht, R. P., *Applied Optics* 37:1690-1701 (1998).
16. Brüggemann, D., Wies, B., Zhang, X. X., Heinze, T., and Knoche, K. F., "CARS Spectroscopy for Temperature and Concentration Measurements in a Spark Ignition Engine," in *Combustion Flow Diagnostics*, D. F. G. Durão, M. V. Heitor, J. H. Whitelaw, and P. O. Witze, eds., Kluwer Academic, Dordrecht, The Netherlands, 1992, pp. 495-511.
17. Lucht R. P., Velur, V. N., Fiechtner, G. J., Carter, C.D., Grinstead, Jr., K. D., Gord, J. R., Danehy, P. M., and Farrow, R. L., *AIAA Journal* 41(3):679-686 (2003).
18. Roy, S., Meyer, T. R., Lucht, R. P., Belovich, V. M., Corporan, E., Gord, J. R., *Combust. Flame* 138, 273-284 (2004).
19. Roy, S., Meyer, T. R., Brown, M. S., Velur, V.N., Lucht, R. P., and Gord, J. R., *Opt. Comm.*, in press (2003).
20. Martinsson, L., Bengtsson, P.-E., and Aldén, M., *Applied Physics B* 62, 29-37 (1996).

21. Thumann, A., Schenk, M., Jonuscheit, J., Seeger, T., and Leipertz, A., *Applied Optics* 36:3500-3505 (1997).
22. Bood, J., Bengtsson, P.-E., and Aldén, M., *Applied Physics B* 70:607-620 (2000).
23. Yueh, F. Y. and Beiting, E. J., *Applied Optics* 27:3233-3243 (1988).
24. Bengtsson, P.-E., Martinsson, L., and Aldén, M., *Applied Spectroscopy* 49:188-192 (1995).
25. Seeger, T. and Leipertz, A., *Applied Optics* 35:2665-2671 (1996).
26. Brackmann, C., Bood, J., Bengtsson, P.-E., Seeger, T., Schenk, M., and Leipertz, A., *Applied Optics* 41:564-572 (2002).
27. M. A. Woodmansee, J. C. Dutton, and R. P. Lucht, *Applied Optics*, **39**, 6243-6256 (2000).
28. Palmer, R. E., The CARSFT Computer Code for Calculating Coherent Anti-Stokes Raman Spectra: User and Programmer Information, Sandia National Laboratories, Livermore, California, Report No. SAND89-8206, 1989.
29. S. F. Hanna, W. D. Kulatilaka, Z. Arp, T. Opatrný, M. O. Scully, J. P. Kuehner, and R. P. Lucht, *Appl. Phys. Lett.* **83**, 1887 (2003).
30. W. D. Kulatilaka, T. N. Anderson, T. L. Bougher, and R. P. Lucht, *Applied Physics B* **80**, 669-680 (2005).

Ballistic imaging of the liquid core for a steady jet in crossflow

Mark A. Linne, Megan Paciaroni, James R. Gord, and Terrence R. Meyer

A time-gated ballistic imaging instrument is used to obtain high-spatial-resolution, single-shot images of the liquid core in a water spray issuing into a gaseous crossflow. We describe further development of the diagnostic technique to improve spatial resolution and present images and statistics for various jets under crossflow experimental conditions (different Weber numbers). Series of these images reveal a near-nozzle flow field undergoing breakup and subsequent droplet formation by stripping. One can also detect signatures of spatially periodic behavior in the liquid core and formation of small voids during breakup. © 2005 Optical Society of America

OCIS codes: 190.3270, 280.1740, 280.2470, 280.2490, 290.7050.

1. Introduction

The process of fuel–air mixture preparation is key to flame stabilization and fuel-conversion efficiency in a wide variety of air- and ground-based power-generation systems. For example, flames in modern gas turbines that are fed by lean premixed prevaporized (LPP) fuel ducts are stabilized in recirculation zones that can shift with changes in load. Flow-field strain rates within the recirculation zones that exceed the extinction strain rate for the local fuel–air mixture can lead to reduced combustion efficiency and reduced static and dynamic stability. Moreover, localized heat release originating from nonuniform fuel-droplet distributions can potentially drive thermoacoustic instabilities, increasing heat transfer to the combustor wall and introducing the potential for significant damage. Mixture preparation has a controlling effect on emissions as well. Overly fuel rich mixing zones can produce large amounts of soot; mixing zones that fall outside the flammability limits are quenched and produce hydrocarbon and CO emis-

sions, and mixing zones near the stoichiometric fuel–air ratio produce high NO_x emissions associated with high temperatures. These performance considerations are all controlled by mixture preparation, a process that is not fully understood.

The work reported here focuses on steady, liquid sprays in crossflow that are relevant to gas-turbine LPP combustors, as one example. The characteristic geometry for an LPP duct incorporates the injection of liquid fuel into a high-temperature and -pressure air stream as depicted schematically in Fig. 1. The balance of aerodynamic drag, liquid inertia, surface tension, and viscous forces induces both deflection and deformation of the jet column. Deflection leads to a curved liquid-jet profile, breaking the liquid column into large segments near the point of curvature (called “column breakup”), and subsequent fragmentation. In contrast, deformation increases the frontal cross section of the jet column and increases the drag, which leads to stripping of smaller ligaments and fragments directly from the column surface (called “surface stripping”). The same forces cause secondary breakup of ligaments and fragments into droplets, which may break down even further before being evaporated. Small droplets are also entrained in the near-wall region owing to the wake flow that develops behind the liquid column.

The relevant global parameter used to capture this balance of forces is the jet Weber number based on the gas density (ρ_g), gas velocity (u_g), jet-orifice diameter (d), and liquid surface tension (σ_l):

$$We_g = \rho_g u_g^2 d / \sigma_l \quad (1)$$

M. A. Linne (Mark.Linne@forbrf.lth.se) and M. Paciaroni (Megan.Paciaroni@forbrf.lth.se) are with the Department of Combustion Physics, Lund Institute of Technology, SE-221 00 Lund, Sweden. J. R. Gord (James.Gord@wpafb.af.mil) is with the Air Force Research Laboratory, Propulsion Directorate, Wright-Patterson Air Force Base, Ohio. T. R. Meyer (Terrence.Meyer@wpafb.af.mil) is with Innovative Scientific Solutions, Inc., Dayton, Ohio 45440.

Received 1 February 2005; revised manuscript received 21 April 2005; accepted 22 April 2005.

0003-6935/05/316627-08\$15.00/0

© 2005 Optical Society of America

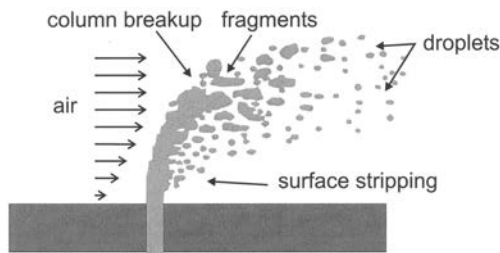


Fig. 1. Schematic of a liquid jet in crossflow of gas.

Gas-turbine-based jets in crossflow typically operate in the range of $100 < We_g < 2000$, which is a range dominated by shear breakup driven by aerodynamic drag. Both column breakup and surface stripping are included within the shear breakup mechanism. Which of the two dominates is determined by the liquid/air momentum flux ratio. Furthermore, liquid viscosity acts in opposition to inertial forces, and it can affect jet penetration heights and jet stability.

Models for liquid jets in crossflow recently developed by Madabhushi¹ and Zuo *et al.*² both utilized a modified version of the wave breakup approach of Reitz³ (the so-called blob model). A number of experimental results have shown, however, that the mechanism of liquid jet in crossflow atomization is quite different from the standard wave breakup approach. Cavaliere and co-workers⁴ showed that the jet evolution is significantly influenced by the onset of a shear breakup mechanism rather than a wave breakup approach. Column breakup's main feature is the appearance of waves on the windward surface of the liquid column, which are then amplified by aerodynamic forces leading to fracture of the column in a wave trough. The onset of observable wave growth usually coincides with an alignment, or at least partial alignment, of the jet with the direction of the airflow. As noted earlier, surface breakup is characterized by stripping of liquid from the surface of the jet. Examination of the breakup process suggests that both the column and surface breakup mechanisms are usually active, but one is dominant, depending on the flow conditions.⁵

While the onset of jet-column breakup is well characterized, the time required to complete the process is more difficult to measure with conventional techniques because of the optical density in this region.⁶ Even the most advanced models still do not account for other important structural features, such as wake effects, and this results in an underprediction of the volume flux in the near-wall region. Dense spray effects on breakup and atomization are also typically ignored, leading to uncertainties in the near field. Errors in the near field can be important when fuel injection is closely coupled to an anchored flame. These problems in understanding remain because there have been no experimental observations of the primary breakup of the liquid core in the dense spray region, because such a core is obscured by a dense fog of droplets. Ballistic imaging can meet this need, pro-

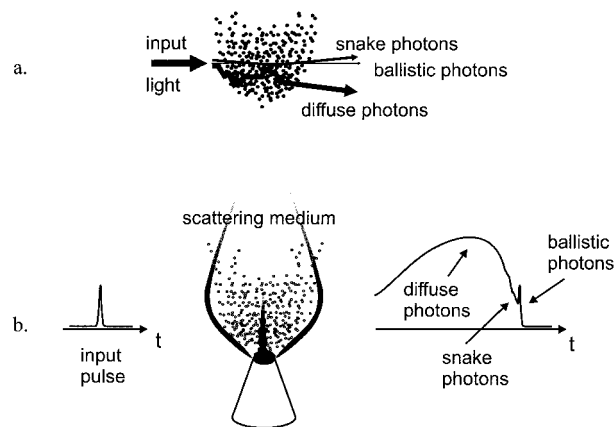


Fig. 2. Schematic of ballistic, snake, and diffuse photons.

viding high-resolution, single-shot images of the liquid core in a dense spray.

2. Single-Shot, Time-Gated, Two-Band Ballistic Imaging

The initial development and evaluation of the basic ballistic imaging instrument used here is described in detail by Paciaroni and Linne.⁷ In this companion paper, we describe further development of the technique and demonstrate its application to a spray.

Ballistic imaging is a form of shadowgraphy that generates images by using light with specific signatures, and there are many ways to do this. When light passes through a highly turbid medium, some of the photons actually pass straight through without scattering, exiting the medium within roughly the same solid angle that they entered (see Fig. 2a). These relatively few photons are termed "ballistic." Because they travel the shortest path, they also exit first (see Fig. 2b). A somewhat larger group of photons is called the "snake" photon group, because they are scattered just once or twice. They exit the medium in the same direction as the input light but with a somewhat larger solid angle than the ballistic photons. Because they travel a bit further, they exit just after the ballistic photons. Light exiting the medium that has scattered multiply ("diffuse photons") has a larger photon number density, but these photons are also scattered into a very large solid angle and they exit last. As a result of their undisturbed path, ballistic photons retain an undistorted image of structures that may be embedded within the turbid medium. If used in a shadowgram arrangement, the ballistic photons can provide diffraction-limited imaging of these structures. Unfortunately, in most highly scattering or absorbing environments, the number of transmitted ballistic photons is often insufficient to provide the necessary signal-to-noise ratio to form an image in a single-shot format. In such a case, the snake photons can be used in imaging, together with the ballistic photons, with little degradation of resolution. In contrast, diffuse photons retain no memory of the structure within the material. If allowed to participate in the formation of an image, the various

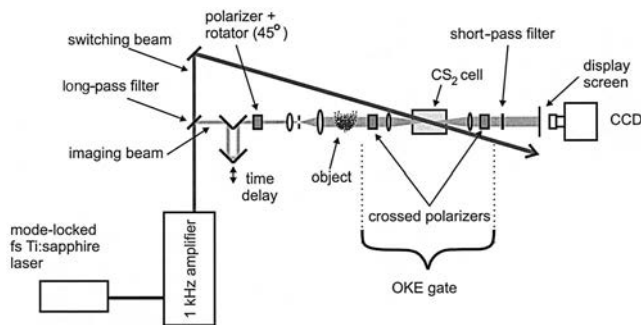


Fig. 3. Schematic of the ballistic imaging system used in this work.

paths these multiply scattered photons take through the material will cause each image point they form to appear as if it came from an entirely different part of the object, and this will seriously degrade resolution. Unfortunately, diffuse photons are the most numerous when light is transmitted through highly turbid media. The problem of obtaining a high-resolution image through highly scattering materials is thus a matter of separating and eliminating the diffuse light from the ballistic and snake light. This can be done by discrimination methods that make use of the properties that identify the ballistic and snake light. As already suggested, the direction taken by transmitted light, together with exit time, can be used to segregate diffuse photons from the imaging photons. In addition, polarization and coherence are both preserved by the ballistic photons, and they can also be used for segregation. Coherence is not used here because snake photons are not well preserved by such techniques, and their contribution is necessary to form a single-shot image.

The system used here was optimized to provide high-resolution, single-shot images of the liquid core in very dense atomizing sprays⁷ by using weak spatial filtering (to select the light exiting at narrow scattering angles) together with time gating. The original design used a spatial filter in front of the camera to reject switching light that was forward scattered. Here we have eliminated that filter, but it is important to point out that any properly designed imaging optical train acts as a weak spatial filter in the sense that it has a defined system aperture and acceptance angle. In time gating, a very fast shutter consisting of an optical Kerr effect (OKE) gate⁸ capable of gating times as short as 2 ps is used to select just the leading edge containing ballistic and snake photons.

The complete system used for this work is shown in Fig. 3. A 1 kHz repetition rate Coherent Legend Ti:sapphire regenerative amplifier, seeded with a Spectra-Physics Tsunami Ti:sapphire mode-locked laser, generates 40 fs, 2.5 mJ pulses centered in wavelength at about 800 nm. The linearly polarized beam is split into OKE gating and imaging beams. In previous work standard dielectric beam splitters were used, but they were replaced by bandpass filters

in this work (for reasons discussed just below). The polarization state of the imaging beam is first linearized, and then the polarization is rotated 45° because the OKE gate relies upon polarization switching. The imaging beam is time delayed by using an adjustable length delay arm, allowing one to control the delay between the arrival of the switching and imaging pulses at the OKE gate, for optimum time gating. The imaging beam then passes through an optics train consisting of a telescope that controls the imaging beam size at the object, a system to relay the beam through the OKE switch, a telescope for imaging onto a display screen, and a second bandpass filter to reject scattered switching light. This optical system was designed and optimized using OSLO, a commercial ray-trace code. By careful choice of available optics, we have ensured that the optical train itself is diffraction limited; there are no spurious aberrations or distortions introduced by the imaging optics themselves.

The OKE gate works in the following manner. When there is no switching pulse present, no image is transferred to the display screen. This is because the OKE gate uses crossed calcite polarizers. The first polarizer in the OKE gate (second polarizer used in the imaging beam) is oriented to pass the polarization orientation of the imaging beam. The second OKE polarizer is oriented normal to the first, blocking an unperturbed imaging beam. The measured extinction ratio of the polarizers is $>10^5$; without a switching pulse present there is $<10^{-5}$ transmission of the imaging beam through the second polarizer. Following the first OKE polarizer, the imaging beam is focused into the Kerr active liquid (CS_2 in this case) with an $F/\#5$ achromat, and then upcollimated with an $F/\#10$ achromat. At the arrival of a switching pulse, the intense electric field of the pulse causes the CS_2 dipoles to align along the polarization vector of the switching beam, creating temporary birefringence in the liquid. This birefringence rotates the polarization of the imaging beam, allowing most of it (70%–75%) to pass through the second polarizer. This OKE-induced birefringence is limited in time by either the duration of the laser pulse or the molecular response time of the Kerr medium, whichever is longer. In our case, the incident laser pulse is much shorter in duration than the molecular relaxation time of 2 ps for CS_2 ; a gate time of 2 ps has been confirmed by direct measurement. Past the OKE gate, the image was relayed to a display screen and the image was captured by a Roper Scientific PI-Max camera.

The system described by Paciaroni and Linne⁷ included a spatial filter at the location of the short-pass filter in Fig. 3. The spatial filter was used because the same wavelength of light was used for switching and imaging, and some switching light was scattered forward into the imaging system. The spatial filter removed most of that interference. A compromise was involved in the choice of aperture for the spatial filter, however, because the aperture must be located at the focal point. That point identifies the Fourier plane,

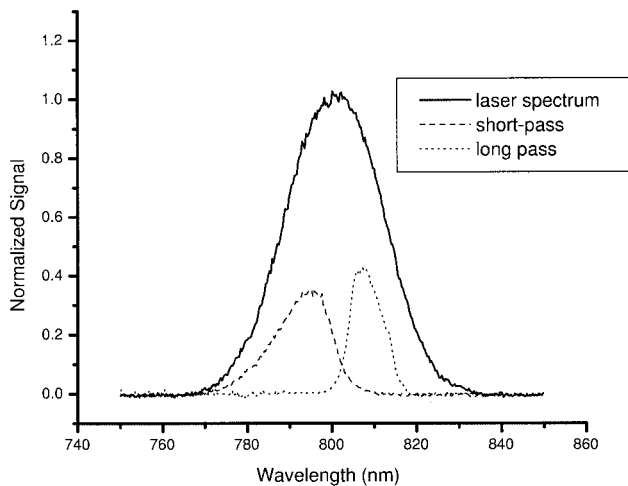


Fig. 4. Spectral schematic of the two-band ballistic imaging approach used in this work.

where the high-spatial-frequency components of the image reside off axis. These high-frequency components are therefore lost if they are blocked by the aperture, and this degrades spatial resolution. Paciaroni and Linne chose an aperture that preserved the high-frequency components, but this allowed some switching light to enter the imaging system. This produced a small but noticeable degradation in contrast, leading to degradation in spatial resolution. It is possible to reject much of this forward scatter by using alternative trapping techniques, but the alignment process must be repeated everytime anything in the imaging system is changed.

Others have used the second harmonic of the laser to switch the OKE gate while imaging with the first harmonic (usually with Nd:YAG at 532 nm and 1.064 μm). This two-wavelength technique allows one to reject scattered switching light with a low-pass optical filter. It was not possible to use that approach here, however, because CS_2 absorbs light at the second harmonic of Ti:sapphire. The amplifier used in the work described here emits over twice the pulse energy at twice the bandwidth of the amplifier used by Paciaroni and Linne. The laser thus offers a related approach for blocking scattered light. A long-pass optical filter was used to split the imaging beam from the switching beam, and a short-pass filter was used to block switching light at the camera. The spatial filter was then removed. The measured spectra of the laser and the two beams used here are shown in Fig. 4. This gave a switching performance similar to the earlier implementation, but it used a simplified optical system. It also improved spatial resolution relative to the resolution of a system using a spatial filter (but otherwise equivalent) by about 1–5 μm . This change was not measured by using the approach described by Paciaroni and Linne.⁷ Rather, a resolution test chart was placed at the object location, and the change in contrast at the camera was simply observed. These figures are therefore not as well established as in the former work.

Paciaroni and Linne performed detailed measurements of the system modulation transfer and point spread functions under various levels of extinction.⁷ They found that this instrument can routinely achieve a spatial resolution around 40–50 μm in a single frame under the very high extinction levels characteristic of a Diesel spray (when using a spatial filter with a 200 μm pinhole). The extinction levels of the jets presented here were not high in comparison to a Diesel spray. The resolution limit for such images is approximately 20–25 μm (when using a spatial filter with a 400 μm pinhole). Again, this figure is approximate as the resolution limit depends upon the actual extinction level, and we have not measured it in this jet. The spatial scale of the imaging system use here was calibrated, however, and when the two-bandwidth approach was used, the features that are clearly observable in the images are of a size consistent with this estimated spatial resolution.

This spatial resolution is superior to former single-frame ballistic imaging cases reported in the literature, but spray modelers require resolution nearer to 10 μm . As a small extension of the former system analysis, therefore, we have evaluated the contribution of each component to this resolution limit. In the two-band instrument the spatial resolution is limited principally by the OKE gate. The switching beam is actually focused weakly into the CS_2 cell for good cell performance (not shown in Fig. 3), and so the induced birefringence is a function of radius moving away from the beam axis. Switching quality thus decreases with position off axis, and this affects resolution in the same way a spatial filter can. This problem can be overcome by increasing the switching pulse energy and increasing the switching beam diameter. Next, crossed polarizers can also remove high-spatial-frequency components. We do not see their contribution at this point, but they could become the next limitation if the spatial filtering effects were removed.

It is worth mentioning that the camera itself does not limit spatial resolution. More common planar imaging systems use a camera that acquires a predefined, diffuse image from within a flowfield located some distance away, and it relies heavily upon the camera lens, image intensifier if one is used, and the architecture of the imaging chip. In contrast, a ballistic image is relayed within a laser beam from the sample volume to a screen. One can use diffraction-limited relay optics to create an image of virtually any size at the screen. The camera can then be adjusted to select a portion of a magnified image. Diffraction then controls spatial resolution for features originating at the sample, not the camera. The camera does impose a limit on spatial dynamic range, however, set by the pixel dimension relative to the overall size of the imaging chip.

3. Spray Experiments

A quasi-steady water jet experiment was developed to demonstrate the diagnostic in a relevant flowfield. It used an accumulator to provide pressurized water

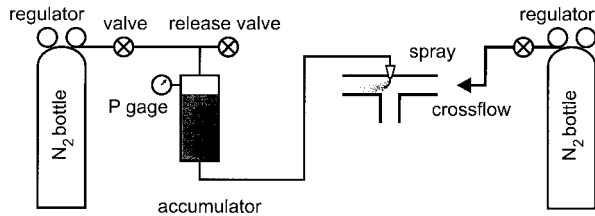


Fig. 5. Schematic of the jet in crossflow apparatus.

(up to 550 kPa) to a nozzle for about 15 min of steady spray time (see Fig. 5). A second nitrogen bottle was used to supply a controllable crossflow of gas at atmospheric pressure. Two simple water nozzles were built to emulate the cases studied by Madabhushi *et al.*¹ The data presented here can not be compared in an easy way with their predictions, as the ballistic images were acquired just 3–4 mm from the jet exit, but they can be used to augment future model development work. The nozzles used here employed simple constant area passages with diameters of 0.789 and 1.722 mm. The nitrogen jet was 4.37 mm diameter in both cases, and it was centered on the water jet before each experiment commenced. The nitrogen flow pattern was not characterized.

The nitrogen and water flow rates were metered simply by providing a constant pressure drop across the orifice that formed either jet. The nitrogen flows were determined by using a calibrated rotameter (calibrated by a mass flow meter), while the water flow rate was measured volumetrically. The various rates were chosen to provide Weber numbers relevant to the model presented by Madabhushi *et al.*¹ The specific properties of each flow studied are detailed in Table 1, where the Reynolds number of the liquid is given by $Re_l = (u_l d)/\nu$ (where ν is the kinematic viscosity), and the momentum flux ratio is given by $(\rho_l u_l^2)/(\rho_g u_g^2)$. Sets of 40 images were acquired for each case. The case with maximum gas velocity, for the jet diameter $d = 7.89 \times 10^{-4}$ m, was not included because there was a question about drift in the nitrogen mass flow rate for that case.

4. Results

An example image from case 2 is shown in Fig. 6. The field of view is approximately 3.5 mm. In the image, one can see dark areas representing a continuous fluid phase and light areas representing the gas phase. After background subtraction, each raw image was normalized by an image of the beam with no

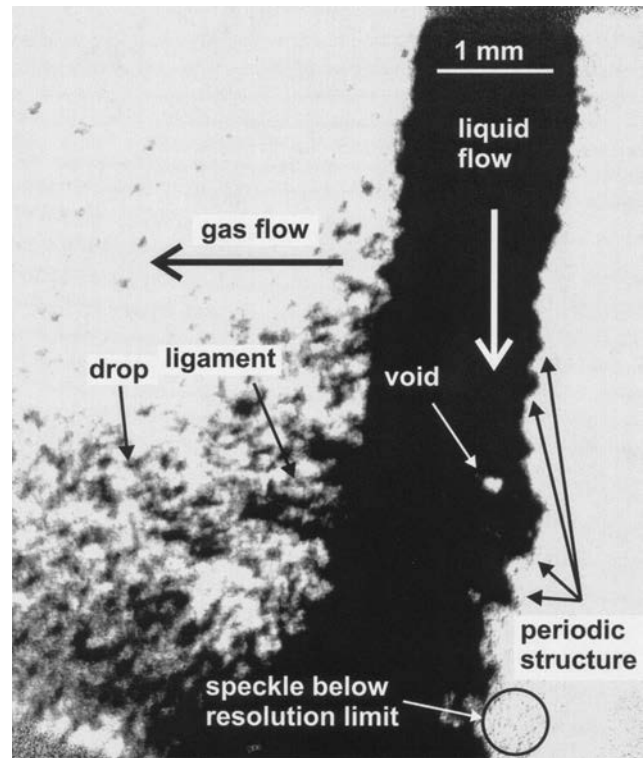


Fig. 6. Example image for case 2.

liquid flow. This removed the laser speckle patterns that were repeatable and flattened the Gaussian profile of the imaging beam. This normalization procedure improved the overall signal-to-noise ratio from 4:1 to 20:1, it provided better visual access to the dark regions of the imaging beam, and it improved droplet detection. A small amount of beam jitter caused a loss of spatial resolution of the order of one micrometer, but this was considered a good compromise given the improvement in overall image quality.

The top of the image in Fig. 6 is the location of the nozzle. The jet issued from the top, and one can see the liquid column breaking up as the liquid flows downward. The gas flow is from right to left in the images. A small amount of laser speckle that is smaller than the resolution limit of the system remains within the gas-phase portion of the image after background subtraction and normalization (see the note in Fig. 6). These should not be interpreted as small droplets. It is also necessary to point out that this spray, while not as dense as an atomizing diesel

Table 1. Jet Run Conditions

Case	Jet Diameter d (m)	Gas Velocity u_g (m/s)	Liquid Velocity u_l (m/s)	We_g	Re_l	Momentum Flux Ratio
1	7.89×10^{-4}	66.7	29.0	56	22,800	161
2	7.89×10^{-4}	100	29.0	126	22,800	72
3	1.73×10^{-3}	70.7	17.4	138	30,100	52
4	1.73×10^{-3}	88.7	17.4	218	30,100	33
5	1.73×10^{-3}	106.7	17.4	316	30,100	23

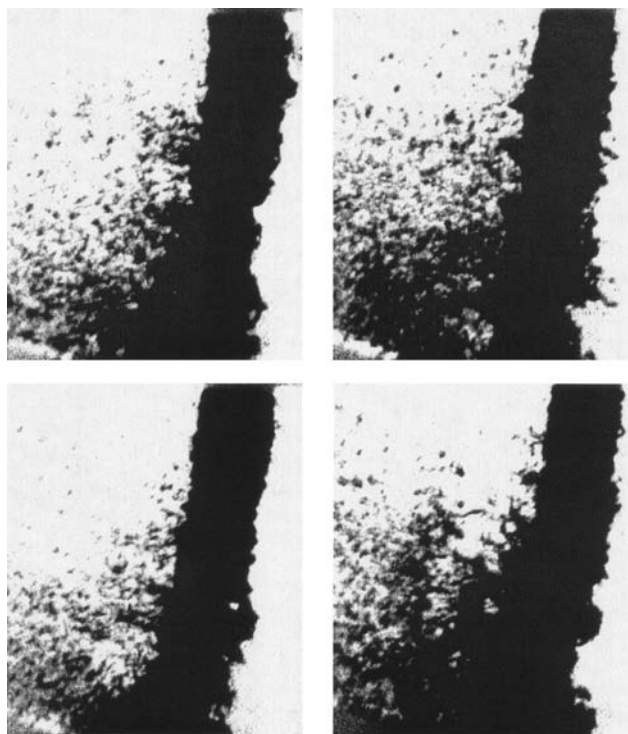


Fig. 7. Shot-to-shot variation for case 2.

fuel spray for example, was quite dense to passive imaging techniques.

The interesting fluid features in Fig. 6 include expansion of the liquid core cross section as it moves downstream, deflection, and perhaps deformation of the jet, appearance of periodic structures along the jet column, evidence for aerodynamic stripping of the jet, and the formation of ligaments, nonspherical primary droplets, and voids. There was some unsteadiness in the spray, as evidenced by the variation from shot to shot in Fig. 7. Variability is diminished in the slower flow case (case 1), and so we speculate that it may be caused by some inherent instability of the nitrogen flow.

The effect of Weber number can be observed in Fig. 8a (case 1) to 8f (case 5). The difference between cases 1 and 2 (Figs. 8a and 8b) differ only in gas velocity. The higher We_g case (Fig. 8b) experiences greater atomization, deflection by the gas, and potentially greater deformation as well. Periodic structures are observed in both cases, but ligaments are larger and more frequent in the higher We_g case. These observations are borne out by statistics taken from the entire collection of images, as presented in Table 2 below.

A larger jet diameter is used to increase the value of We_g for cases 3, 4, and 5. Case 2 (the smaller d case, Fig. 8b) looks quite different from case 3 (the larger d case, Fig. 8c), even though their respective Weber numbers are not very different. This is because the liquid-gas momentum flux ratio changes significantly with the larger jet diameter. Note that case 3 had some very infrequent evidence of bag breakup, as

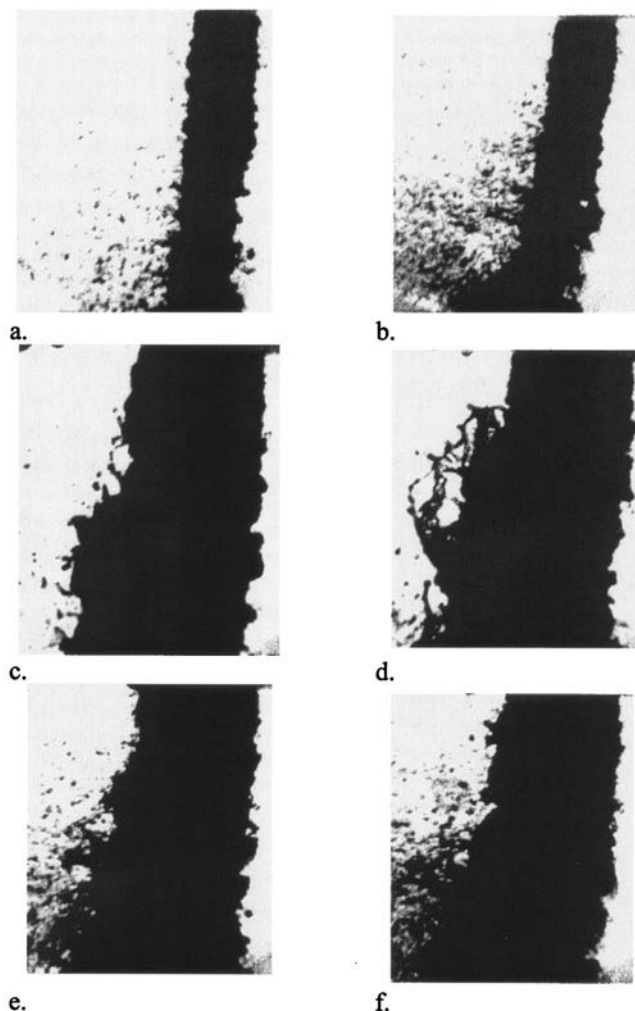


Fig. 8. a, Example spray for case 1; b, case 2; c, case 3; d, evidence for bag breakup in case 3; e, example spray for case 4; f, case 5.

shown in Fig. 8d. Voids are not common in cases 3, 4, and 5, but otherwise they show a progression of features with We_g similar to cases 1 and 2.

The image files were scanned manually for statistics on ligament size and number, droplet size and number, void size and number, and the spatial frequencies of clearly identifiable periodic structures. When the two-dimensional image of a primary droplet was elliptical or oblong, the short dimension was taken.

Figures 9 and 10 contain drop size distributions for the five cases described in Table 1. These data represent averages over all of the images in each case group, presented for a limited number of size classes because the data were extracted manually. It is important to point out that droplets smaller than $20\text{ }\mu\text{m}$ can not be detected by this imaging technique; so the measured distributions necessarily cut off at that point. As shown in the figures, however, most of the distributions fall well above this small cutoff value, except for case 5. The other plots have the approximate shape of a lognormal distribution⁹ with approximately the same average size.

Table 2. Results Extracted from Images

Case	Ave. No. Drops	SMD ^a (μm)	Total No. Voids Obs.	Total No. Ligaments	Periodic Wavelengths ^b (μm)
1	71	46.7	19	54	us: 150,175,200,250,275,300,350 ds: 175,200,225,300
2	96	46.7	39	92	us: 225,300,325 ds: 175,250,300,500
3	29	53.5	14	46	us: 150,225,250,275,300,350,400 ds: 150
4	54	45.6	24	81	us: 150,200,250,300,350,400 ds: 175,250,300,325,375,400
5	108	—	13	78	us: 150,200,250,300,475,600 ds: 225,250,300,325,350,400,750

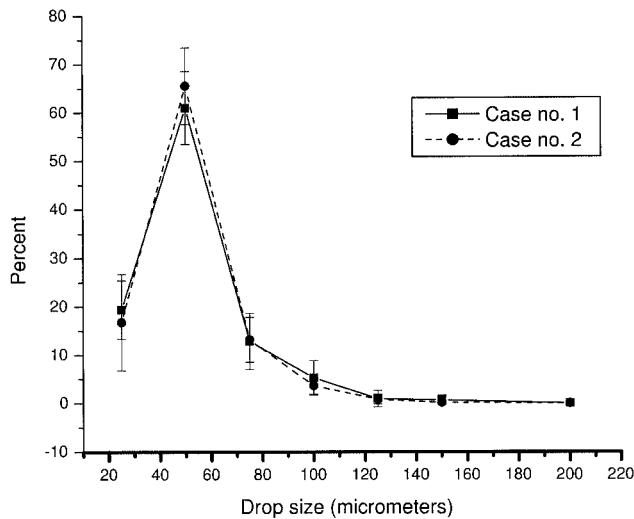
^aSMD, Sauter mean diameter.^bus, upstream side; ds, downstream side.

Fig. 9. Drop size distributions for cases 1 and 2.

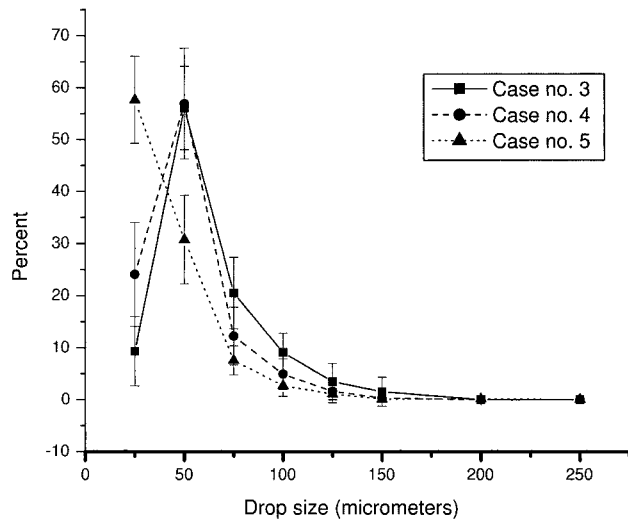


Fig. 10. Drop size distributions for cases 3, 4, and 5.

Table 2 contains a summary of the data extracted from these images. The Sauter mean diameters in the table were inferred by fitting a lognormal distribution to each curve in Figs. 9 and 10 (except for case 5, where there were insufficient data to describe the distribution). Instead of presenting averages for voids and ligaments, the total number observed out of 14 images is presented because there were some images containing neither. The data in the column labeled “Periodic Wavelengths” represent all of the wavelengths for what appeared to be periodic structures in the jets.

Clearly, there are some judgements involved in the manual process of data extraction from these images. Future work will utilize image processing to automate this function, but it is possible to introduce significant errors unless great care is applied to implementation issues such as edge detection. For the time being, therefore, human judgement has been used.

Despite variation in the data, one can extract some preliminary observations. Not surprisingly, the number of droplets and ligaments produced increases with We , while the low We and Re cases produce more voids. The Sauter mean diameter of the primary droplets does not vary significantly for cases 1–4. Case 5 has evolved into a somewhat different regime. It has the largest We and Re , together with the smallest momentum ratio. The droplet size distribution for this case has moved down into a notably smaller size range. Finally, there seems to be an increase in the wavelength of periodic structures with We , but it is not a pronounced trend.

5. Conclusion

Ballistic imaging is a fairly new diagnostic tool for the near field of an atomizing spray. Our latest implementation provides single-shot images with very good spatial resolution, sufficient to extract new information about a highly relevant spray. This initial work reveals a near-nozzle flow field undergoing breakup via stripping. One can also detect signatures of spatially periodic behavior and a few voids. These results will contribute to the development of a physical model that can be included in subroutines of

computational fluid dynamics codes that describe spray breakup.

Future work will focus upon an experiment with upstream gas flow that is more uniform across the jet, and it will be better characterized. More image sequences will be acquired at more locations along the liquid core, and automatic image analysis software will be used to extract higher quality statistics.

Support for this work is provided by a grant from the US Air Force Research Laboratory under grant contract FA8650-04-M-2442. Some of the equipment used was provided by Army Research Office via ARO Project DAAD19-02-1-0221.

References

1. R. K. Madabhushi, M. Y. Leong, and D. J. Hautman, "Simulation of the breakup of a liquid jet in crossflow at atmospheric conditions," *2004 Proceedings of ASME Turbo Expo*, Power for Land, Sea, and Air (American Society of Mechanical Engineers, 2004).
2. B. Zuo, D. L. Black, and D. S. Crocker, "Fuel atomization and drop breakup models for advanced combustion CFD codes," presented at 38th/AIAA/ASME/SAE/ASEE. Joint Propulsion Conference & Exhibit, Indianapolis, Ind., 7–10 July 2002, AIAA paper 2002–4175.
3. R. D. Reitz, "Modeling atomization processes in high-pressure vaporizing sprays," *Atomization Spray Technol.* **3**, 309–337 (1987).
4. A. Cavaliere, R. Ragucci, and C. Noviello, "Bending and break-up of a liquid jet in a high pressure airflow," *Exp. Therm. Fluid Sci.* **27**, 449–454 (2003).
5. J. Becker and C. Hassa, "Breakup and atomization of a kerosene jet in crossflow at elevated pressure," *Atomization Sprays* **12**, 49–67 (2002).
6. M. Rachner, J. Becker, C. Hassa, and T. Doerr, "Modelling of the atomization of a plain liquid fuel jet in crossflow at gas turbine conditions," *Aerosp. Sci. Technol.* **6**, 495–506 (2002).
7. M. Paciaroni and M. Linne, "Single-shot two-dimensional ballistic imaging through scattering media," *Appl. Opt.* **43**, 5100–5109 (2004).
8. L. Wang, P. P. Ho, F. Liu, X. C. Zhang, R. R. Alfano, "Ballistic 2-D imaging through scattering walls using an ultrafast optical Kerr gate," *Science* **253**, 769–771 (1991).
9. A. H. Lefebvre, *Atomization and Sprays* (Hemisphere, 1989).

10 kHz detection of CO₂ at 4.5 μ m by using tunable diode-laser-based difference-frequency generation

Terrence R. Meyer and Sukesh Roy

Innovative Scientific Solutions, Inc., 2766 Indian Ripple Road, Dayton, Ohio 45440

Thomas N. Anderson and Robert P. Lucht

School of Mechanical Engineering, Purdue University, 585 Purdue Mall, West Lafayette, Indiana 47907

Rodolfo Barron-Jimenez*

Department of Mechanical Engineering, Texas A&M University, College Station, Texas 77843

James R. Gord

Air Force Research Laboratory, Propulsion Directorate, Wright-Patterson Air Force Base, Ohio 45433

Received May 12, 2005; revised manuscript received July 22, 2005; accepted July 26, 2005

A compact, high-speed tunable, diode-laser-based mid-infrared (MIR) laser source has been developed for absorption spectroscopy of CO₂ at rates up to 10 kHz. Radiation at 4.5 μ m with a mode-hop-free tuning range of 80 GHz is generated by difference-frequency mixing the 860 nm output of a distributed-feedback diode laser with the 1064 nm output of a diode-pumped Nd:YAG laser in a periodically poled lithium niobate crystal. MIR absorption spectroscopy of CO₂ with a detection limit of 44 ppm m at 10 kHz is demonstrated in a C₂H₄-air laminar diffusion flame and in the exhaust of a liquid-fueled model gas-turbine combustor.

© 2005 Optical Society of America

OCIS codes: 300.6260, 120.1740, 140.2020, 300.1030, 190.1900.

Tunable diode-laser absorption spectroscopy is a mature, relatively low-cost diagnostic approach commonly used in laboratory flames and combustors of practical interest for quantitative measurement of multiple species concentrations and temperature.¹ For the measurement of unsteady phenomena, the most successful approach takes advantage of the high-speed tunability of distributed-feedback (DFB) diode lasers in the near IR for kilohertz-rate detection of H₂O, CO, and CO₂.² Rapid-scan diode lasers for accessing strong electronic transitions in the UV or fundamental bands in the mid-infrared (MIR), however, are still not available, limiting the maximum detection rates of species such as OH, NO, CO, and CO₂.

To tune to the electronic or fundamental vibrational absorption bands of these molecules for enhanced sensitivity and selectivity, researchers have previously used sum-frequency^{3,4} and difference-frequency^{5,6} mixing of slow-scan diode lasers with other high-power laser sources in nonlinear crystals. Wavelengths in the UV and MIR have been achieved with this approach but with data-acquisition bandwidths of ~ 100 Hz or less.¹⁻⁶

By exploiting the new wavelength availability in DFB diode lasers along with sum- or difference-frequency generation, one can achieve high scan rates in the UV and MIR spectral regions while accessing strong absorption bands and avoiding interference from H₂O. Detection of the hydroxyl radical (OH) in the UV with a 20 kHz data-acquisition bandwidth, for example, was recently demonstrated for

the first time by using a laser source based on sum-frequency generation.⁷

In a similar manner, we report the first demonstration to our knowledge of MIR detection of CO₂ at single-scan rates up to 10 kHz with a signal-to-noise ratio of 40:1 by using a DFB diode laser and difference-frequency generation (DFG). Detection rates of 50 kHz are achievable with a signal-to-noise ratio of 20:1. Data are presented in combustion environments with path lengths ranging from 2.5 to 7.5 cm, providing the measurement bandwidth required to track and possibly control unsteady combustor performance characteristics in a variety of applications. Examples of combustion phenomena that require high data-acquisition rates include ignition, blowout, flame holding, and acoustic instability. Furthermore, the wavelength region around 4.5 μ m

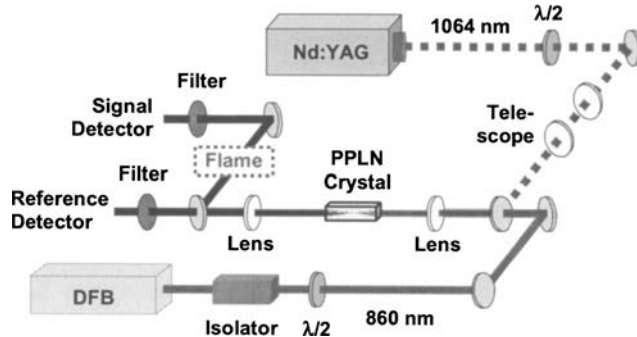


Fig. 1. Schematic of high-speed MIR CO₂-absorption spectroscopy system.

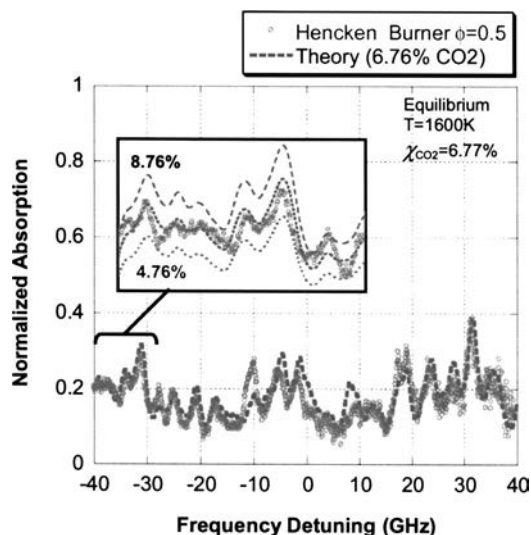


Fig. 2. Broadened CO_2 spectra centered at 2237.87 cm^{-1} in the Hencken burner at $\phi=0.5$. Inset, detailed view of theoretical model compared with experimental data.

holds the potential for simultaneous detection of blended CO_2 and CO spectra, the ratio of which is sought as a useful parameter for combustion monitoring and control.²

The mixing scheme used to achieve MIR wavelengths for absorption by CO_2 and CO is shown in Fig. 1. A 75 mW single-mode DFB diode-laser beam near 860 nm and a 500 mW, diode-pumped Nd:YAG-laser beam at 1064.66 nm are difference-frequency mixed in a 40 mm long periodically poled lithium niobate (PPLN) crystal to attain 420 nW of MIR radiation centered near $4.47 \mu\text{m}$. The DFB diode-laser temperature is varied to achieve a slow-scan DFG center-wavelength range up to 20 nm in the MIR, and DFB diode-laser drive-current modulation is used for rapid mode-hop-free DFG tuning. DFG tuning ranges of 80 and 60 GHz are achieved with drive-current modulation at 2 and 10 kHz. Nonlinearities in time are corrected by using an etalon with a 2 GHz free spectral range. The DFG laser output is directed through the flame as well as to a reference detector for normalization. Standoff detection with spatial filtering and bandpass filters centered at $4.5 \mu\text{m}$ (125 nm FWHM) are used to reduce background thermal radiation prior to detection of the signal and reference beams with cryogenically cooled InSb detectors. Residual background radiation is measured with the laser beams blocked and then subtracted along with photodiode bias prior to normalization. Further details on the DFG setup can be found in Ref. 5.

Theoretical spectra for CO_2 incorporate spectroscopic line parameters from the HITRAN–HITEMP database and apply line broadening to simulate the effects of temperature and pressure.⁵ The temperature is fixed based on coherent anti-Stokes Raman scattering (CARS) data collected previously,⁸ and concentration is allowed to vary during the comparison with experimental CO_2 spectra. The measurement of temperature by using CO_2 spectra at $4.5 \mu\text{m}$ requires further model development⁹ or the detection

of multiple species² and is the subject of ongoing investigation. The data of Fig. 2, collected at 2 kHz in a nearly adiabatic, laminar diffusion flame stabilized over a $25 \text{ mm} \times 25 \text{ mm}$ Hencken burner, demonstrate that the theoretical model adequately predicts many features within the CO_2 absorption spectrum despite its complex nature, with the measured mole fraction of CO_2 closely matching the equilibrium prediction. The inset displays theoretical spectra at $\pm 2\%$ CO_2 mole fraction to illustrate the precision that can be achieved with the current sensor.

Nonaveraged, 10 kHz measurements in the exhaust of a preheated, liquid-fueled, swirl-stabilized, atmospheric-pressure CFM56 gas-turbine combustor at $\phi=0.5$ and $\phi=0.8$ are shown in Fig. 3. Further details of the combustor, which has a 7.6 cm exit diameter exhaust nozzle, can be found in Ref. 8. To our knowledge, this is the first demonstration of 10 kHz MIR absorption spectroscopy in a liquid-fueled combustor, illustrating that it is feasible to apply the DFG sensor to reacting flows of practical interest. Both $\phi=0.5$ and $\phi=0.8$ show good agreement with theoretical comparisons using the HITRAN–HITEMP database and CARS temperatures of 1280 and 1693 K, respectively. The concentrations appear to be within 1% of equilibrium predictions and within 7% of previous measurements by Fourier-transform IR (FTIR) spectroscopy. A scatterplot of 15 scans for $\phi=0.5$ shown in the inset of Fig. 3 illustrates the ability of the sensor to differentiate between the two combustor conditions.

Time-series measurements utilizing 10 kHz data from the Hencken burner and CFM56 combustor at $\phi=0.5$ are shown for comparison in Fig. 4. The CO_2 concentrations are similar in both cases, but data from the CFM56 combustor display a characteristic frequency of $\sim 750 \text{ Hz}$. In contrast, time-series measurements in the Hencken burner are steady with a standard deviation of 2.5%. Assuming there is no sig-

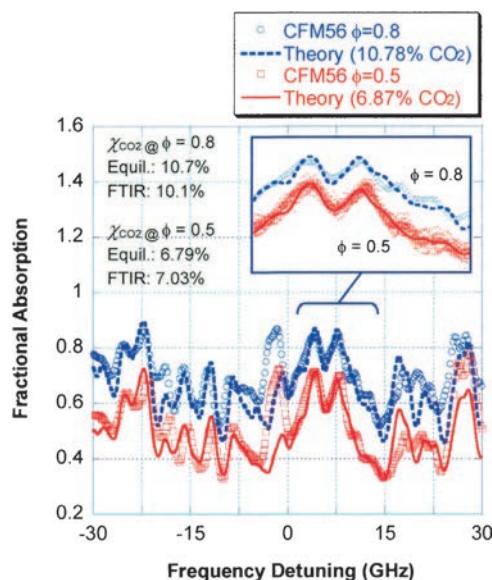


Fig. 3. Broadened CO_2 spectra at 2237.5 cm^{-1} in the CFM56 combustor at $\phi=0.5, 0.8$. The inset for $\phi=0.5$ shows 15-shot data scatter at a 10 kHz scan rate.

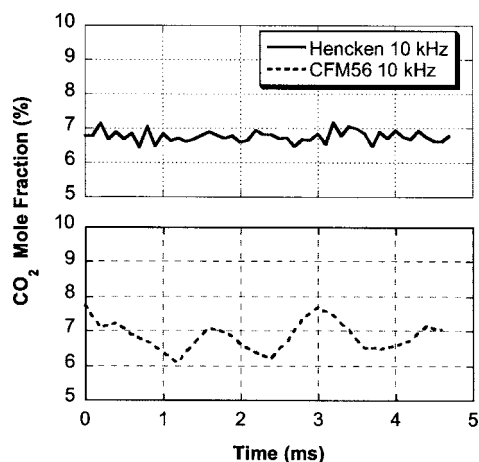


Fig. 4. 10 kHz time-series measurements of CO_2 mole fraction at $\phi=0.5$ in the Hencken burner and CFM56 combustor.

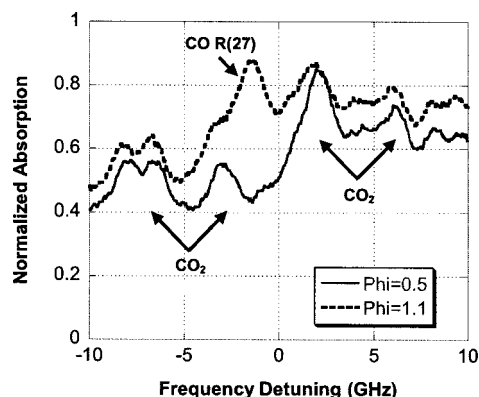


Fig. 5. Demonstration of simultaneous CO_2 and CO measurements centered at 2236.21 cm^{-1} in the CFM56 combustor.

nificant noise contribution from the laminar Hencken flame and for a signal-to-noise ratio of unity, this yields a 10-kHz detection limit of 44 ppm m. Given that CO_2 concentrations are typically of the order of 100,000 ppm in the combustion products, this sensitivity is more than adequate for many combustion-control applications. Nonetheless, it is possible to sacrifice measurement speed for accuracy. Time averaging for 1 s, for example, would lead to a detection limit of approximately 0.44 ppm m. While it is possible to improve the detection limit by time averaging, it is also possible to analyze multiple regions within the wide tuning range to enable detection rates greater than 10 kHz. By tracking five separate regions in Fig. 2, for example, we achieved a 50 kHz measurement rate with a standard deviation of 5% and a detection limit of 83 ppm m.

Finally, note that the potential exists for simultaneous measurement of CO and CO_2 concentrations by operating the sensor near 2236.21 cm^{-1} . This is demonstrated in Fig. 5, which shows measurements in the CFM56 combustor at $\phi=0.5$ and $\phi=1.1$. The $R(27)$ line of CO in the ($\nu''=0, \nu'=1$) band becomes

more prominent as the CO concentration increases from a low to a high equivalence ratio. This facilitates measurement of the CO_2 -to-CO ratio, which can then be maximized to improve combustion efficiency. The tuning range of the DFG laser is sufficient for accurate measurement of the CO_2 concentration, and it may be possible with further model development to isolate the signal contribution from CO. The use of wavelength-modulation spectroscopy may also help to improve the analysis or enable thermometry from blended CO_2 -CO spectral features.⁹

In summary, a newly developed 10 kHz CO_2 absorption-spectroscopy system based on difference-frequency generation of $4.5\text{ }\mu\text{m}$ radiation has been demonstrated successfully in a laboratory flame and in the exhaust of a liquid-fueled combustor. To our knowledge, this is the first demonstration of high-speed absorption spectroscopy of CO_2 in the mid-IR spectral region, as well as the first demonstration of high-speed tunable diode-laser absorption spectroscopy of CO_2 in the exhaust of a liquid-fueled combustor of practical interest. Measured concentrations for a limited data set are within 7% of equilibrium predictions and FTIR measurements, with a 10 kHz detection limit of 44 ppm m. Extension to detection rates as high as 50 kHz as well as simultaneous detection of CO_2 and CO are also demonstrated.

The authors thank Vincent Belovich, Edwin Corporan, and Robert Pawlik of the Air Force Research Laboratory, Propulsion Directorate (AFRLPD), for assistance with the CFM56 combustor rig and FTIR data. Funding was provided by the AFRLPD under contracts F33615-03-D-M2329 and F33615-00-C-2020, and by the Air Force Office of Scientific Research (Julian Tishkoff, Program Manager). T. Meyer's e-mail address is trmeyer@innssi.com.

*Present address, Pranalytica, Inc., 1101, Colorado Avenue, Santa Monica, California 90401.

References

1. M. G. Allen, *Meas. Sci. Technol.* **9**, 545 (1998).
2. M. E. Webber, J. Wang, S. T. Sanders, D. S. Baer, and R. K. Hanson, *Proc. Combust. Inst.* **28**, 407 (2000).
3. D. B. Oh, *Opt. Lett.* **20**, 100 (1995).
4. T. N. Anderson, R. P. Lucht, R. Barron-Jimenez, S. F. Hanna, J. A. Caton, T. Walther, S. Roy, M. S. Brown, J. R. Gord, I. Critchley, and L. Flamand, *Appl. Opt.* **44**, 1491 (2005).
5. R. Barron-Jimenez, T. N. Anderson, J. A. Caton, R. P. Lucht, T. Walther, S. Roy, and J. R. Gord, "Application of a diode-laser-based sensor to carbon monoxide detection in the $4.4\text{--}4.8\text{ }\mu\text{m}$ spectral region," in preparation for submission to *Appl. Phys. B*.
6. D. Richter, D. G. Lancaster, and F. K. Tittel, *Appl. Opt.* **39**, 4444 (2000).
7. T. N. Anderson, R. P. Lucht, T. R. Meyer, S. Roy, and J. R. Gord, *Opt. Lett.* **30**, 1321 (2005).
8. S. Roy, T. R. Meyer, R. P. Lucht, V. M. Belovich, E. Corporan, and J. R. Gord, *Combust. Flame* **138**, 273 (2004).
9. J. T. C. Liu, J. B. Jeffries, and R. K. Hanson, *Appl. Opt.* **43**, 6500 (2004).

Broadband coherent anti-Stokes Raman scattering spectroscopy of nitrogen using a picosecond modeless dye laser

Sukesh Roy and Terrence R. Meyer

Innovative Scientific Solutions, Incorporated, 2766 Indian Ripple Road, Dayton, Ohio 45440

James R. Gord

Air Force Research Laboratory, Propulsion Directorate, Wright-Patterson Air Force Base, Ohio 45433

Received May 13, 2005; revised manuscript received August 7, 2005; accepted August 8, 2005

Broadband picosecond coherent anti-Stokes Raman scattering (CARS) spectroscopy of nitrogen is demonstrated using 145-ps pump and probe beams and a 115-ps Stokes beam with a spectral bandwidth of 5 nm. This is, to our knowledge, the first demonstration of broadband CARS using subnanosecond lasers. The short temporal envelope of the laser pulses and the broadband spectral nature of the Stokes beam will enable nonresonant-background-free, single-shot, or time-dependent spectroscopy in high-pressure or hydrocarbon-rich environments. Successful correlation of room-temperature broadband picosecond N_2 CARS with a theoretical spectrum is presented. © 2005 Optical Society of America

OCIS codes: 320.5390, 120.1740, 140.2050, 190.4380, 300.6230, 300.6290.

Coherent anti-Stokes Raman scattering (CARS) measurements of nitrogen and hydrogen molecules using conventional broadband and modeless nanosecond dye lasers has been widely utilized for thermometry in gaseous flows.^{1–3} The advantage of broadband CARS over narrowband or scanning CARS is that it allows acquisition of single-shot spectra of transient phenomena under unsteady conditions.⁴ A significant drawback of the nanosecond CARS approach, however, is interference of the nonresonant background signal with the resonant CARS signal. This limits the applicability, sensitivity, and accuracy of nanosecond CARS at higher pressures and especially in hydrocarbon-rich environments due to the high nonresonant susceptibility of hydrocarbon compounds. The contribution from the nonresonant background signal is highest when the pump and probe beams are overlapped temporally.^{4–6} In the picosecond regime, it is possible to delay the pump beam temporally with respect to the probe beam to suppress the nonresonant contribution to the CARS signal.

This Letter reports, to our knowledge, the first demonstration of broadband CARS at subnanosecond time scales using a modeless dye laser. Previous investigations of the time-resolved dynamics of atoms or molecules in the picosecond regime have employed optical parametric amplifiers,⁷ synchronously pumped dye lasers,^{5,8} and distributed-feedback dye lasers (DFDLs).^{9,10} These sources, however, are not suitable for single-shot spectroscopic measurements in unsteady flows because of their relatively narrow spectral width and, to our knowledge, have not been utilized for temperature measurements in gaseous environments. In addition to single-shot CARS thermometry in high-pressure, hydrocarbon-rich environments, the broadband picosecond dye laser described here might also be useful for velocity measurements in high-speed flows by using the Raman-excitation

laser-induced electronic fluorescence (RELIEF) technique.¹¹

A schematic diagram of the broadband picosecond CARS system is shown in Fig. 1. The modeless dye laser is pumped by the frequency-doubled, nearly transform-limited pulse width, ~85 mJ/pulse output of a 10-Hz Nd:YAG regenerative amplifier at 532 nm. In contrast to most picosecond dye lasers, the absence of a cavity allows the generation of an output beam without any mode structure. The first cell of the dye laser is side pumped and is followed consecutively by side- and end-pumped amplifier cells. In the current setup, a mixture of R 640 and KR 620 dyes is used to generate the output beam, which is centered at ~607 nm. When used with 532-nm pump beams, this wavelength corresponds to the Stokes beam for

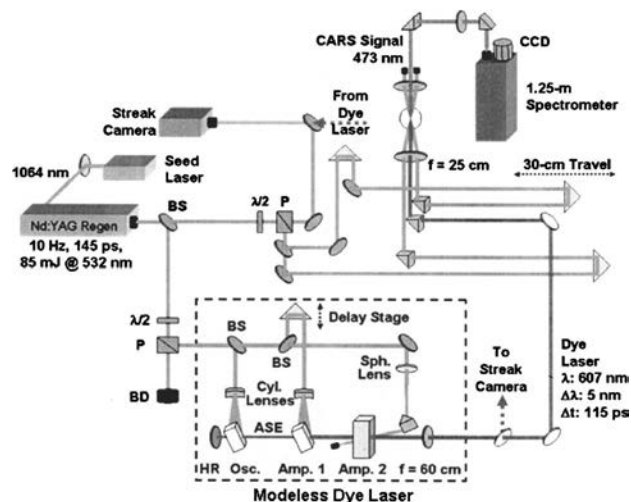


Fig. 1. Schematic diagram of broadband picosecond CARS system. M, mirror; $\lambda/2$, half-wave plate; P, polarizer; BD, beam dump; BS, beam splitter; HR, high reflector; ASE, amplified spontaneous emission.

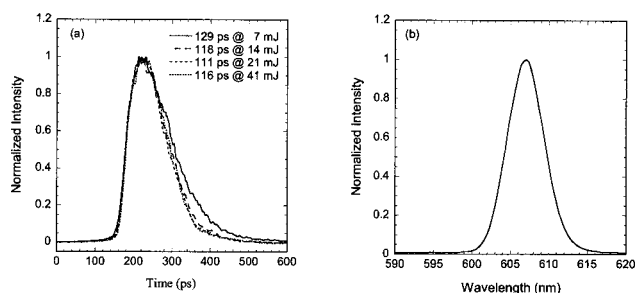


Fig. 2. (a) Temporal profile of dye laser at various pump energies measured with streak camera, (b) spectral profile of dye laser.

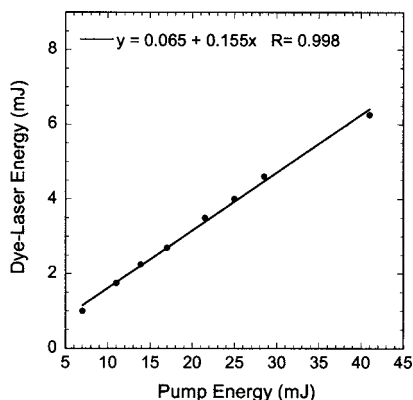


Fig. 3. Dye-laser output energy as function of pump energy.

CARS spectroscopy of nitrogen.⁴ A broadband high reflector placed within 3 mm of the relatively short (~ 12 mm) first cell allows significant temporal overlap between the reflected photons at 607 nm and the ~ 145 ps pump beam at 532 nm within the dye medium. The high reflector provides a preamplified gain of almost a factor of 5 in total energy output. Amplified spontaneous emission (ASE) from the first cell is amplified in the two subsequent cells described previously. The second amplifier cell is end pumped to improve the spatial profile of the beam, and the output is collimated with a 60-cm-focal-length spherical lens. To determine whether ASE from the two amplifier cells contributes significantly to the total output energy, ASE from the first cell was blocked, and the output energy of the dye laser was reduced by at least three orders of magnitude.

The temporal pulse width of the 607-nm-dye-laser beam was measured as a function of pump energy by using a Hamamatsu streak camera (Model C5680-21 with M5676) with a temporal resolution of 10 ps for the selected sweep range of 1 ns. Figure 2(a) shows the temporal profiles of the dye-laser output for different pump energies. The full width half-maximum (FWHM) pulse width of the dye laser is reduced by 9% from 129 ps when the pump energy is increased from 7 to 14 mJ. A further increase in pump energy has no appreciable effect, allowing a consistent pulse width of ~ 115 ps to be maintained. The spectral profile of the dye laser, shown in Fig. 2(b), was measured to have a FWHM of ~ 5 nm with an Ocean Optics spectrometer (Model USB2000) with a resolution of ~ 0.5 nm. This 5 nm bandwidth is necessary to cap-

ture the full spectrum of the nitrogen CARS signal for each laser shot, especially at high temperatures.⁴ The output energy of the dye laser is plotted as a function of the pump energy in Fig. 3. The conversion efficiency of the dye laser is $\sim 15.5\%$ for the entire range of pump energies, implying the medium is not saturated at these energy levels.

The frequency-doubled output of the Nd:YAG regenerative amplifier at 532 nm is used for the pump and probe beams in the nitrogen CARS system, while the dye-laser output at 607 nm is used as the Stokes beam. The pump- and probe-beam energies at the CARS probe volume are 150 μ J, and the energy in the Stokes beam is 800 μ J. The temporal overlap of the pump, probe, and Stokes beams is optimized using translation stages, and the spatial overlap is arranged in a folded BOXCARS geometry, as shown in Fig. 1. The laser beams are focused and recollimated using 300-mm focal length lenses. The spatial resolution defined by the spatial overlap of the beams is estimated to be 30 μ m normal to the beam direction and 1.5 mm in the phase-matching direction. The CARS signal is dispersed by a 1.25 m spectrometer (SPEX 1250M) equipped with a 2400 groove/mm grating. An Andor backilluminated, unintensified CCD camera (Model DU 440BU) with a 2048×512 pixel array is used for acquisition of the CARS spectra. Figure 4 shows a room-air nitrogen spectrum that was averaged over 20 single-shot spectra acquired by using the broadband picosecond CARS system described here. The spectral dispersion of the CARS signal is $0.174 \text{ cm}^{-1}/\text{pixel}$, and the resolution of the CARS detection system is $\sim 0.54 \text{ cm}^{-1}$. Figure 4 also shows a comparison with a theoretical room-temperature spectrum from the Sandia CARSFT code.¹²

In summary, broadband CARS spectroscopy of nitrogen using picosecond lasers has been demonstrated. To our knowledge, this is the first experimental demonstration of broadband picosecond CARS spectroscopy for thermometric purposes. This laser system will allow further investigation of nonresonant-background suppression in high-pressure and hydrocarbon-rich environments¹² for improving the accuracy and sensitivity of CARS thermometry. This system will also allow more detailed

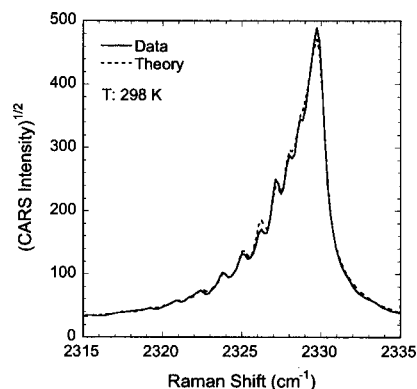


Fig. 4. Experimental and theoretical broadband CARS spectra of nitrogen at room temperature.

studies of the collisional dependence of the CARS signal through variation of the time delay between the pump and the probe beams.

Funding for this research was provided by the Air Force Research Laboratory, Propulsion Directorate, Wright-Patterson Air Force Base, under contract F33615-03-D-2329 and by the Air Force Office of Scientific Research (Julian Tishkoff, Program Manager). S. Roy's e-mail address is sroy@woh.rr.com.

References

1. J. P. Kuehner, M. A. Woodmansee, R. P. Lucht, and J. C. Dutton, *Appl. Opt.* **42**, 6757 (2003).
2. D. R. Snelling, R. A. Sawchuk, and T. Parameswaran, *Appl. Opt.* **33**, 8295 (1994).
3. J. W. Hahn, C. W. Park, and S. N. Park, *Appl. Opt.* **36**, 6722 (1997).
4. A. C. Eckbreth, *Laser Diagnostics for Combustion Temperature and Species*, 2nd ed. (Gordon & Breach, 1996).
5. F. M. Kamga and M. G. Sceats, *Opt. Lett.* **5**, 126 (1980).
6. W. Zinth, A. Lauberau, and W. Kaiser, *Opt. Commun.* **26**, 457 (1978).
7. H. Graener, A. Laubereau, and J. W. Nibler, *Opt. Lett.* **9**, 165 (1984).
8. V. Mozorov, S. Mochalov, A. Olenin, V. Tunkin, and A. Kouzov, *J. Raman Spectrosc.* **34**, 983 (2003).
9. T. Dreier and J. Tobai, *Laser Phys.* **13**, 286 (2003).
10. R. Schwarzwald, P. Monkhouse, and J. Wolfrum, *Chem. Phys. Lett.* **142**, 15 (1987).
11. R. B. Miles and W. R. Lempert, *Annu. Rev. Fluid Mech.* **29**, 285 (1997).
12. R. E. Palmer, "The CARSFT computer code for calculating coherent anti-Stokes Raman spectra: user and programmer information," Report SAND89-8206 (Sandia National Laboratories, 1989).

Time-resolved dynamics of resonant and nonresonant broadband picosecond coherent anti-Stokes Raman scattering signals

Sukesh Roy^{a)} and Terrence R. Meyer

Innovative Scientific Solutions, Inc., 2766 Indian Ripple Road, Dayton, Ohio 45440

James R. Gord

Air Force Research Laboratory, Propulsion Directorate, Wright-Patterson AFB, Ohio 45433

(Received 3 August 2005; accepted 29 November 2005; published online 28 December 2005)

The time-resolved dynamics of resonant and nonresonant broadband picosecond coherent anti-Stokes Raman scattering (CARS) signals in gas-phase media are investigated. For ~ 135 ps pump and probe beams and ~ 106 ps Stokes beams, the magnitude of the nonresonant signals are decreased by more than three orders of magnitude when the probe beam is delayed by ~ 110 ps, whereas the resonant nitrogen CARS signal is reduced only by a factor of 3. Investigation of these time dynamics is important for understanding the optimal time delay for nonresonant background suppression as well as for understanding the collisional and Doppler dependence of the resonant CARS signals. © 2005 American Institute of Physics. [DOI: 10.1063/1.2159576]

Coherent anti-Stokes Raman scattering (CARS) spectroscopy of nitrogen is widely used for temperature measurements in reacting flows and plasmas.^{1,2} In air-breathing combustion environments, measurements of temperature using nitrogen CARS have the advantage that nitrogen is present at high concentrations almost everywhere in the combustor. Most previous CARS thermometric measurements in gas phase or reacting flows have been performed using nanosecond laser pulses. A major limitation of nanosecond-laser-based CARS thermometry is the contribution of the nonresonant signal, which limits the accuracy and degrades the sensitivity of the technique.³ The nonresonant background can be suppressed by polarization selection, but this results in a reduction of the resonant CARS signal by at least a factor of sixteen.³

There have been relatively few demonstrations of picosecond CARS in the gas phase, and all previous measurements in both liquids and gases have been performed using synchronously pumped dye lasers, which do not allow the acquisition of single-shot spectra for unsteady flows.^{4–7} In unsteady flows, where there is significant variation in temperature and density, measurement of the CARS signal using a tunable source such as a synchronously pumped dye laser, optical parametric amplifier, or distributed-feedback dye laser leads to a distortion of the spectra biased toward low temperatures. This is due to the requirement of scanning the dye lasers or the OPA for the acquisition of spectrum covering a bandwidth of ~ 20 – 100 cm^{-1} , especially at temperatures relevant to combustion. We have recently demonstrated picosecond CARS measurements using a broadband modeless dye laser with sufficient bandwidth to excite the full ro-vibrational transition band in a single shot,⁸ thereby enabling nonresonant background suppression while avoiding temperature bias in unsteady flows.

Recently, CARS thermometry using femtosecond laser pulses has also been demonstrated.⁹ Both picosecond and femtosecond CARS systems permit nonresonant background suppression and enable the investigation of molecular-

ensemble collisional dynamics. Relatively straightforward substitution of picosecond lasers into well-established broadband nanosecond CARS systems will enable single-shot thermometry in practical combustion environments; however, femtosecond CARS thermometry will require considerable further development to achieve such measurements.¹⁰

The objective of this work is to investigate the time-resolved dynamics of the broadband picosecond resonant pure-nitrogen CARS signal along with the nonresonant signals from argon, oxygen, and carbon dioxide. This will provide an understanding of the time frame required for effective suppression of the nonresonant contribution to the CARS signal as well as an understanding of the nitrogen-nitrogen collisional-Doppler dephasing and relaxation processes in the ensemble. The dependence of the broadband picosecond CARS signal on pressure and temperature is the subject of ongoing research and will be addressed in a companion letter. The current study is focused on determining the appropriate delay time for the probe beam with respect to the pump beam so as to suppress the nonresonant contribution to the resonant CARS signal. In the liquid phase, time-resolved observation of the resonant and nonresonant contribution to the third-order nonlinear susceptibility using picosecond CARS has been studied by Zinth *et al.*⁶ As expected, the authors observed a distinct temporal behavior for the resonant and nonresonant signals.

The laser wavelengths in the current experiment are selected to excite the rovibrational transition manifold of the nitrogen molecule while being nonresonant to argon, oxygen, and carbon dioxide. The nearly transform-limited frequency-doubled ~ 135 ps output of a Nd:YAG regenerative amplifier at 532 nm is used for the pump and probe beams, and the ~ 106 ps output of a broadband modeless dye laser at 606 nm is used as the Stokes beam. The temporal pulsewidths of the laser beams, measured with a Hamamatsu streak camera (Model C5680-21/M5676), are shown in Fig. 1. Each profile is averaged over ten laser shots. The solid lines shown in Fig. 1 are Gaussian envelopes fitted through the data points and are shown to indicate the deviation of the laser pulsewidths from Gaussian profiles. Further details on

^{a)} Author to whom correspondence should be addressed; electronic mail: sroy@woh.rr.com

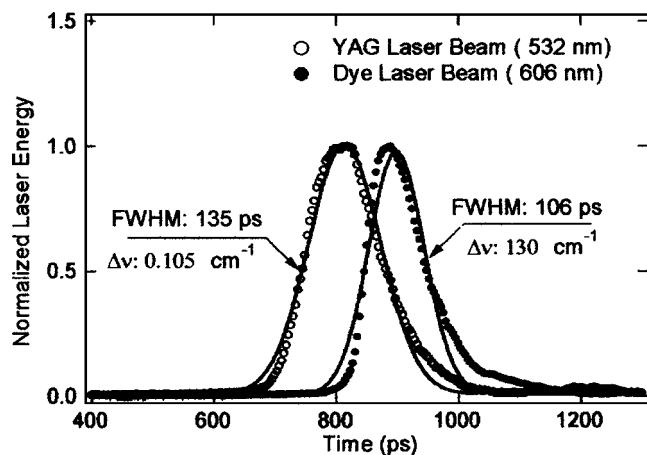


FIG. 1. Temporal profiles of the Nd:YAG and dye-laser beams acquired with a Hamamatsu streak camera. The solid lines are Gaussian profiles fitted through the data points. The profiles are shifted temporally for clarity.

the design and performance of the broadband picosecond CARS system are described elsewhere.⁸

For these experiments, a CARS polarization is induced in the medium by the narrowband pump and the broadband Stokes beams by overlapping them both spatially and temporally. A variable-delay probe beam is then used to investigate the induced polarization. The energy level diagram of the resonant and nonresonant contributions to the CARS signal is shown in Fig. 2.^{1,4} The nonresonant signal appears as a broad background that interferes with and distorts the CARS spectrum. The contribution from the nonresonant background is highest when all the laser beams are overlapped temporally and can significantly affect temperature accuracy, especially in hydrocarbon-rich environments due to the high nonresonant susceptibility of hydrocarbon compounds.

A typical room-temperature CARS spectrum in pure nitrogen and a nonresonant spectrum in pure argon averaged over 100 laser shots are shown in Fig. 3; these spectra are acquired with all laser beams arriving at the probe volume

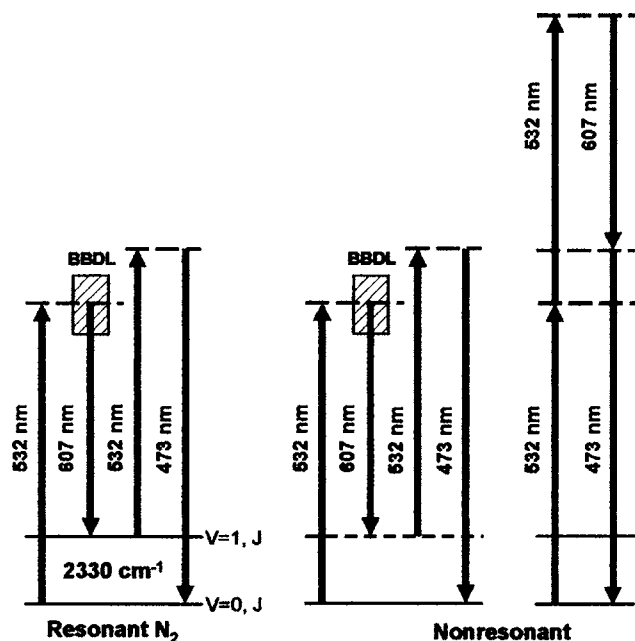


FIG. 2. Energy-level diagrams of the resonant and nonresonant processes that contribute to the CARS signal.

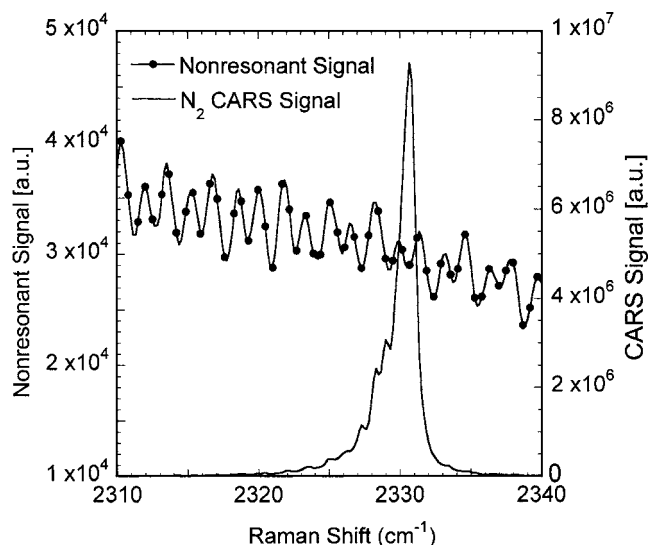


FIG. 3. A typical room temperature CARS spectrum in pure nitrogen and a pure nonresonant spectrum in argon averaged over 100 laser shots.

simultaneously. The nitrogen spectrum represents the overlapping Q -branch transition in the $v=0 \rightarrow v=1$ band in the ground electronic level. Modulation in the nonresonant spectrum is due to etalon effects from the dye cells of the modelless dye laser. The time-resolved resonant CARS signal in pure nitrogen and the nonresonant signal acquired by flowing pure argon, oxygen, and carbon dioxide are shown in Fig. 4 as a function of the time delay between the pump and probe beams. Each data point represents the integrated signal over an entire spectrum, such as that shown in Fig. 3, for a fixed time delay between the pump and probe beams. From Fig. 4, it is evident that the magnitudes of all the nonresonant signals are decreased by more than three orders of magnitude when the probe beam is delayed by ~ 110 ps with respect to the pump beam. Note that the full width half maximum temporal envelope of the Stokes beam is ~ 106 ps while that of the pump or probe beam is ~ 135 ps, as shown in Fig. 1. The magnitude of the resonant CARS signal is highest when the beams are overlapped temporally due to the nonresonant contribution to the resonant CARS signal. The signal decays as the probe beam is delayed with respect to the pump beam due to dephasing of the pump/Stokes-induced polarization. At approximately 130 ps, the slope of decline in the signal

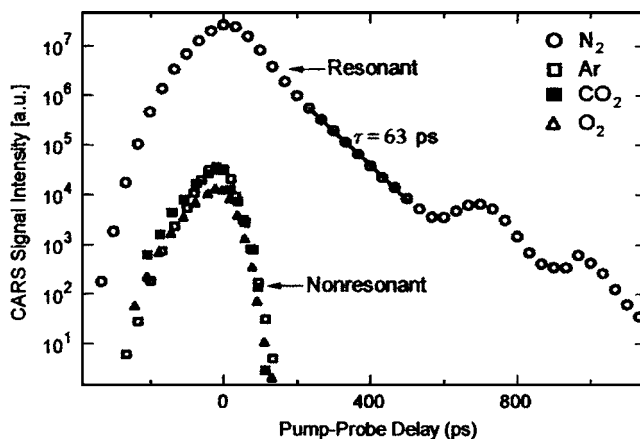


FIG. 4. Time-resolved resonant and nonresonant signals as functions of pump-probe time delay displaying the behavior of the resonant and nonresonant CARS signal.

changes, indicating the disappearance of the nonresonant contribution to the CARS signal.

The data in Fig. 4 indicate the magnitude of the CARS signal is reduced by a factor of 3 while the nonresonant signal is reduced by over three orders of magnitude at ~ 110 ps. Beyond 130 ps, the signal decays exponentially with $\tau=63$ ps due to collision-induced dephasing and rotational energy transfer.¹¹ The oscillation of the signal after ~ 500 ps is due to the constructive and destructive interference between the CARS signal generated from different rovibrational transitions excited by the broadband CARS system dictated by the phase differences between them.

In summary, we demonstrate that the broadband picosecond CARS system described here can be used to suppress the nonresonant contribution preferentially while enabling single-shot measurements typical of broadband nanosecond-laser-based systems. In future work, the time-resolved study described here will be extended to include the effects of Doppler and collisional broadening for a wide range of temperatures and pressures.

Funding for this research was provided by the Air Force Research Laboratory, Propulsion Directorate, Wright-Patterson AFB, under Contract No. F33615-03-D-2329-DO 002, and by the Air Force Office of Scientific Research (Anne Mutsuura, Program Manager).

¹A. C. Eckbreth, *Laser Diagnostics for Combustion Temperature and Species*, 2nd ed. (Gordon and Breach, St. Leonards, Australia, 1996).

²K. Kohse-Hoinghaus and J. B. Jeffries, *Applied Combustion Diagnostics* (Taylor and Francis, New York, 2002).

³A. C. Eckbreth and R. J. Hall, *Combust. Sci. Technol.* **55**, 175 (1981).

⁴F. M. Kamga and M. G. Sceats, *Opt. Lett.* **5**, 126 (1980).

⁵V. Mozorov, S. Mochalov, A. Olenin, V. Tunkin, and A. Kouzov, *J. Raman Spectrosc.* **34**, 983 (2003).

⁶W. Zinth, A. Laubereau, and W. Kaiser, *Opt. Commun.* **26**, 457 (1978).

⁷H. Graener, A. Laubereau, and J. W. Nibler, *Opt. Lett.* **9**, 165 (1984).

⁸S. Roy, T. R. Meyer, and J. R. Gord, *Opt. Lett.* **30**, 3222 (2005).

⁹P. Beaud, H. M. Frey, T. Lang, and M. Motzkus, *Chem. Phys. Lett.* **344**, 407 (2001).

¹⁰T. Long and M. Motzkus, *J. Opt. Soc. Am. B* **19**, 340 (2002).

¹¹G. Knopp, P. Beaud, P. Radi, M. Tulej, B. Bougie, D. Cannavo, and T. Gerber, *J. Raman Spectrosc.* **33**, 861 (2002).

An injection-seeded MHz repetition rate optical parametric oscillator

Naibo Jiang and Walter R. Lempert

Departments of Mechanical Engineering and Chemistry, Ohio State University, Columbus, OH 43202
lempert.1@osu.edu

Gary L. Switzer and Terrence R. Meyer

Innovative Scientific Solutions, Inc., 2766 Indian Ripple Rd., Dayton, OH 45440

James R. Gord

Air Force Research Laboratory, Propulsion Directorate, Wright-Patterson AFB, OH 45433

Abstract: We demonstrate the ability to generate ultra-high frequency sequences of broadly wavelength tunable, high intensity laser pulses using a custom built Optical Parametric Oscillator (OPO) pumped by the third harmonic output of a “burst-mode” Nd:YAG laser. Burst sequences consisting of 6 – 10 pulses separated in time by 6 – 10 microseconds are obtained, with average total conversion efficiency from the 355-nm pump to the 651.5-nm signal and 780-nm idler of approximately 36%. An external cavity diode laser at 780 nm is used to injection seed the OPO cavity, resulting in a time-averaged line width of approximately 200-300 MHz for both the signal and idler waves.

© 2006 Optical Society of America

OCIS codes: (190.4970) Parametric oscillators and amplifiers; (280.2490) Flow diagnostics; (280.1740) Combustion diagnostics

References and links

1. B. Thurow, N. Jiang, M. Samimy, and W. Lempert, “Narrow-linewidth megahertz-rate pulse-burst laser for high-speed flow diagnostics”, *Appl. Opt.* **43**, 5064-5073 (2004), <http://ao.osa.org/abstract.cfm?id=81106>.
2. P. Wu, W. R. Lempert, and R.B. Miles, “MHz pulse-burst laser system and visualization of shock-wave boundary-layer interaction in a Mach 2.5 wind tunnel”, *AIAA J.* **38**, 672-679 (2000), <http://pdf.aiaa.org/jaPreview/AIAAJ/2000/PVJAIMP1009.pdf>.
3. K. Kohse-Hoinghaus and J.B. Jeffries, *Applied Combustion Diagnostics* (Taylor & Francis, New York, 2002).
4. P. Wu, W. R. Lempert, and R.B. Miles, “Tunable pulse-burst laser system for high-speed imaging diagnostics”, AIAA-98-0310, 36th AIAA Aerospace Sciences Meeting, Reno, NV, Jan. 12-15, (1998).
5. J.D. Luff, D.K. Mansfield, S.H. Zaidi, H. Aschoff, J.W. Kuper, and R.B. Miles, “Development of a Tunable Megahertz Pulse-burst Alexandrite Laser System”, AIAA-2003-3746, 34th AIAA Plasmadynamics and Lasers Conference, Orlando, FL, (2003), http://pdf.aiaa.org/preview/CDReadyMPLC03_578/PV2003_3746.pdf.
6. C.F. Kaminski, J. Hult and M. Alden, “High repetition rate planar laser induced fluorescence of OH in a turbulent non-premixed flame”, *Appl. Phys. B.* **68**, 757-760 (1999).
7. W. Koechner, *Solid-State Laser Engineering* (Springer-Verlog, Berlin, 1992).
8. W.R. Bosenberg, W.S. Pelouch and C.L. Tang, “High-efficiency and narrow-linewidth operation of a two-crystal β -BaB₂O₄ optical parametric oscillator”, *Appl. Phys. Lett.*, **55** (19), 1952-1954 (1989).
9. J.A.J. Fitzpatrick, O.V. Checkhlov, J.M.F. Elks, C.M. Western and S.H. Ashworth, “An injection seeded narrow bandwidth pulsed optical parametric oscillator and its application to the investigation of hyperfine structure in the PF radical”, *J. Chem. Phys.*, **115**, 6920-6930 (2001).
10. W. Lee, and W. Lempert, “Enhancement of Spectral Purity of Injection-Seeded Titanium:Sapphire Laser by Cavity Locking and Stimulated Brillouin Scattering”, *Appl. Opt.* **42**, 4320-4326 (2003), <http://ao.osa.org/abstract.cfm?id=73568>.
11. A. Yariv, *Quantum Electronics*, (John Wiley & Sons, New York, 1989).

12. Paul, P.H., Lee, M.P., and Hanson, R.K., "Molecular velocity imaging of supersonic flows using pulsed planar laser-induced fluorescence of NO", *Optics Letters* **14**, 417-419, (1989), <http://ol.osa.org/abstract.cfm?id=9623>.
-

1. Introduction

While there has been enormous progress in recent years in the development and application of a variety of optical diagnostic imaging techniques, the ability to capture time-evolving or volumetric information is severely constrained by limitations of available laser technology. Over the last several years, we have been developing the capability of generating "trains" of 20-30, high-energy Nd:YAG pulses, separated in time by a variable period as short as one microsecond [1,2]. The approach utilizes a low power (order mW) master oscillator, a custom dual Pockel cell pulse "slicer," and a series of flashlamp-pumped amplifiers. In general, it is found that significant energy pulses can be extracted for sequences as long as ~150 microseconds, with total energy per burst sequence of ~1.5 J at the fundamental wavelength of 1064 nm and 2nd/3rd harmonic conversion efficiencies of ~50% and 40%, respectively [1].

In this paper we demonstrate the ability to generate trains of wavelength-tunable pulses using a custom built Optical Parametric Oscillator (OPO), which is the first step toward our goal of developing an ultra-high frame rate Planar Laser-Induced Fluorescence (PLIF) imaging system. PLIF is a powerful diagnostic technique that has been widely employed for studies of combustion and high speed reacting flow [3]. However, since PLIF is based on resonant absorption of radiation, high instantaneous power, wavelength-tunable laser sources are required for time-resolved imaging. While dye and/or solid-state sources, including Nd:YAG-pumped OPOs, are readily available commercially, the published technology on generation of high-speed bursts of such tunable radiation is, to our knowledge, limited to three papers. Wu, et al. [4] pumped a grazing-incidence dye laser with ~0.5 mJ per pulse at 532 nm from an Nd:YAG burst-mode laser, which is similar to that used in the present work. While burst-mode output was obtained, the individual pulse energies were too low to be measured. Luff, et al. [5] have reported an alexanderite system which utilizes the combination of a long pulse (~170 ns) Q-switched oscillator, a Harriott Cell Regenerative Amplifier (for pulse slicing and amplification), and two single-pass amplifiers. Approximately 150 microjoules per pulse, for a 30-pulse sequence with 1- μ s separation at 761 nm was reported. Kaminski, et al. [6] used a set of four commercial double-pulsed Nd:YAG lasers to pump a single commercial dye laser. Starting with 270 mJ per individual pulse at 532 nm, they were able to generate eight pulses at 282 nm, with an average energy of ~1 mJ and a minimum interpulse period of 125 μ sec, constrained by the high intensity pumping requirement of the dye laser.

2. Experiments

Our strategy is to utilize an OPO for the generation of tunable radiation, taking advantage of the fact that the gain decays essentially instantaneously after the passage of each pump pulse within the burst. It was hypothesized that photo-bleaching effects, which severely limit the repetition rate of dye lasers, would therefore be minimal, as would be thermal effects since absorption in BBO at 355 nm is quite low [7]. The custom-built OPO cavity, shown in Fig. 1, was designed specifically for use with the burst mode Nd:YAG pump laser. The OPO "gain" medium consists of a pair of 12-mm-long Type I BBO crystals that are 5-mm \times 7-mm in cross section and are arranged in a linear cavity configuration. The crystals are oriented to provide walk-off compensation between the pump and signal/idler beams, which provides higher effective gain for the relatively small cross sectional area (~2-4 mm²) pump beam [8]. The cavity is doubly resonant on the signal and idler wavelengths, using a broad-band high reflector and output coupler coated for 20 – 30% reflectivity in the wavelength range 600 - 850 nm. The 355-nm pump beam is coupled into and out of the cavity using a pair of 45⁰

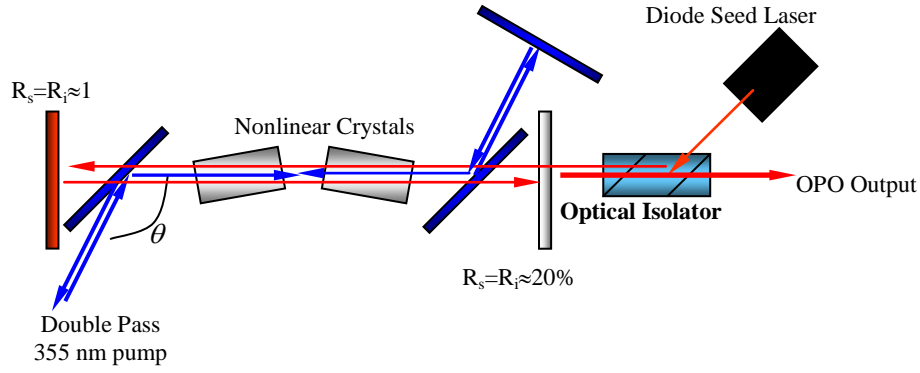


Fig. 1. Schematic diagram of OPO Cavity illustrating injection-seeding and double pass of 355- nm pump beam. Cavity is doubly resonant at signal and idler wavelengths.

dichroic mirrors, which reflect the 355 nm pump beam and transmit the OPO signal and Idler beams. By using a 355-nm 0° reflection mirror, the 355-nm pump beam can be retro-reflected for a second pass through the OPO cavity. Note that double-pass alignment requires very low angular displacement due to the phase-matching requirement. More specifically, angular displacement of the retro-reflected pump is equivalent to changing the BBO crystal angle. Since a 1° angle change affects the OPO signal wavelength by ~ 70 nm, it is clear that careful alignment is required.

The total cavity length is ~ 10 cm, limited by the large size of the current pump mirror mounts. A single-frequency external cavity diode laser is used to injection seed the cavity at either the signal or idler [9] wavelengths, depending upon the experiment. The seed radiation is injected through the output coupler using a Faraday rotation optical isolator, in a manner similar to that employed previously for injection seeding of a Titanium:Sapphire laser [10].

3. OPO Conversion Efficiency

A series of baseline measurements were performed in which the burst-mode pump laser was operated in a manner identical to that used to generate high-frequency pulse trains, but with only a single pulse per burst. The results are summarized in Fig. 2, which show OPO total power conversion efficiencies as a function of input pulse energy when the OPO cavity is operated in double-pass pump configurations. It can be seen that the OPO threshold is ~ 4 mJ, and the conversion efficiency rises rapidly as a function of pulse energy, reaching a plateau of $\sim 35\%$ (total signal + idler) for a pump input energy of ~ 25 mJ. For comparison, the theoretical threshold for single-pass pumping of a doubly resonant OPO cavity can be estimated from the expression [11]

$$I_{th} = \left(\frac{1}{\epsilon_o \mu_o^3} \right)^{1/2} \frac{n_p n_s n_i \left(\cosh^{-1} \frac{1 + R_s R_i}{(R_s + R_i)} \right)^2}{8 \omega_s \omega_i l^2 d_{eff}^2} \quad (1)$$

where ϵ_o and μ_o are permittivity and permeability of free space, respectively, d_{eff} is the effective non-linear coefficient for OPO conversion, equal to 1.98 pm/V, l is the crystal length, R_s and R_i are the reflectivity of the output coupler at the signal and idler wavelengths,

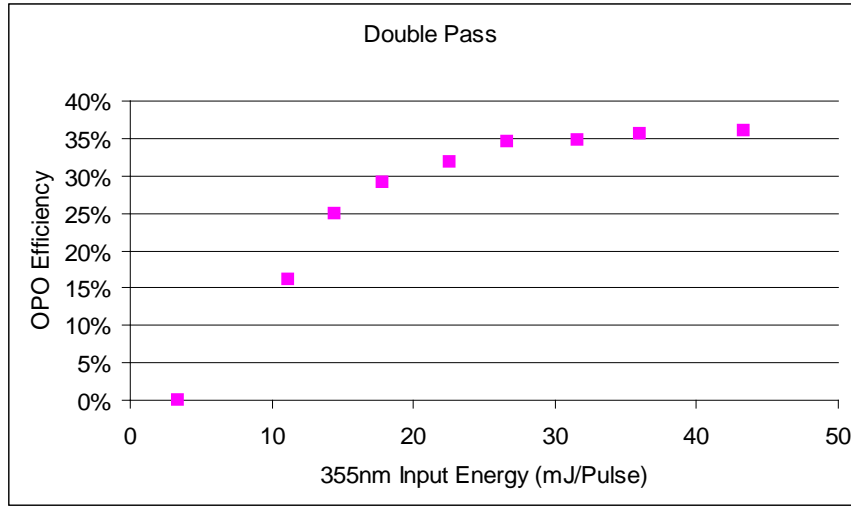


Fig. 2. Conversion efficiency of OPO cavity shown in Fig. 1 for single 355-nm pulse from burst-mode laser system.

respectively. Equation (1) predicts a threshold intensity of $\sim 2.2 \text{ MW/cm}^2$, corresponding to a threshold pump pulse energy of $\sim 1.5 \text{ mJ}$ for our beam of nominal diameter 3.0 mm and pulse duration of 10 ns . This is in quite good agreement with our observed threshold of $\sim 4 \text{ mJ}$. We note that achieving such low threshold implies that the beam spatial quality of the burst mode pump laser is quite good, an issue which was a significant concern prior to performing these measurements. We also point out that low threshold, while always important for nonlinear processes, is particularly critical for burst mode operation of the OPO due to the inherent intensity envelope of the individual pump pulses within the burst. While we have not yet explored this in detail, we note that the pump intensity should be a factor of approximately four greater than threshold for efficient OPO operation [7]. As illustrated in Fig. 2, the plateau in conversion efficiency begins at $\sim 30\%$ for a pump energy of $\sim 17 \text{ mJ}$, which is about four times threshold.

Because our OPO cavity is double resonant, the OPO output includes both signal (651 nm) and idler (780 nm) components with a measured signal idler energy ratio of $0.55:0.45$, which is approximately equal to the ratio of single photon energies. In broad band operation the OPO was operated over a wide range of wavelengths from $\sim 600/869 \text{ nm}$ to $700/720 \text{ nm}$ for the signal/idler respectively. It was found that the OPO output was approximately constant, at least over a signal range of $\pm 50 \text{ nm}$. We also seeded the OPO system at idler wavelengths of 827 nm and 780 nm . In both seeding cases, the OPO conversion efficiency was not significantly changed, but the spectral linewidth was greatly narrowed.

4. Burst Sequences

Operation in burst mode is illustrated in Figs. 3-5, which show some typical single burst sequences for the 355-nm pump and corresponding OPO idler output at 780 nm . Due to limitations in our sampling oscilloscope, the RC time constant was increased to a few microseconds to display the captured burst sequences. The relatively long observed decay of the individual pulses is an artifact of this and does not correspond to the actual ($\sim 6 \text{ nsec}$) individual pulse durations. In each of the illustrated cases, the OPO cavity was operated with injection seeding at the 780-nm idler wavelength. (Unseeded operation gave nearly identical results). Figure 3 illustrates a burst sequence of six pulses, separated in time by $10 \mu\text{s}$. A

variety of additional combinations have been produced ranging from 1 to 12 pulses with 4- to 12- μ s spacing. Note that the displayed pump and OPO output burst sequences were obtained simultaneously, and that a significant effort was made to minimize the non-uniformity of the pulse energy distribution within the burst.

The average instantaneous pump energy for the burst sequence shown in Figure 3 is ~ 31 mJ and the total conversion ratio is $\sim 35\%$. In this case the OPO 651-nm signal energy is ~ 6 mJ per pulse.

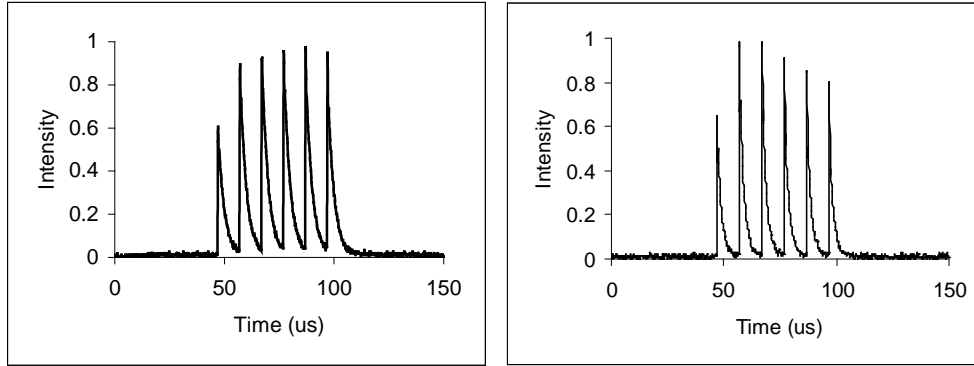


Fig. 3. Typical 6-pulse, 10- μ s-spacing pump (left) and double pass OPO (right) burst sequence. Total OPO conversion efficiency (signal + idler) is 35%. Average single-pulse 355-nm input energy is 31 mJ.

Figure 4 is very similar to Figure 3, except that the number of pulses has been increased to eight. Once again, the input 355 nm pump burst is reasonably uniform. It is also noted that the intensity envelopes of the OPO output follow reasonably the envelopes of the pump pulses. The average pump energy is 26 mJ and the total conversion ratio is 33%.

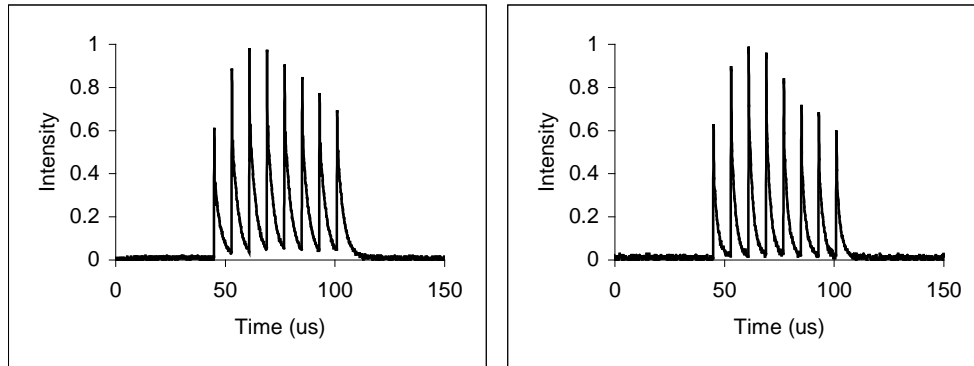


Fig. 4. Typical 8-pulse, 8- μ s-spacing pump (left) and double-pass OPO (right) burst sequence. Total OPO conversion efficiency (signal + idler) is 33%. Average single-pulse 355-nm input energy is 26 mJ.

Figure 5 illustrates another typical case, consisting of 10 pulses with 6 μ s spacing. Again, both the pump and OPO output bursts are reasonably uniform and the intensity envelopes are very similar, which means each pulse has approximately equal conversion ratio. The average pump energy is 16 mJ per pulse, and the OPO conversion efficiency is 32%, which is similar to that observed for the single-pulse case.

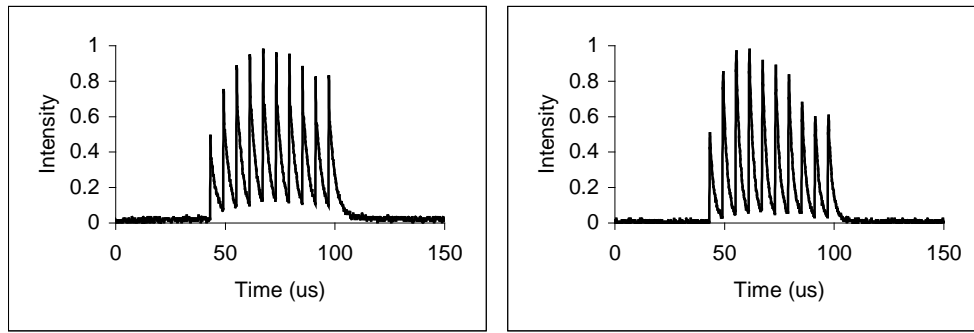


Fig. 5. Typical 10-pulse, 6- μ s-spacing pump (left) and double-pass OPO (right) burst sequence. Total OPO conversion efficiency (signal + idler) is 32%. Average single-pulse 355-nm input energy is 16 mJ.

A variety of additional combinations have been produced ranging from 1 to 12 pulses with 4- to 12- μ s spacing. In all cases total signal + idler conversion efficiency is \sim 30% or more, essentially identical to that obtained using a single pulse. It is also noted that the intensity envelopes of the OPO output follow reasonably, but not precisely, the envelopes of the pump pulses. We attribute this result to the fact that the pump-pulse intensity is significantly above threshold by a factor of four or more. In this regard it is important to note that the pump laser produces bursts with an inherent intensity envelope, particularly when operated at high intensity where gain narrowing is significant. The multiple non-linear steps (2^{nd} / 3^{rd} harmonic followed by OPO) will tend to exacerbate this problem and so it is critical to produce the most uniform pump bursts as possible.

5. OPO Spectral Linewidth

As discussed earlier, a prime motivation for the work presented here is to develop the capability to perform NO-based Planar Laser Induced Fluorescence (PLIF) imaging [12] at ultra-high frame rates. As such an ultimate goal is to mix the OPO signal output with residual 355 nm pump in order to generate tunable burst mode output in the UV range. Our OPO signal output is at 651 nm, a spectral region where it is difficult to obtain diode laser seed sources. A potential solution is to seed at the idler wavelength [8], which for this case is \sim 780 nm.

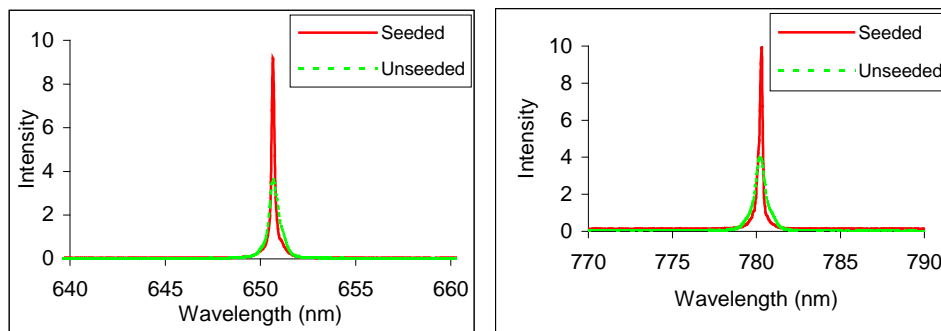


Fig. 6. Low resolution spectra of seeded and unseeded OPO signal (left) and idler output (right). Note that the OPO is seeded at the idler wavelength.

We used an external cavity diode laser (\sim 5 mW at 780 nm) as the seed source. Figure 6 shows typical low resolution spectra, obtained with an available 0.3 m spectrometer, for

seeded and unseeded OPO signal and idler outputs. Notice that both the signal and idler beams are narrowed significantly, from ~ 1 nm to a line width which is very difficult to measure using the low resolution spectrometer.

We have also performed some preliminary measurements using a 2-GHz free spectral range confocal spectrum analyzer, which while not designed for line-width measurements of pulsed lasers can, nonetheless, provide a reasonable estimate. The spectrum analyzer was scanned slowly using a computer generated voltage ramp applied to the controller's external ramp input. An ordinary PIN photodiode captured the transmitted signal which was processed with a boxcar averager and digitized with a computer. A narrow bandpass 780-nm filter was placed directly in front of the detector to avoid stray light at 532 or 355 nm.

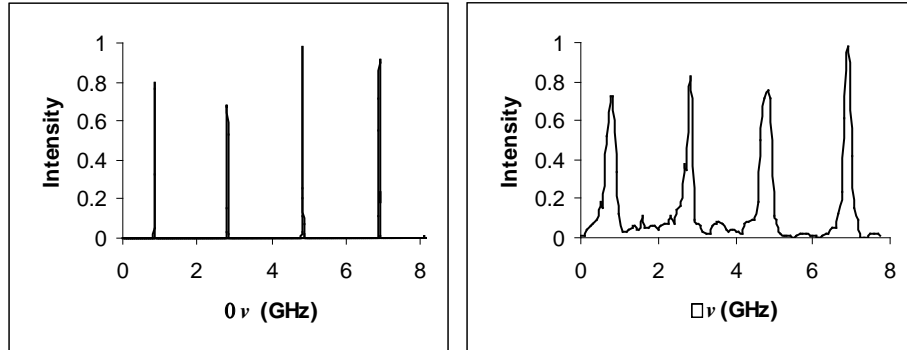


Fig. 7. Etalon trace of cw seed laser (left) and injection-seeded OPO idler output (right) at 780 nm.. Linewidth of seeded OPO output is 200 – 300 MHz, based on 2.0 GHz FSR of etalon.

Figure 7 shows typical traces of the cw seed laser (left) and time averaged pulsed OPO signal output (right). While the OPO signal output traces are admittedly somewhat non-steady, due to a combination of cavity mode stability and drift in the non-stabilized etalon, it is clear that the average line width is a fraction (10 – 15%) of the etalon FSR. We conclude that the time averaged line width is on the order of 200 – 300 MHz. While it is somewhat speculative, it should be noted that the longitudinal mode spacing for our OPO cavity is ~ 1.5 GHz. It is possible, although not conclusively determined, that the weak “peaks” which seem to periodically occur at a position \sim one third of the way between the major transmission peaks could be an indication of lasing on an additional longitudinal mode. We also note that the results from a low-resolution spectrometer showed narrowing line width at the signal wavelength (651.5 nm), when seeded at the 780-nm idler wavelength.

6. Conclusions

We have demonstrated in this paper the ability to generate ultra-high frequency sequences of broadly wavelength-tunable, high-intensity laser pulses using a custom built injection-seeded OPO pumped by the third-harmonic output of a “burst-mode” Nd:YAG laser. Burst sequences consisting of 6 – 10 pulses separated in time by between 6 and 10 μ s are obtained. For a double pass OPO, the average total OPO conversion efficiency is approximately 35%, corresponding to individual 651 nm single pulse energy of ~ 6.0 mJ. An external cavity diode laser at 780 nm is used to injection seed the OPO cavity, resulting in substantial narrowing, from ~ 1 nm to 200-300 MHz for both the signal and idler waves.

Future work will be focused on generation of higher power UV output, as well as on extension of the burst envelop. The latter will be attempted using a long-pulse duration power supply for pumping the Nd:YAG amplifier chain. Preliminary work has indicated that this approach can generate reasonably flat-top gain profiles for durations in the range 0.5 – 1.5 ms.

Acknowledgements

The authors would like to acknowledge Brian Thurow, currently of Auburn University, for his assistance and many useful discussions during his tenure in the Ohio State Gas Dynamics Laboratory. The support of the U.S. Air Force Research Laboratory, Propulsion Directorate under a Phase II Small Business Innovative Research program under contract no. F33615-03-C-2339 is also acknowledged, as well as support from the National Science Foundation (Division of Chemical and Transport Systems), and the Air Force Office of Scientific Research (Program in Unsteady Aerodynamics and Hypersonics).

Water-Vapor Detection Using Asynchronous THz Sampling

MICHAEL S. BROWN,* GREGORY J. FIECHTNER, J. V. RUDD,† DAVID A. ZIMDARS, MATTHEW WARMUTH,‡ and JAMES R. GORD

Innovative Scientific Solutions, Inc., 2766 Indian Ripple Road, Dayton, Ohio 45440-3638 (M.S.B.); Sandia National Laboratories, P.O. Box 969, Livermore, California 94550-0969 (G.J.F.); Picometrix, Inc., 2925 Boardwalk, Ann Arbor, Michigan 48104-6765 (J.V.R., D.A.Z., M.W.); and Air Force Research Laboratory, Propulsion Directorate, Wright-Patterson AFB, Ohio 45433-7251 (J.R.G.)

The use of a fiber-coupled terahertz (THz) transmitter/receiver pair for spectroscopic detection of water vapor is investigated. Transmission signals of an alumina cylinder demonstrate that the measurement approach can be applied in a windowless ceramic combustor. First, a conventional commercial transmitter/receiver pair is used to make measurements for frequencies to 1.25 THz. Water-vapor absorption is clearly evident within the alumina transparency window and is readily modeled using existing databases. A variety of data-acquisition schemes is possible using THz instrumentation. To assess signal-collection techniques, a prototype THz transmitter/receiver pair is then used with the asynchronous optical-sampling (ASOPS) technique to obtain asynchronous THz-sampling signals to 1 THz without the need for an optomechanical delay line. Two mode-locked Ti:sapphire lasers operating at slightly different repetition rates are used for pumping the transmitter and receiver independently to permit a complete time-domain THz signal to be recorded. The resulting repetitive phase walkout is demonstrated by collecting power spectra of room air that exhibit water-vapor absorption.

Index Headings: Terahertz time-domain spectroscopy; THz-TDS; Asynchronous optical sampling; ASOPS; Water vapor.

INTRODUCTION

The field of terahertz (THz) time-domain spectroscopy has developed rapidly, and great strides have been made in the technological innovation of THz sources and detectors. Brief summaries of this rapid evolution can be found in review papers by Nuss and Orenstein¹ and Chen and Zhang.² THz sources provide free-space, low-average-power output (~ 10 nW) that can be coherently or incoherently detected. The low output levels make it possible to analyze detected signals in the linear-dispersion regime.³ With coherent detection, signals that are 1/160th the strength of the incoherent thermal background can be detected.⁴

Terahertz sources and detectors have been used extensively for spectroscopy and imaging.⁵ The short-pulse nature of the time-resolved approach makes it possible to study the dynamics of a wide variety of systems using either THz emission or pump/probe approaches.⁶ THz time-domain spectroscopy has been successfully performed on pure samples of liquid water^{7,8} and of polar^{8,9} and nonpolar¹⁰ solvents. Free-electron transport properties and dynamics in photoionized hexane have been shown to be consistent with the Drude model for the frequency-dependent dielectric function.¹¹ The collision frequency and plasma density of a helium discharge have been measured.¹²

Extraction of both components of the complex dielectric

function can be accomplished using THz time-domain spectroscopy without the need for a Kramers–Kronig analysis,¹³ and fundamental spectral-line-shape studies can be performed as well. Several groups have demonstrated gas-phase absorption spectroscopy. A setup that employs an antenna source along with broadband bolometric detection has been used to detect H₂S, with a detection limit of 30 ppm.¹⁴ Employing an antenna/receiver pair, Harde et al. performed THz time-domain spectroscopy on methyl bromide, methyl chloride, and methyl fluoride. They accurately measured molecular constants and the self-broadening coefficient through a pulse-propagation analysis of the time-resolved THz pulses.^{15,16} A lineshape analysis of the reconstructed absorption revealed a spectrum that bridges the two classical line shape regimes—namely, the van Vleck–Weisskopf and the Lorentzian regimes.^{16,17} Near-real-time part-per-million detection of methyl chloride has recently been demonstrated using a THz–TDS spectrometer based on a White-cell design.¹⁸ While most of the studies published to date have been performed on static-gas samples, preliminary investigations have been conducted in stable flame environments on the detection of hot water molecules.¹⁹ Since a number of passive dielectric and semiconductor materials are semi-transparent in the THz regime, the frequency-dependent absorption and dispersion coefficients can be measured using THz time-domain spectroscopy. Measurement of these coefficients expands the database of information collected with traditional far-infrared (FIR) and microwave techniques and provides a tool for examining the role of intrinsic and impurity charge carriers.²⁰

In the present study, we explore the use of THz time-domain spectroscopy for the investigation of gas-phase spectra in ceramic vessels. Detection of stable major species such as water at the exit plane of a combustor provides a means to assess combustor efficiency. First, we employed a conventional commercial time-domain instrument in which the time delay is scanned optomechanically, with the same laser being used to drive the transmitter and receiver. We then explored the use of electronic synchronization of separate lasers for driving the prototype transmitter and receiver with asynchronous optical sampling (ASOPS). To our knowledge, this technique was first proposed independently by Lill et al.^{21,22} and by Barnes and Lytle.²³ The ASOPS technique has been employed to delay the pulse train from one laser with respect to another,^{24,25} and to delay the outputs between a mode-locked diode laser and a modulated diode laser,²⁶ between a mode-locked laser and a free-running electrical signal,²⁷ and between a mode-locked laser and a free-running microwave source.²⁸ A similar asynchronous-sampling effect can be achieved by splitting the output from a single laser and passing it through two Fabry–Perot interferometers with a slight difference between

Received 14 August 2005; accepted 9 January 2006.

* Author to whom correspondence should be sent. E-mail: michael.brown@wpafb.af.mil.

† Current address: Sandia National Laboratories, P.O. Box 5800, Albuquerque, NM 87123-1153.

‡ Current address: General Dynamics, P.O. Box 134008, Ann Arbor, MI 48113-4008.

their mirror separations. Under measurement conditions where it is desirable or necessary to sweep through the signal rapidly, delays between laser sources generated via optomechanical means can become problematic. Such conditions arise, for example, in the study of molecular energy transfer. To address this concern, we sought to make a THz time-domain measurement using the asynchronous THz-sampling technique, mapping short real-time intervals onto long equivalent-time intervals that can be accommodated more easily during experiments. Recently, Janke et al.²⁹ demonstrated the use of the ASOPS technique to measure the resonant response of a biosensor cavity in the THz spectral region.

The ASOPS technique was originally developed to provide a platform for measurement of rapid excited-state processes in a pump/probe format without the need for an optomechanical delay line.^{30,31} Here, two mode-locked lasers are operated at slightly different repetition rates, producing a controlled relative-phase walkout between the two beams—in effect, a replacement for an optomechanical delay line. Each successive probe pulse samples a longer delay with respect to the previous pump pulse until this delay equals the pump-pulse period; then the cycle is repeated. In this way, a real-time period is scaled to an equivalent-time period by a factor of $f_1/(f_1 - f_2)$, where f_1 and f_2 denote the repetition rates of the two lasers. Synchronous detection is achieved without the need to modulate either beam.³¹ The absence of an optomechanical delay line in the ASOPS approach maintains the spot size of the pump and probe beams constant in the overlap region and eliminates the need to determine “time zero” during wavelength tuning.³⁰ This technique has been successfully employed to measure the excitation and decay dynamics of fluorophores in liquid solution,³¹ gas-phase quenching rates,³² and species concentrations³³ in flames. The use of dual-beam excitation permits determination of the quenching rates required for absolute concentration measurements.³³ The ASOPS technique can also be advantageous for signal-to-noise enhancement. Selection of a sufficiently large beat frequency allows rapid signal averaging combined with high-pass filtering of laser-baseband noise. The sampling time (temporal resolution) is determined by the beat frequency ($\Delta f = f_1 - f_2$) divided by the product of the laser frequencies, $\tau_{\text{samp}} = \Delta f/f_1 f_2$, while the collection time is given by $1/\Delta f$. Hence, to improve signal-to-noise ratios and reduce collection times, it is desirable to maximize the beat frequency. However, this is done at the expense of temporal resolution so a compromise must be reached for each individual measurement. In practice, the beat frequency must satisfy $\Delta f < \tau f_2 F$, where τ denotes the desired temporal resolution and F is the bandwidth of the detection system.²⁴ The ASOPS technique requires a more complicated hardware setup than is often used for pump/probe measurements. However, the payoffs of increased data acquisition rate and increased signal-to-noise ratio through ac coupling of the signal can far outweigh the setup complexity in some measurement scenarios.

THZ INSTRUMENT

Measurements were made using THz-transmitter and receiver modules produced by Picometrix in two platform configurations. The first configuration made use of a commercially available system (T-Ray 2000³⁴) that employs a conventional optomechanical delay line. This typical THz time-domain-spectroscopy platform uses a single femtosecond-laser

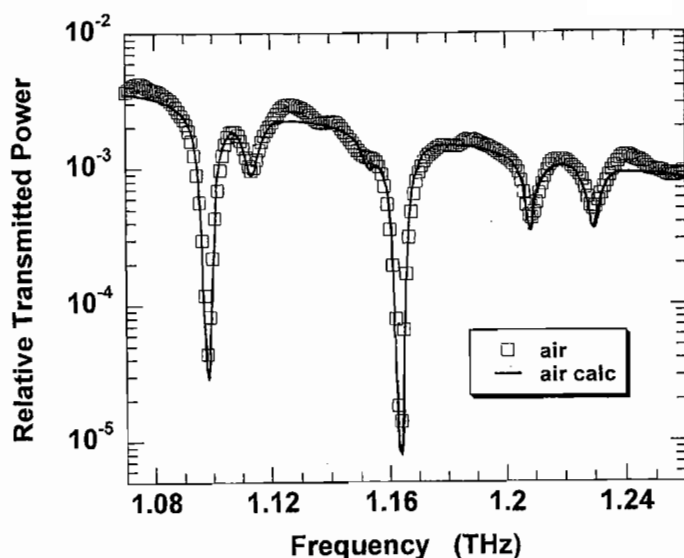


Fig. 1. Measured and calculated absorption spectra in room air with two strong and three weak water-vapor lines.

oscillator to pump both the THz transmitter and the THz receiver. The output of the laser was split, with one half of the energy being directed to the transmitter, and the other half being directed through an optomechanical delay line to the receiver. The THz receiver acts as a time-gated detector. As the optical delay is scanned, the receiver sweeps through the complete THz signal. For the spectrum shown in Fig. 1, the delay was scanned a total of 277 ps at a rate of 5 ps/s. The signal was recorded every 5.1 μm of linear travel, which corresponds to a time step of 17 fs. Four back-to-back sweeps were averaged to yield the raw signal, which was recorded using the commercial software of the T-Ray 2000 system. Processing of the time-domain signals was accomplished off-line using an algorithm described in the Results and Discussion section.

The second configuration employed a prototype transmitter and receiver that were pumped independently by two similar femtosecond-laser oscillators for executing THz-ASOPS measurements. The transmitter and receiver pairs used in both configurations were similar in design, consisting of photoconductive antennae structures with hyper hemispherical lenses. Thus, the modules provided a free-space line-of-sight source and receiver of THz radiation. The collimated transmitter beam had a clear aperture of 4 cm, and for this study the modules were placed at various separations ranging from 18 to 40 cm.

For both experimental platforms, excitation light from the femtosecond oscillator(s) was coupled into the modules using fiber optics. Commercial, mode-locked Ti:sapphire oscillators (Spectra-Physics Tsunamis) delivering ~ 1 W of 800 nm light with a spectral bandwidth of 12 nm were used as the excitation source. Two pairs of half-wave plates and polarization-prism beam splitters were used to control the power delivered to the THz transmitter and receiver. To compensate for group velocity dispersion in the meter-length fibers, the Ti:sapphire beams were double-passed through a pair of transmission gratings prior to their insertion into the fibers. A commercial autocorrelator was used to verify a pulse width of ~ 100 fs at the output of the fibers. The half-wave plates were adjusted such that ~ 70 mW of light from each laser was incident on the grating pair. A loss of ~ 20 mW for each beam was experienced during transmission through the grating assembly.

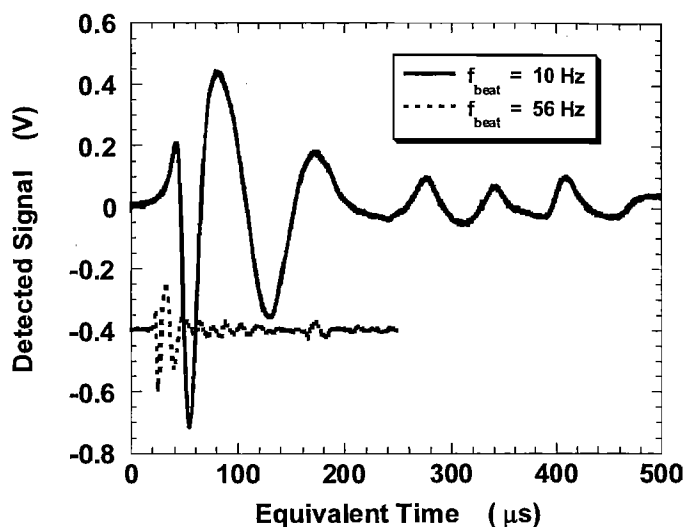


FIG. 2. Raw THz-ASOPS signals taken in room air at beat frequencies of 10 and 56 Hz, with 1 s signal accumulation times. The 56 Hz signal has been offset for clarity.

Losses in the fibers themselves reduced the power delivered to the antennae to ~ 8 mW.

For the THz-ASOPS setup, the laser used to pump the transmitter was passively operated at a repetition rate of $f_1 = 81.336$ MHz. The output of a diode employed to monitor this laser was used as a trigger for the electronics that mode-locked the second laser at a repetition rate of $f_2 = f_1 - \Delta f$. Beat frequencies, Δf , of 10–300 Hz were used in this study. The upper limit was determined by the bandwidth of the amplifier on the receiver and does not represent a limit of the technique itself. In previous ASOPS measurements, beat frequencies of 2–160 kHz have been reported.^{29,33} The receiver module included an amplifier with output directed into a 500 MHz digital oscilloscope for signal viewing and data acquisition. Signal analysis was accomplished off-line. Archived signals were recorded with 1 s dwell times. Each saved sample contained a full sweep of the THz-ASOPS signal in the equivalent-time domain. Conversion of the saved data to the real-time domain was performed in post-collection analysis. The data were obtained by triggering the digital oscilloscope on the signal itself.⁸ With this arrangement all signals have the same time origin, regardless of the target sample, which is convenient for studies of power transmission. If phase information is needed, the oscilloscope can, in principle, be triggered from the second-harmonic signal generated by passing residual light from the two pump lasers through a nonlinear crystal.

RESULTS AND DISCUSSION

In an experiment conducted with the Picometrix T-Ray 2000 system that employs an optomechanical delay line, spectra of ambient water vapor were recorded to 1.25 THz. In reducing the data, zeroes were padded on both the front and the back of the signal to increase the signal length from N to $10N$ points, effectively providing a ten-point interpolation of the signal in the frequency domain following execution of a fast Fourier transform.³⁵ After zero padding, the signal was apodized with

⁸ The steep negative slope of the first signal minimum was used.

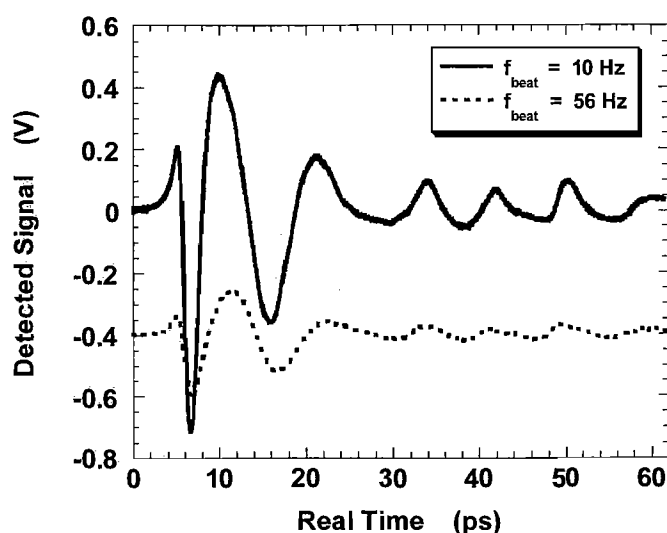


FIG. 3. THz-ASOPS signals of Fig. 2, converted from equivalent time to real time.

a Gaussian window to minimize distortion in the power spectrum and then transformed.^{35,36} The Gaussian window was centered over the raw signal and given a full-width at half-maximum (FWHM) of 240 ps. In Fig. 1 we show the observed power spectrum of ambient water vapor along with a calculation based on the HITRAN database.³⁷ The observed transition linewidths (FWHM) are on the order of 0.012 THz and are easily fit with Lorentzian profiles using the air-broadening coefficients reported in the HITRAN database without the need for instrumental convolution. The amplitude of the observed absorption features is consistent with the separation of the transmitter and receiver (18 cm) and a water-vapor density of $1.9 \times 10^{17} \text{ cm}^{-3}$ (72 °F, 30% relative humidity). In marked contrast, the absorption spectrum of bulk water at room temperature exhibits no sharp spectral features; the absorbance smoothly decreases with increasing frequency between 0.25 and 2.0 THz.³⁸

Similar spectra of water vapor in room air were recorded using the THz-ASOPS platform with the prototype transmitter and receiver heads. The useful spectral bandwidth of these heads does not extend as far as that of the conventional platform; hence, emphasis was placed on spectral features at frequencies below 1 THz. After the temporal signal acquired on the oscilloscope was first scaled from the recorded equivalent time to real time, the data-processing routine described above was also implemented for the THz signals acquired with this platform. Examples of raw THz-ASOPS signals of room air taken at two different beat frequencies are shown in Fig. 2 (equivalent time) and Fig. 3 (real time). For clarity, the 56 Hz signal has been offset in both figures. These time-domain signals, recorded using a 1 s acquisition time, essentially consist of one oscillation of the THz electric field generated by the transmitter. The reduced amplitude of the 56 Hz signal with respect to the 10 Hz signal is real and reflects the operational bandwidth of the receiver/amplifier combination. Methods of improving this bandwidth are under investigation.³⁹ We note that while this beat frequency is small with regard to fast kinetics, the system is well suited for studying long signal delays or long-lived events, such as photon echoes arising from free-induction decay.^{3,16} The measured root mean square (rms)

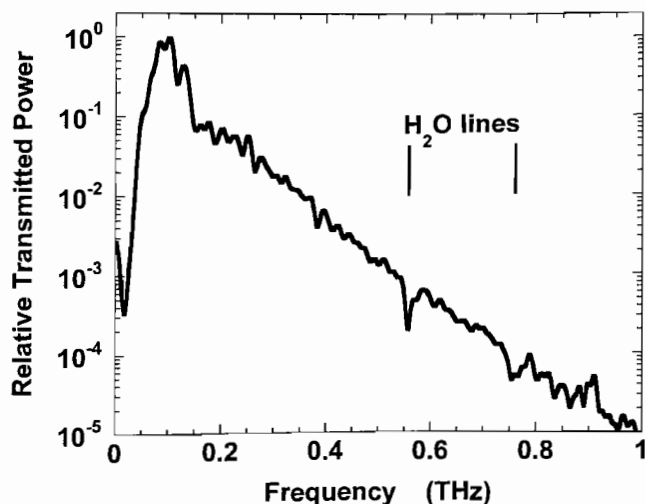


FIG. 4. THz-ASOPS power spectrum of room air taken at a beat frequency of 32 Hz. Two weak water-vapor absorption features are discernible.

noise in the prototype system is observed to be about 14% greater than that of the commercial system.

Figure 4 shows the power spectrum of room air generated from an average of eight 1-s signal acquisitions taken at a beat frequency of 32 Hz. The positions of two weak water-vapor absorption lines are indicated. At room temperature, water has several strong resonances for frequencies greater than 1 THz as well as relatively weak resonances at lower frequencies.⁴⁰ The ratio of the line strength of the transition at 0.75 THz to that at 1.16 THz seen in Fig. 1 is 0.19 at room temperature according to the JPL database.⁴⁰ Under our typical laboratory conditions, the density of water molecules in the air is $\sim 2 \times 10^{17} \text{ cm}^{-3}$. At 300 K the water line at 0.56 THz should have a signal strength 1.5 times that of the feature at 0.75 THz. Our measured ratio of integrated areas is 1.4, with an uncertainty of $\sim 25\%$.

Many materials that are opaque in the visible or near-infrared regions exhibit transparent bands near 1 THz.^{41,42} Since ultraviolet, visible, and infrared spectroscopic studies of high-pressure combustion are hampered by the need for conventional windows in the test article, we chose to examine the THz transparency of a common combustor material found in practical devices, namely, alumina. Figure 5 shows power spectra generated from two series of measurements that were made sequentially. The first series was made on room air and serves as a reference. The second was made on a cylindrical ceramic (alumina) combustor liner with inner and outer diameters of 4.13 cm and 4.76 cm, respectively. Five signals were recorded for each series at a beat frequency of 16 Hz. Between 0.75 and 3 THz, alumina has a nearly constant refractive index of >3 (increasing slightly with frequency), making the liner a cylindrical lens.^{43,44} To minimize refractive losses in transmitting the THz beam through the liner, a 2.5 cm aperture was placed in the beam just in front of the liner; the liner, in turn, was placed as close as possible to the receiver. This limited the ray paths to those that were most normal to the liner surface. Near 1 THz, away from a water resonance, an alumina index of 3.09 and an air index of 1 lead to a reflection loss at each of the air/ceramic interfaces of about 26%.¹¹ As shown in Fig. 5, the combined reflection and absorption losses

¹¹ The index value of 3.09 is an average of the two values at 1 THz reported in Refs. 43 and 44.

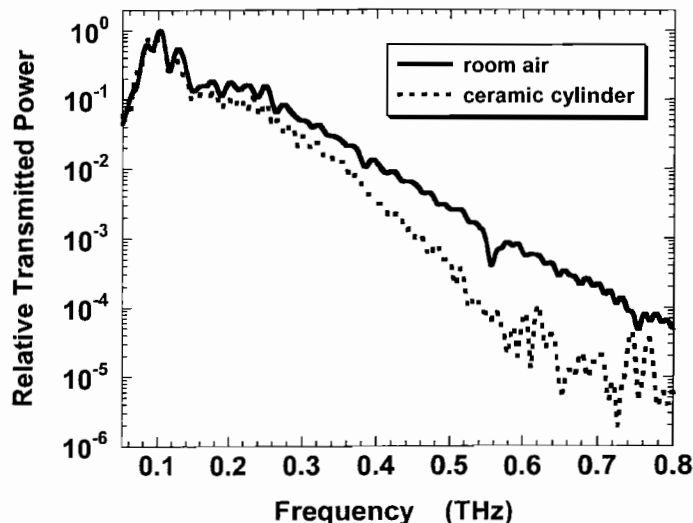


FIG. 5. Relative transmitted power through room air and the ceramic cylinder (4.76 cm o.d., 4.13 cm i.d.). Note the water-absorption line in air signal near 0.56 THz.

in the liner increase steadily with frequency, beginning at about 0.25 THz. Bolivar et al.⁴³ have measured the loss tangent of alumina, which can be converted to an absorption coefficient,⁴⁵ between 0.75 and 3 THz using a thin slab of alumina with minimal lensing issues. Cheville et al.⁴⁴ have made a similar measurement between 0.2 and 2 THz using solid alumina cylinders 3 mm in diameter. The two measurements disagree substantially at low frequency but approach each other at high frequency. Assuming these two measurements bound the expected absorption losses, we estimate transmission values at 0.8, 1.0, and 1.25 THz of 41–91%, 22–44%, and 7–11%, respectively, for our hollow cylinder. Reflective losses from the four interfaces total 70%. Combining the absorptive and reflective losses, we expect a total power transmission of 12–28%, 7–14%, and 2–3% at 0.8, 1.0, and 1.25 THz, respectively. A 10% transmission was observed for the cylinder at 0.8 THz, with the difference probably being due to lensing effects. The alumina transparency window, although narrow, will permit detection of water lines to nearly 1.25 THz, which is significant for potential combustion studies.

Careful interpretation of spectroscopic signals in numerous gas-phase applications demands knowledge of the dynamics of the quantum states involved, including collisional energy transfer. The ASOPS technique provides a pump/probe tool for studying such fast dynamics.^{31,32} Application of the ASOPS approach in the THz regime offers new possibilities in the study of collisional dynamics, such as rotational energy transfer in ground electronic states. For example, a tunable visible or ultraviolet laser could be used to pump population out of a particular quantum ground state. A THz-ASOPS absorption measurement could then be used to determine the collisional re-population of this state. Early in the development of THz time-domain spectroscopy, Greene et al.⁴⁶ demonstrated a pump/probe measurement by combining an optical pump (630 nm beam) with a THz probe. As discussed in Schmittenmaer's review article,⁶ a large number of pump/probe measurements have now been performed using various hardware platforms.

A combination of the ASOPS technique and large-bandwidth THz hardware could provide a valuable tool for

reacting-flow studies. We note that the hardware associated with THz measurements is advancing rapidly. The measurements reported by Janke et al. were performed with a GHz-repetition-rate pump laser.²⁹ For a fixed desired temporal resolution, increasing the laser repetition rate increases the beat frequency and hence the data acquisition rate as well as improving the signal-to-noise ratio.

ACKNOWLEDGMENTS

Funding for this research was provided by the Air Force Research Laboratory, Propulsion Directorate, Wright-Patterson AFB, under Contract Nos. F33615-00-C-2820 and F33615-03-D-2329, and by the Air Force Office of Scientific Research (Dr. Julian Tishkoff, Program Manager). The authors thank Dr. Mark Allen of Physical Sciences, Inc., for the alumina cylinder used during the course of this work.

1. M. C. Nuss and J. Orenstein, in *Millimeter and Submillimeter Wave Spectroscopy of Solids*, G. Gruner, Ed. (Springer, Berlin, 1998), pp. 7–50.
2. Q. Chen and X.-C. Zhang, in *Ultrafast Lasers*, M. Fermann, A. Galvanauskas, and G. Sucha, Eds. (Marcel Dekker, New York, 2003), pp. 521–572.
3. H. Harde and D. Grischkowsky, *J. Opt. Soc. Am. B* **8**, 1642 (1991).
4. M. van Exter and D. Grischkowsky, *IEEE Trans. Microwave Theory Technol.* **38**, 1684 (1990).
5. D. Mittleman, Ed., *Sensing with Terahertz Radiation* (Springer, New York, 2003).
6. C. A. Schmuttenmaer, *Chem. Rev.* **104**, 1759 (2004).
7. L. Thrane, R. H. Jacobsen, P. U. Jepsen, and S. R. Keiding, *Chem. Phys. Lett.* **240**, 330 (1995).
8. J. T. Kindt and C. A. Schmuttenmaer, *J. Phys. Chem.* **100**, 10373 (1996).
9. B. N. Flanders, R. A. Cheville, D. Grischkowsky, and N. F. Scherer, *J. Phys. Chem.* **100**, 11824 (1996).
10. J. E. Pederson and S. R. Keiding, *IEEE J. Quant. Electron.* **28**, 2518 (1992).
11. E. Knoesel, M. Bonn, J. Shan, and T. F. Heinz, *Phys. Rev. Lett.* **86**, 340 (2001).
12. S. P. Jamison, J. Shen, D. R. Jones, R. C. Issac, B. Ersfeld, D. Clark, and D. A. Jaroszynski, *J. Appl. Phys.* **93**, 4334 (2003).
13. M. C. Beard, G. M. Turner, and C. A. Schmuttenmaer, *J. Phys. Chem.* **106**, 7146 (2002).
14. G. Mouret, W. Chen, D. Boucher, R. Bocquet, P. Mounaix, and D. Lippens, *Opt. Lett.* **24**, 351 (1999).
15. H. Harde, N. Katzenellenbogen, and D. Grischkowsky, *J. Opt. Soc. Am. B* **11**, 1018 (1994).
16. H. Harde, R. A. Cheville, and D. Grischkowsky, *J. Phys. Chem. A* **101**, 3646 (1997).
17. H. Harde, N. Katzenellenbogen, and D. Grischkowsky, *Phys. Rev. Lett.* **74**, 1307 (1995).
18. S. A. Harmon and R. A. Cheville, *Appl. Phys. Lett.* **85**, 2128 (2004).
19. R. A. Cheville and D. Grischkowsky, *Opt. Lett.* **23**, 531 (1998).
20. D. Grischkowsky, S. Keiding, M. van Exter, and Ch. Fattinger, *J. Opt. Soc. Am.* **7**, 2006 (1990).
21. E. Lill, S. Schneider, and F. Dorr, *Opt. Commun.* **22**, 107 (1977).
22. E. Lill, S. Schneider, and F. Dorr, *Appl. Phys.* **14**, 399 (1977).
23. W. T. Barnes, Jr., Ph.D. Dissertation, Purdue University, West Lafayette, Indiana (1980).
24. S. Adachi, Y. Takagi, J. Takeda, and K. A. Nelson, *Opt. Commun.* **174**, 291 (2000).
25. J. D. Kafka, J. W. Pieterse, and M. L. Watts, *Opt. Lett.* **17**, 1286 (1992).
26. T. Kanada and D. L. Franzen, *Opt. Lett.* **11**, 4 (1986).
27. K. S. Giboney, S. T. Allen, M. J. W. Rodwell, and J. E. Bowers, *IEEE Photonics Technol. Lett.* **6**, 1353 (1994).
28. T. Löffler, T. Pfeifer, H. G. Roskos, H. Kurz, and D. W. van der Weide, *Microelectron. Eng.* **31**, 397 (1996).
29. C. Janke, M. Forst, M. Nagel, and H. Kurz, *Opt. Lett.* **30**, 1405 (2005).
30. P. A. Elzinga, F. E. Lytle, Y. Jiang, G. B. King, and N. M. Laurendeau, *Appl. Spectrosc.* **41**, 2 (1987).
31. P. A. Elzinga, R. J. Kneisler, F. E. Lytle, Y. Jiang, G. B. King, and N. M. Laurendeau, *Appl. Opt.* **26**, 4303 (1987).
32. G. J. Fiechtner, G. B. King, N. M. Laurendeau, and F. E. Lytle, *Appl. Opt.* **31**, 2849 (1992).
33. G. J. Fiechtner, G. B. King, and N. M. Laurendeau, *Appl. Opt.* **34**, 1117 (1995).
34. J. V. Rudd, D. Zimdars, and M. Warmuth, *Proc. SPIE-Int. Soc. Opt. Eng.* **3934**, 27 (2000).
35. A. G. Marshall and F. R. Verdun, *Fourier Transforms in NMR, Optical, and Mass Spectrometry* (Elsevier, Amsterdam, 1990), Chaps. 2 and 3.
36. J. G. Proakis and D. G. Manolakis, *Digital Signal Processing* (Prentice Hall, Upper Saddleback River, NJ, 1996), Chap. 8.
37. See <http://cfa-www.harvard.edu/HITRAN/>.
38. C. Ronne, P.-O. Astrand, and S. R. Keiding, *Phys. Rev. Lett.* **82**, 2888 (1999).
39. Private communication, M. S. Brown (ISSI, Dayton, OH) and J. Van Rudd (Sandia National Laboratories, Albuquerque, NM).
40. JPL Absorption Library, at <http://spec.jpl.nasa.gov/>.
41. D. M. Mittleman, M. Gupta, R. Neelamani, R. G. Baraniuk, J. V. Rudd, and M. Koch, *Appl. Phys. B* **68**, 1085 (1999).
42. M. N. Afsar, *IEEE Trans. Instrum. Meas.* **IM-36**, 530 (1987).
43. P. H. Bolivar, M. Brucherseifer, J. G. Rivas, R. Gonzalo, I. Ederra, A. L. Reynolds, M. Holker, and P. de Maagt, *IEEE Trans. Microwave Theory Technol.* **51**, 1062 (2003).
44. R. A. Cheville, M. T. Reiten, R. McGowan, and D. R. Grischkowsky, in *Sensing with Terahertz Radiation*, D. Mittleman, Ed. (Springer, Berlin, 2003), pp. 237–293.
45. D. M. Pozar, *Microwave Engineering* (John Wiley and Sons, New York, 1998), Chap. 2.
46. B. J. Greene, J. F. Federici, D. R. Dykaar, A. F. J. Levi, and L. Pfeiffer, *Opt. Lett.* **16**, 48 (1991).

Velocity imaging for the liquid–gas interface in the near field of an atomizing spray: proof of concept

David L. Sedarsky, Megan E. Paciaroni, and Mark A. Linne

Department of Combustion Physics, Lund Institute of Technology, Box 118, Lund 221 00, Sweden

James R. Gord

Propulsion Directorate, Air Force Research Laboratory, Wright-Patterson Air Force Base, Ohio 45433

Terrence R. Meyer

Innovative Scientific Solutions, Inc., Dayton, Ohio 45440

Received October 14, 2005; revised December 9, 2005; accepted December 18, 2005; posted January 12, 2006 (Doc. ID 65395)

We describe adaptation of ballistic imaging for the liquid core of an atomizing spray. To describe unambiguously the forces that act to break apart the liquid core in a spray, one must directly measure the force vectors themselves. It would be invaluable, therefore, to obtain velocity and acceleration data at the liquid–gas interface. We employ double-image ballistic imaging to extract velocity information through the application of image analysis algorithms. This method is shown to be effective for liquid phase droplet features within the resolution limit of the imaging system. In light of these results, it is clear that a three- or four-image implementation of this technique would allow the determination of acceleration, and by extension, information about the forces active in spray breakup. © 2006 Optical Society of America

OCIS codes: 120.1740, 110.2960, 110.7050.

Liquid fuels are commonly used in combustion devices because they have high energy density. To use the fuel effectively, however, it is necessary to disperse the fuel into the airstream by using a spray. Until recently, models describing fuel spray breakup were based on secondary observations of phenomena such as the behavior of droplets on the spray periphery by use of specific spray geometries. These models are therefore semiempirical. The principal missing component required for generation of a fully generic spray breakup model has been an understanding of what happens to the liquid portion of the jet near the centerline, just at the location where it exits into the air (the near field). This problem has persisted because an atomizing fuel spray has a very dense cloud of small droplets shrouding the near field, and this cloud is opaque to normal imaging techniques.

Ballistic imaging was originally applied to biological tissue, and it has been demonstrated with various optical configurations. The first report of ballistic imaging for the liquid core in an atomizing spray described the application, to acquire a single image, of a time-gated instrument to the near field of a water jet in a liquid-oxygen injector.¹ Paciaroni and Linne² and Linne *et al.*³ described a system optimized for spray research: a ballistic imaging instrument capable of acquiring single images in dense sprays with significantly improved spatial resolution.

In this Letter we demonstrate that the instrument can be modified to detect the velocity both of the liquid–gas interface of a spray core and of primary droplets stripped from the core. Moreover, we describe a simple extension that will provide images of the force vectors that act to break apart intact liquid features in sprays.

A full description of the development and evaluation of the ballistic imaging instrument applied here can be found elsewhere.^{2,3} In brief, when light passes through a highly turbid medium, some photons can pass straight through without scattering. These relatively few photons are termed ballistic. Since they travel the shortest path, they exit first. A somewhat larger group of snake photons is scattered only once or twice, and these photons exit the medium traveling in the same direction as the input light with a larger solid angle than the ballistic photons. Since they travel a larger distance, they exit just after the ballistic photons. Photons that have undergone multiple scattering events, termed diffuse photons, are the most numerous in materials with high extinction coefficients. These photons are scattered into a very large solid angle (4π Sr), and they exit last.

The undisturbed path taken by ballistic photons allows the retention of image information regarding structures that may be embedded within the turbid medium. If they are used in a shadowgram arrangement, the ballistic photons can provide a diffraction-limited image of these structures. Unfortunately, in most highly scattering environments the number of transmitted ballistic photons is often insufficient to provide the necessary signal-to-noise ratio to form an image in a single-shot format. In such a case, snake photons, together with ballistic photons, can be used for imaging with little degradation in resolution. The problem of obtaining a high-resolution image through highly turbid media is thus a matter of separating and eliminating diffuse light from ballistic and snake light. This can be done by using discrimination methods that make use of the properties of the transmitted light. In the current work, we use exit time

(via a fast optical Kerr gate) and propagation direction to select the ballistic and snake photons³ (see Fig. 1).

To demonstrate velocity imaging, we adopted a flow system used for liquid jet in cross-flow research by shutting off the gas flow and reducing the liquid flow. This generated a steady sequence of falling droplets, which enabled the 1 kHz laser system to illuminate droplet image pairs with sufficient time resolution between successive images. Sprays will require greater than 1 kHz repetition rates, but such laser systems and cameras are commercially available. The image pairs used for this proof of concept were acquired by use of an interline transfer CCD capable of storing two images spaced as little as $2 \mu\text{s}$ apart.

To extract velocity, we analyzed pairs of ballistic images taken at times t_1 and t_2 , beginning with some image processing. Laser speckle has a distinct small-scale structure that changes from shot to shot. Direct subtraction of a background image introduces aberrant structure because the speckle patterns in one coherently illuminated image do not align well with those in a second image. This difficulty is exacerbated by the fact that speckle from two images can dominate correlation calculations used to extract velocity, leading to erroneous results. Speckle noise must be minimized, therefore, before application of a correlation technique that tracks image features.

We deal with laser speckle by filtering a background image, first by eroding and then by dilating the image, using a circular structuring element. This eliminates small-scale structure in the background image without changing larger features or intensity variations. This adjusted background is used to correct the two source images, effectively eliminating much of the speckle noise. The images are processed as shown in Eq. (1):

$$I_{\text{clean}} = \frac{(I_{\text{raw}} - B_{\text{blank}})}{(B_{\text{adj}} - B_{\text{blank}})}, \quad (1)$$

where I_{raw} is the original image, B_{blank} is an averaged background image with no illumination, and B_{adj} is the illuminated background image adjusted by the aforementioned filtering scheme. Next, the intensity across the image is adjusted to increase contrast and utilize the full dynamic range of the image format. Finally, a median filter is applied to partially remove small features that are below the resolution limit of the imaging system.

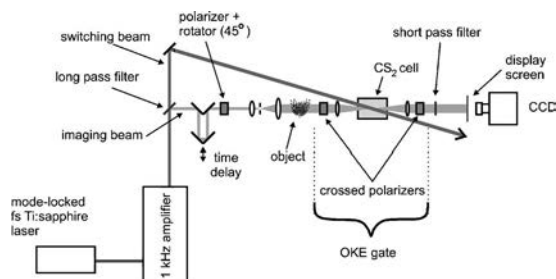


Fig. 1. Schematic of the ballistic imaging instrument used here.

It is necessary to select points of interest within these enhanced images, to track from the image taken at t_1 to the second image at t_2 . We set an appropriate threshold level based on the contents of the images and the droplet and void edges. We use this thresholding process to convert the gray-scale image at t_1 into a two-tone image, such that pixels are either black or white. The Sobel edge-detection algorithm⁴ is applied to this image, leaving only the border pixels of the droplets and voids. These border pixels are selected as investigation points for the correlation step.

The feature offsets between the two droplet images have two components: bulk motion and small-scale motion (including distortions). The bulk motion is especially significant here because the image acquisition rate was necessarily slow. To determine the bulk motion, one must isolate and match the large objects in the image pair, and their centers of mass must be calculated. Each of the investigation points, as determined above, belongs to a large object and is assigned a bulk motion vector calculated from its associated change in location of the center of mass from the first image to the second image.

The entire procedure thus far is in preparation for the correlation step associated with the small-scale motion, which examines a feature (selected investigation point) and determines how it has moved from the first image to the second. The selected investigation points form the center positions used to draw one complete set of correlation windows from the image at time t_1 . We then remove the bulk motion offset for each point at time t_2 to calculate a modified list of points. These adjusted points are used as the center positions of a second set of correlation windows for the image at time t_2 , such that small-scale motion can be extracted via correlation in the absence of any contribution from bulk motion.

It is worth mentioning here that the size of the correlation window is important for obtaining accurate results from this analysis, and some experimentation is required for determining the optimum sizes for various imaging systems. The window size naturally limits the largest small-scale offset that can be calculated. On the other hand, making the window larger can lead to erroneous correlation maxima or introduce edge effects, as the calculated window positions stray over the edge of the image data. These effects must be dealt with carefully when this method is implemented. To ensure accuracy, correlation matches near the values obtained by correlating a source image with background noise should be discarded.

At this stage, the software has calculated the small-scale offset for each investigation point by cross correlating each window centered at an investigation point with its partner window centered at the bulk offset adjusted investigation point. The correct offset is defined as the position that maximizes the correlation. At this point both the bulk and the small-scale offsets for each investigation point have been calculated, so the velocity vector for each feature has been determined.

Results of the method of determining small-scale velocity as applied to an isolated pair of water droplets are shown in Fig. 2. The velocity vectors in the image show how the drop is elongating along its vertical axis and contracting asymmetrically along its horizontal axis as it falls. The motion of the ligament near the lower portion of the drop is also correctly indicated.

It is important to point out that related image analysis techniques have been applied to gas-phase flows for some time. These techniques include Mie scattering from small seeded particles for particle-image velocimetry and Rayleigh or laser-induced fluorescence imaging of gas-phase species. The errors in particle-image velocimetry analysis have been studied in detail and are well understood, but particle-image velocimetry relies on sharp images of single particles that produce distinct correlation peaks. Here, edges are correlated in a way similar to gaseous image velocimetry, and they produce somewhat less-distinct correlation streaks, as discussed in detail by Fielding *et al.*,⁵ Grunefeld *et al.*,⁶ and Tokumaru and Dimotakis.⁷ The principal difference between those techniques and this one is that the gaseous image velocimetry correlations rely on dispersed, gray-scale images for which the correlation must be accomplished across a slowly varying intensity field. Owing to the strong contrast in the signal field, processed ballistic images can be converted into two-tone images with more distinct edges before any correlation is performed. While the issues raised by Fielding *et al.*⁵ should be investigated here as well, the difference just mentioned offers a possibility of less uncertainty. In addition, a sequence of images (e.g., four) would allow some comparison and rationalization of the inferred velocity to be made.

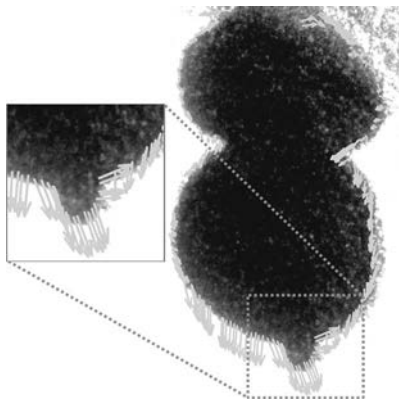


Fig. 2. Droplet image at t_1 with velocity vectors. The droplet diameter is of the order of $500\ \mu\text{m}$.

The results presented here demonstrate that this method is effective in determining velocity information from pairs of ballistic images, provided that the time step from t_1 to t_2 is small enough to allow for sufficiently strong feature correlation. It remains necessary to conduct a more quantitative analysis of the correlation method to determine how each stage in the process affects noise levels in the image and the robustness of the correlation.

If one could obtain at least three or four images taken at sufficiently short intervals it would be possible to apply a similar method to mitigate uncertainties and to obtain acceleration vectors. Laser systems with the appropriate speed are commercially available, and four images can be acquired with two double-image cameras suitably aligned with each other. Other components of the instrument [e.g., the optical Kerr gate (OKE); Fig. 1] are not rate limiting.

From acceleration data, given some knowledge about the composition of the liquid and gas under observation, one could determine the forces acting on the features tracked by our method. This capability can, we believe for the first time, resolve unambiguously the dynamics that break apart the liquid core in the near field.

Support for this research was provided by the U.S. Air Force Research Laboratory under contract FA8650-04-M-2442 (Barry Kiel, Technical Monitor) and by the U.S. Air Force Office of Scientific Research (Anne Matsuura, Program Manager). Some of the equipment was provided by the Army Research Office for project DAAD19-02-1-0221. D. L. Sedarsky is supported by the Swedish Vetenskapsraadet, and M. E. Paciaroni is supported by the Swedish Statens Energimyndigheten. M. A. Linne's e-mail address is mark.linne@forbrf.lth.se.

References

1. P. A. Galland, X. Liang, L. Wang, K. Breisacher, L. Liou, P. P. Ho, and R. R. Alfano, *HTD* (Am. Soc. Mech. Eng.) **321**, 585 (1995).
2. M. Paciaroni and M. Linne, *Appl. Opt.* **43**, 5100 (2004).
3. M. Linne, M. Paciaroni, J. Gord, and T. Meyer, *Appl. Opt.* **44**, 6627 (2005).
4. T. S. Huang, G. J. Yang, and G. Y. Tang, *IEEE Trans. Acoust. Speech, Signal Process.* **ASSP-27**, 13 (1979).
5. J. Fielding, M. Long, G. Fielding, and M. Komiyama, *Appl. Opt.* **40**, 757 (2001).
6. G. Grunefeld, H. Finke, J. Bartelheimer, and S. Kruger, *Exp. Fluids* **29**, 322 (2000).
7. P. T. Tokumaru and P. E. Dimotakis, *Exp. Fluids* **19**, 1 (1995).

RELIEF VELOCIMETRY FOR LARGE-SCALE WIND-TUNNEL FACILITIES

W. Lempert, Y. Zuzeck, M. Uddi, K. Frederickson

*Dept. of Mechanical Engineering
The Ohio State University, Columbus, OH*

S. Roy, T. R. Meyer, S. Gogineni

Innovative Scientific Solutions, Inc., Dayton, OH

J. R. Gord

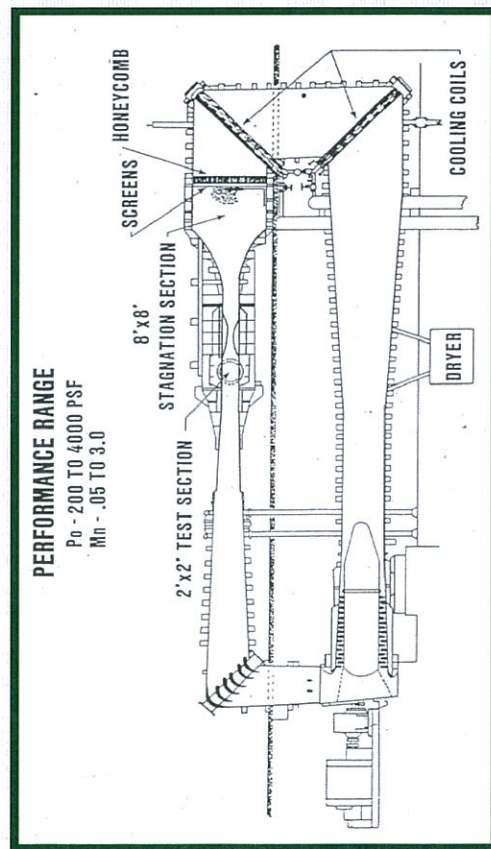
*Air Force Research Laboratory
Wright-Patterson Air Force Base, OH*

Acknowledgments: The authors acknowledge the financial support of Dr. Ryan Schmit of Air Vehicles Directorate at AFRL. This project is funded under SBIR contract.



ISSI

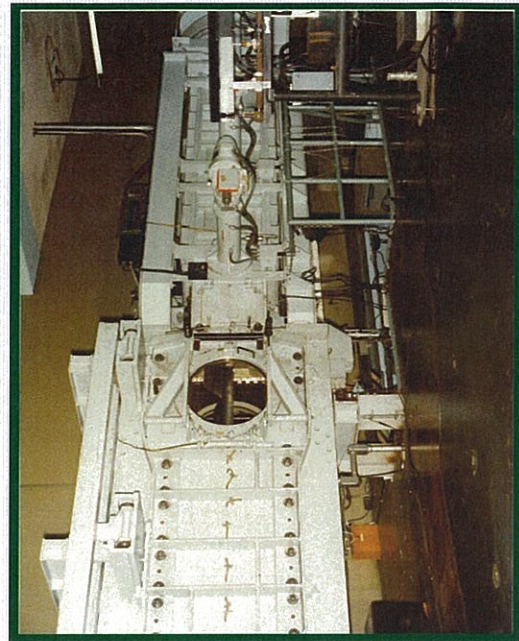
Schematic of the TGF Facility



INSTRUMENTATION REQUIREMENTS FOR AFRL TGF

- High spatial and temporal resolution is highly desirable.
- Reliance on seeding, either particulate or molecular, is highly discouraged.
- Optical access is somewhat restrained.

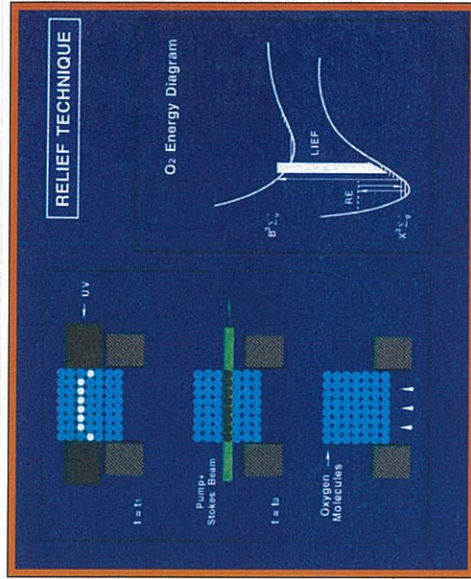
Photograph of the TGF Facility



BRIEF OVERVIEW OF SOME OPTICAL VELOCIMETRY TECHNIQUES

- Laser Doppler Velocimetry
- Particle Image Velocimetry
- Planar Doppler Velocimetry
- Planar Laser Induced Fluorescence
- Filtered Raleigh Scattering
- RELIEF Technique

ILLUSTRATION OF THE BASIC RELIEF FLOW TAGGING VELOCIMETRY CONCEPT



WHY ULTRAFAST FOR RELIEF TECHNIQUE??

While the RELIEF technique has been demonstrated in a wide variety of flows its applicability, in its conventional configuration, to large scale aerodynamic facilities suffers due to the high laser beam intensity requirements. More specifically, the vibrational excitation step, is achieved using what is known as Stimulated Raman Scattering (SRS), the efficiency of which scales as the product of the intensities of two beams termed the Raman "pump" (532 nm) and "Stokes" (581 nm), ie.

$$\frac{dN_{v=1}}{dt} \propto I_{\text{pump}} I_{\text{Stokes}} \quad \text{where the single pulse beam intensity, } I, \text{ is given by } I = \frac{E_{\text{pulse}}}{A \Delta t_{\text{pulse}}}$$

where E_{pulse} is the single pulse energy (in Joules), $A = \pi w_0^2/2$ is the focused beam cross-sectional area, (where w_0 is the focused beam radius or "waist"), and Δt_{pulse} is the pulse duration.

To date all reported RELIEF measurements have been performed using conventional "Q-switched" Nd:YAG laser sources, which have pulse durations of $\sim 10 \times 10^{-9}$ sec (10 nsec) and are limited in total pulse energy to ~ 100 mJ. The required intensity translates to a requirement to focus rather tightly, to beam waists of ~ 25 microns.

WHY ULTRAFAST FOR RELIEF TECHNIQUE?? (contd.)

- The volume element of tagged fluid is relatively small and as such single shot signal levels, while sufficient under typical laboratory conditions, are somewhat marginal for practical applications.
- The length of the tagged fluid element is constrained due to the fundamental property of Gaussian beams relating the waist to the length of the high intensity region of the focused beam.
- Due to the pulse intensity requirements, coupled with constraints related to the Stokes beam generation process, RELIEF measurement to date have been limited to single lines, or in a few cases, to a single cross.
- The intensity required for SRS vibrational excitation is near the dielectric "breakdown" limit of air, and more significantly, to particulate impurities which are often present in large scale facilities.
- The interrogation step requires high power laser radiation that has necessitated the use of ArF excimer lasers, which are rather expensive ($\sim \$200$ K) and more importantly are quite bulky, require toxic chemicals for operation which must be stored in ventilated fume-hoods, are extremely difficult to transport, and can be difficult to maintain. In addition, the 192 nm radiation is inherently problematic, requiring high quality quartz windows for transmission.

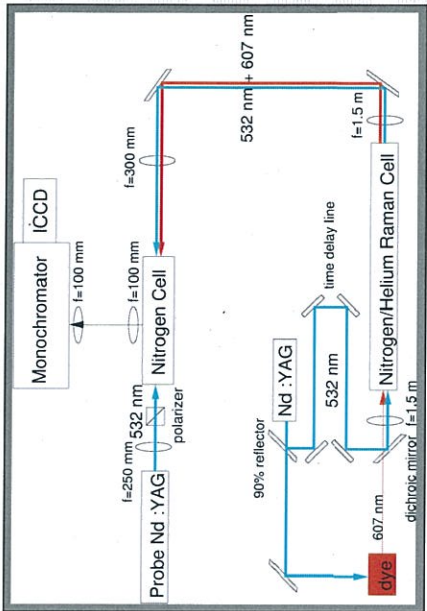
TECHNICAL OBJECTIVES

- Demonstrate that Raman shifting cells, which offer great system simplicity and increased robustness, can be used to generate the required Stokes tagging beam when using psec pulses.
- Show that psec tagging result in efficient vibrational excitation ("tagging) and demonstrate that it enables the use of greatly (~ factor of ten) reduced single pulse energy.
- Demonstrate that the ArF excimer interrogation laser can be replaced with an Nd:YAG-based system.
- Demonstrate the integrated RELIEF system in AFRL Trisomic Facility, especially to study flow patterns in the desired cavity and turret geometries.

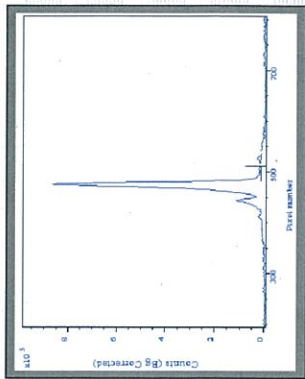
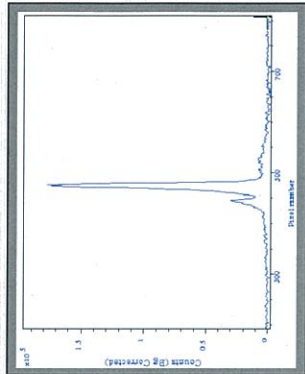
SUMMARY OF N2 RAMAN SHIFTING CELL RESULTS USING 100 psec PULSE DURATION Nd:YAG LASER

532 Input (mJ)	607+707 Output (mJ)	Stokes Conversion	Total Output (mJ)	Loss
1.97	Threshold		1.45	.27
5.09	1.14	.22	2.80	.45
7.29	1.57	.22	3.10	.57
11.16	2.00	.18	3.80	.66
14.96	2.79	.19	4.35	.71
17.69	3.14	.18	4.85	.73
18.23	3.07	.17	4.95	.73

SCHEMATIC DIAGRAM OF N2 V-V KINETICS PUMP/PROBE INSTRUMENT



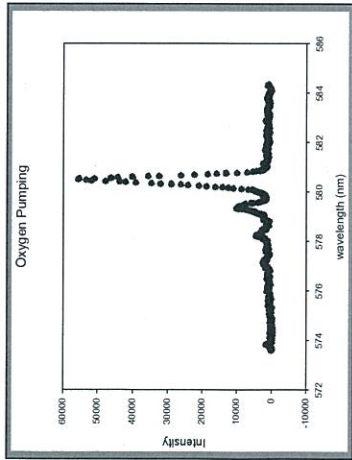
N2 SPONTANEOUS RAMAN SPECTRUM OBTAINED 100 nsec (top) and 3.2 microseconds (bottom) AFTER psec SRS VIBRATIONAL EXCITATION



v''	0	1	2
$f_{v''} - 100 \text{ nsec delay}$	0.70	0.30	
$f_{v''} - 3200 \text{ nsec delay}$	0.73	0.24	0.02 - 0.03

Fractional populations of N2 vibrational levels
 $v=0, 1, \text{ and } 2$

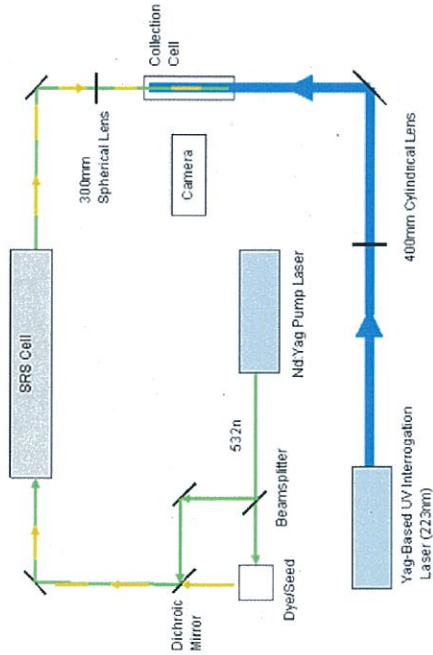
RAMAN SPECTRUM OBTAINED WITH 1 microsecond PUMP/PROBE TIME DELAY CLEARLY SHOWING POPULATION IN O2 VIBRATIONAL LEVELS $v''=0-3$



v''	0	1	2	3
$f_{v''}$	0.89	0.08	0.02	0.008

O₂ vibrational level populations inferred from Raman spectrum

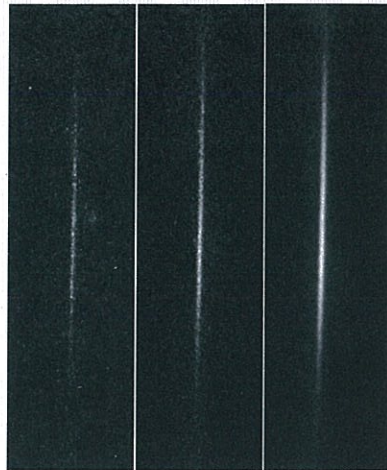
SCHEMATIC DIAGRAM OF PROOF OF CONCEPT Nd:YAG BASED RELIEF INTERROGATION EXPERIMENT



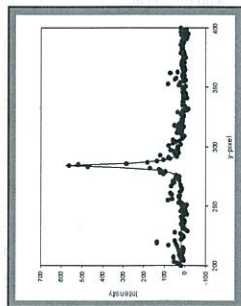
LASER WAVELENGTHS AND PREDICTED RELATIVE RELIEF SIGNAL FOR INTERROGATION FROM VIBRATIONAL LEVELS $v''=1, 3$, and 4

v''	v'	λ (nm)	f_v	f_B	Q Yield	Relative Signal
1	7	192	.170	0.06	5.6×10^{-5}	1.0
3	0	223.4	.010	0.14	3.8×10^{-4}	0.85
4	0	231.1	.005	0.14	3.8×10^{-4}	0.4

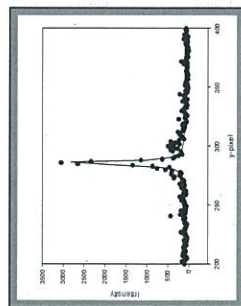
STATIC CELL RELIEF IMAGES INTERROGATED USING Nd:YAG BASED TUNABLE UV LASER IN THE VICINITY OF 223.4nm TO PUMP THE $v''=3 \rightarrow v'=0$ O2 SCHUMANN-RUNGE TRANSITION



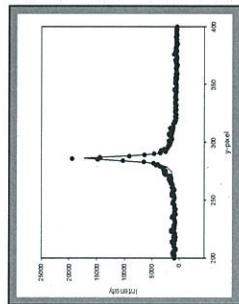
SINGLE VERTICAL SLICES OF GRAY SCALE INTENSITY FROM THE PREVIOUS IMAGES ALONG WITH LEAST SQUARES COMPUTER FIT TO SIMPLE LORENTZIAN LINE SHAPE



$\sigma_v \sim 2 \text{ m/sec}$

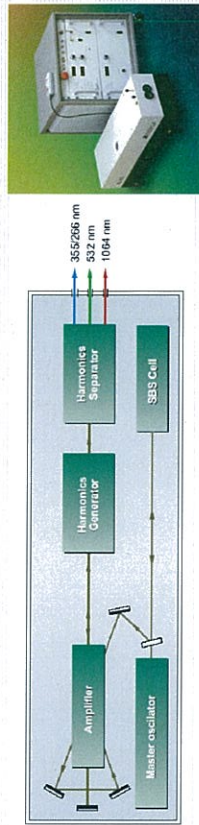


$\sigma_v \sim 1 \text{ m/sec}$

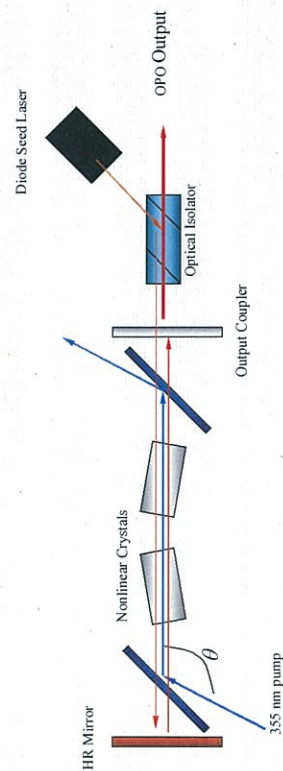


$\sigma_v \sim 1 \text{ m/sec}$

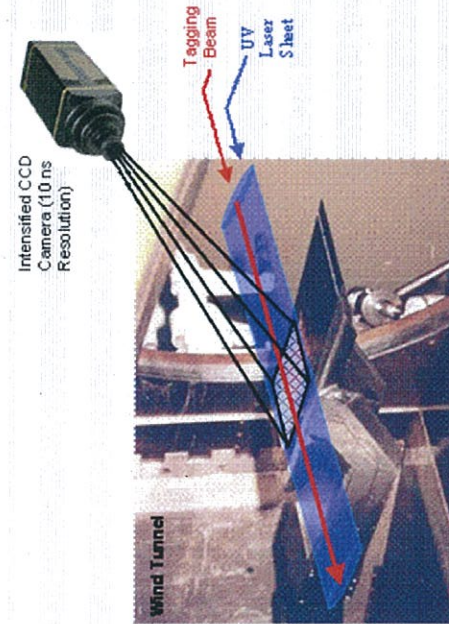
LAYOUT AND PHOTOGRAPH OF EKMA SL300 SERIES SBS PULSE COMPRESSED Nd:YAG LASER SYSTEM



SCHEMATIC DIAGRAM OF INJECTION-SEEDED OPO

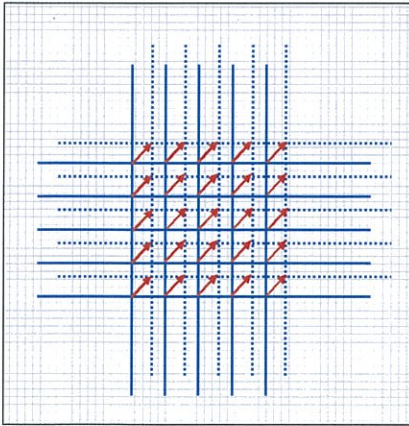


GEOMETRY OF PROOF-OF-CONCEPT DEMONSTRATION



summary

- A novel program to develop ultra-fast technology-based optical Flow Tagging Velocimetry was proposed.
- This diagnostic technique offers great promise, due to recent advances in laser performance, reliability, and cost.



Effects of quenching on electronic-resonance-enhanced coherent anti-Stokes Raman scattering of nitric oxide

Sukesh Roy^{a)}

Innovative Scientific Solutions, Inc., 2766 Indian Ripple Road, Dayton, Ohio 45440

Waruna D. Kulatilaka, Sameer V. Naik, Normand M. Laurendeau, and Robert P. Lucht

Department of Mechanical Engineering, Purdue University, West Lafayette, Indiana 47907

James R. Gord

Air Force Research Laboratory, Propulsion Directorate, Wright-Patterson AFB, Ohio 45433

(Received 11 April 2006; accepted 17 July 2006; published online 8 September 2006)

We investigate the effects of gas-mixture composition on the electronic-resonance-enhanced coherent anti-Stokes Raman scattering (ERE-CARS) signals of nitric oxide (NO). From previous laser-induced fluorescence (LIF) studies, quenching rates are known to change drastically, by factors of 400–800, in mixtures of CO₂/O₂/N₂. The observed ERE-CARS signal remains constant to within 30% whereas LIF signals from NO are predicted to decrease by more than two orders of magnitudes in the same environments. This is very significant for using NO ERE-CARS in high-pressure combustion environments where the electronic quenching rate can vary rapidly as a function of both space and time. © 2006 American Institute of Physics. [DOI: 10.1063/1.2338014]

Nitric oxide (NO) is an important pollutant because of its serious environmental implications. In the atmosphere NO reacts with sunlight to form other nitrogen oxides (NO_x) that ultimately play a role in ground-level smog, acid rain, stratospheric ozone depletion, and global warming. Because more than 95% of atmospheric NO_x originates from combustion processes and 95% of this combustion-formed NO_x is emitted from combustors as NO, a great deal of attention has been devoted to characterizing and reducing NO emissions from combustion equipment. Accurate measurement of NO concentrations [NO] within high-pressure combustors is very difficult but is critical for the minimization of pollutant emissions from power and propulsion systems. Current state-of-the-art measurements of [NO] in high-pressure, liquid-fueled combustors are based on laser-induced fluorescence (LIF); however, a major limitation of LIF is significant quenching of the signal owing to collisions of excited state NO with O₂, CO₂, H₂O, and other molecules.^{1–4}

Coherent anti-Stokes Raman scattering (CARS) is commonly used for measurement of temperature and the concentrations of major species (typically >1%) in reacting flows and plasmas.⁵ Dual- and triple-pump CARS techniques are used for simultaneous measurements of temperature and multiple species concentrations.^{6–9} However, conventional and multiple-pump CARS techniques are not suitable for measuring the concentrations of minor species such as NO because of the strength of the nonresonant four-wave mixing signal compared to the Raman-resonant CARS signal, and because the CARS signal is proportional to the square of number density and drops rapidly with decreasing concentration. The vibrational Raman cross section of NO is 0.2×10^{-30} cm²/sr whereas the Raman cross section of N₂ is 0.46×10^{-30} cm²/sr at 532 nm.⁵

The signal strength for Raman-resonant CARS can be enhanced significantly by tuning one or more of the three CARS laser beams into resonance with an electronic transi-

tion of the molecule. Electronic-resonance-enhanced CARS (ERE-CARS) has been applied to a limited extent for minor-species measurements in flames and plasmas, but the difficulty of interpreting ERE-CARS spectra and the requirement for two or three tunable ultraviolet laser sources have hindered widespread application of this technique.^{10–12} Hanna *et al.*¹³ proposed a variation of the ERE-CARS technique in which visible pump and Stokes laser beams are used to induce a Raman polarization, and an ultraviolet probe beam is scattered from the induced Raman polarization to produce the CARS signal beam. This technique, for which only the ultraviolet probe beam is tuned into resonance with a selected electronic transition of the molecule, is much simpler to implement than ERE-CARS schemes with multiple ultraviolet beams.

The objective of this work is to investigate the effects of variations in electronic quenching rate on the ERE-CARS signal from NO. ERE-CARS measurements were performed in NO/O₂/N₂ or NO/CO₂/N₂ jet flows at room temperature and pressure. The NO concentration was fixed at 1000 ppm for all cases. The composition of the jet-flow buffer gases, either N₂/O₂ or N₂/CO₂, was varied from pure N₂ to 18% N₂/82% O₂ or 18% N₂/82% CO₂, respectively. In this manner the collisional quenching rate for NO was varied by a factor of 400 for the NO/N₂/O₂ jet flows and by a factor of 800 for the NO/N₂/CO₂ jet flows.^{18–20}

An energy-level diagram for the NO ERE-CARS process is shown in Fig. 1. The pump (ω_1) and Stokes (ω_2) beams are visible laser beams with frequencies that are far from resonance with the A²Σ⁺–X²Π electronic transition. The probe beam at frequency ω_3 is at or near an electronic resonance. This wide separation between frequencies ω_1 and ω_3 of the pump and probe beams distinguishes this technique from that employed in previous ERE-CARS experiments,^{10–12} which were performed with the same laser frequency for the pump and probe beams ($\omega_1 = \omega_3$), and with the pump, Stokes, and probe beams at or near electronic resonance.

A schematic diagram of the experimental system is shown in Fig. 2. The laser source for the ω_1 pump beam is an

^{a)} Author to whom correspondence should be addressed; electronic mail: sroy@woh.rr.com

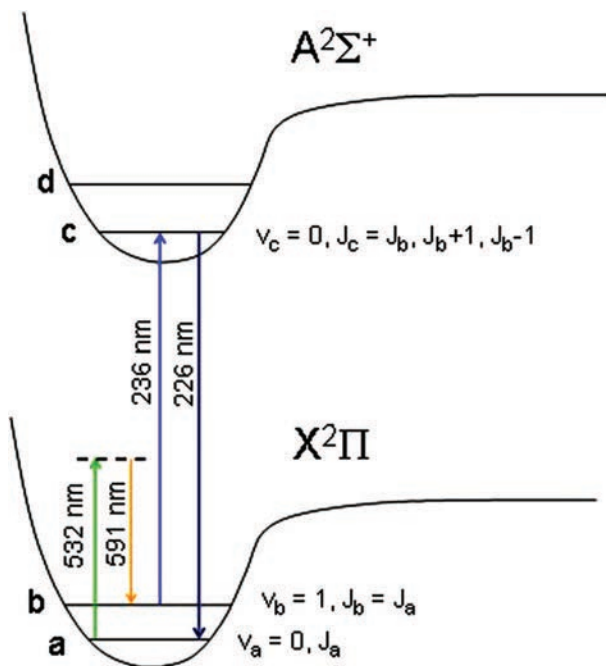


FIG. 1. (Color) Energy-level diagram for the NO ERE-CARS technique. The indicated transitions identify the pump beam ($\lambda_1=532$ nm), Stokes beam ($\lambda_2=591$ nm), ultraviolet probe beam ($\lambda_3=236$ nm), and ERE-CARS signal beam ($\lambda_4=226$ nm).

injection-seeded, Q -switched Nd: Yttrium–aluminum–garnet (YAG) laser with a repetition rate of 10 Hz and a pulse length of 8 ns. The 532-nm Nd:YAG second-harmonic beam is used to pump a tunable, narrowband dye laser to produce laser light at 704 nm. The 704-nm laser radiation is then sum-frequency-mixed with the 355-nm Nd:YAG third-harmonic beam to produce the probe beam (ω_3) at 236 nm. A second, unseeded Nd:YAG laser is used to pump another tunable narrowband dye laser to produce the Stokes beam (ω_2) at a wavelength of 591 nm. The CARS signal (ω_4) at 226 nm is generated using a three-dimensional phase-matching geometry. The energy of the pump, the Stokes, and the probe beams are 2, 2, and 0.2 mJ/pulse, respectively.

A polarization-selection technique is used to suppress the nonresonant background signal.¹³ As shown in Fig. 2, the polarization of all three laser beams is set with respect to the vertical axis. The 236-nm probe beam is vertically polarized, whereas the polarizations of the pump and the Stokes beams

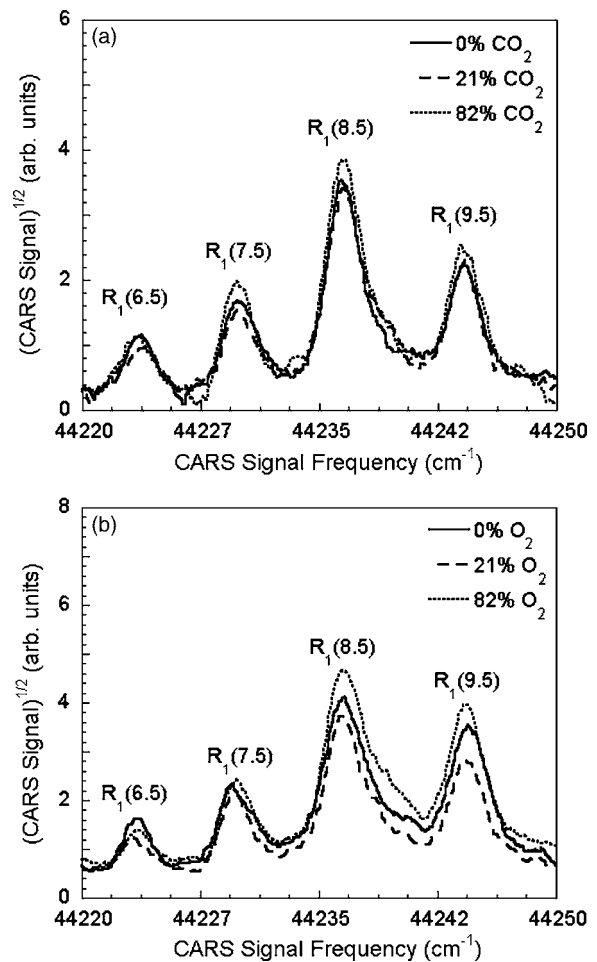


FIG. 3. The square root of the ERE-CARS signal vs CARS signal frequency for (a) three different concentrations of CO_2 in the $\text{NO}/\text{N}_2/\text{CO}_2$ jet flow and (b) three different concentrations of O_2 in the $\text{NO}/\text{N}_2/\text{O}_2$ jet flow. The NO concentration was 1000 ppm for all spectra.

are set at an angle of 60° with respect to the vertical axis. The polarizer in the signal channel is set orthogonal to the polarization of the nonresonant four-wave mixing beam.¹³

ERE-CARS spectra of NO for different concentrations of CO_2 are shown in Fig. 3(a) and for different concentrations of O_2 in Fig. 3(b). The NO concentration for all of these flows was set at 1000 ppm. The ERE-CARS spectra were recorded by tuning the wavelength of the ultraviolet

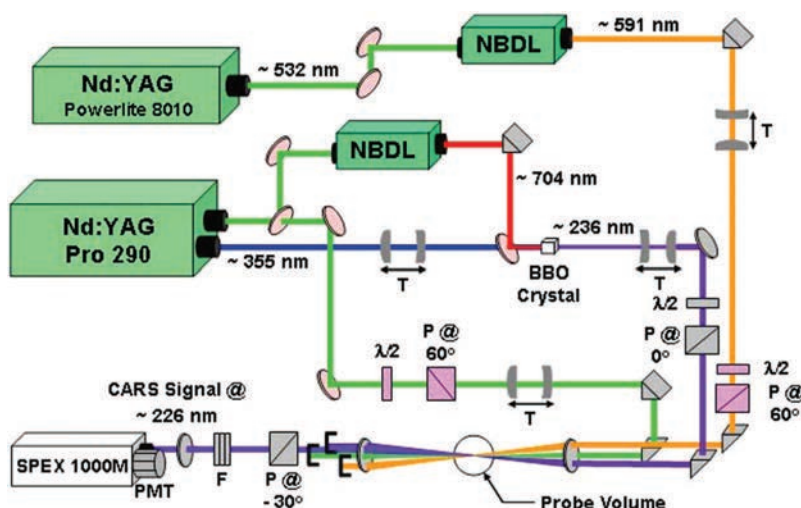


FIG. 2. (Color) Schematic diagram of NO ERE-CARS system. P : polarizer, angles set with respect to the vertical axis; T : telescope; $\lambda/2$: half-wave plate; NBDL: narrowband dye laser; F : filter, composed of four 45° , 215-nm mirrors; PMT: photomultiplier tube.

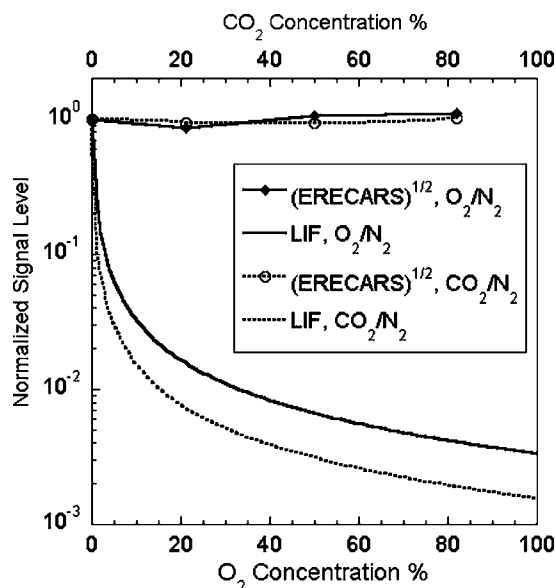


FIG. 4. Dependence of the square root of the ERE-CARS signal and the LIF signal on composition of the NO/N₂/O₂ or NO/N₂/CO₂ jet flow. The NO concentration was 1000 ppm for all ERE-CARS measurements.

probe beam. The Stokes wavelength (vacuum) was held fixed at 591.209 nm; the frequency difference between the pump and Stokes beams was tuned to the Q₁(8.5) Raman transition. The ERE-CARS signal was divided by the ultraviolet probe energy; the square roots of normalized spectra are plotted in Fig. 3. The spectral line notation shown in Fig. 3 corresponds to the electronic transition accessed by the probe laser. The signal is essentially constant despite the large increase in electronic quenching rate as the concentrations of O₂ or CO₂ increase in the jet flow. Although the collisional quenching rate varies drastically with changing O₂ or CO₂ concentrations, the collisional linewidths of the NO transitions are essentially constant. The line-broadening parameter for collisions of NO with O₂ ($\gamma_{12} = 0.265 \pm 0.016 \text{ cm}^{-1}/\text{atm}$) is approximately 10% lower than that for collisions of NO with N₂ ($\gamma_{12} = 0.293 \pm 0.02 \text{ cm}^{-1}/\text{atm}$).^{14–16} The line-broadening parameter for collisions of NO with CO₂ ($\gamma_{12} = 0.303 \pm 0.01 \text{ cm}^{-1}/\text{atm}$) is approximately equal to that for collisions with N₂. The line-broadening parameter γ_{12} is the coherence decay rate owing to both energy-transfer and elastic collisions.

The spectral sum of the square root of the ERE-CARS signal is plotted in Fig. 4 for different concentrations of O₂ and CO₂ in the jet flow. The square root of the ERE-CARS signal is proportional to the number density of NO. The ERE-CARS signal shown in Fig. 4 is calculated by dividing the raw ERE-CARS signal by the probe pulse energy ($\lambda_3 = 236 \text{ nm}$), taking the square root, and then integrating from a signal frequency of 44 190–44 270 cm⁻¹. The spectral sum of the square root of the ERE-CARS signal is then normalized to unity for a jet flow of 1000 ppm NO in 99.9% N₂. The calculated LIF signal from NO is also normalized in the same fashion and plotted in Fig. 4. A comparison of the experimental NO ERE-CARS signal with the calculated NO LIF signal shows the drastic reduction in LIF signal as the O₂ or CO₂ concentrations increase. For the LIF calculations, the quantum efficiency from the A²Σ⁺ electronic level was calculated using a fluorescence lifetime of 206 ns¹⁷ and

quenching cross sections for collisions of NO with N₂, NO, O₂, and CO₂ of 0.0074, 43.0, 25.1, and 60 Å², respectively.^{18–20} The square root of the ERE-CARS signal is nearly independent of the electronic quenching rate. This result confirms a very significant advantage for the application of NO ERE-CARS in high-pressure combustion environments where the collisional quenching rate can vary rapidly as a function of both space and time. Similar quenching independence of ERE-CARS signal of hydroxyl radical (OH) was theoretically suggested by Attal-Treout *et al.*²¹

In summary, we find that the NO ERE-CARS signal is essentially independent of the electronic quenching rate, even when the quenching rate varies by more than two orders of magnitude. The ERE-CARS signal actually increases slightly or remains constant as the O₂ or CO₂ concentration increases. This result is in contrast to the LIF signal, which is inversely proportional to the collisional quenching rate. This finding is very significant for the application ERE-CARS for the detection of NO in high-pressure combustion environments where the electronic quenching rate can vary rapidly as a function of both space and time. Moreover, the proposed ERE-CARS technique also looks promising for the detection of hydrocarbon molecules (such as C₂H₂ and C₆H₆) in reacting flows that are very important for understanding the mechanism of soot formation.

Funding for this research was provided by the Air Force Office of Scientific Research under Contract No. FA9550-05-C-0096 (Dr. Julian Tishkoff, Program Manager), and by the U.S. Department of Energy, Division of Chemical Sciences, Geosciences, and Biosciences, under Grant No. DE-FG02-03ER15391. The authors are grateful to Dr. Terrence R. Meyer of ISSI for helpful discussions and editorial comments.

- ¹C. S. Cooper and N. M. Laurendeau, *Combust. Flame* **123**, 175 (2000).
- ²W. G. Bessler, C. Schulz, T. Lee, D.-I. Shin, M. Hofmann, J. B. Jeffries, J. Wolfrum, and R. K. Hanson, *Appl. Phys. B: Lasers Opt.* **75**, 97 (2002).
- ³S. V. Naik and N. M. Laurendeau, *Combust. Sci. Technol.* **174**, 1 (2002).
- ⁴S. V. Naik and N. M. Laurendeau, *Appl. Phys. B: Lasers Opt.* **B79**, 641 (2004).
- ⁵A. C. Eckbreth, *Laser Diagnostics for Combustion Temperature and Species*, 2nd ed. (Gordon & Breach, St. Leonards, Australia, 1996).
- ⁶R. P. Lucht, *Opt. Lett.* **12**, 78 (1987).
- ⁷S. Roy, T. R. Meyer, M. S. Brown, V. V. Velur, R. P. Lucht, and J. R. Gord, *Opt. Commun.* **224**, 131 (2003).
- ⁸S. Roy, T. R. Meyer, R. P. Lucht, V. B. Belovich, E. Corporan, and J. R. Gord, *Combust. Flame* **138**, 273 (2004).
- ⁹F. Beyrau, A. Bräuer, T. Seeger, and A. Leipertz, *J. Raman Spectrosc.* **34**, 946 (2003).
- ¹⁰A. Pott, T. Doerk, J. Uhlenbusch, J. Ehlbeck, J. Hörschele, and J. Steinwandel, *J. Phys. D* **31**, 2485 (1998).
- ¹¹B. Attal-Trétout, O. O. Schnepf, and J.-P. E. Taran, *Opt. Commun.* **24**, 77 (1978).
- ¹²B. Attal-Trétout, S. C. Schmidt, E. Crété, P. Dumas, and J. P. Taran, *J. Quant. Spectrosc. Radiat. Transf.* **43**, 351 (1990).
- ¹³S. F. Hanna, W. D. Kulatilaka, Z. Arp, T. Opatrný, M. O. Scully, J. P. Kuehner, and R. P. Lucht, *Appl. Phys. Lett.* **83**, 1887 (2003).
- ¹⁴A. Y. Chang, M. D. DiRosa, and R. K. Hanson, *J. Quant. Spectrosc. Radiat. Transf.* **47**, 375 (1992).
- ¹⁵M. D. DiRosa and R. K. Hanson, *J. Mol. Spectrosc.* **164**, 97 (1994).
- ¹⁶P. M. Danehy, E. J. Friedman-Hill, R. P. Lucht, and R. L. Farrow, *Appl. Phys. B: Photophys. Laser Chem.* **57**, 243 (1993).
- ¹⁷J. Luque and D. R. Crosley, *J. Chem. Phys.* **111**, 7405 (1999).
- ¹⁸J. W. Thomam, Jr., J. A. Gray, J. L. Durant, Jr., and P. H. Paul, *J. Chem. Phys.* **97**, 8156 (1992).
- ¹⁹P. H. Paul, J. A. Gray, and J. L. Durant, *AIAA J.* **32**, 1670 (1994).
- ²⁰M. C. Drake and J. W. Ratcliffe, *J. Chem. Phys.* **98**, 3850 (1993).
- ²¹B. Attal-Trétout, P. Berlemont, and J. P. Taran, *Mol. Phys.* **70**, 1, (1990).

R. BARRON-JIMENEZ¹
J.A. CATON¹
T.N. ANDERSON²
R.P. LUCHT^{2,✉}
T. WALTHER³
S. ROY⁴
M.S. BROWN⁴
J.R. GORD⁵

Application of a difference-frequency-mixing based diode-laser sensor for carbon monoxide detection in the 4.4–4.8 μm spectral region

¹ Department of Mechanical Engineering, Texas A&M University, College Station, TX 77843-3123, USA
² School of Mechanical Engineering, Purdue University, West Lafayette, IN 47907-2088, USA
³ Institute for Applied Physics, TU Darmstadt, Schlossgartenstr. 7, 64289 Darmstadt, Germany
⁴ Innovative Scientific Solutions, Inc., 2766 Indian Ripple Rd., Dayton, OH 45440-3638, USA
⁵ Air Force Research Laboratory, Propulsion Directorate, Wright-Patterson Air Force Base, OH 45433-7251, USA

Received: 16 November 2005 / Revised version: 20 April 2006
Published online: 7 June 2006 • © Springer-Verlag 2006

ABSTRACT An all-solid-state continuous-wave (cw) laser system for mid-infrared absorption measurements of the carbon monoxide (CO) molecule has been developed and demonstrated. The single-mode, tunable output of an external-cavity diode laser (ECDL) is difference-frequency mixed with the output of a 550-mW diode-pumped cw Nd:YAG laser in a periodically poled lithium niobate (PPLN) crystal to generate tunable cw radiation in the mid-infrared region. The wavelength of the 860-nm ECDL can be coarse tuned from 860.782 to 872.826 nm, allowing the sensor to be operated in the spectral region 4.4–4.8 μm . CO-concentration measurements were performed in CO/CO₂/N₂ mixtures in a room-temperature gas cell, in the exhaust stream of a well-stirred reactor (WSR) at Wright-Patterson Air Force Base and in a near-adiabatic hydrogen/air CO₂-doped flame. The noise equivalent detection limits were estimated to be 1.1 and 2.5 ppm per meter for the gas cell and flame experiments, respectively. These limits were computed for combustion gas at 1000 K and atmospheric pressure assuming a signal-to-noise ratio of 1. The sensor uncertainty was estimated to be 2% for the gas-cell measurements and 10% for the flame measurements based on the repeatability of the peak absorption.

PACS 07.07.Df; 42.62.Fi; 42.65.Ky; 42.72.Ai

1 Introduction

Increasing concern over the environmental impact of combustion emissions has brought many new governmental regulations in recent years. In response to these restrictions, manufacturers are producing new equipment capable of extremely low levels of pollutant emissions. Currently, advanced power-generating gas turbines emit less than 10 ppm of nitric oxide (NO) and carbon monoxide (CO). These emission levels lie near the lowest detection limit of the current sensor technology.

Diode-laser-based absorption sensors are non-intrusive, and they offer high sensitivity and the potential for combustion control through real-time measurements of trace species.

Several groups have been pursuing research for the detection of CO using tunable infrared diode-laser spectroscopy. Mihalcea et al. [1, 2] developed a diode-laser-based absorption system capable of CO detection using a tunable external-cavity InGaAsP diode laser in the spectral range 1.49–1.58 μm . The CO transitions in the second overtone band (1.3–2 μm region) are four orders of magnitude weaker than those in the fundamental band. Furthermore, the spectral interference from major species such as carbon dioxide (CO₂) and water (H₂O) are very strong in this spectral region, making it difficult to extract quantitative concentration of CO from the experimental spectrum. Several groups [3, 4] have also taken advantage of the CO₂ and H₂O interferences to perform multi-species detection using a similar laser system.

Transition lines in the first-overtone band of CO are one to two orders of magnitude stronger than those in the second-overtone band, and several transitions in the *R* branch are isolated from spectral interferences from CO₂ and H₂O. Wang et al. [5, 6] performed absorption measurements on the first-overtone band of the CO molecule using room-temperature, continuous-wave (cw), single mode InGaAsSb/AlGaAsSb diode lasers operated near 2.3 μm in an atmospheric pressure ethylene/air flame. The concentrations of CO were determined by interrogating two transitions in the first-overtone region. The *R*(30) CO transition at 4343.81 cm⁻¹ was used for measurements in the post-flame region (1.5 cm above the burner surface). The *R*(15) CO transition at 4311.96 cm⁻¹ was used for measurements in the exhaust duct (120-cm-long duct located 79 cm from the burner surface). For measurements in the post-flame zone, CO concentrations in rich flames were in good agreement with the chemical-equilibrium predictions. For direct-absorption measurements in the exhaust, a detection limit of 1.5 ppm-m at 470 K was demonstrated for a measurement time of 0.1 s with a detection bandwidth of 50 kHz. By using wavelength-modulation-spectroscopy techniques, system sensitivity of 0.1 ppm-m was achieved for a total measurement time of 0.4 s and a detection bandwidth of 500 Hz. For some years after this study, no DFB diode lasers were available near 2.3 μm . Currently, distributed feedback (DFB) diode lasers near 2.3 μm are commercially available [7, 8]. Ebert et al. [9] have used this new generation DFB lasers to interrogate the *R*(30) CO transition. They performed direct-absorption measurements of CO con-

✉ Fax: (765) 494-0539, E-mail: lucht@ecn.purdue.edu

centrations in the post-combustion chamber of a hazardous waste incinerator achieving a detection limit of 6.5 ppm for a 1.0 s measurement time through a 2.5 m optical path length.

To access the fundamental band (near 4.6 μm) of carbon monoxide, lead-salt diode-lasers are available and have been extensively used [10–14]. Although successful in detecting CO, the use of in situ sensors based on lead-salt diodes has been limited due to operational complexity, the requirement of cryogenic cooling of the lasers, and multimode operation of the laser system. The recent development of quantum-cascade distributed-feedback (QC-DFB) lasers has allowed spectroscopic monitoring of CO in ambient air and flames [15, 16]; however, cw non-cryogenic versions of these systems are still not available.

A second strategy to obtain mid-infrared radiation is by nonlinear optical parametric frequency conversion; this strategy offers broad tunability, narrow linewidth, broadband parametric gain, efficient continuous-wave (cw) single-pass conversion, near-room-temperature operation, and the use of many mature laser technologies to seed the nonlinear conversion to IR [17]. Several groups have reported spectroscopic measurements of H_2O , CO_2 , CO, NO, C_2H_2 , C_6H_6 , CH_4 , C_2H_4 , OCS [18], and other molecules in the IR region using difference-frequency-mixing (DFM) sources. Schade et al. [19] used a AgGaS_2 crystal to obtain DFM radiation in resonance with line $P(28)$ in the fundamental band of CO at 2022.914 cm^{-1} . In a similar but modular set up, Kelz et al. [20] used the same birefringent nonlinear crystal, AgGaS_2 , to address the spectral region around 4.76 μm . These systems produced low levels of mid-IR radiation from moderate power diode lasers. Schade et al. used 30- and 50-mW input beams to produce 200 nW, while Kelz et al. typically produced >100 nW of mid-IR radiation from 20- and 6-mW beams.

Quasi-phase-matched (QPM) materials have many advantages for the production of mid-infrared radiation through nonlinear conversion. QPM materials (e.g., LiNbO_3 , LiTaO_3 , KTiOPO_4 , RbTiOAsO_4) can be engineered to use the largest nonlinear susceptibility component of the material. The power-conversion efficiency of DFM processes in QPM periodically poled lithium niobate (PPLN) is typically one order of magnitude higher than the conversion efficiency in birefringent materials [18].

Absorption sensors based on the use of a PPLN crystal to produce mid-infrared radiation in a DFM process have been applied for the detection of trace gases [21–23]. Petrov et al. [24] investigated the feasibility of applying of a diode-pumped mid-IR difference-frequency-mixing (DFM) source based on a periodically poled LiNbO_3 (PPLN) crystal to detect atmospheric CO, N_2O , and CO_2 . Their tunable mid-IR DFM source mixed a diode-pumped Nd:YAG ring laser (220 mW at 1064 nm) and 820 mW from a high power GaAlAs tapered amplifier seeded at 860 nm by a diode laser that allows for fast-frequency tuning by means of current modulation. A maximum of 8 μW were measured at 4.5 μm ; however, CO-concentration measurements were typically performed with 3 μW of mid-IR power. With this system Petrov et al. accessed the CO fundamental band at the $R(6)$ transition near 2169 cm^{-1} . The detection sensitivity of 5 ppb – $\text{m}/\sqrt{\text{Hz}}$ was extrapolated based on rms noise meas-

ured in the $2f$ spectra under interference-free conditions in the 4.31–4.63 μm spectral region.

The system described here is based on the DFM of two near-infrared solid-state lasers in a PPLN crystal to produce tunable laser radiation in the 4.2–4.8 μm spectral region. The sensor system takes advantage of a new, compact diode-pumped Nd:YAG laser system and the incorporation of an external-cavity diode laser (ECDL) that allows for frequency tuning. The application of this sensor to mid-infrared, single-pass direct optical absorption measurements of the CO molecule is discussed in this paper. Preliminary CO-concentration measurements have been previously reported in laboratory and real combustion conditions [25] including an operating gas turbine [26]. Three experiments are discussed here. These are: (1) CO/ CO_2 / N_2 mixtures in a room-temperature gas cell, (2) in the exhaust of a well-stirred reactor (WSR), and (3) in a near-adiabatic hydrogen/air CO_2 -doped flame. Spectral interferences were investigated in detail in the CO_2 -doped flame measurements, and CO spectral lines with minimal CO_2 and H_2O absorption interferences were identified. The simplicity and relatively low cost of the DFM-based sensor described here make it an attractive system that is potentially applicable to numerous other interesting molecules in the infrared spectral region.

2 Experimental system and procedure

2.1 CO-sensor system

The schematic diagram of the experimental system is shown in Fig. 1. The mid-IR sensor system is based on DFM of the laser radiation from a 1064-nm, diode-pumped, 500-mW Nd:YAG laser system (IRCL-1064-500-S from CrystaLaser LC) and a tunable, 860-nm ECDL (DL-100 from Topptica Photonics AG) in a periodically poled lithium niobate (PPLN) crystal (Deltronic Crystal Industries Inc.). The PPLN crystal is 40 mm long, 0.5 mm thick, and has a quasi-phase-match period of 22.8 μm .

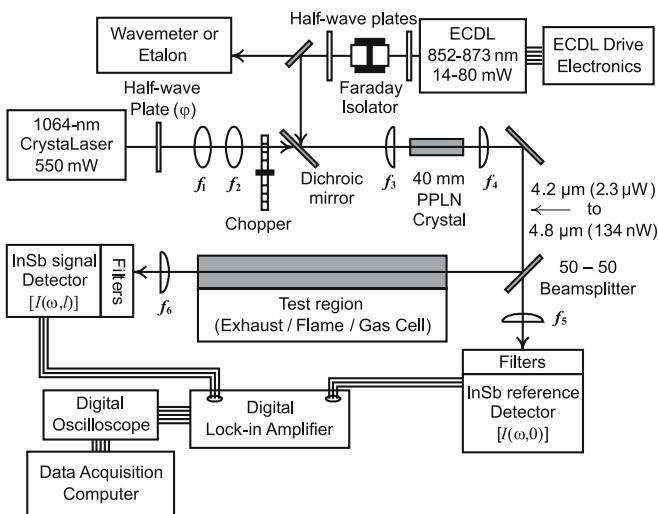


FIGURE 1 Experimental system for the CO-absorption measurements. $f_1 = +25.4\text{ mm}$, $f_2 = +50.2\text{ mm}$, $f_3 = +300\text{ mm}$, $f_4 = +150\text{ mm}$, $f_5 = +200\text{ mm}$, and $f_6 = +150\text{ mm}$

The vacuum wavelength of the 1064-nm Nd:YAG laser was measured to be 1064.664 nm using a Burleigh WA-1000 cw wavemeter. The major advantages of the diode-pumped Nd:YAG system are its excellent beam quality (TEM_{00}), narrow bandwidth (< 10 kHz), stability ($< 2\%$ over 24 h), compactness ($3 \times 3 \times 12$ cm), operability (no special cooling required), and reliability. The wavelength of the ECDL system can be tuned coarsely so that the DFM output beam can be tuned into resonance with various CO transitions in the fundamental band. The bandwidth of the ECDL output radiation was specified by the manufacturer to be ~ 1 MHz. The frequency spectrum of the ECDL was constantly monitored with a Burleigh SA Plus spectrum analyzer (2-GHz free spectral range) as the ECDL output was scanned, typically, over a mode-hop-free tuning range of 12 GHz. The use of a 36-dB Faraday isolator was required to block the back reflections into the ECDL and ensure single-mode operation. With the use of the isolator, no spectral jitter was observed while tuning the ECDL laser.

Several factors were considered to optimize the DFM conversion in the PPLN crystal. Both fundamental beams were carefully overlapped on a dichroic mirror and then focused using a plano-convex 300-mm-focal-length lens in the middle of the PPLN crystal. With this lens, the Rayleigh ranges of the fundamental beams were approximately 17 mm, which is approximately equal to one-half of the length of the PPLN crystal. The waist diameters of the beams were just small enough to be contained within the crystal body. To correct for the different focusing characteristics of the 860-nm and 1064-nm beams, a telescope was used in the 1064-nm beam path to adjust the 1064-nm beam waist position and size. The telescope consisted of two bi-convex lenses with focal lengths of $+25.4$ mm and $+50.2$ mm.

An alignment procedure was developed to ensure proper spatial overlap of the fundamental beams in the crystal. A visible HeNe laser included in the optical path of the 1064-nm beam was used to facilitate the alignment of the sensor. For coarse alignment, two apertures were placed before and after the PPLN crystal. Both input beams were directed through the center of these apertures. Two mirrors in the optical path for each input beam provided enough degrees of freedom to align the lasers through these apertures. Thus, the 860-nm and 1064-nm beams were roughly collinear and focused close to the same axial location. A 150- μm -diameter pinhole was then used to perform more precise alignment of the beams. Since the waist of the input beams was larger than the pinhole diameter, the beam was partially blocked. Maximum power transmission through the pinhole indicated the position of the center of the beam in the radial direction. By comparing the peak transmitted power measurements at different axial locations, we found the beam waist. The waist of the 860-nm beam was determined by the beam diameter and the $f = +300$ mm focusing lens; the waist location of this beam was fixed for a specific ECDL wavelength setting. The axial location of the 1064-nm beam waist was then determined. The spacing of the lenses in the 1064-nm telescope was then adjusted so that the location of the 1064-nm beam waist coincided with the axial location of the 860-nm beam waist. The collinearity of the 1064-nm and 860-nm beams was then checked by using the pinhole in the positions

12.5 mm before and after the waist location. Typically the paths of the 860-nm beam and HeNe laser were adjusted to match the path of the 1064-nm beam. Next, the PPLN crystal was placed in the system with its center at the axial location of the waist of the input beams. The oven that housed the PPLN crystal was mounted on a kinematic mount with five degrees of freedom to allow precise orientation of the PPLN crystal. The constant-temperature oven allowed adjustment of the longitudinal spatial period of the crystal structure to optimize the DFM process for a particular combination of fundamental frequencies. The polarizations of the 1064-nm and 860-nm beams were also adjusted to optimize DFM in the PPLN crystal. Half-wave plates were located in the beam paths upstream of the dichroic mirror to allow adjustment of the polarization of each beam. The 1064-nm Nd:YAG laser power was measured to be 570 mW. However due to the polarization characteristics of the dichroic mirror and the DFM process, the polarization was adjusted to maximize the DFM efficiency, thus sacrificing some power in the transmission through the dichroic mirror. The actual 1064-nm power measured in front of the PPLN entrance face was 320 mW. Similarly, some ECDL power was lost in the reflection from the dichroic mirror because the polarization was adjusted to maximize the DFM efficiency. The power values for the ECDL listed in Table 1 were measured just in front of the PPLN crystal.

The mid-infrared radiation generated in the PPLN crystal was collimated using a plano-convex calcium fluoride (CaF_2) lens ($f = +150$ mm) after exiting the PPLN crystal. The mid-infrared beam was then split into a “signal” beam and a “reference” beam using a 50-50 beamsplitter. The signal beam was directed through the “test region”. In this paper three “test regions” are discussed: i) a gas cell filled with a mixture of CO and other buffer gases, ii) the exhaust of a well-stirred reactor (WSR), and iii) the post-flame region of a hydrogen/air flame doped with CO_2 . The signal beam was focused using a plano-convex CaF_2 lens with a focal length of 150 mm onto a cryogenically cooled InSb detector after passing through a long-wave-pass filter. The reference beam was focused using a plano-convex CaF_2 lens with a focal length of 200 mm onto a second InSb detector, again after being transmitted through a long-wave-pass filter. The filter, with cut off at 3.5 μm , rejected the 860-nm and 1064-nm beams; in addition the InSb detectors had a cut off at 5.4 μm , thus effectively behaving as a broad-band filter.

The detectors used (KISDP-1-J1 from Kolmar Technologies, Inc.) were InSb detectors with an active area of 0.01 cm^2 . The responsivity of both detectors was matched within 5% of each other; the responsivity at peak wavelength was 3.93 A/W. To avoid electrical noise, this model included an integrated transimpedance amplifier. These detectors were cooled with liquid nitrogen to operate at 77 K. The bandwidth of these detectors was 5 MHz nominal at -3 dB and the detection limit $D^* = 6.2 \times 10^{10}$ $\text{cm}(\text{Hz})^{1/2}/\text{W}$. This corresponds to a noise-equivalent-power (NEP) of 4 nW; this NEP is at least 20 times smaller than the generated mid-IR radiation (see Table 1.) The use of cryogenically cooled detectors is convenient but not a limiting factor in the development of the CO-sensor. Currently, there are commercially available detectors that are thermoelectrically cooled and offer detectivities

Experimental Situation	Test CO Transition Name	Position [cm ⁻¹] (μm)	mid-IR generated power [μW]	Diode ID	ECDL Wavelength [nm]	Power [mW]
CO ₂ gas cell measurements [#]	–	2332.990 (4.286)	2.380	JJ82	852.831	80.0
Room-temperature gas cell	<i>R</i> (23)	2224.7127 (4.494)	0.897	JJ82	860.782	58.0
Well Stirred Reactor (WSR)	<i>R</i> (11)	2186.6390 (4.573)	0.089*	2624	863.612	32.3
Hydrogen/air CO ₂ -doped flame	<i>P</i> (19)	2064.3969 (4.844) [‡]	0.134	2624	872.826	14.4

[#] ECDL settings, as delivered

* Output face of the PPLN crystal was chipped

[‡] For this wavelength, the ECDL grating was severely tilted, affecting the cavity performance and beam shape

TABLE 1 Experimental parameters of the CO-sensor for the experiments presented in this study

of $D^* = 1 \times 10^{10} \text{ cm (Hz)}^{1/2}/\text{W}$ [27] for which the shot-noise limit is well under the system performance.

An optical chopper, controlled at 500 Hz, was placed in the path of one of the fundamental beams. The signals from the InSb detectors were processed using lock-in amplifiers (Stanford Research Systems SR830) referenced to the synchronization signal from the optical chopper. The use of the lock-in amplifiers improved the signal-to-noise ratio (SNR) by rejecting the noise components with frequencies different than the chopper frequency. For a mid-infrared power of 250 nW incident on the signal detector, the use of phase-sensitive detection reduced the noise by a factor of three as compared to directly reading the detector signal. The output of the lock-in amplifier was recorded using a computer-controlled digital oscilloscope (Tektronix TDS 3014).

The ECDL was delivered with an optimized wavelength of 852.831 nm and a power output of 80 mW. With this configuration the initial system produced 2.3 μW at 4.286 μm. Later, a diode laser with output centered at 862 nm was purchased and installed in the ECDL assembly. With these two diodes, the ECDL wavelength was coarse tuned within the range 852.8–872.8 nm. Table 1 summarizes the sensor configuration and operating characteristics for the measurements discussed in this paper. In this range the DFM output radiation was close to resonance with transition lines in the *R*- and *P*-branch of the fundamental CO band. Lines tested in the spectral range 4.49–4.84 μm included the *R*(25), *R*(24),

R(23), *R*(20), *R*(11), *P*(18), and *P*(19) transitions, as listed in Table 2.

2.2 Data processing

In general, data processing refers to the comparison of the measured absorption spectrum with the theoretical prediction of Beer's law:

$$\frac{I(\omega, 0) - I(\omega, l)}{I(\omega, 0)} = 1 - \exp(-k_\omega l), \quad (1)$$

where l is the path length, $I(\omega, 0)$ and $I(\omega, l)$ are the spectral intensities at zero and l , respectively, and k_ω is the spectral absorption coefficient given by the product of the line strength and the line profile which accounts for broadening [28]. A computer code for the analysis of the absorption spectrum was developed. For calculation of the absorption spectrum, the line shape was assumed to be a Voigt profile. The Voigt profile was computed using the routine developed by Humlicek [29]. The absorption code incorporates spectroscopic line parameters from the HITRAN/HITEMP database for CO and CO₂, which is an update to the HITRAN96 database [30]. The HITRAN database was updated in 2001 and 2004. The spectral line parameters for the CO molecule were not changed from the 1996 version in the first update [31]. For CO in the fundamental band, the 2004 HITRAN

	$\omega_{0\tau}$ [cm ⁻¹]	$\omega_{0\tau}$ [μm]	$S_\tau(296)$ [cm ⁻¹ /molecule cm ⁻²]	$\gamma_{\text{CO-air}}^0$ [cm ⁻¹ /atm]	$\gamma_{\text{CO-CO}}^0$ [cm ⁻¹ /atm]	$E_{\eta''}$ [cm ⁻¹]	n
<i>R</i> (25)	2230.5258	4.483	5.895×10^{-21}	0.0440	0.0500	1247.0592	0.69
<i>R</i> (24)	2227.6386	4.489	9.011×10^{-21}	0.0445	0.0505	1151.3150	0.69
<i>R</i> (23)	2224.7127	4.494	1.350×10^{-20}	0.0450	0.0510	1059.3718	0.69
<i>R</i> (20)	2215.7044	4.513	4.018×10^{-20}	0.0480	0.0537	806.3828	0.69
<i>R</i> (11)	2186.6390	4.573	3.314×10^{-19}	0.0579	0.0634	253.6672	0.69
<i>P</i> (18)	2068.8469	4.833	6.601×10^{-20}	0.0522	0.0578	656.7892	0.69
<i>P</i> (19)	2064.3969	4.844	4.880×10^{-20}	0.0513	0.0565	729.6774	0.69
<i>P</i> (13)*	2064.5839	4.843	1.282×10^{-23}	0.0574	0.0623	2489.7831	0.69

* This is a hot-band transition from $v'' = 1$ to $v' = 2$, and it can only be detected at high temperatures

TABLE 2 Spectroscopic parameters retrieved from HITRAN database [30] for some selected transitions in the fundamental band of ¹²C¹⁶O. These transitions (τ) correspond to $v'' = 0$ to $v' = 1$ with $\Delta J = \pm 1$

update has improved the accuracy of the collisional broadening coefficients from 2–5% in the 1996 version to 1.3–2.5% of experimental values [32].

The code was designed to calculate the absorption spectrum of CO and CO₂ in a given spectral region using temperature, pressure, path length, and gas-mixture composition as input parameters. It is necessary to consider the gas-mixture composition because of the effect of other species on the collisional broadening of CO. HITRAN provides the coefficients for self- (CO–CO; $\gamma_{\text{CO–CO}}^0$, in $\text{cm}^{-1}/\text{atm}$) and air- (CO–air; $\gamma_{\text{CO–air}}^0$, in $\text{cm}^{-1}/\text{atm}$) collisional broadening at 296 K, as well as the coefficient n of temperature dependence of the air-broadened halfwidth. The collisional broadened half-width at half-maximum (HWHM) [$\gamma(T, P)$] is calculated as suggested by Rothman et al. [30] by

$$\gamma(T, P) = \left(\frac{296}{T} \right)^n \left[\gamma_{\text{CO–air}}^0 (P - P_{\text{CO}}) + \gamma_{\text{CO–CO}}^0 P_{\text{CO}} \right], \quad (2)$$

where T [K] is the gas temperature, P [atm] is the total mixture pressure, and P_{CO} [atm] is the partial pressure for CO.

In the combustion of hydrocarbon fuels, it is reasonably assumed that the molecular composition of the products will be dominated by water, carbon dioxide and nitrogen; none of which is properly accounted for by (2). Proper computation of the collisional broadening of CO requires knowledge of the flame composition and for the target CO transition, the collisional broadening coefficient ($\gamma_{\text{CO–species}}^0$) of CO by every species present in the mixture. To account for the collisional broadening by other species, the correction factors G_{CO} and G_{CO_2} were introduced to correct the collisional width calculated from the HITRAN parameters. $\gamma(T, P)$ is multiplied by the correction factor G_{CO} and the collisional linewidth $\Delta\nu_c$ [cm^{-1}] full-width at half-maximum (FWHM) is calculated by (a similar equation applies for CO₂ absorption)

$$\Delta\nu_c = 2 \cdot \gamma(T, P) \cdot G_{\text{CO}} \quad (3)$$

$G_{\text{CO}} = 1$ corresponds to a gas mixture composed of CO and synthetic air (79% N₂ and 21% O₂). The G_{CO} factor is used as a fitting parameter in the absorption code and to verify the code performance a series of gas-cell measurements were carried with CO/N₂ mixtures. In these measurements, G_{CO} corrected for CO–N₂ broadening as opposed to CO–air; results are shown in Sect. 3.1. It is important to emphasize that the behavior of G_{CO} is very complex since it is dependent on the mixture composition and the particular CO transition being interrogated.

By varying the input parameters, the theoretical absorption spectrum that is the best-fit to the experimental absorption spectrum is found. Depending on the particular experimental conditions, some parameters were known and fixed. The remaining parameters were adjusted in two steps. An evolutionary algorithm [33, 34] was performed for 50 generations with 100 sets per generation. Subsequently, the Levenberg–Marquardt method [35, 36] was applied, initialized by the best-parameters set found by the evolutionary routine.

To assess the sensor detection limit, the rms value of the best fit was calculated. The root-mean-square (rms) refers to the square root of the mean squared deviation of the measured absorption spectrum from the best fit value. The detection

limit was defined for the signal-to-noise (SNR) ratio of one, and the noise quantified by the rms value is an indication of the minimum detectable absorption. To evaluate the detection limit for the sensor, this rms value is considered to be equal to the peak absorption for a given transition under combustion conditions (i.e., CO/air mixture at atmospheric pressure and temperature of 1000 K) for a standard path length of one meter. This standard definition of the detection limit provides a means for comparison of the performance of the sensor under different experimental conditions.

3 Experimental results

The CO-sensor has been tested in a well-controlled room-temperature gas cell and flames in the laboratory. It has also been successfully tested in realistic combustion environments such as the exhaust stream of a well-stirred reactor (WSR).

3.1 Measurements in the room-temperature gas cell

The initial set of CO-absorption measurements was performed in a 30-cm-long gas cell at room-temperature. The cell was filled with known concentrations of CO diluted in nitrogen at various pressures. Room-temperature gas-cell measurements were initially performed to demonstrate the sensor operation and to check the performance of the theoretical code. Numerous CO transitions were investigated in order to identify those that avoid interferences from CO₂ and H₂O molecules at high temperature. For each of these transitions, experiments were performed first in the room-temperature gas cell to confirm the wavelength of the ECDL and the HITRAN/HITEMP spectroscopic line parameters.

For the initial gas-cell measurements, the ECDL grating was tuned using a 1.3-Hz sawtooth function. As a result of this scanning of the grating, the generated mid-IR frequency is tuned back and forth across the absorption feature. Two absorption traces shown in the figures as “Absorption 1” and “Absorption 2” are thus obtained. For these direct-absorption experiments, eight scans were acquired in 3.0 s and averaged using the digital oscilloscope. The Tektronix digital oscilloscope has a resolution of 10 000 data points, and binning 10 neighboring data points in software reduced the read noise. It was verified that this binning process did not affect the spectral line shapes.

Hanna et al. [25, 37] describe the basic data-analysis technique used in our CO-absorption work. For gas-cell measurements Hanna et al. acquired the signal and reference traces for absorbing conditions in the gas cell. The cell was then evacuated and filled with clean air, then signal and reference traces were acquired again. The spectral transmission was then obtained by dividing the ratio of the signal to the reference traces under absorbing conditions by the ratio of the signal to the reference traces under non-absorbing conditions (cell filled with air). This technique requires a measurement with non-absorbing gas in the test region. In some experimental situations, such as in the exhaust of a gas turbine engine, it is not possible or feasible to turn the engine on and off. Under these conditions a slightly different scheme was used. The unattenuated portions of the signal scan [$I(\omega, l)$] were fit using a third-degree polynomial [$p(\omega)$]. To compute the

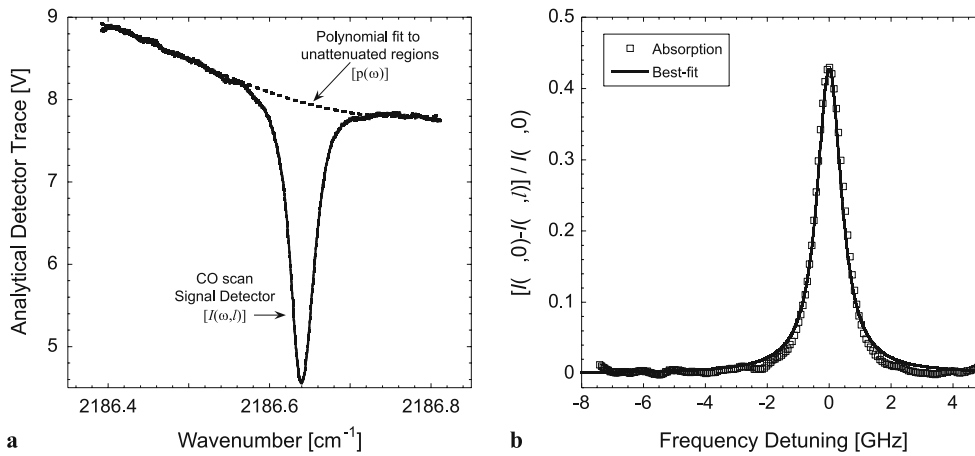


FIGURE 2 Normalization scheme. Panel (a) signal detector traces acquired for the absorbing conditions of the test region and the polynomial fit to the unattenuated portions of the signal trace. (b) The resulting absorption with its best-fit theoretical shape

third-degree polynomial, the unattenuated regions must be distinguishable from the regions with absorption features and the scanning range of the system must be large enough to resolve the wings of the transition line.

Figure 2a shows the raw CO transmission data recorded from the signal detector. The unattenuated regions for the trace were identified between 2186.4 to 2186.54 cm^{-1} and 2186.74 to 2186.82 cm^{-1} . Figure 2a includes the fitted polynomial to the unattenuated regions. The absorption in Fig. 2b was computed using

$$\frac{I(\omega, 0) - I(\omega, l)}{I(\omega, 0)} = 1 - \frac{I(\omega, l)|_{\text{CO scan}}}{p(\omega)}. \quad (4)$$

The scanning range of the ECDL in the CO-sensor system allowed the determination of unattenuated regions of the absorption scans. The polynomial fit technique was employed for the gas-cell measurements.

Figure 3 shows experimental and theoretical spectra for the $R(23)$ transition of the fundamental band of CO at 2224.7127 cm^{-1} when the gas cell was filled with a mixture of 1010 ppm CO in a buffer gas of N_2 at pressures of 6.66 kPa and 13.33 kPa. The specific operating conditions for the sensor are listed in Table 1. This gas mixture was prepared by Matheson as a “certified standard” with an accuracy of 2%. The gas cell was at room temperature, and the best fit of the data corresponds to an average theoretical CO concentration

of 1004 ppm. The estimated uncertainty in the experimental measurements for the CO concentration is less than 20 ppm or 2% of the CO mole fraction of 1010 ppm. This estimate is indicative of the best-fit concentration values obtained from a series of experiments performed on different days and for different transitions. The experimental uncertainty is in part due to the uncertainties of the pressure gage, uncertainties in the theoretical model, and baseline level fluctuations due to long-term drifts in laser power or optical alignment. This experimental value is still in good agreement with the certified gas-mixture concentration, and, as can be seen on Fig. 3, the theoretical spectral line shape, intensity, and line width are in excellent agreement with the experimental line shape.

For the gas-cell measurements, the rms noise in the baseline was measured to be 0.0017, which corresponds to a noise detection limit of 1.1 ppm per meter path length in gas at combustion conditions i.e., 1000 K and 1 atm. This assumes a signal-to-noise (SNR) ratio of 1 at the detection limit.

The HITRAN [30] database shows that the CO-absorption lines in the R branch of the fundamental band are separated by approximately 3 cm^{-1} , which is larger than the mode-hop-free tuning range of the ECDL. It was not possible to scan over two neighboring CO transitions, and it was, therefore, difficult to verify the wavelength of the generated mid-IR beam. By adding CO_2 to the CO/ N_2 mixture in the gas cell, some weak

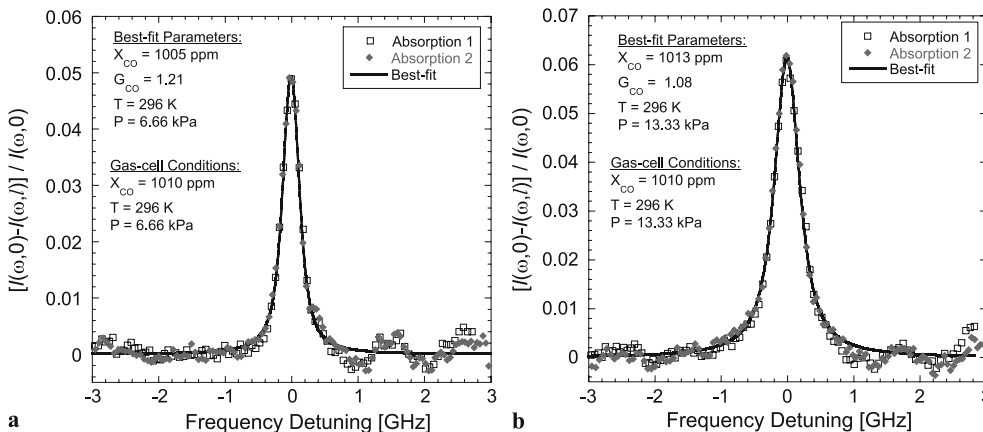


FIGURE 3 Comparison of the measured and calculated $R(23)$ transition in the fundamental band of CO at 2224.7127 cm^{-1} . The 0.32-m-long, room-temperature gas cell was filled with a mixture of 1010 ppm CO and N_2 at pressures of (a) 6.66 kPa and (b) 13.33 kPa

CO_2 transitions appeared within the mid-IR scanning range. The resulting spectrum included both CO and CO_2 transitions, and the wavelength of the DFM-generated mid-infrared radiation was thus verified.

Several $\text{CO}/\text{N}_2/\text{CO}_2$ mixtures were probed in a series of room-temperature experiments in the gas cell. Two of the resulting spectra are shown in Fig. 4. The $R(23)$ transition of CO is shown at 0 GHz frequency detuning, while the absorption line observed at approximately -6 GHz corresponds to the CO_2 transition $P(51)$ at 2224.519 cm^{-1} . In this experiment the gas cell was filled with a mixture of CO/N_2 until the gas-cell pressure reached 13.33 kPa. CO_2 was then added until the gas-cell pressure reached 14.66 or 22.66 kPa. For a final pressure of 14.66 kPa, the mixture composition was 918 ± 30 ppm, $90.8 \pm 2.3\%$, and $9.09 \pm 2.3\%$ for CO, N_2 , and CO_2 , respectively. For the final pressure of 22.66 kPa, the concentrations of CO, N_2 and CO_2 were calculated to be 594 ± 18 ppm, $58.7 \pm 1.3\%$, and $41.17 \pm 1.3\%$ respectively. The uncertainties in these calculations were based on the estimated accuracy of the pressure transducer and the published uncertainty in the composition of the certified mixture. From the spectra shown in Fig. 4, it is evident that the agreement between measured and theoretical line positions, intensities, and concentrations falls within the estimated experimental uncertainties.

For the gas-cell measurements, the correction factor G_{CO} accounts for the fact that nitrogen (N_2) is the buffer gas and not air as assumed in the HITRAN-based absorption code. From a series of measurements on transition $R(23)$ in the gas cell, the average of the best-fit G_{CO} value was 1.11. With this G_{CO} , the N_2 -broadened halfwidth coefficient ($\gamma_{\text{CO}-\text{N}_2}^0$) was calculated to be $0.0502\text{ cm}^{-1}/\text{atm}$. This value is 2.41% lower than the value reported by Varghese and Hanson [11], but 3.43%, 7.18%, and 6.25% higher than the values from Hartmann et al. [38], Predoi-Cross et al. [39], and Sinclair et al. [40] respectively.

For the $\text{CO}/\text{N}_2/\text{CO}_2$ mixture experiments the average best-fit value of G_{CO} was 1.093, thus accounting for the inclusion of CO_2 in the mixture. By using the measured $\gamma_{\text{CO}-\text{N}_2}^0$ for $R(23)$ the CO_2 -broadened halfwidth coefficient ($\gamma_{\text{CO}-\text{CO}_2}^0$) was calculated to be $0.0461\text{ cm}^{-1}/\text{atm}$. This number agrees within 4.3% of the value computed by Hartmann et al. [38] of $0.0465\text{ cm}^{-1}/\text{atm}$, obtained by interpolation for $J = 23$.

Experimental data for the $\gamma_{\text{CO}-\text{CO}_2}^0$ value have been published [41–43] for CO lines in the fundamental band for $J \leq 19$. Our measurements for $\gamma_{\text{CO}-\text{CO}_2}^0$ cannot be directly compared.

3.2 Measurements in the exhaust of a well-stirred reactor (WSR)

In order to demonstrate the sensor in a more realistic combustion environment, CO-measurements were performed in the exhaust stream of a well-stirred reactor (WSR) at Wright-Patterson Air Force Base (WPAFB). The CO-sensor was mounted on a 0.6-m by 1.2-m optical breadboard, and an aluminum enclosure was built to shield the optics from the environment (i.e., particles, heating, radiation). During testing, a flow of dry air was directed into the enclosure to maintain a stable operating temperature. Vibrations were reduced by mounting the sensor on an optical bench and vibration isolation pads.

The exhaust gases from the WSR exited through a 5-cm-diameter, 30-cm-long ceramic tube. The mid-infrared beam was directed along the diameter of the tube approximately 3 mm above the tube exit. A B-type thermocouple with 0.02-mm-diameter wires was placed in the exhaust at the same height as the beam but about 4 mm to the side. An extractive probe was located in the center of the exhaust stream approximately 2 cm above the beam height. The probe was operated in conjunction with non-dispersive IR (NDIR) analyzer (VIA 510 from Horiba Instruments). The uncertainty of this probe-analyzer system was estimated to be 3%. With this instrumentation, the diode-laser-based measurements were compared with the data from extractive sampling.

High-temperature spectral calculations were performed using the HITRAN database, and it was observed that the presence of CO_2 introduces significant spectral interference for the CO fundamental band R -branch transitions for J values higher than 14. To avoid CO_2 interferences, the $R(11)$ CO transition at 2186.6390 cm^{-1} was selected for the absorption measurements. The 852-nm ECDL was coarse-tuned to 863.612 nm to achieve mid-IR generation at 2186.6390 cm^{-1} (see Table 1). The 852-nm diode laser in the ECDL was replaced with an 862-nm diode. The new diode was operated at 863.612 nm with 32.3 mW and exhibited

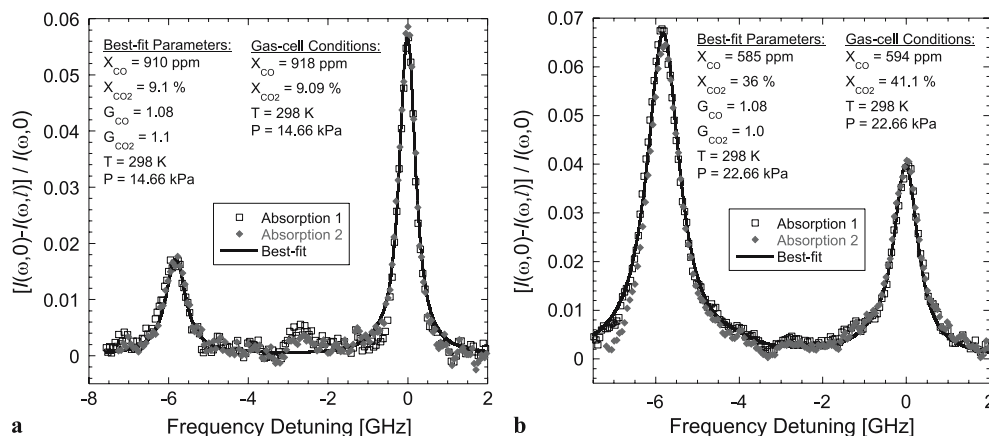


FIGURE 4 Comparison of the measured and calculated absorption for the CO transition $R(23)$ can be observed at 0 GHz frequency detuning. The absorption line observed at approximately -6 GHz corresponds to the $P(51)$ transition from the CO_2 molecule at 2224.519 cm^{-1} . For these experiments the 0.32-m-long gas cell was filled with a mixture of $\text{CO}/\text{N}_2/\text{CO}_2$ at labeled concentrations for pressures (a) 14.66 kPa and (b) 22.66 kPa

a mode-hop-free tuning range of 14 GHz. With this power, the expected mid-IR power was calculated to be 410 nW, a power drop of 46% based on the mid-infrared power of 900 nW obtained using 58 mW from the ECDL at 860.782 nm. The mid-infrared power obtained using the 863.612 nm ECDL was 89 nW, almost a factor of five lower than expected. A small chip in the PPLN crystal face was discovered at the WSR facility during alignment of the CO-sensor, and this was later determined to be the primary cause of the low mid-infrared power.

Given the operational conditions of the reactor, the CO-absorption transitions were broadened to the extent that the spectra did not exhibit any regions where attenuation was negligible, and it was not possible to perform a good polynomial fit for $I(\omega, 0)$. The oscilloscope trace of the reference detector was used in the data-reduction process to determine $I(\omega, 0)$. To account for the background flame emission, the half-wave plate in the 1064-nm beam path was detuned ($\Delta\varphi$) 45° so that the mid-IR generated in the PPLN was completely cancelled. The oscilloscope trace recorded for this condition served as the baseline for the signal and reference detectors. The difference between signal-detector $[I(\omega, l)]$ trace and its baseline $[I(\omega, l)|_{\Delta\varphi=45^\circ}]$ was normalized by the difference between the reference-detector $[I'(\omega, 0)]$ trace and its baseline $[I'(\omega, 0)|_{\Delta\varphi=45^\circ}]$. In general, the output of the lock-in amplifier was different for the signal and reference traces, and it was necessary to include a scaling factor in the expression for the absorption. This factor is the ratio in the denominator of the right-hand side of

$$\frac{I(\omega, 0) - I(\omega, l)}{I(\omega, 0)} = 1 - \frac{I(\omega, l) - I(\omega, l)|_{\Delta\varphi=45^\circ}}{\left[\frac{I'(\omega, 0) - I'(\omega, 0)|_{\Delta\varphi=45^\circ}}{I'(\omega_1, 0) - I'(\omega_1, 0)|_{\Delta\varphi=45^\circ}} \right]} \quad (5)$$

where ω_1 is the frequency at which $I'(\omega, 0)$ is maximum. By using this scaling factor, the reference detector trace was projected as the trace of the signal detector when no absorption occurs. This technique assumes that the shapes of the signal and reference traces were the same if no absorption occurred. It was found that the unattenuated signal trace and the reference trace were equal to better than 1% over the entire spec-

tral scan. Therefore the error induced by this data-processing scheme was minimal.

Figure 5 shows the comparison of the measured and calculated CO-absorption line shape for the $R(11)$ transition in the fundamental band at $2186.6390 \text{ cm}^{-1}$. The reactor was operated using ethylene at equivalence ratios of $\Phi = 1.40$ and $\Phi = 1.75$. Due to high CO concentration, almost 100% of the signal beam was absorbed at the line center. Measurements could not be made at lower levels of CO because of operational limitations of the WSR. Due to thermal considerations, the WSR can only be operated at very fuel-lean ($\Phi = 0.4$ to 0.75) or very fuel-rich ($\Phi = 1.4$ to 1.75) conditions. At lean operating conditions, the CO concentration was expected to fall in the range 30 to 60 ppm, with CO_2 levels within 6 to 7%. Under these conditions, spectral interference from CO_2 was strong enough to obscure the CO transitions. The low signal-to-noise ratio of the measurements due to the low mid-infrared power and the short path length through the flame were also factors in our inability to observe the CO transition under fuel-lean conditions.

For the fuel-rich conditions, the only visible species in the recorded spectra was CO. While CO_2 is present in the exhaust stream, its concentration was comparable to the CO concentration, and the intensity of the CO_2 transitions in this spectral region are two orders of magnitude smaller than those for CO. The CO_2 concentration, thus, has no effect on the fitting procedure. The CO concentrations determined from the best-fit theoretical parameters for experimental curves obtained from several absorption scans under different fuel-rich conditions agreed to within 15% with the results obtained from the extractive probe in conjunction with a NDIR analyzer. Similar discrepancies between probe and diode-laser measurements have been reported previously by Schoenung and Hanson [44], although Nguyen et al. [45] have reported that extractive sampling probes underestimate CO concentration by a factor of 10.

The temperatures reported in Fig. 5 are the readings from the thermocouple and were not corrected for radiation because the thermocouple was located at a different position than the beam path. They were only used as an initial guess for the best-fit procedure. The resulting best-fit temperatures were consistent to within 100 K for the WSR experiments. Notice that for the best fit on Fig. 5, the G_{CO} factor is larger

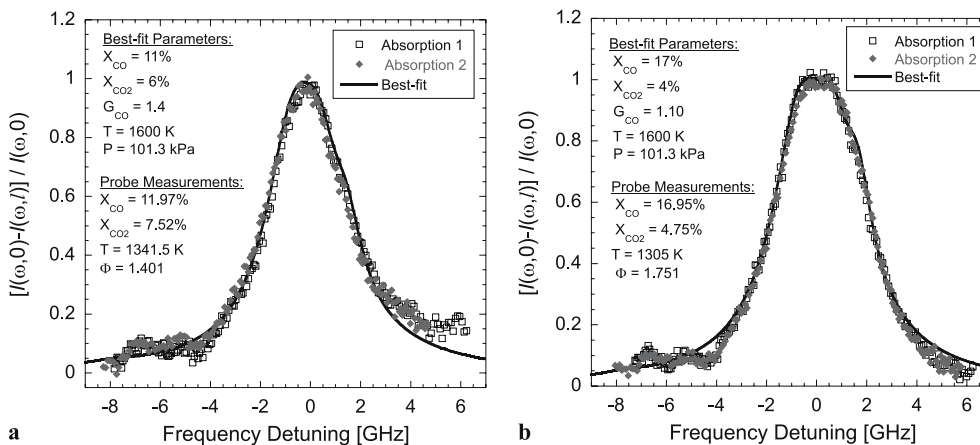


FIGURE 5 Comparison of the measured and calculated CO-absorption line shape for the $R(11)$ transition in the fundamental band at $2186.6390 \text{ cm}^{-1}$. Measurements were performed 3 mm over the exhaust of the WSR at WPAFB over an absorption path length of 5 cm. Reactor was run fuel-rich (a) $\Phi = 1.401$ and (b) $\Phi = 1.751$

than 1 and accounts for line broadening by species other than CO and air. Notice also that the G_{CO} is reduced as expected when the CO_2 -to-CO concentration ratio decreases towards higher equivalence ratios.

For the WSR measurements, the intrinsic noise to the best fit (rms) was calculated to be 0.039. This corresponds to a detection limit of 21 ppm-m for gas at 1000 K, assuming a SNR of 1. The decrease in sensitivity during the field measurements is due in part to noise and vibrations from the combustion equipment. However, the low value of the generated mid-IR power due to the chipped PPLN crystal was the most significant factor in the increase of the detection limit.

3.3 Measurements in $\text{H}_2/\text{air}/\text{CO}_2$ flames

CO measurements were also performed in near adiabatic $\text{H}_2/\text{air}/\text{CO}_2$ flames to investigate high-temperature CO_2 interferences in detail and identify CO lines with minimal interferences. The detection of CO in high-temperature hydrocarbon/air flames using diode-laser probes has been reported by many groups [10, 12, 44, 46, 47]. CO concentrations in these flames are adjusted by controlling the equivalence ratio. CO concentrations in the range of 1% to 15% are measured, and at the edge of the flames the CO concentrations are the lowest. Recently, Wehe et al. [16] used a rich hydrogen/air diffusion flame to simulate the exhaust of a gas turbine. Their flame was cooled with added nitrogen to achieve a temperature of approximately 1150 K, measured with a thermocouple.

CO_2 was seeded into the burner and CO was formed by dissociation. In this flame Wehe et al. reported a measurement of 27 ppm of CO in a 1.2-m folded path length using a quasi-cw quantum-cascade laser at 4.62 μm .

In the current study, a $\text{H}_2/\text{air}/\text{CO}_2/\text{N}_2$ flame was stabilized on a Hencken burner. The flame produced by the Hencken burner is flat, uniform, steady, and nearly adiabatic [48]. A hydrogen/air flame with added CO_2 and N_2 allows for adjustment of the CO concentrations by varying the CO_2 flow and adjustment of the flame temperature by varying the N_2 flow. This flame was ideal for testing of the CO-sensor since in addition to controlling the CO concentration it also offered a high temperature environment with a high concentration of CO_2 .

To perform CO-concentration measurements in the flames, the ECDL was coarse tuned to 872.826 nm so that the generated mid-IR radiation was in resonance with the $P(19)$ transition in the fundamental vibrational band of CO at 2064.3969 cm^{-1} [30]. Tuning the mid-IR radiation to the wavelength of this particular transition was advantageous because of the absence of CO_2 absorption lines in this region. Furthermore, within the scanning range of the sensor the $P(13)$ transition of the $v:2 \leftarrow 1$ band at 2064.583 cm^{-1} emerges at high temperatures, offering independent verification of the mid-IR wavelength and the opportunity for performing two-line thermometry.

To address the P branch, some modifications to the sensor layout were performed. A different PPLN crystal with

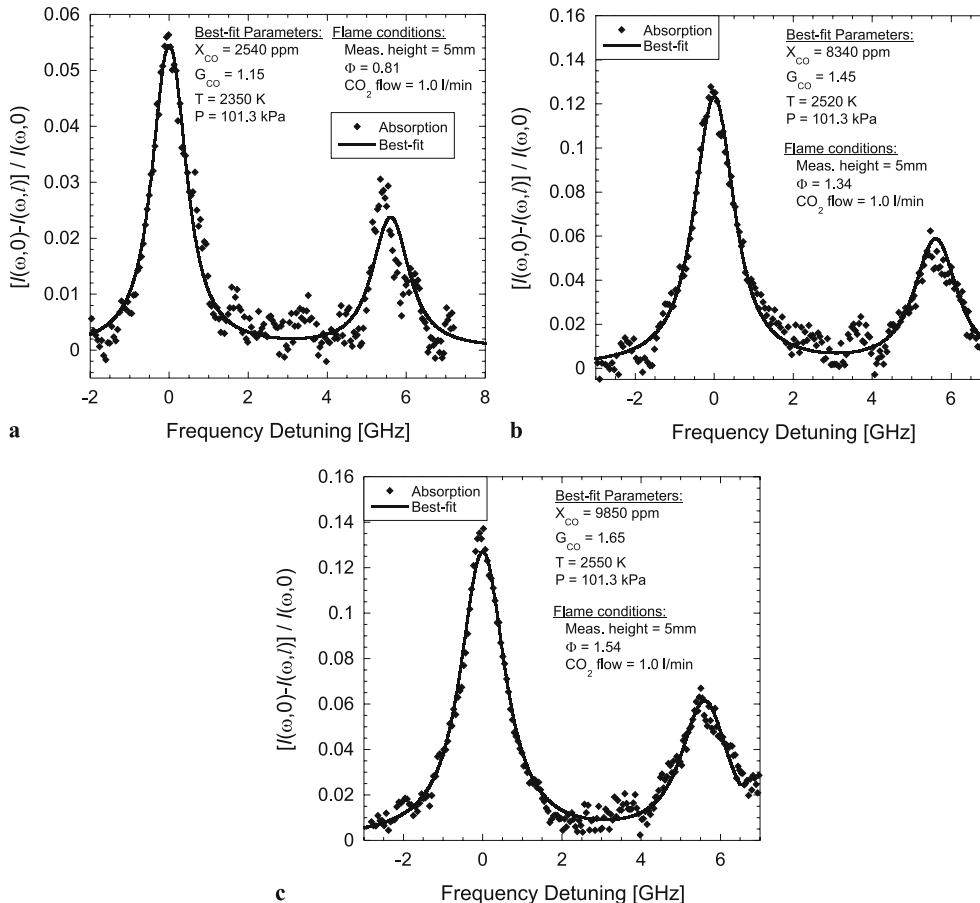


FIGURE 6 Comparison of measured and calculated CO-absorption line shapes for the $P(19)$ (at 0 GHz) transition in the fundamental band at 2064.3969 cm^{-1} and the $P(13)$ (at 5.5 GHz) transition of the $v:2 \leftarrow 1$ band at 2064.583 cm^{-1} [30]. CO-absorption measurements were performed at 5 mm from the surface of the Hencken burner through a path length of 5 cm. The equivalence ratio of these flames is (a) $\phi = 0.81$, (b) $\phi = 1.34$, and (c) $\phi = 1.54$. The composition of the hydrogen/air flames is given in Table 3. For these flames the inlet CO_2 flow is 1.01/min

Φ	Burner inlet flows [l/min]				X_{CO_2} [%]*	X_{CO} [ppm] (meas. at 5 mm)	Fig.
	H ₂	Air	N ₂	CO ₂			
0.81	25	72	0	1	1.02	2540	6a
1.15	23	65	28	2	1.69	4500	7a
	23	65	28	3.5	2.93	5820	7b
	23	65	28	4.9	4.06	9400	7c
1.34	40	85	20	1	0.68	8340	6b
	40	85	20	2	1.36	7040	—
	40	85	20	3	2.03	11 900	—
1.54	32.3	67.9	28.8	1	0.77	9850	6c
	32.3	67.9	28.8	1.9	1.45	7220	—
	32.3	67.9	28.8	2.5	1.90	9990	—
	32.3	67.9	28.8	3.4	2.57	15 790	—

* Calculated mole fraction of carbon dioxide in the reactants

TABLE 3 Composition of the flames stabilized in the Hencken burner

a quasi-phase-match period of 22.1 μm was used to achieve DFM generation in the 4.8- μm region. The ECDL grating was severely tilted in order to obtain laser radiation at 872.862 nm from the diode laser with a nominal wavelength of 862 nm. The severe tilting of the grating caused the power of the ECDL to decrease to 14.4 mW while the shape of the beam was distorted. The ECDL tuning capabilities were degraded so that the scanning frequency was reduced to 260 mHz to obtain about 9 GHz of single-mode hop-free tuning range in only the region of the scan where the laser frequency was decreasing. Under these conditions the generated beam at 4.8 μm had

a power of 134 nW as compared to 2.38 μW at 4.2 μm (see Table 1). For the flame measurements, data were acquired for a time period of 13.4 s. Typically, seven traces were consecutively acquired and averaged by the software. Binning of ten neighboring data points was performed to reduce oscilloscope read noise.

Due to the limited scanning range and the presence of two CO transitions, the recorded spectra acquired using the signal detector did not exhibit any regions with negligible attenuation needed to perform a polynomial fit for $I(\omega, 0)$. Instead of a polynomial fit, the signal detector was used to record $I(\omega, 0)$ since the burner can be easily extinguished and then reignited. The flame was ignited and data were recorded with the signal detector $[I(\omega, l)]$. To account for flame emissions, the mid-IR generation was cancelled (see Sect. 3.2) and the baseline spectrum was acquired $[I(\omega, l)|_{\Delta\varphi=45^\circ}]$. The baseline was subtracted from the signal trace. Then the flame was extinguished and an oscilloscope trace of the signal detector was acquired with no flame and no CO in the test region (similar concept as in Hanna et al. [25]). Absorption was then calculated using

$$\frac{I(\omega, 0) - I(\omega, l)}{I(\omega, 0)} = 1 - \frac{[I(\omega, l) - I(\omega, l)|_{\Delta\varphi=45^\circ}]_{\text{flame}}}{[I(\omega, l) - I(\omega, l)|_{\Delta\varphi=45^\circ}]_{\text{no-flame}}} \quad (6)$$

A series of CO-concentration measurements were performed in different flames as described in Table 3. The flames were stabilized at equivalence ratios of $\Phi = 0.81, 1.15, 1.34, 1.54$

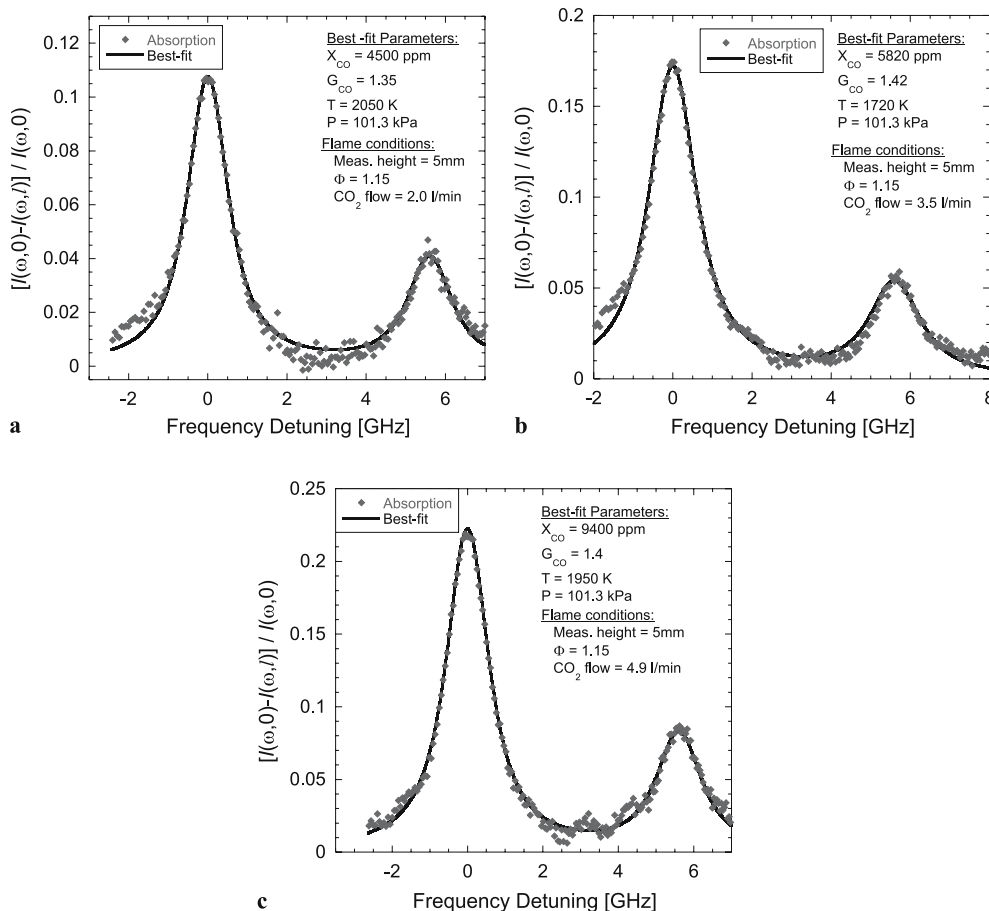


FIGURE 7 Comparison of the measured and calculated CO-absorption line shapes for the $P(19)$ (at 0 GHz) transition in the fundamental band at 2064.3969 cm^{-1} and the $P(13)$ (at 5.5 GHz) transition of the $v:2 \leftarrow 1$ band at 2064.583 cm^{-1} [30]. Measurements were performed 5 mm above the surface of the Hencken burner in a fuel-rich ($\Phi = 1.15$) hydrogen/air CO_2 -doped flame. The path length through the flame was estimated to be 5 cm. Flames composition is given in Table 3. The flow of dopant CO_2 was adjusted to (a) 2.0 l/min, (b) 3.5 l/min, and (c) 4.9 l/min to change the CO content of the flame

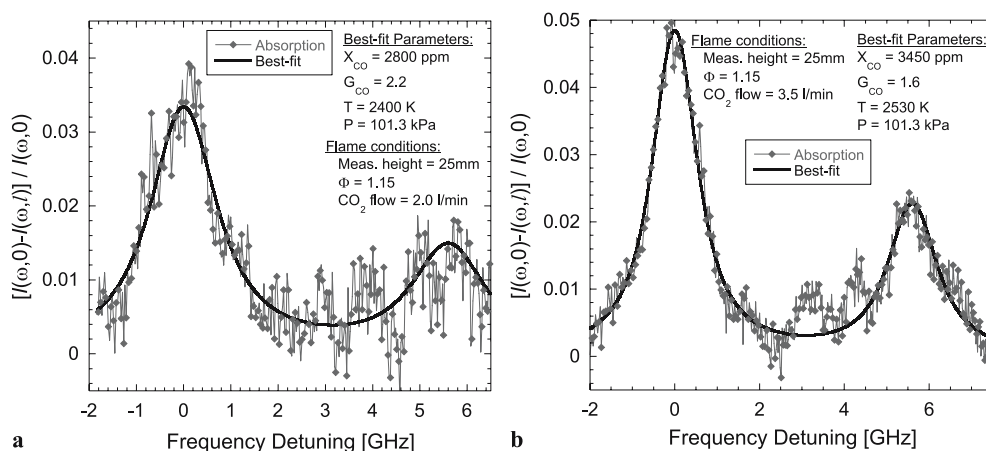


FIGURE 8 Comparison of the measured and calculated CO-absorption line shapes for the $P(19)$ (at 0 GHz) fundamental band transition at 2064.3969 cm^{-1} and the $P(13)$ (at 5.5 GHz) transition of the $v:2 \leftarrow 1$ band at 2064.583 cm^{-1} [30]. Measurements were performed 25 mm above the surface of the Hencken burner. The path length through the flame was estimated to be 5 cm. Panels (a), (b) compare directly to the corresponding panels of Fig. 7

for CO_2 flow rates of 1.0 to 4.9 standard liters per minute (SLM). For these flames, the diode-laser sensor was used to measure flame CO concentrations in the range of 2540 ppm to 16% at 5 mm from the burner surface.

Figures 6, 7, and 8 show the measured and calculated absorption spectra for the $P(19)$ fundamental band and $P(13)$ $v:2 \leftarrow 1$ band CO transitions at 0 and 5.5 GHz frequency detuning, respectively. Measurements were performed at 5 mm from the burner surface. The absorption path length through the flame was 5 cm, corresponding to a single pass. Figure 6 shows three different flames with equivalence ratios of a) 0.81, b) 1.34, and c) 1.54. For these flames the flow rate of carbon dioxide was 1.0 SLM. The lower measured CO concentration and flame temperature were observed for the flame with $\Phi = 0.81$. The flow rates used to produce the $\Phi = 0.81$ flame were at the limit of the burner stability, and the flame was close to the blow-off limit. Under these conditions the flame was difficult to operate. To achieve stable flames with lower CO concentrations, several fuel-oxidizer ratios were tried. Figure 7 present fuel-rich flames with an equivalence ratio of 1.15. The fuel stream was prepared by mixing 23.0

SLM of hydrogen (H_2) and 28.0 SLM of nitrogen (N_2). The air flow and the CO_2 flow were mixed to form the oxidizer stream. In this series of experiments, the air flow was 65.0 SLM and the CO_2 flow rate was varied from 2.0 to 4.9 SLM.

Figures 6 and 7 show the comparison of the experimental CO spectrum with the best-fit theoretical spectrum for measurements at 5 mm from the burner surface. As shown in Figs. 6 and 7, the theoretical spectral line shape, intensity, and line width of both absorption features are in excellent agreement with the experimental data. The rms noise standard deviation of the experimental spectrum from the best-fit theoretical spectrum shown in Figs. 6 and 7 was measured to be 0.004. Assuming $\text{SNR} = 1$ the detection limit was computed to be 2.5 ppm-m for gas at 1000 K. Based on the repeatability of the data from several tests under identical flow conditions, the uncertainty of the peak absorption was estimated to be on the order of 10%. For the $\Phi = 1.15$ flame measurements at an axial distance of 5 mm, the G_{CO} parameter had an average value of 1.42. As discussed, the G_{CO} parameter depends on the flame products which in turn are a function of the reactants composition and flame temperature. In Fig. 6, the line-broadening factor varies between 1.15 and 1.65 for different flame compositions.

Measurements were also performed at 25 mm from the surface of the burner. Figure 8 a and b show the recorded spectra at 25 mm for comparison with panels a and b of Fig. 7, respectively. It can be seen that the CO concentration at the 25-mm location dropped approximately 40% from the 5-mm location while the rms noise maintained the same 0.004 value.

Figure 9 summarizes the measured CO concentration in the series of the tested flames. It shows the measured CO concentration at 5 mm as a function of the reactant CO_2 mole fraction. It is observed that for each flame ($\Phi = 1.15, 1.34, 1.54$) the measured CO concentration reaches a minimum and then increases as the inlet CO_2 flow to the burner is increased. Recall that the CO concentration in the combustion products depends on the flame temperature and the availability of carbon dioxide. As the input amount of CO_2 to the flame increases, the flame temperature is reduced and less CO is produced. As more CO_2 is added to the burner, more CO is produced and, as indicated by the sharp gradient in CO concentration for $X_{\text{CO}_2} > 1.4\%$, the production of CO is dominated by the availability of CO_2 . Numerical simulations of the Hencken burner

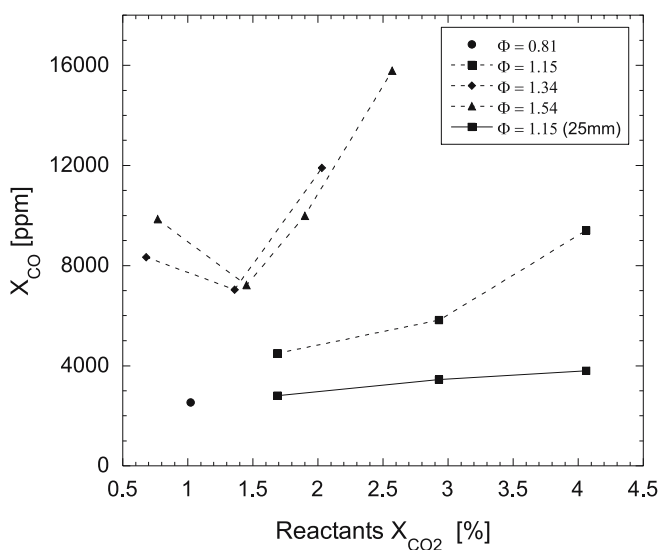


FIGURE 9 Measured CO concentration for the $\text{H}_2/\text{air}/\text{CO}_2$ flames as a function of the CO_2 mole fraction in the inlet flow. Measurements were performed with the mid-infrared sensor at 5 mm from the top of the burner

flames are required to corroborate the measured values of CO concentration and flame temperature.

4 Summary and future work

A diode-laser-based sensor system for mid-infrared single-pass direct-absorption measurements of CO has been demonstrated. The system produces mid-IR radiation in the 4.4–4.8 μm spectral region by difference-frequency mixing of radiation from a near-infrared ECDL and a compact Nd:YAG laser in a PPLN crystal. The system was tested in different experiments that demonstrate its operation and ability to detect CO in CO/N₂/CO₂ mixtures, under combustor exhaust conditions, and in high-temperature post-flame regions with high CO₂ concentrations. This paper presents direct absorption measurements of the fundamental band CO transitions $R(23)$, $R(11)$, and $P(19)$ at 2224.7127, 2186.6390, and 2064.3969 cm^{-1} respectively.

For the CO-absorption measurements in the room-temperature gas cell, the uncertainty of the sensor was estimated to be on the order of 2%. The current detection limit of the system in a laboratory environment was computed to be 1.1 ppm for a 1-m path length through 1000 K combustion gas in a laboratory controlled environment. In similar conditions (i.e. 1 m, 1000 K, 101.3 kPa,) the minimum detectable absorbance for the system described by Mihalcea et al. [2] would correspond to a detection limit of 8470 ppm. This is due to the fact that the interrogated transition $R(13)$ in the second overtone is 1000 times weaker than transitions in the fundamental band. By addressing the $R(15)$ CO transition of the first overtone band, the DFB based system described by Wang et al. [6] yielded a minimum detectable absorbance that corresponds to a detection limit of 1.75 ppm at similar conditions. Line $R(15)$ in the first overtone is 10 times weaker than line $R(23)$ in the fundamental band. Wang et al. [6] system used a DFB laser that allows faster scanning and more power (i.e. 20 mW), thus compensating for the weakness of the addressed transition. These comparisons are only for direct absorption measurements whereas, more sophisticated detection schemes improve the detection limit of the instruments.

The CO-sensor system was also successfully tested in a real combustion environment in the exhaust of the well-stirred reactor (WSR) at Wright-Patterson Air Force Base (WPAFB). CO-concentration measurements in the WSR exhaust agreed to within 15% with extractive probe and NDIR measurements. The estimated CO detection limit was 21 ppm-m for gas at 1000 K. The observed drastic increase in the detection limit was directly related to the reduction of generated mid-infrared power. The reduced power was caused primarily by a chip on the PPLN crystal face. The WSR absorption measurements are an excellent demonstration of the operation of the sensor for measurements with short path length through a very high temperature combustion exhaust.

Finally, CO-absorption measurements were performed on near-adiabatic H₂/air/CO₂/N₂ flames. In the 4.8- μm spectral region, spectral interferences of CO₂ and H₂O were investigated in detail and CO transitions with minimal CO₂ spectral interference were identified. The transition $P(19)$ in the fundamental band at 2064.3969 cm^{-1} and the transition

$P(13)$ of the $v:2 \leftarrow 1$ band at 2064.5839 cm^{-1} were probed offering the possibility of two-line thermometry, which also reduces the uncertainty in the spectral-fitting process. The experimental and theoretical line shapes and intensities are in excellent agreement. The line broadening parameter was about 40% greater than the value for air at the same temperature. The noise equivalent detection limit for the sensor for the hydrogen/air CO₂-doped flame experiments was determined to be 2.5 ppm-m at 1000 K gas. Numerical simulations of the Hencken-burner flames will be performed for comparison with the absorption measurements.

To enhance the sensitivity of the CO-sensor, an increase in the generated mid-IR power and better noise discrimination are required. Future plans include substitution of the diode laser to improve the mid-IR generation, as well as implementation of wavelength-modulation spectroscopy (WMS) or frequency-modulation spectroscopy (FMS) [49]. To increase the scanning rate and the mode-hop-free tuning range, the use of a DFB laser is required. To access the P -branch of the CO fundamental band by DFM, an 860-nm DFB diode-laser has to be mixed with a 1047-nm Nd:YLF laser source. These two laser sources had been recently substituted into the CO-sensor system described, and CO-concentration measurements have been performed on the exhaust stream of liquid-fueled CFM-56 gas-turbine model combustor at WPAFB. These experiments will be discussed in a forthcoming publication. The simplicity, generality, and relative low cost of the DFM-based CO-absorption sensor strategy described and tested in this study is potentially applicable to numerous other interesting species in the mid-IR spectral region.

ACKNOWLEDGEMENTS The authors would like to thank Scott Stouffer and Mike Arstingstall at Wright-Patterson AFB for their help in performing the WSR exhaust experiments. This research was supported by the Air Force Research Laboratory, Propulsion Directorate, Wright-Patterson AFB through Innovative Scientific Solutions, Inc. under Contract No. F33615-00-C-2020, F33615-03-D-M2329, by the Air Force Office of Scientific Research (Dr. Julian Tishkoff, Program Monitor), and by the U.S. EPA STAR Program under Project No. R-82818001.

REFERENCES

- 1 R.M. Mihalcea, D.S. Baer, R.K. Hanson, Meas. Sci. Technol. **9**, 327 (1998)
- 2 R.M. Mihalcea, D.S. Baer, R.K. Hanson, Appl. Opt. **36**, 8745 (1997)
- 3 D.M. Sonnenfroh, M.G. Allen, Appl. Opt. **36**, 3298 (1997)
- 4 J.J. Nikkari, J.M. DiIorio, M.J. Thomson, Appl. Opt. **41**, 446 (2002)
- 5 J. Wang, M. Maiorov, J.B. Jeffries, D.Z. Garbuzov, J.C. Connolly, R.K. Hanson, Meas. Sci. Technol. **11**, 1576 (2000)
- 6 J. Wang, M. Maiorov, D.S. Baer, D.Z. Garbuzov, J.C. Connolly, R.K. Hanson, Appl. Opt. **39**, 5579 (2000)
- 7 Sacher Lasertechnik, LLC (Buena Park CA, 2005) [<http://www.sacher.de/index.php>]
- 8 Frankfurt Laser Co. (Friedrichsdorf Germany, 2005) [<http://www.frlaserco/index.htm>]
- 9 V. Ebert, H. Teichert, P. Strauch, T. Kolb, H. Seifert, J. Wolfrum, Proc. Combust. Inst. **30**, 1611 (2005)
- 10 P.L. Varghese, R.K. Hanson, J. Quantum Spectrosc. Radiat. Transf. **26**, 339 (1981)
- 11 P.L. Varghese, R.K. Hanson, J. Quantum Spectrosc. Radiat. Transf. **24**, 479 (1980)
- 12 J.H. Miller, S. Elreedy, B. Ahvazi, F. Woldu, P. Hassanzadeh, Appl. Opt. **32**, 6082 (1993)
- 13 H.S. Lowry, C.J. Fisher, J. Quantum Spectrosc. Radiat. Transf. **31**, 575 (1984)
- 14 R.G. Daniel, K.L. McNesby, A.W. Miziolek, Appl. Opt. **35**, 4018 (1996)

- 15 A.A. Kosterev, F.K. Tittel, R. Köhler, C. Gmachl, F. Capasso, D.L. Sivco, A.Y. Cho, S. Wehe, M.G. Allen, *Appl. Opt.* **41**, 1169 (2002)
- 16 S. Wehe, M.G. Allen, X. Liu, J.B. Jeffries, R.K. Hanson, AIAA Paper No. 2003-0588 (2003)
- 17 T.J. Kulp, S.E. Bisson, R.P. Bambha, T.A. Reichardt, U.-B. Goers, K.W. Aniolek, D.A.V. Kliner, B.A. Richman, K.M. Armstrong, R. Sommers, R. Schmitt, P.E. Powers, O. Levi, T. Pinguet, M. Fejer, J.P. Kopolow, L. Goldberg, T.G. Mcrae, *Appl. Phys. B* **75**, 317 (2002)
- 18 W. Chen, D. Boucher, F.K. Tittel, *Recent Res. Dev. Appl. Phys.* **5**, 27 (2002)
- 19 W. Schade, T. Blanke, U. Willer, C. Rempel, *Appl. Phys. B* **63**, 99 (1996)
- 20 T. Kelz, A. Schumacher, M. Nägele, B. Sumpf, H.-D. Kronfeldt, *J. Quantum Spectrosc. Radiat. Transf.* **61**, 591 (1999)
- 21 D. Richter, D.G. Lancaster, R.F. Curl, W. Neu, F.K. Tittel, *Appl. Phys. B* **67**, 347 (1998)
- 22 M. Seiter, M.W. Sigrist, *Infrared Phys. Technol.* **41**, 259 (2000)
- 23 K.P. Petrov, R.F. Curl, F.K. Tittel, *Appl. Phys. B* **66**, 531 (1998)
- 24 K.P. Petrov, L. Goldberg, W.K. Burns, R.F. Curl, F.K. Tittel, *Opt. Lett.* **21**, 86 (1996)
- 25 S.F. Hanna, R. Barron-Jimenez, T.N. Anderson, R.P. Lucht, J.A. Caton, T. Walther, *Appl. Phys. B* **75**, 113 (2002)
- 26 T.N. Anderson, R. Barron-Jimenez, J.A. Caton, R.P. Lucht, S. Roy, M.S. Brown, J.R. Gord, T. Walther, I. Critchley, L. Flamand, In *Proc. ASME Summer Heat Transfer Conference HT2003-47532* (2003)
- 27 VIGO System S.A. (Warsaw Poland, 2005) [<http://www.vigo.com.pl>]
- 28 R.P. Lucht, R.C. Peterson, N.M. Laurendeau, *Fundamentals of Absorption Spectroscopy for Selected Diatomic Flame Radicals* (School of Mechanical Engineering, Purdue University, West Lafayette, Indiana, 1978)
- 29 J. Humlicek, *J. Quantum Spectrosc. Radiat. Transf.* **21**, 309 (1979)
- 30 L.S. Rothman, C.P. Rinsland, A. Goldman, S.T. Massie, D.P. Edwards, J.-M. Flaud, A. Perrin, C. Camy-Peyret, V. Dana, J.Y. Mandin, J. Schroeder, A. McCann, R.R. Gamache, R.B. Wattson, K. Yoshino, K.V. Chance, K.W. Jucks, L.R. Brown, V. Nemtchinov, P. Varanasi, *J. Quantum Spectrosc. Radiat. Transf.* **60**, 665 (1998)
- 31 L.S. Rothman, A. Barbe, D.C. Bennef, L.R. Brown, C. Camy-Peyret, M.R. Carleer, K. Chance, C. Clerbaux, V. Dana, V.M. Devi, A. Fayt, J.-M. Flaud, R.R. Gamache, A. Goldman, D. Jacquemart, K.W. Jucks, W.J. Lafferty, J.-Y. Mandin, S.T. Massie, V. Nemtchinov, D.A. Newnham, A. Perrin, C.P. Rinsland, J. Schroeder, K.M. Smith, M.A.H. Smith, K. Tang, R.A. Toth, J. Vander Auwera, P. Varanasi, K. Yoshino, *J. Quantum Spectrosc. Radiat. Transf.* **82**, 5 (2003)
- 32 L.S. Rothman, D. Jacquemart, A. Barbe, D.C. Benner, M. Birk, L.R. Brown, M.R. Carleer, C. Chackerian Jr, K. Chance, L.H. Coudert, V. Dana, V.M. Devi, J.-M. Flaud, R.R. Gamache, A. Goldman, J.-M. Hartmann, K.W. Jucks, A.G. Maki, J.-Y. Mandin, S.T. Massie, J. Orphal, A. Perrin, C.P. Rinsland, M.A.H. Smith, J. Tennyson, R.N. Tolchenov, R.A. Toth, J. Vander Auwera, P. Varanasi, G. Wagner, *J. Quantum Spectrosc. Radiat. Transf.* **96**, 139 (2005)
- 33 A. Wolf, *Aufbau eines Diodenlaser-basierten UV-Absorptionssensors für Stickstoffmonoxid* (Institute for Applied Physics, TU Darmstadt, Darmstadt, Germany, June 2003)
- 34 D.B. Fogel, *IEEE Trans. Neural Netw.* **5**, 3 (1994)
- 35 W.H. Press, S.A. Teukolsky, W.T. Vetterling, B.P. Flannery, *Numerical Recipes in FORTRAN 77: The Art of Scientific Computing, Vol. 1 of FORTRAN Numerical Recipes* (Cambridge University Press, Cambridge, 2001)
- 36 W.H. Press, S.A. Teukolsky, W.T. Vetterling, B.P. Flannery, *Numerical Recipes in FORTRAN 90: The Art of Parallel Scientific Computing, Vol. 2 of FORTRAN Numerical Recipes* (Cambridge University Press, Cambridge, 2002)
- 37 R. Barron-Jimenez, T.N. Anderson, J.A. Caton, R.P. Lucht, T. Walther, S. Roy, M.S. Brown, J.R. Gord, AIAA Paper No. 03-0402 (2003)
- 38 J.M. Hartmann, L. Rosenmann, M.Y. Perrin, J. Taine, *Appl. Opt.* **27**, 3063 (1988)
- 39 A. Predoi-Cross, C. Luo, P.M. Sinclair, J.R. Drummond, A.D. May, *J. Mol. Spectrosc.* **198**, 291 (1999)
- 40 P.M. Sinclair, P. Duggan, R. Berman, A.D. May, J.R. Drummond, *J. Mol. Spectrosc.* **181**, 41 (1997)
- 41 J.P. Bouanich, *J. Quantum Spectrosc. Radiat. Transf.* **13**, 953 (1973)
- 42 P. Varanasi, *J. Quantum Spectrosc. Radiat. Transf.* **15**, 191 (1975)
- 43 T. Nakazawa, M. Tanaka, *J. Quantum Spectrosc. Radiat. Transf.* **28**, 409 (1982)
- 44 S.M. Shoenung, R.K. Hanson, *Combust. Sci. Technol.* **24**, 227 (1981)
- 45 Q.V. Nguyen, B.L. Edgar, R.W. Dibble, A. Gulati, *Combust. Flame* **100**, 395 (1995)
- 46 B. Rosier, P. Gicquel, D. Henry, A. Coppalle, *Appl. Opt.* **27**, 360 (1988)
- 47 R.R. Skaggs, J.H. Miller, *Combust. Flame* **100**, 430 (1995)
- 48 R.D. Hancock, K.E. Bertagnolli, R.P. Lucht, *Combust. Flame* **109**, 323 (1997)
- 49 J.A. Silver, *Appl. Opt.* **31**, 707 (1992)

Measurement of nitric oxide concentrations in flames by using electronic-resonance-enhanced coherent anti-Stokes Raman scattering

Waruna D. Kulatilaka, Ning Chai, Sameer V. Naik, Normand M. Laurendeau, and Robert P. Lucht

School of Mechanical Engineering, Purdue University, West Lafayette, Indiana 47907

Joel P. Kuehner

Department of Physics and Engineering, Washington & Lee University, Lexington, Virginia 24450

Sukesh Roy

Innovative Scientific Solutions, Inc., 2766 Indian Ripple Road, Dayton, Ohio 45440

James R. Gord

Air Force Research Laboratory, Propulsion Directorate, Wright-Patterson Air Force Base, Ohio 45433

Received June 19, 2006; revised August 1, 2006; accepted August 14, 2006;
posted August 29, 2006 (Doc. ID 72149); published October 26, 2006

We have measured nitric oxide (NO) concentrations in flames by using electronic-resonance-enhanced coherent anti-Stokes Raman spectroscopy (ERE-CARS). Visible pump and Stokes beams were tuned to a Q-branch vibrational Raman resonance of NO. A UV probe beam was tuned into resonance with specific rotational transitions in the ($v''=1, v'=0$) vibrational band in the $A^2\Sigma^+-X^2\Pi$ electronic transition, thus providing a substantial electronic-resonance enhancement of the resulting CARS signal. NO concentrations were measured at levels down to 50 parts in 10^6 in H_2 /air flames at atmospheric pressure. NO was also detected in heavily sooting C_2H_2 /air flames at atmospheric pressure with minimal background interference.

© 2006 Optical Society of America

OCIS codes: 300.6230, 120.1740.

Performing accurate nitric oxide (NO) concentration measurements in high-pressure, high-temperature combustion media is a challenging task. Laser-induced fluorescence (LIF) has been applied quantitatively to high-pressure combustion devices up to 60 bars.^{1–3} Application of LIF is complicated because of fluorescent interferences³ from other species such as O_2 and hydrocarbon fragments, absorption of the UV laser beam, and electronic quenching of the LIF signal.^{4,5} In addition to LIF, degenerate four-wave mixing (DFWM),^{6,7} polarization spectroscopy (PS),⁸ and coherent anti-Stokes-Raman spectroscopy⁹ (CARS) have also been investigated for detecting NO in flames and plasmas. We have previously demonstrated three-laser, electronic-resonance-enhanced coherent anti-Stokes-Raman spectroscopy (ERE-CARS) as a promising technique for measuring NO concentrations.¹⁰ In this Letter, we present what we believe is the first ERE-CARS measurements of NO in flames. A detection limit of 50 parts in 10^6 (ppm) has been demonstrated in atmospheric pressure H_2 /air flames. We have also applied ERE-CARS to NO measurements in atmospheric pressure heavily sooting C_2H_2 /air flames.

For the ERE-CARS experiments, we use visible pump ($\lambda_1=532$ nm) and Stokes ($\lambda_2=591$ nm) beams. The frequency difference between these two beams is tuned to a Q-branch Raman resonance in the $v''=0 \rightarrow v''=1$ vibrational transition of the $X^2\Pi$ electronic level of NO. The Raman polarization created in the medium is then probed by using a UV probe beam

($\lambda_3=236$ nm), which is tuned to be in electronic resonance with a rotational transition in the $v''=1, v'=0$ vibrational band of the $A^2\Sigma^+-X^2\Pi$ electronic transition of NO. The ERE-CARS signal generated at 226 nm is thus in resonance with rotational transitions in the $v'=0 \rightarrow v''=0$ band of the same electronic transition. The energy level diagram for the ERE-CARS process is shown in Fig. 1.

The NO ERE-CARS experimental apparatus is shown in Fig. 2. The pump beam at $\lambda_1=532$ nm is the second-harmonic output of an injection-seeded, Q-switched Nd:YAG laser with a repetition rate of 10 Hz and a pulse width of 8 ns (FWHM). The 532 nm output is also used to pump a tunable, narrowband, dye laser operating at ~ 704 nm using LDS 698 laser dye. The output from this dye laser is then sum-frequency mixed with the 355 nm, third-harmonic output from the same injection-seeded Nd:YAG laser using a β -barium borate (β -BBO) crystal, thus generating 236 nm laser radiation. The 236 nm beam acts as the probe for the NO ERE-CARS process. The second harmonic of an unseeded Nd:YAG laser is used to pump a second tunable, narrowband, dye laser containing Rhodamine 610 laser dye. The 591 nm beam from this second dye laser is the Stokes beam. The three laser beams are focused to approximately a diameter of 200 μ m and overlap over an axial distance of approximately 6 mm. The laser pulse energies used are 12, 15, and 0.5 mJ for the pump, Stokes, and probe beams, respectively. The Stokes beam and probe beam linewidths are approximately 0.1 cm^{-1} .

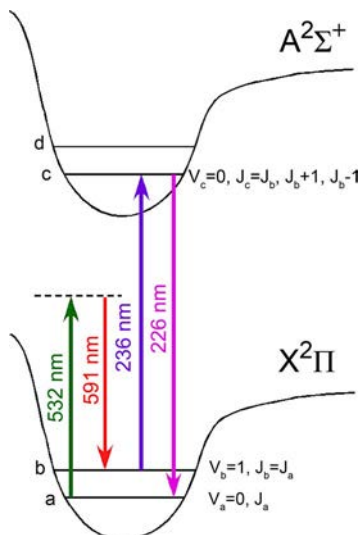


Fig. 1. (Color online) Energy level diagram for NO ERE-CARS.

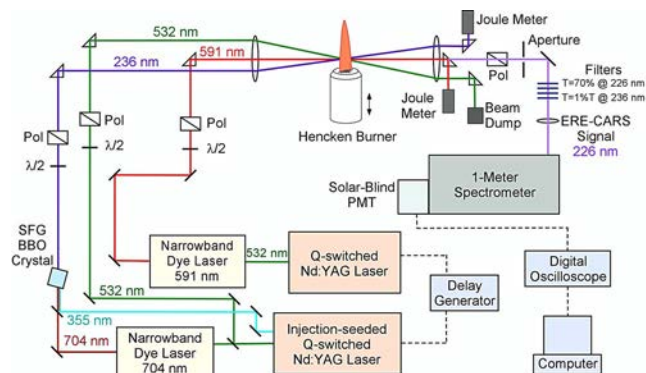


Fig. 2. (Color online) NO ERE-CARS experimental apparatus.

The nonresonant background is suppressed by using a polarization technique.¹⁰

We demonstrated the applicability of ERE-CARS at high temperature by performing NO concentration measurements in an atmospheric pressure H_2 /air flame at an equivalence ratio (Φ) of 1.0. The H_2 /air flame was stabilized on a 25 mm \times 25 mm Hencken calibration burner.¹¹ Known quantities of NO were seeded into the air flow to establish accurate NO concentrations in the flame. The probe volume was located 6 mm above the burner surface. At this location, the flame temperature is approximately 2300 K, and the predicted flame-generated NO concentration is very low, of the order of 10 ppm.¹² Hence the NO concentration at this location is determined primarily by the seeding level. The seed NO concentration was varied from 0 to approximately 1000 ppm. The resulting ERE-CARS spectra for different seeding levels are shown in Fig. 3. The spectra shown in Fig. 3 were recorded by scanning the Stokes laser while fixing the wavelength of the UV probe laser in resonance with the $Q_{11}(13.5)$ transition in the (0,1) band of the $A^2\Sigma^+-X^2\Pi$ transition. From these scans, we conclude that our NO detection limit is 50 ppm.

ERE-CARS spectra can be obtained either by scanning the probe frequency with the Stokes frequency

fixed or by scanning the Stokes frequency with a fixed probe frequency. For the flame measurements, we chose to scan the Stokes frequency by using a fixed UV probe frequency. This frequency-scanning method was selected because fluorescence interferences, from NO itself and from other flame species such as O, O_2 ,^{13,14} and soot, result largely from UV resonances. When the frequency of the UV radiation is unchanged during a spectral scan, as for the Stokes scans, these fluorescence interferences contribute a constant background. The resulting baseline on the ERE-CARS signal is subtracted to obtain a background-corrected ERE-CARS signal. During Stokes scans, we first block the UV probe beam at the beginning for a short period of time and then block the Raman pump beam toward the end of the scan. By so doing, we can determine the background levels resulting from fluorescence interferences and/or scattered UV probe radiation.

The ERE-CARS signal is plotted as a positive quantity above zero by subtracting background interferences as shown in Figs. 3(a)–3(f). The background-corrected ERE-CARS signal was integrated between

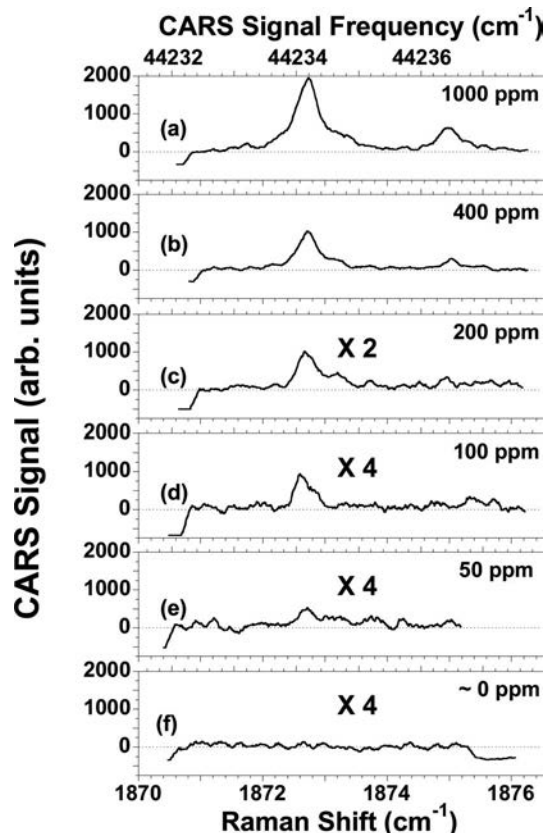


Fig. 3. ERE-CARS spectra recorded at a height of 6 mm above the burner surface by seeding 0–1000 ppm NO into an H_2 /air flame at $\Phi=1.0$ stabilized over the Hencken burner. The spectra (c)–(f) are multiplied by the factors shown and plotted on the same scale. The spectral curve at the Raman shift of 1872.74 cm^{-1} corresponds to the $Q_{11}(13.5)$ Raman transition and the $Q_{11}(13.5)$ UV resonant transition at 44,234.2 cm^{-1} . The spectral line at the Raman shift of 1875.00 cm^{-1} corresponds to the $Q_{11}(7.5)$ Raman transition and the $R_{11}(7.5)$ UV resonant transition at 44,236.45 cm^{-1} .

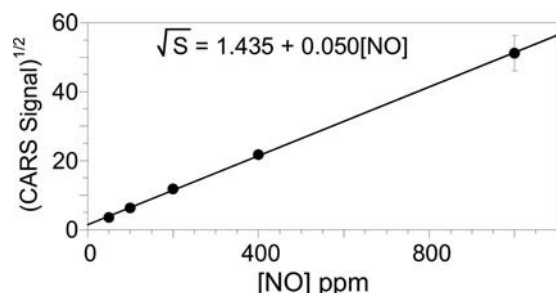


Fig. 4. Square root of integrated NO ERE-CARS signal as a function of NO concentration in NO-seeded H_2 /air flame. The spectra shown in Fig. 3 were integrated as discussed in the text to obtain the data points.

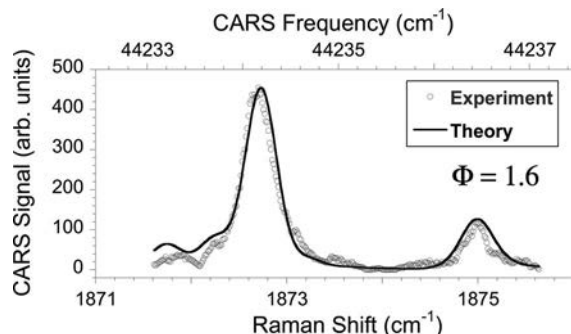


Fig. 5. NO ERE-CARS spectrum recorded at a height of 55 mm above the burner surface in a C_2H_2 /air flame at $\Phi = 1.6$ stabilized on the Hencken burner. The flame was heavily sooting at the measurement location.

the Raman shifts of $1872\text{--}1874\text{ cm}^{-1}$. The square root of the integrated ERE-CARS signal is plotted as a function of the NO concentration in Fig. 4. The data points lie along a straight line nearly passing through the origin, indicating that, as expected, the ERE-CARS signal is proportional to the square of the NO number density.

ERE-CARS was also successfully applied to the detection of flame-generated NO (no seeding) in H_2 /air flames and C_2H_2 /air sooting flames stabilized on the Hencken burner. The ERE-CARS technique has the advantage of excellent species selectivity, since both Raman and electronic resonance conditions must be satisfied to generate an ERE-CARS signal. Background-free detection is possible in heavily sooting flames by scanning the Stokes frequency while fixing the UV probe frequency. A spectrum recorded in a heavily sooting C_2H_2 /air flame at $\Phi = 1.6$ is shown in Fig. 5. The theoretical spectral line shape was calculated using the modified Sandia CARSFT code¹⁵ at a flame temperature of 2300 K. Measurement of NO in such heavily sooting flames by other techniques such as LIF would be very difficult owing to substantial broadband UV fluorescence interferences from hydrocarbon fragments.

In summary, we have demonstrated detection of NO concentrations down to 50 ppm in flames by using ERE-CARS. Very strong, background-corrected ERE-CARS signals were also detected from heavily sooting C_2H_2 /air flames. We have also found that the ERE-CARS signal is nearly unaffected by collisional quenching from other flame species such as O_2 and

CO_2 (Ref. 16) and remains nearly constant with increasing pressure.¹⁷ In future work, we will explore the potential for single-laser-shot ERE-CARS measurements and develop a two-channel system for simultaneous detection of the ERE-CARS and nonresonant background signals, which will allow us to correct for factors such as laser beam absorption.

Funding for this research was provided by the Air Force Office of Scientific Research under contract FA9550-05-C-0096 (Julian Tishkoff, program manager), by the Air Force Research Laboratory, Propulsion Directorate, Wright-Patterson Air Force Base under contract F33615-03-D-2329, and by the U.S. Department of Energy, Office of Basic Energy Sciences, Division of Chemical Sciences, Geosciences, and Biosciences under grant DE-FG02-03ER15391. W. D. Kulatilaka's email address is wkulatil@purdue.edu.

References

1. C. S. Cooper and N. M. Laurendeau, *Combust. Flame* **123**, 175 (2000).
2. S. V. Naik and N. M. Laurendeau, *Combust. Sci. Technol.* **176**, 1809 (2004).
3. W. G. Bessler, C. Schluz, T. Lee, J. B. Jefferies, and R. K. Hanson, *Appl. Opt.* **42**, 4922 (2003).
4. J. W. Daily, W. G. Bessler, C. Schluz, V. Sick, and T. B. Settersten, *AIAA J.* **43**, 458 (2005).
5. P. H. Paul, J. A. Gray, J. L. Durant, Jr., and J. W. Thoman, Jr., *Chem. Phys. Lett.* **259**, 508 (1996).
6. R. L. Vander Wal, R. L. Farrow, and D. J. Rakestraw, in *Twenty-Fourth Symposium (International) on Combustion* (The Combustion Institute, 1992), p. 1653.
7. A. J. Grant, P. Ewart, and C. T. Stone, *Appl. Phys. B* **74**, 105 (2002).
8. B. Löfstedt, R. Fritzson, and M. Aldén, *Appl. Opt.* **35**, 2140 (1996).
9. A. Pott, T. Dorek, J. Uhlenbusch, J. Ehlbeck, J. Hörschele, and J. Steinwandl, *J. Phys. D* **31**, 2485 (1998).
10. S. F. Hanna, W. D. Kulatilaka, Z. Arp, T. Opatrný, M. O. Scully, J. P. Kuehner, and R. P. Lucht, *Appl. Phys. Lett.* **83**, 1887 (2003).
11. W. D. Kulatilaka, R. P. Lucht, S. F. Hanna, and V. R. Katta, *Combust. Flame* **137**, 523 (2004).
12. V. R. Katta, Innovative Scientific Solutions, Inc., 2766 Indian Ripple Road, Dayton, Ohio 45440 (personal communication).
13. I. J. Wysong, J. B. Jefferies, and D. R. Crosley, *Opt. Lett.* **14**, 767 (1989).
14. Q. V. Nguyen, R. W. Dibble, C. D. Carter, G. J. Fiechtner, and R. S. Barlow, *Combust. Flame* **105**, 499 (1996).
15. R. E. Palmer, *The CARSFT Computer Code for Calculating Coherent Anti-Stokes Raman Spectra: User and Programmer Information*, Sandia National Laboratories Report SAND89-8206 (Sandia National Laboratories, 1989).
16. S. Roy, W. D. Kulatilaka, S. V. Naik, N. M. Laurendeau, R. P. Lucht, and J. R. Gord, *Appl. Phys. Lett.* **89**, 104105 (2006).
17. W. D. Kulatilaka, N. Chai, S. Roy, S. V. Naik, N. M. Laurendeau, R. P. Lucht, J. P. Kuehner, and J. R. Gord, "Effects of pressure variations on electronic-resonance-enhanced coherent anti-Stokes Raman scattering of nitric oxide," submitted to *Opt. Commun.*

Femtosecond coherent anti-Stokes Raman scattering measurement of gas temperatures from frequency-spread dephasing of the Raman coherence

Robert P. Lucht^{a)}

School of Mechanical Engineering, Purdue University, West Lafayette, Indiana 47907

Sukesh Roy

Innovative Scientific Solutions, Inc., 2766 Indian Ripple Road, Dayton, Oklahoma 45440

Terrence R. Meyer

Department of Mechanical Engineering, Iowa State University, Ames, Iowa 50011

James R. Gord

Air Force Research Laboratory, Propulsion Directorate, Wright-Patterson AFB, Oklahoma 45433

(Received 20 September 2006; accepted 17 November 2006; published online 20 December 2006)

Gas-phase temperatures and concentrations are measured from the magnitude and decay of the initial Raman coherence in femtosecond coherent anti-Stokes Raman scattering (CARS). A time-delayed probe beam is scattered from the Raman polarization induced by pump and Stokes beams to generate CARS signal; the dephasing rate of this initial coherence is determined by the temperature-sensitive frequency spread of the Raman transitions. Temperature is measured from the CARS signal decrease with increasing probe delay. Concentration is found from the ratio of the CARS and nonresonant background signals. Collision rates do not affect the determination of these quantities. © 2006 American Institute of Physics. [DOI: [10.1063/1.2410237](https://doi.org/10.1063/1.2410237)]

We demonstrate the measurement of gas-phase temperature from the frequency-spread dephasing of the induced Raman coherence in femtosecond coherent anti-Stokes Raman scattering (CARS) spectroscopy. The initial decay rate of the coherence is very sensitive to temperature and is not affected by collision rates or Stark shifts, two factors which significantly complicate frequency-domain nanosecond CARS measurements. By performing these measurements in the first few picoseconds after the impulsive pump-Stokes excitation of the Raman transitions, the CARS signal strength is maximized and collisions have no effect on the determination of species concentration and temperature. In addition, concentration is determined from the initial magnitude of the Raman coherence induced by the pump and Stokes beams.

Although the potential of femtosecond CARS for spectroscopic gas-phase measurements has been demonstrated in several recent experiments,^{1–6} it is still far less developed than nanosecond CARS as a gas-phase diagnostic technique, and significant questions remain concerning the advantages and disadvantages of the two techniques. Initial experiments were directed primarily at extracting parameters of spectroscopic interest from time-averaged spectra obtained from pure gas mixtures of H₂ and N₂ in cells,^{2,4,6} although temperature measurements were also demonstrated.^{2,3,5} Temperature was determined from the dependence of the CARS signal as a function of probe-delay time, and in the case of N₂ the CARS signal was acquired and analyzed for several hundred picoseconds after pump-Stokes excitation of the Raman coherence.^{2,3} One study was reported in which temperature was determined from a CARS spectrum obtained in an atmospheric-pressure flame.³

The current experiments were performed using a 1 kHz repetition rate, high-pulse-energy femtosecond laser system. The seed pulse from a mode-locked Ti:sapphire laser is regeneratively amplified in a Ti:sapphire amplifier pumped by a 20 W Nd:YLF laser at 527 nm to yield a 45 fs, 800 nm output pulse. The pulse energy of the amplified fundamental beam at 800 nm is approximately 2.5 mJ. The nearly Fourier-transform-limited frequency bandwidth of the 45 fs fundamental output of the regenerative amplifier is approximately 220 cm⁻¹ full width at half maximum (FWHM). Part of the 800 nm beam is used to pump the optical parametric amplifier to produce a 1350 nm beam, which is then frequency doubled to produce a 675 nm beam with approximately 20 μJ/pulse. The 675 nm beam is divided to provide the pump and probe beams for the CARS system. The energies for the pump, Stokes, and probe beams measured just before the CARS probe volume were 6, 25, and 6 μJ/pulse, respectively. The pump, Stokes, and probe beam polarizations were linear and parallel.

The CARS process is initiated by the generation of a Raman coherence in the medium by the Fourier-transform-limited pump and Stokes pulses, which arrive at the probe volume at the same time. The CARS signal is then generated by directing a time-delayed probe beam into the CARS probe volume using a three-dimensional phase-matching geometry. The frequency difference between the 675 nm pump beam and 800 nm Stokes beam is 2330 cm⁻¹, corresponding to the fundamental vibrational Raman band of nitrogen. Because of the broad bandwidth of the pump and Stokes pulses, different rovibrational transitions in the Raman band are impulsively excited with approximately the same efficiency. These rovibrational Raman coherences are initially in phase, but begin to oscillate out of phase with each other after impulsive excitation due to slight differences in their frequencies.

^{a)} Author to whom correspondence should be addressed; FAX: (765) 494-0539; electronic mail: lucht@purdue.edu

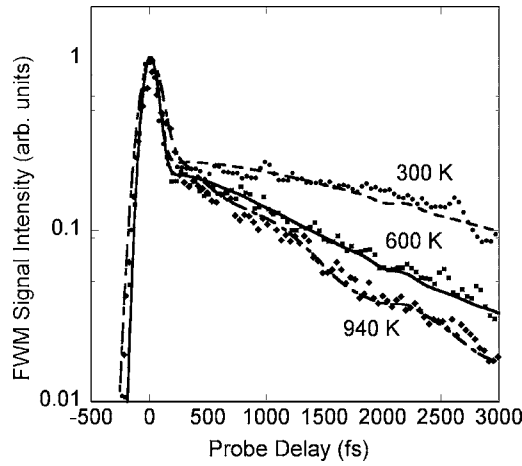


FIG. 1. FWM signal intensity vs probe time delay for air at temperatures of 300, 600, and 940 K. The pressure was 1 bar for all three temperatures.

The dependence of the femtosecond CARS signal on probe-delay time for three different temperatures is shown in Fig. 1. The measurements were performed in a heated gas cell at atmospheric pressure and temperatures of 300, 600, and 940 K (the maximum temperature for the cell). The theoretical curves are in excellent agreement with the experimental data for all three temperatures. The theoretical curves were calculated by convolving the time-delayed probe beam with the Raman and nonresonant components of the macroscopic polarization,

$$S(\tau) = \int_{-\infty}^{+\infty} I_{\text{pr}}(t - \tau) [P_{\text{res}}(t) + P_{\text{nres}}(t)]^2 dt, \quad (1)$$

where $S(\tau)$ is the four-wave mixing (FWM) signal strength, the probe pulse is centered at delay time τ , and the probe irradiance $I_{\text{pr}}(t - \tau)$ is assumed to have a Gaussian pulse shape and peaks at $t = \tau$. The nonresonant polarization is assumed to be directly proportional to the instantaneous amplitudes of the pump and Stokes beams, which are assumed to have Gaussian pulse shapes with maxima at $t = 0$,

$$P_{\text{nres}}(t) = \alpha E_p(t) E_s(t), \quad (2)$$

where α is an arbitrary scaling parameter for the nonresonant FWM signal. In calculating the Raman polarization $P_{\text{res}}(t)$, we assume that the polarization amplitude for each Raman transition i increases linearly with the integrated product of the pump and Stokes amplitudes and that the polarization amplitude is proportional to the population difference ΔN_i between the lower and upper levels and to the Raman cross section $(d\sigma/d\Omega)_i$. Furthermore, we assume that the pump and Stokes pulses are Fourier transform limited such that the various Raman transitions are oscillating in phase at time $t = 0$. The Raman polarization is thus given by

$$P_{\text{res}}(t) = \beta \left[\int_{-\infty}^t E_p(t') E_s(t') dt' \right] \times \sum_i \left\{ \Delta N_i \left(\frac{d\sigma}{d\Omega} \right)_i \cos(\omega_i t) \exp(-\Gamma_i t) \right\}, \quad (3)$$

where β is an arbitrary scaling parameter. After impulsive excitation by the pump and Stokes beams, the polarization for the various Raman transitions oscillates with angular frequency ω_i and decays due to dephasing collisions with a rate

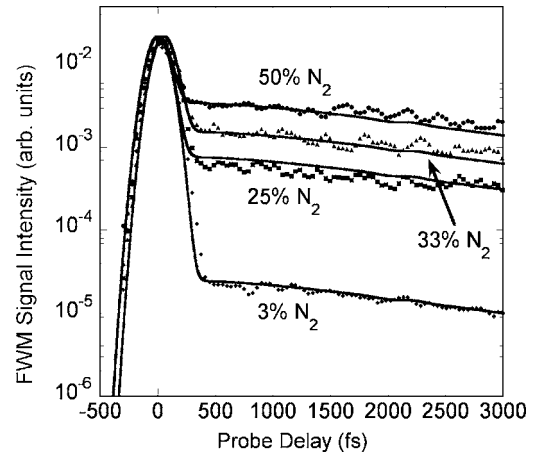


FIG. 2. FWM signal intensity vs probe time delay for N_2/Ar mixtures with N_2 concentrations of 50%, 33%, 25%, and 3%. The mixtures were at a temperature of 300 K and a pressure of 1 bar.

constant of Γ_i , the Raman linewidth. The parameters for each Raman transition for given temperatures and pressures are obtained from the Sandia CARS spectral-fitting code.⁷ The contributions of Q -, O -, and S -branch transitions are considered, although the contribution of the Q -branch transitions is dominant.

In Fig. 1 the data are scaled so the FWM signals are set to a value of 1.0 at $t = 0$ fs. At $t = 200$ fs, the nonresonant FWM signal has decayed significantly and the FWM signal is dominated by the CARS signal. The ratio of the peak FWM signal at $t = 0$ fs to the CARS signal at $t = 200$ fs is approximately the same for all three signal traces because the coherences for the various Raman transitions are excited impulsively and oscillate nearly in phase at $t = 200$ fs. The fact that this ratio is approximately equal for all three temperatures indicates that all the Raman transitions are excited with the same phase, as would be expected for near-transform-limited pulses.⁸ The excitation of the Raman coherence is discussed in detail by Scully *et al.*⁹

For longer delay times, the CARS signal decays because the Raman coherences for the various transitions oscillate at slightly different frequencies, resulting in a decay of the initial macroscopic Raman polarization. At higher temperatures the N_2 population is spread over a greater range of rovibrational levels. Consequently, the rate at which the initial polarization decays is faster because the frequency spread of the transitions that contribute to the initial macroscopic Raman polarization is greater (similarly, Hayden and Chandler¹⁰ observed very different initial decay times for benzene and 1,3,5-hexatriene because of the different frequency widths of the room-temperature Q -branch vibrational bands for these species). For N_2 CARS Q -branch transitions at atmospheric pressure and temperature, the collisional linewidth $\Gamma_i/\pi c$ (FWHM) is approximately 0.1 cm^{-1} , corresponding to a characteristic dephasing collision time of 106 ps. Consequently, dephasing collisions are completely negligible for the time scale shown in Fig. 1.

The FWM signal is plotted versus probe delay in Fig. 2 for room-temperature N_2/Ar mixtures with different concentrations of N_2 . The ratios β/α of the resonant to nonresonant scaling factors for the curves shown in Fig. 2 are 0.61, 0.40, 0.28, and 0.06 for the mixtures of 50%, 33%, 25%, and 3% N_2 in Ar, respectively. Given the value of 0.61 for the ratio β/α for 50% N_2 in Ar, the theoretical values of the ratio β/α

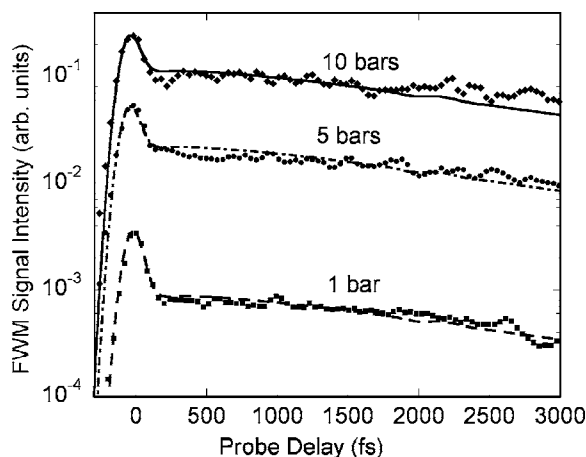


FIG. 3. FWM signal intensity vs probe time delay for air at a temperature of 300 K and pressures of 1, 5, and 10 bars.

for 33%, 25%, and 3% N_2 are 0.39, 0.29, and 0.033, respectively, taking into account the slightly different nonresonant susceptibilities of N_2 and Ar.¹¹ Only the scaling factor for the 3% N_2 in Ar mixture varies by more than 10% from its expected value, which could be due to the fact that the N_2 mass-flow meter was near the lower end of its operating range. Even for the 3% N_2 in Ar mixture, the nonresonant FWM signal is negligible compared to the N_2 CARS signal for probe delays greater than 300 fs. The detection limit for femtosecond CARS may be much lower than for nanosecond CARS because the detection limit for femtosecond CARS will be determined by photon shot-noise statistics. For N_2 at atmospheric temperature and pressure, the total number of resonant CARS photons generated at 200 fs after the initial excitation is approximately 50 000 photons/pulse (calculated using typical values for the quantum efficiency and gain of the photomultiplier tube). The current femtosecond CARS system should thus be capable of detecting species at concentrations of less than 2000 ppm.

The pressure dependence of the femtosecond CARS signal is shown in Fig. 3. The resonant femtosecond CARS signal is proportional to the square of the pressure. In contrast, for nanosecond CARS, the peak signal intensity for an isolated Raman transition is independent of pressure because of the opposite effects of increasing species number density and increasing collisional linewidth. For the N_2 band head in nanosecond CARS, the signal increases approximately linearly with pressure above atmospheric pressure because of

the effects of overlapping transitions and collisional narrowing.¹²

In summary, gas-phase temperature and concentration were determined from the temporal dependence of the femtosecond CARS signal in the first few picosecond after impulsive pump-Stokes excitation. A time-delayed probe beam was used to generate the CARS signal. In the first few picosecond after pump-Stokes excitation of the Raman coherence, the CARS signal is close to its peak level, and collisions have virtually no effect on the signal. Consequently, temperature and concentration can be determined with low detection limits using a simple theoretical treatment provided that the Raman transition frequencies and cross sections are known. No knowledge of the Raman linewidths and no spectral convolutions of the laser and Raman linewidths are required in the analysis of the femtosecond CARS signal to determine these parameters. The high signal levels that we observed indicate that single-shot femtosecond CARS measurements in flames using the chirped-pulse technique demonstrated by Lang and Motzkus⁵ should be quite feasible.

Funding for this research was provided by the National Science Foundation (Award No. 0413623-CTS) and by the Air Force Office of Scientific Research. The authors acknowledge the expert assistance of Kyle D. Frische and Keith D. Grinstead of Innovative Scientific Solutions, Inc. Stimulating discussions with Marlan O. Scully are gratefully acknowledged.

¹T. Lang, K.-L. Kompa, and M. Motzkus, *Chem. Phys. Lett.* **310**, 65 (1999).

²T. Lang, M. Motzkus, H. M. Frey, and P. Beaud, *J. Chem. Phys.* **115**, 5418 (2001).

³P. Beaud, H.-M. Frey, T. Lang, and M. Motzkus, *Chem. Phys. Lett.* **344**, 407 (2001).

⁴H. Skenderović, T. Buckup, W. Wohlleben, and M. Motzkus, *J. Raman Spectrosc.* **33**, 866 (2002).

⁵T. Lang and M. Motzkus, *J. Opt. Soc. Am. B* **19**, 340 (2002).

⁶G. Knopp, P. Radi, M. Tulej, T. Gerber, and P. Beaud, *J. Chem. Phys.* **118**, 8223 (2003).

⁷R. E. Palmer, Sandia National Laboratories Report No. SAND89-8206, 1989.

⁸N. Dudovich, D. Oron, and Y. Silberberg, *Nature (London)* **418**, 512 (2002).

⁹M. O. Scully, G. W. Kattawar, R. P. Lucht, T. Opatrny, H. Pillof, A. Rebane, A. V. Sokolov, and M. S. Zubairy, *Proc. Natl. Acad. Sci. U.S.A.* **99**, 10994 (2002).

¹⁰C. C. Hayden and D. W. Chandler, *J. Chem. Phys.* **103**, 10465 (1995).

¹¹A. C. Eckbreth, *Laser Diagnostics for Combustion Temperature and Species*, 2nd ed. (Gordon and Breach, Amsterdam, 1996), p. 345.

¹²S. M. Green, P. J. Rubas, M. A. Paul, J. E. Peters, and R. P. Lucht, *Appl. Opt.* **37**, 1690 (1998).

Measurements of NO and OH Concentrations in Vitiated Air Using Diode-Laser-Based Ultraviolet Absorption Sensors

Thomas N. Anderson¹ and Robert P. Lucht²
Purdue University, West Lafayette, Indiana 47907

Terrence R. Meyer³, Tarun Mathur,⁴ and Keith D. Grinstead, Jr.⁵
Innovative Scientific Solutions, Inc., Dayton, Ohio 45440

and

James R. Gord⁶, Mark Gruber⁷, and Campbell D. Carter⁸
Air Force Research Laboratory, Propulsion Directorate, Wright-Patterson AFB, Ohio 45433

Diode-laser-based sensors were implemented to measure the concentrations of nitric oxide (NO) and hydroxyl (OH) radicals in the vitiated inlet airflow of a model scramjet combustor. The sensors utilized sum-frequency-mixed sources consisting of a fixed-frequency 532-nm laser and a tunable diode laser to generate ultraviolet radiation for absorption spectroscopy with electronic transitions of OH and NO. Sensitive, interference-free, absolute measurements were possible, enabling the first measurements of both species in a model scramjet combustor using diode-laser-based sensors. With wavelength-modulation spectroscopy, no absorption by OH was evident in the vitiated airflow, verifying that the OH concentration was below the 0.2-ppm detection limit of the sensor. Concentrations of NO were measured to be 200-1100 ppm for the vitiator conditions tested.

Nomenclature

A	=	nozzle area
A^*	=	nozzle area at throat
M	=	Mach number
p	=	static pressure
p_0	=	stagnation pressure
T	=	static temperature
T_0	=	stagnation temperature
x	=	position along flow direction
k	=	specific heat ratio

I. Introduction

VITIATION has long been used to simulate high-Mach number flight conditions for ground tests of supersonic propulsion systems. In the vitiation process, air is heated to flight conditions by combusting fuel with air and adding oxygen to maintain the oxygen content of normal air. Many parameters of flight air can be closely simulated with the vitiated air such as Mach number, total enthalpy, oxygen content, and stagnation temperature. In addition,

¹ Research Assistant, School of Mechanical Engineering, 585 Purdue Mall, MS 1288, and AIAA Student Member.

² Professor, School of Mechanical Engineering, 585 Purdue Mall, MS 1288, and AIAA Associate Fellow.

³ Assistant Professor, Dept. of Mechanical Engineering, Iowa State Univ., Ames, Iowa; AIAA Associate Fellow.

⁴ Research Engineer; AIAA Senior Member.

⁵ Research Chemist; AIAA Member.

⁶ Principal Research Chemist; AIAA Associate Fellow.

⁷ Senior Aerospace Engineer; AIAA Associate Fellow.

⁸ Senior Aerospace Engineer; AIAA Associate Fellow.

vitiation is easier, less expensive, and more efficient than other heating techniques such as arc heating and thermal storage. However, the combustion process in the vitiator alters the composition of the air, adding H_2O , CO_2 , OH, NO, and CO.

Many studies have demonstrated that these “contaminants” in vitiated air can significantly affect combustion behavior. For example, several groups have demonstrated accelerated ignition in supersonic combustion in the presence of small levels of OH,^{1,2} NO,²⁻⁵ and other species.⁷⁻⁹ It is likely that these contaminants also affect other combustion parameters such as flame holding or stability, although no studies are available to verify these effects. If the composition of vitiated air is significantly different than that of normal air experienced in flight, then the results of supersonic ground tests might not be valid for actual flight conditions.

In order to assess the impact of contaminants from vitiation, the actual composition of vitiated air must first be measured. Optical sensors provide a convenient, non-intrusive means for measuring the concentration of the various contaminants. In particular, diode-laser-based sensors are rugged enough to survive the harsh environments of many supersonic combustion test cells, and these sensors provide absolute measurements of species concentration.

Water vapor is the most readily accessible molecule to study with diode-laser-based sensors because of the many water vapor transitions that coincide with telecommunications lasers. Three separate groups have previously used diode-laser-based sensors to measure water vapor concentration and temperature in model scramjet combustors.⁹⁻¹¹ All three previous measurements demonstrated that diode-laser-based sensors can be employed in model scramjet combustors if sufficient care is taken to mitigate beam-steering effects from the high-speed flow. Nitric oxide (NO) has also been measured in a hypersonic wind tunnel using a cryogenically-cooled lead-salt diode laser.¹² However, these previous NO measurements were severely affected by boundary layers around the supersonic flow, and the NO mole fraction measurements were only accurate to within an order of magnitude due to noise. No measurements of hydroxyl (OH) radical concentration have been demonstrated in vitiated air with a diode-laser-based sensor.

In the experiments described in this paper, we have used diode-laser-based sensors to measure NO and OH concentrations in the vitiated inlet air of a model scramjet combustor at Wright-Patterson Air Force Base in Dayton, Ohio. By employing newly developed diode-laser-based sensors that allow us to probe strong electronic transitions of NO and OH in the ultraviolet (UV) spectral region,¹³⁻¹⁶ we were able to quantify the concentrations of both molecules in the vitiated air. To the authors’ knowledge, these experiments represent the first reported measurements of NO and OH in vitiated air using diode-laser-based sensors. Quantitative measurements of both these species provide much-needed information on the composition of the vitiated airflow to determine the actual effects on combustion in the model scramjet combustor.

II. Scramjet Facility

The model scramjet combustor facility at Wright-Patterson AFB is used to study supersonic fuel injection, flameholding, ignition, and inlet-combustor isolation in scramjet propulsion systems.¹⁷ A diagram of the scramjet facility is shown in Figure 1. Details of the facility can be found in Gruber *et al.*¹⁷ and Mathur *et al.*¹⁸ and references therein. A continuous flow of preheated air at 13.6 kg/s, 5.2 MPa, and 920 K is supplied by the Research Air Facility at Wright-Patterson AFB. The supply air is heated further in a sudden expansion vitiator that was fueled with natural gas. Make-up oxygen is added to the vitiated air to replenish the oxygen burned during combustion in the vitiator. The stagnation temperature and pressure of the vitiated air is measured with probes in the water-cooled instrumentation section just downstream of the vitiator. The high-temperature, high-pressure air is then compressed from axisymmetric (254-mm diameter) to two-dimensional (57.2 x 177.8 mm) before being expanded through the facility nozzle to Mach 2.5.

After the expansion, the vitiated airflow passes through two isolator sections to contain the pre-combustion pressure rise before entering the model scramjet combustor. The combustor section has fused-silica windows to allow optical access for the diode-laser-based sensor measurements, as shown in the photograph in Figure 1. Optics for the sensor measurements were mounted on optical breadboards mounted beside the windows. The layout of the optics at the combustor section is described in the next section.

After the combustor section, the airflow is routed through a calorimeter and then out of the test cell through an exhaustor. The composition of the vitiated airflow was monitored throughout the tests with a commercial gas analyzer (ECOM America, Ltd.), and air was sampled from a probe located at the exit of the combustor section. The static pressure along the flow path in the combustor section was measured with pressure taps. Flow section areas were also known at every point along the flow path in the combustor section. Using either the static pressures or the flow section areas along with the stagnation conditions at the combustor inlet, the Mach numbers at the measurement locations were calculated for analysis of the diode-laser-based sensor data. The calculations are discussed in Section IV.

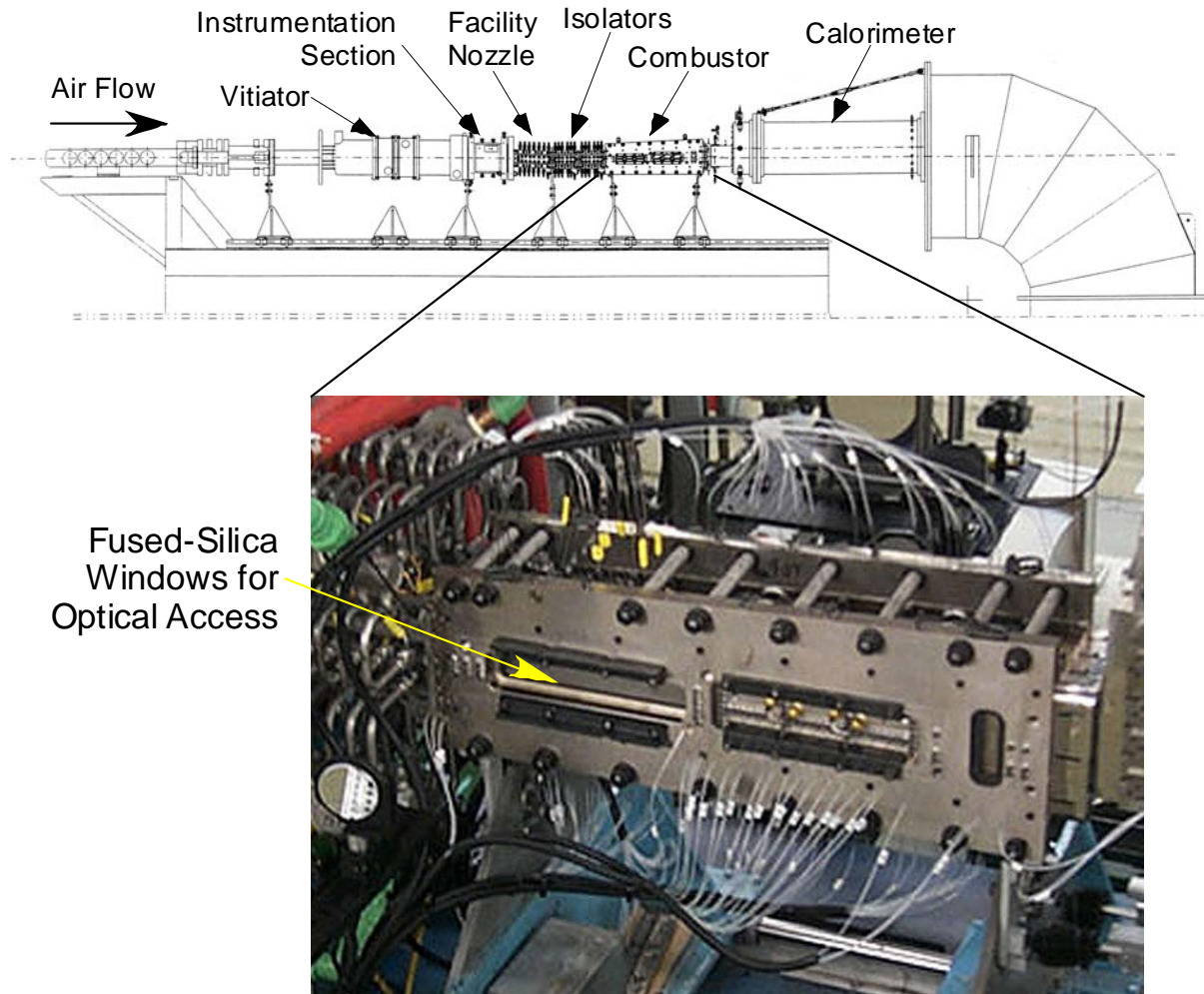


Figure 1. Schematic diagram of the scramjet facility at Wright-Patterson Air Force Base in Dayton, Ohio, and a photograph of the combustor section where OH and NO measurements were performed.

III. Diode-Laser-Based Sensor Systems

The two diode-laser-based sensors used to measure NO and OH in the scramjet have been previously developed and demonstrated.¹³⁻¹⁶ Detailed descriptions of the sensors are available in Refs. 13-16, but the general layout of each sensor is briefly discussed here along with the modifications required for measurements in the scramjet facility. Both sensors utilize sum-frequency mixing to generate tunable UV radiation that is used to perform absorption spectroscopy of OH and NO. They utilize a common architecture in which a high-power, fixed-frequency, 532-nm laser is mixed with a tunable diode laser in a beta-barium borate (β -BBO) crystal. For performing absorption spectroscopy, part of the generated UV radiation is measured immediately as a reference and the remainder is coupled into an optical fiber to simplify the transmission of the beam through the scramjet combustor.

A. OH Sensor

In the OH sensor, around 35 mW of 763-nm radiation from a rapidly-tunable distributed feedback (DFB) diode laser (Sacher Lasertechnik) is mixed with 5 W of 532-nm radiation from a frequency-doubled, Nd:YVO₄ laser (Coherent Verdi). A schematic diagram of the system is shown in Figure 2. Typically, around 25 μ W of UV is generated at a wavelength of 313.5 nm, which is in resonance with the (0,0) band of the $A^2\Sigma^+-X^2\Pi$ electronic

transition of OH. The UV is separated from the fundamental beams using two mirrors HR-coated for 310 nm, and then split with a 70/30 beamsplitter. The 30% reflected is sent directly through a colored-glass filter (UG-11; 3-mm thick) and onto a UV-enhanced Si photodiode (Advanced Photonix) to provide the reference intensity as the laser is current tuned. The remaining 70% of the UV radiation transmitted through the beamsplitter is reflected once more with a 310-nm mirror and then coupled into a 2-m-long, 600- μm -core-diameter, fused silica optical fiber (Ocean Optics; P600-2-UV/VIS). The entire optical system was built on a 61-cm x 61-cm breadboard.

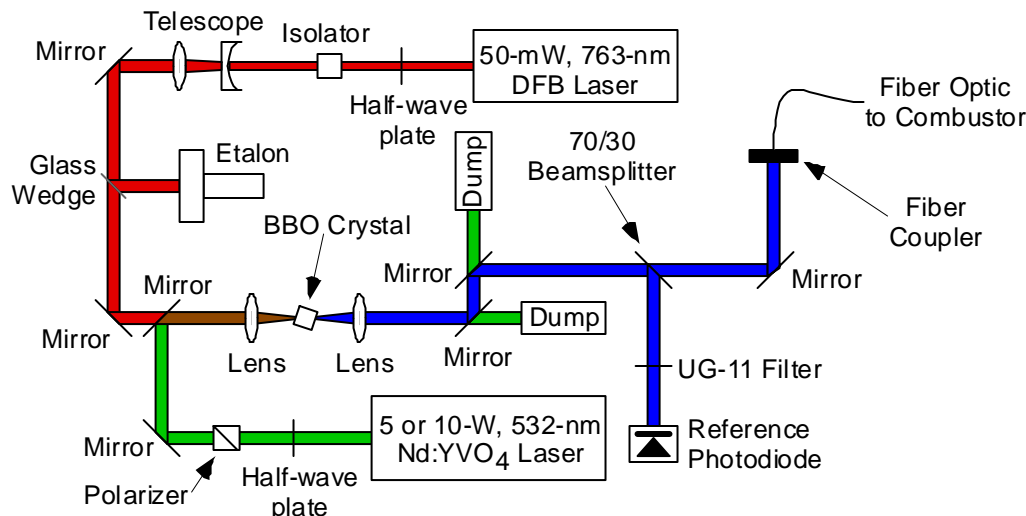


Figure 2. Schematic diagram of the diode-laser-based sensor used to measure OH concentration.

At the combustor section, the UV beams for both OH and NO measurements were directed as shown in Figure 3. For the OH sensor, the 313.5-nm radiation in the fiber was sent to an optical breadboard mounted beside the scramjet combustor section. The laser system was placed on a cart away from the combustor to reduce vibrations and to maintain a stable operating temperature. At the test section, the UV beam exited the fiber through a fused-silica fiber coupler mounted in a 6-axis mount. An $f=75\text{-mm}$ lens was placed approximately 75 mm from the end of the fiber coupler to collimate the UV beam as it passed through the combustor. The beam diameter on the windows was roughly 2.2 cm. The UV beam was located approximately 32 cm downstream from the nozzle exit. After passing through the fused-silica windows, the beam was reflected back through the 22.86-cm-wide

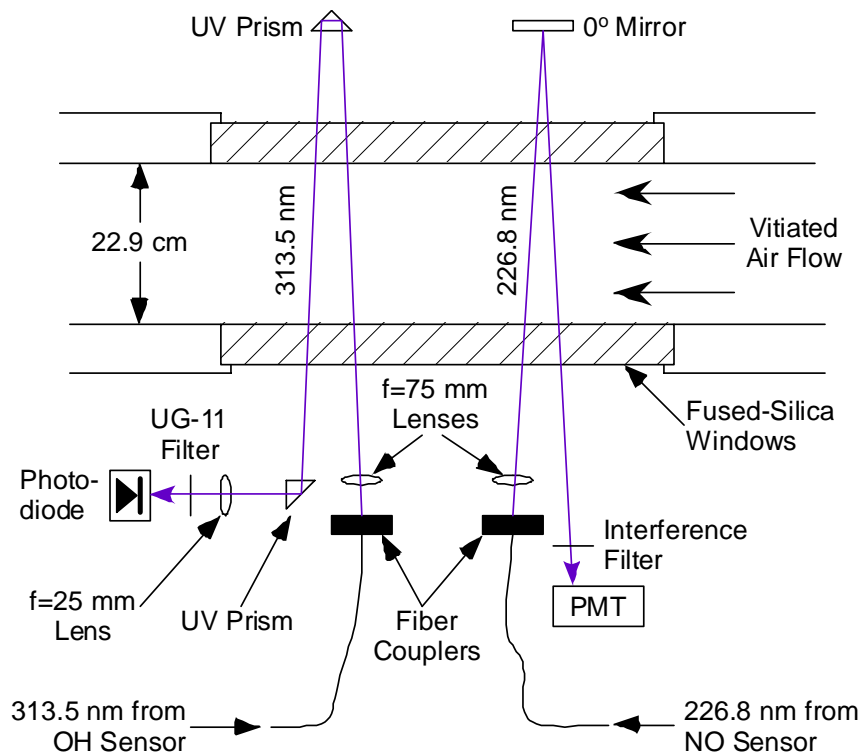


Figure 3. Schematic diagram of the optical layout in the scramjet combustor for measurements of OH and NO with diode-laser-based sensors.

combustor using a 2.54-cm x 2.54-cm fused-silica prism that was AR-coated for 248-355 nm. A second prism was used to direct the beam to an $f=25$ -mm lens to focus the beam onto the photodetector. A 3-mm-thick UG-11 filter was placed before the photodetector to block the fundamental laser radiation and room light. The remainder of the optics in the OH sensor were the same as for the previous configuration described in Meyer *et al.* and Anderson *et al.*^{15,16} It should be noted that the beamsplitter and reference detector were still in place to attempt direct absorption measurements in addition to WMS measurements.

Control and modulation of the OH sensor were performed remotely from inside the control room. The data acquisition computer was located in the research cell next to the sensors, and the computer was controlled remotely with a PC extender. Second-harmonic detection with wavelength-modulation spectroscopy (2f WMS) was used, and the 2f-WMS lineshapes were acquired and processed as described in Anderson.²⁰ The DFB laser was modulated with a signal composed of a 50-kHz sine wave (0.42-V amplitude) added to a 10-Hz triangle-wave function (0.7-V amplitude). The photodiode signal was demodulated through the lock-in amplifier (Stanford Research Systems, SR850) and recorded with the computer. All spectra were averaged over 100 complete cycles of the triangle-wave function to decrease the noise. The lock-in amplifier settings were the following: 300 μ s time constant, 500 μ V sensitivity, 24 dB/oct filter slope, 143.8° phase angle, and maximum dynamic reserve. The 300- μ s time constant represents a filter bandwidth of 260 Hz, and when averaged over 100 sweeps, the final detection bandwidth is 2.6 Hz.

B. NO Sensor

For the NO sensor, the tunable laser is an external cavity diode laser (ECDL) at 395-nm (Toptica Photonics), as shown in Figure 4. Around 11 mW of radiation from this laser is mixed with 100 mW of 532-nm radiation from a diode-pumped, intracavity-frequency-doubled Nd:YAG laser (CrystalLaser). Approximately 325 nW of UV is generated at 226.8 nm to probe transitions in the (0,0) band of the $A^2\Sigma-X^2\Pi$ electronic transition of NO. The UV is recollimated after the crystal and then split with a 50/50 beamsplitter. The reflected beam is used as a reference and is sent through two interference filters centered at 228 nm (Andover) and onto a solar-blind photomultiplier tube (PMT; Hamamatsu, R7154). Two filters were required to adequately block the 395-nm radiation since the PMT is relatively sensitive to radiation at this wavelength. The transmitted beam is fiber coupled into a 2-m-long, 600- μ m-core-diameter, fused silica optical fiber (Ocean Optics; P600-2-UV/VIS) to send to the test section. This entire optical system was built on a 45.7-cm x 45.7-cm breadboard, which is substantially smaller than the 61-cm x 122-cm breadboard used previously for this sensor.¹⁴ The smaller packaging facilitated transport of the sensor and simplified the setup near the scramjet facility since the breadboard could be placed on the same table with the OH sensor.

NO sensor measurements were performed using direct absorption spectroscopy where the wavelength of the UV radiation was slowly tuned over the transition by changing the angle of the diffraction grating in the ECDL. A

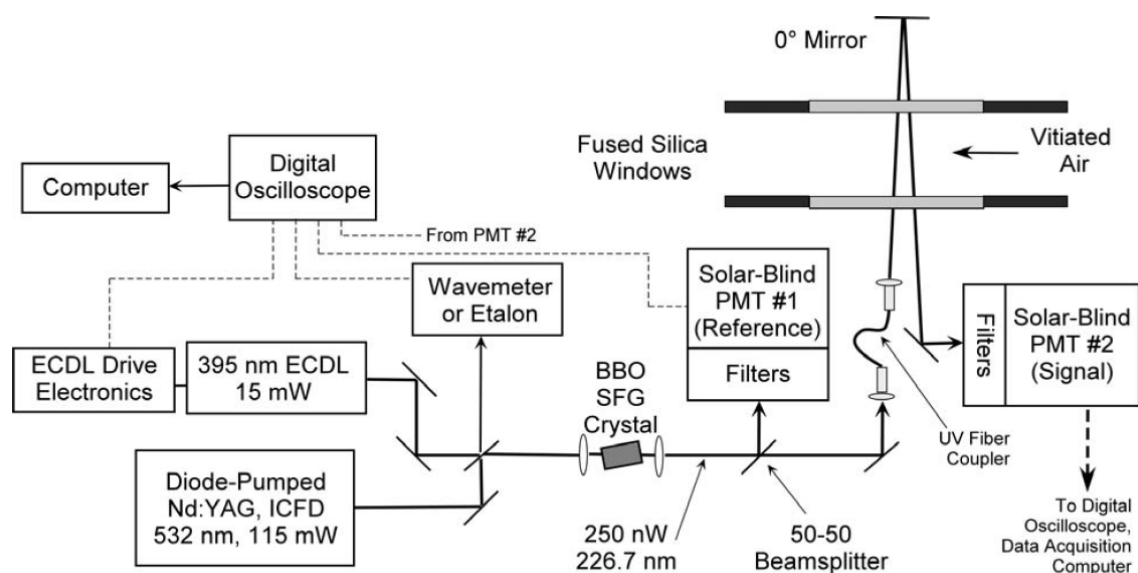


Figure 4. Schematic diagram of NO sensor system for scramjet experiments.

simultaneous correction of the injection current was also required to prevent mode hops during tuning. A 20-Hz triangle-wave function was output from the AI/AO card, and the voltage was doubled with a 2x amplifier to an amplitude of 15 V; this voltage was applied directly to the laser head to modulate the piezoelectric crystal that moves the diffraction grating. A second triangle-wave function with an amplitude of 0.165 V was generated with the AI/AO card and applied to the ECDL controller to modulate the injection current of the laser. With this configuration, a 15 GHz mode-hop-free tuning range was achieved. A larger tuning range could be achieved if a larger amplifier were available to overcome the ± 10 V limitation of the AI/AO card. Further details of the wavelength scanning technique are discussed in Anderson *et al.*¹⁹

The optical layout for the NO sensor at the combustor section is shown in Figure 3. UV radiation at 226.8 nm from the optical fiber was pitched across the combustor test section with a fused-silica fiber coupler mounted on a 6-axis mount. All optics were attached to a breadboard mounted next to the scramjet combustor. The NO sensor was placed on a table several feet away from the flow facility to shield the sensor from vibrations and high temperatures. Like the OH sensor, an $f=75$ -mm fused-silica lens was used to collimate the light from the coupler to maintain a constant beam diameter of roughly 3 cm throughout the two passes through the combustor. A 0° mirror for 226 nm was used on the opposite side of the combustor to reflect the UV beam back through the combustor and onto the PMT. Two narrowband interference filters (Andover 228FS10-25) were placed before the PMT to block the fundamental radiation and room lights. The UV beam for the NO sensor measurements was located approximately 21.9 cm downstream of the facility isolator exit.

As with the OH sensor, the NO sensor was controlled remotely from a computer inside the control room. The computer with the DAQ system was placed next to the sensor and controlled from inside the control room using a PC extender. This allowed us to use short BNC cables for control and acquisition with the sensor. The ECDL was controlled using the two-signal scheme described above to achieve a mode-hop-free tuning range of 15 GHz. An etalon was also simultaneously recorded to monitor the frequency change of the ECDL during the scans. The laser was scanned at 20 Hz and 100 scans were averaged to reduce noise. Photocurrents from the PMTs were detected across 50-k Ω resistors and filtered with the filter/preamplifiers using a cutoff frequency of 1 kHz and amplified with a gain of 5x on the signal PMT voltage and 50x on the reference PMT voltage. Detector and etalon signals were recorded using the DAQ system and processed according to the procedure described in Anderson *et al.*¹⁴ Fuel flow for the vitiator was cut off between every other condition to record air scans to be used in the normalization. The ECDL wavelength was adjusted to 395.2819 nm to probe the $P_2(9)$ transition (for NO) at 44084.69 cm^{-1} .

IV. Results

A. OH Measurements

The 2f-WMS data were recorded in the vitiated air for vitiator temperatures from 1000 to 1389 K. The averaged raw 2f-WMS signal recorded at the scramjet combustor for a vitiator temperature of 1389 K is shown in Figure 5. The averaged raw 2f-WMS signal acquired in hot air immediately after shutting off the vitiator is also shown in Figure 5. Taking the difference of the two scans, it is evident that there is no absorption by OH in the vitiated air. The 2f-WMS feature resulting from absorption of the 763-nm beam by oxygen provides a convenient frequency reference to ensure that the UV wavelength is correct. Using this frequency reference, a theoretical OH 2f-WMS lineshape was generated and compared with the corrected experimental 2f-WMS signal in Figure 6.

The theoretical 2f-WMS lineshape in Figure 6 was calculated for 1 ppm of OH at the measured pressure and calculated temperature (see Section IV.B for temperature calculations) at the beam location inside the scramjet combustor test section. The collision width was estimated for air at the measured temperature. All parameters used in the theoretical calculation are included in Figure 6. The three parameters for the WMS lineshape were calculated from calibration of the sensor based on a modulation voltage amplitude of 0.42 V. Details of the calibration are available in Anderson.²⁰

From Figure 6, it is clear that there is no detectable absorption by OH in the vitiated air, even at the highest vitiator temperature. Therefore, the OH mole fraction is below the detection limit of the OH sensor in the current configuration. To estimate the detection limit, the peak 2f-WMS signal for 1 ppm is noted to be 0.43 V from Figure 6 for the 0.457-m path length through the test section. The noise in the corrected 2f-WMS spectrum in Figure 6 has a standard deviation of approximately 0.1 V. Thus, the detection limit (for SNR=1) of the OH sensor is ~ 0.2 ppm for the path length and conditions in the scramjet combustor test section. For comparison with the detection limit in previous configurations, this corresponds to a detection limit of 0.1 ppm-m OH in 700-K gas at a 0.1-Hz rate. In a 10-second averaging time, the detection limit for the WMS configuration during laboratory experiments was 0.04 ppm-m.²⁰

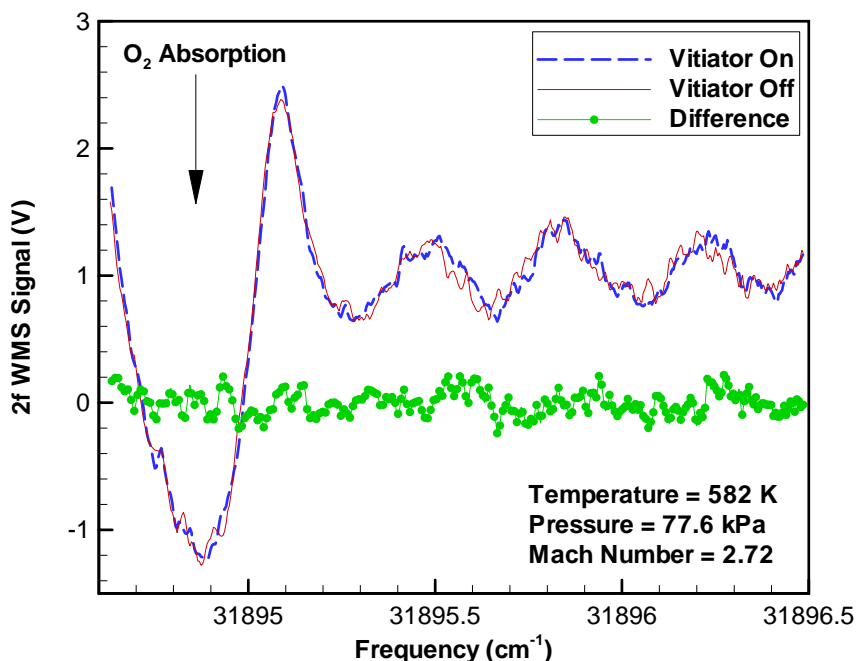


Figure 5. Raw 2f-WMS signals acquired with the OH sensor with the vitiator on and off and the difference of the two signals for a vitiator stagnation temperature of 1389 K. The static temperature, static pressure, and Mach number at the measurement location are shown. The 2f-WMS signal resulting from absorption of the 763-nm beam by oxygen before the crystal is indicated.

For vitiator stagnation temperatures of 1000 K to 1389 K, no OH was observed in the vitiated air with the OH sensor. Thus, we have demonstrated that the OH levels in the vitiated airflow at the combustor test section in the scramjet facility are below 0.2 ppm. Most numerical studies have shown that much greater levels of OH than these are required to significantly affect ignition chemistry in supersonic combustors.^{1,2} Therefore, our measurements indicate that vitiator-generated OH should not affect the results of ground tests using the scramjet facility. This proof that OH is negligible in the vitiated airflow increases the confidence in past and future results with the model scramjet combustor at Wright-Patterson Air Force Base.

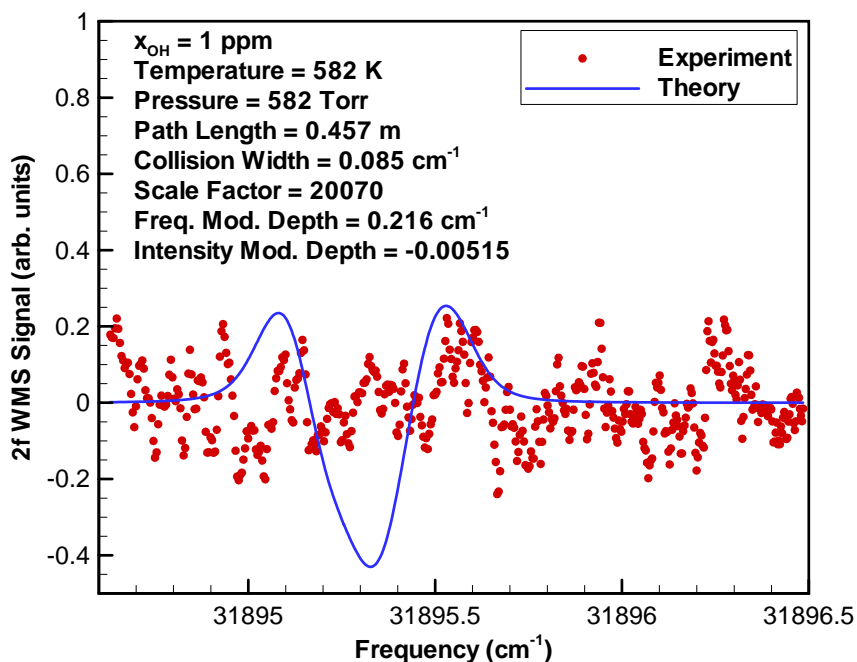


Figure 6. Corrected 2f-WMS signal (difference from Figure 5) and theoretical 2f-WMS signal for 1 ppm of OH at the conditions for the scan in Figure 5.

B. NO Measurements

Five different vitiator conditions were tested during the scramjet experiments so that the stagnation temperatures at the vitiator exit ranged from 1000 K to 1389 K. The static temperature, pressure, and Mach number of the air at the location of the 226-nm beam in the combustor section are shown in Table 1 for each vitiator condition. Pressure taps were located along the length of the combustor section to directly measure the static pressure at the beam location, and the pressures reported in Table 1 are single-shot measurements at each condition. No thermocouples were placed in the combustor test section, however, and two different methods were used to estimate the static temperature at the 226-nm beam location. In Method A, we used the static pressure to estimate the static temperature, T , at the beam location with the equation²¹

$$T = T_0 \left(\frac{p}{p_0} \right)^{(k-1)/k},$$

where T_0 is the stagnation temperature at the facility-nozzle exit, p is the static pressure at the NO beam location, p_0 is the stagnation pressure at the vitiator exit, and k is the specific heat ratio. In Method B, we used the area ratio between the nozzle area at the beam location [$A(x)$] and the nozzle area at the throat (A^*) to calculate the Mach number by iterating the equation²¹

$$\frac{A(x)}{A^*} = \frac{1}{M} \left[\frac{1 + \frac{k-1}{2} M^2}{1 + \frac{k-1}{2}} \right]^{(k+1)/2(k-1)},$$

where M is the Mach number at the beam location. Using the calculated Mach number at the beam location, the local static temperature is calculated using

$$T = T_0 \left[1 + \frac{k-1}{2} M^2 \right]^{-1}.$$

The temperatures calculated using each method are within 5% of each other, as listed in Table 1. NO mole fractions were calculated using both temperatures to investigate the influence of temperature. However, the temperatures calculated using Method B were assumed to be more accurate since the flow section areas were known precisely whereas the measured static pressures used in Method A were only single-shot measurements and therefore were susceptible to larger fluctuations.

Absorption spectra of NO in the vitiated air for two vitiator stagnation temperatures are shown in Figure 7. The theoretical lineshapes for these and all spectra in the scramjet experiments were calculated by fixing the temperature and pressure to the values from Table 1. The transmission scale factor was also fixed to unity since no broadband attenuation was observed in the signals. Only the NO mole fraction and collision width were allowed to vary to optimize the fit. At the lowest two vitiator temperatures, the theoretical lineshapes agree closely with the

Table 1. Conditions of the vitiated airflow in the model scramjet combustor at the location of the 226-nm beam for NO measurements for the vitiator stagnation temperatures tested.

Vitator Stagnation Temp. (K)	Static Temp. at Test Location (K) ^a	Static Temp. at Test Location (K) ^b	Static Pressure at Location (kPa)	Mach Number at Test Location
1000	410	390	62.0	2.61
1111	466	436	64.8	2.58
1222	526	496	65.0	2.58
1333	593	559	66.2	2.57
1389	619	587	65.9	2.57

^aCalculated using the static pressure measured at the beam location

^bCalculated using the flow-section area at the beam location.

experimental lineshapes, as demonstrated in Figure 7(a). Unfortunately, the agreement between theoretical and experimental absorption lineshapes worsens as the vitiator temperature increases. The spectra from the highest three vitiator temperatures become asymmetric on the low-frequency side, as illustrated in the spectrum in Figure 7(b) for the highest vitiator temperature. On the high-frequency side of the spectra, the experimental and theoretical

absorption lineshapes agree closely, and reasonable values of NO mole fraction and collision width can be extracted from the fit to only the high-frequency portion of the lineshapes.

The NO mole fractions determined from the spectral fits at each condition are shown in Figure 8. Gas temperatures calculated using the area ratios (Method B) were used for the results in Figure 8. The temperatures calculated using Method A resulted in NO mole fractions that were 6-9% higher than those in Figure 8. As mentioned earlier, the temperatures (and therefore NO mole fractions) determined using Method B are believed to be most accurate, so the NO mole fractions in Figure 8 represent the most accurate measurement of NO at each vitiator temperature. As seen in Figure 8, the diode-laser-based sensor measurements of NO agree closely with measurements from the ECOM analyzer for lower vitiator temperatures. At higher temperatures, we believe that the diode-laser-sensor measurements are not as sensitive because the UV beam is almost completely attenuated after two passes through the vitiated air stream. Future tests are planned with only a single pass through the combustor to re-examine the high-temperature conditions.

In addition to NO mole fractions, we also compare the observed collision widths to calculations for air at the pressure and temperature for

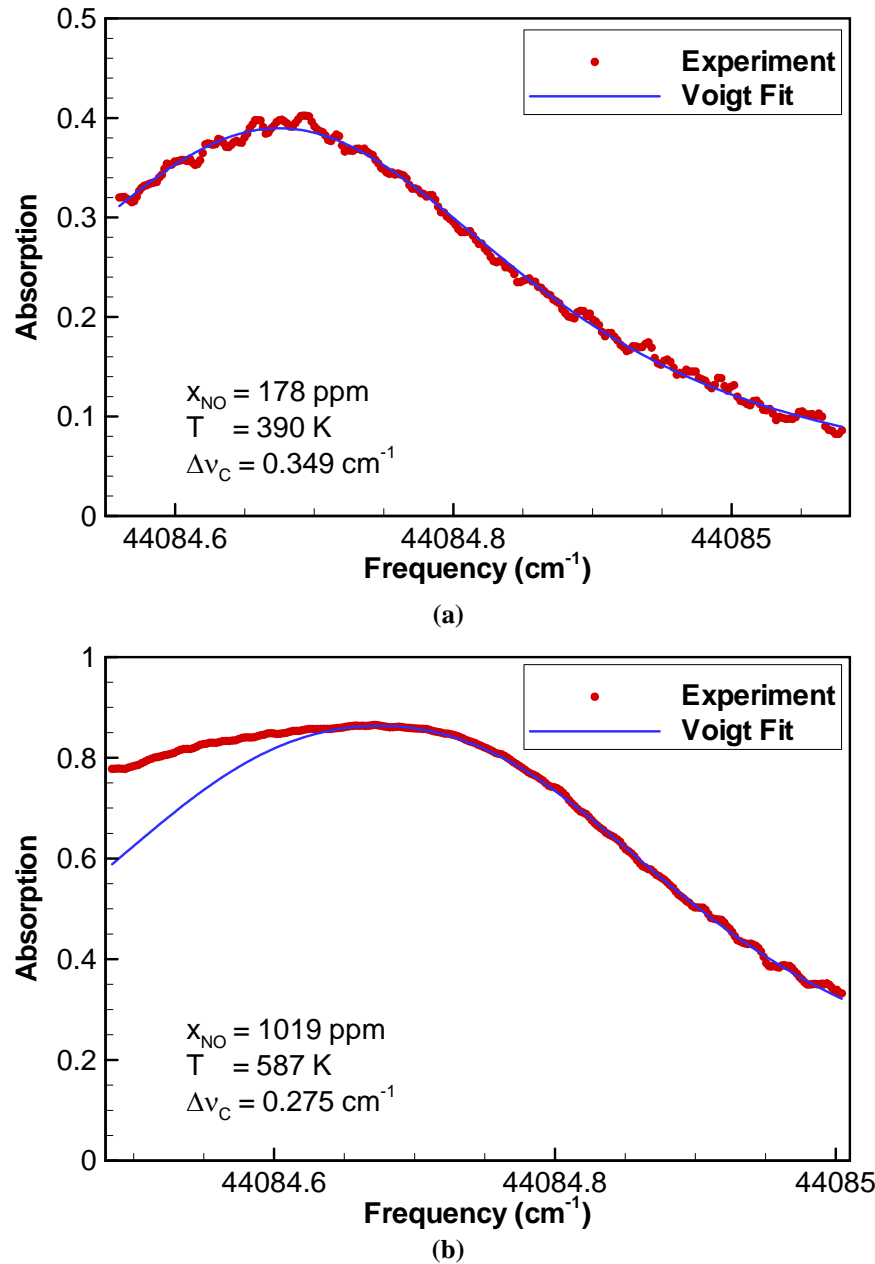


Figure 7. Averaged absorption spectra acquired with the NO sensor in the vitiated airflow for the scramjet combustor for vitiator stagnation temperatures of a) 1000 K and b) 1389 K. Both spectra were acquired in 2.5 seconds (40 Hz, 100 sweeps averaged).

each condition. Collision-broadening coefficients for NO broadened by N_2 and O_2 were calculated using expressions from Chang *et al.*²² and DiRosa *et al.*,²³ and the total collision width was summed according to expressions in the references. The calculated collision widths for NO in air (79% N_2 and 21% O_2 by volume) were

consistently around 20% smaller than the actual collision widths. The reason for the discrepancy in collision widths is unknown at this time.

Another phenomenon was also observed in the NO spectra acquired in the vitiated airflow. As seen in the experimental absorption spectra in Figure 9, there is a shift in the line center to higher frequencies as the vitiator temperature increases. In this figure, the absorption lineshape for the 1000-K case was shifted to the actual line center frequency (44084.69 cm^{-1}), and all the remaining spectra were shifted by the same amount to illustrate the magnitude of the frequency shift. By comparing the etalon fringes for each case, a shift of only 0.013 cm^{-1} was observed in the laser frequency between the lowest and highest vitiator temperatures. The observed frequency difference between line center of the 1000-K and 1389-K spectra is $\sim 0.08 \text{ cm}^{-1}$. Thus, the actual shift in line center frequency is approximately 0.07 cm^{-1} between the lowest and highest vitiator temperature spectra.

At present, neither the asymmetry nor the excessive collision widths can be readily explained. The effects of potential boundary layers in the flow were investigated, but even severe gradients in pressure, velocity, and temperature did not cause significant broadening or shift in simulated path-averaged spectra. Previous studies of temperature and pressure gradients in the scramjet combustor have shown relatively uniform profiles.¹⁷ Another

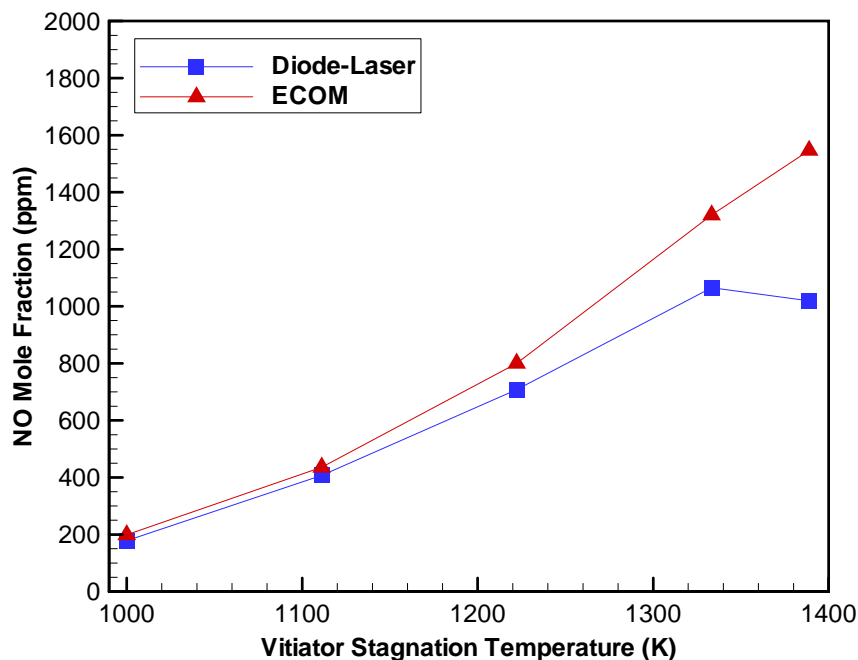


Figure 8. Variation of measured NO mole fractions with vitiator stagnation temperature as measured with the diode-laser sensor and commercial gas analyzer (ECOM).

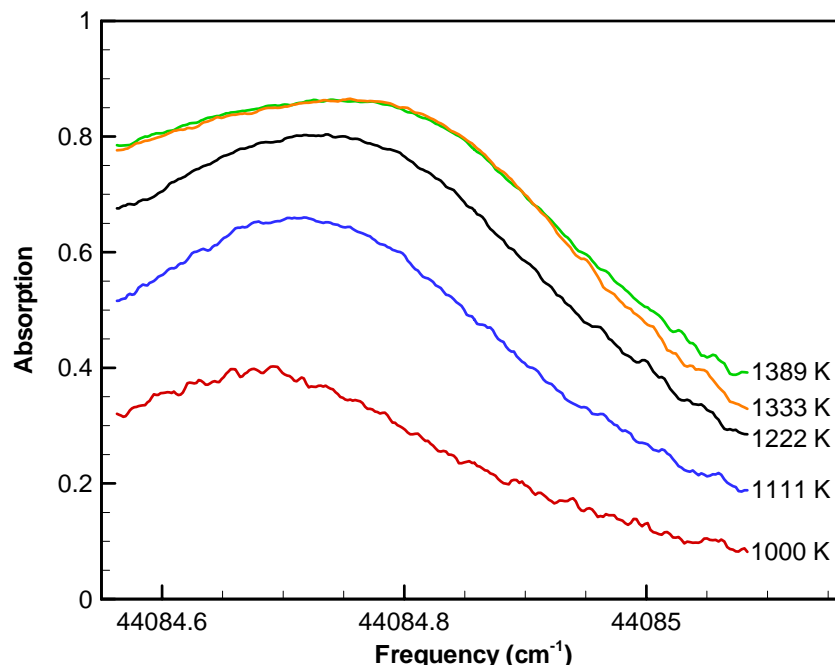


Figure 9. Averaged experimental absorption spectra for all conditions tested in the scramjet experiments. The spectrum for the 1000 K case was shifted to the correct absolute frequency, and the remaining spectra were shifted by the same amount to show the line shift with increasing vitiator temperature.

possibility is absorption by an interfering species. However, most species that are present in appreciable amounts in the vitiated air display only broadband absorption in this spectral region. No transmission scale was necessary in the spectral fits to the NO absorption data, so this possibility is not likely either. Further experiments are planned to investigate the causes of these phenomena.

Nonetheless, the NO mole fractions measured with the diode-laser sensor provide reasonable estimates for the NO contamination in the vitiated airflow for each vitiator condition. Using these data, researchers using the scramjet combustor at Wright-Patterson AFB can begin to calculate the effect on future hypersonic combustion experiments in the facility.

V. Conclusion

Measurements of both OH and NO concentrations have been performed using newly developed diode-laser-based sensors. The sensors are based on sum-frequency-mixing of a high-power, fixed-frequency, 532-nm laser with a tunable diode laser in a BBO crystal. The resulting UV radiation is in resonance with electronic transitions of NO or OH to perform absorption spectroscopy with little interference from other molecules and significantly enhanced sensitivity due to the strong absorption cross sections. The sensors are rugged enough to be used under harsh conditions (e.g., supersonic combustion rigs), and they can be operated remotely via a computer interface.

Concentrations of NO and OH were measured in the vitiated airflow of a model scramjet combustor at Wright-Patterson Air Force Base in Dayton, Ohio. No absorption by OH was evident in the vitiated airflow, quantifying for the first time that the OH mole fraction is less than 0.2 ppm in the vitiated air used to simulate flight conditions in the scramjet facility. The results from these experiments validate previous studies in the scramjet facility, which have all assumed that OH is negligible in the vitiated airflow. For NO, diode-laser-based sensor measurements indicated that NO mole fractions of 180-1100 ppm were present in the vitiated airflow for vitiator stagnation temperatures of 1000-1389 K, respectively. NO absorption spectra were broader than predicted by 20% at all conditions, and a systematic shift of the line-center frequency to higher frequencies was observed with increasing vitiator stagnation temperature. No explanation has been identified for these two phenomena. Excellent signal-to-noise ratios were achieved with the sensor during the experiments, with a detection noise of 0.8% for a 2.5-second averaging time. In the vitiator exhaust conditions, this corresponds to a detection limit of approximately 2 ppm-m (at 500 K, 60 kPa).

Both sets of experiments represent the first application of diode-laser-based sensors for measurements of NO or OH in a model scramjet combustor. With knowledge of the concentrations of these two species in the vitiated airflow, researchers can examine the impact of vitiator contamination on the results of ground tests using the scramjet facility.

Acknowledgments

The authors acknowledge the support of the Air Force Office of Scientific Research (AFOSR), Julian Tishkoff (Program Manager).

References

- ¹R. B. Edelman and L. J. Spadaccini. Theoretical effects of vitiated air contamination on ground testing hypersonic airbreathing engines. *Journal of Spacecraft and Rockets*, 6:1442-1447, 1969.
- ²B. Han, C. J. Sung, and M. Nishioka. Effects of vitiated air on hydrogen ignition in a high-speed laminar mixing layer. *Combustion Science and Technology*, 176:305-330, 2004.
- ³C. J. Sung, J. G. Li, G. Yu, and C. K. Law. Chemical kinetics and self-ignition in a model supersonic hydrogen-air combustor. *AIAA Journal*, 37:208-214, 1999.
- ⁴Y. Tan, C. G. Fotache, and C. K. Law. Effects of NO on the ignition of hydrogen and hydrocarbons by heated counterflowing air. *Combustion and Flame*, 119:346-355, 1999.
- ⁵W. R. Laster and P. E. Sojka. Autoignition of H₂-air: the effect of NO_x addition. *Journal of Propulsion and Power*, 5:385-390, 1989.
- ⁶T. Mitani. Ignition problems in scramjet testing. *Combustion and Flame*, 101:347-359, 1995.
- ⁷T. Mitani, T. Hiraiwa, S. Sato, S. Tomioka, T. Kanda, and K. Tani. Comparison of scramjet engine performance in Mach 6 vitiated and storage-heated air. *Journal of Propulsion and Power*, 13:635-642, 1997.
- ⁸T. Sander, A. Lyubar, T. Sattelmayer, and E. A. Shafranovsky. Influence of the burnout in vitiators on ignition limits in scramjet combustors. *AIAA Journal*, 42:319-325, 2004.
- ⁹J. T. C. Liu, G. B. Rieker, J. B. Jeffries, M. R. Gruber, C. D. Carter, T. Mathur, and R. K. Hanson, "Near-infrared diode laser absorption diagnostic for temperature and water vapor in a scramjet combustor," *Applied Optics*, Vol. 44, No. 31, 6701-6711 (2005).

- ¹⁰B. L. Upschulte, M. F. Miller, and M. G. Allen. Diode laser sensor for gasdynamic measurements in a model scramjet combustor. *AIAA Journal*, 38:1246-1252, 2000.
- ¹¹A. D. Griffiths and A. F. P. Houwing. Diode laser absorption spectroscopy of water vapor in a scramjet combustor. *Applied Optics*, 44:6653-6659, 2005.241
- ¹²A. Mohamed, B. Rosier, D. Henry, Y. Louvet, and P. L. Varghese. Tunable diode laser measurements on nitric oxide in a hypersonic wind tunnel. *AIAA Journal*, 34:494-499, 1996.
- ¹³S. F. Hanna, R. Barron-Jimenez, T. N. Anderson, R. P. Lucht, J. A. Caton, T. Walther, "Diode-laser-based ultraviolet absorption sensor for nitric oxide," *Applied Physics B*, Vol. 75, 113-117 (2002).
- ¹⁴T. N. Anderson, R. P. Lucht, R. Barron-Jimenez, S. F. Hanna, J. A. Caton, T. Walther, S. Roy, M. S. Brown, J. R. Gord, I. Critchley, and L. Flamand. Combustion exhaust measurements of nitric oxide with an ultraviolet diode-laser-based absorption sensor. *Applied Optics*, 44:1491-1502, 2005.
- ¹⁵T. N. Anderson, R. P. Lucht, T. R. Meyer, S. Roy, and J. R. Gord, "Diode-laser-based ultraviolet-absorption sensor for high-speed detection of the hydroxyl radical," *Optics Letters*, Vol. 30, 1321-1323 (2005).
- ¹⁶T. R. Meyer, S. Roy, T. N. Anderson, J. D. Miller, V. R. Katta, R. P. Lucht, and J. R. Gord, "Measurements of OH mole fraction and temperature up to 20 kHz by using a diode-laser-based UV absorption sensor," *Applied Optics*, Vol. 44, No. 31, 6729-6740 (2005).
- ¹⁷M. Gruber, J. Donbar, K. Jackson, T. Mathur, R. Baurle, D. Eklund, and C. Smith. Newly developed direct-connect high-enthalpy supersonic combustion research facility. *Journal of Propulsion and Power*, 17:1296-1304, 2001.
- ¹⁸T. Mathur, M. Gruber, K. Jackson, J. Donbar, W. Donaldson, T. Jackson, and F. Billig. Supersonic combustion experiments with a cavity-based fuel injector. *Journal of Propulsion and Power*, 17:1305-1312, 2001.
- ¹⁹T. N. Anderson, R. P. Lucht, S. Priyadarsan, K. Annamalai, and J. A. Caton, "In situ measurements of nitric oxide in coal-combustion exhaust using a sensor based on a widely-tunable external-cavity GaN diode laser," *Applied Optics* (in press).
- ²⁰T. N. Anderson, "Diode-Laser-Based Sensors for Flame Diagnostics and Combustion-Emissions Monitoring," PhD Dissertation, School of Mechanical Engineering, Purdue University, West Lafayette, IN, 2006.
- ²¹Robert W. Fox and Alan T. McDonald. *Introduction to Fluid Mechanics*. 4th ed., John Wiley & Sons, Inc., New York, New York, 1992.
- ²²A. Y. Chang, M. D. DiRosa, and R. K. Hanson. Temperature dependence of collision broadening and shift in the NO A←X (0,0) band in the presence of argon and nitrogen. *Journal of Quantitative Spectroscopy and Radiative Transfer*, 47:375-390, 1992.
- ²³M. D. DiRosa and R. K. Hanson. Collision-broadening and -shift of NO $\gamma(0,0)$ absorption lines by H₂O, O₂, and NO at 295 K. *Journal of Molecular Spectroscopy*, 164:97-117, 1994.

2007 AIAA Aerospace Sciences Meeting and Exhibit
8-11 January, 2007. Reno, Nevada

AIAA 2007-1301

A Robust Procedure for the Analysis of Non-Evenly Spaced Velocity Time-Series Data

Kyle B. Garwick, 2Lt, USAF; Amy Lynch; James R. Gord, Ph.D.; Barry V. Kiel
Air Force Research Laboratory, Propulsion Directorate
Wright Patterson Air Force Base

Terrence R. Meyer, Ph.D.
Innovative Scientific Solutions, Inc.
Dayton, OH

ABSTRACT

Laser Doppler Velocimetry (LDV) is an important tool for validation of computational fluid-dynamics models in high-enthalpy bluff-body flows. Unlike hotwire anemometry, however, high-speed LDV data must be unevenly sampled in time and cannot be analyzed using a standard Discrete Fast Fourier Transform (DFFT). Instead, data from LDV has traditionally been processed with the Lomb Algorithm, which is a normalized periodogram representing a linear least squares approximation of the linear regression of periodic functions. The Lomb Algorithm can be computationally inefficient because a sufficiently large number of frequencies must be chosen to produce accurate results. In this paper, spectral analysis with the Lomb Algorithm is compared to data processed using a piecewise interpolation scheme developed using MATLAB[®]. A series of known input signals are generated to provide a baseline for this comparison. Successful implementation in the wake of a bluff-body is discussed. Such alternative schemes are straightforward to implement, can be easily tailored for each flow application to extract the relevant low- and high-frequency modes, and may be more attractive for applications such as real time spectral analysis or combustion control.

NOMENCLATURE

CFD	Computational Fluid Dynamics	St	Strouhal Number
DFFT	Discrete Fast Fourier Transform	t	Time
FFT	Fast Fourier Transform	TKE	Turbulent Kinetic Energy
L	Reference Length	U, u	Velocity
LES	Large Eddy Simulation	u_{sim}	Simulated Velocity
LDV	Laser Doppler Velocimetry	\bar{u}	Mean Velocity
LPT	Low Pressure Turbine	σ^2	Variance or Root Mean Square
N	Number of Data Points	ω	Frequency
P_n	Normalized Periodiogram		
RMS	Root Mean Square		

1 INTRODUCTION

Computational Fluid Dynamics (CFD) is increasingly utilized as an engineering tool for combustion research. Accurate CFD data can only be realized through extensive code validation with experimental data. Hussain's (1983) discussion of "triple decomposition" gives us insight as to how to validate these codes. Hussain decomposes turbulent flow into three components; the mean or time independent portion of the flow, the coherent structures, and the non-coherent structures. In turbulent flows, it is necessary to resolve all three aspects for accurate comparisons between model predictions and experimental data.

When comparing coherent structures, frequency domain data of the fluctuating velocity is an excellent comparison. The coherent vortex shedding then can be easily discerned from the plot of the transformed data. The frequencies are represented non-dimensionally using the bluff-body width and the inlet velocity by the Strouhal Number, St , as shown in equation (1).

$$St = \frac{\omega L}{U} \quad (1)$$

The relationship between the coherent and non-coherent can best be seen through the energy cascade seen in the TKE spectrum, determined by calculating the turbulent kinetic energy as a function of time and transforming that data into frequency space. The TKE spectrum is normalized by the Kolmogorov scales, the smallest turbulent scales which have a dissipative effect on the flow (Tennekes & Lumley, 1990). Normalizing in this fashion demonstrates the effect of flow Reynolds number on the coherent large-scale structures and turbulent kinetic energy. As Reynolds number increases, energy is stored increasingly within the large scales of the flow.

This data can be gathered by non-intrusive laser diagnostic systems such as Laser-Doppler Velocimetry (LDV). LDV gathers velocity data through airflow by using lasers to track seed particles through a test rig. This data is time-series, but not often for a uniform time step. The focus of this paper is to validate data reduction procedures that result in the most robust way to characterize the coherent structures in the turbulent wake of a bluff body. This analysis will focus on the frequency and Strouhal data. Future endeavors will examine the non-coherent structures such as TKE Spectrum. A cubic interpolation procedure is developed and compared to the Lomb Algorithm, which has often been used to analyze such data. The major problem with the Lomb Algorithm is the dependence of the method on high data rates, which often become difficult to attain in a combustor flow. A piecewise cubic interpolation, as described in this paper can provide more versatility when dealing with low data rates. This paper will use a series of known signals to validate the piecewise cubic interpolation and then the code will be applied to experimental data from LDV measurements of a bluff-body in cold flow situations. The results will be compared to the same data processed by the Lomb Algorithm. This comparison will use LDV data with both high and low data rates to illustrate the robustness of each code.

2 EXPERIMENTAL PROCEDURES

2.1 LDV PROCEDURES

A two-component laser-Doppler velocimetry (LDV) system (TSI, Inc.) was employed for measuring instantaneous velocity at various conditions in the wake region of the bluff body. The primary advantages of the LDV technique include excellent accuracy (typically ~1% for velocity) and high data rate (up to 30 kHz), making it an ideal non-intrusive diagnostic approach for recording unsteady fluid velocity and for quantitative comparison with numerical simulations. A number of previous publications have discussed the theory and operating principles of LDV (Goldstein, 1983). Only the details relevant for data analysis and model validation are included here.

The LDV optical layout is shown in Figure 1. The LDV system is driven by an argon-ion laser with 514.5 nm and 488 nm output beams. The two wavelengths are used to generate orthogonal interference fringes for measuring two components of velocity from the same probe volume. Signals from particle scattering off the 514.5-nm and 488-nm beams are collected in back-scatter mode, separated in the multicolor receiver, and processed by the burst correlator to provide velocity information. Air is seeded with 1- μm aluminum oxide (Al_2O_3) particles just upstream of the test section.

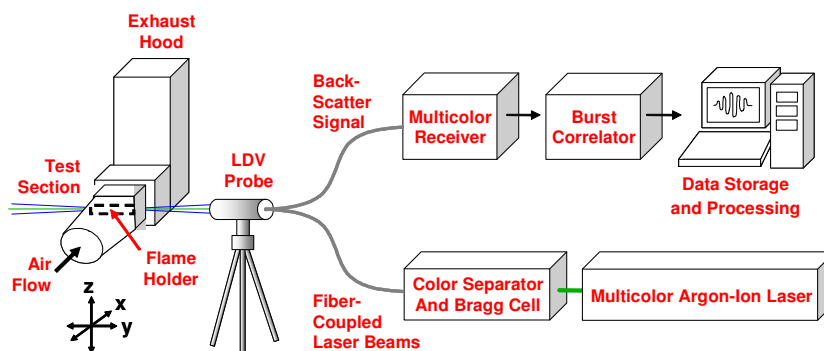


Figure 2-1. Laser Doppler Velocimetry

Approximately 8000 data points per location were recorded for each component of velocity for a number of flow conditions and locations downstream of the flame holder. The test section had to be cleaned periodically due to collection of seed particles on the windows inside the test section. Cleaning the windows prevents erroneous readings due to the thin layer of seed that collects on these surfaces. In order to acquire sufficient data to characterize the non-coherent portion of the turbulent flow, care was taken to ensure that data rates were ≥ 1000 Hz. Achieving these data rates required random time sampling in which data were collected at the arrival time of each particle-scattering signal rather than at regular time intervals.

2.2 KNOWN SIGNAL GENERATION

In order to validate the techniques used to interpolate the random time-series data obtained in an LDV system, a baseline must first be established. Using MATLAB[®], a series of “known” signals was generated at a data rate of 20 KHz. This general equation was used for signal generation,

$$u_{sim} = \sin(2\omega\pi t) \quad (2)$$

Equation (2) generates a simple sine wave based on a known frequency, ω , and a given time, t . u_{sim} is the simulated velocity measurement given by the right hand side of equation (2). The data rate of 20 KHz was chosen to provide enough points to create a comprehensive data set that can be very versatile in testing the ability of the data reduction technique presented in this report. Each signal is over a time interval of 3 seconds. The signal generation is characterized by a constant time step of 5×10^{-5} at first. After the basic signal is created, these signals will be randomized and will no longer have equivalent time steps. Further explanation of the data reduction process using these known signals will be explained below.

2.3 TEST FACILITY

A 12 MW experimental combustion facility located in the Atmospheric Pressure Combustion Research Complex was used for the experiments. This facility is owned and operated by the Propulsion Directorate of the Air Force Research Laboratory (AFRL), Wright Patterson Air Force Base, OH. The facility is capable of simulating the exit conditions of the Low-Pressure Turbine (LPT) of legacy, pipeline, and future high performance fighters. The facility provides a uniform velocity and temperature profile ($\pm 3\%$), and 6% turbulence intensity at the inlet of the test section. This facility is an atmospheric pressure facility.

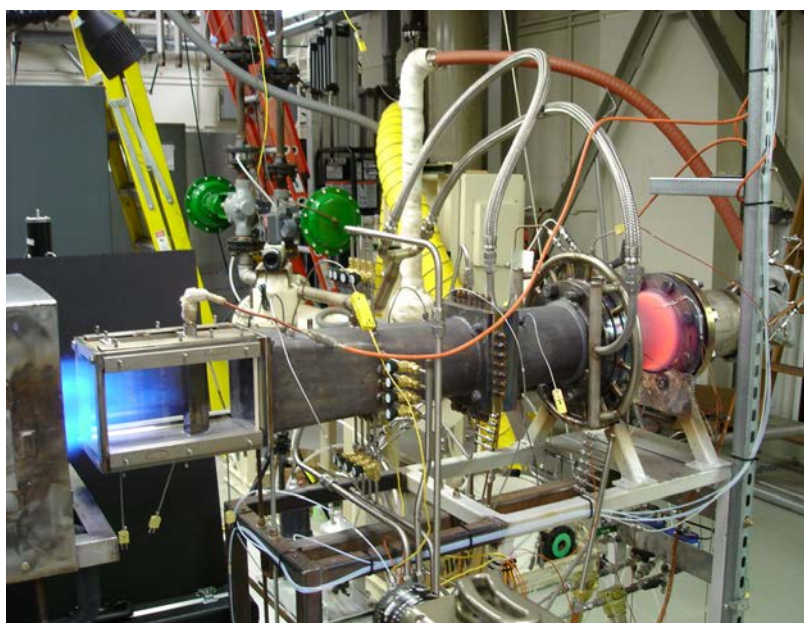


Figure 2-2. Atmospheric Combustion Research Facility

Experiments were conducted on two baseline bluff-bodies in this rig over a range of Reynolds numbers from 10,000 to 55,000. The bluff bodies used were a closed and open v-gutter, as shown in figure 2-3. In these experiments, LDV data were collected at numerous points in the wake of the bluff bodies.

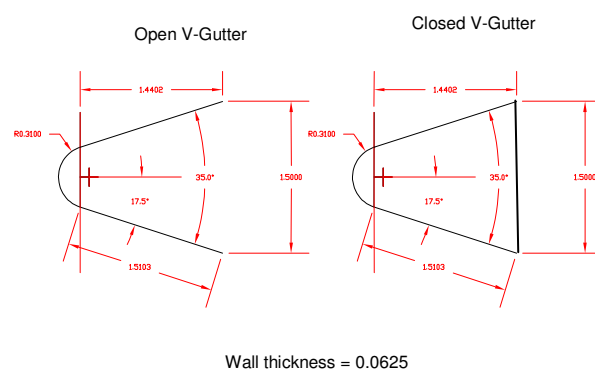


Figure 2-3. Open and Closed V-Gutter Bluff Bodies

3 DATA ANALYSIS

3.1 MATLAB[®] INTERPOLATION PROCEDURE

In an effort to reduce the computational overhead required in reducing hundreds of sets of LDV data for LES validation, alternative processing techniques were formulated using the windowing, interpolation, and DFFT tools available in MATLAB[®]. These DFFT tools require the velocity data have a constant time step and require that the random LDV data be re-sampled. This is done by creating a histogram of all the time steps between data and choosing a representative time step based on the results. There are many options available in choosing this representative time step. For this analysis, the median time step found in the data is used to complete the interpolation.

There are many perils to such data interpolation. Gaps in the raw time series can be interpreted by the DFFT as false frequencies if the interpolation is not robust. Small gaps in the data will result in false frequencies in the high frequency portion of the transformed data, leading to errors in the non-coherent portion of the TKE spectrum. Large gaps in the data will result in false frequencies in the low frequency portion of the transformed data. These errors make it difficult to extract the true shedding frequency of coherent structures. Windowing techniques can be used in an attempt to eliminate the false frequencies resulting from large gaps in the data. The accuracy of the interpolation scheme and the interpolated time step were varied in an attempt to eliminate the issues associated with errors in the TKE spectrum.

Discrete data may be considered to be a truncated portion of a continuous stream of data (Jong, 1982). The truncation results in "leakage," and is analogous to a rectangular window being applied to the continuous data. This is equivalent to convolving the frequency domain data with the transform of a square function. In the frequency domain, a square window is represented by a Gaussian type central curve with several side lobes. One solution to this problem is to average several DFFTs of shorter subsets of the original data record. This procedure, though, sacrifices accuracy because less data is used to compute each DFFT. Another solution to this problem is to apply another window to the discrete data that tends to counteract the effect of the square window already convolved onto the discrete data. Several windows available in MATLAB[®] were applied to the data and comparisons were made to the Lomb Algorithm and to the known data sets. The one used in the interpolation code is the Blackman-Harris window.

Several interpolation schemes are available in MATLAB[®]. The function "interp1", has interpolation flags for nearest neighbor, linear, cubic spline, and piecewise. Each of these techniques was used to interpolate the LDV data and comparisons to the Lomb Algorithm and the known signals. The cubic Hermite interpolation had by far the best comparison with the other two methods.

3.2 KNOWN SIGNAL AND INTERPOLATION CODE VALIDATION

Once the known signal is created and the FFT of the constant time step data is verified for the specified shedding frequency a random vector is employed to pull various values of the raw data to create a known set time series data with an uneven time step. This new set of data is then applied to the interpolation scheme. This is important in proving that the interpolation code can provide a useful tool for

reducing time-series data when the time step is random. By using the known signals, the resultant shedding frequency will be known, and the shedding frequency given by the code should be close to the known frequency established when creating the signals.

3.3 LOMB ALGORITHM

Data generated by LDV is collected from the scattered light of solid seed particles in the flow. The scattered light collected in the process is typically randomly spaced in time. To obtain frequency domain information from the unevenly spaced data, several techniques have been applied by Clark et al. (1985), Ardian and You (1987), Veynante and Candel (1988), and Chao and Leu (1992). The Shannon or Lomb Algorithm has been one method traditionally employed (Clark et al., 1985; Veynante and Candel, 1988).

When employing the Lomb Algorithm, the first step is to determine the mean (equation (3)) and variance (equation (4)), or root mean square (rms), of the data set.

$$\bar{u} = \frac{1}{N} \sum_1^N u_i \quad (3)$$

$$\sigma^2 = \frac{1}{N-1} \sum_1^N (u_i - \bar{u})^2 \quad (4)$$

Next, a normalized periodogram is obtained.

$$P_n(\omega) = \frac{1}{2\sigma^2} \left\{ \frac{\sum_j [(u_i - \bar{u}) \cos \omega(t_j - \tau)]^2}{\sum_j \cos \omega(t_j - \tau)} + \frac{\sum_j [(u_i - \bar{u}) \sin \omega(t_j - \tau)]^2}{\sum_j \sin \omega(t_j - \tau)} \right\} \quad (5)$$

Where τ is defined as:

$$\tan(2\omega\tau) = \frac{\sum_j \sin(2\omega t_j)}{\sum_j \cos(2\omega t_j)} \quad (6)$$

The normalized periodogram, P_n , is mathematically equivalent to the equation for the harmonic linear least square approximation of the linear regression of sines and cosines of the data. In linear regression the data is weighted point wise and the error is minimized with least squares. This differs from the DFFT of evenly distributed data weighted equally on each time interval. Point-wise weighting thus offers an advantage when the data has a non-constant interval.

To adequately resolve the coherent and non-coherent portions of the turbulent data, sufficient resolution and accuracy are required. When using a liner regression-type algorithm such as the Lomb algorithm, "false frequencies" are a consequence of poor resolution. False frequencies will result in an inaccurate reproduction of the TKE spectrum (Mueller et al., 1998). The accuracy of the Lomb Algorithm, and inherently the probability of a false frequency, is solely a function of the number of frequencies, ω_i , that are used in the regression. The greater the number of frequencies used in the regression the lower the probability of a false frequency and the higher the accuracy of the TKE spectrum. Because of this,

the Lomb Algorithm can be a very robust analysis tool if the turbulent data contains coherent and non-coherent spectra over a large frequency range. The Lomb algorithm typically is not very accurate for a low sampling rate. The Lomb algorithm calculations used in this experiment is contained in an executable C-Code developed by at Propulsion Directorate, AFRL, WPAFB, OH. After the initial interpolation using the Lomb algorithm, shedding frequency and Strouhal data can be analyzed using MATLAB®.

3.4 COMPARISON PROCEDURE

In this analysis, only the u-component of the velocity will be considered, since the concern is only with the comparison between the two methods of interpolation. As described earlier, the sets of known signals will be randomized for an uneven time step and then fed into the interpolation code. This will show that the interpolation code can provide viable results in non-evenly spaced time-series data. Next, the LDV data will be fed to the interpolation code as well as to the LOMB algorithm. Comparisons will be made based on the results for Strouhal Number and shedding frequency between the codes.

4 RESULTS AND CONCLUSIONS

4.1 INTERPOLATION CODE VALIDATION

To validate the interpolation code, three known signals were created. The signals were created with a known frequency of 73Hz, 535Hz and 1310Hz, respectfully. These signals originally were created with a constant time step of 5×10^{-5} seconds. Theses signals were created and then a DFFT was performed on each signal to show that the frequency was indeed correct. Then the signal was randomized, creating an uneven time step in the known data. This non-evenly spaced signal was run through the interpolation code to see if the interpolation could pick out the frequency in the signal. For each of the three signals, a typical data rate of 4.5 to 5 kHz was used to randomize the data. This data rate is typical of useful LDV data. This method was run on all three signals and the results are shown in table 4-1.

Table 4-1. Interpolation Code Validation for Known Signals

Known Frequency	Interpolated Frequency	Percent Error
73 Hz	73.54	-0.747
535 Hz	534.07	0.1723
1310 Hz	1309.4	0.046

It can be seen that the interpolation code does a good job picking out the correct frequencies when applied to the randomized known signals, all result in less than a percent of error. Figure 4-1 and 4-2 below show the DFFT of the know signal and the DFFT of the randomized known signal, respectively, of the 535 Hz generated signal.

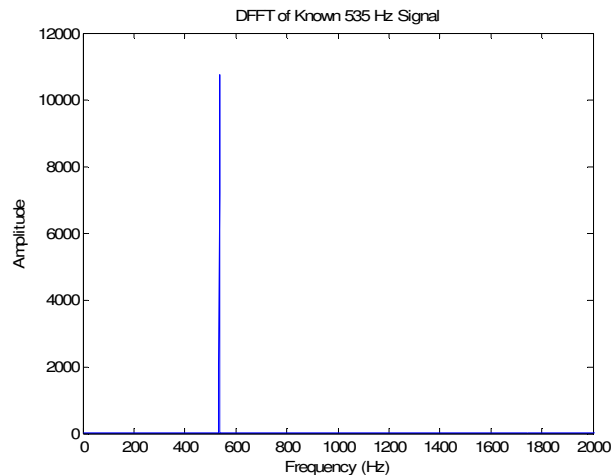


Figure 4-1. DFFT of Known 535 Hz Signal

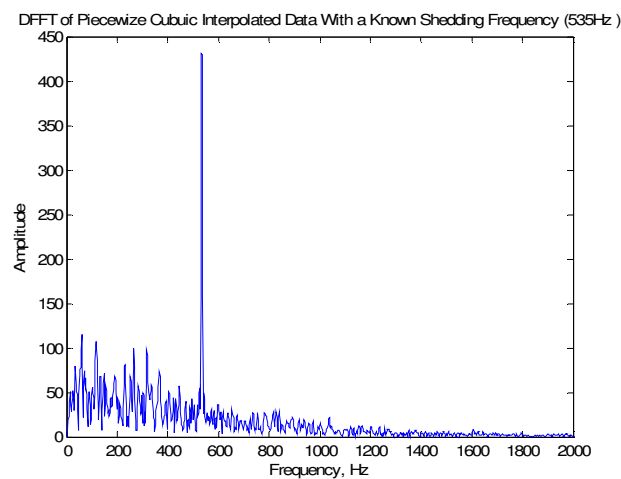


Figure 4-2. DFFT of Randomized 535 Hz Signal

4.2 COMPARISON OF INTERPOLATION CODE TO LOMB ALGORITHM

Next, the interpolation code is run for actual LDV data collected in the research rig described above. This data is also reduced using the LOMB algorithm. The results were then compared. Many sets of LDV data were tested in this method. Six will be highlighted in this paper. The table below shows the LDV data sets and the subsequent comparison between the two methods. The comparison is based on the Strouhal number obtained from the LDV data.

Table 4-2. Interpolation Code Results Compared with LOMB Algorithm.

Data Rate	Reynolds Number	Closed/Open Gutter?	Interpolation Strouhal Number	LOMB Algorithm Strouhal Number	Percent Error
910Hz	40,000	Closed	0.0301	0.1015	70.345
953Hz	40,000	Closed	0.0145	0.0026	-457.692
1939Hz	40,000	Closed	0.2846	0.2842	-0.1407
4456Hz	40,000	Closed	0.2898	0.2888	-0.3463
7660Hz	40,000	Closed	0.2902	0.2886	-0.5544
9989Hz	40,000	Closed	0.2966	0.2951	-0.5083

The data is separated according to data rate as shown above. For LDV data of a low data rate (less than 1000Hz), neither code produces very promising results. In the figures below, the LDV data is shown in frequency space. Neither figure shows any discernable characteristic frequency.

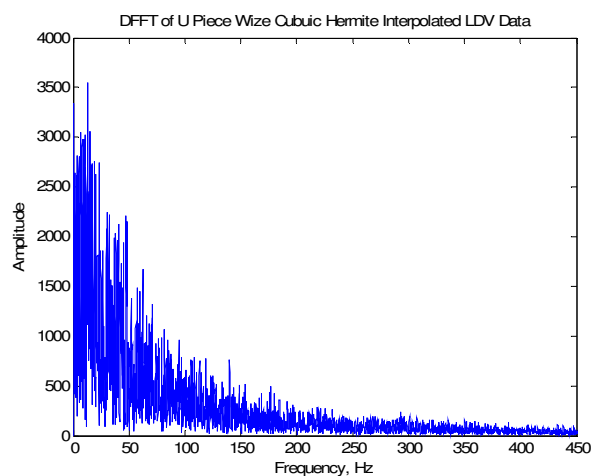


Figure 4-3 DFFT of LDV Data with Low Sampling Rate (Interpolation)

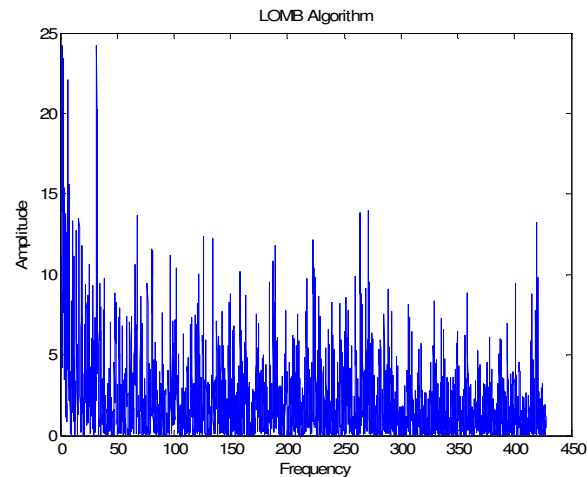


Figure 4-4. DFFT of LDV Data with Low Sampling Rate (LOMB)

In the LOMB plot, a peak occurs at about 30Hz, but that can be assumed to be a false frequency due to the low data rate. The interpolation plot doesn't produce any information of real use, as the maximum value occurs around 0Hz and continues to decline with increasing frequency. Therefore, it can be concluded that LDV data that has less than a 1kHz sampling rate is useless in gaining useful velocity data in the flow.

LDV data that has a 'normal' data sampling rate (1000Hz-6000Hz) was tested using both methods and the results were much more promising. In both cases, the percent error between the two methods was less than 1%. The figures below show the interpolation and LOMB FFTs, respectively, of the data taken at 1939Hz sampling rate.

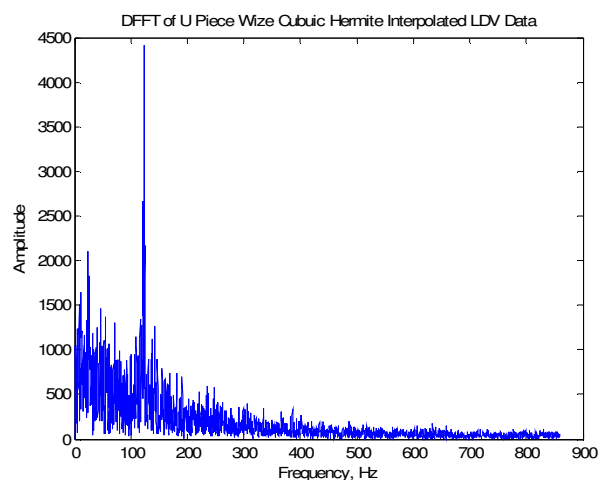


Figure 4-5. DFFT of LDV Data with a Nominal Sampling Rate (Interpolation)

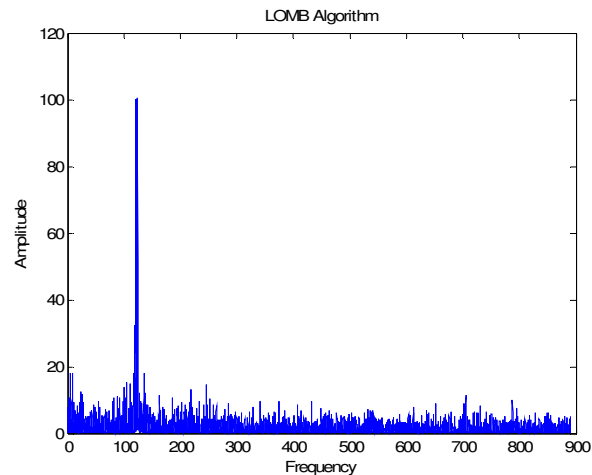


Figure 4-6. DFFT of LDV Data with a Nominal Sampling Rate (LOMB)

The last two sets of data highlighted here are LDV data sets at a relatively high data sampling rate (greater than 6000Hz). These data sets produced similar results to the nominal data rates, as can be expected. The errors were once again less than 1% in each case. As the sampling rate gets higher, both methods should improve in accuracy. Since there are more samplings per second, the relative time step becomes closer and closer to being uniform, thus making the decision for the interpolation time step much easier. The figures below show the FFTs of the interpolation and LOMB algorithm, respectively, for the high data sampling rate of 7660Hz.

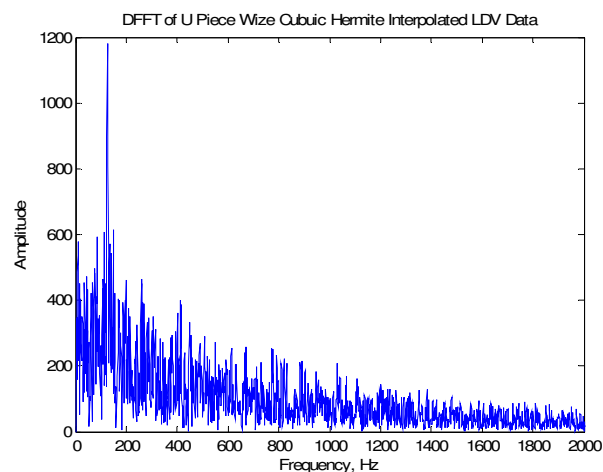


Figure 4-7. DFFT of LDV Data with a High Sampling Rate (Interpolation)

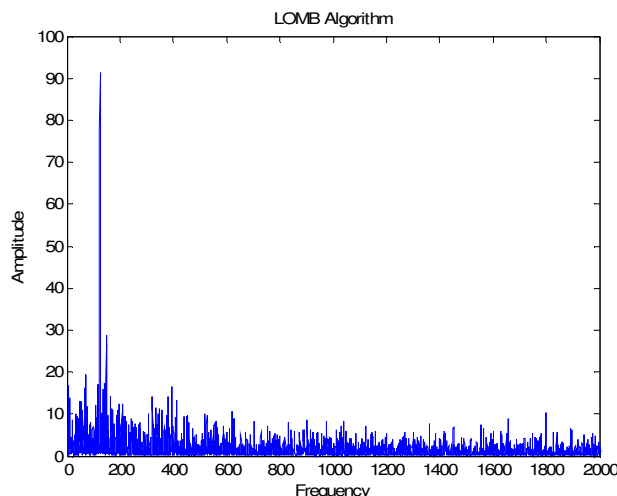


Figure 4-8. DFFT of LDV Data with a High Sampling Rate (LOMB)

5. RECOMMENDATIONS

From the results above, it can be seen that the interpolation reduction code presented in this paper can serve as a robust method to reduce non-evenly spaced, time-series LDV data into frequency space data and provide useful results. The LOMB algorithm is still a suitable method to produce the same results, but the simplicity in the interpolation can prove to be more versatile when dealing with false frequencies or gaps in the data. Now that, the interpolation code has shown the ability to produce frequency information from LDV data, the next step is to look at the interpolation time step used. For the interpolation to improve, especially at low data rates, the correct interpolation time step must be chosen. Also, the potential of false frequencies in the data is still a problem. Future endeavors will look at ways to identify where these false frequencies occur and how to filter them out of the signal.

6. REFERENCES

- Adrian, R. and Yao, C., "Power Spectra of Fluid Velocities measured by Laser Doppler Velocimetry," *Experiments in Fluids*, Vol. 5, pp. 17-28.
- Benedict, L., Nobach, H., and Tropea, C. (2000) "Estimation of Turbulent Velocity Spectra from Laser Doppler Data." *Measurement Science and Technology*. Vol. 11, pp. 1089-1104.
- Numerical Recipes in C: The Art of Scientific Computing (1992), Cambridge University Press, pp. 575-584.
- Chao, Y. and Leu, j. (1992), "A Fractal Reconstruction Method for LDV Spectral Analysis", *Experiments in Fluids*, Vol. 13, pp. 91-97.
- Clark, J., Palmer, M., and Lawrence, P. (1985), "A Transformation Method for the Reconstruction of Functions from Non-uniformly Spaced Samples," *IEEE Transactions, Acoustic Speech Signal Processing*, Vol. 33, pp. 1151-1165.
- Goldstein, R. J. (1983), "Laser Velocimetry," in Fluid Mechanics Measurements, Hemisphere Publishing Corporation, Washington D.C., pp. 155-244.

Incropera, F. and DeWitt, D. (2002) Fundamentals of Heat and Mass Transfer, pp. 331-339.

Jong, M. (1982), Methods of Discrete Signal and System Analysis, McGraw Hill Book Company, pp. 295-296.

Muller, E., Nobach, H., and Tropea, C. (1998) "Model Parameter Estimation from Non-Equidistant Sampled Data Sets at Low Data Rates." *Measurement Science and Technology*. Vol. 9, pp. 435-441.

Roshko, A. (1954), "On the Drag and Shedding Frequency Two Dimensional Bluff Bodies," NACA TN 3169.

Tennekes, H. and Lumley, J. (1990), A First Course in Turbulence, MIT Press.

Veynante, D. and Candel, S. (1988), "Application of non-linear Spectral analysis and Signal Reconstruction to LDV," *Experiments in Fluids*, Vol. 6, pp. 534-540.

N. CHAI¹
S.V. NAIK¹
W.D. KULATILAKA¹
N.M. LAURENDEAU¹
R.P. LUCHT^{1,✉}
S. ROY²
J.R. GORD³

Detection of acetylene by electronic resonance-enhanced coherent anti-Stokes Raman scattering

¹ School of Mechanical Engineering, Purdue University, West Lafayette, IN 47907, USA

² Innovative Scientific Solutions, Inc., 2766 Indian Ripple Road, Dayton, OH 45440, USA

³ Air Force Research Laboratory, Propulsion Directorate, Wright-Patterson AFB, OH 45433, USA

Received: 30 November 2006/Revised version: 5 March 2007
Published online: 16 May 2007 • © Springer-Verlag 2007

ABSTRACT We report the detection of acetylene (C_2H_2) at low concentrations by electronic resonance-enhanced coherent anti-Stokes Raman scattering (ERE-CARS). Visible pump and Stokes beams are tuned into resonance with Q-branch transitions in the ν_2 Raman band of acetylene. An ultraviolet probe beam is tuned into resonance with the $\tilde{A}-\tilde{X}$ electronic transition of C_2H_2 , resulting in significant electronic resonance enhancement of the CARS signal. The signal is found to increase significantly with rising pressure for the pressure range 0.1–8 bar at 300 K. Collisional narrowing of the spectra appears to be important at 2 bar and above. A detection limit of approximately 25 ppm at 300 K and 1 bar is achieved for our experimental conditions. The signal magnitudes and the shape of the C_2H_2 spectrum are essentially constant for UV probe wavelengths from 233.0 to 238.5 nm, thus indicating that significant resonant enhancement is achieved even without tuning the probe beam into resonance with a specific electronic resonance transition.

PACS 42.65.Dr; 42.62.Fi; 42.65.-k

1 Introduction

Coherent anti-Stokes Raman scattering (CARS) is a useful and accurate technique for performing spatially resolved measurements of temperature and major-species concentrations [1, 2]. CARS can be used for simultaneous measurement of multiple species concentrations and temperature in a single laser shot when using appropriate broadband laser sources [3]. The detection limit for CARS is typically 1000 ppm or greater at atmospheric pressure [1], even for well-optimized CARS systems with polarization background subtraction.

Electronic resonance-enhanced (ERE) CARS was first demonstrated for dilute solutions of diphenyloctatetraene in benzene [4]. Several molecules and radicals have been investigated via ERE-CARS including I_2 [5, 6], NO_2 [7, 8], C_2 [9–11], S-tetrazine vapor [12], OH [13], and CH [14]. Hanna et al. [15] demonstrated ERE-CARS for nitric oxide

(NO) by implementing a dual-pump CARS approach and observed significant resonance enhancement. Kulatilaka et al. [16] employed ERE-CARS to monitor NO concentrations in a combustion environment. A detection limit of approximately 50 ppm was demonstrated in a hydrogen-air flame, thus confirming the utility of ERE-CARS for measurements of minor species in reacting flows. Kulatilaka et al. [17] subsequently investigated pressure-scaling and saturation effects for NO ERE-CARS. The ERE-CARS signal for NO was found to increase with rising pressure up to 2 bar and to remain nearly constant thereafter up to 8 bar.

Measurements of acetylene (C_2H_2) concentration are important for understanding many combustion processes. Acetylene plays an important role in the chemical kinetics of both soot initiation and growth [18, 19], and also in the formation of polycyclic aromatic hydrocarbons [19]. Measurements of acetylene, moreover, are useful for understanding surface chemistry related to chemical vapor deposition as well as to carbon-nanotube synthesis via combustion [20].

2 Experimental description

The energy-level diagram for the C_2H_2 ERE-CARS process is shown in Fig. 1. The frequency difference between the pump beam at a vacuum wavelength $\lambda_1 = 532.215$ nm (18789.4 cm⁻¹) and the Stokes beam at $\lambda_2 \cong 594$ nm (16815 cm⁻¹) corresponds to a Raman shift of 1974 cm⁻¹ – the frequency of the bandhead for the ν_2 band of acetylene. The Raman polarization induced in the medium is detected using an ultraviolet (UV) probe beam at $\lambda_3 \cong 236$ nm (42370 cm⁻¹). The ERE-CARS signal is near resonance with various ro-vibrational bands in the $\tilde{A}-\tilde{X}$ electronic transition of C_2H_2 [21–23], and has a wavelength $\lambda_{CARS} \cong 225.5$ nm (44350 cm⁻¹). Acetylene is a linear molecule in its ground electronic state with five fundamental vibrations [24], and has a planar trans-bent geometry in its lowest excited singlet state [21]. Among five fundamental vibrations in the ground electronic state, three are Raman-active; the other two are infrared-active. The ν_2 band at 1974 cm⁻¹ corresponds to symmetric stretching of the molecule and is the strongest of the three Raman-active modes [24]. The complete ν_2 Raman band of acetylene can be acquired by scanning λ_2 for fixed λ_1 and λ_3 .

✉ Fax: +1-765-494-0539, E-mail: lucht@ecn.purdue.edu

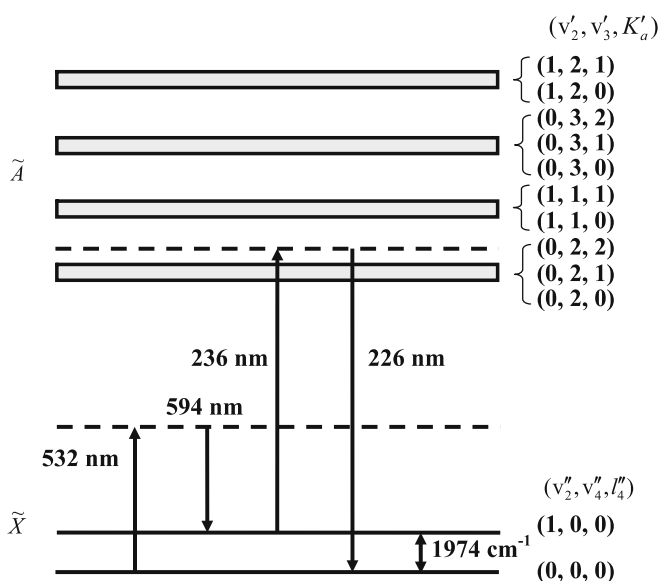


FIGURE 1 Energy-level diagram for the C_2H_2 ERE-CARS process

2.1 Optical system

The experimental apparatus for our C_2H_2 ERE-CARS measurements is shown in Fig. 2. The second-harmonic output of an injection-seeded, Q-switched Nd:YAG laser (Spectra-Physics Model Quanta Ray PRO 290-10) is split via a 90/10 beam splitter. Ninety percent of the second-harmonic beam is employed to pump a tunable, narrowband dye laser (Continuum Model ND 6000), which produces an output beam at a wavelength of approximately 704 nm. LDS 698 laser dye is used within the ND 6000 dye laser. The remaining 10% of the second-harmonic beam is used as the pump beam (ω_1). The repetition rate of the laser is 10 Hz, and the temporal pulse length is approximately 8 ns at full-width at half-maximum (FWHM).

The third-harmonic output at 355 nm of the same injection-seeded Spectra-Physics Nd:YAG laser is sum-frequency mixed with the Continuum dye-laser output at 704 nm, generating a tunable UV probe beam (ω_3) at 236 nm. A beta-barium-borate (β -BBO) crystal mounted in an Inrad Auto-tracker III is used for the sum-frequency mixing process. This tunable UV source, whose maximum energy is ~ 4 mJ/pulse, constitutes the probe beam (λ_3). Finally, the second-harmonic output of an unseeded Nd:YAG laser (Continuum Model Precision PRO 9010) is used to pump another tunable, narrowband dye laser (Lumonics Model SpectrumMaster). Rhodamine 610 laser dye is employed to generate the Stokes beam (ω_2) near 594 nm.

The two Nd:YAG lasers are synchronized using a digital delay generator (SRS Model DG 535) so that all three beams overlap temporally with a peak deviation of less than 1 ns. A combination of a half-wave plate and a polarizer is placed within each beam path to control the pulse energy. The polarizer is also used to set the desired polarization for each beam. The pump beam and the Stokes beam are linearly polarized, with the polarization axis set at 60° with respect to the vertical axis. The UV probe beam is vertically polarized. A three-dimensional folded BOXCARS geometry is employed to satisfy the phase-matching requirement [25].

A 50-mm diameter, 500-mm focal-length, UV-grade fused-silica lens is used to focus the three beams. However, to obtain better signal-to-noise ratios while maintaining reasonable spatial resolution, the beams are overlapped about 25 mm away from their focal plane. This spatial overlap also reduces saturation effects for both the Raman and electronic transitions [12] because of reduced laser irradiances at the probe volume. The length of the resulting probe volume is about 6 mm. The diameters of all three beams at the probe volume are approximately $200 \mu\text{m}$, as measured by translating a razor blade across the overlap region while monitoring the transmitted power of each laser.

The three input beams and the signal beam are recollimated using another 50-mm diameter, 500-mm focal-length lens. The Stokes beam (λ_2) is directed into a wavemeter (High Finesse Model WS-6) to record its wavelength when scanning the Stokes dye laser. The pump beam (λ_1) is trapped using a beam dump. The UV probe beam (λ_3) is directed onto a pyroelectric joulemeter (Molelectron Model J3-05). The UV probe pulse energy is recorded continuously so that shot-to-shot fluctuations in the UV-beam energy can be accounted for in subsequent data analysis.

The ERE-CARS signal and the non-resonant four-wave-mixing signal are directed through an analyzing polarizer of high rejection ratio. The transmission axis of the analyzer is set perpendicular to the polarization direction of the non-resonant signal, thus minimizing non-resonant interferences. The analyzing polarizer is mounted on a high-resolution rotation stage to achieve the best possible suppression of non-resonant background. Light scattered from the UV beam at 236 nm is blocked using four band-pass filters [15], as shown in Fig. 2. The signal beam at ~ 225.5 nm is isolated using a 1-m spectrometer (SPEX Model 1000M) and collected via a solar-blind photomultiplier tube (PMT-Hamamatsu Model R7154).

2.2 Flow and pressure systems

For measurements of the detection limit, we employ a jet flow of acetylene in a buffer gas of nitrogen. Molecular mixing is ensured by combining a gas flow of 1000 ppm C_2H_2 in N_2 with an additional flow of pure N_2 sufficiently far upstream of the nozzle. The diameter of the nozzle producing the jet flow is approximately 10 mm. Careful adjustments are made to ensure that the probe volume is completely encompassed by the jet.

The pressure-scaling experiments are performed in a pressure vessel which can accommodate pressures up to 8 bar. The inlet of the vessel is connected to a gas bottle containing 1000 ppm C_2H_2 in N_2 . In addition, the outlet of the vessel is connected to a vacuum pump. It is ensured that no residual mixture remained in the vessel prior to refilling of the vessel at each pressure.

3 Results and discussion

The ERE-CARS signal is acquired while scanning the frequency of the Stokes dye laser and fixing that of the UV probe beam. In past ERE-CARS measurements of nitric oxide [15, 16], we have performed both UV scans (λ_2 fixed, λ_3 varying) and Stokes scans (λ_2 varying, λ_3 fixed). However,

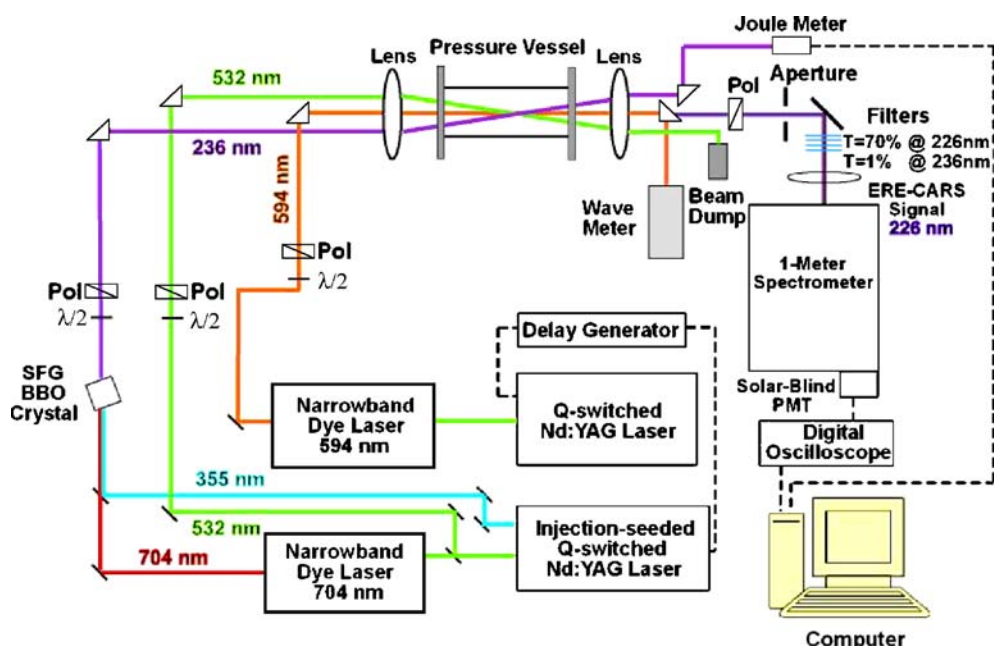


FIGURE 2 Experimental system for C_2H_2 ERE-CARS

for this work, we present only Stokes scans. UV scans are performed but yield essentially constant signals owing to the broad character of the electronic resonance interaction. The ERE-CARS signal is averaged over 10 laser shots and subsequently corrected for shot-to-shot UV (λ_3) fluctuations via division by the UV energy. It is observed that the fluctuations in the Stokes laser beam (λ_2) are negligible.

Spectral v_2 band structures for 1% C_2H_2 at 0.05 atm and 300 K for various pulse energies of both the pump beam (ω_1) and Stokes beam (ω_2) are shown in Figs. 3 and 4. The Sandia CARSFT code [26] is used to calculate theoretical CARS spectra for given laser linewidths at the specified temperature

and pressure. The CARSFT calculations do not include any effects of saturation. Figure 3 shows a comparison between theoretical and measured spectra for the same experimental conditions at fixed energy levels for ω_1 and ω_2 . Good agreement is achieved between theory and experiment. The remaining differences between theory and experiment are probably due to slight saturation of the experimental spectrum. The odd rotational lines are well resolved in Fig. 3, but the even rotational lines are not evident. The linewidth (FWHM) of the pump beam (λ_1) is $\sim 0.003 \text{ cm}^{-1}$; in comparison, that of both the Stokes beam (λ_2) and the UV probe beam (λ_3) is approximately 0.1 cm^{-1} . From Fig. 3, we observe that the odd rotational lines have FWHMs of approximately 0.1 cm^{-1} . By comparing the two cases in Fig. 4, we find clear evidence

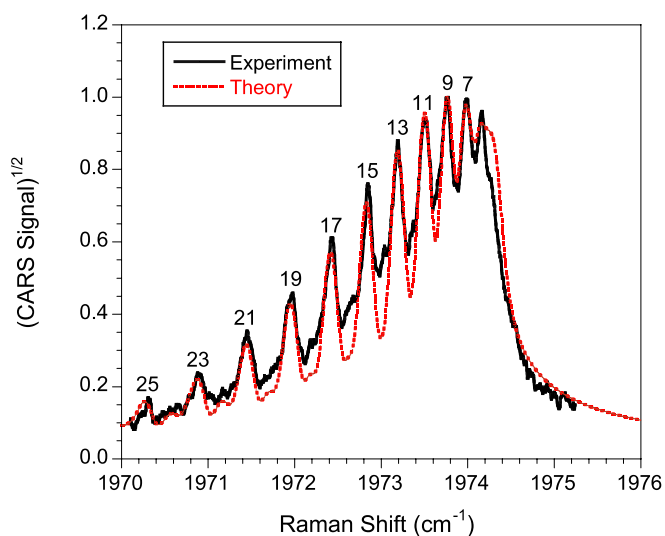


FIGURE 3 Comparison between experimental and theoretical C_2H_2 ERE-CARS spectra for 1% C_2H_2 in buffer N_2 gas at 0.05 bar and 300 K. The experimental spectrum is obtained for pulse energies of 2 mJ/pulse, 2 mJ/pulse, and 0.5 mJ/pulse for the pump, Stokes, and probe beams, respectively. The theoretical linewidths are 0.01 cm^{-1} and 0.15 cm^{-1} for the pump and Stokes beams, respectively. The Q-branch lines with odd rotational quantum number $J \geq 7$ are labeled

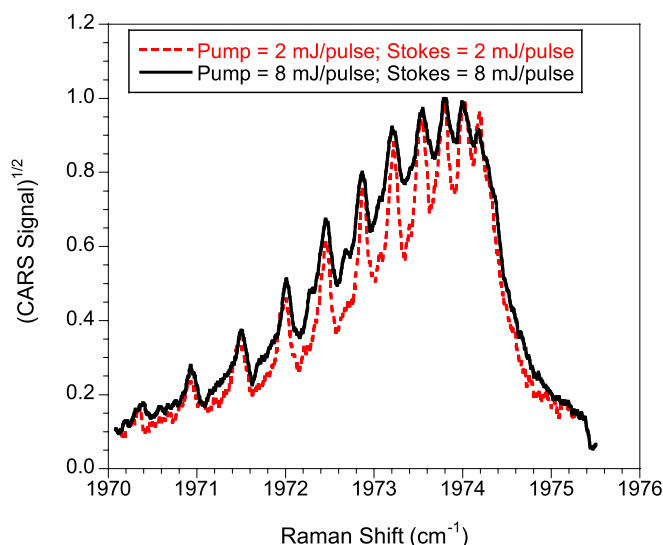


FIGURE 4 Saturation broadening of C_2H_2 ERE-CARS spectra at 0.05 bar and 300 K for 1% C_2H_2 in N_2 . The pulse energy of the UV probe beam (ω_3) is 0.5 mJ/pulse for both measurements

for saturation broadening of the Raman resonances at higher pump and Stokes laser irradiances.

Figure 5 shows a comparison of theoretical and experimental ERE-CARS spectra of C_2H_2 for the ν_2 Raman band at various UV probe wavelengths from 233.0 nm to 238.5 nm. From Fig. 5, we observe no significant change in the ERE-CARS spectrum as a function of UV wavelengths. The rovibrational structure of the acetylene $\tilde{A}-\tilde{X}$ electronic transition is discussed in detail by Innes [21] and Watson et al. [22]. The initial and final levels of the fundamental Q-branch transition at 1974 cm^{-1} are characterized by $(v_2'' = 0, v_4'' = 0, l_4'' = 0)$ and $(v_2' = 1, v_4' = 0, l_4' = 0)$, respectively. Watson et al. [22] and Innes [21] list the frequencies and the approximate transition strengths between the $(v_2'' = 0, v_4'' = 0, l_4'' = 0)$ band in the \tilde{X} level and various vibrational bands in the \tilde{A} level. The bands in the \tilde{A} level that are connected with the ground $(v_2'' = 0, v_4'' = 0, l_4'' = 0)$ band are listed in Table 1. The band frequency, strength (S = strong, M = medium, W = weak,

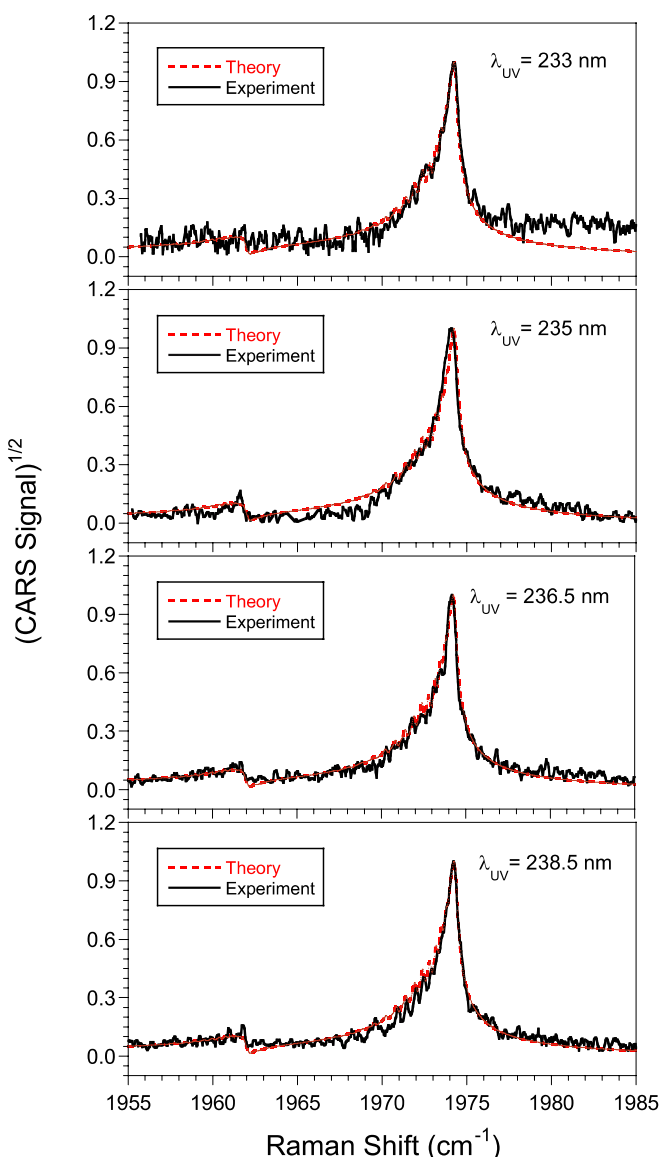


FIGURE 5 C_2H_2 ERE-CARS spectra at 1.0 atm and 300 K in a jet flow of 1% C_2H_2 in buffer N_2 . The UV probe wavelength varies from 233.0 nm to 238.5 nm

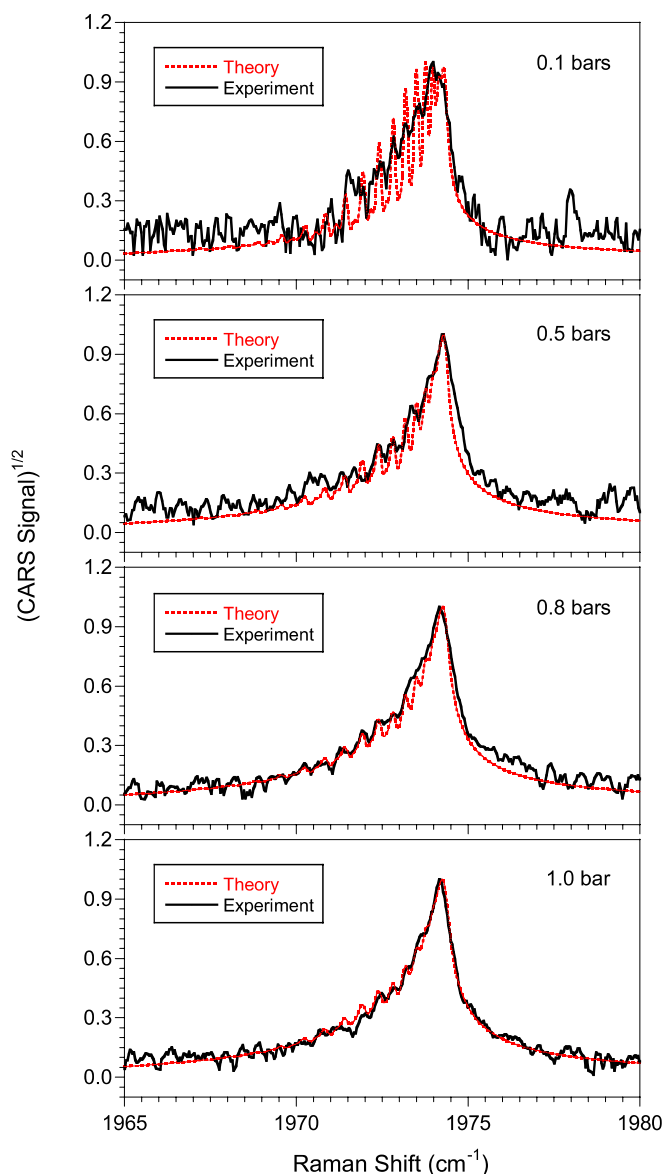


FIGURE 6 C_2H_2 ERE-CARS spectra at four different sub-atmospheric pressures. The spectra are recorded for a mixture of 1000 ppm C_2H_2 in N_2 buffer gas inside the pressure vessel. For all spectra, the UV probe wavelength $\lambda_3 = 236\text{ nm}$. The pulse energies for the pump, Stokes, and probe beams are 8.0, 8.0, and 0.5 mJ/pulse, respectively

VW = very weak), and corresponding UV probe wavelength are listed for exact resonance with a given band. Neither Watson et al. [22] nor Innes [21] provide any information on transitions from the $(v_2'' = 1, v_4'' = 0, l_4'' = 0)$ band in the \tilde{X} level.

Although it appears from Table 1 that we should have observed a significant increase in signal for $\lambda_3 = 236.5\text{ nm}$ as compared to the other probe wavelengths investigated, no significant change is observed in the ERE-CARS spectrum. In fact, the maximum signal strength is found near 236 nm, so that most of the measurements reported in this paper are obtained with a probe wavelength of 236 nm.

ERE-CARS measurements for the ν_2 Raman band of C_2H_2 are also performed for pressures ranging from sub-atmospheric (0.1 bar) to above atmospheric (8 bar) at 300 K. Figure 6 shows comparisons between theoretical and experimental spectra at different sub-atmospheric pressures from

0.1 to 1 bar, while Fig. 7 shows similar comparisons at pressures from 2 to 8 bar. We find, as expected, that individual rotational lines blend into a band structure as the pressure rises. In general, the theoretical and experimental spectra agree well for pressures less than 2 bar. The experimental spectrum at 0.1 bar is not as clearly resolved as the theoretical spectrum. This result is almost certainly due to the higher level of saturation for the Raman transitions at lower pressure. For pressures higher than 1 bar, the experimental spectra are narrower than the theoretical spectra. This trend becomes more pronounced at higher pressures. The implication is that significant collisional narrowing occurs at pressures above 2 bar; unfortunately, the CARSFT code does not include a collisional narrowing model for C_2H_2 . The experimental spectra tend to be more symmetric at higher pressures as compared with the the-

\tilde{A} band (v'_2, v'_3, K'_a)	$\tilde{\nu}$ (cm^{-1})	Strength	λ_3 (nm)
(0, 1, 0)	43 245.12	S	242.30
(0, 1, 1)	43 258.05	S	242.22
(0, 1, 2)	43 296.75	W	242.00
(0, 1, 3)	43 360.94	VW	241.62
(1, 0, 0)	43 584.45	W	240.32
(1, 0, 1)	43 596.31	M	240.26
(0, 2, 0)	44 275.27	M	236.40
(0, 2, 1)	44 289.35	S	236.32
(0, 2, 2)	44 331.40	W	236.09
(1, 1, 0)	44 631.78	M	234.42
(1, 1, 1)	44 644.45	M	234.35
(0, 3, 0)	45 285.72	S	230.88
(0, 3, 1)	45 301.13	S	230.80
(0, 3, 2)	45 347.15	M	230.56
(1, 2, 0)	45 662.68	M	228.89
(1, 2, 1)	45 676.42	S	228.82

TABLE 1 Bands in the \tilde{A} level connected with the ($v''_2 = 0, v''_4 = 0, l''_4 = 0$) band in the \tilde{X} level

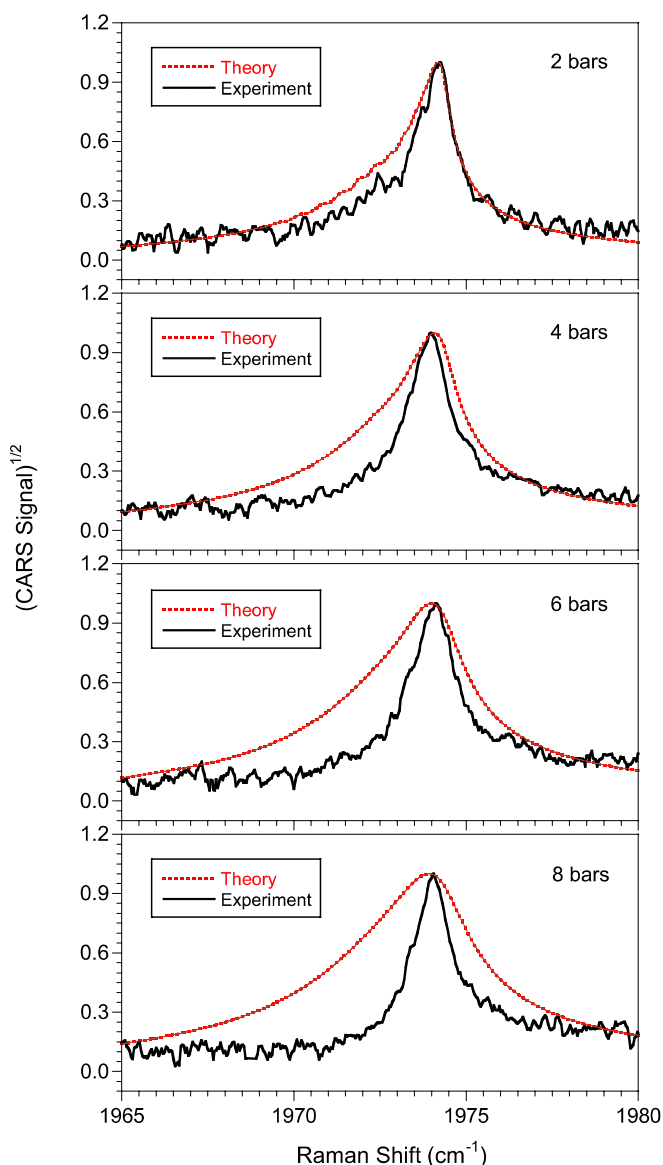


FIGURE 7 C_2H_2 ERE-CARS spectra at pressures from 2 to 8 bar. All spectra are recorded for a mixture of 1000 ppm C_2H_2 in N_2 buffer gas inside the pressure vessel. The UV probe wavelength λ_3 and the pulse energies are the same as for Fig. 6

oretical spectra, again presumably due to strong collisional narrowing.

For the spectra shown in Figs. 6 and 7, the square root of the ERE-CARS signal is integrated in the Raman shift range from 1970 cm^{-1} to 1978 cm^{-1} and plotted as a function of pressure in Fig. 8. Figure 8 shows that the square root of the integrated ERE-CARS signal increases sharply with increasing pressure from 0.1 to 4 bar and then increases gradually beyond 5 bar. The spectral scans are repeated at pressures of 1, 4, 5, and 7 bar. From these repeated measurements, we conclude that the square root of the integrated ERE-CARS signal is repeatable to within 5%. Baum et al. [27] performed acetylene absorption measurements in the wavelength range 189–229 nm for a path length of 127 mm. They found that the absorbance near 226 nm is negligibly small at 1 atm for a C_2H_2 concentration of 630 ppm. Therefore, despite changes in number density and the effects of line broadening, we conclude that the effects of UV absorption can be neglected for our experiments up to 8 bar.

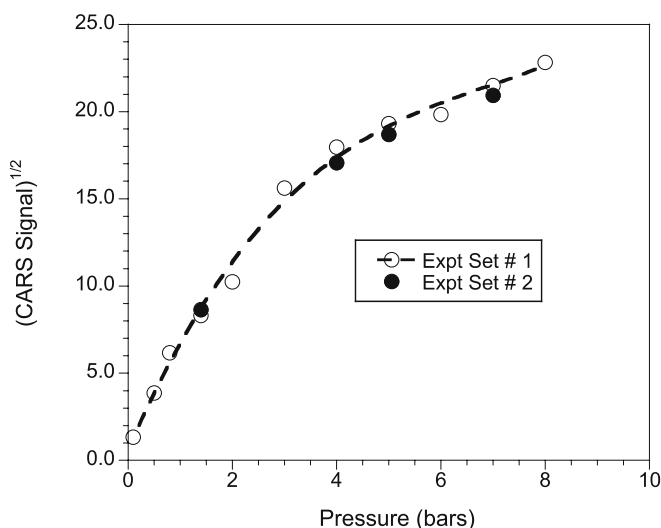


FIGURE 8 Variation of the square root of the integrated C_2H_2 ERE-CARS signal with increasing pressure in the pressure range 0.05–8 bar

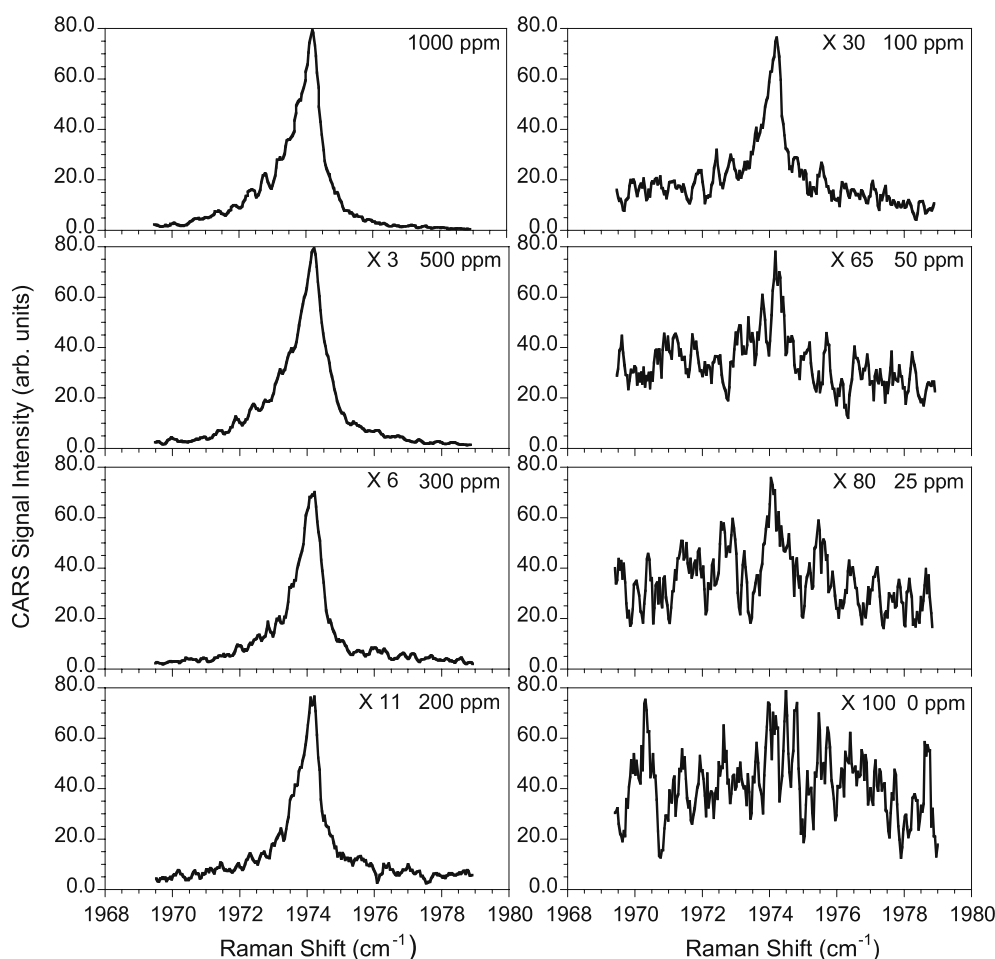


FIGURE 9 C_2H_2 ERE-CARS detection-limit measurements at 1 atm and 300 K in a jet flow of 1000 ppm C_2H_2 in N_2 buffer gas, diluted with additional N_2 . For all spectra, the pulse energies for the pump, Stokes, and probe beams are 8, 8, and 2 mJ/pulse, respectively. The probe wavelength is 236.0 nm

As mentioned previously, acetylene displays an essentially constant electronic coupling with the ($v_2'' = 1$, $v_4'' = 0$, $l_4'' = 0$) level in the ground electronic state, thus yielding nearly the same resonance enhancement in the pressure range 0.1–8 bar. This factor, combined with strong collisional narrowing at high pressures, results in a substantial increase in the ERE-CARS signal with rising pressures for a constant mole fraction of C_2H_2 . The gradual increase in square root of the integrated ERE-CARS signal beyond 5 bar is presumably due to broadening of the Raman transitions at higher pressures.

As indicated previously, the detection limit for CARS can be improved by several orders of magnitude by tuning the UV laser beam to a suitable electronic resonance. Figure 9 shows ERE-CARS spectra over the ν_2 Raman band for different C_2H_2 concentrations. A mixture of 1000 ppm C_2H_2 in N_2 buffer gas is diluted with additional N_2 to establish the given concentration levels. The measurements are performed in a jet flow produced from a nozzle. We established a C_2H_2 detection limit of 25 ppm upon suppressing the non-resonant signal from the N_2 buffer gas. This result suggests that ERE-CARS has excellent potential for minor-species measurements, even in reacting flows.

Figure 10 shows that the square root of the integrated ERE-CARS signal (1970 cm^{-1} –1978 cm^{-1}) varies linearly with acetylene concentration at atmospheric pressure. This

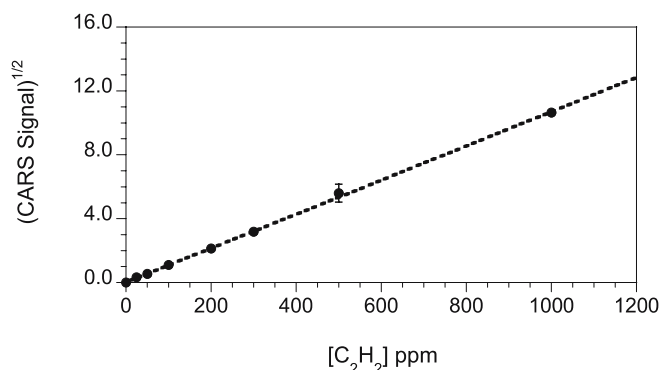


FIGURE 10 Square root of integrated C_2H_2 ERE-CARS signal as a function of C_2H_2 concentration in a jet flow at 1 atm. A typical error bar of 10% is shown at a concentration of 500 ppm

result verifies the expected theoretical behavior, as indicated by $I_{\text{CARS}} \propto |\chi^{(3)}|^2$, where I_{CARS} is the irradiance of the CARS signal and $\chi^{(3)}$ is the third-order nonlinear susceptibility [4].

4 Conclusions and future work

Electronic resonance-enhanced coherent anti-Stokes Raman scattering (ERE-CARS) has been applied to obtain acetylene spectra at pressures ranging from 0.1 to 8 bar.

The acetylene ERE-CARS signal is found to rise sharply with increasing pressure from 0.1 to 4 bar, but more gradually from 5 to 8 bar. As expected, the square root of the integrated ERE-CARS signal at 1 atm and 300 K varies linearly with C_2H_2 concentration. The detection limit under these conditions is found to be approximately 25 ppm. No significant changes in spectral signature or signal levels are observed as the UV probe wavelength is varied from 233.0 to 238.5 nm.

We plan to apply ERE-CARS for measurement of C_2H_2 profiles in high-pressure counter-flow diffusion flames in the Purdue high-pressure flame facility [28]. Quantitative analysis of these profiles will require either calibration or the incorporation of a collisional narrowing model [29–31] for C_2H_2 in the CARSFT code.

ACKNOWLEDGEMENTS Funding for this research program was provided by the U.S. Department of Energy, Division of Chemical Sciences, Geosciences, and Biosciences, under Grant No. DE-FG02-03ER15391, by the Air Force Office of Scientific Research under Contract No. FA9550-05-C-0096 (Dr. Julian Tishkoff, Program Manager), and by the Air Force Research Laboratory, Propulsion Directorate, Wright-Patterson Air Force Base, under Contract No. F33615-03-D-2329.

REFERENCES

- 1 A.C. Eckbreth, *Laser Diagnostics for Combustion Temperature and Species* (Gordon and Breach Publishers, Amsterdam, 1996)
- 2 A.C. Eckbreth, G.M. Dobbs, J.H. Stufflebeam, P.A. Tellex, *Appl. Opt.* **23**, 1328 (1984)
- 3 R.P. Lucht, *Opt. Lett.* **12**, 78 (1987)
- 4 B. Hudson, W. Hetherington III, S. Cramer, I. Chabay, G.K. Klauminzer, *Proc. Nat. Acad. Sci.* **73**, 3798 (1976)
- 5 B. Attal, O.O. Schnepf, J.-P.E. Taran, *Opt. Commun.* **24**, 77 (1978)
- 6 A. Beckman, H. Fietz, P. Baierl, W. Kiefer, *Chem. Phys. Lett.* **86**, 140 (1982)
- 7 D.M. Guthals, K.P. Gross, J.W. Nibler, *J. Chem. Phys.* **70**, 2393 (1979)
- 8 M.E. McIlwain, J.C. Hindman, *J. Chem. Phys.* **73**, 68 (1980)
- 9 K.P. Gross, D.M. Guthals, J.W. Nibler, *J. Chem. Phys.* **70**, 4673 (1979)
- 10 W.M. Hetherington III, G.M. Korenowski, K.B. Eisenthal, *Chem. Phys. Lett.* **77**, 275 (1981)
- 11 D.A. Greenhalgh, *Appl. Opt.* **22**, 1128 (1983)
- 12 T.J. Aartsma, W.H. Hesselink, D.A. Wiersma, *Chem. Phys. Lett.* **71**, 424 (1980)
- 13 B. Attal-Trétout, S.C. Schmidt, E. Crété, P. Dumas, J.P. Taran, *J. Quantum Spectrosc. Radiat. Transf.* **43**, 351 (1990)
- 14 T. Doerk, P. Jauernik, S. Hadrich, B. Pfelzer, J. Uhlenbusch, *Opt. Commun.* **118**, 637 (1995)
- 15 S.F. Hanna, W.D. Kulatilaka, Z. Arp, T. Opatrny, M.O. Scully, J.P. Kuehner, R.P. Lucht, *Appl. Phys. Lett.* **83**, 1887 (2003)
- 16 W.D. Kulatilaka, N. Chai, S.V. Naik, N.M. Laurendeau, R.P. Lucht, J.P. Kuehner, S. Roy, J.R. Gord, *Opt. Lett.* **31**, 3357 (2006)
- 17 W.D. Kulatilaka, N. Chai, S.V. Naik, N.M. Laurendeau, R.P. Lucht, J.P. Kuehner, S. Roy, J.R. Gord, *Opt. Commun.* **274**, 441 (2007)
- 18 I. Glassman, *Proc. Combust. Inst.* **22**, 295 (1988)
- 19 H. Richter, J.B. Howard, *Prog. Energ. Combust. Sci.* **26**, 565 (2000)
- 20 J.M. Bonard, M. Croci, C. Klinke, F. Conus, I. Arfaoui, T. Stöckli, A. Chatelain, *Phys. Rev. B* **67**, 085412 (2003)
- 21 K.K. Innes, *J. Chem. Phys.* **22**, 863 (1954)
- 22 J.K.G. Watson, M. Herman, J.C. Van Craen, R. Colin, *J. Mol. Spectrosc.* **95**, 101 (1982)
- 23 B.A. Williams, J.W. Fleming, *Appl. Phys. B* **75**, 883 (2002)
- 24 R.P. Lucht, R.L. Farrow, R.E. Palmer, *Combust. Sci. Technol.* **45**, 261 (1986)
- 25 A.C. Eckbreth, *Appl. Phys. Lett.* **32**, 421 (1978)
- 26 R.E. Palmer, The CARSFT Computer Code For Calculating Coherent Anti-Stokes Raman Spectra: User and Programmer Information, Sandia National Laboratories Report SAND89-8206, Livermore, CA (1989)
- 27 M.M. Baum, S. Kumar, A.M. Lappas, P.D. Wagner, *Rev. Sci. Instrum.* **74**, 3104 (2003)
- 28 C.D. Carter, G.B. King, N.M. Laurendeau, *Rev. Sci. Instrum.* **60**, 2606 (1989)
- 29 R.G. Gordon, R.P. McGinnis, *J. Chem. Phys.* **49**, 2455 (1968)
- 30 R.G. Gordon, R.P. McGinnis, *J. Chem. Phys.* **55**, 4898 (1971)
- 31 M.L. Koszykowski, R.L. Farrow, R.E. Palmer, *Opt. Lett.* **10**, 478 (1985)

Effects of pressure variations on electronic-resonance-enhanced coherent anti-Stokes Raman scattering of nitric oxide

Waruna D. Kulatilaka ^{a,*}, Ning Chai ^a, Sameer V. Naik ^a, Sukesh Roy ^b,
Normand M. Laurendeau ^a, Robert P. Lucht ^a, Joel P. Kuehner ^c, James R. Gord ^d

^a School of Mechanical Engineering, Purdue University, West Lafayette, IN 47907, United States

^b Innovative Scientific Solutions, Inc., 2766 Indian Ripple Road, Dayton, OH 45440, United States

^c Department of Physics and Engineering, Washington and Lee University, Lexington, VA 24450, United States

^d Air Force Research Laboratory, Propulsion Directorate, Wright-Patterson AFB, OH 45433, United States

Received 13 October 2006; received in revised form 3 February 2007; accepted 8 February 2007

Abstract

The effects of pressure variations on the electronic-resonance-enhanced coherent anti-Stokes Raman scattering (ERE-CARS) signal of nitric oxide (NO) were studied at pressures ranging from 0.1 to 8 bar. ERE-CARS signals were recorded in a gas cell filled with a mixture of 300 ppm NO in N₂ buffer gas at room temperature. The ERE-CARS signal was found to increase with rising pressure up to 2 bar and to remain nearly constant thereafter. The spectra recorded at different cell pressures were modeled using a modified version of the Sandia CARSFT code. Laser-saturation effects were accounted for by systematically varying the theoretical ultraviolet probe-laser linewidth. Excellent agreement was obtained between theory and experiment for the pressure-scaling behavior of the ERE-CARS signal of NO. This finding, along with a negligible influence of electronic quenching on the ERE-CARS signal, provides strong incentive for the application of ERE-CARS to measurements of NO concentrations in high-pressure combustion environments.

© 2007 Elsevier B.V. All rights reserved.

PACS: 42.62.Fi; 42.65.Dr; 82.33.Vx

1. Introduction

Coherent anti-Stokes Raman scattering (CARS) is a well established diagnostic technique for measuring temperature and major species concentrations in reacting flows [1]. Recently, CARS techniques have been demonstrated for the simultaneous measurement of multiple species concentrations [2–4]. CARS has also been investigated both experimentally [4,5] and theoretically [6] for concentration and temperature measurements in high-pressure environments. At high pressures, collisional narrowing effects have a direct impact on the shape and intensity of CARS spectra [7–9]. Additional influences include laser-saturation [9–12],

Stark broadening [12,13] and stimulated Raman pumping [13]. Interference effects between different rotational lines have been studied theoretically for high-resolution CARS spectra of oxygen (O₂), nitrogen (N₂) and nitric oxide (NO) over a range of spectral bandwidths [14]. Theoretical and experimental investigations of line interference effects in vibrational Q-branch spectra of N₂ and CO have also been conducted using stimulated Raman spectroscopy [15]. Rotational collisional narrowing in the NO fundamental Q-branch was the subject of a prior investigation in the pressure range 20–100 kPa [16].

CARS has been applied to high-resolution spectroscopy of NO by Doerk and co-workers [17,18]. However, traditional vibrational or rotational CARS techniques have limited sensitivity and thus are not suitable for detection of minor species in flames and plasmas. This difficulty can be overcome by tuning one or more of the pump, Stokes,

* Corresponding author. Present address: Sandia National Laboratories, Livermore, CA 94551, United States. Tel.: +1 925 2943527.

E-mail address: wdkulat@sandia.gov (W.D. Kulatilaka).

and probe beams into resonance with an electronic transition of the molecule. The resulting CARS signal exhibits a significant resonance enhancement. Electronic-resonance-enhanced coherent anti-Stokes Raman scattering (ERE-CARS) has previously been applied to both OH [19] and CH [20]. In our own work, we have demonstrated ERE-CARS of NO [21] and have demonstrated NO detection limits of 50 ppm or better in atmospheric-pressure flames [22]. Further details of our ERE-CARS experiments can be found in two recent publications [22,23].

In this paper, we describe the pressure-scaling behavior of the NO ERE-CARS signal. ERE-CARS spectra of NO were recorded using a gas cell at pressures ranging from 0.1 to 8 bar at room temperature. Near-background-free detection has been demonstrated using a frequency-scanning method incorporated into these experiments [22]. The ERE-CARS technique can be used to perform quantitative measurements of NO concentration in high-pressure combustion environments for which traditional laser-induced fluorescence (LIF) techniques become less accurate and more complicated, primarily owing to electronic quenching and background interferences [24–27].

2. ERE-CARS experimental procedure

Our ERE-CARS technique is an extension of the dual-pump CARS method previously developed for simulta-

neous detection of two major species [2]. The energy level diagram for the ERE-CARS process is shown in Fig. 1. We use visible pump ($\lambda_1 = 532$ nm) and Stokes ($\lambda_2 = 591$ nm) beams which are far from the $A^2\Sigma^+ - X^2\Pi$ electronic resonance of NO. The frequency difference between these two beams is tuned to a Q-branch Raman resonance in the $v'' = 0 \rightarrow v'' = 1$ vibrational transition of the $X^2\Pi$ electronic level of NO. The Raman polarization created in the medium is then probed using an ultraviolet (UV) probe beam ($\lambda_3 = 236$ nm). The wavelength of the UV beam is selected to be at or near electronic resonance with rotational transitions in the $v' = 1 \rightarrow v' = 0$ vibrational band of the $A^2\Sigma^+ - X^2\Pi$ electronic transition of NO. The ERE-CARS signal generated at 226 nm is thus in resonance with rotational transitions in the $v' = 0 \rightarrow v' = 0$ band of the same electronic transition. Consequently, a dramatic increase in the ERE-CARS signal occurs because of electronic resonance enhancement. Our ERE-CARS approach differs from previous such methods owing to the wide separation maintained between the wavelengths of the pump and probe beams [21].

The experimental apparatus used for our pressure-scaling studies of the NO ERE-CARS signal is shown in Fig. 2. The pump beam at $\lambda_1 = 532$ nm is the second-harmonic output of an injection-seeded, Q-switched Nd:YAG laser (Spectra-Physics Model Quanta Ray PRO 290-10) with a repetition rate of 10 Hz and a pulse width of approximately 8 ns (FWHM). This Nd:YAG laser is equipped with active-feedback-control systems to obtain both excellent pointing stability (BeamLok) and minimum divergence (D-Lok) of the output laser beams. Approximately 250 mJ of the 532-nm output from the same Nd:YAG laser is used to pump a tunable, narrow-band dye laser (Continuum Model ND 6000). This dye laser is operated using LDS 698 laser dye. The output wavelength of the dye laser is approximately 704 nm, and the pulse energy is approximately 20 mJ. LDS 698 is a very stable laser dye and the spatial mode of the dye laser beam is near-Gaussian. The 704-nm laser radiation is subsequently sum-frequency mixed with approximately 25 mJ of the 355-nm, third-harmonic output of the same injection-seeded Nd:YAG laser to generate UV radiation at 236 nm. A beta-barium borate (β -BBO) crystal mounted inside an Inrad Autotracker III is used for sum-frequency generation (SFG). Employing this scheme, we can obtain tunable, 236-nm UV radiation with excellent spatial mode structure and with pulse energies up to 4 mJ. This 236-nm beam acts as the probe beam for the NO ERE-CARS process.

The second-harmonic output of an unseeded Nd:YAG laser (Continuum Model Powerlite Precision II 9010) is used to pump a second tunable, narrow-band dye laser (Lumonics Model SpectrumMaster) containing Rhodamine 610 laser dye. The 591-nm output beam from this second dye laser is the Stokes beam. The two Nd:YAG pump lasers are synchronized electronically so that all three pulses overlap within 1 ns at the probe volume. A half-waveplate/polarizer combination was included in each of

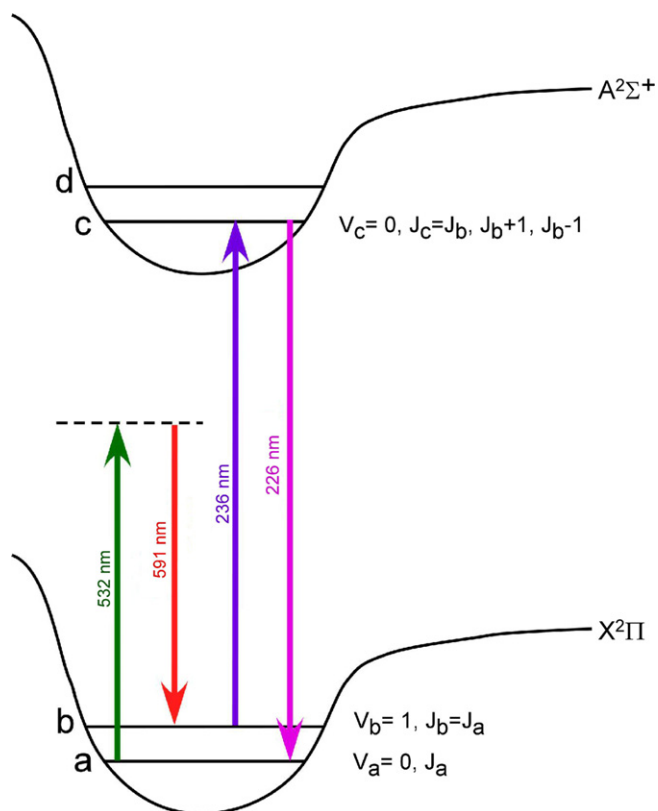


Fig. 1. Energy-level diagram for NO ERE-CARS.

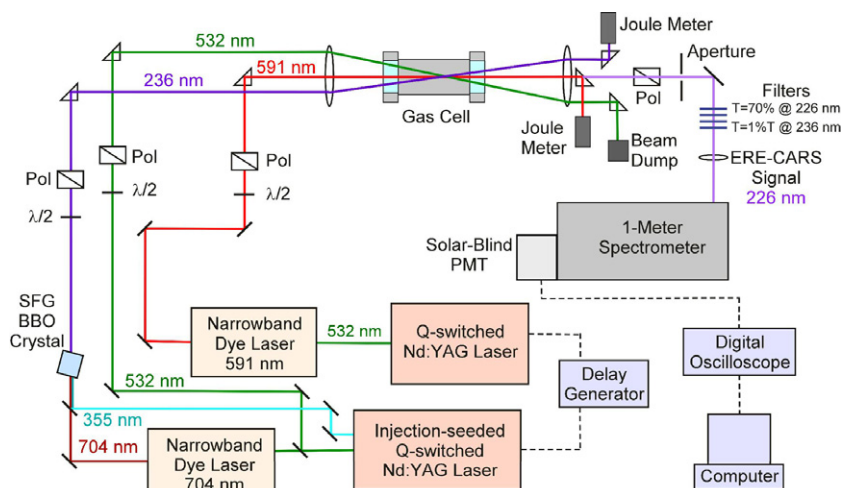


Fig. 2. NO ERE-CARS experimental apparatus.

the three ERE-CARS beam paths so that pulse energies can be controlled and specific polarizations maintained for each beam. Two telescopes were placed in the Stokes and UV probe beams, respectively (not shown in Fig. 2 for clarity), so that, by adjusting the lens separation, the focal planes of all three beams could be made to overlap at the ERE-CARS probe volume. Phase-matching was achieved by using the usual three-dimensional folded BOX-CARS geometry.

The three ERE-CARS beams were focused into the probe volume using a 50-mm diameter, 500-mm focal-length, UV-grade fused silica lens. The diameters at the overlap region of the three beams were approximately 200 μm . The beams were crossed about 25 mm away from the focal plane and the effective interaction length was measured to be approximately 6 mm. We selected the length for the probe volume so that we could generate significant ERE-CARS signals while maintaining reasonable spatial resolution and avoiding significant saturation of the Raman and electronic transitions. If required, better spatial resolution could be achieved by crossing the laser beams much closer to their focal plane.

A gas cell containing a 300-ppm mixture of NO in N_2 buffer gas was positioned at the probe volume. The ERE-CARS signal beam was recollimated using an additional 50-mm diameter, 500-mm focal-length lens. The polarizations of the three incoming beams were arranged such that the non-resonant four-wave-mixing signal could be suppressed using a polarizer placed along the signal beam. The polarization technique used to suppress the non-resonant background is described in a previous publication [21]. Scattered UV probe radiation within the ERE-CARS channel was blocked using four 45°, Nd:YAG fifth-harmonic laser mirrors placed at normal incidence to the beam [21]. The signal was transmitted through a 1-m spectrometer and detected using a solar-blind photomultiplier tube (PMT) connected to a digital oscilloscope and a personal computer.

3. Results and discussion

Pressure-scaling of the NO ERE-CARS signal was investigated at room temperature. Spectra were recorded by scanning the Stokes wavelength while fixing the UV wavelength so that we could precisely account for fluorescence interferences in the signal channel [22]. The pressure dependence of the ERE-CARS signal was studied for two different sets of laser-pulse energies. For the low-energy case, the pulse energies were 5 mJ, 5 mJ, and 0.25 mJ for the pump, Stokes, and UV probe beams, respectively. For the high-energy case, the pulse energies were 12.5 mJ, 11.5 mJ, and 0.6 mJ for the above three beams, respectively. The pulse energies for the low-energy case were chosen so that we obtained signals with signal-to-noise ratios greater than 10 for all pressures. The pulse energies for the high-energy case were approximately twice those of the low-energy case. Spectra were recorded using a gas cell filled with 300 ppm NO in N_2 buffer gas for a range of pressures varying from 0.1 to 8 bar.

The ERE-CARS probe volume was located 160 mm in front of the exit window of the gas cell to ensure that the spot sizes of the beams at the exit plane would be large enough to prevent window damage. As a result, significant absorption of the ERE-CARS signal occurs within the gas cell. The theoretical absorption was calculated at the wavelength of the ERE-CARS signal for each pressure, using a computer code [28] incorporating spectroscopic parameters from LIFBASE [29]. From such calculations, all NO ERE-CARS signals were corrected for absorption in the cell.

The ERE-CARS signals are plotted in Fig. 3 after subtracting constant LIF background interferences. The spectra recorded for the low-energy case are shown in panels a–h of Fig. 3. Similarly, the spectra recorded for the high-energy case are shown in panels i–p. Panels a–j, and also i–p, are scaled by the factors shown so that all plots employ the same ordinate. The spectral line of Fig. 3 is a blend of the Raman transitions $Q_{11}(1.5)$, $Q_{11}(2.5)$,

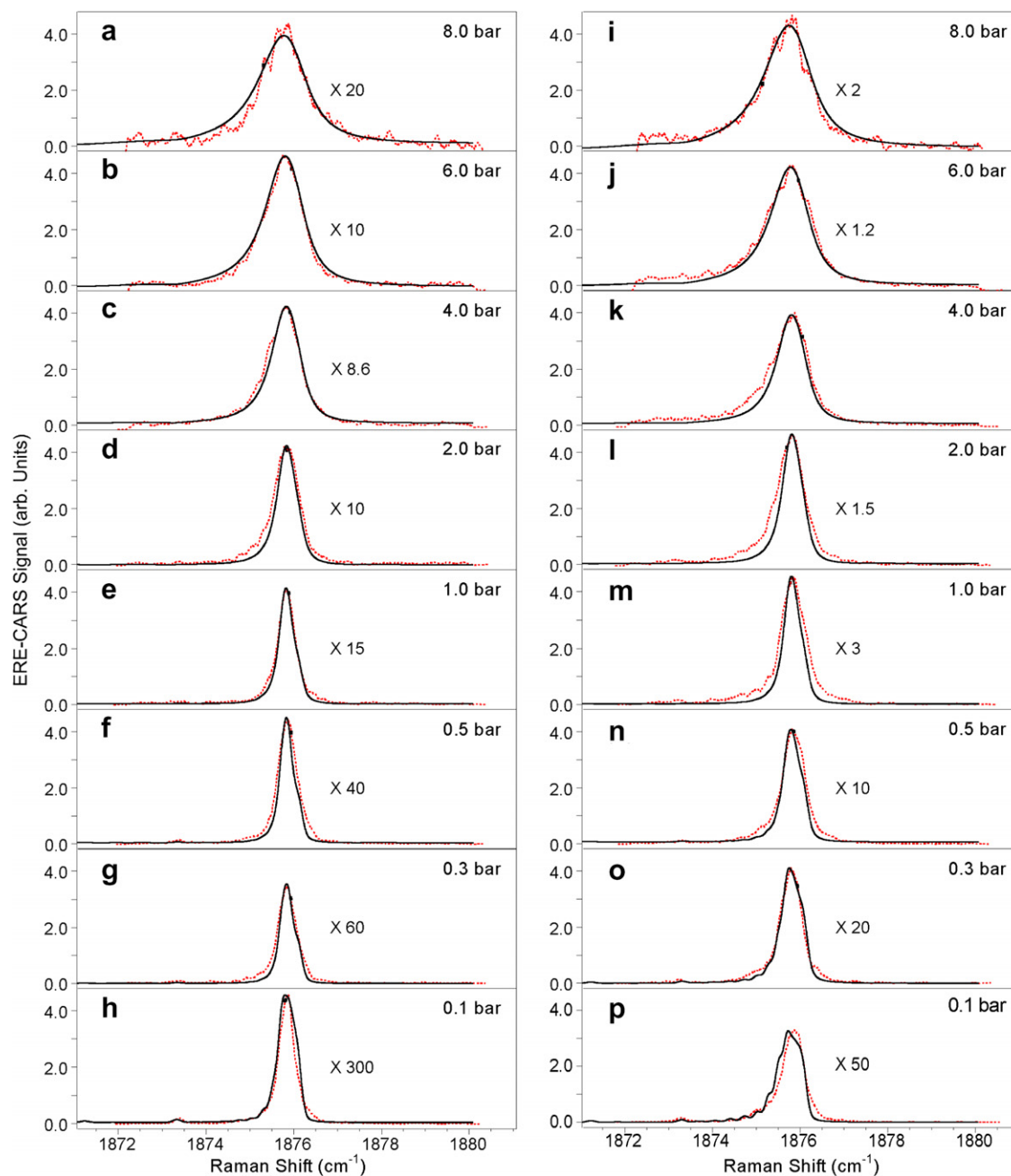


Fig. 3. Theoretical and experimental ERE-CARS spectra for different pressures at room temperature. The spectra shown in panels a–h are recorded using low pulse energies, while the spectra in panels i–p are recorded using high pulse energies. Experimental spectra are shown by dotted lines, while the theoretical spectra are shown by solid lines.

$Q_{11}(3.5)$ and $Q_{11}(4.5)$ at Raman shifts of 1876.03, 1875.95, 1875.82 and 1875.66 cm^{-1} , respectively. The UV probe is electronically resonant with $Q_{11}(1.5)$, $Q_{11}(2.5)$ and $Q_{11}(3.5)$ lines at frequencies 44197.94, 44197.52 and 44197.72 cm^{-1} , respectively.

The ERE-CARS spectra have been modeled using a perturbative (low laser irradiance) analysis. The Sandia CARSFT code [30] was modified for simulation of the ERE-CARS spectra, with NO spectral data obtained from LIFBASE [29] and from previous high-resolution CARS measurements [14,16]. In particular, the ERE-CARS code was employed to model spectra for both

the UV probe and Stokes scans. The ERE-CARS code, at this stage of development, does not include a rigorous treatment of saturation, which is a very important effect in our measurements, especially below atmospheric-pressure. The effects of saturation are modeled by performing calculations with variable UV probe-frequency widths. For the pressure-scaling experiments, good agreement was obtained between theory and experiment in terms of both the spectral shape and intensity of the ERE-CARS signal. For calculating theoretical ERE-CARS spectra, we used a UV probe-frequency width, $\Delta\omega_3$, described by

$$\Delta\omega_3 = \Delta\omega_{30} \left(1 + \frac{E_L}{E_{\text{sat}}} \right), \quad (1)$$

where the UV probe-frequency width, $\Delta\omega_{30} = 0.2 \text{ cm}^{-1}$, when the UV pulse energy E_L (in mJ) is significantly smaller than the saturation UV pulse energy, E_{sat} (in mJ). The saturation UV pulse energy can be taken as directly proportional to the total pressure, P (in bars), and thus can be written as

$$E_{\text{sat}} = \beta P, \quad (2)$$

where β is a suitable constant of proportionality (mJ/bar). Hence, Eq. (1) can be written as

$$\Delta\omega_3 = \Delta\omega_{30} \left(1 + \frac{E_L}{\beta P} \right). \quad (3)$$

The value of $\beta = 0.25 \text{ mJ/bar}$ was used to fit both the high- and low-UV-pulse-energy spectra. Minor variations in β do not have significant effects on the shape of the spectral lines. The theoretical spectra calculated using UV probe-frequency widths given by Eq. (3) over a range of pressures from 0.1 to 8 bar are shown by the solid lines in Fig. 3 for the low- and high-energy cases. The theoretical line shapes calculated using this approach agree very well with those obtained experimentally for both the high- and low-energy cases. The assumption of a broadened UV probe linewidth yields the correct pressure dependence for the ERE-CARS spectra and signal levels between pressures of 0.1 and 8 bar. However, the effects of significantly larger UV probe linewidths used at lower pressures are seen clearly in the theoretical spectrum shown in Fig. 3p. The structure in this spectrum results from the increased resonance enhancement for higher- J Raman transitions due to the large UV probe linewidth calculated using Eq. (3).

The background-corrected ERE-CARS signal was integrated between Raman shifts of $1874\text{--}1878 \text{ cm}^{-1}$ for each pressure. The square root of the integrated ERE-CARS signal is plotted as a function of pressure in Fig. 4 for

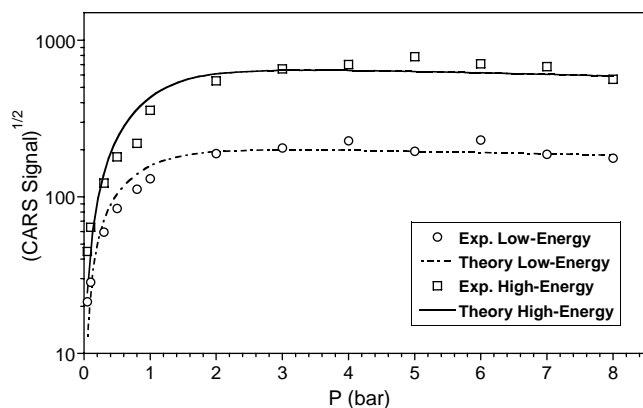


Fig. 4. Integrated ERE-CARS signal as a function of pressure. The squares and the line passing through them are for the high-energy case while the circles and the line passing through them are for the low-energy case, as described in the text. Theoretical line shapes are calculated by integrating theoretical spectra for the same Raman-shift range, $1874\text{--}1878 \text{ cm}^{-1}$.

the two different laser-energy cases described earlier. The spectral scans were repeated at pressures of 0.5, 2, 5, and 8 bar for the high-energy case to verify repeatability of our experiments. The integrated ERE-CARS signal is repeatable to within 5% for all of the repeated spectra. In each case, the theoretical pressure-dependence curve is obtained by integrating the theoretical spectra for the same Raman-shift range and is scaled at 1 bar to obtain a good fit with the experiments.

The square root of the ERE-CARS signal increases very rapidly with pressure up to 2 bar and remains nearly constant for 2–8 bar. The rapid increase in ERE-CARS signal with pressure up to 2 bar is a result of the dependence of the ERE-CARS signal on the square of the NO number density and of the decrease in the extent of saturation of the Raman and UV probe transitions as the pressure rises. A minor drop in signal is observed as the pressure increases above 3 bar, both in theory and experiment. This behavior arises from broadening of the UV probe transition as pressure increases, resulting in a reduction in the effective electronic resonance enhancement. Consequently, in contrast to regular N_2 CARS [7], no significant enhancement is observed in the ERE-CARS signal for our NO experiments owing to collisional narrowing with rising pressure.

In contrast to ERE-CARS, laser-induced fluorescence (LIF) manifests a significant decrease in signal with increasing pressure as the pressure rises from 0.1 to 2 bar. In contrast to ERE-CARS, the reduction in signal arises mostly from broadening of the UV pump transition [24,25]. The LIF signal and the ERE-CARS signal are compared as functions of pressure in Fig. 5. The two signals are normalized to a value of unity at 1 bar for easy comparison. LIF signals were calculated on a per-molecule basis at each pressure using the spectroscopic package LIF-SIM [31]. These signals were then multiplied by the corresponding pressure to account for the linear rise in number density with increasing pressure. Above 2 bar, the LIF signal is nearly constant as a function of pressure, similar to

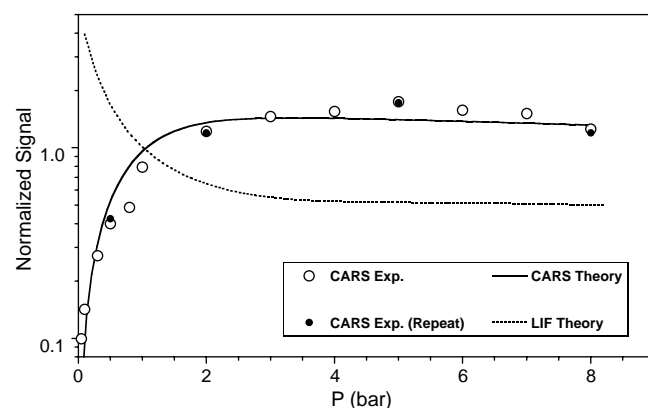


Fig. 5. ERE-CARS signal for the high-energy case (solid line) and LIF signal (dotted line) for the same conditions, as a function of pressure. The two signals are normalized to a value of unity at 1 bar for easy comparison. The experimental ERE-CARS data points are shown by open circles and the repeated data points are shown by solid circles.

the behavior of the ERE-CARS signal. We should note that, in the presence of collision partners such as O₂ and CO₂, the actual LIF signal would be much lower than with N₂ as a collision partner. In contrast, the ERE-CARS signal would remain nearly unaffected by any changes in electronic quenching [23].

4. Conclusions and future work

In summary, we have investigated pressure-scaling of the ERE-CARS signal for NO up to 8 bar. The ERE-CARS signal rises rapidly with increasing pressure up to 2 bar and remains nearly constant thereafter. Excellent agreement was obtained between theoretical and experimental pressure-scaling behavior for the ERE-CARS signal of NO. Saturation effects were modeled using the modified SANDIA CARSFT code by incorporating a systematic variation of the UV-laser linewidth.

We have previously developed a computer code based on direct numerical integration of the time-dependent density–matrix equations to model the ERE-CARS process [10]. The density–matrix approach allows us to account for saturation effects in a rigorous manner. At present, we are using this code to model NO ERE-CARS spectra with various levels of saturation; the results will be discussed in a future publication.

Acknowledgements

Funding for this research was provided by the Air Force Office of Scientific Research under Contract No. FA9550-05-C-0096 [Program Monitor: Dr. Julian Tishkoff], by the Air Force Research Laboratory, Propulsion Directorate, Wright-Patterson Air Force Base, under Contract No. F33615-03-D-2329, and by the US Department of Energy, Division of Chemical Sciences, Geosciences, and Biosciences, under Grant No. DE-FG02-03ER15391.

References

- [1] A.C. Eckbreth, *Laser Diagnostics for Combustion Temperature and Species*, Gordon and Breach Publishers, Amsterdam, 1996.
- [2] R.P. Lucht, *Opt. Lett.* 12 (1987) 78.
- [3] S. Roy, T.R. Meyer, M.S. Brown, V.N. Velur, R.P. Lucht, J.R. Gord, *Opt. Commun.* 224 (2003) 131.
- [4] M. Schenk, T. Seeger, A. Leipertz, *Appl. Opt.* 39 (2000) 6918.
- [5] S.M. Green, P.J. Rubas, M.A. Paul, J.E. Peters, R.P. Lucht, *Appl. Opt.* 37 (1998) 1690.
- [6] M.J. Papac, J.D. Posner, D. Dunn-Rankin, *Appl. Spectrosc.* 57 (2003) 93.
- [7] R.J. Hall, J.F. Verdick, A.C. Eckbreth, *Opt. Commun.* 35 (1980) 69.
- [8] T. Dreier, G. Schiff, A.A. Suvernev, *J. Chem. Phys.* 100 (1994) 6275.
- [9] V.N. Zadkov, N.I. Koroteev, *Chem. Phys. Lett.* 105 (1984) 108.
- [10] R.P. Lucht, R.L. Farrow, *J. Opt. Soc. Am. B* 5 (1988) 1243.
- [11] R.L. Farrow, R.P. Lucht, *Opt. Lett.* 11 (1986) 374.
- [12] R. Bombach, B. Hemmerling, W. Hubschmid, *Chem. Phys.* 144 (1990) 265.
- [13] M.A. Woodmansee, R.P. Lucht, J.C. Dutton, *AIAA J.* 40 (2002) 1078.
- [14] J. Laane, W. Kiefer, *J. Raman Spectrosc.* 9 (1980) 353.
- [15] G.J. Rosasco, W. Lempert, W.S. Hurst, *Chem. Phys. Lett.* 97 (1993) 435.
- [16] W. Lempert, G.J. Rosasco, W.S. Hurst, *J. Chem. Phys.* 81 (1984) 4241.
- [17] A. Pott, T. Doerk, J. Uhlenbusch, J. Ehlbeck, J. Hörschele, J. Steinwandel, *Appl. Spectrosc.* 51 (1997) 1360.
- [18] T. Doerk, J. Ehlbeck, R. Jedamzik, J. Uhlenbusch, J. Hörschele, J. Steinwandel, *J. Phys. D: Appl. Phys.* 31 (1998) 2485.
- [19] B. Attal-Trétout, S.C. Schmidt, E. Crété, P. Dumas, J.P. Taran, *J. Quant. Spectrosc. Rad. Trans.* 43 (1990) 351.
- [20] T. Doerk, M. Hertl, B. Pfler, S. Hädrich, P. Jauernik, J. Uhlenbusch, *Appl. Phys. B* 64 (1997) 111.
- [21] S.F. Hanna, W.D. Kulatilaka, Z. Arp, T. Opatrný, M.O. Scully, J.P. Kuehner, R.P. Lucht, *Appl. Phys. Lett.* 83 (2003) 1887.
- [22] W.D. Kulatilaka, N. Chai, S.V. Naik, N.M. Laurendeau, R.P. Lucht, J.P. Kuehner, S. Roy, J.R. Gord, *Opt. Lett.* 31 (2006) 3357.
- [23] S. Roy, W.D. Kulatilaka, S.V. Naik, N.M. Laurendeau, R.P. Lucht, J.R. Gord, *Appl. Phys. Lett.* 89 (2006) 104.
- [24] R.V. Ravikrishna, S.V. Naik, C.S. Cooper, N.M. Laurendeau, *Combust. Sci. Technol.* 176 (2004) 1.
- [25] S.V. Naik, N.M. Laurendeau, *Appl. Phys. B* 79 (2004) 641.
- [26] W.G. Bessler, C. Schulz, T. Lee, J.B. Jeffries, R.K. Hanson, *Appl. Opt.* 42 (2003) 4922.
- [27] G.C. Martin, C.J. Mueller, C.F. Lee, *Appl. Opt.* 45 (2006) 2089.
- [28] T.N. Anderson, R.P. Lucht, R. Barron-Jimenez, S.F. Hanna, J.A. Caton, T. Walther, S. Roy, M.S. Brown, J.R. Gord, I. Critchley, L. Flamand, *Appl. Opt.* 44 (2005) 1491.
- [29] J. Luque, D.R. Crosley, LIFBASE: database and spectral simulation (version 1.5), SRI International Report MP 99-009, 1999.
- [30] R.E. Palmer, The CARSFT computer code for calculating coherent anti-Stokes Raman spectra: user and programmer information, Sandia National Laboratories Report SAND89-8206, Livermore, CA, 1989.
- [31] W.G. Bessler, C. Schulz, V. Sick, J.W. Daily: a versatile modeling tool for nitric oxide LIF spectra, in: *Proceedings of the 3rd Joint Meeting of the US Sections of the Combustion Institute*, Chicago, March 16–19, 2003, Paper PI05. <<http://www.lifsim.com>>.

Detection of atomic hydrogen in flames using picosecond two-color two-photon-resonant six-wave-mixing spectroscopy

Waruna D. Kulatilaka,¹ Robert P. Lucht,¹ Sukesh Roy,² James R. Gord,³ and Thomas B. Settersten^{4,*}

¹School of Mechanical Engineering, Purdue University, West Lafayette, Indiana 47907

²Innovative Scientific Solutions Incorporated, 2766 Indian Ripple Road, Dayton, Ohio 45440

³Air Force Research Laboratory, Propulsion Directorate, Wright-Patterson Air Force Base, Ohio 45433

⁴Combustion Research Facility, Sandia National Laboratories, Livermore, California 94551

*Corresponding author: tbsette@sandia.gov

Received 8 September 2006; accepted 28 November 2006;
posted 14 December 2006 (Doc. ID 74773); published 12 June 2007

We report an investigation of two-color six-wave-mixing spectroscopy techniques using picosecond lasers for the detection of atomic hydrogen in an atmospheric-pressure hydrogen–air flame. An ultraviolet laser at 243 nm was two-photon-resonant with the $2S_{1/2} \leftarrow 1S_{1/2}$ transition, and a visible probe laser at 656 nm was resonant with H_{α} transitions ($n = 3 \leftarrow n = 2$). The signal dependence on the polarization of the pump laser was investigated for a two-beam polarization-spectroscopy experimental configuration and for a four-beam grating configuration. A direct comparison of the absolute signal and background levels in the two experimental geometries demonstrated a significant advantage to using the four-beam grating geometry over the simpler two-beam configuration. Picosecond laser pulses provided sufficient time resolution to investigate hydrogen collisions in the atmospheric-pressure flame. Time-resolved two-color laser-induced fluorescence was used to measure an $n = 2$ population lifetime of 110 ps, and time-resolved two-color six-wave-mixing spectroscopy was used to measure a coherence lifetime of 76 ps. Based on the collisional time scale, we expect that the six-wave-mixing signal dependence on collisions is significantly reduced with picosecond laser pulses when compared to laser pulse durations on the nanosecond time scale. © 2007 Optical Society of America

OCIS codes: 300.6420, 300.6500, 020.1670, 020.2070, 280.1740.

1. Introduction

Atomic hydrogen is an important species in reacting flows because of its high reactivity and diffusivity. For example, in low-pressure diamond-synthesis environments, hydrogen atoms play a significant role in determining the growth rate and quality of the diamond film [1]; in nonpremixed flames interacting with vortices, the time evolution of the hydrogen atom concentration closely follows that of the heat release during the interaction and therefore, will reveal information concerning the heat-release rate during the interaction processes [2]. Moreover, hydrogen atoms may play an important role in the

formation of soot in hydrocarbon combustion [3]. Therefore the measurement of atomic-hydrogen concentration in flames is of fundamental importance in understanding the relevant chemical, heat, and mass transfer processes.

Laser-induced fluorescence (LIF) is the most commonly used technique for detecting atomic hydrogen in reacting flows. Single-photon excitation of hydrogen atoms from the ground state is not possible in practical reacting flows because the excitation wavelengths lie in the vacuum UV where the medium is optically thick. Multiphoton excitation schemes obviate this problem by shifting the excitation wavelengths to the UV or visible spectral regions. Various multiphoton LIF schemes have been employed for detection of the hydrogen atom in reacting flows [1,3–10]. Czarnetzki *et al.* [10] compared different schemes

employing multiphoton excitation to the $n = 3$ and $n = 4$ levels and subsequent detection of the Balmer-line fluorescence.

Coherent techniques also have been used for the detection of atomic hydrogen in flames and plasmas. Demonstrated techniques include two-photon polarization spectroscopy [11–14], two-photon-resonant four-wave-mixing spectroscopy [15], two-color laser-induced grating spectroscopy [16], and two-color, two-photon laser-induced polarization spectroscopy [17]. All these techniques rely on two-photon-resonant four-wave-mixing [11–15] or six-wave-mixing [16,17] processes, which generate a signal via the third-order nonlinear susceptibility, $\chi^{(3)}$, or the fifth-order nonlinear susceptibility, $\chi^{(5)}$, respectively. In all these experiments, the wave-mixing signals were detected either in a two-beam, laser-induced polarization spectroscopy (PS) configuration [11–14,17] or in a four-beam grating configuration, which requires phase matching [15,16].

Proponents of the coherent techniques have indicated that these approaches have the potential to be more quantitative than LIF because the signals depend only on the total dephasing rate of a transition rather than on specific population relaxation processes such as collisional quenching, which can depend strongly on the particular colliding species and not just on the total density of colliders [14,15]. An additional advantage of the coherent technique lies in the fact that the signal propagates as a laserlike beam. This characteristic enables extremely effective spatial discrimination against the background flame emission and enables measurements on systems where limited optical access precludes the implementation of a fluorescence-based diagnostic.

Among the coherent techniques, the PS configuration is the easiest to implement, requiring a single pump and a single probe beam, which are crossed in the sample. In this two-beam configuration, the nonlinear interaction generates an electric field component that is orthogonal to the probe beam polarization and propagates collinearly with the probe beam. This component is selectively detected as the signal by using a polarization analyzer. With the exception of the recent work by Kulatilaka *et al.* [17], all previous measurements of atomic hydrogen employing the PS configuration used the same laser wavelength for the pump and probe beams [11–14]. The lasers were two-photon-resonant with the $2S_{1/2} \leftarrow 1S_{1/2}$ transition. These single-color PS experiments generate signals via $\chi^{(3)}$, but compared to resonant four-wave-mixing spectroscopy, the nonlinear interaction is weaker because of the low oscillator strength of the two-photon transition.

Kulatilaka *et al.* [17] detected atomic hydrogen using two-color PS (TC-PS). As in the single-color PS experiments, a pump beam excites $2S_{1/2} \leftarrow 1S_{1/2}$ via two-photon-resonant absorption, but in this case the probe laser resonantly couples the $n = 2$ and $n = 4$ levels, generating the signal at 486 nm via $\chi^{(5)}$. The single-photon-resonant probe step benefits from

the high oscillator strength of the H_β transition. Because this is a two-color technique, the background from scattered 243 nm pump photons is efficiently suppressed by placing a spectral filter in front of the detector.

More generally in these coherent wave-mixing techniques, the grating or phase-matched geometry can be used [15,16]. In this configuration, the pump laser is split into two beams of nominally equal intensity. The two pump beams and the probe beam are crossed in the sample. The crossed beams produce a spatially varying coherence, which generates the signal beam in the phase-matched direction [15,16]. Because the detected polarization is not constrained to be orthogonal to the probe polarization, as it is for the PS configuration, it is possible to detect signals generated by scattering the probe beam off pump-induced population gratings. In contrast, the PS configuration relies on pump-induced optical anisotropy to rotate the probe polarization. We expect that optical anisotropy is relatively weak in comparison with the total population that can be excited to $n = 2$, and we speculated that it would be possible to generate signals larger than those in the PS configuration by scattering off population gratings. Accordingly, one goal of the current work is to compare directly the maximum signal levels that can be generated in the two-beam and the four-beam configurations under identical conditions.

Additional goals of the current work are to investigate the use of picosecond lasers for TC-6WM detection of atomic hydrogen in an atmospheric-pressure flame and to characterize the collisional time scales relevant to this application. These goals are motivated by the assumption that the sensitivity of the technique to variations in the collisional environment can be significantly reduced by shortening the time scale of the wave-mixing process so that it is shorter than that of characteristic collision times. This assumption extrapolates from the results of earlier studies of the collisional dependence of single-photon-resonant PS [18]. In the theoretical and experimental efforts of Reichardt *et al.* [18], it was shown that for a resonance that is primarily Doppler broadened, the PS signal for copropagating pump and probe beams scales as $(\gamma\Gamma)^{-2}$ for a long-pulse laser, where γ is the coherence dephasing rate, and Γ is the inverse of the excited-state lifetime. The authors demonstrated that the collisional dependence can be significantly reduced by using laser pulses with a pulse width shorter than the characteristic collision times. In this case, the PS signal scales as γ^{-1} . Furthermore, for a saturating pump beam, the short-pulse PS signal is found to be nearly independent of the collision rate [18,19].

In the current work, we used TC-LIF and TC six-wave-mixing spectroscopy (TC-6WM) techniques to detect atomic hydrogen in an atmospheric-pressure hydrogen–air flame. We used picosecond lasers to provide sufficient time resolution to characterize the collisional time scales in the flame. The objectives of

this experiment were (1) to characterize the polarization dependence of TC-6WM signals in the two-beam TC-PS configuration [17] and in the four-beam grating configuration [16]; (2) to compare directly the signals produced in the two experimental configurations; and (3) to measure the $n = 2$ population lifetime using time-resolved TC-LIF and the $n = 2$ coherence lifetime using time-resolved TC-6WM.

2. Experimental Procedure

Hydrogen atoms were probed in the postflame region of an atmospheric-pressure, hydrogen–air flame, which was stabilized on a rectangular Hencken burner, similar to that detailed in Ref. 17. The flame equivalence ratio was set to 1.1 for all the experiments. For a hydrogen–air flame of equivalence ratio 1.1 stabilized over the Hencken burner, the estimated flame temperature is 2400 K and the H-atom mole fraction is 0.003, both calculated using the UNICORN code taking into account the geometry of the burner [17]. The corresponding H-atom number density is $9.1 \times 10^{15} \text{ cm}^{-3}$. For most experiments, however, we used additional nitrogen dilution to prevent the burner surface from overheating. At this condition, equilibrium calculations [20] predict a flame temperature of 2190 K and an H-atom number density of $2.7 \times 10^{15} \text{ cm}^{-3}$.

An energy level diagram for hydrogen is shown in Fig. 1, and the pump and probe transitions used in the current experiment are indicated by arrows. A picosecond pump laser was used to excite hydrogen atoms via the $2S_{1/2} \leftarrow 1S_{1/2}$ two-photon transition at 243 nm. A time-delayed picosecond probe laser, tuned to single-photon H_α transitions ($n = 3 \leftarrow n = 2$) at 656 nm, was used to probe the evolution of the excited atoms in the $n = 2$ manifold of states. The probe laser effectively drives all electric-dipole-allowed transitions that couple $n = 2$ states to $n = 3$ states because the Doppler broadening in the flame (approximately 0.5 cm^{-1} at 656 nm) and the laser linewidth are sufficiently large that the $2S$ – $2P$ splitting and fine structure are unresolved.

The experimental system, shown in Fig. 2, was designed to allow simultaneous detection of TC-LIF and TC-6WM signals in either the TC-PS or the phase-matched configuration. The pump and probe laser pulses were produced with two independently

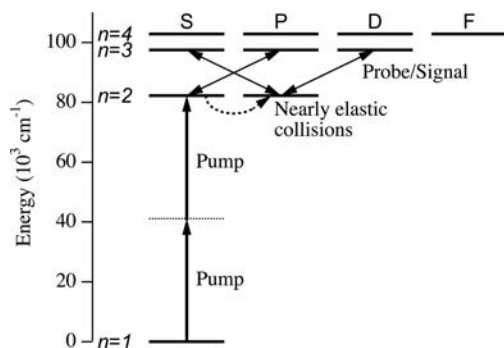


Fig. 1. Energy level diagram.

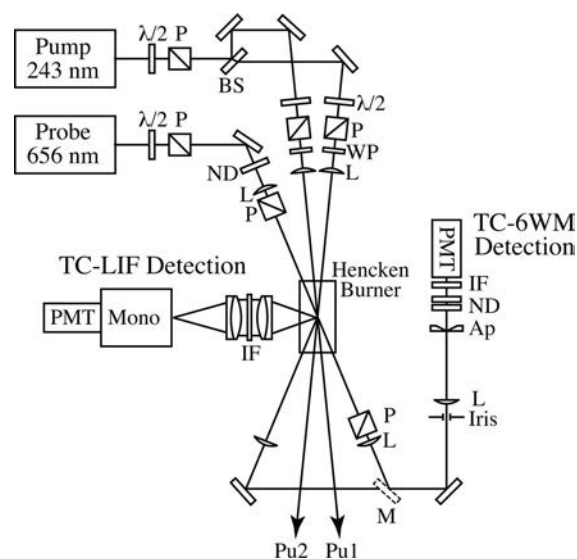


Fig. 2. Experimental arrangement: $\lambda/2$, half-wave plate; P, α -BBO polarizer; BS, beam splitter; ND, neutral-density filter; L, lens; WP, half- or quarter-wave plate; M, kinetically mounted mirror; Ap, aperture; IF, 656 nm interference filter; Mono, monochromator.

pumped distributed-feedback dye lasers (DFDLs) similar to the design described in Ref. 21. The relative delay between the pump and the probe pulses was electronically controlled with a resolution of 20 ps. The UV pump laser pulses were produced by frequency tripling in β -barium borate (BBO) crystals the output of an amplified DFDL operating at 729.40 nm. The fundamental output of the second amplified DFDL, tuned to 656.46 nm, was used as the probe laser. We estimate that the pump and probe pulse widths were of the order of 45 and 75 ps, respectively.

The UV beam was formed into two pump beams (Pu1 and Pu2) of approximately equal intensity using a dielectric beam splitter. The two beams were crossed with a full angle of 2° in the postflame region of the flame. The combination of a half-wave plate and a polarizer was used to control the energy of each pump beam. Pump beam energies were monitored using pyroelectric joulemeters, and the pulse energy in each beam was typically 5–10 μJ . A 500 mm focal length lens in each beam focused the beams to their intersection, and an optical delay line in one of the UV beam paths enabled the optimization of the temporal overlap of the two pump pulses at the flame. Quarter- and half-wave plates were used to set the polarization state of each beam independently.

The visible probe beam propagated in the same horizontal plane as the two pump beams and was focused to their intersection using a 750 mm focal length lens. The pulse energy was adjusted using the combination of a half-wave plate and a polarizer. When necessary, the pulse energy was further attenuated using neutral-density filters. Typically, the probe pulse energy was reduced to approximately 50 nJ. The probe beam path was separated by approximately 5° from the plane bisecting the two pump

beams. According to the 6WM phase-matching condition [16], the 656 nm signal beam emerged from the flame separated from the probe beam with a full angle of approximately 10° . A 300 mm focal length lens focused the signal beam through a $500\text{ }\mu\text{m}$ aperture to reduce scattered light. The signal beam subsequently passed through a H_α interference filter and neutral-density filters before detection by a photomultiplier tube (PMT). The photocurrent was integrated by using a charge-integrating amplifier and digitized.

The probe was linearly polarized by an α -BBO polarizer placed prior to the flame. A crossed analyzer was placed in the probe beam after the flame so that the TC-PS signal could be detected. The measured extinction ratio was better than 10^{-7} . For detection of the TC-PS signal, one of the pump beams was blocked, ensuring that the four pump photons required for the 6WM process originated from the same beam. A kinetically mounted mirror (see Fig. 2) deflected the TC-PS signal beam to the PMT.

The TC-LIF signal at 656 nm was collected normal to the pump beam direction using an $f/3$ achromatic doublet. A second doublet focused the fluorescence to the entrance slit of a $1/8\text{ m}$ monochromator, which served as a spectral filter. Additionally, a H_α interference filter was placed between the two lenses for additional background rejection. The fluorescence was detected by a PMT, and the output of this PMT was processed in the same way as that of the TC-6WM detector.

3. Results and Discussion

The dependences of the TC-PS and TC-LIF signals on the polarization of the pump beam were investigated in the two-beam experimental configuration. The probe beam was always vertically polarized, and the signal was detected as the horizontal polarization component propagating in the probe beam direction. In the first experiment, the polarization of the pump beam (Pu1) was varied by rotating a zero-order quarter-wave plate located after the polarizer in the pump beam. When the wave-plate axis was oriented either vertically or horizontally, the pump polarization remained vertical. Rotating the wave plate by 45° with respect to the vertical direction produced nominally circular polarization, and other wave-plate orientations produced elliptical polarization. The TC-PS and TC-LIF signals were recorded as functions of the quarter-wave-plate orientation and are shown in Fig. 3. For the data shown in Fig. 3, the probe pulse energy was approximately $6\text{ }\mu\text{J}$; a similar dependence was observed with a probe pulse energy of approximately 50 nJ , although the signal fluctuations were larger.

Maximum values of TC-PS and TC-LIF signals were generated when the pump polarization was linear. In the limit of pure circular polarization, two-photon excitation to $2S_{1/2}$ is forbidden, and both the LIF and the polarization signals should be zero. In some measurements, very small, nonzero signals were

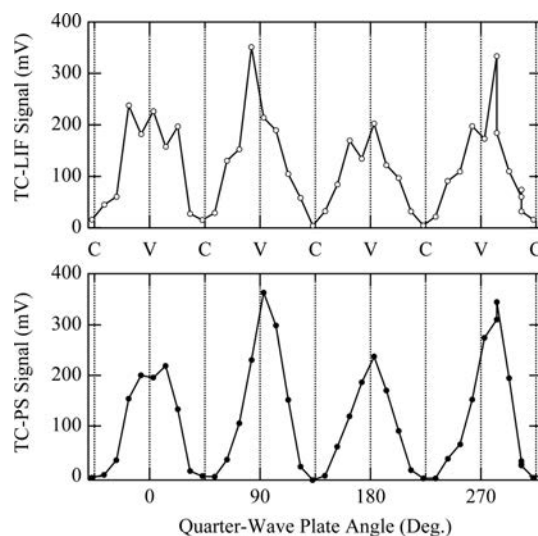


Fig. 3. TC-PS and TC-LIF signals as a function of the rotation of a quarter-wave plate in the Pu1 beam. Pu1 polarization is indicated along the abscissa; V, linear vertical; C, circular.

observed with the quarter-wave plate set to produce circular polarization, indicating that the pump polarization actually was slightly elliptical at these settings. We characterized the purity of the circular polarization of the pump beam using the procedure outlined in Ref. 22. For this measurement, the axis of the quarter-wave plate was oriented 45° to the vertical direction to generate nominally circular polarization. A second polarizer, placed after the quarter-wave plate in the pump beam path, was rotated while monitoring the laser energy transmitted through it. Using the formula given in Ref. 22, the purity of the circular polarization was greater than 98%.

The authors of the earlier investigation of TC-PS detection of atomic hydrogen indicated that their experimental configuration used a circularly polarized pump beam [17]. Based on our current observations, we infer that their signal was generated by a slight ellipticity of the pump polarization owing to imperfections in the optical arrangement. We expect that significantly larger signals would have resulted if linear pump polarization had been used and that a sensitivity much higher than that reported is possible.

A second experiment investigated the dependence of the TC-PS signal on the orientation of a linearly polarized pump beam. In this case, the probe pulse energy was approximately 60 nJ , and a zero-order half-wave plate was used to rotate the polarization of Pu1. The purity of the resulting linear polarization was analyzed and confirmed to be better than 99.95%. The TC-PS signal is plotted as a function of the rotation of the half-wave plate in Fig. 4. The half-wave-plate angle, θ , is defined such that 0° and 45° correspond to the vertical and horizontal pump polarizations, respectively. There is a clear modulation of the signal with θ , and the data are fit using the function $y(\theta) = y_0 + a_0 \sin 4\theta$ (solid curve). Vertical and horizontal pump polarizations produce similar

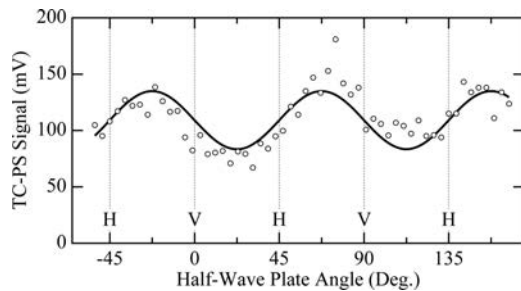


Fig. 4. TC-PS signal as a function of the rotation of a half-wave plate in the Pu1 beam. Pu1 polarization is indicated along the abscissa; H, horizontal; V, vertical.

signals, and the signal level increases or decreases by approximately 25% when the pump polarization is $\pm 45^\circ$ with respect to the probe polarization. At this point, we do not have an explanation for this dependence, and we will investigate the behavior in future theoretical development. In any case, we do not observe a strong dependence on the angle between the pump and the probe polarizations, and we can assert that the TC-PS signal produced using vertically polarized pump and probe beams is representative to within 25% of the maximum signal possible with the two-beam configuration.

A third experiment investigated the signal dependence on the polarization of the two pump beams in the four-beam grating geometry. The population grating created by the two-pump-beam geometry gives rise to a coherent signal separated from the probe direction by 10° . The large spatial separation of the probe and signal beams enables virtually background-free TC-6WM signal detection; the measured signal-to-background ratios were larger than 10^6 . Half-wave plates were used to rotate the linear polarization of each pump beam. We investigated combinations of pump-beam polarizations that were oriented at 0° (vertical), 90° (horizontal), or $\pm 45^\circ$ with respect to the probe polarization (vertical). The probe pulse energy was approximately 55 nJ.

We observed a strong dependence of the TC-6WM grating signal on the angle between the polarizations of the two pump beams, as shown in Fig. 5. The maximum signal was generated when the pump polarizations were orthogonal, and the minimum signal was observed for parallel pump polarizations. The corresponding TC-LIF signals are plotted in the top panel of Fig. 5. The TC-LIF signal, which is proportional to the density of atoms excited to $n = 2$, has exactly the opposite dependence on the angle between the polarizations of the two pump beams. For a fixed angle between the two pump-beam polarizations, no systematic dependence on the angle between the pump and the probe polarizations was observed for either the TC-6WM signal or the TC-LIF signal. For example, the signals agreed to within the experimental scatter when both pump beams were polarized 0° , 90° , or 45° with respect to the probe polarization.

Signals obtained with the TC-PS configuration were directly compared to the TC-6WM signals

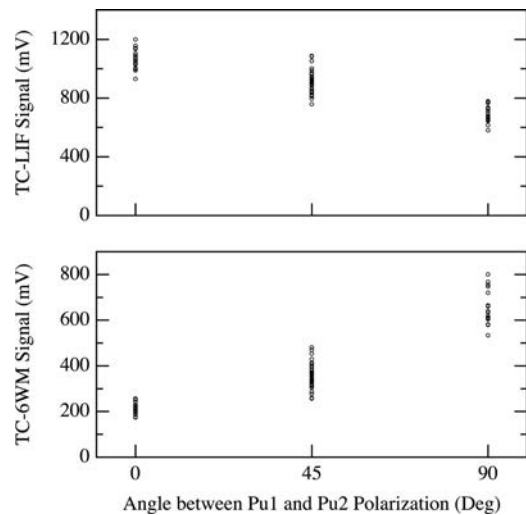


Fig. 5. TC-6WM (four-beam configuration) and TC-LIF signals as a function of the angle between the polarization of the two pump beams.

shown in Fig. 5 by inserting the kinetically mounted mirror in the probe beam path (see Fig. 2) and blocking one of the pump beams. This procedure enabled rapid switching between the two configurations, ensuring that the experimental conditions were the same for the two measurements. With both pump beams and the probe beam polarized vertically, the TC-PS configuration using Pu1 or Pu2 (see Fig. 2) produced a signal between 5 and 7 mV. This signal level can be compared to the peak signal of approximately 660 mV obtained with orthogonal pump polarizations in the grating configuration of TC-6WM. We conclude that maximum signal levels generated in the four-beam grating geometry are approximately 2 orders of magnitude larger than those generated in the two-beam TC-PS geometry. Furthermore, the peak signal-to-background ratio for the grating configuration was in excess of 6×10^6 , compared to only 10^2 for the TC-PS configuration.

In the previous nanosecond TC-PS experiment [17], it was possible to detect H-atom mole fractions as low as 10^{-4} (with number density of approximately $3.5 \times 10^{14} \text{ cm}^{-3}$) when the polarization of the pump beam was not optimized for maximum signal. Based on the current results, we expect that the signals in the previous experiment would increase by more than 2 orders of magnitude if the grating configuration were employed. We conclude, therefore, that at least a 1 order of magnitude improvement in the H-atom detection limit is possible [17].

Finally, we conducted pump-probe studies of collisions affecting the pump-induced population and coherences in $n = 2$ by delaying the probe pulse with respect to the pump pulses. In this case, both pump beams and the probe beam were linearly polarized in the vertical direction. The TC-LIF and TC-6WM signals were simultaneously recorded and are plotted as a function of the delay between the pump and the probe pulses in Fig. 6. The large dynamic range in

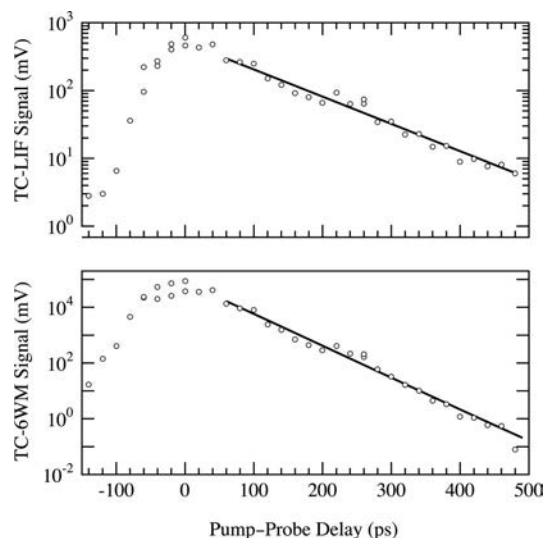


Fig. 6. TC-6WM and TC-LIF signals as a function of the delay between pump and probe pulses. Single-exponential fits to the data in the tails of the decay are shown as solid lines.

these measurements was achieved by placing calibrated neutral-density filters in front of the two detectors. The largest signals shown for the TC-6WM signal, for example, were acquired with an optical density of nearly 3, and thus the scaled signals shown in Fig. 6 correspond to measured signals of approximately 100 mV.

A single-exponential function was used to fit the data in the tail of the TC-LIF signal decay. The exponential time constant was approximately 110 ps. Because the probe laser cannot resolve the $2S$ – $2P$ splitting, the measurement is not sensitive to collisional mixing of the $2S$ – $2P$ levels, and we interpret the TC-LIF decay constant as the $n = 2$ lifetime. The excited states can decay by radiative relaxation and nonradiative quenching. Radiative relaxation from $n = 2$ is dominated by Ly_{α} emission ($2P \rightarrow 1S$), which has a natural lifetime of 1.6 ns. Radiative relaxation from $2S$ to $1S$ via a single-photon transition is forbidden, and the natural lifetime of the $2S$ level is 0.12 s. The lifetime measured in the current experiment is, therefore, primarily determined by nonradiative quenching with a rate of approximately $8.5 \times 10^9 \text{ s}^{-1}$.

Although there have been no prior measurements of the $n = 2$ lifetime in flames, our measurement is comparable to time-resolved measurements of H_{α} fluorescence decays from $n = 3$ in atmospheric-pressure flames [23]. Furthermore, assuming that quenching is dominated by collisions with H_2O , we estimate a quenching rate constant for H_2O of $0.9 \times 10^{-8} \text{ cm}^3 \text{ s}^{-1}$. This value agrees remarkably well with the results of Meier *et al.* [24], although their measured quenching rates were for $H(n = 3)$, not $H(n = 2)$, in collisions with H_2O . We expect that the large nonradiative quenching rate for H_2O may be attributable to resonant energy transfer. The B – X transition of H_2O is excited by Ly_{α} radiation, leading to rapid dissocia-

tion. The primary dissociation products are $H(1S)$, $OH(A)$, and $OH(X)$ [25]. Evidence of resonant energy transfer was presented by Goldsmith [8], who observed a significant increase in $OH(A)$ and $OH(X)$ following two-photon 243 nm excitation of $H(2S)$ in a H_2 – O_2 flame.

The best-fit value for the exponential time constant for a single-exponential fit to the TC-6WM data was approximately 38 ps. Because the TC-6WM signal scales as $|\chi^{(5)}|^2$, we infer that the time constant describing the coherence decay is twice this value, or approximately 76 ps. The coherence decays slightly faster than the population because it is destroyed not only by electronic quenching collisions, but also by dephasing collisions, which do not cause a population loss from the $n = 2$ manifold of states. The dephasing collisions can include elastic m_F -scrambling collisions and nearly elastic collisions causing transitions between the $2S_{1/2}$, $2P_{1/2}$, and $2P_{3/2}$ levels. Based on the measured population loss rate, the rate dephasing collisions is approximately $4.1 \times 10^9 \text{ s}^{-1}$.

4. Conclusion

We have performed a detailed study of the effects of pump beam polarization on TC-6WM signals generated by atomic hydrogen in an atmospheric-pressure flame. The maximum signal for the two-beam TC-PS configuration was produced when the pump beam was linearly polarized. We observed a weak signal dependence on the orientation, with respect to the probe polarization, of the linearly polarized pump beam. The maximum signal for the four-beam grating configuration was produced when the two linearly polarized pump beams had orthogonal polarization. In this case, there was no observable signal dependence on the rotation of the pump polarizations with respect to that of the probe beam.

The maximum signals generated with the four-beam grating configuration were 2 orders of magnitude larger than those produced in the TC-PS configuration. Furthermore, signal-to-background ratios in the former configuration were $>10^4$ larger than those observed for TC-PS. Considering that excellent sensitivity was demonstrated in a previous diagnostic application of TC-PS using a nonoptimal pump polarization [17], we expect dramatically improved diagnostic performance using the four-beam grating configuration of TC-6WM.

Collisional studies of $n = 2$ were performed using time-resolved TC-LIF and TC-6WM (in the grating configuration). Rapid collisional quenching of $n = 2$ was characterized by an exponential time constant of 110 ps. TC-6WM measurements indicated that the $n = 2$ coherence decayed with an exponential time constant of 76 ps. We infer that the combined rate of elastic and nearly elastic collisions that dephase the pump-induced coherence is approximately 50% of the rate of electronic quenching collisions. Because the collision time scale is of the order of, or slightly longer than, the pulse width of our lasers, we expect a significantly reduced collision dependence in the

signal generation process in comparison to that predicted for pulses of nanosecond duration.

The results of these experiments indicate significant potential for sensitive detection of atomic hydrogen using TC-6WM and suggest that insensitivity to collisions in atmospheric pressure systems is possible by using lasers with pulse widths that are tens of picoseconds or less. Furthermore, the results motivate future theoretical efforts toward a deeper understanding of the signal generation process in TC-6WM approaches.

Funding for this research was provided by the U.S. Department of Energy, Office of Basic Energy Sciences, Division of Chemical Sciences, Geosciences, and Biosciences. Sandia is a multiprogram laboratory operated by Sandia Corporation, a Lockheed Martin Company, for the U.S. Department of Energy's National Nuclear Security Administration under contract DE-AC04-94AL85000. J. R. Gord and S. Roy acknowledge support by the Air Force Research Laboratory, Propulsion Directorate, Wright-Patterson Air Force Base, under contract F33615-03-D-2329 and by the Air Force Office of Scientific Research.

References

1. K. E. Bertagnolli, R. P. Lucht, and M. N. Bui-Pham, "Atomic hydrogen concentration profile measurements in stagnation-flow diamond-forming flames using three-photon excitation laser-induced fluorescence," *J. Appl. Phys.* **83**, 2315–2326 (1998).
2. P.-H. Renard, J. C. Rolon, D. Thévenin, and S. Candel, "Investigations of heat release, extinction, and time evolution of the flame surface for a nonpremixed flame interacting with a vortex," *Combust. Flame* **117**, 189–205 (1999).
3. S. J. Harris, A. M. Weiner, R. J. Blint, and J. E. M. Goldsmith, "Concentration profiles in rich and sooting ethylene flames," in *Proceedings of the Twenty-First Symposium (International) on Combustion* (Combustion Institute, 1986), pp. 1033–1045.
4. R. P. Lucht, J. T. Salmon, G. B. King, D. W. Sweeney, and N. M. Laurendeau, "Two-photon-excited fluorescence measurement of hydrogen atoms in flames," *Opt. Lett.* **8**, 365–367 (1983).
5. M. Aldén, A. L. Schawlow, S. Svanberg, W. Wendt, and P. L. Zhang, "Three-photon-excited fluorescence detection of atomic hydrogen in an atmospheric-pressure flame," *Opt. Lett.* **9**, 211–213 (1984).
6. J. T. Salmon and N. M. Laurendeau, "Absolute concentration measurements of atomic hydrogen in subatmospheric premixed $H_2/O_2/N_2$ flat flames with photoionization controlled-loss spectroscopy," *Appl. Opt.* **26**, 2881–2891 (1987).
7. J. T. Salmon and N. M. Laurendeau, "Concentration measurements of atomic hydrogen in subatmospheric premixed $C_2H_4/O_2/Ar$ flat flames," *Combust. Flame* **74**, 221–231 (1988).
8. J. E. M. Goldsmith, "Photochemical effects in 243 nm two-photon excitation of atomic hydrogen in flames," *Appl. Opt.* **28**, 1206–1213 (1989).
9. J. E. M. Goldsmith and N. M. Laurendeau, "Single-laser two-step fluorescence detection of atomic hydrogen in flames," *Opt. Lett.* **15**, 576–578 (1990).
10. U. Czarnetzki, K. Miyazaki, T. Kajiwara, K. Muraoka, M. Maeda, and H. F. Döbele, "Comparison of various two-photon excitation schemes for laser-induced fluorescence spectroscopy in atomic hydrogen," *J. Opt. Soc. Am. B* **11**, 2155–2162 (1994).
11. J. Seidel, "Theory of two-photon polarization spectroscopy of plasma-broadened hydrogen L_α line," *Phys. Rev. Lett.* **57**, 2154–2156 (1986).
12. K. Danzmann, K. Grützmacher, and B. Wende, "Doppler-free 2-photon polarization-spectroscopic measurement of the Stark-broadened profile of the hydrogen L_α line in a dense plasma," *Phys. Rev. Lett.* **57**, 2151–2153 (1986).
13. R. Dux, K. Grützmacher, M. I. de la Rosa, and B. Wende, "Absolute determination of local ground-state densities of atomic hydrogen in nonlocal-thermodynamic-equilibrium environments by two-photon polarization spectroscopy," *Phys. Rev. E* **51**, 1416–1427 (1995).
14. K. Grützmacher, M. I. de la Rosa, A. B. Gonzalo, M. Steiger, and A. Steiger, "Two-photon polarization spectroscopy applied for quantitative measurements of atomic hydrogen in atmospheric pressure flames," *Appl. Phys. B* **76**, 775–785 (2003).
15. J. A. Gray and R. Trebino, "Two-photon-resonant four-wave-mixing spectroscopy of atomic hydrogen in flames," *Chem. Phys. Lett.* **216**, 519–524 (1993).
16. J. A. Gray, J. E. M. Goldsmith, and R. Trebino, "Detection of atomic hydrogen by two-color laser-induced grating spectroscopy," *Opt. Lett.* **18**, 444–446 (1993).
17. W. D. Kulatilaka, R. P. Lucht, S. F. Hanna, and V. R. Katta, "Two-color, two-photon laser-induced polarization spectroscopy (LIPS) measurements of atomic hydrogen in near-adiabatic, atmospheric pressure hydrogen/air flames," *Combust. Flame* **137**, 523–537 (2004).
18. T. A. Reichardt, F. DiTeodoro, R. L. Farrow, S. Roy, and R. P. Lucht, "Collisional dependence of polarization spectroscopy with a picosecond laser," *J. Chem. Phys.* **113**, 2263–2269 (2000).
19. S. Roy, R. P. Lucht, and T. A. Reichardt, "Polarization spectroscopy using short-pulse lasers: Theoretical analysis," *J. Chem. Phys.* **116**, 571–580 (2002).
20. W. C. Reynolds, *The element potential method for chemical equilibrium analysis: implementation in the interactive program STANJAN*, Tech. Rep. Stanford University Report ME 270 HO No. 7 (Stanford University, 1986).
21. X. L. Chen, B. D. Patterson, and T. B. Settersten, "Time-domain investigation of OH ground-state energy transfer using picosecond two-color polarization spectroscopy," *Chem. Phys. Lett.* **388**, 358–362 (2004).
22. J. B. Norman and R. W. Field, "Collision-induced angular-momentum reorientation and rotational energy-transfer in $CaF(A^2\Pi_{1/2})$ -Ar thermal collisions," *J. Chem. Phys.* **92**, 76–89 (1990).
23. S. Agrup, F. Ossler, and M. Aldén, "Measurements of collisional quenching of hydrogen-atoms in an atmospheric-pressure hydrogen oxygen flame by picosecond laser-induced fluorescence," *Appl. Phys. B* **61**, 479–487 (1995).
24. U. Meier, K. Kohse-Höinghaus, and T. Just, "H and O atom detection for combustion applications: study of quenching and laser photolysis effects," *Chem. Phys. Lett.* **126**, 567–573 (1986).
25. D. H. Mordaunt, M. N. R. Ashfold, and R. N. Dixon, "Dissociation dynamics of $H_2O(D_2O)$ following photoexcitation at the Lyman- α wavelength (121.6 nm)," *J. Chem. Phys.* **100**, 7360–7375 (1994).

Theory of femtosecond coherent anti-Stokes Raman scattering spectroscopy of gas-phase transitions

Robert P. Lucht^{a)} and Paul J. Kinnius*School of Mechanical Engineering, Purdue University, West Lafayette, Indiana 47907-2088*

Sukesh Roy

Innovative Scientific Solutions, Inc., 2766 Indian Ripple Road, Dayton, Ohio 45440

James R. Gord

Air Force Research Laboratory, Propulsion Directorate, Wright-Patterson AFB, Ohio 45433

(Received 9 March 2007; accepted 29 May 2007; published online 31 July 2007)

A theoretical analysis of coherent anti-Stokes Raman scattering (CARS) spectroscopy of gas-phase resonances using femtosecond lasers is performed. The time-dependent density matrix equations for the femtosecond CARS process are formulated and manipulated into a form suitable for solution by direct numerical integration (DNI). The temporal shapes of the pump, Stokes, and probe laser pulses are specified as an input to the DNI calculations. It is assumed that the laser pulse shapes are 70 fs Gaussians and that the pulses are Fourier-transform limited. A single excited electronic level is defined as an effective intermediate level in the Raman process, and transition strengths are adjusted to match the experimental Raman polarizability. The excitation of the Raman coherence is investigated for different Q -branch rotational transitions in the fundamental 2330 cm^{-1} band of diatomic nitrogen, assuming that the pump and Stokes pulses are temporally overlapped. The excitation process is shown to be virtually identical for transitions ranging from $Q(2)$ to $Q(20)$. The excitation of the Raman coherences is also very efficient; for laser irradiances of $5 \times 10^{17}\text{ W/m}^2$, corresponding approximately to a $100\text{ }\mu\text{J}$, 70 fs pulse focused to $50\text{ }\mu\text{m}$, approximately 10% of the population of the ground Raman level is pumped to the excited Raman level during the impulsive pump-Stokes excitation, and the magnitude of the induced Raman coherence reaches 40% of its maximum possible value. The theoretical results are compared with the results of experiments where the femtosecond CARS signal is recorded as a function of probe delay with respect to the impulsive pump-Stokes excitation. © 2007 American Institute of Physics. [DOI: 10.1063/1.2751184]

I. INTRODUCTION AND MOTIVATION

A theoretical investigation of femtosecond coherent anti-Stokes Raman scattering (CARS) spectroscopy is discussed. Femtosecond CARS offers some significant potential advantages compared with nanosecond CARS, i.e., CARS as usually performed with nanosecond pump and Stokes lasers. These potential advantages include (1) the capability of performing real-time temperature and species measurements at data rates of 1 kHz or greater, and (2) the absence of any effect of collisions in the determination of temperature and concentration from the femtosecond CARS signal. We have recently performed experiments demonstrating the capability of measuring temperature and concentration from the dependence of femtosecond CARS signal as a function of probe delay after impulsive pump-Stokes excitation.¹ The theoretical analysis discussed in this paper was performed to investigate the physics of the femtosecond CARS process in detail, both to simulate the experimental results and to develop strategies for further optimization of the femtosecond CARS experiment.

The potential for real-time measurements at frequencies

of interest in turbulent flames is the result of the recent commercial availability of femtosecond laser systems with pulse energies up to a few millijoules and with repetition rates of 1 kHz up to at least 5 kHz. If techniques for acquiring single-pulse temperatures and concentrations can be developed, time series measurements can be performed in turbulent flames and flows at data rates that are comparable to or greater than turbulent fluctuation frequencies. The potential for significant noise reduction also exists as a result of the nearly Fourier-transform-limited character of the spectrum of the femtosecond laser pulse. A Fourier-transform-limited laser pulse with a temporal duration of 70 fs has a spectral width of approximately 200 cm^{-1} , about the same as a typical broadband dye laser used as the Stokes beam for broadband CARS. The major source of noise in a broadband CARS experiment performed with nanosecond lasers is the shot-to-shot spectral noise in the broadband Stokes dye laser. The spectrum of the femtosecond laser, on the other hand, is much more stable from shot to shot because it is nearly Fourier-transform limited.

Femtosecond lasers have been applied for nonlinear spectroscopy in a number of experiments in recent years. Femtosecond CARS microscopy has been demonstrated for probing cell structure,²⁻⁴ solids,⁵⁻⁷ and liquids.⁷⁻¹¹ The use of

^{a)} Author to whom correspondence should be addressed. Tel.: 765-494-5623; Fax: 765-494-0539. Electronic mail: lucht@purdue.edu

femtosecond CARS to detect bacterial spores such as anthrax was proposed by Scully *et al.*¹² and demonstrated in recent experiments by Pestov *et al.*¹³

Femtosecond CARS was first demonstrated as a probe of dynamics in gas-phase molecules by Hayden and Chandler¹⁴ and Schmitt *et al.*¹⁵ Meyer and Engel¹⁶ used a wave-packet approach to analyze femtosecond CARS experiments on gas-phase I₂. A series of notable recent experiments has been directed primarily at extracting parameters of spectroscopic interest from time-averaged spectra obtained from H₂ and N₂ in cells.^{17–20} Femtosecond CARS was also used to measure ortho/para deuterium concentration ratios.²¹ The potential of femtosecond CARS as a gas-phase temperature measurement diagnostic has been explored in a few experiments.^{1,19,22}

In almost all of these previous gas-phase femtosecond CARS experiments, the spectral information in the CARS signal was obtained by using a time-delayed probe beam to detect the beating of the different Raman transitions that were coherently excited by the pump and Stokes beams. In these experiments, the time delay between the probe beam and the pump-Stokes excitation was varied by scanning a translation stage slowly and recording the CARS signal as a function of the probe time delay. The spectral information contained in the CARS signal can be extracted by Fourier analysis of the temporal variation of the CARS intensity versus probe time delay. Alternatively, the experimental data can be compared with a direct calculation of the CARS intensity as a function of probe time delay. In most of these previous experiments, the region of interest in terms of probe time delay was always tens of picoseconds after the pump-Stokes interaction when the excited Raman transitions were oscillating out of phase, resulting in a beating pattern from which spectroscopic parameters were extracted by Fourier analysis.

In our femtosecond CARS experiments,¹ probe time delays of a few picoseconds are used to measure the initial decay of the Raman coherence induced by the impulsive pump-Stokes excitation. The rate at which this giant initial coherence decays is controlled by the frequency range for which Raman transitions with significant strength are excited. As temperature increases and more energy levels of the N₂ molecule are populated, the frequency range increases. As this frequency range increases, the induced Raman coherence decays faster because the excited Raman transitions begin to oscillate out of phase more quickly; we refer to this decay of the initial Raman coherence as frequency-spread dephasing. The impulsive pump-Stokes excitation process of this giant coherence and its initial decay due to frequency-spread dephasing are the focus of this paper. In particular, we show that for Fourier-transform-limited pump and Stokes pulses, the *Q*-branch transitions of the fundamental band of N₂ are excited to the same degree and have the same phase immediately after the impulsive pump-Stokes excitation process. The calculation of the subsequent decay of the femtosecond CARS signal as a function of probe delay is shown to be in excellent agreement with experimental results. The implications of the results of these DNI calculations for the design of future experiment are discussed.

II. DENSITY MATRIX ANALYSIS FOR THE INTERACTION OF A TWO-STATE RESONANCE WITH MONOCHROMATIC LASER RADIATION

The time-dependent density matrix equations for a multistate system irradiated by laser radiation are given by^{23–25}

$$\frac{\partial \rho_{jj}}{\partial t} = -\frac{i}{\hbar} \sum_m (V_{jm} \rho_{mj} - \rho_{jm} V_{mj}) - \Gamma_j \rho_{jj} + \sum_m \Gamma_{mj} \rho_{mm}, \quad (1)$$

$$\frac{\partial \rho_{nj}}{\partial t} = -\rho_{nj}(i\omega_{nj} + \gamma_{nj}) - \frac{i}{\hbar} \sum_m (V_{nm} \rho_{mj} - \rho_{nm} V_{mj}), \quad (2)$$

where the diagonal matrix element ρ_{jj} is the occupation probability for state *j*, proportional to the population of state *j*, and the off-diagonal matrix element ρ_{nj} describes the coherence between states *n* and *j*. In Eqs. (1) and (2), \hbar is Planck's constant (J s), Γ_{mj} is the population transfer rate (s⁻¹) from state *m* to state *j*, $\Gamma_j = \sum_m \Gamma_{jm}$ is the total population transfer rate (s⁻¹) from state *j* to all other states *m*, ω_{nj} is the resonance frequency (s⁻¹) between states *n* and *j*, and γ_{nj} is the collisional dephasing rate (s⁻¹) of the coherence. The coherence is dephased by both population transfer collisions and by pure dephasing collisions, so $\gamma_{nj} \geq \Gamma_n + \Gamma_j$. The interaction term V_{mj} (J) is given by^{23,24}

$$V_{mj} = -\boldsymbol{\mu}_{mj} \cdot \mathbf{E}(\mathbf{r}, t), \quad (3)$$

where $\boldsymbol{\mu}_{mj} = \langle \psi_m | \boldsymbol{\mu} | \psi_j \rangle$ is the electric dipole matrix element (C m) and $\mathbf{E}(\mathbf{r}, t)$ is the laser electric field (J/C m). The laser field is given by

$$\begin{aligned} \mathbf{E}(\mathbf{r}, t) = & \frac{1}{2} \hat{e}_1 A_1(\mathbf{r}, t) \exp[+i(\mathbf{k}_1 \cdot \mathbf{r} - \omega_1 t)] \\ & + \frac{1}{2} \hat{e}_2 A_2(\mathbf{r}, t) \exp[+i(\mathbf{k}_2 \cdot \mathbf{r} - \omega_2 t)] \\ & + \frac{1}{2} \hat{e}_3 A_3(\mathbf{r}, t) \exp[+i(\mathbf{k}_3 \cdot \mathbf{r} - \omega_3 t)] + \text{c.c.}, \end{aligned} \quad (4)$$

where \hat{e}_1 , \hat{e}_2 , and \hat{e}_3 are the complex unit vectors for the pump, Stokes, and probe fields. These unit vectors describe the polarization states of the fields ($\hat{e}_i \cdot \hat{e}_i^* = 1$), \mathbf{r} is the position vector (m), $A_i(\mathbf{r}, t)$ is the slowly varying amplitude function (J/C m) for the electric field of the *i*th laser, \mathbf{k}_i (m⁻¹) is the propagation vector, and ω_i (s⁻¹) is the angular frequency. In the development below, we will solve the density matrix equations at $\mathbf{r}=0$. The CARS signal will be determined from the induced polarization component at frequency $\omega_4 = \omega_1 - \omega_2 + \omega_3$.

The density matrix model is now specialized to investigate the femtosecond CARS process in the *Q* branch of the nitrogen molecule. The general structure of the model is depicted schematically in Fig. 1. In the development of the density matrix equations, energy levels will be designated using upper case letters and quantum states will be designated using lower case letters. Levels *G* and *E* are specific rotational levels in vibrational levels in the ground $X^1\Sigma_g^+$ ground electronic level of N₂; the lower case letters *g* and *e* will be used to designate Zeeman states in levels *G* and *E*, respectively. The rotational quantum numbers for levels *G* and *E* are equal, $J_G = J_E$, and the vibrational quantum numbers are related by $v_E = v_G + 1$. An effective (fictitious) electronic level κ with $1\Sigma_u^+$ character is defined as the intermedi-

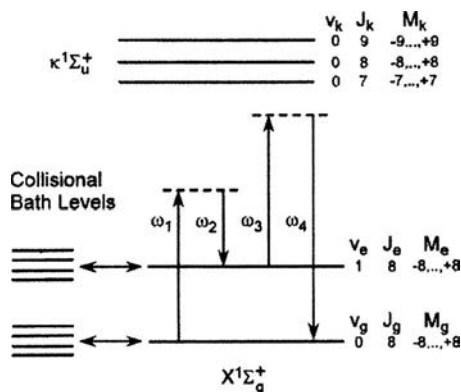


FIG. 1. Schematic diagram of the energy level structure for the femtosecond CARS calculations for the $Q(8)$ transition in the fundamental (1,0) Raman band of the nitrogen molecule. The $\kappa^1\Sigma_u^+(v=0) \rightarrow X^1\Sigma_g^+(v=0, 1, 2, 3, \text{ and } 4)$ transition strengths were varied to match the Raman cross section of N_2 .

ate level for the Q -branch Raman transitions. Only the ground vibrational manifold of this excited electronic level is included in the calculations. In general, there are numerous excited electronic levels that are single-photon coupled with the upper and lower energy levels, E and G , respectively, of the Raman process. Inclusion of all of these excited electronic energy levels in the femtosecond CARS code is computationally intractable, and in any case, the transition strengths between these excited electronic energy levels and energy levels in the $X^1\Sigma_g^+$ ground electronic level are not known with much accuracy. Consequently, we adjust the vibrational oscillator strengths for transitions between the effective level κ and the vibrational levels in the $X^1\Sigma_g^+$ ground electronic level so that the calculated Raman polarizability²⁶ $(\alpha_{zz})_{GE}^2$,

$$\begin{aligned} (\alpha_{zz})_{GE}^2 &= \sum_{g,e} \left| \sum_k \left\{ \frac{\mu_{zek}\mu_{zkg}}{\hbar(\omega_{kg}-\omega_1)} + \frac{\mu_{zek}\mu_{zkg}}{\hbar(\omega_{ke}+\omega_1)} \right\} \right|^2 \\ &= \left(\frac{\partial \sigma}{\partial \Omega} \right)_{zz} \frac{16\pi^2 \varepsilon_0^2 c^4}{\omega_s^4}, \end{aligned} \quad (5)$$

matches the experimental value of $4.0 \times 10^{-83} \text{ C}^4 \text{ m}^4/\text{J}^2$ as determined from Raman cross section data for the fundamental ($v_G=0 \rightarrow v_E=1$) band of nitrogen listed in Schrötter and Klöckner.²⁷ The electronic energy and rotational constant for the $\kappa^1\Sigma_u^+(v=0)$ level were chosen to match the values for the $g^1\Sigma_u^+(v=0)$ level of N_2 as given by Tilford and Wilkinson.²⁸ The $\kappa^1\Sigma_u^+(v=0) \rightarrow X^1\Sigma_g^+(v)$ vibrational oscillator strengths were adjusted so that the Raman polarizability is proportional to $v+1$, where v is the vibrational quantum number (in the $X^1\Sigma_g^+$ electronic level) for the lower energy level of the Raman transition. In Fig. 1, the level $J_G=8$ is coupled with $J_K=7$ and $J_K=9$ by single-photon transitions; the $J_G=8$ to $J_K=8$ transition is not allowed for the $^1\Sigma_u^+ \rightarrow ^1\Sigma_g^+$ transitions. Level $J_E=8$ is also coupled with $J_K=7$ and $J_K=9$ by single-photon transitions. The rotational line strengths for the $\kappa^1\Sigma_u^+(v=0) \rightarrow X^1\Sigma_g^+(v)$ transitions were calculated from formulas in Ref. 29.

The density matrix equations for the different coherences among states g , e , and k in levels G , E , and K , respectively, and for the populations of these states are now derived and

manipulated into a form suitable for numerical analysis. For the single-photon coherences ρ_{kg} and ρ_{ke} , the pump, Stokes, and probe laser frequencies are very far from resonance, and we will calculate these terms using the steady state approximation. For the Raman coherences ρ_{eg} , on the other hand, the steady state approximation is not applicable and the density matrix equation must be solved by direct numerical integration (DNI). The development of the equations suitable for numerical analysis for the coherence and population density matrix elements is described in the following sections and in more detail in the Appendix.

A. Density matrix elements for transition between states g in ground level G and states k in excited level K

From Eq. (2), the time dependence of the coherence density matrix element ρ_{kg} is given by

$$\begin{aligned} \frac{\partial \rho_{kg}(t)}{\partial t} &= \dot{\rho}_{kg} = -\rho_{kg}(i\omega_{kg} + \gamma_{kg}) \\ &\quad - \frac{i}{\hbar} \sum_{g'} (V_{kg'}\rho_{g'g} - \rho_{kg}V_{g'g}) \\ &\quad - \frac{i}{\hbar} \sum_e (V_{ke}\rho_{eg} - \rho_{ke}V_{eg}) \\ &\quad - \frac{i}{\hbar} \sum_{k'} (V_{kk'}\rho_{k'g} - \rho_{kk}V_{k'g}). \end{aligned} \quad (6)$$

Eliminating terms that are zero because the radiative interaction terms are zero ($V_{g'g}=V_{kk'}=V_{eg}=0$), we obtain

$$\dot{\rho}_{kg} = -\rho_{kg}(i\omega_{kg} + \gamma_{kg}) - \frac{i}{\hbar} \sum_{g'} V_{kg'}\rho_{g'g} - \frac{i}{\hbar} \sum_e V_{ke}\rho_{eg}. \quad (7)$$

We have also assumed that $\rho_{kk'}$ is negligibly small in the absence of electronic resonance effects. The density matrix coherence terms ρ_{kg} , ρ_{kg} , and ρ_{eg} are now expressed as products of slowly varying amplitude terms and oscillatory exponential terms:

$$\rho_{kg}(t) = \sigma_{kg}(t)\exp(-i\omega_1 t) + \eta_{kg}(t)\exp(-i\omega_4 t), \quad (8)$$

$$\rho_{ke}(t) = \sigma_{ke}(t)\exp(-i\omega_2 t) + \eta_{ke}(t)\exp(-i\omega_3 t), \quad (9)$$

$$\rho_{eg}(t) = \sigma_{eg}(t)\exp[-i(\omega_1 - \omega_2)t]. \quad (10)$$

The single-photon-resonance terms ρ_{kg} and ρ_{ke} are expanded in terms of two different frequencies that are important for different steps in the CARS interaction. The coherence term ρ_{kg} takes part in both the pump interaction and the probe interaction, and the coherence term ρ_{ke} takes part in the Stokes interaction and the signal generation process. Substituting Eqs. (8) and (10) into Eq. (7) and then rearranging the equation, we obtain

$$\begin{aligned} &\dot{\sigma}_{kg}\exp(-i\omega_1 t) - i\omega_1\sigma_{kg}\exp(-i\omega_1 t) \\ &\quad + \dot{\eta}_{kg}\exp(-i\omega_4 t) - i\omega_4\eta_{kg}\exp(-i\omega_4 t) \\ &= -[\sigma_{kg}\exp(-i\omega_1 t) + \eta_{kg}\exp(-i\omega_4 t)][i\omega_{kg} + \gamma_{kg}] \end{aligned}$$

$$-\frac{i}{\hbar} \sum_{g'} V_{kg'} \rho_{g'g} - \frac{i}{\hbar} \sum_e V_{ke} \sigma_{kg} \exp[-i(\omega_1 - \omega_2)t], \quad (11)$$

where we have used the relation

$$\dot{\rho}_{kg} = \dot{\sigma}_{kg} \exp(-i\omega_1 t) - i\omega_1 \sigma_{kg} \exp(-i\omega_1 t) + \dot{\eta}_{kg} \exp(-i\omega_4 t) - i\omega_4 \eta_{kg} \exp(-i\omega_4 t). \quad (12)$$

Multiplying Eq. (11) by $\exp(+i\omega_4 t)$, we obtain

$$\begin{aligned} & \dot{\sigma}_{kg} \exp[-i(\omega_1 - \omega_4)t] - i\omega_1 \sigma_{kg} \exp[-i(\omega_1 - \omega_4)t] + \dot{\eta}_{kg} \\ &= -[\sigma_{kg} \exp[-i(\omega_1 - \omega_4)t] + \eta_{kg}][i(\omega_{kg} - \omega_4) + \gamma_{kg}] \\ & - \frac{i}{\hbar} \sum_{g'} V_{kg'} \rho_{g'g} \exp(+i\omega_4 t) \\ & - \frac{i}{\hbar} \sum_e V_{ke} \sigma_{eg} \exp[-i(\omega_1 - \omega_2 - \omega_4)t]. \end{aligned} \quad (13)$$

The terms containing σ_{kg} and $\dot{\sigma}_{kg}$ oscillate at the optical frequency $\omega_1 - \omega_4$ in Eq. (13) and are eliminated using the rotating wave approximation to give us

$$\begin{aligned} \dot{\eta}_{kg} = & -\eta_{kg}[i(\omega_{kg} - \omega_4) + \gamma_{kg}] \\ & - \frac{i}{\hbar} \sum_{g'} V_{kg'} \rho_{g'g} \exp(+i\omega_4 t) \\ & - \frac{i}{\hbar} \sum_e V_{ke} \sigma_{eg} \exp(+i\omega_3 t), \end{aligned} \quad (14)$$

where we have used the relation $\omega_3 = -\omega_1 + \omega_2 + \omega_4$. The resonant interaction terms $V_{kg'}$, V_{ke} , $V_{kk'}$, and V_{kg} are given by

$$V_{kg'} = V_{kg'}^{(-)} + V_{kg'}^{(+)}, \quad (15)$$

$$V_{ke} = V_{ke}^{(-)} + V_{ke}^{(+)}, \quad (16)$$

where

$$\begin{aligned} V_{kg'}^{(-)} = & -\frac{1}{2} \boldsymbol{\mu}_{kg'} \cdot [\hat{e}_1 A_1(t) \exp(-i\omega_1 t) + \hat{e}_2 A_2(t) \exp(-i\omega_2 t) \\ & + \hat{e}_3 A_3(t) \exp(-i\omega_3 t)] \\ = & V_{kg'}^{(-1)} \exp(-i\omega_1 t) + V_{kg'}^{(-2)} \exp(-i\omega_2 t) \\ & + V_{kg'}^{(-3)} \exp(-i\omega_3 t), \end{aligned} \quad (17)$$

$$\begin{aligned} V_{kg'}^{(+)} = & -\frac{1}{2} \boldsymbol{\mu}_{kg'} \cdot [\hat{e}_1^* A_1^*(t) \exp(+i\omega_1 t) + \hat{e}_2^* A_2^*(t) \exp(+i\omega_2 t) \\ & + \hat{e}_3^* A_3^*(t) \exp(+i\omega_3 t)] \\ = & V_{kg'}^{(+1)} \exp(+i\omega_1 t) + V_{kg'}^{(+2)} \exp(+i\omega_2 t) \\ & + V_{kg'}^{(+3)} \exp(+i\omega_3 t), \end{aligned} \quad (18)$$

and the other components $V_{ke}^{(-)}$ and $V_{ke}^{(+)}$ are defined in a similar fashion. Substituting Eqs. (15) and (16) into Eq. (14) and keeping only those terms that do not oscillate at optical frequencies (again using the rotating wave approximation), we obtain

$$\dot{\eta}_{kg} = -\eta_{kg}[i(\omega_{kg} - \omega_4) + \gamma_{kg}] - \frac{i}{\hbar} \sum_e V_{ke}^{(-3)} \sigma_{eg}. \quad (19)$$

For the case where $|\omega_{kg} - \omega_4| \gg \gamma_{kg}$, we can assume that the polarization η_{kg} is given by the steady state solution, $\dot{\eta}_{kg} = 0$. In this case, solving for the real and imaginary components of η_{kg} , we obtain

$$\begin{aligned} 0 = & -(\eta_{kg}^r + i\eta_{kg}^i)[i(\omega_{kg} - \omega_4) + \gamma_{kg}] \\ & - \frac{i}{\hbar} \sum_e (V_{ke}^{(-3r)} + iV_{ke}^{(-3i)})(\sigma_{eg}^r + i\sigma_{eg}^i), \end{aligned} \quad (20)$$

$$\begin{aligned} 0 = & -\eta_{kg}^r \gamma_{kg} + \eta_{kg}^i (\omega_{kg} - \omega_4) + \frac{1}{\hbar} \sum_e (V_{ke}^{(-3r)} \sigma_{eg}^i \\ & + V_{ke}^{(-3i)} \sigma_{eg}^r) = -\eta_{kg}^r \gamma_{kg} + \eta_{kg}^i (\omega_{kg} - \omega_4) + \alpha_{3keg}, \end{aligned} \quad (21)$$

$$\begin{aligned} 0 = & -\eta_{kg}^i \gamma_{kg} - \eta_{kg}^r (\omega_{kg} - \omega_4) + \frac{1}{\hbar} \sum_e (-V_{ke}^{(-3r)} \sigma_{eg}^r \\ & + V_{ke}^{(-3i)} \sigma_{eg}^i) = -\eta_{kg}^i \gamma_{kg} - \eta_{kg}^r (\omega_{kg} - \omega_4) + \beta_{3keg}, \end{aligned} \quad (22)$$

where

$$\alpha_{3keg} = \frac{1}{\hbar} \sum_e (V_{ke}^{(-3r)} \sigma_{eg}^i + V_{ke}^{(-3i)} \sigma_{eg}^r) \quad (23)$$

and

$$\beta_{3keg} = \frac{1}{\hbar} \sum_e (-V_{ke}^{(-3r)} \sigma_{eg}^r + V_{ke}^{(-3i)} \sigma_{eg}^i). \quad (24)$$

Solving Eq. (22) for η_{kg}^i , we obtain

$$\eta_{kg}^i = -\frac{\eta_{kg}^r (\omega_{kg} - \omega_4) + \beta_{3keg}}{\gamma_{kg}}. \quad (25)$$

Substituting Eq. (25) into Eq. (21), we obtain

$$\begin{aligned} \eta_{kg}^r = & \frac{\eta_{kg}^i (\omega_{kg} - \omega_4) + \alpha_{3keg}}{\gamma_{kg}} \\ = & -\frac{\eta_{kg}^r (\omega_{kg} - \omega_4)^2}{\gamma_{kg}^2} + \frac{(\omega_{kg} - \omega_4) \beta_{3keg}}{\gamma_{kg}^2} + \frac{\alpha_{3keg}}{\gamma_{kg}}. \end{aligned} \quad (26)$$

Rearranging we obtain

$$\eta_{kg}^r = \frac{(\omega_{kg} - \omega_4) \beta_{3keg} + \gamma_{kg} \alpha_{3keg}}{[\gamma_{kg}^2 + (\omega_{kg} - \omega_4)^2]}. \quad (27)$$

Substituting Eq. (30) into Eq. (28), we obtain

$$\begin{aligned} \eta_{kg}^i = & -\frac{(\omega_{kg} - \omega_4)}{\gamma_{kg}} \left\{ \frac{(\omega_{kg} - \omega_4) \beta_{3keg} + \gamma_{kg} \alpha_{3keg}}{[\gamma_{kg}^2 + (\omega_{kg} - \omega_4)^2]} \right\} + \frac{\beta_{3keg}}{\gamma_{kg}} \\ = & -\left\{ \frac{[(\omega_{kg} - \omega_4)^2 / \gamma_{kg}] \beta_{3keg} + (\omega_{kg} - \omega_4) \alpha_{3keg}}{[\gamma_{kg}^2 + (\omega_{kg} - \omega_4)^2]} \right\} \\ & + \frac{[\gamma_{kg}^2 + (\omega_{kg} - \omega_4)^2] \beta_{3keg}}{\gamma_{kg} [\gamma_{kg}^2 + (\omega_{kg} - \omega_4)^2]}. \end{aligned} \quad (28)$$

Rearranging and canceling terms, we obtain

$$\eta_{kg}^i = \frac{\gamma_{kg}\beta_{3keg} - (\omega_{kg} - \omega_4)\alpha_{3keg}}{\gamma_{kg}^2 + (\omega_{kg} - \omega_4)^2}. \quad (29)$$

Multiplying Eq. (11) by $\exp(+i\omega_1 t)$, we obtain

$$\begin{aligned} & \dot{\sigma}_{kg} - i\omega_1 \sigma_{kg} + \dot{\eta}_{kg} \exp[-i(\omega_4 - \omega_1)t] \\ & - i\omega_4 \eta_{kg} \exp[-i(\omega_4 - \omega_1)t] \\ & = -\{\sigma_{kg} + \eta_{kg} \exp[-i(\omega_4 - \omega_1)t]\}[i\omega_{kg} + \gamma_{kg}] \\ & - \frac{i}{\hbar} \sum_{g'} V_{kg'} \rho_{g'g} \exp(+i\omega_1 t) \\ & - \frac{i}{\hbar} \sum_e V_{ke} \sigma_{eg} \exp(+i\omega_2 t). \end{aligned} \quad (30)$$

Substituting for the radiative interaction terms and eliminating terms that oscillate at optical frequencies, we obtain

$$\begin{aligned} \dot{\sigma}_{kg} &= -\sigma_{kg}[i(\omega_{kg} - \omega_1) + \gamma_{kg}] - \frac{i}{\hbar} \sum_{g'} V_{kg'}^{(-1)} \rho_{g'g}^r \\ & - \frac{i}{\hbar} \sum_e V_{ke}^{(-2)} \sigma_{eg}. \end{aligned} \quad (31)$$

Rewriting Eq. (31) in terms of real and imaginary components, we obtain

$$\begin{aligned} \dot{\sigma}_{kg}^r + i\dot{\sigma}_{kg}^i &= -(\sigma_{kg}^r + i\sigma_{kg}^i)[i(\omega_{kg} - \omega_1) + \gamma_{kg}] \\ & - \frac{i}{\hbar} \sum_{g'} (V_{kg'}^{(-1r)} + iV_{kg'}^{(-1i)}) (\rho_{g'g}^r + i\rho_{g'g}^i) \\ & - \frac{i}{\hbar} \sum_e (V_{ke}^{(-2r)} + iV_{ke}^{(-2i)}) (\sigma_{eg}^r + i\sigma_{eg}^i). \end{aligned} \quad (32)$$

Solving for the real component of $\dot{\sigma}_{kg}$, we obtain

$$\begin{aligned} \dot{\sigma}_{kg}^r &= \sigma_{kg}^i(\omega_{kg} - \omega_1) - \sigma_{kg}^r \gamma_{kg} + \frac{1}{\hbar} \sum_{g'} (V_{kg'}^{(-1r)} \rho_{g'g}^i \\ & + V_{kg'}^{(-1i)} \rho_{g'g}^r) + \frac{1}{\hbar} \sum_e (V_{ke}^{(-2r)} \sigma_{eg}^i + V_{ke}^{(-2i)} \sigma_{eg}^r) \\ & = \sigma_{kg}^i(\omega_{kg} - \omega_1) - \sigma_{kg}^r \gamma_{kg} + \alpha_{1kg'g} + \alpha_{2keg}, \end{aligned} \quad (33)$$

where

$$\alpha_{1kg'g} = \frac{1}{\hbar} \sum_{g'} (V_{kg'}^{(-1r)} \rho_{g'g}^i + V_{kg'}^{(-1i)} \rho_{g'g}^r) \quad (34)$$

and

$$\alpha_{2keg} = \frac{1}{\hbar} \sum_e (V_{ke}^{(-2r)} \sigma_{eg}^i + V_{ke}^{(-2i)} \sigma_{eg}^r). \quad (35)$$

Solving for the imaginary component of $\dot{\sigma}_{kg}$, we obtain

$$\begin{aligned} \dot{\sigma}_{kg}^i &= -\sigma_{kg}^r(\omega_{kg} - \omega_1) - \sigma_{kg}^i \gamma_{kg} + \frac{1}{\hbar} \sum_{g'} (-V_{kg'}^{(-1r)} \rho_{g'g}^r \\ & + V_{kg'}^{(-1i)} \rho_{g'g}^i) + \frac{1}{\hbar} \sum_e (-V_{ke}^{(-2r)} \sigma_{eg}^r + V_{ke}^{(-2i)} \sigma_{eg}^i) \\ & = -\sigma_{kg}^r(\omega_{kg} - \omega_1) - \sigma_{kg}^i \gamma_{kg} + \beta_{1kg'g} + \beta_{2keg}, \end{aligned} \quad (36)$$

where

$$\beta_{1kg'g} = \frac{1}{\hbar} \sum_{g'} (-V_{kg'}^{(-1r)} \rho_{g'g}^r + V_{kg'}^{(-1i)} \rho_{g'g}^i) \quad (37)$$

and

$$\beta_{2keg} = \frac{1}{\hbar} \sum_e (-V_{ke}^{(-2r)} \sigma_{eg}^r + V_{ke}^{(-2i)} \sigma_{eg}^i). \quad (38)$$

Because of the large detuning for the density matrix elements σ_{kg}^r and σ_{kg}^i , we can assume that the steady state solution will be valid for these terms. We can, therefore, solve for these density matrix elements. Setting $\dot{\sigma}_{kg}^r = \dot{\sigma}_{kg}^i = 0$ and solving Eq. (39) for σ_{kg}^i , we obtain

$$\sigma_{kg}^i = -\sigma_{kg}^r \frac{(\omega_{kg} - \omega_1)}{\gamma_{kg}} + \frac{\beta_{1kg'g} + \beta_{2keg}}{\gamma_{kg}}. \quad (39)$$

Substituting Eq. (39) into Eq. (33), we obtain

$$\begin{aligned} 0 &= \left[-\sigma_{kg}^r \frac{(\omega_{kg} - \omega_1)}{\gamma_{kg}} + \frac{\beta_{1kg'g} + \beta_{2keg}}{\gamma_{kg}} \right] (\omega_{kg} - \omega_1) \\ & - \sigma_{kg}^r \gamma_{kg} + \alpha_{1kg'g} + \alpha_{2keg}. \end{aligned} \quad (40)$$

Solving Eq. (40) for σ_{kg}^r , we obtain

$$\sigma_{kg}^r = \frac{(\beta_{1kg'g} + \beta_{2keg})(\omega_{kg} - \omega_1) + \gamma_{kg}(\alpha_{1kg'g} + \alpha_{2keg})}{(\omega_{kg} - \omega_1)^2 + \gamma_{kg}^2}. \quad (41)$$

Substituting Eq. (41) into Eq. (39), we obtain:

$$\begin{aligned} \sigma_{kg}^i &= - \left[\frac{(\beta_{1kg'g} + \beta_{2keg})(\omega_{kg} - \omega_1) + \gamma_{kg}(\alpha_{1kg'g} + \alpha_{2keg})}{(\omega_{kg} - \omega_1)^2 + \gamma_{kg}^2} \right] \\ & \times \frac{(\omega_{kg} - \omega_1)}{\gamma_{kg}} + \frac{\beta_{1kg'g} + \beta_{2keg}}{\gamma_{kg}} \\ & = \frac{-(\omega_{kg} - \omega_1)(\alpha_{1kg'g} + \alpha_{2keg}) + \gamma_{kg}(\beta_{1kg'g} + \beta_{2keg})}{(\omega_{kg} - \omega_1)^2 + \gamma_{kg}^2}. \end{aligned} \quad (42)$$

B. Summary of the equations for the density matrix elements for the CARS interaction

The detailed derivation of the time-dependent density matrix equation for the other coherence and population terms is presented in the Appendix. Because of the large magnitude of the detuning parameters $(\omega_{ke} - \omega_2)$ and $(\omega_{ke} - \omega_3)$, the density matrix elements σ_{ke} and η_{ke} that describe the single-photon-induced coherences between level K and level E are assumed to be in steady state. The real and imaginary components of σ_{ke} are given by

$$\sigma_{ke}^r = \frac{(\beta_{1ke} + \beta_{2ke'e})(\omega_{ke} - \omega_2) + (\alpha_{1ke} + \alpha_{2ke'e})\gamma_{ke}}{(\omega_{ke} - \omega_2)^2 + \gamma_{ke}^2}, \quad (43)$$

$$\sigma_{ke}^i = [-\sigma_{ke}^r(\omega_{ke} - \omega_2) + \beta_{1ke} + \beta_{2ke'e}]/\gamma_{ke}, \quad (44)$$

where

$$\alpha_{1ke} = \frac{1}{\hbar} \sum_g [V_{kg}^{(-1r)} \sigma_{ge}^i + V_{kg}^{(-1i)} \sigma_{ge}^r], \quad (45)$$

$$\alpha_{2ke'e} = \frac{1}{\hbar} \sum_{e'} [V_{ke'e}^{(-2r)} \rho_{e'e}^i + V_{ke'e}^{(-2i)} \rho_{e'e}^r], \quad (46)$$

$$\beta_{1ke} = \frac{1}{\hbar} \sum_g [-V_{kg}^{(-1r)} \sigma_{ge}^r + V_{kg}^{(-1i)} \sigma_{ge}^i], \quad (47)$$

$$\beta_{2ke'e} = \frac{1}{\hbar} \sum_{e'} [-V_{ke'e}^{(-2r)} \rho_{e'e}^r + V_{ke'e}^{(-2i)} \rho_{e'e}^i]. \quad (48)$$

The real and imaginary components of η_{ke} are given by

$$\eta_{ke}^i = [-\eta_{ke}^r(\omega_{ke} - \omega_3) + \beta_{3ke'e}]/\gamma_{ke}, \quad (49)$$

$$\eta_{ke}^r = \frac{\alpha_{3ke'e}\gamma_{ke} + \beta_{3ke'e}(\omega_{ke} - \omega_3)}{\gamma_{ke}^2 + (\omega_{ke} - \omega_3)^2}, \quad (50)$$

where

$$\alpha_{3ke'e} = \frac{1}{\hbar} \sum_{e'} (V_{ke'e}^{(-3r)} \rho_{e'e}^i + V_{ke'e}^{(-3i)} \rho_{e'e}^r), \quad (51)$$

$$\beta_{3ke'e} = \frac{1}{\hbar} \sum_{e'} (-V_{ke'e}^{(-3r)} \rho_{e'e}^r + V_{ke'e}^{(-3i)} \rho_{e'e}^i). \quad (52)$$

The steady state assumption is made only for the single-photon coherence terms σ_{kg} , η_{kg} , σ_{ke} , and η_{ke} ; for these terms, the frequency component of interest as shown in Eqs. (8) and (9) is very far from the single-photon resonance frequency for the transition. For the other coherence terms and for the population terms, the steady state approximation is not made. The density matrix equations that describe the time development of σ_{eg} , the two-photon-induced Raman coherence term for transitions between ground level G and excited level E , are given by

$$\begin{aligned} \dot{\sigma}_{eg}^r = & \sigma_{eg}^i[\omega_{eg} - (\omega_1 - \omega_2)] - \sigma_{eg}^r\gamma_{eg} + \frac{1}{\hbar} \sum_k [V_{ek}^{(+2r)} \sigma_{kg}^i \\ & + V_{ek}^{(+2i)} \sigma_{kg}^r + V_{ek}^{(+3r)} \eta_{kg}^i + V_{ek}^{(+3i)} \eta_{kg}^r - \sigma_{ek}^r V_{kg}^{(-1i)} \\ & - \sigma_{ek}^i V_{kg}^{(-1r)}], \end{aligned} \quad (53)$$

$$\begin{aligned} \dot{\sigma}_{eg}^i = & -\sigma_{eg}^r[\omega_{eg} - (\omega_1 - \omega_2)] - \sigma_{eg}^i\gamma_{eg} + \frac{1}{\hbar} \sum_k [-V_{ek}^{(+2r)} \sigma_{kg}^r \\ & + V_{ek}^{(+2i)} \sigma_{kg}^i - V_{ek}^{(+3r)} \eta_{kg}^r + V_{ek}^{(+3i)} \eta_{kg}^i + \sigma_{ek}^r V_{kg}^{(-1r)} \\ & - \sigma_{ek}^i V_{kg}^{(-1i)}]. \end{aligned} \quad (54)$$

The density matrix equations that describe the time development of the Zeeman state coherence terms $\rho_{ee'}$ for level E and $\rho_{gg'}$ for level G are given by

$$\begin{aligned} \dot{\rho}_{e'e}^r = & \rho_{e'e}^i\omega_{e'e} - \rho_{e'e}^r\gamma_{e'e} + \frac{1}{\hbar} \sum_k (V_{e'k}^{(+2r)} \sigma_{ke}^i + V_{e'k}^{(+2i)} \sigma_{ke}^r \\ & - \sigma_{e'k}^r V_{ke}^{(-2i)} - \sigma_{e'k}^i V_{ke}^{(-2r)}), \end{aligned} \quad (55)$$

$$\begin{aligned} \dot{\rho}_{e'e}^i = & -\rho_{e'e}^r\omega_{e'e} - \rho_{e'e}^i\gamma_{e'e} + \frac{1}{\hbar} \sum_k (-V_{e'k}^{(+2r)} \sigma_{ke}^r + V_{e'k}^{(+2i)} \sigma_{ke}^i \\ & + \sigma_{e'k}^r V_{ke}^{(-2r)} - \sigma_{e'k}^i V_{ke}^{(-2i)}), \end{aligned} \quad (56)$$

$$\begin{aligned} \dot{\rho}_{g'g}^r = & +\rho_{g'g}^i\omega_{g'g} - \rho_{g'g}^r\gamma_{g'g} + \frac{1}{\hbar} \sum_k (V_{g'k}^{(+1r)} \sigma_{kg}^i + V_{g'k}^{(+1i)} \sigma_{kg}^r \\ & - \sigma_{g'k}^r V_{kg}^{(-1i)} - \sigma_{g'k}^i V_{kg}^{(-1r)}), \end{aligned} \quad (57)$$

$$\begin{aligned} \dot{\rho}_{g'g}^i = & -\rho_{g'g}^r\omega_{g'g} - \rho_{g'g}^i\gamma_{g'g} + \frac{1}{\hbar} \sum_k (-V_{g'k}^{(+1r)} \sigma_{kg}^r \\ & + V_{g'k}^{(+1i)} \sigma_{kg}^i + \sigma_{g'k}^r V_{kg}^{(-1r)} - \sigma_{g'k}^i V_{kg}^{(-1i)}). \end{aligned} \quad (58)$$

The density matrix equations that describe the time development of the state populations ρ_{ee} for level E and ρ_{gg} for level G are given by

$$\begin{aligned} \dot{\rho}_{ee} = & -\Gamma_e \rho_{ee} + \sum_m \Gamma_{me} \rho_{mm} + \frac{2}{\hbar} \sum_k (V_{ek}^{(+2r)} \sigma_{ke}^i + V_{ek}^{(+2i)} \sigma_{ke}^r) \\ & + \frac{2}{\hbar} \sum_k (V_{ek}^{(+3r)} \eta_{ke}^i + V_{ek}^{(+3i)} \eta_{ke}^r), \end{aligned} \quad (59)$$

$$\begin{aligned} \dot{\rho}_{gg} = & -\Gamma_g \rho_{gg} + \sum_m \Gamma_{mg} \rho_{mm} + \frac{2}{\hbar} \sum_k (V_{gk}^{(+1r)} \sigma_{kg}^i + V_{gk}^{(+1i)} \sigma_{kg}^r). \end{aligned} \quad (60)$$

Both the population term ρ_{kk} and the Zeeman state coherence term $\rho_{kk'}$ for level K are assumed to be negligible.

C. Solution of the density matrix equations for the CARS interaction

The time-dependent equations for the coherence and population terms, Eqs. (53)–(60), are solved by direct numerical integration. A variable-order Adams-Bashforth-Moulton predictor-corrector method³⁰ is used to integrate these differential equations. The time-dependent electric field amplitudes $A_1(t)$, $A_2(t)$, and $A_3(t)$ for the pump, Stokes, and probe beams are input parameters for the numerical calculations. They are modeled using 100 fs Gaussian envelopes, resulting in laser irradiance pulse shapes that are 70 fs Gaussian pulses, approximately the same as for the pulses produced by our laser system.¹ The difference in the central frequencies between the pump and Stokes beams is set to a value of 2330 cm⁻¹, the nominal value for the Raman Q branch of the N₂ fundamental band. The frequency of the pump and probe beams is set to the same value. The pulses are assumed to be Fourier-transform limited. The peak irra-

diance for each of the pulses is also specified as an input parameter. The step size used in the calculations is 1.0 fs.

D. Calculation of the CARS signal at frequency ω_4

The CARS signal results from the Fourier component of the radiating polarization $\mathbf{P}(t) = \text{Tr}[\boldsymbol{\mu}\rho(t)] = \sum_{k,g} [\boldsymbol{\mu}_{kg}\rho_{gk}(t) + \boldsymbol{\mu}_{gk}\rho_{kg}(t)]$ induced in the medium at frequency $\omega_4 = \omega_1 - \omega_2 + \omega_3$. The radiation that is produced by this oscillating polarization is polarized as a function of the unit polarization vectors \hat{e}_1 , \hat{e}_2 , and \hat{e}_3 of the input fields and the polarization properties of the CARS resonance. We can calculate the field radiated with arbitrary unit vector \hat{e}_4 by analyzing the frequency spectrum of the dot product of \hat{e}_4 and the radiating polarization. The component of the induced polarization along the direction of \hat{e}_4 is given by

$$\begin{aligned} P_4(\omega_4, t) &= \hat{e}_4 \cdot [\boldsymbol{\mu}_{kg}\rho_{gk} + \boldsymbol{\mu}_{gk}\rho_{kg}] \\ &= \hat{e}_4 \cdot [\boldsymbol{\mu}_{kg}\eta_{gk} \exp(+i\omega_4 t) \\ &\quad + \boldsymbol{\mu}_{gk}\eta_{kg} \exp(-i\omega_4 t)]. \end{aligned} \quad (61)$$

Multiplying through by $\exp(+i\omega_4 t)$, we obtain the amplitude $P_{40}(\omega_4, t)$ of the polarization at frequency ω_4

$$P_{40}(\omega_4, t) = \hat{e}_4 \cdot \boldsymbol{\mu}_{gk}\eta_{kg}. \quad (62)$$

The amplitude of the CARS signal will be proportional to $P_{40}(\omega_4, t)$, and in the absence of the nonresonant background contribution, the CARS signal will be proportional to $P_{40}(\omega_4, t)P_{40}^*(\omega_4, t)$. The actual magnitude of the CARS signal will depend on the phase-matching angles for the pump, Stokes, and probe beams, and on the effective interaction length of the phase-matched beams. For perfect phase matching ($\mathbf{k}_4 = \mathbf{k}_1 - \mathbf{k}_2 + \mathbf{k}_3$), the time development of the polarization at the signal frequency ω_4 will be the same at each spatial location in the overlap region except for a spatial phase factor. Because of this spatial phase factor, the field radiated at frequency ω_4 by the induced polarization will interfere constructively in the direction $\mathbf{k}_1 - \mathbf{k}_2 + \mathbf{k}_3$. It is not necessary to perform a spatial integration for the calculations performed in this paper because the CARS signal frequency is distinct from the frequencies of the pump, Stokes, and probe beams.

III. IMPULSIVE PUMP-STOKES EXCITATION OF Q-BRANCH RESONANCES IN NITROGEN

The results of calculations for different $Q(J)$ transitions in the fundamental band are shown in Fig. 2. The quantities plotted are the real and imaginary components of σ_{EG} and the magnitude of σ_{EG} , where

$$\sigma_{EG} = \sum_{e,g} \sigma_{eg}. \quad (63)$$

The summation in Eq. (63) is over all Zeeman states in the upper and lower levels of the Raman transition. The coherence density matrix elements plotted in Fig. 2 are normalized by dividing by $(\rho_{GG})^0$, the population of level G prior to pump-Stokes excitation. As is shown in Fig. 2(a), for the $Q(2)$ transition, the real part of the coherence element σ_{EG} is

very small compared to the imaginary part after the excitation of the Raman coherence by 70 fs pump and Stokes pulses. Recall from Eq. (10) that

$$\sigma_{eg} = \rho_{eg} \exp[+i(\omega_1 - \omega_2)t]. \quad (64)$$

In Fig. 2(a), the resonance frequencies for all transitions eg are 2329.8 cm^{-1} , very close to the input difference frequency of $\omega_1 - \omega_2 = 2330 \text{ cm}^{-1}$. The induced coherence ρ_{EG} oscillates with a frequency $\omega_{EG} \cong \omega_1 - \omega_2$, and consequently, as shown in Fig. 2(a), the relative magnitudes of the real and imaginary components of σ_{EG} change only very slowly after impulsive pump-Stokes excitation. Rewriting Eqs. (53) and (54) for the case of negligible laser power, as would be the case after the pump-Stokes laser excitation, we obtain

$$\dot{\sigma}_{eg}^r = \sigma_{eg}^i [\omega_{eg} - (\omega_1 - \omega_2)] - \sigma_{eg}^r \gamma_{eg}, \quad (65)$$

$$\dot{\sigma}_{eg}^i = -\sigma_{eg}^r [\omega_{eg} - (\omega_1 - \omega_2)] - \sigma_{eg}^i \gamma_{eg}. \quad (66)$$

For the $Q(2)$ transition, the term $\omega_{eg} - (\omega_1 - \omega_2)$ is very small and the relative magnitudes of the real and imaginary components of σ_{EG} remain essentially unchanged for several picoseconds following pump-Stokes excitation. The relative magnitudes of the real and imaginary components of σ_{EG} define the phase of the coherence. For the time scale shown in Fig. 2, the dephasing of the induced coherences due to collisions is negligible, and the magnitude of the normalized coherence, $|\sigma_{EG}|/(\rho_{GG})^0$, is essentially constant. The magnitude of the coherence is given by

$$|\sigma_{EG}| = \sqrt{(\sigma_{EG}^r)^2 + (\sigma_{EG}^i)^2}. \quad (67)$$

The results of similar calculations for the $Q(5)$ transition are shown in Fig. 2(b). Note that the normalized magnitude of the induced Raman coherence, $|\sigma_{EG}|/(\rho_{GG})^0$, is nearly the same as for the $Q(2)$ transition. Also, more variation in the phase of the coherence is evident for the $Q(5)$ transition, although the phase of σ_{EG} is still nearly constant over the time interval shown. The results for the $Q(10)$, $Q(15)$, and $Q(20)$ coherences are shown in Figs. 2(c)–2(e), respectively. Note that the normalized magnitude of the coherence, $|\sigma_{EG}|/(\rho_{GG})^0$, is nearly the same for all five transitions. For these transitions, changes in the phase of σ_{EG} , however, become increasingly evident as the $\omega_{eg} - (\omega_1 - \omega_2)$ term increases. The phase of these transitions is related to the ratio of the real and imaginary components of the coherence amplitude σ_{EG} . In Fig. 3, the quantity $\sigma_{EG}'/|\sigma_{EG}|$ is plotted as a function of time for the $Q(5)$, $Q(10)$, and $Q(20)$ Raman transitions. It is evident that at approximately 2200 fs after impulsive pump-Stokes excitation, the Raman coherences for $Q(5)$ and $Q(20)$ transitions are out of phase by 180° and interfere destructively in terms of contributing to the macroscopic Raman polarization.

The excited level populations ρ_{EE} and normalized excited level populations $\rho_{EE}/(\rho_{GG})^0$ for the $Q(2)$, $Q(5)$, $Q(10)$, $Q(15)$, and $Q(20)$ transitions are plotted in Fig. 4. The excited level populations for the various Raman Q -branch transitions are different because of differences in the initial population $(\rho_{GG})^0$ for each of the initial levels J_G , but again the temporal behavior and the magnitude of the normalized ex-

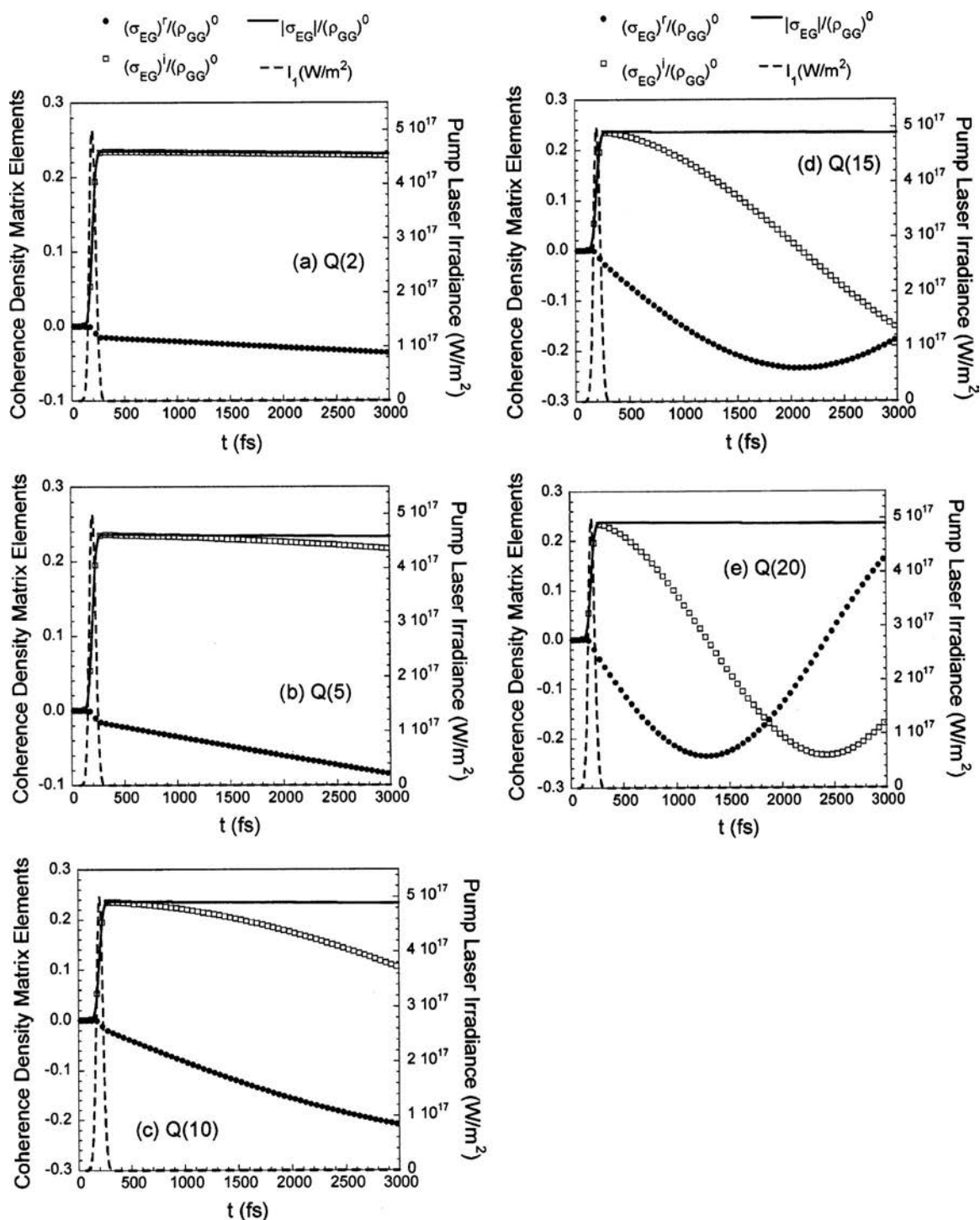


FIG. 2. Temporal dependence of the real and imaginary components and the magnitude of the induced Raman coherence for the (a) $Q(2)$, (b) $Q(5)$, (c) $Q(10)$, (d) $Q(15)$, and (e) $Q(20)$ transitions in the fundamental (1,0) band of N_2 . The coherence matrix elements are normalized by dividing by the population of level G prior to laser excitation. The difference between the central frequencies of the pump and Stokes lasers is 2330 cm^{-1} . The Raman frequencies for the $Q(2)$, $Q(5)$, $Q(10)$, $Q(15)$, and $Q(20)$ transitions are 2329.8, 2329.4, 2328.0, 2325.8, and 2322.7 cm^{-1} , respectively. The collisional dephasing rate for each Raman transition is $5 \times 10^9\text{ s}^{-1}$, corresponding to a Raman linewidth of 0.053 cm^{-1} . The pump and Stokes laser temporal pulse shapes are both Gaussian with widths of 70 fs (full width at half maximum). The pump and Stokes pulses are overlapped exactly in time. The peak irradiance for both the pump and Stokes pulses is $5 \times 10^{17}\text{ W/m}^2$.

cited level populations at the conclusion of the impulsive pump-Stokes excitation are essentially identical for each of the transitions.

The normalized magnitude $|\sigma_{EG}|/(\rho_{GG})^0$ of the induced coherence is near the maximum possible value of 0.5 for the two-level EG system.³¹ As shown in Fig. 2, the normalized

magnitude $|\sigma_{EG}|/(\rho_{GG})^0$ increases monotonically during the pump-Stokes excitation to a value of approximately 0.24 for all five Q -branch transitions. The effect of higher pump and Stokes irradiances on the induced coherence and excited level population is shown for the $Q(5)$ transition in Fig. 5. The onset of Rabi beating in the induced Raman coherence is

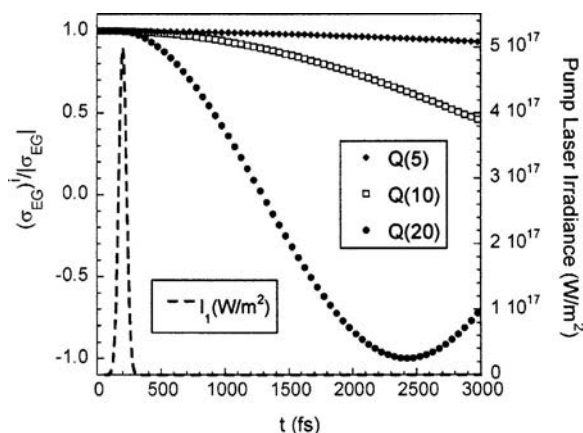


FIG. 3. Temporal dependence of the phase of the induced Raman coherence for the $Q(5)$, $Q(10)$, and $Q(20)$ transitions in the fundamental (1,0) band of N_2 . The collisional dephasing rate and the pump and Stokes pulse parameters are the same as given in the caption of Fig. 2.

clearly evident at pump and Stokes laser irradiance levels of $2 \times 10^{18} \text{ W/m}^2$, as shown in Fig. 5(a). Although the normalized magnitude $|\sigma_{EG}|/(\rho_{GG})^0$ reaches a value of 0.4 during the pump-Stokes excitation, the normalized magnitude of the Raman coherence decreases from this peak value and reaches a value of 0.3 at the conclusion of the pump-Stokes excitation. At pump and Stokes laser irradiance levels of 10^{19} W/m^2 , the Rabi beating in the induced Raman coherence is very strong and exhibits numerous strong oscillations within the temporal envelope of the pump and Stokes beams. At the conclusion of the pump-Stokes excitation, the magnitude of the normalized coherence is lower for laser irradiance levels of 10^{19} W/m^2 than for laser irradiance levels of $2 \times 10^{18} \text{ W/m}^2$.

The normalized population of the excited level, $\rho_{EE}/(\rho_{GG})^0$, reaches a value of 0.7 at the conclusion of the pump-Stokes excitation for laser irradiance levels of $2 \times 10^{18} \text{ W/m}^2$, as shown in Fig. 5(c). The magnitude of the

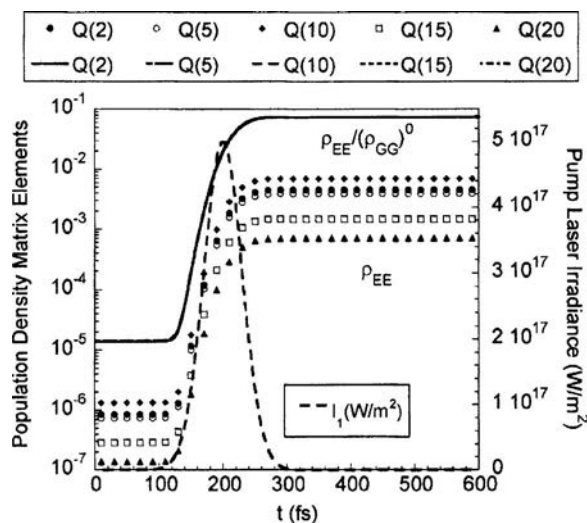


FIG. 4. Temporal dependence of the excited state populations and the normalized excited populations for the $Q(2)$, $Q(5)$, $Q(10)$, $Q(15)$, and $Q(20)$ transitions in the fundamental (1,0) Raman band of N_2 . The collisional dephasing rate and the pump and Stokes pulse parameters are the same as given in the caption of Fig. 2.

coherence $|\sigma_{EG}|$ begins to decrease when the level population is inverted, i.e., $\rho_{EE}/(\rho_{GG})^0 > 0.5$, as can be seen by comparing Figs. 5(a) and 5(c). Rabi oscillations in the excited level population are clearly evident for laser irradiance levels of 10^{19} W/m^2 , as shown in Fig. 5(d).

IV. FEMTOSECOND CARS SIGNAL GENERATION: INTERACTION OF THE PROBE LASER WITH THE INDUCED RAMAN COHERENCE

The CARS signal results from the scattering of the probe beam from the induced Raman coherence. We have performed measurements of temperature and concentration in room air and gas cells,¹ and more recently, in flames³² by monitoring the decay of the femtosecond CARS signal as a function of probe delay with respect to the impulsive pump-Stokes excitation. The results of a probe delay scan for N_2 CARS in room air is shown in Fig. 6. Both the CARS signal from the fundamental (1,0) Raman band of N_2 and the nonresonant background contribute to the observed four-wave mixing (FWM) signal. The calculated FWM signal is also shown. The agreement between the experimental data and the DNI calculations is excellent.

The calculated FWM signal amplitude is proportional to the sum of the CARS polarization amplitude, as given in Eq. (62), and the nonresonant background polarization amplitude,

$$A_{\text{FWM}} \propto (\hat{e}_4 \cdot \mu_{gk} \eta_{kg}) + \beta \chi_{\text{NR}} A_1(t) A_2(t) A_3(t). \quad (68)$$

The CARS signal polarization amplitude $\hat{e}_4 \cdot \mu_{gk} \eta_{kg}$ has both real and imaginary components, but the nonresonant background polarization amplitude $\beta \chi_{\text{NR}} A_1(t) A_2(t) A_3(t)$ is purely real [we assume that the laser amplitudes $A_1(t)$ are real without loss of generality]. The scaling parameter β is adjusted in the calculations to fit the experimental data. For the calculations shown in Fig. 6, $\beta = 0.175$; we are still investigating the departure of β from the expected value of 1.0. We have noted that the ratio of the nonresonant peak in the FWM signal to the resonant signal does vary by a factor of at least 2 from day to day, and this appears to be the result of day-to-day variation in laser pulse parameters.

We performed a series of DNI calculations to investigate the effect of variations in the pump and Stokes laser irradiances on the calculated FWM signal. The calculated FWM signal (CARS+NR), CARS signal, and pump irradiance profile are shown in Figs. 7(a)–7(e) for values 10^{34} , 2.5×10^{34} , 2.5×10^{35} , 4×10^{36} , and $10^{38} \text{ W}^2/\text{m}^4$, respectively, for the product $I_{\text{pump}}^{\text{pk}} I_{\text{Stokes}}^{\text{pk}}$ of the peak irradiances for the pump and Stokes beams. Note that for the values of 10^{34} , 2.5×10^{34} , and $2.5 \times 10^{35} \text{ W}^2/\text{m}^4$ for the pump-Stokes peak irradiance product, the ratio of the peak in the CARS+NR signal to the CARS signal is nearly constant. For $I_{\text{pump}}^{\text{pk}} I_{\text{Stokes}}^{\text{pk}} = 2.5 \times 10^{35} \text{ W}^2/\text{m}^4$, the normalized excited level population reaches a value of approximately 0.07 as a result of the pump-Stokes excitation, as shown in Fig. 4. At higher values of $I_{\text{pump}}^{\text{pk}} I_{\text{Stokes}}^{\text{pk}}$, saturation effects start to become important. As shown in Figs. 7(d) ($I_{\text{pump}}^{\text{pk}} I_{\text{Stokes}}^{\text{pk}} = 4 \times 10^{36} \text{ W}^2/\text{m}^4$) and 7(e) ($I_{\text{pump}}^{\text{pk}} I_{\text{Stokes}}^{\text{pk}} = 10^{38} \text{ W}^2/\text{m}^4$), the ratio of the CARS+NR signal peak to the CARS signal increases drastically. This effect is also shown in Fig. 8, where the normalized CARS

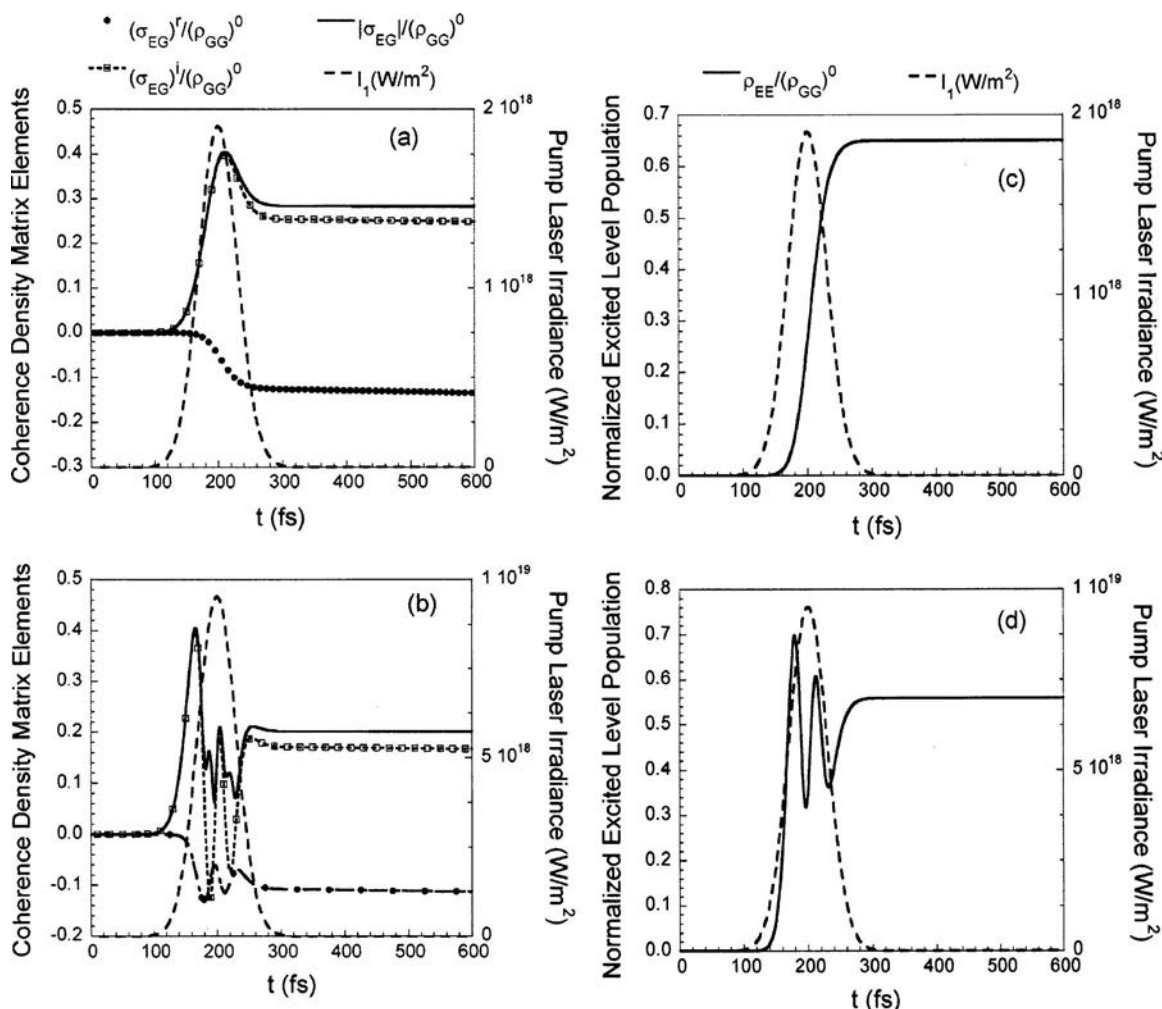


FIG. 5. Response of the $Q(5)$ Raman transition to excitation at two different irradiance levels. The real and imaginary components and the magnitude of the induced Raman coherence are plotted in (a) and (b) for peak pump and Stokes irradiances of 2×10^{18} and 10^{19} W/m², respectively. The normalized excited level population is plotted in (c) and (d) for peak pump and Stokes irradiances of 2×10^{18} and 10^{19} W/m², respectively. The $Q(5)$ transition frequency is 2329.4 cm^{-1} , and the difference between the central frequencies of the pump and Stokes lasers is 2330 cm^{-1} . All resonance and laser parameters are the same as listed in the caption of Fig. 2 except for the peak irradiances for the pump and Stokes pulses.

signal is plotted for four different values of $I_{\text{pump}}^{\text{pk}} I_{\text{Stokes}}^{\text{pk}}$. The normalized CARS signal shown in Fig. 8 is calculated by dividing the CARS signal shown in Figs. 7(a) and 7(c)–7(e) by $I_{\text{pump}}^{\text{pk}} I_{\text{Stokes}}^{\text{pk}}$ and then normalizing the data to the peak value for $I_{\text{pump}}^{\text{pk}} I_{\text{Stokes}}^{\text{pk}} = 2.5 \times 10^{35} \text{ W}^2/\text{m}^4$ (the curve for $I_{\text{pump}}^{\text{pk}} I_{\text{Stokes}}^{\text{pk}} = 2.5 \times 10^{34} \text{ W}^2/\text{m}^4$ is not shown for reasons of clarity because it is nearly identical with the $I_{\text{pump}}^{\text{pk}} I_{\text{Stokes}}^{\text{pk}} = 10^{34} \text{ W}^2/\text{m}^4$ curve). The drastic decrease in the normalized CARS signal for $I_{\text{pump}}^{\text{pk}} I_{\text{Stokes}}^{\text{pk}} = 4 \times 10^{36} \text{ W}^2/\text{m}^4$ and $I_{\text{pump}}^{\text{pk}} I_{\text{Stokes}}^{\text{pk}} = 10^{38} \text{ W}^2/\text{m}^4$ is evident from Fig. 8; for $I_{\text{pump}}^{\text{pk}} I_{\text{Stokes}}^{\text{pk}} = 10^{38} \text{ W}^2/\text{m}^4$, the CARS signal has decreased by three orders of magnitude due to saturation effects.

The data shown in Fig. 6 were acquired using pump, Stokes, and probe laser pulse energies of 10, 100, and $10 \mu\text{J}$, respectively. The pulse width for these pulses, measured using an autocorrelator, was approximately 70 fs. The estimated focal diameter for the pulses was $50 \mu\text{m}$. Assuming top-hat spatial profiles, the calculated peak irradiance for these pulses is approximately 5×10^{16} , 5×10^{17} , and $5 \times 10^{16} \text{ W/m}^2$, respectively, indicating that the experimental values of $I_{\text{pump}}^{\text{pk}} I_{\text{Stokes}}^{\text{pk}}$ were about an order of magnitude below the saturation threshold in our experiments.

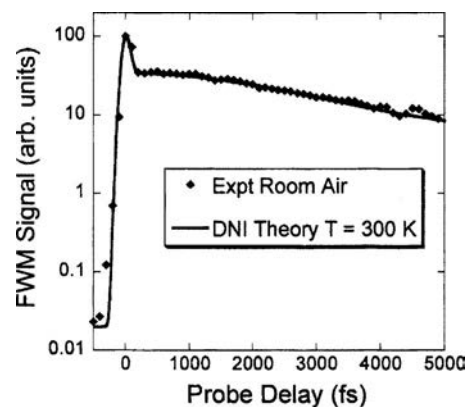


FIG. 6. Comparison of the results from the measurement of the FWM signal as a function of probe delay and DNI theoretical calculations for room air. For the experiment, the pump, Stokes, and probe pulse energies were 10, 100, and $10 \mu\text{J}$, respectively. The measured pulse widths were approximately 70 fs. For the calculations, the peak irradiances for the pump, Stokes, and probe beams were 5×10^{16} , 5×10^{17} , and $5 \times 10^{16} \text{ W/m}^2$, respectively, corresponding to an estimated $50 \mu\text{m}$ focal diameter for each beam. The collisional dephasing rate and the laser pulse parameters for the calculations are the same as given in the caption of Fig. 2.

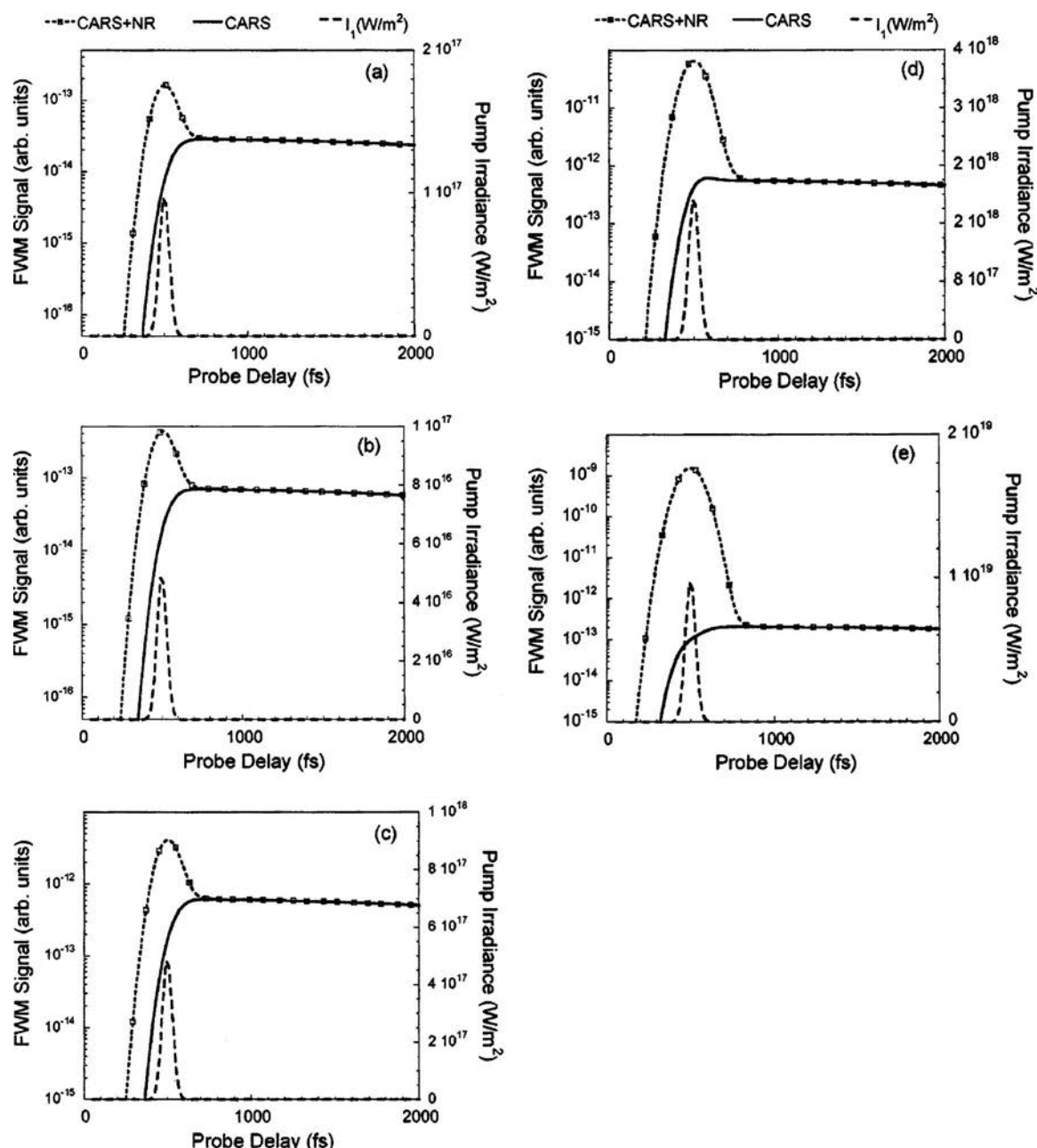


FIG. 7. Calculation of the CARS signal from N_2 and CARS plus nonresonant background signal from room air. The peak irradiances for the pump, Stokes, and probe beams were (a) 10^{17} , 10^{17} , and 10^{15} W/m^2 , respectively; (b) 5×10^{16} , 5×10^{17} , and 10^{15} W/m^2 , respectively; (c) 5×10^{17} , 5×10^{17} , and 10^{15} W/m^2 , respectively; (d) 2×10^{18} , 2×10^{18} , and 10^{15} W/m^2 , respectively; and (e) 10^{19} , 10^{19} , and 10^{15} W/m^2 , respectively. The collisional dephasing rate and the laser pulse parameters for the calculations are the same as given in the caption of Fig. 2.

V. CONCLUSIONS AND FUTURE WORK

We have performed a theoretical analysis of the femtosecond CARS process to support our ongoing experimental efforts^{1,32} to develop techniques for temperature and concentration measurements. The DNI calculation methods that we have developed are ideal for the numerical modeling of the interaction of femtosecond laser radiation with both single-photon and two-photon (including Raman) molecular resonances. This interaction is inherently far from steady state, which is usually assumed for perturbative analyses. The temporal pulse shapes of the lasers and the laser irradiances are input parameters in the DNI numerical modeling. The DNI results should be applicable for laser irradiances less than the

irradiances required for dielectric breakdown; for air at standard temperature and pressure conditions, the breakdown threshold for 810 nm, 110 fs laser pulses was determined to be approximately 3×10^{20} W/m^2 by Qin *et al.*³³ We determined that the Raman transitions are significantly saturated for pump and Stokes irradiances greater than 10^{20} W/m^2 .

One aspect of the DNI modeling that bears further investigation is the validity of the rotating wave approximation. We have used this approximation extensively in developing the equations for the numerical analysis. The optical frequency is 3.748×10^{14} Hz for 800 nm laser radiation, and there are approximately 26 complete optical cycles within the 70 fs full width at half maximum of the laser pulses.

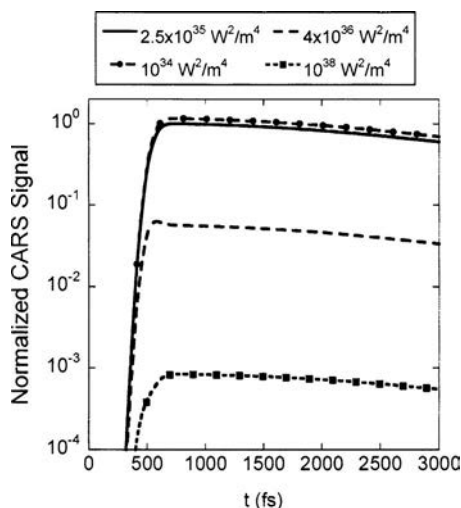


FIG. 8. Normalized N_2 CARS signal from room air. The CARS signal for peak irradiances of $I_{\text{pump}} = I_{\text{Stokes}} = 5 \times 10^{17} \text{ W/m}^2$ is the base case. For each curve, the calculated CARS signal is divided by the peak CARS signal for the base case, and by the normalized peak irradiance product $I_{\text{pump}}^{\text{pk}} I_{\text{Stokes}}^{\text{pk}} / 2.5 \times 10^{35}$. The peak irradiance products $I_{\text{pump}}^{\text{pk}} I_{\text{Stokes}}^{\text{pk}}$ for each curve are indicated in the legend. The collisional dephasing rate and the laser pulse parameters for the calculations are the same as given in the caption of Fig. 2.

Therefore, it seems that the rotating wave approximation will still be valid, at least for cases where saturation effects are not significant. The Raman coherence in Fig. 5(b) exhibits temporal structure with characteristic time of a few tens of femtoseconds. We will examine this approximation in future numerical studies. Although the equations for the numerical analysis will be more complicated when derived without this approximation, the numerical time step for the calculations discussed above was either 1.0 or 2.0 fs. The numerical time step will not have to be lowered significantly as a result of NOT using the rotating wave approximation.

The theoretical work that we have performed has important implications for the development of femtosecond CARS as a diagnostic tool for gas-phase media. First of all, the two-photon Raman resonance can be excited very effectively with the 70 fs laser pulses, even though the frequency bandwidth of the laser radiation is more than a factor of 1000 greater than the Raman linewidths of the N_2 Q -branch transitions. For the femtosecond CARS experiments that we have performed, the irradiance product $I_{\text{pump}}^{\text{pk}} I_{\text{Stokes}}^{\text{pk}}$ is within an order of magnitude of the value of approximately $5 \times 10^{35} \text{ W}^2/\text{m}^4$, at which Raman saturation effects begin to become significant. In addition, the different excited Raman coherences are oscillating with the same phase, resulting in a giant Raman coherence, just after the impulsive pump-Stokes excitation. We had assumed that the different transitions were oscillating in phase, following impulsive pump-Stokes excitation in our previous work,¹ and our numerical computations have confirmed this, at least for Fourier-transform-limited pump and Stokes pulses. The DNI calculations thus provide a quantitative framework for estimating signal levels for femtosecond CARS diagnostic techniques.

We will investigate the effect of processes leading to non-Fourier-transform-limited pulses, such as chirp, on the impulsive pump-Stokes excitation process in future numeri-

cal studies. In addition, the use of pulse shaping to selectively excite specific vibrational modes and/or to discriminate against the nonresonant background has been demonstrated in previous experiments.^{5,8-10,34-39} The DNI approach is ideally suited for theoretical studies of the effects of non-Fourier-transform-limited pulses on femtosecond CARS signal generation and for the evaluation of different pulse shaping strategies. Time-dependent phase, frequency, and polarization of the input laser beams can all be incorporated easily into the DNI calculations.

The calculations discussed in this paper were all performed for parallel, linear polarizations of the pump, Stokes, probe, and CARS signal beams. In future studies, polarization effects will be included so that, for example, polarization techniques for nonresonant background suppression can be investigated. The structure of the excited intermediate levels will be altered by adding an effective (fictitious) $\xi^1\Pi_u$ electronic level and adjusting the strengths of the $\xi^1\Pi_u-X^1\Sigma_g^+$ and $\kappa^1\Sigma_u^+X^1\Sigma_g^+$ transitions until the correct values for both the N_2 Raman cross section and depolarization ratio are obtained.

Single-laser-shot CARS temperature measurements using a chirped pulse probe beam have been performed by Lang and Motzkus,¹⁹ the chirped pulse detection technique was also demonstrated by Knutsen *et al.*¹¹ We have performed some preliminary single-laser-shot experiments with a chirped pulse probe beam, and the observed signal levels are promising for the acquisition of single-shot spectra from flame media. Our computational results indicate that for the present commercial femtosecond laser system that we are using,³² the magnitude of the Raman coherences are close to their maximum possible values as a result of the impulsive pump-Stokes excitation. The generated CARS signal can still be increased by increasing the probe beam irradiance, however, especially for a chirped pulse probe beam. The demonstration of single-shot femtosecond CARS temperature measurements from combustion media at data rates of 1 kHz or greater is a major goal of this research, and the DNI calculations discussed in this paper are of great value for defining the necessary laser properties and experimental strategies for these high-data-rate temperature measurements.

ACKNOWLEDGMENTS

Funding for this research was provided by the National Science Foundation, Combustion and Plasmas Program, under Award No. 0413623-CTS, by the U.S. Department of Energy, Division of Chemical Sciences, Geosciences and Biosciences, under Grant No. DE-FG02-03ER15391, by the Air Force Office of Scientific Research, and by the Air Force Research Laboratory, Propulsion Directorate, Wright-Patterson Air Force Base, under Contract No. F33615-03-D-2329. Stimulating discussions with Professor Marlan O. Scully are gratefully acknowledged.

APPENDIX: DERIVATION OF THE TIME-DEPENDENT DENSITY MATRIX EQUATIONS

1. Density matrix elements for transition between states k in excited level K and states e in excited level E

The density matrix elements that describe the single photon induced coherence between level K and level E are given by

$$\begin{aligned}\dot{\rho}_{ke} = & -\rho_{ke}(i\omega_{ke} + \gamma_{ke}) - \frac{i}{\hbar} \sum_g (V_{kg}\rho_{ge} - \rho_{kg}V_{ge}) \\ & - \frac{i}{\hbar} \sum_{e'} (V_{ke'}\rho_{e'e} - \rho_{ke'}V_{e'e}) \\ & - \frac{i}{\hbar} \sum_{k'} (V_{kk'}\rho_{k'e} - \rho_{kk'}V_{k'e}).\end{aligned}\quad (\text{A1})$$

Eliminating terms that are zero due to a zero value for the electric-dipole-moment matrix element or very small in magnitude due to the negligible populations of levels K and S , we obtain

$$\begin{aligned}\dot{\rho}_{ke} = & -\rho_{ke}(i\omega_{ke} + \gamma_{ke}) - \frac{i}{\hbar} \sum_g V_{kg}\rho_{ge} - \frac{i}{\hbar} \sum_{e'} V_{ke'}\rho_{e'e} \\ & - \frac{i}{\hbar} \sum_{k'} V_{kk'}\rho_{k'e}.\end{aligned}\quad (\text{A2})$$

Substituting Eqs. (9) and (10) into Eq. (A2), we obtain

$$\begin{aligned}\dot{\rho}_{ke} \exp(-i\omega_2 t) - i\omega_2 \rho_{ke} \exp(-i\omega_2 t) + \dot{\eta}_{ke} \exp(-i\omega_3 t) \\ - i\omega_3 \eta_{ke} \exp(-i\omega_3 t) \\ = -[\sigma_{ke} \exp(-i\omega_2 t) + \eta_{ke} \exp(-i\omega_3 t)](i\omega_{ke} + \gamma_{ke}) \\ - \frac{i}{\hbar} \sum_g V_{kg}\sigma_{ge} \exp[+i(\omega_1 - \omega_2)t] \\ - \frac{i}{\hbar} \sum_{e'} V_{ke'}\rho_{e'e} - \frac{i}{\hbar} \sum_{k'} V_{kk'}\sigma_{k'e} \exp(-i\omega_2 t).\end{aligned}\quad (\text{A3})$$

Multiplying through by $\exp(+i\omega_2 t)$ and rearranging, we obtain

$$\begin{aligned}\dot{\sigma}_{ke} + \dot{\eta}_{ke} \exp[+i(\omega_2 - \omega_3)t] - i\omega_3 \eta_{ke} \exp[+i(\omega_2 - \omega_3)t] \\ = -\{\sigma_{ke} + \eta_{ke} \exp[+i(\omega_2 - \omega_3)t]\}(i\omega_{ke} - \omega_2) + \gamma_{ke} \\ - \frac{i}{\hbar} \sum_g V_{kg}\sigma_{ge} \exp(+i\omega_1 t) \\ - \frac{i}{\hbar} \sum_{e'} V_{ke'}\rho_{e'e} \exp(+i\omega_2 t) \\ - \frac{i}{\hbar} \sum_{k'} V_{kk'}\sigma_{k'e}.\end{aligned}\quad (\text{A4})$$

Substituting Eqs. (15) and (16) into Eq. (A4) and eliminating terms that oscillate at optical frequencies, we obtain

$$\begin{aligned}\dot{\sigma}_{ke} = & -\sigma_{ke}[i(\omega_{ke} - \omega_2) + \gamma_{ke}] - \frac{i}{\hbar} \sum_g V_{kg}^{(-1)} \sigma_{ge} \\ & - \frac{i}{\hbar} \sum_{e'} V_{ke'}^{(-2)} \rho_{e'e}.\end{aligned}\quad (\text{A5})$$

Writing the density matrix elements and radiative interaction terms in terms of real and imaginary components and assuming steady state ($\dot{\sigma}_{ke}=0$), we obtain

$$\begin{aligned}0 = & -(\sigma_{ke}^r + i\sigma_{ke}^i)[i(\omega_{ke} - \omega_2) + \gamma_{ke}] \\ & - \frac{i}{\hbar} \sum_g [V_{kg}^{(-1r)} + iV_{kg}^{(-1i)}](\sigma_{ge}^r + i\sigma_{ge}^i) \\ & - \frac{i}{\hbar} \sum_{e'} [V_{ke'}^{(-2r)} + iV_{ke'}^{(-2i)}](\rho_{e'e}^r + i\rho_{e'e}^i).\end{aligned}\quad (\text{A6})$$

Solving for the real and imaginary components, we obtain

$$0 = \sigma_{ke}^i(\omega_{ke} - \omega_2) - \sigma_{ke}^r \gamma_{ke} + \alpha_{1ke} + \alpha_{2ke'e}, \quad (\text{A7})$$

$$0 = -\sigma_{ke}^r(\omega_{ke} - \omega_2) - \sigma_{ke}^i \gamma_{ke} + \beta_{1ke} + \beta_{2ke'e}, \quad (\text{A8})$$

where

$$\alpha_{1ke} = \frac{1}{\hbar} \sum_g [V_{kg}^{(-1r)} \sigma_{ge}^i + V_{kg}^{(-1i)} \sigma_{ge}^r], \quad (\text{A9})$$

$$\alpha_{2ke'e} = \frac{1}{\hbar} \sum_{e'} [V_{ke'}^{(-2r)} \rho_{e'e}^i + V_{ke'}^{(-2i)} \rho_{e'e}^r], \quad (\text{A10})$$

$$\beta_{1ke} = \frac{1}{\hbar} \sum_g [-V_{kg}^{(-1r)} \sigma_{ge}^r + V_{kg}^{(-1i)} \sigma_{ge}^i], \quad (\text{A11})$$

$$\beta_{2ke'e} = \frac{1}{\hbar} \sum_{e'} [-V_{ke'}^{(-2r)} \rho_{e'e}^r + V_{ke'}^{(-2i)} \rho_{e'e}^i]. \quad (\text{A12})$$

Solving for σ_{ke}^r and σ_{ke}^i , we obtain

$$\sigma_{ke}^r = \frac{(\beta_{1ke} + \beta_{2ke'e})(\omega_{ke} - \omega_2) + (\alpha_{1ke} + \alpha_{2ke'e})\gamma_{ke}}{(\omega_{ke} - \omega_2)^2 + \gamma_{ke}^2}, \quad (\text{A13})$$

$$\sigma_{ke}^i = [-\sigma_{ke}^r(\omega_{ke} - \omega_2) + \beta_{1ke} + \beta_{2ke'e}]/\gamma_{ke}. \quad (\text{A14})$$

Multiplying Eq. (A3) through by $\exp(+i\omega_3 t)$ and rearranging, we obtain

$$\begin{aligned}\dot{\sigma}_{ke} \exp[+i(\omega_3 - \omega_2)t] - i\omega_2 \sigma_{ke} \exp[+i(\omega_3 - \omega_2)t] + \dot{\eta}_{ke} \\ = -\{\sigma_{ke} \exp[+i(\omega_3 - \omega_2)t] + \eta_{ke}\}(i\omega_{ke} - \omega_3) + \gamma_{ke} \\ - \frac{i}{\hbar} \sum_g V_{kg}\sigma_{ge} \exp[+i(\omega_1 - \omega_2 + \omega_3)t] \\ - \frac{i}{\hbar} \sum_{e'} V_{ke'}\rho_{e'e} \exp(+i\omega_3 t) \\ - \frac{i}{\hbar} \sum_{k'} V_{kk'}\sigma_{k'e} \exp[+i(\omega_3 - \omega_2)t].\end{aligned}\quad (\text{A15})$$

Substituting Eqs. (15) and (16) into Eq. (A15) and eliminating terms that oscillate at optical frequencies, we obtain

$$\dot{\eta}_{ke} = -\eta_{ke}[i(\omega_{ke} - \omega_3) + \gamma_{ke}] - \frac{i}{\hbar} \sum_{e'} V_{ke'}^{(-3)} \rho_{e'e}^{(-3)}. \quad (\text{A16})$$

Writing Eq. (A16) in terms of real and imaginary components assuming steady state ($\dot{\eta}_{ke}=0$), we obtain

$$0 = -(\eta_{ke}^r + i\eta_{ke}^i)[i(\omega_{ke} - \omega_3) + \gamma_{ke}] - \frac{i}{\hbar} \sum_{e'} (V_{ke'}^{(-3r)} + iV_{ke'}^{(-3i)})(\rho_{e'e}^r + i\rho_{e'e}^i). \quad (\text{A17})$$

Equating real and imaginary components in Eq. (A17), we obtain

$$\begin{aligned} \eta_{ke}^r \gamma_{ke} - \eta_{ke}^i(\omega_{ke} - \omega_3) &= \frac{1}{\hbar} \sum_{e'} (V_{ke'}^{(-3r)} \rho_{e'e}^i + V_{ke'}^{(-3i)} \rho_{e'e}^r) \\ &= \alpha_{3ke'e}, \end{aligned} \quad (\text{A18})$$

$$\begin{aligned} \eta_{ke}^r(\omega_{ke} - \omega_3) + \eta_{ke}^i \gamma_{ke} &= \frac{1}{\hbar} \sum_{e'} (-V_{ke'}^{(-3r)} \rho_{e'e}^r + V_{ke'}^{(-3i)} \rho_{e'e}^i) \\ &= \beta_{3ke'e}. \end{aligned} \quad (\text{A19})$$

Solving Eq. (A19) for η_{ke}^i , we obtain

$$\eta_{ke}^i = [-\eta_{ke}^r(\omega_{ke} - \omega_3) + \beta_{3ke'e}]/\gamma_{ke}. \quad (\text{A20})$$

Substituting Eq. (A20) into Eq. (A18) and solving for η_{ke}^r , we obtain

$$\eta_{ke}^r = \frac{\alpha_{3ke'e} \gamma_{ke} + \beta_{3ke'e}(\omega_{ke} - \omega_3)}{\gamma_{ke}^2 + (\omega_{ke} - \omega_3)^2}. \quad (\text{A21})$$

2. Density matrix elements for transition between states *e* in excited level *E* and states *g* in ground level *G*

The density matrix elements that describe the two-photon-induced transitions between ground level *G* and excited level *E* are given by

$$\begin{aligned} \dot{\rho}_{eg} &= -\rho_{eg}(i\omega_{eg} + \gamma_{eg}) - \frac{i}{\hbar} \sum_{g'} (V_{eg'} \rho_{g'g} - \rho_{eg'} V_{g'g}) \\ &\quad - \frac{i}{\hbar} \sum_{e'} (V_{ee'} \rho_{e'g} - \rho_{ee'} V_{e'g}) \\ &\quad - \frac{i}{\hbar} \sum_k (V_{ek} \rho_{kg} - \rho_{ek} V_{kg}). \end{aligned} \quad (\text{A22})$$

Substituting using Eqs. (8)–(10), rearranging, and eliminating terms that are negligible, we obtain

$$\begin{aligned} \dot{\sigma}_{eg} \exp[-i(\omega_1 - \omega_2)t] - i(\omega_1 - \omega_2) \sigma_{eg} \exp[-i(\omega_1 - \omega_2)t] \\ = -\sigma_{eg} \exp[-i(\omega_1 - \omega_2)t](i\omega_{eg} + \gamma_{eg}) \\ - \frac{i}{\hbar} \sum_k \{V_{ek}[\sigma_{kg} \exp(-i\omega_1 t) + \eta_{kg} \exp(-i\omega_4 t)] \\ - [\sigma_{ek} \exp(+i\omega_2 t) + \eta_{ek} \exp(+i\omega_3 t)]V_{kg}\}. \end{aligned} \quad (\text{A23})$$

Multiplying through by $\exp[+i(\omega_1 - \omega_2)t]$ and rearranging, we obtain

$$\begin{aligned} \dot{\sigma}_{eg} &= -\sigma_{eg}\{i[\omega_{eg} - (\omega_1 - \omega_2)] + \gamma_{eg}\} \\ &\quad - \frac{i}{\hbar} \sum_k V_{ek}\{\sigma_{kg} \exp(-i\omega_2 t) \\ &\quad + \eta_{kg} \exp[-i(\omega_4 - \omega_1 + \omega_2)t]\} \\ &\quad + \frac{i}{\hbar} \sum_k \{\sigma_{ek} \exp(+i\omega_1 t) \\ &\quad + \eta_{ek} \exp[+i(\omega_3 + \omega_1 - \omega_2)t]\}V_{kg}. \end{aligned} \quad (\text{A24})$$

Using the relation $\omega_4 = \omega_1 - \omega_2 + \omega_3$, we can rewrite Eq. (A24) as

$$\begin{aligned} \dot{\sigma}_{eg} &= -\sigma_{eg}\{i[\omega_{eg} - (\omega_1 - \omega_2)] + \gamma_{eg}\} \\ &\quad - \frac{i}{\hbar} \sum_k V_{ek}[\sigma_{kg} \exp(-i\omega_2 t) + \eta_{kg} \exp(-i\omega_3 t)] \\ &\quad + \frac{i}{\hbar} \sum_k [\sigma_{ek} \exp(+i\omega_1 t) + \eta_{ek} \exp(+i\omega_4 t)]V_{kg}. \end{aligned} \quad (\text{A25})$$

Substituting for the radiative interaction terms using Eqs. (15) and (16) and keeping only those terms that do not oscillate at optical frequencies, we obtain

$$\begin{aligned} \dot{\sigma}_{eg} &= -\sigma_{eg}\{i[\omega_{eg} - (\omega_1 - \omega_2)] + \gamma_{eg}\} \\ &\quad - \frac{i}{\hbar} \sum_k (V_{ek}^{(+2)} \sigma_{kg} + V_{ek}^{(+3)} \eta_{kg} - \sigma_{ek} V_{kg}^{(-1)}), \end{aligned} \quad (\text{A26})$$

$$\begin{aligned} \dot{\sigma}_{eg}^r + i\dot{\sigma}_{eg}^i &= -(\sigma_{eg}^r + i\sigma_{eg}^i)\{i[\omega_{eg} - (\omega_1 - \omega_2)] + \gamma_{eg}\} \\ &\quad - \frac{i}{\hbar} \sum_k [(V_{ek}^{(+2r)} + iV_{ek}^{(+2i)})(\sigma_{kg}^r + i\sigma_{kg}^i) \\ &\quad + (V_{ek}^{(+3r)} + iV_{ek}^{(+3i)})(\eta_{kg}^r + i\eta_{kg}^i) \\ &\quad - (\sigma_{ek}^r + i\sigma_{ek}^i)(V_{kg}^{(-1r)} + iV_{kg}^{(-1i)})], \end{aligned} \quad (\text{A27})$$

$$\begin{aligned} \dot{\sigma}_{eg}^r &= \sigma_{eg}^i[\omega_{eg} - (\omega_1 - \omega_2)] - \sigma_{eg}^r \gamma_{eg} + \frac{1}{\hbar} \sum_k [V_{ek}^{(+2r)} \sigma_{kg}^i \\ &\quad + V_{ek}^{(+2i)} \sigma_{kg}^r + V_{ek}^{(+3r)} \eta_{kg}^i + V_{ek}^{(+3i)} \eta_{kg}^r - \sigma_{ek}^r V_{kg}^{(-1i)} \\ &\quad - \sigma_{ek}^i V_{kg}^{(-1r)}], \end{aligned} \quad (\text{A28})$$

$$\begin{aligned} \dot{\sigma}_{eg}^i &= -\sigma_{eg}^r[\omega_{eg} - (\omega_1 - \omega_2)] - \sigma_{eg}^i \gamma_{eg} + \frac{1}{\hbar} \sum_k [-V_{ek}^{(+2r)} \sigma_{kg}^r \\ &\quad + V_{ek}^{(+2i)} \sigma_{kg}^i - V_{ek}^{(+3r)} \eta_{kg}^r + V_{ek}^{(+3i)} \eta_{kg}^i + \sigma_{ek}^r V_{kg}^{(-1r)} \\ &\quad - \sigma_{ek}^i V_{kg}^{(-1i)}]. \end{aligned} \quad (\text{A29})$$

3. Density matrix elements for coherence between states e' in excited level E and states e in excited level E

The density matrix elements that describe the coherence between states e and e' in excited level E , where $e \neq e'$, are given by

$$\begin{aligned}\dot{\rho}_{e'e} = & -\rho_{e'e}(i\omega_{e'e} + \gamma_{e'e}) - \frac{i}{\hbar} \sum_g (V_{e'g}\rho_{ge} - \rho_{e'g}V_{ge}) \\ & - \frac{i}{\hbar} \sum_{e''} (V_{e'e''}\rho_{e''e} - \rho_{e'e''}V_{e''e}) \\ & - \frac{i}{\hbar} \sum_k (V_{e'k}\rho_{ke} - \rho_{e'k}V_{ke}).\end{aligned}\quad (\text{A30})$$

The radiative interaction terms are zero for many of these transitions

$$\dot{\rho}_{e'e} = -\rho_{e'e}(i\omega_{e'e} + \gamma_{e'e}) - \frac{i}{\hbar} \sum_k (V_{e'k}\rho_{ke} - \rho_{e'k}V_{ke}).\quad (\text{A31})$$

Using Eq. (9), we obtain

$$\begin{aligned}\dot{\rho}_{e'e} = & -\rho_{e'e}(i\omega_{e'e} + \gamma_{e'e}) - \frac{i}{\hbar} \sum_k [V_{e'k}\sigma_{ke} \exp(-i\omega_2 t) \\ & - \sigma_{e'k} \exp(+i\omega_2 t)V_{ke}].\end{aligned}\quad (\text{A32})$$

Substituting for the radiative interaction terms and neglecting terms that oscillate at optical frequencies, we obtain

$$\dot{\rho}_{e'e} = -\rho_{e'e}(i\omega_{e'e} + \gamma_{e'e}) - \frac{i}{\hbar} \sum_k [V_{e'k}^{(+2)}\sigma_{ke} - \sigma_{e'k}V_{ke}^{(-2)}].\quad (\text{A33})$$

Solving for the real and imaginary parts of $\rho_{e'e} = \rho_{e'e}^r + i\rho_{e'e}^i$, we obtain

$$\begin{aligned}\dot{\rho}_{e'e}^r + i\dot{\rho}_{e'e}^i = & -(\rho_{e'e}^r + i\rho_{e'e}^i)(i\omega_{e'e} + \gamma_{e'e}) \\ & - \frac{i}{\hbar} \sum_k [(V_{e'k}^{(+2r)} + iV_{e'k}^{(+2i)})(\sigma_{ke}^r + i\sigma_{ke}^i) \\ & - (\sigma_{e'k}^r + i\sigma_{e'k}^i)(V_{ke}^{(-2r)} + iV_{ke}^{(-2i)})],\end{aligned}\quad (\text{A34})$$

$$\begin{aligned}\dot{\rho}_{e'e}^r = & \rho_{e'e}^i\omega_{e'e} - \rho_{e'e}^r\gamma_{e'e} + \frac{1}{\hbar} \sum_k (V_{e'k}^{(+2r)}\sigma_{ke}^i + V_{e'k}^{(+2i)}\sigma_{ke}^r \\ & - \sigma_{e'k}^rV_{ke}^{(-2i)} - \sigma_{e'k}^iV_{ke}^{(-2r)}),\end{aligned}\quad (\text{A35})$$

$$\begin{aligned}\dot{\rho}_{e'e}^i = & -\rho_{e'e}^r\omega_{e'e} - \rho_{e'e}^i\gamma_{e'e} + \frac{1}{\hbar} \sum_k (-V_{e'k}^{(+2r)}\sigma_{ke}^r + V_{e'k}^{(+2i)}\sigma_{ke}^i \\ & + \sigma_{e'k}^rV_{ke}^{(-2r)} - \sigma_{e'k}^iV_{ke}^{(-2i)}).\end{aligned}\quad (\text{A36})$$

4. Density matrix elements for coherence between states g' in ground level G and states g in ground level G

The density matrix elements that describe the coherence between states g and g' in ground level G , where $g \neq g'$, are given by

$$\begin{aligned}\dot{\rho}_{g'g} = & -\rho_{g'g}(i\omega_{g'g} + \gamma_{g'g}) - \frac{i}{\hbar} \sum_{g''} (V_{g'g''}\rho_{g''g} - \rho_{g'g''}V_{g''g}) \\ & - \frac{i}{\hbar} \sum_e (V_{g'e}\rho_{eg} - \rho_{g'e}V_{eg}) \\ & - \frac{i}{\hbar} \sum_k (V_{g'k}\rho_{kg} - \rho_{g'k}V_{kg}).\end{aligned}\quad (\text{A37})$$

The radiative interaction terms are zero for many of these transitions

$$\dot{\rho}_{g'g} = -\rho_{g'g}(i\omega_{g'g} + \gamma_{g'g}) - \frac{i}{\hbar} \sum_k (V_{g'k}\rho_{kg} - \rho_{g'k}V_{kg}).\quad (\text{A38})$$

Using Eq. (8), we obtain

$$\begin{aligned}\dot{\rho}_{g'g} = & -\rho_{g'g}(i\omega_{g'g} + \gamma_{g'g}) - \frac{i}{\hbar} \sum_k [V_{g'k}\sigma_{kg} \exp(-i\omega_1 t) \\ & - \sigma_{g'k} \exp(+i\omega_1 t)V_{kg}].\end{aligned}\quad (\text{A39})$$

Substituting for the radiative interaction terms and neglecting terms that oscillate at optical frequencies, we obtain

$$\dot{\rho}_{g'g} = -\rho_{g'g}(i\omega_{g'g} + \gamma_{g'g}) - \frac{i}{\hbar} \sum_k [V_{g'k}^{(+1)}\sigma_{kg} - \sigma_{g'k}V_{kg}^{(-1)}].\quad (\text{A40})$$

Solving for the real and imaginary parts of $\rho_{g'g} = \rho_{g'g}^r + i\rho_{g'g}^i$, we obtain

$$\begin{aligned}\dot{\rho}_{g'g}^r + i\dot{\rho}_{g'g}^i = & -(\rho_{g'g}^r + i\rho_{g'g}^i)(i\omega_{g'g} + \gamma_{g'g}) \\ & - \frac{i}{\hbar} \sum_k [(V_{g'k}^{(+1r)} + iV_{g'k}^{(+1i)})(\sigma_{kg}^r + i\sigma_{kg}^i) \\ & - (\sigma_{g'k}^r + i\sigma_{g'k}^i)(V_{kg}^{(-1r)} + iV_{kg}^{(-1i)})],\end{aligned}\quad (\text{A41})$$

$$\begin{aligned}\dot{\rho}_{g'g}^r = & +\rho_{g'g}^i\omega_{g'g} - \rho_{g'g}^r\gamma_{g'g} + \frac{1}{\hbar} \sum_k (V_{g'k}^{(+1r)}\sigma_{kg}^i + V_{g'k}^{(+1i)}\sigma_{kg}^r \\ & - \sigma_{g'k}^rV_{kg}^{(-1i)} - \sigma_{g'k}^iV_{kg}^{(-1r)}),\end{aligned}\quad (\text{A42})$$

$$\begin{aligned}\dot{\rho}_{g'g}^i = & -\rho_{g'g}^r\omega_{g'g} - \rho_{g'g}^i\gamma_{g'g} + \frac{1}{\hbar} \sum_k (-V_{g'k}^{(+1r)}\sigma_{kg}^r \\ & + V_{g'k}^{(+1i)}\sigma_{kg}^i + \sigma_{g'k}^rV_{kg}^{(-1r)} - \sigma_{g'k}^iV_{kg}^{(-1i)}).\end{aligned}\quad (\text{A43})$$

5. Density matrix element for population of states e in excited level E

The density matrix element for the population of state e in excited level E is given by

$$\begin{aligned}\dot{\rho}_{ee} = & -\Gamma_e \rho_{ee} + \sum_m \Gamma_{me} \rho_{mm} - \frac{i}{\hbar} \sum_g (V_{eg} \rho_{ge} - \rho_{eg} V_{ge}) \\ & - \frac{i}{\hbar} \sum_k (V_{ek} \rho_{ke} - \rho_{ek} V_{ke}) - \frac{i}{\hbar} \sum_{e'} (V_{ee'} \rho_{e'e} - \rho_{ee'} V_{e'e}).\end{aligned}\quad (\text{A44})$$

Simplifying by deleting terms that are zero or negligible gives us

$$\dot{\rho}_{ee} = -\Gamma_e \rho_{ee} + \sum_m \Gamma_{me} \rho_{mm} - \frac{i}{\hbar} \sum_k (V_{ek} \rho_{ke} - \rho_{ek} V_{ke}). \quad (\text{A45})$$

Substituting using Eqs. (9), we obtain

$$\begin{aligned}\dot{\rho}_{ee} = & -\Gamma_e \rho_{ee} + \sum_m \Gamma_{me} \rho_{mm} - \frac{i}{\hbar} \sum_k \{V_{ek} [\sigma_{ke} \exp(-i\omega_2 t) \\ & + \eta_{ke} \exp(-i\omega_3 t)] - [\sigma_{ek} \exp(+i\omega_2 t) \\ & + \eta_{ek} \exp(+i\omega_3 t)] V_{ke}\}.\end{aligned}\quad (\text{A46})$$

Substituting for the radiative interaction terms using Eqs. (15) and (16) and eliminating terms that oscillate at optical frequencies, we obtain

$$\begin{aligned}\dot{\rho}_{ee} = & -\Gamma_e \rho_{ee} + \sum_m \Gamma_{me} \rho_{mm} - \frac{i}{\hbar} \sum_k [V_{ek}^{(+2)} \sigma_{ke} - \sigma_{ek} V_{ke}^{(-2)}] \\ & - \frac{i}{\hbar} \sum_k [V_{ek}^{(+3)} \eta_{ke} - \eta_{ek} V_{ke}^{(-3)}].\end{aligned}\quad (\text{A47})$$

Writing Eq. (A47) in terms of real and imaginary components, we obtain

$$\begin{aligned}\dot{\rho}_{ee} = & -\Gamma_e \rho_{ee} + \sum_m \Gamma_{me} \rho_{mm} - \frac{i}{\hbar} \sum_k [(V_{ek}^{(+2r)} + iV_{ek}^{(+2i)}) \\ & \times (\sigma_{ke}^r + i\sigma_{ke}^i) - (\sigma_{ek}^r + i\sigma_{ek}^i)(V_{ke}^{(-2r)} + iV_{ke}^{(-2i)})] \\ & - \frac{i}{\hbar} \sum_k [(V_{ek}^{(+3r)} + iV_{ek}^{(+3i)})(\eta_{ke}^r + i\eta_{ke}^i) - (\eta_{ek}^r + i\eta_{ek}^i) \\ & \times (V_{ke}^{(-3r)} + iV_{ke}^{(-3i)})].\end{aligned}\quad (\text{A48})$$

Solving for $\dot{\rho}_{ee}$,

$$\begin{aligned}\dot{\rho}_{ee} = & -\Gamma_e \rho_{ee} + \sum_m \Gamma_{me} \rho_{mm} - \frac{i}{\hbar} \sum_k (V_{ek}^{(+2r)} \sigma_{ke}^r - V_{ek}^{(+2i)} \sigma_{ke}^i \\ & - \sigma_{ek}^r V_{ke}^{(-2r)} + \sigma_{ek}^i V_{ke}^{(-2i)}) - \frac{i}{\hbar} \sum_k (V_{ek}^{(+3r)} \eta_{ke}^r - V_{ek}^{(+3i)} \eta_{ke}^i \\ & - \eta_{ek}^r V_{ke}^{(-3r)} + \eta_{ek}^i V_{ke}^{(-3i)}) + \frac{1}{\hbar} \sum_k (V_{ek}^{(+2r)} \sigma_{ke}^i + V_{ek}^{(+2i)} \sigma_{ke}^r \\ & - \sigma_{ek}^i V_{ke}^{(-2i)} - \sigma_{ek}^r V_{ke}^{(-2r)}) + \frac{1}{\hbar} \sum_k (V_{ek}^{(+3r)} \eta_{ke}^i + V_{ek}^{(+3i)} \eta_{ke}^r \\ & - \eta_{ek}^i V_{ke}^{(-3i)} - \eta_{ek}^r V_{ke}^{(-3r)}).\end{aligned}$$

$$- \eta_{ek}^r V_{ke}^{(-3i)} - \eta_{ek}^i V_{ke}^{(-3r)}). \quad (\text{A49})$$

It is not immediately obvious that the imaginary terms in Eq. (A49) are zero. However, the radiative interaction terms are described by relations such as

$$V_{ek}^{(+2)} = -\frac{1}{2} \boldsymbol{\mu}_{ek} \cdot (\hat{\mathbf{e}}_2^* A_2^*) = -\frac{1}{2} (\boldsymbol{\mu}_{ke})^* \cdot (\hat{\mathbf{e}}_2 A_2)^* = (V_{ke}^{(-2)})^* \quad (\text{A50})$$

and

$$V_{ek}^{(+3)} = -\frac{1}{2} \boldsymbol{\mu}_{ek} \cdot (\hat{\mathbf{e}}_3^* A_3^*) = -\frac{1}{2} (\boldsymbol{\mu}_{ke})^* \cdot (\hat{\mathbf{e}}_3 A_3)^* = (V_{ke}^{(-3)})^*. \quad (\text{A51})$$

Substituting Eqs. (A50) and (A51) into Eq. (A49), we obtain

$$\begin{aligned}\dot{\rho}_{ee} = & -\Gamma_e \rho_{ee} + \sum_m \Gamma_{me} \rho_{mm} + \frac{2}{\hbar} \sum_k (V_{ek}^{(+2r)} \sigma_{ke}^i + V_{ek}^{(+2i)} \sigma_{ke}^r) \\ & + \frac{2}{\hbar} \sum_k (V_{ek}^{(+3r)} \eta_{ke}^i + V_{ek}^{(+3i)} \eta_{ke}^r).\end{aligned}\quad (\text{A52})$$

6. Density matrix element for population of state g in excited level G

The density matrix element for the population of state g in ground level G is given by

$$\begin{aligned}\dot{\rho}_{gg} = & -\Gamma_g \rho_{gg} + \sum_m \Gamma_{mg} \rho_{mm} - \frac{i}{\hbar} \sum_{g'} (V_{gg'} \rho_{g'g} - \rho_{gg'} V_{g'g}) \\ & - \frac{i}{\hbar} \sum_k (V_{gk} \rho_{kg} - \rho_{gk} V_{kg}) - \frac{i}{\hbar} \sum_e (V_{ge} \rho_{eg} - \rho_{ge} V_{eg}).\end{aligned}\quad (\text{A53})$$

Simplifying by deleting terms that are zero or negligible gives us

$$\dot{\rho}_{gg} = -\Gamma_g \rho_{gg} + \sum_m \Gamma_{mg} \rho_{mm} - \frac{i}{\hbar} \sum_k (V_{gk} \rho_{kg} - \rho_{gk} V_{kg}). \quad (\text{A54})$$

Substituting using Eq. (8), we obtain

$$\begin{aligned}\dot{\rho}_{gg} = & -\Gamma_g \rho_{gg} + \sum_m \Gamma_{mg} \rho_{mm} - \frac{i}{\hbar} \sum_k \{V_{gk} [\sigma_{kg} \exp(-i\omega_1 t) \\ & + \eta_{kg} \exp(-i\omega_4 t)] - [\sigma_{gk} \exp(+i\omega_1 t) \\ & + \eta_{gk} \exp(+i\omega_4 t)] V_{kg}\}.\end{aligned}\quad (\text{A55})$$

Substituting for the radiative interaction terms using Eq. (15) and eliminating terms that oscillate at optical frequencies, we obtain

$$\dot{\rho}_{gg} = -\Gamma_g \rho_{gg} + \sum_m \Gamma_{mg} \rho_{mm} - \frac{i}{\hbar} \sum_k [V_{gk}^{(+1)} \sigma_{kg} - \sigma_{gk} V_{kg}^{(-1)}]. \quad (\text{A56})$$

Writing Eq. (A56) in terms of real and imaginary components, we obtain

$$\begin{aligned} \dot{\rho}_{gg} = & -\Gamma_g \rho_{gg} + \sum_m \Gamma_{mg} \rho_{mm} - \frac{i}{\hbar} \sum_k [(V_{gk}^{(+1r)} + iV_{gk}^{(+1i)}) \\ & \times (\sigma_{kg}^r + i\sigma_{kg}^i) - (\sigma_{gk}^r + i\sigma_{gk}^i)(V_{kg}^{(-1r)} + iV_{kg}^{(-1i)})]. \end{aligned} \quad (\text{A57})$$

Solving for $\dot{\rho}_{gg}$, we obtain

$$\begin{aligned} \dot{\rho}_{gg} = & -\Gamma_g \rho_{gg} + \sum_m \Gamma_{mg} \rho_{mm} + \frac{1}{\hbar} \sum_k (V_{gk}^{(+1r)} \sigma_{kg}^i + V_{gk}^{(+1i)} \sigma_{kg}^r \\ & - \sigma_{gk}^r V_{kg}^{(-1i)} - \sigma_{gk}^i V_{kg}^{(-1r)}) + \frac{i}{\hbar} \sum_k (-V_{gk}^{(+1r)} \sigma_{kg}^r \\ & + V_{gk}^{(+1i)} \sigma_{kg}^i + \sigma_{gk}^r V_{kg}^{(-1r)} - \sigma_{gk}^i V_{kg}^{(-1i)}). \end{aligned} \quad (\text{A58})$$

Again we can use the relation $V_{gk}^{+1} = (V_{kg}^{-1})^*$ to eliminate the imaginary terms in Eq. (A58) to obtain

$$\dot{\rho}_{gg} = -\Gamma_g \rho_{gg} + \sum_m \Gamma_{mg} \rho_{mm} + \frac{2}{\hbar} \sum_k (V_{gk}^{(+1r)} \sigma_{kg}^i + V_{gk}^{(+1i)} \sigma_{kg}^r). \quad (\text{A59})$$

¹R. P. Lucht, S. Roy, T. R. Meyer, and J. R. Gord, Appl. Phys. Lett. **89**, 251112 (2006).

²A. Zumbusch, G. R. Holtom, and X. S. Xie, Phys. Rev. Lett. **82**, 4142 (1999).

³J.-X. Cheng, A. Volkmer, and X. S. Xie, J. Opt. Soc. Am. B **19**, 1363 (2002).

⁴J.-X. Cheng and X. S. Xie, J. Phys. Chem. B **108**, 827 (2004).

⁵N. Dudovich, D. Oron, and Y. Silberberg, Nature (London) **418**, 512 (2002).

⁶A. Rebane, M. Drobizhev, M. Kruk, A. Karotki, I. Tehver, and M. Scully, J. Mod. Opt. **52**, 1243 (2005).

⁷Y. Huang, A. Dogariu, Y. Avitzour, R. K. Murawski, D. Pestov, M. C. Zhi, A. V. Sokolov, and M. O. Scully, J. Appl. Phys. **100**, 124912 (2006).

⁸D. Oron, N. Dudovich, D. Yelin, and Y. Silberberg, Phys. Rev. Lett. **88**, 063004 (2002).

⁹D. Oron, N. Dudovich, D. Yelin, and Y. Silberberg, Phys. Rev. A **65**, 043408 (2002).

¹⁰S.-H. Lim, A. G. Caster, and S. R. Leone, Phys. Rev. A **72**, 041803 (2005).

¹¹K. P. Knutsen, J. C. Johnson, A. E. Miller, P. B. Petersen, and R. J. Saykally, Chem. Phys. Lett. **387**, 436 (2004).

¹²M. O. Scully, G. W. Kattawar, R. P. Lucht, T. Opatrný, H. Pilloff, A. Rebane, A. V. Sokolov, and M. S. Zubairy, Proc. Natl. Acad. Sci. U.S.A.

99, 10994 (2002).

¹³D. Pestov, R. A. Murawski, G. O. Ariunbold *et al.*, Science **316**, 265 (2007).

¹⁴C. C. Hayden and D. W. Chandler, J. Chem. Phys. **103**, 10465 (1995).

¹⁵M. Schmitt, G. Knopp, A. Materny, and W. Kiefer, J. Phys. Chem. A **102**, 4059 (1998).

¹⁶S. Meyer and V. Engel, J. Raman Spectrosc. **31**, 33 (2000).

¹⁷T. Lang, K.-L. Kompa, and M. Motzkus, Chem. Phys. Lett. **310**, 65 (1999).

¹⁸T. Lang, M. Motzkus, H. M. Frey, and P. Beaud, J. Chem. Phys. **115**, 5418 (2001).

¹⁹T. Lang and M. Motzkus, J. Opt. Soc. Am. B **19**, 340 (2002).

²⁰H. Skenderović, T. Buckup, W. Wohlleben, and M. Motzkus, J. Raman Spectrosc. **33**, 866 (2002).

²¹G. Knopp, K. Kirch, P. Beaud, K. Mishima, H. Spitzer, P. Radi, M. Tulej, and T. Gerber, J. Raman Spectrosc. **34**, 989 (2003).

²²P. Beaud, H.-M. Frey, T. Lang, and M. Motzkus, Chem. Phys. Lett. **344**, 407 (2001).

²³M. Sargent III, M. O. Scully, and W. E. Lamb, Jr., *Laser Physics* (Addison-Wesley, Reading, MA, 1974).

²⁴R. W. Boyd, *Nonlinear Optics*, 2nd ed. (Academic, Amsterdam, 2003).

²⁵D. Marcuse, *Principles of Quantum Electronics* (Academic, New York, 1980).

²⁶D. A. Long, *The Raman Effect: A Unified Treatment of the Theory of Raman Scattering by Molecules* (Wiley, West Sussex, 2002), pp. 49–152.

²⁷H. W. Schrötter and H. W. Klöckner, in *Raman Spectroscopy of Gases and Liquids*, edited by A. Weber (Springer-Verlag, Berlin, 1979).

²⁸S. G. Tilford and P. G. Wilkinson, J. Mol. Spectrosc. **12**, 231 (1964).

²⁹I. Kovacs, *Rotational Structure in the Spectra of Diatomic Molecules* (American Elsevier, New York, 1969).

³⁰L. F. Shampine, *Numerical Solution of Ordinary Differential Equations* (Chapman and Hall, New York, 1994).

³¹M. Jain, H. Xia, G. Y. Yin, A. J. Merriam, and S. E. Harris, Phys. Rev. Lett. **77**, 4326 (1996).

³²S. Roy, P. J. Kinnus, R. P. Lucht, and J. R. Gord, Opt. Commun., to be published.

³³Y.-D. Qin, H. Yang, C.-J. Zhu, and Q. Gong, Appl. Phys. B: Lasers Opt. **71**, 581 (2000).

³⁴A. M. Weiner, D. E. Leaird, G. P. Wiederrecht, and K. A. Nelson, J. Opt. Soc. Am. B **8**, 1264 (1990).

³⁵V. V. Lozovoy, B. I. Grimberg, E. J. Brown, I. Pastirk, and M. Dantos, J. Raman Spectrosc. **31**, 41 (2000).

³⁶D. Oron, N. Dudovich, and Y. Silberberg, Phys. Rev. Lett. **89**, 273001 (2002).

³⁷D. Oron, N. Dudovich, and Y. Silberberg, Phys. Rev. Lett. **90**, 213902 (2003).

³⁸N. Dudovich, D. Oron, and Y. Silberberg, J. Chem. Phys. **118**, 9208 (2003).

³⁹D. Oron, N. Dudovich, and Y. Silberberg, Phys. Rev. A **70**, 023415 (2004).

Improving Signal-to-Interference Ratio in Rich Hydrocarbon–Air Flames Using Picosecond Coherent Anti-Stokes Raman Scattering

TERRENCE R. MEYER,* SUKESH ROY, and JAMES R. GORD

Department of Mechanical Engineering, Iowa State University, Ames, Iowa 50011 (T.R.M.); Innovative Scientific Solutions, Inc., 2766 Indian Ripple Road, Dayton, Ohio 45440 (S.R.); and Air Force Research Laboratory, Propulsion Directorate, Wright-Patterson AFB, Ohio 45433 (J.R.G.)

There is growing interest in the use of short-pulse lasers for coherent anti-Stokes Raman scattering (CARS) to minimize non-resonant background (NRB) contributions in a variety of applications. Using time-coincident picosecond (ps) pump and Stokes beams and a time-delayed ps probe beam, we show that a three orders of magnitude reduction in NRB interference can be achieved in rich hydrocarbon–air flames while preserving 60% to 80% of the CARS signal. This represents a significant improvement in signal-to-interference ratio compared with previous measurements in room temperature air and is attributable to reduced rates of collisional dephasing and relaxation at flame temperatures. Measurements within the flame zone of a laminar flat-flame burner are used to investigate the characteristics of time-coincident and probe-delayed broadband ps N_2 -CARS spectra for C_2H_4 –air equivalence ratios of 0.5 to 1.2. Up to three ro-vibrational bands of N_2 are excited with each laser shot using 135 ps pump and 106 ps Stokes beams, and the CARS signal is generated using a 135 ps probe beam delayed by 165 ps. The enhanced signal-to-interference ratio achieved in the current work is one to two orders of magnitude higher than that previously achieved using polarization-selection techniques without sensitivity to the effects of birefringence caused by density gradients or test cell windows. Moreover, the use of a 135 ps laser source in this study enables frequency domain “broadband” CARS with sufficient resolution to extract ro-vibrational spectral features under various flame conditions. The effect of probe delay and NRB suppression on characteristics of these broadband CARS spectra are investigated, and evidence of preferential collisional dephasing and relaxation of different ro-vibrational transitions is not detected. This is a promising but preliminary result to be investigated further in future work.

Index Headings: Coherent anti-Stokes Raman scattering; CARS; Picosecond; Ultrafast; Non-resonant background; Hydrocarbon–air flames.

INTRODUCTION

Coherent anti-Stokes Raman scattering (CARS) measurements of temperature and major-species number density have been demonstrated in a wide array of practical combusting flows, including internal combustion engines, jet engines, propellant burners, and industrial furnaces.^{1–4} The CARS signal, which is obtained through stimulated Raman pumping

and coherent scattering, is several orders of magnitude greater than spontaneous Raman scattering. It is ideal for measurements in flames with significant broadband emission because the signal is coherent and can be captured efficiently using offset detection. Under stoichiometric, fuel-rich, or high-pressure conditions, however, the increased non-resonant background (NRB) contribution from hydrocarbon species can affect the accuracy of number-density measurements and can lead to an overestimate of temperature.

Because of its impact on CARS spectroscopy, non-resonant susceptibility has been measured extensively for gaseous species commonly found in hydrocarbon–air flames.² Published uncertainties are $\pm 10\%$ and are most reliable in premixed flames and in well-mixed combustion products when the reactant composition is known *a priori*. In the mixing region of diffusion flames, the variation in non-resonant susceptibility from the oxidizer to the fuel stream can be as high as 1000% for hydrocarbon–air combustion. This leads to a certain degree of subjectivity with regard to CARS spectral analysis and limits the ability to extract quantitative information in turbulent flames. Suppressing the generation of NRB, therefore, is highly advantageous for improving the accuracy and detection limit of CARS measurements.

Previously, the most effective means of suppressing the NRB contribution for ro-vibrational CARS made use of the polarization sensitivity of CARS signals.^{5–7} The angular separation in the resonant and non-resonant signals can be optimized by selecting appropriate pump and Stokes field polarizations, and an analyzer can be used to collect the desired signal. Unfortunately, this approach reduces the CARS signal by at least a factor of 16 because the resonant signal decreases when the pump and Stokes polarizations are angularly separated. Manipulation of the polarization-dependent properties of the ro-vibrational CARS signal can improve detectability, therefore, but it is not effective under photon-limited conditions.² Non-resonant background suppression based on polarization selection^{5,8} may also be problematic in high-pressure practical combustors because of polarization scrambling from density gradients and window birefringence, where the typical window thickness can be three to four inches.

Received 30 April 2007; accepted 8 August 2007.

* Author to whom correspondence should be sent. E-mail: trm@iastate.edu.

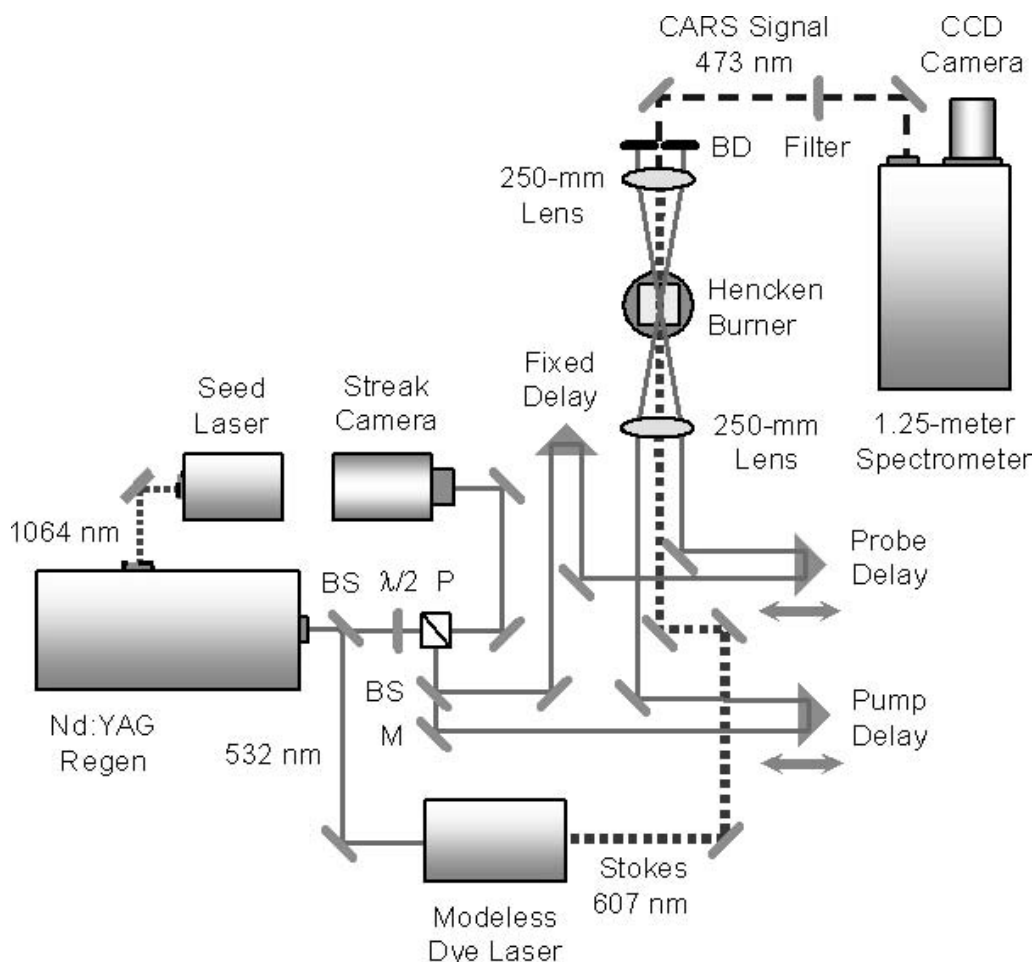


FIG. 1. Schematic diagram of broadband ps CARS system. Symbols: (BS) beam splitter, ($\lambda/2$) half-wave plate, (P) polarizer, (M) mirror, (\leftrightarrow) translation stage, and (BD) beam dump.

Alternatively, NRB suppression can be achieved using ultrashort (femtosecond or picosecond) pulses by delaying the probe beam with respect to the pump and Stokes beams.^{9–13} The objective of the current work is to investigate the use of “broadband” picosecond (ps) CARS in hydrocarbon–air flames, which combines time domain NRB suppression, commonly employed in the femtosecond regime, with the high spectral resolution frequency domain approach of nanosecond CARS. We have recently demonstrated ps N₂-CARS measurements with high spectral resolution in room air¹² and studied the time-resolved dynamics of spectrally integrated resonant and non-resonant signals.¹³ Previous data obtained in room air indicate that it is possible to reduce the NRB signal by more than three orders of magnitude with a corresponding factor of three drop in CARS signal intensity through appropriate selection of the CARS probe delay. However, it is expected that temperature dependent collisional dephasing and relaxation will significantly slow the rate of CARS signal decay in combusting flows, helping to avoid significant losses in CARS signal with increasing probe delay. This is advantageous not only for NRB suppression under photon-limited conditions, but also for enabling the use of 50 to 200 ps lasers to achieve broadband CARS with sufficient resolution to extract ro-vibrational spectral features.

The current measurements address two primary questions with regard to probe-delayed ps N₂-CARS spectra in

hydrocarbon–air flames, including (1) the effect of flame conditions on the ideal operating parameters for enhancing signal-to-interference ratio, and (2) the relative effect of probe delay and NRB suppression on excited-state ro-vibrational N₂-CARS spectra, including evidence of preferential collisional dephasing and relaxation for various ro-vibrational transitions. However, we do not present absolute improvements in temperature accuracy or precision, as we show from this work that a more advanced, time-dependent theoretical model is required for analytical comparison with spectra from non-time-coincident N₂-CARS beams. Other research using ps CARS has focused on solid-state chemical reactions or shock propagation studies,^{14–16} neither of which are directly useful for this purpose. Hence, the current work focuses on quantitative measurements of signal-to-interference ratio, with qualitative observation of the time-dependent ro-vibrational N₂-CARS spectral features.

EXPERIMENTAL

Optical System. The broadband ps CARS experimental arrangement shown in Fig. 1 is described in previous publications,^{12,13} and only a brief summary is included here for reference. A fraction of the energy from a 10 Hz, frequency-doubled, Nd:YAG regenerative amplifier (Coherent, Inc.) at 532 nm is used to pump a modeless dye laser to

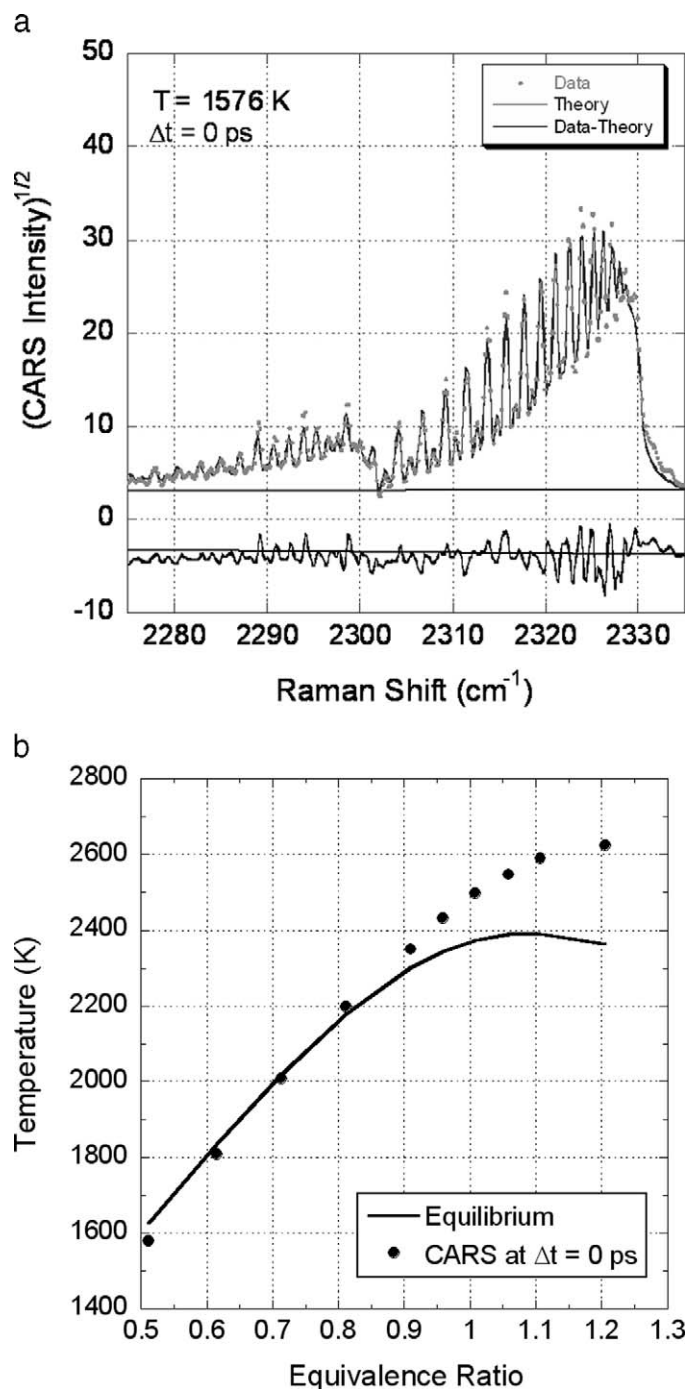


FIG. 2. (a) Experimental and theoretical broadband ps N_2 -CARS spectra at $\phi = 0.5$ with time-coincident beams and (b) temperatures acquired from $\phi = 0.5$ to 1.2 with time-coincident beams.

generate the Stokes beam at 606 nm. The output of the dye laser has a full-width at half-maximum (FWHM) bandwidth of ~ 5 nm, FWHM pulse width of 106 ps, and output energy set to 800 μJ (out of a 5 mJ maximum). The nearly transform-limited beam at 532 nm has a FWHM pulse width of ~ 135 ps and is split into pump and probe beams, each with an energy set to 150 μJ (out of an 8 mJ maximum). The pump, probe, and Stokes beams are arranged in a folded BOXCARS geometry, and the temporal overlap is adjusted using translation stages in the paths of the pump and probe beams. The spatial resolution

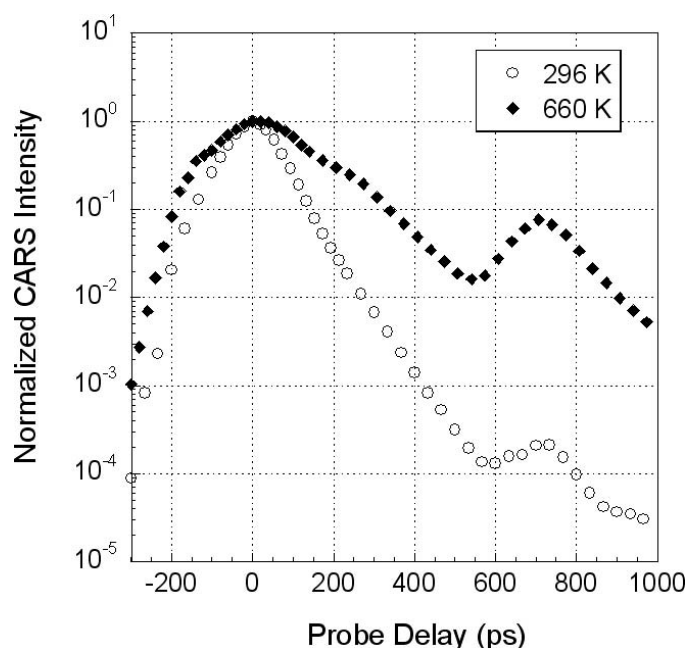


FIG. 3. CARS signal decay as a function of probe delay in a heated cell. Signals are normalized to the signal at a probe delay of zero.

is estimated to be 30 μm in the direction normal to the beam and 1.5 mm in the phase-matching direction. The CARS signal is dispersed by a 1.25 m spectrometer (SPEX 1250M) with a 2400 grooves/mm grating, and the spectrum is recorded using a back-illuminated, unintensified 2048×512 pixel array charge-coupled device (CCD) camera with full vertical binning (Andor Technologies Model DU 440BU). Single-shot CARS signal intensities recorded with this camera and using the beam energies stated above lead to full-scale signal-to-noise ratios of at least 1600:1 and 1000:1 for the time-coincident and time-delayed configurations, respectively, for all flame conditions. The spectral dispersion of the CARS signal is $0.174 \text{ cm}^{-1}/\text{pixel}$, and the resolution of the CARS detection system is $\sim 0.54 \text{ cm}^{-1}$. This is similar to the spectral resolution for nanosecond systems,³ indicating that the ps pump- and probe-laser bandwidth of $\sim 0.12 \text{ cm}^{-1}$ is sufficient to resolve the rovibrational transitions under the current flame conditions.

Test Section. Measurements are performed within the product zone at a height 12 mm above a flat C_2H_4 -air flame stabilized over a Hencken burner. The flat flame actually consists of a series of small diffusion flames whose products mix thoroughly within a few millimeters of the burner surface.¹⁷ This test configuration enables measurements in an idealized diffusion flame with well-mixed products of known composition and non-resonant susceptibility. Flow rates are adjusted to match those of previous temperature measurements,¹⁷ and the equivalence ratio (ϕ) is varied from 0.5 to 1.2 to illustrate the relative effect of the NRB at lean and rich conditions.

RESULTS AND DISCUSSION

Time-Coincident Coherent Anti-Stokes Raman Scattering Spectra. A typical 100-shot-average N_2 -CARS spectrum acquired using the ps laser system with time-coincident beams is shown in Fig. 2a, along with a theoretical fit from the Sandia CARSFT code.¹⁸ CARSFT spectra are plotted using the

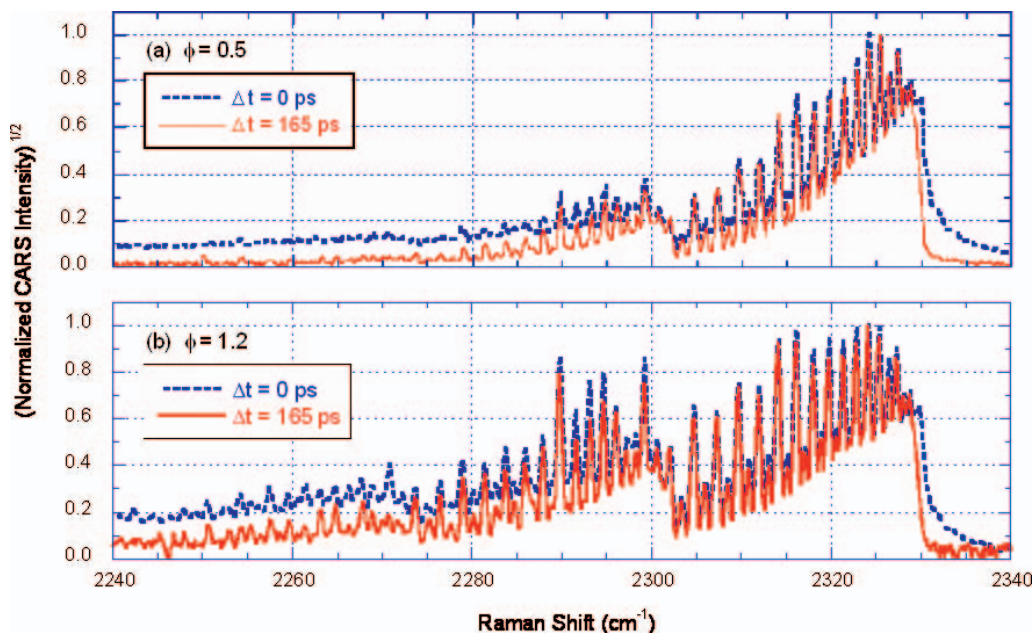


FIG. 4. Comparison of time-coincident and probe-delayed experimental broadband ps N₂-CARS spectra at (a) $\phi = 0.5$ and (b) $\phi = 1.2$.

square-root of signal intensity, which is proportional to the difference in number density between coupled vibrational levels. The spectrum in Fig. 2a is quite similar to broadband spectra obtained using nanosecond lasers with similar peak intensities, and the measured flame temperature is within 2% of the equilibrium value predicted for $\phi = 0.5$. Hence, the laser pulse widths in the current work can be used to generate high-resolution frequency domain CARS spectra that can be analyzed using the steady-state CARSFT model when the pump, Stokes, and probe beams are time coincident.

To illustrate the effect of NRB contributions on conventional CARS signal analysis, Fig. 2b shows the variation in ps CARS temperature measurements from $\phi = 0.5$ to 1.2 using time-coincident beams and assuming values of the non-resonant susceptibility² based on experimentally validated equilibrium predictions of the product composition.¹⁷ The temperature accuracy is within 50 K from $\phi = 0.5$ to 0.8, with a temperature overshoot that increases from 50 to 250 K from $\phi = 0.9$ to 1.2, respectively. Because the actual flame temperature does not

vary significantly in this latter range of equivalence ratios, it is likely that this overshoot is caused by the increased contribution of the NRB from unburned hydrocarbons.¹⁹

During the spectral fitting process for the data in Fig. 2b, the magnitude of the non-resonant susceptibility was scaled by up to 30% based on the expected product composition for rich C₂H₄-air combustion. One approach to improving temperature accuracy under rich conditions is to allow the NRB to “float” during the spectral fitting process rather than fixing its value to match that of the expected product composition. In this case, the non-resonant susceptibility of the converged solution is ~30–40% higher than that expected from the product composition. This approach improves the temperature accuracy by ~20–50 K, although the measured temperature is still over 200 K above the adiabatic flame temperature at $\phi = 1.2$. Reducing the temperature overshoot to within 100 K requires an additional 150% increase in the non-resonant susceptibility beyond that of the converged solution, which implies *a priori* knowledge of the flame temperature to “determine” the NRB level.

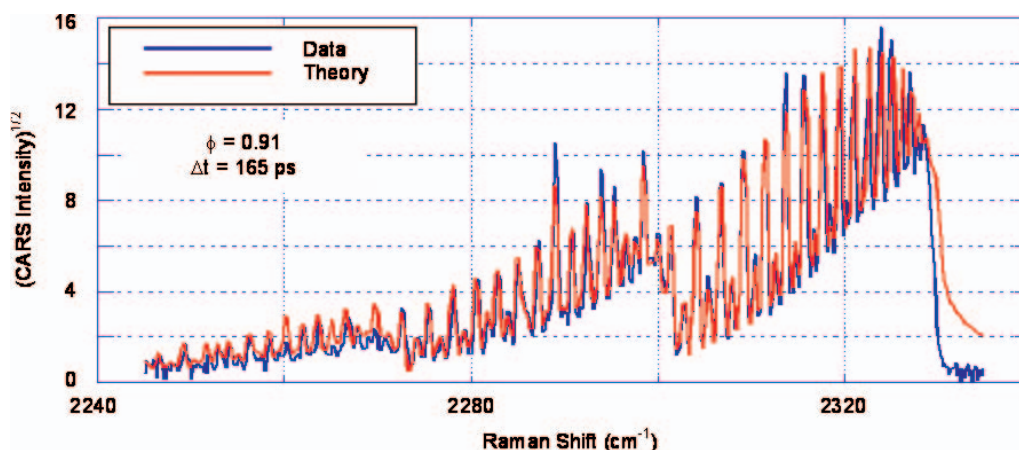


FIG. 5. Experimental and theoretical broadband ps N₂-CARS spectra at $\phi = 0.91$ with a probe delay of 165 ps.

Non-Resonant Background Suppression. As discussed earlier, the use of polarization selection for reducing the NRB signals in ro-vibrational CARS is problematic under photon-limited conditions^{5–7} and when significant sources of birefringence are present in the test section. In the current work, a five orders of magnitude reduction in NRB signal can be achieved with a probe delay of 165 ps, which at room temperature is accompanied by a factor of 15 drop in CARS signal intensity.¹³ At higher temperatures, however, the resonant CARS signal is expected to decay more slowly because of the reduced rate of collisional dephasing and relaxation.²⁰ This is illustrated clearly in Fig. 3, which shows the normalized ps CARS signal decay as a function of probe delay in a heated cell. The decay rate of the CARS signal at 660 K is only a factor of 2.5 rather than a factor of 15 for a probe delay of 165 ps.

The results of the temperature cell study indicate that relatively high CARS signal levels may be maintained with significant probe delays under flame conditions. Normalized, 100-shot-average ps CARS spectra collected in the flat flame burner at $\phi = 0.5$ and 1.2 with time-coincident beams and with a probe-beam delay of 165 ps are shown in Fig. 4. The first two ro-vibrational bands of N_2 are visible at $\phi = 0.5$, and up to three ro-vibrational bands are visible at $\phi = 1.2$. Non-resonant-background suppression while using a time-delayed probe beam is most apparent along the lower range of the rotational transitions below 2300 cm^{-1} . Odd- J rotational lines that are obscured by non-resonant contributions in the case of time-coincident beams appear more prominent when using a time-delayed probe beam.

The relative effect of the NRB contribution increases dramatically for higher ro-vibrational bands, thereby altering the relative magnitude of rotational transitions and providing a possible explanation for the temperature overshoot shown in Fig. 2b. The impact of NRB suppression on CARS measurements under signal limited conditions is most evident within the N_2 hot bands in Fig. 4 between 2280 to 2290 cm^{-1} . These plots enable one to better distinguish the NRB level from the baseline signal. It is possible to observe that the signal-to-interference ratio of the probe-delayed CARS signal is significantly higher than that of the time-coincident signal, with a background that approaches the limit of the spectral resolution in the former case. The CARS-signal intensities in Figs. 4a and 4b are reduced by 45% and 40%, respectively, leading to a five orders of magnitude drop in NRB signal while retaining a significant fraction of the CARS signal. The increase in signal-to-interference ratio for the full range of flame conditions is two orders of magnitude higher than for the use of polarization selection in ro-vibrational CARS.⁵ In addition, the suppression of NRB achieved with a time-delayed ps probe beam should have little or no dependence on polarization scrambling due to density gradients and window birefringence in combustors of practical interest.

The level of improvement in signal-to-interference ratio is obviously dependent upon the flame conditions and the selection of laser pulse widths and probe delay. For the current conditions, the selection of a shorter probe delay would still enable a three orders of magnitude reduction in NRB signal while preserving 60% to 80% of the CARS signal intensity. At high pressures, collisional dephasing rates will increase and it may be beneficial to use a shorter probe delay. In this case, laser pulse widths on the order of 50 to 80 ps would allow comparable NRB suppression with a reduced probe-beam

delay to preserve CARS signal intensity. The increase in laser linewidth would not adversely affect measurement resolution because of the increase in ro-vibrational linewidths at higher pressure. The preservation of CARS signal intensity is important for signal-limited conditions, as is often the case for single-shot measurements in turbulent diffusion flames.

Broadband Background-Free N_2 Coherent Anti-Stokes Raman Scattering Spectra. Although this work demonstrates effective NRB suppression in hydrocarbon–air flames, it is important to determine whether the time decay of the CARS polarization due to collisions will significantly distort the ro-vibrational spectra. It is not entirely certain, for example, that differences in the spectral profiles shown previously in Fig. 4 do not stem from preferential collisional dephasing and relaxation for different ro-vibrational transitions. To address this issue, Fig. 5 compares the experimental N_2 -CARS spectrum for a time delay of 165 ps with a theoretical spectrum using the CARSFT code assuming steady-state conditions and zero NRB contribution. The theoretical spectrum was obtained using the equilibrium flame temperature for an equivalence ratio of 0.91 and does not include numerical fitting with the experimental data. However, the ability of the theoretical spectrum to capture the overall ro-vibrational structure of the experimental data in Fig. 5 implies that the effect of collisions does not significantly distort the relative intensity of the CARS signal for different J -levels and vibrational bands during the first 165 ps for atmospheric-pressure flames. There is an apparent mismatch, however, between the experimental and theoretical spectra near the baseline of the N_2 CARS bandhead. This mismatch is not likely attributable to NRB suppression since the CARSFT code presumes zero NRB. It may be due, instead, to the destructive interference of two or three states that are simultaneously excited by the near-transform-limited 0.12 cm^{-1} bandwidth pump beam and the 130 cm^{-1} bandwidth Stokes beam. This mismatch prevents successful fitting with the steady-state CARSFT code and indicates that a more advanced theoretical model, currently under development, is required to account for the time-dependent N_2 -CARS signal decay.

CONCLUSION

The suppression of NRB in broadband ps N_2 -CARS spectra has been investigated in hydrocarbon–air flames of varying equivalence ratio. Improvements of at least four orders of magnitude in signal-to-background ratio can be achieved by delaying the 135 ps probe beam by 165 ps with respect to the 135 ps pump and 106 ps Stokes beams. This strategy, which achieves greater NRB suppression than polarization-based techniques while preserving a higher percentage of the CARS signal, has the potential to significantly enhance the performance of CARS thermometry in high-pressure, turbulent, liquid-fueled combustors of practical interest by overcoming the known limitations of nanosecond-based, time-coincident systems. Use of ps, transform-limited pulses also enables frequency-domain CARS for minimizing bias errors due to density fluctuations. Future work includes theoretical analyses of non-resonant-background-free CARS spectra, initially with hydrogen CARS, as well as implementation in high-pressure combustors of practical interest.

ACKNOWLEDGMENTS

The authors thank R. Lucht, R. Farrow, and L. Rahn for helpful discussions regarding short-pulse CARS. Funding for this research was provided by the Air Force Research Laboratory, Propulsion Directorate, Wright-Patterson AFB,

1. L. P. Goss, "Cars Instrumentation for Combustion Applications", in *Instrumentation for Flows with Combustion*, A. Taylor, Ed. (Academic Press Ltd., London, 1993), Chap. 4, p. 251.
2. A. C. Eckbreth, *Laser Diagnostics for Combustion Temperature and Species* (Gordon and Breach, St. Leonards, Australia, 1996), 2nd ed., p. 281.
3. S. Roy, T. R. Meyer, R. P. Lucht, V. M. Belovich, E. Corporan, and J. R. Gord, *Combust. Flame* **138**, 273 (2004).
4. T. R. Meyer, S. Roy, R. P. Lucht, and J. R. Gord, *Combust. Flame* **142**, 52 (2005).
5. L. A. Rahn, L. J. Zych, and P. L. Mattern, *Opt. Commun.* **39**, 249 (1979).
6. R. L. Farrow, P. L. Mattern, and L. A. Rahn, "Crossed-Beam Background-Free CARS Measurements in a Methane Diffusion Flame," AIAA Paper 81-0182 (American Institute of Aeronautics and Astronautics, Reston, Virginia, 1981).
7. A. C. Eckbreth and R. J. Hall, *Combust. Sci. Technol.* **25**, 175 (1981).
8. F. Vestin, M. Afzelius, C. Brackman, and P.-E. Bengtsson, *Proc. Combust. Inst.* **30**, 1673 (2006).
9. R. P. Lucht, S. Roy, T. R. Meyer, and J. R. Gord, *Appl. Phys. Lett.* **89**, 251112 (2006).
10. R. P. Lucht, *Science* (Washington, D.C.) **316**, 207 (2007).
11. D. Pestov, R. K. Murawski, G. O. Ariunbold, X. Wang, M. Zhi, A. V. Sokolov, V. A. Sautenkov, Y. V. Rostovtsev, A. Dogariu, Y. Huang, and M. Scully, *Science* (Washington, D.C.) **316**, 265 (2007).
12. S. Roy, T. R. Meyer, and J. R. Gord, *Opt. Lett.* **30**, 3222 (2005).
13. S. Roy, T. R. Meyer, and J. R. Gord, *Appl. Phys. Lett.* **87**, 264103 (2005).
14. D. E. Hare and D. D. Dlott, *Appl. Phys. Lett.* **64**, 715 (1994).
15. S. A. Hambir, J. Franken, D. E. Hare, E. L. Chronister, B. J. Baer, and D. D. Dlott, *J. Appl. Phys.* **81**, 2164 (1997).
16. Y. Yang, S. A. Hambir, and D. D. Dlott, *Shock Waves* **12**, 129 (2002).
17. T. R. Meyer, S. Roy, T. N. Anderson, J. D. Miller, V. R. Katta, R. P. Lucht, and J. R. Gord, *Appl. Opt.* **44**, 6729 (2005).
18. R. E. Palmer, Report SAND89-8206, Sandia National Laboratories, Livermore, California (1989).
19. S. P. Kearney and M. N. Jackson, "Dual-Pump CARS Thermometry in Sooting Acetylene-Fueled Flames," AIAA Paper 2006-0432 (American Institute of Aeronautics and Astronautics, Reston, Virginia, 2006).
20. G. Knopp, P. Beaud, P. Radi, M. Tulej, B. Bougie, D. Cannavo, and T. Gerber, *J. Raman Spectrosc.* **33**, 861 (2002).

Effect of Collisions on Time-Delayed Picosecond Coherent anti-Stokes Raman Scattering (ps-CARS) Spectroscopy

James R. Gord¹, Paul Hsu², and Sukesh Roy²

¹*Air Force Research Laboratory, Propulsion Directorate, Wright-Patterson AFB, Ohio 45433*

²*Innovative Scientific Solutions, Inc., 2766 Indian Ripple Road, Dayton, OH 45440*

Email: james.gord@wpafb.af.mil, [Tel: 937-255-3115](tel:937-255-3115), Fax: 937-255-1125

The effect of collisions on the measured temperatures using time-delayed ps-CARS is investigated. In ps-CARS the probe beam is delayed wrt the pump and Stokes beams in order to suppress the nonresonant background.

©2007 Optical Society of America

OCIS codes: (300.6230) Coherent anti-Stokes Raman scattering; (020.2070) Effects of collisions; (270.1670) Coherent optical effects

Coherent anti-Stokes Raman scattering (CARS) measurements of nitrogen and hydrogen molecules using conventional broadband and modeless nanosecond dye lasers have been widely utilized for thermometry in gaseous flows [1]. A significant drawback of the nanosecond CARS approach, however, is interference of the nonresonant background (NRB) signal with the resonant CARS signal. This limits the applicability, sensitivity, and accuracy of nanosecond CARS in hydrocarbon-rich environments due to the high nonresonant susceptibility of hydrocarbon compounds. The contribution from the nonresonant background signal is highest when the pump and probe beams are overlapped temporally [2-3]. In the picosecond regime, it is possible to delay the probe beam temporally with respect to the pump beam in order to suppress the nonresonant contribution to the CARS signal. It is also possible to study vibrational energy transfer (VET) and rotational energy transfer (RET) in non-equilibrium hypersonic flows.

The time-resolved dynamics of resonant broadband picosecond coherent anti-Stokes Raman scattering (CARS) signals in gas-phase media are investigated. From our previous work on N₂ CARS we have found that, for ~135-ps pump and probe beams and ~106-ps Stokes beams, the magnitude of the nonresonant signals are decreased by more than three orders of magnitude when the probe beam is delayed by ~110 ps, whereas the resonant N₂ CARS signal is reduced only by a factor of three [1]. This finding was significant for the application of broadband ps-CARS in heavily sooting hydrocarbon flames, where it is very difficult to estimate the nonresonant susceptibility for the extraction of temperatures from experimental spectra [2]. The other unique feature of the picosecond CARS system that makes it ideal for fiber coupling in harsh environment application is the requirement of only ~200 μ J of energy for the pump and probe beams as compared to 25 mJ of energy per laser beam generally required in nanosecond laser-based CARS.

However, there is a fundamental question regarding the distortion of the time-delayed spectrum that needs to be resolved before ps-CARS could be used for temperature measurements. Does the time-delayed spectrum get distorted enough during the first 200 ps, because of the variation of relaxation rates for different transitions that constitute the spectrum, to yield a completely different temperature? The time for which spectral distortion could be negligible will depend on the relevant pressure. The current work focuses on answering this question by analyzing the time-delayed spectrum of H₂ molecule for various pressures and temperatures. The rotational lines of H₂ molecule are well separated thus would allow

investigating the J-dependent relaxation rates and thereby the temperature evaluated from the resultant time-delayed spectrum.

Measurements were performed in an atmospheric-pressure, near-adiabatic hydrogen-air flame stabilized over a Hencken burner. Temperature was varied by changing the equivalence ratio (ϕ) of the flame (equivalence ratio is defined as the ratio of actual fuel-to-air over fuel-to-air

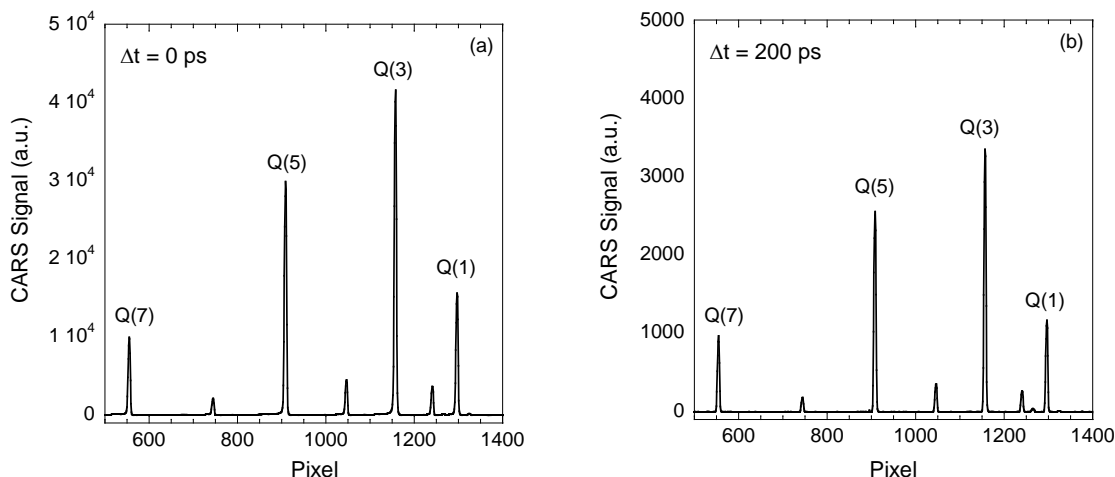


Fig. 1: H₂ CARS spectra in a nearly adiabatic laboratory flame at an equivalence ratio of 1.2. (a) Probe beam is temporally overlapped with the pump and Stokes beams and (b) probe was delayed by 200 ps wrt the pump and Stokes beams.

for the stoichiometric condition). Time-delayed CARS spectra are acquired by delaying the probe beam wrt the pump and Stokes beams. The CARS spectra of H₂ for $\phi = 1.2$ acquired at 0-ps delay and 200-ps delay are shown in Fig. 1. The Q-branch transitions of

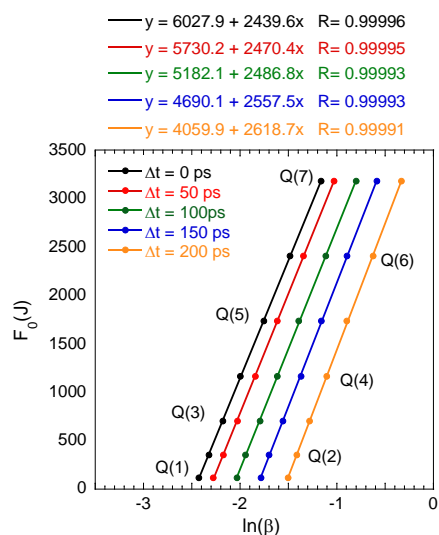


Fig. 2: Boltzmann plots of H₂ CARS spectra for different probe delays wrt the pump and Stokes beams.

equilibrium assumption. As shown in Fig. 2, the values of the temperatures extracted from time-

$v' = 1 \rightarrow v'' = 0$ vibrational band shown in Fig. 1 are used to extract temperatures using Boltzmann plot. The main purpose of this work is to find out whether the temperature extracted from 0-ps delayed spectrum is significantly different from the temperature extracted from 200-ps delayed spectrum. Moreover, we also would like to know what the optimum delay between the probe and the excitation beams is that introduces minimum uncertainty along with significant nonresonant background signal reduction. The extracted temperature will be significantly different if the dephasing and relaxation rate of each Q-branch transitions significantly differs from each other. The Boltzmann plots of H₂ CARS spectra for different probe delays wrt the pump and Stokes beams are shown in Fig. 2. Q(1) to Q(7) transitions of H₂ molecule in the $v' = 1 \rightarrow v'' = 0$ vibrational band are used to extract the temperature. The slope of the Boltzmann plot yields the temperature based on the

delayed spectra are changing with the probe delay. This showed that if the probe beam is delayed by 200 ps, there will be a 7% variation in the value of the reported temperature as compared to the temporally overlapped condition, typical in ns CARS. However, one needs not to use a 200 ps time delay to suppress the nonresonant background. For 100-ps time-delay the temperature variation is less than 2% with more than three order-of-magnitudes nonresonant signal reduction [2].

In order to understand the underlying physics of the change in temperature with the probe delay the relaxation rates of each Q-branch transitions are measured. Time-resolved CARS signal of Q-branch transitions for the flame condition reported here is shown in Fig. 3. These

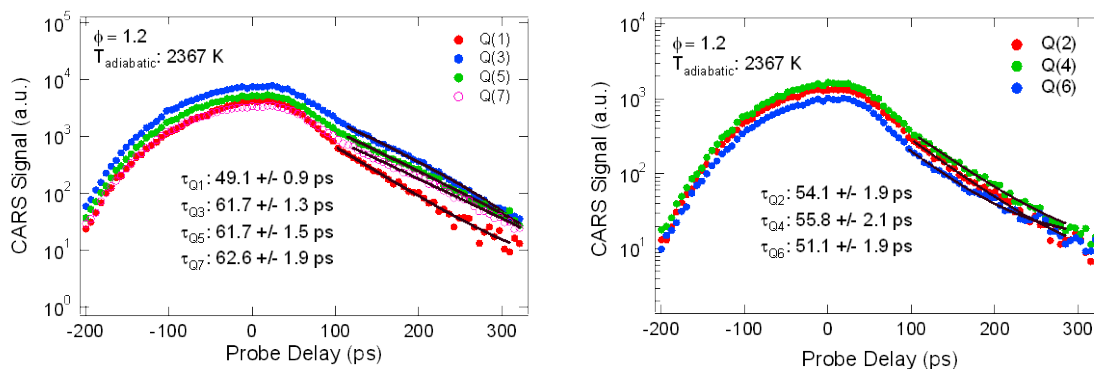


Fig. 3: Temporal evolution of the Q-branch transitions of H₂ molecule for an equivalence ratio of 1.2.

plots reveal the dephasing and relaxation rates of each rotational level (J). It is evident that for the extreme case, the coherence decay rates of Q(1) and Q(7) vary by ~27%. However, for most of the transitions the coherence decay rates vary by less than 10% wrt each other. The variation of the Q(1) and Q(7) rates may also be affected by low signal-to-noise ratio.

This research will pave the way for the application of ps-CARS in harsh chemically reacting flows and will also allow assigning an upper bound on temperature measurement accuracy for time-delayed CARS spectra.

Funding for this research was provided by the Air Force Office of Scientific Research and by the Air Force Research Laboratory, Propulsion Directorate, Wright-Patterson Air Force Base under Contract No. F33615-03-D-2329.

References:

1. A. C. Eckbreth, Laser Diagnostics for Combustion Temperature and Species. Amsterdam: Gordon and Breach. pp 596, 2nd ed. (1996)
2. S. Roy, T. R. Meyer, and J. R. Gord, Opt. Lett. 30, 3222 (2005)
3. S. Roy, T. R. Meyer, and J. R. Gord, Appl. Phys. Lett. 87, 264103 (2005)
4. T. R. Meyer, S. Roy, and J. R. Gord, "Improving Signal-to-Interference Ratio in Rich Hydrocarbon-Air Flames Using Picosecond Coherent Anti-Stokes Raman Scattering", Appl. Spectrosc. (in press, September 2007)

Fs-CARS for High-Bandwidth, Collision-Free Temperature Measurements

Sukesh Roy¹, Paul J. Kinnius², Robert P. Lucht², and James R. Gord³

¹*Innovative Scientific Solutions, Inc., 2766 Indian Ripple Road, Dayton, OH 45440*

²*Department of Mechanical Engineering, Purdue University, West Lafayette, IN 47907*

³*Air Force Research Laboratory, Propulsion Directorate, Wright-Patterson AFB, Ohio 45433*

E-mail: sroy@woh.rr.com, Tel: 937-255-3115, Fax: 937-656-4110

Fs-laser-based time-resolved coherent anti-Stokes Raman scattering (CARS) spectroscopy of nitrogen is used to measure temperature at 1 kHz. The first few ps of the time-resolved CARS signal are free of collisions for pressures up to 20 bar.

©2007 Optical Society of America

OCIS codes: (300.6230) Coherent anti-Stokes Raman scattering; (020.2070) Effects of collisions; (270.1670) Coherent optical effects

CARS spectroscopy is widely used for temperature and major-species-concentration measurements in reacting flows and plasmas [1]. Because of the phase-matching requirement and laser-like nature of the signal, CARS is ideally suited for reacting flows with significant background emission because the CARS signal can be easily isolated spectrally, spatially, and temporally from the flame emission. The technique also provides spatially and temporally resolved information with high accuracy.

Time-resolved fs-CARS has been used for the first time by Leonhardt et al. to study the molecular beat phenomena in liquid phase benzene, cyclohexane, and pyridine [2]. Hayden and Chandler [3] first used fs-CARS for investigating the molecular vibrational dynamics of ground-state gas-phase benzene and 1,3,5-hexatriene. The use of fs laser systems for CARS spectroscopy has three significant potential advantages: (1) reduction or elimination of the nonresonant contribution to the CARS signal when the probe beam is delayed with respect to the pump beam, (2) reduction or elimination of the effects of collisions on the CARS signal, thereby

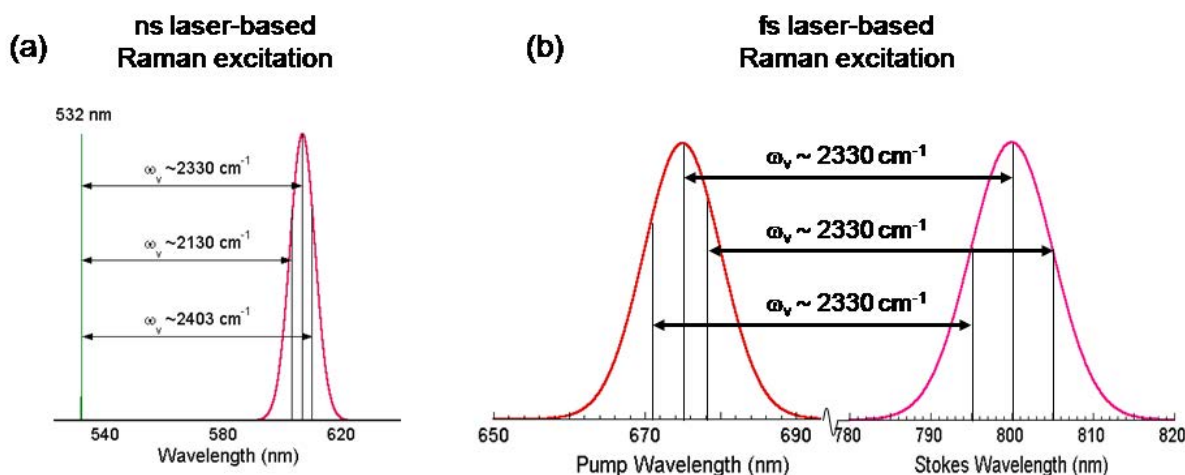


Figure 1. Raman excitation scheme for gas-phase N_2 molecule using (a) ns-laser-based multiplex CARS and (b) fs pump and Stokes lasers.

reducing modeling uncertainty and increasing signal-to-noise ratio, and (3) the capability of generating signals at rates of 1 kHz or greater. The reduction or elimination of the nonresonant background and collisional effects will greatly simplify the modeling of CARS spectra and improve accuracy by eliminating the need for information concerning Raman linewidths [4-5].

Schematic diagrams of the Raman-excitation processes with ns and fs lasers are shown in Fig. 1. In CARS, the wavelengths of the pump and Stokes beams are chosen such that the pump-Stokes frequency difference matches a Raman resonance frequency of the molecule. For the nitrogen molecule, the Raman resonance frequency for the $v''=0$ to $v'=1$ band is approximately 2330 cm^{-1} . This excitation process creates a Raman coherence in the medium, resulting in a shifted signal when the medium is probed by another laser beam. In multiplex CARS using ns lasers, a narrowband pump beam and a broadband Stokes beam are employed for simultaneous excitation of numerous transitions in the ro-vibrational Raman band of the molecule. As shown in Fig. 1(a), in ns-CARS each pair of pump and Stokes frequencies is resonant with only one transition. For fs-CARS, however, multiple pump-Stokes pairs contribute to the excitation of the same transition, thereby creating a significant Raman coherence in the medium [6-7] despite the large frequency bandwidths of the pump and Stokes beams. Numerous Raman transitions are excited with the same phase when the pump and Stokes beams are nearly Fourier transform-limited. This in-phase impulsive excitation creates a very large coherence in the medium, which then decays as a result of the slight frequency differences between the neighboring transitions. This decay rate can be used to determine the temperature [4].

Time-resolved fs-CARS signals of nitrogen as a function of probe-pulse delay with respect to the pump pulse at various equivalence ratios are shown in Fig. 2. The decay of the Raman coherence during the first few ps after the initial impulsive excitation by the nearly transform-limited pump and Stokes laser pulses is the focus of our experiments. The effects of collisions on this time scale are not important for pressures less than 20 bar. It is evident from the figure that the rate at which the signal decays increases with flame equivalence ratio and temperature. The signal decays faster with increasing temperature because of the contributions of more

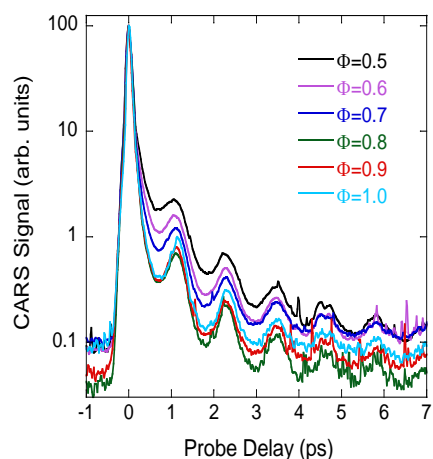


Figure 2. Time-resolved fs-CARS signal for various equivalence ratios (ϕ).

transitions over a wider frequency range to the initial Raman coherence. This results from redistribution of the population to higher energy levels with increasing temperature. The spectrally broad, nearly transform-limited pump and Stokes pulses simultaneously excite all the transitions accessible within the bandwidth of the lasers. The resulting coherence decays thereafter as a result of the slight frequency mismatches between neighboring transitions. The signal reaches a maximum value at a probe delay of zero because of the contribution from both resonant and nonresonant signals. In Fig. 2 all signals were normalized to a peak intensity of 100 at time zero. The oscillatory behavior of the signal is qualitatively similar for temperatures in the range 1600 - 2400 K. The characteristic frequency of the oscillations observed in Fig. 2 is approximately 900 GHz, which corresponds to the beat frequency between the $v'=1 \rightarrow v''=0$ and $v'=2 \rightarrow v''=1$ vibrational bands and also between the $v'=2 \rightarrow v''=1$ and $v'=3 \rightarrow v''=2$ vibrational bands.

Single-shot temperature measurements were performed by chirping the ~ 75 fs probe pulse to ~ 2.4 ps and capturing the resulting signal with an unintensified CCD camera. Time-resolved CARS signals were generated because of the interaction of the coherence, established by the pump and Stokes beams, with the chirped probe beam, where the time-delay is encoded in the wavelengths of the probe beam. The signal that is dispersed with a 0.3-m spectrometer and recorded with the CCD camera is the Fourier transform of the time-resolved CARS signal. The acquisition rate of the camera prevented us from taking data at 1 kHz; 5-shot averaged data are shown in Fig. 3. Figure 3(a) and 3(b) show the chirped CARS signal of N_2 at a flame temperature of ~ 1500 K when the probe beam was temporally coincident with the excitation beams and the probe beam was temporally delayed wrt the excitation beams by 3 ps, respectively. The oscillation due to the beating between the various vibrational modes is clearly evident in Fig. 3(b). The signal-to-noise ratio of the 5-shot averaged spectrum clearly displays the potential of this technique for single-shot temperature measurements at 1 kHz at flame temperatures. We are currently evaluating other cameras for acquisition of single-shot spectra.

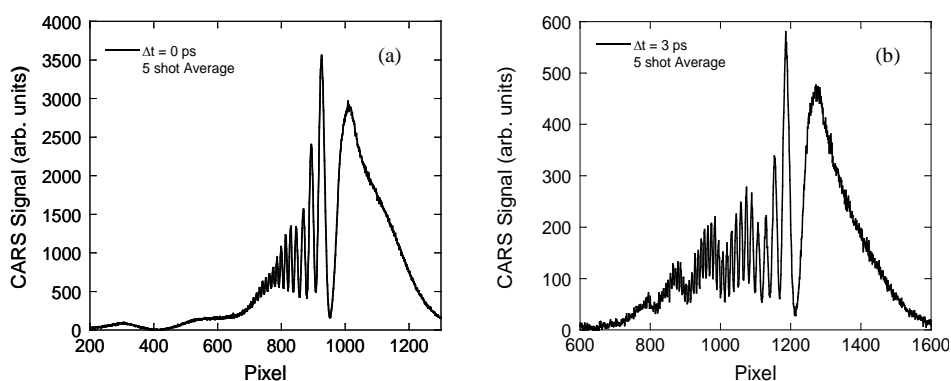


Fig. 3: 5-shot averaged chirped N_2 CARS signals acquired in an atmospheric-pressure, near-adiabatic, hydrogen-air diffusion flame for an equivalence ratio of 0.5. (a) The probe beam is time coincident with the excitation beams and (b) the probe beam is delayed 3-ps wrt the excitation beams.

Current research activities in our laboratory are designed to address these key issues: (1) single-shot temperature measurements at rates of 1 kHz or greater using a spectrally chirped probe pulse, (2) influence of other molecules excited by the broadband fs-laser pulses on measurements of temperature and species concentrations, and (3) concentration measurements of minor species such as C_2H_2 , C_6H_6 , and other flame molecules and radicals using shaped laser pulses.

Funding for this research was provided by the Air Force Office of Scientific Research; by the Air Force Research Laboratory, Propulsion Directorate, Wright-Patterson Air Force Base under Contract No. F33615-03-D-2329; and by the National Science Foundation, Combustion and Plasma Program under Award No. 0413623-CTS.

References:

1. A. C. Eckbreth, *Laser Diagnostics for Combustion Temperature and Species*. Amsterdam: Gordon and Breach., 2nd ed. (1996)
2. R. Leonhardt, W. Holzapfel, W. Zinth, W. Kaiser, *Chem. Phys. Lett.* 133, 373 (1987)
3. C. C. Hayden, D. W. Chandler, *J. Chem. Phys.* 103, 10465 (1995)
4. R. P. Lucht, S. Roy, T. R. Meyer, J. R. Gord, *Appl. Phys. Lett.* 89, 251112 (2006)
5. S. Roy, P. J. Kinnius, R. P. Lucht, J. R. Gord, *Opt. Comm.*, doi:10.1016/j.optcom.2007.09.040 (2007)
6. R. P. Lucht, *Science* 316, 207 (2007)
7. R. P. Lucht, P. J. Kinnius, S. Roy, J. R. Gord, *J. Chem. Phys.* 127, 044316 (2007)

Insensitivity of electronic-resonance-enhanced coherent anti-Stokes Raman scattering (ERE-CARS) to electronic quenching

Anil K. Patnaik,¹ Sukesh Roy,¹ Robert P. Lucht,² and James R. Gord³

¹Innovative Scientific Solutions, Inc., 2766 Indian Ripple Road, Dayton, OH 45440

²Department of Mechanical Engineering, Purdue University, West Lafayette, IN 47907

³Air Force Research Laboratory, Propulsion Directorate, Wright-Patterson AFB, Ohio 45433

E-mail: anil@imssi.com

Abstract: The insensitivity of ERE-CARS signal to collisional quenching is investigated. It is observed that the strong laser pulse helps in keeping both the excited-state population and the ground-state coherence reasonably high, even with significant quenching.

©2007 Optical Society of America

OCIS codes: (300.6230) Coherent anti-Stokes Raman scattering; (020.2070) Effects of collisions; (270.1670) Coherent optical effects

Spectroscopic measurement of a target species in a high-pressure combustor environment is strongly affected by collisions of this species with other molecules present in the combustor. One of the major effects of such collisions is electronic quenching, which is the decay of the excited-electronic-state population to unwanted molecular states. Such quenching leads to major limitations in the current state-of-art technique that is based on laser-induced fluorescence (LIF), causing the signal to drop by a few orders of magnitude [1]. On the other hand, coherent anti-Stokes Raman scattering (CARS) has been used increasingly as a very common laser diagnostics technique for measuring the temperature and concentration of the major species [2-3]. The recent development of electronic-resonance-enhanced CARS (ERE-CARS) [4], where one or more of the applied lasers in CARS is tuned to an electronic transition, has lead to resonant enhancement of the CARS signal, allowing the ERE-CARS technique to be used also for spectroscopic measurement of minor species [5]. Recently, it has been demonstrated that unlike the LIF signal, the ERE-CARS signal of nitric oxide (NO) in a mixture of CO₂/O₂/N₂ is unaffected by the strong electronic quenching that is caused by the gas mixtures [1].

It is intriguing that although both the ERE-CARS and the LIF signals are obtained from the emitted radiation via de-excitation of the excited state, LIF turns out to be extremely sensitive to excited electronic quenching, whereas the ERE-CARS signal is not affected by it. In this paper, we present a theoretical investigation of the insensitivity of ERE-CARS to strong electronic quenching, as opposed to the strong drop of the LIF signal.

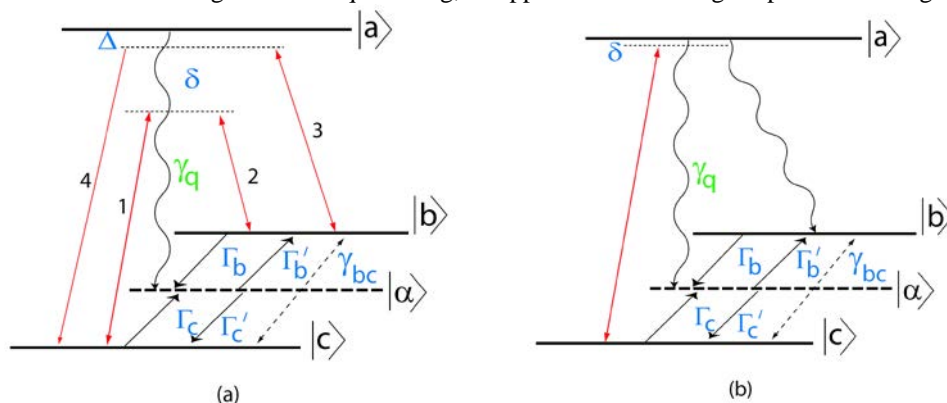


Fig. 1. Model schemes to compare the effect of electronic quenching on the diagnostic signal via (a) CARS and (b) LIF method. Electronic quenching is modeled by an incoherent decay γ_q to a fictitious state $|\alpha\rangle$ that represents all of the molecular states those are not of interest. The applied fields are denoted by 1-3, and the CARS signal in (a) is represented by 4. The ground-state mixing rates are denoted by Γ_i and Γ'_i , and the coherence dephasing is represented by γ_{bc} . Detuning of the lasers from their respective transitions are given by δ and Δ .

To understand the effect of quenching on ERE-CARS and LIF, we have devised a new model scheme that incorporates all of the prime physical processes involved in the experiment on NO [1]. We consider a three-level scheme [see Fig. 1(a)], where the excited state $|a\rangle$ corresponds to the $v = 0$ vibrational state in the $A^2\Sigma^+$ electronic

state of NO, and the states $|b\rangle$ and $|c\rangle$ represent the $v = 0, 1$ states of the ground electronic state $X^2\Pi$. We introduce a fictitious state $|\alpha\rangle$ that takes into account all physical processes that are unaccounted for in the simplified three-level model. The state $|\alpha\rangle$ accounts for electronic quenching from the excited electronic state to unwanted states via radiative or non-radiative transitions occurring as a result of the mixing of the ground-state population due to collision with other molecules. Note that, unlike in [1], we do not consider any rotational transitions in this calculation since this will add no new physics to the current investigation. The corresponding scheme for LIF is shown in Fig. 1(b). The symbols used in the figure are described in the figure caption.

To describe the molecular dynamics, we derive a density matrix equation for the above model scheme

$$\frac{\partial \rho}{\partial t} = -\frac{i}{\hbar}[H, \rho] + \text{spontaneous decay, quenching and dephasing terms} \quad (1)$$

Where, ρ represents the density matrix and H is the Hamiltonian of the molecule + laser-molecule interaction. The density matrix elements ρ_{ij} represent population of the i^{th} state if $i = j$ and coherence between states i and j for $i \neq j$. We use the following approximations to derive the dynamic equations for the density matrix elements:

- a. To separate various polarizations that are oscillating at different frequencies, we make the transformations

$$\begin{aligned} \rho_{ab} &\rightarrow \sigma_{ab} \text{Exp}[-i\nu_2 t] + \eta_{ab} \text{Exp}[-i\nu_3 t], \\ \rho_{ac} &\rightarrow \sigma_{ac} \text{Exp}[-i\nu_1 t] + \eta_{ac} \text{Exp}[-i\nu_4 t], \\ \text{and } \rho_{bc} &\rightarrow \sigma_{bc} \text{Exp}[-i(\nu_1 - \nu_2)t]. \end{aligned} \quad (2)$$

Here, ν_j represents the frequencies of the input fields ($j \rightarrow 1$ to 3) and the CARS signal field ($j = 4$).

- b. We assume that detuning of the fields 1 and 2 to be very large compared to the energy separation between the states $|b\rangle$ and $|c\rangle$, i.e., $\delta \gg (E_b - E_c)/\hbar$. We use the well known rotating wave approximation to eliminate highly oscillating terms such as $e^{i\delta t}$.

Furthermore, we use Maxwell-Bloch equations to describe the propagation of the CARS/LIF signal through the medium. However, because of the limited scope of this short paper, we present only the results of the atomic evolution that essentially capture the physics of the quenching effect on both the ERE-CARS and the LIF signals.

Below, we present the results of the numerical calculation for both the CARS and the LIF configurations. It is well known that the LIF signal is proportional to the excited-state population ρ_{aa} , whereas the CARS signal depends on the magnitude of the ground-state coherence $|\rho_{bc}|$. We present the time evolution of the excited-state population in Fig. 2 for both the CARS and the LIF configurations and that of the ground-state coherence for the CARS configuration in Fig. 3. We have used all the parameters close to their experimental [1] values, except that here we consider a continuous-wave laser as opposed to the nanosecond laser used in the above experiment for purposes of describing our objective easily and effectively. A detailed calculation with nanosecond laser pulses will be published elsewhere. To permit a good comparison, all of the parameters are scaled with spontaneous decay rate γ of the excited-state $A^2\Sigma^+$ of NO. The quenching rate γ_q changes significantly with the composition of the gas mixture $\text{CO}_2/\text{O}_2/\text{N}_2$. For our numerical calculation, we considered three different values: $\gamma_q = \gamma$, 10γ , and 100γ .

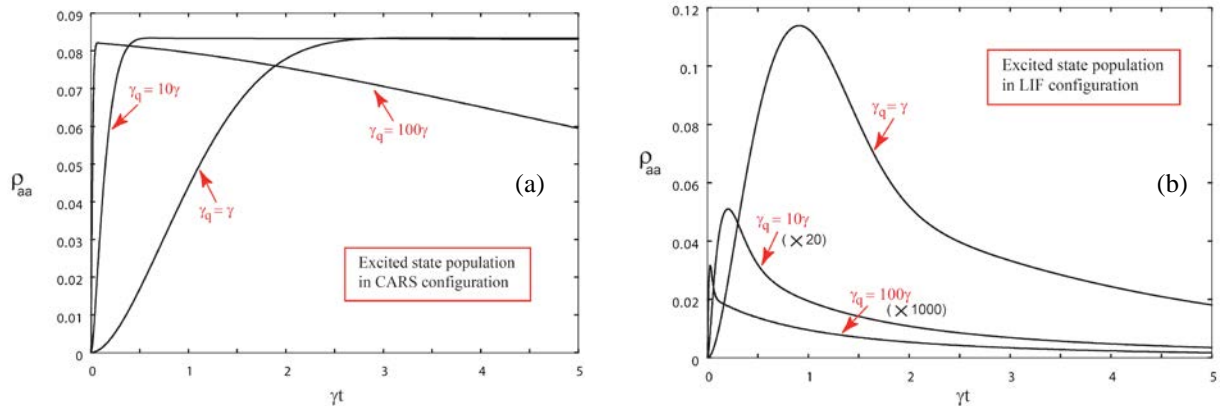


Fig. 2. Insensitivity of excited-state population in CARS configuration (a) compared to that in LIF configuration (b). The population changes only a few percent in the CARS configuration with an increase in γ_q , but in the LIF configuration, the population is depleted by several orders of magnitude. The x-axis represents real time scaled with the excited state decay time γ^{-1} .

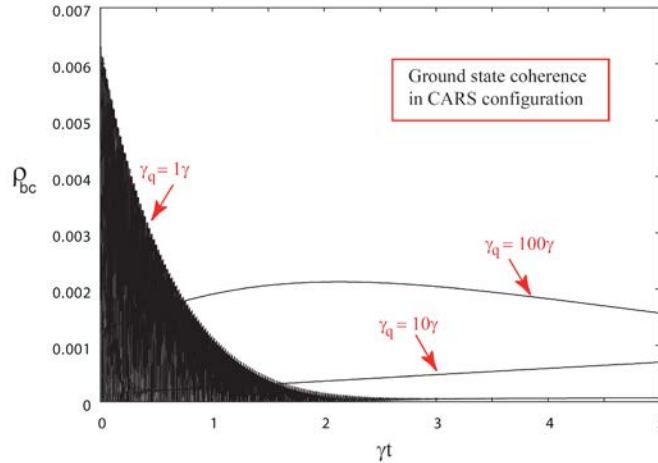


Fig. 3. Ground-state coherence in CARS configuration. Most strikingly, the magnitude of the coherence in the long time limit increases with the excited-state quenching rate. The x-axis represents real time scaled with the excited state decay time γ^{-1} .

In the CARS configuration, the Rabi frequencies [given as $\vec{d} \cdot \vec{E} / \hbar$ (d and E_i representing dipole moment and electric fields, respectively)] corresponding to the pump and Stokes fields [fields 1 and 2 in Fig. 1(a)] are taken to be 1000γ , and the probe is considered to have an order of magnitude less intensity than 1 and 2. The detuning of fields 1 and 2 from the excited transition is $\delta = 5 \cdot 10^5 \gamma$. The electronic-quenching rates are assumed to affect equally to the decay rates from $|a\rangle$ to $|b\rangle$ and $|c\rangle$. The ground-state vibrational population redistribution rates Γ_j and Γ_j' and also the coherence dephasing rate γ_{bc} , are taken to be $\Gamma_j = \Gamma_j' = \gamma_{bc} = \gamma_q/2$. It clearly shown in Fig. 2(a) that in the CARS configuration, the excited-state population is not depleted significantly with an increase in quenching rate and also survives for a longer period of time. Furthermore, larger γ_q accelerates the process of reaching a steady value with increasing γ_q , and also corresponding large rate of population redistribution help to overcome the strong Rabi flopping caused by the probe field, which resonantly transfers population between states $|b\rangle$ and $|a\rangle$. However, in Fig. 2(b), in the LIF configuration, the excited-state population is strongly depleted by a few orders of magnitude with an increase in γ_q . The Rabi frequency of the LIF pumping field is taken to be γ to avoid saturation and detuning is $\delta=0$.

In Fig. 3, we present the evolution of the ground-state coherence for different γ_q values. For small γ_q , the strong Rabi flopping due to the reasonably strong probe field dominates during the initial period of ρ_{bc} and attains a steady-state value later. For larger $\gamma_q = \gamma$, the initial Rabi flopping is reduced. However, we find a striking and unexpected result--for larger γ_q the steady-state values of ρ_{bc} are higher than that for $\gamma_q = \gamma$. We confirmed this result with our extensive numerical checks, including those with our independent numerical program for the steady-state values. We understand this result to be a combined effect of the strong coherent pumping ability and the electronic quenching associated with strong ground-state population redistribution. However, further increase in γ_q results in a sharp decrease in the steady state of ρ_{bc} when quenching dominates the re-pumping fields (result not shown in Fig. 3). Note that “no” spatial propagation is considered here. However, the time evolution of ρ_{aa} and ρ_{bc} , presented here enhances the understanding of the observed insensitivity of the CARS signal to the electronic quenching rate.

In summary, we have shown explicitly that the excited-state population and the ground-state coherence in a CARS configuration are not affected strongly by the excited-state electronic quenching. In fact, strikingly, in the long time limit, we observed an increase in the magnitude of ground state coherence with γ_q up to a certain value. This is attributed to our ability to re-pump strongly the excited state in the CARS configuration. On the other hand, the LIF configuration suffers from very large depletion of the excited-state population with an increase in γ_q . That is because, larger re-pumping field cannot be used in LIF where the transition quickly saturates, even with a much weaker field.

Funding for this research was provided by the Air Force Office of Scientific Research under Contract No. FA9550-07-C-0036 (Dr. Julian Tishkoff, Program Manager) and by the U.S. Department of Energy, Division of Chemical Sciences, Geosciences, and Biosciences, under Grant No. DE-FG02-03ER15391.

- [1] S. Roy, W. D. Kulatilaka, S. Naik, N. M. Laurendeau, R. P. Lucht, and J. R. Gord, *Appl. Phys. Lett.* **89**, 104105 (2006).
- [2] K. Kohse-Hoinghaus, *Prog. Energy Combust. Sci.* **20**, 203 (1994).
- [3] A. C. Eckbreth, *Laser Diagnostics for Combustion Temperature and Species* (2nd Ed.) (Taylor and Francis, NY, 1996).
- [4] B. Atal-Tretout, O. O. Schnepp, and J.-P.E. Taran, *Opt. Commun.* **24**, 77 (1978).
- [5] S. F. Hanna, W. D. Kulatilaka, Z. Arp, T. Opatrny, M. O. Scully, J. P. Kuehner, and R. P. Lucht, *Appl. Phys. Lett.* **83**, 1887 (2003).

Femtosecond Coherent Anti-Stokes Raman Scattering Measurement of Gas-Phase Species and Temperature

Robert P. Lucht and Paul J. Kinnius

*School of Mechanical Engineering, Purdue University, West Lafayette, Indiana 47907-2088
lucht@purdue.edu, Tel: (765) 494-5623, Fax: (765) 494-0539*

Sukesh Roy

Innovative Scientific Solutions, Inc., Dayton, Ohio 45440-3638

James R. Gord

Air Force Research Laboratory, Propulsion Directorate, Wright-Patterson Air Force Base, Ohio 45433-7103

Abstract: The use of femtosecond lasers for coherent anti-Stokes Raman scattering measurements in gases is reviewed. Coupling of femtosecond laser radiation with gas-phase resonances, determination of temperature from frequency-spread dephasing, and single-shot measurements are discussed.

OCIS codes: (300.6230) Spectroscopy, coherent anti-Stokes Raman scattering; (300.6530) Spectroscopy, ultrafast; (300.6390) Spectroscopy, molecular; (120.1740) Combustion Diagnostics

Introduction

The use of femtosecond lasers for coherent anti-Stokes Raman spectroscopy (CARS) of molecules in the gas phase offers some significant potential advantages compared with nanosecond (ns) CARS; i.e., CARS as usually performed with ns pump and Stokes lasers. These potential advantages include (1) the capability of performing real-time temperature and species measurements at data rates significantly greater than 1 kHz and (2) the absence of any effect of collisions in the determination of temperature and concentration from the fs CARS signal. We have performed recently experiments demonstrating the capability of measuring temperature and concentration from the dependence of fs CARS signal as a function of probe delay after impulsive pump-Stokes excitation [1,2]. The acquisition of strong CARS signals from gas-phase species using fs lasers would at first glance seem to be quite difficult. For room air conditions, typical Raman line widths are 0.1 cm^{-1} while the frequency bandwidth of a Fourier-transform-limited 100-fs laser pulse is 150 cm^{-1} . However, there are numerous frequency pairs within the spectral envelopes of the pump and Stokes lasers that can contribute to the excitation of the Raman resonance, which is a two-photon transition. Consequently, the excitation of gas-phase Raman resonances is quite efficient, as discussed in detail by Lucht et al. [3].

Several fs CARS experiments have been reported in the literature, e.g. [4,5]. In the majority of these studies, the signal is obtained by scanning the time delay of the probe beam with respect to the pump and Stokes beams, which typically are timed to arrive simultaneously at the probe volume. The probe signal as a function of time is then typically Fourier analyzed to determine spectroscopic parameters, collision broadening parameters, etc. In our experiments [1,2], temperature and species concentration were determined from the decay of the CARS signal in the first few picoseconds (ps) after the impulsive pump-Stokes Raman pumping. The CARS signal in these initial few ps is much stronger because the Raman transitions contribute coherently because they are excited with the same phase by the impulsive pump-Stokes excitation. After a few ps they begin to oscillate out of phase due to the differences in the transition frequencies of the various Raman resonances; we refer to this phenomenon as frequency-spread dephasing. The frequency-spread dephasing time decreases with temperature because the frequency spread of transitions that contribute to the Raman coherence increases with increasing temperature.

The potential for real-time measurements at frequencies of interest in turbulent flames is the result of the recent commercial availability of fs laser systems with pulse energies of up to a few mJ and with repetition rates of up to 20 kHz, and the expected availability of commercial systems in the near future with repetition rates approaching 100 kHz. If techniques for acquiring single-pulse temperatures and concentrations can be developed, time series measurements can be performed in turbulent flames and flows at data rates that are comparable to or greater than turbulent fluctuation frequencies. We have performed some initial fs CARS experiments with a chirped probe beam as illustrated in Fig. 1. To perform single-pulse fs-CARS measurements, the probe pulse is chirped by directing it through a 30-cm length of heavy flint glass as discussed by [6]. The chirped probe pulse length is approximately 2 picoseconds (ps). The central wavelength of the probe beam decreases during the laser pulse due to dispersion in

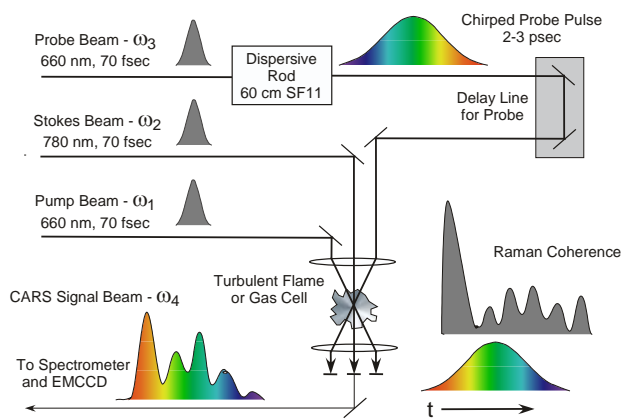


Fig. 1. Schematic diagram of the chirped-probe-pulse fs-CARS experiment.

the flint glass rod. Consequently, the wavelength of the fs-CARS signal beam also decreases as a function of time with respect to the beginning of the probe pulse. The fs-CARS signal beam is directed into a spectrometer and the spectrum is recorded for each laser shot on a charge-coupled device (CCD) camera. The temporal behavior of the Raman coherence can then be determined from the spectrum of the fs-CARS signal. The chirped probe pulse allows us to map the temporal behavior of the Raman coherence into the spectrum of the CARS signal. The time delay between the chirped probe pulse and the pump and Stokes beams is adjusted using the same mechanical stage that is used for the scanned probe beam experiments. Chirped probe experiments were performed for room temperature nitrogen and

for mixtures of nitrogen and carbon monoxide. For each setting of the mechanical translation stage, a spectrum from pure argon was also recorded; pure argon has a purely nonlinear response. Measurements were also performed in flames stabilized on a near-adiabatic burner. In these initial experiments, the spectra were not collected on a single-shot basis due to the limited readout rate of the CCD camera. However, excellent signal-to-noise ratios were observed for five-shot averaged spectra from flames, and the acquisition of single-shot spectra will be demonstrated in the near future.

The experimental results were modeled by solving the time-dependent density matrix equations using the direct numerical integration (DNI) techniques discussed in Ref. 3. The pump and Stokes pulses are modeled as Fourier-transform-limited 70 fs pulses. The probe beam is modeled as a linearly chirped pulse with a 3-ps Gaussian envelope for the electric-field amplitude. The time-dependent electric field of the CARS signal field is calculated using the DNI code for specified temperature and nitrogen concentration. However, in the experiment the CARS signal is detected using a spectrometer. In the theoretical modeling, the CARS spectrum is calculated by performing a Fourier transform on the time-dependent CARS signal from the DNI solution of the density matrix equations. Our initial results show good agreement between experimental and theoretical chirped probe fs CARS spectra. More detailed characterization of the properties of the chirped probe pulse may be required to obtain better agreement between theory and experiment. The comparison of theory and experiment will be discussed in detail during the presentation.

Acknowledgments

Funding for this research was provided by the Air Force Office of Scientific Research (Dr. Julian Tishkoff, Program Manager), and by the Air Force Research Laboratory, Propulsion Directorate, Wright-Patterson Air Force Base, under Contract No. F33615-03-D-2329, by the National Science Foundation, Combustion and Plasmas Program under Award Number 0413623-CTS, and by the U.S. Department of Energy, Division of Chemical Sciences, Geosciences and Biosciences, under Grant No. DE-FG02-03ER15391, .

References

- [1] R. P. Lucht, S. Roy, T. R. Meyer, and J. R. Gord, *Appl. Phys. Lett.* **89**, 251112 (2006).
- [2] S. Roy, P. J. Kinnius, R. P. Lucht, and J. R. Gord, *Opt. Commun.*, accepted for publication (2008)
- [3] R. P. Lucht, P. J. Kinnius, S. Roy, and J. R. Gord, "Theory of Femtosecond Coherent Anti-Stokes Raman Scattering for Gas-Phase Transitions," *J. Chem. Phys.* **127**, 044316 (2007).
- [4] T. Lang, K.-L. Kompa, and M. Motzkus, *Chem. Phys. Lett.* **310**, 65-72 (1999).
- [5] H. Skenderović, T. Buckup, W. Wohlleben, and M. Motzkus, *J. Raman Spectrosc.* **33**, 866-871 (2002).
- [6] T. Lang and M. Motzkus, "Single-Shot Femtosecond Coherent Anti-Stokes Raman Scattering Thermometry," *J. Opt. Soc. Am. B* **19**, 340-344 (2002).

Perturbative theory and modeling of electronic-resonance-enhanced coherent anti-Stokes Raman scattering spectroscopy of nitric oxide

Joel P. Kuehner,^{1,a)} Sameer V. Naik,² Waruna D. Kulatilaka,² Ning Chai,² Normand M. Laurendeau,² Robert P. Lucht,^{2,3} Marlan O. Scully,^{3,4} Sukesh Roy,⁵ Anil K. Patnaik,⁵ and James R. Gord⁵

¹Department of Physics and Engineering, Washington and Lee University, Lexington, Virginia 24450, USA

²School of Mechanical Engineering, Purdue University, West Lafayette, Indiana 47907, USA

³The Institute for Quantum Studies, Texas A&M University, College Station, Texas 77843, USA

⁴Applied Physics & Materials Science Group, Princeton University, Princeton, New Jersey 08544, USA

⁵Air Force Research Laboratory, Propulsion Directorate Wright Patterson AFB, Ohio 45433, USA

(Received 20 December 2007; accepted 24 March 2008; published online 7 May 2008)

A theory is developed for three-laser electronic-resonance-enhanced (ERE) coherent anti-Stokes Raman scattering (CARS) spectroscopy of nitric oxide (NO). A vibrational Q -branch Raman polarization is excited in the NO molecule by the frequency difference between visible Raman pump and Stokes beams. An ultraviolet probe beam is scattered from the induced Raman polarization to produce an ultraviolet ERE-CARS signal. The frequency of the ultraviolet probe beam is selected to be in electronic resonance with rotational transitions in the $A^2\Sigma^+ \leftarrow X^2\Pi$ (1,0) band of NO. This choice results in a resonance between the frequency of the ERE-CARS signal and transitions in the (0,0) band. The theoretical model for ERE-CARS NO spectra has been developed in the perturbative limit. Comparisons to experimental spectra are presented where either the probe laser was scanned with fixed Stokes frequency or the Stokes laser was scanned with fixed probe frequency. At atmospheric pressure and an NO concentration of 100 ppm, good agreement is found between theoretical and experimental spectral peak locations and relative intensities for both types of spectra. Factors relating to saturation in the experiments are discussed, including implications for the theoretical predictions. © 2008 American Institute of Physics. [DOI: 10.1063/1.2909554]

I. INTRODUCTION

Electronic-resonance-enhanced (ERE) coherent anti-Stokes Raman scattering (CARS) spectra of nitric oxide (NO) have been investigated theoretically and experimentally by employing a three-laser or dual-pump CARS method.¹ This paper explores the details and capabilities of a developed theory for the ERE-CARS process. With increased attention on combustion emissions and pollutant formation² and the use of NO tracers in flowfield mixing studies,³ the need has arisen for a diagnostic technique capable of probing low number density levels (~ 10 ppm) of radical species such as NO. Moreover, strong interest exists in studying thermally generated NO in hypersonic flowfields, as knowledge of NO concentration at elevated temperature levels would provide insight into the reaction rates required for modeling these flowfields.⁴ Beyond the effects on the flowfield, NO formation has been demonstrated as an excellent flowfield tracer in hypersonic flows.⁵ Finally, developments in the area of national security have prompted a need for techniques that not only can detect minor species, pollutants, and toxins but that can do so rapidly.^{6,7} ERE-CARS is a possible solution to these problems, as it is capable of probing low molecular number density levels on a relatively short time scale. These advantages have generated recent interest in the ERE-CARS

technique for other molecules⁸ and is the reason why we have focused our efforts at this time on adapting the ERE-CARS method for NO.

Figure 1 represents the energy-level diagram for the three-laser process utilized in this CARS method. Visible Raman pump and Stokes beams induce a Raman transition through a virtual state that is far from resonance with the $A^2\Sigma^+ \leftarrow X^2\Pi$ electronic transition of NO. The third laser beam, termed the ultraviolet “probe” beam, has a frequency that probes the Raman resonance through the first excited electronic state of NO. Usually, this third beam is termed a “pump” beam. This nomenclature arose in the CARS literature because, in most CARS experiments, the ω_1 and ω_3 beams are produced from the same laser beam, i.e., $\omega_1 = \omega_3$, and each beam serves as a probe for the Raman polarization pumped by the other. However, for the case shown in Fig. 1, the ω_3 beam does not participate in the generation of a Raman polarization in the medium and is thus referred to as the probe beam. In this manner, the CARS method employed in this study is a modified version of the dual-pump CARS process previously investigated for the simultaneous detection of two species.^{9,10}

Typically, the application of CARS for minor species detection and measurement is limited by coherent interference of the nonresonant background and the CARS signal from the Raman resonance of interest. The inherent nonresonant background susceptibility from major species, such as

^{a)}Author to whom correspondence should be addressed. Tel.: (540) 458-8153. FAX: (540) 458-8884. Electronic mail: kuehnerj@wlu.edu.

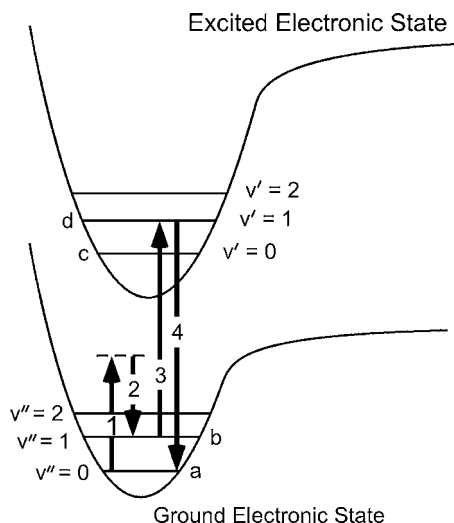


FIG. 1. CARS energy-level diagram including electronic resonances.

diatomic nitrogen (N_2), dominates the susceptibility when the Raman species is present in low concentration. This problem is magnified for molecules such as NO that possess relatively weak Raman cross-sections, resulting in an additional reduction in signal level compared to N_2 .¹¹ The use of polarization techniques to suppress the nonresonant background has been demonstrated; however, the application of such techniques results in a reduction in signal strength by at least a factor of 16.¹² Therefore, polarization techniques are beneficial, but increases in the Raman resonant signal strength must be performed simultaneously.

Since the late 1970's, a few groups have investigated the potential of ERE-CARS for minor species measurements in flames or plasmas.¹³ The term electronic-resonance-enhanced is used to indicate that the frequency of the pump, probe, and/or Stokes beam are tuned near resonance with an electronic transition of the molecule. The electronic resonance can increase the resonant CARS signal considerably, minimizing concerns associated with the nonresonant background. The current technique differs from previous ERE-CARS investigations^{14–16} in that the frequency of the Raman pump (ω_1) and ultraviolet probe (ω_3) beams are well separated. As a result, the Raman process and electronic process are, in a sense, uncoupled.

In the past, the pump, Stokes, and probe beam frequencies were all in or near electronic resonance, a case termed “triple resonance.”^{17,18} Triple resonance spectra are difficult to interpret, because weaker double resonances appear near the major peaks.¹⁹ In almost all of these investigations, the intensity of any ultraviolet beam is restricted so as to maintain both Raman and electronic transitions within the perturbative regime, i.e., so that laser-induced population transfer is negligible for both the Raman and electronic transitions. However, the intensities of the visible pump and Stokes beams in this experiment are high enough that stimulated Raman pumping is expected to be a significant effect, and the Raman polarization that is established in the medium by the visible pump and Stokes beams is close to the maximum that can be attained without saturating the transition. The use of visible pump and Stokes beams simplifies the experimen-

tal implementation and theoretical treatment of ERE-CARS without sacrificing detection sensitivity. Additional benefits of Raman excitation with visible beams are that it permits easier interpretation of the features in the spectra and more transitions can be probed simultaneously.

Other techniques, such as laser-induced fluorescence (LIF), degenerate four-wave mixing (DFWM), and laser-induced polarization spectroscopy (PS) have proven useful for probing minor species; however, ERE-CARS has advantages over these techniques when the medium is at high pressure or when multiple species are present. For instance, to interpret an experimental LIF spectrum for concentration measurements, the collision partners must be identified.² DFWM can be independent of quenching rates,²⁰ but it loses sensitivity compared to ERE-CARS at increased pressure levels.²¹ Similar to DFWM, PS can also be affected by collision rates.¹³ Hence, ERE-CARS is a preferable technique at high pressure or when quenching is problematic.

Additionally, at elevated temperatures and/or pressures, the LIF or DFWM spectra of various species can overlap, resulting in uncertainty as to which molecule is being probed.^{22,23} As implemented in these experiments, ERE-CARS has enhanced selectivity compared to LIF and DFWM because of the requirement for simultaneous Raman and electronic resonance for signal generation. This benefit in conjunction with minimized effects owing to pressure and varying collision partners make ERE-CARS a very attractive prospect.

II. EXPERIMENTAL SYSTEM

The experimental system for NO ERE-CARS measurements is shown schematically in Fig. 2. A *Q*-switched Nd:yttrium aluminum garnet (YAG) laser (Continuum 9010) with a repetition rate of 10 Hz and a pulse duration of approximately 7 ns was used to pump a narrowband, tunable dye laser (Lumonics), with Rhodamine 610 dye as the lasing medium. The dye laser output was centered near 590 nm with a frequency bandwidth of approximately 0.08 cm^{-1} and supplied the source for the Stokes beam (ω_2). The 532 nm pump beam (ω_1) for the CARS process was generated using a second injection-seeded, *Q*-switched Nd:YAG laser (Spectra-Physics 290-10). A narrowband dye laser (Continuum ND6000) was also pumped using this 532 nm output to produce tunable radiation in the vicinity of 704 nm; the laser dye used here was LDS 698. This radiation was mixed with the 355 nm third-harmonic output of the injection-seeded Nd:YAG laser to generate the probe beam (ω_3) near 236 nm. A feedback-controlled frequency conversion system (INRAD Autotracker III) with a β -BBO nonlinear crystal was used for the sum-frequency-mixing process. The full-width at half-maximum (FWHM) frequency bandwidth of the single-axial-mode pump beam ($\omega_1=532\text{ nm}$) was 0.003 cm^{-1} while the bandwidth of the ultraviolet probe beam ($\omega_3=236\text{ nm}$) was approximately 0.1 cm^{-1} .

A three-dimensional phase-matching scheme was employed to generate the ultraviolet, 226 nm ERE-CARS signal. The BOXCAR geometry²⁴ is slightly modified from the case of CARS performed with all visible beams. The patterns

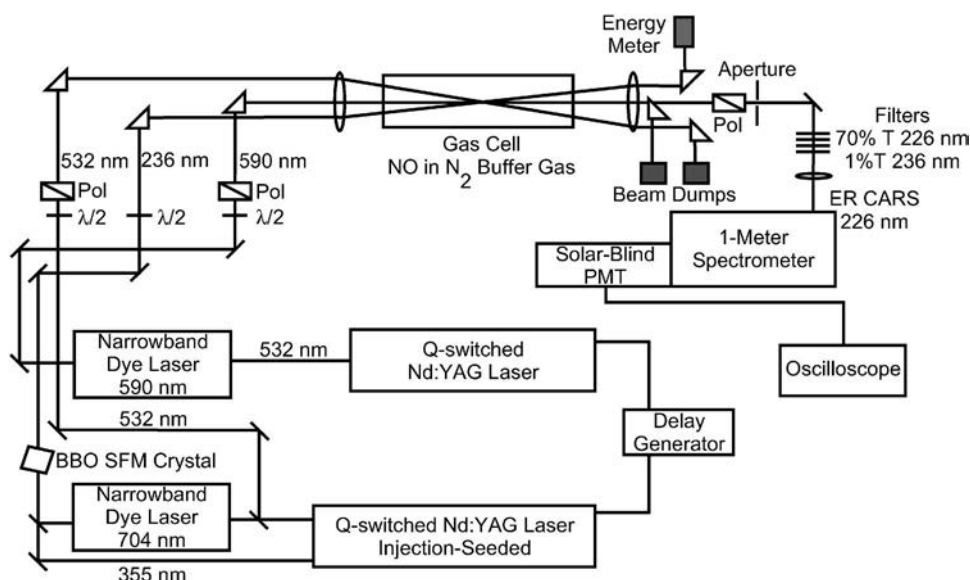


FIG. 2. Experimental system for the NO ERE-CARS system.

of the three laser beams on the focusing lens and of the laser beams and the CARS signal beam on the collimating lens are shown in Fig. 3. As a consequence of the large difference in momentum of the ultraviolet and visible photons interacting in the CARS process, the ultraviolet probe beam is much closer to the axis joining the centers of the input and output lenses than the visible pump and Stokes beams. The ultraviolet CARS signal beam is also generated much closer to this axis.

During a typical experiment, pulse energies of 5 mJ were used for the visible pump and Stokes beams. The maximum pulse energy of the ultraviolet probe beam was 0.25 mJ. The beams were focused at the probe volume and recollimated after interaction, along with the ERE-CARS signal, using a pair of 500 mm, focal-length lenses. At this point, beam dumps were used to capture the visible pump and Stokes beams. A joulemeter (Molelectron J3-05) monitored the pulse energy of the ultraviolet probe beam after interaction. Four 215 nm dielectric mirrors, designed to be used at 45° incidence, and a set of apertures filtered the ERE-CARS signal. By utilizing the 215 nm mirrors at 0° incidence, a low-pass filter is formed that transmits 70% at 226 nm but only 1% at 236 nm, thereby significantly reducing background interference from the ultraviolet probe beam. The ERE-CARS signal was further isolated by a 1 m spectrometer (SPEX). The resulting signal intensity was collected using a solar-blind-photomultiplier tube (Hamamatsu R166)

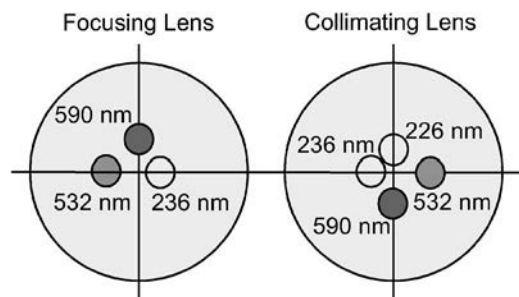


FIG. 3. Phase-matching geometry employed in the NO ERE-CARS system.

and oscilloscope (Tektronix TDS5054B). The joulemeter and photomultiplier output were recorded on a shot-by-shot basis during which time either the Stokes- or the probe-beam frequency was scanned under computer control.

In addition to interference caused by scattered background from the ultraviolet probe beam, the ERE-CARS signal contained significant contributions from the nonresonant four-wave-mixing background signal, as discussed earlier. Therefore, once the ERE-CARS signal was located and an optimal system alignment was obtained, a polarization technique¹ was utilized to suppress the nonresonant background. This polarization arrangement is demonstrated in Fig. 4. The ultraviolet probe beam was vertically polarized, while the axes of the visible pump and Stokes beams were rotated 60° to the vertical. This generates an almost vertically polarized ERE-CARS signal, and at the same time, caused the polarization of the nonresonant background to be rotated 30° to the vertical. To take advantage of this technique, an α -BBO analyzer was placed in the signal channel such that the transmission axis was perpendicular to the nonresonant

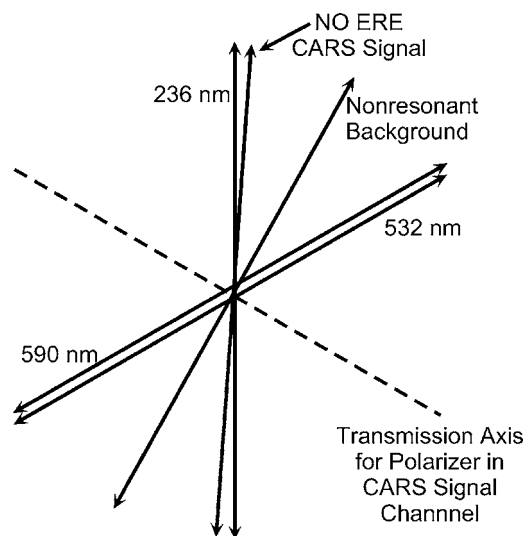


FIG. 4. Polarization arrangement for ERE-CARS detection.

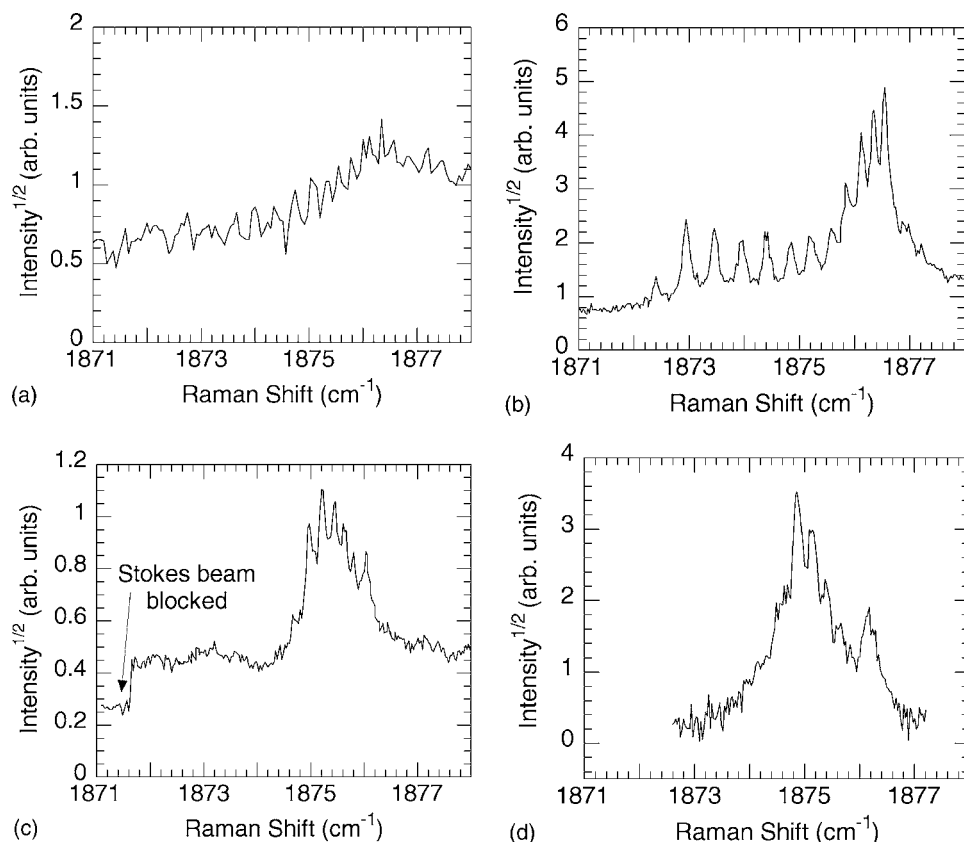


FIG. 5. Experimental NO ERE-CARS spectra demonstrating electronic resonance enhancement at room temperature and subatmospheric pressure for the following conditions (a) $\omega_3 = 42\,140.75\text{ cm}^{-1}$ and 1% NO, (b) $\omega_3 = 42\,194.09\text{ cm}^{-1}$ and 1% NO, (c) $\omega_3 = 42\,337.00\text{ cm}^{-1}$ and 1000 ppm NO, and (d) $\omega_3 = 42\,342.92\text{ cm}^{-1}$ and 1000 ppm NO.

background polarization. This significantly reduced the nonresonant background signal. While this diminishes the ERE-CARS signal as well, the overall effect is a considerable increase in signal-to-noise ratio (SNR).

III. EXPERIMENTAL DEMONSTRATION OF ELECTRONIC RESONANCE ENHANCEMENT

The initial NO ERE-CARS experiments were performed with a room-temperature, subatmospheric mixture of 1% NO in a buffer gas of N_2 (10 000 ppm). The NO ERE-CARS spectrum shown in Fig. 5(a) was recorded by scanning the Stokes dye laser beam with a fixed ultraviolet probe-beam frequency ω_3 of $42\,140.75\text{ cm}^{-1}$ (237.3 nm). For this probe frequency, there is some electronic resonance enhancement, but the probe frequency is below the electronic transition frequency for the ($v_b=1$ and $v_d=0$) vibrational band. The spectrum shown in Fig. 5(b) was recorded by scanning the Stokes dye laser beam with a fixed ultraviolet probe-beam frequency closer to resonance ($42\,194.09\text{ cm}^{-1}$ or 237.0 nm). The enhancement upon electronic resonance is clearly evident.

The ERE-CARS signal frequency ω_4 is readily absorbed by 1% NO. Therefore, as the frequency ω_3 is scanned further into electronic resonance, the NO concentration in the gas cell was decreased by a factor of 10 to 1000 ppm. The results of this change are shown in Fig. 5(c), which represents a spectrum recorded for a fixed ultraviolet probe-beam frequency of $42\,337.00\text{ cm}^{-1}$ (236.2 nm). The spectrum shown in Fig. 5(d) was acquired with all beams vertically polarized. The Stokes beam was blocked at the beginning of the scan for a Raman shift range of $1871.1\text{--}1871.6\text{ cm}^{-1}$; hence, the

increase in signal level at 1871.6 cm^{-1} is due to the nonresonant background. For subsequent recording of ERE-CARS spectra, the polarization scheme shown in Fig. 4 was used to suppress the nonresonant background. A typical spectrum recorded with polarization suppression is shown in Fig. 5(d) for 1000 ppm NO and a fixed probe-beam frequency of $42\,342.9\text{ cm}^{-1}$.

IV. PERTURBATIVE THEORY FOR ERE-CARS

Theoretical studies of the third-order polarization susceptibility in the perturbative limit (low input laser powers) have been previously developed and tested for ERE-CARS.^{18,25–28} Bloembergen *et al.*²⁵ and Oudar and Shen²⁶ both performed a perturbation expansion of the density matrix for the system. Eesley²⁷ employed Hellwarth diagrams as a basis for the derivation, and Druet *et al.*²⁸ used a time-ordered diagrammatic approach. A review of these theories is found in Attal-Trétout *et al.*¹⁸ Line strength calculations for various Hund's coupling cases for OH, C_2 , CH,¹⁹ and for I_2 (Ref. 29) have also been performed. While significant work has been done to model the aforementioned molecular species, applying these models to NO requires some additional considerations. Because NO is closer to a pure Hund's case (a), the satellite branches in the absorption spectrum are much stronger for higher values of the rotational quantum number J as opposed to OH.¹⁹ This introduces new transitions into the spectrum, which must be accounted for in the model.

The form of the polarization susceptibility modeled here is derived from the general third-order susceptibility given by Prior for all four-wave mixing processes.³⁰ The double-

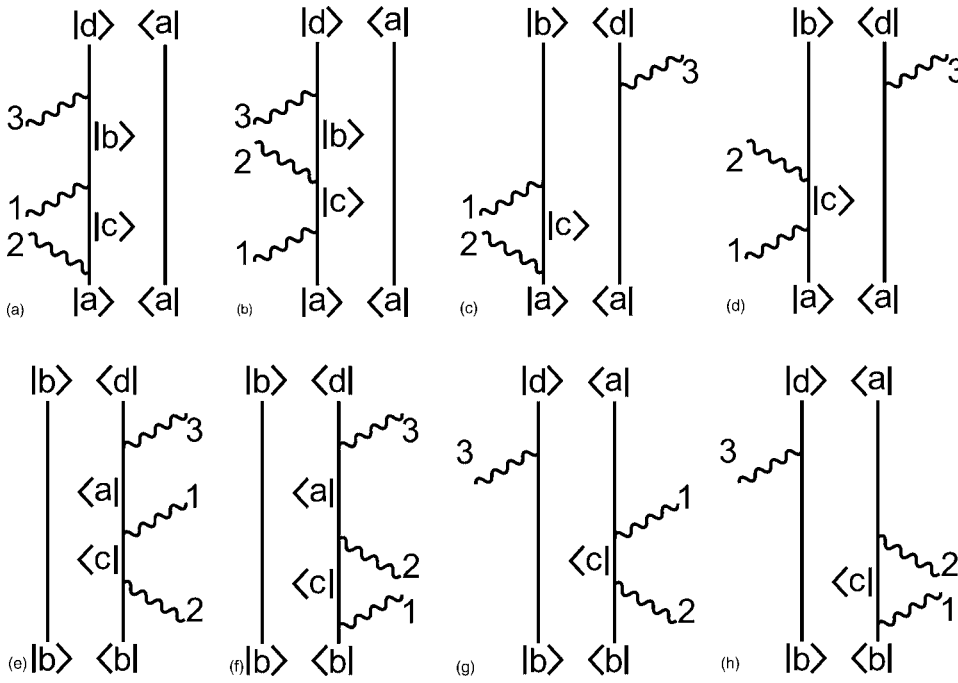


FIG. 6. Double-sided Feynman diagrams for the ERE-CARS process corresponding to the following terms in Prior: (Ref. 30) (a) 3, (b) 4, (c) 21, (d) 24, (e) 9, (f) 10, (g) 39, and (h) 42.

sided Feynman diagrams concerning Raman resonances between levels a and b (see Fig. 1) are displayed in Fig. 6. These diagrams are similar to previous time-ordered diagrams;¹⁴ however, this presentation accounts for nondegenerate pump beams. In particular, Figs. 6(b), 6(d), 6(e), and 6(g) correspond to Figs. 1(a), 1(b), 2(a), and 2(b) in Attal *et al.*,¹⁴ respectively. Assuming levels c and d are initially unpopulated, the diagrams of Fig. 6 result in a reduction of the general form as follows (in units of m^2/V^2)

$$\begin{aligned} \chi_{\text{CARS}}(\omega_4; \omega_1, -\omega_2, \omega_3) &= \chi_{\text{NR}} + \frac{N}{4\pi\epsilon_0\hbar^3} \sum_{a,b} \left\{ \left(\frac{1}{\omega_{ba} - (\omega_1 - \omega_2) - i\Gamma_{ba}} \right) \right. \\ &\times \sum_d \left(\frac{\mu_{4da}\mu_{3bd}}{\omega_{da} - \omega_4 - i\Gamma_{da}} + \frac{\mu_{3da}\mu_{4bd}}{\omega_{db} + \omega_4 + i\Gamma_{db}} \right) \\ &\times \left[\sum_c \rho_{aa}^{(0)} \left(\frac{\mu_{1cb}\mu_{2ac}}{\omega_{ca} + \omega_2 - i\Gamma_{ca}} + \frac{\mu_{2cb}\mu_{1ac}}{\omega_{ca} - \omega_1 - i\Gamma_{ca}} \right) \right. \\ &\left. \left. - \sum_c \rho_{bb}^{(0)} \left(\frac{\mu_{2cb}\mu_{1ac}}{\omega_{cb} - \omega_2 + i\Gamma_{cb}} + \frac{\mu_{1cb}\mu_{2ac}}{\omega_{cb} + \omega_1 + i\Gamma_{cb}} \right) \right] \right\}, \end{aligned} \quad (1)$$

where N is the total population being probed, ϵ_0 is the permittivity of free space, \hbar is Planck's constant, $\rho_{ii}^{(0)}$ is the fractional population of the state i , ω_{ij} is defined as $(E_i - E_j)/\hbar$ with E_i being the energy associated with state i , ω_k is the frequency of laser beam k , Γ_{ij} is the dephasing rate for the electric dipole transition between states i and j , and μ_{kij} is defined as

$$\mu_{kij} = \hat{e}_k \cdot \vec{\mu}_{ij}, \quad (2)$$

where $\vec{\mu}_{ij}$ is the dipole matrix element for the transition $i \rightarrow j$, and \hat{e}_k is the normalized polarization vector for laser

beam k . The form of Eq. (1) is in agreement with others in the literature.¹⁸ The remaining susceptibility terms not shown in Eq. (1) arise from Raman resonances between levels other than a and b and one- and two-photon transitions. These excluded terms are small in magnitude, largely frequency-independent as compared to the terms shown, and can be accounted for in χ_{NR} , the nonresonant susceptibility.²⁸

Considering the case shown in Fig. 1, it is evident that $\omega_{cb} \equiv \omega_{ca} - \omega_1 + \omega_2$ and $\omega_{ca}, \omega_{cb} \gg \omega_1, \omega_2$. Therefore, Eq. (1) can be reduced to

$$\begin{aligned} \chi_{\text{CARS}}(\omega_4; \omega_1, -\omega_2, \omega_3) &= \chi_{\text{NR}} + \frac{N}{4\pi\epsilon_0\hbar^3} \sum_{a,b} \left\{ \left(\frac{1}{\omega_{ba} - (\omega_1 - \omega_2) - i\Gamma_{ba}} \right) \right. \\ &\times \sum_d \left(\frac{\mu_{4da}\mu_{3bd}}{\omega_{da} - \omega_4 - i\Gamma_{da}} + \frac{\mu_{3da}\mu_{4bd}}{\omega_{db} + \omega_4 + i\Gamma_{db}} \right) \\ &\times \left[\sum_c (\rho_{aa}^{(0)} - \rho_{bb}^{(0)}) \left(\frac{\mu_{1cb}\mu_{2ac}}{\omega_{cb} + \omega_1} + \frac{\mu_{2cb}\mu_{1ac}}{\omega_{ca} - \omega_1} \right) \right] \right\}. \end{aligned} \quad (3)$$

The final summation in brackets has the form of a spontaneous Raman cross-section (in units of m^2/sr) for excitation at ω_1 ³¹

$$\begin{aligned} \left(\frac{\partial \alpha}{\partial \Omega} \right)_{ab} &= \frac{\omega_2^4}{(4\pi\epsilon_0)^2 c^4} \left| \sum_c \left(\frac{\mu_{1cb}\mu_{2ac}}{\hbar(\omega_{cb} + \omega_1)} \right. \right. \\ &\left. \left. + \frac{\mu_{2cb}\mu_{1ac}}{\hbar(\omega_{ca} - \omega_1)} \right) \right|^2. \end{aligned} \quad (4)$$

Equation (3) can then be recast as

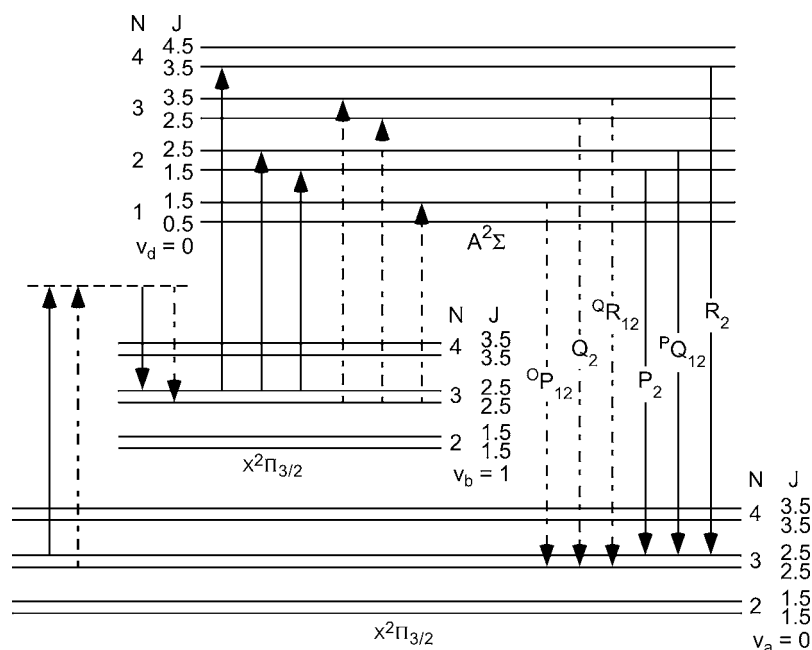


FIG. 7. Energy-level diagram of the ERE-CARS process for the $X^2\Pi_{3/2}$ ground electronic state of NO.

$$\begin{aligned} \chi_{\text{CARS}}(\omega_4; \omega_1, -\omega_2, \omega_3) &= \chi_{\text{NR}} + \frac{N}{4\pi\epsilon_0\hbar^3} \sum_{a,b} \left\{ \left(\frac{1}{\omega_{ba} - (\omega_1 - \omega_2) - i\Gamma_{ba}} \right) \right. \\ &\times \sum_d \left(\frac{\mu_{4da}\mu_{3bd}}{\omega_{da} - \omega_4 - i\Gamma_{da}} + \frac{\mu_{3da}\mu_{4bd}}{\omega_{db} + \omega_4 + i\Gamma_{db}} \right) \\ &\times \left[(\rho_{aa}^{(0)} - \rho_{bb}^{(0)}) \sqrt{\frac{(4\pi\epsilon_0)^2 \hbar^2 c^4}{\omega_2^4} \left(\frac{\partial \alpha}{\partial \Omega} \right)_{ab}} \right] \Bigg\}, \quad (5) \end{aligned}$$

where c is the speed of light. Observing for the electronic resonance case in Fig. 1 that $\omega_{da} \approx \omega_4$, the second term in the second line of Eq. (5) is nonresonant and can be absorbed into χ_{NR} . Rearranging, Eq. (5) now becomes

$$\begin{aligned} \chi_{\text{CARS}}(\omega_4; \omega_1, -\omega_2, \omega_3) &= \chi_{\text{NR}} \\ &+ \frac{Nc^2}{\hbar^2\omega_2^2} \sum_{a,b,d} \left\{ \left(\frac{\partial \alpha}{\partial \Omega} \right)_{ab}^{1/2} \left(\frac{(\rho_{aa}^{(0)} - \rho_{bb}^{(0)})}{\omega_{ba} - (\omega_1 - \omega_2) - i\Gamma_{ba}} \right) \right. \\ &\times \left(\frac{\mu_{4da}\mu_{3bd}}{\omega_{da} - \omega_4 - i\Gamma_{da}} \right) \Bigg\}. \quad (6) \end{aligned}$$

This equation is employed in modeling the ERE-CARS spectra presented herein. To compare the theoretical spectra with the acquired data, convolutions must be performed to account for the finite laser linewidths used in the experiment. Three convolutions were conducted: One each for the pump, the Stokes, and the probe beams. Gaussian profiles were assumed for each laser beam. The third convolution is unique to this ERE-CARS process, and has not been applied in previous models, in which a convolution for the Stokes beam is typically applied.³² Once the convolutions are completed, the magnitude of the complex susceptibility can be compared to the data.

As seen from Fig. 1, if ω_3 is tuned into resonance with ω_{bd} , then ω_4 will be resonant with ω_{da} . The enhancement

resulting from this electronic resonance enables the detection of weak Raman transitions of molecules such as NO, even at low concentrations. Improvements in the detection limit on the order of 10^2 – 10^8 can be achieved.²⁸ In addition, species selectivity for the CARS process is strengthened by this electronic resonance. For the standard CARS process, the Raman resonance criterion is

$$\omega_1 - \omega_2 = \omega_{ba}. \quad (7)$$

For the ERE-CARS process under consideration in this study, the electronic resonance criterion is

$$\omega_4 = \omega_{da}. \quad (8)$$

The extra selectivity provided by two resonance requirements can eliminate interferences from overlapping spectra of molecules, such as the $A \leftarrow X$ fluorescence band of NO with the Schumann–Runge system of O_2 .²²

Equation (6) is now considered in light of the specific energy-level diagram for the $\Pi_{3/2}$ ground state of NO shown in Fig. 7. A similar schematic could be presented for the $X^2\Pi_{1/2}$ state. Only the Raman Q -branch was probed during the experiments; therefore, the S - and O -branches are not included in the diagram. For the case under consideration in Fig. 7, $v_d=0$. In accordance with the selection rules for Raman transitions, two distinct Raman Q -branch transitions can occur, corresponding to either parity of the lower rotational levels. To distinguish between parity levels, the transitions starting from negative parity ground states are shown with solid lines, whereas those that originate from positive parity states are shown with dashed lines. The Raman transition occurs through a virtual state, as only the ultraviolet probe beam is in electronic resonance. Once the molecule is excited to its first vibrational level ($v_b=1, J_b$), three electronic transitions can couple the molecule to the $A^2\Sigma$ state for a specific rotational level and parity. Each of the electronic transitions is matched with a corresponding electronic transition that returns the molecule to the ground state. The large dif-

ference in frequency between the pump and probe-beams separates the Raman process from the electronic process; thus, the enhancement of the Raman process is well defined, which assists in reducing the complexity of the model.

To apply the model, the Raman cross-section was calculated from values provided by Schrötter and Klöckner.¹¹ The same cross-section was used for both electronic ground states of NO, as a previous study of NO CARS determined the values to be essentially the same.³³ Resonance effects between ω_4 and ω_{da} were evaluated using the dipole matrix elements μ_{3bd} and μ_{4da} . These matrix elements were calculated following the formulae in Hilborn³⁴ incorporating spectroscopic data from LIFBASE.³⁵ The spontaneous emission coefficient A_{21} , used to calculate the matrix elements, was divided by a factor of three to account for isotropic emission and the fact that the Zeeman effect was not explicitly taken into account, as used previously by Siegman.³⁶ The Raman shift (ω_{ba}) was based on the constants of Huber and Herzberg³⁷ and of Laane and Kiefer.³⁸ The electronic transition frequencies ω_{da} were taken from LIFBASE.³⁵

The Raman linewidths (cm^{-1}) Γ_{ba} (FWHM) were obtained from Doerk *et al.* as follows³⁹

$$\Gamma_{ba} = 0.12 \left(\frac{T_{\text{ref}}}{T} \right) \left(\frac{P}{P_{\text{ref}}} \right), \quad (9)$$

where $T_{\text{ref}} = 298$ K and $P_{\text{ref}} = 1$ atm. The electronic transition linewidth Γ_{da} was calculated from a combination of the Doppler and collisional widths. The collisional width was approximated as

$$\Gamma_{da,c} = 0.6P, \quad (10)$$

where $\Gamma_{da,c}$ has units of cm^{-1} and P has units of atm. The above relation is an approximation to the work of Chang *et al.*⁴⁰ and is in agreement with other studies in the literature.^{20,41} The Doppler width for the electronic resonance transitions is based on the standard theory¹³ and at room temperature is approximately⁴¹ $\Gamma_{da,D} = 0.1 \text{ cm}^{-1}$. The total linewidth was then approximated by

$$\Gamma_{da} = \sqrt{\Gamma_{da,c}^2 + \Gamma_{da,D}^2}. \quad (11)$$

V. DEFINITION OF AN EFFECTIVE INTERMEDIATE RAMAN LEVEL

To address the contribution to the susceptibility in Eq. (6) from the numerous excited electronic states of NO, we define an effective electronic level for the calculations. We use the general transition polarizability to determine the characteristics of the effective electronic level. The transition polarizability can be related to the Raman cross-section of Eq. (4) by

$$\left(\frac{\partial \alpha}{\partial \Omega} \right)_{ab} = \frac{\omega_2^4}{(4\pi\epsilon_0)^2 c^4} \overline{(\alpha_{zz})_{ab}^2}. \quad (12)$$

Therefore, the transition polarizability is found to be

$$\overline{(\alpha_{zz})_{ab}^2} = \left| \sum_c \left(\frac{\mu_{1cb}\mu_{2ac}}{\hbar(\omega_{cb} + \omega_1)} + \frac{\mu_{2cb}\mu_{1ac}}{\hbar(\omega_{ca} - \omega_1)} \right) \right|^2. \quad (13)$$

The summation over c includes only the possible intermediate states that have single-photon allowed transitions with both states a and b . The polarizability for a transition between an initial rotational level A and final rotational level B is found by summing over all possible Zeeman states a and b ,

$$\overline{(\alpha_{zz})_{AB}^2} = \frac{1}{(2J_A + 1)} \sum_{a,b} \left| \sum_c \left(\frac{\mu_{1cb}\mu_{2ac}}{\hbar(\omega_{cb} + \omega_1)} + \frac{\mu_{2cb}\mu_{1ac}}{\hbar(\omega_{ca} - \omega_1)} \right) \right|^2. \quad (14)$$

In general, the Raman cross-section or transition polarizability cannot be calculated directly, especially for molecules such as NO which possesses numerous excited levels that are connected with the $X^2\Pi$ ground state through single-photon transitions. In addition, many vibrational levels in each of these electronic levels are connected with the $v''=0$ and $v''=1$ vibrational levels in the $X^2\Pi$ state by transitions with significant oscillator strengths. Beyond the sheer number of transitions that would have to be accounted for, the oscillator strengths for most of these transitions are not well known. This is especially the case for electronic levels above the $E^2\Sigma^+$ level of NO.

Consequently, we chose one effective electronic level ($C^2\Pi$), aside from the $A^2\Sigma^+$ state, to act as an intermediate level in the Raman transition by representing all of the non-resonant excited electronic levels. The oscillator strengths, and thus the dipole matrix elements, of the (0,0) and (0,1) bands in the $C^2\Pi \leftarrow X^2\Pi$ electronic manifold were artificially enhanced so as to obtain the literature value¹¹ of the transition polarizability for the fundamental (1,0) band of the Q -branch of NO in the $X^2\Pi$ state. In particular, the values of the dipole matrix elements for this band were increased by a factor of 2.2 from the values of Luque and Crosley.³⁵ The calculation for Eq. (14) was performed by summing only over states c in the $v=0$ vibration-rotation bands of the $A^2\Sigma^+$ and $C^2\Pi$ levels.

VI. ENHANCEMENT FACTOR

Because a primary advantage of employing ERE-CARS over CARS is the enhancement in signal level, a parameter that quantifies this increase was developed as part of the study. The resulting enhancement factor or $\delta(\omega_4)$ is defined as

$$\delta(\omega_4) = \frac{\chi_{\text{CARS}}(\omega_4; \omega_1, -\omega_2, \omega_3)}{\chi_{\text{CARS}}((2\omega_1 - \omega_2); \omega_1, -\omega_2, \omega_1)}, \quad (15)$$

where the denominator represents the degenerate pump-beam case $\omega_1 = \omega_3$. The enhancement factor is used to evaluate the reduction in detection limit resulting from electronic resonance enhancement. This factor is proportional to the increase in CARS susceptibility and thus inversely proportional to the NO detection limit. The CARS signal is proportional to the square of the enhancement factor.

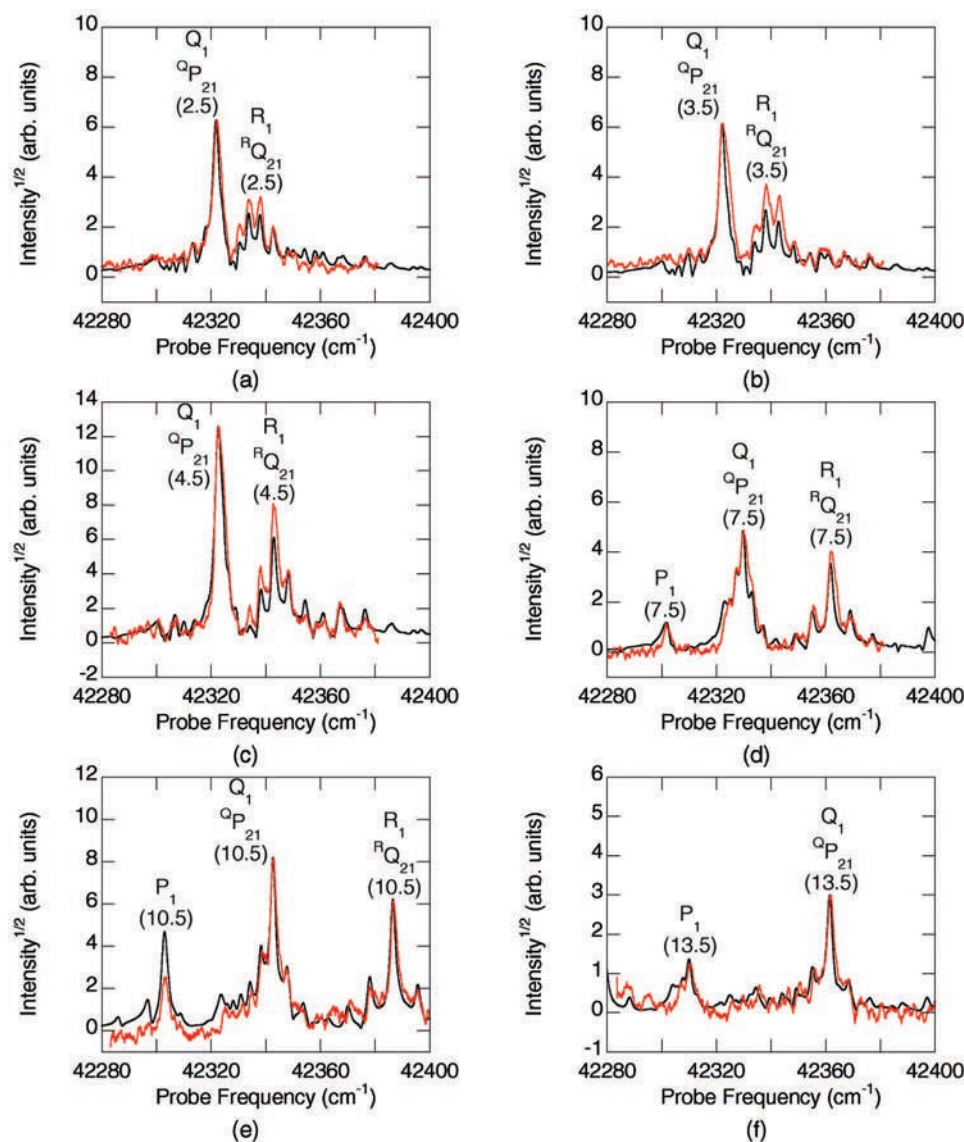


FIG. 8. (Color) Comparison of theoretical (black line) and experimental (red line) ERE-CARS spectra generated for a pressure of 1.0 atm, a concentration of 100 ppm NO, and for Raman shifts and Raman transitions of (a) 1875.95 cm⁻¹, Q₁(2.5), (b) 1875.82 cm⁻¹, Q₁(3.5), (c) 1875.66 cm⁻¹, Q₁(4.5), (d) 1875.00 cm⁻¹, Q₁(7.5), (e) 1874.02 cm⁻¹, Q₁(10.5), and (f) 1872.74 cm⁻¹, Q₁(13.5).

VII. RESULTS

During the experiments, either the Stokes or the ultraviolet probe-beam frequency was scanned to produce a CARS spectrum. These two spectrum types were acquired experimentally and theoretically modeled and are referred to as “Stokes scans” or “probe scans” to indicate which laser beam was tuned across the spectrum. Because the spectral features of these scan types differ, the results will be covered in separate sections.

For clarity, a notation is introduced here, similar to that found in the literature,¹⁸ to denote the overall ERE-CARS transition. The notation begins by listing the Raman transition with a subscript [1 for $\Pi_{1/2}$ and 2 for $\Pi_{3/2}$ (Ref. 42)] to indicate the Π state of the molecule. The final electronic transition is identified next following the notation of Mavrodineanu and Boiteux.⁴³ The value of J_a in the ground state is then listed in parentheses. Therefore, processes involving transitions on the far right and second from far right in Fig. 7 would be denoted by $Q_2R_2(2.5)$ and $Q_2^PQ_{12}(2.5)$, respectively.

A. Results for probe scans

Figure 8 shows comparisons between theoretical and experimental spectra for six atmospheric probe-scan cases. For these scans, the probe frequency was tuned over the approximate range of 42 280–42 400 cm⁻¹ (236.5–237.0 nm). The spectra encompass fixed Stokes frequencies that correlate to Raman shifts between 1872.74 and 1875.95 cm⁻¹. The data were acquired at room temperature using a concentration of 100 ppm NO in N₂.

As shown in Fig. 8, good agreement exists between the theoretical and experimental spectra for all fixed Raman shifts. Spectral peak locations and relative intensities are well represented. While a good match generally occurs in linewidths, we should note that the theoretical spectra were generated using Stokes and probe linewidths of 0.08 and 1.0 cm⁻¹, respectively. This probe linewidth is wider than that estimated experimentally. The enhanced linewidth indicates the presence of saturation in the electronic process $b \rightarrow d$ (see Fig. 7) and highlights the necessity of a triple convolution in generating the theoretical spectra. These results confirm that the model is capable of calculating theoretical

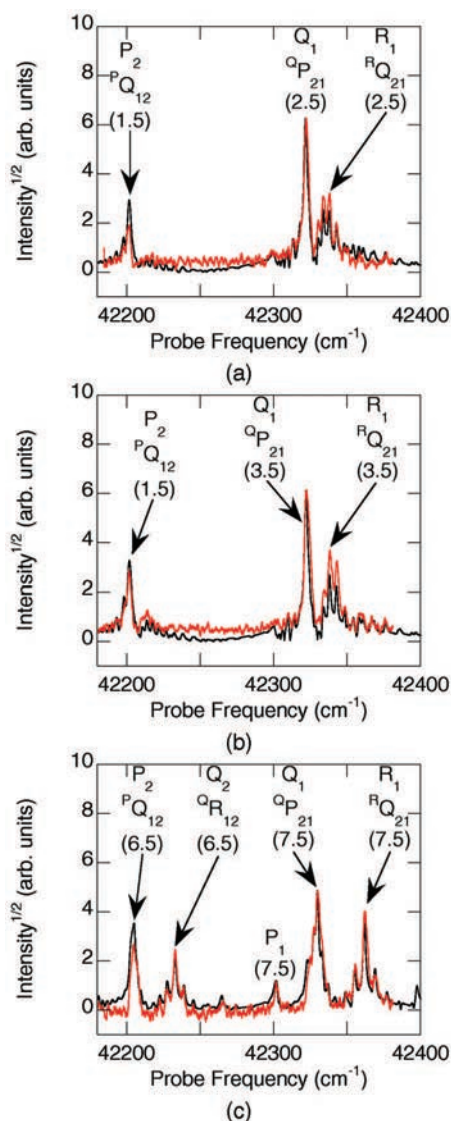


FIG. 9. (Color) Comparison of theoretical (black line) and experimental (red line) ERE-CARS spectra generated for a pressure of 1.0 atm, a concentration of 100 ppm NO, and for Raman shifts and Raman transitions of (a) 1875.95 cm^{-1} , $Q_1(2.5)/Q_2(1.5)$, (b) 1875.82 cm^{-1} , $Q_1(3.5)/Q_2(1.5)$, and (c) 1875.00 cm^{-1} , $Q_1(7.5)/Q_2(6.5)$.

spectra in good agreement with experimental spectra, and, more importantly, that the essential physics of the ERE-CARS process are captured by the model.

Figure 9 displays three probe-scan cases over an extended probe-frequency range. These three cases correspond to those shown in Figs. 8(a), 8(b), and 8(d). By expanding the scale, the spectra now encompass resonances in the $\Pi_{3/2}$ ground state. The amplitude variation between the spectra of Figs. 8 and 9 occurs because the frequency difference $\omega_1 - \omega_2$ is in resonance with different rotational levels. For the expanded spectra, the $\Pi_{1/2}$ transitions correspond to the peaks on the righthand side of each spectrum and the $\Pi_{3/2}$ transitions are on the lefthand side. As an example, the major peaks in Fig. 9(a) are marked and correspond to the following transitions from left to right: $Q_2P_2(1.5) + Q_2^PQ_{12}(1.5)$, $Q_1Q_1(2.5) + Q_1^QP_{21}(2.5)$, and $Q_1R_1(2.5) + Q_1^RQ_{21}(2.5)$. Similar transitions occur in Figs. 9(b) and 9(c), with the transition Q_1P_1 appearing in Fig. 9(c) for $J_1 = 7.5$.

The relative intensities within a given Π state are generally predicted with good accuracy. However, the relative intensities between Π states, i.e., on the right and left sides of the spectra, are not in complete agreement with the experimental spectra. This is primarily due to a decrease in probe-beam power during the scan, which arises from the short lifetime of the LDS698 laser dye employed in the experiments. The experimental spectra were normalized by dividing by the measured probe-beam power, but this procedure might not be the most accurate normalization approach if the electronic resonance was saturated. In addition, the two Π states may not have the same Raman cross-section, as assumed for our calculations.

The enhancement factor associated with each spectrum in Fig. 8 is shown in Fig. 10. Because of the isolated electronic resonances that dominate each spectrum, the spectral behavior of the enhancement factor is very similar to its corresponding spectrum. As can be seen from Fig. 10, the electronic resonance for the ERE-CARS process provides an enhancement in signal strength by a factor of approximately 1000 compared to a typical CARS process. This significant enhancement permits the CARS signal to be detected above the nonresonant background.

B. Results for Stokes scans

Figure 11 displays comparisons between theoretical and experimental spectra for three atmospheric Stokes-scan cases. The experimental spectra were acquired by scanning the Stokes frequency over a Raman shift range of $1872.5\text{--}1877.5\text{ cm}^{-1}$ for three different fixed ultraviolet probe-beam frequencies. The experimental spectra were obtained for the same diagnostic conditions as for the probe-scan spectra shown in Fig. 8 (1.0 atm and 100 ppm NO). The theoretical spectra were generated using a smaller probe-beam linewidth (0.08 cm^{-1}) and an identical Stokes-beam linewidth. This behavior indicates that the effects of saturation occurring in the electronic process are not significant for Stokes-scan spectra. As the probe-beam frequency is fixed, the convolution with the Stokes beam linewidth becomes the dominant factor in determining the shape of the Stokes-scan spectra.

The theoretical spectra in Fig. 11 are in good agreement with the experimental results. Because of the numerous Q -branch transitions probed and the three possible electronic transitions at or near resonance for each case (see Fig. 7), the Stokes scans include a greater number of enhanced transitions as compared to the probe scans. These transitions overlap and interfere, and thus appear as a single wide peak. This merging results from the frequency spacing of the NO Q -branch Raman lines, which is far less than the frequency spacing of the electronic transitions, and the use of visible pump and Stokes beams. Similar to the probe scans, the spectral shape of the experimental Stokes scans changes as the ultraviolet probe-beam frequency is varied. The modeled spectra capture these spectral changes well for all cases.

The behavior of the Stokes-scan spectra can be explained by considering the dominant transitions as the probe frequency is changed for each scan. Only transitions arising

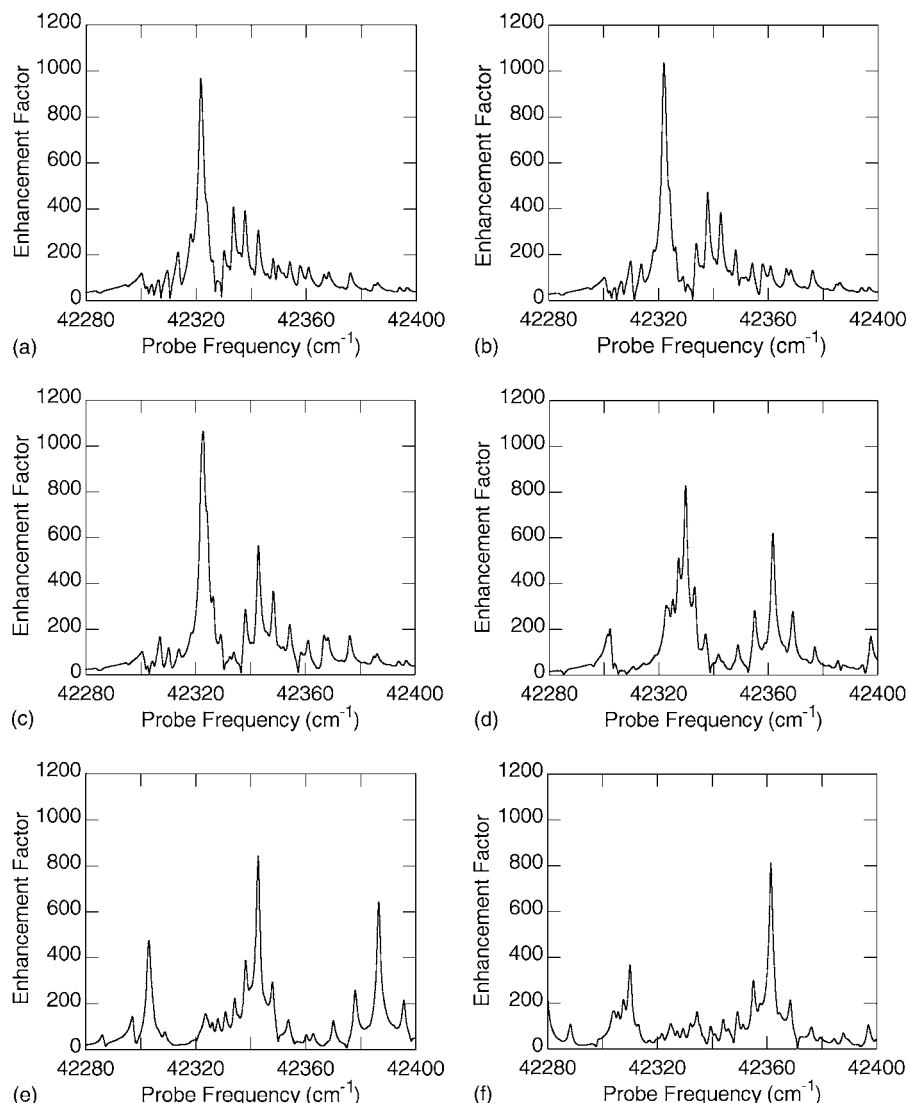


FIG. 10. Enhancement factor for a pressure of 1.0 atm, a concentration of 100 ppm NO, and for Raman shifts of (a) 1875.95 cm^{-1} , (b) 1875.82 cm^{-1} , (c) 1875.66 cm^{-1} , (d) 1875.00 cm^{-1} , (e) 1874.02 cm^{-1} , and (f) 1872.74 cm^{-1} .

from the $\Pi_{1/2}$ state are probed using these diagnostic parameters. Starting with Fig. 11(a), the ERE-CARS process is in strong resonance with the Q_1Q_1 and the $Q_1^Q P_{21}$ transitions for $J=1.5-5.5$, with the dominant peak occurring for $J=4.5$. As the probe beam is shifted to higher frequencies, these resonances move to higher values of J , with a maximum intensity occurring at $J=7.5$ and a shift to the left of the dominant peak, as shown in Fig. 11(b). Simultaneously, a new set of resonances appears on the righthand side of the spectrum, corresponding to Q_1R_1 and $Q_1^R Q_{21}$ for $J=1.5-2.5$. These two sets of resonances continue to shift to the left as the probe frequency rises, as displayed in Fig. 11(c), with the maximum intensity occurring for $J=10.5$ and $J=4.5$ for the left and right peaks, respectively.

The spectral response of NO is clearly detectable over the nonresonant background even at this low concentration and the model is capable of predicting the spectrum for these thermodynamic conditions for both types of scans. The SNR for the spectra shown in Figs. 8 and 11 is approximately 10, and as such, the detection limit is estimated to be less than 10 ppm. In comparison, using polarization CARS, Pott *et al.*⁴⁴ report a detection limit of 200 ppm with a SNR of approximately unity.

Figure 12 displays the enhancement factors corresponding to the Stokes scan spectra shown in Fig. 11. As with the probe scans, the spectral shape of the enhancement factor is similar to the corresponding spectrum. Moreover, the enhancement magnitude is similar to that of the probe scans, near a factor of 1000.

VIII. CONCLUSIONS

In conclusion, the ERE-CARS process has been demonstrated both experimentally and theoretically for NO. The good agreement between the experimental and theoretical spectra for both the probe and Stokes scans highlights the capabilities of the theoretical model developed and described in this paper. The predicted line positions match closely with those of the transitions in the experimental spectra. The relative intensities corresponding to each Π state are approximately correct, and good comparisons occurred between spectra encompassing both Π states. This theory complements the sensitivity of the experimental setup, which was able to obtain NO spectra for a concentration of 100 ppm at a SNR of 10. This low detection limit makes the technique viable for many practical applications. In addition, the en-

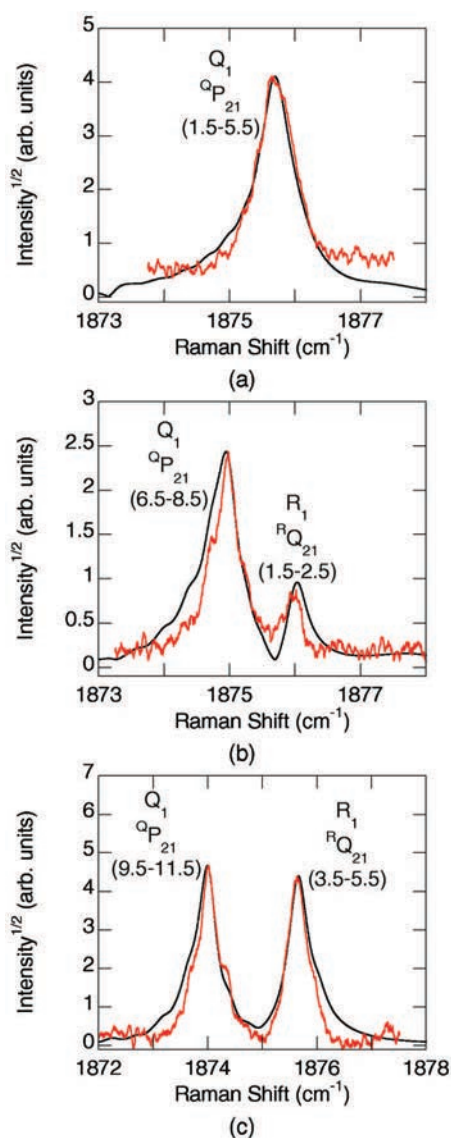


FIG. 11. (Color) Comparison of theoretical (black line) and experimental (red line) ERE-CARS spectra for a pressure of 1.0 atm, a concentration of 100 ppm, and probe frequencies of (a) 42 322.61 cm^{-1} , (b) 42 330.41 cm^{-1} , and (c) 42 343.00 cm^{-1} .

hancement factor illustrates the advantages of employing ERE-CARS over the degenerate pump-beam case.

Another advantage of ERE-CARS is increased species selectivity. This feature can be demonstrated from the results presented for both the probe and Stokes scans. As shown in Fig. 8, only a few dominant transitions occur for each configuration of probe and Stokes frequencies. While an increased number of transitions occur for the Stokes-scan spectra (Fig. 11), it is clear from all cases that not all Raman Q -branch transitions can be probed and enhanced simultaneously. Therefore, if the entire range of transitions for one molecule cannot be satisfied completely, it is very unlikely that the probe and Stokes frequencies chosen will satisfy the selection criteria for two molecules simultaneously. This benefit of ERE-CARS is just as important as the enhancement in signal strength, because a strong signal arising from multiple species can be just as difficult to analyze as a weak, indiscernible signal.

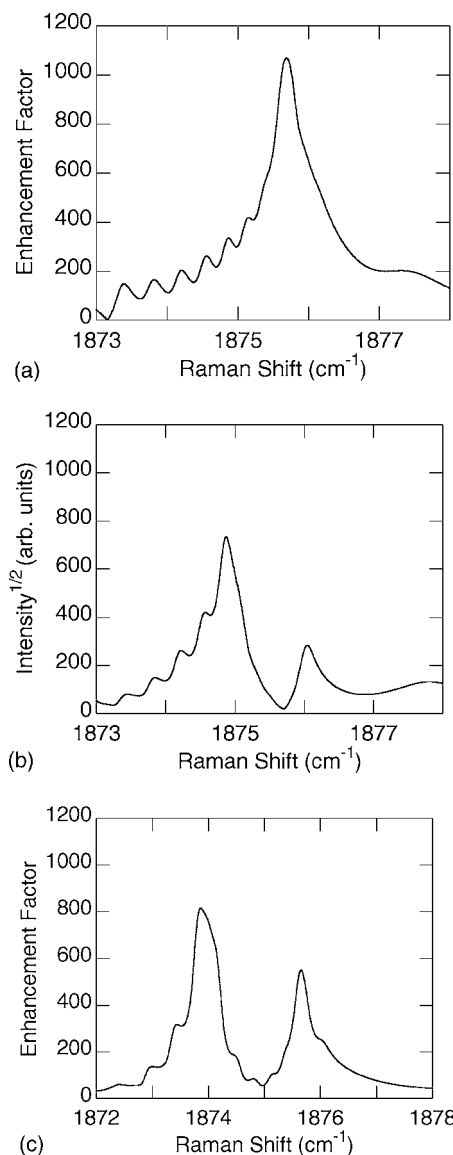


FIG. 12. Enhancement factor for a pressure of 1.0 atm, a concentration of 100 ppm, and probe frequencies of (a) 42 322.61 cm^{-1} , (b) 42 330.41 cm^{-1} , and (c) 42 343.00 cm^{-1} .

ACKNOWLEDGMENTS

Funding for this research was provided by a Phase II STTR SB00207 from the Air Force Office of Scientific Research (Dr. Julian Tishkoff, Program Manager) under Contract No. FA9550-07-C-0036, by the U.S. Department of Energy, Division of Chemical Sciences, Geosciences and Biosciences, under Grant No. DE-FG02-03ER15391, and by the Air Force Research Laboratory, Propulsion Directorate, Wright-Patterson Air Force Base, under Contract No. F33615-03-D-2329. Additional support is gratefully acknowledged from the Defense Advanced Research Project Agency and the U.S. Army Research Office.

¹S. F. Hanna, W. D. Kulatilaka, Z. Arp, T. Opatrný, M. O. Scully, J. P. Kuehner, and R. P. Lucht, *Appl. Phys. Lett.* **83**, 1887 (2003).

²W. Meier, A. O. Vydrov, V. Bergmann, and W. Stricker, *Appl. Phys. B: Lasers Opt.* **63**, 79 (1996).

³T. R. Meyer, G. F. King, G. C. Martin, R. P. Lucht, F. R. Schauer, and J. C. Dutton, *Exp. Fluids* **32**, 603 (2002).

- ⁴D. Bose and G. V. Candler, *J. Thermophys. Heat Transfer* **12**, 214 (1998).
- ⁵P. M. Danehy, P. Mere, M. J. Gaston, S. O'Byrne, P. C. Palma, and A. F. P. Houwing, *AIAA J.* **39**, 1320 (2001).
- ⁶M. O. Scully, G. W. Kattawar, R. P. Lucht, T. Opatrný, H. Pilloff, A. Rebane, A. V. Sokolov, and M. S. Zubairy, *Proc. Natl. Acad. Sci. U.S.A.* **99**, 10994 (2002).
- ⁷G. Beadie, J. Reintjes, M. Bashkansky, T. Opatrny, and M. O. Scully, *J. Mod. Opt.* **50**, 2361 (2003).
- ⁸M. Bruchhausen, J. Voigt, T. Doerk, S. Hädrich, and J. Uhlenbusch, *J. Mol. Spectrosc.* **201**, 70 (2000).
- ⁹R. P. Lucht, *Opt. Lett.* **12**, 78 (1987).
- ¹⁰R. P. Lucht, V. Velur-Natarajan, C. D. Carter, K. D. Grinstead, Jr., J. R. Gord, P. M. Danehy, G. J. Fiechtner, and R. L. Farrow, *AIAA J.* **41**, 679 (2003).
- ¹¹H. W. Schrötter and H. W. Klöckner, *Raman Spectroscopy of Gases and Liquids*, edited by A. Weber (Springer-Verlag, Berlin, 1979), pp. 123–166.
- ¹²L. J. Rahn, L. A. Zych, and P. L. Mattern, *Opt. Commun.* **30**, 249 (1979).
- ¹³A. C. Eckbreth, *Laser Diagnostics for Combustion Temperature and Species* (Gordon and Breach, Amsterdam, 1996).
- ¹⁴B. Attal, O. O. Schnepf, and J.-P. E. Taran, *Opt. Commun.* **24**, 77 (1978).
- ¹⁵T. Doerk, P. Jauernik, S. Hädrich, B. Pfelzer, and J. Uhlenbusch, *Opt. Commun.* **118**, 637 (1995).
- ¹⁶T. Doerk, M. Hertl, B. Pfelzer, S. Hädrich, P. Jauernik, and J. Uhlenbusch, *Appl. Phys. B: Lasers Opt.* **64**, 111 (1997).
- ¹⁷B. Attal-Trétout, S. C. Schmidt, E. Crété, P. Dumas, and J. P. Taran, *J. Quant. Spectrosc. Radiat. Transf.* **43**, 351 (1990).
- ¹⁸B. Attal-Trétout, P. Berlemont, and J. P. Taran, *Mol. Phys.* **70**, 1 (1990).
- ¹⁹B. Attal-Trétout, P. Monot, and K. Müller-Dethlefs, *Mol. Phys.* **73**, 1257 (1991).
- ²⁰P. M. Danehy, E. J. Friedman-Hill, R. P. Lucht, and R. L. Farrow, *Appl. Phys. B: Photophys. Laser Chem.* **57**, 243 (1993).
- ²¹H. Bervas, B. Attal-Trétout, S. Le Boiteux, and J. P. Taran, *J. Phys. B* **25**, 949 (1992).
- ²²B. E. Battles and R. K. Hanson, *J. Quant. Spectrosc. Radiat. Transf.* **54**, 521 (1995).
- ²³V. Krüger, M. Dumont, S. Le Boiteux, Y. J. Picard, F. Chaussard, and B. Attal-Trétout, *Phys. Rev. A* **64**, 012717 (2001).
- ²⁴A. C. Eckbreth, *Appl. Phys. Lett.* **32**, 421 (1978).
- ²⁵N. Bloembergen, H. Lotem, and R. T. Lynch, Jr., *Indian J. Pure Appl. Phys.* **16**, 151 (1978).
- ²⁶J.-L. Oudar and Y. R. Shen, *Phys. Rev. A* **22**, 1141 (1980).
- ²⁷G. L. Eesley, *Coherent Raman Spectroscopy* (Pergamon, Oxford, 1981).
- ²⁸S. A. J. Druet, B. Attal, T. K. Gustafson, and J. P. Taran, *Phys. Rev. A* **18**, 1529 (1978).
- ²⁹I. Aben, W. Ubachs, G. van der Zwan, and W. Hogervorst, *Mol. Phys.* **76**, 591 (1992).
- ³⁰Y. Prior, *IEEE J. Quantum Electron.* **QE-20**, 37 (1984).
- ³¹R. J. Hall and A. C. Eckbreth, *Laser Appl.* **5**, 213 (1984).
- ³²R. E. Palmer, *The CARSFT computer code for calculating coherent anti-Stokes Raman spectra: User and programmer information*, Sandia Report No. SAND89-8206, 1989 (unpublished).
- ³³A. Beckmann, H. Fietz, W. Kiefer, and J. Laane, *Phys. Rev. A* **24**, 2518 (1981).
- ³⁴R. C. Hilborn, *Am. J. Phys.* **50**, 982 (1982).
- ³⁵J. Luque and D. R. Crosley, *LIFBASE: Database and Spectral Simulation Program* (Version 1.6), SRI International Report No. MP 99-009, 1999 (unpublished).
- ³⁶A. E. Siegman, *Lasers* (University Science Books, Mill Valley, 1986).
- ³⁷K. P. Huber and G. Herzberg, *Molecular Spectra and Molecular Structure, IV. Constants of Diatomic Molecules* (Van Nostrand Reinhold, New York, 1979).
- ³⁸J. Laane and W. Kiefer, *J. Raman Spectrosc.* **9**, 353 (1980).
- ³⁹T. Doerk, J. Ehlbeck, R. Jedamzik, J. Uhlenbusch, J. Hörschele, and J. Steinwandel, *Appl. Spectrosc.* **51**, 1360 (1997).
- ⁴⁰A. Y. Chang, M. D. DiRosa, and R. K. Hanson, *J. Quant. Spectrosc. Radiat. Transf.* **47**, 375 (1992).
- ⁴¹S. F. Hanna, R. Barron-Jimenez, T. N. Anderson, R. P. Lucht, J. A. Caton, and T. Walther, *Appl. Phys. B: Lasers Opt.* **75**, 113 (2002).
- ⁴²G. Herzberg, *Molecular Spectra and Molecular Structure, I. Spectra of Diatomic Molecules* (Van Nostrand, Princeton, 1950).
- ⁴³R. Mavrodineanu and H. Boiteux, *Flame Spectroscopy* (Wiley, New York, 1965).
- ⁴⁴A. Pott, T. Doerk, J. Uhlenbusch, J. Ehlbeck, J. Hörschele, and J. Steinwandel, *J. Phys. D* **31**, 2485 (1998).



ANNUAL
REVIEWS **Further**

Click [here](#) for quick links to Annual Reviews content online, including:

- Other articles in this volume
- Top cited articles
- Top downloaded articles
- Our comprehensive search

Applications of Ultrafast Lasers for Optical Measurements in Combusting Flows*

James R. Gord,¹ Terrence R. Meyer,²
and Sukesh Roy¹

¹Air Force Research Laboratory, Propulsion Directorate, Wright-Patterson Air Force Base, Ohio 45433; email: james.gord@wpafb.af.mil, sroy@woh.rr.com

²Mechanical Engineering Department, Iowa State University, Ames, Iowa 50011; email: trm@iastate.edu

Annu. Rev. Anal. Chem. 2008. 1:663–87

First published online as a Review in Advance on March 18, 2008

The *Annual Review of Analytical Chemistry* is online at anchem.annualreviews.org

This article's doi:
10.1146/annurev.anchem.1.031207.112957

Copyright © 2008 by Annual Reviews.
All rights reserved

1936-1327/08/0719-0663\$20.00

*The U.S. Government has the right to retain a nonexclusive, royalty-free license in and to any copyright covering this paper.

Key Words

combustion diagnostics, laser-induced fluorescence, pump/probe, ballistic imaging, coherent anti-Stokes Raman scattering, wave mixing

Abstract

Optical measurement techniques are powerful tools for the detailed study of combustion chemistry and physics. Although traditional combustion diagnostics based on continuous-wave and nanosecond-pulsed lasers continue to dominate fundamental combustion studies and applications in reacting flows, revolutionary advances in the science and engineering of ultrafast (picosecond- and femtosecond-pulsed) lasers are driving the enhancement of existing diagnostic techniques and enabling the development of new measurement approaches. The ultrashort pulses afforded by these new laser systems provide unprecedented temporal resolution for studies of chemical kinetics and dynamics, freedom from collisional-quenching effects, and tremendous peak powers for broad spectral coverage and nonlinear signal generation. The high pulse-repetition rates of ultrafast oscillators and amplifiers allow previously unachievable data-acquisition bandwidths for the study of turbulence and combustion instabilities. We review applications of ultrafast lasers for optical measurements in combusting flows and sprays, emphasizing recent achievements and future opportunities.

CARS: coherent anti-Stokes Raman scattering

RFWM: resonant four-wave mixing

1. INTRODUCTION

Propulsion systems represent a substantial fraction of the cost, weight, and complexity of aircraft and spacecraft. The vast majority of these propulsion systems are powered through fuel combustion; therefore, the detailed study of fundamental combustion phenomena has emerged as a highly relevant and important field of endeavor. Today's combustion scientists and engineers devote much of their work to improving propulsion-system performance while simultaneously reducing pollutant emissions. Increasing the affordability, maintainability, and reliability of these critical propulsion systems is a major driver of activity as well.

Although our efforts in the Combustion and Laser Diagnostics Research Complex at Wright-Patterson Air Force Base are focused primarily on combustion phenomena associated with air-breathing and rocket propulsion, a host of other applications drive advances in combustion science as well. These include internal-combustion engines, land- and sea-based power generation, industrial processing, combustion-based synthesis, waste incineration, and fire safety, for example. Clean, efficient combustion technologies and alternative fuels (e.g., Fischer-Tropsch fuels and biofuels) are critical for meeting current and future energy demands while reducing our dependence on fossil fuels and minimizing such environmental impacts as smog, particulates, acid rain, greenhouse gases, and global warming.

Advanced measurement techniques that exploit lasers and optics have become well-established tools for characterizing combusting flows (1–4). Such noninvasive measurement approaches are often ideally suited for visualizing complex reacting flows and quantifying key chemical-species concentrations, temperature, and fluid-dynamic parameters. The fundamental information these techniques provide is essential for achieving a detailed understanding of the chemistry and physics of combustion processes.

Many successful optical measurements achieved to date in combusting flows have been based on the use of conventional continuous-wave and nanosecond-pulsed laser systems, including Q-switched Nd:YAG lasers, excimer lasers, and associated YAG- and excimer-pumped dye lasers. These systems have been the workhorses in most experiments involving such optical measurement techniques as planar laser-induced fluorescence, particle-image velocimetry, laser-induced incandescence, coherent anti-Stokes Raman scattering (CARS) spectroscopy, and resonant four-wave mixing (RFWM). These laser systems afford high pulse energies required for sheet lighting in planar techniques and for nonlinear interactions such as those in CARS and RFWM. They also provide the relatively narrow spectral bandwidths required for spectroscopic studies of key gas-phase combustion species (e.g., OH, CH, NO, and CO).

Although the impact of continuous-wave and nanosecond-pulsed lasers systems on the modern science of combustion measurements is undeniable, continuing revolutionary advances in the science and engineering of ultrafast lasers (i.e., picosecond- and femtosecond-pulsed lasers) (5–8) have enhanced the capabilities and utility of existing combustion-diagnostic techniques while enabling the development and application of new measurement methodologies previously unachievable. Early

practitioners pioneered ultrafast combustion measurements based on modelocked argon-ion and Nd:YAG lasers with synchronously pumped dye lasers, but the advent of modelocked titanium:sapphire (Ti:sapphire) oscillators and amplifier systems based on regenerative and multipass configurations and chirped-pulse amplification has changed the landscape dramatically, accelerating the development and application of new ultrafast laser-based combustion diagnostics.

Regardless of the architecture, two key features of ultrafast lasers are responsible for the tremendous utility they afford for combustion measurements: ultrashort pulses and high pulse-repetition rates. Myriad beneficial characteristics stem from the ultrashort picosecond and femtosecond pulses delivered by modern ultrafast laser systems. These advantages of ultrashort pulses are realized in terms of the time resolution achievable and the temporal duration of the optical combustion measurements. In addition, ultrashort pulses enable tremendous instantaneous power from laser systems of moderate to low average power.

The time resolution afforded by ultrafast laser systems has been exploited to study the kinetics and dynamics of combustion chemistry and energy-transfer processes. Investigators have used separation in time of various pump and probe pulses to discriminate against nonresonant background signals, enhancing measurement sensitivity and selectivity and enabling the determination of key minor-species concentrations. Because of the ultrashort duration of some of these measurements, signals can be acquired that are largely free of collisional and pressure effects. This key feature of ultrafast combustion measurements addresses one of the major limitations of conventional nanosecond-pulsed diagnostics, and it enables quantitative measurements of parameters such as number densities and temperature in high-pressure, turbulent flames characteristic of most practical combustion devices. In these systems the collisional-quenching environment is typically highly inhomogeneous and rapidly changing in both space and time.

The instantaneous power from these ultrafast laser systems has been exploited to drive many desirable nonlinear phenomena. Researchers have utilized such nonlinearities to expand the spectral coverage available from these laser systems and to achieve various novel higher-order signals based on multiple-wave mixing. Amplified Ti:sapphire-based systems can deliver usable radiation throughout an impressive spectral region across the ultraviolet (UV), visible, and infrared. Through continuing advances involving laser-matter interactions and higher-order harmonic generation, extreme UV radiation and X-rays can be produced for diagnostic applications. At the opposite end of the spectrum, terahertz radiation has been generated using ultrafast lasers and applied to combustion measurements. Nonlinear signal generation in combusting flows has been explored with ultrafast lasers and wave-mixing techniques that include polarization spectroscopy (PS), CARS, and RFWM (described in detail below).

Many ultrafast laser systems deliver very high pulse-repetition rates. Modelocked oscillators feature repetition rates of the order ~ 100 GHz, and commercially available amplifiers deliver pulses at rates up to 1–300 kHz. Fluctuation timescales of the order 1–100 μ s characterize the high-pressure, turbulent combustion environments found in most practical devices. Although conventional 10-Hz, nanosecond-pulsed laser

PS: polarization spectroscopy

systems can be used to study these turbulent combustion environments, they provide only probability density functions for combustion parameters and cannot capture time correlations describing fluctuating turbulent combustion. Investigators have used measurements based on high-repetition-rate, ultrafast laser systems, conversely, to capture probability density functions, as well as time series, time correlations, and power spectral densities (PSDs) describing the frequency content of turbulent phenomena of interest.

In the sections below, we review the advantages of ultrafast laser systems for optical combustion measurements with special emphasis on applications involving ultrafast laser-induced fluorescence (LIF), linear pump/probe techniques, time-gated ballistic imaging, ultrafast CARS spectroscopy, and resonant and Raman PS and wave mixing. Advances stemming from the ultrashort pulses and high pulse-repetition rates provided by ultrafast lasers are evident throughout these applications.

2. ULTRAFAST LASER-INDUCED FLUORESCENCE

LIF has been used extensively for measurements of minor-species concentrations and gas temperature in reacting and nonreacting flows (1–4). Measurements of minor species are important for understanding flame chemistry and validating models of ignition, heat release, flame propagation, pollutant formation, and flame extinction. The availability of picosecond lasers for time-resolved LIF has played a critical role in the study of energy-transfer processes, in extending LIF measurements to the deep UV, and in improving the quantitative nature of LIF in unknown quenching environments.

The quantitative interpretation of LIF signals requires detailed knowledge of molecular energy-transfer processes such as electronic quenching, rotational energy transfer (RET), and vibrational energy transfer. One can easily investigate these processes, which compete with the radiative decay of the excited state, at low pressures using nanosecond lasers (9). At atmospheric pressure, however, transfer rates must be measured with picosecond resolution given gas collision rates that yield fluorescence lifetimes of the order 1 ns.

A typical setup for OH LIF comprises a chirped-pulse amplified Ti:sapphire laser system (1.5-ps pulse width, 0.5 mJ per pulse) that is frequency tripled to the UV near 284 nm (1-ps pulse width, 20 μ J per pulse) (10). Other investigators have used a Raman-excimer laser in combination with stimulated Brillouin scattering (11), passive and active modelocking in combination with stimulated Brillouin scattering (12), or regenerative amplification with or without a distributed-feedback dye laser (13, 14) to achieve ~ 100 -ps pulses with sufficient spectral resolution (of the order 0.5 cm^{-1} at atmospheric pressure) to isolate individual rotational transitions. Another advantage of picosecond lasers is the ability to access species such as H atoms (12), O atoms (15, 16), CO (17), and NO (18) through two-photon excitation. Typical detection schemes include fast photomultiplier tubes, streak cameras, and fast-gated optical imagers for time-resolved studies of collisional quenching, RET, and vibrational energy transfer (9–18).

In addition to fundamental studies of energy-transfer processes for LIF, ultrafast lasers have also been applied for quantitative measurements in flames of practical

interest. In particular, a number of researchers have used fluorescence lifetimes for quantitative measurements of minor-species concentrations in flames in which the temperature and colliding-species concentrations may be unknown. These lifetimes, which are largely dominated by collisional quenching for atmospheric-pressure flames, are typically of the order $\sim 1\text{--}3$ ns and require the use of a picosecond laser for sufficient time resolution. Application of this approach is particularly important in unsteady, turbulent flames. Studies have been performed for vortex/flame interactions (19) and two-dimensional imaging (20) using picosecond LIF with streak cameras. In turbulent flames, it is also desirable to compute the PSD to analyze the frequency content of number-density fluctuations. To obtain longer time series for PSD measurements of minor species, one can employ a picosecond Ti:sapphire oscillator along with a multichannel photon-counting system for on-the-fly quenching corrections based on fluorescence-lifetime measurements (21, 22). This eliminates uncertainties due to the variation of temperature and colliding-species concentrations in turbulent flames. Time-series measurements have been made for CH (23) and OH (24), as well as OH and temperature (25). **Figure 1** shows a schematic of the optics layout and time-gating approach for the latter, and **Figure 2** shows typical time-resolved OH and temperature measurements in a vortex/flame burner.

Picosecond lasers have been instrumental in improving our understanding of molecular energy-transfer processes in LIF. In addition, picosecond LIF has proven to be useful in turbulent flames in which LIF signals are influenced by local variations in the rate of collisional quenching.

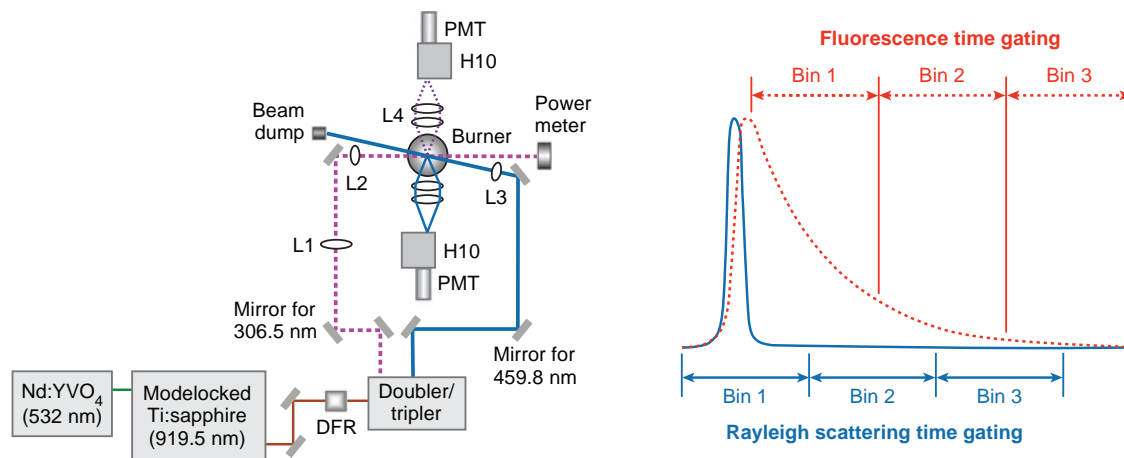
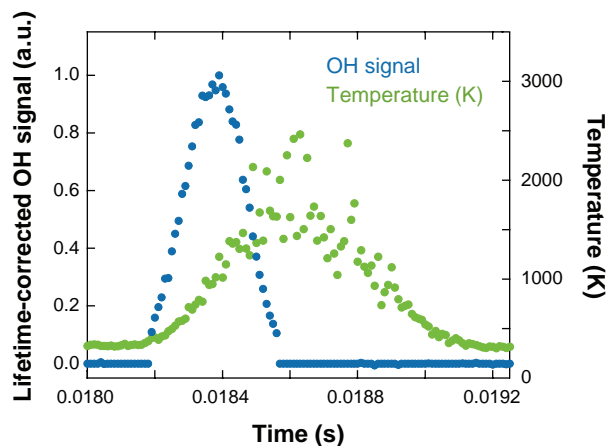


Figure 1

Optical layout (*left panel*) and time-gating diagram (*right panel*) for simultaneous Rayleigh scattering and lifetime-corrected OH laser-induced fluorescence. Bins 1–3 integrate over 3.5-ns bins to detect Rayleigh scattering and resolve fluorescence lifetime assuming single exponential decay. Abbreviations used: DFR, double Fresnel rhomb; H10, 0.1-m monochromator; L1, 1-m lens; L2, 20-cm lens; L3, 20-cm lens; L4, 15-cm lens; PMT, photomultiplier tube. Figure reprinted with permission from Reference 25. Copyright 2007, Optical Society of America.

Figure 2

Simultaneous measurements of temperature and lifetime-corrected OH laser-induced fluorescence during vortex/flame interaction.



3. LINEAR PUMP/PROBE TECHNIQUES

A number of groups have developed and applied linear pump/probe techniques to measure absolute number densities of key species as well as temperature in combusting flows. These techniques are linear in the sense that the combustion analyte under study interacts linearly with the pump beam (i.e., a one-photon pump-analyte interaction) and linearly with the probe beam (i.e., a one-photon probe-analyte interaction). Typically in these experiments, the pump beam interacts with the analyte in a linear, one-photon absorption process, transferring some population from the ground electronic state to an excited electronic state, thereby creating a transient hole in the ground-state population and a transient excited-state population. The probe beam subsequently interacts with this transient population distribution through one or more of three processes, based in large part on the spectral characteristics of the probe beam. A probe beam spectrally resonant with ground-state absorption features of the analyte experiences a transient reduction in absorption upon interaction with the pump-modified population distribution. This is manifested as a transient gain in the transmitted intensity of the probe beam. A probe beam spectrally resonant with emission features of the analyte experiences a transient enhancement through stimulated emission upon interaction with the pump-modified population distribution. This is also manifested as a transient gain in the transmitted intensity of the probe beam. A probe beam spectrally resonant with excited-state absorption features of the analyte experiences a transient increase in absorption upon interaction with the pump-modified population distribution. This is manifested as a transient bleach in the transmitted intensity of the probe beam. As the redistribution of population induced by the pump beam relaxes in time, so too do the transient phenomena associated with the probe-beam transmission.

In practice investigators often observe these transient phenomena experimentally by modulating the pump-beam intensity. This modulation is transferred from the pump beam to the analyte population distribution and thereby onto the probe beam. Lock-in detection of the transmitted probe beam reveals the extent of modulation

transfer from the pump beam to the probe beam, and the lock-in signal scales linearly with the analyte concentration. The time delay between the pump and probe beams can be adjusted to explore the temporal characteristics of the population-relaxation dynamics.

Lytle and coworkers (26, 27) developed and applied an ingenious scheme for scanning the pump/probe delay and exploring the temporal evolution of the population relaxation using a technique they termed asynchronous optical sampling (ASOPS). In ASOPS, two separate laser oscillators are used—one for the pump beam and one for the probe beam. The optical cavities of the two oscillators are adjusted to slightly different lengths such that the two oscillators operate at slightly different pulse-repetition rates. This difference in pulse-repetition rates is manifested as a repetitive phase walkout between the pump and probe pulses that repeats at Δf , the difference between the two pulse-repetition rates. A no-moving-parts pump/probe delay is achieved without the need for an optomechanical delay line (see **Figure 3**).

The ASOPS technique complements the LIF techniques described in Section 2 above and similar to those techniques can be used to measure absolute number densities and explore the detailed, time-evolving collisional-quenching environments in turbulent combustion through the determination of the population lifetime decay. Fiechtner and coworkers (28–31) applied ASOPS to the measurement of atomic sodium and OH in various laboratory flames. They developed rate-equation models to extract quantitative number densities and collisional-quenching rates from these ASOPS experiments (30, 32).

Fiechtner & Linne (33) pursued a simplified pump/probe arrangement with a fixed pump/probe delay rather than a scanning delay. Although this approach does not reveal the temporal evolution of population relaxation, it can be configured to yield measurements of absolute number densities of key chemical species free from the effects of collisional quenching, provided the fixed pump/probe delay is set such that the probe beam interacts with the pump-modified analyte on a timescale that is short with respect to the collisional timescale. In this fashion, Settersten and coworkers

ASOPS: asynchronous optical sampling

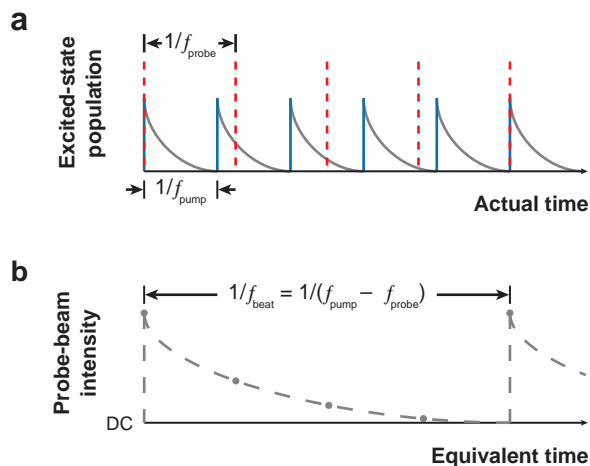


Figure 3
 Conceptual asynchronous optical sampling timing diagram depicting (a) excited-state population and (b) probe-beam intensity upon stimulated emission. Pump pulses are indicated in blue, and probe pulses are indicated in red.

(34, 35) achieved measurements of potassium and other species in various laboratory flames and modeled the characteristics of the pump/probe signal using rate equations and density-matrix equations (34–37). By forming the pump beam into a laser light sheet and crossing that pump-beam sheet with an upcollimated probe beam in a premixed methane-air flame maintained on a Meeker-type burner, Linne et al. (38) achieved ultrafast linear pump/probe two-dimensional imaging of potassium seeded into the flame.

Advances in ultrafast laser systems have driven tremendous innovations in sensing with terahertz radiation (39). We can also consider terahertz time-domain spectroscopy (THz-TDS) as a linear pump/probe technique, although the pump and probe interactions differ from those discussed above. In the pump/probe experiments described above, the pump and probe beams interact directly with the analyte; however, the pump and probe beams serve different purposes in THz-TDS. In these experiments, the pump beam from a femtosecond-pulsed laser interacts with a target material to generate broadband terahertz radiation, either through photoconduction in a biased semiconductor (e.g., low-temperature-grown GaAs) or through optical rectification (a process described in detail in Reference 39) in a nonlinear medium. When the pulsed terahertz radiation generated in this fashion is transmitted through an absorbing analyte, the spectral and temporal characteristics of the terahertz pulse are modified through linear absorption processes. The probe beam is utilized for time-gated detection of the transmitted terahertz pulse, either through photoconductive or electro-optic sampling. By scanning the pump/probe delay, one can capture the temporal characteristics of the transmitted terahertz pulse, and the Fourier transformation of that pulse yields its frequency-resolved transmission spectrum from which terahertz absorption features of the analyte are determined.

Cheville & Grishchkowsky (40, 41) measured species concentrations and temperature in premixed propane-air flames with THz-TDS techniques based on a traditional optomechanical scanning delay line for variation of the pump/probe delay. Brown et al. (42) adopted the ASOPS scheme described above for H₂O-vapor measurements with a no-moving-parts pump/probe delay. The potential for future applications of THz-TDS in combustion is promising. The terahertz spectral region is rich in absorption features of interest for the quantification of key combustion species (especially H₂O) and temperature. Furthermore, hydrocarbon fuels and carbonaceous soot exhibit little or no absorption in this spectral region, suggesting that THz-TDS should be an ideal technique for measurements in liquid-hydrocarbon-fueled, highly sooting combustion environments such as those characteristic of most practical devices.

4. TIME-GATED BALLISTIC IMAGING

As light propagates through a turbid medium, its direction, polarization, and phase are altered owing to gradients in the index of refraction. Diffuse photons pass through the sample volume with significant multiple scattering events and emerge with a shift in location and direction. This is shown schematically in **Figure 4a** and leads to the blurring of internal features within the medium. Snake photons are altered to a

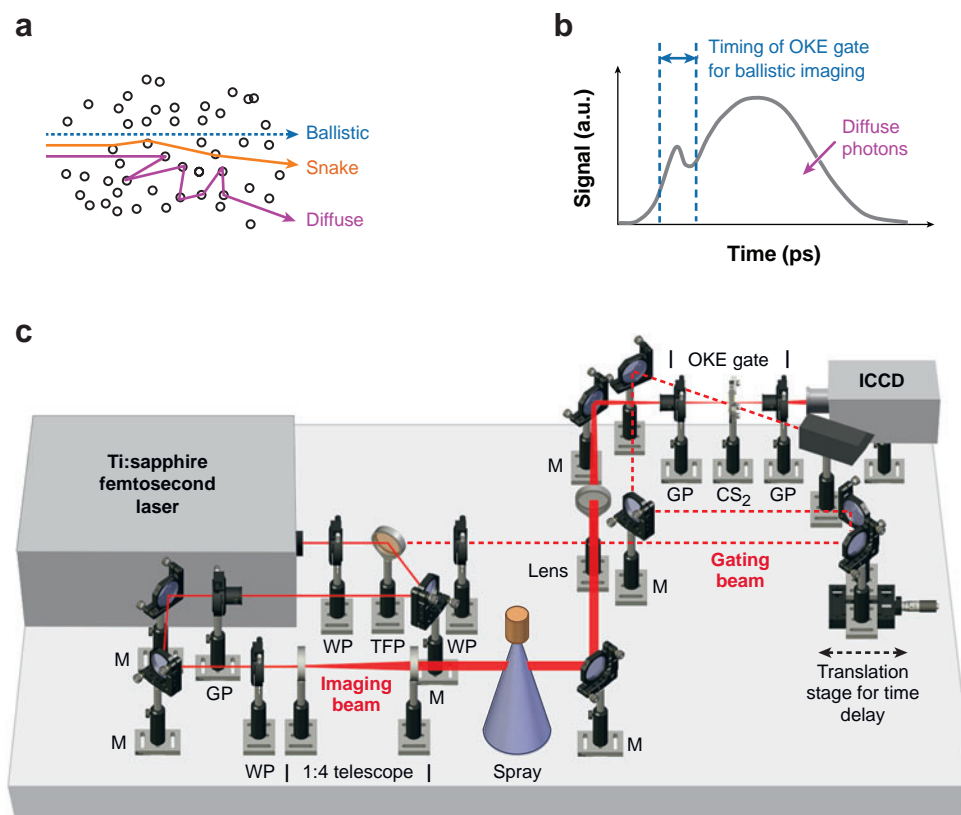


Figure 4

Conceptual picture of (a) ballistic, snake, and diffuse photons; (b) time trace of signal on detector; and (c) optical layout for time-gated ballistic-photon imaging. Abbreviations: GP, Glan polarizer; ICCD, intensified charge-coupled device camera; M, mirror; OKE, optical Kerr effect; TFP, thin film polarizer; WP, half-wave plate.

lesser degree as they propagate with relatively few scattering events, whereas ballistic photons pass through without deviation and maintain their direction of propagation, polarization, and phase.

Interest in utilizing ballistic photons for imaging applications is driven by the possibility that one could use visible and infrared light sources to image turbid media without the need for ionizing radiation or synchrotron sources. The general approach is to separate ballistic or snake photons from diffuse photons using differences in direction, polarization, coherence, or temporal properties of the light passing through the medium. It is possible, for example, to employ a spatial filter to reduce photons that have lost collimation or confocal properties after exiting the sample volume (43, 44). Polarization gating involves the use of an analyzer rather than a spatial filter (45, 46), whereas coherence gating can be accomplished using nonlinear mixing processes (e.g., second-harmonic generation or holography) to discriminate against scattered photons (47–50).

In many cases, spatial filtering and polarization gating may not provide sufficient discrimination against diffuse photons, whereas coherence gating may be too restrictive in that it can eliminate all but the ballistic photons. For unsteady multiphase flows, it is often necessary to use both snake and ballistic photons to have sufficient signal levels for instantaneous two-dimensional imaging of transient mixing processes. One approach, enabled by the availability of ultrafast lasers, is to distinguish photons based on passage time through the turbid medium. A femtosecond laser beam that undergoes significant scattering exits with longer pulse width (order picosecond) because diffuse photons travel a longer path through the sample volume. This longer path is shown schematically in **Figure 4a** along with a conceptual view in **Figure 4b** of short time gating to discriminate against diffuse photons.

Early work on time-domain photon discrimination demonstrated that one could use picosecond lasers to achieve gate widths on the order of 7–10 ps using an optical Kerr-effect (OKE) time gate consisting of a CS₂ cell placed between a pair of crossed polarizers (51–53). Birefringence with a short relaxation time is induced in the CS₂ upon excitation with an ultrafast laser pulse, allowing light to pass through the crossed polarizers through adjustment of a translation stage to vary the time delay between the imaging and gating beams. Investigators have used this approach for discriminating against diffuse photons in a number of applications (54, 55). With the availability of amplified femtosecond laser systems, it has become possible to achieve time gates as short as 2 ps with high transmission efficiency (56–60).

Figure 4c shows an example of the optical setup for time-gated ballistic imaging. The linearly polarized 1 mJ per pulse output of a 1 kHz repetition rate Ti:sapphire amplifier with 80-fs pulse width is split 90% and 10% into gating and imaging beams, respectively, using a wave plate–polarizer combination. The imaging path includes a Glan polarizer, a half-wave plate, and a beam-expanding telescope. After passing through a dense spray, the imaging beam is weakly focused through the OKE gate, then spatially filtered, and relay imaged directly into an intensified charge-coupled device camera. The gating beam passes through a half-wave plate and a mechanical time-delay stage before arriving at the 1-cm-thick, 2.5-cm-diameter CS₂ cell. The induced birefringence across the imaging beam is kept fairly constant within the CS₂ cell because the imaging beam is relatively small (<500-μm diameter) and passes through the centroid of the relatively large gating beam (~6-mm diameter). The transmission efficiency of the OKE gate is ~30% when activated by the 80-fs laser pulse, which is sufficient for signal-to-leakage ratios of ~20:1. This arrangement allows instantaneous two-dimensional imaging of turbid media, in this case a liquid spray. Laser sources with repetition rates as high as 10 kHz with 1 mJ per pulse are now available and will enable ballistic imaging at unprecedented data rates.

This approach has been used for measurements of liquid breakup phenomena in diesel sprays (58), liquid jets in gaseous crossflow (59), and coaxial rocket injectors. **Figure 5** shows an example of coaxial rocket injectors, comparing a rocket spray shadowgram with and without time gating. Internal structures that were previously not visible due to diffuse scattering are revealed with the use of ultrafast time gating. This has implications for the study of liquid jet breakup and gas-liquid mixing processes in multiphase reacting flows.

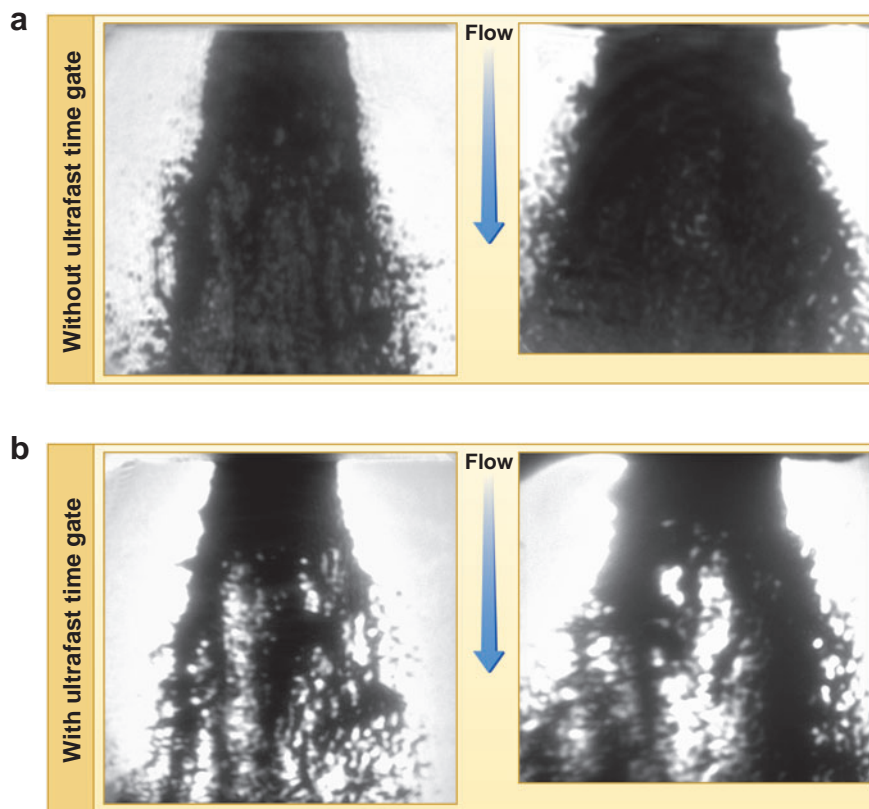


Figure 5

Sample images of rocket spray (*a*) without ultrafast time gate and (*b*) with ultrafast time gate. Flow is from top to bottom.

Advances in ultrafast laser technology have led to significant growth in the implementation of time-gated ballistic-imaging systems for visualizing hidden structures in optically dense media. A number of innovations such as two-color ballistic imaging (59) and dual-pulse ballistic imaging for velocimetry (60) have also been demonstrated recently. Future work could involve the use of three or more consecutive pulses to acquire the acceleration of interfacial regions as well as velocity within dense media. Finally, efforts are underway to use Monte Carlo simulations to predict the properties of ultrafast laser–light propagation through scattering media (61), including implementation for cases with inhomogeneously distributed scatterers.

5. ULTRAFAST COHERENT ANTI-STOKES RAMAN SCATTERING SPECTROSCOPY

CARS spectroscopy is widely used for temperature and major-species-concentration measurements in reacting flows and plasmas (1–3). Because of the phase-matching

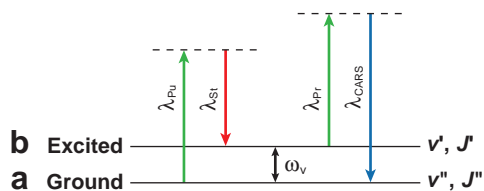


Figure 6

Energy-level diagram for coherent anti-Stokes Raman scattering signal-generation process, where *a* and *b* denote ground and excited levels of molecule, respectively, and ω_v corresponds to vibrational frequency of molecule. Here v' and J' refer to excited-state vibrational and rotational quantum number, respectively, and v'' and J'' refer to ground-state vibrational and rotational quantum number, respectively.

requirement and laser-like nature of the signal, CARS is ideally suited for reacting flows with significant background emission because one can easily isolate the CARS signal spectrally, spatially, and temporally from the flame emission. The technique also provides spatially and temporally resolved information with high accuracy.

An energy-level diagram for the CARS signal-generation process is shown in **Figure 6**. In CARS the wavelengths of the pump and Stokes beams are chosen to excite either the vibrational or rotational transitions of the molecule. We can also describe this excitation process as creating coherence in the medium with a pump-Stokes pair after which the coherence evolves according to the interaction of the molecules with the surrounding medium. When a probe beam interacts with the excited molecules, it is scattered at an anti-Stokes-shifted frequency to yield the CARS signal.

Until recently most of the CARS work in reacting flows was performed using nanosecond lasers to determine gas temperature and the concentrations of major species such as N_2 , O_2 , CO_2 , CO , H_2 , and H_2O (1, 62–65). Electronic-resonance-enhanced CARS using nanosecond lasers has also been demonstrated for determining the concentration of flame radicals such as OH , NO , and C_2H_2 (66–68). Traditional nanosecond CARS uses a narrowband ($\sim 0.001\text{ cm}^{-1}$) transform-limited pump laser and a broadband ($\sim 150\text{ cm}^{-1}$) Stokes laser to excite the entire rovibrational manifold of the molecule (**Figure 7a**). For example, a narrowband laser at 532 nm and a broadband laser at $\sim 607\text{ nm}$ excite the rovibrational energy levels of N_2 , which is typically targeted for temperature measurements because of its abundance in air-fed reacting flows. The band head of the $v'=1 \rightarrow v''=0$ transition in the ground electronic state falls at $\sim 2330\text{ cm}^{-1}$. As shown in **Figure 7a**, only one pump-Stokes pair contributes to the excitation of the coherence for a particular transition. However, nanosecond CARS has several disadvantages that challenge its application in high-pressure, turbulent reacting flows: (a) interference of the nonresonant background signal with the resonant signal, which affects the accuracy and sensitivity of the measurements, especially for hydrocarbon-fueled combustion (1, 69); (b) the low repetition rates of the lasers used, which complicate efforts to study the temporal characteristics of turbulent flames and explore combustion instabilities; and (c) the need to understand the collisional environment and associated

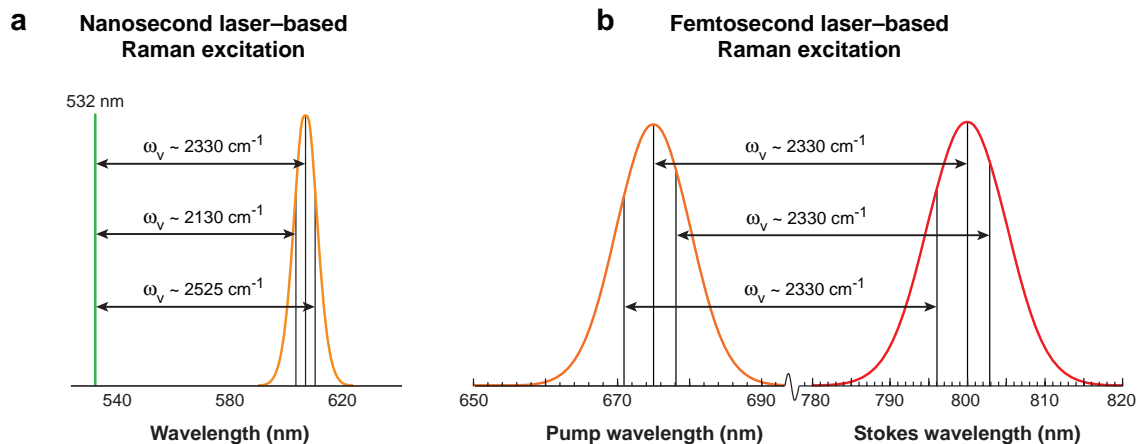


Figure 7

Raman excitation scheme for gas-phase N_2 using (a) nanosecond laser-based multiplex coherent anti-Stokes Raman scattering and (b) femtosecond pump and Stokes lasers.

dephasing and relaxation processes for quantitative interpretation of the CARS signal.

The use of ultrafast lasers to address these issues in reacting flows has been the subject of continuing research activities in the Air Force Research Laboratory's Combustion and Laser Diagnostics Research Complex at Wright-Patterson Air Force Base. In picosecond or femtosecond CARS, nonresonant background signals are observed only when all three laser beams are temporally and spatially coincident. These nonresonant interferences can be suppressed by delaying the probe beam with respect to the Raman-excitation beams. Roy et al. (69) performed picosecond multiplex CARS experiments with the probe beam delayed by ~ 150 ps with respect to the Raman-excitation beams. In this arrangement, the nonresonant background signal is reduced by more than three orders of magnitude, whereas the resonant signal is reduced by only a factor of three to yield a tremendous improvement in signal-to-noise ratio. However, in picosecond CARS, the quantitative interpretation of the signal still requires some knowledge of the collisional physics, and the repetition rate of the lasers used in these particular experiments is only of the order 10–20 Hz.

Femtosecond CARS spectroscopy has the potential to overcome the problems associated with nanosecond CARS for combustion applications, as evidenced by recent studies of femtosecond CARS in noncombusting environments (70–75). When two femtosecond laser pulses are used to create coherence in the medium (as in the case of CARS), the ground and excited states are coupled efficiently because of the availability of a large number of pump-Stokes pairs within the bandwidth of the laser pulses contributing to the excitation of the same coherence (**Figure 7b**) (75). **Figure 7** shows pump-Stokes pairs for the excitation of N_2 in the ground electronic state, as mentioned above. This specific feature of femtosecond laser-based Raman excitation, along with the suppression of the nonresonant background using a delayed probe

beam, holds the potential for making the femtosecond CARS technique suitable for detecting minor species in reacting flows. Moreover, femtosecond CARS allows measurements to be made at rates of 1 kHz or greater and time-resolved CARS signals to be acquired over a time period that is short with respect to the collisional timescale, thereby eliminating the need to understand collisional broadening, line narrowing, and other dephasing and relaxation processes due to collisions.

Dantus et al. (76) eloquently describe the excitation of vibrational and rotational coherences by femtosecond lasers and the subsequent decay of these coherences either through frequency-spread dephasing or loss of alignment. Initially it was anticipated that the large bandwidths characteristic of femtosecond lasers would be problematic for molecular spectroscopy in reacting flows because of the associated lack of selectivity (broadband excitation of many transitions of one or more molecules) and relatively inefficient coupling of these spectrally broad pulses to individual transitions as compared with coupling of narrowband nanosecond pulses more closely matched to the line width of these transitions. However, the excitation process depicted in **Figure 7b** and recent research activities in this field have shown that the bandwidth of femtosecond lasers is actually an advantage rather than a hindrance.

In 1987 femtosecond CARS was first used to study molecular beat phenomena in liquid-phase benzene, cyclohexane, and pyridine (77); subsequently, Hayden & Chandler (78) demonstrated its application to the investigation of gas-phase molecular dynamics. Lang et al. (71) focused their work with femtosecond CARS on determining the molecular parameters and gas-phase temperature from the time-resolved oscillatory pattern of the Raman coherence following pump-Stokes excitation of H₂. They determined those parameters from the width and relative heights of the coherence recurrence peaks. The measurement of temperature from these peaks at ~320 ps, as described by Lang et al. (70), requires a detailed understanding of the collisional dephasing and relaxation physics of the probe molecule within its surrounding environment. Researchers have also used femtosecond CARS to make measurements in dense media to investigate RET processes (72), to determine the concentrations of *ortho*- and *para*-deuterium (79), and to measure single-shot temperature by probing H₂ using a chirped probe pulse (80). The technique has also been used for microscopy (81), the selective control of molecular structure (82), detection of bacterial spores (83), and investigation of the ground- and excited-state dynamics of molecules (84).

The focus of our efforts is the application of time-resolved femtosecond CARS for temperature measurements in high-temperature flames, based on the frequency-spread dephasing rate after the initial impulsive excitation of the Raman coherence in N₂ by femtosecond pump and Stokes beams. After the initial excitation, all in-phase Raman coherences excited by the nearly transform-limited laser pulses begin to oscillate out of phase with respect to each other as a result of slight differences in their frequencies. Because of the frequency differences between the neighboring transitions, the resulting coherence begins to dephase; the dephasing rate depends on temperature only and is completely insensitive to collisions (73). **Figure 8** shows time-resolved femtosecond CARS signals during the first few picoseconds after the initial impulsive excitation as a function of temperature. The coherence dephases at a faster rate with increasing temperature as a result of the contribution

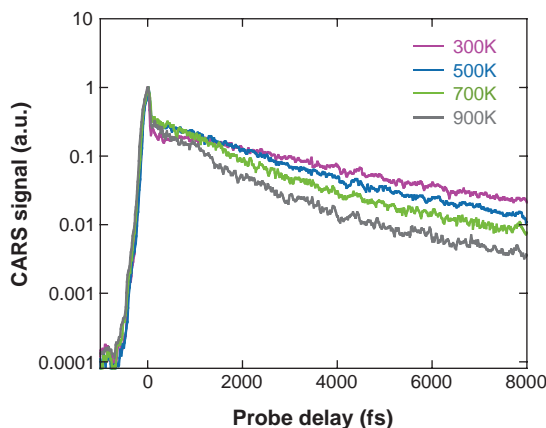


Figure 8

Temperature-dependent time-resolved femtosecond coherent anti-Stokes Raman scattering signal of N₂ (73).

from many energy levels; higher rotational and vibrational levels are populated with increasing temperature according to the Boltzmann distribution. Roy and colleagues (73–74) reported detailed theoretical and experimental results related to this concept and discussed the application of this technique in reacting flows (75). They found the estimated absolute accuracy and precision of the measurement technique to be ± 40 K and ± 50 K, respectively, over the temperature range 1500–2500 K (75). **Figure 9** illustrates the temporal evolution of time-resolved femtosecond CARS signals during the first few picoseconds after the initial excitation as a function of pressure. It is evident from **Figure 9** that the coherence dephasing rate during the first few picoseconds is insensitive to collisions. However, collisions begin to influence the dephasing rates when the pressure is increased beyond 20 bar (72). We have designed current research activities in our laboratory to address these key issues: (a) single-shot temperature measurements at rates of 1 kHz or greater using a spectrally chirped probe pulse, (b) the influence of other molecules excited by the broadband femtosecond laser pulses on measurements of temperature and species

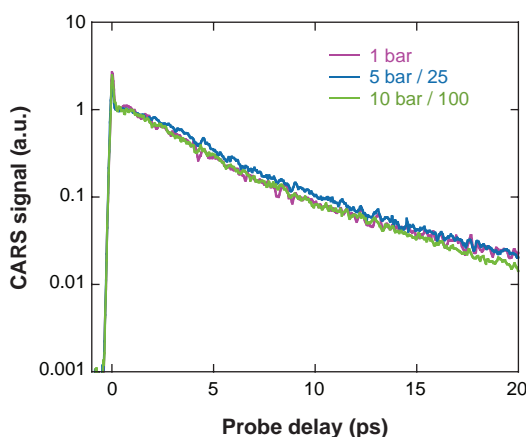


Figure 9

Pressure dependence of time-resolved N₂ femtosecond coherent anti-Stokes Raman scattering signal during first few picoseconds after impulsive excitation of the coherence.

concentrations, and (c) concentration measurements of minor species such as C_2H_2 , C_6H_6 , and other flame molecules and radicals using shaped laser pulses.

6. RESONANT AND RAMAN-INDUCED POLARIZATION SPECTROSCOPY AND WAVE MIXING

PS has emerged as a valuable spectroscopic tool for measuring the concentrations of minor species such as OH, CH, and NH in reacting flows (1–3, 85–88) and plasmas (89). PS is a nonlinear pump/probe technique in which the probe beam is linearly polarized prior to interacting with the medium of interest. PS uses either a circularly or a linearly polarized pump beam for selective pumping of the population from the ground to the excited states; in the latter case, the pump-beam polarization is rotated 45° with respect to the probe-beam polarization. Because of the anisotropy induced by the pump beam, the probe-beam polarization becomes slightly elliptical or slightly rotated while passing through the medium. As a consequence, some of the probe beam leaks through a polarization analyzer whose transmission axis is orthogonal to the original probe-beam polarization; this leakage is the PS signal. To illustrate the introduction of anisotropy by selective pumping, **Figure 10** shows an energy-level diagram of the $P_1(2)$ transition of OH. A linearly polarized pump beam couples the $\Delta M = 0$ transitions, and a right or left circularly polarized pump beam couples either the $\Delta M = +1$ or the $\Delta M = -1$ transitions, respectively.

Two distinct advantages of using ultrafast lasers for PS are (a) the reduction in collisional dependence and (b) the determination of the state-specific rotational, orientation, and alignment relaxation rates from time-resolved measurements. Roy and colleagues (86, 91) showed that when using an ultrafast laser (laser pulse width $\tau_L < \tau_C$ characteristic collision time), the collision-rate dependence of the PS signal is significantly decreased as compared with that in the long-pulse laser case

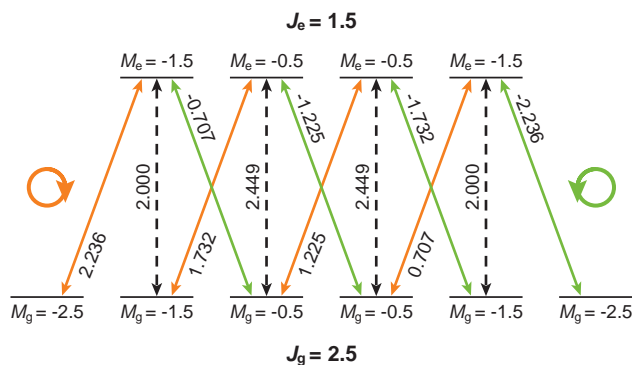


Figure 10

Energy-level diagram for Zeeman state structure of $P_1(2)$ transition. Allowed $\Delta M = 0$ transitions are indicated by dashed arrows; $\Delta M = \pm 1$ transitions are indicated by solid arrows. J and M represent rotational and projection quantum numbers, respectively. Strengths and phases of transitions are indicated by numerical value of x or z components of geometry-dependent part of the dipole matrix element (90). Figure redrawn from Reference 91.

($\tau_L > \tau_C$) for a nonsaturating pump beam. For a saturating pump beam, the picosecond PS signal is nearly independent of collisions (91).

The polarization-dependent selective pumping shown in **Figure 10** creates various types of anisotropies such as orientation and alignment in the medium with relaxation rates due to elastic (M_J changing) and inelastic RET collisions that can significantly affect the resulting PS signal and signals associated with other laser techniques that exploit laser-induced anisotropy. Orientation, which describes the net helicity or spin of the system, and alignment, which describes the spatial distribution of angular momentum, are proportional to the dipole and quadrupole moments of the angular momentum distributions, respectively (92). To illustrate the anisotropies created by the pump laser, **Figure 11** shows the population distribution in the excited Zeeman states for the $P_1(8)$ transition of OH. **Figure 11a** shows the oriented distribution of the excited-state population when pumped by a right circularly polarized beam, whereas **Figure 11b** shows the aligned distribution when pumped by a linearly polarized beam. The population distribution is shown for a time at which the 100-ps (full width at half-maximum) pump laser reaches the peak intensity of $5 \times 10^9 \text{ W m}^{-2}$ and was calculated using the density-matrix numerical code described by Roy et al. (91).

The use of picosecond lasers enables experimental investigation of the rates at which these anisotropies are destroyed in collisional environments. Dreizler and colleagues (93, 94) used PS and RFWM to determine the population, orientation, and alignment relaxation rates of OH in reacting flows. The RFWM technique, in which the two pump photons originate from two different pump beams, is similar to PS, in which both pump photons originate from the same pump beam. Unlike PS, the RFWM technique allows measurements of the population, orientation, and alignment relaxation rates independently through the control of polarization settings for

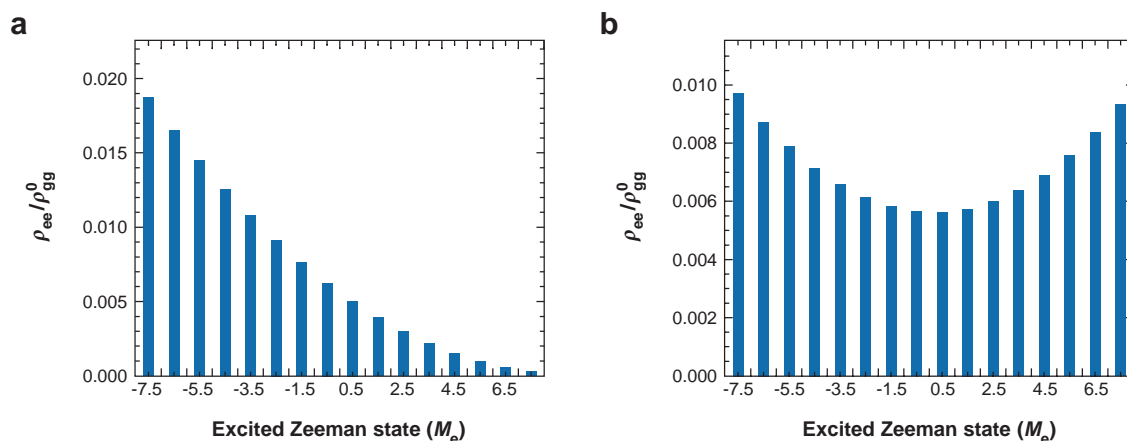


Figure 11

Population distribution in excited Zeeman states for $P_1(8)$ transition pumped by (a) right circularly polarized beam and (b) linearly polarized beam. ρ_{gg}^0 is ground-state population at $t = 0$ s.

each laser beam. In an experiment in which both pump and probe beams are resonant with the same transitions, the measured relaxation rates have a contribution from both the ground and the excited states as reported by Dreizler and colleagues (93, 94). To measure the ground-state orientation and alignment relaxation rates of OH, Chen and coworkers (95) and Costen & McKendrick (96) employed two-color PS in which the pump and probe beams are coupled through an intermediate level in the ground electronic state. Chen & Settersten (97) also demonstrated two-color RFWM for determining the ground-state population, orientation, and alignment relaxation rates by varying the polarization of two pump beams and the probe beam independently. Recently, picosecond laser-based, two-color, two-photon PS was used for the detection of atomic hydrogen in an atmospheric-pressure H_2 -air flame; because of its high reactivity and diffusivity, the hydrogen atom plays an important role in combustion chemical kinetics (98).

Femtosecond laser-based Raman-induced PS and degenerate four-wave mixing were used to study the ground-level RET in N_2 , O_2 , and CO_2 (99, 100). The broadband femtosecond lasers create a rotational wave packet by simultaneously exciting multiple rotational Raman transitions. The delayed probe beam then probes the misalignment and realignment of this rotational coherence due to elastic and inelastic collisions. These studies will have a significant impact in determining the RET rates for species relevant to reacting flows. Raman-induced degenerate four-wave mixing of H_2 , in which the rotational transitions of H_2 were excited using a sub-20-fs laser pulse, has also been used to determine temperature from the relative intensities of the beat frequencies between the Stokes and anti-Stokes transitions (101).

7. CONCLUSION

Revolutionary ultrafast laser technologies are redefining the combustion-diagnostics arena. Unprecedented new measurement capabilities are emerging as researchers exploit the ultrashort pulses and high pulse-repetition rates delivered by these systems. This review highlights recent advances in ultrafast LIF, linear pump/probe techniques, time-gated ballistic imaging, ultrafast CARS, and resonant and Raman-induced PS and wave mixing. Continuing developments of ultrafast laser systems promise to provide further reductions in cost, size, and complexity with increased robustness and stability and improved user-friendliness. All these enhancements will allow the transition of ultrafast laser-based combustion diagnostics from the laboratory to the field for applications that include test-cell and shop-floor measurements, nondestructive evaluation/inspection, and onboard sensing and control.

SUMMARY POINTS

1. Detailed studies of combustion chemistry and physics are critical for the continued advancement of numerous combustion-related applications, including propulsion, power generation, industrial processing, waste incineration, and fire safety.

2. Optical combustion diagnostics are ideal tools for noninvasive characterization of reacting and nonreacting flows.
3. Although continuous-wave and nanosecond-pulsed lasers are the current sources of choice for most combustion diagnostics, emerging ultrafast (picosecond- and femtosecond-pulsed) laser technologies are driving new developments in combustion measurements.
4. Ultrashort pulses enable time-resolved measurements with unprecedented temporal resolution and freedom from collisional effects that plague measurements with nanosecond-pulsed lasers. Peak powers achievable with these pulses allow nonlinear frequency conversion, expanding the spectral coverage of these systems to new heights. Similarly, these peak powers enable nonlinear signal generation in combusting systems with lasers of moderate to low average power.
5. High pulse-repetition rates afforded by ultrafast oscillators and amplifiers provide the data-acquisition bandwidth necessary to study the temporal evolution of turbulent fluctuations and combustion instabilities. Time series and PSDs can be constructed to characterize these flame phenomena.
6. Ultrafast combustion measurements achieved to date include LIF, linear pump/probe measurements, time-gated ballistic imaging, CARS, PS, and wave mixing. In many cases the ultrafast variants described in this review enjoy numerous and significant advantages over their continuous-wave and nanosecond-pulsed analogs.
7. Continuing and future developments of ultrafast lasers hold tremendous promise for even greater spectral coverage, single-shot high-speed measurements, and application to complex real-world systems for test-cell and shop-floor measurements, nondestructive evaluation/inspection, and on-board sensing and control.

DISCLOSURE STATEMENT

The authors are not aware of any biases that might be perceived as affecting the objectivity of this review.

ACKNOWLEDGMENTS

The authors gratefully acknowledge editorial assistance provided by Ms. Marian Whitaker and continuing long-term financial support and encouragement from Dr. Julian Tishkoff, Air Force Office of Scientific Research. We also gratefully recognize a host of outstanding colleagues and collaborators with whom we have interacted over the course of the past many years. Their tremendous expertise and enthusiasm have contributed immeasurably to many of the efforts described in this review. Of particular note are the contributions of Dr. G.J. Fiechtner, Prof. G.B. King, Dr. M.A. Linne, Prof. R.P. Lucht, and Dr. T.B. Settersten.

LITERATURE CITED

1. Eckbreth AC. 1996. *Laser Diagnostics for Combustion Temperature and Species*. Amsterdam: Gordon & Breach. 596 pp. 2nd ed.
2. Kohse-Höinghaus K, Jeffries JB. 2002. *Applied Combustion Diagnostics*. New York: Taylor & Francis. 705 pp.
3. Linne MA. 2002. *Spectroscopic Measurement: An Introduction to the Fundamentals*. New York: Academic. 414 pp.
4. Laurendeau NM. 2005. *Statistical Thermodynamics: Fundamentals and Applications*. New York: Cambridge Univ. Press. 448 pp.
5. Diels J-C, Rudolph W. 2006. *Ultrashort Laser Pulse Phenomena*. New York: Academic. 680 pp. 2nd ed.
6. Rullière C, ed. 2005. *Femtosecond Laser Pulses: Principles and Experiments*. New York: Springer. 426 pp. 2nd ed.
7. Fermann ME, Galvanauskas A, Sucha G. 2003. *Ultrafast Lasers: Technology and Applications*. New York: Marcel Dekker. 784 pp.
8. Hobbs PCD. 2000. *Building Electro-Optical Systems: Making It All Work*. New York: Wiley & Sons. 727 pp.
9. Hartlieb AT, Markus D, Kreutner W, Kohse-Höinghaus K. 1997. Measurement of vibrational energy transfer of OH ($A^2\Sigma^+$, $v' = 1 \rightarrow 0$) in low pressure flames. *Appl. Phys. B* 65:81–91
10. Beaud P, Radi PP, Franzke D, Frey H-M, Mischler B, et al. 1998. Picosecond investigation of the collisional deactivation of OH $A^2\Sigma^+$ ($v' = 1$, $N' = 4$, 12) in an atmospheric-pressure flame. *Appl. Opt.* 37:3354–67
11. Nielsen T, Bormann F, Burrows M, Andresen P. 1997. Picosecond laser-induced fluorescence measurement of rotational energy transfer of OH $A^2\Sigma^+$ ($v' = 2$) in atmospheric pressure flames. *Appl. Opt.* 36:7960–69
12. Agrup S, Ossler F, Aldén M. 1995. Measurements of collisional quenching of hydrogen atoms in an atmospheric-pressure hydrogen oxygen flame by picosecond laser-induced fluorescence. *Appl. Phys. B* 61:479–87
13. Settersten TB, Patterson BD, Kronmayer H, Sick V, Schulz C, Daily JW. 2006. Branching ratios for quenching of nitric oxide $A^2\Sigma^+$ ($v' = 0$) to $X^2\Pi$ ($v'' = 0$). *Phys. Chem. Chem. Phys.* 8:5328–38
14. Brockhinke A, Kreutner W, Rahmann U, Kohse-Höinghaus K, Settersten TB, Linne MA. 1999. Time-, wavelength-, and polarization-resolved measurements of OH $A^2\Sigma^+$ picosecond laser-induced fluorescence in atmospheric-pressure flames. *Appl. Phys. B* 69:477–85
15. Agrup S, Aldén M. 1994. Two-photon laser-induced fluorescence and stimulated emission measurements from oxygen atoms in a hydrogen/oxygen flame with picosecond resolution. *Opt. Commun.* 113:315–23
16. Frank JH, Chen X, Patterson BD, Settersten TB. 2004. Comparison of nanosecond and picosecond excitation for two-photon laser-induced fluorescence imaging of atomic oxygen in flames. *Appl. Opt.* 43:2588–97
17. Settersten TB, Dreizler A, Farrow RL. 2002. Temperature- and species-dependent quenching of CO B probed by two-photon laser-induced fluorescence using a picosecond laser. *J. Chem. Phys.* 117:3173–79

18. Settersten TB, Patterson BD, Gray JA. 2006. Temperature- and species-dependent quenching of NO $A^2\Sigma^+$ ($v' = 0$) probed by two-photon laser-induced fluorescence using a picosecond laser. *J. Chem. Phys.* 124:234308
19. Brockhinke A, Bülter A, Rolon JC, Kohse-Hoinghaus K. 2001. ps-LIF measurements of minor species concentration in a counter diffusion flame interactive with a vortex. *Appl. Phys. B* 72:491–96
20. Ossler F, Metz T, Martinsson L, Aldén M. 1998. Two-dimensional visualization of fluorescence lifetimes by use of a picosecond laser and a streak camera. *Appl. Opt.* 37:2303–14
21. Klassen MS, Thompson BD, Reichardt TA, King GB, Laurendeau NM. 1994. Flame concentration measurements using picosecond time-resolved laser-induced fluorescence. *Combust. Sci. Technol.* 97:391–403
22. Pack SD, Renfro MW, King GB, Laurendeau NM. 1999. Laser-induced fluorescence triple-integration method applied to hydroxyl concentration and fluorescence lifetime measurements. *Combust. Sci. Technol.* 140:405–25
23. Renfro MW, King GB, Laurendeau NM. 2000. Scalar time-series measurements in turbulent CH₄/H₂/N₂ nonpremixed flames: CH. *Combust. Flame* 122:139–50
24. Renfro MW, King GB, Laurendeau NM. 1999. Quantitative hydroxyl concentration time-series measurements in turbulent nonpremixed flames. *Appl. Opt.* 38:4596–608
25. Meyer TR, King GB, Gluesenkamp M, Gord JR. 2007. Simultaneous high-speed measurement of temperature and lifetime-corrected OH laser-induced fluorescence in unsteady flames. *Opt. Lett.* 32:2221–23
26. Elzinga PA, Lytle FE, Jiang Y, King GB, Laurendeau NM. 1987. Pump/probe spectroscopy by asynchronous optical sampling. *Appl. Spectrosc.* 41:2–4
27. Elzinga PA, Kneisler RJ, Lytle FE, Jiang Y, King GB, Laurendeau NM. 1987. Pump/probe method for fast analysis of visible spectral signatures utilizing asynchronous optical sampling. *Appl. Opt.* 26:4303–9
28. Kneisler RJ, Lytle FE, Fiechtner GJ, Jiang Y, King GB, Laurendeau NM. 1989. Asynchronous optical sampling: a new combustion diagnostic for potential use in turbulent, high-pressure flames. *Opt. Lett.* 14:260–62
29. Fiechtner GJ, King GB, Laurendeau NM, Lytle FE. 1992. Measurements of atomic sodium in flames by asynchronous optical sampling: theory and experiment. *Appl. Opt.* 31:2849–64
30. Fiechtner GJ. 1992. *Quantitative concentration measurements in atmospheric-pressure flames by picosecond pump/probe absorption spectroscopy*. PhD thesis. Purdue Univ.
31. Fiechtner GJ, King GB, Laurendeau NM. 1995. Quantitative concentration measurements of atomic sodium in an atmospheric hydrocarbon flame with asynchronous optical sampling. *Appl. Opt.* 34:1117–26
32. Fiechtner GJ, King GB, Laurendeau NM. 1995. Rate-equation model for quantitative concentration measurements in flames by picosecond pump-probe absorption spectroscopy. *Appl. Opt.* 34:1108–16

33. Fiechtner GJ, Linne MA. 1994. Absolute concentrations of potassium by picosecond pump/probe absorption in fluctuating, atmospheric pressure flame. *Combust. Sci. Technol.* 100:11–27
34. Settersten TB. 1999. *Picosecond pump/probe diagnostics for combustion*. PhD thesis. Colo. School of Mines
35. Settersten TB, Linne MA. 2002. Picosecond pump-probe absorption spectroscopy in gases: models and experimental validation. *Appl. Opt.* 41:2869–78
36. Settersten T, Linne M, Gord J, Fiechtner G. 1999. Density matrix and rate equation analyses for picosecond pump/probe combustion diagnostics. *ALAA J.* 37:723–31
37. Settersten TB, Linne MA. 2002. Modeling pulsed excitation for gas-phase laser diagnostics. *J. Opt. Soc. Am. B* 19:954–64
38. Linne MA, Morse DC, Skilowitz JL, Fiechtner GJ, Gord JR. 1995. Two-dimensional pump-probe imaging in reacting flows. *Opt. Lett.* 20:2414–16
39. Mittleman D, ed. 2003. *Sensing with Terahertz Radiation*. New York: Springer. 337 pp.
40. Cheville RA, Grischkowsky D. 1995. Far-infrared, terahertz time-domain spectroscopy of flames. *Opt. Lett.* 20:1646–48
41. Cheville RA, Grischkowsky D. 1998. Observation of pure rotational absorption spectra in the ν_2 band of hot H_2O in flames. *Opt. Lett.* 23:531–33
42. Brown MS, Fiechtner GJ, Rudd JV, Zimdars DA, Warmuth M, Gord JR. 2006. Water-vapor detection using asynchronous THz sampling. *Appl. Spectrosc.* 60:261–65
43. Schmitt JM, Knüttel A, Yadlowsky M. 1994. Confocal microscopy in turbid media. *J. Opt. Soc. Am. A* 11:2226–35
44. Kempe M, Genack AZ, Rudolph W, Dorn P. 1997. Ballistic and diffuse light detection in confocal and heterodyne imaging systems. *J. Opt. Soc. Am. A* 14:216–23
45. Demos SG, Alfano RR. 1996. Temporal gating in highly scattering media by the degree of optical polarization. *Opt. Lett.* 21:161–63
46. Mujumdar S, Ramachandran H. 2004. Imaging through turbid media using polarization modulation: dependence on scattering anisotropy. *Opt. Commun.* 241:1–9
47. Fujimoto JG, De Silvestri S, Ippen EP, Puliafito CA, Margolis R, Oseroff A. 1986. Femtosecond optical ranging in biological systems. *Opt. Lett.* 11:150–52
48. Yoo KM, Xing Q, Alfano RR. 1991. Imaging objects hidden in highly scattering media using femtosecond second-harmonic-generation cross-correlation time gating. *Opt. Lett.* 16:1019–21
49. Bordenave E, Abraham E, Jonusauskas G, Oberlé J, Rullière C. 2002. Longitudinal imaging in biological tissues with a single laser shot correlation system. *Opt. Exp.* 10:35–40
50. Kippelen B, Marder SR, Hendrickx E, Maldonado JL, Guillemet G, et al. 1998. Infrared photorefractive polymers and their applications for imaging. *Science* 279:54–57
51. Duguay MA, Mattick AT. 1971. Ultrahigh speed photography of picosecond light pulses and echoes. *Appl. Opt.* 10:2162–70

52. Sala K, Richardson MC. 1975. Optical Kerr effect induced by ultrashort pulses. *Phys. Rev. A* 12:1036–47
53. Ho PP, Alfano RR. 1979. Optical Kerr effect in liquids. *Phys. Rev. A* 20:2170–87
54. Wang L, Ho PP, Liu C, Zhang G, Alfano RR. 1991. Ballistic 2-D imaging through scattering walls using an ultrafast optical Kerr gate. *Science* 253:769–71
55. Galland PA, Liang X, Wang L, Breisacher K, Liou L, et al. 1995. Time-resolved optical imaging of jet sprays and droplets in highly scattering medium. *Proc. Am. Soc. Mech. Eng.* HTD-321:585–88
56. Paciaroni M, Linne M. 2004. Single-shot, two-dimensional ballistic imaging through scattering media. *Appl. Opt.* 43:5100–9
57. Paciaroni M, Linne M, Hall T, Delplanque J-P, Parker T. 2006. Single-shot two-dimensional ballistic imaging of the liquid core in an atomizing spray. *At. Sprays* 16:51–70
58. Linne M, Paciaroni M, Hall T, Parker T. 2006. Ballistic imaging of the near field in a diesel spray. *Exp. Fluids* 40:836–46
59. Linne MA, Paciaroni M, Gord JR, Meyer TR. 2005. Ballistic imaging of the liquid core for a steady jet in crossflow. *Appl. Opt.* 44:6627–34
60. Sedarsky DL, Paciaroni ME, Linne MA, Gord JR, Meyer TR. 2006. Velocity imaging for the liquid-gas interface in the near field of an atomizing spray: proof of concept. *Opt. Lett.* 31:906–8
61. Wang X, Wang LV, Sun C-W, Yang C-C. 2003. Polarized light propagation through scattering media: time-resolved Monte Carlo simulations and experiments. *J. Biomed. Opt.* 8:608–17
62. Roy S, Meyer TR, Brown MS, Velur VN, Lucht RP, Gord JR. 2003. Triple-pump coherent anti-Stokes Raman scattering (CARS): temperature and multiple-species concentration measurements in reacting flows. *Opt. Commun.* 224:131–37
63. Meyer TR, Roy S, Lucht RP, Gord JR. 2005. Dual-pump dual-broadband CARS for exhaust-gas temperature and CO₂-O₂-N₂ mole-fraction measurements in model gas-turbine combustors. *Combust. Flame* 142:52–61
64. Hall RJ, Shirley JA. 1983. Coherent anti-Stokes Raman spectroscopy of water vapor for combustion diagnostics. *Appl. Spectrosc.* 37:196–202
65. Rahn LA, Zych LJ, Mattern PL. 1979. Background-free CARS studies of carbon monoxide in a flame. *Opt. Commun.* 30:249–52
66. Attal-Trétout B, Schmidt SC, Crété E, Dumas P, Taran JP. 1990. Resonance CARS of OH in high-pressure flames. *J. Quant. Spectrosc. Radiat. Transf.* 43:351–64
67. Roy S, Kulatilaka WD, Naik SV, Laurendeau NM, Lucht RP, Gord JR. 2006. Effects of quenching on electronic-resonance-enhanced coherent anti-Stokes Raman scattering of nitric oxide. *Appl. Phys. Lett.* 89:104105
68. Chai N, Naik SV, Kulatilaka WD, Laurendeau NM, Lucht RP, et al. 2007. Detection of acetylene by electronic resonance-enhanced coherent anti-Stokes Raman scattering. *Appl. Phys. B* 87:731–37
69. Roy S, Meyer TR, Gord JR. 2005. Time-resolved dynamics of resonant and non-resonant broadband picosecond coherent anti-Stokes Raman scattering signals. *Appl. Phys. Lett.* 87:264103

70. Lang T, Motzkus M, Frey HM, Beaud P. 2001. High resolution femtosecond coherent anti-Stokes Raman scattering: determination of rotational constants, molecular anharmonicity, collisional line shifts, and temperature. *J. Chem. Phys.* 115:5418–26
71. Lang T, Kompa KL, Motzkus M. 1999. Femtosecond CARS on H₂. *Chem. Phys. Lett.* 310:65–72
72. Knopp G, Beaud P, Radi P, Tulej M, Bougie B, et al. 2002. Pressure-dependent N₂ Q-branch fs-CARS measurements. *J. Raman Spectrosc.* 33:861–65
73. Lucht RP, Roy S, Meyer TR, Gord JR. 2006. Femtosecond coherent anti-Stokes Raman scattering measurement of gas temperatures from frequency-spread dephasing of the Raman coherence. *Appl. Phys. Lett.* 89:251112
74. Lucht RP, Kinnius PJ, Roy S, Gord JR. 2007. Theory of femtosecond coherent anti-Stokes Raman scattering spectroscopy of gas-phase resonant transitions. *J. Chem. Phys.* 127:044316
75. Roy S, Kinnius PJ, Lucht RP, Gord JR. 2008. Temperature measurements in reacting flows by time-resolved femtosecond coherent anti-Stokes Raman scattering (fs-CARS) spectroscopy. *Opt. Commun.* 281:319–25
76. Dantus M, Bowman RM, Zewail AH. 1990. Femtosecond laser observations of molecular vibration and rotation. *Nature* 343:737–39
77. Leonhardt R, Holzapfel W, Zinth W, Kaiser W. 1987. Terahertz quantum beats in molecular liquids. *Chem. Phys. Lett.* 133:373–77
78. Hayden CC, Chandler DW. 1995. Femtosecond time-resolved studies of coherent vibrational Raman scattering in large gas-phase molecules. *J. Chem. Phys.* 103:10465–72
79. Knopp G, Kirch K, Beaud P, Mishima K, Spitzer H, et al. 2003. Determination of the ortho-/para deuterium concentration ratio with femtosecond CARS. *J. Raman Spectrosc.* 34:989–93
80. Lang T, Motzkus M. 2002. Single-shot femtosecond coherent anti-Stokes Raman-scattering thermometry. *J. Opt. Soc. Am. B* 19:340–44
81. Cheng JX, Xie XS. 2004. Coherent anti-Stokes Raman scattering microscopy: theory, instrumentation, and applications. *J. Phys. Chem. B* 108:827–40
82. Weiner AM, Leaird DE, Wiederrecht GP, Nelson KA. 1990. Femtosecond pulse sequences used for optical manipulation of molecular motion. *Science* 247:1317–19
83. Scully MO, Kattawar GW, Lucht RP, Opatrný T, Pilloff H, et al. 2002. FAST CARS: engineering a laser spectroscopic technique for rapid identification of bacterial spores. *Proc. Nat. Acad. Sci. USA* 99:10994–1001
84. Schmitt M, Knopp G, Materny A, Kiefer W. 1998. The application of femtosecond time-resolved coherent anti-Stokes Raman scattering for the investigation of ground and excited state molecular dynamics of molecules in the gas phase. *J. Phys. Chem. A* 102:4059–65
85. Demtröder W. 2002. *Laser Spectroscopy*. New York: Springer. 987 pp. 3rd ed.
86. Reichardt TA, Teodoro FD, Farrow RL, Roy S, Lucht RP. 2000. Collisional dependence of polarization spectroscopy with a picosecond laser. *J. Chem. Phys.* 113:2263–69

87. Keifer J, Li Z, Zetterberg J, Linvin M, Aldén M. 2007. Simultaneous laser-induced fluorescence and sub-Doppler polarization spectroscopy of the CH radical. *Opt. Commun.* 270:347–52
88. Tobai J, Dreier T. 1999. Measurement of relaxation times of NH in atmospheric pressure flames using picosecond pump-probe degenerate four-wave mixing. *J. Mol. Struct.* 480–481:307–10
89. Danzmann K, Grützmacher K, Wende B. 1986. Doppler-free two-photon polarization-spectroscopic measurement of the Stark-broadened profile of the hydrogen La line in a dense plasma. *Phys. Rev. Lett.* 57:2151–53
90. Sargent M III, Scully MO, Lamb WE Jr. 1974. *Laser Physics*. Boulder, CO: Westview Press. 464 pp.
91. Roy S, Lucht RP, Reichardt TA. 2002. Polarization spectroscopy using short-pulse lasers: theoretical analysis. *J. Chem. Phys.* 116:571–80
92. Zare RN. 1988. *Angular Momentum: Understanding Spatial Aspects in Chemistry and Physics*. New York: Wiley & Sons. 368 pp.
93. Dreizler A, Taddy R, Suvernev AA, Himmelhaus M, Dreier T, Foggi P. 1995. Measurement of orientational relaxation times of OH in a flame using picosecond time-resolved polarization spectroscopy. *Chem. Phys. Lett.* 240:315–23
94. Taddy R, Dreizler A, Suvernev AA, Dreier T. 1997. Measurement of orientational relaxation times of OH ($A^2\Sigma-X^2\Pi$) transitions in atmospheric pressure flames using picosecond time-resolved nonlinear spectroscopy. *J. Mol. Struct.* 410–411:85–88
95. Chen X, Patterson BD, Settersten TB. 2004. Time-domain investigation of OH ground-state energy transfer using picosecond two-color polarization spectroscopy. *Chem. Phys. Lett.* 388:358–62
96. Costen ML, McKendrick KG. 2005. Orientation and alignment moments in two-color polarization spectroscopy. *J. Chem. Phys.* 122:164309
97. Chen X, Settersten TB. 2007. Investigation of OH $X^2\Pi$ collisional kinetics in a flame using picosecond two-color resonant four-wave-mixing spectroscopy. *Appl. Opt.* 46:3911–20
98. Kulatilaka WD, Lucht RP, Roy S, Gord JR, Settersten TB. 2007. Detection of atomic hydrogen in flames using picosecond two-color two-photon-resonant six-wave-mixing spectroscopy. *Appl. Opt.* 46:3921–27
99. Morgan M, Price W, Hunziker L, Ludowise P, Blackwell M, Chen Y. 1993. Femtosecond Raman-induced polarization spectroscopy studies of rotational coherence in O₂, N₂ and CO₂. *Chem. Phys. Lett.* 209:1–9
100. Frey HM, Beaud P, Gerber T, Mischler B, Radi PP, Tzannis AP. 1999. Femtosecond nonresonant degenerate four-wave mixing at atmospheric pressure and in a free jet. *Appl. Phys. B* 68:735–39
101. Hornung T, Skenderovic H, Kompa KL, Motzkus M. 2004. Prospect of temperature determination using degenerate four-wave mixing with sub-20 fs pulses. *J. Raman Spectrosc.* 35:934–38



Contents

A Personal Journey of Discovery: Developing Technology and Changing Biology <i>Lee Hood</i>	1
Spectroscopic and Statistical Techniques for Information Recovery in Metabonomics and Metabolomics <i>John C. Lindon and Jeremy K. Nicholson</i>	45
Mass Spectrometry for Rapid Characterization of Microorganisms <i>Plamen A. Demirev and Catherine Fenselau</i>	71
Scanning Electrochemical Microscopy <i>Shigeru Amemiya, Allen J. Bard, Fu-Ren F. Fan, Michael V. Mirkin, and Patrick R. Unwin</i>	95
Novel Detection Schemes of Nuclear Magnetic Resonance and Magnetic Resonance Imaging: Applications from Analytical Chemistry to Molecular Sensors <i>Elad Harel, Leif Schröder, and Shoujun Xu</i>	133
Chemical Cytometry: Fluorescence-Based Single-Cell Analysis <i>Daniella Cohen, Jane A. Dickerson, Colin D. Whitmore, Emily H. Turner, Monica M. Palcic, Ole Hindsgaul, and Norman J. Dovichi</i>	165
Chemical Analysis of Single Cells <i>Laura M. Borland, Sumith Kottegoda, K. Scott Phillips, and Nancy L. Allbritton</i>	191
Ion Chemistry in the Interstellar Medium <i>Theodore P. Snow and Veronica M. Bierbaum</i>	229
Plasma Diagnostics for Unraveling Process Chemistry <i>Joshua M. Stillabn, Kristina J. Trevino, and Ellen R. Fisher</i>	261
Biomolecule Analysis by Ion Mobility Spectrometry <i>Brian C. Bobrer, Samuel I. Merenbloom, Stormy L. Koeniger, Amy E. Hilderbrand, and David E. Clemmer</i>	293
In Vitro Electrochemistry of Biological Systems <i>Kelly L. Adams, Maja Puchades, and Andrew G. Ewing</i>	329

Current Applications of Liquid Chromatography/Mass Spectrometry in Pharmaceutical Discovery After a Decade of Innovation <i>Bradley L. Ackermann, Michael J. Berna, James A. Eckstein, Lee W. Ott, and Ajai K. Chaudhary</i>	357
Optical Probes for Molecular Processes in Live Cells <i>Yoshio Umezawa</i>	397
Cell Culture Models in Microfluidic Systems <i>Ivar Meyvantsson and David J. Beebe</i>	423
Peptides in the Brain: Mass Spectrometry–Based Measurement Approaches and Challenges <i>Lingjun Li and Jonathan V. Sweedler</i>	451
Analysis of Atmospheric Aerosols <i>Kimberly A. Prather, Courtney D. Hatch, and Vicki H. Grassian</i>	485
Multiplexed Spectroscopic Detections <i>Kyle D. Bake and David R. Walt</i>	515
Terrestrial Analysis of the Organic Component of Comet Dust <i>Scott A. Sandford</i>	549
High-Resolution Mass Spectrometers <i>Alan G. Marshall and Christopher L. Hendrickson</i>	579
Surface-Enhanced Raman Spectroscopy <i>Paul L. Stiles, Jon A. Dieringer, Nilam C. Shah, and Richard P. Van Duyne</i>	601
Time-Resolved Microdialysis for In Vivo Neurochemical Measurements and Other Applications <i>Kristin N. Schultz and Robert T. Kennedy</i>	627
Applications of Ultrafast Lasers for Optical Measurements in Combusting Flows <i>James R. Gord, Terrence R. Meyer, and Suresh Roy</i>	663
Matrix-Assisted Laser Desorption/Ionization Imaging Mass Spectrometry for the Investigation of Proteins and Peptides <i>Kristin E. Burnum, Sara L. Frappier, and Richard M. Caprioli</i>	689
Formation and Characterization of Organic Monolayers on Semiconductor Surfaces <i>Robert J. Hamers</i>	707
Nanoscope Porous Sensors <i>John J. Kasianowicz, Joseph W.F. Robertson, Elaine R. Chan, Joseph E. Reiner, and Vincent M. Stanford</i>	737

Combining Self-Assembled Monolayers and Mass Spectrometry for Applications in Biochips <i>Zachary A. Gurard-Levin and Milan Mrksich</i>	767
Liposomes: Technologies and Analytical Applications <i>Aldo Jesorka and Owe Orwar</i>	801
Fundamentals of Protein Separations: 50 Years of Nanotechnology, and Growing <i>David A. Egas and Mary J. Wirth</i>	833
Functional and Spectroscopic Measurements with Scanning Tunneling Microscopy <i>Amanda M. Moore and Paul S. Weiss</i>	857
Coherent Anti-Stokes Raman Scattering Microscopy: Chemical Imaging for Biology and Medicine <i>Conor L. Evans and X. Sunney Xie</i>	883

Measurements of Nitric Oxide Concentration in Flames Using Broadband Stokes Electronic-Resonance-Enhanced (ERE) Coherent Anti-Stokes Raman Scattering

N. Chai¹, A. Satija¹, S. V. Naik¹, R. P. Lucht¹, N. M. Laurendeau¹, S. Roy², J. R. Gord³

¹School of Mechanical Engineering, Purdue University, West Lafayette, IN 47907

²Innovative Scientific Solutions, Inc., 2766 Indian Ripple Road, Dayton, OH 45440

³Air Force Research Laboratory, Propulsion Directorate, Wright-Patterson AFB, OH 45433

Why Use Broadband Stokes ERE CARS in Flames?

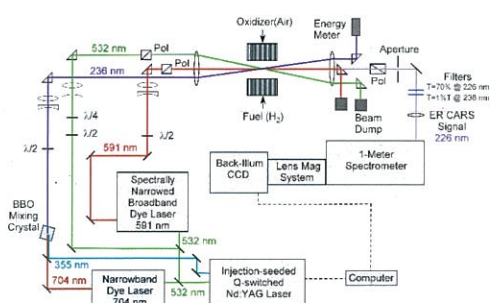
Coherent anti-Stokes Raman scattering (CARS) is a well-established technique for combustion and plasma diagnostics.

Normal CARS has a detection limit of 1% in flames even under well optimized conditions.

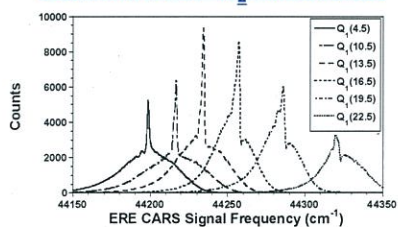
Electronic-Resonance-Enhanced (ERE) CARS can be used to detect minor species. We use visible pump and Stokes beams, ultraviolet probe beam.

The use of a broadband Stokes laser enables single-laser-shot detection for potential application in turbulent flames.

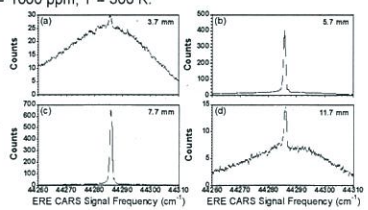
Broadband Vibrational ERE-CARS



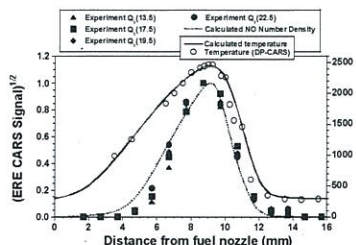
ERE CARS NO Concentration Measurements in Laminar Counter-Flow H₂/Air Flames



Stokes beam centered at ~ 591 nm, probe beam corresponding to Q-branch Raman transition in the (0, 1) band of A²Σ⁺ - X²Π electronic system of NO. [NO] = 1000 ppm, T = 300 K.

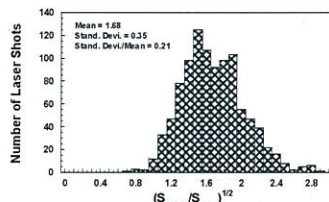


Single-laser-shot measurements of NO in laminar counter-flow H₂/air diffusion flame. Detection limit ~ 30 ppm.



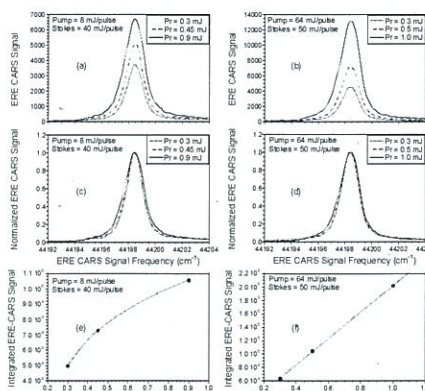
Comparison between experiment (ERE-CARS) and theory (OPPDIF with GR13.0). Experimental data were corrected for Boltzmann fraction. Dual pump CARS temperature is also shown.

Single-Laser-Shot Statistics

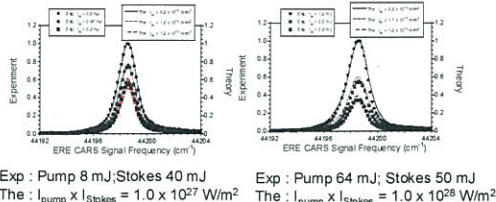


Saturation Effects in ERE CARS

Saturation in ERE-CARS is an important issue. Both the two-photon-induced Raman transition and the one-photon induced electronic probe transition in NO can be saturated.



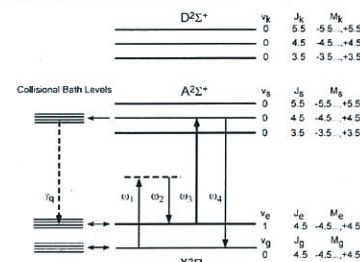
Saturation of the one-photon induced electronic transition is less evident with enhanced pumping of the two-photon induced Raman transition.



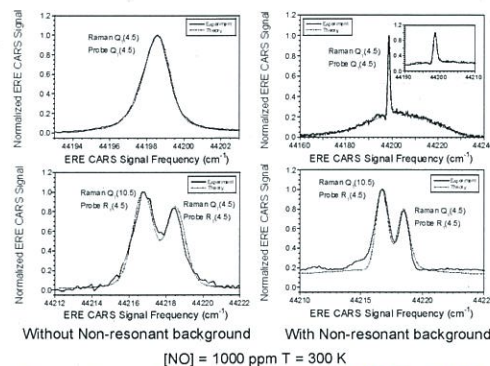
Exp: Pump 8 mJ; Stokes 40 mJ
The: $p_{\text{pump}} \times I_{\text{Stokes}} = 1.0 \times 10^{27} \text{ W/m}^2$

Exp: Pump 64 mJ; Stokes 50 mJ
The: $p_{\text{pump}} \times I_{\text{Stokes}} = 1.0 \times 10^{28} \text{ W/m}^2$

Time-Dependent Density Matrix Theory of ERE CARS



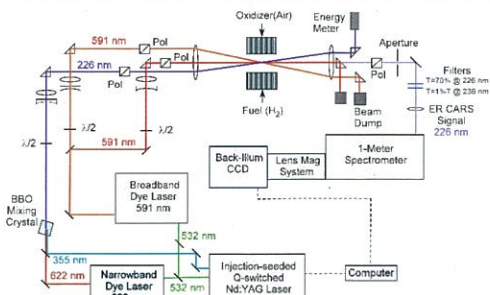
ERE CARS process is modeled using a fictitious electronic level as the intermediate level in the Raman process (D²Σ⁺). The transition strengths are adjusted to give the correct Raman cross section. The electronic-resonance-enhancement is modeled using A²Σ⁺ level which is directly coupled by the probe beam



Without Non-resonant background With Non-resonant background

[NO] = 1000 ppm T = 300 K

Broadband Pure-Rotational ERE-CARS



Funding for this research was provided by the Air Force Office of Scientific Research under Contract No. FA9550-07-C-0036 (Dr. Julian Tishkoff, Program Manager) and by the Air Force Research Laboratory, Propulsion Directorate, Wright-Patterson Air Force Base, under Contract No. F33615-03-D-2329, and by the U.S. Department of Energy, Division of Chemical Sciences, Geosciences and Biosciences, under Grant No. DE-FG02-03ER15391. We thank Mr. Mathew Thariyan, Mr. Vijaykumar Ananthanarayanan, and Mr. Aizaz Bhuiyan for providing us with the dual-pump CARS temperature measurements.

Theory of Femtosecond Coherent Anti-Stokes Raman Scattering (CARS) Spectroscopy for Gas-Phase Transitions

Robert P. Lucht,¹ Paul J. Kinnius,¹ Sukesh Roy,² James R. Gord³

¹School of Mechanical Engineering, Purdue University, West Lafayette, IN 47907

²Innovative Scientific Solutions, Inc., 2766 Indian Ripple Road, Dayton, OH 45440

³Air Force Research Laboratory, Propulsion Directorate, Wright-Patterson AFB, OH 45433

Why Use Femtosecond Lasers for CARS in Flames?

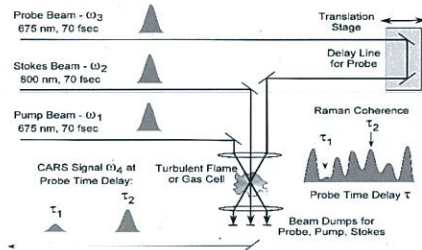
Nsec CARS using (typically) a Q-switched Nd:YAG laser and broadband dye laser is a well-established technique for combustion and plasma diagnostics.

Fsec lasers have much higher repetition rates than nsec Q-switched Nd:YAG lasers: > 1-100 kHz versus ~10 Hz.

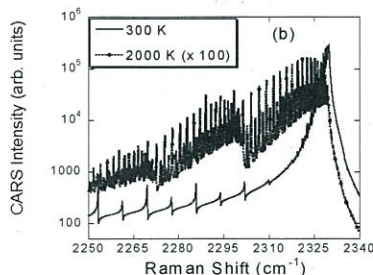
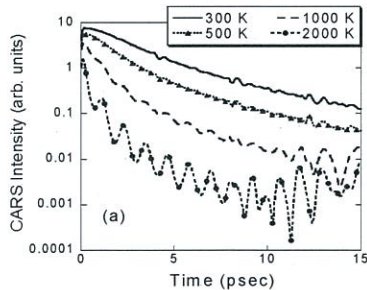
But can we obtain a sufficient signal on a single laser shot to make measurements in turbulent environments? And how do we extract temperature and concentration from the signal?

How effectively can Raman transitions with line width ~ 0.1 cm⁻¹ be excited by the fs pump and Stokes beams with bandwidths of 200 cm⁻¹?

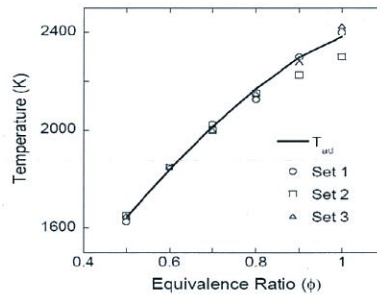
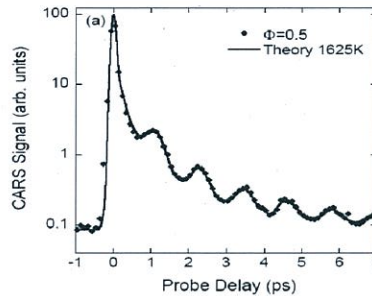
Probe-Delay-Scan Fs CARS



Calculated Probe Delay Scans – Signal Decay Due to Frequency-Spread Dephasing – No Effect of Collisions



Fs CARS Temperature Measurements in Near-Adiabatic H₂/Air Flames

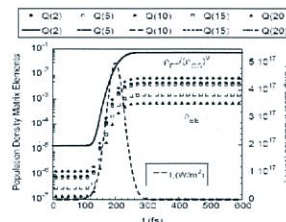


Modeling of the experimental scans above accomplished with a 1-page computer code, don't need to know Raman linewidths. Measured flame temperatures very close to adiabatic.

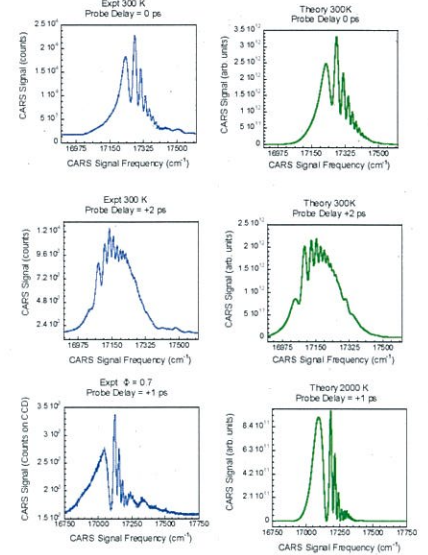
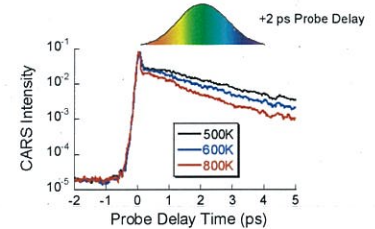
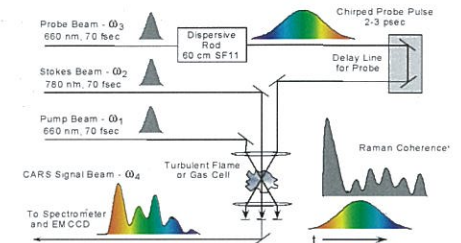
Time-Dependent Density Matrix Theory of Fs CARS

CARS process is modeled using a fictitious electronic level as the intermediate level in the Raman process. The transition strengths are adjusted to give the correct Raman cross section. Fs pump and Stokes excite the Raman transitions very effectively. Commercial systems can saturate N₂ Q-branch transitions.

$$\begin{aligned}\rho_{kg}(t) &= \sigma_{kg}(t) \exp(-i\omega_1 t) + \eta_{kg}(t) \exp(-i\omega_2 t) \\ \rho_{ke}(t) &= \sigma_{ke}(t) \exp(-i\omega_2 t) + \eta_{ke}(t) \exp(-i\omega_3 t) \\ \rho_{eg}(t) &= \sigma_{eg}(t) \exp[-i(\omega_1 - \omega_2)t]\end{aligned}$$



Single-Shot Fs CARS



Chirped-probe fs CARS process results in very high signal levels in flames, single-shot quite feasible. Data acquisition rates of 1 kHz have now been demonstrated. Laser systems with rep rates up to 100 kHz now under development.

Funding for this research was provided by the National Science Foundation, Combustion and Plasmas Program under Award Number 0413623-CTS, by the U.S. Department of Energy, Division of Chemical Sciences, Geosciences and Biosciences, under Grant No. DE-FG02-03ER15391, by the Air Force Office of Scientific Research, and by the Air Force Research Laboratory, Propulsion Directorate, Wright-Patterson Air Force Base, under Contract No. F33615-03-D-2329.

Single-laser-shot detection of nitric oxide in reacting flows using electronic resonance enhanced coherent anti-Stokes Raman scattering

Ning Chai,^{1,a)} Sameer V. Naik,¹ Normand M. Laurendeau,¹ Robert P. Lucht,¹
Sukesh Roy,² and James R. Gord³

¹*School of Mechanical Engineering, Purdue University, West Lafayette, Indiana 47907-2088, USA*

²*Innovative Scientific Solutions, Inc., 2766 Indian Ripple Road, Dayton, Ohio 45440, USA*

³*Air Force Research Laboratory, Propulsion Directorate, Wright-Patterson AFB, Ohio 45433, USA*

(Received 2 May 2008; accepted 25 July 2008; published online 4 September 2008)

Single-laser-shot electronic resonance enhanced coherent anti-Stokes Raman scattering (ERE-CARS) spectra of nitric oxide (NO) were generated using the 532 nm output of an injection-seeded Nd:YAG (yttrium aluminum garnet) laser as the pump beam, a broadband dye laser at approximately 591 nm as the Stokes beam, and a 236 nm narrowband ultraviolet probe beam. Single-laser-shot ERE-CARS spectra of NO were acquired in an atmospheric-pressure hydrogen/air counterflow diffusion flame. The single-shot detection limit in this flame was found to be approximately 30 ppm, and the standard deviation of the measured NO concentration was found to be approximately 20% of the mean. © 2008 American Institute of Physics.

[DOI: [10.1063/1.2973166](https://doi.org/10.1063/1.2973166)]

The quantitative measurement of concentration of pollutant NO in combustion environments is a challenging task. Laser-induced fluorescence (LIF) has been studied extensively for measurements of NO.^{1–4} Several difficulties with LIF have been investigated including interferences from O₂, CO₂ and other species,^{2,5,6} electronic quenching of the NO fluorescence signal via binary collisions,⁷ and ultraviolet (UV) absorption of both the excitation beam and the NO fluorescence signal.

We have recently applied electronic resonance enhanced coherent anti-Stokes Raman scattering (ERE-CARS) for detection of NO in atmospheric and high-pressure environments.^{8–11} The ERE-CARS signal was found to be nearly independent of electronic quenching for two important colliders, O₂ and CO₂.^{8,9} Detection of NO via ERE-CARS in a highly sooting acetylene-air flame was reported for NO concentrations down to approximately 50 ppm.¹⁰ The excellent spectral selectivity of ERE-CARS enables detection of NO despite the presence of multiple interferences such as broadband fluorescence from soot. Finally, the NO ERE-CARS signal was found to be insensitive to variations in collision rates for a laminar H₂/air counterflow flame.¹¹ These findings make ERE-CARS a potentially powerful tool for measurements of NO in practical combustion systems. However, for our previous ERE-CARS measurements of NO, we used a narrowband dye laser (DL) as the Stokes laser beam. Frequency scanning of the Stokes beam across a specified Raman-shift range was necessary to acquire a complete spectrum.

In this paper, we discuss single-shot measurements. The narrowband DL employed for the Stokes beam was replaced with a broadband DL (BBDL) and the ERE-CARS signal was detected using a back-illuminated charge-coupled device (CCD) camera system instead of a photomultiplier tube. The single-shot ERE-CARS system was used for measurements of NO in a counterflow, nonpremixed H₂/air flame at atmo-

spheric pressure. Such measurements are an important step toward application of ERE-CARS for single-shot measurements in practical combustors.

The energy level diagram for ERE-CARS of NO has been discussed elsewhere.¹¹ The 532 nm pump beam and the broadband Stokes beam at 591 nm were used to excite *Q*-branch Raman resonances in the (0,1) band of the ground electronic state of NO. An UV probe beam at approximately 236 nm was scattered from the *Q*-branch Raman resonances excited by the 532 nm pump and 591 nm Stokes beams to generate the ERE-CARS signal. One or two Raman transitions, among the multiple *Q*-branch transitions excited by the pump and Stokes beams, were selectively enhanced by tuning the probe beam into resonance with transitions in the (0,1) vibrational band in the $A^2\Sigma^+ - X^2\Pi$ electronic transition. The CARS signal beam was generated at a wavelength of approximately 226 nm. The wide separation in wavelength between the pump and probe beams distinguishes the current approach from previous ERE-CARS experiments.^{12–16} The bandwidths [full width at half maximum (FWHM)] of the pump, Stokes, and probe beams were approximately 0.003, 50, and 0.1 cm⁻¹, respectively.

An injection-seeded *Q*-switched Nd:YAG (yttrium aluminum garnet) laser (Spectra-Physics model Quanta-Ray 290–10) with repetition rate of 10 Hz was used to generate the pump, Stokes, and probe beams involved in the ERE-CARS process. The energy of the second harmonic output at 532 nm from this laser was 800 mJ/pulse, and that of the third harmonic output at 355 nm was 150 mJ/pulse. The 532 nm beam was directed onto a 50/50 beam splitter. Approximately 20% of the transmitted energy was directed into the probe volume as the pump laser beam. The remaining 80% of the transmitted energy was used to pump a narrowband DL using LDS698 laser dye. The 704 nm output from the narrowband DL was then sum-frequency mixed with the 355 nm third harmonic Nd:YAG output in a beta-barium-borate nonlinear optical crystal to produce the UV probe beam at 236 nm.

^{a)}Author to whom correspondence should be addressed. Electronic mail: nchai@purdue.edu.

The reflected beam from the 50/50 beam splitter was used to pump a spectrally narrowed broadband Stokes DL. Approximately 20% of the reflected energy was used to pump a tunable spectrally narrowed BBDL oscillator. Two prisms were used to disperse the output laser beam in the horizontal plane within the BBDL oscillator cavity. The back mirror of the cavity was a flat full reflector and the front mirror was a wedged flat glass that served as the output coupler. The center wavelength of the BBDL was tuned to 591 nm by changing the angle of the back mirror of the oscillator cavity in the horizontal plane. The two dispersing prisms served to narrow the bandwidth (FWHM) of the output BBDL beam from 300 to 50 cm^{-1} . The remaining 80% of the energy was used to pump two amplifier stages. A mixture of rhodamine 610 and 640 was used in both oscillator and amplifier stages.

The polarization of the pump and Stokes beams was set at 60° with respect to the vertical axis, and the polarization of the probe beam was set at 0° with respect to the vertical axis. This polarization configuration permits complete suppression of the accompanying nonresonant four-wave-mixing signal if desired.¹⁷ All three beams were focused using a fused-silica lens with a focal length of 500 mm. The estimated spatial resolution is approximately 1 mm along the beam path. The maximum energy levels for the pump, Stokes, and probe beams in the probe volume were 60, 50, and 1.2 mJ/pulse, respectively. All three beams and the generated ERE-CARS signal beam were recollimated using another fused-silica lens with a focal length of 500 mm.

The ERE-CARS signal beam was passed through an analyzing polarizer and a filter. The filter had a transmittance of 1% at 236 nm and 70% at 226 nm. A 1 m spectrometer (Horiba Jobin Yvon model SPEX 1000M) with a customized grating (3600 grooves/mm) blazed at the desired signal wavelength was used to separate the signal beam. A combination of a UV camera lens (Nikon model Nikkor 105 mm $f/4.5$ UV) and another positive planoconvex UV lens with a focal length of 500 mm was used as a relay system to further increase the spectral resolution of the detection system. The spectral dispersion on the CCD chip was measured to be approximately 0.14 $\text{cm}^{-1}/\text{pixel}$. An unintensified CCD camera (Andor Technology model DU440-BU) was used to detect the ERE-CARS signal.

The experimental procedures for single-shot ERE-CARS were actually more straightforward than for our previous narrowband ERE-CARS measurements of NO.⁸ For the scanning ERE-CARS experiments, acquisition of a single spectrum required 15–20 min; for the BBDL ERE-CARS experiments, spectra were acquired at a rate of 10 Hz. The effect of scattered light from the UV probe beam was also greatly reduced because the CARS signal was spectrally resolved, and the wavelength peak for scattered light was considerably removed from the ERE-CARS signal pixels.

Figure 1 shows the NO ERE-CARS signal for six different Raman transitions measured in a jet for 1000 ppm NO diluted with N_2 at 300 K with an exposure time of 10 s. As the frequency of the probe beam was changed from $Q_1(4.5)$ up to $Q_1(22.5)$ within the $\gamma(0,1)$ band of A-X electronic system of NO, different Q-branch Raman transitions of $Q_1(4.5)$ up to $Q_1(22.5)$ were selectively enhanced. Consequently, the frequency of the peak of the ERE-CARS signal also changed as the probe frequency was changed.

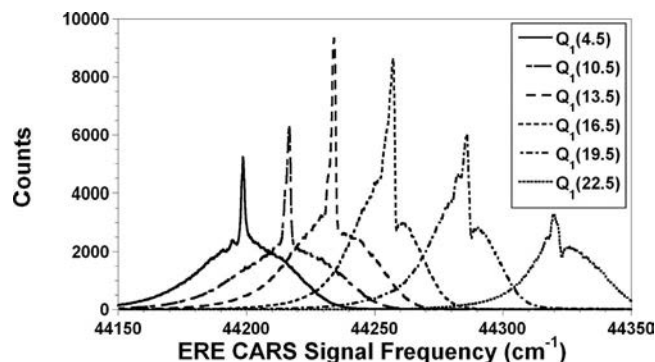


FIG. 1. ERE-CARS signals for six different Raman transitions at 300 K: $Q_1(4.5)$, $Q_1(10.5)$, $Q_1(13.5)$, $Q_1(16.5)$, $Q_1(19.5)$, and $Q_1(22.5)$. The UV probe frequency was fixed at 42 322.89, 42 342.68, 42 361.46, 42 386.12, 42 416.63, and 42 452.95 cm^{-1} , corresponding to $Q_1(4.5)$, $Q_1(10.5)$, $Q_1(13.5)$, $Q_1(16.5)$, $Q_1(19.5)$, and $Q_1(22.5)$ electronic transitions in the $\gamma(0,1)$ band within the $A^2\Sigma^+ - X^2\Pi$ electronic system of NO.

Figure 2 shows single-shot ERE-CARS signals at various distances from the fuel nozzle in a H_2/air counterflow diffusion flame with a global strain rate of 20 s^{-1} at 1 atm. The energy levels for the pump, Stokes, and probe beams were 16, 40, and 0.9 mJ/pulse, respectively. The predicted NO concentration using OPPDIF¹⁸ at a distance of 3.7 mm from the fuel nozzle is 30 ppm. On this basis, a single-shot detection limit of approximately 30 ppm was estimated. The nonresonant four-wave-mixing signal was not suppressed completely so as to normalize the resonant ERE CARS signal with respect to the nonresonant signal to improve shot-to-shot signal reproducibility. This technique also provides the potential for quantitative concentration measurements using the nonresonant background signal as a reference.¹⁹

Figure 3 shows the comparison between the measured broadband ERE-CARS signals and the calculated NO concentration profile for the same H_2/air counterflow diffusion flame. The temperature profile was calculated using the same code. The temperature profile was measured in a separate dual-pump CARS experiment.

The measured NO spectra were acquired with an exposure time of 10 s. A sloping baseline was drawn across the bottom of the resonant line, e.g., from 44 283 to 44 289 cm^{-1} for the $Q_1(19.5)$ line, as shown in Fig. 2(d). The ERE-CARS signal was determined by integrating over

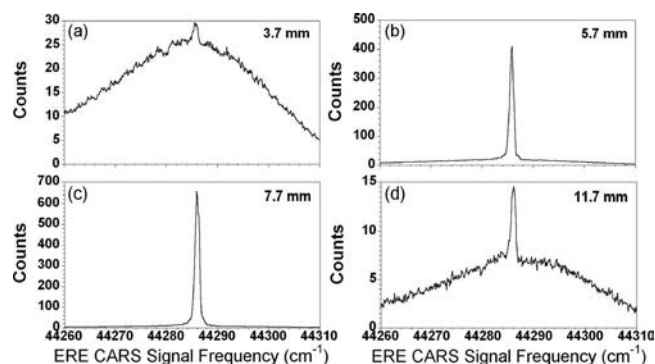


FIG. 2. Single-shot ERE-CARS signal of NO at various distances away from fuel nozzle in the H_2/air counterflow diffusion flame at 1 atm. The frequency of the probe beam was fixed at 42 416.63 cm^{-1} , corresponding to the $Q_1(19.5)$ transition in the $\gamma(0,1)$ band within the $A^2\Sigma^+ - X^2\Pi$ electronic system of NO. The analyzing polarizer was intentionally tuned so as to leak a portion of the nonresonant four-wave-mixing signal.

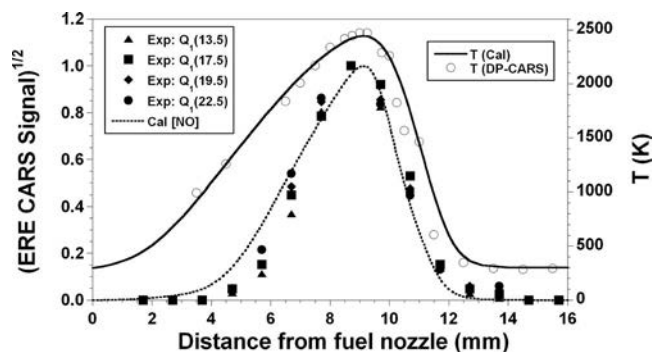


FIG. 3. Comparison between measured broadband ERE-CARS signal using four different Raman transitions and the calculated (OPPDIF) NO concentration profile for the same H₂/air counterflow diffusion flame. Also shown is the comparison between calculated temperature and measured temperature profile in a separate dual-pump CARS experiment.

approximately 6 cm⁻¹ range across the resonant line above the fitted sloping baseline. This method may cause errors at low NO concentrations because of the modulation of the nonresonant signal to the resonant signal. We are currently developing a computer code to fit the experimental spectra and to account rigorously for the modulation of the ERE-CARS signal with the nonresonant background. The Boltzmann-fraction-corrected square root of the integrated ERE-CARS signal is assumed to be proportional to the number density of NO. The ERE-CARS measurements and the predicted profile of NO number density are in fair agreement. The FWHM of the measured profiles with four different sets of Raman and electronic transitions are in good agreement with the FWHM of the calculated profile.

The good agreement observed between the experimental and calculated profiles shown in Fig. 3 is an indication that the ERE-CARS signal level is not affected by the variation in collision rates, including electronic quenching through the flame zone. This insensitivity to collision rates may be a consequence of saturating both the Raman and electronic transitions. We are exploring saturation effects in the ERE-CARS process using time dependent density matrix modeling.²⁰

Because of fluctuations in the laser-pulse energy and multimode characteristics of the Stokes and probe beams involved in the single-shot ERE-CARS process, the peak magnitude of the signal fluctuates from shot to shot. Figure 4 shows a histogram of the square root for the ratio of the integrated ERE-CARS signal and nonresonant four-wave-mixing signal for 1000 single-shot spectra. The standard deviation of this ratio was approximately 20% of the mean. The predicted NO concentration and temperature at this position are 210 ppm and 1750 K, respectively. Similar results were obtained at other locations close to the peak NO position. Single-shot ERE-CARS is thus a promising diagnostic technique for turbulent flames.

Funding for this research was provided by the Air Force Office of Scientific Research under Contract No. FA9550-07-C-0036 (Dr. Julian Tishkoff, Program Manager) and by the Air Force Research Laboratory, Propulsion Directorate, Wright-Patterson Air Force Base, under Contract

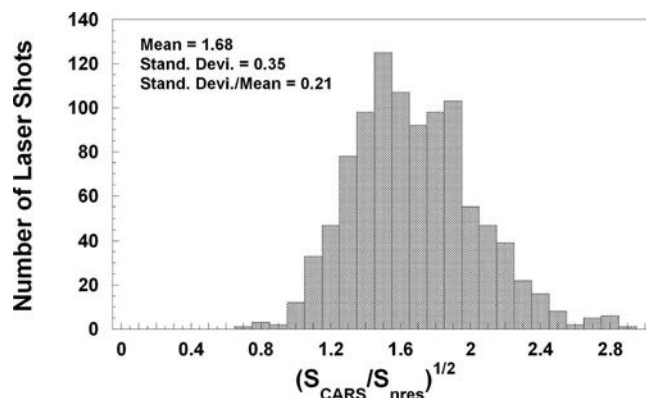


FIG. 4. Histogram of square root for ratio of integrated ERE-CARS signal and nonresonant four-wave-mixing signal for 1000 single-shot spectra acquired at a distance of 10.7 mm from the fuel nozzle for the same flame as described in Fig. 2. The ERE-CARS signal was integrated approximately 4 cm⁻¹ over the resonant line above the sloping baseline (S_{CARS}); the nonresonant four-wave-mixing signal was integrated over approximately 4 cm⁻¹ located 8 cm⁻¹ away from the resonant peak (S_{nres}). The energy levels for the pump, Stokes, and probe beams were 64, 43, and 1.0 mJ/pulse, respectively. The frequency of the probe beam was fixed at 42 416.63 cm⁻¹, corresponding to the Q₁(19.5) transition in the γ(0,1) band within the A²Σ⁺–X²Π electronic system of NO.

No. F33615-03-D-2329. We thank Mr. M. Thariyan, Mr. V. Ananathanarayanan, and Mr. A. Bhuiyan for providing us with the CARS temperature measurements.

- ¹J. R. Reisel and N. M. Laurendeau, *Combust. Sci. Technol.* **98**, 137 (1994).
- ²M. D. Di Rosa, K. G. Klavuhn, and R. K. Hanson, *Combust. Sci. Technol.* **118**, 257 (1996).
- ³C. S. Cooper and N. M. Laurendeau, *Appl. Phys. B* **70**, 903 (2000).
- ⁴W. G. Bessler, C. Schulz, T. Lee, J. B. Jeffries, and R. K. Hanson, *Appl. Opt.* **42**, 4922 (2003).
- ⁵W. G. Bessler, C. Schulz, T. Lee, J. B. Jeffries, and R. K. Hanson, *Chem. Phys. Lett.* **375**, 344 (2003).
- ⁶K. C. Smyth, C. R. Shaddix, and D. A. Everest, *Combust. Flame* **111**, 185 (1997).
- ⁷P. H. Paul, J. A. Gray, J. L. Durant, Jr., and J. W. Thoman, Jr., *Chem. Phys. Lett.* **259**, 508 (1996).
- ⁸S. Roy, W. D. Kulatilaka, S. V. Naik, N. M. Laurendeau, R. P. Lucht, and J. R. Gord, *Appl. Phys. Lett.* **89**, 104105 (2006).
- ⁹A. K. Patnaik, S. Roy, R. P. Lucht, and J. R. Gord, "Collisional effects on molecular dynamics in electronic-resonance-enhanced CARS," *J. Mod. Opt.* (to be published).
- ¹⁰W. D. Kulatilaka, N. Chai, S. V. Naik, N. M. Laurendeau, R. P. Lucht, S. Roy, and J. R. Gord, *Opt. Lett.* **31**, 3357 (2006).
- ¹¹N. Chai, W. D. Kulatilaka, S. V. Naik, N. M. Laurendeau, R. P. Lucht, J. P. Kuehner, S. Roy, V. R. Katta, and J. R. Gord, *Appl. Phys. B* **88**, 141 (2007).
- ¹²B. Attal, O. O. Schnepp, and J. P. E. Taran, *Opt. Commun.* **24**, 77 (1978).
- ¹³T. Doerk, P. Jauernik, S. Hädrich, B. Pfelzer, and J. Uhlenbusch, *Opt. Commun.* **118**, 637 (1995).
- ¹⁴T. Doerk, M. Hertl, B. Pfelzer, S. Hädrich, P. Jauernik, and J. Uhlenbusch, *Appl. Phys. B* **64**, 111 (1996).
- ¹⁵B. Attal-Tretout, S. C. Schmidt, E. Crete, P. Dumas, and J. R. Taran, *J. Quant. Spectrosc. Radiat. Transf.* **43**, 351 (1990).
- ¹⁶B. Attal-Tretout, P. Berlemont, and J. P. Taran, *Mol. Phys.* **70**, 1 (1990).
- ¹⁷S. F. Hanna, W. D. Kulatilaka, Z. Arp, T. Opatrný, M. O. Scully, J. P. Kuehner, and R. P. Lucht, *Appl. Phys. Lett.* **83**, 1887 (2003).
- ¹⁸A. E. Lutz, R. J. Kee, J. F. Grcar, and F. M. Rupley, Sandia National Laboratories Report No. SAND96-8243, 1996.
- ¹⁹R. L. Farrow, R. P. Lucht, G. L. Clark, and R. E. Palmer, *Appl. Opt.* **24**, 2241 (1985).
- ²⁰R. P. Lucht, P. J. Kinnus, S. Roy, and J. R. Gord, *J. Chem. Phys.* **127**, 044316 (2007).

Collisional effects on molecular dynamics in electronic-resonance-enhanced CARS

Anil K. Patnaik^{a,b,*}, Sukesh Roy^a, Robert P. Lucht^c and James R. Gord^a

^aAir Force Research Lab., Propulsion Directorate, Wright-Patterson AFB, OH, USA;

^bDepartment of Physics, Wright State University, Dayton, OH, USA; ^cDepartment of Mechanical Engineering, Purdue University, West Lafayette, IN, USA

(Received 11 March 2008; final version received 22 August 2008)

The role of collisional decay on the evolution of molecular coherence and excited-state population in an electronic-resonance-enhanced coherent anti-Stokes Raman scattering (ERE-CARS) configuration is studied. A four-level model scheme is proposed and a density-matrix equation is derived to determine the system evolution. It is shown that even for significantly large collisional decays, a suitable (rather strong) probe-laser intensity prevents significant depletion of the excited-state population and enhances the ground-state coherence. A physical understanding is developed for the reported insensitivity [Roy et al. *Appl. Phys. Lett.* **2006**, 89, 104105] of the ERE-CARS signal to the rate of collisional decay at the excited electronic level.

Keywords: coherent anti-Stokes Raman scattering; collision; electronic quenching; molecular coherence; molecular dynamics

1. Introduction

Spectroscopic measurement of a target species in a high-pressure environment is strongly affected by collisions of that species with other molecules in the medium. One of the major effects of such collisions is electronic quenching – the de-population of the excited electronic state to molecular states other than the state of interest, e.g. to a vibrational or rotational state in the ground electronic state [1]. Collisional quenching is a major concern for state-of-the-art spectroscopic measurement techniques [2]. Until the mid-1990s only two methods were considered to perform well in high-pressure (but not necessarily high-quenching) environments [3]: (i) all-resonant coherent anti-Stokes Raman scattering (CARS), where a pump and a Stokes field drive a coherence in vibrational levels in the ground electronic level of the target molecule and a third field (all of them being resonant to the excited coupling transition) scatters off the coherence to generate the CARS signal [4], and (ii) laser-induced fluorescence (LIF), where a laser resonantly populates the excited electronic state followed by the fluorescence, which is detected through a filter or monochromator to derive the spectroscopic information [5]. While the LIF signal is

*Corresponding author. Email: anil.patnaik@wright.edu

proportional to the population in the excited state, the CARS signal is dependent on the square of the ground-state coherence. Since both the excited-state population and the ground-state coherence are sensitive to electronic quenching, all-resonant CARS and LIF both are also sensitive to quenching [6]. Particularly in the LIF method, a rapid decay of the excited-state population due to collisional quenching causes a corresponding drop in signal [7,8]. Early spectroscopic measurement of OH showed that the detection sensitivity of all-resonant CARS in a high-pressure environment is roughly equivalent to that of LIF [6,9]. Recently a variant of all-resonant CARS named as electronic-resonance-enhanced CARS (ERE-CARS) was proposed [10]. In this technique both the pump and Stokes fields are far off-resonance from the excited state but are on two-photon resonance with the two ground states; the third (probe) field is resonant to the excited electronic transition. From the ERE-CARS measurement of nitric oxide (NO), a quantitative assessment of minor species concentration was demonstrated [10]. ERE-CARS measurements have also been performed in a high-pressure NO cell [11]. In high pressure combustor environments, the traditional LIF technique becomes less accurate and more complicated [12], primarily due to electronic quenching and background interference [13]. Resonant CARS and ERE-CARS have been used to detect NO and several other combustion radicals [6,9,10,14,15]. A detailed theoretical study has been performed for ERE-CARS spectroscopy of NO [16]. The ERE-CARS technique using fs-pulses has been employed for rapid detection of bacterial spores in the atmosphere [17].

In recent work [18] by some of the authors of this paper, ERE-CARS detection of NO was performed in NO/O₂/N₂ and NO/CO₂/N₂ jet flows at room temperature. With the NO concentration fixed, the electronic quenching rate was varied by a factor of 800 (maximum). It was observed that the CARS signal, unlike the LIF signal, was rather insensitive to the strong quenching. It is intriguing that although both the ERE-CARS and the LIF signals originate from the radiation emitted via the decay of the excited state, LIF is extremely sensitive to the electronic quenching, whereas the ERE-CARS signal is not. The only difference is that the emission in the former case is coherent and that in the latter case is incoherent.

In the present paper, we theoretically investigate the relative insensitivity of the ERE-CARS signal to strong electronic quenching, as opposed to the order-of-magnitude reduction in the LIF signal. A generic four-level model (see Figure 1) is proposed. The primary goal of such a simplified model is to develop a physical understanding of and enable a comparison between the quenching effects on the ERE-CARS and LIF systems. The system dynamics is described by deriving equations for the density-matrix elements that are solved numerically to study the time evolution of the relevant population and coherence. We show that by suitably choosing the intensity of the probe laser in the ERE-CARS configuration, even stronger ground state coherence is obtained with enhanced collisional quenching. The effect of collisional quenching on the excited-state population in the ERE-CARS and LIF configurations is compared to emphasize the significance of ERE-CARS as a robust spectroscopic tool in a high-quenching environment. For numerical purpose we have used parameters corresponding to the experiment [18] on ERE-CARS of NO in a jet flow with CO₂/O₂/N₂ as quenchers. However, the conclusions drawn here are valid for any generalized ERE-CARS system.

The organization of the paper is as follows. In Section 2, we discuss our proposed model scheme and derive equations of dynamics, both for the ERE-CARS and

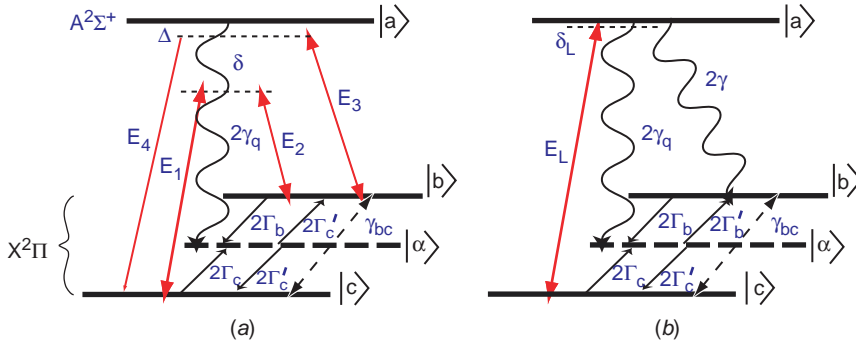


Figure 1. Model schemes for comparing effect of collisions on diagnostic signal via (a) CARS and (b) LIF methods. Energy levels correspond to molecular states of NO. Electronic quenching is depicted as incoherent decay $2\gamma_q$ to a pseudo state $|\alpha\rangle$ that collectively represents all the molecular states not of interest. Applied fields are denoted by E_i ($i \rightarrow 1, 2, 3$), and the CARS signal in (a) is represented by E_4 . Ground-state mixing rates are denoted by $2\Gamma_j$ and $2\Gamma'_j$, and coherence dephasing is represented by γ_{bc} . Detuning of lasers from their respective transitions are given by δ and Δ , as shown in the figures. Electric field and its detuning in the LIF method are denoted by E_L and δ_L , respectively. (The color version of this figure is included in the online version of the journal.)

LIF systems. In Section 3, we present numerical results to show the evolution of the population and coherence and discuss how quenching could affect the spectroscopic signal. In Section 4, we summarize the results.

2. The model and its dynamics

We propose the four-level model (see Figure 1) that depicts the energy states of the NO molecule for studying the ERE-CARS and LIF processes. The excited-state $|a\rangle$ corresponds to a particular rotational level J in the $v=0$ vibrational level in the $A^2\Sigma^+$ electronic state of NO, and the states $|b\rangle$ and $|c\rangle$ represent particular J levels in the $v=0, 1$ levels of the ground electronic state $X^2\Pi$. We introduce a pseudo energy level $|\alpha\rangle$ that collectively takes into account all molecular processes that are unaccounted for in a simplified three-level Λ scheme, e.g. (a) electronic quenching (with a quenching rate $2\gamma_q$) from the excited state $|a\rangle$ to unwanted vibrational and rotational states in the ground electronic states and (b) radiative or non-radiative transitions to and from $|b\rangle$ and $|c\rangle$ due to the mixing of the ground-state population with rates $2\Gamma'_i$ and $2\Gamma_i$, respectively. The coherence dephasing rate is given by γ_{bc} .

The applied fields E_1 (pump field) and E_2 (Stokes field) are on two-photon resonance with the $|b\rangle \leftrightarrow |c\rangle$ transition, and their detuning from state $|a\rangle$ is δ , which is considered to be much larger than any linewidth parameters in the system. The probe field E_3 , which is near resonant to the $|a\rangle \leftrightarrow |b\rangle$ transition with a detuning Δ , beats with the Raman coherence ρ_{bc} (generated by the pump and Stokes fields) to produce the ERE-CARS signal E_4 . Thus, the total field involved in the interaction with the molecule is given as

$$E(z, t) = \sum_{i=1}^4 \hat{e}_i |E_i(z)| \exp[-i(\nu_i t - k_i z)] + c.c., \quad (1)$$

where the three input fields at $z=0$ are given by $E_i(z=0, t) = \hat{e}_i |E_{i_0}(t)| \exp(-i\nu_i t) + c.c.$ ($i=1, 2, 3$), and $E_4(z=0)=0$. Here \hat{e}_i is the unit vector along the direction of the field E_i . The laser frequency and the wave vector of the field E_i are given by ν_i and k_i , respectively. All of the fields are assumed to be broad nanosecond pulses (as in the experiment [18]), and the field amplitudes are assumed to be time independent. To describe the molecular dynamics, we derive a density-matrix equation for the above system, given by

$$\frac{\partial \rho}{\partial t} = -\frac{i}{\hbar} [H, \rho] + \text{decay and dephasing contributions}, \quad (2)$$

where ρ represents the density matrix. The semi-classical Hamiltonian H , corresponding to the molecule and the laser-molecule interaction, is given as

$$H \equiv \hbar(\omega_{ac}|a\rangle\langle a| + \omega_{bc}|b\rangle\langle b| + \omega_{\alpha c}|\alpha\rangle\langle\alpha|) - \hbar \left[\{\Omega_1 \exp(-i\nu_1 t) + \Omega_4 \exp(-i\nu_4 t)\} |a\rangle\langle c| + \{\Omega_2 \exp(-i\nu_2 t) + \Omega_3 \exp(-i\nu_3 t)\} |a\rangle\langle b| + H.c. \right]. \quad (3)$$

Here $\hbar\omega_{jc}$ is the energy separation of the state $|j\rangle$ ($j \rightarrow a, b, \alpha$) from the ground state $|c\rangle$. The Rabi coupling between the lasers and the molecule is given by $\Omega_i = f_{aj} R_{aj} (d_{aj} E_i / \hbar)$, where the field E_i couples the states $|a\rangle$ and $|j\rangle$ (for $j \rightarrow b, c$) having the dipole-matrix element d_{aj} . The Frank-Condon overlap factor and rotational overlap between the ro-vibrational states $|a\rangle$ and $|j\rangle$ are given by f_{aj} and R_{aj} , respectively. Note that the anti-resonant terms, such as $\Omega_i \exp(-i\nu_i t) |b\rangle\langle a|$ ($i \rightarrow 1, 2, 3$) etc., have already been eliminated from the interaction part in the Hamiltonian. Using Equations (2) and (3), and inserting the phenomenological decay coefficients, the dynamical equations for the density-matrix elements of the ERE-CARS system are obtained as

$$\begin{aligned} \frac{\partial \rho_{aa}}{\partial t} &= -(4\gamma + 2\gamma_q) \rho_{aa} + i(\Omega_1 \sigma_{ca} + \Omega_4 \eta_{ca}) - i(\Omega_1^* \sigma_{ac} + \Omega_4^* \eta_{ac}) \\ &\quad + i(\Omega_2 \sigma_{ba} + \Omega_3 \eta_{ba}) - i(\Omega_2^* \sigma_{ab} + \Omega_3^* \eta_{ab}), \\ \frac{\partial \sigma_{ab}}{\partial t} &= -[(2\gamma + \gamma_q + \Gamma_b) + i(\delta + \Delta)] \sigma_{ab} + i\Omega_2 (\rho_{bb} - \rho_{aa}) + i\Omega_1 \tilde{\rho}_{cb}, \\ \frac{\partial \eta_{ab}}{\partial t} &= -[(2\gamma + \gamma_q + \Gamma_b) + i\Delta] \eta_{ab} + i\Omega_3 (\rho_{bb} - \rho_{aa}) + i\Omega_4 \tilde{\rho}_{cb}, \\ \frac{\partial \sigma_{ac}}{\partial t} &= -[(2\gamma + \gamma_q + \Gamma_c) + i(\delta + \Delta)] \sigma_{ac} + i\Omega_1 (\rho_{cc} - \rho_{aa}) + i\Omega_2 \tilde{\rho}_{bc}, \\ \frac{\partial \eta_{ac}}{\partial t} &= -[(2\gamma + \gamma_q + \Gamma_c) + i\Delta] \eta_{ac} + i\Omega_4 (\rho_{cc} - \rho_{aa}) + i\Omega_3 \tilde{\rho}_{bc}, \\ \frac{\partial \rho_{bb}}{\partial t} &= -2\Gamma_b \rho_{bb} + 2\gamma \rho_{aa} + 2\Gamma'_b \rho_{\alpha\alpha} - i(\Omega_2 \sigma_{ba} + \Omega_3 \eta_{ba}) + i(\Omega_2^* \sigma_{ab} + \Omega_3^* \eta_{ab}), \\ \frac{\partial \tilde{\rho}_{bc}}{\partial t} &= -(\Gamma_b + \Gamma_c + \gamma_{bc}) \tilde{\rho}_{bc} + i(\Omega_2^* \sigma_{ac} + \Omega_3^* \eta_{ac}) - i(\Omega_1 \sigma_{ba} + \Omega_4 \eta_{ba}), \\ \frac{\partial \rho_{cc}}{\partial t} &= -2\Gamma_c \rho_{cc} + 2\gamma \rho_{aa} + 2\Gamma'_c \rho_{\alpha\alpha} - i(\Omega_1 \sigma_{ca} + \Omega_4 \eta_{ca}) + i(\Omega_1^* \sigma_{ac} + \Omega_4^* \eta_{ac}), \\ \frac{\partial \rho_{\alpha\alpha}}{\partial t} &= -2(\Gamma'_b + \Gamma'_c) \rho_{\alpha\alpha} + 2\Gamma_b \rho_{bb} + 2\Gamma_c \rho_{cc} + 2\gamma_q \rho_{aa}. \end{aligned} \quad (4)$$

Here, the matrix element ρ_{ij} represents the coherence between states $|i\rangle$ and $|j\rangle$ (for $i \neq j$) and the population of the state $|i\rangle$ (for $i = j$). Note that $\rho_{ij} \equiv \rho_{ji}^*$. The following approximations are used to derive the above Equations (4):

- (1) To separate various polarizations that are oscillating at different frequencies, we make the transformations

$$\begin{aligned}\rho_{ab} &\rightarrow \sigma_{ab} \exp(-i\nu_2 t) + \eta_{ab} \exp(-i\nu_3 t), \\ \rho_{ac} &\rightarrow \sigma_{ac} \exp(-i\nu_1 t) + \eta_{ac} \exp(-i\nu_4 t), \\ \text{and } \rho_{bc} &\rightarrow \tilde{\rho}_{bc} \exp[-i(\nu_1 - \nu_2)t].\end{aligned}\quad (5)$$

Here both σ_{ij} and η_{ij} represent the coherence between states $|i\rangle$ and $|j\rangle$ that are oscillating at different frequencies.

- (2) We use the rotating-wave approximation to eliminate the fast oscillatory terms. Furthermore, we assume that the fields \mathbf{E}_1 and \mathbf{E}_2 are far off-resonance from the excited electronic state $|a\rangle$ such that $\delta \gg \omega_{bc}$ and also the detuning δ is much larger than any other decay or dephasing parameters. Hence, the large oscillation terms $\exp(i\delta t)$ are eliminated compared to their strong resonant counterparts. We will drop the tilde sign in $\tilde{\rho}_{bc}$ in the remainder of the paper for the sake of brevity.

Various decay and dephasing rates are involved in the above equations: (1) the spontaneous decay rates from the state $|a\rangle$ to the states $|b\rangle$ and $|c\rangle$ are represented by 2γ , (2) the electronic quenching rate $2\gamma_q$ represents the decay from state $|a\rangle$ to the pseudo state $|\alpha\rangle$, (3) the incoherent non-radiative population transfers between the various ground vibrational and rotational states from (to) the states $|b\rangle$ and $|c\rangle$ are represented by $2\Gamma_b$ ($2\Gamma'_c$) and $2\Gamma_c$ ($2\Gamma'_c$), and (4) the coherence dephasing rate is given by γ_{bc} . Note that we have ignored the pure-elastic dephasing terms involving the optical transitions in the above equations. Pure optical dephasing could play an important role in certain molecules where dephasing rate becomes larger than RET. We will discuss such a situation elsewhere.

To obtain an approximate estimation of the CARS field Ω_4 , we use the Maxwell–Bloch equation in the slowly varying envelope approximation [19]

$$\frac{\partial \Omega_4}{\partial z} = i \frac{3}{4\pi} N \gamma \lambda_{ac}^2 \eta_{ac}, \quad (6)$$

that describes the spatial evolution of the CARS signal while propagating through the medium. Here, N is the number density of the target molecule, and λ_{ac} is the wavelength of the transition $|a\rangle \leftrightarrow |c\rangle$. Note that we have ignored the time dependence of the field because we consider all of our fields to be CW. Assuming that the probe field is strong and on resonance with the $|a\rangle \leftrightarrow |c\rangle$ transition and that the CARS field is negligibly small, an approximate solution can be obtained for the CARS signal intensity as

$$I_{\text{CARS}} \cong \left[\frac{3N\gamma\lambda_{ac}^2 z}{4\pi(2\gamma + \gamma_q + \Gamma_c)} \right]^2 |E_3|^2 |\rho_{bc}|^2. \quad (7)$$

Thus, the signal generation is strongly influenced by the ground-state coherence as the CARS intensity is proportional to $|\rho_{bc}|^2$. On the other hand, the LIF signal is only proportional to the excited-state population ρ_{aa} . The inverse dependence of I_{CARS} on the

square of the quenching rate $2\gamma_q$ is the cause of concern for the decline in detection sensitivity of the ERE-CARS method that is observed in strong quenching environments [3,6]. We will discuss the details of the effect of quenching on the ERE-CARS configuration in the next section.

For completeness, we also present the equations for the density-matrix elements corresponding to the LIF model configuration shown in Figure 1(b)

$$\begin{aligned}
 \frac{\partial \rho_{aa}}{\partial t} &= -(4\gamma + 2\gamma_q)\rho_{aa} + i\Omega_L \rho_{ca} - i\Omega_L^* \rho_{ac}, \\
 \frac{\partial \rho_{ac}}{\partial t} &= -[(2\gamma + 2\gamma_q + \Gamma_c) + i\delta_L]\rho_{ac} + i\Omega_L(\rho_{cc} - \rho_{aa}), \\
 \frac{\partial \rho_{bb}}{\partial t} &= -2\Gamma_b \rho_{bb} + 2\gamma \rho_{aa} + 2\Gamma'_b \rho_{\alpha\alpha}, \\
 \frac{\partial \rho_{cc}}{\partial t} &= -2\Gamma_c \rho_{cc} + 2\gamma \rho_{aa} + 2\Gamma'_c \rho_{\alpha\alpha} - i\Omega_L \rho_{ca} + i\Omega_L^* \rho_{ac}, \\
 \frac{\partial \rho_{\alpha\alpha}}{\partial t} &= -2(\Gamma'_b + \Gamma'_c)\rho_{\alpha\alpha} + 2\Gamma_b \rho_{bb} + 2\Gamma_c \rho_{cc} + 2\gamma_q \rho_{aa}.
 \end{aligned} \tag{8}$$

Note that since only one field E is present in the LIF configuration, we do not need to use the transformation given earlier in Equation (5) to derive the above Equations (8). Here $\Omega_L = f_{ac}(d_{ac}E_L/\hbar)$ is the Rabi frequency of the pumping field E coupled to the transition $|c\rangle \leftrightarrow |a\rangle$.

3. Effect of quenching on the evolution of population and coherence

In this section, we present the numerical results for both the CARS and the LIF configurations solving Equations (4) and (8), respectively. To emphasize the effect of the quenching rate ($2\gamma_q$) on the ERE-CARS and LIF configurations, in Figure 2 we present the time evolution of the excited-state population for both configurations. We have chosen all of the parameters to be close to their experimental values in [18]. To enable a good

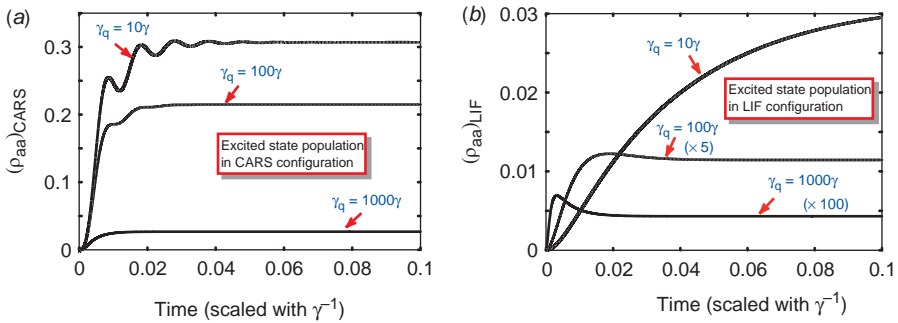


Figure 2. Evolution of excited-state population in (a) CARS configuration and (b) LIF configuration. Population changes only a few percent in the CARS configuration when γ_q increases by an order of magnitude; however, in the LIF configuration, for the same range of quenching, population is depleted by several orders of magnitude. The x -axis represents real time scaled with excited-state decay time γ^{-1} . (The color version of this figure is included in the online version of the journal.)

comparison, all of the parameters are scaled with the spontaneous decay rate γ of the excited state $A^2\Sigma^+$ of NO. The quenching rate γ_q changes significantly with the composition of the gas mixture $\text{CO}_2/\text{O}_2/\text{N}_2$ [20]. For our numerical calculation, we consider three values of electronic quenching: $\gamma_q = 10\gamma$, 100γ , and 1000γ . The lifetime of the excited state is $(2\gamma)^{-1} = 206 \text{ ns}$ [21]. The ground-state population distribution from $|b\rangle$ and $|c\rangle$ to the state $|\alpha\rangle$ is assumed to be $\Gamma'_j = \Gamma_{\text{RET}} \equiv 10^3\gamma$; where the rotational-energy-transfer (RET) rate for NO is $2\Gamma_{\text{RET}} \approx 10^{10} \text{ s}^{-1}$ [22]. Moreover, the population-transfer rate from $|\alpha\rangle$ to the participating ground states $|b\rangle$ and $|c\rangle$, represented by $2\Gamma_j$, is slightly slower than $2\Gamma_{\text{RET}}$. Certain difficulties exist [23] assigning values to these parameters of our model from the known experimental data [22], which we hope to address in future work. However, for simplicity we assume here $\Gamma_j \approx \Gamma'_j/10 \equiv 100\gamma$. Note that due to the presence of a closely lying rotational manifold near each of the levels $|b\rangle$ and $|c\rangle$ under consideration, the elastic coherence-dephasing rate γ_{bc} is almost negligible compared to the inelastic dephasing rates (via Γ_j and Γ'_j) and hence can be ignored [24].

In the CARS configuration, the Rabi frequencies of the pump and Stokes fields are taken to be the same $\Omega_1 = \Omega_2 = \Omega = 1000\gamma$, and the intensity of the probe is considered to be an order of magnitude less intense than that of $|E_1|^2$ and $|E_2|^2$. The detunings are $\delta = 5 \times 10^5\gamma$ and $\Delta = 0$. From Figure 2(a) the excited-state population in the ERE-CARS configuration is depleted only by an order of magnitude when the quenching rate is increased by two orders of magnitude. However, the excited-state population in the LIF configuration, shown in Figure 2(b), is reduced by more than three orders of magnitude for the same increase in γ_q . The LIF pumping field is considered to be on resonance with the $|a\rangle \leftrightarrow |c\rangle$ transition. The corresponding Rabi frequency is taken to be $\Omega_L = 10\gamma$. Stronger LIF pumping is avoided to prevent saturation of the transition. Thus, the excited state population in ERE-CARS is clearly far less sensitive to collisional quenching than that in LIF.

Furthermore, from Equation (7), the ERE-CARS signal is proportional to $|\rho_{bc}|^2$ for stronger Ω_3 . We examine the time evolution of ρ_{bc} in Figure 3 for different values of γ_q . For a lower quenching rate $\gamma_q = 10\gamma$, the Rabi flopping due to the strong probe field dominates during the initial period of ρ_{bc} and later attains steady state. For even larger $\gamma_q \gg \gamma$, the initial Rabi flopping is reduced, and steady state is reached more rapidly. This is due to the fact that the high population-redistribution rates (Γ_i and Γ'_i are large compared to γ) along with stronger quenching help to overcome the strong Rabi flopping caused by the probe field, which resonantly transfers population between states $|b\rangle$ and $|a\rangle$. Furthermore, it may be observed that for a higher quenching rate, the steady-state value of $|\rho_{bc}|$ is larger than that for the low quenching rates. This is a *counter-intuitive result* because usually one would expect a weaker ground-state coherence with an increase in incoherent processes in the system (i.e. for larger γ_q). We confirmed this result with our systematic numerical checks. This result can be understood as the combined effect of the strong coherent pumping, the electronic quenching from the excited state, and also the associated strong ground-state population redistribution. However, when the quenching is increased further, i.e. for $\gamma_q > 1000\gamma$, a sharp decrease in the steady state of ρ_{bc} occurs (not shown here). In the latter case the quenching dominates the repumping field. From Equation (7) it is clear that an increase in quenching rate would reduce the CARS signal. However, the observed increase in ρ_{bc} for larger γ_q could compensate for the loss of signal due to

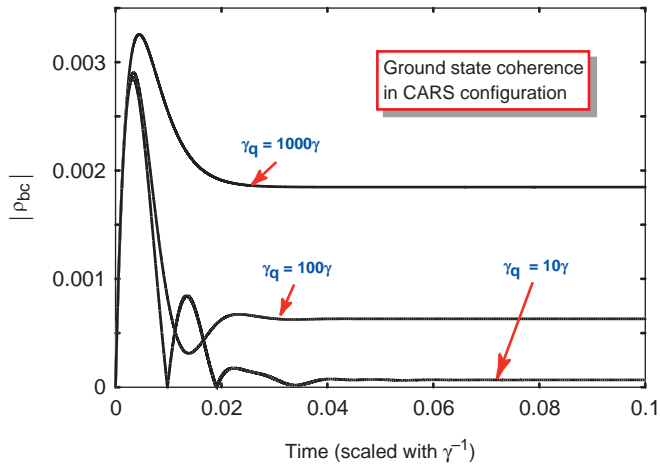


Figure 3. Ground-state coherence in the CARS configuration. Most strikingly, magnitude of coherence in long-time limit increases with excited-state quenching rate. The x -axis represents real time scaled with excited-state decay time γ^{-1} . (The color version of this figure is included in the online version of the journal.)

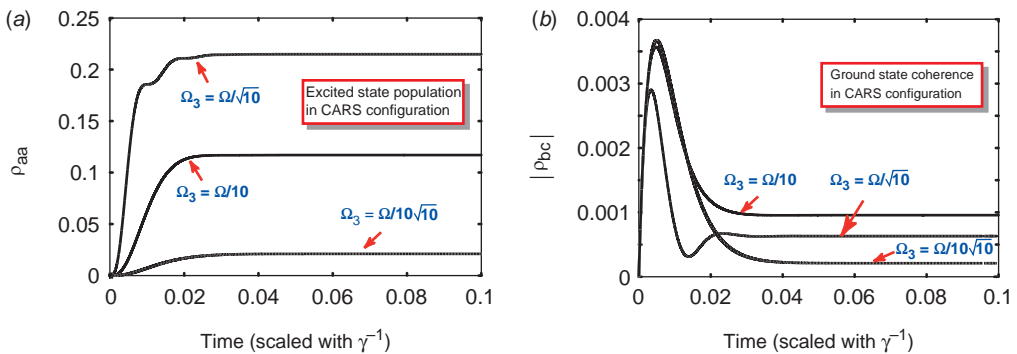


Figure 4. Evolution of population and coherence for fixed value of quenching $\gamma_q = 100\gamma$ with different probe field intensities. Role of probe field as effective repumping field is evident. The x -axis represents real time scaled with excited-state decay time γ^{-1} . (The color version of this figure is included in the online version of the journal.)

collisional quenching and might even cause an effective increase in the ERE-CARS signal. Also any decrease in the CARS signal could be compensated by increasing the probe intensity $|E_3|^2$. A similar constructive role of collisional quenching has been discussed by Lucht et al. [25] in a completely different configuration of two-level degenerate four-wave mixing (DFWM), where the quenching favors generation of DFWM signal but collisional dephasing does not.

To facilitate a discussion of the role of the repumping (probe) field, we plotted the evolution of both ρ_{aa} and ρ_{bc} for different values of Ω_3 with fixed values of $\gamma_q = 100\gamma$ and $\Omega = 1000\gamma$ in Figure 4. An increase in Ω_3 clearly increases the excited-state population.

However, the ground-state coherence does not always increase with an increase in Ω_3 , e.g. for $\Omega_3 = 100(10^{1/2})\gamma$, $|\rho_{bc}|$ is weaker than for $\Omega_3 = 100\gamma$. This can be understood as follows: an increase in Ω_3 coherently repumps $|a\rangle$, followed by the incoherent decays. Then a rapid population redistribution occurs among the ground states, which are then pumped by E_1 and E_2 , leading to an increase in $|\rho_{bc}|$. However, if Ω_3 is extremely strong, the repumping is too rapid to excite the population to $|a\rangle$, even before a significant coherence $|\rho_{bc}|$ can be established. Therefore, for each value of γ_q , there exists an optimal repumping field for which $|\rho_{bc}|$ reaches a maximum. In the presence of two strong resonant fields, the effects of collisional ground-state dephasing and population redistribution on the fluorescence in a three-level atomic system has been discussed in [26].

4. Summary

In summary, we have shown that the excited-state population and the ground-state coherence in an ERE-CARS configuration are not strongly affected by excited-state electronic quenching. In the long-time limit, we observed a counter-intuitive effect – an increase in the ground-state coherence can occur with an increase in collisional-quenching rate. This is attributed to our ability to strongly repump the excited state in the CARS configuration. We also show that for a given set of quenching and ground-state population redistribution rates, there exists an optimal value of the repumping field that can generate maximum coherence. On the other hand, the LIF configuration suffers from several-orders-of-magnitude depletion of the excited-state population with an increase in quenching rate. Our numerical results along with the approximate expression obtained for the NO ERE-CARS signal provides a physical understanding of the observed insensitivity of ERE-CARS of NO to collisions reported in [18].

Acknowledgements

We are extremely thankful to Dr T.B. Settersten for many interesting discussions on various incoherent processes in NO and for providing us crucial parameters to validate our proposed model for NO. Funding for this research was provided by the Air Force Office of Scientific Research under Contract No. FA9550-07-C-0036 (Dr Julian Tishkoff, Program Manager) and by the US Department of Energy, Division of Chemical Sciences, Geosciences, and Biosciences, under Grant No. DE-FG02-03ER15391.

References

- [1] Eckbreth, A.C. *Laser Diagnostics for Combustion Temperature and Species*; Gordon and Breach Publishers: Amsterdam, 1996.
- [2] Kohse-Höinghaus, K.; Meier, U.; Attal-Trétout, B. *Appl. Opt.* **1990**, *29*, 1560–1569.
- [3] Kohse-Höinghaus, K. *Prog. Energy Combust. Sci.* **1994**, *20*, 203–279.
- [4] Attal-Trétout, B.; Berlmont, P.; Taran, J.P. *Mol. Phys.* **1990**, *70*, 1–51.
- [5] Crosley, D.R. *Combust. Flame.* **1989**, *78*, 153–167.
- [6] Attal-Trétout, B.; Schmidt, S.C.; Crété, E.; Dumas, P.; Taran, J.P. *J. Quant. Spectrosc. Radiat. Transf.* **1990**, *43*, 351–364; Attal-Trétout, B.; Bouchardy, P.; Magre, P.; Pealat, M.; Taran, J.P. *Appl. Phys. B* **1990**, *51*, 17–24.

- [7] Ravikrishna, R.V.; Naik, S.V.; Cooper, C.S.; Laurendeau, N.M. *Combust. Sci. Technol.* **2004**, *176*, 1–21; Naik, S.V.; Laurendeau, N.M. *Appl. Phys. B* **2004**, *79*, 641–651.
- [8] Bessler, W.G.; Schulz, C.; Lee, T.; Jeffries, J.B.; Hanson, R.K. *Appl. Opt.* **2003**, *42*, 4922–4936; Martin, G.C.; Mueller, C.J.; Lee, C.F. *Appl. Opt.* **2006**, *45*, 2089–2100.
- [9] Attal, B.; D  bare, D.; M  ller-Dethlefs, K.; Taran, J.P. *Rev. Phys. Appl.* **1983**, *18*, 39–50.
- [10] Hanna, S.F.; Kulatilaka, W.D.; Arp, Z.; Opatrny, T.; Scully, M.O.; Kuehner, J.P.; Lucht, R.P. *Appl. Phys. Lett.* **2003**, *83*, 1887–1889.
- [11] Kulatilaka, W.D.; Chai, N.; Naik, S.V.; Roy, S.; Laurendeau, N.M.; Lucht, R.P.; Kuehner, J.P.; Gord, J.R. *Opt. Commun.* **2007**, *274*, 441–446.
- [12] Lucht, R.P.; Sweeney, D.W.; Laurendeau, N. *Combust. Sci. Technol.* **1985**, *42*, 259–281; Eckberth, A.C.; Bonczyk, P.A.; Verdiek, J.F. *Prog. Energy Combust. Sci.* **1979**, *5*, 253–322.
- [13] Battles, B.E.; Hanson, R.K. *J. Quant. Spectrosc. Radiat. Transf.* **1995**, *54*, 521–537.
- [14] Attal-Tr  tout, B.; Schnepf, O.O.; Taran, J.P. *Opt. Commun.* **1978**, *24*, 77–82.
- [15] Chai, N.; Naik, S.V.; Kulatilaka, W.D.; Laurendeau, N.M.; Lucht, R.P.; Roy, S.; Gord, J.R. *Appl. Phys. B* **2007**, *87*, 731–737.
- [16] Kuehner, J.P.; Naik, S.V.; Kulatilaka, W.D.; Chai, N.; Laurendeau, N.M.; Lucht, R.P.; Patnaik, A.K.; Scully, M.O.; Roy, S.; Gord, J.R. *J. Chem. Phys.* **2008**, *128*, 174308-1–12.
- [17] Scully, M.O.; Kattawar, G.W.; Lucht, R.P.; Opatrny, T.; Pilloff, H.; Rebane, A.; Sokolov, A.V.; Zubairy, M.S. *Proc. Nat. Acad. Sci.* **2002**, *99*, 10994–11001; Beadie, G.; Reintjes, J.; Bashkansky, M.; Opatrny, T.; Scully, M.O. *J. Mod. Opt.* **2003**, *50*, 2361–2368.
- [18] Roy, S.; Kulatilaka, W.D.; Naik, S.; Laurendeau, N.M.; Lucht, R.P.; Gord, J.R. *Appl. Phys. Lett.* **2006**, *89*, 104105-1–3.
- [19] Scully, M.O.; Zubairy, M.S. *Quantum Optics*; Cambridge University Press: Cambridge, UK, 1997.
- [20] Drake, M.C.; Ratcliffe, J.W. *J. Chem. Phys.* **1993**, *98*, 3850–3865.
- [21] Reisel, J.R.; Carter, C.D.; Laurendeau, N.M. *J. Quant. Spectrosc. Radiat. Transf.* **1992**, *47*, 43–54; Lucht, R.P.; Roy, S.; Reichardt, T.A. *Prog. Energy Combust. Sci.* **2003**, *29*, 115–137.
- [22] Settersten, T.B.; Patterson, B.D.; Kronmayer, H.; Sick, V.; Schulz, C.; Daily, J.W. *Phys. Chem. Chem. Phys.* **2006**, *8*, 5328–5338.
- [23] Settersten, T.B., Sandia National Laboratory. Private discussion, 2008.
- [24] Lucht, R.P.; Farrow, R.L. *J. Opt. Soc. Am. B* **1988**, *5*, 1243–1252; Farrow, R.L.; Sitz, G.O. *J. Opt. Soc. Am. B* **1989**, *6*, 865–870.
- [25] Lucht, R.P.; Farrow, R.D.; Rakestraw, D.J. *J. Opt. Soc. Am. B* **1993**, *10*, 1508–1520.
- [26] Patnaik, A.K.; Hsu, P.S.; Agarwal, G.S.; Welch, G.R.; Scully, M.O. *Phys. Rev. A* **2007**, *75*, 023807-1–6.



Development of a nearly transform-limited, low-repetition-rate, picosecond optical parametric generator

Paul S. Hsu, Sukesh Roy*, James R. Gord

Air Force Research Laboratory, Propulsion Directorate, Wright-Patterson AFB, OH 45433-7251, USA

ARTICLE INFO

Article history:

Received 30 July 2008

Received in revised form 12 September 2008

Accepted 12 September 2008

PACS:

42.60.-v

42.65.Yj

42.65.Re

42.60.jf

ABSTRACT

A low-repetition-rate (10-Hz), picosecond (ps) optical parametric generator (OPG) seeded at the idler wavelength with a high-power diode laser is demonstrated. The output of the OPG at ~ 566 nm is amplified in dye cells, resulting in signal enhancement by more than three orders of magnitude. The nearly transform-limited beam at ~ 566 nm has a pulsewidth of ~ 170 ps, with an overall output of ~ 2.3 mJ/pulse. The laser is tuned either by tuning the nonlinear crystal or the seed-laser current. The applications of such a simple, compact, high-performance, tunable ps laser system for linear and nonlinear spectroscopies are outlined.

© 2008 Elsevier B.V. All rights reserved.

1. Introduction

Tunable picosecond (ps) lasers with moderate (<10 -GHz) spectral resolution are useful for time-resolved spectroscopy. For example, these lasers enable spectral resolution of closely lying vibrational levels [1], provide high temporal resolution for the study of fast dynamics in high-temperature and -pressure conditions [2,3], and improve the signal-to-noise ratio in the coherent anti-Stokes Raman scattering (CARS) through suppression of the nonresonant background [4]. Furthermore, the use of short pulse lasers enables efficient nonlinear processes with low pulse energy often below the material-damage threshold [5] and, making it possible to deliver the laser beams through fiber optics in harsh environments [6]. Several sources for non-parametric generation of tunable ps light are available, including external injection-seeded Fabry–Perot laser diodes [7,8], semiconductor lasers [9], and dye lasers [10]. Parametric light generators that employ nonlinear crystals are distinct from non-parametrically tunable radiation sources because of their high output energy and large tuning range [11,12].

The application of tunable ps lasers for high-resolution linear and nonlinear spectroscopic techniques, such as laser-induced fluorescence (LIF) [3], polarization spectroscopy (PS) [13], and electronic-resonance-enhanced coherent anti-Stokes Raman scattering (ERE-CARS) spectroscopy [14] requires high output energy with a nearly transform-limited bandwidth. It would also be advanta-

geous for sources to be widely tunable so that broad spectral ranges could be covered for spectroscopic applications. For example, these ps laser-based spectroscopic techniques could be used for detecting the temperature and concentration of OH, CH, NO and other molecules in reaction flows.

Unlike parametric processes employing nanosecond (ns) lasers [15,16], where parametric gain can be enhanced by multiple round-trip interactions, in a low-repetition-rate ps optical parametric generator (OPG), parametric gain is limited to a single-pass interaction because of the short interaction time of the laser pulse with the nonlinear medium. Furthermore, in this OPG, line-narrowing also must be accomplished during the single-pass interaction time. Tunable, ps optical parametric amplifiers (OPA) that have been reported to date are generally characterized by low-output-pulse energy (~ 100 μ J) and broad spectral width (>300 GHz) [17,18]. Several high-output-pulse energy (~ 1 mJ/pulse) ps OPA systems are commercially available, but the spectral width is typically >120 GHz [19]. The state-of-the-art tunable ps laser system is based on a Nd:YAG-pumped distributed-feedback dye laser (DFDL), which provides nearly transform-limited pulses (~ 5 GHz) of 100-ps duration at a repetition-rate of 20 Hz [3,10]. However, DFDL-based tunable ps laser systems require very sophisticated alignment and maintenance and are extremely sensitive to mechanical disturbances.

In this letter, we describe the development of a robust Nd:YAG-pumped tunable ps laser system using an OPG assisted by a high-power injection-seeded laser, that provides nearly transform-limited pulses (time-bandwidth product <1.4) of ~ 170 ps duration at a repetition-rate of 10 Hz. The pulsewidth of the tunable laser

* Corresponding author. Tel.: +1 937 255 3115; fax: +1 937 656 4110.
E-mail address: sroy@woh.rr.com (S. Roy).

is limited by the pulsedwidth of the pump laser. We have demonstrated that the OPG signal pulses can be significantly amplified in the pulsed dye amplifiers (PDA). Coarse tuning of the laser system is achieved by tuning the temperature or the piezo of the seed-

laser, whereas fine tuning of the order ~ 50 GHz is achieved by tuning the injection current of the seed-laser. The proposed OPG-PDA system is extremely robust and requires no day-to-day alignment as long as the pump laser is stable.

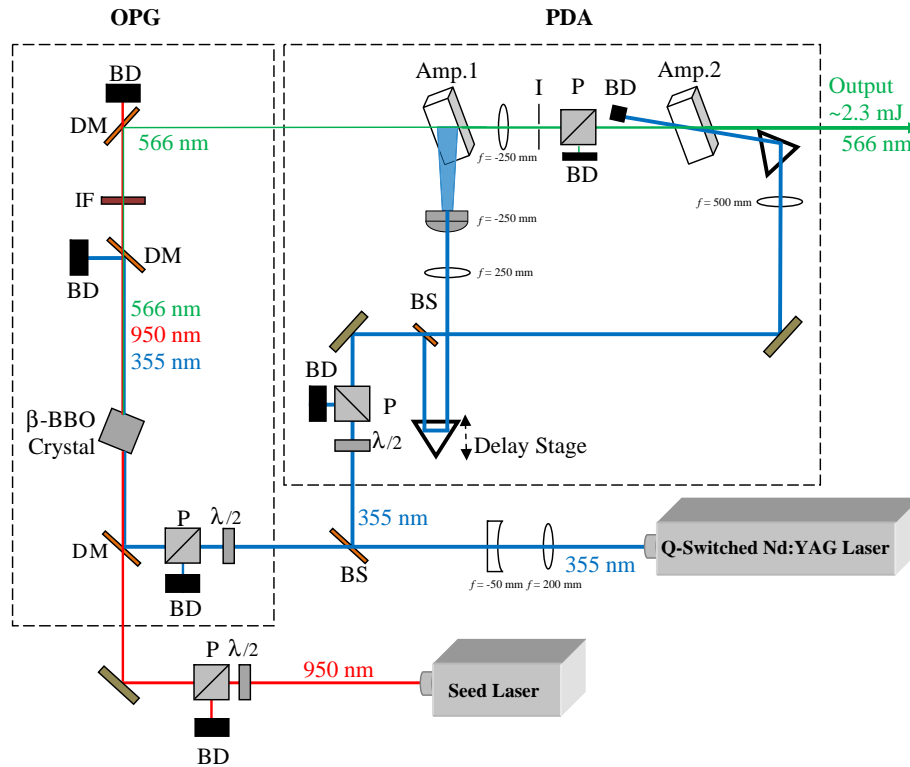


Fig. 1. Schematic diagram of tunable ps laser system. $\lambda/2$, Half-wave plate; P, polarizer; BD, beam dump; BS, beam splitter; DM, dichroic mirror; I, iris; IF, interference filter.

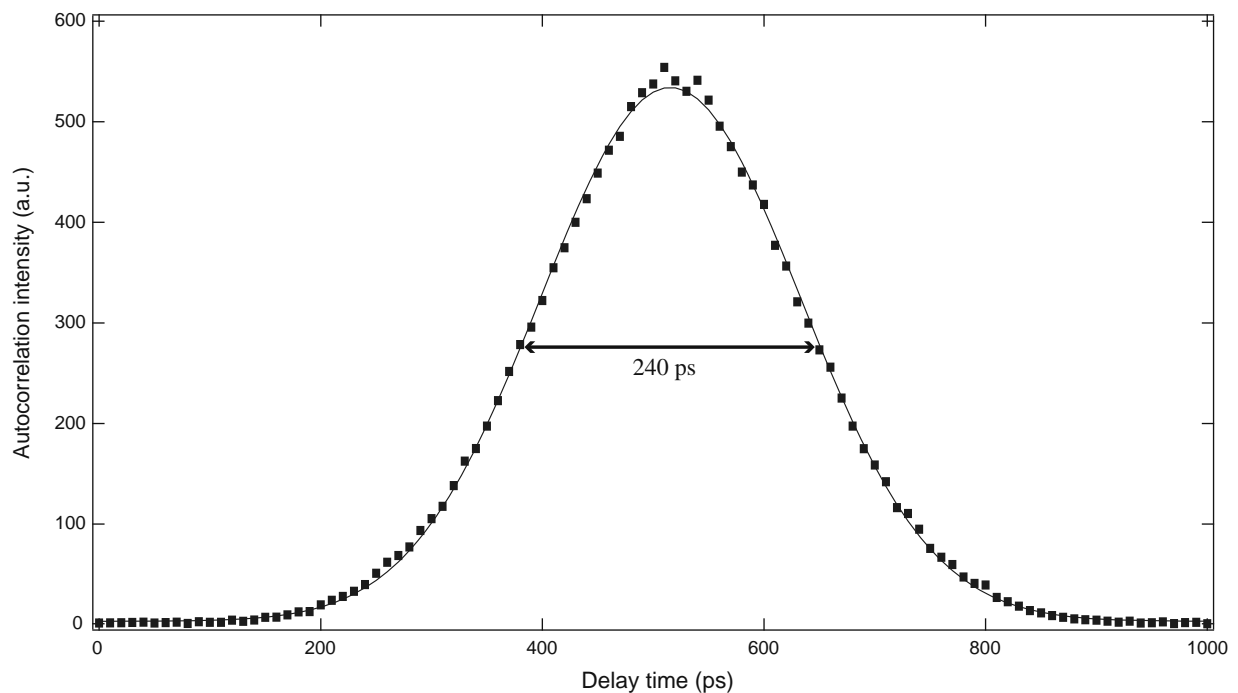


Fig. 2. Autocorrelation trace (symbols) and Gaussian fit (curve) of amplified-OPG signal at 566 nm with seeding at idler wavelength. Autocorrelation width is 240 ps, corresponding to pulsewidth of 170 ps.

2. Experimental setup and results

The system consists of two stages: (1) OPG, where the tunable, nearly transform-limited ps pulse is produced and (2) PDA, where the OPG signal pulse is amplified. A schematic diagram of the ps OPG system is shown in Fig. 1. A Nd:YAG laser (EKSPLA SL300) at 355 nm is used to pump the OPG and PDA systems with a pulse energy of ~ 90 mJ. The repetition-rate and the pulsewidth of the pump laser at 355 nm are 10 Hz and ~ 150 ps, respectively. The Nd:YAG output is nearly transform-limited (single-longitudinal-mode oscillator) and has excellent top-hat beam quality. In the current setup, generations of OPG signal radiation with ~ 1 μ J/pulse from an injection-seeded β -BBO crystal was demonstrated using a 17-mJ pump and a 630-mW diode laser as the CW seed source at an idler wavelength of ~ 950 nm. The purpose of the injection seeding at the idler wavelength for OPG is to avoid spectrum interference in the subsequent amplification processes [16,20]. The spectral component at the idler frequency is blocked ahead of the PDA stage by a dichroic mirror. The observed OPG signal is well-shaped and does not contain the component of the seed-laser. To match the seed-laser beam size, the pump beam is down-collimated to 2-mm diameter in the BBO crystal. The BBO crystal is cut at an angle of 30° to the optical axis. The crystal length is 10 mm, and the faces are 8 mm square in cross section (normal to the beam-propagation direction) with MgF_2 protective coatings. To minimize thermal fluctuations, the BBO crystal is installed in a temperature-controlled crystal holder. The maximum energy out of the injection-seeded OPG signal at ~ 566 nm is only a few μ J.

For amplification, the OPG signal is injection-seeded into two dye cells that are side- and end-pumped by a portion of the 355-nm laser beams. The temporal overlap between the OPG signal photons and the ~ 150 -ps pump beam in the first dye cell is achieved using a delay stage. The second amplifier cell is end-pumped to improve the spatial profile of the beam. To reduce amplification of the amplified spontaneous emission (ASE) in the second dye cell, a polarizer and an iris are placed after the first dye cell to filter most of the ASE generated from the first dye cell. In the current setup, Rhodamine 590 dye is used to amplify the OPG beam at ~ 566 nm. The OPG signal is amplified by more than three orders of magnitude through the dye cells.

The pulse duration of the amplified-OPG pulses was measured using a multi-shot scanning autocorrelator (EKSPLA AC532/1064). The average autocorrelation-pulse profile of the amplified-OPG signal is shown in Fig. 2. For a Gaussian profile an autocorrelation width of ~ 240 ps corresponds to a temporal pulse width of ~ 168 ps. The spectral profile of the OPG signal, shown in Fig. 3a,

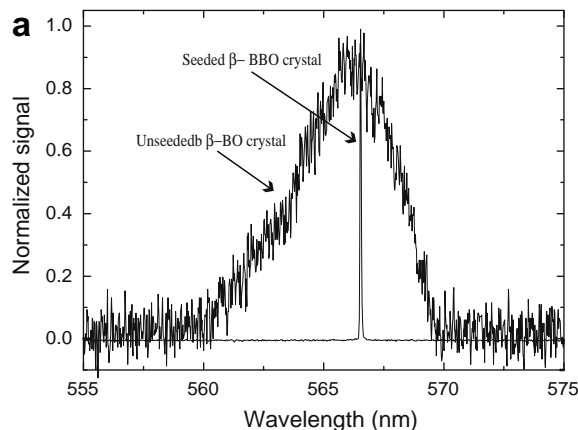


Fig. 3. (a) Spectrum of light emitted from unseeded BBO crystal and seeded BBO crystal. (b) Image of transmission pattern of amplified-OPG signal through solid etalon (30-GHz FSR, 330 finesse).

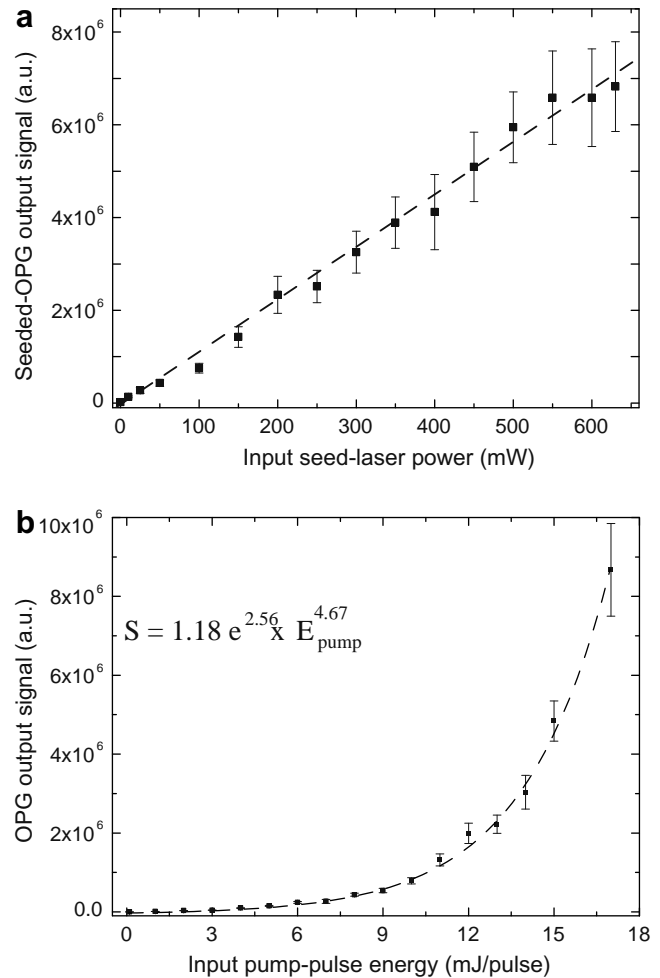
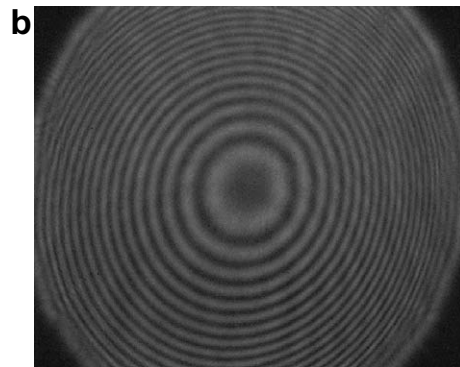


Fig. 4. (a) Intensity of signal output from seeded BBO crystal as function of seed-laser power with constant pump-pulse energy of 17 mJ. (b) Intensity of signal output from seeded BBO crystal as function of pump-pulse energy of 355-nm beam with constant seed-laser power of 630 mW. Symbols represent experimental data and dashed line is linear fit.

was measured with an ocean optics spectrometer (Model USB4000). The FWHM of the unseeded- and seeded-OPG signals was observed to be ~ 5 nm and ~ 0.02 nm, respectively, with a resolution ~ 0.02 nm. The limited spectral resolution of the spectrom-



eter prevented full resolution of the linewidth of the seeded-OPG signal. To determine the bandwidth of the OPG signal accurately, a solid etalon with FSR of 33 GHz and finesse of 330 was used. The interference fringes recorded with a commercial CCD camera are shown in Fig. 3b. By analyzing the spacing between the interference fringes from the etalon transmission [21], the linewidth of the amplified-OPG signal was found to be 8.32 ± 0.648 GHz. The linewidth is approximately a factor of two broader than the linewidth of the pump beam, which was measured to be 4.37 ± 0.8 GHz. The output energy of the ~ 1 μ J/pulse OPG signal was amplified to ~ 2.3 mJ/pulse using two stages of dye amplifications. The pre-amplifier was side-pumped with ~ 22 mJ/pulse energy, and the final amplifier was end-pumped with ~ 33 mJ/pulse energy. The intensity of the OPG signal from the seeded BBO crystal as a function of the seed-laser power is shown in Fig. 4a. Typically 10-mW seed power is required for an ordinary ns laser-based OPO or OPA system [15,16]. However, we discovered that such low seed power is not sufficient to assist the parametric process during the single trip in the nonlinear crystal. It is shown in Fig. 4a that with a rather intense seed-laser the OPG signal increases by more than two orders of magnitude when the seed-laser power is increased from 10 mW to 630 mW. The results show that effective parametric gain for the ps single-pass OPG can be achieved only with a substantial flux of seed photons. The OPG signal shows a linear dependence on seed-laser power; however, for seed-laser powers greater than 550 mW, the signal begins to saturate. The saturation could not be resolved properly because of limited seed-laser power. The dependence of the OPG signal intensity on the pump-pulse energy with a 630-mW seed beam at the idler wavelength is shown in Fig. 4b. From an exponential fit it is observed that the signal beam intensity is proportional to the pump-pulse energy raised to a power of ~ 4.67 . For the unseeded OPG the pump-energy threshold is ~ 10 mJ, whereas with a seed power of ~ 630 mW, the required threshold pump-energy is reduced to ~ 100 μ J. The large fluctuations shown in Fig. 4 are due to the instability of the pump laser at high power.

3. Conclusions

To summarize, we have demonstrated the operation of a low-repetition-rate ps OPG assisted by a high-power seed-laser at the idler wavelength. The output of the OPG signal is amplified by

more than three orders of magnitude in pulsed dye amplifiers. The resulting signal beam is nearly transform-limited and should be very useful for performing linear and nonlinear time-resolved spectroscopy where a broadly tunable laser source is required.

Acknowledgments

The authors gratefully acknowledge fruitful discussions with Dr. A.K. Patnaik of Wright State University and ISSI and Dr. T.B. Settersten of Sandia National Laboratories. Funding for this research was provided by the Air Force Office of Scientific Research under Contract No. FA9550-07-C-0036 (Dr. Julian Tishkoff, Program Manager) and by the Air Force Research Laboratory, Propulsion Directorate, Wright-Patterson Air Force Base under Contract No. F33615-03-D-2329.

References

- [1] A.C. Eckbreth, Laser Diagnostics for Combustion Temperature and Species, second ed., Gordon & Breach, 1996.
- [2] R. Schwarzwald, P. Monkhouse, J. Wolfrum, Chem. Phys. Lett. 142 (1987) 15.
- [3] T.B. Settersten, B.D. Patterson, J.A. Gray, J. Chem. Phys. 124 (2006) 234308.
- [4] S. Roy, T.R. Meyer, J.R. Gord, Appl. Phys. Lett. 87 (2005) 264103.
- [5] W.H. Lowdermilk, D. Milam, IEEE J. Quant. Electron. 17 (1981) 1888.
- [6] D.P. Hand, J.D. Entwistle, R.R.J. Maier, A. Kuhn, C.A. Greated, J.D.C. Jones, Meas. Sci. Technol. 10 (1999) 239.
- [7] M. Zhang, D. Wang, W. Jin, M.S. Demokan, Opt. Eng. 41 (2002) 1747.
- [8] A.M. Clarke, P.M. Anandarajah, L.P. Barry, IEEE Photon. Technol. Lett. 16 (2004) 2344.
- [9] A. Fragemann, V. Pasiskevicius, F. Laurell, Opt. Express 13 (2005) 6482.
- [10] P.P. Yaney, D.A.V. Kliner, P.E. Schrader, R.L. Farrow, Rev. Sci. Instrum. 71 (2000) 1296.
- [11] R.A. Ganeev, T. Usmanov, J. Appl. Spectrosc. 64 (1997) 544.
- [12] M.H. Dunn, M. Ebrahimzadeh, Science 286 (1999) 1513.
- [13] T.A. Reichardt, F.D. Teodoro, R.L. Farrow, S. Roy, R.P. Lucht, J. Chem. Phys. 113 (2000) 2263.
- [14] S.F. Hanna, W.D. Kulatilaka, Z. Arp, T. Opatrný, M.O. Scully, J.P. Kuehner, R.P. Lucht, Appl. Phys. Lett. 83 (2003) 1887.
- [15] S. Wu, V.A. Kapinus, G.A. Blake, Opt. Commun. 159 (1999) 74.
- [16] W.D. Kulatilaka, T.N. Anderson, T.L. Bougher, R.P. Lucht, Appl. Phys. B 80 (2005) 669.
- [17] X.D. Zhu, L. Deng, Appl. Phys. Lett. 61 (1992) 1490.
- [18] M. Tiihonen, V. Pasiskevicius, F. Laurell, Opt. Express 14 (2006) 8728.
- [19] For example: Ekspla PG 500 Series, <<http://www.ekspla.com/en/main/products/17/21?pid=441>>.
- [20] H. Luo, L. Qian, P. Yuan, H. Zhu, S. Wen, Opt. Express 13 (2005) 9747.
- [21] K.K. Lehmann, D. Romanini, J. Chem. Phys. 105 (1996) 10263 (the validity for determining spectral width of short laser pulse by using an etalon is rigorously described in this reference).

CFD Based Global Chemistry Predictions for Normal and Inverse Laminar Ethane Jet Diffusion Flames under Oxygen Enhancement and Gravity-Variation.

Pramod Bhatia^{*,a}, V. R. Katta^b, P.B. Sunderland^c, S.S. Krishnan^d and J. P. Gore^a

^a*School of Mechanical Engineering, Purdue University, West Lafayette, IN 47907, USA*

^b*Innovative Scientific Solutions, Inc., 2766 Indian Ripple Road, Dayton, OH 45440-3638, USA*

^c*National Center for Microgravity Research, Cleveland, OH 44135, USA*

^d*Department of Mechanical Engineering, Purdue School of Engineering and Technology, IUPUI, 723 W. Michigan Street, Indianapolis, IN 46202, USA*

Abstract

Global calculations involving five species, at four different fuel compositions, for ethane jet diffusion and inverse-diffusion flames in earth gravity and in microgravity conditions are made using an axisymmetric, time dependent computational fluid dynamics code. Computations were compared with the experimental data obtained from NASA Glenn Research Center. Enhancement in oxygen resulted in increased flame temperatures. There was no significant change in inverse-diffusion flame lengths (based on maximum temperature) with oxygen enhancement and gravity variation.

Introduction

Jet diffusion and inverse-diffusion flames have been of great interest for past few decades. Both the configurations can arise on earth [1] and in space. Oxygen-enrichment and gravity-variation can have significant affect on the flame properties. For example, equilibrium calculations show that the adiabatic flame temperature for ethane increases from 2250 K in air to 3082 K in oxygen (Table 1) i.e., an increase of about 37% in the presence of oxygen compared to air. Also, the normal jet diffusion non-buoyant flames are reported to be longer than buoyant flames [2]

Objective(s)

The objectives of this study are to understand and predict flame behavior under:

- Microgravity (μ -g) and 1-g environments.
- Oxygen-enrichment.
- Normal and inverse diffusion flame configurations.

One-step global-chemistry version of the axisymmetric computational tool developed by Katta [3, 4] was used. Comparisons between steady-state computational results and experimental data [5] are presented. Ethane fuel (1.0 mole fraction) was used to examine the effects of oxygen-enhancement (0.21, 0.3, 0.5 and 1.0; mole fraction) in nitrogen. Normal gravity and zero gravity computations were completed for inverse-diffusion flames. Table 1 summarizes the eleven steady-state computations. Transient computations were also completed for CASE 1.

The computational model is the one developed by Katta [3,4]. The present simulations involved a round 5.5 mm burner, quiescent ambient gas at 0.98 bars and 298 K under enhanced-oxygen conditions. Five species involved in the global chemistry calculations are: Ethane (C_2H_4), Oxygen (O_2), Nitrogen (N_2), H_2O and Carbon-dioxide (CO_2).

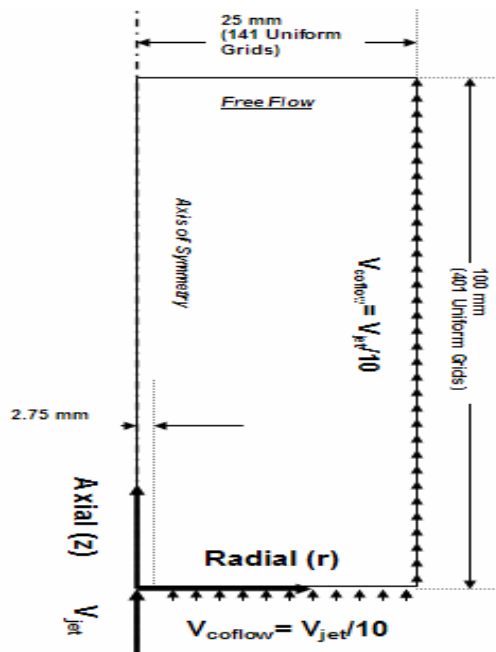


Figure 1. Computational Domain

*Corresponding author: Tel +1-765-743-3409, Email: bhatia@purdue.edu (Pramod Bhatia)
Proceedings of the 2004 Technical Meeting of the Central States Section of the Combustion Institute

Figure 1 presents the geometry of the axisymmetric computational domain. The computational domain extending 100 mm X 25 mm in the axial (z) and radial (r) directions, respectively, is represented by a staggered, uniform 401 X 141 grid system. The co-flow velocity is set at $1/10^{\text{th}}$ of the jet velocity. Tables 1 summarize the boundary conditions. The aero-thermo-physical properties (viscosity, specific heat, thermal conductivity, mass diffusivity, and heat of formation) for the species were assumed to vary with temperature [4]. The global reaction rates were optimized in the past for normal diffusion flames for combustion with air. Radiation heat losses were neglected as a first step.

Results and discussion

Table 1 gives the summary of the eleven computed cases. Figure 2 shows the axial velocity profiles at the centerline plotted as a function of distance from the burner exit. Upstream of the flame tip, the axial velocity increases for all cases because of the volumetric expansion caused by the combustion heat release. Beyond the flame tip the axial velocities increase with distance for the 1-g cases (Figures 2 & 5.1-8), whereas it decreases for the 0-g (Figure 2 & 5.9-11) cases as expected. These effects are expected because of the high product temperatures leading to lower density and resultant buoyant accelerations in the 1-g cases, in contrast to the deceleration caused by shear forces for the 0-g cases. These effects decrease with downstream distance and the axial velocities start approaching uniform profiles.

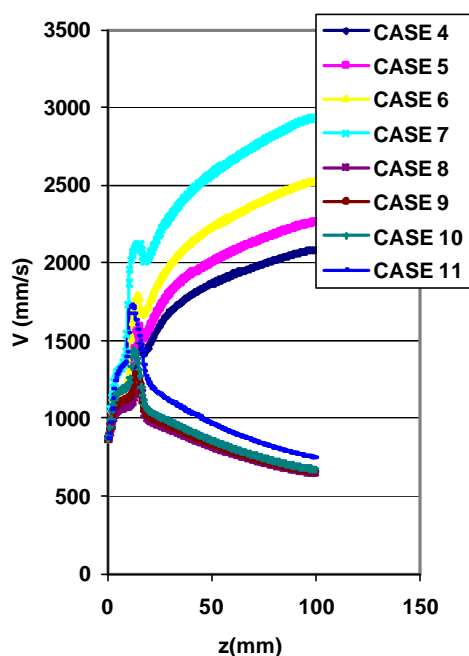


Figure 2. Axial-Velocity Vs. z (r=0)

No significant differences in maximum flame temperatures and maximum temperature based flame lengths were observed between 1-g and 0-g inverse-diffusion flames, with identical oxygen mole fractions.

The temperature (Figure 3) and fuel mass fraction (Figure 4) along the axial direction (at $r=0$) show similar values for the 1-g and 0-g inverse-diffusion flames. As expected, the flame temperatures increase with an increase in the inlet oxygen mole fraction. The centerline C_2H_6 mass fraction values increase in a similar manner for all inverse diffusion flames and decrease monotonically for all normal diffusion flames (Figure 4).

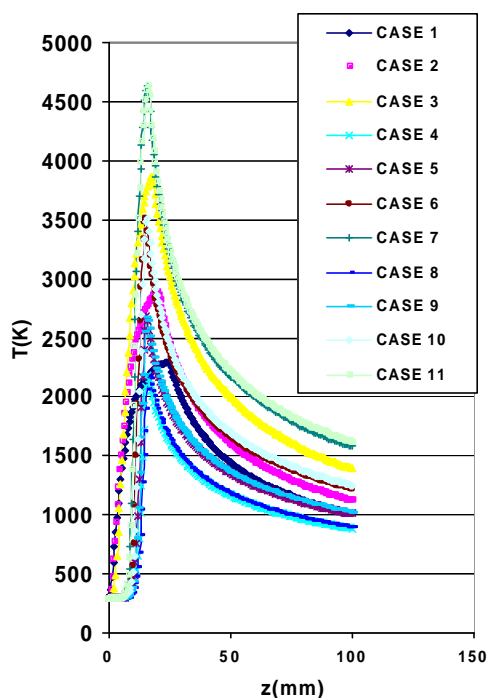


Figure 3. Temperature Vs. z (at r=0)

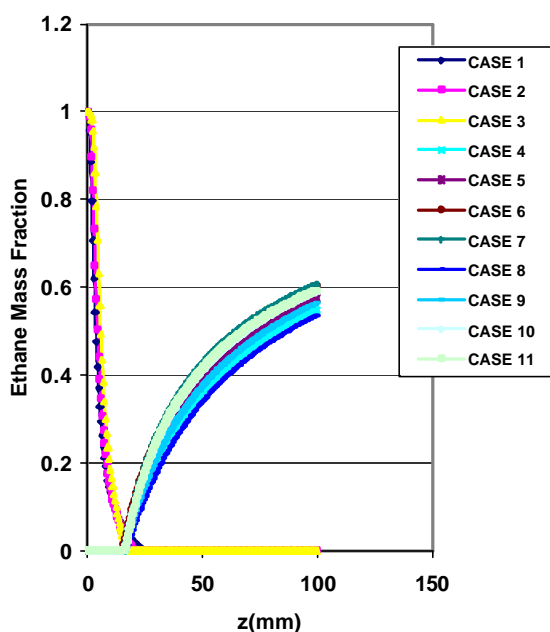


Figure 4. C_2H_4 Mass Fraction Vs. z ($r=0$)

Figures 5.1 to 5.11 show flame photographs from Ref. [5] and temperature contours and velocity vectors from the present computations. The comparisons can only be qualitative because of the differences in the quantities being displayed as well as the differences between the boundary conditions in the experiments and the computations. Final converged unsteady computations conducted for CASE 1 show no significant differences with the results obtained from its steady computations.

Figures 5.1 to 5.11 show remarkable qualitative similarities between the shapes and locations of color changes observed in the flame photographs and contour changes observed in the calculated temperature contour plots. These trends are encouraging but more work is needed as discussed in the following.

A comparison of the adiabatic equilibrium temperatures for the different cases presented in Table 1 with the maximum temperatures computed by the present global chemistry model and approximate thermo-physical property assumptions reveals significant differences with increases in oxygen concentrations. The calculated maximum temperatures are much higher than the adiabatic equilibrium temperatures. This is caused by the current assumption of specific heats and the limitations of global kinetic steps which appear to prevent high temperature dissociation which may be prevalent in oxygen enriched flames. Experimental measurements of temperature distributions and improved computations

with detailed chemistry and radiation models are necessary to resolve these issues.

Conclusion

Computations were performed for ethane fueled laminar gas-jet diffusion flames, emphasizing the effects of oxygen enhancement, gravity, and inverse burning on velocity and temperature profiles. The mole fraction of oxygen in the oxidizer was varied from 0.21-1. Qualitative comparisons were performed with the experimental results [5]. The major findings were:

1. As expected, oxygen-enhanced conditions caused increase in flame temperatures and gas velocities.
2. For inverse-diffusion flames, gravity has relatively small influences on the flame temperature and fuel mass fraction distributions.
3. The axial velocities increase significantly before the flame tip for the normal and zero gravity flames as a result of expansion caused by heat release. Beyond the flame tip the velocities increase for the 1-g flames whereas they decrease for 0-g flames.
4. In case of inverse diffusion flames, the gravity-variation and oxygen-enhancement had no significant effect on the flame length (based on maximum temperature).
5. Comparisons of maximum temperatures based on present thermo-physical properties and global kinetic rates with adiabatic equilibrium temperatures show that the computations may be overestimating the non-equilibrium effects by underestimating the rates of dissociation reactions. Temperature measurements and detailed chemistry and thermo-physical property calculations are necessary to address these issues.

Acknowledgements

This work is supported by NASA Glenn Research Center. Special thanks to Dave Seaman, Bill Whitson and Chinh Le for helping in facilitating computations.

References

- [1] C.E. Baukal, in: C.E. Baukal (Ed.), Oxygen-Enhanced Combustion, CRC Press, Boca Raton, 1998, pp. 2-42.
- [2] P.B. Sunderland, B. J. Mendelson, Z.-G. Yuan, and D.L. Urban, (1999) "Shapes of Buoyant and Nonbuoyant Laminar Jet Diffusion Flames," Combust. Flame, Vol. 116, pp. 376-385.

- [3] V. R. Katta, L. P. Goss and W. M. Roquemore, "Effect of nonunity Lewis number and finite-rate chemistry on the dynamics of a hydrogen-air jet diffusion flame" Combustion and Flame, Vol. 96, pp. 60-74, 1994
- [4] W. M. Roquemore; V. R. Katta, Role of Flow Visualization in the development of UNICORN, Journal of Visualization, Vol 3/4 (2000), Pg 257-272.
- [5] P. B. Sunderland, S. S. Krishnan and J. P. Gore; Effects of oxygen enhancement and gravity on normal and inverse laminar jet diffusion flames, Combustion and Flame, Volume 136, Issues 1-2, January 2004, Pages 254-256

Table 1. Summary of computed cases

	GRAVITY	DIFFUSION	INLET O ₂ MOLE FRACTION	JET VELOCITY (mm/s)	FLAME LENGTH (mm) BASED ON T _{max}	T _{max} (K)	T (K) ADIABATIC
CASE 1	1-g	Normal	0.21	24	24	2300	2250
CASE 2	1-g	Normal	0.3	74	20	2900	2553
CASE 3	1-g	Normal	0.5	124	17.7	3870	2839
CASE 4	1-g	Inverse	0.21	866	16	2190	2250
CASE 5	1-g	Inverse	0.3	866	15.2	2690	2553
CASE 6	1-g	Inverse	0.5	866	15.2	3510	2839
CASE 7	1-g	Inverse	1.0	866	15.8	4640	3082
CASE 8	0-g	Inverse	0.21	866	15.3	2180	2250
CASE 9	0-g	Inverse	0.3	866	15.8	2680	2553
CASE10	0-g	Inverse	0.5	866	15.8	3510	2839
CASE11	0-g	Inverse	1.0	866	15.3	4630	3082

Figure 5.1 – 11 Comparisons between Computational and Experimental Results.

(Left: Experimental Results [5]; Right: Computational Results: Temperature and velocity profiles)

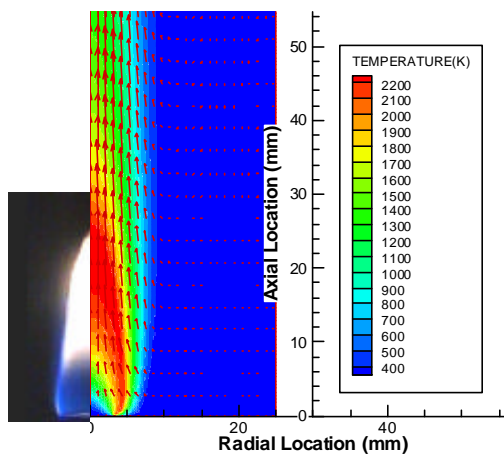


Figure 5.1 : Case 1

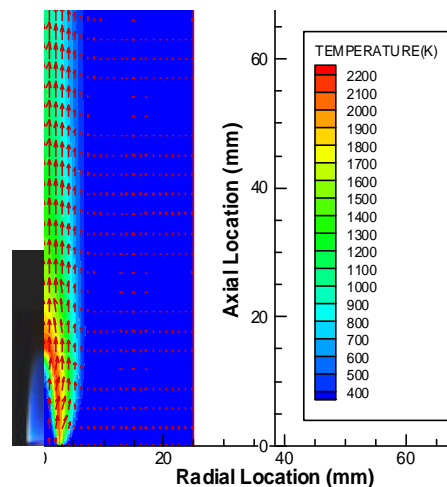


Figure 5.4 : Case 4

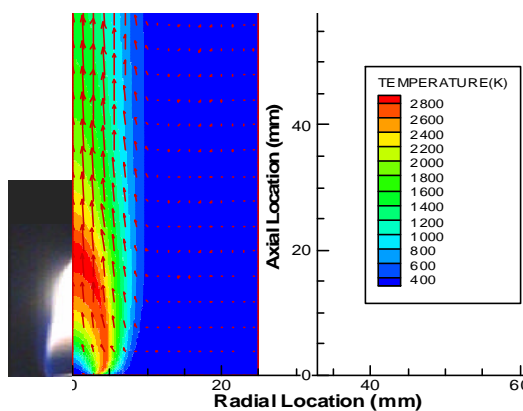


Figure 5.2 : Case 2

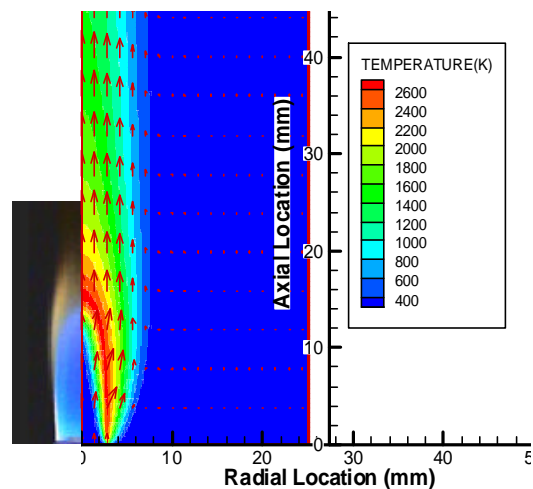


Figure 5.5 : Case 5

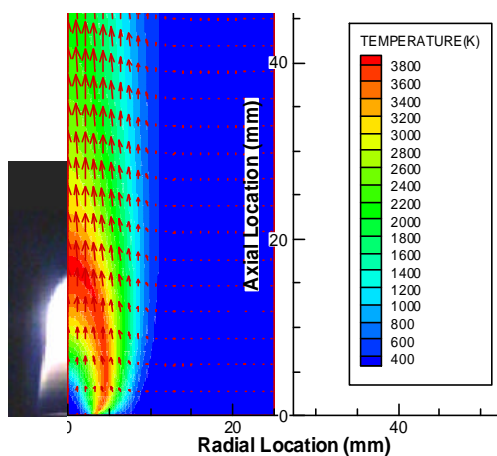


Figure 5.3 : Case 3

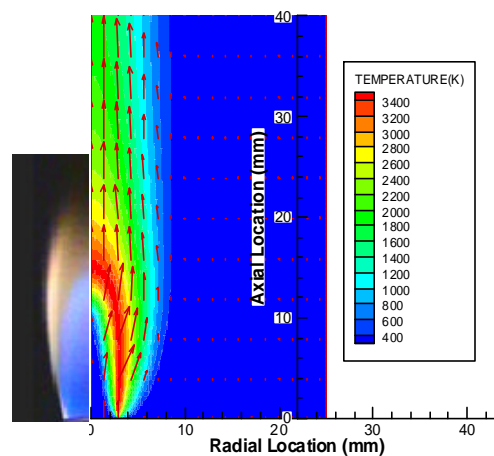


Figure 5.6 : Case 6

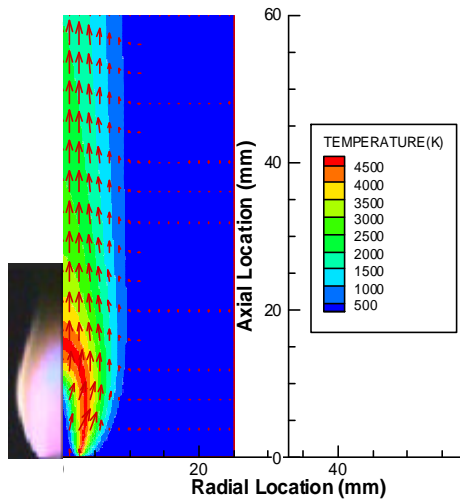


Figure 5.7 : Case 7

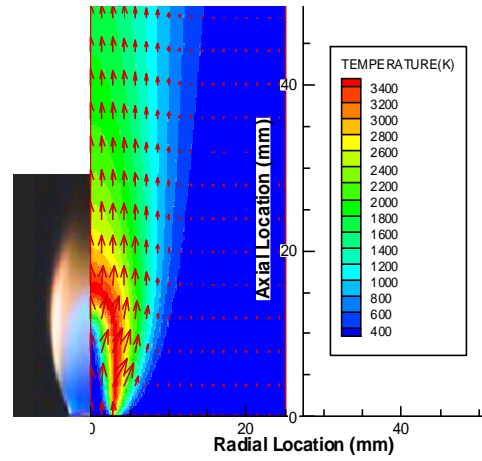


Figure 5.10 : Case 10

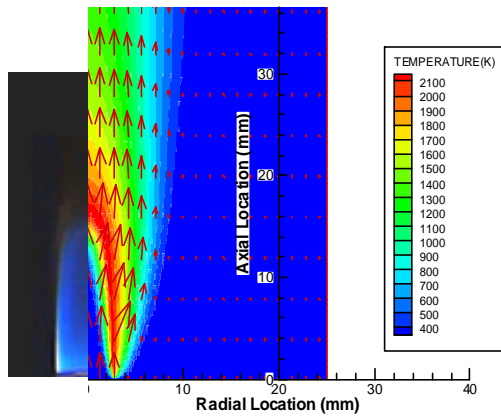


Figure 5.8 : Case 8

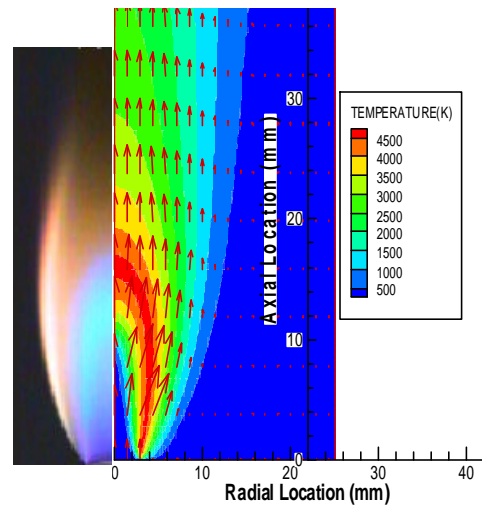


Figure 5.11 : Case 11

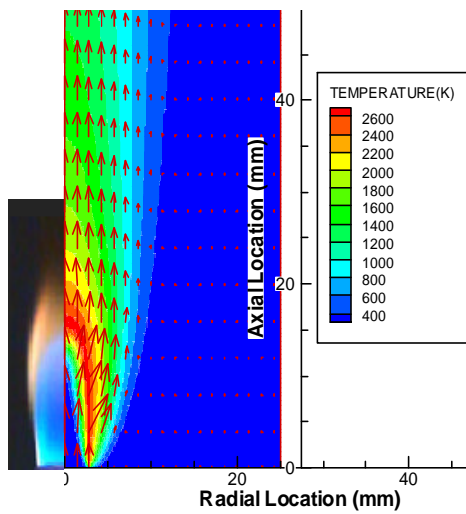


Figure 5.9: Case 9

Macro- vs. Micro-Vortex/Flame Interactions in Hydrogen Diffusion Flames

V. R. Katta* and T. R. Meyer
Innovative Scientific Solutions, Inc
2766 Indian Ripple Road
Dayton, OH 45440

J. R. Gord and W. M. Roquemore
Air Force Research Laboratory
Propulsion Directorate
Wright-Patterson Air Force Base, OH 45433

Abstract

Validity of the flamelet theory is examined by studying vortex/flame interactions in a hydrogen/air opposing-jet diffusion flame. The dynamic changes to the flame structure during the interaction process are investigated. Vortices are injected toward the flame surface from the air side. A centimeter-size vortex is made to interact with a 7.0-mm-thick flame, and a micron-size vortex is made to interact with a 2.4-mm-thick flame. High vortex propagation velocities are used for creating rapid flame extinction in both cases. Irrespective of the vortex propagation velocity, the larger vortex tends to create a wrinkled flame representative of a strained laminar flamelet, while the smaller vortex tends to replace the local fluid in the flame zone with the constituent fluid and create a distributed reaction zone. As the micron-size vortex is larger than the Kolmogorov length scale, a significant part of the fluid-chemistry interactions in turbulent diffusion flames may, therefore, be represented by distributed reaction zones rather than laminar flamelets.

Introduction

According to flamelet theory [1], the local instantaneous composition and temperature of the mixture in a nonpremixed system can be modeled as being the same as those in a stretched laminar diffusion flame. The mixture fraction and scalar dissipation rate are then used in linking the turbulent flame structure to that of the laminar flames. At a critical value of scalar dissipation rate, the laminar diffusion flame extinguishes due to large mixture fraction gradients. The reaction zone in physical space becomes so narrow that diffusive heat loss will lead to quenching. This scalar-dissipation-rate analogy has been used in flamelet theories in modeling extinction and ignition phenomena in turbulent flames. The unsteady effects in the reaction zone are usually considered by incorporating the unsteady diffusion of reactants and heat conduction [2]. Flamelet theories have been successfully applied to the modeling of various nonpremixed flame systems [3].

A necessary condition for flamelet concepts to apply is that the reaction zone must be thinner than the smallest scale of the turbulence, which is the Kolmogorov length scale. Performing asymptotic expansion for high Damkohler numbers for hydrogen flames, Bilger [4] derived an expression for reaction rate and argued that flamelets are not asymptotically thin due to the influence of reverse reactions; that is, the reaction zones are equilibrium broadened. Even though, the regular asymptotic analysis and the non-reacting experimental

data used by Bilger [4] are not ideal for judging the validity of the flamelet theories, they certainly raise important issues about the applicability of the flamelet theories to the turbulent-combustion process. It has been widely recognized that highly-resolved measurements and numerical simulations are needed for addressing the existence of laminar flamelets in turbulent-flow environments [5].

A numerical investigation is performed in the present study to aid the understanding of the extinction process associated with laminar flamelets and, thereby, verify the applicability of the laminar flamelet theory. Vortex/flame interactions, which are often considered to be the building blocks of statistical theories of turbulence, are utilized for establishing highly strained flamelets. These interactions were studied in the past for understanding the effects of curvature on unsteady flames [6]. In particular, experiments designed by Roberts et al. [7] and by Rolon et al. [8] have generated considerable interest, especially because of their unique ability to inject a well-characterized vortex toward the flame surface. In numerous investigations performed using the Rolon burner, the size and strength of the vortex have been varied in attempts to understand global features such as scale [9,10] and origin [11] effects and localized features such as annular-quenching [12] and nonadiabatic-equilibrium-temperature [13,14] phenomena.

Several mathematical models have also been developed for the study of the interaction between a planar flame and an induced vortex. In a majority of

*Corresponding Author, yrkatta@innssi.com

these models, it was assumed that an artificially created vortex pair (generated by specifying the vorticity field) interacts with a flat flame formed in a parallel flow. Although such an assumption has advantages in exploring interesting aspects of vortex/flame interactions, investigations employing these synthesized vortices do not represent actual interactions in opposing-jet flames and hence, cannot facilitate direct comparisons between predictions and measurements. To overcome these difficulties, two- and three-dimensional computational-fluid-dynamics models that incorporate detailed chemical kinetics (CFDC) have been developed [15,16]. Complete simulation of the opposing-jet flame using multi-dimensional models not only eliminated concerns regarding the simplified analyses but also provided a valuable tool for studying vortex/flame interactions. In the present investigation, a well-tested CFDC model [17] was used for understanding the flame structure near extinction and for testing the validity of flamelet theories.

Numerical Model

Time-dependent, axisymmetric Navier-Stokes equations written in the cylindrical-coordinate (z - r) system are solved along with species- and energy-conservation equations [16]. A detailed-chemical-kinetics model is used to describe the hydrogen-air combustion process. This model consists of thirteen species--namely, H_2 , O_2 , H , O , OH , H_2O , HO_2 , H_2O_2 , N , NO , NO_2 , N_2O , and N_2 . A detailed-chemical-kinetics model having 74 reactions among the constituent species is used; the rate constants for this H_2 - O_2 - N_2 reaction system were obtained from Ref. [18].

Temperature- and species-dependent property calculations are incorporated. The governing equations are integrated on a nonuniform staggered-grid system. An orthogonal grid having rapidly expanding cell sizes in both the axial and radial directions is employed. The finite-difference forms of the momentum equations are obtained using an implicit QUICKEST scheme [16], and those of the species and energy equations are obtained using a hybrid scheme of upwind and central differencing. At every time step the pressure field is calculated by solving the pressure Poisson equations simultaneously and utilizing the LU (Lower and Upper diagonal) matrix-decomposition technique. This model, called UNICORN (UNsteady Ignition and COmbustion with ReactionNs), has been extensively validated [17] by simulating various steady and unsteady counterflow [12] and coflow [16,19] jet diffusion flames and by comparing the results with experimental data.

Burner Details:

The opposing-jet-flame burner used for these studies was designed by Rolon [8]. The burner assembly consists of 25-mm-diameter nozzles (d_o), 40-mm-diameter outer

nozzles (D_o), and syringe tubes of 0.2-mm to 5-mm diameter (d_i). A flat flame is formed between the fuel and air jets having velocities of 0.69 and 0.5 m/s, respectively. An annular nitrogen flow of 0.1 m/s is used from both the fuel and air side nozzles. The hydrogen-to-nitrogen ratio employed for the fuel jet is 0.38. Only the region between the lower and upper nozzle exits was modeled in the present study. The fuel (d_o), air (d_o), nitrogen (D_o), and injection (d_i) jet diameters used in the simulations were identical to those used in the experiment. A comparison between experimental and numerical data for these conditions is available in the literature [14].

Results and Discussion

Calculations for the steady-state axisymmetric flame were made using a non-uniform 401 x 301 mesh system distributed over a physical domain of 40 x 40 mm, which yielded a mesh spacing of 0.1 mm in both the axial (z) and the radial (r) directions in the region of interest. A flat profile for the velocity is used at the exit of the each nozzle. The air-side strain rate along the stagnation line calculated from the rate of change in the axial velocity (u) with respect to the distance (z) is 48 s^{-1} . The peak temperature of 1560 K of this weakly strained flame is only slightly lower than the corresponding adiabatic-equilibrium flame temperature of 1598 K. The flame thickness based on temperature is 7.0 mm.

A centimeter-size vortex is generated on the air side by injecting air from the 5.0-mm diameter central injection tube. The interaction between the vortex and the flame is shown in Figs. 1(a)-(c) at three different phases. In order to have a rapid interaction, the fluid was introduced from the injection tube at a velocity of 160 m/s. When the vortex was far away from the flame [Fig. 1(a)] the structure of the latter was unaltered. The vortex has grown to 1.2 cm in diameter by the time it starts penetrating through the flame [Fig. 1(b)], and the flame thickness has reduced to ~ 2.0 mm. The flame is wrinkled (dimpled) before being extinguished at the center. In fact, flame wrinkling and thickness did not change much with vortices injected at a wide range of velocities. Finally, the flame is extinguished at the center and the vortex penetrates through the hole as shown in Fig. 1(c). This interaction process follows flamelet theory as the vortex increased the oxidizer fluxes into the flame zone and eventually extinguishes the flame when cooling becomes dominant.

The large-vortex/flame interaction suggests that flame thickness decreases to ~ 2 mm before the flame is extinguished. That means, in order to verify the validity of the flamelet theory, a sub-millimeter vortex must be injected toward the flame surface. To preserve the grid resolution for simulations of micron-size-vortex/flame interactions, a stationary opposing-jet flame is established between nozzles that are separated by 4 mm.

A grid system having 800 x 336 nodes and a spacing of 4 μm in the z and r directions is utilized. The generated steady-state flame has a thickness of ~ 2.4 mm based on the temperature profile. The vortex on the air side is generated by injecting fluid through an 80- μm diameter nozzle at a velocity of 75 m/s. The interaction between the micron-size vortex and the flame at three instants is shown in Figs. 1(d)-(f).

As expected, the vortex did not perturb the flame when it was far away as shown in Fig. 1(d). Interestingly, unlike the large-vortex/flame-interaction case, the micron-size vortex penetrated through the flame without wrinkling or dimpling the reaction zone [Fig. 1(e)]. The vortex grew to ~ 0.3 mm in diameter when it was penetrating through the flame. On the other hand, when the vortex was emerging from the flame zone, it carried hot products with it as seen in Fig. 1(f). This interaction process did not follow the typical flamelet theory. The flame is not stretched by the vortex at any instant.

To highlight the differences between the two vortex/flame interactions, evolutions of temperature, reactant concentrations, and OH concentration along the centerline are plotted in Figs. 2 and 3 for the large- and micron-size cases, respectively. Figure 2(a) shows the flame-thinning process associated with the large-vortex/flame interaction. On the other hand, the knife-edge pattern in temperature distribution in Fig. 3(a) suggests that the hot gases are replaced by the micron-size vortex. As described in our previous paper [14], the small-size vortices quickly become reactant deficient, entrain combustion products and carry high-temperature gases with them [green colored fluid between 0.1 and 0.2 ms in Fig. 3(a)]. Similarly, the diffusion process is evident in the reactant-evolution plots [Figs. 2(a) and 2(b)] shown for the large-vortex case, while discontinuous-type reactant propagation is seen in Figs. 3(b) and 3(c) for the micron-size case.

The flame structures at different instants are shown in Figs. 4 and 5 for the large- and micron-size vortex/flame interaction cases, respectively. The small kinks in the velocity profiles of the large-vortex case result from the combustion process due to volumetric expansion. The temperature profiles at different instants in Fig. 4(b) represent those of a stretched flame. Thickness and peak temperature decreased as the flame was stretched and translated (and wrinkled). On the other hand, during most of the micron-size-vortex/flame-interaction process, the flame temperature upstream of the vortex head was not perturbed [Fig. 5(b)]. When the vortex came out of the flame zone, it carried hot products with it. These temperature profiles suggest that the flame is not being stretched by the vortex.

The heat-release-rate profiles shown in Fig. 4(c) represent that of a stretched laminar flame. The peak heat release rate increased as the flame was stretched by the large-size vortex. Interestingly, the heat release rate near

the head of the micron-size vortex increased significantly [at 64 and 80 μs in Fig. 5(c)] even though it was not perturbed in the upstream locations. The peak values are clipped in Fig. 5(c) for clarity. At 64 μs the heat release rate increased to 3130 J/cm³/s, while at 80 μs it increased to 11,600 J/cm³/s. In comparison, the peak heat release rate only increased to 290 J/cm³/s in the case of a large-vortex/flame interaction. The super-high reactivity (40 times greater) in the micron-size vortex/flame interaction results from the mixing of products and air—not from flame stretch.

The micron-size vortex used in this study reached 0.3 mm in diameter when it was passing through the flame zone. This is much larger than the Kolmogorov length scale of 0.03 mm obtained based on the turbulence Reynolds number and length-scales of 500 and 3 mm, respectively. This implies that a significant portion of the length scales in a turbulent reacting flow promote mixing in the reaction zone rather than wrinkling the reaction layer. In other words, a significant part of the turbulence-chemistry interaction might not follow laminar flamelet theory.

Acknowledgment:

This work was supported, in part, by the Air Force Office of Scientific Research (Dr. Julian Tishkoff, Technical Monitor).

References:

1. N. Peters, *Proc. Combust. Inst.* 21 (1986) 1231-1256.
2. B. Cuenot, F. N. Egolfopoulos, and T. Poinso, *Combust. Theory Modeling* 4 (2000) 77-97.
3. S. K. Liew, K. N. C. Bray, J. B. Moss, *Comb. Flame*, 56 (1984) 199-213.
4. R. W. Bilger, *Proc. Combust. Inst.* 22 (1988) 475-488.
5. N. Peters, *Prog. Astronautics Aeronautics* 135 (1991) 155-182.
6. P. H. Paul, and H. N. Najm, *Proc. Combust. Inst.* 27 (1998) 43-51.
7. W. L. Roberts, J. F. Driscoll, M. C. Drake, J. W. Ratcliffe, *Proc. Combust. Inst.* 24 (1992) 169-177.
8. J. C. Rolon, F. Aguerre, S. Candel, *Combust. Flame* 100 (1995) 422.
9. P. H. Renard, D. Thevenin, J. C. Rolon, S. Candel, *Prog. Energy Combust. Sci.* 26 (2000) 225-282.
10. D. Thevenin, P. H. Renard, G. J. Fiechtner, J. R. Gord, J. C. Rolon, *Proc. Combust. Inst.* 28 (2000) 2101-2108.
11. V. R. Katta, and W. M. Roquemore, *Proc. Combust. Inst.* 28 (2000) 2055-2062.
12. V. R. Katta, C. D. Carter, G. J. Fiechtner, W. M. Roquemore, J. R. Gord, and J. C. Rolon, *Proc. Combust. Inst.* 27 (1998) 587-594.
13. K. Yoshida, and T. Takagi, *Proc. Combust. Inst.* 27 (1998) 685.
14. V. R. Katta, T. R. Meyer, J. R. Gord, and W. M. Roquemore, *Combust. Flame* 132 (2003) 639.
15. M. D. Smooke, A. Ern, M. A. Tanoff, B. A. Valdati, R. K. Mohammed, D. F. Marran, M. B. Long, *Proc. Combust. Inst.* 26 (1996) 2161-2168.
16. V. R. Katta, L. P. Goss, W. M. Roquemore, *AIAA J.* 32 (1994) 84.
17. W. M. Roquemore and V. R. Katta, *J. Visualization* 2 (2000) 257.
18. M. Frenklach, H. Wang, M. Goldenberg, G. P. Smith, D. M. Golden, C. T. Bowman, R. K. Hanson, W. C. Gardiner, V. Lissianski, Gas Research Institute Technical Report No. GRI-95/0058 (Gas Research Institute, Chicago), November 1, 1995.
19. V. R. Katta and W. M. Roquemore, *AIAA J.* 36 (1998) 2044.

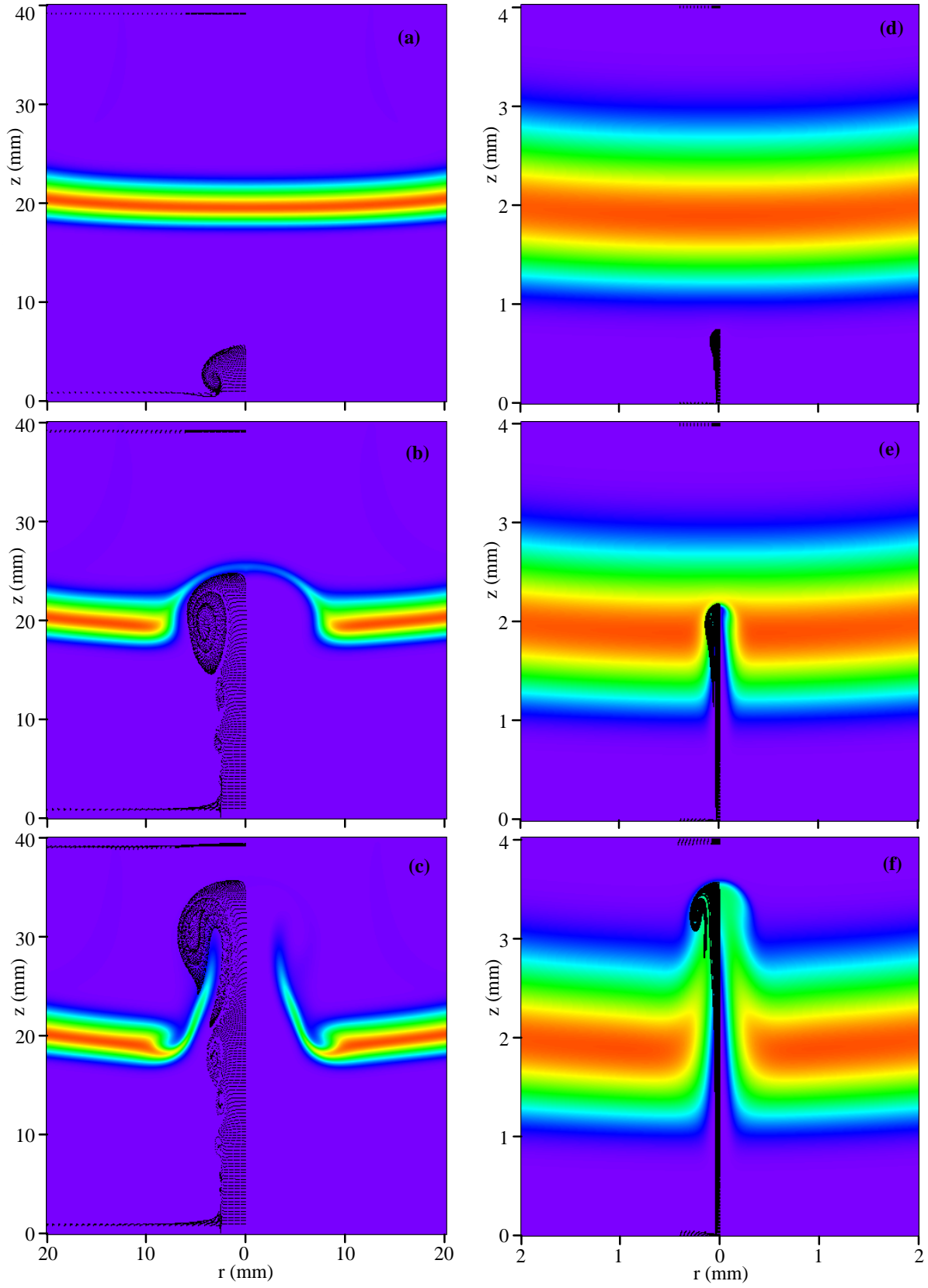


Fig. 1. Interaction of diffusion flame (a), (b), and (c) with large-size vortex and (d), (e), and (f) with micron-size vortex.

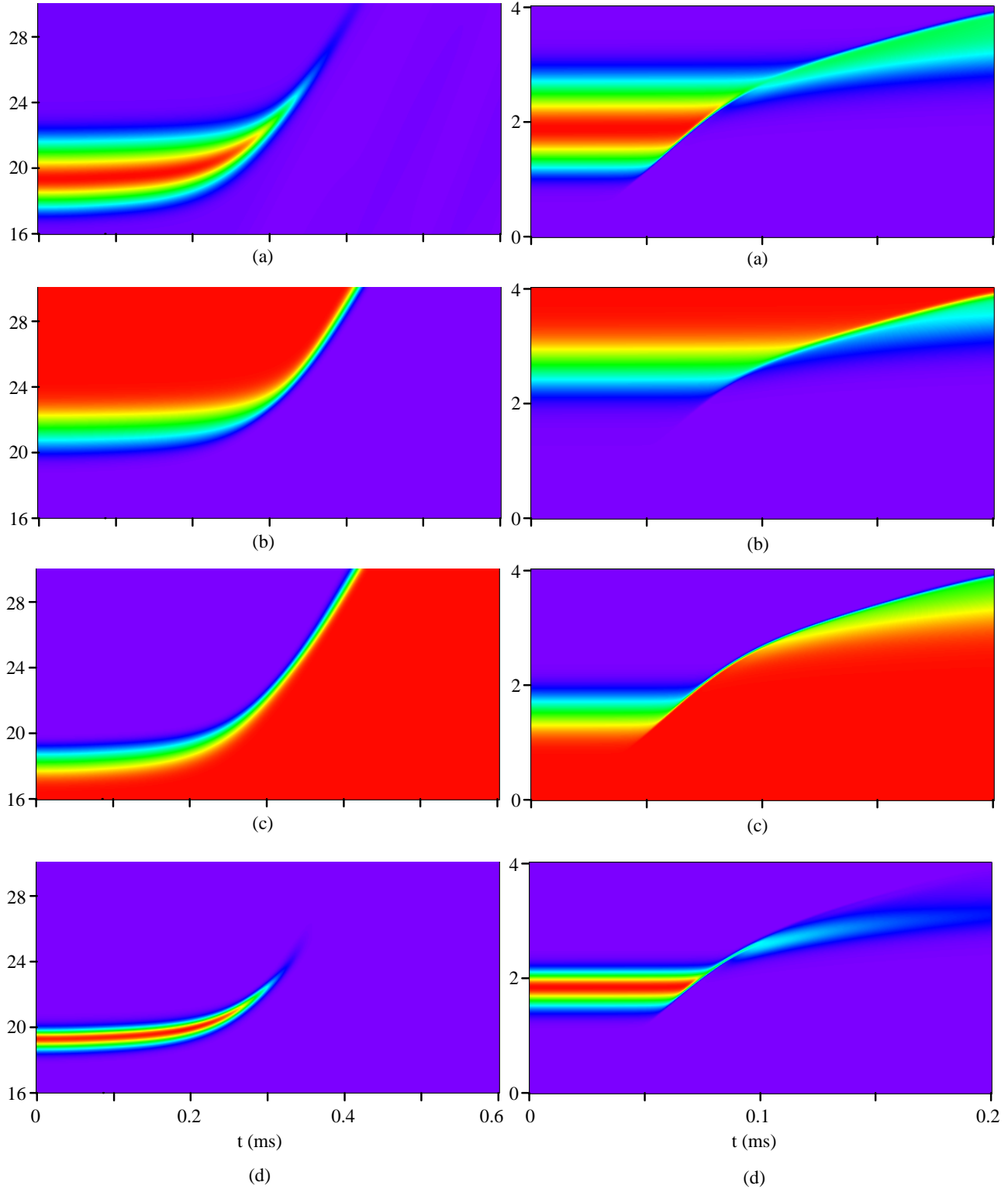


Fig. 2. Evolution of flame structure along centerline during interaction with cm-size vortex. (a) Temperature, (b) fuel concentration, (c) oxygen concentration, (d) OH concentration.

Fig. 3. Evolution of flame structure along centerline during interaction with micron-size vortex. (a) Temperature, (b) fuel concentration, (c) oxygen concentration, and (d) OH concentration.

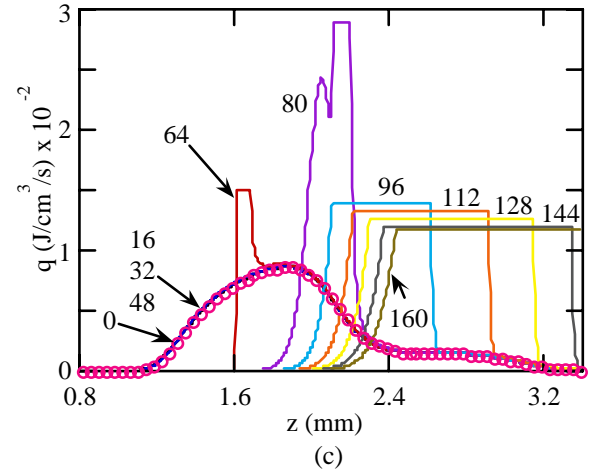
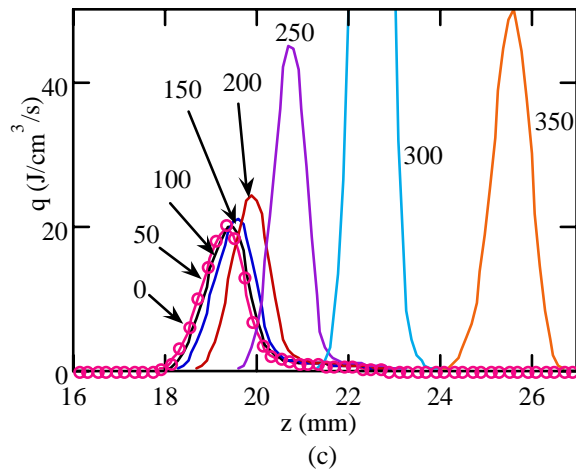
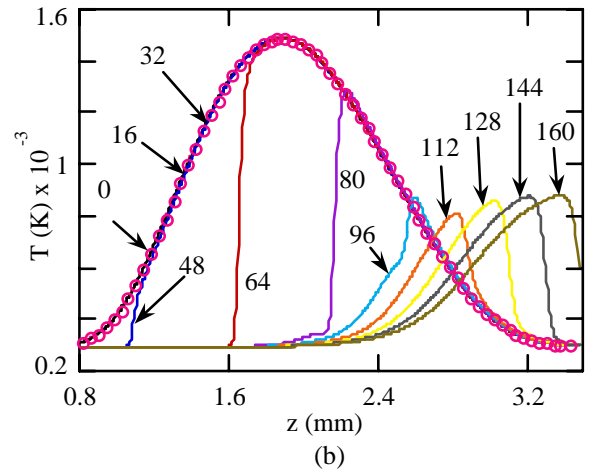
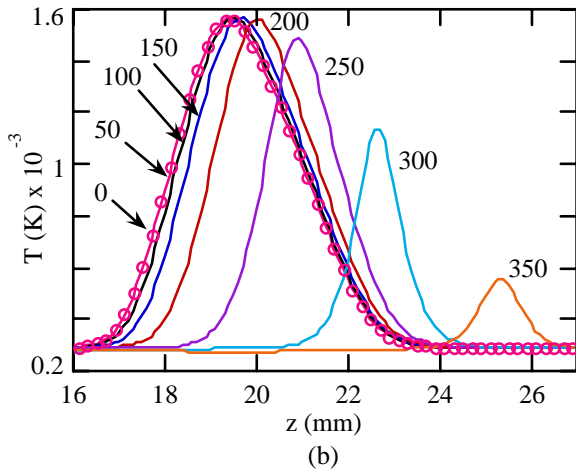
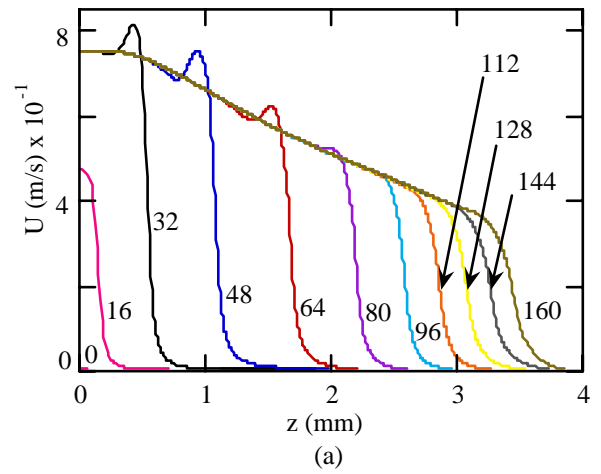
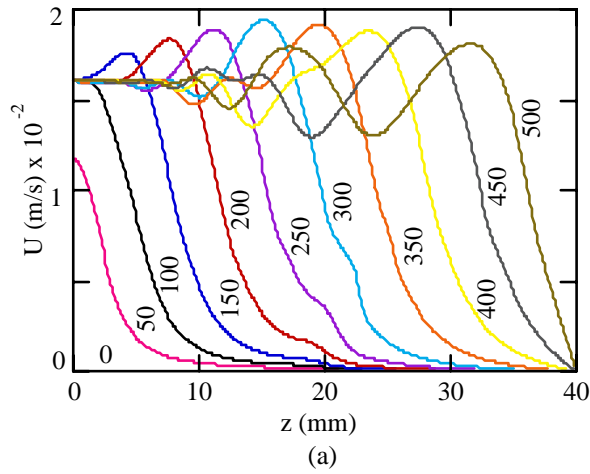


Fig. 4. (a) Velocity, (b) temperature, and (c) heat release rate at various instants during large-size-vortex/flame interaction. Numbers represent interaction time in μs .

Fig. 5. (a) Velocity, (b) temperature, and (c) heat release rate at various instants during micron-size-vortex/flame interaction. High values in heat release rate are clipped for clarity. Numbers represent interaction time in μs .

GT2004-54165

SIMULATION OF PAHS IN TRAPPED-VORTEX COMBUSTOR

Viswanath R. Katta
Innovative Scientific Solutions
2766 Indian Ripple Road
Dayton, OH 45440-3638
vrkatta@innssi.com

William M. Roquemore
Propulsion Directorate
Air Force Research Laboratory
Wright-Patterson Air Force Base, OH 45433-7103
melvyn.roquemore@wpafb.af.mil

ABSTRACT

Residence time and thermo-chemical environment are important factors in determining soot-formation characteristics of jet engine combustors. For understanding the chemical and physical structure of the soot formed in these combustors knowledge on flow dynamics and formation of polycyclic aromatics-hydrocarbons (PAHs) is required. A time-dependent, detailed-chemistry computational-fluid-dynamic (CFD) model is developed for the simulation of the reacting flows in a trapped-vortex combustor. The axisymmetric trapped-vortex combustor of Hsu et al. was modeled by replacing injection holes with injection slots. Ethylene-air mixtures were used as fuel. Several calculations were made by varying the equivalence ratio and velocity of the main flow. Unsteady simulations revealed that the shear-layer vortices established outside the cavity flow enhance mixing of benzene in the wake region of the afterbody. However, in all the cases considered here, majority of the PAH species are produced in the cavity region. While fuel-rich condition resulted lower amounts of PAHs in the cavity region, soot is produced more in this region.

INTRODUCTION

Unsteady flow in and around cavity-type geometries occurs in a variety of applications such as slotted wind tunnels, slotted flumes, bellows-type configurations, and aircraft-engine and airframe components. In particular, the unsteady flow in aircraft combustors restricts fuel-lean operation and degrades flame-stability characteristics. Hsu et al. [1] have proposed a simple, compact, and efficient method of using cavities to stabilize combustion. Since this concept uses a vortex that is trapped in a cavity [2] to stabilize the flame, it is referred as the Trapped-Vortex (TV) concept.

Experimental investigations of Hsu et al. [1] indicated that a trapped-vortex combustor operates most efficiently when fuel and air are injected directly into the

cavity. However, direct injection of mass (air and/or fuel) into the cavity could alter the geometrical criterion derived for locking vortices inside passive cavities (i.e., without injection). Because of this direct injection cavity flow in a trapped-vortex combustor experiences higher residence times and fuel-rich environment and may lead to increased production of pollutants and soot.

Considerable progress has been made in recent years in understanding the chemical and physical aspects of soot formation in hydrocarbon flames. After the first aromatic rings (such as benzene and small PAHs) are formed in the gas phase, acetylene and other molecules react with these small PAHs to form larger PAHs [3]. The first soot particles are thought to be formed when two or more PAHs react to form a three dimensional particle. This process is known as particle inception [4]. The soot particles formed interact with the gas-phase molecules by the addition of acetylene to their surfaces (surface growth) and by the reaction with molecular oxygen and/or hydroxyl radical (oxidation). Another process thought to increase soot mass is the collision of PAHs with a soot particle.

Several experimental and numerical investigations of soot formation have been performed using coflow and counterflow diffusion flames [5-8]. A few have focused on the importance of soot particle pathways (i.e., residence time, temperature, and chemistry) [9,10]. Santoro et al. [9] used soot volume fraction, temperature, and velocity measurements from an ethylene-air jet diffusion flame to examine the soot growth process along individual particle paths. Based on experimental data, they argued that the soot formation rate increases in the annular region of the flame due to an increase in residence time. Lin and Faeth [10] found that the direction of soot particle movement with respect to the flame sheet is important. They argued that if soot particles forming on the fuel rich side of the flame remained entrained in the fuel-rich region for a long time

before crossing the flame surface, then surface growth could be enhanced. In contrast, Lin and Faeth [10] argued that the amount of soot generated could be reduced if the soot particle is made to cross the flame surface quickly. Recent calculations of Katta et al. [11] have suggested that presence of large-scale structures in dynamic flames could influence the way PAH species are formed and hence, could impact the amount of soot produced. The purpose of this paper is to develop a time-dependent numerical model with detailed chemistry to examine the influence of large-scale structures on soot formation in combustors.

Various attempts have been made in the past to develop models for soot predictions. Some of these models are detailed, and have been calibrated against experimental data obtained in laminar, premixed or diffusion flames of simple configurations. For example, Frenklach and coworkers [12] proposed a detailed kinetic model of soot formation and validated [12,13] using measurements of laminar, premixed flames while Mauss, Bockhorn and their coworkers [14,15] established a different detailed soot model that was tested in laminar, counter-flow diffusion flames. The detailed kinetic soot model consists of 1) gas-phase chemistry and 2) kinetics describing the particle growth and destruction processes. The gas-phase chemistry describes the formation of PAHs [16,17]. The particle growth and destruction involve inception/ nucleation of particles resulting from coagulation of PAHs and are modeled via a set of surface reactions [12-15], and particle coagulation is modeled based on the method of moments [12-15] or the discrete-sectional method [18,19].

The complexity and the uncertainties associated with the detailed kinetic soot models made their application limited to simple laminar flames. On the other hand, for the simulation of turbulent combustor flows, a variety of simplified soot models that can be easily implemented into design codes have been proposed [20]. The most widely used models are based on the assumption that soot consists of particles with monodisperse size distribution. Then the soot formation, coupled directly to the fuel concentration, is modeled by one or two equations: one for the particle volume fraction and the other for the particle number density.

Leung et al. [21] argued that the intermediate species contributing to the soot particle formation should be connected to at least the pyrolysis kinetics of the fuel. For simplicity, they assumed acetylene to be the intermediate species and proposed a simplified soot model combined with the gas-phase kinetics of fuel pyrolysis for counterflow, ethylene and propane flames [21] as well as coflow, methane flames [22]. The results showed that with this approach good agreement with measured data for soot volume fraction, particle growth and number density could be obtained. In the present work, a model similar to that of Leung et al. [21] is used for the predictions of soot formation in combustors.

In the present work, numerical simulations for the reacting flows in a trapped-vortex combustor for different equivalence ratios were made using a well-

tested CFD code UNICORN. A detailed chemical kinetics model for PAH formation and a two-step model for soot formation was incorporated. Numerical results obtained for unsteady flames with different equivalence ratios are compared.

COMBUSTOR DESCRIPTION

The geometry chosen for the present study is similar to that of the trapped-vortex combustor designed by Hsu et al. [1]. Figure 1, obtained using a normal photographic camera with long exposure time, shows the flame and the combustor geometry for operation under a primary equivalence ratio (defined as fuel-to-air ratio injected into the cavity relative to the ratio required for stoichiometric combustion) of 4.4. The combustor consists of a 70-mm-diameter flat cylindrical forebody enclosed in an annular cylindrical tube having an 80-mm inner diameter. An afterbody disc having diameter and thickness of 50.8 and 20 mm, respectively, is attached to the forebody using a 9-mm-diameter centerbody. The size of the cavity formed between the forebody and the afterbody is varied by moving the latter toward or away from the former. Airflow over this body develops vortices inside the cavity and behind the afterbody; normally these vortices shed, and the flow becomes dynamic in nature. The velocity of the air in the annular gap between the forebody and the surrounding tube is varied between 10 and 40 m/s. Primary air and fuel are injected into the cavity from the afterbody. Fuel and air are carried to the afterbody through a central tube that connects the afterbody to the forebody. A grid system having 301X121 grid points with varying space is used to represent the axisymmetric trapped-vortex combustor in Fig. 1. Variations in the grid spacing in the axial (z) and radial (r) directions were allowed in such a way that the grid points are clustered in the cavity and near the walls.

In the experiments of Hsu et al. [1] fuel and air were introduced into the cavity from concentric holes on the afterbody. However, in the present axisymmetric simulations, these injection holes are grouped into three annular ring jets with the fuel jet sandwiched between the air jets. Based on the hole size and mean distance from the centerline, the reconstructed annular jets of 1.5-mm thickness are located in the afterbody. The centers of these three annular jets (A, B, and C in Fig. 1) are located 11, 14, and 19 mm from the axis of symmetry, respectively. While Jets A and C represent that of air, Jet B represents that of fuel. Exit velocities for air jets A and C are 2.0 m/s, and that for the fuel jet is either 0.625 m/s for case 1 or 1.625 m/s for case 2. These injections of fuel and primary air along with a 20-m/s main air flow resulted in global (or overall) equivalence ratios of 0.05 and 0.13 for case 1 and case 2, respectively. The corresponding primary equivalence ratios in the cavity are 2.11 and 5.5, respectively.

MATHEMATICAL MODEL

A time-dependent, axisymmetric mathematical model known as UNICORN (Unsteady Ignition and Combustion using ReactionNs) [23,24] is used to simulate

the potentially unsteady combustions flows considered in this study. It solves for u - and v -momentum equations, continuity, and enthalpy- and species-conservation equations on a staggered-grid system. The body-force term due to the gravitational field is included in the axial-momentum equation for simulating vertically mounted flames. A clustered mesh system is employed to trace the large gradients in flow variables near the flame surface. A detailed chemical-kinetics model of Wang and Frenklach [25] is incorporated into UNICORN for the investigation of PAH formation in C_2H_4 flames. It consists of 99 species and 1066 elementary-reaction steps. Thermo-physical properties such as enthalpy, viscosity, thermal conductivity, and binary molecular diffusion of all the species are calculated from the polynomial curve fits developed for the temperature range 300 - 5000 K. Mixture viscosity and thermal conductivity are then estimated using the Wilke and Kee expressions, respectively. Molecular diffusion is assumed to be of the binary-diffusion type, and the diffusion velocity of a species is calculated using Fick's law and the effective-diffusion coefficient of that species in the mixture. Turbulence is modeled using k - ϵ approach. A simple radiation model based on the optically thin-media assumption is incorporated into the energy equation. Only radiation from CH_4 , CO , CO_2 , H_2O , and soot is considered in the present study [26].

The finite-difference forms of the momentum equations are obtained using an implicit QUICKST scheme [27], and those of the species and energy equations are obtained using a hybrid scheme of upwind and central differencing. At every time step, the pressure field is accurately calculated by solving all the pressure Poisson equations simultaneously and using the LU (Lower and Upper diagonal) matrix-decomposition technique. The boundary conditions are treated in the same way as that reported in earlier papers [28].

Soot Model

Computational soot models based on the fundamental physics of soot formation and oxidation are not yet available. The research groups around Moss and Lindstedt have made some progress in modeling soot formation using semiempirical models based on the mechanisms of particle inception, agglomeration, surface growth, and oxidation. The two groups utilized two equation models with transport equations for particle number density, N_s , and soot mass fraction, Y_s . These equations can be written for unsteady flow as

$$\frac{\partial \rho N_s}{\partial t} + \nabla \cdot (\rho \mathbf{V} N_s) - \nabla \cdot (\rho \mathbf{D}_{N_s} \nabla N_s) = \omega_{N_s} \quad (1)$$

$$\frac{\partial \rho Y_s}{\partial t} + \nabla \cdot (\rho \mathbf{V} Y_s) - \nabla \cdot (\rho \mathbf{D}_s \nabla Y_s) = \omega_s \quad (2)$$

where \mathbf{V} is the velocity vector, ρ is density, D is the molecular diffusion coefficient, and ω is the production term from chemical reactions. The two source terms in Eqs. 1 and 2 are obtained using Lindstedt's model [29],

which is based on the simplifying assumption that nucleation and growth are first-order functions of acetylene concentrations. The underlying chemical reactions for nucleation and growth are similar and given as



with the reaction rates

$$r_1 = k_1(T) [C_2H_2]$$

and

$$r_2 = k_2(T) f(A_s) [C_2H_2]$$

for nucleation and growth, respectively, where $f(A_s)$ denotes a functional dependence on soot surface area per unit volume. Brookes and Moss [30] analyzed the functional dependence of the soot growth rate on A_s and found that under simplified conditions with no soot oxidation and radiation the appropriate functional dependence is linear and therefore $f(A_s)$ is set equal to A_s .

The reaction steps for O_2 and OH oxidation can be written as



The reaction rates for equations (4) and (5) are approximated by $r_3 = k_3(T) A_s [O_2]$ and $r_4 = k_4(T) A_s [OH]$.

The expression for O_2 oxidation is essentially the one derived by Lee et al. [31]. Reaction rate constants for OH attack on soot particles are taken from Bradley et al. [32] and a collision efficiency of 0.04 [33] is assumed.

Using the above expressions, the source terms for soot mass fraction and particle density can be obtained from

$$\begin{aligned} \omega_s = & 2k_1(T) [C_2H_2] M_s + 2k_2(T) A_s [C_2H_2] M_s \\ & - k_3(T) A_s [O_2] M_s - k_4(T) A_s [OH] M_s \end{aligned} \quad (6)$$

and

$$\begin{aligned} \omega_{N_s} = & 2k_1(T) [C_2H_2] N_a/n_{c,min} \\ & - 2C_a (d_p)^{1/2} (6\sigma_B T/\rho_s)^{1/2} (\rho_{N_s})^2 \end{aligned} \quad (7)$$

The last term on the right of Eq. 7 accounts for the decrease in particle number density by particle agglomeration. Here $\sigma_B = 1.38 \times 10^{-23}$ J/K is the Boltzmann constant, M_i is the molecular weight of species i , $N_A = 6.0232 \times 10^{26}$ is the Avogadro number, $C_a = 9$ is the agglomeration constant, and $n_{c,min} = 60$ is the minimum particle number required for particle nucleation. The density of the soot particles (ρ_s) is assumed to be 1800 kg/m^3 . The particle surface area is defined by

$$A_s = \pi (d_p)^2 \rho N_s \quad (8)$$

with the particle diameter, d_p , given as

$$d_p = (6 Y_s / \pi \rho_s N_s). \quad (9)$$

Finally, soot volume fraction (f_v) is calculated from soot mass fraction using the relationship $f_v = \rho Y_s / \rho_s$.

RESULTS AND DISCUSSION

Model Validation Studies:

The CFD model UNICORN has been extensively validated in the past by simulating various steady and unsteady counterflow [23,34] and coflow [23,35] jet diffusion flames and by comparing the results with experimental data. This gives confidence that UNICORN can simulate the structure of dynamic flames accurately. However, the integration of C_2H_4 and PAH chemistry into UNICORN needs to be validated to establish the accuracy of the present predictions. Validation is achieved by simulating the burner-stabilized flame extensively investigated by Harris et al. [36] and Wang and Frenklach. [25]

The flame chosen is a premixed $C_2H_4/O_2/Ar$ flame with an equivalence ratio of 2.76. The velocity of the cold reactants is 7.8 cm/s. The $Ar:O_2$ mole ratio is 79:21. Two-dimensional calculations for this burner-stabilized flame are made by enforcing periodic boundary conditions at the two boundaries in the axial (z) direction and by using the measured temperature profile as input. These two-dimensional calculations eventually resulted in a one-dimensional flame with all the variations in the radial direction diminished.

Variations in concentrations of several species with respect to flame height are compared with experimental data in Fig. 2. The temperature profile used in these calculations has a peak value of 1657 K [Fig. 2(a)]. The calculations predict the proper trends in major species concentrations, such as the decrease in O_2 and C_2H_4 concentrations and the increase in CO and CO_2 concentrations. However, the computed concentrations for H_2 are somewhat lower than the measurements. This discrepancy was also observed by Wang and Frenklach [25] while modeling this flame using CHEMKIN and was attributed to the higher concentrations of OH obtained with the present chemical mechanism.

The experimental and measured mole fractions of CH_4 , C_2H_2 , C_4H_4 , and C_4H_6 at different heights are compared in Fig. 2(b). The key intermediate species are generally predicted well by the model. The computed peak concentrations of these species are within a factor of two of the measured values, which is probably within the experimental uncertainty. Similarly, the predicted concentration profiles of one-ring aromatics compare well with the measured ones shown in Fig. 2(c). The steady rise of aromatics is typical of C_2H_4 burner-

stabilized flames and is well reproduced by the Wang/Frenklach mechanism. Based on the comparisons shown in Fig. 2 it is assumed that the modified UNICORN model can reasonably simulate an C_2H_4 flame.

Trapped-Vortex Combustor Flows:

Calculations for the axisymmetric trapped-vortex combustor described earlier (Fig. 1) were made for two equivalence-ratio cases. No swirl to the main or primary flows was used. The computed instantaneous flow field for cavity equivalence ratio of 2.11 (case 1) is shown in Fig. 3(a) by plotting velocity vectors and iso-temperature contours in the left and right halves, respectively. Computed flow in the cavity, which resulted from the net effect of recirculation created by the main flow and the penetrating flow of the injection jets, is nearly in steady state. The structure of a trapped vortex is not apparent in the velocity field as the injection jets modified the stationary (trapped) vortex established in the cavity by the main flow and the size of the cavity. Temperature field also indicates that the flow of combustion products from the cavity over the disk is associated with only weak unsteady shedding. This was confirmed by making animation of the time-dependent solution. The shedding frequency is 1165 Hz. The weak vortex shedding from the cavity suggests that the global vortex structure in the cavity represents a locked vortex. Note that the design strategy used by Hsu et al. [1] for determining the cavity size was based on the conditions for obtaining locked vortices in cold flows without primary injection. For this cavity size, cold-flow calculations also showed locked vortices within the cavity and behind the afterbody. Absence of strong vortex shedding from the cavity, noted from the reacting flow calculations made with primary injection (Fig. 3), suggests that the locked-vortex criterion obtained using cold annular flow yields locked vortices (overall) in the reacting flow case also. Additional calculations must be performed with different cavity sizes before a general conclusion can be reached regarding locked vortices in cold and reacting flows. The near confinement of OH field to cavity region [Fig. 3(b)] suggests that most of the combustion is taking place within the cavity and products are only mixing with the main airflow in the downstream locations. Similarly, most of the PAH species present only in the cavity region. However, benzene [Fig. 3(c)] and phenyl radical seem to accumulate in the region downstream of the afterbody and the amount of accumulation is influenced by the vortex shedding (or large-scale mixing) in the shear layer.

The instantaneous soot volume fraction and the number density are shown on the left and right halves of Fig. 3(d), respectively. Significant amount of soot is formed in the cavity region and some of it is destroyed through oxidation in the downstream locations. Soot particles are also growing in size in the relatively low velocity region downstream of the afterbody.

Calculations made for the fuel-rich condition (case 2) with an equivalence ratio of 5.5 are shown in Fig. 4. Here, the air injection into the cavity and that of primary were not changed when compared to those used in case 1. Instead, fuel injection rate was increased to achieve the fuel-rich condition. Overall, the flame became longer with burning taking place up to ~ 80 mm downstream of the afterbody. As expected, with the higher heat release in this fuel-rich case, the shedding frequency for the shear-layer vortices has decreased to 820 Hz.

Reduced amounts of PAHs have formed in the cavity region for this condition and the excess fuel is generating additional PAHs in the downstream locations. However, as seen in Fig. 4(d), the soot produced in the cavity region is more than that obtained in case 1 [Fig. 3(d)]. This is in support with the experiments which indicated that the fuel-rich conditions yield higher soot in the cavity.

CONCLUSIONS

A time-dependent, axisymmetric, detailed-chemistry CFD model was developed for the simulation of combustor flows inside a trapped-vortex combustor. PAH formation was simulated using the 99-species, 1066-reactions mechanism of Wang and Frenklach. Soot formation is modeled using a two-variable approach and turbulence is modeled using k and ϵ equations. The CFD model (UNICORN) was validated by simulating a burner-stabilized premixed flame and comparing the results with measurements. The axisymmetric trapped-vortex combustor of Hsu et al. was modeled by replacing injection holes with injection slots. Several calculations were made by varying the equivalence ratio (by changing the fuel flow) and velocity of the main flow. Unsteady simulations captured the shear-layer vortices established between the higher primary air-jet velocity and the cavity flow. In all the cases considered here, majority of the PAH species are produced in the cavity region. However, benzene and biphenyl seem to accumulate in the wake region of the forebody. Fuel-rich condition resulted lower amounts of PAHs in the cavity region. On the other hand, significant amount of soot is produced in this region.

ACKNOWLEDGEMENTS

Financial support for this work was provided by Strategic Environmental Research and Development Program (SERDP, Charles Pellerin), the Air Force Office of Scientific Research (AFOSR, Julian Tishkoff) and the Air Force Contract #F33615-00-C-2068 (Vince Belovich).

REFERENCES

- Hsu, K. Y., Goss, L. P., Trump, D. D., and Roquemore, W. M., "Characteristics of a Trapped-Vortex Combustor," *Journal of Propulsion and Power*, Vol. 14, No. 1, 1998.
- Little, B. H., and Whipkey, R. R., "Locked Vortex Afterbodies," *Journal of Aircraft*, Vol. 16, No. 5, 1979, pp. 296-302.
- Richter, H. and Howard, J. B., *Prog. Energy Combust. Sci.* 26:565 (2000)
- Kennedy, I. M., *Prog. Energy Combust. Sci.* 23:95 (1997)
- Kaplan, C. R., and Kilasanath, K., *Combustion and Flame*, Vol. 124, 2001, pp. 275-294.
- Smooke, M. D., Mcenally, C. S., Pfefferle, L. D., Hall, R. J., and Colket, M. B., *Combustion and Flame*, Vol. 117, 1999, pp. 117-139.
- Sugiyama, G., *Proceedings of the Combustion Institute*, The Combustion Institute, PA, Vol. 25, 1994, pp. 601-608.
- Du, J., and Axelbaum, R. L., *Combustion and Flame*, Vol. 100, 1995, pp. 367-375.
- Santoro, R. J., Yeh, T. T., Horvath, J. J., and Semerjian, H. G., *Combustion Science and Technology*, Vol. 53, 1987, pp. 89-115.
- Lin, K.-C., and Faeth, G. M., *Journal of Propulsion and Power*, Vol. 12, 1996, pp. 10-17.
- Katta, V. R., Blevins, L. G., and Roquemore, W. M., *PAH Formation in an Inverse Diffusion Flame*, AIAA Paper No. 2003-0666, Reno, NV, 2003.
- Frenklach, M. and Wang, H., *Twenty-third Symposium (International) on Combustion*, The Combustion Institute, Pittsburgh, 1991, pp.1559-1566.
- Frenklach, M. and Wang, H., in *Soot Formation in Combustion: Mechanisms and Models* (H. Bockhorn, Ed.), Springer-Verlag, Heidelberg, 1994, pp.165-189.
- Mauss, F., Schäfer, T. and Bockhorn, H., *Combust. Flame* 99:697-705 (1994).
- Mauss, F. and Bockhorn, H., *Z. Phys. Chem.* 188:45 (1995).
- Haynes, B.S. and Wagner, H. GG., *Prog. Energy Combust. Sci.* 7:229-273 (1981).
- Calcote, H.F., *Combust. Flame* 42:215-242 (1981).
- Colket, M.B. and Hall, R.J., in *Soot Formation in Combustion: Mechanisms and Models* (H. Bockhorn, Ed.), Springer-Verlag, Heidelberg, 1994, pp.442-468.
- Hall, R.J., Smooke, M.D. and Colket, M.B., in *Physical and Chemical Aspects of Combustion: A Tribute to Irvin Glassman* (F.L. Dryer and R.F. Sawyer, Eds.), Gordon and Breach, Amsterdam, 1997, pp.189-230.
- Hiroyasu, H., Kadota, T. and Arai, M., *Bulletin of the JSME* 26:569-575 (1983).
- Leung, K.M., Lindstedt, R.P. and Jones, W.P., *Combust. Flame* 87:289-305 (1991).
- Lindstedt, R.P., in *Soot Formation in Combustion: Mechanisms and Models* (H. Bockhorn, Ed.), Springer-Verlag, Heidelberg, 1994, pp.417-439.
- Roquemore W. M., and Katta, V. R., *Journal of Visualization*, in press Jan. 2000.
- Katta, V. R., and Roquemore, W. M., *Combustion and Flame*, Vol. 100, No. 1, 1995, p. 61.
- Wang, H., and Frenklach, M., *Combustion and Flame*, Vol. 110, No. 1, 1997, p. 173.

26. Annon., Computational Submodels, International Workshop on Measurement and Computation of Turbulent Nonpremixed Flames., <http://www.ca.sandia.gov/tdf/Workshop/Submodels.html>, 2001.
27. Katta, V. R., Goss, L. P., and Roquemore, W. M., *AIAA Journal*, Vol. 32, No. 1, 1994, p. 84.
28. Katta, V. R., Goss, L. P., and Roquemore, W. M., *Int. J. Num. Methods Heat Fluid Flow*, Vol. 4, No. 5, 1994, p. 413.
29. Lindstedt, P. R., in *Soot Formation in Combustion* (H. Bockhorn, Ed.), Springer Verlag, Heidelberg, 1994, p. 417.
30. Brookes, S. J., and Moss, J. B., *Combust. Flame*, 116:486 (1999).
31. Lee, K. B., Thring, M. W., and Beer, J. M., *Combust. Flame* 6:137 (1962).
32. Bradley, D., Dixon-Lewis, G., El-Din Habik, S., and Mushi, E. M. J., *Twentieth Symposium (International) on Combustion*, The Combustion Institute, Pittsburgh, 1984, p. 931.
33. Puri, R., Santoro, R. J., and Smyth, K. C., *Combust. Flame* 97:125 (1994).
34. Katta, V. R., Carter, C. D., Fiechtner, G. J., Roquemore, W. M., Gord, J. R., and Rolon, J. C., in *Twenty-seventh Symposium (International) on Combustion*, The Combustion Institute, Pittsburgh, PA, 1998, p. 98.
35. Katta, V. R., and Roquemore W. M., *AIAA Journal*, Vol. 36, No. 11, 1998, p. 2044.
36. Harris, S., Weiner, A. M., and Blint, R., *Combustion and Flame*, Vol. 72, 1988, pp. 91-109.

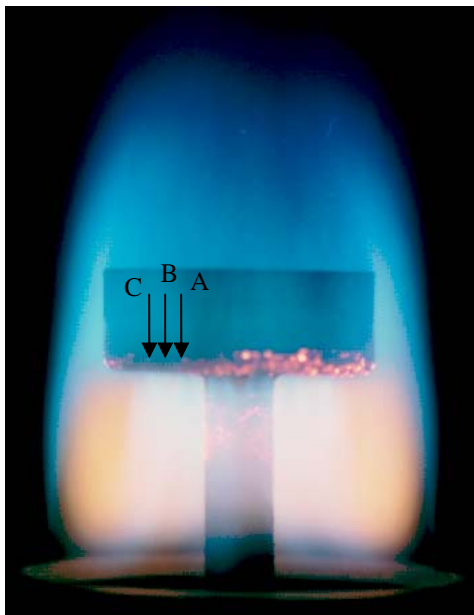


Fig. 1. Direct photograph of the trapped-vortex combustor.

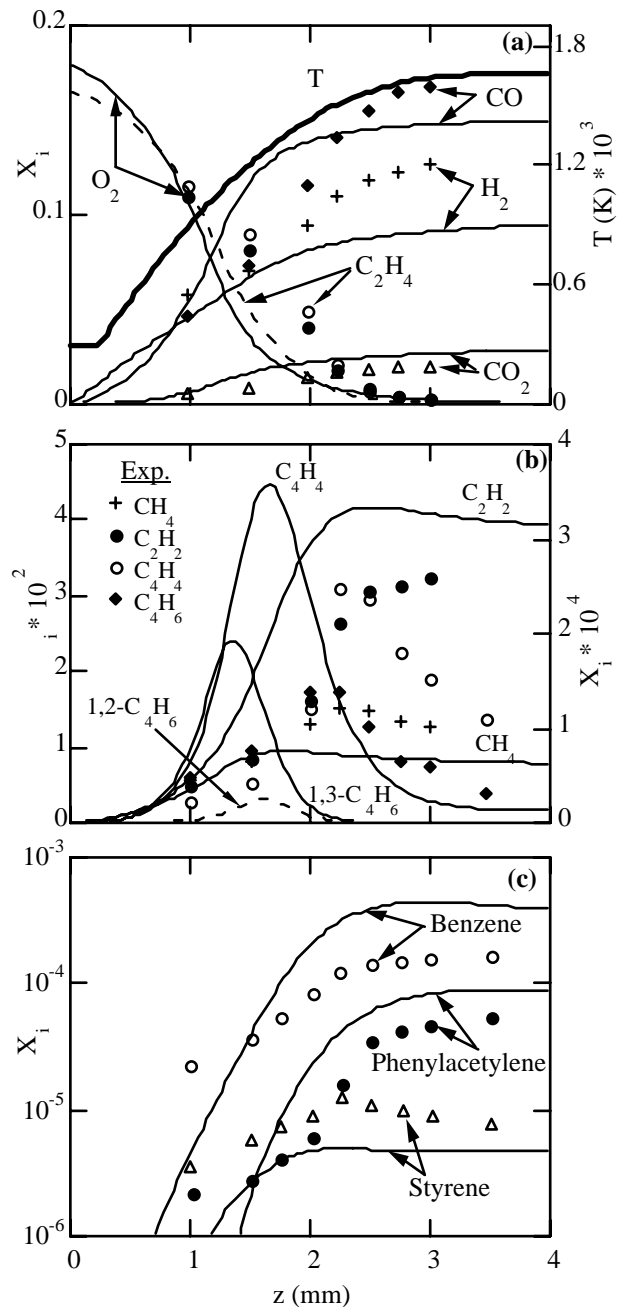
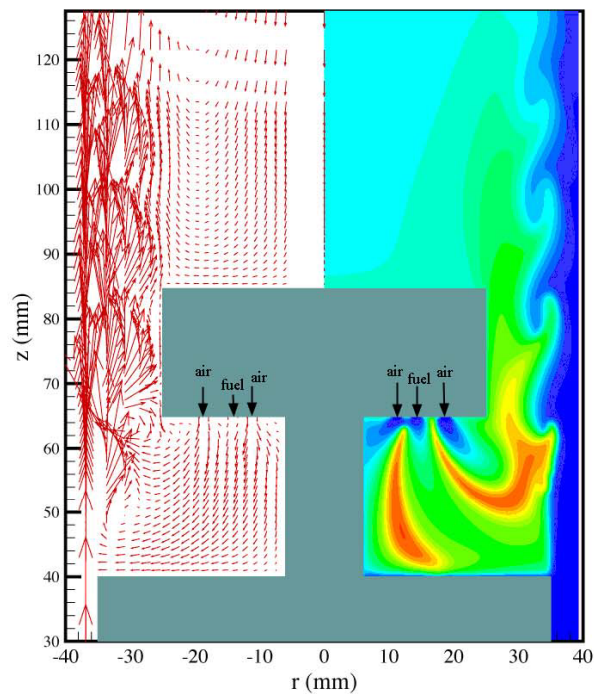
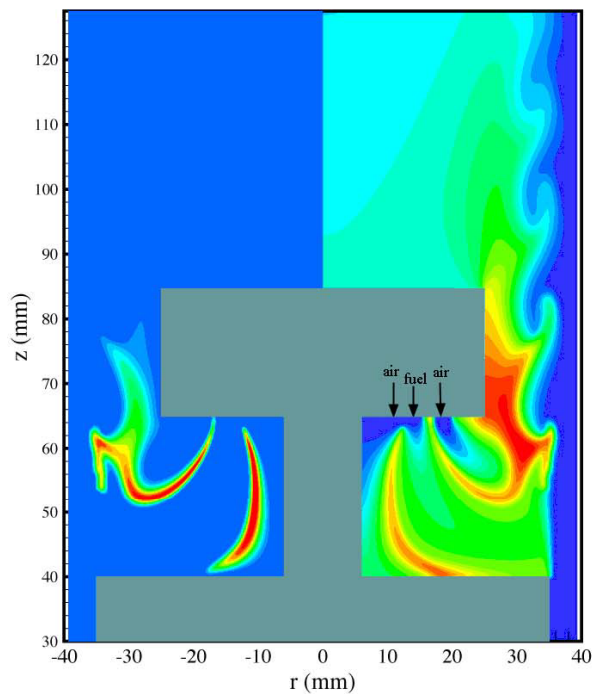


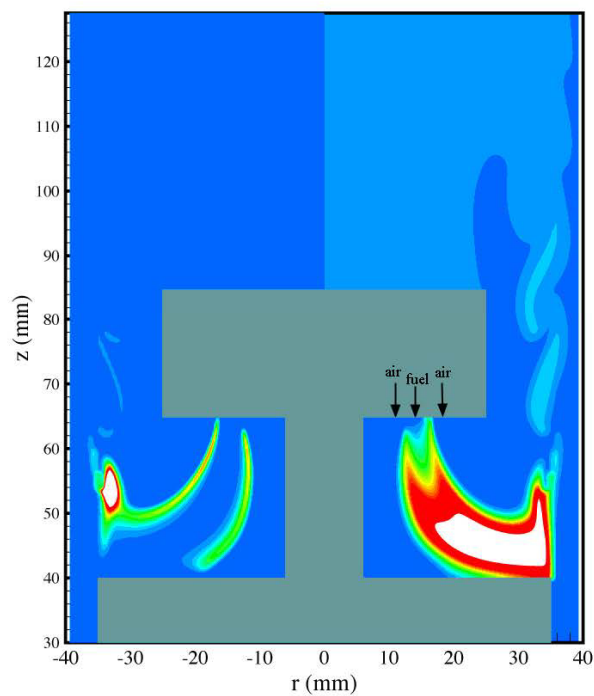
Fig. 2. Comparison between measured and computed species distributions for the burner-stabilized premixed flame. Calculations for this one-dimensional flame were made using UNICORN and by imposing temperature profile shown in (a).



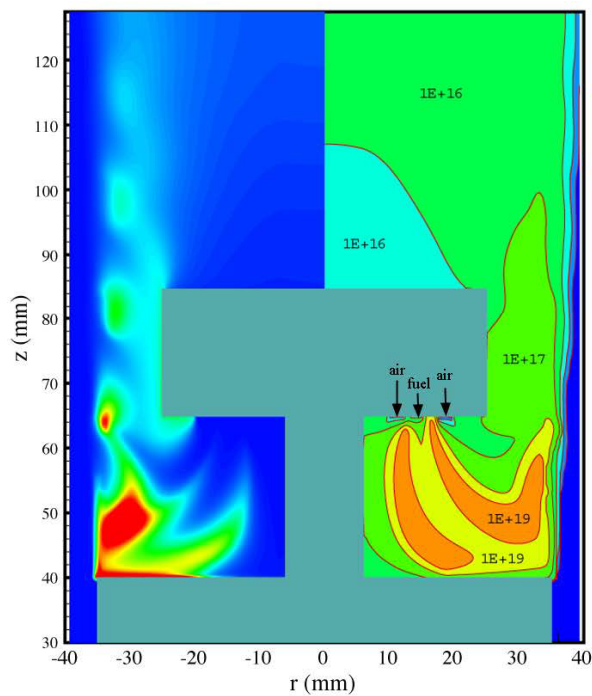
(a)



(b)

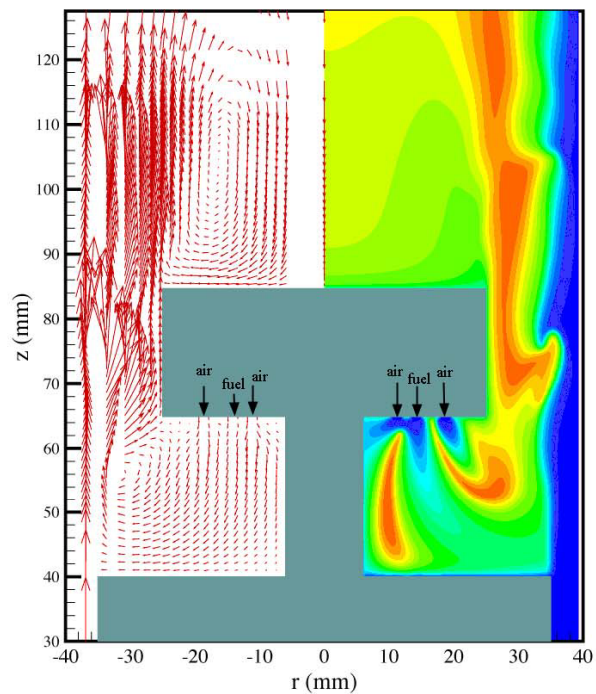


(c)

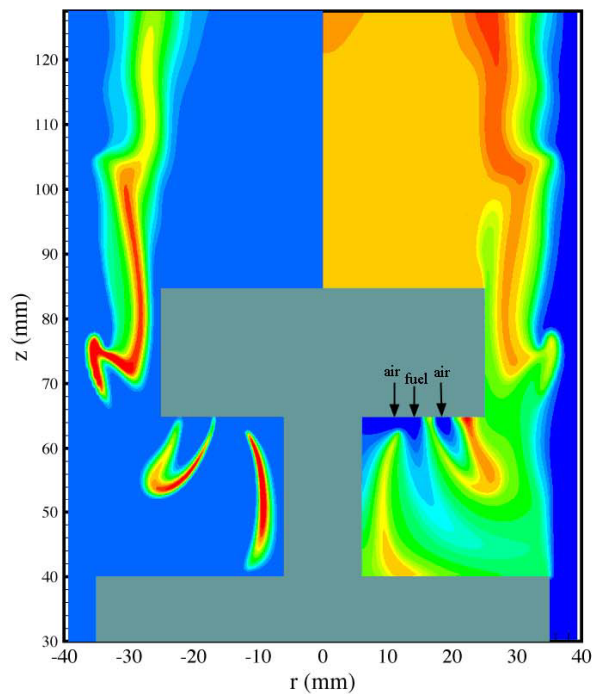


(d)

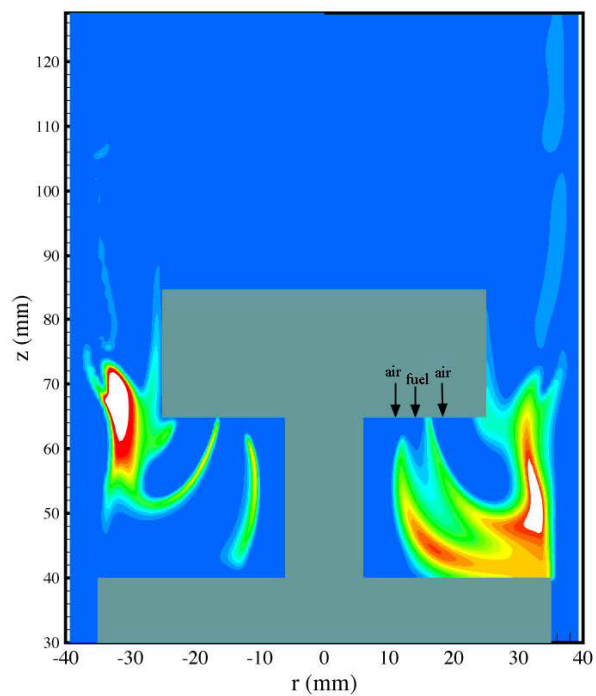
Fig. 3. Flow field obtained for stoichiometry condition. (a) Velocity and temperature, (b) mole fractions of OH (left) and CO₂ (right), (c) mole fractions of phenyl (left) and benzene (right), (d) soot volume fraction (left) and no. density (right)



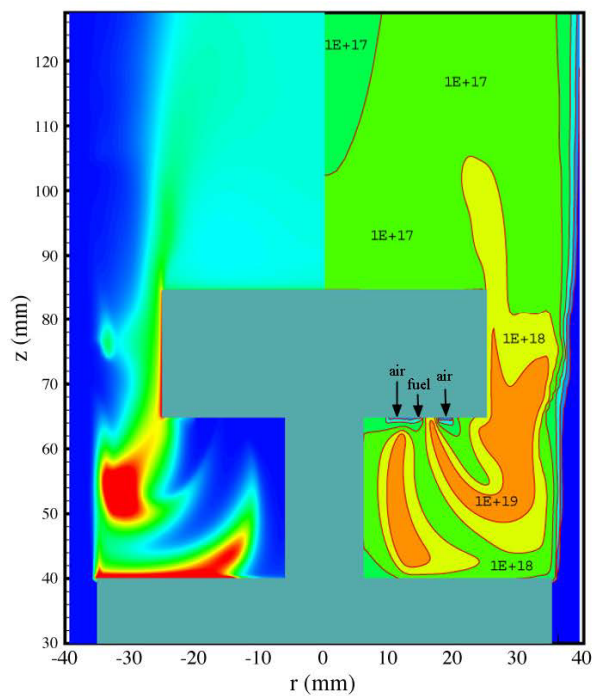
(a)



(b)



(c)



(d)

Fig. 4. Flow field obtained for a fuel-rich condition. (a) Velocity and temperature, (b) mole fractions of OH (left) and CO₂ (right), (c) mole fractions of phenyl (left) and benzene (right), (d) soot volume fraction (left) and no. density (right)

Gravity, radiation, and coflow effects on partially premixed flames

Xiao Qin^{a)}

Department of Mechanical and Aerospace Engineering, Princeton University, Princeton, New Jersey 08544

Ishwar K. Puri^{b)} and Suresh K. Aggarwal

Department of Mechanical and Industrial Engineering, University of Illinois at Chicago, 842 West Taylor Street, Chicago, Illinois 60607-7022

Viswanath R. Katta^{c)}

Innovative Scientific Solutions, Inc., Dayton, Ohio 45440

(Received 6 November 2003; accepted 4 May 2004; published online 1 July 2004)

Our objective is to characterize gravity effects on the structure of laminar methane–air partially premixed flames through detailed simulations. We examine the heat loss due to radiation from similar flames that are established at various gravitational accelerations and coflow velocities. Radiation is modeled using the optically thin assumption that provides a limiting value for the radiation heat transfer. We have validated the simulations with measurements in a representative 1-g flame. The predictions are in good agreement with the measured reaction zone topologies and temperature distributions. The simulations show that when the gravitational acceleration for a representative 1-g partially premixed double flame is instantaneously decreased to zero, it is possible to establish a nearly steady 0-g flame in roughly 2.2 s. The overall effect of radiation on the structure of the 1-g flame is relatively insignificant in contrast to the corresponding 0-g flame. Due to radiation effects, the heights of both the inner premixed and outer nonpremixed reaction zones in the 0-g double flame increase, and the heat release rate intensity near the premixed reaction zone tip decreases. When radiation effects are not included in the simulations, the peak temperatures are nearly the same for the 1-g and 0-g flames. However, with radiation the difference in these temperatures is significant. The decrease in the peak temperature due to radiation for the 0-g flame is nearly five times larger than for the 1-g flame. The value of the radiation fraction for 0-g flames without coflow can be as large as 50%, although it drops significantly in the presence of a coflow. While the flowfields upstream of the inner premixed reaction zone are nearly identical for 1-g and 0-g double flames, they are markedly different in the regions between the two reaction zones as well as downstream of the outer nonpremixed reaction zone. The maximum flame temperatures and local heat-release rates increase as the gravitational acceleration increases, while the radiation fractions and inner flame heights decrease. The flickering frequency also increases from 14.7 Hz at 1-g to 41.4 Hz at 10-g and follows the correlation $St \propto Fr^{-0.57}$ that is in accord with a previous compilation of normal gravity data. The radiation Damköhler number is inversely proportional to the Froude number. The radiation fraction decreases with increasing coflow, and the differences between the maximum flame temperatures and heat-release rates for 1-g and 0-g flames become less pronounced. Results for triple flames are in accord with those for double flames. © 2004 American Institute of Physics. [DOI: 10.1063/1.1764835]

I. INTRODUCTION

Partially premixed flames (PPFs) are hybrid flames containing multiple reaction zones. They can exploit the advantages of both nonpremixed and premixed flames regarding safety, lower pollutant emission levels, and flame stability.^{1,2} A detailed understanding of the structure of PPFs is important from both practical and scientific considerations. Unwanted fires can originate in a partially premixed mode when

a pyrolyzed or evaporated fuel forms an initial mixture with the ambient air.³ Partially premixed flames occur in many applications including gas-fired domestic burners, industrial furnaces, and Bunsen burners. Partial premixing also occurs under other circumstances, such as in turbulent combustion due to local extinction and reignition processes,⁴ in lifted flames,^{5,6} and in practical spray systems due to the presence of locally fuel vapor-rich regions.^{7,8} Partially premixed combustion may also be encountered in future space applications or spaceship fires,^{9,10} and thus it is meaningful to investigate gravitational effects on PPFs from this perspective.

The effects of gravity on premixed and nonpremixed flames have been extensively investigated over the last decade. Law and Faeth,¹⁰ Kono *et al.*,¹¹ and Ronney¹² have provided detailed reviews of experimental and computational

^{a)}Telephone: 609-258-7975; fax: 609-258-6123. Electronic mail: xqin@princeton.edu

^{b)}Author to whom correspondence should be addressed. Telephone: 312-355-3317; fax: 312-996-8664. Electronic mail: ikpuri@uic.edu

^{c)}Telephone: 937-255-8781; fax: 937-429-9734. Electronic mail: Viswanath.Katta@wpafb.af.mil

studies dealing with such 1-*g* and microgravity (μ -*g*) flames under different configurations. However, the corresponding literature regarding PPFs under 1-*g* and μ -*g* conditions is sparse. It is known that PPFs contain multiple reaction zones and their structure is determined by the transport and thermochemical interactions between these reaction zones.^{1,2,13–15} We have previously presented computational results of gravity effects on these interactions. For double flames, i.e., PPFs containing an inner rich premixed and an outer nonpremixed reaction zone, we observed that the absence of gravity increases the spatial separation between the reaction zones, since diffusive transport is enhanced relative to advection as buoyant entrainment of the oxidizer is eliminated.¹³ These effects increase the effective flame volume in a μ -*g* flame compared to its 1-*g* counterpart. In addition, the spatial characteristics of the inner premixed region were found to be mostly unaffected by the gravitational acceleration, while the outer nonpremixed zones exhibited significant differences. Another investigation indicated that the overall structure of a triple flame is determined by interactions between its three reaction zones, which can be influenced by changes in the mean velocity, equivalence ratio, and gravitational acceleration.¹⁴ While the inner rich premixed reaction zone is weakly influenced by gravity, the central nonpremixed and outer lean premixed reaction zones exhibit significant differences at 0-*g* and 1-*g*.

Since the high temperature regions are much broader for PPFs at 0-*g*, thermal radiation effects can become significant as the role of gravity is diminished. The radiative cooling time τ_{rad} for a gaseous volume of combustion products that is initially at its adiabatic flame temperature T_f is $\tau_{\text{rad}} = [\gamma/(\gamma - 1)]P/[4\sigma K_p(T_f^4 - T_0^4)]$,¹² where γ is the heat capacity ratio, P the pressure, σ the Stefan–Boltzmann constant, K_p the Planck mean absorption coefficient, and T_0 the ambient temperature. Assuming $P = 1$ atm, $K_p = 56 \text{ cm}^{-1}$, $\gamma = 1.35$, $T_0 = 298 \text{ K}$, and partially premixed flame temperatures to vary from 1650 to 2200 K (in the inner premixed and outer nonpremixed reaction zones), the corresponding τ_{rad} values lie in the range 0.3–0.09 s. The diffusive transport time scale can be represented as $\tau_d = \delta^2/\alpha$ and the corresponding buoyant transport time scale as $\tau_b \approx L/V_b$, where δ is the transport zone thickness, α the thermal diffusivity, and L the representative length. $V_b \approx [gL(\Delta\rho/\rho)]^{1/2}$ is the buoyancy-induced velocity (g is the gravity acceleration constant and ρ the density). In general, $\Delta\rho/\rho \approx 1$, so that $\tau_b \approx (L/g)^{1/2}$.¹² Representative values for α and g are taken to be $1.5 \text{ cm}^2 \text{ s}^{-1}$ and 980 cm s^{-2} , respectively. For $1 \leq L \leq 10 \text{ cm}$, τ_b varies from 0.03 to 0.1 s. For τ_d to lie within these bounds, $\delta = 2\text{--}4 \text{ mm}$. This thickness depends on the level of partial premixing and the velocities of the reactant streams. Therefore, if the transport zone thickness exceeds 4 mm (as is the norm in the flames that we have investigated¹⁴), $\tau_b < \tau_d$, i.e., gravitational effects overwhelm transport effects. Radiation effects are of less significance in normal gravity, since $\tau_b < \tau_{\text{rad}}$. However, $\tau_b \rightarrow \infty$ as $g \rightarrow 0$, implying that radiation effects may be significant under microgravity conditions. Moreover, since the role of molecular transport becomes more important as the gravitational acceleration is reduced, it is also possible that $\tau_{\text{rad}} \approx \tau_d$.

A careful investigation of the interactions between transport, buoyancy, and thermal radiation should increase our understanding of PPFs. It is important to quantify these effects under different flow conditions. The objective of this investigation is to examine gravity effects on the structure of laminar methane–air PPFs. We will focus on quantifying the heat loss due to radiation by comparing the results for flames established at various gravitational accelerations and the competing influence of coflow-induced advection.

II. NUMERICAL METHOD

A. Governing equations

The computational model is based on the algorithm developed by Katta *et al.*¹⁶ and the simulation method is described in detail elsewhere.^{1,13–15} The numerical model solves time-dependent governing equations for an axisymmetric reacting flow. Using cylindrical coordinates, these equations can be written in the form

$$\begin{aligned} \frac{\partial(\rho\Phi)}{\partial t} + \frac{\partial(\rho v\Phi)}{\partial r} + \frac{\partial(\rho u\Phi)}{\partial z} \\ = \frac{\partial}{\partial r} \left(\Gamma^\Phi \frac{\partial\Phi}{\partial r} \right) + \frac{\partial}{\partial z} \left(\Gamma^\Phi \frac{\partial\Phi}{\partial z} \right) - \frac{\rho v\Phi}{r} + \frac{\Gamma^\Phi}{r} \frac{\partial\Phi}{\partial r} + S^\Phi. \end{aligned} \quad (1)$$

Here t is the time, and u and v represents the axial (z) and radial (r) velocity components, respectively. The general form of the equation represents conservation of mass, momentum, species, or energy conservation equation, depending on the variable used for Φ . The transport coefficient Γ^Φ and source terms S^Φ appearing in the above equation are provided in Table 1 of Ref. 1. Introducing the overall species conservation equation and the perfect gas state equation completes the set of equations. In addition, a sink term based on an optically thin gas assumption is included in the energy equation to account for thermal radiation in the flame. This is described in the following section. The methane–air chemistry is modeled using a detailed mechanism that considers 24 species and 81 elementary reactions.¹⁷ The mechanism has been validated for the computation of premixed flame speeds and the structure of nonpremixed and PPFs.^{18,19}

Figure 1 presents the geometry of the axisymmetric coannular burner and computational domain. The computational domain of $100 \times 50 \text{ mm}^2$ in the axial (z) and radial (r) directions, respectively, is represented by a staggered, non-uniform (401×151)-grid system. The inner burner wall of 0.8 mm thickness is simulated by an insert body maintained at an isothermal temperature. The outflow boundaries in both directions are located sufficiently far from the respective inflow and symmetric boundaries so that the propagation of boundary-induced disturbances is minimized. At the inflow boundary, the fully developed pipe flow in the inner tube and flat-velocity profiles outside the inner tube (when outer flow velocity V_{out} is not zero) were used. The temperature and species mass fraction profiles are assumed to be uniform at the inflow boundary.

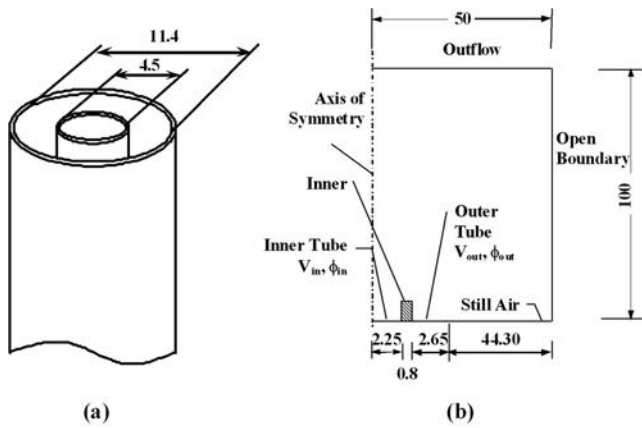


FIG. 1. A schematic diagram of the axisymmetric burner (a) and computational domain (b). The dimensions are in unit of millimeter.

B. Thermal radiation model

An optically thin radiation model has been frequently used in combustion simulations, including investigations on the flammability limit for premixed flames,^{20–22} NO_x formation,^{23,24} flame structure,²⁵ and extinction¹⁸ of PPFs. According to the optically thin approximation, the sink term due to the radiation heat loss q_{rad} is²⁶

$$q_{\text{rad}} = -4\sigma K_p(T^4 - T_0^4), \quad (2)$$

where T is the local flame temperature. K_p accounts for the absorption and emission from the participating gaseous species CO₂, H₂O, CO, and CH₄, and is expressed as

$$K_p = P \sum_k X_k K_{p,k}, \quad (3)$$

where $K_{p,k}$ denotes the mean absorption coefficient of species k . Its value is obtained by using a polynomial approximation to the experimental data provided in Ref. 27.

The radiation fraction χ_{rad} is taken as the ratio of total radiation heat loss Q_{rad} to total heat released Q (heat of combustion), i.e.,

$$\chi_{\text{rad}} = Q_{\text{rad}}/Q. \quad (4)$$

The heat of combustion is calculated by integrating the local heat-release rate in the volume encompassed by the computational domain, i.e.,

$$Q = \int_V q dV \approx \sum_{i,j=1}^{NI,NJ} q_{i,j} \Delta V_{i,j}, \quad (5)$$

where V is the volume of the computational domain, $\Delta V_{i,j} = \pi(r_{i+1,j}^2 - r_{i,j}^2)(z_{i,j+1} - z_{i,j})$, NI and NJ are the numbers of grid points in the axial and radial directions, respectively, and $q_{i,j}$ is the local heat-release rate expressed as

$$q = q_{i,j} = \sum_{k=1}^K H_k \omega_k, \quad (6)$$

where H_k and ω_k is enthalpy and net production rate of k th species, respectively. The total radiation heat loss can be obtained by integrating the local radiation heat loss over the volume, i.e.,

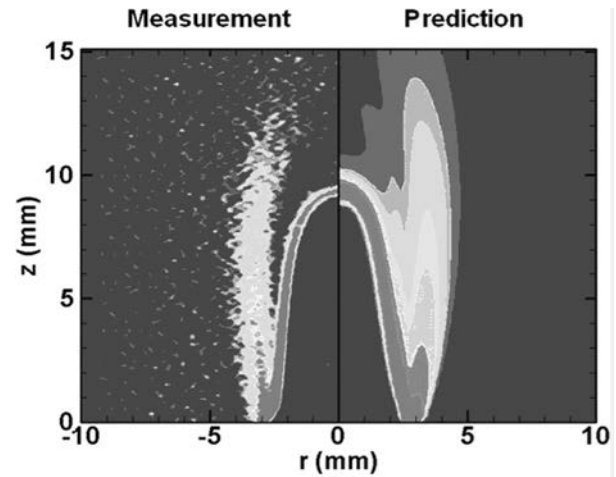


FIG. 2. Comparison between measured C_2^* -chemiluminescence intensity (left) and predicted heat-release rates (right) for a methane–air double flame of $\phi_{\text{in}}=2.0$ and $\phi_{\text{out}}=0$, with $V_{\text{in}}=0.6 \text{ m s}^{-1}$ and $V_{\text{out}}=0.5 \text{ m s}^{-1}$.

$$Q_{\text{rad}} = \int_V q_{\text{rad}} dV \approx \sum_{i,j=1}^{NI,NJ} q_{\text{rad}} \Delta V_{i,j}. \quad (7)$$

III. RESULTS AND DISCUSSION

A. Validation of numerical model

The numerical model has been previously validated for both burner-stabilized and lifted methane–air PPFs.^{2,28} Additional validation of the model is provided herein by comparing the predicted and measured flame topologies and temperature distributions for a 1-g partially premixed methane–air double flame. Figure 2 presents a comparison of the predicted heat-release rate contours with the experimentally obtained C_2^* -chemiluminescence intensities for this flame. The flow conditions are $\phi_{\text{in}}=2.0$, $V_{\text{in}}=0.6 \text{ m s}^{-1}$, $\phi_{\text{out}}=0$, and $V_{\text{out}}=0.5 \text{ m s}^{-1}$, where ϕ_{in} and ϕ_{out} are the mixture equivalence ratios of the inner and outer tubes, while V_{in} and V_{out} the mean flow velocities as of the inner and outer tubes, respectively. The optically thin radiation model was included in this simulation. We have found the C_2^* -chemiluminescence to be a good marker of the heat-release and reaction zones.²⁸ In Fig. 2, the C_2^* -chemiluminescence image for the flame is normalized by multiplying each pixel intensity by a constant value, which is the ratio of the maximum heat-release rate to the maximum pixel intensity. The measurement and prediction are in good agreement with respect to the topologies of both the inner rich premixed and outer nonpremixed reaction zones. Both the simulated heat-release rates and the chemiluminescence image indicate that the reaction intensities peak at the flame base, where the inner and outer reactions are merged. This high reactivity region has been termed as the “reaction kernel” by Takahashi *et al.*²⁹ Its presence is due to the combined effects of flame curvature and premixing that primarily occur in the vicinity of the burner rim. The reaction intensity decreases along the side of the inner premixed zone, and the heat-release rate also progressively decreases downstream along the outer nonpremixed reaction zone. The nonpre-

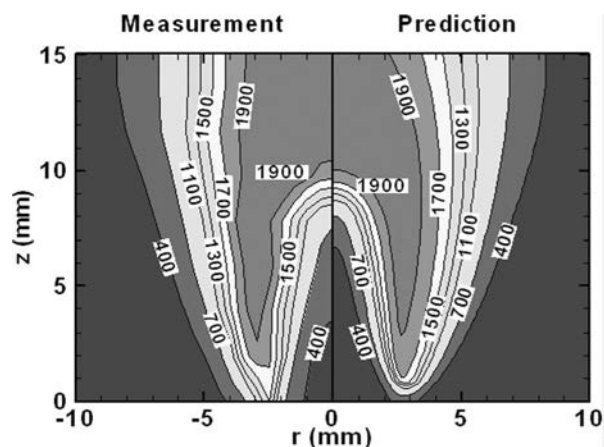


FIG. 3. Comparison between predicted (left) and measured (right) temperature distributions for the flame corresponding to Fig. 2.

mixed reaction zone exhibits a weak tip, as shown in Fig. 2, for both the chemiluminescence image and the simulation.

Figure 3 presents a comparison between the measured and predicted temperature distributions for the flame considered in Fig. 2. The measurements are made using rainbow Schlieren deflectometry.³⁰ The measured temperatures show evidence of a small amount of heat transfer to the burner rim, which is not shown by the predictions due to the imposed boundary conditions. Regardless of this upstream discrepancy, there is generally good agreement between the measured and predicted temperatures at downstream locations. Both the measurement and the prediction indicate that the premixed reaction zone is relatively thin, and the region with the highest temperatures lies between the inner premixed and outer nonpremixed reaction zones. The measured maximum temperature is slightly higher (2159 K vs 2021 K) than the corresponding predicted value. This is attributed to the uncertainties in both the measurements and predictions (e.g., related to the chemical mechanism and the thermodynamic and transport properties). The maximum measurement error lies near the centerline on the rich side of the inner premixed flame because of a constant refractivity assumption.³¹

B. Simulations of 0-g PPFs

Since the numerical solution employs a time-dependent algorithm, two different approaches can be employed to obtain a stable PPF at 0-g. One is to ignite the mixture at the beginning of a 0-g simulation and allow it to attain a steady state structure. The other approach is to first simulate a steady flame at 1-g, and then change the gravitational acceleration to zero and continue the time marching until a steady 0-g flame is obtained. The experimental analogs of both methods have been used in drop-tower experiments and their differences have been discussed by Bahadori *et al.*³² They observed that laminar jet nonpremixed flames did not reach steady state as the temperature fields were still evolving at the end of the drop period. Urban *et al.*³³ and Lin *et al.*³⁴ conducted long-duration tests in the space shuttle and observed that nonpremixed soot-containing hydrocarbon flames were almost twice as long as μ -g flames observed in

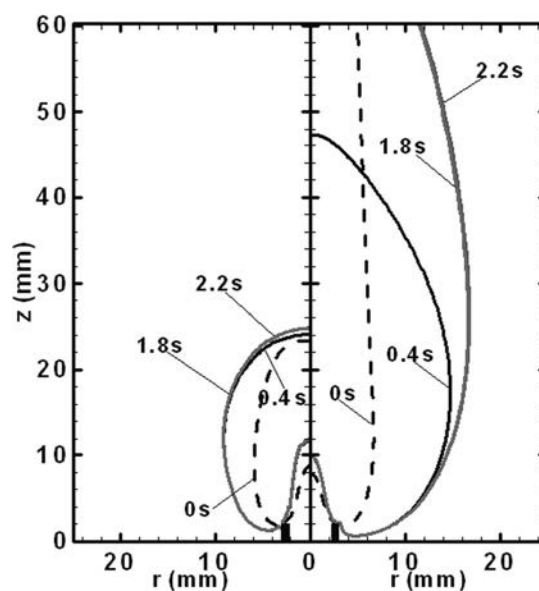


FIG. 4. Temporal evolution of the selected heat-release rate (left) and temperature contours (right) for a 0-g PPF at the conditions of $\phi_{in}=2.5$, $V_{in}=0.3 \text{ m s}^{-1}$, $\phi_{out}=0$, and $V_{out}=0$. The heat-release rate contour has a value of $100 \text{ kJ m}^{-3} \text{ s}^{-1}$, while the temperature contour has a value of 600 K.

ground-based drop-tower facilities. Similar trends may be expected for PPFs and it is worthwhile to examine these transient aspects in order to understand the influence of changing gravitational acceleration.

Figure 4 presents the temporal evolution for a 0-g PPF simulated using the second approach, i.e., when a stable 1-g flame is subjected to a sudden 0-g condition at $t=0$. The evolution is shown in terms of a selected value of heat-release rate contour ($100 \text{ kJ m}^{-3} \text{ s}^{-1}$) and an isotherm contour (600 K) plotted at different times. The flow conditions are $\phi_{in}=2.5$, $V_{in}=0.3 \text{ m s}^{-1}$, $\phi_{out}=0$, and $V_{out}=0$. The initial 1-g flame at $t=0$ is represented by broken lines. It becomes rounder and broader during its evolution to a steady 0-g flame. The inner premixed reaction zone reaches steady state rapidly, but the outer nonpremixed flame evolves over a longer duration. In addition, the heat-release rate reaches steady state much faster than the temperature. For example, the specified heat-release rate contour at 0.4 s is near that at 1.8 s and 2.2 s, but the temperature contour at $t=0.4 \text{ s}$ appears to be still developing. Since $\tau_d \approx \tau_{rad}$, the isotherm is influenced both by diffusion and radiation. Nonetheless, the isotherms at 1.8 s and 2.2 s are nearly identical, suggesting that a nearly steady state is established at 2.2 s. Therefore, the “steady” 0-g flames discussed in the following sections are those corresponding to $t=2.2 \text{ s}$.

C. Effect of radiation on 1-g and 0-g flames

Figure 5 presents the flame structures in terms of the heat-release rate and temperature contours for 1-g and 0-g flames simulated with and without the radiation model. The flow conditions are the same as for the flame in Fig. 4. All flames exhibit a double-flame structure. For the 1-g flames [cf. Figs. 5(a) and 5(b)], the heat-release rate contours indicate that the heights of both the inner premixed and outer

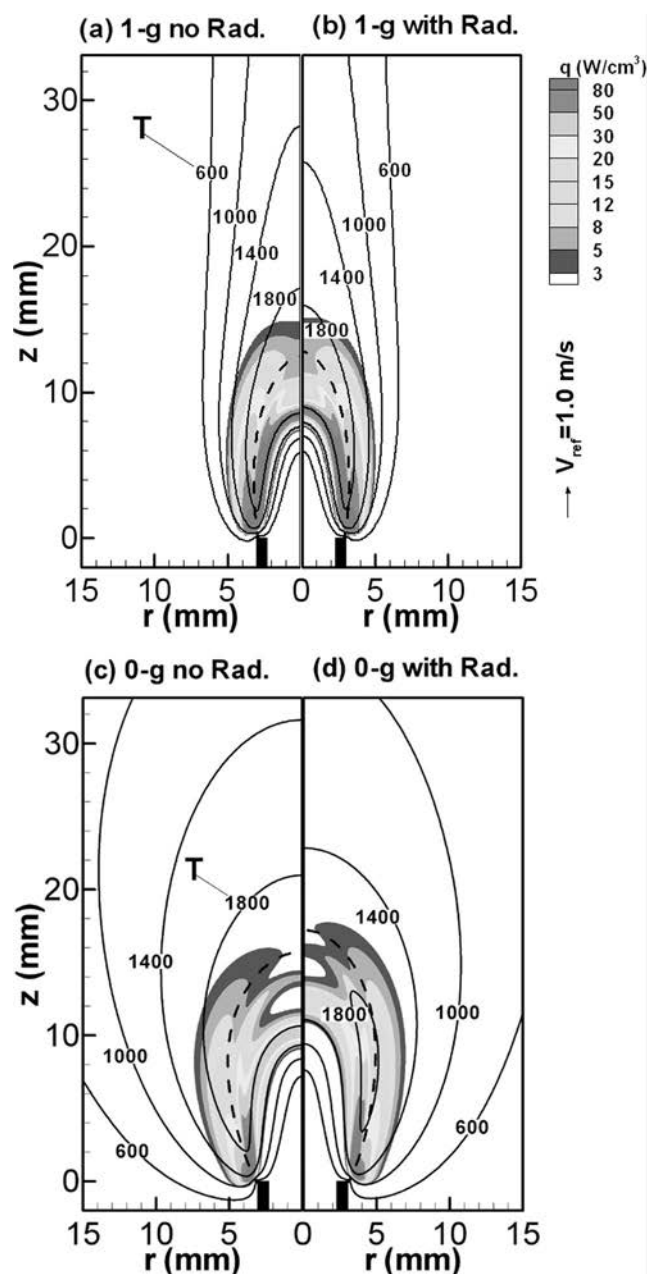


FIG. 5. Double-flame structure in terms of the heat-release rate and temperature contours for flames of (a) 1-g without radiation, (b) 1-g with radiation, (c) 0-g without radiation, and (d) 0-g with radiation. The dashed line represents the stoichiometric mixture fraction line. The flow conditions are the same as those in Fig. 4.

nonpremixed zones slightly increase when radiation is accounted for, implying a small increase in the chemical time. Radiation also decreases the temperature in the high-temperature regions, as indicated by the intersection of the 1400 K and 1800 K isotherms with the centerline. However, the overall effect of radiation on the structure of the 1-g flame is of less significance than on the 0-g flame. As indicated by the heat-release rate contours [cf. Figs. 5(c) and 5(d)], when radiation is addressed, the heights of both the inner premixed and outer nonpremixed reaction zones increase by about 2 mm ($>10\%$). In addition, the heat-release rate intensity near the flame tip decreases, and the region

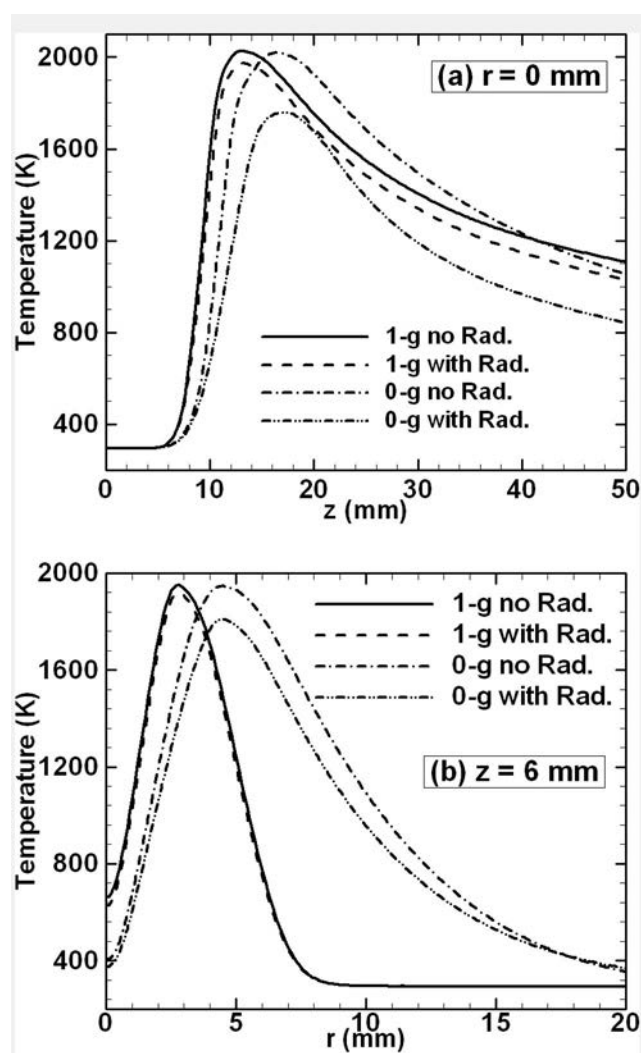


FIG. 6. Temperature profiles along the centerline (a) and along a radial cut at $z = 6$ mm (b) for both the 1-g and 0-g flames discussed in Fig. 5.

occupied by the 1800 K isotherm shrinks from that without radiation. The decreases in the flame temperature and the global reaction rate due to radiation produce a relatively longer and thicker flame at 0-g. Radiation also decreases the thermal and mass diffusivities through reduced temperatures.

Figures 5(c) and 5(d) show the existence of a weak heat-release peak between the inner rich premixed and outer nonpremixed reaction zones. The stoichiometric mixture fraction contour ξ_{st} (defined according to Bilger³⁵) is identified by a dashed line in these figures in order to clarify the location of the nonpremixed reaction zone. This ξ_{st} contour passes through the region that lies between the maxima in the inner premixed and outer nonpremixed heat-release zones. Comparing our results with Fig. 4(f) in Ref. 25, similar weak reaction zones occur in both investigations, although the burner configuration and flow conditions are different.

Figure 6 presents temperature profiles along the centerline and along a radial segment at $z = 6$ mm for both the 1-g and 0-g flames discussed in Fig. 5. The temperature profiles reach peak values downstream of the inner premixed reaction zone and thereafter exhibit a gradual decrease. The shift in the maximum temperature locations for the 0-g flame is in-

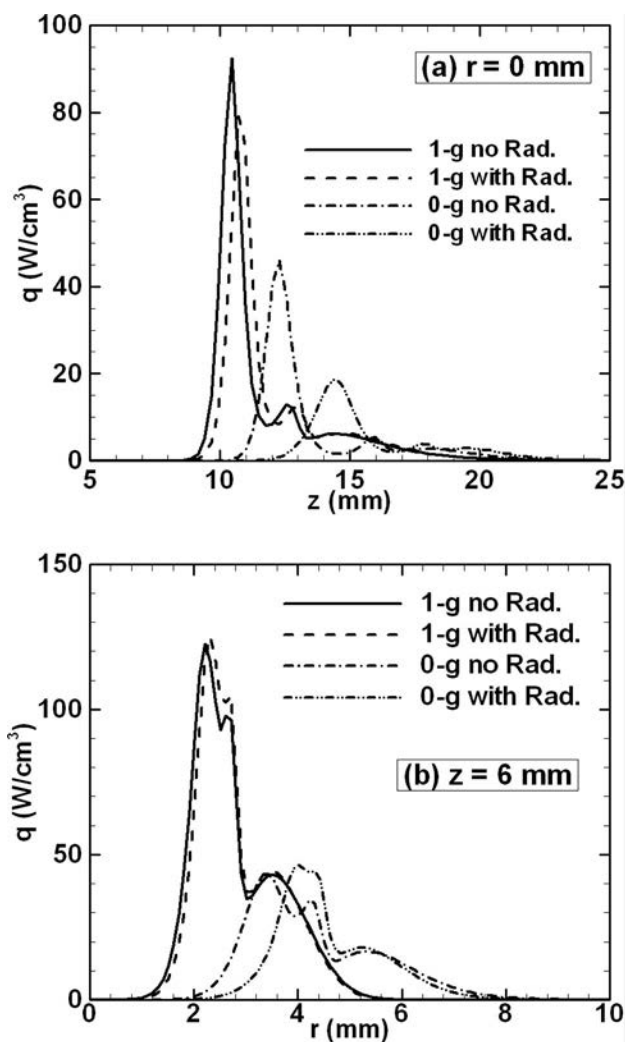


FIG. 7. Heat-release rate profiles along the centerline (a) and along a radial cut at $z = 6$ mm (b) for both the 1-g and 0-g flames discussed in Fig. 5.

dicative of the increase in the flame height. Without radiation, the peak temperatures are essentially identical for the 1-g and 0-g flames (2028 K vs 2020 K). However, when radiation is included, the difference between these two temperatures is significant [1973 K (1-g) vs 1760 K (0-g), respectively]. The decrease in the peak temperature caused by considering radiation heat loss is 260 K for the 0-g flame compared to 55 K for the 1-g flame. Clearly, radiation effects on PPFs are significantly enhanced in 0-g condition. This is also due to the larger reaction volume for the 0-g PPF in comparison to the 1-g flame [cf. Figs. 6(a) and 6(b)].

Figure 7 presents heat-release rate profiles for these flames. Their peaks along the centerline [cf. Fig. 7(a)] occur at the inner premixed flame tip, while the two peaks in the radial profiles [cf. Fig. 7(b)] occur in the inner premixed and outer nonpremixed reaction zones, respectively. In the absence of radiation the peak heat-release rates for the 0-g flames are only one-half of those for the 1-g flames. This difference can be attributed to two factors: first, the 0-g flame is spatially broader and longer than the 1-g flame; second, the reactivity at the premixed flame tip is weaker for the 0-g flame due to a decrease in oxidizer advection in the

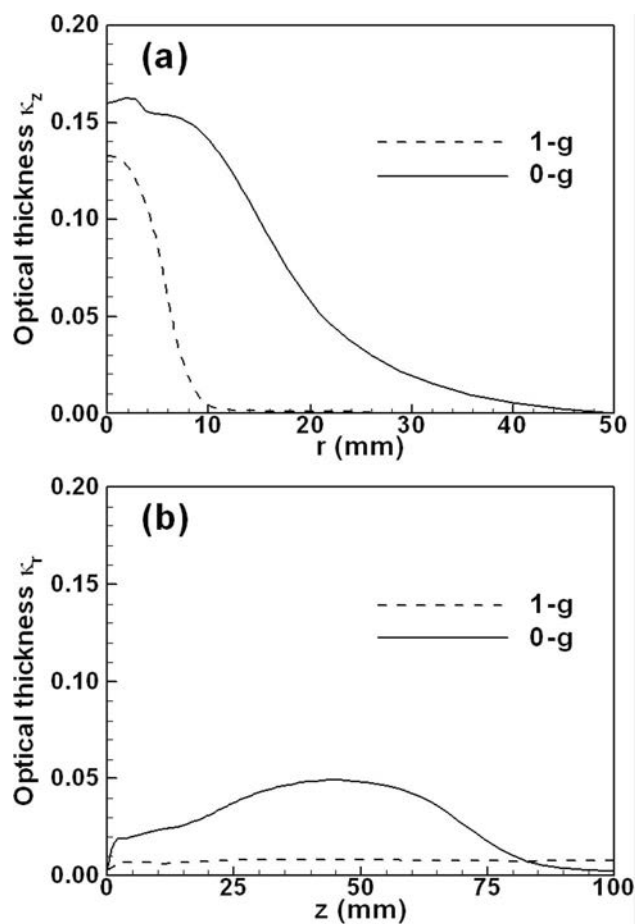


FIG. 8. Variation of optical thickness κ_z (a) and κ_r (b) for the flames corresponding to Figs. 5(b) and 5(d), respectively.

absence of buoyancy. This figure also corroborates the results discussed in the context of Figs. 5 and 6. For the 0-g flames, the peak heat-release rates when radiation is addressed are less than half of those without radiation, indicating that the reactivity at the premixed flame tip is significantly weakened by radiation. Another observation from a comparison of radial heat-release rate profiles in Fig. 7(b) is that radiation does not have a significant effect on the magnitude of the radial heat-release rates in 1-g and 0-g PPFs; instead, it shifts the peaks further away from the centerline.

D. Validity of the optically thin gas assumption

In order to assess the validity of the optically thin gas assumption, the optical thickness in the axial direction (κ_z) is calculated by²⁶

$$\kappa_z(r) = \int_0^Z K_p dz, \quad (8)$$

and in the radial direction (κ_r) by

$$\kappa_r(z) = \int_0^R K_p dr, \quad (9)$$

where R and Z are the computational domain lengths in the radial and axial directions, respectively. Figure 8 presents the variation of κ_z and κ_r for the flames corresponding to Figs. 5(b) and 5(d), respectively.

TABLE I. Properties of double flames under different gravity levels and coflow. For all the cases, $\phi_{in}=2.5$, $V_{in}=0.3 \text{ m s}^{-1}$, and $\phi_{out}=0$.

V_{out} (m s^{-1})	Gravity (g)	T_{max} (K)	q_{max} (W cm^{-3})	Q (W)	Q_{rad} (W)	χ_{rad} (%)	$\kappa_{z,max}$	H (mm)
0	1	1974	632	32.78	3.03	9.2	0.132	10.7
0	0	1760	268	32.02	16.17	50.5	0.162	14.4
0.3	1	1989	1008	32.90	2.69	8.2	0.130	8.2
0.3	0	1954	890	32.78	7.51	22.9	0.149	8.6
0.6	0	1990	1264	32.66	4.02	12.3	0.135	9.7
1.0	0	2008	1454	33.31	2.36	7.1	0.128	7.3

5(b) and 5(d). The value of κ_z is much larger than that of κ_r , since the Planck mean coefficients are functions of the local species concentrations and temperatures, and because the flames are optically thicker in the axial direction than in the radial direction. The fact that κ_z is larger than κ_r is also due to the high concentration of CH_4 , H_2O , CO , and CO_2 along the axial segment that is considered. The optical thickness is significantly larger for the 0- g flame than for the 1- g flame. The peak values of κ_z occur near the centerline and are 0.132 and 0.162 for the 1- g and 0- g flames, respectively. Although these values are not insignificant, they are nevertheless much smaller than unity and thus justify the optically thin gas assumption.

The global effect of radiation on 1- g and 0- g PPFs is summarized in Table I, which presents the simulated values of the maximum flame temperature T_{max} , maximum heat-release rate q_{max} , heat of combustion Q , total radiation heat loss Q_{rad} , radiation fraction χ_{rad} , maximum axial optical thickness $\kappa_{z,max}$, and inner flame height H (which is defined by the location of peak heat-release rate along the centerline) for six flames. The simulated radiation fraction values for 1- g flames are in good agreement with those reported in literature for laminar methane-air nonpremixed flames.³⁶ It is logical that corresponding values for PPFs should be of the same order. A comparison of χ_{rad} for 1- g and 0- g flames again demonstrates that the effect of radiation on PPFs is significantly enhanced in the absence of gravity for which the χ_{rad} value can be as high as 50.5%, although it drops to 22.9% in the presence of a coflow at 0.3 m s^{-1} . The optically thin gas model is known to overpredict the radiation heat loss in flames. Nevertheless, it provides a limiting value for the radiation loss, and can be used to compare the effects of radiation in 1- g and 0- g flames.

E. Effect of gravity on double-flame structure

Our previous investigations^{13,14} have examined the gravitational effects on partially premixed flames without considering thermal radiation. Since the preceding results clearly demonstrate that the effect of thermal radiation on flames is significantly enhanced under 0- g conditions, differences between the 1- g and 0- g flames would be greatly enhanced when radiation is addressed. Figure 9 presents velocity vectors, and temperature and heat-release rate contours for the 1- g and 0- g flames discussed in Fig. 5. The base of the 0- g flame moves further away from the centerline and stabilizes below the burner rim. The height of the inner pre-

mixed reaction zone is significantly longer than for the 1- g flame (14.4 vs 10.7 mm). The flame base displacement occurs due to the entrainment of air. In 1- g , entrainment produces a flow that pushes the flame closer to the centerline and also pulls the flame base radially inward toward the burner wall. In 0- g , the flame base remains away from the centerline due to the absence of the buoyant flow. The maximum flame temperature and heat-release rate are significantly lower in the absence of gravity (cf. Table I) and the flame occupies more volume. For example, when we assume the flame is described by the volume occupied by temperatures $T \geq 1000 \text{ K}$ then the volume of the 0- g flame is 3.9 times larger than that of the 1- g flame (i.e., $9.298 \text{ vs } 2.381 \text{ cm}^3$).

For the 1- g flame, the Froude number ($\text{Fr} = V_{in}^2 / GD$, here G is gravity level of unity g and D is the inner tube diameter) has a value of 2, implying that the gravitational and inertial effects are of similar magnitude. The velocity vector plots in Fig. 9 indicate that while flow fields upstream of the inner premixed reaction zone are nearly identical for the 1- g and 0- g flames they are markedly different in regions between the two reaction zones as well as downstream of the outer nonpremixed reaction zone. For the 1- g flame, buoyancy accelerates the products (CO and H_2 from the in-

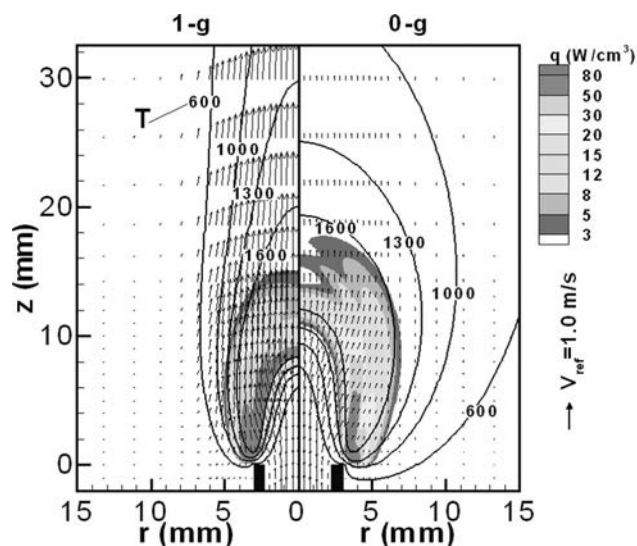


FIG. 9. Velocity vector fields, temperature, and heat-release rate contours for the 1- g and 0- g flames discussed in the context of Figs. 5(b) and 5(d), respectively.

TABLE II. Properties of double flames under different gravity levels. For all the cases, $\phi_{in}=2.5$, $V_{in}=0.3 \text{ m s}^{-1}$, $\phi_{out}=0$, and $V_{out}=0$.

Gravity (g)	T_{max} (K)	q_{max} (W cm $^{-3}$)	Q_{rad} (W)	χ_{rad} (%)	H (mm)	f (Hz)	Fr
0	1760	268	16.17	50.56	14.4		
0.1	1898	349	6.85	21.4	10.6		20.4
1	1974	632	3.03	9.21	9.1	12.8	2.0
2	1991	834	2.25	6.85	8.2	18.9	1.0
3	1997	952	2.02	6.08	7.8	23.7	0.68
5	2013	1181	1.51	4.55	7.1	33.3	0.4
10	2054	1964	1.14	3.21	6.3	41.4	0.2

ner premixed zone, and CO_2 and H_2O from the outer non-premixed zone) downstream of the two respective reaction zones. In addition, the buoyant entrainment bends the velocity vectors toward the centerline. This causes the outer reaction zone to move closer to the inner reaction zone, making the 1-g flame more compact than the 0-g flame.

Table II lists the properties of the double flame described in Fig. 4 at different levels of gravitational acceleration, i.e., 0-g, 0.1-g, 1-g, 2-g, 3-g, 5-g, and 10-g. At and above 1-g, the flame is unsteady; therefore, average values of T_{max} , q_{max} , Q_{rad} , χ_{rad} , and H are provided in italics. The maximum flame temperatures and local heat-release rates increase as the gravitational acceleration increases, while the radiation fractions and inner flame heights (H) decrease. The flickering frequency f also increases from 14.7 Hz at 1-g to 41.4 Hz at 10-g. Figure 10 presents the relationship between the inverse Froude number and the Strouhal number ($St=fD/V_{in}$) of the flickering flames under various gravitational accelerations. The results of premixed flames of Durox *et al.*³⁷ and nonpremixed flames of Arai *et al.*³⁸ are also plotted for comparison. The solid line represents the correlation $St \propto Fr^{-0.57}$ provided by Hamins *et al.*³⁹ through a large compilation of normal gravity data from a variety of flames. Our results are in good agreement with those of Durox *et al.*³⁷ and closely follow the correlation of Hamins *et al.*³⁹ The nonpremixed flame results of Arai *et al.*³⁸ also fall along the slope. This implies that flickering at enhanced gravity is in-

fluenced by the same physical factors as under normal gravity conditions,³⁹ and the instability mechanism responsible for the buoyancy-induced flame flickering is independent of the boundary conditions and flame configurations.

Besides the radiation fraction, the radiation intensity can also be expressed by the radiation (fourth) Damköhler number, which compares the heat generated by chemical reaction to the heat lost by radiation, i.e., $Da_{rad}=Q/Q_{rad} \sim \tau_{rad}/\tau_{chem}$. As $Da_{rad} \rightarrow 1$, the radiation heat loss becomes significant. The chemical reaction time scale τ_{chem} is related to the flow time of the gas through the radiating volume. It can be shown that $\tau_{rad} \sim (X_f Q/c_p T - 1)^{-1} = f(X_f, T)$, where c_p is the specific heat capacity and X_f the fuel mole fraction. Therefore, $Da_{rad} \sim V(g)f(X_f, T)$, where $V(g)$ is the effective velocity as a function of gravity and T is a function of X_f . The radiative heat loss increases with a decrease in $V(g)$ or increase of T . The Froude number is also a significant non-dimensional parameter for the radiation importance related by the Damköhler number. It can be shown that $Da_{rad} \sim (1 + Fr^{-1})f(X_f, T)$. This indicates that the Damköhler number is inversely proportional to the Froude number. As Fr increases, which occurs during the transition from 1-g to μ -g, Da_{rad} decreases, which means the relative significance of radiation increases.

F. Effect of coflow and inner jet velocities on double-flame structures

In order to examine the effect of coflow on the structures of 1-g and 0-g PPFs, we have simulated flames with coflow velocities $V_{out}=0.3, 0.6$, and 1.0 m s^{-1} . There is little difference between these flames, and all flames become shorter and more compact. Figure 11 presents velocity vectors along with temperature and heat-release rate contours for the flame with $V_{out}=0.3 \text{ m s}^{-1}$. The coflow velocity is assumed to have a top hat velocity profile that ends at the outer burner wall. The outer ambient flow is considered to be quiescent air with an axial velocity 0.001 m s^{-1} at the inflow boundary. Other conditions pertaining to this flame are $\phi_{in}=2.5$, $V_{in}=0.3 \text{ m s}^{-1}$, and $\phi_{out}=0$. Although, the presence of a coflow makes both the 1-g and 0-g flames shorter and more compact, its influence is more pronounced on the 0-g flame. The flame base is pushed closer to the centerline by the presence of the coflow and the difference in the structures of 1-g and 0-g flames is less significant as the coflow velocity is increased. Table I presents some global properties of

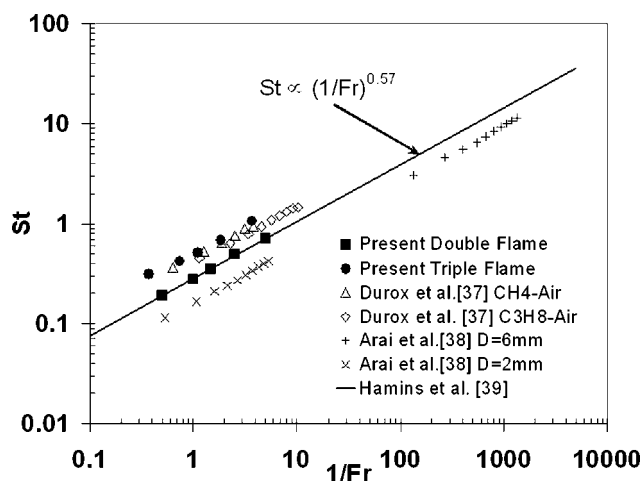


FIG. 10. Relationship between the inverse Froude number and the Strouhal number of flickering flames under various gravity levels.

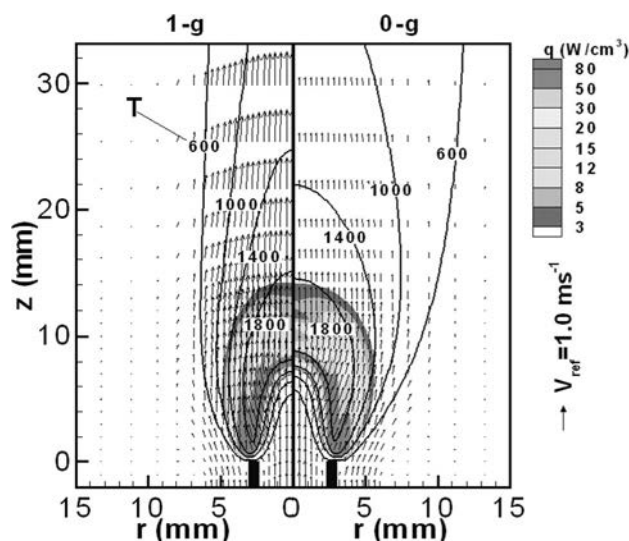


FIG. 11. Effect of coflow on the structure of 1-g and 0-g double flames in terms of velocity vector fields, temperature, and heat-release rate contours for the condition of $\phi_{in}=2.5$, $V_{in}=0.3 \text{ m s}^{-1}$, $\phi_{out}=0$, and $V_{out}=0.3 \text{ m s}^{-1}$.

these flames. Both the maximum flame temperature and heat-release rate become larger in the presence of a coflow, since it increases the advective oxidizer flux, thus enhancing the global reaction rate. Takahashi and Katta have reported a similar “blowing effect” for laminar methane jet nonpremixed flames.⁴⁰ The radiation fraction also decreases with increasing coflow, and the differences between the maximum flame temperatures and heat-release rates for the 1-g and 0-g flames become less pronounced.

Figure 12 illustrates the effect of varying inner jet velocities on the 1-g and 0-g PPFs. The heat-release rate contours, velocity vectors, and isotherms are presented for three cases: (a) $V_{in}=0.1 \text{ m s}^{-1}$, (b) 0.4 m s^{-1} , and (c) 0.8 m s^{-1} . Other conditions are $\phi_{in}=2.5$, $\phi_{out}=0$, and $V_{out}=0$. The values of the Froude number of the 1-g flames for these three cases are 0.23, 3.63, and 14.51, respectively. For all cases, the heights of the inner and outer reaction zones increase as the jet velocity is increased. The dependence of the inner flame height on the reactant velocity is attributed to the constant residence time, which is determined by the reaction time that essentially depends only on the equivalence ratio. The increase in the height of the outer flame is attributed to the strong synergistic interaction between the two flames and to the enhanced advection fluxes of CO and H_2 from the inner reaction zone. The difference between the 1-g and 0-g flame heights is more significant at higher jet velocities. At 0-g, the weaker air entrainment and the enhancement of radiation heat loss due to the absence of buoyant acceleration cause the flame heights to increase further for larger inner flow rates.

The volume of the high temperature region increases with a higher jet velocity. The volumes occupied by temperatures greater than 1000 K (V_{1000}) for the three jet velocities are calculated and listed in Table III, along with fraction of heat lost due to thermal radiation. As the jet velocity increases eightfold from 0.1 to 0.8 m s^{-1} , the value of V_{1000}

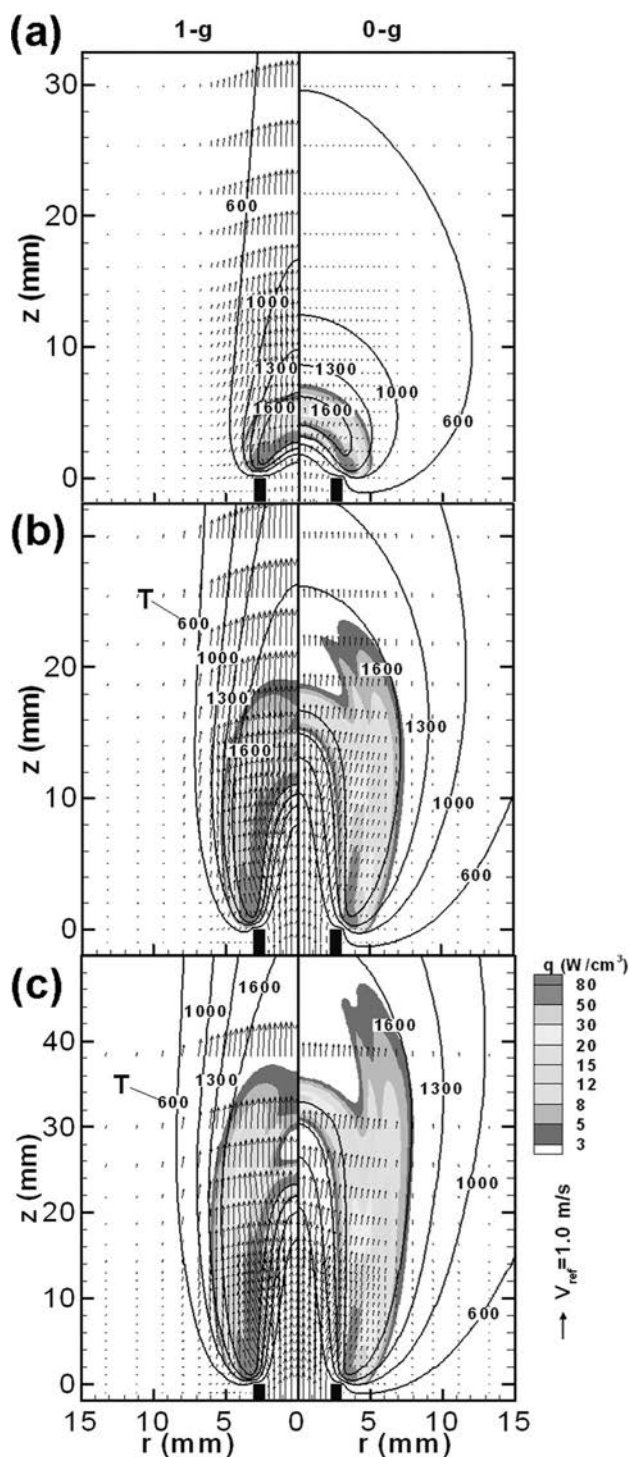


FIG. 12. Effect of inner jet velocities on the 1-g and 0-g PPFs. The heat-release rate contours, velocity vectors, and isotherms are presented for three cases: (a) $V_{in}=0.1 \text{ m s}^{-1}$, (b) 0.4 m s^{-1} , and (c) 0.8 m s^{-1} . Other conditions are $\phi_{in}=2.5$, $\phi_{out}=0$, and $V_{out}=0$.

increases roughly 24 times from 0.4 to 9.54 cm^3 at 1-g, but the influence on the radiative heat flux fraction is smaller, since it increases from 5.38% to 12.8%. The 0-g flames also experience a similar effect. At 0-g, for all three jet velocities, the values of V_{1000} are about 3.4 times larger than their 1-g counterparts, while the radiation fractions are approxi-

TABLE III. Radiation fraction and thermal field volume for the flames shown in Fig. 12.

V_{in} (m s ⁻¹)	1-g		0-g	
	χ_{rad} (%)	V_{1000} (cm ³)	χ_{rad} (%)	V_{1000} (cm ³)
0.1	5.38	0.40	32.19	1.38
0.4	10.27	3.75	53.13	13.69
0.8	12.80	9.54	51.87	32.21

mately five times larger. These results exhibit no explicit correlation between V_{1000} and χ_{rad} .

G. Gravity effect on burner-stabilized triple flames

Figure 13 compares a burner-stabilized 1-g triple flame with its 0-g counterpart at the conditions $\phi_{in}=2.5$, $V_{in}=0.6$ m s⁻¹, $\phi_{out}=0.35$, and $V_{out}=0.5$ m s⁻¹. These axisymmetric triple flames are more compact and shorter with less space between the three reaction zones as compared to the planar triple flames described in Refs. 2 and 14. The effect of gravity on the flame shape of the axisymmetric triple flame is not significant due to the presence of the coflow as explained in the preceding section. However, gravity strongly influences flame instability, especially in outer lean premixed and central nonpremixed flames. The isotherms and velocity vectors in Fig. 13 show that the outer lean premixed reaction zone at 1-g is influenced by the evolution of a vortex. The vortex moves downstream and interacts with the lean premixed flame, thereby interfering with the inner nonpremixed reaction zone. The 0-g triple flame is stable and no oscillations are observed in the heat-release

rate contours. The velocity vectors also show no vortex-induced air entrainment and downstream acceleration in the 0-g flame.

Table IV presents the properties of similar triple flames (to that described in Fig. 13) under different gravitational accelerations. Average values of T_{max} , q_{max} , Q_{rad} , χ_{rad} , and H are provided in *italics*. Similar to the double flames, as the gravitational acceleration increases, the maximum flame temperature and local heat-release rate increase, and the radiation fraction and inner flame height decrease. The flickering frequency of the triple flames is larger than that of the double flames under the same gravitational acceleration. The relationship between the inverse Froude number and the Strouhal number for these flames is also shown in Fig. 10. The data lie above the correlation of Hamins *et al.*³⁹ but still follow the power law relationship showing that the flickering mechanisms for both triple and double flames are similar.

IV. CONCLUSIONS

The effects of gravity, radiation heat loss, and coflow on burner-stabilized methane–air partially premixed double and triple flames are numerically investigated in the range from 0-g to 10-g. The model employs a detailed description of methane–air chemistry, thermodynamic, and transport properties, with the effect of thermal radiation modeled by the optically thin assumption.

(1) Gravity has a significant effect on the outer nonpremixed reaction zone in the case of double flames, and on both the outer nonpremixed and lean premixed zones in the case of triple flames. The flames are steady due to the absence of buoyancy at zero and 0.1-g; while at 1-g and larger gravitational accelerations (up to 10-g) both double and triple flames are unsteady. The flickering frequency increases with increasing gravitational acceleration. The correlation between the Strouhal number and the Froude number for

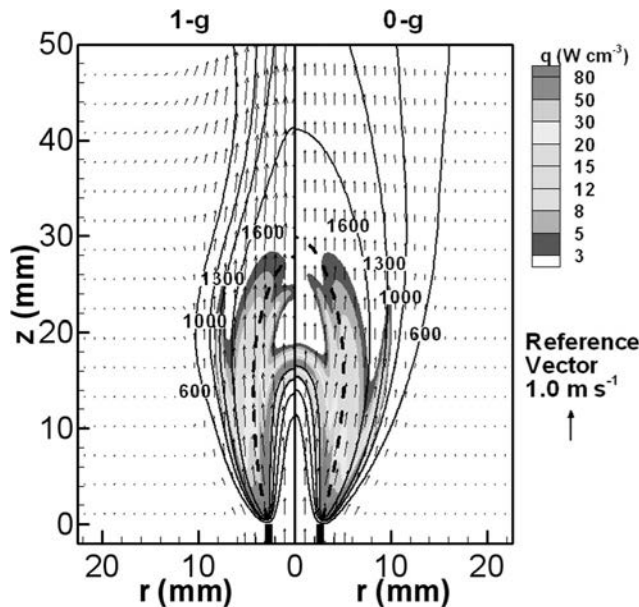


FIG. 13. Effect of gravity on the structures of burner-attached triple flames in terms of velocity vectors fields, temperature, and heat-release rate contours. The dashed line represents the stoichiometric mixture fraction line. The flow conditions are $\phi_{in}=2.5$, $V_{in}=0.6$ m s⁻¹, $\phi_{out}=0.35$, and $V_{out}=0.5$ m s⁻¹.

TABLE IV. Properties of triple flames at different conditions. For all the cases, $\phi_{in}=2.5$, $V_{in}=0.6$ m s⁻¹, $\phi_{out}=0.35$, and $V_{out}=0.5$ m s⁻¹.

Gravity (g)	T_{max} (K)	q_{max} (W cm ⁻³)	Q_{rad} (W)	χ_{rad} (%)	H (mm)	f (Hz)
0	1980	1047	31.02	30.13	16.8	
0.1	1982	1059	23.53	22.76	16.7	
1	2002	1135	13.12	12.59	16.5	15.2
2	2020	1246	9.43	9.44	16.0	20.4
3	2027	1298	9.19	8.71	15.8	24.3
5	2042	1402	7.01	7.29	15.6	32.1
10	2052	1628	4.79	4.45	15.3	51.7

both the double and triple flames follow the relation $St \propto Fr^{-0.57}$, which is in good agreement with a previous compilation of normal gravity data from a variety of flames.

(2) The radiation effect is significantly smaller for PPFs at 1-g or higher gravitational accelerations than in hypogravity. The value of radiation fraction χ_{rad} decreases from ~ 0.1 to ~ 0.04 in the range from 1-g to 10-g. However, thermal radiation effects become significant for 0-g flames for which χ_{rad} can be as large as 0.5, since the flame volume increases as buoyancy is lowered. This causes the flame temperature to decrease and results in weaker chemical reactivity. In addition, the heights of both the inner premixed and outer nonpremixed reaction zones in the 0-g PPFs become higher due to the reduced chemical activity caused by thermal radiation.

(3) The radiation (fourth) Damköhler number, which compares heat generated to the heat lost by radiation, illustrates the significance of radiation through the relation $Da_{rad} \sim (1 + Fr^{-1})f(X_f, T)$. Its value decreases (i.e., relative significance of radiation increases) as Fr increases (e.g., during the transition from 1-g to 0-g).

(4) The effect of the coflow is to counteract the effect of gravity on PPFs, since it enhances the oxidizer advection to the nonpremixed reaction zone and, thus, increases the overall reaction rate. We show that $Da_{rad} \sim V(g)f(X_f, T)$, which implies that the radiative heat loss decreases (or the Da_{rad} increases) with an increase in the mean flow velocity.

(5) The simulations of 1-g to 0-g PPFs indicate that the radiation-chemistry interactions are significantly enhanced in the absence of gravity, implying that the microgravity conditions are well suited for a fundamental investigation of such interactions.

ACKNOWLEDGMENTS

This research was supported by the National Science Foundation Combustion and Plasma Systems Program for which Dr. Thomas Chapman is the Program Director and by the NASA Microgravity Research Division for which Dr. Uday Hegde serves as the technical monitor. We thank Dr. X. Xiao for assisting with the deflectometry measurements.

- ¹Z. Shu, S. K. Aggarwal, V. R. Katta, and I. K. Puri, "A numerical investigation of the flame structure of an unsteady inverse partially premixed flame," *Combust. Flame* **111**, 296 (1997).
- ²R. Azzoni, S. Ratti, S. K. Aggarwal, and I. K. Puri, "The structure of triple flames stabilized on a slot burner," *Combust. Flame* **119**, 23 (1999).
- ³A. Hamins, K. Konishi, P. Borthwick, and T. Kashiwagi, "Global properties of gaseous pool fires," *Proc. Combust. Inst.* **26**, 1429 (1996).
- ⁴N. Peters, "Partially premixed diffusion flamelets in non-premixed turbulent combustion," *Proc. Combust. Inst.* **20**, 353 (1984).
- ⁵B. Rogg, F. Behrendt, and J. Warnatz, "Turbulent non-premixed combustion in partially premixed diffusion flamelets with detailed chemistry," *Proc. Combust. Inst.* **21**, 1533 (1986).
- ⁶B. J. Lee and S. H. Chung, "Stabilization of lifted tribrachial flames in a laminar nonpremixed jet," *Combust. Flame* **109**, 163 (1997).
- ⁷J. P. Gore, W. H. Meng, and J. H. Jang, "Droplet flames in reactive environments," *Combust. Flame* **82**, 126 (1990).
- ⁸M. C. Drake, D. T. French, and T. D. Fansler, "Advanced diagnostics for minimizing hydrocarbon emissions from a direct-injection gasoline engine," *Proc. Combust. Inst.* **26**, 2581 (1986).
- ⁹K. R. Sacksteder, "The implications of experimentally controlled gravitational accelerations for combustion science," *Proc. Combust. Inst.* **23**, 1589 (1990).

- ¹⁰C. K. Law and G. M. Faeth, "Opportunities and challenges of combustion in microgravity," *Prog. Energy Combust. Sci.* **20**, 65 (1994).
- ¹¹M. Kono, K. Ito, T. Niioka, T. Kadota, and J. Sato, "Current state of combustion research in microgravity," *Proc. Combust. Inst.* **26**, 1189 (1996).
- ¹²P. D. Ronney, "Understanding combustion processes through microgravity research," *Proc. Combust. Inst.* **27**, 2485 (1998).
- ¹³Z. Shu, C. W. Chun, S. K. Aggarwal, V. R. Katta, and I. K. Puri, "Gravity effects on steady two-dimensional partially premixed methane-air flames," *Combust. Flame* **118**, 91 (1999).
- ¹⁴R. Azzoni, S. Ratti, I. K. Puri, and S. K. Aggarwal, "Gravity effects on triple flames: Flame structure and flow instability," *Phys. Fluids* **11**, 3449 (1999).
- ¹⁵S. K. Aggarwal, I. K. Puri, and X. Qin, "A numerical and experimental investigation of 'inverse' triple flames," *Phys. Fluids* **13**, 265 (2001).
- ¹⁶V. R. Katta, L. P. Goss, and W. M. Roquemore, "Effect of nonunity Lewis number and finite-rate chemistry on the dynamics of a hydrogen-air jet diffusion flame," *Combust. Flame* **96**, 60 (1994).
- ¹⁷N. Peters, in *Reduced Kinetic Mechanisms for Applications in Combustion Systems*, Lecture Notes in Physics Vol. m15, edited by N. Peters and B. Rogg (Springer, Berlin, 1993), pp. 3–14.
- ¹⁸H. Xue and S. K. Aggarwal, "Effects of reaction mechanisms on structure and extinction of partially premixed flames," *AIAA J.* **39**, 637 (2001).
- ¹⁹Z. Shu, V. R. Katta, I. K. Puri, and S. K. Aggarwal, "Effects of C2-chemistry on the structure of partially premixed methane-air flames," *Combust. Sci. Technol.* **157**, 185 (2000).
- ²⁰K. N. Lakshminah, P. J. Paul, and H. S. Mukunda, "On the flammability limit and heat loss in flames with detailed chemistry," *Proc. Combust. Inst.* **23**, 433 (1990).
- ²¹C. J. Sung and C. K. Law, "Extinction mechanisms of near-limit premixed flames and extended limits of flammability," *Proc. Combust. Inst.* **26**, 865 (1996).
- ²²H. Guo, Y. Ju, K. Maruta, T. Niioka, and F. Liu, "Radiation extinction limit of counterflow premixed lean methane-air flames," *Combust. Flame* **109**, 639 (1997).
- ²³R. V. Ravikrishna and N. M. Laurendeau, "Laser-induced fluorescence measurements and modeling of nitric oxide in counterflow partially premixed flames," *Combust. Flame* **122**, 474 (2000).
- ²⁴R. S. Barlow, A. N. Karpetis, J. H. Frank, and J. Y. Chen, "Scalar profiles and NO formation in laminar opposed-flow partially premixed methane/air flames," *Combust. Flame* **127**, 2021 (2001).
- ²⁵B. A. V. Bennett, C. S. McEnally, L. D. Pfefferle, and M. D. Smooke, "Computational and experimental study of axisymmetric coflow partially premixed methane/air flames," *Combust. Flame* **123**, 522 (2000).
- ²⁶R. Siegel and J. R. Howell, *Thermal Radiation Heat Transfer* (Hemisphere, New York, 1981).
- ²⁷N. Smith, J. Gore, J. Kim, and Q. Tang, Radiation Models, International Workshop on Measurement and Computation of Turbulent Nonpremixed Flames (<http://www.ca.sandia.gov/tdf/Workshop/Submodels.html>) (2001).
- ²⁸Z. Shu, B. J. Krass, C. W. Choi, S. K. Aggarwal, V. R. Katta, and I. K. Puri, "An experimental and numerical investigation of the structure of steady two-dimensional partially premixed methane-air flames," *Proc. Combust. Inst.* **27**, 625 (1998).
- ²⁹F. Takahashi, W. J. Schmolli, and V. R. Katta, "Attachment mechanisms of diffusion flames," *Proc. Combust. Inst.* **27**, 675 (1998).
- ³⁰X. Xiao, I. K. Puri, and A. Agrawal, "Temperature measurements in steady axisymmetric partially premixed flames by use of rainbow Schlieren deflectometry," *Appl. Opt.* **41**, 1922 (2002).
- ³¹X. Qin, X. Xiao, I. K. Puri, and S. K. Aggarwal, "Effects of varying composition on temperature reconstructions obtained from refractive index measurements in flames," *Combust. Flame* **128**, 121 (2002).
- ³²M. Y. Bahadori, R. B. Edelman, D. P. Stocker, and S. L. Olson, "Ignition and behavior of laminar gas-jet diffusion flames in microgravity," *AIAA J.* **28**, 236 (1990).
- ³³D. L. Urban, Z. G. Yuan, P. B. Sunderland, G. T. Linteris, J. E. Voss, K. C. Lin, Z. Dai, K. Sun, and G. M. Faeth, "Structure and soot properties of nonbuoyant ethylene/air laminar jet diffusion flames," *AIAA J.* **36**, 1346 (1998).
- ³⁴K. C. Lin, G. M. Faeth, P. B. Sunderland, D. L. Urban, and Z. G. Yuan, "Shapes of nonbuoyant round luminous hydrocarbon/air laminar jet diffusion flames," *Combust. Flame* **116**, 415 (1999).
- ³⁵R. W. Bilger, "The structure of turbulent nonpremixed flames," *Proc. Comb. Inst.* **22**, 475 (1988).
- ³⁶G. H. Markstein, "Relationship between smoke point and radiant emission

- from buoyant turbulent and laminar diffusion flames,” *Proc. Combust. Inst.* **20**, 1055 (1984).
- ³⁷D. Durox, T. Yuan, F. Baillot, and J. M. Most, “Premixed and diffusion flames in a centrifuge,” *Combust. Flame* **102**, 501 (1995).
- ³⁸M. Arai, H. Sato, and K. Amagai, “Gravity effects on stability and flickering motion of diffusion flames,” *Combust. Flame* **118**, 293 (1999).
- ³⁹A. Hamins, J. C. Yang, and T. Kashiwagi, “An experimental investigation of the pulsation frequency of flames,” *Proc. Combust. Inst.* **24**, 1695 (1992).
- ⁴⁰F. Takahashi and V. R. Katta, “Reaction kernel structure and stabilizing mechanisms of jet diffusion flames in microgravity,” *Proc. Combust. Inst.* **29**, 2509 (2002).

EFFECT OF DILUENTS ON LIFTED PARTIALLY PREMIXED FLAMES IN NORMAL AND MICROGRAVITY: A NUMERICAL INVESTIGATION

Alejandro M. Briones, Suresh K. Aggarwal*, and Viswanath R. Katta†

University of Illinois at Chicago

Department of Mechanical and Industrial Engineering, Chicago, IL 60607

ABSTRACT

The effect of fuel stream dilution on the liftoff characteristics of partially premixed flames (PPFs) under 1- and 0-g conditions is investigated. Lifted methane-air PPFs are established in axisymmetric coflowing jets using different diluents and dilution levels. A time-accurate, implicit algorithm that uses a detailed description of the chemistry and includes radiation effects is used for the simulations. The predictions are validated through a comparison of the flame reaction zone topologies and liftoff heights. The effects of diluents and gravity on the flame liftoff height, topology, and base structure are characterized. The predominantly inert agents CO_2 and N_2 are considered because of their flame suppressant characteristics. Results indicate that under identical conditions a lifted 0-g PPF is stabilized closer to the burner compared to the 1-g flame, and the CO_2 dilution is more effective in detaching the flame from the burner in comparison with the N_2 dilution. Additionally, the 1-g lifted flames exhibit well-organized oscillations due to buoyancy-induced instability, while the corresponding 0-g flames exhibit steady state behavior.

INTRODUCTION

Partially premixed flames (PPFs) are established when a fuel rich gas stream flows adjacent to a fuel lean stream. The associated concentration gradients support flames with multiple reaction zones. In general, a rich premixed flame is established in the fuel rich zone and a nonpremixed flame outside of this region. Often a lean premixed flame is also established in the fuel lean region. Then, the nonpremixed flame is located between the rich and lean premixed flames. PPFs can be described as hybrid flames with the characteristics of both nonpremixed and premixed flames. Consequently, by using partial premixing, one can exploit the advantages of both nonpremixed and premixed flames regarding safety, emissions control, and flame stability.

Unwanted fires can originate in a partially premixed mode when a pyrolyzed or evaporated fuel forms an initial fuel rich mixture with the ambient air. Flames in such incipient fires are diluted and partially premixed with oxidation products such as CO_2 as well as with partial oxidation products such as CO and H_2 . Flame liftoff is important since in many cases fires do not necessarily “sit” on surfaces. i.e., they can consist of lifted flames for various reasons such as dilution, oxidizer starvation, high velocity pyrolyzed jets, etc. Partially premixed combustion is also important in space applications, particularly due to fire safety considerations [1,2]. Fire in a spacecraft or in an extraterrestrial base can lead to mission termination and/or loss of life. The advent of longer duration missions to the space increases the likelihood of mishaps that result from fire. Therefore, development of efficient fire suppressants and procedures for use in spacecraft environments represents a critical task. For these reasons studying partially premixed flames under normal and partial gravity conditions is important.

The extinguishment of a flame could be achieved by decreasing the flame temperature to a point that no free radicals are formed (thermal effect), and decreasing the concentration of free radicals and thus interrupting the flame chemistry of chain reactions (chemical effect). Therefore, fire suppressants could be of those affecting the flames thermally and/or chemically. Fire suppressants such as halogenated compounds extinguish fire mainly by chemical means and therefore the ability of the compound to remove free radicals is important. Halon 1301 is currently used worldwide for fire protection in earth or in spacecraft. However, it is regulated by international agreements (Montreal Protocol [3]) because of concerns with their destructive effect on the stratospheric ozone layer. The regulations have intensified the research for new fire suppressants, but the search for a new fire-extinguishing agent with all the desirable properties of Halon 1301 has not been successful. Vahdat et al. [4] have experimentally and theoretically investigated extinction using binary fire suppressants. These compounds were of organic compound/nitrogen nature. Although these mixtures seemed to be very promising, halogenated compounds such as CF_3Br (Halon 1301) were still found to be more efficient fire suppressants. By contrast, inert gases extinguish fire primarily through thermal effect; thus, heat capacity plays an important role in lowering the flame temperature. Numerous investigations have shown that when an inert gas such as N_2 or CO_2 is diluted with fuel, they promote lifting of the flame, while further increase in dilution leads to extinction through blowout [5,6]. Katta et al. [6] have extensively studied the extinguishment characteristics of CO_2 as a fire-suppressing agent using a coflowing nonpremixed configuration. They showed that flames under microgravity conditions required more dilution compared to flames under normal gravity.

Most of the early work on flame suppression was carried out in premixed flames [7], as the burning velocity provides a convenient parameter for characterizing suppressant effectiveness. More recently, both coflow and counterflow

* Corresponding author; e-mail: ska@uic.edu, tel: 1-312-996-2235, fax: 1-312-413-0447

† Innovative Scientific Solutions, Inc., 2766 Indian Ripple Road, Dayton, OH 45440-3638, USA

configurations have been employed for studying the structure and the extinction mechanism of nonpremixed flames [6,8, 9]. Previous investigations [10,11,12] have focused on the suppression of low strain rate nonpremixed flames in a counterflow configuration for laminar flames using different diluents and showed that CF_3Br was the most efficient inhibitor compared with other diluents such as N_2 and CO_2 . To study fire suppressants, it is needed to determine the extinguishing concentrations of a flame for several chemical compounds and/or inert gas. Experimentally, this process is expensive and time consuming. However, a method to computationally estimate the effectiveness of a given inhibitor would compare flame liftoff height for flames at the same conditions, but using different diluents. Therefore, a flame liftoff height is important to assess the effectiveness of diluents in inhibiting the flame. The objective of this paper is to numerically investigate the effect of different diluents on the liftoff and blowout characteristics of PPFs under 1- and 0-g conditions. Lifted methane-air PPFs are established in axisymmetric coflowing jets that are also diluted with inert gases at various levels of partial premixing. Dilution is applied either in the fuel jet flow or in the air coflow stream. A coflow configuration with equal jet and coflow velocities is employed in order to minimize the effects of the jet shear layer on the flame liftoff behavior. The flames are simulated using a time-accurate, implicit algorithm that uses detailed descriptions of chemistry and transport. The effects of diluents, dilution, and gravity on the flame liftoff height, topology, base structure, and oscillation frequency are analyzed.

NUMERICAL METHOD

The computational model is based on the algorithm developed by Katta et al. [13] and the simulation method is described in detail elsewhere [14,15]. The numerical model solves the time-dependent governing equations for unsteady reacting flows in a two-dimensional planar or axisymmetric configuration. In axisymmetric coordinates, these equations are:

$$\frac{\partial(\mathbf{r}\Phi)}{\partial t} + \frac{\partial(\mathbf{r}v\Phi)}{\partial r} + \frac{\partial(\mathbf{r}u\Phi)}{\partial z} = \frac{\partial}{\partial r} \left(\Gamma^\Phi \frac{\partial \Phi}{\partial r} \right) + \frac{\partial}{\partial z} \left(\Gamma^\Phi \frac{\partial \Phi}{\partial z} \right) - \frac{\mathbf{r}v\Phi}{r} + \frac{\Gamma^\Phi}{r} \frac{\partial \Phi}{\partial r} + S^\Phi$$

Here t denotes the time, u and v represent the axial (z) and radial (r) velocity components, respectively. The general form of the equation represents conservation of mass, momentum, species, or energy conservation equation, depending on the variable used for Φ . The diffusive transport coefficient Γ^Φ and source terms S^Φ appearing in the above equation is provided in Table 1 of Ref. 14. Introducing the overall species conservation equation and the state equation completes the set of equations. In addition, a sink term based on an optically thin gas assumption is included in the energy equation to account for thermal radiation from the flame [20]. The sink term due to the radiation heat loss is expressed as $q_{rad} = -4\sigma K_p (T^4 - T_o^4)$

[16] where T denotes the local flame temperature. The term K_p accounts for the absorption and emission from the participating gaseous species (CO_2 , H_2O , CO and CH_4) and is expressed as $K_p = P \sum_k X_i K_{p,i}$ where $K_{p,i}$ denotes the mean

absorption coefficient of the k^{th} species. Its value is obtained by using a polynomial approximation to the experimental data provided in Ref.17. The methane-air chemistry is modeled using a detailed mechanism that considers 24 species and 81 elementary reactions [18]. The mechanism has been validated for the computation of premixed flame speeds and the detailed structure of both nonpremixed and partially premixed flames [14,15,19,20,21].

The computational domain of $150 \times 100 \text{ mm}^2$ in the axial (z) and radial (r) directions, respectively, is represented by a staggered, non-uniform (301×101) grid system. The reported results are grid independent. An isothermal insert simulates the inner $2 \times 1 \text{ mm}$ burner wall. The boundary conditions used here can be found elsewhere [5, 14, 15]:

RESULTS AND DISCUSSION

Validation of Numerical Model

The numerical model has been previously validated for both burner-stabilized and lifted methane-air PPFs [5, 15,22, 29]. Additional validation is provided by comparing the predicted heat release rates and measured reaction zone intensities for 1- and 0-g 25% N_2 -diluted and 10% CO_2 -diluted lifted partially premixed flames, as shown in Fig. 1. The experimentally obtained images of the 1- and 0-g lifted flames presented in Fig. 1 have been converted into reaction rate intensities. The reaction rates are very large near the flame base. The peak values of the predicted heat release rate and the measured intensity are similar at the flame base, where the inner and outer reaction regions are merged. Care is taken in comparing the 1-g flames at the same time, since they are subject to buoyancy-induced oscillations. The measured and predicted reaction zone topographies are in relatively good agreement as are the flame liftoff heights. However, there is more discrepancy between the predicted and experimental flame length. Both the simulations and measurements show that in the absence of gravity both the liftoff and flame heights decrease.

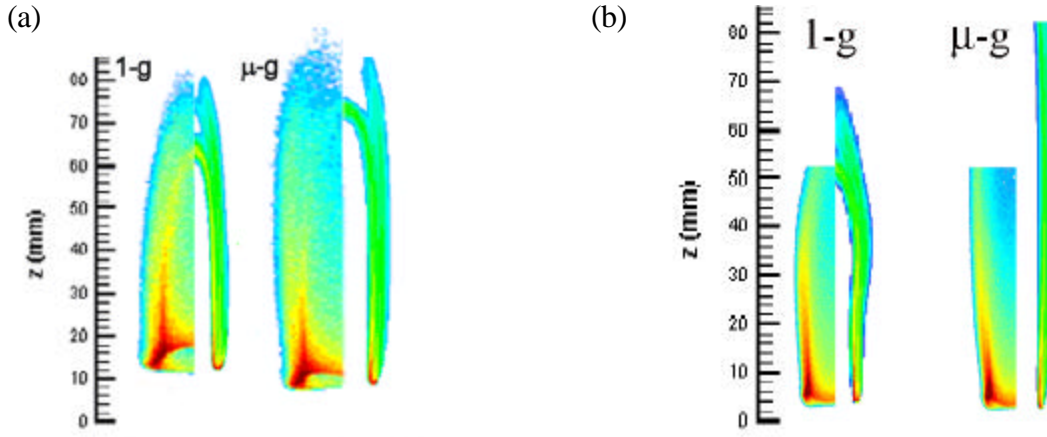


Figure 1: Comparison of post-processed experimentally obtained images (i.e., converted into reaction rate contours) (on the left) and predicted heat release rate contours (on the right) for (a) 25% N_2 -diluted and (b) 10% CO_2 -diluted, lifted 1-g and m-g PPFs established at $f=2.25$, $V_{in}=V_{out}=50$ cm/s.

Modified Flame Index

Previous investigations have distinguished the various reaction zones in PPFs based on their spatial locations [14,23]. In lifted flames, however, the premixing ahead of the flame front can be relatively small depending upon the liftoff height. Consequently, it can be difficult to distinguish the reaction zones visually. In order to spatially resolve the various reaction zones in the lifted PPFs more clearly, we have developed a method based on a modified flame index. Takeno and co-workers [24] have suggested the use of such an index based on the scalar product of the gradients of fuel and oxidizer mass fractions, which distinguishes between the premixed and nonpremixed reaction zones. Their flame index is defined as [24] $G_{FO} = \nabla Y_F \cdot \nabla Y_O$. Here Y_F denotes the fuel mass fraction and Y_O the oxidizer mass fraction. Domingo et al. [25] normalized this flame index as $x_p = 1/2(1 + G_{FO}/|G_{FO}|)$, such that $x_p = 1$ and 0 represent the premixed and nonpremixed reaction zones, respectively. In our investigation, we modified the Domingo et al. [25] flame index based on the local mixture fraction such that it can also distinguish between the rich and lean premixed reaction zones.

It is well known that the stoichiometric mixture fraction f_s lies within the nonpremixed reaction zone [26]. Therefore, the rich and lean premixed zones are located in the inner and outer regions in which the local mixture fraction f is larger and smaller than f_s , respectively. Accordingly, we can define a modified flame index $x_M = ((f - f_s)/|f - f_s|) \cdot 1/2(1 + G_{FO}/|G_{FO}|)$. Here the mixture fraction is defined following Bilger [27]. With this definition $x_M = 1$ represents the rich premixed zone, -1, the lean premixed zone, and ± 0.5 or 0 (depending upon the fuel under consideration) for the nonpremixed zone. If the fuel is completely consumed in the premixed zones, which is normally the case for PPFs burning hydrocarbon fuels [14, 15, 21], $x_M = \pm 0.5$, with +0.5 and -0.5 values corresponding to the nonpremixed regions adjacent to the rich premixed and lean premixed zones, respectively. The value of $x_M = 0$ for PPFs burning hydrogen, since the fuel is partially consumed in the premixed reaction zone with the remaining fuel being consumed in the nonpremixed zone [28]. Identification of the various reaction zones is more relevant in regions of high reactivity, i.e., where the heat release rates are significant. Therefore, we have computed the flame index in regions where the heat release rate is at least 1% of the maximum heat release rate.

The use of the modified flame index to identify different reaction zones in a PPF has been employed before [5,29]. We have computed the detailed flame structure for N_2 -diluted at 1- and 0-g PPFs established at $\phi=2.50$, $V_{in}=V_{out}=50$ cm/s. Table 1 presents the liftoff height and flame base structures for different levels of dilution. The flame base structure transitions from a triple to a double flame structure as the flame liftoff height decreases [5]. In addition, the flame liftoff height increases as the amount of dilution is increased. Importantly, it is required more dilution of N_2 to liftoff the flame at 0-g than at 1-g. While the 0-g flame remains attached with 14% N_2 dilution, the 1-g flame is already detached from the burner and lifted 6.1mm at the same dilution and diluent conditions.

Table 1 Diluted 1- and 0-g N₂-diluted PPFs established at $f=2.50$, $V_{in}=V_{out}=50$ cm/s.

Gravity condition	Dilution % (by vol.)	Liftoff height (mm)	Flame base structure
1-g	25.00	12.5	Triple structure
1-g	14.00	6.10	Double structure
1-g	7.5	0.00	Double structure
0-g	25.00	7.10	Double structure
0-g	14.00	0.00	Double structure
0-g	7.5	0.00	Double structure

Furthermore, we have computed the detailed flame structure for N₂- and CO₂-diluted flames established at 1- and 0-g PPFs established at $\phi=2.50$, $V_{in}=V_{out}=50$ cm/s. Table 2 presents the liftoff heights, flame lengths, and flame base structures for the cases under investigation. CO₂ is more effective to lift the flame with a lower dilution level, it produces a larger liftoff height compared to the flame diluted with N₂, which implies that CO₂ may be a better fire suppressant agent compared to N₂.

Table 2 Diluted 1- and 0-g PPFs established at $f=2.50$, $V_{in}=V_{out}=50$ cm/s.

Gravity condition	Diluent	Dilution % (by vol.)	Liftoff height (mm)	Flame length (mm)	Flame base structure
1-g	N ₂	25	12.5	68	Triple structure
0-g	N ₂	25	7.10	86	Double structure
1-g	CO ₂	15	29	81	Triple structure
0-g	CO ₂	15	5.00	110	Double structure

Effect of diluents on the structure of PPFs

Figure 2 presents the flame structure in terms of the iso-temperature and CO₂ mass fraction contours for 1-g and 0-g N₂- and CO₂-diluted flames. Note that for both the N₂- and CO₂-diluted flames, CO₂ mass fraction has been normalized using its dilution value in the fuel stream ($Y_{CO_2} = 0.2288$). The 0-g PPFs are broader, longer, and have larger volume than the corresponding 1-g flames. Therefore, the radiative heat loss from 0-g flames is significantly greater than that from 1-g flames; therefore, lowering the temperature. For example, both the N₂- and CO₂-diluted flames under normal gravity shows that they reached a maximum temperature above 1800 K (i.e., 1809 K for N₂-diluted and 1813 K for CO₂-diluted PPF), while under microgravity peak temperatures fall below 1800 K (i.e., 1786 K for N₂-diluted and 1776 K for CO₂-diluted PPF). As mentioned before, the liftoff height decreases under 0-g conditions compared with corresponding 1-g flames.

As indicated in Fig. 2, for CO₂-diluted flames under both 1- and 0-g conditions, the CO₂ mass fraction first decreases from the burner exit to the flame front, and then increased inside the flame due to the production of CO₂ mostly in the nonpremixed zone. This CO₂ production peaks near the flame tip. The production of CO₂ in the N₂-diluted PPFs under both 1- and 0-g conditions is relatively constant along the nonpremixed zone in comparison with the CO₂-diluted PPFs. As expected, both the diluents, N₂ and CO₂, show no chemical effect on the flame.

Figures 3 and 4 present the temperature and axial velocity profiles along the

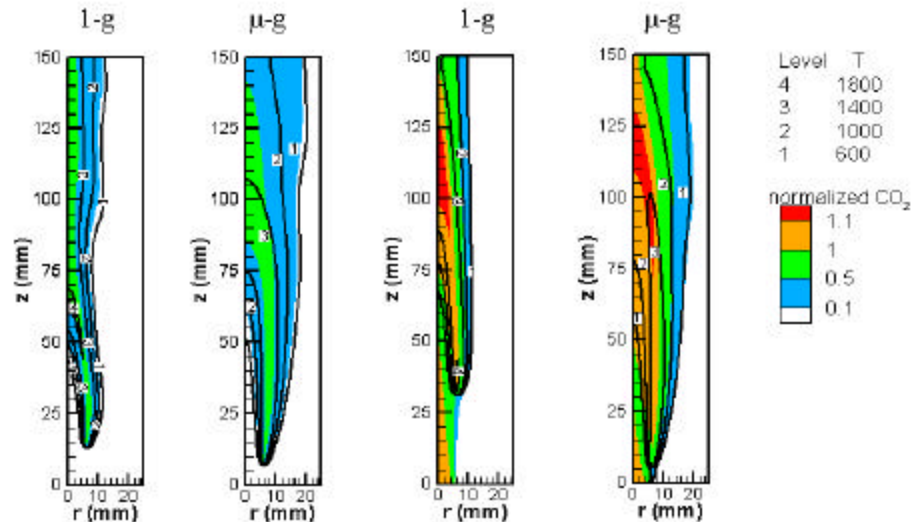


Figure 2: Temperature and normalized CO₂ mass fraction contours for 1- and 0-g lifted PPFs established at $f=2.50$, $V_{in}=V_{out}=50$ cm/s, and 25% N₂- (on the left) and 15% CO₂-dilution (on the right).

stoichiometric mixture fraction line as a function of axial distance from the burner for the flames discussed in the context of Fig. 2. These profiles indicate notable similarity in the base structures of 1-g N_2 - and CO_2 -diluted, and 0-g N_2 - and CO_2 -diluted flames, respectively. Although the temperature profiles between 1- and 0-g flames are very similar, there are differences between the 1- and 0-g axial velocity profiles. At 1-g, the local flow velocity increases due to buoyant acceleration displaying a parabolic profile and the flame is stabilized at a higher axial location to balance the flame propagation speed with the local flow velocity. These parabolic axial velocity profiles along the stoichiometric mixture fraction indicate that normal gravity PPFs exhibit well-organized oscillations. In addition, the entrainment caused by buoyant acceleration leads to larger mixing, which decreases the mixture fraction gradient [5]. This in turn modifies the flame propagation speed and thereby the liftoff height. On the other hand, the higher liftoff height of 1-g flames induces greater mixing of fuel into the oxidizer stream. Both of these effects, i.e., higher liftoff height and the buoyant entrainment, lead to enhanced mixing in the case of 1-g flames.

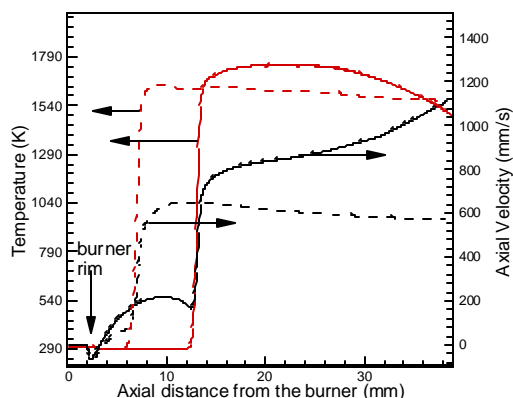


Figure 3: Temperature and axial velocity profiles along the stoichiometric mixture fraction as function of the axial distance from the burner for 25% N_2 -diluted PPFs under 1- and 0-g established at $f=2.50$, $V_{in}=V_{out}=50$ cm/s.

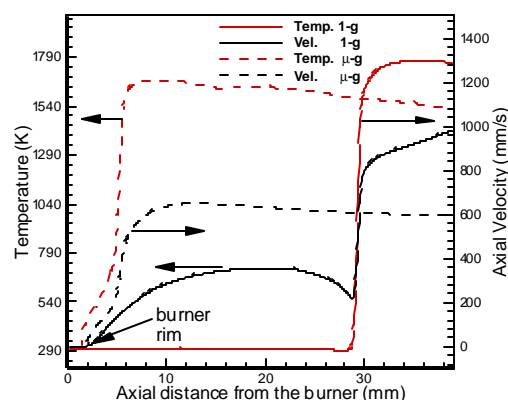


Figure 4: Temperature and axial velocity profiles along the stoichiometric mixture fraction as function of the axial distance from the burner for 15% CO_2 -diluted PPFs under 1- and 0-g established at $f=2.50$, $V_{in}=V_{out}=50$ cm/s.

CONCLUSIONS

We have presented a computational investigation on the liftoff characteristics of diluted partially premixed flames (PPFs) under 1- and 0-g conditions. Lifted methane-air PPFs have been established in axisymmetric coflowing jets using nitrogen and carbon dioxide dilution. A time-accurate, implicit algorithm that uses a detailed description of methane-air chemistry and includes radiation effects is used for simulations. Predictions are validated through a comparison of the flame reaction zone topologies, liftoff heights, and flame lengths. The effects of diluents are discussed.

1. The CO_2 -diluted PPF is more effective in detaching the flame since less dilution is required to obtain the same liftoff height compared with N_2 -dilution. This implies that CO_2 may be a better fire suppressant agent compared with N_2 .
2. For PPFs diluted with N_2 or CO_2 (in the fuel jet) it is observed that 1-g flames are lifted higher than their corresponding 0-g flames. This occurs because the buoyant acceleration and entrainment accelerate the gases and consequently the lifted flame is stabilized farther away from the burner. The stabilization location is determined by the balance between the local flow velocity and flame speed.
3. The 0-g PPFs are broader, longer, and have larger volume than the corresponding 1-g flames. As a consequence, the radiative heat loss from 0-g flames is significantly greater than that from 1-g flames. This lowers the flame temperature, the flame speed decreases, buoyant acceleration is inhibited, and the liftoff height of 0-g flames decreases.
4. The 1-g lifted flames exhibit well-organized oscillations due to a buoyancy-induced instability while the corresponding μ -g flames exhibit steady state behavior.

ACKNOWLEDGMENTS

This research was supported by the NASA Microgravity Research Division through Grant No. NCC3-688 for which Dr. Kurt Sacksteder serves as the technical monitor. We thank Mr. Andrew Lock for providing us the experimental data.

REFERENCE

1. K. R. Sacksteder, *Proc. Combust. Inst.* 23 (1990) 1589.
2. C. K. Law, G. M. Faeth, *Prog. Energy Combust. Sci.* 20 (1994) 65.
3. UNEP, *Montreal Protocol on Substances that Deplete the Ozone Layer*, 2004.
4. N. Vahdat, Y. Zou, M. Collins, *Fire Safety J.* 38 (2003) 553-567.
5. A. J. Lock, A. M. Briones, X. Qin, S. K. Aggarwal, I. K. Puri, U. Hegde, Submitted to *Combust. Flame* (2004).
6. V.R. Katta, F. Takahashi, and G.T. Linteris, *Combust. Flame* 137 (2004) 506-522.
7. V. Babushok, W. Tsang, G. T. Linteris, D. Reinelt, *Combust. Flame* 115 (1998) 551-560.
8. J. E. Siow, N. M. Laurendeau, *Combust. Flame* 136 (2004) 16-24.
9. M. A. Macdonald, T. M. Jayaweera, E. M. Fisher, F. C. Gouldin, *Combust. Flame* 116 (1999) 166-176.
10. N. Vora, J. E. Siow, and N.M. Laurendeau, *Combust. Flame* 126 (2001) 1393-1401.
11. M. Bundy, A. Hamins, K. Y. Lee, *Combust. Flame* 133 (2003) 299-310.
12. A. Hamins, D. Trees, K. Seshadri, and H. K. Chelliah, *Combust. Flame* 99 (1994) 221-230.
13. V. R. Katta, L. P. Goss, and W. M. Roquemore, *Combust. Flame* 96 (1994) 60-74.
14. Z. Shu, S. K. Aggarwal, V. R. Katta, I. K. Puri, *Combust. Flame* 111 (1997) 276-295.
15. R. Azzoni, S. Ratti, I. K. Puri, S. K. Aggarwal, *Phys. Fluids* 11 (1999) 3449-40.
16. R. Siegel, and J. R. Howell, *Thermal Radiation Heat Transfer*, Hemisphere Publishing Corporation, New York, 1981.
17. B. J. Lee, S. H. Chung, S. H., *Combust. Flame* 109 (1997) 163-172.
18. N. Peters, *Reduced Kinetic Mechanisms for Applications in Combustion Systems*, Lecture Notes in Physics, Vol. m15, edited by N. Peters and B. Rogg, (Springer, Berlin, 1993), pp. 3-14.
19. Z. Shu, C. Choi, S. K. Aggarwal, V. Katta, I. K. and Puri, *Combust. Flame*. 118 (1999) 91-107.
20. X. Qin, I. K. Puri, and S. K. Aggarwal, V. R. Katta, *Phys. Fluids* 16 (2004) 2963-2974.
21. H. Xue, S. K. Aggarwal, *AIAA Journal* 39 (2001) 637.
22. Z. Shu, B. Krass, C. Choi, S. K. Aggarwal, V. Katta, and I. K. Puri, *Proc. Combust. Inst.* 27 (1998) 625-632.
23. A. J. Lock, R. Ganguly, I. K. Puri, S. K. Aggarwal, U. Hedge, *Proc. Combust. Inst.*, 30 To appear (2004).
24. H. Yamashita, M. Shimada, and T. Takeno, *Proc. Combust. Inst.* 26 (1996) 27-34.
25. P. Domingo, L. Vervisch, J. Réveillon, Submitted to the *Combustion and Flame*, 2004.
26. S. K. Aggarwal, I. K. Puri, *AIAA Journal* 36 (1998) 1190-1199.
27. R. W. Bilger, *Proc. Combust. Inst.* 22 (1988) 475-488.
28. A. Briones, S. K. Aggarwal, *Int. J. Hydrogen Energy* 30 (2005) 327-339.
29. A. Lock, I. Puri, S. Aggarwal, U. Hegde, 43rd *AIAA Aerospace Sciences Meeting and Exhibit* (2005) AIAA-2005-0147.

Numerical Studies on Ultra-Lean Methane Premixed Flames

V. R. Katta*

Innovative Scientific Solutions, Inc.
2766 Indian Ripple Road
Dayton, OH 45440

Z. Cheng and R. W. Pitz

Mechanical Engineering Department
Vanderbilt University
Nashville, TN 37235

Lean combustion has potential advantages in limiting NO_x and particulate emissions and in improving fuel-consumption efficiency. The major difficulty in achieving and sustaining lean combustion in aircraft engines is associated with the flame-stability problem. A numerical study is performed in this paper on a counterflow-premixed-flame system for understanding the stability of the ultra lean methane/air mixture. A time-dependent, axisymmetric mathematical model known as UNICORN (UNsteady Ignition and COMbustion using ReactionNs) is used for the two-dimensional simulation of premixed flames associated with this opposing-jet burner. Sub-limit lean methane/air flames are supported in this burner by the products generated by a lean hydrogen/air premixed flame. A detailed chemical-kinetics model GRI-V1.2 (developed by the Gas Research Institute) is used for simulating the double-flame structure formed between the methane/air and hydrogen/air mixtures. Extinction of methane flame is obtained by increasing the applied stretch rate on both the flames. Numerical results are compared with the experimental data. Role of the radicals diffusing from the stable hydrogen flame in stabilizing the unstable lean methane flame is discussed.

INTRODUCTION:

Lean combustion is currently under investigation due to its potential advantages in limiting thermal NO_x emissions and in reducing fuel consumption. It has been used in gas turbines and direct injection spark ignition (DISI) engines. But a critical problem is that lean combustion tends to produce unburned hydrocarbon pollutants. For example, in DISI engines, ultra-lean combustion is achieved by charge stratification. The fuel/air mixture is inhomogeneous, leading to the simultaneous formation of lean, rich and stoichiometric regions. For the inhomogeneous reactants, Haworth et al. [1] simulated turbulent inhomogeneous combustion in DISI engines and found that hydrocarbon-rich fragments and oxidizer penetrate behind the primary heat-release zone to form a secondary reaction zone. Flames occurring in an inhomogeneously mixed fuel and air region are examples of partially premixed combustion. Some of this partially premixed mixture is so lean that it doesn't burn. But this ultra lean mixture may still react if hot products interact

with it. That is, under certain conditions, the lean mixture region can burn and thus reduce the potential pollutants. The interaction of lean mixture with hot products needed to maintain the lean region burning is the focus of this work. Partially premixed flames have been studied widely. In particular, the downstream interaction between two premixed streams was investigated by Sohrab et al. [2]. Most practical flames are stretched. The stretch effect combined with other aspects such as the effect of Lewis number or curvature will modify flame structure significantly [3, 4]. Considering the various conditions that exist simultaneously in inhomogeneous fuel/air reaction, a set of CH₄/air flames with a wide range of equivalence ratios and stretch rates impinging upon downstream hot products are studied experimentally and numerically. The opposed jet burner generates counterflow flames that are widely used to study chemical kinetics and species transport under aerodynamic stretch. Using the opposed jet flames, partially premixed CH₄/air versus air flame structures were investigated [5, 6]. Lean partially premixed CH₄ and C₃H₈ flame structures versus hot products have also been investigated [7, 8]. In general, premixed flames [9, 10] are much less sensitive to stretch than diffusion flames [11]. In the present work, stretch effects on the flame structure of lean CH₄/air mixtures are studied using a two-dimensional, detailed transport, complex chemistry numerical model.

NUMERICAL MODEL:

A time-dependent, axisymmetric mathematical model known as UNICORN (Unsteady Ignition and Combustion using ReactionNs) [12,13] is used to simulate the potentially unsteady jet diffusion flames considered in this study. It solves for u- and v-momentum equations, continuity, and enthalpy- and species-conservation equations on a staggered-grid system. A clustered mesh system is employed to trace the large gradients in flow variables near the flame surface. A detailed chemical-kinetics model (GRI Version 1.2) of Gas Research Institute [14] is incorporated into UNICORN for the investigation of methane flames. It consists of 32 species and 346 elementary-reaction steps. Thermo-physical properties such as enthalpy, viscosity, thermal conductivity, and binary molecular diffusion of all the species are calculated from the polynomial curve fits developed for the temperature range 300 - 5000 K. Mixture

*Corresponding Author: vrkatta@erinet.com

Proceedings of 4th Joint Meeting of the U. S. Sections of the Combustion Institute, 2005.

viscosity and thermal conductivity are then estimated using the Wilke and Kee expressions, respectively. Molecular diffusion is assumed to be of the binary-diffusion type, and the diffusion velocity of a species is calculated using Fick's law and the effective-diffusion coefficient of that species in the mixture. A simple radiation model based on the optically thin-media assumption [15] is incorporated into the energy equation. Only radiation from CH_4 , CO , CO_2 , and H_2O is considered in the present study. Due to lack of any soot modeling in the present study radiation from soot is not considered. This simplification could result in only slightly higher flame temperatures in the lean flames considered in the present study.

The finite-difference forms of the momentum equations are obtained using an implicit QUICKEST scheme [16], and those of the species and energy equations are obtained using a hybrid scheme of upwind and central differencing. At every time step, the pressure field is accurately calculated by solving all the pressure Poisson equations simultaneously and using the LU (Lower and Upper diagonal) matrix-decomposition technique. The boundary conditions are treated in the same way as that reported in earlier papers [17].

EXPERIMENT:

The opposed jet burner used in this study was designed by Seshadri et al. [18] and has been used extensively for hydrogen- and hydrocarbon-fueled diffusion flames and for hydrocarbon-fueled premixed flames. With the honeycomb inserts, rather than wire screens, it has also been used for the studies of lean H_2 /air premixed flames [19]. The burner system consists of 25-mm diameter inner nozzles that are separated by 12.6 mm. Methane and air mixture was issued from one nozzle while hydrogen and air mixture was issued from the other. Measurements of major species and temperature were made along the centerline using a nonintrusive, Raman diagnostic system [19]. Experiments were performed for various equivalence ratios and stretch rates. Details of eight flames that were classified into three groups are described in Ref. [19]. All these flames used fuel jets of 300K-inlet temperature. Group A includes three flames with the same CH_4 /air mixtures (with an equivalence ratio 0.68) and lean H_2 /air mixtures (with an equivalence ratio 0.28) but subjected to different stretch rates.

RESULTS AND DISCUSSION:

Two-dimensional calculations for the opposing jet lean-premixed flames are made using UNICORN code. A grid system having 421X101 node points is used for describing the physical space between the burner nozzles. Flat velocity profiles are used at the nozzle exits. Results obtained along the stagnation line for the three flames in Group A are compared with the measurements in Figs. 1-3, respectively. The global stretch rates (defined as twice the velocity difference divided by nozzle separation) applied on these flames are 90 s^{-1} , 136 s^{-1} , and 204 s^{-1} . As seen from Figs. 1-3, calculations have yielded double-flame structure for all the three applied stretch rates. Methane/air mixture produced

a flame on the left side with temperature greater than 1600 K and hydrogen/air mixture produced a flame on the right side with a temperature of about 1300 K. As the applied stretch rate on these flames increased the peak temperatures and the separation between the two flame locations decreased.

Calculations compared well with the measurements for the 90 s^{-1} and 136 s^{-1} global stretch rate cases (Figs. 1 and 2). The double-flame structure was well reproduced. However, significant differences exist between the predictions and measurements for the 204 s^{-1} case (Fig. 3). The temperature and concentrations of CO and CO_2 predicted by the model for this case are significantly higher than the measured values. In fact, calculations resulted in a double-flame structure at this stretch rate (204 s^{-1}) while measurements indicate a single-flame structure. Calculations were repeated with different grid sizes to make sure that the noted differences in flame structure are not associated with the grid resolution. Interestingly, calculations made by Cheng et al. [19] using OPDIFF code also resulted in a double-flame structure under this stretch rate.

The ability of the numerical model in predicting single-flame structure is tested through simulating other flames in Groups B and C discussed in Ref. [19]. Results obtained for $\Phi_{\text{CH}_4} = 0.54$, $\Phi_{\text{H}_2} = 0.28$ flame at a global stretch rate of 90 s^{-1} are compared with the measurements in Fig. 4. Note that methane flame is extinguished at this stretch rate and only the hydrogen flame is present. Calculations reproduced the single-flame structure well.

Calculations of the $\Phi_{\text{CH}_4} = 0.68$, $\Phi_{\text{H}_2} = 0.28$ flame in Fig. 3 at 204 s^{-1} stretch rate yielding a double-flame structure while the measurements show the presence of only hydrogen flame. For understanding this discrepancy between the prediction and measurement additional calculations are performed for this flame. Typically, flames with finite rate chemistry are calculated from an initial solution that is either generated by a global-chemistry model or constructed from a known solution at different flow conditions. Some times finite-rate calculations are also performed from cold-flow solution and by using high-temperature ignition spot. In the present study, calculations for the flame at a given stretch rate are performed from a known solution at lower stretch rate. Considering the possibility of this approach leading to a double-flame structure in Fig. 3, calculations for this flame are repeated by using an initial flame at higher stretch rate and that has only hydrogen flame (as in Fig. 4). Interestingly, a second solution for the flame in Fig. 3 is obtained. The computed results are shown in Fig. 5 along with the measured values. This computed single-flame structure matched well with the flame obtained in the experiments.

The numerical experiments performed for the $\Phi_{\text{CH}_4} = 0.68$, $\Phi_{\text{H}_2} = 0.28$, $k_{\text{global}} = 204 \text{ s}^{-1}$ flame suggests that under certain conditions flames can have two stable states. For understanding this dual-state characteristics of the lean premixed methane flames, calculations for the $\Phi_{\text{CH}_4} = 0.68$, $\Phi_{\text{H}_2} = 0.28$ flame are performed from a low-stretch-rate condition and gradually increasing the stretch rate. The peak temperature and CO_2 concentrations are shown in Fig. 6 for various stretch rates. As expected, temperature decreased

from 1750 K with stretch rate. At about 260 s^{-1} global stretch rate the flame temperature drastically decreased to 1350 K and any further increase in stretch rate increased the temperature slightly. Actually, at 260 s^{-1} global stretch rate the methane flame started extinguishing and at higher stretch rates only hydrogen flame survived yielding single-flame structure.

Calculations performed by decreasing the stretch rate followed the same path till the stretch rate reached a value of 300 s^{-1} . Further reduction in stretch rate did not yield the double-flame structure that was obtained with decreasing-stretch-rate approach. In fact, methane flame could not be established even for stretch rates as low as 60 s^{-1} . This behavior is also found in a slightly richer flame ($\Phi_{\text{CH}_4} = 0.81$, $\Phi_{\text{H}_2} = 0.28$). The variations in peak temperature and CO_2 concentrations with increasing stretch rate for this flame are shown in Fig. 7. Note that the flame response to decreasing stretch rate is similar to that shown in Fig. 6; however, it is not plotted in Fig. 7 due to incomplete calculations.

Two-dimensional structures of the $\Phi_{\text{CH}_4} = 0.68$, $\Phi_{\text{H}_2} = 0.28$, $k_{\text{global}} = 204\text{ s}^{-1}$ flame in different states are shown in Fig. 8. The double-flame structure is shown on the left half and the single-flame structure is shown on the right half. Methane/air mixture is flowing from the bottom and hydrogen/air mixture is flowing from top. As seen from velocity field (Fig. 8a) the stagnation point (zero velocity location) is shifted toward hydrogen jet when the methane flame is established in State A. The volumetric expansion associated with methane flame caused such a shift in stagnation point. The temperature (Fig. 8b) and OH concentration (Fig. 8c) fields further suggest that the hydrogen flame established on the hydrogen-fuel side of the stagnation point is also shifted with the establishment of methane flame.

The structure of $\Phi_{\text{CH}_4} = 0.68$, $\Phi_{\text{H}_2} = 0.28$ flame in State A along stagnation line is shown in Fig. 9. Temperature and heat release rate along the stagnation line are shown in Fig. 9a and the rates of destruction of reactants are shown in Fig. 9b. The concentrations and rates of production of CH_3 and OH radicals are shown in Fig. 9c. Even though the hot products generated along the methane and hydrogen flames are getting mixed and resulting a monotonically decreasing temperature from former to latter, the two flames are chemically well separated. Heat release and reactant consumption associated with each flame are occurring locally and independently. However, abundant species such as OH radicals generated at one flame are transported to the other flame; which might be having some secondary effects on local chemical kinetics.

Even though methane flame is extinguished in the State-B solution, part of the methane/air mixture is consumed near the hydrogen flame. The structure of $\Phi_{\text{CH}_4} = 0.68$, $\Phi_{\text{H}_2} = 0.28$ flame in State B along stagnation line is shown in Fig. 10. Heat-release-rate profile (Fig. 10a) in the shoulder region of the hydrogen flame is modified due to the burning of methane/air mixture. However, such burning is not triggering chain-branching reactions of methane-oxygen system and consequently methane flame is not established.

The rates of destruction of reactants in State-B solution are shown in Fig. 10b while the concentrations and rates of production of CH_3 and OH radicals are shown in Fig. 10c. A very weak, but distinct, methane combustion is taking place in the shoulder region of the hydrogen flame. For example, the peak production rate of CH_3 radical in State-B solution ($\sim 2.5\text{ mole/cm}^3/\text{s}$) is only half of that established in the State-A solution.

ACKNOWLEDGEMENTS:

Financial support for this work was provided by the Air Force Office of Scientific Research (AFOSR, Julian Tishkoff) and the Air Force Contract #F33615-00-C-2068 (Vince Belovich).

REFERENCES:

1. D.C. Haworth, R.J. Blint, B. Cuenot, and T.J. Poinso, *Combust. Flame* 121 (3) (2000) 395-417.
2. S.H. Sohrab, Z.Y. Ye, C.K. Law, *Proc. Combust. Inst.* 20 (1984) 1957-1965.
3. C.K. Law, *Proc. Combust. Inst.*, 22 (1988) 1381-1402.
4. D.M. Mosbacher, J.A. Wehrmeyer, R.W. Pitz, C.J. Sung and J.L. Byrd, *Proc. Combust. Inst.* 29 (2002) 1479-1486.
5. M.A. Tanoff, M.D. Smooke, R.J. Osborne, T.M. Brown, R.W. Pitz, *Proc. Combust. Inst.* 26 (1996) 1121-1128.
6. R.S. Barlow, A.N. Karpetis, J.H. Frank, and J.-Y. Chen, *Combust. Flame* 127 (2001) 2102-2118.
7. J.A. Wehrmeyer, Z. Cheng, D.M. Mosbacher, R.W. Pitz, and R. Osborne, *Combust. Flame* 128 (3) (2002) 232-241.
8. Z. Cheng, J.A. Wehrmeyer, and R.W. Pitz, 38th AIAA/ASME/SAE/ASEE Joint Propulsion Conference, AIAA 2002-4021, Indianapolis, IN, 2002.
9. C.J. Sung, J.B. Liu, and C.K. Law, *Combust. Flame* 106 (1-2) (1996) 168-183.
10. C.K. Law, C.J. Sung, G. Yu and R.L. Axelbaum, *Combust. Flame* 98 (1-2) (1994) 139-154.
11. C.J. Sung, G. J.B. Liu, and C.K. Law, *Combust. Flame* 102 (4) (1995) 481-492.
12. Roquemore W. M., and Katta, V. R., *Journal of Visualization* 2 (2000) 257-272.
13. Katta, V. R., and Roquemore, W. M., *Combustion and Flame*, Vol. 100, No. 1, 1995, p. 61.
14. G.P. Smith, D.M. Golden, M. Frenklach, N.W. Moriarty, B. Eiteneer, M. Goldenberg, C.T. Bowman, R.K. Hanson, S. Song, W.C. Jr. Gardiner, V.V. Lissianski, and Z. Qin, <http://www.me.berkeley.edu/gri-mech>.
15. Annon., Computational Submodels, International Workshop on Measurement and Computation of Turbulent Nonpremixed Flames, <http://www.ca.sandia.gov/TNF/radiation.html>, 2001.
16. Katta, V. R., Goss, L. P., and Roquemore, W. M., *AIAA Journal*, Vol. 32, No. 1, 1994, p. 84.
17. Katta, V. R., Goss, L. P., and Roquemore, W. M., *Int. J. Num. Methods Heat Fluid Flow*, Vol. 4, No. 5, 1994, p. 413.

- 18.K. Seshadri, I. Puri, and N. Peters, *Combust. Flame* 61 (3) (1985) 237-249.
- 19.Cheng, Z., Wehrmeyer J. A, and Pitz, R. W., Lean or Ultra Lean Stretched Planar Methane/Air Flames, to be published in *Proc. Combust. Inst.*, 30 (2004)

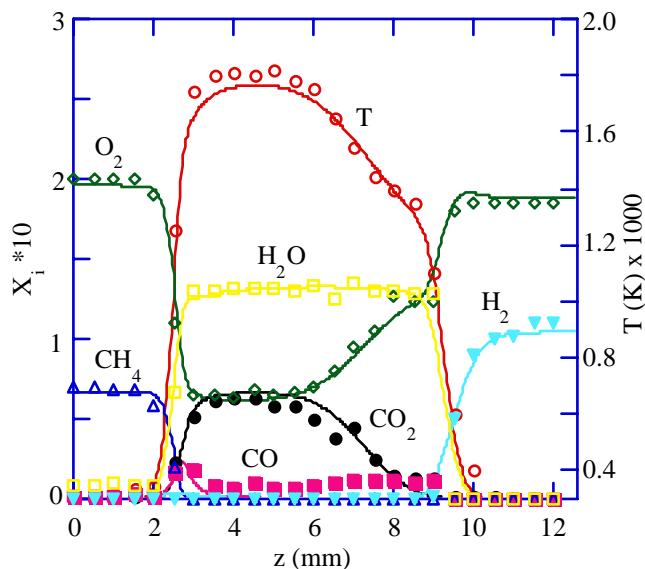


Fig. 1. Computed (lines) and measured (symbols) temperature and species distributions along stagnation line for $\Phi_{CH_4} = 0.68$, $\Phi_{H_2} = 0.28$, $k_{global} = 80 \text{ s}^{-1}$ flame.

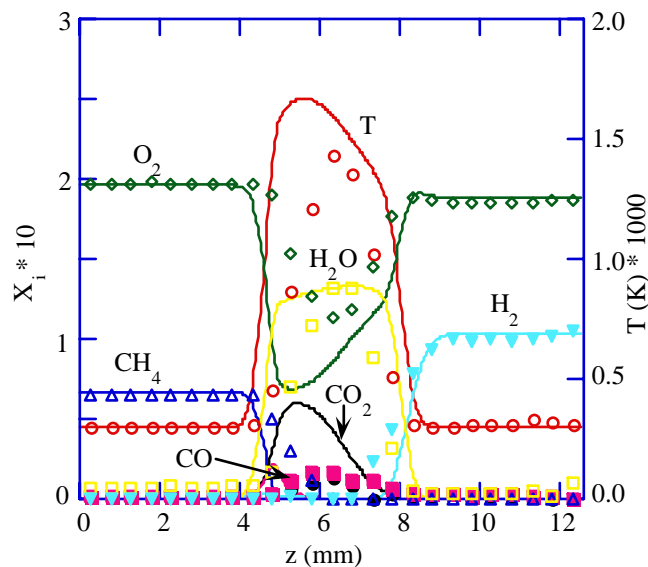


Fig. 3. Computed (lines) and measured (symbols) temperature and species distributions along stagnation line for $\Phi_{CH_4} = 0.68$, $\Phi_{H_2} = 0.28$, $k_{global} = 204 \text{ s}^{-1}$ flame.

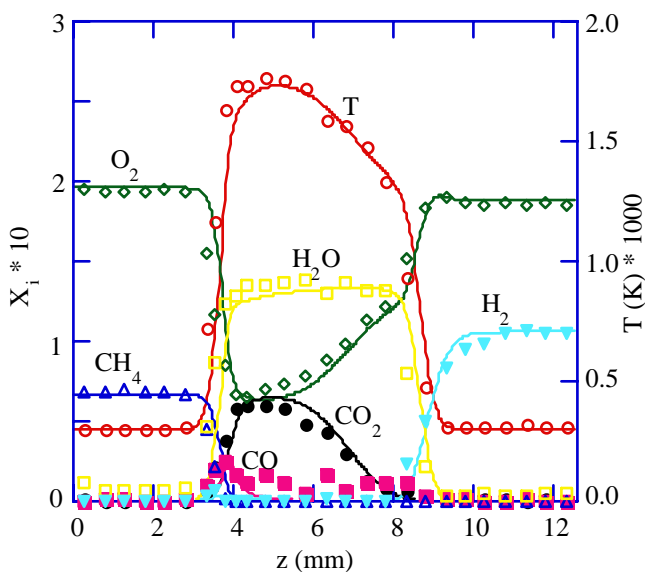


Fig. 2. Computed (lines) and measured (symbols) temperature and species distributions along stagnation line for $\Phi_{CH_4} = 0.68$, $\Phi_{H_2} = 0.28$, $k_{global} = 136 \text{ s}^{-1}$ flame.

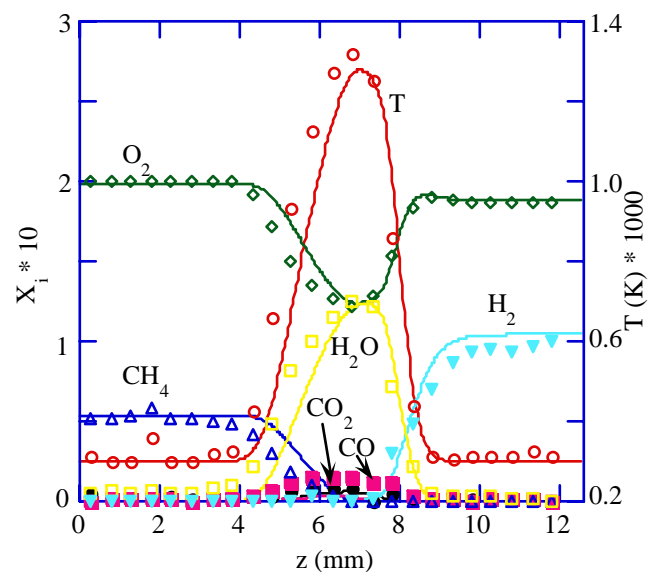


Fig. 4. Computed (lines) and measured (symbols) temperature and species distributions along stagnation line for $\Phi_{CH_4} = 0.54$, $\Phi_{H_2} = 0.28$, $k_{global} = 90 \text{ s}^{-1}$ flame.

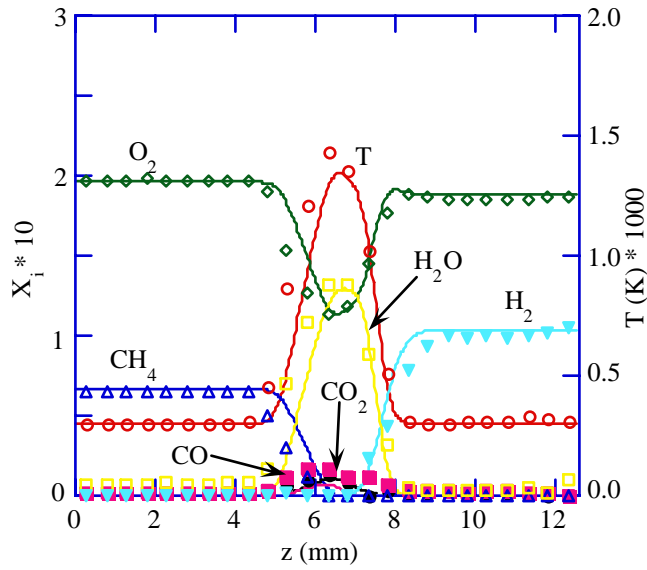


Fig. 5. Computed (lines) second state of the $\Phi_{\text{CH}_4} = 0.68$, $\Phi_{\text{H}_2} = 0.28$, $k_{\text{global}} = 204 \text{ s}^{-1}$ flame. Symbols show measurements.

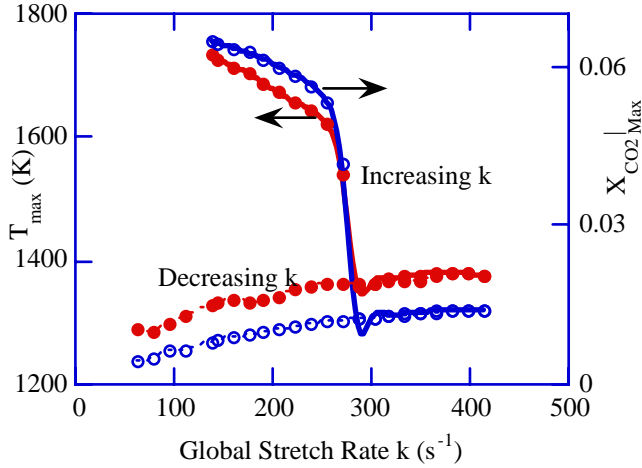


Fig. 6. Variation of peak temperature (solid circles) and CO_2 (open circles) concentration with increasing (solid lines) and decreasing (broken lines) stretch rates for flame in Fig. 1.

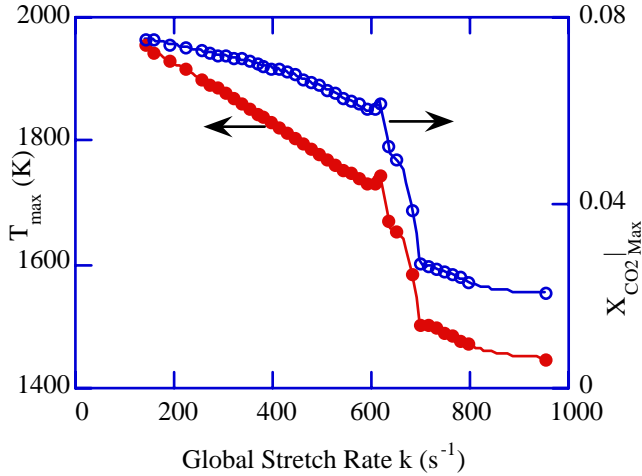


Fig. 7. Variation of peak temperature (solid circles) and CO_2 (open circles) concentration with increasing stretch rates for $\Phi_{\text{CH}_4} = 0.81$, $\Phi_{\text{H}_2} = 0.28$ flame.

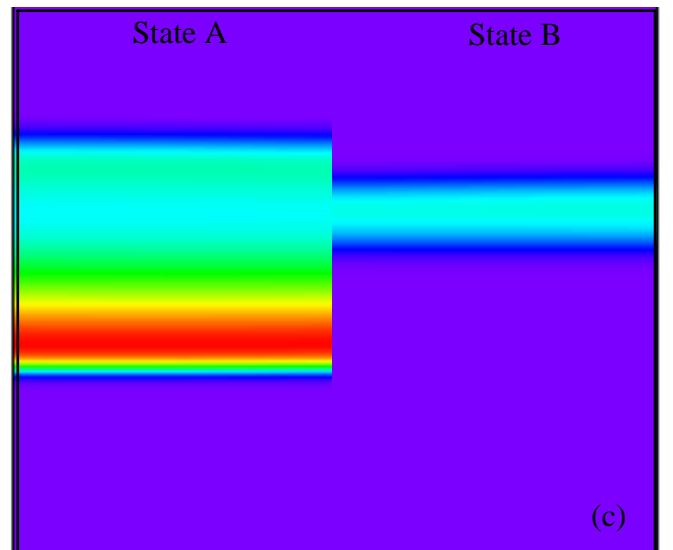
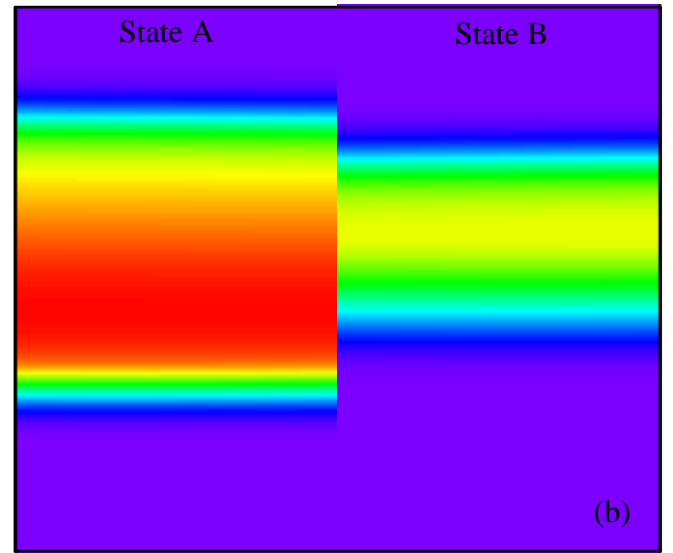
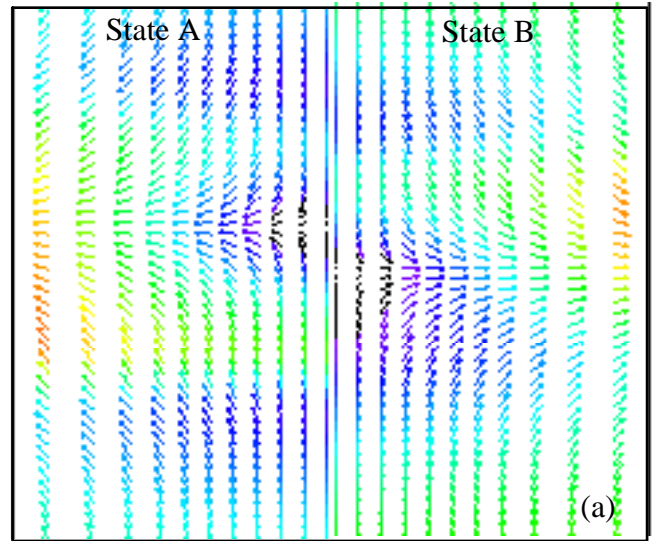


Fig. 8. Two states of $\Phi_{\text{CH}_4} = 0.68$, $\Phi_{\text{H}_2} = 0.28$ flame shown between $z = 2$ and 10 mm and between $r = 0$ and 4 mm . (a) Velocity field, (b) temperature and (c) OH concentration

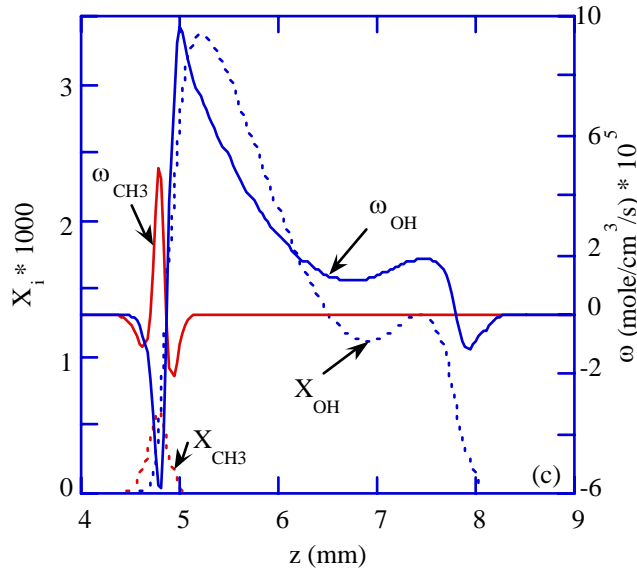
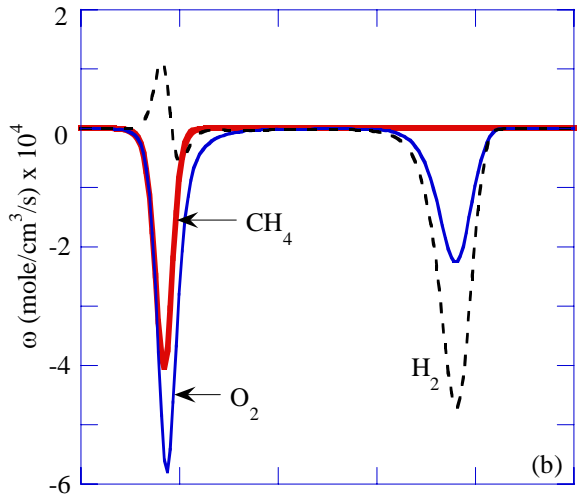
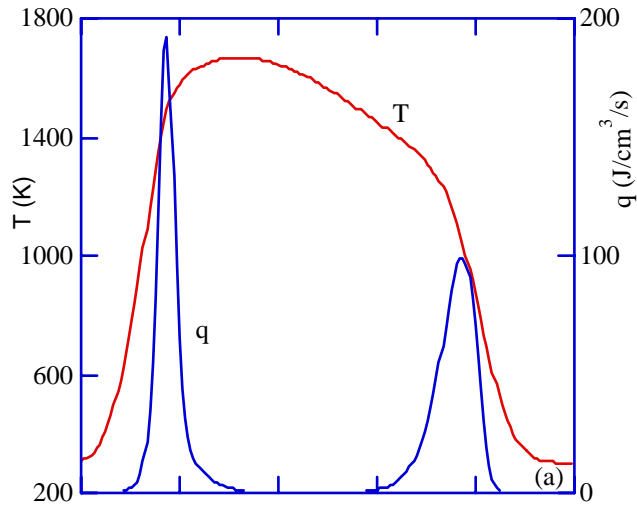


Fig. 9. Structure of $\Phi_{\text{CH}_4} = 0.68$, $\Phi_{\text{H}_2} = 0.28$ flame in State A along stagnation line. (a) Temperature and heat release rate, (b) rates of production of reactants, and (c) concentrations and rates of production of CH_3 and OH radicals.

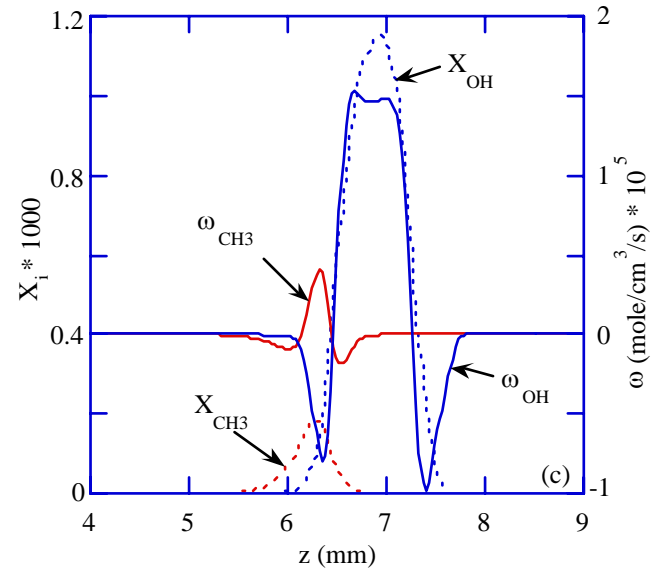
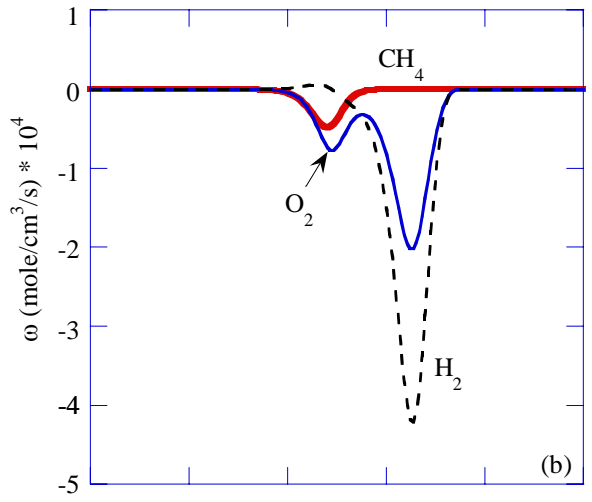
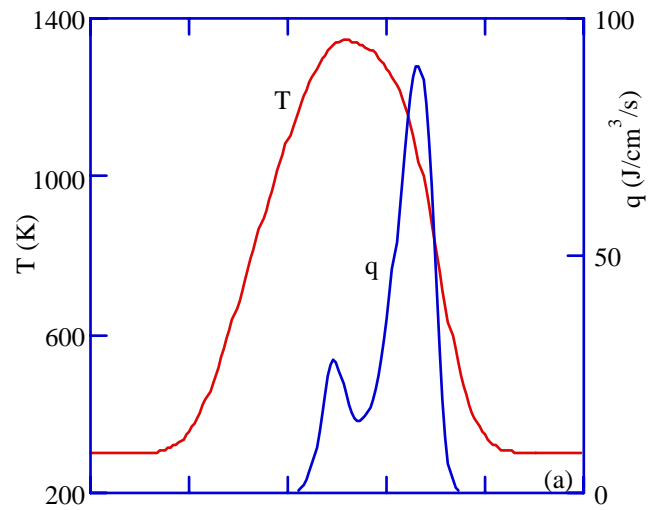


Fig. 10. Structure of $\Phi_{\text{CH}_4} = 0.68$, $\Phi_{\text{H}_2} = 0.28$ flame in State B along stagnation line. (a) Temperature and heat release rate, (b) rates of production of reactants, and (c) concentrations and rates of production of CH_3 and OH radicals.

Effect of Nitromethane on Soot Formation in Heptane Jet Diffusion Flame

V. R. Katta*

Innovative Scientific Solutions, Inc.
2766 Indian Ripple Road
Dayton, OH 45440

and

W. M. Roquemore

Air Force Research Laboratory
Propulsion Directorate
Wright-Patterson Air Force Base, OH 45433

Residence time and thermo-chemical environment are important factors in the soot-formation processes of jet diffusion flames. For understanding the chemical and physical structure of the soot formed in jet flames knowledge on flow dynamics of diffusion flames is required. A time-dependent, axisymmetric mathematical model known as UNICORN (Unsteady Ignition and Combustion using ReactionNs) is used for the simulation of Heptane/Air unsteady jet diffusion flames. A detailed chemical-kinetics model is incorporated into UNICORN for the investigation of PAH formation in heptane flames. It consists of up to 197 species and 2800 elementary-reaction steps. A simple soot model based on two conservation equations and acetylene concentration is used for estimating soot production in these flames. The effect of nitromethane on the PAH species and soot formed in these flames is investigated by incorporating nitromethane chemistry. Small amounts of nitromethane are added to fuel jet.

INTRODUCTION:

Considerable progress has been made in recent years in understanding the chemical and physical aspects of soot formation in hydrocarbon flames. After the first aromatic rings (such as benzene and small PAHs) are formed in the gas phase, acetylene and other molecules react with these small PAHs to form larger PAHs [1]. The first soot particles are thought to be formed when two or more PAHs react to form a three dimensional particle. This process is known as particle inception [2]. The soot particles formed interact with the gas-phase molecules by the addition of acetylene to their surfaces (surface growth) and by the reaction with molecular oxygen and/or hydroxyl radical (oxidation). Another process thought to increase soot mass is the collision of PAHs with a soot particle.

Several experimental and numerical investigations of soot formation have been performed using coflow and counterflow diffusion flames [3-6]. A few have focused on the importance of soot particle pathways (i.e., residence time, temperature, and chemistry) [7,8]. Santoro et al. [7] used soot volume fraction, temperature, and velocity measurements from an ethylene-air jet diffusion flame to examine the soot growth process along individual particle

paths. Based on experimental data, they argued that the soot formation rate increases in the annular region of the flame due to an increase in residence time. Lin and Faeth [8] found that the direction of soot particle movement with respect to the flame sheet is important. They argued that if soot particles forming on the fuel rich side of the flame remained entrained in the fuel-rich region for a long time before crossing the flame surface, then surface growth could be enhanced. In contrast, Lin and Faeth [8] argued that the amount of soot generated could be reduced if the soot particle is made to cross the flame surface quickly. Recent calculations of Katta et al. [9] have suggested that presence of large-scale structures in dynamic flames could influence the way PAH species are formed and hence, could impact the amount of soot produced. The purpose of this paper is to investigate the influence of additives on soot formation in jet diffusion flames.

Various attempts have been made in the past to develop models for soot predictions. Some of these models are detailed, and have been calibrated against experimental data obtained in laminar, premixed or diffusion flames of simple configurations. For example, Frenklach and coworkers [10] proposed a detailed kinetic model of soot formation and validated [10,11] using measurements of laminar, premixed flames while Mauss, Bockhorn and their coworkers [12,13] established a different detailed soot model that was tested in laminar, counter-flow diffusion flames. The detailed kinetic soot model consists of 1) gas-phase chemistry and 2) kinetics describing the particle growth and destruction processes. The gas-phase chemistry describes the formation of PAHs [14,15]. The particle growth and destruction involve inception/ nucleation of particles resulting from coagulation of PAHs and are modeled via a set of surface reactions [10-13], and particle coagulation is modeled based on the method of moments [10-13] or the discrete-sectional method [16,17].

The most widely used soot models are based on the assumption that soot consists of particles with monodisperse size distribution. Then the soot formation, coupled directly to the fuel concentration, is modeled by one or two equations: one for the particle volume fraction and the other for the particle number density. Leung et al. [18] argued that the intermediate species contributing to the soot particle formation should be connected to at least the pyrolysis kinetics of the fuel. For simplicity, they assumed acetylene

*Corresponding Author: vrkatta@erinet.com

Proceedings of 4th Joint Meeting of the U. S. Sections of the Combustion Institute, 2005.

to be the intermediate species and proposed a simplified soot model combined with the gas-phase kinetics of fuel pyrolysis for counterflow, ethylene and propane flames [18] as well as coflow, methane flames [19]. The results showed that with this approach good agreement with measured data for soot volume fraction, particle growth and number density could be obtained. In the present work, a model similar to that of Leung et al. [18] is used for the predictions of soot formation in jet diffusion flames.

NUMERICAL MODEL:

A time-dependent, axisymmetric mathematical model known as UNICORN (Unsteady Ignition and Combustion using ReactionNs) [20,21] is used to simulate the potentially unsteady combustions flows considered in this study. It solves for u- and v-momentum equations, continuity, and enthalpy- and species-conservation equations on a staggered-grid system. The body-force term due to the gravitational field is included in the axial-momentum equation for simulating vertically mounted flames. A clustered mesh system is employed to trace the large gradients in flow variables near the flame surface. A detailed chemical-kinetics model developed by NIST [22] is incorporated into UNICORN for the investigation of PAH formation in heptane flames. It consists of 197 species and 2800 elementary-reaction steps. Thermo-physical properties such as enthalpy, viscosity, thermal conductivity, and binary molecular diffusion of all the species are calculated from the polynomial curve fits developed for the temperature range 300 - 5000 K. Mixture viscosity and thermal conductivity are then estimated using the Wilke and Kee expressions, respectively. Molecular diffusion is assumed to be of the binary-diffusion type, and the diffusion velocity of a species is calculated using Fick's law and the effective-diffusion coefficient of that species in the mixture. A simple radiation model based on the optically thin-media assumption is incorporated into the energy equation. Only radiation from CH₄, CO, CO₂, H₂O, and soot is considered in the present study.

The finite-difference forms of the momentum equations are obtained using an implicit QUICKEST scheme [23], and those of the species and energy equations are obtained using a hybrid scheme of upwind and central differencing. At every time step, the pressure field is accurately calculated by solving all the pressure Poisson equations simultaneously and using the LU (Lower and Upper diagonal) matrix-decomposition technique. The boundary conditions are treated in the same way as that reported in earlier papers [24].

Soot Model

This study utilized a two-equation model for soot with transport equations for particle number density, N_s , and soot mass fraction, Y_s . These equations can be written for unsteady flow as

$$\frac{\partial N_s}{\partial t} + \nabla \cdot (\rho V N_s) - \nabla \cdot (\rho D_{N_s} \nabla N_s) = \omega_{N_s} \quad (1)$$

$$\frac{\partial Y_s}{\partial t} + \nabla \cdot (\rho V Y_s) - \nabla \cdot (\rho D_s \nabla Y_s) = \omega_s \quad (2)$$

where \mathbf{V} is the velocity vector, ρ is density, D is the molecular diffusion coefficient, and ω is the production term from chemical reactions. The two source terms in Eqs. 1 and 2 are obtained using Lindstedt's model [25], which is based on the simplifying assumption that nucleation and growth are first-order functions of acetylene concentrations. The underlying chemical reactions for nucleation and growth are similar and given as



with the reaction rates

$$r_1 = k_1(T) [C_2H_2] \text{ and } r_2 = k_2(T) f(A_s) [C_2H_2]$$

for nucleation and growth, respectively, where $f(A_s)$ denotes a functional dependence on soot surface area per unit volume. Brookes and Moss [26] analyzed the functional dependence of the soot growth rate on A_s and found that under simplified conditions with no soot oxidation and radiation the appropriate functional dependence is linear and therefore $f(A_s)$ is set equal to A_s .

The reaction steps for O₂ and OH oxidation can be written as



The reaction rates for equations (4) and (5) are approximated by $r_3 = k_3(T) A_s [O_2]$ and $r_4 = k_4(T) A_s [OH]$.

The expression for O₂ oxidation is essentially the one derived by Lee et al. [27]. Reaction rate constants for OH attack on soot particles are taken from Bradley et al. [28] and a collision efficiency of 0.04 [29] is assumed.

Using the above expressions, the source terms for soot mass fraction and particle density can be obtained from

$$\omega_s = 2k_1(T) [C_2H_2] M_s + 2k_2(T) A_s [C_2H_2] M_s - k_3(T) A_s [O_2] M_s - k_4(T) A_s [OH] M_s \quad (6)$$

and

$$\omega_{N_s} = 2k_1(T) [C_2H_2] N_a/n_{c,min} - 2C_a (d_p)^{1/2} (6\sigma_B T/\rho_s)^{1/2} (\rho_{N_s})^2 \quad (7)$$

The last term on the right of Eq. 7 accounts for the decrease in particle number density by particle agglomeration. Here $\sigma_B = 1.38 \times 10^{-23}$ J/K is the Boltzmann constant, M_i is the molecular weight of species i , $N_A = 6.0232 \times 10^{26}$ is the Avogadro number, $C_a = 9$ is the agglomeration constant, and $n_{c,min} = 60$ is the minimum particle number required for particle nucleation. The density of the soot particles (ρ_s) is assumed to be 1800 kg/m³. The particle surface area is defined by

$$A_s = \pi (d_p)^2 N_s \quad (8)$$

with the particle diameter, d_p , given as

$$d_p = (6 Y_s / \pi \rho_s N_s). \quad (9)$$

Finally, soot volume fraction (f_v) is calculated from soot mass fraction using the relationship $f_v = \rho Y_s / \rho_s$.

RESULTS AND DISCUSSION

The CFD model UNICORN has been extensively validated in the past by simulating various steady and unsteady counterflow and coflow jet diffusion flames and by comparing the results with experimental data. This gives confidence that UNICORN can simulate the structure of dynamic flames accurately. However, the integration of heptane and PAH chemistry into UNICORN needs to be validated. This is achieved by simulating partially premixed opposing jet flames of Berta et al. [30]. Computed solutions obtained for a flame with global strain rate of 50 s^{-1} and fuel-stream equivalence ratio of 4 are compared with the experimental data in Fig. 1. Predictions for temperature and various species including benzene seem to follow the measurements.

Calculations are performed for a jet diffusion flame with fuel jet and coflow air velocities of 0.05 m/s and 0.2 m/s, respectively. The fuel jet diameter is 1 cm. Pure fuel (100% heptane) and bended fuel (80% heptane + 20% toluene) are used as fuels. Effect of nitromethane on soot formation in these flames is studied by adding various amounts of nitromethane to the fuel jet. Two-dimensional calculations are performed using a grid system with 151×101 nodes on a physical domain of $150 \times 50 \text{ mm}$.

Results obtained for 100% heptane flame are shown in Figs. 2-4. Distributions of soot mass fraction in these flames are shown in Fig. 2. Peak value corresponding to white color is $\sim 3\%$ of the total gas mass. Regions shaded with white represent flame locations where soot mass fraction has increased beyond 3% level. As seen from Fig. 2 soot is increasing with the addition of nitromethane. However, addition of nitromethane is also reducing the flame height and flame diameter. Consequently, increase in local soot concentration may not necessarily result into an increase in total soot generated in these flames. For investigating this possibility, flame structures in radial and axial directions are shown in Figs. 3 and 4. The axial velocity and temperature profiles obtained at a height of 60 mm (Fig. 3) indicate that the flame diameter decreases with the addition of nitromethane. Flame is also accelerating at the centerline due to volumetric expansion resulting from higher temperature. As seen from Fig. 4a heptane is more rapidly consumed in the presence of nitromethane. Consistent with the increase in soot mass fraction, peak concentrations of benzene, acetylene and biphenyl are increasing with the addition of nitromethane.

In order to assess the overall effect of nitromethane in these jet flames, mass fractions of heptane, benzene,

acetylene and biphenyl are integrated over the flame cross section at different flame heights and the results are shown in Figs. 4c and 4d. Interestingly, net mass fractions of benzene, acetylene and biphenyl are decreasing with the addition of nitromethane. This suggests that even though nitromethane increases the local concentrations of PAH species and soot in a jet flame, the over all production of these species is actually decreased.

Results obtained for 80% heptane+20% toluene fuel blend are shown in Figs. 5-7. Even though addition of nitromethane flame up to 18% yielded stable flames, addition of 20% nitromethane destabilized the flame base and the flame became extinguished in time. The soot image shown in Fig. 5 for the 20% nitromethane case is an instantaneous solution obtained during the blowout process. Similar to the pure heptane flames, local soot mass fraction increased with the addition of nitromethane in the blend-fuel case also. Due to the reduction in the flame size, the net production of benzene, acetylene and biphenyl are decreased with the addition of nitromethane.

ACKNOWLEDGEMENTS

Financial support for this work was provided by Strategic Environmental Research and Development Program (SERDP, Charles Pellerin), the Air Force Office of Scientific Research (AFOSR, Julian Tishkoff) and the Air Force Contract #F33615-00-C-2068 (Vince Belovich).

REFERENCES:

1. Richter, H. and Howard, J. B., *Prog. Energy Combust. Sci.* 26:565 (2000)
2. Kennedy, I. M., *Prog. Energy Combust. Sci.* 23:95 (1997)
3. Kaplan, C. R., and Kilasanath, K., *Combustion and Flame*, Vol. 124, 2001, pp. 275-294.
4. Smooke, M. D., Mecnally, C. S., Pfefferle, L. D., Hall, R. J., and Colket, M. B., *Combustion and Flame*, Vol. 117, 1999, pp. 117-139.
5. Sugiyama, G., *Proceedings of the Combustion Institute*, The Combustion Institute, PA, Vol. 25, 1994, pp. 601-608.
6. Du, J., and Axelbaum, R. L., *Combustion and Flame*, Vol. 100, 1995, pp. 367-375.
7. Santoro, R. J., Yeh, T. T., Horvath, J. J., and Semerjian, H. G., *Combustion Science and Technology*, Vol. 53, 1987, pp. 89-115.
8. Lin, K.-C., and Faeth, G. M., *Journal of Propulsion and Power*, Vol. 12, 1996, pp. 10-17.
9. Katta, V. R., Blevins, L. G., and Roquemore, W. M., *PAH Formation in an Inverse Diffusion Flame*, AIAA Paper No. 2003-0666, Reno, NV, 2003.
10. Frenklach, M. and Wang, H., *Twenty-third Symposium (International) on Combustion*, The Combustion Institute, Pittsburgh, 1991, pp.1559-1566.
11. Frenklach, M. and Wang, H., in *Soot Formation in Combustion: Mechanisms and Models* (H. Bockhorn, Ed.), Springer-Verlag, Heidelberg, 1994, pp.165-189.
12. Mauss, F., Schäfer, T. and Bockhorn, H., *Combust. Flame* 99:697-705 (1994).
13. Mauss, F. and Bockhorn, H., *Z. Phys. Chem.* 188:45 (1995).
14. Haynes, B.S. and Wagner, H. GG., *Prog. Energy Combust. Sci.* 7:229-273 (1981).
15. Calcote, H.F., *Combust. Flame* 42:215-242 (1981).

16. Colket, M.B. and Hall, R.J., in *Soot Formation in Combustion: Mechanisms and Models* (H. Bockhorn, Ed.), Springer-Verlag, Heidelberg, 1994, pp.442-468.
17. Hall, R.J., Smooke, M.D. and Colket, M.B., in *Physical and Chemical Aspects of Combustion: A Tribute to Irvin Glassman* (F.L. Dryer and R.F. Sawyer, Eds.), Gordon and Breach, Amsterdam, 1997, pp.189-230.
18. Leung, K.M., Lindstedt, R.P. and Jones, W.P., *Combust. Flame* 87:289-305 (1991).
19. Lindstedt, R.P., in *Soot Formation in Combustion: Mechanisms and Models* (H. Bockhorn, Ed.), Springer-Verlag, Heidelberg, 1994, pp.417-439.
20. Roquemore W. M., and Katta, V. R., *Journal of Visualization*, in press Jan. 2000.
21. Katta, V. R., and Roquemore, W. M., *Combustion and Flame*, Vol. 100, No. 1, 1995, p. 61.
22. Tsang W., and Babushok, V., "Detailed mechanism for PAH species" *manuscript in preparation*, National Institute of Standards and Technology, Gaithersburg, MD, 2004
23. Katta, V. R., Goss, L. P., and Roquemore, W. M., *AIAA Journal*, Vol. 32, No. 1, 1994, p. 84.
24. Katta, V. R., Goss, L. P., and Roquemore, W. M., *Int. J. Num. Methods Heat Fluid Flow*, Vol. 4, No. 5, 1994, p. 413.
25. Lindstedt, P. R., in *Soot Formation in Combustion* (H. Bockhorn, Ed.), Springer Verlag, Heidelberg, 1994, p. 417.
26. Brookes, S. J., and Moss, J. B., *Combust. Flame*. 116:486 (1999).
27. Lee, K. B., Thring, M. W., and Beer, J. M., *Combust. Flame* 6:137 (1962).
28. Bradley, D., Dixon-Lewis, G., El-Din Habik, S., and Mushi, E. M. J., *Twentieth Symposium (International) on Combustion*, The Combustion Institute, Pittsburgh, 1984, p. 931.
29. Puri, R., Santoro, R. J., and Smyth, K. C., *Combust. Flame* 97:125 (1994).
30. P. Berta, Puri. I. K., Aggarwal, S. K., Partially Premixed n-Heptane/Air Counterflow Flames, 2004 Spring Technical Meeting, Central States Section of the Combustion Institute, 21-23 March, 2004, Austin, Texas.

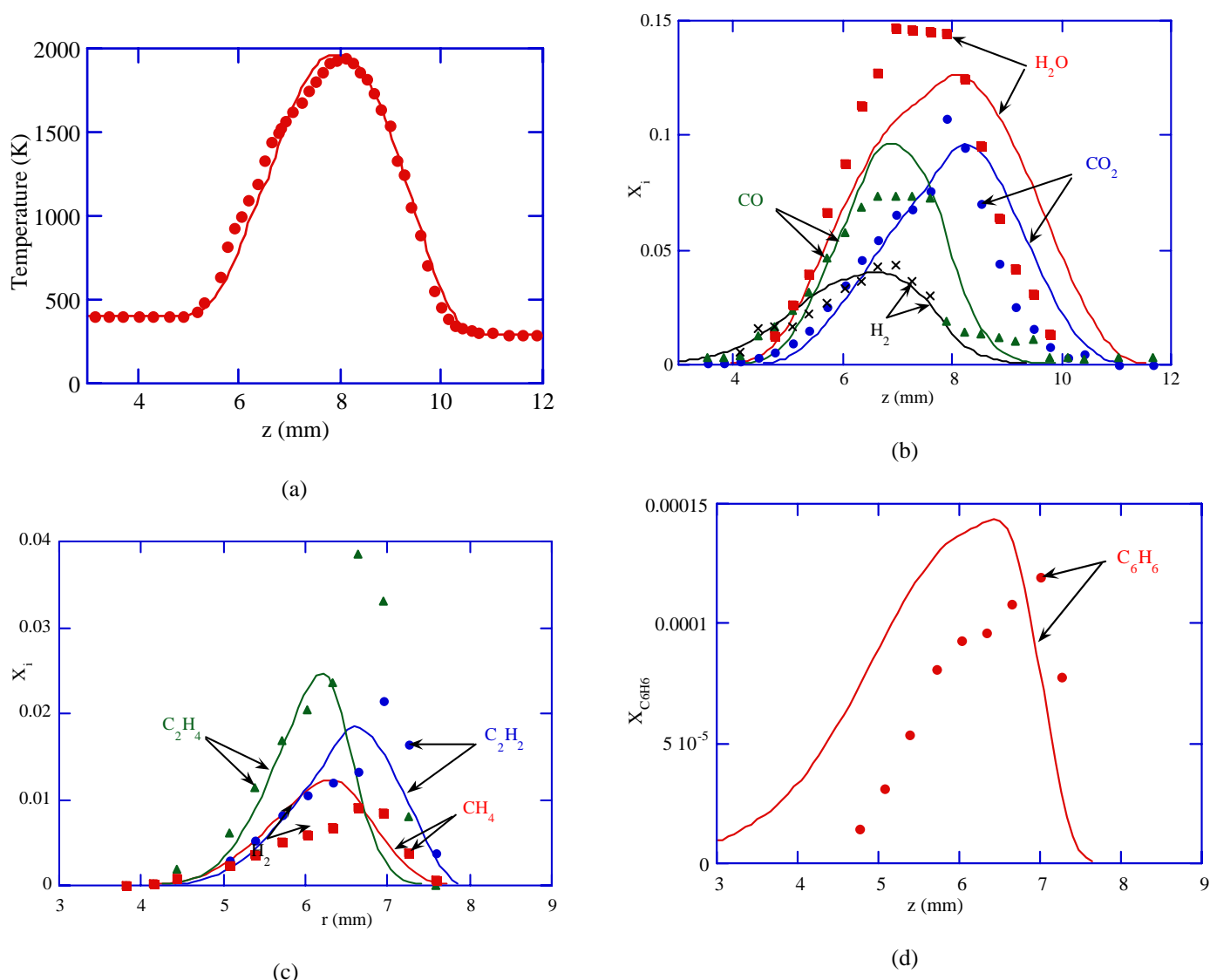


Fig. 1. Comparison of predicted (lines) and measured (symbols) flame structures of partially premixed opposing jet diffusion flame. Experimental data were made by Berta et al [30]. (a) Temperature, (b) molar concentrations of CO, CO₂, H₂O, H₂, (c) molar concentrations of CH₄, C₂H₂, C₂H₄, and (d) benzene concentration along the stagnation line.

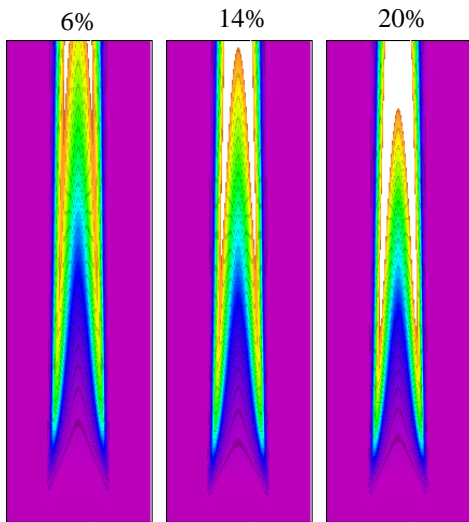


Fig. 2 Soot distribution in a jet diffusion flame with different levels of nitromethane added to heptane fuel jet. Each image represents 120 mm height. Excess soot is marked in white.

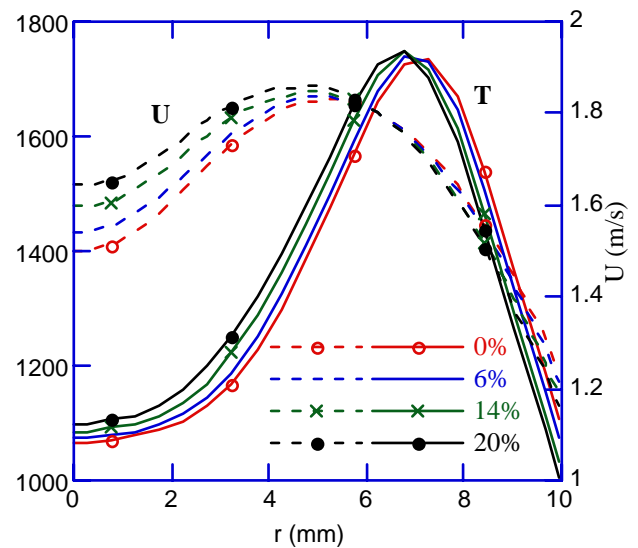


Fig. 3. Distributions of axial velocity and temperature at a height of 60 mm above the burner.

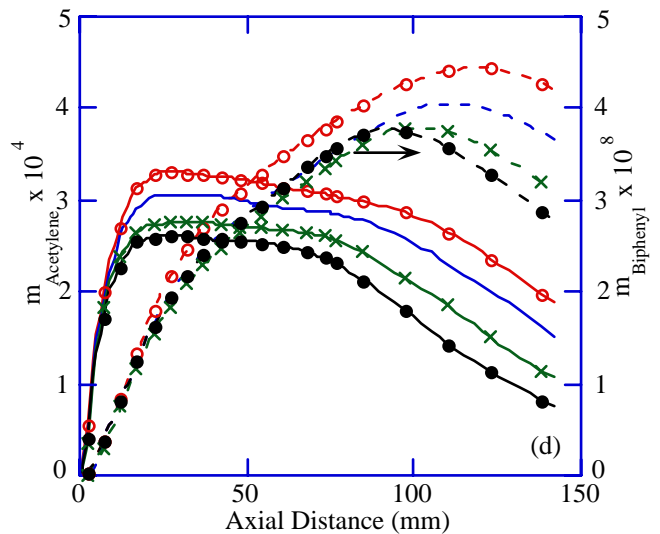
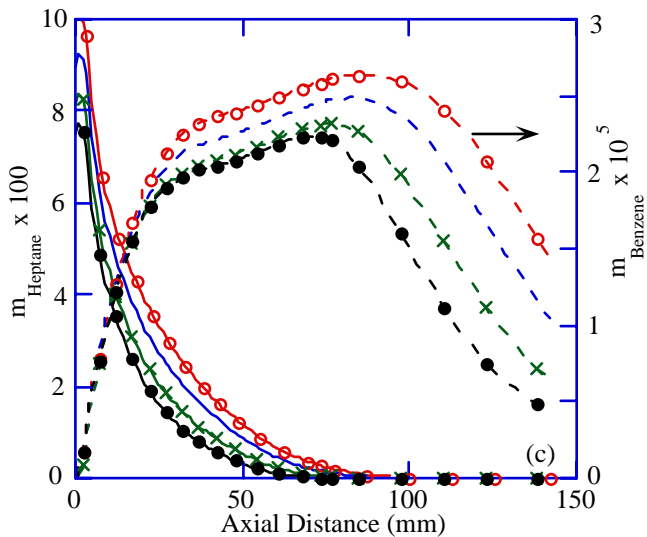
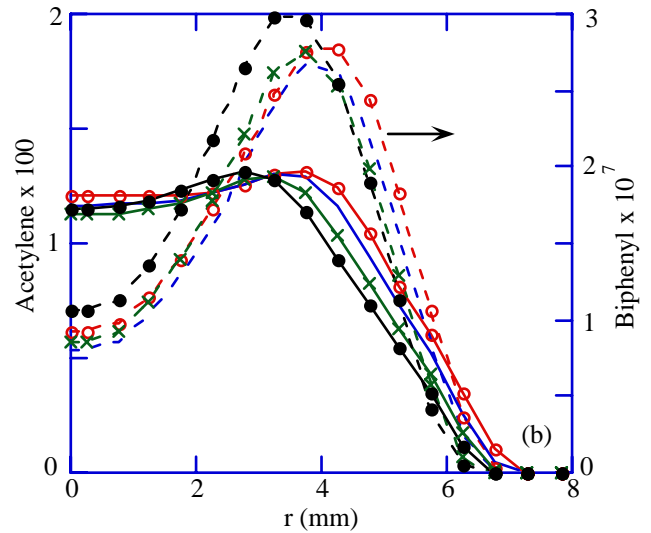
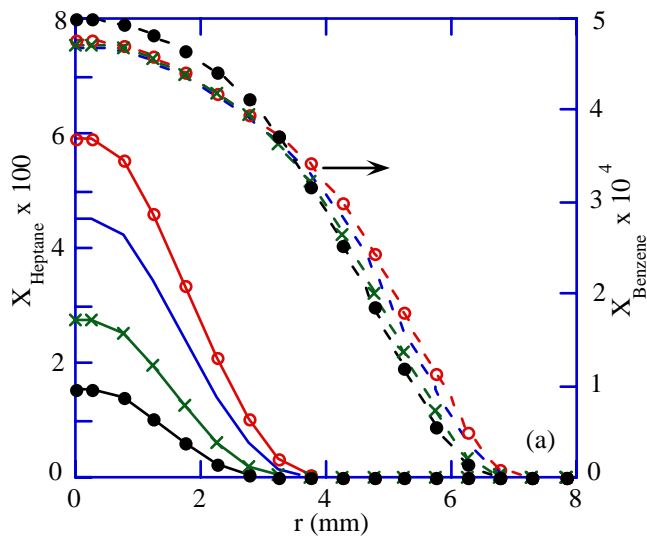


Fig. 4. Heptane decomposition and formation of benzene, acetylene and biphenyl for various concentrations of nitromethane. Lines with open circles, no symbols, crosses, and solid circles represent 0, 6, 14, and 20 % nitromethane, respectively. Figs. (a) and (b) represent flame structure at a height of 60 mm. Figs. (c) and (d) represent total mass fractions at different heights.

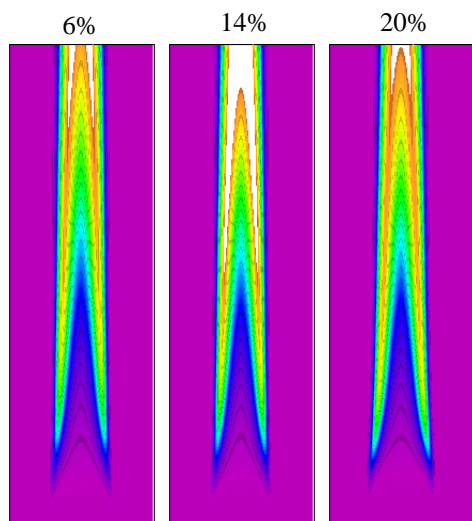


Fig. 5 Soot distribution in heptane+toluene flame with different levels of nitromethane added to fuel. Each image represents 120 mm height. Excess soot is marked in white.

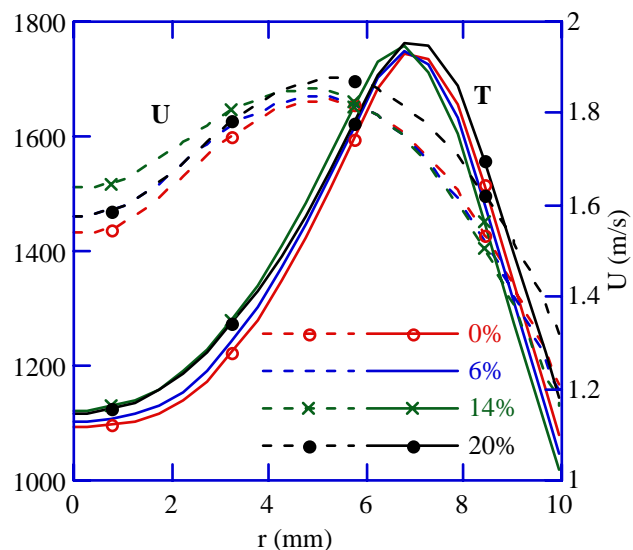


Fig. 6. Distributions of axial velocity and temperature at a height of 60 mm above the base for heptane+toluene flame.

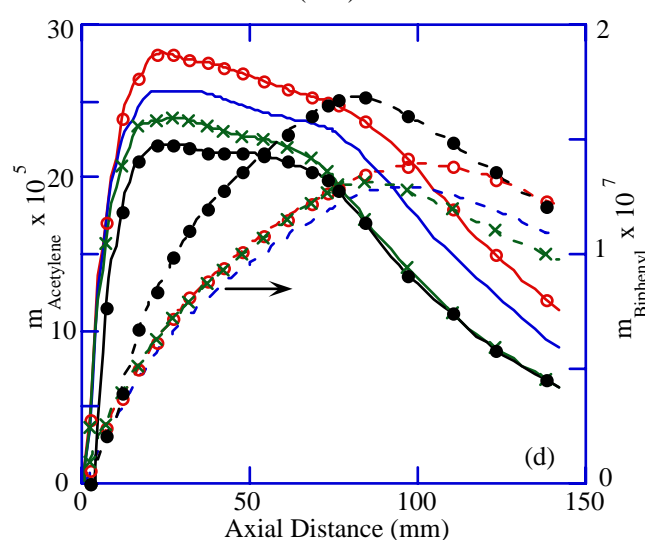
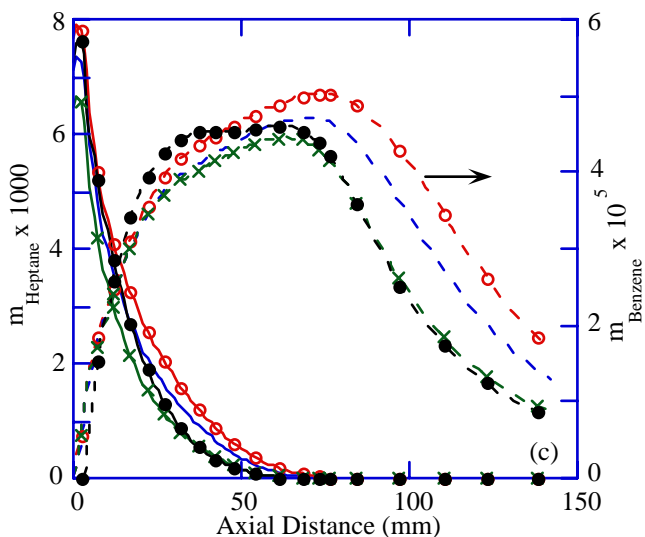
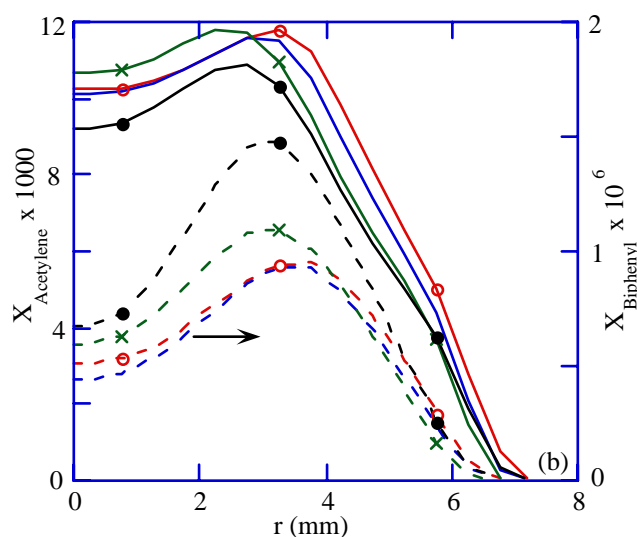
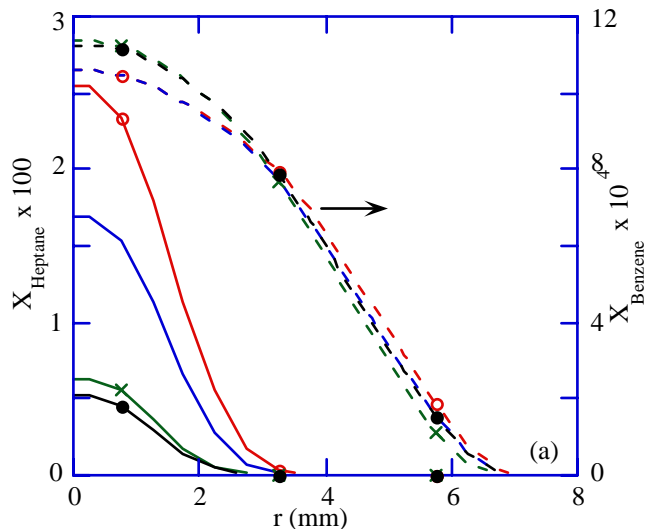


Fig. 7. Heptane decomposition and formation of benzene, acetylene and biphenyl in heptane+toluene flame. Lines with open circles, no symbols, crosses, and solid circles represent 0, 6, 14, and 20 % nitromethane added to the fuel jet, respectively. Figs. (a) and (b) represent flame structure at a height of 60 mm. Figs. (c) and (d) represent total mass fractions at different heights.

CFD Based Global and Detailed Chemistry Predictions for Inverse Laminar Ethane Jet Diffusion Flames under Oxygen Enhancement and Gravity Variation.

Pramod Bhatia^{*a}, V. R. Katta^b, S.S. Krishnan^c, P.B. Sunderland^d and J. P. Gore^a

^a*School of Mechanical Engineering, Purdue University, West Lafayette, IN 47907, USA*

^b*Innovative Scientific Solutions, Inc., 2766 Indian Ripple Road, Dayton, OH 45440-3638, USA*

^c*Department of Mechanical Engineering, Purdue School of Engineering and Technology, IUPUI,
723 W. Michigan Street, Indianapolis, IN 46202, USA*

^d*Department of Fire Protection Engineering, University of Maryland, College Park, MD 20742, US*

Abstract

Global chemistry calculations (involving five species) and detailed chemistry calculations (involving 99 species including PAH and 1066 reactions) at four different oxidizer compositions (21, 30, 50 and 100 % O₂ mole fraction in N₂), for ethane inverse jet diffusion flames in earth gravity and in microgravity conditions were made using an axisymmetric, time dependent computational fluid dynamics code. Computations were compared with the experimental photographs of microgravity and 1-g flames. Enhancement in oxygen resulted in increased flame temperatures. Calculations reveal that oxygen enhancement causes an increase in PAH, CO and C₂H₂ emission for earth gravity inverse diffusion flames, whereas they decrease for microgravity inverse diffusion flames. However their maximum PPM (by mass) in general increases with oxygen enhancement and gravity reduction. The flame width also increased with oxygen enhancement and gravity reduction.

Nomenclature

Og_IDF_{xx}	Inverse diffusion flame under microgravity with oxidizer composed, respectively, of xx and (100 - xx) mole % of O ₂ and N ₂ .
$1g_IDF_{xx}$	Inverse diffusion flame under normal gravity with oxidizer composed, respectively, of xx and (100 - xx) mole % of O ₂ and N ₂ .
% Production (xxx)	Net mass production rate of "xxx" species (calculated at the domain exit) $\times 100$
D	Jet mass inflow Burner's inner diameter
Fr	Froude Number $\left(= \frac{V_0^2}{g \cdot D} \right)$
$L_{f, comp}$	Computed flame length.
$L_{f, exp}$	Experimental flame length
PPM	Parts per million (by mass)
Re	Reynolds number based on D and V ₀
\dot{Q}	Heat release rate, for complete combustion using low heating value of fuel.
$T(K)$	Temperature in Kelvin
$T_{ad}(K)$	Adiabatic flame temperature in Kelvin
$T_{max}(K)$	Maximum computed flame Temperature in Kelvin
V	Axial velocity
V_0	Jet velocity
V_{co}	Co-flow velocity
W_{comp}	Computed flame width
W_{exp}	Experimental flame width
z	Axial distance from the burner tip
Z_0	z at r = 0

Introduction

Laminar jet diffusion flames are fundamental to combustion. Their study has contributed to myriad advances in combustion science, including the development of theoretical, computational, and diagnostic combustion tools. Laminar jet flames are pertinent to the turbulent flames of more practical interest. These flames were one of the first flame configurations to be observed in microgravity (Edelman et al. 1972 [1] and references therein). This work and subsequent studies by Bahadori and co-workers [2, 3] were mostly confined to measurements of luminous flame shapes. These early efforts involved tests in the NASA 2.2- and 5.2-second drop facilities. These studies considered only normal diffusion flames burning in air. Bahadori et al. (1993) considered microgravity methane and propane gas jet flames burning in various pressure ambients of 15-50% O₂ in N₂ [3]. They noted that increased oxygen concentrations led to shorter flames and increased soot concentrations.

Blevins et al. (2001) considered laminar ethylene inverse diffusion flames for soot structure and chemical analysis in 1-g [4]. Sunderland et al. (2003) studied pure oxygen ethylene diffusion flames in normal and inverse spherical configurations [5]. However, they used diluted fuel and their objective was to study flame structure and hydrodynamic effects under microgravity conditions. Van-Hulle (2002) studied turbulent methane diffusion flames with two oxidizers: air and oxygen [6].

Hence, both jet diffusion and inverse diffusion flames have been studied with great interest over the past few decades. Both configurations can arise on earth [7] and in space. Oxygen enrichment and gravity variation can have significant effect on flame properties. For example, the 2000 species equilibrium calculations show that the adiabatic flame temperature for ethane increases from 2250 K in air to 3082 K in oxygen i.e., an increase of about 37% in the presence of oxygen compared to air. Also, normal jet diffusion non-buoyant flames are reported to be longer than buoyant flames [8].

*Corresponding author: Tel +1-765-743-1434, Email: bhatiap@purdue.edu (Pramod Bhatia)

Proceedings of 4th Joint Meeting of the U. S. Sections of the Combustion Institute, 2005

Objectives

In the present work the primary objectives are to understand and predict inverse diffusion flame behavior under:

- (a) Microgravity (0-g) and earth-gravity (1-g) environments.
- (b) Varying levels of oxygen in the oxidizer.

The calculations have been performed using global-chemistry (5 species and 1 reaction) and detailed-chemistry (99 species and 1066 reactions mechanism involving Polycyclic Aromatic Hydrocarbons (PAHs) [9]) using the axi-symmetric computational tool developed by Katta [10, 11, 12]. Comparisons between steady-state computational results and experimental flame photographs [13] (not presented here) were made. Ethane fuel (1.0 mole fraction) was used to examine the effects of oxygen-enhancement (0.21, 0.3, 0.5 and 1.0 mole fraction) in nitrogen. Table 1 summarizes the test conditions for the performed computations.

Computational Model

A steady state version of time-dependent, axisymmetric computational fluid dynamics (CFD) model known as UNICORN (Unsteady Ignition and Combustion using ReactionNs) [10, 11] is used to simulate the steady jet inverse diffusion flames considered in this study. It solves for u- and v- momentum equations, continuity, and enthalpy- and species-conservation equations using cylindrical coordinates on a staggered-grid system. Introducing the overall species conservation equation and the perfect gas state equation completes the set of equations. In addition, the detailed chemistry calculations also include a sink term based on an optically-thin gas assumption (accounting for the absorption and emission from the gaseous species CO_2 , H_2O , CO and CH_4) in the energy equation to account for thermal radiation in the flame. The effect of radiation heat losses were, however, neglected for global chemistry computations.

The body-force term due to the gravitational field is included in the axial-momentum equation for simulating normal gravity flames. A clustered mesh system is employed for the computations to trace the large gradients in flow variables near the flame surface. Detailed chemical-kinetics model of Wang and Frenklach [9] incorporated into UNICORN [10, 11] is used for investigation of PAH formation in Ethane (C_2H_6) flames. It consists of 99 species and 1066 elementary-reaction steps. Five species involved in the global chemistry calculations are: ethane (C_2H_6), oxygen (O_2), nitrogen (N_2), H_2O and carbon dioxide (CO_2). Thermo-physical properties such as enthalpy, viscosity, thermal conductivity, and binary molecular diffusion of all the species are calculated from polynomial curve fits developed for the temperature range 300 – 5000 K. Mixture viscosity and thermal conductivity are then estimated using the Wilke and Kee expressions, respectively. Molecular diffusion is assumed to be binary diffusion, and the diffusion velocity of species is calculated using Fick's law and the effective-diffusion coefficient of that species in the mixture. The finite-difference forms of the momentum equations are obtained using an implicit QUICKEST scheme [17], and those of the species and energy equations are obtained using a hybrid scheme of upwind and central differencing. The pressure field is accurately calculated by solving all the pressure Poisson equations simultaneously and using the Lower and Upper diagonal matrix-decomposition technique. The boundary

conditions are treated in the same way as that reported in earlier papers [18].

The CFD model UNICORN has been extensively validated in the past by simulating various steady and unsteady counterflow [19, 11] and coflow [17, 19, 20] jet diffusion flames and by comparing the results with experimental data. This gives confidence that UNICORN can simulate flame structure and other parameters accurately.

Computational Domain

The present simulations involved a round 5.5 mm diameter burner, quiescent ambient gas at 0.98 bar and 298 K under enhanced-oxygen conditions. Figure 1 presents the geometry of the axisymmetric computational domain. The computational domain extending 100 mm x 50 mm in the axial (z) and radial (r) directions, respectively, is represented by a staggered, clustered 401 x 191 grid system. The co-flow velocity is set at 1/10th of the jet velocity. The effect of round 5.5 mm diameter burner on flow dynamics is modeled by including an adiabatic rectangular body of thickness 0.45 mm and height 5 mm inside the computational domain.

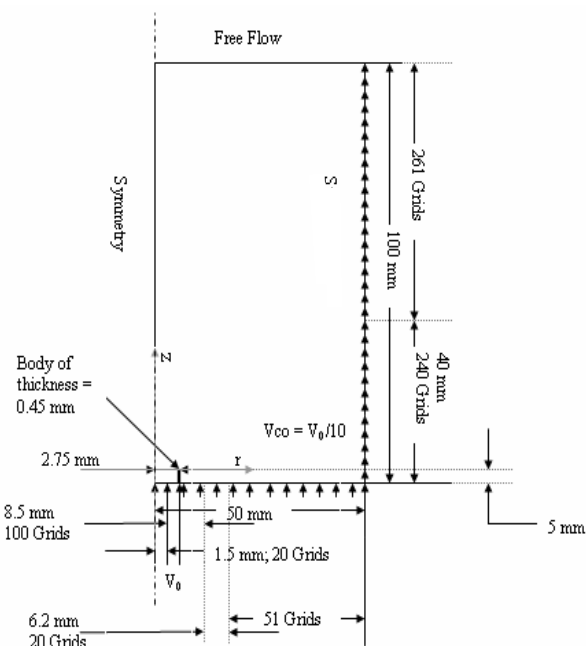


Figure 1. Computational Domain

Results and discussion

Figures 2 and 3 show the axial velocity profiles at the centerline plotted as a function of distance from the burner exit. Upstream of the flame tip, the axial velocity increases for all cases because of the volumetric expansion caused by the combustion heat release. Beyond the flame tip the axial velocities increase with distance for the 1-g cases whereas they decrease for the 0-g cases, because of the high product temperatures leading to lower density and resultant buoyant accelerations in the normal gravity cases, in contrast to the deceleration caused by shear forces for the microgravity cases. These effects decrease with downstream distance and the axial velocities start approaching uniform profiles.

The values of flame lengths and widths are presented in Table 2. The flame lengths and widths from the computations are calculated based on the following definitions: Flame length was defined as the distance between the burner

tip and the location of the peak temperature along the centerline. Flame width was defined as twice the maximum radial distance of the maximum temperature location from the centerline. The experimental flame lengths and widths were obtained from Ref. [13]. These flame lengths correspond to blue regions, except for case 3 (1g_IDF50) and case 7 (0g_IDF50), which are luminous lengths. All experimental widths correspond to blue regions.

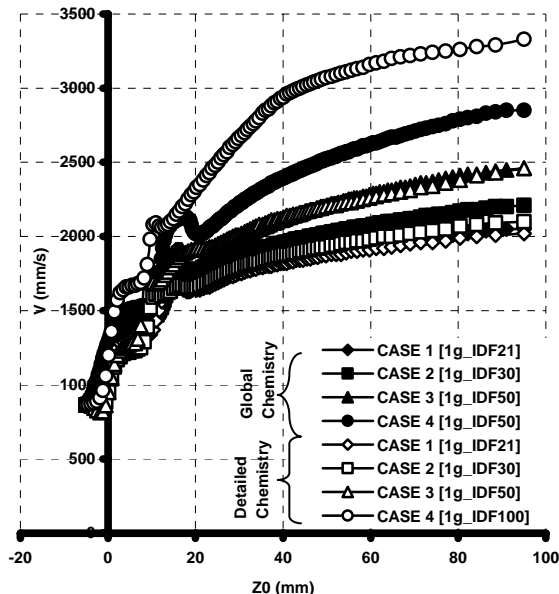


Figure 2. Centerline axial velocity plot for 1-g inverse diffusion flames (Detailed and Global Chemistry)

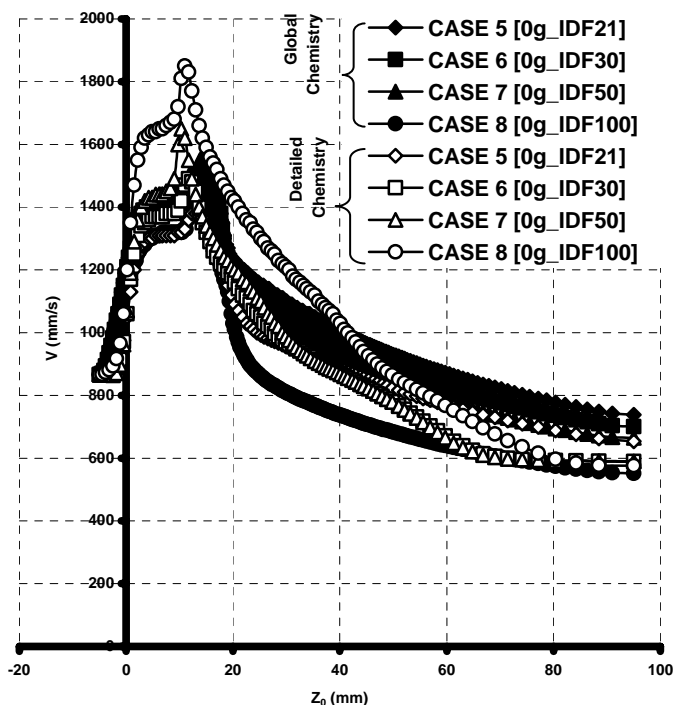


Figure 3. Centerline axial velocity plot for 0-g inverse diffusion flames (Detailed and Global Chemistry)

Global chemistry computations revealed that with identical oxygen mole fraction there are no significant differences in maximum flame temperatures and the maximum temperature-based-flame lengths increase very slightly for 0-g inverse diffusion flames in comparison to the 1-g inverse-diffusion flames (Table 2). Results from detailed chemistry computations also follow a similar trend except for cases 2 and 3 (intermediate O_2 concentrations), where the 1-g flame lengths are significantly lower than their 0-g counterparts. The detailed chemistry predictions are closer to the experimental results in view of an expected logarithmic relationship between stoichiometry and flame length. Flame widths increase with gravity and oxygen enhancement.

For global chemistry computations the temperature (Figure 4 & 5) along the axial direction (at $r=0$) show similar values for both 1-g and 0-g inverse-diffusion flames. The flame temperatures increase with an increase in the inlet oxygen mole fraction. Also, because of many step reactions, the detailed chemistry computations predict a much wider high temperature zone when compared to the corresponding global chemistry results. Detailed chemistry computations also reveal that because of larger velocities and resultant mixing for 1-g flames this zone is relatively thinner for them. Pure oxygen 1-g flames however show an opposite trend. This is because of their excessive large downstream velocity leading to thermal convection in the axial direction. Thickness of this zone however increases with oxygen enhancement.

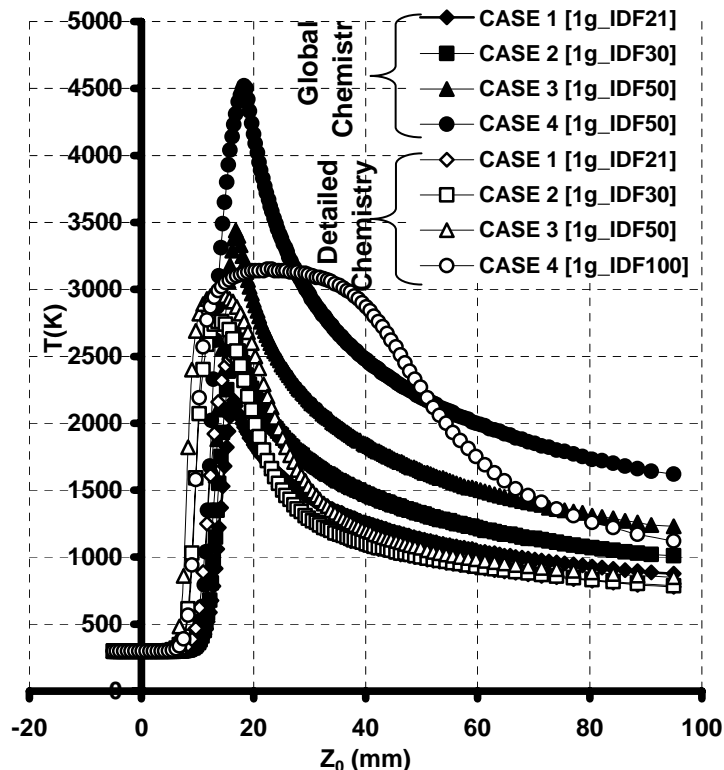


Figure 4. Centerline temperature plot for 1-g inverse diffusion flames (Detailed and Global Chemistry)

The flame temperature contours were compared with the experimental flame photographs from Ref. [13]. The comparisons were only qualitative because of the differences in the quantities being compared as well as the differences between the boundary conditions in the experiments and the computations. These comparisons showed excellent

qualitative similarities between the shapes and locations of color changes observed in the flame photographs and contour changes observed in the calculated temperature contour plots. These trends are encouraging but because of space limitation they are not presented in this paper

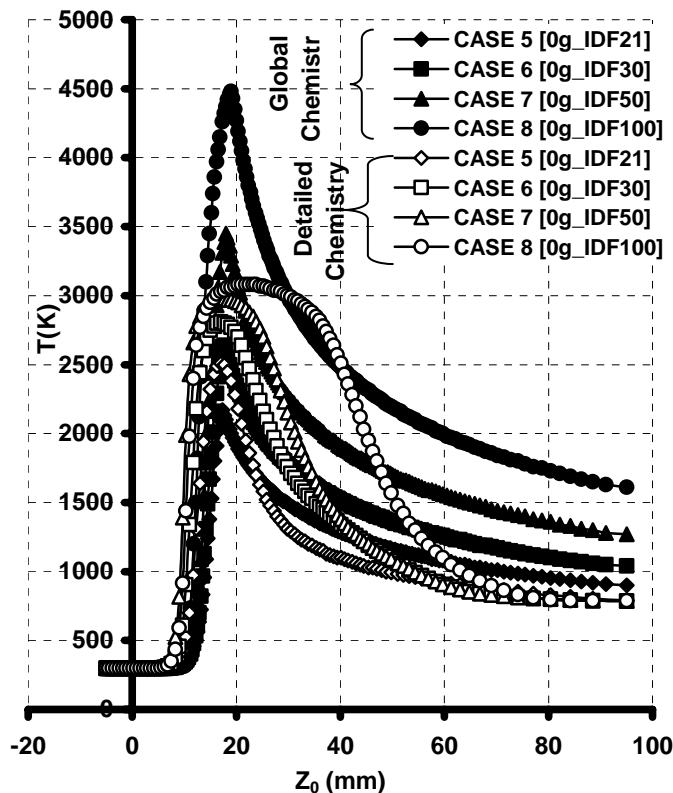


Figure 5. Centerline temperature plot for 0-g inverse diffusion flames (Detailed and Global Chemistry)

Calculation of species production (as mass percent of jet inflow) and maximum PPM are, respectively, presented in figures 6 (a – e) and 7(a – e). These figures reveal that for 1-g flames, PAHs (soot precursors) and acetylene production increase with oxygen enhancement. These species are indicator of soot production so for 1-g inverse diffusion flames soot production will increase with oxygen enhancement. Further, for these flames the emission of harmful gases such as CO and PAH increase with oxygen enhancement. For 0-g inverse diffusion flames, there is no significant change in the emission of these species with oxygen concentration. Species maximum PPM plots (figure 7(a – f)) for 0-g flames show similar trends as that of 1-g flames. This indicates that these flames can be more sooting and harmful at high oxygen concentrations. Also, the observed appearance of maximum PAH outside the flame surface on the fuel side is supported by the Ref. [12].

Conclusions

Computations were performed for ethane fueled laminar gas-jet diffusion flames, emphasizing the effects of oxygen enhancement and gravity under inverse burning. The mole fraction of oxygen in the oxidizer was varied from 0.21-1. Qualitative comparisons were performed with the experimental results [13]. The major findings were:

1. Oxygen-enhanced conditions caused increase in flame temperatures and gas velocities.

2. The axial velocities increase significantly before the flame tip for the 1-g and 0-g flames as a result of expansion caused by heat release. Beyond the flame tip the velocities increase for the 1-g flames (due to buoyancy) whereas they decrease for 0-g flames (due to shear).
3. Flame widths increase with gravity and oxygen enhancement.
4. Computational results indicate that both 1-g and 0-g inverse diffusion flames can be more sooting and can emit harmful gases at high oxygen concentrations.

Acknowledgements

This work is supported by NASA Glenn Research Center under the technical management of M. K. King and D. P. Stocker. Special thanks to Dave Seaman, Bill Whitson and Chinh Le for helping in facilitating computations.

References

1. R. B. Edelman, O. F. Fortune, G. Weilerstein, T. H., Cochran, J. B Haggard, Proc. Combust. Inst. 14 (1972) 399-412.
2. M. Y. Bahadori, R. B. Edelman, D. P. Stocker, S. L. Olson, AIAA J. 28 (1990), 236-244.
3. M. Y. Bahadori, D. P. Stocker, D. F. Vaughan, L. Zhou, R. B. Edelman: Combustion and Spectroscopy (FA Williams ed.) Pergamon Press, Oxford, 1993, 49-66.
4. L.G. Blevins, R.A. Fletcher, B.A. Benner, E.B. Steel, and G.W. Mulholland, Proceedings of the Combustion Institute 29:2325 (2002).
5. P.B. Sunderland, R.L. Axelbaum, D.L. Urban, B.H. Chao, and S. Liu, Combustion and Flame 132:25-33 (2003).
6. P. Van-Hulle, M. Talbaut, M. Weill, A. Coppalle, Meas. Sci. Technol. 13 (2002) 375 – 382.
7. C.E. Baukal, in: C.E. Baukal (Ed.), Oxygen-Enhanced Combustion, CRC Press, Boca Raton, 1998, p. 2-42.
8. P.B. Sunderland, B. J. Mendelson, Z.-G. Yuan, D.L. Urban, Combust. Flame 116 (3) (1999) 376-385.
9. H. Wang, M. Frenklach, Combust. Flame 110 (1) (1997) 173-221
10. V. R. Katta, L. P. Goss and W. M. Roquemore, Combust. Flame 96 (1-2) 1994 60-74
11. W. M. Roquemore, V. R. Katta, J. Visualization 2 (3/4) (2000) 257-272.
12. V. R. Katta, L. G. Blevins and W. M. Roquemore 41st ASME, AIAA 2003-0666
13. P.B. Sunderland, S.S. Krishnan, and J.P. Gore, Combustion and Flame 136:254-256 (2004).
14. Z. Shu, S. K Aggarwal, V. R. Katta, I. K. Puri, Combust. Flame, 111 (4) (1997) 296-311
15. R. Siegel, J. R. Howell, Thermal Radiation Heat Transfer, Hemisphere, New York, 1981.
16. N. Smith, J. Gore, J. Kim, Q. Tang, Radiation Models, International Workshop on Measurement and Computation of Turbulent Nonpremixed Flames, <http://www.ca.sandia.gov/tdf/Workshop/Submodels.html>, 2001.
17. V. R. Katta, L. P. Goss and W. M. Roquemore, AIAA J., 32 (1) (1994) 84

18. V. R. Katta, L. P. Goss, W. M. Roquemore, Int. J. Num. Methods Heat Fluid Flow, 4 (5) (1994) 413
19. V. R. Katta, C. D. Carter, G. J. Fiechtner, W. M. Roquemore, J. R. Gord, J. C. Rolon, Proceedings of the Combustion Institute 27, (1998) p. 587-594
20. X. Qin, I. K. Puri, S. K. Aggarwal, V. R. Katta, Phy. Fluids, 6 (8) 2004 2963-2974.
21. M.Y. Bahadori, D.P. Stocker, L. Zhou, U. Hegde, Combust. Sci. and Tech., 167 2001 169-186

Table 1. Test Conditions

CASES	GRAVITY	DIFFUSION	INLET O ₂ MOLE FRACTION	V ₀ (mm/s)	Fr	Re	\dot{Q} (W)
CASE 1 [1g_IDF21]	1-g	Inverse	0.21	866	13.9	312	72
CASE 2 [1g_IDF30]	1-g	Inverse	0.3	866	13.9	310	102
CASE 3 [1g_IDF50]	1-g	Inverse	0.5	866	13.9	310	171
CASE 4 [1g_IDF100]	1-g	Inverse	1.0	866	13.9	311	342
CASE 5 [0g_IDF21]	0-g	Inverse	0.21	866	∞	312	72
CASE 6 [0g_IDF30]	0-g	Inverse	0.3	866	∞	310	102
CASE 7 [0g_IDF50]	0-g	Inverse	0.5	866	∞	310	171
CASE 8 [0g_IDF100]	0-g	Inverse	1.0	866	∞	311	342

Table 2. Flame Lengths, widths and maximum temperatures

CASES	L _{f, comp} (mm) Global Chemistry	L _{f, comp} (mm) Detailed Chemistry	L _{f, exp} (mm)	W _{comp} (mm) Global Chemistry	W _{comp} (mm) Detailed Chemistry	W _{exp} (mm)	T _{max} (K) Global Chemistry	T _{max} (K) Detailed Chemistry	T _{ad} (K) GLOBAL CALCULATIONS 5 SPECIES	T _{ad} (K) CEA CALCULATIONS 2000 SPECIES
CASE 1 [1g_IDF21]	16.5	16.3	14	5.0	5.2	---	2170	2490	2382	2250
CASE 2 [1g_IDF30]	16.5	14.2	13	5.2	5.4	----	2650	2760	2977	2553
CASE 3 [1g_IDF50]	16.8	13.7	14	6.0	6.0	----	3440	2970	3981	2839
CASE 4 [1g_IDF100]	18.2	19	17	7.6	7.6	----	4520	3150	5491	3082
CASE 5 [0g_IDF21]	17.3	17	16	5.0	5.4	6	2170	2509	2382	2250
CASE 6 [0g_IDF30]	17.7	17.1	14	5.4	5.6	6	2640	2808	2977	2553
CASE 7 [0g_IDF50]	18	17.7	15	6.4	7.8	7.3	3450	2978	3981	2839
CASE 8 [0g_IDF100]	19	20.3	19	9	9.4	10	4480	3080	5491	3082

Fig. 6 (a)

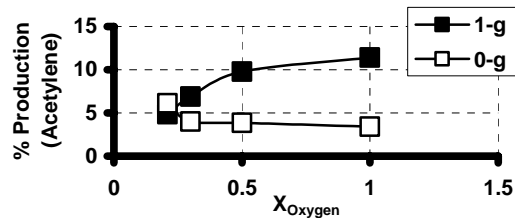


Fig. 6 (b)

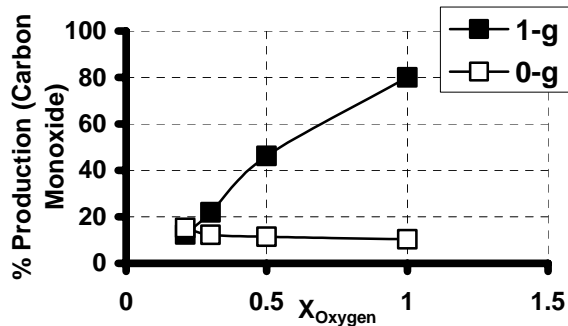


Fig. 6 (c)

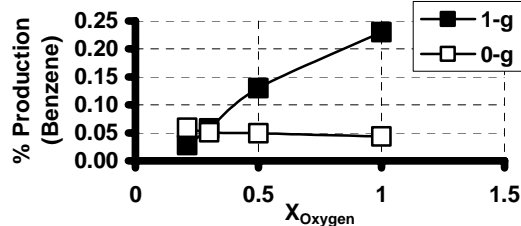


Fig. 6 (d)

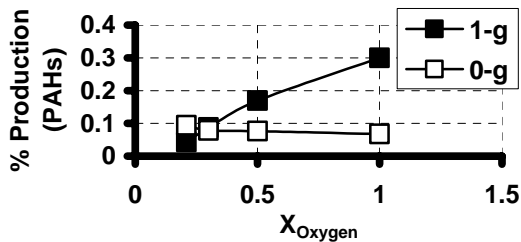


Fig. 6 (e)

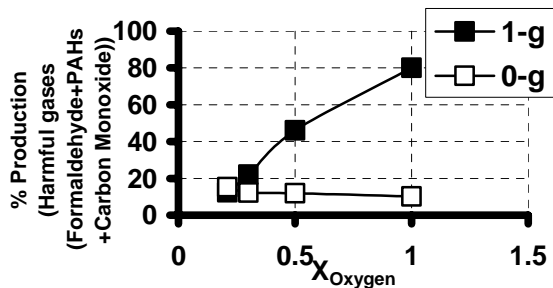


Figure 6: Relevant species' Production by mass as a percent of jet inflow vs. inflow oxygen mole fraction

Fig. 7 (a)

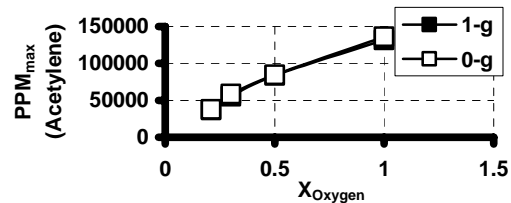


Fig. 7 (b)

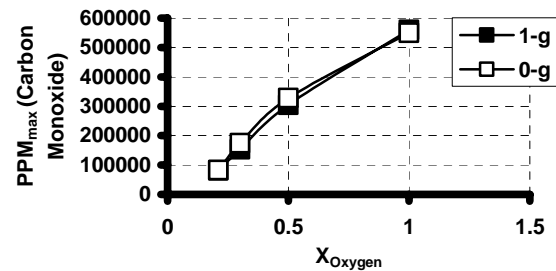


Fig. 7 (c)

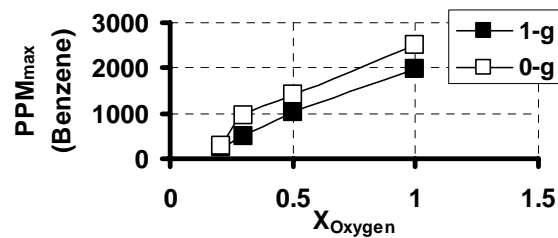


Fig. 7 (d)

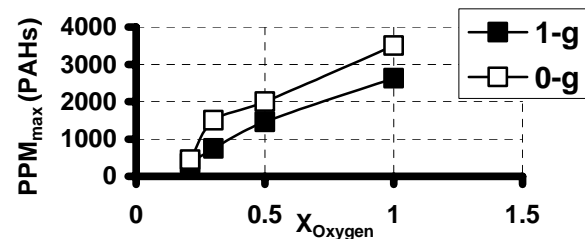


Fig. 7 (e)

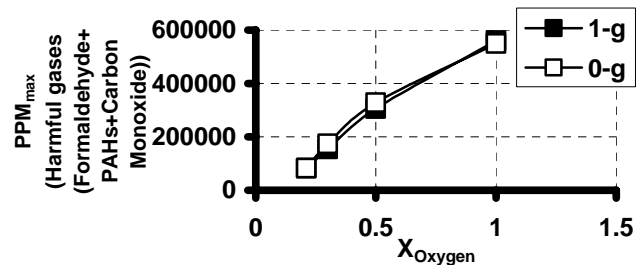


Figure 7: Maximum PPM by mass of relevant species' vs. inflow oxygen mole fraction

STUDIES ON SOOT FORMATION IN A MODEL GAS-TURBINE COMBUSTOR

Viswanath R. Katta* and Terrence R. Meyer
Innovative Scientific Solutions, Inc.
2766 Indian Ripple Road
Dayton, OH 45440-3638

Christopher Montgomery
Reaction Engineering International
77 West 200 South, Suite 210
Salt Lake City, UT 84101

William M. Roquemore
Propulsion Directorate
Air Force Research Laboratory
Wright-Patterson Air Force Base, OH 45433

ABSTRACT

Residence time and thermo-chemical environment are important elements in the soot-formation processes in combustors, especially which use swirl for flame stabilization. For understanding the chemical and physical structure of the soot formed in these combustors knowledge on flow dynamics and formation of polycyclic aromatic hydrocarbons (PAHs) is required. A time-dependent, detailed-chemistry computational-fluid-dynamic (CFD) model is developed for the simulation of the reacting flows in a model swirl-stabilized combustor. While commercial JP-8 fuel was used in the experiments, a 6-component surrogate mixture was used in the calculations for mimicking the JP-8-fuel combustion. Detailed chemical kinetics were used for the simulation of combustion as well as formation of PAH species. Several calculations were made for different equivalence ratios obtained by varying the fuel jet velocity and by keeping the airflow unaltered. Turbulent-flow simulations revealed that two recirculation zones that are separated by the air jet establish in the swirl-stabilized combustor. Stabilization of flames between the air jets and the recirculation zones depends on the equivalence ratio. For the highly fuel-lean cases ($\phi = 0.65$) flame is stabilized between the air jet and the central recirculation zone and for the fuel-rich cases flame is stabilized between the air jets and the corner recirculation zone. However, both flames seem coexist for slightly fuel-lean cases ($\phi = 0.85$). Predicted OH concentration fields are

compared with the OH images obtained using planar-laser-induced-fluorescence (PLIF) technique. Probe measurements made in the exhaust products are also compared.

INTRODUCTION

Swirling jets are commonly used in gas-turbine engines to achieve compact, stable, and efficient combustion. The flowfield in the primary zone of a swirl combustor is characterized by recirculation zones with high shear stresses and turbulent intensities that result in vortex breakdown and motion of large-scale flow structures.^{1,2} These unsteady fluid elements and recirculation zones can significantly increase the formation of pollutants such as carbon monoxide (CO), nitric oxide (NO), unburned hydrocarbons (UHC), and soot.³⁻⁵ However, the mechanisms that lead to enhanced pollutants formation in swirl-stabilized, liquid-fueled combustors are not fully understood. Previous experimental investigations have relied on exhaust-gas measurements and parametric studies to gain insight into the effects of various input conditions on soot loading.⁶⁻¹⁰ Much of the fundamental knowledge concerning soot formation is derived from theoretical investigations of laminar diffusion flames,^{11,12} with only a limited number of studies being focused on turbulence effects.^{13,14} The importance of considering unsteadiness and fluid-flame interactions was demonstrated by Shaddix et al.,¹⁴ who found that a forced unsteady methane/air diffusion flame produced a four-fold increase in soot volume fraction (as a result of increased particle size) as compared with a steady flame having the same mean fuel-flow velocity. Recent calculations of Katta et al.¹⁵ have suggested that presence of large-scale structures in dynamic

* Corresponding Author: vrkatta@erinet.com

This paper is declared a work of the U. S. Government and is not subjected to copyright protection in the U.S.

flames could influence the way polycyclic-aromatic-hydrocarbon (PAH) species are formed and; thereby, could impact the amount of soot produced. The goal of the current investigation is to simulate and understand soot formation in the highly dynamic environment of a modeled swirl-stabilized, liquid-fueled combustor.

Soot is an undesirable combustion product and its formation represents one of the most complex chemical systems in flames. Considerable progress has been made in recent years in understanding the chemical and physical aspects of soot formation in hydrocarbon flames. Soot particles containing several thousands of carbon atoms are formed from simple fuel molecules within a few milliseconds. After the first aromatic rings (such as benzene and small PAHs) are formed in the gas phase, acetylene and other molecules react with these small PAHs to form larger PAHs¹⁶. The first soot particles are thought to be formed when two or more PAHs react to form a three dimensional particle. This process is known as particle inception¹⁷. The soot particles interact with the gas-phase molecules by the addition of acetylene to their surfaces (surface growth) and react with molecular oxygen and/or hydroxyl radical (oxidation). Another process thought to increase soot mass is the collision of PAHs with a soot particle. Accurate predictions for soot formation in swirl combustors should consider all these processes and the effects of flow unsteadiness and recirculation zones on these processes.

Various attempts have been made in the past to develop models for soot predictions¹⁷. Some of these models are detailed, and have been calibrated against experimental data obtained in laminar, premixed or diffusion flames of simple configurations. For example, Frenklach and coworkers¹⁸ proposed a detailed kinetic model of soot formation and validated^{18,19} using measurements of laminar, premixed flames while Mauss, Bockhorn and their coworkers^{20,21} established a different detailed soot model that was tested in laminar, counter-flow diffusion flames. The detailed kinetic soot model consists of 1) gas-phase chemistry and 2) kinetics describing the particle growth and destruction processes. The gas-phase chemistry describes the formation of PAHs^{22,23}. The particle growth and destruction involve inception/ nucleation of particles resulting from coagulation of PAHs and are modeled via a set of surface reactions,¹⁸⁻²¹ and particle coagulation is modeled based on the method of moments¹⁸⁻²¹ or the discrete-sectional method.^{24,25}

The complexity and the uncertainties associated with the detailed kinetic soot models made their application limited to simple laminar flames. On the other hand, for the simulation of turbulent combustor flows, a variety of simplified soot models that can be easily implemented into design codes have been proposed²⁶. The most widely used models are based on the assumption that soot consists of particles with mono-disperse size distribution. Then the soot formation, coupled directly to the fuel concentration, is modeled by one or two equations: one for the particle volume fraction and the other for the particle number density.

Leung et al.²⁷ argued that the intermediate species contributing to the soot particle formation should be

connected to at least the pyrolysis kinetics of the fuel. For simplicity, they assumed acetylene to be the intermediate species and proposed a simplified soot model combined with the gas-phase kinetics of fuel pyrolysis for counterflow, ethylene and propane flames²⁷ as well as coflow, methane flames²⁸. The results showed that with this approach good agreement with measured data for soot volume fraction, particle growth and number density could be obtained. In the present work, a model similar to that of Leung et al.²⁷ is used for the prediction of soot formation in swirl-stabilized combustors fueled with JP-8 fuel. Detailed chemical kinetics for JP-8 fuel and the two-step soot model are incorporated into a well-tested CFD code UNICORN. Numerical results obtained for combusting flows with different equivalence ratios and swirl velocities are compared.

MATHEMATICAL MODEL

A time-dependent, axisymmetric mathematical model known as UNICORN (Unsteady Ignition and Combustion using ReactionNs)^{29,30} is used for simulating the turbulent combusting flows in the model swirl combustor. It solves for u- and v-momentum equations, continuity, and enthalpy- and species-conservation equations on a staggered-grid system. A clustered mesh system is employed to trace the large gradients in flow variables near the flame surface. A detailed chemical-kinetics model of Violi et al.³¹ is incorporated into UNICORN for the investigation of soot formation in JP-8 flames. It consists of 161 species and 1538 reaction steps. JP-8 fuel is considered as a surrogate mixture of 30% (by volume) n-dodecane ($\text{n-C}_{12}\text{H}_{26}$), 20% n-tetradecane ($\text{n-C}_{14}\text{H}_{30}$), 10% of iso-octane ($\text{I-C}_8\text{H}_{18}$), 20% of methylcyclohexane MCH (C_7H_{14}), 5% of tetralin ($\text{C}_{10}\text{H}_{12}$), and 15% of m-xylene (C_8H_{10}). Thermo-physical properties such as enthalpy, viscosity, thermal conductivity, and binary molecular diffusion of all the species are calculated from the polynomial curve fits developed for the temperature range 300 - 5000 K. Mixture viscosity and thermal conductivity are then estimated using the Wilke and Kee expressions, respectively. Molecular diffusion is assumed to be of the binary-diffusion type, and the diffusion velocity of a species is calculated using Fick's law and the effective-diffusion coefficient of that species in the mixture. Turbulence is modeled using k- ϵ approach. A simple radiation model based on the optically thin-media assumption is incorporated into the energy equation for treating radiation heat loss from gaseous species³². Only CH_4 , CO , CO_2 , and H_2O are considered as radiating species in the present study. Heat losses from soot particles are computed assuming blackbody radiation from the carbonaceous soot particles.³³

The finite-difference forms of the momentum equations are obtained using an implicit QUICKEST scheme³⁴, and those of the species, energy, k and ϵ equations are obtained using a hybrid scheme of upwind and central differencing. At every time step, the pressure field is accurately calculated by solving all the pressure Poisson equations simultaneously and using the LU (Lower and Upper

diagonal) matrix-decomposition technique. The boundary conditions are treated in the same way as that reported in earlier papers³⁵.

Soot Model

Computational soot models based on the fundamental physics of soot formation and oxidation are not yet available. The research groups around Moss and Lindstedt have made some progress in modeling soot formation using semiempirical models based on the mechanisms of particle inception, agglomeration, surface growth, and oxidation. Both the groups utilized two equation models with transport equations for particle number density, N_s , and soot mass fraction, Y_s . These equations can be written for unsteady flow as

$$\frac{\partial N_s}{\partial t} + \nabla \cdot (\rho \mathbf{V} N_s) - \nabla \cdot (\rho D_{N_s} \nabla N_s) = \omega_{N_s} \quad (1)$$

$$\frac{\partial Y_s}{\partial t} + \nabla \cdot (\rho \mathbf{V} Y_s) - \nabla \cdot (\rho D_s \nabla Y_s) = \omega_s \quad (2)$$

where \mathbf{V} is the velocity vector, ρ is density, D is the molecular diffusion coefficient, and ω is the production term from chemical reactions. The two source terms in Eqs. 1 and 2 are obtained using Lindstedt's model³⁶, which is based on the simplifying assumption that nucleation and growth are first-order functions of acetylene concentrations. Soot oxidation was considered primarily due to the presence of O_2 and OH . Finally, soot agglomeration was treated as a source term in Eq. 2.

The simulations presented here are performed on a AMD Opteron Personal Computer with 2.0 GB of memory. Typical execution time is ~40 s/time-step for the swirl-stabilized-combustor simulations. Steady state solutions are typically obtained in about 20,000 time steps starting from the solution obtained using the global combustion chemistry model.

RESULTS AND DISCUSSION

Studies on Jet Diffusion Flames:

The CFD model UNICORN has been extensively validated in the past by simulating various steady and unsteady counterflow^{29,37} and coflow^{29,38} jet diffusion flames and by comparing the results with experimental data. This gives confidence that UNICORN can simulate the structure of dynamic flames accurately. However, the integration of JP-8 chemistry into UNICORN needs to be validated to establish the accuracy of the present predictions. For this purpose a number of calculations are performed for simple jet diffusion flames for which qualitative understanding has been established.

The flame chosen is a pure diffusion flame formed between gaseous JP-8 fuel and air. The velocity of the fuel injected from a 1.0-cm diameter tube at room temperature is varied between 1.0 and 3.0 cm/s, while that of the annulus air is fixed at 10 cm/s. Axisymmetric calculations for this

jet diffusion flame are performed on a non-uniform grid system of 151x71. Fuel and air jets are separated by a 0.5-mm-thick tube wall which is treated as an isothermal one at 600 K, which is a reasonable assumption for the simulation of attached flames.

Results obtained for three fuel-jet velocities are shown in Fig. 1. The iso-temperature plots in Fig. 1(a) suggest that significant preheating of fuel is taking place at all velocity conditions. Flames are, in general, burning intensely in the shoulder region with a slightly cooled flame tip. As expected flame height is linearly increased with fuel jet velocity. The peak temperature is about 2000 K. It is important to note that the presence of tube wall was critical in obtaining attached flames even for the low velocities used in these simulations.

Concentration distributions of benzene, an important species in soot formation, are shown in Fig. 2 for the three velocity cases considered. Even though, the overall distribution of benzene is increasing with the velocity the peak mole fraction (0.0014) is decreasing—suggesting that soot index decreases with fuel jet velocity. The two step-soot model used in the present study also predicts a decrease in soot concentration with velocity as shown in Fig. 3. These observations on flame height and temperature and soot distributions for different fuel jet velocities are in agreement with the general observations of jet diffusion flames.

Decomposition of parent fuel components along the centerline is shown in Fig. 4 for 0.01-m/s fuel jet velocity case. Preheating of fuel promoted endothermic reactions and decomposed parent species of JP-8 surrogate rather slowly till a flame height of 10 mm. At this location, ignition is taking place and consumption of the remaining parent species occurring rather quickly. Interestingly, among all the parent species, consumption of m-xylene is noticeably slower, even though, the low-temperature decomposition of this species was similar to that of other species.

Studies Swirl-Stabilized-Combustor:

The near-field structure of swirl-stabilized flames is highly dependent upon the characteristics of the fuel injector and the geometry of the surrounding flame tube. The injector configuration used in the modeled swirl-stabilized combustor is a generic swirl-cup liquid-fuel injector studied at the Atmospheric-Pressure Combustor-Research Complex of the Air Force Research Laboratory's Propulsion Directorate.³⁹ It employs pressure atomization and dual-radial, counter-swirling co-flows of air to entrain the fuel, promote droplet break-up, and enhance mixing. The near-axisymmetric, conical flame obtained under overall-fuel-lean operating conditions is shown in Fig. 5(a). It composed of an outer droplet-vaporization/preheat region (A) and an inner turbulent flame brush region (B).⁴⁰ The flame is stabilized by a recirculation zone (C) that brings hot combustion products upstream along the centerline. The 40-mm-exit-diameter swirl cup is installed at the entrance of a 15.25 cm × 15.25 cm square-cross-section flame tube, as shown in Fig. 5(b). After exiting the primary flame zone,

the combustion products are allowed to mix thoroughly along the 48-cm long flame tube before entering a 43-cm-long, 5.7-cm exit-diameter exhaust nozzle that is designed to create a uniform exhaust-gas temperature and concentration profiles.

Changes in overall equivalence ratio from $\phi = 0.5$ to 1.15 were achieved in the experiments⁴¹ by varying the pressure drop across the fuel-spray nozzle from about 1.5 to 10 atm, which resulted in fuel mass flow rates of 1.0 to 2.2 g/s, respectively. The fuel flow rate is measured using a Max Machinery positive-displacement flow meter with $\pm 0.5\%$ full-scale accuracy. The airflow system consists of three Sierra 5600 SLPM mass flow controllers with $\pm 1\%$ full-scale accuracy. The inlet air is heated to 450 K with a constant flow rate of ~ 0.028 kg/s. The air-pressure drop across the combustor dome was ~ 4.8 to 5.2% of the main supply. Most of the airflow enters the combustor through the swirl-cup injector, but a small percentage enters through aspiration holes along the aft wall. No liner air jets are used in the secondary zone; therefore, the fuel-air ratio depends almost entirely on the flow rates through the injector cup.

The combustor is optically accessible via 75-mm-wide quartz windows along the top and sides for in-situ laser-based diagnostics. In addition, a sampling probe for measuring particulate counts is located at the exit of the combustor.

Axisymmetric mathematical model for the swirl-stabilized combustor is constructed using a 17.2-cm diameter, 48-cm long chimney and with thin tubes separating the fuel and air flows at the combustor entrance. Gaseous JP-8 fuel is injected at the center while the two outer air jets are forced into the combustor with counter swirling motions. The computational domain was discretised using a non-uniform grid system of 251x126.

Calculations for the swirl-stabilized combustor shown in Fig. 5 are made for different equivalence ratios. Flow fields obtained for a fuel-lean and for a fuel-rich condition are shown in Figs. 6(a) and 6(b), respectively. The nozzle geometry incorporated in the model is also shown in these figures. Gaseous JP-8 is injected from a 4-mm hole at the center with an axial velocity of 15 m/s and swirl angle of 70° . Such high swirl angle for the fuel jet was used in order for representing the cone angle of the liquid spray. Fuel jet is immediately surrounded with a 2-mm-thick wall and then a high-speed air jet with axial velocity of 100 m/s and a swirl angle of -30° . A second air jet of 100 m/s is issued through the 5 mm annulus gap between the nozzle walls at a velocity of 100 m/s and at a swirl angle of 45° . The velocity of the fuel jet was changed for achieving different equivalence-ratio conditions. The two cases in Fig. 6 are obtained with fuel velocities of 15 and 30 m/s, which correspond to equivalence ratios of 0.65 and 1.15, respectively.

As shown in Fig. 6 the swirling air jets are merging together and expanding radially as they propagate downstream. Such radial expansion of high momentum air jets has created two toroidal recirculation regions; one in the corner and the other one at the center. Interestingly, when the fuel jet velocity is increased from 15 m/s to 30

m/s, the height of the corner recirculation zone decreased while that of the center recirculation zone increased. Note the shift in jet impinging location on the combustor wall from 12 cm to 10 cm in Figs. 6(a) and 6(b), respectively. This suggests that the high swirl associated with the fuel jet is also contributing to the expansion of the air jets and such contribution increases with the fuel jet momentum (or velocity). Decrease in corner-recirculation-zone length improves the stability characteristics of the combustor. However, an increase in the length of the center recirculation zone might also contribute to additional pollutants formation due to increase in residence time.

Combustion characteristics associated with 0.65-equivalence-ratio case are shown in Fig. 7. Iso-temperature contours are shown in color in Fig. 7(a) while the concentration distributions of soot, benzene, and OH are shown in Figs. 7(b), 7(c), and 7(d), respectively. Under this fuel-lean condition, flame is anchored in the region between the air jets and the center recirculation zone. While the peak flame temperature is ~ 2100 K, the temperature of the exhaust products at the combustor exit decreased significantly due to their mixing with the excess air. Very little soot is produced [Fig. 7(b)] under this fuel-lean condition, which qualitatively agrees with the experiments [Fig. 5(a)]. Both the benzene and OH are confined to the high-temperature flame zone and very little of these species are found in the exhaust products. The OH-concentration distribution obtained in the experiments using PLIF technique is shown in the insert next to Fig. 7(d). The corresponding location for the experimental OH image in the combustor is marked with a square in Fig. 7(d). The v-shaped OH distribution supports the prediction that the flame is sandwiched between the air jets and the central recirculation zone and that almost all of OH is confined to this flame region.

The overall equivalence ratio has been increased to 0.85 when the velocity of the fuel jet is increased to 20 m/s. The predicted combustion field for this fuel-lean condition is shown in Fig. 8. Significant change in flame structure could be noticed when comparing the temperature distributions in Figs. 7(a) and 8(a). At an equivalence ratio of 0.85, not only a flame is established between the air jets and the central recirculation zone, similar to that seen with 0.65-equivalence-ratio case, but also a flame is established between the air jets and the corner recirculation zone. Part of the fuel injected at the center is carried by the air jets into the corner recirculation zone and establishes the second flame when this fuel mixes with the air jet. Even though the peak flame temperature remained at 2100 K, the temperature of the exhaust products increased for 0.85-equivalence-ratio case. Interestingly, very little soot and benzene are produced under this fuel-lean condition also. However, experiments have shown some soot generation under 0.85-equivalence-ratio condition. It is speculated that the dynamic behavior of the central recirculation zone might be contributing to the production of pollutants and soot⁴¹. Use of k- ϵ turbulence model and the relatively coarse grid system in the calculations might have dissipated the flow oscillations and yielded a steady flow field, which,

in turn, might have contributed to the elimination of soot. Further calculations with fine grid system are required for capturing the large-scale dynamic behavior of the central recirculation region. However, the overall flame structure is well captured in the present simulations. A comparison between the predicted-OH distribution [Fig. 8(d)] and the experimentally obtained PLIF-OH image (insert in Fig. 8) suggests that the model has correctly captured the two-flame structure and the excess amount of OH radicals in the central recirculation zone.

Soot production has significantly increased when the equivalence ratio was increased to 1.15. The fuel jet velocity corresponding to this condition is 30 m/s and the simulated flow field was shown in Fig. 6(b). The predicted combustion field is shown in Fig. 9. In contrast to the fuel-lean cases, corner recirculation zone has become the hottest region in the fuel-rich case. Flame is anchored between the air jets and the corner recirculation zone. More interestingly, the flame established between the air jets and the central recirculation zone in the fuel-lean cases has disappeared in the fuel-rich case. This is more evident in the OH plot in Fig. 8(d). OH is formed along the outer edge of the corner recirculation zone and is not connected at the center. The OH-PLIF image obtained in the experiments (insert in Fig. 8) support the prediction that the flame established along the central recirculation zone in fuel-lean conditions is extinguished under fuel-rich conditions.

As expected, significant amount of soot has been generated for the fuel-rich condition [Fig. 8(b)]. Experiments [Fig. 5(b)] have confirmed this prediction. Interestingly, not much soot is produced in the corner recirculation zone, even though it is found to be the hottest region. This is mainly because of the local equivalence ratio within the corner recirculation region. The fuel entrained into this zone is not sufficient to make it fuel rich. In contrast, the central recirculation zone became fuel rich and contributed to decrease in temperature and increase in soot production.

Temperature and species distributions along the centerline of the combustor are plotted in Fig. 10 for different equivalence-ratio cases. Inline with the images shown in Figs. 7-9, OH is present in the central recirculation zone only for fuel-lean conditions and its concentration decreases with decrease in equivalence ratio [Fig. 10(a)]. Measurements made in the exhaust gases⁴² for fuel-lean cases are shown in Fig. 10 with large filled symbols. The predicted exhaust temperatures are ~ 150 K higher than the measurements for both the 0.65 and 0.85 equivalence-ratio cases. The lower exhaust temperatures in the experiments could have resulted from the radiation losses from the 43-cm long exhaust nozzle inserted at the end of the combustor. On the other hand, excellent agreement is found for CO₂/N₂ and O₂/N₂ ratios for these two cases as seen in Fig. 10(b).

CONCLUSIONS

A time-dependent, axisymmetric, detailed-chemistry CFD model was developed for the simulation of combustor flows inside a model swirl-stabilized combustor. Combustion chemistry and PAHs formation associated with JP-8 fuel are simulated using the 161-species, 1538-reactions mechanism of Violi et al.³¹. Soot formation is modeled using a two-variable approach and turbulence is modeled using k and ϵ equations. The CFD code (UNICORN) was tested through the simulation of a laminar jet diffusion flame for different fuel jet velocities. The swirl-stabilized combustor with a square chimney was modeled as an axisymmetric combustor. Several calculations were made by varying the equivalence ratio (by changing the fuel flow) and by keeping the swirl and air flow constant.

The high swirl used for the fuel and air jets in the combustor expanded the air jets rapidly and created corner and central recirculation zones. Increasing equivalence ratio via increasing fuel jet velocity decreased the size of the corner recirculation zone and increased that of the central recirculation zone. For highly fuel-lean cases ($\phi = 0.65$) flame is stabilized in between the air jets and the central recirculation zone, resulting a v-shaped flame structure. For slightly fuel-lean cases ($\phi = 0.85$) two flames are stabilized. While the first one is formed in between the air jets and the central recirculation zone, the second one is formed between the air jets and the corner recirculation zone from the excess fuel transported along the combustor walls. For all the fuel-rich cases, the first flame between the air jets and the central recirculation zone could not be stabilized, leaving the combustor to operate on the flame anchored in between the air jets and corner recirculation zone. This resulted in an open-v-shaped flame structure. The very little quantities of soot predicted for the fuel-lean cases and the rapid increase of soot with equivalence ratio for fuel-rich cases qualitatively agree with the experimental observations. The measurements made for temperature, CO₂, and O₂ in the exhaust gases matched with the predictions. The combustion chemistry of Violi et al.³¹ for JP-8 fuel seems a reliable mechanism that can be easily incorporated into multi-dimensional CFD codes.

ACKNOWLEDGEMENTS

Financial support for this work was provided by the Air Force Office of Scientific Research (AFOSR, Julian Tishkoff), the Air Force Contracts #F33615-00-C-2329 (Vince Belovich) and #F33615-03-C-2338 (Edwin Corporan).

REFERENCES

1. Kim, W.-W., Menon, S., and Mongia, H. (1999), "Large-eddy simulation of a gas turbine combustor flow," *Combust. Sci. Technol.* 143:25-62.
2. Wang, S., Hsieh, S.-Y., and Yang, V., "Numerical simulation of gas turbine swirl-stabilized injector dynamics," AIAA paper 2001-0334, 2001.
3. Heitor, M. V., and Whitelaw, J. H. (1986), "Velocity, Temperature, and Species Characteristics of the Flow in a Gas-Turbine Combustor," *Combust. Flame* 64:1-32.
4. Bicen, A. F., Tse, D. G. N., and Whitelaw, J. H. (1990), "Combustion characteristics of a model can-type combustor," *Combust. Flame* 80:111-125.
5. Held, T. J., Mueller, M. A., Li, S.-C., and Mongia, H., "Data-driven model for NO_x, CO and UHC emissions for a dry low emissions gas turbine combustor," AIAA paper 2001-3425, 2001.
6. Eckerle, W. A., "Soot loading in a generic gas turbine combustor," AIAA paper 87-0297, 1987.
7. Fang, T. C., Megaridis, C. M., Sowa, W. A., and Samuelson, G. S. (1998), "Soot morphology in a liquid-fueled swirl-stabilized combustor," *Combust. Flame* 112:312-328.
8. Snelling, D. R., Thomson, K. A., Smallwood, G. J., and Gulder, O. L. (1999), "Two-dimensional imaging of soot volume fraction in laminar diffusion flames," *Appl. Opt.* 38:2478-1485.
9. Black, J. D. (1999), "Laser induced incandescence measurements of particles in aero-engine exhausts," EUROPTO Conference on Environmental Sensing and Applications, Munich, Germany, pp. 209-215.
10. Jenkins, T. P., Bartholomew, J. L., DeBarber, P. A., Yang, P., Seitzman, J. M., and Howard, R. P., "A laser-induced incandescence system for measuring soot flux in aircraft engine exhausts," AIAA paper 2002-3736, 2002.
11. Santoro, R. J., Yeh, T. T., Horvath, J. J., and Semerjian, H. G. (1987), "The transport and growth of soot particles in laminar diffusion flames," *Combust. Sci. Technol.* 53:89-115.
12. Urban, D. L., and Faeth, G. M., "Soot research in combustion science: introduction and review of current work," AIAA paper 2001-0322, 2001.
13. Won, Y.-H., Kamimoto, T., Kobayashi, H., and Kosaka, H., "2-D soot visualization in unsteady spray flame by means of laser sheet scattering technique," SAE Tech. Paper 910223, 1991.
14. Shaddix, C. R., Harrington, J. E., and Smyth, K. C. (1994), "Quantitative Measurements of Enhanced Soot Production in a Flickering Methane / Air Diffusion Flame," *Combust. Flame* 99:723-732.
15. Katta, V. R., Blevins, G. L., and Roquemore, W. M., *Combustion and Flame*, Vol. 142, 2005, pp. 33-51.
16. Richter, H. and Howard, J. B., *Prog. Energy Combust. Sci.* 26:565 (2000)
17. Kennedy, I. M., *Prog. Energy Combust. Sci.* 23:95 (1997).
18. Frenklach, M. and Wang, H., *Twenty-third Symposium (International) on Combustion*, The Combustion Institute, Pittsburgh, 1991, pp.1559-1566.
19. Frenklach, M. and Wang, H., in *Soot Formation in Combustion: Mechanisms and Models* (H. Bockhorn, Ed.), Springer-Verlag, Heidelberg, 1994, pp.165-189.
20. Mauss, F., Schäfer, T. and Bockhorn, H., *Combust. Flame* 99:697-705 (1994).
21. Mauss, F. and Bockhorn, H., *Z. Phys. Chem.* 188:45 (1995).
22. Haynes, B.S. and Wagner, H. G.G., *Prog. Energy Combust. Sci.* 7:229-273 (1981).
23. Calcote, H.F., *Combust. Flame* 42:215-242 (1981).
24. Colket, M.B. and Hall, R.J., in *Soot Formation in Combustion: Mechanisms and Models* (H. Bockhorn, Ed.), Springer-Verlag, Heidelberg, 1994, pp.442-468.
25. Hall, R.J., Smooke, M.D. and Colket, M.B., in *Physical and Chemical Aspects of Combustion: A Tribute to Irvin Glassman* (F.L. Dryer and R.F. Sawyer, Eds.), Gordon and Breach, Amsterdam, 1997, pp.189-230.
26. Hiroyasu, H., Kadota, T. and Arai, M., *Bulletin of the JSME* 26:569-575 (1983).
27. Leung, K.M., Lindstedt, R.P. and Jones, W.P., *Combust. Flame* 87:289-305 (1991).
28. Lindstedt, R.P., in *Soot Formation in Combustion: Mechanisms and Models* (H. Bockhorn, Ed.), Springer-Verlag, Heidelberg, 1994, pp.417-439.
29. Roquemore W. M., and Katta, V. R., *Journal of Visualization*, in press Jan. 2000.
30. Katta, V. R., and Roquemore, W. M., *Combustion and Flame*, Vol. 100, No. 1, 1995, p. 61.
31. Violi, A., Yan, S., Eddings, E. G., Sarofim, A. F., Gratata, S., Faravelli, T., and Ranzi, E., "Experimental Formulation and Kinetic Model for JP-8 Surrogate Mixtures," *Combustion Science and Technology*, 174:339-417, 2002..
32. Annon., Computational Submodels, International Workshop on Measurement and Computation of Turbulent Nonpremixed Flames., <http://www.ca.sandia.gov/tdf/Workshop/Submodels.html>, 2001.
33. Guo, H., Liu, F., Smallwood, G. J., *Combustion Theory and Modeling*, Vol. 8, 2004, pp. 475-489.
34. Katta, V. R., Goss, L. P., and Roquemore, W. M., *AIAA Journal*, Vol. 32, No. 1, 1994, p. 84.
35. Katta, V. R., Goss, L. P., and Roquemore, W. M., *Int. J. Num. Methods Heat Fluid Flow*, Vol. 4, No. 5, 1994, p. 413.
36. Lindstedt, P. R., in *Soot Formation in Combustion* (H. Bockhorn, Ed.), Springer Verlag, Heidelberg, 1994, p. 417.
37. Katta, V. R., Carter, C. D., Fiechtner, G. J., Roquemore, W. M., Gord, J. R., and Rolon, J. C., in *Twenty-seventh Symposium (International) on Combustion*, The Combustion Institute, Pittsburgh, PA, 1998, p. 98.
38. Katta, V. R., and Roquemore W. M., *AIAA Journal*, Vol. 36, No. 11, 1998, p. 2044.
39. Roy, S., Meyer, T. R., Lucht, R. P., Belovich, V. M., Corporan, E., and Gord, J. R., "Temperature and CO₂ concentration measurements in the exhaust stream of liquid-fueled combustor using dual-pump coherent anti-Stokes Raman scattering (CARS) spectroscopy," submitted for publication in *Combust. Flame*, 2003.
40. Lee, K., and Chehroudi, B. (1995), "Structure of a swirl-stabilized spray flame relevant to gas turbine and furnaces," *J. Prop. Power* 11:1110-1117.
41. Meyer, T. R., Roy, S., Gogineni, S. P., Belovich, V. M., Corporan, E., and Gord, J. R., "OH-PLIF and Soot Volume Fraction Imaging in the Reaction Zone of a Liquid-Fueled Gas-Turbine Combustor", *Proceedings of ASME Turbo Expo 2004*, Paper No. GT2004-54318.
42. Roy, S., Meyer, T. R., Lucht, R. P., Belovich, V. M., Corporan, E., and Gord, J. R., *Combustion and Flame*, Vol. 138, 2004, pp. 273-284.

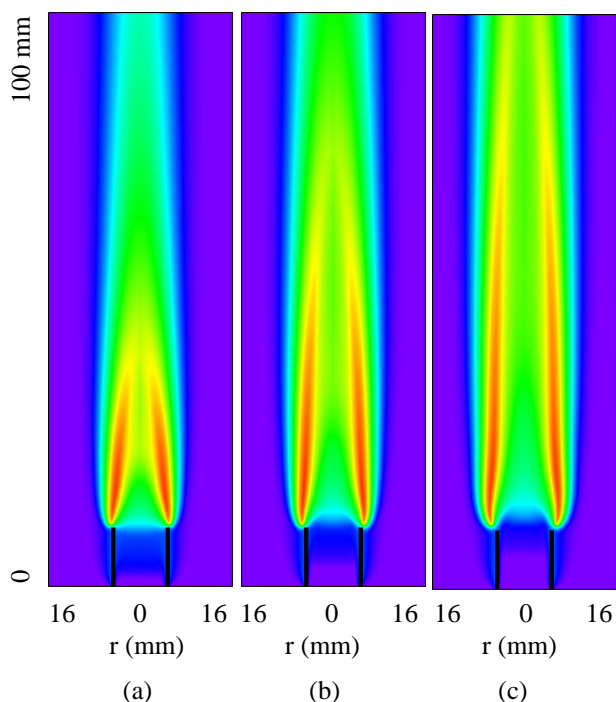


Fig. 1. Co-axial jet diffusion flames of JP-8 fuel at (a) 0.01 m/s, (b) 0.02 m/s, and (c) 0.03 m/s. Iso-temperature contours are shown between 300 K (purple) and 2000 K (red).

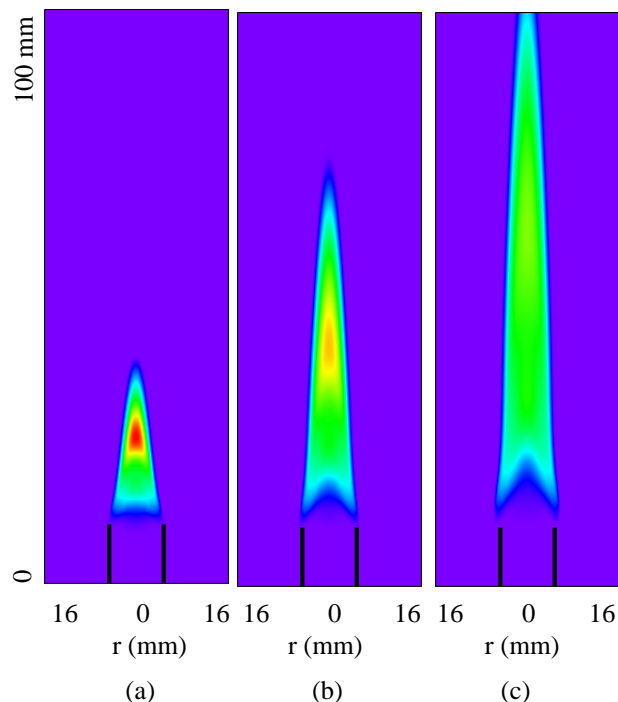


Fig. 2. Benzene concentration in JP-8 co-axial, jet diffusion flames. Fuel-jet velocities are (a) 0.01 m/s, (b) 0.02 m/s, and (c) 0.03 m/s. Red color indicates peak concentration of 0.14 %.

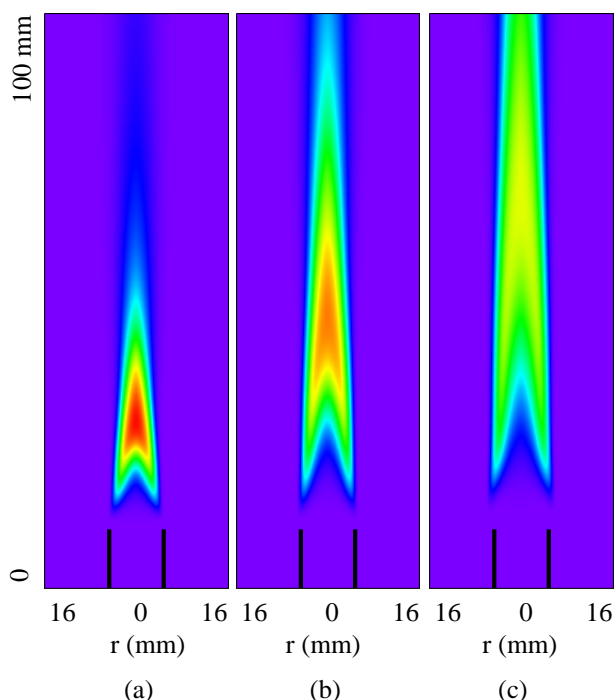


Fig. 3. Soot volume fraction in JP-8 fueled, co-axial, jet diffusion flames at (a) 0.01 m/s, (b) 0.02 m/s, and (c) 0.03 m/s. Red color indicates peak volume fraction of 5%.

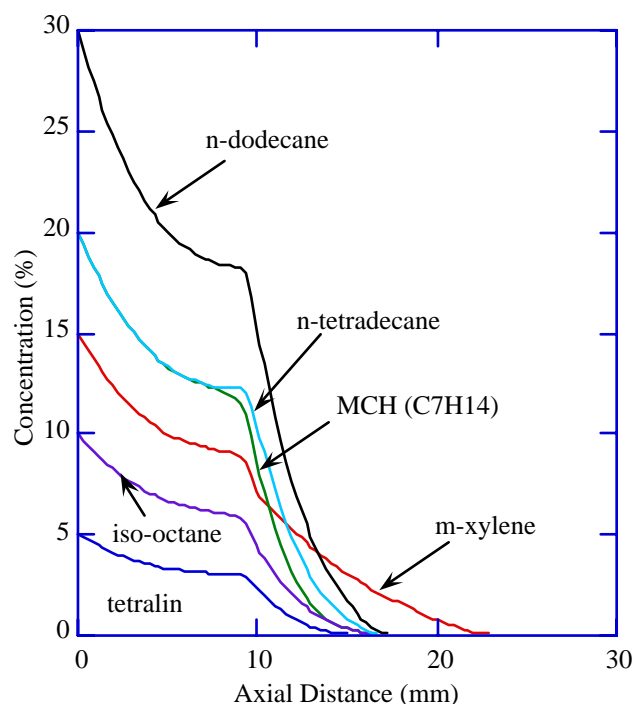


Fig. 4. Decomposition of parent species of JP-8 surrogate fuel with height in a co-axial, jet diffusion flame of 0.01-m/s fuel jet velocity.

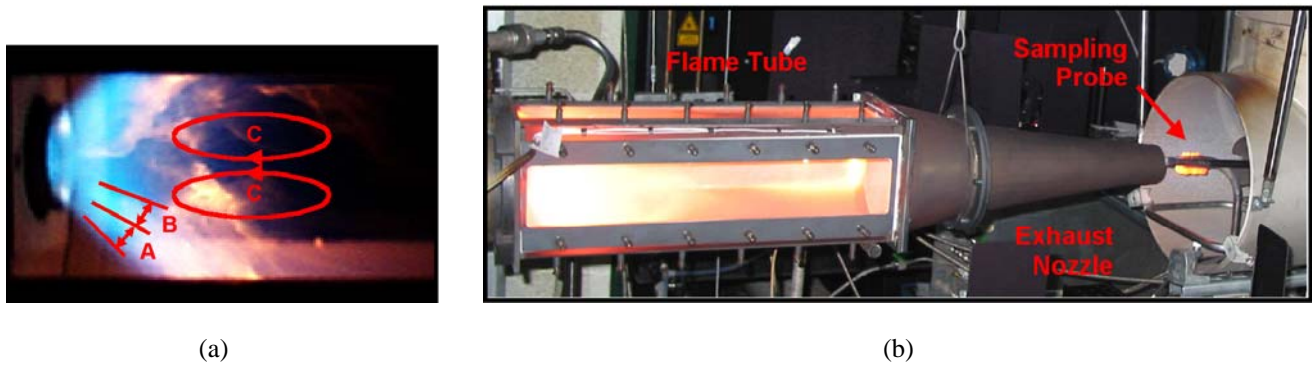


Fig. 5. Operation of JP-8 fueled, swirl-stabilized, model gas-turbine combustor under different equivalence-ratio conditions. (a) Photograph of the near-field flame structure under fuel-lean conditions and (b) photograph of the flame and test rig under fuel-rich conditions.

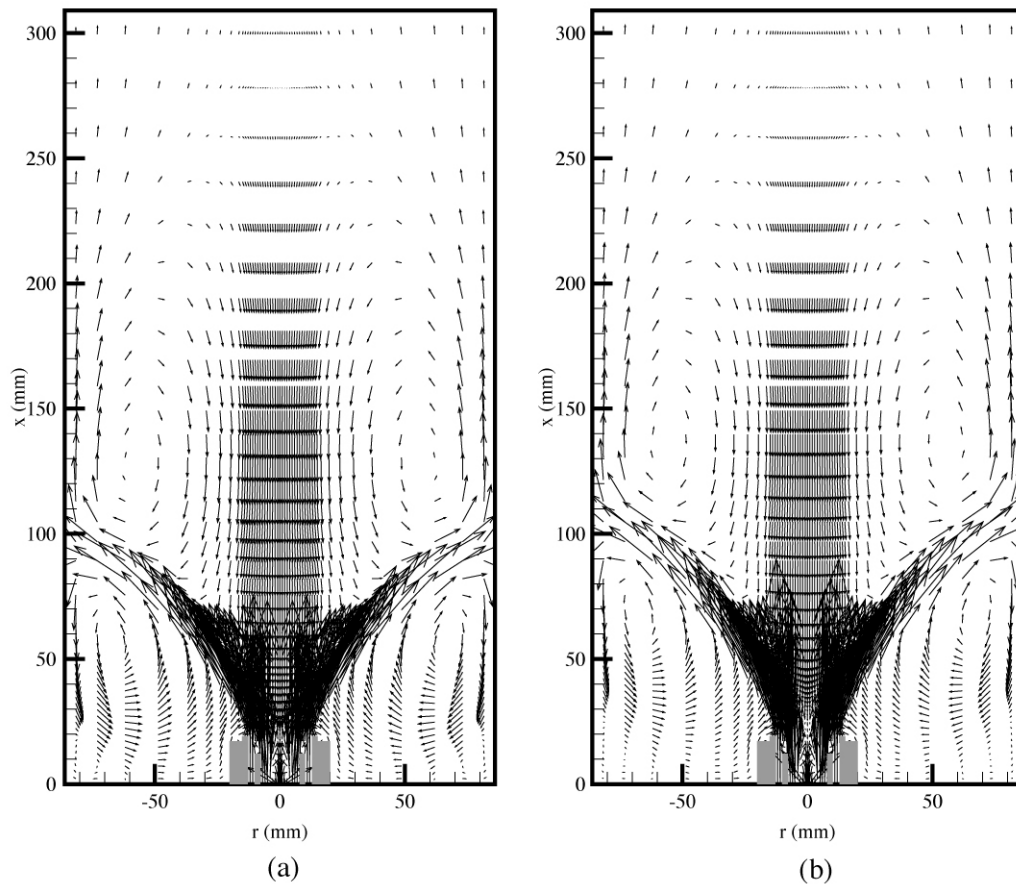


Fig. 6. Axi-symmetric simulations of swirl-stabilized, model gas-turbine combustor with detailed chemistry for JP-8 fuel. Velocity fields obtained for overall equivalence ratios of (a) 0.65 and 1.15. Change in overall equivalence ratio was obtained by varying the fuel jet issued from the center.

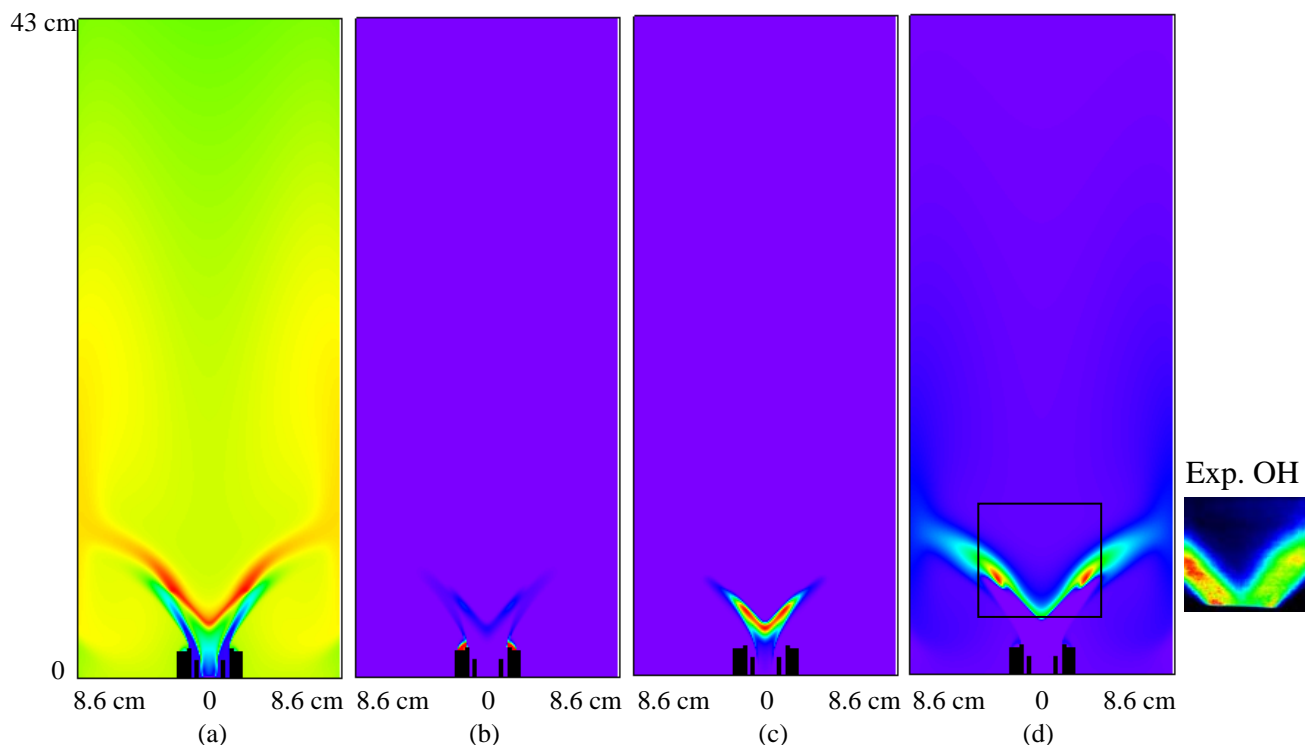


Fig. 7. Flame structure and species distributions of swirl-stabilized, model gas-turbine combustor operating under fuel-lean equivalence ratio of 0.65. Distributions of (a) temperature with red indicating a peak value of 2100 K, (b) soot volume fraction with a peak value of 0.2 %, (c) benzene concentration with a peak value of 0.15 %, and (d) OH concentration with a peak value of 0.5 %. Insert shows the OH-PLIF image obtained in the experiments.

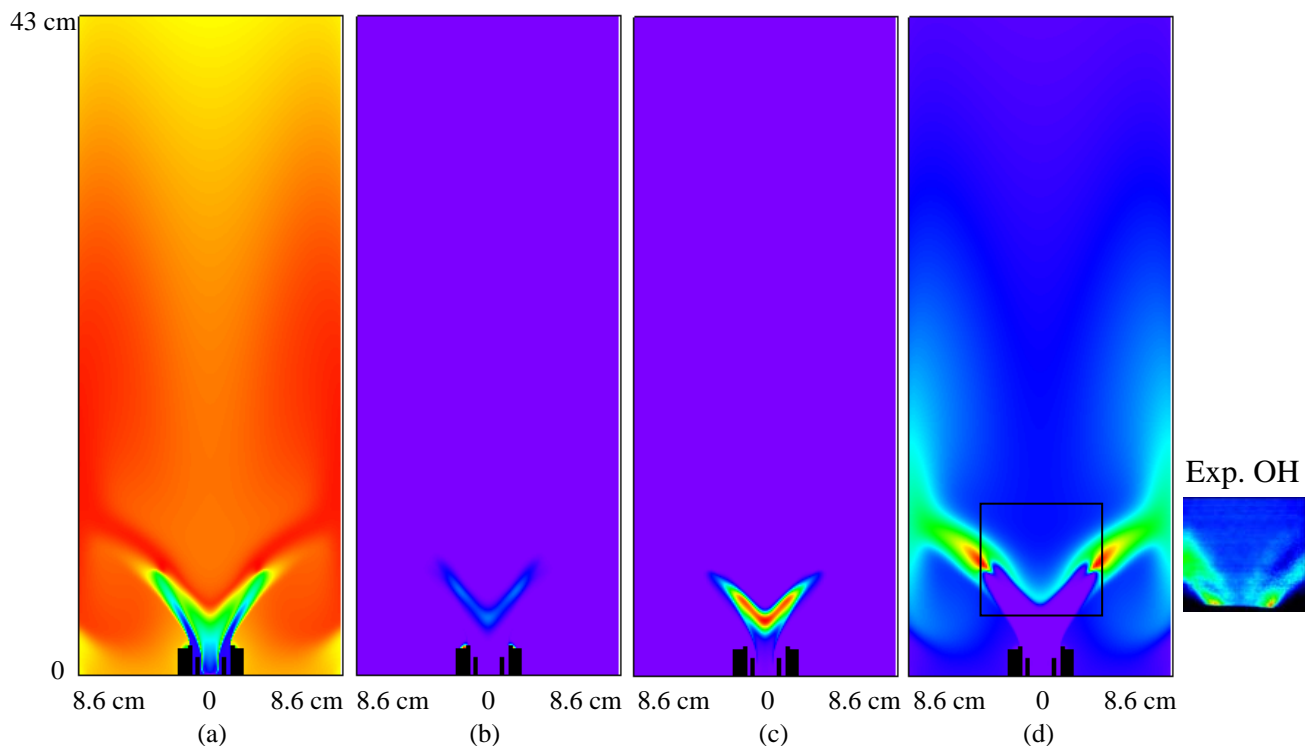


Fig. 8. Flame structure and species distributions of swirl-stabilized, model gas-turbine combustor operating under fuel-lean equivalence ratio of 0.85. Distributions of (a) temperature with red indicating a peak value of 2100 K, (b) soot volume fraction with a peak value of 0.2 %, (c) benzene concentration with a peak value of 0.15 %, and (d) OH concentration with a peak value of 0.5 %. Insert shows the OH-PLIF image obtained in the experiments.

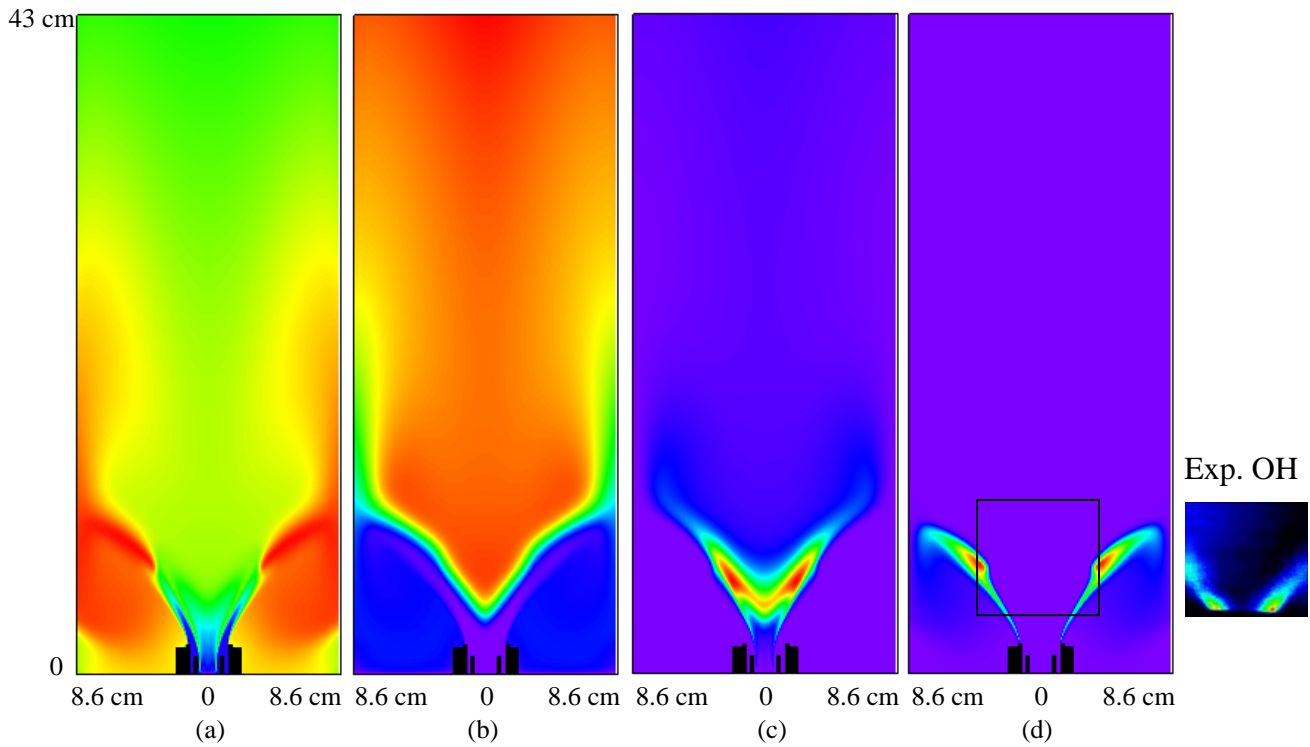


Fig. 9. Flame structure and species distributions of swirl-stabilized, model gas-turbine combustor operating under fuel-lean equivalence ratio of 1.15. Distributions of (a) temperature with red indicating a peak value of 2100 K, (b) soot volume fraction with a peak value of 0.8 %, (c) benzene concentration with a peak value of 0.15 %, and (d) OH concentration with a peak value of 0.5 %. Insert shows the OH-PLIF image obtained in the experiments.

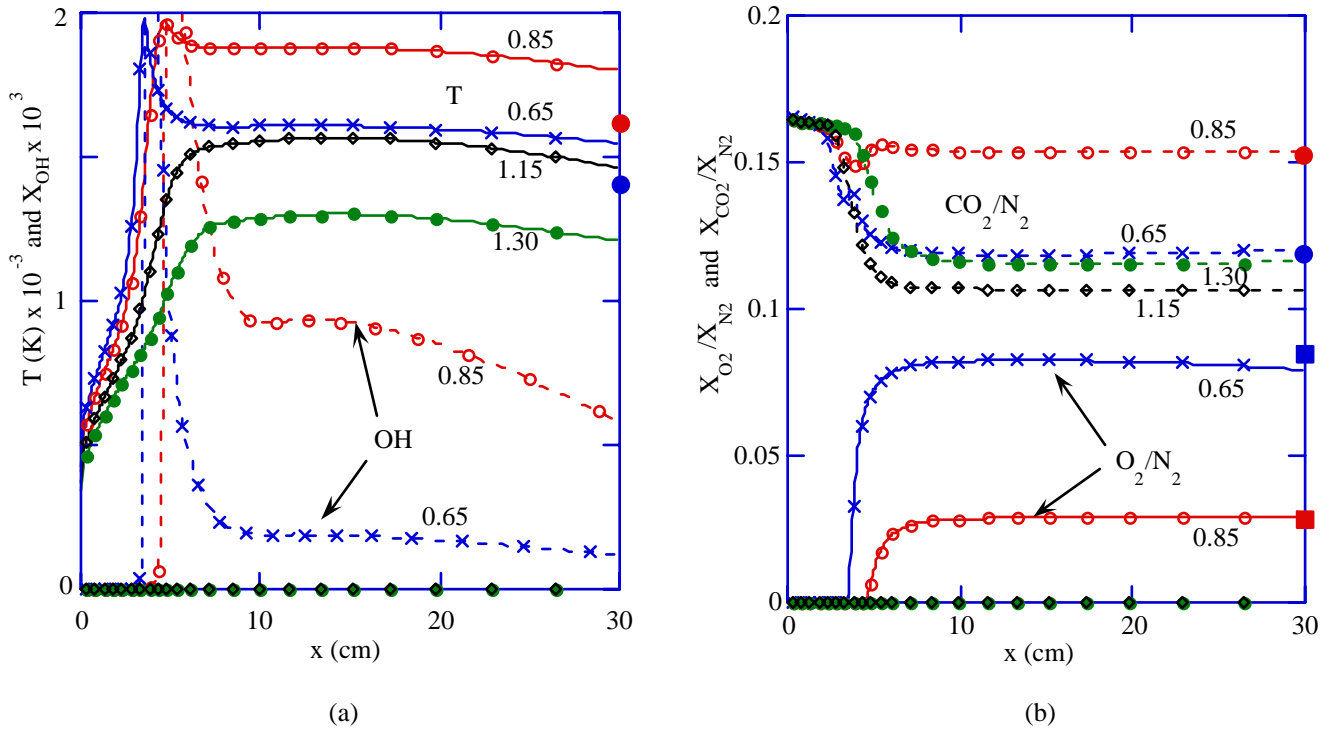


Fig. 10. Distributions of temperature and species concentrations along the centerline of the combustor computed under different equivalence-ratio conditions. (a) Variations of temperature and OH concentration, and (b) variations of O_2 and CO_2 concentrations normalized with local N_2 concentration. Large symbols indicate experimental data of Roy et al.⁴²

Micro-Vortex/Flame Interactions and Their Implications in Turbulent-Flame Modeling

V. R. Katta¹, T. R. Meyer¹, J. R. Gord² and W. M. Roquemore²

¹Innovative Scientific Solutions, Inc
2766 Indian Ripple Road, Dayton, OH 45440, USA

²Air Force Research Laboratory
Propulsion Directorate, Wright-Patterson Air Force Base, OH 45433, USA

Abstract

Laminar flamelet theory is often used for representing the structure of a turbulent diffusion flame. Limitations of such representation are examined by studying various vortex/flame interactions in a hydrogen/air opposing-jet diffusion flame. Vortices are injected from the air side toward the flat flame formed between the fuel and air jets. A centimetre-size vortex is made to interact with a 7.0-mm-thick flame and a micron-size vortex is made to interact with a 2.4-mm-thick flame. Sufficiently high vortex propagation velocities are used for creating flame extinction in both cases. While the larger vortices, irrespective of their propagation velocity, tend to create a wrinkled, strained flame before causing extinction--representing a laminar flamelet, the smaller vortices tend to replace the local fluid in the flame zone with the constituent fluid and destroyed the flame structure--representing a distributed reaction zone. As the micron-size vortex is larger than the Kolmogorov length scale, a portion of the possible turbulent processes (events) in a hydrogen diffusion flame must be viewed as distributed reaction zones.

Introduction

According to flamelet theory [1], the local instantaneous composition and temperature of the mixture in a nonpremixed system can be modeled as being the same as those in a stretched laminar diffusion flame. The mixture fraction and scalar dissipation rate are then used in linking the turbulent flame structure to that of the laminar flames. At a critical value of scalar dissipation rate, the laminar diffusion flame extinguishes due to large mixture fraction gradients. The reaction zone in physical space becomes so narrow that diffusive heat loss will lead to quenching. This scalar-dissipation-rate analogy has been used in flamelet theories in modeling extinction and ignition phenomena in turbulent flames. The unsteady effects in the reaction zone are usually considered by incorporating the unsteady diffusion of reactants and heat conduction [2]. Flamelet theories have been successfully applied to the modeling of various nonpremixed flame systems [3].

A necessary condition for flamelet concepts to apply is that the reaction zone must be thinner than the smallest scales of the turbulence which is Kolmogorov length scale. Performing asymptotic expansion for high Damkohler numbers for hydrogen flames, Bilger [4] derived an expression for reaction rate and argued that flamelets are not asymptotically thin due to the influence of reverse reactions; that is, the reaction zones are equilibrium broadened. Even though, the regular asymptotic analysis and the non-reacting experimental data used by Bilger [4] are not ideal for judging the validity of the flamelet theories, they certainly raised important issues about the applicability of the flamelet theories to the turbulent-combustion process. It has been widely recognized that highly-resolved measurements and numerical simulations are needed for addressing the existence of laminar flamelets in turbulent-flow environment [5].

A numerical investigation is performed in the present study to aid the understanding of the extinction process associated with laminar flamelets and, thereby, verify the validity of the laminar flamelet theory. Vortex/flame interactions, which are often considered to be the building blocks of statistical theories of turbulence, are utilized for establishing highly strained flamelets. These interactions were studied in the past for understanding the effects of curvature on unsteady flames [6]. In particular, experiments designed by Roberts et al. [7] and by Rolon et al. [8] have generated considerable interest, especially because of their unique ability to inject a well characterized vortex toward the flame surface. Numerous investigations have been performed using Rolon burner and by varying the size and strength of the vortex in attempts to understand global features such as scale [9,10] and origin [11] effects and localized features such as annular-quenching [12] and nonadiabatic-equilibrium-temperature [13,14] phenomena.

Complete simulation of the opposing-jet flame using multi-dimensional models not only eliminate concerns regarding the simplified analyses but also provide a valuable tool for studying vortex/flame interactions. Several two- and three-dimensional computational-fluid-dynamics models with detailed chemical kinetics (CFDC) have been developed [15,16] for the study of the interaction between a planar flame formed in counterflow burners and an induced vortex. In the present investigation, a well-tested CFDC model [17] was used for understanding the flame structure near extinction and for testing the validity of flamelet theories.

Numerical Model

Time-dependent, axisymmetric Navier-Stokes equations written in the cylindrical-coordinate (z - r) system are solved along with species- and energy-conservation equations [16]. A detailed-chemical-kinetics model is used to describe the hydrogen-air combustion process. This model consists of thirteen species--namely, H_2 , O_2 , H , O , OH , H_2O , HO_2 ,

H₂O₂, N, NO, NO₂, N₂O, and N₂. A detailed-chemical-kinetics model having 74 reactions among the constituent species is used; the rate constants for this H₂-O₂-N₂ reaction system were obtained from Ref. [18].

Temperature- and species-dependent property calculations are incorporated. The governing equations are integrated on a nonuniform staggered-grid system. An orthogonal grid having rapidly expanding cell sizes in both the axial and radial directions is employed. The finite-difference forms of the momentum equations are obtained using an implicit QUICKEST scheme [16] and those of the species and energy equations are obtained using a hybrid scheme of upwind and central differencing. At every time step the pressure field is calculated by solving the pressure Poisson equations simultaneously and utilizing the LU (Lower and Upper diagonal) matrix-decomposition technique. This model, called UNICORN (UNsteady Ignition and COmbustion with ReactionNs), has been extensively validated [17] by simulating various steady and unsteady counterflow [12] and coflow [16,19] jet diffusion flames and by comparing the results with experimental data.

Burner Details

The opposing-jet-flame burner used for these studies was designed by Rolon [8]. The burner assembly consists of 25-mm-diameter nozzles (d_o), 40-mm-diameter outer nozzles (D_o), and syringe tubes of 0.2-mm to 5-mm diameter (d_i). A flat flame is formed between the fuel and air jets having velocities of 0.69 and 0.5 m/s, respectively. An annular nitrogen flow of 0.1 m/s is used from both the fuel and air side nozzles. The hydrogen-to-nitrogen ratio employed for the fuel jet is 0.38. Only the region between the lower and upper nozzle exits was modeled in the present study. The fuel (d_o), air (d_o), nitrogen (D_o), and injection (d_i) jet diameters used in the simulations were identical to those used in the experiment.

Results and Discussion

Calculations for the steady-state axisymmetric flame were made using a non-uniform 401 x 301 mesh system distributed over a physical domain of 40 x 40 mm, which yielded a mesh spacing of 0.1 mm in both the axial (z) and the radial (r) directions in the region of interest. Flat profile for the velocity is used at the exit of the each nozzle. The air-side strain rate along the stagnation line calculated from the rate of change in the axial velocity (u) with respect to the distance (z) is 48 s⁻¹. The peak temperature of 1560 K of this weakly strained flame is only slightly lower than the corresponding adiabatic-equilibrium flame temperature of 1598 K. The flame thickness based on temperature is 7.0 mm.

A centimeter-size vortex is generated on the air side by injecting air from the 5.0-mm diameter central injection tube. Several vortex/flame interactions are obtained by injecting air at different velocities. In general, the propagation velocity of the vortex emerging from the nozzle decreases as it travels toward the flame surface. If the vortex propagation velocity becomes low by the time it reaches the flame surface, the interaction generates a weakly stretched and wrinkled flame. Note that stretch rate inversely corresponds to the flame thickness. Consequently, during the interaction between a centimeter-size vortex and the flame surface, the thickness of the latter decreases. As the vortex propagation velocity increases with the air injection, wrinkling of the flame surface decreases while stretch rate increases and flame thickness decreases further. For a sufficiently high propagation velocity, vortex extinguishes the flame locally and penetrates through the hole formed on the flame surface. Only interactions that extinguish the flame are considered in the present study.

Interaction of a large vortex injected from the 5-mm diameter nozzle with a air jet velocity of 30 m/s revealed that the vortex grows to ~1.2 cm in diameter by the time it starts penetrating through the flame and the flame thickness reduces to ~2.0 mm. Flame becomes wrinkled before it is being extinguished at the center. In fact, flame wrinkling and thickness did not change much with vortices injected over a wide range of velocities (20 ~ 160 m/s). Finally, flame is extinguished at the center and vortex has penetrated through the hole. This interaction process follows the description given by flamelet theory as the vortex increases the oxidizer fluxes into the flame zone and eventually extinguishes the flame when cooling becomes dominant.

The interaction between a large-vortex and the flame surface suggests that flame thickness decreases to ~2 mm before it is being extinguished. That means, in order to verify the validity of the flamelet theory, a sub-millimeter vortex must be injected toward the flame surface. To preserve the grid resolution for the simulation of micron-size-vortex/flame interaction, a stationary opposing-jet flame is established between nozzles that are separated by 4 mm. A grid system having 800 x 336 nodes and a spacing of 4 μ m in z and r directions is utilized. The generated steady-state flame has a thickness of ~2.4 mm based on temperature profile. Vortex on the air side is generated by injecting fluid through an 80- μ m diameter nozzle at a velocity of 30 m/s. The interaction between the micron-size vortex and the flame at an instant (200 μ s after the start of air injection) is shown in Fig. 1. Instantaneous distributions of temperature and OH concentration are shown in the left and right halves, respectively. Vortex structure is also shown in these figures by plotting instantaneous locations of the particles injected from the exit of the air jet nozzle.

The size of the micro vortex injected from the 80- μ m-diameter nozzle increased as it passed through the flame. The core of the vortex has reached a diameter of 540 μ m in 200 μ s. Micron-sized vortices seem to grow rapidly in the flame zone compared to the centimeter-sized vortices. Unlike in large-vortex/flame-interaction case, the micron-size vortex in Fig. 1 has penetrated through the flame without wrinkling the latter. On the other hand, micro vortices entrain

significant amount of products and carry with it as seen in Fig. 1. As described in our previous paper [14], the small size vortices quickly become reactant deficient, entrain combustion products and carry high-temperature gases with it [green color fluid that represents a temperature of ~ 800 K within the vortex in Fig. 1]. This interaction process did not follow the typical flamelet theory. Flame is not stretched by the vortex at any instant.

The flame structures at different instants are shown in Figs. 2 and 3 for the centimeter- and micron-size vortex/flame interaction cases, respectively. The temperature profiles at different instants in Fig. 2(a) represent those of a stretched flame. Thickness and peak temperature decreased as the flame is stretched and shifted (while flame is wrinkled). On the other hand, during the most of the micron-size-vortex/flame-interaction process the flame temperature upstream of the vortex head was not perturbed [Fig. 3(a)]. When the vortex came out of the flame zone, it carried hot products with it. These temperature profiles suggest that flame is not being stretched by the vortex.

The heat-release-rate profiles shown in Fig. 2(b) represent that of a stretched laminar flame. Peak heat release rate increased as the flame is stretched by the large-size vortex. Interestingly, heat release rate near the head of the micron-size vortex [Fig. 3(b)] has increased an order of magnitude more than that was seen in centimetre-size vortex/flame interaction. The super-high reactivity (20 times more heat release rate) in micron-size vortex/flame interaction is resulting from mixing of products and air—not from the flame stretch.

Super reactivity in the case of micron-size vortex/flame interaction is also evident in the production rates of OH and H species [Figs. 2(c) and 2(d)]. In a stretched flame (as in the case of centimetre-size vortex) both the production and destruction of these species increased with stretch rate [Figs. 3(c) and 3(d)]. However, as the micron-size vortex rapidly introduces fresh air into the products, production rate of OH [Fig. 2(c)] increased significantly while destruction of this species is nearly unperturbed. Similarly, destruction of H radical [Fig. 2(d)] is significantly enhanced in the micron-size vortex case while production of it was nearly unperturbed.

The micron-size vortex used in this study reached 0.3 mm in diameter when it was passing through the flame zone. This is much larger than the Kolmogorov length scale of 0.03 mm obtained based on turbulence Reynolds number and length-scales of 500 and 3 mm, respectively. This implies that significant portion of length scales in a turbulent reacting flow promote mixing in the reaction zone rather than wrinkling the reaction layer. In other words, a significant part of turbulence-chemistry interaction can not follow laminar flamelet theory.

Acknowledgment

This work was supported, in part, by the Air Force Office of Scientific Research (Dr. Julian Tishkoff, Technical Monitor).

References

1. N. Peters, *Proc. Combust. Inst.* 21 (1986) 1231-1256.
2. B. Cuenot, F. N. Egolfopoulos, and T. Poinsot, *Combust. Theory Modeling* 4 (2000) 77-97.
3. S. K. Liew, K. N. C. Bray, J. B. Moss, *Comb. Flame*, 56 (1984) 199-213.
4. R. W. Bilger, *Proc. Combust. Inst.* 22 (1988) 475-488.
5. N. Peters, *Prog. Astronautics Aeronautics* 135 (1991) 155-182.
6. P. H. Paul, and H. N. Najm, *Proc. Combust. Inst.* 27 (1998) 43-51.
7. W. L. Roberts, J. F. Driscoll, M. C. Drake, J. W. Ratcliffe, *Proc. Combust. Inst.* 24 (1992) 169-177.
8. J. C. Rolon, F. Aguerre, S. Candel, *Combust. Flame* 100 (1995) 422.
9. P. H. Renard, D. Thevenin, J. C. Rolon, S. Candel, *Prog. Energy Combust. Sci.* 26 (200) 225-282.
10. D. Tevenin, P. H. Renard, G. J. Fiechtner, J. R. Gord, J. C. Rolon, *Proc. Combust. Inst.* 28 (2000) 2101-2108.
11. V. R. Katta, and W. M. Roquemore, *Proc. Combust. Inst.* 28 (2000) 2055-2062.
12. V. R. Katta, C. D. Carter, G. J. Fiechtner, W. M. Roquemore, J. R. Gord, and J. C. Rolon, *Proc. Combust. Inst.* 27 (1998) 587-594.
13. K. Yoshida, and T. Takagi, *Proc. Combust. Inst.* 27 (1998) 685.
14. V. R. Katta, T. R. Meyer, J. R. Gord, and W. M. Roquemore, *Combust. Flame* 132 (2003) 639.
15. M. D. Smooke, A. Ern, M. A. Tanoff, B. A. Valdati, R. K. Mohammed, D. F. Marran, M. B. Long, *Proc. Combust. Inst.* 26 (1996) 2161-2168.
16. V. R. Katta, L. P. Goss, W. M. Roquemore, *AIAA J.* 32 (1994) 84.
17. W. M. Roquemore and V. R. Katta, *J. Visualization* 2 (2000) 257.
18. M. Frenklach, H. Wang, M. Goldenberg, G. P. Smith, D. M. Golden, C. T. Bowman, R. K. Hanson, W. C. Gardiner, V. Lissianski, Gas Research Institute Technical Report No. GRI-95/0058 (Gas Research Institute, Chicago), November 1, 1995.
19. V. R. Katta and W. M. Roquemore, *AIAA J.* 36 (1998) 2044.

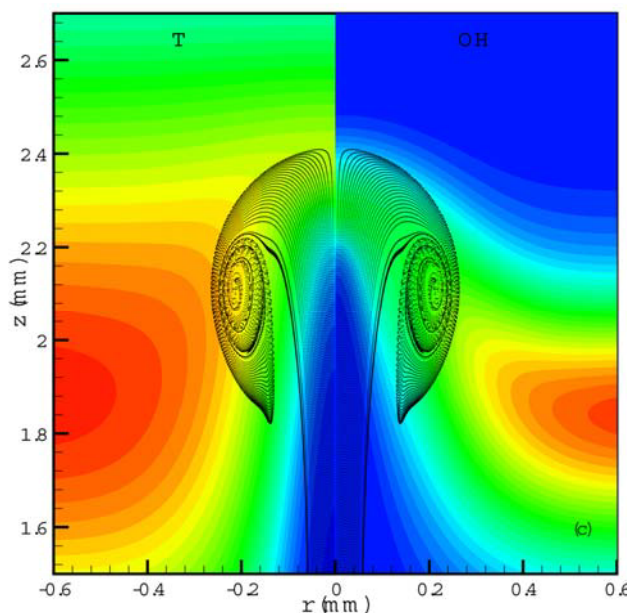


Fig. 1. Interaction of micro vortex with flame surface at 200 μ s. In each image instantaneous locations of particles are superimposed on temperature and OH-concentration fields on left and right halves, respectively.

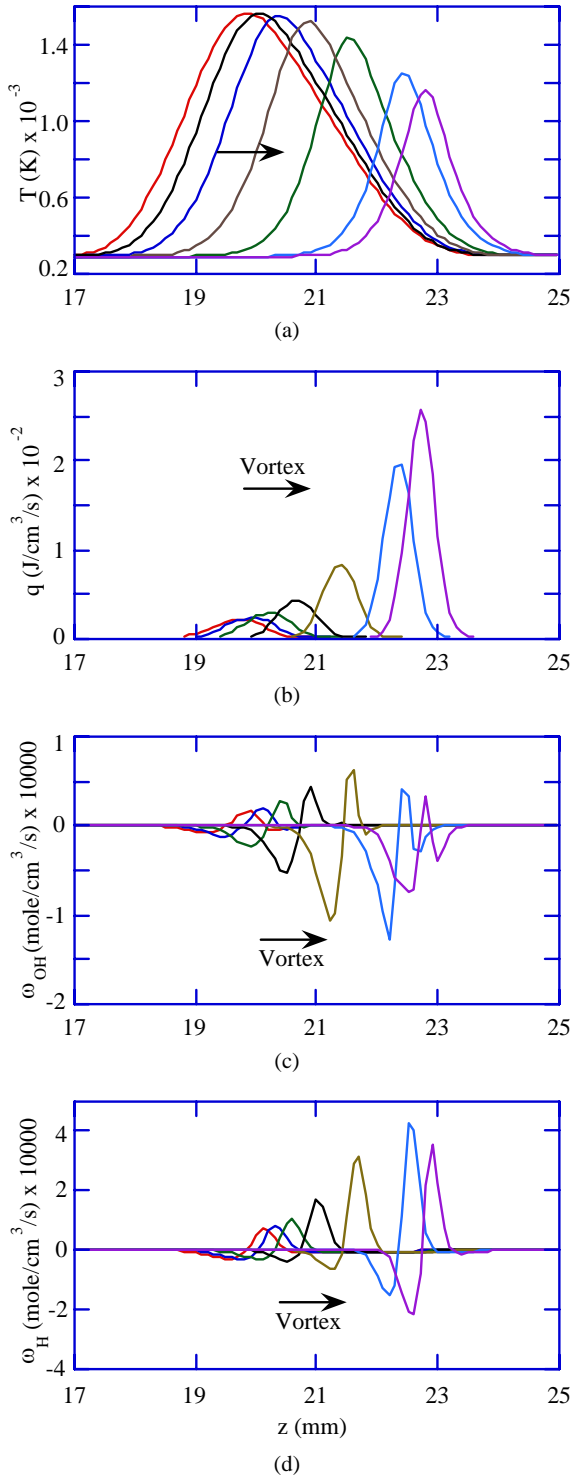


Fig. 2. Interaction of a large-size vortex with the flame surface. Variations in flame structure along the stagnation line as a centimetre-size vortex passes through the flame surface. Distributions of (a) temperature, (b) heat release rate, (c) rate of production of OH molecules, and (d) rate of production of H atoms plotted at different phases of the interaction between $t = 500 \mu\text{s}$ and 2 ms .

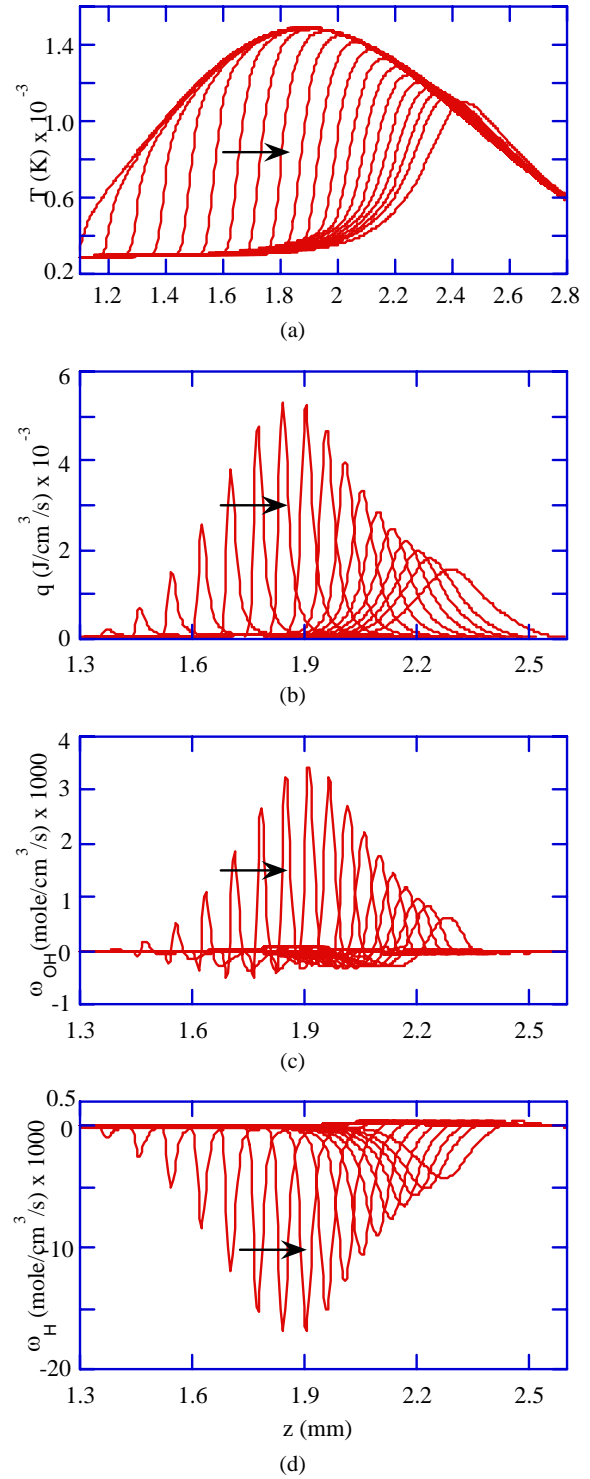


Fig. 3. Variations in flame structure along the stagnation line as a micro vortex passes through the flame surface. Distributions of (a) temperature, (b) heat release rate, (c) rate of production of OH molecules, and (d) rate of production of H atoms plotted at different phases of the interaction between $t = 100 \mu\text{s}$ and $240 \mu\text{s}$. Vortex motion is from left to right.

A numerical investigation of flame liftoff, stabilization, and blowout

Alejandro M. Briones and Suresh K. Aggarwal^{a)}

Department of Mechanical and Industrial Engineering, University of Illinois at Chicago, Chicago, Illinois 60607

Viswanath R. Katta

Innovative Scientific Solutions, Inc., 2766 Indian Ripple Road, Dayton, Ohio 45440

(Received 13 September 2005; accepted 28 February 2006; published online 17 April 2006)

The effects of fuel stream dilution on the liftoff, stabilization, and blowout characteristics of laminar nonpremixed flames (NPFs) and partially premixed flames (PPFs) are investigated. Lifted methane-air flames were established in axisymmetric coflowing jets. Because of their flame suppression characteristics, two predominantly inert agents, CO_2 and N_2 , were used as diluents. A time-accurate, implicit algorithm that uses a detailed description of the chemistry and includes radiation effects is used for the simulations. The predictions are validated using measurements of the reaction zone topologies and liftoff heights of both NPF and PPF. While an undiluted PPF is stabilized at the burner rim, characterized by significant radical destruction and heat loss to the burner, the corresponding undiluted NPF is lifted and stabilized in a low-velocity region extending from the wake of the burner. Detailed comparison of diluted NPF with PPF reveals that the base structures of both the flames are similar and exhibit a double flame structure in the near-field region, where the flame stabilization depends on a balance between the reaction rate and the scalar dissipation rate, which could also be interpreted as a balance between the edge-flame speed undergoing its local scalar dissipation rate and the local flow velocity. As diluent concentration is increased, the flames become weaker, move downstream along the stoichiometric mixture fraction line, and stabilize at a location where they can find a local flow field that has a lower scalar dissipation rate. Further increase of the diluent concentration moves the flames further downstream into the far-field region, where both the NPF and PPF exhibit a triple flame structure, and the flame stabilization mechanism also involves a balance between the triple flame speed and local flow velocity. The PPFs, however, shift to a higher liftoff height and blow out at a lower diluent concentration compared to the NPF, which can withstand larger amounts of dilution. In addition, both NPF and PPF are stabilized at lower liftoff heights and blowout at a lower diluent concentration, when they are diluted with N_2 compared to that with CO_2 . The observed effects of fuel stream dilution and partial premixing on flame liftoff and blowout can be explained using the existing flame stabilization theories. © 2006 American Institute of Physics.

[DOI: [10.1063/1.2191851](https://doi.org/10.1063/1.2191851)]

INTRODUCTION

Flame liftoff and blowout are important for both fundamental and practical considerations. In a coflow jet configuration, depending on fuel jet and coflow conditions (i.e., velocity, dilution, and amount of premixing), flames can be stabilized either at the burner or they can be lifted and stabilized downstream of the burner. Moreover, as liftoff height increases, the flame structure can transition from a nonpremixed flame to a double flame containing two reaction zones, and then to a triple flame containing three reaction zones, i.e., a lean premixed zone, a rich premixed zone, and a nonpremixed zone.¹ Phillips² first described these lifted triple flames. Subsequently, several stabilization criteria for lifted jet diffusion flames have been proposed.^{3–8}

Most previous studies have based the flame stabilization mechanism in terms of a balance between the local flow

velocity and the tribrachial flame speed. Chung and Lee³ employed a cold jet theory,⁹ and derived a theoretical formula for liftoff height and blowout conditions of nonpremixed jet flames. Their analysis showed that the Schmidt number (Sc) plays an important role in flame liftoff, and stable lifted flames are possible only for fuels for which $Sc > 1$. Increasing the fuel flow rate increases the liftoff height for propane and n-butane flames ($Sc > 1$) and decreases it for methane and ethane flames ($0.5 < Sc < 1$), implying that methane and ethane flames blowout directly in the burner-stabilized mode. However, Kioni *et al.*¹⁰ and Plessing *et al.*¹¹ established lifted methane flames using nitrogen dilution and investigated the effect of strain rate. Ghosal and Vervisch¹² demonstrated analytically that a lifted laminar flame is possible for a fuel for which Sc is greater than a critical value Sc_{cr} , which is less than unity. For values of $Sc < Sc_{cr}$, they showed that a lifted flame is subcritical and can only survive in a narrow parametric region. In a subsequent study, Lee *et al.*¹³ investigated the effect of partial premixing on flame liftoff and blowout for propane and

^{a)} Author to whom all correspondence should be addressed. Electronic address: ska@uic.edu

n-butane flames, and observed that the jet velocity at flame liftoff and blowout decreases as the level of partial premixing is increased.

Ruetsch *et al.*⁵ reported that the effect of heat release on lifted triple flames provides an upper bound for the flame speed. Increasing the heat release and reducing the mixture fraction gradient increases the flame speed over that of the corresponding planar premixed flame. Buckmaster¹⁴ demonstrated that in a special case of unity Lewis number (Le), the edge flame speed (U_F) increases with decreasing scalar dissipation rate (χ) in a linear form, $U_F/S_L^0 = 1 - \chi/\chi^0$, where χ^0 is the scalar dissipation rate when U_F is zero. Chen and Bilger⁶ reported that the flame propagation speed (U_p) increases monotonically with decreasing χ along the stoichiometric mixture fraction contour. They combined the above theories to propose a general expression for the triple flame propagation velocity, $U_p/S_L^0 = (\rho_u/\rho_b)1/2[1 - (\chi_{st}/\chi_a)^m]$, where the correlation constants m and χ_a are determined from a linear regression analysis. This equation is consistent with the argument that U_p/S_L^0 is bounded by the heat release for small scalar dissipation rates. Based on the above flame stabilization theories, most previous investigations have focused on determining the critical inlet flow velocities for flame liftoff and blowout. However, the liftoff and blowout characteristics of NPFs, and especially those of PPFs, with respect to the effects of diluents, have not been extensively investigated. This provided the major motivation for the present study.

The flame stabilization theories³⁻⁶ described above are based on the tribrachial flame speed hypothesis. Takahashi and Katta⁸ reported, however, that flames stabilized near the burner do not exhibit a triple flame structure, and therefore the flame stabilization cannot be explained in terms of the tribrachial flame speed. Instead they hypothesized that a lifted nonpremixed flame is stabilized by a reaction kernel, in which a subtle balance is maintained between the residence time and reaction time. They also highlighted the importance of detailed chemistry in simulating flame liftoff and stabilization, as global chemistry, which neglects the radical reactions, led to an incorrect understanding of the flame base or reaction kernel structure.

Studies dealing with the effects of diluents on the liftoff and blowout characteristics of flames are also important for practical considerations. For instance, Halon 1301 is currently used worldwide for fire protection, but because of concerns with its effect on the stratospheric ozone layer, it is regulated by international agreements (Montreal Protocol¹⁵). While these regulations have intensified research for new fire suppressants, the search for a new fire-extinguishing agent with all the desirable properties of Halon 1301 has not been successful so far. Vahdat *et al.*¹⁶ investigated flame extinction using binary fire suppressants of organic compounds mixed with nitrogen. Although these mixtures appear to be promising, halogenated compounds such as CF_3Br (Halon 1301) are still found to be more efficient. The inert gases extinguish fire primarily through the thermal effect, and thus being harmless to the environment, provide justification for studying their effects on lifted flames.

The major objective of our investigation is to character-

ize the effects of fuel stream dilution and partial premixing on flame liftoff, stabilization, and blowout. Lifted methane-air nonpremixed (NPF) and partially premixed flames (PPFs) are established in axisymmetric coflowing jets. The flames are simulated using a time-accurate, implicit algorithm that uses detailed descriptions of chemistry and transport. Results of simulations are used to (i) distinguish between the burner-stabilized and lifted flames in terms of velocity profiles along the stoichiometric mixture fraction line and heat transfer from the flame to the burner, (ii) perform a detailed comparison of the structures of NPF and PPF in terms of the various reaction zones near the flame base; the base flame structure is important for the flame stabilization criteria, (iii) examine the flame stabilization criteria for lifted flames stabilized in both the near-field and far-field regions, and (iv) characterize the effectiveness of two common fire suppression agents, N_2 and CO_2 , in extinguishing the NPFs and PPFs.

Depending on the liftoff height, diluent concentration, and other conditions, the liftoff behavior of nonpremixed jet flames falls into three different categories:¹⁷ (i) both liftoff and blowout occurring in the laminar region, (ii) liftoff occurring in the laminar region, but blowout in the turbulent region, and (iii) both liftoff and blowout occurring in the turbulent region. In the present study, we focus on the liftoff and blowout occurring in the laminar region of coflowing jets. A coflow jet configuration is employed, since it provides more stable flow conditions compared to free jets, and also facilitates the treatment of boundary conditions.

THE COMPUTATIONAL MODEL

The computational model is based on the algorithm developed by Katta *et al.*¹⁸ and the simulation method is described in detail elsewhere.^{19,20} The numerical model solves the time-dependent governing equations for unsteady reacting flows in an axisymmetric configuration. The governing equations can be written in a generalized form as

$$\begin{aligned} & \frac{\partial(\rho\Phi)}{\partial t} + \frac{\partial(\rho v\Phi)}{\partial r} + \frac{\partial(\rho u\Phi)}{\partial z} \\ &= \frac{\partial}{\partial r} \left(\Gamma^\Phi \frac{\partial\Phi}{\partial r} \right) + \frac{\partial}{\partial z} \left(\Gamma^\Phi \frac{\partial\Phi}{\partial z} \right) - \frac{\rho v\Phi}{r} + \frac{\Gamma^\Phi}{r} \frac{\partial\Phi}{\partial r} + S^\Phi. \end{aligned}$$

Here t denotes the time, and u and v represent the axial (z) and radial (r) velocity components, respectively. The general form of the equation represents conservation of mass, momentum, species, or energy conservation equation, depending on the variable used for Φ . The diffusive transport coefficient Γ^Φ and source terms S^Φ appearing in the above equation are provided in Table 1 of Ref. 19. Introducing the overall species conservation equation and the state equation completes the set of equations. In addition, a sink term based on an optically thin gas assumption is included in the energy equation to account for thermal radiation from the flame.²⁵ The sink term is expressed as $q_{rad} = -4\sigma K_p(T^4 - T_o^4)$,²¹ where T denotes the local flame temperature, and K_p accounts for the absorption and emission from the participating gaseous

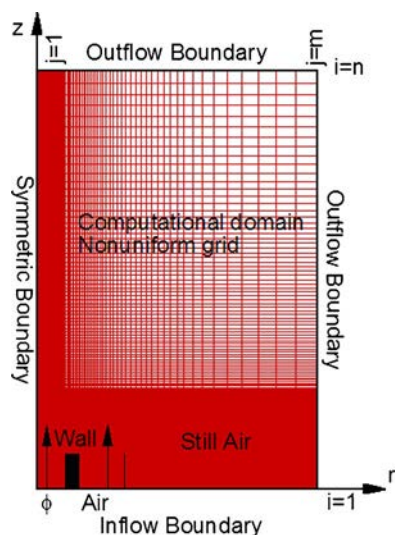


FIG. 1. Schematic of the computational domain and boundary conditions.

species (CO_2 , H_2O , CO and CH_4), and is expressed as $K_p = P \sum X_i K_{p,i}$, where $K_{p,i}$ denotes the mean absorption coefficient of the k th species. Its value is obtained by using a polynomial approximation to the experimental data provided in Ref. 21.

The thermodynamic and transport properties appearing in the governing equations are considered to be temperature- and species-dependent. The thermal conductivity and viscosity of the individual species are estimated based on Chapman–Enskog collision theory, following which those of the mixture are determined using the Wilke semiempirical formulas.²² Chapman–Enskog theory and the Lennard–Jones potentials are used to estimate the binary-diffusion coefficient between each species and nitrogen. The methane–air chemistry is modeled using a detailed mechanism that considers 24 species and 81 elementary reactions.²³ The major species included in the mechanism are CH_4 , O_2 , CO_2 , CO , CH_2O , H_2 , H_2O , C_2H_2 , C_2H_4 , C_2H_6 , and N_2 , while the radical species include CH_3 , CH_2 , CH , CHO , H , O , OH , HO_2 , H_2O_2 , C_2H , C_2H_3 , C_2H_5 , and CHCO . The mechanism has been validated previously for the computation of premixed flame speeds and the detailed structure of both nonpremixed and partially premixed flames.^{19,20,24–26}

While the finite-difference forms of the momentum equations are obtained using the QUICKEST scheme,²⁷ those of the species and energy are obtained using a hybrid scheme of upwind and central differencing. The pressure field is calculated at every time step by solving all of the pressure Poisson equations simultaneously and using the LU (lower and upper diagonal) matrix-decomposition technique.

Figure 1 illustrates the computational domain. It consists of $150 \text{ mm} \times 100 \text{ mm}$ in the axial (z) and radial (r) directions, respectively, and is represented by a staggered, non-uniform grid system. The reported results are grid-independent, as discussed in the next section. An isothermal insert simulates the inner $2 \times 1 \text{ mm}$ burner wall. The boundary conditions used here can be found elsewhere.^{19,20} Both

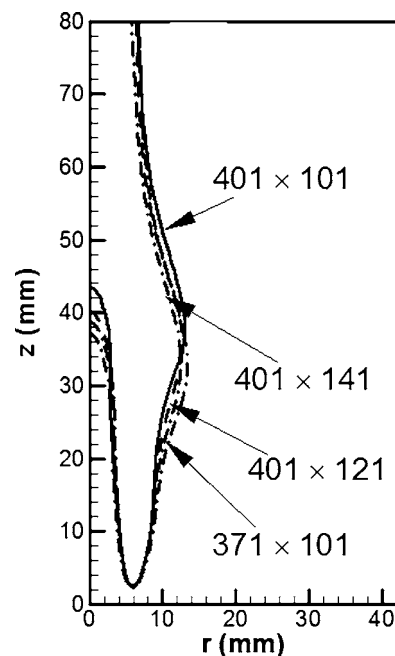


FIG. 2. Temperature isocontour of 1000 K for a CO_2 -diluted partially premixed flame computed using four different grids. For all cases, the flame is computed using the same initial conditions.

the inner and outer jets are set with a constant and uniform velocity of 50 cm/s. The inner jet issues fuel-air mixture at equivalence ratios of $\phi = \infty$ (pure fuel) and 2.25 for the simulation of nonpremixed and partially premixed flames, respectively, while the outer jet issues air. The diluent (CO_2 or N_2) is introduced through the inner jet, and its concentration is varied in order to investigate the flame liftoff, stabilization, and blowout phenomena.

The two base cases simulated correspond to undiluted NPF and PPF. These two base flames are obtained starting from the respective global-chemistry ($\text{CH}_4 + \text{O}_2 \rightarrow \text{CO}_2 + \text{H}_2\text{O}$) solutions as initial conditions and by performing detailed-chemistry calculations for sufficiently long times (~ 10000 time steps corresponding to 2 s).²³ Once the undiluted flames are established, diluents are gradually added until blowout is reached. Blowout is achieved when a critical concentration of diluents moves the flames further downstream rapidly and out of the computational domain, as described by Katta *et al.*²⁸

RESULTS AND DISCUSSION

Validation of numerical model

Egolfopoulos and Law²⁹ demonstrated that by minimizing the effect of numerical diffusivity through mesh refinement, the computed flame speed, which plays a key role in flame stabilization, converges to a grid-independent value. Results of numerical simulations to achieve grid independence for the present case are illustrated in Fig. 2, which presents an isotherm contour (1000 K) for a typical CO_2 -diluted PPF computed using four different grids, i.e., 371×101 , 401×101 , 401×121 , and 401×141 . The mole fraction of CO_2 added to the fuel stream is 5% for this case. For all four grids, the calculations begin using the same ini-

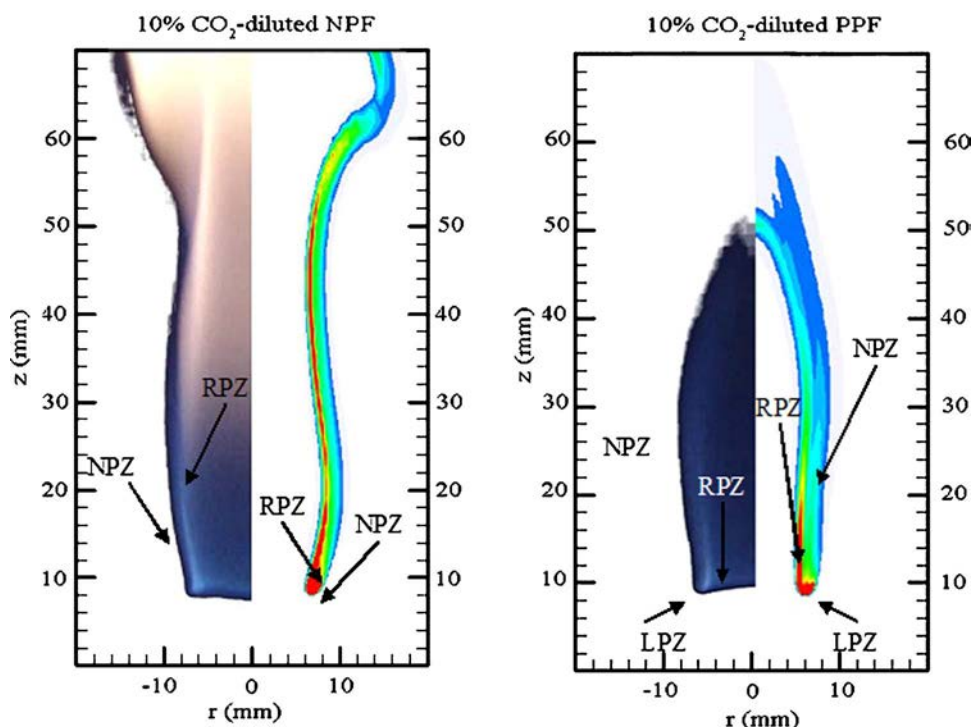


FIG. 3. Comparison of predicted heat release rate contours (right) and measured luminosity contours (left) for the 10% CO_2 -diluted nonpremixed (NPF) and partially premixed flames (PPF). The rich premixed, nonpremixed, and lean premixed reaction zones are represented by RPZ, NPZ, and LPZ, respectively.

tial conditions. Grid lines are clustered near the flame surfaces (not shown) to resolve the steep gradients of the dependent variables. The differences between the results computed using these four grids are small, suggesting the convergence of the simulated flame. Therefore, the minimum grid spacing used for our simulations is 0.103 mm in the z direction and 0.150 mm in the r direction corresponding to a 401×101 grid. In order to further assure that both the temperature and radical species layers are sufficiently resolved in our simulations, we plotted (not shown) the radial profiles of temperature and CH radical near the lifted flame base (at an axial distance of 10.0 mm from the flame base). The thicknesses of the temperature and CH radical layers computed from these profiles were found to be 7.9 and 1.2 mm, respectively. We also computed the structure of the corresponding PPF established at $\phi=2.25$ in a counterflow (one-dimensional) configuration, and found (not shown) that the temperature and CH radical layers had thicknesses of 7.7 and 1.5 mm, and contained 47 and 10 grid points, respectively. These results provided additional confirmation that both the temperature and radical layers are sufficiently resolved in our simulations.

The numerical model has been previously validated using experimental data for a variety of steady and unsteady flames, including opposed-jet diffusion flames,³⁰ burner-stabilized flames,^{20,31,32} and lifted flames.^{7,28} Katta *et al.*³⁰ compared the predicted OH concentrations in opposed-jet flames with the measurements from planar laser-induced fluorescence (PLIF), and showed good agreement. Shu *et al.*³¹ reported good agreement between the predicted and the measured velocity fields using PIV, as well as between the predicted heat release rate contours and the measured C_2^* -chemiluminescence images, for methane-air partially premixed flames. Azzoni *et al.*²⁰ reported similarly good agree-

ment for triple flames stabilized on a slot burner. Likewise, Takahashi *et al.*⁷ reported good agreement between the predicted and measured velocity fields using particle imaging velocimetry (PIV) for methane-air jet diffusion flames under near-lifting conditions. Recently, Katta *et al.*²⁸ accurately predicted the minimum diluent concentration for blowout of methane-air cup-burner flames.

In the present study, we provide additional validation of the numerical model by comparing the predicted heat release rate contours with the measured luminosity contours for CO_2 -diluted lifted nonpremixed and partially premixed flames. As shown in Fig. 3, the numerical model reproduces the measured flame topology and liftoff height for both NPF and PPF. Both flames are located about 9 mm above the burner rim. Mixing of the reactants is enhanced in the wake region above the burner rim, allowing entrainment of air into the fuel side. Consequently, the NPF exhibits a double flame structure containing a rich premixed zone and a nonpremixed zone, while the PPF exhibits a triple flame structure. The locations of the various reaction zones are well predicted by the numerical model. The detailed flame structure for these cases is discussed in a later section. As these flames are established at normal gravity, both the simulations and measurements exhibit well-organized oscillations, induced by buoyant acceleration, and so care is taken in comparing the two flames at the same phase angle. In the NPF, the buoyant acceleration of hot gases outside the flame surface causes shear-layer rollup, leading to the formation of a toroidal vortex that interacts with the flame surface at locations downstream of the flame base. On the other hand, the PPF does not indicate this toroidal vortex ring; instead, the flame pinches off when the flame tip reaches its maximum amplitude. The blue color in the experimental images represents the flame shape and the bright yellow in the NPF corre-

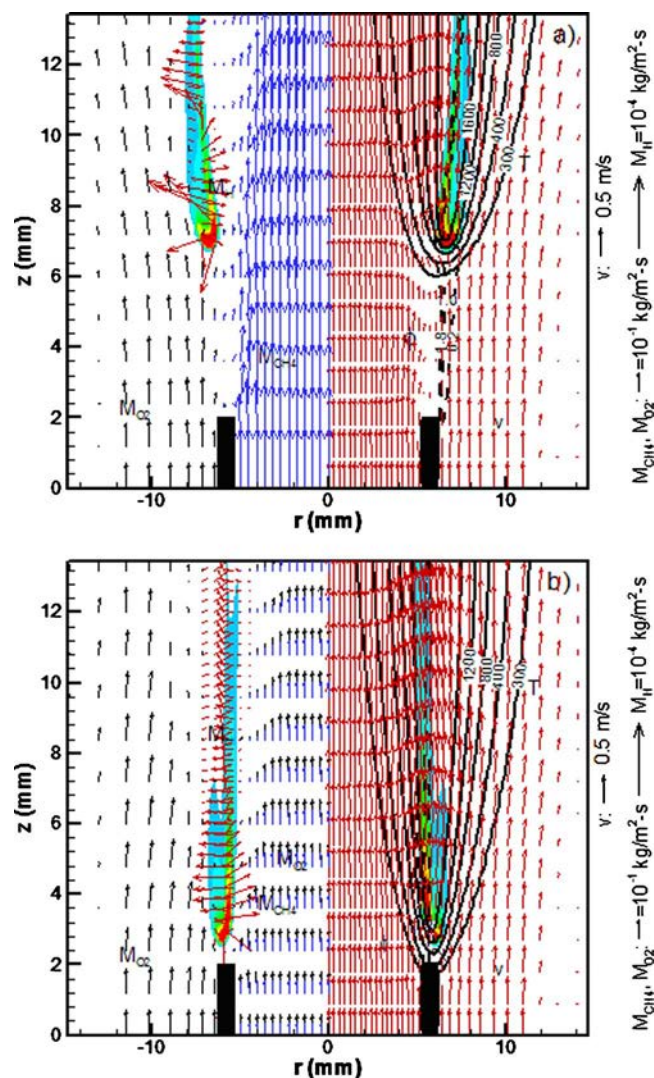


FIG. 4. Computed temperature contours (T), equivalence ratio contours (ϕ), heat release rate contours (q), velocity vectors (v), and mass flux vectors of CH_4 (M_{CH_4}), O_2 (M_{O_2}), and H -atoms (M_{H}) for the undiluted (a) NPF and (b) PPF. The mass flux vectors are shown on the left side, while q -contours are shown on both sides of the axis of symmetry.

sponds to the soot-containing region. Notice that the flame luminosity is greatly diminished in the PPF, implying a significant reduction in soot volume fraction due to partial pre-mixing. Although the numerical model does not account for soot formation, which enhances thermal radiation, the liftoff heights between the experiments and simulations match quite well. This is mainly due to a lack of soot in the flame-base region and, hence, ignoring soot and the related thermal radiation in the numerical simulations did not affect the accuracy of the predicted flame base structure.

Structure of undiluted nonpremixed and partially premixed flames

Figure 4 presents the computed flame structures of the undiluted NPF and PPF in terms of temperature contours (T) (in solid lines), equivalence ratio contours (ϕ) (in broken lines), and velocity vectors (v) on the right side and mass flux vectors (M_{CH_4} , M_{O_2} , and M_{H}) on the left side of the axis

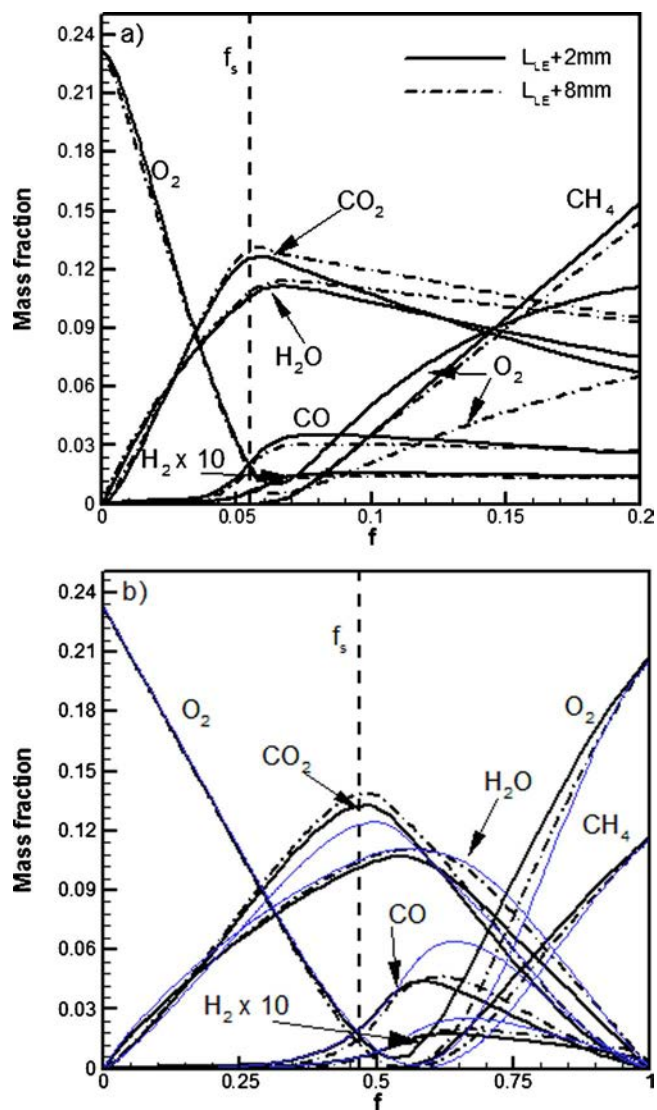


FIG. 5. State relationships in terms of scalar profiles at two axial locations with respect to mixture fraction (f) for the (a) NPF and (b) PPF discussed in the context of Fig. 4. An analogous steady counterflow flame at $\phi=2.25$ and strain rate of 100 s^{-1} is also shown for comparison with the coflow PPF in Fig 5(b). The thin blue lines represent the results from the counterflow flame. The vertical dashed line represents the stoichiometric mixture fraction (f_s).

of symmetry. The heat release rate contours (q) (in rainbow color scheme) are shown on both sides. As noted earlier, these flames at normal gravity exhibit well-organized oscillations. Consequently, the plots in Fig. 4 depict the instantaneous flame structure. For the NPF, the flame base is lifted and stabilized in a low-velocity region that extends from the wake of the burner rim. The mixing of the reactants is enhanced in the wake region, as indicated by the overlapping of CH_4 and O_2 mass flux vectors and the equivalence ratio contours. The flame is located on the air side, where the flame reaches stoichiometric conditions. The heat release rate contours show the high reactivity region near the flame base. The velocity vectors show the thermal expansion, as well as the axial acceleration, as the flow approaches the hot flame. Because the flame base was formed on the air side (due to the low value of stoichiometric ratio for methane fuel and

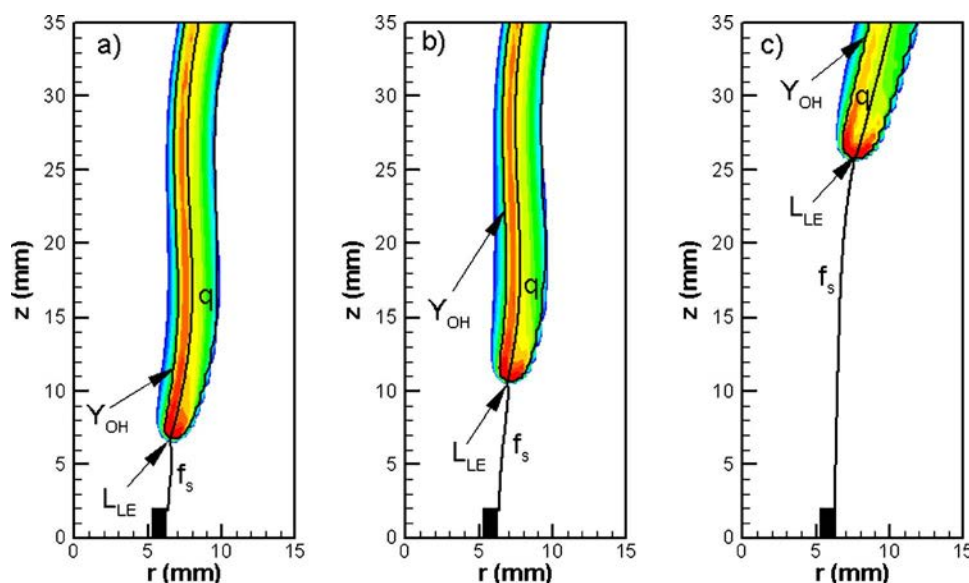


FIG. 6. Predicted heat release rate contours (q), stoichiometric mixture fraction line (f_s), and OH mass fraction (Y_{OH}) contours for three cases: (a) undiluted, (b) 15% CO_2 -diluted, and (c) 30% CO_2 -diluted NPFs. The location of the leading edge is indicated by L_{LE} .

oxygen), the mass flux of O_2 dominates compared to that of CH_4 . Consequently, the high oxygen concentration that surrounds the flame base and the H atoms that diffuse in every direction enhance the chain-branching reaction $\text{H} + \text{O}_2 \rightarrow \text{OH} + \text{O}$, as discussed by Takahashi and Katta.⁸

In summary, the NPF is lifted and stabilized downstream of the burner on the oxidizer side with negligible heat transfer to the burner, while the PPF is stabilized at the burner rim with a significant heat transfer to the burner, as indicated by the temperature contours near the burner rim in Fig. 4(b). This implies that partial premixing affects flame stabilization near the burner rim. This can be expected since the flame stabilization near the burner has been argued to depend upon the leakage of oxygen to the fuel side.^{33,34} Since oxygen is already present in the fuel stream for the PPF, its stabilization behavior is expected to be different from that of the corresponding NPF. These two flames also provide a clear distinction between the characteristics of the lifted and burner-stabilized flames.

In order to further examine the structures of the two flames depicted in Fig. 4, we present in Fig. 5 the state relationships in terms of the profiles of major reactant and product species (CH_4 , O_2 , H_2O , and CO_2), and “intermediate” fuel species (H_2 and CO) with respect to the mixture fraction (f).³⁵ Here $f=1$ and 0 indicate the fuel and oxidizer sides, respectively. Scalar profiles for a counterflow flame simulation at $\phi=2.25$ and strain rate 100 s^{-1} are also included for comparison with the coflow PPF. As discussed by Smooke³⁶ and Naha and Aggarwal,³⁷ partially premixed combustion can be grouped into two distinct regimes, namely a double-flame regime and a merged-flame regime. In the first regime, a PPF contains two physically separated reaction zones, while in the second regime, the two reaction zones are nearly merged. In both the coflow and counterflow PPFs [cf. Fig. 5(b)], the incoming CH_4 and O_2 from the fuel side are completely consumed in the rich premixed zone before reaching the stoichiometric mixture fraction (f_s). The “intermediate” fuel species CO and H_2 are formed in the rich premixed zone, and then transported and consumed in the nonpremixed

zone. The CO_2 and H_2O mass fractions, however, peak near the rich premixed zone, indicating a nearly merged-flame structure. The NPF also shows a similar flame structure in terms of the relative locations of the consumption of reactants and the peak intermediate species. The smaller f_s value for NPFs implies that more mixing is required for establishing these flames compared to that of PPFs. Also, note that the mass fraction of oxygen penetrating into the fuel side of NPF, $Y_{\text{O}_2} \sim 0.12$, is comparable to the corresponding value, $Y_{\text{O}_2} \sim 0.20$, for PPF. Since state relationships of both NPF and PPF are similar, these flames contain a nearly merged flame structure corresponding to a (double) partially premixed flame.

Effect of dilution on the lifted flame structure

Figure 6 presents the global flames structure of CO_2 -diluted NPFs in terms of the heat release rate (q), stoichiometric mixture fraction (f_s), and OH mass fraction (Y_{OH}) contours for three different dilution levels. The flame leading edge (L_{LE}) is defined as the intersection of the stoichiometric mixture fraction (f_s) line and the flame surface, which is represented by a specific OH mass fraction contour (i.e., $Y_{OH} = 2 \times 10^{-5}$), following Qin *et al.*³⁸ As expected, the liftoff height (L_f), which is taken as the distance from the burner rim to L_{LE} , increases, and L_{LE} shifts radially outward with increasing diluent concentration.

Previous investigations have generally distinguished the various reaction zones in jet flames based on their spatial locations.^{19,39} In lifted flames, however, the premixing ahead of the flame front can be relatively small depending upon the liftoff height, and it may be difficult to distinguish between the double and triple flame structures at the flame base. This distinction, however, is important in the context of examining the flame stabilization mechanisms. In order to spatially resolve the various reaction zones of the flames more clearly, we employ the modified flame index (ξ_M) developed in our previous investigation,¹

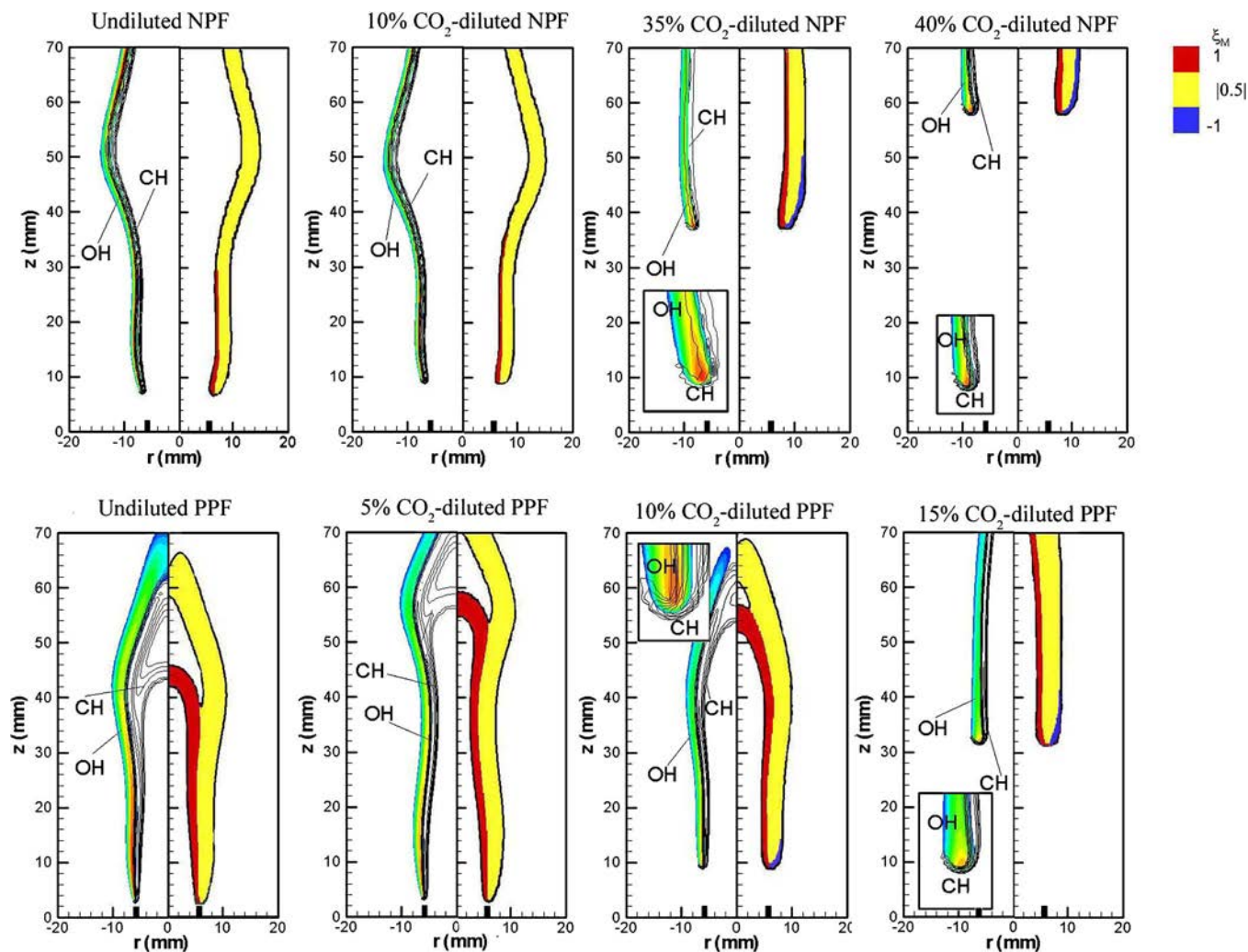


FIG. 7. Flame structures of various CO_2 -diluted NPFs and PPFs are shown through the modified flame index (ξ_M) contours (right), the OH (color rainbow) and CH (monochrome) mass fraction contours (left). For NPFs, a double flame structure [with a rich premixed zone (RPZ) and a nonpremixed zone (NPZ)] is indicated for 0% and 10% CO_2 -dilutions, and a triple flame structure for 35% and 40% CO_2 -dilutions. For PPFs, a double flame structure is indicated for 0% and 5% CO_2 -dilutions, and a triple flame structure for 10% and 15% CO_2 -dilutions.

$$\xi_M = \left(\frac{f - f_s}{|f - f_s|} \right) \cdot \frac{1}{2} \left(1 + \frac{G_{FO}}{|G_{FO}|} \right).$$

Here the mixture fraction (f) is defined following Bilger,³⁵ and G_{FO} is the flame index proposed by Takeno and co-workers.⁴⁰ With this definition, $\xi_M = 1$ represents a rich premixed zone, -1 a lean premixed zone, and $|0.5|$ a nonpremixed zone for hydrocarbon flames. Since identification of the various reaction zones is more relevant in regions of high reactivity, i.e., where the heat release rates are significant, we have computed ξ_M only in regions where the heat release rate is at least 1% of the maximum heat release rate.

Figure 7 presents ξ_M contours as well as the OH (rainbow color) and CH (monochrome) mass fraction contours for NPFs and PPFs established at various CO_2 -dilution concentrations. The CH and OH mass fractions have previously been used to indicate the flame structure in counterflow configuration.^{36,41} Whereas the OH mass fraction peaks in the nonpremixed reaction zone when the flame exhibits a nearly merged flame structure, the CH mass fraction peaks in

the premixed reaction zones. Therefore, OH and CH contours can also be used to visualize the flame structure, in addition to the modified flame index (ξ_M). As noted earlier, the undiluted NPF is lifted and stabilized at an axial location downstream of the burner rim wake. As the diluent concentration increases, L_f increases, and there is a transition from a double flame to a triple flame structure, characterized by the appearance of a lean premixed zone indicated by the blue color and the presence of CH in the outermost region of the flame base (i.e., the lean premixed zone). In contrast, for low diluent concentrations, the PPF is stabilized at the burner rim and exhibits a double flame structure. As the diluent concentration increases, the PPF is lifted. Further increase in diluent concentration increases L_f , and additional mixing in the region between burner rim and flame leads to a transition from a double flame to a triple flame structure. The lean premixed zone becomes more pronounced as L_f increases with the increase in diluent concentration. Therefore, the base structure of a lifted flame depends largely on L_f , which in turn de-

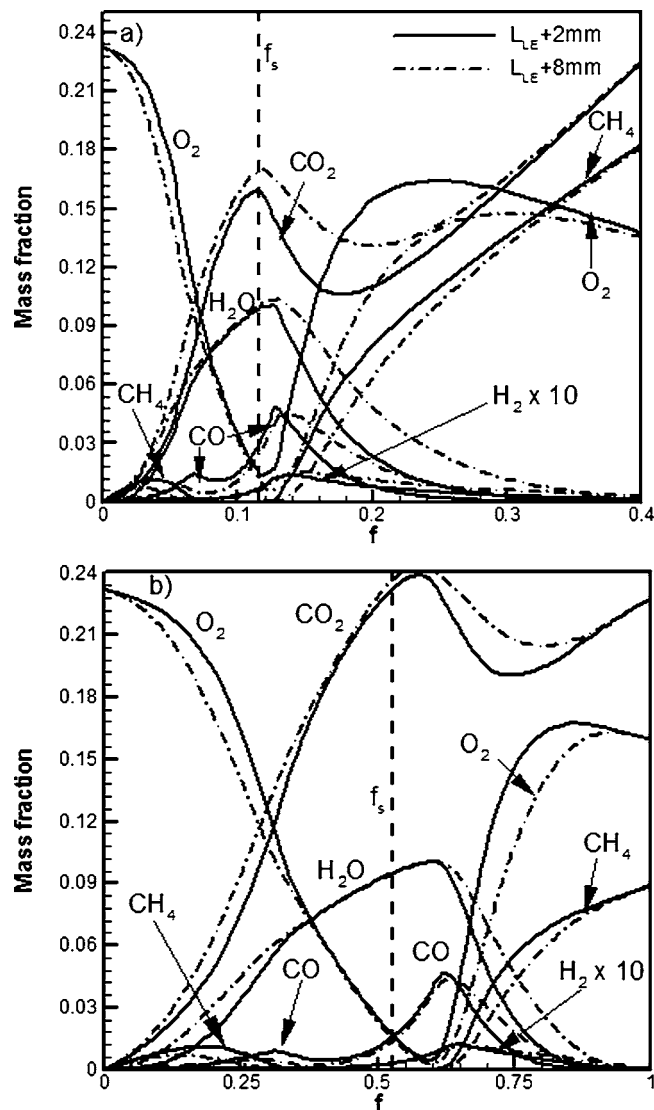


FIG. 8. State relationships in terms of scalar profiles with respect to mixture fraction (f) at two axial locations for (a) 20% CO_2 -diluted NPF and (b) 10% CO_2 -diluted PPF. The vertical dashed line represents the stoichiometric mixture fraction (f_s) value.

depends on mixture composition (i.e., diluent concentration, partial premixing, and premixing outside the nozzle^{38,42}), jet velocity, coflow velocity, and nozzle shape.

Figure 8 presents the detailed structure of a 20% CO_2 -diluted NPF and a 10% CO_2 -diluted PPF. State relationships are presented for the major reactant and product species (CH_4 , O_2 , H_2O , and CO_2) and the “intermediate” fuel species (H_2 and CO) with respect to f ³⁵ at two axial locations. The existence of a rich premixed zone in both the flames is indicated by the relatively high mass fraction of O_2 on the fuel side ($Y_{\text{O}_2} \sim 0.16$). In this zone, both CH_4 and O_2 are completely consumed, producing “intermediate” fuel species H_2 and CO , which are transported and oxidized in the nonpremixed zone to form CO_2 and H_2O . The nonpremixed zone is located near $f=f_s$, as indicated by the peak mass fractions of CO_2 and H_2O . The leakage of CH_4 to the air side leads to the formation of a lean premixed reaction zone, which is located near $f=0.07$ and 0.3 for the NPF and PPF and

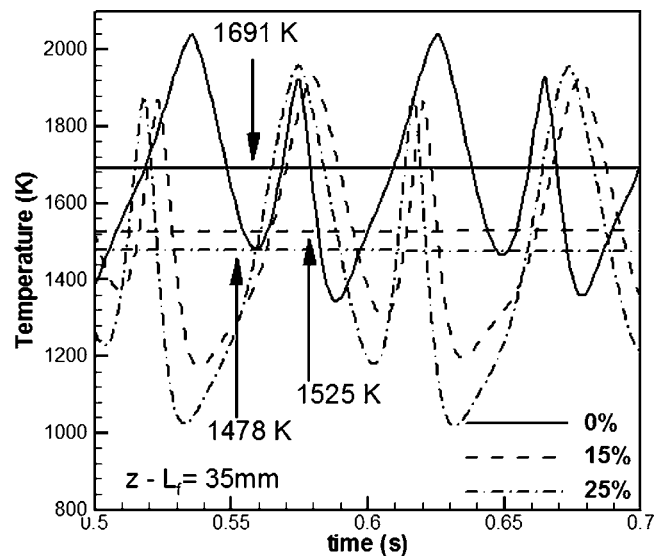


FIG. 9. Temporal evolution of temperature for undiluted, 15% CO_2 -diluted, and 25% CO_2 -diluted NPFs. The horizontal lines indicate the time-averaged temperature. The temperature values are taken 35 mm above the leading edge of each flame.

PPF, respectively. The existence of a lean premixed zone is also illustrated by the comparison of flame structures depicted in Figs. 6 and 8. The location of the lean premixed zone is indicated by the second (smaller) CO and H_2O peaks in both NPF and PPF in Fig. 8. These peaks are located near $f=0.07$ and 0.3 for the NPF and PPF, respectively.

Buoyancy-induced flame oscillations

As noted earlier, the flames simulated in the present study exhibit well-organized oscillations induced by buoyant acceleration. In order to characterize these oscillations, Fig. 9 presents the temporal evolution of temperature at a location 35 mm above the flame leading edge for three CO_2 -diluted NPFs. The interaction between the flame surface and the toroidal vortex, formed by buoyant acceleration of hot gases outside the flame surface, leads to oscillations in temperature. As the diluent concentration is increased and the flame is stabilized at a further downstream location, the amplitude of oscillation increases, while the frequency of oscillation remains nearly constant in the range 15–20 Hz. (The amplitude of oscillation refers to the amplitude of temperature variation at the probing point.) In addition, the mean temperature decreases, indicating a reduction in flame reactivity with increased dilution.

Effects of partial premixing and dilution on flame liftoff and blowout

In order to characterize the effects of partial premixing and diluents, the variation of flame liftoff height with diluent mole fraction is presented in two different formats. Figure 10 depicts the effect of partial premixing by plotting the liftoff height versus the amount of dilution in N_2 -diluted flames [Fig. 10(a)] and CO_2 -diluted flames [Fig. 10(b)], while Fig. 11 compares the effectiveness of N_2 and CO_2 diluents in

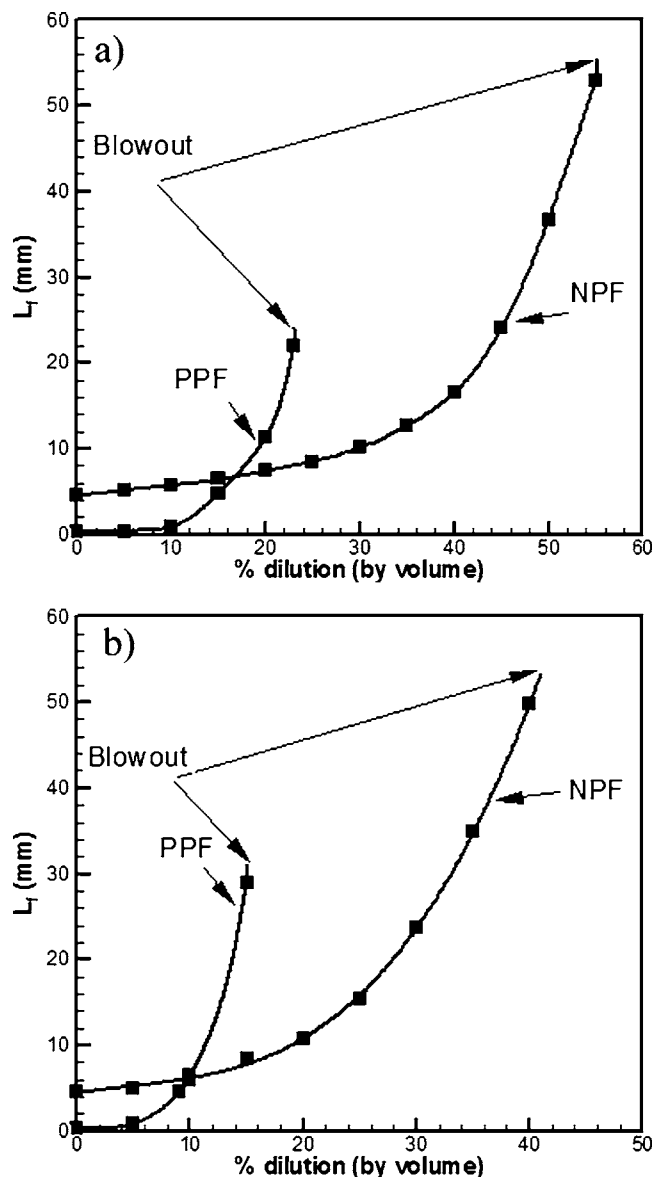


FIG. 10. Lift-off height (L_f) plotted as a function of diluent mole fraction for the N_2 - (a) and CO_2 -diluted (b) NPFs and PPFs. The blowout conditions are also shown.

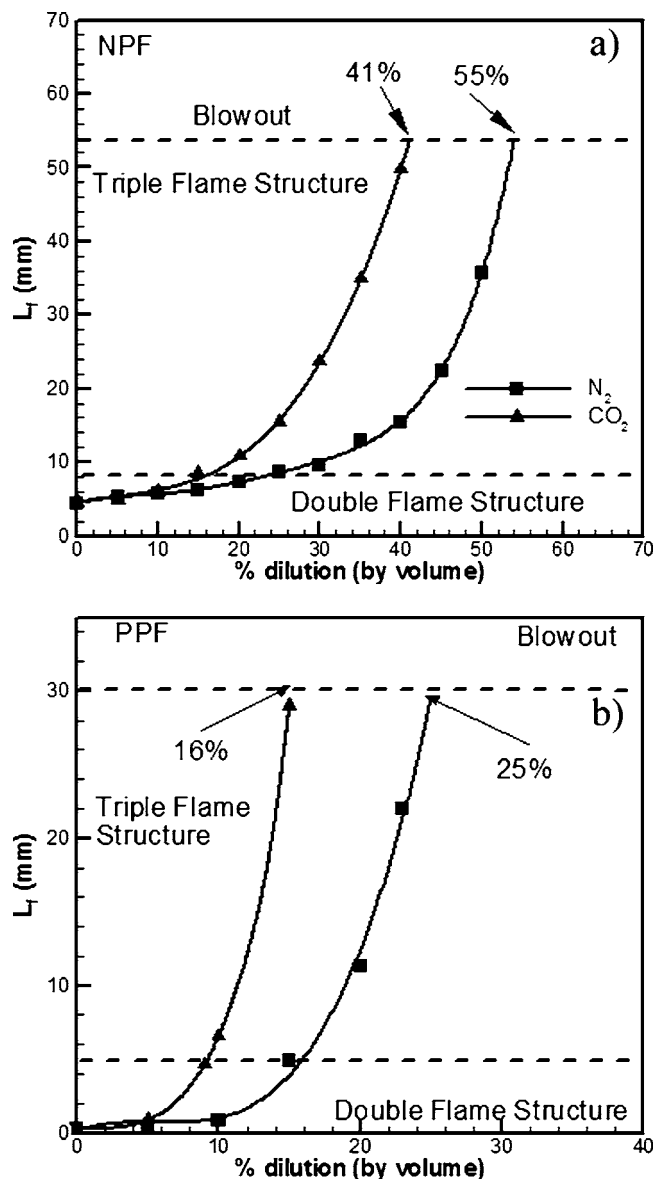


FIG. 11. Lift-off height (L_f) plotted as a function of diluent mole fraction for N_2 - and CO_2 -diluted NPFs (a) and PPFs (b). The double flame, triple flame, and blowout regions are also shown.

causing flame liftoff and blowout in NPF [Fig. 11(a)] and PPF [Fig. 11(b)]. Important observations are as follows:

- (1) As noted earlier, the undiluted NPF is lifted and stabilized downstream of the burner rim, while the corresponding PPF is stabilized at the burner rim. With the addition of diluent, the liftoff height of NPF first increases gradually, and then quite rapidly until the blowout occurs (cf. Fig. 10). In contrast, the PPF first lifts off from the burner rim due to local extinction caused by dilution, which reduces heat transfer to the rim and the rate of H-atom destruction. Once the flame is lifted, its liftoff height increases much more rapidly compared to that of a NPF. Consequently, its liftoff height exceeds that of a NPF, and the diluent mole fraction required for its extinction (through blowout) is significantly smaller than that for a NPF. For the results presented in Fig. 10, the CO_2 dilutions required for the extinction of PPF and

NPF are 16% and 41%, respectively. The corresponding values for N_2 dilution are 25% and 55%, respectively. In addition, a PPF blows out at a lower height compared to a NPF. The superior blowout characteristics of NPFs are due to the higher amount of fuel contained in the fuel jet, which leads to a lower scale dissipation rate for these flames.

- (2) The addition of diluent in the fuel jet reduces the chemical activity in the flame base, as indicated by the reduced temperature. As the flame gets weaker, it shifts further downstream to a stabilization location corresponding to a lower scalar dissipation rate (χ), defined as $\chi = 2D_{F-mix}(\nabla f)^2$, where D_{F-mix} is the fuel diffusivity with respect to the mixture. Figure 12 presents χ plotted versus the axial position along the stoichiometric mixture fraction line for various NPFs and PPFs. For each case, the flame is located at the minimum χ value. The addi-

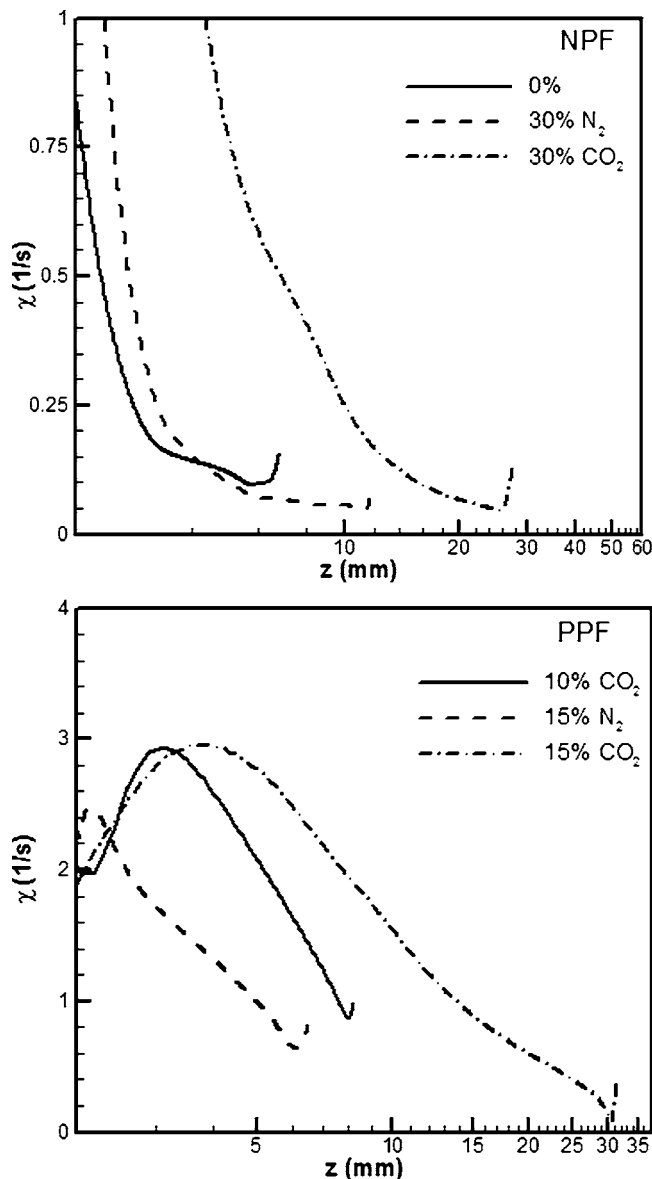


FIG. 12. Scalar dissipation rate (χ) plotted versus the axial position (z) along the stoichiometric mixture fraction line for N_2 - and CO_2 -diluted NPFs (top) and PPFs (bottom).

tion of diluent increases the local scalar dissipation rate while decreasing the flame reactivity. (The effect of fuel stream dilution on the flame reactivity and scalar dissipation rate is further discussed in the next section.) Consequently, the flame moves downstream to a location of smaller χ in order to achieve a balance between scalar dissipation rate and reaction rate. For a mole fraction of CO_2 greater than 41% (or that of N_2 greater than 55%), the NPF blows out as it cannot find a stabilization point within the computational domain [cf. Fig. 11(a)]. The corresponding mole fractions of CO_2 and N_2 for the blowout of PPFs are 16% and 25%, respectively. The existence of a triple flame structure at the flame base also plays an important role in the stabilization of lifted flames in the far field region. This aspect is discussed in the next section.

(3) For low diluent concentrations, the PPF is located at a

lower axial position compared to the NPF. However, as the diluent concentration exceeds a critical value, the PPF shifts to a higher axial location compared to the NPF. Thus, a PPF exhibits a greater sensitivity to fuel stream dilution compared to a NPF (cf. Figs. 10 and 11).

- (4) For the same diluent mole fraction, CO_2 -diluted flames are lifted higher compared to N_2 -diluted flames. Moreover, the diluent mole fraction required for the extinguishment (through blowout) of CO_2 -diluted flames is smaller than for N_2 -diluted flames, although their liftoff heights at extinction are generally similar for the two cases. As discussed in the next section, this can be attributed to the fact that CO_2 dilution increases the scalar dissipation rate and simultaneously decreases the reaction rate by a larger amount compared to that caused by N_2 dilution.
- (5) In the far field region or near the blowout conditions, the liftoff height increases at a faster rate compared to that in the near field. This could be due to the fact that the fuel stream dilution increases the scalar dissipation rate and/or decreases the reaction rate in a nonlinear manner. In addition, both the NPFs and PPFs stabilized in the far field region have a triple flame structure at the base, and a balance between the triple flame speed and local flow velocity also plays a role in the stabilization of these flames. This aspect is further discussed in the next section.
- (6) A previous investigation²⁸ demonstrated that with air stream dilution, methane-air NPFs blow out in a burner-attached mode or in a lifted mode close to the burner. Our simulations indicate that it is possible to establish lifted methane-air NPFs using fuel stream dilution.

Flame stabilization mechanism

Flame liftoff and stabilization are complex processes involving transport, partial premixing, flame propagation, scalar dissipation, and extinction.^{33,34} The stabilization of lifted nonpremixed laminar flames has generally been explained based on the existence of a triple flame structure at the base of a lifted flame, and a dynamic balance between the triple flame speed and the local flow velocity.⁴⁻⁶ This stabilization mechanism is more meaningful for flames that are stabilized in the far field. For flames stabilized in the near field, Takahashi and Katta⁸ hypothesized stabilization by the existence of a reaction kernel in which a dynamic balance is maintained between the characteristic reaction rate and scalar dissipation rate. In order to examine these hypotheses in the context of the present simulations, we computed the scalar dissipation rate and flame speed for various N_2 - and CO_2 -diluted flames.

Figure 12 presents the scalar dissipation rate (χ) versus axial position along the stoichiometric mixture fraction line for several simulated flames. As noted earlier, the flame is stabilized at a location of minimum χ . The effect of fuel stream dilution is to decrease the flame reactivity, as illustrated by the decrease in flame temperature (cf. Fig. 8), and increase the local scalar dissipation rate. The increase in χ is

due to the fact that the fuel stream dilution increases the stoichiometric mixture fraction value (f_s), and thereby shifts the f_s contour from oxidizer region to mixing layer region, which is characterized by large mixture fraction gradients (∇f). Consequently, as the diluent mole fraction is increased, the flame shifts downstream and radially outward to a location of smaller χ in order to achieve a balance between scalar dissipation rate and reaction rate. This stabilization mechanism is consistent with the hypothesis proposed by Takahashi and Katta,⁸ and can also be interpreted as a balance between the edge-flame speed (U_F) and the local flow velocity.⁴³ In fact, the edge flame speed (U_F) has been reported to be a function of the scalar dissipation rate (χ).¹⁴ In addition, the stabilization mechanism can also be used to explain why PPFs are lifted higher than NPF, and CO₂-diluted flames are lifted higher than N₂-diluted flames. As indicated in Fig. 12, the scalar dissipation rate is higher for PPFs compared to that for NPFs. Consequently, PPFs are lifted higher and blow out at a smaller diluent mole fraction compared to PPFs. Similarly, CO₂ dilution decreases flame reactivity, due to the thermal effect, and increases scalar dissipation rate by a larger amount compared to that with N₂ dilution. Consequently, CO₂-diluted flames are lifted higher and blow out at a lower diluent mole fraction compared to N₂-diluted flames.

As discussed earlier, as the flame liftoff height increases, a triple flame structure develops at the flame base (cf. Fig. 7). For these flames, we computed the flame speed (S_L) at the base (triple point) by using the relation^{44,45}

$$S_L = -\frac{1}{\rho|\nabla\varphi|}[\nabla \cdot (\rho D \nabla \varphi) + \omega_\varphi],$$

where the scalar φ is represented by temperature. Figure 13(a) presents the variation of S_L with diluent mole fraction for N₂- and CO₂-diluted NPFs and PPFs. As the diluent mole fraction is increased, the flame speed increases, and the flame is stabilized further downstream in order for S_L to match the local flow velocity. Our results are consistent with those reported by previous researchers. For instance, Kioni *et al.*¹⁰ measured the velocity of a lifted triple flame and found it to be well above the unstretched laminar flame speed of the corresponding stoichiometric premixed fuel-air mixture. In the context of the present study, it should be noted that as the diluent mole fraction is increased, the unstretched laminar flame speed decreases, while the triple flame speed increases, indicating that the ratio of triple flame speed to unstretched laminar flame speed can vary significantly depending upon the mixture and flow conditions. Our results are also in accord with the analysis of Buckmaster,¹⁴ who demonstrated analytically that the flame edge speed (or S_L) increases as the scalar dissipation rate decreases. As noted earlier, with the increase in diluent mole fraction, the scalar dissipation rate (χ) at the flame edge decreases (cf. Fig. 12), and, consequently, the triple flame speed (S_L) increases, as indicated in Fig. 13(a).

The variation of S_L with diluent mole fraction can also be explained from the fact that lifted flames in the present study are positively stretched (at the flame base) and there is a positive correlation between the flame speed and the

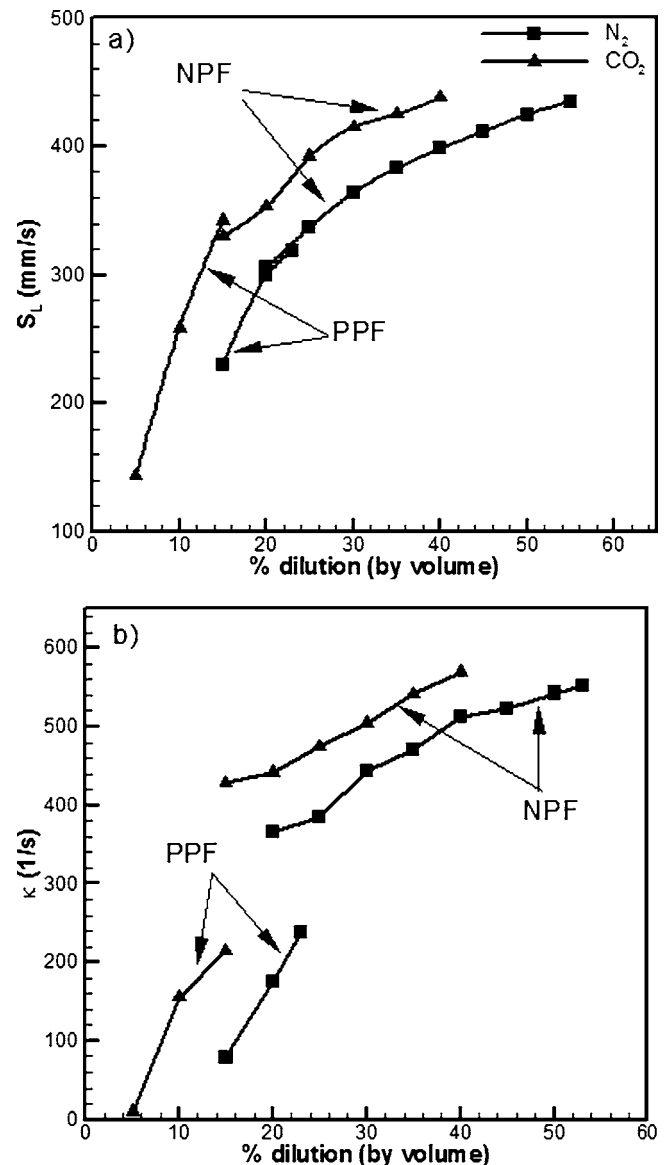


FIG. 13. Stretched laminar flame speed (a) and flame stretch (b) at the flame leading edge (L_{LE}) plotted as a function of diluent mole fraction for the N₂- and CO₂-diluted NPFs and PPFs.

stretch. Figure 13(b) presents the variation of stretch (κ) with the diluent mole fraction for the cases shown in Fig. 13(a). The flame stretch is computed using the relation⁴⁴

$$k = \nabla \cdot \mathbf{V}_{fluid} - \mathbf{n} \cdot \nabla \mathbf{V}_{fluid} + S_L (\nabla \cdot \mathbf{n}).$$

For both the nonpremixed and partially premixed flames, as the flame is lifted higher with the increase in diluent mole fraction, the stretch increases. Moreover, the stretch is higher for CO₂-diluted flames compared to that for N₂-diluted flames, and for NPFs compared to that for PPFs. The correlation between flame speed (S_L) and stretch (κ) is shown in Fig. 14, which presents S_L versus κ for various flames discussed in the context of Fig. 13.

There is a positive correlation between S_L and κ , since these flames are positively stretched and the Lewis number (Le) at the flame base is less than unity. As discussed by Qin *et al.*,⁴⁶ the stoichiometric equivalence ratio and the stoichio-

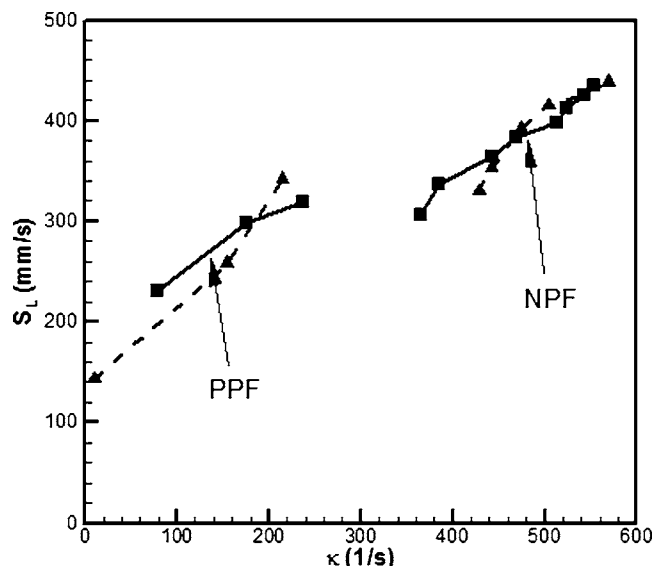


FIG. 14. Stretched laminar flame speed versus flame stretch for various lifted flames discussed in the context of Fig. 13.

metric mixture fraction contours coincide in the cold region, but diverge just ahead of the flame due to product formation. Consequently, the stoichiometric mixture fraction contour leads to a localized lean mixture at the flame base, and for lean CH_4/air mixtures, $\text{Le} < 1.0$. Thus, for the positively stretched flame base, its convex nature toward the fresh mixture defocuses the heat, while focusing the deficient species (methane). For $\text{Le} < 1.0$, the focusing effect dominates, leading to a positive correlation between flame speed and stretch. Since κ increases with the increase in diluent mole fraction, S_L also increases, as indicated in Fig. 14. In addition, as shown in Fig. 13, κ is higher for CO_2 -diluted flames compared to that for N_2 -diluted flames, and for NPFs compared to that for PPFs. Consequently, S_L is higher for CO_2 -diluted flames compared to that for N_2 -diluted flames, and for NPFs compared to that for PPFs.

CONCLUSIONS

We have presented a computational investigation of the flame liftoff, stabilization, and blowout characteristics of nonpremixed (NPF) and partially premixed flames (PPF). Lifted methane-air flames were established in axisymmetric coflowing jets using N_2 and CO_2 as diluents. A time-accurate, implicit algorithm that uses a detailed description of methane-air chemistry and includes an optically thin radiation model was used for simulations. The predictions were validated using measurements of the reaction zone topologies and liftoff heights for both NPF and PPF. Detailed numerical simulations were then used to examine the effects of dilution and partial premixing on the flame liftoff, stabilization, and blowout characteristics, and to analyze previous theories for the stabilization of lifted flames. Important observations are as follows:

- (1) The undiluted NPF is lifted and stabilized in a low-velocity region downstream of the burner rim, while the corresponding PPF is stabilized at the burner rim, char-

acterized by significant radical destruction and heat loss to the burner. With the addition of diluent, the liftoff height of NPF first increases gradually, and then quite rapidly until the flame blows out, as it cannot find a stabilization point within the computational domain. In contrast, the PPF first lifts off from the burner rim due to local extinction caused by dilution. Once the flame is lifted, its liftoff height increases much more rapidly compared to that of a NPF. Consequently, its liftoff height exceeds that of a NPF, and the diluent mole fraction required for its extinction (through blowout) is significantly smaller than that for a NPF. In addition, a PPF blows out at a lower height compared to a NPF. The superior blowout characteristics of NPFs are due to the higher amount of fuel contained in the fuel jet, which leads to a lower scalar dissipation rate for these flames.

- (2) For flames stabilized in the near field, both NPFs and PPFs exhibit a double flame structure, and their stabilization mechanism involves a balance between reaction rate and scalar dissipation rate, which can also be interpreted as the balance between the edge-flame speed undergoing its local scalar dissipation rate and the local flow velocity. As the diluent concentration is increased, the local scalar dissipation rate increases while the flame reactivity decreases. Consequently, the flame moves downstream along the stoichiometric mixture fraction line to an axial location where it can withstand a lower scalar dissipation rate. Further increase in diluent concentration moves the flame into the far field region, where both NPFs and PPFs exhibit a triple flame structure. Here the flame stabilization also depends on a balance between the triple flame speed and the local flow velocity at the base, and the liftoff height increases more rapidly with increasing diluent concentration. In addition, the flames are positively stretched at the base, and there is a positive correlation between the flame speed and the stretch.
- (3) The NPFs and PPFs simulated in the present study exhibit well-organized oscillations induced by buoyant acceleration. As the diluent concentration is increased and the flame is stabilized at a further downstream location, the amplitude of oscillation increases, while the frequency of oscillation remains nearly constant in the range 15–20 Hz.
- (4) For the same diluent mole fraction, CO_2 -diluted flames are lifted higher compared to N_2 -diluted flames. Moreover, the diluent mole fraction required for the extinguishment (through blowout) of CO_2 -diluted flames is smaller than that for N_2 -diluted flames. This can be attributed to the fact that CO_2 dilution increases the scalar dissipation rate and decreases the reaction rate by a larger amount compared to that caused by N_2 dilution.

ACKNOWLEDGMENTS

This research was supported by the NASA Microgravity Research Division through Grant No. NCC3-688 for which Dr. Uday Hegde and Dr. Kurt Sacksteder serve as the tech-

nical monitors. We thank Andrew Lock for providing the experimental images used for validating the numerical model.

- ¹A. J. Lock, A. M. Briones, X. Qin, S. K. Aggarwal, I. K. Puri, and U. Hegde, "Lift-off characteristics of partially premixed flames under normal and microgravity conditions," *Combust. Flame* **143**, 159 (2005).
- ²H. Phillips, Flame in a buoyant methane layer, *Proc. Combust. Inst.* **10**, 1277 (1965).
- ³S. H. Chung and B. J. Lee, "On the characteristics of laminar lifted flames in a nonpremixed jet," *Combust. Flame* **86**, 62 (1991).
- ⁴B. J. Lee and S. H. Chung, "Stabilization of lifted tribrachial flames in a laminar nonpremixed jet," *Combust. Flame* **109**, 163 (1997).
- ⁵G. R. Ruetsch, L. Vervisch, and A. Liñán, "Effects of heat release on triple flames," *Phys. Fluids* **7**, 1454 (1995).
- ⁶Y.-C. Chen and R. W. Bilger, "Stabilization mechanisms of lifted laminar flames in axisymmetric jet flows," *Combust. Flame* **122**, 377 (2000).
- ⁷F. Takahashi, W. J. Schmoll, and V. R. Katta, "Attachment mechanism of diffusion flames," *Proc. Combust. Inst.* **27**, 675 (1998).
- ⁸F. Takahashi and V. R. Katta, "A reaction kernel hypothesis for the stability limit of methane jet diffusion flames," *Proc. Combust. Inst.* **28**, 2071 (2000).
- ⁹H. Schlichting, *Boundary Layer Theory*, 2nd ed. (McGraw-Hill, New York, 1979).
- ¹⁰P. N. Kioni, B. Rogg, K. N. C. Bray, and A. Liñán, "Flame spread in laminar mixing layers: The triple flame," *Combust. Flame* **95**, 276 (1993).
- ¹¹T. Plessing, P. Terhoeven, N. Peters, and M. S. Mansour, "An experimental and numerical study of a laminar triple flame," *Combust. Flame* **115**, 335 (1998).
- ¹²S. Ghosal and L. Vervisch, "Stability diagram for lift-off and blowout of a round jet laminar diffusion flame," *Combust. Flame* **123**, 646 (2001).
- ¹³B. J. Lee, M. S. Cha, and S. H. Chung, "Characteristics of laminar lifted flames in a partially premixed jet," *Combust. Sci. Technol.* **127**, 55 (1997).
- ¹⁴J. Buckmaster, "Edge-flames," *J. Eng. Math.* **31**, 269 (1997).
- ¹⁵UNEP, Montreal Protocol on Substances that Deplete the Ozone Layer, 2004.
- ¹⁶N. Vahdat, Y. Zou, and M. Collins, "Fire-extinguishing effectiveness of new binary agents," *Fire Saf. J.* **38**, 553 (2003).
- ¹⁷B. J. Lee, J. S. Kim, and S. H. Chung, "Effect of dilution on the liftoff and non-premixed jet flames," *Proc. Combust. Inst.* **25**, 1175 (1994).
- ¹⁸V. R. Katta, L. P. Goss, and W. M. Roquemore, "Effect of nonunity Lewis number and finite-rate chemistry on the dynamics of a hydrogen-air jet diffusion flame," *Combust. Flame* **96**, 60 (1994).
- ¹⁹Z. Shu, S. K. Aggarwal, V. R. Katta, and I. K. Puri, "A numerical investigation of the flame structure of an unsteady inverse partially premixed flame," *Combust. Flame* **111**, 276 (1997).
- ²⁰R. Azzoni, S. Ratti, I. K. Puri, and S. K. Aggarwal, "Gravity effects on triple flames: Flame structure and flow instability," *Phys. Fluids* **11**, 3449 (1999).
- ²¹R. Siegel and J. R. Howell, *Thermal Radiation Heat Transfer* (Hemisphere Publishing Corporation, New York, 1981).
- ²²R. C. Reid, J. M. Prausnitz, and B. E. Poling, *The Properties of Gases and Liquids* (McGraw-Hill, New York, 1987).
- ²³N. Peters, *Reduced Kinetic Mechanisms for Applications in Combustion Systems*, Lecture Notes in Physics Vol. m15, edited by N. Peters and B. Rogg (Springer, Berlin, 1993), pp. 3–14.
- ²⁴Z. Shu, C. Choi, S. K. Aggarwal, V. Katta, and I. K. Puri, "Gravity effects on steady two-dimensional partially premixed methane-air flames," *Combust. Flame* **118**, 91 (1999).
- ²⁵X. Qin, I. K. Puri, S. K. Aggarwal, and V. R. Katta, "Gravity, radiation, and coflow effects on partially premixed flames," *Phys. Fluids* **16**, 2963 (2004).
- ²⁶H. Xue and S. K. Aggarwal, "Effects of reaction mechanisms on structure and extinction of partially premixed flames," *AIAA J.* **39**, 637 (2001).
- ²⁷V. R. Katta, L. P. Goss, and W. M. Roquemore, "Numerical investigation of transitional H_2/N_2 jet diffusion flames," *AIAA J.* **32**, 84 (1994).
- ²⁸V. R. Katta, F. Takahashi, and G. T. Linteris, "Suppression of cup-burner flames using carbon dioxide in microgravity," *Combust. Flame* **137**, 506 (2004).
- ²⁹F. N. Egolfopoulos and C. K. Law, "An experimental and computational study of the burning rates of ultra-lean to moderately-rich $H_2/O_2/N_2$ laminar flames with pressure variations," *Proc. Combust. Inst.* **23**, 333 (1990).
- ³⁰V. R. Katta, T. R. Meyer, M. S. Brown, J. R. Gord, and W. M. Roquemore, "Extinction criterion for unsteady, opposing-jet diffusion flames," *Combust. Flame* **137**, 198 (2004).
- ³¹Z. Shu, B. Krass, C. Choi, S. K. Aggarwal, V. Katta, and I. K. Puri, "An experimental and numerical investigation of the structure of steady two-dimensional partially premixed methane-air flames," *Proc. Combust. Inst.* **27**, 625 (1998).
- ³²R. Azzoni, S. Ratti, S. K. Aggarwal, and I. K. Puri, "The structure of triple flames stabilized on a slot burner," *Combust. Flame* **119**, 23 (1999).
- ³³N. Peters and F. A. Williams, "Lift-off characteristics of turbulent diffusion jet flames," *AIAA J.* **21**, 423 (1983).
- ³⁴W. M. Pitts, "Assessment of theories for the behavior and blowout of lifted turbulent jet diffusion flames," *Proc. Combust. Inst.* **22**, 809 (1988).
- ³⁵R. W. Bilger, "The structure of turbulent nonpremixed flames," *Proc. Combust. Inst.* **22**, 475 (1988).
- ³⁶M. A. Tanoff, M. D. Smooke, R. J. Osborne, T. M. Brown, and R. W. Pitz, "The sensitive structure of partially premixed methane-air vs. air counterflow flames," *Proc. Combust. Inst.* **26**, 1121 (1996).
- ³⁷S. Naha and S. K. Aggarwal, "Fuel effects on NO_x emissions in partially premixed flames," *Combust. Flame* **139**, 90 (2004).
- ³⁸X. Qin, I. K. Puri, and S. K. Aggarwal, "Characteristics of lifted triple flames stabilized in the near field of a partially premixed axisymmetric jet," *Proc. Combust. Inst.* **29**, 1565 (2002).
- ³⁹A. J. Lock, R. Ganguly, I. K. Puri, S. K. Aggarwal, and U. Hedge, "Gravity effects on partially premixed flames: An experimental-numerical investigation," *Proc. Combust. Inst.* **30**, 511 (2004).
- ⁴⁰H. Yamashita, M. Shimada, and T. Takeno, "A numerical study on flame stability at the transition point of jet diffusion flames," *Proc. Combust. Inst.* **26**, 27 (1996).
- ⁴¹H. Guo, F. Liu, and G. J. Smallwood, "A numerical study on NO_x formation in laminar counterflow CH_4 /air triple flames," *Combust. Flame* **143**, 282 (2005).
- ⁴²S. H. Won, S. H. Chung, M. S. Cha, and B. J. Lee, "Lifted flame stabilization in developing and developed regions of coflow jets for highly diluted propane," *Proc. Combust. Inst.* **28**, 2093 (2000).
- ⁴³S. H. Won, J. Kim, K. J. Hong, M. S. Cha, and S. H. Chung, "Stabilization mechanism of lifted flame edge in the near field of coflow jets for diluted methane," *Proc. Combust. Inst.* **30**, 339 (2004).
- ⁴⁴X. Qin, C. W. Choi, A. Mukhopadhyay, I. K. Puri, S. K. Aggarwal, and V. R. Katta, "Triple flame propagation and stabilization in a laminar axisymmetric jet," *Combust. Theory Modell.* **8**, 293 (2004).
- ⁴⁵A. Mukhopadhyay and I. K. Puri, "An assessment of stretch effects on a flame tip using the thin flame and thick flame formulations," *Combust. Flame* **133**, 499 (2003).
- ⁴⁶X. Qin, An investigation of unsteady partially premixed flames, Ph.D. thesis, The University of Illinois at Chicago, 2003.

Trimethylphosphate as Soot Reducing Additive—A Numerical Study on Jet Flames

V. R. Katta*

Innovative Scientific Solutions Inc
2766 Indian Ripple Road
Dayton, OH 45440-3638

William M. Roquemore
Propulsion Directorate
Air Force Research Laboratory
Wright-Patterson Air Force Base, OH 45433

Abstract

Doping of organophosphorus compounds into flames produce phosphor-bearing species, which are known to catalytically recombine radicals such as H, O, and OH and, thereby, reduce the chemical activity in the flame zone. While such scenario for decreasing chemical activity is well being used for inhibiting the flames, the possibility of its application for reducing soot in the flames needs to be explored. A time-dependent, axisymmetric mathematical model known as UNICORN (Unsteady Ignition and Combustion using ReactionNs) is used for studying the effects of trimethyl phosphate (TMP) on soot production in various flames. A detailed chemical-kinetics model consisting 238 species and 3178 elementary reaction steps is incorporated into UNICORN for the simulation of heptane flames doped with TMP. Using the same code TMP added methane and propane flames are also simulated. Effects of TMP in coaxial diffusion and premixed jet flames are investigated by varying the amount of additive in the fuel jet. Premixed flames are found to be more sensitive to the presence of TMP. As expected, the burning velocity of the fuel is significantly reduced. However, an increase in soot production is also observed. In contrast, TMP is less effective in diffusion flames, but decreases soot when sufficient amount is added. Stability of the diffusion flame is not affected much by the presence of TMP in the fuel jet. The contrasting behavior of TMP in premixed and diffusion flames appeared similarly in methane, propane and heptane flames.

Introduction

Research on fire suppression during the early 1970s was focused on finding alternative additives as the use of super effective halogenated compounds was found to be impractical due to the corrosive effect on halogen acids on engines. Halogenated hydrocarbons were, later on, banned from their use as fire suppressants owing to their role in atmospheric ozone depletion [1]. The search for effective replacements has led to a family of organophosphorus compounds, which showed considerable promise as flame inhibitors [2-4]. Fortuitously, some researchers have found that the sooting characteristics of the flames they have been studying seem to be altered when small quantities of phosphorus compounds were added [5]. From the fire-suppression works it is known that small phosphor-bearing species such as HOPO_2 and HOPO produced from the organophosphorus compounds alter the flame chemistry by catalytically recombining the key flame radicals, especially H, O, and OH. As the concentrations of these radical species are also crucial in the formation of polycyclic aromatic hydrocarbons (PAHs) and in the soot

oxidation process, it is natural to expect alteration to the sooting behavior of the flames when organophosphorus compounds are added.

A numerical and experimental study was initiated at Wright Laboratory for evaluating the effectiveness of trimethyl phosphate (TMP) and dimethyl methyl phosphate (DMMP) in reducing soot in various flames. Present paper describes the numerical study conducted using TMP as soot suppressing additive. Both the premixed and diffusion flames are considered. Effectiveness of TMP in methane, propane and heptane flames is also studied.

Numerical Model

A time-dependent, axisymmetric mathematical model known as UNICORN (Unsteady Ignition and Combustion using ReactionNs) [6,7] is used to simulate the potentially unsteady combustions flows considered in this study. It solves for u- and v-momentum equations, continuity, and enthalpy- and species-conservation equations on a staggered-grid system. The body-force term due to the gravitational field is included in the axial-momentum

* Corresponding author: vrkatta@erinet.com

Proceedings of the 2006 Technical Meeting of the Central States Section of The Combustion Institute

equation for simulating vertically mounted flames. A clustered mesh system is employed to trace the large gradients in flow variables near the flame surface. A detailed chemical-kinetics model developed by NIST [8] is incorporated into UNICORN for the investigation of PAH formation in heptane flames. The combustion inhibition chemistry of TMP developed by LLNL [9] is also incorporated. The combined mechanism consists of 238 species and 3178 elementary-reaction steps. Thermo-physical properties such as enthalpy, viscosity, thermal conductivity, and binary molecular diffusion of all the species are calculated from the polynomial curve fits developed for the temperature range 300 - 5000 K. Mixture viscosity and thermal conductivity are then estimated using the Wilke and Kee expressions, respectively. Molecular diffusion is assumed to be of the binary-diffusion type, and the diffusion velocity of a species is calculated using Fick's law and the effective-diffusion coefficient of that species in the mixture. A simple radiation model based on the optically thin-media assumption is incorporated into the energy equation [10]. Only radiation from CH₄, CO, CO₂, H₂O, and soot is considered in the present study.

The finite-difference forms of the momentum equations are obtained using an implicit QUICKEST scheme [11], and those of the species and energy equations are obtained using a hybrid scheme of upwind and central differencing. At every time step, the pressure field is accurately calculated by solving all the pressure Poisson equations simultaneously and using the LU (Lower and Upper diagonal) matrix-decomposition technique. The boundary conditions are treated in the same way as that reported in earlier papers [12].

This study utilized a two-equation model for soot with transport equations for particle number density, N_s , and soot mass fraction, Y_s . These equations can be written for unsteady flow as

$$\frac{\partial N_s}{\partial t} + \nabla \cdot (\rho \mathbf{V} N_s) - \nabla \cdot (\rho D_{N_s} \nabla N_s) = \omega_{N_s} \quad (1)$$

$$\frac{\partial Y_s}{\partial t} + \nabla \cdot (\rho \mathbf{V} Y_s) - \nabla \cdot (\rho D_s \nabla Y_s) = \omega_s \quad (2)$$

where \mathbf{V} is the velocity vector, ρ is density, D is the molecular diffusion coefficient, and ω is the production term from chemical reactions. The two source terms in Eqs. 1 and 2 are obtained using Lindstedt's model [13,14], which is based on the simplifying assumption that nucleation and growth are first-order functions of acetylene concentrations.

Results and Discussion

The CFD model UNICORN has been extensively validated in the past by simulating various steady and

unsteady counterflow and coflow jet diffusion flames and by comparing the results with experimental data. This gives confidence that UNICORN can simulate the structure of dynamic flames accurately. The integration of heptane and PAH chemistry into UNICORN was validated [15] by simulating counterflow partially premixed flames of Berta et al. [16]. Predictions for temperature and various species including benzene matched well with the measurements [15].

The code developed for the simulation of TMP effects on heptane flames could also be used for the simulation of methane, propane, or ethylene flames doped with TMP. Calculations are made for a propane flame with an equivalence ratio (ϕ) of 1.5. Fuel-air-TMP mixture is issued from a 6-mm-diameter tube at an average exit velocity of 0.5 m/s. Parabolic velocity profile which gives a peak value of 1.0 m/s is imposed at the exit of the tube. A low-speed (0.01 m/s), coannular airflow is used in the region outside the flame. Distributions of temperature and soot volume fraction for the base flame (with no added TMP) are shown in Figs. 1(a) and 1(b), respectively. Similarly, distributions for 0.1% added TMP are shown in Figs. 1(c) and 1(d) and those for 1.0% TMP are shown in Figs. 1(e) and 1(f). A common color scheme is used for each variable based on the peak value obtained from all the flames. As the peak soot concentration produced in the flame with 1% TMP [Fig. 1(f)] is nearly two orders more than that of the base flame [Fig. 1(b)], the linear color scale did not show the soot distribution in the latter flame.

As seen from Fig. 1, addition of TMP to the propane premixed flame is decreasing the burning velocity and increasing the soot formation. The burning velocity computed based on the inner cone area [Fig. 1(a)] for the $\phi = 1.5$ flame is about 0.20 m/s. In comparison the measured burning velocity at stoichiometry is 0.41 m/s [17]. Based on the inner cone areas in Figs. 1(c) and 1(e) the burning velocity has decreased by 45% and 56% when TMP was added by 0.1% and 1.0%, respectively. Decrease in burning velocity also resulted in an increase in flame-standoff distance. This decrease compare favorably with that measured for stoichiometric flame [9]. Addition of TMP has significantly increased soot formation [Figs. 1(b), 1(d), and 1(f)].

Calculations are made for the propane jet diffusion flame with various amounts of TMP added to the fuel jet. Results obtained for a 0.01-m/s-jet-velocity case are shown in Fig. 2. Interestingly, TMP has very little effect on the stability of the diffusion flame for concentrations up to 1%. However, soot has decreased by about 20%. This is in contrast with the premixed flame in which soot increased with the addition of TMP. Similar calculations were made for a higher fuel jet velocity (0.1 m/s) and found that TMP has negligible impact either on the stability or on the soot production even for concentrations up to 1%.

The predicted effects of TMP in propane premixed and diffusion flames matched qualitatively with those obtained in the experiments [5]. Both calculations and experiment yielded increase in soot and flame inhibition for premixed flames and decrease in soot for diffusion flames. Calculations made with methane fuel also resulted similar trends. Results obtained for a diffusion flame are shown in Fig. 3. Even though, the flame stability is not affected much with the addition of TMP, soot has decreased more significantly than that noted in propane flames (Fig. 2). However, quick experiments conducted for methane diffusion flame suggested an increase in soot production with TMP [5].

Calculations for heptane premixed and diffusion flames are performed with various amounts of TMP added to the fuel. The diameter of the fuel tube was 12 mm and the fuel jet velocity was 0.005 m/s. Even with this low fuel velocity the diffusion flame formed is longer than those obtained for methane and propane fuels. In consistent with the other diffusion flame calculations, due to the length, the simulated heptane flame is insensitive to the added TMP. Results obtained for the base flame (0% TMP) are shown in Fig. 4 in the form of temperature and soot and nitric-oxide concentration distributions. Variations along the centerline for different amounts of added TMP are shown in Fig. 5. Flame structures are identical for 0% and 0.1% TMP cases. However, a trace amount of deviation is observed for the 1% case. Interestingly, NO has decreased significantly when 1% TMP is added.

Structures of the heptane premixed flame for 0%, 0.1% and 1.0% TMP concentrations are shown in Figs. 6, 7, and 8, respectively. The fuel equivalence ratio is 2.0 and the fuel jet velocity is 1 m/s. As expected from the other premixed calculations, burning velocity for heptane fuel has also decreased with the addition of TMP. Based on the inner cone surface areas burning velocity has decreased by 5% when 0.1% TMP was added and decreased by 19% with 1% TMP. As expected, concentration of OH decreased and that of soot increased with the amount of TMP. The radical recombination promoted by the P-based species caused OH concentration to decrease. The increase in soot concentration correlates to that in benzene concentration. Significant reduction in NO is also noted. It seems TMP reduces NO production in both premixed and diffusion flames.

The results of all the simulations made with methane, propane and heptane fuels are summarized in Table 1. In general, soot is enhanced in premixed flames and suppressed in diffusion flames when TMP is added. Premixed flames are more sensitive to the presence of TMP compared to diffusion flames. And also, large flames are less sensitive to TMP compared to the small ones. Among the fuels studied, methane is more sensitive

than propane which is more sensitive than heptane to the presence of TMP.

Table 1: Effect of TMP on soot formation in various flames

Fuel	Soot in	
	Premixed Flame	Diffusion Flame
Methane	Enhanced significantly	No change in large flames Decreased in small flames
Propane	Enhanced significantly	No change in large flames Decreased significantly in small flames
Heptane	Enhanced	No change for small amounts of TMP Decreased for large amounts of TMP

Conclusions

Organophosphorus compounds inhibit flames via generating small P-bearing species, which catalytically recombine key flame radicals and reduce chemical activity in the flame zone. Such enhancement in radical recombination could also lead to changes in sooting characteristics. A time-dependent, axisymmetric mathematical model known as UNICORN (Unsteady Ignition and Combustion using ReactionNs) was used for the investigation of trimethyl phosphate (TMP) effects on soot production in various flames. A detailed chemical-kinetics model was incorporated into UNICORN for the simulation of heptane flames doped with TMP. It consists of 238 species and 3178 elementary-reaction steps. A simple soot model based on two conservation equations and acetylene concentration was used for estimating soot production in these flames. Effects of TMP in diffusion and premixed flames were investigated by varying the amount of additive in the fuel jet. Methane, propane and heptane flames were considered.

Premixed flames are more sensitive to the presence of TMP. However, increased amounts of soot are produced with the addition of TMP. In contrast, TMP is less effective in diffusion flames, but decreases soot when sufficient amount is added. The burning velocity of a premixed flame is significantly reduced with the addition of TMP while it has negligible effect on the stability of a diffusion flame. The contrasting behavior of TMP in premixed and diffusion flames appeared in the same way in methane, propane and heptane flames.

Acknowledgements

Financial support for this work was provided by Strategic Environmental Research and Development Program (SERDP, Charles Pellerin), the Air Force Office of Scientific Research (AFOSR, Julian Tishkoff) and the Air Force Contract #F33615-00-C-2068 (Vince Belovich).

References

1. Halon Replacements: Technology and Science (Miziolek, A. W., and Tsang, W., Eds), ACS Symp. Ser. 611, Washington, DC, 1995.
2. Noto, T., Babushok, V. I., Hamins, A., Tsang, W., Combustion and Flame, 1998, Vol. 112, No. 1/2, pp. 147-160.
3. Lask, G., Wagner, H. Gg., Influence of additives on the velocity of laminar flames, 8th Symposium (International) on Combustion, 1960, pp. 432-438.
4. Rosser, W. A. Jr., Inami, S. H., Wisc, H., Combustion and Flame, 1966, Vol. 10, No. 3, pp. 287-294.
5. Hastic, J. W., Bonnell, D. W., Molecular Chemistry of Inhibited Combustion Systems, NBSIR 80-2169, 1980.
6. Roquemore W. M., and Katta, V. R., *Journal of Visualization*, in press Jan. 2000.
7. Katta, V. R., and Roquemore, W. M., *Combustion and Flame*, Vol. 100, No. 1, 1995, p. 61.
8. Tsang W., and Babushok, V., "Detailed mechanism for PAH species" *manuscript in preparation*, National Institute of Standards and Technology, Gaithersburg, MD, 2004.
9. Korobeinichev, O. P., Shvartsberg, V. M., Shmakov, A. G., Bolshova, T. A., Jayaweera, T. M., Melius, C. F., Pitz, W. J. and Westbrook, C. K., "Flame Inhibition by Phosphorus-Containing Compounds in Lean and Rich Propane Flames," *Proceedings of the Combustion*, vol. 30, pp. 2350-2357, 2004.
10. Katta, V. R., Goss, L. P., and Roquemore, W. M., *AIAA Journal*, Vol. 32, No. 1, 1994, p. 84.
11. Katta, V. R., Goss, L. P., and Roquemore, W. M., *Int. J. Num. Methods Heat Fluid Flow*, Vol. 4, No. 5, 1994, p. 413.
12. Annon., Computational Submodels, International Workshop on Measurement and Computation of Turbulent Nonpremixed Flames, <http://www.ca.sandia.gov/TNF/radiation.html>, (2001).
13. Lindstedt, R.P., in *Soot Formation in Combustion: Mechanisms and Models* (H. Bockhorn, Ed.), Springer-Verlag, Heidelberg, 1994, pp.417-439.
14. Leung, K.M., Lindstedt, R.P. and Jones, W.P., *Combust. Flame* 87:289-305 (1991).
15. Katta, V. R., and Roquemore, W. M., Effect of nitromethane on soot formation in heptane jet diffusion flame, *Proceedings of 4th Joint Meeting of the U. S. Sections of the Combustion Institute*, 2005.
16. P. Berta, Puri. I. K., Aggarwal, S. K., Partially Premixed n-Heptane/Air Counterflow Flames, 2004 Spring Technical Meeting, Central States Section of the Combustion Institute, 21-23 March, 2004, Austin, Texas.
17. Dyakov, I. V., Konnov, A. A., de Ruyck, J., Bosschaart, K. J., Brock, E. C. M., and de Goey, L. P. H., *Combustion Science and Technology*, Vol. 172, 2001, pp. 81-96.

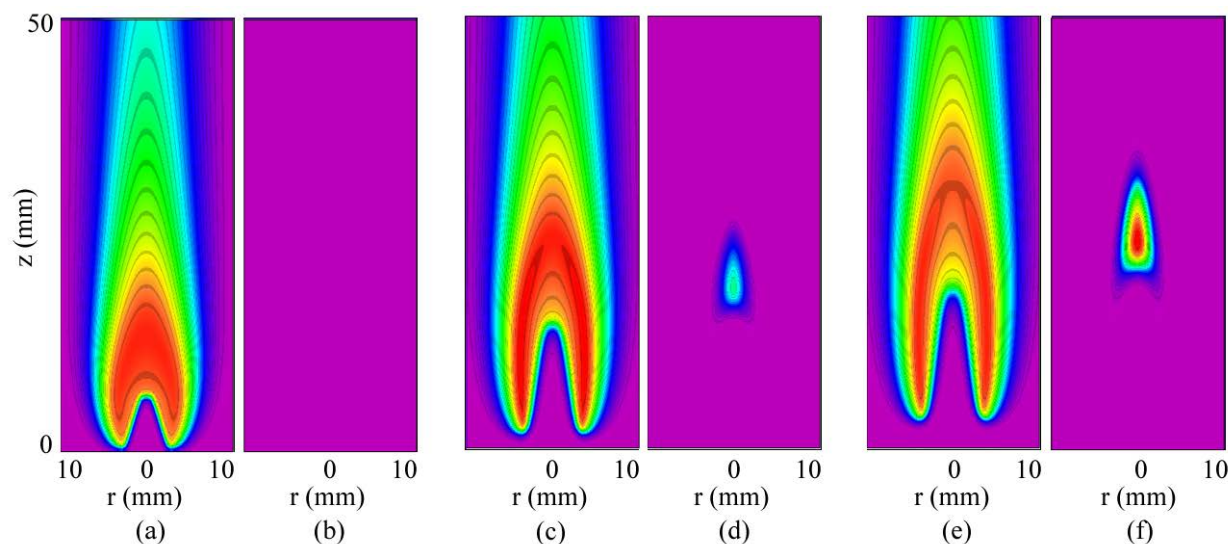


Fig. 1. Effect of TMP on premixed propane flame. Mixture of propane, air and TMP with $\phi = 1.5$ is issued from a 6-mm tube at 0.5 m/s. Distributions of (a) temperature and (b) soot volume fraction for base flame with 0% TMP. (c) and (d) for the flame with 0.1% TMP and (e) and (f) are for the flame with 1% TMP.

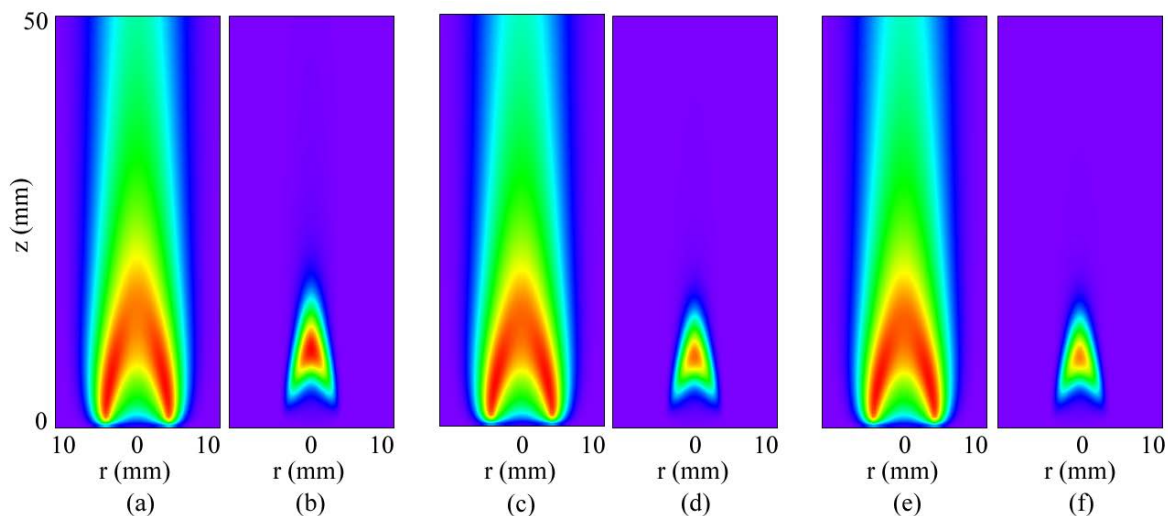


Fig. 2. Effect of TMP on propane jet diffusion flame. Distributions of (a) temperature and (b) soot volume fraction for base flame with 0% TMP, (c) and (d) for the flame with 0.1% TMP, and (e) and (f) are for the flame with 1% TMP.

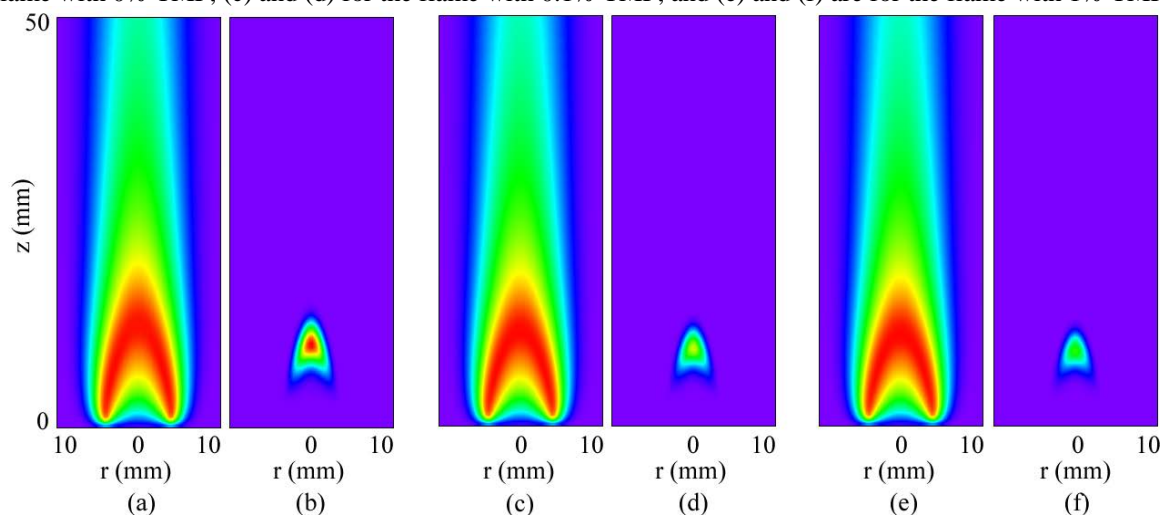


Fig. 3. Effect of TMP on methane jet diffusion flame. Distributions of (a) temperature and (b) soot volume fraction for base flame with 0% TMP, (c) and (d) for the flame with 0.1% TMP, and (e) and (f) are for the flame with 1% TMP.

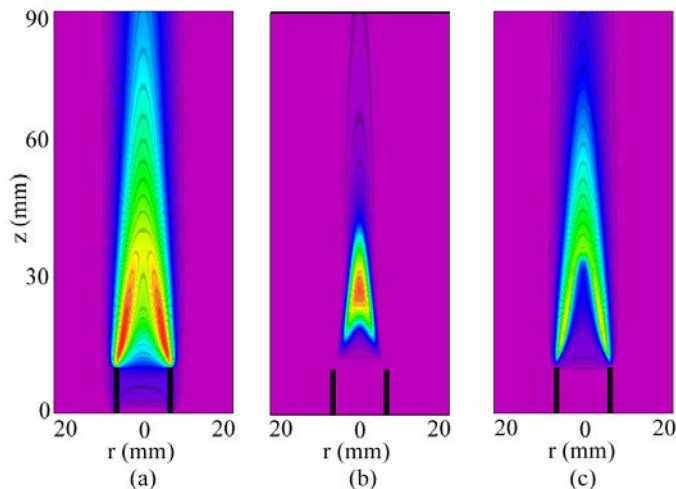


Fig. 4. Heptane jet diffusion flame. Distributions of (a) temperature, (b) soot volume fraction and (c) NO concentration.

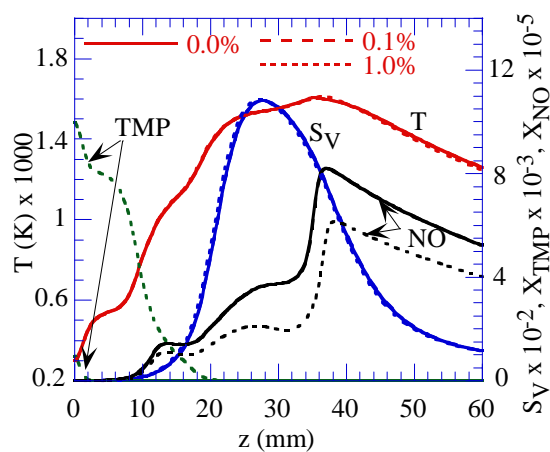


Fig. 5. Effect of TMP on heptane jet diffusion flame. Distributions of T and species along the centerline.

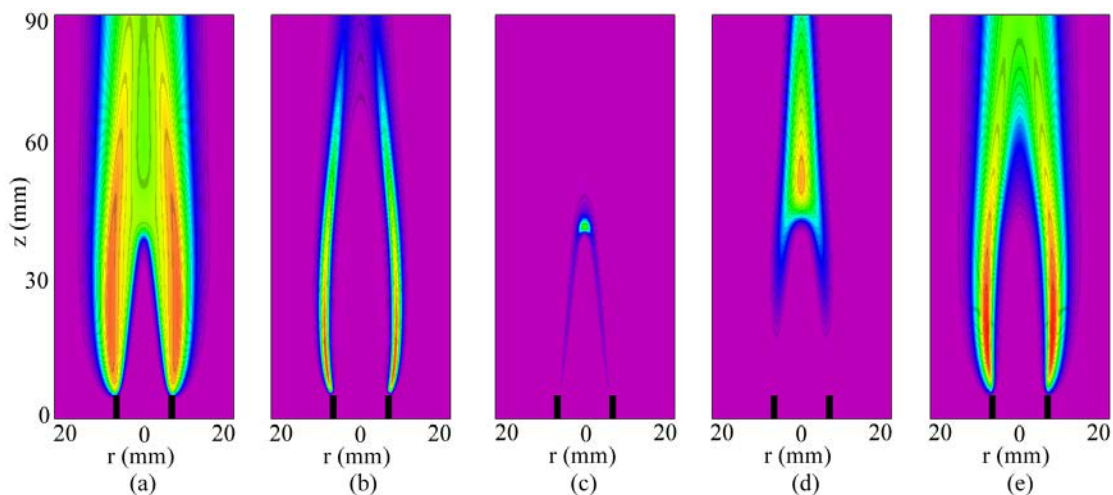


Fig. 6. Heptane premixed flame with 0% TMP. Mixture of heptane and air with $\phi = 2.0$ is issued from a 13-mm tube at 1.0 m/s. Distributions of (a) temperature, (b) OH, (c) benzene, (d) soot volume fraction, and (e) NO.

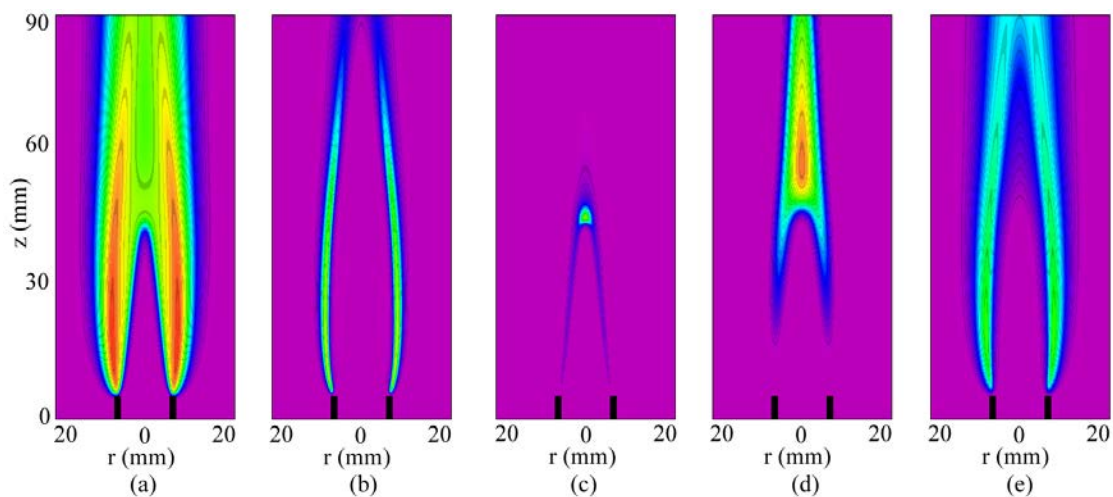


Fig. 7. Heptane premixed flame with 0.1% TMP. Mixture of heptane and air with $\phi = 2.0$ is issued from a 13-mm tube at 1.0 m/s. Distributions of (a) temperature, (b) OH, (c) benzene, (d) soot volume fraction, and (e) NO.

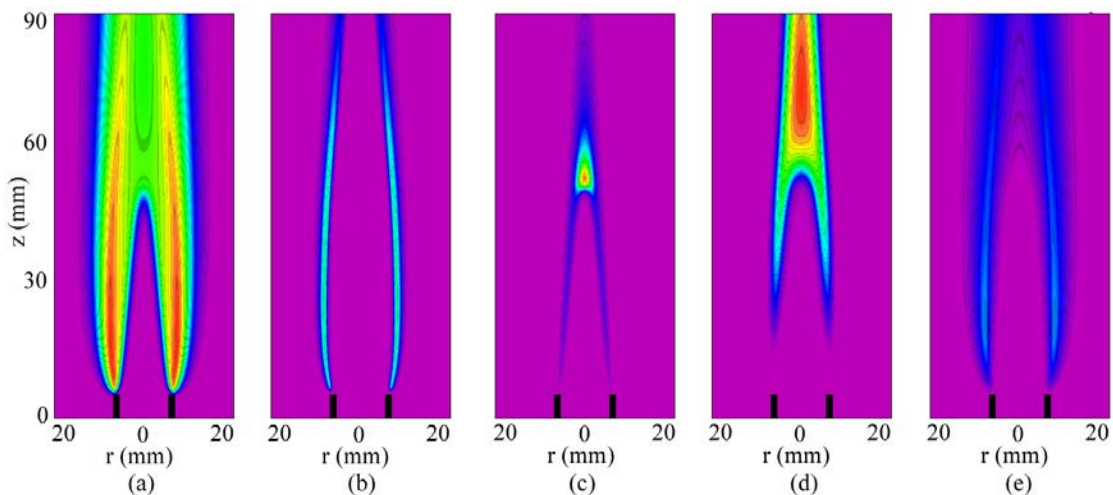


Fig. 8. Heptane premixed flame with 1.0% TMP. Mixture of heptane and air with $\phi = 2.0$ is issued from a 13-mm tube at 1.0 m/s. Distributions of (a) temperature, (b) OH, (c) benzene, (d) soot volume fraction, and (e) NO.

Effects of H₂-Enrichment on Flame Propagation Characteristics of Methane-Air Flames

A.M. Briones, S.K. Aggarwal¹

Department of Mechanical and Industrial Engineering

University of Illinois at Chicago

Chicago, Illinois

and

V.R. Katta

Innovative Scientific Solutions, Inc.

Dayton, Ohio

Abstract

Lean burning of hydrocarbons yields exceptionally low pollutant emissions and superior combustion characteristics. For most hydrocarbon fuels, however, burning in the lean regime results in stability problems because of lean flammability limits. Hydrogen is an alternate fuel. The use of pure hydrogen, however, in a practical combustor is limited due to problems with storage, low volumetric heating value, and flashback, making the use of pure hydrogen very difficult and dangerous. For this reason, a hydrogen-hydrocarbon fuel blend may be a practical solution. Previous investigations have mainly focused on studying the effects of hydrogen addition to hydrocarbon flames using simplified configurations (e.g. counterflow 1-D flames and freely propagating flames). However, for most combustors, flames are exposed to both hydrodynamic and curvature-induced stretch, and oscillations that drastically affect their flammability and emission characteristics. In this investigation, methane-air flames are established on axisymmetric coflowing jets with fuel-air mixture introduced through the inner burner and air through the coannular burner. The effect of H₂-enrichment on flame propagation is investigated for a wide range of conditions. A time-accurate, implicit algorithm that uses a detailed description of the flame chemistry (GRI-Mech 1.2) and includes radiation effects is utilized for simulations. The addition of hydrogen affects both the flame propagation characteristics through preferential-diffusion instability and its inherent high flame speed.

Introduction

There is a world-wide growing interest to move towards a hydrogen-based economy due to many potential advantages of hydrogen fuel over conventional fossil fuels. Apart from being environmentally clean, hydrogen represents potentially an unlimited source of energy since it can be readily formed from water through electrolysis, as well as from fossil fuels through partial oxidation and reforming. In addition, it has higher energy per unit mass (about 2.6 times that of gasoline), superior ignition characteristics, and significantly wider flammability limits compared to hydrocarbon fuels. However, due to its high flammability and low volumetric energy density, many important issues pertaining to hydrogen safety and storage are still being addressed. Numerous efforts are currently underway focusing on the use of hydrogen in various propulsion and energy applications, including fuel cells and hydrogen-based IC engines [1,2,3]. In this context, blending hydrogen with hydrocarbon fuels also represents a promising approach to increase the use of hydrogen, and improve the emission and performance of various combustion systems [4,5,6]. Such an approach is justified further by recognizing that there is no intrinsic reason to achieve zero CO₂ emission

because the hydrosphere have tremendous capacity to absorb CO₂, which, after all, is also produced through various natural processes such as wildland fires. Studies reported by Al-Baghdadi [4], Choudhuri and Gollahalli [5], Kumar et al. [6], and Naha and Aggarwal [7] have shown that using blends of hydrogen and hydrocarbon fuels can improve both the emission and combustor performance.

In response to the interest in establishing a hydrogen economy to mitigate the global warming problem, there have been considerable activities in the development of hydrogen-fueled internal combustion engines [8]. However, due to the high reactivity of hydrogen, and the need for supercharging, hydrogen-fueled engines are prone to pre-ignition and knock, and could potentially emit high levels of NO_x [9]. Most of the previous fundamental studies on hydrogen/hydrocarbon combustion have been directed toward the possibility of using hydrogen as an additive to facilitate ignition and to enhance combustion intensity [10]. There has been, however, considerably low activity on the study of the propagation characteristics of hydrogen/hydrocarbon flames.

Our objective in this context is to examine the effects of H₂-enrichment on the propagation of

¹ Corresponding author. Fax: 312-413-0447. Tel: 312-404-7824. email: ska@uic.edu

nonpremixed flames that are ignited downstream of a burner in the non-uniform mixture of an axisymmetric jet. A comprehensive, time-dependent computational model is used to simulate the transient ignition and flame propagation phenomena. The model employs a detailed description of methane–air chemistry and transport properties. In addition, the transition of a propagating triple flame into a double flame is examined by following the dominant reactions.

Physical-Numerical Model

The computational model is based on the algorithm developed by Katta et al. [11] and the simulation method is described in detail elsewhere [12,13]. The numerical model solves the time-dependent governing equations for unsteady reacting flows in an axisymmetric configuration. The governing equations can be written in a generalized form as:

$$\frac{\partial(\rho\Phi)}{\partial t} + \frac{\partial(\rho v\Phi)}{\partial r} + \frac{\partial(\rho u\Phi)}{\partial z} = \frac{\partial}{\partial r} \left(\Gamma^\Phi \frac{\partial\Phi}{\partial r} \right) + \frac{\partial}{\partial z} \left(\Gamma^\Phi \frac{\partial\Phi}{\partial z} \right) - \frac{\rho v\Phi}{r} + \frac{\Gamma^\Phi}{r} \frac{\partial\Phi}{\partial r} + S^\Phi$$

Here t denotes the time, and u and v represent the axial (z) and radial (r) velocity components, respectively. The general form of the equation represents conservation of mass, momentum, species, or energy conservation equation, depending on the variable used for Φ . The diffusive transport coefficient Γ^Φ and source terms S^Φ appearing in the above equation is provided in Table 1 of Ref. 12. Introducing the overall species conservation equation and the state equation completes the set of equations. In addition, a sink term based on an optically thin gas assumption is included in the energy equation to account for thermal radiation from the flame.¹⁸ The sink term is expressed as¹⁴ where T denotes the local flame temperature, an

$q_{rad} = -4\sigma K_p (T^4 - T_o^4)$ d
 K_p accounts for the absorption and emission from the participating gaseous species (CO_2 , H_2O , CO and CH_4), and is expressed as

$$K_p = P \sum_k X_i K_{p,i}$$

where $K_{p,i}$ denotes the mean absorption coefficient of the k^{th} species. Its value is obtained by using a polynomial approximation to the experimental data provided in Ref. 14.

The thermodynamic and transport properties appearing in the governing equations are considered to be temperature and species dependent. The thermal conductivity and viscosity of the individual species are estimated based on Chapman–Enskog collision theory, following which those of the mixture are determined using the Wilke semi-empirical formulas.¹⁵ Chapman–Enskog theory and the Lennard-Jones potentials are used to estimate the binary-diffusion coefficient between each species and nitrogen. The methane–air chemistry is modeled using a detailed mechanism that considers 32 species and 346 elementary reactions.¹⁶ The major species included in the mechanism are CH_4 , O_2 , CO_2 , CO , CH_2O , H_2 , H_2O , C_2H_2 , C_2H_4 , C_2H_6 , CH_3OH , Ar , and N_2 , while the radical species include CH_3 , CH_2 , CH , CHO , H , O , OH , HO_2 , H_2O_2 , C_2H , C_2H_3 , C_2H_5 , CHCO , C , $\text{CH}_2(\text{s})$, CH_2OH , CH_3O , CH_2CO , and HCCOH . The mechanism has been validated previously for the computation of premixed flame speeds and the detailed structure of both nonpremixed and partially premixed flames [12,13,17,18,19].

While the finite-difference forms of the momentum equations are obtained using QUICKEST scheme [20], those of the species and energy are obtained using a hybrid scheme of upwind and central differencing. The pressure field is calculated at every time step by solving all of the pressure Poisson equations simultaneously and using the LU (lower and upper diagonal) matrix-decomposition technique.

Figure 1 illustrates the computational domain. It consists of 100 mm×50 mm in the axial (z) and radial (r) directions, respectively, and is represented by a staggered, non-uniform grid system. The reported results are grid independent, as discussed in the next section. The minimum grid spacing is 0.075mm in the r -direction and 0.090mm in the z -direction. An isothermal insert simulates the inner 2×0.8 mm burner wall. The boundary conditions used here can be found elsewhere [12,13]. The inner and outer jets are set with a constant and uniform velocity of 10cm/s, and 30 cm/s. The inner jet issues hydrogen/methane mixtures, while the outer jet issues air.

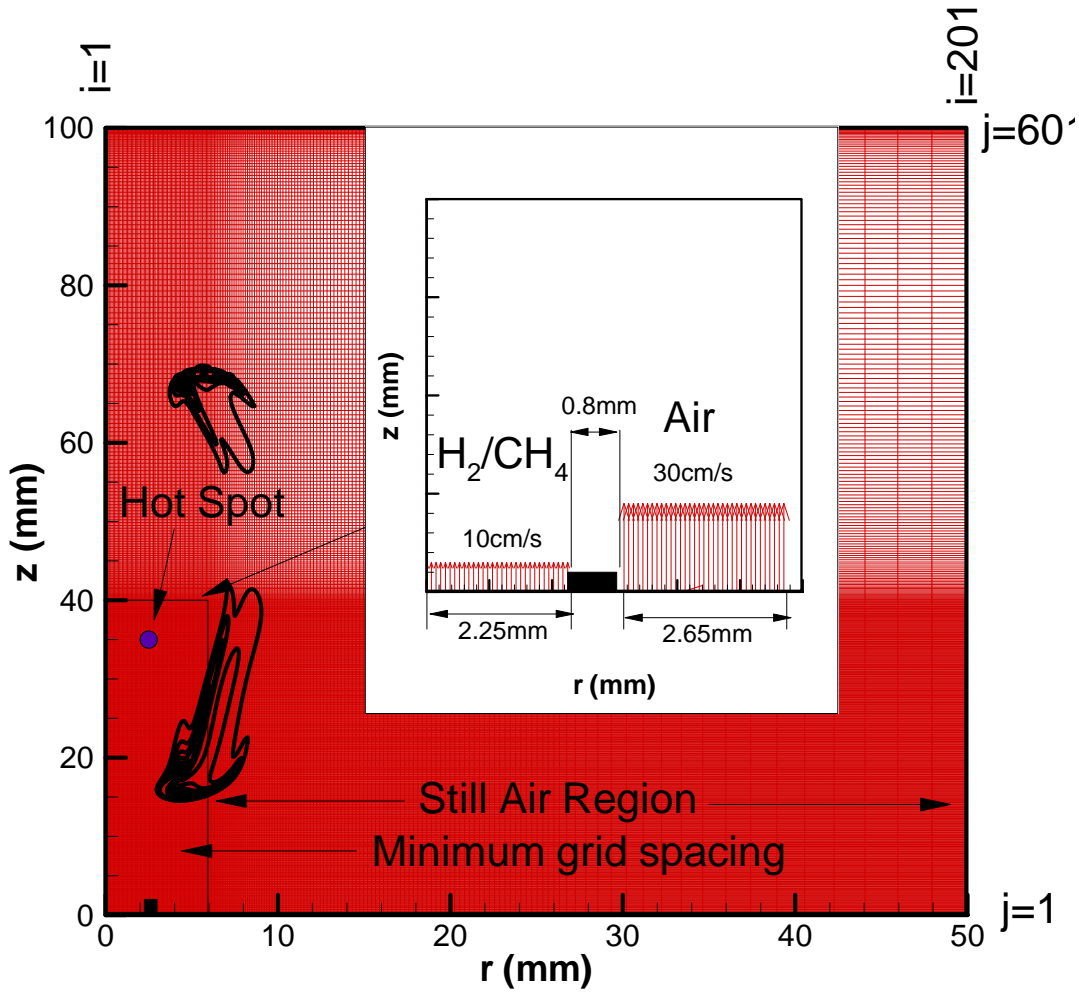


Figure 1. Schematic of the computational grid used in the simulations. The small rectangle shows the minimum grid spacing region where the propagation flamefront is located. Schematic of the computational domain is also shown.

Results and Discussion

Hydrogen-methane mixture with a mean burner exit velocity $V = 0.1 \text{ ms}^{-1}$ was introduced from the inner tube, and an air stream with a mean velocity of 0.3 ms^{-1} was supplied from the outer tube. The observations from this configuration allowed us to examine the formation and propagation of a triple flame in a nonpremixed jet. Hydrogen-methane mixtures were ignited at a 35mm height downstream of the burner exit.

Figure 2 presents the simulated results of transient ignition and flame propagation processes of a nonpremixed CH_4 flame (Flame A) (left) and a nonpremixed 25% H_2 -75% CH_4 flame (Flame B) (right), which are represented through the heat release rate contours. To ignite the mixture, a rectangular zone of area 2 mm^2 centered at $z = 35 \text{ mm}$ was set to an initial temperature of 2000 K. Also, the radical H and OH

mass fractions were set to 0.005 in this zone. After a short period (i.e. less than 2ms), these conditions were removed and the flame developed by itself. In general, two reacting volumes (or kernels) are formed following ignition. One propagates downstream and is quickly extinguished. The other propagates upstream towards the burner and develops into a triple flame, which is the focus of this investigation. The triple point is clearly established by $t \sim 5 \text{ ms}$ and a well-defined triple flame develops at $\sim 13 \text{ ms}$. The RP and LP reaction zones, as well as the NP reaction zone that is located between the RP and LP reaction zones, can be readily identified in the 13.125 and 37.5ms images. As the flame propagates upstream, the inner RP and the NP reaction zones become longer, and globally they both appear to move more slowly than the triple point or leading edge of the flame. Simultaneously, the flame curvature around the triple point increases significantly. When the triple flame approaches the burner and is stabilized near its

exit, it transforms into a double flame due to the absence of the mixing layer; i.e. the outer LP reaction

The snapshots on the right presents the simulated

stabilization near the burner exit in the form of a double flame are clearly indicated in the simulations. In addition, Flame B propagates much faster than Flame

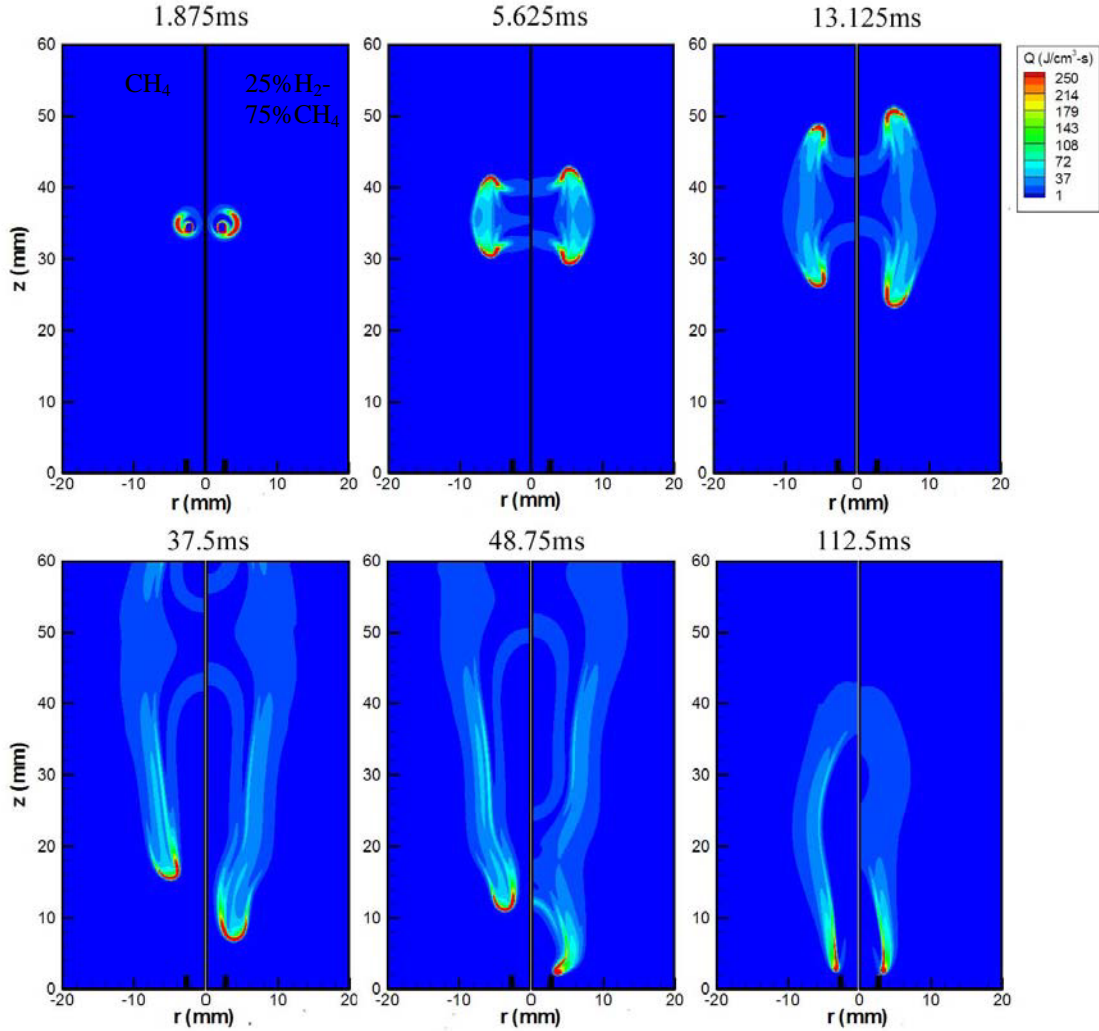


Figure 2. Simulated images showing the temporal evolution of ignition and flame propagation in terms of heat release rate contours for a nonpremixed CH_4 flame (Flame A) (left) and a nonpremixed $25\%\text{H}_2$ - $75\%\text{CH}_4$ flame (Flame B). Each image contains fourteen contours beginning from a value of $1 \text{ J/cm}^3\text{-s}$ with successive $18 \text{ J/cm}^3\text{-s}$.

results of transient ignition and flame propagation processes of a nonpremixed $25\%\text{H}_2$ - $75\%\text{CH}_4$ flame (Flame B). These processes are represented through the heat release rate contours for the same incremental time corresponding to Flame A. The transient processes associated with the formation of the triple flame, and its

A. For example, the base of Flame B is located at $\sim 22\text{mm}$ at 13.125ms after ignition, while Flame A is located at $\sim 26\text{mm}$. Both flames propagate nearly evenly. Here, use of the term “even” implies that the flames propagate along a linear path.

In the presentation more results will be shown regarding temporal evolutions, flame speeds, propagating velocities, hydrodynamic stretch, and curvature-induced stretch for many nonpremixed hydrogen/methane flames.

Conclusions

The characteristics of propagating nonpremixed hydrogen/methane flames have been investigated numerically. Numerical simulations were based on a comprehensive, time-dependent computational model that employs a detailed description of methane-air chemistry and transport properties.

The simulations indicate that the flame leading edge or triple point, which can be defined by the intersection of the stoichiometric mixture fraction line and the specific OH isocontour, propagates along the stoichiometric mixture fraction line. This result is in accord with the previous investigations concerning flame liftoff and downstream propagation.

Hydrogen addition causes that the flame propagates faster upstream in comparison with the flame with pure methane.

References

- 1 J.W. Heffel, *Int. J. of Hydrogen Energy* 2003;28(8):901-908.
- 2 D. M. Kabat, J. W. Heffel, *Int. J. of Hydrogen Energy* 2002;27(10):1093-1102.
- 3 J.W. Heffel, *Int. J. of Hydrogen Energy* 2003;28(11):1285-1292.
- 4 M.A.S. Al-Baghdadi, *Renewable Energy* 2003;28(9):1471-1478.
- 5 A.R. Choudhuri, S. R. Gollahalli, *Int. J. of Hydrogen Energy* 2000;25(5):451-462.
- 6 M.S. Kumar, A. Ramesh, B. Nagalingam, *Int. J. of Hydrogen Energy* 2003;28(10):1143-1154.
- 7 Naha S., Aggarwal, S. K., Submitted to *Combust. Flame* 2003.
- 8 J.M. Ogden, *Int. J. Hydrogen Energy* 24 (1999) 709–730.
- 9 R.J. Natkin, X. Tang, B. Boyer, B. Otmans, A. Denlinger, J.W. Heffel, SAE Paper 2003-01-0631.
- 10 C.K. Law, O.C. Kwon, *Int. J. Hydrogen Energy* 29 (2004) 867–879.
- 11 V. R. Katta, L. P. Goss, W. M. Roquemore, "Effect of nonunity Lewis number and finite-rate chemistry on the dynamics of a hydrogen-air jet diffusion flame," *Combust. Flame* **96**, 60 (1994).
- 12 Z. Shu, S. K. Aggarwal, V. R. Katta, I. K. Puri, "A numerical investigation of the flame structure of an unsteady inverse partially premixed flame," *Combust. Flame* **111**, 276 (1997).
- 13 R. Azzoni, S. Ratti, I. K. Puri, S. K. Aggarwal, "Gravity effects on triple flames: Flame structure and flow instability," *Phys. Fluids* **11**, 3449 (1999).
- 14 R. Siegel, J. R. Howell, *Thermal Radiation Heat Transfer*, Hemisphere Publishing Corporation, New York, 1981.
- 15 R. C. Reid, J. M. Prausnitz, B. E. Poling, *The properties of gases and liquids*, McGraw-Hill, New York, 1987.
- 16 M. Frenklach, H. Wang, C.-L. Yu, M. Goldenberg, C.T. Bowman, R.K. Hanson, D.F. Davidson, E.J. Chang, G.P. Smith, D.M. Golden, W.C. Gardiner and V. Lissianski, http://www.me.berkeley.edu/gri_mech/; and Gas Research Institute Topical Report: M. Frenklach, H. Wang, M. Goldenberg, G.P. Smith, D.M. Golden, C.T. Bowman, R.K. Hanson, W.C. Gardiner and V. Lissianski, 'GRI-Mech---An Optimized Detailed Chemical Reaction Mechanism for Methane Combustion,' Report No. GRI-95/0058, November 1, 1995.
- 17 Z. Shu, C. Choi, S. K. Aggarwal, V. Katta, I. K. and Puri, "Gravity effects on steady two-dimensional partially premixed methane-air flames," *Combust. Flame* **118**, 91 (1999).
- 18 X. Qin, I. K. Puri, and S. K. Aggarwal, V. R. Katta, "Gravity, radiation, and coflow effects on partially premixed flames," *Phys. Fluids* **16**, 2963 (2004).
- 19 H. Xue, S. K. Aggarwal, "Effects of reaction mechanisms on structure and extinction of partially premixed flames," *AIAA J.* **39**, 637 (2001).
- 20 V. R. Katta, L. P. Goss, W. M. Roquemore, "Numerical investigation of transitional H₂/N₂ jet diffusion flames," *AIAA J.* **32**, 84 (1994).

Hysteresis in a Counterflow Premixed Flame System

V. R. Katta*

Innovative Scientific Solutions Inc.
2766 Indian Ripple Road
Dayton, OH 45440-3638

Shengteng Hu, Peiyong Wang and Robert W. Pitz
Mechanical Engineering Department
Vanderbilt University
Nashville, TN 37235

William M. Roquemore and James Gord
Propulsion Directorate
Air Force Research Laboratory
Wright-Patterson Air Force Base, OH 45433

Abstract

The response of the counterflow flame system established between lean-methane-air and lean-hydrogen-air streams to stretch is investigated. A two-dimensional model known as UNICORN is used. Detailed measurements for temperature and species concentrations are obtained along the centerline. Numerical simulations have identified the hysteresis property of this flame system, which was later confirmed by the experiments. For the given flow conditions the flame system can have more than one stable operating mode, however the actual operating mode depends on the way the flow conditions were obtained. For understanding such hysteresis behavior of the counterflow flames, simulations are performed by increasing and decreasing stretch rates. When stretch rate on the flame system is increased, the flame transitions from a double-flame to a single-flame structure due to the aerodynamic-cooling process. When stretch rate is decreased, the flame doesn't transition back to its double-flame structure due to stretch effects on molecular diffusion—leading to hysteresis. Flames established with various lean methane-air mixtures are studied for determining the range for possessing hysteresis. It is found that flame system exhibits hysteresis only for methane-air mixtures leaner than $\phi=0.811$. However, for $0.811 > \phi > 0.74$, decrease in stretch increases flame temperature due to a decrease in stretch-induced cooling and eventually returns the flame structure to a double-flame one. In this narrow range of ϕ (0.74-0.811) hysteresis in counterflow premixed flames is temporary, which establishes a hysteresis loop with respect to stretch rate.

Introduction

Lean combustion is of interest due to its potential advantages in limiting thermal NO_x emissions and in increasing fuel consumption efficiency. Typically, diluted fuel-air mixtures are obtained through either available excess air or exhaust-gas recirculation. Lean combustion has been used in gas turbines and direct injection spark ignition (DISI) engines. However, a critical problem in using lean combustion is that it tends to produce unburned hydrocarbon pollutants. For example, in DISI engines, ultra-lean combustion is achieved by charge stratification. The fuel/air mixture is inhomogeneous, leading to the simultaneous formation of lean, rich and stoichiometric regions. For the inhomogeneous reactants, Haworth et al. [1] simulated turbulent inhomogeneous combustion in DISI engines and found that hydrocarbon-rich fragments

and oxidizer penetrate behind the primary heat-release zone to form a secondary reaction zone and, thereby, pollutants. Flames occurring in an inhomogeneously mixed fuel and air regions are also examples of partially premixed combustion. Some of this partially premixed mixture is so lean that it doesn't burn. However, such ultra-lean mixtures may still combust if hot products interact with it. That is, under certain conditions, the lean mixture region can burn and thus reduce the potential pollutants. Therefore, it is important to understand the interaction of lean mixture with hot products that are needed to maintain the lean region burning [2-6]. In the present work, stretch effects on the flame structure of lean CH₄/air mixtures are studied using a two-dimensional, detailed transport, complex chemistry numerical model and non-intrusive experimental techniques.

* Corresponding author: vrkatta@erinet.com

Proceedings of the 2006 Technical Meeting of the Central States Section of The Combustion Institute

Numerical Model

A time-dependent, axisymmetric mathematical model known as UNICORN (Unsteady Ignition and Combustion using ReactionNs) [7,8] is used for the simulation of the unsteady counterflow flames. It solves for axial- and radial-momentum equations, continuity, and enthalpy- and species-conservation equations on a staggered-grid system. A clustered mesh system is employed to trace the large gradients in flow variables near the flame surface. A detailed chemical-kinetics model (GRI Version 1.2) of Gas Research Institute [9] is incorporated into UNICORN. It consists of 32 species and 346 elementary-reaction steps. Molecular diffusion is assumed to be of the binary-diffusion type, and the diffusion velocity of a species is calculated using Fick's law and the effective-diffusion coefficient of that species in the mixture. A simple radiation model based on the optically thin-media assumption is used. Only radiation from CH_4 , CO , CO_2 , and H_2O is considered in the present study. The details of the numerical scheme used for solving the governing partial differential equations and the boundary conditions are given in References 10 and 11.

Experiment

The counterflow burner used in this study was designed by Seshadri et al. [12]. The schematic diagram of the burner along with the supplied flows is shown in Fig. 1. The burner system consists of 25-mm diameter inner nozzles that are separated by 12.6 mm. Methane-air mixture issues from the top nozzle while hydrogen-air mixture issues from the bottom nozzle. A low-speed nitrogen flow issues from the bottom outer nozzle protecting the flame from the room-air disturbances. The exhaust products flow into a top outer nozzle that is under suction. The top nozzle is water-cooled and the exit temperature for all the gasses is 300 K. Measurements of major species and temperature were made along the centerline using a non-intrusive, Raman-scattering diagnostic system [6,13]. Experiments were performed for various equivalence ratios and stretch rates. Details of eight flames that were classified into three groups are given in Ref. [13]. For example, Group A includes three flames with the same CH_4/air mixture (with an equivalence ratio of 0.68) and lean H_2/air mixture (with an equivalence ratio of 0.28) but subjected to different stretch rates [13].

Results and Discussion

Two-dimensional calculations for the premixed flame system in Fig. 1 were made on a grid system having 421×101 node points in the axial (z) and radial (r) directions, respectively. Flat velocity profiles were used at the nozzle exits. Computed temperature and OH-concentration distributions for a typical flame are shown in Fig. 1. The global stretch rate (the ratio between twice

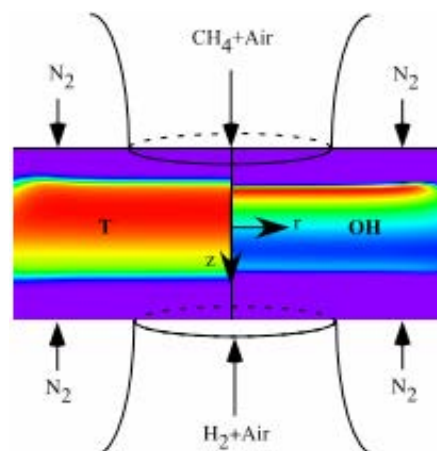


Fig. 1. Premixed flame system that exhibits hysteresis. Typical temperature and OH-concentration distributions under low-strain-rate conditions are shown.

the velocity difference and the nozzle separation) applied on this flame was 90 s^{-1} . Even though the computational domain was extended to 20 mm in the radial direction, only the data up to 15 mm is shown in Fig. 1. Calculations have yielded a double-flame structure with methane flame (lower) burning more intensely than the hydrogen one (upper). The former flame is also shorter (in the radial direction) than the latter. Detailed comparisons made between the computed and measured temperature and species profiles along the centerline [14,15] suggested that UNICORN code with GRI-V1.2 chemical kinetics predicts the flame structure accurately.

The premixed flame system shown in Fig. 1 is simulated first by performing calculations for a low-stretch-rate flame using the global-chemistry solution as the initial data and then performing calculations for the specific stretch rate using the previously obtained solution as the initial data. In general, if the counterflow premixed flames do not possess hysteresis, one could also obtain flame in Fig. 1 by performing calculations using previously obtained higher-stretch-rate flame as initial data. Numerical studies performed for different methane-air equivalence ratios suggested that the flame system in Fig. 1 only has hysteresis for certain lean conditions. For example, calculations performed for the counterflow premixed flame with $\phi_{\text{CH}_4} > 0.811$ are independent of the initial conditions used. Computed flames are obtained for several stretch rates using increasing-stretch-rate approach for $\phi_{\text{CH}_4} = 0.811$ flame and the results are plotted in Fig. 2 in the form of peak-temperature (T_f) variation with respect to the applied stretch rate (open symbols and broken line). Calculations are repeated for this flame for all the stretch-rate cases starting from the highest-stretched flame and then by decreasing the stretch rate. Results of these calculations are shown in Fig. 2 with

cross symbols and the solid line. For lower stretch rates (regime I) this flame system possesses two flames, one on the methane side and the other on the hydrogen side, and for higher stretch rates (regime III) it possesses only the methane-side flame. Transition from double-flame structure to single-flame structure occurs between the global stretch rates of 620 and 700 s^{-1} . More importantly, the flame system at a given stretch rate possesses either a double-flame or a single-flame structure, which is independent of the solution methodology. Peak temperature (T_p) along the centerline computed for various stretch rates for $\phi_{\text{CH}_4}=0.76$ flame system are shown in Fig. 3. Data computed with increasing-stretch-rate approach are shown with open circles and those computed with decreasing-stretch-rate approach are shown with crosses. Broken and solid lines are drawn, for clarity, through the circles and crosses, respectively. The flame system exhibits a unique double-flame structure for all the stretch rates $< 410 \text{ s}^{-1}$ (regime I) and a unique single-flame structure for stretch rates $\geq 510 \text{ s}^{-1}$ (regime III). However, for stretch rates in between 410 and 510 s^{-1} the flame system can have either a double-flame structure, if the calculations are made following the increasing stretch rate approach, or a single-flame structure, if the calculations are made following the decreasing stretch rate approach. Consequently, the flame system is known to possess a hysteresis property. Figure 3 further suggests that the flame system jumps back and forth between the double-flame and single-flame structures as the applied stretch rate is cyclically varied. This behavior establishes a hysteresis loop. Interestingly, when the methane-air equivalence ratio was decreased to 0.74, the flame system exhibits permanent hysteresis as shown in Fig. 4. For all the stretch rates $> 440 \text{ s}^{-1}$ (regime III) flame system has a unique solution independent of how that stretch rate was arrived at. There is a slight scatter in the temperature data as the planar flames formed in the counterflow burner tend to oscillate weakly. For all the stretch rates $< 440 \text{ s}^{-1}$ the flame system has two stable states; namely, the double-flame state (regime I) and the single-flame state (regime II). Therefore, flame temperature for stretch rates $< 440 \text{ s}^{-1}$ depends on the way the stretch rate was achieved, i.e., through increasing or decreasing.

Reasons for the products-supported premixed flames to exhibit double-state behavior can be understood by studying the differences in the flow and chemical structures of the flame systems formed under different stretch-rate regimes. Flames in regimes marked as I, II, and III in Fig. 4 for CH_4/air equivalence ratio of 0.74 are considered for this purpose. While regimes I and II represent double-flame and single-flame systems, respectively, at a stretch rate of 250 s^{-1} , regime III represents the system with single flame at a stretch rate of 600 s^{-1} . Temperature, velocity, and heat release rate distributions along the centerline for the flames in regimes I, II, and III are shown using solid lines in Figs. 5(a), 6(a),

and 7(a), respectively. Concentrations of H and CH radicals and oxygen consumption rates for the three flames are shown using solid lines in Figs. 5(b), 6(b), and 7(b), respectively. Production rates for OH and H_2 in the three flames are shown using solid lines in Figs. 5(c), 6(c), and 7(c), respectively. Stagnation points are marked with $U=0$ lines. Broken lines in Figs. 5, 6, and 7 represent the data obtained for the flame systems stretched 10% more than those in I, II, and III (i.e., 275, 275, and 660 s^{-1}), respectively.

As shown in Fig. 5, both methane and hydrogen flames are present in regime I flames. Heat release rate and temperature generated by the methane flame are higher than those generated by the 0.28-equivalence-ratio hydrogen flame. Because of the counterflow configuration, heat generated by the hotter methane flame heats the cooler hydrogen flame [16]. Consequently, the temperature of the methane flame is lower and that of the hydrogen flame is higher compared to their respective adiabatic flame temperatures. Heat release rate and oxygen consumption rate indicate that the reaction zones of the two flames are well separated. However, temperature and H-mole-fraction distributions suggest a strong interaction between the two flames through product species. These flames come closer when the stretch rate on the system increases (compare solid and broken lines in Fig. 5), which results in more interaction between the two flames. As a result, the temperature of the methane flame decreases further and that of hydrogen flame increases further; which, as shown in Figs. 2-4, translates into a decrease in peak temperature of the flame system with stretch rate (for regime I flames).

Extinction temperature for hydrogen flames ($\sim 1150 \text{ K}$) is less than that of methane flames ($\sim 1500 \text{ K}$). As a result, methane flame extinguishes first when the temperature of the methane-air/hydrogen-air flame system decreases and the structure of the double-flame system transitions into a single-flame one (regime II) as shown in Fig. 6. Unburned methane gas in this mode diffuses into the products generated by the hydrogen flame and a part of it gets decomposed (low-temperature chemistry) and releases a small amount of heat. Significant drops in oxygen consumption rate and CH and H mole fractions also suggest incomplete combustion of methane fuel. Nevertheless, reaction zones for the two fuels came close to each other and interact directly. Note the peak in heat release rate from methane decomposition appearing on the hydrogen side of the stagnation point. As diffusion fluxes increase with stretch rate, heat release rate and temperature also increase (compare the solid and broken lines in Fig. 6). This translates into an increase in peak temperature of the flame system with stretch rate (for regime II flames) as shown in Fig. 4.

Either from regime I or regime II, at higher stretch rates the flame system moves into regime III. Methane fuel diffuses into the products of the hydrogen flame and

participates in the low-temperature chemistry. According to the flamelet theory for nonpremixed combustion [17] reaction-zone temperature decreases, even though heat release rate continues to increase, with stretch rate due to reduced reaction-zone thickness and, thereby, increased heat losses (compare solid and broken lines in Fig. 7). This translates into a decrease in peak temperature of the flame system with stretch rate (for regime III flames) as shown in Figs. 2-4.

Hysteresis of the counterflow premixed flames can be explained by considering their characteristics in different regimes (I, II and III). In the laboratory, high-energy ignition sources such as a blowtorch establish the flame with methane and hydrogen burning in regime I. When the stretch rate is increased, the flame temperature decreases due to aerodynamic heat loss and, if the methane flame extinguishes, the flame system transitions to a single-flame one. Such a transition occurs at relatively low stretch rates in regime II for leaner methane/air mixtures. When stretch rate on the flame system with single flame (regime II) decreases, the flame temperature also decreases due to a drop in diffusion fluxes. The flame system remains in regime II as the temperature of the methane-air mixture cannot attain the ignition value. Therefore, for leaner methane/air mixtures, the flame system allows two stable operating states at a given stretch rate and exhibits hysteresis. When stretch rate on a moderately lean flame ($\phi_{CH_4} > 0.811$) in regime I is increased then it transitions into a flame in regime III. If stretch rate of this flame is decreased, then the flame temperature increases due to a drop in stretch-induced cooling (flamelet description) and if the local temperature reaches the ignition value then the flame system transitions to a regime-I flame. For these equivalence ratios, the flame system doesn't exhibit hysteresis.

Conclusions

The counterflow flame system established between lean-methane-air and lean-hydrogen-air streams was investigated. A two-dimensional model known as UNICORN was used for the simulation. GRI version 1.2 chemical kinetics involving 32 species and 346 one-way elementary reactions was used. Detailed measurements for temperature and species concentrations were obtained along the centerline. The hysteresis property of this flame system was first identified in numerical simulations and was later confirmed by experiments.

Calculations for various lean methane-air mixtures were performed to understand the hysteresis of the counterflow premixed flame system. Aerodynamic and chemical structures of the flames at different stretch rates were obtained through increasing-stretch-rate and decreasing-stretch-rate approaches. It was found that flame system exhibits hysteresis for methane-air mixtures leaner than 0.811. Hysteresis of the flame is associated with its double-state behavior. When the stretch on the

flame system is increased, it transitions from a double-flame to a single-flame structure due to aerodynamic cooling. When the stretch on the flame is decreased, it doesn't transition back to the double-flame structure due to stretch effects on molecular diffusion. However, for $0.811 > \phi_{CH_4} > 0.74$, decreasing the stretch increases the flame temperature due to a decrease in stretch-induced cooling and returns the flame structure to a double-flame one. In this narrow range of equivalence ratios (0.74-0.81) hysteresis in counterflow premixed flames is temporary, which establishes a hysteresis loop.

Acknowledgements

Financial support for the computational work was provided by the Air Force Office of Scientific Research (AFOSR, Julian Tishkoff) and the Air Force Contract #F33615-00-C-2068 (Vince Belovich). Financial support for the experimental work was provided by the National Science Foundation (Grant No. CTS-0314704).

References

1. D. C. Haworth, R. J. Blint, B. Cuenot, and T. J. Poinot, *Combust. Flame* 121 (3) (2000) 395-417.
2. S. H. Sohrab, Z. Y. Ye, C. K. Law, *Proc. Combust. Inst.* 20 (1984) 1957-1965.
3. M. A. Tanoff, M. D. Smooke, R. J. Osborne, T. M. Brown, R. W. Pitz, *Proc. Combust. Inst.* 26 (1996) 1121-1128.
4. R. S. Barlow, A. N. Karpetis, J. H. Frank, and J.-Y. Chen, *Combust. Flame* 127 (2001) 2102-2118.
5. J. A. Wehrmeyer, Z. Cheng, D. M. Mosbacher, R. W. Pitz, and R. Osborne, *Combust. Flame* 128 (3) (2002) 232-241.
6. Z. Cheng, J. A. Wehrmeyer, and R. W. Pitz, 38th AIAA/ASME/SAE/ASEE Joint Propulsion Conference, AIAA 2002-4021, Indianapolis, IN, 2002.
7. W. M. Roquemore, and V. R. Katta, *Journal of Visualization* 2 (2000) 257-272.
8. V. R. Katta, and W. M. Roquemore, *Combustion and Flame*, Vol. 100, No. 1, (1995), p. 61.
9. G. P. Smith, D. M. Golden, M. Frenklach, N. W. Moriarty, B. Eiteneer, M. Goldenberg, C. T. Bowman, R. K. Hanson, S. Song, W. C. Jr. Gardiner, V. V. Lissianski, and Z. Qin, <http://www.me.berkeley.edu/gri-mech>.
10. V. R. Katta, L. P. Goss, and W. M. Roquemore, *AIAA Journal*, Vol. 32, No. 1, (1994), p. 84.
11. V. R. Katta, L. P. Goss, and W. M. Roquemore, *Int. J. Num. Methods Heat Fluid Flow*, Vol. 4, No. 5, (1994), p. 413.
12. K. Seshadri, I. Puri, and N. Peters, *Combust. Flame* 61 (3) (1985) 237-249.
13. Z. Cheng, J. A. Wehrmeyer, and R. W. Pitz, *Proc. Combust. Inst.*, 30 (2005) 285-293.
14. V. R. Katta, Z. Cheng, R. W. Pitz, Proceedings of the 4th Joint Meeting of the U. S. Sections of the Combustion Institute, Philadelphia, PA, March 21-23, (2005).
15. V. R. Katta, S. Hu, P. Wang, R. W. Pitz, W. M. Roquemore, and J. R. Gord, Submitted to 31st International Symposium on Combustion.
16. C. J. Sung and C. K. Law, AIAA Paper, Presented at the Aerospace Sciences Meeting and Exhibit, Reno, NV, Jan. 12-16, 1993.
17. N. Peters, *Proc. Combust. Inst.* 21 (1986) 1231-1256.

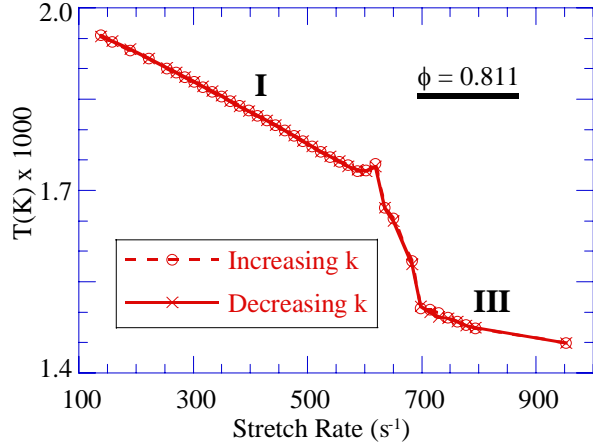


Fig. 2. Temperature of a premixed flame system formed between counter-flowing CH₄-air ($\phi=0.811$) and H₂-air ($\phi=0.28$) jets at different stretch rates.

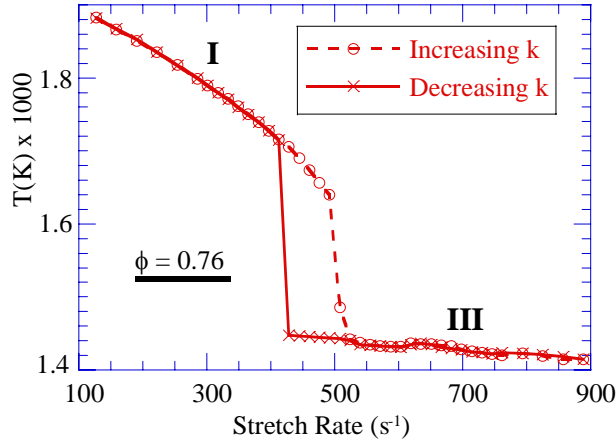


Fig. 3. Changes in temperature for increasing and decreasing stretch on the premixed flame system when the CH₄-air equivalence ratio is 0.76.

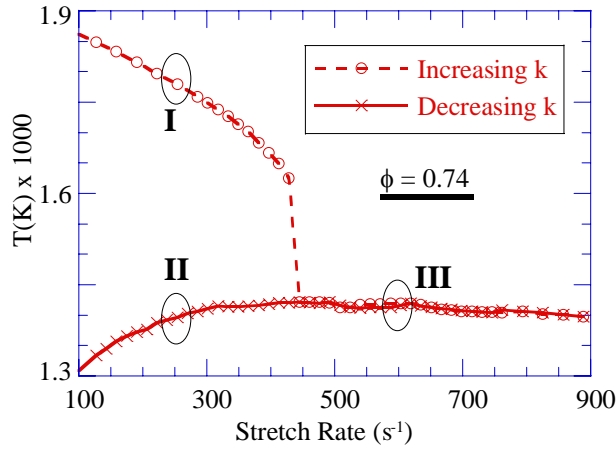


Fig. 4. Changes in temperature for increasing and decreasing stretch on the premixed flame system when CH₄-air equivalence ratio was further decreased to 0.74.

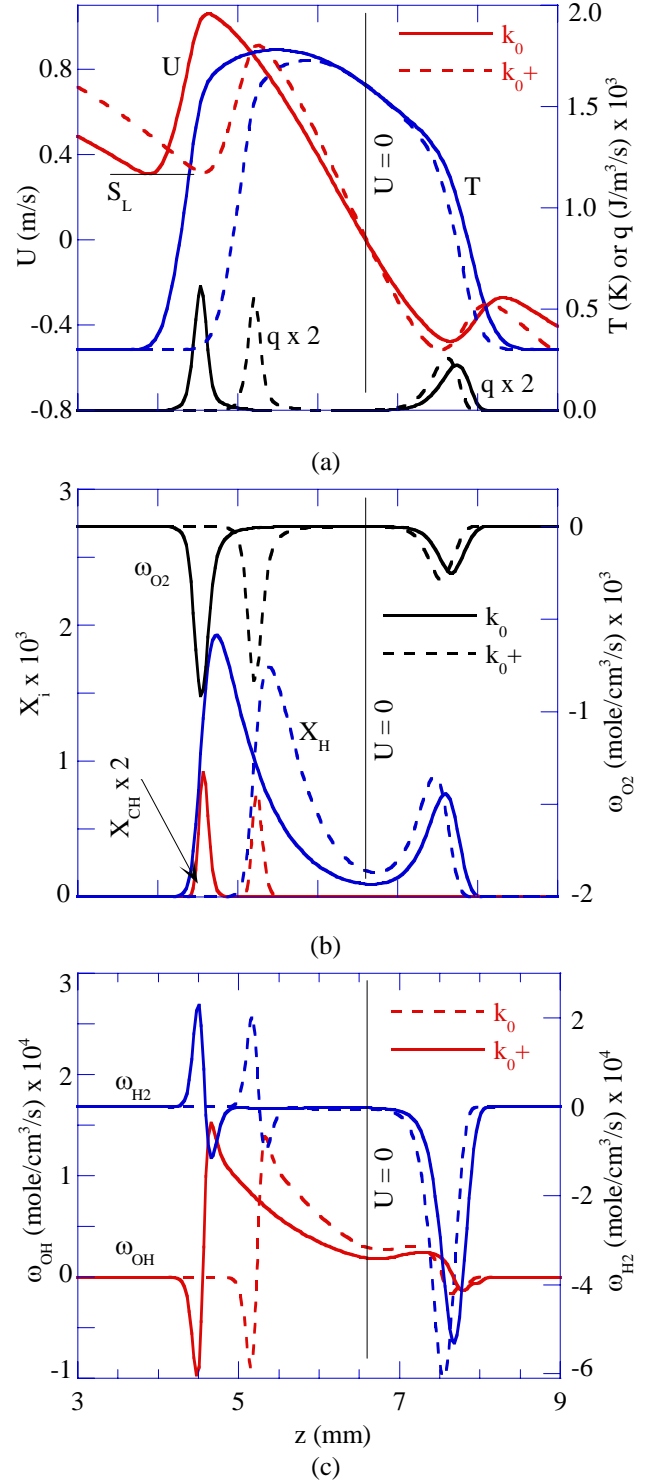


Fig. 5. Changes in flame structure due to perturbation in stretch rate when the flame system in Fig. 4 ($\phi_{\text{CH}_4}=0.74$) is operating in regime I at a stretch rate of 250 s⁻¹. Radial distributions of (a) velocity, temperature and heat release rate, (b) H and CH mole fractions and O₂ consumption rate, and (c) OH and H₂ production and destruction rates.

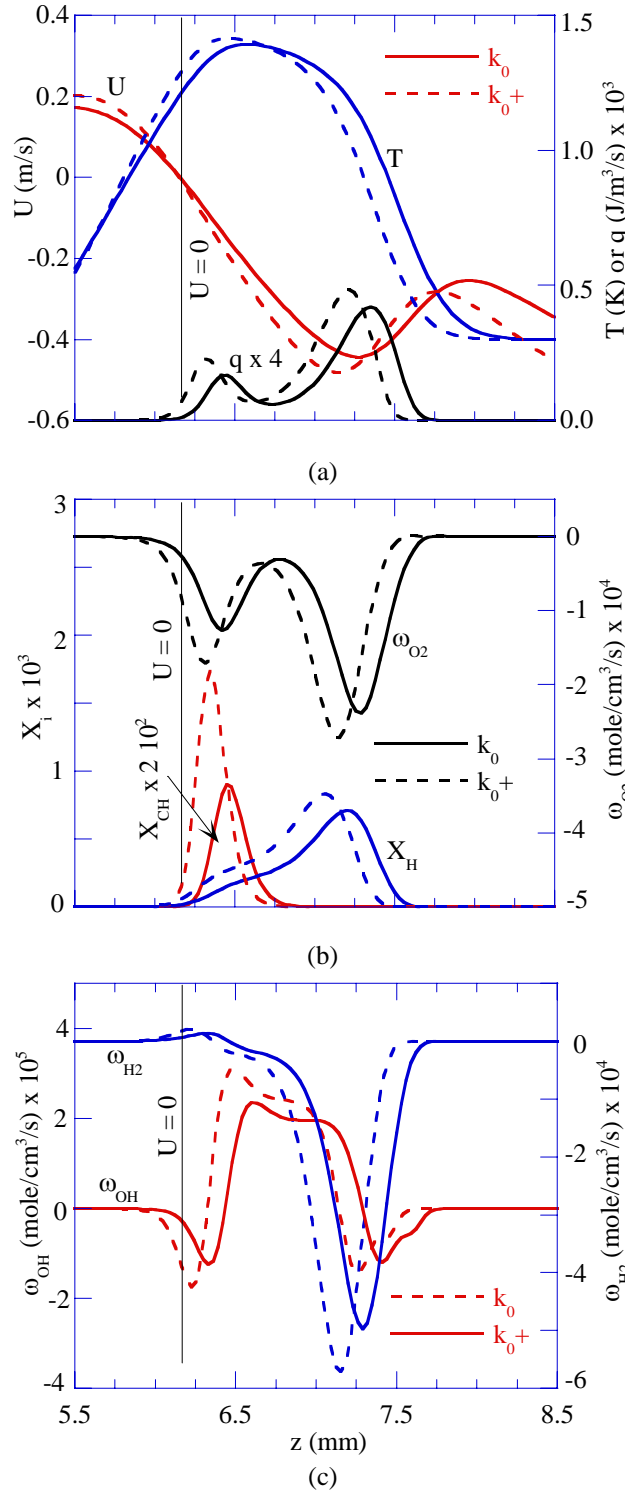


Fig. 6. Changes in flame structure due to perturbation in stretch rate when the $\phi_{CH4}=0.74$ flame system is operating in regime II at a stretch rate of 250 s^{-1} . Radial distributions of (a) velocity, temperature and heat release rate, (b) H and CH mole fractions and O_2 consumption rate, and (c) OH and H_2 production and destruction rates.

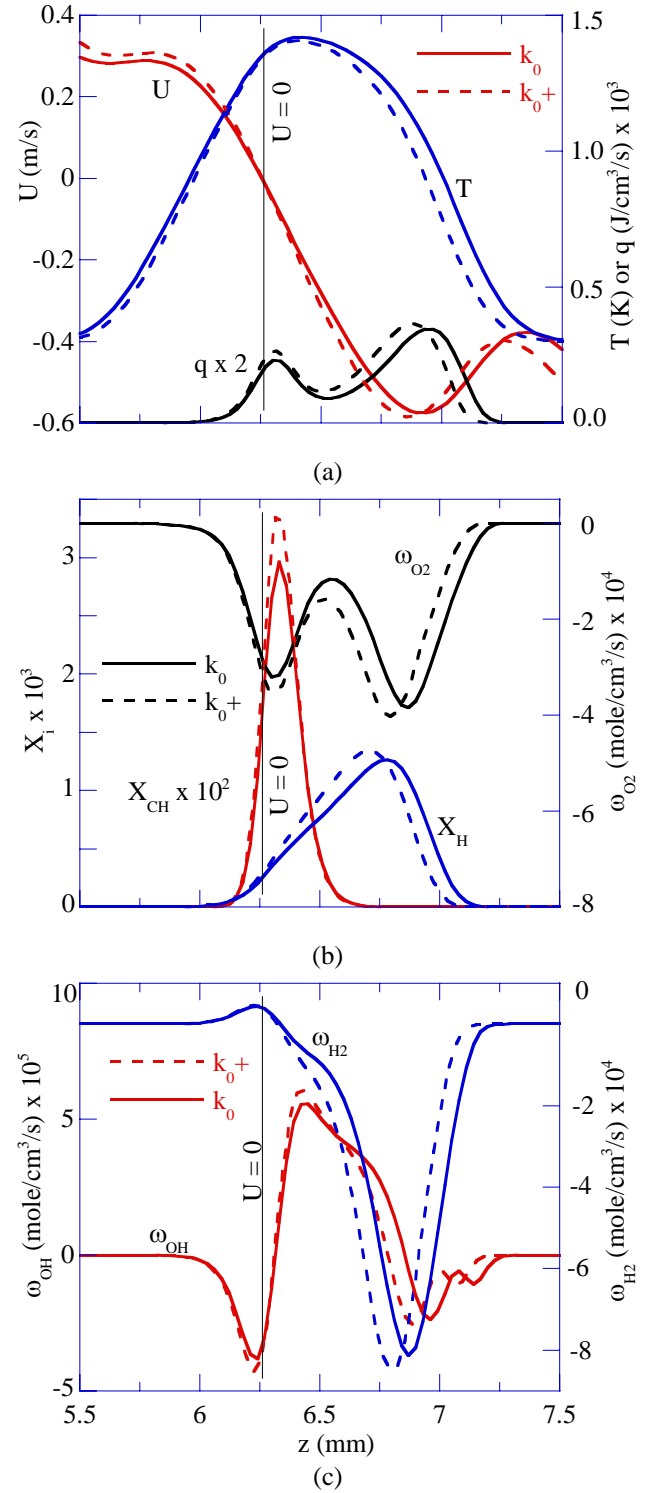


Fig. 7. Changes in flame structure due to perturbation in stretch rate when the flame system in Fig. 4 ($\phi_{CH4}=0.74$) is operating at a stretch rate of 600 s^{-1} . Radial distributions of (a) velocity, temperature and heat release rate, (b) H and CH mole fractions and O_2 consumption rate, and (c) OH and H_2 production and destruction rates.

Comparison of Chemical-Kinetics Models for JP-8 Fuel in Predicting Premixed and Nonpremixed Flames

Viswanath R. Katta*
Innovative Scientific Solutions, Inc.
2766 Indian Ripple Road
Dayton, OH 45440-3638

Mohamad Mawid, Balu Sekar, Edwin Corporan,
Joseph Zelina, and William M. Roquemore
Propulsion Directorate
Air Force Research Laboratory
Wright-Patterson Air Force Base, OH 45433

Christopher J. Montgomery
Reaction Engineering International
77 West 200 South, Suite 210
Salt Lake City, UT 84101

Computational-fluid-dynamics-(CFD)-based predictions are presented for an opposed jet nonpremixed flame and laminar nonpremixed and premixed coaxial jet flames burning vaporized JP-8 fuel. Results are presented for four published chemical kinetic mechanisms for JP-8. The first JP-8 kinetic mechanism is identified as the Violi-Small mechanism (161 reactions and 1538 reactions); the second is the Violi-Large mechanism (216 species and 9654 reactions); the third is the Zhang mechanism (208 species and 2186 reactions); and the fourth is the Mawid mechanism (226 species and 3230 reactions). There are three surrogate fuels associated with the Mawid mechanism. Differences and similarities in laminar flame structure and stability, resulting from the calculations using the four JP-8 mechanisms, are discussed. Calculations with the Violi-Small and Violi-Large mechanisms predicted extinction strain rates that are within 90% of a published measurement. The flames obtained with the Zhang mechanism are found to be the most difficult to extinguish, and those obtained with the Mawid mechanism are the easiest to extinguish. Calculations with the Zhang mechanism yielded the highest stability for the nonpremixed jet flame and the highest flame velocity for the stoichiometric mixture of JP-8 and air in the premixed jet flame. The Mawid mechanism resulted in coaxial nonpremixed jet flames that are more stable than those obtained with the Violi mechanisms, yet the flame velocities predicted by the Mawid mechanism for the premixed jet flame are lower than those predicted by the Violi mechanisms. Calculations with the Mawid mechanism using surrogate mixtures 1 and 3 resulted in very different limiting strain rates for the opposed-jet flame; however, for the premixed jet flame, the computed flame velocities are nearly the same for these mixtures. Numerical experiments are also performed to understand the sensitivity of the parent compounds used in Mawid mechanism for possible changes in their concentrations. Direct comparisons of the calculations with experiments are very limited because published data on these simple laboratory flames burning JP-8 are almost nonexistent. Indeed, these predictions are presented with the anticipation that they will stimulate experiments that will aid in obtaining suitable kinetic mechanisms for JP-8 flames.

* Corresponding Author, vrkatta@erinet.com

I. Introduction

With the declining supply of petroleum and its rising cost, it seems inevitable that the United States Air Force will transition to non-petroleum, alternative jet fuels derived from tar sands, coal, or shale. A near-term transition possibility is to mix the alternative fuel with JP-8, the primary aviation fuel used by the United States Air Force. Over time, the quantity of JP-8 would be reduced to zero. It is expected that the chemical composition and physical properties of the alternative fuels will be different from those of JP-8. This will impact the combustion characteristics of the fuel. The ability to predict the combustion characteristics of future blends of JP-8 requires a reliable chemical kinetic model for JP-8. To achieve this, several significant technical challenges must be overcome.

JP-8 is a mixture of hundreds, if not thousands, of hydrocarbons.^{1,2} It has been processed to meet a specification that covers a broad range of physical properties that include boiling range/volatility, heat of combustion, and freeze point. There is also a limit on the concentration of aromatic compounds. The JP-8 specification can be satisfied by many different hydrocarbon mixtures. Indeed, each batch of JP-8 can usually be a different chemical mixture.³ This is a significant impediment in developing “a” chemistry model for JP-8. A popular approach to solving this problem is to establish a surrogate fuel that represents a “typical” JP-8. A surrogate fuel is a well-defined mixture of a few hydrocarbon compounds whose relative concentrations can be adjusted such that the combustion characteristics of the mixtures become similar to those of a typical JP-8.² Chemical-kinetics models for the surrogate mixture are then developed based on the models established for the individual components of the mixture.

Development of chemical-kinetics models for JP-8 surrogate fuels is a formidable task given their complex composition. A surrogate fuel is usually developed based on chemical class distribution and by matching physical properties such as volatility, density, boiling point, and molecular weight.⁴⁻⁷ Schulz⁷ proposed a 12-component surrogate mixture for JP-8. Other investigators have also proposed surrogates for jet fuels.^{8,9-11} During combustion, the high molecular weight compounds undergo a sequential reduction to lower molecular weight hydrocarbons. Thus, the chemical-kinetics mechanisms for the surrogate fuels include reactions for the lower molecular weight compounds. The kinetics also includes pyrolysis and oxidation reactions that convert large molecules to radicals and smaller molecules. Condensation and dealkylation reactions that govern the growth of polycyclic aromatic hydrocarbons (PAHs) and soot are also included.^{1,12} The semi-detailed or lumped approach reduces the overall complexity of the resulting chemical-kinetics model both in terms of equivalent species and lumped or equivalent reactions.¹³ Even the semi-detailed models for surrogate fuels can involve hundreds of species and thousands of reactions. Incorporating them into CFD-based models and then making predictions for reacting flows in burners is very challenging.

Detailed simulations for the flame structure and predictions for the flame characteristics (ignition, extinction, flame speed, and stability) are essential for the development of any chemical-kinetics model. Simulations for the shock-tube, perfectly-stirred-reactor (PSR), and well-stirred-reactor (WSR) flames are often performed using zero-dimensional codes such as CHEMKIN,¹⁴ LSENS¹⁵ and STANJAN.¹⁶ Opposed jet flames and the burner-stabilized premixed flames are often treated as one-dimensional problems. Codes such as OPPDIF,¹⁷ RUN1DL,¹⁸ and CANTERA¹⁹ are used for these types of calculations. The performance of a chemical-kinetics model must also be evaluated for its ability to simulate multi-dimensional coaxial premixed and nonpremixed flames. However, multi-dimensional codes are computationally less stable and more expensive and time-consuming to operate. This paper presents computations performed with a robust and efficient CFD code that can handle large chemical-kinetics mechanisms.

UNICORN is a continually evolving two-dimensional numerical model that is being developed hand in hand with validation experiments.^{20,21} Recently, UNICORN has been modified so that it can be used to effectively and efficiently simulate the dynamic characteristics of nonpremixed and premixed flames using very large chemical kinetic mechanisms. This paper presents predictions for an opposed jet nonpremixed flame and laminar nonpremixed and premixed coaxial jet flames burning vaporized JP-8 fuel. Computations are given for four published chemical kinetic mechanisms for JP-8. The first JP-8 kinetic mechanism is identified as the Violi small mechanism (161 reactions and 1538 reactions); the second is the Violi large mechanism (216 species and 9654 reactions); the third is the Zhang mechanism (208 species and 2186 reactions); and the fourth is the Mawid mechanism (226 species and 3230 reactions). There are three surrogate mixtures associated with the Mawid mechanism. Differences and similarities in laminar flame structure and stability resulting from the calculations using the four JP-8 mechanisms are discussed. Numerical experiments are also performed to understand the sensitivity of the parent compounds used in Mawid mechanism for possible changes in their concentrations.

Ideally, we would like to evaluate the different kinetic mechanisms by comparing the calculations with experimental data. Unfortunately, published fundamental JP-8 flame data are almost nonexistent. This is due, in part, to the problems associated with the gasification of the fuel. Partial vaporization, preferential evaporation, and

condensation can introduce some bias in the experimental data. Thus, experiments with JP-8 and its surrogates strive for complete gasification in a way that doesn't change their chemical composition. Recently, Holley et al.,²² Humer et al.,¹³ and Agosta et al.⁸ have established standardized procedures for vaporizing liquid fuels and have started benchmark experiments for evaluating chemical-kinetics models. Other researchers are also conducting fundamental flame experiments with a "typical" JP-8 fuel and different surrogates. Indeed, it is anticipated that future experiments will provide the data needed to evaluate predictions like those presented in this paper.

II. Mathematical Model

A time-dependent, axisymmetric mathematical model known as UNICORN (Unsteady Ignition and Combustion using ReactionNs)^{20,21} is used for simulating different types of laminar flames. It solves for u- and v-momentum equations, continuity, and enthalpy- and species-conservation equations on a staggered-grid system. A clustered mesh system is employed in each case to trace the large gradients in flow variables near the flame surface. Four different detailed chemical-kinetics models, namely Violi-Small,²² Violi-Large,⁹ Zhang,¹⁰ and Mawid^{11,23-27} are incorporated into UNICORN for the evaluation of their abilities in predicting different types of JP-8 flames. Violi-Small mechanism consists of 161 species and 1538 reactions (some of them are lumped), Violi-Large mechanism consists of 216 species and 9654 reactions (some of them are lumped), Zhang mechanism consists of 208 species and 2186 elementary reactions, and Mawid mechanism consists of 226 species and 3230 elementary reactions. While the first three mechanisms use their own surrogate mixtures for representing JP-8 fuel, Mawid mechanism offers the usage of one of the three surrogate mixtures developed at Wright Laboratory.¹¹ The details of the surrogate mixtures used in these mechanisms are listed in Table 1. Note that the surrogate mixture used in Violi mechanisms is identical to the second mixture (Surrogate-2) used in Mawid mechanism. Due to lack of sufficient experimental data, none of these mechanisms was sufficiently validated and due to the large sizes, multi-dimensional simulations for laminar flames using these mechanisms have not yet been made.

Thermo-physical properties such as enthalpy, viscosity, thermal conductivity, and binary molecular diffusion of all the species are calculated from the polynomial curve fits developed for the temperature range 300 - 5000 K. Mixture viscosity and thermal conductivity are then estimated using the Wilke and Kee expressions, respectively. Molecular diffusion is assumed to be of the binary-diffusion type, and the diffusion velocity of a species is calculated using Fick's law and the effective-diffusion coefficient of that species in the mixture. A simple radiation model based on the optically thin-media assumption is incorporated into the energy equation for treating radiation heat loss from gaseous species²⁸. Only CH₄, CO, CO₂, and H₂O are considered as radiating species in the present study. Heat losses from soot particles are computed assuming blackbody radiation from the carbonaceous soot particles.²⁹

The finite-difference forms of the momentum equations are obtained using an implicit QUICKEST scheme,²¹ and those of the species, energy, and other scalar equations are obtained using a hybrid scheme of upwind and central differencing. At every time step, the pressure field is accurately calculated by solving all the pressure Poisson equations simultaneously and using the LU (Lower and Upper diagonal) matrix-decomposition technique. The boundary conditions are treated in the same way as that reported in earlier papers.³⁰

Computational soot models based on the fundamental physics of soot formation and oxidation are not yet available. The research groups around Moss³¹ and Lindstedt³² have made some progress in modeling soot formation using semi-empirical models based on the mechanisms of particle inception, agglomeration, surface growth, and oxidation. Soot model in UNICORN is based on a two-equation model with transport equations for particle number density, N_s , and soot mass fraction, Y_s . The source terms in these soot transport equations are obtained using Lindstedt's model,³² which is based on the simplifying assumption that nucleation and growth are first-order functions of acetylene concentrations. Soot oxidation was considered primarily due to the presence of O₂ and OH. Finally, soot agglomeration was treated as a source term in the soot number density equation.

The simulations presented here are performed on a single cpu, AMD Opteron Personal Computer with 2.0 GB of memory. Typical execution time is ~30 s/time-step for the coaxial nonpremixed flame simulations. Steady state solutions are typically obtained in about 2,000 time steps starting from the solution obtained using the global combustion chemistry model.

III. Results and Discussion

Typically, chemical-kinetics models developed for a given fuel are tested for their accuracy by comparing the predictions made for quantities such as ignition delay times, laminar flame speeds, extinction limits, and flame structures with the measured values. It is also known that out of these different characteristic parameters flame ignition and extinction are more sensitive to the chemical kinetics of the fuel. As discussed earlier, the chemical kinetics available in the literature for JP-8 fuel are not sufficiently validated due to lack of experimental data and

their abilities for predicting multidimensional flames are so far untested due to the computational difficulties associated with these large mechanisms. Development of UNICORN code for large mechanisms has made the way for accomplishing the latter task while the advances in vaporization techniques for liquid fuels have paved the way for filling the former.

A. Opposed Jet Flames

Recently, Holley et al.²² have obtained ignition limits for JP-8 fuels and extinction limits for JP-8 nonpremixed flames through conducting opposed-jet experiments. Single, planar nonpremixed flame was established by flowing a heated fuel/N₂ jet against an O₂ jet. The exit diameter (D) for the fuel and the oxidizer nozzles through which the respective jets were issued was 14 mm. The distance between the fuel and oxidizer nozzles was 14 mm (L). Holley et al.²² obtained extinction limits for the nonpremixed flame formed between the fuel and oxidizer jets by changing the fuel/N₂ ratio while keeping the flow rates; thereby, the strain rate on the flame, constant. For example, Holley et al.²² determined that JP-8 fuel extinguishes at 155-s⁻¹ global strain rate ($\Delta V/L$) when the fuel/N₂ ratio was decreased to 0.0802.

Axisymmetric calculations are performed for the opposed jet flame of Holley et al. using the UNICORN code and different chemical-kinetics mechanisms for JP-8 fuel. The physical domain between the two nozzles (14 mm in the axial direction and 20 mm in the radial direction) is represented using a 201x31 grid system. This resulted in a uniform grid spacing of 70 μ m across the flame. The fuel/N₂ ratio used in the calculations is 0.08. The temperatures of the fuel and oxidizer streams are set to the measured values of 394 and 294 K, respectively. A low-speed N₂ flow at 294 K is allowed outside the fuel and oxidizer streams for shielding the flame. Initially a stable flame is established for a low-strain-rate case of 28.6 s⁻¹. The corresponding fuel and oxidizer velocities are 0.2 and 0.2 m/s, respectively. Calculations are repeated on this flame by gradually increasing the strain rate (velocities) till the flame along the centerline is extinguished. The entire procedure starting from establishing an initial flame to obtaining an extinguished flame is repeated with each chemical-kinetics mechanism and surrogate mixture.

Results obtained for the 115-s⁻¹ strained flame using Violi-Small and Mawid mechanisms are shown in Fig. 1 on the left and right halves, respectively. Surrogate-2 is used with Mawid mechanism for representing JP-8 fuel. Velocity fields are superimposed on temperature distributions in Fig. 1. Heated fuel is issued from the bottom nozzle while O₂ is issued from the top. Since the density of the heated fuel is lower than that of the O₂, the flame is slightly shifted from the mid plane ($z = 7$ mm) toward the fuel nozzle. The flame is formed on the fuel side of the stagnation plane ($U=0$ surface). The peak temperature obtained with Mawid mechanism is ~ 80 K lower than that obtained with Violi-Small mechanism. However, the flame widths obtained with these two mechanisms are nearly the same.

The response of the flame to increases in strain rate predicted by different chemical-kinetics models is shown in Fig. 2. The peak temperature along the centerline ($r = 0$) is plotted at different strain rates. Due to increase in heat transport and chemical nonequilibrium, the temperature of the flame decreased with strain rate. Data from each chemical-kinetics model terminates at the extinction limit. The measured extinction limit of 150 s⁻¹ is also shown in Fig. 2 with a vertical box. The width of the box corresponds to the experimental uncertainty of 3.5% reported by Holley et al.²² Calculations with Mawid mechanism are made using three different surrogate mixtures. Note that Surrogate-2 is identical to the JP-8 fuel representation used in Violi mechanisms. In general, calculations with the different mechanisms resulted in variations in peak temperature of 120 K for weakly strained flames. As the strain increases, the variation in peak temperature also increases. Among the six chemical-kinetics models considered (Table 1), the Violi mechanisms seemed to provide the most realistic extinction strain rates. Both the Violi-Small and Violi-Large mechanisms yielded nearly the same relationship between peak temperature and strain rate. At the higher strain rates, these two mechanism result in small but gradual deviation in peak temperature. The extinction strain rate of 136 s⁻¹ predicted by these two mechanisms is within 90% of the measured value.

The all-elementary-reaction-based model developed by Zhang yielded the most stubborn flame from extinction point of view, even though the flame itself is not as strong (based on peak temperature) as the ones predicted by the semi-elementary-reaction-based mechanisms of Violi. Extinction in opposed jet flames occurs solely due to a sudden drop in chemical activity, which will be triggered by the temperature. Strain rate, on the other hand, makes the temperature of the flame to decrease via heat transport. Consequently, even though the temperature of the flame at 136 s⁻¹ strain rate obtained with the Zhang mechanism is lower than that obtained with the Violi mechanisms, flame did not extinguish in the former calculation due to the chemical-kinetics mechanism used. Eventually, the Zhang mechanism results in flame extinction when the peak temperature drops below 1565 K. This occurred at a global strain rate of ~ 247 s⁻¹.

The importance of an accurate surrogate mixture for representing JP-8 fuel is evident from the calculations made with the Mawid mechanism. The three different surrogate mixtures resulted in different temperature-strain-rate relationships (Fig. 2). Surrogate-1 yielded the lowest flame temperatures, and they decreased rapidly with strain rate.

Surrogates 2 and 3 yielded nearly the same extinction limits with the latter mixture having an extinction limit that is nearer to the measured value. Interestingly, the flame temperature predicted with Surrogate-2 is higher than that predicted with Surrogate-3, when the strain rate is low, but when the strain rate is high, the temperature is lower. Table 1 suggests that the major difference among the surrogate mixtures that could affect the performance of Surrogate-1 is the presence of hexadecane (10.2%), cyclooctane (4.7%), meththynaphthalene (3.9%), tetramethylbenzene (4.4%), and butylbenzene (4.6%). A numerical experiment conducted by systematically removing these compounds suggested that removal of hexadecane from the Surrogate-1 mixture significantly increases the flame temperature (~ 108 K) and the extinction limit predicted by Mawid mechanism.

The chemical structures of the flames obtained with the Violi-Small mechanism and the Mawid mechanism with Surrogate-2 at a global strain rate of 115 s^{-1} are shown in Figs. 3 and 4, respectively. The fuel description used in the Violi mechanism is identical to that of Surrogate-2. Decomposition of parent species, production of intermediate fuels such as C_3H_8 , C_2H_4 , CH_4 , and H_2 , and the generation of radical species OH are shown in Figs. 3 and 4. Note that even though the flame widths are identical, the peak temperatures predicted by these two chemical mechanisms differ by ~ 70 K, and the flame in Fig. 4 is at its extinction limit while the strain applied on the flame in Fig. 3 is well below its extinction limit. The chemical structures in Figs. 3 and 4 reveal some significant differences between the Violi and Mawid mechanisms. 1) Iso-octane and xylene are decomposing much faster and MCH is decomposing much slower in the Mawid mechanism, 2) propane produced by the Mawid mechanism is nearly an order of magnitude lower than that produced by the Violi mechanism, and 3) H_2 is generated slightly more by the Mawid mechanism.

Flame widths calculated from temperature distributions along the centerline ($r = 0$) are shown in Fig. 5 for different strain rates. As expected, width of the opposing-jet flame decreased nearly exponentially with strain rate. However, all calculations resulted in nearly the same flame widths under various strain-rate conditions--suggesting that the low-temperature reactions used in these mechanisms must be comparable to each other. Another important fact illustrated in Fig. 5 is that the limiting width of the flame (prior to extinction) is determined by the chemical kinetics and not by the strain rate. For example, at a strain rate of 120 s^{-1} , the flame width obtained with the Mawid mechanism with Surrogate-3 is at the extinction limit. However, the same flame widths obtained with the Violi mechanisms are slightly wider than their limiting values and that obtained with the Zhang mechanism is significantly wider than its limiting value. This observation is in contrast with the general belief, formed based on laminar flamelet theory, that flames become infinitely thin prior to extinction.

Figure 6 shows the variations in peak flame temperatures with strain rate for the 500-K preheated fuel. The fuel/ N_2 mass ratio is kept at 0.08, the same value used for the calculations shown in Fig. 2. A slight increase in temperature may be noted when the strain rate was increased initially. As all the mechanisms predicted such increase in peak temperature it is believed to be occurring due to some physical mechanism rather than a chemical phenomenon. The preheated fuel comes closer to the stagnation plane when the strain rate on the flame is increased, which, in turn, tends to increase the flame temperature. When this increase in temperature overcomes the decrease in temperature due to stretch effect the flame temperature increases with strain rate. At higher strain rates, the flame-stretch effects dominate in reducing the flame temperature up to extinction. The extinction order among the chemical-kinetics mechanisms did not change even at this elevated fuel temperature. On strain-rate scale, Mawid mechanisms with Surrogate-1 fuel extinguished first at 120 s^{-1} , Mawid mechanism with Surrogate-2 fuel next at 170 s^{-1} , Mawid mechanism with Surrogate-3 at 180 s^{-1} , Violi-Small mechanism at 202 s^{-1} , and finally Zhang mechanism extinguished the flame at 374 s^{-1} .

B. Coaxial Nonpremixed Flames

Flat flames obtained in opposed jet configurations provide a good platform for testing the chemical-kinetics mechanisms. However, unlike most practical flames, opposing-jet flames do not have stability issues, as they do not possess leading edges. The role of chemical kinetics in the stability of jet flames is significant and, therefore, proposed chemical-kinetics mechanisms must also be tested for their ability in predicting nonpremixed jet flames as well. The advantage of codes like UNICORN is that once a chemical-kinetics mechanism is incorporated they can be used for the simulation of both opposed and coaxial jet flames.

Calculations for a JP-8 coaxial nonpremixed jet flame are performed using the four chemical-kinetics models considered in the present work. The simulated burner has a central fuel tube of 0.6-cm radius and is surrounded by a 5-cm radius coflowing air. Preheated fuel- N_2 mixture at 500 K and with 90% fuel by mass is issued at a velocity of 2 cm/s. The coannular flow consists of room-temperature air and is issued at a velocity of 5 cm/s. These low-velocity conditions were chosen so that stable flames are established with all the four chemical-kinetics models. A computational grid of 151×61 is used for discretizing the physical domain of 10 cm x 5 cm in axial and radial directions, respectively. Grid clustering is used for placing most of the grid lines in the flame zone. Initial conditions

(flame) for the detailed-chemistry calculations were obtained from the simulations using a global-chemistry UNICORN code.

Results for the coaxial nonpremixed jet flame obtained with the Violi-Small, Violi-Large, and the Zhang models are shown in Figs. 7(a), 7(b), and 7(c), respectively. Here, iso contours of methylcyclohexane (dashes) and H₂ (solid lines) are superimposed on the temperature distribution (in rainbow color) on the left half of each figure. Iso contours of benzene (dashes), OH (solid lines) and temperature (in color) are shown on the right halves. The OH concentration is multiplied by 100. Similar plots prepared from the data obtained using the Mawid mechanism with Surrogate-1, Surrogate-2, and Surrogate-3 mixtures are shown in Figs. 8(a), 8(b), and 8(c), respectively.

In general, all six models predict nearly the same flame shape with the base region burning hotter than the tip region. The flames are slightly shifted from the inlet boundary as imposed by the stability criterion for nonpremixed jet flames. However, there are several important differences in these predictions. The Violi-Small and Violi-Large mechanisms result in nearly the same flame structure with the exception that the large mechanism generates more H₂ and benzene inside the flame and MCH extends farther into the core region [Figs. 7(a) and 7(b)]. The thermal layer (flame thickness) is wider for the Violi-Large flame, which resulted hotter core region in Fig. 7(b). As expected from the opposed-jet-flame calculations (Fig. 2), The coaxial nonpremixed flame predicted by the Zhang mechanism [Fig. 7(c)] is much closer to the inflow boundary compared to those predicted by the other models. This is anticipated based on the higher extinction strain rate for Zhang mechanism shown in Fig. 2. Even though, the benzene concentration is 1% in the surrogate mixture as prescribed by the Zhang mechanism, it is all being consumed quickly in the core region and does not enhance the benzene produced in the flame region [Fig. 7(c)].

The flame tips and the core region of the coaxial nonpremixed flames predicted by the Mawid mechanism are hotter than those predicted by the Violi or Zhang mechanism. Although the Mawid mechanism for Surrogate-1 yielded the largest separation between the flame base and the inflow boundary [Fig. 8(a)], the other two surrogates yielded flames closer to the inflow boundary than those obtained with Violi mechanisms. This is not expected based on the extinction-strain-rate data shown in Fig. 2. This anomaly in stability of the coaxial nonpremixed flames and the extinction of the opposed jet flames obtained with surrogates 1 and 2 may result from the differences in fuel concentrations (8% in opposed-jet and 90% in coaxial-jet cases) used for these two types of flames.

C. Coaxial Premixed Flames

Flame speed is another characteristic parameter of fuel-air mixture, which needs to be represented accurately by the chemical kinetics employed. For understanding the flame-speed characteristics of the chemical-kinetics mechanisms calculations are performed for a Bunsen-type coaxial premixed flame using the four models listed in Table 1. To allow for possible flashbacks in premixed systems a 5-mm-long fuel tube is included in the calculations. The inner and outer radii of the tube are 5.6 and 6.6 mm, respectively. Preheated (500 K) fuel and air mixture at stoichiometric proportion exits the fuel tube with an average velocity of 1.2 m/s. A parabolic, fully developed velocity profile is assumed at the inlet of the fuel tube. Results obtained with Violi-Small, Violi-Large, and Zhang models are shown in Figs. 9(a), 9(b), and 9(c), respectively. Iso contours of methylcyclohexane (in dashes) and H₂ (in solid lines) are superimposed on the temperature distribution (in rainbow color) on the left half of each figure. Iso contours of benzene (dashes), OH (solid lines) and temperature (in color) are shown on the right halves. The concentration of OH shown in these figures was enhanced 100 times. Similar plots prepared from the data obtained using Mawid mechanism with Surrogate-1, Surrogate-2, and Surrogate-3 mixtures are shown in Figs. 10(a), 10(b), and 10(c), respectively.

Since the velocity profiles used in all the calculations shown in Figs. 9 and 10 are the same, the surface area of the inner cone (or the height of the inner cone for equal base diameters) directly represents the flame speed. As seen from Figs. 9(a) and 9(b) the Violi-Small and Violi-Large mechanisms yielded identical inner cones and, hence, have the same flame speeds. Only a minor difference in the burning intensity at the inner cone tip is observed for the premixed flames predicted by these two mechanisms (See Figs. 9(a) and 9(b)). On the other hand, the Zhang mechanism resulted in flashback and flame propagated into the fuel tube. Also, the flame appears to be stabilized at the inlet boundary through altering the flow fluxes (rates). This seems unrealistic. Flashback resulted because of the higher flame velocity predicted by this chemical-kinetics mechanism. This is consistent with the higher extinction strain rate in Fig. 2 and the shortest separation between the flame base and the inflow boundary in Fig. 7(c).

The inner cone of the premixed flame predicted by the Mawid mechanism with Surrogate-1 mixture is nearly twice longer and, hence, half the flame speed than those predicted by the Violi mechanisms. Such prediction again is consistent with the findings made for the Mawid mechanism with opposed- and coaxial-nonpremixed-jet flames. Interestingly, Surrogates 2 and 3 with the Mawid mechanism also resulted in nearly a 50% decrease in flame

velocities. The post combustion region (i.e., the region outside the inner cone) is nearly the same in all the flames except that predicted by Zhang mechanism.

IV. Summary

A time-dependent, detailed-chemistry CFD model (UNICORN) is developed for utilizing large chemical-kinetics mechanisms that are required for the prediction of different types of reacting flows associated with JP-8 fuel. Performances of four detailed-chemical-kinetics models, namely Violi-Small (161 species and 1538 reactions), Violi-Large (216 species and 9654 reactions), Zhang (208 species and 2186 reactions), and Mawid (226 species and 3230 reactions) for mimicking JP-8 fuel are evaluated using UNICORN and through the simulation of opposed jet nonpremixed, coaxial nonpremixed jet, and coaxial premixed jet flames. Characteristics of three different surrogate mixtures for JP-8 fuel with 6 or 12 compounds are investigated using Mawid mechanism. The extinction characteristics of the chemical-kinetics models and surrogate mixtures are studied through the simulation of opposed jet nonpremixed flames. Violi-Small and Violi-Large mechanisms resulted in limiting extinction strain rates that are close (within 90%) to a measurement. While the flames obtained with Zhang mechanism were found to be the most difficult ones to extinguish, those obtained with Surrogate-1 mixture in Mawid mechanism were easy to extinguish. Numerical experiments performed for the sensitivity of individual compounds in Surrogate-1 mixture suggested that removal of hexadecane improves the extinction limit for the flame significantly. The stability characteristics are assessed from the simulations of coaxial nonpremixed jet flames and the flame-speed properties are evaluated by simulating Bunsen-type premixed flames. Zhang mechanism yielded highest stability for the nonpremixed jet flame and highest flame velocity for the stoichiometric mixture of JP-8 and air. Surrogates 2 and 3 in Mawid mechanism resulted coaxial nonpremixed jet flames that are more stable than those obtained with Violi mechanisms yet, the flame velocities predicted by Mawid mechanism are lower than those predicted by Violi mechanisms. Surrogates 1 and 3 in Mawid mechanism resulted very different limiting strain rates for opposed jet flame, however the flame velocities computed with these surrogates are nearly the same.

V. Acknowledgments

Financial support for this work was provided by the Air Force Office of Scientific Research (AFOSR, Julian Tishkoff), the Air Force Contracts F33615-00-C-2329 (Vince Belovich) and F33615-03-C-2338 (Edwin Corporan).

VI. References

1. Anon, Workshop on Combustion Simulation Databases for real Transportation Fuels, J. W. Hudgens (Ed.), NIST Gaithersburg, Maryland, 2003.
2. Ranzi, E., Faravelli, T., Frassoldati, A., and Granata, s., IEC 44 (2005) 5170-5183.
3. Defense Energy Support Center, Petroleum Quality Information System, annual fuel property surveys, <http://www.desc.dla.mil/DCM/DCMPage.asp?pageid=99>, 1994-2004.
4. Edwards, T. and Maurice, L. Q., Journal of Propulsion and Power 17 (2001) 461-466
5. Wood, C. P., McDonell, V. G., Smith, R. a., Samuelson, G. S., J. Propulsion and Power, Vol. 5, No. 4, 1989, pp. 399-405.
6. Farmer, R. C., Anderson, P. G., Cheng, G. C., Myruski, B. L., Pike, R. W., "Propulsion Chemistry for CFD Applications," Final Report on Contract NAS8-40574, National Aeronautics and space administration, Marshal Space Flight Center, AL, Sept., 1997.
7. Schulz, W., ACS Petroleum Chemistry Division Preprints 37 (2) (1991) 383-392.
22. Holley, A. T., Dong. Y., Andac, M. G., Egolfopoulos, F. N., "Ignition and extinction of Non-premixed Flames of Single-Component Liquid Hydrocarbons, Jet Fuels, and their Surrogates," to be published in Proceedings of the Combustion Institute 31 (2006).
8. Agosta, A., Cernansky, N. P., Miller, D. L., Faravelli, T., and Ranzi, E., Experimental Thermal and Fluid Science 28 (2004) 701-708.

9. Violi, A., Yan, S., Eddings, E. G., Sarofim, A. F., Granata, S., Faravelli, T., Ranzi, E., "Experimental Formulation and Kinetic Model for JP-8 Surrogate Mixtures," *Combustion Science and Technology* 174 (2002) 399-417.
10. Zhang, H., Ph. D. Thesis, Department of Chemical Engineering, University of Utah, 2005.
11. Mawid, M. A., Park, T. W., Sekar, B., and Arana, C., "Development and Validation of a Detailed JP-8 Fuel Chemistry Mechanism," AIAA Paper 2002-3876, 38th AIAA Joint Propulsion Conference, Indianapolis, Indiana, July 7-10, 2002.
12. Tsang, W., *Data Science Journal* (2004) 3 (1-9).
13. Humer, S., Frassoldati, A., Granata, S., Faravelli, T., Ranzi, E., Seiser, R., Seshadri, K., "Experimental and Kinetic Modeling Study of Combustion of JP-8, its Sorrogates and Reference Compounds in Laminar Nonpremixed Flows," to be published in *Proceedings of the Combustion Institute* 31 (2006).
14. Kee, R. J., Miller, J. A., Jefferson, T. H., "CHEMKIN: A General-Purpose, Problem-Independent, Transportable, Fortran, Chemical Kinetic Code Package," Technical Report SAND80-8003, Sandia National Laboratories, 1980.
15. Radhakrishnan, K., "LSENS--A General Chemical Kinetics and sensitivity Analysis Code for Homogeneous Gas-Phase Reactions," NASA Reference Publication 1328, NASA, 1994.
16. Reynolds, W. C., "STANJAN Version 3.95," Stanford University, September 1993.
17. Lutz, A. E., Kee, R. J., Grcar, J. F., and Rupley, F. M., "OPPDIF: A Fortran Program for Computing Opposed-flow Diffusion Flames," SAND96-8243, Sandia National Laboratories, CA (1996)
18. Rogg, B., "RUN1DL—The Cambridge Universal Laminar Flamelet Computer Code," in *Reduced Kinetic Mechanisms for Applications in Combustion Systems*, N. Peters and B. Rogg (Eds), *Lecture Notes in Physics* m15, Springer-Verlag, Heidelberg, Germany, 1993, pp. 350-351.
19. Goodwin, D. G., "CANTERA: An Open-Source, Object-Oriented Software Suite for Combustion," Division of Engineering and Applied Science, California Institute of Technology, CA, (2000)
20. Roquemore W. M., and Katta, V. R., "Role of Flow Visualization in the Development of UNICORN," *Journal of Visualization* 2 (2000) 257-272.
21. Katta, V. R., Goss, L. P., and Roquemore, W. M., *AIAA Journal*, Vol. 32, No. 1, 1994, p. 84.
22. Montgomery, C. J., Zhao, W., Tam, C. -J., Eklund, D. R., and Chen, J.-Y., "CFD Simulations of a 3-D Scramjet Flameholder using Reduced Chemical Kinetic Mechanisms," AIAA Paper 2004-3874, 40th AIAA/ASME/SAE/ASEE Joint Propulsion Conference and Exhibit, Fort Lauderdale, Florida, July 11-14, 2004.
23. Mawid, M. A., Park, T. W., Sekar, B., and Arana, C., "Development of Detailed Chemical Kinetic Mechanisms for Ignition/Oxidation of JP-8/Jet-A/JP-7 Fuels," ASME Paper 2003-GT-38932, ASME Turbo Expo, Atlanta, Georgia, June 16-19, 2003.
24. Mawid, M. A., Park, T. W., Sekar, B., and Arana, C., "Development and Validation of Detailed and Reduced Chemical Kinetic Mechanisms for Oxidation of JP-8/Jet-A/JP-7 Fuels," ISABE-2003-1028, XVI ISABE Proceedings, Cleveland, Ohio, August 31 – September 5, 2003.
25. Mawid, M. A., Park, T. W., Sekar, B., and Arana, C., "Importance of Surrogate JP-8/Jet-A Fuel Composition in Detailed Chemical Kinetics Development," AIAA Paper 2004-4207, 40th AIAA/ASME/SAE/ASEE Joint Propulsion Conference and Exhibit, Fort Lauderdale, Florida, July 11-14, 2004.

26. Mawid, M. A. and Sekar, B., "Development of a Detailed Jp-8/Jet-A Chemical Kinetic Mechanism For High Pressure Conditions In Gas Turbine Combustors", GT-2006-90478, Proceedings of ASME Turbo Expo 2006, May 8-11, Barcelona, Spain.
27. Mawid, M. A., Park, T. W., Sekar, B., and Arana, C., "Detailed Chemical Kinetic Modeling of JP-8/Jet-A Ignition and Combustion," GT2005-68829, Proceedings of ASME Turbo Expo, Reno, NV, June 6-9, 2005.
28. Annon., Computational Submodels, International Workshop on Measurement and Computation of Turbulent Nonpremixed Flames, <http://www.ca.sandia.gov/TNF/radiation.html>, (2001).
29. Guo, H., Liu, F., Smallwood, G. J., Combustion Theory and Modeling, Vol. 8, 2004, pp. 475-489.
30. Katta, V. R., Goss, L. P., and Roquemore, W. M., *Int. J. Num. Methods Heat Fluid Flow*, Vol. 4, No. 5, 1994, p. 413.
31. Mauss, F., Schäfer, T. and Bockhorn, H., *Combust. Flame* 99:697-705 (1994).
32. Lindstedt, R.P., in *Soot Formation in Combustion: Mechanisms and Models* (H. Bockhorn, Ed.), Springer-Verlag, Heidelberg, 1994, pp.417-439.

Table 1. Representation of JP-8 Fuel in Various Chemical-Kinetics Models.

Fuel Components	Violi-Small Mechanism	Violi-Large Mechanism	Zhang Mechanism	Mawid Mechanism		
				Surrogate-1	Surrogate-2	Surrogate-3
n-decane (n-C ₁₀ H ₂₂)	0	0	0	16.2	0	25
n-dodecane (n-C ₁₂ H ₂₆)	30	30	73.5	21	30	25
n-tetradecane (n-C ₁₄ H ₃₀)	20	20	0	15.6	20	20
n-hexadecane (n-C ₁₆ H ₃₄)	0	0	0	10.2	0	0
i-octane (I-C ₈ H ₁₈)	10	10	5.5	5.7	10	5
Cyclooctane (c-C ₈ H ₁₆)	0	0	0	4.7	0	0
Methylnaphthalene MCH (C ₁₁ H ₁₀)	20	20	10	5.1	20	5
1-methylnaphthalene (C ₁₁ H ₁₀)	0	0	0	3.9	0	0
Tetralin (C ₁₀ H ₁₂)	5	5	0	4.1	5	0
1,2,4,5-tetramethylbenzene (C ₉ H ₁₂)	0	0	0	4.4	0	0
Butylbenzene (C ₁₀ H ₁₄)	0	0	0	4.6	0	0
m-xylene (C ₈ H ₁₀)	15	15	0	4.5	15	0
Toluene (C ₇ H ₈)	0	0	10	0	0	20
Benzene (C ₆ H ₆)	0	0	1	0	0	0
Molecular Weight	144.38	144.38	151.3	156.87	144.38	146.89

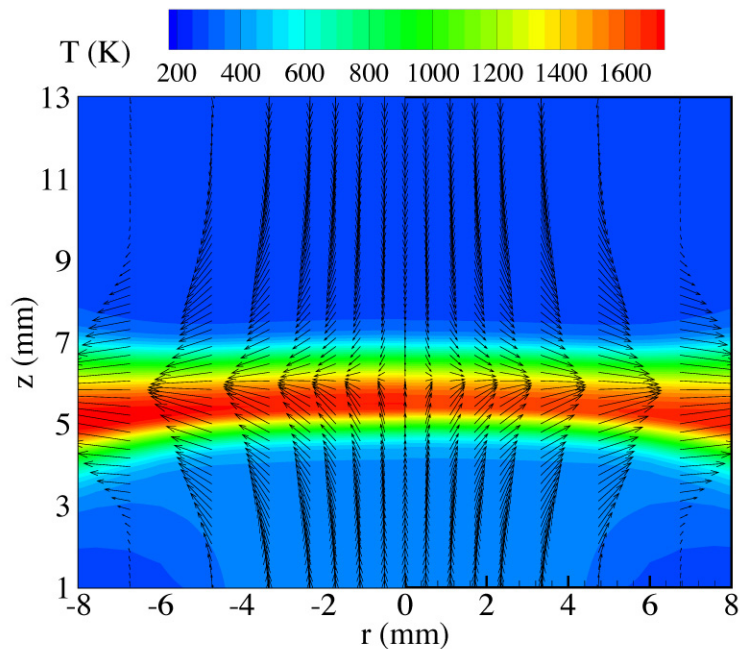


Fig. 1. Opposing-jet nonpremixed JP-8 flame. Temperature and velocity fields obtained with Violi-Small mechanism are shown on the left half and those obtained with Mawid's mechanism are shown on the right half.

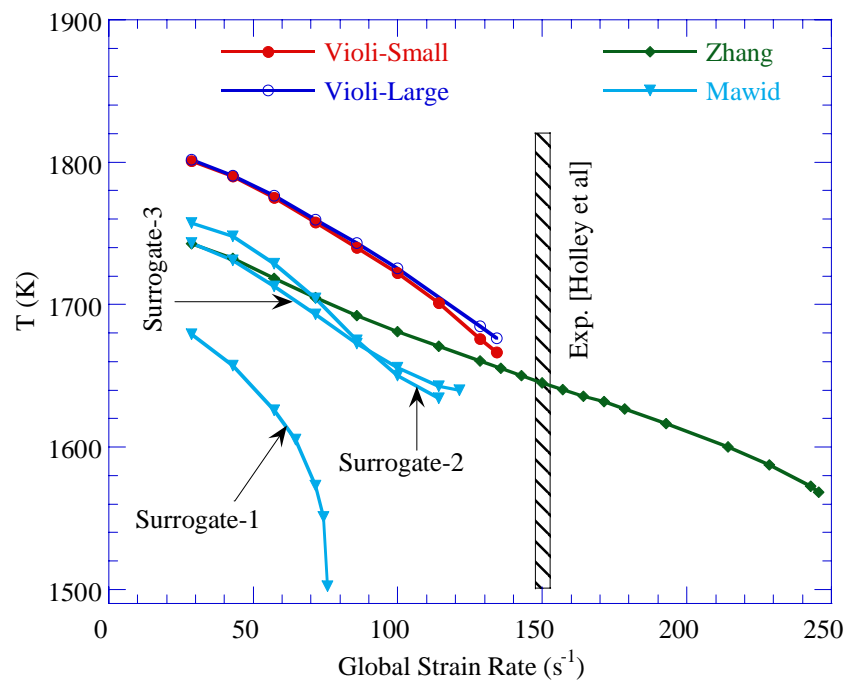


Fig. 2. Variations of peak temperature of a nonpremixed JP-8 flame with strain rate obtained using different chemical-kinetics mechanisms. Fuel/N₂ mass ratio and temperature on the fuel stream are 0.08 and 394 K, respectively. Extinction with a given chemical-kinetics model occurred for all strain rates greater than the right most value shown for each curve. Measured extinction strain rate is shown with a vertical bar.

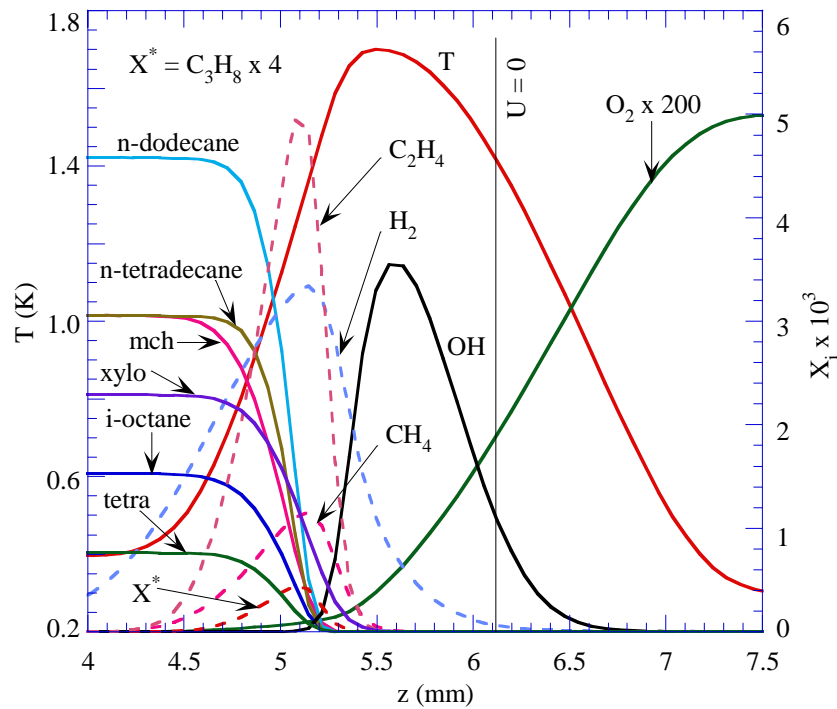


Fig. 3. Temperature and species distributions, predicted using Violi-Small chemical-kinetics mechanism, along the centerline of the opposing-jet nonpremixed JP-8 flame with a global strain rate is 115 s^{-1} .

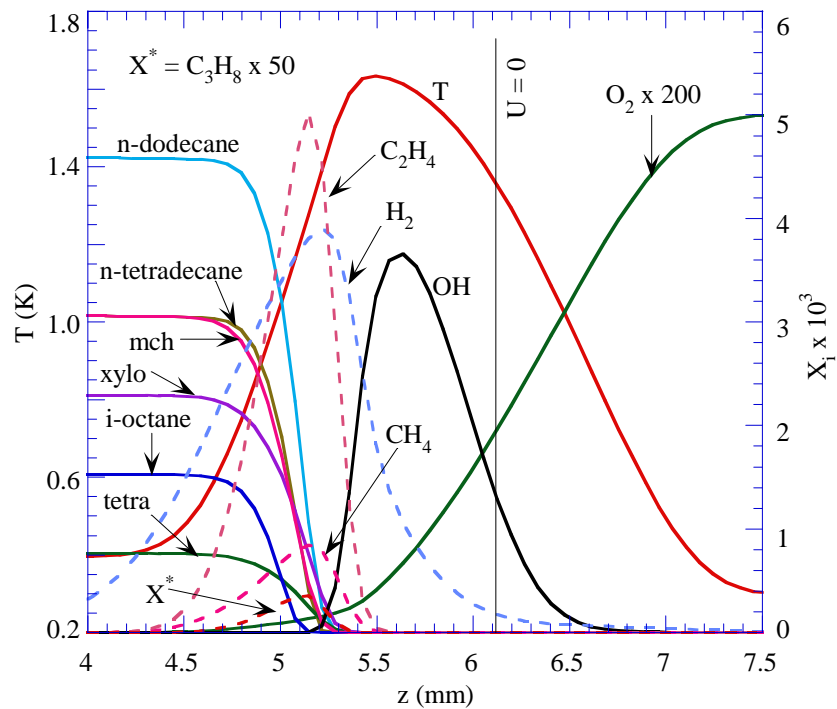


Fig. 4. Temperature and species distributions, predicted using Mawid chemical-kinetics mechanism, along the centerline of the opposing-jet nonpremixed JP-8 flame with a global strain rate is 115 s^{-1} .

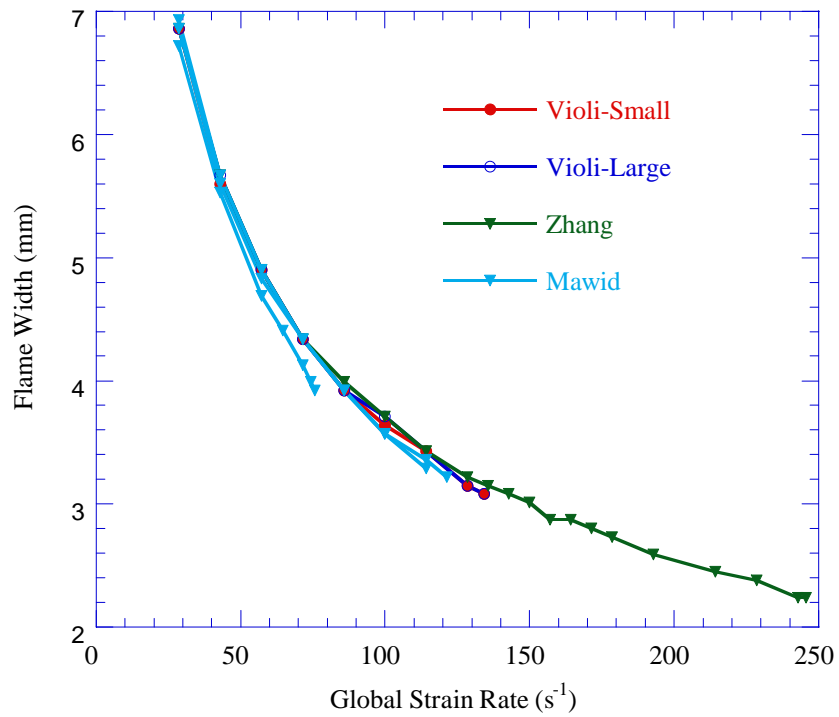


Fig. 5. Variations of width (based on temperature distribution) of a nonpremixed JP-8 flame with strain rate obtained using different chemical-kinetics mechanisms. Fuel/ N_2 mass ratio in the fuel stream is 0.08.

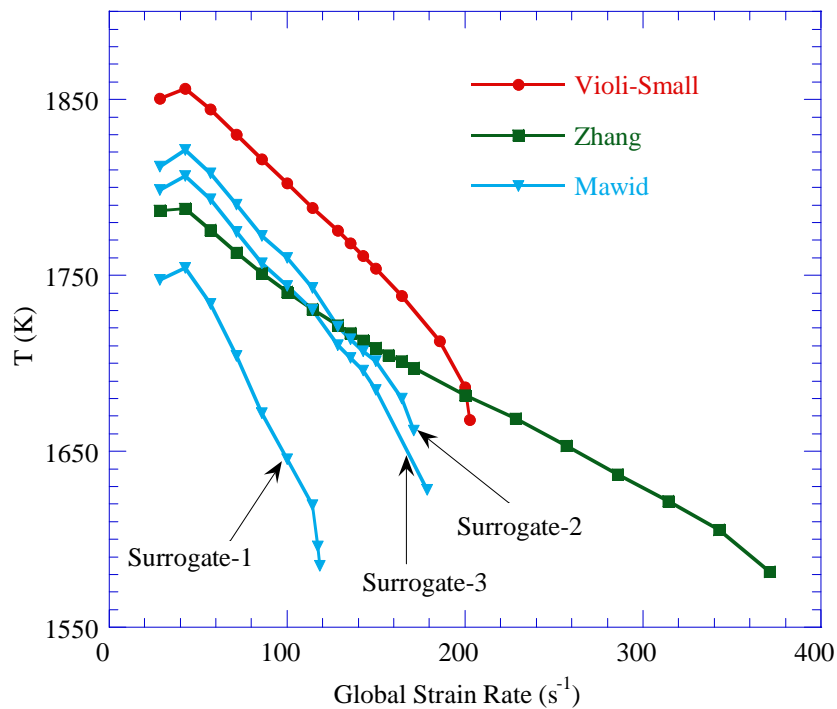


Fig. 6. Variations of peak temperature of nonpremixed JP-8 flame with strain rate obtained using different chemical-kinetics mechanisms. Fuel/ N_2 mass ratio and temperature on the fuel stream are 0.08 and 500 K, respectively.

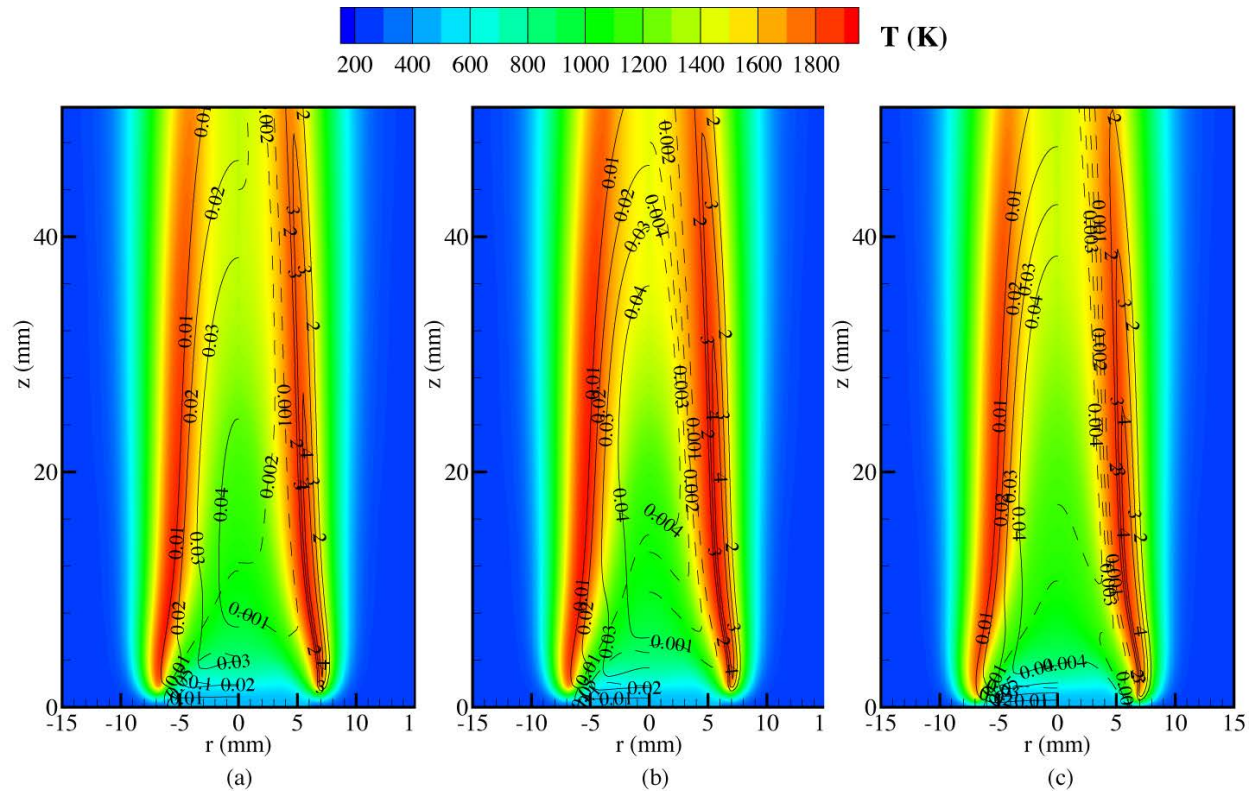


Fig. 7. Structure of JP-8 nonpremixed jet flame predicted using (a) Violi-Small, (b) Violi-Large, and (c) Zhang mechanisms. Iso contours of MCH (dashes) and H₂ (solid) are superimposed on temperature distribution on the left half and iso contours of benzene (dashes) and OH (solid) are superimposed on the right half.

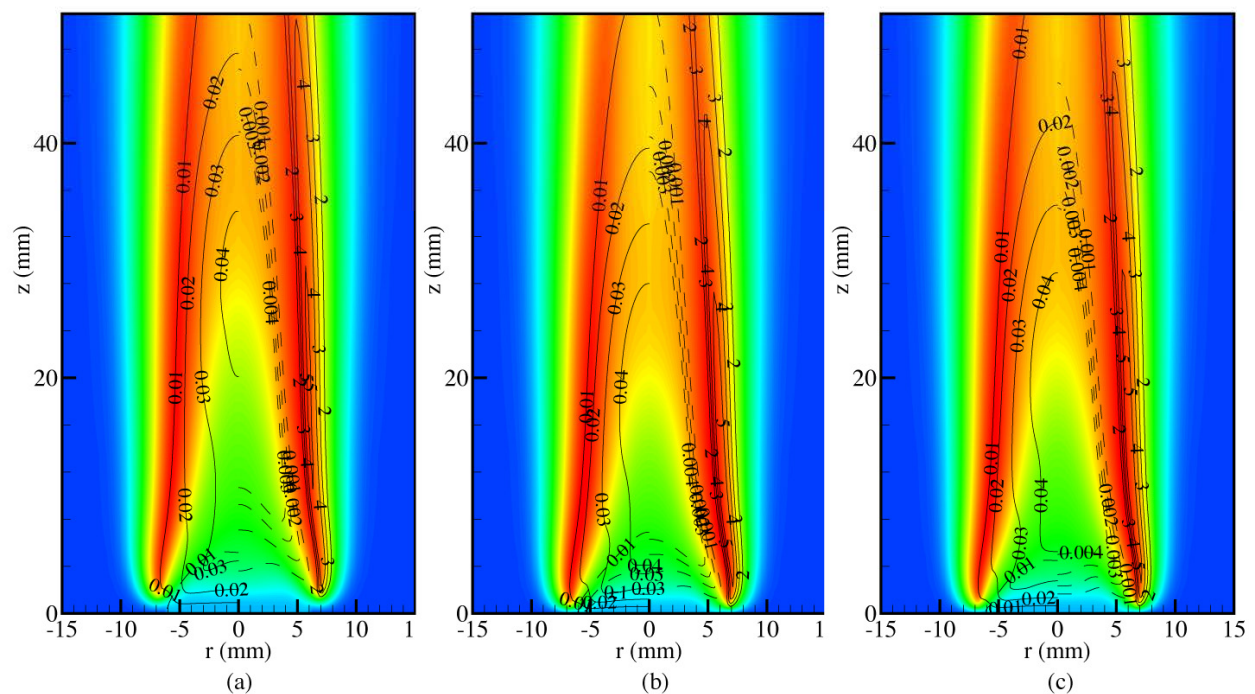


Fig. 8. Structure of JP-8 nonpremixed jet flame predicted using Mawid mechanism with (a) surrogate-1, (b) surrogate-2, and (c) surrogate-3 mixtures. Iso contours of MCH (dashes) and H₂ (solid) are superimposed on temperature distribution on the left half and iso contours of benzene (dashes) and OH (solid) are superimposed on the right half.

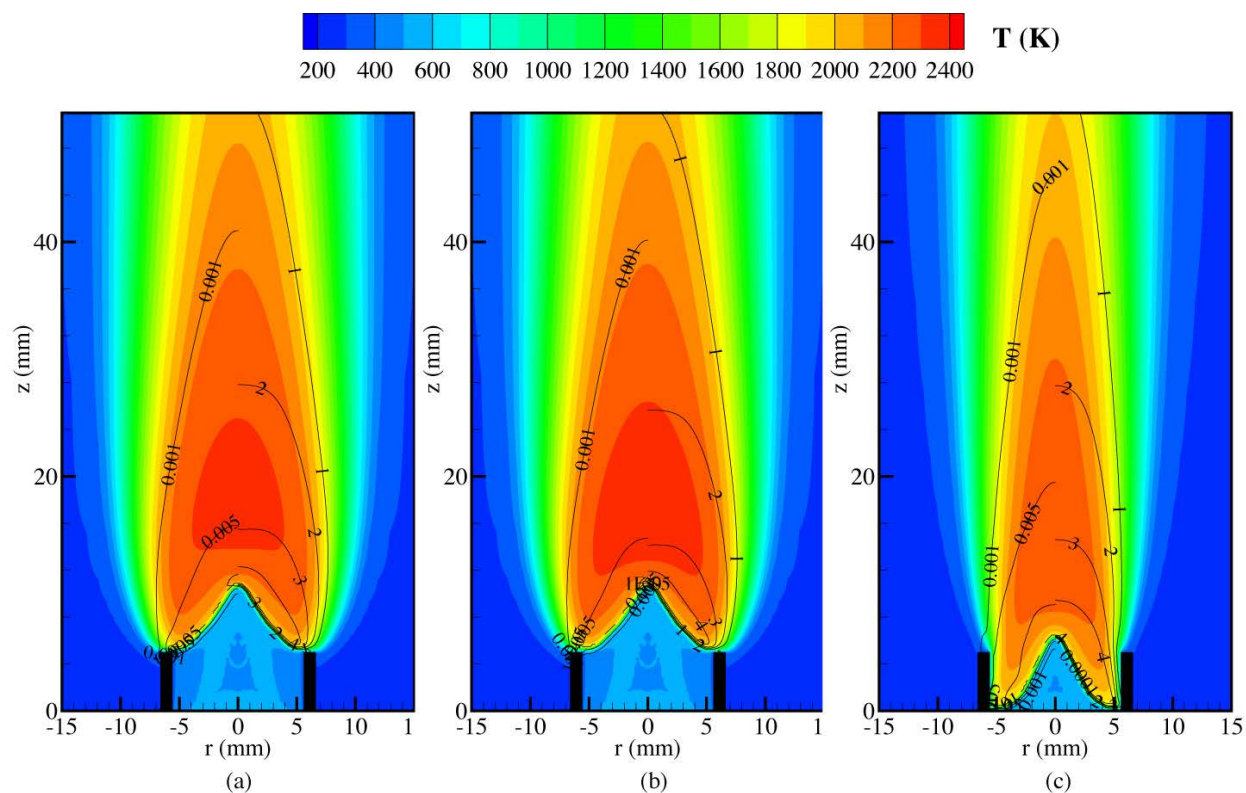


Fig. 9. Structure of stoichiometric JP-8 premixed flame predicted using (a) Violi-Small, (b) Violi-Large, and (c) Zhang mechanisms. Iso contours of MCH (dashes) and H₂ (solid) are superimposed on temperature distribution on the left half and iso contours of benzene (dashes) and OH (solid) are superimposed on the right half.

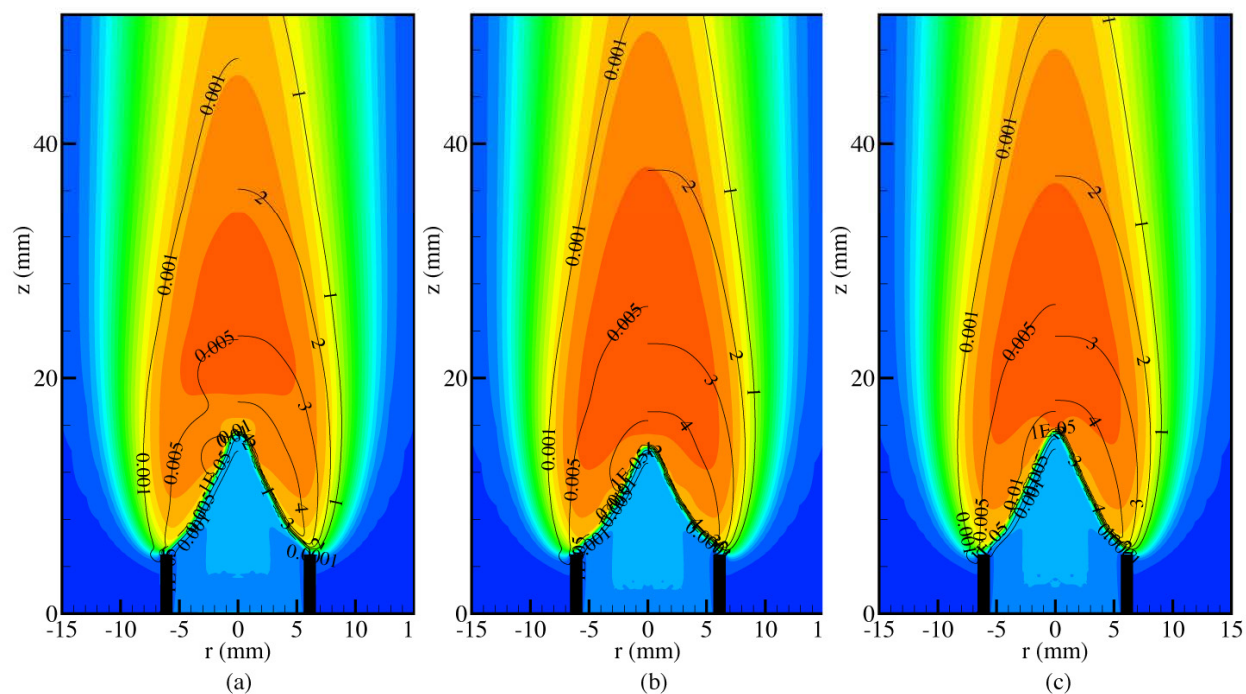


Fig. 10. Structure of stoichiometric JP-8 premixed flame predicted using Mawid mechanism with (a) surrogate-1, (b) surrogate-2, and (c) surrogate-3 mixtures. Iso contours of MCH (dashes) and H₂ (solid) are superimposed on temperature distribution on the left half and iso contours of benzene (dashes) and OH (solid) are superimposed on the right half.

Numerical Studies on Soot Mitigation in a Model Gas-Turbine Combustor

Viswanath R. Katta* and Terrence R. Meyer
Innovative Scientific Solutions, Inc.
2766 Indian Ripple Road
Dayton, OH 45440-3638

Christopher J. Montgomery
Reaction Engineering International
77 West 200 South, Suite 210
Salt Lake City, UT 84101

William M. Roquemore
Propulsion Directorate
Air Force Research Laboratory
Wright-Patterson Air Force Base, OH 45433

A time-dependent, detailed-chemistry, computational-fluid-dynamics (CFD) model is developed for the evaluation of the performance of a soot-reducing additive in a model swirl-stabilized combustor. While commercial JP-8 fuel was used in the experiments, a 6-component surrogate mixture was used in the calculations for mimicking the JP-8-fuel combustion. Di-tertiary-butyle-peroxide (DTBP) additive, which is known for improving the ignition characteristics of hydrocarbon fuels, was tested for its ability in reducing the soot. Detailed chemical kinetics were used for the simulation of JP-8+DTBP combustion and the consequent formation of PAH species. Calculations were made for different equivalence ratios obtained through varying the fuel jet velocity while keeping the airflow unaltered. Turbulent-flow simulations with the base JP-8 fuel revealed that significant amount of soot is formed for fuel-rich conditions while no or negligible soot is formed for equivalence ratios less than 0.8. Addition of DTBP for the fuel-rich operating conditions resulted in only a marginal decrease in the amount of soot formed. Its effect on fuel-lean operation of the combustor is also found to be negligible. However, DTBP seems to be more effective in reducing the soot when the combustor is operating in the neighborhood of stoichiometric conditions. Consistent with these results, calculations made for a simple jet diffusion flame also revealed that DTBP has no effect on soot formation when it was added to the fuel jet.

I. Introduction

SWIRLING jets are commonly used in gas-turbine engines to achieve compact, stable, and efficient combustion. The flowfield in the primary zone of a swirl combustor is characterized by recirculation zones with high shear stresses and turbulent intensities that result in vortex breakdown and motion of large-scale flow structures.^{1,2} These unsteady fluid elements and recirculation zones can significantly increase the formation of pollutants such as carbon monoxide (CO), nitric oxide (NO), unburned hydrocarbons (UHC), and soot.³⁻⁵ However, the mechanisms that lead to enhanced pollutants formation in swirl-stabilized, liquid-fueled combustors are not fully understood. Previous experimental investigations have relied on exhaust-gas measurements and parametric studies to gain insight into the effects of various input conditions on soot loading.⁶⁻¹⁰ Much of the fundamental knowledge concerning soot formation is derived from theoretical investigations of laminar diffusion flames,^{11,12} with only a limited number of studies being focused on turbulence effects.^{13,14} The importance of considering unsteadiness and fluid-flame interactions was demonstrated by Shaddix et al.,¹⁴ who found that a forced unsteady methane/air diffusion flame

* Corresponding Author, vrkatta@erinet.com

produced a four-fold increase in soot volume fraction (as a result of increased particle size) as compared with a steady flame having the same mean fuel-flow velocity. Recent calculations of Katta et al.¹⁵ have suggested that presence of large-scale structures in dynamic flames could influence the way polycyclic-aromatic-hydrocarbon (PAH) species are formed and; thereby, could impact the amount of soot produced.

A quick control on the soot produced by the liquid-fueled combustors can be achieved through the use of additives. Properly designed additives suppress soot emissions via two paths: destruction of soot particles previously formed, or prevention of inception reactions. The latter offers a potential order of magnitude soot reduction; hence it is desirable to develop and tailor jet fuel formulations to mitigate particulate formation. The di-tertbutyl peroxide (DTBP) has been shown experimentally to alter both gas-phase combustion¹⁶ and soot production. Drop-tube¹⁷ experimental results indicated that adding DTBP to the fuel could reduce the amount of soot produced. The goal of the current investigation is to simulate and understand the effects of DTBP on soot formation in the highly dynamic environment of a modeled swirl-stabilized, liquid-fueled combustor.

Various attempts have been made in the past to develop models for soot predictions. Some of these models are detailed, and have been calibrated against experimental data obtained in laminar, premixed or diffusion flames of simple configurations. For example, Frenklach and coworkers¹⁸ proposed a detailed kinetic model of soot formation and validated^{18,19} using measurements of laminar, premixed flames while Mauss, Bockhorn and their coworkers^{20,21} established a different detailed soot model that was tested in laminar, counter-flow diffusion flames. The detailed kinetics based soot model consists of 1) gas-phase chemistry and 2) kinetics describing the particle growth and destruction processes. The gas-phase chemistry describes the formation of PAHs.^{22,23} The particle growth and destruction involve inception/ nucleation of particles resulting from coagulation of PAHs and are modeled via a set of surface reactions,¹⁸⁻²¹ and particle coagulation is modeled based on the method of moments¹⁸⁻²¹ or the discrete-sectional method.^{24,25}

The complexity and the uncertainties associated with the detailed kinetic soot models made their application limited to simple laminar flames. On the other hand, for the simulation of turbulent combustor flows, a variety of simplified soot models that can be easily implemented into design codes have been proposed.²⁶ The most widely used models are based on the assumption that soot consists of particles with mono-disperse size distribution. Then the soot formation, coupled directly to the fuel concentration, is modeled by one or two equations: one for the particle volume fraction and the other for the particle number density.

Leung et al.²⁷ argued that the intermediate species contributing to the soot particle formation should be connected to at least the pyrolysis kinetics of the fuel. For simplicity, they assumed acetylene to be the intermediate species and proposed a simplified soot model combined with the gas-phase kinetics of fuel pyrolysis for counterflow, ethylene and propane flames²⁷ as well as coflow, methane flames.²⁸ The results showed that with this approach good agreement with measured data for soot volume fraction, particle growth and number density could be obtained. In the present work, a model similar to that of Leung et al.²⁷ is used for the prediction of soot formation in swirl-stabilized combustors fueled with JP-8 fuel. Detailed chemical kinetics for JP-8 fuel and DTBP additive and the two-step soot model are incorporated into a well-tested CFD code UNICORN. Numerical results obtained for combusting flows with different equivalence ratios and additive concentrations are compared.

II. Mathematical Model

A time-dependent, axisymmetric mathematical model known as UNICORN (Unsteady Ignition and Combustion using ReactionNs)^{29,30} is used for simulating the turbulent combusting flows in the model swirl combustor. It solves for u- and v-momentum equations, continuity, and enthalpy- and species-conservation equations on a staggered-grid system. A clustered mesh system is employed to trace the large gradients in flow variables near the flame surface. A detailed chemical-kinetics model of Violi et al.³¹ is incorporated into UNICORN for the investigation of soot formation in JP-8 flames. It consists of 161 species and 1538 reaction steps. For the investigation of the effects of adding DTBP a detailed chemical-kinetics model developed by Bozzelli³² is also incorporated.

The O-O bond in DTBP is weak, with bond energy of about 43.5 kcal/mol. At high temperatures, DTBP dissociates quickly to form two tertiary butoxy radicals, which, in turn, form acetone and CH₃ radical. Acetone decomposes at high temperatures to form two methyl radicals and CO or will react with the radical pool or O₂ to form an acetonyl radical. Further reactions of the acetonyl radical produce additional methyl radicals, O, and OH. DTBP may also react with the radical pool or O₂ to form hydrocarbon peroxide radicals. Further reactions of these radicals release energy and produce methyl, O, and OH radicals through chain-branching processes. All these processes are represented via elementary reaction steps within the DTBP chemical-kinetics mechanism, which consists of 95 species in addition to those used in the JP-8 mechanism and 724 additional reactions. Thus, DTBP can speedup ignition via exothermically enhancing the radical pool. The enhanced radical pool can also decrease soot production by speeding oxidation of soot precursor species and of the soot particles themselves. Decreasing the

ignition time may increase or decrease soot production depending on the system.

DTBP additive is added to the JP-8 fuel jet of the swirl combustor in small proportions. JP-8 fuel is considered as a surrogate mixture of 30% (by volume) n-dodecane ($n\text{-C}_{12}\text{H}_{26}$), 20% n-tetradecane ($n\text{-C}_{14}\text{H}_{30}$), 10% of iso-octane ($\text{I-C}_8\text{H}_{18}$), 20% of methylcyclohexane MCH (C_7H_{14}), 5% of tetralin ($\text{C}_{10}\text{H}_{12}$), and 15% of m-xylene (C_8H_{10}). Thermo-physical properties such as enthalpy, viscosity, thermal conductivity, and binary molecular diffusion of all the species are calculated from the polynomial curve fits developed for the temperature range 300 - 5000 K. Mixture viscosity and thermal conductivity are then estimated using the Wilke and Kee expressions, respectively. Molecular diffusion is assumed to be of the binary-diffusion type, and the diffusion velocity of a species is calculated using Fick's law and the effective-diffusion coefficient of that species in the mixture. Turbulence is modeled using k- ϵ approach. A simple radiation model based on the optically thin-media assumption is incorporated into the energy equation for treating radiation heat loss from gaseous species.³³ Only CH_4 , CO , CO_2 , and H_2O are considered as radiating species in the present study. Heat losses from soot particles are computed assuming blackbody radiation from the carbonaceous soot particles.³⁴

The finite-difference forms of the momentum equations are obtained using an implicit QUICKEST scheme,³⁵ and those of the species, energy, k and ϵ equations are obtained using a hybrid scheme of upwind and central differencing. At every time step, the pressure field is accurately calculated by solving all the pressure Poisson equations simultaneously and using the LU (Lower and Upper diagonal) matrix-decomposition technique. The boundary conditions are treated in the same way as that reported in earlier papers.³⁶

Soot Model:

Computational soot models based on the fundamental physics of soot formation and oxidation are not yet available. The research groups around Moss and Lindstedt have made some progress in modeling soot formation using semiempirical models based on the mechanisms of particle inception, agglomeration, surface growth, and oxidation. Both the groups utilized two equation models with transport equations for particle number density, N_s , and soot mass fraction, Y_s . These equations can be written for unsteady flow as

$$\frac{\partial \rho N_s}{\partial t} + \nabla \cdot (\rho \mathbf{V} N_s) - \nabla \cdot (\rho D_{N_s} \nabla N_s) = \omega_{N_s} \quad (1)$$

$$\frac{\partial \rho Y_s}{\partial t} + \nabla \cdot (\rho \mathbf{V} Y_s) - \nabla \cdot (\rho D_s \nabla Y_s) = \omega_s \quad (2)$$

where \mathbf{V} is the velocity vector, ρ is density, D is the molecular diffusion coefficient, and ω is the production term from chemical reactions. The two source terms in Eqs. 1 and 2 are obtained using Lindstedt's model,³⁶ which is based on the simplifying assumption that nucleation and growth are first-order functions of acetylene concentrations. Soot oxidation was considered primarily due to the presence of O_2 and OH . Finally, soot agglomeration was treated as a source term in Eq. 2.

The simulations presented here are performed on AMD Opteron Personal Computer with 2.0 GB of memory. Typical execution time is ~50 s/time-step for the swirl-stabilized-combustor simulations. Steady state solutions are typically obtained in about 20,000 time steps starting from the solution obtained using the global combustion chemistry model.

III. Results and Discussion

A. Studies on Jet Diffusion Flames

The CFD model UNICORN has been extensively validated in the past by simulating various steady and unsteady counterflow^{29,38} and coflow^{29,39} jet diffusion flames and by comparing the results with the experimental data. This gives confidence that UNICORN can simulate the structure of dynamic flames accurately. However, the integration of JP-8 chemistry (with and without DTBP kinetics) into UNICORN needs to be validated to establish the accuracy of the present predictions. For this purpose a number of calculations were performed for simple jet diffusion flames for which qualitative understanding has been established.

The flame chosen is a pure diffusion flame formed between gaseous JP-8 fuel and air. The velocity of the fuel injected from a 1.0-mm diameter tube at room temperature is 0.2 m/s, while that of the annulus air is fixed at 0.05 m/s. DTBP additive is added to the fuel jet by replacing the equal amount of JP-8 such that the exit velocity of the

fuel jet is not altered. Axisymmetric calculations for this jet diffusion flame are performed for various concentrations of DTBP on a non-uniform grid system of 151x71.

Results obtained for the base flame (without adding any DTBP) are shown in Fig. 1. The iso-temperature plot in Fig. 1(a) suggests that significant preheating of fuel prior to entering into the flame zone is taking place. Flame, in general, is burning intensely in the shoulder region with a significantly cooled flame tip. The peak temperature is about 2000 K. Distribution of the soot formed in this flame is shown in Fig. 1(b). As expected, significant amount of soot is produced at the flame tip, which gradually burned off in the downstream locations.

Variations of temperature and soot volume fraction along the centerline ($r = 0$) at different heights for several concentrations of DTBP are shown in Fig. 2(a). Note, the temperature at the flame tip is only about 1500 K and the peak soot concentration is located slightly downstream of the flame tip. Radiation from soot and preferential heat transport due to non-unity Lewis numbers are causing this drop in flame temperature at the tip from 2000 K. Addition of DTBP has only marginal effects on the diffusion flame. In general, temperature is increasing and soot is decreasing with the addition of DTBP, however, these changes became pronounced only for DTBP concentration of 30%. At this high concentration of DTBP soot in the exhaust gases has been reduced by $\sim 50\%$ even though the peak value hasn't changed much. It should be recalled that this additive is known for reducing the ignition delay time and its effects on soot reduction are unknown. As expected, ignition along the centerline in the jet diffusion flame is enhanced with the addition of DTBP while the final temperature in the exhaust remained nearly the same.

Decomposition of DTBP and production of benzene along the centerline are shown in Fig. 2(b). Most of the added additive is consumed in the preheating region of the fuel (i.e., $T < 1000$ K) prior to the formation of benzene. Figure 2(b) further suggests that the peak concentration of benzene is decreasing with the addition of DTBP, which means that the soot reduction observed with this additive is occurring through a decrease in formation rate rather than through increase in soot destruction rate.

B. Studies Swirl-Stabilized-Combustor

The near-field structure of swirl-stabilized flames is highly dependent upon the characteristics of the fuel injector and the geometry of the surrounding flame tube. The injector configuration used in the modeled swirl-stabilized combustor is a generic swirl-cup liquid-fuel injector studied at the Atmospheric Pressure Combustor Research Complex of the Air Force Research Laboratory's Propulsion Directorate.⁴⁰ It employs pressure atomization and dual-radial, counter-swirling co-flows of air to entrain the fuel, promote droplet break-up, and enhance mixing. The model gas-turbine combustor contains a swirl cup, flame tube and exhaust nozzle and the details of the combustor are provided in the Refs. 40 and 41. The 40-mm-exit-diameter swirl cup is installed at the entrance of a 15.25 cm \times 15.25 cm square-cross-section flame tube. After exiting the primary flame zone, the combustion products are allowed to mix thoroughly along the 48-cm long flame tube before entering a 43-cm-long, 5.7-cm exit-diameter exhaust nozzle that is designed to create a uniform exhaust-gas temperature and concentration profiles.

Axisymmetric mathematical model for the swirl-stabilized combustor is constructed using a 17.2-cm diameter, 48-cm long chimney and with thin tubes separating the fuel and air flows at the combustor entrance. Gaseous JP-8 fuel along with DTBP additive is injected at the center while the two outer air jets are forced into the combustor with counter swirling motions. The computational domain was discretized using a non-uniform grid system of 251x126.

Calculations for the swirl-stabilized combustor are made for different equivalence ratios and additive concentrations. It was found that the effectiveness of DTBP in highly fuel-rich conditions is very limited. However, as the equivalence ratio is decreased the effectiveness of DTBP also increased. Results for a marginally fuel-rich condition ($\phi = 1.15$) are shown in Fig. 3. Temperature distributions inside the combustor are plotted in Figs. 3(a) and 3(b) for no additive case and 5% DTBP case, respectively. The nozzle geometry incorporated in the model is also shown in these figures. Gaseous JP-8 (or JP-8+DTBP) is injected from a 4-mm hole at the center with an axial velocity of 40 m/s and swirl angle of 70° . Such high swirl angle for the fuel jet was used in order for representing the cone angle of the liquid spray. Fuel jet is immediately surrounded with a 2-mm-thick wall and then a high-speed air jet with axial velocity of 100 m/s and a swirl angle of -30° . A second air jet of 100 m/s is issued through the 5 mm annulus gap between the nozzle walls at a velocity of 100 m/s and at a swirl angle of 45° . The velocity of the fuel jet was changed for achieving different equivalence-ratio conditions.

The swirling air jets merge and expand radially as they propagate downstream. Such radial expansion of high momentum air jets created two torroidal recirculation regions—one in the corner and the other one at the center. Typically, flames can establish along either or both of these recirculation zones.⁴² The temperature field in Fig. 3(a) suggests that the corner recirculation zone has become the hottest region for this fuel-rich case. Flame is anchored between the air jets and the corner recirculation zone and no flame was established between the air jets and the central recirculation zone.⁴² This was more evident in the OH plot (not shown here).

Addition of 5% DTBP has not changed the temperature significantly. Figure 3(b) indicates a slight increase in temperature in the region where the air jets are impinging the combustor wall ($z \sim 11$ cm). Soot produced in the combustor with and without DTBP is shown in Figs. 3(c) and 3(d). Significant amount of soot is generated under these fuel-rich operating conditions. Even though some soot is found in the corner recirculation zones, most of it is actually generated in the central recirculation zone and carried into the former. Significant soot growth has occurred in the region downstream of the central recirculation zone ($z > 25$ cm).

A comparison of soot distributions obtained with and without DTBP [Figs. 3(c) and 3(d)] suggests that 5% addition of DTBP has significantly reduced the soot levels. In fact, reduction in soot is evident in all regions of the combustor. Such soot reduction was not observed either in the jet diffusion flames or in the combustor flows under high ϕ conditions.

Distributions of temperature and various species along the centerline are shown in Figs. 4(a) and 4(b) for different amounts of DTBP. Similar to the results obtained for a jet diffusion flame (Fig. 2) addition of DTBP has also increased the centerline temperature in the swirl-stabilized combustor. However, DTBP seems to be more effective in the combustor than in jet diffusion flame. The low concentrations of OH along the centerline suggest that flame is not established. Interestingly, acetylene concentration has increased in certain regions and decreased in other; whereas, soot was reduced everywhere.

The mass integrated soot and various species at different axial locations are shown in Figs. 5(a) and 5(b). With the addition of 5% DTBP soot mass has decreased by $\sim 23\%$ at $z = 30$ cm. On the other hand, further increase in DTBP did not cause much reduction in soot. Similarly, PAH species such as benzene and Phenol have also decreased with the addition of DTBP.

Effect of adding 5% DTBP to swirl-stabilized combustor operating under stoichiometric ($\phi = 1.0$) conditions is shown in Fig. 6. Fuel jet velocity used for this condition was 30 m/s. Temperature distributions obtained with and without DTBP are shown in Figs. 6(a) and 6(b), respectively. Significant amounts of combustion products are entrained into the corner recirculation zone, which, in turn, are supporting the flame. Addition of DTBP increased the temperature in both the recirculation regions. Soot formed under stoichiometric conditions is shown in Fig. 6(c) without the addition of DTBP and in Fig. 6(d) with the addition of 5% DTBP. Significant reduction in soot was obtained in this case.

Distributions of temperature and species concentrations along the centerline are shown in Figs. 7(a) and 7(b). Temperature of the central recirculation zone has increased by ~ 150 K with the addition of 5% DTBP. More significantly, another flame has established at the upstream tip of the central recirculation zone as evident in OH profile. This suggests that DTBP additive is improving ignition in the swirl-stabilized combustor. Average mass fractions of soot and other species at several cross sections along the combustor length are plotted in Figs. 8(a) and 8(b). Soot mass under stoichiometric conditions has decreased by $\sim 70\%$ with the addition of 5% DTBP. Interestingly, benzene and phenol PAHs have not changed much with the addition of DTBP. This is, in part, due to the rapid burn-off of these species in high-temperature combustion products in the central recirculation zone.

IV. Summary

A time-dependent, axisymmetric, detailed-chemistry CFD model was developed for the evaluation of the performance of di-tertiary-butyl-peroxide (DTBP) as soot reducing additive in a model swirl-stabilized combustor. Combustion chemistry and PAHs formation associated with JP-8+DTBP fuel are simulated using the 256-species, 2262-reactions mechanism of Violi et al³¹ and Bozzelli³². Soot formation is modeled using a two-variable approach and turbulence is modeled using k and ϵ equations. The CFD code (UNICORN) was tested through the simulation of a laminar jet diffusion flame for different fuel jet velocities. The swirl-stabilized combustor with a square chimney was modeled as an axisymmetric combustor. Several calculations were made by varying the equivalence ratio (by changing the fuel flow) and for various concentrations of DTBP additive.

DTBP additive was found to be ineffective in changing sooting characteristics of a jet diffusion flame. However, only a slight reduction in soot was observed when DTBP was added at 30% level. The high swirl used for the fuel and air jets in the swirl-stabilized combustor expanded the air jets rapidly and created corner and central recirculation zones. In general, addition of DTBP to the swirl-stabilized combustor increased the recirculation-zone temperatures. For slightly fuel-rich case ($\phi = 1.15$) flame was stabilized in between the air jets and the corner recirculation zone. Addition of 5% DTBP to this fuel-rich combustor flow reduced the soot by 23%. On the other hand, addition of 5% DTBP to the combustor operating at stoichiometric conditions reduced the soot by 70%. DTBP also caused the flame to establish between the air jets and the central recirculation zone. DTBP additive was found to improve ignition characteristics of a model gas-turbine combustor and, simultaneously, to reduce the soot formation. However, its effectiveness in reducing soot has decreased with equivalence ratio for fuel-rich operating conditions.

Acknowledgments

Financial support for this work was provided by the Air Force Office of Scientific Research (AFOSR, Julian Tishkoff), the Air Force Contracts #F33615-00-C-2329 (Vince Belovich) and #F33615-03-C-2338 (Edwin Corporan).

References

1. Kim, W.-W., Menon, S., and Mongia, H. (1999), "Large-eddy simulation of a gas turbine combustor flow," *Combust. Sci. Technol.* 143:25-62.
2. Wang, S., Hsieh, S.-Y., and Yang, V., "Numerical simulation of gas turbine swirl-stabilized injector dynamics," AIAA paper 2001-0334, 2001.
3. Heitor, M. V., and Whitelaw, J. H. (1986), "Velocity, Temperature, and Species Characteristics of the Flow in a Gas-Turbine Combustor," *Combust. Flame* 64:1-32.
4. Bicen, A. F., Tse, D. G. N., and Whitelaw, J. H. (1990), "Combustion characteristics of a model can-type combustor," *Combust. Flame* 80:111-125.
5. Held, T. J., Mueller, M. A., Li, S.-C., and Mongia, H., "Data-driven model for NO_x, CO and UHC emissions for a dry low emissions gas turbine combustor," AIAA paper 2001-3425, 2001.
6. Eckerle, W. A., "Soot loading in a generic gas turbine combustor," AIAA paper 87-0297, 1987.
7. Fang, T. C., Megaridis, C. M., Sowa, W. A., and Samuelsen, G. S. (1998), "Soot morphology in a liquid-fueled swirl-stabilized combustor," *Combust. Flame* 112:312-328.
8. Snelling, D. R., Thomson, K. A., Smallwood, G. J., and Gulder, O. L. (1999), "Two-dimensional imaging of soot volume fraction in laminar diffusion flames," *Appl. Opt.* 38:2478-1485.
9. Black, J. D. (1999), "Laser induced incandescence measurements of particles in aero-engine exhausts," EUROPTO Conference on Environmental Sensing and Applications, Munich, Germany, pp. 209-215.
10. Jenkins, T. P., Bartholomew, J. L., DeBarber, P. A., Yang, P., Seitzman, J. M., and Howard, R. P., "A laser-induced incandescence system for measuring soot flux in aircraft engine exhausts," AIAA paper 2002-3736, 2002.
11. Santoro, R. J., Yeh, T. T., Horvath, J. J., and Semerjian, H. G. (1987), "The transport and growth of soot particles in laminar diffusion flames," *Combust. Sci. Technol.* 53:89-115.
12. Urban, D. L., and Faeth, G. M., "Soot research in combustion science: introduction and review of current work," AIAA paper 2001-0322, 2001.
13. Won, Y.-H., Kamimoto, T., Kobayashi, H., and Kosaka, H., "2-D soot visualization in unsteady spray flame by means of laser sheet scattering technique," SAE Tech. Paper 910223, 1991.
14. Shaddix, C. R., Harrington, J. E., and Smyth, K. C. (1994), "Quantitative Measurements of Enhanced Soot Production in a Flickering Methane / Air Diffusion Flame," *Combust. Flame* 99:723-732.
15. Katta, V. R., Blevins, G. L., and Roquemore, W. M., *Combustion and Flame*, Vol. 142, 2005, pp. 33-51.
16. Mack, J. H., Dibble, R. W., Buchholz, B. A., and Flowers, D. L., "The Effect of the Di-Tertiary Butyl Peroxide (DTBP) Additive on HCCI Combustion of Fuel Blends of Ethanol and Diethyl Ether," SAE Technical paper 2005-01-2135, (2005).
17. Kobayashi, H., Howard, J. B., and Sarofim, A. F., "Coal Devolatilization at High Temperatures," *Sixteenth Symposium (International) on Combustion*, The Combustion Institute, Pittsburgh, pp. 411-425.
18. Frenklach, M. and Wang, H., *Twenty-third Symposium (International) on Combustion*, The Combustion Institute, Pittsburgh, 1991, pp.1559-1566.
19. Frenklach, M. and Wang, H., in *Soot Formation in Combustion: Mechanisms and Models* (H. Bockhorn, Ed.), Springer-Verlag, Heidelberg, 1994, pp.165-189.
20. Mauss, F., Schäfer, T. and Bockhorn, H., *Combust. Flame* 99:697-705 (1994).
21. Mauss, F. and Bockhorn, H., *Z. Phys. Chem.* 188:45 (1995).
22. Haynes, B.S. and Wagner, H. GG., *Prog. Energy Combust. Sci.* 7:229-273 (1981).
23. Calcote, H.F., *Combust. Flame* 42:215-242 (1981).
24. Colket, M.B. and Hall, R.J., in *Soot Formation in Combustion: Mechanisms and Models* (H. Bockhorn, Ed.), Springer-Verlag, Heidelberg, 1994, pp.442-468.
25. Hall, R.J., Smooke, M.D. and Colket, M.B., in *Physical and Chemical Aspects of Combustion: A Tribute to Irvin Glassman* (F.L. Dryer and R.F. Sawyer, Eds.), Gordon and Breach, Amsterdam, 1997, pp.189-230.
26. Hiroyasu, H., Kadota, T. and Arai, M., *Bulletin of the JSME* 26:569-575 (1983).
27. Leung, K.M., Lindstedt, R.P. and Jones, W.P., *Combust. Flame* 87:289-305 (1991).

28. Lindstedt, R.P., in *Soot Formation in Combustion: Mechanisms and Models* (H. Bockhorn, Ed.), Springer-Verlag, Heidelberg, 1994, pp.417-439.
29. Roquemore W. M., and Katta, V. R., *Journal of Visualization*, 2 (2000) 257-272.
30. Katta, V. R., and Roquemore, W. M., *Combustion and Flame*, Vol. 100, No. 1, 1995, p. 61.
31. Violi, A., Yan, S., Eddings, E. G., Sarofim, A. F., Gratata, S., Faravelli, T., and Ranzi, E., "Experimental Formulation and Kinetic Model for JP-8 Surrogate Mixtures," *Combustion Science and Technology*, 174:339-417, 2002..
32. Bozzeli, J., Private communications, 2005.
33. Annon., Computational Submodels, International Workshop on Measurement and Computation of Turbulent Nonpremixed Flames., <http://www.ca.sandia.gov/TNF/Workshop/radiation.html>, (2001).
34. Guo, H., Liu, F., Smallwood, G. J., *Combustion Theory and Modeling*, Vol. 8, 2004, pp. 475-489.
35. Katta, V. R., Goss, L. P., and Roquemore, W. M., *AIAA Journal*, Vol. 32, No. 1, 1994, p. 84.
36. Katta, V. R., Goss, L. P., and Roquemore, W. M., *Int. J. Num. Methods Heat Fluid Flow*, Vol. 4, No. 5, 1994, p. 413.
37. Lindstedt, P. R., in *Soot Formation in Combustion* (H. Bockhorn, Ed.), Springer Verlag, Heidelberg, 1994, p. 417.
38. Katta, V. R., Carter, C. D., Fiechtner, G. J., Roquemore, W. M., Gord, J. R., and Rolon, J. C., in *Twenty-seventh Symposium (International) on Combustion*, The Combustion Institute, Pittsburgh, PA, 1998, p. 98.
39. Katta, V. R., and Roquemore W. M., *AIAA Journal*, Vol. 36, No. 11, 1998, p. 2044.
40. Roy, S., Meyer, T. R., Lucht, R. P., Belovich, V. M., Corporan, E., and Gord, J. R., "Temperature and CO₂ concentration measurements in the exhaust stream of liquid-fueled combustor using dual-pump coherent anti-Stokes Raman scattering (CARS) spectroscopy," submitted for publication in *Combust. Flame*, 2003.
41. Meyer, T. R., Roy, S., Gogineni, S. P., Belovich, V. M., Corporan, E., and Gord, J. R., "OH-PLIF and Soot Volume Fraction Imaging in the Reaction Zone of a Liquid-Fueled Gas-Turbine Combustor", Proceedings of ASME Turbo Expo 2004, Paper No. GT2004-54318.
42. Katta, V. R., Meyer, T. R., Montgomery, C., and Roquemore, W. M., "Studies on Soot Formation in a Model Gas-Turbine Combustor," AIAA Paper 2005-3777, 41st AIAA/ASME/SAE/ASEE Joint Propulsion Conference and Exhibit, Tucson, AZ, July 10-13, 2005.

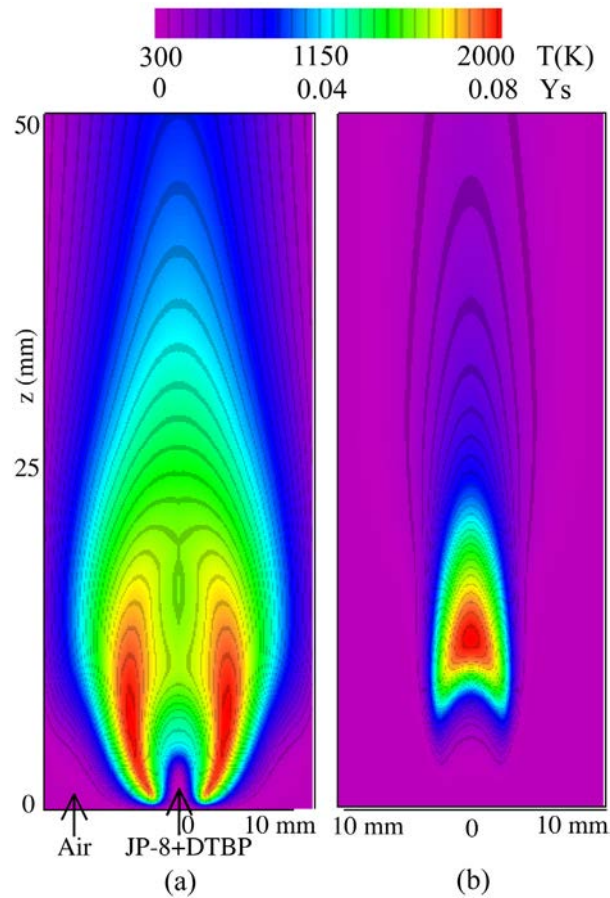


Fig. 1. Jet diffusion flame used for the investigation of additive effects on soot formation. (a) Temperature, and (b) soot-mass-fraction distributions of the base flame.

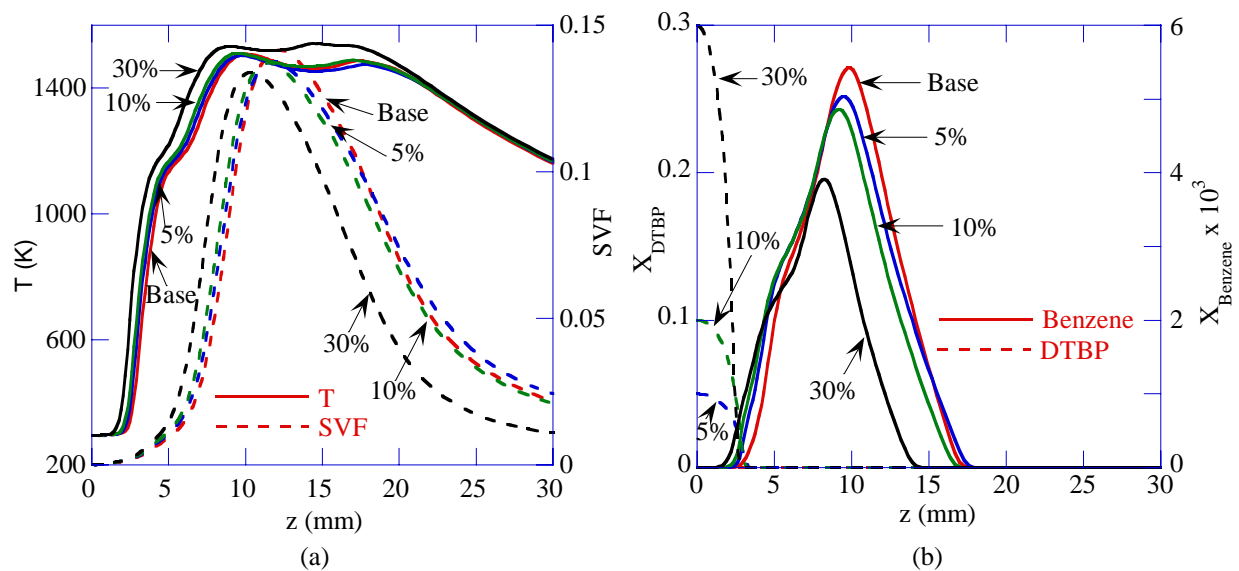


Fig. 2. (a) Distributions of temperature and soot volume fraction and (b) consumption of DTBP and production of benzene along the centerline of the jet diffusion flame for different concentrations of DTBP.

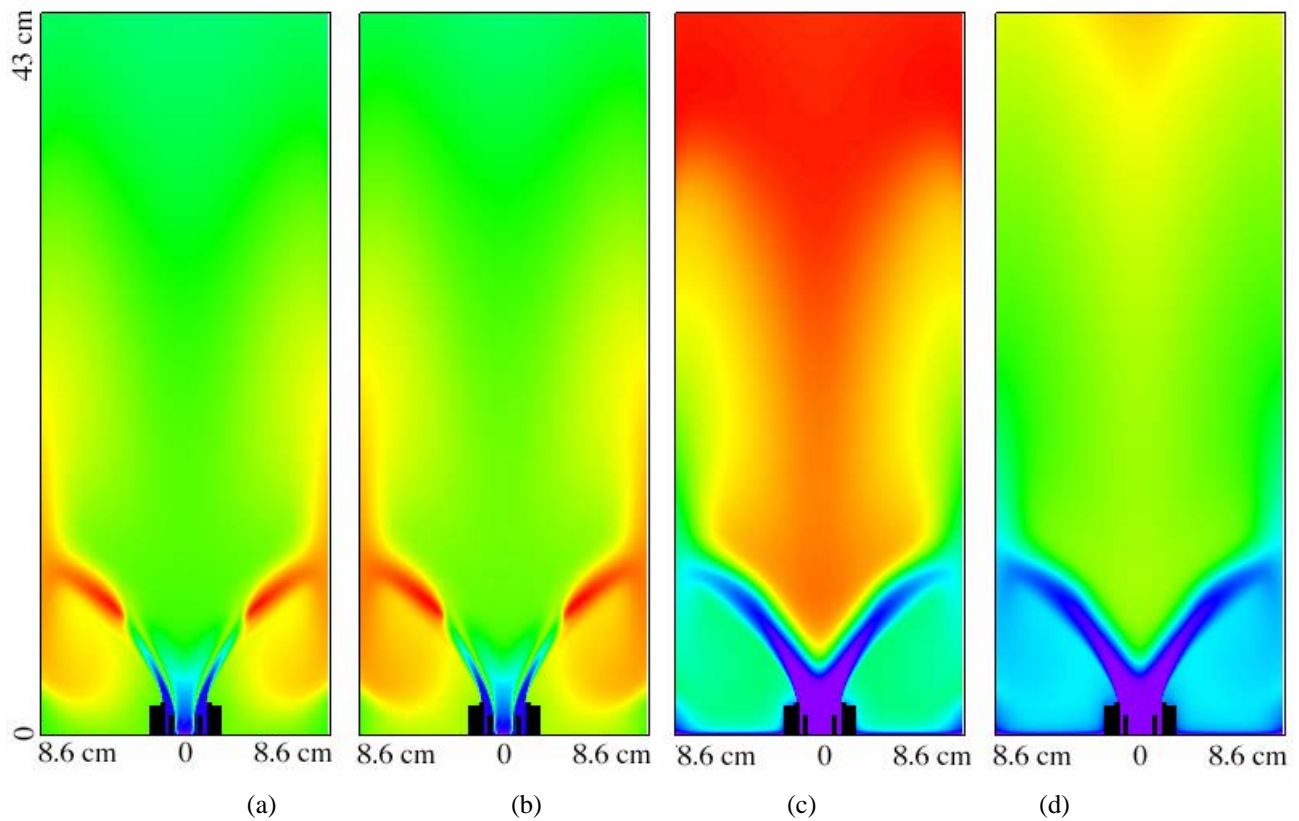


Fig. 3. Effect of DTBP in swirl-stabilized combustor operating at $\phi = 1.15$. Distributions of (a) temperature and (c) soot mass fraction when no additive was added; (b) and (d) are those when 5% DTBP was added.

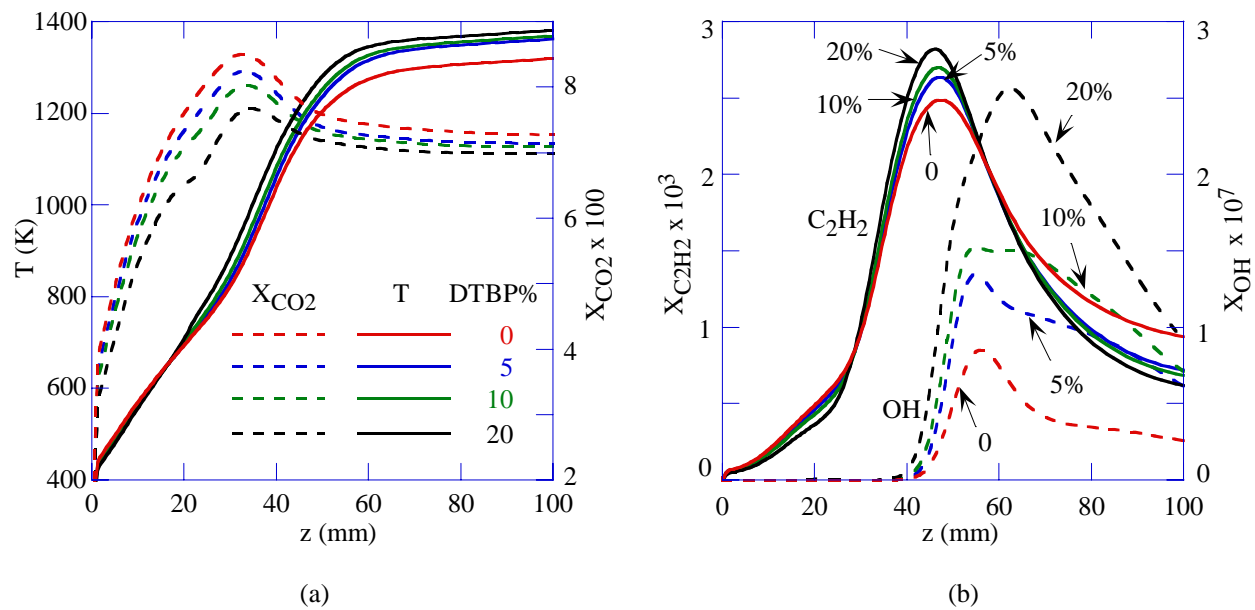


Fig. 4. Distributions of temperature and species concentrations along the centerline for various amounts of DTBP added to the fuel jet. $\phi = 1.15$

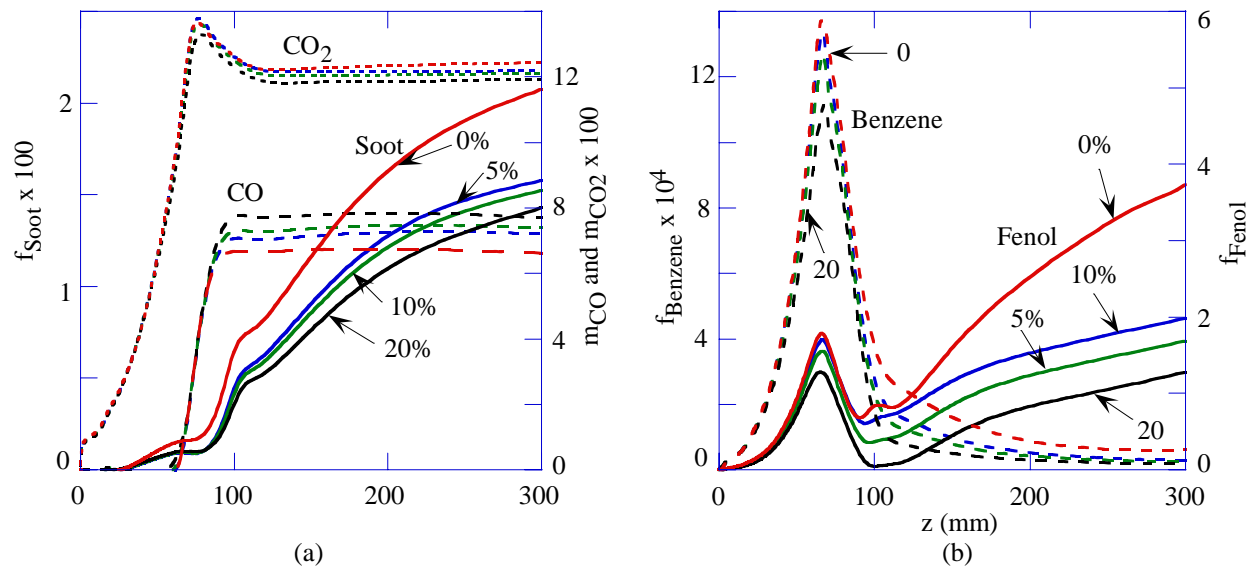


Fig. 5. Net mass fractions of soot and other species at different axial locations for various amounts of DTBP added to the fuel jet. $\phi = 1.15$.

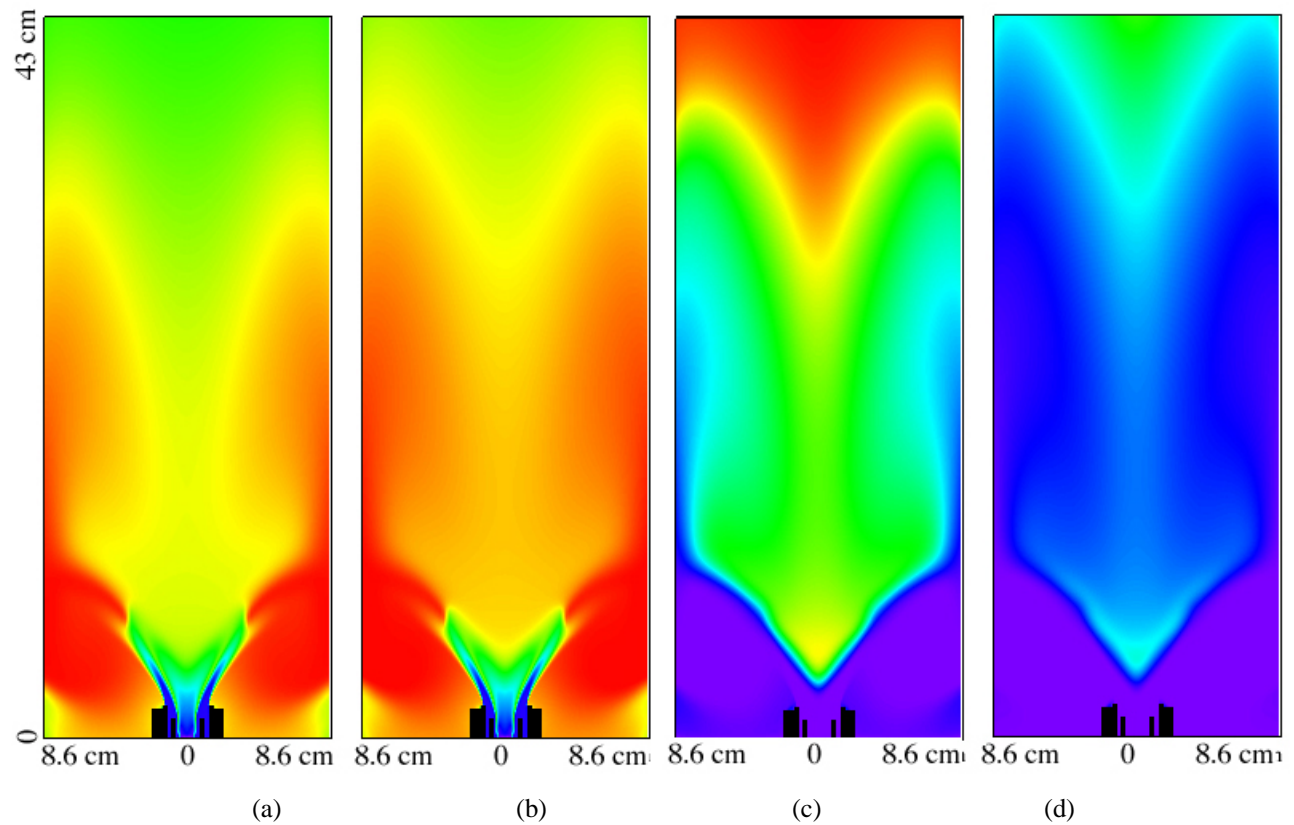


Fig. 6. Effect of DTBP in swirl-stabilized combustor operating at $\phi = 1.00$. Distributions of (a) temperature and (c) soot mass fraction when no additive was added; (b) and (d) are those when 5% DTBP was added.

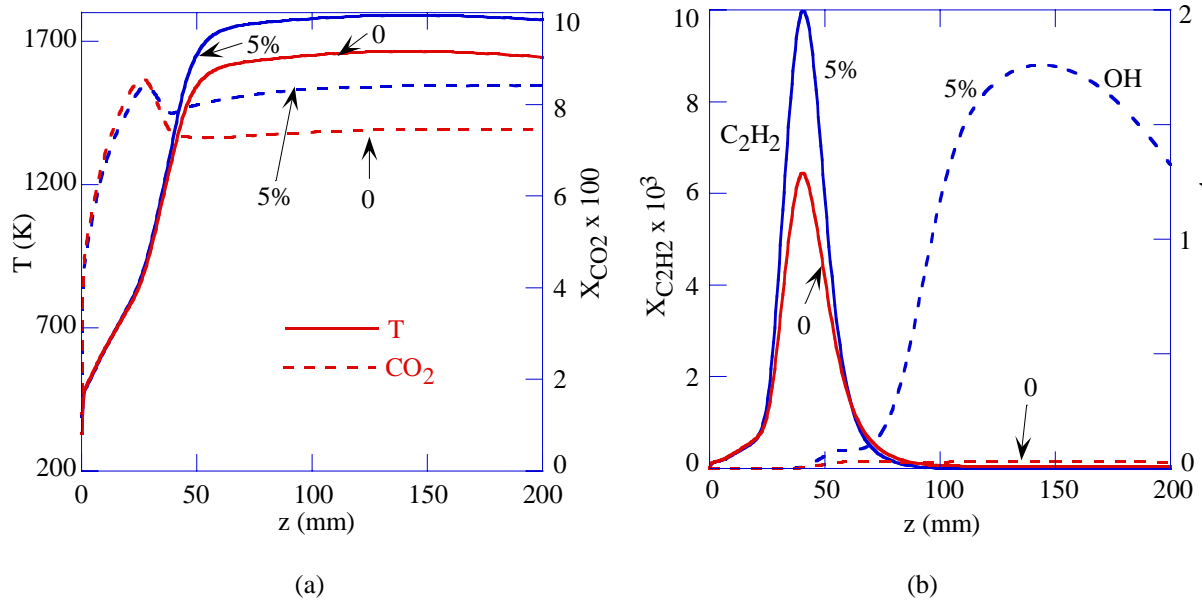


Fig. 7. Distributions of temperature and species concentrations along the centerline for various amounts of DTBP added to the fuel jet. $\phi = 1.0$

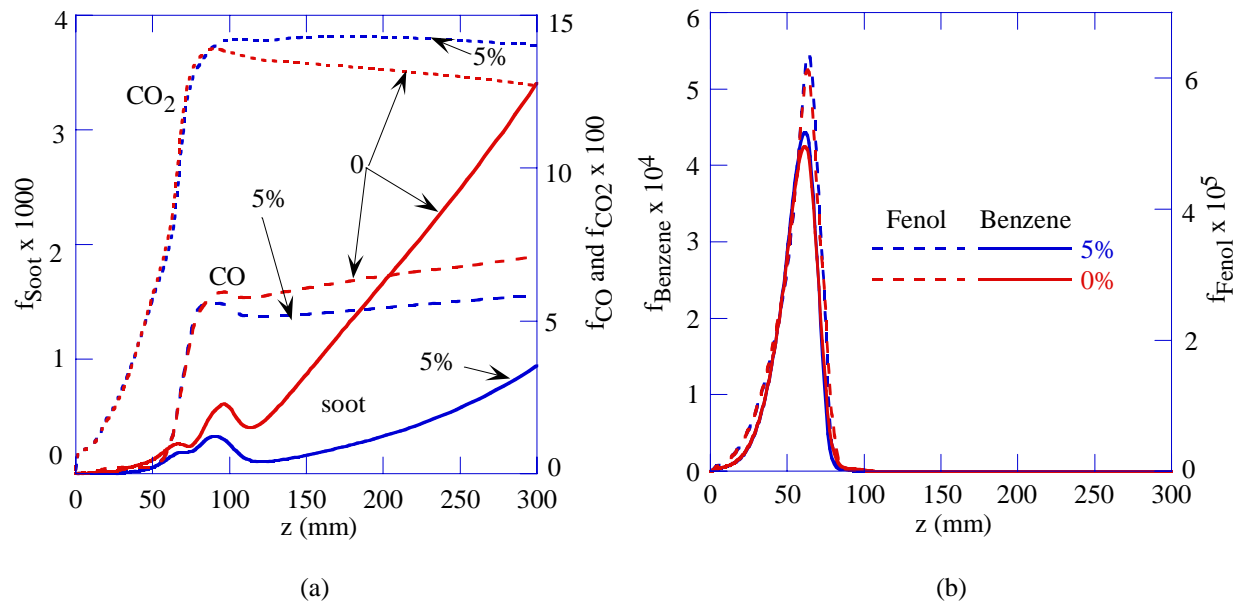


Fig. 8. Net mass fractions of soot and other species at different axial locations for various amounts of DTBP added to the fuel jet. $\phi = 1.0$

Numerical Study of Evolution of Strongly Forced Axisymmetric Laminar Cold-Flow Jets

V. V. Barve,* O. A. Ezekoye,† and N. T. Clemens‡
University of Texas at Austin, Austin, Texas 78712

and

V. R. Katta§
Innovative Scientific Solutions, Inc., Dayton, Ohio 45440-3638

Periodic jet forcing presents interesting opportunities for jet mixing for a variety of applications. In this work, simulations are performed to study the effect of high-amplitude forcing on laminar jets ($Re = 100$) with net mass flux. For the cases presented in this work, we look at the effects of simulating the internal nozzle and show that assumptions about the nozzle flow have a large effect on the downstream flow evolution. Studies are performed on strongly forced axisymmetric jets in two geometries: 1) jets issuing perpendicularly from a flat wall and 2) jets issuing from a straight tube (nozzle). The amplitude and frequency of the forcing function are varied to study vortex creation and subsequent evolution downstream of the jet. For example, cases in which the peak jet velocity is three to four times the mean jet velocity are examined. The near-nozzle region was of particular interest due to the strong mixing processes occurring there. We discuss how nozzle flow processes modify the creation of downstream large-scale vortical structures. An interesting result of this work is that the strongest forcing cases possess some striking similarities to synthetic jets. For such cases, the flow reversal processes at the jet exit plane are investigated.

Nomenclature

A	=	amplitude of forcing
D	=	nozzle diameter
f	=	frequency of forcing
g	=	gravitational acceleration
Q	=	volumetric flow rate across cross section at distance x downstream of nozzle
Q_e	=	volumetric flow rate across nozzle exit
Re	=	Reynolds number, $U_0 D / \nu$
r	=	radial distance
Sr	=	Strouhal number, $f D / U_{\max}$
U_{\max}	=	maximum axial velocity (occurs at 25% phase)
U_0	=	time-averaged axial velocity
X	=	axial distance at which velocity oscillations are less 5% of time-averaged velocity
x	=	axial distance
ν	=	kinematic viscosity
ρ	=	density

I. Introduction

JET mixing is improved in laminar flows by unsteady forcing. The ability to increase the mixing rate for laminar flows is important in the development of mesoscale reactors of various types. In some small-scale (laminar) combustion reactors, acoustically excited and pulsed-flow flames have been shown to have significantly different characteristics in terms of flame length and luminosity when compared to nonpulsed flames. Forced jets have been stud-

ied in the literature for their ability to modify the flowfield and increase the jet entrainment rates. Significantly more work has been performed in the analysis of turbulent pulsed jets as compared to laminar jets because of the obvious technological applications of turbulent jets. However, with increased miniaturization of reactors of all types, the requirement for mixing in small-scale and laminar flows becomes more of an issue.^{1,2} In addition, there may be similarities between turbulent and laminar unsteadily forced jets, and insights from one flow regime may aid in interpretation of observations in another regime. As such, we will review some of the more relevant turbulent unsteadily forced literature in this paper. The seminal work by Crow and Champagne³ showed that jet forcing increased the entrainment rates for turbulent jets. They also found a preferred excitation mode at $Sr = 0.3$; note that their Strouhal number is based on the mean jet exit velocity and forcing frequency. Hill and Greene⁴ and Vermuelen et al.⁵ have also reported increased mixing rates and entrainment with periodically forced jets.

Marzouk et al.⁶ performed simulations on weakly forced laminar jets. (The amplitude was less than 20% of the mean velocity.) The jet velocity profiles revealed that the effects of the forcing were restricted to the core of the jet. Also, they observed that the extent of the area affected by the forcing depended on the forcing frequency.

The forcing amplitudes used in all of the aforementioned cases did not fully modulate the flow, that is, the forcing amplitude was always less than 100%, and so there was no flow reversal at the nozzle exit. Increasing the forcing amplitude to the point where the flow is fully modulated allows for much more interesting flow dynamics. In reacting systems, such as that in the work of Shaddix et al.,⁷ where a laminar reacting jet was periodically/acoustically forced, significant changes occurred in the flame characteristics. Later, particle image velocimetry (PIV) data for the same experimental conditions were acquired by Papadopoulos et al.,⁸ and they showed that during certain phases, negative velocities are present in the near-nozzle region for moderately and strongly forced flames. This indicated that the fluid was being sucked back into the nozzle. Also, shadowgraphs indicated a strong mixing of the cool and hot regions due to the forcing. In other work, Muramatsu and Era⁹ studied the mixing of pulsed CO₂ gas issuing from a round nozzle into still air. Velocity and concentration measurements revealed a phase lag between concentration and velocity, with the concentration changing after the velocity. Also, the mixing of gases was greatly enhanced near the nozzle exit and the mass fraction of the CO₂ at the nozzle exit

Received 1 June 2005; revision received 21 October 2005; accepted for publication 29 December 2005. Copyright © 2006 by the American Institute of Aeronautics and Astronautics, Inc. All rights reserved. Copies of this paper may be made for personal or internal use, on condition that the copier pay the \$10.00 per-copy fee to the Copyright Clearance Center, Inc., 222 Rosewood Drive, Danvers, MA 01923; include the code 0001-1452/06 \$10.00 in correspondence with the CCC.

*Graduate Research Assistant, Department of Mechanical Engineering.

†Professor, Department of Mechanical Engineering; dezekoye@mail.utexas.edu.

‡Professor, Department of Aerospace Engineering. Associate Fellow AIAA.

§Senior Engineer, 2766 Indian Ripple Road. Associate Member AIAA.

was found to be lower than unity, indicating that air from the surroundings was being ingested into the nozzle during parts of the cycle.

It can be argued that synthetic jets, jets with zero net mass flux, can be considered to be a limiting case of strongly forced periodic jets, where the forcing amplitude is infinitely larger than the mean velocity. The flowfield developed by synthetic jets has been discussed in detail in the literature by Smith and Glezer,¹⁰ Cater and Soria,¹¹ and Glezer and Amitay.¹² Cater and Soria¹¹ commented that synthetic jets are a special case of fully pulsed jets where the mean velocity of the jet is zero due to the pulsing action. They found that turbulent synthetic jets have similar cross-stream velocity profiles as steady jets, but with different spreading and decay rates. Direct numerical simulation studies by Rizzetta et al.¹³ and Lee and Goldstein¹⁴ of the synthetic jets used in the experiments of Smith and Glezer¹⁰ provided further insight into the flowfield development of slot jets. Rizzetta et al.¹³ presented two- and three-dimensional computational results. They simulated the oscillating membrane by applying a moving boundary condition and found that the flow in the cavity becomes periodic after several cycles. As a result, periodic velocity profiles could be used as the boundary condition at the slot exit to simulate the forcing action. The two-dimensional calculations by Lee and Goldstein¹⁴ showed that the Reynolds number affected the slot exit flow profile, whereas the Strouhal number affected the jet evolution downstream of the slot. Bera et al.¹⁵ used PIV to examine both pulsed jets, that is, strongly forced jets with net mass flux, and synthetic jets under identical forcing conditions and found that the synthetic jets have more lateral expansion than the pulsed jets.

In this study, two exit flow conditions are examined in terms of their influence on forced laminar jet evolution. We study forced laminar wall jets (issuing perpendicular to the wall) with top-hat exit velocity profiles and with fully developed velocity profiles. We also examine a jet flow issuing from a nozzle, that is, a straight tube five diameters in length, embedded in the computational domain. For both types of problems, the forcing frequency and the forcing amplitude are varied to examine their effects on jet evolution.

II. Numerical Scheme

A finite volume computational fluid dynamics (CFD) code, UNICORN, was used for the computations. This code solves the two-dimensional axisymmetric form of the unsteady conservation of momentum and conservation of mass equations using a staggered grid, where velocities take face values and where pressure and den-

sity are cell centered,

$$\frac{\partial \rho}{\partial t} + \nabla \cdot (\rho \mathbf{V}) = 0 \quad (1)$$

$$\rho \frac{\partial \mathbf{V}}{\partial t} + \rho \mathbf{V} \cdot \nabla \mathbf{V} = -\nabla P + \rho \mathbf{g} - \nabla \cdot \bar{\tau} \quad (2)$$

The implicit form of the QUICKEST scheme is used for discretization of the momentum equation, and the pressure projection method is used to close the pressure/mass conservation relationship. The finite difference scheme is third-order accurate in space and third-order accurate in time. Katta et al.¹⁶ provide further details about the numerical schemes and the individual terms in the discretized form of the continuity and momentum equations. The time-step size in the calculations is limited by the Courant–Friedrichs–Lewy condition, viz.,

$$u(\Delta t / \Delta x) \leq 1 \quad (3)$$

The iterative alternate direction implicit scheme is used to solve the momentum equations. The iterations are stopped once the values of the velocity components converge to a small value:

$$(\varphi^n - \varphi^{n-1}) / \varphi^{n-1} \leq 10^{-5} \quad \text{or} \quad \varphi^n - \varphi^{n-1} \leq 10^{-5} \quad (4)$$

where φ is the velocity component.

The pressure Poisson equation is set up based on the continuity equation and is solved directly using the lower–upper decomposition method.

Two physical situations (domains) were modeled in this study. The first one, shown in Fig. 1a, involves a wall jet in which the computational domain is stretched to 12 cm in the radial direction and 40 cm in the axial direction. A nonuniform grid, with 410 points in the axial direction and 224 points in the radial direction, was used. The grid lines were clustered in the shear-layer region near the jet exit and varied in size from 0.01 to 0.4 cm axially and from 0.01 to 0.17 cm radially. Outflow (zero-gradient) boundary conditions are applied at the right side and top boundaries, whereas symmetry boundary conditions are applied along the centerline. The bottom side incorporates the wall jet; an inlet velocity boundary condition is specified over the radial extent of 0.5 cm, and the wall boundary condition covers the remainder of the boundary.

The second domain (Fig. 1b) is an extension of the first domain to explore the effects of a nozzle. Once again the diameter of the jet is kept at 1 cm, but the nozzle extends 5 cm into the domain. The

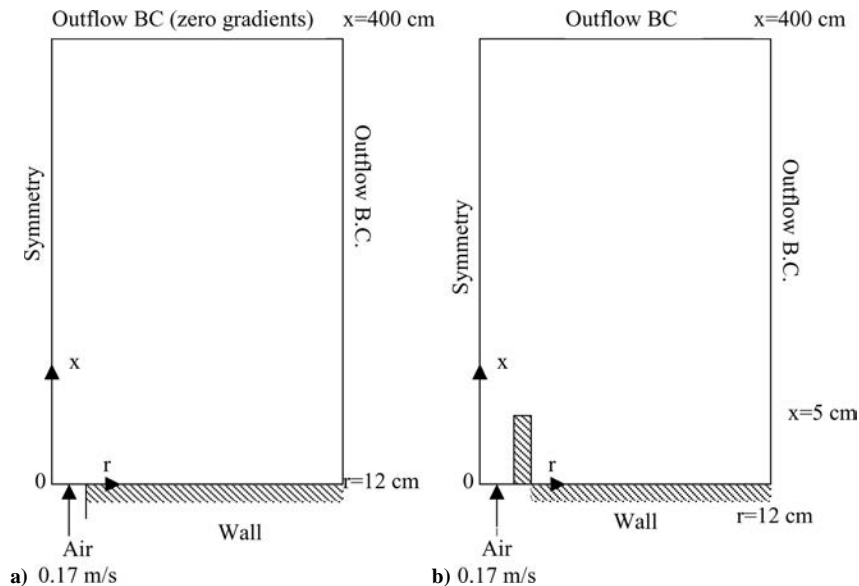


Fig. 1 Schematic of computational domain (not to scale): a) computational domain of wall jet and b) domain for nozzle jet.⁵⁴⁹

Table 1 Different conditions (amplitude and frequency) and geometries examined

Geometry	U_0	$Re(U_0 D/\nu)$	A , %	f , Hz	Sr (fD/U_{\max})
Wall jet	0.17	100	200	2.5	0.049
Wall jet	0.17	100	200	5	0.098
Wall jet	0.17	100	200	10	0.196
Wall jet	0.17	100	200	16	0.314
Wall jet	0.17	100	200	50	0.98
Wall jet	0.17	100	200	100	1.961
Wall jet	0.17	100	200	200	3.922
Wall jet	0.17	100	200	500	9.804
Wall jet	0.17	100	300	5	0.074
Wall jet	0.17	100	300	50	0.735
Wall jet	0.17	100	300	100	1.471
Wall jet	0.17	100	300	200	2.941
Wall jet	0.17	100	300	500	7.353
Wall jet	0.17	100	1000	50	0.267
Wall jet	0.51	300	200	50	0.327
Wall jet	0.51	300	200	500	3.268
Wall jet	0.51	300	300	500	2.451
Wall jet	0.34 (FD) ^a	100	200	5	0.049
Wall jet	0.34 (FD)	100	200	50	0.49
Wall jet	0.34 (FD)	100	200	500	4.902
Nozzle	0.17	100	200	5	0.098
Nozzle	0.17	100	200	50	0.98
Nozzle	0.17	100	200	500	9.804

^aFD indicates fully developed velocity profile, with the peak velocity being listed. All other cases have top-hat velocity profile.

nozzle wall thickness was 0.1 cm. The domain extends 400 cm from the nozzle tip in the axial direction and 12 cm from the centerline in the radial direction. Once again, outflow boundary conditions are applied to the top and left side boundaries and a symmetry boundary condition was applied at the centerline. In this case, the jet velocity at the bottom of the nozzle was described.

A steady-state jet was simulated to benchmark the code and the numerical scheme. This involved an air jet issuing out into quiescent surroundings (air). This steady-state jet solution then served as the initial condition for the forced jets. For all of the simulations, properties of air at 300 K and 1 atm were used. The baseline case is a steady jet with a top-hat velocity profile of magnitude 17 cm/s. The diameter of the jet was 1 cm and the Reynolds number, $Re = U_0 D/\nu$, was 100. U_0 is the jet exit axial velocity and D is the jet diameter. The forcing cases involved using a velocity function of the form $u = U_0[1 + A \sin(2\pi ft)]$. This function gives a period-averaged velocity of U_0 . Based on the amplitude of forcing, there are two regimes for forced jets, the low forcing regime, which has amplitudes less than or equal to 100%, $A < 1$, and the high forcing regime, with amplitudes greater than 100%, $A \geq 1$, and for which flow reversal occurs. One expects the high-amplitude forcing to produce effects quite different than those with low forcing. For the forcing cases the simulations were terminated once time-periodic solutions were obtained.

Table 1 lists the different cases examined in this study. The nondimensional frequency is the Strouhal number, which is defined as $Sr = fD/U_{\max}$, where f is the forcing frequency and U_{\max} is the peak velocity along the centerline at the jet exit.

III. Results

A. Low-Amplitude Forcing

The normalized axial velocity profile for the benchmark steady jet is shown in Fig. 2. Although not shown in Fig. 2, the results are similar to those obtained in a similar computational study by Pai and Hsieh.¹⁷ The axial velocity scales as x^{-1} in the far-field region as suggested by Schlichting.¹⁸ The Schlichting solution, adjusted for the point source of momentum as suggested by Andrade and Tsien,¹⁹ is also shown in Fig. 2.

In Fig. 2 the normalized axial velocity profile for a case identical to that performed by Marzouk et al.⁶ is included. The Marzouk et al. case is a low-amplitude forcing problem, $A = 10\%$, with $Sr = 0.273$ and the 25% phase shown. This particular phase has the maximum

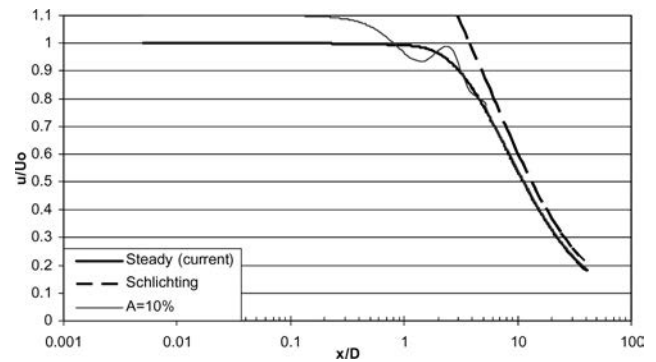


Fig. 2 Validation of centerline velocity, u/U_0 , with axial distance, x/D , for steady jets and low-amplitude forcing laminar jets; current steady jet data, $Re = 100$, are compared with analytical solution given by Schlichting,¹⁸ and the low-amplitude forcing case, $A = 10\%$, matches data from Marzouk et al.⁶

jet exit velocity of all of the phases. Consistent with the results by Marzouk et al.,⁶ the forcing effects on the axial velocity along the centerline seem to disappear beyond a distance of 8–10 diameters downstream of the orifice, and beyond this downstream distance the profile matches that of the steady-state case. The varying velocity field along the centerline indicates the presence of vortical structures being created at the jet orifice. The decay of the oscillations in the velocity profile indicates that the forcing seems to affect only the jet near-field region and that, farther downstream, the oscillations are attenuated.

B. High-Amplitude Forcing

1. Wall Jets (Without Nozzle)

With higher-amplitude forcing, one expects that the structures generated at the jet entrance plane would get larger and stronger. To examine this, computations with 200 and 300% forcing amplitude over a range of frequencies were performed. Figure 3 shows contour plots of the vorticity field along with the velocity vectors for a steady jet and for five different phases for the forced jet at 200% amplitude forcing and 5 Hz frequency ($Sr = 0.098$). In the steady jet (top left) the vorticity peaks near the orifice (orifice radius of 5 mm) due to the large velocity gradient at the jet exit plane associated with the top-hat profile. As expected, farther downstream, the vorticity magnitudes are reduced as the vorticity diffuses radially outward. For the forced jet, as we move sequentially over the forcing time period, the vorticity field reveals that vortices are being shed off of the orifice edge. The sequence shows the generation of vortices at the orifice edge, followed by their ejection from the near-orifice region and their subsequent convection downstream. This sequence suggests that this case exhibits similarities to an impulsively started jet because the vortices grow in size with downstream distance and convect downstream without interacting with each other. The sequence for a high-frequency forcing case, $f = 50$ Hz and $Sr = 0.98$, at the same amplitude, $A = 200\%$, is shown in Fig. 4. Here too the vortices are ejected from the orifice edge; however, these vortices are not entirely convected downstream. It appears that some parts of the structures are instead pulled back into the orifice. This is in contrast to the low forcing frequency case shown in Fig. 3 where the vortices are convected downstream.

Figure 5a shows the centerline axial velocities normalized by the average exit velocity at five phases for a forcing amplitude $A = 200\%$ and frequency $f = 5$ Hz, corresponding to $Sr = 0.098$. The normalized time-averaged centerline axial velocity profile along the centerline has also been plotted. As expected, the increased forcing amplitude transmits the forcing effects farther downstream as compared to the low-amplitude forcing case (Fig. 2). The normalized time-averaged centerline velocity is larger than unity, over almost 20 diameters ($20D$) downstream, suggesting that the jet volumetric flow rate is larger than that of the steady jet (Fig. 2). Figure 5b shows the same plot for a case with 200% amplitude forcing, but at a higher forcing frequency of $f = 50$ Hz corresponding to $Sr = 1$. This forcing frequency is 10 times the forcing frequency of the

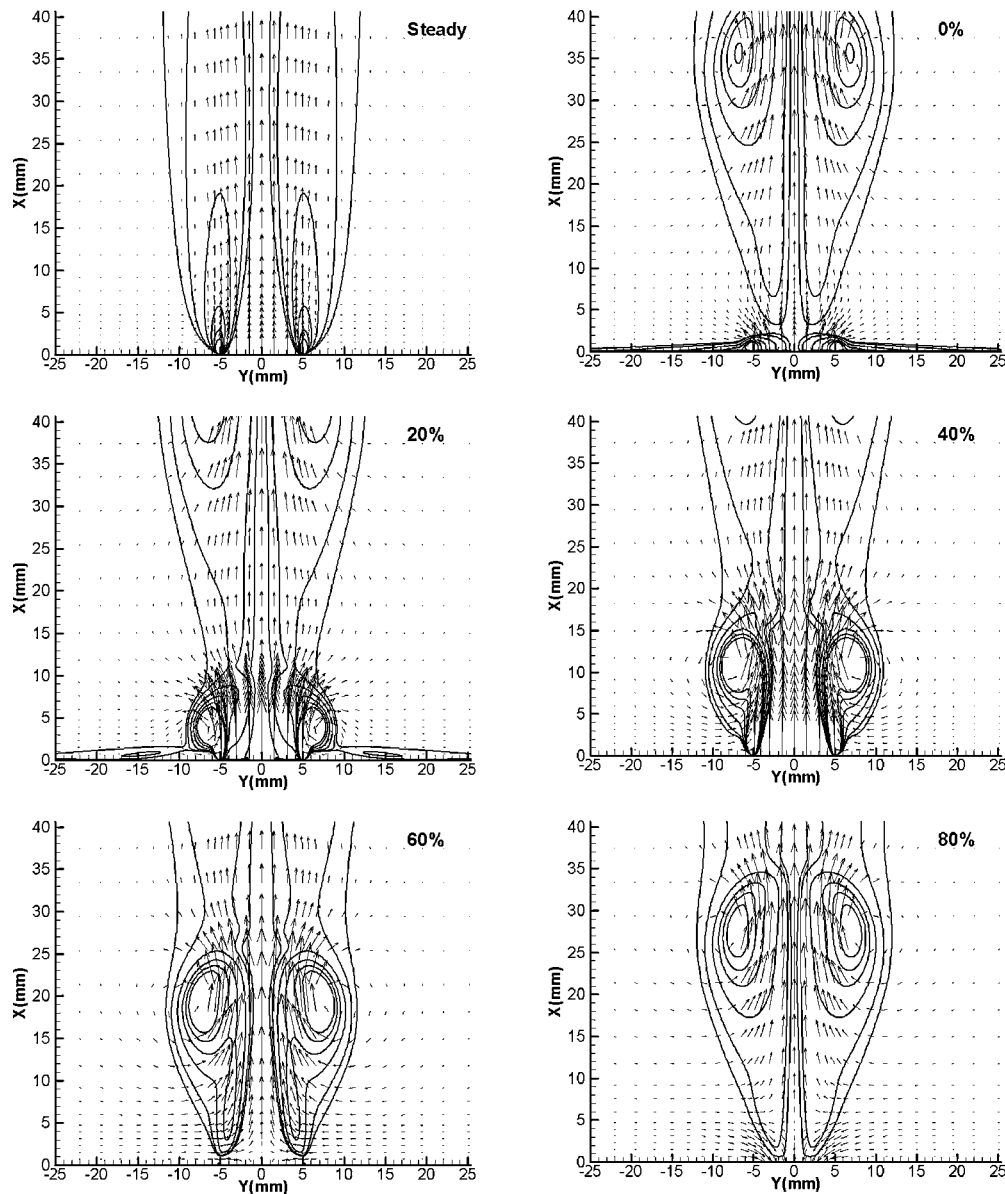


Fig. 3 Vorticity contour plots and instantaneous velocity field for case with forcing amplitude 200% at 5 Hz, $Sr = 0.098$; steady case and five different phases, 0, 20, 40, 60, and 80%, are shown.

case in Fig. 5a, and the increase in frequency affects the region of oscillating flow quite dramatically and shrinks this region closer to the orifice plane. The distance over which the normalized time-averaged centerline axial velocity exceeds unity is slightly smaller (approximately $10D$ downstream) than the low-frequency case, and the peak value of the normalized time-averaged centerline velocity with $Sr = 1$ is higher than that with $Sr = 0.1$. Also, from Figs. 5a and 5b, one can see a region near the orifice plane where the axial velocities are negative. This region is larger for the low-frequency case ($\sim 0.4D$ – $0.5D$) than for the high-frequency case ($\sim 0.2D$). Careful viewing of the velocity field time sequences shows that the region in the flowfield where the axial velocity is zero, that is, where the axial velocity changes from negative to positive, is a stagnation point separating a region close to the orifice plane, over which the flow reversal effects dominate the flowfield, and another region away from the orifice over which the flow reversal does not effectively control the flowfield. The velocity vectors in Fig. 3 at the 60 and 80% phase clearly show a stagnation point near the nozzle. This stagnation point is only seen during certain phases (60 and 80% phase) and is created and destroyed over the forcing period. This effect was examined over a range of frequencies (effectively Strouhal number) with

a forcing amplitude of 200%. As the forcing frequency increased, the distance over which flow reversal was observed to be reduced. This trend indicates that the forcing frequency appears to be a key factor in the evolution of the velocity field.

On changing the forcing amplitude to 300%, the same trends were observed. An increase in frequency led to a reduction of the region over which the forcing effects were observed. Figure 6 shows the results for the time-averaged centerline axial velocities (normalized by the corresponding peak time averaged centerline velocity), for 300% amplitude forcing and at three different forcing frequencies: 5, 50, and 500 Hz (corresponding to $Sr = 0.074$, 0.74, and 7.4). We normalize by U_{max} so that we can fit the normalized values in the range from 0 to 1 and compare the different forcing frequency cases. The steady-state profile has also been plotted for comparison. The low-frequency case starts to decay much farther downstream than the steady-state case or the high-frequency forcing cases. Also, the high-frequency forcing cases decay with downstream distance, almost like the steady-state jet. This observation again reinforces the notion that the high frequencies seem to localize the effects of the forcing in the near-orifice region, whereas in the far field the jet behaves similar to a steady jet.

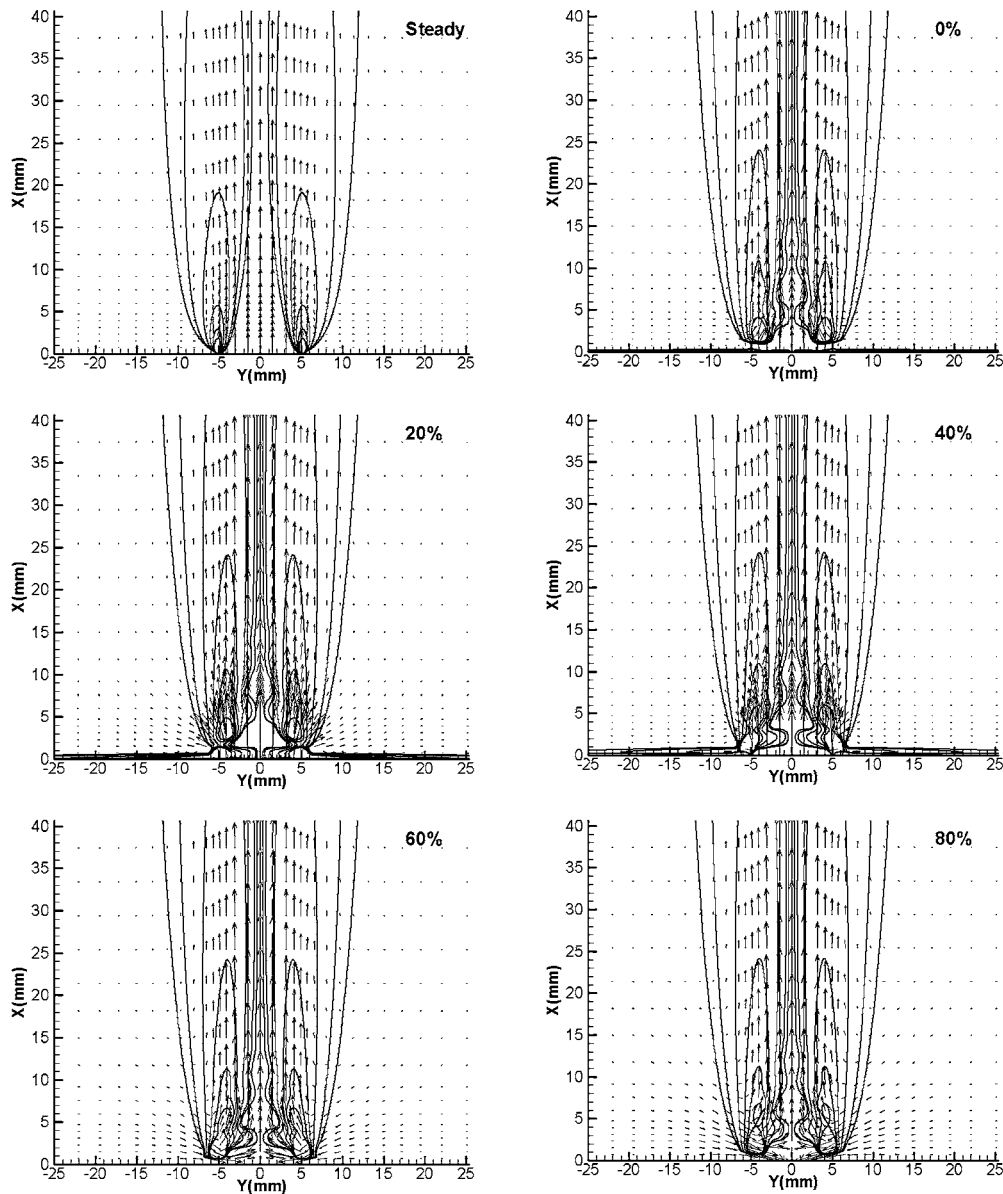


Fig. 4 Vorticity contour plots and instantaneous velocity field for case with forcing amplitude 200% at 50 Hz, $Sr=0.98$; steady case and five different phases, 0, 20, 40, 60, and 80%, are shown.

Figure 7 shows the time-averaged normalized centerline axial velocity as a function of downstream distance. The profiles have been normalized by their peak values. Figure 7a shows the case of 200 and 300% forcing at a 5-Hz forcing frequency, $Sr = 0.098$ and 0.074 , respectively. As expected, the effects of the higher-amplitude forcing, 300%, are felt farther downstream as compared to the low-amplitude forcing at this 5-Hz forcing frequency. For the same forcing amplitudes at a higher frequency, $f = 500$ Hz, no such difference is observed (Fig. 7b), suggesting that differences between 300 and 200% forcing are negligible for high-frequency forcing. Also, at this high frequency, the forced jets decay in a similar manner as the steady jet, even though the normalizing parameter U_{\max} for the two amplitudes and the steady case is different.

In the 200% forcing cases discussed earlier (Figs. 3 and 4), the only difference between the two cases is the forcing frequency. With high-frequency forcing, although the vortices are being generated, they do not seem to have sufficient time to escape the near-field region that exhibits reverse flow. A comparison of the timescales for vortex generation and vortex convection helps us to explain these characteristics. The vortices are generated essentially over the first half of the forcing cycle, giving a vortex generation timescale of $T/2$

[or $1/(2f)$]. The timescale of the convection of the vortices can be thought of as L^*/V^* , where L^* is length of the near-nozzle region that the vortex needs to escape with a characteristic velocity V^* . From Figs. 5a and 5b, along the centerline, the negative velocities are observed over less than $0.5D$. Taking $0.5D$ as the length scale L^* and the peak velocity at the jet exit, U_{\max} , as velocity scale V^* gives a vortex convection timescale of $D/2U_{\max}$. U_{\max} appears to be the best choice for the velocity scale because the vortices are shed at the instant at which the velocity peaks. After this peak, the velocity at the jet exit starts to decrease, causing the vortex to separate off of the edge of the orifice. The ratio of the two timescales, vortex generation vs vortex convection, gives U_{\max}/fD , which is just the inverse of the Strouhal number.

If the Strouhal number is greater than unity, the vortex generation time is less than the vortex convection time, and the vortices are not shed fast enough to be convected downstream. For a Strouhal number less than one, the vortex generation time is larger than the convection time, and the vortices have enough time to be convected downstream. Gharib et al.²⁰ and Rosenfeld et al.²¹ have used a similar scaling analysis in their study of impulsively started jets and refer to the inverse of the Strouhal number as a “formation time.” When the

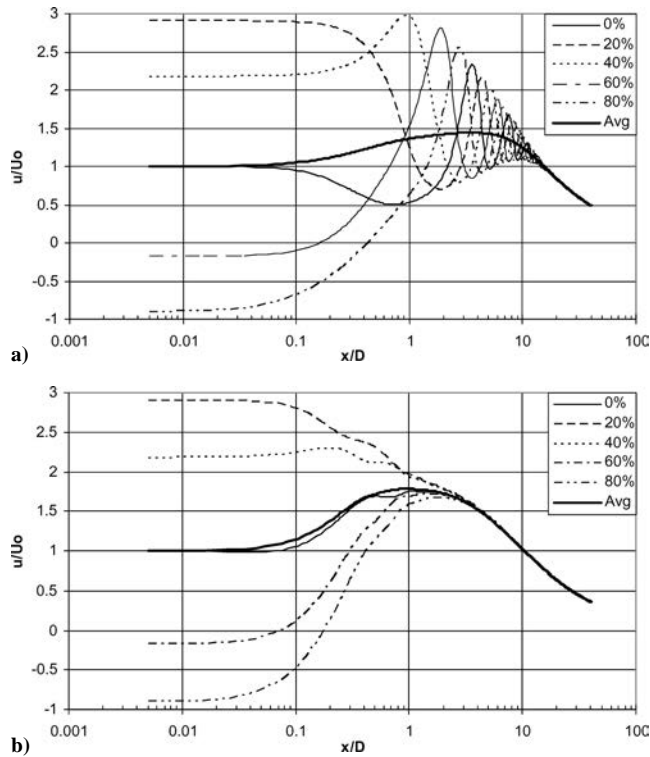


Fig. 5 Centerline velocity vs downstream distance for 200% amplitude forcing at a) 5 Hz, $Sr = 0.1$, for five different phases and b) 50 Hz, $Sr = 1$, for five different phases; time-averaged velocity over cycle also shown, and centerline axial velocity is normalized by mean velocity at jet exit.

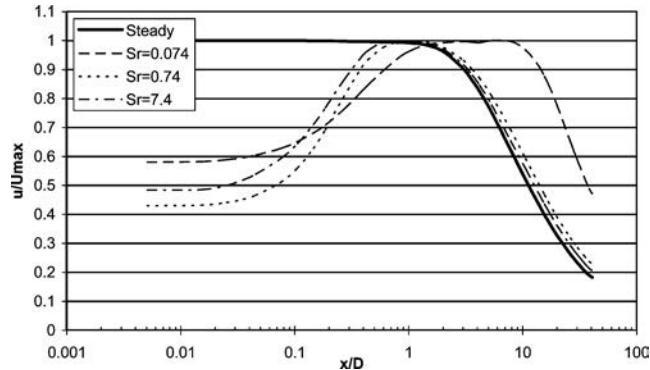


Fig. 6 Time-averaged centerline velocity as function of axial distance with 300% amplitude forcing for Strouhal numbers of 0.074, 0.74, and 7.4; decay of centerline velocity is shown and peak velocity is function of Strouhal number.

terminology by Gharib et al.²⁰ is used, a short stroke is detrimental to seeing vortex effects downstream because, first, $U_{max}/2f$ will not create a fully formed vortex. Then, this poorly formed vortex with weak circulation, and, thus, weak induced velocity, is at a distance/stroke $L = U_{max}/2f$ from the nozzle that is smaller than the critical distance L^* from the nozzle required for a vortex to escape flow reversal. Thus, the two effects together of a weak circulation (incompletely formed vortex) and reverse flow make it less likely that the vortex effects will be felt downstream.

If the Strouhal number is the controlling parameter in periodically forced jets, then at any given forcing frequency f a sufficiently high jet exit velocity U_{max} should exist such that the Strouhal number is less than unity and the vortices would be convected downstream. These higher velocities can be obtained at the jet exit by using stronger (higher-amplitude) forcing, regardless of the frequencies. To test this hypothesis, a case with the same forcing frequency, $f = 50$ Hz, as that shown in Figs. 4 and 5b, where the vortices are

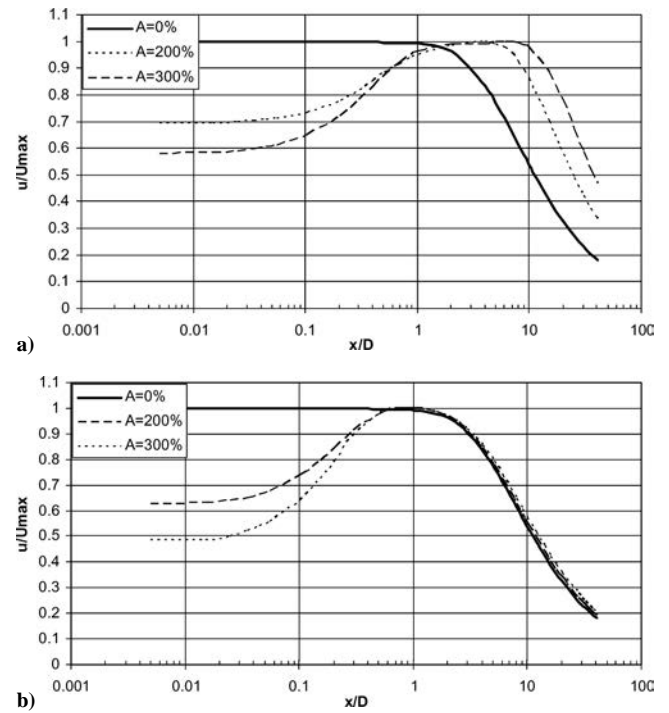


Fig. 7 Time-averaged centerline velocity vs axial distance for a) $f = 5$ Hz and b) $f = 50$ Hz for different amplitudes (200 and 300%).

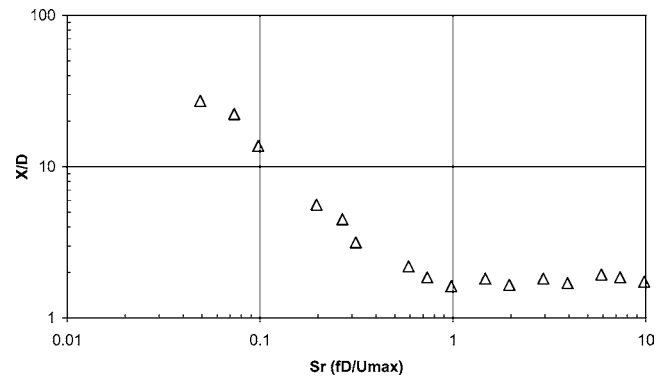


Fig. 8 Axial distance X/D at which velocity oscillations at centerline are no longer seen vs Strouhal number, fD/U_{max} .

not convected downstream, but with a higher forcing amplitude of 1000% instead of 200%, was examined. This case gives a Strouhal number of 0.267 and the vortices were convected downstream of the near-nozzle region, confirming our hypothesis.

Amplitude and frequency modulation appear to control the creation and convection of the vortices, which might prove useful in controlling jet properties. Figure 8 shows the normalized downstream distance, X/D , where the velocity oscillations along the centerline decay to 5% of the time-averaged value for different Strouhal numbers. This downstream distance is an indicator of the distance over which the forcing effects persist for different forcing cases. Figure 8 shows two distinct domains divided by $Sr = 1$. In the region where the Strouhal number is less than one, the downstream decay distance decreases with increasing Strouhal number and scales as $x^{-0.85}$. Beyond $Sr = 1$, the downstream decay distance does not vary with Strouhal number, reflecting the localization of the forcing effects in the near-nozzle region.

2. Velocity Profile Effects

Another effect that was considered is the jet exit velocity profile. The 200% amplitude forcing simulations with frequencies of 5, 50, and 500 Hz were repeated with a parabolic (fully developed) profile at the orifice exit. The average flow rate was matched to

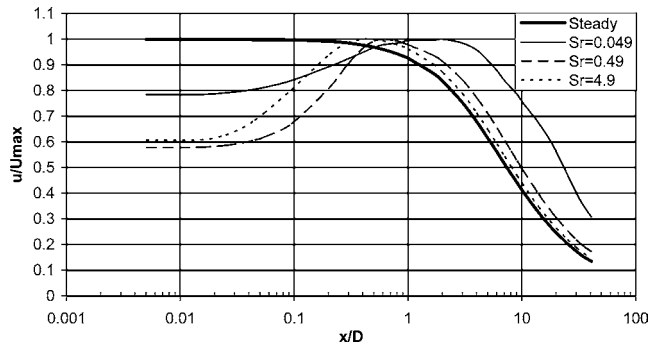


Fig. 9 Time-averaged normalized centerline velocity vs downstream distance for 200% forcing with parabolic velocity profile.

a steady jet with $Re = 100$. The forcing function was of the form $u = U_0(r)[1 + A \sin(2\pi ft)]$, where $U_0(r)$ is the fully developed Poiseuille velocity profile. Note that, in reality, the forcing frequency would have to be very slow to allow a fully developed profile to exist at the orifice exit. However, we examine this profile as a computational exercise. Figure 9 shows the normalized jet exit velocity, U/U_{\max} , along the centerline for three different forcing frequencies (5, 50, and 500 Hz) at 200% amplitude forcing. Here the time-averaged velocity is normalized by the peak value of the time-averaged velocity. As we discussed in the preceding sections, for low-frequency forcing, the oscillations persist farther downstream, whereas with high-frequency forcing (high Strouhal number), the effects are localized. Also, for the high-frequency forcing cases, the normalized velocity decays with axial distance just like the steady case. All of these results are similar to those observed with the top-hat profile, suggesting that the forced jet evolution is relatively insensitive to the exact character of the velocity profiles.

3. Nozzle Jets

The next step in the study involved modeling the presence of a nozzle in the computational domain. This domain was shown in Fig. 1b. Kim et al.²² reported the velocity profiles for an acoustically forced jet. They observed from the velocity profiles at the nozzle exit and within the nozzle that the radial velocity profile was relatively flat and that large gradients existed near the nozzle walls. For our simulations, a top-hat forcing velocity boundary condition was applied at the bottom of the nozzle, that is, at $x = 0$. Figure 10a shows the axial velocity profiles at a location two diameters (2 cm) into the nozzle for a case with 200% amplitude forcing and 50-Hz frequency. An unsteady component of the axial velocity field was also calculated by subtracting off of the corresponding steady-state velocity field. This unsteady axial velocity is shown in Fig. 10b. Consistent with Kim et al.,²² the profiles show high velocity gradients near the nozzle wall, whereas the profiles are flat over the rest of the cross section. The boundary-layer thickness is approximately 1 mm, which is consistent with a scaling estimate for the Stokes layer at this frequency, $\delta \sim \sqrt{\nu/f}$.

Figures 11 and 12 are the vorticity contour and velocity vector plots for 200% amplitude forcing at 5 and 50 Hz, respectively, for the nozzle-resolved calculations. The steady case contour plot is also shown. For the low-forcing-frequency case, the vortices are generated and ejected from the nozzle tips and then convect downstream. During later parts of the cycle, the negative velocities at the nozzle exit can be seen. The axisymmetric geometry of the nozzle results in the fluid being sucked into the nozzle, mainly along the nozzle edge. As a result, during the first half of the cycle where the nozzle exit velocities are positive, the fluid is pushed out over the entire face of the nozzle exit. Over the second half of the cycle, the fluid is sucked into the nozzle primarily along the nozzle walls. Here too, the flowfield generates a stagnation point above the nozzle exit (80% phase case), separating the regions of negative velocity and positive velocity. The high frequency, $f = 50$ Hz, case shows similar results, although the vortices are not convected downstream.

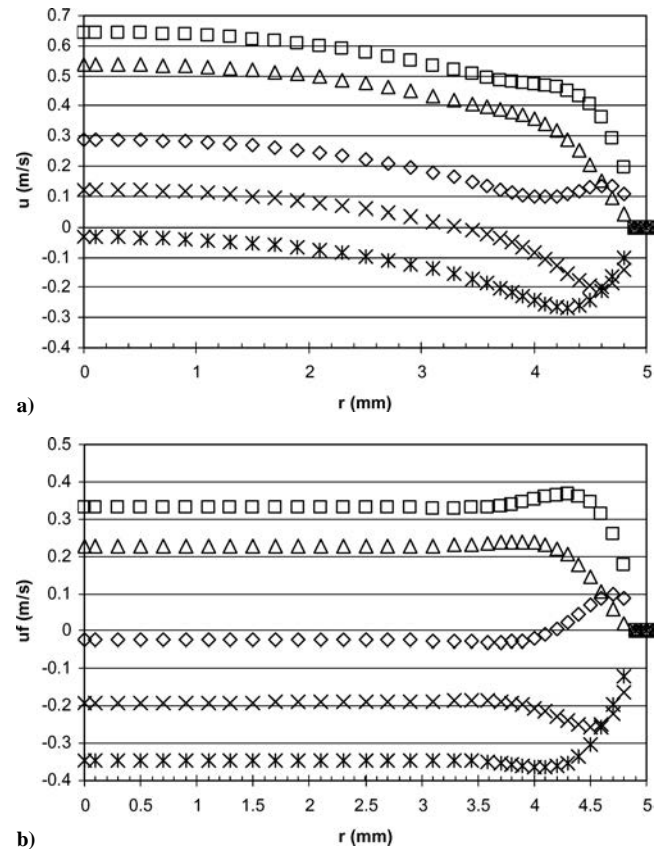


Fig. 10 Plot of a) axial velocity u and b) forced component u_f of axial velocity vs radial distance r at cross section two-dimensional distance within nozzle for 200% amplitude forcing at $f = 5$ Hz, $Sr = 0.098$: \diamond , 0%; \square , 20%; \triangle , 40%; \times , 60%; and $*$, 80%.

Figures 13a and 13b show the axial and radial velocity profiles at the first (downstream) grid-point location after the nozzle exit location for forcing at $Sr = 0.098$. The axial velocity profiles at the different phases over the period of forcing show that the effect of the forcing is first felt at the nozzle edge, and then the effects diffuse toward the centerline. In other words, there appears to be a lag along the cross section, and the forcing effects on the velocity in the center lag the effects at the nozzle edge/wall. The steady-state axial velocity profile has also been plotted as a reference. The steady-state axial velocity profile is essentially a fully developed profile based on the entrance length L_e estimate for flow through a pipe, $L_e \sim 0.06 Re D$. The radial velocity profiles explain the lag effects seen in the axial velocity profile. Negative radial velocities indicate fluid motion toward the centerline, whereas positive values indicate fluid motion away from the centerline. During the 60 and 80% phases, the radial velocity is negative, indicating fluid motion toward the centerline. Also, the 0% phase radial velocity is positive as was the 0% phase axial velocity indicating the jet outflow.

Figure 14a shows the normalized centerline axial velocity as a function of the downstream distance for 200% amplitude forcing at 5-Hz frequency, $Sr = 0.098$. The steady-state and the time-averaged profiles have also been plotted for comparison. As has been described earlier, the axial velocity has been normalized by the mean axial velocity of the forcing function at the bottom of the nozzle, $x = 0$. Note that the nozzle length is five diameters, and hence, the centerline time-averaged axial velocity increases throughout the nozzle. This increase is simply the evolution of the top-hat profile to a Poiseuille profile. The 60% phase velocity profile shows that the axial velocity turns from negative to positive within the nozzle. Immediately downstream of the nozzle exit the time-averaged velocity is larger than the steady-state velocity profile, showing the effect of the redirected ingested mass. Figure 14b is the corresponding plot for high-frequency forcing, $Sr = 0.98$. Just as in the case with the

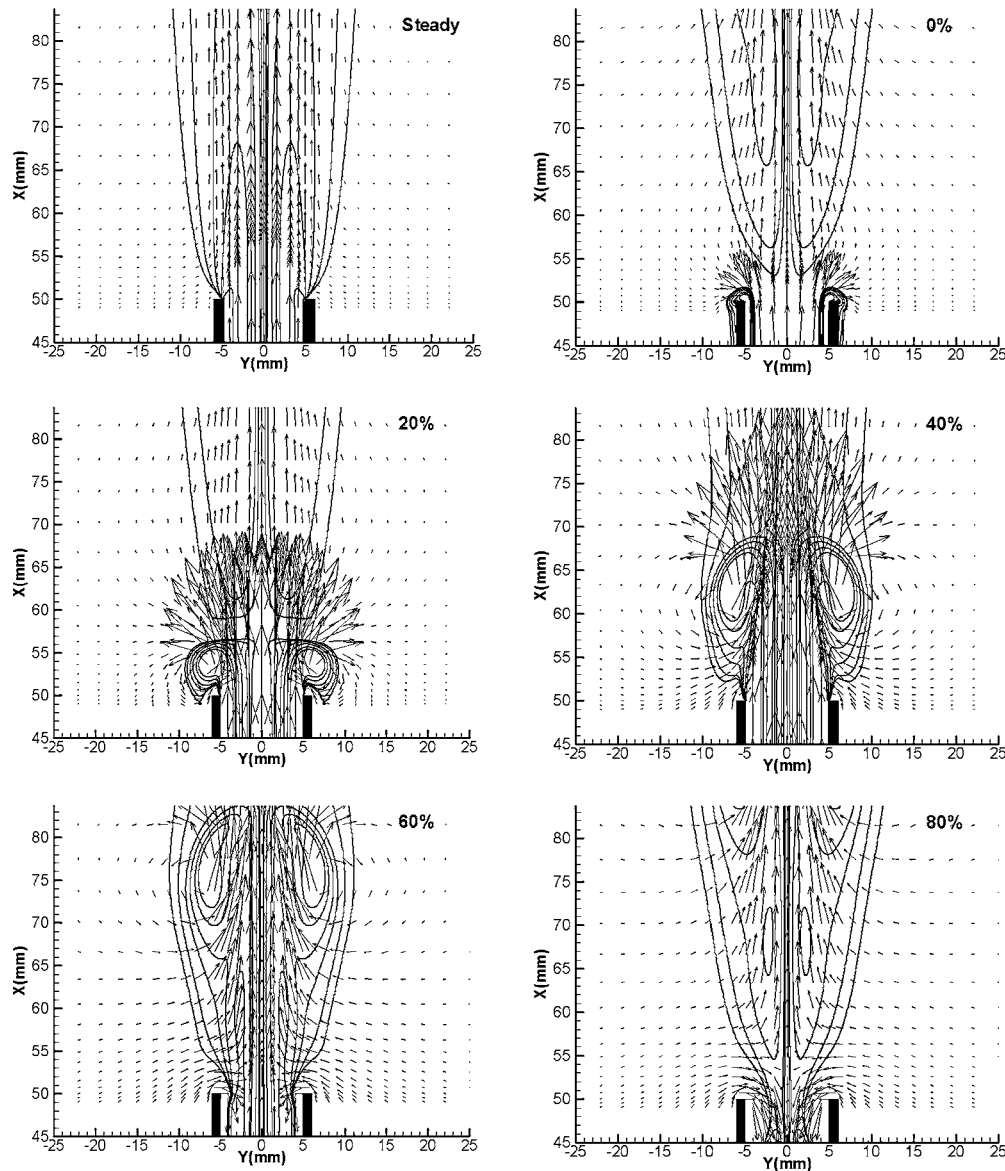


Fig. 11 Vorticity contour plots and instantaneous velocity field for case with forcing amplitude 200% at 5 Hz, $Sr = 0.098$; steady case and five different phases, 0, 20, 40, 60, and 80%, are shown (vorticity values per second).

wall jets, the high-frequency forcing limits the effects of the forcing to the near-nozzle region. Also, the time-averaged velocity profile matches the steady-state profile more closely.

In both (high- and low-frequency-forcing) cases, the peak time-averaged velocities do not differ much from the peak steady-state velocity. This is different from the earlier wall-jet cases, in which the nozzle was not modeled. Note that the peak centerline velocity in the forced and the unforced cases occurs at the nozzle exit. The exit velocity profiles from Fig. 13a show that the centerline axial velocity varies between about 0.65 and -0.15 m/s, whereas the steady-state velocity is about 0.35 m/s. Superficially, this appears to be inconsistent with 200% amplitude forcing. One might believe that 200% forcing of a steady flow with centerline velocity of 0.35 m/s would result in a range of centerline axial velocities from 1.05 to -0.35 m/s. This is not the case. We force a top-hat profile located at the bottom of the nozzle at 200%. The forcing velocity boundary condition at the bottom of the nozzle has a top-hat profile that varies from 0.51 to -0.17 m/s for the case shown in Fig. 13a. Because the profile is flat at the bottom of the nozzle, the centerline axial velocity increases due to the no-slip condition along the nozzle walls. This results in the increase of the positive centerline velocity from 0.51 to 0.65 m/s. However, the peak negative velocity only changes from -0.17 to -0.15 m/s because the strongest negative velocities are seen near the nozzle walls (Fig. 11; 60 and 80% phase).

A comparison of the velocity profiles of the forced jets, with and without the nozzle, is shown in Fig. 15 for a forcing amplitude of 200%. The centerline axial velocity profile of the jets as a function of the downstream distance is plotted. In the case of the jet with the nozzle, the downstream distance has been offset by the nozzle length, so that the downstream distances in both the cases are from the jet exit plane tip. For the low-forcing-frequency case, the velocity profiles with and without the nozzle match one another beyond 10 diameters. This is because the vortices have decayed at these far downstream locations, and the jets now behave as steady jets. However, the high-frequency cases do not match one another over the domain considered. Earlier results (without the nozzle) showed that at high-frequency forcing the jet decays in a similar manner to a steady jet. The steady-state jet exit velocity profile in Fig. 13a shows that the jet, in the case with the nozzle, is close to fully developed. The steady centerline axial velocity decay profiles for the top-hat and parabolic profiles are shown in Fig. 16. These profiles are very similar to those observed in the high-frequency-forcing cases in Fig. 15. Thus, the difference in the high-frequency-axial-velocity profiles can be explained based on the spanwise exit velocity profile. Generally, jets with top-hat and fully developed profiles develop differently because the top-hat profile jet has more initial axial momentum than the fully developed jet with the same mass flux and, hence, decays more slowly than the fully developed jet.

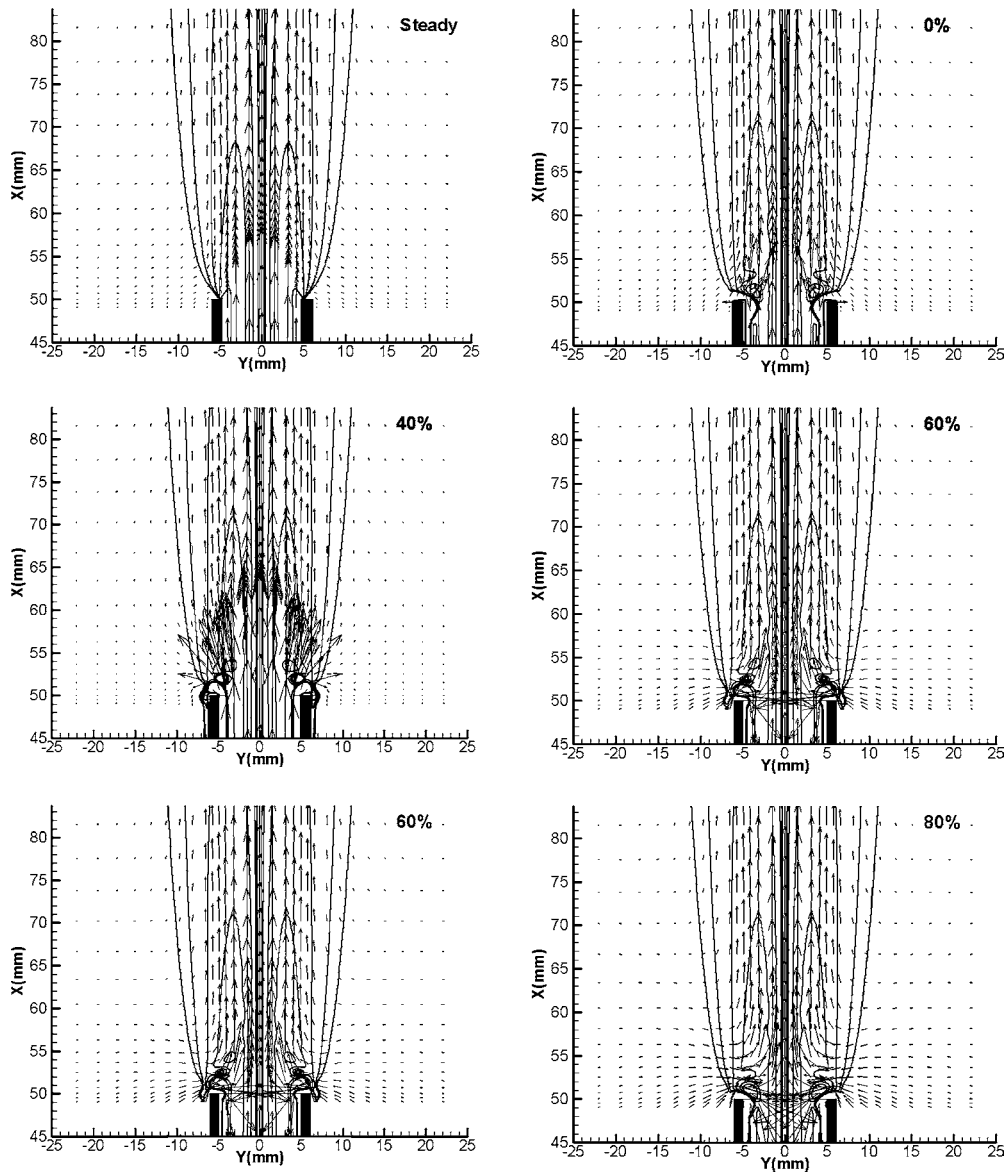


Fig. 12 Vorticity contour plots and instantaneous velocity field for case with forcing amplitude 200% at 50 Hz, $Sr = 0.98$; steady case and five different phases, 0, 20, 40, 60, and 80%, are shown.

C. Jet Spread and Entrainment

Figure 17 shows the half-width of the jet as a function of downstream distance for the steady jet and 200% amplitude forcing jets. The half-width of the jet is the radial distance at which the axial velocity is one-half of the centerline axial velocity. The steady jet half-width compares well with the half-width in Ref. 17. Figure 17 shows that the forced jets do not spread as quickly as the steady jet. The spread rates are calculated at downstream locations where the velocity oscillations have disappeared, and the jet appears to behave like a steady jet. Because there is increased average momentum flux and increased induced volumetric flow rate for the pulsed jet at locations where the pulsed jet is steady, it appears to be a higher-Reynolds-number jet than a steady jet with the same mass flow rate. The lower spread rate appears to be a result of this higher effective Reynolds number of the pulsed jets because it is well known that steady laminar jets spread more slowly as the Reynolds number is increased.

The forced jets are expected to have higher flow rates than steady jets because the forcing action would bring in more fluid from the surroundings. In the current study the entrainment is quantified by the ratio of the volumetric flow rate Q at a downstream cross section to the volumetric flow rate at the nozzle exit Q_e . The volumetric flow

rate at a given cross section was calculated as

$$Q = 2\pi \int_0^\infty u(r)r dr \quad (5)$$

Figure 18 shows the entrainment as a function of downstream distance for the 200% forcing cases. The steady-state case has also been plotted for comparison. In the steady case, the slope of the entrainment curve flattens out with downstream distance. This has been observed by Abdel-Hameed and Bellan²³ in simulations of rectangular jets with Reynolds numbers in the 400–600 range. The volumetric flow rate calculations for the forced jets were made at the downstream distances at which the unsteady effects have decayed. For the forced jet cases, the entrainment varies linearly with downstream distance, and at any downstream distance the entrainment in forced jets is higher than that for the steady jet. The forced jets are narrower as compared to the steady jet (Fig. 17) and have higher axial velocities (Figs. 5a and 5b). The forcing action at the orifice edge causes fluid to be sucked into the orifice over part of the forcing period and then pushed out over the remainder of the period. Separation at the orifice plane causes the jet to have higher average axial momentum than the equivalent steady jet with the same mass

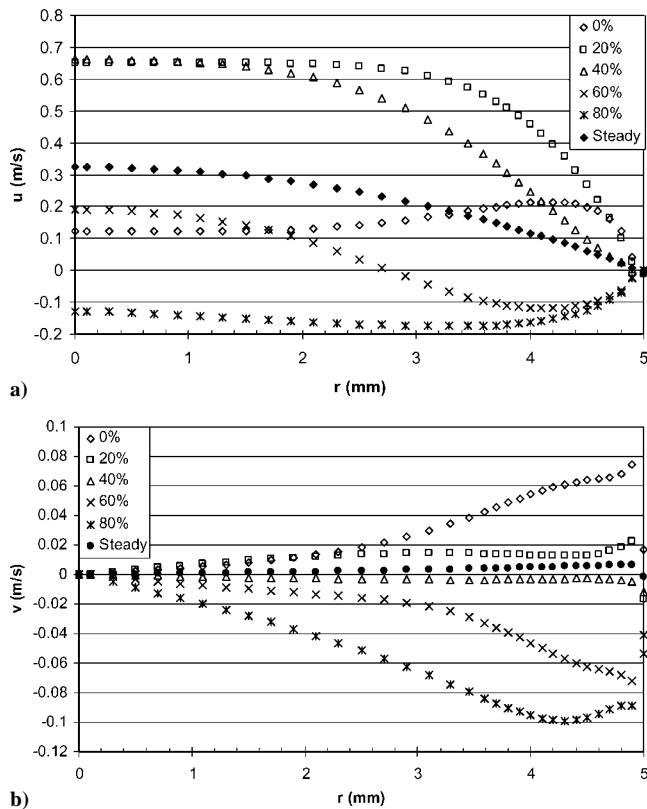


Fig. 13 Velocity profiles a) axial and b) radial at first grid point after nozzle exit for five different phases with 200% amplitude forcing at $f = 5$ Hz, $Sr = 0.098$, and corresponding no-forcing (steady) profile.

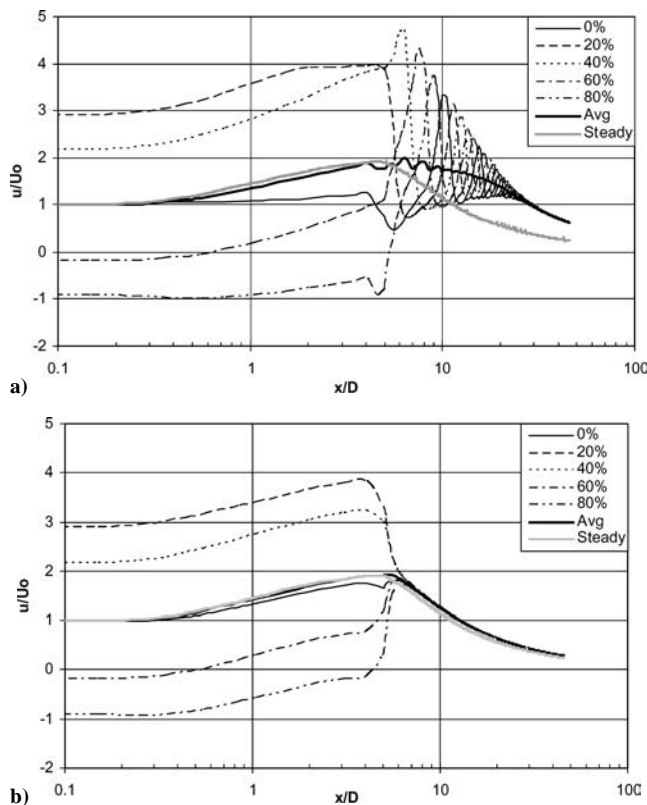


Fig. 14 Centerline axial velocity vs downstream distance for 200% amplitude forcing at a) 5 Hz, $Sr = 0.098$, and b) 50 Hz, $Sr = 0.98$, for five different phases; time-averaged velocity over cycle and steady-state velocity profile are also shown, with centerline axial velocity normalized by mean velocity at bottom of nozzle.

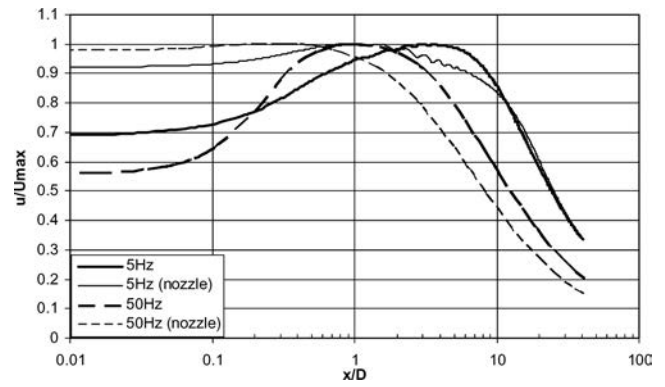


Fig. 15 Comparison of normalized time-averaged centerline axial velocity profiles along centerline, with and without the nozzle for 200% amplitude forcing.

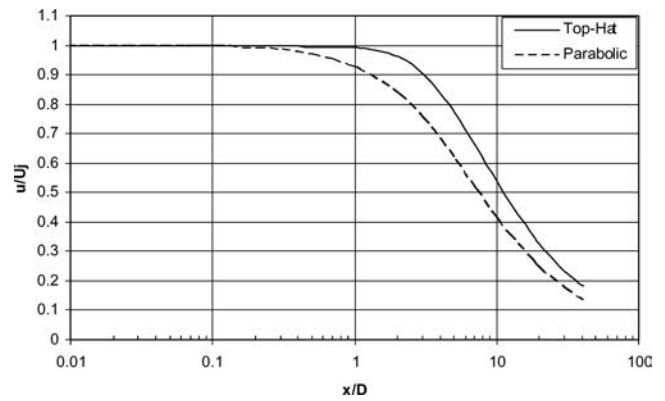


Fig. 16 Centerline axial velocity profiles for steady jets with parabolic profile and top-hat profile.

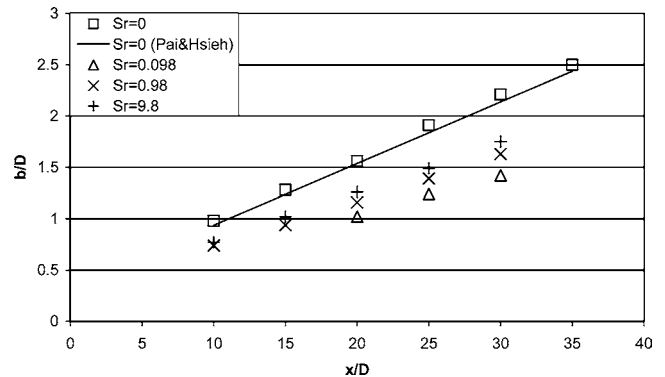


Fig. 17 Half-width of jet as function of downstream distance for 200% amplitude forcing at $Sr = 0.098$, 0.98, and 9.8.

flux. Stated differently, even though the time-averaged flow rate for the forced jets is the same as the flow rate for the steady jet, the directional flow rate (flow rate of the fluid being pushed out) for the forced jets over the time period is higher than the flow rate for the steady jet. This increased flow rate is seen in the higher volumetric flow rates for the forced jets.

Also, the slopes for forced jets are different compared to that of the steady jet. These slopes represent a nondimensional entrainment rate, $D/Q_0(dQ/dx)$. For steady laminar jets, the volumetric flow rate at any downstream distance as given by Schlichting¹⁸ is $Q = 8\pi \nu x$. The entrainment rate for the Schlichting correlation is

$$\frac{dQ}{dx} = 8\pi \nu$$

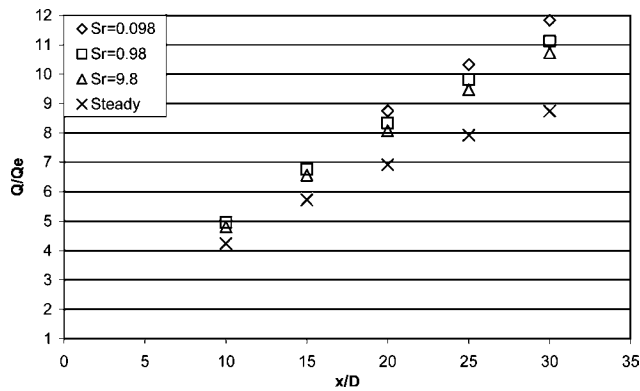


Fig. 18 Entrainment as function of downstream distance for 200% amplitude forcing at $Sr = 0.098$, 0.98 , and 9.8 .

and nondimensionally,

$$\frac{D}{Q_0} \frac{dQ}{dx} = 8\pi \nu \frac{D}{Q_0} = 8\pi \nu \frac{4D}{\pi D^2 U_0} = 32 \frac{\nu}{U_0 D} = \frac{32}{Re} \quad (6)$$

For $Re = 100$, the Schlichting nondimensional entrainment rate is 0.32. In our steady jet calculations, this corresponding value over $x/D < 10$ is 0.324. For the forced cases, the entrainment rates are higher as compared to that of the steady jet. The nondimensional entrainment rate for the steady jet at $x/D = 25$ is 0.18, whereas the corresponding values for the forced jets are 0.3, 0.27, and 0.265 for $Sr = 0.098$, 0.98 , and 9.8 , respectively.

IV. Conclusions

Simulations of strongly forced axisymmetric jets using a finite volume based CFD code have been performed. The code was benchmarked by simulating a steady jet and low-amplitude forcing jets. The forced jets were simulated using a periodically varying jet axial velocity boundary condition. The peak velocities for the forced jets were three to four times the mean velocity and the forcing frequencies varied from 5 to 500 Hz. The creation and convection of vortices from orifice and nozzle exit planes were studied. The results showed that the Strouhal number was the critical parameter for the downstream evolution of the forced jets. For jets with a Strouhal number less than unity, the vortices were found to convect downstream, whereas with a higher Strouhal number, the forcing effects were localized to the near exit region. Also, for jets forced at high Strouhal number the far-field centerline axial velocity scales with the downstream distance similar to that of a steady jet. The jet exit velocity profile (fully developed or top hat) did not affect these trends, and similar trends were observed for jets issuing from a nozzle (tube five diameters in length). The forced jets were seen to spread slower than steady jets of equivalent mass flow rate. The entrainment calculations showed an increase in volumetric flow rate and entrainment rates for forced jets.

Acknowledgments

This work was supported by the National Science Foundation under Grant CTS-0308589 and NASA under Grant NNC04AA04A.

References

- ¹Meldrum, D. R., and Holl, M. R., "Microscale Bioanalytical Systems," *Science*, Vol. 297, Aug. 2002, pp. 1197, 1198.

- ²Lee, Y.-K., Deval, J., Tabeling, P., and Ho, C.-M., "Chaotic Mixing in Electrokinetically and Pressure Driven Micro Flows," *Proceedings of the Micro Electro Mechanical Systems (MEMS)*, Inst. of Electrical and Electronics Engineers, New York, 2001, pp. 483–486.
- ³Crow, S. C., and Champagne, F. H., "Orderly Structure in Jet Turbulence," *Journal of Fluid Mechanics*, Vol. 48, 1971, pp. 547–591.
- ⁴Hill, W. G., Jr., and Greene, P. R., "Increased Turbulent Mixing Rates Obtained by Self-Excited Acoustic Oscillations," *Journal of Fluids Engineering*, Ser. 1, Vol. 99, No. 3, 1977, pp. 520–525.
- ⁵Vermuelen, P. J., Rainville, P., and Ramesh, V., "Measurements of the Entrainment Coefficient of Acoustically Pulsed Axisymmetric Free Air Jets," *Journal of Engineering for Gas Turbines and Power*, Vol. 114, April 1992, pp. 409–415.
- ⁶Marzouk, S., Mhiri, H., Golli, S. E., Palec, G. L., and Bournot, P., "Numerical Study of a Heated Pulsed Axisymmetric Jet in a Laminar Mode," *Numerical Heat Transfer*, Pt. A, Vol. 43, No. 4, 2003, pp. 409–429.
- ⁷Shaddix, C. R., Harrington, J. E., and Smyth, K. C., "Quantitative Measurements of Enhanced Soot Production in a Flickering Methane/Air Diffusion Flame," *Combustion and Flame*, Vol. 99, No. 3–4, 1994, pp. 723–732.
- ⁸Papadopoulos, G., Bryant, R. A., and Pitts, W. M., "Flow Characterization of Flickering Methane/Air Diffusion Flames Using Particle Image Velocimetry," *Experiments in Fluids*, Vol. 33, No. 3, 2002, pp. 472–481.
- ⁹Muramatsu, A., and Era, Y., "Mixing of Carbon Dioxide Gas and Air by a Pulsating Jet with a Reversed Flow," *Proceedings of the 4th ASME/JSME Joint Fluids Engineering Conference*, FEDSM2003-45232, Vol. 2, Pt. D, American Society of Mechanical Engineers, New York, 2003, pp. 2689–2696.
- ¹⁰Smith, B. L., and Glezer, A., "The Formation and Evolution of Synthetic Jets," *Physics of Fluids*, Vol. 10, No. 9, 1998, pp. 2281–2297.
- ¹¹Cater, J. E., and Soria, J., "The Evolution of Round Zero-Net-Mass-Flux Jets," *Journal of Fluid Mechanics*, Vol. 472, 2002, pp. 167–200.
- ¹²Glezer, A., and Amitay, M., "Synthetic Jets," *Annual Review of Fluid Mechanics*, Vol. 34, 2002, pp. 503–529.
- ¹³Rizzetta, D. P., Visbal, M. R., and Stanek, M. J., "Numerical Investigation of Synthetic Jet Flowfields," *AIAA Journal*, Vol. 37, No. 8, 1999, pp. 919–927.
- ¹⁴Lee, C. Y., and Goldstein, D. B., "Two-Dimensional Synthetic Jet Simulation," *AIAA Journal*, Vol. 40, No. 3, 2002, pp. 510–516.
- ¹⁵Bera, J. C., Michard, M., Grosjean, N., and Comte-Bellot, G., "Flow Analysis of Two-Dimensional Pulsed Jets by Particle Image Velocimetry," *Experiments in Fluids*, Vol. 31, No. 5, 2001, pp. 519–532.
- ¹⁶Katta, V. R., Goss, L. P., and Roquemore, W. M., "Numerical Investigations of Transitional H_2/N_2 Jet Diffusion Flames," *AIAA Journal*, Vol. 32, No. 1, 1994, pp. 84–94.
- ¹⁷Pai, S. I., and Hsieh, T., "Numerical Solution of Laminar Jet Mixing with and Without Free Stream," *Applied Scientific Research*, Vol. 27, No. 1, 1972, pp. 39–62.
- ¹⁸Schlichting, H., *Boundary-Layer Theory*, 7th ed., McGraw-Hill, New York, 1979, pp. 230–234.
- ¹⁹Andrade, E. N., and Tsien, L. C., "The Velocity-Distribution in a Liquid into Liquid Jet," *Proceedings of the Physical Society of London*, Vol. 49, No. 4, 1937, pp. 381–391.
- ²⁰Gharib, M., Rambod, E., and Shariff, K., "A Universal Time Scale for Vortex Ring Formation," *Journal of Fluid Mechanics*, Vol. 360, 1998, pp. 121–140.
- ²¹Rosenfeld, M., Rambod, E., and Gharib, M., "Circulation and Formation of Laminar Vortex Rings," *Journal of Fluid Mechanics*, Vol. 376, 1998, pp. 297–318.
- ²²Kim, T. K., Park, J., and Shin, H. D., "Mixing Mechanism near the Nozzle Exit in a Tone Excited Non-Premixed Jet Flame," *Combustion Science and Technology*, Vol. 89, No. 1–4, 1993, pp. 83–100.
- ²³Abdel-Hameed, H., and Bellan, J., "Direct Numerical Simulations of Two-Phase Laminar Jet Flows with Different Cross Section Injection Geometries," *Physics of Fluids*, Vol. 14, No. 10, 2002, pp. 3655–3674.

K. Fujii
Associate Editor

Characteristics of Propagating H₂-Enriched CH₄-Air Flames

Alejandro M. Briones¹ and Suresh K. Aggarwal.²
University of Illinois at Chicago, Chicago, IL 60607

and

Viswanath R. Katta³
Innovative Scientific Solutions, Inc. Dayton, OH 45440

The effects of H₂ enrichment on the propagation of laminar CH₄-air triple flames in axisymmetric coflowing jets are numerically investigated. A comprehensive, time-dependent computational model, which employs a detailed description of chemistry and transport, is used to simulate the transient ignition and flame propagation phenomena. Flames are ignited in a jet-mixing layer far downstream of the burner. Following ignition, a well-defined triple flame is formed that propagates upstream with nearly constant flame displacement speed towards the burner along the stoichiometric mixture fraction line. As the flame approaches the burner, it transitions to a double flame, and subsequently to a burner-stabilized nonpremixed flame. Predictions are validated using measurements of the flame displacement speed. Detailed simulations are used to examine the effects of H₂ enrichment on the propagation characteristics of CH₄-air triple flames. As H₂ concentration in the fuel blend is increased, the flame displacement and propagation speeds increase progressively due to the enhanced chemical reactivity, diffusivity, and preferential diffusion caused by H₂ addition. In addition, the flammability limits associated with the triple flames are progressively extended with the increase in H₂ concentration. The flame structure and flame dynamics are also markedly modified by H₂ enrichment, which substantially increases the flame curvature and mixture fraction gradient, as well as the hydrodynamic and curvature-induced stretch near the triple point. For all the H₂-enriched methane-air flames investigated in this study, there is a negative correlation between flame speed and stretch, with the flame speed decreasing almost linearly with stretch, consistent with previous studies. The effect of H₂ addition is to modify the flame sensitivity to stretch, as it decreases the Markstein number (Ma) and increases the flame tendency towards diffusive-thermal instability (i.e. $Ma \rightarrow 0$). These results are consistent with the previously reported experimental results for outwardly propagating spherical flames burning a mixture of natural gas and hydrogen.

¹ Graduate Research Assistant, Mech. Indust. Eng. Dept., 842 W. Taylor St. (ERF 2039) Chicago, IL, 60608.

² Professor, Mech. Indust. Eng. Dept., 842 W. Taylor St. (ERF 2039) Chicago, IL, 60608, AIAA Member.

³ Scientist, Innovative Scientific Solutions, Inc., Dayton, OH 45440.

I. Introduction

There is a worldwide interest in developing hydrogen-based combustion systems, due to growing environmental concerns and deteriorating supply-demand scenario with regards to fossil fuels. Fossil fuels are non-renewable and major source of pollutants, including CO_2 , NO_x , UHC, and soot. In contrast, hydrogen represents a potentially unlimited source of energy that is environmentally clean, with NO_x being the major undesirable pollutant. There are, however, significant difficulties associated with hydrogen storage due to its high flammability limits, low ignition energy, and low volumetric energy content. There are also many unresolved issues with regards to H_2 combustion, such as knock, detonation, pre-ignition, and flashback. In this context, hydrogen-hydrocarbon fuel blends offer a very promising alternative, as they can synergistically resolve the storage and combustion problems associated with hydrogen and the emission problems associated with fossil fuel combustion. Consequently, there has been considerable interest in investigating the combustion and emission characteristics of hydrogen-hydrocarbon fuel blends.

Several studies have been reported on the performance and emission characteristics of internal combustion engines using hydrogen-fossil fuel blends. These include studies dealing with a diesel engine using hydrogen-vegetable oil blend [1], and spark ignition engines using hydrogen-gasoline blend [2,3], hydrogen-natural gas blend [4,5,6,7,8], and hydrogen-methanol blend [9]. Bauer and Forest [10] investigated the effect of hydrogen addition on the performance of methane-fueled vehicles. It was shown that the wide flammability limits of hydrogen makes it possible to run SI engines at lower equivalence ratios using a hydrogen-methane blend, which lowers cylinder temperature and thereby NO_x emission. Al-Baghdadi [11] also observed a significant reduction in NO_x production in spark ignition engines when a hydrogen-ethanol mixture was used instead of gasoline.

Flame studies using hydrogen-hydrocarbon fuel blends have also been reported. Choudhuri and Gollahali [12] performed an experimental-numerical investigation of hydrogen-natural gas jet diffusion flames, and observed a reduction in soot concentration and emission index of CO (EICO), but an increase in EINO with hydrogen addition. Rortveit et al. [13] reported an experimental-numerical study of NO_x emissions in counterflow methane-hydrogen nonpremixed flames. Naha et al. [14,15] studied the emission characteristics of hydrogen-methane and hydrogen-n-heptane fuel blends using a counterflow flame, and observed significant reduction in NO_x emission in hydrogen-n-heptane flames. Fotache et al. [16] investigated the ignition characteristics of hydrogen-enriched methane flames at various pressures, and identified three ignition limits, namely (i) hydrogen-assisted ignition, (ii) transition, and (iii) hydrogen-dominated ignition. Huang et al. [17] measured the flame speeds for natural gas-hydrogen mixtures, and observed that the increase in H_2 content increases the flame speed exponentially, while the Markstein length transitions from positive to negative implying tendency towards diffusive-thermal instability. Law et al. [18] examined the effect of adding propane to hydrogen at different pressures, and observed that propane reduces the tendency towards diffusive-thermal instability, whereas a pressure increase promotes diffusive-thermal instability causing flame front wrinkling and higher flame speeds. Schefer [19] investigated the stabilization of hydrogen-enriched methane-air swirl-stabilized premixed flames. It was shown that hydrogen addition reduces the lean stability limit, allowing stable burner operation at lower flame temperature that is in turn beneficial for achieving lower NO_x emission. Similarly, Hawkes and Chen [20] studied hydrogen-enriched lean premixed methane air flames, and reported that hydrogen addition increases flame resistance to quenching, but also increases tendency towards diffusive-thermal instability. In addition, the NO emission was observed to increase while CO emission decreased with hydrogen addition.

Our literature review indicates that while many important combustion and emission characteristics of hydrogen-hydrocarbon fuel blends have been investigated, the flame propagation characteristics of such fuel blends have not been examined in previous studies. A fundamental understanding of the flame propagation characteristics of various fuel blends is important for the design of future combustion devices, such as spark ignition engines and gas turbine combustors, burning fuel blends. These characteristics are also important for the design of flame arrestors, which require laminar flame speed data for different fuel blends over a wide range of conditions. For example, a venturi flame arrestor employs a flow restriction to increase the mixture velocity above the flame propagation speed in order to capture a propagating flame.

In this paper, we report a fundamental investigation on the propagation characteristics of H_2 -enriched CH_4 -air flames in a laminar nonpremixed jet. The major objective is to examine the effects of H_2 enrichment on the propagation characteristics of CH_4 -air flames in nonuniform mixtures in which the flame is subjected to flow nonuniformity and mixture fraction gradients, as well as curvature-induced, hydrodynamic, and unsteady stretch effects. A propagating flame is established by igniting the fuel-air mixture in the far field of a jet issuing a H_2 - CH_4 mixture in a coflowing air jet. The ignition event is simulated by providing a small high-temperature zone containing small amounts of H and OH radicals. This high-temperature zone generates an ignition kernel that

propagates upstream and rapidly develops into a triple flame, which then propagates upstream towards the burner rim. The effects of hydrogen enrichment on the propagation characteristics of this triple flame are investigated using a comprehensive computational model that includes detailed descriptions of transport and chemistry. The choice of this configuration is based on several considerations. First this configuration is relevant to many combustion systems, including gas turbines and internal combustion engines [21]. Second, it is difficult to establish lifted H_2 -air or CH_4 -air flames in a jet configuration due to the high mass diffusivity of these fuels ($Sc < 1$) [22]. Third, the present configuration is well suited to examine the propagation characteristics of triple flames established using hydrogen-methane fuel blends, and to characterize the effects of hydrogen on stretch-flame speed interactions. Finally, investigations of triple flame propagation in laminar jets provide fundamental information for the understanding and modeling of turbulent flames. For instance, the stabilization [23,24] and propagation [25,26] of turbulent flames often involve triple flames, which are subjected to a wide range of mixture fraction gradient, stretch, and partial premixing. Consequently, several previous studies have investigated the effects of jet velocity [22,26], coflow velocity [27], partial premixing [25,28,29], heat release [30], and dilution [28,29] on laminar flame stabilization and propagation. However, the flame propagation characteristics associated with fuel blends have not yet been investigated.

It is important to note that a similar configuration involving triple flames has been employed in previous studies. Ruetsch et al. [30] reported the first numerical investigation of triple flames and thus laid the foundation for such studies. They showed that heat release redirects the flow ahead of the triple flame, reducing the flow velocity along the stoichiometric mixture fraction line, which reaches a local minimum just ahead of the triple flame. For a lifted triple flame, this local minimum flow velocity was defined as the flame propagation speed (S_{tri}) at the triple point, while the upstream flow velocity was defined as the far-field or global flame speed (U_F). In addition, it was shown that the global flame speed increases with the decrease in mixture fraction gradient, and in the limit of small mixture fraction gradient, the U_F/S_{tri} ratio is proportional to the square root of the density ratio of unburnt to burnt mixtures ($\sqrt{\rho_u/\rho_b}$) across the flame. Qin et al. [25] and Ko and Chung [26] investigated the propagation of CH_4 -air triple flames in laminar jets and observed that the flame displacement speed (V_f), which is the flame velocity in laboratory coordinates, remains nearly constant during propagation, while the flame propagation speed (S_{tri}) decreases with flame stretch and mixture fraction gradient. In addition, S_{tri} was found to be about two times the laminar stoichiometric unstretched flame speed (S_L^0), while it was observed to be considerably higher (3-6 times) in turbulent jets [31]. It is also interesting to note that in both laminar [25,26] and turbulent flows [32] it was observed that an increase in jet velocity decreases the flame displacement speed but increases the propagation speed, and that the flame propagation speed decreases with axial position due to the increase in mixture fraction gradient and flame curvature. This further highlights the fact that investigations of laminar triple flames can provide insight into the stabilization and propagation of turbulent flames.

Im and Chen [33] investigated the propagation of H_2 -air triple flames in a nonpremixed jet. Similar to previous studies [30,34], the global flame speed was found to be proportional to the square root of the density ratio across the flame. Another important observation from this study was that for H_2 -air mixtures, the flame is shifted towards the air side and becomes asymmetric with respect to the stoichiometric mixture fraction ($f_s=0.0285$) line,⁴ since f_s is much smaller than 0.5. Consequently, the triple point, located at the intersection of stoichiometric mixture fraction line and flame surface, does not coincide with the flame leading edge, which is located at the local minimum flame curvature. This shift between the triple point and the leading edge is important in the context of determining the triple flame speed, since the experimental studies have generally reported the flame speeds at the leading edge [35], while the numerical investigations have computed these speeds at the triple point [25,29,33]. While this shift is also observed for hydrocarbon flames, it becomes more pronounced for hydrogen flames, and therefore, relevant for fuel blends containing hydrogen.

The preceding literature review indicates that several investigations have been reported dealing with the propagation of triple flames in the context of pure fuels. However, the flame propagation characteristics of fuel blends have not been examined as yet.

II. Computational Model

The numerical model is based on the solution of the time-dependent governing equations for a two-dimensional unsteady reacting flow [36,37]. Using cylindrical coordinates (r,z) these equations can be written as:

⁴ Note that for $f_s=0.5$ the flame will be symmetric with respect to the stoichiometric mixture fraction line, and the locations of the triple point and the flame leading edge will coincide.

$$\frac{\partial(\rho\Phi)}{\partial t} + \frac{\partial(\rho v\Phi)}{\partial r} + \frac{\partial(\rho u\Phi)}{\partial z} = \frac{\partial}{\partial r} \left(\Gamma^\Phi \frac{\partial\Phi}{\partial r} \right) + \frac{\partial}{\partial z} \left(\Gamma^\Phi \frac{\partial\Phi}{\partial z} \right) - \frac{\rho v\Phi}{r} + \frac{\Gamma^\Phi}{r} \frac{\partial\Phi}{\partial r} + S^\Phi \quad (1)$$

Here t denotes the time, ρ the density, and u and v the axial (z) and radial (r) velocity components, respectively. The general form of the equation represents conservation of mass, momentum, species, or energy conservation, depending on the variable used for Φ . The diffusive transport coefficient Γ^Φ and source terms S^Φ are described in Ref. 36. Introducing the overall species conservation equation and the state equation completes the equation set. A sink term based on an optically thin gas assumption was included in the energy equation to account for thermal radiation from the flame [38] in the form $q_{rad} = -4\sigma K_p (T^4 - T_o^4)$ [39] where T denotes the local flame

temperature, and K_p accounts for the absorption and emission from the participating gaseous species (CO_2 , H_2O , CO and CH_4) expressed as $K_p = P \sum_k X_i K_{p,i}$ where $K_{p,i}$ denotes the mean absorption coefficient of the k^{th} species, σ is the Stephen-Boltzmann constant, and T_o is the ambient temperature. The value of $K_{p,i}$ is obtained using a polynomial approximation to the experimental data provided in Ref. 39.

The thermodynamic and transport properties appearing in the governing equations are temperature and species dependent. The thermal conductivity and viscosity of the individual species were based on Chapman–Enskog collision theory, following which those of the mixture are determined using the Wilke semi-empirical formulas [40] Chapman–Enskog theory and the Lennard-Jones potentials were used to estimate the binary-diffusion coefficient between each species and nitrogen. The methane–air chemistry is modeled using a detailed mechanism that considers 31 species and 346 elementary reactions [41]. The major species included in the mechanism are CH_4 , O_2 , CO_2 , CO , CH_2O , H_2 , H_2O , C_2H_2 , C_2H_4 , C_2H_6 , CH_3OH , and N_2 , while the radical species include CH_3 , CH_2 , CH , CHO , H , O , OH , HO_2 , H_2O_2 , C_2H , C_2H_3 , C_2H_5 , CHCO , C , $\text{CH}_2(\text{s})$, CH_2OH , CH_3O , CH_2CO , and HCCOH . The mechanism has been validated previously for the computation of premixed flame speeds and the detailed structure of premixed and nonpremixed flames [42,43,44].

The finite-difference forms of the momentum equations are obtained using QUICKST scheme [45], while those of the species and energy are obtained using a hybrid scheme of upwind and central differencing. The pressure field is calculated at every time step by solving all of the pressure Poisson equations simultaneously and using the LU (lower and upper diagonal) matrix-decomposition technique.

Figure 1 illustrates the computational domain. It consists of 100 mm×50 mm in the axial (z) and radial (r) directions, respectively, and is represented by a staggered, non-uniform grid system. The reported results are grid independent, as discussed in the next section. The minimum grid spacing is 0.05 mm in both the r - and z -directions. An isothermal insert (2×0.8 mm) simulates the inner burner wall. The temperature at the burner wall was set at 300K. The inner and outer jets are set with a constant and uniform velocity of 10cm/s and 30 cm/s, respectively. The inner jet issues a H_2 - CH_4 mixture, while the outer jet issues air. A propagating flame is established by igniting the fuel-air mixing layer in the far field (35mm above the burner rim). The ignition event is simulated by providing a small high-temperature zone with a temperature of 2000K and a rectangular cross-sectional area of 2mm², and containing small amounts of H and OH radicals. This high-temperature zone generates an ignition kernel that propagates upstream and rapidly develops into a triple flame, which then propagates upstream towards the burner rim and eventually stabilizes at the rim. Detailed numerical algorithm is developed to determine the

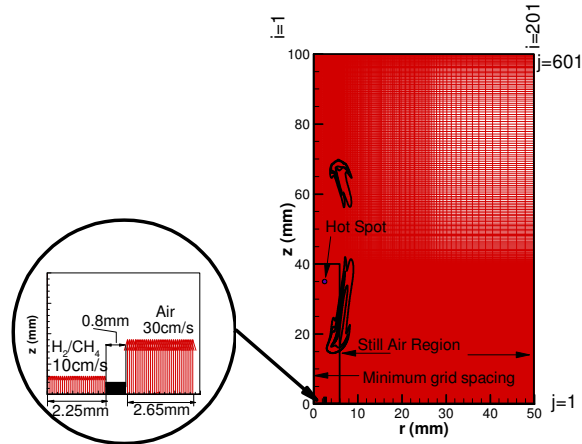


Figure 1: Schematic of the computational grid used in the simulations. The small rectangle shows the minimum grid spacing region where the propagation flame front is located. Schematic of the computational domain is also shown.

propagation characteristics of this flame, such as flame displacement and propagation speeds, flame structure and dynamics near the triple point, and flame stretch-speed interactions.

III. Results and Discussion

A. Validation of Numerical Model

The algorithm used for the simulation of propagating flames has been extensively validated in previous studies, using experimental data from burner-stabilized flames [36,46], lifted partially premixed flames [37], and propagating partially premixed flames [25]. The validation has included the comparison of the predicted and measured flame topology, liftoff heights (L_f), temperature, velocity and concentration fields, and flame displacement speed (V_f). In the following section, we will provide an additional validation by comparing the predicted and measured [47] flame displacement speed (V_f) of a propagating CH₄-air triple flame.

B. Ignition and Flame Propagation

Figure 2 presents the simulated results of transient ignition, flame propagation, and flame attachment for a propagating CH₄-air triple flame in terms of heat release rate contours. The first image at $t=0$ ms corresponds to an instant when the high-temperature ignition source is removed, while the subsequent images show the formation and propagation of a triple flame. Following ignition, two reacting volumes (or kernels) are formed, as indicated by the image at $t=3$ ms. One propagates downstream and is quickly extinguished. The other propagates upstream towards the burner and develops into a triple flame, which is the focus of this investigation. The triple flame structure develops at $t=18$ ms. The flame propagates in a quasi-steady manner, i.e., at near-constant flame displacement speed (V_f), from $z=25$ mm to $z=4$ mm, exhibiting a well-defined triple flame structure as indicated in the snapshot at 48ms. The three reaction zones, namely the rich premixed zone (RPZ), the lean premixed zone (LPZ), and the nonpremixed zone (NPZ), can be readily identified in the 18ms and 48ms images. As the flame approaches the burner rim (i.e. $z=4$ mm), the length of the RPZ shortens, and the flame transitions to a double flame, as the LPZ

disappears. The flame reaches the burner rim at 88 ms, and during its stabilization at the rim, the RPZ extinguishes and the flame transitions from a double flame to a steady nonpremixed flame.

Figure 3 presents the flame displacement speed (V_f) during propagation as a function of flame position (d_f) for the 0% H₂-, 25% H₂-, 50% H₂-, and 75% H₂-enriched CH₄-air flames. The instantaneous flame displacement speed is obtained by calculating rate of change of axial position of the triple point with time (i.e. $V_f = (\Delta z)_{tr}/\Delta t$). Following Won et al. [35] the flame surface, which is needed for determining the triple point, is chosen to be the iso-contour

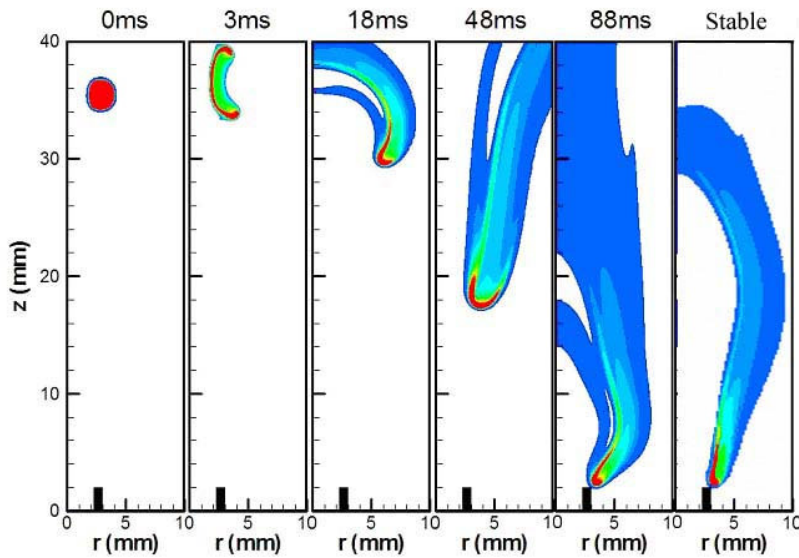


Figure 2: Simulated results showing the temporal evolution of ignition and flame propagation in terms of heat release rate contours for the pure CH₄-air flame.

of 0.0727 H₂O mass fraction. The measured flame displacement speed as a function of flame position for a propagating CH₄-air triple flame, taken from Ref. [47], is also shown in the figure. There is good agreement between the predicted and measured flame displacement speeds. Both predictions and measurements indicate that V_f is nearly independent of time. Our predictions are also consistent with the measurements of Ko and Chung [26] for propagating CH₄-air triple flames with different jet inlet velocities. The flame displacement speed decreases as the flame gets close to the burner rim ($d_f \sim 2-3$ mm) and tends to zero as the flame stabilizes at the rim. In addition, results

in Fig. 3 indicate that as the amount of H_2 in the fuel blend is increased, the flame displacement speed progressively increases, and the flame reaches the burner rim in shorter time. The increase in V_f is due to an increase in the flame propagation speed, S_{tri} (discussed later), which in turn is due the enhanced chemical reactivity, diffusivity, and preferential diffusion effects caused by H_2 enrichment. The aspects dealing with the effects of H_2 enrichment on the flame propagation characteristics, including stretch-flame speed interactions, are further discussed in Section 3.4.

C. Flame Base Structure

In order to spatially resolve the various reaction zones of the propagating flame more clearly, we have previously developed a modified flame index [28,29], defined as

$$\xi_M = \left(\frac{f - f_s}{|f - f_s|} \right) \cdot \frac{1}{2} \left(1 + \frac{G_{FO}}{|G_{FO}|} \right) \quad (2)$$

Here the mixture fraction (f) is defined following Bilger [48], and G_{FO} is the flame index proposed by Takeno and coworkers [49]. With this definition, $\xi_M = 1$ represents a rich premixed zone, -1 a lean premixed zone, and 0.5 a nonpremixed zone for hydrocarbon flames. Since identification of the various reaction zones is more relevant in regions of high reactivity, i.e. where the heat release rates are significant, we have computed ξ_M only in regions where the heat release rate is at least 1% of the maximum heat release rate.

Figure 4 presents ξ_M contours for propagating CH_4 -air flames established with different H_2 enrichment. The contours are shown when the flames are at two different positions, the first one at $z=17$ mm corresponding to quasi-steady propagation, and the second one near the burner rim ($z \approx 2$) when the flames are in the attachment process at the burner rim. For all the four cases considered, the ξ_M contours clearly indicate that during quasi-steady flame propagation, the flames exhibit a triple flame structure at the flame base. The LPZ is weakened with H_2 addition as indicated by the reduction of the lean premixed wing. For all the four cases, as the flames get close to the burner rim, the LPZ extinguishes and the triple flame transitions to a double flame containing the rich premixed (RPZ) and nonpremixed (NPZ) zones. As these four flames are stabilized at the burner rim, the RPZ gets extinguished due to insufficient mixing near the rim, and the flames exhibit a single (NPZ) flame structure.

Since H_2 -air premixed flames exhibit wider flammability limits than typical hydrocarbon-air premixed flames, it is relevant to examine the effect of H_2 enrichment on the flammability limits of propagating CH_4 -air triple flames. Figure 5 presents the four flames, discussed in the context of Fig. 4, in terms of heat release rate contours, streamlines, and equivalence ratio contours. The equivalence ratio is computed using $\phi = (f(1-f_s)/(f_s(1-f)))$, which implies that the stoichiometric line ($\phi=1.0$) coincides with the stoichiometric mixture fraction (f_s) line. Previous investigations [47] have used an equivalence ratio $\phi_u = Y_F/(vY_{O_2})$, where v is the stoichiometric fuel-air mass ratio) based on the reactants' mass fractions in the unburnt mixture. However, the propagating triple flame structure is better characterized using ϕ instead of ϕ_u , since $\phi_u=1.0$ line does not coincide with f_s in the burnt region, although it does in the unburnt region. For the 0% H_2 -enriched flame, the region of high reactivity (red color) extends from $\phi=0.46$ to $\phi=1.58$, which correspond, respectively, to the lean and rich flammability limits of CH_4 -air premixed flames. [50,51,52]. There is, however, still significant reactivity beyond these ϕ values, implying that a triple flame extends the flammability limits due to synergistic interactions among the three reaction zones. The H_2 enrichment further extends these flammability limits, since it enhances flame reactivity as well as interactions between the reaction zones. For instance, for the 75% H_2 -enriched flame, the region of high reactivity (red color) extends from

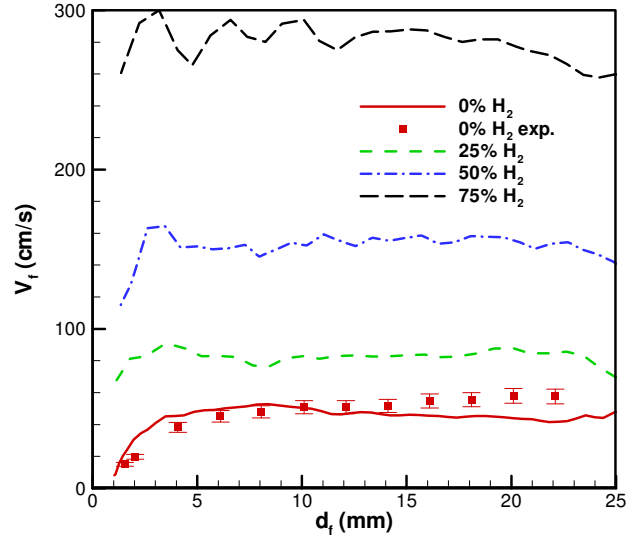


Figure 3: Predicted axial propagation velocity (V_f) as a function of axial position from the burner rim (d_f) for the 0% H_2 -, 25% H_2 -, 50% H_2 -, and 75% H_2 -enriched CH_4 -air propagating flames. The measured axial displacement flame speed (V_f) for a CH_4 -air propagating flames is also included for validation of the numerical simulations.

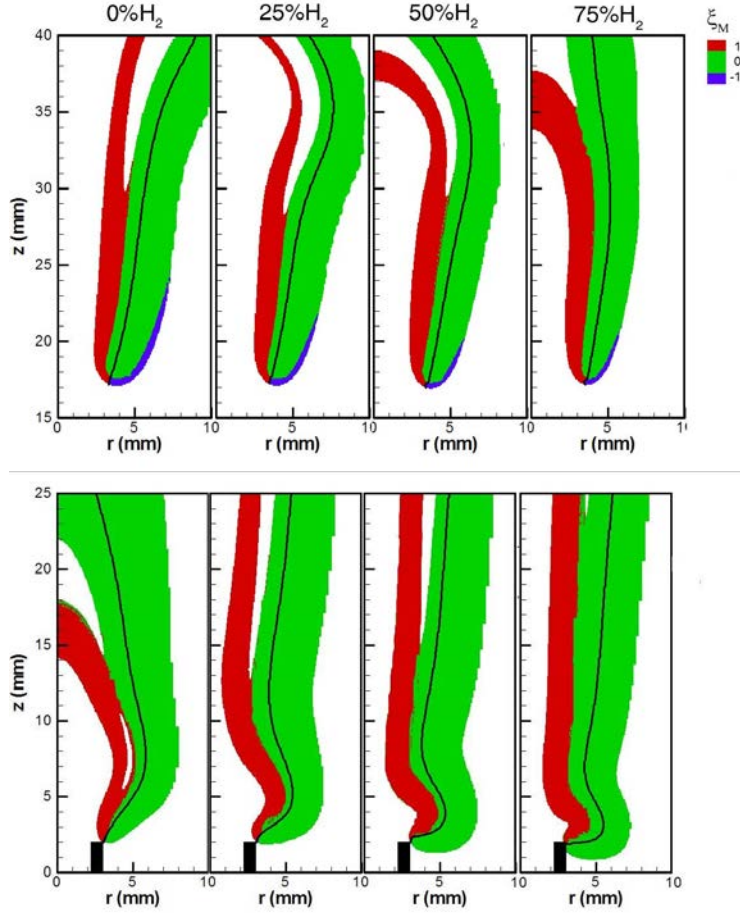


Figure 4. Flame structures of various H₂-enriched CH₄-air flames are shown through the modified flame index (ξ_M) contours during quasi-steady flame propagation (a) and flame attachment (b).

preferential diffusion. The preferential diffusion effect can be demonstrated by comparing the structure of H₂-enriched propagating triple flames along the stoichiometric mixture fraction with that of the corresponding stoichiometric planar flames.

Lateral diffusion of heat and species plays an important role in determining the structure of propagating triple flames. With fuel blends (say) containing fuels A and B with unequal diffusivities, preferential diffusion of fuel species can lead to localized regions of higher concentration of fuel A compared to B, and this may significantly affect the flame propagation characteristics. This preferential diffusion effect becomes more significant in propagating triple flames compared to that in planar flames due to the presence of

$\phi=0.14$ to $\phi=2.54$. H₂ addition also increases both the mixture fraction gradient and flame curvature, as indicated by the collapsed ϕ lines near the flame base. Moreover, since H₂ enrichment decreases the stoichiometric mixture fraction (f_s), the flame becomes more asymmetric with respect to $\phi=1.0$ line. For example, f_s is 0.055 for the 0%H₂-flame, and decreases to 0.044 for the 75%H₂-enriched flame. Consequently, the flow divergence ahead of the flame base becomes more asymmetric with increasing H₂ content. Therefore, the effect of H₂ enrichment is to significantly extend the flammability limits, decrease the radius of curvature at the triple flame base, increase the mixture fraction gradient, and make the flow divergence more asymmetric with respect to the stoichiometric line. These effects influence the flame dynamics, as discussed in the following sections.

D. Stoichiometric Flame Structure

Our simulations indicate that in addition to the enhanced flammability limits, H₂ enrichment also causes a significant increase in the flame propagation speed of triple flames. Since the flame speed is strongly influenced by preferential mass diffusion effects, we examine in this section the effect of H₂ enrichment on

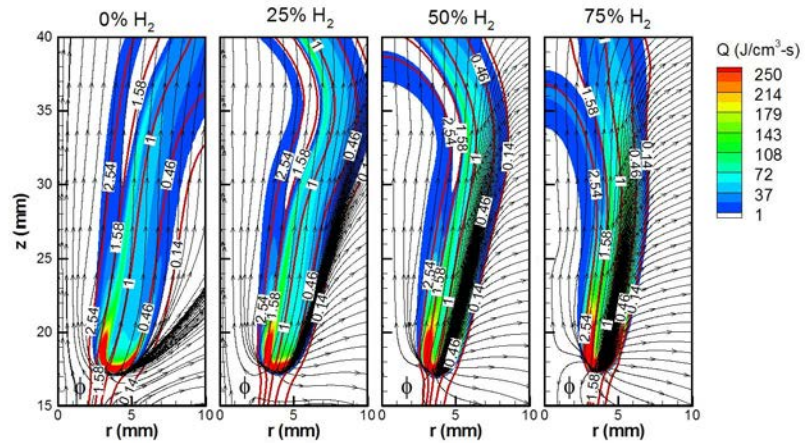


Figure 5: Computed heat release rate contours (rainbow scheme) (q), equivalence ratio contours (red lines) (ϕ), and flow field streamlines (black lines) (v) for 0%H₂-, 25%H₂-, 50%H₂-, and 75%H₂-enriched CH₄-air propagating flames.

lateral diffusion. In order to characterize this effect, we compare the structure of H_2 -enriched propagating triple flames along the stoichiometric mixture fraction with that of the corresponding stoichiometric planar flames. Figure 6 presents these flame structures in terms of the temperature, axial velocity, and major species (CH_4 , O_2 , H_2O , H_2 ,

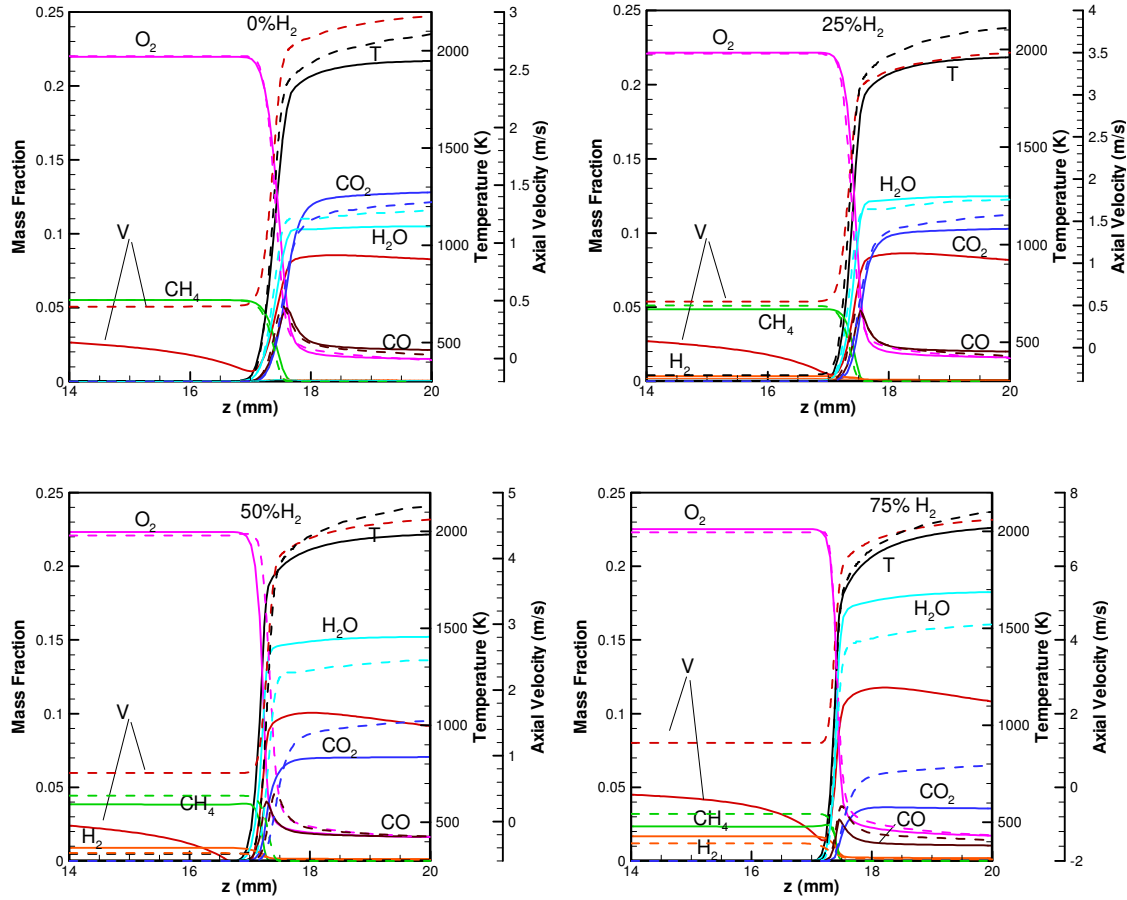


Figure 6. Comparison of the temperature, axial velocity, reactants (CH_4 , H_2 , and O_2), and products (CO_2 , CO , and H_2O) mass fraction profiles between the instantaneous flame structure along the stoichiometric mixture fraction line of simulated axisymmetric propagating triple flames (solid) discussed in the context of Fig. 7 and the corresponding stoichiometric planar flames (dashed). Both structures are superimposed at the location of the maximum heat release rate peak.

CO_2 , and CO) profiles for the four H_2 -enriched triple flames (discussed in the context of Figs. 4 and 5) and the corresponding stoichiometric planar flames. The two structures are superimposed at the location of the maximum heat release rate. The peak flame temperature for triple flames is lower than that for the corresponding planar premixed flames, and this may be attributed to the effects of lateral heat transport and stretch in triple flames. The peak flame temperature, however, increases with H_2 addition for both triple and planar premixed flames.

The presence of preferential diffusion in the case of triple flames can be observed by comparing the CH_4 and H_2 mass fraction profiles for the triple flames and the corresponding planar flames in Fig. 6. For the 0% H_2 -enriched case, the CH_4 mass fraction profiles for the triple flame is almost identical to that for the planar premixed flame. However, with increasing H_2 enrichment, the CH_4 mass fraction becomes increasingly smaller while H_2 mass fraction becomes larger in triple flames than those in planar flames, indicating the preferential diffusion of H_2 over that of CH_4 . The reduction in CH_4 mass fraction due to preferential diffusion is further indicated by the reduced CO and CO_2 mass fractions and the increased H_2O mass fractions for the triple flames compared to those for the planar flames. Therefore, the preferential diffusion of H_2 in H_2 -enriched propagating triple flames leads to localized higher concentration of hydrogen, which enhances the flame propagation speed.

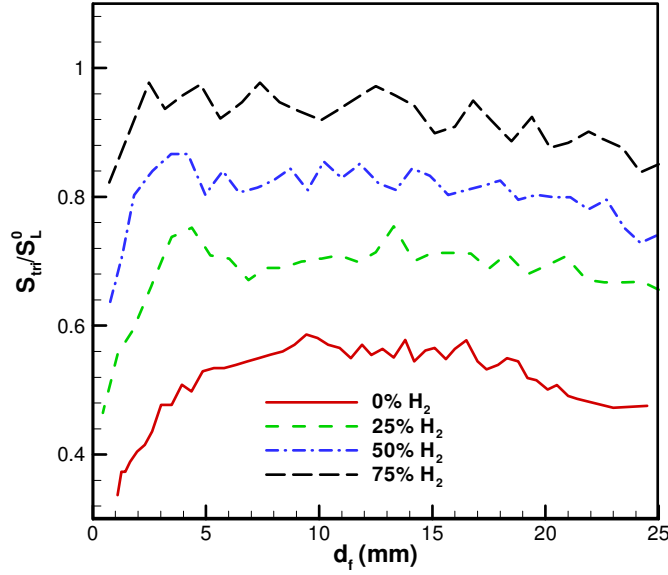


Figure 7: Normalized flame propagation speed (S_{tri}/S_L^0) plotted as a function of distance from the burner rim (d_f) for the 0% H_2 -, 25% H_2 -, 50% H_2 -, and 75% H_2 -enriched CH_4 -air propagating flames.

33, 53]:

$$S_d^* = \frac{\rho S_d}{\rho_u}, S_d = \left(\frac{1}{\rho |\nabla \phi|} [\nabla \cdot (\rho D \nabla \phi) + \omega_\phi] \right) \quad (3a)$$

$$\kappa_h = \nabla \cdot \mathbf{V}_{fluid} - \mathbf{nn} : \nabla \mathbf{V}_{fluid} \quad (3b)$$

$$\kappa_c = S_d (\nabla \cdot \mathbf{n}) \quad (3c)$$

$$\kappa = \kappa_h + \kappa_c \quad (3d)$$

In Eq. (3a) the scalar ϕ is represented by the H_2O mass fraction ($Y_{H_2O}=0.0727$ [26]). Note that a density-weighted flame speed (S_d^*) is being used following Im and Chen [33]. Here S_d^* represents the local flame speed along the flame surface, while S_d^* at the triple point yields the flame propagation speed (S_{tri}). In addition, the far-field flame speed (U_F), which represents the global triple flame speed is evaluated using [33,54]:

$$U_F - U_0 = S_{tri} - U_e = V_f \quad (4)$$

Here U_0 is the local maximum flow velocity along the stoichiometric mixture fraction line (f_s) ahead of the flame, which is not affected by flow divergence, whereas U_e is the local minimum flow velocity along f_s ahead of the flame. Note that if the flame were to be stabilized as a lifted flame, its displacement speed is zero ($V_f=0$), and then $U_F=|U_0|$ and $S_{tri}=|U_e|$.

Figure 7 presents the normalized flame propagation speed (S_{tri}/S_L^0) as a function of distance from the burner rim (d_f) for the four H_2 -enriched CH_4 -air triple flames. Here S_L^0 is the stoichiometric unstretched planar flame speed, which is computed for each of the four H_2 -enriched flames using the Chemkin package [55] with GRI 1.2 chemistry model [41]. The S_L^0 values for the four flames are provided in Table 1. Several important observations can be made from this figure. First, with increasing H_2 enrichment, S_{tri} increases due to the enhanced chemical reactivity, diffusivity, and preferential diffusion caused by H_2 addition. Second, the ratio S_{tri}/S_L^0 is less than unity, implying that the effect of stretch is to reduce the flame speed for these flames. This aspect is further discussed later in this section. Third, the difference between S_{tri} and S_L^0 is reduced with increasing H_2 enrichment, implying that the flame becomes less sensitive to stretch rate with H_2 addition. Finally, S_{tri} varies during flame propagation. Both of these aspects are also discussed later in this section.

Another important observation from Fig. 6 is that the axial velocity in the case of triple flames reaches a minimum ahead of the flame due to the flow divergence effect. This minimum velocity is associated with the triple flame propagation speed (S_{tri}). For stationary lifted triple flames, Ruetsch et al. [30] and Im and Chen [33] have shown this minimum velocity to be close to the stoichiometric planar flame speed (S_L). However, for upstream propagating triple flames, this minimum velocity becomes negative (cf. Fig. 6) due to flow reversal ahead of the flame. This is consistent with the results reported by Qin et al. [25]. As the amount of H_2 in the fuel blend is increased, the minimum flow velocity increases in magnitude, indicating that the flame propagation speed also increases.

E. Flame Dynamics at the Triple Point

In order to examine the flame dynamics and stretch-flame speed interactions, the flame speed (S_{tri}), and the hydrodynamic (κ_h), curvature-induced (κ_c), and total (κ) stretch rates at the triple point are extracted from our simulations, using the following equations [25,

Ruetsch et al. [30] and Im and Chen [33] showed that U_F/S_{tri} is proportional to the square root of the density ratio (i.e. $\sqrt{(\rho_u/\rho_b)}$) for small mixture fraction gradients. In order to confirm this relationship for our simulations, we present in Fig. 8 the normalized far-field flame speed (U_F/S_{tri}) as a function of flame position (d_f) for the flames discussed in the context of Fig. 5. It is interesting to note that for all H_2 -enriched flames, $U_F/S_{tri} \approx 2.5$ during quasi-steady flame propagation. Our simulations also indicate that the square root of the density ratio remains nearly constant ($\sqrt{(\rho_u/\rho_b)} \approx 2.6$) for all the four flames during propagation. While Ruetsch et al. [30] and Im and Chen [33] reported this relationship for triple flames under idealized conditions, our simulations demonstrate a similar relationship under more complex conditions. For instance, Ruetsch et al. [30] used global chemistry with constant thermodynamics and transport properties to establish perfectly symmetric non-buoyant propagating triple flames in a uniform flow field, while our simulations include detailed chemistry as well as variable transport and

	S_L^0 (mm/s)	δ_L^0 (mm) ¹
0% H_2 -100% CH_4	400.0	0.47
25% H_2 -75% CH_4	497.0	0.44
50% H_2 -50% CH_4	693.0	0.37
75% H_2 -25% CH_4	1163.0	0.33

Table 1. Unstretched flame speeds (S_L^0) and thicknesses (δ_L^0) of H_2 -enriched CH_4 -air stoichiometric planar premixed flames, computed using the Chemkin package and GRI-Mech. 1.2 chemistry model.

number is given by $Ka = \delta_L^0 \cdot \kappa / S_{tri}$, and the Markstein number (Ma) is equal to the negative of the slope of each curve in this figure. The flame propagation speed decreases almost

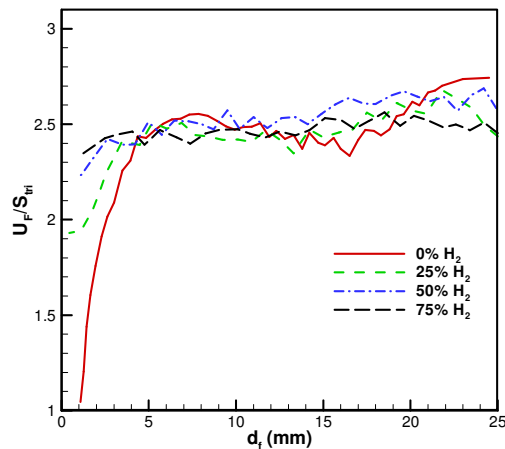


Figure 8. Normalized far-field flame speed (U_F/S_{tri}) as a function of distance from the burner rim (d_f) for the 0% H_2 -, 25% H_2 -, 50% H_2 -, and 75% H_2 -enriched CH_4 -air propagating flames.

decrease in the slope (i.e. $-Ma$). This is consistent with the results shown in Fig. 7. Previous experimental and numerical studies have shown that the flame speed decreases linearly with stretch for stoichiometric outwardly propagating spherical CH_4 -air and H_2 -air flames ($Ka > 0$), and that the latter is less sensitive to stretch [56,57]. Therefore, our results are consistent with those reported in the cited studies. Our results are also consistent with the experimental results of Huang et al. [17] who observed that

thermodynamic properties, and show that the flow redirection effect (i.e., $U_F/S_{tri} \approx \sqrt{(\rho_u/\rho_b)}$) is observed for propagating triple flames under more complex conditions, such as nonuniform flow field, presence of buoyancy, flame radiation, and asymmetric flow divergence upstream of the flame.

In order to examine the stretch-flame speed interactions, we present in Fig. 9, the normalized flame propagation speed (S_{tri}/S_L^0) as a function of Karlovitz number (Ka) for the flames discussed in the context of Fig. 7. Based on the flame stretch theory, $S_L^0/S_{tri} = 1 + MaKa$ [56], where the Karlovitz

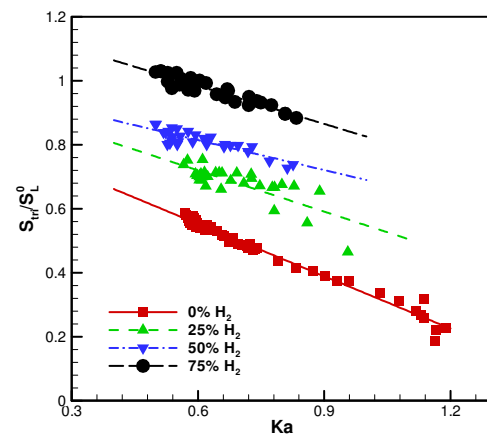


Figure 9. Normalized flame propagation speed (S_{tri}/S_L^0) as a function of Karlovitz number (Ka) for the flames discussed in the context of Fig. 7.

for outwardly propagating spherical flames burning a stoichiometric mixture of natural gas and hydrogen with air, the increase in H_2 content decreases the Markstein number, implying greater tendency towards diffusive-thermal instability.

IV. Conclusions

The effects of H_2 enrichment on the flame structure, dynamics, and stretch-flame speed interactions for propagating triple flames are characterized.

1. Following ignition, a well-defined triple flame is formed that propagates upstream with a nearly constant displacement speed (V_f) along the stoichiometric mixture fraction line. As this flame approaches the burner, it transitions to a double flame, and subsequently to a nonpremixed flame as it stabilizes at the burner rim. With increase in H_2 concentration in the fuel blend, both the flame displacement speed and propagation speed (S_{tri}) increase progressively due to the enhanced chemical reactivity, diffusivity, and preferential diffusion caused by H_2 enrichment.
2. The propagating triple flame structure is substantially modified with H_2 enrichment, which increases the flame curvature and mixture fraction gradient near the triple point. The addition of H_2 also enhances interactions between the reaction zones, which extend the flammability limits associated with CH_4 -air triple flames. In addition, H_2 enrichment makes the flow divergence ahead of the flame more asymmetric with respect to the stoichiometric mixture fraction line. Consequently, the triple point does not coincide with the flame leading edge, which is located at the local minimum flame curvature. This distinction is important in the context of determining the flame propagation speed (S_{tri}), since experimental studies have generally reported the flame speeds at the leading edge, while numerical investigations have reported these values at the triple point.
3. The flame dynamics at the triple point is also significantly modified with H_2 enrichment. In addition to the enhancement in flame propagation speed (S_{tri}), H_2 addition considerably increases both the hydrodynamic and curvature-induced stretch, and hence the total stretch. Moreover, the stretch-flame speed interactions are substantially modified, as H_2 enrichment reduces the flame sensitivity to stretch, i.e., it decreases the Markstein number (Ma) and increases flame tendency towards diffusive-thermal instability (i.e. $Ma \rightarrow 0$). These results are consistent with the previously reported experimental results for outwardly propagating premixed spherical flames burning a stoichiometric mixture of natural gas and hydrogen with air.
4. For all the H_2 enriched methane-air flames investigated in this study, the flame propagation speed decreases linearly with stretch. This is consistent with previous studies which have shown a negative correlation between flame speed and stretch for stoichiometric CH_4 -air and H_2 -air premixed flames with an effective Lewis number greater than one. While S_{tri} decreases linearly with stretch, the ratio U_f/S_{tri} (U_f being the far-field flame speed) is found to be proportional to the square root of the unburned to burned density ratio ($\sqrt{(\rho_u/\rho_b)}$). This is an important result because it implies that the flame stretch theory and flow redirection effect, which have previously been discussed in the context of idealized flame configurations, also apply to more complex flames such as H_2 -enriched CH_4 -air triple flames propagating in a non-uniform flow field.

V. References

1. M. S. Kumar, A. Ramesh, B. Nagalingam, "Use of Hydrogen to Enhance the Performance of a Vegetable Oil Fuelled Compression Ignition Engine," *Int. J. Hydrogen Energy* 28, 1143 (2003).
2. F. W. Hoehn, R. L. Baisly, M. W. Dowdy, "Advances in Ultra Lean Combustion Technology using Hydrogen-Enriched Gasoline", *Proc. 10th Intersociety Energy Conversion Conf.*, Newark, DE, USA, Paper 759173, 1975.
3. E. Sher, Y. Hacohen, "Measurements and Predictions of the Fuel Consumption and Emissions of a Spark Ignition Engine Fueled with Hydrogen-Enriched Gasoline," *Proc. Inst. Mech. Eng.* 203, 155 (1989).
4. V. Raman, J. Hansel, J. Fulton, F. Lynch, D. Bruderly, "Hythane—An Ultra Clean Transportation Fuel, Hydrogen Fuel for Surface Transportation," SAE Publication, p. 47-56, 1996.
5. B. Nagalingam, F. Duebel, K. Schmillen, "Performance Study using Natural Gas, Hydrogen-Supplemented Natural Gas and Hydrogen in AVL Research Engines," *Int. J. Hydrogen Energy* 8, 715 (1983).
6. M. R. Swain, M. J. Yusuf, Z. Dulger, M. N. Swain, "The Effects of Hydrogen Addition on Natural Gas Engine Operation," SAE Paper 932775, 1993.
7. G. A. Karim, I. Wierzb, Y. Al-Alousi, "Methane-Hydrogen Mixtures as Fuels," *Int. J. Hydrogen Energy* 21, 625(1996).

8. R. L. Hoekstra, Van Blarigan, P. N. Mulligan, "NO_x Emissions and Efficiency of Hydrogen, Natural Gas, and Hydrogen-Natural Gas Blended Fuels," SAE Paper 961103.
9. F. Schafer, "An Investigation of the Addition of Hydrogen to Methanol on the Operation of an Unthrottled Otto Engine," SAE Paper 810776, 1996.
10. C. G. Bauer, T.W. Forest, "Effect of Hydrogen Addition on the Performance of Methane-Fueled Vehicles. Part II: Driving Cycle Simulations," Int. J. Hydrogen Energy 26, 71 (2001).
11. M.A.S. Al-Baghdadi, "Hydrogen-Ethanol Blending as an Alternative Fuel of Spark Ignition Engines," Renewable Energy 28, 1471 (2002).
12. A. R. Choudhuri, S. R. Gollahali, "Intermediate Radical Concentration in Hydrogen-Natural Gas Blended Fuel Jet Flames," Int. J. Hydrogen Energy 4, 1293 (2004).
13. G.J. Rortveit, J.E. Hustad, F.A. Williams, "NO_x Formation in Diluted CH₄/H₂ Counterflow Diffusion Flames," Proc. 6th Int. Conf. Tech. Combust. Clean Environment, Porto, Portugal, 2000.
14. S. Naha, S. K. Aggarwal, "Fuel Effects on NO_x Emissions in Partially Premixed Flames, Combust. Flame 139, 90 (2004).
15. S. Naha, A. M. Briones, S. K. Aggarwal, "Effect of Fuel Blends on Pollutant Emissions in Flames," Combust. Sci. Tech. 177, 183 (2005).
16. C. G. Fotache, T. G. Kreutz, C. K. Law, "Ignition of Hydrogen-Enriched Methane Heated by Air," Combust. Flame 114, 436 (1998).
17. Z. Huang, Y. Zhang, K. Zeng, B. Liu, Q. Wang, D. Jiang, "Measurements of Laminar Burning Velocities for Natural Gas-Hydrogen-Air Mixtures," Combust. Flame 146, 302 (2006).
18. C.K. Law, G. Jomass, J.K. Bechtold, "Cellular Instabilities of Expanding Hydrogen/propane Spherical Flames at Elevated Pressures: Theory and Experiment," Proc. Combust. Inst. 30, 159 (2005).
19. R.W. Schefer "Hydrogen Enrichment for Improved Lean Flame Stability," Int. J. Hydrogen Energy 28, 1131 (2003).
20. E.R. Hawkes, J. H. Chen, "Direct Numerical Simulation of Hydrogen-Enriched Lean Premixed Methane-Air Flames," Combust. Flame 138, 242 (2004).
21. P.F. Flynn, R.P. Durrett, G.L. Hunter, A.O. Loye, O.C. Akinyemi, J.E. Dec, C.K. Westbrook, "Diesel Combustion: An Integrated View Combining Laser Diagnostics, Chemical Kinetics, and Empirical Validation," 1999 SAE Paper 1999-01-0509.
22. B.J. Lee, S.H. Chung, "Stabilization of Lifted Tribrachial Flames in a Laminar Nonpremixed Jet," Combust. Flame 109, 163 (1997).
23. H. Phillips, "Flame in a Buoyant Methane Layer," Proc. Combust. Inst. 10, 1277 (1965).
24. P. N. Kioni, B. Rogg, K. N. Bray, A. Liñán, "Flame Spread in Laminar Mixing Layers: The Triple Flame," Combust. Flame 95, 276(1993).
25. X. Qin, C.W. Choi, A. Mukhopadhyay, I.K. Puri, S.K. Aggarwal, V.R. Katta, "Triple Flame Propagation and Stabilization in a Laminar Axisymmetric Jet," Combust. Theory Modelling 8, 293 (2004).
26. Y.S. Ko, S.H. Chung, "Propagation of Unsteady Tribrachial Flames in Laminar Non-Premixed Jets," Combust. Flame 118, 151(1999).
27. J. Lee, S. H. Won, S. H. Jin, S. H. Chung, "Lifted Flames in Laminar Jets of Propane in Coflow Air," Combust. Flame 135, 449(2003).
28. A.J. Lock, A.M. Briones, X. Qin, S.K. Aggarwal, I.K. Puri, U. Hegde, "Liftoff Characteristics of Partially Premixed Flames under Normal and Microgravity Conditions," Combust. Flame 143, 159 (2005).
29. A.M. Briones, S.K. Aggarwal, V.R. Katta, "A Numerical Investigation of Flame Liftoff Stabilization, and Blowout," Phys. Fluids 18, 1 (2006).
30. G.R. Ruetsch, L. Vervisch, A. Liñán, "Heat Release Effects on Triple Flames," Phys. Fluids 7, 1447 (1995).
31. S.F. Ahmed, E. Mastorakos, "Spark Ignition of Lifted Turbulent Jet Flames," Combust. Flame 146, 215(2006).
32. S.F. Ahmed, E. Mastorakos, "Spark Ignition of Lifted Turbulent Jet Flames," Combust. Flame 146, 215(2006).
33. H.G. Im, J.H. Chen, "Structure and Propagation of Triple Flames in Partially Premixed Hydrogen-Air Mixtures," Combust. Flame 119, 436 (1999).
34. I.K. Puri, S.K. Aggarwal, S. Ratti, R. Azzoni, "On the Similitude between Lifted and Burner-Stabilized Triple Flames: A Numerical and Experimental Investigation," Combust. Flame 124, 311 (2001).
35. S.H. Won, J. Kim, K.J. Hong, M.S. Cha, S.H. Chung, "Stabilization Mechanism of Lifted Flame Edge in the Near Field of Coflow Jets for Diluted Methane," Proc. Combust. Inst. 30, 339 (2005).

36. Z. Shu, S. K. Aggarwal, V. R. Katta, I. K. Puri, "Flame-Vortex Dynamics in an Inverse Partially Premixed Combustor: The Froude Number Effects," *Combust. Flame* 111, 276 (1997).
37. R. Azzoni, S. Ratti, I. K. Puri, S. K. Aggarwal, "Gravity Effects on Triple Flames: Flame Structure and Flow Instability," *Phys. Fluids* 11, 3449 (1999).
38. X. Qin, I. K. Puri, S. K. Aggarwal, V. R. Katta, "Gravity, Radiation, and Coflow Effects on Partially Premixed Flames," *Phys. Fluids* 16, 2963(2004).
39. R. Siegel, J. R. Howell, *Thermal Radiation Heat Transfer*, Hemisphere Publishing Corporation, New York, 1981.
40. R. C. Reid, J. M. Prausnitz, B. E. Poling, *The properties of gases and liquids*, McGraw-Hill, New York, 1987.
41. M. Frenklach, H. Wang, C.-L. Yu, M. Goldenberg, C.T. Bowman, R.K. Hanson, D.F. Davidson, E.J. Chang, G.P. Smith, D.M. Golden, W.C. Gardiner and V. Lissianski, http://www.me.berkeley.edu/gri_mech/; and Gas Research Institute Topical Report: M. Frenklach, H. Wang, M. Goldenberg, G.P. Smith, D.M. Golden, C.T. Bowman, R.K. Hanson, W.C. Gardiner and V. Lissianski, 'GRI-Mech---An Optimized Detailed Chemical Reaction Mechanism for Methane Combustion,' Report No. GRI-95/0058, November 1, 1995.
42. F.N. Egolfopoulos, D.L. Zhu, C. K. Law, "Experimental and Numerical Determination of Laminar Flame Speeds: Mixtures of C₂-Hydrocarbons with Oxygen and Nitrogen," *Proc. Combust. Inst.* 23, 471 (1990).
43. D.E. Heard, J.B. Jeffries, G.P. Smith, D.R. Crosley, "LIF Measurements in Methane/Air Flames of Radicals Important in Prompt-NO Formation," *Combust. Flame* 88, 137 (1992).
44. V. R. Katta, F. Takahashi, G. T. Linteris, "Suppression of Cup-burner Flames Using Carbon Dioxide in Microgravity," *Combust. Flame* 137, 506 (2004).
45. V. R. Katta, L. P. Goss, W. M. Roquemore, "Numerical Investigation of Transitional Jet Diffusion Flames," *AIAA J.* 32, 84 (1994).
46. Z. Shu, B. Krass, C. Choi, S. K. Aggarwal, V. Katta, I. K. Puri, "An Experimental and Numerical Investigation of the Structure of Steady Two-Dimensional Partially Premixed Methane-Air Flames," *Proc. Combust. Inst.* 27, 625 (1998).
47. X. Qin, *An Investigation of Unsteady Partially Premixed Flames*, Ph.D. Thesis, University of Illinois at Chicago, 2004.
48. R. W. Bilger, "The Structure of Turbulent Nonpremixed Flames," *Proc. Combust. Inst.* 22 475.
49. H. Yamashita, M. Shimada, T. Takeno, "A Numerical Study on Flame Stability at Transition Point of Jet Diffusion Flames," *Proc. Combust. Inst.* 26, 27 (1996).
50. H.C. Barnett, R.R. Hibbard (eds.), "Basic Consideration in the Combustion of Hydrocarbon Fuels with Air," NACA Report 1300, 1959.
51. M.G. Zabetakis, *Flammability Characteristics of Combustible Gases and Vapors*, U.S. Bureau of Mines, Bulletin 627, 1965.
52. I. Wierzbna, B.B. Ale, "Rich Flammability Limits of Fuel Mixtures Involving Hydrogen at Elevated Temperatures," *Int. J. Hydrogen Energy* 25, 75 (2000).
53. A. Mukhopadhyay, I.K. Puri, "An Assessment of Stretch Effects on a Flame Tip Using Thin Flame and Thick Flame Formulations," *Combust. Flame* 133, 499 (2003).
54. G.R. Ruetsch, J.E. Broadwell, "Effects of Confinement on Partially Premixed Flames," Center for Turbulence Research, Annual Res. Briefs, 1995.
55. R.J. Kee, F.M. Rupley, J.A. Miller, M.E. Coltrin, J.F. Grcar, E. Meeks, H. K. Moffat, A. E. Lutz, G. Dixon-Lewis, M. D. Smooke, J. Warnatz, G. H. Evans, R. S. Larson, R. E. Mitchell, L. R. Petzold, W. C. Reynolds, M. Caracotsios, W. E. Stewart, P. Glarborg, C. Wang, C. L. McLellan, O. Adigun, W. G. Houf, C. P. Chou, S. F. Miller, P. Ho, P. D. Young and D. J. Young, CHEMKIN Release 4.0.2, Reaction Design, San Diego, CA (2005).
56. M.I. Hassan, K.T. Aung, G.M. Faeth, "Measured and Predicted Properties of Laminar Premixed Methane/Air Flames at Various Parameters," *Combust. Flame* 115, 539 (1998).
57. O. C. Kwon, G. M. Faeth, "Flame/Stretch Interactions of Premixed Hydrogen-Fueled Flames: Measurements and Predictions," *Combust. Flame* 124, 590 (2001).



Investigations on double-state behavior of the counterflow premixed flame system

Viswanath R. Katta ^{a,*}, Shengteng Hu ^b, Peiyong Wang ^b,
Robert W. Pitz ^b, William M. Roquemore ^c, James R. Gord ^c

^a Innovative Scientific Solutions, Inc., 2766 Indian Ripple Road, Dayton, OH 45440, USA

^b Mechanical Engineering Department, Vanderbilt University, Nashville, TN 37235, USA

^c Propulsion Directorate, Air Force Research Laboratory, Wright Patterson Air Force Base, OH 45433, USA

Abstract

The counterflow flame system established between lean-methane–air and lean-hydrogen–air streams is investigated experimentally and numerically. A two-dimensional model known as UNICORN was used for the simulation. Detailed measurements for temperature and species concentrations were obtained along the centerline using Raman spectroscopy. A double-state behavior for this flame system was identified in the numerical simulations, which was later confirmed by the experiments. For the given flow conditions, the flame system can have either a single-flame or a double-flame structure depending on the way those conditions were achieved. Detailed comparisons were made between measurements and calculations for the two flame structures. Calculations for various lean methane–air mixtures and stretch rates were performed to understand the double-state behavior of counterflow premixed flames. It was found that the flame system exhibits double-state behavior only for leaner ($\phi_{\text{CH}_4} < 0.74$) methane–air mixtures. Aerodynamic and chemical structures of the flames in different stretch-rate regimes were analyzed. When stretch rate on the flame system is increased, the flame transitions from a double-flame to a single-flame structure due to aerodynamic-cooling process. When stretch rate is decreased, the flame does not transition back to the double-flame structure due to stretch effects on molecular diffusion. However, for ($\phi_{\text{CH}_4} > 0.81$), decrease in stretch rate increases flame temperature due to lack of stretch-induced cooling and returns the flame structure to a double-flame one. For a narrow range of equivalence ratios (0.74–0.81) counterflow premixed flames exhibit a hysteresis property.

© 2006 The Combustion Institute. Published by Elsevier Inc. All rights reserved.

Keywords: Premixed flames; Extinction; Stretch rate; Double states; Lean combustion

1. Introduction

Lean combustion is of interest due to its potential advantages in limiting thermal NO_x emissions and in increasing fuel consumption efficiency.

Typically, diluted fuel–air mixtures are obtained through either available excess air or exhaust-gas recirculation. Lean combustion has been used in gas turbines and direct injection spark ignition (DISI) engines. However, a critical problem in using lean combustion is that it tends to produce unburned hydrocarbon pollutants. For example, in DISI engines, ultra-lean combustion is achieved by charge stratification. The fuel/air mixture is

* Corresponding author. Fax: +1 937 656 4110.
E-mail address: vrkatta@erinet.com (V.R. Katta).

inhomogeneous, leading to the simultaneous formation of lean, rich and stoichiometric regions. For the inhomogeneous reactants, Haworth et al. [1] simulated turbulent inhomogeneous combustion in DISI engines and found that hydrocarbon-rich fragments and oxidizer penetrate behind the primary heat-release zone to form a secondary reaction zone and, thereby, pollutants. Flames occurring in an inhomogeneously mixed fuel and air regions are also examples of partially premixed combustion. Some of this partially premixed mixture is so lean that it does not burn. However, such ultra-lean mixtures may still combust if hot products interact with it. That is, under certain conditions, the lean mixture region can burn and thus reduce the potential pollutants. The focus of this work is to study interaction of lean mixture with hot products that are needed to maintain the lean region burning. Partially premixed flames have been studied widely. In particular, the downstream interaction of two premixed streams was investigated by Sohrab et al. [2]. On the other hand, most practical flames are stretched to different extents. The stretch effects combined with other aspects such as the effect of Lewis number or curvature will modify flame structure significantly [3,4]. Considering the various conditions that exist simultaneously in inhomogeneous fuel/air reaction, a set of CH_4 /air flames with a wide range of equivalence ratios and stretch rates impinging upon counterflowing hot products are studied experimentally and numerically. The opposed jet burner that generates nearly flat flames are widely used to study chemical kinetics and species transport under aerodynamic stretch. Using the counterflow jet flames, partially premixed CH_4 /air versus air flame structures were investigated [5,6]. Structures of the lean partially premixed CH_4 and C_3H_8 flames established between the fuels and the hot products have also been investigated [7–9]. In general, premixed flames [10,11] are much less sensitive to stretch than diffusion flames [12]. In the present work, stretch effects on the flame structure of lean CH_4 /air mixtures are studied using a two-dimensional, detailed transport, complex chemistry numerical model.

2. Numerical model

A time-dependent, axisymmetric mathematical model known as UNICORN (Unsteady Ignition and Combustion using ReactionNs) [13,14] is used for the simulation of the unsteady counterflow premixed flames. It solves for axial- and radial-momentum equations, continuity, and enthalpy- and species-conservation equations on a staggered-grid system. A clustered mesh system is employed to trace the large gradients in flow variables near the flame surface. A detailed chemical-

kinetics model (GRI Version 1.2) of Gas Research Institute [15] is incorporated into UNICORN for the investigation of methane–hydrogen flames. It consists of 32 species and 346 elementary-reaction steps. Thermo-physical properties such as enthalpy, viscosity, thermal conductivity, and binary molecular diffusion of all the species are calculated from the polynomial curve fits developed for the temperature range 300–5000 K. Mixture viscosity and thermal conductivity are then estimated using the Wilke and Kee expressions, respectively. Molecular diffusion is assumed to be of the binary-diffusion type, and the diffusion velocity of a species is calculated using Fick's law and the effective-diffusion coefficient of that species in the mixture. A simple radiation model based on the optically thin-media assumption [16] is incorporated into the energy equation. Only radiation from CH_4 , CO , CO_2 , and H_2O is considered in the present study. Radiation from soot is not considered, which is justified for the nearly non-sooting lean premixed flames studied.

The finite-difference forms of the momentum equations are obtained using an implicit QUICK-EST scheme [17], and those of the species and energy equations are obtained using a hybrid scheme of upwind and central differencing. At every time step, the pressure field is accurately calculated by solving all the pressure Poisson equations simultaneously and using the LU (Lower and Upper diagonal) matrix-decomposition technique. The computational domain is bounded between sets of inflow boundaries in the axial direction and between the axis of symmetry and outflow boundaries in the radial direction. The boundary conditions are treated in the same way as that reported in earlier papers [17,18].

3. Experiment

The counterflow burner used in this study was designed by Seshadri et al. [19] which has been extensively considered for hydrogen- and hydrocarbon-fueled diffusion flames and for hydrocarbon-fueled premixed flames. With the honeycomb inserts, rather than wire screens, it has also been used for the studies of lean H_2 /air premixed flames [20]. The schematic diagram of the burner along with the supplied flows is shown in Fig. 1. The burner system consists of 25-mm diameter inner nozzles that are separated by 12.6 mm. Methane–air mixture was issued from the top nozzle while hydrogen–air mixture was issued from the bottom nozzle. The honeycomb flow straighteners inserted in the flow supplies yielded uniform exit velocities [20]. A low-speed nitrogen flow was issued from the top and bottom outer nozzles for protecting the flame from the room-air disturbances. The exit temperature for all the gases was 300 K. Measurements of major

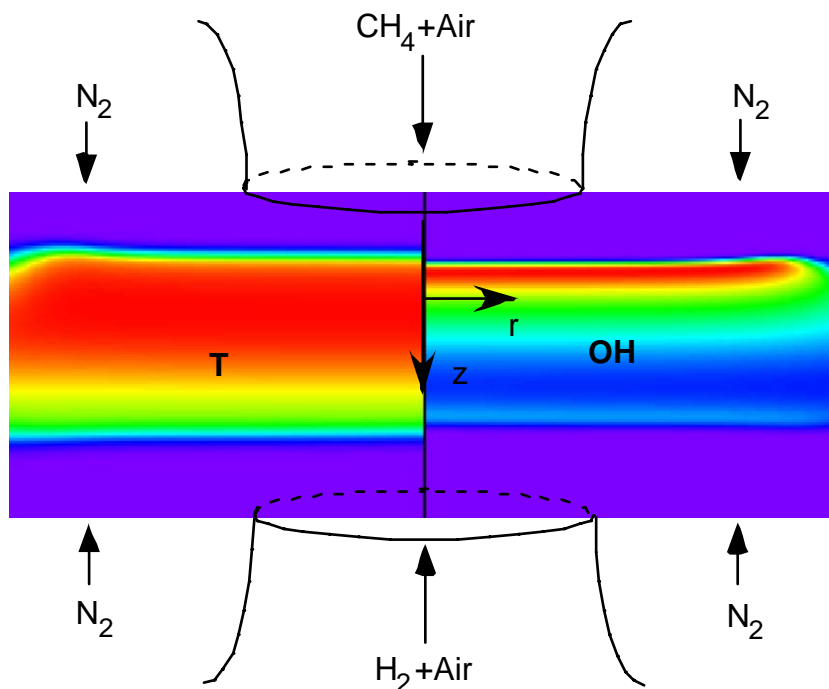


Fig. 1. Premixed flame system used for the investigation of products-supported lean combustion. Typical temperature and OH-concentration distributions are shown in the left and right halves, respectively.

species and temperature were made along the centerline using a non-intrusive, Raman-scattering diagnostic system [8,20]. Experiments were performed for various equivalence ratios and stretch rates. Details of eight flames that were classified into three groups are given in Ref. [20]. For example, Group A includes three flames with the same CH_4/air mixture (with an equivalence ratio of 0.68) and lean H_2/air mixture (with an equivalence ratio of 0.28) but subjected to different stretch rates [20]. In this study, two additional flames are measured with a slightly leaner CH_4/air mixture ($\phi = 0.64$).

4. Results and discussion

Two-dimensional calculations for the premixed flame system developed between the upper and lower nozzles were made using UNICORN code on a grid system that has 421×101 node points in the axial (z) and radial (r) directions, respectively. Flat velocity profiles were used at the nozzle exits. Computed results in the form of temperature and OH-concentration distributions for a typical flame in Group A are shown in Fig. 1. The global stretch rate (defined as the ratio between twice the velocity difference and the nozzle separation) applied on this flame was 90 s^{-1} . Even though the computational domain was

extended to 20 mm in the radial direction, only the data up to 15 mm is shown in Fig. 1. Calculations have yielded a double-flame structure with methane flame (lower) burning more intensely than the hydrogen one (upper). Former flame is also shorter (in the radial direction) than the latter. Detailed comparisons made between the computed and measured temperature and species profiles along the centerline [21] suggested that UNICORN code with GRI-V1.2 chemical kinetics predicts the flame structure accurately.

Increasing the velocities of the hydrogen- and methane-fuel jets increases the applied stretch rate on the double-flame system and decreases the separation between the two flames. At a certain stretch rate, the methane flame extinguishes and the flame system switches from a double-flame structure to a single-flame one. Interestingly, significant differences developed between the predictions and measurements when the stretch rate was increased to 204 s^{-1} . While experiments produced a single flame, calculations have predicted a double-flame structure. Repeated calculations with different grid sizes and for stretch rates slightly higher and lower than 204 s^{-1} failed to predict the single-flame structure. Note that calculations made by Cheng et al. [20] using OPPDIF code also resulted in a double-flame structure for this stretch-rate condition. Their efforts in using different chemical kinetics models have also failed.

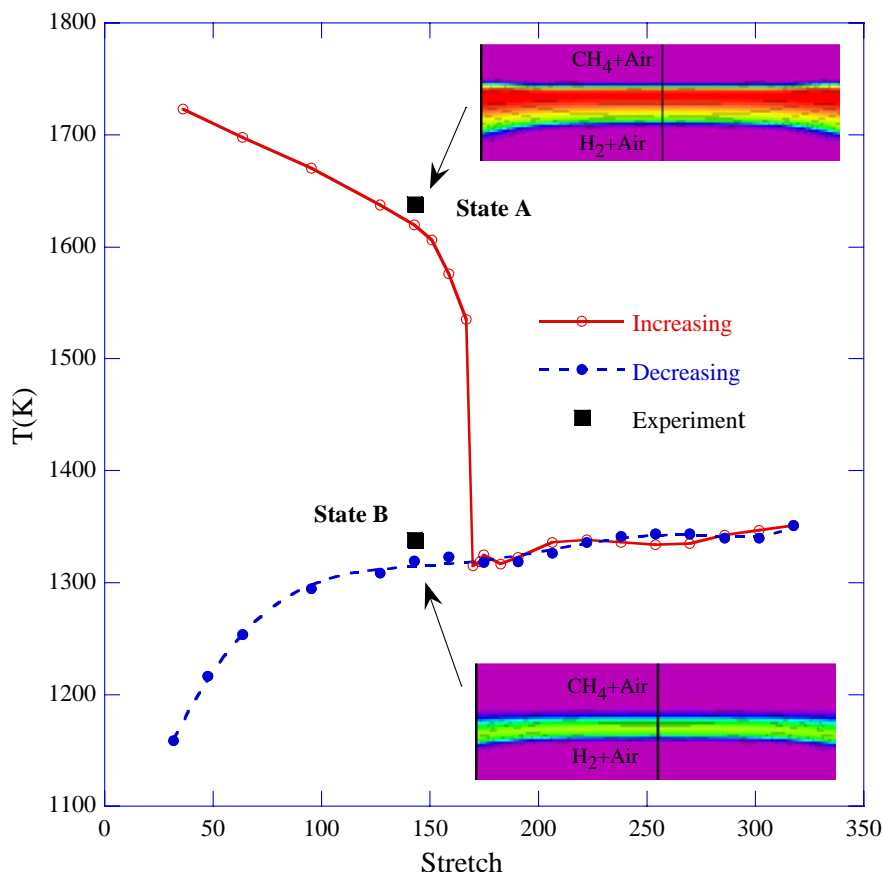


Fig. 2. Response of a premixed flame formed between counter-flowing methane–air and hydrogen–air jets to increasing (open circles) and decreasing (solid circles) strain rates. $\Phi_{\text{CH}_4} = 0.64$, $\Phi_{\text{H}_2} = 0.28$. Insets show the temperature images of two stable states under identical conditions.

Additional calculations are performed for understanding the discrepancy between the predicted and measured flame structures for the 204-s^{-1} -stretch-rate case. Typically, finite-rate chemistry calculations for a flame are performed using an initial solution that is either generated by a global-chemistry model or constructed from a known solution at different flow conditions. Occasionally, such calculations are also performed from a cold-flow solution and by using a high-temperature ignition spot. In the present study, calculations for the flame at a given stretch rate are performed from a known solution at a lower stretch rate. Note that this approach resulted in accurate predictions of the double-flame structure for low-stretch-rate cases and the single-flame structure for the high-stretch-rate cases, but failed to predict the single-flame structure for the low-stretch-rate 204-s^{-1} case. While repeating the calculations for the 204-s^{-1} case using different initial conditions, accidentally one calculation was provided with a high-stretch-rate flame as initial solution. Surprisingly, that calculation converged

to a single-flame structure – just the way that was seen in the experiments, and gave the first indication for the existence of two stable states for the methane–air/hydrogen–air flame system.

For understanding the double-state behavior of the counterflow premixed flames, experimental and numerical studies are performed on a flame system with $\Phi_{\text{CH}_4} = 0.64$, $\Phi_{\text{H}_2} = 0.28$. Calculations are performed first for a low-stretch-rate case using the global-chemistry solution as the initial data and then for higher-stretch-rate cases using previously obtained solution as the initial data. Calculations are repeated for all the stretch-rate cases starting from the highest-stretched flame and then by decreasing the stretch rate. Peak temperature (T_f) along the centerline computed for various stretch rates are shown in Fig. 2. Data computed with increasing-stretch-rate approach are shown with open circles and those computed with decreasing-stretch-rate approach are shown with solid circles. Solid and broken lines are drawn through the symbols for clarity. For all the stretch rates $\geq 168\text{ s}^{-1}$ flame

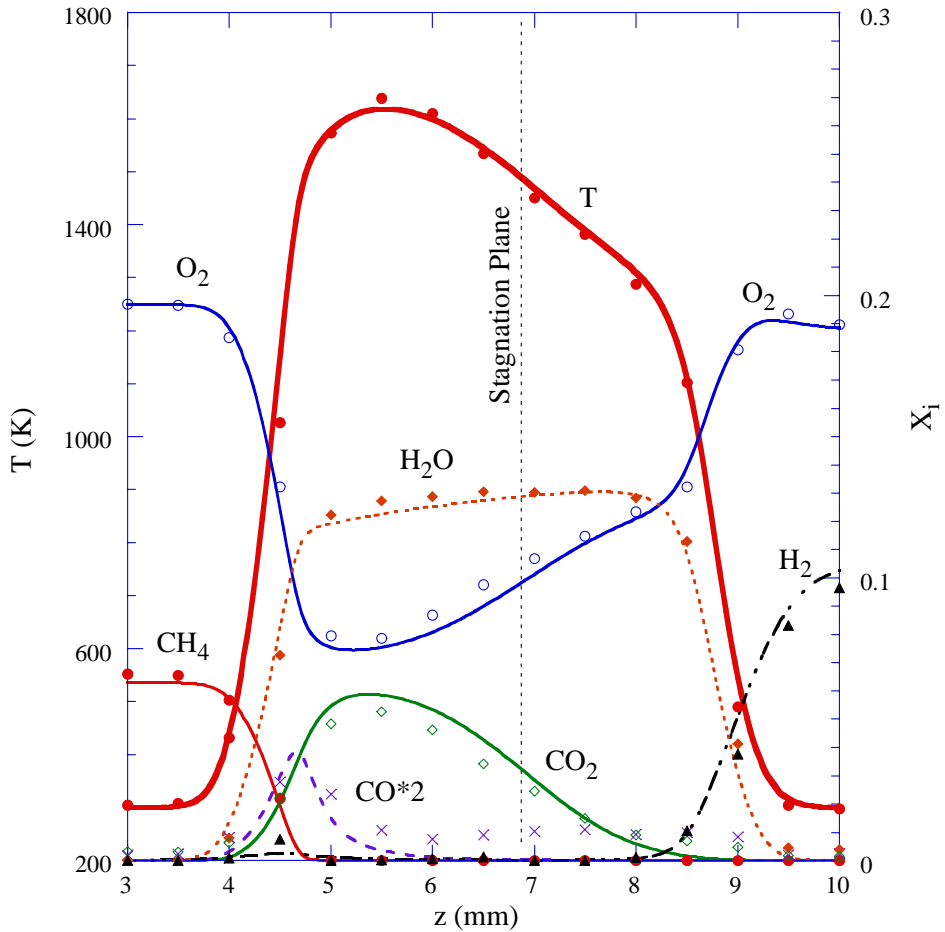


Fig. 3. Computed (lines) and measured (symbols) temperature and species distributions along stagnation line for the flame in State A. $\phi_{\text{CH}_4} = 0.64$, $\phi_{\text{H}_2} = 0.28$, $k_{\text{global}} = 143 \text{ s}^{-1}$ flame.

system has a unique solution independent of how that strain rate was arrived at. There is a slight scatter in the temperature data as the planar flames formed in the counterflow burner tend to oscillate weakly. For all the stretch rates $< 168 \text{ s}^{-1}$ flame system has two stable states; namely, A and B. Therefore, flame temperature in this regime depends on the way the stretch rate was achieved, i.e., through increasing or decreasing. Note, the double-state behavior is also confirmed with OPPDIF code and using increasing- and decreasing-stretch-rate approaches.

Experiments for the $\phi_{\text{CH}_4} = 0.64$ – $\phi_{\text{H}_2} = 0.28$ flame system at a given stretch rate are performed first by establishing the flame using a blow torch and then significantly perturbing the flame using a metal wire. Inline with the computations, experiments have also shown the existence of two stable states. The two peak temperatures measured for the 143 s^{-1} -stretch-rate case are shown in Fig. 2 using solid squares. Good agreement between predictions and experiments was found for both

states (A and B). Computed-flame images in terms of temperature distributions corresponding to these states are shown in Fig. 2 as insets. Several observations can be noted from the flame behavior:

1. Transition from state A to B occurs sharply with a small change in stretch rate.
2. Once the flame system is in state B, it is not possible to bring it back to state A through changing stretch rate. State A was achieved through the use of global-chemistry solution as initial condition in the calculations and through the use of flame torch for ignition in the experiment.
3. Peak temperature decreases (from 1722 K) with stretch rate when the flame system is in state A and increases (from 1160 K) when it is in state B.

Detailed comparisons between the predicted and measured structures of the 143 s^{-1} -stretch-rate

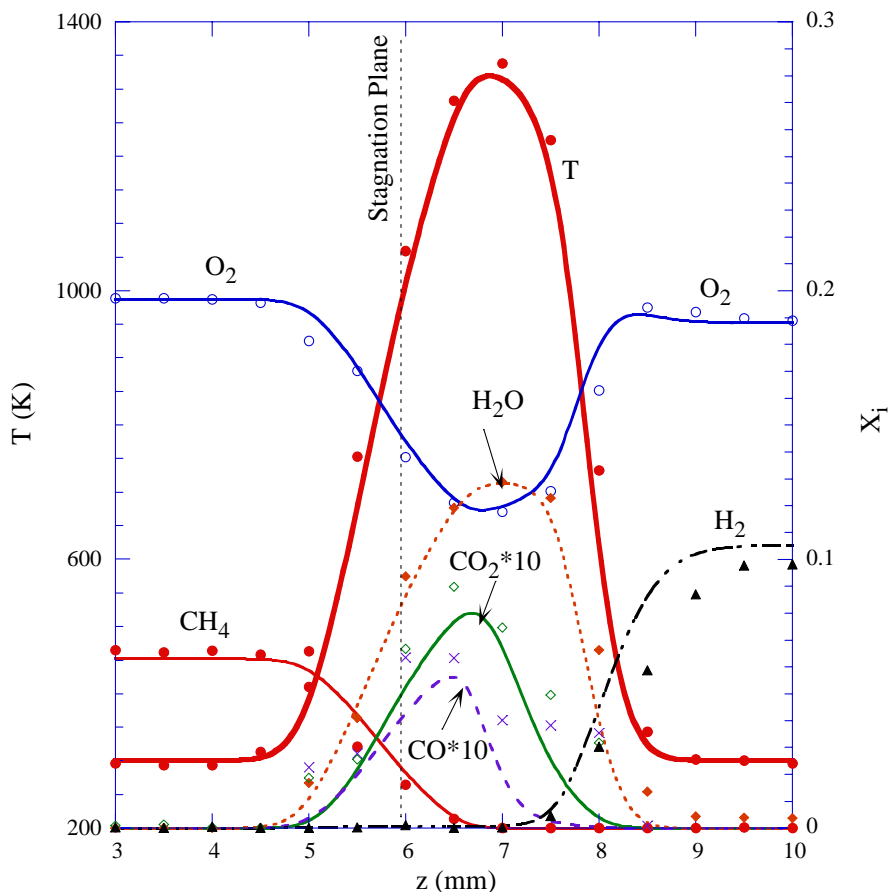


Fig. 4. Computed (lines) and measured (symbols) temperature and species distributions along stagnation line for the flame in State B. $\Phi_{\text{CH}_4} = 0.64$, $\Phi_{\text{H}_2} = 0.28$, $k_{\text{global}} = 143 \text{ s}^{-1}$ flame.

flame system for states A and B are shown in Figs. 3 and 4, respectively. Temperature and species distributions along the centerline are compared. Here, z is the distance from the top nozzle. Locations of the stagnation points are indicated with vertical lines. Note that the flow and boundary conditions for the flame systems shown in Figs. 3 and 4 are identical. The only difference between these two flame systems is in the way they were arrived at, i.e., in the initial conditions. The double-flame structure of state A (Fig. 3) is well reproduced. The methane–air mixture produced a flame on the left side ($z \sim 5.4 \text{ mm}$) of the stagnation point with a peak temperature of $\sim 1720 \text{ K}$ and the hydrogen–air mixture produced a flame on the right side ($z \sim 8.1 \text{ mm}$) with a temperature of $\sim 1300 \text{ K}$. When the flame system is operating in state B (Fig. 4), the methane flame extinguished and only the hydrogen flame is established at $z \sim 7 \text{ mm}$ with a peak temperature of $\sim 1320 \text{ K}$. Due to lack of methane combustion only trace amounts of CO and CO_2 are produced. Complete depletion of methane in Fig. 4 is resulting from the counterflow

geometry rather than from combustion. Over all, very good agreement between experiment and calculations is achieved for the flames in the two different states.

>The major distinction between the flames in states A and B is that methane is burning in one state (A) and is not in the other (B). This means that the temperature resulting from hydrogen–air combustion is not sufficient for igniting the methane–air mixture with $\Phi = 0.64$. It is known that ignition temperature for fuel-lean mixture decreases with equivalence ratio. Therefore, for a particular equivalence ratio >0.64 the counterflow premixed flame system may not exhibit double-state behavior. For verifying this hypothesis a series of calculations are performed by using methane–air mixtures with different equivalence ratios. Both the increasing- and decreasing-stretch-rate approaches are used. Equivalence ratio for H_2/air mixture was not changed ($\Phi_{\text{H}_2} = 0.28$).

Computed peak flame temperatures along the centerline for various CH_4/air equivalence ratios

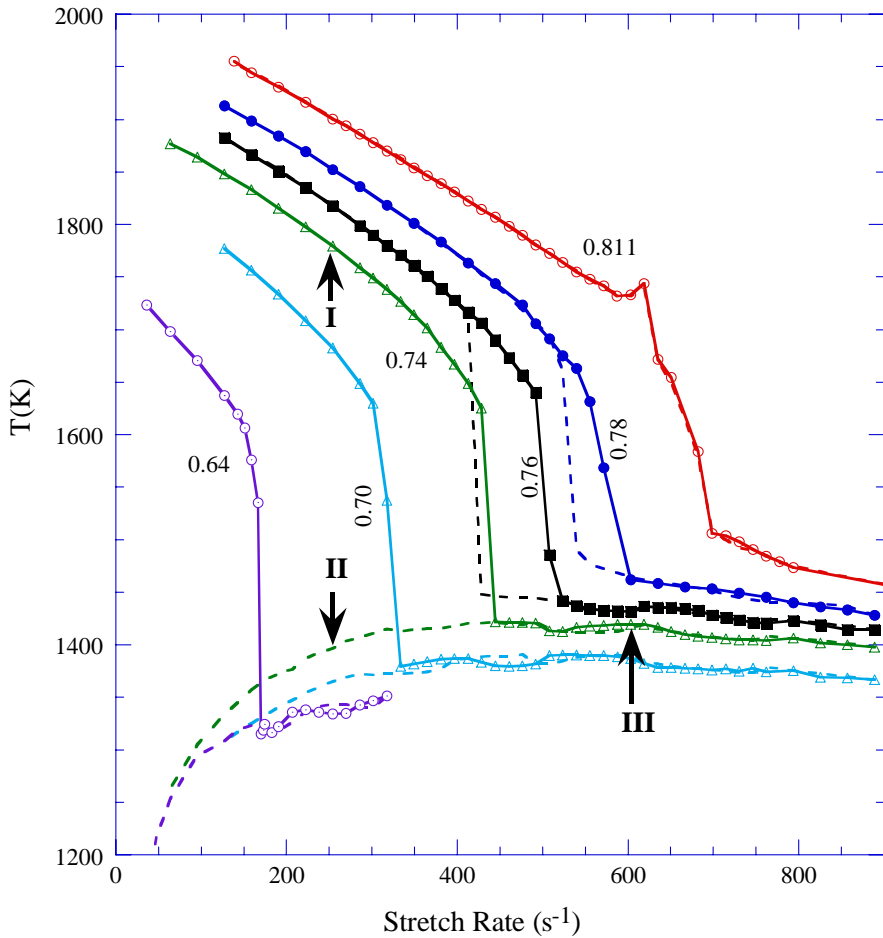


Fig. 5. Response of various premixed flames formed between counter-flowing methane–air and hydrogen–air jets to increasing (symbols) and decreasing (broken lines) strain rates. Φ_{CH_4} is varied while Φ_{H_2} is kept constant at 0.28.

are shown at different stretch rates in Fig. 5. Symbols represent the data obtained while increasing the stretch rate and solid lines are the curves fitted through this data. Broken lines represent the curves passing through the data obtained while decreasing the stretch rate. The transition at which flame system jumps from state A to B is shifted to higher stretch rates as the CH_4/air equivalence ratio is increased. Moreover, transition took place over a wider range of stretch rates in higher CH_4/air -equivalence-ratio cases. Unlike in the case of $\Phi_{\text{CH}_4} = 0.64$, where flame system exhibited double-state behavior, the decreasing-stretch-rate data (broken line) for $\Phi_{\text{CH}_4} = 0.811$ followed the increasing-stretch-rate data (solid line) – suggesting that the flame system did not possess double-state behavior. Nevertheless, the flame system still has a double-flame structure for stretch rates $< 610 \text{ s}^{-1}$ and a single-flame structure (with methane flame being extinguished) for stretch rates $> 700 \text{ s}^{-1}$. More interestingly, for

intermediate CH_4/air equivalence ratios such as 0.76 and 0.78, flame system exhibits hysteresis. For example, in $\Phi_{\text{CH}_4} = 0.76$ case, flame system stays in state A (double-flame state) until the stretch rate is increased beyond 500 s^{-1} , but it does not come back to state A from state B until the stretch rate is decreased to 430 s^{-1} . Such a brief hold back in state B could lead to combustion-induced noise if stretch rate on the flame system were cyclically varied as in unsteady counterflow experiments [22,23].

Reasons for the products-supported premixed flames to exhibit double-state behavior can be understood by studying the differences in flow and chemical structures of flame systems formed under different stretch-rate regimes. Flames in regimes marked as I, II, and III in Fig. 5 for CH_4/air equivalence ratio of 0.74 are considered for this purpose. While regimes I and II represent flames in states A and B, respectively, at a stretch rate of 250 s^{-1} , regime III represents the flame in

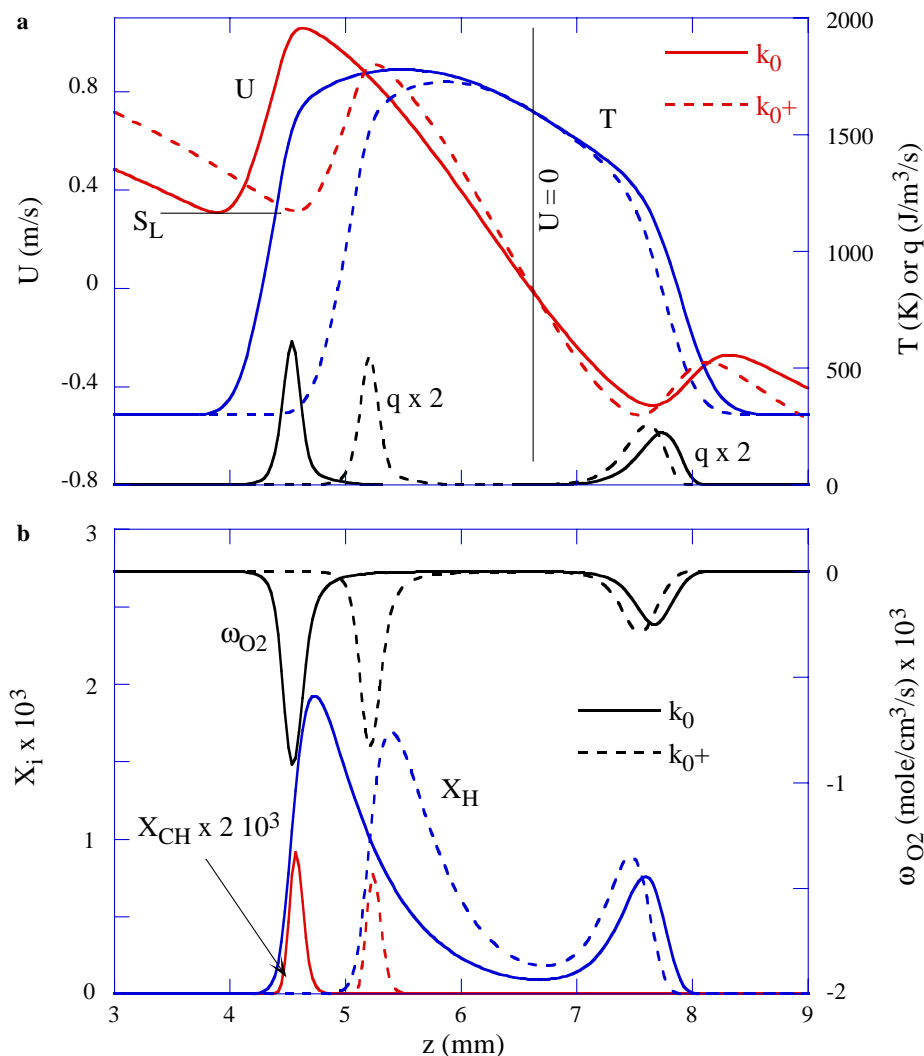


Fig. 6. Changes in flame structure to perturbation in strain rate when State A flame is established under low-strain-rate conditions. $\Phi_{CH_4} = 0.74$, $\Phi_{H_2} = 0.28$, and $k_0 = 250 \text{ s}^{-1}$. Distributions of (a) velocity, temperature and heat release rate, and (b) H and CH mole fractions and O_2 consumption rate. Broken lines represent the flame structure for $k_0^+ = 275 \text{ s}^{-1}$.

state B at a stretch rate of 600 s^{-1} . Temperature, velocity, and heat release rate distributions along the centerline for the flames in regimes I, II, and III are shown using solid lines in Figs. 6a, 7a, and 8a, respectively. Concentrations of H and CH radicals and oxygen consumption rates for the three flames are shown using solid lines in Figs. 6b, 7b, and 8b, respectively. Stagnation points are marked with $U = 0$ lines. Broken lines in Figs. 6–8 represent the data obtained for the flame systems stretched 10% more than those in I, II, and III (i.e., 275, 275, and 660 s^{-1}), respectively.

As shown in Fig. 6, both methane and hydrogen flames are present in regime-I flames. Heat

release rate and temperature generated by the methane flame are higher than those generated by the 0.28-equivalence-ratio hydrogen flame. Because of the counterflow configuration heat generated by the hotter methane flame heats the cooler hydrogen flame [24]. Consequently, the temperature of the methane flame is lower and that of the hydrogen flame is higher compared to their respective adiabatic flame temperatures. Note the less-than-unity Lewis number of the hydrogen fuel further increases the flame temperature when the flame is stretched [4]. Heat release rate and oxygen consumption rate indicate that the reaction zones of the two flames are well separated. However, temperature and

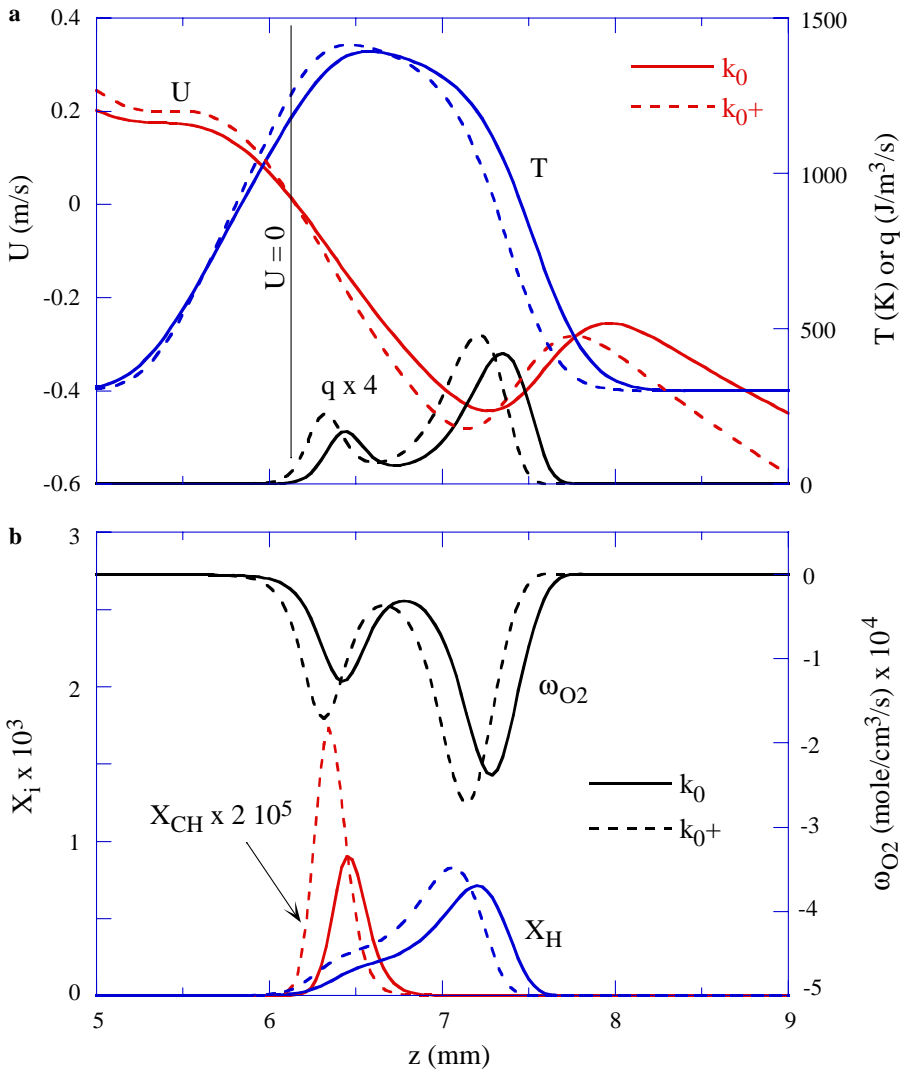


Fig. 7. Changes in flame structure to perturbation in strain rate when State B flame is established under low-strain-rate conditions. $\Phi_{CH_4} = 0.74$, $\Phi_{H_2} = 0.28$, and $k_0 = 250 \text{ s}^{-1}$. Distributions of (a) velocity, temperature and heat release rate, and (b) H and CH mole fractions and O_2 consumption rate. Broken lines represent the flame structure for $k_0^+ = 275 \text{ s}^{-1}$.

H-mole-fraction distributions suggest a strong interaction between the two flames through product species. These flames come closer when the stretch rate on the system increases (compare solid and broken lines in Fig. 6), which results in more interaction between the two flames. As a result, the temperature of the methane flame decreases further and that of hydrogen flame increases further; which, as shown in Figs. 2 and 5, translates into a decrease in peak temperature of the flame system with stretch rate (for regime I flames).

Extinction temperature for hydrogen flames ($\sim 1150 \text{ K}$) [25] is less than that of methane flames ($\sim 1500 \text{ K}$) [26]. As a result, the methane flame extinguishes first when the temperature of the meth-

ane-air/hydrogen-air flame system decreases and the structure of the double-flame system transitions into a single-flame one (regime II) as shown in Fig. 7. Unburned methane gas in this mode diffuses into the products generated by the hydrogen flame and a part of it gets decomposed (low-temperature chemistry) and releases a small amount of heat. Significant drop in oxygen consumption rate and CH and H mole fractions also suggest incomplete combustion of methane fuel. Nevertheless, reaction zones for the two fuels came close to each other and interacting directly. Note the peak in heat release rate from methane decomposition appearing on the hydrogen side of the stagnation point. As diffusion fluxes increase with stretch rate, heat release rate and temperature also increase (compare

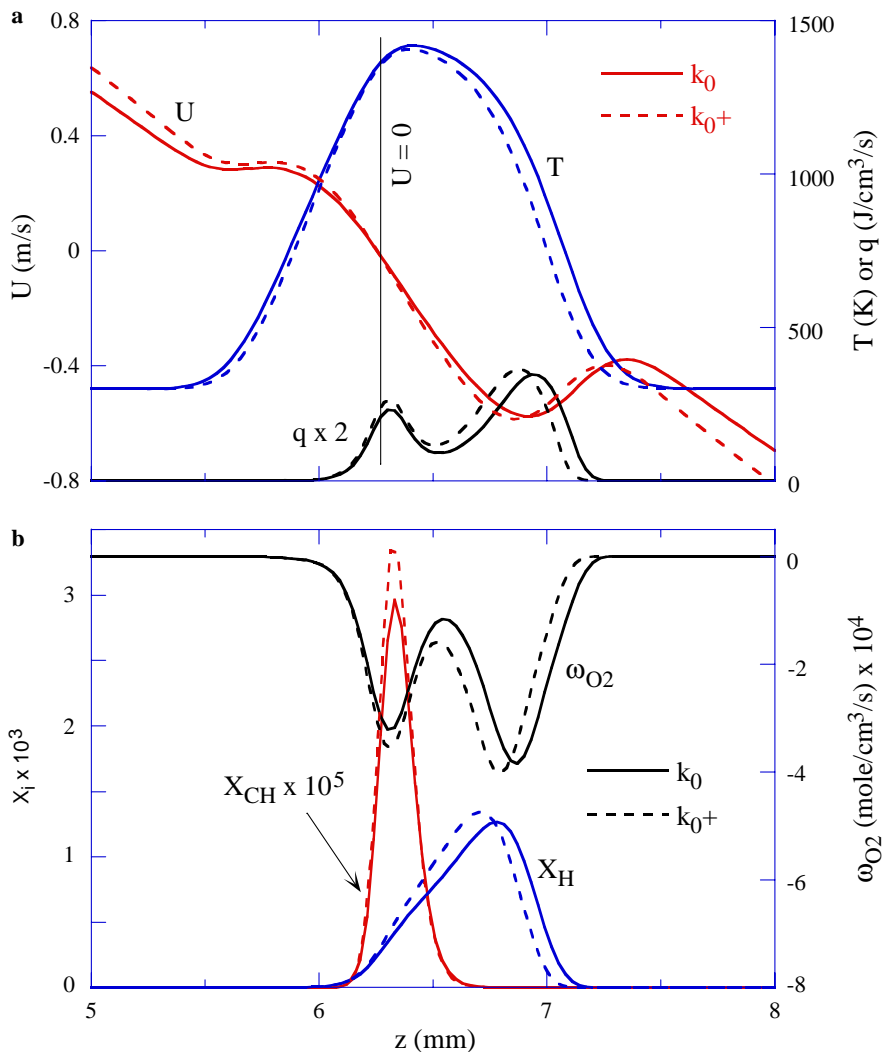


Fig. 8. Changes in flame structure to perturbation in strain rate when flame is established under high-strain-rate conditions. $\phi_{CH_4} = 0.74$, $\phi_{H_2} = 0.28$, $k_0 = 620 \text{ s}^{-1}$. Distributions of (a) velocity, temperature and heat release rate, and (b) H and CH mole fractions and O_2 consumption rate. Broken lines represent the flame structure for $k_0^+ = 660 \text{ s}^{-1}$.

the solid and broken lines in Fig. 7). This translates into an increase in peak temperature of the flame system with stretch rate (for regime II flames) as shown in Figs. 2 and 5.

Either from regime I or regime II, at higher stretch rates the flame system moves into regime III. Methane fuel diffuses into the products of the hydrogen flame and participates in low-temperature chemistry. According to flamelet theory for non-premixed combustion [27] reaction-zone temperature decreases, even though heat release rate continues to increase, with stretch rate due to reduced reaction-zone thickness and, thereby, increased heat losses (compare solid and broken lines in Fig. 8). This translates into a decrease in peak temperature of the flame system with stretch

rate (for regime III flames) as shown in Figs. 2 and 5.

Double-state behavior of counterflow premixed flames can be explained by considering their characteristics in different regimes (I, II and III). High-energy ignition sources such as a blow torch establish state-A flames with methane and hydrogen burning in regime I. When stretch rate is increased, flame temperature decreases due to aerodynamic heat loss and the flame system transitions to state B when the methane flame extinguishes. Such a transition occurs at relatively low stretch rates in regime II for leaner methane/air mixtures. When stretch rate on a state-B flame with $\phi_{CH_4} < 0.74$ (regime II) decreases, the flame temperature also decreases due to a drop

in diffusion fluxes. The flame remains in state B as the temperature can not reach the ignition value for the methane–air mixture. Therefore, for leaner methane/air mixtures, the flame system allows two stable states at a given stretch rate and exhibits double-state behavior. When stretch rate on a moderately lean state-A flame ($\phi_{\text{CH}_4} > 0.74$) increases it transitions into state B in regime III. If stretch rate of this state-B flame is decreased, then flame temperature increases due to drop in stretch-induced cooling (flamelet description) and the flame system transitions to state A when flame temperature reaches its ignition value. For these equivalence ratios, the flame system does not exhibit double-state behavior.

5. Conclusions

The counterflow flame system established between lean-methane–air and lean-hydrogen–air streams was investigated experimentally and numerically. A two-dimensional model known as UNICORN was used for the simulation. GRI version 1.2 chemical kinetics involving 32 species and 346 one-way elementary reactions was used. Detailed measurements for temperature and species concentrations were obtained along the centerline using Raman spectroscopy. A double-state behavior for this flame system was first identified in the numerical simulations, which was later confirmed by the experiments. A good agreement between measurements and calculations was obtained for the flame in different states.

Calculations for various lean methane–air mixtures were performed to understand the double-state behavior of the counterflow premixed flames. Aerodynamic and chemical structures of the flames at different stretch rates were obtained through increasing-stretch-rate and decreasing-stretch-rate approaches. It was found that flame system exhibits double-state behavior only for leaner ($\phi_{\text{CH}_4} < 0.74$) methane–air mixtures. When stretch rate is increased, the flame transitions from a double-flame to a single-flame structure due to aerodynamic cooling. When stretch rate is decreased, the flame does not transition back to the double-flame structure due to stretch effects on molecular diffusion. However, for $\phi_{\text{CH}_4} > 0.74$, decrease in stretch rate increases flame temperature due to a decrease in stretch-induced cooling and returns the flame structure to a double-flame one. For a narrow range of equivalence ratios (0.74–0.81) counterflow premixed flames exhibited a hysteresis property.

Acknowledgments

Financial support for the computational work was provided by the Air Force Office of Scientific

Research (AFOSR, Julian Tishkoff) and the Air Force Contract #F33615-00-C-2068 (Vince Belovich). Financial support for the experimental work was provided by the National Science Foundation (Grant No. CTS-0314704).

References

- [1] D.C. Haworth, R.J. Blint, B. Cuenot, T.J. Poinso, *Combust. Flame* 121 (3) (2000) 395–417.
- [2] S.H. Sohrab, Z.Y. Ye, C.K. Law, *Proc. Combust. Inst.* 20 (1984) 1957–1965.
- [3] C.K. Law, *Proc. Combust. Inst.* 22 (1988) 1381–1402.
- [4] D.M. Mosbacher, J.A. Wehrmeyer, R.W. Pitz, C.J. Sung, J.L. Byrd, *Proc. Combust. Inst.* 29 (2002) 1479–1486.
- [5] M.A. Tanoff, M.D. Smooke, R.J. Osborne, T.M. Brown, R.W. Pitz, *Proc. Combust. Inst.* 26 (1996) 1121–1128.
- [6] R.S. Barlow, A.N. Karpetis, J.H. Frank, J.-Y. Chen, *Combust. Flame* 127 (2001) 2102–2118.
- [7] J.A. Wehrmeyer, Z. Cheng, D.M. Mosbacher, R.W. Pitz, R. Osborne, *Combust. Flame* 128 (3) (2002) 232–241.
- [8] Z. Cheng, J.A. Wehrmeyer, R.W. Pitz, in: 38th AIAA/ASME/SAE/ASEE Joint Propulsion Conference, AIAA 2002-4021, Indianapolis, IN, 2002.
- [9] N. Darabiha, S.M. Candel, V. Giovangigli, M.D. Smooke, *Combust. Sci. Technol.* 60 (1988) 267–284.
- [10] C.J. Sung, J.B. Liu, C.K. Law, *Combust. Flame* 106 (1–2) (1996) 168–183.
- [11] C.K. Law, C.J. Sung, G. Yu, R.L. Axelbaum, *Combust. Flame* 98 (1–2) (1994) 139–154.
- [12] C.J. Sung, G.J.B. Liu, C.K. Law, *Combust. Flame* 102 (4) (1995) 481–492.
- [13] W.M. Roquemore, V.R. Katta, *J. Visualizat.* 2 (2000) 257–272.
- [14] V.R. Katta, W.M. Roquemore, *Combust. Flame* 100 (1) (1995) 61.
- [15] G.P. Smith, D.M. Golden, M. Frenklach, et al., 2001. Available from: <http://www.me.berkeley.edu/gri-mech>.
- [16] Annon., Computational Submodels, International Workshop on Measurement and Computation of Turbulent Nonpremixed Flames. Available from: <http://www.ca.sandia.gov/TNF/radiation.html>.
- [17] V.R. Katta, L.P. Goss, W.M. Roquemore, *AIAA J.* 32 (1) (1994) 84.
- [18] V.R. Katta, L.P. Goss, W.M. Roquemore, *Int. J. Num. Meth. Heat Fluid Flow* 4 (5) (1994) 413.
- [19] K. Seshadri, I. Puri, N. Peters, *Combust. Flame* 61 (3) (1985) 237–249.
- [20] Z. Cheng, J.A. Wehrmeyer, R.W. Pitz, *Proc. Combust. Inst.* 30 (2005) 285–293.
- [21] V.R. Katta, Z. Cheng, R.W. Pitz, in: Proceedings of the 4th Joint Meeting of the US Sections of the Combustion Institute, Philadelphia, PA, 21–23 March 2005.
- [22] H.G. Im, C.K. Law, J.S. Kim, F.A. Williams, *Combust. Flame* 100 (1995) 21–30.
- [23] F.N. Egolfopoulos, C.S. Campbell, *J. Fluid Mech.* 318 (1996) 1–29.
- [24] C.J. Sung, C.K. Law, AIAA Paper, in: Presented at the Aerospace Sciences Meeting and Exhibit, Reno, NV, 12–16 January 1993.

- [25] V.R. Katta, T.R. Meyer, M.S. Brown, J.R. Gord, W.M. Roquemore, *Combust. Flame* 137 (2004) 198–221.
- [26] V.R. Katta, W.M. Roquemore, *Extinction in Methane–air Counterflow Diffusion Flame—A Direct Numerical Study*, Central States section Meeting of the Combustion Institute, St. Louis, Paper No. 80, 1996, pp. 449–454.
- [27] N. Peters, *Proc. Combust. Inst.* 21 (1986) 1231–1256.

5th US Combustion Meeting
Organized by the Western States Section of the Combustion Institute
and Hosted by the University of California at San Diego
March 25-28, 2007.

Predictions on Sooting Behavior of Recirculation-Zone-Supported Flames

V. R. Katta¹ and W. M. Roquemore²

¹*Innovative Scientific Solutions, Inc, 2766 Indian Ripple Road,
Dayton, OH 45440-3638, USA*

²*Air Force Research Laboratory, Propulsion Directorate,
Wright Patterson Air Force Base, OH 45433-7251, USA*

The primary and secondary recirculation zones, which are formed in between the fuel and oxidizer jets of a centerbody burner, transport fuel across the centerbody to the oxidizer jet and establish a flame anchored to the rim of the centerbody. Experimentally it was found that the sooting characteristics of a centerbody burner change dramatically when the operating conditions are altered systematically. A time-dependent, axisymmetric, detailed-chemistry CFD model is developed for the studies of soot in a 46-mm-diameter centerbody burner. Combustion and PAH formation are simulated using Wang-Frenklach (99 species and 1066 reactions) and NIST (197 species and 2800 reactions) mechanisms. Soot is simulated using a two-equation model of Linstedt. Calculations are performed for different flow conditions in which concentration of ethylene was reduced gradually without altering the fuel and oxidizer flow rates. Numerical experiments are performed for determining the effect of soot radiation on flame structure. The flame weakening in the transition region of the leading and trailing flame sections is found to result from soot radiation. Amazingly similar flame and soot structures are obtained with the two chemical-kinetics mechanisms considered.

1. Introduction

Particulate matter with particle sizes of 2.5 microns or less (PM_{2.5}) is perhaps the most important of all air pollutant because these small particles can penetrate deep into the lungs and cause significant health problems. In 2005, the EPA proposed revisions to the National Ambient Air Quality Standards (NAAQS) that would reduce the PM_{2.5} 24-hour standard from 65 $\mu\text{g}/\text{m}^3$ to 35 $\mu\text{g}/\text{m}^3$. Essentially all of the solid particles (soot) produced in gas turbine engines are PM_{2.5} emissions. Indeed, the major source of PM_{2.5} emissions produced by the Department of Defense (DoD) is gas turbine engine powered aircraft. In 2004, DoD aircraft produced about 4.2×10^{10} kg of PM_{2.5} emissions. This corresponds to the production of about 2.1×10^{23} soot particles. Much of these emissions occur in local areas around active air bases.

The formation, growth, transport, and burnout of soot are perhaps the most complex and least understood processes in flames and combustion systems. Soot particles containing several-thousand carbon atoms are formed in flames from simple fuel molecules within a few microseconds [1]. However, these soot precursor particles on a much longer time scale interact with the gas-phase molecules during the surface-growth process, colloid with each other in the agglomeration process and react with oxygenated species in the oxidation process. All of these

chemical and physical two-phase processes occur simultaneously in typical nonpremixed or premixed flames. In gas turbine combustors, these processes are further complicated by the burning of practical fuels, consisting of thousands of species, and the actions of turbulent flow. There is a significant science base for understanding the soot processes; however, it is inadequate to provide accurate soot models that can aid in the design of future low sooting gas turbine combustors burning current and future alternative fuels. Thus, there is a pressing need to expand the science base in ways that foster the development and evaluation of accurate CFD models for designing low sooting combustion systems.

The Strategic Environmental Research and Development Program (SERDP) office recently started a comprehensive fundamental soot research initiative involving five principal research groups and eight supporting groups. The objectives of these coordinated programs are: (1) to aid the DoD in meeting current and future NAAQS PM_{2.5} regulations and (2) to establish the fundamental science base needed to develop and validate soot models that can be used to design low PM_{2.5} emission combustor in future gas turbine engines burning practical hydrocarbon fuels. One of the SERDP sponsored programs involves a strongly coupled, mutually supportive experimental and simulation effort that investigates soot processes in different burners. The burner designs progress in complexity in a way that the effects of chemical kinetics, diffusion, flame stretch, recirculation, and turbulence on the soot processes can be systematically studied. The computational part of this effort is to use a state-of-the-art, Navier-Stokes based 2D CFD code to aid in designing experiment, predicting and interpreting results, and evaluating soot and chemistry models for the suite of burners. The CFD code used for this purpose is called UNICORN (UNsteady Ignition and COMbustion using ReactionNs) [2,3].

This paper describes the simulations performed by UNICORN using a simple soot model for the centerbody flames. Predictions for the changes in flame and soot characteristics when the fuel is diluted with nitrogen are presented. Effects of soot radiation on flame and soot structures are also presented. Calculations are performed using two detailed chemical-kinetics models for assessing the predictive capabilities of the state-of-the-art mechanisms for ethylene combustion. Rather extensive calculations and the comparisons made with the experimental flames are presented in a companion paper that evaluates the suitability of a centerbody for studying sooting process [4].

2. Mathematical Model

A time-dependent, axisymmetric mathematical model known as UNICORN (Unsteady Ignition and Combustion using ReactionNs) [2,3] is used for the simulation of the unsteady combusting flows in the centerbody combustor. It solves for u- and v-momentum equations, continuity, and enthalpy- and species-conservation equations on a staggered-grid system. The body-force term due to the gravitational field is included in the axial-momentum equation for simulating vertically mounted flames. A clustered mesh system is employed to trace the steep gradients in flow variables near the flame surface. A detailed chemical-kinetics model developed by Wang and Frenklach [5] is incorporated into UNICORN for the investigation of PAH and soot formation in ethylene flames. It consists of 99 species and 1066 elementary-reaction steps. A more comprehensive mechanism that involves 197 species and 2800 reactions [6], developed by NIST, has also been incorporated into UNICORN code for validation and future use purposes. Thermo-physical properties such as enthalpy, viscosity, thermal conductivity, and binary molecular diffusion of all the species are calculated from the polynomial curve fits developed for

the temperature range 300 - 5000 K. Mixture viscosity and thermal conductivity are then estimated using the Wilke and Kee expressions, respectively. Molecular diffusion is assumed to be of the binary-diffusion type, and the diffusion velocity of a species is calculated using Fick's law and the effective-diffusion coefficient of that species in the mixture. A simple radiation model based on the optically thin-media assumption is incorporated into the energy equation [7]. Only radiation from CH₄, CO, CO₂, H₂O, and soot is considered in the present study. Soot radiation is modeled as blackbody type [8].

Computational soot models based on the fundamental physics of soot formation and oxidation are not yet available. The research groups around Moss [9] and Lindstedt [10] have made some progress in modeling soot formation using semi-empirical models based on the mechanisms of particle inception, agglomeration, surface growth, and oxidation. Both the groups utilized two equation models with transport equations for particle number density, N_s , and soot mass fraction, Y_s . The source terms in these soot transport equations are obtained using Lindstedt's model [10], which is based on the simplifying assumption that nucleation and growth are first-order functions of acetylene concentrations. Soot oxidation was considered primarily due to the presence of O₂ and OH. Finally, soot agglomeration was treated as a source term in the soot number density equation.

The finite-difference forms of the momentum equations are obtained using an implicit QUICKEST scheme [11,12], and those of the species and energy equations are obtained using a hybrid scheme of upwind and central differencing. At every time step, the pressure field is accurately calculated by solving all the pressure Poisson equations simultaneously. The LU (Lower and Upper diagonal) matrix-decomposition technique is used. The boundary conditions are treated in the same way as that reported in earlier papers [13]. This model has been extensively validated [2] by simulating various steady and unsteady counterflow [14-16] and coflow [17,18] jet diffusion flames and by comparing the results with experimental data.

3. Results and Discussion

The geometry of the centerbody burner was described in detail in Ref. 4. It consists of a 46-mm-diameter disc enclosed in a cylindrical chimney with an annular gap of 17 mm. A 7.6-mm-diameter jet is located at the center of the disc through which fuel (a mixture of ethylene and nitrogen) is injected at a velocity of 1.25 m/s. A mixture of air and nitrogen is flowed through the annular gap also at the same velocity. Calculations for the flames of the centerbody burner are made using a 301x161 grid system.

Simulations are performed on a Personal Computer with 2.0 GB of memory. Execution times strongly depend on the number of species considered in the model and the grid size. Typically with 99 species and 1066 reactions (Wang-Frenklach model) on a 301X161 grid system simulations took ~30 s/time-step on AMD-Opteron-250 computer. Steady state solution for each case is obtained in about 10,000 time steps.

In order to understand the flame structures associated with the centerbody burner, calculations are made for two fuel-flow cases. While pure ethylene is used as fuel for the first case, a 44-percent-diluted ethylene-nitrogen mixture is used for the second case. For both cases less sooty flames are obtained by reducing the oxygen concentration in the annular flow. The oxygen-to-nitrogen ratio used in the annular flow is 0.20 (which is achieved by adding 25% nitrogen to air).

Note, the fuel and oxidizer jet velocities are held constant at 1.25 m/s with uniform distribution for both cases.

Results obtained for pure-fuel case are shown in Fig. 1. Axisymmetric representation of the flame is used while displaying the data. Centerbody with fuel- and oxidizer-jet openings is displayed at the bottom of each of the figures 1(a) and 1(b). While velocity vectors are superimposed on the temperature field on the left half of 1(a), streamlines are superimposed on soot-volume-fraction distribution on the right half. Similarly, iso-concentration contours of ethylene (black lines) and OH (red lines) are superimposed on oxygen concentration field on the left half of 1(b) and those of benzene are superimposed on acetylene concentration field on the right half. Streamlines and velocity vectors show the two recirculation zones associated with the centerbody flames. These recirculation zones are formed due to the separation between the fuel and oxidizer jets. However, due to the differences in the momentum, the recirculation zone closer to the oxidizer jet (primary recirculation zone, PRZ) is much larger than the one closer to the fuel jet (secondary recirculation zone, SRZ). These recirculation zones play a vital role in transporting fuel toward oxidizer and in establishing a flame along the outer edge of the centerbody. The leading portion of the flame curves along the outer edge of the PRZ and then transitions into the trailing nonpremixed jet flame when PRZ is terminated at $z \sim 30$ mm. Even though it is not that obvious, the SRZ and the PRZ terminate at the same height. Both temperature and OH profiles suggest that flame is becoming weak in this transition region.

As seen in Fig. 1(a), most of the soot is located within the PRZ and is not symmetrically distributed within the recirculation zone. This suggests that soot is formed in PRZ rather than formed somewhere else and transported into the recirculation zone. In fact, a significant portion of the fuel-side flame zone is within PRZ and all most all of the acetylene is produced along the outer edge of the PRZ, which is then transported toward its center. As the soot model used in the current simulations is based on acetylene, soot in Fig. 1(a) is also being generated and grown within the PRZ. Interestingly, soot doesn't seem to accumulate in the SRZ. Velocity vectors and streamlines in Fig. 1(a) suggest that the flow is nearly parallel to the flame surface and turns inward as it approaches the end of the recirculation zone. The flow pattern and residence times need to be analyzed to better understand the sooting behavior of the centerbody flames.

Results obtained for the diluted-fuel case are shown in Fig. 2. The shown variables and the display schemes used are identical to those used in Fig. 1. As expected, the addition of nitrogen in the fuel decreases the flame temperature. Interestingly, the decrease in soot volume is more dramatic than what one would expect based on changes in temperature. A quick look at the velocity and temperature fields suggest that the flame surface has moved into the core of the vortex especially the section where it transitioned from recirculation-supported leading flame to normal nonpremixed trailing flame. Such flame movement can be expected as the stoichiometric surface shifts closer to the fuel jet with fuel dilution. On the other hand, the sizes of the PRZ and SRZ in the diluted-fuel case are nearly the same as those in the pure-fuel case with the heights being ~ 30 mm. Since the recirculation zones behind the centerbody are established due to the fuel and oxidizer jets, they are not affected by the fuel dilution (molecular weights of nitrogen and ethylene being the same). However, as the viscosity of the fluid in the upper portion of the recirculation zones decreased due to lower flame temperature, the centers of the recirculation zones moved downstream in the diluted-fuel case. Consequently, with fuel dilution, flame surface shifts toward the center of the PRZ; while, the latter moves downstream (closer to the

flame surface). The changes in flame-recirculation-zone interaction [4] led to a dramatic decrease in soot formation in diluted-fuel case.

Radial distributions of temperature and axial velocity along the centers of the PRZs for pure-fuel and diluted-fuel cases (heights of 9 and 11 mm, respectively) are shown in Fig. 3(a). The distributions of soot volume fraction and number density are shown in Fig. 3(b). The radial locations of the centers of the PRZs are marked on the velocity profiles with solid circles. As noted earlier, the structure of the recirculation zone did not change much with fuel dilution. The flame temperature decreased by ~ 120 K while the gas temperature at the PRZ center increased over 200 K. A three-fold decrease in soot volume fraction due to nitrogen addition to fuel is noted in Fig. 3(b). Soot number density, which peaks on the fuel side of the peak-temperature location, decreased by 50%. Even though the soot number density increased in the core region of PRZ with fuel dilution, the soot volume decreased dramatically.

The centerbody flames seem to produce a significant amount of soot in the leading portion of the flame and within the recirculation zones. Computations for these flames were performed assuming that radiative heat loss from soot follows that of a blackbody. Such an assumption is known to over estimate the actual losses. To determine the effect of soot radiation on the flames shown in Figs. 1 and 2 calculations are repeated by turning it off. Flame and soot structures obtained without soot radiation are shown in Figs. 4(a) and 4(b) for the pure- and diluted-fuel cases, respectively. Note the changes in the scales used for the color maps for these figures compared to those used in 1 and 2.

As expected, the flame temperature decreased by as much as 100 K when the soot radiation was considered in the model. The decrease was more in the sooty pure-fuel flame. This drop in flame temperature could be responsible for the significant decrease in soot concentration predicted with soot radiation turned on. Even though the flame structures were significantly changed due to soot radiation, the recirculation zones (PRZ and SRZ) were not significantly affected. Interestingly, the flame weakening, in the leading-flame-to-trailing-flame transition region observed in Figs. 1 and 2, disappeared when soot radiation was ignored. The soot volume distributions in Figs. 4(a) and 4(b) do not indicate any increase in soot in this region. It is not clear why temperature in this transition region was more affected by soot radiation than in the leading-flame or trailing-flame regions. Moreover, even though the soot levels in diluted-fuel case are one-third of those in pure-fuel case, the flame-weakening behavior is similar in both the flames—suggesting that soot radiation itself is not responsible for such behavior.

Calculations for the pure-fuel and diluted-fuel cases are also performed using a more comprehensive chemical-kinetics model developed by NIST for ethylene fuel. Temperature, soot and species structures obtained for pure-fuel case are shown in Fig. 5 and those for the diluted-fuel case are shown in Fig. 6. Variables shown and the display schemes used for these figures are identical to those used in Fig. 1. Amazingly identical flame structures are obtained with Wang-Frenklach and NIST mechanisms for both the flame cases. The soot structures are also very similar. However, acetylene and benzene concentrations predicted by NIST mechanism are notable lower than those predicted by Wang-Frenklach mechanism. Such a discrepancy in the predictions of these two mechanisms was previously noted in heptane opposing-jet flames studies [19]. Detailed measurements are required for sorting out the differences in these predictions, which will be the focus of our future work.

4. Conclusions

In a companion paper [4], it was experimentally found that the sooting characteristics of a centerbody burner could change dramatically with changes in operating conditions. UNICORN was successful in predicting the change in shape of the sooting flame. This paper describes the UNICORN code and provides predictions of the sooting characteristics not reported in [4]. A time-dependent, axisymmetric, detailed-chemistry CFD model is used to simulate the ethylene-air combustion in a 5.6-mm-diameter centerbody burner. Combustion and PAH formation are simulated using Wang-Frenklach (99 species and 1066 reactions) and NIST (197 species and 2800 reactions) mechanisms. Soot is simulated using a two-equation model of Linstedt. Calculations are performed for different flow conditions in which concentration of ethylene was reduced gradually without altering the fuel and oxidizer flow rates. The structures of the primary and secondary recirculation zones that are formed between the fuel and oxidizer jets are not greatly affected by this dilution. However, as the fuel dilution increased, the flame formed outside the PRZ moved into the recirculation zone and altered the sooting characteristics. Numerical experiments are performed for determining the effect of soot radiation on flame structure. The flame weakening in the transition region of the leading and trailing flame sections is found to result from soot radiation. Amazingly similar flame and soot structures were obtained with the two chemical-kinetics mechanisms used in this study.

Acknowledgments

Financial support for this work was provided by Strategic Environmental Research and Development Program (SERDP, Charles Pellerin), the Air Force Office of Scientific Research (AFOSR, Julian Tishkoff) and the Air Force Contract #F33615-00-C-2068 (Vince Belovich).

References

1. Kennedy, I. M., *Prog. Energy Combust. Sci.* 23:95 (1997)
2. Roquemore W. M., and Katta, V. R., *Journal of Visualization*, 2 (2000) 257.
3. Katta, V. R., Blevins, L. G., and Roquemore, W. M., *Combust. Flame* 142:33-51 (2005).
4. Roquemore, M., Katta, V., Belovich, V., Pawlik, R., Lynch, A., Miller, J., Stouffer, S., Justinger, G., Zelina, J., Roy, S., and Gord, J., "Experimental and Numerical Studies of Centerbody Flames," Paper No. P44, 5th US Combustion Meeting Organized by the Western States Section of the Combustion Institute and Hosted by the University of California at San Diego, March 25-28, 2007.
5. Wang, M., and Frenklach, *Combustion and Flame* 110 (1997) 173.
6. Tsang W., and Babushok, V., "Detailed mechanism for PAH species" *manuscript in preparation*, National Institute of Standards and Technology, Gaithersburg, MD, 2004
7. Annon., Computational Submodels, International Workshop on Measurement and Computation of Turbulent Nonpremixed Flames, <http://www.ca.sandia.gov/TNF/radiation.html>, (2001).
8. Guo, H., Liu, F., Smallwood, G. J., *Combustion Theory and Modeling*, Vol. 8, 2004, pp. 475-489.
9. Mauss, F., Schäfer, T. and Bockhorn, H., *Combust. Flame* 99:697-705 (1994).

10. Lindstedt, R.P., in *Soot Formation in Combustion: Mechanisms and Models* (H. Bockhorn, Ed.), Springer-Verlag, Heidelberg, 1994, pp.417-439.
11. Leonard, B. P., *Comput. Meth. Appl. Mech. Eng.* 19:59 (1979).
12. Katta, V. R., Goss, L. P., and Roquemore, W. M., *AIAA Journal*, Vol. 32, No. 1, 1994, p. 84.
13. Katta, V. R., Goss, L. P., and Roquemore, W. M., *Int. J. Num. Methods Heat Fluid Flow*, Vol. 4, No. 5, 1994, p. 413.
14. Katta, V. R., Meyer, T. R., Brown, M. S., Gord, J. R., and Roquemore, W. M., *Combust. Flame* 137 (2004) 198-221.
15. Katta, V. R., Carter, C. D., Fiechtner, G. J., Roquemore, W. M., Gord, J. R., and Rolon, J. C., *Proc. Combust. Inst.* 27:587-594 (1998).
16. Katta, V. R., Meyer, T. R., Gord, J. R., and Roquemore, W. M., *Combust. Flame* 132:639 (2003).
17. Katta, V. R., and Roquemore, W. M., *AIAA J.* 36:2044 (1998).
18. Grisch, F., Attal-Tretout, B., Bouchardy, P., Katta, V. R., and Roquemore, W. M., *J. Nonlin. Opt. Phys. Mater.* 5:505 (1996).
19. Katta, V. R., and Roquemore, W. M., “Effect of Nitromethane on Soot Formation in Heptane Jet Diffusion Flame”, Proceedings of 4th Joint Meeting of the U. S. Sections of the Combustion Institute, 2005.

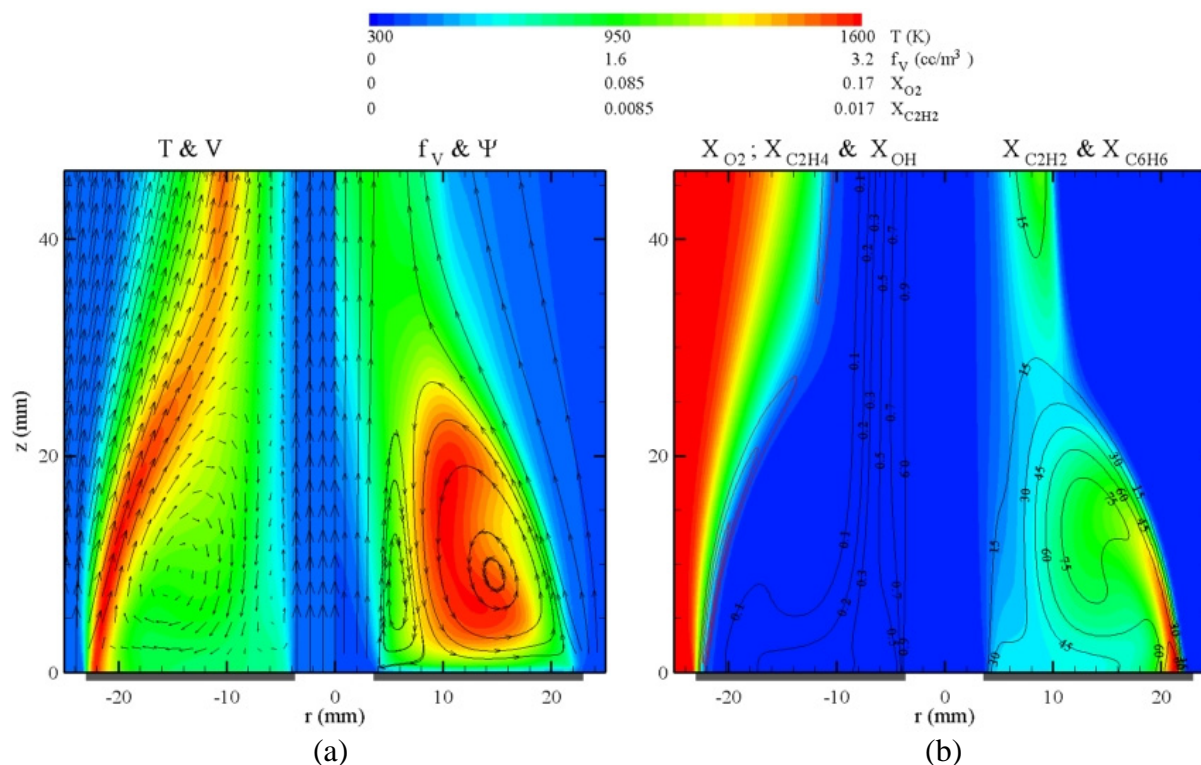


Fig. 1. Centerbody flame with pure fuel calculated using detailed chemical kinetics. (a) Velocity vectors and streamlines are superimposed on temperature (left half) and soot-volume-fraction (right half) fields, respectively. (b) Iso contours of ethylene and benzene are superimposed on oxygen (left) and acetylene (right) fields, respectively. Red contours represent OH.

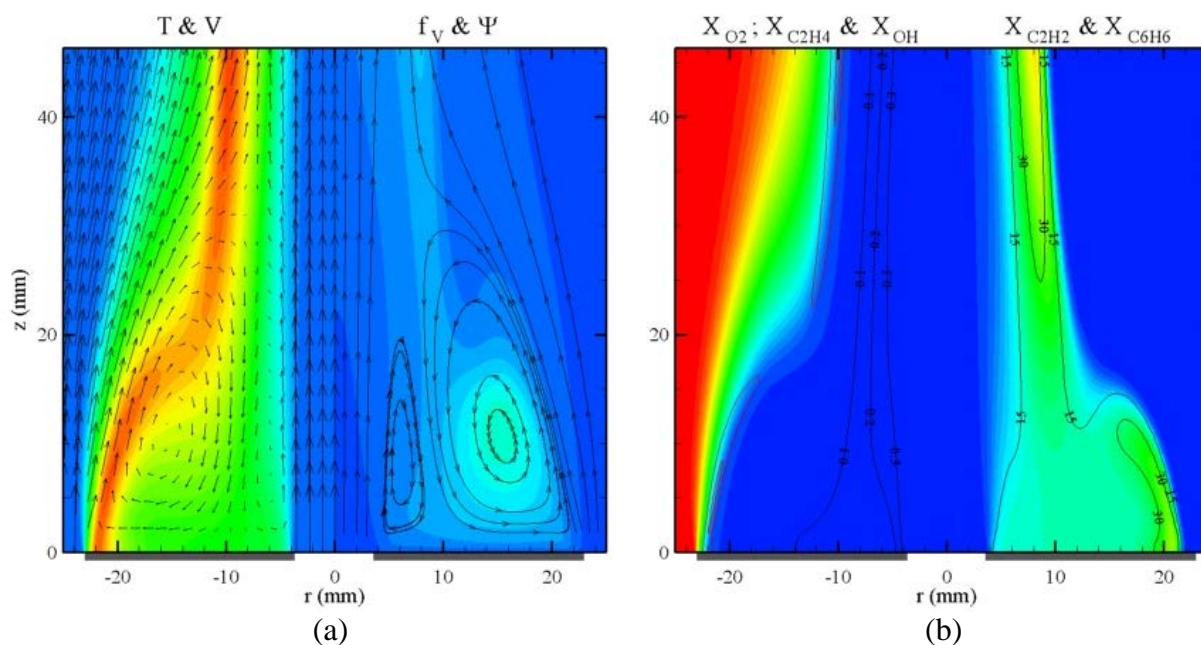


Fig. 2. Centerbody flame with diluted fuel. Velocity, temperature, streamlines and soot volume fraction are shown in (a) and ethylene, oxygen, OH, acetylene and benzene are shown in (b). Color scales are same as the ones used in Fig. 1.

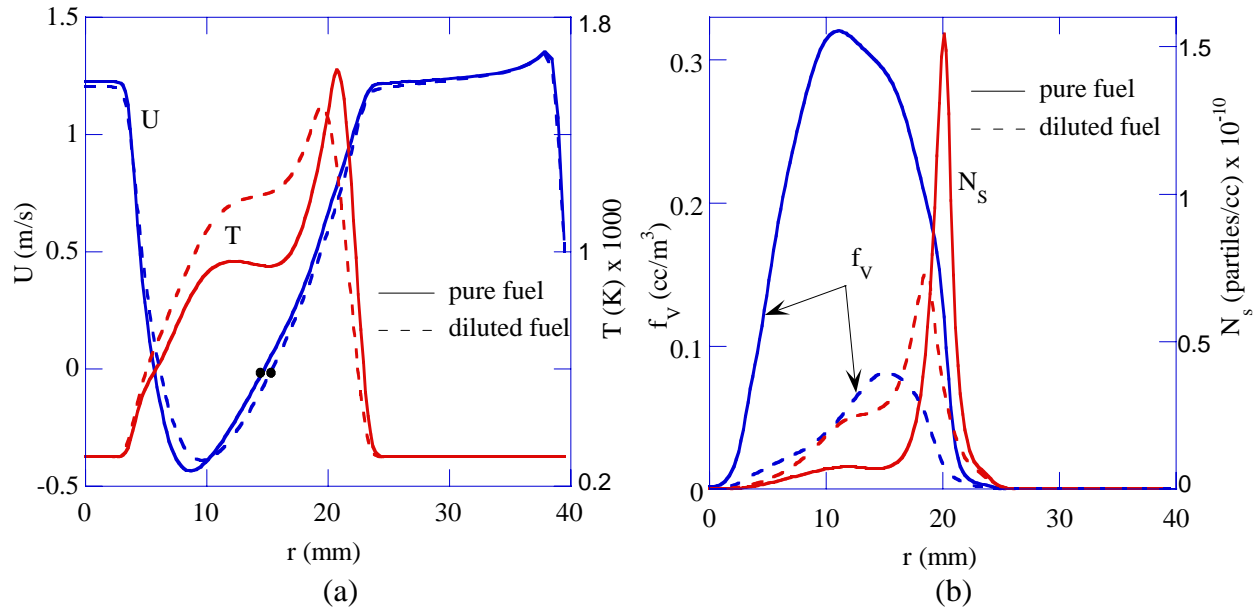


Fig. 3. Effect of fuel dilution on (a) flame and vortex structure and (b) soot and particle distributions. Vortex centers are shown in (a) with filled circles.

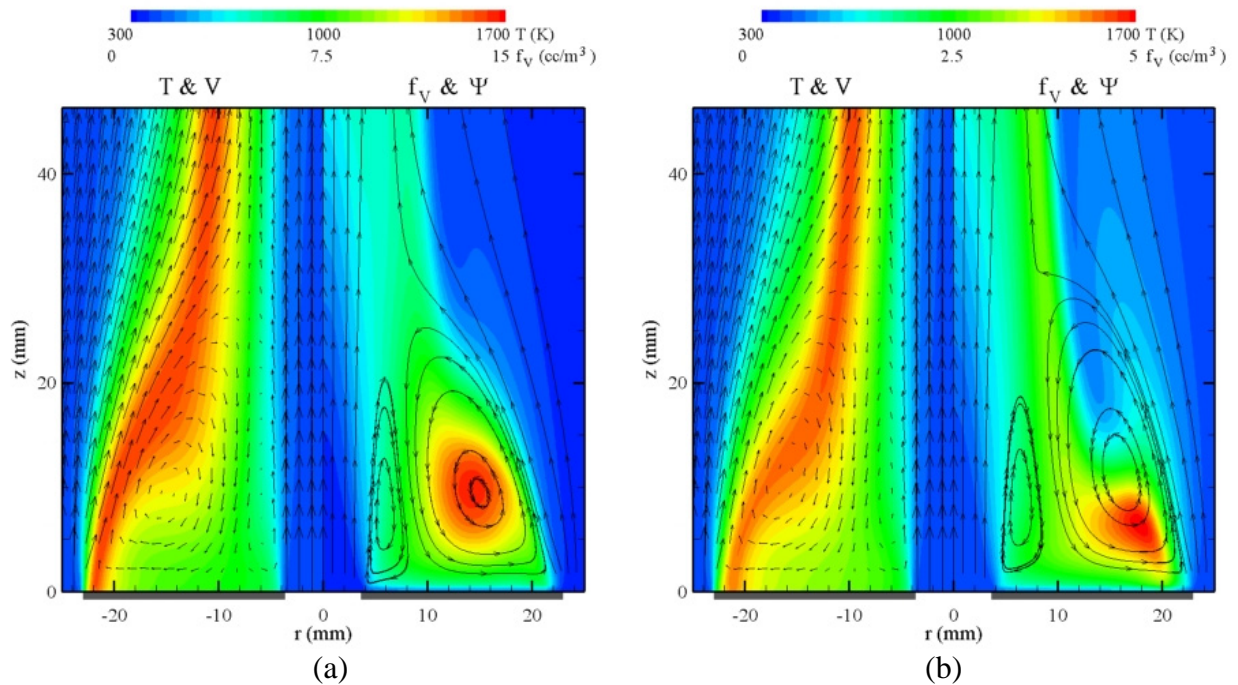


Fig. 4. The effects of radiation on flame structure and soot formation in pure-fuel (a) and diluted-fuel (b) cases. Velocity and streamlines are superimposed on temperature (left half) and soot-volume-fraction (right half) fields, respectively. Note the changes in the ranges used for the variables.

5th US Combustion Meeting
Organized by the Western States Section of the Combustion Institute
and Hosted by the University of California at San Diego
March 25-28, 2007.

Experimental and Numerical Studies of Centerbody Flames

M. Roquemore¹, V. Katta³, V. Belovich¹, R. Pawlik¹, A. Lynch¹, J. Miller¹,
S. Stouffer², G. Justinger², J. Zelina¹, S. Roy³, and J. Gord¹

¹*Air Force Research Laboratory, Propulsion Directorate,
Wright-Patterson AFB OH 45433-7251, USA*

²*University of Dayton Research Institute,
Dayton OH 45469-0114, USA*

³*Innovative Scientific Solutions, Inc. (ISSI),
Dayton OH 45440-3638, USA*

This paper describes the preliminary evaluation of a centerbody burner as a tool for developing and evaluating soot models. The burner consists of a 46-mm diameter disk symmetrically located in an 80-mm diameter annular quartz duct. A 7.6-mm diameter fuel jet is located at the center of the disk. A mixture of air and excess nitrogen is supplied to the annular duct at a flow rate of 250 SLPM. Ethylene fuel, mixed with nitrogen, is supplied to the central fuel jet at a flow rate of 3.4 SLPM. Three flames are studied. They have the same air and fuel velocity (1.2 m/s) and similar vortex characteristics. Different sooting flame characteristics are achieved by varying the N₂ dilution in the fuel and air. For example, with no N₂ dilution almost the entire surface of the flame is sooting. The two flames with N₂ dilution have donut and ring shaped sooting structures. All three of the flames have the interesting characteristic that the soot path lines have spiraling trajectories that terminate at the center of the recirculation zone. Simulations, using a 2D, CFD-based code (UNICORN), correctly estimate the structures of the recirculation and flame zones. Also, reasonable estimates are presented for the global structure of the unusual sooting surfaces of the three flames. This is somewhat surprising consider the rudimentary soot model used in UNICORN. However, the soot model is not sufficiently developed to capture the spiral trajectories of the soot particles. The spiraling path lines are correctly estimated using a particle-tracing program and flow field data from UNICORN. Other computational experiments are presented that give insights into the interesting sooting characteristics of these flames.

1. Introduction

Particulate matter with particle sizes of 2.5 microns or less (PM_{2.5}) is perhaps the most important air pollutant because these small particles can penetrate deep into the lungs and cause significant health problems. In 2005, the EPA proposed revisions to the National Ambient Air Quality Standards that would reduce the PM_{2.5} 24-hour standard from 65 $\mu\text{g}/\text{m}^3$ to 35 $\mu\text{g}/\text{m}^3$. Essentially all of the solid particles (soot) produced in gas turbine engines are PM_{2.5} emissions. Indeed, the major source of PM_{2.5} emissions produced by the Department of Defense (DoD) is gas turbine engine-powered aircraft. In 2004, DoD

aircraft produced about 4.2×10^{10} kg of PM_{2.5} emissions. This corresponds to the production of about 2.1×10^{23} soot particles. Much of these emissions occur in local areas around active air bases.

The formation, growth, transport, and burnout of soot are perhaps the most complex and least understood processes in flames and combustion systems. Soot precursor particles containing several thousand-carbon atoms are formed a few microseconds in simple flames. However, on a much longer time-scale the soot precursor particles interact with gas-phase molecules during the surface-growth process, collide with each other in the agglomeration process, and react with oxygenated species in the oxidation process. All of these chemical and physical two-phase processes occur simultaneously in typical nonpremixed or premixed flames. In gas turbine combustors, these processes are further complicated by burning practical fuels, consisting of thousands of species, and the actions of turbulent flow. There is a significant science base for understanding the soot processes; however, it is inadequate to provide accurate soot models that can aid in the design of future low-sooting gas turbine combustors burning current and future alternative fuels. Thus, there is a pressing need to expand the science base in ways that foster the evaluation and development of accurate CFD models for designing low-sooting combustion systems.

The Strategic Environmental Research and Development Program (SERDP) office recently started a comprehensive soot research initiative to meet the scientific challenges facing the Department of Defense in meeting current and future NAAQS PM_{2.5} regulations in and around airbases. The objective of the SERDP program is to establish the fundamental science base needed to develop and validate soot models that can be used to design low PM_{2.5} emission combustors in future gas turbine engines burning practical hydrocarbon fuels. The SERDP program involves five principal research groups and eight supporting groups. One of the SERDP sponsored programs involves a strongly coupled, mutually supportive experimental and simulation effort that investigates soot processes in different burners. The burner designs progress in complexity in such a way that the effects of chemical kinetics, diffusion, flame stretch, recirculation, and turbulence on the soot processes can be systematically studied. A centerbody burner was selected to study the effects of a laminar recirculation zone on the soot processes.

The centerbody configuration, also referred to in the literature as a bluff-body burner or coannular jets with a large separation, is selected for these studies because it has been used for many years to aid the evaluation and development of combustion models (Roquemore, 1983), (Sturgess 1984), (Correa, 1992), (Fallot, 1997), (Liu, 2005), (Kempf, 2006), and (Merci, 2006). It has a simple geometry with clean inlet conditions for modeling, clear optical access for use of laser diagnostics, and can be operated at conditions that give radically different flow fields and flame structures for evaluating and developing models. The ability to dramatically change the flow field by changing the inlet flow rates was first observed by (Yule 1980) for non-reacting flows and by others in reacting flows (Roquemore 1980), (Masri 1984), (Dally 1998), (Namazian 1989), (Esquiva-Dano 2001). In this paper, the effects due to changing the flow field are not exploited. Instead, laminar flames are studied in which the flow fields are about the same

but their sooting surfaces are radically different. To our knowledge, a centerbody burner has never been used to study soot at similar laminar flow conditions.

This paper presents a preliminary evaluation of the suitability of the centerbody burner for studying soot. Experimental images of three unusually shaped sooting flames are compared with soot predictions made with a 2D simulation called UNICORN (UNsteady Ignition and COMbustion using ReactionNs). The visualized sooting flame structures, flow fields, and soot transport are compared with predictions made with UNICORN.

2. Simulations and Modeling (UNICORN)

UNICORN (UNsteady Ignition and COMbustion using ReactionNs) code is a time-dependent, axisymmetric mathematical model, which is used for the simulation of steady and unsteady reacting flows. It has been developed over a fourteen-year period (Katta, 1993) and has evolved hand-in-hand with experiments designed to test its ability to predict ignition, extinction, stability limits, and the dynamic and steady state characteristics of diffusion and premixed flames burning various fuels (Roquemore and Katta, 2000). UNICORN uses the simplified soot model by (Lindstedt, 1994) and a detailed chemical kinetics model for ethylene (Wang and Frenklach, 1997). A simple radiation model based on the optically thin-media assumption is incorporated into the energy equation for treating radiation heat loss from gaseous species (Annon, 2001). Only CH_4 , CO , CO_2 , and H_2O are considered as radiating species in the present study. Heat losses from soot particles are computed assuming blackbody radiation from the carbon soot particles (Guo, 2004). A more detailed description of UNICORN is given in (Katta 2004 and 2007).

3. Experimental Set-up

The experimental set-up is shown in Fig. 1. The centerbody is contained in a vertical wind tunnel designed to provide a smooth flow into the test section. The centerbody is a 46-mm diameter disk with a 7.6-mm diameter fuel jet located at its center. The centerbody is symmetrically mounted in an 80-mm ID quartz tube that extends 25 cm from the face of the centerbody. Ethylene fuel is used in these studies because a detailed chemistry mechanism exists (Wang, 1997), and because it has been widely used in soot studies (Smooke, et al. 2005). A YAG laser and cylindrical lens are used to form a laser sheet for visualizing the soot characteristics of the flames. Mie scattering images from soot particles are collected with a digital camera mounted normal to the laser sheet.

The experiments are designed so the laminar flow fields are about the same for the different flow conditions. However, the sooting flame structures are dramatically different. The volumetric flow rate of the mixture of air and excess nitrogen in the annular duct is 250 SLPM, and the flow rate for the ethylene fuel and nitrogen mixture in the central fuel jet is 3.4 SLPM. Since the molecular weight of ethylene is about the same as air and nitrogen, maintaining the same flow rates for the different experiments is equivalent to maintaining constant momentum in the air and fuel jets. Because of this, the

recirculation zone established by the centerbody has about the same size and shape for the different flames. Nitrogen addition is used to change the soot characteristics of the flames by dilution/chemistry effects. The average velocity of the air and fuel is about 1.2 m/s for all of the experiments. According to (Roquemore, 1986), this flow condition would correspond to a fuel jet that penetrates the recirculation zone established by the annular air jet.

Results and Discussion

The purpose of this paper is to determine if the centerbody burner is suitable for long-term soot studies and evaluating soot models. In the past, we have extensively used visualization techniques to study flames and evaluate models such as UNICORN (Roquemore and Katta 2000). Simple flames were selected that had distinguishing features that could be easily visualized. A model that could not capture the distinguishing features obviously needed additional work. Although this approach is not sufficient for evaluating models, it does demonstrate a necessary requirement that the models correctly predict unusual flame features. This strategy of studying simple flames with distinguishing characteristics is adopted for this preliminary evaluation of UNICORN and a simple soot model.

Dramatically different sooting flame structures can be achieved by changing the N_2 dilution in the fuel and/or air jets. This is illustrated by comparing the flame photographs shown in Figs 2a, 3a, and 4a. The yellow flame represents the sooting surfaces. In Fig. 2a, the sooting surface starts about 1 mm above the face of the centerbody and appears to follow the shear layer of the recirculation zone. A blue flame is located along the outer rim of the sooting flame surface. It results from chemiluminescence of species such as CH and C_2 and is a reasonable marker for the stoichiometric flame surface. In all three flames, soot forms on the fuel rich side of the stoichiometric surface just as one would expect for diffusion flames.

The sooting surface of the flame shown in Fig. 3a has a donut shape. The base of the soot surface has lifted about 6 mm and the attached blue flame is anchored about 1 mm above the centerbody face. This donut shaped sooting surface is obtained by adding N_2 to the air and fuel in a way that keeps their total flow rates constant. Further decreasing the fuel flow and increasing N_2 results in a thin, soot ring structure and an attached blue flame as noted in Fig. 4a. These unusual flame structures are well suited for evaluating UNICORN and the soot model. However, some caution must be used in comparing photographed and computed flames. Only the outer edges of the observed and computed flame surfaces should be compared. This is because the flame photographs are 2D images of 3D surfaces, and the presented calculations are 2D cross sections through the center of the flame. The only locations where the images overlap are at the outer surfaces.

Parts (b) and (c) of Figures 2, 3, 4 present the calculated temperature, fuel volume fraction, soot volume fraction, and the soot radiation intensity contours along with the velocity vector fields. The calculated velocity vectors and fuel volume fraction contours give insight into the flow field and the processes involved in establishing and maintaining a flame. For example, the fuel mass fraction contours on the right side of the (b) figures illustrates how a small fraction of the fuel is entrained into the recirculation zone, mixed with hot products, and transported radially outward along the centerbody face where it mixes with the annular air and ignites and burns at stoichiometric conditions. This high-temperature, stoichiometric flame can be directly compared with the blue flames in the photographs in Figs. 2a-4a. The yellow flames in the photographs are due to blackbody radiation from the soot particles and can be directly compared with the computed radiation intensity from the soot. However, the radiation intensity depends exponentially on temperature so that a small quantity of soot in the higher temperature regions can dominate the soot radiation pattern. Thus, the calculated radiation intensities do not indicate the regions of highest soot concentration as shown by the soot volume fraction contours in the (c) images. The flame photographs and the contour plots have a one-to-one scaling, so they can be directly compared.

UNICORN calculations capture the unusual shapes of the sooting flames and many of the details of the combustion process. This is noted by using enlarged transparent overlays to compare the observed and computed flames in Figs. 2-4. When this is done, the computed soot radiation intensity in Fig. 2c and the blue flame in Fig. 2a overlay almost perfectly. A near perfect overlay is also obtained when the observed sooting flame surface in Fig. 2a is compared with the computed radiation intensity surface in Fig. 2c. The calculations show that the radiation intensity surface is just inside the high temperature flame surface shown in Fig. 2b just as observed in the flame photograph. Similar overlay comparisons of the flame surfaces in Figs. 3 and 4 also show reasonable agreement. Indeed, the calculated soot radiation intensities have similar donut and ring type sooting structures as those observed in the flame photographs. The major difference is that the calculated radiation intensities are displaced several millimeters downstream of the observed donut and ring surfaces. The agreement is surprisingly good considering the simple nature of the soot model.

UNICORN predicts that the highest soot concentrations are located inside the recirculation zone. This is noted in the calculated soot volume fraction contours shown in Figs. 2c-4c. The soot is also predicted to be concentrated around the vortex center, as shown by the superimposed velocity vector fields. This prediction can be evaluated using Mie scattering from a 2D laser sheet.

Laser sheet-lit images in Figures 5a and 6a show soot path lines that spiral towards the center of the recirculation zone. The soot appears to form near the centerbody face and can be easily tracked as the particles progress towards the vortex center. The soot tends to accumulate at the vortex center where visual observations indicate they either burn up or grow to the point that they fall to the centerbody face. This very unusual phenomenon is

not new. It was observed more than 20 years ago in studies with a similar centerbody burn on an Air Force Office of Scientific Research program (Roquemore, 1986). However, its' importance to soot studies was not recognized. The current version of UNICON cannot directly simulate this spiraling motion since soot is treated as a gas in the current model.

It is intriguing to consider what causes the spiral trajectories of the soot particles shown in Figs. 5a and 6a. To explore possible answers to this question, a particle-tracking program embedded in UNICORN is used (Katta, 2005). It is a Lagrangian-based program with Newtonian particle dynamics and includes drag, thermophoretic (Goldhirsch, 1983), and gravitational forces. This particle-tracking program is used to explore the path lines of particles released in the sooting zone of the flames.

It is evident from Fig. 5b that 5-micron diameter carbon particles, released at the location where the UNICORN calculations show soot is first formed, follow spiral path lines like the soot particles observed in Fig. 5a. There are other interesting details that are also captured in the path-line calculations. For example, the center and size of the observed and computed vortices are almost identical and the spiral tracks have similar characteristics. In Fig. 5a, the widths of the path lines are broader where the particles turn and start their downward motion towards the centerbody. The widths of the path lines become narrower as the particles approach the vortex center. This phenomenon is captured by the calculation as noted by the path lines on the right side of Fig. 5b. In this figure, more particles are released over a slightly wider region than is shown by the image on the left side of Fig. 5b. This implies that the broadening results from the number of soot particles and, to a lesser extent, the region in which they are produced. Since the particle-tracking program does not have a mechanism for destroying the particles, the observed narrowing of the path lines must result from some other effect that is not currently understood.

The nature of the forces causing the spiral particle path lines in Figs. 5a and 6a is not clearly understood. Spiral trajectories for heavy particles in a Burgers vortex have been calculated by (Marcu, 1995). They found that if the Stokes number is less than $16 \pi^2 A$ where A is equal to ν / Γ (viscosity/circulation), then the radially outward centrifugal force is less than the inward drag force. When this happens, the particles spiral towards the vortex center. This analysis does not directly apply to our problem because the fluid in a spiraling Burgers vortex is transported towards the vortex center, which is not the case for the centerbody-stabilized vortex. However, the spiral motion does depend on particle size. Figure 7a illustrates what happens when massless particles are released close to the centerbody face in the shear region where the calculations show soot is first formed. The black lines are the particle tracks. The massless particles do not spiral toward the vortex center but form a closed path that follows the outer region of the recirculation zone. Particle-tracking calculations (not presented) with 0.05, 1, and 5-micron diameter carbon particles result in spiral path lines. However, the calculated particle tracks shown in Fig. 7b illustrate that 50-micron diameter carbon particles have

sufficient momentum to carry them down stream without being entrained into the recirculation zone. Thus, there is a range of particle sizes that will exhibit a spiral motion. Perhaps the type of nondimensional analysis performed by (Marcu, 1995) when applied to a bluff-body stabilized vortex can provide the conditions resulting in spiral path lines.

The particles experience several forces that could contribute to their spiral motion. These forces include drag, thermophoresis, shear, and gravity. For the particles to spiral towards the vortex center, these forces must interact in a way that produces a net centripetal (inward directed) force. The two major forces are believed to be thermophoresis and drag. Their interaction could be very simple. Drag causes the particles to lose energy, and the thermophoresis pushes them towards the vortex center. The result is a spiraling motion of the particles. More studies are planned to determine if this simple explanation is correct.

The soot in the donut flame also has a spiral motion as noted in Fig. 6a. However, the path lines are different from those in Fig. 5a in that they have a very tight spiral that is almost contained in the sooting donut structure. UNICORN with particle-tracking calculations shown in Fig. 6b capture some but not all of observed details. For example, UNICORN correctly predicts the location of the vortex center, but the particle tracks are about the same size as those calculated for the full sooting flame show in Fig. 5a. Thus, the tightly spiraling path lines shown in Fig. 6a are not predicted. For the sooting ring flame shown in Fig. 4a, close visual inspection reveals that the soot particles have a very tight spiral trajectory that is about the same size as the sooting ring structure. Visual observations show that the sooting ring is actually distributed around the vortex center ring of the axisymmetric recirculation zone. UNICORN with particle tracking does not predict this very tight spiral motion.

Soot oxidation or burn-up may be responsible for the tight spiral motion in the donut and ring flames. The sooting, donut flame is formed by adding N_2 to both the fuel and air. The sooting ring is formed when more N_2 is added to the fuel. For nonpremixed jet flames, adding N_2 to the fuel causes the stoichiometric flame surface to move towards the centerline of the burner. This also appears to happen in the centerbody flame. The flame surfaces in Figs. 3 and 4 move towards the burner center line as the N_2 is added to the fuel. This is evident in both the flame photographs and the computed temperature contours shown in Figs. 3 and 4. Thus, adding N_2 brings the flame surface closer to the vortex center. In the ring shape, sooting flame (Fig. 4a), the actual flame surface appears to pass through the vortex center. For this case, consider what happens to the soot particles as they spiral around the vortex center. The particles with the larger radii must pass through the high-temperature flame zone. If these particles are burned up in the high-temperature flame, they will vanish and so will their path lines. Indeed, the only path lines that will be observed are those close to the vortex center that don't pass through the high-temperature flame or, if they do, their travel time is sufficiently small that they are not completely oxidized. Thus, we believe that soot particles with large radii

burn-up as they pass through the flame zone. This leaves only the particles with small radii that do not pass through the flame. They appear as tight spirals observed for the donut and ring flames.

Summary and Conclusions

Dramatically different sooting, laminar flames can be established with a centerbody burner. These flames have different sooting structures and other interesting features that make them desirable for soot model evaluation and development. For example, three flames, with different N₂ dilution in the fuel and air, exhibit full, donut, and ring-shaped sooting structures. Furthermore, the soot particle entrainment into the recirculation is an interesting phenomenon. Their path lines spiral toward the vortex center in all of the flames. However, the spiral path lines are more tightly wrapped for the donut flame than for the fully sooting flame. The spiral path for the ring flame is wrapped so tight that it is only about the size of the sooting ring. The different sooting flame shapes are calculated with UNICORN with an accuracy that is surprising good considering the rudimentary nature of the soot model. UNICORN treats the soot as large gas molecules and does not currently predict the path lines of actual soot particles. Thus, UNICORN could not directly predict the spiral motion of the soot particles. However, it has a particle-tracking program that did indirectly simulate the spiral motion by tracking 5-micron diameter carbon particles that are released in a region where soot starts to form. The particle-tracking program did not correctly calculate the tight spiral motion of the donut and ring sooting flames. The tight spirals may result because soot particles, in large orbits about the vortex center, tend to burn up as they pass through the high-temperature flame, thus leaving only the particles with smaller radii (tighter orbits) around the vortex center. The spiral path lines of the soot are postulated to result as the drag force reduces the energy of the particles and the thermophoretic force pushes them towards the vortex center. However, there are other factors that must be considered. For example, particle-tracking calculations show that massless particles follow a closed path around the recirculation zone and do not spiral towards the center, whereas the inertia of 50-micron diameter carbon particles carries them downstream without being entrained into the recirculation zone. Thus, there is a size range that has not been well quantified in which particles will not have a spiral motion. More detailed studies of these flames are planned in the future.

Acknowledgments

The authors wish to acknowledge the financial support of Dr. Chuck Pellerin of the SERDP program office and the Turbine Engine Division of the Propulsion Directorate of the Air Force Research Laboratory. We also appreciate insightful discussions with Prof. Paul Newton of the University of Southern California on the motion of particles in a Burgers vortex. We would also like to thank Mr. Jack Yoder for making the illustration of the experimental set-up. The authors appreciate editorial changes made by Ms. Gayle Byrd.

References

- Annon. (2001), *Computational Submodels, International Workshop on Measurement and Computation of Turbulent Nonpremixed Flames*, <http://www.ca.sandia.gov/tdf/Workshop/Submodels.html>, 2001.
- Correa, S. M., Gulati, A., (1992), *Measurements and Modeling of a Bluff-Body Stabilized Flame*, Combustion and Flame, 89, 2, 195-213.
- Dally, B. B., and Masri, A. R., (1998), *Instantaneous and Mean Compositional Structure of Bluff-Body Stabilized Nonpremixed Flames*, Combustion and Flame, 114, 119-148.
- Esquiva-Dano, H. T., et al., (2001), *Influence of a Bluff-Body's Shape on the Stabilization Regime of Non-Premixed Flames*, Combustion and Flame, 127, 2167-2180.
- Fallot, L. (1997), *Modeling Finite-Rate Chemistry Effects in Nonpremixed Turbulent Combustion: Test on the Bluff-Body Stabilized Flame*, Combustion and Flame, 110, 298-318.
- Goldhirsch, Isaac, and Ronis, David (1983), *Theory of Thermophoresis I. General Considerations and Mode-Coupling Analysis*, Physical Review A, 27, 3, March 1983.
- Guo, H., Liu, F., and Smallwood, G. J. (2004), *Combustion Theory and Modeling*, Vol. 8, pp. 475-489.
- Katta, V. R., and Roquemore, W. M. (2004), *Simulation of PAHs in Trapped-Vortex Combustor*, GT2004-54165, Proceedings of ASME Turbo Expo 2004, June 14-17, Vienna, Austria.
- Katta, V. R., Blevins, L. G., and Roquemore, W. M., (2005), *Dynamics of an Inverse Diffusion Flame and its Role in Polycyclic-Aromatic-Hydrocarbon and Soot Formation*, Combustion and Flame, 142, 33-51.
- Katta, V. R. (2007), *Predictions on Sooting Behavior of Recirculation-Zone Supported Flames*, Paper # D 37, 5th US Combustion Meeting.
- Kempf, A., et al., (2006), *Large-Eddy Simulation of a Bluff-Body Stabilized Nonpremixed Flame*, Combustion and Flame, 144, 170-189.
- Lindstedt, R. P. (1994), *Simplified Soot Nucleation and Surface Growth Steps for Non-Premixed Flames*, in *Soot Formation in Combustion: Mechanisms and Models* (H. Bockhorn, Ed.), Springer-Verlag, Heidelberg, pp. 417-439.
- Liu, Kai, et al., (2005), *Calculations of Bluff-Body Stabilized Flames Using a Joint Probability Density Function Model with detailed Chemistry*, 141, 89-117.
- Masri, A. R., and Bilger, R. W., (1984), *Twentieth Symposium (International) on Combustion*, The Combustion Institute, Pittsburgh, 319-320.
- Marcu, B, Meiburg, E. and Newton, P. K., (1995), *Dynamics of Heavy Particles in a Burgers Vortex*, Phys. Fluids, 7, 2, 400-410.
- Merci, Bart, et al., (2006), *Comparative Study of Micromixing Models in Transported Scalar PDF Simulations of Turbulent Nonpremixed Bluff-Body Flame*, Combustion and Flame, 144, 109-130.
- Namazian, et al., (1989), *Nonpremixed Bluff-Body Burner Flow and Flame Imaging Study*, Exp. in Fluids, 8, 3-4, 216-228.
- Roquemore, et al., (1980), *Preliminary Evaluation of a Combustor for Use in Modeling and Diagnostics Development*, ASME Publication 80-GT-93.

Roquemore, et al., (1984), *Utilization of Laser Diagnostics to Evaluate Combustor Models*, AGARD CP 353, 19, p. 36-1.

Roquemore, et al., (1986), *A Study of a Bluff-body Combustor Using Laser Sheet Lighting*, *Experiments in Fluids*, 4, 205-213.

Roquemore and Katta (2000), *Role of Flow Visualization in the Development of UNICORN*, *J. of Visualization*, 2, pp. 257-272.

Smooke, M. D., et al. (2005), *Soot Formation in Laminar Diffusion Flames*, *Combustion and Flame*, 143, 613-628.

Sturgess, G. J., and McManus, K. R., (1984), *Calculations of turbulent mass transport in a bluff-body diffusion-flame combustor*, American Institute of Aeronautics and Astronautics, Aerospace Sciences Meeting, 22nd, Reno, NV, Jan. 9-12, 1984.

Wang, H., and Frenklach, M., (1997), *A Detailed Kinetic Modeling Study of Aromatics Formation in Laminar Premixed Acetylene and Ethylene Flames*, *Combustion and Flame*, 110:173-221.

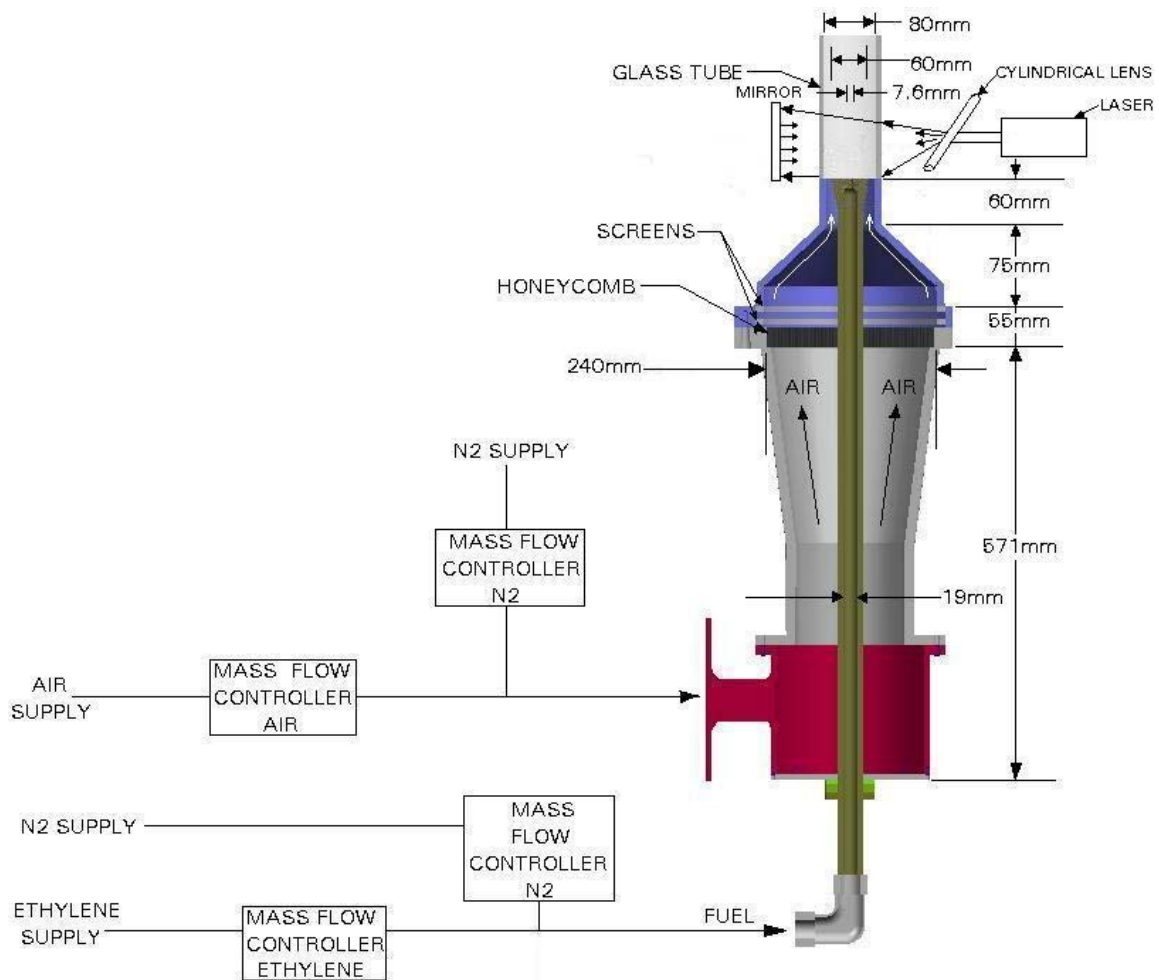


Figure 1. Experimental set-up showing flow controllers, test section, and laser sheet lighting arrangement. A digital camera (not shown) is set up normal to the laser sheet.

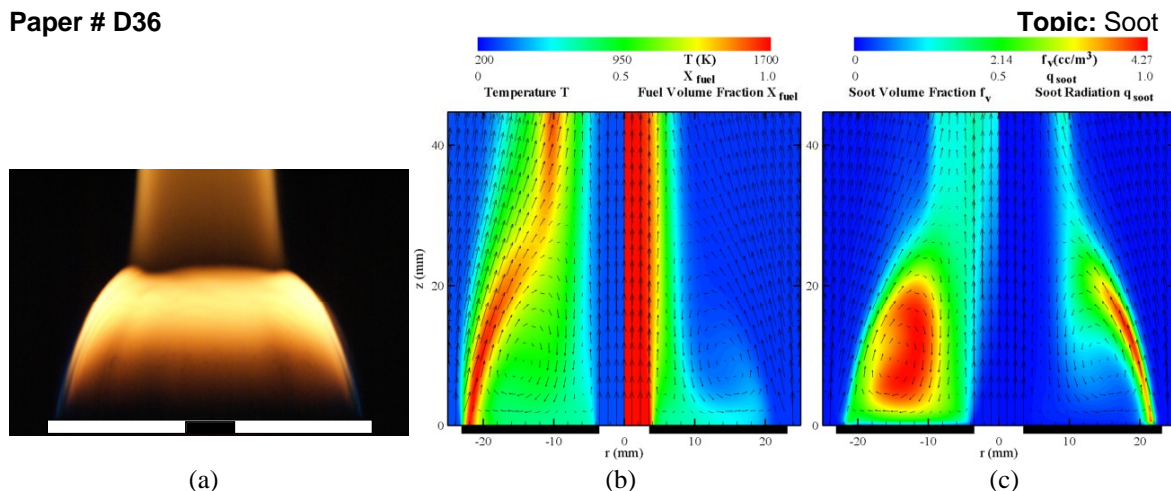


Figure 2. (a) Photograph of sooting flame structure for an airflow rate of 250 SLPM and fuel flow rate of 3.4 SLPM. UNICORN calculations of: (b) temperature (left) and fuel volume fraction (right); and (c) relative soot volume (left) and normalized soot radiation intensity (right).

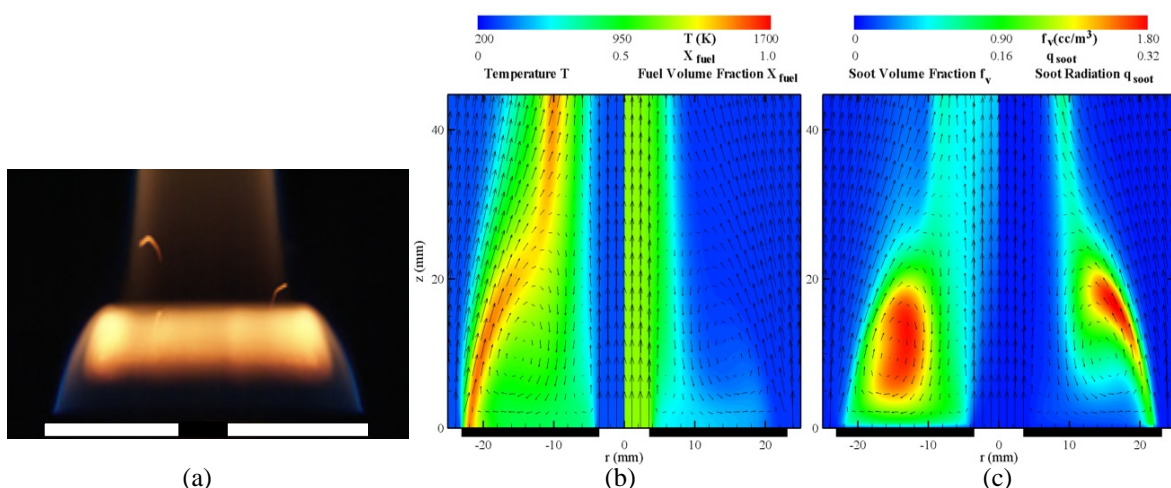


Figure 3. (a) Photograph of sooting flame structure for an airflow rate of 200 SLPM and 50 SLPM N_2 and fuel flow rate of 2.1 SLPM and 1.3 SLPM N_2 . UNICORN calculations of: (b) temperature (left) and fuel volume fraction (right); and (c) relative soot volume (left) and normalized soot radiation intensity (right).

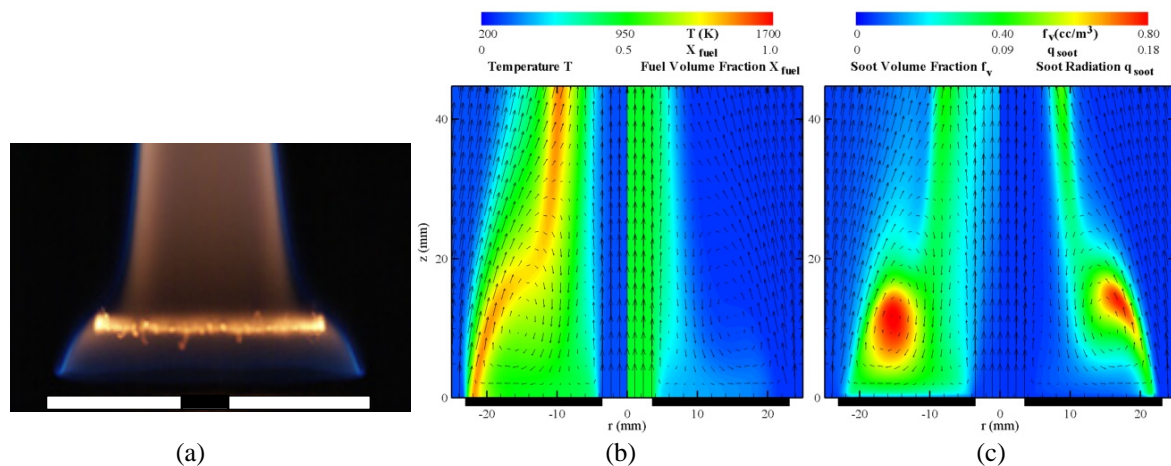


Figure 4. (a) Photograph of sooting flame structure for an airflow rate of 200 SLPM and 50 SLPM N_2 and fuel flow rate of 1.5 SLPM and 1.9 SLPM N_2 . UNICORN calculations of: (b) temperature (left) and fuel volume fraction (right); and (c) relative soot volume (left) and normalized soot radiation intensity (right).

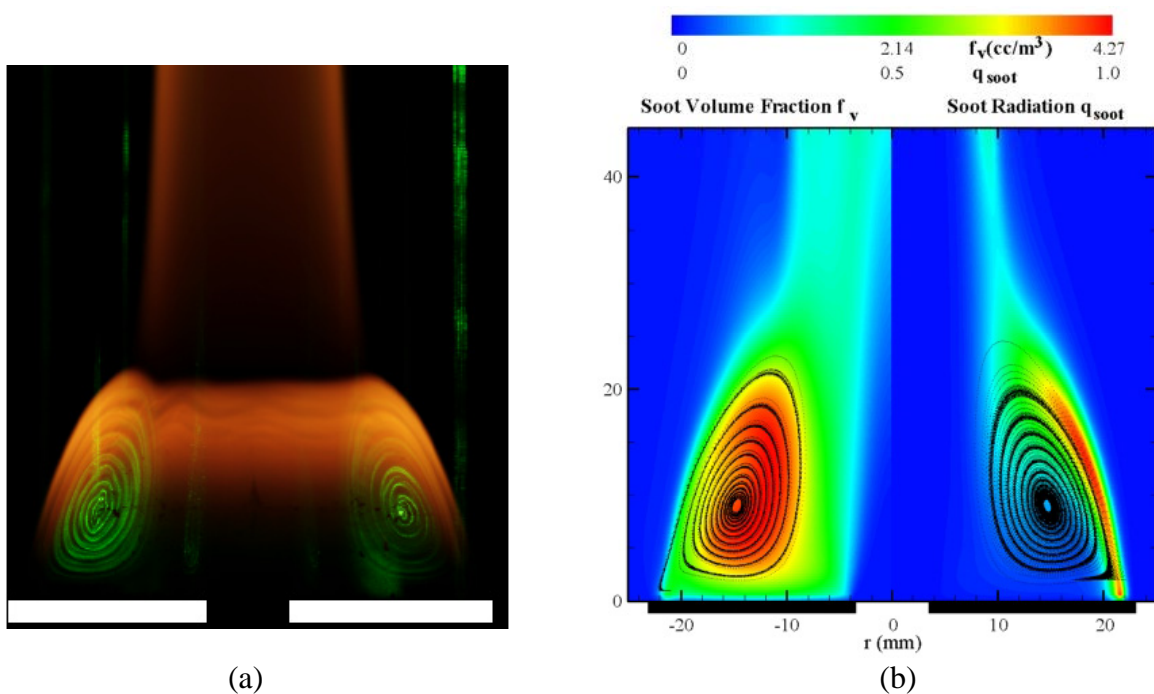


Figure 5. (a) Photograph of sooting flame and laser sheet image of the soot structure for an airflow rate of 250 SLPM and fuel flow rate of 3.4 SLPM. (b) Cross section of the computed path of 5-micron carbon particles released where the computations estimate the soot is initially formed. Flow conditions of (a) and (b) are the same.

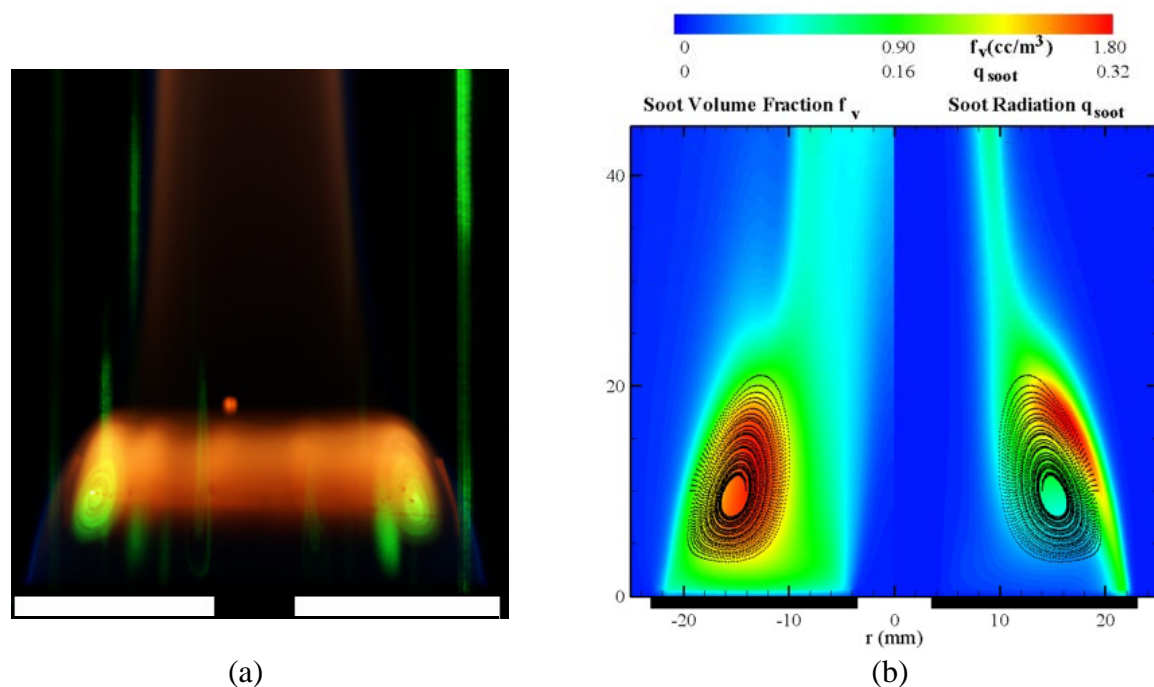


Figure 6. (a) Photograph of sooting flame and laser sheet image of the soot structure for an airflow rate of 200 SLPM and 50 SLPM N_2 and fuel flow rate of 2.1 SLPM and 1.3 SLPM N_2 . (b) Cross section of the computed path of 5-micron carbon particles released where the computations estimate the soot is initially formed. Flow conditions of (a) and (b) are the same.

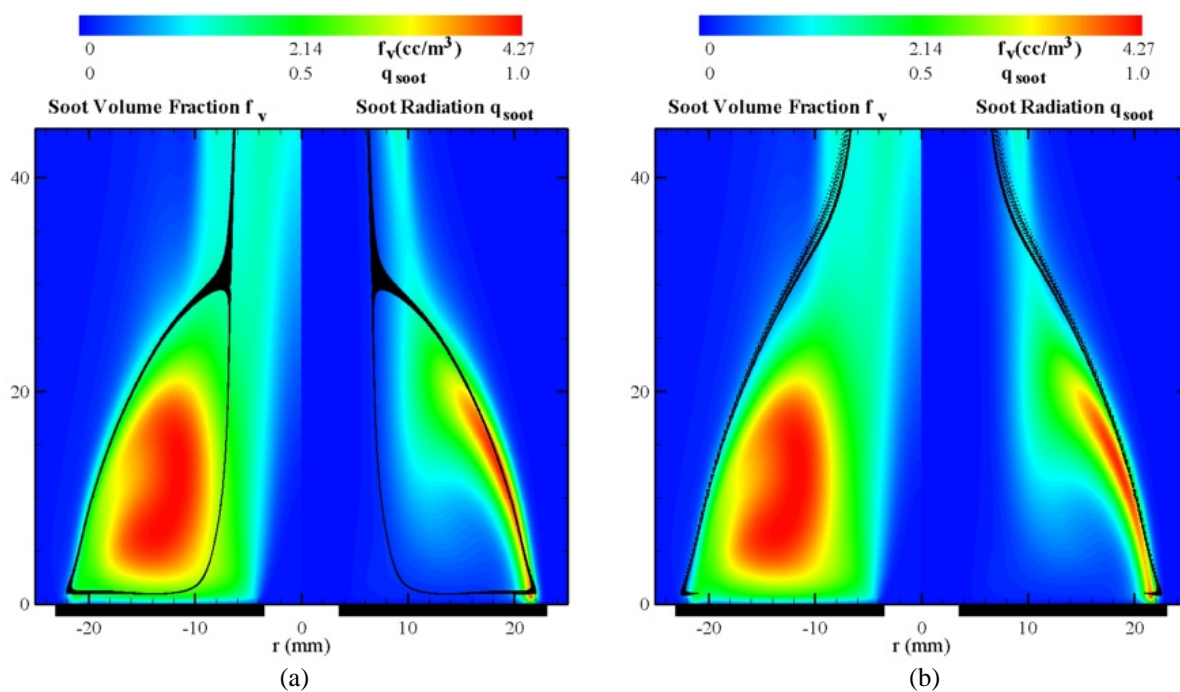


Figure 7. UNICORN calculations of: (a) tracks of mass-less particles and (b) tracks of 50-micron diameter carbon particles. Soot volume fraction is shown on the left side of each figure and soot radiation intensity is shown on the right side. Calculations are for an airflow rate of 250 SLPM and fuel flow rate of 3.4 SLPM.

Can Nonpremixed Stretched Flames Become Infinitely Thin?

Viswanath R. Katta¹, William M. Roquemore², James R. Gord²

¹Innovative Scientific Solutions Inc,
2766 Indian Ripple Road, Dayton, OH 45440, USA

²Propulsion Directorate, Air Force Research Laboratory,
Wright Patterson Air Force Base, OH 45433, USA

1 Introduction

Laminar flamelet is an asymptotic concept introduced by Peters [1] for describing turbulent flames. If the relevant chemical time scales are short compared to the convection and diffusion time scales, according to flamelet concept, combustion takes place within asymptotically thin layers embedded in the turbulent flow. In other words, laminar flamelet concept allows turbulent fluctuations in a reaction layer to be treated as variations to the flame structure rather than deviations to the structure itself. The usefulness of laminar flamelet concept in modeling turbulent flames comes from the assumption that the local instantaneous composition and temperature of the mixture in a nonpremixed system could be modeled as being the same as those in a stretched laminar flame [2]. The mixture fraction and scalar dissipation rate are commonly used in linking the turbulent flame structure to that of the laminar flame. At a critical value of scalar dissipation rate laminar nonpremixed flame extinguishes due to large mixture fraction gradients. The reaction zone in physical space under such critical conditions becomes so narrow that diffusive heat loss will lead to quenching. This scalar-dissipation-rate analogy has been used in flamelet theories in modeling extinction and ignition phenomena in turbulent flames. Flamelet theories have been successfully applied to the modeling of various nonpremixed flame systems [3].

A necessary condition for the flamelet concepts to be applied is that the reaction zone must be thinner than the smallest scales of the turbulence, which is Kolmogorov length scale. Performing asymptotic expansion for high Damkohler numbers for hydrogen flames, Bilger [4] derived an expression for reaction rate and argued that flamelets are not asymptotically thin due to the influence of reverse reactions; which means that the reaction zones must be broadened due to chemical equilibrium. Even though, the regular asymptotic analysis and the non-reacting experimental data used by Bilger [4] are not ideal for judging the validity of the flamelet theories, they certainly raised important issues about the applicability of the flamelet theories to the turbulent-combustion process. It has been widely recognized that highly resolved measurements and numerical simulations are needed for addressing the existence of laminar flamelets in turbulent-flow environment [5].

Recent numerical simulations of micro-vortex/flame interactions [6] suggested that vortices that are smaller than a millimeter in size cannot stretch a laminar nonpremixed flame. Instead, they destroy the flame structure during the interaction process. Even though these findings pose questions on the validity of the laminar flamelet concept, they could not disapprove the existence of infinitely thin reaction layers. A weak hydrogen-air nonpremixed flame is aerodynamically stretched in the present study for identifying the limits, if any, on the reaction layer thickness. The effect of chemical equilibrium on reaction layer thickness is also investigated.

2 Mathematical Model

A time-dependent axisymmetric model known as UNICORN (UNsteady Ignition and COmbustion using ReactionNs) [7] is used for the simulations of steady flames associated with an opposed-jet burner. This model solves the Navier-Stokes and species- and energy-conservation equations written in the cylindrical-coordinate (z -

r) system. A detailed-chemical-kinetics model is employed for describing the hydrogen-air combustion process. This model consists of 13 species--namely, H_2 , O_2 , H , O , OH , H_2O , HO_2 , H_2O_2 , N , NO , NO_2 , N_2O , and N_2 --and 74 elementary reactions (37 forward and 37 backward) among the constituent species. The rate constants for this H_2 - O_2 - N_2 reaction system were obtained from Ref. [8].

Temperature- and species-dependent property calculations are incorporated in the model. The governing equations are integrated on a nonuniform staggered-grid system. An orthogonal grid having rapidly expanding cell sizes in both the axial and the radial directions is employed. The finite-difference forms of the momentum equations are obtained using an implicit QUICKEST scheme [9], and those of the species and energy equations are obtained using a hybrid scheme of upwind and central differencing. At every time step, the pressure field is calculated by solving the pressure Poisson equations simultaneously and utilizing the LU (Lower and Upper diagonal) matrix-decomposition technique. UNICORN has been validated previously by simulating various steady and unsteady opposed and coflow jet nonpremixed flames [7,10].

The opposed-jet-flow burner, shown in Fig. 1, consists of two concentric nozzle systems. Fuel (a mixture of hydrogen and nitrogen) is issued from the top nozzle ($d_0 = 20$ mm) while air is issued from the bottom. Low speed nitrogen shroud flows ($D_0 = 30$ mm) are used for both the fuel and air jets. The top and bottom nozzles are separated by 20 mm. A flat nonpremixed flame is formed between the fuel and air jets in the neighborhood of the stagnation plane. The weak flame established with hydrogen-to-nitrogen ratio of 0.38 is aerodynamically stretched by increasing the fuel and air jet velocities simultaneously. The z - r coordinate system and a typical computed flame are shown in Fig. 1. Note, only one half of the flame shown in this figure is calculated. A non-uniform 801×51 mesh system distributed over a physical domain of 20×20 mm in the region between the upper and lower nozzles is used. An uniform mesh spacing of 0.02 mm in the axial (z) direction across the flame width and a rapidly increasing grid spacing in the radial (r) direction starting from 0.02 mm spacing at the axis of symmetry are achieved with this grid system.

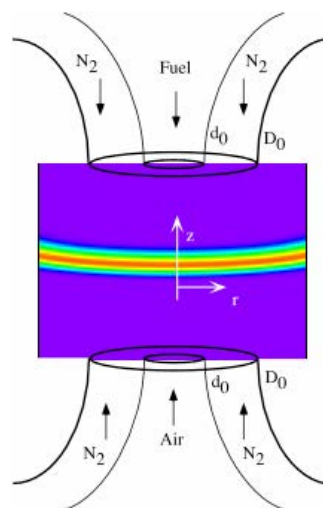


Fig. 1. Schematic diagram of the opposed-jet-flow burner modeled.

3 Results and Discussion

The steady-state flame shown in Fig. 1 represents a weakly stretched laminar flame obtained with fuel and air jet velocities of 0.4 and 0.3 m/s, respectively. As the velocities of the fuel and air jets increased, flame becomes thinner and its temperature decreases. Flame extinguishes for a critical set of velocities. Variations in flame (peak) temperature and peak heat-release rate along the centerline with respect to scalar dissipation rate at stoichiometry (χ_{st}) are shown in Fig. 2 for velocities ranging from 0.3 m/s through 21 m/s. Scalar dissipation rate (χ) is calculated from mixture-fraction formulation of Bilger [4] and using $1 \text{ m}^2/\text{s}$ for diffusion coefficient [11]. Results are labeled with “normal kinetics” while the open circles represent the values of the maximum-stretched flame. Further stretching of the flame resulted in extinguishment. The opposed-jet flame shown in Fig. 1 extinguished when the temperature dropped to 1140 K at which the scalar dissipation rate was 1.12 s^{-1} . To understand the role of chemical equilibrium on flame structure, calculations for the opposed-jet flame are repeated after increasing or decreasing the rates of the chemical reactions. Three sets of data with modified reaction rates are shown in Fig. 2. Results obtained after reducing the rates of the 37 forward reactions by half are shown with dash-dot lines, those obtained after doubling the rates of the forward reactions are shown in broken lines, and those obtained after doubling the rates of both the forward and reverse reactions are shown in thin lines. Changes in reaction rates affected not only the maximum stretch rate that can be applied on this flame but also the temperature at which extinction takes place. In general, temperature and heat release rates at extinction are higher with faster reactions. At a given scalar dissipation rate (χ_{st}) temperature and heat release rate of the flame increase with the reactivity of the system and such increase is more pronounced at higher χ_{st} .

This behavior can be explained from the chemical-nonequilibrium state of the flame. Increase in reaction rates enhances reactivity in the flame zone and, thereby, shifts the flame more into equilibrium.

Flame thickness estimated based on the full width of the temperature profile is shown in Fig. 3 for different χ_{st} values and for different chemical kinetics. Thicknesses of the flame at the time of extinction are marked with open circles. As the stretch rate increased on the steady opposed-jet flame, its thickness decreased as suggested by the laminar flamelet theory. However, contrary to the assumption that stretched flames become infinitely thin prior to extinction, flame thicknesses at extinction obtained with normal, reduced and enhanced kinetics are all within the range of 1 and 2 mm. More interestingly, the thickness Vs χ_{st} plot suggests that flame thickness is asymptotically approaching a finite value (~ 1 mm).

One could argue that temperature profile may not necessarily represent the reaction zone thickness as the it will be influenced by the thermal and molecular diffusive transport. Typically, intermediate radical species such as OH, O, and H that have short lifespan are confined to reaction zones. Variations of flame thicknesses obtained from the full width of OH and O radical distributions are shown in Figs. 4 and 5, respectively. For a given scalar dissipation rate, reaction zone thicknesses obtained from OH and O radical distributions are about one half of that obtained from temperature. Figs. 4 and 5 suggest that the radical-based reaction-zone thicknesses are also asymptotically approaching a finite value as the scalar dissipation rate on the flame is increased. It is important to note that even the smallest thickness of 0.5 mm represents a radical profile that has been resolved with a large number (25) of grid points, and hence, the asymptotic thicknesses shown in Figs. 3-5 are not limited by the grid distribution.

An examination of Figs. 4 and 5 further reveals that when the forward reaction rates (k_f) are reduced by half, the thickness of the reaction zone has increased for the similarly stretched flames (equal scalar dissipation rates). When the forward reaction rates are increased by 100% the reaction zone thickness decreased for the similarly stretched flames. On the other hand, when the reverse reaction rates (k_b) are also doubled the reaction zone thickness did not change much. This suggests that the flames calculated using twice the normal reaction rates are in chemical equilibrium and any further increase in reaction rates doesn't decrease the reaction-zone thickness. Which means flames are broadened (from infinitely thin reaction zone) not due to finite-rate chemistry, but due to equilibrium condition.

Calculations made with different reaction rates suggest that a minimum reaction zone thickness exists for flames that are aerodynamically stretched. For the hydrogen flame considered in this study, the minimum reaction zone thickness is in the range 0.5-1.0 mm, depending on the radical species used for obtaining the thickness. Consequently, flamelet theory cannot be applied to hydrogen-air nonpremixed flames for turbulent fluctuation length scales that are smaller than 0.5 mm. This was also evident in our previous studies [6] on vortex/flame interactions in which vortices smaller than 0.5 mm in diameter failed in stretching the flame.

4 Conclusions

A numerical study has been performed for determining the minimum possible thickness for a nonpremixed hydrogen-air flame. The flat flame formed between the counter flowing fuel and air jets is stretched through increasing jet velocities. A time-dependent model, known as UNICORN, that incorporates 13 species and 74 reactions among the constituent species has been used for the simulation of opposed-jet hydrogen-air nonpremixed flame. Numerical experiments were performed through changing the reaction rates. It is found that a nonpremixed flame can only be stretched to a minimum thickness prior to its extinction. Contrary to the flamelet description for laminar stretched flames, the reaction zone thickness for a hydrogen-air nonpremixed flame can asymptotically reach a value in the range 0.5-1.0 mm, depending on the radical species used for measuring the thickness. This finding has an important bearing on turbulence modeling based on flamelet theory.

References

- [1] N. Peters, *Proc. Combust. Inst.* 21 (1986) 1231-1256.
- [2] N. Peters, Length Scales in Laminar and Turbulent Flames, in Numerical Approaches to Combustion Modeling, (Eds. E. S. Oran and J. P. Boris), Progress in Astronautics and aeronautics, Vol. 135, 1991, Washington, D. C.

- [3] S. K. Liew, K. N. C. Bray, J. B. Moss, *Comb. Flame*, 56 (1984) 199-213.
- [4] R. W. Bilger, *Proc. Combust. Inst.* 22 (1988) 475-488.
- [5] N. Peters, *Prog. Astronautics Aeronautics* 135 (1991) 155-182.
- [6] V. R. Katta, T. R. Meyer, J. R. Gord, and W. M. Roquemore, Micro-Vortex/Flame interactions and Their Implication in Turbulent-Flame Modeling, 2005 Technical Meeting of the eastern States section of the Combustio Institute, Orlando, FL, Nov. 13-15, 2005.
- [7] W. M. Roquemore and V. R. Katta, *J. Visualization* 2 (2000) 257.
- [8] M. Frenklach, H. Wang, M. Goldenberg, G. P. Smith, D. M. Golden, C. T. Bowman, R. K. Hanson, W. C. Gardiner, V. Lissianski, Gas Research Institute Technical Report No. GRI-95/0058 (Gas Research Institute, Chicago), November 1, 1995.
- [9] V. R. Katta, L. P. Goss, W. M. Roquemore, *AIAA J.* 32 (1994) 84.
- [10] V. R. Katta and W. M. Roquemore, *AIAA J.* 36 (1998) 2044.
- [11] V. R. Katta, T. R. Meyer, M. S. Brown, J. R. Gord, and W. M. Roquemore, *Combust. Flame* 137 (2004) 198-221.

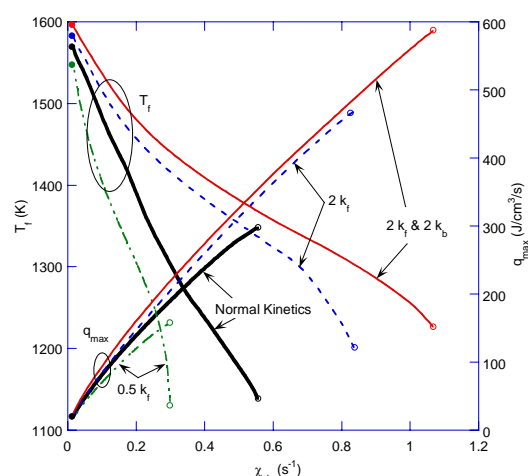


Fig. 2. Response of a steady state flame to aerodynamic stretch for different (fast vs slow) chemical kinetics.

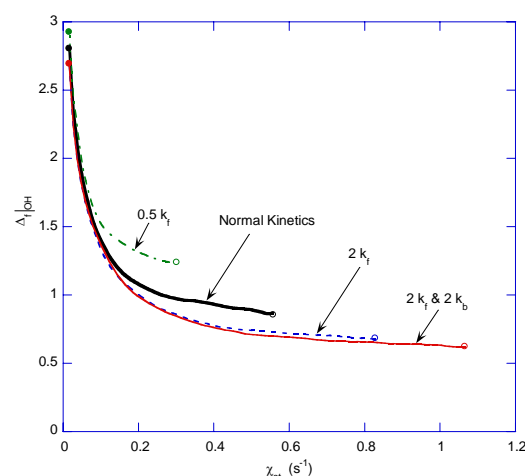


Fig. 4. Thickness (based on OH concentration) of a steady state flame at different stretch rates.

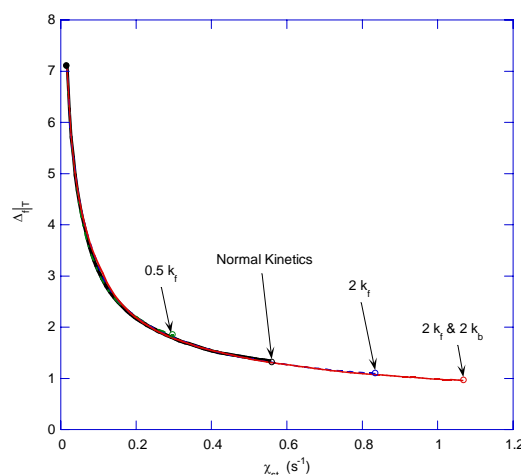


Fig. 3. Thickness (based on Temperature) of a steady state flame at different stretch rates and with different (fast vs slow) chemical kinetics.

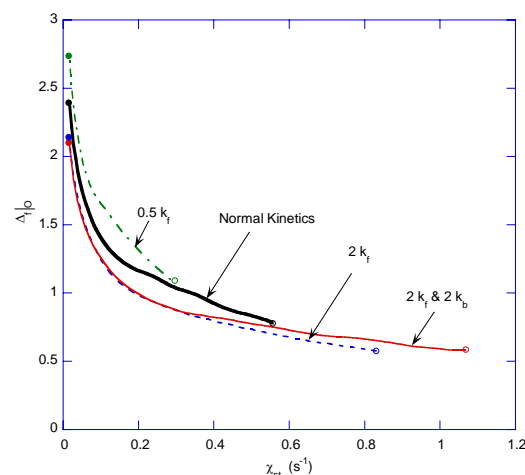


Fig. 5. Thickness (based on O concentration) of a steady state flame at different stretch rates.

Evaluation of Chemical Kinetics Models for Heptane Combustion

Viswanath R. Katta*

Innovative Scientific Solutions, Inc., Dayton, OH, 45440

and

William M. Roquemore†

Propulsion Directorate, Wright-Patterson Air Force Base, OH, 45433

Computational fluid dynamic (CFD) -based predictions are presented for nonpremixed and premixed flames burning vaporized heptane fuel. Three chemical kinetics models are incorporated into a time-dependent, two-dimensional, detailed-chemistry, CFD model known as UNICORN. The first mechanism is the San Diego (SD) mechanism (52 species and 544 reactions), the second one is the Lawrence Livermore National Laboratory (LLNL) mechanism (160 species and 1540 reactions), and the third one is the National Institute of Standards and Technology (NIST) mechanism (197 species and 2926 reactions). Numerical models are validated through simulating an opposing-jet nonpremixed flame that was previously studied experimentally. Models are also tested for their accuracies in predicting strain-induced extinction and autoignition. Compared to traditional one-dimensional models for opposing-jet flames, two-dimensional simulations are found to give results closer to the experimental values. All three mechanisms are reasonably close to each other in predicting co-axial jet nonpremixed and premixed flames. SD mechanism is found to be slightly stiffer than the other two mechanisms, especially in solving for premixed combustion. While LLNL kinetics resulted in a steady Bunsen-type premixed flame, SD and NIST mechanisms yielded cellular-type flame structures for the same flow conditions.

I. Introduction

Detailed chemical kinetics for describing combustion of higher hydrocarbon fuels involves several hundred species and several thousand elementary reactions. The need for more accurate and presumably larger chemical-kinetic mechanism is being strongly driven by the escalating costs of petroleum-based fuels and the need to develop alternate fuels. Indeed, new fuel mechanisms are being rapidly developed. Traditionally, such newly developed mechanisms are validated through the simulations of zero- and one-dimensional flames using codes such as RUN1DL,¹ OPPDIF,² and CHEMKIN³ and comparing the results with the available experimental data. Extensive experimental data for the intermediate species concentrations are required for obtaining a reasonably calibrated kinetics mechanism. However, it is not always feasible to obtain concentrations of the numerous hydrocarbon intermediates generated during the combustion of complex hydrocarbon fuels. As a result, validation of newly developed complex chemical-kinetics mechanisms using traditional approaches can only be partially performed.

One of the dangers in using partially validated mechanisms is that the simulations for a reacting flow under certain conditions may look reasonable, but may result in poor simulations under different conditions. This was demonstrated by Katta et al.⁴ using recently developed mechanisms for JP-8 fuels. Three JP-8 mechanisms were investigated. One came from Ranzi's group, the second one from University of Utah, and the third one came from the Propulsion Directorate of the Air Force Research Laboratory (AFARL/PR). These three mechanisms were

* Senior Engineer, vrkatta@erinet.com, 2766 Indian Ripple Road, AIAA Associate Fellow.

† Senior Scientist, melvyn.roquemore@wpafb.af.mil, Building 5, 1950 Fifth Street, AIAA Fellow.

developed independently and validated using the limited experimental data on ignition delay and flame speeds. The Violi mechanism (Ranzi's group)⁵ has 161 species and 1538 reactions, which includes some global-type reactions, the University of Utah mechanism⁶ has 208 species and 2186 reactions, and the Mawid mechanism (AFRL/PR)⁷ has 216 species and 3000 reactions. These three mechanisms were incorporated into UNICORN and calculations were performed for a variety of two-dimensional flame systems. It was found that the flame structures predicted by these mechanisms were radically different from each other and more importantly the blowout characteristics of a nonpremixed flame varied significantly from mechanism to mechanism. Disappointingly, the partially validated chemistry models were found to be of only limited use in the simulations of multidimensional flames. Thus, there exists a great need for validating these complex mechanisms through the simulation of multidimensional flames using robust and efficient CFD codes that can handle large chemical-kinetics mechanisms.⁸

Chemical-kinetic-mechanisms that describe oxidation of n-heptane (n-c7H16) have been developed by numerous investigators.⁹⁻¹⁰ n-Heptane is a primary reference fuel for octane rating in internal combustion engines. Extensive experimental work has been performed for validating/developing detailed mechanisms for n-heptane.¹¹⁻¹² However, these mechanisms were not tested for their ability to predict multi-dimensional flames. This is, in part, due to lack of detailed experimental data in laboratory jet flames and, in part, due to lack of robust CFD models that can perform multi-dimensional calculations using large chemical kinetics. UNICORN is a time-dependent two-dimensional numerical model that is being developed for simulating the dynamic characteristics of nonpremixed and premixed flames using very large chemical kinetic mechanisms.⁸ This paper describes the predictions made for n-heptane flames using three detailed chemical kinetics models.

II. Mathematical Model

UNICORN (UNsteady Ignition and COmbustion using ReacTiONs) code^{13,14} is a time-dependent, axisymmetric mathematical model, which is used for the simulation of unsteady reacting flows. It is capable of performing direct numerical simulations (DNS) and has been developed over a ten-year period. Its evolution has been in conjunction with experiments conducted to test its ability to predict ignition, extinction, stability limits, and the dynamic characteristics of nonpremixed and premixed flames of various fuels. It solves for u- and v-momentum equations, continuity, and enthalpy- and species-conservation equations on a staggered-grid system. The body-force term due to the gravitational field is included in the axial-momentum equation for simulating vertically mounted flames. A clustered mesh system is employed to trace the large gradients in flow variables near the flame surface. Three detailed chemical-kinetics models developed for heptane- combustion are incorporated. First one is San Diego (SD) mechanism.¹⁵ It consists of 52 species and 544 elementary reactions. The second one is Lawrence Livermore National Laboratory (LLNL) mechanism.¹⁶ It consists of 160 species and 1540 reactions. And the third one is National Institute of Standards and Technology (NIST) mechanism.¹⁷ It consists of 197 species and 2926 reactions. Thermo-physical properties such as enthalpy, viscosity, thermal conductivity, and binary molecular diffusion of all the species are calculated from the polynomial curve fits developed for the temperature range 300 - 5000 K. Mixture viscosity and thermal conductivity are then estimated using the Wilke and Kee expressions, respectively. Molecular diffusion is assumed to be of the binary-diffusion type, and the diffusion velocity of a species is calculated using Fick's law and the effective-diffusion coefficient of that species in the mixture. A simple radiation model based on the optically thin-media assumption is incorporated into the energy equation.¹⁸ Only radiation from CH₄, CO, CO₂, and H₂O is considered in the present study.

The finite-difference forms of the momentum equations are obtained using an implicit QUICKEST scheme,^{19,20} and those of the species and energy equations are obtained using a hybrid scheme of upwind and central differencing. At every time step, the pressure field is accurately calculated by solving all the pressure Poisson equations simultaneously and using the LU (Lower and Upper diagonal) matrix-decomposition technique. Different types of boundary conditions such as adiabatic wall, isothermal wall, symmetric surface, outflow, and inflow can be applied to the boundaries of the computational domain.²¹

The simulations presented here are performed on a single cpu, AMD Opteron Personal Computer with 2.0 GB of memory. Typical execution time is ~30 s/time-step for the coaxial-nonpremixed-flame simulations. Steady state solutions are typically obtained in about 2,000 time steps starting from the solution obtained using the global combustion chemistry model.

III. Results and Discussion

Multidimensional-flame simulations using UNICORN can be performed on a Personal Computer with 2.0 GB of memory. Execution times strongly depend on the number of species considered in the chemical-kinetics model and

the grid size. The calculations made with different heptane chemical kinetics models are presented in the following subsections:

A. Validations for Flame Structure

The opposing-jet flame considered for validating the numerical models is formed between pre-vaporized heptane and air jets. This flame represents a weakly stretched laminar flame and the experiments were carried out by Seiser et al.¹¹ The burner for gaseous reactants is made up of two opposing ducts with inner diameters of 22.2 mm through which reactants are introduced. The distance between the ducts is 10 mm. The mixture of n-heptane vapor and nitrogen is introduced from the bottom duct while air is introduced from the top duct. The temperatures of the fuel and air jets are 338 and 298 K, respectively. Experiments were conducted for different strain rates (velocities) and measurements for temperature and species were made along the burner centerline. For model validation purpose the data obtained at strain rate of 150 s^{-1} is considered.

$$\text{StrainRate } a = \frac{2|V_2|}{L} \left(1 + \frac{|V_1|}{|V_2|} \sqrt{\frac{|\rho_1|}{|\rho_2|}} \right)$$

Here, V_1 and V_2 represent the velocities of the fuel and air, respectively and ρ_1 and ρ_2 represent the respective densities. L is the separation between the fuel and oxidizer ducts. Fuel is composed of 15% heptane and 85% nitrogen. The fuel and air velocities used for the 150-s^{-1} flame are 0.342 and 0.375 m/s, respectively. Two-dimensional simulations for the flowfield between the upper and lower ducts are performed using a 301×41 variable grid system. This grid yielded a mesh spacing of $33 \mu\text{m}$ across the flame surface in the axial direction. Calculations for this flame are performed using the three chemical kinetics models. The three steady state flames obtained are shown in Fig. 1. Temperature distributions color-coded with rainbow color scheme (red and violet representing 300 and 1700 K, respectively) are shown in Fig. 1. The nonpremixed flame formed between the two reactant ducts is slightly curved upward toward air duct. All three mechanisms resulted in nearly identical flames in shapes and sizes.

Temperature and axial-velocity distributions along the centerline across the flame are shown in Fig. 2. While the computed profiles are shown with lines temperature measurements obtained by Seiser et al.¹¹ are plotted with solid symbols. Even though the moments of the fuel and oxidizer jets were matched, the stagnation plane (plane perpendicular to the centerline and passing through $U = 0$ location) is located $\sim 0.5 \text{ mm}$ away from the midsection toward the fuel duct. The peak-temperature surface is located $\sim 0.2 \text{ mm}$ away from the midsection toward the air duct, which is also the case in the experiments. All three mechanisms resulted in nearly identical temperature and velocity profiles. Calculated temperature profiles compare well with measured one. Maximum temperature predicted by NIST mechanism is $\sim 40 \text{ K}$ lower than that obtained with SD or LLNL mechanism.

Distributions of fuel, oxygen, H_2O , and CO_2 along the centerline are shown in Fig. 3 along with the measured one. Once again, all three models predicted nearly the same distributions for these species. Comparisons with experiment are also reasonable. However, this is not the case for the other species such as fuel and radical species. Distributions of H_2 , CO and $\text{C}_2\text{H}_2 + \text{C}_2\text{H}_4$ are shown in Fig. 4 and those of CH_4 , C_3H_6 and C_2H_6 are shown in Fig. 5. In general, models are over predicting the concentrations for all these species. Note similar discrepancies between measurements and calculations were also obtained with a one-dimensional model CHEMKIN in conjunction with a shortened version of SD mechanism.¹¹ While SD and NIST mechanisms predict the same H_2 concentrations LLNL mechanism is resulting in $\sim 25\%$ more. Differences in the predictions made by the three mechanisms may be noted for all the species shown in Figs. 4 and 5. However, these differences did not cause any deviations in the overall flame structures shown in Figs. 1 and 2. It will be interesting to see the impact of these differences on the structures of the co-axial premixed and nonpremixed jet flames.

B. Validations for Strain-Induced Extinction

Using the burner described in the previous section Seiser et al.¹² have obtained strain rates for extinguishing the flames. Selecting a particular value for the n-heptane-nitrogen ratio in the fuel jet and a matching ratio (based on flame-sheet location) for the air and nitrogen in the oxidizer jet Seiser et al.¹² obtained critical conditions for extinction. They performed these experiments by varying the fuel and oxidizer jet velocities while allowing only a small change in the flame location by matching the momentums of these jets. Calculations with UNICORN code with SD, LLNL, and NIST mechanisms are performed for obtaining critical extinction conditions for a specific n-heptane-nitrogen ratio. The temperatures of the fuel and oxidizer streams are 345 and 298 K, respectively. Fuel is composed of 28.2% n-heptane and 71.8% nitrogen by volume. Oxidizer is composed of 20.5% oxygen and 79.5%

nitrogen. Reactant ducts are separated by 10 mm. Calculations with the three mechanisms are repeated by gradually increasing the fuel and oxidizer jet velocities until the flame is extinguished. Incremental changes to the velocities were decreased as the flame approaches extinction conditions. Due to an imbalance between the heat produced in the flame and heat transported away from the flame, maximum temperature decreases with strain rate (or velocity). A typical strained flame obtained at near-extinction limit is shown in Fig. 6. Since only the central part of the flame is strained due to the impinging reactant jets maximum temperature decreased only in this region. Flame became thin, but not infinitely thin, compared to the weakly strained one in Fig. 1.

Results obtained in the form of changes to the maximum temperature with increase in strain rate are shown in Fig. 7. Strain rate measured for the critical flame (just prior to extinction) is also shown in Fig. 7 with a hatched rectangle. Significant differences are found in the flame responses predicted by the three mechanisms. LLNL mechanism is giving the most stable flame with a critical extinction strain rate of 447 s^{-1} . This compares well with the measured value of 460 s^{-1} . NIST mechanism, which predicts lower maximum temperatures (Fig. 2), resulted in flame extinction for a strain rate of 340 s^{-1} . SD mechanism, which predicts higher temperatures in weakly strained flames (Fig. 2), resulted in extinction for a strain rate of 405 s^{-1} . Interestingly, one-dimensional calculations performed for this flame using LLNL mechanism by Seiser et al.¹² obtained an extinction strain rate of 520 s^{-1} which is $\sim 13\%$ higher than the measured value. The two-dimensional simulations performed in this study using the same mechanism resulted extinction strain rate that is only 3% lower than the measurements. This suggests that the one-dimensional assumption for the flowfield at higher strain rates is not appropriate. Such differences in extinction conditions between the one-d and two-d simulations were also noted by Katta et al.²² in partially premixed flames.

C. Validations for Autoignition

Using opposing-jet flame configuration Seiser et al.¹² have conducted autoignition experiments. They issued n-heptane-nitrogen mixture from the bottom duct and heated air from the top duct. Autoignition condition was reached by gradually increasing the air temperature. The volume fraction of n-heptane in the fuel jet was kept constant at 15% while the fuel temperature is maintained at 378 K . Experiments were performed for different strain rates. For validation purpose calculations for this configuration are performed for a strain rate of 400 s^{-1} . Two-dimensional simulations using SD, LLNL, and NIST mechanisms are performed by gradually increasing the air temperature. Since autoignition depends not only on temperature but also on induction time, calculations for this problem must be performed sufficiently long in time—beyond the time required for establishing a steady-state flowfield. Temperature distribution obtained for a 1282-K -airflow case is shown in Fig. 8. This is computed using SD mechanism and flame has not been established, as autoignition did not take place. However, when the airflow temperature is increased by another degree to 1283 K autoignition took place.

Heated air mixes with the relatively cold fuel in the region surrounding the stagnation plane. Mixing of fuel and oxygen also simultaneously takes place. A combination of local equivalence ratio, strain rate and temperature determines the whether autoignition takes place or not. Therefore, one should not refer air temperature itself to as autoignition temperature and the ability of a chemical kinetics mechanism in predicting autoignition must be assessed by simulating the entire flowfield. Two-dimensional calculations are performed using three mechanisms. It is observed that temperature and OH concentration in the mixing region increase exponentially with air temperature. Therefore, for tracing autoignition process, computed results in the form of maximum temperature and OH concentration at different air temperatures are shown in Fig. 9. The conditions at which autoignition took place in the calculations are marked with solid circles. The air temperature at which autoignition took place in the experiment is shown with hatched rectangle. Among the three mechanisms, NIST one is predicting autoignition process closer to the experiment. One-dimensional calculations performed with LLNL mechanism¹² resulted autoignition when air temperature was 1237 K . Two-dimensional calculation with the same mechanism predicted (Fig. 9) autoignition at 1264 K . In comparison experiment has suggested 1204-K air temperature for autoignition. However, there is about 50 K error margin associated with the measurements made by Seiser et al.¹²

D. Simulation of a Co-Axial Jet Premixed Flame

Flame speed is another characteristic parameter of fuel-air mixture, which needs to be represented accurately by the chemical kinetics employed. For understanding the flame-speed characteristics of the chemical-kinetics mechanisms calculations are performed for a Bunsen-type coaxial premixed flame using the three kinetics models. To allow for possible flashbacks in premixed systems a 5-mm -long fuel tube is included in the calculations. The inner and outer radii of the tube are 5.6 and 6.4 mm , respectively. Preheated stoichiometric fuel and air mixture at 400 K exits the fuel tube at an average velocity of 1.6 m/s . A parabolic, fully developed velocity profile is assumed at the inlet of the fuel tube. A computational grid of 201×107 is used for discretizing the physical domain of $20 \text{ cm} \times 5 \text{ cm}$ in axial and radial directions, respectively. While calculations with LLNL and NIST mechanisms were carried

with a time-step of 0.05 ms, calculations with SD mechanisms had to be carried with a time-step of 0.02 ms due to the difficulties with convergence. Results obtained with SD, LLNL, and NIST mechanisms are shown in Figs. 10, 11, and 12, respectively. Temperature distributions color-coded with rainbow scheme (violet representing 300 K and red representing 2300 K) are shown in 10a, 11a, and 12a. Similarly, H₂-mole-fraction distributions between 0 and 0.002 are shown in b figures, O₂-mole-fraction distributions between 0 and 0.233 are shown in c figures and OH-mole-fraction distributions between 0 and 0.005 are shown in d figures.

Since the velocity profiles used in all the calculations shown in Figs. 10-12 are the same, the surface area of the inner cone (or the height of the inner cone for equal base diameters) directly represent the flame speed. As seen from Figs. 10a and 12a the SD and NIST mechanisms yielded nearly identical inner cone shapes and heights and, hence, have the same flame speeds. Both are exhibiting cellular flame structures. In fact, calculations with these two mechanisms did not reach a steady-state solution. On the other hand, calculations made with LLNL mechanism resulted in a steady flow with a smooth flame surface. Also, burning velocity estimated from inner cone height of Fig. 11c is nearly 20% less than that obtained with the other two mechanisms. These differences and similarities in burning velocities obtained with different mechanisms are inconsistent with the extinction and autoignition properties obtained previously.

E. Simulation of a Co-Axial Jet Nonpremixed Flame

Flat flames obtained in opposing-jet configurations provide a good platform for testing the chemical-kinetics mechanisms. However, unlike most practical flames, opposing-jet flames do not have stability issues, as they do not possess leading edges. The role of chemical kinetics in the stability of jet flames is significant and, therefore, proposed chemical-kinetics mechanisms must also be tested for their ability in predicting nonpremixed jet flames as well. The advantage of codes like UNICORN is that once a chemical-kinetics mechanism is incorporated they can be used for the simulation of both opposing- and coaxial-jet flames.

Calculations for n-heptane coaxial nonpremixed jet flame are performed using the three chemical-kinetics models considered in the present work. The simulated burner has a central fuel tube of 0.6-cm radius and is surrounded by a 5-cm radius coflowing air. Preheated n-heptane at 400 K is issued at a velocity of 2.2 cm/s. Coannular flow consists of room-temperature air issued at a velocity of 9.2 cm/s. Such low-velocity conditions were chosen so that stable flames are established with all the three chemical-kinetics models. A computational grid of 201x71 is used for discretizing the physical domain of 20 cm x 5 cm in axial and radial directions, respectively. Grid clustering is used for placing most of the grid lines in the flame zone. Initial conditions (flame) for the detailed-chemistry calculations are obtained from the simulation using a global-chemistry UNICORN code. Calculations with all three mechanisms were carried using a time-step of 0.05 ms.

Results for the coaxial nonpremixed jet flame obtained with the SD, LLNL, and NIST mechanisms are shown in Figs. 13, 14, and 15, respectively. Temperature distributions color-coded with rainbow scheme (violet representing 300 K and red representing 2100 K) are shown in 13a, 14a, and 15a. Similarly, H₂-mole-fraction distributions between 0 and 0.004 are shown in b figures, O₂-mole-fraction distributions between 0 and 0.233 are shown in c figures and OH-mole-fraction distributions between 0 and 0.003 are shown in d figures.

In general, all three models predict nearly the same flame shape with tips burning hotter than the bases. The flames are anchored to the burner rim on the outer edge. There are several differences in these predictions. LLNL mechanism predicts higher H₂ concentration inside the flame than that predicted by NIST mechanism, which is higher than that predicted by SD mechanism. First part of this difference is consistent with the predictions made for the opposing-jet flame (Fig. 4); however, the second part is not. In opposing jet flame both the SD and NIST mechanisms yielded nearly the same H₂ concentrations. OH predicted by NIST mechanism is lower than those predicted by the other two mechanisms. Oxygen tends to leak from the flame base into the fuel jet for SD and NIST mechanisms while flame base is tightly anchored to the burner rim in LLNL simulation. This is consistent with the burning velocities obtained with Bunsen-type-premixed-flame calculations.

IV. Conclusion

A computational study was performed to elucidate the differences in the combustion characteristics predicted by different detailed chemical kinetics modes for n-heptane fuel. Three chemical kinetics models are considered in the present study. They are 1) San Diego (SD) mechanism (52 species and 544 reactions), 2) Lawrence Livermore National Laboratory (LLNL) mechanism (160 species and 1540 reactions), and 3) National Institute of Standards and Technology (NIST) mechanism (197 species and 2926 reactions). These mechanisms were incorporated into a time-dependent, two-dimensional, detailed-chemistry, computation-fluid-dynamics model known as UNICORN.

Numerical models are validated through simulating an opposing-jet nonpremixed flame that was previously studied experimentally. Models are also tested for their accuracies in predicting strain-induced extinction and autoignition. Compared to traditional one-dimensional models for opposing-jet flames, two-dimensional simulations are found to give results closer to the experimental values. Predictions are made for two-dimensional nonpremixed and premixed jet flames burning vaporized heptane fuel. All three mechanisms are reasonably close to each other in predicting co-axial jet nonpremixed and premixed flames. SD mechanism is found to be slightly stiffer than the other two mechanisms, especially in solving for premixed combustion. While LLNL kinetics resulted in a steady Bunsen-type premixed flame, SD and NIST mechanisms yielded cellular-type flame structures for the same flow conditions.

Acknowledgments

Financial support for this work was provided by the Air Force Office of Scientific Research (AFOSR, Julian Tishkoff), Strategic Environmental Research and Development Program (SERDP, Bruce Sartwell), and the Air Force Contract #F33615-03-D-2329 (Vince Belovich).

References

1. Rogg, B., "RUN1DL—The Cambridge Universal Laminar Flamelet Computer Code," in *Reduced Kinetic Mechanisms for Applications in Combustion Systems*, N. Peters and B. Rogg (Eds), Lecture Notes in Physics m15, Springer-Verlag, Heidelberg, Germany, 1993, pp. 350-351.
2. Lutz, A. E., Kee, R. J., Grcar, J. F., and Rupley, F. M., "OPPDIF: A Fortran Program for Computing Opposed flow Diffusion Flames," SAND96-8243, Sandia National Laboratories, CA (1996)
3. Kee, R. J., Miller, J. A., Jefferson, T. H., "CHEMKIN: A General-Purpose, Problem-Independent, Transportable, Fortran, Chemical Kinetic Code Package," Technical Report SAND80-8003, Sandia National Laboratories, 1980.
4. Katta, V. R., Mawid, M., Sekar, B., Corporan, E., Zelina, J., Roquemore, W. M., and Montgomery, C. J., "Comparison of Chemical-Kinetics Models for JP-8 Fuel in Predicting Premixed and Nonpremixed Flames," AIAA-2006-4745, 42nd AIAA/ASME/SAE/ASEE Joint Propulsion Conference and Exhibit, Sacramento, CA, July 9-12, 2006.
5. Violi, A., Yan, S., Eddings, E. G., Sarofim, A. F., Granata, S., Faravelli, T., Ranzi, E., "Experimental Formulation and Kinetic Model for JP-8 Surrogate Mixtures," *Combustion Science and Technology* 174 (2002) 399-417.
6. Zhang, H., Ph. D. Thesis, Department of Chemical Engineering, University of Utah, 2005.
7. Mawid, M. A., Park, T. W., Sekar, B., and Arana, C., "Detailed Chemical Kinetic Modeling of JP-8/Jet-A Ignition and Combustion," GT2005-68829, Proceedings of ASME Turbo Expo, Reno, NV, June 6-9, 2005.
8. Katta, V. R., and Roquemore, W. M., "Calculation of Multidimensional Flames Using Large chemical Kinetics," AIAA-2007-4418, 37th AIAA Fluid Dynamics conference and exhibit, Miami, FL, June 25-28, 2007.
9. Westbrook, C. K., Warnatz, J., and Pitz, W. J., *Proc. Combust. Inst.* 22:893-901 (1988).
10. Lindstedt, P., *Proc. Combust. Inst.* 27:269-285 (1998).
11. Seiser, R., Truett, L., Trees, D., and Seshadri, K., "Structure and Extinction of Non-Premixed n-Heptane Flames," *Proc. Combust. Inst.* 27:649-657 (1998).
12. Seiser, R., Pitsch, H., Seshadri, K., Pitz, W. J., and Curran, H. J., "Extinction and Autoignition of n-Heptane in Counterflow Configuration," *Proc. Combust. Inst.* 28:2029-2037 (2000).
13. Roquemore W. M., and Katta, V. R., *Journal of Visualization*, 2 (2000) 257-272.
14. Katta, V. R., and Roquemore, W. M., "Simulation of Dynamic Methane jet Diffusion Flames Using Finite Rate Chemistry Models," *AIAA Journal*, Vol. 36, No. 11, 1998, p. 2044-2054.
15. <http://www-mae.ucsd.edu/~combustion/cermech/Heptane-Reactions/>
16. http://www-cmls.llnl.gov/?url=science_and_technology-chemistry-combustion-nc7h16_reduced_mechanism
17. Tsang, W., *Data Science Journal* (2004) 3 (1-9).
18. Anon, Computational Submodels, International Workshop on Measurements and Computation of Turbulent Nonpremixed Flames. Available at <http://www.ca.sandia.gov/TNF/radiation.html>.
19. Leonard, B. P., *Comput. Meth. Appl. Mech. Eng.* 19:59 (1979).
20. Katta, V. R., Goss, L. P., and Roquemore, W. M., *AIAA Journal*, Vol. 32, No. 1, 1994, p. 84.
21. Katta, V. R., Goss, L. P., and Roquemore, W. M., *Int. J. Num. Methods Heat Fluid Flow*, Vol. 4, No. 5, 1994, p. 413.
22. Katta, V. R., Hu, S., Wang, P., Pitz, R., Roquemore, W. M., and Gord, J., "Investigations on Double-State Behaviour of the Counterflow Premixed flame system," *Proc. Combust. Inst.* 31:1055-1066 (2007).

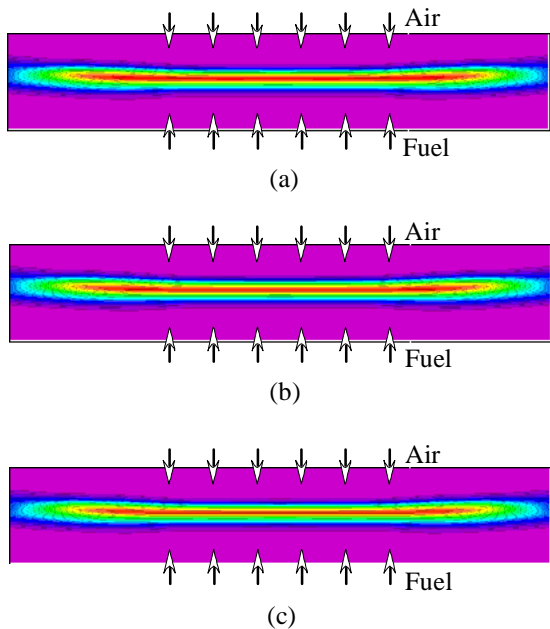


Fig. 1. Opposing-jet non-premixed heptane flame simulated using (a) SD mechanism, (b) LLNL mechanism, (c) NIST mechanism. Global strain rate is 150 s^{-1} . Temperature distributions are shown between 300 and 1700 K.

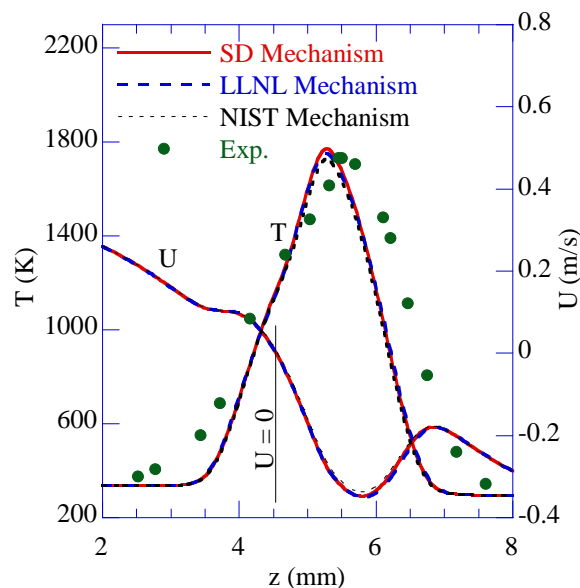


Fig. 2. Distributions of temperature and axial velocity plotted along the centerline. Lines represent profiles computed using different chemical kinetics mechanisms and symbols represent measurements of Seiser et al.¹¹ Global strain rate is 150 s^{-1} .

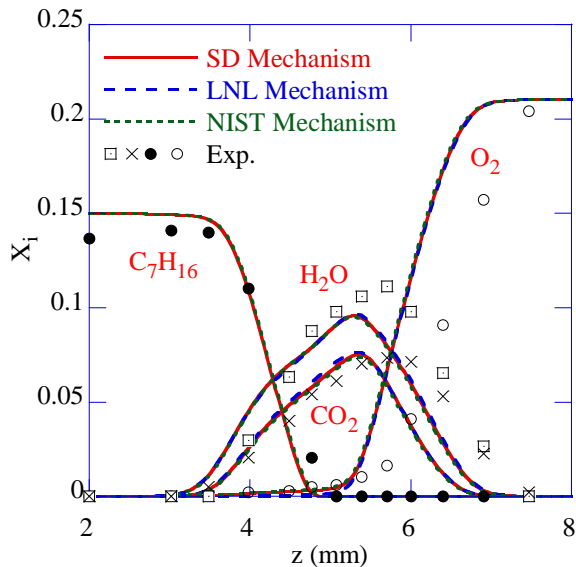


Fig. 3. Distributions of fuel, oxygen, H_2O , and CO_2 plotted along the centerline. Lines represent profiles computed using different chemical kinetics mechanisms and symbols represent measurements of Seiser et al.¹¹ Global strain rate is 150 s^{-1} .

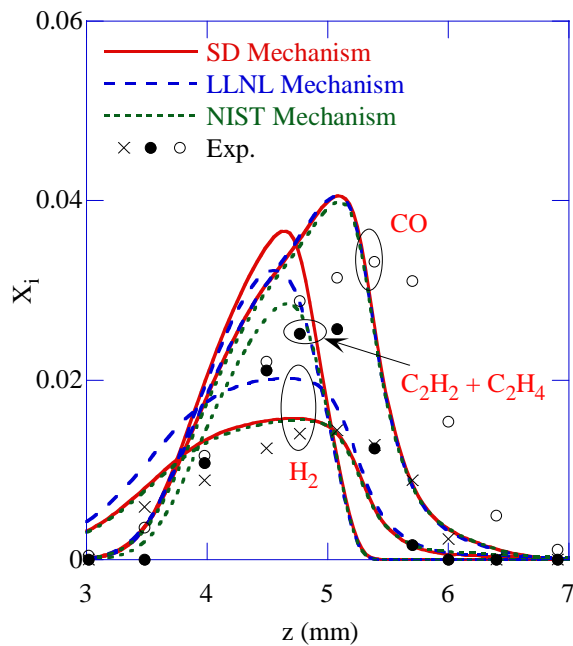


Fig. 4. Distributions of intermediate fuel species H_2 , $\text{C}_2\text{H}_2 + \text{C}_2\text{H}_4$, and CO plotted along the centerline. Lines represent profiles computed using different chemical kinetics mechanisms and symbols represent measurements of Seiser et al.¹¹ Global strain rate is 150 s^{-1} .

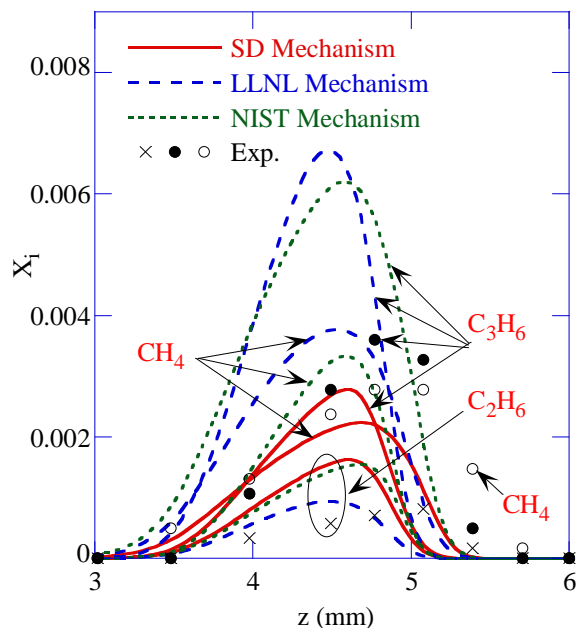


Fig. 5. Distributions of intermediate species CH_4 , C_3H_6 , and C_2H_6 plotted along the centerline. Lines represent profiles computed using different chemical kinetics mechanisms and symbols represent measurements of Seiser et al.¹¹ Global strain rate is 150 s^{-1} .

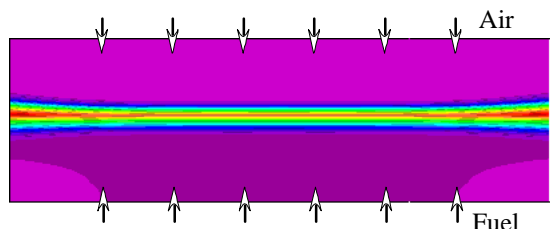


Fig. 6. Near-extinction opposing-jet non-premixed heptane flame simulated using SD mechanism. Global strain rate is 408 s^{-1} . Temperature distribution is shown between 300 and 1800 K.

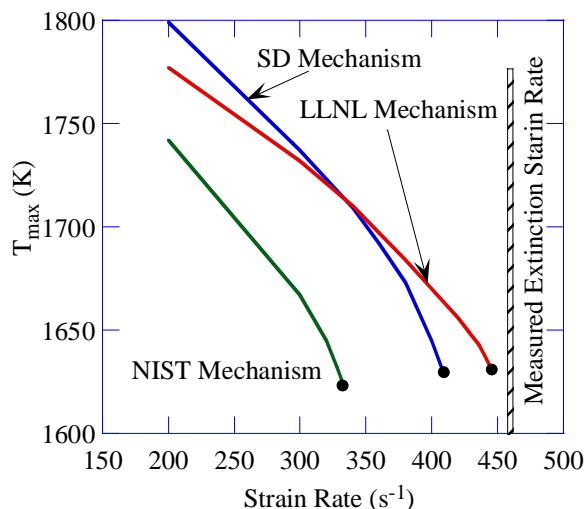


Fig. 7. Maximum flame temperatures obtained at different strain rates. Solid circles represent extinction conditions.

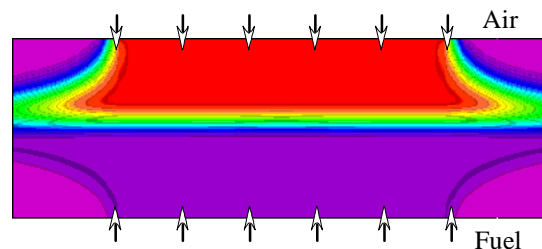


Fig. 8. Temperature distribution between the opposing jets of premixed heptane-air fuel and 1282-K air. Global strain rate is 400 s^{-1} . Temperature distribution is shown between 300 and 1300 K.

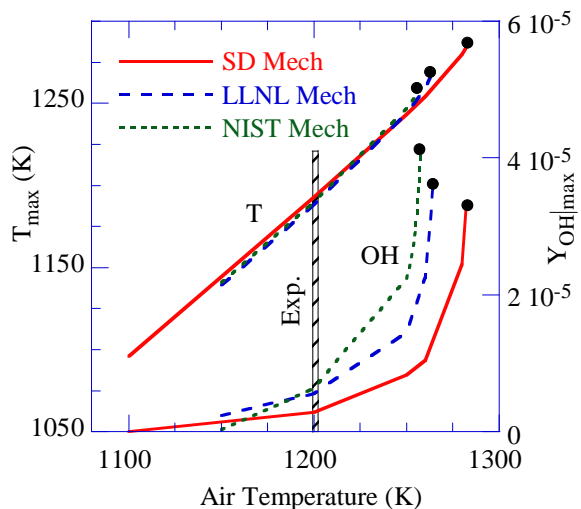


Fig. 9. Maximum temperatures and OH concentrations obtained for different air temperatures. Solid circles represent ignition conditions.

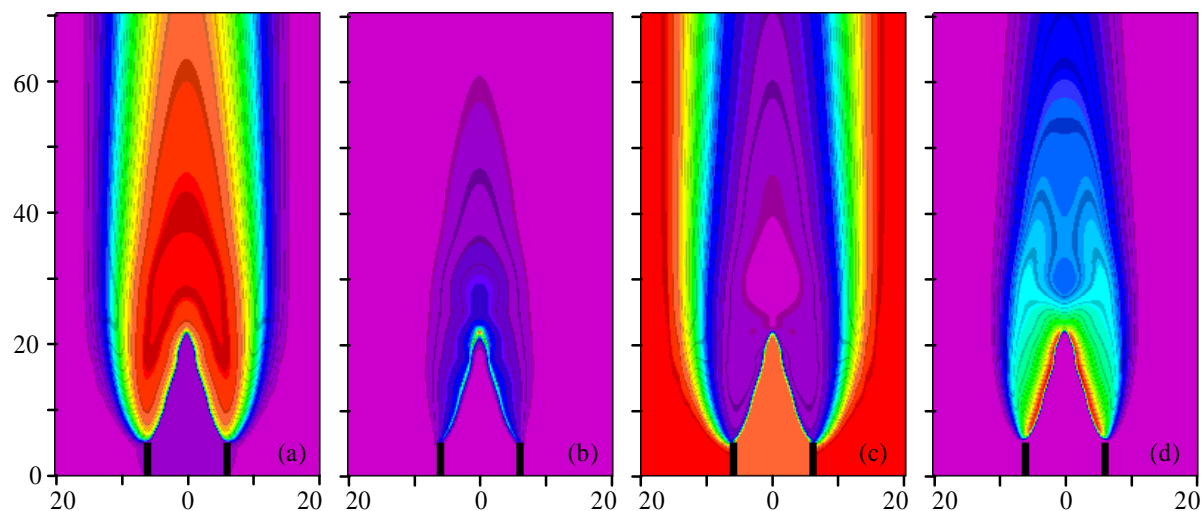


Fig. 10. Premixed flame calculated using SD mechanism. Distributions of (a) T, (b) H₂, (c) O₂, and (d) OH

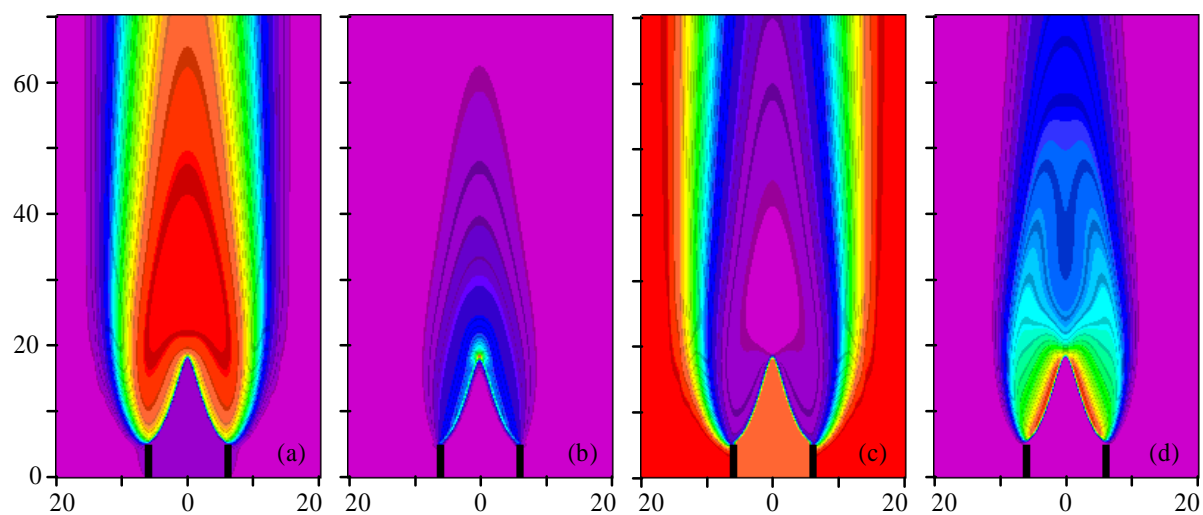


Fig. 11. Premixed flame calculated using LLNL mechanism. Distributions of (a) T, (b) H₂, (c) O₂, and (d) OH

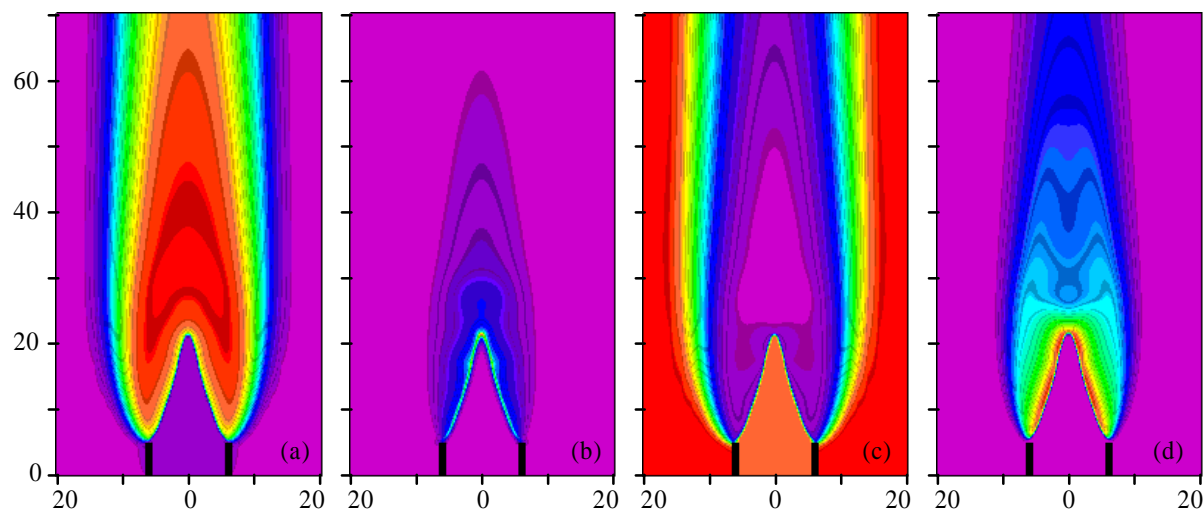


Fig. 12. Premixed flame calculated using NIST mechanism. Distributions of (a) T, (b) H₂, (c) O₂, and (d) OH

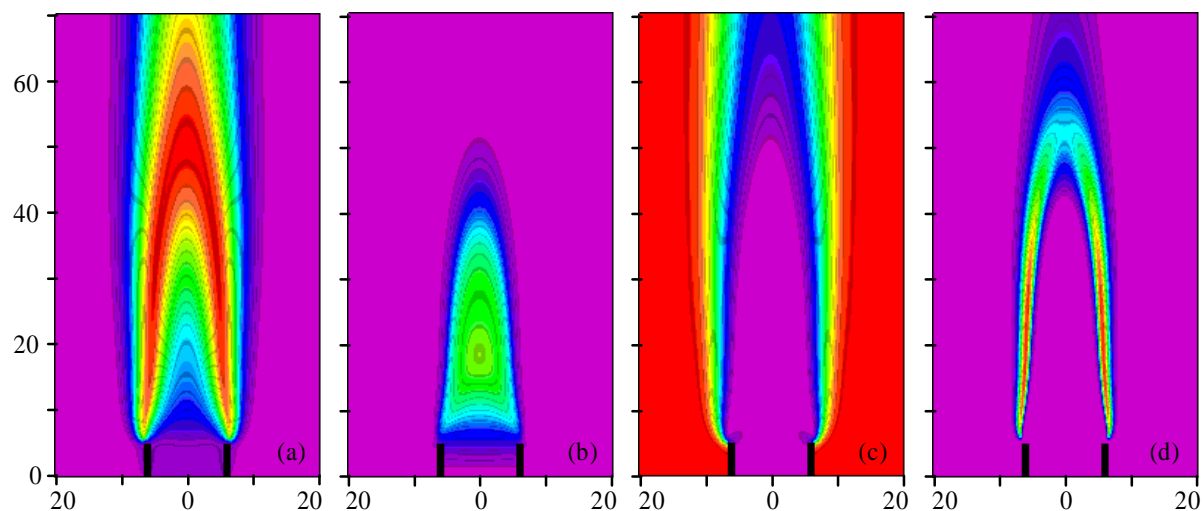


Fig. 13. Non-premixed flame calculated using SD mechanism. Distributions of (a) T, (b) H₂, (c) O₂, and (d) OH

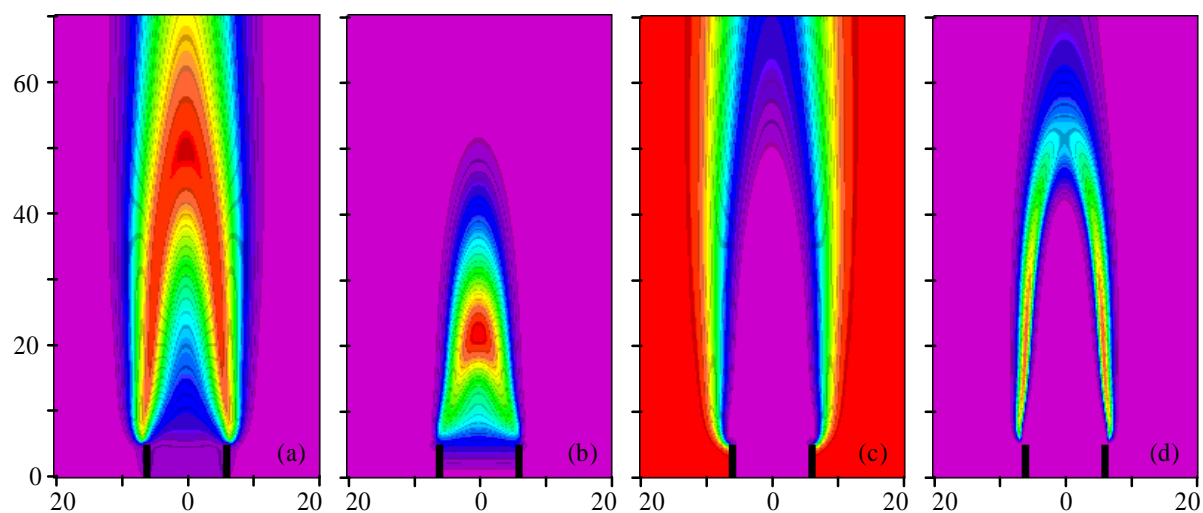


Fig. 14. Non-premixed flame calculated using LLNL mechanism. Distributions of (a) T, (b) H₂, (c) O₂, and (d) OH

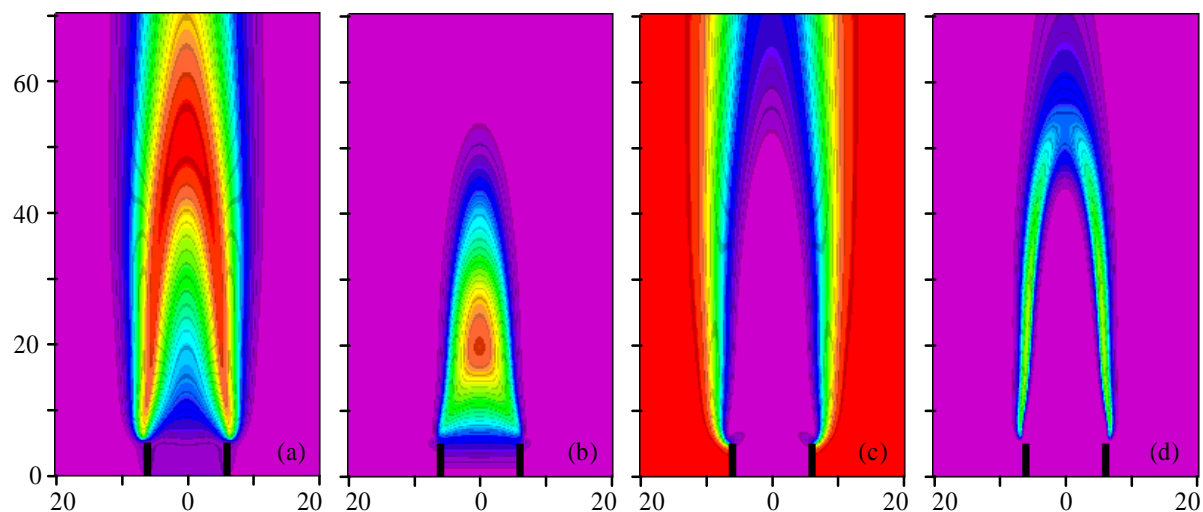


Fig. 15. Non-premixed flame calculated using NIST mechanism. Distributions of (a) T, (b) H₂, (c) O₂, and (d) OH

Comparison of Chemical-Kinetics Mechanisms through Predicting a Nonpremixed Ethylene Jet Flame

V. R. Katta*

Innovative Scientific Solutions Inc
2766 Indian Ripple Road
Dayton, OH 45440-3638

W. M. Roquemore
Propulsion Directorate
Air Force Research Laboratory
Wright-Patterson Air Force Base, OH 45433

R. J. Santoro
Department of Mechanical Engineering
Pennsylvania State University
University Park, PA 16802

Abstract

As the detailed chemical-kinetics mechanisms are usually developed and validated through the simulation of zero- and one-dimensional flames, their performance in predicting a multidimensional flame must be tested prior to using them in a combustor design. Predictive capabilities of various detailed chemical-kinetics mechanisms for ethylene-air combustion are investigated in this paper through the simulation of a nonpremixed jet flame. A time-dependent, axisymmetric mathematical model is used for the flame simulation. Five detailed chemical-kinetics models; namely, 1) Wang-Frenklach mechanism (99 species and 1066 reactions), 2) Wang-Colket mechanism (171 species and 2002 reactions), 3) San Diego (SD) mechanism (52 species and 544 reactions), 4) NIST mechanism (197 species and 2926 reactions), and 5) LLNL mechanism (160 species and 1540 reactions) are considered. A two-equation soot model is used in conjunction with the detailed-chemistry models for the simulation of sooty ethylene flames. Calculations are made with and without soot for identifying the impact of soot model on the chemistry models and vice versa. It is found that all the five chemistry models predict a nonpremixed jet flame equally well when soot was not considered. However, when soot was included predictions deviated from each other and San Diego mechanism yielded results that are closest to the experiment.

Introduction

Detailed chemical kinetics for describing combustion of hydrocarbon fuels involves several hundred species and several thousand elementary reactions. Traditionally, mechanisms are developed and validated through the simulations of zero- and one-dimensional flames using codes such as RUN1DL [1], OPPDIF [2], and CHEMKIN [3] and comparing the results with the available experimental data from shock tube, opposing-jet burner, premixed-flat-flame burner, etc. Extensive experimental data for the concentrations of intermediate species are required for obtaining a reasonably calibrated kinetics mechanism. However, it is not always feasible to obtain concentrations of the numerous hydrocarbon intermediates and, as a result validation of complex chemical-kinetics mechanisms is often partially performed. On the other hand, chemical-kinetics mechanisms are developed, in part, for the simulation of

flames in aircraft combustors, which are multidimensional in nature. It is risky to make predictions for a practical flame using a partially validated chemical kinetics without knowing how it performs under convection-diffusion environment. A two dimensional, nonpremixed ethylene flame is simulated in this paper using five detailed chemical kinetics models and the results are compared with the experimental data. Details of these simulations and comparisons are described in this paper.

A two-dimensional numerical model known as UNICORN (Unsteady Ignition and Combustion using ReactionNs) [4] that has the capability to incorporating large detailed chemical-kinetics mechanisms was developed at AFRL/RZ for the simulation of dynamic nonpremixed and premixed jet flames. This model is being used for studying flame systems and evaluating large chemical mechanisms and soot models on programs sponsored by the Air Force Office of Scientific Research

* Corresponding author: vrkatta@erinet.com

Proceedings of the 2008 Technical Meeting of the Central States Section of The Combustion Institute

(AFOSR) and the Strategic Environmental Research and Development Program (SERDP).

Numerical Model

A time-dependent, axisymmetric mathematical model known as UNICORN (Unsteady Ignition and Combustion using ReactionS) [4, 5] is used for simulating co-axial jet nonpremixed flames. It solves for u- and v-momentum equations, continuity, and enthalpy- and species-conservation equations on a staggered-grid system. The body-force term due to the gravitational field is included in the axial-momentum equation for simulating vertically mounted flames. A clustered mesh system is employed to trace the large gradients in flow variables near the flame surface. Five detailed chemical-kinetics models available in the literature for ethylene combustion are incorporated into UNICORN for the investigation of sooty nonpremixed flames. The first mechanism considered is Wang-Frenklach mechanism [6]. It consists of 99 species and 1066 elementary reactions. This mechanism has been extensively validated using shock-tube and flat-flame-burner data. The second one is Wang-Colket mechanism [7]. It has been developed from Wang-Frenklach mechanism by considering wider range of experimental data [8]. It consists of 171 species and 2002 elementary reactions. Third one is San Diego (SD) mechanism [9]. It consists of 52 species and 544 elementary reactions. The fourth one is National Institute of Standards and Technology (NIST) mechanism [10]. It consists of 197 species and 2926 reactions. The fifth one is Lawrence Livermore National Laboratory (LLNL) mechanism [11]. It consists of 160 species and 1540 reactions.

Thermo-physical properties such as enthalpy, viscosity, thermal conductivity, and binary molecular diffusion of all the species are calculated from the polynomial curve fits developed for the temperature range 300 - 5000 K. Mixture viscosity and thermal conductivity are then estimated using the Wilke and Kee expressions, respectively. Molecular diffusion is assumed to be of the binary-diffusion type, and the diffusion velocity of a species is calculated using Fick's law and the effective-diffusion coefficient of that species in the mixture. A simple radiation model based on the optically thin-media assumption is incorporated into the energy equation [12]. Radiation from only CH₄, CO, CO₂, and H₂O is considered. Radiation from soot is treated as that from a blackbody [13].

The finite-difference forms of the momentum equations are obtained using an implicit QUICKEST scheme [5] and those of the species and energy equations are obtained using a hybrid scheme of upwind and central differencing. At every time step, the pressure field is accurately calculated by solving all the pressure Poisson equations simultaneously and using the LU (Lower and Upper diagonal) matrix-decomposition technique. The boundary conditions are treated in the same way as that reported in earlier papers [14].

This study utilized a two-equation model for soot with transport equations for particle number density, N_s , and soot mass fraction, Y_s . These equations can be written for unsteady flow as

$$\frac{\partial \rho N_s}{\partial t} + \nabla \cdot (\rho \mathbf{V} N_s) - \nabla \cdot (\rho D_{N_s} \nabla N_s) = \omega_{N_s} \quad (1)$$

$$\frac{\partial \rho Y_s}{\partial t} + \nabla \cdot (\rho \mathbf{V} Y_s) - \nabla \cdot (\rho D_s \nabla Y_s) = \omega_s \quad (2)$$

where \mathbf{V} is the velocity vector, ρ is density, D is the molecular diffusion coefficient, and ω is the production term from chemical reactions. The two source terms in Eqs. 1 and 2 are obtained using Lindstedt's model [15], which is based on the simplifying assumption that nucleation and growth are first-order functions of acetylene concentrations.

Results and Discussion

Sooting characteristics of a vertically mounted laminar nonpremixed ethylene-air jet flame were studied experimentally by Santoro et al [16, 17]. The atmospheric pressure, co-annular burner used in those experiments consists of 11.1-mm-inner-diameter fuel tube with a wall thickness of 0.8 mm which is enclosed in a 102-mm-inner-diameter brass cylinder. Several inserts such as ceramic honeycomb, brass screens and glass beads were used in the annular gap between the two tubes to give uniform exit velocity for the air flowing through this gap. The fuel tube, which extends 2.5 mm above the burner surface, is also partially filled with glass beads for flow conditioning. A 46-cm-long glass chimney is mounted on the outer brass cylinder for protecting the flame from room-air disturbances. Details of the experimental procedure and the measurement techniques are given in References 16.

Detailed temperature and species measurements were obtained for a nonpremixed flame in which pure ethylene was issued at a velocity of 3.91 cm/s from the fuel tube. Coannular flow consists of room-temperature air issued at a velocity of 8.8 cm/s. Calculations for this flame are performed using the five chemical-kinetics models; namely, Wang-Frenklach, Wang-Colket, San Diego, NIST and LLNL mechanisms listed previously. A computational grid of 301x101 is used for discretizing the physical domain of 46 cm x 5.1 cm. Grid clustering is used for placing most of the grid lines in the flame zone. As a result the grid spacing obtained in the flame zone is 0.2 mm in both axial and radial directions. Initial conditions (flame) for the detailed-chemistry calculations were obtained from the simulation performed using a global-chemistry UNICORN code. Calculations with all five mechanisms are carried using a time-step of 0.05 ms.

None of the five chemical-kinetics models considered in the present study were developed taking sooting

characteristics into account. The two-equation soot model described earlier is added to each of these five chemical-kinetics models for predicting soot in nonpremixed flames. Since soot affects other species concentrations directly through its formation and oxidation and indirectly through heat radiation, it is important to understand the performance of a chemical-kinetics mechanism with and without having soot model added to it. Hence, calculations for the ethylene nonpremixed flame are first performed without adding the soot model and the results are compared with the measurements in Figs. 1 and 2.

Predicted and measured radial distributions of temperature and CO_2 mole fraction are compared at 15-mm, 40-mm, and 70-mm above the fuel-tube tip in Figs. 1(a), 1(b), and 1(c), respectively. Amazingly, all five chemical-kinetics mechanisms resulted in similar distributions at all heights--with San Diego mechanism giving slightly higher temperatures. On the other hand, some differences in the predicted concentration distributions for species such as CO and C_2H_2 may be noted in Fig. 2. For example, San Diego mechanism is giving higher CO concentrations while LLNL mechanism is predicting higher C_2H_2 concentrations.

Figures 1 and 2 also illustrate the discrepancies that exist in both temperature and species concentrations when compared with the experimental data. Such discrepancy, in general, got worsened with height in the flame. At 70 mm, measured temperatures are lower than the predictions by as much as 500 K. However, considering the fact that the predicted temperatures are close to the measurements in the flame zone ($r \sim 6.5$ mm) near the burner exit ($z < 15$ mm), it may be concluded on ad hoc basis that radiation from soot is affecting the temperature distribution in the flame. Calculations are then repeated for the same flame using the five chemical-kinetics mechanisms listed previously and by adding the two-equation soot model. Results in the form of temperature and species distributions at different heights in the flame are shown in Figs. 3 and 4.

A dramatic decrease in temperatures is observed when calculations considered soot in the flame. At 70 mm, predicted peak temperatures matched well with the measurements. Even though the temperatures predicted using different chemical-kinetics models with soot are in general closer to the measured values the variations among the predictions are much larger than those observed when soot was not considered (Fig. 1). Interestingly, no improvement in the predictions of species (CO_2 and CO) concentrations was achieved by considering soot. Drop in predicted temperatures below the measured values closer to the burner exit (at $z = 15$ and 40 mm) suggest an over correction for the radiation from soot. Consistently, all five models have over predicted the amount of soot near the burner exit. Also, the two-equation soot model, independent of the chemical kinetics used, failed to predict the shape of the soot distribution. While measurements suggest a shoulder-like

soot distribution models have predicted bell-shaped distributions, especially, in the downstream locations. Among the five chemical-kinetics mechanisms considered, level of soot concentration predicted by San Diego mechanism compared better with the measurements. Such an assessment on San Diego mechanism holds good even for the temperature and species predictions.

Impact of soot on temperature is shown in Fig. 5 through plotting temperature distributions with and without considering soot in Figs. 5(a) and 5(b), respectively. Data obtained with San Diego mechanism was used. Predicted soot-volume-fraction distribution is shown in Fig. 5(c). When soot was not considered peak (or flame) temperature remained the same at different heights. Radiation from soot cooled the flame with height and transformed it into an open-tipped (flame tip burning less intensely) one.

Plots similar to those shown in Fig. 5 were generated using the data obtained with Wang-Frenklach mechanism and are shown in Fig. 6. The major difference in the predictions made with San Diego and Wang-Frenklach mechanisms is in the distribution and magnitude of soot volume fraction. Latter mechanism not only predicted higher amounts of soot in the flame but also provided significant delay in the generation of soot near the burner exit.

Conclusions

Predictive capabilities of various detailed chemical-kinetics mechanisms were investigated through the simulation of a nonpremixed ethylene-air jet flame. This flame was investigated experimentally in the past and detailed measurements for temperature and species concentrations are available. A time-dependent, axisymmetric mathematical model known as UNICORN (Unsteady Ignition and Combustion using ReactionNs) was used for the flame simulation. Five detailed chemical-kinetics models; namely, 1) Wang-Frenklach mechanism (99 species and 1066 reactions), 2) Wang-Colket mechanism (171 species and 2002 reactions), 3) San Diego (SD) mechanism (52 species and 544 reactions), 4) NIST mechanism (197 species and 2926 reactions, and 5) LLNL mechanism (160 species and 1540 reactions) were considered. A two-equation soot model was used for simulating the sooty ethylene flame.

Initial calculations made without adding the soot model revealed that all five mechanisms result in flame structures that are close to each other. However, the predicted temperatures were found to be significantly higher, especially in the downstream locations, than the measured ones. Inclusion of soot model improved the temperature predictions but no significant improvement in the prediction of species concentrations was achieved. Among the five mechanisms, San Diego mechanism with two-equation soot model resulted in soot and temperature that were closest to the measurements. On the other hand,

none of the mechanisms was able to predict the experimentally observed shoulder-like soot distribution.

Acknowledgements

Financial support for this work was provided by Strategic Environmental Research and Development Program (SERDP, Bruce Sartwell), the Air Force Office of Scientific Research (AFOSR, Julian Tishkoff) and the Air Force Contract #F33615-00-C-2068 (Vince Belovich and Tim Edwards).

References

1. Rogg, B., "RUN1DL—The Cambridge Universal Laminar Flamelet Computer Code," in *Reduced Kinetic Mechanisms for Applications in Combustion Systems*, N. Peters and B. Rogg (Eds), Lecture Notes in Physics m15, Springer-Verlag, Heidelberg, Germany, 1993, pp. 350-351.
2. Lutz, A. E, Kee, R. J., Grcar, J. F., and Rupley, F. M., "OPPDIF: A Fortran program for computing opposed flow diffusion flames," SAND96-8243, Sandia National Laboratories, Livermore, CA (1996).
3. Kee, R. J., Miller, J. A., and Jefferson, T. H., "CHEMKIN: A general-purpose, problem-independent, transportable, Fortran, chemical kinetic code package," Technical Report SAND80-8003, Sandia National Laboratories, Livermore, CA, 1980.
4. Roquemore, W. M., and Katta, V. R., *Journal of Visualization* 2 (2000) 257-272.
5. Katta, V. R., Goss, L. P., and Roquemore, W. M., *AIAA Journal* 32 (1) (1994) 84.
6. Wang, H., and Frenklach, M., *Combustion and Flame* 110 (1) (1997) 173.
7. Wang, H., and Colket, M., Private Communications (2007).
8. Jomaas, G., Zheng, X. L., Zhu, D. L., and Law, C. K., *Proceedings of the Combustion Institute* 30 (2005) 193-200.
9. <http://www.mae.ucsd.edu/~combustion/cermech/Heptane-Reactions/>
10. Tsang, W., *Data Science Journal* 3 (2004) 1-9.
11. http://www-cmls.llnl.gov/?url=science_and_technology-chemistry-combustion-nc7h16_reduced_mechanism.
12. Annon., Computational Submodels, International Workshop on Measurement and Computation of Turbulent Nonpremixed Flames, <http://www.ca.sandia.gov/TNF/radiation.html>, (2001).
13. Guo, H., Liu, F., Smallwood, G. J., *Combustion Theory and Modeling* 8 (2004) 475-489.
14. Katta, V. R., Goss, L. P., and Roquemore, W. M., *International Journal of Numerical Methods for Heat and Fluid Flow* 4 (5) (1994) 413.
15. Lindstedt, R.P., in *Soot Formation in Combustion: Mechanisms and Models* (H. Bockhorn, Ed.), Springer-Verlag, Heidelberg, 1994, pp.417-439.
16. Santoro, R. J., and Semerjian, H. G., and Dobbins, R. A., *Combustion and Flame* 51 (1983) 203-218.
17. Santoro, R. J., and Semerjian, H. G., *Proceedings of the Combustion Institute* 20 (1984) 997-1006.

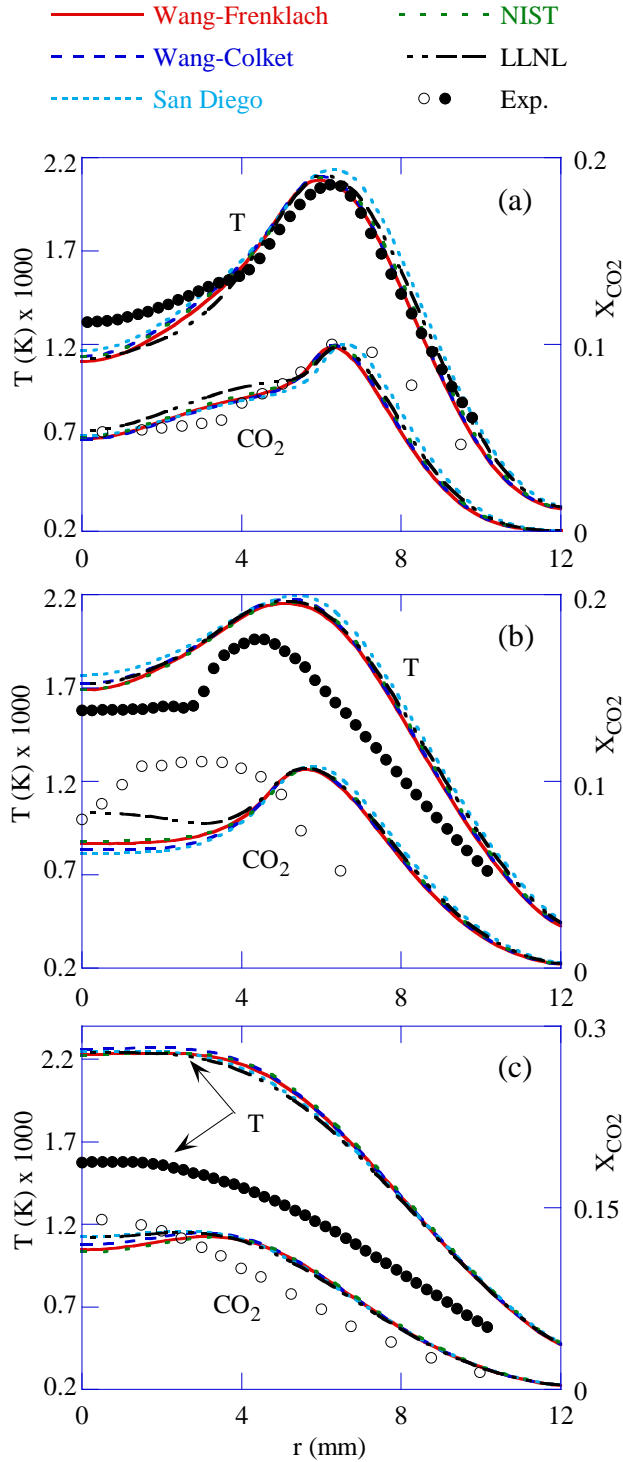


Fig. 1. Comparison of radial distributions of temperature and CO₂ mole fraction obtained using several chemical-kinetics mechanisms and measurements at (a) 15-mm, (b) 40-mm, and (c) 70-mm flame heights. Simulations are made without incorporating soot sub-model.

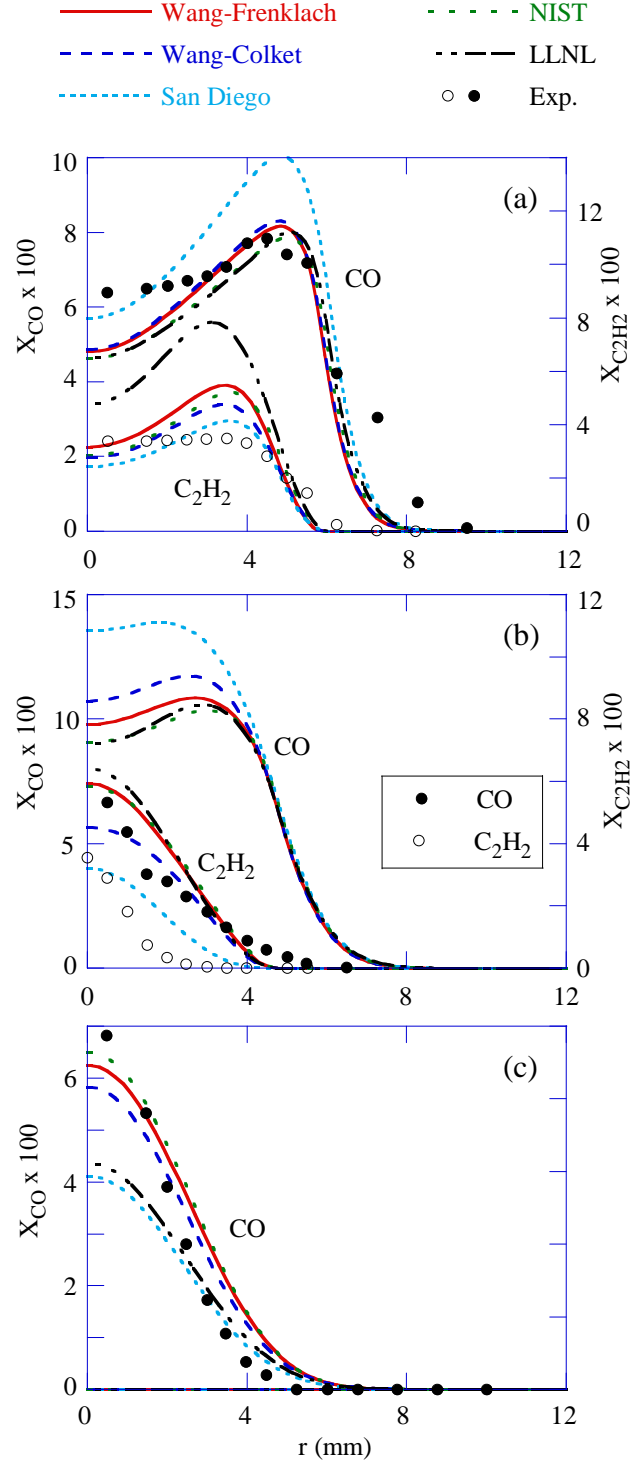


Fig. 2. Comparison of radial distributions of CO and C₂H₂ mole fractions obtained using several chemical-kinetics mechanisms and measurements at (a) 15-mm, (b) 40-mm, and (c) 70-mm flame heights. Simulations are made without incorporating soot sub-model.

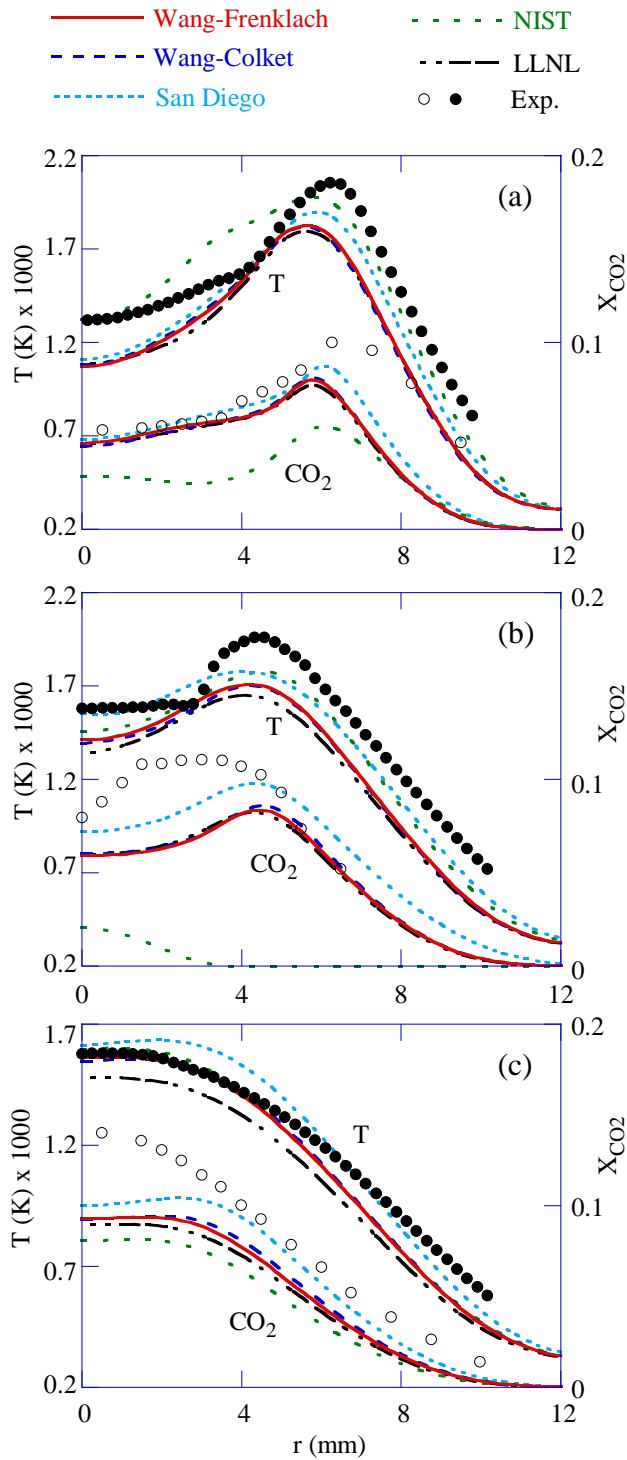


Fig. 3. Comparison of radial distributions of temperature and CO₂ mole fraction obtained using several chemical-kinetics mechanisms and measurements at (a) 15-mm, (b) 40-mm, and (c) 70-mm flame heights. Simulations are made after incorporating a two-equation soot sub-model.

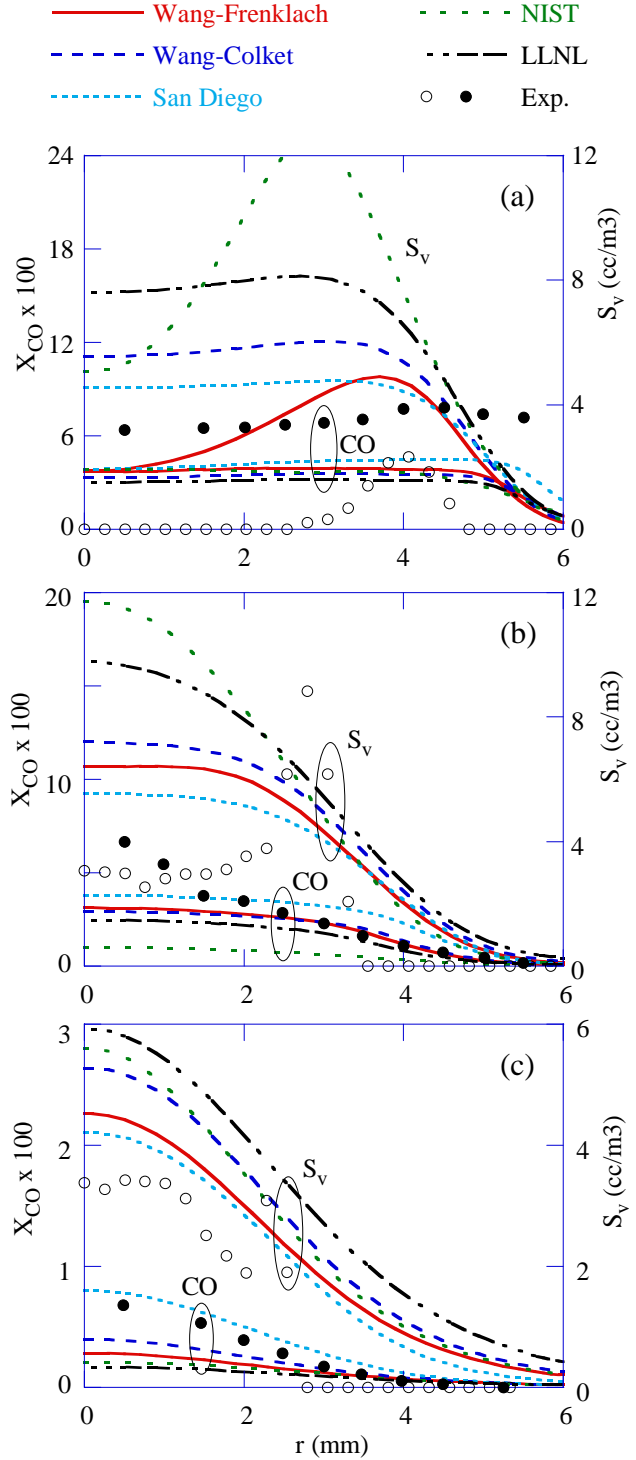


Fig. 4. Comparison of radial distributions of CO mole fraction and soot volume fraction obtained using several chemical-kinetics mechanisms and measurements at (a) 15-mm, (b) 40-mm, and (c) 70-mm flame heights. Simulations are made after incorporating a two-equation soot sub-model.

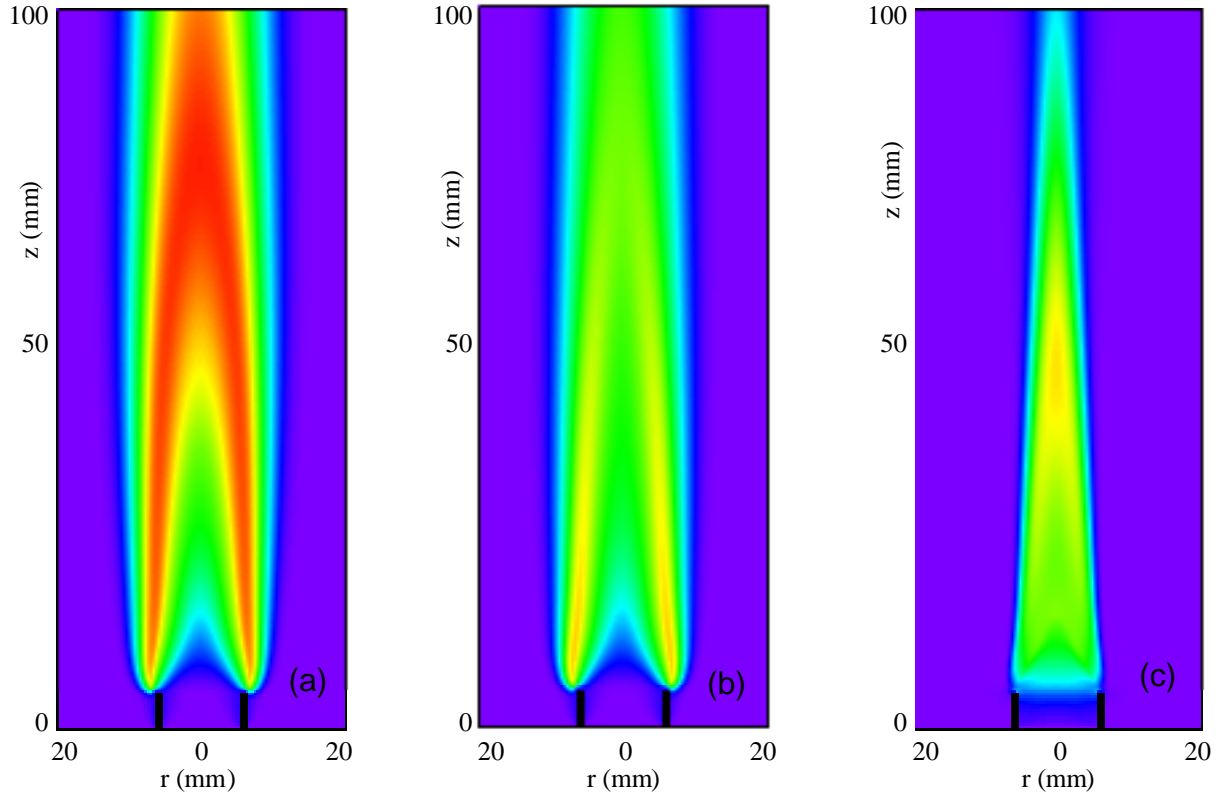


Fig. 5. Flame structure simulated using San Diego mechanism. (a) Temperature obtained without soot sub-model, and (b) temperature, and (c) soot volume fraction obtained with soot sub-model.

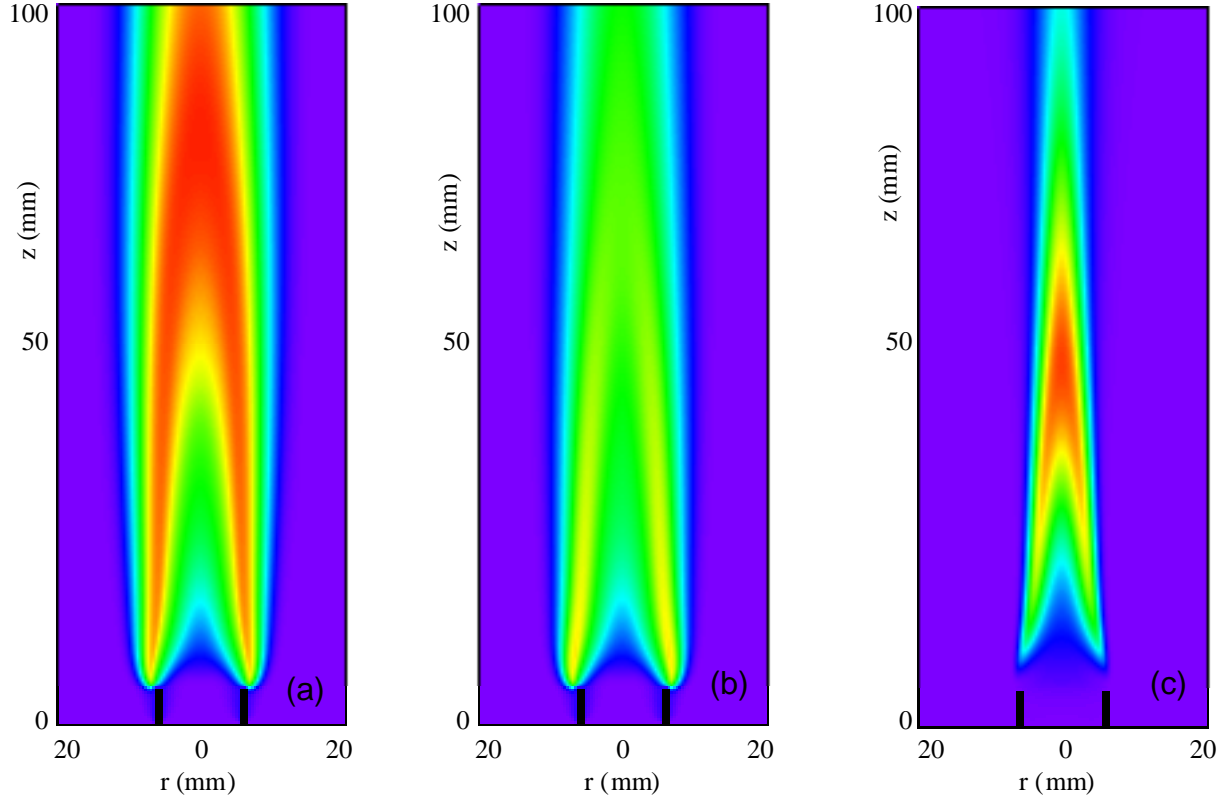


Fig. 6. Flame structure simulated using Wang-Frenklach mechanism. (a) Temperature obtained without soot sub-model, and (b) temperature and (c) soot volume fraction obtained with soot sub-model.

Effects of H₂ enrichment on the propagation characteristics of CH₄–air triple flames

Alejandro M. Briones^a, Suresh K. Aggarwal^{a,*}, Viswanath R. Katta^b

^a Department of Mechanical and Industrial Engineering, University of Illinois at Chicago, Chicago, IL 60607, USA

^b Innovative Scientific Solutions, Inc., 2766 Indian Ripple Road, Dayton, OH 45440, USA

Received 12 March 2007; received in revised form 27 January 2008; accepted 22 February 2008

Available online 7 April 2008

Abstract

The effects of H₂ enrichment on the propagation of laminar CH₄–air triple flames in axisymmetric coflowing jets are numerically investigated. A comprehensive, time-dependent computational model, which employs a detailed description of chemistry and transport, is used to simulate the transient ignition and flame propagation phenomena. Flames are ignited in a jet-mixing layer far downstream of the burner. Following ignition, a well-defined triple flame is formed that propagates upstream along the stoichiometric mixture fraction line with a nearly constant displacement velocity. As the flame approaches the burner, it transitions to a double flame, and subsequently to a burner-stabilized nonpremixed flame. Predictions are validated using measurements of the displacement flame velocity. As the H₂ concentration in the fuel blend is increased, the displacement flame velocity and local triple flame speed increase progressively due to the enhanced chemical reactivity, diffusivity, and preferential diffusion caused by H₂ addition. In addition, the flammability limits associated with the triple flames are progressively extended with the increase in H₂ concentration. The flame structure and flame dynamics are also markedly modified by H₂ enrichment, which substantially increases the flame curvature and mixture fraction gradient, as well as the hydrodynamic and curvature-induced stretch near the triple point. For all the H₂-enriched methane–air flames investigated in this study, there is a negative correlation between flame speed and stretch, with the flame speed decreasing almost linearly with stretch, consistent with previous studies. The H₂ addition also modifies the flame sensitivity to stretch, as it decreases the Markstein number (Ma), implying an increased tendency toward diffusive–thermal instability (i.e. $Ma \rightarrow 0$). These results are consistent with the previously reported experimental results for outwardly propagating spherical flames burning a mixture of natural gas and hydrogen.

© 2008 The Combustion Institute. Published by Elsevier Inc. All rights reserved.

Keywords: Hydrogen–methane blends; Propagating triple flames; Diffusive–thermal instability; Preferential diffusion; Stretch–flame speed interactions

1. Introduction

There is a worldwide interest in developing hydrogen-based combustion systems, due to growing environmental concerns and the deteriorating supply–demand scenario with regard to fossil fuels. Fossil fuels are nonrenewable and a major source of pollutants,

* Corresponding author. Fax: +1 312 413 0441.
E-mail address: ska@uic.edu (S.K. Aggarwal).

including CO_2 , NO_x , UHC, and soot. In contrast, hydrogen represents a potentially unlimited source of energy that is environmentally clean, with NO_x being the major undesirable pollutant. There are, however, significant difficulties associated with hydrogen storage due to its high flammability limits, low ignition energy, and low volumetric energy content. There are also many unresolved issues with regard to H_2 combustion, such as knock, detonation, preignition, and flashback. In this context, hydrogen–hydrocarbon fuel blends offer a very promising alternative, as they can synergistically resolve the storage and combustion problems associated with hydrogen and the emission problems associated with fossil fuel combustion. Consequently, there has been considerable interest in investigating the combustion and emission characteristics of hydrogen–hydrocarbon fuel blends.

Several studies have been reported on the performance and emission characteristics of internal combustion engines using hydrogen–fossil fuel blends. These include studies dealing with a diesel engine using a hydrogen–vegetable oil blend [1] and spark ignition engines using a hydrogen–gasoline blend [2,3], a hydrogen–natural gas blend [4–8], and a hydrogen–methanol blend [9]. Bauer and Forest [10] investigated the effect of hydrogen addition on the performance of methane-fueled vehicles. It was shown that the wide flammability limits of hydrogen makes it possible to run SI engines at lower equivalence ratios using a hydrogen–methane blend, which lowers cylinder temperature and thereby NO_x emission. Al-Baghdadi [11] also observed a significant reduction in NO_x production in spark ignition engines when a hydrogen–ethanol mixture was used instead of gasoline.

Flame studies using hydrogen–hydrocarbon fuel blends have also been reported. Choudhuri and Gollahali [12] performed an experimental–numerical investigation of hydrogen–natural gas jet diffusion flames and observed a reduction in the soot concentration and emission index of CO (EICO), but an increase in EINO with hydrogen addition. Rortveit et al. [13] reported an experimental–numerical study of NO_x emissions in counterflow methane–hydrogen nonpremixed flames. Naha et al. [14,15] studied the emission characteristics of hydrogen–methane and hydrogen–*n*-heptane fuel blends using a counterflow flame, and observed significant reduction in NO_x emission in hydrogen–*n*-heptane flames. Fotache et al. [16] investigated the ignition characteristics of hydrogen-enriched methane flames at various pressures and identified three ignition limits, namely (i) hydrogen-assisted ignition, (ii) transition, and (iii) hydrogen-dominated ignition. Huang et al. [17] measured the flame speeds for natural gas–hydrogen mixtures and observed that the increase in H_2 content

increases the flame speed exponentially, while the Markstein length transitions from positive to negative, implying a tendency toward diffusive–thermal instability. Law et al. [18] examined the effect of adding propane to hydrogen at different pressures and observed that propane reduces the tendency toward diffusive–thermal instability, whereas a pressure increase promotes diffusive–thermal instability, causing flame front wrinkling and higher flame speeds. Schefer [19] investigated the stabilization of hydrogen-enriched methane–air swirl-stabilized premixed flames. It was shown that hydrogen addition reduces the lean stability limit, allowing stable burner operation at lower flame temperature that is in turn beneficial for achieving lower NO_x emission. Similarly, Hawkes and Chen [20] studied hydrogen-enriched lean premixed methane–air flames and reported that hydrogen addition increases flame resistance to quenching, but also increases the tendency toward diffusive–thermal instability. In addition, the NO emission was observed to increase, while the CO emission decreased with hydrogen addition.

Our literature review indicates that while many important combustion and emission characteristics of hydrogen–hydrocarbon fuel blends have been investigated, the flame propagation characteristics of such fuel blends have not been examined. A fundamental understanding of the flame propagation characteristics of various fuel blends is important for the design of future combustion devices, such as spark ignition engines and gas turbine combustors, burning fuel blends. These characteristics are also important for the design of flame arrestors, which require laminar flame speed data for different fuel blends over a wide range of conditions. For example, a Venturi flame arrestor employs a flow restriction to increase the local mixture velocity above the local triple flame speed in order to capture a propagating flame.

In this paper, we report a fundamental investigation on the propagation characteristics of H_2 -enriched CH_4 -air flames in a laminar nonpremixed jet. The major objective is to examine the effects of H_2 enrichment on the propagation characteristics of CH_4 -air flames in nonuniform mixtures in which the flame is subjected to flow nonuniformity and mixture fraction gradients, as well as curvature-induced, hydrodynamic, and unsteady stretch effects. A propagating flame is established by igniting the fuel–air mixture in the far field of a jet issuing a H_2 - CH_4 mixture in a coflowing air jet. The ignition event is simulated by providing a small high-temperature zone containing small amounts of H and OH radicals. This high-temperature zone generates an ignition kernel that propagates upstream and rapidly develops into a triple flame, which then propagates upstream to-

ward the burner rim. The effects of hydrogen enrichment on the propagation characteristics of this triple flame are investigated using a comprehensive computational model that includes detailed descriptions of transport and chemistry. The choice of this configuration is based on several considerations. First, this configuration is relevant to many combustion systems, including gas turbines and internal combustion engines [21]. Second, it is difficult to establish lifted H_2 –air or CH_4 –air flames in a jet configuration due to the high mass diffusivity of these fuels ($Sc < 1$) [22]. Third, the present configuration is well suited to examine the propagation characteristics of triple flames established using hydrogen–methane fuel blends and to characterize the effects of hydrogen on stretch–flame speed interactions. Finally, investigations of triple flame propagation in laminar jets provide fundamental information for the understanding and modeling of turbulent flames. For instance, the stabilization [23,24] and propagation [25,26] of turbulent flames often involve triple flames, which are subjected to a wide range of mixture fraction gradient, stretch, and partial premixing. Consequently, several previous studies have investigated the effects of jet velocity [22,26], coflow velocity [27], partial premixing [25,28,29], heat release [30], and dilution [28,29] on laminar flame stabilization and propagation. However, the flame propagation characteristics associated with fuel blends have not yet been investigated.

It is important to note that a similar configuration involving triple flames has been employed in previous studies. Ruetsch et al. [30] reported the first numerical investigation of triple flames and thus laid the foundation for such studies. They showed that heat release redirects the flow ahead of the triple flame, reducing the flow velocity along the stoichiometric mixture fraction line, which reaches a local minimum just ahead of the triple flame. For a lifted triple flame, this local minimum flow velocity was defined as the local (triple) flame speed (S_{tri}) [30,31] at the triple point, while the upstream flow velocity was defined as the far field or global flame speed (U_F) [30,31]. In addition, it was shown that the global flame speed increases with the decrease in mixture fraction gradient, and in the limit of small mixture fraction gradient, the U_F/S_{tri} ratio is proportional to the square root of the density ratio of unburnt to burnt mixtures ($\sqrt{\rho_u/\rho_b}$) across the flame. Qin et al. [25] and Ko and Chung [26] investigated the propagation of CH_4 –air triple flames in laminar jets and observed that the instantaneous displacement flame velocity (V_f),¹ which is

the flame velocity in laboratory coordinates, remains nearly constant during propagation, while the local triple flame speed (S_{tri}) decreases with flame stretch and mixture fraction gradient. In addition, the global flame speed (U_F) was found to be about twice the laminar stoichiometric unstretched flame speed (S_L^0), while it was observed to be considerably higher (3–6 times) in turbulent jets [32]. It is also interesting to note that in both laminar [25,26] and turbulent flows [32] it was observed that an increase in jet velocity decreases the displacement flame velocity but increases the local flame speed, and that the local flame speed decreases with axial position due to the increase in mixture fraction gradient and flame curvature. This further highlights the fact that investigations of laminar triple flames can provide insight into the stabilization and propagation of turbulent flames.

Im and Chen [33] investigated the propagation of H_2 –air triple flames in a nonpremixed jet. Similarly to previous studies [30,34], the global flame speed was found to be proportional to the square root of the density ratio across the flame. Another important observation from this study was that for H_2 –air mixtures, the flame is shifted toward the air side and becomes asymmetric with respect to the stoichiometric mixture fraction ($f_s = 0.0285$) line,² since f_s is much smaller than 0.5. Consequently, the triple point, located at the intersection of the stoichiometric mixture fraction line and the flame surface, does not coincide with the flame leading edge, which is located at the local minimum flame curvature. This shift between the triple point and the leading edge is important in the context of determining the triple flame speed, since the experimental studies have generally reported the flame speeds at the leading edge [35], while the numerical investigations have computed these speeds at the triple point [25,29,33]. While this shift is also ob-

S_{tri} is also referred as the edge speed in Ref. [31], as the local displacement speed in Ref. [33], and as the flame propagation speed in Ref. [25]. Similarly, U_F is also referred as the stabilization speed in Ref. [33] and as the relative propagation speed in Ref. [32]. In addition, V_f is referred as the flamefront propagation velocity in Ref. [25] and as the net flame velocity in Ref. [32]. Here, we define S_{tri} as the local triple flame speed, U_F as the global flame speed, and V_f as the displacement flame velocity. Note that we use the term “speed” when referring to flame properties (i.e., relative velocities with respect to the incoming jet flow velocity such as S_{tri} and U_F), whereas the term “velocity” is used for absolute velocities (i.e., measured from a fixed coordinate system such as V_f).

² Note that for $f_s = 0.5$ the flame will be symmetric with respect to the stoichiometric mixture fraction line, and the locations of the triple point and the flame leading edge will coincide.

¹ It is important to note the inconsistencies in the definitions of S_{tri} , U_F , and V_f used in the literature. For instance,

served for hydrocarbon flames, it becomes more pronounced for hydrogen flames, and therefore relevant to fuel blends containing hydrogen.

The preceding discussion indicates that several previous studies have focused on the propagation of triple flames in the context of pure fuels. However, the flame propagation characteristics of fuel blends have not been examined as yet.

2. Computational model

The numerical model is based on the solution of the time-dependent governing equations for a two-dimensional unsteady reacting flow [36,37]. Using cylindrical coordinates (r, z), these equations can be written as

$$\begin{aligned} \frac{\partial(\rho\Phi)}{\partial t} + \frac{\partial(\rho v\Phi)}{\partial r} + \frac{\partial(\rho u\Phi)}{\partial z} \\ = \frac{\partial}{\partial r} \left(\Gamma^\Phi \frac{\partial\Phi}{\partial r} \right) + \frac{\partial}{\partial z} \left(\Gamma^\Phi \frac{\partial\Phi}{\partial z} \right) \\ - \frac{\rho v\Phi}{r} + \frac{\Gamma^\Phi}{r} \frac{\partial\Phi}{\partial r} + S^\Phi. \end{aligned} \quad (1)$$

Here t denotes the time, ρ the density, and u and v the axial (z) and radial (r) velocity components, respectively. The general form of the equation represents conservation of mass, momentum, species, or energy conservation, depending on the variable used for Φ . The diffusive transport coefficient Γ^Φ and source terms S^Φ are described in Ref. [36]. Introducing the overall species conservation equation and the state equation completes the equation set. A sink term based on an optically thin gas assumption was included in the energy equation to account for thermal radiation from the flame [38] in the form $q_{\text{rad}} = -4\sigma K_p(T^4 - T_0^4)$ [39], where T denotes the local flame temperature, and K_p accounts for the absorption and emission from the participating gaseous species (CO_2 , H_2O , CO , and CH_4) expressed as $K_p = P \sum_k X_k K_{p,i}$, where $K_{p,i}$ denotes the mean absorption coefficient of the k th species, σ is the Stefan–Boltzmann constant, and T_0 is the ambient temperature. The value of $K_{p,i}$ is obtained using a polynomial approximation to the experimental data provided in Ref. [39].

The thermodynamic and transport properties appearing in the governing equations are temperature- and species-dependent. The thermal conductivity and viscosity of the individual species were based on Chapman–Enskog collision theory, following which those of the mixture are determined using the Wilke semiempirical formulas [40]. Chapman–Enskog theory and the Lennard–Jones potentials were used to estimate the binary diffusion coefficient between each species and nitrogen. The methane–air chemistry is

modeled using a detailed mechanism that considers 31 species and 346 elementary reactions [41]. The major species included in the mechanism are CH_4 , O_2 , CO_2 , CO , CH_2O , H_2 , H_2O , C_2H_2 , C_2H_4 , C_2H_6 , CH_3OH , and N_2 , while the radical species include CH_3 , CH_2 , CH , CHO , H , O , OH , HO_2 , H_2O_2 , C_2H , C_2H_3 , C_2H_5 , CHCO , C , $\text{CH}_2(\text{s})$, CH_2OH , CH_3O , CH_2CO , and HCCOH . The mechanism has been validated previously for the computation of premixed flame speeds and the detailed structure of premixed and nonpremixed flames [42–44].

The finite-difference forms of the momentum equations are obtained using the QUICKEST scheme [45], while those of the species and energy are obtained using a hybrid scheme of upwind and central differencing. The pressure field is calculated at every time step by solving all of the pressure Poisson equations simultaneously and using the LU (lower and upper diagonal) matrix-decomposition technique.

Fig. 1 illustrates the computational domain. It consists of 100×50 mm in the axial (z) and radial (r) directions, respectively, and is represented by a staggered, nonuniform grid system. The reported results are grid-independent, as discussed in the next section. The minimum grid spacing is 0.05 mm in both the r - and z -directions. It is important to note that we have examined the grid resolution issues in a previous study [29] and found that a minimum grid spacing of 0.05 is sufficient to resolve the H and CH radical layers. An isothermal insert (2×0.8 mm) simulates the inner burner wall. The temperature at the burner wall was set at 300 K. The inner and outer jets are set with constant and uniform velocities of 10 and 30 cm/s, respectively. The inner jet issues a H_2 – CH_4 mixture, while the outer jet issues air. A propagating flame is established by igniting the fuel–air mixing layer in the far field (35 mm above the burner rim). The ignition event is simulated by providing a small high-temperature zone with a temperature of 2000 K and a rectangular cross-sectional area of 2 mm^2 , and containing small amounts of H and OH radicals. This high-temperature zone generates an ignition kernel that propagates upstream and rapidly develops into a triple flame, which then propagates upstream toward the burner rim and eventually stabilizes at the rim. A detailed numerical algorithm is developed to determine the propagation characteristics of this flame, which include the instantaneous displacement flame velocity and propagation speeds (i.e., local and global flame speeds), flame structure and dynamics near the triple point, and flame stretch–speed interactions for various levels of H_2 enrichment.

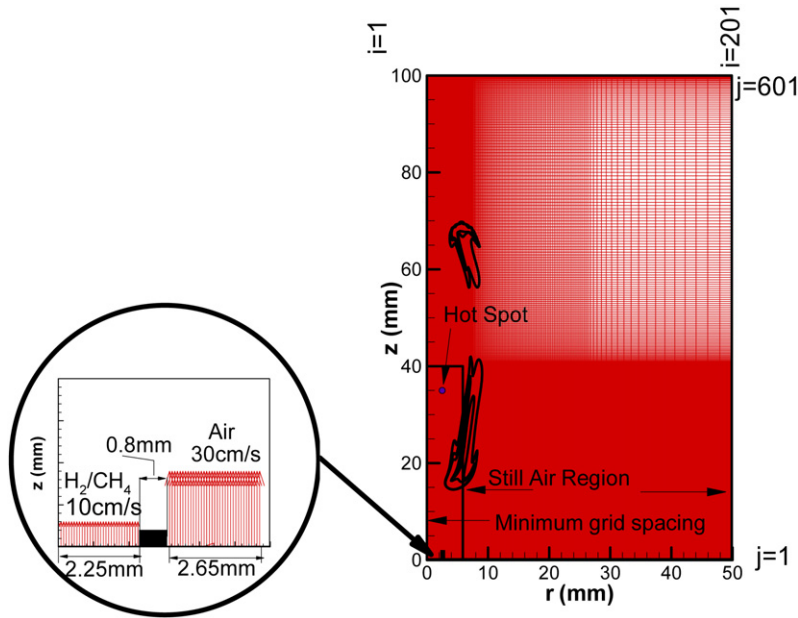


Fig. 1. Schematic of the computational grid used in the simulations. The small rectangle shows the minimum grid spacing region where the propagation flame front is located. A schematic of the computational domain is also shown.

3. Results and discussion

3.1. Validation of numerical model

The algorithm used for the simulation of propagating flames has been extensively validated in previous studies, using experimental data from burner-stabilized flames [36,46], lifted partially premixed flames [37], and propagating partially premixed flames [25]. The validation has included the comparison of the predicted and measured flame topology, liftoff heights (L_f), temperature, velocity and concentration fields, and instantaneous displacement flame velocity (V_f). In the following section, we will provide an additional validation by comparing the predicted and measured [47] displacement flame velocity (V_f) of a propagating CH_4 -air triple flame.

3.2. Ignition and flame propagation

Fig. 2 presents the simulated results of transient ignition, flame propagation, and flame attachment for a propagating CH_4 -air triple flame in terms of heat release rate contours. The first image at $t = 0$ ms corresponds to an instant when the high-temperature ignition source is removed, while the subsequent images show the formation and propagation of a triple flame. Following ignition, two reacting volumes (or kernels) are formed, as indicated by the image at $t = 3$ ms. One propagates downstream and is quickly extinguished. The other propagates upstream toward

the burner and develops into a triple flame, which is the focus of this investigation. The triple flame structure develops at $t \sim 18$ ms. The flame propagates in a quasi-steady manner, i.e., at near-constant displacement flame velocity (V_f), from $z = 25$ mm to $z = 4$ mm, exhibiting a well-defined triple flame structure, as indicated in the snapshot at 48 ms. The three reaction zones, namely the rich premixed zone (RPZ), the lean premixed zone (LPZ), and the nonpremixed zone (NPZ), can be readily identified in the 18- and 48-ms images. As the flame approaches the burner rim (i.e., $z \approx 4$ mm), the length of the RPZ decreases, and the flame transitions to a double flame; i.e., the LPZ extinguishes. The flame reaches the burner rim at 88 ms, and during its stabilization at the rim, the RPZ extinguishes and the flame transitions from a double flame to a steady nonpremixed flame.

In Fig. 3, we present the temporal variation of axial flame position with respect to the burner rim ($d_f = z - 2$ mm) for the propagating 0% H_2 -, 25% H_2 -, 50% H_2 -, and 75% H_2 -enriched CH_4 -air triple flames. As the amount of H_2 in the fuel blend is increased, the displacement flame velocity increases, as expected, and the time taken for the flame to reach the burner rim decreases considerably. In addition, the simulations indicate that for all four flames depicted in Fig. 3, the axial flame position (d_f) varies almost linearly with time. This behavior is consistent with the measurements reported by Ko and Chung [26], who showed that the flame position of propagating lami-

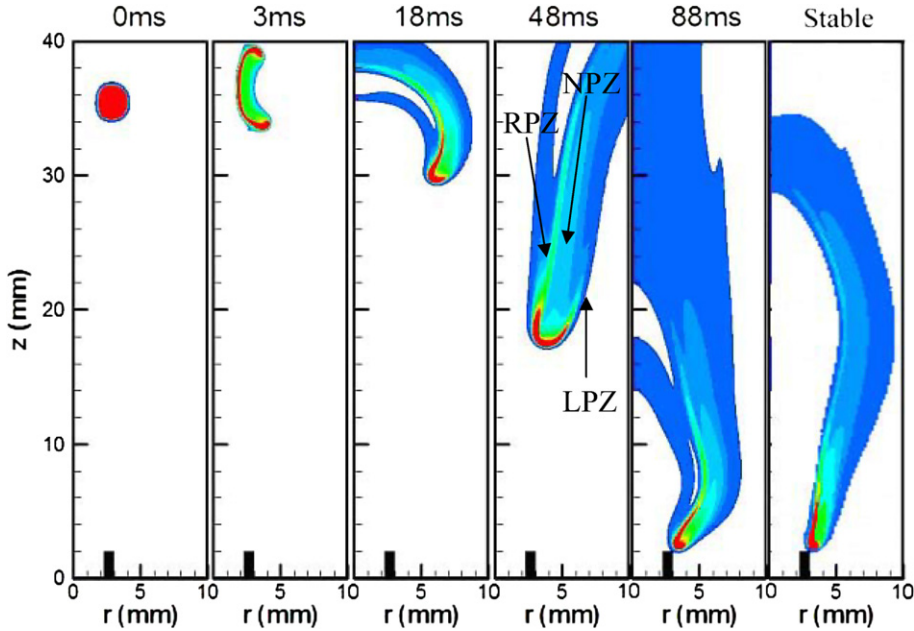


Fig. 2. Simulations showing the temporal evolution of ignition and flame propagation in terms of heat release rate contours for the pure CH₄–air flame. The three reaction zones, i.e., the rich premixed (RPZ), nonpremixed (NPZ), and lean premixed (LPZ) zones, are indicated in the snapshot at $t = 48$ ms.

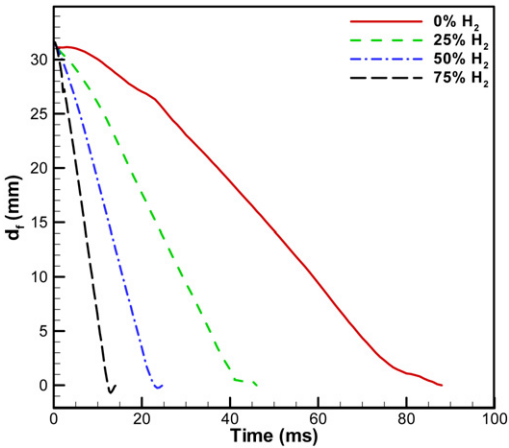


Fig. 3. Axial flame position (d_f) as a function of time for the 0%, 25%, 50%, and 75% H₂-enriched CH₄–air propagating flames.

nar CH₄–air triple flames in nonpremixed jets varies linearly with time regardless of the jet inlet velocity.

Fig. 4 presents the instantaneous displacement flame velocity (V_f) as a function of flame position (d_f) for the four H₂-enriched CH₄–air flames discussed in the context of Fig. 3. The displacement flame velocity is obtained by calculating the rate of change of axial position of the triple point with time (i.e., $V_f = (\Delta z)_{\text{tri}} / \Delta t$). Note here that based on our simulations the radial component of the displacement flame

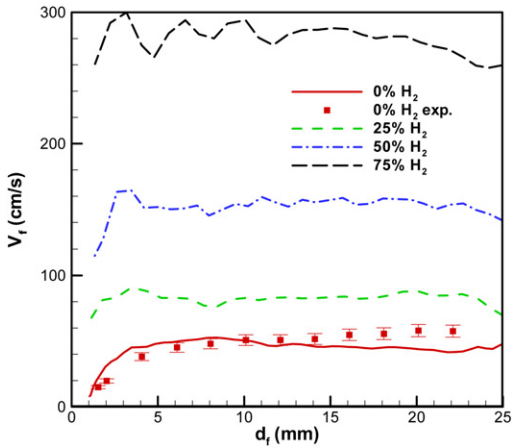


Fig. 4. Predicted displacement flame velocity (V_f) as a function of axial distance from the burner rim (d_f) for the 0%, 25%, 50%, and 75% H₂-enriched CH₄–air propagating flames. The measured V_f for a CH₄–air propagating flames from Ref. [47] is also shown for validation of the numerical model.

velocity is negligible (i.e., $V_f = V_{f,z}$). The flame surface, which is needed for determining the triple point, is chosen to be the isocontour of the 0.0727 H₂O mass fraction, following Won et al. [35]. The measured displacement flame velocity as a function of flame position for a propagating CH₄–air triple flame, taken from Ref. [47], is also shown in the figure. There is

good agreement between the predicted and measured values. Both predictions and measurements indicate that V_f is nearly independent of time. Our predictions are also consistent with the measurements of Ko and Chung [26] for propagating CH₄–air triple flames with different jet inlet velocities. The displacement flame velocity decreases as the flame gets close to the burner rim ($d_f \sim 2\text{--}3\text{ mm}$) and tends to zero as the flame stabilizes at the rim. In addition, results in Fig. 4 indicate that as the amount of H₂ in the fuel blend is increased, V_f progressively increases, and the flame reaches the burner rim in a shorter time (cf. Fig. 3). The increase in V_f is due to an increase in the local triple flame speed, S_{tri} (discussed later), which in turn is due to the enhanced chemical reactivity, diffusivity, and preferential diffusion effects caused by H₂ enrichment. The aspects dealing with the effects of H₂ enrichment on the flame propagation characteristics, including stretch–flame speed interactions, are discussed in Section 3.4.

3.3. Flame base structure

In order to spatially resolve the various reaction zones of the propagating flame more clearly, we have previously developed a modified flame index [28,29], defined as

$$\xi_M = \left(\frac{f - f_s}{|f - f_s|} \right) \cdot \frac{1}{2} \left(1 + \frac{G_{\text{FO}}}{|G_{\text{FO}}|} \right). \quad (2)$$

Here the mixture fraction (f) is defined following Bilger [31], and G_{FO} is the flame index proposed by Takeno and co-workers [48]. Note that G_{FO} can only distinguish between premixed and nonpremixed reaction zones, while with the modified definition (i.e., Eq. (2)), $\xi_M = 1$ represents a rich premixed zone, -1 a lean premixed zone, and $|0.5|$ a nonpremixed zone for hydrocarbon flames. Since identification of the various reaction zones is more relevant in regions of high reactivity, i.e., where the heat release rates are significant, we have computed ξ_M only in regions where the heat release rate is at least 1% of the maximum heat release rate.

Fig. 5 presents ξ_M contours for propagating CH₄–air flames established with different H₂ enrichment. The contours are shown when the flames are at two different positions, one at $z = 17\text{ mm}$ corresponding to quasi-steady propagation, and the other near the burner rim ($z \approx 2$) when the flames are in the attachment process at the burner rim. For all four cases considered, the ξ_M contours clearly indicate that during quasi-steady flame propagation, the flames exhibit a triple flame structure at the flame base. The LPZ is weakened with H₂ addition, as indicated by the reduction of the lean premixed wing. For all the four cases, as the flames get close to the burner rim, the

LPZ extinguishes and the triple flame transitions to a double flame containing the rich premixed (RPZ) and nonpremixed (NPZ) zones. As these four flames are stabilized at the burner rim, the RPZ gets extinguished due to insufficient mixing near the rim, and the flames exhibit a single (NPZ) flame structure.

In order to further examine the structures of the four flames depicted in Fig. 5 during quasi-steady flame propagation, we present in Fig. 6 the radial profiles of heat release rate and reactant species (CH₄, H₂, and O₂) mass fractions at an axial location $z = 20\text{ mm}$ near the flame base. The heat release rate profiles have been used in previous investigations [28, 49,50] to identify the global flame structure. For all four flames, the heat release rate profiles exhibit three distinct peaks, indicating a triple flame structure. The triple flame structure is also indicated by the CH₄, H₂, and O₂ mass fraction profiles. The effect of H₂ enrichment is to increase the heat release rate in all three reaction zones and to reduce the spatial distance between the nonpremixed and lean premixed reaction zones, and thereby enhance interaction between them.

Since H₂–air premixed flames exhibit wider flammability limits than typical hydrocarbon–air premixed flames, it is relevant to examine the effect of H₂ enrichment on the flammability limits of propagating CH₄–air triple flames. Fig. 7 presents the four flames, discussed in the context of Fig. 5, in terms of the instantaneous heat release rate contours, streamlines,³ and equivalence ratio contours. The equivalence ratio is computed using $\phi = (f(1 - f_s)/(f_s(1 - f)))$, which implies that the stoichiometric line ($\phi = 1.0$) coincides with the stoichiometric mixture fraction (f_s) line. Previous investigations [47] have used a different equivalence ratio, namely $\phi_u = Y_F/(\nu Y_{\text{Ox}})$, where ν is the stoichiometric fuel–air mass ratio, based on the reactants' mass fractions in the unburnt mixture. However, the propagating triple flame structure is better characterized using ϕ , since the $\phi_u = 1.0$ line does not coincide with f_s in the burnt region, although it does in the unburnt region. For the 0% H₂-enriched flame, the region of high reactivity (red color) extends from $\phi = 0.46$ to $\phi = 1.58$, which correspond, respectively, to the lean and rich flammability limits of CH₄–air premixed flames [51–53]. There is, however, still significant reactivity beyond these ϕ values, implying that a triple flame extends the flammability limits due to synergistic interactions among the three reaction zones. The H₂ enrichment further extends these flammability limits, since it enhances flame reactivity as well as interactions between the re-

³ For propagating flames, which represent a dynamic system, streamlines are simply used here to indicate an instantaneous snapshot of the flow field.

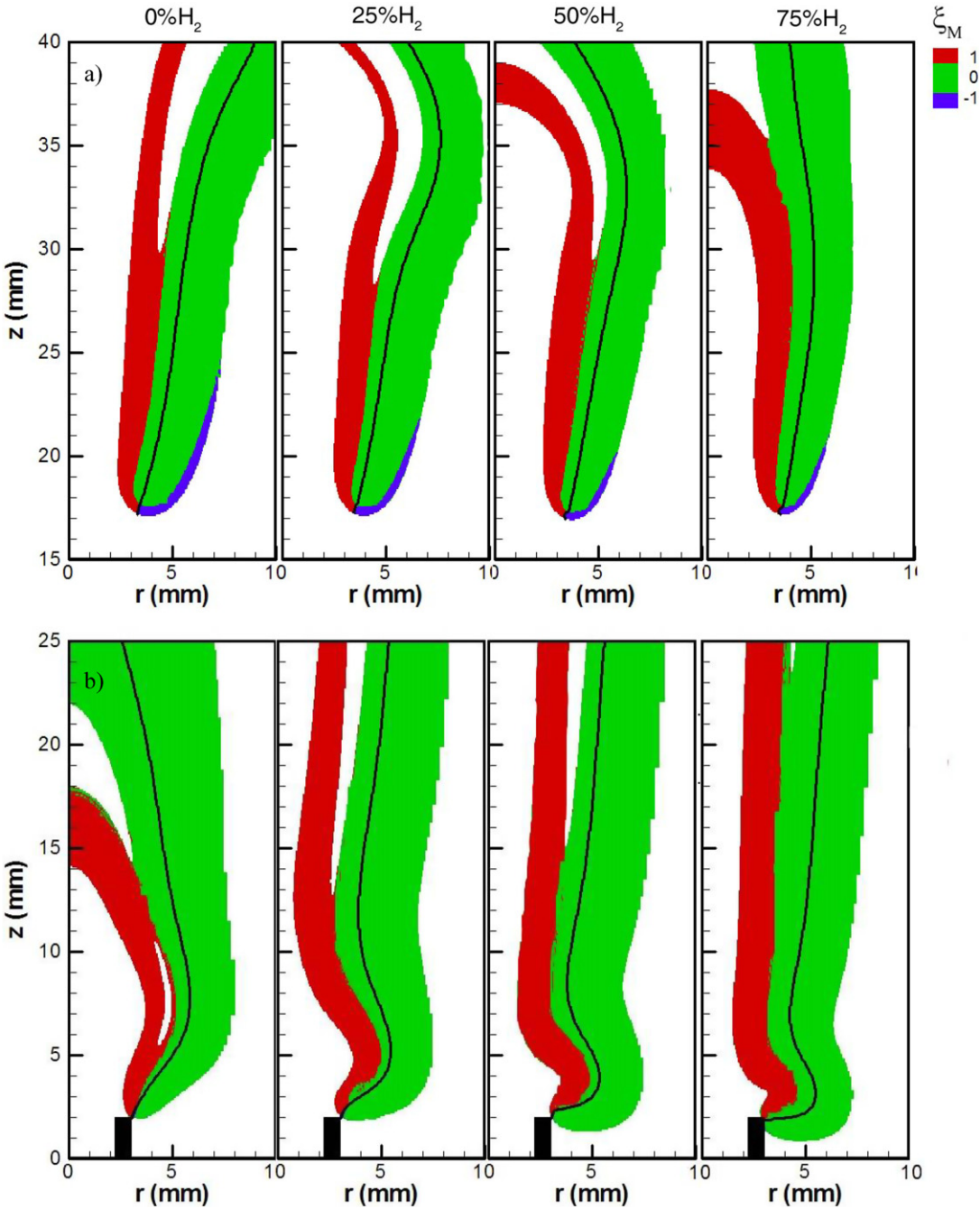


Fig. 5. Flame structures of various H₂-enriched CH₄-air flames are shown through the modified flame index (ξ_M) contours during quasi-steady flame propagation (a) and flame attachment (b).

action zones. For instance, for the 75% H₂-enriched flame, the region of high reactivity (red color) extends from $\phi = 0.14$ to $\phi = 2.54$. H₂ addition also increases both the mixture fraction gradient and the flame curvature, as indicated by the collapsed ϕ lines near the flame base. Moreover, since H₂ enrichment decreases the stoichiometric mixture fraction (f_s), the

flame becomes more asymmetric with respect to the $\phi = 1.0$ line. For example, f_s is 0.055 for the 0% H₂-flame, and decreases to 0.044 for the 75% H₂-enriched flame. Consequently, the flow divergence ahead of the flame base becomes more asymmetric with increasing H₂ content. Therefore, the effect of H₂ enrichment is to significantly extend the flamma-

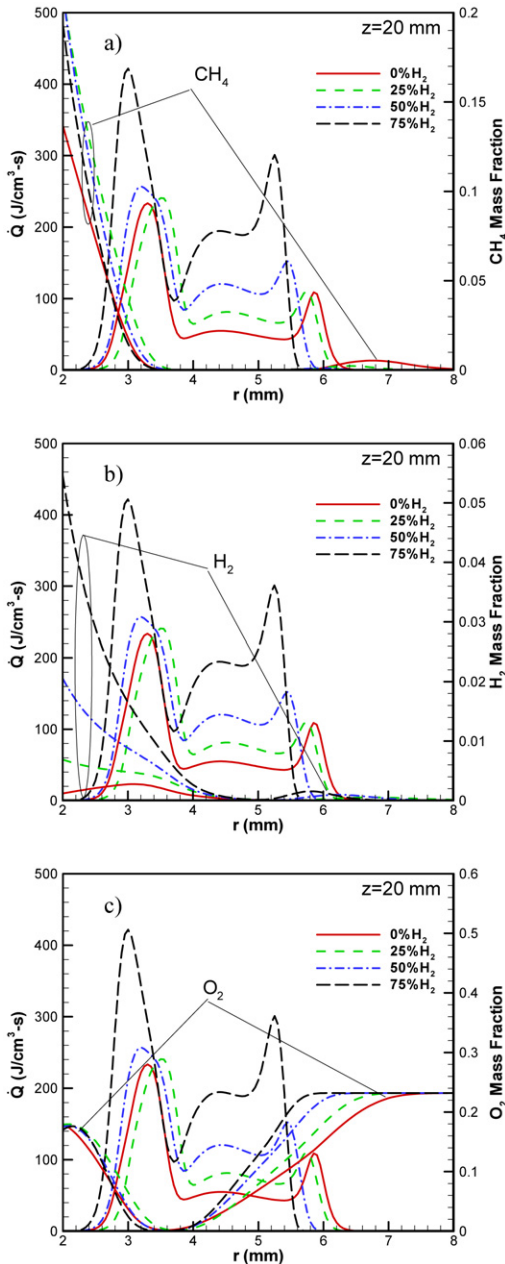


Fig. 6. Flame structure in terms of heat release rate and (a) CH_4 , (b) O_2 , and (c) H_2 radial profiles as a function of radial distance from the centerline (r) for the 0%, 25%, 50%, and 75% H_2 -enriched CH_4 -air propagating flames.

bility limits, decrease the radius of curvature at the triple flame base, increase the mixture fraction gradient, and make the flow divergence more asymmetric with respect to the stoichiometric line. These effects influence the flame dynamics, as discussed in the following sections.

Table 1

Lean and rich flammability limits of H_2 -enriched CH_4 -air planar and triple flames

	Planar flames		Triple flames	
	ϕ_{LEAN}	ϕ_{RICH} [53]	ϕ_{LEAN}	ϕ_{RICH}
0% H_2 –100% CH_4	0.46 [51]	1.58	0.30	2.0
25% H_2 –75% CH_4	–	1.66	0.20	2.4
50% H_2 –50% CH_4	–	1.84	0.14	2.9
75% H_2 –25% CH_4	–	2.00	0.10	3.7
100% H_2 –0% CH_4	0.14 [52]	2.54	–	–

In order to further quantify the effect of H_2 enrichment on the flammability limits of propagating CH_4 -air triple flames, Fig. 8 presents the heat release rate profiles for the four flames as a function of equivalence ratio in the radial direction at an axial location ($z = 20$ mm) near the flame base. As the amount of H_2 in the fuel blend is increased, both the lean and rich flammability limits widen considerably. For instance, the rich flammability limit increases from 2.0 (for the 0% H_2 -enriched flame) to 3.7 (for the 75% H_2 -enriched flame), while the lean flammability limit increases from 0.3 to 0.1. Table 1 summarizes the lean and rich flammability limits of planar and triple flames.⁴ As mentioned before, the triple flame structure exhibits a wider flammability limit than the corresponding planar premixed flames. In addition, the equivalence ratio corresponding to the local maximum heat release rate in the NPZ shifts to the leaner mixture with H_2 enrichment. For instance, these equivalence ratios are $\phi = 0.9$ and 0.8 for the 0% and 75% H_2 -enriched flames, respectively. Consequently, the locations of the local maximum heat release rate and the triple point, which is at the stoichiometric line, do not coincide, and the difference becomes more pronounced with the increase in H_2 enrichment. This has implications for accurately determining the flame speed and stretch-flame speed interactions for propagating triple flames.

3.4. Stoichiometric flame structure and preferential diffusion effect

Our simulations indicate that in addition to the enhanced flammability limits, H_2 enrichment also causes a significant increase in the local flame speed of triple flames. Since the flame speed is strongly influenced by preferential mass diffusion effects, we examine in this section the effect of H_2 enrichment on preferential diffusion. The preferential diffusion

⁴ The rich and lean flammability limits for each propagating flame are obtained at 2.5% of the maximum heat release rate.

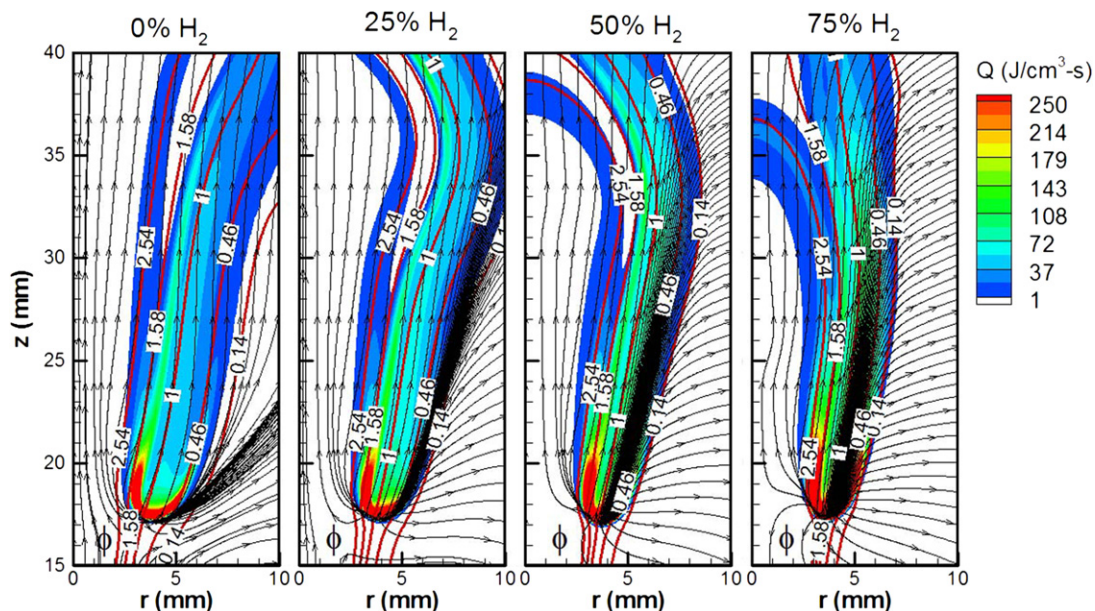


Fig. 7. Computed heat release rate contours (rainbow scheme) (q), equivalence ratio contours (red lines) (ϕ), and flow field streamlines (black lines) (v) for 0%, 25%, 50%, and 75% H_2 -enriched CH_4 -air propagating flames.

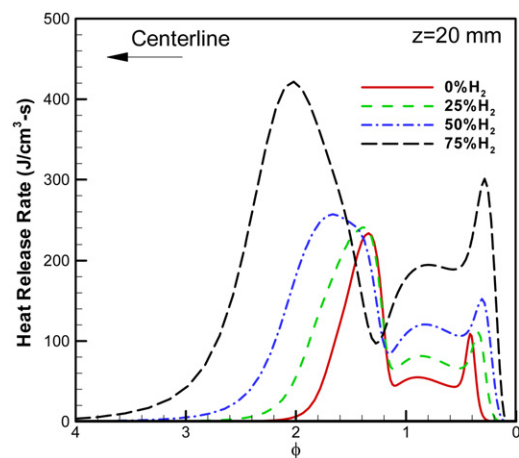


Fig. 8. State relationships in terms of heat release rate radial profiles as a function of equivalence ratio (ϕ) at an axial location of $z = 20$ mm for 0%, 25%, 50%, and 75% H_2 -enriched CH_4 -air propagating flames in the context of Fig. 7.

effect can be demonstrated by comparing the structure of H_2 -enriched propagating triple flames along the stoichiometric mixture fraction with that of the corresponding stoichiometric planar flames.

Lateral diffusion of heat and species plays an important role in determining the structure of propagating triple flames. With fuel blends (say) containing fuels A and B with unequal diffusivities, preferential diffusion of fuel species can lead to localized

regions of higher concentration of fuel A compared to fuel B, and this may significantly affect the flame propagation characteristics. This preferential diffusion effect becomes more significant in propagating triple flames than in planar flames due to the presence of lateral diffusion. In order to characterize this effect, we compare the structure of H_2 -enriched propagating triple flames along the stoichiometric mixture fraction with that of the corresponding stoichiometric planar flames. Fig. 9 presents these flame structures in terms of the temperature, axial velocity, and major species (CH_4 , O_2 , H_2O , H_2 , CO_2 , and CO) profiles for the four H_2 -enriched triple flames (discussed in the context of Figs. 7 and 8) and the corresponding stoichiometric planar flames. The two structures are superimposed at the location of the maximum heat release rate. The stoichiometric planar premixed flames were computed using the freely propagating flame simulator of CHEMKIN 4.0 [54] with GRI-Mech 1.2 [41]. The peak flame temperature for triple flames is lower than that for the corresponding planar premixed flames, and this may be attributed to the effects of lateral heat transport and stretch in triple flames. The peak flame temperature, however, increases with H_2 addition for both triple and planar premixed flames.

The presence of preferential diffusion in the case of triple flames can be observed by comparing the CH_4 and H_2 mass fraction profiles for the triple flames and the corresponding planar flames in Fig. 9. For the 0% H_2 -enriched case, the CH_4 mass fraction profiles for the triple flame is almost identical to that

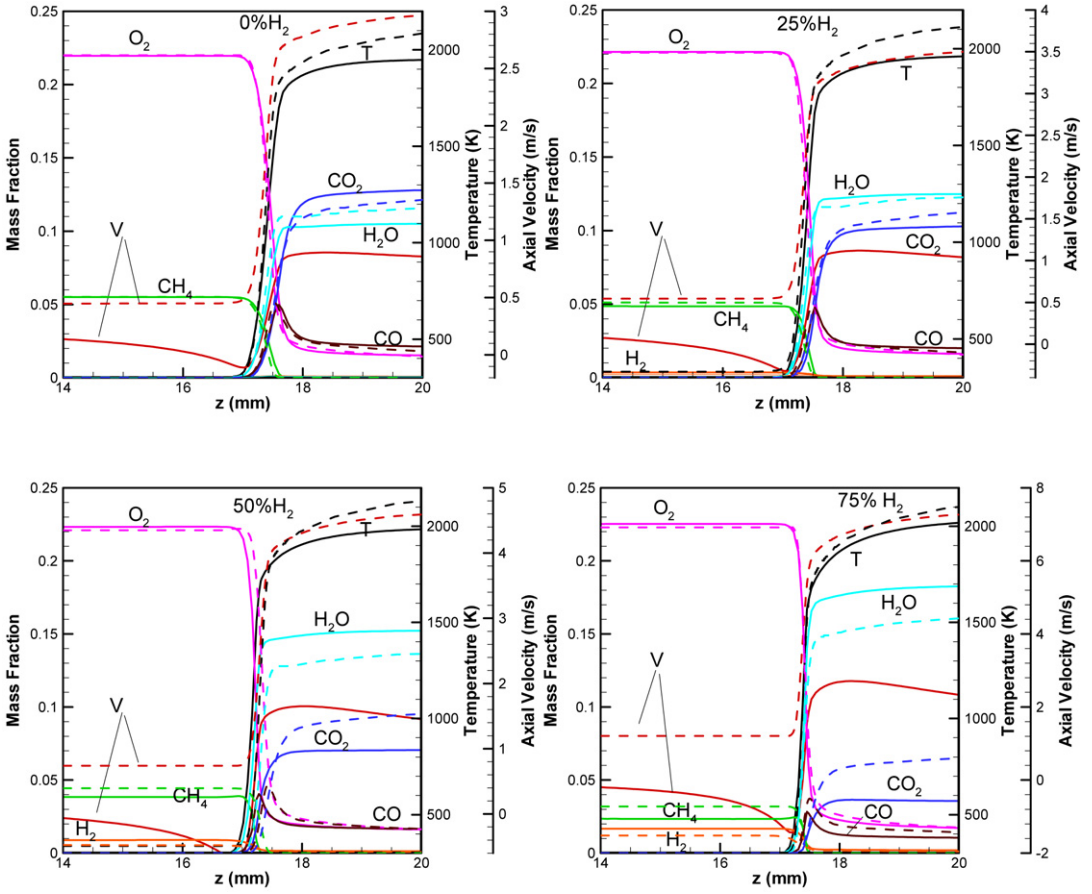


Fig. 9. Comparison of the temperature, axial velocity, and reactants (CH_4 , H_2 , and O_2) and products (CO_2 , CO , and H_2O) mass fraction profiles between the instantaneous flame structure along the stoichiometric mixture fraction line of simulated axisymmetric propagating triple flames (solid) discussed in the context of Fig. 7 and the corresponding stoichiometric planar flames (dashed). The two structures are superimposed at the location of the maximum heat release rate peak.

for the planar premixed flame. However, with increasing H_2 enrichment, the CH_4 mass fraction becomes increasingly smaller while the H_2 mass fraction becomes larger in triple flames than in planar flames, indicating the preferential diffusion of H_2 over CH_4 . The reduction in the CH_4 mass fraction due to preferential diffusion is further indicated by the reduced CO and CO_2 mass fractions and the increased H_2O mass fractions for the triple flames compared to those for the planar flames. Therefore, the preferential diffusion of H_2 in H_2 -enriched propagating triple flames leads to localized higher concentration of hydrogen, which enhances the local flame speed (S_{tri}).

Another important observation from Fig. 9 is that the axial flow velocity in the case of triple flames reaches a minimum ahead of the flame due to the flow divergence effect. This minimum velocity is associated with the local triple flame speed (S_{tri}). For stationary lifted triple flames, Ruetsch et al. [30] and Im and Chen [33] have shown this minimum velocity

to be close to the stoichiometric planar flame speed (S_L). However, for upstream propagating triple flames this minimum velocity becomes negative (cf. Fig. 9) due to flow reversal ahead of the flame. This is consistent with the results reported by Qin et al. [25]. As the amount of H_2 in the fuel blend is increased, the minimum flow velocity increases in magnitude, indicating that the local triple flame speed also increases.

3.5. Flame dynamics at the triple point

In order to examine the flame dynamics and stretch–flame speed interactions, the local flame speed (S_{tri}) and the hydrodynamic (κ_h), curvature-induced (κ_c), and total (κ) stretch rates at the triple point are extracted from our simulations, using the following equations [25,33,55]:

$$S_d^* = \frac{\rho S_d}{\rho_u}, \quad S_d = \left(\frac{1}{\rho |\nabla \varphi|} [\nabla \cdot (\rho D \nabla \varphi) + \omega_\varphi] \right), \quad (3a)$$

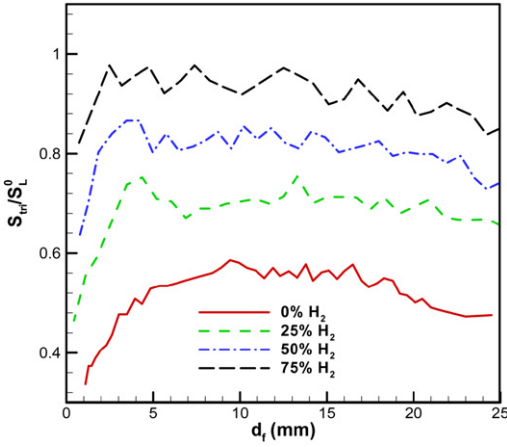


Fig. 10. Normalized local (triple) flame speed (S_{tri}/S_L^0) plotted as a function of distance from the burner rim (d_f) for the 0%, 25%, 50%, and 75% H_2 -enriched CH_4 -air propagating flames.

$$\kappa_h = \nabla \cdot V_{fluid} - nn : \nabla V_{fluid}, \quad (3b)$$

$$\kappa_c = S_d(\nabla \cdot n), \quad (3c)$$

$$\kappa = \kappa_h + \kappa_c. \quad (3d)$$

In Eq. (3a) the scalar φ is represented by the H_2O mass fraction ($Y_{H_2O} = 0.0727$ [26]). Note that a density-weighted flame speed (S_d^*) is being used, following Im and Chen [33]. Here S_d^* represents the local flame speed along the flame surface, while S_d^* at the triple point yields the local triple flame speed (S_{tri}). In addition, the global flame speed (U_F) is evaluated using [33,56]

$$U_F - U_0 = S_{tri} - U_e = V_f. \quad (4)$$

Here U_0 is the local maximum flow velocity along the stoichiometric mixture fraction line (f_s) ahead of the flame, which is not affected by flow divergence, whereas U_e is the local minimum flow velocity along f_s ahead of the flame. Note that if the flame were to be stabilized as a lifted flame, its displacement flame velocity would be zero ($V_f = 0$), and then $U_F = |U_0|$ and $S_{tri} = |U_e|$.

Fig. 10 presents the normalized local triple flame speed (S_{tri}/S_L^0) as a function of distance from the burner rim (d_f) for the four H_2 -enriched CH_4 -air triple flames. Here S_L^0 is the stoichiometric unstretched planar flame speed, which is computed for each of the four H_2 -enriched flames using the CHEMKIN package [54] with the GRI 1.2 chemistry model [41]. The S_L^0 values for the four flames are provided in Table 2. Several important observations can be made from this figure. First, with increasing H_2 enrichment, S_{tri} increases due to the enhanced chemical reactivity, diffusivity, and preferential diffusion

Table 2

Unstretched flame speeds (S_L^0) and thicknesses (δ_L^0) of H_2 -enriched CH_4 -air stoichiometric planar premixed flames, computed using the CHEMKIN package [54] and the GRI-Mech. 1.2 [41] chemistry model

	S_L^0 (mm/s)	δ_L^0 (mm) ^a
0% H_2 –100% CH_4	400.0	0.47
25% H_2 –75% CH_4	497.0	0.44
50% H_2 –50% CH_4	693.0	0.37
75% H_2 –25% CH_4	1163.0	0.33

^a Flame thickness was obtained using the gradient method: $\delta_L^0 = (T_{max} - T_{min}) / (dT/dx)_{max}$. Here T is the temperature and x is the axial distance in a one-dimensional configuration.

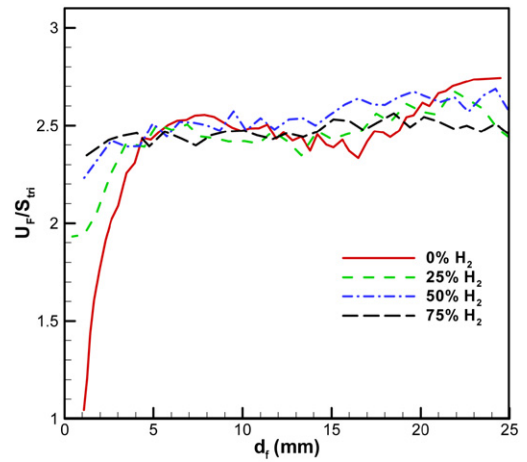


Fig. 11. Normalized global flame speed (U_F/S_{tri}) as a function of distance from the burner rim (d_f) for the 0%, 25%, 50%, and 75% H_2 -enriched CH_4 -air propagating flames.

caused by H_2 addition. Second, the ratio S_{tri}/S_L^0 is less than unity, implying that the effect of stretch is to reduce the flame speed for these flames. Third, the difference between S_{tri} and S_L^0 is reduced with increasing H_2 enrichment, implying that the flame becomes less sensitive to stretch rate with H_2 addition. Finally, S_{tri} varies during flame propagation. These aspects are further discussed later in this section.

Ruetsch et al. [30] and Im and Chen [33] have shown that U_F/S_{tri} is proportional to the square root of the density ratio (i.e., $\sqrt{(\rho_u/\rho_b)}$) in the limit of small mixture fraction gradient. In order to confirm this relationship for our simulations, we present in Fig. 11 the normalized far-field flame speed (U_F/S_{tri}) as a function of flame position (d_f) for the flames discussed in the context of Fig. 10. It is interesting to note that for all H_2 -enriched flames, $U_F/S_{tri} \approx 2.5$ during quasi-steady flame propagation. Our simulations also indicate that the square root of the density ratio remains nearly constant ($\sqrt{(\rho_u/\rho_b)} \approx 2.6$) for

all four flames during propagation. While Ruetsch et al. [30] and Im and Chen [33] reported this relationship for triple flames under idealized conditions, our simulations demonstrate a similar relationship under more complex conditions. For instance, Ruetsch et al. [30] used global chemistry with constant thermodynamics and transport properties to establish perfectly symmetric nonbuoyant propagating triple flames in a uniform flow field, while our simulations include detailed chemistry as well as variable transport and thermodynamic properties and show that the flow redirection effect (i.e., $U_F/S_{tri} \approx \sqrt{(\rho_u/\rho_b)}$) is observed for propagating triple flames under more complex conditions, such as nonuniform flow field, presence of buoyancy, flame radiation, and asymmetric flow divergence upstream of the flame.

Fig. 12 presents the hydrodynamic (κ_h), curvature-induced (κ_c), and total (κ) stretch at the triple point plotted as a function of distance from the burner rim (d_f) for the four flames discussed in the context of Fig. 10. As the H_2 enrichment is increased, both κ_h and κ_c and, consequently, the total stretch increase considerably. The increase in κ_h can be attributed to the increased heat release rate at the flame base (cf. Figs. 6, 7, and 8) due to H_2 enrichment, which in turn increases the normal component of flow velocity across the flame front, while the tangential component remains nearly constant. This flow redirection effect, which bends the streamlines toward the stoichiometric mixture fraction line, is responsible for flow divergence ahead of the flame (cf. Fig. 9). The increase in curvature-induced stretch with H_2 enrichment is due to the increase in flame curvature ($\nabla \cdot n$), as discussed in the context of Fig. 7.

It is worth mentioning that the stretch rates for the CH_4 -air flame studied here are comparable to those reported by Qin et al. [25] and Ko and Chung [26] for propagating CH_4 -air triple flames. For instance, the curvature-induced stretch in the present study is comparable to those reported in the cited studies. While the hydrodynamic stretch (κ_h) is comparable to that reported by Qin et al. [25], it is considerably higher than that reported by Ko and Chung [26]. The difference could be related to the different flow conditions, especially the jet velocity and the absence of coflow in the cited study [26].

In order to examine the stretch-flame speed interactions, we present in Fig. 13 the normalized local triple flame speed (S_{tri}/S_L^0) as a function of the Karlovitz number (Ka) for the flames discussed in the context of Fig. 10. Based on the flame stretch theory, $S_L^0/S_{tri} = 1 + Ma Ka$ [57], where the Karlovitz number is given by $Ka = \delta_L^0 \cdot \kappa/S_{tri}$, and the Markstein number (Ma) is equal to the negative of the slope of each curve in this figure. The local triple flame speed decreases almost linearly with increasing Ka

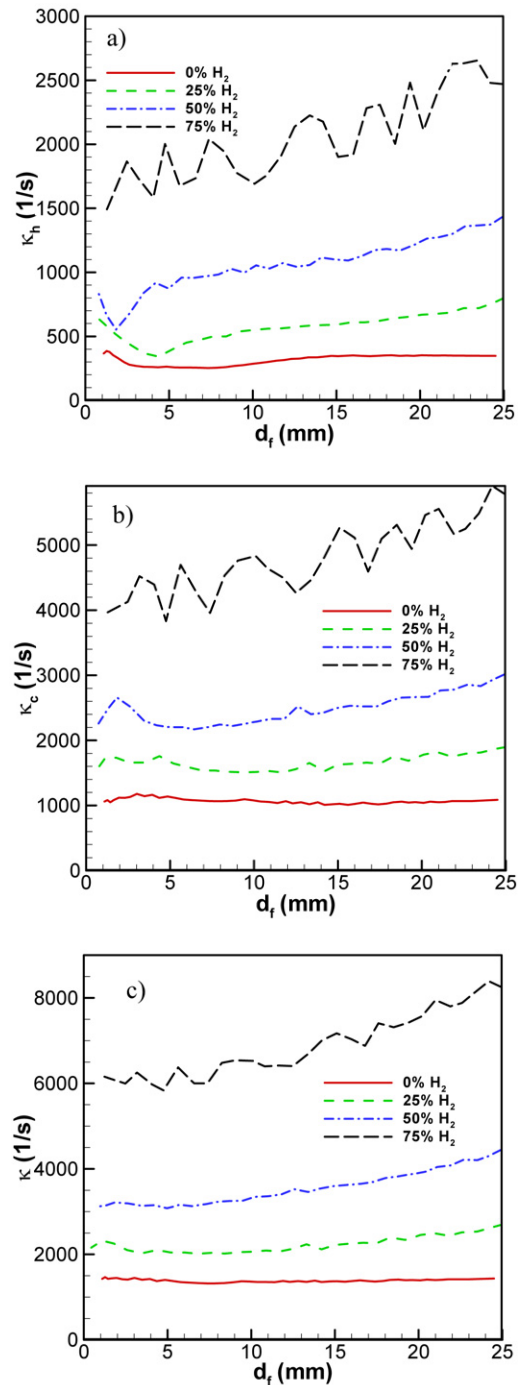


Fig. 12. (a) Hydrodynamic (κ_h), (b) curvature-induced (κ_c), and (c) total (κ) stretch rates at the triple point plotted as a function of distance from the burner rim (d_f) for the propagating 0%, 25%, 50%, and 75% H_2 -enriched CH_4 -air triple flames.

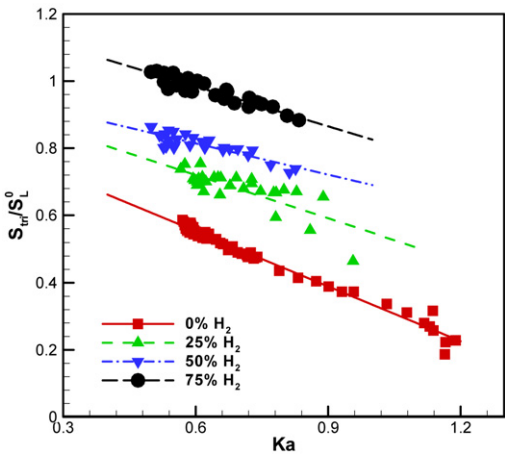


Fig. 13. Normalized local (triple) flame speed (S_{tri}/S_L^0) as a function of Karlovitz number (Ka) for the flames discussed in the context of Fig. 10.

for all cases, implying that these flames are diffusive–thermally stable [57,58]. This result is also consistent with the results reported in Ref. [25] concerning flame speed–stretch interactions in a propagating partially premixed methane–air flame. For a positively stretched flame base, its convex nature toward the fresh mixture defocuses the heat, while focusing the deficient reactant. Thus, for $Le > 1.0$, the defocusing effect dominates, leading to a negative correlation between local triple flame speed and stretch. In addition, Fig. 13 indicates that the propagating triple flames become less sensitive to stretch (i.e., less diffusive–thermally stable) as H_2 enrichment increases, as indicated by the decrease in the slope (i.e., $-Ma$). This is consistent with the results shown in Fig. 10. Previous experimental and numerical studies have shown that the flame speed decreases linearly with stretch for stoichiometric outwardly propagating spherical CH_4 –air and H_2 –air flames ($Ka > 0$), and that the latter is less sensitive to stretch [57,58]. Therefore, our results are consistent with those reported in the cited studies. Our results are also consistent with the experimental results of Huang et al. [17], who observed that for outwardly propagating spherical flames burning a stoichiometric mixture of natural gas and hydrogen with air, the increase in H_2 content decreases the Markstein number, implying increased tendency toward diffusive–thermal instability.

To characterize the effects of curvature and mixture fraction gradient on triple flame propagation, Fig. 14 presents the normalized local triple flame speed (S_{tri}/S_L^0) as a function of $\delta_L^0 \cdot \nabla \cdot n$ and Da^{-1} , which are, respectively, the dimensionless flame curvature and the dimensionless mixture fraction gradient. Following Ruetsch et al. [30], Da is computed

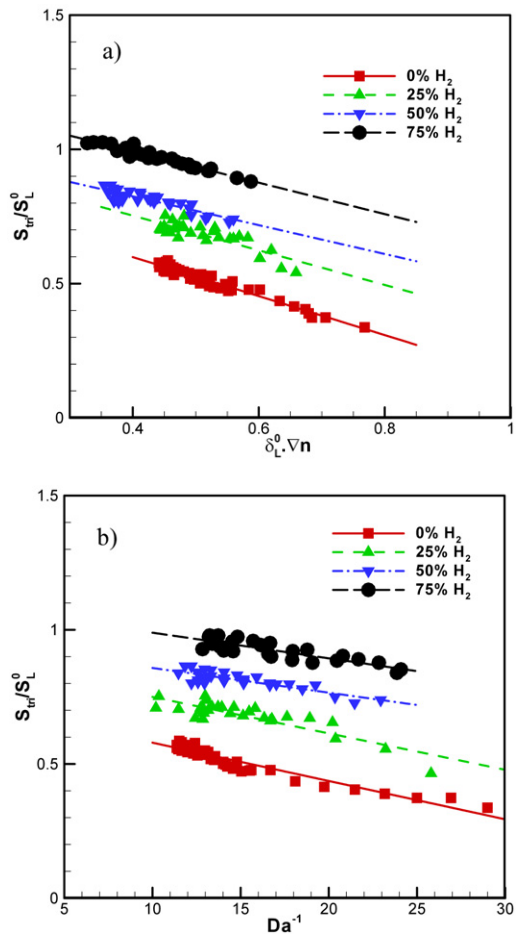


Fig. 14. Normalized local (triple) flame speed (S_{tri}/S_L^0) as a function of (a) dimensionless flame curvature ($\delta_L^0 \cdot \nabla n$) and (b) inverse Damköhler number (Da^{-1}) for the flames discussed in the context of Fig. 10.

at the location of the local minimum flow velocity along f_s . Results indicate a linear correlation between S_{tri}/S_L^0 and $\delta_L^0 \cdot \nabla n$ and between S_{tri}/S_L^0 and Da^{-1} for all the four cases. As $\delta_L^0 \cdot \nabla n$ increases, S_{tri}/S_L^0 decreases, since the premixed wings are weakened and the propagating triple flame structure resembles more that of a nonpremixed flame. Similarly, with increasing Da^{-1} , S_{tri}/S_L^0 decreases. The response of the local triple flame speed to curvature and mixture fraction gradient is consistent with previous investigations [25,26,30]. Generally, the effect of H_2 enrichment is to reduce the flame’s sensitivity to curvature and mixture fraction gradient, as indicated by a decrease in the respective slopes.

Finally, in order to isolate the effect of H_2 enrichment on Markstein numbers (Ma) from that of flame structure, Table 3 summarizes the Markstein numbers for triple flames discussed in the context of Fig. 13

Table 3

Summary of Markstein numbers (Ma) for H₂-enriched CH₄-air planar and triple flames

	Markstein numbers (Ma)	
	Planar flames ^a	Triple flames
0% H ₂ –100% CH ₄	0.42	0.55
25% H ₂ –75% CH ₄	0.26	0.43
50% H ₂ –50% CH ₄	0.19	0.31
75% H ₂ –25% CH ₄	0.11	0.39

^a Computed under stoichiometric conditions.

and the corresponding counterflow (twin) premixed flames. The Markstein numbers for the latter flames are computed using the CHEMKIN package [54] with the GRI 1.2 chemistry model [41]. The methodology is described in Ref. [59]. An important observation from this table is that triple flames have higher Ma than the corresponding premixed flames, indicating greater sensitivity to stretch and higher diffusive–thermal stability for triple flames.

4. Conclusions

We have presented a numerical investigation on the propagation characteristics of H₂-enriched CH₄-air flames in a nonpremixed jet. Propagating triple flames are established in axisymmetric coflowing jets by igniting the fuel–air mixture at a downstream location. A time-accurate implicit algorithm that uses detailed descriptions of transport and CH₄-air chemistry is used for simulations. The predictions are validated using measurements of the instantaneous displacement flame velocity. The effects of H₂ enrichment on the flame structure, dynamics, and stretch–flame speed interactions for propagating triple flames are characterized.

1. Following ignition, a well-defined triple flame is formed that propagates upstream along the stoichiometric mixture fraction line with a nearly constant displacement flame velocity (V_f). As the flame approaches the burner, it transitions to a double flame and subsequently to a nonpremixed flame, and stabilizes at the burner rim. With increased H₂ concentration in the fuel blend, both V_f and S_{tri} (local triple flame speed) increase progressively due to the enhanced chemical reactivity, diffusivity, and preferential diffusion caused by H₂ enrichment.
2. The propagating triple flame structure is substantially modified by H₂ enrichment, which increases the flame curvature and mixture fraction gradient near the triple point. The addition of H₂ also enhances interactions between the reac-

tion zones, which extend the flammability limits associated with CH₄-air triple flames. In addition, H₂ enrichment makes the flow divergence ahead of the flame more asymmetric with respect to the stoichiometric mixture fraction line. Consequently, the triple point does not coincide with the flame leading edge, which is located at the local minimum flame curvature. This distinction is important in the context of determining S_{tri} , since experimental studies have generally reported flame speeds at the leading edge, while numerical investigations have reported these values at the triple point.

3. The flame dynamics at the triple point is also significantly modified by H₂ enrichment. In addition to the enhancement in local triple flame speed (S_{tri}), H₂ addition considerably increases both the hydrodynamic and curvature-induced stretch, and hence the total stretch. Moreover, the stretch–flame speed interactions are substantially modified, as H₂ enrichment reduces the flame sensitivity to stretch; i.e., it decreases the Markstein number (Ma) and thus increases the flame tendency toward diffusive–thermal instability (i.e., $Ma \rightarrow 0$). These results are consistent with the previously reported experimental results for outwardly propagating premixed spherical flames burning a stoichiometric mixture of natural gas and hydrogen with air.
4. For all the H₂-enriched methane–air flames investigated in this study, the local triple flame speed decreases linearly with stretch. This is consistent with previous studies that have shown a negative correlation between flame speed and stretch for stoichiometric CH₄-air and H₂-air premixed flames with an effective Lewis number greater than one. While S_{tri} decreases linearly with stretch, the ratio U_F/S_{tri} (U_F being the global flame speed) is found to be proportional to the square root of the unburned to burned density ratio ($\sqrt{(\rho_u/\rho_b)}$). This is an important result because it implies that the flame stretch theory and flow redirection effect, which have previously been discussed in the context of idealized flame configurations, also apply to more complex flames such as H₂-enriched CH₄-air triple flames propagating in a nonuniform flow field.
5. Results also indicate that the flammability limits associated with triple flames are significantly wider than those associated with the corresponding planar premixed flames. Triple flames also exhibit higher sensitivity to stretch and greater diffusive–thermal stability than their corresponding stoichiometric planar premixed flames.

References

- [1] M.S. Kumar, A. Ramesh, B. Nagalingam, *Int. J. Hydrogen Energy* 28 (2003) 1143–1154.
- [2] F.W. Hoehn, R.L. Baisly, M.W. Dowdy, in: *Proc. 10th Intersociety Energy Conversion Conf.*, Newark, DE, USA, Paper 759173, 1975.
- [3] E. Sher, Y. Hacohen, *Proc. Inst. Mech. Eng.* 203 (1989) 155–162.
- [4] V. Raman, J. Hansel, J. Fulton, F. Lynch, D. Bruderly, SAE Publication, 1996, pp. 47–56.
- [5] B. Nagalingam, F. Duebel, K. Schmillen, *Int. J. Hydrogen Energy* 8 (1983) 715–720.
- [6] M.R. Swain, M.J. Yusuf, Z. Dulger, M.N. Swain, SAE Paper 932775, 1993.
- [7] G.A. Karim, I. Wierzba, Y. Al-Alousi, *Int. J. Hydrogen Energy* 21 (1996) 625–631.
- [8] R.L. Hoekstra, P. Van Blarigan, P.N. Mulligan, SAE Paper 961103.
- [9] F. Schafer, SAE Paper 810776, 1996.
- [10] C.G. Bauer, T.W. Forest, *Int. J. Hydrogen Energy* 26 (2001) 71–77.
- [11] M.A.S. Al-Baghdadi, *Renewable Energy* 28 (2002) 1471–1478.
- [12] A.R. Choudhuri, S.R. Gollahali, *Int. J. Hydrogen Energy* 4 (2004) 1293–1302.
- [13] G.J. Rortveit, J.E. Hustad, F.A. Williams, in: *Proc. 6th Int. Conf. Tech. Combust. Clean Environment*, Porto, Portugal, 2000.
- [14] S. Naha, S.K. Aggarwal, *Combust. Flame* 139 (2004) 90–105.
- [15] S. Naha, A.M. Briones, S.K. Aggarwal, *Combust. Sci. Technol.* 177 (2005) 183–220.
- [16] C.G. Fotache, T.G. Kreutz, C.K. Law, *Combust. Flame* 110 (1997) 429–440.
- [17] Z. Huang, Y. Zhang, K. Zeng, B. Liu, Q. Wang, D. Jiang, *Combust. Flame* 146 (2006) 302–311.
- [18] C.K. Law, G. Jomass, J.K. Bechtold, *Proc. Combust. Inst.* 30 (2005) 159–167.
- [19] R.W. Schefer, *Int. J. Hydrogen Energy* 28 (2003) 1131–1141.
- [20] E.R. Hawkes, J.H. Chen, *Combust. Flame* 138 (2004) 242–258.
- [21] P.F. Flynn, R.P. Durrett, G.L. Hunter, A.O. Loye, O.C. Akinyemi, J.E. Dec, C.K. Westbrook, SAE Paper 1999-01-0509, 1999.
- [22] B.J. Lee, S.H. Chung, *Combust. Flame* 109 (1997) 163–172.
- [23] H. Phillips, *Proc. Combust. Inst.* 10 (1965) 1277–1283.
- [24] P.N. Kioni, B. Rogg, K.N. Bray, A. Liñán, *Combust. Flame* 95 (1993) 276–290.
- [25] X. Qin, C.W. Choi, A. Mukhopadhyay, I.K. Puri, S.K. Aggarwal, V.R. Katta, *Combust. Theory Modelling* 8 (2004) 293–314.
- [26] Y.S. Ko, S.H. Chung, *Combust. Flame* 118 (1999) 151–163.
- [27] J. Lee, S.H. Won, S.H. Jin, S.H. Chung, *Combust. Flame* 135 (2003) 449–462.
- [28] A.J. Lock, A.M. Briones, X. Qin, S.K. Aggarwal, I.K. Puri, U. Hegde, *Combust. Flame* 143 (2005) 159–173.
- [29] A.M. Briones, S.K. Aggarwal, V.R. Katta, *Phys. Fluids* 18 (2006) 043603.
- [30] G.R. Ruetsch, L. Vervisch, A. Liñán, *Phys. Fluids* 7 (1995) 1447–1454.
- [31] R.W. Bilger, *Proc. Combust. Inst.* 22 (1988) 475–488.
- [32] S.F. Ahmed, E. Mastorakos, *Combust. Flame* 146 (2006) 215–231.
- [33] H.G. Im, J.H. Chen, *Combust. Flame* 119 (1999) 436–454.
- [34] I.K. Puri, S.K. Aggarwal, S. Ratti, R. Azzoni, *Combust. Flame* 124 (2001) 311–325.
- [35] S.H. Won, J. Kim, K.J. Hong, M.S. Cha, S.H. Chung, *Proc. Combust. Inst.* 30 (2005) 339–347.
- [36] Z. Shu, S.K. Aggarwal, V.R. Katta, I.K. Puri, *Combust. Flame* 111 (1997) 276–286.
- [37] R. Azzoni, S. Ratti, I.K. Puri, S.K. Aggarwal, *Phys. Fluids* 11 (1999) 3449–3464.
- [38] X. Qin, I.K. Puri, S.K. Aggarwal, V.R. Katta, *Phys. Fluids* 16 (2004) 2963–2974.
- [39] R. Siegel, J.R. Howell, *Thermal Radiation Heat Transfer*, Hemisphere Publishing Corporation, New York, 1981.
- [40] R.C. Reid, J.M. Prausnitz, B.E. Poling, *The Properties of Gases and Liquids*, McGraw–Hill, New York, 1987.
- [41] M. Frenklach, H. Wang, C.-L. Yu, M. Goldenberg, C.T. Bowman, R.K. Hanson, D.F. Davidson, E.J. Chang, G.P. Smith, D.M. Golden, W.C. Gardiner, V. Lissianski, http://www.me.berkeley.edu/gri_mech/; and Gas Research Institute Topical Report: M. Frenklach, H. Wang, M. Goldenberg, G.P. Smith, D.M. Golden, C.T. Bowman, R.K. Hanson, W.C. Gardiner, V. Lissianski, GRI-Mech—An Optimized Detailed Chemical Reaction Mechanism for Methane Combustion, Report No. GRI-95/0058, November 1, 1995.
- [42] F.N. Egolfopoulos, D.L. Zhu, C.K. Law, *Proc. Combust. Inst.* 23 (1990) 471–478.
- [43] D.E. Heard, J.B. Jeffries, G.P. Smith, D.R. Crosley, *Combust. Flame* 88 (1992) 137–148.
- [44] V.R. Katta, F. Takahashi, G.T. Linteris, *Combust. Flame* 137 (2004) 506–522.
- [45] V.R. Katta, L.P. Goss, W.M. Roquemore, *AIAA J.* 32 (1994) 84–94.
- [46] Z. Shu, B. Krass, C. Choi, S.K. Aggarwal, V. Katta, I.K. Puri, *Proc. Combust. Inst.* 27 (1998) 625–632.
- [47] X. Qin, Ph.D. thesis, University of Illinois at Chicago, 2004.
- [48] H. Yamashita, M. Shimada, T. Takeno, *Proc. Combust. Inst.* 26 (1996) 27–34.
- [49] H. Guo, F. Liu, G.J. Smallwood, *Combust. Flame* 143 (2005) 282–298.
- [50] A.M. Briones, S. Som, S.K. Aggarwal, *Combust. Flame* 149 (2007) 448–462.
- [51] H.C. Barnett, R.R. Hibbard (Eds.), *NACA Report 1300*, 1959.
- [52] M.G. Zabetakis, U.S. Bureau of Mines, *Bulletin* 627, 1965.
- [53] I. Wierzba, B.B. Ale, *Int. J. Hydrogen Energy* 25 (2000) 75–80.
- [54] R.J. Kee, F.M. Rupley, J.A. Miller, M.E. Coltrin, J.F. Grcar, E. Meeks, H.K. Moffat, A.E. Lutz, G. Dixon-Lewis, M.D. Smooke, J. Warnatz, G.H. Evans, R.S. Larson, R.E. Mitchell, L.R. Petzold, W.C. Reynolds, M. Caracotsios, W.E. Stewart, P. Glarborg, C. Wang, C.L. McLellan, O. Adigun, W.G. Houf, C.P. Chou, S.F.

- Miller, P. Ho, P.D. Young, D.J. Young, CHEMKIN Release 4.0.2, Reaction Design, San Diego, CA, 2005.
- [55] A. Mukhopadhyay, I.K. Puri, *Combust. Flame* 133 (2003) 499–502.
- [56] G.R. Ruetsch, J.E. Broadwell, Annual Res. Briefs, Center for Turbulence Research, 1995.
- [57] M.I. Hassan, K.T. Aung, G.M. Faeth, *Combust. Flame* 115 (1998) 539–550.
- [58] O.C. Kwon, G.M. Faeth, *Combust. Flame* 124 (2001) 590–610.
- [59] C.K. Wu, C.K. Law, *Proc. Combust. Inst.* 20 (1985) 1941–1949.

GT2008-50853

NUMERICAL STUDIES ON CAVITY-INSIDE-CAVITY-SUPPORTED FLAMES IN ULTRA COMPACT COMBUSTORS

Viswanath R. Katta^{*}, Joeseeph Zelina, and William M. Roquemore

**Air Force Research Laboratory
Propulsion Directorate
Wright-Patterson Air Force Base, OH 45433-7103**

^{*}Innovative Scientific Solutions Inc., Dayton, OH

ABSTRACT

Cavities are incorporated in the designs of the future gas-turbine combustors for providing flame stability and, thereby, for improving the lean blowout characteristics. Recently, a Cavity-inside-cavity (CIC) design was proposed for the Air Force Research Laboratory's ultra compact combustor (UCC). Numerical studies are performed in the present study to understand the dynamics of the CIC-supported flames. The complex CIC that was used in the actual hardware has been simplified for making it amenable to two-dimensional models. Calculations are performed for the modified CIC using a two-dimensional, unsteady, reacting flow code known as UNICORN. Direct numerical simulations and calculations using $k-\epsilon$ turbulence model are performed. A fast, global-chemistry model is used for studying the flame dynamics inside and in the wake region of CIC. Calculations are performed for several CIC geometries generated through varying the width of the cavity. The design CIC is found oversized for the secondary (circumferential) airflow used in UCCs. A detailed chemistry model is also used for understanding the blowout characteristics of the CIC-supported flames.

INTRODUCTION

Gas turbine engines have continued to improve with innovations in making them smaller, more efficient and environmentally friendly. Studies [1] have indicated that reheating of the combustion products between the high- and low-pressure turbine stages in a gas turbine engine could improve the specific thrust by as much as 50%. However, as a

conventional combustor is too large to be incorporated for providing the extra heat between the two turbine stages, new technologies such as Ultra Compact Combustor (UCC) that can maintain high-efficiency burning in an extremely short length are being developed [2,3]. In the original design of UCC a cavity runs around the outer circumference of the turbine inlet guide vanes. For improving the lean blowout and stability characteristics of the UCC a second cavity, referred to as cavity-inside-cavity (CIC), is channeled inside the primary one [4,5]. Entire fuel used in UCC is injected through this cavity. Additional air jets are also provided in CIC for increasing fuel-air mixing and for creating a stable vortical flow inside the cavity. Because of these fuel and air injections into the cavity and the high-speed secondary air flowing in the circumferential direction over the cavity makes the design of CIC complicated.

Unsteady flow in and around cavity-type geometries occurs in a variety of applications such as slotted wind tunnels, slotted flumes, bellows-type configurations, and aircraft-engine and airframe components. In particular, the unsteady flow in aircraft combustors restricts fuel-lean operation and degrades flame-stability characteristics. Hsu et al. [6] have proposed a simple, compact, and efficient method of using cavities to stabilize combustion. Since this concept uses a vortex that is trapped in a cavity [7] to stabilize the flame, it is referred as the Trapped-Vortex (TV) concept. Experimental investigations of Hsu et al. [6] indicated that a trapped-vortex combustor operates most efficiently when fuel and air are injected directly into the cavity. However, direct injection of mass (air and/or

fuel) into the cavity could alter the geometrical criterion derived for locking vortices inside passive cavities (i.e., without injection). Because of this direct injection cavity flow in a trapped-vortex combustor experiences higher residence times and fuel-rich environment and may lead to increased production of pollutants and soot. Therefore, in order to reap the benefits of trapping a vortex inside the cavity while not creating excessively long residence times for unmixed fuel, cavity size must be determined while considering the fuel and air injection schemes.

In the present work, numerical simulations for the reacting flows associated with a CIC for different equivalence ratios are made using a well-tested CFD code UNICORN [8]. A detailed chemical kinetics model for gas-phase reactions and a two-step model for soot formation are incorporated. A global, infinitely fast chemical kinetics is also used for performing optimization studies on CIC geometry. Numerical results obtained for unsteady flames with different CIC geometries are compared.

MODEL CONFIGURATION

The ultra-compact combustor (UCC) conceptually integrates the traditional combustor with the preceding compressor exit guide vanes and the following turbine inlet guide vanes. Details of the UCC design established at Air Force Research Laboratory (AFRL) are given in References 2 and 3. For improving the flame-stability and lean-blowout characteristics, this design included novel geometrical features such as cavity-in-cavity (CIC). The basic idea of CIC has stemmed from AFRL's trapped-vortex-combustor concept [6,7], which successfully used a cavity for trapping the recirculation vortex that generally moves around in the wake region of a flame holder. The CIC used in AFRL's UCC is described in Reference 5. A schematic diagram of the CIC is shown in Fig. 1a. CICs are drilled in the longitudinal direction at the top surface of a circumferential main cavity. Secondary air is injected in the circumferential direction at the top surface of the main cavity. The primary air of the combustor flowing across the circumferential cavity and the secondary air flowing across the CIC in the circumferential direction make the overall flowfield highly three-dimensional. However, the strong secondary air inside the circumferential cavity is expected to shield the CIC from the primary air and, consequently, flow inside a CIC could be assumed as two dimensional with the third direction coinciding with the longitudinal direction of the combustor. With this assumption, flowfield associated with a CIC is modeled as a two-

dimensional one as shown in Fig. 1b. Velocities for the secondary air (40 m/s), driver jet A (28 m/s), driver jet B (19 m/s), and fuel jet F (1.0 m/s) are obtained by matching the flow rates used in the experiment [5]. Note that the circular holes through which these jets were issued in the experiment are treated as slots in the current two-dimensional modeling. The widths of jets A and B are set as 1 mm and that of fuel jet F is set as 3 mm. It is also assumed that operation of one CIC doesn't influence the operation the other in its neighborhood. Fuel is injected into CIC with a recess at the top plate for mimicking spray-nozzle mounting. CIC shown in Fig. 1b is modeled with a non-uniform grid system having 251X151 points and with a minimum spacing of 0.1 mm.

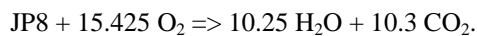
NUMERICAL MODEL

UNICORN (UNsteady Ignition and Combustion using ReactionNs) code [8,9] is a time-dependent, two-dimensional mathematical model used for the simulation of unsteady reacting flows. It is capable of performing direct numerical simulations (DNS) and has been developed over a ten-year period. Its evolution has been in conjunction with experiments conducted for testing its ability to predict ignition, extinction, stability limits, and the dynamic characteristics of nonpremixed and premixed flames of various fuels [10-13]. It solves for u- and v-momentum equations, continuity, and enthalpy- and species-conservation equations on a staggered-grid system. A clustered mesh system is employed to trace the large gradients in flow variables near the flame surface. Detailed chemical-kinetics models for various fuels are incorporated. Thermo-physical properties such as enthalpy, viscosity, thermal conductivity, and binary molecular diffusion of all the species are calculated from the polynomial curve fits developed for the temperature range 300 - 5000 K. Mixture viscosity and thermal conductivity are then estimated using the Wilke and Kee expressions, respectively. Molecular diffusion is assumed to be of the binary-diffusion type, and the diffusion velocity of a species is calculated using Fick's law and the effective-diffusion coefficient of that species in the mixture. A simple radiation model based on the optically thin-media assumption is incorporated into the energy equation. Radiation from CH₄, CO, CO₂, H₂O, and soot is considered [14]. Soot is modeled using the two-equation methodology proposed by Lindstedt [15].

The finite-difference forms of the momentum equations are obtained using an implicit QUICKST scheme[9], and those of the species and energy equations are obtained using a hybrid scheme of upwind and central differencing. At every time step,

the pressure field is accurately calculated by solving all the pressure Poisson equations simultaneously and using the LU (Lower and Upper diagonal) matrix-decomposition technique. Different types of boundary conditions such as adiabatic wall, isothermal wall, symmetric surface, outflow, and inflow can be applied to the boundaries of the computational domain [16].

Two chemical kinetics models for JP-8-fuel-air combustion are used. One is an infinitely fast, global-type reaction mechanism involving five species, namely fuel, O₂, CO₂, H₂O, and N₂. The second chemical-kinetics model is Violi's detailed mechanism [17], which consists of 161 reactions and 1538 reactions (some of them are lumped). Gaseous JP-8 fuel in both these mechanisms is treated as a surrogate mixture of six parent species (n-dodecane 30%, n-tetradecane 20%, 1-octane 10%, methylnaphthalene 20%, tetralin 5% and m-xylene 15%) that is developed at AFRL [18]. The global reaction for this surrogate mixture is



While global-chemistry model is used for optimizing the size of the cavity, Violi's detailed-chemical-kinetics model for JP-8 fuel is used for investigating the blowout characteristics of the design cavity. Since the prediction of blowout phenomenon depends on the extinction characteristics of the chemistry model used, Violi mechanism is examined for its ability to simulate the extinction process of an opposing-jet nonpremixed flame. The physical domain modeled between the opposing fuel (mixture of gaseous JP-8 and N₂) and air jets (14 mm in the axial direction and 20 mm in the radial direction) is represented using a 201x31 grid system, which resulted in a uniform grid spacing of 70 μm across the flame. The fuel/N₂ ratio used is 0.08. Experiments for this flame were conducted by Holley et al [19]. Temperatures of the fuel and oxidizer streams are set to the measured values of 394 and 294 K, respectively. Initially a stable flame is established for a low-strain-rate case of 28.6 s⁻¹ and then calculations are repeated by gradually increasing the strain rate (velocities) until the flame along the centerline is extinguished.

The predicted flame response to increase in strain rate up to extinction limit is shown in Fig. 2. Here, the peak temperature along the centerline ($r = 0$) is plotted at different strain rates. Due to chemical nonequilibrium, temperature of the flame decreased with strain rate. The measured extinction limit of 150 s⁻¹ is shown with a vertical box. Width of the box corresponds to the experimental uncertainty of 3.5% reported by Holley et al [19]. Violi mechanism

simulated the flame extinction process reasonably well with the predicted extinction strain rate of 136 s⁻¹ being within 90% of the measured value.

RESULTS AND DISCUSSION

Calculations for the cavity-in-cavity geometry shown in Fig.1 are performed using the previously described detailed kinetics model and also with a global, infinitely fast chemistry model. As the latter model is simple and fast, it is used for conducting parametric studies in search for an optimum cavity configuration while the computationally intensive former model is used for understanding the flame blowout characteristics. Direct numerical simulations (without using any turbulence model) for the unsteady flowfields associated with the design-size CIC are shown in Figs. 3a and 3b. While the instantaneous velocity is shown in Fig. 3a the temperature field at the same instant is shown in Fig. 3b. The flow recirculation established in the cavity due to the high-speed secondary airflow is confined close to the front cavity wall. The driver jets (A and B) are ejected out of the cavity near the aft wall. The recirculation vortex is unsteady and makes the driver jets to flutter. Interestingly, the recirculation zone did not extend into the top half (wall side) of the cavity, which is filled with the fuel injected from the top wall. Fuel is eventually ejected out of the cavity along with the driver jets. Two non-premixed flames are established (Fig. 3b) along the interfaces between the fuel and driver air jets in the cavity region and then a wake flame is established between the excess fuel ejected out of the cavity and the secondary air jet. The unsteady recirculation vortex is making the flames to wrinkle. Steady-state results obtained after using k- ϵ turbulence model (Figs. 3c and 3d) also suggest that the upper half of the cavity is free from strong recirculating flows. Figure 3d suggests that the two flames emanating from the cavity are smoothly rolling back on to the downstream cavity wall. Both the direct numerical simulations and k- ϵ calculations suggest that the volume of the cavity is more than what is required for trapping the recirculation zones. Flow of combustion products along the downstream cavity wall suggests that it could influence the flow passing over the next CIC. However, for simplicity purpose such effects are neglected in the present study and pure air is assumed to be flowing over the CIC.

Fuel-Air Mixing:

Fuel is injected into CIC with a recession from the bottom wall for mimicking the spray-nozzle mounting. For improved combustion efficiency and lower pollutant formation it is desirable to mix fuel with air as quickly as possible. However, as seen

from Fig. 3, the weaker recirculation in the cavity is not able to effectively transport air into the fuel-jet recession and delays fuel-air mixing. To determine whether a lower or higher fuel flow rate would entrain any air into the fuel-jet-recession region, calculations for 0.5 m/s and 2.0 m/s fuel jet velocities are carried out. Results in the form of instantaneous temperature distributions for these two cases are shown in Figs. 4a and 4b, respectively. In general, flames are becoming longer in the axial direction with increase in the fuel flow into the cavity. From these calculations it is clear that changing the fuel jet velocity did not increase flow recirculation into the upper half of the cavity and air is not brought into this region. Consequently, flames are not established in the upper half of the cavity. However, a comparison among flames in Figs. 4a, 3a and 4b (with increasing fuel-jet velocity) suggests that the wake flame becomes steadier when the fuel flow rate is increased. This should be expected as the design CIC seems larger than the required one for trapping the recirculation vortex and additional fuel into the cavity makes it aerodynamically smaller and, thereby, reducing vortex shedding into the wake flame.

For determining the impact of the fuel-jet recession on the flame dynamics, calculations are repeated after removing the fuel-jet recession. Results in the form of temperature distributions for 1.0 m/s and 2.0 m/s fuel jet velocities are shown in Figs. 5a and 5b, respectively. A comparison of flames obtained with fuel-jet recession (Figs. 3a and 4b) and without (Figs. 5a and 5b) for the same flow conditions indicates that the fuel-jet recession has minimal effect on the flame stability.

Optimization of Main Cavity:

Knowing that the main cavity in Fig. 1 is oversized for the secondary air used in ultra compact combustors, an attempt has been made for determining the correct size for CIC for a stable combustion. Calculations are repeated after increasing or decreasing the width of the cavity while not altering the size and location of the fuel injection, height of the cavity and other flow conditions. Several calculations are made for the cavity widths ranging between 5.4 mm and 12.2 mm. Typical results in the form of instantaneous temperature distributions for 5.4, 6.2, 8.2, and 12.2 mm cavities are shown in Figs. 6a, 6b, 6c, and 6d, respectively. Also, results shown in Fig. 3a for 10.2-mm cavity should be viewed in between Figs. 6c and 6d as a part of this study. Note that no effort was made in synchronizing these results to a particular phase of the flowfield.

Temperature fields in Figs 6 and 3a indicate that irrespective of the width of the cavity the bottom half of the cavity, especially in and around the fuel-jet injector, entrained very little air or combustion products. To a lesser significance, it may also be noted that the recirculation zone in the lower half of the 12.2-mm cavity has penetrated slightly deeper into the cavity. This indicates that a much wider cavity is required in order the recirculation zone to fill it completely. These calculations further suggest that the designed cavity not only is oversized but also has a height-to-width ratio that is more than needed. A comparison among the instantaneous temperature fields in Fig. 6 and 3a reveals that the cavity and wake flows are becoming more dynamic as the width of the cavity is increased. However, a further analysis based on Fourier time-frequency decomposition revealed that flow unsteadiness decreased first with the cavity width and then increased with further increase in the cavity width—suggesting that there exist an optimum width for the cavity in Fig.1 for stable combustion.

Dynamic characteristics of the flow are quantified by first recording the fluctuations in temperatures at different locations inside the cavity and within the wake flow over a period of 50 ms and then analyzing the data using Fourier-time-frequency-decomposition technique. Temperature data collected at a location $z = 27$ mm and $h = 19$ mm for various cavity widths are shown in Fig. 7a and their power spectral densities (PSD) are shown in Fig. 7b. This location, marked as P in Fig. 1, is close to the aft face of the cavity and is within the shear layer of the secondary air and cavity flow. The PSDs are normalized to the peak value. Figure 7a shows that temperature fluctuations are most severe when cavity width is 12.2 mm and minimum when it is 6.2 mm. The design cavity width of 10.2 mm yielded temperature fluctuations that are only slightly weaker than those obtained for 12.2-mm cavity and are significantly larger compared to those obtained for 6.2-mm cavity. The smallest cavity (5.4 mm) also resulted in temperature fluctuations that are larger than those obtained for 6.2-mm cavity. The fundamental frequency of temperature fluctuations for larger cavities (10.2 and 12.2 mm) is ~ 2100 Hz and it increased to ~ 2800 Hz for 5.4-mm cavity. PSD for 6.2-mm case is negligibly small. Strengths of both fundamental and first-harmonic frequencies have decreased with cavity size.

Temperature data collected at a location (marked as Q in Fig. 1) slightly inside the cavity ($z = 27$ mm, $h = 20$ mm) are shown in Fig. 8. Amplitude of the temperature fluctuations is lowest at this location also when the cavity width is 6.2 mm. However, this minimum amplitude is significantly larger than that

obtained at location P. The PSD plot in Fig. 8b obtained at location Q also shows that the fluctuations with 6.2-mm cavity are weaker than those obtained with the other three cavities. Interestingly, the maximum amplitude for the fluctuations in the design cavity (10.2-mm width) appeared for the first harmonic frequency (~ 4300 Hz). This could be due to a strong vortex splitting occurring inside the cavity.

Finally, the dynamics of the flow in the wake regions of the cavities are shown in Fig. 9. Temperature fluctuations collected at point R in Fig. 1 ($z = 50$ mm, $h = 18$ mm) are shown in Fig. 9a. Even at this location the amplitude of fluctuation is minimum (at least during some cycles) for 6.2-mm cavity. Interestingly, a strong sub-harmonic frequency (~ 1100 Hz) has appeared for this cavity.

Calculations with Detailed Chemical kinetics:

Results obtained with fast, global chemistry suggested that flow inside the design cavity (10.2-mm width) is unsteady due to the dynamics of a loosely trapped recirculation zone. Such unsteadiness could cause flame blow out, however flames shown in Figs. 3-6 are stabilized inside the cavity. This false stability could be arising from the infinitely fast chemistry used for those simulations. For understanding the ability of the flames in getting stabilized under the dynamic environment inside the 10.2-mm cavity, calculations have been performed with the detailed-chemical-kinetics model described earlier. Due to the large number (162) of species used in this mechanism, each calculation took more than 300 hours of computer time. A parametric study for design optimization based on such detailed mechanism requires significant amount computer resources and is beyond the scope of the current paper. However, calculations can be done using this mechanism for understanding flame stability characteristics for a given cavity geometry.

Detailed chemistry calculations are performed for the 10.2-mm cavity and results at two instants are shown in Fig 10. Blowout did not occur for this fuel flow rate of 1.0 m/s. Instantaneous velocity, temperature, fuel (NC12)-concentration and CO-concentration fields at time t_0 are shown in Figs. 10a, 10b, 10c, and 10d, respectively and those obtained 0.2 ms later are shown in Figs. 10e, 10f, 10g, and 10h, respectively. Dynamics of the cavity and wake flows obtained with the detailed-chemistry model are similar to those obtained with the fast-chemistry model (Fig. 3). A comparison of velocity fields in Figs. 10a and 10e shows that the dynamics of the unsteady recirculation vortex, which causes the cavity and wake flow to become unsteady. The

strong recirculation vortex pinches a part of the flame and rolls with it. Under weakly and moderately dynamic conditions, such flame pinching (Fig. 10b) occurs only during a fraction of vortex-roll-up cycle and flame gets re-establishes as shown in Fig. 10f.

As seen in fast-chemistry simulations, calculations with detailed chemistry also restricted the recirculation zone to the lower half of the cavity. As a result, the upper half of the cavity is filled with fuel (Figs. 10c and 10g). The dynamic recirculation vortex is rolling along the interface of the fuel and air around the mid-section of the cavity and pushing fuel into air stream intermittently. These blobs of fuel pockets are getting burned as they travel downstream (Fig. 10g) in the wake of the cavity flow. Pockets of combustion product CO in the cavity region (Figs. 10d and 10h) also provide evidence for intermittent burning taking place in the current cavity geometry.

CONCLUSIONS

Calculations for a cavity-inside-cavity (CIC) were performed using a two-dimensional, unsteady, reacting flow code known as UNICORN. Direct numerical simulations and calculations using $k-\epsilon$ turbulence model were performed. A fast, global chemistry was used for studying the dynamics of the flow associated with CIC and for optimizing its size. A detailed-chemistry model was used for understanding the blowout characteristics of the CIC-supported flames.

- 1) The design CIC seems oversized for the secondary (circumferential) airflow used in ultra compact combustors.
- 2) The recirculation vortex and its dynamics are confined to the lower half of the cavity. Fuel injected from the upper wall of the cavity filled the space in the upper half. Due to lack of air entrainment into this region, no flames were formed inside and around the fuel injection location.
- 3) In order to fill the cavity with air for better fuel-air mixing, its height must be reduced and for properly trapping the recirculation vortex within the cavity, its width must be reduced.
- 4) A parametric study conducted by changing the width of the cavity suggested that an optimum size would be ~ 6.2 mm for minimizing the flow unsteadiness.
- 5) The dynamics of the recirculation vortex fragments the flame inside the cavity, however, flame blowout was not observed for the fuel flow rate considered.

ACKNOWLEDGEMENTS

Financial support for this work was provided by the Air Force Office of Scientific Research (AFOSR, Julian Tishkoff) and the Air Force Contract #F33615-03-D-2329 (Vince Belovich).

REFERENCES

- [1] W. A. Sirignano, F. Liu, J. Prop. & Power 15 (1999) 111-118.
- [2] R. A. Anthenien, R. A. Mantz, W. M. Roquemore, G. J. Sturgess, 2nd Joint Meeting of the US Sections of the Combustion Institute, Oakland, CA, March (2001).
- [3] J. Zelina, D. T. Shouse, R. D. Hancock, "Ultra-Compact Combustors for Advanced Gas Turbine Engines," ASME IGTI 2004-GT-53155.
- [4] R. A. Anthenien, J. Zelina, Proceedings of the 2006 Technical Meeting of the Central States Section of the Combustion Institute, Cleveland, OH, April (2006).
- [5] J. Zelina, W. Anderson, D. T. Shouse, ASME IGTI 2008-50090, to be presented.
- [6] Hsu, K. Y., Goss, L. P., Trump, D. D., and Roquemore, W. M., "Characteristics of a Trapped-Vortex Combustor," Journal of Propulsion and Power, Vol. 14, No. 1, 1998.
- [7] Roquemore, W. M., Shouse, D., Burns, D., Johnson, A., Cooper, C., Duncan, B., Hsu, K-Y., Katta, V. R., Sturgess, G. T., and Vihinen, I., "Trapped Vortex Combustor Concept for Gas Turbine Engines," AIAA-2001-0483.
- [8] Roquemore W. M., and Katta, V. R., *Journal of Visualization*, 2 (2000) 257-272.
- [9] Katta, V. R., Goss, L. P., and Roquemore, W. M., *AIAA Journal*, Vol. 32, No. 1, 1994, p. 84.
- [10] katta
- [11] Katta, V. R., and Roquemore, W. M., *Combustion and Flame*, Vol. 100, No. 1, 1995, p. 61.
- [12] Katta, V. R., Carter, C. D., Fiechtner, G. J., Roquemore, W. M., Gord, J. R., and Rolon, J. C., in *Twenty-seventh Symposium (International) on Combustion*, The Combustion Institute, Pittsburgh, PA, 1998, p. 98.
- [13] Katta, V. R., Blevins, L. G., and Roquemore, W. M., PAH Formation in an Inverse Diffusion Flame, *Combustion and Flame*, Vol. 142, 2005, pp. 33-51.
- [14] Annon., Computational Submodels, International Workshop on Measurement and Computation of Turbulent Nonpremixed Flames., <http://www.ca.sandia.gov/tdf/Workshop/Submodels.html>, 2001.
- [15] Lindstedt, R.P., in *Soot Formation in Combustion: Mechanisms and Models* (H. Bockhorn, Ed.), Springer-Verlag, Heidelberg, 1994, pp.417-439.
- [16] Katta, V. R., Goss, L. P., and Roquemore, W. M., *Int. J. Num. Methods Heat Fluid Flow*, Vol. 4, No. 5, 1994, p. 413.
- [17] Violi, A., Yan, S., Eddings, E. G., Sarofim, A. F., Granata, S., Faravelli, T., Ranzi, E., "Experimental Formulation and Kinetic Model for JP-8 Surrogate Mixtures," *Combustion Science and Technology* 174 (2002) 399-417.
- [18] Schulz, W., ACS Petroleum Chemistry Division Preprints 37 (2) (1991) 383-392.
- [19] Holley, A. T., Dong, Y., Andac, M. G., Egolfopoulos, F. N., "Ignition and extinction of Non-premixed Flames of Single-Component Liquid Hydrocarbons, Jet Fuels, and their Surrogates," in *Thirty-First Symposium (International) on Combustion*, The Combustion Institute, Pittsburgh, PA, 2006.

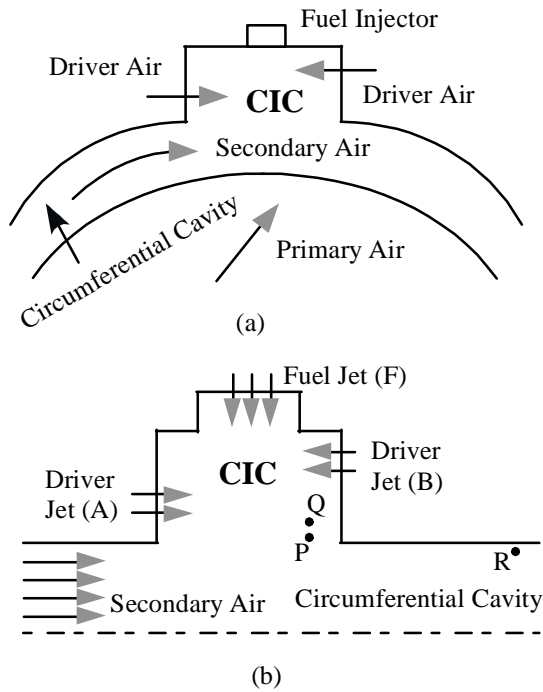


Fig. 1. (a) Schematic diagram of CIC used in UCC. (b) Two-dimensional model of simplified CIC.

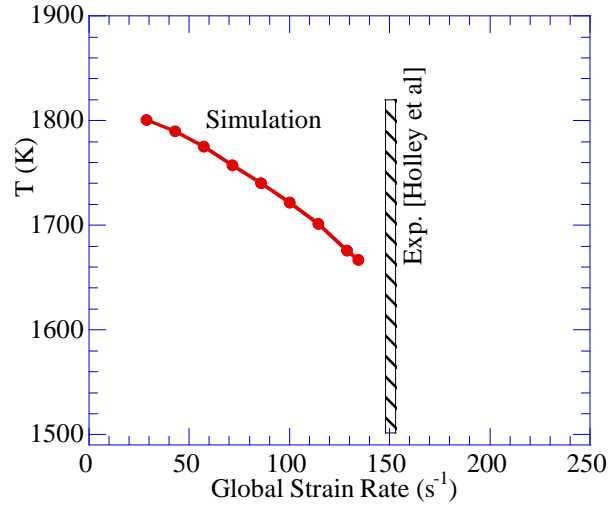


Fig. 2. Predicted temperature of an opposing-jet non-premixed flame under different stretch conditions up to extinction. Calculations are made using Violi detailed-kinetics mechanism. Gaseous JP-8 fuel was used in the experiment and calculations. Measured extinction strain rate is shown with vertical bar.

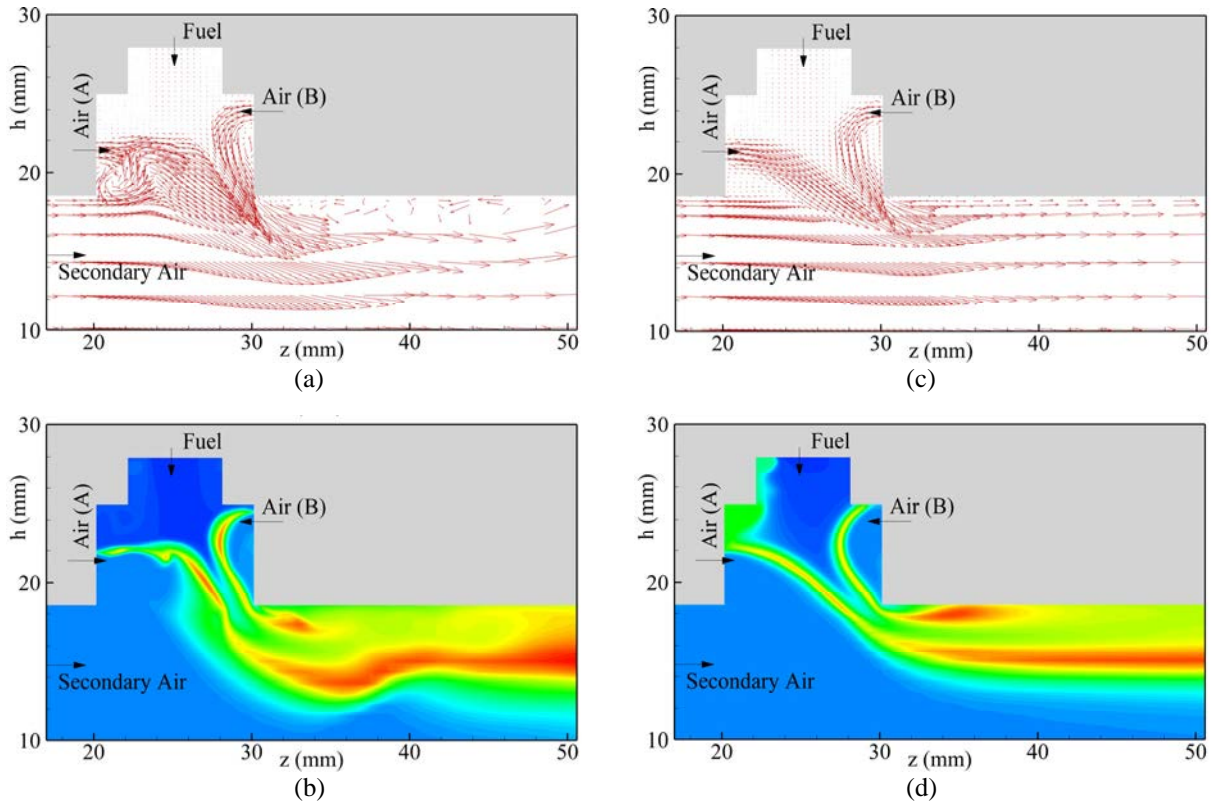


Fig. 3. Computed flowfields for the 10.2-mm-size design cavity. Instantaneous (a) velocity and (b) temperature fields obtained with direct numerical simulations and (c) velocity and (d) temperature fields obtained from the simulations utilizing $k-\epsilon$ turbulence model.

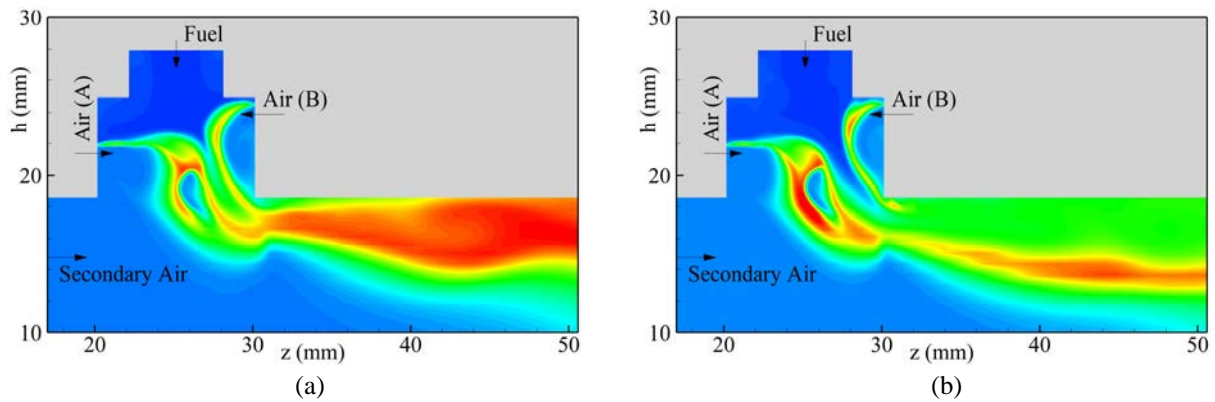


Fig. 4. Instantaneous temperature fields obtained for (a) 0.5 and (b) 2.0 m/s fuel jets. Cavity width is 10.2 mm.

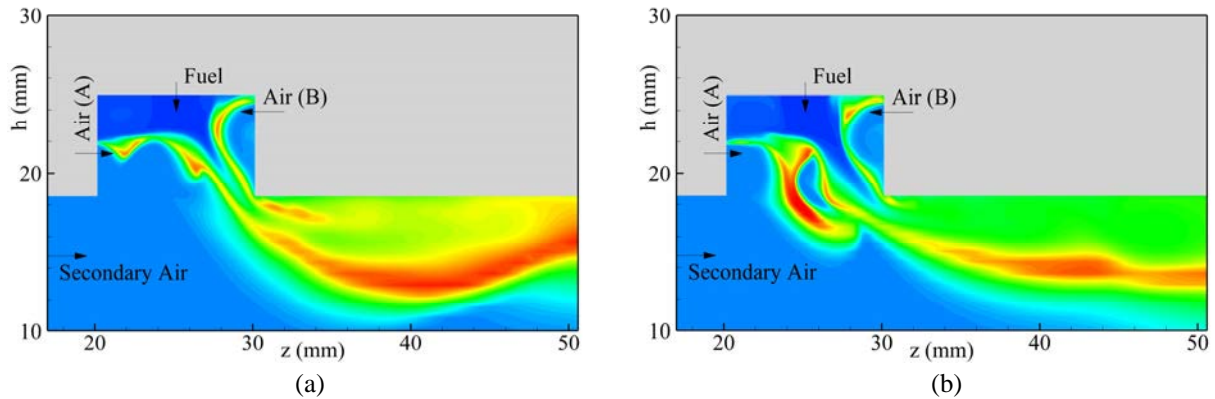


Fig. 5. Instantaneous temperature field without fuel-jet recession when fuel velocity was (a) 1.0 or (b) 2.0 m/s.

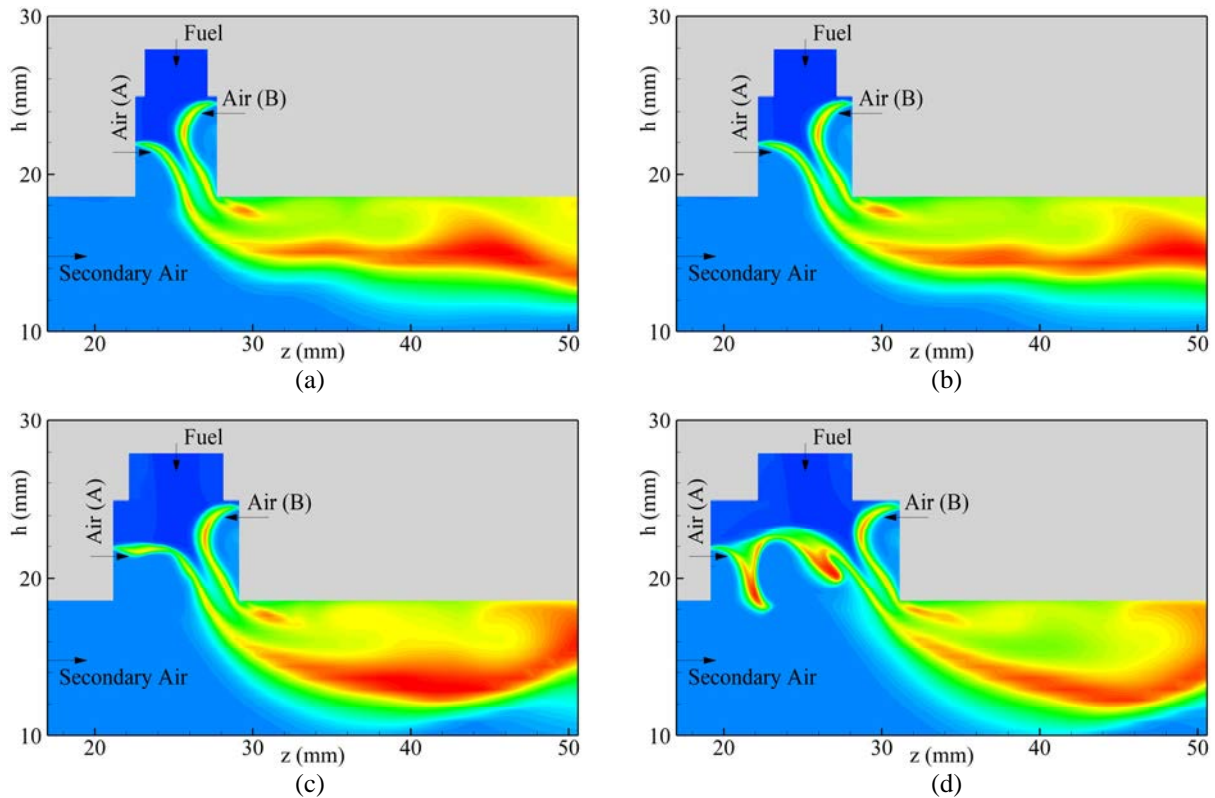


Fig. 6. Instantaneous temperature fields obtained for (a) 5.4, (b) 6.2, (c) 8.2, and (d) 12.2 mm wide cavities.

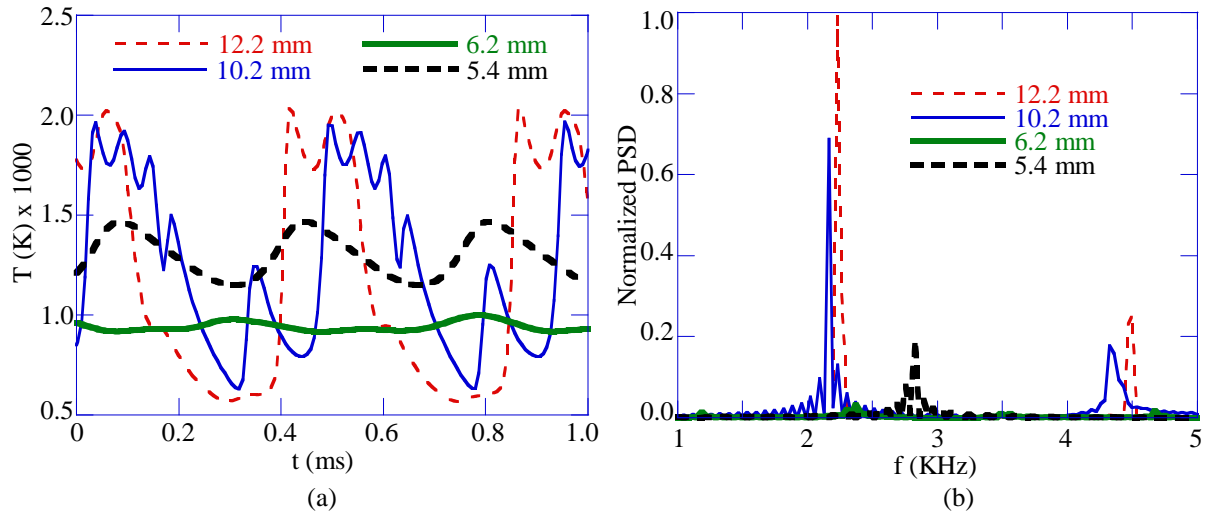


Fig. 7. (a) Temperature signal and its (b) power spectral density obtained at a point (27 mm x 19 mm) in cavity.

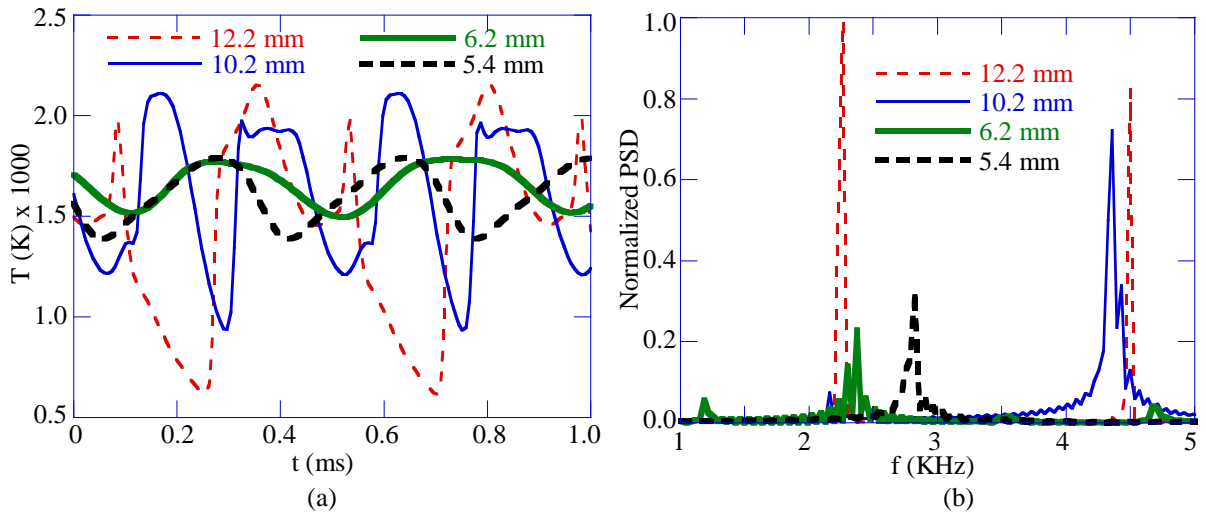


Fig. 8. (a) Temperature signal and its (b) power spectral density obtained at a point (27 mm x 20 mm) in cavity.

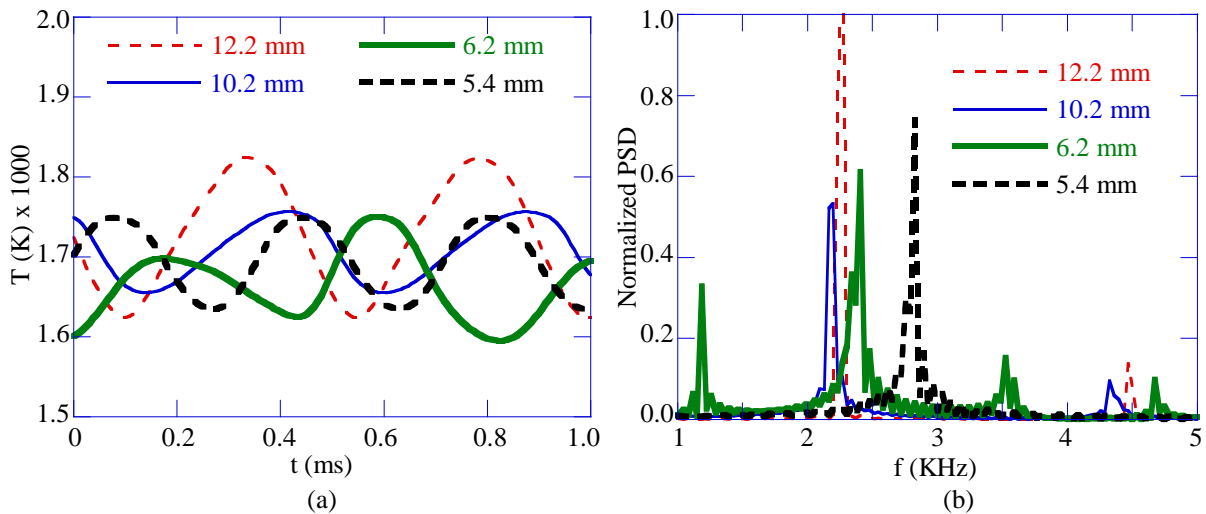


Fig. 9. (a) Temperature signal and its (b) power spectral density obtained at a point (50 mm x 18 mm) in the wake of the cavity.

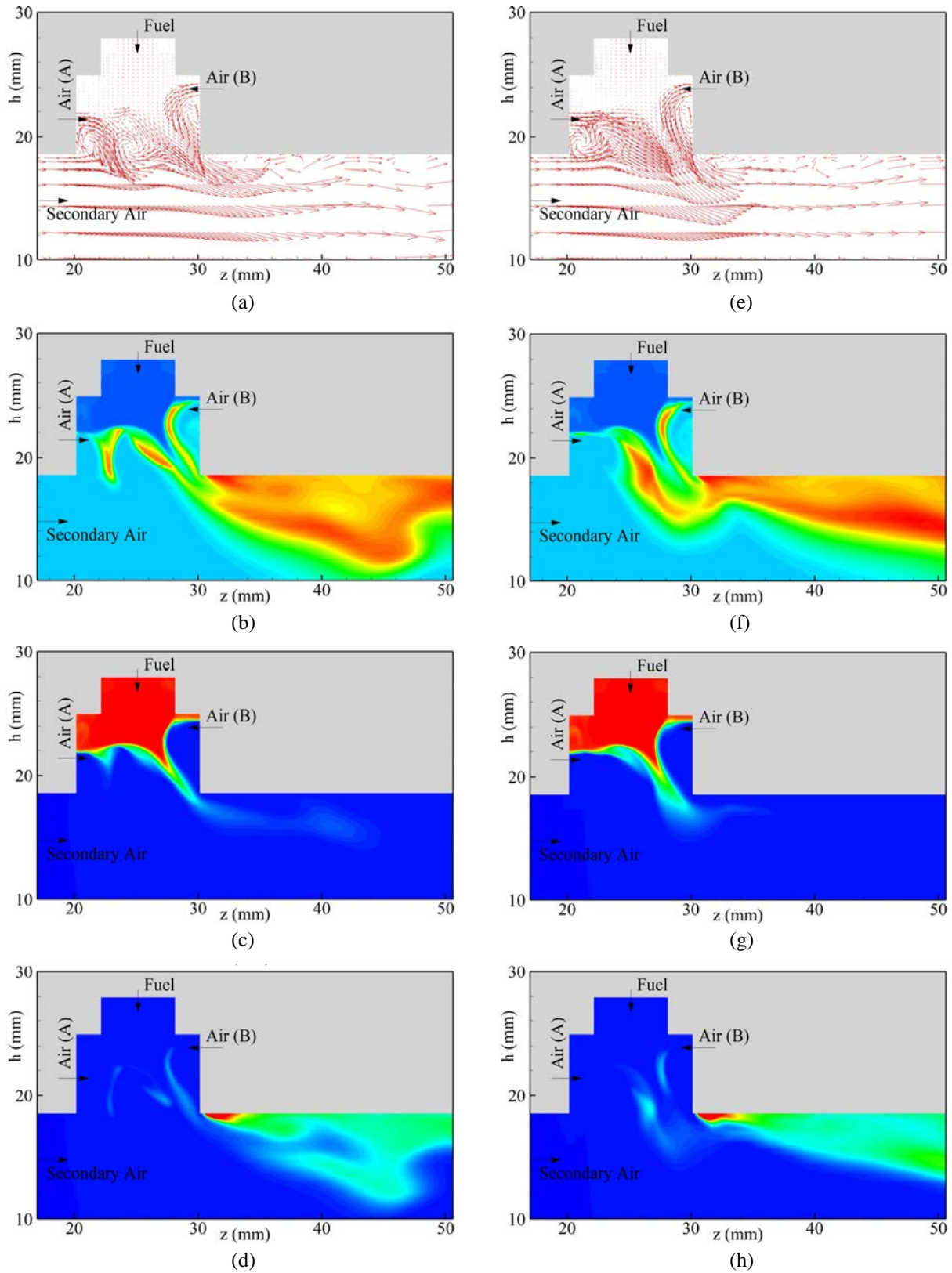


Fig. 10. Flowfields for the 10.2-mm-size cavity at two different instants obtained through direct numerical simulations with detailed chemical kinetics. Instantaneous (a) and (e) velocity, (b) and (f) temperature, (c) and (g) NC12 concentration, and (d) and (h) CO concentration fields obtained at t_0 and $t_0 + 0.2$ ms, respectively.

Stability of Lifted Flames in Centerbody Burner

V. R. Katta*

Innovative Scientific Solutions Inc
2766 Indian Ripple Road
Dayton, OH 45440-3638

W. M. Roquemore

Propulsion Directorate
Air Force Research Laboratory
Wright-Patterson Air Force Base, OH 45433

Abstract

The centerbody burner was designed with an objective of understanding the coupled processes of soot formation, growth, and burn-off through decoupling them using recirculation zones. Experimentally it was found that sooting characteristics of the centerbody burner could alter dramatically with the changes in operating conditions. One of the interesting operating regimes; in which, flame lifts off and forms a column of soot, was identified when oxygen in the oxidizer stream was sufficiently reduced. This paper describes the numerical studies performed for understanding the lifted flames of the centerbody burner. A time-dependent, axisymmetric, detailed-chemistry CFD model (UNICORN) is used. Combustion and PAH formation are modeled using Wang-Frenklach (99 species and 1066 reactions) mechanism and soot is simulated using a two-equation model of Lindstedt. Calculations have reasonably predicted the structure of the lifted flame. The predicted flame lift-off height matches well with that of the experiment. Recirculation zones formed between the flame base and the centerbody transport fuel and its lighter fragments formed in the lifted flame region toward the face of the centerbody. Mixing of oxygen and fuel and its fragments between the flame base and centerbody establishes a premixed flame in the flame-base region. Numerical studies are conducted by increasing and decreasing the coannular flow velocity for determining the stability of the lifted flames.

Introduction

The formation, growth, transport, and burnout of soot are perhaps the most complex and least understood processes in flames and combustion systems. Soot particles containing several-thousand carbon atoms are formed in flames from simple fuel molecules within a few microseconds [1]. However, these soot precursor particles on a much longer time scale interact with the gas-phase molecules during the surface-growth process, colloid with each other in the agglomeration process and react with oxygenated species in the oxidation process. All of these chemical and physical two-phase processes occur simultaneously in flames. In gas turbine combustors, these processes are further complicated by the burning of practical fuels, consisting of thousands of species, and the actions of turbulent flow. There is a significant science base for understanding the soot processes; however, it is inadequate to provide accurate soot models that can aid in the design of future low sooting gas turbine combustors. Thus, there is a pressing need to expand the science base in ways that foster the development and evaluation of accurate CFD models for designing low sooting combustion systems.

The Strategic Environmental Research and Development Program (SERDP) office recently started a comprehensive fundamental soot research initiative involving a suite of burners [2]. The designs of these burners progress in complexity in a way that the effects of chemical kinetics, diffusion, flame stretch, recirculation, and turbulence on the soot processes can be systematically studied. The computational part of this effort is to use a state-of-the-art, Navier-Stokes based CFD code (UNICORN) [3] to aid in designing experiment, predicting and interpreting results, and evaluating soot and chemistry models.

The centerbody burner [2], one of the few designs selected in the suite of burners for studying soot, consists of an annular oxidizer jet and a central fuel jet separated by a bluff body. The formation of recirculation zones in this burner [4] provides a mechanism for decoupling various soot processes and investigating them individually. Initial experiments by varying the nitrogen dilution in the fuel and/or oxidizer jets [2] suggested that very different flames with fully, donut-shaped, or ring-type soot layers could be obtained. Recent experiments have further revealed that a lifted flame with a column of

* Corresponding author: vrkatta@erinet.com

soot extending into the relatively cold regions between the flame base and the face of the bluff body can also be obtained.

Lifted flames established in the shear layers of co-axial jets of fuel and oxidizer were studied by several investigators [5, 6], mainly for understanding the stabilization mechanisms [7, 8]. However, as the recirculation zones in centerbody burner provide additional complexity to the stability of the lifted flame, further studies must be performed for understanding the centerbody lifted flames. This paper describes the simulations performed by UNICORN using a simple soot model for the centerbody lifted flames. Predictions for the changes in flame and soot characteristics when the oxidizer is diluted with nitrogen are presented. Structure of the base of the lifted flame is studied. Effects of oxidizer velocity on flame lift-off height are investigated.

Numerical Model

A time-dependent, axisymmetric mathematical model known as UNICORN (Unsteady Ignition and Combustion using ReactionNs) [3, 9] is used for the simulation of the unsteady combustions in the centerbody combustor. It solves for u - and v -momentum equations, continuity, and enthalpy- and species-conservation equations on a staggered-grid system. The body-force term due to the gravitational field is included in the axial-momentum equation for simulating vertically mounted flames. A clustered mesh system is employed to trace the steep gradients in flow variables near the flame surface. A detailed chemical-kinetics model developed by Wang and Frenklach [10] is incorporated into UNICORN for the investigation of PAH and soot formation in ethylene flames. It consists of 99 species and 1066 elementary-reaction steps. Thermo-physical properties such as enthalpy, viscosity, thermal conductivity, and binary molecular diffusion of all the species are calculated from the polynomial curve fits developed for the temperature range 300 - 5000 K. Mixture viscosity and thermal conductivity are then estimated using the Wilke and Kee expressions, respectively. Molecular diffusion is assumed to be of the binary-diffusion type, and the diffusion velocity of a species is calculated using Fick's law and the effective-diffusion coefficient of that species in the mixture.

Soot in the flame is simulated after assuming it as a gaseous species and through the solution of two conservation equations—one for the soot volume fraction and the other for soot number density. Soot nucleation, agglomeration and oxidation processes are modeled following Lindstedt approach [11]. A simple radiation model for gaseous species, based on the optically thin-media assumption, is incorporated into the energy equation [12]. Only radiation from CH_4 , CO , CO_2 , and H_2O is considered in the present study. Radiation from soot is modeled assuming it as blackbody type [13].

The finite-difference forms of the momentum equations are obtained using an implicit QUICKEST scheme [9], and those of the species and energy equations are obtained using a hybrid scheme of upwind and central differencing. At every time step, the pressure field is accurately calculated by solving all the pressure Poisson equations simultaneously and using the LU (Lower and Upper diagonal) matrix-decomposition technique. The boundary conditions are treated in the same way as that reported in earlier papers [14]. This model has been extensively validated [3] by simulating various steady and unsteady counterflow [15, 16] and coflow [17, 18] jet diffusion flames and by comparing the results with experimental data.

Results and Discussion

The geometry of the centerbody burner was described in detail in Ref. 2. It consists of a 46-mm-diameter disc enclosed in a cylindrical chimney with an annular gap of 17 mm. A 7.6-mm-diameter hole is made at the center of the disc through which fuel (a mixture of ethylene and nitrogen) is injected at a velocity of 1.25 m/s. A mixture of air and nitrogen is flowed through the annular gap, also at a velocity of 1.25 m/s.

Concentrations of nitrogen in the fuel and oxidizer streams are varied for obtaining different types of flames. For example, as discussed in Ref. 2, dilution of fuel jet transforms a fully sooty flame into a donut-type sooty flame and subsequent dilution of oxidizer jet results in a ring-type sooty flame. Further experiments revealed that a lifted flame with a column of soot establishes when oxygen concentration in the oxidizer becomes sufficiently low. Direct photograph of the flame obtained with 14.7% oxygen in the oxidizer stream is shown in Fig. 1. No nitrogen flow was used in the fuel stream. Glow from the flame has illuminated the 46-mm-diameter centerbody. Flame has lifted off from the face of the centerbody and stabilized at about 13 mm away from it. Radiation from CH and other ionized species that earmarks the reaction zone may be identified from the blue regions in Fig. 1. A column of soot that is extended all the way to the face of the centerbody can be identified from orange color. Note that this flame is very sensitive to the flow conditions and a small variation in flow velocity or nitrogen dilution could transition it into an oscillating flame.

Calculations for the lifted flame shown in Fig. 1 are made using a 451x251 grid system. Concentrations of ethylene in the fuel jet and oxygen in the oxidizer jet are 100 and 14.7 percents, respectively. Velocities of the jets are 1.25 m/s. Simulations are performed on a Personal Computer with 2.0 GB of memory. Execution times strongly depend on the number of species considered in the chemical-kinetics model and the grid size. Typically, with 99 species and 1066 reactions (Wang-Frenklach model) on a 451X251 grid system, simulations took ~50 s/time-step on AMD-Opteron-250 computer. Even

though, time-dependent simulations are performed assuming that the resulting flowfield could be unsteady by nature, only steady state solutions are resulted in about 10,000 time steps.

Results obtained for the lifted flame are shown in Fig. 1. Axisymmetric representation of the flame is used while displaying the data. While iso-concentration contours of ethylene (solid gray lines), oxygen (broken lines) and OH (solid black lines) are superimposed on temperature field in the left half, streamlines are superimposed on temperature field in the right half. Location of the stoichiometric surface is marked with a solid white line. The two recirculation-type vortices associated with the centerbody flames may be identified from the streamlines. These recirculation vortices are formed due to the separation between the fuel and oxidizer jets. However, due to the differences in the momentum, recirculation vortex closer to the oxidizer jet is much larger than the one closer to the fuel jet. These recirculation vortices play a vital role in transporting fuel across the centerbody toward the oxidizer jet and in establishing a nonpremixed flame near the oxidizer jet.

Calculations have predicted a lifted flame with the flame base shifted ~ 13 mm from the centerbody. This lift-off height matches well with that observed in the experiment (Fig. 1). Flame is stabilized on the outer edge of the oxidizer-side recirculation zone where flow (streamlines) is diverging. Stoichiometric surface (white line) in the flame region also matches well with the outer edge of the blue region in Fig. 1. Higher concentration of OH radical (black contour lines) near the flame base suggests the formation of a reaction kernel [19, 20]. Fuel transported by the recirculation vortices is mixing with oxygen in the inner region of the oxidizer jet and forming a partially premixed region upstream of the flame base.

Detailed structure of the flame base is shown in Fig. 3. Here, calculated CH distribution is shown in rainbow color palette. Iso contours of temperature and acetylene are superimposed using black and gray lines, respectively. Velocity vectors are also shown in this figure. The hook-type CH –concentration distribution in two dimensions matches well with the toroidal-type flame ring captured in the three-dimensional photograph of the experiment (Fig. 1). As depicted by acetylene distribution, ethylene fuel is decomposing into smaller fuel fragments in the flame region, which are then transported into the region between the flame base and centerbody by the recirculation vortices. Consequently, flame is established from the combustion of oxygen and fuel fragments such as methane, hydrogen and acetylene. This is evident from the deviation in the location of peak-CH-concentration region from the stoichiometric surface computed using ethylene and oxygen (white line) near the flame base. Thus, the recirculation zones are playing a vital role in transporting fuel and its lighter fragments upstream of the flame base and in stabilizing it.

Structure of the flame base is shown in Fig. 4 through plotting radial distributions of temperature, axial velocity, and reactants and intermediate-species concentrations. Note the difference in the ranges for radial distances used in Fig. 4(a) and 4(b). The small peak in temperature at $r = 20$ mm is resulting from combustion. High temperature (~ 1300 K) in the regions $r < 20$ mm is resulting from the products that transported by the recirculation zones. Significant mixing of fuel fragments and oxygen is taking place in the region upstream of the flame base, which forms a premixed flame at $r = 21$ mm as evident from the sudden increase in axial velocity. Consumption of lighter fuels (H_2 and CH_4), ethylene and oxygen at this location [$r = 21$ mm in Fig. 4(b)] also suggest the presence of a premixed flame.

For understanding the stability of the lifted flame in Fig. 2, calculations are repeated by increasing or decreasing the coflow air-nitrogen velocity. For each new velocity, flame base has shifted to a new location and became stabilized. Flame and flowfields at higher coflow velocity ($O_{\text{oxidizer}} = 1.4$ m/s) are shown in Fig. 5 and those for a lower coflow velocity ($O_{\text{oxidizer}} = 1.0$ m/s) are shown in Fig. 6. As expected, coflow velocity has changed the sizes of the oxidizer-side and fuel-side recirculation zones. Increasing coflow velocity destabilized the flame in Fig. 2. However, as the flame retreats from its stable location, more fuel (original and its fragments) mixes with oxygen and leads for a stronger premixed flame, and thereby, establishes a new stabilization location for the flame base. This can be identified from the sharper flame-base region in Fig. 5 compared to that in Fig. 6.

Movements of flame base and the center of the oxidizer-side recirculation-zone with coflow velocity are plotted in Fig. 7. Overall, response of the recirculation zone center to the changes in coannular flow velocity is weaker than that of the flame base. Interestingly, flame base and recirculation zone center are located at the same radial distance for $O_{\text{oxidizer}} < 1.2$ m/s. For higher velocities flame base moves closer toward the center than the center of the recirculation zone. Note lifted flame in the experiment (Fig. 1) became unsteady for small changes in flow conditions. On the other hand, calculations have resulted in a new stable flame when the flow conditions are modified. Reason for this difference will be investigated in the future.

Conclusions

Sooting characteristics of a centerbody burner could change dramatically with changes in operating conditions. It was experimentally found that flame lifts off and forms a column of soot when oxygen in the oxidizer stream was sufficiently reduced. This paper describes the numerical studies performed for the lifted flames of the centerbody burner. A time-dependent, axisymmetric, detailed-chemistry CFD model (UNICORN) was used to simulate the ethylene-air combustion in a 5.6-mm-diameter

centerbody burner. Combustion and PAH formation were modeled using Wang-Frenklach (99 species and 1066 reactions) mechanism. Soot was simulated using a two-equation model of Lindstedt. Calculations have predicted the structure of the lifted flame reasonably well. The predicted lift-off height matched well with that of the experiment. It was found that fuel and its lighter fragments formed in the lifted flame region transported upstream toward the face of the centerbody by the recirculation zones. Mixing of oxygen and fuel and its fragments between the flame base and the face of the centerbody established a premixed flame in the flame-base region. While experiments have indicated that stability of the lifted flames is highly sensitive to the operating conditions, numerical studies conducted by increasing and decreasing the coannular flow velocity suggested that a stable flame could be established at a new location for the given velocity condition. Further experimentation and computation are needed for resolving this discrepancy.

Acknowledgements

Financial support for this work was provided by Strategic Environmental Research and Development Program (SERDP, Bruce Sartwell), the Air Force Office of Scientific Research (AFOSR, Julian Tishkoff) and the Air Force Contract #F33615-03-D-2329 (Vince Belovich).

References

- Kennedy, I. M., *Progress in Energy and Combustion Science* 23:95 (1997)
- Roquemore, M., Katta, V., Belovich, V., Pawlik, R., Lynch, A., Miller, J., Stouffer, S., Justinger, G., Zelina, J., Roy, S., and Gord, J., "Experimental and Numerical Studies of Centerbody Flames," Paper No. P44, Proceedings of the 5th US National Combustion Meeting, San Diego, March 25-28, 2007.
- Roquemore W. M., and Katta, V. R., *Journal of Visualization*, 2 (2000) 257.
- Katta, V. R., and Roquemore, W. M., "Predictions on Sooting Behavior of Recirculation-Zone-Supported Flames," D37, Proceedings of the 5th US Combustion Meeting, San Diego, March 25-28, 2007.
- Ko, Y. S., Chung, S. H., Kim, G. S., and Kim, S. W., *Combust. Flame* 123:430 (2000).
- Qin, X., Choi, C. W., Mukhopadhyay, A., Puri, I. K., Aggarwal, S. K., and Katta, V. R., *Combustion Theory and Modeling* 8 (2004) 293-314.
- Robson, K., and Wilson, M. J. G., *Combustion and Flame* 13 (1969) 626-634.
- Takahashi, F., Schmoll, W. J., and Katta, V. R., *Proceedings of the Combustion Institute* 27 (1998) 675-684.
- Katta, V. R., Goss, L. P., and Roquemore, W. M., *AIAA Journal* 32 (1) (1994) 84.
- Wang, M., and Frenklach, *Combustion and Flame* 110 (1997) 173.
- Lindstedt, R.P., in *Soot Formation in Combustion: Mechanisms and Models* (H. Bockhorn, Ed.), Springer-Verlag, Heidelberg, 1994, pp.417-439.
- Annon., Computational Submodels, International Workshop on Measurement and Computation of Turbulent Nonpremixed Flames, <http://www.ca.sandia.gov/TNF/radiation.html>, (2001).
- Guo, H., Liu, F., Smallwood, G. J., *Combustion Theory and Modeling* 8 (2004) 475-489.
- Katta, V. R., Goss, L. P., and Roquemore, W. M., *International Journal Numerical Methods in Heat and Fluid Flow* 4 (5) (1994) 413.
- Katta, V. R., Carter, C. D., Fiechtner, G. J., Roquemore, W. M., Gord, J. R., and Rolon, J. C., *Proceedings of the Combustion Institute* 27:587-594 (1998).
- Katta, V. R., Meyer, T. R., Gord, J. R., and Roquemore, W. M., *Combustion and Flame* 132:639 (2003).
- Katta, V. R., and Roquemore, W. M., *AIAA Journal* 36:2044 (1998).
- Grisch, F., Attal-Tretout, B., Bouchardy, P., Katta, V. R., and Roquemore, W. M., *Journal of Nonlinear Optical Physics and Mater* 5:505 (1996).
- Takahashi, F., and Katta, V. R., *Proceedings of the Combustion Institute* 29 (2002) 2509-2518.
- Takahashi, F., and Katta, V. R., *Proceedings of the Combustion Institute* 30 (2005) 383-390.



Fig. 1. Photograph of lifted flame obtained in centerbody burner with pure ethylene central fuel jet and coannular flow of nitrogen-diluted air.

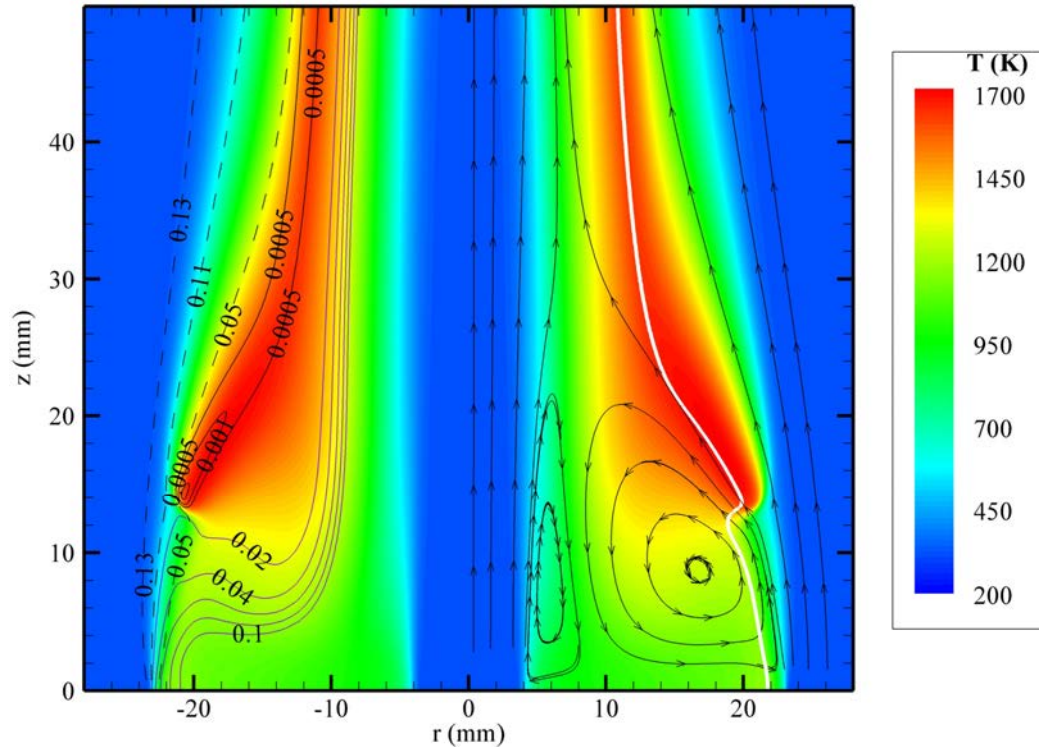


Fig. 2. Computed lifted flame of centerbody burner. Iso contours of OH (black solid lines), ethylene (gray solid lines), and oxygen (broken lines) and streamlines are superimposed on left and right halves, respectively of color temperature map. Location of stoichiometric surface is marked with white line on right half.

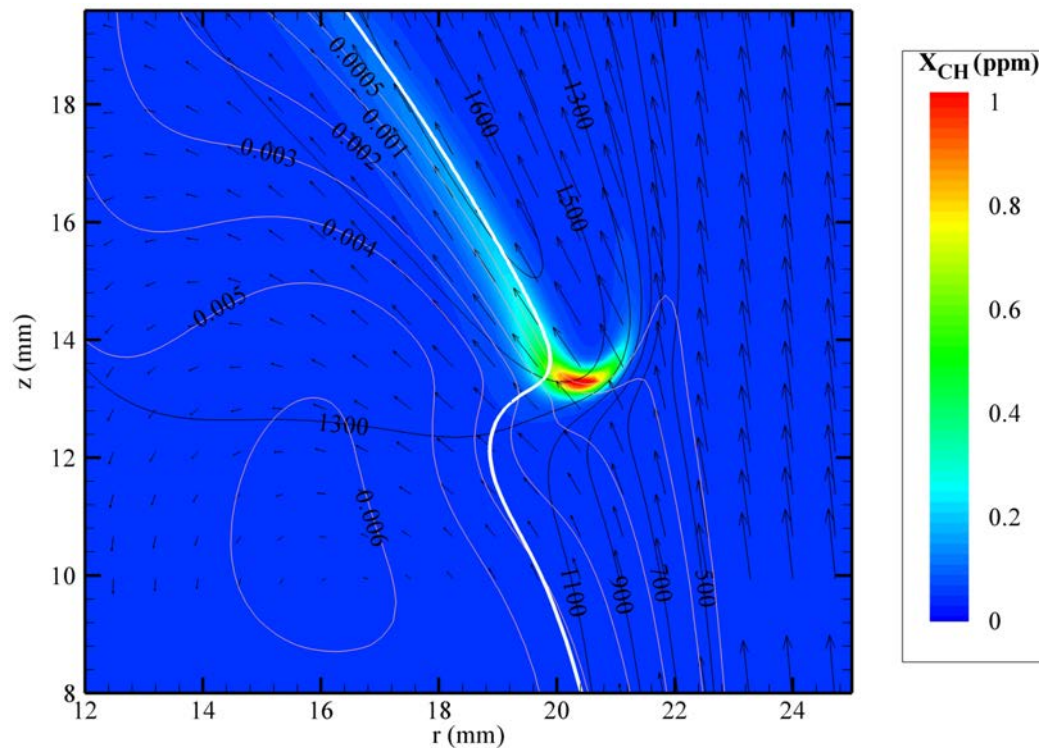


Fig. 3. Close-up view of lifted flame base. Velocity field and iso contours of temperature (black solid lines) and acetylene (gray solid lines) are superimposed on color map of CH concentration. Location of stoichiometric surface is marked with white line.

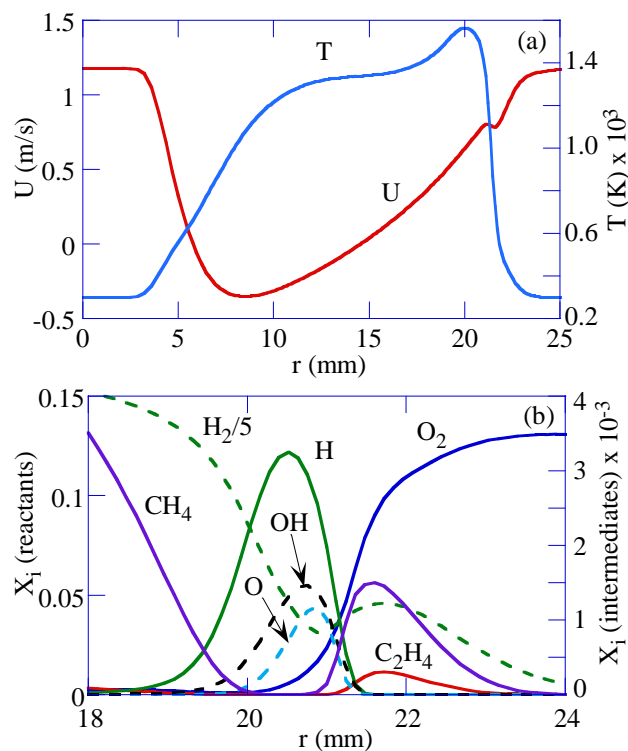


Fig. 4. Structure of lifted flame base. Radial distributions of (a) temperature and axial velocity and (b) concentrations of reactants and intermediate species at a height of 13.8 mm above centerbody plate.

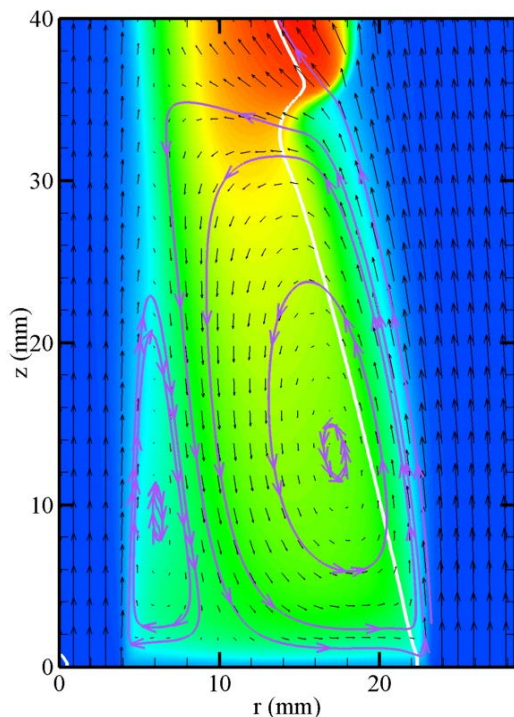


Fig. 5. Lifted flame for higher coannular flow. Velocity field and streamlines are superimposed on color temperature map. Stoichiometry is shown with white line.

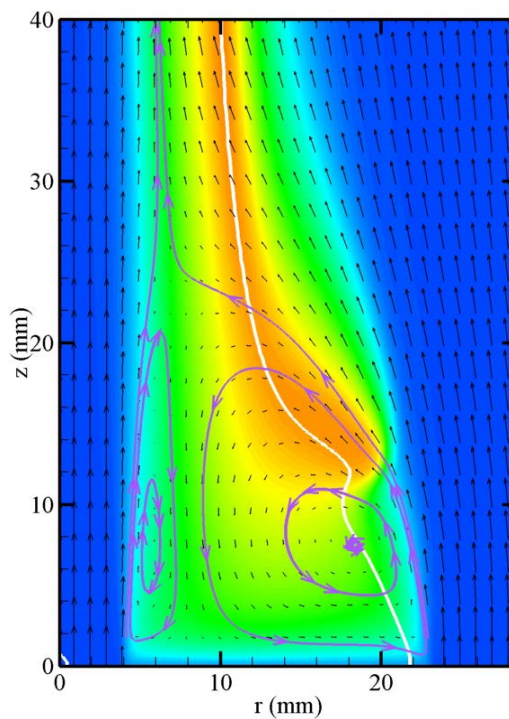


Fig. 6. Lifted flame simulated for lower coannular nitrogen-air flow. Velocity field and streamlines (gray solid lines) are superimposed on color temperature map. Stoichiometric surface is shown with white line.

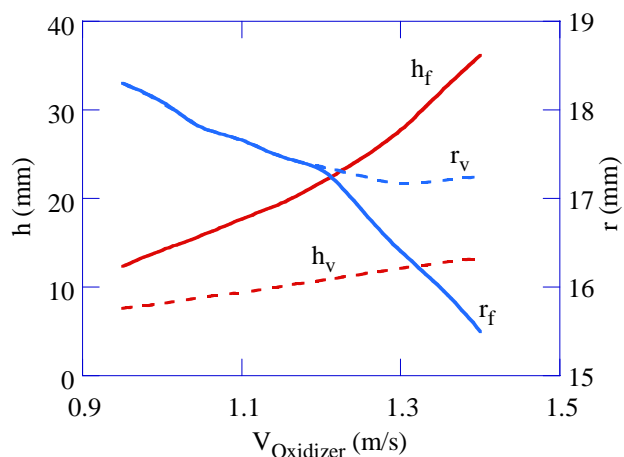


Fig. 7. Changes in height (h) and radius (r) of flame base location and recirculation zone center with respect to increase in coannular nitrogen-air velocity.

Calculation of Multidimensional Flames Using Large Chemical Kinetics

Viswanath R. Katta*

Innovative Scientific Solutions, Inc., Dayton, Ohio 45440

and

William M. Roquemore†

U.S. Air Force Research Laboratory, Wright-Patterson Air Force Base, Ohio 45433

DOI: 10.2514/1.33131

A time-dependent, two-dimensional, detailed-chemistry computational fluid dynamics model, known as UNICORN (unsteady ignition and combustion using reactions), is used for solving complex flame problems. The unique features incorporated in UNICORN for handling extremely large chemical kinetics with ease and efficiency are discussed. A submixture concept that is used for evaluating transport properties is described. This concept increases the computational speed by a factor of five for a 208-species mechanism and is expected to have even higher efficiency with larger mechanisms. An implicit treatment for certain reaction-rate terms applied during the solution of species-conservation equations is described. Moving the reaction-rate source terms to the left-hand side of the partial differential equations eases the stiffness problem that is typically associated with combustion chemical kinetics. Computational speeds are further improved in UNICORN by completely integrating the chemical-kinetics mechanisms with the solution algorithm. A software-generated computational fluid dynamics approach is used to avoid the tedious and near-impossible task of manually integrating a large chemical-kinetics mechanism into a computational fluid dynamics code. Several calculations demonstrating the abilities of the UNICORN code are presented. Chemical-kinetics mechanisms up to 366 species and 3700 reaction steps are incorporated, and simulations for unsteady multidimensional flames are performed on personal computers. Making use of the robustness and efficiency of the UNICORN code, detailed chemical mechanisms developed for JP-8 fuel are tested for their accuracy, and a parametric study on the role of parent species of a surrogate mixture in predicting flame extinguishment is performed. Ease of changing chemical kinetics in the UNICORN code is demonstrated through the investigation of effects of additives in JP-8 fuel.

Nomenclature

C_i	= chemical symbol for the i th species
D_{ij}	= diffusion coefficient in a binary mixture of the i th and j th species
$D_{i,\text{mix}}$	= binary-diffusion coefficient of the i th species in a mixture
$f(Y_i)$	= first variable used in the modified species-conservation equation
$g(Y_i)$	= second variable used in the modified species-conservation equation
I_i^j	= availability of the i th species in the reactants of the j th reaction
J_i^j	= availability of the i th species in the products of the j th reaction
k_j	= rate of the j th reaction
M_i	= molecular weight of the i th species
N_s	= number of species in the chemical kinetics
N_R	= number of reactions in the chemical kinetics
p	= pressure
r	= radial distance
T	= temperature
t	= time

u	= axial velocity component
\mathbf{V}	= velocity
v	= radial velocity component
X_i	= mole fraction of the i th species
X_{\min}	= minimum mole fraction in submixture
Y_i	= mass fraction of the i th species
z	= axial distance
Δ_{fT}	= flame thickness based on temperature distribution
$\Delta_{f\text{OH}}$	= flame thickness based on hydroxyl-radical distribution.
δ_i	= error in the i th species in percent
$\partial/\partial t$	= differential operator with respect to t
η	= simulation time
η_0	= simulation time when $X_{\min} = 0$
$\lambda_i, \lambda_{\text{mix}}$	= thermal conductivity of the i th species and mixture, respectively
μ_i, μ_{mix}	= viscosity of the i th species and mixture, respectively
$\nu'_{i,j}$	= stoichiometric coefficient for the i th species appearing as reactant in the j th reaction
$\nu''_{i,j}$	= stoichiometric coefficient for the i th species appearing as product in the j th reaction
ρ	= density
ϕ, ϕ'	= functions
χ_{st}	= scalar dissipation rate at stoichiometry
$\Omega^{(1,1)*}$	= reduced collision integral
ω	= production rate
∇	= Laplace operator

Presented as Paper 4418 at the 37th AIAA Fluid Dynamics Conference and Exhibit, Miami, FL, 25–28 June 2007; received 28 June 2007; revision received 7 March 2008; accepted for publication 17 March 2008. This material is declared a work of the U.S. Government and is not subject to copyright protection in the United States. Copies of this paper may be made for personal or internal use, on condition that the copier pay the \$10.00 per-copy fee to the Copyright Clearance Center, Inc., 222 Rosewood Drive, Danvers, MA 01923; include the code 0001-1452/08 \$10.00 in correspondence with the CCC.

*Senior Engineer, 2766 Indian Ripple Road; vrkatta@erinet.com. AIAA Associate Fellow.

†Senior Scientist, Propulsion Directorate, Building 5, 1950 Fifth Street; melvyn.roquemore@wpafb.af.mil. AIAA Fellow.

I. Introduction

DETAILED chemical kinetics for describing combustion of aviation fuels involves several hundred species and several thousand elementary reactions. The need for more accurate and presumably larger chemical-kinetics mechanisms is strongly driven by the escalating cost of petroleum-based fuels and the need to

develop alternative and Fischer–Tropsch fuels. Indeed, new fuel mechanisms are being developed at a rapid pace. Traditionally, such newly developed mechanisms are validated through the simulations of zero- and one-dimensional flames using codes such as RUN1DL [1], OPPDIF [2], and CHEMKIN [3] and comparing the results with available experimental data. Extensive experimental data for the intermediate species concentrations are required for obtaining a reasonably calibrated kinetics mechanism. However, in many cases, it is not feasible to obtain concentrations of the numerous hydrocarbon intermediates that are generated during the combustion of complex hydrocarbon fuels such as JP-8. As a result, newly developed, complex chemical-kinetics mechanisms can be only validated partially using traditional approaches.

One of the risks in using partially validated mechanisms is that the simulations for a reacting flow under one set of conditions may appear to be reasonable, whereas under a different set of conditions they may be poor. This was demonstrated by Katta et al. [4] using recently developed mechanisms for JP-8 fuels. Three JP-8 mechanisms were investigated: one from Ranzi's group at Politecnico di Milano, the second from the University of Utah, and the third from the Propulsion Directorate of the Air Force Research Laboratory (AFRL/RZ). These mechanisms were developed independently and validated using the limited experimental data on ignition delay times and flame speeds. The Violi mechanism (Ranzi's group) [5] has 161 species and 1538 reactions, including some global-type reactions; the University of Utah mechanism [6] has 208 species and 2186 reactions, and the Mawid Mechanism (AFRL/RZ) [7] has 216 species and 3000 reactions. These three mechanisms were incorporated in UNICORN [8] (unsteady ignition and combustion using reactions), and calculations were performed for a variety of two-dimensional flame systems. It was found that the flame structures predicted by these mechanisms were radically different and, more important, that the blowout characteristics of a nonpremixed flame varied significantly from mechanism to mechanism. Disappointingly, the partially validated chemistry models were found to be of only limited use in the simulation of multidimensional flames.

Thus, a second-level validation must be performed on partially validated chemistry models through the simulation of two- or three-dimensional flames and by comparing the global features such as flame shape, size, and liftoff height. As these global quantities can easily be measured in the laboratory, a second-level validation for the detailed-chemistry models can be performed if computational fluid dynamics (CFD) codes that can incorporate large-chemical-kinetics mechanisms and perform simulations for multidimensional flames are available.

Advances in computer hardware technology and the need to improve the understanding of combustion phenomena such as flame stability, pollutant formation, and lean blowout have led to the development of CFD codes with detailed chemical kinetics [9–11]. However, due to the fact that computational time increases significantly with the size of the chemical-kinetics mechanism used, CFD code developments are limited to either simple fuels, such as hydrogen [12], methane [13], and ethylene [14], that are described with smaller detailed mechanisms (less than 100 species) or to complex fuels such as propane [15], heptane [16], and JP-8 [17] that are described with reduced mechanisms (tens of species).

A two-dimensional numerical model known as UNICORN [8], which has the capability to incorporate detailed chemical-kinetics mechanisms, has been developed at AFRL/RZ for the simulation of dynamic, nonpremixed, and premixed jet flames. This model is being used for studying flame systems and evaluating large chemical mechanisms and soot models on programs sponsored by the U.S. Air Force Office of Scientific Research and the Strategic Environmental Research and Development Program.

The present paper describes extension of the UNICORN code to incorporate very large chemical-kinetics mechanisms and to simulate multidimensional flames efficiently and accurately. Various simulations that were performed for demonstrating the capabilities of the modified UNICORN code are discussed.

II. Mathematical Model

The UNICORN code [8,18] is a time-dependent, axisymmetric mathematical model that is used for the simulation of unsteady reacting flows. It is capable of performing direct numerical simulations and has been developed over a 10-year period. Its evolution has been in conjunction with experiments conducted to test its ability to predict ignition, extinction, stability limits, and the dynamic characteristics of nonpremixed and premixed flames of various fuels. It solves for u - and v -momentum equations, and continuity, and enthalpy- and species-conservation equations on a staggered-grid system. The body-force term due to the gravitational field is included in the axial-momentum equation for simulating vertically mounted flames. A clustered mesh system is employed to trace the large gradients in flow variables near the flame surface. Detailed chemical-kinetics models for various fuels are incorporated. Thermophysical properties such as enthalpy, viscosity, thermal conductivity, and binary molecular diffusion of all of the species are calculated from the polynomial curve fits developed for the temperature range 300–5000 K. Mixture viscosity and thermal conductivity are then estimated using the Wilke [19] and Kee [20] expressions, respectively. Molecular diffusion is assumed to be of the binary-diffusion type, and the diffusion velocity of a species is calculated using Fick's law and the effective-diffusion coefficient of that species [21] in the mixture. A simple radiation model based on the optically thin-media assumption is incorporated into the energy equation.

The finite-difference forms of the momentum equations are obtained using an implicit QUICKEST (quadratic upstream interpolation for convective kinematics with estimated streaming terms) scheme [18,22], which is fourth-order accurate in space and third-order accurate in time. The species and energy equations are discretized using a hybrid scheme of upwind and central differencing, which is second-order accurate in both time and space. At every time step, the pressure field is accurately calculated by solving all of the pressure Poisson equations simultaneously and using the lower and upper diagonal matrix-decomposition technique. The overall accuracy of the calculations made by the UNICORN code is estimated to be second-order or better in both time and space. As demonstrated in the past [23], it is possible to simulate two-dimensional turbulent flows (where no significant variation in flow variables exists in the third dimension) using UNICORN. However, for brevity, the scope of the present paper is limited to steady and unsteady laminar flames. Different types of boundary conditions such as adiabatic wall, isothermal wall, symmetric surface, outflow, and inflow can be applied to the boundaries of the computational domain [24].

III. Computational Procedure

In theory, the mathematical model described previously is sufficient for the simulation of multidimensional flames using large chemical kinetics. However, because of limitations on computational resources and difficulties associated with incorporating chemical-kinetics models, to obtain a multidimensional-flame solution using a large chemical-kinetics mechanism within a reasonable amount of time is a daunting task. Four computational techniques have been incorporated in UNICORN to make it efficient and robust in simulating multidimensional flames on personal computers.

A. Nonuniform Grid System

The accuracy of a simulation performed using a finite-difference scheme depends on the grid resolution. Typically, one obtains a grid-independent solution by performing calculations on increasingly finer meshes until the solution attains quasi-steady state (mesh independent). The finite-difference forms of the governing equations in the UNICORN code are obtained on a nonuniform, orthogonal mesh system and are solved using semi-implicit procedures [18]. These procedures, due to fewer restrictions on the time step, allow the use of rapidly expanding grid sizes in both the axial and the radial directions. Because the reaction-zone of a flame is confined to a

narrow region within the high-temperature zone, grid distribution must be sufficiently fine in that region. Variable grid systems are constructed a priori while enforcing clustering of grid points in the neighborhoods of the reaction zones, while allowing the grid spacing to expand rapidly as the grid points are located away from these regions. This facilitates the use of a minimum number of grid points for the simulation of a given flame. Calculations are made first on a coarse-grid system and then on a fine-mesh system, using the previously obtained solution as the initial conditions. The implicit procedures used in the UNICORN code permit stable calculations, even when large variations in grid spacing are present between the coarse- and fine-mesh systems. Overall, fewer grid points and systematic progress toward a fine-mesh solution allow the UNICORN code to perform multidimensional simulations with large chemical kinetics efficiently.

B. Calculation of Transport Properties

As described previously, the transport properties for the mixture are calculated using Wilke's [19] and Kee's [20] empirical expressions. Mixture thermal conductivity λ_{mix} and viscosity μ_{mix} can be calculated as follows for a mixture with N_s species:

$$\lambda_{\text{mix}} = \sum_{i=1}^{N_s} \lambda_i \left[1 + \frac{1.065}{2\sqrt{2}X_i} \sum_{k \neq i}^{N_s} X_k \phi_{ik} \right]^{-1} \quad \text{with} \quad (1)$$

$$\phi_{ik} = \frac{[1 + (\lambda_i^0/\lambda_k^0)^{1/2}(M_i/M_k)^{1/4}]^2}{[1 + M_i/M_k]^{1/2}}$$

$$\mu_{\text{mix}} = \sum_{i=1}^{N_s} \mu_i \left[1 + \frac{\sqrt{2}}{4X_i} \sum_{k \neq i}^{N_s} X_k \phi'_{ik} \right]^{-1} \quad \text{with} \quad (2)$$

$$\phi'_{ik} = \frac{[1 + (\mu_i/\mu_k)^{1/2}(M_i/M_k)^{1/4}]^2}{[1 + M_i/M_k]^{1/2}}$$

Here, λ_i and μ_i are thermal conductivity and viscosity of the individual species, respectively, and M_i and X_i are species molecular weight and concentration, respectively. Similarly, the effective-diffusion coefficient of the i th species in a mixture [21] is calculated using the empirical expression

$$D_{i,\text{mix}} = \frac{1 - X_i}{\sum_{j \neq i}^{N_s} X_j/D_{ij}} \quad \text{with} \quad (3)$$

$$D_{ij} = \frac{2.628 \cdot 10^{-3}}{p\rho^2 \Omega_{i,j}^{(1,1)*}} \left[\frac{T^3(M_i + M_j)}{2M_i M_j} \right]^{1/2}$$

D_{ij} is the binary-diffusion coefficient between species i and j , and $\Omega_{i,j}^{(1,1)*}$ is the reduced collision integral. Calculation of the mixture transport properties for systems with a large number of species is laborious and requires far more computational time than that required for solving the conservation equations or the reaction rates. Examination of Eqs. (1) and (2) suggests that, in a system having N_s species, ϕ and ϕ' must be evaluated $(N_s^2 - N_s)$ number of times at each grid point. For example, in a system of 300 chemical species, ϕ and ϕ' must be evaluated 89,700 times each, which is nearly 18 times more than the number of calculations required for evaluating reaction rates for 5000 reactions. As N_s increases, evaluation of λ_{mix} and μ_{mix} becomes increasingly time consuming. However, in multidimensional-flame calculations, most of the species will be present in trace amounts in regions away from the flame zone and only in parts per million levels in the flame zone. Because trace concentrations of species do not affect the thermal conductivity or viscosity of the mixture, it is possible to increase the speed of the calculations by considering only those species that are in significant concentrations. This can be accomplished by creating a submixture at every grid point through elimination of all species that are below a specified concentration in the entire mixture and then evaluation of transport properties using only the submixture. Note that diffusion coefficients

$D_{i,\text{mix}}$ are evaluated by using Eq. (3) and considering all of the species in the mixture, because the benefit of using the submixture in this case is minimal.

In the simulation of a two-dimensional nonpremixed jet flame, increasing the speed of the calculations through use of the submixture concept is demonstrated in Fig. 1. A 208-species, 1093-reaction, chemical-kinetics model for JP-8 fuel is used for this demonstration. Calculations for the flame are repeated by changing the minimum concentration allowed in the submixture. The computational time for each simulation is normalized with that required by the original simulation that considered all of the species while evaluating the transport properties. The minimum concentration allowed in the submixture is shown in log scale on the horizontal axis. For each simulation percentage error, δ_i is obtained first by calculating the difference in the concentration of the i th species predicted with the submixture concept and that of the original simulation and then by normalizing this difference to the original value. Errors estimated based on the peak H radical and byphenyl poly-aromatic-hydrocarbon concentrations at a flame height of 4 cm are shown in Fig. 1. Note that errors in the concentrations of major species, temperature, and velocity are negligible.

A dramatic reduction in calculation time (by a factor of five) is achieved by considering species whose concentrations are $>10.0^{-03}$ for transport-property evaluation purposes, whereas the errors introduced are $<1\%$ in minor- and trace-species concentrations. It is important to note that the reduction shown in Fig. 1 is for the entire flame simulation (not just for the transport-property calculation) which gives some indication of the large percentage of computational time required for calculating mixture transport properties alone. Because the increase in speed of calculation is proportional to the square of the number of species, the benefit of using submixtures becomes more pronounced as the number of species in the chemical-kinetics model increases.

C. Handling Stiff Equations

Species-conservation equations can be written as following using Fick's law of diffusion for binary mixtures and the effective-diffusion coefficient $D_{i,\text{mix}}$ for the i th species in the mixture.

$$\frac{\partial \rho Y_i}{\partial t} + \nabla \cdot [\rho Y_i \mathbf{V} - \rho D_{i,\text{mix}} \nabla Y_i] = \dot{\omega}_i \quad (4)$$

Here, the source term $\dot{\omega}_i$ is the rate of production of the i th species that must be calculated from the adopted chemical-kinetics mechanism, which is written in the following form:

$$\sum_{i=1}^{N_s} \nu'_{i,j} C_i \xrightarrow{k_j} \sum_{i=1}^{N_s} \nu''_{i,j} C_i \quad j = 1, N_R \quad (5)$$

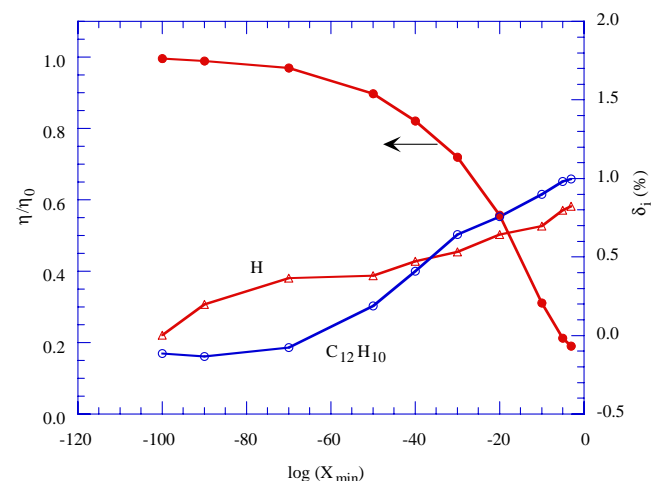


Fig. 1 Computational time required and associated errors for different minimum concentrations allowed in submixture domain. 663

Here, C_i represents chemical symbol for the i th species and N_R represents the total number of reactions in the chemical-kinetics mechanism. Note that all reactions in the mechanism are written as forward reactions.

In general, because of the high reaction rates (and, hence, large $\dot{\omega}_i$ values) associated with the combustion processes, species-conservation equations become very stiff; traditionally, small time steps are used in solving Eq. (4) to overcome this stiffness problem. However, such an approach places severe restrictions on multidimensional-flame simulations because the flow time scales associated with certain domains such as recirculation and coflow-entrainment regions are several orders of magnitude larger than the chemical time scales. Therefore, special techniques are required for solving Eq. (4) with larger time steps in multidimensional-flame simulations. After expanding the source terms into destruction and production terms, Eq. (4) can be rewritten as

$$\begin{aligned} \frac{\partial \rho Y_i}{\partial t} + \nabla \cdot [\rho Y_i \mathbf{V} - \rho D_{i,\text{mix}} \nabla Y_i] \\ = - \sum_{j=1}^{N_R} (v'_{i,j} - v''_{i,j}) k_j \prod_{m=1}^{N_s} \left(\frac{Y_m}{M_m} \right)^{v'_{m,j}} \end{aligned} \quad (6)$$

and then as

$$\begin{aligned} \frac{\partial \rho Y_i}{\partial t} + \nabla \cdot [\rho Y_i \mathbf{V} - \rho D_{i,\text{mix}} \nabla Y_i] \\ = - \sum_{j=1}^{N_R} (v'_{i,j} - v''_{i,j}) k_j I_i^j \left(\frac{Y_i}{M_i} \right)^{v'_{i,j}} \prod_{\substack{m=1 \\ m \neq i}}^{N_s} \left(\frac{Y_m}{M_m} \right)^{v'_{m,j}} \\ - \sum_{j=1}^{N_R} (v'_{i,j} - v''_{i,j}) k_j J_i^j \prod_{m=1}^{N_s} \left(\frac{Y_m}{M_m} \right)^{v'_{m,j}} \end{aligned} \quad (7)$$

where $I_i^j = 1$ if the i th species is a reactant in the j th reaction, otherwise $I_i^j = 0$, and where $J_i^j = 1$ if the i th species is a product in the j th reaction, otherwise $J_i^j = 0$.

Because the mass fraction of the i th species explicitly appears in the destruction terms (first set of terms on the right-hand side) of Eq. (7), they can be shifted to the left-hand side of the equation for treating them implicitly. Species-conservation equations are then rewritten, after linearizing the destruction terms with respect to Y_i , as

$$\begin{aligned} \frac{\partial \rho Y_i}{\partial t} + \nabla \cdot [\rho Y_i \mathbf{V} - \rho D_{i,\text{mix}} \nabla Y_i] \\ + \sum_{j=1}^{N_R} (v'_{i,j} - v''_{i,j}) k_j I_i^j \left(\frac{Y_i}{M_i} \right) \left(\frac{Y_i}{M_i} \right)^{(v'_{i,j}-1)} \prod_{\substack{m=1 \\ m \neq i}}^{N_s} \left(\frac{Y_m}{M_m} \right)^{v'_{m,j}} \\ = - \sum_{j=1}^{N_R} (v'_{i,j} - v''_{i,j}) k_j J_i^j \prod_{m=1}^{N_s} \left(\frac{Y_m}{M_m} \right)^{v'_{m,j}} \end{aligned} \quad (8)$$

which then takes the following implicit form in terms of Y_i :

$$\frac{\partial \rho Y_i}{\partial t} + \nabla \cdot [\rho Y_i \mathbf{V} - \rho D_{i,\text{mix}} \nabla Y_i] + f(Y_i) \cdot Y_i = g(Y_i) \quad (9)$$

Here, $f(Y_i)$ and $g(Y_i)$ are functions of chemical-kinetics parameters and species mass fractions. Values of these functions are calculated from the data available after the previous time step's solution.

Special care must be taken when the i th species appears in both the reactants and the products of a reaction. Implicit treatment of the destruction terms significantly enhances the stability of the numerical scheme [25] and allows time steps much larger than those allowed by Eq. (9). However, because $f(Y_i)$ and $g(Y_i)$ in Eq. (9) are temporarily treated as constants based on the previous time step's data, the solution procedure previously described for the species-conservation equations represents a semi-implicit algorithm. Note, a fully implicit algorithm can be derived by constructing Jacobian matrices for all of the species involved in the production and

destruction terms in Eq. (6), but such procedures become memory and computational-time intensive and may become restrictive in performing multidimensional-flame simulations [26]. Because the primary goal for the development of the UNICORN code is to simulate multidimensional flames using large chemical-kinetics mechanisms, memory-intensive fully implicit algorithms were not used.

D. Incorporating Large Chemical Kinetics

Detailed chemical-kinetics for describing combustion of aviation fuels could involve hundreds of species and thousands of reactions. Such large mechanisms can be used for performing multidimensional reacting-flow simulations by either calculating the reaction rates $\dot{\omega}_i$ in Eq. (4) at each grid point, through calling a mechanism subroutine (such as CHEMKIN) [27] or integrating the mechanism with a CFD code [28,29]. Because the former approach does not require any manipulation of the chemical-kinetics mechanism that has been supplied in a standard format (for example, CHEMKIN format [3]), it eliminates any possible errors in using the chemical-kinetics mechanism for a multidimensional-flame simulation. However, such a calling-mechanism approach puts a significant burden on computational resources. Also, it may become an impractical approach for even a moderately large mechanism, mainly due to the fact that general-purpose codes such as CHEMKIN perform a number of overhead calculations each time they are called. Furthermore, the calling-mechanism approach requires the chemical source terms to be treated explicitly, as in Eq. (4), which is known for its limitations in handling stiff reactions.

Incorporating large chemical-kinetics mechanisms in a CFD code, either through Eq. (4) or Eq. (9), is a formidable task and highly susceptible to typographical and programming errors. Moreover, the implicit treatment of the reaction-rate terms in Eq. (9) and the need for continuous evaluation of functions $f(Y_i)$ and $g(Y_i)$ (as and when new information about a species is available) to ensure a stable-solution procedure make the large chemical-kinetics mechanism incorporation extremely difficult. Because of these difficulties, scientists/engineers rarely use large mechanisms for performing multidimensional reacting-flow simulations. As described in the previous subsection, the UNICORN code was developed based on an implicit algorithm for chemical reactions, and the reaction mechanism must be integrated with the code.

UNICORN uses an innovative approach to achieve efficient calculations for reacting flows with large chemical-kinetics mechanisms. This approach involves the development of a logic program that "reads" a chemical mechanism of any size into UNICORN and automatically configures it in such a way that the calculations run efficiently. To understand this approach, one must realize that UNICORN is optimized for each kinetic mechanism to ensure that reacting flows using the mechanism can be computed efficiently and accurately. Some background is required to understand, in general, how this is accomplished. The UNICORN code is developed based on an implicit algorithm for chemical reactions, which requires that the reaction mechanisms be integrated with the code. During the early development stages of UNICORN, small chemical mechanisms for fuels such as hydrogen and methane were incorporated manually: a very cumbersome and time-consuming task. For example, the total time required for incorporating a 21-species, 81-reaction mechanism into UNICORN was about a month, including the time for debugging and finding and correcting typographical and programming errors. Such developmental time was expected to increase to several months for medium-size mechanisms with less than 100 species. This seemed to be an impractical approach for large mechanisms with more than 200 species. To circumvent this problem, a special logic program has been written that directly reads the chemical-kinetics data that are prepared and distributed in standard CHEMKIN format and writes an efficient, robust version of the UNICORN code for that chemistry. With this approach, a UNICORN code that is optimized for a specific chemical-kinetics model can be developed in a few hours, independent of its size.

The logic program that generates a new UNICORN code in FORTRAN language for the given chemical-kinetics model directly reads the kinetics data prepared in standard CHEMKIN format. This logic program has been rigorously tested on smaller mechanisms to ensure that it generates an error-free UNICORN code for the given chemistry. In this way, human involvement in preparing the CFD code is minimized; hence, errors associated with it are eliminated. Using this software-generated CFD strategy (i.e., accurate development of a modified UNICORN code), a number of reacting-flow simulations have been performed. These include 1) ethylene flames with 99 species and 1066 reactions [30], 2) propane flames with 105 species and 1200 reactions [31], 3) methane + halon flames with 92 species and 1644 reactions [32], and 4) heptane flames with 366 species and 3698 reactions [33].

IV. Results and Discussion

Multidimensional-flame simulations using UNICORN can be performed on a personal computer with 2.0 GB of memory. Execution times depend strongly on the number of species considered in the chemical-kinetics model and the grid size. The ease of use and efficiency of the UNICORN code in handling stiff and large chemical kinetics are demonstrated in the following subsections.

A. Studies on Flame Thickness

The opposing-jet flame shown in Fig. 2 is formed between hydrogen and air jets and represents a weakly stretched laminar flame. The fuel and air jet velocities used are 0.4 and 0.3 m/s, respectively. A 13-species, 74-reaction H_2 - O_2 - N_2 chemical-kinetics model is used for simulating this flame. As the velocities of the fuel and air jets increase, the flame becomes thinner and its temperature decreases. The flame extinguishes for a critical set of velocities (or strain rates or scalar dissipation rates). Two theories are used to describe the flame-extinction process. According to laminar-flamelet theory [34], the reaction layer of a flame becomes infinitely thin before the flame is extinguished. On the other hand, the distributed-reaction-zone theory of Bilger [35] suggests that the reaction layers are broadened because of chemical equilibrium and that flames cannot be stretched to infinitely thin surfaces. Let us consider the opposing-jet flame shown in Fig. 2 for understanding the flame-

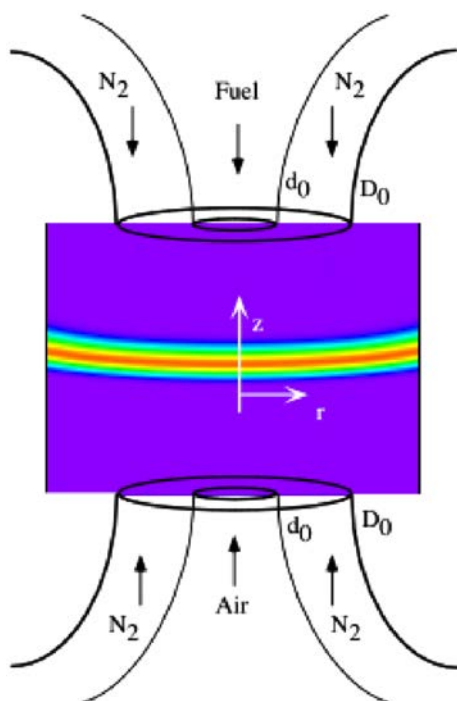


Fig. 2 Opposing-jet nonpremixed flame subjected to strain rates up to extinction limit.

extinction process and, particularly, the limits, if any, for flame thickness.

Numerical experiments are performed through increasing the reaction rates in an attempt to approach asymptotically infinitely thin reaction zones. Increasing the reaction rates renders the species-conservation equations stiffer and challenges the numerical algorithm in handling stiff equations. Four sets of data with modified reaction rates are shown in Fig. 3. The results of flame-thickness estimates based on the full width of the temperature profile at various scalar dissipation rates χ_{st} are shown in Fig. 3. Thicknesses of the flame at the time of extinction are marked with open circles. Flame thicknesses obtained after reducing the rates of the 37 forward reactions by one-half are shown with dash-dot lines, whereas that obtained after doubling the rates of the forward reactions is shown with a broken line. Note that increasing or decreasing the forward reaction rates alone (without changing the reverse reaction rates) in a chemical-kinetics mechanism could alter the equilibrium characteristics of the chemical system; hence, such studies should be strictly limited to evaluating the stability of the numerical scheme. Results obtained after doubling the rates of the forward and reverse reactions are shown with thin lines, and those obtained after increasing the rates of both the forward and reverse reactions by an order of magnitude are shown with dotted lines. Changes in reaction rates affect not only the maximum scalar dissipation rate (or stretch rate) that can be applied on this flame, but also the temperature at which extinction takes place. In general, temperature and heat release rates at extinction are higher with faster reactions. At a given scalar dissipation rate χ_{st} , the temperature and heat release rate of the flame increases with the reactivity of the system. The increase is more pronounced at higher χ_{st} . This behavior can be explained considering the chemical-nonequilibrium state of the flame. An increase in the reaction rates enhances the reactivity in the flame zone and, thereby, shifts the flame more into equilibrium.

Figure 3 suggests that the thickness of the steady opposed-jet flame decreases, as described by the laminar-flamelet theory, when the stretch rate is increased. However, contrary to the assumption that stretched flames become infinitely thin before extinction, flame thicknesses at extinction obtained with normal, reduced, and enhanced kinetics are all within the range of 1 and 2 mm. More interestingly, the thickness vs χ_{st} plot suggests that flame thickness is asymptotically approaching a finite value (~ 1 mm).

One could argue that the temperature profile might not necessarily represent the reaction-zone thickness because it is influenced by the thermal and molecular diffusive transports. Typically, intermediate radical species such as OH, O, and H that have a short life span are confined to reaction zones. Variations of flame thicknesses obtained from the full width of OH radical distributions are shown in Fig. 4. For a given scalar dissipation rate, reaction-zone thicknesses obtained from OH radical distributions are about one-half of those

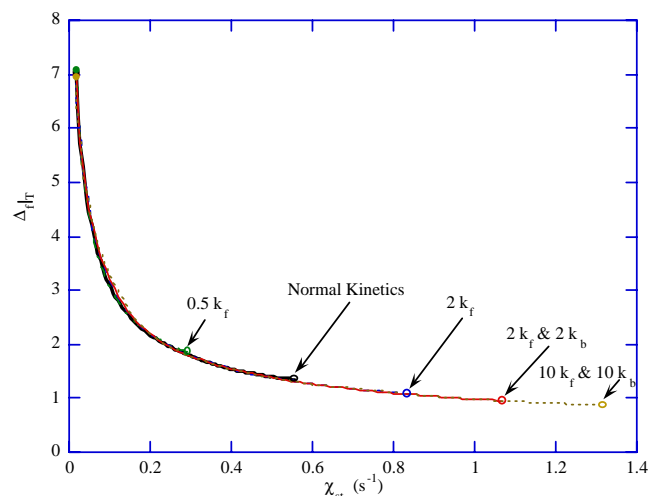


Fig. 3 Thickness of steady-state flame at different stretch rates obtained from temperature.

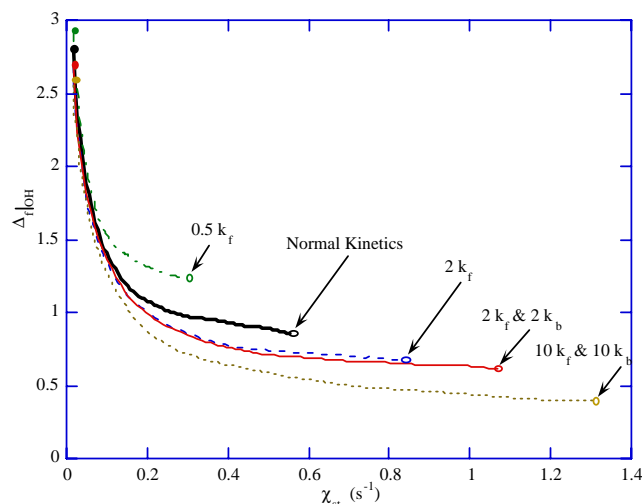


Fig. 4 Thickness of steady-state flame at different stretch rates obtained from OH concentration.

obtained from temperature. Figure 4 suggests that the radical-based reaction-zone thicknesses are also asymptotically approaching a finite value as the scalar dissipation rate on the flame is increased. It is important to note that even the smallest thickness of 0.5 mm represents a radical profile that has been resolved with a large number (25) of grid points; hence, the asymptotic thicknesses shown in Figs. 3 and 4 are not limited by the grid distribution.

Calculations made with different reaction rates suggest that a minimum thickness exists for the reaction zone of a flame that is aerodynamically stretched. For the hydrogen flame considered in this study, the minimum reaction-zone thickness is in the range 0.5–1.0 mm, depending on the radical species used for obtaining the thickness. A similar study of methane flames also suggested that the minimum reaction-zone thickness (based on OH distribution) for those flames is also ~ 0.5 mm.

B. Studies on Ethylene–Air Jet Nonpremixed Flames

Calculations for an inverse diffusion flame (IDF) were made with UNICORN using three chemical-kinetics models for ethylene–air

combustion. The first model is proposed by Wang and Frenklach [36] and consists of 99 species and 1066 elementary-reaction steps; the second is developed by the National Institute of Standards and Technology (NIST) and consists of 225 species and 1634 elementary reactions [37]; the third is a more comprehensive mechanism assembled by NIST and consists of 366 species and 3698 reactions [37]. Note that all of these mechanisms for ethylene–air combustion are well validated for high-temperature chemical processes, and one should expect similar flame shapes and temperature and major-product-concentration distributions. Larger mechanisms contain additional chemical kinetics required for predicting pollutant formation. The simulated IDF burner consists of a 1-cm-diam central air jet and a 3-cm-diam coannular fuel jet [31,38]. The air and ethylene flow velocities are 35 cm/s and 7 cm/s, respectively. Axisymmetric calculations were made on a physical domain of 200×50 mm using a 401×121 nonuniform grid system. The steady-state flames obtained with the three mechanisms are shown in the left halves of Figs. 5a–5c in plots of isotemperature gray-scale distributions. The three mechanisms predicted the same flame height and peak temperature (2440 K). Typical execution times for these calculations are 30 s/time step with the Wang–Frenklach mechanism, 65 s/time step with the NIST smaller mechanism, and 114 s/time step with the NIST larger mechanism. Steady-state flames were obtained in about 2000 time steps, starting from the solution obtained with a global-chemistry UNICORN code.

Various studies of normal jet nonpremixed flames (i.e., with the fuel jet at the center) suggest that when the annular airflow is low (<40 cm/s), the flame tends to flicker with the development of buoyancy-induced vortices outside the flame surface. Generally, the flickering frequency for these flames is independent of or weakly dependent on fuel-jet diameter, fuel type, and airflow velocity. The low annular fuel velocity of ~ 7 cm/s and the high-enthalpy ethylene fuel (flame temperatures are about 2400 K) used for the IDF create an appropriate environment for flame flicker. To investigate the possibility that the IDF oscillates naturally, unsteady calculations were performed for the same flow conditions using all three chemical-kinetics mechanisms. Surprisingly, the unsteady simulations resulted in a flame with large vortices forming outside the flame surface. Stably oscillating unsteady flames were obtained within 10,000 time steps of the calculations. Instantaneous temperature fields of the unsteady IDF that were simulated using the three mechanisms are shown in the right halves of Figs. 5a–5c.

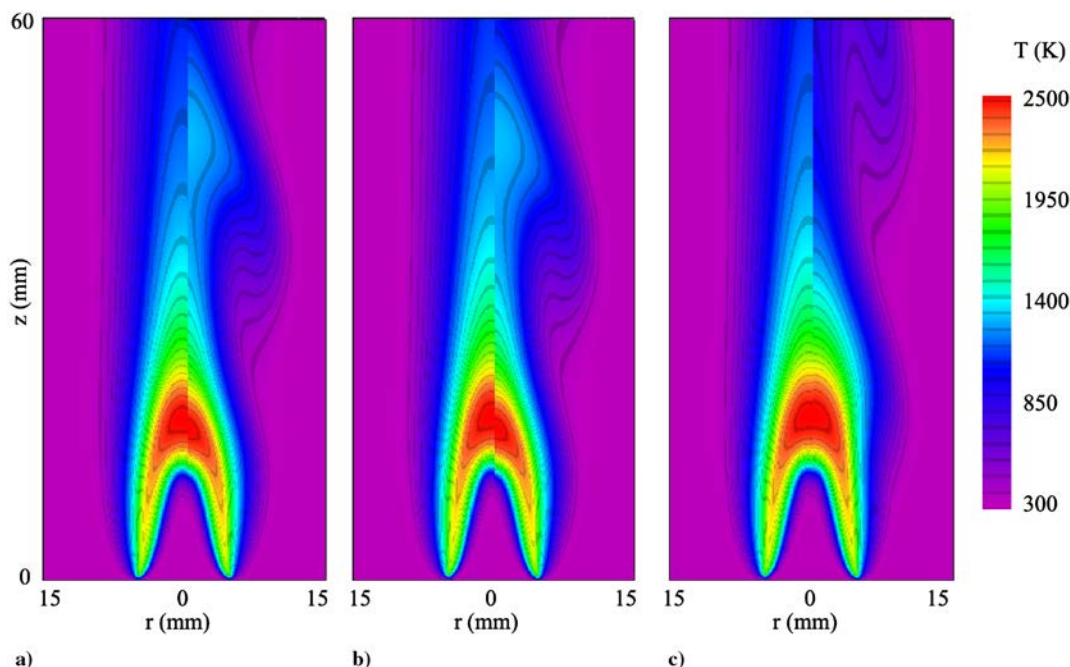


Fig. 5 Steady-state (left) and unsteady (right) ethylene–air, inverse nonpremixed flames simulated using a) Wang–Frenklach, b) NIST, and c) enhanced NIST mechanisms. Temperature distributions are shown.

Whereas the phases of the flames in Figs. 5a and 5b are matched, the phase of the flame in 5c is selected such that it is 180 deg from the other two. The unsteady temperature field upstream of the flame tip ($0 < z < 18$ mm) plotted in Fig. 5c is similar to that of the steady-state flames shown in Figs. 5a–5c. However, the large vortical structure ~ 30 mm in length that formed in the downstream location distorted the temperature field of the unsteady flame. When this vortical structure moved closest to the burner surface ($z = 0$), it squeezed the high-temperature region and made the flame temporarily shorter in Figs. 5a and 5b than the steady-state flame. Calculation time for the unsteady simulation performed with the 366-species, 3698-reaction mechanism was ~ 128 s/time step, and the solution in Fig. 5c was plotted after 15 days of calculations.

Benzene concentrations predicted by the three ethylene–air combustion models (Wang–Frenklach, NIST, and comprehensive NIST) are shown in Figs. 6a–6c, respectively. Steady-state and unsteady solutions are shown on the left and right halves of these images, respectively. Although nearly identical temperatures are predicted by the Wang–Frenklach and the two NIST mechanisms (Fig. 5), the benzene concentrations predicted by these mechanisms are quite different. The Wang–Frenklach mechanism yielded only $\sim 50\%$ of benzene that was predicted by the two NIST mechanisms. Although peak benzene concentration in the steady-state flame was established near the flame tip ($z \sim 20$) in the Wang–Frenklach mechanism (left half of Fig. 6a), it was established near the flame base in the NIST mechanisms (left halves of Figs. 6b and 6c). Interestingly, the buoyant vortex formed outside the flame surface in the unsteady simulation (Fig. 6b) has increased the benzene concentration significantly near its leading edge ($z \sim 45$ in Fig. 6b). Obtaining near identical solutions (Figs. 5 and 6) with different-size chemical-kinetics mechanisms is as expected and demonstrates the accuracy of the UNICORN code in incorporating large chemical-kinetics mechanisms.

C. Studies on JP-8–Air Nonpremixed Jet Flames

Axisymmetric calculations were performed for the opposing-jet JP-8 flame (similar to that shown in Fig. 2) using the UNICORN code. Four detailed chemical-kinetics models, namely, Violi-small [5], Violi-large [5], Zhang [6], and Mawid [7], were used for representing JP-8–air combustion. The Violi-small mechanism

consists of 161 reactions and 1538 reactions (some of them are lumped) [5]. The Violi-large mechanism consists of 216 species and 9654 reactions (some of them are also lumped). The Zhang mechanism [6] consists of 208 species and 2186 elementary reactions. The Mawid mechanism [7] consists of 226 species and 3230 elementary reactions. Whereas the first three mechanisms use their own surrogate mixtures for representing JP-8 fuel, the Mawid mechanism employs one of the three surrogate mixtures developed at AFRL/RZ [39]. The chemical compositions of these surrogate mixtures are given in Table 1. The physical domain between the two nozzles (14 mm in the axial direction and 20 mm in the radial direction) was represented using a 201×31 grid system, which resulted in a uniform grid spacing of $70 \mu\text{m}$ across the flame. The fuel/ N_2 ratio used in the calculations was 0.08. Experiments for this flame were conducted by Holley et al. [40]. The temperatures of the fuel and oxidizer streams were set to the measured values of 394 and 294 K, respectively. Initially, a stable flame was established for a low-strain-rate case of 28.6 s^{-1} . The corresponding fuel and oxidizer velocities were 0.2 and 0.2 m/s, respectively. Calculations for this flame were repeated by gradually increasing the strain rate (velocities) until the flame along the centerline was extinguished. The entire procedure, starting from establishing an initial flame to obtaining an extinguished flame, was repeated with each chemical-kinetics mechanism and surrogate mixture.

The flame response to an increase in strain rate predicted by different chemical-kinetics models is shown in Fig. 7. Here, the peak temperature along the centerline ($r = 0$) is plotted at different strain rates. Because of chemical nonequilibrium, the temperature of the flame decreased with strain rate. Data from each chemical-kinetics-model calculation up to the extinction limit are shown in Fig. 7. The measured extinction limit of 150 s^{-1} is shown with a vertical box. The width of the box corresponds to the experimental uncertainty of 3.5% reported by Holley et al. [40]. Calculations with the Mawid mechanism [7] were made using three surrogate mixtures identified as surrogate 1, surrogate 2, and surrogate 3. JP-8 fuel represented in the Violi mechanisms [5] is identical to surrogate 1. Among the four chemical-kinetics models considered, the Violi mechanisms predicted extinction strain rate more accurately than the other two. The Violi-small and the Violi-large mechanisms yielded nearly the same relationship between peak temperature and strain rate. A small but gradual deviation in peak temperature at higher strain rates

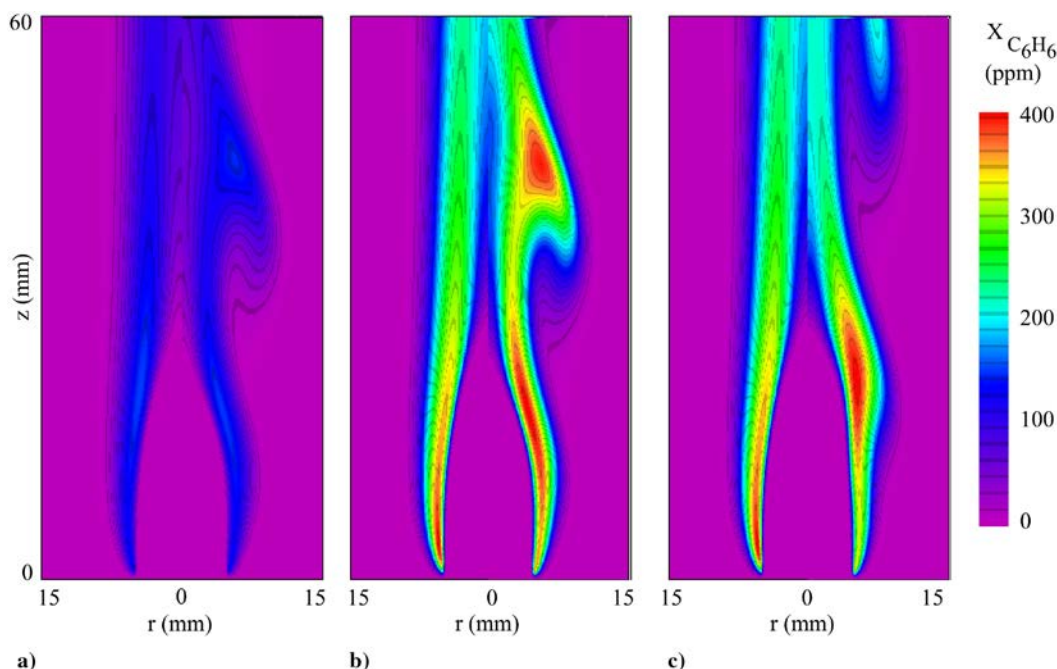


Fig. 6 Benzene concentrations in ethylene–air, inverse nonpremixed flames shown in Fig. 5. Calculations made with a) Wang–Frenklach, b) NIST, and c) enhanced NIST mechanisms.

Table 1 Representation of JP-8 fuel in various chemical-kinetics models

Fuel components	Violi-small mechanism [5]	Violi-large mechanism [5]	Zhang mechanism [6]	Mawid mechanism [7]		
				Surrogate 1	Surrogate 2	Surrogate 3
<i>n</i> -decane (<i>n</i> -C10H22)	0	0	0	16.2	0	25
<i>n</i> -dodecane (<i>n</i> -C12H26)	30	30	73.5	21	30	25
<i>n</i> -tetradecane (<i>n</i> -C14H30)	20	20	0	15.6	20	20
<i>n</i> -hexadecane (<i>n</i> -C16H34)	0	0	0	10.2	0	0
<i>i</i> -octane (I-C8H18)	10	10	5.5	5.7	10	5
Cyclooctane (c-C8H16)	0	0	0	4.7	0	0
Methylnaphthalene MCH (C11H10)	20	20	10	5.1	20	5
1-methylnaphthalene (C11H10)	0	0	0	3.9	0	0
Tetralin (C10H12)	5	5	0	4.1	5	0
1, 2, 4, 5-tetramethylbenzene (C9H12)	0	0	0	4.4	0	0
Butylbenzene (C10H14)	0	0	0	4.6	0	0
<i>m</i> -xylene (C8H10)	15	15	0	4.5	15	0
Toluene (C7H8)	0	0	10	0	0	20
Benzene (C6H6)	0	0	1	0	0	0
Molecular weight	144.38	144.38	151.3	156.87	144.38	146.89

predicted by these two mechanisms should be noted. The extinction strain rate of 136 s^{-1} predicted by these two mechanisms is within 90% of the measured value.

The elementary-reaction-based model developed by Zhang [6] yielded the most stubborn flame from an extinction point of view, even though the flame itself was not as strong (based on peak temperature) as the ones predicted by the semi-elementary-reaction-based mechanisms of Violi [5]. The importance of an accurate surrogate mixture for representing JP-8 fuel is evident from the calculations made with the Mawid mechanism [7]. The three surrogate mixtures yielded different temperature-strain-rate relationships (Fig. 7). Surrogate 1 yielded the lowest flame temperatures, which decreased further and rather rapidly with strain rate. Surrogates 2 and 3 yielded nearly the same extinction limits, with the latter mixture resulting in a slightly closer extinction limit when compared with the measured value. Interestingly, the flame temperature predicted with surrogate 2 was higher than that predicted with surrogate 3 when the strain rate was low, and lower when the strain rate was high. The major difference among the surrogate mixtures is that surrogate 1 contains additional parent compounds such as hexadecane (10.2%), cyclooctane (4.7%), methylnaphthalene (3.9%), tetramethylbenzene (4.4%), and butylbenzene (4.6%). A numerical experiment was conducted by systematically removing these compounds from surrogate 1. Calculations were repeated for the opposing-jet flame for different stretch rates; the results are shown in Fig. 8 and suggest that removal of hexadecane from the surrogate 1 mixture significantly increases the flame temperature ($\sim 108 \text{ K}$) and the extinction limit predicted by the Mawid mechanism.

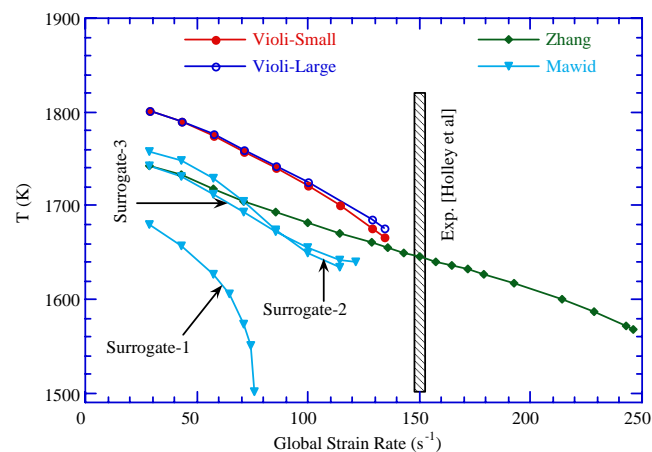


Fig. 7 Variations of peak temperature of nonpremixed, opposing-jet JP-8 flame with strain rate obtained using different chemical-kinetics mechanisms. Measured extinction strain rate is shown with vertical bar.

Calculations for a JP-8 coaxial nonpremixed jet flame were performed using the four chemical-kinetics models. The simulated burner has a central fuel tube of 0.6 cm radius and is surrounded by a 5 cm radius coflowing air. A preheated fuel- N_2 mixture at 500 K and with 90% fuel by mass was issued at a velocity of 2 cm/s. The coannular flow consisted of room-temperature air and was issued at a velocity of 5 cm/s. A computational grid of 151×61 was used for discretizing the physical domain of $10 \times 5 \text{ cm}$ in axial and radial directions. Grid clustering was used for placing most of the grid points in the flame zone. Initial conditions (flame) for the detailed chemistry calculations were obtained from the simulation using a global-chemistry UNICORN code.

Results for the coaxial nonpremixed jet flame obtained with the Violi-small, Violi-large [5], and Zhang [6] models are shown in Figs. 9a–9c, respectively. Here, isocontours of methylcyclohexane (in dashes) and H_2 (in solid lines) are superimposed on the temperature distribution (in gray scale) on the left half of each figure. Isocontours of benzene (dashes), OH (solid lines), and temperature (in gray scale) are shown on the right halves.

In general, all three chemistry models predicted nearly the same flame shape, with the base region burning hotter than the tip region. Flames are slightly shifted from the inlet boundary as imposed by the stability criterion of the nonpremixed jet flames. However, several important differences exist in these predictions. The Violi-small and Violi-large mechanisms [5] resulted in nearly the same flames, except that the latter mechanism generated more H_2 and benzene inside the flame, and methylnaphthalene (MCH) was present in locations slightly farther downstream in the core region (Figs. 9a and 9b). The thermal layer (flame thickness) is wider for the Violi-large

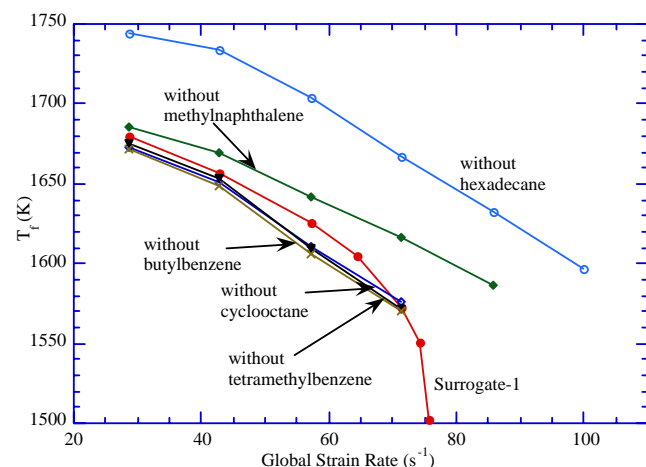


Fig. 8 Influence of parent compounds in surrogate 1 mixture of Mawid's [7] JP-8 mechanism on predicting flame extinction.

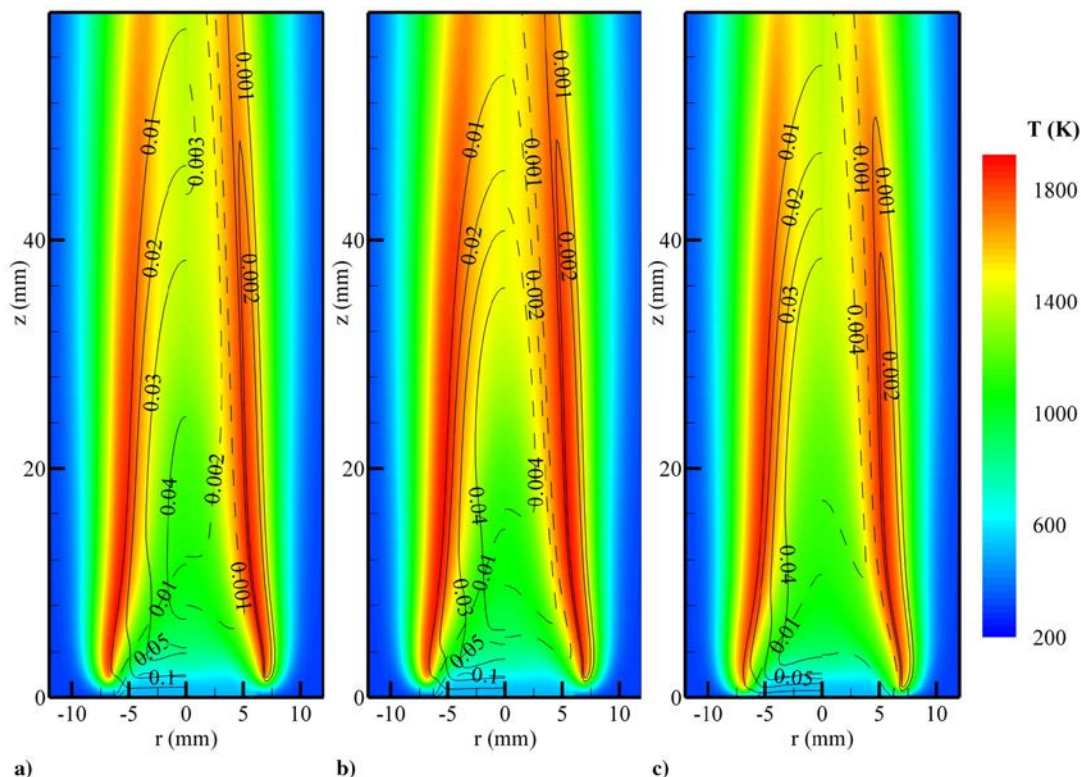


Fig. 9 Structure of JP-8 nonpremixed flame predicted using a) Violi-small, b) Violi-large, [5], and c) Zhang [6] mechanisms. Isocontours of MCH (dashed) and H_2 (solid) superimposed on temperature distribution on left half; isocontours of benzene (dashed) and OH (solid) superimposed on right half.

flame, which resulted in a hotter core region in Fig. 9b. As expected from the opposing-jet-flame calculations (Fig. 7), which suggested a much higher extinction strain rate for the Zhang mechanism [6], the coaxial nonpremixed flame predicted by this mechanism (Fig. 9c) is much closer to the inflow boundary than those predicted by the other models. Although there was 1% benzene in the surrogate mixture of the Zhang mechanism, it was all being consumed quickly in the core

region and did not enhance the benzene produced in the flame region (Fig. 9c).

D. Studies on Effect of Di-Tertiary-Butyl-Peroxide on JP-8 Flames

Di-Tertiary-Butyl-Peroxide (DTBP) additive is known for improving the ignition characteristics of hydrocarbon fuels. It has

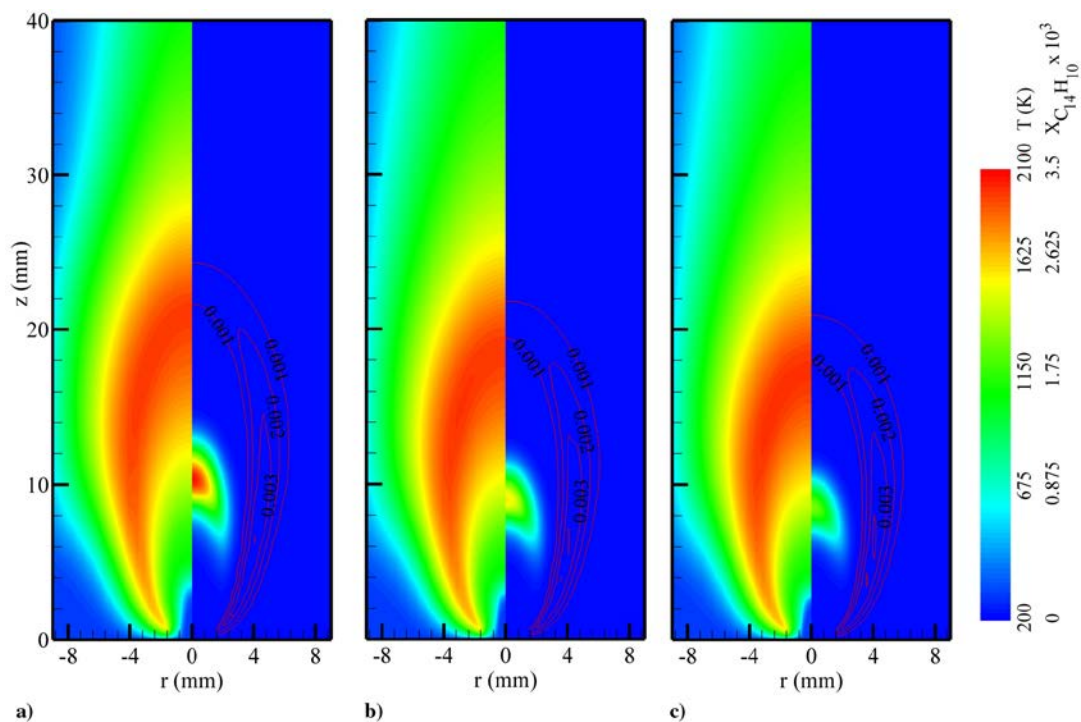


Fig. 10 Effect of DTBP additive on a) low-speed, nonpremixed jet flame, b) base flame, and c) flames with 10 and 15% additive added to fuel jet, respectively. Temperature distributions shown on left half of each flame; phenanthrene $C_{14}H_{10}$ (gray scale) and OH (contours) concentrations shown on right half.

been shown experimentally that the addition of DTBP alters gas-phase combustion [41] and, in some cases, soot production. Drop-tube [42] experimental results indicated that adding DTBP to fuel could reduce the amount of soot produced. For investigating the effects of DTBP on a JP-8 flame, a detailed chemical-kinetics model developed by Bozzelli [43], consisting of 98 species and 724 additional reactions, was added to the Zhang JP-8 mechanism [6]. The final Zhang–Bozzelli chemical-kinetics model derived for studying the effects of DTBP on JP-8 fuel has 306 species and 2910 reactions. The flame chosen for this study was a pure nonpremixed flame formed between gaseous JP-8 fuel and air. The velocity of the fuel, injected from a 1.0-mm-diam tube at room temperature, was 0.2 m/s. The annulus air velocity was 0.05 m/s. DTBP additive was added to the fuel jet by replacing an equal amount of JP-8, such that the exit velocity of the fuel jet was not altered. Axisymmetric calculations for this nonpremixed jet flame were performed for various concentrations of DTBP on a nonuniform grid system of 151×71 .

Results obtained for the base flame (without addition of DTBP) are shown in Fig. 10a, and those for the flames with 10 and 15% DTBP added to the fuel jet are shown in Figs. 10b and 10c, respectively. Whereas gray-scale distributions of isothermality are shown on the left halves of these figures, gray-scale distributions of phenanthrene ($C_{14}H_{10}$) are shown on the right halves. Distributions of the OH radical are superimposed in the right halves of the images. Phenanthrene was selected as a representative polycyclic-aromatic-hydrocarbon species that traces soot inception and growth. Figure 10a suggests that significant preheating of fuel before entering the flame zone is taking place. The flame, in general, is burning intensely in the tip region, with lower temperatures in the shoulder region. The peak temperature is about 2000 K. Fuel at room temperature exists for only a distance of ~ 5 mm in the fuel jet, at which location low-temperature ignition is taking place. Parent compounds of the JP-8 surrogate are decomposing into lower hydrocarbon fuels (such as C_2H_4 , CH_4 , and H_2) between this ignition location and the flame surface (peak-temperature location). Almost all of the phenanthrene produced in this flame is located upstream of the flame tip. Based on the phenanthrene distribution, it is expected that soot in this flame will develop along the axis of symmetry and in the neighborhood of the flame tip. The effects of DTBP on JP-8 fuel appear to be marginal. Addition of 10% DTBP reduced the flame size slightly (~ 2 mm in height), as shown in Fig. 10b. As expected, DTBP improved the ignition characteristics of the fuel. Note a decrease in the height of the room-temperature fuel jet and an increase in the OH concentration when 10% DTBP was added. Interestingly, phenanthrene concentration decreased by $\sim 50\%$. These effects became more pronounced, as shown in Fig. 10c, when 15% DTBP was added to the fuel jet. To confirm this, further studies must be conducted using DTBP chemistry along with other JP-8 chemical kinetics (Violi-large [5], and Mawid [7]). The robust UNICORN code is capable of performing multidimensional calculations for a nonpremixed jet flame using these mechanisms.

V. Conclusions

The multidimensional CFD model UNICORN has been extensively validated in the past by simulating various steady and unsteady opposing- and coflowing-jet premixed and nonpremixed flames, and by comparing the results with experimental data [8], lending confidence in the accuracy of the simulations made using UNICORN for the structures of dynamic flames. To prepare for current and future demands for simulations of multidimensional flames established from commercial fuels, a robust and efficient UNICORN code that could handle large chemical-kinetics mechanisms with ease was developed. Following a software-generated CFD approach, a separate UNICORN code for a given chemical-kinetics mechanism was prepared. This approach virtually eliminated the human errors that occur when incorporating large chemical-kinetics mechanisms in a CFD code. The efficiency of the UNICORN code has been improved through the use of a submixture

concept while evaluating transport properties and rapidly expanding grid systems. The robustness of the UNICORN code has been improved by making use of an implicit approach for solving species-conservation equations with large chemical source terms. Several sample simulations have been presented for demonstrating the abilities of the UNICORN code in handling very large chemical-kinetics mechanisms. Handling of stiffness, caused by the large source terms associated with combustion chemistry, has been demonstrated in the study on laminar-flamelet theory for stretched laminar nonpremixed flames where limits on flame thickness were examined through increasing the reaction rates by an order of magnitude. Efficiency of the calculations was demonstrated by conducting a parametric study on the role of parent compounds of a JP-8 surrogate mixture in predicting flame extinguishment. Retention of the accuracy of the UNICORN code while using very large chemical-kinetics mechanisms was demonstrated by simulating a naturally oscillating buoyant nonpremixed flame using models with 99 species, 1066 reactions; 225 species, 1634 reactions; and 366 species, 3698 reactions. Ease of incorporating large chemical-kinetics models was demonstrated in a study of additive effects on a JP-8 flame conducted by merging Zhang's JP-8 mechanism [6] with Bozzelli's Di-Tertiary-Butyl-Peroxide mechanism [43].

Acknowledgments

Financial support for this work was provided by the U.S. Air Force Office of Scientific Research (Julian Tishkoff), the Strategic Environmental Research and Development Program (Charles Pellerin), and U.S. Air Force Contract no. F33615-03-D-2329 (Tim Edwards and Vince Belovich). The authors thank Marian Whitaker for editorial help.

References

- [1] Rogg, B., "RUN1DL: The Cambridge Universal Laminar Flamelet Computer Code," *Reduced Kinetic Mechanisms for Applications in Combustion Systems*, edited by N. Peters and B. Rogg, Lecture Notes in Physics m15, Springer-Verlag, Heidelberg, Germany, 1993, pp. 350–351.
- [2] Lutz, A. E., Kee, R. J., Grcar, J. F., and Rupley, F. M., "OPPDIF: A Fortran Program for Computing Opposed Flow Diffusion Flames," Sandia National Lab. SAND96-8243, 1996.
- [3] Kee, R. J., Miller, J. A., and Jefferson, T. H., "CHEMKIN: A General-Purpose, Problem-Independent, Transportable, Fortran, Chemical Kinetic Code Package," Sandia National Lab. TR SAND80-8003, 1980.
- [4] Katta, V. R., Mawid, M., Sekar, B., Corporan, E., Zelina, J., Roquemore, W. M., and Montgomery, C. J., "Comparison of Chemical-Kinetics Models for JP-8 Fuel in Predicting Premixed and Nonpremixed Flames," *42nd AIAA/ASME/SAE/ASEE Joint Propulsion Conference and Exhibit*, AIAA Paper 2006-4745, July 2006.
- [5] Violi, A., Yan, S., Eddings, E. G., Sarofim, A. F., Granata, S., Faravelli, T., and Ranzi, E., "Experimental Formulation and Kinetic Model for JP-8 Surrogate Mixtures," *Combustion Science and Technology*, Vol. 174, Nos. 1–12, 2002, pp. 399–417. doi:10.1080/00102200215080
- [6] Zhang, H., Ph. D. Dissertation, Dept. of Chemical Engineering, Univ. of Utah, Salt Lake City, UT, May 2005.
- [7] Mawid, M. A., and Sekar, B., "Detailed Chemical Kinetic Modeling of JP-8/Jet-A Ignition in High Pressure Shock Tube," *42nd AIAA/ASME/SAE/ASEE Joint Propulsion Conference and Exhibit*, AIAA Paper 2006-5102, July 2006.
- [8] Roquemore, W. M., and Katta, V. R., "Role of Flow Visualization in the Development of UNICORN," *Journal of Visualization*, Vol. 2, Nos. 3–4, 2000, pp. 257–272.
- [9] Briones, A. M., Aggarwal, S. K., and Katta, V. R., "Numerical Investigation of Flame Lift-off, Stabilization, and Blowout," *Physics of Fluids*, Vol. 18, No. 4, 2006, p. 043603. doi:10.1063/1.2191851
- [10] Anna, A. D., Kent, J. H., and Santoro, R. J., "Investigation of Species Concentration and Soot Formation in a Co-Flowing Diffusion Flame of Ethylene," *Combustion Science and Technology*, Vol. 179, Nos. 1–2, 2007, pp. 355–369. doi:10.1080/00102200600812419

- [11] Liu, F., Guo, H., Smallwood, G. J., and Gulder, O. L., "Numerical Modeling of Soot Formation and Oxidation in Laminar Coflow Non-Smoking and Smoking Ethylene Diffusion Flame," *Combustion Theory and Modeling*, Vol. 7, No. 2, 2003, pp. 301–315.
doi:10.1088/1364-7830/7/2/305
- [12] Mizobuchi, Y., Shinjo, J., Ogawa, S., and Takeno, T., "Numerical Study on the Formation of Diffusion Flame Islands in a Turbulent Hydrogen Jet Lifted Flame," *Proceedings of the Combustion Institute*, Vol. 30, No. 1, 2005, pp. 611–619.
doi:10.1016/j.proci.2004.08.142
- [13] Kaplan, C. R., and Kailasanath, K., "Flow-Field Effects on Soot Formation in Normal and Inverse Methane-Air Diffusion Flames," *Combustion and Flame*, Vol. 124, Nos. 1–2, 2001, pp. 275–294.
doi:10.1016/S0010-2180(00)00196-6
- [14] Bennett, B. A. V., Mecnally, C. S., Pfefferle, L. D., and Smooke, M., "Computational and Experimental Study of Axisymmetric Coflow Partially Premixed Ethylene/Air Flames," *Combustion and Flame*, Vol. 127, Nos. 1–2, 2001, pp. 2004–2022.
doi:10.1016/S0010-2180(01)00306-6
- [15] Haworth, D. C., Cuenot, B., and Poinot, T., "Direct Numerical Simulation and Modeling for Lean Stratified Propane-Air Flames," *Combustion and Flame*, Vol. 128, Nos. 1–2, 2002, pp. 1–21.
doi:10.1016/S0010-2180(01)00328-5
- [16] Maroteaux, F., Noel, L., and Ahmed, A., "Numerical Investigations on Methods to Control the Rate of Heat Release of HCCI Combustion Using Reduced N-Heptane with Multidimensional CFD Code," *Combustion Theory and Modeling*, Vol. 11, No. 4, 2007, pp. 501–525.
doi:10.1080/13647830600952891
- [17] Ebrahimi, H., and Malo-Molina, F., "Numerical Investigation of 2-D and 3-D Multitube Pulse Detonation Using H₂ and JP8 Fuel," *42nd AIAA Aerospace Sciences Meeting and Exhibit*, AIAA Paper 2004-0465, Jan. 2004.
- [18] Katta, V. R., Goss, L. P., and Roquemore, W. M., "Numerical Investigations of Transitional H₂/N₂ Jet Diffusion Flames," *AIAA Journal*, Vol. 32, No. 1, 1994, p. 84.
- [19] Wilke, C. R., "Viscosity Equation for Gas Mixtures," *Journal of Chemical Physics*, Vol. 18, No. 4, April 1950, pp. 517–519.
doi:10.1063/1.1747673
- [20] Hirschfelder, J. O., Curtiss, C. F., and Bird, R. B., *Molecular Theory of Gases and Liquids*, Wiley, New York, 1954.
- [21] Williams, F. A., *Combustion Theory*, Perseus, Reading, MA, 1985.
- [22] Leonard, B. P., "Stable and Accurate Convective Modeling Procedure Based on Quadratic Upstream Interpolation," *Computational Methods in Applied Mechanical Engineering*, Vol. 19, 1979, p. 59.
- [23] Katta, V. R., and Roquemore, W. M., "Numerical Studies on Trapped-Vortex Concepts for Stable Combustion," *Transactions of the ASME: Journal of Engineering for Gas Turbines and Power*, Vol. 120, April 1998, p. 60.
doi:10.1115/1.2818088
- [24] Katta, V. R., Goss, L. P., and Roquemore, W. M., "Simulation of Vortical Structures in a Jet Diffusion Flame," *International Journal of Numerical Methods for Heat and Fluid Flow*, Vol. 4, No. 5, 1994, p. 413.
doi:10.1108/EUM00000000004046
- [25] Liang, L., Kong, S.-C., Jung, C., and Reitz, R. D., "Development of Semi-Empirical Solver for Detailed Chemistry In Internal Combustion Engine Simulations," *Journal of Engineering for Gas Turbines and Power*, Vol. 129, No. 1, 2007, pp. 271–278.
doi:10.1115/1.2204979
- [26] Smooke, M. D., "Numerical Modeling of Laminar Diffusion Flames," edited by E. S. Oran and J. P. Boris, Vol. 135, Progress in Astronautics and Aeronautics, AIAA, Washington, D.C., 1991, pp. 183–223.
- [27] Ito, T., Hosaka, T., Senda, J., and Fujimoto, H., "Numerical Investigation of Soot Formation in Diesel Jet Flame Using Detailed Kinetic Model," *Transactions of the Japan Society of Mechanical Engineers, Series B*, Vol. 71, No. 701, 2005, pp. 288–294.
- [28] Hilbert, R., and Thevenin, D., "Autoignition of Turbulent Non-Premixed Flames Investigated Using Direct Numerical Simulations," *Combustion and Flame*, Vol. 128, Nos. 1–2, 2002, pp. 22–37.
doi:10.1016/S0010-2180(01)00330-3
- [29] Yoshida, K., and Takagi, T., "Transient Local Extinction and Reignition Behavior of Diffusion Flames Affected by Flame Curvature and Preferential Diffusion," *Proceedings of the Combustion Institute*, Vol. 27, 1998, pp. 685–692.
- [30] Katta, V. R., Blevins, L. G., and Roquemore, W. M., "Dynamics of an Inverse Diffusion Flame and Its Role in Polycyclic-Aromatic-Hydrocarbon and Soot Formation," *Combustion and Flame*, Vol. 142, Nos. 1–2, 2005, pp. 33–51.
doi:10.1016/j.combustflame.2005.02.006
- [31] Katta, V. R., and Roquemore, W. M., "Simulation of Unsteady Flows in an Axisymmetric Research Combustor Using Detailed-Chemical Kinetics," *34th AIAA/ASME/SAE/ASEE Joint Propulsion Conference and Exhibit*, AIAA Paper 98-3766, July 1998.
- [32] Katta, V. R., Takahashi, F., and Linteris, G. T., "Fire-Suppression Characteristics of CF₃H in a Cup Burner," *Combustion and Flame*, Vol. 144, No. 4, 2006, pp. 645–661.
doi:10.1016/j.combustflame.2005.09.006
- [33] Katta, V. R., and Roquemore, W. M., "Effect of Nitromethane on Soot Formation in Heptane Jet Diffusion Flame," *Fourth Joint Combustion Meeting of the U. S. Sections of the Combustion Institute*, Combustion Inst. Paper 198, March 2005.
- [34] Peters, N., "Laminar Flamelet Concepts in Turbulent Combustion," *Proceedings of the Combustion Institute*, Vol. 21, 1986, pp. 1231–1256.
- [35] Bilger, R. W., "The structure of turbulent nonpremixed flames," *Proceedings of the Combustion Institute*, Vol. 22, 1988, pp. 475–488.
- [36] Wang, H., and Frenklach, M., "Detailed Kinetic Modeling Study of Aromatics Formation in Laminar Premixed Acetylene and Ethylene Flames," *Combustion and Flame*, Vol. 110, No. 1, 1997, p. 173.
doi:10.1016/S0010-2180(97)00068-0
- [37] Tsang, W., "Progress in the Development of Combustion Kinetics Databases for Liquid Fuels," *Data Science Journal*, Vol. 3, Jan. 2004, pp. 1–9.
doi:10.2481/dsj.3.1
- [38] Blevins, L. G., Fletcher, R. A., Benner, B. A., Steel, E. B., and Mulholland, G. W., "Existence of Young Soot in the Exhaust of Inverse Diffusion Flames," *Proceedings of the Combustion Institute*, Vol. 29, No. 2, 2002, pp. 2325–2333.
doi:10.1016/S1540-7489(02)80283-8
- [39] Schulz, W., "Oxidation Products of a Surrogate JP-8 Fuel," *ACS Petroleum Chemistry Division Preprints*, Vol. 37, No. 2, 1991, pp. 383–392.
- [40] Holley, A. T., Dong, Y., Andac, M. G., and Egolfopoulos, F. N., "Ignition and Extinction of Non-Premixed Flames of Single-Component Liquid Hydrocarbons, Jet Fuels, and Surrogates," *Proceedings of the Combustion Institute*, Vol. 31, No. 1, 2007, pp. 1205–1213.
doi:10.1016/j.proci.2006.07.208
- [41] Mack, J. H., Dibble, R. W., Buchholz, B. A., and Flowers, D. L., "Effect of the Di-Tertiary Butyl Peroxide (DTBP) Additive on HCCI Combustion of Fuel Blends of Ethanol and Diethyl Ether," *Society of Automation Engineers TP 2005-01-2135*, 2005.
- [42] Kobayashi, H., Howard, J. B., and Sarofim, A. F., "Coal Devolatilization at High Temperatures," *Proceedings of the Combustion Institute*, Vol. 16, 1976, pp. 411–425.
- [43] Montgomery, C., Sarofim, A., Preciado, I., Marsh, N., Eddings, E., and Bozzelli, J., "Experimental and Numerical Investigation of Soot-Reducing Fuel Additives," *41st AIAA/ASME/SAE/ASEE Joint Propulsion Conference and Exhibit*, AIAA Paper 2005-4472, July 2005.

C. Kaplan
Associate Editor

Asymmetric Expansion of detonation Wave in an Array of Tubes

Viswanath R. Katta*

Innovative Scientific Solutions, Inc., Dayton, OH, 45440

One of the important design criteria in the development of Pulse Detonation Engines (PDEs) is to reliably transition detonation generated in the ignition tube into a larger main tube in a shortest distance possible. It is thought that asymmetrically aligning the ignition and main tubes would enhance detonation transition. An exploratory numerical study was conducted for understanding detonation expansion in asymmetrically joined tube assemblies. A computational fluid dynamics (CFD) code based on flux corrected transport is used for the simulation of two-dimensional detonation wave formed from a pair of ignition sources in a smaller ignition tube and expanded into a larger main tube. A large number of geometries obtained by varying the tube sizes and offsets (asymmetry) are investigated. It is found that expansion of detonation destroys its cellular structure and generates strong triple-shock points near the walls. Asymmetric expansion creates triple-shock points that are stronger than those generated in symmetric expansion. Interaction of strong triple-shock points with walls often leads to galloping detonations. For severe expansion ratios symmetric configuration resulted in a deflagration wave (failed detonation) while asymmetric configurations yielded successful detonation transition from ignition tube to main tube.

I. Introduction

Pulse Detonation Engines (PDEs) operate with a higher thermal efficiency than the conventional, constant-pressure combustion engines [1]. PDEs also provide a very high specific impulse thrust at operating frequencies of few hundred Hz. They can be designed without the use of any rotating machinery or valves in the flow path. However, the design and operation of the PDEs are complicated by the unsteady, high-speed, pulsed combustion. To reduce the deflagration-to-detonation transition (DDT) time several conceptual procedures have been proposed. The combustible mixture in the main chamber can be ignited using detonation wave that was generated in a much-smaller, pre-detonation (or ignition) chamber. The primary concern in such approach is the success of the transmission of detonation wave from pre-detonation chamber to main chamber. Previous studies have indicated that the maximum expansion a detonation can successfully go through is of the order of 100%--placing a severe restriction on the detonation-tube diameter [2]. In order to achieve detonation in large-size tubes, innovative techniques need to be developed for improving the detonations (such as overdriven detonations) in the ignition chamber and for reliably transitioning detonation into the main chamber. One of the concepts thought about for providing a reliable transmission of detonation into a larger main chamber was to join the ignition chamber to the main chamber with a degree of asymmetry. It is believed that the complex wave structures generated during asymmetric expansion of cellular detonation wave would eventually strengthen the detonation itself. This problem of sustaining detonation in large-diameter tubes is investigated in the present paper using numerical techniques.

The detailed cellular structure of gaseous detonations has been studied using experimental techniques since 1960's. However, only in the late 1970's Taki and Fujiwara [3] and later Oran et al. [4] were able to numerically simulate the cellular detonation structure for the two-dimensional case. Both the experiments and simulations have identified that the number of cells in a cellular detonation wave is a consequence of the chemistry of the problem which is characterized by the reaction-zone length scale. The cell size was also found to be independent of the

*Senior Engineer, Associate Fellow of AIAA

channel width. After Taki and Fujiwara's first simulation [3] a number of numerical studies using cellular detonations have been performed during the past two decades [5-7].

An important concern in using cellular detonation wave as a source for the burning of the reactants stems from the stability of the cellular detonation wave. Experimentally it was found that the stability of the detonation wave increases with tube diameter. For example, a sudden increase in the tube diameter may not quench the detonation if the diameter is greater than thirteen cell widths [8]. As shown by St-Cloud et al. [9] and Moen et al. [10], a finite perturbation may lead to complete destruction of one-cell-width detonations. Therefore, a small but sudden expansion of detonation (or ignition) hotspot may result in a deflagration wave. Similarly sudden expansion of a detonation with fewer cells may also result in deflagration combustion. In the present numerical paper, expansion of detonation wave in asymmetrically joined tube assemblies are studied through systematically changing the diameters and offset between the ignition and main tubes. Numerical results are analyzed through the generation of movies of the instantaneous pressure fields in the tubes.

II. Mathematical Model

The conservation equations for mass, momentum, energy and the two progress variables are solved in Cartesian coordinate system [11]. The gas mixture considered in the numerical investigations is a stoichiometric hydrogen-oxygen fuel diluted with Ar/He by 70%. This mixture is known to generate a very stable detonation [3]. The hydrogen-oxygen reactions are represented by the two-step reaction mechanism of Korobeinikov [12]. This model has been successfully applied in the past for addressing various two-dimensional unsteady detonation problems [3,13]. The Chapman-Jouguet (C-J) Mach number of the premixed gas mixture considered is 4.8. The speed of sound, which is used for non-dimensionalizing velocities, in the unburned mixture is 529.16 m/s.

The present simulations used an explicit 2nd-order MacCormack predictor-corrector technique with 4th-order FCT (Flux Corrected Transport) scheme for capturing the shock waves accurately. Grid systems up to 3001x451 points are constructed with a criterion of $\Delta x = \Delta y = 2L^*/9$. Here, L^* is the induction length--a characteristic distance related to the unburned gas mixture. For the hydrogen-oxygen mixture considered in the present study L^* is 0.2933 cm. The cell width λ of a stably propagating detonation simulated with this mixture is ~ 2.60 cm. Note that this cell width is independent of the size of the tube used. Consequently all the dimensions reported in this paper are non-dimensionalized with λ . Every calculation is started after filling the channel with combustible mixture and then by igniting the mixture at specified regions. For the ignition purpose, two circular areas of 9-grid-points radius each are selected near the closed end of the ignition tube and then replaced the fuel mixture within this region with the combustion products. In constant-width channels, a stably propagating multi-dimensional detonation wave establishes as the combustion products push the flame front.

III. Results and Discussion

The detonation code employed for the current investigation on detonation wave propagation through asymmetrically placed tubes was previously used in performing studies on detonation propagation in various size straight tubes [14], tubes with porous walls [15] and tubes with obstructions [16]. The deflagration-to-detonation process in a tube having a width of λ was successfully simulated using a single ignition point. The stably propagating detonation wave with two transverse waves was successfully established from a single ignition spot after ~ 1000 time steps. The interaction between the transverse and detonation wave resulted in two triple-shock points and, thereby, a single detonation cell. Detonation velocities obtained at the upper and lower walls and at the mid-section showed that the reflection of a triple-shock point from the wall and the interactions between two triple-shock points result in locally increased propagation velocity. However, the average non-dimensional propagation velocity of the detonation was 4.96, which is close to the Chapman-Jouguet (C-J) velocity for the mixture considered. The geometry considered for studying detonation propagation from a small ignition tube with a width of H_1 to the main tube with a width of H_2 is shown in Fig. 1. These two tubes are attached such a way that their symmetric planes are offset by δ . The lengths of the ignition and main tubes are 24λ and 48λ , respectively. Two ignition sources are provided near the closed end of the ignition tube. Ignition sources are enclosed in open cavities such that the reflections from cavity walls provide quicker transition from ignition-induced deflagration wave to final detonation wave. Even though one ignition source is sufficient for initiating detonation in a small tube, two ignition sources are used in the present study for making sure that a stable propagating detonation wave establishes in the wide range of ignition-tube widths considered. This is demonstrated in Figs. 2-4.

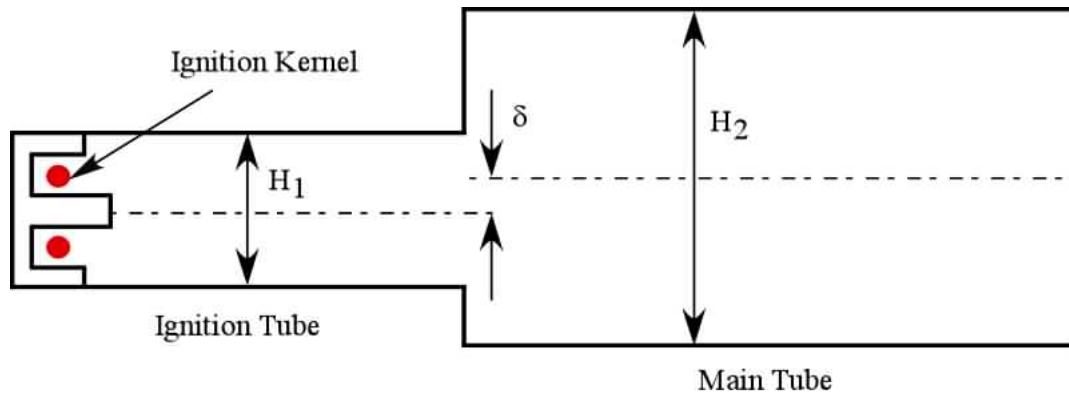


Fig. 1. Schematic diagram of the tube array used for studying detonation transition from small (ignition) tube to large (main) tube.

A. Detonation Initiation

Calculations for detonation formation in a 3.6λ -wide ignition tube were performed using a grid system of 151×1001 . Results in the form of instantaneous pressure distributions in different sections of the tube are shown in Fig. 2. Ignition kernels have grown to the extent of interacting with the cavity walls in $3 \mu\text{s}$ [Fig. 2(a)]. The shock waves emanated from the cavities established a detonation front by the time combustion reached half way in the ignition tube [Fig. 2(b)]. A stably propagating detonation with 7-8 triple-shock points (~ 3.5 cells) developed by the time it reached the exit of the ignition tube. The structure of the detonation wave exiting the ignition tube is shown in Fig. 2(c). The high-pressure regions in this figure represent interaction between two triple-shock points. Detonation initiation and propagation in a 4.8λ -wide ignition tube are shown in Fig. 3. These calculations are performed using a 201×1001 grid-system. Ignition sources provided in this calculation were identical to those used in 3.6λ calculation. For accommodating the smaller cavities in the wider ignition tube the widths of the cavity walls were increased [Fig. 3(a)]. This resulted in additional expansion when shock waves emanated from the cavities. However, a strong detonation wave was established in the mid-section of the ignition tube [Fig. 3(b)]. The detonation wave exiting the tube has about ten triple-shock points [Fig. 3(c)]. Note that unlike in Fig. 2(c) the triple-shock points in Fig. 3(c) are not evenly spaced. This suggests that the detonation wave has not sufficiently developed in the 24λ -long ignition tube. In contrast, calculations made for a 6λ -wide ignition tube resulted in an under-developed detonation by the time combustion front reached the tube exit [Fig. 4(c)]. Pressure distribution in Fig. 4(c) suggests only about 10 triple-shock points that are unevenly distributed developed on the detonation front. Note that a stably propagating detonation front should have 12 triple-shock points in this 6λ -wide tube. The development of fewer triple-shock points may be understood by examining the detonation structure at the mid-section of the tube [Fig. 4(b)]. Significant expansion of shock waves while exiting the cavities due to thicker walls [Fig. 4(a)] quenched the detonation near the symmetry plane. Collision of triple-shock points near the tube walls generated strong triple-shock points. These strong triple-shock points in a longer ignition tube should generate additional cells and should yield a stably propagating detonation with 7-8 cells.

B. Detonation Propagation in Main Tube

A number of calculations were performed for understanding detonation transition from ignition tube to main tube using the three ignition tubes described in Figs. 2-3 and various main tube sizes. Details of the tube sizes and layouts are summarized in Table 1. Note, offset (δ/λ) zero means ignition and main tubes are symmetrically attached and maximum δ/λ for each tube combination represents a configuration in which lower walls of the tubes are aligned (Fig. 1). Different grid systems were used for accommodating tube widths listed in Table 1. However, the grid resolution of 42 points per λ in both the longitudinal and vertical directions was maintained in all the calculations. Each calculation was started with ignition sequence and continued till the detonation wave front reaches the exit of the main tube, which represents $\sim 800 \mu\text{s}$ real time and 25,000 computational time-steps. Instantaneous pressure fields were stored after every 200 time-steps ($6.2 \mu\text{s}$ real time) of calculations. Results were analyzed through the

movies of pressure fields for understanding the dynamic characteristics of detonation propagation from ignition tube to main tube.

Table 1: Geometrical details of ignition and main tubes used in various simulations.

Tube Combination	Initiation Tube (H_1/λ)	Main Tube (H_2/λ)	Offset (δ/λ)
1	3.6	4.8	0, 0.12, 0.24, 0.36, 0.48, 0.6
2	3.6	6	0, 0.12, 0.24, 0.36, 0.48, 0.6, 0.72, 0.84, 0.96, 1.08, 1.2
3	3.6	7.2	0, 0.6, 1.2, 1.8
4	3.6	8.4	0, 0.6, 1.2, 1.8, 2.4
5	3.6	9.6	0, 0.6, 1.2, 1.8, 2.4, 3.0
6	3.6	10.8	0, 0.6, 1.2, 1.8, 2.4, 3.0, 3.6
7	3.6	12	0, 1.2, 2.4, 3.6, 4.2
8	3.6	13.2	0, 0.6, 1.2, 2.4, 3.6, 4.8
9	4.8	6	0, 0.12, 0.24, 0.36, 0.48, 0.6
10	4.8	7.2	0, 0.12, 0.24, 0.36, 0.48, 0.6, 0.72, 0.84, 0.96, 1.08, 1.2
11	4.8	8.4	0, 0.6, 1.2, 1.8
12	4.8	9.6	0, 0.6, 1.2, 1.8, 2.4
13	6	7.2	0, 0.24, 0.48, 0.6
14	6	8.4	0, 0.24, 0.48, 0.72, 0.96, 1.2
15	6	9.6	0, 0.6, 1.2, 1.8
16	6	10.8	0, 0.6, 1.2, 1.8, 2.4

The following observations are made from the simulations listed in Table 1:

Tube Combination 1. Calculations for the symmetric configuration ($\delta/\lambda = 0$) yielded smooth expansion of detonation from ignition tube to main tube. Initially, where the tubes were joined, the 3-4-cell detonation wave front reduced to one-cell wave. However, as the detonation propagated in the main tube additional cells started developing. Detonation neither locally nor temporally became deflagration wave. When a small offset of 0.12 was introduced to the tube assembly, detonation wave front still reduced to one-cell structure; however, one out of the two triple shock points that made-up the cellular structure became much stronger. Even though additional cells were developed while the detonation propagated in the main tube, the stronger triple-shock point led to galloping waves [15] near the walls, which destroyed the cellular structure of the detonation front. As detonation propagated further triple-shock point got weaker and new cells started establishing. Expansion into a 0.24-offset tube reduced the detonation wave to a one-triple-shock-point structure, i.e. half a cell. However, the surviving triple point is much stronger than those observed in the previous cases. Interaction of this strong triple-shock point with the tube walls led to galloping detonations, which then caused the detonation front to attain multi-cell structure. Interestingly, when the offset was increased to 0.36, no galloping detonations were observed. In fact, multiple cells were present on detonation front throughout the expansion process. Further increase in offset (to 0.48) enhanced cell destruction and the process of making one triple-shock point stronger than the rest. A galloping detonation also occurred. On the other hand, a stably propagating multi-cell detonation wave front with all the triple-shock points of nearly the same strength was established by the time it reached the exit of the main tube. The 0.6-offset case was similar to the 0.48-offset case, except that more galloping detonation events occurred in the former.

Tube Combination 2. Expansion through the symmetrically placed tubes ($\delta/\lambda = 0$) reduced the multi-cell-detonation structure to single-cell one. Both the triple-shock points that created the cell structure to the detonation wave front were stronger than those observed in a stably propagating detonation case. Interestingly, detonation front quickly settled into a stably propagating multi-cell structure (~ 12 triple-shock points). When an offset of 0.12 was introduced to the tube assembly these two triple-shock points got merged into a single strong triple-shock point. Stably propagating detonation was quickly established in this case also. No galloping detonations were observed. The 0.24-offset case was similar to the 0.12-offset case except that more triple-shock points (12 vs 10) were

established by the time detonation reached the end of the main tube. Even more triple-shock points were established in 0.36-offset case (14 vs 12). Such increase in the number of triple-shock points continued for the 0.48-offset case (16 vs 14). The two triple-shock points got merged into a single one when offset was increased to 0.6. This led to the formation of strong galloping detonation. In fact, cells were created while the detonation wave front was accelerating in the galloping detonation event. This offset also produced 16 triple-shock points on the detonation front when it reached the exit of the main tube. More but gradually weakening galloping detonation events occurred when the offset was increased to 0.72. It is also observed that galloping detonations tend to destroy the existing cells on a detonation front while simultaneously establishing newer cells. When the offset was increased to 0.84 detonation wave nearly became deflagration wave on one side and galloping detonation on the other side during the expansion process. A stably propagating wave structure was established by the time detonation reached the exit plane of the main tube. The 0.96 and 1.08-offset cases were similar to 0.84-offset case. In all these three cases majority of the detonation front became deflagration wave with no cellular structure. However, galloping detonation events re-established the detonation wave. 1.2-offset case was similar to previous one.

Tube Combination 3. Similar to previous cases, triple-shock points during the symmetric expansion of detonation in this tube combination also merged into two; thus, yielding a single-cell detonation front. Multiple cells were later on developed through cell-splitting process and transition of detonation wave from ignition tube to main tube was smooth. In the 0.6- and 1.2-offset cases, one triple-shock point got significantly stronger than the other point. Stronger one resulted in galloping detonations whenever it interacted with the tube walls. After several collisions at the wall these triple points yielded multi-cell structure rather dramatically. With 1.8 offset expansion of detonation into larger main tube resulted in a single triple-shock point. This led to some delay in the establishment of multiple cells. However, when they appeared it happened rather quickly. In general more cells developed as the tubes offset is increased.

Tube Combination 4. The symmetric expansion is shown in Fig. 5. Instantaneous pressure fields are plotted at three sections of the main tube. As seen Fig. 5(a) detonation wave front lost all the cells when it went through the geometrical expansion. Note that (as shown in Fig. 1) the detonation exited from the ignition tube had 3-4 cells. However, two strong triple-shock points were survived near the tube walls. Propagation of detonation with these two triple-shock points resulted in a single-cell structure [Fig. 5(b)] for some distance. However, through cell-splitting process detonation wave front with nearly 10 cells was established by the time it reached the exit of the tube [Fig. 5(c)]. When the offset of the ignition and main tubes was increased to 1.2, one triple-shock point got stronger than the other [Fig. 6(a)]. As shown in Fig. 6(b) propagation of stronger triple-shock created new cells. However, when the triple-shock point got too strong it also destroyed the existing cells [Fig. 6(c)]. Asymmetric and insufficiently developed detonation front established at the end of the main tube. Process of detonation expansion is shown in Fig. 7(a) for the 2.4-offset case. Triple-shock points on a detonation wave front become weaker when the detonation is subjected to expansion. However, the slowed-down triple-shock points get focused on to the upstream wall and generate a strong triple-shock point. This is shown in Fig. 7(b). Further collisions of this surviving triple-shock point with the walls generate multi-cell detonation front through cell splitting and/or generating new cells as shown in Fig. 7(c).

Tube Combination 5. Two triple-shock points were formed in the symmetric-expansion case. However, since the expansion ratio (H_2/H_1) for this combination is high (~ 2.7) detonation is not completely developed by the time it reached the exit of the main tube. Reminiscence of the initial strong triple-shock point is evident on the detonation front at the exit. In 0.6-offset case the strong triple-shock point produced strong explosion-type events latter in the tube. These events destroyed the already present cells and created the new ones. As a result at the exit plane detonation possessed a structure with only one strong triple-shock point. The 1.2-offset case is similar to previous one, but more cells were developed toward exit. The triple-shock point got stronger when the offset was increased to 1.8, which eventually led to the development of a stable detonation front at the exit of the main tube. While the results obtained with 2.4 offset are similar to those calculated with 1.8 offset, creation of new cells and destruction of older cells are more evident in the former case. Detonation was not quite well developed at the exit when the offset was increased to the maximum value of 2.4. Galloping detonations started establishing in this case.

Tube Combination 6. One strong triple-shock point established during symmetric expansion of the detonation wave into 10.8λ -wide tube. This resulted in a fully developed detonation front in the main tube toward the exit. Calculations with offset suggested that detonation front development gets delayed with offset initially and then gets accelerated with further increase in offset.

Tube Combination 7. Detonation front nearly decayed into deflagration wave for the symmetric case. However, the surviving triple-shock points could able to re-establish the detonation wave front, which further develops into a stable wave by the time it reaches the exit of the main tube. Initial excessive decay of detonation wave was not

evident when tubes were joined with some offset. Detonation develops into a stable wave front for all the offset conditions.

Tube Combination 8. Detonation failed to expand into the main tube that is 3.7 times wider than the ignition tube when it was attached symmetrically. Instantaneous pressure fields obtained at different sections of the main tube are shown in Fig. 8. The two triple-shock points developed from the merging of triple-shock points on the detonation front exited from the ignition tube during the initial expansion process [Fig. 8(a)] did not gain sufficient energy for triggering a galloping detonation, which is needed for re-establishing a decaying detonation wave. The detonation wave gradually decayed into a deflagration wave [Figs. 8(b)-8(d)]. However, when a small offset (0.6) was provided to the tube assembly, one triple-shock point got stronger while the other one got weaker [Fig. 9(a) and 9(b)]. The stronger triple-shock point was able to re-establish the detonation as shown in Fig. 9(c). The galloping detonation developed new cells [Fig. 9(c)] and finally established a stable detonation by the time it reached the exit plane [Fig. 9(d)]. Even though detonation failed for 1.2-offset case it has survived for longer period of time than the symmetric one did. Detonations were successfully established for all other offset cases. Instantaneous pressure fields obtained with 3.6 offset are shown in Figs. 10(a)-10(d).

Tube Combination 9. Detonation exited from the 4.8λ -wide ignition tube transitioned into a 6λ -wide main tube smoothly when the tubes were attached symmetrically. In contrast to the previous cases with smaller ignition tube, detonation front lost only a few cells during expansion when it emanated from a larger ignition tube. Number of cells increased as the detonation propagated in the main tube. A small offset (0.12) to the tube assembly developed stronger triple points on one side of the detonation wave and made it curved. Detonation became flat as it propagated downstream. Stronger triple-shock point in 0.24-offset case seems to destroy the weaker ones. However, it generated new cells once it gathered enough strength. Detonation is still developing at the exit. In 0.36-offset case the strong triple-shock point completely destroyed the other triple-shock points. However, it produced new cells whenever its interaction with the walls produced strong explosions. Behavior of detonation expansion with other two offsets (0.48 and 0.6) was similar to that observed with smaller offsets.

Tube Combination 10. Smooth transition of detonation wave from ignition tube to main tube was obtained with symmetric configuration. However, detonation front was not quite well developed by the time it reached the exit. For conditions with offset, in general, stronger triple points developed as the wave expanded asymmetrically. Number of stronger triple points decreased with offset. At the same time strength of the survived triple point increased with offset. Strong triple-shock points tend to destroy the existing cells and generate new ones.

Tube Combination 11. Near smooth transition of detonation was obtained in symmetric case. Slightly stronger triple-shock points were developed initially. Much stronger triple-shock points were developed in 0.6-offset case however they got dissipated to regular strength quickly. Stable detonation front wave was established in main tube rather quickly. With 1.2 offset all triple-shock points gradually merged into one strong triple-shock point. Because of this at some section in the main tube detonation front contained only one triple-shock point and the rest of the wave was smooth. Nevertheless, such smooth wave did not stay long. It convoluted into multi-cell structure rather dramatically. Detonation propagation in 1.8-offset case followed that of 1.2-offset case.

Tube Combination 12. Near smooth transition of detonation was obtained in symmetric case. Slightly stronger triple-shock points were developed initially. Two strong triple-shock points have developed in 0.6-offset case. These points destroyed the other triple-shock points and cells. However, they did not develop new cells in the main tube length considered. Nevertheless, detonation was sustained. In 1.2-offset case, merging of all the triple-shock points resulted in a strong explosion near the wall and established a stable detonation wave. Structure of the detonation wave near the exit was similar to that obtained with symmetric expansion. Merging of triple-shock points transformed most of the detonation wave into deflagration wave in 2.4-offset case. However, a strong explosion associated with the united triple-shock point re-established detonation. Strong explosion also created cellular structure to the wave front.

Tube Combination 13. Detonation exited from the 6λ -wide ignition tube transitioned into a 7.2λ -wide main tube smoothly when the tubes were attached symmetrically. However, detonation wave was developed partially with fewer cells (less than the one expected for a 7.2λ -wide tube). Detonation might develop the remaining cells in a longer tube. Interestingly, small offset (0.12) in tube arrangement did not cause much a deviation to detonation propagation from symmetric expansion. However, strong triple-shock points have established when offset was increased to 0.36. Propagation of these stronger triple-shock points did not cause the other triple-shock points to weaken. Detonation front was partially developed by the time it exited from the main tube. Results for 0.6-offset case were similar to those obtained with 0.36 offset.

Tube Combination 14. Detonation is significantly distorted while going through symmetric expansion. Stronger triple-shock points have developed which then destroyed or weakened the existing cells while generating new ones. Detonation expansion in 0.24-offset case established one strong triple point. Rest of the detonation became cell-free.

Detonation propagated in this mode for two channel widths before new cells start establishing on the smooth part of the wave front. 0.48- and 0.72-offset cases were similar to 0.24 case except that the detonation front never became smooth as in the former ones. Triple-shock point in 0.72- and 1.2-offset cases did not get intensified and as a result detonation retained its cellular structure through out the propagation.

Tube Combination 15. Results for this tube combination were similar to those obtained for combination 14 except that more orderly detonations developed for higher offsets for this tube combination.

Tube Combination 16. Symmetric detonation propagation from the 6λ -wide ignition tube into a 10.8λ -wide main tube is shown in Fig. 11. Detonation was significantly distorted and a strong triple-shock point was established at the mid-section of the main tube [Fig. 11(b)]. Detonation front at the exit of the tube [Fig. 11(c)] is still developing as the presence of a stronger triple-shock point continues to alter the cell structure. Partial development of detonation is more pronounced in the tube arrangements with some offsets (Figs. 12 and 13).

Times taken by detonation fronts in various tube configurations listed in Table 1 are plotted in Figs. 14, 15 and 16. In each case times are calculated starting from ignition till the detonation front reached first the mid-section of the main tube and then the end section. Variations in detonation arrival times with respect to tubes offset for 3.6λ -wide ignition tube are shown in Fig. 14. Even though, as discussed earlier, significant variations were noted in detonation structures during their propagation in tubes with different offsets, the arrival times shown in Fig. 14 are more or less independent of the tubes offset. This confirms the fact that the cellular structure of a detonation wave does not alter the average wave propagation speed. Numerically it was confirmed that propagation speeds of planar one-dimensional and cellular two-dimensional detonation waves are same and equal to Chapman-Jouguet speed [3]. However, expansion of detonation wave into wider tubes created partially weakened detonations (for example Figs. 9 and 10) which may reduce the average propagation speeds. This is evident in the Figs. 15 and 16 in which detonation arrival times are plotted with respect to tube expansion ratios. Detonation arrival times are increasing with expansion ratio. A comparison of arrival times in Figs. 15(a) and 15(b) suggests that the average detonation propagation speed decreased (or arrival times increased) more when tubes are joined with some offset. However, as noted in Fig. 15(a), the survival chance for the detonation to expand into a wider tube increases if tubes are joined with some offset.

IV. Conclusion

A computational study was performed for understanding detonation expansion into a main tube from a smaller ignition tube. A computational fluid dynamics (CFD) code based on flux-corrected transport is used for the simulation of two-dimensional detonation waves. Detonations are initiated in ignition tubes using two circular ignition sources enclosed in open cavities. Ignition tube is joined to the main tube with a specified offset creating asymmetric expansion for the detonation wave. A number of ignition-main-tube configurations are obtained through changing the tube sizes and offsets. Results are analyzed from the movies of pressure fields generated for each case. In general, expansion of detonation destroys its cellular structure and generates strong triple-shock points. It is found that asymmetric expansion creates triple-shock points that are stronger than those generated in symmetric expansion. Interaction of these stronger triple-shock points with walls often led to galloping detonations. However, the average propagation speed is not changed much with asymmetric nature of the tube assembly. For severe expansion ratios symmetric configuration resulted in a deflagration wave (failed detonation) while asymmetric configurations yielded successful detonation transition from ignition tube to main tube.

Acknowledgments

Financial support for this work was provided by the Air Force Office of Scientific Research (AFOSR, Dr. Julian Tishkoff) and the Air Force Contract #F33615-03-D-2329 (Dr. Fred Schauer). Author also thanks Drs. Fred Schauer and John Hoke for providing stimulating technical discussions.

References

- [1] Schauer, F., Stutrud, J., and Bradley, R. "Detonation Initiation Studies and Performance Results for Pulsed Detonation Engine Applications." AIAA Paper No. 2001-129, *39th AIAA Aerospace Sciences Meeting & Exhibit*, 8-11 January 2001, Reno, NV.
- [2] Katta, V. R., Chin, L. P., and Schauer, F., 17th International Colloquium on the Dynamics of Explosions and Reactive Systems, Heidelberg, Germany, July 25-30, 1999.
- [3] Taki, S., and Fujiwara, T., AIAA J. 16, 73 (1978).
- [4] Oran, E. S., Young, T. R., Boris, J. P., Picone, J. M., and Edwards, D. H., Ninteenth Symposium (International) on Combustion, P. 573, The Combustion Institute, PA, 1982.

- [5] Pantow, E.G., Fischer, M., and Kratzel, Th., "Decoupling and Recoupling of Detonation Waves Associated with Sudden Expansion," *Shock Waves*, Vol. 6, pp. 131-137, 1996.
- [6] Tangirala, V. E., Varatharajan, B., Pinard, P. F., and Dean, A. J., AIAA 2004-1209, 42nd AIAA Aerospace Sciences Meeting and exhibit, 5-8 Jan 2004, Reno, NV
- [7] Gamezo, V.N., Ogawa, T., and Oran, E.S., "Numerical Simulations of Flame Propagation and DDT in Obstructed Channels Filled with Hydrogen-Air Mixture," *Proceedings of the Combustion Institute* 30, pp. 2462-2471, 2007.
- [8] Glassman, I., *Combustion*, 3rd Edition, 1996, p.259
- [9] Saint-Cloud, J. P., Guerraud, C., Brochet, C., and Manson, N., *Astronautica Acta.*, 17, 487 (1972).
- [10] Moen, I. O., Donato, M., Knystautas, R., and Lee, J. H., Eighteenth Symposium (International) on Combustion, p. 1615, The Combustion Institute.
- [11] Taki, S., and Fujiwara, T., "Numerical Simulation of Triple Shock Behavior of Gaseous Detonation," *Proceedings of the Combustion Institute*, Vol. 18, 1981, pp. 1671-1681.
- [12] Korobeinikov, V., Levin, V., Markov, V., and Chernyi, G., *Astronautica Acta*, Vol. 17, No. 4&5, p. 529, 1972.
- [13] Hopper, D. R., King, P., Schauer, F. R., Katta, V. R., and Hoke, J. L., "Detonation Propagation Across an Asymmetric Step expansion," AIAA Paper 2007-5078, 43rd AIAA/ASME/SAE/ASEE Joint Propulsion Conference & Exhibit, July 8-11, 2007, Cincinnati, OH.
- [14] Fujiwara, T., and Katta, V. R., "Propagation Mechanism of Detonation—Three-Dimensional Phenomena," *Proceedings of the International Symposium on Computational Fluid Mechanics*, Aug. 28-31, Nagoya, Japan, pp. 531-536.
- [15] Katta, V. R., Fujiwara, T., and Lee, J. H., *Memoirs of the Faculty of Engineering, Nagoya University*, Vol. 40, No. 1, 1988.
- [16] Katta, V.R., Tucker, K.C., Hoke, J., Schauer, F., "Initiation of Detonation in a Large Tube," *19th International Colloquium on the Dynamics of Explosions and Reactive Systems*, Hakone, Japan, July 2 – August 1, 2003.

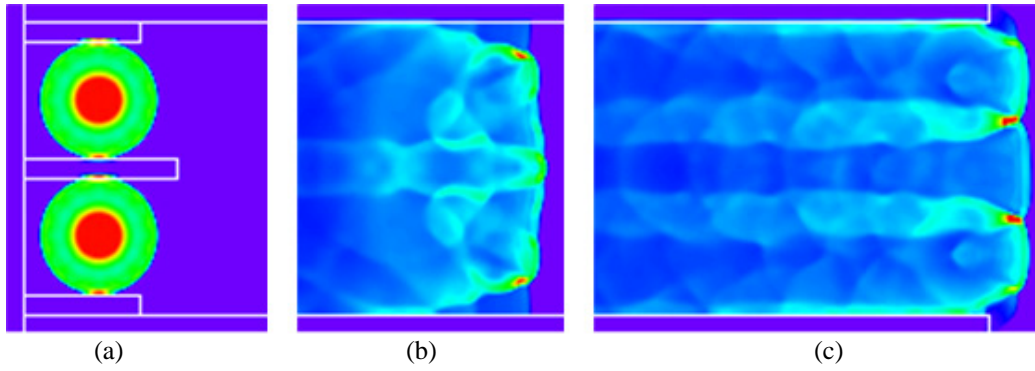


Fig. 2. Initiation and formation of detonation inside a 3.6λ -wide ignition tube. (a) Ignition kernel $3\ \mu\text{s}$ after the ignition. Structure of detonation wave inside ignition tube when it is at mid section (b) and while exiting (c).

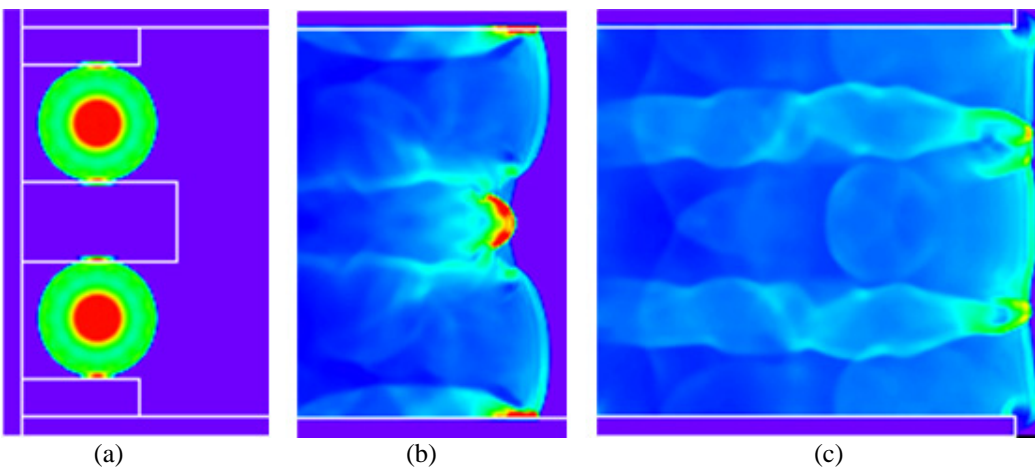


Fig. 3. Initiation and formation of detonation inside a 4.8λ -wide ignition tube. (a) Ignition kernel $3\ \mu\text{s}$ after the ignition. Structure of detonation wave inside ignition tube when it is at mid section (b) and while exiting (c).

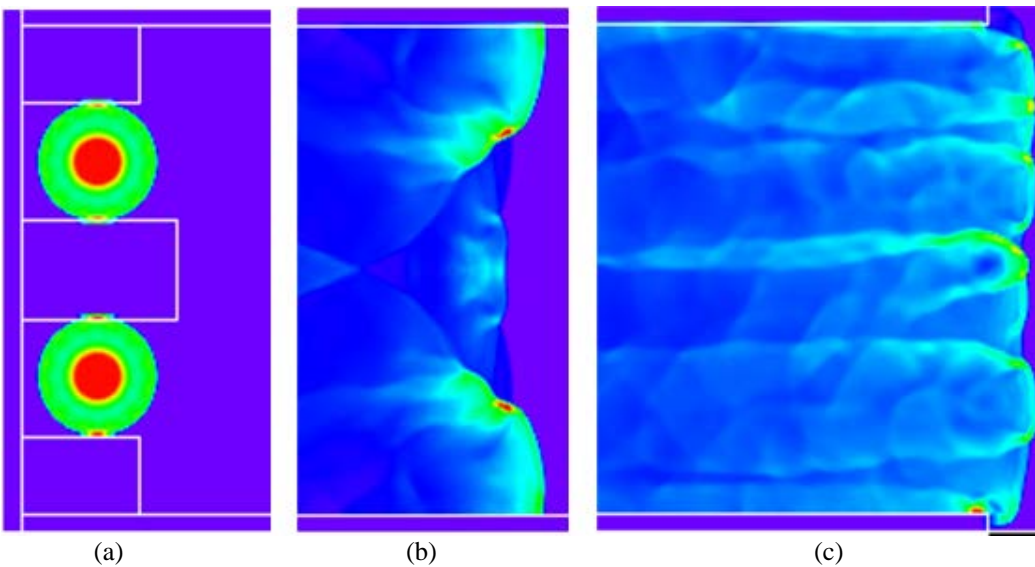


Fig. 4. Initiation and formation of detonation inside a 6λ -wide ignition tube. (a) Ignition kernel $3\ \mu\text{s}$ after the ignition. Structure of detonation wave inside ignition tube when it is at mid section (b) and while exiting (c).

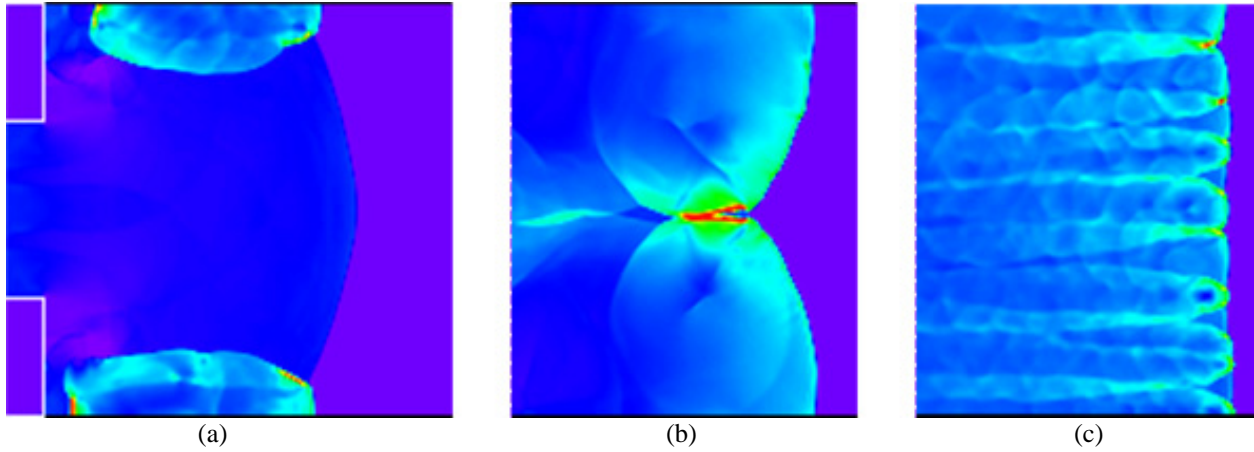


Fig. 5. Propagation of detonation from 3.6λ -wide ignition tube to 8.4λ -wide main tube. $\delta/\lambda = 0$. Detonation wave structure (a) while going through expansion, (b) at mid-section of main tube, and (c) at exit.

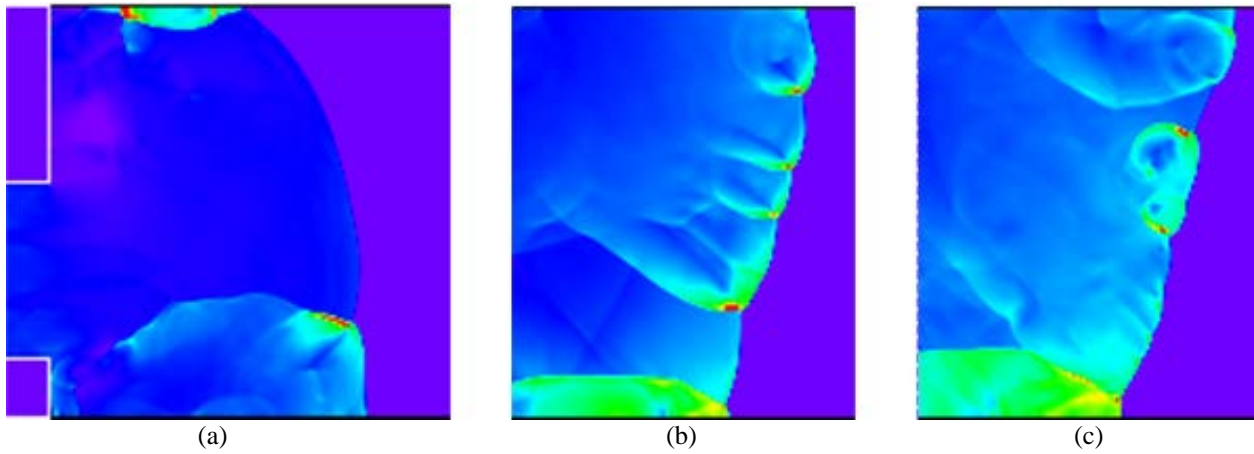


Fig. 6. Propagation of detonation from 3.6λ -wide ignition tube to 8.4λ -wide main tube. $\delta/\lambda = 1.2$. Detonation wave structure (a) while going through expansion, (b) at mid-section of main tube, and (c) at exit.

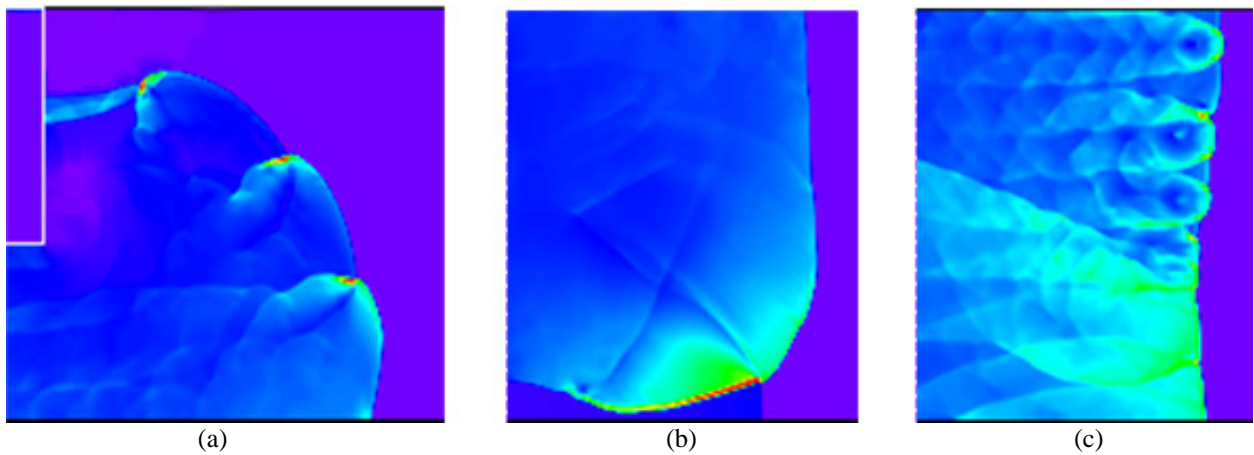


Fig. 7. Propagation of detonation from 3.6λ -wide ignition tube to 8.4λ -wide main tube. $\delta/\lambda = 2.4$. Detonation wave structure (a) while going through expansion, (b) at mid-section of main tube, and (c) at exit.

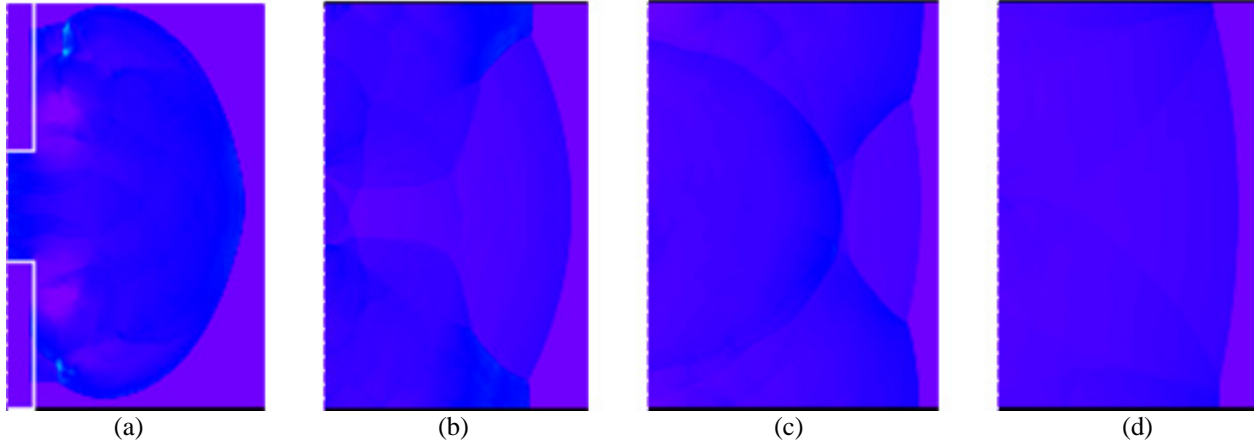


Fig. 8. Propagation of detonation from 6λ -wide ignition tube to 13.2λ -wide main tube. $\delta/\lambda = 0$. Detonation wave structure (a) while going through expansion and (b) 124 μs , (c) 230 μs , and (d) 550 μs later.

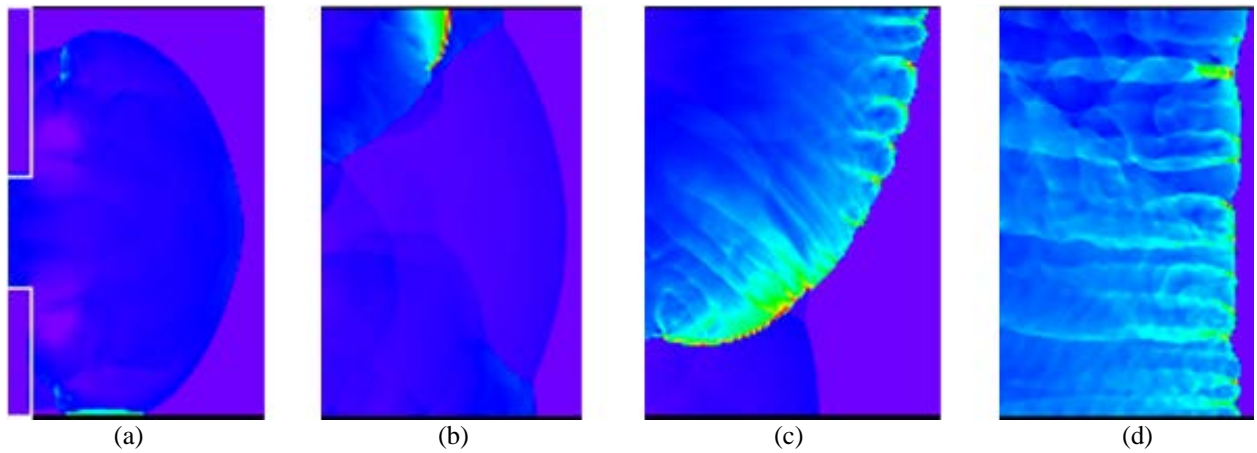


Fig. 9. Propagation of detonation from 3.6λ -wide ignition tube to 13.2λ -wide main tube. $\delta/\lambda = 0.6$. Detonation wave structure (a) while going through expansion and (b) 124 μs , (c) 230 μs , and (d) 550 μs later.

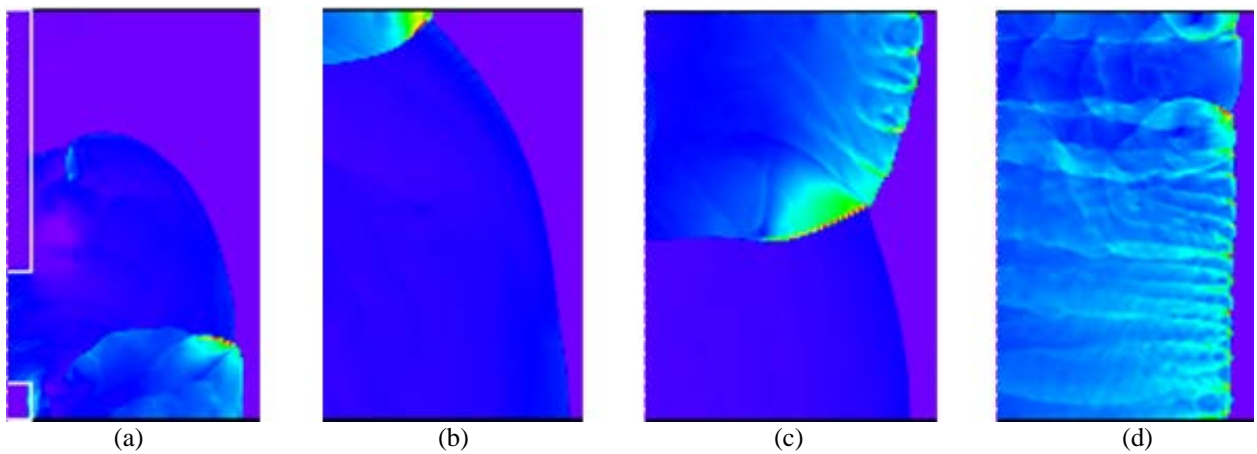


Fig. 10. Propagation of detonation from 3.6λ -wide ignition tube to 13.2λ -wide main tube. $\delta/\lambda = 3.6$. Detonation wave structure (a) while going through expansion and (b) 124 μs , (c) 230 μs , and (d) 550 μs later.

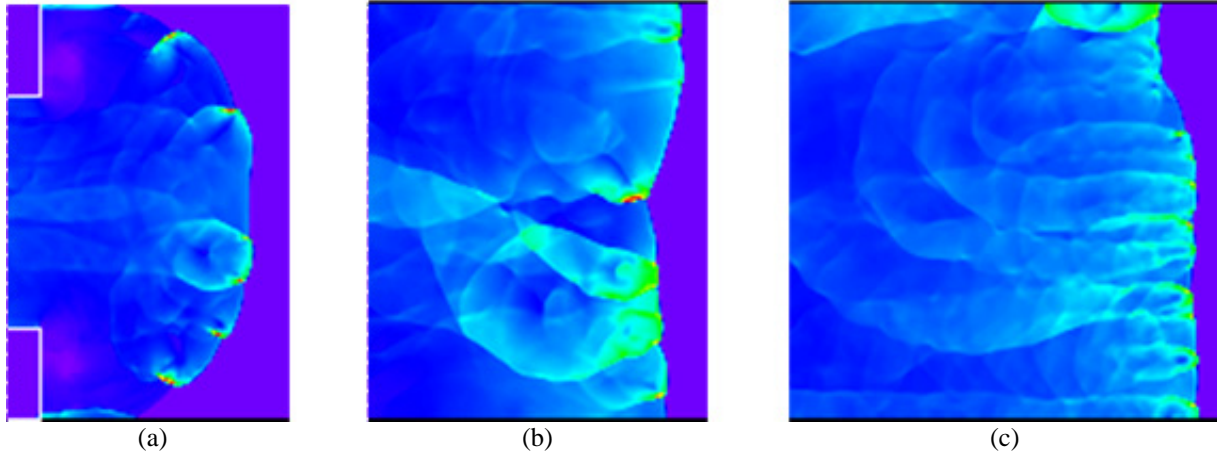


Fig. 11. Propagation of detonation from 6λ -wide ignition tube to 10.8λ -wide main tube. $\delta/\lambda = 0$. Detonation wave structure (a) while going through expansion and (b) $300\ \mu\text{s}$ and (c) $400\ \mu\text{s}$ later.

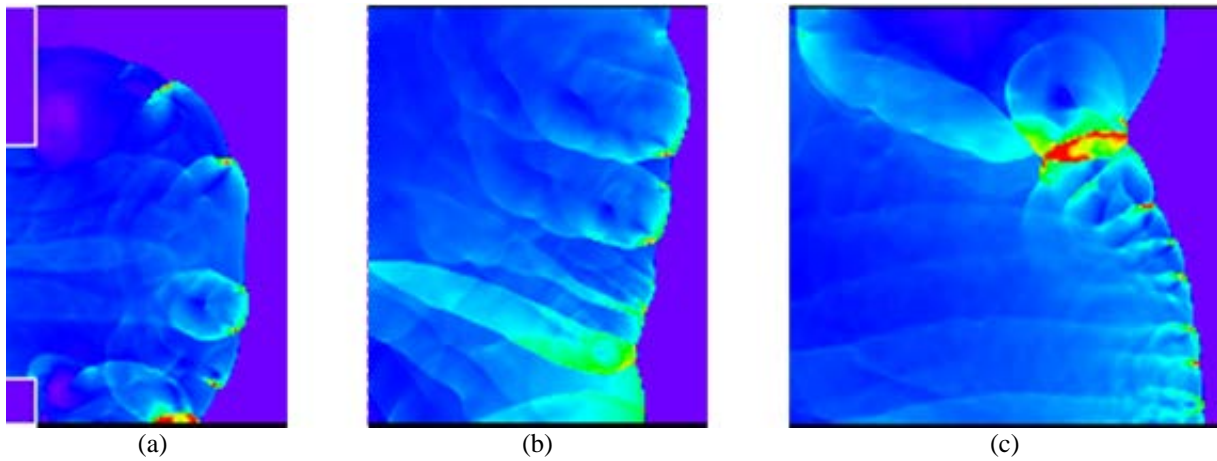


Fig. 12. Propagation of detonation from 6λ -wide ignition tube to 10.8λ -wide main tube. $\delta/\lambda = 1.2$. Detonation wave structure (a) while going through expansion and (b) $300\ \mu\text{s}$ and (c) $400\ \mu\text{s}$ later.

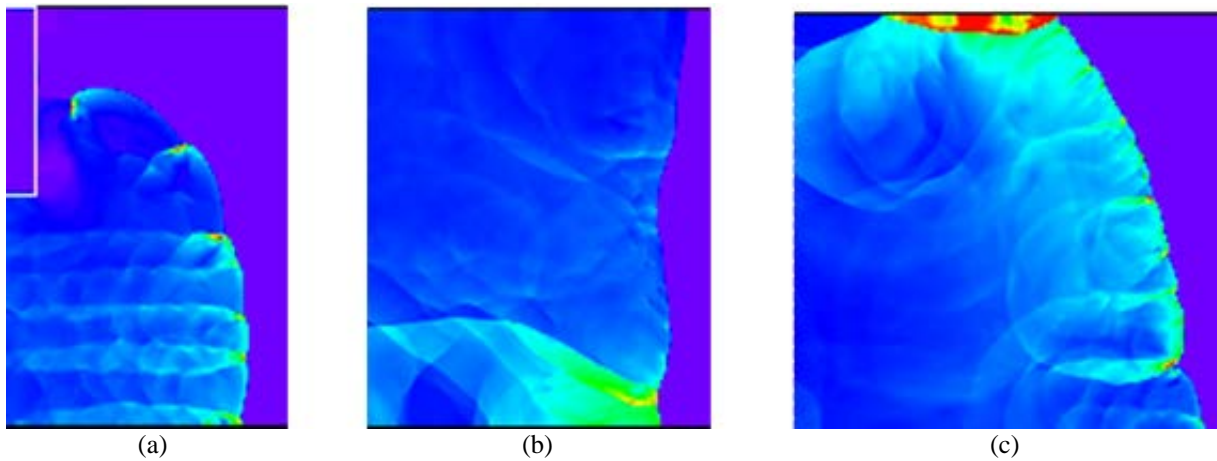


Fig. 13. Propagation of detonation from 6λ -wide ignition tube to 10.8λ -wide main tube. $\delta/\lambda = 2.4$. Detonation wave structure (a) while going through expansion and (b) $300\ \mu\text{s}$ and (c) $400\ \mu\text{s}$ later.

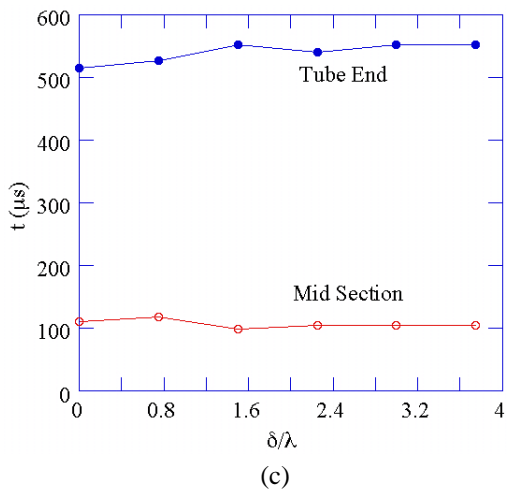
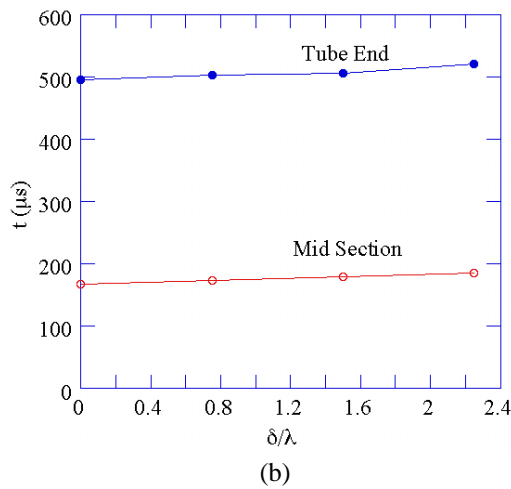
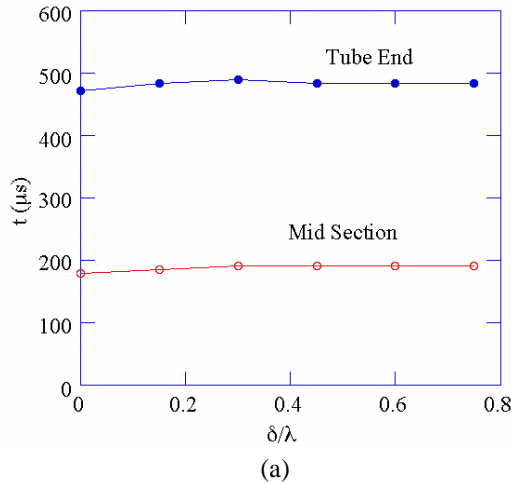


Fig. 14. Times required for detonation front for reaching mid- and end-sections of main tube for different tube offsets. Ignition tube width is 3.6λ . Main tube widths are (a) 4.8λ , (b) 7.2λ , and (c) 9.6λ .

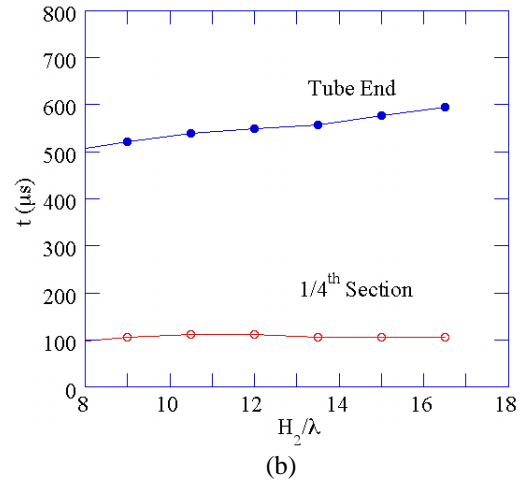
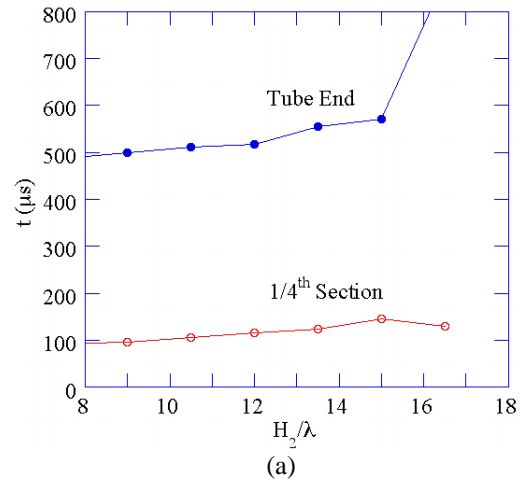


Fig. 15. Times required for detonation front for reaching 1/4th- and end-sections of main tube for different tube widths. Ignition tube width is 3.6λ . Tube-offsets are (a) 0 and (b) maximum.

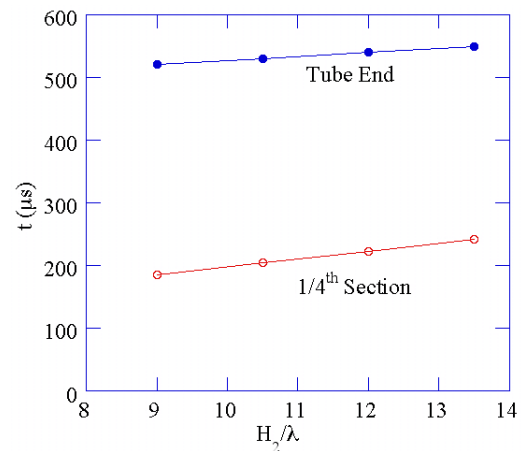


Fig. 16. Times required for detonation front for reaching 1/4th- and end-sections of main tube for different tube widths. Ignition tube width is 6λ . Tube-offset is zero.

DYNAMICS OF VORTEX-FLAME INTERACTIONS AND IMPLICATIONS FOR TURBULENT COMBUSTION

T. R. Meyer,^{*} V.R. Katta,[†] and M. S. Brown,[‡]
Innovative Scientific Solutions, Inc.
2766 Indian Ripple Road, Dayton, OH 45440-3638, USA
937-904-4007, trmeyer@innssi.com

J. R. Gord,[§] and W. M. Roquemore,[¶]
Air Force Research Laboratory, Propulsion Directorate
1790 Loop Road North, Wright-Patterson Air Force Base, OH 45433-7103, USA

A. Lemaire,[#] K. Zähringer,^{**} and J.C. Rolon,^{††}
École Centrale Paris, Laboratoire d'EM2C
Grande Voie des Vignes, 92295 Chatenay-Malabry Cedex, France

Abstract

Vortex-flame interactions are used to study the dynamics of unsteady laminar flamelet burning in non-premixed gaseous and two-phase flows. Such interactions provide a tractable numerical and experimental regime in which turbulent-like phenomena can be evaluated. This work explores a number of fundamental parameters that have implications for the study of turbulent combustion, including scalar dissipation, unsteady flame thickness, unsteady strain rate, and a new parameter recently proposed to characterize local extinction. Particular attention is paid to time-dependent (dynamic) phenomena, such as unsteadiness and flame movement, that may play a significant role in turbulent combustion modeling and validation. Results indicate that a variety of features can result in non-idealized flamelet behavior in near-unity-Lewis number flames. The sensitivity of mixture fraction state relationships to vortex-flame effects is analyzed and discussed.

^{*}Research Engineer, Member AIAA

[†]Senior Scientist, Associate Fellow AIAA

[‡]Physicist, Senior Member AIAA

[§]Principal Research Chemist, Associate Fellow AIAA

[¶]Senior Scientist, Fellow AIAA

[#]Post-Doctoral Student, Nonmember

^{**}Research Engineer, Nonmember

^{††}Professor, Nonmember

This paper is declared a work of the U.S. Government and is not subject to copyright protection in the United States.

Introduction

Vortex-flame interactions are often considered as fundamental building blocks for statistical theories of turbulence. Such interactions subject the flame surface not only to unsteadiness, but also to deformation. A number of experimental and theoretical investigations have considered the effects of curvature on unsteady flames [1,2]. Experiments designed by Roberts et al., [3] and by Rolon [4] have succeeded in producing well-characterized, repeatable vortex-flame interactions that can be used to verify computational and phenomenological models.

During studies in which a flame surface is subjected to stretch, deformation, and translation, a number of surprising features of flamelet behavior have been discovered: (1) moving curved flames can withstand strain rates that are much higher than steady extinction limits would suggest, and (2) that vortices coming from the air side can quench the flame much easier than the ones coming from the fuel side. The effects of vortex size have been studied by Takagi et al. [5] and Yoshida and Takagi [6], who investigated curvature effects on temperature by injecting micro jets toward the flame surface. Additional studies by Lee et al. [7] and Finke and Grunefeld [8] also considered the effects of curvature and preferential diffusion on flame temperature and extinction. Such studies have demonstrated the importance of considering both unsteadiness and flame geometry on flamelet behavior.

The combination of a repeatable combustor flowfield for experimentation and a laminar flow regime for the use of numerical models with complex chemistry has provided a means of bridging the gap with state-of-the-art turbulence models with simplified

chemistry. Modern K- ϵ and large-eddy simulations (LES), for example, often use a single parameter, referred to as the mixture fraction, to track the progress of chemical reactions. Temperature and species concentrations are assumed to be a direct function of this variable through “state relationships.” The latter can take the form of look-up tables with corrections for Lewis number effects, steady/unsteady strain, and scalar dissipation.

While simplified numerical models make turbulent combustion calculations more tractable, flamelet models have also been used to improve the ability of advanced experimental diagnostics to track dynamic flame behavior. In experiments used to verify the performance of LES models, flamelet models have been used to infer the mixture fraction based on the measurement of a single species such as the hydroxyl radical (OH). In this case, vortex-flame dynamics can play a significant role not only in bridging the gap between laminar and turbulent combustion models, but also in bridging the gap between available experimental diagnostics and relevant parameters for code validation.

The goal of the current work is to study how the coupling between unsteady fluid dynamics and flame chemistry can be used to improve turbulent combustion models as well as advanced combustion diagnostic techniques that rely on flamelet assumptions to infer the progress of flame chemistry. We first demonstrate the ability of numerical and experimental vortex-dynamics studies to capture a variety of interactions that are common in turbulent combustion but which are not easily captured in combustion models with simplified chemistry. We then discuss the implications of these dynamics for turbulent combustion models and experiments. More specifically, we explore the following areas: (1) the role of scalar dissipation, flame thickness, and unsteady strain on local flame extinction for a variety of fuel fractions, vortex sizes, and vortex velocities in methane-air flames, (2) differences or similarities in extinction behavior between single and colliding vortices (a.k.a. moving versus stationary dynamically strained flames), and (3) the behavior of certain experimental observables for model validation in dynamically strained environments.

Experimental Method

The opposing-jet-flow burner used for the studies of unsteady flame structures was designed by Rolon [9] and is shown in Fig. 1. The colliding vortex configuration shown on the left is used for methane-air flames, while the single vortex configuration on the right is used for both gaseous methane-air flames as well as droplet-seeded two-phase vortex-flame interactions. The burner system and experimental set-

up is described in detail in Refs. [9-13]. A flat flame is formed between the fuel and air jets having velocities of 0.5 to 1.0 m/s. The fuel-to-nitrogen ratio is varied to achieve various global mixture fractions. Vortices are shot toward the flame surface from either the fuel side or the air side, or simultaneously from both sides using a piston actuation system. In the colliding vortex configuration, vortices from the air and fuel sides are timed to meet at the flame and keep the flame stationary during the extinction process. Different sizes of fuel- and air-side vortices are achieved simply by changing the size of the vortex injection tube. The different vortex and flame conditions used in this study are listed in Table 1 for reference.

The laser-based measurement system consists of planar laser-induced fluorescence (PLIF) imaging of OH and CH, as well as simultaneous particle-image velocimetry (PIV), as shown in Fig. 2. Precise timing between the lasers, cameras, and piston driving events allows vortex repeatability on the same order as the computational time scales. Further details on the experimental diagnostics system can be found in Refs. [12-14].

Table 1. Vortex-flame conditions.

Run #	# of Vortices	Vortex Injection Tube Dia. (mm)	Vortex Vel. (m/s)	Fuel mass frac., Y _f
1	1	0.4	9	0.465
2	1	3.4	5	0.465
3	1	5	3	0.465
4	1	5	5	0.465
5	1	5	9	0.465
6	2	5	1	0.417
7	2	5	1	0.465
8	2	5	3	0.417
9	2	5	3	0.465
10	2	5	5	0.1967
11	2	5	5	0.305
12	2	5	5	0.417
13	2	5	5	0.465
14	2	5	5	0.515
15	2	5	7	0.465
16	2	5	9	0.465

Computational Method

Time-dependent, axisymmetric Navier-Stokes equations written in the cylindrical-coordinate (z - r) system are solved along with species- and energy-conservation equations [15]. A detailed-chemical-kinetics model has been used to describe the methane-air combustion process using 31 species and the GRI 1.2 chemistry model.

Temperature- and species-dependent property calculations are incorporated. The governing equations are integrated on a non-uniform staggered-grid system. An orthogonal grid having rapidly expanding cell sizes in both the axial and radial directions is employed to place more grid points in the strained flame region. The finite-difference forms of the momentum equations are obtained using an implicit QUICKEST scheme, [16,17] and those of the species and energy equations are obtained using a hybrid scheme of upwind and central differencing. At every time step, the pressure field is calculated by solving the pressure Poisson equations simultaneously and utilizing the LU (Lower and Upper diagonal) matrix-decomposition technique. This model, called UNICORN (UNsteady Ignition and COMbustion with ReactionNs), has been extensively validated [18] by simulating various steady and unsteady counterflow [19] and coflow [14,20,21] jet diffusion flames and by comparing the results with experimental data.

Results and Discussion

Model Validation

A typical experimental image of the millimeter-size-vortex/flame interaction is shown in Fig. 3. This represents the OH concentration field captured using PLIF measurement technique. It clearly shows the significant increase in OH concentration in the head region of the vortex. Results obtained from the calculations made for the millimeter-size-vortex/flame interaction in Fig. 3 are shown on the right-hand side of the experimental image. Calculations have also predicted the significant increase in the concentration of OH in the head region. The computed OH distribution matches qualitatively with the uncorrected experimental OH-PLIF data. The somewhat broad and diffused distribution of OH in the vortex-head region of the experiment could be attributed to the alignment of laser sheet to the axis of the injection tube. The inner and outer radii of the protrusion of the OH layer that occurred due to the vortex motion are only ~ 0.3 and 0.7 mm, respectively; which are of the order of the laser-sheet thickness (~ 0.4 mm). Any small misalignment of the laser sheet to the centerline of the OH protrusion could capture the OH that is present

circumferentially and make the fluorescence image blurry.

Both in the experiment and calculation, the interaction between millimeter-size vortex and flame resulted in local quenching of the latter along the stagnation line during the early stages and then the flame was reconnected within 1 ms. Calculations as well as experiments [22] made with different injection velocities resulted in very similar interaction sequences; namely, quenching, re-ignition, and an increase in temperature above the adiabatic value in the head region of the vortex.

Results for the colliding vortex configuration are shown in Fig. 4. Here, a 2-mm sized vortex is shot from above and a 5-mm sized vortex is shot from below. The flame extinguishes upon collision of the two vortices, and the flame is then entrained in the combined vortex structure. The flame morphology and timing are remarkably similar in both the computations and the experiment, showing that the numerical model adequately captures the spatially-evolving features of the flow. In order to maintain a more stationary flame, calculations on same-sized vortices have subsequently been used.

Invariant Flame Extinction Criteria

Flame extinction is an important parameter affecting the flame surface density in turbulent flames, although it is not easily considered in turbulent combustion models. In addition, mechanisms that lead to flame extinction also alter reaction rate and combustion efficiency. As vortices interact with a flame, flame intermediates such as the OH radical begin to decrease slowly at first, then drop quickly during the extinction process, as shown in Fig. 5. The CH radical, on the other hand, grows in intensity as the vortex approaches and increases chemical reaction rates. CH then declines more steeply than OH as flame chemistry comes to an abrupt halt. The entire extinction process can take fractions of a millisecond to several milliseconds depending on the imposed strain rate and exact chemical pathway. CH extinguishes slightly earlier than OH, a feature has also been observed in a number of experiments using OH and CH PLIF in turbulent methane-air flames [23,24]. In these experiments, intense regions of CH were found to correspond strongly with intense regions of OH, and CH was rarely found to extinguish without OH being extinguished as well. Such studies indicate that CH is a sensitive marker for flame extinction. In addition, CH layer thickness can be used for LES model validation. Temperature is another marker that is used to assess flame progress, but as shown in Fig. 6, there is a significant phase lag between the response of OH and

CH and that of Temperature. We find it useful, therefore, to consider the use of OH and CH as quantitative markers for flame extinction. In particular, we find that for the conditions listed in Table 1, the extinction flame temperature for OH and CH is about 1350K and 1450K, respectively, to within $\pm 5-7\%$. In the current work, the moment of extinction is determined by fitting a line to the last 20-40% of the OH vs. time plot and determining the zero crossing.

In terms of combustion modeling, however, it is useful to consider variables that are typically tracked in simplified chemistry models. Several parameters have been suggested in the literature. We will consider three as follows: a strain rate – temperature relation, scalar dissipation, and characteristic reactive layer thicknesses.

The following strain rate - temperature relation was first proposed by Katta et al. [25] based on results in a hydrogen-air unsteady counterflow diffusion flames:

$$\sigma = T_{\infty} \frac{K_a}{\left(\frac{dT}{dt}\right)_{ext}}$$

It is generally understood that the strain rate, K , acting on the flame will increase reactant flux into the flame zone. At lower strain rates, the chemical kinetics can consume all the reactants entering the flame zone. However, at higher strain rates, chemistry may not keep-up with the reactant fluxes and, there by, flame cooling occurs. As the strain rate (either air or fuel side) represents only the reactant fluxes transported into the flame zone it does not account for the changes in non-equilibrium chemistry that is taking place in highly stained flames.

Katta and coworkers found that this parameter, which is proportional to the air-side strain rate, K_a , and inversely proportional to the temperature-drop rate, gave a unique value at the extinction condition for all the flames considered in Ref. [25]. Some difference was noted for the case of a moving flame as opposed to a stationary flame. In the current work, we also found a difference between stationary and moving flames, as shown in Fig. 7. The difference in these two conditions is consistent with the finding of Katta et al. [25] of a different value σ for moving versus stationary flames.

As an alternative to the aforementioned extinction criterion, σ , the scalar dissipation rate has also been used as a measure of flame extinction. While strain rate alone cannot capture the response of the inner reaction zone to induced vortex perturbation, scalar dissipation is a measure of the scalar gradient field as follows:

$$\chi = 2 D_{eff} \left[\left(\frac{d\xi}{dz} \right)^2 + \left(\frac{d\xi}{dr} \right)^2 \right]$$

where D_{eff} is the thermal diffusivity and the mixture fraction, ξ , is defined as the mass fraction of material that originated from the fuel stream. It has a value which ranges from zero in the oxidizer stream to unity in the fuel stream. Because it represents the scalar gradient field, it accounts for the time integrated effects of strain rate and is more directly coupled to the progress of the reaction. This is especially true for lower turbulence levels for which the flame surface may not be aligned with the direction of principal strain. It has been proposed by Santoro et al. [26] as a quasi-universal extinction criterion, although it is not trivial to measure.

For the calculations reported here, the value of scalar dissipation at the stoichiometric surface was recorded as the overall reaction rate also peaks at this location. The data are shown in Fig. 8 for a set of conditions with only one air-side vortex and a set of conditions with vortices from both the fuel and air sides. Note that the while the case with only one vortex is fairly invariant, the case with two vortices shows an upward trend with higher levels of the air-side strain rate. This means that the flame can withstand higher levels of scalar dissipation before extinguishing as the vortex velocity increases. This trend is consistent with the findings of Ref. [25] in hydrogen-air dual-vortex-flame interactions.

Because of the difficulty in measuring scalar dissipation, Santoro et al. [26] have proposed using a mixing layer thickness a substitute for scalar dissipation. They argue that since the inverse of the scalar gradient is proportional to the mixing layer thickness, the mixing layer thickness can be used as an invariant extinction criterion. They report that the unsteady mixing layer thickness at extinction is very similar to that achieved in a quasi-steady manner. Since it is difficult to achieve strain rates that are typical in turbulent flows using a quasi-steady approach, it is also of interest to determine if this scaling is invariant to a number of different conditions. Fig. 9 shows an example of the change in layer thicknesses for CH, OH, and temperature during a vortex-flame interaction. Each computed value is normalized to the layer thickness in a steady flame. Note that OH and temperature are much more affected by the approaching vortex than CH. This agrees with the results of Refs. [23] and [24], who found that the CH layer thickness remained equal to that of their laminar counterparts. These were not conclusive, however, because of the limited spatial resolution of their imaging system. It is also interesting to note that temperature and OH follow nearly identical trends. The OH mole fraction is also plotted in Fig. 9 to indicate the time of extinction. After this time, the layer thickness of OH and CH are no longer meaningful. It is also interesting to note in the

right-hand figure that the change in OH and temperature thickness is nearly invariant with vortex velocity, size, fuel composition, and whether there are one or two vortices. The values of CH, although expected to be higher than OH and temperature, are unrealistically high because they were measured at the time of OH extinction when all the CH has nearly disappeared.

Consideration of Experimental Observables

Because of the availability of laser absorption lines and powerful Q-switched pulsed lasers, PLIF of species such as OH and CH are commonly used to characterize unsteady flames. In a series of papers from the same authors as Refs. [23] and [34], OH and CH PLIF was measured along with instantaneous velocity to characterize the structure of turbulent diffusion flames. It is of interest that flame extinction and flame stabilization can play a significant role in moderately turbulent flows. In particular, they found that the principal axis of strain was often aligned normal to the flame surface in the downstream region of $Re > 19,000$ combustion flows. Thus, the single and dual-vortex arrangement used here and discussed above is of direct relevance to turbulent combustion. Nonetheless, it is also of interest to use this burner configuration to improve the ability of planar single-shot or point-wise time-series measurements to gain insight into the accuracy of state-of-the-art turbulent combustion models.

It is already apparent that the OH layer thickness can be used as an analogy to the temperature thickness in terms of its dynamic behavior. For the strain rate – temperature criterion described earlier, it may also be possible to use measurements of CH and OH decay rates as analogies to the temperature decay rate. Evidence for this was found by Lemaire et al. [27], who showed that increasing strain rates increased the rate of CH decay in gaseous and two-phase vortex-flame interactions. These results are shown in Fig. 10 for which the Rates of CH decay increase with measured peak strain rates of 919, 1687, 1461, and 2363 s^{-1} for Vortices 1A, 2A, 2B, and 4A, respectively [27]. Calculations for similar conditions were performed in the current work, and an increased rate of decay of CH with increasing vortex strength is apparent in Fig. 11 (left). The correlation between the rate of decay of CH and OH with that of temperature is shown on the right in Fig. 11. It is notable that this correlation is somewhat good for most conditions of Table 1. This indicates that in addition to layer thickness, an analogy exists between temperature and CH/OH time dynamics. It should be noted that CH and OH are not the only experimental observables that may be of some use.

Other quantities such as HCO and CH₂O have also been proposed [26].

In addition to the time dynamics of layer thickness and decay rate, it is also useful to study vortex-induced perturbations in state relationships use to extract mixture fraction from time-series measurements of OH and CH [28-30]. In figure 12, three phases of vortex-flame are shown for run condition 2 (Table 1) – the steady state level, profiles when CH is at 50% of the steady value and at 5% of the steady value. Note that the CH and OH layers peak at lower values of the mixture fraction during vortex perturbation from the air-side, indicating that the flame intermediates are being produced at an effectively leaner condition due to the influx of oxidizer. Note also that the OH and CH layers broaden with respect to mixture fraction during the interaction. In particular, for example, a steady state relationship would not allow CH to exist below a mixture fraction of 0.1, according to Fig. 12. Yet, during vortex perturbation, CH persists down to nearly 0.05. The opposite effect may take place for vortices impinging from the fuel side. This could have a significant impact on the power spectral densities that are synthesized from flamelet manifolds for comparison with OH and CH time series data for LES model validation. It would be of interest to study the effects of dual-vortex perturbation on the state relationship as well. This gives some idea as to potential impact that vortex-flame events can have on transient state relationships between combustion intermediates and the mixture fraction.

A final consideration for how vortex-flame interactions can affect experimental observables in terms of the transient quenching rate imposed on measured species [30]. Not only can the temperature change dramatically during an extinction event, for example, but the distribution of quenching species may also change due to changes in reactant influx. Figure 13 shows the time-dependent quenching rate for OH (left) and CH (right) during the vortex flame interaction of Run 2. Note that the quenching rates for both are remarkably minor for much of the interaction. It is only toward the end of the perturbation that the quenching rate for OH drops significantly and that for CH increases. The effect of the change is quenching rate is best expressed in terms of the change in fluorescence quantum efficiency, which for weak laser perturbation is simply $A/(A+Q)$, where A is the coefficient for spontaneous emission and Q is the total quenching rate from all species. The effect on the species profiles near flame extinction are shown in Fig. 14, with the CH “observed” during an experiment overpredicting CH levels and OH being underpredicted. Note that the quenching rate for CH in particular are not known at low temperatures, although measurements are currently

underway in ongoing vortex-flame experiments.

Conclusions

Vortex dynamics for a number of non-premixed flame configurations were explored in order to determine relevant parameters for use in flamelet and mixture fraction approaches to turbulent combustion modeling. Several possible invariant extinction criteria are discussed, including a strain rate – temperature parameter, scalar dissipation, and species layer thicknesses. The latter was found to be the most promising in that it was most invariant for the conditions studied here. In addition, a number of features of interest to turbulent combustion model validation using experimental observables such as OH and CH were discussed. These include layer thicknesses, decay rates versus temperature decay rates, mixture fraction state relationships, and fluorescence quenching. The discussion should also apply to other experimental observables, a subject of ongoing research. The use of unsteady vortex-flame perturbations has, therefore been shown to be quite useful in helping to bridge the gap between laminar combustion models with complex chemistry and turbulent fluid dynamics models with simplified chemistry.

Acknowledgments

This work was supported by U. S. Air Force Contracts F33615-95-C-2507, F33615-97-C-2702, and F33615-00-C-2608, and French DGA / ONERA PEA-number 98703-TITAN in a French-U.S. collaborative program. Additional funding was provided by the U.S. Air Force Office of Scientific Research with Dr. Julian Tishkoff as Program Manager.

References

1. Paul, P. H., and Najm, H. N., *Proc. Combust. Inst.* 27: 43-50 (1998).
2. Patnaik, G., and Kailasanath, K., *Proc. Combust. Inst.* 27: 711-717 (1998).
3. Roberts, W. L., Driscoll, J. F., Drake, M. C., Ratcliffe, J. W., *Proc. Combust. Inst.* 24: 169-176 (1992).
4. Rolon, J. C., Aguerre, F., and Candel, S., *Combust. Flame* 100:422 (1995).
5. Takagi, T., Yoshikawa, Y., Yoshida, K., Komiyama, M., and Kinoshita, S., *Proc. Combust. Inst.* 26:1101-1110 (1996).
6. Yoshida, K., and Takagi, T., *Proc. Combust. Inst.* 27:685-692 (1998).
7. Lee, J. C., Frozakis, C. E., and Boulouchos, K., “Numerical Study of an Opposed-Jet H₂-Air Diffusion Flame-Vortex Interactions,” Seventeenth International Colloquium on the Dynamics of Explosions and reactive Systems (ICDERS), Heidelberg, Germany, July 25-30, 1999.
8. Finke, H., and Grunefeld, G., *Proc. Combust. Inst.* 28:2133-2140 (2000).
9. Rolon, J. C., Aguerre, F., and Candel, S., *Combust. Flame* 100:422 (1995).
10. Katta, V.R.; Carter, C.D.; Fiechtner, G.J.; Roquemore, W.M.; Gord, J.R.; Rolon, J.C., *Proc Combust Inst* 27:587-594 (1998).
11. Katta, V.R.; Meyer, T.R.; Gord, J.R.; Roquemore, WM (2003) *Combust Flame* 132:639-651.
12. Fiechtner, G.J.; Katta, V.R.; Carter, C.D.; Gord, J.R.; Roquemore, WM; Rolon, J.C., *J Visualization* 3:96 (2000a).
13. Fiechtner, G.J.; Renard, P.H.; Carter, C.D.; Gord, J.R.; Rolon, J.C., *J Visualization* 2(3/4):331-342 (2000b).
14. Lemaire, A.L.; Meyer, T.R.; Zähringer, K., Rolon, J.C., Gord, J.R., *Appl. Opt.* 42(12):2063-2072 (2003).
15. Katta, V. R., and Roquemore, W. M., *Combust. Flame* 100:61 (1995).
16. Frenklach, M., Wang, H., Goldenberg, M., Smith, G. P., Golden, D. M., Bowman, C. T., Hanson, R. K., Gardiner, W. C., V. Lissianski, V., Gas Research Institute Technical Report No. GRI-95/0058, November 1, 1995.
17. Leonard, B. P., *Comput. Meth. Appl. Mech. Eng.*, 19:59 (1979).
18. Katta, V. R., Goss, L. P., and Roquemore, W. M., *AIAA J.*, 32:84 (1994).
19. Roquemore, W. M., and Katta, V. R., *Journal of Visualization*, 2:257 (2000).
20. Katta, V. R., Carter, C. D., Fiechtner, G. J., Roquemore, W. M., Gord, J. R., and Rolon, J. C., *Proc. Combust. Inst.* 27: 587-594 (1998).
21. Grisch, F., Attal-Tretout, B., Bouchardy, P., Katta, V. R., and Roquemore, W. M., *J. Nonlin. Opt. Phys. Mater* 5:505 (1996).
22. Renard, P. H., Thevenin, D., Rolon, J. C., and Candel, S., *Prog. Energy Combust. Sci.* 26:225-282 (2000).
23. Watson, K. A., Lyons, K. M., Donbar, J. M., and Carter, C.D., *Combust. Flame* 123:252-265 (2000).
24. Ratner, A., Driscoll, J. F., Donbar, J. M., Carter, C. D., Mullin, J. A., *Proc. Combust. Inst.* 28:245-252 (2000).
25. Katta, V. R., Meyer, T. R., Brown, M. S., Gord, J. R., and Roquemore, W. M., submitted for publication in *Combust. Flame* (2003), was AIAA paper 2002-0479.
26. Santoro, V. S., Kyritsis, D. C., Linan, A., Gomez,

- A., *Proc. Combust. Inst.* 28:2109-2126 (2000).
27. Lemaire, A., Meyer, T. R., Zähringer, K., Gord, J. R., and Rolon, J. C., *Exp. Fluids*, in press (2003).
 28. Renfro, M. W., Gore, J. P., Laurendeau, N. M., *Combust. Flame* 129:120-135 (2002).
 29. Renfro, M. W., Guttenfelder, W. A., King, G. B., Laurendeau, N. M., *Combust. Flame* 123:389-401 (2000).
 29. Renfro, M. W., King, G. B., Laurendeau, N. M., *Combust. Flame* 122:139-150 (2000).
 30. Tamura, M., Berg, P. A., Harrington, J. E., Luque, J., Jeffries, J. B., Smith, G. P., and Crosley, D. R., *Combust. Flame* 114:502-514 (1998).

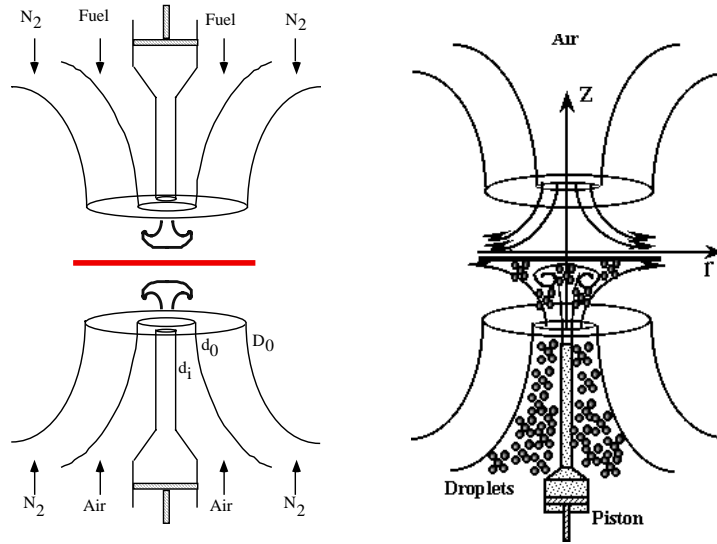


Fig. 1. Schematics of single-phase, dual-vortex (left) and two-phase, single-vortex (right) vortex-flame apparatus.

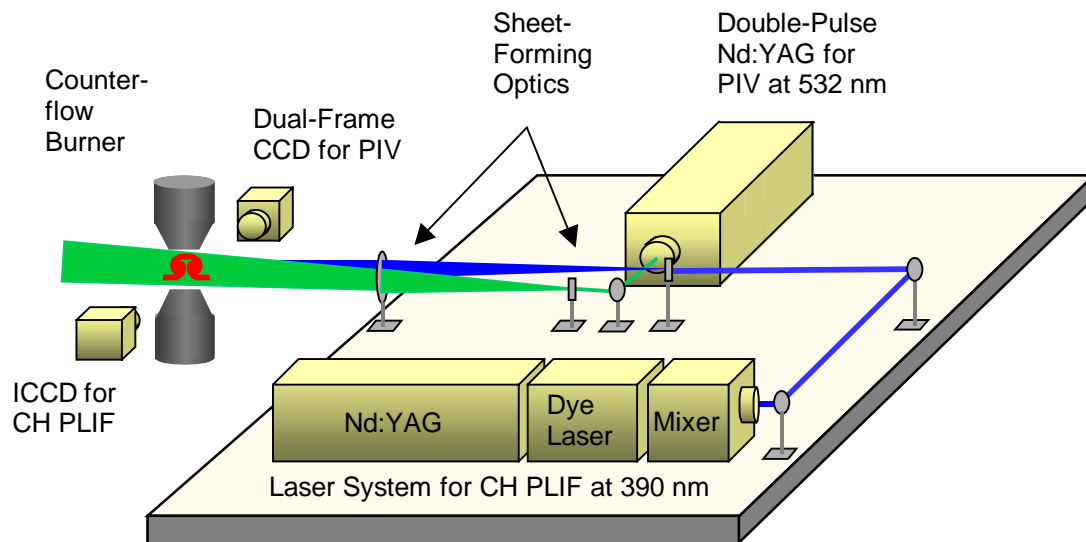


Fig. 2. Schematic of the OH/CH LIF and PIV measurement scheme.

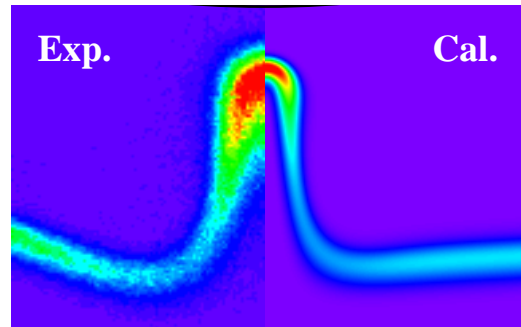


Fig. 3. Comparison of experimental and calculated OH distribution during a mm-size vortex-flame interaction. The high-intensity region at the tip of the perturbation represents a region of super-adiabatic flame temperature.

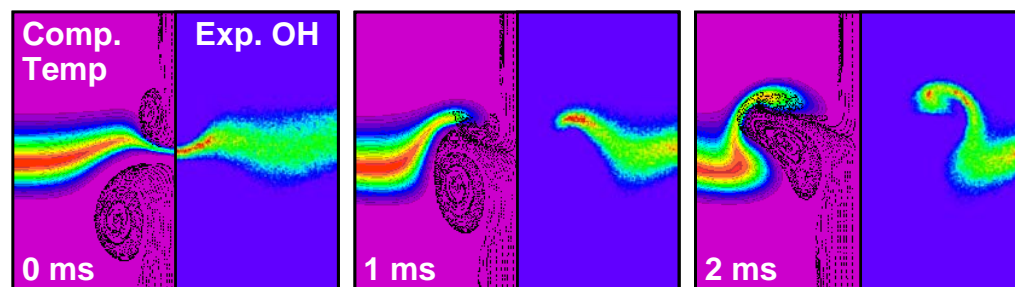


Fig. 4. Comparison of computed temperature and experimental OH distribution during the collision of 5-mm and 2-mm vortices at the flame surface.

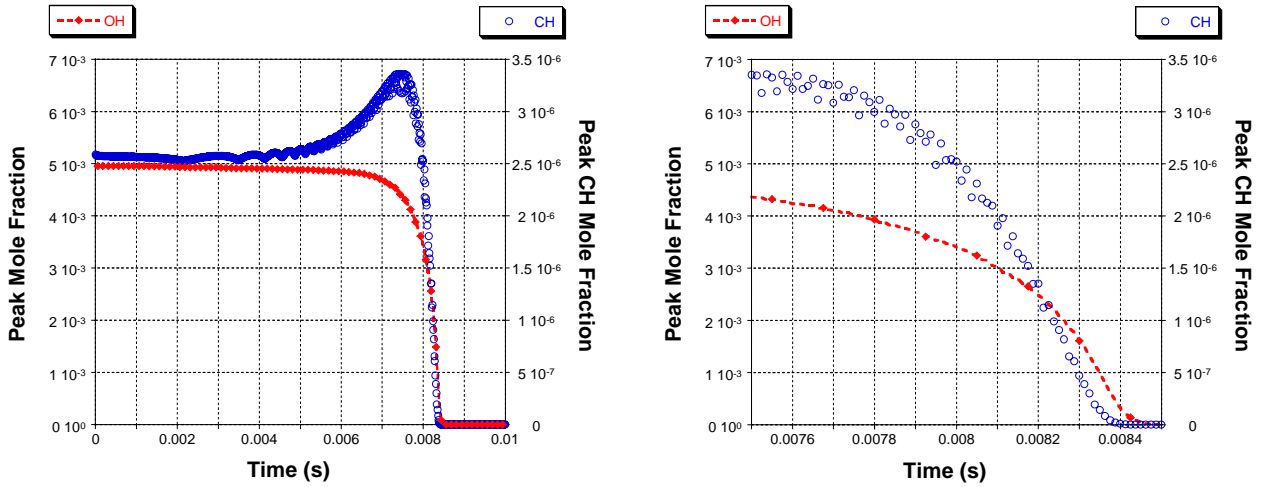


Fig. 5. Effect of vortex interaction on the peak of the OH and CH layers. Right-hand figure is a temporally more resolved version of the left-hand figure.

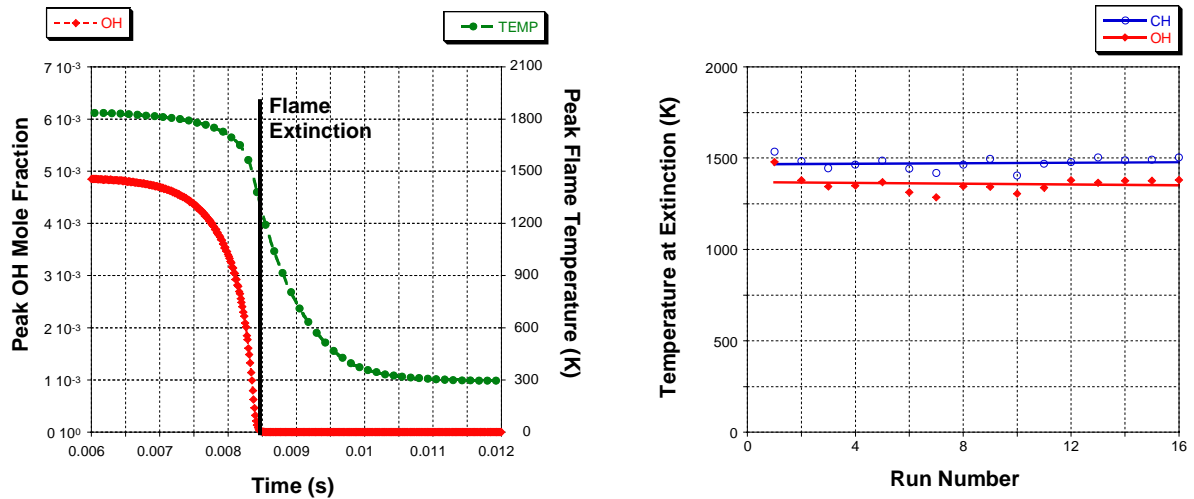


Fig. 6. Lag in temperature as compared to OH during the extinction process. Left-hand figure shows that OH extinction takes place while at a fairly high temperature (1300-1400K) . Right-hand figure shows that extinction temperature is nearly constant for various vortex velocities, mixture fractions, and sizes. CH extinguishes sooner than OH, as indicated by its higher extinction flame temperature.

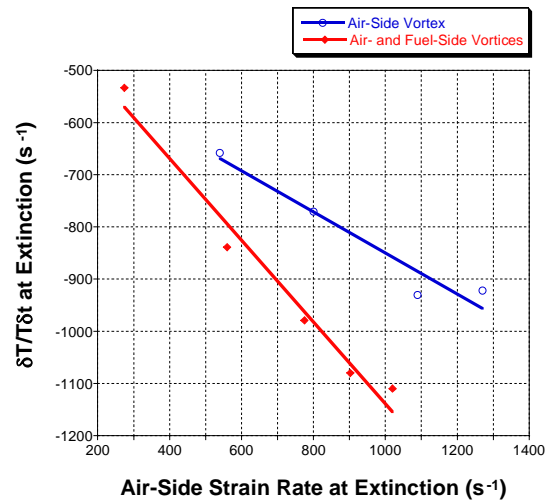


Fig. 7. Test of the strain rate temperature relation proposed as an extinction criterion. The proportionality of the rate of temperature change to the air-side extinction strain rate is encouraging, but variations are found for moving flames perturbed by one vortex as opposed to a stationary flame perturbed by two vortices.

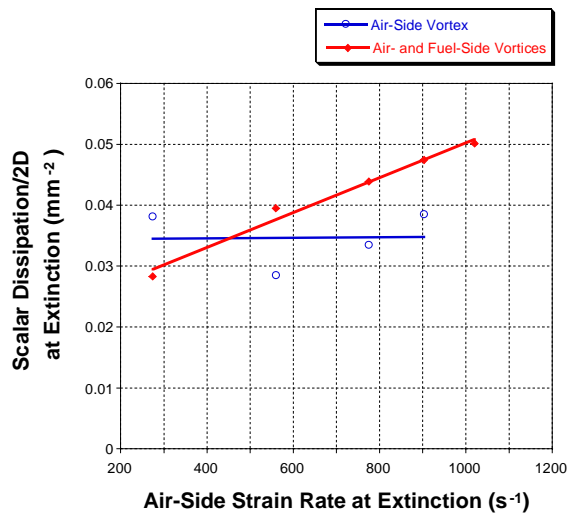


Fig. 8. Different calculation of scalar dissipation rate at the stoichiometric surface for the single and dual-vortex configurations.

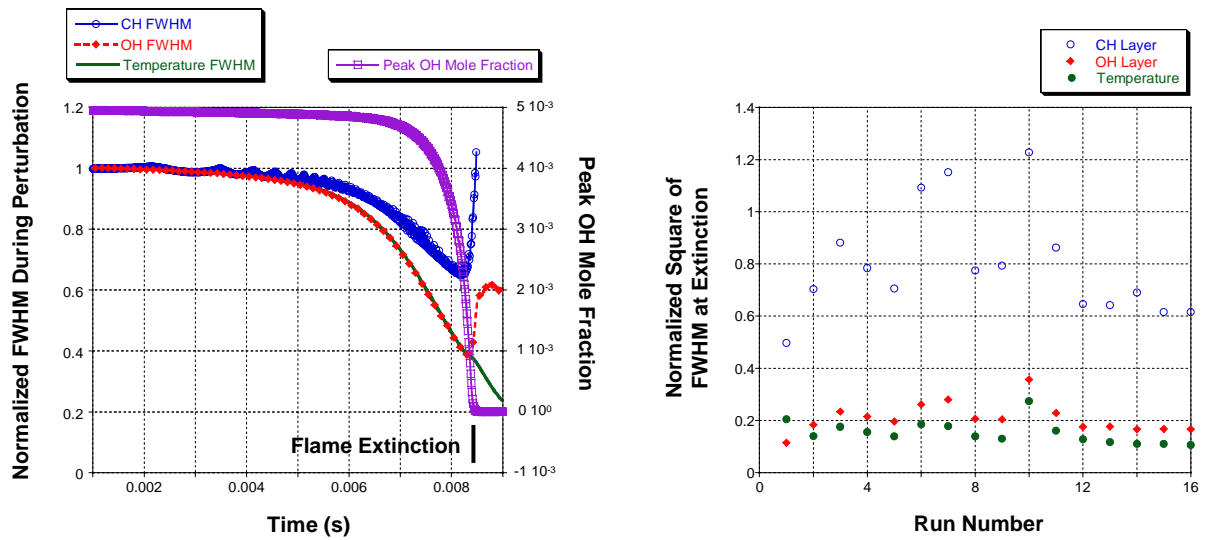


Fig. 9. Time dependence of CH, OH, and temperature thicknesses during vortex flame interaction. Values in left figure are normalized to the thickness in the steady flame, values in the right figure are the values at extinction squared (by analogy with scalar dissipation).

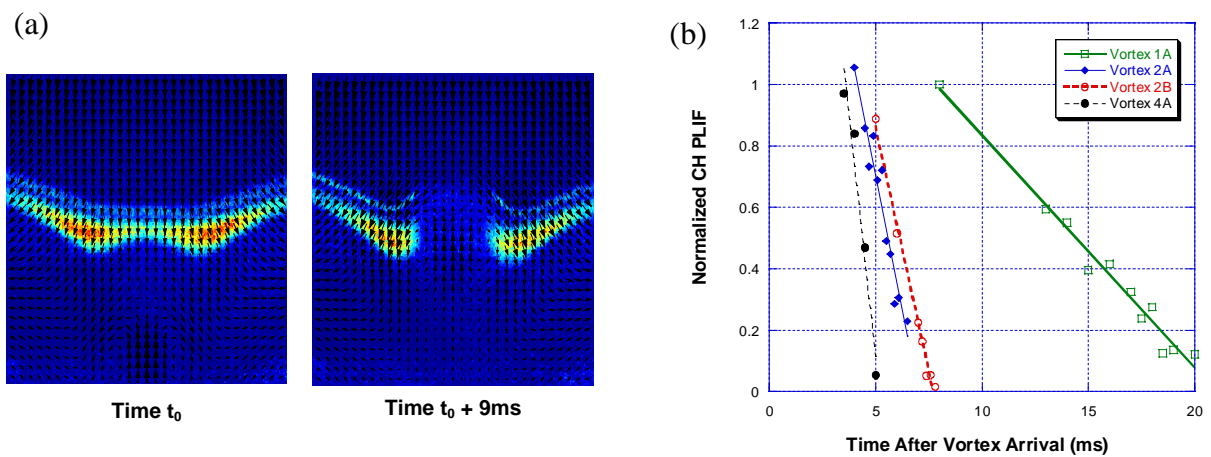


Fig. 10. Example of two-phase vortex-flame interaction from the Ref. [14] using simultaneous CH PLIF and particle image velocimetry (PIV). Rates of CH decay in the figure increase with measured peak strain rates of 919, 1687, 1461, and 2363 s^{-1} for Vortices 1A, 2A, 2B, and 4A, respectively.

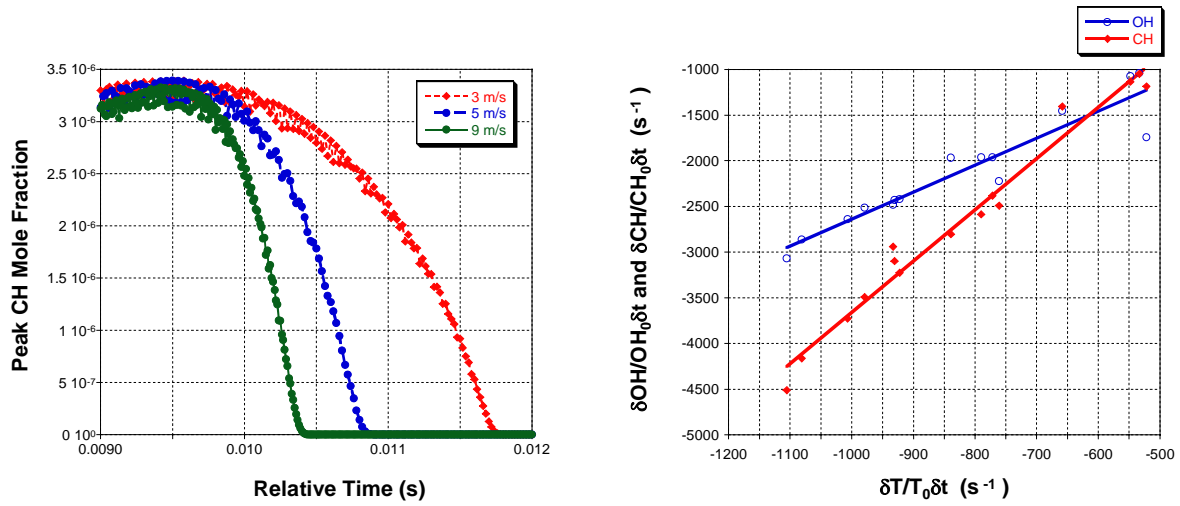


Fig. 11. Increase in CH decay rate for stronger vortex perturbations (left) and correlation between CH and OH decay rates with that of temperature for conditions from Table 1.

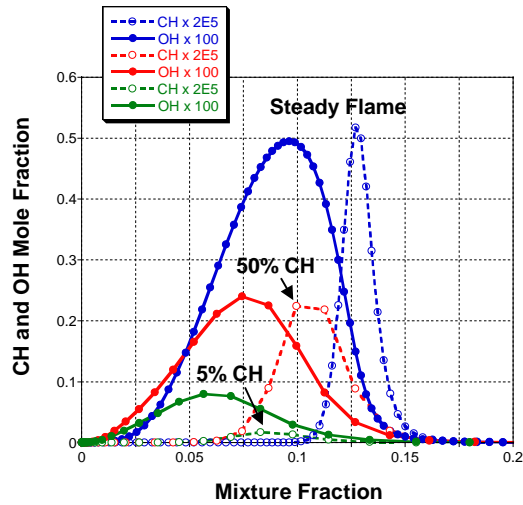


Fig. 12. State relationship for CH and OH with respect to mixture fraction for three phases of vortex-flame interaction – steady flame, when CH mole fraction is 50% of steady level, and when CH mole fraction is at 5% of steady level.

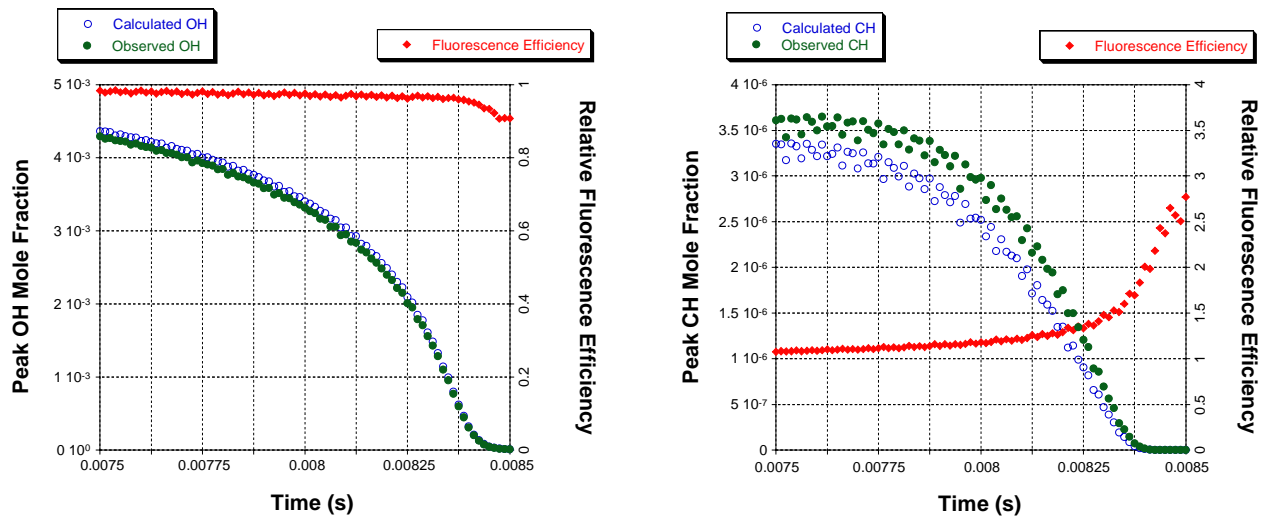


Fig. 13. Variation of quenching rate and its effect on the normalized signals observed in an LIF experiment for OH (left) and CH (right). The effect is more pronounced as the flame nears extinction.

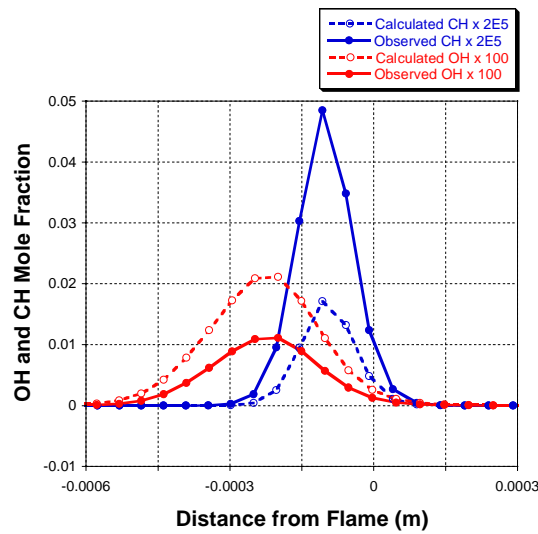


Fig. 14. Effect of flame product distribution on spatial fluorescence quenching profile when the CH level is 5% of that in the steady condition. Note very little change in the spatial profiles. The observed CH signal near extinction overpredicts the actual CH, while the observed OH underpredicts the actual OH.

Vortex Induced Extinction of Non-Premixed Counterflow Flames

A.Lemaire^{1,2}, K. Zähringer^{1,2*}, T. Meyer³, J. Gord⁴ and J.C. Rolon¹

¹Laboratoire E.M2.C., Ecole Centrale Paris, FRANCE

²now at : LSS, Universität Magdeburg, GERMANY

³Innovative Scientific Solutions Inc., Dayton, Ohio, USA

⁴Air Force Research Laboratory, Wright-Patterson Air Force Base, Ohio, USA

Abstract

In this experimental study, unsteady strain rate effects on the extinction process of a laminar strained two-phase flame are pursued during flame/vortex interaction, investigating simultaneously the flow field by Particle Imaging Velocimetry (PIV), and the reaction zone by Planar Laser Induced Fluorescence (PLIF) of the CH radical. The influence on the aerodynamic extinction limits for different vortex parameters and for different single- and two-phase flames is examined. The influence of different flames on the vortex flow is also investigated.

Introduction

The understanding of laminar flamelets is of great interest for turbulent combustion research [1-3], since turbulent combustion can take place in the laminar flamelet regime, depending on the relative scales of the flame front and of the flow perturbations [4]. Extensive studies of laminar strained flames improved the knowledge of the coupling between aerodynamics, diffusion processes and chemical kinetics.

However in reality, turbulent combustion takes place in highly unsteady flows. The characteristic time scales of the flow perturbations, due to small scales, can be of the same order as the time scales of diffusion and reaction. Thus coupling occurs that cannot be approached by steady analyses [5; 6]. Many studies have been carried out to investigate the effects of time-dependent strain on the flame. Darabiha [7] showed for calculations of an unsteady hydrogen/air opposed-jet flame with detailed chemistry and transport, that the flame response decreases when the frequency of strain rate oscillations increases. He observed that the flame can exist beyond the steady-state extinction limit for high frequencies and high strain rates. Delays between the forcing oscillation and the flame structure response appear. Using detailed chemistry and transport calculations of an unsteady methane/air opposed-jet flame, Egolfopoulos [8] obtained the same results and explained the flame response delay by diffusion processes in the diffusive flame layer and accumulation of reactants.

The flame front in turbulent non-premixed flames might be strained unsteadily, but also be curved. The interaction between a non-premixed counterflow flame and a vortex takes into account these processes and is thus a well-suited configuration for investigations [9]. Studies report the strain rate influence [10; 11] during gaseous vortex-flame interaction. Yoshida *et al.* [12] studied experimentally and numerically a counterflow

diffusion hydrogen/air flame strained by an impinging micro-jet. They found that the flame can resist to a high strain rate up to 5-10 times the quasi-steady extinction strain rate.

Studying multi-phase turbulent combustion is of great practical and fundamental interest. In many practical applications, fuel is introduced in a liquid form, modifying strongly the combustion process. In multi-phase turbulent flames, many phenomena are coupled, such as atomization, evaporation, molecular and turbulent mixing and chemical kinetics. Understanding and modeling of this coupling is a present challenge [13].

In this paper, simultaneous laser diagnostics are used to study the interaction between an *n*-heptane spray, a vortex ring and a non-premixed counterflow methane/air flame. The first studies of two-phase vortex-flame interactions in counterflow diffusion flames were reported by Santoro *et al.* [14; 15]. They compared vortex-induced perturbation and quasi-steady perturbation using PLIF of formaldehyde and laser Doppler velocimetry (LDV). They found that strain rates induced by air-side gaseous vortices are larger than quasi-steady strain rates, by over a factor of two, for a range of inlet oxidizer mass fractions.

The goal of the current investigation is to study the aerodynamic extinction limits of gaseous and two-phase flame fronts, submitted to unsteady strain and curvature. A flat non-premixed flame is established near the stagnation plane of a counterflow burner, and fuel-side vortices are introduced. The behavior of the reaction zone is studied using CH planar laser-induced fluorescence (PLIF), and vortex-induced strain rate is measured using particle-image velocimetry (PIV). Initial work in this configuration [16] focused primarily on the experimental technique and discerning the effects of global mixture ratio (i.e. fuel composition). Further work [17] investigated, through the qualitative CH

* Corresponding author: katharina.zaehringer@vst.uni-magdeburg.de

Associated Web site: <http://www.uni-magdeburg.de/isut/LSS>

Proceedings of the European Combustion Meeting 2003

concentrations and flame surface evolutions during the flame/vortex interaction, the liquid phase effects on the combustion process and the response of the flame submitted to strain. This study showed that the maximum peak strain rate is a relevant parameter for the extinction process. Here we focus on flame extinction limits by analysing in particular the unsteady effects on the extinction strain rate.

Experimental set-up

Burner

The burner set-up consists of a counterflow burner with air in the upper and fuel in the lower stream. The experimental device was previously modified from a gaseous counterflow burner design [18] to include a piston-actuated vortex injection system [19] and a monodisperse spray generator [16].

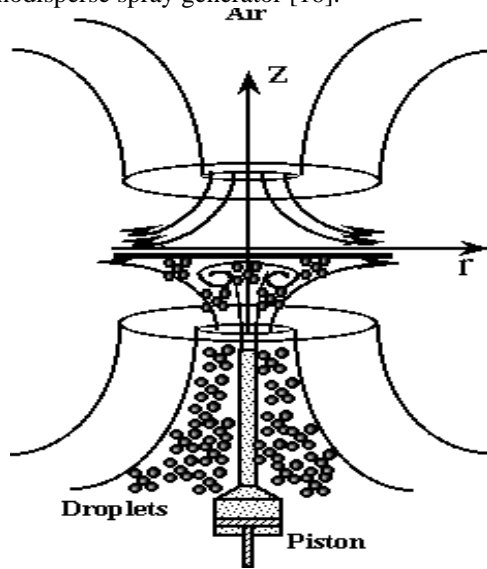


Figure 1 : Counterflow burner used for two-phase vortex-flame experiments.

The burner (Figure 1) consists of two axisymmetric, 20-mm diameter counterflow nozzles, with air in the upper flow and the nitrogen-fuel mixture in the lower flow. A 40-mm diameter flow of nitrogen surrounds each nozzle to shield the flame from ambient disturbances. The nozzles are separated by 30 mm. In our study the global strain rate imposed by the steady injection velocities is set to about 90 s^{-1} . The fuel is composed of methane diluted with nitrogen and seeded with n-heptane droplets produced by an atomizer system, creating a mono-disperse spray of $2.5\text{-}\mu\text{m}$ mean diameter droplets for the current flow conditions. The spray is diluted to a non-dense condition with a volumetric density of $9 \times 10^6 \text{ cm}^{-3}$.

Flame	Y_f	Ω (%)	Φ
M	0.26	0	4.43
D1	0.27	43	4.43
D2	0.21	52	3.44

Table 1 : Inlet flow conditions for steady strained flames.

The inlet flow conditions used in this investigation can be characterized by a number of parameters as listed in Table 1. They include the fuel mass fraction Y_f , the ratio Ω between the mass of n-heptane droplets and the total mass of fuel and the global mixture ratio Φ . The case M refers to a flame with no n-heptane seeding, cases D1 and D2 refer to two-phase flames.

Along the centerline of the fuel nozzle, a vortex injection tube is added, fed by an electronical piston-actuation system. This controls the volume ejected and the ejection time, in order to generate vortices of varying strength. Different vortex sizes can be created by changing the diameter of the injection tube. The vortex generation is then controlled by the vortex tube diameter d and by the expulsing velocity v_{ex} of the jet creating the vortex. These are listed in the Table 2 for different vortices. The expulsing velocity v_{ex} is calculated, based on incompressible fluid behavior, from the rise time of the piston, the volume expelled and the vortex tube diameter.

Vortex	T1	T2	t1	t2
d (mm)	3.7	3.7	2	2
v_{ex} (m/s)	0.35	0.46	0.44	1.2

Table 2 : Vortex generation conditions.

PIV system

In the current study, the vortex flow-field and the strain acting on the flame have been determined by digital cross-correlation PIV. Silicon-dioxide particles are used as seeding material in the air stream, while the n-heptane droplets are used to collect the Mie scattering from the fuel stream. The particle and droplet Stokes numbers in flows of characteristic perturbation times up to $700 \mu\text{s}$ (corresponding to strain rates of 1500 s^{-1}), are as low as 0.04, thus assuring that these tracers can follow our flows and are well-suited for the PIV measurements.

A double-pulsed Nd:YAG laser generates the overlapping 532-nm PIV-beams with an energy of 200 mJ per beam (Fig. 2). The beams are expanded using a lens combination forming a sheet of 0.5 mm thickness. The pulse intervals are varied from $50 \mu\text{s}$ to $200 \mu\text{s}$ depending on the speed of the vortex. A dual-frame 1008x1018 array Kodak Megaplug ES1.0 camera is used to acquire the two PIV images through an AF Micro Nikkor 105 mm f/2.8 lens and a 36-mm extension ring. Thus a magnification ratio of 2.2:1 image-to-CCD is achieved.

Mie scattering images are processed using an adaptative mesh technique with a commercially available PIV software. A final 32×32 pixel interrogation region and 50% overlap are used, giving a resolution of $290 \mu\text{m}$ for non-reactive flows, while, for reactive flows, a final 8×8 pixel interrogation region without overlap is achieved giving a resolution of $143 \mu\text{m}$.

CH system

The optical arrangement for the detection of the CH radical by PLIF is also presented in Fig. 2. The laser

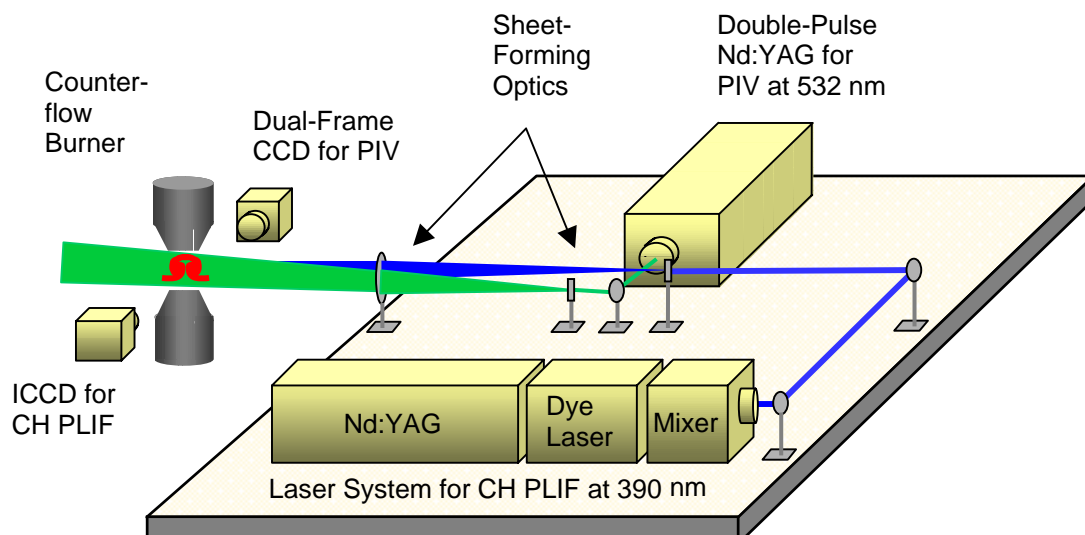


Figure 2 : Schematic of the simultaneous CH PLIF/PIV system.

system is composed of a Nd:YAG laser (1064 nm), doubled to 532 nm and pumping a tunable dye laser (Rhodamine 640). The dye-laser beam is frequency mixed with the Nd:YAG fundamental to obtain a wavelength (389.5 nm) corresponding to the $Q_1(5)$ transition of the $B^2\Sigma^-X^2\Pi$ (0,0) absorption band. The pulse duration is about 7 ns, with a mean energy of 15 to 20 mJ.

The beam is formed into a laser sheet that matches with the laser sheets from the PIV lasers in the axis of the burner. The CH laser sheet has a height of about 2 cm and a thickness of 0.3 mm. The energy distribution inside the CH laser sheet has been measured by Rayleigh scattering from nitrogen and Mie scattering from the droplets and the power density variation inside the region observed by the camera does not exceed 5%. In order to further minimise the effects of laser-sheet intensity variations and molecular quenching of CH, the laser energy is chosen to nearly saturate the CH transition. Note that the intention of this study is not a quantitative determination of CH concentrations, but the qualitative observation of vortex-flame interaction and extinction.

Fluorescence from the A-X (0,0) and A-X (1,1) bands around 430 nm is recorded using a 512x512 array PI-Max intensified CCD camera with a 58-mm f/1.2 Noct-Nikkor lens, giving a pixel measurement area of $100 \times 100 \mu\text{m}^2$. The CH-layer thickness is about 250 μm . A combination of a 410-nm high-pass and a 450-nm low-pass filter are used to separate the CH LIF signal from background scattering.

Synchronisation system

The precise synchronization of several events, including vortex generation, three laser pulses, and three camera exposures is needed for these simultaneous CH PLIF and PIV experiments. The master delay generator is driven by the 10-Hz second pulse of the double-pulse PIV laser. It then triggers the piston driver, CH-PLIF

laser system, and DANTEC PIV controller. The latter drives the PIV camera and lasers to ensure that all events occur simultaneously. The CH laser pulse occurs between the two PIV laser pulses to avoid light scattering from particles.

Various phases of the development of the vortex-flame interaction can be imaged by adjusting the relative timing between piston actuation and laser diagnostics. The initial time of the vortex-flame interaction is defined as the time when the vortex starts to perturb the CH layer.

Results for non-reactive flows

Figure 3 presents the velocity field superposed to the vorticity field in the case of the non-reactive vortex t_2 (see Table 2) for two different times during the vortex life time.

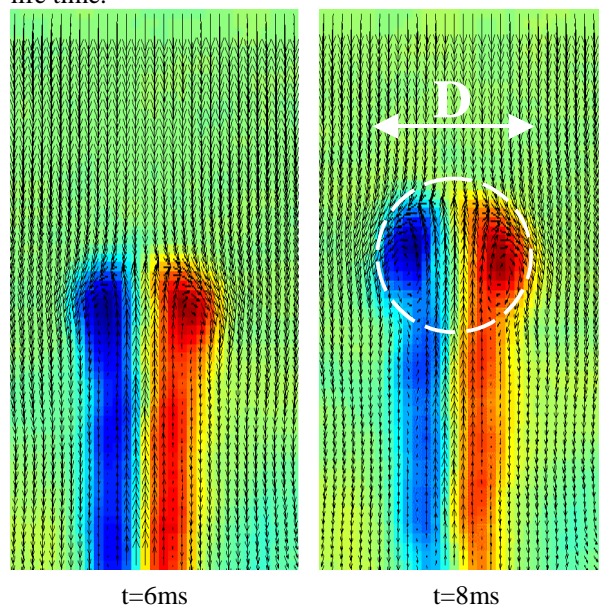


Figure 3 : Velocity and vorticity fields for vortex t_2 in the non-reacting case.

Note that the velocity vectors are presented in the reference frame of the vortex by subtracting the vortex translation velocity of about 1 m/s. This frame of reference highlights the circulating flow pattern and makes it easier to determine the vortex position as a function of time. The vorticity field exhibits the vortex core and also the shear layer created by the gas expulsion.

The non-reactive vortex is characterised by two parameters : the vortex size D and the strain rate Λ_{nr} . The size D of the vortex is determined from the vorticity field as shown on the right side of figure 3. The local strain rate Λ_{nr} is deduced from the velocity field. Since flame extinction in the current experiments is observed to take place at the centerline, the relevant strain rate induced by the vortex is defined at the axis by the following formulation :

$$\Lambda = -\frac{\partial u_z}{\partial z}$$

where z is the axial coordinate and u_z is the vertical component of velocity. The peak strain rate occurs near the stagnation point in the convective frame of reference. The strain rate Λ_{nr} for the non-reactive flows is chosen equal to the maximum value of the peak strain rate during the vortex evolution. It takes a value of 840 s^{-1} in the case of the vortex t2. The PIV resolution of $290 \text{ }\mu\text{m}$ leads to 6 measuring points across the velocity gradient thickness of about 1.5 mm. Results from vortex size and strain rate determination for the other vortices are shown in Table 3.

Results for reactive flows

Our aim is to study the dynamic response, and especially the extinction, of single- and two-phase non-premixed flames submitted to an unsteady strain. The extinction is, in particular, investigated through aerodynamic extinction limits and focuses on unsteady effects of the perturbation on the extinction limits. For this, two values of the strain rate during the flame/vortex interaction are measured : one Λ_r relevant for the aerodynamic reactive perturbation, another one Λ_q relevant for the extinction process. The first is defined, in the same manner as for the non-reactive flows, by the maximal value of the peak strain rate during the vortex evolution. The second one is measured at the moment of flame extinction, the flame extinction being depicted by the CH layer extinction. Data from CH PLIF diagnostics effectively localise the diffusion flame front and extinction zones (extinction signal refers to a signal that falls to the level of background noise) of the two-phase flame.

Figure 4 presents the extinction process occurring during the interaction between the two-phase flame D1 (see Table 1) and the vortex t1 (see Table 2). The flame is visualised by the CH fluorescence, while the flow is visualised by the velocity field. This interaction sequence is a superposition of CH PLIF and PIV data obtained by averaging on 10 single laser pulses.

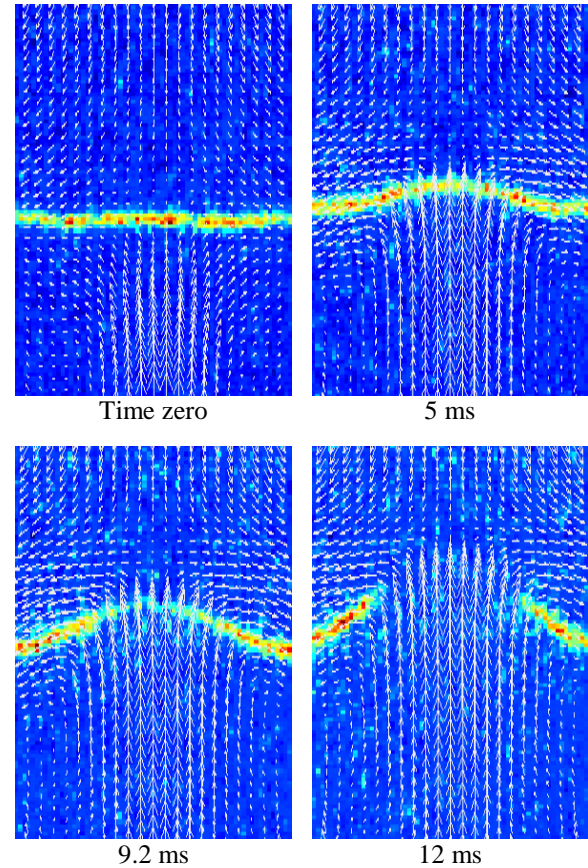


Figure 4 : CH fluorescence and velocity fields during extinction for flame D1 and vortex t1.

At 5ms, the flame is clearly wrinkled but has not yet been extinguished. In fact the flame moves towards the stoichiometry line, that is deformed by the fuel vortex. At 9.2 ms, the flame intensity is clearly decreasing at the centerline and extinction is fully established at 12 ms, allowing the droplet-laden vortex to continue past the flame. The vortex-induced extinction occurs with an extinction strain rate Λ_q of 260 s^{-1} , while the characteristic reactive perturbation strain rate Λ_r is around 400 s^{-1} .

The velocity increase, due to the high vortex speed, increases the gradients and then the species diffusion velocities. The chemical kinetics can become the limiting process against the molecular diffusion transport. If the heat losses used for heating of the cold reactants, becomes higher than the heat released by the chemical reactions, flame extinction occurs. The vortex induced extinction process reveals the finite rate of chemical kinetics.

Figure 5 shows the axial velocity profile (crosses), combined with the vaporization front (dotted line) and CH peak (plain line) positions during the same interaction as figure 4 at two different times : 5 ms and 10 ms after the initial time, corresponding respectively to the occurrence of the maximal strain rate and to the extinction time.

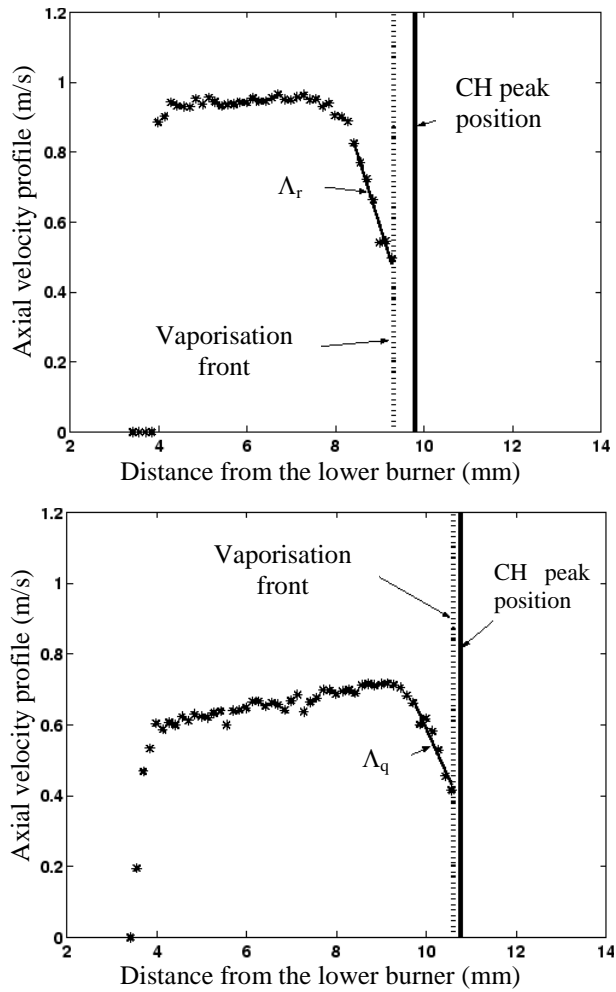


Figure 5 : Axial velocity profiles, peak CH and vaporisation front positions for the determination of strain rates (flame D1, vortex t1).

As the PIV measurements on the fuel side are obtained from Mie scattering of the volatile n-heptane droplets, velocity determination beyond the vaporization front is not possible. At the axis, the flow can locally be described by the Euler equation as a potential flow. Thus the velocity gradient (the strain rate) is constant from the external border of the flames thermo-diffusive layer to the evaporation front [18]. Then the two strain rates Λ_r and Λ_q can be measured at the borderline of the evaporation front. The very small interrogation mesh

size of 8x8 pixel gives a resolution of 143 μm , with about 5 measurement points in the velocity gradient thickness. Strain rate results for the other vortices are shown in Table 3.

Discussion of results

The results of our study are listed in Table 3 for some typical interactions between gaseous or two-phase flames and aerodynamic vortex perturbations. The abbreviation n.e. refers to an interaction without any flame extinction.

The different strain rate values show that the extinction strain rate is not constant for an identical flame, contrary to the quasi-steady flame regime. The flame response to a quasi-steady strain variation is often represented by the S-curve [20]. The flame extinguishes at a fixed value of the strain rate, this value depending only on the initial mixture. In an unsteady regime, the extinction strain rate is no more constant and tends to increase with the characteristic strain imposed to the flame. The extinction limit then depends not only on the initial mixture composition, but also strongly on the aerodynamic perturbation. This can be explained by the fact that the flame response is limited by the diffusion time, corresponding to the transfer time of the aerodynamic information from the outer region of the thermo-diffusive layer, to the inner reactive layer. During this time delay the strain imposed at the external flame layer continues to grow.

The strain rate values listed in Table 3 also show that the extinction strain rate is not always lower for the two-phase flame D1 than for the corresponding gaseous flame M, as it is observed in steady flames [21]. It shows again that the unsteadiness plays an important role in the extinction process.

Another aspect of vortex/flame interaction is the influence of the flame on the aerodynamic field. This study is achieved by comparing the vortex-induced strain rate in the non-reactive flow Λ_{nr} and in the reactive flow Λ_r . These different values are listed in Table 3 for different vortices and flames. In the case of the gaseous flame M, the strain rate is decreased by the presence of the flame, passing from a value of 380 s^{-1} to 330 s^{-1} in the case of the interaction with the vortex T1 and from a value of 470 s^{-1} to 460 s^{-1} in the case of the interaction with the vortex T2. This can be explained by viscous dissipation of the vortex flow in the high

Vortex	D (mm)	Λ_{nr} (1/s)	Flame M		Flame D1		Flame D2	
			Λ_r (1/s)	Λ_q (1/s)	Λ_r (1/s)	Λ_q (1/s)	Λ_r (1/s)	Λ_q (1/s)
T1	6	380	330	290	420	330		
T2	6	470	460	420	530	520		
t1	3.5	840			350	n.e.	400	260
t2	3.5	1270			1300	1300	1100	1100

Table 3 : Vortex diameter and strain rate determined for non-reactive and reactive flows, as well as for extinction in gaseous and two-phase flames.

temperature region imposed by the flame.

While the presence of the flame in the case of gaseous flows tends to decrease the vortex-induced strain rate, it seems that, in the case of the two-phase flame D1, the gas expansion due to evaporation is the preponderant phenomenon. This leads to the increase of the vortex-induced strain rate, passing from a value of 380 s^{-1} to 420 s^{-1} in the case of the interaction with the vortex T1, and from a value of 470 s^{-1} to 530 s^{-1} in the case of the interaction with the vortex T2.

The flame influence on vortices of different sizes can also be analysed in the case of the flame D1. The smaller non-reactive vortex t1 (3.5mm) imposes a much higher strain rate (840 s^{-1}) than the non-reactive vortex T2 of 6mm size (470 s^{-1}). However in the presence of the flame D1 the strain rate imposed by the small vortex t1 falls down to 350 s^{-1} , corresponding to a vortex kinetic energy loss of 80 %. This shows that the small structure experiences a higher kinetic energy dissipation due to the high flame temperature.

Conclusions

In this study the vortex strain induced extinction behavior of purely gaseous and of n-heptane two-phase flames has been examined.

Extinction limits do not only depend on the flame composition, but even more on the parameters of the perturbation. The faster is the perturbation, the higher is the difference between the unsteady case extinction strain rate and the extinction limit of the quasi-steady flame.

The viscous dissipation of the kinetic energy strongly modifies the flow in the vicinity of the flame. These losses are more important if the vortex is small, modifying the energy transfers between turbulence scales.

Acknowledgements

This work was supported by U.S. Air Force Contract F33615-00-C-2068 and French DGA / ONERA PEA-number 98703-TITAN in a French-U.S. collaborative program.

References

- [1] Libby, P. A. and Williams, F. A., *Comb. Flame* 44:287-303 (1982).
- [2] Peters, N., *Prog. Energy Combust. Sci.* 10:221-252 (1984).
- [3] Law, C. K., *Proc. Comb. Inst.* 22:1381-1402 (1988).
- [4] Peters, N., *Proc. Comb. Inst.* 21:1231-1250 (1986).
- [5] Carrier, G. F., F.E.Fendell and Marble, F. E., *SIAM J. Appl. Math.* 28:463-499 (1975).
- [6] Linán, A. and Crespo, A., *Combust. Sci. Tech.* 14:95-117 (1976).
- [7] Darabiha, N., *Combustion Science and Technology* 86:163-181 (1992).
- [8] Egolfopoulos, F. N., *International Journal of Energy Research* 24:989-1010 (2000).

- [9] Renard, P. H., Thévenin, D., Rolon, J. C. and Candel, S., *Prog. Energ. Combust. Sci.* 26:225-282 (2000).
- [10] Katta, V. R., Carter, C. D., Fiechtner, G. J., Roquemore, W. M., Gord, J. R. and Rolon, J. C., *Proc. Comb. Inst.* 27:587-594 (1998).
- [11] Meyer, T. R., Fiechtner, G., Gogineni, S. P., Rolon, J. C., Carter, C. D. and Gord, J. R., *Exp. Fluids* in press (2003).
- [12] Yoshida, K. and Takagi, T., *Proc. Comb. Inst.* 27:685-692 (1998).
- [13] Veynante, D. and Vervisch, L., *Prog. Energy Combust. Sci.* 28:193-266 (2002).
- [14] Santoro, V. S., Kyritsis, D. C. and Gomez, A., *Proc. Comb. Inst.* 28:1023-1030 (2000a).
- [15] Santoro, V. S., Kyritsis, D. C., Linán, A. and Gomez, A., *Proc. Comb. Inst.* 28:2109-2116 (2000b).
- [16] Lemaire, A., Meyer, T. R., Zähringer, K., Rolon, J.-C. and Gord, J. R., *Applied Optics* 42:2063-2071 (2003).
- [17] Lemaire, A., Meyer, T. R., Zähringer, K., Gord, J. R. and Rolon, J.-C., *Experiments in Fluids*, in press (2003).
- [18] Rolon, J. C., Veynante, D., Martin, J. P. and Durst, F., *Experiments in Fluids* 11:313-324 (1991).
- [19] Rolon, J. C., Aguerre, F. and Candel, S., *Combustion and Flame* 100:422-429 (1995).
- [20] Linán, A., *Acta Astron.* 1:1007-1039 (1974).
- [21] Santoro, V. S., Kyritsis, D. C. and Gomez, A., *ICDERS*, Heidelberg, Germany (1999).

PIV/PLIF investigation of two-phase vortex–flame interactions: effects of vortex size and strength

A. Lemaire, T. R. Meyer, K. Zähringer, J. R. Gord, J. C. Rolon

36

Abstract The evolution of flame surface area and rate of CH layer extinction are measured during the interaction of a two-phase counterflow diffusion flame with fuel-side vortices of varying size and strength. Planar laser-induced fluorescence (PLIF) of CH is used to mark the flame front and particle-image velocimetry (PIV) is used to measure the strain rate field at various phases of the interaction process. Vortices of similar initial circulation but differing in size showed widely disparate peak strain rates and CH decay rates because of varying levels of flame-induced vortex dissipation. Vortex size is also found to have a significant effect on flame surface area evolution during and after extinction, with the presence of droplets playing a significant role in the latter. Implications of these results for the fundamental understanding of vortex–flame interactions are discussed.

1

Introduction

In the flamelet description of turbulent non-premixed combustion, local strain and curvature increase the scalar dissipation rate and can result in local flame extinction, reduced overall reaction rates, and decreased flame stability (Peters 1986). A number of experimental studies have used well-controlled vortices to perturb steady H₂–air counterflow diffusion flames and simulate this unsteady extinction process in a repeatable manner, as reviewed by Renard et al. (2000). These studies have been used to

generate turbulent combustion diagrams (Thévenin et al. 2000) as well as to study the time evolution of flame surface area (Renard et al. 1999) and strain rate (Katta et al. 1998; Meyer et al. 2003) during gaseous vortex–flame interaction.

The goal of the current investigation is to study the extinction process during *two-phase* vortex–flame interaction. A flat non-premixed flame is established near the stagnation plane of a counterflow burner, and *fuel-side vortices* are introduced using an electronically actuated piston. The behavior of the reaction zone is studied using CH planar laser-induced fluorescence (PLIF), and the vortex-induced strain rate is measured using particle-image velocimetry (PIV). Initial work in this configuration (Lemaire et al. 2003) focused primarily on demonstrating the experimental technique and discerning the effects of global mixture ratio (i.e. fuel composition). Here, the flame surface evolution and the relative CH mole fraction as a function of time relative to vortex perturbation are reported while keeping the global mixture ratio constant and varying the vortex size and strength. Results are presented for methane–air flames with and without the addition of *n*-heptane droplets.

The first studies of two-phase vortex–flame interactions in counterflow diffusion flames were reported by Santoro et al. (2000a, 2000b), who used methanol–air spray flames to avoid the effects of H₂ preferential diffusion and to capture flame phenomena found in practical devices. They compared vortex-induced perturbation and quasi-steady perturbation using PLIF of formaldehyde and laser Doppler velocimetry (LDV). They found paradoxically that strain rates induced by air-side gaseous vortices are larger than *quasi-steady* strain rates by over a factor of 2 for a range of inlet oxidizer mass fractions. Follow-up work by Kyritsis et al. (2002) showed that scalar dissipation of mixture fraction is a more dominant parameter controlling the extinction process. Nonetheless, strain rate remains an important parameter in that it is more easily measured than scalar dissipation in turbulent flames.

The use of CH PLIF as a marker for the flame front serves multiple goals. The CH radical has been widely used as a marker for the non-premixed flame zone because it appears in a narrow region of the flame near the location of peak temperature (Donbar et al. 2000; Han and Mungal 2000). Unlike the premixed study of Nguyen and Paul (1996), measurements of OH and CH PLIF in diffusion flames indicate that CH does not exhibit “false” flame extinctions (Donbar et al. 2000). The relative CH number density during vortex–flame interaction is of further

Received: 16 October 2002 / Accepted: 23 February 2003

Published online: 9 May 2003

© Springer-Verlag 2003

A. Lemaire, K. Zähringer, J. C. Rolon (✉)
Laboratoire d'EM2C, Ecole Centrale Paris, 92295 Grande Voie des
Vignes, Chatenay-Malabry Cedex, France
E-mail: rolon@em2c.ecp.fr

T. R. Meyer
Innovative Scientific Solutions, Inc., 2766 Indian Ripple Road,
Dayton, OH, 45440-3638, USA

J. R. Gord
Air Force Research Laboratory, Propulsion Directorate, Wright-
Patterson Air Force Base, OH45433-7103, USA

The authors would like to acknowledge the help and advice of Dr. V.R. Katta of Innovative Scientific Solutions, Inc. and Dr. C.D. Carter of the Air Force Research Laboratory. This work was supported by U.S. Air Force Contract No. F33615-00-C-2068 and French DGA/ONERA PEA-No. 98703-TITAN in a French–U.S. collaborative program.

interest because of the important role of CH in the formation of prompt NO and soot pollutants, its role in NO_x reburning (Thoman and McIlroy 2000), and as a means for optimizing multidimensional numerical simulations with complex chemical kinetic models.

2 Experimental apparatus

The burner apparatus and diagnostic approach were previously described by Lemaire et al. (2003). Thus, only a brief description is included here for reference, with minor changes relevant for this study.

2.1 Burner apparatus

The experimental device used for this work was previously modified from a gaseous counterflow burner design (Rolon et al. 1991) to include a piston-actuated vortex injection system (Rolon et al. 1995). Several experimental studies using this apparatus have been reported previously in the literature (Renard et al. 1999; Fiechtner et al. 2000). As shown in Fig. 1, the burner consists of two axisymmetric, 20-mm diameter counterflow nozzles, with air in the upper flow and a nitrogen–fuel mixture in the lower flow. A 40-mm diameter shroud flow of nitrogen surrounds each nozzle to shield the flame from ambient disturbances. The nozzle separation is set to 30 mm in this case. Vortex tubes of 2 mm and 3.7 mm are added along the centerline of the fuel nozzle, fed by an electronically controlled piston-actuation system. Vortices of varying strength can be generated by controlling the size, stroke, and rise time of the piston. Only the piston stroke is varied here. The resulting vortex circulation has been found to be equal to the square of the ejected fluid volume divided by the piston rise time and the fourth power of the vortex tube diameter (Maxworthy 1972). The vortex rotational and convection velocities have been found to be proportional to the circulation divided by the vortex tube diameter (Roberts and Driscoll 1991; Roberts et al. 1993). The relevant vortex properties for the current work are listed in Table 1. They include vortices with equal circulation but differing size, and vortices with equal size but differing circulation.

The main modification to the burner apparatus for the current two-phase vortex–flame experiments is the addition of a nitrogen-jet atomizer in the fuel stream, described previously by Rolon et al. (1991) and similar to the apparatus characterized by Durox et al. (1999). This atomizer produces a monodisperse field of droplets of about 2.43–2.83 μm in diameter for the current flow con-

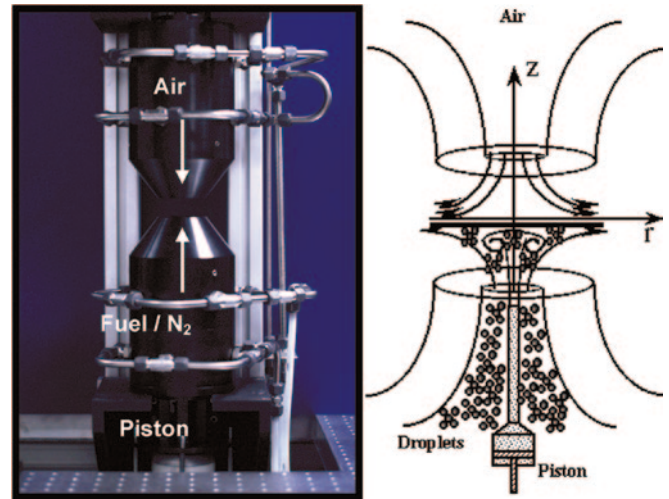


Fig. 1. Jet in coflow burner used for two-phase vortex–flame experiments

ditions. The spray is further diluted to a nondense condition with methane and additional nitrogen to a volumetric density of $9 \times 10^6 \text{ cm}^{-3}$.

The various inlet flow conditions used in this investigation can be characterized by a number of parameters as listed in Table 1. These include the volume ejected by the piston, theoretical vortex circulation, measured peak strain rate along the centerline, CH decay rate normalized to 1/ms, mass fraction of methane in the fuel y , and steady nozzle velocities, v_{Ox} and v_{fuel} . The global mixture ratio, defined as the ratio of the initial mass fraction of fuel to oxygen divided by the corresponding stoichiometric ratio, is 4.43 for all conditions, as is the piston rise time of 10 ms. Cases 1A and 2A differ in piston stroke and thus ejected volume and circulation. Case 2B, with no *n*-heptane seeding, is the gaseous analog of Case 2A. Cases 3A and 4A have smaller vortex tube diameters and differ only in piston stroke.

2.2 PIV–PLIF system

Simultaneous diagnostics are performed to characterize the vortex–flame interaction, with PIV used to assess the dynamic effect of the vortical flow field on the flame structure as visualized by CH PLIF.

Particle image velocimetry is performed using silicon dioxide particles (1–5 μm) in the air stream and *n*-heptane droplets in the fuel stream. The use of Mie scattering from the *n*-heptane fuel droplets for PIV avoids problems with agglomeration of solid seed particles in the unvaporized

Table 1. Vortex properties and flow parameters used in the experiments. Global mixture ratio is 4.43 and piston rise time is 10 ms for all cases

Case	Vortex tube diam. (mm)	Ejected volume (mm ³)	Circulation (cm ² /s)	Meas. peak strain (s ^{−1})	CH decay rate (ms ^{−1})	Mass frac. of methane in fuel y	v_{Ox} (m/s)	v_{fuel} (m/s)
1A	3.7	37.9	7.7	919	0.076	0.57	0.7	0.5
2A	3.7	49.2	13	1687	0.350	0.57	0.7	0.5
2B	3.7	49.2	13	1461	0.317	1.0	0.7	0.5
3A	2	13.9	13	845	–	0.57	0.59	0.61
4A	2	37.9	90	2363	0.625	0.57	0.59	0.61

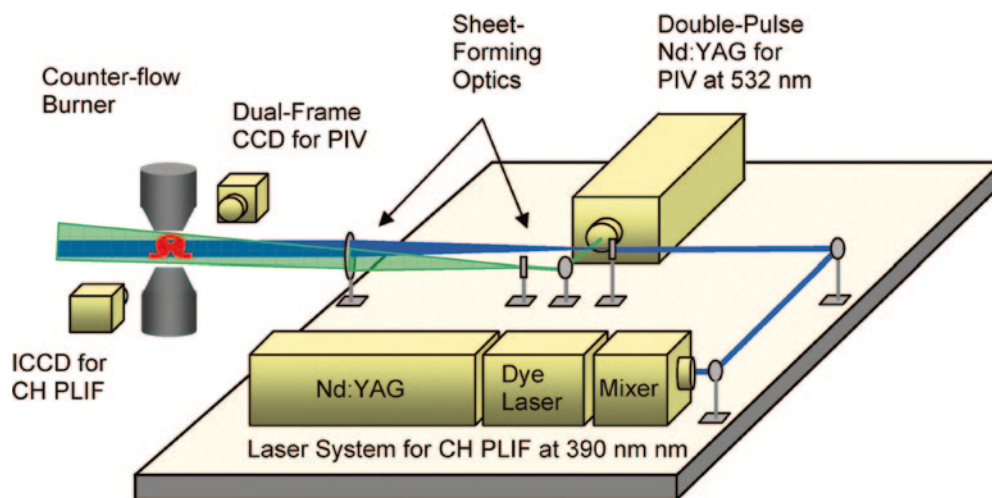


Fig. 2. Schematic of the simultaneous PIV/PLIF system

fuel. Overlapping 532-nm beams are generated using a double-pulsed Nd:YAG laser (Fig. 2) and are formed into 0.5-mm thick vertical sheets using cylindrical ($f=-12.7$ mm) and spherical lenses ($f=500$ mm). Reasonable particle displacements for various vortex convection velocities are achieved by varying the pulse interval from 0.050 ms to 0.2 ms. The PIV images are collected using a dual-frame 1008×1018 (9.07 mm×9.16 mm) array ICCD camera (Kodak Megaplug ES1.0) equipped with an AF 105-mm $f/2.8$ lens (Micro Nikkor) and a 36-mm extension ring. The image-to-CCD magnification ratio is about 2.2:1. Postprocessing is performed using custom designed software from Innovative Scientific Solutions (USA). An adaptive mesh is used to obtain typical pixel interrogation regions of 32×32 with 50% overlap. This results in a 62×62 vector field across each image.

CH PLIF is achieved using the $Q_1(5)$ transition (389.5 nm) in the $B^2\Sigma^- - X^2\Pi(0,0)$ absorption band of CH, obtained by frequency mixing the output of a Nd:YAG-pumped tunable narrow-band dye laser (rhodamine 640) with the Nd:YAG fundamental (1064 nm). Laser pulses of about 7 ns in duration and mean energies between 15 and 20 mJ are formed into 2-cm high x 0.3-mm thick sheets that are superposed with the PIV laser sheets. The energy distribution inside the CH laser sheet was controlled by Rayleigh scattering from nitrogen and Mie scattering from the droplets. The flame position is placed in the central region of the laser sheet and remains in this region during the entire vortex–flame interaction. The power density variation inside the measurement region does not exceed 5%. In order to further minimize the effects of laser-sheet intensity variations, laser fluence is adjusted so as to partially saturate the CH transition. As shown in Fig. 3, the CH PLIF signal is in the nonlinear regime by 4.5 MW/cm² (1 mJ).

Fluorescence is collected from the A–X (0,0) and A–X (1,1) bands around 430 nm while using a combination of 410-nm high-pass and 450-nm low-pass filters to minimize interferences from background scattering. The CH PLIF signal is collected using a 2×2 binned 512×512 array intensified CCD camera (PI-Max) with a 58-mm $f/1.2$ lens (Noct-Nikkor) and 20-mm extension ring. An image-to-CCD magnification ratio of 1.85:1 (20 mm×20 mm region)

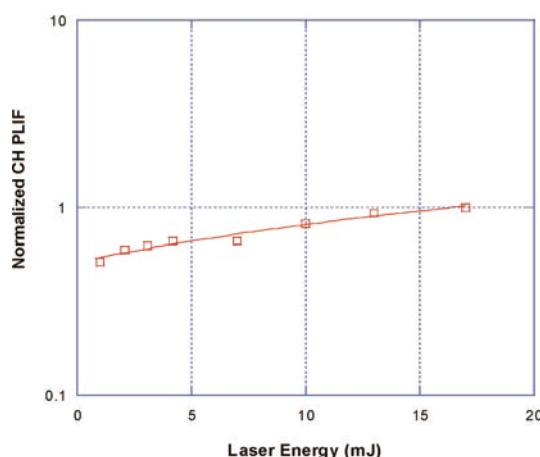


Fig. 3. CH PLIF intensity as a function of laser power. A nearly saturated regime is used in this study with laser powers between 15 and 20 mJ

is achieved with a pixel measurement area of 100×100 μm^2 . The limiting resolution based on the Nyquist criterion and modulation transfer function (MTF) of the lens is found to be about 234 μm . This is the smallest structure that the camera can faithfully discern and is only slightly better than the *steady* CH layer thickness of about 250 μm . The current set-up cannot distinguish, therefore, between a decrease in CH layer intensity and CH layer thickness, although these effects can be considered analogous for the purposes of discussing CH layer extinction.

An important source of uncertainty in the CH signal during vortex–flame interaction arises from temperature-dependent fluorescence quenching rates. Based on results of a numerical simulation of a steady counterflow flame with complex chemistry, the main CH quenching species (H_2O , CO, N_2 , and CO_2) are fairly constant in the region where CH is present. Quenching from O_2 and CH_4 nearly offset each other in the CH region, and temperature varies by less than 3%. Thus, the CH profile does not require significant corrections because of variations in temperature and quenching species across the unperturbed flame. The overall effect of quenching variations on the CH profile and CH fluorescence efficiency *during flame*

perturbation is minimized by operating in a high-energy regime. Finally, variation in the Boltzman fraction for the $Q_1(5)$ transition of CH is on the order of +25% for the temperature range applicable during flame extinction (from 1700 to 1100 K). While nontrivial, such uncertainty also does not significantly detract from the main focus of this study, which is the qualitative observation of CH number density during vortex–flame interaction.

Simultaneous CH PLIF and PIV requires the synchronization of several events, including vortex generation, three laser pulses, and three camera exposures. The timing of the CH laser pulse occurs 20 μ s before the second PIV laser pulse to avoid particle scattering on the camera used for CH PLIF. The vortex–flame interaction can then be imaged at various phases of its development by adjusting the relative timing of piston actuation and laser diagnostics. The initial time of the vortex–flame interaction is defined when the vortex starts to perturb the CH layer.

3 Results and discussion

The velocity profile induced by vortex 2A (Table 1) at 4.5 ms after the vortex arrives at the flame front is shown in Fig. 4 (right). Note that the vectors are an average of five images and are presented in the reference frame of the vortex by subtracting a convection velocity of about 0.56 m/s. This frame of reference highlights the circulating flow pattern. Since flame extinction in the current experiments is observed to take place at the centerline, the relevant normal strain rate induced by the vortex is defined as dv/dy , where v is the vertical component of velocity, and y is the axial coordinate. The vortex imposes high velocities on the fuel side of the flame. Then the velocity decreases quickly as the flame is being approached, where it reaches a minimum. The number of velocity vectors through the flame is not enough to catch the thermal dilatation due to the high flame temperature. However the extinction process induced by high strain

rates is pursued in this study, and the relevant strain is measured in the near convective region of the outer flame diffusive layer. The peak normal strain rate of about 1700 s^{-1} that occurs during the fast velocity decrease is located prior to the preheat zone of the flame. Therefore no corrections for thermophoretic effects were necessary on the measured peak strain rate, as accurate velocity measurements can be performed prior to the flame preheat layer (Sung et al. 1994). The standard deviation caused by vortex repeatability is on the order of about 7% for velocity and 15% for peak normal strain rate. Adequacy of PIV resolution is demonstrated as the velocity and strain rate are found to be “grid independent” for interrogation regions of 32×32 or less. Peak normal strains along the centerline *during* vortex–flame interaction are calculated using 32×32 interrogation regions and are reported in Table 1 for all of the flow conditions used in this study. Values measured at the instant of flame extinction may have undergone significant dissipation because of heat release and are not necessarily representative of the relevant strain rate for extinction. In addition to peak strain rate, vortex circulation is used to help determine the effects of vortex size and strength on flame surface development and CH layer extinction.

The time evolution of the perturbed counterflow flame as a function of time after vortex arrival is shown in Fig. 5 for vortex 2A. The velocity field is superposed on the CH fluorescence pattern. The CH layer is located above a strong fluorescence signal from species on the fuel side of the flame. Based on a numerical simulation with complex chemistry, this layer of fluorescence corresponds to the location of polycyclic aromatic hydrocarbons (PAH). The PAH are formed around the droplet cloud, between the cold spray and the high temperature flame, where the *n*-heptane evaporates. Interference from this layer is minimized by spatial separation with CH (Fig. 5), and by the fact that its fluorescence is strongly diminished by the approaching vortex. When the vortex is interacting with

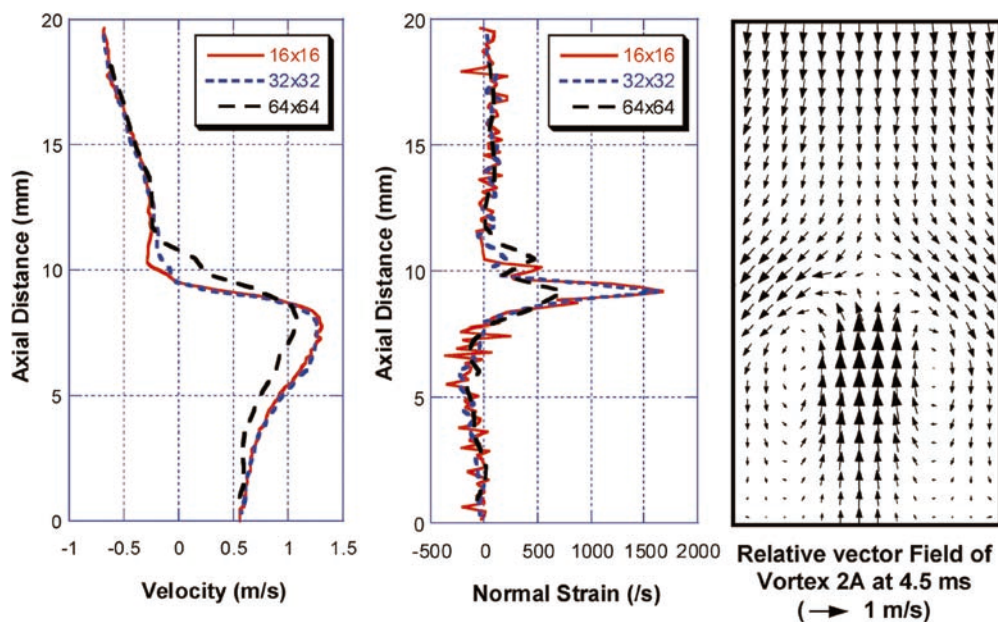


Fig. 4. Comparison of velocity and normal strain rate for vortex 2A (Table 1) using different PIV interrogation regions. Interrogation regions of 32×32 pixels (3 vectors/mm) or 16×16 pixels (6 vectors/mm) are shown to be adequate for computing peak strain rates. Overlap parameter is 50%

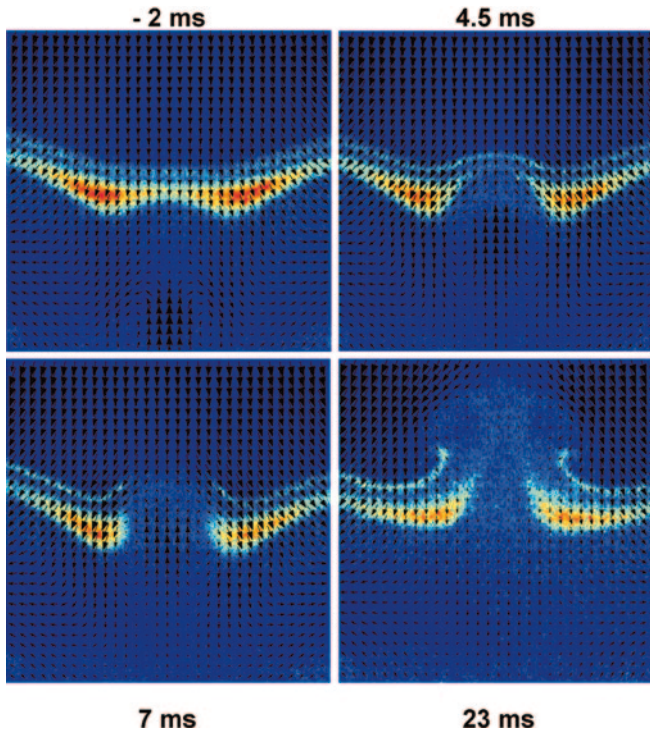


Fig. 5. Sample CH PLIF/PIV sequence of vortex 2A (Table 1) showing the vortex–flame interaction at various phases of evolution. Times are relative to when the vortex first wrinkles the flame

the flame the PAH layer disappears, and only the CH layer remains until the flame extinguishes in the center. In describing the evolution of the CH layer in Fig. 5, time zero is defined as the time at which the vortex starts to perturb the counterflow flame. At 4.5 ms, the flame is clearly wrinkled but has not yet been extinguished. The flame decreases in intensity after this point until extinction is fully established between 5 to 7 ms, allowing the droplet-laden vortex to continue past the flame. The vortex core remains under the flame until 8 ms and passes through the flame between 8 ms and 13 ms. A slight outline of the vortex is visible at 23 ms due to Mie scattering.

In order to obtain qualitative information about the effects of the vortex on the flame, one can calculate the time evolution of the flame surface shown in Fig. 6 and the CH layer centerline intensity shown in Fig. 7 from experimental images. Data from CH PLIF diagnostics effectively localize the diffusion flame front and extinction zones (extinction signal refers to signal that falls to the background noise). One can define the flame front position by following the maxima of CH intensity for an average of ten images. Once the flame front is determined, each segment between two points is treated as an elementary area and is rotated about the axis of symmetry using the Guldin theorem. The total flame surface is the sum of the elementary areas and is normalized by the value of the nonperturbed flame. The CH intensity data was calculated using a region of 4×6 pixels at the centerline of the CH front averaging on ten images.

The centerline CH intensity plotted as a function of time (Fig. 7) during extinction indicates that the process is nearly linear with respect to time. The slope of the curve

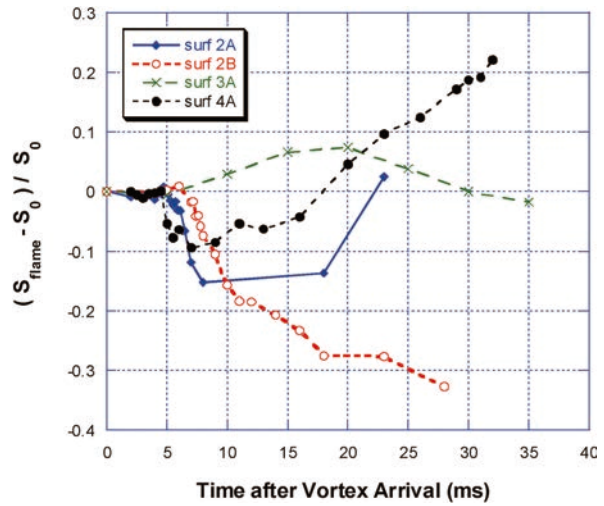


Fig. 6. Evolution of normalized flame surface area during vortex–flame interaction. Vortex and flame conditions refer to Table 1

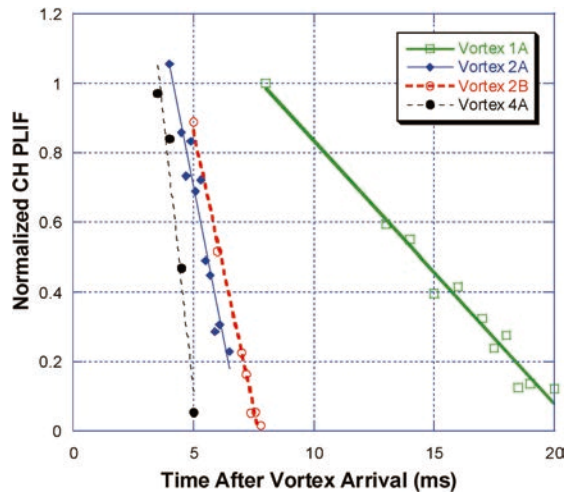


Fig. 7. Relative CH number density during CH layer extinction. Vortex and flame conditions refer to Table 1

represents the extinction rate. The vortex velocity field induces a decrease of the flame surface and of the centerline CH intensity. Comparing flame surface evolutions, measured extinction rates and maximum peak normal strain rates, one may show that when the peak normal strain rate increases, the flame surface and the CH intensity during extinction decrease prior and faster in any cases presented in Fig. 6 and 7. We may say that the peak normal strain rate is sufficient to predict the extinction of the CH layer and is the main controlling parameter of extinction for the vortices studied in this paper. Comparing cases 2A and 2B, two-phase effects can be underlined, especially through the earlier decrease of the flame surface and the higher extinction rate in the case of the two-phase flame. This supports the finding of Santoro and Gomez (2002), who found that the latent heat of vaporization of the droplets works to reduce flame temperatures and weaken the flat counterflow flame. The faster extinction of the two-phase flame can be explained by heat losses

due to evaporation, lower chemical activity of *n*-heptane compared to methane, and higher strain rate due to the expansion of evaporated *n*-heptane. The peak normal strain rate measured is indeed higher in the two-phase case (CH decay rate of 0.35 s^{-1}) than in the gaseous case (CH decay rate of 0.32 s^{-1}). As the droplets used in this experiment are very small the inertia effect on extinction is probably negligible. However, as shown by the plateau and the following increase of flame surface of case 2A, the two-phase flame reignition is faster. Case 2B, where the flame is not doped by *n*-heptane droplets, does not show the constant plateau, and the flame surface area continues to decrease. The two-phase flame surface increase is not due to reconnection, but occurs because the edges of the flame are entrained by the vortex after extinction, thereby increasing the total surface area. This can be explained by the excess of unburned *n*-heptane droplets in case 2A, which evaporate and contribute to the formation of a cylindrical flame around the axis. The two-phase case 4A, which uses the smaller vortex tube of 2 mm, exhibits the same flame surface evolution characteristics as case 2A, except that since the vortex is faster, the extinction and reignition processes are faster due to the fact that the vortex-induced strain passes through the flame field faster. One can notice that, still comparing cases 2A and 4A, the larger vortex of case 2A results in a stronger decrease in flame surface from the initial nonperturbed flame during extinction. This is due to the fact when the flame/vortex impact area is larger, a larger flame area is perturbed, wrinkled, and extinguished. Cases 2A and 3A have similar vortex circulation but different vortex sizes. Despite having higher vortex velocity (recall, vortex rotational and convection velocity \sim circulation/tube diameter), no extinction takes place for the smaller vortex of case 3A. Thus, the flame surface area increases in case 3A because of flame wrinkling and decays back to its original level after the vortex is dissipated (Fig. 6). This means that a higher velocity vortex (as in case 3A) does not always extinguish the flame easier (compared to case 2A). Thus, vortex circulation is not sufficient to predict extinction. As the vortex size determines the flame/vortex impact area, the vortex size corresponds to the area where the local dynamic strain rate acts upon the flame. Larger areas of vortex-induced strain lead to higher flame sensitivity to extinction. In addition, smaller vortices are more subject to the effects of viscous dissipation induced by heat release. In fact, vortex 3A has the lowest effective maximum peak normal strain rate, even lower than case 1A for which the vortex circulation and convective velocity are very low. As alluded to earlier, this may be due to the higher level of energy dissipation experienced by smaller vortices.

Case 3A can be contrasted with case 4A, which has the same vortex size as 3A but experiences flame extinction because of a significantly higher peak normal strain rate. It is worth noting, however, that the level of normal strain and rate of CH layer extinction is also somewhat low for Case 4A, considering that its circulation is about sevenfold that of the other cases. This is consistent with vortices of smaller size being more susceptible to energy dissipation due to heat release. This is confirmed by the velocity and strain rate data presented in Figs. 8 and 9,

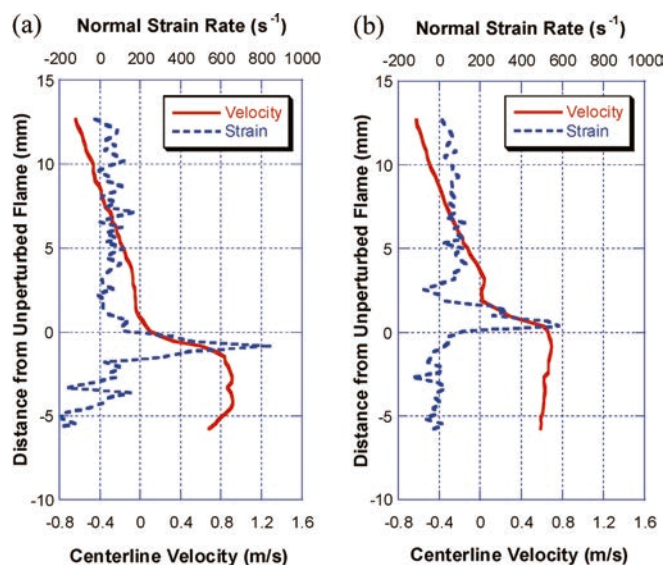


Fig. 8. Centerline profiles of velocity and normal strain rate for vortex 3A (Table 1) at (a) 5 ms and (b) 10 ms after the initiation of vortex interaction

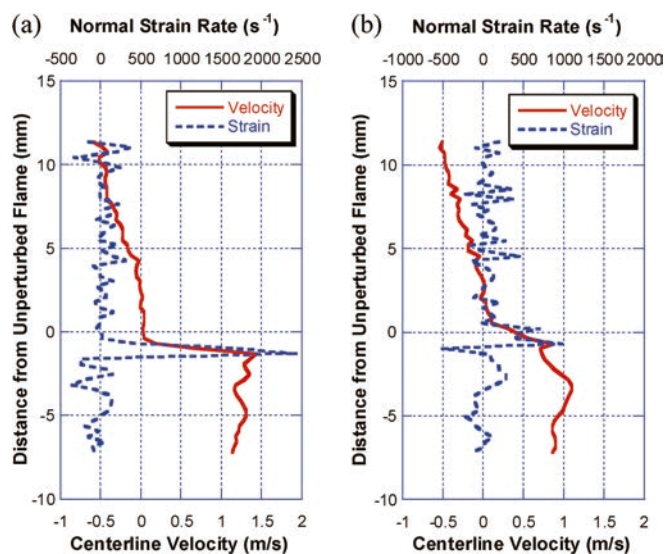


Fig. 9. Centerline profiles of velocity and normal strain rate for vortex 4A (Table 1) at (a) 3 ms and (b) 3.5 ms after the initiation of vortex interaction

for which cases 3A and 4A, respectively, are highly dissipated after interaction with the counterflow flame. The strain rate in case 4A drops by 60%, for example, within 0.5 ms. This is in contrast with the large but slow vortex of case 1A (not shown), which maintains its strain rate level for nearly the entire 20 ms of the flame-extinction process.

It seems, therefore, that the peak strain rate located in the near-convective region of the flame diffusive layer is a significant controlling parameter that accounts for both initial vortex circulation as well as vortex size. This is supported by the clear relationship between peak strain rate and the rate of CH layer extinction shown in Fig. 10.

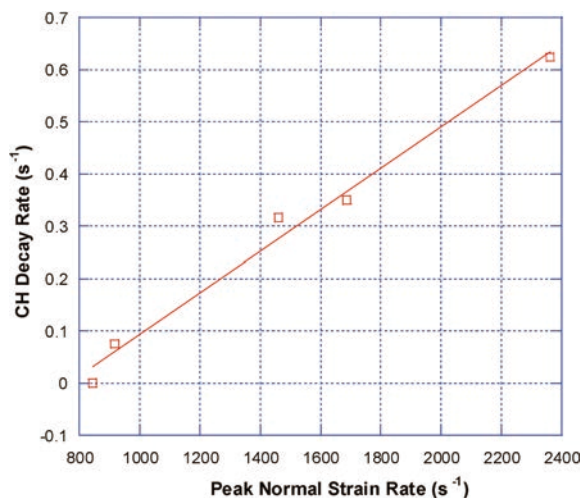


Fig. 10. Relationship between peak normal strain and CH layer decay rate (values shown in Table 1)

4

Conclusions

The interaction between a vortex and a two-phase non-premixed flame has been studied using simultaneous CH PLIF and PIV diagnostics. Under high strain fields as induced by a vortex, the disappearance of the PAH signal allows one to discriminate the CH layer. Using an adaptive mesh technique, the PIV system was shown to have adequate resolution for measurements of peak normal strain during vortex–flame interaction. We deduced from these measurements the time evolution of some flame–vortex interaction parameters with single- and two-phase counterflow diffusion flames.

The results of the present investigation show that micron-sized droplets convected by vortices strongly affect the postextinction flame surface development. In addition, the presence of unburned *n*-heptane droplets causes faster reignition after the vortex passing through the flame. The effects of vortex size and velocity are studied in the context of flame surface area evolution and flame extinction. We deduce from this study that extinction is not uniquely determined by convection velocity, vortex size, and circulation, but by a combination of these factors. In contrast, the flame experiences rapid extinction rates for vortices inducing high normal strain rates. It has been shown that in the vortex–flame interactions studied in this paper, the peak normal strain rate is the main controlling parameter for the flame extinction. The rate of CH extinction can be described conveniently by a single value since the drop in CH mole fraction is found to be sufficiently linear with respect to time for a variety of conditions.

Based on this investigation, CH PLIF and PIV are shown to be excellent techniques for evaluating vortex-induced flame perturbations in hydrocarbon–air systems. Future work on the current data set includes processing of a wider range of fuel compositions and vortex conditions for the development of combustion diagrams and for the extraction of more conclusive empirical trends.

References

- Donbar JM, Driscoll JF, Carter CD (2000) Reaction zone structure in turbulent non-premixed jet flames from CH–OH PLIF images. *Combust Flame* 122:1–19
- Durox D, Ducruix S, Lacas F (1999) Flow seeding with an air nebulizer. *Exp Fluids* 27:408–413
- Fiechtner GJ, Renard PH, Carter CD, Gord JR, Rolon JC (2000) Injection of single and multiple vortices in an opposed-jet burner. *J Visualization* 2:331–341
- Han D, Mungal MG (2000) Simultaneous measurement of velocity and CH layer distribution in turbulent nonpremixed flames. *Proc Combust Inst* 28:261–267
- Katta VR, Carter CD, Fiechtner GJ, Roquemore WM, Gord JR, Rolon JC (1998) Interaction of a vortex with a flat flame formed between opposing jets of hydrogen and air. *Proc Combust Inst* 27:587–594
- Kyritsis DC, Santoro VS, Gomez A (2002) Quantitative scalar dissipation rate measurements in vortex perturbed counterflow diffusion flames. In: *Proc twenty-ninth symposium (international) on combustion*, Sapporo, Japan 2002
- Lemaire A, Meyer TR, Zähringer K, Rolon JC, Gord JR (2003) Vortex-induced flame extinction in two-phase counterflow diffusion flames using CH PLIF and PIV. *Appl Opt* (in press)
- Maxworthy T (1972) The structure and stability of vortex rings. *J Fluid Mech* 51:15–32
- Meyer TR, Fiechtner GJ, Gogineni SP, Rolon JC, Carter CD, Gord JR (2003) PLIF/PIV study of vortex-induced annular extinction in counterflow H₂–air diffusion flames. *Exp Fluids* (in press)
- Nguyen QV, Paul PH (1996) The time evolution of a vortex–flame interaction observed via planar imaging of CH and OH. *Proc Combust Inst* 26:357–364
- Peters N (1986) Laminar flamelet concepts in turbulent combustion. In: *Proc twenty-first symposium (international) on combustion*. The Combustion Institute, Pittsburgh, PA, pp 1231–1250
- Renard PH, Rolon JC, Thévenin D, Candel S (1999) Investigations of heat release extinction and time evolution of the flame surface for a non-premixed flame interacting with a vortex. *Combust Flame* 117:189–205
- Renard PH, Thévenin D, Rolon JC, Candel S (2000) Dynamics of flame/vortex interactions. *Prog Energy Combust Sci* 26:225–282
- Roberts W, Driscoll J (1991) A laminar vortex interacting with a premixed flame-measured formation of pockets of reactants. *Combust Flame* 87:245–256
- Roberts W, Driscoll J, Drake M, Goss L (1993) Images of the quenching of the flame by a vortex to quantify regimes of turbulent combustion. *Combust Flame* 94:58–69
- Rolon JC, Aguerre F, Candel S (1995) Experiments on the interaction between a vortex and a strained diffusion flame. *Combust Flame* 100:422–429
- Rolon JC, Veynante D, Martin JP, Durst F (1991) Counter jet stagnation flows. *Exp Fluids* 11:313–324
- Santoro VS, Gomez A (2002) Extinction and reignition in counterflow diffusion spray flames interacting with laminar vortices. In: *Proc twenty-ninth symposium (international) on combustion*, Sapporo, Japan 2002
- Santoro VS, Kyritsis DC, Gomez A (2000a) An experimental study of vortex–flame interaction in counterflow spray diffusion flames. *Proc Combust Inst* 28:1023–1030
- Santoro VS, Kyritsis DC, Linan A, Gomez A (2000b) Vortex-induced extinction behavior in methanol gaseous flames: a comparison with quasi-steady extinction. *Proc Combust Inst* 28:2109–2116
- Sung CJ, Law CK, Axelbaum RL (1994) Thermophoretic effects on seeding particles in LDV measurements of flames. *Combust Sci Tech* 99:119–132
- Thévenin D, Renard PH, Fiechtner GJ, Gord JR, Rolon JC (2000) Regimes of non-premixed flame–vortex interactions. *Proc Combust Inst* 28:2101–2108
- Thoman JW, McIlroy A (2000) Absolute CH radical concentrations in rich low-pressure methane–oxygen–argon flames via cavity ring-down spectroscopy of the A2D–X2P transition. *J Chem Phys A* 104:4953–4961

Simultaneous PLIF/PIV investigation of vortex-induced annular extinction in H₂-air counterflow diffusion flames

T.R. Meyer, G.J. Fiechtner, S.P. Gogineni, J.C. Rolon, C.D. Carter, J.R. Gord

Abstract High-temporal-resolution measurements of scalars and velocity are used to study vortex-induced annular (off-centerline) flame extinction during the interaction of a propagating vortex with an initially stationary counterflow hydrogen-air diffusion flame. Such an extinction process differs from classical one-dimensional descriptions of strained flamelets in that it captures the effects of flame curvature as well as dynamic strain. Planar laser-induced fluorescence (PLIF) measurements of the hydroxyl radical (OH) are used to track flame development, and simultaneous particle-image velocimetry (PIV) is used to characterize the two-dimensional flow-field. Measurements reveal differences in local normal strain rate profiles along and across the reaction zone and indicate that vortex-induced curvature in the annular region may initiate the extinction process. In addition, the

effect of local flame extinction on vortex evolution and dissipation is determined from measured vorticity data.

Keywords Counterflow, Vortex, Flame, Extinction, Diffusion flame

1 Introduction

It is well-recognized that vortices occur readily in turbulent flows. Recent laser-based measurements of species and velocity in turbulent diffusion flames have revealed that vortical structures play a significant role in local flame extinction, curvature, thickness, and stabilization (Watson et al. 1999; Donbar et al. 2001). Detailed studies of vortical structures in fully turbulent flames are difficult because those structures must be tracked in both space and time with respect to the flame front. Alternatively, fundamental turbulent flame behavior can be represented by the interaction of a laminar, non-premixed flame with a repeatable, spatially propagating toroidal vortex (Rolon et al. 1995; Samaniego and Mantel 1999). The resulting data can be used to investigate the effects of unsteady strain and curvature or to identify fundamental regimes of vortex-flame interaction (Katta et al. 1998; Fiechtner et al. 1999; Renard et al. 2000; Thévenin et al. 2000; Katta et al. 2003; Lemaire et al. 2003).

While extinction in such vortex-flame studies has typically been observed to take place at a point located at the leading edge of the vortex, Katta et al. (1998) predicted that flame extinction can occur in an annular pattern away from the centerline under certain experimental conditions. Experimental observation of this annular extinction was first reported in a collaborative publication between scientists at the Air Force Research Laboratory and École Centrale Paris (Thevenin et al. 2000), with a view toward establishing various regimes of vortex-induced wrinkling and extinction. The current work focuses on the annular extinction itself as an archetype for flamelet behavior under the influence of two-dimensional flowfields. Therefore, the current investigation of off-centerline extinction emphasizes flame dynamics induced by vortex rotation in addition to flow unsteadiness. We provide a detailed description of the experimental apparatus used to observe the annular extinction and present possible reasons for its occurrence. In addition, we examine the effects of flame extinction or the lack thereof on the vorticity magnitude and discuss the degree of coupling between the flame front and vortex flowfield.

Received: 25 September 2002 / Accepted: 25 July 2003
Published online: 22 November 2003
© Springer-Verlag 2003

T.R. Meyer (✉), S.P. Gogineni
Innovative Scientific Solutions, Inc.,
2766 Indian Ripple Road, Dayton,
OH 45440, U.S.A
E-mail: Terrence.Meyer@wpafb.af.mil

G.J. Fiechtner
Sandia National Laboratories,
7011 East Avenue, MS9951, Livermore,
CA 94550, U.S.A

J.C. Rolon
Laboratoire E.M2.C, CNRS/École Centrale Paris,
92295, Chatenay-Malabry Cedex, Paris, France

C.D. Carter, J.R. Gord
Air Force Research Laboratory,
Propulsion Directorate,
Wright-Patterson Air Force Base,
OH 45433, U.S.A

The authors thank Dr. W. M. Roquemore, Dr. V. R. Katta, Dr P. H. Renard, and Prof. D. Thévenin for guidance and valuable discussions. The authors also thank Dr. R. D. Hancock and Capt. I. Vihinen for assistance in assembling the burner, and Mr. K. D. Grinstead and Dr. J. M. Donbar for technical assistance in setting up the experiments. Finally, the authors thank Prof. G. Mungal of Stanford University for providing the StanPIV software. This work was supported by U. S. Air Force Contracts F33615-95-C-2507, F33615-97-C-2702, and F33615-00-C-2068. Additional funding was provided by the U.S. Air Force Office of Scientific Research with Dr. Julian Tishkoff as Program Manager.

These goals are accomplished using detailed measurements of the time-dependent velocity and concentration fields in a non-premixed flame supported by air and fuel in a counterflow burner configuration (Rolon et al. 1995). Here, a piston is used to inject vortices of varying strength, and the hydrogen fuel is diluted with nitrogen at various levels to study the effect of global mixture ratio. Planar laser-induced fluorescence (PLIF) of the hydroxyl radical (OH) is used to mark the flame front, and two-color particle-image velocimetry (PIV) is employed to characterize the vortex structure. Recently, several researchers have conducted a number of joint PLIF/PIV experiments in unsteady flames. Rehm and Clemens (1997) have made OH-PLIF and PIV measurements in a hydrogen jet flame. Joint scalar and velocity-field measurements were performed by Frank et al. (1996), Donbar et al. (2001), and Kothnur et al. (2002) in turbulent flames, and by Hasselbrink and Mungal (1998) and Watson et al. (1999, 2002) in lifted methane-air diffusion flames. The present simultaneous OH-PLIF and PIV measurements are the non-premixed counterpart of the vortex-flame studies of Driscoll et al. (1994) and Mueller et al. (1995). To explore the time-dependent nature of the vortex-flame interactions, a synchronization scheme for precise control of relative timing between the laser diagnostics and vortex-flame event is also implemented. A temporal resolution of 10 μ s is achieved with this scheme, allowing the annular extinction to be observed at various phases of its evolution.

2 Experimental

2.1 Counterflow burner

Several experimental facilities have been implemented to study vortex-flame interactions, as reviewed by Renard et al. (2000). For the experiments described in this paper, a vortex is injected into a flame supported at the mid-plane of an opposed-jet burner (Rolon et al. 1995) with 25 mm diameter upper and lower nozzles separated by 40 mm. A diagram of the burner is shown in Fig. 1. The fuel, consisting of hydrogen diluted with nitrogen, flows from the upper nozzle; air flows from the lower nozzle. This configuration differs from conventional counterflow flames in that a tube with 5 mm inner diameter is installed concentrically within the lower nozzle. This tube is attached to a cylinder containing a solenoid-driven piston that forces a vortex to emerge from the tube and collide with the flat counterflow flame.

Since vortex formation in non-reacting flow has been the subject of intense study for many years, a considerable amount of information is available to aid in characterizing the injected vortices. As fluid is pumped impulsively from a nozzle or orifice, a single vortex forms, followed by additional vortices in the production of a starting jet (Garside et al. 1943). For a cylindrical volume of fluid that emanates from a nozzle having length L and diameter D , Gharib et al. (1998) and Shusser et al. (1998) have shown that the maximum circulation attainable by a vortex ring is reached for $L/D \sim 4$, and that for larger ratios additional trailing vortex rings form. For the present 5 mm nozzle,

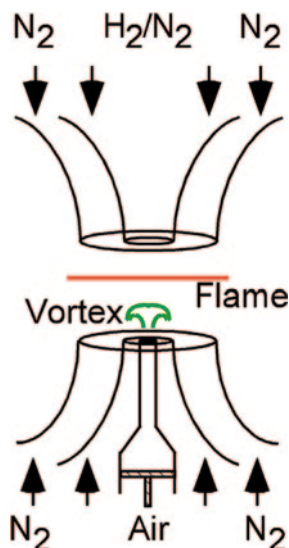


Fig. 1. Schematic of the non-premixed counterflow vortex-flame burner

the volume that a vortex can contain, as estimated from the results of Gharib et al., is $\sim 0.4 \text{ cm}^3$. The vortex generator used in the present study can sweep a maximum volume of $\sim 2.5 \text{ cm}^3$, for a maximum attainable L/D ratio of ~ 25 . For the experiments described here, comparatively strong vortices are generated using a 10 ms piston rise time.

Since the aim of the present study is to produce vortex-flame events that are similar to those achieved in the computations of Katta et al. (1998), the piston is allowed to travel through its maximum range, but the tube is placed such that the diagnostics are triggered before additional vortices exit the tube. Models that rely on an artificially created vortex pair by specifying the vortex field (Ashurst 1993; Poinso et al. 1987; Rutland et al. 1991) may not be well represented by our experimental conditions because of the geometry and vorticity field associated with a time-evolving pulsed jet. A detailed discussion of vortex formation in our apparatus is given elsewhere (Fiechtner et al. 2000a, 2000b), with emphasis on the importance of matching experimental conditions and boundary conditions during comparison of experimental data and model predictions.

Vortex conditions are monitored carefully to avoid multiple-vortex or turbulent conditions by examining scattering images that are acquired with a charge-coupled device (CCD) camera. Vortex visualization is accomplished during alignment of the vortex nozzle using PLIF of acetone (Fiechtner et al. 1998); a vaporizer is installed temporarily between the vortex tube and the mass-flow controller for this purpose. Because acetone changes the fuel content and character of the counterflow flames, this visualization is only performed to determine the non-reacting vortex properties.

The laminar vortices produced experimentally travel upward within the surrounding oxidizer flow. A flow of air is supplied to the vortex tube such that in the absence of a vortex, the exit velocity matches the velocity of the air emanating from the surrounding nozzle. To minimize the

impact of room-air disturbances, upper and lower guard flows of nitrogen are supported through outer nozzles, which are concentric with the respective upper (fuel) and lower (air) inner nozzles. The hydrogen, nitrogen-diluent, and air flows are furnished by mass-flow controllers with respective full-scale ranges of 20, 20, and 30 l/min. A continuous flow of air is provided to the vortex tube by a 5 l/min controller, while the guard flows for the upper and lower guard (outer) nozzles are furnished by two 50 l/min mass-flow controllers. The flow rates of the controllers are accurate to $\pm 1\%$ of the full-scale range. The experiments have been repeated for three flame conditions (Table 1).

Seed particles are introduced into the burner flows when digital PIV measurements of the vortex velocity are performed. Three particle seeders are installed – one after the air mass-flow controller, a second after the vortex-air mass-flow controller, and a third after the junction where the hydrogen and nitrogen gases are mixed. Each flow is seeded with hollow spherical ceramic particles with an approximate mean diameter of 2.4 μm . PLIF experiments are also performed with unseeded flows to ensure that there are no significant differences with results from experiments with seeded flows.

2.2

PLIF/PIV system

A review of PLIF fundamentals can be found in Eckbreth (1988). The PLIF system in the current experiment includes a frequency-doubled, Q-switched Nd:YAG laser that is used to pump a dye laser; this dye laser, in turn, is frequency doubled. The UV radiation is directed through a telescope that is adjusted to produce a light sheet with a height that matches as nearly as possible the 40 mm burner separation. The resulting beam thickness is $\sim 300 \mu\text{m}$, which corresponds to the full width (defined as the distance between the locations of the 25% peak-intensity points).

Hydroxyl radicals absorb the laser radiation at 281.3 nm via the $R_1(8.5)$ transition of the (1,0) band in the A-X system. For flame temperatures ranging from 1100–2200 K, the Boltzmann population fraction for this transition varies by only 10%. Therefore, large changes in OH PLIF signal within this temperature range can be attributed to changes in OH number density rather than changes in the Boltzmann population fraction for the $R_1(8.5)$ transition. The OH PLIF signal is expected to drop significantly below 1100 K and mark flame extinction, both because of a drop in the Boltzmann population fraction for the $R_1(8.5)$ transition and because chemical reactions are expected to cease below this temperature (Croonenbroek 1996; Renard et al. 1999; Rolon et al. 1996).

Table 1. Flow rates (LPM) at 21.5°C and 724 mmHg for the three flames studied in the current investigation. $X_{\text{H}_2-\text{in}-\text{N}_2}$ is the volume fraction of hydrogen in nitrogen diluent

Gas	Flame type A	Flame type B	Flame type C
H ₂ (SLPM)	5.31	4.67	4.04
N ₂ diluent (SLPM)	17.0	17.0	17.1
$X_{\text{H}_2-\text{in}-\text{N}_2}$	0.24	0.22	0.17
Air (SLPM)	11.2	11.2	11.2

After laser excitation of the $R_1(8.5)$ transition, fluorescence from the A-X (1,1) and (0,0) bands is detected normal to the laser sheet through Schott WG-295 and UG-11 colored-glass filters using a 105 mm focal-length f/4.5 UV lens. The resulting UV fluorescence is recorded on an intensified CCD camera with an intensifier gate width of 100 ns. CCD pixels are binned in 2×2 groups; the result is an effective array size of 288×192 pixels, with an imaged area of 25.6×38.4 mm². The bottom of the image is flush with the surface of the lower nozzle. A color table is used, with a maximum value set to 100% of the maximum signal for each image. The low-signal color of 10% is at least two standard deviations above the mean background. Therefore, in cases where “extinction” of the OH layer is observed, this term refers to signal levels that fall below this minimum value and are therefore assigned the last color in the table.

In studies of vortex-flame interactions conducted by other investigators (see, for example, Najm et al. 1998 and Paul et al. 1998), LIF was assumed to mark a quantity such as heat release or burning rate. In the present experiments OH images are obtained for the direct comparison of certain spatial and temporal features and for comparison with the flame structure predicted by Katta et al. (1998); therefore, no attempt is made to correlate the images with other quantities, although it has been shown recently that the OH concentration may be a good indicator of flame extinction in this configuration (Renard et al. 1999). This is confirmed experimentally through qualitative Rayleigh scattering images under similar conditions, although no attempt is made to determine the exact moment of flame extinction due to the added uncertainty of increased OH fluorescence quenching at depressed temperatures.

An introduction to PIV can be found in Raffel et al. (1998). Measurements of the velocity field in the current work are carried out using digital two-color PIV (Gogineni et al. 1998). A color digital CCD with an array of 3060×2036 pixels is used with an imaged area of 26.0×39.0 mm² (roughly matching the PLIF field of view). The color CCD camera for PIV and the intensified CCD array for OH PLIF are aligned using a transparent mask printed with a graduated scale. Further alignment between images is performed after each experiment in post-processing; a transformation in two-dimensional space is applied to the PIV images relative to the PLIF images resulting in a final viewing area of 24.5×36.0 mm². Two lasers are employed, with one PIV light sheet being produced by frequency doubling the output of a Q-switched Nd:YAG laser (30 mJ/pulse at the test section). The remainder of this beam is used to pump the dye laser that is frequency doubled to excite OH. The second PIV light sheet is produced by pumping a dye laser (employing DCM laser dye) with a second frequency-doubled, Q-switched Nd:YAG laser; this results in laser radiation at 640 nm (40 mJ/pulse at the test section). The thickness of both the red and the green light sheets is set to $\sim 700 \mu\text{m}$ in the probe region. Due to the size and axisymmetric geometry of the vortex flowfield, significant gradients are not expected across this laser-sheet thickness. A digital delay generator is used to drive the timing of the two lasers such that the red pulses are delayed precisely with respect

to the green ones. In the absence of a vortex, the underlying counterflow velocity field is probed with red pulses that are delayed by up to 1 ms with respect to the corresponding green pulses. For the most rapid vortices studied, the delay between red and green pulses is reduced to 10 μ s. The camera shutter is set to open for 1/15 s to permit detection of both laser pulses by the color CCD while minimizing interferences from flame emission and ambient light.

Velocity vectors are calculated using custom-designed software developed at Stanford (StanPIV – Hasselbrink 1999). This software incorporates several improvements to standard (single-pass) PIV algorithms and allows recursive estimation of the velocity field. A correlation area of 32 \times 32 pixels is used in the calculation, corresponding to a correlation area of 0.067 cm² and a spatial resolution of 400 μ m. The latter corresponds to four or five vectors across the unperturbed OH layer. Spurious vectors are filtered using a consistency filter that rejects vectors for which the square root of $(\Delta x_i - \Delta x_o)^2 + (\Delta y_i - \Delta y_o)^2$ is greater than about one-tenth of the distance across an interrogation region for three of the eight nearest neighbors. Here, Δx and Δy are the cross-correlation distances, the subscript i denotes the eight nearest neighbors, and the subscript o denotes the vector being filtered. The values of the vectors that are invalidated by the filter are interpolated.

2.3

High-temporal-resolution synchronization scheme

Because data on the time-dependent nature of the vortex-flame interactions are to be analyzed in conjunction with simultaneous scalar and velocity data, precise synchronization of several experimental events is required. These events include the generation and propagation of vortices,

production of laser pulses, and activation of the PIV-camera shutter and PLIF-camera intensifier. As explained in the following discussion, the current synchronization scheme, shown in Fig. 2, was developed to avoid the inherent jitter caused by long term delays in conventional delay generators. This problem arises when trying to synchronize the 0.5 s delay of piston actuation from an arbitrary-waveform generator (AWG) to the fifth pulse of a 10 Hz laser trigger from a digital delay generator (DDG). The jitter between 10 Hz clock outputs is one part in 10⁴, corresponding to a jitter of 50 μ s over the 0.5 s period. For this reason, attempts to synchronize the piston and 10 Hz clock severely limit the temporal resolution available to “freeze” the vortex-flame events, and require an intensifier gate width larger than 50 μ s (which leads to an unacceptable level of background flame emission).

When the DDG is triggered externally, however, the jitter between the trigger and a delayed DDG output pulse is 60 ps plus the output delay divided by 10⁸. Over the 0.5 s period between the first and fifth laser pulses, this corresponds to a jitter of only 5 ns. Therefore, a 10 Hz clock is added to the system for driving the lasers, and an externally triggered master DDG is used to impose a low-jitter 0.5 s delayed pulse, which pre-emptively triggers the fifth pulse of the 10 Hz clock (note the 50 Ω power combiner in Fig. 2). This approach reduces the jitter in the timing of the fifth laser pulse from 50 μ s to <10 ns while maintaining the nominal 10 Hz repetition rate required by the lasers. The coincidence unit in Fig. 2 ensures that pre-emptive triggering occurs only when an initiation pulse is output from the PLIF camera controller.

Other outputs of the master DDG are delayed suitably and directed to the image detectors. For PIV experiments, the width of a TTL pulse is adjusted using a gate generator that closes a relay to trigger the digital PIV camera system.

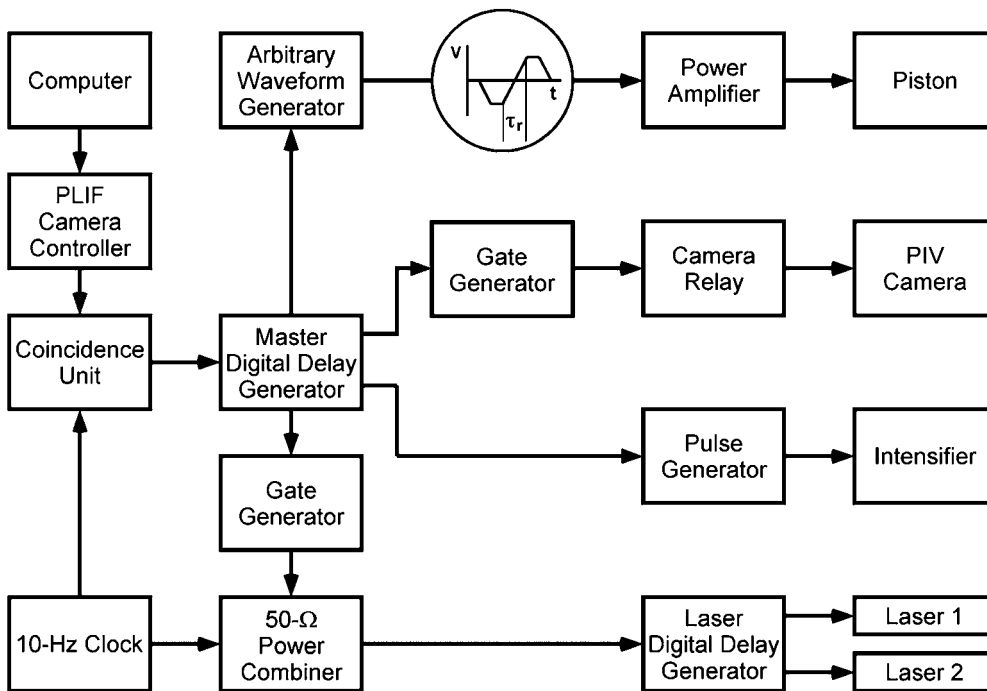


Fig. 2. Block diagram of the high-temporal-resolution synchronization scheme enabling vortex imaging repeatability to within 10 μ s

For simultaneous PLIF experiments, another master-DDG output triggers a pulse generator that, in turn, activates the intensifier of an ICCD camera.

The scheme depicted in Fig. 2 provides precise control of the relative timing between the laser diagnostics and the vortex-flame event. To explore the temporal evolution of the event, data are captured utilizing the following phase-locked timing sequence: 1) an image is recorded, 2) the delay between vortex production and the laser/camera events is adjusted, and 3) another vortex is initiated and a second image recorded. This process is repeated to acquire numerous images that are obtained at increasing delays. An animation is then created by assembling the individual images in temporal order.

3 Results and discussion

The temporal sequence of OH PLIF images during an annular extinction is shown in Fig. 3 for Flame A in Table 1. The temporal delay between images is $10\ \mu\text{s}$, and the vortex velocity is $11.5\ \text{m/s}$. The off-centerline break in the OH layer shown in these figures is very similar in structure to that observed numerically by Katta et al. (1998), attesting to the predictive capability of their code. The $10\ \mu\text{s}$ temporal delay used to resolve the extinction process demonstrates the success of the synchronization scheme for repeatable imaging of high-speed vortices and is similar to that employed in the computations. In the following discussion, we present PLIF/PIV data for cases

with and without flame extinction to highlight various features of the vortex-flame interaction process. We then present more detailed calculations of the normal strain field and discuss the annular extinction in greater detail.

Simultaneous images of OH PLIF overlaid with instantaneous velocity vectors from PIV are shown in Figs. 4 and 5 for cases with no flame extinction (weaker vortex) and with flame extinction (stronger vortex), respectively. Inflow conditions match those of Flame C in Table 1. Each OH PLIF image is normalized to the peak signal level within the unperturbed region of the flame. The velocity vectors plotted here correspond to the reference frame of the vortex and are obtained by subtracting its convection velocity. The number of vectors is reduced by 60% for presentation purposes. Figures 4 and 5 also show vorticity distributions computed by central differencing of the velocity field.

For the case with no flame extinction, shown in Fig. 4, the vortex velocity is about $4\ \text{m/s}$, and images are separated by $9\ \text{ms}$. As the vortex approaches, the flame surface becomes highly wrinkled and wraps around the leading edge of the vortex. The flame then burns across the vortex rollers without being extinguished and continues propagating along the vortex column, as shown in the central and right-most frames of Fig. 4a. The location of the vortex structure is shown more clearly in the vorticity plots of Fig. 4b. The case with flame extinction is shown in Fig. 5, with a time spacing between frames of $6\ \text{ms}$. The vortex shown in Fig. 5a breaks the OH layer as it advances

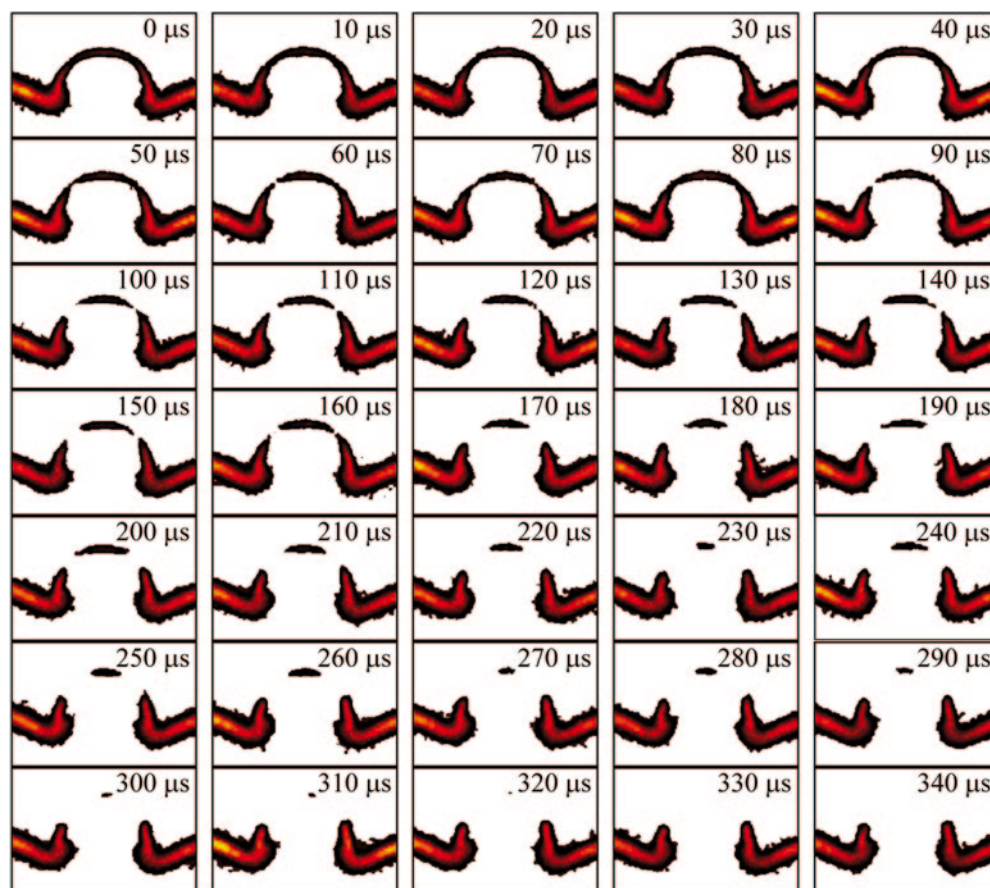


Fig. 3. Sequence of OH PLIF images with a temporal delay between images of $10\ \mu\text{s}$. Conditions are for Flame A (see Table 1) and incoming vortex convection velocity of $11.5\ \text{m/s}$

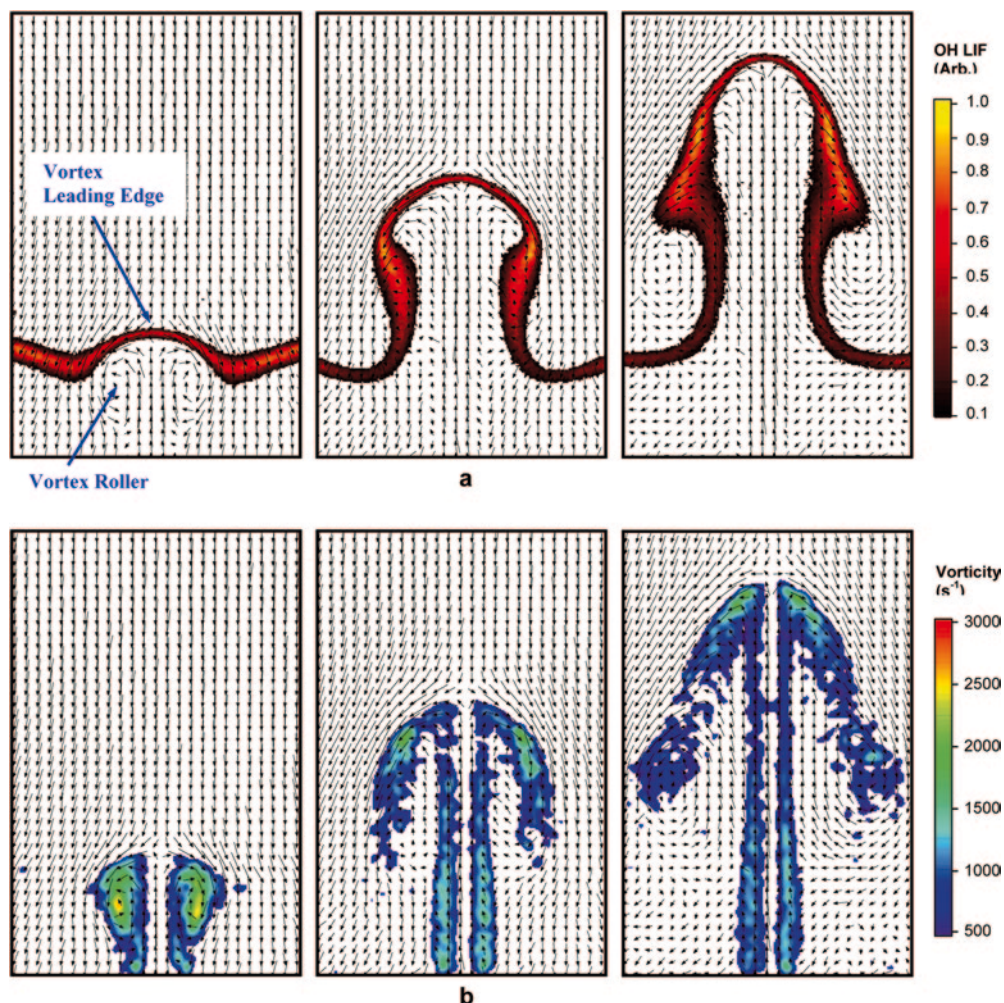


Fig. 4. a Simultaneous OH-PLIF and velocity distributions for a case with no flame extinction; b superposed velocity and vorticity distributions. Conditions are for Flame C (see Table 1) and an incoming vortex convection velocity of 4 m/s. Images are 24.5 mm wide×36 mm high, progress in time is from left to right, and images are spaced 9 ms apart

toward the upper nozzle, after which the flame propagates into the vortex rollers and begins to reconnect.

The following is a frame-by-frame comparison of Figs. 4 and 5 to illustrate the effect of flame extinction on the vortex flowfield. The plot of vorticity in the left-most frame of Fig. 5b shows that the vortex is stronger than that of Fig. 4b. As a consequence, the vortex in the central frame of Fig. 5b induces a local flame extinction and is able to sustain its rotation. By comparison, the vortex in the central frame of Fig. 4b is dissipated because of interaction with the flame and a corresponding increase in viscosity for the combustion products. In the right-most frame of Fig. 5b, however, the locally quenched flame begins to reconnect, and the overtaken vortex is even more strongly dissipated than the vortex of Fig. 4b. This suggests that the laminarization of local turbulence in non-premixed flames can be achieved through different mechanisms for vortices of varying strength, with reconnection playing a significant role for vortices that are strong enough to induce a local flame extinction.

Details of the flame extinction process are not evident in Fig. 5 because of the relatively large time spacing between images. To explore this process in more detail, simultaneous OH PLIF and velocity vectors are plotted in Fig. 6 for three images during the interaction of an 8.25 m/s vortex with Flame B from Table 1. The flame begins to

thin in an annular region as the vortex approaches in the left-most frame. A clear break in the OH layer is then observed in the central frame. Regions I-III in Fig. 6 are located 0–10 mm along the OH layer, with the centerline (Region I) located at 0 mm and the annulus (Region II) located at about 5 mm.

Fig. 7a contains line plots of the relative OH-PLIF signal and velocity gradient normal to the flame surface, dU_n/dR ; data are from the left-most image of Fig. 6, where U_n and R are the velocity and spatial components, respectively, normal to the flame surface. From this definition, dU_n/dR represents the compressional-strain component across the flame. The abscissa of Fig. 7a represents the distance along the center of the OH layer from Region I to Region III. The velocity gradient is calculated using a combination of central differencing and linear interpolation between grid points. Increasing the vector density by a factor of two did not significantly alter the measured strain rates, indicating that the velocity gradients are adequately resolved by the 32×32 interrogation regions used here. Based on noise in the velocity data, the uncertainty in measured strain rates is estimated to be $\pm 10\%$. In Fig. 7a, where strain rates are plotted with respect to the OH layer, errors in PIV/OH image registration lead to a final uncertainty of about $\pm 15\%$. In terms of shot-to-shot fluctuations in vortex strength and

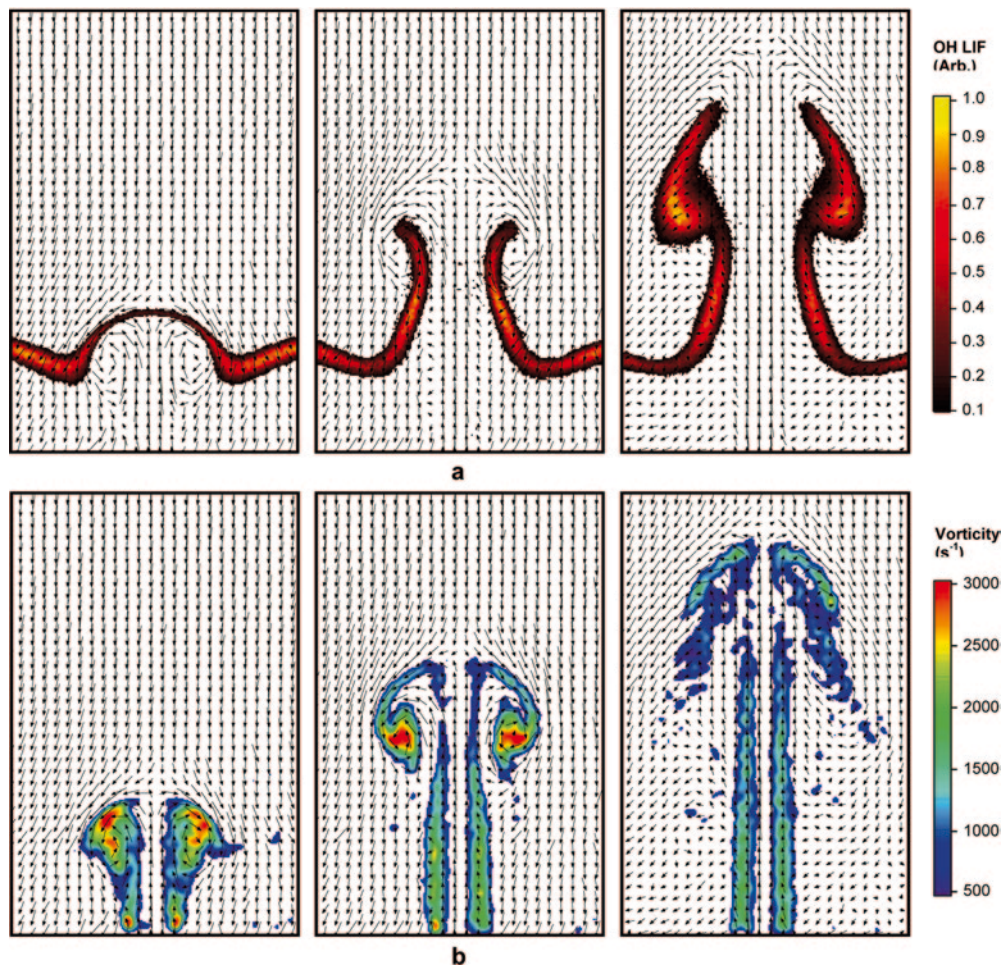


Fig. 5. a Simultaneous OH-PLIF and velocity distributions for a case with flame extinction; b superposed velocity and vorticity distributions. Conditions are for Flame C (see Table 1) and an incoming vortex convection velocity of 5 m/s. Images are 24.5 mm wide×36 mm high, progress in time is from left to right, and images are spaced 6 ms apart

trajectory, these strain rate measurements are considered to be repeatable to within $\pm 25\%$.

According to the plot of relative OH signal in Fig. 7a, flame extinction begins to occur near Region II in an annular region away from the jet centerline and within a region of maximum dU_n/dR . By reviewing the left-most image of Fig. 6, it is clear that this off-axis compressional strain is induced by the tangential velocity of the rotating vortex. To compare further the strain rates acting upon the flame in the centerline and annular regions, line plots of dU_n/dR across the flame in Regions I and II, respectively,

are shown in Fig. 7b for comparison. Unlike in Fig. 7a, the abscissa of Fig. 7b represents the distance from the center of the OH layer. The value of dU_n/dR toward the *fuel side* of the OH layer is slightly higher in the annular region than at the centerline, with measured peak values that are within 10% of those predicted by Katta et al. (1998). In contrast, the experimental and computed *air side* strain rates are lower at the annular extinction location than at the centerline. The spatially integrated strain rate across the flame is also about 10–15% lower at the annular extinction location than at the centerline. Uncertainties in

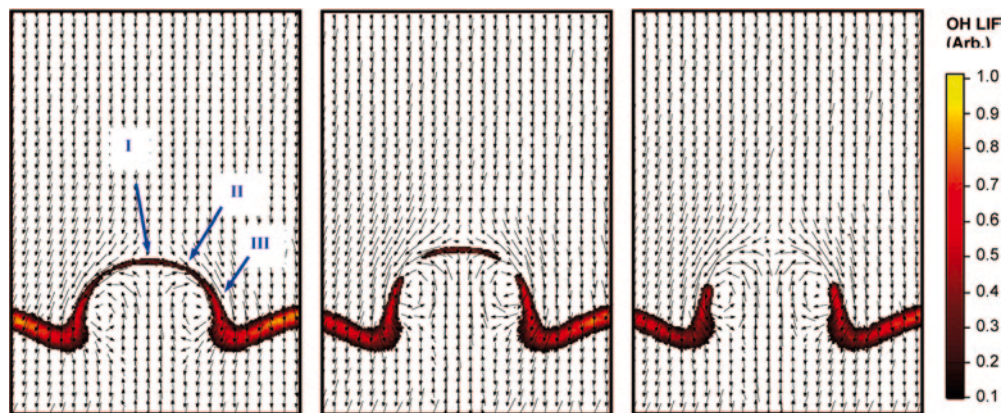


Fig. 6. Simultaneous OH PLIF and velocity distributions for Flame B (see Table 1) and an incoming vortex convection velocity of 8.25 m/s. Images are 24.5 mm wide×36 mm high, progress in time is from left to right, and images are spaced 0.3 ms apart to show three stages of the extinction process. Symbols I-III represent regions located 0–10 mm along the flame front

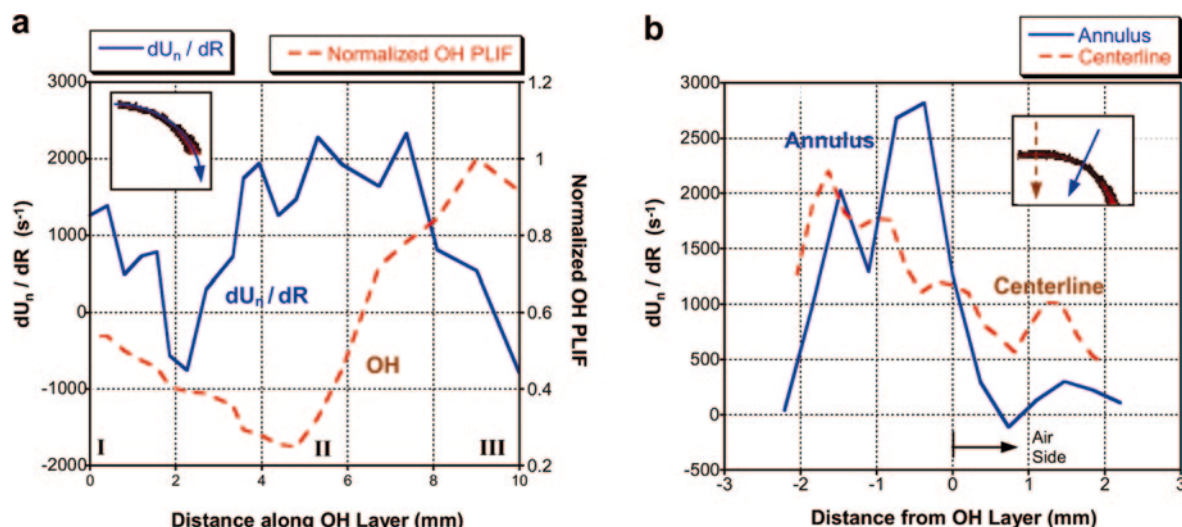


Fig. 7. a Velocity gradient normal to the flame surface (dU_n/dR) and the normalized OH fluorescence signal *along* the flame from Region I to III from the left-most image of Fig. 6; b velocity

gradient normal to the flame surface measured *across* Regions I (centerline) and II (annular region) from the left-most image of Fig. 6

the velocity measurements due to thermophoresis (Sung et al. 1996) are not expected to alter this analysis significantly because strain rates are reported relative to the OH layer and, presumably, relative to an isocontour of temperature.

These data indicate that the local strain rate may not be the controlling parameter in the initiation of annular flame extinction. Katta et al. (1998) argued instead that the annular extinction may result from increased local curvature and preferential diffusion. It is apparent from the central frame of Fig. 6, for example, that flame extinction is initiated in Region II near a location of maximum curvature. By fitting the flame profile along 5 mm sectors at the centerline and annulus, the flame radius for each region was calculated to be about 10 mm and 5 mm, respectively, to within $\pm 5\%$. Due to higher curvature in the annular region, thermal diffusion per unit area is reduced on the fuel side by a factor of four compared to the centerline region, while preferential diffusion of hydrogen would bring an influx of cool, fuel-rich gases into the annular flame zone and depress the reaction rate. In contrast with the flame structure of Fig. 6 noted above, the leftmost image of the non-extinguished flame of Fig. 4a shows no apparent increase in curvature in the annular region. Correspondingly, the flame in Fig. 4a is slightly thinner at the centerline than at the annulus, further indicating that local variations in curvature may play a dominant role in the initiation of flame extinction for the current flow regime.

4 Conclusions

The interaction of a toroidal vortex with a flat, counter-flow, hydrogen-air diffusion flame captures a number of important processes in turbulent combustion, including vortex-induced flame wrinkling, stretch, normal strain, and unsteadiness. To first order, centerline flame extinction at the leading edge of the vortex simulates the effects of unsteadiness and flame stretch. In the current

study, off-centerline strain rates and curvature induced by the rotational component of the approaching vortex were determined using simultaneous OH PLIF and PIV. Analysis of local normal strain rates *along* the OH layer shows slightly higher magnitudes near the annular region where flame extinction is first observed, but measurements across the flame show a more complex strain rate distribution. In contrast, high local curvature in the annular region is shown to correlate well with the initiation of flame extinction. To assess the effects of flame extinction on the flowfield, plots of vorticity calculated from the PIV data are used to show that the case with flame extinction has higher initial vortex strength, but experiences greater levels of dissipation at later times during flame reconnection. Therefore, the ability to obtain measurements of scalars and velocity in a time-correlated sequence is demonstrated to be particularly useful in studying the coupled effects of fluid dynamics and flame chemistry in dynamically-strained, curved flamelets. Such conditions more closely simulate the fluid-chemistry interactions that are typical in turbulent diffusion flames.

References

- Ashurst WT (1993) *Combust Sci Technol* 92:87
- Croonenbroek T (1996) PhD Thesis, Laboratoire E.M2.C, CNRS and École Centrale Paris
- Donbar JM, Driscoll JF, Carter CD (2001) *Combust Flame* 125(4):1239–1257
- Driscoll JF, Sutkus DJ, Roberts WML, Post ME, Goss LP (1994) *Combust Sci Technol* 96:213–229
- Eckbreth AC (1996) *Laser diagnostics for combustion temperature and species*, 2nd edn. Gordon and Breach, The Netherlands
- Fiechtner GJ, Carter CD, Grinstead KD, Gord JR, Roquemore WM, Rolon JC (1998) Flame-vortex interactions in a non-premixed H_2/N_2 /air counterflow burner. AIAA Paper 98-3770
- Fiechtner GJ, Carter CD, Katta VR, Gord JR, Donbar JM, Rolon JC (1999) Regimes of interaction between a non-premixed hydrogen-air flame and an isolated vortex. AIAA Paper 99-0320
- Fiechtner GJ, Katta VR, Carter CD, Gord JR, Roquemore WM, Rolon JC (2000a) *J Visual-Japan* 3(2):96

- Fiechtner GJ, Renard PH, Carter CD, Gord JR, Rolon JC (2000b) *J Visual-Japan* 2(3/4):331–342
- Frank JH, Lyons KM, Long MB (1996) *Combust Flame* 107:1–12
- Garside JE, Hall AR, Townsend DTA (1943) *Nature* 152:748
- Gharib M, Rambod E, Shariff K (1998) *J Fluid Mech* 360:121–140
- Gogineni S, Goss L, Pestian D, Rivir R (1998) *Exp Fluids* 25:320–328
- Hasselbrink E (1999) Transverse jets and jet flames: structure, scaling, and effects of heat release. PhD Thesis, Stanford University, Stanford, CA
- Hasselbrink EF, Mungal MG (1998) *P Combust Inst* 27:1167–1173
- Katta VR, Carter CD, Fiechtner GJ, Roquemore WM, Gord JR, Rolon JC (1998) *P Combust Inst* 27:587–594
- Katta VR, Meyer TR, Gord JR, Roquemore WM (2003) *Combust Flame* 132:639–651
- Kothnur PS, Tsurikov MS, Clemens NT, Donbar JM, Carter CD (2002) *P Combust Inst* 29:1921–1927
- Lemaire A, Meyer TR, Zähringer K, Rolon JC, Gord JR (2003) *Appl Optics* 42(12):2063–2071
- Mueller CJ, Driscoll JF, Sutkus DJ, Roberts WL, Drake MC, Smooke MD (1995) *Combust Flame* 100:323–331
- Najm HN, Paul PH, Mueller CJ, Wyckoff PS (1998) *Combust Flame* 113:312–332
- Paul PH, Najm HN (1998) *P Combust Inst* 27:43–50
- Poinsot T, Trouve A, Veynante D, Candel S, Esposito E (1987) *J Fluid Mech* 177:265–292
- Raffel M, Willert C, Kompenhans J (1998) *Particle image velocimetry: a practical guide*. Springer, Berlin Heidelberg New York
- Rehm JE, Clemens NT (1998) *P Combust Inst* 27:1113–1120
- Renard P-H, Rolon JC, Thévenin D, Candel S (1999) *Combust Flame* 117:189–205
- Renard PH, Thevenin D, Rolon JC, Candel S (2000) *Prog Energ Combust* 26:225–282
- Rolon JC, Aguerre F, and Candel S (1995) *Combust Flame* 100:422–429
- Rolon JC, Darabiha N, Croonenbroek T, Dagusé Th, Martin JP (1996) Quantitative LIF and Rayleigh measurements of temperature and absolute concentration of OH radical in strained diffusion flames. 8th International Symposium on Applications of Laser Techniques to Fluid Mechanics, Lisbon, Portugal
- Rutland CJ, Ferziger JH (1991) *Combust Flame* 84:343–360
- Samaniego JM, Mantel T (1999) *Combust Flame* 118:537–556
- Shusser M, Gharib M, Mohseni K (1999) A new model for inviscid vortex ring formation. AIAA Paper 99-3805
- Sung CJ, Kistler JS, Nishioka M, Law CK (1996) *Combust Flame* 105:189–201
- Thévenin D, Renard PH, Fiechtner GJ, Gord JR, Rolon JC (2000) *P Combust Inst* 28:2101–2108
- Watson KA, Lyons KM, Donbar JM, Carter CD (1999) *Combust Flame* 117:257–271
- Watson KA, Lyons KM, Carter CD, Donbar JM (2002) *P Combust Inst* 29:1905–1912

Influence of Spray-Flame Structure on Soot Formation in Gas-Turbine Combustors

T.R. Meyer,* S. Roy, and S.P. Gogineni
Innovative Scientific Solutions, Inc.
Dayton, OH 45440-3638

J.R. Gord
Air Force Research Laboratory, Propulsion Directorate
Wright-Patterson Air Force Base, OH 45433-7103

Abstract

Simultaneous measurements of OH planar laser-induced fluorescence (PLIF) and laser-induced incandescence (LII) are used to characterize the flame structure and soot formation process in the reaction zone of a swirl-stabilized, liquid-fueled gas-turbine combustor. Studies are performed at atmospheric pressure with heated inlet air and overall equivalence ratios ranging from 0.5 to 1.15. At low equivalence ratios ($\phi < 0.8$), large-scale structures entrain rich pockets of fuel and air deep into the flame layer; at higher equivalence ratios, these pockets grow in size and prominence, escape the OH-oxidation zone, and serve as sites for soot inception.

Introduction

Flame stabilization in gas-turbine engines is typically achieved with the aid of a recirculation zone established behind an air-swirl/liquid-fuel injector. The turbulent swirling motion that results from both the air flow and liquid injection process is characterized by high shear stresses and turbulent intensities that result in vortex breakdown and large-scale unsteady motions.^{1,2} Thus, the same turbulent process used for flame stabilization also generates unsteadiness that is known to play a key role in the formation of pollutant emissions such as carbon monoxide (CO), nitric oxide (NO), and unburned hydrocarbons (UHC).³⁻⁵

The impact of unsteady effects on soot formation was demonstrated by Shaddix et al.,⁶ who found that a forced methane/air diffusion flame produced a four-fold increase in soot volume fraction (as a result of increased particle size) as compared with a steady flame having the same mean fuel-flow velocity. In addition to unsteady effects, it has also been shown that the heterogeneous droplet distribution resulting from the injection process can lead to significant local variations in fuel-air ratio.^{7,8} In swirl-stabilized spray flames, therefore, soot can be formed under conditions that are locally fuel rich even though the overall equivalence ratio may be fuel lean.

A review of the literature indicates that relatively few studies have been performed on the effects of the spray-flame structure on soot formation.⁹⁻¹¹ Understanding these fundamental processes is increasingly important for minimizing particulate emissions and thermal loading in modern high-performance gas-turbine engines.

The goal of the current investigation is to study the effects of unsteadiness and local flame structure on soot formation within the turbulent two-phase reaction zone of a swirl-stabilized combustor. This is accomplished through simultaneous imaging of the soot volume fraction and hydroxyl-radical (OH) distribution using laser-induced incandescence (LII) and OH planar laser-induced fluorescence (PLIF), respectively. Residual Mie scattering from large droplets, which appears in the OH images but does not preclude signal interpretation, is used to a limited extent as a spray diagnostic.

Swirl-Stabilized Combustor

The injector configuration shown in Fig. 1(a) is a generic swirl-cup liquid-fuel injector used in ongoing fuel studies at the Atmospheric-Pressure Combustor-Research Complex of the Air Force Research Laboratory's Propulsion Directorate.¹² It employs pressure atomization and dual-radial, counter-swirling-air co-flows to entrain the fuel, promote droplet break-up, and enhance mixing. The 40-mm-exit-diameter swirl cup is installed at the entrance of a 15.25 cm \times 15.25 cm square-cross-section flame tube. After exiting the primary flame zone, pictured in Fig. 1(b), the combustion products are allowed to mix thoroughly along the 48-cm long flame tube before entering a 43-cm-long, 5.7-cm exit-diameter exhaust nozzle.

Changes in overall equivalence ratio from $\phi = 0.5$ to 1.15 were achieved in the current study by varying the pressure drop across the fuel-spray nozzle from about 1.5 to 10 atm, which resulted in fuel mass flow rates of 1.0 to 2.2 g/s, respectively. The fuel flow rate is measured using

* Corresponding author: trmeyer@innssi.com

Associated Web site: <http://www.innssi.com>

Proceedings of the 2004 Technical Meeting of the Central States Section of The Combustion Institute

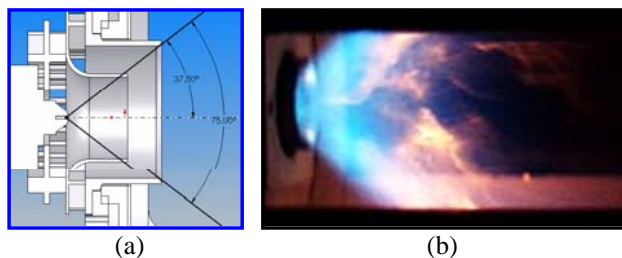


Fig. 1. (a) Dual-radial swirl-injector geometry and (b) photograph of near-field flame structure.

a Max Machinery positive-displacement flow meter with $\pm 0.5\%$ full-scale accuracy. The air-flow system consists of three Sierra 5600 SLPm mass flow controllers with $\pm 1\%$ full-scale accuracy. The inlet air is heated to 450 K with a constant flow rate of ~ 0.028 kg/s. The air-pressure drop across the combustor dome was ~ 4.8 to 5.2% of the main supply. Most of the air flow enters the combustor through the swirl-cup injector, but a small percentage enters through aspiration holes along the aft wall. No liner air jets are used in the secondary zone; therefore, the fuel-air ratio depends almost entirely on the flow rates through the injector cup.

The combustor is optically accessible via 75-mm-wide quartz windows along the top and sides for in-situ laser-based diagnostics.

Measurement System

The use of OH as a flame marker is typical in studies of soot formation in diffusion flames because of its close correlation with flame temperature.^{13,14} The current OH-PLIF measurement system uses a 330- μm wide sheet tuned to the $Q_1(9)$ transition at 283.922 nm (in air), which has less than a $\pm 2.5\%$ variation in the ground-level Boltzmann fraction from 1600 to 2400K. This range of temperatures coincides with the equilibrium conditions one would expect for JP-8 fuel at equivalence ratios used in this study ($\phi = 0.5$ to 1.15).¹⁵

Fluorescence in the linear regime is collected from about 306 to 320 nm via the (1,1) and (0,0) bands of OH using an intensified charge-coupled device (ICCD) camera oriented approximately along the normal to the sheet. Two 1-mm thick WG295 Schott Glass filters are used in front of the camera lens to reduce scattering from droplets at 283.922 nm, and a UG11 filter is employed to nearly eliminate flame emission, scattering from the LII laser wavelength of 532 nm, and fluorescence from polycyclic-aromatic-hydrocarbon (PAH) compounds. A 105-mm-focal-length $f/4.5$ UV lens is employed to collect the OH fluorescence, and an intensifier gate width of 20 ns is used to capture the OH signal. Images are typically collected with 2x2 binning to obtain adequate resolution (512x512) and framing rate (1.4 Hz). The pixel viewing

area in each 2x2 superpixel is $200 \times 200 \mu\text{m}^2$. OH PLIF signal corrections (typ. $\pm 15\%$) in the axial direction are performed in post-processing based on measurements of the laser-sheet profile after each run.

For measurements with low laser irradiance, the effect of collisional quenching on fluorescence efficiency must also be considered. As a result of offsetting effects in the equilibrium combustion products of JP-8, the rate of collisional quenching is found to be fairly constant for equivalence ratios of less than unity. Under rich conditions the conversion of CO to CO_2 decreases substantially and leads to an increase in collisional quenching and a decrease in fluorescence efficiency. In the liquid-spray region where lean and rich pockets of fuel can co-exist, qualitative signal interpretation must take into account a possible variation of $\pm 30\%$ in fluorescence efficiency.¹⁶

Mie scattering was obtained using the same optical setup as that for the OH LIF system. When tuned on and off the OH absorption line, as shown in Figs. 2(a) and (b), the intense, highly localized droplet scatter can be distinguished from the large, more uniformly distributed OH layers. Large droplet clusters appear primarily near the injector exit, and single droplets with trailing flames are often observed traveling into the recirculation region, as shown in Fig. 2(a). The trailing flames of these droplets do not appear in the off-line images nor at higher equivalence ratios and, therefore, are not attributable to scattering off of fuel vapor or fluorescence from broadband sources such as PAH compounds. It was found that two WG295 color-glass filters and parallel-polarization detection would provide optimal OH LIF sensitivity while minimizing the likelihood of damaging the ICCD because of intense levels of droplet scattering.

The LII system employed in the current study for soot-volume-fraction imaging operates in the saturated regime (measured $> 200 \text{ mJ/cm}^2$) to reduce the effect of laser-intensity variations. In this regime, the uncertainty in relative soot-volume-fraction measurements is estimated

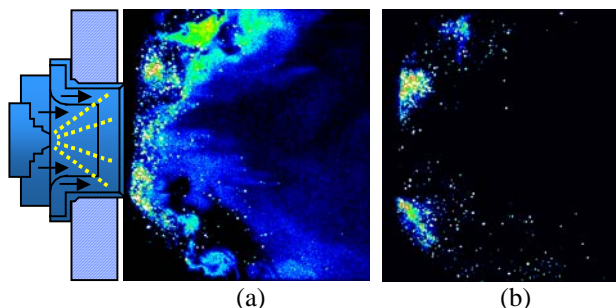


Fig. 2. Raw signal from OH PLIF and droplet Mie scattering while on $Q_1(9)$ line of (1,0) band in A-X system (left) and droplet Mie scattering while off the OH line (right). Overall equivalence ratio is 0.7.

to be about $\pm 10\%$ for the full width of the 700- μm thick laser sheet.

After excitation by a laser pulse at 532 nm, the LII signal from superheated soot is detected using a 1024 \times 1024 ICCD camera and an f/1.2, 58-mm-focal-length glass lens. After 4 \times 4 pixel binning, the measurement resolution is about 575 \times 575 μm^2 . A 500 nm short-pass filter is used for detection from 415 to 500 nm, which reduces contributions from nascent soot particles, OH fluorescence/chemiluminescence, and red-shifted fluorescence from PAH compounds. The relatively short-lived PAH fluorescence is also minimized by employing a time-delayed detection scheme. Scattering from the 532-nm laser source is eliminated through the use of a 532-nm zero-degree reflective mirror in addition to the 500-nm short-pass filter and delayed detection. A camera delay of 20 ns after the laser pulse was found to reduce laser scatter to nearly the background level while maintaining LII signal-to-noise ratios greater than 20:1. The LII signal decayed quickly within the first 200 ns after the laser pulse. Using a gate width of 50 ns, errors due to particle size effects are expected to be minimal (5-10%).¹⁷

Results and Discussion

The average and instantaneous OH distributions at overall equivalence ratios (ϕ) ranging from 0.5 to 1.15 are shown in Figs. 3(a) to 3(d). All images are background subtracted and corrected for laser-sheet intensity variations and laser-sheet divergence. The effect of laser attenuation is evident in the lower flame region, with signal levels that are 10% less than the upper flame region. The false color scale is common for all images and varies from 5% to 100% of the maximum OH signal as determined by probability density functions at $\phi = 0.5$.

Two main features of the flame structure become apparent when analyzing the series of images in Fig. 3. The first is that the flame structure evolves from a single- to multi-layer reaction zone. The second is the prominent role that turbulence plays in determining this structure.

A classical five-zone description of pressure-jet hollow-cone spray combustion¹⁸ consists of a dense spray, primary flame zone, rich-premix zone, rich secondary combustion zone, and a recirculation zone. The dense spray region in the near field is dominated by fuel vapor and cannot support combustion. The primary zone is formed by the combustion of fuel vapor from small droplets. A rich-premix zone is then formed along the spray direction due to evaporation of larger droplets. This is followed by rich combustion and product recirculation.

For the current injector geometry, the primary reaction zone is highly perturbed by large-scale structures that entrain reactants across the entire width of the flame layer, as shown in the instantaneous image of Fig. 3(a). At higher equivalence ratios, these turbulent motions become more prominent and the primary flame zone, labeled in Fig. 3(b), becomes more intermittent. Also, an

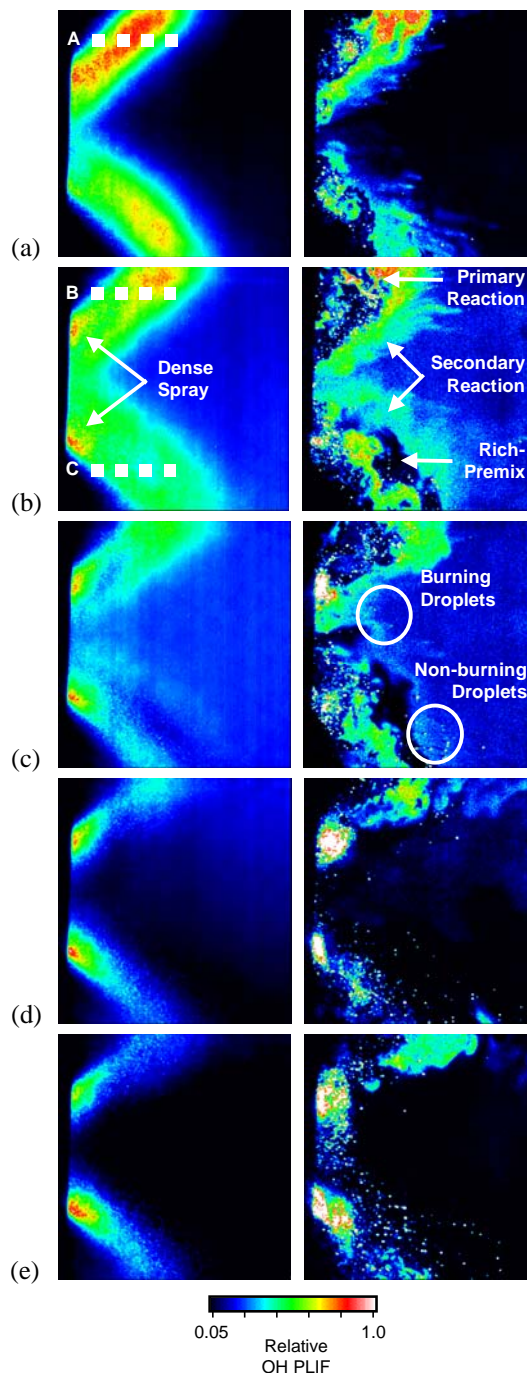


Fig. 3. 200-shot average (left) and instantaneous (right) OH PLIF images at equivalence ratios of (a) 0.5, (b) 0.7, (c) 0.8, (d) 1.0, and (e) 1.15. False-color scale from 5% to 100% of the peak average (4100) and instantaneous (5250) counts at $\phi = 0.5$.

intermittent rich-premix region is formed along the inner cone of the spray, as labeled in Fig. 3(b). This region comes into direct contact with the recirculation zone and reacts with any available oxygen, thereby establishing a

secondary flame zone as labeled in Fig. 3(b). At $\phi = 0.5$, the primary and secondary reaction zones are essentially merged, and a gradual separation in the flame layers takes place at higher equivalence ratios. This phenomenon is most visible in the lower half of the average image in Fig. 3(c), where the primary and secondary reaction zones are completely separated by the rich-premix zone. Since the air-flow rate is held constant for all test conditions in this study, these dynamics can be attributed to the behavior of the liquid spray as the injection pressure is increased. Experiments and computations based on gaseous-fuel injection, therefore, may not capture this behavior.

To further elucidate the role of intermittency and the character of the rich-premix region, it is useful to present probability density functions (PDFs) of the OH PLIF signal. PDFs are mathematically defined as histograms with areas normalized to unity. They are helpful in highly intermittent flames for which the ensemble average does not accurately represent the instantaneous field. For example, they can be used to detect whether an increase in OH signal results from an increase in OH within large-scale structures or from an increase in their frequency of occurrence. They can also be used to discriminate against Mie scattering, which occurs with much higher camera counts than the OH PLIF.

Figures 4(a) and 4(b) show PDF data for $\phi = 0.5$ and 0.7, respectively, across the upper flame zone just above the dense spray, as shown in Fig. 3. Each profile in Fig. 4 represents a different downstream position, as noted in the legend. At each point, signals from 0 to 6000 counts from 200 images are tabulated into bins of 200 counts. The contribution from droplet scattering, which typically occurs with tens of thousands of counts per pixel, is not significant at these locations since the PDFs drop to zero by 5000-6000 counts.

The PDF profiles for $\phi = 0.5$ in Fig. 4(a) change significantly from 12 - 34.8 mm because of changes in large-scale structure dynamics across the flame. The PDFs at 12 and 19.6 mm are bimodal in character, with the low-signal peak representing cases when the measurement point is outside of a flame structure and the high-signal peak representing cases when the measurement point is within a flame structure. As one crosses the center of the flame layer, the PDFs are increasingly weighted toward the high-signal peak. Note that both the low and high signal peaks are remain “stationary” from 12 mm to 27.2 mm, indicating that the fluid composition within the large scale-structures is nearly constant in this region. Beyond 27.2 mm, the PDFs take on a “marching” character. Specifically, the PDF profiles are shifting to lower signal levels, indicating that large-scale entrainment of unburned reactant is reduced in this region.

The PDF profiles for the upper flame at $\phi = 0.7$ follow the same trends as for those at $\phi = 0.5$. This is evident in Fig. 4(b) in which the PDFs from $x = 12 - 27.2$ mm are weighted more and more to the high-signal peak. The

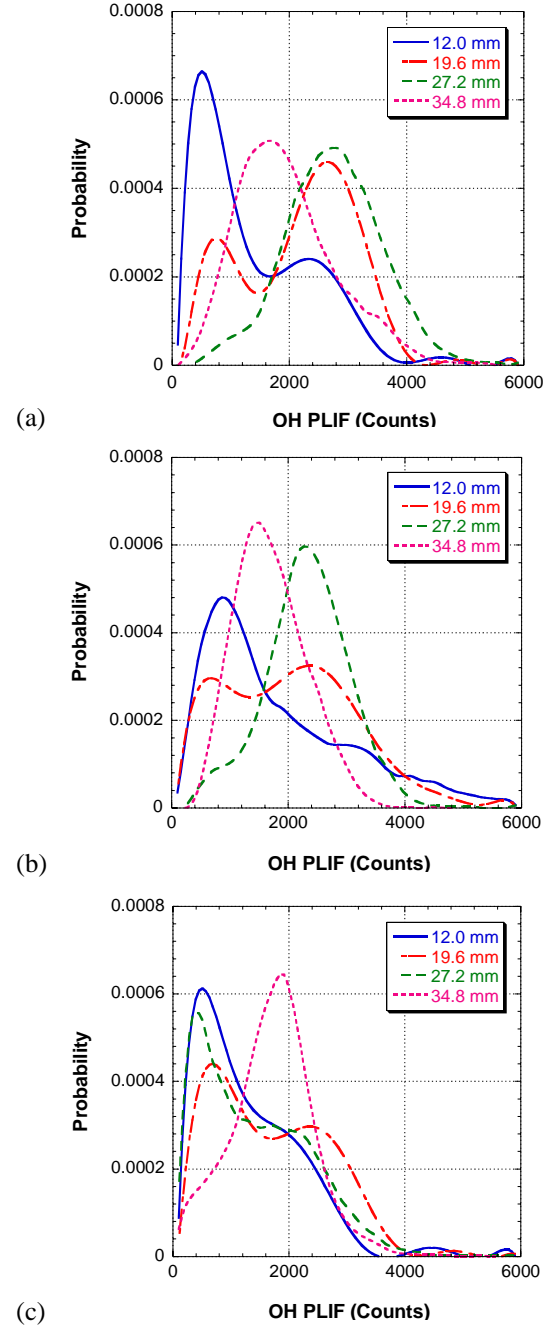


Fig. 4. Probability density functions of OH PLIF at (a) Line A, (b) Line B, and (c) Line C as marked in Fig. 3.

PDFs for the lower flame in Fig. 4(c), however, mark the emergence of the rich-premix zone at 27.2 mm. Rather than shifting to the high-signal peak, the PDF profile at this location shifts back to the low signal peak and is similar to the profile shown at 12 mm. This indicates that the rich-premix region between the primary and secondary zones is similar in terms of large-scale

structure dynamics to the unburned reactant layer along the outer cone of the spray flame.

Based on this understanding of the turbulent flame structure, it is of interest to determine the location of soot inception, how it evolves, and the dynamic behavior that controls the rate of soot production. Based on the results reported by Shaddix et al.⁶ in forced flames, it is likely that the turbulent flow structure reported in the previous section will have a significant impact on soot production.

Figures 5(a) – 5(c) show simultaneous images of OH PLIF and soot volume fraction from LII at $\phi = 0.8, 1.0$, and 1.15 . The OH PLIF images have the same false color scale shown in Fig. 3, while the LII signal is plotted using color contours defined by a reverse color scale shown in Fig. 5. Analysis of these images reveals an inverse correlation between soot volume fraction and OH PLIF signal. An exception is in the dense spray region where low levels of LII interference are detected due to residual droplet scattering. Increasing the time delay for LII detection reduces this scatter but also significantly reduces the detection of soot incandescence. Instead it is sufficient to note that most of the LII signal is detected in regions that are free of droplet Mie scattering (as detected with the OH PLIF camera) and is attributable to the presence of soot. The LII signal is also not likely to come from PAH fluorescence, which would appear more consistently and have peak signals near the spray region. Background images collected without the laser sheet show that the contribution from nascent soot incandescence is less than 5%.

For all flow conditions studied here, soot is most often generated along the inner cone of the flame. Not unexpectedly, this corresponds to the intermittent rich-premix zone discussed in the previous section. This is particularly evident in Fig. 5(a), where soot is shown propagating out of this region and into the recirculation zone. It is interesting note that soot is seldom observed within intermittent regions of low OH signal in the central and outer cone. This is not surprising since there are likely to be higher levels of oxygen and OH available for soot oxidation in this region.

From observation of simultaneous OH PLIF and LII data, as shown in Fig. 5, it is evident that the rate of soot production increases significantly with overall equivalence ratio. The mechanisms for this increased production can now be assessed given knowledge of how the soot is formed and how it evolves. As noted in the previous discussion, large-scale turbulent motions increase the prominence of the rich-premix zones as the injection pressure is increased. In addition, the secondary reaction zone is weakened as the equivalence ratio in the recirculation zone increases. Even at lower overall equivalence ratios ($\phi \sim 0.8$), intermittency can result in locally rich regions within the recirculation zone.

Due to a slight asymmetry in the conical flame structure, the lower spray region displays a weaker

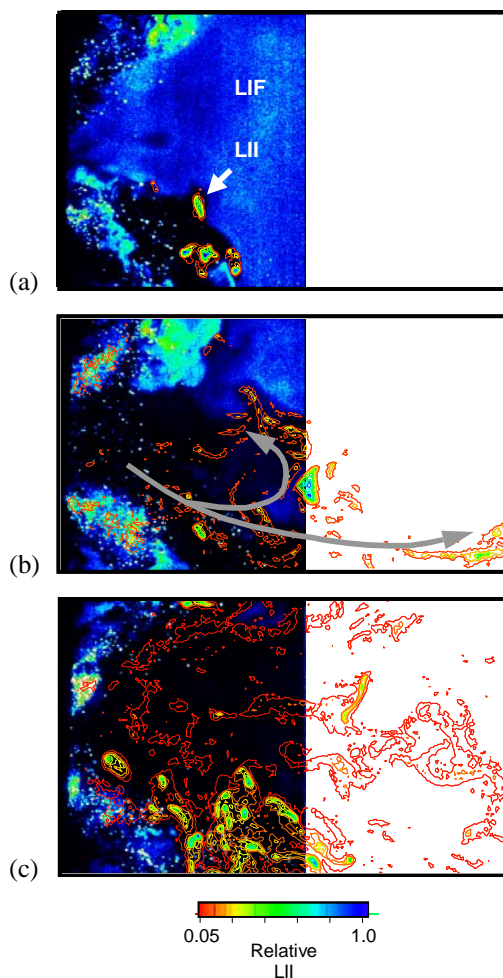


Fig. 5. Overlay of OH PLIF and LII images at an equivalence ratios of (a) 0.8, (b) 1.0, and (c) 1.15. OH PLIF false-color map same as for Fig. 3. LII shown in false-color contours from 5% to 100% of the peak signal in each image.

secondary reaction zone and, by inference, locally richer conditions. In the lower flame of Fig. 5(a), for example, there is very little in the way of a secondary reaction zone. Correspondingly in Fig. 3(c), large droplets are shown entering the recirculation zone with burning wakes in the upper half while droplets entering the recirculation zone in the lower half do not. Locally rich conditions in this lower flame region allow soot produced in the rich-premix zone to escape the flame layer and undergo a much slower oxidation process. In fact, soot production takes place almost exclusively in the lower half of the combustor for all equivalence ratios, as shown in Fig. 5.

These observations illustrate the impact of non-homogeneous fuel-air distributions on soot production. Unsteady motions induced by large-scale structures enhance soot production to the extent that they allow rich

pockets of fuel and air to escape the primary flame layer and enter the oxygen- and OH-starved recirculation zone.

Conclusions

A simultaneous OH PLIF and planar LII system was developed, tested, and demonstrated in a liquid-fuel swirl-stabilized combustor. These combined diagnostics provide phenomenological evidence of soot-formation mechanisms in this highly turbulent environment by mapping the instantaneous flame zone and soot volume fraction.

It was found that large-scale structures play a key role in the soot formation process. Intermittent regions of rich premixed regions of fuel and air develop between the primary flame layer and recirculation zone that serve as sites for soot inception. The rate of soot production is dependent upon the frequency and spatial extent of these regions; the rate of soot oxidation is dependent upon the presence of a secondary reaction zone as well as the availability of oxygen and OH in this zone. Hence, the overall soot volume fraction is highly sensitive to the dynamics of the injection process as well as to the local, unsteady equivalence ratio. Experimental and numerical studies in gaseous combustors may not capture these dynamics properly.

Acknowledgements

We thank Dr. V.M. Belovich, Dr. E. Corporan, Dr. M. Dewitt, M. Arstingstall, and C. Frayne for assistance with the combustor facility. We also gratefully acknowledge useful discussions with Viswanath Katta regarding soot formation in unsteady flames. Funding for this research was provided by the U. S. Air Force Research Laboratory, Propulsion Directorate, Wright-Patterson AFB, under Contract Nos. F33615-00-C-2068 and F33615-D-03-M2829, and by the Air Force Office of Scientific Research [Program Monitor: Dr. Julian Tishkoff].

References

- Kim, W.-W., Menon, S., and Mongia, H., "Large-eddy simulation of a gas turbine combustor flow," *Combust. Sci. Technol.* 143:25-62 (1999).
- Wang, S., Hsieh, S.-Y., and Yang, V., "Numerical simulation of gas turbine swirl-stabilized injector dynamics," AIAA paper 2001-0334, 2001.
- Heitor, M. V., and Whitelaw, J. H., "Velocity, Temperature, and Species Characteristics of the Flow in a Gas-Turbine Combustor," *Combust. Flame* 64:1-32 (1986).
- Bicen, A. F., Tse, D. G. N., and Whitelaw, J. H., "Combustion characteristics of a model can-type combustor," *Combust. Flame* 80:111-125 (1990).
- Held, T. J., Mueller, M. A., Li, S.-C., and Mongia, H., "Data-driven model for NO_x, CO and UHC emissions for a dry low emissions gas turbine combustor," AIAA paper 2001-3425, 2001.
- Shaddix, C. R., Harrington, J. E., and Smyth, K. C., "Quantitative Measurements of Enhanced Soot Production in a Flickering Methane / Air Diffusion Flame," *Combust. Flame* 99:723-732 (1994).
- Allen, M. G., and Hanson, R. K., "Digital imaging of species concentration fields in spray flames," *Proc. Combust. Inst.* 21:1755-1762 (1986).
- Bellan, J., and Harstad, K., "Evaporation, Ignition, and Combustion of Nondilute Clusters of Drops," *Combust. Flame* 79:272-286 (1990).
- Fang, T. C., Megaridis, C. M., Sowa, W. A., and Samuelsen, G. S., "Soot morphology in a liquid-fueled swirl-stabilized combustor," *Combust. Flame* 112:312-328 (1998).
- Barbella, R., Beretta, F., Ciajolo, A., D'Alessio, A., Prati, M. V., and Tamai, R., "Spray-swirl interaction and early pyrolysis of kerosene and light oils spray flames produced by simplex pressure atomizer," *Proc. Combust. Inst.* 22:1983-1990 (1988).
- Brown, M. S., Meyer, T. R., Gord, J. R., Belovich, V. M., and Roquemore, W. M., "Laser-induced incandescence measurements in the reaction zone of a model gas turbine combustor," AIAA paper 2002-0393, 2002.
- Roy, S., Meyer, T. R., Lucht, R. P., Belovich, V. M., Corporan, E., and Gord, J. R., "Temperature and CO₂-concentration measurements in the exhaust stream of a liquid-fueled combustor using dual-pump coherent anti-Stokes Raman scattering (CARS) spectroscopy," Submitted for publication in *Combust. Flame*, 2004.
- Smyth, K. C., Miller, J. H., Dorfman, R. C., Mallard, W. G., and Santoro, R. J., "Soot inception in a methane/air diffusion flame as characterized by detailed species profiles," *Combust. Flame* 62:157-181 (1985).
- Cignoli, F., Benecchi, S., and Giorgio, Z., "Simultaneous one-dimensional visualization of OH, polycyclic aromatic hydrocarbons, and soot, in a laminar diffusion flame," *Opt. Lett.* 17:229-231 (1992).
- Turns, S. R., "An Introduction to Combustion," McGraw-Hill, New York, 1996.
- Meyer, T. R., Roy, S., Belovich, V. M., Corporan, E., and Gord, J. R., "Simultaneous planar LII, OH PLIF and droplet Mie scattering in swirl-stabilized spray flames," Submitted for publication in *Appl. Opt.*, 2004.
- Ni, T., Pinson, J. A., Gupta, S., and Santoro, R. J., "Two-dimensional imaging of soot volume fraction by the use of laser-induced incandescence," *Appl. Opt.* 34:7083-7091 (1995).
- Chigier, N. A., "The atomization and burning of liquid fuel sprays," *Prog. Energy Combust. Sci.* 2:97-114 (1976).

Extinction criterion for unsteady, opposing-jet diffusion flames

V.R. Katta,^{a,*} T.R. Meyer,^a M.S. Brown,^a J.R. Gord,^b and W.M. Roquemore^b

^a Innovative Scientific Solutions, Inc., 2766 Indian Ripple Road, Dayton, OH 45440, USA

^b Air Force Research Laboratory, Propulsion Directorate, Wright–Patterson Air Force Base, OH 45433, USA

Received 25 April 2003; received in revised form 29 January 2004; accepted 9 February 2004

Abstract

Dynamic flames are known to survive at strain rates that are much higher than those associated with steady-state flames. A numerical and experimental investigation is performed to aid the understanding of the extinction process associated with unsteady flames. Spatially locked unsteady flames in an opposing-jet-flow burner are established and stretched by simultaneously driving one vortex from the air side and another from the fuel side. Changes in the structure of the flame during its interaction with the incoming vortices and with the instability-generated secondary vortices are investigated using a time-dependent computational-fluid-dynamics-with-chemistry (CFDC) code known as UNICORN (UNsteady Ignition and COMbustion with ReactionNs). The combustion process is simulated using a detailed-chemical-kinetics model that incorporates 13 species and 74 reactions. Slow-moving vortices produce a wrinkled but continuous flame, while fast-moving vortices create a locally quenched flame with its edge wrapped around the merged vortical structures. In an attempt to characterize the observed quenching process, five variables—namely, air-side, fuel-side, and stoichiometric strain rates and maximum and stoichiometric scalar dissipation rates—are investigated. It is found that these characteristic parameters cannot be used to describe the quenching process associated with unsteady flames. The flow and chemical nonequilibrium states associated with the unsteady flames are responsible for changes in the extinction values of these traditional characteristic variables. However, even though the quenching values of the scalar dissipation rates increase with the velocity of the incoming vortices, the variations are much smaller than those observed in the strain rates. It is proposed that a variable that is proportional to the air-side strain rate and inversely proportional to the rate of change in the flame temperature can be used to characterize the unsteady quenching process uniquely.

© 2004 The Combustion Institute. Published by Elsevier Inc. All rights reserved.

Keywords: Extinction; Unsteady flames; Turbulent flames; Diffusion flames; Vortex–flame interaction; Nonequilibrium flows

1. Introduction

Studies of the structure of unsteady flames are important for gaining an understanding of fundamental combustion processes. Such studies provide insight into turbulent-combustion phenomena and aid the development and evaluation of simplified models that

can be used in design codes for practical combustion systems. Unsteady flames associated with turbulent combustion are subjected to stretching that varies with time; typically, the time scale for the changes in strain rate is comparable to those of the chemical (e.g., reaction time) and physical (e.g., diffusion time) responses of the system. Because of the resulting nonequilibrium environment, the structure of a stretched unsteady flame differs from that of a stretched steady-state flame.

* Corresponding author.

E-mail address: vrkatta@erinet.com (V.R. Katta).

Numerous experimental and numerical investigations [1–3] have been performed to quantify the scalar structure of steady-state, aerodynamically strained, planar, counterflow diffusion flames. Such studies have not only provided benchmark experimental data but also yielded valuable insight into the steady-state behavior of the planar flame that is subjected to stretch (or strain) rates up to the extinction limits. In practical combustion devices, flames are subjected to severe unsteadiness that results from the random motion of the vortices [4,5]. To retain the analytical and experimental simplicity offered by planar diffusion flames, however, the unsteady flame structure is also investigated in counterflow flames by fluctuating the fuel and air jets simultaneously and sinusoidally [6–8]. Although the results have indicated that unsteady flames can be stretched beyond the steady-state extinction limit [9], these studies are mainly focused on understanding the behavior of the flame when subjected to moderate-amplitude fluctuations in strain rate [7], reactant composition [7,10], and partial premixing [11]. Since the extinction strain rate, in general, is higher than the maximum strain rate at which ignition can occur, temporal flame extinction at any time within the fluctuation cycle in a periodically oscillating counterflow flame could lead to complete flame extinction. Consequently, strain rates that are lower than the extinction limit are often used in the periodically oscillating-flame experiments.

Using numerical simulations Ghoniem et al. [12] have demonstrated that partial extinction and reignition can occur in a periodically oscillating counterflow flame when it is subjected to a high-amplitude, high-frequency perturbation. Recently, Egolfopoulos [13] provided a detailed analysis of unsteady counterflow flames and concluded that even though the flame response to strain-rate perturbations diminishes at higher frequencies, the substantial transient effects that still exist in the flame zone lead to partial extinction and reignition. Following these findings, Cuenot et al. [14] proposed the following extinction criterion: for an unsteady flame to be extinguished, the applied strain rate should not only exceed the critical steady-state extinction value but also remain higher over a characteristic time.

The unsteady extinction criterion proposed by Cuenot et al. [14] uses global quantities such as applied strain rate, crossover temperature, and characteristic time, which are readily available for periodically oscillating-counterflow-flame configurations. However, in the case of flames stretched by vortices, such global quantities cannot easily be estimated since the local strain rate and characteristic-time scale strongly depend on the evolution of the vortex (note that entrainment modifies the vortex-propagation velocity) in the given flowfield. Therefore, an unsteady

extinction criterion based on local quantities is also required for the prediction of extinction during a vortex/flame interaction process.

During vortex/flame interactions, which are often considered to be the building blocks of statistical theories of turbulence, the flame surface is subjected not only to unsteadiness but also to deformation. To investigate the effects of curvature on unsteady flames, both theoretical and experimental studies have been initiated [15–18]. In particular, experiments designed by Roberts et al. [19] and by Rolon et al. [20] have generated considerable interest, especially because of their unique ability to inject a well-characterized vortex toward the flame surface. Numerous investigations have been performed by varying the size and strength of the vortex in opposing-jet burners [20] in attempts to understand global features such as scale [21,22] and origin [23] effects and localized features such as annular-quenching [24] and non-adiabatic-equilibrium-temperature [25,26] phenomena.

Recent studies on vortex/flame interactions by Katta and Roquemore [23] revealed that the extinction strain rate of an unsteady flame is dependent on whether the flame is traveling or stationary. By issuing vortices from the fuel and air sides of an opposing-flow jet diffusion flame, they simulated traveling and stationary unsteady flames. In the traveling unsteady flame, not only the strain rate on the flame but also the flame location was changed with time; in the stationary unsteady flame, on the other hand, the strain rate was varied with time by locking its position spatially. The latter unsteady flames, established by issuing vortices simultaneously from the air and fuel sides, offered a pathway to understanding the unsteady-flame structure near extinction.

Several investigators have developed models [17, 27,28] for the study of the interaction between a planar flame and an induced vortex. In all of these models, it was assumed that an artificially created (by specifying the vorticity field) vortex pair interacts with a flat flame formed in a parallel flow. Although this assumption has advantages in exploring interesting aspects of vortex/flame interactions, investigations employing these synthesized vortices do not represent actual interactions in opposing-jet flames and, hence, cannot facilitate direct comparisons between predictions and measurements, making verification of the former very difficult.

Recent advances in computer hardware and the need to improve the understanding of combustion phenomena under complex practical situations have led to the development of two- and three-dimensional computational-fluid-dynamics models that incorporate detailed chemical kinetics (CFDC) [29,30]. Complete simulation of the opposing-jet flame using multidimensional models not only eliminated concerns

regarding the simplified analyses but also provided a valuable tool for studying vortex/flame interactions in premixed [19,31] and diffusion [20,24] flames. In the present investigation, a well-tested CFDC model was used to understand the unsteady flame structure near extinction and to characterize the extinction process.

2. Mathematical model

A time-dependent axisymmetric model known as UNICORN (UNsteady Ignition and COMbustion with ReactionNs) [32] was used for the simulation of unsteady flames associated with an opposing-jet-flow burner. This model solves the Navier–Stokes and species- and energy-conservation equations written in the cylindrical-coordinate (z – r) system. A detailed-chemical-kinetics model is employed to describe the hydrogen–air combustion process. This model consists of 13 species—namely, H_2 , O_2 , H , O , OH , H_2O , HO_2 , H_2O_2 , N , NO , NO_2 , N_2O , and N_2 —and 74 elementary reactions among the constituent species. The rate constants for this H_2 – O_2 – N_2 reaction system were obtained from Ref. [33].

Temperature- and species-dependent property calculations are incorporated into the model. The governing equations are integrated on a nonuniform staggered-grid system. An orthogonal grid having rapidly expanding cell sizes in both the axial and the radial directions is employed. The finite-difference forms of the momentum equations are obtained using an implicit QUICKEST scheme [34,35], and those of the species and energy equations are obtained using a hybrid scheme of upwind and central differencing. At every time step, the pressure field is calculated by solving the pressure Poisson equations simultaneously and utilizing the LU (lower and upper diagonal) matrix-decomposition technique. UNICORN has been validated previously by simulating various steady and unsteady counterflow [23,24,27] and coflow [30,36] jet diffusion flames.

3. Results and discussion

3.1. Burner details

The opposing-jet-flow burner used for the investigations of unsteady-flame structures was designed by Rolon, is shown in Fig. 1, and is described in detail in Ref. [20]. A flat flame is formed between fuel and air jets having velocities of 0.69 and 0.5 m/s, respectively. The hydrogen-to-nitrogen ratio used for the fuel jet is 0.38. Unsteady flames are established by injecting vortices simultaneously from the fuel

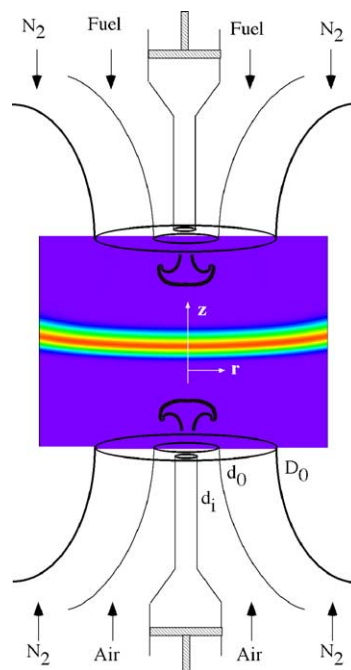


Fig. 1. Schematic diagram of the opposing-jet-flow burner used for investigations of double-vortex/flame interactions. Nitrogen-diluted hydrogen fuel and air were introduced from upper and lower nozzles, respectively. The structure of the steady-state flame is also shown in the form of the iso-temperature distribution.

and air sides. The collision of these vortices with the flame surface, in general, imposes unsteady stretch on the flame. Such a collision involving stronger vortices may also quench the flame locally and generate multiple vortices. Studies were performed to investigate various types of vortex-collision/flame interactions by incorporating different sizes of fuel- and air-side injection tubes and varying the injection durations. Air-side vortices were generated by injecting a specified amount of air through the syringe tube (Fig. 1) and then through a 5.0-mm-diameter injection tube. On the other hand, fuel-side vortices were generated by injecting a specified amount of fuel through the syringe tube and then through either a 2.0-mm- or a 5.0-mm-diameter injection tube. Two types of interactions—namely, unsteady nonstationary and unsteady stationary—are treated in the present paper. The z – r coordinate system used for the simulation of flames associated with the Rolon burner is shown in Fig. 1. Calculations for these axisymmetric flames were made using a nonuniform 601×301 mesh system distributed over a physical domain of 40×40 mm, which yielded a mesh spacing of 0.05 mm in both the axial (z) and the radial (r) directions in the region between the two nozzles.

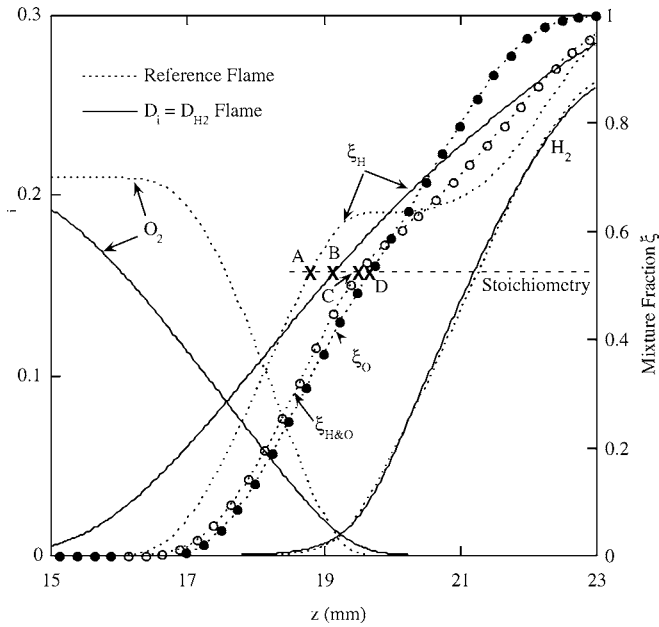


Fig. 2. Steady-state flame structures along the centerline for the reference flame (broken lines) and “ $D_1 = D_{H_2}$ ” flame (solid lines). Points A–D represent mixture fractions at stoichiometric conditions.

3.2. Steady-state flame structure

Prior to the injection of vortices, a flat flame is simulated for the experimental conditions described earlier. The computed steady-state flame in the form of isotherm distributions is shown in Fig. 1, along with the schematic diagram of the burner. Note that the gravitation force in this simulation is neglected. The slight upward curvature of the flame surface develops as a result of the lower density of the hydrogen fuel. Apparently, the velocity difference used for the fuel and air jets (0.69 vs 0.5 m/s, respectively) did not provide a perfect balance of momentum for the two jets, resulting in a slight shift in the flame location from the burner mid-plane toward the air jet (lower nozzle). The flame structure along the centerline (also known as the stagnation line in this opposing-jet-flow configuration) is shown in Figs. 2–4 and is referred to as the reference flame. The fuel, oxygen, and mixture-fraction (ξ) distributions are represented in Fig. 2 by broken lines (reference flame). As a result of nonequilibrium chemistry, hydrogen and oxygen coexist in an overlap region that is ~ 2 mm thick. Although several forms of mixture-fraction definition are available in the literature [37], no particular form has an advantage over the others in describing the flame structure, and in many studies a particular form of mixture fraction is selected over others as a matter of convenience [38]. The one used in the present study is based on the mass fraction of fluid that originates from the fuel jet at a given lo-

cation [37]. In hydrogen flames this mixture fraction (ξ_H) is computed from the following equation:

$$\xi_H = \frac{w_{H_2}}{Y_{H_2}^0} \left[\left(\frac{Y_{H_2}}{w_{H_2}} + \frac{Y_{H_2O}}{w_{H_2O}} + \frac{Y_{H_2O_2}}{w_{H_2O_2}} \right) + \frac{1}{2} \left(\frac{Y_H}{w_H} + \frac{Y_{OH}}{w_{OH}} + \frac{Y_{HO_2}}{w_{HO_2}} \right) \right]. \quad (1)$$

Here, Y_i represents the mass fraction of the i th species, w_i represents the molecular weight of the i th species, and the superscript 0 represents the state in the fuel jet. The stoichiometric value of the mixture fraction (ξ_{stoich}), calculated based on the flow conditions used in this study, is 0.5264. This stoichiometric condition is established (Location A in Fig. 2) on the oxygen-rich side of the reaction zone.

Fig. 2 shows that the mixture fraction for the reference flame did not increase monotonically from zero on the air side ($z = 0$) to unity on the fuel side ($z = 40$ mm). Rather, it reached a peak value at about $z = 19.5$ mm and then stayed at a plateau before rising to unity. This nonmonotonic behavior suggests that the laminar flame shown in Fig. 1 cannot be uniquely described in the mixture-fraction domain. For example, several locations on the flame along the centerline have the same mixture-fraction value of 0.63 (Fig. 2), while the temperatures at these locations vary between 1195 and 1510 K.

The nonmonotonic variation in mixture fraction across the flame, shown in Fig. 2, is specific to the hydrogen/air opposing-jet flow considered in this study.

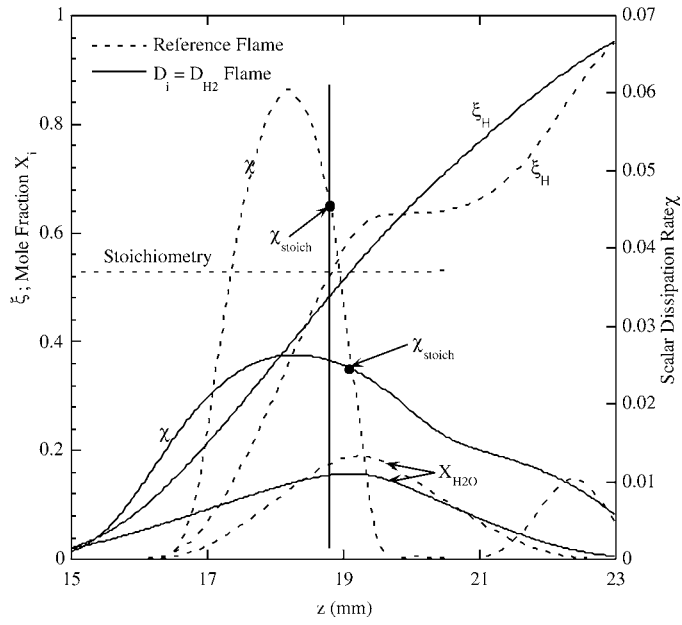


Fig. 3. Mixture fraction and scalar dissipation rate along the centerline for the reference flame (broken lines) and “ $D_i = D_{H_2}$ ” flame (solid lines).

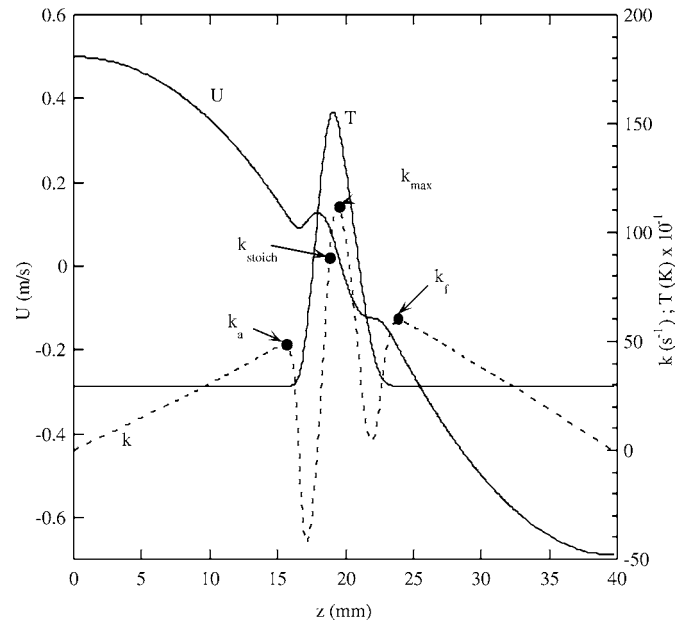


Fig. 4. Velocity, temperature, and strain rate along the centerline for the steady-state flame shown in Fig. 1.

To investigate whether such behavior appears in other forms of mixture fractions, variations of mixture fractions obtained from the elemental mass fractions of the oxygen atom (ξ_O) [37] and the hydrogen and oxygen atoms ($\xi_{H\&O}$) [39] are displayed in Fig. 2 using solid and open symbols, respectively. Note that the latter form of mixture fraction was proposed by Bilger [39] to take into account the preferential-diffusion ef-

fects associated with hydrogen flames. The stoichiometric mixture fraction for all three forms is 0.5264. The mixture fraction (ξ_O) obtained using the element originating from the oxidizer jet (which is O) increases smoothly with distance, and stoichiometry occurs at $z = 19.66$ mm (Location C), which is on the fuel side of the reaction zone. As expected, the mixture fraction ($\xi_{H\&O}$) calculated based on elements

originating from both the fuel and the oxidizer jets falls between ξ_H and ξ_O , and stoichiometry occurs at $z = 19.45$ mm (Location D).

Since the mixture fraction is extensively used in characterizing the structure of a diffusion flame, it is useful to identify the underlying flame properties for the nonmonotonic behavior of the mixture fraction. In laminar nonpremixed flames, mixing takes place through diffusion only; and if the diffusivities of all species are equal, then the mixture fraction becomes an independent variable with respect to the choice of species. However, in hydrogen flames the diffusivity of hydrogen (into nitrogen) is approximately three times that of oxygen, and the mixture fraction does not become an independent variable ($\xi_H \neq \xi_O \neq \xi_{H\&O}$), as shown in Fig. 2. To demonstrate the preferential-diffusion effect on mixture fraction, calculation of the steady flame in Fig. 1 is repeated by assuming that the diffusion coefficients of all of the species are identical to that of hydrogen and by enforcing the $Le = 1$ condition for heat transport. The distributions of fuel and oxygen concentrations and the mixture fraction for the “ $D_i = D_{H_2}$ ” flame are shown in Fig. 2 with solid lines. The flame became thicker than the reference flame as a result of increased oxygen diffusion. In this “ $D_i = D_{H_2}$ ” flame, the mixture fraction was monotonically increased to unity from zero, and the stoichiometric value (0.5264) appeared at $z = 19.1$ mm (Location B), where the mole fraction of oxygen is nearly twice that of hydrogen.

In the reference flame oxygen diffuses much more slowly (~ 0.3 times) than hydrogen. Because of this lower diffusivity, the oxygen-concentration profile on the air side is steeper (Fig. 2) than that in the “ $D_i = D_{H_2}$ ” flame; this, in turn, causes the mixture-fraction (ξ_H) profile to be steeper on the air side. Similarly, water diffuses more slowly in the reference flame than in the “ $D_i = D_{H_2}$ ” flame. This increases the water concentration in the flame zone (Fig. 3) and, thereby, the local value of the mixture fraction—leading to a peak in the profile. Note that the stoichiometric value of the mixture fraction in the reference flame appears at a location that is slightly shifted from the stoichiometric condition based on the reactant mole fraction (i.e., $X_{O_2} = 2X_{H_2}$) toward the air side. In fact, none of the mixture-fraction definitions yielded stoichiometric conditions at their respective stoichiometric values.

The scalar dissipation rate χ is often used to characterize a stretched diffusion flame. Based on the mixture fraction, χ is defined as

$$\chi = 2D \left[\left(\frac{d\xi}{dz} \right)^2 + \left(\frac{d\xi}{dr} \right)^2 \right]. \quad (2)$$

Here, D is the diffusion coefficient and, for simplicity, may be considered to be $1 \text{ m}^2/\text{s}$. Variations of the scalar dissipation rate and the mole fractions of H_2O along the centerline are shown in Fig. 3 for both the reference and the “ $D_i = D_{H_2}$ ” flames. The steep gradient in ξ_H in the former flame resulted in values of χ that were significantly higher than those obtained in the latter flame. Furthermore, the reference flame exhibits more than one peak in the χ distribution; this is true for all of the scalar-dissipation-rate profiles that were obtained for this flame by employing various mixture-fraction definitions. The existence of double peaks in the scalar dissipation rate is a particular characteristic of a diffusion flame in which preferential-diffusion and non-unity-Lewis-number effects are significant. The stoichiometric values of the scalar dissipation rates for both reference and “ $D_i = D_{H_2}$ ” flames are indicated in Fig. 3 by solid circles. In both flames the maximum scalar dissipation rates occur on the air side of the stoichiometric location. The peak value of χ in the reference flame is about 20% higher than that at stoichiometric location and appears ~ 1 mm on the air side. Since there is no particular advantage in using one form of scalar dissipation rate over the other for characterizing a hydrogen diffusion flame, the scalar dissipation rate calculated from Eq. (1) is used in the present study for convenience.

The velocity, temperature, and strain-rate distributions along the centerline for the steady flame are shown in Fig. 4. Several investigators have used strain rate to characterize an opposing-flow jet diffusion flame. However, as seen in Fig. 4, this flame has no single (or unique) strain rate. The various strain rates that can be defined for this flame are as follows:

- (1) global strain rate based on nozzle separation and exit velocities ($k_{\text{glob}} = 29.75 \text{ s}^{-1}$),
- (2) air-side strain rate ($k_a = 48.9 \text{ s}^{-1}$),
- (3) fuel-side strain rate ($k_f = 59.6 \text{ s}^{-1}$),
- (4) strain rate at the stoichiometric surface ($k_{\text{stoich}} = 68.9 \text{ s}^{-1}$),
- (5) peak strain rate ($k_{\text{max}} = 112.5 \text{ s}^{-1}$).

The air- and fuel-side strain rates are obtained from the locations where the temperature initially begins to increase from room conditions on the respective sides. In a steady-state flame, as shown in Fig. 4, the air- and fuel-side strain rates match the local peak values on the respective sides of the flame zone. However, such a criterion does not necessarily hold in the case of unsteady flames. Therefore, k_a and k_f are obtained from the temperature gradient rather than the peak values for all of the unsteady flames discussed in the present paper.

The steady-state flame shown in Fig. 2 represents a weakly strained laminar flame. The peak strain rate

on the fuel side is greater than that on the air side as a result of the difference in the density of the two jets. Even at this low strain rate, the fuel and oxidizer are not completely consumed simultaneously in the flame zone. In an overlap region of ~ 2 mm, both H_2 and O_2 are present (cf. Fig. 2). The flame (peak-temperature region) is located at $z = 19.2$ mm, and its temperature of 1560 K is only slightly lower than the corresponding adiabatic equilibrium temperature of 1598 K.

The steady-state strain rate of the opposing-jet flame can be increased by gradually increasing the velocities of the fuel and air jets. Calculations were repeated with the jet velocities being varied, and it was found that a stable steady-state flame could be obtained for fuel and air jet velocities of 16 and 14 m/s, respectively. These velocities yielded an air-side strain rate (k_a), a fuel-side strain rate (k_f), and a strain rate at the stoichiometric surface (k_{stoich}) of 1410, 1678, and 2460 s^{-1} , respectively. The maximum scalar dissipation rate (χ_{max}) and the scalar dissipation rate at the stoichiometric surface (χ_{stoich}) for this extinction condition are 1.28 and 0.78, respectively. The corresponding peak (flame) temperature was 1130 K. The extinction strain rate and flame temperature agree favorably with calculations made by Gutheil et al. [40]. A small increase in either air- or fuel-jet velocity from these extinction limits first caused the flame temperature to decrease below 1130 K and then caused the flame to extinguish, with its temperature reaching 300 K in <1 ms. Based on these calculations a steady-state-extinction criterion of 1130 K has been established and was used in the later studies on unsteady flame extinction. Analysis of unsteady flames (shown in a later section) suggested that the 1130-K criterion for defining extinction is valid for unsteady flames also.

An unsteady strain rate was imposed on the flame shown in Fig. 1 by issuing vortices simultaneously from the fuel (top) and air (bottom) nozzles. Various unsteady flames were generated by injecting air and fuel through the respective syringe tubes in such a way that the peak values of the exit velocities were in the range of 2–19 m/s. In the following sections, the dynamics associated with these vortices is discussed, followed by the changes to the flame structure caused by the impingement.

3.3. Interaction with colliding vortices of different sizes

Vortices are shot toward the flame surface simultaneously from the air and fuel sides by injecting a specified amount (2.2 cm^3) of air and fuel through the respective syringe tubes. The flame-quenching process with colliding vortices of different sizes is studied by injecting air through a 5-mm-diameter injection

tube and fuel through a 2-mm-diameter injection tube. Evolution of the vortices and their interaction with the flame surface depend on the injection duration. In general, with shorter injection durations, the generated vortices travel faster toward the flame surface and affect its structure as the local-flow time scales approach the chemical time scales. Calculations and measurements are performed to capture the colliding-vortex/flame-interaction process for various injection velocities.

While calculations for peak injection velocities of <2 m/s yielded flames that were stretched and wrinkled but not extinguished anywhere, calculations for higher velocities resulted in flame quenching along the stagnation line and propagation of the flame edge into the multivortex flowfield. Experiments were also performed for some of the injection conditions in an attempt to understand the flame-quenching pattern during the vortex–flame–vortex interaction process. The computed and experimental results for the $+5/-5$ m/s injection case at different stages of the interaction process are shown in Fig. 5. The computed temperature and OH-concentration distributions are plotted on the left and right halves of Figs. 5a–5c. The instantaneous locations of the particles that were released from the air and fuel nozzles are also shown in these figures to aid visualization of the flow structures. Air injected from the 5-mm-diameter tube generated a vortex, and it grew to 12 mm in diameter by the time (8.1 ms) it reached the flame surface (Fig. 5a). Similarly, during the same time period, the fuel vortex grew to 5 mm from its initial size of 2 mm. The collision of these two vortices at the flame surface stretched the flame. The temperature of the flame along the stagnation line decreased to 1140 K, which is near the quenching limit of 1130 K. In another millisecond, the double-vortex/flame interaction completely quenched the flame that was sandwiched between the vortices in the region around the centerline (Fig. 5b). As the vortices continued to push against each other in the hole formed on the flame surface, the edge of the flame wrinkled and propagated into the fuel vortex, as evident in Fig. 5c. Similar behavior was observed in the OH-concentration distributions obtained in the experiment through the use of the planar laser-induced-fluorescence (PLIF) technique (Figs. 5d–5f). Details of the PLIF measurements made in the Rolon burner are given in Refs. [41,42]. Considering the difficulties associated with the alignment of the small tubes that were separated by 40 mm, the symmetric nature of the flowfield obtained in the experiments during the double-vortex/flame interactions is reasonable. The predictions are qualitatively in good agreement with the measurement results. The injection velocities for the vortices in the present calculations were estimated

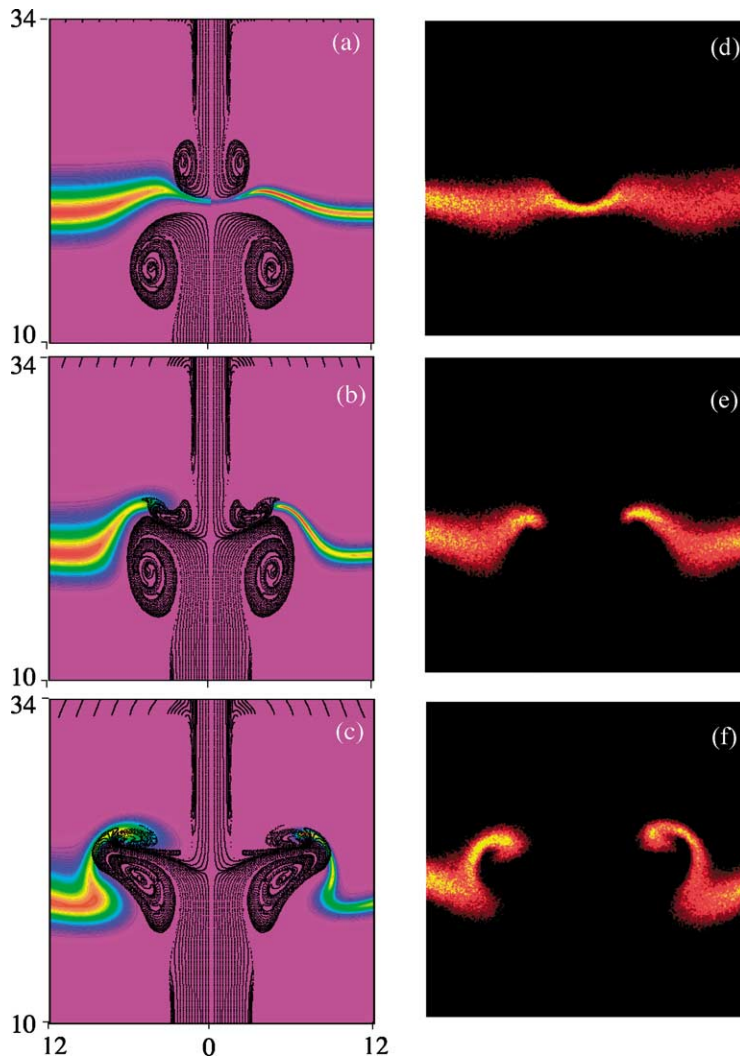


Fig. 5. Comparison of simulated ((a), (b), and (c)) and measured ((d), (e), and (f)) double-vortex/flame interactions at various instants. Particle locations are superimposed on temperature (left) and OH (right) fields of computed data. Raw data from PLIF of OH shown in experimental images. (a) and (d) at t_0 ms, (b) and (e) at $t_0 + 1$ ms, and (c) and (f) $t_0 + 2$ ms.

from the total amounts of fluid used for injections in the experiment—not from the actual velocities—which may have contributed to the discrepancy noted between the experiments and calculations in Fig. 5.

The collision of vortices of different sizes at the flame surface not only generated unsteady stretching on the flame but also shifted the flame location during the interaction process. As discussed earlier and in Ref. [23], the translation velocity of the flame during a vortex/flame-interaction process alters the extinction strain rate, thereby complicating the relationship between the unsteady strain rate and extinction. To alleviate this problem, investigations were performed by injecting vortices of the same size from the fuel and air sides simultaneously. This was achieved through

the utilization of 5-mm-diameter injection tubes on both the air and the fuel sides.

3.4. Interaction with colliding vortices of the same size

A wide range of strain rates was imposed on the flame by forcing vortices from the fuel- and air-injection tubes simultaneously by (1) changing the maximum injection velocity and (2) changing the rise times, as shown in Fig. 6. Here, the imposed velocity with respect to time at the exit of the air-injection tube is shown for different injection schemes. Identical negative-velocity profiles were superimposed on the steady flow emanating from the fuel-injection tube.

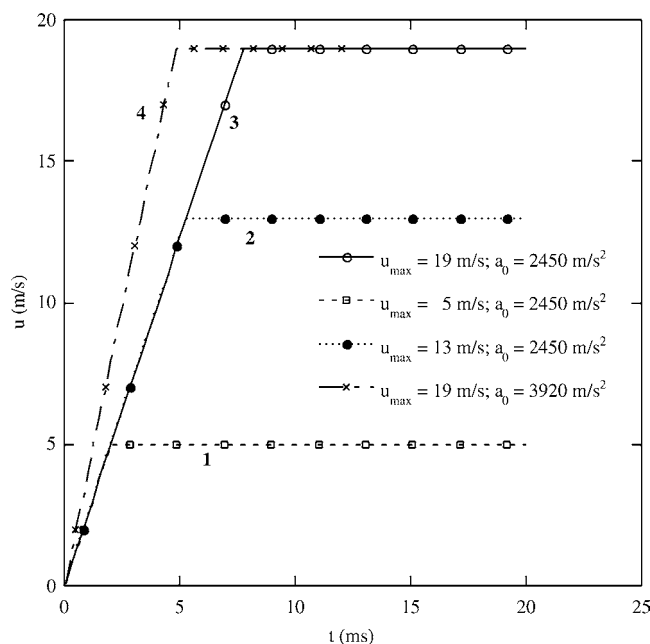


Fig. 6. Imposed velocity profiles at exits of fuel and air nozzles for generating various types of double-vortex/flame interactions.

In the case where the maximum velocity (u_{\max}) was changed, the rate of increase (a_0) for the imposed velocity was set at 2450 m/s^2 (for example, 1, 2, and 3 in Fig. 6); and in the case where the rise times were changed, the maximum velocity was set at 19 m/s (for example, 3 and 4 in Fig. 6). Calculations were performed for each case until the interaction reduced the flame temperature to 1000 K , which was well below the extinction temperature of 1130 K .

Vortex and flame structures at two instants for two cases with different maximum velocities are shown in Fig. 7. In both cases, the rate of increase for the superimposed velocity was set at 2450 m/s^2 , and the maximum velocities were set equal to 5 m/s for the first case (Figs. 7a and 7b) and 13 m/s for the second case (Figs. 7c and 7d). Temperature is shown on the left side, and OH-concentration distributions are shown on the right. Instantaneous locations of the particles are superimposed on the temperature-OH plots to display the structures of the fuel and air vortices. The imposed velocity functions that generate these vortices are shown as Profiles 1 and 2 in Fig. 6. The injection velocity with a 5-m/s maximum value, failed to cause flame extinction. The temperature decreased to 1190 K in 8.35 ms (Fig. 7b) and then remained at this value during the remainder of the interaction process. It is evident from Fig. 7 that the flame did not travel axially while being stretched between the fuel- and air-side vortices for both velocity cases. In fact, for all of the velocity cases considered for colliding vortices of the same size, the flame did not travel while

being dynamically stretched; this established a stationary unsteady (no translational component) strain rate on the flame. The flame in the 13-m/s -maximum-velocity case was nearly extinguished at the centerline in 6.1 ms (Fig. 7d), and the temperature decreased to 1190 K .

3.5. Unsteady flame structure

The flame structures along the centerline at three instants for the $+13/-13\text{-m/s}$ interaction case are shown in Fig. 8. As the flame was being stretched, its thickness and temperature decreased, while the peak-temperature location remained nearly the same ($z \sim 19.2 \text{ mm}$). Also, the reactant fluxes (gradients) near the flame zone increased with flame stretch. The amounts of fuel and oxygen crossing the flame (Fig. 8) due to nonequilibrium chemistry increased with flame stretch. The variations in strain rate, mixture fraction, and scalar dissipation rate along the centerline at 5.7 and 6.1 ms are shown in Figs. 9 and 10, respectively. The important quantities k_a , k_f , k_{stoich} , χ_{stoich} , and χ_{\max} are represented in these figures by filled circles. While the strain-rate distributions in the flame that is sandwiched between the two vortices are quite different from that of the steady-state flame, the scalar-dissipation-rate distributions in unsteady and steady-state flames remain similar. Even though the strain rate has increased significantly ($\sim 2000 \text{ s}^{-1}$) on both sides of the flame at 5.7 ms (Fig. 9), this high strain rate has not yet applied on the flame surface. Air- and fuel-side strain rates have increased only to

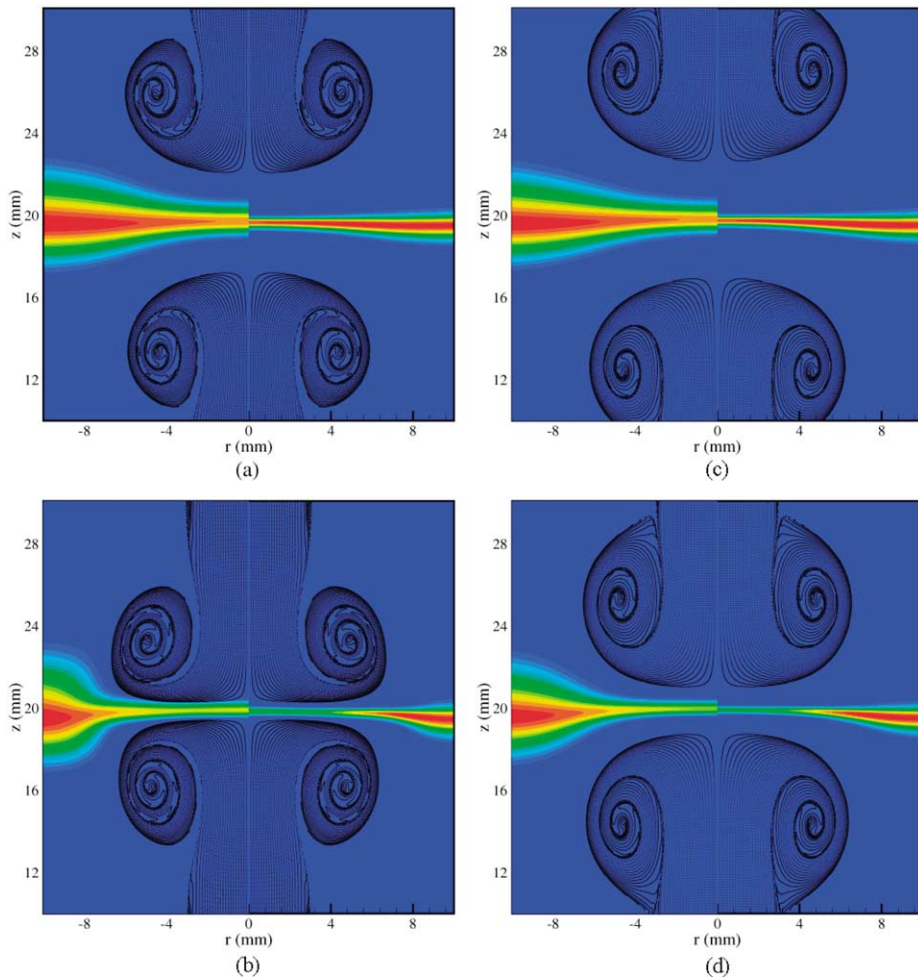


Fig. 7. Interaction of equal-sized counter-traveling vortices with flame at different instants: (a) and (b) for 5-m/s and (c) and (d) for 13-m/s peak-injection-velocity cases. Isotherm and OH-mole-fraction contours are plotted on the left and right sides, respectively.

1120 and 1416 s^{-1} , respectively, while the maximum scalar-dissipation rate has increased to 1.03 s^{-1} .

At $t = 6.1 \text{ ms}$ the flame temperature decreased to 1150 K, and quenching of the flame was not observed. However, the air- and fuel-side strain rates increased to values that were well above the corresponding steady-state strain rates for extinction. Interestingly, the stoichiometric value of the scalar-dissipation rate deviated significantly from its maximum value (Fig. 10).

3.6. Extinction criterion for unsteady flames

The unsteady hydrogen flame is considered to be extinguished when its temperature falls below 1130 K, based on the steady-state-extinction criterion discussed earlier. Defining an extinction criterion for unsteady flames based on a critical temperature

seems appropriate since the chemical kinetics and the heat-release rate (or temperature) are closely associated and such a criterion is often used in determining the extinction concentrations for fire-extinguishing agents [43,44]. The accuracy of this approach is evaluated in this section by investigating several unsteady flames under near-extinction conditions. Variations of flame temperature and heat-release rate with time during a slow, a moderate, and a fast vortex/flame interaction are shown in Fig. 11a. Similarly, the variations in peak production and destruction rates of the OH radical are shown in Fig. 11b, and those of the H radical are shown in Fig. 11c.

As the stretch on the flame is increased, increasingly more reactants are forced into the flame zone. As a result, (1) consumption of reactants in the flame zone increases—yielding an increase in the heat-release rate—and (2) the temperature decreases as

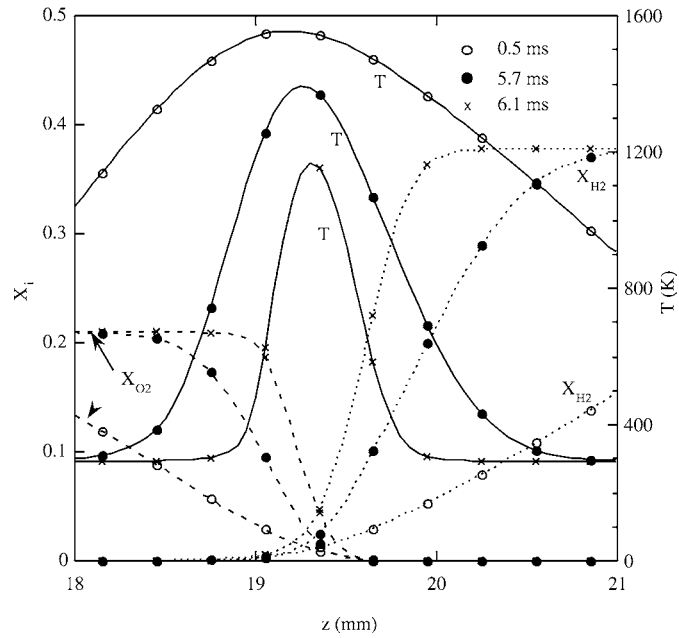


Fig. 8. Instantaneous structures of flame during double-vortex/flame interaction produced using 13-m/s injection velocity.

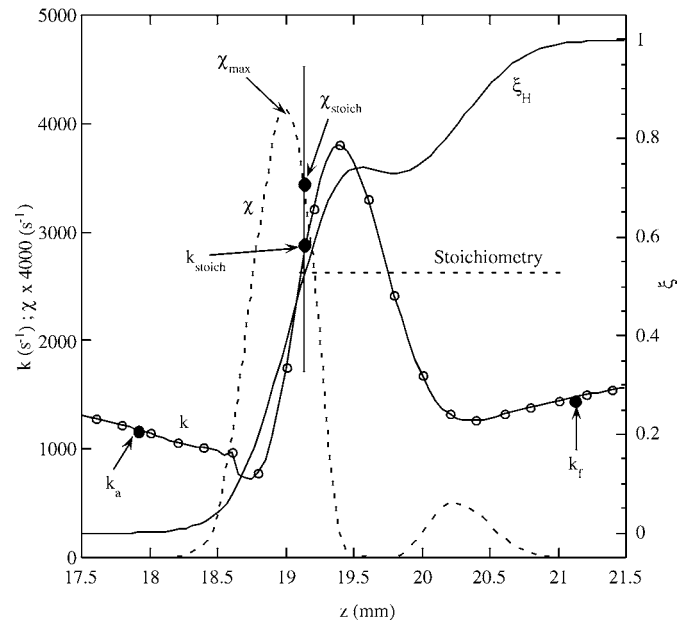


Fig. 9. Mixture fraction, scalar dissipation rate, and strain rate along the centerline at $t = 6$ ms during double-vortex/flame interaction produced using a 13-m/s injection velocity.

a result of the inability of the flame to consume (burn) all of the reactants. An increase in reactant consumption also increases the production and destruction rates for all of the species, with the exception of the OH radical. The production rate of OH decreases monotonically, as shown in Fig. 11b, to zero as the flame is stretched. In any case, once the

flame begins to extinguish, all the quantities in Fig. 11 decrease rapidly. It is important to note that extinction of a flame is not an instantaneous event but a process which takes place over a period of time. In flame studies, however, the instant at which the extinction process begins is of most interest and is the one investigated in the present study. In steady-state

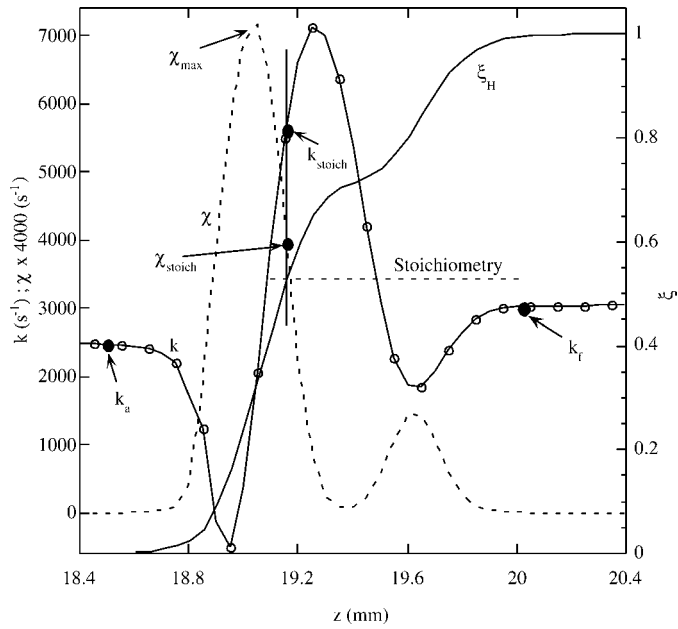


Fig. 10. Mixture fraction, scalar dissipation rate, and strain rate along the centerline at $t = 7$ ms during double-vortex/flame interaction produced using 13-m/s injection velocity.

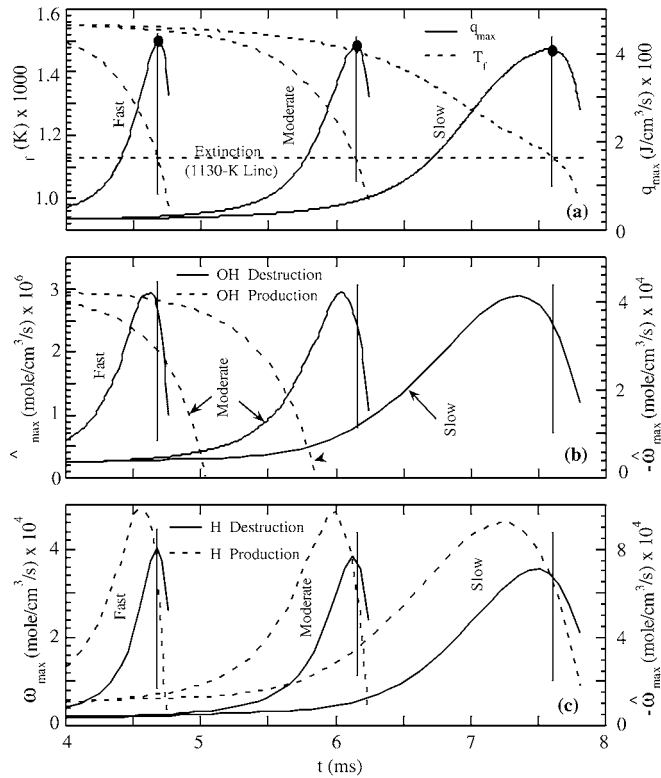


Fig. 11. Changes in characteristic flame quantities in the neighborhood of extinction when the flame is subjected to slow-, moderate-, and fast-changing strain rates. (a) Temperature and heat release rate, (b) OH production and destruction rates, (c) H production and destruction rates.

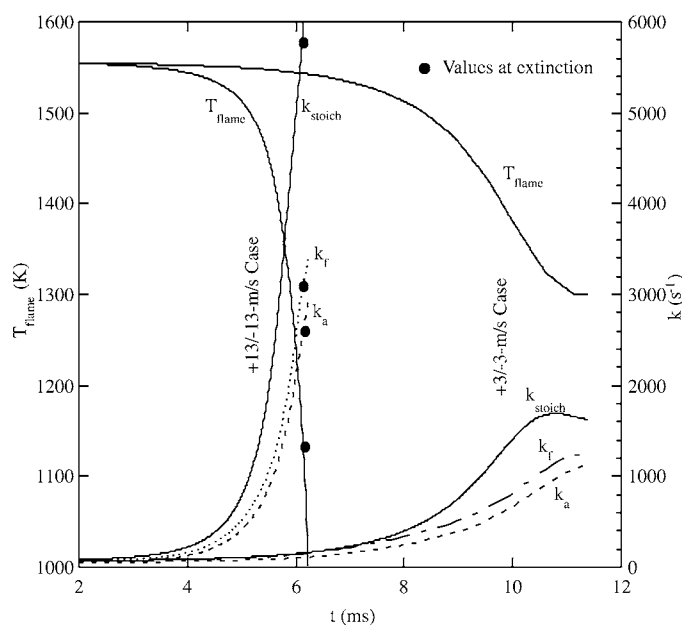


Fig. 12. Variations of flame temperature and strain rates with time during two double-vortex/flame interactions.

flames it was observed that the temperature and heat-release rate increase with stretch rate and that the extinction process begins when the flame temperature decreases to 1130 K. As evident from Fig. 11a, the heat-release rate in unsteady flames also reaches a maximum value when the temperature decreases to 1130 K, and any further decrease in temperature is associated with a sharp decrease in heat-release rate. This temperature/heat-release-rate behavior is the same in all of the unsteady flames simulated using a wide range of vortex velocities (or vortex/flame-interaction times) and strongly correlates with the behavior observed in steady-state flames. Consequently, the 1130-K criterion found in steady-state flames is extended to unsteady flames for determining the time at which extinction begins. Interestingly, OH and H destruction rates (Figs. 11b and 11c) reach their peak values slightly before the temperature decreases to 1130 K, and production of OH ceases ~ 1 ms prior to this event. For the fast vortex/flame interaction, OH production ceased at $t = 3.6$ ms and was not apparent in Fig. 11b.

3.7. Characterization of extinction in unsteady flames

Simulations made for various double-vortex/flame interactions resulted in local flame extinction along the centerline. Traditionally, extinction is characterized by the strain rate imposed on the flames [1,3]. However, it has been shown by several authors that the strain rates at which unsteady flames are extin-

guished are significantly higher than those at which steady-state flames are extinguished [9,23]. Since the strain rate has been found to be an inadequate quantity for describing the extinction behavior of an unsteady flame, several researchers have examined other variables that might be used for this purpose. The variable often used is the scalar dissipation rate [45]. The results obtained for double-vortex/flame interactions in the present study were used to investigate the adequacy of the strain rate and scalar-dissipation rate for describing the quenching process associated with unsteady flames.

3.8. Vortices with different injection masses

The double-vortex/flame interaction shown in Figs. 7a and 7b stretched the flame significantly but did not cause flame extinction. On the other hand, the interaction shown in Figs. 7c and 7d caused local extinction. These two interactions were obtained by injecting fluids at different peak velocities. The changes in temperature and various strain rates during these interaction processes are shown in Fig. 12. When the injection peak velocity was 3 m/s, the flame temperature gradually decreased to ~ 1300 K and then remained at that level, accompanied by some weak oscillations (~ 20 K in magnitude). Typically, soon after the collision at the flame surface, the double vortices generate secondary vortices; this, in turn, creates oscillations in the flame temperature. Nevertheless, for this injection the flame was not extinguished. The air-side strain rate increased, as expected, with time dur-

ing the double-vortex/flame interaction and reached a maximum value of 1080 s^{-1} . This value is well below the steady-state extinction strain rate of 1410 s^{-1} ; hence, flame quenching would not be expected for this injection condition. The fuel-side strain rate and that at the stoichiometric location also increased with time during the interaction process. Interestingly, the stoichiometric strain rate began to deviate increasingly from k_a and k_f as the flame was stretched.

Similar plots for the 13-m/s peak-injection-velocity case are also shown in Fig. 12. In this case the flame temperature decreased rapidly to room temperature, with flame quenching occurring at $\sim 1130 \text{ K}$. As discussed earlier, this temperature limit was obtained from the steady-state quenching study. The temperature and various strain rates at the instant of flame extinction are indicated by solid circles in Fig. 12 for the 13-m/s peak-injection case. It should be noted that the air-side strain rate at the time of extinction is $\sim 2600 \text{ s}^{-1}$, which is nearly twice that required to quench the flame in a steady-state manner. The air- and fuel-side strain rates seem to increase at the same rate during the interaction process; the stoichiometric strain rate, on the other hand, increases much more rapidly, and the value at extinction ($\sim 5750 \text{ s}^{-1}$) is nearly 2.3 times that obtained for a steady-state flame.

To aid the understanding of the extinction behavior of an unsteady flame, the temperature and strain-rate behavior for all of the peak-injection-velocity cases are plotted in Figs. 13 and 14, respectively. Flame extinction is observed only for the cases with peak injection velocities greater than 5 m/s. As the peak injection velocity is increased above this value, the flame temperature decreases rapidly. However, the response of the flame to the changes in peak injection velocity diminishes at higher peak values. For example, the decrease in temperature remains nearly the same for the 12- and 13-m/s peak-injection cases. Note that all of the double-vortex/flame interactions shown in Figs. 13 and 14 were obtained by imposing the same rate of increase for different peak-injection-velocity cases, as shown in Fig. 6. This suggests that in the higher peak-injection-velocity cases, the primary vortex growth—and, thereby, flame extinction—occurs prior to the injection velocity actually reaching the peak value, which renders a further increase in the maximum velocity trivial with regard to the flame-extinction process.

The increases in air-side strain rate (k_a) during various double-vortex/flame interactions are shown in Fig. 14. The extinction conditions for cases with peak injection velocity $> 5 \text{ m/s}$, determined based on the 1130-K temperature limit, are indicated by filled circles. The envelope passing through these circles separates the flame from its extinction state. In gen-

eral, the strain rate at which extinction takes place increases with applied maximum injection velocity. It is also evident from this figure that an opposing-jet flame survives at a strain rate that is much higher than the steady-state extinction limit (1410 s^{-1})—if the flame is subjected to that strain rate rapidly. In other words, the faster the flame stretches, the higher the strain rate it can withstand without being quenched. Similar behavior was observed in other characteristic parameters such as k_f , k_{stoich} , χ_{max} , and χ_{stoich} .

Vortices generated using a fixed rate of increase ($a_0 = 2450 \text{ m/s}^2$) in injection velocity traveled toward the flame surface and caused the flame to stretch. However, as evident in Figs. 13 and 14, the stretch applied on the flame surface did not increase in proportion to the peak value of the injection velocity, and the maximum imposed air-side strain rate was limited to $\sim 2635 \text{ s}^{-1}$ because of the apparent saturation in vortex-penetration velocity. Vortices generated with peak values $> 10 \text{ m/s}$ caused extinction prior to the injection velocity reaching its specified peak value; thus, the peak value became trivial with regard to the quenching process. To circumvent this saturation problem, vortices were generated by injecting fluid at different rates of increase in the injection velocity ($2450\text{--}4900 \text{ m/s}^2$) and by maintaining the peak injection velocity at 19 m/s, as shown in Fig. 6. Such a high peak value was chosen to ensure that extinction would occur prior to the injection velocity reaching the peak value even at the slowest rate of injection (2450 m/s^2).

3.9. Vortices with the same injection mass

Calculations for the double-vortex/flame interactions were made using the above-mentioned constant-peak-velocity injection scheme. The changes in flame temperature along the centerline during the interaction process for all of the cases are plotted in Fig. 15. The extinction process in the flame was considered to begin when the temperature decreased to 1130 K. Further decrease in temperature after the flame is locally extinguished results from the diffusion and conduction of products and heat, respectively, from the flame zone. As expected, the flame responds uniquely to changes in the acceleration of fluid injection. The time at which extinction occurs is inversely proportional to the rate of increase (a_0) in the injection velocity.

The changes in air-side strain rate during the vortex/flame-interaction process are shown in Fig. 16 for various a_0 cases. The strain rates at which extinction took place were obtained from the 1130-K-cutoff criterion and are indicated by filled circles in this figure. A linear decrease in extinction strain rate with time can be observed. All of the interactions in Fig. 16 occur more rapidly than those in Fig. 14 and are

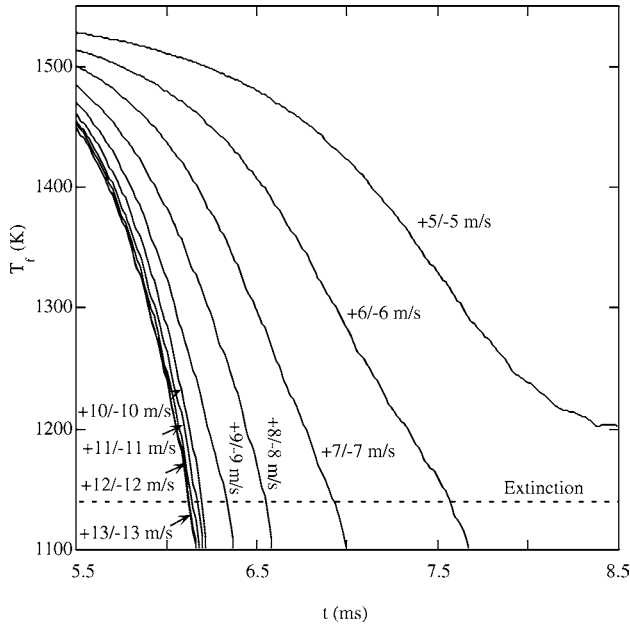


Fig. 13. Variations of flame temperature with time for double-vortex/flame interactions simulated using various peak injection velocities.

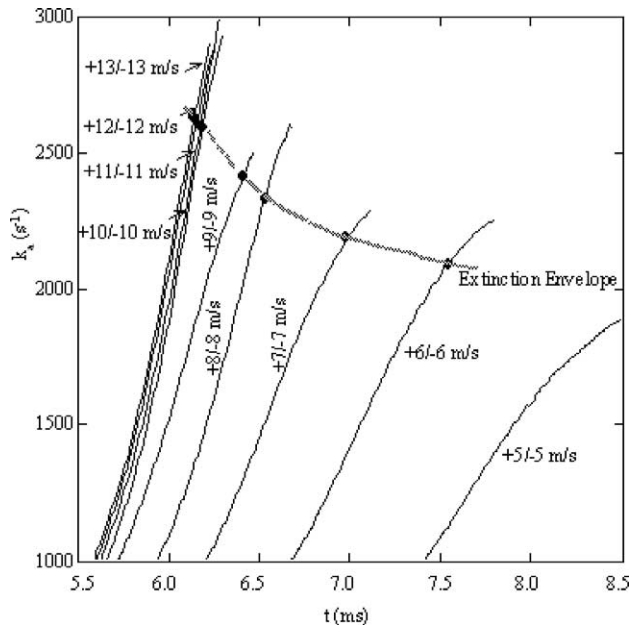


Fig. 14. Variations of air-side strain rate with time for double-vortex/flame interactions simulated using various peak injection velocities.

sustained to much higher air-side strain rates. The extinction strain rate increased from 2600 to 3200 s^{-1} when the injection-fluid accelerations were increased from 2450 to 4900 m/s^2 . The data in Figs. 14 and 16 clearly indicate that using a unique value of air-side strain rate, one cannot predict the quenching condi-

tion of an unsteady flame. In other words, the value of the air-side strain rate at which extinction occurs in an unsteady flame depends on the rate at which the flame was strained. Changes in fuel-side and stoichiometric strain rates with time for various double-vortex/flame interactions (for $u_{\text{max}} = 19 \text{ m/s}$ cases) are plotted

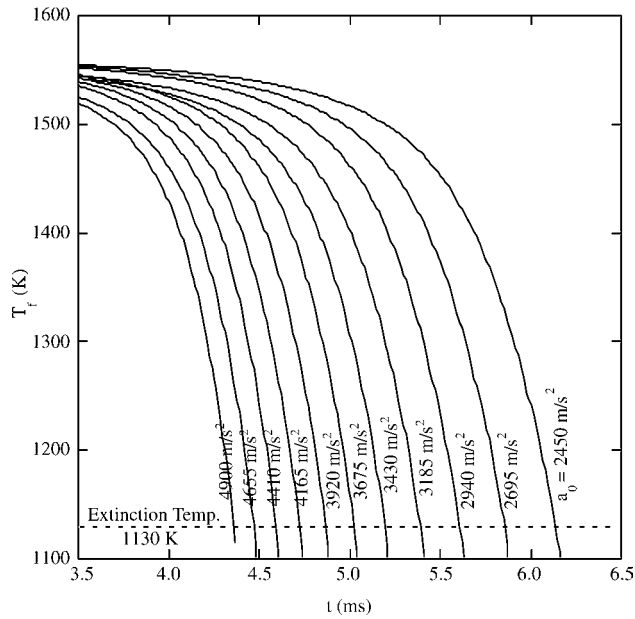


Fig. 15. Variations of flame temperature with time for double-vortex/flame interactions simulated using various rates of increase in injection velocity.

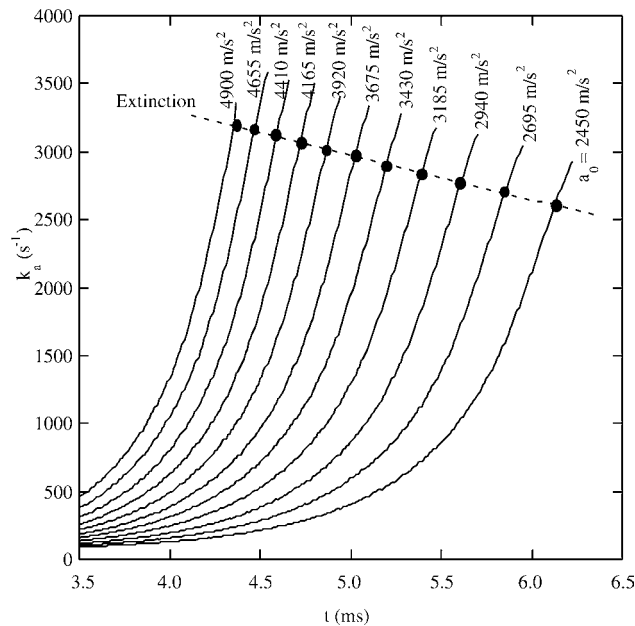


Fig. 16. Variations of air-side strain rate with time for double-vortex/flame interactions simulated using various rates of increase in injection velocity. Extinction values based on the 1130-K-temperature criterion are indicated by solid circles.

in Figs. 17 and 18, respectively. Similar to the behavior of the air-side strain rate, both the fuel-side and the stoichiometric strain rates increase with time. It is important to note that these extinction-strain-rate values (obtained from the 1130-K-cutoff criterion and indicated by solid circles) also decrease with time—similar to the behavior of the air-side strain-

rate values. Figs. 15–17 suggest that none of these strain rates can characterize an unsteady extinction process uniquely. However, among the three strain rates, the air-side one is the least sensitive to unsteadiness. It decreased by only 585 s^{-1} when the vortex interaction time was increased by 1.77 ms, while the fuel-side and stoichiometric strain rates decreased by

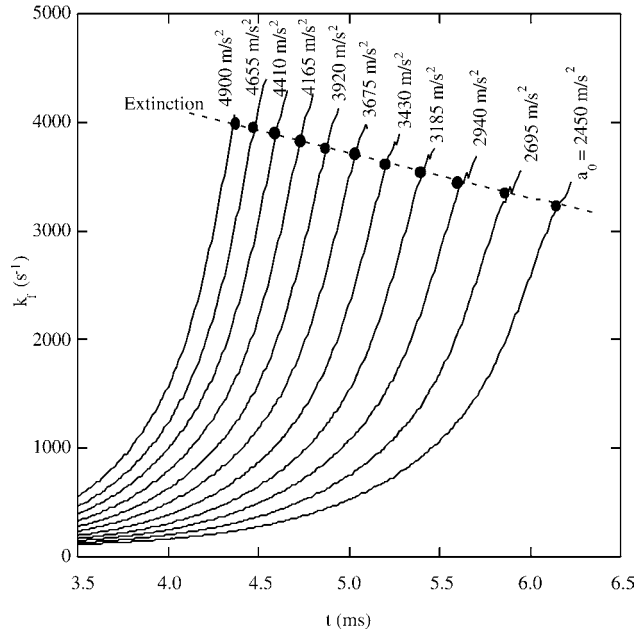


Fig. 17. Variations of fuel-side strain rate with time for double-vortex/flame interactions simulated using various rates of increase in injection velocity. Extinction values based on the 1130-K-temperature criterion are indicated by solid circles.

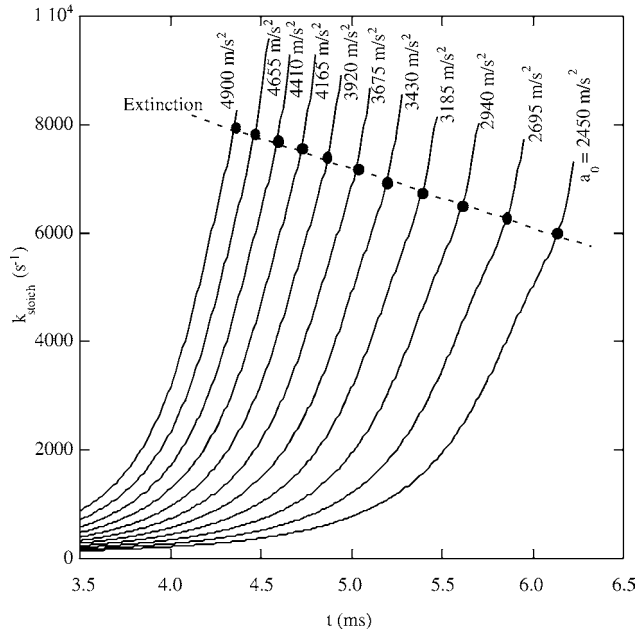


Fig. 18. Variations in strain rate at the stoichiometric location with time for double-vortex/flame interactions simulated using various rates of increase in injection velocity. Extinction values based on the 1130-K-temperature criterion are indicated by solid circles.

860 and 2000 s⁻¹, respectively. The reason for the dependence of extinction strain rate on vortex–flame interaction time is explained below.

The structures along the centerline of a slowly strained flame ($a_0 = 2450 \text{ m/s}^2$) and a rapidly

strained flame ($a_0 = 4099 \text{ m/s}^2$) just prior to extinction are compared in Fig. 19. The fuel and oxygen fluxes (gradients) into the flame zone, the temperature distributions, and the widths are nearly identical for both flames (Fig. 19a). The mixture-fraction (ξ_H) dis-

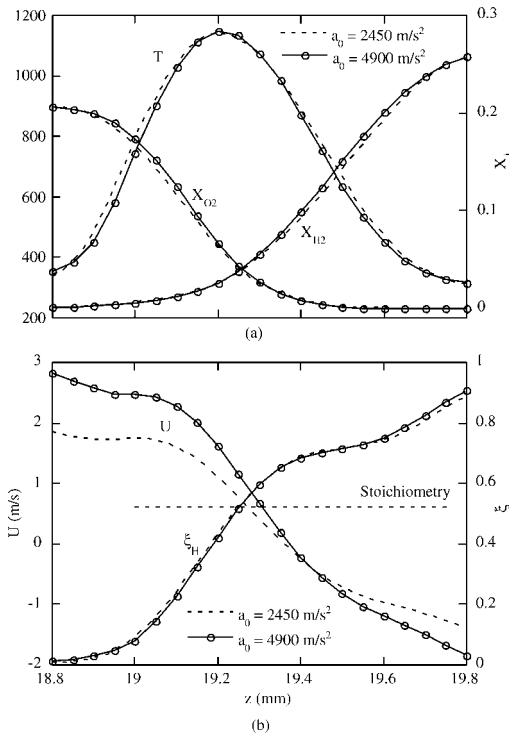


Fig. 19. Comparison of structures along the centerlines of slowly and rapidly strained flames at time of extinction. (a) Temperature and reactant mole fractions; (b) velocity and mixture fraction.

tributions are also quite similar, as shown in Fig. 19b. For all practical purposes, based on the temperature and species distributions, one might consider these two flames to be chemically identical. However, as shown in Fig. 19b, their flow structures are quite different. The rapidly strained flame is subjected to higher velocity gradients (solid line) across the reaction zone than the slowly strained flame (broken line). Since strain rate describes the flow structure, the air-side, fuel-side, and stoichiometric strain rates are all higher for the former flame. That means that even though the chemical structures of the two flames are identical, the strain rates acting on them can be different if the flow structures are different.

In a diffusion flame, fuel and oxygen consumed in the reaction zone enter through convection and diffusion. On the other hand, convective flow also influences the fuel (or oxygen) distribution and, thereby, modifies the diffusion flux. For example, an increase in convective flow in the z direction in Fig. 19a brings more fresh oxygen into the flame zone; this, in turn, increases the oxygen-concentration gradient, eventually increasing the diffusive flux of oxygen into the flame zone. When a vortex travels toward the flame surface, it induces convective flow upstream

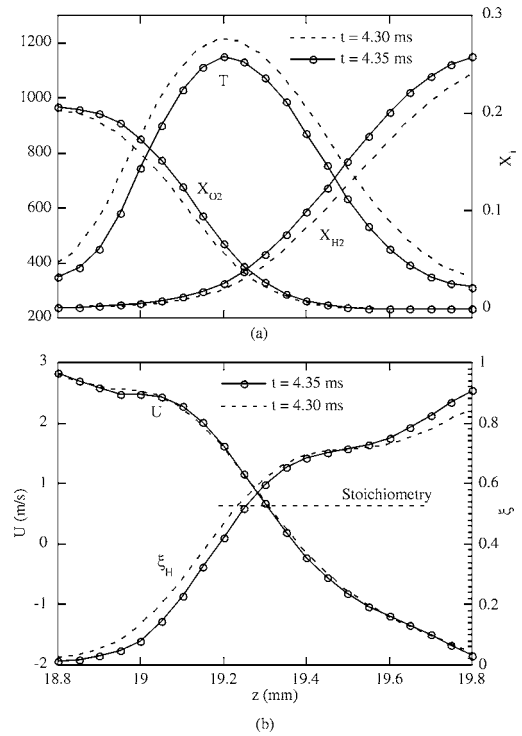


Fig. 20. Comparison of structures along the centerline at two instants near extinction for a rapidly strained flame. (a) Temperature and reactant mole fractions; (b) velocity and mixture fraction.

of the vortex through a pressure wave. Consequently, through diffusion, the fluid in the vortex will be distributed in the region surrounding the vortex. However, since diffusion velocities are only on the order of 0.4 m/s (in a 0.8-mm -thick flame), a considerable delay will occur between the fluid diffusion and the velocity imposition—leading to a flow-nonequilibrium situation. The delay between the imposed velocity and the resulting diffusion was also observed by Egolfopoulos and Campbell [7] and Takahashi and Katta [46] in moderately strained flames.

The two flames shown in Fig. 19 are in a flow-nonequilibrium state, with diffusion not yet fully adjusted to the imposed velocity. As the delay between the diffusion and the imposed velocity increases with vortex-convection speed, the rapidly strained flame requires a longer period of time to achieve equilibrium than the slowly strained flame; the result is identical chemical but different flow structures.

To further verify the hypothesis concerning the flow-nonequilibrium situation in unsteady flames, the structures along the centerline for the rapidly strained flame ($a_0 = 4900 \text{ m/s}^2$) at two instants are shown in Fig. 20. While the data represented by solid lines at $t = 4.35 \text{ ms}$ are those shown in Fig. 19 for this flame, those represented by broken lines were ob-

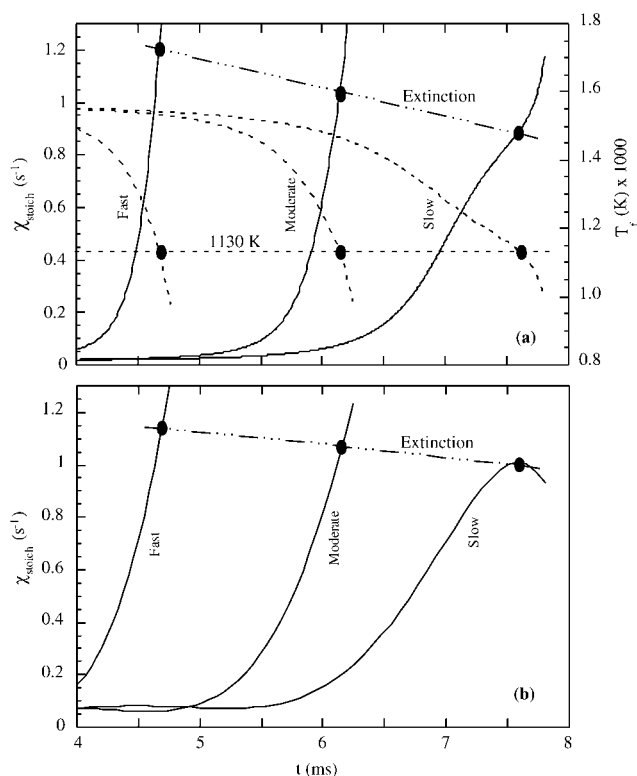


Fig. 21. Changes in scalar dissipation rates at stoichiometry in the neighborhood of extinction when flame is subjected to slow-, moderate-, and fast-changing strain rates. Scalar dissipation rates are calculated using mixture fractions defined based on (a) Bilger's formula [39] and (b) Eq. (1).

tained 0.05 ms earlier in the double-vortex/flame-interaction process. Although the vortices on the fuel and air sides of the flame have moved very near each other by $t = 4.3$ ms, the velocity has not changed appreciably during the following 0.05 ms (Fig. 20b) of interaction. However, as observed in Fig. 20a, the diffusion layer moved ~ 0.02 mm toward the peak-temperature location. This movement is consistent with that estimated based on a diffusion velocity of 0.4 m/s. The increased fuel and oxygen flux into the reaction zone cooled the flame (decrease in T) and reduced the reactant consumption (increased amounts of fuel and oxygen at the stoichiometric surface).

Since the strain rate computed at a flame location represents the flow structure at that location and because of the flow nonequilibrium discussed previously, an accurate description of the quenching process using strain rate alone is not possible, as demonstrated in Figs. 14, 16, 17, and 18. In contrast, however, since the scalar dissipation rate (defined in Eq. (2)) represents the overall diffusion process, this rate calculated at a flame location could be used to describe the quenching process.

As described previously, Eq. (2) yields different forms of the scalar dissipation rate, depending on the

mixture-fraction definition used. The sensitivities of the three scalar dissipation rates (obtained based on ξ_H , ξ_O , and ξ_{H+O}) to the stretching time period of an unsteady flame are compared by computing these rates for the three vortex/flame interactions (slow, moderate, and fast) described in Fig. 11. In general, all of the four scalar-dissipation-rate profiles along the stagnation line during these three vortex/flame interactions are similar to the ones shown in Figs. 9 and 10, with two peaks occurring in the flame zone—one near the stoichiometric location and the other on the fuel side of the flame zone. The variations of scalar dissipation rate at stoichiometry with time during the three vortex/flame interactions are shown in Fig. 21. Only scalar dissipation rates obtained with Bilger's mixture fraction (ξ_{H+O}) and H-element-based mixture fraction (ξ_H) are shown here (Figs. 21a and 21b, respectively). It should be recalled from Fig. 2 that the stoichiometric location of the Bilger's mixture fraction is nearest to the peak-reactivity location ($2X_{H_2} = X_{O_2}$ location), while that of the H-element-based mixture fraction is farthest from it. Extinction values determined based on the 1130-K criterion are also shown in Fig. 21. It is evident from this figure that the extinction scalar dissipation rates ob-

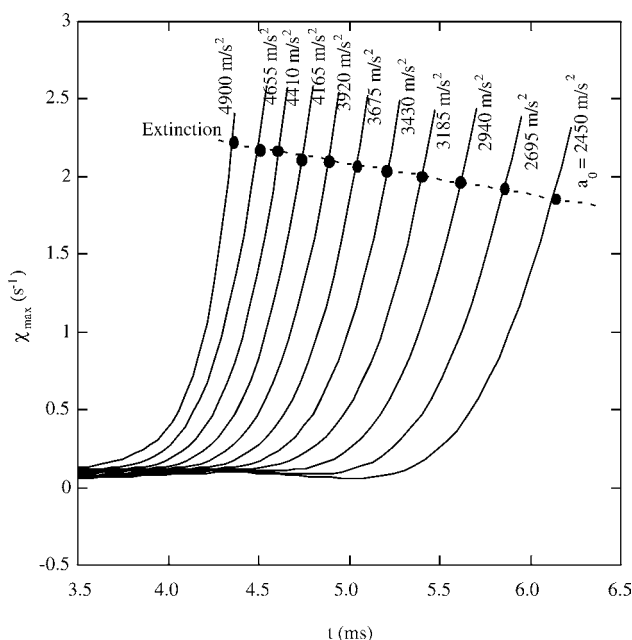


Fig. 22. Variations of the peak scalar dissipation rate with time for double-vortex/flame interactions simulated using different rates of increase in injection velocity. Extinction values based on the 1130-K-temperature criterion are indicated by solid circles.

tained with $\xi_{\text{H}\&\text{O}}$ (Fig. 21a) are more sensitive to the vortex/flame-interaction time than those obtained with ξ_{H} . In fact, based on sensitivity to interaction time (or vortex speed), the scalar dissipation rate obtained using ξ_{H} was least sensitive, followed by that obtained with $\xi_{\text{H}\&\text{O}}$, and, finally, that obtained with ξ_{O} . Because of the lowest sensitivity, the scalar dissipation rate obtained with ξ_{H} is used for the evaluation of the scalar dissipation rate for describing the extinction of unsteady flames.

Variations in the maximum value of the scalar dissipation rate and the local value at the stoichiometric surface with time are plotted for each double-vortex/flame-interaction case in Figs. 22 and 23, respectively. The respective values at extinction for all of the unsteady flames, determined based on the 1130-K criterion, are represented by filled circles. From Figs. 22 and 23, it is apparent that the scalar dissipation rates χ_{\max} and χ_{stoich} also failed to characterize the extinction process in unsteady flames uniquely, which means that extinction in unsteady flames cannot be predicted using scalar dissipation rates. However, the variations in extinction values with respect to the changes in fluid-injection velocity seem to be smaller for scalar dissipation rates than for strain rates. The ranges in unsteady extinction values of various characteristic variables used in the present study are shown in Table 1, along with the percentage increases from the respective steady-state limits. The extinction values for χ_{\max} in unsteady flames range from 1.85 to 2.215 s^{-1} and are higher only by 45

to 73% than the limit obtained in steady-state flames (1.28 s^{-1}). Among all of the characterizing variables, χ_{stoich} most nearly represents the unsteady extinction process, with only a variation of 30 to 53% from the steady-state limit.

3.10. Unified characterization of extinction in unsteady flames

The fact that the scalar dissipation rate describes unsteady flame extinction more closely than the strain rate can be understood by considering the chemical and flow nonequilibrium processes that develop in these flames. As the strain rate on the flame is increased, through diffusion, increasingly more reactants are transported into the reaction zone. At lower strain rates, the chemical kinetics can consume all of the entering reactants. However, at higher rates of strain, the chemistry cannot cope with the large reactant fluxes and, therefore, flame cooling occurs. As discussed previously, the strain rate represents reactant fluxes transported into the reaction zone only in the case of steady-state flames. When flow non-equilibrium occurs, the strain rate does not take into account the time lag between the diffusion and convection processes and, hence, cannot represent the extinction process. Since the scalar dissipation rate describes the diffusion process, it is less sensitive to the flow nonequilibrium that develops in unsteady flames. However, the scalar dissipation rate can represent the chemical kinetics in the flame zone only

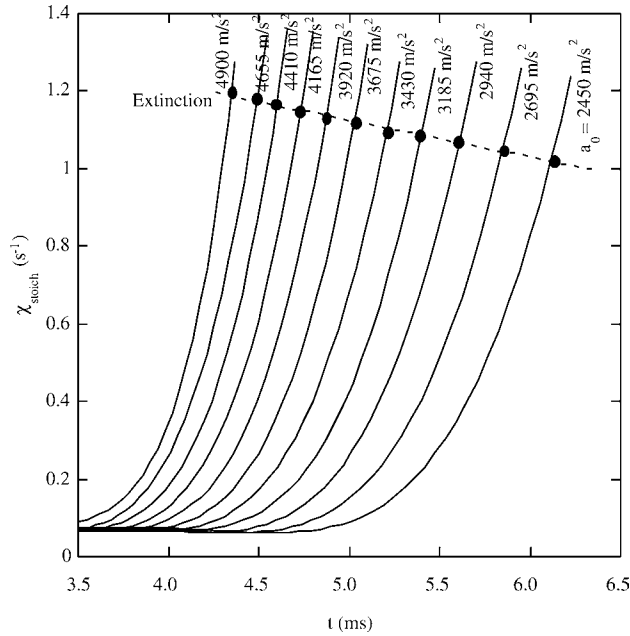


Fig. 23. Variations of the scalar dissipation rate at stoichiometry with time for double-vortex/flame interactions simulated using various rates of increase in injection velocity.

Table 1
Values of various characteristic variables at extinction in unsteady flames

Characteristic variable	Steady-state extinction limit (s^{-1})	Values at extinction in unsteady flames	
		Actual variation (s^{-1})	Percent variation above steady-state limit
k_a	1410	2610–3195	85–127
k_f	1678	3240–4000	93–138
k_{stoich}	2460	5950–7950	142–223
χ_{max}	1.28	1.85–2.215	45–73
χ_{stoich}	0.78	1.02–1.193	30–53

when the diffusion time scale is far greater than the chemical (reaction) time scale—which exists in unstretched flames where the reactions are limited by the diffusion process. When chemical nonequilibrium occurs (chemistry-limited situation), the scalar dissipation rate does not take into account the time lag between the diffusion and chemical kinetics and, hence, fails to represent the extinction process. Nevertheless, since the scalar-dissipation rate reflects changes in diffusion more accurately than the strain rate, the former describes the unsteady extinction process more accurately.

To represent the unsteady-extinction process uniquely, one must consider a variable that takes into account both the flow- and the chemical-nonequilibrium processes. Since the strain rate or scalar-dissipation rate can be used to estimate the former, a parameter that can be used to estimate the latter is required. If one assumes that no delay exists between chemi-

cal kinetics and heat-release rate, then dT_f/dt (rate of decrease in flame temperature) represents the rate of change in chemical kinetics and, in other words, the rate of change in the chemical-nonequilibrium state. Vortices that move more rapidly result in higher dT_f/dt values at extinction, and those that move more slowly result in lower dT_f/dt values. Therefore, by defining a variable that is proportional to the air-side strain rate and inversely proportional to the temperature-decrease rate (dT_f/dt), one can obtain a universal value for identifying the quenching process in unsteady flames.

By considering both the chemical and flow non-equilibrium states of an unsteady flame, a new variable (σ) is defined as the ratio of the strain rate to the rate of change in flame temperature as follows:

$$\sigma = T_\infty \frac{k_a - k_{a0}}{dT_f/dt} \tag{3}$$

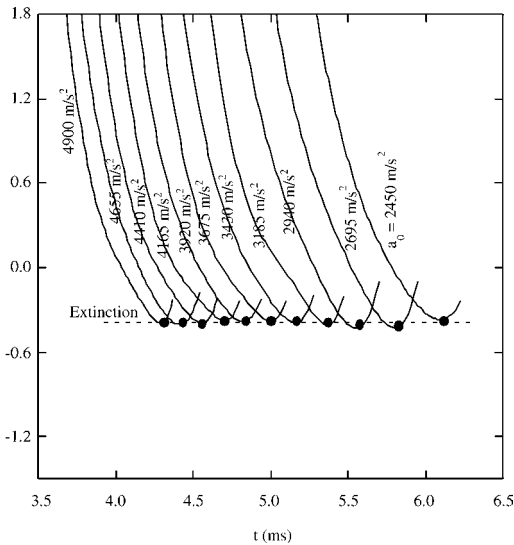


Fig. 24. Variations of the new variable σ with time for double-vortex/flame interactions simulated using various rates of increase in injection velocity.

Here, T_f is the flame (peak) temperature, and k_{a0} is the steady-state air-side extinction strain rate. Values of σ computed at several instants during various vortex/flame interactions are plotted in Fig. 24. In each case as the vortices issued from the fuel and air sides approach the flame surface, σ decreases with interaction time, crosses zero when the instantaneous strain rate reaches the steady-state extinction limit, reaches a minimum value, and then begins to increase. Interestingly, the minimum values of σ for all of the double-vortex/flame-interaction cases are the same—0.39. The striking feature of σ became evident when the extinction condition for each interaction case was plotted in Fig. 24 (filled circles). The extinction conditions coincided with the minima in σ .

The behavior of σ in Fig. 24 can be interpreted as follows: (1) the value of σ at extinction (0.39) is independent of the interaction time scales, and (2) the extinction condition represents the minima in the t -vs- σ profile. The first observation suggests that the new variable σ can be used to characterize the extinction process in unsteady flames—extinction occurs when $\sigma = 0.39$ in any unsteady flame considered in this study. The second observation suggests that extinction in a flame occurs when the behavior of σ with respect to t becomes reversed (changing from decreasing to increasing). Since no extinction criterion was used when plotting variations of σ with respect to t , the natural development of minima at the extinction point suggests that the 1130-K-temperature criterion used in this study for defining the extinction state is fairly accurate. Any extinction criterion based on a flame temperature other than 1130 K

would shift the filled circles in Fig. 24 from the minima locations. The values of σ calculated for the double-vortex/flame interactions simulated with different peak-injection velocities (Figs. 13 and 14) are in the range 0.39–0.4. However, σ calculated for the case of the traveling unsteady flame (Fig. 5) is ~ 0.3 , suggesting the need to consider flame movement in the quenching criterion. Interestingly, a variable similar to σ obtained using the scalar dissipation rate in the numerator for representing flow nonequilibrium failed to predict the extinction process of the unsteady flames; in other words, its extinction value depends on the interaction time.

4. Conclusions

Unsteady flames are often studied to gain a better understanding of turbulent-flame structures; such studies facilitate the development of accurate turbulence-chemistry interaction models. An experimental and numerical study has been performed to identify the time-dependent flame structure that develops during an interaction between multiple vortices and the flame surface. A time-dependent model, known as UNICORN, that incorporates 13 species and 74 reactions among the constituent species has been used for the simulation of unsteady flames resulting from multivortex/flame interactions in opposing-flow hydrogen jet diffusion flames. In the past this model has been validated by direct simulation of several steady-state and unsteady axisymmetric counterflow and coflow jet diffusion flames. Phase-locked experiments were conducted, and OH-concentration measurements were made using the PLIF technique.

A steady-state opposing-flow jet flame was first established using the Rolon-burner geometry. Several unsteady flames were then obtained by forcing vortices toward the flame surface from both sides simultaneously using injection tubes placed in the fuel and air nozzles. When the fuel- and air-side vortices were of different sizes, the double-vortex/flame interaction yielded a traveling unsteady flame. The computed flame-extinction process and the propagation of flame edge into the fuel-side vortex compared favorably with the experimental results. To investigate the differences between the steady-state and dynamic extinction processes, stationary unsteady flames were established by forcing equal-sized vortices from the fuel and air nozzles.

It was found that the air-side strain rate, fuel-side strain rate, strain rate at stoichiometric location peak scalar dissipation rate, and scalar dissipation rate at stoichiometric location cannot be used to characterize the quenching process associated with unsteady flames. In general, the extinction values of these vari-

ables in unsteady flames are higher than the respective ones in steady-state flames, and the differences increase with vortex speed. Analysis of flame structures just prior to extinction revealed that dynamic flames encounter flow and chemical nonequilibrium environments. The former arises as a result of the time lag between the diffusion and convection processes, while the latter develops as a result of the time lag between the chemical kinetics and diffusion. Since strain rates represent neither of these nonequilibrium processes, the values of these characteristic parameters at flame extinction are found to vary significantly with vortex/flame interaction time. Even though the scalar dissipation rates represent the flow nonequilibrium accurately, the values of these characteristic parameters at flame extinction also increase with vortex/flame interaction time; however, their variations are much smaller than those observed in strain rates. A new variable (σ) that is proportional to the air-side strain rate and inversely proportional to the rate of change in the flame temperature is proposed to characterize the unsteady extinction process. During a double-vortex/flame interaction, it is found that σ decreases with time, reaches a minimum value at extinction, and then increases again. All of the stationary unsteady flames investigated in the present study were found to be extinguished when the value of σ , independent of the vortex/flame interaction time, reached 0.39. On the other hand, traveling unsteady flames appear to be extinguished at a lower σ value.

Acknowledgments

This work was supported, in part, by the Air Force Office of Scientific Research (Dr. Julian Tishkoff, Technical Monitor). The experimental setup shown in Fig. 1 was designed and built at the Air Force Research Laboratory by Drs. P.H. Renard, J.C. Rolon, and G.J. Fiechtner under a Joint US–French Collaborative Program. The authors acknowledge Marian Whitaker for editorial assistance.

References

- [1] R.J. Kee, J.A. Miller, G.H. Evans, G. Dixon-Lewis, *Proc. Combust. Inst.* 22 (1988) 1479–1486.
- [2] G. Dixon-Lewis, *Proc. Combust. Inst.* 23 (1990) 305–324.
- [3] H.K. Chelliah, C.K. Law, T. Ueda, M.D. Smooke, F.A. Williams, *Proc. Combust. Inst.* 23 (1990) 503–510.
- [4] H.C. Hottel, W.R. Hawthorne, *Proc. Combust. Inst.* 3 (1949) 254–266.
- [5] W.M. Roquemore, L.-D. Chen, L.P. Goss, W.F. Lynn, in: R. Borghi, S.N.B. Murthy (Eds.), *Turbulent Reactive Flows*, in: *Lecture Notes in Engineering*, vol. 40, Springer-Verlag, Berlin, 1989, p. 49.
- [6] N. Darabiha, *Combust. Sci. Technol.* 86 (1992) 163–181.
- [7] F.N. Egolfopoulos, C.S. Campbell, *J. Fluid Mech.* 318 (1996) 1–29.
- [8] H.G. Im, C.K. Law, J.S. Kim, F.A. Williams, *Combust. Flame* 100 (1995) 21–30.
- [9] T.M. Brown, R.W. Pitz, C.J. Sung, *Proc. Combust. Inst.* 27 (1998) 703–710.
- [10] T. Shamim, A. Atreya, *Combust. Flame* 121 (2000) 59–74.
- [11] T. Shamim, A. Atreya, *Combust. Flame* 123 (2000) 241–251.
- [12] A.F. Ghoniem, M.C. Soteriou, B.M. Cetegen, O.M. Kino, *Proc. Combust. Inst.* 24 (1992) 223–230.
- [13] F.N. Egolfopoulos, *Int. J. Energy Res.* 24 (2000) 989–1010.
- [14] B. Cuenot, F.N. Egolfopoulos, T. Poinso, *Combust. Theory Modeling* 4 (2000) 77–97.
- [15] P.H. Paul, H.N. Najm, *Proc. Combust. Inst.* 27 (1998) 43–50.
- [16] G. Patnaik, K. Kailasanath, *Proc. Combust. Inst.* 27 (1998) 711–717.
- [17] W.T. Ashurst, *Combust. Sci. Technol.* 92 (1993) 87–103.
- [18] V.S. Santoro, D.C. Kyritsis, A. Linan, A. Gomez, *Proc. Combust. Inst.* 28 (2000) 2109–2116.
- [19] W.L. Roberts, J.F. Driscoll, M.C. Drake, J.W. Ratcliffe, *Proc. Combust. Inst.* 24 (1992) 169–176.
- [20] J.C. Rolon, F. Aguerre, S. Candel, *Combust. Flame* 100 (1995) 422–429.
- [21] P.H. Renard, D. Thevenin, J.C. Rolon, S. Candel, *Prog. Energy Combust. Sci.* 26 (2000) 225–282.
- [22] D. Tevenin, P.H. Renard, G.J. Fiechtner, J.R. Gord, J.C. Rolon, *Proc. Combust. Inst.* 28 (2000) 2101–2108.
- [23] V.R. Katta, W.M. Roquemore, *Proc. Combust. Inst.* 28 (2000) 2055–2062.
- [24] V.R. Katta, C.D. Carter, G.J. Fiechtner, W.M. Roquemore, J.R. Gord, J.C. Rolon, *Proc. Combust. Inst.* 27 (1998) 587–594.
- [25] K. Yoshida, T. Takagi, *Proc. Combust. Inst.* 27 (1998) 685–692.
- [26] V.R. Katta, T.R. Meyer, J.R. Gord, W.M. Roquemore, *Combust. Flame* 132 (2003) 639–651.
- [27] T. Poinso, A. Trounev, D. Veynante, S. Candel, E. Esposito, *J. Fluid Mech.* 177 (1987) 265.
- [28] D. Thevenin, P.H. Renard, J.C. Rolon, S. Candel, *Proc. Combust. Inst.* 26 (1996) 1079–1086.
- [29] M.D. Smooke, A. Ern, M.A. Tanoff, B.A. Valdati, R.K. Mohammed, D.F. Marran, M.B. Long, *Proc. Combust. Inst.* 26 (1996) 2161–2168.
- [30] V.R. Katta, W.M. Roquemore, *AIAA J.* 36 (11) (1998) 2044–2054.
- [31] V.R. Katta, W.M. Roquemore, Calculation of premixed methane–air flame using detailed chemical kinetics, in: *Proceedings of the 1998 Technical Meeting of the Central States Section of the Combustion Institute*, The Combustion Institute, Pittsburgh, PA, 1998.
- [32] W.M. Roquemore, V.R. Katta, *J. Visualization* 2 (3/4) (2000) 257–272.
- [33] M. Frenklach, H. Wang, M. Goldenberg, G.P. Smith, D.M. Golden, C.T. Bowman, R.K. Hanson, W.C. Gardiner, V. Lissianski, *Gas Research Institute Techni-*

- cal Report No. GRI-95/0058, Gas Research Institute, Chicago, November 1, 1995.
- [34] B.P. Leonard, *Comput. Methods Appl. Mech. Eng.* 19 (1) (1979) 59–98.
- [35] V.R. Katta, L.P. Goss, W.M. Roquemore, *AIAA J.* 32 (1) (1994) 84–94.
- [36] F. Grisch, B. Attal-Tretout, P. Bouchardy, V.R. Katta, W.M. Roquemore, *J. Nonlinear Opt. Phys. Mater.* 5 (3) (1996) 505–526.
- [37] J. Warnatz, U. Maas, R.W. Dibble, *Combustion, Physical and Chemical Fundamentals, Modeling and Simulation, Experiments, Pollutant Formation*, Springer-Verlag, Heidelberg, 1996, p. 127.
- [38] R.W. Bilger, Turbulent flows with nonpremixed reactants, in: P.A. Libby, F.A. Williams (Eds.), *Turbulent Reacting Flows*, in: *Topics in Applied Physics*, vol. 44, Springer-Verlag, New York, 1980, p. 65.
- [39] R.W. Bilger, *Proc. Combust. Inst.* 22 (1988) 475–488.
- [40] E. Gutheil, G. Balakrishnan, F.A. Williams, in: N. Peters, B. Rogg (Eds.), *Lecture Notes in Physics*, Springer-Verlag, New York, 1993, p. 177.
- [41] G.T. Fiechtner, P.H. Renard, C.D. Carter, J.R. Gord, J.C. Rolon, *J. Visualization* 2 (2000) 331–342.
- [42] G.T. Fiechtner, C.D. Carter, K.D. Grinstead, J.R. Gord, W.M. Roquemore, J.C. Rolon, Flame–vortex interactions in a non-premixed H_2/N_2 /air counterflow burner, in: 34th AIAA/ASME/SAE/ASEE Joint Propulsion Conference & Exhibit, Cleveland, OH, 1998, AIAA 98-3770.
- [43] R.S. Sheinson, J.E. Penner-Hahn, D. Indritz, *Fire Safety J.* 15 (1989) 437–450.
- [44] A.F. Roberts, B.W. Quince, *Combust. Flame* 20 (1973) 245–251.
- [45] D.C. Kyritsis, V.S. Santoro, A. Gomez, Measurements and computations of scalar dissipation rate in vortex perturbed counterflow diffusion flame, in: *Proceedings of the 2001 Technical Meeting of the Eastern States Section of the Combustion Institute*, The Combustion Institute, Hilton Head, SC, 2001, pp. 320–323.
- [46] F. Takahashi, V.R. Katta, *J. Propulsion Power* 11 (1) (1995) 170–177.

GT2004-54318

OH PLIF AND SOOT VOLUME FRACTION IMAGING IN THE REACTION ZONE OF A LIQUID-FUELED MODEL GAS-TURBINE COMBUSTOR

Terrence R. Meyer, Sukesh Roy, and Sivaram P. Gogineni
Innovative Scientific Solutions, Inc.
2766 Indian Ripple Road
Dayton, OH 45440-3638

Vincent M. Belovich, Edwin Corporan, and James R. Gord
Air Force Research Laboratory/PRTC
1790 Loop Road North
Wright-Patterson Air Force Base, OH 45433

ABSTRACT

Simultaneous measurements of OH planar laser-induced fluorescence (PLIF) and laser-induced incandescence (LII) are used to characterize the flame structure and soot formation process in the reaction zone of a swirl-stabilized, JP-8-fueled model gas-turbine combustor. Studies are performed at atmospheric pressure with heated inlet air and primary-zone equivalence ratios from 0.55 to 1.3. At low equivalence ratios ($\phi < 0.9$), large-scale structures entrain rich pockets of fuel and air deep into the flame layer; at higher equivalence ratios, these pockets grow in size and prominence, escape the OH-oxidation zone, and serve as sites for soot inception. Data are used to visualize soot development as well as to qualitatively track changes in overall soot volume fraction as a function of fuel-air ratio and fuel composition. The utility of the OH-PLIF and LII measurement system for test rig diagnostics is further demonstrated for the study of soot-mitigating additives.

Keywords: Gas-Turbine Combustor, Swirl-Stabilized, Spray Flame, Soot Volume Fraction, LII, PLIF.

INTRODUCTION

Swirl-stabilized liquid-spray injectors are commonly used in gas-turbine engines to achieve compact, stable, and efficient combustion. The flowfield in the primary zone of such a spray flame is characterized by high shear stresses and turbulent intensities that result in vortex breakdown and large-scale unsteady motions.^{1,2} These unsteady motions are known to play a key role in the formation of pollutant emissions such as carbon monoxide (CO), nitric oxide (NO), and unburned hydrocarbons (UHC).³⁻⁵ Considerably less is known, however, about the mechanisms that lead to soot formation in swirl-stabilized liquid-fueled combustors. Previous investigations

have relied on exhaust-gas measurements and parametric studies to gain insight into the effects of various input conditions on soot loading.⁶⁻¹⁰ Much of the fundamental knowledge concerning soot formation is derived from investigations of laminar diffusion flames,^{11,12} with only a limited number of studies having focused on unsteady effects.^{13,14} The importance of considering unsteadiness and fluid-flame interactions was demonstrated by Shaddix et al.,¹⁴ who found that a forced methane/air diffusion flame produced a four-fold increase in soot volume fraction (as a result of increased particle size) as compared with a steady flame having the same mean fuel-flow velocity.

The goal of the current work is to study soot formation in the highly dynamic environment of a swirl-stabilized JP-8-fueled model combustor. This is accomplished by simultaneous imaging of the soot volume fraction and hydroxyl-radical (OH) distribution using laser-induced incandescence (LII) and OH planar laser-induced fluorescence (PLIF), respectively. Residual Mie scattering from large droplets, which appears in the OH images but does not preclude signal interpretation, is used to a limited extent as a spray diagnostic.

The utility of LII for two-dimensional imaging of soot volume fraction has been demonstrated in a number of investigations^{15,16} and has been implemented in aircraft engine exhaust streams.^{9,10} Brown et al.¹⁷ performed planar LII for soot-volume-fraction imaging in the reaction zone of a model gas-turbine combustor; their measurements demonstrated LII in the primary reaction zone but did not image the turbulent flame structure near the exit of the swirl cup. In the current work, we extend the work of Brown et al.¹⁷ by performing LII at the exit of the swirl cup and by the addition of OH PLIF.

The use of OH as a flame marker is typical in studies of soot formation in diffusion flames because of its close correlation with flame temperature.^{18,19} It has also been

employed in a number of investigations of swirl-stabilized combustors.^{20,21} The use of laser-saturated OH LIF for *quantitative* measurements has also been demonstrated,^{22,23} although saturation is quite difficult in the case of planar measurements. In the current investigation we demonstrate semi-quantitative measurements in the recirculation region using excitation levels well below saturation. OH-PLIF measurements in the liquid-spray region are more qualitative because of simultaneous droplet scattering and non-equilibrium conditions.

The performance and accuracy of the planar LII and OH-PLIF systems are characterized in the current work and described below. Instantaneous, averaged, and statistical data from OH PLIF are then employed to provide insight into the turbulent nature of the swirl-stabilized spray flame at various equivalence ratios. The physical processes that govern the soot formation process are visualized using simultaneous OH PLIF, LII, and droplet Mie scattering. Finally, the overall soot volume fraction in the primary zone is tracked as a function of fuel composition.

NOMENCLATURE

A_{OH}	– Rate of spontaneous emission (s^{-1})
F_B	– Boltzmann fraction
N_{OH}	– Number density of OH molecules (m^{-3})
Q_{OH}	– Collisional quenching rate (s^{-1})
S_{OH}	– relative OH-PLIF signal
η	– fluorescence efficiency
ϕ	– Equivalence ratio

EXPERIMENTAL SET UP

A. Swirl-Stabilized Combustor

The near-field structure of swirl-stabilized flames is highly dependent upon the characteristics of the fuel injector and the geometry of the surrounding flame tube. The injector configuration shown in Fig. 1 is a generic swirl-cup liquid-fuel injector used in ongoing fuel studies at the Atmospheric-Pressure Combustor-Research Complex of the Air Force Research Laboratory's Propulsion Directorate.²⁴ It employs a pressure-swirl atomizer (Delavan model 27710-8) with a nominal flow number of 1.6. The 4-cm exit diameter nozzle is centrally located in a 15.25 cm x 15.25 cm square cross-section dome-type combustor. The spray impinges upon a filming surface and is surrounded by dual-radial, counter-swirling-air co-flows to entrain the fuel, promote droplet break-up, and enhance mixing. The resulting three-dimensional conical flame, shown in Fig. 1(b), is composed of several zones including an outer droplet-vaporization/preheat region, an inner turbulent flame brush region, and a recirculation zone that brings hot combustion products upstream along the centerline.²⁵ After exiting the primary flame zone, the combustion products are allowed to mix thoroughly along the 48-cm long flame tube before entering a 43-cm-long, 5.7-cm exit-diameter exhaust nozzle that is designed to create a uniform exhaust-gas temperature and concentration profile.

Changes in overall equivalence ratio from $\phi = 0.5$ to 1.15 (primary zone equivalence ratio from $\phi = 0.55$ to 1.3) were achieved in the current study by varying the pressure drop across the fuel-spray nozzle from about 1.5 to 10 atm, which

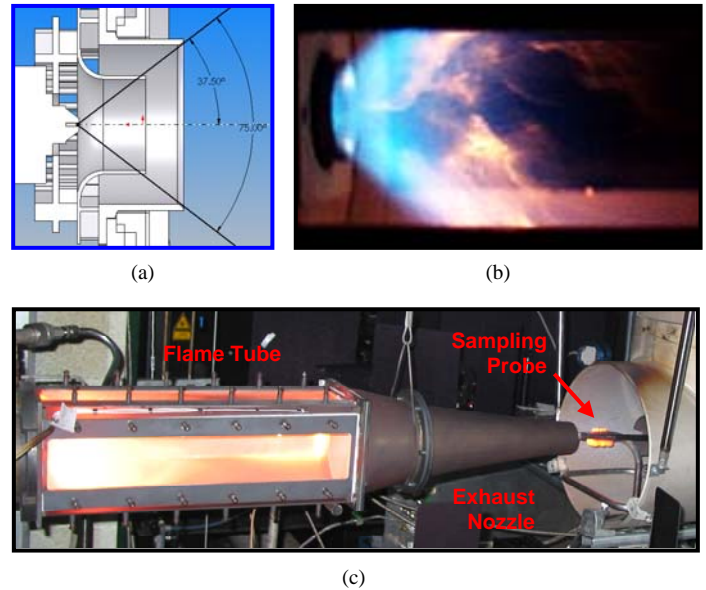


Fig. 1. (a) Dual-radial swirl-injector geometry used in the current study (b) photograph of near-field flame structure, and (c) photograph of the test rig.

resulted in fuel mass flow rates of 1.0 to 2.2 g/s, respectively. The fuel flow rate is measured using a Max Machinery positive-displacement flow meter with $\pm 0.5\%$ full-scale accuracy. The air-flow system consists of three Sierra 5600 SLPM mass flow controllers with $\pm 1\%$ full-scale accuracy. The inlet air is heated to 450 K with a constant flow rate of ~ 0.028 kg/s. The air-pressure drop across the combustor dome was ~ 4.8 to 5.2% of the main supply. Most of the air flow enters the combustor through the swirl-cup injector, but a small percentage enters through aspiration holes along the aft wall. No liner air jets are used in the secondary zone; therefore, the fuel-air ratio depends almost entirely on the flow rates through the injector cup.

The combustor is optically accessible via 75-mm-wide quartz windows along the top and sides for in-situ laser-based diagnostics. In addition, particulate emissions at the exit of the exhaust nozzle are characterized using a TSI Model 3022A Condensation Nuclei Counter (CNC) to provide a count of particles per unit volume (particle number density), and a TSI Model 3936 Scanning Mobility Particle Sizer (SMPS) to obtain the particle size distribution. Particulate emissions are captured and transported to the analytical instruments via an oil-cooled probe, which consists of three concentric tubes with three fluid passages. The outermost passage flows recirculating cooling oil, which is kept at 150°C for all tests. The middle annulus provides particle-free dry dilution air, and the center passage transports the diluted sample to the instruments. The probe is installed facing the flow in the center and near the exit of the combustor to help capture a “representative” sample of the exhaust and avoid diluting or contaminating with surrounding air. The sample line is heated to 75°C, and the sample is diluted at the probe tip to help prevent water condensation and particulate loss to the wall due to high wall-sample temperature gradients. Sharp bends in the sample line were avoided to reduce particle loss.

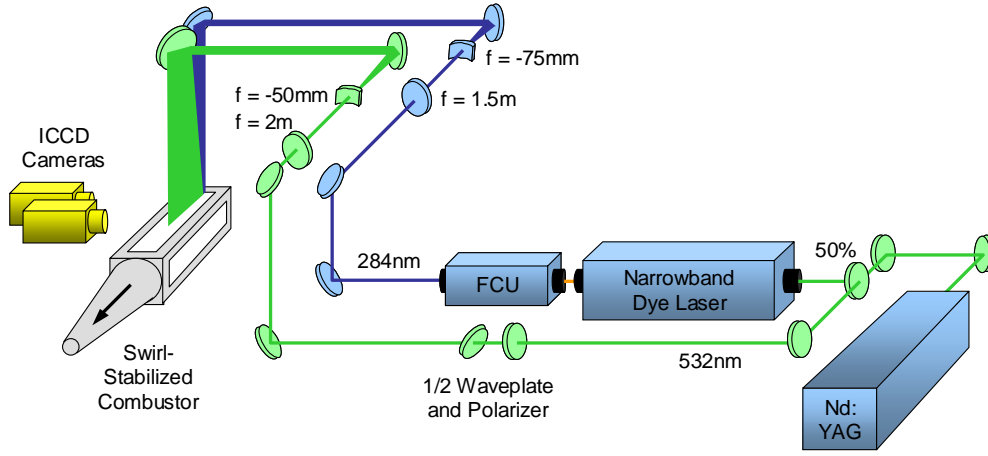


Fig. 2. Experimental setup for simultaneous OH PLIF and LII in an atmospheric-pressure, swirl-stabilized, liquid fueled, model gas-turbine combustor.

B. OH-PLIF System

A review of PLIF fundamentals can be found in Eckbreth (1996).²⁶ As shown in the optical set-up in Fig. 2, 50% of the laser energy from a frequency-doubled, Q-switched Nd:YAG laser (Spectra-Physics Pro290) is used to pump a dye laser (Sirah Precision Scan), the output of which is frequency doubled to obtain wavelengths in the (1,0) band of the OH A-X system. The dye laser is tuned to the $Q_1(9)$ transition at 283.922 nm (in air), which has less than a $\pm 2.5\%$ variation in the ground-level Boltzmann fraction, F_B , from 1600 to 2400K. This range of temperatures coincides with the equilibrium conditions one would expect for JP-8 fuel at equivalence ratios used in this study (primary zone $\phi = 0.55 - 1.3$).²⁷ Considering the full range of possible temperatures from 1100 to 2400K within typical lean and rich flammability limits,²⁸ the Boltzmann fraction for this transition varies by up to $\pm 12.5\%$. The maximum laser energy available for OH PLIF was 24 mJ. A 1.5-m-focal-length spherical plano-convex lens and a -75-mm-focal-length plano-concave lens are used to form a laser sheet that enters the combustor through the top window. The laser-sheet thickness is 330 μm at full-width-half-max (FWHM) as measured by translating a knife-edge across the beam. The sheet width is ~ 7 cm, with a 3° full-angle divergence. A near top-hat sheet-width profile that drops to zero laser energy within about 1 mm is obtained by clipping the wings of the laser sheet at the last turning mirror above the combustor.

Fluorescence is collected from about 306 to 320 nm via the (1,1) and (0,0) bands of OH using an intensified charge-coupled device (ICCD) camera (Princeton Instruments PI-MAX SB) oriented approximately along the normal to the sheet. Two 1-mm thick WG295 Schott Glass filters are used in front of the camera lens to reduce scattering from droplets at 283.922 nm, and a UG11 filter is employed to nearly eliminate flame emission, scattering from the LII laser wavelength of 532nm, and fluorescence from polycyclic-aromatic-hydrocarbon (PAH) compounds. A 105-mm-focal-length f/4.5 UV lens is employed to collect the OH fluorescence, and an intensifier gate width of 20 ns is used to capture the OH signal. Images are typically collected with 2x2 binning to obtain adequate resolution (512x512) and framing rate (1.4 Hz). The pixel viewing area in each 2x2 superpixel is $200 \times 200 \mu\text{m}^2$.

Based on the dimensions of the OH-PLIF laser sheet and total laser energy of 24 mJ, it is estimated that the laser irradiance of $1.36 \times 10^7 \text{ W/cm}^2$ is two to three orders of magnitude lower than the 90-95% saturation level.^{22,23} The OH-PLIF signal is, therefore, linearly related to laser-energy variations. OH-PLIF signal corrections (typ. $\pm 15\%$) in the axial direction are performed in post-processing based on measurements of the laser-sheet profile after each run. Signal variation (typ. $\pm 3\%$) due to the 3° laser-sheet expansion in the cross-stream direction is also corrected in post-processing. Corrections are not made for laser-energy attenuation due to OH absorption and droplet scattering; this leads to signal uncertainties of $\pm 10\%$ in the lower region of each image. The effect of this error is substantially reduced in the upper half of the combustor where most of the data in this study is extracted. Shot-to-shot fluctuations in laser energy add an estimated $\pm 5\%$ uncertainty, as determined from data collected in a laminar diffusion flame with the same OH-PLIF system.

For measurements with low laser irradiance, the effect of collisional quenching on fluorescence efficiency must also be considered. For a given imaging system and laser irradiance, the OH-PLIF signal, S_{OH} , from each pixel volume is proportional to the number density of OH, N_{OH} , and the fluorescence efficiency, η .²⁶

$$S_{OH} \approx N_{OH} \eta = N_{OH} \frac{A_{OH}}{A_{OH} + Q_{OH}} \quad (1)$$

The fluorescence efficiency is proportional to the rate of spontaneous emission, A_{OH} , from molecules in the excited state and inversely proportional to the rate at which excited molecules are depleted via spontaneous emission and collisional quenching, Q_{OH} . Collisional quenching is a function of the temperature-, pressure-, and species-dependent quenching coefficient as well as the number density of the species.²⁹ As a result of offsetting effects in the equilibrium combustion products of JP-8, the rate of collisional quenching is found to be fairly constant for equivalence ratios of less than unity. Under rich conditions the conversion of CO to CO_2 decreases substantially and leads to an increase in collisional quenching and a decrease in fluorescence efficiency. In regions

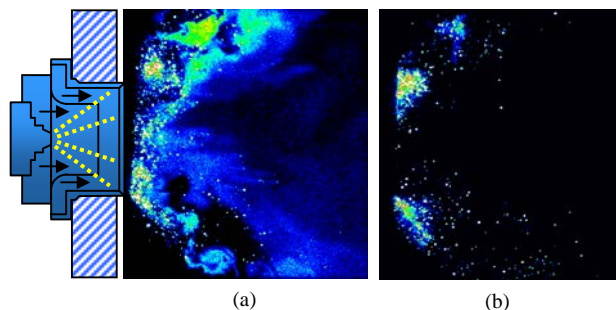


Fig. 3. Raw signal from (a) OH PLIF and droplet Mie scattering while on $Q_1(9)$ line of (1,0) band in A-X system and (b) droplet Mie scattering while off the OH line. Overall $\phi = 0.7$.

where equilibrium assumptions are valid, the LIF signal can be used along with Eqn. 1 and the Boltzmann fraction, F_B , to determine the relative OH number density; this will be discussed further in the results section. In the liquid-spray region where lean and rich pockets of fuel can co-exist, qualitative signal interpretation is problematic since the fluorescence efficiency could vary by more than $\pm 30\%$ based on local conditions.

C. Mie-Scattering

Mie scattering was obtained using the same setup as for the OH-PLIF system. It was found that two WG295 color-glass filters (CVI Laser) and parallel-polarization detection would provide optimal OH LIF sensitivity while minimizing the likelihood of damaging the ICCD because of intense levels of droplet scattering. When tuned off the OH absorption line, as shown in Fig. 3(b), the intense, highly localized droplet scatter can be distinguished from the large, more uniformly distributed OH layers. Large droplet clusters appear primarily near the injector exit, and single droplets with trailing flames are often observed traveling into the recirculation region, as shown in Fig. 3(a). The trailing flames of these droplets do not appear in the off-line images nor at higher equivalence ratios and, therefore, are not attributable to scattering off of fuel vapor or fluorescence from broadband sources such as PAH compounds. The droplet-scattering signal intensity is about one order of magnitude higher than that of the OH PLIF, but it occurs primarily at isolated points. The OH-PLIF signal levels (determined from probability density functions) are assigned to a false-color table from black to red, while the Mie scattering signals are above this range and appear in white.

D. LII System

Some of the first two-dimensional visualizations of soot volume fraction using LII were performed by Santoro and co-workers¹⁵ and by Vander Wal and Weiland.¹⁶ The effects of various parameters such as laser fluence, laser-sheet profile, detection wavelength, camera gate width, and camera gate delay have been explored in a number of follow-up investigations.³⁰⁻³² A list of reviews on the subject is provided by Urban and Faeth.¹² The LII optical layout employed in the current study is shown schematically in Fig. 2, where 50% of the energy from a frequency-doubled Nd:YAG is formed into a sheet using a 2-m plano-convex spherical lens and a -50-mm plano-concave cylindrical lens. The FWHM thickness of the

laser sheet is about 700 μm within the measurement volume, as measured by traversing a knife-edge across the sheet. As is the case for the OH LIF laser sheet, the long 2-m-focal-length lens is used to minimize variations in laser-sheet thickness within the measured region. The sheet width is ~ 14 cm, with a full angle divergence of 6° within the test section. An overall tilt of 5° is used to overlap the LII and PLIF laser sheets. The wings of the LII sheet are clipped prior to the last turning mirror to generate a near top-hat profile that drops to zero laser energy within about 2 mm. To reduce systematic errors due to intensity variations in the laser sheet and due to laser extinction in the measurement volume, the LII system is operated in the saturated regime, measured in the current system to be above 200 mJ/cm^2 . This saturation regime, found at similar fluence levels in the literature,^{30,32} reduces the uncertainty in the relative soot volume fraction measurements to about $\pm 10\%$ for the full width of the laser sheet.

The LII signal is detected using a 1024 \times 1024 ICCD camera (Princeton Instruments PI-MAX SB-MG) and an f/1.2, 58-mm-focal-length glass lens. After 4 \times 4 pixel binning, the measurement resolution is about 575 \times 575 μm^2 . A 500 nm short-pass filter (CVI Laser) is used for detection from 415 to 500 nm, which reduces contributions from nascent soot particles, OH fluorescence/chemiluminescence, and red-shifted fluorescence from PAH compounds. The relatively short-lived PAH fluorescence is also minimized by employing a time-delayed detection scheme. Scattering from the 532-nm laser source is eliminated through the use of a 532-nm zero-degree reflective mirror in addition to the 500-nm short-pass filter and delayed detection. Light leakage from flame luminosity while the ICCD intensifier is gated off is minimized through the use of a 25-ms-gate Uniblitz shutter. During post-processing the residual background signal from flame luminosity is subtracted from each image. A color scale is chosen with a minimum value corresponding to 5% above the background and a maximum value of 100% of the peak in each image.

To optimize the timing of LII detection, data were collected in the swirl-stabilized flame for a number of camera-intensifier-gate delays and widths. A camera delay of 20 ns after the laser pulse was found to reduce laser scatter to nearly the background level while maintaining LII signal-to-noise ratios greater than 20:1. The LII signal decayed quickly within the first 200 ns after the laser pulse. The long decay in signal after 200 ns is dominated by larger, slow-cooling particles. Using a gate width of 50 ns, errors due to particle size effects are estimated to be on the order of 5-10%.³⁰

E. Combined LIF/LII System

The OH-PLIF and LII cameras are synchronized using an external delay generator driven by the advanced Q-switch TTL output of the Nd:YAG laser. The precise camera delay required to capture each image is imposed using an onboard timing generator in each ICCD controller. The laser pulses are coincident to within several nanoseconds so that no fluid movement occurs between LIF and LII detection. Because of spatial constraints within the test cell, both cameras are positioned on the same side of the combustor at slight 3.5° angles to overlap the two imaged regions. The PLIF image area overlaps the left half of the LII image nearest the injector cup in order to minimize off-axis defocusing. After camera alignment, registration images are collected for use in post-processing.

RESULTS AND DISCUSSION

A. Average and Instantaneous Flame Structure

The average and instantaneous OH distributions at overall equivalence ratios (ϕ) ranging from 0.5 to 1.15 are shown in Figs. 4(a) to 4(f). All images are background subtracted and corrected for laser-sheet intensity variations and laser-sheet divergence. The effect of laser attenuation is evident in the lower flame region, with signal levels that are 10% less than the upper flame region. The false color scale is common for all images and varies from 5% to 100% of the maximum OH signal as determined by probability density functions at $\phi = 0.5$.

Two main features of the flame structure become apparent when analyzing the series of images in Fig. 4. The first is that the flame structure evolves from a single- to multi-layer reaction zone. The second is the prominent role that turbulence plays in determining this structure.

A classical five-zone description of pressure-jet hollow-cone spray combustion³³ consists of a dense spray, primary flame zone, rich-premix zone, rich secondary combustion zone, and a recirculation zone. The dense spray region in the near field is dominated by fuel vapor and cannot support combustion. The primary zone is formed by the combustion of fuel vapor from small droplets. A rich-premix zone is then formed along the spray direction due to evaporation of larger droplets. This is followed by rich combustion and product recirculation.

For the current injector geometry, the primary reaction zone is highly perturbed by large-scale structures that entrain reactants across the entire width of the flame layer, as shown in the instantaneous image of Fig. 4(a). At higher overall ϕ , these turbulent motions become more prominent and the primary flame zone, labeled in Fig. 4(c), becomes more intermittent. Also, an intermittent rich-premix region is formed along the inner cone of the spray, as labeled in Fig. 4(c). This region comes into direct contact with the recirculation zone and reacts with any available oxygen, thereby establishing a secondary flame zone as labeled in Fig. 4(c). At overall $\phi = 0.5$, the primary and secondary reaction zones are essentially merged, and a gradual separation in the flame layers takes place at higher equivalence ratios. This phenomenon is most visible in the lower half of the average image in Fig. 4(d), where the primary and secondary reaction zones are completely separated by the rich-premix zone. Since the air-flow rate is held constant for all test conditions in this study, these dynamics may be attributable to the behavior of the liquid spray as the injection pressure is increased, as well as to changes in local equivalence ratio. Experiments and computations based on gaseous-fuel injection, therefore, may not capture this behavior.

To further elucidate the role of intermittency and the character of the rich-premix region, it is useful to present probability density functions (PDFs) of the OH-PLIF signal. PDFs are mathematically defined as histograms with areas normalized to unity. They are helpful in highly intermittent flames for which the ensemble average does not accurately represent the instantaneous field. For example, they can be used to detect whether an increase in OH signal results from an increase in OH within large-scale structures or from an increase in their frequency of occurrence. They can also be used to discriminate against Mie scattering, which occurs with much higher camera counts than the OH PLIF.

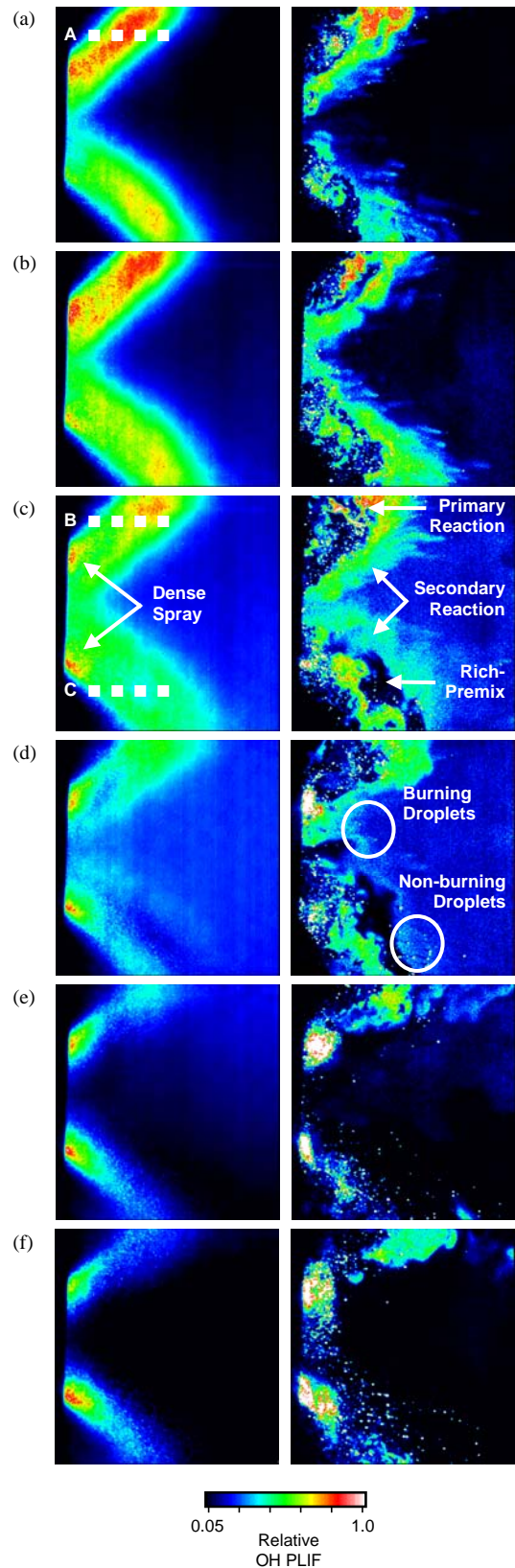


Fig. 4. 200-shot average (left) and instantaneous (right) OH-PLIF images at overall ϕ of (a) 0.5, (b) 0.6, (c) 0.7, (d) 0.8, (e) 1.0, and (f) 1.15. False-color scale from 5% to 100% of the peak average (4100) and instantaneous (5250) counts at $\phi = 0.5$.

Figures 5(a) and 5(b) show PDF data for overall $\phi = 0.5$ and 0.7, respectively, across the upper flame zone just above the dense spray, as shown in Fig. 4. Each profile in Fig. 5 represents a different downstream position, as noted in the legend. At each point, signals from 0 to 6000 counts from 200 images are tabulated into bins of 200 counts. The contribution from droplet scattering, which typically occurs with tens of thousands of counts per pixel, is not significant at these locations since the PDFs drop to zero by 5000-6000 counts.

The PDF profiles for overall $\phi = 0.5$ in Fig. 5(a) change significantly from 12 - 34.8 mm because of changes in large-scale structure dynamics across the flame. The PDFs at 12 and

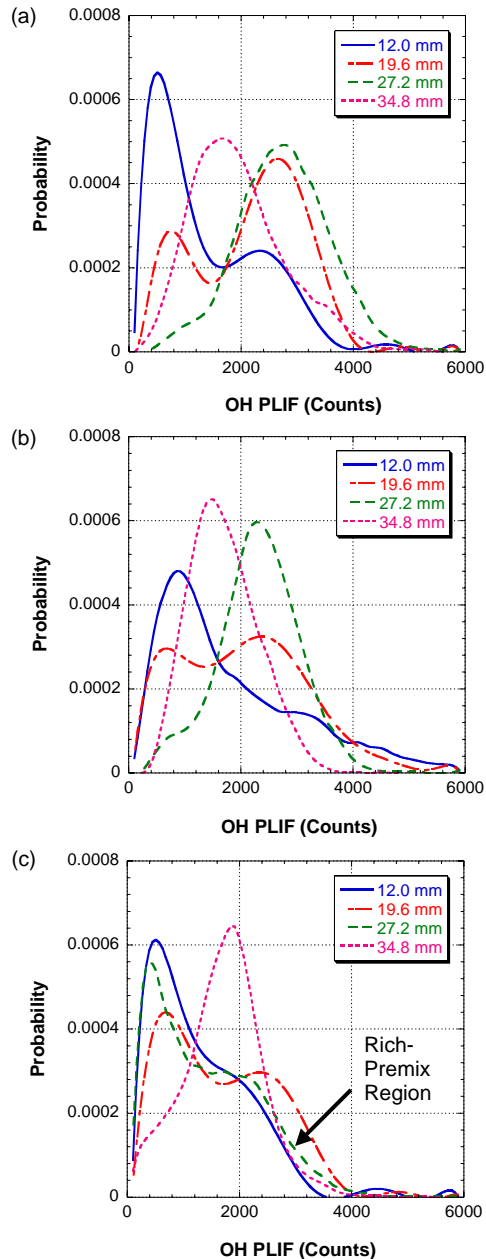


Fig. 5. Probability density functions of OH PLIF at (a) Line A, (b) Line B, and (c) Line C as marked in Fig. 4.

19.6 mm are bimodal in character, with the low-signal peak representing cases when the measurement point is outside of a flame structure and the high-signal peak representing cases when the measurement point is within a flame structure. As one crosses the center of the flame layer, the PDFs are increasingly weighted toward the high-signal peak such that the low signal peak is almost not visible at 27.2 mm. Note that both the low and high signal peaks remain “stationary” from 12 mm to 27.2 mm, indicating that the fluid composition within the large scale-structures is nearly constant in this region. Beyond this point, the PDFs take on a “marching” character. Specifically, the PDF profiles are shifting to lower signal levels. This indicates that the influence of large-scale entrainment of unburned reactant is reduced in this region. Strikingly similar behavior is found in the PDFs of non-reacting turbulent jets, with stationary PDFs in regions dominated by large-scale structures and marching PDFs in regions dominated by gradient mixing.^{34,35}

The PDF profiles for the upper flame at overall $\phi = 0.7$ follow the same trends as for those at overall $\phi = 0.5$. This is evident in Fig. 5(b) in which the PDFs from $x = 12 - 27.2$ mm are weighted more and more to the high-signal peak. The PDFs for the lower flame in Fig. 5(c), however, mark the emergence of the rich-premix zone at 27.2 mm. Rather than shifting to the high-signal peak, the PDF profile at this location shifts back to the low signal peak and is similar to the profile shown at 12 mm. This indicates that the rich-premix region between the primary and secondary zones is similar in terms of large-scale structure dynamics to the unburned reactant layer along the outer cone of the spray flame.

B. Soot Formation Process

While understanding the average and instantaneous flame structure is important for the purpose of validating turbulent models of gas turbine combustion, another main goal of the current analysis is to determine how soot is formed in swirl-stabilized liquid-spray flames. In particular, it is of interest to determine the location of soot inception, how it evolves, and the dynamic behavior that controls the rate of soot production. Based on the results reported by Shaddix et al.¹⁴ in forced flames, it is likely that the turbulent flow structure reported in the previous section will have a significant impact on soot production.

Figures 6(a) – 6(c) show simultaneous images of OH PLIF and soot volume fraction from LII at overall $\phi = 0.8, 1.0$, and 1.15. The OH-PLIF images have the same false color scale shown in Fig. 4, while the LII signal is plotted using color contours defined by a reverse color scale shown in Fig. 6. Analysis of these images reveals an inverse correlation between soot volume fraction and OH-PLIF signal. An exception is in the dense spray region where low levels of LII interference are detected due to residual droplet scattering. Increasing the time delay for LII detection reduces this scatter but also significantly reduces the detection of soot incandescence. Instead it is sufficient to note that most of the LII signal is detected in regions that are free of droplet Mie scattering (as detected with the OH-PLIF camera) and is attributable to the presence of soot. The LII signal is also not likely to come from PAH fluorescence, which would appear more consistently and have peak signals near the spray region. Background images

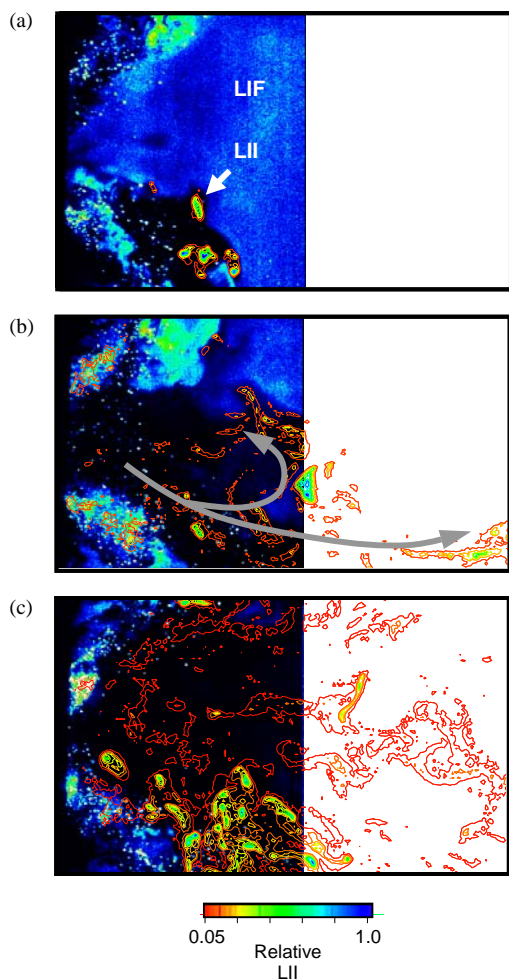


Fig. 6. Overlay of OH-PLIF and LII images at overall ϕ of (a) 0.8, (b) 1.0, and (c) 1.15. OH-PLIF false-color map same as for Fig. 4. LII shown in false-color contours from 5% to 100% of the peak signal in each image.

collected without the laser sheet show that the contribution from nascent soot incandescence is less than 5%.

For all flow conditions studied here, soot is most often generated along the inner cone of the flame. Not unexpectedly, this corresponds to the intermittent rich-premix zone discussed in the previous section. This is particularly evident in Fig. 6(a), where soot is shown propagating out of this region and into the recirculation zone. It is interesting to note that soot is seldom observed within intermittent regions of low OH signal in the primary zone. This is not surprising since there are likely to be higher levels of oxygen and OH available for soot oxidation in this region.

From observation of simultaneous OH-PLIF and LII data, as shown in Fig. 6, it is evident that the rate of soot production increases significantly with overall equivalence ratio. The mechanisms for this increased production can now be assessed given knowledge of how the soot is formed and how it evolves. As noted in the previous discussion, large-scale turbulent motions increase the prominence of the rich-premix zones as the injection pressure is increased. In addition, the secondary reaction zone is weakened as the equivalence ratio in the

recirculation zone increases. Even at lower overall equivalence ratios, intermittency can result in locally rich regions within the recirculation zone, particularly in the lower spray region of the current set up. In the lower flame of Fig. 6(a), for example, there is very little in the way of a secondary reaction zone. In Fig. 4(d), large droplets are shown entering the recirculation zone with burning wakes in the upper half while droplets entering the recirculation zone in the lower half do not. Locally rich conditions allow soot produced in the rich-premix zone to escape the flame layer and undergo a much slower oxidation process.

The sensitivity of the rate of soot production to the local flame structure is illustrated serendipitously in the current work by the asymmetry in the upper and lower halves of the spray flame. As noted earlier, the rich-premix region is much more prominent in frequency and spatial extent in the lower spray region. In fact, soot production takes place almost exclusively in the lower half of the combustor for all equivalence ratios, as shown in Fig. 6. This asymmetry, which could result from misalignment of the injector nozzle, is also detected in time-averaged images of flame emission and is not due to uncertainties in the current measurement system.

C. Applications

The combined use of planar LII and OH PLIF has been shown in the previous discussion to provide valuable physical insight into soot formation in the current flame environment. It is also of interest to determine whether the simultaneous OH-PLIF and LII diagnostic can be useful for tracking changes in flame composition and soot production with various combustor inlet conditions – namely, equivalence ratio and fuel composition. In studies of soot mitigating additives, for example, it is important to determine whether changes in soot production result from changes in the chemical or physical properties of the fuel.

Figures. 7 and 8 demonstrate the ability of the OH-PLIF and LII systems to track local equivalence ratio and soot production, respectively. Using a region in the recirculation zone that is free of droplet scatter, the time- and spatially averaged OH-PLIF signal is computed with respect to equivalence ratio. This provides a calibration for JP-8 that can be used to qualitatively track changes in equivalence ratio. Fig. 7 is not plotted versus overall equivalence ratio, but with respect to an equilibrium calculation²⁷ for JP-8 fuel. The validity of equilibrium assumptions in this region have been proposed in previous investigations of can-type gas turbine combustors.^{3,4} The temperatures and species concentrations from this equilibrium calculation were then used to calculate the effect of LIF efficiency and Boltzmann fraction on OH-PLIF signals. Encouragingly, the fit to the equilibrium calculation is quite good, even under rich conditions for which quenching corrections are most uncertain.

The fit of OH-PLIF signals to equilibrium calculations, shown in Fig. 7, indicates that the *local* equivalence ratio is 13.5% higher than the *overall* equivalence ratio. In other words, stoichiometric conditions in the recirculation zone are expected for *overall* equivalence ratios of $\phi = 0.88$. This is not surprising since images collected at these equivalence ratios show a transition from burning to non-burning wakes behind droplets that enter the recirculation zone. Differences in local and overall equivalence ratio may be partially due to air from the

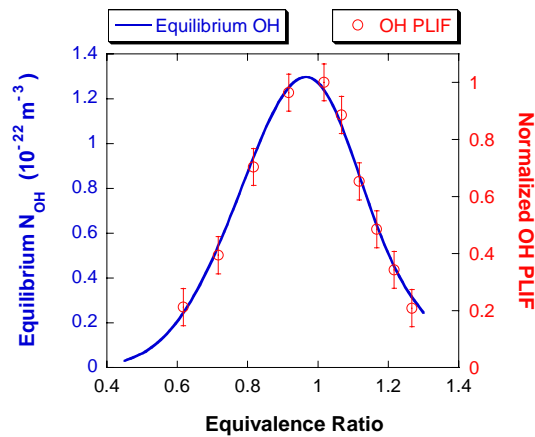


Fig. 7. Equivalence-ratio dependence of equilibrium OH number density compared with OH-PLIF data in the recirculation zone. Confidence intervals set to $\pm 5\%$ of the peak value.

aspiration holes of the aft wall escaping the primary flame zone or due to incomplete mixing in the primary flame-recirculation region.

In Fig. 8, the temporally and spatially averaged relative soot volume fraction is plotted as a function of overall equivalence ratio for the current spray flame. The LII data show an exponential rise in soot volume fraction with equivalence ratio. The sampling probe displays a threshold effect at about $\phi = 1.0$, below which soot in the exhaust is effectively oxidized due to long residence times and the presence of excess air. In the primary zone of the combustor, there is less time to oxidize the soot. In addition, the primary zone is locally higher in equivalence ratio than in the exhaust.

Fig. 8 also shows the results of an LII experiment performed with a longer gate width of 200ns as opposed to 50ns. This was performed to assess the sensitivity of the data to particle-size effects -- a bias toward higher particle sizes would be expected for the longer gate duration of 200 ns. Because of normalization, this bias appears as a slight decrease in signal at lower equivalence ratios for which particle sizes are expected to be smaller. The effect appears to be minimal, indicating that detection with a 50 ns gate is also free of particle-size effects.

Since the dependence of soot on equivalence ratio is exponential, slight changes in equivalence ratio could easily be mistaken for changes in soot particle counts in the exhaust stream. This highlights the importance of tracking equivalence ratio while performing studies of soot-mitigating additives. An example is shown in Fig. 9 where methyl acetate is added to the fuel during a test. Note the large decrease in soot volume fraction during methyl-acetate addition, as measured by LII; this corresponded to a large decrease in particle counts from the sampling probe. Note also the increase in OH-PLIF signal; according to the results of Fig. 7, this indicates that the fuel mixture which initially had an overall $\phi = 1.05$ (local $\phi = 1.19$) is becoming leaner. A certain ambiguity exists, however, because the final equivalence ratio could lie on either side of the peak OH signal. Using the exponential fit to the data in Fig. 8, however, the change in LII signal corresponds to an

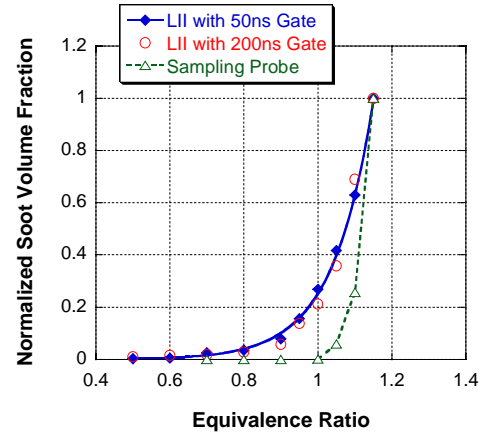


Fig. 8 Effect of overall ϕ on normalized soot volume fraction. LII measurements using a camera gate of 50 ns are fit with an exponential function. Data from sampling probe acquired at exit of exhaust nozzle.

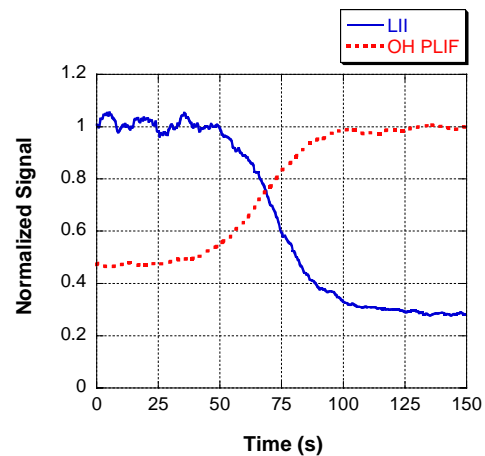


Fig. 9. Effect of methyl acetate ($C_3H_6O_2$) addition to JP-8 fuel on LII and OH-PLIF signals in primary flame zone of swirl-stabilized combustor. Signals averaged for 100 shots.

equivalence ratio that is slightly on the rich side of the OH peak. An overall equivalence-ratio decrease of 0.123 due to methyl-acetate addition is measured to within 1% for both the OH-PLIF and LII data, and to within 10% of flow calculations. The agreement between OH-PLIF and LII data indicates that methyl acetate in the current work did not have an effect on soot production, except for its effect on equivalence ratio. One can envision, therefore, the use of a combined LIF and LII system to track the performance of soot-mitigating additives without uncertainties in equivalence ratio.

SUMMARY

A simultaneous OH-PLIF and planar LII system was developed, tested, and demonstrated in a JP-8-fueled, liquid-spray swirl-stabilized combustor. These combined diagnostics provide phenomenological evidence of soot-formation

mechanisms in this highly turbulent environment by mapping the instantaneous flame zone and soot volume fraction.

It was found that large-scale structures play a key role in the soot formation process. Intermittent regions of rich premixed regions of fuel and air develop between the primary flame layer and recirculation zone that serve as sites for soot inception. The rate of soot production is dependent upon the frequency and spatial extent of these regions; the rate of soot oxidation is dependent upon the presence of a secondary reaction zone as well as the availability of oxygen and OH in this zone. Hence, the overall soot volume fraction may be highly sensitive to the dynamics of the injection process as well as to the local, unsteady equivalence ratio. Experimental and numerical studies in gaseous combustors may not capture these dynamics properly.

The utility of the OH-PLIF and LII system was also demonstrated for studies of soot formation with fuel-mitigating additives. OH PLIF is used to assess changes in flame structure and to track qualitative changes in local equivalence ratio. LII is used to track the time- and spatially averaged soot volume fraction.

The use of these combined diagnostics provides unique information on the soot formation process in highly turbulent two-phase flows and represents a unique application to practical combustors. To permit more definitive conclusions concerning the initiation of soot formation, future effort will include the use of double-pulse laser operation to image soot evolution.

ACKNOWLEDGMENTS

We thank Matthew Dewitt, Mike Arstinstall, and Chuck Frayne for technical assistance with the combustor facility. We also gratefully acknowledge useful discussions with Viswanath Katta regarding soot formation in unsteady flames. Funding for this research was provided by the U. S. Air Force Research Laboratory, Propulsion Directorate, Wright-Patterson AFB, under Contract Nos. F33615-00-C-2068, F33615-D-03-M2829, and F33615-00-C-3020, and by the Air Force Office of Scientific Research [Program Monitor: Dr. Julian Tishkoff].

REFERENCES

- Kim, W.-W., Menon, S., and Mongia, H. (1999), "Large-eddy simulation of a gas turbine combustor flow," *Combust. Sci. Technol.* 143:25-62.
- Wang, S., Hsieh, S.-Y., and Yang, V., "Numerical simulation of gas turbine swirl-stabilized injector dynamics," AIAA paper 2001-0334, 2001.
- Heitor, M. V., and Whitelaw, J. H. (1986), "Velocity, Temperature, and Species Characteristics of the Flow in a Gas-Turbine Combustor," *Combust. Flame* 64:1-32.
- Bicen, A. F., Tse, D. G. N., and Whitelaw, J. H. (1990), "Combustion characteristics of a model can-type combustor," *Combust. Flame* 80:111-125.
- Held, T. J., Mueller, M. A., Li, S.-C., and Mongia, H., "Data-driven model for NO_x, CO and UHC emissions for a dry low emissions gas turbine combustor," AIAA paper 2001-3425, 2001.
- Eckerle, W. A., "Soot loading in a generic gas turbine combustor," AIAA paper 87-0297, 1987.
- Fang, T. C., Megaridis, C. M., Sowa, W. A., and Samuelsen, G. S. (1998), "Soot morphology in a liquid-fueled swirl-stabilized combustor," *Combust. Flame* 112:312-328.
- Snelling, D. R., Thomson, K. A., Smallwood, G. J., and Gulder, O. L. (1999), "Two-dimensional imaging of soot volume fraction in laminar diffusion flames," *Appl. Opt.* 38:2478-1485.
- Black, J. D. (1999), "Laser induced incandescence measurements of particles in aero-engine exhausts," EUROPTO Conference on Environmental Sensing and Applications, Munich, Germany, pp. 209-215.
- Jenkins, T. P., Bartholomew, J. L., DeBarber, P. A., Yang, P., Seitzman, J. M., and Howard, R. P., "A laser-induced incandescence system for measuring soot flux in aircraft engine exhausts," AIAA paper 2002-3736, 2002.
- Santoro, R. J., Yeh, T. T., Horvath, J. J., and Semerjian, H. G. (1987), "The transport and growth of soot particles in laminar diffusion flames," *Combust. Sci. Technol.* 53:89-115.
- Urban, D. L., and Faeth, G. M., "Soot research in combustion science: introduction and review of current work," AIAA paper 2001-0322, 2001.
- Won, Y.-H., Kamimoto, T., Kobayashi, H., and Kosaka, H., "2-D soot visualization in unsteady spray flame by means of laser sheet scattering technique," SAE Tech. Paper 910223, 1991.
- Shaddix, C. R., Harrington, J. E., and Smyth, K. C. (1994), "Quantitative Measurements of Enhanced Soot Production in a Flickering Methane / Air Diffusion Flame," *Combust. Flame* 99:723-732.
- Quay, B., Lee, T.-W., Ni, T., and Santoro, R. J. (1994), "Spatially Resolved Measurements of Soot Volume Fraction Using Laser-Induced Incandescence," *Combust. Flame* 97:384-392.
- Vander Wal, R. L., and Weiland, K. J. (1994), "Laser-induced incandescence: Development and characterization towards a measurement of soot-volume fraction," *Appl. Phys. B* 59:445-452.
- Brown, M. S., Meyer, T. R., Gord, J. R., Belovich, V. M., and Roquemore, W. M., "Laser-induced incandescence measurements in the reaction zone of a model gas turbine combustor," AIAA paper 2002-0393, 2002.
- Smyth, K. C., Miller, J. H., Dorfman, R. C., Mallard, W. G., and Santoro, R. J. (1985), "Soot inception in a methane/air diffusion flame as characterized by detailed species profiles," *Combust. Flame* 62:157-181.
- Cignoli, F., Benecchi, S., and Giorgio, Z. (1992), "Simultaneous one-dimensional visualization of OH, polycyclic aromatic hydrocarbons, and soot, in a laminar diffusion flame," *Opt. Lett.* 17:229-231.
- Shih, W.-P., Lee, J. G., and Santavicca, D. A. (1996), "Stability and emissions characteristics of a lean premixed gas turbine combustor," in the Twenty-Sixth Symposium (International) on Combustion (The Combustion Institute), pp. 2771-2778.
- Foglesong, R. E., Frazier, T. R., Flamand, L. M., Peters, J. E., and Lucht, R. P., "Flame structure and emissions characteristics of a lean premixed gas turbine combustor," AIAA paper 99-2399, 1999.
- Lucht, R. P., Sweeney, D. W., and Laurendeau, N. M. (1983), "Laser-saturated fluorescence measurements of OH concentration in flames," *Combust. Flame* 50:189-205.

23. Carter, C. D., King, G. B., and Laurendeau, N. M. (1992), "Saturated fluorescence measurements of the hydroxyl radical in laminar high-pressure C₂H₆/O₂/N₂ flames," *Appl. Opt.* 31:1511-1522.
24. Roy, S., Meyer, T. R., Lucht, R. P., Belovich, V. M., Corporan, E., and Gord, J. R., "Temperature and CO₂ concentration measurements in the exhaust stream of liquid-fueled combustor using dual-pump coherent anti-Stokes Raman scattering (CARS) spectroscopy," submitted for publication in *Combust. Flame*, 2003.
25. Lee, K., and Chehroudi, B. (1995), "Structure of a swirl-stabilized spray flame relevant to gas turbine and furnaces," *J. Prop. Power* 11:1110-1117.
26. Eckbreth, A. C. (1996), "Laser diagnostics for combustion temperature and species," 2nd Ed., Gordon and Breach Publishers, The Netherlands.
27. Turns, S. R. (1996), "An Introduction to Combustion," McGraw-Hill, New York.
28. Lefebvre, A. H. (1999), "Gas turbine combustion," 2nd Ed., Taylor and Francis, Philadelphia, PA.
29. Tamura, M., Berg, P. A., Luque, J., Harrington, J. E., Smith, G. P., Jeffries, J. B., and Crosley, D. R. (1998), "Collisional quenching of NO A, CH A, and OH A in low pressure hydrocarbon flames," *Combust. Flame* 114:502-514.
30. Ni, T., Pinson, J. A., Gupta, S., and Santoro, R. J. (1995), "Two-dimensional imaging of soot volume fraction by the use of laser-induced incandescence," *Appl. Opt.* 34:7083-7091.
31. Bryce, D. J., Ladommatos, N., and Zhao, H. (2000), "Quantitative investigation of soot distribution by laser-induced incandescence," *Appl. Opt.* 39:5012-5022.
32. Michelsen, H. A. (2003), "Understanding and predicting the temporal response of laser-induced incandescence from carbonaceous particles," *J. Chem. Phys.* 118:7012-7045.
33. Chigier, N. A. (1976), "The atomization and burning of liquid fuel sprays," *Prog. Energy Combust. Sci.* 2:97-114.
34. Karasso, P. S., and Mungal, M. G. (1997), "Scalar mixing and reaction in plane liquid shear layers," *J. Fluid Mech.* 323:23-63.
35. Meyer, T. R., Dutton, J. C., and Lucht, R. P. (2001), "Experimental study of the mixing transition in a gaseous axisymmetric jet," *Phys. Fluids* 13:3411-3424.

Temperature and CO₂ concentration measurements in the exhaust stream of a liquid-fueled combustor using dual-pump coherent anti-Stokes Raman scattering (CARS) spectroscopy

Sukesh Roy^{a,*}, Terrence R. Meyer^a, Robert P. Lucht^b, Vincent M. Belovich^c,
Edwin Corporan^c, James R. Gord^c

^a Innovative Scientific Solutions, Inc., 2766 Indian Ripple Road, Dayton, OH 45440, USA

^b Department of Mechanical Engineering, Purdue University, West Lafayette, IN 47907, USA

^c Air Force Research Laboratory, Propulsion Directorate, Wright-Patterson Air Force Base, OH 45433, USA

Received 18 August 2003; received in revised form 6 April 2004; accepted 20 April 2004

Available online 2 July 2004

Abstract

Single-shot, dual-pump coherent anti-Stokes Raman scattering (CARS) measurements of N₂ and CO₂ were performed in the exhaust stream of a swirl-stabilized JP-8-fueled combustor under sooting conditions. The combustor is designed to study particulate formation and particle-size distributions for different flame conditions and therefore is operated at near-stoichiometric overall fuel–air ratios. Various jet fuels and additive concentrations were studied. These conditions pose a significant challenge for temperature measurements using standard N₂ CARS due to strong flame emission and absorption of the CARS signal by the C₂ Swan band. With the dual-pump CARS technique employed in this study, the N₂ CARS signal is generated at a wavelength (496 nm) that is not absorbed by C₂, and concentration measurements of CO₂ can be performed. The standard deviations of the single-shot temperature measurements were approximately 3–4% of the mean values for equivalence ratios ranging from 0.4 to 1.1, whereas those of the single-shot CO₂ concentration measurements were between 9 and 20% of the mean values. Previous single-shot temperature and CO₂ concentration measurements using dual-pump CARS in this liquid-fueled combustor were limited to an equivalence ratio of 0.45, with standard deviations in temperature of about 5–6% of the mean value of 1143 K (Lucht et al., AIAA J. 41 (4) (2003) 679–686). The current study demonstrates a significant improvement in the applicability of single-shot CARS temperature and CO₂ concentration measurements to practical, swirl-stabilized combustors under sooting conditions.

© 2004 The Combustion Institute. Published by Elsevier Inc. All rights reserved.

Keywords: Coherent anti-Stokes Raman scattering; Liquid-fueled combustor; Sooting flames; Temperature measurements

1. Introduction

Coherent anti-Stokes Raman scattering (CARS) spectroscopy has been widely used for measuring the

temperature and concentration of major species in reacting flows [1]. Measurements have also been performed using CARS to determine the temperature in practical combustors and internal-combustion engines [2–8]. Measurements of temperature using N₂ CARS in practical combustors have the advantage that N₂ is present almost everywhere at high concentrations.

* Corresponding author. Fax: +937-656-4110.
E-mail address: sukesh@innssi.com (S. Roy).

However, applying the N_2 CARS technique to the measurement of temperature in practical combustors is always challenging, mainly due to the following: (1) interference from highly luminous environments, (2) steering of the laser beams due to density gradients, and (3) absorption of the CARS signal by the strong C_2 Swan bands [1,9]. Interference from flame luminosity can be minimized using either a mechanical shutter in front of the spectrometer [10] or an interline-transfer charge-coupled-device (CCD) camera for data acquisition [11]. In practical combustors with highly sooting environments, the effect of beam steering can be greatly reduced by arranging the CARS beams in a collinear fashion rather than in a folded BOXCARS geometry [1]. The absorption of the CARS signal by the strong C_2 Swan band can be avoided by shifting the CARS signal generation to a different wavelength region.

Dual-pump CARS, first proposed by Lucht [12], allows one to shift the N_2 CARS signal output away from 473 nm by shifting one of the pump frequencies away from 532 nm. This technique also allows simultaneous concentration measurements of a second species, such as O_2 , CO_2 , H_2 , or CO , in addition to the temperature measurements. The wavelength of the second pump beam is selected so that the CARS spectra for the two species under study are observed at nearly the same frequency, enabling detection with a single spectrometer and CCD camera and eliminating systematic errors due to the wavelength dependence of the detection-system efficiency. The dual-pump CARS technique has been applied to the simultaneous measurement of N_2 – O_2 [12,13], N_2 – H_2 [14], N_2 – CH_4 [15], and N_2 – CO_2 [16].

The dual-pump CARS technique was applied by Lucht et al. [17] in the exhaust stream of a practical combustor to measure temperature and CO_2 concentration from a single laser shot. However, those measurements were limited to an overall equivalence ratio (ϕ) of less than 0.5. Several other CARS techniques, such as triple-pump CARS [18], dual-broadband rotational CARS [19–21], and simultaneous vibrational and rotational CARS [22–25], have also been used for temperature and multiple-species concentration measurements.

The current N_2 – CO_2 dual-pump CARS system exhibited excellent accuracy for single-shot temperature and CO_2 concentration measurements in an atmospheric-pressure, near-adiabatic hydrogen–air flame seeded with CO_2 and stabilized on a Hencken burner [18]. The standard deviations of the measured single-shot temperatures and the CO_2 concentrations in this calibration flame were approximately 2.3 and 6% of the mean values, respectively, for a wide range of equivalence ratios ($\phi = 0.25$ to $\phi = 1.2$). The objectives of this investigation were to use the same

system as in Ref. [18] to perform single-shot temperature and CO_2 concentration measurements in the exhaust stream of a liquid-fueled practical combustor under sooting conditions. Measurements were performed for a number of different jet fuels and additive concentrations over a wide range of equivalence ratios ($\phi = 0.4$ to $\phi = 1.1$). These measurements are used to provide benchmark temperature and CO_2 statistical distributions in the exit plane of the combustor and to evaluate the effects of particulate-mitigating additives on flame chemistry. These measurements are also used to assess the viability of future dual-pump CARS measurements in the reaction zone of the combustor under sooting conditions. These data complement laser-induced incandescence (LII) and planar laser-induced fluorescence (PLIF) measurements of soot volume fraction and OH-radical concentrations, respectively, which are ongoing in the current combustor.

2. Experimental setup

2.1. Atmospheric-pressure, swirl-stabilized combustor

The planar sector rig, shown in Fig. 1a, is used in the Atmospheric-Pressure Combustor Research Complex of the U.S. Air Force Research Laboratory to study the performance characteristics of model gas-turbine-engine combustors. In addition to conventional temperature and sampling probes, it has optical access on three sides for in situ laser-based diagnostics. The air-flow system consists of three Sierra 5600 SLPM mass-flow controllers with $\pm 1\%$ full-scale accuracy and is capable of supplying up to 14,200 SLPM of heated air at 530 K. In this investigation air to the combustor was heated to 450 K, and the flow rate was held constant at approximately 0.0283 kg/s. The air-pressure drop across the combustor dome was approximately 5% of the main supply. The fuel system is capable of supplying both liquid and gaseous fuels and is configured for the current effort to study the performance characteristics of jet-fuel variants and particulate-mitigating additives using a single swirl-cup injector similar to a General Electric CFM56. The fuel flow rate is measured using a Max Machinery positive-displacement flow meter with $\pm 0.5\%$ full-scale accuracy. Changes in equivalence ratio from 0.4 to 1.1 are achieved by varying the pressure drop across the fuel-spray nozzle from 0.9 to 8.2 atm, resulting in fuel mass-flow rates of 0.8 to 2.1 g/s. The injector and the (15.25 \times 15.25)-cm cross-section flame tube are designed to simulate the swirl-stabilized flame structure and residence time of a conventional gas-turbine-

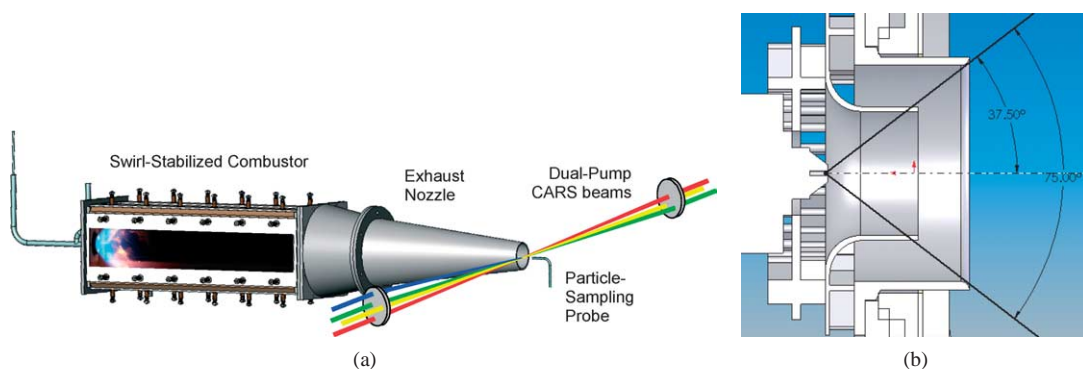


Fig. 1. (a) Illustration of the atmospheric-pressure, swirl-stabilized combustor used for studies of jet-fuel variants and particulate-mitigating additives. The dual-pump CARS probe volume for measurements of temperature and CO_2 concentration is placed at the exit plane of the exhaust nozzle just upstream of the particle-sampling probe. (b) Schematic diagram of the swirl-injector geometry used in this study.

engine combustor. A schematic diagram of the swirl injector used in this study is shown in Fig. 1b. The swirl-cup liquid-fueled injector used in the current study employs pressure atomization and dual-radial counter-swirling-air co-flows to entrain the fuel, promote droplet break-up, and enhance mixing. After exiting the primary flame zone, the combustion products are allowed to mix thoroughly along the 48-cm-long flame tube before entering a 43-cm long, 5.7-cm exit-diameter exhaust nozzle designed to create a uniform exhaust-gas temperature and concentration profile.

The performance characteristics of three jet-fuel variants were studied, including JP-8, JP-8X45, and a semi-synthetic jet fuel. Each has a different hydrogen-to-carbon ratio and aromatic content, as discussed further below. In addition, data were collected for various additive candidates consisting of organophosphates, organometallics, and other compounds used for particulate mitigation. A particle-sampling probe was placed at the exit of the convergent exhaust nozzle to extract and transport the sample to the particulates instrumentation for measuring the number density, mass, and size distribution of soot compounds simultaneously with the CARS temperature and concentration data.

In Fig. 1a flow is from left to right, and the injector swirl cup can be seen in the back wall of the combustor. Chemiluminescence from CH (light blue) appears near the cup, along with soot luminescence (light red). The dual-pump CARS measurement volume, defined by the focal point and laser-beam crossing location, was placed at the center of the exhaust-nozzle exit plane, just upstream of the particle-sampling probe. At higher equivalence ratios (>0.7), thermal loading from flame radiation becomes significant, and it is necessary to thermally isolate the CARS optics and detection system. Failure to do so results in progressive deterioration of the CARS signal-to-noise ratio.

After final beam-alignment procedures and thermal isolation, dual-pump CARS data were typically collected for several hours with minimal adjustments to the optical system.

2.2. Dual-pump CARS system

The experimental schematic and energy-level diagrams of the dual-pump CARS system for the simultaneous detection of N_2 and CO_2 molecules are shown in Figs. 2a and 2b, respectively. An injection-seeded Nd:YAG laser (Spectra Physics Pro 290) is used to pump a narrowband dye laser and a broadband dye laser while also providing a 532-nm CARS pump beam. The repetition rate of the Nd:YAG laser is 10 Hz with a pulse width (FWHM) of approximately 10 ns. The frequency spectrum is single-longitudinal-mode due to injection seeding, and the linewidth (FWHM) of the 532-nm output is 0.001 cm^{-1} . The frequency spectrum of the broadband dye laser that serves as the Stokes beam for each of the generated CARS signals is centered at approximately 608 nm with an approximate bandwidth of 200 cm^{-1} . The narrowband dye laser provides laser radiation at approximately 560 nm. The bandwidth of the narrowband dye laser beam is $\sim 0.06 \text{ cm}^{-1}$. The combination of the 532-nm pump beam with the 607-nm Stokes beam produces rovibrational N_2 Raman polarization that coherently scatters the 560-nm pump beam, yielding an N_2 CARS signal near 496 nm. At the same time, the 560-nm pump beam and the 607-nm Stokes beam produce CO_2 Raman polarization that scatters the 532-nm pump beam, yielding a CO_2 CARS signal that also appears near 496 nm. The narrowband dye laser is tuned slightly to spectrally separate the N_2 and CO_2 CARS signals. The energy in each pump beam at the CARS probe volume is approximately 25 mJ, and the energy in the Stokes

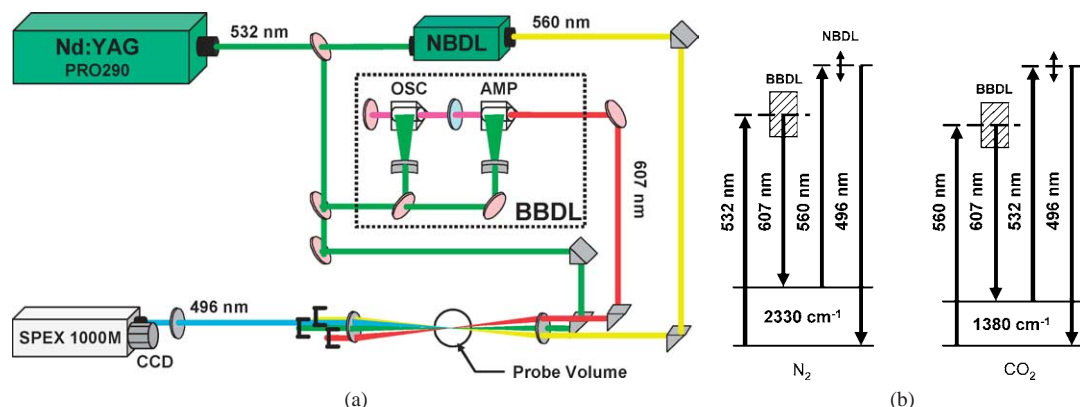


Fig. 2. (a) Schematic diagram of the dual-pump CARS system for the simultaneous measurement of temperature and the concentrations of N_2 and CO_2 at the exhaust stream of a liquid-fueled combustor. (b) Energy-level diagram for the N_2 – CO_2 dual-pump CARS system.

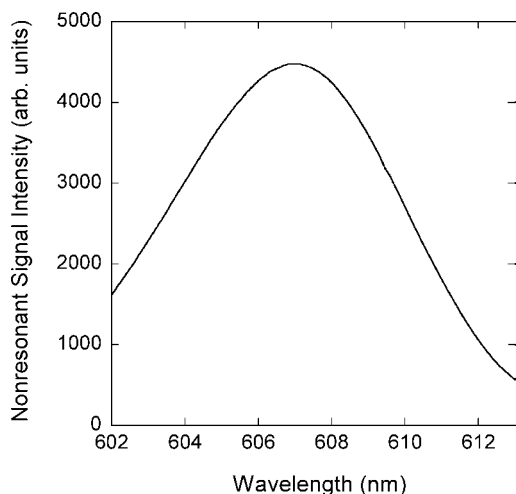


Fig. 3. Typical nonresonant spectrum for the CARS setup. The spectrum was acquired by placing the CARS probe volume within an open argon flow tube. The spectrum shown above was averaged over 200 laser shots.

beam is approximately 15 mJ. The pump and Stokes beams are arranged in a folded BOXCARS geometry. The laser beams are focused and recollimated using 500-mm focal-length lenses. The estimated spatial resolution of the measurements is $\sim 30 \mu\text{m}$ normal to the beam direction and $\sim 1.5 \text{ mm}$ in the phase-matching direction.

The CARS signals are dispersed by a 1.0-m spectrometer (SPEX 1000M) equipped with a 2400-groove/mm grating. An Andor back-illuminated, unintensified CCD camera (Model DU 440BU) with a (2000×512) -pixel array is used to acquire the CARS signals. The spectral dispersion of the CARS signals is $0.17 \text{ cm}^{-1}/\text{pixel}$, and the resolution of the CARS detection system is approximately 0.54 cm^{-1} .

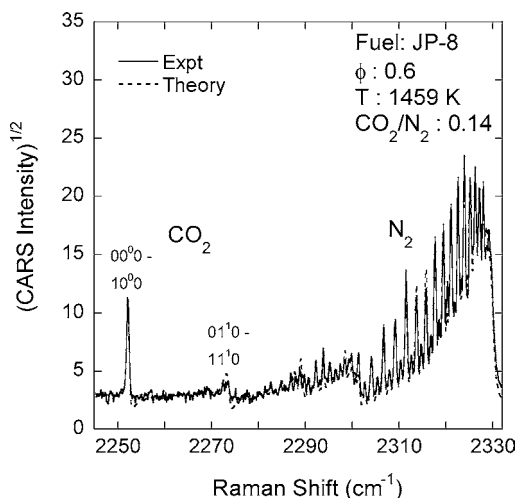


Fig. 4. Single-shot N_2 – CO_2 dual-pump CARS spectrum acquired in the exhaust stream of a JP-8-fueled combustor for an equivalence ratio of 0.6. The solid line represents the experimental spectrum, and the dotted line represents the theoretical spectrum calculated using the Sandia CARSFT code.

The resolution of the CARS system was evaluated by fitting the experimental CARS spectrum from room air with that of a theoretical one using the Sandia CARSFT code [26].

The CARS spectra are normalized using a nonresonant spectrum to account for the effects of spectral variations in dye power [1]. The nonresonant spectrum is recorded by placing the beam-overlap region within an open argon flow tube. A typical nonresonant spectrum for the current setup is shown in Fig. 3. The dye-laser spectrum is very stable over the course of the experiment; the nonresonant spectra acquired on different days are essentially identical.

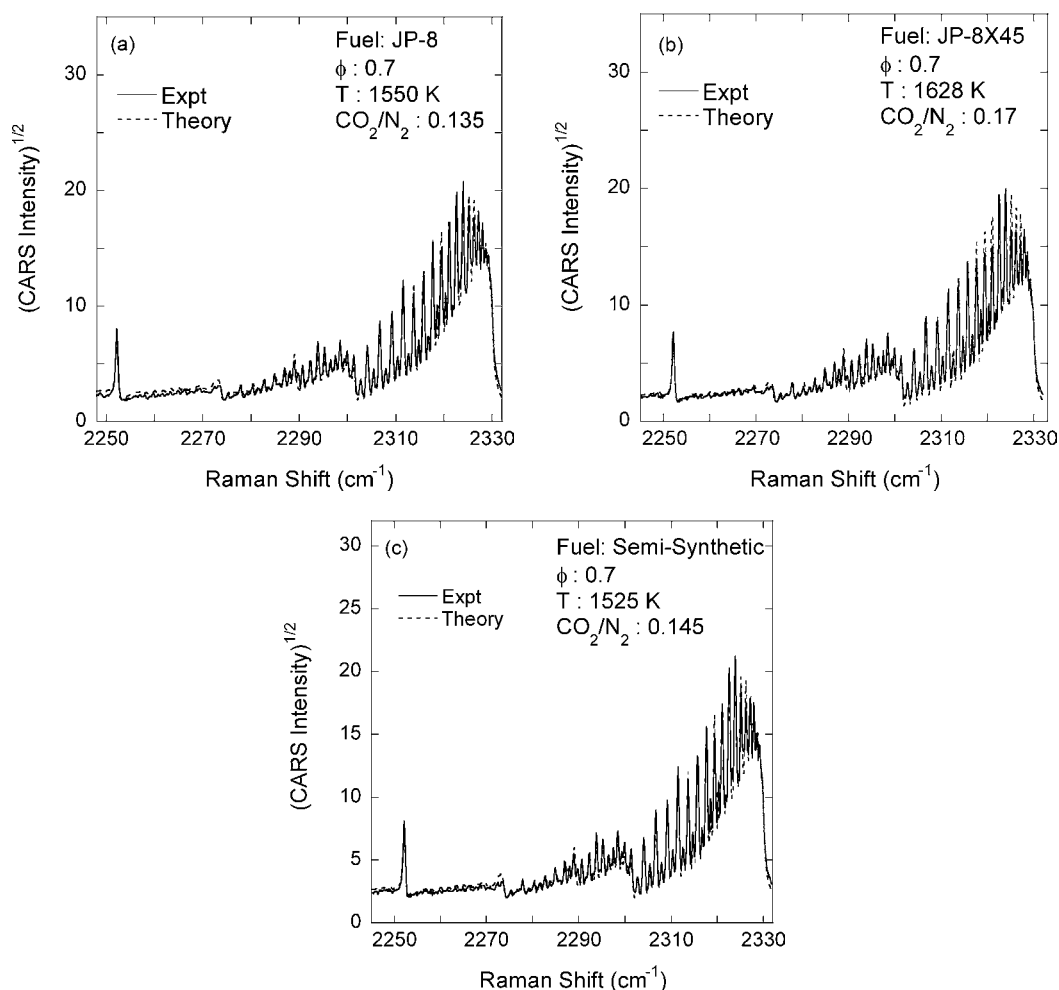


Fig. 5. N_2 – CO_2 dual-pump CARS spectra for three jet fuels for an equivalence ratio of 0.7. Each spectrum was averaged over 100 laser shots.

3. Results and discussion

Temperature and CO_2 concentration measurements were performed in the exhaust stream of the swirl-stabilized liquid-fueled combustor (see Fig. 1) over a wide range of equivalence ratios for the three jet fuels using N_2 – CO_2 dual-pump CARS spectroscopy. This CARS system exhibited excellent accuracy, as determined from temperature and CO_2 concentration measurements in a calibrated flame [18]. The calibrated flame was a laminar, premixed near-adiabatic hydrogen–air flame seeded with CO_2 and stabilized on a Hencken burner. Measurements were performed at atmospheric pressure. The standard deviations of the measured single-shot temperatures and CO_2 concentrations in the calibrated flame were 2.3 and 6% of the mean values, respectively, for a wide range of equivalence ratios [18]. Measurements in the liquid-fueled combustor were performed immediately

after measurements in the calibrated flame without altering the CARS system. The day-to-day repeatability of the dual-pump CARS system for the same combustor-flow conditions was found to be approximately $\pm 1\%$ for measured temperatures and $\pm 2\%$ for measured CO_2 concentrations.

The jet fuels used for this experiment were JP-8, JP-8X45, and semisynthetic fuel. The semisynthetic fuel consists of 50% JET-A and 50% coal-derived compounds. JP-8X45 is a high-energy-density fuel that is high in aromatics and cycloparaffins. JP-8 is standard military jet fuel, which consists of commercial JET-A fuel with additives. The carbon-to-hydrogen ratios for JP-8, JP-8X45, and semisynthetic fuels are 0.52, 0.6, and 0.5, respectively. The aromatic content of the JP-8, JP-8X45, and semisynthetic fuels is 15.9, 40.8, and 10.0%, respectively, measured using a standard ASTM D3343-95 method (Annual Book of ASTM Standards, Vol. 05.02, Sect. 5, 1998).

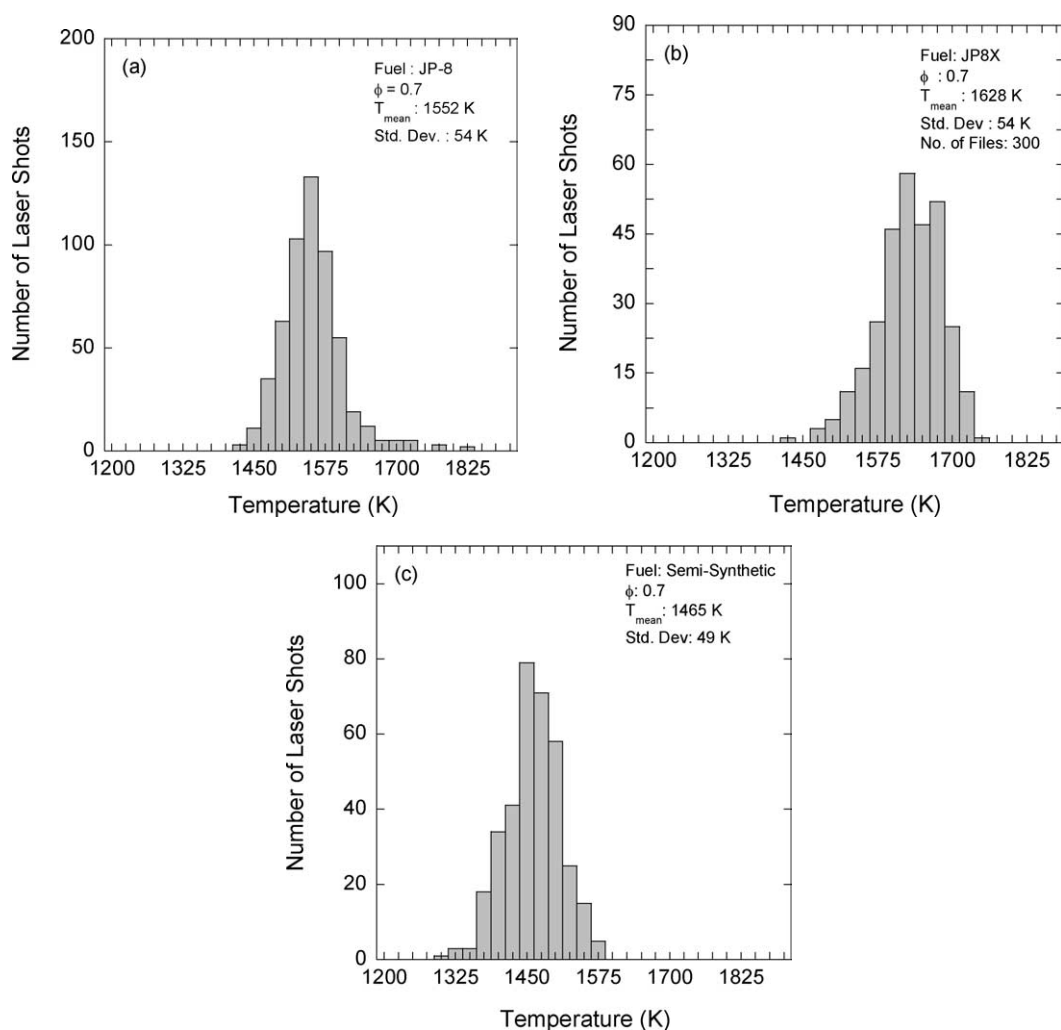


Fig. 6. Probability density functions (PDFs) of temperature determined from single-shot N_2 - CO_2 dual-pump CARS spectra in the exhaust stream of the combustor for three jet fuels for an equivalence ratio of 0.7.

The objectives of this study were to perform single-shot temperature and CO_2 concentration measurements at high equivalence ratios under sooting conditions. Previous single-shot temperature and CO_2 concentration measurements using dual-pump CARS in the exhaust stream of this combustor were limited to an equivalence ratio of 0.45 [17]. Based on the current work, it is concluded that this limitation was primarily due to misalignment of the CARS system at high equivalence ratios due to increased heat loading. This misalignment decreased CARS signal levels, significantly reducing the signal-to-noise ratio. In addition to the work of Lucht et al. [17], conventional coherent anti-Stokes Raman scattering of N_2 has previously been used to measure single-shot temperatures in the reaction zone of a JP-8-fueled combustor under *lean conditions* [2]. The success of the

current measurements under stoichiometric and even rich conditions was achieved by using high-quality optical mounts and by minimizing heat loading of the optical system. Use of ultra-high-resolution mirror mounts (Newport Model 610) for all of the CARS beams helped to increase the signal-to-noise ratio of the N_2 - CO_2 dual-pump CARS signal by at least one order of magnitude. Heat loading to the optics and mounts was minimized significantly by careful heat shielding and also by use of cooling fans at strategic locations. In addition to thermal isolation of the CARS system, increased spatial filtering of the CARS signal beam was necessary to reduce contributions from luminous combustion products at high equivalence ratios. Following these procedures, it was found after combustor shut-down that the room-temperature dual-pump CARS signal was reduced by

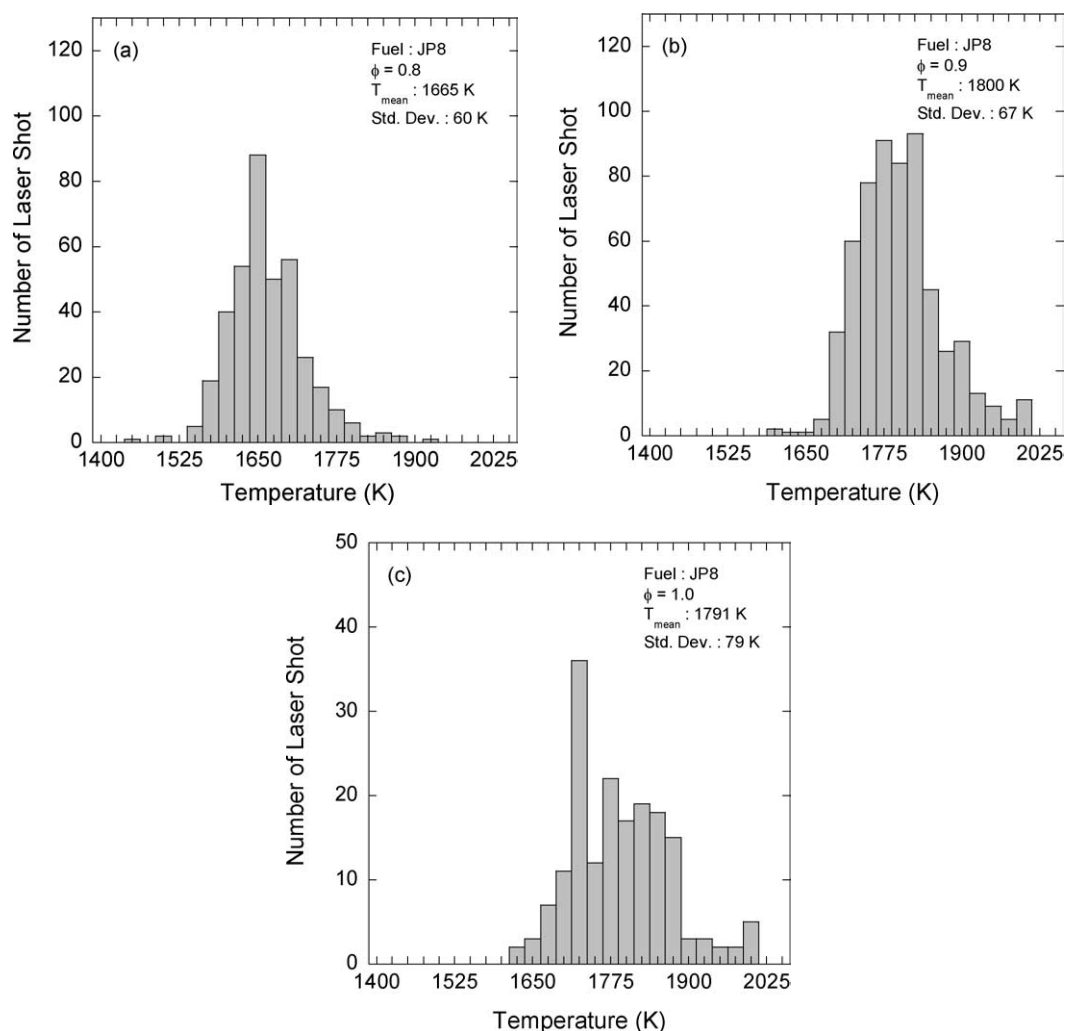


Fig. 7. Probability density functions (PDFs) of temperature determined from single-shot N_2 – CO_2 dual-pump CARS spectra acquired at the exhaust of the JP-8-fueled combustor for three equivalence ratios.

only 20% after approximately 7 h of combustor operation.

A typical single-shot dual-pump N_2 – CO_2 CARS spectrum acquired in the exhaust stream of the JP-8-fueled combustor for an equivalence ratio of 0.6 is shown in Fig. 4. The solid line represents the experimental CARS signal, and the dotted line represents the theoretical CARS spectrum calculated using the Sandia CARSFT code [26]. The temperature and relative CO_2 concentration were evaluated by comparing the experimental spectrum with a theoretical one. Fig. 5 shows the N_2 – CO_2 CARS spectra for the three jet fuels for an equivalence ratio of 0.7. Each spectrum was averaged over 100 laser shots. As is evident from Fig. 5, JP-8X45 produces the highest temperature, likely due to the fuel's high aromatic/carbon content. Semisynthetic fuel, which consists of 50%

coal-derived compounds and 50% JP-8 fuel, is the least sooting among the three (due to its lower aromatic content) and displays the lowest temperature. Temperatures were obtained by fitting only the N_2 part of the spectrum. Probability density functions (PDFs) of the single-shot temperature measurements for the three jet fuels are shown in Fig. 6. The overall equivalence ratio for these measurements was 0.7. The standard deviations of these temperature measurements were within 3–4% of the mean values.

PDFs of temperature and CO_2 and N_2 concentration ratios for the JP-8-fueled combustor derived from single-shot data for three equivalence ratios are shown in Figs. 7 and 8, respectively. CO_2 concentrations are presented with respect to the N_2 concentrations. In CARS, in order to determine the exact concentrations of the interested species one has to know the

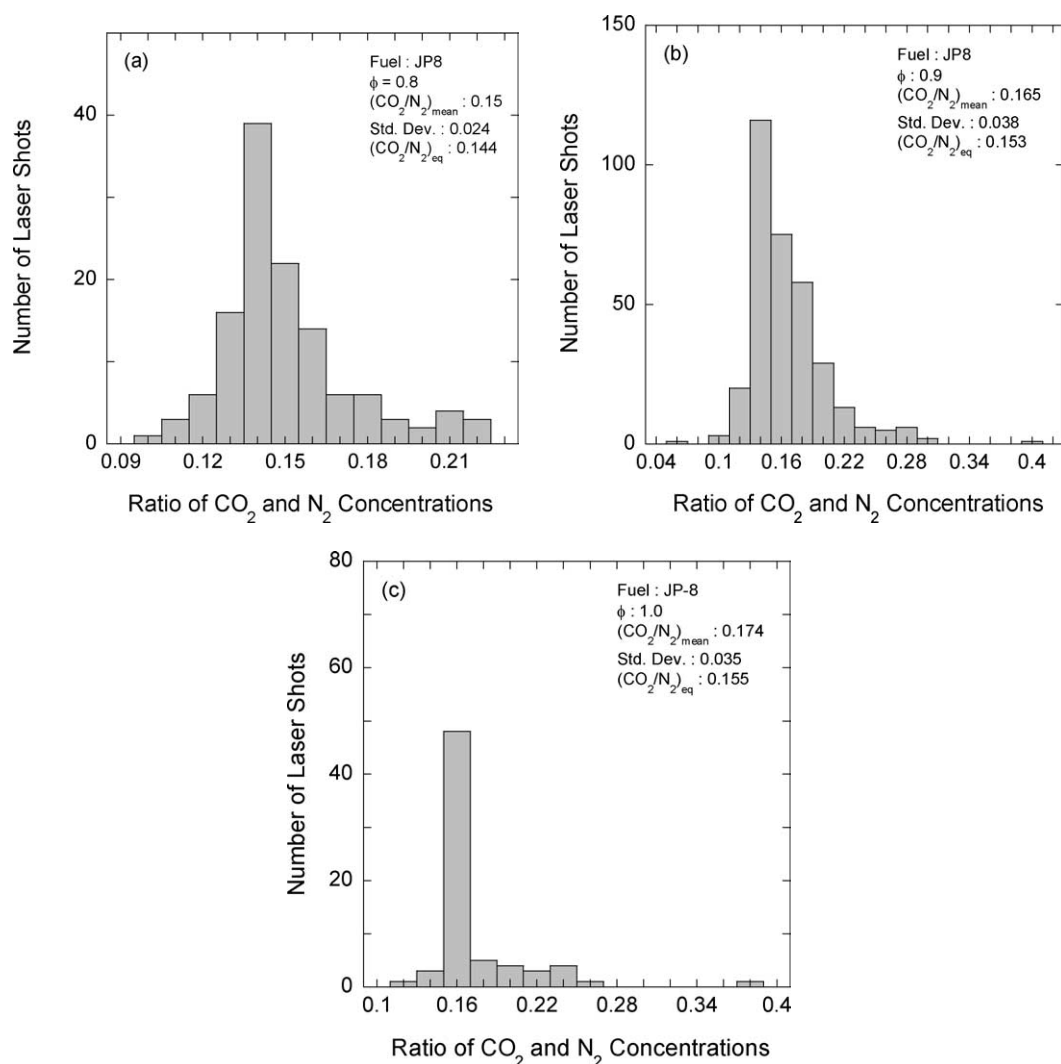


Fig. 8. Probability-density functions (PDFs) of the ratio of CO_2 and N_2 concentrations determined from single-shot N_2 – CO_2 dual-pump CARS spectra acquired at the exhaust of the JP-8-fueled combustor for three equivalence ratios.

nonresonant susceptibility of the medium, which is possible only if most of the major combustion products are known. In practical liquid-fueled combustor, it is almost impossible to know the concentrations of various hydrocarbons and other species, all of which will contribute to the generation of nonresonant signal. That is why in dual-pump CARS the ratio of the concentrations of the two major species is shown, as both species concentrations are determined with respect to the same nonresonant background. One also can get an approximate idea about the mole fraction of the second species if the nitrogen concentration is assumed. In Ref. [17], the authors assumed the nitrogen concentration to be 74% and calculated the CO_2 mole fraction from the evaluated ratio of CO_2 and N_2 concentrations. The liquid-fueled combustor

data shown in Ref. [17] were limited to very low equivalence ratios for which this assumption might be reasonable. The results of near-stoichiometric equivalence ratios presented here are significantly higher than the equivalence ratios of any previous measurements performed in this combustor, single-shot or time-averaged [2,17]. These figures show that the current setup can also be used to acquire flow-field statistics at high equivalence ratios under *unsteady* sooting conditions. The standard deviations for the measured temperatures and CO_2 and N_2 concentration ratios as determined from single-shot, dual-pump N_2 – CO_2 CARS spectra are approximately 3–4 and 9–20% of the mean values, respectively. These standard deviations are larger than those measured in the calibration flame (2.3 and 6%, respectively) due in

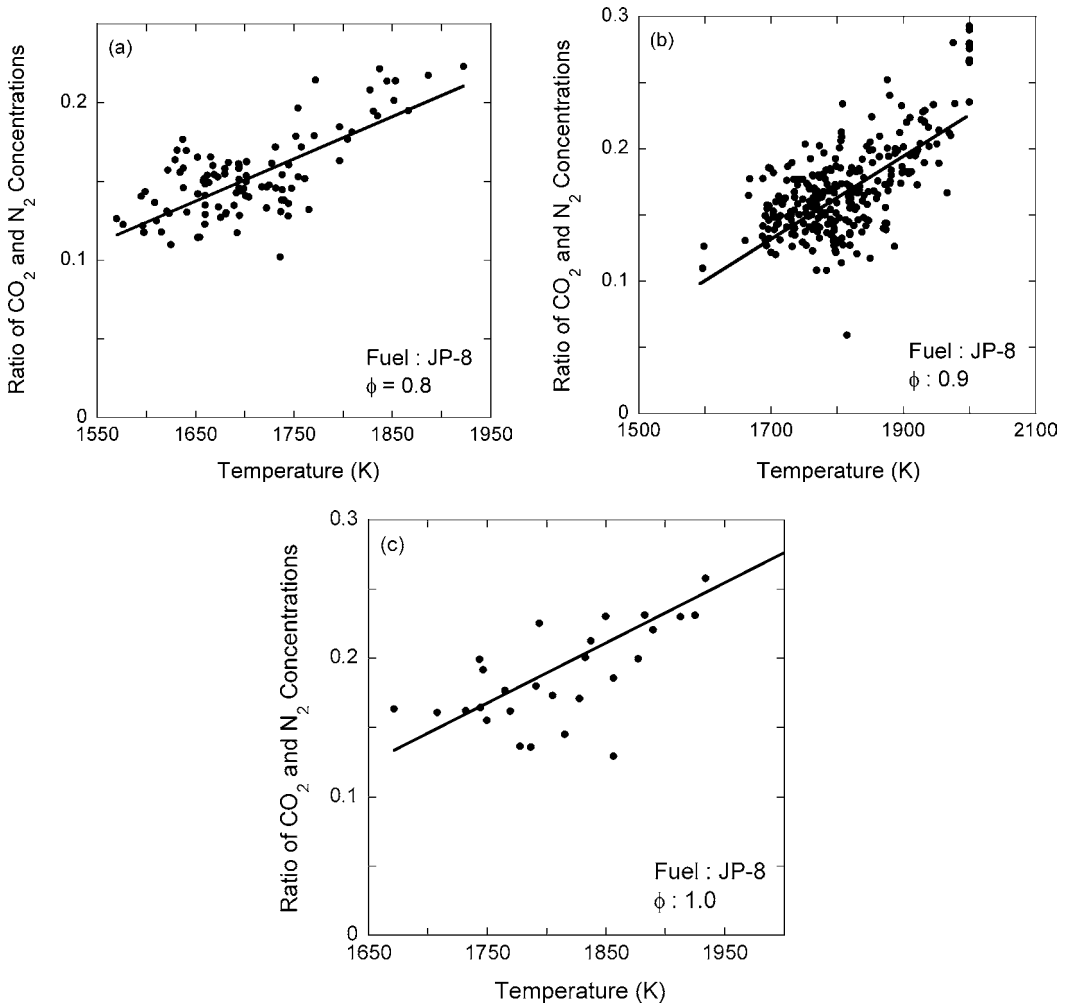


Fig. 9. Correlations of temperature and CO_2 and N_2 concentration ratios for the single-shot CARS data for three equivalence ratios in the exhaust stream of the JP-8-fueled combustor.

part to reduced signal-to-noise ratios, as well as to increased unsteadiness and spatial variations in the swirl-stabilized combustor. The increase in combustor unsteadiness is verified in Fig. 9, which shows correlation diagrams for the measured CO_2 concentrations and gas-phase temperatures determined from the single-shot, dual-pump N_2 – CO_2 spectra for three equivalence ratios. A least-squares fit through the data points shows a correlated increase in CO_2 concentration with temperature, indicating that temperature fluctuations are accompanied by shot-to-shot fluctuations in equivalence ratio.

The temperature and the ratio of CO_2 and N_2 concentration measurements for all three fuels are summarized in Figs. 10a and 10b, respectively. The increase in the standard deviation of the CO_2 mole fraction with equivalence ratio could be attributed to combustor unsteadiness or CARS system uncertainty,

as discussed above. As discussed before, the CARS system has an inherent temperature uncertainty of $\sim 2\%$ determined from the measurements in a calibrated flame. The rest of the uncertainty in temperature measurements will be due to the combustor unsteadiness. Both the temperature and the CO_2 concentration increase monotonically with equivalence ratio (ϕ) before reaching a maximum near an equivalence ratio of 1.0, as expected. The temperature and the CO_2 concentration begin to decrease beyond $\phi = 1.0$. Based on C/H ratio, CO_2 concentrations for JP-8X should be higher than JP-8 or the semisynthetic fuel, as confirmed in Fig. 10b, while the semisynthetic fuel should be slightly lower than JP-8, contrary to the results shown in Fig. 10b. The CO_2 concentrations were evaluated by fitting the experimental N_2 – CO_2 dual-pump spectra to theoretical spectra. The fitting results depend on the quality of the acquired spectra.

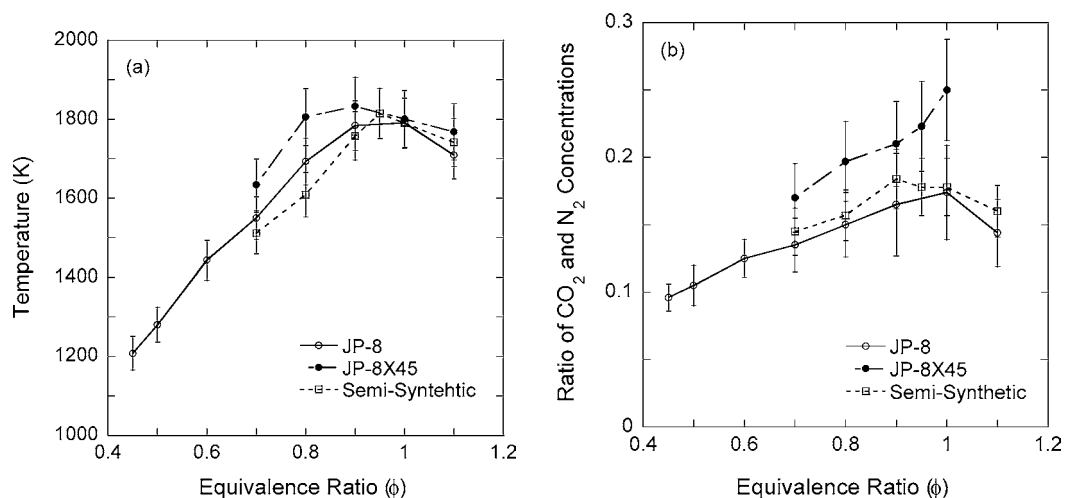


Fig. 10. (a) Temperature profiles and (b) ratio of CO_2 and N_2 concentration profiles in the exhaust stream of a liquid-fueled, swirl-stabilized combustor for different jet fuels. The uncertainties were calculated based on the analysis of single-shot, N_2 – CO_2 dual-pump CARS spectra.

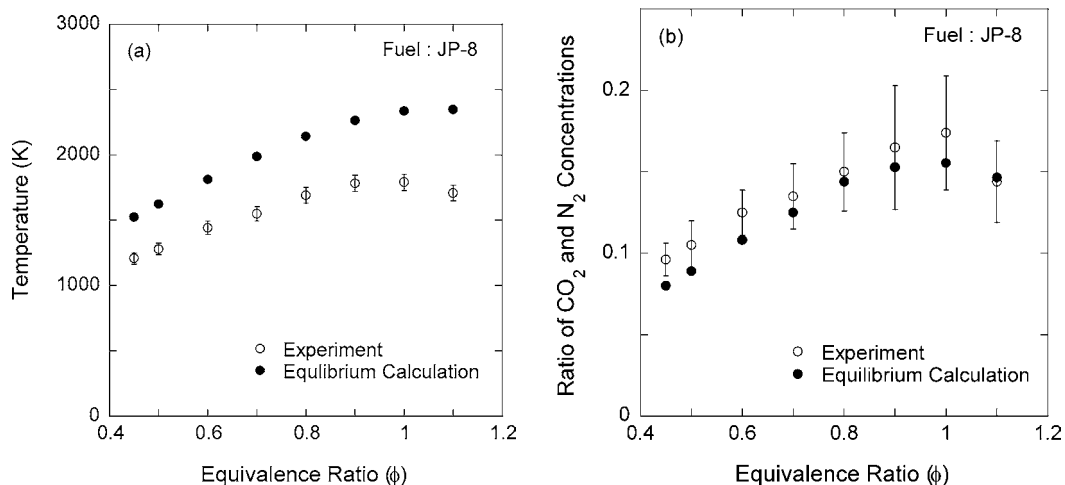


Fig. 11. Comparison of the experimental results with the equilibrium calculations for JP-8 fuel (a) temperature profiles and (b) ratios of CO_2 and N_2 concentration profiles.

The baselines of the spectra acquired for the semisynthetic fuel were very noisy due to strong background scattered light. Because of the limited stock of the semisynthetic fuel, we did not get a chance to repeat the experiments with this fuel. However, we were able to reduce the background scattered light and the flame luminosity at high equivalence ratios significantly by placing apertures at strategic locations during the experiments with JP-8 fuel. Due to this added spatial filtering, the quality of the spectra acquired for the JP-8 fuel is excellent.

A comparison with theoretical JP-8 temperature and CO_2/N_2 data from an equilibrium combustion code [27] is shown in Figs. 11a and 11b, respectively.

The molecular formula of JP-8 fuel is $\text{C}_{10.9}\text{H}_{20.9}$ and the heat of formation is -2.48×10^5 kJ/K (private communication, T. Edwards, U.S. Air Force Research Laboratory, Wright–Patterson Air Force Base, 2001). The measured temperatures are lower than the adiabatic flame temperatures by 21% during lean combustor operation and by 28% under the richest conditions ($\phi = 1.1$). The increase in this discrepancy at higher equivalence ratios is expected, due to increased heat losses at higher temperatures via heat conduction and soot radiation. The unsteadiness of the flame and the spatial averaging during the measurements also contribute to the discrepancy between the measured and the calculated temperatures shown in Fig. 11a. The

Table 1

Summary of the additive study results with JP-8 fuel at two different equivalence ratios

Additive conc. (mg/L)	$\phi = 0.7$ Fuel: JP-8, additive: KLEEN			$\phi = 1.1$ Fuel: JP-8, additive: KLEEN		
	Exhaust temp. (K)	CO ₂ /N ₂	Particle count change (%)	Exhaust temp. (K)	CO ₂ /N ₂	Particle count change (%)
0	1540 ± 49	0.135 ± 0.020	–	1699 ± 64	0.144 ± 0.025	–
7800	1549 ± 51	0.142 ± 0.022	11.1	1709 ± 62	0.130 ± 0.028	–
15,600	1560 ± 48	0.128 ± 0.020	28.3	1708 ± 72	0.150 ± 0.022	–19.1
31,200	1558 ± 51	0.144 ± 0.018	44.0	1724 ± 70	0.134 ± 0.032	–31.3

measured CO₂/N₂ concentrations follow the correct trend with equivalence ratio, but are about 15% too high under lean conditions. Under stoichiometric to rich conditions, the difference between measured and theoretical CO₂/N₂ concentrations decreases to about 7–9%. These discrepancies are mostly due to issues related to the spectral modeling of the CO₂ CARS spectra [17,18]. These modeling issues are the subject of ongoing investigation and are beyond the scope of the current work.

As stated earlier, the effects of particulate-mitigating additives on temperature and CO₂ concentrations were also studied. It was hypothesized that these additives might alter the flame temperature via soot reduction or changes in flame chemistry. The additive used with JP-8 fuel is known as “KLEEN.” The results of the additive study with JP-8 fuel using dual-pump N₂–CO₂ CARS are summarized in Table 1. The current dual-pump CARS data show no significant change in the exhaust temperature or CO₂ concentration for various levels of additive concentrations with JP-8 fuel. These additives affect the particle count significantly, but seem to do so through a mechanism that does not alter the final state of the combustion products (i.e., temperature and CO₂). This implies that other parameters, such as combustion efficiency and CO emissions, might also remain relatively unchanged with additive concentration. A more careful study in the primary flame zone where soot production takes place is necessary for more definitive conclusions regarding the effects of additives on flame chemistry, and is the subject of ongoing investigation. These measurements show that the precision of the current CARS system is ideally suited for fuel and additive studies in the exhaust stream (as in the current work) or in the primary flame zone (for future work).

4. Conclusions

Single-shot temperature and CO₂ concentration measurements were performed in the exhaust stream

of a swirl-stabilized, liquid-fueled combustor using dual-pump N₂–CO₂ CARS spectroscopy. Experiments were performed with three different jet fuels for equivalence ratios ranging from 0.4 to 1.1 under low to high sooting conditions. Dual-pump CARS allows the measurement of temperature, along with the concentration of a second species (in the present case, CO₂) with respect to the N₂ concentration. The standard deviations of the measured temperature and CO₂ mole fraction as determined from single-shot, dual-pump N₂–CO₂ CARS spectra are approximately 3–4 and 9–20% of the mean values, respectively, for a wide range of equivalence ratios. The wide variation in the single-shot CO₂ concentration is due, in part, to the variation in temperature, as shown in Fig. 9. For a fixed equivalence ratio, the CO₂ mole fraction clearly shows an upward trend with temperature, as expected. Both the temperature and the CO₂ concentration increase with equivalence ratio and reach a maximum value near an equivalence ratio of 1.0 before beginning to decrease because of excess fuel. Measurements of temperature and CO₂ concentration for a variety of particulate-mitigating additives show no significant changes within the experimental error of the current CARS system. The dual-pump approach will allow us to pursue future CARS measurements in the reaction zone of the combustor under sooting conditions along with laser-induced incandescence (LII) and planar laser-induced fluorescence (PLIF) measurements to quantify soot formation and to study unsteady flame characteristics.

Acknowledgments

Funding for this research was provided by the U.S. Air Force Research Laboratory, Propulsion Directorate, Wright-Patterson AFB, under Contracts F33615-00-C-2068, F33615-03-D-M2329, and F33615-00-C-2020, and by the Air Force Office of Scientific Research (Dr. Julian Tishkoff, Program Manager).

References

- [1] A.C. Eckbreth, *Laser Diagnostics for Combustion Temperature and Species*, second ed., Gordon & Breach, Amsterdam, 1996.
- [2] F. Takahashi, J.W. Schmoll, G.L. Switzer, D.T. Shouse, *Proc. Combust. Inst.* (1994) 183–191.
- [3] J. Bood, P.-E. Bengtsson, F. Mauss, K. Burgdorf, I. Denbratt, *SAE Paper No. 971669*, 1997, pp. 1–12.
- [4] L.P. Goss, D.D. Trump, B.G. MacDonald, G.L. Switzer, *Rev. Sci. Instrum.* 54 (1983) 563–571.
- [5] S.P. Heneghan, M.D. Vangsness, *Rev. Sci. Instrum.* 62 (9) (1991) 2093–2099.
- [6] D. Ball, H.S. Driver, R.J. Hutcheon, R.D. Lockett, G.N. Robertson, *Opt. Eng.* 33 (9) (1994) 2870–2874.
- [7] P.M.J. Hughes, R.J. Lacelle, T. Parameswaran, *Combust. Sci. Technol.* 105 (1995) 131–145.
- [8] D.N. Klimenko, W. Clauss, M. Oswald, J. Smith, W. Mayer, *J. Raman Spectrosc.* 33 (2002) 900–905.
- [9] W.P. Stricker, in: K. Kohse-Höinghaus, J.B. Jeffries (Eds.), *Applied Combustion Diagnostics*, Taylor & Francis, New York, 2002, p. 182.
- [10] S. Roy, W.D. Kulatilaka, R.P. Lucht, N.G. Glumac, T. Hu, *Combust. Flame* 130 (2002) 261–276.
- [11] S. Roy, G. Ray, R.P. Lucht, *Appl. Opt.* 40 (2001) 6005–6011.
- [12] R.P. Lucht, *Opt. Lett.* 12 (1987) 78–80.
- [13] R.D. Hancock, F.R. Schauer, R.P. Lucht, R.L. Farrow, *Appl. Opt.* 36 (1997) 3217–3226.
- [14] F.R. Schauer, PhD thesis, University of Illinois at Urbana–Champaign, Urbana, IL, 1998.
- [15] S.M. Green, P.J. Rubas, M.A. Paul, J.E. Peters, R.P. Lucht, *Appl. Opt.* 37 (1989) 1690–1701.
- [16] D. Brüggemann, B. Wies, X. Zhang, T. Heinze, K.F. Knoche, in: D.F.G. Durão, M.V. Heitor, J.H. Whitelaw, P.O. Witze (Eds.), *Combustion Flow Diagnostics*, Kluwer Academic, Dordrecht, 1992, p. 495.
- [17] R.P. Lucht, V.N. Velur, G.J. Fiechtner, C.D. Carter, K.D. Grinstead Jr., J.R. Gord, P.M. Danehy, R.L. Farrow, *AIAA J.* 41 (4) (2003) 679–686.
- [18] S. Roy, T.R. Meyer, M.S. Brown, V.N. Velur, R.P. Lucht, J.R. Gord, *Opt. Commun.* 224 (2003) 131–137.
- [19] L. Martinsson, P.-E. Bengtsson, M. Aldén, *Appl. Phys. B* 62 (1996) 29–37.
- [20] A. Thumann, M. Schenk, J. Jonuscheit, T. Seeger, A. Leipertz, *Appl. Opt.* 36 (1997) 3500–3505.
- [21] J. Bood, P.-E. Bengtsson, M. Aldén, *Appl. Phys. B* 70 (2000) 607–620.
- [22] F.Y. Yueh, E.J. Beiting, *Appl. Opt.* 27 (1988) 3233–3243.
- [23] P.-E. Bengtsson, L. Martinsson, M. Aldén, *Appl. Spectrosc.* 49 (1995) 188–192.
- [24] T. Seeger, A. Leipertz, *Appl. Opt.* 35 (1996) 2665–2671.
- [25] C. Brackmann, J. Bood, P.-E. Bengtsson, T. Seeger, M. Schenk, A. Leipertz, *Appl. Opt.* 41 (2002) 564–572.
- [26] R.E. Palmer, *The CARSFT computer code for calculating coherent anti-Stokes Raman spectra: user and programmer information*, Report SAND89-8206, Sandia National Laboratories, Livermore, CA, 1989.
- [27] S.R. Turns, *An Introduction to Combustion*, McGraw-Hill, New York, 1996.

Studies of Hydroxyl Distribution and Soot Formation in Turbulent Spray Flames

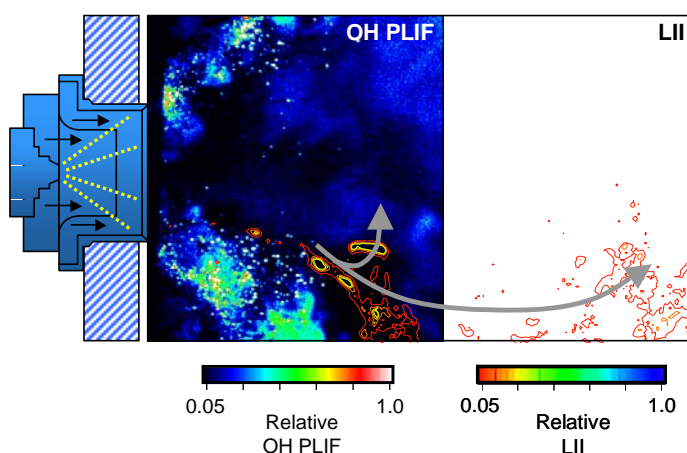
James R. Gord,¹ Terrence R. Meyer,² Sukesh Roy,² Sivaram P. Gogineni²

¹Air Force Research Laboratory, Propulsion Directorate
Wright-Patterson Air Force Base, OH 45433-7103, USA

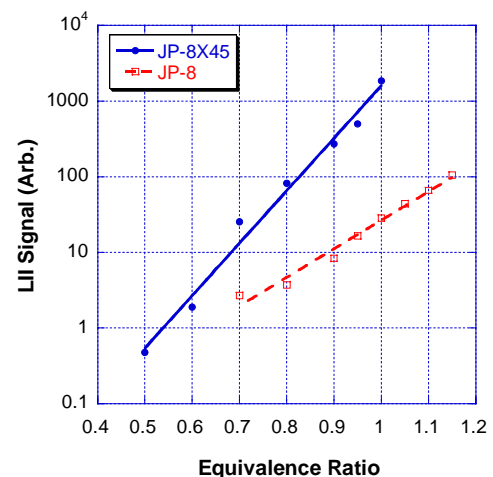
²Innovative Scientific Solutions, Inc.
2766 Indian Ripple Road, Dayton, OH 45440-3638, USA

Abstract

A measurement system that combines several laser-based imaging techniques is developed for characterizing the instantaneous flame structure and soot-formation mechanisms in an atmospheric-pressure, swirl-stabilized, liquid-fueled, model gas-turbine combustor. Planar laser-induced incandescence (LII) is used to map the soot volume fraction and planar laser-induced fluorescence (PLIF) of the hydroxyl radical (OH) is used to image the flame zone. Mie scattering, which appears as an interference in the OH PLIF signal, is used to a limited extent as a spray diagnostic. Optimal excitation and detection parameters to enable the simultaneous use of these techniques in turbulent spray flames are discussed, along with analyses of potential sources of error. The data indicate that the flame in the near field of the swirl-stabilized injector is highly perturbed by large-scale structures and that fluid-flame interactions have a significant impact on soot formation. Rich pockets of fuel and air along the interface between the spray flame and recirculation zone serve as locations for soot inception, as shown below (left). The effect of local equivalence ratio is determined from qualitative analysis of the OH-PLIF data and comparison with equilibrium calculations in the recirculation region. Spatially averaged LII measurements demonstrate that soot volume fraction in the primary flame zone increases exponentially with equivalence ratio. This is illustrated in the semi-log plot shown below (right) for two different jet fuels. Preliminary results suggest that soot formation in the primary zone is strongly dependent on fuel aromatic content.



Simultaneous OH-PLIF (left half) and laser-induced incandescence (full image) at overall equivalence ratio of 1.0 for JP-8-fueled, swirl-stabilized spray flame.



Comparison of relative soot-volume fraction as a function of equivalence ratio for two different jet fuels.

1. Introduction

Swirl-stabilized, liquid-spray injectors are commonly used in gas-turbine engines to achieve compact, stable, and efficient combustion. The flowfield in the primary zone of such a spray flame is characterized by high shear stresses and turbulent intensities that result in vortex breakdown and large-scale unsteady motions.^{1,2} These unsteady motions are known to play a key role in the formation of pollutant emissions such as carbon monoxide (CO), nitric oxide (NO), and unburned hydrocarbons (UHC).³⁻⁵ Considerably less is known, however, about the mechanisms that lead to soot formation in swirl-stabilized, liquid-fueled combustors. Previous investigations have relied on exhaust-gas measurements and parametric studies to gain insight into the effects of various input conditions on soot loading.⁶⁻¹⁰ Much of the fundamental knowledge concerning soot formation is derived from investigations of laminar diffusion flames,^{11,12} with only a limited number of studies having focused on unsteady effects.^{13,14} The importance of considering unsteadiness and fluid-flame interactions was demonstrated by Shaddix et al.,¹⁴ who found that a forced methane/air diffusion flame produced a four-fold increase in soot volume fraction (as a result of increased particle size) as compared with a steady flame having the same mean fuel-flow velocity.

The goal of the current investigation is to study soot formation in the highly dynamic environment of a swirl-stabilized, liquid-fueled combustor. This is accomplished using simultaneous imaging of the soot volume fraction, hydroxyl-radical (OH) distribution, and droplet pattern in the primary reaction zone using laser-induced incandescence (LII), OH planar laser-induced fluorescence (PLIF), and droplet Mie scattering, respectively. The utility of LII for two-dimensional imaging of soot volume fraction has been demonstrated in laboratory investigations^{15,16} as well as in aircraft-engine exhausts.^{9,10} Brown et al.¹⁷ performed planar LII for soot-volume-fraction imaging in the reaction zone of a gas-turbine combustor; their preliminary measurements employed LII alone for demonstration purposes and did not image the turbulent flame structure near the exit of the swirl cup. In the current work, we extend the work of Brown et al.¹⁷ by performing LII at the exit of the swirl cup and by adding OH-PLIF and Mie scattering diagnostics.

The use of OH as a flame marker is typical in studies of soot formation in diffusion flames because of its close correlation with flame temperature.^{18,19} It has also been employed in a number of investigations of swirl-stabilized combustors.^{20,21} The use of laser-saturated OH LIF for *quantitative* measurements has also been demonstrated,^{22,23} although saturation is quite difficult in the case of planar measurements. In the current investigation, we demonstrate qualitative measurements in the recirculation region using excitation levels well below saturation. OH-PLIF measurements in the liquid-spray region are more uncertain because of simultaneous droplet scattering and non-equilibrium conditions, although meaningful measurements are possible with careful consideration of potential errors.

The performance and accuracy of the planar LII, OH-PLIF, and Mie scattering systems are characterized in the current work and described below. The combined use of LII, OH PLIF, and droplet Mie scattering is then shown to provide insight into the unsteady physical processes that govern soot formation in gas turbine engines. OH PLIF is employed to track local equivalence ratio and the effects of flame chemistry. Finally, the current measurement system is demonstrated to be useful in assessing the performance soot-mitigating additives.

2. Experimental Setup

2.1 Swirl-Stabilized Combustor

The near-field structure of swirl-stabilized flames is determined by the characteristics of the fuel injector and the geometry of the surrounding flame tube. As shown in Fig. 1, the swirl-cup, liquid-fuel injector used in the current study employs pressure atomization and dual-radial, counter-swirling-air co-flows to entrain the fuel, promote droplet break-up, and enhance mixing. The 4.3-cm-exit-diameter swirl cup is installed at the entrance of a 15.25-cm \times 15.25-cm square-cross-section flame tube, as shown in Fig. 2. After exiting the primary flame zone, the combustion products are allowed to mix thoroughly along the 48-cm long flame tube before entering a 43-cm-long, 5.7-cm-exit-diameter exhaust nozzle that is designed to create uniform exhaust-gas-temperature and concentration profiles.

The combustor shown in Fig. 2 is used in the Atmospheric-Pressure Combustor-Research Complex of the Air Force Research Laboratory's Propulsion Directorate to study the performance characteristics of model gas-turbine-engine fuels and fuel additives. An overview of the facility is available in the literature,²⁵ although certain aspects relevant to the current work are described here for reference. Changes in overall equivalence ratio from $\phi = 0.5$ to 1.15 are achieved in the current study by varying the pressure drop across the fuel-spray nozzle from about 1.5 to 10 atm, which results in fuel mass-flow rates of 1.0 to 2.2 g/s, respectively. The fuel flow rate is measured using a Max Machinery positive-displacement flow meter with $\pm 0.5\%$ full-scale accuracy. The air-flow system consists of three Sierra 5600 SLPM mass-flow controllers with $\pm 1\%$ full-scale accuracy. The inlet air is heated to 450 K with a constant flow rate of ~ 0.028 kg/s. The air-pressure drop across the combustor dome is ~ 4.8 to 5.2% of the main supply. Most of the air flow enters the combustor through the swirl-cup injector, but a small percentage enters through aspiration holes along the aft wall. No liner air jets are used in the secondary zone; therefore, the fuel-air ratio depends almost entirely on the flow rates through the injector cup.

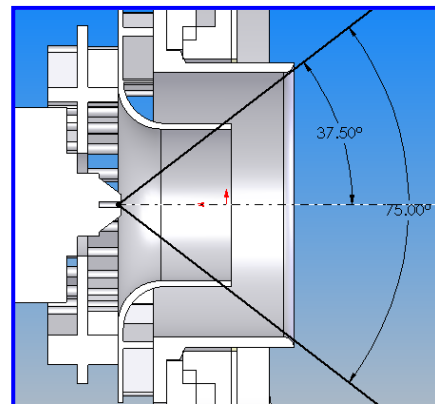


Fig. 1. Center-mounted swirl injector with dual-air counterswirlers.

The combustor is optically accessible via 75-mm-wide quartz windows along the top and sides for *in-situ*, laser-based diagnostics. In addition, a sampling probe for measuring particle number density (counts per cubic centimeter) via a condensation nuclei counter (CNC) is located at the exit of the combustor.

2.2. OH-PLIF System

A review of PLIF fundamentals can be found in Eckbreth (1996).²⁶ As shown in the optical set-up in Fig. 2, 50% of the laser energy from a frequency-doubled, Q-switched Nd:YAG laser (Spectra-Physics Pro290) is used to pump a dye laser (Sirah Precision Scan), the output of which is frequency doubled to obtain wavelengths in the (1,0) band of the OH A-X system. The dye laser is tuned to the $Q_1(9)$ transition at 283.922 nm (in air), which has less than $\pm 2.5\%$ variation in the ground-level Boltzmann fraction from 1600 to 2400 K. As shown in Fig. 3, this range of temperatures coincides with the equilibrium conditions expected for JP-8 fuel at equivalence ratios used in this study ($\phi = 0.5$ to 1.15).²⁷ Considering the full range of temperatures from 1100 to 2400 K, which are within typical lean and rich flammability limits,²⁸ the Boltzmann fraction for this transition varies by up to $\pm 12.5\%$.

The maximum laser energy available for OH PLIF is 24 mJ. A 1.5-m-focal-length spherical plano-convex lens and a -75-mm-focal-length plano-concave lens are used to form a laser sheet that enters the combustor through the top window. The laser-sheet thickness is 330 μm at full-thickness-half-max (FTHM) as measured by translating a knife edge across the beam.

A 7-cm, top-hat-like sheet-width profile that transitions to zero laser energy within about 1 mm is obtained by clipping the wings of the laser sheet at the last turning mirror above the combustor. The sheet is slowly expanding with a 3° full-angle divergence.

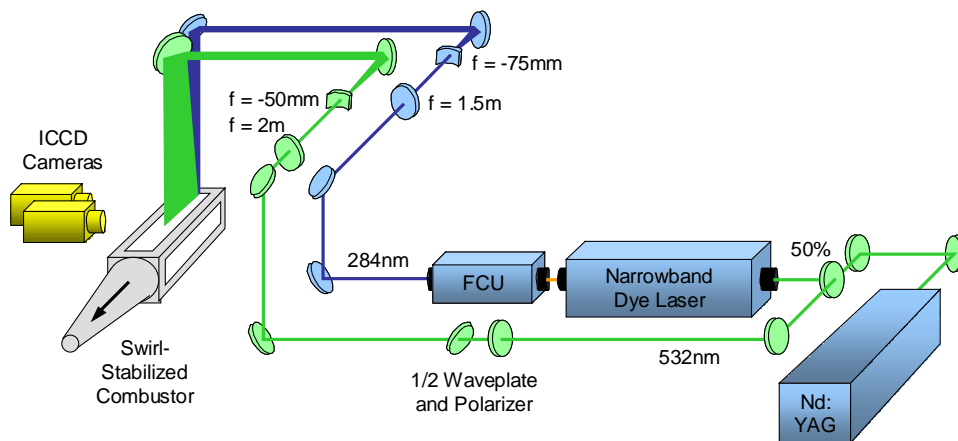


Fig. 2. Optical set up for simultaneous OH PLIF and LII.

Fluorescence is collected from about 306 to 320 nm via the (1,1)

and (0,0) bands of OH using an intensified charge-coupled-device (ICCD) camera (Princeton Instruments PI-MAX SB) oriented slightly off-normal to the sheet. Two 1-mm WG295 Schott Glass filters are used in front of the camera lens to reduce scattering from droplets at 283.922 nm. A UG11 filter nearly eliminates flame emission, scattering from the LII laser at 532 nm, and fluorescence from polycyclic aromatic hydrocarbons (PAH's). A 105-mm-focal-length f/4.5 UV lens is used to collect the OH fluorescence. An intensifier gate width of 20 ns is used to capture the OH signal. Images are typically collected with 2x2 binning (512x512) to obtain adequate resolution and framing rate. The pixel viewing area in each 2x2 superpixel is 200x200 μm^2 . Table 1 summarizes the OH-PLIF optical parameters.

Based on the dimensions of the OH-PLIF laser sheet and total available laser energy of 24 mJ, it is estimated that the maximum laser irradiance of $1.36 \times 10^7 \text{ W/cm}^2$ is two to three orders of magnitude lower than that required to achieve 90-95% saturation.^{22,23} The OH-PLIF signal is, therefore, linearly related to laser-energy variations. OH-PLIF signal corrections (typ. $\pm 15\%$) in the axial direction are performed in post processing, based on measurements of the laser-sheet profile after each run. Signal variation (typ. $\pm 3\%$) due to the 3° laser-sheet expansion in the cross-stream direction is also corrected in post processing. Corrections are not made for laser-energy attenuation due to OH absorption and droplet scattering; this leads to signal uncertainties of $\pm 10\%$ in the lower region of each image. The effect of this error is substantially reduced in the upper half of the combustor, where most of the data in this study is extracted. Shot-to-shot fluctuations in laser energy add an estimated $\pm 5\%$ uncertainty, as determined from data collected in a laminar diffusion flame with the same OH-PLIF system.

For measurements with low laser irradiance, the effect of collisional quenching on fluorescence efficiency must also be considered. For a given imaging system and laser irradiance, the OH-PLIF signal, S_{OH} , from each pixel volume is proportional to the OH number density, N_{OH} , and the fluorescence efficiency, η ,²⁶ as shown in Eqn. 1.

$$S_{OH} \approx N_{OH} \eta = N_{OH} \frac{A_{OH}}{A_{OH} + Q_{OH}} \quad (1)$$

The fluorescence efficiency is proportional to the rate of spontaneous emission, A_{OH} , from molecules in the excited state and inversely proportional to the rate at which excited molecules are depleted via spontaneous emission and collisional quenching, Q_{OH} . Collisional quenching is a function of the temperature- and pressure-dependent quenching coefficient as well as the number densities of the quenching species.²⁹ As a result of offsetting effects in the equilibrium combustion products of JP-8, the collisional quenching rate is found to be fairly constant for equivalence ratios less than unity, as shown in Fig. 3. Under rich conditions the conversion of CO to CO_2 decreases substantially, leading to an increase in collisional quenching and a decrease in fluorescence efficiency. In regions where equilibrium assumptions are valid, the LIF signal can be used along with Eqn. 1 and the Boltzmann distribution to determine the relative OH number density; this will be discussed further in the Results Section. In the liquid-spray region where lean and rich pockets co-exist, qualitative signal interpretation is problematic since signal efficiency can vary by more than $\pm 30\%$, according to Fig. 3.

Mie scattering is obtained using the same optical setup as that for the OH-PLIF system. It is found that optical filters and the use of parallel polarization in the detection scheme can reduce but not altogether eliminate droplet scattering. It is found that two WG295 color-glass filters (CVI Laser) and parallel-polarization detection provide optimal OH-PLIF sensitivity while minimizing

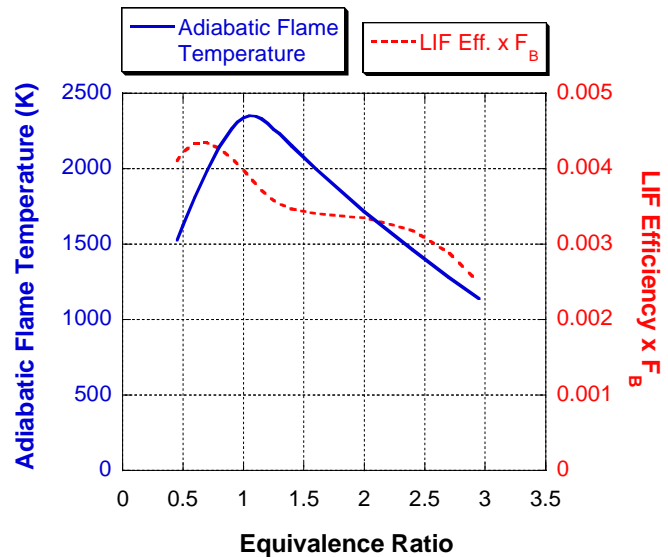


Fig. 3. Adiabatic-flame-temperature calculations assuming equilibrium combustion products along with OH-LIF efficiency multiplied by the Boltzmann fraction for JP-8 fuel at various equivalence ratios.

the likelihood of damaging the ICCD due to intense levels of droplet scattering. When the laser is tuned off the OH absorption line, as shown in Fig. 4, the intense, highly localized droplet scatter can be distinguished from the large, more uniformly distributed OH layers. Large droplet clusters appear primarily near the injector exit, and single droplets with trailing flames are often observed traveling into the recirculation region. The trailing flames of these droplets do not appear in the off-line images and, therefore, are not attributable to scattering from fuel vapor or fluorescence from broadband sources such as PAH compounds. The droplet-scattering signal intensity is about one order of magnitude

higher than that of the OH PLIF, but the signal occurs primarily at isolated points. A false-color table is selected, therefore, based on probability density functions of OH PLIF. The full range of OH-PLIF signal levels is assigned colors from black to red, while the Mie scattering signals are above this range and appear in white.

2.3. LII System

Some of the first two-dimensional visualizations of soot volume fraction using LII were performed by Santoro and co-workers¹⁵ and by Vander Wal and Weiland.¹⁶ The effects of various parameters such as laser fluence, laser-sheet profile, detection wavelength, camera gate width, and camera gate delay have been explored in a number of follow-up investigations.³⁰⁻³² A list of reviews on the subject is provided by Urban.¹²

The LII optical layout employed in the current study is shown schematically in Fig. 2, where 50% of the energy from a frequency-doubled Nd:YAG is formed into a sheet using a 2-m plano-convex spherical lens and a -50-mm plano-concave cylindrical lens. The FTHM of the laser sheet is about 700 μm within the measurement volume, as measured by traversing a knife edge across the sheet. As is the case for the OH-PLIF laser sheet, the long 2-m-focal-length lens is used to minimize variations in laser-sheet thickness within the measured region. The sheet width is ~ 14 cm, with wings that are clipped prior to the last turning mirror to generate a top-hat-like profile that transitions to zero laser energy within about 2 mm. The sheet has a full angle divergence of 6° within the test section. An overall tilt of 5° is used to overlap the LII and PLIF laser sheets. The laser-fluence distribution varies by $\pm 15\%$ over the first 7 cm of the sheet, corresponding to the region where PLIF and Mie scattering are measured. Over the remaining 7 cm of the sheet, the laser fluence decreases more quickly from a peak of 460 mJ/cm^2 to a minimum of 180 mJ/cm^2 . To reduce systematic errors due to laser-sheet-width intensity variations in the downstream half of the laser sheet and due to laser extinction in the measurement volume, the LII system is operated in the saturated regime. A saturation fluence near 200 mJ/cm^2 , shown in Fig. 5, agrees with previous measurements in the literature.^{30,32} Figure 5 indicates that the uncertainty in the relative soot-volume-fraction measurements is within $\pm 10\%$ over the full width of the laser sheet.

The LII signal is detected using a 1024 \times 1024 ICCD camera (Princeton Instruments PI-MAX SB-MG) and an f/1.2, 58-mm-focal-length glass lens. After 4 \times 4 pixel binning, the measurement resolution is about 575 \times 575 μm^2 . A 500-nm

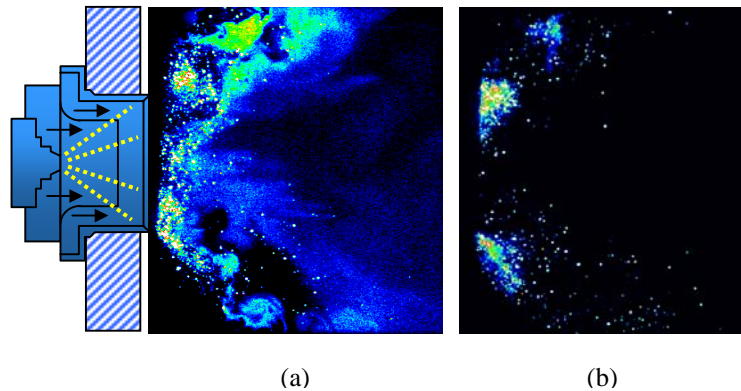


Fig. 4. Raw signal from (a) OH PLIF and droplet Mie scattering while on $Q_1(9)$ line of (1,0) band in A-X system and (b) droplet Mie scattering while off the OH line. Overall $\phi = 0.7$.

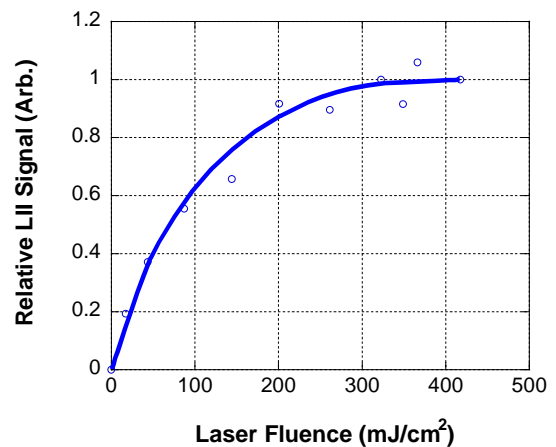


Fig. 5. LII saturation curve from averaged images in a swirl-stabilized combustor at overall $\phi = 1.1$. Solid line is for guidance only.

Table 1. Summary of OH-PLIF optical parameters for optimal detection in the primary flame zone.

	OH-PLIF Parameter	Criteria
Camera gate width	20 ns	Minimize flame emission
Camera delay	0 ns	Maximize signal
Excitation wavelength	283.922 nm	Temperature insensitivity
Detection wavelength	306 - 320 nm	Minimize scatter and flame emission
Length of meas. volume	2.5"	Visualize primary flame zone
Thickness of meas. volume	330 μm	High resolution and laser fluence
Laser fluence	30 - 40 mJ/cm^2	Maximize signal

Table 2. Summary of LII optical parameters for optimal detection in the primary flame zone.

	LII Parameter	Criteria
Camera gate width	50 ns	Minimize particle-size bias
Camera delay	20 ns	Minimize scatter/PAH fluorescence
Excitation wavelength	532 nm	Safety and beam quality
Detection wavelength	415 - 500 nm	Minimize PAH and wavelength effects
Length of meas. volume	5"	Visualize primary flame zone & beyond
Thickness of meas. volume	700 μm	Adequate resolution and meas. volume
Laser fluence	200 - 420 mJ/cm^2	Saturate signal

short-pass filter (CVI Laser) is used for detection from 415 to 500 nm, which reduces contributions from nascent soot particles, OH fluorescence/chemiluminescence, and red-shifted fluorescence from PAH compounds. The relatively short-lived PAH fluorescence is also minimized by employing a time-delayed detection scheme. Scattering from the 532-nm laser source is eliminated by using a 532-nm zero-degree reflective mirror with the 500-nm short-pass filter and delayed detection. Light leakage from flame luminosity while the ICCD intensifier is gated off is minimized through the use of a 25-ms-gate Uniblitz shutter. During post processing the residual background signal from flame luminosity is subtracted from each image. A color scale is chosen with a minimum value 5% above the background and a maximum value at 100% signal.

To optimize the timing of LII detection, data are collected in the swirl-stabilized flame for a number of camera-intensifier-gate delays and widths. A camera delay of 20 ns after the laser pulse is found to reduce laser scatter to nearly the background level while maintaining LII signal-to-noise ratios greater than 20:1. The LII signal decays quickly within the first 200 ns after the laser pulse, as shown in Fig. 6. The long decay in signal after 200 ns is dominated by larger, slow-cooling particles. With a gate width of 50 ns, errors due to particle-size effects are estimated to be on the order of 5-10%.³⁰ Table 2 summarizes the optical parameters used for LII.

2.4. Combined LIF/LII System

The OH-PLIF and LII cameras are synchronized using an external delay generator (Stanford Research Systems DG535) driven by the advanced Q-switch TTL output of the Nd:YAG laser. The laser pulses are separated by only a few nanoseconds to avoid fluid movement during LIF and LII detection. The precise camera delay required to capture each image is imposed using a timing generator in each ICCD controller. Because of spatial constraints within the test cell, both cameras are positioned on the same side of the combustor at 3.5° to normal to overlap the two imaged regions. This angle is minimized by placing the LIF image to the far right of the camera viewing area and using a relatively large LII viewing area. Thus, the PLIF image area overlaps the left half of the LII image nearest the injector cup. After camera alignment, registration images are collected prior to each run for use in post processing. At higher equivalence ratios (>0.7), thermal loading from flame radiation is significant, and heat shielding is employed to reduce misalignment of the LII/LIF optics. During each run the OH-PLIF and LII sheets are checked periodically using burn paper and adjusted to ensure that the laser-intensity distributions and positions have not changed.

3. Results and Discussion

3.1. Instantaneous Flame Structure

The average OH distribution at $\phi = 0.5$ is shown in Fig. 7(a). All images are background subtracted and corrected for laser-sheet intensity variations and laser-sheet divergence. A slight asymmetry is apparent in the upper and lower halves, with the effects of laser attenuation being evident in the lower half of the image.

The intermittency and spatial inhomogeneity of the instantaneous flame structure is shown by the OH-PLIF images in Figs. 7(b) and 7(c). These images indicate that the fuel-preheat and reactant-mixing layers are highly turbulent. The instantaneous thickness of the OH layer varies significantly because of fluid entrainment from large-scale vortex structures. These structures are shed from the shear layer that is anchored on the lip of the outer air swirler; they enhance the mixing process, bring fresh reactants into the outer conical flame, and can reach across the flame layer and be a source of local flame extinction and intermittency. The latter is more prominent in Fig. 7(c), which shows an instantaneous OH-PLIF image at $\phi = 0.9$ with no contiguous flame in the viewing area. The size of the

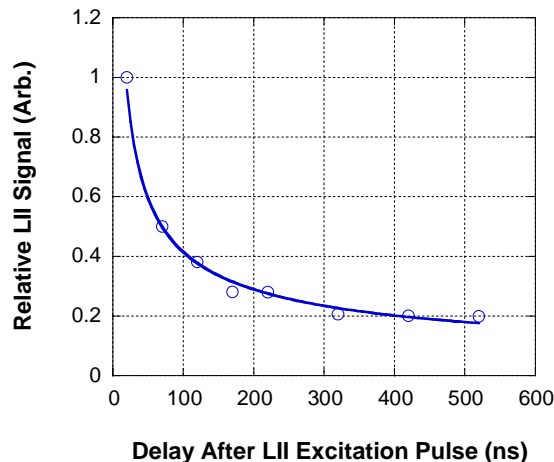


Fig. 6. Power-law time dependence of LII signal in swirl-stabilized combustor at $\phi = 1.1$.

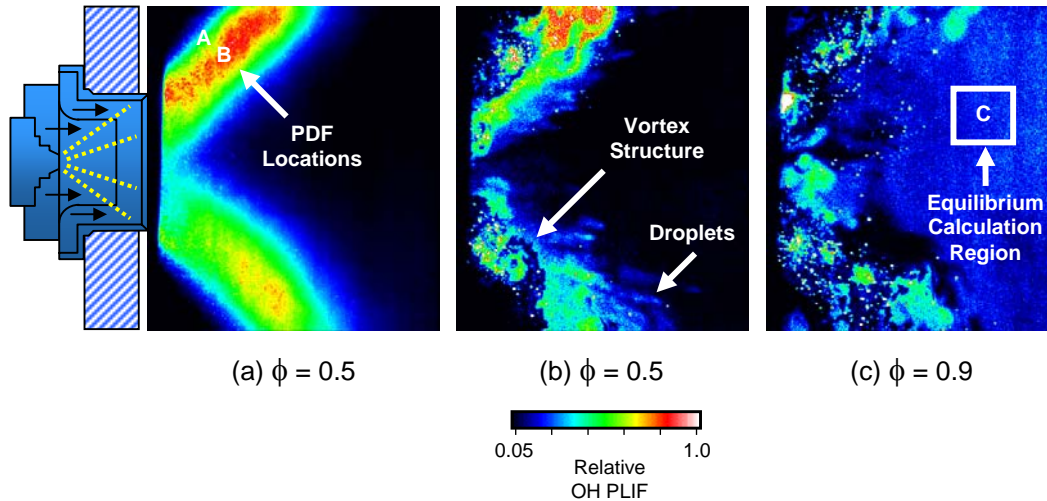


Fig. 7. Post-processed OH-PLIF images: (a) time-averaged image at overall $\phi = 0.5$, (b) instantaneous image at overall $\phi = 0.5$, and (c) instantaneous image at overall $\phi = 0.9$. Horizontal and vertical extent of signal is 4 to 70 mm from injector exit and -39 to 39 mm from injector centerline, respectively.

structures in Figs. 7(b) and 7(c) that are generated during the turbulent cascade from large to small scales ranges from about 0.5 mm to the entire width of the flame layer. Since the air-flow rate is held constant, much of this intermittency can be attributed to the behavior of the liquid spray as it impinges upon and sheds off the lip of the outer air swirler. This indicates that experiments and computations based on gaseous-fuel injection would not capture the significant changes in large-scale-structure dynamics induced by increased liquid-fuel injection.

To quantify the intermittency of the primary flame layer, probability density functions (PDF's) of OH PLIF signals are computed and plotted in Fig. 8 for Locations A and B shown in Fig. 7(a). Bin sizes of 200 counts are used along with 200 images. Normalization is performed only for data in the range 0 - 6000 counts, which is below the range typically observed from droplet Mie scattering. Location A is within the mixing layer dominated by large-scale turbulent structures, while Location B is within the central region of the outer conical flame. The PDF's at both locations show bimodal distributions but with opposite peaks. At Location A high levels of intermittency lead to a primary peak with low signal counts and a secondary peak with 3000-3500 counts. At Location B low-signal counts have decreased in probability and high-signal counts have increased in probability, indicating that large-scale structures seldom bring fresh reactants to this point in the flame at $\phi = 0.5$.

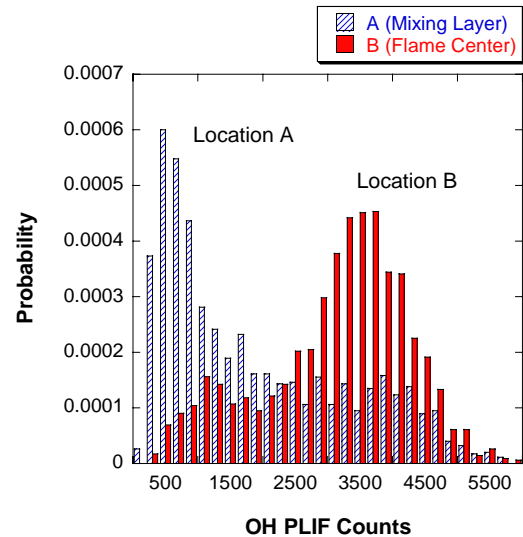


Fig. 8. Probability density functions (PDF's) of the corrected OH-PLIF signal at Location A (mixing layer) and Location B (flame center) shown in the average image of Fig. 7(a).

3.2. Determination of Local Equivalence Ratio

Figures 7(b) and 7(c) also show the distribution of droplets marked by Mie scattering. This signal, which scales as the droplet diameter squared, is biased toward larger droplets and cannot be used to interpret the true size distribution. However, it can be used as a qualitative marker for those large droplets that escape the initial preheat zone. Interestingly, the droplets in Fig. 7(b) have trailing flames, which indicates that evaporation and mixing with available oxygen is occurring in their wakes. Figure 7(c), however, shows droplets entering the recirculation zone without trailing flames. Since the temperature, evaporation, and reaction rates are expected to be higher in this

region for the higher equivalence ratio of Fig. 7(c), the absence of trailing flames indicates a lack of available oxygen for combustion. This is somewhat surprising since the combustor is operating at *overall* lean equivalence ratios in both Figs. 7(b) and 7(c).

In fact, it can be shown that the *local* equivalence ratio for the case of Fig. 7(c) is higher than the *overall* value of 0.9. Using a region in the recirculation zone that is free of droplet scatter [see Fig. 7(c)], an equilibrium calculation²⁷ is performed for JP-8 fuel at equivalence ratios varying from 0.5 to 1.15. The validity of equilibrium assumptions in this region has been proposed in previous investigations of can-type gas-turbine combustors.^{3,4} The temperatures and species concentrations from this equilibrium calculation are then used to calculate the effects of LIF efficiency and Boltzmann fraction on OH-PLIF signals, as shown previously in Fig. 3. The fit of OH-PLIF signals to equilibrium calculations, shown in Fig. 9, indicates that the local equivalence ratio is 13.5% higher than the overall equivalence ratio. Thus, the stoichiometric condition in the primary flame zone occurs for *overall* equivalence ratios between 0.8 and 0.9. Correspondingly, images collected at these equivalence ratios show a transition from burning to non-burning wakes behind droplets. The occurrence of locally rich conditions near the primary flame zone may be due in part to air from the aspiration holes of the aft wall escaping the primary flame zone or due to incomplete mixing in the flame recirculation region. The significance of this finding for understanding soot formation mechanisms and evaluating differences with sampling-probe data in the exhaust stream are discussed below.

3.3. Soot-Formation Mechanisms

Figure 10 shows two instantaneous LII contour plots at $\phi = 1.0$ overlaid with OH-PLIF images that are collected simultaneously. It should be noted that these LII images are typical for about 5% of the data set. More commonly, the spatial extent of the LII signal from highly concentrated soot pockets encompasses less than 1% of the primary flame zone. Images such as those in Fig. 10, therefore, account for the “turbulent flame brush” that may be responsible for most of the soot production in liquid-spray flames. The flow patterns noted in the figure are derived using observations from high-speed digital images collected in the same combustor. Soot is generated along the inner cone of the flame in regions of low OH-PLIF intensity. A portion of the soot is advected along the outer path of the recirculation zone, while a portion appears to enter immediately into the recirculation zone.

Most of the LII signal is detected in regions that are free of droplet Mie scattering (as detected with the OH-PLIF camera) and is attributable to the presence of soot. Some of the LII signal does occur in regions of high Mie scattering, indicating that some, if not most, of the signal near the injector exit cannot be attributed to the presence of soot. The LII signal is not likely to come from PAH fluorescence, which should occur prior to the 20-ns gate delay and would appear more consistently near the spray region.

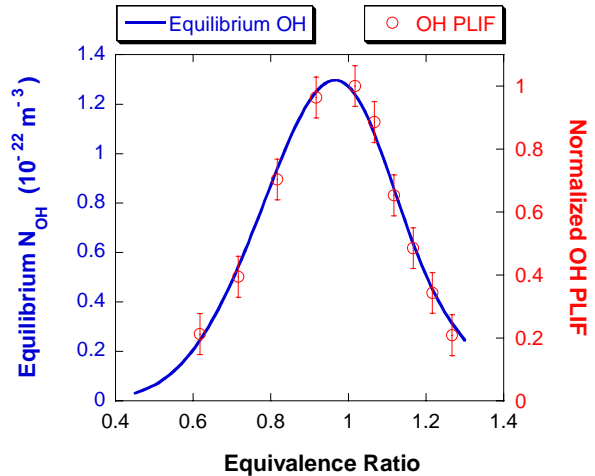


Fig. 9. Theoretical OH number density compared with OH-PLIF data in the recirculation zone [Region C in Fig. 7(c)]. OH-PLIF data are corrected for variations in fluorescence efficiency and Boltzmann fraction with ϕ (see Fig. 3).

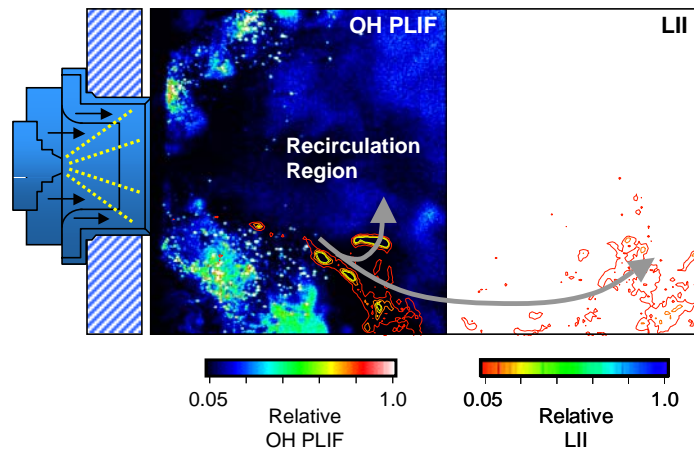


Fig. 10. Simultaneous OH PLIF (left half) and laser-induced incandescence (full image) at overall equivalence ratio of 1.0.

Background images collected without the laser sheet show that the contribution from nascent soot incandescence is less than 5%.

Thus, it is likely that soot formation is, in fact, initiated along the downstream region of the conical flame adjacent to the recirculation zone. The absence of OH PLIF in this region is quite evident in the lower half of the spray flame at low and high overall equivalence ratios [see Fig. 7(c) at $\phi = 0.9$], regardless of whether LII is detected. This region likely contains a rich mixture of fuel and air that escapes the main spray cone because of turbulent interactions. At low overall equivalence ratios [see Fig. 7(b) at $\phi = 0.9$], soot formed within this rich mixture may be oxidized by oxygen and hydroxyl radicals before entering the recirculation zone. At high equivalence ratios, soot formation is aided both by a drop in temperature and by the lack of an oxidizing partner. The soot formed in Region B is advected either downstream or into the recirculation zone.

3.4. Averaged Soot-Volume-Fraction Measurements

The combined use of planar LII, OH PLIF, and Mie scattering has been shown above to provide physical insight into soot formation in the current flame environment. Data described in the discussion that follows demonstrate the utility of LII and OH PLIF for studying the effects of fuel-inlet conditions on soot production. This is illustrated in Fig. 11, where the temporally and spatially averaged relative soot volume fraction is plotted as a function of overall equivalence ratio for the current spray flame. The LII data show an exponential increase in soot volume fraction with equivalence ratio. The sampling probe CNC data display a threshold effect at about $\phi = 1.0$, below which soot in the exhaust is effectively oxidized due to long residence times and greater quantities of O_2 and OH. In the primary zone of the combustor, there is less time to oxidize the soot. In addition, the local ϕ is higher in the primary zone than in the exhaust.

The LII experiment is also performed at two camera gate widths to assess the sensitivity of the data to particle-size effects. A bias toward higher particle sizes for the longer gate duration of 200 ns would be expected. Because of normalization, this bias appears as a slight decrease in signal at lower equivalence ratios for which particle sizes are expected to be smaller. This effect appears to be minimal in Fig. 11 (to within experimental uncertainty), suggesting that detection with a 50-ns gate is also free of significant particle-size effects.

The current measurement system is presently being used to study the effects of particulate-mitigating additives and varying fuel type on soot formation in swirl-stabilized combustors. Figure 12, for example, shows a comparison of the relative soot volume fraction for JP-8 and JP-8X45 (45% aromatic content). The JP-8 data from Fig. 11 are rescaled to that of JP-8X45 to allow a comparison on a semi-log plot. Both show an exponential increase with equivalence ratio, with the soot volume fraction of JP-8X45 varying between one to two orders of magnitude higher in the primary flame zone than that of JP-8.

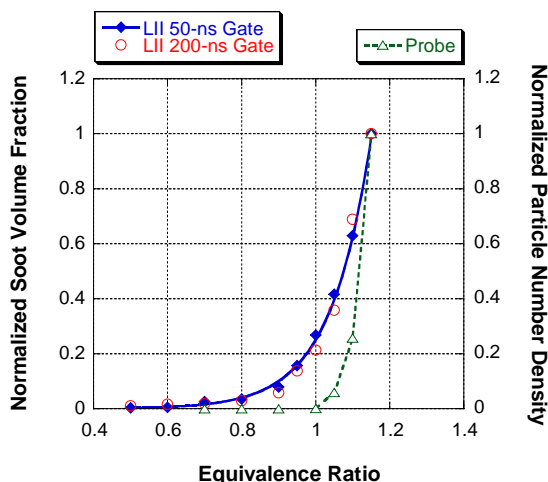


Fig. 11. LII and CNC data. LII measurements with camera gate of 50 ns are fit with exponential function.

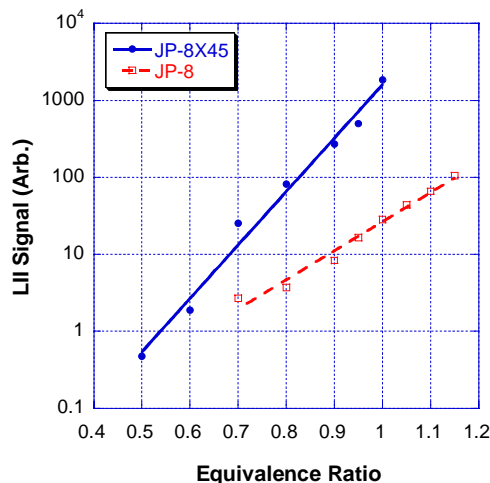


Fig. 12. Relative soot volume fraction for two different jet fuels.

4. Conclusions

A simultaneous planar LII, OH-PLIF, and Mie-scattering system is developed, tested, and demonstrated in a JP-8-fueled, liquid-spray, swirl-stabilized combustor. These combined diagnostics permit phenomenological characterization of soot-formation mechanisms in this highly turbulent environment by mapping the soot volume fraction, instantaneous flame zone, and fuel-droplet behavior. It is found that large-scale structures play a key role in flame intermittency and that soot formation is a strong function of spray-flame interactions as well as local equivalence ratio. Experimental and numerical studies in gaseous-fueled combustors may not capture these dynamics properly. Soot formation in the inner conical flame region correlates with regions of low OH PLIF and droplet Mie scattering. A qualitative study of equivalence-ratio effects on the OH-PLIF signals shows that equilibrium assumptions can be used for OH-signal correction in the recirculation zone. LII data indicate an exponential dependence on equivalence ratio with a strong dependence on fuel aromatic content. Future work includes a broader survey of fuel additives and fuel types.

Acknowledgments

We thank Dr. Vincent Belovich, Dr. Edwin Corporan, Dr. Matthew DeWitt, Dr. Viswanath Katta, and Theodore Williams for their technical input, as well as Michael Arstingstall and Charles Frayne for assistance with the combustor facility. Funding for this research was provided by the Air Force Research Laboratory, Propulsion Directorate, Wright-Patterson AFB, under Contract Nos. F33615-00-C-2068, F33615-D-03-M2829, and F33615-00-C-3020, and by the Air Force Office of Scientific Research (Dr. Julian Tishkoff, Program Monitor).

References

1. W.-W. Kim, S. Menon, and H. Mongia, "Large-eddy simulation of a gas turbine combustor flow," *Combust. Sci. Technol.* **143**, 25-62 (1999).
2. S. Wang, S.-Y. Hsieh, and V. Yang, "Numerical simulation of gas turbine swirl-stabilized injector dynamics," AIAA paper 2001-0334 (American Institute of Aeronautics and Astronautics, Reston, VA, 2001).
3. M. V. Heitor, and J. H. Whitelaw, "Velocity, Temperature, and Species Characteristics of the Flow in a Gas-Turbine Combustor," *Combust. Flame* **64**, 1-32 (1986).
4. A. F. Bicen, D. G. N. Tse, and J. H. Whitelaw, "Combustion Characteristics of a Model Can-Type Combustor," *Combust. Flame* **80**, 111-125 (1990).
5. T. J. Held, M. A. Mueller, S.-C. Li, and H. Mongia, "Data-driven model for NO_x, CO and UHC emissions for a dry low emissions gas turbine combustor," AIAA paper 2001-3425 (American Institute of Aeronautics and Astronautics, Reston, VA, 2001).
6. W. A. Eckerle, "Soot loading in a generic gas turbine combustor," AIAA paper 87-0297 (American Institute of Aeronautics and Astronautics, New York, NY, 1987).
7. T. C. Fang, C. M. Megaridis, W. A. Sowa, and G. S. Samuelsen, "Soot morphology in a liquid-fueled swirl-stabilized combustor," *Combust. Flame* **112**, 312-328 (1998).
8. D. R. Snelling, K. A. Thomson, G. J. Smallwood, and O. L. Gulder, "Two-dimensional imaging of soot volume fraction in laminar diffusion flames," *Appl. Opt.* **38**, 2478-1485 (1999).
9. J. D. Black, "Laser Induced Incandescence Measurements of Particles in Aero-Engine Exhausts," SPIE Vol. 3821, EUROPTO Conference on Environmental Sensing and Applications, Munich, Germany (1999).
10. T. P. Jenkins, J. L. Bartholomew, P. A. DeBarber, P. Yang, J. M. Seitzman, and R. P. Howard, "A laser-induced incandescence system for measuring soot flux in aircraft engine exhausts," AIAA paper 2002-3736 (American Institute of Aeronautics and Astronautics, Reston, VA, 2002).
11. R. J. Santoro, T. T. Yeh, J. J. Horvath, and H. G. Semerjian, "The transport and growth of soot particles in laminar diffusion flames," *Combust. Sci. Technol.* **53**, 89-115 (1987).
12. D. L. Urban and G. M. Faeth, "Soot research in combustion science: introduction and review of current work," AIAA paper 2001-0322 (American Institute of Aeronautics and Astronautics, Reston, VA, 2001).
13. Y.-H. Won, T. Kamimoto, H. Kobayashi, and H. Kosaka, "2-D soot visualization in unsteady spray flame by means of laser sheet scattering technique," SAE Tech. Paper 910223 (Society of Automotive Engineers, Warrendale, PA, 1991).

14. C. R. Shaddix, J. E. Harrington, and K. C. Smyth, "Quantitative Measurements of Enhanced Soot Production in a Flickering Methane / Air Diffusion Flame," *Combust. Flame* **99**, 723-732 (1994).
15. B. Quay, T.-W. Lee, T. Ni, and R. J. Santoro, "Spatially Resolved Measurements of Soot Volume Fraction Using Laser-Induced Incandescence," *Combust. Flame* **97**, 384-392 (1994).
16. R. L. Vander Wal and K. J. Weiland, "Laser-induced incandescence: Development and characterization towards a measurement of soot-volume fraction," *Appl. Phys. B* **59**, 445-452 (1994).
17. M. S. Brown, T. R. Meyer, J. R. Gord, V. M. Belovich, and W. M. Roquemore, "Laser-induced incandescence measurements in the reaction zone of a model gas turbine combustor," AIAA paper 2002-0393 (American Institute of Aeronautics and Astronautics, Reston, VA, 2002).
18. K. C. Smyth, J. H. Miller, R. C. Dorfman, W. G. Mallard, and R. J. Santoro, "Soot inception in a methane/air diffusion flame as characterized by detailed species profiles," *Combust. Flame* **62**, 157-181 (1985).
19. F. Cignoli, S. Benecchi, and Z. Giorgio, "Simultaneous one-dimensional visualization of OH, polycyclic aromatic hydrocarbons, and soot in a laminar diffusion flame," *Opt. Lett.* **17**, 229-231 (1992).
20. W.-P. Shih, J. G. Lee, and D. A. Santavicca, "Stability and emissions characteristics of a lean premixed gas turbine combustor," in the Twenty-Sixth Symposium (International) on Combustion (The Combustion Institute, Pittsburgh, PA, 1996).
21. R. E. Foglesong, T. R. Frazier, L. M. Flamand, J. E. Peters, and R. P. Lucht, "Flame structure and emissions characteristics of a lean premixed gas turbine combustor," AIAA paper 99-2399 (American Institute of Aeronautics and Astronautics, Reston, VA, 1999).
22. R. P. Lucht, D. W. Sweeney, and N. M. Laurendeau, "Laser-saturated fluorescence measurements of OH concentration in flames," *Combust. Flame* **50**, 189-205 (1983).
23. C. D. Carter, G. B. King, and N. M. Laurendeau, "Saturated fluorescence measurements of the hydroxyl radical in laminar high-pressure C₂H₆/O₂/N₂ flames," *Appl. Opt.* **31**, 1511-1522 (1992).
24. K. Lee and B. Chehroudi, "Structure of a swirl-stabilized spray flame relevant to gas turbine and furnaces," *J. Propul. Power* **11**, 1110-1117 (1995).
25. S. Roy, T. R. Meyer, R. P. Lucht, V. M. Belovich, E. Corporan, and J. R. Gord, "Temperature and CO₂-concentration measurements in the exhaust stream of a liquid-fueled combustor using dual-pump coherent anti-Stokes Raman scattering (CARS) spectroscopy," *Combust. Flame*, submitted for publication (2003).
26. A. C. Eckbreth (1996), "Laser diagnostics for combustion temperature and species," 2nd Ed., Gordon and Breach Publishers, The Netherlands.
27. S. R. Turns (1996), "An Introduction to Combustion," McGraw-Hill, New York.
28. A. H. Lefebvre (1999), "Gas turbine combustion," 2nd Ed., Taylor and Francis, Philadelphia, PA.
29. M. Tamura, P. A. Berg, J. Luque, J. E. Harrington, G. P. Smith, J. B. Jeffries, and D. R. Crosley, *Combust. Flame* **114**, 502-514 (1998).
30. T. Ni, J. A. Pinson, S. Gupta, and R. J. Santoro, "Two-dimensional imaging of soot volume fraction by the use of laser-induced incandescence," *Appl. Opt.* **34**, 7083-7091 (1995).
31. D. J. Bryce, N. Ladommatos, and H. Zhao, "Quantitative investigation of soot distribution by laser-induced incandescence," *Appl. Opt.* **39**, 5012-5022 (2000).
32. H. A. Michelsen, "Understanding and predicting the temporal response of laser-induced incandescence from carbonaceous particles," *J. Chem. Phys.* **118**, 7012-7045 (2003).

INFLUENCE OF FUEL TYPE AND OPERATING CONDITIONS ON PARTICULATES IN GAS-TURBINE COMBUSTORS

**Sarah K. Chelgren, Vincent M. Belovich, Edwin Corporan,
and James R. Gord**

Air Force Research Laboratory, Propulsion Directorate
1790 Loop Road North
Wright-Patterson Air Force Base, OH 45433

Matthew J. DeWitt

University of Dayton Research Institute
1790 Loop Road North
Wright-Patterson Air Force Base, OH 45433

Sukesh Roy and Terrence R. Meyer

Innovative Scientific Solutions, Inc.
2766 Indian Ripple Road
Dayton, OH 45440

ABSTRACT

A study to characterize the production of particulate-matter (PM) emissions is performed in a liquid-fueled model gas-turbine combustor while varying fuel type and operating conditions. Laser-induced incandescence (LII), OH planar laser-induced fluorescence (PLIF), and laser Mie scattering are used to track soot volume fraction, measure local equivalence ratio, and visualize droplet scattering in the reaction zone, respectively. A condensation nuclei counter (CNC) is employed to provide particle number density (PND) in the exhaust stream of the combustor, and a scanning mobility particle sizer (SMPS) is used to obtain particle-size distribution. In-situ and ex-situ PM emissions are measured for fuel aromatic content that varies from 0-45% by volume as well as for paraffinic fuels low in

aromatic and heteroatomic content. Consistent with results of previous studies, fuels containing aromatics, which have been shown to promote PM production, produce higher quantities of soot than straight-chain hydrocarbons. Laser-based measurements show a significant correlation among physical flame structure, fuel type, and particle number density.

Keywords: Gas-Turbine Combustor, Fuels, Soot, Particulates, Laser Diagnostics.

INTRODUCTION

During the past several years, increased concern has been expressed regarding the impact of aircraft emissions on the environment and public health. Despite the technological advances made during the past 50 years in attempts to reduce emissions from

aircraft turbine engines, the total emissions of the global aviation fleet have not decreased. This is due to the growth in the aviation industry and the increased demand for global transportation services, which was projected to increase at a rate of 3–5% per year before the September 11, 2001 terrorist attacks (1).

Aircraft emissions include primary combustion products that are present at the engine exit and secondary emissions produced in the atmosphere via chemical reactions. The aircraft emissions of primary concern are CO₂, soot particulates, and nitrogen and sulfur oxides. Although aircraft particulate-matter (PM) exhaust, at an estimated emission index (EI) of 0.04 g/kg-fuel (2), is a small fraction of the overall aircraft emissions, numerous studies have shown that these particles have serious environmental and health implications (3). Most of the PM emissions from turbine engines are smaller than 2.5 µm in diameter (PM_{2.5}); these are considered to be the most harmful since they can easily enter the respiratory system and cause respiratory and cardiovascular problems. Additionally, fine carbon particles tend to absorb unburned hydrocarbons (specifically, polycyclic aromatic hydrocarbons—PAH) that are carcinogenic and potentially can be absorbed in the lungs.

The Environmental Protection Agency (EPA) has recently adopted a revision of the PM regulation to require more stringent regulation of PM_{2.5} emissions (3). Additional guidelines include Executive Order 13148 (April 2000), Greening the Government Through Leadership in Environmental Management, that calls for a 40% - 50% reduction in pollutants by the end of 2006. Environmentally, soot particulates contribute to the formation of photochemical smog and provide nuclei for the formation of liquid droplets in the atmosphere that contribute to the formation of contrails and potential climate change.

The Turbine Engine Division's Combustion Branch at the Air Force Research Laboratory (AFRL) has taken an active role in characterizing combustion processes and flame structure (4). In the present work, the chemical and physical characteristics of several types of fuels were studied to explore their impact on the PM emissions from a CFM 56 combustor. The effort was focused on the relationship between aromatic content and PM production. Previous studies have been conducted on this relationship using a T63 combustor (5). In the present study, preliminary results have been

processed for four of the fuels tested. These results will help to elucidate the fuel characteristics—physical and/or chemical—that impact PM.

Swirl-stabilized liquid-spray injectors are commonly used in gas-turbine engines to achieve compact, stable, and efficient combustion. The flowfield in the primary zone of such a spray flame is characterized by high shear stresses and turbulent intensities that result in vortex breakdown and large-scale unsteady motions (6,7). These unsteady motions are known to play a key role in the formation of pollutant emissions such as carbon monoxide (CO), nitric oxide (NO), and unburned hydrocarbons (UHC) (8-10). Considerably less is known, however, about the mechanisms that lead to soot formation in swirl-stabilized, liquid-fueled combustors. Previous investigations have relied on exhaust-gas measurements and parametric studies to gain insight into the effects of various input conditions on soot loading (11-15). Much of the fundamental knowledge concerning soot formation is derived from investigations of laminar diffusion flames (16,17) with only a limited number of studies having focused on unsteady effects (18,19). The importance of considering unsteadiness and fluid-flame interactions was demonstrated by Shaddix et al. (19) who found that a forced methane/air diffusion flame produced a four-fold increase in soot volume fraction (as a result of increased particle size) as compared with a steady flame having the same mean fuel-flow velocity.

The goal of the current work was to study soot formation in the highly dynamic environment of a swirl-stabilized model combustor. This was accomplished by simultaneous imaging of the soot volume fraction and the hydroxyl-radical (OH) distribution using laser-induced incandescence (LII) and OH planar laser-induced fluorescence (PLIF), respectively. Residual Mie scattering from large droplets, which appears in the OH images but does not preclude signal interpretation, was used to a limited extent as a spray diagnostic. Probe data taken downstream of the combustor were also used for comparison. These data were taken at a different location, allowing possible confirmation of trends observed in the flame structure and comparison of in-situ and ex-situ results.

The utility of LII for two-dimensional imaging of soot volume fraction has been demonstrated in a number of investigations (20,21) and has been implemented in aircraft-engine exhaust streams

(14,15). Brown et al. (22) performed planar LII for soot-volume-fraction imaging in the reaction zone of a model gas-turbine combustor; their measurements demonstrated LII in the primary reaction zone but did not image the turbulent flame structure near the exit of the swirl cup. In the current work, we extend the work of Brown et al. (22) by performing LII at the exit of the swirl cup and by using OH PLIF as well.

The use of OH as a flame marker is typical in studies of soot formation in diffusion flames because of its close correlation with flame temperature (23,24). It has also been employed in a number of investigations of swirl-stabilized combustors (25,26). The use of laser-saturated OH LIF for *quantitative* measurements has also been demonstrated (27,28), although saturation is quite difficult in the case of planar measurements. In the current investigation we demonstrated semi-quantitative measurements in the recirculation region using excitation levels well below saturation. OH-PLIF measurements in the liquid-spray region are more qualitative because of simultaneous droplet scattering and non-equilibrium conditions.

The performance and accuracy of the planar LII and OH-PLIF systems were characterized in the current work and are described below. Instantaneous and averaged data from OH PLIF were then employed to provide insight into the turbulent nature of the swirl-stabilized spray flame at various equivalence ratios. The physical processes that govern the soot-formation process were visualized using simultaneous OH PLIF, LII, and droplet Mie scattering. Finally, the overall normalized intensity in the primary zone was tracked as a function of fuel composition.

EXPERIMENTAL

A. Swirl-Stabilized Combustor

The near-field structure of swirl-stabilized flames is highly dependent upon the characteristics of the fuel injector and the geometry of the surrounding flame tube. The injector configuration shown in Fig. 1 is a generic swirl-cup liquid-fuel injector used in ongoing fuel studies at the Atmospheric-Pressure Combustor-Research Complex of the Air Force Research Laboratory's Propulsion Directorate (29). It employs a pressure-swirl atomizer (Delavan Model 27710-8) with a nominal flow number of 1.6. The 4-cm exit diameter nozzle is centrally located in

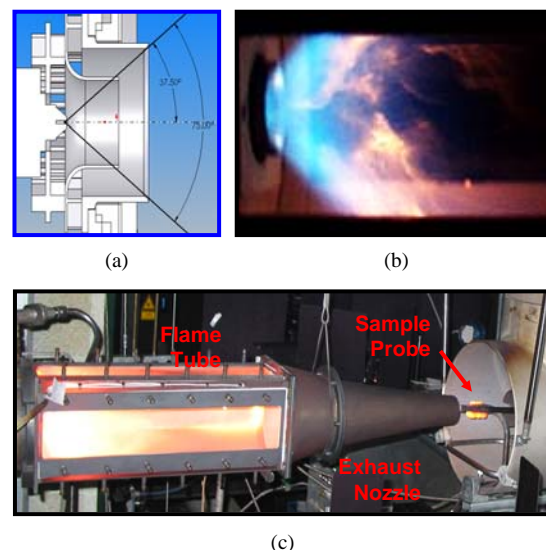


Fig. 1. (a) Dual-radial swirl-injector geometry (current study), (b) photograph of near-field flame structure, and (c) photograph of the test rig.

a 15.25-cm x 15.25-cm square cross-section dome-type combustor. The spray impinges upon a filming surface and is surrounded by dual-radial, counter-swirling-air co-flows to entrain the fuel, promote droplet breakup, and enhance mixing. The resulting three-dimensional conical flame [shown in Fig. 1(b)] is composed of several zones, including an outer droplet-vaporization/preheat region, an inner turbulent flame-brush region, and a recirculation zone that brings hot combustion products upstream along the centerline (30). After exiting the primary flame zone, the combustion products are allowed to mix thoroughly along the 48-cm-long flame tube before entering a 43-cm-long, 5.7-cm-exit-diameter exhaust nozzle that is designed to create a uniform exhaust-gas temperature and concentration profile.

Changes in overall equivalence ratio from $\Phi = 0.5$ to 1.10 (primary-zone equivalence ratio from $\Phi = 0.55$ to 1.3) were achieved in the current study by varying the pressure drop across the fuel-spray nozzle from about 1.5 to 10 atm, which resulted in fuel mass flow rates of 1.0 to 2.2 g/s, respectively. The fuel flow rate was measured using a Max Machinery positive-displacement flow meter with $\pm 0.5\%$ full-scale accuracy. The air-flow system consisted of three Sierra 5600 SLPM mass flow controllers with $\pm 1\%$ full-scale accuracy. The inlet air was heated to 450 K with a constant flow rate of ~ 0.028 kg/s. The air-pressure drop across the

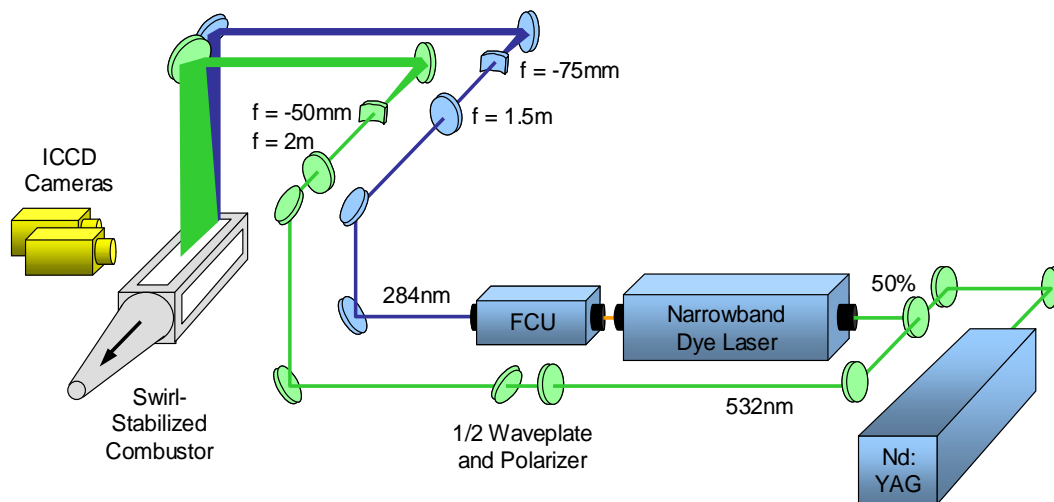


Fig. 2. Experimental setup for simultaneous OH PLIF and LII in an atmospheric-pressure, swirl-stabilized, liquid fueled, model gas-turbine combustor.

combustor dome was ~ 4.8 - 5.2% of the main supply. Most of the air flow entered the combustor through the swirl-cup injector, but a small percentage entered through aspiration holes along the aft wall. No liner air jets were used in the secondary zone; therefore, the fuel-air ratio depended almost entirely on the flow rates through the injector cup. The combustor is optically accessible via 75-mm-wide quartz windows along the top and sides for in-situ laser-based diagnostics.

B. OH-PLIF System

A review of PLIF fundamentals can be found in Eckbreth (1996) (31). As shown in the optical set-up in Fig. 2, 50% of the laser energy from a frequency-doubled, Q-switched Nd:YAG laser (Spectra-Physics Pro290) is used to pump a dye laser (Sirah Precision Scan), the output of which is frequency doubled to obtain wavelengths in the (1,0) band of the OH A-X system. The dye laser is tuned to the $Q_1(9)$ transition at 283.922 nm (in air), which exhibits less than a $\pm 2.5\%$ variation in the ground-level Boltzmann fraction, F_B , from 1600 to 2400K. This range of temperatures coincides with the equilibrium conditions one would expect for JP-8 fuel at the equivalence ratios used in this study (primary zone $\Phi = 0.55 - 1.3$) (32). The maximum laser energy available for OH PLIF was 24 mJ. A 1.5-m-focal-length, spherical plano-convex lens and a -75 -mm-focal-length plano-concave lens are used to form a laser sheet that enters the combustor through the top

window. The laser-sheet thickness is $330\text{ }\mu\text{m}$ at full-width-half-max (FWHM). The sheet width is $\sim 7\text{ cm}$, with a 3° full-angle divergence. A near top-hat sheet-width profile that drops to zero laser energy within about 1 mm is obtained by clipping the wings of the laser sheet at the last turning mirror above the combustor.

Fluorescence is collected from about 306-320 nm via the (1,1) and (0,0) bands of OH using an intensified charge-coupled device (ICCD) camera (Princeton Instruments PI-MAX SB) oriented approximately along the normal to the sheet. Two 1-mm-thick WG295 Schott Glass filters are used in front of the camera lens to reduce scattering from droplets at 283.922 nm, and a UG11 filter is employed to eliminate most of the flame emission, scattering from the LII laser wavelength of 532 nm, and fluorescence from PAH compounds. A 105-mm-focal-length $f/4.5$ UV lens is employed to collect the OH fluorescence, and an intensifier gate width of 20 ns is used to capture the OH signal. Images are typically collected with 2×2 binning to obtain adequate resolution (512×512) and framing rate (1.4 Hz). The pixel viewing area in each 2×2 superpixel is $200 \times 200\text{ }\mu\text{m}^2$.

The laser irradiance of $1.36 \times 10^7\text{ W/cm}^2$ is two to three orders of magnitude lower than the 90-95% saturation level (27,28). The OH-PLIF signal is, therefore, linearly related to laser-energy variations. Corrections were not made for laser-energy attenuation due to OH absorption and droplet

scattering; this led to signal uncertainties of $\pm 10\%$ in the lower region of each image. The effect of this error is substantially reduced in the upper half of the combustor where most of the data in this study were extracted. Shot-to-shot fluctuations in laser energy add an estimated $\pm 5\%$ uncertainty, as determined from data collected in a laminar diffusion flame with the same OH-PLIF system.

For measurements with low laser irradiance, the effect of collisional quenching on fluorescence efficiency must also be considered. For a given imaging system and laser irradiance, the OH-PLIF signal, S_{OH} , from each pixel volume is proportional to the number density of OH, N_{OH} , and the fluorescence efficiency, η .²⁶

$$S_{OH} \approx N_{OH} \eta = N_{OH} \frac{A_{OH}}{A_{OH} + Q_{OH}} \quad (1)$$

The fluorescence efficiency is proportional to the rate of spontaneous emission, A_{OH} , from molecules in the excited state and inversely proportional to the rate at which excited molecules are depleted via spontaneous emission and collisional quenching, Q_{OH} . Collisional quenching is a function of the temperature-, pressure-, and species-dependent quenching coefficient as well as the number density of the species (33). As a result of offsetting effects in the equilibrium combustion products of JP-8, the rate of collisional quenching is found to be fairly constant for equivalence ratios less than unity. Under rich conditions the conversion of CO to CO₂ decreases substantially, which leads to an increase in collisional quenching and a decrease in fluorescence efficiency. In regions where equilibrium assumptions are valid, the LIF signal can be used along with Eq. (1) and the Boltzmann fraction, F_B , to determine the relative OH number density; this will be discussed further in the Results and Discussion Section. In the liquid-spray region where lean and rich pockets of fuel can co-exist, qualitative signal interpretation is problematic since the fluorescence efficiency may vary by more than $\pm 30\%$, based on local conditions.

C. Mie Scattering

Mie scattering was obtained using the same setup as that for the OH-PLIF system. It was found that two WG295 color-glass filters (CVI Laser) and parallel-polarization detection would provide optimal OH LIF sensitivity while minimizing the likelihood of damaging the ICCD because of intense

levels of droplet scattering. Large droplet clusters appear primarily near the injector exit, and single droplets with trailing flames are often observed traveling into the recirculation region. The trailing flames of these droplets appear neither in the off-line images nor at higher equivalence ratios and, therefore, are not attributable to scattering from fuel vapor or fluorescence from broadband sources such as PAH compounds. The droplet-scattering signal intensity is about one order of magnitude higher than that of the OH PLIF, but it occurs primarily at isolated points. The OH-PLIF signal levels (determined from probability density functions) are assigned to a false-color table from black to red, while the Mie scattering signals are above this range and appear in white.

D. LII System

Some of the first two-dimensional visualizations of soot volume fraction using LII were performed by Santoro and co-workers (20) and by Vander Wal and Weiland (21). Urban and Faeth (17) published reviews regarding the effects of various parameters such as laser fluence and profile as well as camera gate width and delay. The LII optical layout employed in the current study is shown schematically in Fig. 2, where 50% of the energy from a frequency-doubled Nd:YAG is formed into a sheet using a 2-m plano-convex spherical lens and a -50-mm plano-concave cylindrical lens. The FWHM thickness of the laser sheet is about 700 μm within the measurement volume. As is the case for the OH LIF laser sheet, the long 2-m-focal-length lens is used to minimize variations in laser-sheet thickness within the measured region. The sheet width is ~ 14 cm, with a full angle divergence of 6° within the test section. The wings of the LII sheet are clipped prior to the last turning mirror to generate a near top-hat profile that drops to zero laser energy within about 2 mm. To reduce systematic errors due to intensity variations in the laser sheet and laser extinction in the measurement volume, the LII system is operated in the saturated regime, which is measured in the current system to be above 200 mJ/cm^2 . This saturation regime, found at similar fluence levels in the literature, (34,35) reduces the uncertainty in the relative soot-volume-fraction measurements to about $\pm 10\%$ for the full width of the laser sheet.

The LII signal is detected using a 1024×1024 ICCD camera (Princeton Instruments PI-MAX SB-MG) and an f/1.2 58-mm-focal-length glass lens.

After 4x4 pixel binning, the measurement resolution is about $575 \times 575 \mu\text{m}^2$. A 500-nm short-pass filter (CVI Laser) is used for detection from 415 to 500 nm, which reduces contributions from nascent soot particles, OH fluorescence/chemiluminescence, and red-shifted fluorescence from PAH compounds. The relatively short-lived PAH fluorescence is also minimized by employing a time-delayed detection scheme. Scattering from the 532-nm laser source is eliminated through the use of a 532-nm zero-degree reflective mirror, in addition to the 500-nm short-pass filter and delayed detection. Light leakage from flame luminosity while the ICCD intensifier is gated off is minimized through the use of a 25-ms-gate Uniblitz shutter. A camera delay of 20 ns after the laser pulse was found to reduce laser scatter to almost nearly the background level while maintaining LII signal-to-noise ratios greater than 20:1. The LII signal decayed quickly within the first 200 ns after the laser pulse. The long decay in signal after 200 ns is dominated by larger, slow-cooling particles. Using a gate width of 50 ns, errors due to particle-size effects are estimated to be on the order of 5-10% (34).

E. Combined LIF/LII System

The OH-PLIF and LII cameras are synchronized using an external delay generator that is driven by the advanced Q-switch TTL output of the Nd:YAG laser. The precise camera delay required to capture each image is imposed using an onboard timing generator in each ICCD controller. The laser pulses are coincident to within several nanoseconds so that no fluid movement occurs between LIF and LII detection. Because of spatial constraints within the test cell, both cameras are positioned on the same side of the combustor at slight 3.5° angles to overlap the two imaged regions. The PLIF image area overlaps the left half of the LII image nearest the injector cup in order to minimize off-axis defocusing. After camera alignment, registration images are collected for use in post-processing.

F. Ex-Situ Measurements and Instrumentation

PM and gaseous emissions were measured to quantify the effect of fuel composition and equivalence ratio on the relative production rates and selectivities of the exhaust constituents. Specifically,

combination of these ex-situ results with those obtained in the primary zone of the combustor will significantly assist in deconvoluting the complicated physical and chemical mechanisms that influence PM and emission production. Two oil-cooled probes facing the exhaust flow immediately downstream of the converging end-adaptor were installed to obtain “representative” samples of the engine exhaust. One probe, used for on-line quantitation of the PM aerosol characteristics, introduced dilution air at the probe tip to prevent particle loss to the wall, water condensation, and saturation of the analytical equipment. The diluted sample was drawn to the analytical instruments via a vacuum pump; dilution air and sample flows were controlled using high-precision Brooks 5850i mass-flow controllers. The PND (count of particles per unit volume) was quantified using a TSI Model 3022A CNC and a MetOne Model 237B Laser Particle Counter (LPC)—the CNC is used to quantify small-diameter (<300 nm) particles, while the LPC is used to quantify large-diameter (300-5000 nm) particles. A TSI Model 3936 Scanning Mobility Particle Sizer (SMPS) used to classify the particles by size has a measurement range of 7-1000 nm. For these tests, more than 99.9% of the PND was <300 nm in size; therefore, the PND quantified using the CNC will be used for subsequent comparison.

The undiluted sample was used for further off-line characterization of the PM emissions and quantitation of major and minor gaseous species. Particulate samples were collected on quartz and paper filters for off-line analysis, which includes determination of the engine smoke number, temperature-programmed oxidation to characterize the relative carbon composition, and analysis of absorbed PAHs via Gas Chromatography/Mass Spectrometry (GC/MS). Gaseous emissions were quantified using an MKS MultiGas 2030 Fourier-Transform Infrared (FTIR)-based gas analyzer, a Horiba FIA-510 total hydrocarbon analyzer, and a M&C PMA-10 oxygen analyzer. The FTIR analyzer quantifies non-symmetric gaseous species at parts-per-billion (ppb) to percent sensitivity. The MultiGas 2030 can simultaneously analyze more than 30 gases and perform analysis in gas streams containing up to 30% water.

Fuel	H/C ratio	% Aromatic	Sulfur (ppm)	Surface Tension (dynes/cm) @ 22°C	Density (kg/m ³) @ 60°F	Viscosity (cSt) @ 40°C	Flash Point (°C)
JP-8X 45 (high in aromatics & cycloparaffins)	1.67	40.8	400	31.5	889	1.74	57
JP-8X 20 (high in aromatics & cycloparaffins)	1.78	18.5	100	27.5	856	1.77	53
JP-8 (POSF-3773)	1.91	15.9	700	28.0	800	1.24	60
MCH (methylcyclohexane)	2.00	0.0	0	25.1	770	0.75	-3
JP-8/Isopar H (50/50) (fuel blend)	2.02	7.3	300	24.9	780	1.30	50
Semi-Synthetic (50% coal-derived & 50% Jet A)	2.02	10.0	400	26.0	788	1.28	54
Isopar H (iso-paraffin solvent)	2.14	<0.01	0	24.1	780	1.38	54
Norpar-13 (normal-paraffin solvent)	2.15	0.03	0	27.0	784	1.82	97
Isopar M (iso-paraffin solvent)	2.15	<0.05	0	24.5	790	2.24	93

Fig. 3. Properties of fuels studied.

G. Fuels

Properties of the fuels investigated are shown in Fig. 3. These fuels were selected to study the impact of major constituents in JP-8 on particulate emissions. The JP8-X45 and JP8-X20 are experimental fuels developed in the mid-1980s under an Air Force sponsored program to provide an economical high energy density fuel to replace JP-10 (a single component missile fuel) (36). These JP8-X fuels were made by hydrotreating light cycle oil—a highly aromatic by-product of catalytic cracking of petroleum—to obtain a fuel high in naphthenes (cycloparaffins). The main difference between JP8 and the JP8-X fuels is the larger quantity of normal and branched paraffinic components and the lower concentration of cyclic (both aromatic and cycloparaffin) compounds in JP8. The semi-synthetic fuel is a 50/50 blend of Jet-A with a coal-derived Fischer-Tropsch fuel. Roets et al. provide a detailed description of the fuel (37). The neat synthetic fuel, produced in Sasolburg, South Africa, is high in iso-paraffins and contains zero aromatics. Based on the amount of aromatics in the 50/50 blend, the Jet-A fuel in the semi-synthetic fuel contains approximately 20% aromatics by volume. The Exxon solvents Norpar-13, Isopar M, and Isopar H were tested to evaluate paraffinic fuels with zero aromatic content.

RESULTS AND DISCUSSION

A. LII and Mie Scattering

The fuels were evaluated in the liquid-fueled CFM-56 combustor at atmospheric conditions to investigate the production of PM emissions while varying fuel type and operating conditions. LII and LIF techniques were compared with trends observed from a CNC which provided PND in the exhaust stream of the combustor. The effects of the chemical characteristics of these fuels on particulate formation are discussed below.

Results were obtained by first averaging each data set of images (800 images using LII and 200 images using LIF) into a single averaged image for each run. This averaged image was then corrected by subtracting the average background file. Specific regions of interest (ROI) were selected for each run. These ROI were consistent for each data set on a given day to enable a better comparison of runs. Statistics were run and average intensity recorded. Representative LII data can be seen in Fig. 4. The false-color scale is common for all images and varies from 5 to 100% of the maximum signal. Dense regions are shown as white regions of high intensity, whereas regions of low intensity are blue in color.

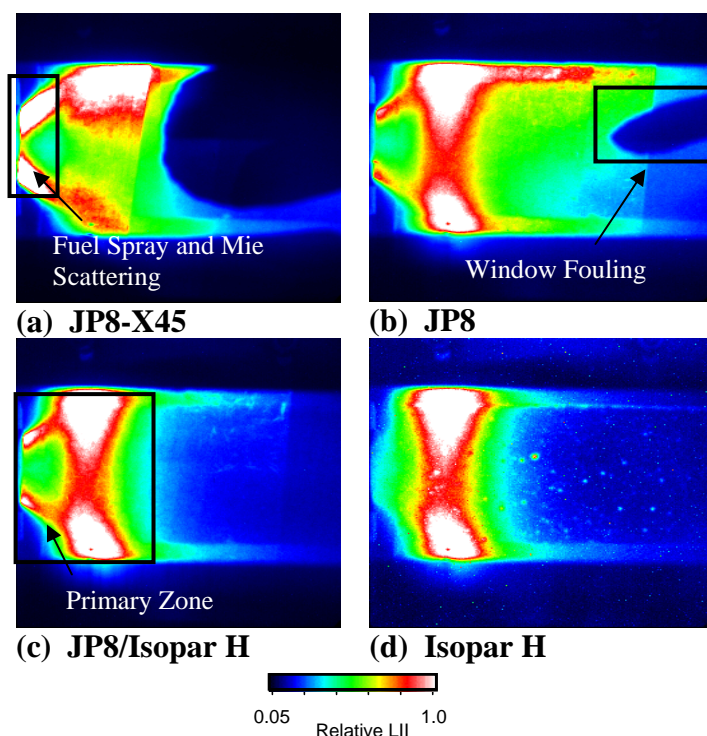


Fig. 4. LII images are representative of a) JP8-X45, b) JP8, c) JP8/Isopar H (50/50) blend, d) and Isopar H. False-color scale from 5 to 100% of peak average at an equivalence ratio of 1.10.

Mie scattering can be used for qualitative tracking of changes in spray characteristics and soot production, as illustrated in Fig. 4. Four fuels are shown, all at an equivalence ratio of 1.1. JP8-X45 has a dense, high-intensity fuel spray as compared with standard JP8 and JP8/Isopar H (50/50) blend. Isopar H has no apparent high-intensity region in the fuel-spray zone. This may be the result of the changing fuel physical characteristics and their effects on injection pressure and atomization. Soot production for these four fuels also follows a similar trend, probably due to their chemical structure. For JP8-X45, a significant soot formation is observed on the quartz viewing window, beginning at an equivalence ratio of 0.9. This dark region indicates where the ICCD cameras were unable to capture the incandescence phenomenon because of window fouling. For standard JP8 the soot formation is also obvious, but not to the extent observed for X45.

Four critical factors in soot development are chemical structure, fuel atomization, prevalence of oxidant, and temperature. The importance of chemical structure is apparent in a comparison of fuels with various aromatic levels. As illustrated in

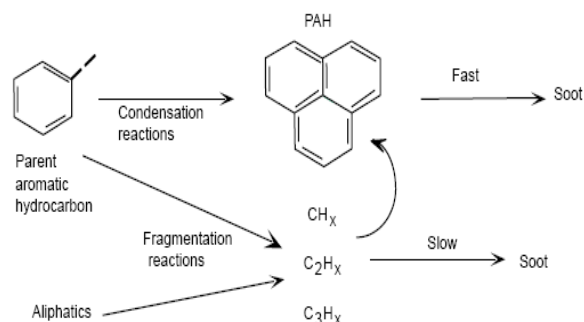


Fig 5. Simplified soot-formation mechanism (38).

Fig. 5, compounds with a parent aromatic hydrocarbon have faster reaction rates, thus accelerating the rate of soot production. Aliphatic compounds must undergo additional reaction steps to form a ring structure, consequently delaying soot formation. Fuels with high levels of aromatic and cycloparaffin content, such as JP8-X45, are higher in normalized intensity than fuels such as JP8, Isopar H, and JP-8/Isopar H (50/50) blend, which are lower in aromatic content. This can be seen in Fig. 6 where data trends were normalized to the highest JP8 signal. This normalized intensity is indicative of relative soot production.

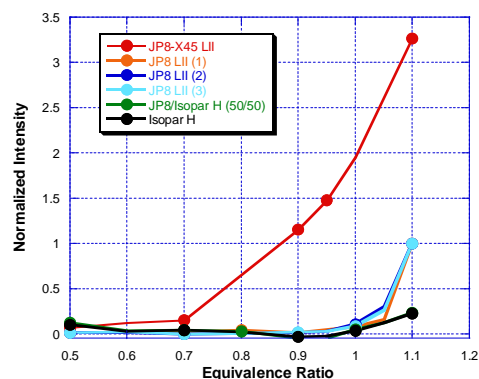


Fig. 6. Normalized intensity as a function of equivalence ratio for LII (days 1, 2, and 3 respectively). Intensity is normalized to maximum JP8.

Several results of significance are illustrated in Fig. 6. The JP8-X45 has a substantially greater normalized intensity (more than three times as high) than JP8 alone. Furthermore, the Isopar and the JP-8/Isopar H (50/50) blend are lower in normalized intensity than JP8. These outcomes are expected from their chemical structure. JP8-X45 has the

highest aromatic content and, therefore, would be expected to be the highest soot producer; Isopar H and its blend have minimal levels of aromatics and are anticipated to have a lower level of soot production. It is also important to note the high degree of reproducibility among the JP8 fuels, even though they were run on different days, as demonstrated in Fig. 7.

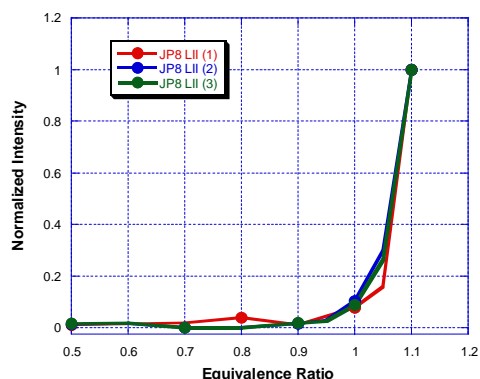


Fig. 7. Comparison of JP8 LII data over multiple testing days.

A correlation can be established between soot formation and aromatic content, as shown in Fig. 8. Normalized intensity increases with percent aromatic content, indicating greater soot formation. Furthermore, each equivalence ratio follows approximately the same trend. This indicates that fuel structure or composition is a major driving force in soot formation. This relationship can also be used to validate the trends observed in Fig. 5, where soot formation and locations of high intensity increase with percent aromatic content. At lower aromatic content, greater variations can be observed as a function of equivalence ratio. These differences may be attributable to spray atomization and droplet formation, which can only be observed using in-situ techniques.

In-situ techniques have the capability to image flame characteristics and soot production in the primary flame zone, where soot first begins to develop. Ex-situ techniques, such as probes, are point measurements performed at the exit of the combustor. These methods can be employed to confirm basic trends observed in-situ.

Fuel and probe comparisons were made for the fuels studied. Standard JP8 data collected over multiple days using LII were plotted versus ex-situ probe data by normalizing JP8 to the maximum signal (see Fig. 9). An exponential trend was

observed as equivalence ratio increased; this was also demonstrated by Lynch et al. (39). Good agreement between normalized JP8 LII results and probe data prompted similar LII/probe comparisons for the remaining fuels.

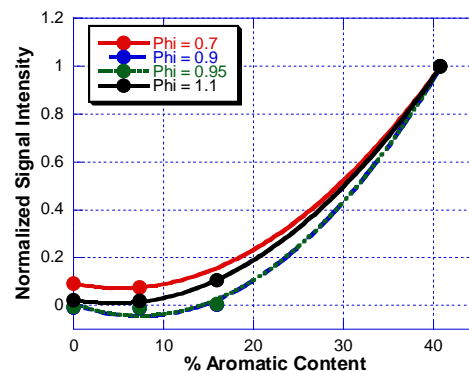


Fig. 8. Normalized signal increases with aromatic content. Four trends are shown as different equivalence ratios.

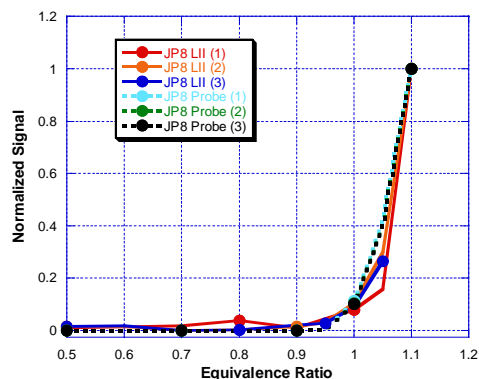


Fig. 9. Comparison of data of JP8 and probe for three successive test days represented as 1, 2, and 3.

At equivalence ratios below 0.7, JP8-X45 LII intensity values showed close agreement with probe data; however, above 0.7 substantial differences were observed. One source of variance could be the large amount of soot formation on the window, which prevented data collection in this region. If a larger ROI were permissible, LII intensity might increase which would result in closer agreement. Thresholds were also noted to occur at different equivalence ratios, 0.7 and 0.9 respectively, for data collected using LII and probe methods, as can be observed in Fig. 10. The threshold indicates where soot formation begins exponential growth, as further explained by OH PLIF. Probe and LII data for the JP8/Isopar H (50/50) blend, Fig. 11, show better

agreement at higher equivalence ratios than previously observed with JP8-X45.

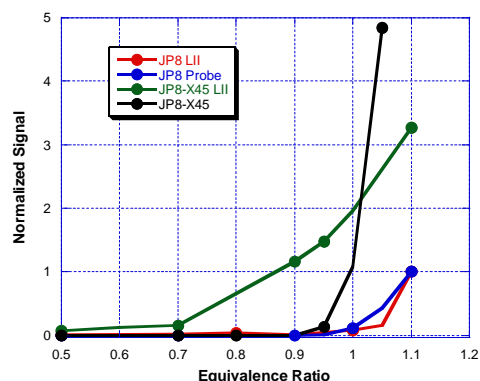


Fig. 10. Comparison of data from JP8-X45, JP8, and probe normalized to maximum JP8.

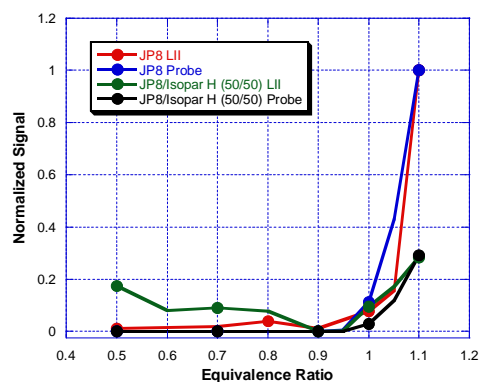


Fig. 11. Comparison of data from JP8/Isopar H (50/50), JP8, and probe normalized to maximum JP8.

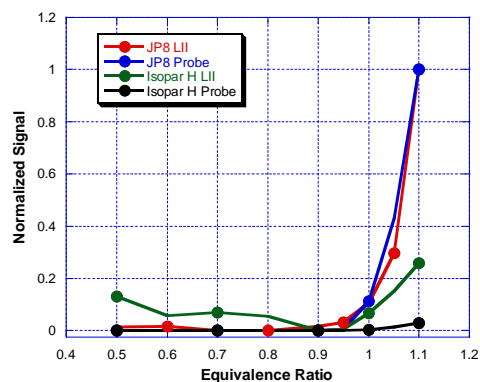


Fig. 12. Comparison of data from JP8, Isopar H, and probe normalized to maximum JP8.

Fluctuations at fuel-lean conditions, observed in Isopar H in Fig 12, may be a result of temperature variations that affect soot oxidation. Additionally, at fuel-rich conditions particle burnout may result in a deviation between probe and LII intensity. Particle burnout occurs as longer residence times are achieved in the flame tube, allowing more mixing to

occur and increasing the reaction time. Particle size may also affect burnout. This relationship will be examined more closely in further studies.

B. LIF

OH PLIF is used to assess changes in flame structure and to track qualitative changes in local equivalence ratio. OH is often used as an indicator of flame temperature (Lynch et al. (39)).

Maximum normalized OH-PLIF intensity occurs at an overall equivalence ratio between 0.8 and 0.9, which can be observed in similar graphs for different fuels with various chemical properties (Fig. 13).

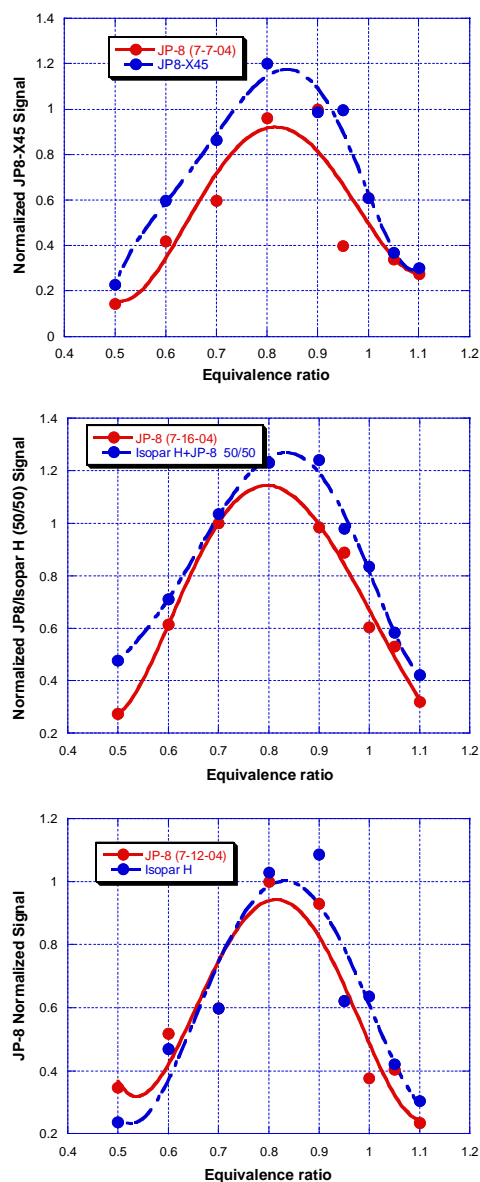


Fig. 13. OH PLIF data trends for the four fuels. Signal normalized to maximum JP8.

Lynch et al. (39) note a peak equilibrium OH signal occurring at an equivalence ratio of 1.0. Similarly occurring peaks for different fuels clearly demonstrate the comparability of data sets due to similar local-equivalence-ratio trends between fuels.

When comparing LIF and LII data, one important trend which can be observed in Fig. 14, should be noted. As the ratio of fuel to air increases, the OH signal, indicating the presence of oxidizing agents, also increases and eventually forms a bell-shaped curve. At the maximum of the OH bell curve, the lowest LII signal is observed. As the OH signal decreases, the LII signal begins to increase, and eventually becomes exponential. An inverse relationship exists between the LIF and LII signal, as first discussed by Lynch et al. (39). The peak OH indicates the greatest prevalence of oxidizing agents; however, as the equivalence ratio increases, the lack of oxidizing agent leads to increased soot production.

This oxidizing agent can be tracked using single-shot LIF data, as shown in Fig. 15. These single-shot images provide qualitative information concerning the flame structure. The presence or absence of droplet formation can be easily noted when examining Mie scattering in these images. The JP8-X45 fuel has the greatest amount of droplet formation, and standard JP8 has only a minimal amount. Isopar H has no droplets, perhaps due to better atomization and more fuel breakup. Isopar H also has no clearly defined primary zone. The JP8/Isopar (50/50) blend does exhibit a distinct primary zone as well as fuel droplets although not to the extent of JP8-X45 and JP8. Larger amounts of oxidant, represented as green in the figure, exist in the fuel-rich regions of JP8 as compared to JP8-X45. However, the largest amount of oxidant in the fuel-rich regions is found upon examination of Isopar H, as denoted by the higher OH signal. This trend is also observed in the recirculation zone where the impact made on soot can be significant. Isopar H has a significant amount of OH in the recirculation zone, which leads to greater oxidation. JP8 has minimal amounts of OH in this zone, again correlating with soot trends observed earlier. JP8/Isopar H (50/50) blend has OH levels greater than standard JP8 although not as prevalent as with Isopar H. JP8-X45 has negligible amounts of OH in the recirculation zone, supporting the greater production of soot observed in LII data.

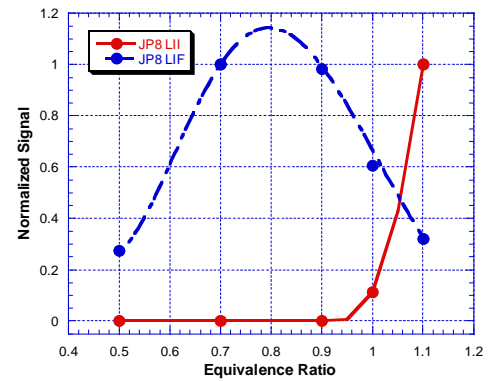


Fig. 14. Comparison of LII and LIF data trends.

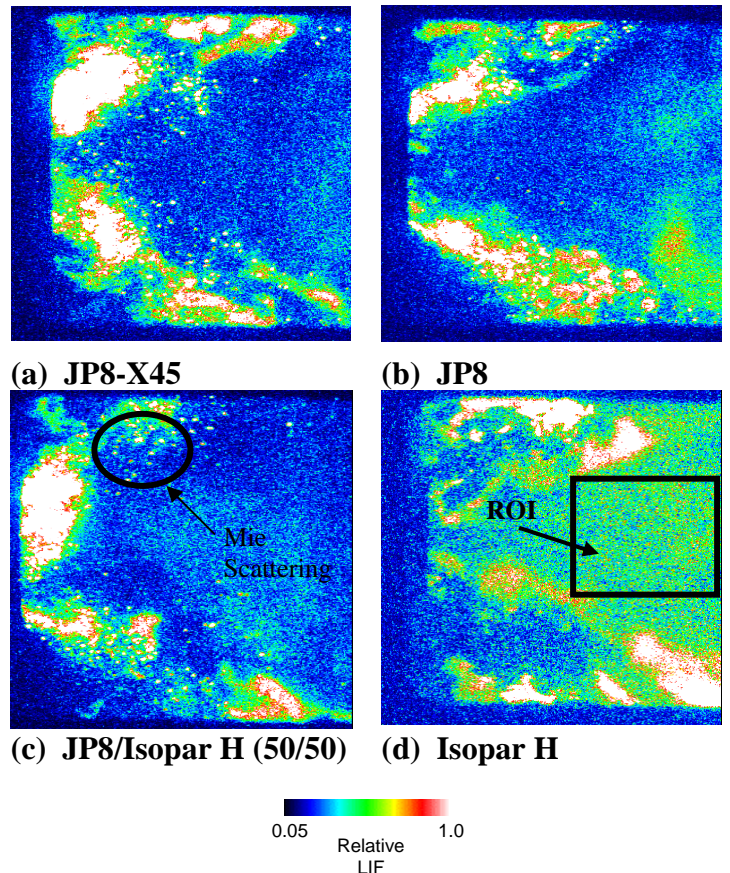


Fig. 15. Single shot LIF data at an equivalence ratio of 1.10 for a) JP8-X45, b) JP8, c) JP8/Isopar H (50/50), d) and Isopar H. Also shown is a typical ROI.

CONCLUSIONS

LII/LIF techniques can provide valuable insight into combustion processes and flame structure. These techniques allow in-situ measurements such as in the present study imaging of fuel spray and flame structure that are not possible with current ex-situ methods; however, ex-situ measurements provide valuable quantitative data for comparison purposes.

LII/LIF can be used qualitatively and semi-quantitatively for utilities such as tracking OH concentrations, locations of soot formation, and spray characteristics.

Preliminary results show a correlation between OH levels, soot production, and chemical structure. Regions of high OH intensity, indicating greater levels of oxidant, correspond to regions of lower soot production. Another indicator of lowered soot production is minimal aromatic content. Preliminary results exhibit a trend with soot production exponentially increasing with aromaticity (Fig. 8).

ACKNOWLEDGMENTS

The authors would like to acknowledge Mr. Joe Miller of Universal Technology Corporation and Ms. Amy Lynch of the Air Force Research Laboratory (AFRL) for their technical support. This work is supported by AFRL/PRTC and AFRL/PRTG and CEVV (Civil Engineering Pollution Control). The work of UDRI is supported by the Air Force Research Laboratory (AFRL) under cooperative research agreement number F33615-03-2-2347.

REFERENCES

1. National Research Council, 2002, "The Greener Skies: Reducing Environmental Impacts of Aviation."
2. International Civil Aviation Organization, 1995, "Aircraft Exhaust Emissions," *Annex 16*, Vol. II, Second Ed.
3. National Research Council, 1998, "Research Priorities for Airborne Particulate Matter, 1. Immediate Priorities and a Long-Range Research Portfolio," National Academy Press.
4. Corporan, E., Roquemore, W. M., Jacobson, A., Harrison, W. E., and Phelps, D., 2002, "Air Force Programs to Reduce Particulate Emissions from Aircraft," AIAA 2002-3722, AIAA Joint Propulsion Conference.
5. Corporan, E., Monroig, O., Wagner, M., DeWitt, M. J., "Influence of Fuel Chemical Composition on Particulate Matter Emissions of a Turbine Engine," ASME paper GT2004-54335, 2004.
6. Kim, W.-W., Menon, S., and Mongia, H. (1999), "Large-eddy simulation of a gas turbine combustor flow," *Combust. Sci. Technol.* 143:25-62.
7. Wang, S., Hsieh, S.-Y., and Yang, V., "Numerical simulation of gas turbine swirl-stabilized injector dynamics," AIAA paper 2001-0334, 2001.
8. Heitor, M. V., and Whitelaw, J. H. (1986), "Velocity, Temperature, and Species Characteristics of the Flow in a Gas-Turbine Combustor," *Combust. Flame* 64:1-32.
9. Bicen, A. F., Tse, D. G. N., and Whitelaw, J. H. (1990), "Combustion characteristics of a model can-type combustor," *Combust. Flame* 80:111-125.
10. Held, T. J., Mueller, M. A., Li, S.-C., and Mongia, H., "Data-driven model for NO_x, CO and UHC emissions for a dry low emissions gas turbine combustor," AIAA paper 2001-3425, 2001.
11. Eckerle, W. A., "Soot loading in a generic gas turbine combustor," AIAA paper 87-0297, 1987.
12. Fang, T. C., Megaridis, C. M., Sowa, W. A., and Samuelsen, G. S. (1998), "Soot morphology in a liquid-fueled swirl-stabilized combustor," *Combust. Flame* 112:312-328.
13. Snelling, D. R., Thomson, K. A., Smallwood, G. J., and Gulder, O. L. (1999), "Two-dimensional imaging of soot volume fraction in laminar diffusion flames," *Appl. Opt.* 38:2478-1485.
14. Black, J. D. (1999), "Laser induced incandescence measurements of particles in aero-engine exhausts," EUROPTO Conference on Environmental Sensing and Applications, Munich, Germany, pp. 209-215.
15. Jenkins, T. P., Bartholomew, J. L., DeBarber, P. A., Yang, P., Seitzman, J. M., and Howard, R. P., "A laser-induced incandescence system for measuring soot flux in aircraft engine exhausts," AIAA paper 2002-3736, 2002.
16. Santoro, R. J., Yeh, T. T., Horvath, J. J., and Semerjian, H. G. (1987), "The transport and growth of soot particles in laminar diffusion flames," *Combust. Sci. Technol.* 53:89-115.
17. Urban, D. L., and Faeth, G. M., "Soot research in combustion science: introduction and review of current work," AIAA paper 2001-0322, 2001.
18. Won, Y.-H., Kamimoto, T., Kobayashi, H., and Kosaka, H., "2-D soot visualization in unsteady spray flame by means of laser sheet scattering technique," SAE Tech. Paper 910223, 1991.
19. Shaddix, C. R., Harrington, J. E., and Smyth, K. C. (1994), "Quantitative Measurements of Enhanced Soot Production in a Flickering

- Methane / Air Diffusion Flame," *Combust. Flame* 99:723-732.
20. Quay, B., Lee, T.-W., Ni, T., and Santoro, R. J. (1994), "Spatially Resolved Measurements of Soot Volume Fraction Using Laser-Induced Incandescence," *Combust. Flame* 97:384-392.
 21. Vander Wal, R. L., and Weiland, K. J. (1994), "Laser-induced incandescence: Development and characterization towards a measurement of soot-volume fraction," *Appl. Phys. B* 59:445-452.
 22. Brown, M. S., Meyer, T. R., Gord, J. R., Belovich, V. M., and Roquemore, W. M., "Laser-induced incandescence measurements in the reaction zone of a model gas turbine combustor," AIAA paper 2002-0393, 2002.
 23. Smyth, K. C., Miller, J. H., Dorfman, R. C., Mallard, W. G., and Santoro, R. J. (1985), "Soot inception in a methane/air diffusion flame as characterized by detailed species profiles," *Combust. Flame* 62:157-181.
 24. Cignoli, F., Benecchi, S., and Giorgio, Z. (1992), "Simultaneous one-dimensional visualization of OH, polycyclic aromatic hydrocarbons, and soot, in a laminar diffusion flame," *Opt. Lett.* 17:229-231.
 25. Shih, W.-P., Lee, J. G., and Santavicca, D. A. (1996), "Stability and emissions characteristics of a lean premixed gas turbine combustor," in the Twenty-Sixth Symposium (International) on Combustion (The Combustion Institute), pp. 2771-2778.
 26. Foglesong, R. E., Frazier, T. R., Flamand, L. M., Peters, J. E., and Lucht, R. P., "Flame structure and emissions characteristics of a lean premixed gas turbine combustor," AIAA paper 99-2399, 1999.
 27. Lucht, R. P., Sweeney, D. W., and Laurendeau, N. M. (1983), "Laser-saturated fluorescence measurements of OH concentration in flames," *Combust. Flame* 50:189-205.
 28. Carter, C. D., King, G. B., and Laurendeau, N. M. (1992), "Saturated fluorescence measurements of the hydroxyl radical in laminar high-pressure C₂H₆/O₂/N₂ flames," *Appl. Opt.* 31:1511-1522.
 29. Roy, S., Meyer, T. R., Lucht, R. P., Belovich, V. M., Corporan, E., and Gord, J. R., "Temperature and CO₂ concentration measurements in the exhaust stream of liquid-fueled combustor using dual-pump coherent anti-Stokes Raman scattering (CARS) spectroscopy," submitted for publication in *Combust. Flame*, 2003.
 30. Lee, K., and Chehroudi, B. (1995), "Structure of a swirl-stabilized spray flame relevant to gas turbine and furnaces," *J. Prop. Power* 11:1110-1117.
 31. Eckbreth, A. C. (1996), "Laser diagnostics for combustion temperature and species," 2nd Ed., Gordon and Breach Publishers, The Netherlands.
 32. Turns, S. R. (1996), "An Introduction to Combustion," McGraw-Hill, New York.
 33. Tamura, M., Berg, P. A., Luque, J., Harrington, J. E., Smith, G. P., Jeffries, J. B., and Crosley, D. R. (1998), "Collisional quenching of NO A, CH A, and OH A in low pressure hydrocarbon flames," *Combust. Flame* 114:502-514.
 34. Ni, T., Pinson, J. A., Gupta, S., and Santoro, R. J. (1995), "Two-dimensional imaging of soot volume fraction by the use of laser-induced incandescence," *Appl. Opt.* 34:7083-7091.
 35. Michelsen, H. A. (2003), "Understanding and predicting the temporal response of laser-induced incandescence from carbonaceous particles," *J. Chem. Phys.* 118:7012-7045.
 36. Hall, L. W., 1987, "Production of Jet Fuel Samples from Light Cycle Oil and Light Pyrolysis Oil," AFWAL-TR-87-2001.
 37. Roets, P., Botha, J. J., Moses, C. A., and Stavinoha, L. L., 1998, "Stability and Handling of Sasol Semi-Synthetic Jet Fuel," Proceedings of the International Conference on Stability and Handling of Liquid Fuels, 6th, Vancouver, B. C., Oct. 13-17, 1997, Vol. 2, pp. 789-804.
 38. Lefebvre, A. H., 1983, "Gas Turbine Combustion," 1st Edition.
 39. Lynch, A. C., Belovich, V. M., Corporan, E., Gord, J. R., Roy, S., and Meyer, T. R., "Application of Laser Imaging for Studies of Particulate Formation in Gas-Turbine Combustion," AFRC-JFRC 2004.

APPLICATION OF LASER IMAGING FOR STUDIES OF PARTICULATE FORMATION IN GAS-TURBINE COMBUSTION

Amy C. Lynch, James R. Gord, Edwin Corporan, Vincent M. Belovich
Air Force Research Laboratory, Propulsion Directorate
1950 Fifth Street
Wright-Patterson Air Force Base, OH 45433

Terrence R. Meyer, Sukesh Roy
Innovative Scientific Solutions, Inc.
2766 Indian Ripple Road
Dayton, OH 45440

ABSTRACT

The goal of the current investigation is to study soot formation in the highly dynamic environment of a swirl-stabilized, liquid-fueled combustor. This is accomplished using simultaneous imaging of the soot volume fraction and hydroxyl-radical (OH) distribution in the primary reaction zone using laser-induced incandescence (LII) and OH planar laser-induced fluorescence (PLIF), respectively. Residual droplet Mie scattering is also detected in the OH-PLIF diagnostic system and is used to a limited extent as a spray diagnostic. The performance and accuracy of the planar LII and OH-PLIF systems are characterized in the current work and demonstrated in studies of jet fuels and soot-mitigating additives. Preliminary analyses of the data indicate that the flame in the near field of the injector is highly perturbed by large-scale structures and that fluid-flame interactions have a significant impact on local equivalence ratio and soot formation. Rich pockets of fuel and air along the interface between the spray flame and recirculation zone serve as locations for soot inception. The effect of local equivalence ratio is determined from semi-quantitative analysis of the OH-PLIF data and good agreement with equilibrium calculations in the recirculation region. Spatially

averaged LII measurements demonstrate that soot volume fraction in the primary flame zone increases exponentially with equivalence ratio, and are compared with particle-sampling data collected in the exhaust stream.

Keywords: Gas-Turbine Combustor, Soot, LII, OH, PLIF.

INTRODUCTION

Swirl-stabilized liquid-spray injectors are commonly used in gas-turbine engines to achieve compact, stable, and efficient combustion. The flowfield in the primary zone of such a spray flame is characterized by high shear stresses and turbulent intensities that result in vortex breakdown and large-scale unsteady motions.^{1,2} These unsteady motions are known to play a key role in the formation of pollutant emissions such as carbon monoxide (CO), nitric oxide (NO), and unburned hydrocarbons (UHC).³⁻⁵ Considerably less is known, however, about the mechanisms that lead to soot formation in swirl-stabilized liquid-fueled combustors. Previous investigations have relied on exhaust-gas measurements and parametric studies to gain insight into the effects of various input conditions on soot

loading.⁶⁻¹⁰ Much of the fundamental knowledge concerning soot formation is derived from investigations of laminar diffusion flames,^{11,12} with only a limited number of studies having focused on unsteady effects.^{13,14} The importance of considering unsteadiness and fluid-flame interactions was demonstrated by Shaddix et al.,¹⁴ who found that a forced methane/air diffusion flame produced a four-fold increase in soot volume fraction (as a result of increased particle size) as compared with a steady flame having the same mean fuel-flow velocity.

The goal of the current work is to study soot formation in the highly dynamic environment of a swirl-stabilized JP-8-fueled model combustor. This is accomplished by simultaneous imaging of the soot volume fraction and hydroxyl-radical (OH) distribution using laser-induced incandescence (LII) and OH planar laser-induced fluorescence (PLIF), respectively. Residual Mie scattering from large droplets, which appears in the OH images but does not preclude signal interpretation, is used to a limited extent as a spray diagnostic.

The utility of LII for two-dimensional imaging of soot volume fraction has been demonstrated in a number of investigations^{15,16} and has been implemented in aircraft engine exhaust streams.^{9,10} Brown et al.¹⁷ performed planar LII for soot-volume-fraction imaging in the reaction zone of a model gas-turbine combustor; their measurements demonstrated LII in the primary reaction zone but did not image the turbulent flame structure near the exit of the swirl cup. In the current work, we extend the work of Brown et al.¹⁷ by performing LII at the exit of the swirl cup and by the addition of OH PLIF.

The use of OH as a flame marker is typical in studies of soot formation in diffusion flames because of its close correlation with flame temperature.^{18,19} It has also been employed in a number of investigations of swirl-stabilized combustors.^{20,21} The use of laser-saturated OH LIF for *quantitative* measurements has also been demonstrated,^{22,23} although saturation is quite difficult in the case of planar measurements. In the current investigation we demonstrate semi-quantitative measurements in the recirculation region using excitation levels well below saturation. OH-PLIF measurements in the liquid-spray region are more qualitative because of simultaneous droplet scattering and non-equilibrium conditions.

The performance and accuracy of the planar LII and OH-PLIF systems are characterized in the

current work and described below. Instantaneous, averaged, and statistical data from OH PLIF are then employed to provide insight into the turbulent nature of the swirl-stabilized spray flame at various equivalence ratios. The physical processes that govern the soot formation process are visualized using simultaneous OH PLIF, LII, and droplet Mie scattering. Finally, the overall soot volume fraction in the primary zone is tracked as a function of fuel composition.

NOMENCLATURE

- A_{OH} – Rate of spontaneous emission (s^{-1})
- F_B – Boltzmann fraction
- N_{OH} – Number density of OH molecules (m^{-3})
- Q_{OH} – Collisional quenching rate (s^{-1})
- S_{OH} – relative OH-PLIF signal
- η – fluorescence efficiency
- Φ – Equivalence ratio

EXPERIMENTAL SET UP

A. Swirl-Stabilized Combustor

The near-field structure of swirl-stabilized flames is highly dependent upon the characteristics of the fuel injector and the geometry of the surrounding flame tube. The injector configuration shown in Fig. 1 is a generic swirl-cup liquid-fuel injector used in ongoing fuel studies at the Atmospheric-Pressure Combustor-Research Complex of the Air Force Research Laboratory's Propulsion Directorate.²⁴ It employs a pressure-swirl atomizer (Delavan model 27710-8) with a nominal flow number of 1.6. The 4-cm exit diameter nozzle is centrally located in a 15.25 cm x 15.25 cm square cross-section dome-type combustor. The spray impinges upon a filming surface and is surrounded by dual-radial, counter-swirling-air co-flows to entrain the fuel, promote droplet break-up, and enhance mixing. The resulting three-dimensional conical flame, shown in Fig. 1(b), is composed of several zones including an outer droplet-vaporization/preheat region, an inner turbulent flame brush region, and a recirculation zone that brings hot combustion products upstream along the centerline.²⁵ After exiting the primary flame zone, the combustion products are allowed to mix thoroughly along the 48-cm long flame tube before entering a 43-cm-long, 5.7-cm exit-diameter exhaust nozzle that is designed to create a uniform exhaust-gas temperature and concentration profile.

Changes in overall equivalence ratio from $\Phi = 0.5$ to 1.15 (primary zone equivalence ratio from $\Phi = 0.55$ to 1.3) were achieved in the current study by varying the pressure drop across the fuel-spray nozzle from about 1.5 to 10 atm, which resulted in fuel mass flow rates of 1.0 to 2.2 g/s, respectively. The fuel flow rate is measured using a Max Machinery positive-displacement flow meter with $\pm 0.5\%$ full-scale accuracy. The air-flow system consists of three Sierra 5600 SLPM mass flow controllers with $\pm 1\%$ full-scale accuracy. The inlet air is heated to 450 K with a constant flow rate of ~ 0.028 kg/s. The air-pressure drop across the combustor dome was ~ 4.8 to 5.2% of the main supply. Most of the air flow enters the combustor through the swirl-cup injector, but a small percentage enters through aspiration holes along the aft wall. No liner air jets are used in the secondary zone; therefore, the fuel-air ratio depends almost entirely on the flow rates through the injector cup.

The combustor is optically accessible via 75-mm-wide quartz windows along the top and sides for in-situ laser-based diagnostics. In addition, particulate emissions at the exit of the exhaust nozzle are characterized using a TSI Model 3022A Condensation Nuclei Counter (CNC) to provide a count of particles per unit volume (particle number density), and a TSI Model 3936 Scanning Mobility Particle Sizer (SMPS) to obtain the particle size distribution. Particulate emissions are captured and transported to the analytical instruments via an oil-cooled probe, which consists of three concentric tubes with three fluid passages. The outermost passage flows recirculating cooling oil, which is kept at 150°C for all tests. The middle annulus provides particle-free dry dilution air, and the center passage transports the diluted sample to the instruments. The probe is installed facing the flow in the center and near the exit of the combustor to help capture a “representative” sample of the exhaust and avoid

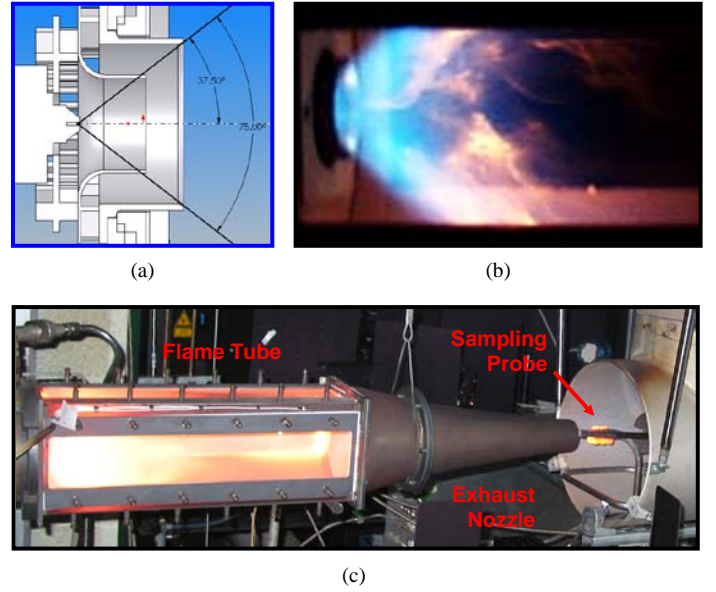


Fig. 1. (a) Dual-radial swirl-injector geometry used in the current study (b) photograph of near-field flame structure, and (c) photograph of the test rig.

diluting or contaminating with surrounding air. The sample line is heated to 75°C, and the sample is diluted at the probe tip to help prevent water condensation and particulate loss to the wall due to high wall-sample temperature gradients. Sharp bends in the sample line were avoided to reduce particle loss.

B. OH-PLIF System

A review of PLIF fundamentals can be found in Eckbreth (1996).²⁶ As shown in the optical set-up in Fig. 2, 50% of the laser energy from a frequency-doubled, Q-switched Nd:YAG laser (Spectra-Physics Pro290) is used to pump a dye laser (Sirah Precision Scan), the output of which is frequency doubled to obtain wavelengths in the (1,0) band of the OH A-X system. The dye laser is tuned to the $Q_1(9)$ transition at 283.922 nm (in air), which has less than a $\pm 2.5\%$ variation in the ground-level Boltzmann fraction, F_B ,

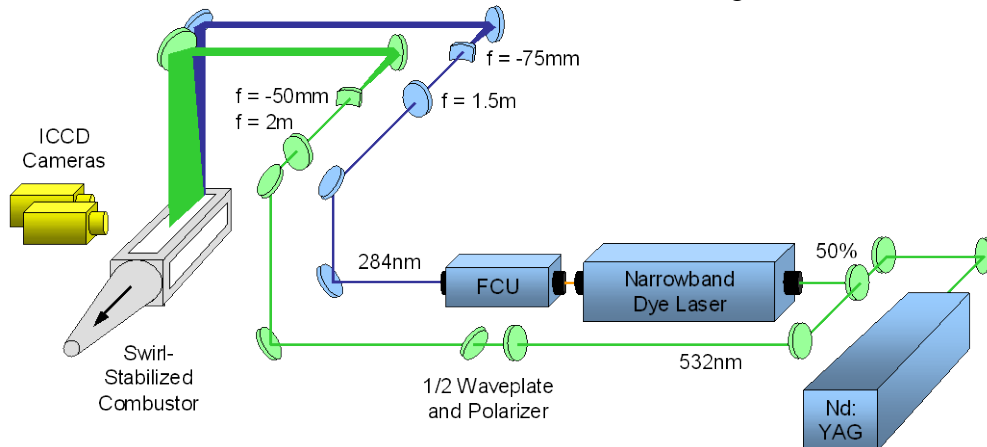


Fig. 2. Experimental setup for simultaneous OH PLIF and LII in an atmospheric-pressure, swirl-stabilized, liquid fueled, model gas-turbine combustor.

from 1600 to 2400K. This range of temperatures coincides with the equilibrium conditions one would expect for JP-8 fuel at equivalence ratios used in this study (primary zone $\Phi = 0.55 - 1.3$).²⁷ Considering the full range of possible temperatures from 1100 to 2400K within typical lean and rich flammability limits,²⁸ the Boltzmann fraction for this transition varies by up to $\pm 12.5\%$. The maximum laser energy available for OH PLIF was 24 mJ. A 1.5-m-focal-length spherical plano-convex lens and a -75-mm-focal-length plano-concave lens are used to form a laser sheet that enters the combustor through the top window. The laser-sheet thickness is 330 μm at full-width-half-max (FWHM) as measured by translating a knife-edge across the beam. The sheet width is ~ 7 cm, with a 3° full-angle divergence. A near top-hat sheet-width profile that drops to zero laser energy within about 1 mm is obtained by clipping the wings of the laser sheet at the last turning mirror above the combustor.

Fluorescence is collected from about 306 to 320 nm via the (1,1) and (0,0) bands of OH using an intensified charge-coupled device (ICCD) camera (Princeton Instruments PI-MAX SB) oriented approximately along the normal to the sheet. Two 1-mm thick WG295 Schott Glass filters are used in front of the camera lens to reduce scattering from droplets at 283.922 nm, and a UG11 filter is employed to nearly eliminate flame emission, scattering from the LII laser wavelength of 532nm, and fluorescence from polycyclic-aromatic-hydrocarbon (PAH) compounds. A 105-mm-focal-length f/4.5 UV lens is employed to collect the OH fluorescence, and an intensifier gate width of 20 ns is used to capture the OH signal. Images are typically collected with 2x2 binning to obtain adequate resolution (512x512) and framing rate (1.4 Hz). The pixel viewing area in each 2x2 superpixel is $200 \times 200 \mu\text{m}^2$.

Based on the dimensions of the OH-PLIF laser sheet and total laser energy of 24 mJ, it is estimated that the laser irradiance of $1.36 \times 10^7 \text{ W/cm}^2$ is two to three orders of magnitude lower than the 90-95% saturation level.^{22,23} The OH-PLIF signal is, therefore, linearly related to laser-energy variations. OH-PLIF signal corrections (typ. $\pm 15\%$) in the axial direction are performed in post-processing based on measurements of the laser-sheet profile after each run. Signal variation (typ. $\pm 3\%$) due to the 3° laser-sheet expansion in the cross-stream direction is also

corrected in post-processing. Corrections are not made for laser-energy attenuation due to OH absorption and droplet scattering; this leads to signal uncertainties of $\pm 10\%$ in the lower region of each image. The effect of this error is substantially reduced in the upper half of the combustor where most of the data in this study is extracted. Shot-to-shot fluctuations in laser energy add an estimated $\pm 5\%$ uncertainty, as determined from data collected in a laminar diffusion flame with the same OH-PLIF system.

For measurements with low laser irradiance, the effect of collisional quenching on fluorescence efficiency must also be considered. For a given imaging system and laser irradiance, the OH-PLIF signal, S_{OH} , from each pixel volume is proportional to the number density of OH, N_{OH} , and the fluorescence efficiency, η .²⁶

$$S_{\text{OH}} \approx N_{\text{OH}} \eta = N_{\text{OH}} \frac{A_{\text{OH}}}{A_{\text{OH}} + Q_{\text{OH}}} \quad (1)$$

The fluorescence efficiency is proportional to the rate of spontaneous emission, A_{OH} , from molecules in the excited state and inversely proportional to the rate at which excited molecules are depleted via spontaneous emission and collisional quenching, Q_{OH} . Collisional quenching is a function of the temperature-, pressure-, and species-dependent quenching coefficient as well as the number density of the species.²⁹ As a result of offsetting effects in the equilibrium combustion products of JP-8, the rate of collisional quenching is found to be fairly constant for equivalence ratios of less than unity. Under rich conditions the conversion of CO to CO_2 decreases substantially and leads to an increase in collisional quenching and a decrease in fluorescence efficiency. In regions where equilibrium assumptions are valid, the LIF signal can be used along with Eqn. 1 and the Boltzmann fraction, F_B , to determine the relative OH number density; this will be discussed further in the results section. In the liquid-spray region where lean and rich pockets of fuel can co-exist, qualitative signal interpretation is problematic since the fluorescence efficiency could vary by more than $\pm 30\%$ based on local conditions.

C. Mie-Scattering

Mie scattering was obtained using the same setup as for the OH-PLIF system. It was found that two WG295 color-glass filters (CVI Laser) and parallel-

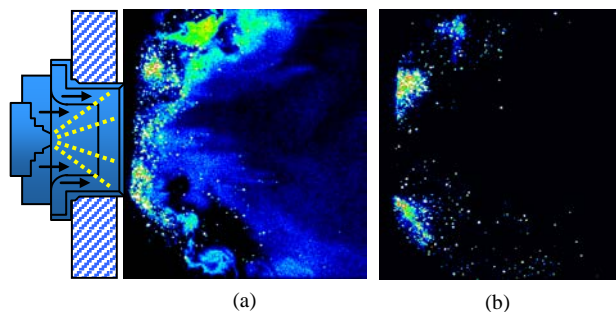


Fig. 3. Raw signal from (a) OH PLIF and droplet Mie scattering while on $Q_1(9)$ line of (1,0) band in A-X system and (b) droplet Mie scattering while off the OH line. Overall $\phi = 0.7$.

polarization detection would provide optimal OH LIF sensitivity while minimizing the likelihood of damaging the ICCD because of intense levels of droplet scattering. When tuned off the OH absorption line, as shown in Fig. 3(b), the intense, highly localized droplet scatter can be distinguished from the large, more uniformly distributed OH layers. Large droplet clusters appear primarily near the injector exit, and single droplets with trailing flames are often observed traveling into the recirculation region, as shown in Fig. 3(a). The trailing flames of these droplets do not appear in the off-line images nor at higher equivalence ratios and, therefore, are not attributable to scattering off of fuel vapor or fluorescence from broadband sources such as PAH compounds. The droplet-scattering signal intensity is about one order of magnitude higher than that of the OH PLIF, but it occurs primarily at isolated points. The OH-PLIF signal levels (determined from probability density functions) are assigned to a false-color table from black to red, while the Mie scattering signals are above this range and appear in white.

D. LII System

Some of the first two-dimensional visualizations of soot volume fraction using LII were performed by Santoro and co-workers¹⁵ and by Vander Wal and Weiland.¹⁶ The effects of various parameters such as laser fluence, laser-sheet profile, detection wavelength, camera gate width, and camera gate delay have been explored in a number of follow-up investigations.³⁰⁻³² A list of reviews on the subject is provided by Urban and Faeth.¹² The LII optical layout employed in the current study is shown schematically in Fig. 2, where 50% of the energy from a frequency-doubled Nd:YAG is formed into a

sheet using a 2-m plano-convex spherical lens and a -50-mm plano-concave cylindrical lens. The FWHM thickness of the laser sheet is about $700 \mu\text{m}$ within the measurement volume, as measured by traversing a knife-edge across the sheet. As is the case for the OH LIF laser sheet, the long 2-m-focal-length lens is used to minimize variations in laser-sheet thickness within the measured region. The sheet width is ~ 14 cm, with a full angle divergence of 6° within the test section. An overall tilt of 5° is used to overlap the LII and PLIF laser sheets. The wings of the LII sheet are clipped prior to the last turning mirror to generate a near top-hat profile that drops to zero laser energy within about 2 mm. To reduce systematic errors due to intensity variations in the laser sheet and due to laser extinction in the measurement volume, the LII system is operated in the saturated regime, measured in the current system to be above $200 \text{ mJ}/\text{cm}^2$. This saturation regime, found at similar fluence levels in the literature,^{30,32} reduces the uncertainty in the relative soot volume fraction measurements to about $\pm 10\%$ for the full width of the laser sheet.

The LII signal is detected using a 1024×1024 ICCD camera (Princeton Instruments PI-MAX SB-MG) and an f/1.2, 58-mm-focal-length glass lens. After 4×4 pixel binning, the measurement resolution is about $575 \times 575 \mu\text{m}^2$. A 500 nm short-pass filter (CVI Laser) is used for detection from 415 to 500 nm, which reduces contributions from nascent soot particles, OH fluorescence/chemiluminescence, and red-shifted fluorescence from PAH compounds. The relatively short-lived PAH fluorescence is also minimized by employing a time-delayed detection scheme. Scattering from the 532-nm laser source is eliminated through the use of a 532-nm zero-degree reflective mirror in addition to the 500-nm short-pass filter and delayed detection. Light leakage from flame luminosity while the ICCD intensifier is gated off is minimized through the use of a 25-ms-gate Uniblitz shutter. During post-processing the residual background signal from flame luminosity is subtracted from each image. A color scale is chosen with a minimum value corresponding to 5% above the background and a maximum value of 100% of the peak in each image.

To optimize the timing of LII detection, data were collected in the swirl-stabilized flame for a number of camera-intensifier-gate delays and widths. A camera delay of 20 ns after the laser pulse was found to reduce laser scatter to nearly the

background level while maintaining LII signal-to-noise ratios greater than 20:1. The LII signal decayed quickly within the first 200 ns after the laser pulse. The long decay in signal after 200 ns is dominated by larger, slow-cooling particles. Using a gate width of 50 ns, errors due to particle size effects are estimated to be on the order of 5-10%.³⁰

E. Combined LIF/LII System

The OH-PLIF and LII cameras are synchronized using an external delay generator driven by the advanced Q-switch TTL output of the Nd:YAG laser. The precise camera delay required to capture each image is imposed using an onboard timing generator in each ICCD controller. The laser pulses are coincident to within several nanoseconds so that no fluid movement occurs between LIF and LII detection. Because of spatial constraints within the test cell, both cameras are positioned on the same side of the combustor at slight 3.5° angles to overlap the two imaged regions. The PLIF image area overlaps the left half of the LII image nearest the injector cup in order to minimize off-axis defocusing. After camera alignment, registration images are collected for use in post-processing.

RESULTS AND DISCUSSION

A. Average and Instantaneous Flame Structure

The average and instantaneous OH distributions at overall equivalence ratios (Φ) ranging from 0.5 to 1.15 are shown in Figs. 4(a) to 4(f). All images are background subtracted and corrected for laser-sheet intensity variations and laser-sheet divergence. The effect of laser attenuation is evident in the lower flame region, with signal levels that are 10% less than the upper flame region. The false color scale is common for all images and varies from 5% to 100% of the maximum OH signal as determined by probability density functions at $\Phi = 0.5$.

Two main features of the flame structure become apparent when analyzing the series of images in Fig. 4. The first is that the flame structure evolves from a single- to multi-layer reaction zone. The second is the prominent role that turbulence plays in determining this structure.

A classical five-zone description of pressure-jet hollow-cone spray combustion³³ consists of a dense spray, primary flame zone, rich-premix zone, rich secondary combustion zone, and a recirculation zone. The dense spray region in the near field is

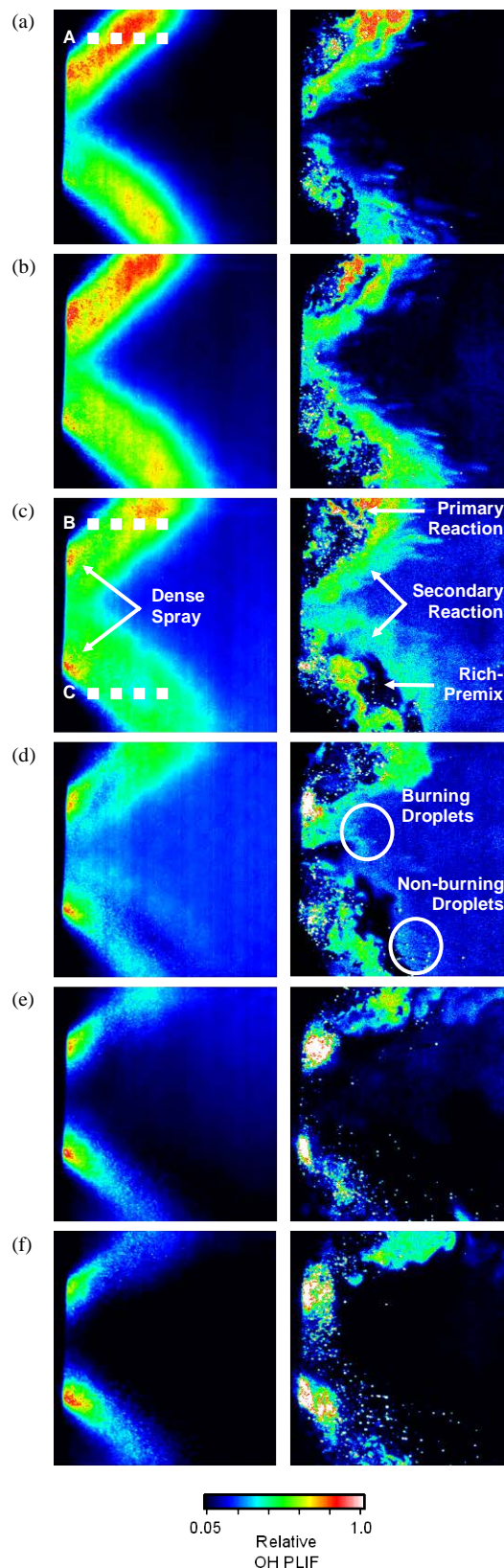


Fig. 4. 200-shot average (left) and instantaneous (right) OH-PLIF images at overall ϕ of (a) 0.5, (b) 0.6, (c) 0.7, (d) 0.8, (e) 1.0, and (f) 1.15. False-color scale from 5% to 100% of the peak average (4100) and instantaneous (5250) counts at $\phi = 0.5$.

dominated by fuel vapor and cannot support combustion. The primary zone is formed by the combustion of fuel vapor from small droplets. A rich-premix zone is then formed along the spray direction due to evaporation of larger droplets. This is followed by rich combustion and product recirculation.

For the current injector geometry, the primary reaction zone is highly perturbed by large-scale structures that entrain reactants across the entire width of the flame layer, as shown in the instantaneous image of Fig. 4(a). At higher overall Φ , these turbulent motions become more prominent and the primary flame zone, labeled in Fig. 4(c), becomes more intermittent. Also, an intermittent rich-premix region is formed along the inner cone of the spray, as labeled in Fig. 4(c). This region comes into direct contact with the recirculation zone and reacts with any available oxygen, thereby establishing a secondary flame zone as labeled in Fig. 4(c). At overall $\Phi = 0.5$, the primary and secondary reaction zones are essentially merged, and a gradual separation in the flame layers takes place at higher equivalence ratios. This phenomenon is most visible in the lower half of the average image in Fig. 4(d), where the primary and secondary reaction zones are completely separated by the rich-premix zone. Since the air-flow rate is held constant for all test conditions in this study, these dynamics may be attributable to the behavior of the liquid spray as the injection pressure is increased, as well as to changes in local equivalence ratio. Experiments and computations based on gaseous-fuel injection, therefore, may not capture this behavior.

To further elucidate the role of intermittency and the character of the rich-premix region, it is useful to present probability density functions (PDFs) of the OH-PLIF signal. PDFs are mathematically defined as histograms with areas normalized to unity. They are helpful in highly intermittent flames for which the ensemble average does not accurately represent the instantaneous field. For example, they can be used to detect whether an increase in OH signal results from an increase in OH within large-scale structures or from an increase in their frequency of occurrence. They can also be used to discriminate against Mie scattering, which occurs with much higher camera counts than the OH PLIF.

Figures 5(a) and 5(b) show PDF data for overall $\Phi = 0.5$ and 0.7, respectively, across the upper flame zone just above the dense spray, as shown in Fig. 4.

Each profile in Fig. 5 represents a different downstream position, as noted in the legend. At each point, signals from 0 to 6000 counts from 200 images are tabulated into bins of 200 counts. The contribution from droplet scattering, which typically occurs with tens of thousands of counts per pixel, is not significant at these locations since the PDFs drop to zero by 5000-6000 counts.

The PDF profiles for overall $\Phi = 0.5$ in Fig. 5(a) change significantly from 12 - 34.8 mm because of changes in large-scale structure dynamics across the flame. The PDFs at 12 and 19.6 mm are bimodal in character, with the low-signal peak representing cases when the measurement point is outside of a flame structure and the high-signal peak representing cases when the measurement point is within a flame structure. As one crosses the center of the flame layer, the PDFs are increasingly weighted toward the high-signal peak such that the low signal peak is almost not visible at 27.2 mm. Note that both the low and high signal peaks remain “stationary” from 12 mm to 27.2 mm, indicating that the fluid composition within the large scale-structures is nearly constant in this region. Beyond this point, the PDFs take on a “marching” character. Specifically, the PDF profiles are shifting to lower signal levels. This indicates that the influence of large-scale entrainment of unburned reactant is reduced in this region. Strikingly similar behavior is found in the PDFs of non-reacting turbulent jets, with stationary PDFs in regions dominated by large-scale structures and marching PDFs in regions dominated by gradient mixing.^{34,35}

The PDF profiles for the upper flame at overall $\Phi = 0.7$ follow the same trends as for those at overall $\Phi = 0.5$. This is evident in Fig. 5(b) in which the PDFs from $x = 12 - 27.2$ mm are weighted more and more to the high-signal peak. The PDFs for the lower flame in Fig. 5(c), however, mark the emergence of the rich-premix zone at 27.2 mm. Rather than shifting to the high-signal peak, the PDF profile at this location shifts back to the low signal peak and is similar to the profile shown at 12 mm. This indicates that the rich-premix region between the primary and secondary zones is similar in terms of large-scale structure dynamics to the unburned reactant layer along the outer cone of the spray flame.

B. Soot Formation Process

While understanding the average and instantaneous flame structure is important for the purpose of validating turbulent models of gas turbine combustion, another main goal of the current analysis is to determine how soot is formed in swirl-stabilized liquid-spray flames. In particular, it is of interest to determine the location of soot inception, how it evolves, and the dynamic behavior that controls the rate of soot production. Based on the results reported by Shaddix et al.¹⁴ in forced flames, it is likely that the turbulent flow structure reported in the previous section will have a significant impact on soot production.

Figures 6(a) – 6(c) show simultaneous images of OH PLIF and soot volume fraction from LII at overall $\Phi = 0.8, 1.0$, and 1.15 . The OH-PLIF images have the same false color scale shown in Fig. 4, while the LII signal is plotted using color contours defined by a reverse color scale shown in Fig. 6. Analysis of these images reveals an inverse correlation between soot volume fraction and OH-PLIF signal. An exception is in the dense spray region where low levels of LII interference are detected due to residual droplet scattering. Increasing the time delay for LII detection reduces this scatter but also significantly reduces the detection of soot incandescence. Instead it is sufficient to note that most of the LII signal is detected in regions that are free of droplet Mie scattering (as detected with the OH-PLIF camera) and is attributable to the presence of soot. The LII signal is also not likely to come from PAH fluorescence, which would appear more consistently and have peak signals near the spray region. Background images collected without the laser sheet show that the contribution from nascent soot incandescence is less than 5%.

For all flow conditions studied here, soot is most often generated along the inner cone of the flame. Not unexpectedly, this corresponds to the intermittent rich-premix zone discussed in the previous section. This is particularly evident in Fig. 6(a), where soot is shown propagating out of this region and into the recirculation zone. It is interesting to note that soot is seldom observed within intermittent regions of low OH signal in the primary zone. This is not surprising since there are likely to be higher levels of oxygen and OH available for soot oxidation in this region.

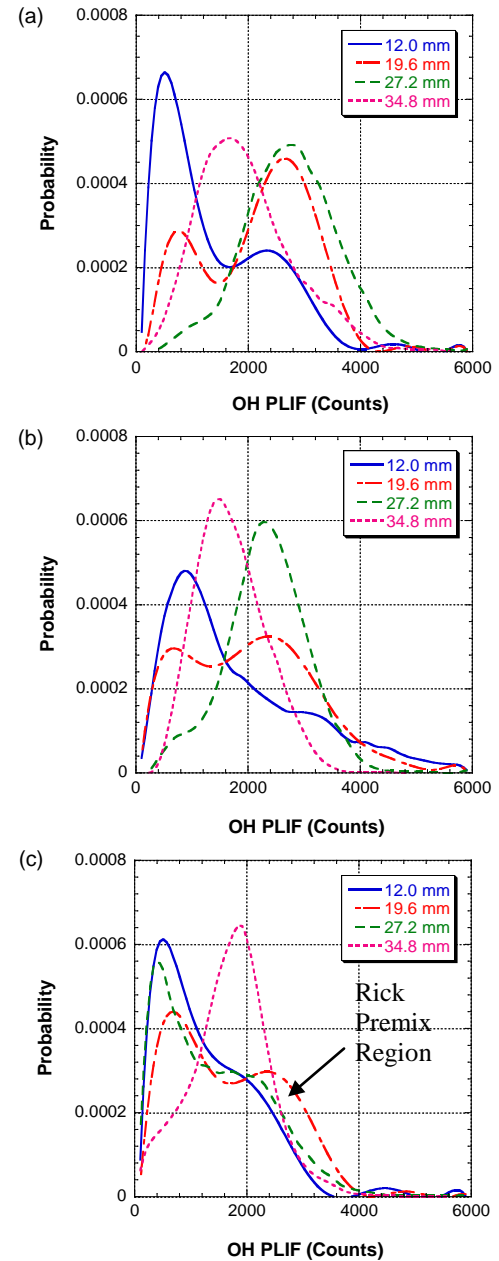


Fig. 5. Probability density functions of OH PLIF at (a) Line A, (b) Line B, and (c) Line C as marked in Fig. 4.

From observation of simultaneous OH-PLIF and LII data, as shown in Fig. 6, it is evident that the rate of soot production increases significantly with overall equivalence ratio. The mechanisms for this increased production can now be assessed given knowledge of how the soot is formed and how it evolves. As noted in the previous discussion, large-scale turbulent motions increase the prominence of the rich-premix zones as the injection pressure is increased. In addition, the secondary reaction zone is weakened as

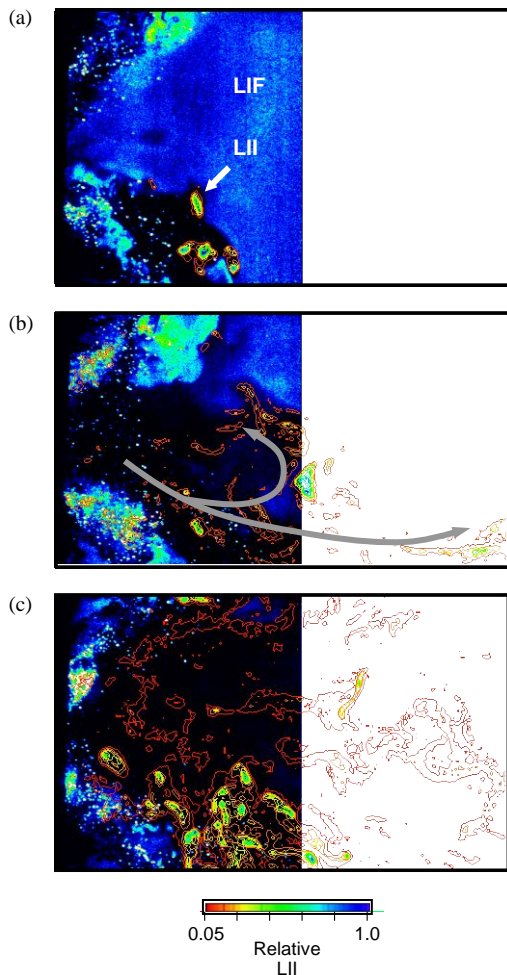


Fig. 6. Overlay of OH-PLIF and LII images at overall ϕ of (a) 0.8, (b) 1.0, and (c) 1.15. OH-PLIF false-color map same as for Fig. 4. LII shown in false-color contours from 5% to 100% of the peak signal in each image.

the equivalence ratio in the recirculation zone increases. Even at lower overall equivalence ratios, intermittency can result in locally rich regions within the recirculation zone, particularly in the lower spray region of the current set up. In the lower flame of Fig. 6(a), for example, there is very little in the way of a secondary reaction zone. In Fig. 4(d), large droplets are shown entering the recirculation zone with burning wakes in the upper half while droplets entering the recirculation zone in the lower half do not. Locally rich conditions allow soot produced in the rich-premix zone to escape the flame layer and undergo a much slower oxidation process.

The sensitivity of the rate of soot production to the local flame structure is illustrated serendipitously in the current work by the asymmetry in the upper and lower halves of the spray flame. As noted

earlier, the rich-premix region is much more prominent in frequency and spatial extent in the lower spray region. In fact, soot production takes place almost exclusively in the lower half of the combustor for all equivalence ratios, as shown in Fig. 6. This asymmetry, which could result from misalignment of the injector nozzle, is also detected in time-averaged images of flame emission and is not due to uncertainties in the current measurement system.

C. Applications

The combined use of planar LII and OH PLIF has been shown in the previous discussion to provide valuable physical insight into soot formation in the current flame environment. It is also of interest to determine whether the simultaneous OH-PLIF and LII diagnostic can be useful for tracking changes in flame composition and soot production with various combustor inlet conditions – namely, equivalence ratio and fuel composition. In studies of soot mitigating additives, for example, it is important to determine whether changes in soot production result from changes in the chemical or physical properties of the fuel.

Figures. 7 and 8 demonstrate the ability of the OH-PLIF and LII systems to track local equivalence ratio and soot production, respectively. Using a region in the recirculation zone that is free of droplet scatter, the time- and spatially averaged OH-PLIF signal is computed with respect to equivalence ratio. This provides a calibration for JP-8 that can be used to qualitatively track changes in equivalence ratio. Fig. 7 is not plotted versus overall equivalence ratio, but with respect to an equilibrium calculation²⁷ for JP-8 fuel. The validity of equilibrium assumptions in this region have been proposed in previous investigations of can-type gas turbine combustors.^{3,4} The temperatures and species concentrations from this equilibrium calculation were then used to calculate the effect of LIF efficiency and Boltzmann fraction on OH-PLIF signals. Encouragingly, the fit to the equilibrium calculation is quite good, even under rich conditions for which quenching corrections are most uncertain.

The fit of OH-PLIF signals to equilibrium calculations, shown in Fig. 7, indicates that the *local* equivalence ratio is 13.5% higher than the *overall* equivalence ratio. In other words, stoichiometric conditions in the recirculation zone are expected for *overall* equivalence ratios of $\Phi = 0.88$. This is not

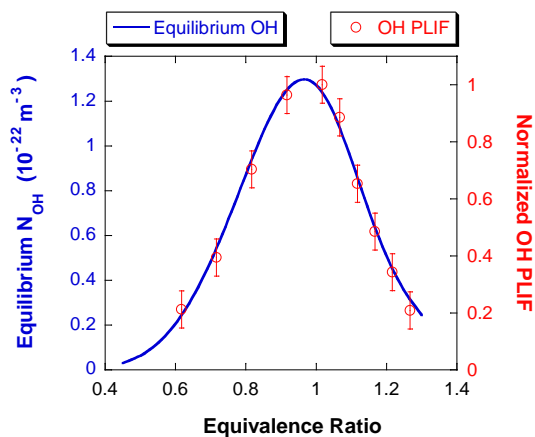


Fig. 7. Equivalence-ratio dependence of equilibrium OH number density compared with OH-PLIF data in the recirculation zone. Confidence intervals set to $\pm 5\%$ of the peak value.

surprising since images collected at these equivalence ratios show a transition from burning to non-burning wakes behind droplets that enter the recirculation zone. Differences in local and overall equivalence ratio may be partially due to air from the aspiration holes of the aft wall escaping the primary flame zone or due to incomplete mixing in the primary flame-recirculation region.

In Fig. 8, the temporally and spatially averaged relative soot volume fraction is plotted as a function of overall equivalence ratio for the current spray flame. The LII data show an exponential rise in soot volume fraction with equivalence ratio. The sampling probe displays a threshold effect at about $\Phi = 1.0$, below which soot in the exhaust is effectively oxidized due to long residence times and the presence of excess air. In the primary zone of the combustor, there is less time to oxidize the soot. In addition, the primary zone is locally higher in equivalence ratio than in the exhaust.

Fig. 8 also shows the results of an LII experiment performed with a longer gate width of 200ns as opposed to 50ns. This was performed to assess the sensitivity of the data to particle-size effects -- a bias toward higher particle sizes would be expected for the longer gate duration of 200 ns. Because of normalization, this bias appears as a slight decrease in signal at lower equivalence ratios for which particle sizes are expected to be smaller. The effect appears to be minimal, indicating that detection with a 50 ns gate is also free of particle-size effects.

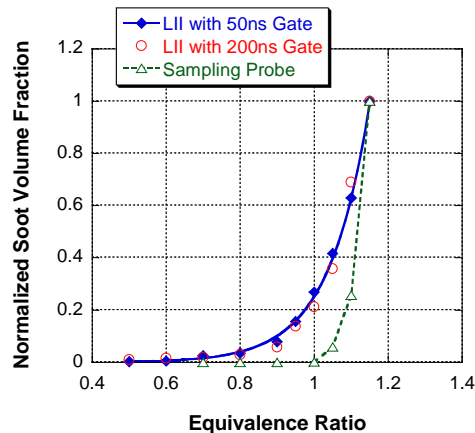


Fig. 8 Effect of overall ϕ on normalized soot volume fraction. LII measurements using a camera gate of 50 ns are fit with an exponential function. Data from sampling probe acquired at exit of exhaust nozzle.

Since the dependence of soot on equivalence ratio is exponential, slight changes in equivalence ratio could easily be mistaken for changes in soot particle counts in the exhaust stream. This highlights the importance of tracking equivalence ratio while performing studies of soot-mitigating additives. An

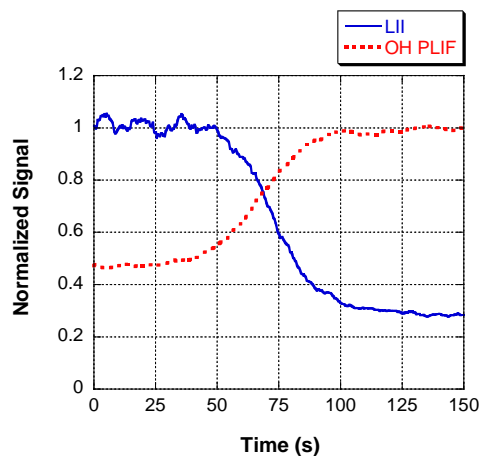


Fig. 9. Effect of methyl acetate ($C_3H_6O_2$) addition to JP-8 fuel on LII and OH-PLIF signals in primary flame zone of swirl-stabilized combustor. Signals averaged for 100 shots.

example is shown in Fig. 9 where methyl acetate is added to the fuel during a test. Note the large decrease in soot volume fraction during methyl-acetate addition, as measured by LII; this corresponded to a large decrease in particle counts from the sampling probe. Note also the increase in OH-PLIF signal; according to the results of Fig. 7, this indicates that the fuel mixture which initially

had an overall $\Phi = 1.05$ (local $\Phi = 1.19$) is becoming leaner. A certain ambiguity exists, however, because the final equivalence ratio could lie on either side of the peak OH signal. Using the exponential fit to the data in Fig. 8, however, the change in LII signal corresponds to an equivalence ratio that is slightly on the rich side of the OH peak. An overall equivalence-ratio decrease of 0.123 due to methyl-acetate addition is measured to within 1% for both the OH-PLIF and LII data, and to within 10% of flow calculations. The agreement between OH-PLIF and LII data indicates that methyl acetate in the current work did not have an effect on soot production, except for its effect on equivalence ratio. One can envision, therefore, the use of a combined LIF and LII system to track the performance of soot-mitigating additives without uncertainties in equivalence ratio.

SUMMARY

A simultaneous OH-PLIF and planar LII system was developed, tested, and demonstrated in a JP-8-fueled, liquid-spray swirl-stabilized combustor. These combined diagnostics provide phenomenological evidence of soot-formation mechanisms in this highly turbulent environment by mapping the instantaneous flame zone and soot volume fraction.

It was found that large-scale structures play a key role in the soot formation process. Intermittent regions of rich premixed regions of fuel and air develop between the primary flame layer and recirculation zone that serve as sites for soot inception. The rate of soot production is dependent upon the frequency and spatial extent of these regions; the rate of soot oxidation is dependent upon the presence of a secondary reaction zone as well as the availability of oxygen and OH in this zone. Hence, the overall soot volume fraction may be highly sensitive to the dynamics of the injection process as well as to the local, unsteady equivalence ratio. Experimental and numerical studies in gaseous combustors may not capture these dynamics properly.

The utility of the OH-PLIF and LII system was also demonstrated for studies of soot formation with fuel-mitigating additives. OH PLIF is used to assess changes in flame structure and to track qualitative changes in local equivalence ratio. LII is used to track the time- and spatially averaged soot volume fraction.

The use of these combined diagnostics provides unique information on the soot formation process in highly turbulent two-phase flows and represents a unique application to practical combustors. To permit more definitive conclusions concerning the

initiation of soot formation, future effort will include the use of double-pulse laser operation to image soot evolution.

ACKNOWLEDGMENTS

We thank Matthew Dewitt, Mike Arstinstall, and Chuck Frayne for technical assistance with the combustor facility. We also gratefully acknowledge useful discussions with Viswanath Katta regarding soot formation in unsteady flames. Funding for this research was provided by the U. S. Air Force Research Laboratory, Propulsion Directorate, Wright-Patterson AFB, under Contract Nos. F33615-00-C-2068, F33615-D-03-M2829, and F33615-00-C-3020, and by the Air Force Office of Scientific Research [Program Monitor: Dr. Julian Tishkoff].

REFERENCES

1. Kim, W.-W., Menon, S., and Mongia, H. (1999), "Large-eddy simulation of a gas turbine combustor flow," *Combust. Sci. Technol.* 143:25-62.
2. Wang, S., Hsieh, S.-Y., and Yang, V., "Numerical simulation of gas turbine swirl-stabilized injector dynamics," AIAA paper 2001-0334, 2001.
3. Heitor, M. V., and Whitelaw, J. H. (1986), "Velocity, Temperature, and Species Characteristics of the Flow in a Gas-Turbine Combustor," *Combust. Flame* 64:1-32.
4. Bicen, A. F., Tse, D. G. N., and Whitelaw, J. H. (1990), "Combustion characteristics of a model can-type combustor," *Combust. Flame* 80:111-125.
5. Held, T. J., Mueller, M. A., Li, S.-C., and Mongia, H., "Data-driven model for NO_x, CO and UHC emissions for a dry low emissions gas turbine combustor," AIAA paper 2001-3425, 2001.
6. Eckerle, W. A., "Soot loading in a generic gas turbine combustor," AIAA paper 87-0297, 1987.
7. Fang, T. C., Megaridis, C. M., Sowa, W. A., and Samuelsen, G. S. (1998), "Soot morphology in a liquid-fueled swirl-stabilized combustor," *Combust. Flame* 112:312-328.
8. Snelling, D. R., Thomson, K. A., Smallwood, G. J., and Gulder, O. L. (1999), "Two-dimensional imaging of soot volume fraction in laminar diffusion flames," *Appl. Opt.* 38:2478-1485.
9. Black, J. D. (1999), "Laser induced incandescence measurements of particles in aero-

- engine exhausts," EUROPTO Conference on Environmental Sensing and Applications, Munich, Germany, pp. 209-215.
10. Jenkins, T. P., Bartholomew, J. L., DeBarber, P. A., Yang, P., Seitzman, J. M., and Howard, R. P., "A laser-induced incandescence system for measuring soot flux in aircraft engine exhausts," AIAA paper 2002-3736, 2002.
 11. Santoro, R. J., Yeh, T. T., Horvath, J. J., and Semerjian, H. G. (1987), "The transport and growth of soot particles in laminar diffusion flames," *Combust. Sci. Technol.* 53:89-115.
 12. Urban, D. L., and Faeth, G. M., "Soot research in combustion science: introduction and review of current work," AIAA paper 2001-0322, 2001.
 13. Won, Y.-H., Kamimoto, T., Kobayashi, H., and Kosaka, H., "2-D soot visualization in unsteady spray flame by means of laser sheet scattering technique," SAE Tech. Paper 910223, 1991.
 14. Shaddix, C. R., Harrington, J. E., and Smyth, K. C. (1994), "Quantitative Measurements of Enhanced Soot Production in a Flickering Methane / Air Diffusion Flame," *Combust. Flame* 99:723-732.
 15. Quay, B., Lee, T.-W., Ni, T., and Santoro, R. J. (1994), "Spatially Resolved Measurements of Soot Volume Fraction Using Laser-Induced Incandescence," *Combust. Flame* 97:384-392.
 16. Vander Wal, R. L., and Weiland, K. J. (1994), "Laser-induced incandescence: Development and characterization towards a measurement of soot-volume fraction," *Appl. Phys. B* 59:445-452.
 17. Brown, M. S., Meyer, T. R., Gord, J. R., Belovich, V. M., and Roquemore, W. M., "Laser-induced incandescence measurements in the reaction zone of a model gas turbine combustor," AIAA paper 2002-0393, 2002.
 18. Smyth, K. C., Miller, J. H., Dorfman, R. C., Mallard, W. G., and Santoro, R. J. (1985), "Soot inception in a methane/air diffusion flame as characterized by detailed species profiles," *Combust. Flame* 62:157-181.
 19. Cignoli, F., Benecchi, S., and Giorgio, Z. (1992), "Simultaneous one-dimensional visualization of OH, polycyclic aromatic hydrocarbons, and soot, in a laminar diffusion flame," *Opt. Lett.* 17:229-231.
 20. Shih, W.-P., Lee, J. G., and Santavicca, D. A. (1996), "Stability and emissions characteristics of a lean premixed gas turbine combustor," in the Twenty-Sixth Symposium (International) on Combustion (The Combustion Institute), pp. 2771-2778.
 21. Foglesong, R. E., Frazier, T. R., Flamand, L. M., Peters, J. E., and Lucht, R. P., "Flame structure and emissions characteristics of a lean premixed gas turbine combustor," AIAA paper 99-2399, 1999.
 22. Lucht, R. P., Sweeney, D. W., and Laurendeau, N. M. (1983), "Laser-saturated fluorescence measurements of OH concentration in flames," *Combust. Flame* 50:189-205.
 23. Carter, C. D., King, G. B., and Laurendeau, N. M. (1992), "Saturated fluorescence measurements of the hydroxyl radical in laminar high-pressure C₂H₆/O₂/N₂ flames," *Appl. Opt.* 31:1511-1522.
 24. Roy, S., Meyer, T. R., Lucht, R. P., Belovich, V. M., Corporan, E., and Gord, J. R., "Temperature and CO₂ concentration measurements in the exhaust stream of liquid-fueled combustor using dual-pump coherent anti-Stokes Raman scattering (CARS) spectroscopy," submitted for publication in *Combust. Flame*, 2003.
 25. Lee, K., and Chehroudi, B. (1995), "Structure of a swirl-stabilized spray flame relevant to gas turbine and furnaces," *J. Prop. Power* 11:1110-1117.
 26. Eckbreth, A. C. (1996), "Laser diagnostics for combustion temperature and species," 2nd Ed., Gordon and Breach Publishers, The Netherlands.
 27. Turns, S. R. (1996), "An Introduction to Combustion," McGraw-Hill, New York.
 28. Lefebvre, A. H. (1999), "Gas turbine combustion," 2nd Ed., Taylor and Francis, Philadelphia, PA.
 29. Tamura, M., Berg, P. A., Luque, J., Harrington, J. E., Smith, G. P., Jeffries, J. B., and Crosley, D. R. (1998), "Collisional quenching of NO A, CH A, and OH A in low pressure hydrocarbon flames," *Combust. Flame* 114:502-514.
 30. Ni, T., Pinson, J. A., Gupta, S., and Santoro, R. J. (1995), "Two-dimensional imaging of soot volume fraction by the use of laser-induced incandescence," *Appl. Opt.* 34:7083-7091.
 31. Bryce, D. J., Ladommatos, N., and Zhao, H. (2000), "Quantitative investigation of soot distribution by laser-induced incandescence," *Appl. Opt.* 39:5012-5022.
 32. Michelsen, H. A. (2003), "Understanding and predicting the temporal response of laser-induced

- incandescence from carbonaceous particles," *J. Chem. Phys.* 118:7012-7045.
33. Chigier, N. A. (1976), "The atomization and burning of liquid fuel sprays," *Prog. Energy Combust. Sci.* 2:97-114.
34. Karasso, P. S., and Mungal, M. G. (1997), "Scalar mixing and reaction in plane liquid shear layers," *J. Fluid Mech.* 323:23-63.
35. Meyer, T. R., Dutton, J. C., and Lucht, R. P. (2001), "Experimental study of the mixing transition in a gaseous axisymmetric jet," *Phys. Fluids* 13:3411-3424.

Investigation of a dynamic diffusion flame of H₂ in air with laser diagnostics and numerical modeling

F. Grisch^{a,*}, B. Attal-Tretout^a, A. Bresson^a, P. Bouchardy^a, V.R. Katta^b,
W.M. Roquemore^c

^a *Département Mesures Physiques, Office National d'Etudes et de Recherches Aéronautiques,
Fort de Palaiseau, 91761 Palaiseau Cedex, France*

^b *Innovative Scientific Solutions, Inc., 2766 Indian Ripple Road, Dayton, OH 45440-3638, USA*

^c *Air Force Research Laboratory, Wright-Patterson Air Force Base, OH 45433, USA*

Received 29 July 2003; received in revised form 1 August 2004; accepted 6 August 2004

Available online 8 September 2004

Abstract

Detailed studies of flame–vortex interactions play a vital role in improving our understanding of turbulent combustion. A combined experimental and numerical study was conducted on a low-speed, buoyant, jet diffusion flame of hydrogen in air to investigate the vortex–flame interaction and the effects of preferential diffusion on the flame's structure. A time-dependent, axisymmetric mathematical model with detailed transport processes and a chemical-kinetics mechanism was used to simulate the dynamics of the flame. Single-shot measurements of temperature and the concentrations of molecular hydrogen (H₂), the pollutant nitric oxide (NO), atomic oxygen (O), atomic hydrogen (H), and the hydroxyl radical (OH) were made using optical techniques such as coherent anti-Stokes Raman scattering, degenerate four-wave mixing, and planar laser-induced fluorescence. Temperature and mole fractions of different species are presented in two-dimensional contour maps and compared with the numerical predictions. The model predicted the behavior of the experimentally observed dynamic flame quite well, including variations in temperature and molar concentrations of fuel and tracer species such as H, OH, and NO. Discrepancies in the concentration of O atoms were also noted.

© 2004 The Combustion Institute. Published by Elsevier Inc. All rights reserved.

Keywords: Diffusion flame; Flame–vortex interaction; CARS; LIF; DFWM

1. Introduction

Studies of diffusion flames are of both theoretical and engineering importance in improving our understanding of fundamental combustion processes by providing insight into turbulent combustion phenomena, which facilitate the development and eval-

uation of simplified models for use in design codes for practical systems. Consequently, since the pioneering work of Hottel and Hawthorne [1], jet diffusion flames have become one of the most extensively investigated flame systems. Over the past 2 decades a significant amount of data on statistical parameters such as fluctuations in velocity, temperature, and concentration in turbulent combustion processes have been obtained through the use of single-point and planar-imaging techniques [2]. Although these measurements have greatly increased our understand-

* Corresponding author. Fax: 33-1-69-93-61-82.

E-mail address: frederic.grisch@onera.fr (F. Grisch).

ing of the interactions of turbulence and the chemistry, several important physical–chemical processes, such as the role of strained/stretched laminar flamelets and the existence of distributed reaction zones, are not yet adequately understood. This is particularly true for the periodically oscillating laminar and near-transitional jet flames, in which the interactions of large-scale, organized buoyancy-induced vortices on the air side and Kelvin–Helmholtz-type vortices on the fuel side of the flame alter the flame’s structure significantly and in different ways. Knowledge of these flame–vortex interactions is essential for improving the accuracy of existing models, such as those using laminar-flamelet approaches.

The coupling between the unsteady fluid dynamics and combustion processes associated with vortex–flame interactions has been investigated recently using a time-dependent, fluid-dynamics model with detailed chemistry [3,4] known as UNICORN (unsteady ignition and combustion with reactions) [5]. Application of this model to a low-speed, dynamic diffusion flame of hydrogen and air produced rather surprising results, which could not be explained with intuitive arguments. These studies suggested that the temperature along a flame’s surface changes during a vortex–flame interaction; for example, it increases in the compressed regions and decreases in the stretched regions when an air-side vortex interacts with the flame. The latter variation could be explained by means of flamelet theory, which suggests that the temperature of a diffusion flame decreases when the stretch on the flame is increased; however, the former variation, i.e., an increase in temperature in the compressed regions, could not be explained with intuitive reasoning. In fact, simulations [3,4] have predicted a temperature increase of ~ 100 K above the adiabatic value in the compressed regions. By performing various numerical experiments, Katta et al. [3] concluded that the Lewis number not being unity, in conjunction with the concave curvature (with respect to the fuel) in the compressed region, results in an increase in temperature above the adiabatic-equilibrium value. These numerical studies also showed that preferential mass diffusion, a Lewis number not equal to unity, and flame curvature all affect not only the local temperature but also the local species’ concentrations. In particular, concentrations of species with diffusion coefficients lower than that of the fuel tend to be diminished, while those of species with diffusion coefficients higher than that of the fuel tend to be increased. These predictions suggest the importance of understanding the relative roles of various processes taking place during a vortex–flame interaction, i.e., a precursor to studies of turbulence–chemistry interactions.

The rather surprising and counterintuitive predictions of UNICORN for the variations in temperature

and [NO] [3] in an unsteady diffusion flame of hydrogen and air have been validated by conducting two independent experimental studies, one by Carter et al. [5,6] and the other by Grisch et al. [7]. In both experiments phase-locked measurements of temperature and species’ concentrations were conducted, making use of the fact that the interaction between the flame’s surface and the outer vortex generated as a result of buoyancy forces occurs periodically at ~ 15 Hz. While the same flame system was employed in both studies, the laser-induced fluorescence (LIF) technique was used in the former [5,6] and the degenerate-four-wave-mixing (DFWM) technique was used in the latter [7] for measuring [NO]. Both measurements yielded higher [NO] in the flame-bulge regions and lower concentrations in the squeezed regions—confirming the predictions made by UNICORN.

While the strong dependence of NO production on temperature caused the NO concentration to vary significantly during the flame–vortex interaction, lesser degree variations in intermediate species such as H, O, and OH, predicted by UNICORN, result from preferential diffusion. Since the variations in the concentrations of radicals have an important bearing on the turbulent-flame structure, the predictions made using UNICORN with regard to the variations in these concentrations must also be verified.

The objective of the present study was to investigate the structure of the low-speed hydrogen–air diffusion flame in detail using experimental and computational techniques. This effort is an extension of an earlier study of vortex–flame interactions [7] comparing modeling predictions and the temperatures and [NO] using coherent anti-Stokes Raman-scattering (CARS) and DFWM techniques, respectively. An extended database is established below for investigating the impact of vortex–flame interactions on the concentrations of fuel and radicals and for further evaluating the predictions of UNICORN. The database includes optical measurements of $[H_2]$, $[H]$, and $[OH]$; these species are believed to be the key ones in the oxidation and processes occurring in this flame. The temporal and spatial evolutions of the vortex–flame interactions were investigated by phase-locking the measurements and using different single-shot laser diagnostics either separately or in combination. CARS was used to measure temperature and $[H_2]$, and DFWM and LIF were used for the concentrations of NO and radicals.

2. Numerical model

A time-dependent, axisymmetric mathematical model, known as UNICORN, was used for the simulation of vertically mounted, unsteady, jet diffusion

flames. Full Navier–Stokes equations written in cylindrical coordinates were solved along with species- and energy-conservation equations [8]. A detailed chemical-kinetics model derived from GRI-V2.0 [9] (using only the elements H, O, and N) was employed to describe the combustion of hydrogen in air. This model involved 13 species (H_2 , O_2 , H, O, OH, H_2O , HO_2 , H_2O_2 , N, NO, NO_2 , N_2O , and N_2) and 74 elementary reactions. Temperature- and species-dependent properties were incorporated. The governing equations were integrated on a nonuniform staggered-grid system. An orthogonal grid having rapidly expanding cell sizes in both the axial and the radial directions was employed. The finite-difference forms of the momentum equations were obtained using an implicit QUICKEST scheme [8,10], and those of the species and energy equations were obtained using a hybrid scheme of upwind and central differencing. At every time step, the pressure field was calculated by solving the Poisson equations for pressure simultaneously and utilizing the lower and upper diagonal matrix-decomposition technique.

Unsteady axisymmetric calculations for the buoyant jet diffusion flames were made on a physical domain of 400×150 mm, utilizing a 201×71 nonuniform grid system, which yielded 1.0- and 0.1-mm grid spacings in the flame zone in the z and r directions, respectively. The computational domain was bounded by the axis of symmetry and a free-flow boundary in the radial direction and by the inflow and outflow planes in the axial direction. The outer boundary in the z direction was located sufficiently far from the burner exit (~ 40 fuel-jet diameters) that propagation of boundary-induced disturbances into the region of interest was minimal. Flat velocity profiles were imposed at the fuel- and air-inflow boundaries, while an extrapolation procedure with weighted zero- and first-order terms was used to estimate the flow variables at the outflow boundary. Details of the boundary conditions have been given [11].

3. Experimental procedure

The burner was an assembly of concentric tubes, with the fuel-jet nozzle located at the center. Uniform, low-turbulence annular-air flow was delivered around the central fuel jet through a nozzle ($\varnothing = 150$ mm) with a divergent section and a flow straightener. A short, tapered contour nozzle ($\varnothing = 10$ mm) was used for delivering fuel composed of 78 vol% hydrogen and 22% nitrogen. The exit velocities for the fuel and air jets were 3.55 m/s and 37.9 cm/s, respectively. The low annular-air velocity used in these studies is known to generate vortices, which convect outside the flame's surface at a frequency of 14.8 Hz [7].

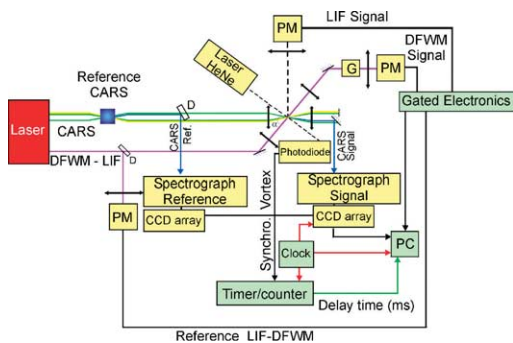


Fig. 1. CARS/DFWM/LIF experimental setup.

A conventional laser system (Fig. 1) consisting of CARS/DFWM/LIF spectrometers was used for the simultaneous single-shot measurements of temperature and concentrations of trace species. Two benches were mounted on a single table to deliver the pump and Stokes beams required for multiplex CARS and the UV beam necessary to monitor the species' concentrations by DFWM and/or LIF [7]. The first bench comprises a frequency-doubled injection-seeded Nd:YAG laser and a broadband dye laser for generating the pump and Stokes beams, respectively, required for multiplex CARS [12]. For the excitation of the N_2 Raman transitions, the Stokes beam is centered at 607.3 nm, with a broadband emission of 60 cm^{-1} full width at half maximum (FWHM) bandwidth. For the measurements of $[\text{H}_2]$, the Q branches of the Raman emission were probed using LDS698 dye diluted in ethanol. A bandwidth of 200 cm^{-1} was achieved for these measurements. The second laser bench consisted of a tunable narrow-band dye laser, pumped by a multimode Nd:YAG laser, frequency doubled in a BBO crystal to generate the UV beam with a FWHM of 0.12 cm^{-1} . The laser repetition rate was 10 Hz with 10-ns laser pulses, and both laser systems were synchronized within a temporal jitter < 10 ns.

The CARS and UV beams were focused colinearly at the probe volume. A planar BOXCARS arrangement was used for the CARS beams, and referencing and nonresonant background cancellation were applied systematically [12]. The CARS beams were focused in the flame with a lens (300-mm focal length), which yielded a 3-mm-long, 100- μm -diameter probe volume. The available energies in this probe volume were 35 mJ at 532 nm, 2.5 mJ at 607 nm, and 2 mJ at 683 nm. Reference and sample CARS spectra were dispersed in separate spectrographs and detected using two 512-diode arrays. A folded BOXCARS arrangement was used for the DFWM beams along with a crossed-polarization arrangement to obtain an optimal signal-to-noise ratio involving one-photon resonance [13]. A UV lens with a long focal

length (900 mm) was used for DFWM. Lenses with a short-focal length (300 mm) were used for excitation of O and H atoms by two-photon absorption, followed by fluorescence emission.

The angle between the UV and the CARS beam axes was limited to 5° to ensure that a quasi-perfect coincidence of both probe volumes was achieved. The superposition of the DFWM, LIF, and CARS probe volumes was adjusted using a 200- μm -diameter pinhole, inserted at the beam focus, and mounted on three translation stages. The pinhole was positioned carefully in the three dimensions to achieve superposition of the beams with an accuracy of approximately $\pm 20\text{ }\mu\text{m}$. With a beam separation of 22 mm, the DFWM probe volume represents a region 10 mm long and 200 μm in diameter. The DFWM and LIF signals were detected on two separate channels on the laser path and at right angles to it. Spatial filtering and a dichroic polarizer were used on the signal path for DFWM; the DFWM signal was detected with a UV photomultiplier. The fluorescence signals were collected at $f/2$ by a fused-silica lens and focused onto a 1-mm-i.d. optical fiber. The spatial resolution in the flame then corresponded to a cylinder 1 mm long and 200 μm in diameter. For the fluorescence of free atoms of O, RG780 and RG665 colored-glass filters, with a narrow-band interference filter centered at 860 nm, were used along with a red-sensitive photomultiplier for separating the fluorescence emission from the scattered laser light and the emission from water vapor in the flame. To detect H atoms a combination of OG-530 and narrow-band interference filters was employed, along with a red-sensitive photomultiplier. Part of the UV beam was also detected on a reference channel to monitor the laser-power fluctuations from shot to shot.

Planar laser-induced fluorescence was used to probe OH. The frequency-doubled output of the laser (282.75 nm) was formed into a thin sheet using a combination of cylindrical and spherical lenses. Fluorescence emission from excited OH was collected by a UV camera lens placed at a right angle to the laser sheet and using UG5 and WG295 filters and recorded onto the 512×512 -pixel CCD array of a Princeton Imax intensified camera. The size of the region imaged was $50 \times 50 \times 0.2\text{ mm}^3$. A reference signal allowed monitoring of the laser-sheet profile energy for each laser shot. For this purpose a partial reflection induced by a parallel plate illuminated liquid acetone contained in a glass cell. The fluorescence signal emitted by acetone was collected at the bottom portion of the ICCD array, together with OH-fluorescence images.

Instantaneous measurements in the periodically oscillating jet diffusion flame were obtained using the following procedure: the frequency of the outer vor-

tices was monitored by passing a He–Ne laser beam through the outer part of the flame and detecting the beam wandering using a PIN photodiode. The phase angles at which single-shot measurements were performed were obtained by measuring the delay between the laser pulses and the periodic signal generated by the PIN photodiode using a counter/timer (Hewlett–Packard). Point measurements were made in the flame by translating the burner to the specified axial (z) and radial (r) locations. The radial position was changed in coarse steps of 1 mm. For each location single-point measurements were recorded in real time over several successive cycles of the buoyant vortices. Typically, sequences of 500 laser shots were recorded with a laser repetition rate of 9.8 Hz to obtain a sampling time of $\sim 1\text{ ms}$. Instantaneous images of OH were acquired at a selected axial position by phase-locking the laser pulse with the vortex displacement.

4. Measurement methodology

Flame temperatures were derived from the observed Q branch of the CARS spectrum of N_2 , which was fitted to a library of theoretical shapes [14]. The accuracy of the temperature measurements obtained under stable conditions is approximately $\pm 10\text{ K}$ at room temperature and $\pm 30\text{ K}$ at 2000 K, with standard deviations of 5 and 2%, respectively.

The concentration of the fuel, H_2 , was determined from the integrated area of the H_2 CARS signal after calibrating the system in an ambient flow in which $[\text{H}_2]$, the temperature, and the pressure were all known. The temperature, which was required for determining the absolute concentrations of species, was derived simultaneously from the experimental single-shot H_2 CARS spectrum with a Boltzmann diagram technique [15]. The accuracy of instantaneous measurements of concentration was $\sim 10\%$.

[NO] was measured by DFWM. The basic physics of DFWM has been previously presented in the context of optics and spectroscopy [16] and its application to combustion diagnostics has been reviewed [17, 18]. In these measurements the excitation frequency is tuned to the $Q_1(21.5) + S_{21}(10.5)$ transitions of the $A^2\Sigma^+ - X^2\Pi(0,0)$ band of the γ system [19]. These lines are well isolated from the O_2 Schumann–Runge transitions, present in this spectral range, and yielded good signal strength over a wide range of temperatures. Using one-photon resonance in NO, it was shown that optimal sensitivity was achieved with a pump beam lying just at the level of the saturation threshold of the stronger rotational line under study. The DFWM signal intensity is then given by

$$S^{\text{DFWM}} \propto N^2(T) F^{\text{DFWM}}(T, S, \gamma_{\text{coll}}(T)),$$

where N is the number density. The function F was calculated for each of the temperatures involved in the CARS library according to the variation of the γ_{coll} collision linewidths with temperature using a saturation model adapted for the range of energy employed. During the present experiments, the energies at the sample volume for the pump beams were fixed at 23 μJ , i.e., approximately one-half the saturation intensity of NO [19].

The fluorescence of OH was obtained using excitation of the $Q_1(5)$ line in the $X^2\Pi-A^2\Sigma^+(1,0)$ transition near 282.75 nm. The probe-volume beam energy was limited to $< 10 \mu\text{J}$ to ensure that fluorescence was within the linear-excitation regime. Measurement of the local [OH] relied upon the proportionality between the fluorescence intensity and [OH]. Thus, the observed signal intensity S_{LIF} can be written as

$$S_{\text{LIF}} \propto N(T) F^{\text{LIF}}(T, \gamma_{\text{coll}}(T)),$$

where the function F^{LIF} summarizes the influences of the spontaneous-emission rates and the collision-energy transfer processes. The total quenching rate was estimated for lean- and rich-flame conditions using the data of Paul et al. [20] and the gas composition and temperature obtained from calculations of adiabatic equilibrium.

Since the DFWM and LIF signals were temperature-dependent, the absolute number densities of NO and OH were calibrated in flames in which the species' concentrations, the temperature, and the pressure were known. The calibration of the NO signal was performed in a laminar, premixed flame of $\text{H}_2 + \text{air}$ burning on a porous burner [7]. The equivalence ratio was 0.43 and the temperature was 1350 K. The flame was doped with 280 ppm of NO. This calibration assumed that most of the doped NO passed through the flame zone without participating in the reburn reactions and that the amount of natural NO is small compared to the doped amount. The former assumption is supported by the experimental studies of: (1) Cattolica et al. [21], who suggest that at low pressures no significant amount of doped NO will be removed from a burner-stabilized flame (similar to the one used in the present study for calibration purposes), and (2) Schulz et al. [22], who suggest that measurements of [NO] by LIF must be calibrated under fuel-lean conditions and with NO-dopant levels of > 200 ppm. Furthermore, the calculations performed using the CHEMKIN and PREMIX codes [23,24] indicated that [NO] in the burnt gases is within 2% of the doped level. Based on this, the relative accuracy of the measurements of [NO] was estimated to be $\sim 5\%$ [7].

For [OH] calibrations, the porous burner was operated at an H_2/air equivalence ratio of 0.9 to provide

a near-stoichiometric premixed flame. The fluorescence intensity of OH was recorded as a function of height above the porous surface. This curve gave the relative [OH] along the flame's axis. The accuracy of a relative concentration was estimated by performing a series of 500 single-shot measurements for each location. Analysis of the resultant reactive-Mie-scattering (RMS) deviations led to an uncertainty of $\sim 10\%$. Absolute calibration was performed by comparing the experimental and calculated profiles simulated with the PREMIX code. The detailed chemical-kinetics model derived from GRI-V2.0 (using only H, O, and N elements) was employed to describe the combustion of hydrogen + air. To take into account heat losses from the flame, the experimental temperatures measured by CARS at various heights were supplied as input data to the PREMIX calculations. The resultant accuracy of the temperature measurements was obtained on a series of 500 single-shot measurements, which yielded an uncertainty of $\pm 2\%$. Although the flame model uses a detailed chemical-kinetic model, which has been validated on several types of flames, we estimate the present uncertainty on the absolute [OH] to be $\sim 20\%$.

To measure their concentration, O atoms were excited to the $3p^3P$ state by two-photon absorption of 226-nm radiation. The processes originating from $J = 2$ were probed preferentially [16]. The experiments were performed by exciting the $J' = 0, 1, 2$ triplet components of the excited state. The O-atom fluorescence was monitored at 844.6 nm from the $3p^3P$ excited state down to the $3s^3S$ intermediate state. In contrast to the excitation of NO, the energy of the pump beam was set at 900 μJ , which is far below the saturation-intensity limit of the two-photon process under conditions of an atmospheric-pressure flame. The two-photon transition $1s^2S-3d^2D$ of the H atom was excited by a UV beam tuned to 205.1 nm by tripling the fundamental emission of the rhodamine dye. The fluorescence was monitored at 656.3 nm from the $n = 3$ excited state to the $n = 2$ intermediate state. As for O atoms, the energy of the pump laser was fixed at 1.2 mJ to induce strong fluorescence signals. For an O atom, saturation and photodissociation processes are not limiting for the input energy.

As a result of their high reactivity, the radicals O and H are, in general, found only in high-temperature regions. Thus, the fluorescence of O and H in flames becomes quasi-insensitive to the temperature. The conversion of the fluorescence signal of an atomic species to the number density is given by

$$N_f = N_{\text{cal}} \frac{S_f}{S_{\text{cal}}} \frac{R_{\text{cal}}^2}{R_f^2},$$

where N , S , and R are the number density, the fluorescence signal, and the energy of the laser beam,

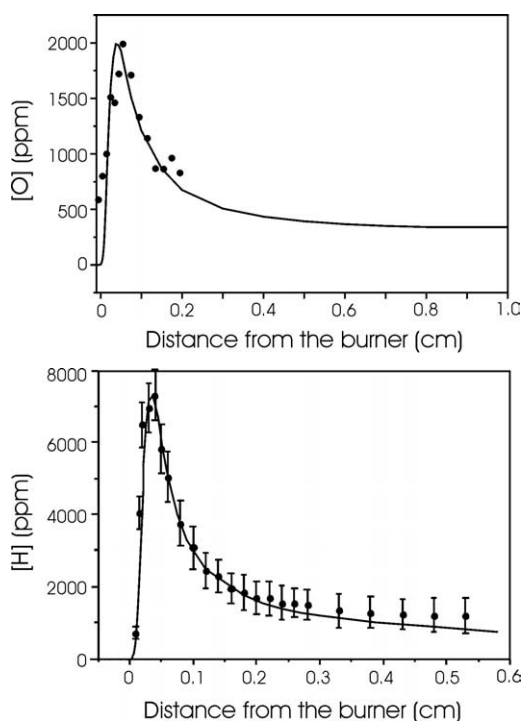


Fig. 2. Absolute O concentration (top) and absolute H concentration (bottom) in $\Phi = 0.9$, atmospheric-pressure, premixed H_2/air flame. Symbols represent experimental results; lines represent simulations performed with flame model [23,24].

respectively; the subscripts f and cal denote the sample and calibration flames, respectively. Absolute calibration of the fluorescence signal from an atomic species was performed with a strategy similar to that used for OH. As shown in Fig. 2, the concentration profiles of O and H measured in the calibration flame are very similar to those obtained in the simulations. The rescaling procedure provided an absolute value for the peak concentration, which was later used to calibrate the measurements in the buoyant flame. This value was responsible for the final uncertainty in the measurements of [O] and [H]. It was estimated that the absolute accuracy is less than a factor of 2. Concerning the relative accuracy, it is also important to note that measurements of [O] and [H] in the calibration flame exhibited large shot-to-shot fluctuations due to: (1) real-time fast variations in [O] and [H] in the reaction zone, (2) shot-to-shot fluctuations of the LIF signals caused by the weak signal-to-noise ratio, and (3) the squared dependence of two-photon LIF signals on laser energy. Taking into account these sources of error, the relative accuracy of [O] and [H] was deduced from the standard variation of fluorescence intensity recorded on statistical data of 300 single-shot measurements. The re-

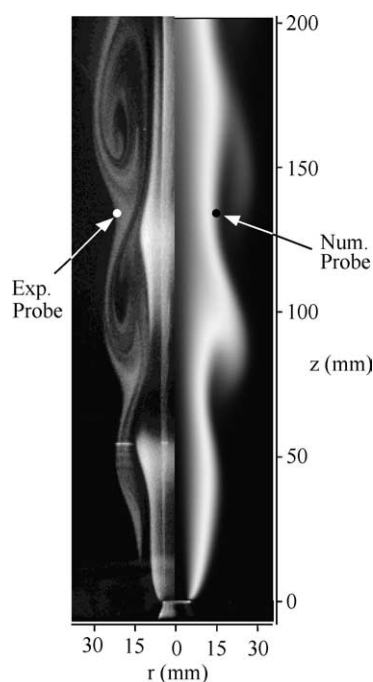


Fig. 3. Structure of low-speed, buoyant, jet diffusion flame. Instantaneous image obtained using reactive-Mie-scattering technique shown on left half; instantaneous temperature distribution obtained using UNICORN model shown on right half.

sulting uncertainty was then estimated to be $\pm 20\%$ (see Fig. 2).

5. Results and discussion

Measured and computed instantaneous images of the flame are shown in Fig. 3 on the left and right halves, respectively. The dynamic flame structure is evident from this figure, and a comparison of computed and measured images suggests that the model captured the important features of this low-speed flame. Both the measurements and the calculations show two toroidal vortical structures outside the flame's surface, convecting downstream, and a third one just forming at ~ 50 mm above the nozzle. The computed convective frequency of ~ 15 Hz for the vortices is in good agreement with the measured value (~ 14.8 Hz). The experimental image was obtained using a RMS technique [25]. The bright region in this image (left half of Fig. 3) is the luminous flame surface, as captured simultaneously with Mie-scattered light. As described earlier, the time-dependent simulation for this low-speed jet diffusion flame was made using UNICORN on a 201×71 grid system. It is important to note that no external perturbation was used in this simulation and that the buoyant acceleration of

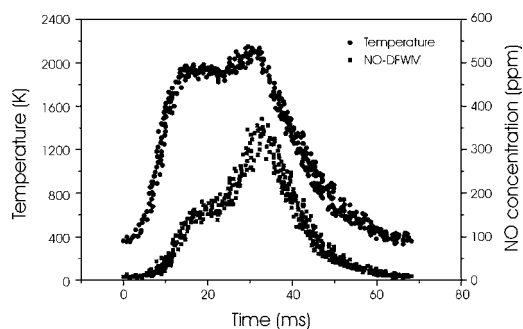


Fig. 4. Profiles of temperature and NO concentration with respect to time in buoyant diffusion flame at location $r = 15.5$ mm and $z = 135$ mm.

hot gases along the flame's surface is responsible for the formation of the outer vortices [3,4,8].

Variations in temperature and concentrations of the species were recorded simultaneously as a function of time over a vortex-crossing period at different locations in the flame. For validating the model, a location with axial and radial distances of 135 and 15.5 mm, respectively, was chosen. This location is marked with filled circles in Fig. 3 on both the experimental and the simulated images. As the vortices travel past this probe location, hot combustion products convect not only in the axial direction but also in the radial direction. Typical time-dependent profiles of measured temperature and [NO] at this location are shown in Fig. 4 with solid circles and squares, respectively. These profiles represent the data in the bulge region during the vortex–flame interaction. The presence of low-temperature gas (~ 400 K) during certain periods suggests that the probe is located outside (on the air side) of the flame.

The two peaks in the temperature–time plot (Fig. 4) are highly reproducible and represent stretched and compressed flamelets [7]. When the flame is bulged in the braid region of a vortex pair, the flame section (flamelet) that is being pulled outward by the lower vortex becomes compressed, and the flame section being pushed inward by the upper vortex becomes stretched. This means, with reference to time, that the flame section crossing the probe location first ($t \sim 13$ ms) represents the stretched flame (due to the upper vortex) and the one crossing later ($t \sim 30$ ms) represents the compressed flame (due to the lower vortex). Supporting the prediction of Katta et al. [3,4] the experimental temperature of the compressed flamelet is higher than that of the stretched flamelet, with a temperature difference of ~ 100 K. The variation in [NO], in general, follows that of temperature. However, because of the nonlinear dependence of NO production on temperature, the former nearly doubles when the latter increases by ~ 100 K in the compressed flamelet.

Contour plots of the measured parameters in space and time were constructed from the individual time profiles recorded at several radial locations. About 10 single-shot measurements were averaged at each temporal (phase) and spatial position, i.e., at a specified height (135 mm from the burner) and a specified radius (1-mm intervals from the center); about 10 measurements were made every 1 ms during the flame-flicker period (~ 65 ms) and averaged to obtain one value in the contour map. Computed evolutions of temperature and species' concentrations at a height of 135 mm were obtained by storing these quantities at several instants during one flicker cycle. Fig. 5 compares the measured and computed values for temperature and concentrations of H_2 , OH, H, NO, and O.

Experimentally, it was observed that islands of high temperature (Fig. 5a) and high [NO] (Fig. 5e) developed in the compressed region of the flame bulge (~ 40 ms). It is interesting to note that the location of the NO peak was shifted slightly by a few millimeters in the radial direction from that of the peak temperature. Similar observations were made from the simulations presented on the right halves of Figs. 5a and 5e, which accurately captured the flame bulge, both spatially and temporally. The maximum temperatures of ~ 2150 K in the measurements and ~ 2250 K in the simulations developed at the same location on the flame bulge. In the stretched region of the flame, measurements also showed a peak temperature drop of ~ 100 K, which is consistent with the simulations. [NO] followed the temperature, with the peak located in the bulge region, as predicted in the calculations. Note that these calculations were made prior to the experiments.

The difference in the peak [NO] (~ 510 ppm in the experiment and ~ 600 ppm in the calculation) is thought to result, in part, from the higher temperature (by 100 K) obtained in the calculations and, in part, from the chemical kinetics used in the calculations for forming NO. Note that only thermal NO, which is a strong function of temperature, derived from the GRI-V2.0 mechanism was used in these calculations. The more recent release of the GRI-V3.0 mechanism contains minor changes to the chemistry of $H_2 + O_2 + N_2$, and the calculation repeated for this low-speed jet diffusion flame using the GRI-V3.0 mechanism yielded nearly identical results. In fact, the difference of only 90 ppm between the measured and the calculated [NO] is less than would be expected with a 100 K difference in flame temperature; however, the simple thermal NO mechanism used in the model seems to reduce this difference.

A comparison of the measured and computed values of [OH] and [H] (see Figs. 5c and 5d, respectively) also shows good agreement. OH was mainly present in a relatively narrow region characterized

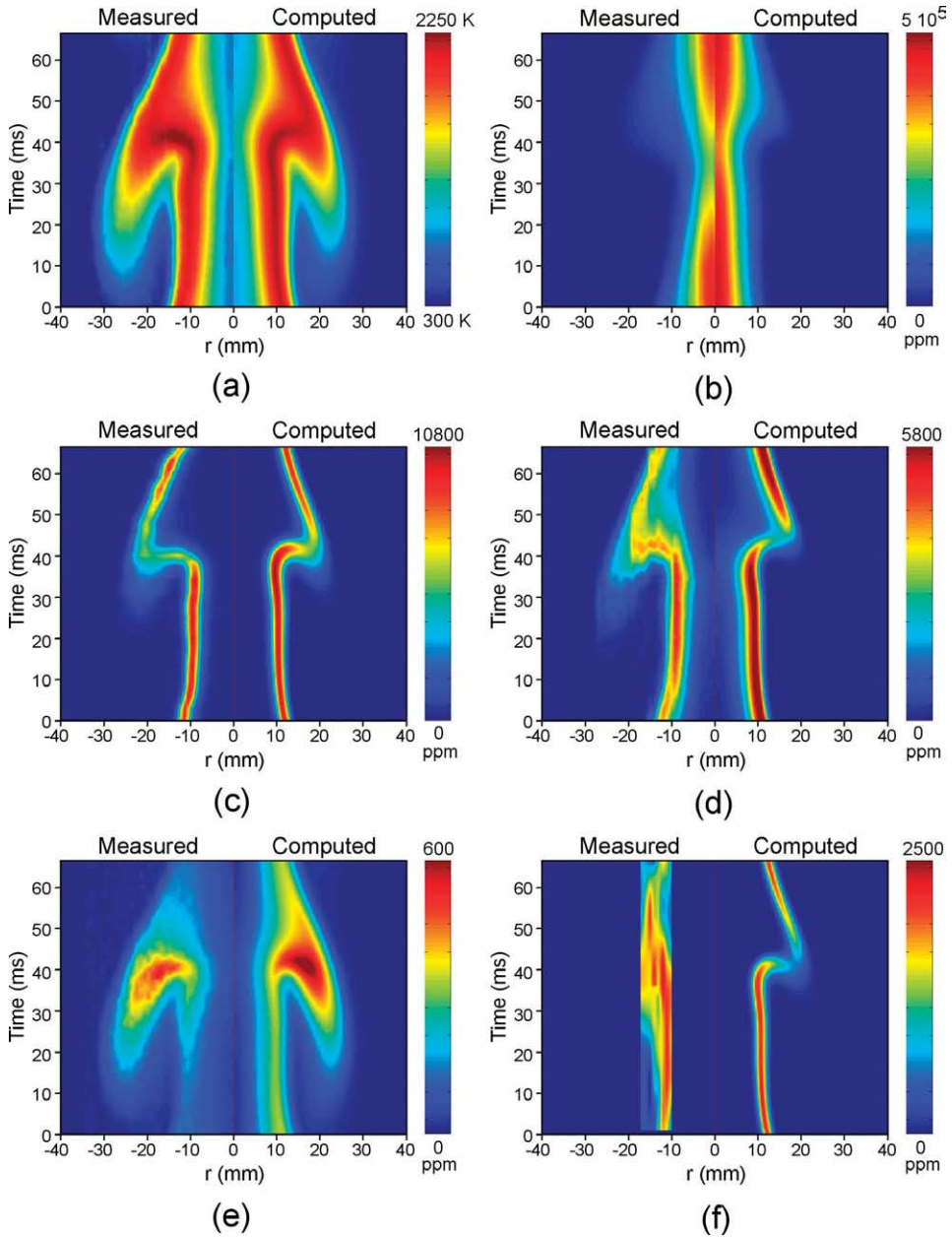


Fig. 5. Contour plots of measured (left) and computed (right) flow-field parameters in space (radius) and time at 135 mm downstream of jet exit: (a) temperature, (b) H_2 concentration, (c) OH concentration, (d) H concentration, (e) NO concentration, and (f) O concentration. Experimental O concentration is multiplied by a factor of 3.

by its high temperature, i.e., the region enclosed by the $T = 1800$ K contour. In contrast to the observed distribution of [NO], the peak value of [OH] (10,800 ppm) in the experiment was found to develop in the stretched region. Such behavior in [OH] was observed in the simulations (shown in the right half of Fig. 5c) performed prior to the experiment [3,4] and before Katta et al. [3] argued that the preferential

diffusion of lighter species is responsible for the increasing [OH] in the stretched region where the temperature is lower. Fig. 5d shows that free H atoms are also confined to the high-temperature region of the flame, with a peak in their concentration developing in the stretched region. In general, the measured distribution of [H] follows that predicted. However, small discrepancies in the shape and peak values of

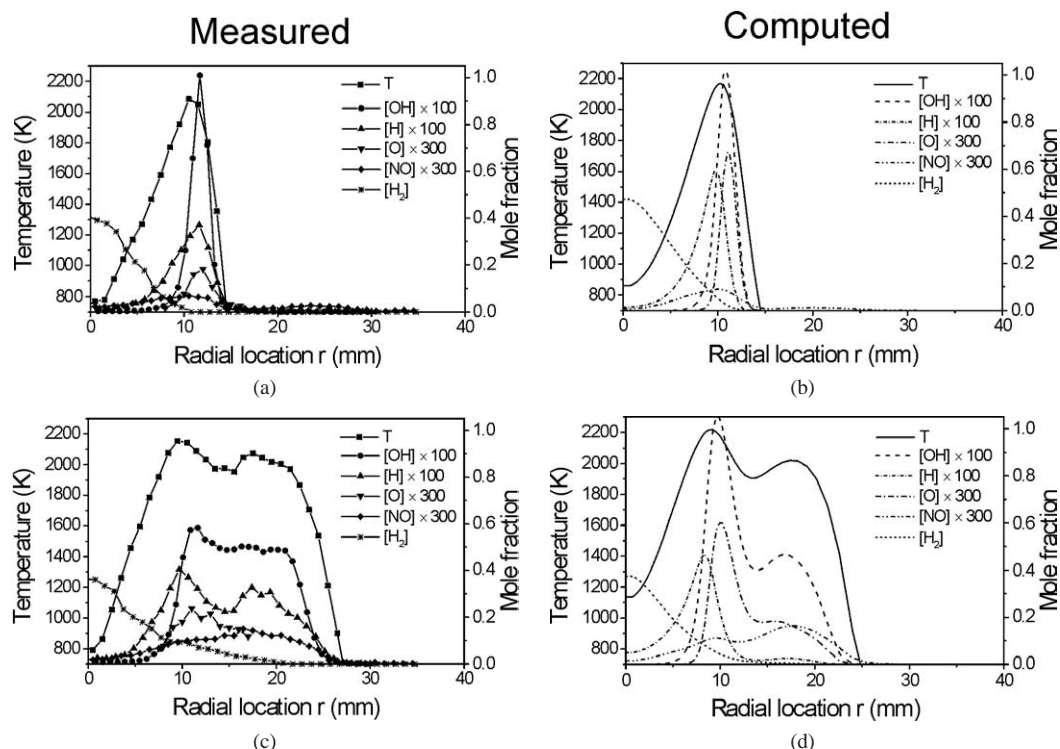


Fig. 6. Flame structure at (a) $t = 5$ ms and (b) $t = 39$ ms, corresponding to stretched and compressed regions, respectively. Measured (left) and computed (right) radial distributions of temperature and mole fractions of H_2 , OH, O, H, and NO are plotted.

the measurements and predictions can also be noted. First, the region where [H] was measured was quite broad compared to the calculated one; second, the measured peak concentration was lower than the calculated one by 20%. Nevertheless, it may be recalled that the error margin in the measurements of [H] using the LIF technique is also $\sim 20\%$.

The predicted concentration distribution of fuel (H_2) matches well with the measurements. Calculations have even predicted the variations in $[H_2]$ due to thinning of concentrations in the stretched region and the presence of islands of concentration in the compressed region. Furthermore, a comparison of Figs. 5b and 5d corroborates that the formation of H is well correlated with the consumption of fuel, whatever the location in the flame.

Fig. 5f suggests that atomic O is mainly present along the steep temperature gradient on the air side of the flame, i.e., outwardly shifted compared to the high-temperature zone. The computations show similar behavior in the spatial distribution of [O]; however, a considerable discrepancy on absolute concentration is noted (a factor of 3 difference). Such a large discrepancy between the measured and the predicted [O] cannot be explained by the uncertainty in the measurements. It may result from the assumption made in the measurements that the quenching effects are sim-

ilar in the calibrated premixed flame and the dynamic jet diffusion flame. It is also possible that the chemical kinetics used in the present model may not be sufficient to yield accurate [O] in dynamic flames.

The structure of the dynamic flame at instants of 5 and 39 ms, corresponding to the stretched and compressed flames, respectively, are shown in Fig. 6 in plots of radial distributions of temperature and species' concentrations. Note that the data shown in Fig. 6 are quite different from those in Fig. 4, even though some similarities exist. With reference to the instantaneous flame image in Fig. 3, the data in Fig. 6 represent the instantaneous structure of the flame along the radial line passing through the probe location at $t = 5$ ms (Fig. 6a) and at $t = 39$ ms (Fig. 6b). On the other hand, the data in Fig. 4 represent the time evolution of temperature and species at one probe location. However, the data at $r = 15.5$ mm in Figs. 6a and 6b correspond to those data at $t = 5$ and 39 ms, respectively, in Fig. 4. By plotting the measurements and the predictions on the left and the right halves, respectively, the species concentrations and temperature profiles can be easily compared in Figs. 6a and 6b, respectively.

The spatial distributions of the temperatures agree very closely between the computations and the experiments. Experimentally, the flame structure is quite

narrow in the stretched region, as expected, because of an increase in reactant fluxes (stretch effect). Because these fluxes decrease in the compressed-flame region, the structure of the flame in this region becomes broadened (Fig. 6b). The temperature profile in the compressed region exhibits two peaks, with a difference of ~ 100 K: one located adjacent to the fuel jet and the other located in the flame-bulge region.

Observation of the [O] and [OH] profiles in the stretched region (Fig. 6a) suggests that these species are formed on the lean side of the flame in a relatively thin zone, with their peak locations being shifted slightly from the peak temperature. In contrast, the production of H appears on the rich side of the flame. Fig. 6a also suggests that a good correlation between the consumption of fuel and the production of H with temperature is obtained in the measurements. As with the measured temperatures, the agreement between the computed and the measured concentration profiles is very good. The evolutions and locations of the spatial distribution of every concentration were well predicted. However, calculations indicate that much more O and H is formed in the front flame; this is in contrast to the distributions observed experimentally.

In the compressed region [OH] exhibits a broad profile, with a peak located on the lean side of the flame. The peak [OH] is 40% lower than that in the stretched flamelet. The peak in [O] appears at the same location as the peak in [OH]; however, the production of O seems to decrease, despite the presence of a high local temperature and [OH] in the flame-bulge region. Comparison of the [O] profiles of Figs. 6a and 6b also shows an increase of 30% in the peak concentration in the compressed region. On the other hand, [H] exhibits a two-peak structure, which follows closely the temperature profile, with a 15% variation over the same temperature range. As noted previously, H production shows good correlation with the consumption of fuel, which decreases gradually over the width of the flame bulge. In contrast to the stretched region, substantial differences are noted between the computations and the measurements in terms of maximum concentrations. The modeling results (Fig. 6b) show that the concentrations of radicals exhibit a well-defined, two-peak structure with a peak intensity located on the rich side of the flame (i.e., at a radial location of 11 mm, where we still denote the presence of the stretched flame), as was the case with the experimental results. The peak [OH] and [O] are overestimated by a factor of ~ 1.8 relative to the experimental values. We also note that the calculated [H] agree quite well with experiment at $r = 11$ mm, while a large discrepancy is noted in the flame-bulge region ($r = 17.5$ mm). The reason for these discrepancies could be attributed to some aspects of the consumption of H_2 , not correctly accounted for. For in-

stance, the modeling results show a faster decrease of fuel over the width of the flame, which could then modify the distribution of the intermediate species via the main branching reactions $H + O_2 \rightarrow OH + O$ and $OH + H_2 \rightarrow H_2O + H$.

Finally, [NO] closely follows the temperature, with the peak in the former being located in the bulge region. The large [NO] in the compressed flame arises, in part, from the transport of the NO generated in other regions of the flame. The decrease of [O] and the increase of [NO] in the bulge region also illustrate the effect of the Zeldovich mechanism, which governs the thermal production of NO. In particular, O may react with the nitrogen present in large quantities in this zone to form NO. As discussed by Katta et al. [3,4], these observations can be attributed to the preferential-diffusion effects in hydrogen diffusion flames arising from the unequal diffusion velocities. It was found that preferential diffusion enhances the chemical effects, when the vortex is on the air side. The direct effect of stretch on the flamelet is an increase in the fluxes of reactants into the flame zone and that of compression is a decrease in them. Thus, in conjunction with the preferential-diffusion effects, this was predicted to increase the production of lighter species such as OH, O, and H in the stretched region but to decrease it in the compressed region. The experiments performed in the present study support those predictions. In contrast, the maximum [NO] was found in the compressed flamelet as a result of its sensitivity to the temperature and longevity.

6. Conclusion

Unsteady flames are often studied to gain an understanding of turbulent-flame structures to permit the development of accurate models of the interaction of turbulence and chemistry. An experimental and computational study was conducted in a low-speed, H_2 /air, jet diffusion flame in which temperature and species change rapidly during flame-vortex interactions. A time-dependent CFD code (UNICORN) incorporating detailed transport coefficients and a chemical-kinetics mechanism was used for the simulation of these buoyancy-dominated dynamic flames. Single-shot measurements of temperature and species' concentrations were made using different laser-based techniques. This study showed that a vertically mounted, dynamic, jet diffusion flame can be accurately characterized using computational methods and advanced optical-diagnostic measurement techniques. In this combined numerical and experimental study, detailed measurements, which were cross-verified for their accuracy, were obtained. The temporally and spatially resolved measurements of

temperature and concentrations of H_2 , H, O, OH, and NO established a database for the H_2 /air jet diffusion flame, which can be used for the development and improvement of the model. The measurements captured the depletion of radicals, such as H, O, and OH, where the flame was compressed and the buildup of these species where stretching occurred, as predicted by the UNICORN model. The contradictory behavior of temperature and [NO], which increase/decrease in the compressed/stretched flame location, respectively, was also quantified by time-resolved measurements. The techniques demonstrated in this study for measuring absolute concentrations of radicals and molecules during a vortex–flame interaction can be used to identify the important chemical pathways in diffusion flames.

Acknowledgments

This work was supported, in part, by the Direction Générale de l'Armement. The numerical effort was supported by the Air Force Office of Scientific Research (Dr. Julian Tishkoff, Technical Monitor). The authors acknowledge Marian Whitaker for editorial assistance.

References

- [1] H.C. Hottel, W.R. Howthorne, *Proc. Combust. Inst.* 3 (1949) 254–266.
- [2] A.R. Masri, R.W. Dibble, R.S. Barlow, *Prog. Energy Combust. Sci.* 22 (1996) 307–362.
- [3] V.R. Katta, W.M. Roquemore, *Combust. Flame* 96 (1994) 60–74.
- [4] V.R. Katta, W.M. Roquemore, *Combust. Flame* 100 (1995) 61–70.
- [5] W.M. Roquemore, V.R. Katta, *J. Visualization* 2 (2000) 257–272.
- [6] C.D. Carter, L.P. Goss, K.Y. Hsu, V.R. Katta, D.D. Trump, in: *Proceedings of the Combined Central States/Western States/Mexican National Sections Meeting of the Combustion Institute*, April 23–26, 1995.
- [7] F. Grisch, B. Attal-Tretout, P. Bouchardy, V.R. Katta, W.M. Roquemore, *J. Nonlin. Opt. Phys. Mater.* 5 (1996) 505–526.
- [8] V.R. Katta, L.P. Goss, W.M. Roquemore, *AIAA J.* 32 (1994) 84–94.
- [9] M. Frenklach, H. Wang, M. Goldenberg, G.P. Smith, D.M. Golden, C.T. Bowman, R.K. Hanson, W.C. Gardiner, V. Kissianski, Report No. GRI-95/0058, Gas Research Institute, Chicago, 1995.
- [10] B.P. Leonard, *Comput. Methods Appl. Mech. Eng.* 19 (1979) 59–98.
- [11] V.R. Katta, L.P. Goss, W.M. Roquemore, *Int. J. Num. Methods Heat Fluid Flow* 4 (1994) 413–424.
- [12] S. Druet, J.P. Taran, *Prog. Quant. Electron.* 7 (1981) 1–72.
- [13] Y. Prior, *Appl. Opt.* 19 (1980) 1741–1746.
- [14] M. Péalat, P. Magre, P. Bouchardy, G. Collin, *Appl. Opt.* 30 (1991) 1263–1273.
- [15] S. Candel, G. Herding, R. Snyder, P. Scoufflaire, C. Rolon, L. Vingert, M. Habiballah, F. Grisch, M. Péalat, P. Bouchardy, D. Stepowsky, A. Cessou, P. Colin, *J. Prop. Power* 14 (1998) 826–834.
- [16] R.A. Fisher (Ed.), *Optical Phase Conjugation*, Academic Press, New York, 1983.
- [17] R.L. Farrow, D.J. Rakestraw, *Science* 257 (1992) 1894–2000.
- [18] K. Kohse-Höinghaus, *Prog. Energy Combust. Sci.* 20 (1994) 203–279.
- [19] G.N. Robertson, K. Kohse-Höinghaus, S. Le Boiteux, F. Aguerre, B. Attal-Tretout, *J. Quant. Spectrosc. Radiat. Transfer* 55 (1996) 71–101.
- [20] P.H. Paul, J.A. Gray, J.W. Durant, J.W. Thoman, *AIAA J.* 32 (1994) 1670–1675.
- [21] R.J. Cattolica, J.A. Cavolowsky, T.G. Mataga, *Proc. Combust. Inst.* 22 (1988) 1165–1173.
- [22] C. Schulz, V. Sick, U.E. Meier, J. Heinze, W. Stricker, *Appl. Opt.* 38 (1999) 1434–1443.
- [23] R.J. Kee, F.M. Rupley, J.A. Miller, Report No. SAND89-8009, Sandia National Laboratories, 1989.
- [24] R.J. Kee, J.F. Grear, M.D. Smooke, J.A. Miller, Report No. SAND85-8240, Sandia National Laboratories, 1985.
- [25] W.M. Roquemore, L.D. Chen, L.P. Goss, W.F. Lynn, in: R. Borghi, S.N.B. Murthy (Eds.), *Turbulent Reactive Flows*, in: *Lecture Notes in Engineering*, vol. 40, Springer-Verlag, Berlin, 1989, p. 49.



ELSEVIER

Available online at www.sciencedirect.com

SCIENCE @ DIRECT®

Proceedings of the Combustion Institute 30 (2005) 475–483

Proceedings
of the
Combustion
Institute

www.elsevier.com/locate/proci

Unsteady effects on flame extinction limits during gaseous and two-phase flame/vortex interactions

A. Lemaire^{a,b}, K. Zähringer^b, T.R. Meyer^c, J.C. Rolon^{a,*}

^a Laboratoire EM2C, Ecole Centrale Paris and CNRS, Grande Voie des Vignes, F-92295 Châtenay-Malabry, France

^b Lehrstuhl für Strömungsmechanik und Strömungstechnik, Otto-von-Guericke Universität Magdeburg, Postfach 4120, D-39016 Magdeburg, Germany

^c Innovative Scientific Solutions, Inc., 2766 Indian Ripple Road, Dayton, OH 45440-3638, USA

Abstract

In highly fluctuating flows, it happens that high values of the strain-rate do not induce extinction of the flame front. Unsteady effects minimize the flame response to rapidly varying strain fields. In the present study, the effects of time-dependent flows on non-premixed flames are investigated during flame/vortex interactions. Gaseous flames and spray flames in the external sheath combustion regime are considered. To analyse the flame/vortex interaction process, the velocity field and the flame geometry are simultaneously determined using particle imaging velocimetry and laser-induced fluorescence of the CH radical. The influence of vortex flows on the extinction limits for different vortex parameters and for different gaseous and two-phase flames is examined. If the external perturbation is applied over an extended period of time, the extinction strain-rate is that corresponding to the steady-state flame, and this critical value mainly depends on the fuel and oxidizer compositions and the injection temperature. If the external perturbation is applied during a short period of time, extinction occurs at strain-rates above the steady-state extinction strain-rate. This deviation appears for flow fluctuation timescales below steady flame diffusion timescales. This behaviour is induced by diffusive processes, limiting the ability of the flame to respond to highly fluctuating flows. With respect to unsteady effects, the spray flames investigated in this article behave essentially like gaseous flames, because evaporation takes place in a thin layer before the flame front. Extinction limits are only slightly modified by the spray, controlling process being the competition between aerodynamic and diffusive timescales.

© 2004 The Combustion Institute. Published by Elsevier Inc. All rights reserved.

Keywords: Non-premixed; Spray; Vortex/flame; Extinction; Unsteadiness

1. Introduction

In non-premixed turbulent flames, chemistry and diffusion processes do not respond to rapidly varying strain fields [1]. The flame acts like a filter, and the scalar fields are only affected by low-frequency,

perturbations. When the characteristic timescales of the flow perturbations are comparable to those of diffusion and reaction [2], it is necessary to abandon the steady-state analyses and consider time-dependent effects [3,4]. This aspect is illustrated by experiments of unsteadily strained flames [5,6]. Unsteady effects have also been investigated using time-dependent calculations of strained flames with complex chemistry [7–9] or activation energy asymptotics [10]. It is shown in

* Corresponding author. Fax: +33 147 02 80 35.

E-mail address: rolon@em2c.ecp.fr (J.C. Rolon).

these various studies that, when the frequency of the flow field fluctuation increases, a time-lag appears between the forcing perturbation and the flame response. Above a cut-off frequency the flame response decreases rapidly. It has been observed that the flame can exist beyond the steady-state extinction limit if the modulation frequency is sufficiently high. This is explained to result from an accumulation of reactants in the diffusive layer due to the unsteady straining imposed by the flow [11]. These studies show that the flame response to unsteady strain-rate depends on the fluctuation frequency, the amplitude of this oscillation (related to the maximum strain-rate acting on the flame front), and the initial mean strain-rate. In the present study this dependence is investigated in the case of flame/vortex interactions.

Vortex/flame interactions are often considered to typify elementary processes of turbulent combustion. During successive interactions, the flame front is submitted to a variable strain field, possibly inducing extinction [12–14]. The fact that a non-premixed flame interacting with a vortex can resist to strain-rates up to 5–10 times the quasi-steady extinction strain-rate [12] once more reveals the importance of unsteadiness in the flame response. The flame response to unsteady strain-rate constitutes a central issue in turbulent combustion [15]. Since the extinction process plays an important role in flame stabilization processes [16], it is of importance to analyse the transition between the non-reacting and the burning state [17]. The present study focuses on the local extinction of non-premixed flames and on the influence of the flow unsteadiness on the flame extinction limits during flame/vortex interactions.

In many practical applications, fuel is introduced in a liquid form, usually as a spray. This modifies the combustion process. Multi-phase turbulent flames typically involve a large set of coupled phenomena such as atomization, dispersion, vaporization, molecular, and turbulent mixing, and chemical reactions. Understanding and modelling of such coupled flow fields is a difficult task. It is, for example, possible to use flamelet concepts for non-premixed turbulent flames extended to spray conditions as discussed in [18]. Understanding the interaction between unsteady laminar flows, sprays, and non-premixed flames may be useful to this type of modelling.

The present study aims at providing information on such processes by considering the interaction between a vortex ring and a non-premixed two-phase counterflow flame. Spray combustion is considered for non-dense droplet clouds in the external sheath combustion regime. The spray vaporizes in an evaporation layer bounding the spray, and the flame is fed by pre-evaporated reactant fluxes. Initial studies of a similar configuration were reported by Santoro et al. [19,20]. It

was found that two-phase flames interacting with a vortex sustain instantaneous strain-rates higher than those required for quasi-steady extinction. This conclusion was obtained by comparing two extinction modes, one being the quasi-steady state, the other a vortex-induced situation. In the present experiments, different vortex-induced perturbations interacting with flames are compared to understand how unsteady effects influence the flame response to strain-rate. A non-premixed flat flame is first established near the stagnation plane of a counterflow burner, and vortices are introduced on the fuel-side. The behaviour of the reaction zone is studied using planar laser-induced fluorescence (PLIF) of the CH radical, and vortex-induced strain-rate is simultaneously measured using particle-image velocimetry (PIV). Previous studies were undertaken using qualitative CH concentration and flame surface evolutions during flame/vortex interactions. The influence of the liquid phase on flame extinction and re-ignition is considered in [21]. The strain-rate history is a key parameter in the extinction process. The present study deals with unsteady effects on gaseous and two-phase flame response by analysing the strain-rate at extinction for different unsteady vortex flows.

2. Experimental setup

2.1. Burner device

The experimental device, derived from an initial steady gaseous counterflow burner [22], includes a piston-actuated vortex injection system [23] and a monodisperse spray generator [21].

The burner (Fig. 1) comprises two axisymmetric opposite nozzles of 20-mm diameter, with air in the upper flow and a nitrogen–fuel mixture in the lower flow. The distance between the nozzle outlets is set to 30 mm. The global strain-rate imposed by the steady gaseous injection velocities is kept constant at 90 s^{-1} following the definition of

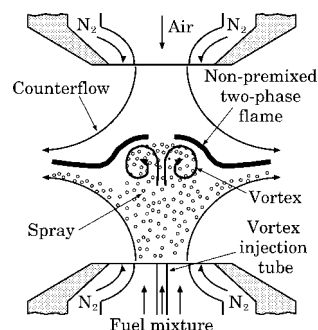


Fig. 1. Schematic representation of a two-phase flame/vortex interaction in opposed-jets burner.

Seshadri and Williams [24]. The fuel mixture is composed of methane diluted with nitrogen and seeded with 2.5 μm -diameter *n*-heptane droplets. The spray is diluted to a non-dense condition. The number of droplets per cubic centimetre is roughly estimated to 10^7 cm^{-3} . This estimation is done at the 2 cm-diameter outlet of the burner from flowmeter data without taking account of the part of evaporated *n*-heptane. The inlet steady flow conditions are characterized by the inflow fuel mass fraction $Y_{f,0}$, the mass ratio Ω between the liquid mass, and the total fuel mass and the global mixture ratio Φ . This last quantity is defined as $\Phi = s Y_{f,0} / Y_{ox,0}$ where s is the stoichiometric mass ratio of the reaction, and $Y_{f,0}$ and $Y_{ox,0}$ are, respectively, the inflow fuel and oxidizer mass fractions. Inlet flow conditions are listed in Table 1. Case **M** refers to a purely gaseous methane flame, cases **D** and **E** refer to *n*-heptane droplet-seeded flames. Flame **D**, with *n*-heptane seeding, is the two-phase analog of flame **M**, while flame **E** differs from flame **D** by a higher mass ratio of liquid fuel and a lower global mixture ratio.

Vortices are generated along the centreline of the fuel nozzle by an injection tube, fed by an electronic piston-actuation system. This tube is supplied by a flow derivation from the main fuel flow such that, in the absence of a vortex the exit velocity matches the steady flow velocity. The piston-actuation system controls the volume ejected and the ejection time, to generate vortices of varying strengths. Different vortex sizes are obtained by changing the diameter d of the injection tube, as listed in Table 1. The non-reactive vortices are characterized by two parameters: the vortex size D and the translational velocity U_T . These parameters are determined from the vorticity field measured by PIV, as explained in [25] and are also listed in Table 1.

Figure 2 shows a typical interaction between a non-premixed flame, a spray, and a vortex (in the case of flame **E** interacting with vortex **d**). As CH fluorescence intensity is very low, the flame front is observed in Fig. 2 by induced fluorescence of the OH radical. This allows to visualize on the same image the spray, entrained by the vortex flow, interacting with the flame front. The central part of the flame is extinguished, allowing the droplet-laden vortex to continue past the flame.

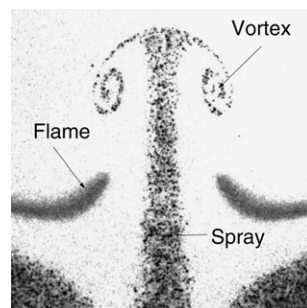


Fig. 2. Two-phase flame/vortex interaction visualized by OH fluorescence and light scattering on the droplet cloud in the case of the two-phase flame **E** ($Y_{f,0}=0.21$ and $\Omega=52\%$) interacting with vortex **d** ($D=3.5 \text{ mm}$ and $U_T=1.6 \text{ m/s}$).

2.2. CH visualization and velocity measurements

The flame front is visualized by laser-induced fluorescence of the CH radical, while the vortex flow-field and the strain-rate acting on the flame are determined by a digital cross-correlation PIV technique. Many details on the set-up are given in [21], only a brief description is included below.

The CH radical is excited at a wavelength of 389.5 nm corresponding to the $Q_1(5)$ transition of the $\text{B}^2\Sigma^- \leftarrow \text{X}^2\Pi(0,0)$ CH absorption band. To minimize the effects of laser-sheet intensity non-uniformities and molecular quenching of CH, the laser energy is chosen to nearly saturate the CH transition. Note that the intention of this study is not a quantitative determination of CH concentrations, but the qualitative observation of vortex/flame interactions and especially the extinction-induced CH decrease [21]. Fluorescence from the A–X (0,0) and A–X (1,1) bands is recorded using an intensified CCD camera, each CCD pixel corresponding to a measurement area of $100 \times 100 \mu\text{m}^2$. Then, the image resolution ($230 \mu\text{m}$) is only slightly smaller than the steady CH-layer thickness of about $250 \mu\text{m}$. The current set-up cannot discriminate, therefore, between a decrease of intensity or thickness of the CH layer, but these effects can be considered analogous for the purpose of discussing CH layer extinction.

To perform PIV measurements, silicon-dioxide particles are seeded in the air stream, while the

Table 1

(Left part) Inlet flow conditions of single- and two-phase steady strained flames, case **M** refers to a purely gaseous methane flame, and cases **D** and **E** refer to *n*-heptane droplet-seeded flames

Flames	M	D	E	Vortices	a	b	c	d	A	B
$Y_{f,0}$	0.26	0.27	0.21	d (mm)	2	2	2	2	3.7	3.7
Ω (%)	0	43	52	D (mm)	3.5	3.5	3.5	3.5	6	6
Φ	4.43	4.43	3.44	U_T (m/s)	0.39	0.74	1.0	1.6	0.46	0.53

(Right part) Vortex properties.

n-heptane droplets scatter the light from the fuel stream. The particle and droplet Stokes numbers in flows with characteristic perturbation times down to 0.5 ms (corresponding to strain-rates of 2000 s^{-1}) are as low as 0.06. Thus, these tracers and droplets follow the flow induced by the vortex and are well suited for PIV measurements. The two overlapping PIV laser sheets match with the CH-pumping laser sheet on the burner axis. The PIV pulse intervals are varied from 50 to 200 μs depending on the vortex speed. A dual-frame camera is used to acquire the two light scattering images. PIV images are processed with a commercially available software using an adaptive mesh technique from an initial 64×64 pixel interrogation area to a final 8×8 pixel interrogation area. This gives a vector spacing of 143 μm . Standard vector rejection techniques are applied with less than 6% of outliers.

A synchronization system ensures that signals controlling all the experimental devices are linked together. With appropriate time delays, the CH-pumping laser is fired between the two PIV laser pulses to avoid light scattering from particles. Various phases of a vortex/flame interaction can be imaged by adjusting the relative time-lag between piston actuation and laser shots.

3. Results and discussion

3.1. Extinction process

Figure 3 presents two times during the extinction process induced by the interaction between two-phase flame **E** and vortex **b** (Table 1). This interaction sequence is described by superposing CH PLIF and PIV data, each obtained by phase-averaging 10 images. For the purpose of this visualization, velocity data, not available in

the neighbourhood of the flame, are interpolated across the flame front. The initial time t_0 is defined as the moment when the vortex starts to perturb the CH layer. The flame is clearly wrinkled, 7.8 ms after the initial time t_0 (Fig. 3A). In fact, the reactive front follows the stoichiometric line, which is deformed by the vortex. Until the flame extinguishes, the CH layer intensity and thickness decrease on the centreline. Flame extinction is initiated 10 ms after the beginning of the interaction and is observed in the central part of the flame 0.5 ms later in Fig. 3B.

Figures 4B and C) shows the axial velocity profile (crosses) measured by PIV, along with the positions of the CH front (plain line) and the evaporation front (dotted line) during the same interaction as visualized in Fig. 3. Plots correspond to the time $t_0 + 5$ ms and to the extinction time $t_0 + 10$ ms. The relative CH layer and evaporation front positions indicate that the droplets get closer to the flame as their velocity is augmented by the vortex flow induced on the fuel side of the flame. This velocity decreases rapidly towards the stagnation plane, imposing a high strain-rate to the flame. The high vortex speed steepens the gradients and augments the species diffusion velocities. The reaction rate can then become the limiting process compared to the molecular diffusion fluxes. If the heat losses to the cold reactants exceed the heat released by the chemical reactions, flame extinction occurs. Extinction induced by increasing the strain-rate acting on the flame front reveals the finite rate of chemical kinetics.

3.2. Strain-rate determination

To examine the influence of unsteady effects on the extinction limits, it is interesting to determine two values of the strain-rate during the flame/vortex interaction: the first, A , characterizes the aerodynamic perturbation imposed to the flame, the second, A_q , defines the extinction limit. The characteristic strain-rate A is defined as the maximum value of the strain-rate during the temporal vortex evolution. The extinction strain-rate A_q is measured at the moment of flame extinction, defined in the present study as CH layer extinction.

Figure 4 shows how these two values are determined from the experimental axial velocity profiles. Since flame extinction is observed on the centreline, the effective strain-rate induced by the vortex is defined on the axis as the z -derivative of the vertical velocity component v , leading to $-\partial v / \partial z$. In the case of gaseous flames, strain-rates acting on the flame front are measured on the fuel side prior to the flame preheat layer avoiding the influence of the thermal gas expansion (Fig. 4A). In the case of two-phase flames, as shown in Figs. 4B and C, velocity measurements beyond the vaporization front are not possible due to the

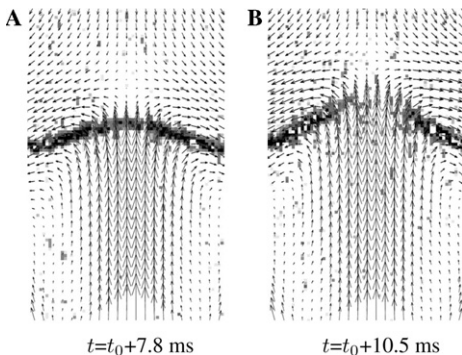


Fig. 3. Flame front visualized by CH fluorescence and velocity fields during the extinction of the two-phase flame **E** ($Y_{f,0} = 0.21$ and $\Omega = 52\%$) interacting with vortex **b** ($D = 3.5$ mm and $U_T = 0.74$ m/s), t_0 refers to the beginning of the interaction.

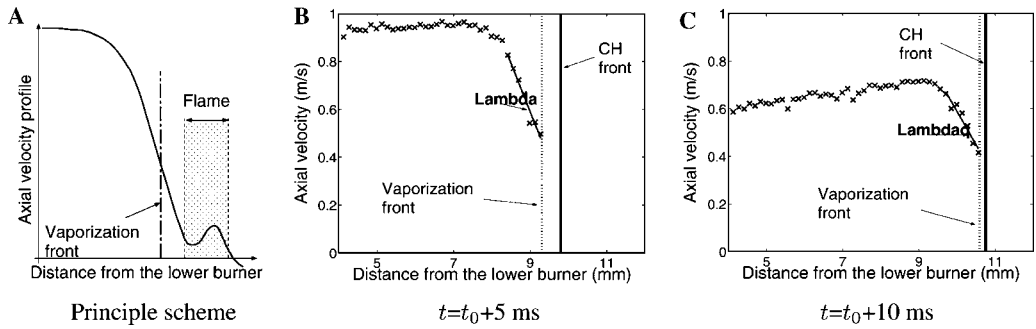


Fig. 4. (A) Idealized representation of the axial velocity profile. (B,C) Experimental axial velocity profiles (crosses), along with CH peak (plain line) and vaporization front (dotted line) positions, corresponding to the measurements of: (B) the maximum strain-rate A , (C) the extinction strain-rate A_q , during the interaction between flame E and vortex b.

evaporation of droplets that serve as tracers. Since the flow can locally be described by the Euler equation as a potential flow [22], the velocity gradient is constant in the outer region of the flame including the evaporation front (Fig. 4A). The strain-rate is therefore measured on the borderline of the evaporation front. The velocity profile is then linearly fitted upstream the evaporation front (upstream the preheat layer in the case of gaseous flames), and the strain-rate is obtained from the slope of the fitted line (Figs. 4B and C). No correction for thermophoretic effects is necessary since these strain-rate measurements are carried out prior to the flame preheat layer [26].

In the case of the interaction visualized in Fig. 3, between two-phase flame E and vortex b, the vortex-induced extinction occurs at a strain-rate A_q of 260 s^{-1} , 10 ms after the initial time, while the characteristic perturbation strain-rate A is equal to 400 s^{-1} . The flame does not extinguish at a maximum value of the strain-rate, as it could be expected. This is probably due to the kinetic energy dissipation in the flame neighbourhood.

The strain-rate results are listed in Table 2 where the abbreviation ‘n.ext.’ refers to a flame/vortex interaction, which does not lead to flame extinction. These results show that, for identical flame compositions, the extinction strain-rate increases with an increase in the vortex-induced strain-rate imposed to the flame. For example, two-phase flame E interacting with three identical-sized vortices extinguishes at strain-rates vary-

ing from 270 to 1300 s^{-1} depending on the vortex speed. The extinction limit thus depends not only on the initial mixture composition, as for steady flames, but also on the strain rate history.

3.3. Unsteady effects in flame response to variable strain

The results listed Table 2 can be analysed regarding timescales. In unsteadily strained flat flame, the amplitude of the flow perturbation and the fluctuation frequency are independent variables. However, in the flame/vortex interaction, these two parameters are proportional. A faster vortex imposes a higher strain-rate to the flame. This is typical of turbulent fluctuations where the characteristic eddy turn-over is inversely proportional to the strain-rate. Then the characteristic perturbation time τ_f (which is proportional to the vortex residence time) is defined as the inverse of the maximum strain-rate A ($\tau_f = 1/A$). Figure 5 presents the flame response in terms of aerodynamic extinction limits as a function of the characteristic perturbation time τ_f . In this figure, square, circle, triangle symbols correspond, respectively, to gaseous flame M, two-phase flame D, and two-phase flame E. The hollow and filled symbols relate to a vortex size D of 3.5 and 6 mm, respectively. Figure 5 shows two limiting behaviours of the flame response to the strain-rate. The first limit is the quasi-steady extinction regime [27]. For long perturbation

Table 2

Characteristic perturbation strain-rate A and extinction strain-rate A_q for different flames and vortices of Table 1

	Vortices (s^{-1})	a	b	c	d	A	B
Gaseous flame M	A	—	—	—	—	330	460
	A_q	—	—	—	—	290	420
Two-phase D	A	—	350	1300	1350	420	530
	A_q	—	n.ext.	1300	1350	330	520
Two-phase flame E	A	300	400	1100	1300	—	—
	A_q	n.ext.	270	1100	1300	—	—

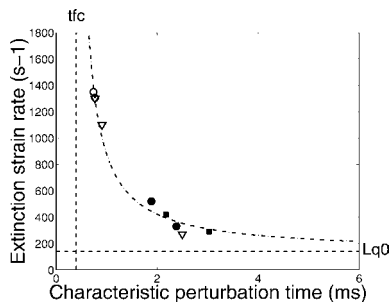


Fig. 5. The importance of unsteady effects is outlined by plotting the extinction strain-rate A_q as a function of the characteristic perturbation time $\tau_f = 1/\Lambda$.

times, the extinction strain-rates tend to a constant value represented by the dashed horizontal line. In Fig. 5, this value corresponds to the quasi-steady extinction strain-rate of flame **M**, equal to $\Lambda_q^0 = 140 \text{ s}^{-1}$. The second limit indicates that a flame behaves like a low pass filter [8,6]. Analytical expressions of the flame response to unsteady strain-rate exhibit the existence of a cut-off frequency, above which the flame response decreases rapidly [10,15]. As a consequence, if the characteristic perturbation timescale decreases, the strain-rate necessary to induce the flame extinction increases. This behaviour corresponds to a vertical asymptote, represented by the vertical dashed line in Fig. 5. The dependence of the extinction strain-rate on the flow timescale can be modelled by a hyperbolic curve defined as $(A_q - A_q^0)(\tau_f - \tau_f^c) = C$ (C is a constant close to unity), where Λ_q^0 and τ_f^c correspond, respectively, to the horizontal and vertical asymptotes. The best fit of the hyperbolic curve (dash-dotted curve) in Fig. 5 is plotted with the values $\tau_f^c = 0.4 \text{ ms}$ and $C = 0.45$. Below this curve, flame extinction does not appear. Figure 6 shows extinction strain-rate results obtained by Brown et al. [6] plotted versus the characteristic flow time. Experiments consist of a counterflow non-premixed methane/air flame

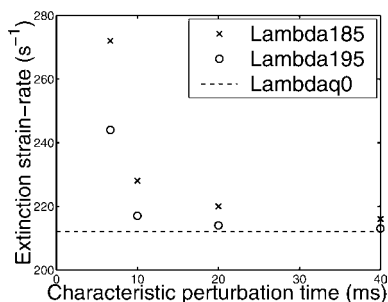


Fig. 6. Extinction strain-rate results obtained by Brown et al. [6] plotted versus the flow timescale. This data representation confirms the flame behaviour submitted to varying-strain observed in our experiments.

of composition ($Y_{f,0} = 0.27$) close to flame **M**, submitted to forcing velocity oscillations from 25 to 150 Hz for different initial mean strain-rates Λ_0 of 185 s^{-1} (crosses) and 195 s^{-1} (circles). Strain-rates measured in [6] are determined as proposed in [24] from the jet exhaust velocities. This differs from the method adopted in the present study and explains the difference in the strain-rate values. The steady-state extinction occurs at a strain-rate of $\Lambda_q^0 = 212 \text{ s}^{-1}$, represented in Fig. 6 by the horizontal dashed line. The characteristic time is taken to be the inverse of the oscillation frequency. Experiments described by Brown et al. [6] on unsteadily strained flat flames confirm that the extinction strain-rate depends on the flow timescale following the hyperbolic behaviour observed in the present study. Figure 6 shows also that the initial steady strain-rate influences the flame response to unsteady strain-rate. For initial highly strained flames, the extinction strain-rate deviates to a lesser extent from the steady-state value.

Extinction strain-rate results obtained in [6] for a mean strain-rate of 185 s^{-1} (crosses in Fig. 6) show a deviation $(A_q - A_q^0)/A_q^0$ of the extinction strain-rate A_q from the steady value A_q^0 smaller than 4% for perturbation times longer than 20 ms. Deviations from the steady-state increase to 10% and 30% for perturbation times down to 10 and 7 ms, respectively. Our results for flame **M** show deviations from the steady-state up to 110% and 230% for perturbation times of 3 and 2 ms, respectively. The experimental results show that there is a critical value of the characteristic perturbation time, under which the extinction strain-rate deviates from the steady-state extinction limit. Beyond this value the flame behaves in a quasi-steady manner, while below the same unsteady effects appear. In non-premixed flames, diffusion fluxes control heat and mass transfer in the flame neighbourhood. The flame structure therefore depends on diffusion processes and associated timescales. The characteristic time τ_m of the diffusive molecular transport can be defined as the inverse of the scalar dissipation rate χ ($\chi = 2D|\nabla Z|_{st}^2$ with a molecular diffusion coefficient D for methane/air flame **M** of around $0.3 \text{ cm}^2/\text{s}$). The Z -gradient $|\nabla Z|_{st}$ can be approximated by the inverse of the flame thickness δ , leading to $\tau_m = \delta^2/2D$. The flame thickness deduced from the OH layer distribution and estimated from OH fluorescence results is $\delta \approx 1 \text{ mm}$ for the steady flame **M**. The species diffusion time τ_m is then around 20 ms for methane/air flame **M**. It appears that the critical value of the characteristic perturbation time under which the extinction strain-rate deviates from the steady-state extinction limit corresponds to the flame diffusion time τ_m . This is confirmed by the results plotted in Fig. 6. The more strained the initial flame, the shorter is the flame diffusion time. In that case, the deviation

from the steady-state appears for shorter flow timescales, as shown in Fig. 6. Unsteady effects derive from a competition between the flow perturbations and the ability of the diffusive layer to follow these variations. If flow timescales become very small compared to diffusion timescales, the inner reaction zone becomes totally insensitive to the flow perturbations, corresponding to the asymptotic value τ_f .

Figure 5 shows that, in the external sheath combustion regime, spray flame responds to variable strain-rates like gaseous flames. Even for highly penetrating vortices, droplets do not interact individually with the flame. The spray vanishes in the evaporation layer, and the flame is fed by gaseous reactant fluxes. With respect to unsteady effects, only diffusive timescales are modified by the spray shifting slightly the critical value of the flow time, above which the flame does not respond in a quasi-steady manner.

Figure 5 also shows that the strain-rate is a key parameter in the extinction process. The flame curvature effect appears to be weak. This is so because, first, the vortex sizes are much larger than the flame thickness, second, the hydrocarbon flames extinguish quite rapidly and, as shown in Fig. 3, the flame is not highly wrinkled at extinction.

Finally, it can be observed from CH images, not shown in the present article, that the spray flame **D** extinguishes earlier than the gaseous flame **M** when submitted to a vortex of identical generation conditions. This may be due to heat losses associated with droplet evaporation [19]. However, another explanation can be proposed for the extinction of unsteady two-phase flames. As the vortex approaches the flame, droplet evaporation leads to gas expansion and then the two-phase vortex imposes a higher strain-rate to the flame as shown in Table 2. Thus, during flame/vortex interactions, the apparent weakness of the spray flames can also be explained by the higher strain-rates exerted on the two-phase flames. On the other hand, unsteady two-phase flames submitted to faster perturbations sustain extinction strain-rates higher than those characterizing gaseous flames. This indicates once more that unsteadiness plays a major role in the extinction process.

4. Conclusions

Vortex-strain-induced extinction of gaseous and two-phase flames has been examined by simultaneous measurements of the velocity field and the flame geometry. These flow and flame characteristics have been obtained by particle image velocimetry and laser-induced fluorescence of CH radical. These experiments show that extinction of unsteady flames does not only depend on the instantaneous value of the strain-rate, above which

the flame extinguishes, but is also related to the history of the perturbation. Considering initial and boundary conditions of unsteady flames, extinction limits not only depend on initial flame composition and temperature—as for steady extinction mode, but also depend on the characteristic perturbation time. The faster the perturbation, the further the extinction limit is extended beyond the quasi-steady-state extinction limit. From the longest to the shortest perturbation timescales, the flame extinction strain-rate varies from the steady-state value to high values of 10 times the steady value. In fact, non-premixed flames submitted to varying-strain fields extinguish at strain-rates following a hyperbolic dependence with the flow timescale, where the steady-state extinction strain-rate and the fluctuation time below which the flame is not affected by flow perturbations are the asymptotic limits. Experiments show that deviation from the quasi-steady state extinction appears when perturbation timescales become smaller than diffusion timescales. Unsteady effects in non-premixed combustion originate in diffusive processes by means of mass accumulation in the diffusive layer. It is believed that the diffusive layer acts as a buffer between the convective region of the flow and the inner reactive flame layer. Diffusion processes shift the extinction limits so that the extinction conditions are modified. In highly fluctuating flows, unsteady effects strongly influence the flame response and must be considered to predict extinction processes correctly. In the present experiments, we have chosen small monodisperse droplet conditions to separate effects of droplet piercing through the flame front. In this case, as the evaporation takes place in a thin layer before the reaction front, the flame is fed only by gaseous reactant fluxes. With respect to unsteady effects, spray flames burning in the external sheath combustion regime behave therefore like gaseous flames. The extinction strain-rates are slightly modified by the presence of the spray, controlling process being the competition between aerodynamic and diffusive timescales.

Acknowledgments

The authors wish to acknowledge Pr. S. Candel and Dr. J. Gord for helpful discussions. This work was supported by the DGA and ONERA within the PEA number 982703 - TITAN.

References

- [1] J.M. Donbar, J.F. Driscoll, C.D. Carter, *Combust. Flame* 125 (2001) 1239–1257.
- [2] N. Peters, *Turbulent Combustion*. Cambridge University Press, 2000.
- [3] G.F. Carrier, F.E. Fendell, F.E. Marble, *SIAM J. Appl. Math.* 28 (1975) 463–499.

- [4] D.C. Haworth, M.C. Drake, S.B. Pope, R.J. Blint, *Proc. Combust. Inst.* 22 (1988) 589–597.
- [5] J.S. Kistler, C.J. Sung, T.G. Kreutz, C.K. Law, M. Nishioka, *Proc. Combust. Inst.* 26 (1996) 113–120.
- [6] T.M. Brown, R.W. Pitz, C.J. Sung, *Proc. Combust. Inst.* 27 (1998) 703–710.
- [7] N. Darabiha, *Combust. Sci. Technol.* 86 (1992) 163–181.
- [8] F.N. Egolfopoulos, C.S. Campbell, *J. Fluid, Mech.* 318 (1996) 1–29.
- [9] C.J. Sung, C.K. Law, *Combust. Flame* 123 (2000) 375–388.
- [10] B. Cuenot, F.N. Egolfopoulos, T. Poinot, *Combust. Theory Model* 4 (2000) 77–97.
- [11] F.N. Egolfopoulos, *Int. J. Energy Res.* 24 (2000) 989–1010.
- [12] K. Yoshida, T. Takagi, *Proc. Combust. Inst.* 27 (1998) 685–692.
- [13] D. Thévenin, P.H. Renard, G. Fiechtner, J.R. Gord, J.C. Rolon, *Proc. Combust. Inst.* 28 (2000) 2101–2108.
- [14] V.R. Meyer, T.R. Katta, M.S. Brown, J.R. Gord, W.M. Roquemore, A. Lemaire, K. Zähringer, J.C. Rolon, in: *39th AIAA/ASME/SAE/ASEE Joint Propulsion Conference and Exhibit*. Huntsville, USA, 2003.
- [15] S. Candel, *Proc. Combust. Inst.* 29 (2002), 1–28.
- [16] L. Vervisch, *Proc. Combust. Inst.* 28 (2000) 11–24.
- [17] R.W. Bilger, *Proc. Combust. Inst.* 22 (1988) 475–488.
- [18] C. Hollmann, E. Gutheil, *Combust. Sci. Technol.* 135 (1998) 175–192.
- [19] V.S. Santoro, D. Kyritsis, A. Gomez, in: *17th International Colloquium on the Dynamics of Explosions and Reactive Systems*. Heidelberg, Germany, 1999.
- [20] V.S. Santoro, D.C. Kyritsis, A. Gomez, *Proc. Combust. Inst.* 28 (2000) 1023–1030.
- [21] A. Lemaire, T.R. Meyer, K. Zähringer, J.C. Rolon, J.R. Gord, *Exp. Fluids* 36 (2003) 36–42.
- [22] J.C. Rolon, D. Veynante, J.P. Martin, F. Durst, *Exp. Fluids* 11 (1991) 313–324.
- [23] P.H. Renard, D. Thévenin, J.C. Rolon, S. Candel, *Prog. Energy Combust. Sci.* 26 (3) (2000) 225–282.
- [24] K. Seshadri, F.A. Williams, *Int. J. Heat Mass Transf.* 21 (2) (1978) 251–253.
- [25] A. Lemaire, K. Zähringer, T.R. Meyer, J.R. Gord, J.C. Rolon, in: *2nd European Combustion Meeting*. Orléans, France, 2003.
- [26] C.J. Sung, C.K. Law, R.L. Axelbaum, *Combust. Sci. Technol.* 99 (1994) 119–132.
- [27] A. Liñán, *Acta Astro.* 1 (1974) 1007–1039.

Comments

Katharina Kohse-Höinghaus, University of Bielefeld, Germany. Your results about the correlation of extinction and strain rate are very interesting. There is ample literature about extinction parameters in counterflow diffusion burners. Would you regard this data now as lower limits of strain rates for extinction?

Reply. The correlation between extinction and strain rate is effectively now well established. The fundamental relevance of this study, we believe, is the experimental evidence of the existence of two extinction asymptotes limits, one lower and well known as the quasi-steady extinction limits, and another highest, corresponding to highly unsteady interactions (short characteristic perturbation time). The deviation from the quasi-steady state extinction is controlled by the competition between the perturbation time scales, and diffusion time scales. These data show the flammability domain, or the lower limits of strain rates for extinction, under the influence of different aerodynamics conditions.

●
Michael Drake, General Motors, USA. Is the amount of liquid fuel added enough to lead to a lower temperature of the fuel stream due to vaporization? What effect would this have on extinction limits?

Reply. Answer to this question is essentially included in the original paper, concerning the amount of liquid fuel added (see Section 2, Experimental setup), and the effects this has on the extinction limits (see Section 4, Conclusions, two last sentences). Summarizing, in this

paper, spray combustion is considered for non-dense droplet clouds in the external sheath combustion regime, in which the extinction strain-rates are slightly modified by the presence of the spray, controlling process being the competition between aerodynamic and diffusive time-scales. For a more detailed analysis on the influence of the liquid phase on flame extinction and re-ignition, we recommend our previous work using qualitative CH concentration and flame surface evolutions during flame/vortex interactions in (Ref. [21] in paper).

●
Robert Pitz, Vanderbilt University, USA. You found that the extinction of unsteady diffusion flames could depend on the history of the strain rate. Would a better indicator of extinction in unsteady laminar diffusion flames be the value of the scalar dissipation at the flame surface?

Reply. While we agree on the importance of the scalar dissipation rate as been a better indicator of extinction in unsteady laminar diffusion flames, this does not necessarily detract from the significance of strain rate history, which has a significant impact on scalar dissipation and is directly connected to strain rate in unsteady counter-flow flames. It is the primary focus of this work. It is also somewhat early to declare that scalar dissipation is a universal criterion for extinction. A study performed by the group at Yale [1], for example, showed that the scalar dissipation rate at extinction was as much as 26% higher than the value for quasi-steady extinction. This variation could be greater for other flame/vortex

conditions. A numerical study by Katta et al. [2], for example, found differences between steady and unsteady scalar dissipation rates at extinction of up to 73%.

References

- [1] D.C. Kyritsis, V.S. Santoro, A. Gomez, *Proc. Combust. Inst.* 29 (2002) 1679–1685.
- [2] V.R. Katta, T.R. Meyer, M.S. Brown, J.R. Gord, W.M. Roquemore, *Combust. Flame* 137 (2004) 198–221.



David Hagen, Vast Power Systems ILC, USA. Do you see or expect any surface area related quenching of radicals on drop surfaces compared to enthalpic or evaporation rate or strain rate-quenching phenomena [1]?

Reference

- [1] G.O. Thomas, *Combust. Flame* 130 (2002) 147–162.

Reply. In order to obtain qualitative information about the effects of the vortex on the flame, one can calculate the time evolution of the flame surface and the CH layer centerline intensity from experimental

images. Data from CH PLIF diagnostics effectively localize the diffusion flame front and extinction zones (extinction signal refers to signal that falls to the background noise). One can define the flame front position by following the maxima of CH intensity for an average of about 10 images. Comparing flame surface evolutions, measured extinction rates, and maximum peak normal strain rates, one may show that when the peak normal strain rate increases, the flame surface and the CH intensity during extinction decrease prior and faster in any cases we studied. We may say that the peak normal strain rate is sufficient to predict the extinction of the CH layer and is the main controlling parameter of extinction for the vortices studied in this paper. The rate of CH extinction can be described conveniently by a single value since the drop in CH mole fraction is found to be sufficiently linear with respect to time for a variety of conditions. In all cases studied in this work, quenching of radicals (OH and CH in our measurements) on drop surfaces were well correlated to a strain rate-quenching phenomena. Indeed, it can be observed from CH images (see our previous work Ref. [21] in paper) that spray flame extinguishes earlier than the gaseous flame when submitted to a vortex of identical generation conditions. This may be effectively due to enthalpy associated with droplet evaporation rate (Ref. [1] in Pitz reply).

Simultaneous planar laser-induced incandescence, OH planar laser-induced fluorescence, and droplet Mie scattering in swirl-stabilized spray flames

Terrence R. Meyer, Sukesh Roy, Vincent M. Belovich, Edwin Corporan, and James R. Gord

Simultaneous planar laser-induced incandescence, hydroxyl radical planar laser-induced fluorescence, and droplet Mie scattering are used to study the instantaneous flame structure and soot formation process in an atmospheric pressure, swirl-stabilized, liquid-fueled, model gas-turbine combustor. Optimal excitation and detection schemes to maximize single-shot signals and avoid interferences from soot-laden flame emission are discussed. The data indicate that rich pockets of premixed fuel and air along the interface between the spray flame and the recirculation zone serve as primary sites for soot inception. Intermittent large-scale structures and local equivalence ratio are also found to play an important role in soot formation. © 2005 Optical Society of America

OCIS codes: 120.0120, 290.0290, 300.0300, 120.1740, 300.2530.

1. Introduction

Swirl-stabilized liquid-spray injectors are commonly used in gas-turbine engines to achieve compact, stable, and efficient combustion. The flow field in the primary zone of such a spray flame is characterized by high shear stresses and turbulent intensities that result in vortex breakdown and large-scale unsteady motions.^{1,2} These unsteady motions are known to play a key role in the formation of pollutant emissions such as carbon monoxide (CO), nitric oxide (NO), and unburned hydrocarbons.^{3–5} Less is known, however, about the mechanisms that lead to soot formation in swirl-stabilized, liquid-fueled combustors. Previous investigations have relied on exhaust-gas measurements and parametric studies to gain insight into the effects of various input conditions on soot loading.^{6–10} Much of the fundamental knowledge concerning soot formation is derived from investigations of laminar diffusion flames,¹¹ with only a limited number of studies having focused on internal combustion en-

gines and unsteady effects.^{12–14} The importance of considering unsteadiness and fluid-flame interactions was demonstrated by Shaddix *et al.*,¹⁴ who found that a forced methane-air diffusion flame produced a fourfold increase in soot volume fraction (as a result of increased particle size) as compared with a steady flame having the same mean fuel flow velocity.

The goal of the current investigation is to study soot formation in the highly dynamic environment of a swirl-stabilized, liquid-fueled combustor. This is accomplished by simultaneous imaging of the soot volume fraction, hydroxyl radical (OH) distribution, and spray pattern in the primary reaction zone by use of laser-induced incandescence (LII), OH planar laser-induced fluorescence (PLIF), and droplet Mie scattering, respectively. The utility of LII for two-dimensional imaging of soot volume fraction has been demonstrated in laboratory investigations^{15,16} as well as in aircraft engine exhausts.^{9,10} Brown *et al.*¹⁷ performed planar LII for soot-volume-fraction imaging in the reaction zone of a gas-turbine combustor; their preliminary measurements employed LII alone for demonstration purposes and did not image the turbulent flame structure near the exit of the swirl cup. In this paper we extend the research of Brown *et al.*¹⁷ by performing LII at the exit of the swirl cup and by adding OH PLIF and Mie-scattering diagnostics.

Use of OH as a flame marker is typical in studies of soot formation in diffusion flames because of its close correlation with flame temperature.^{18,19} It has also been employed in a number of investigations of swirl-

T. R. Meyer (trmeyer@innssi.com) and S. Roy are with Innovative Scientific Solutions, Incorporated, Dayton, Ohio 45440. V. M. Belovich, E. Corporan, and J. R. Gord are with the U.S. Air Force Research Laboratory, Propulsion Directorate, Wright-Patterson Air Force Base, Ohio 45433.

Received 22 December 2003; revised manuscript received 28 June 2004; accepted 6 October 2004.

0003-6935/05/030445-10\$15.00/0

© 2005 Optical Society of America

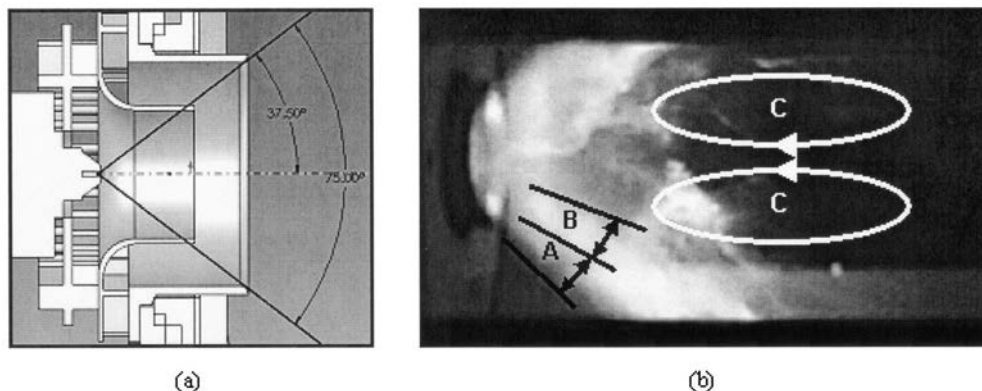


Fig. 1. (a) Swirl injector geometry used in the current study, and (b) photograph of near-field flame structure. Flow is left to right. Regions A–C depict the fuel evaporation and preheat zone, the turbulent flame brush, and the recirculation region, respectively.

stabilized combustors.^{20,21} Use of laser-saturated OH laser-induced fluorescence (LIF) for quantitative measurements has also been demonstrated,^{22,23} although saturation is quite difficult in the case of planar measurements. In the current investigation, we demonstrate qualitative measurements in the recirculation region using excitation levels well below saturation. OH PLIF measurements in the liquid-spray region are more uncertain because of simultaneous droplet scattering and nonequilibrium conditions, although meaningful measurements are possible with careful consideration of potential errors.

The performance and accuracy of the planar LII, OH PLIF, and Mie-scattering systems are characterized in this paper and described below. The combined use of LII, OH PLIF, and droplet Mie scattering is then shown to provide insight into the unsteady physical processes that govern soot formation in gas-turbine engines. OH PLIF is employed to track the local equivalence ratio and the effects of flame chemistry. Finally, the current measurement system is demonstrated to be useful for the assessment of the performance of soot-mitigating additives.

2. Experimental Setup

A. Swirl-Stabilized Combustor

The near-field structure of swirl-stabilized flames is determined by the characteristics of the fuel injector and the geometry of the surrounding flame tube. As shown in Fig. 1, the swirl-cup, liquid-fuel injector used in the current study employs pressure atomization and dual-radial, counterswirling air coflows to entrain the fuel, promote droplet breakup, and enhance mixing. The resulting three-dimensional conical flame, shown in Fig. 1(b), is composed of an outer droplet vaporization and preheat region (A) and an inner turbulent flame-brush region (B).²⁴ The flame is stabilized by a recirculation zone (C) that brings hot combustion products upstream along the centerline. The 4.3-cm-exit-diameter swirl cup is installed at the entrance of a 15.25 cm × 15.25 cm square cross-section flame tube, as shown in Fig. 2. After exiting the primary flame zone, the combustion prod-

ucts are allowed to mix thoroughly along the 48-cm-long flame tube before entering a 43-cm-long, 5.7-cm-exit-diameter exhaust nozzle that is designed to create uniform exhaust-gas temperature and concentration profiles.

The combustor shown in Fig. 2 is used in the Atmospheric-Pressure Combustor Research Complex of the U.S. Air Force Research Laboratory's Propulsion Directorate to study the performance characteristics of model gas-turbine engine fuels and fuel additives. An overview of the facility is available in the literature,²⁵ although certain aspects relevant to the current study are described here for reference. We achieved the changes in the overall equivalence ratio from $\phi = 0.5$ to 1.15 by varying the pressure drop across the fuel-spray nozzle from approximately 1.5 to 10 atm, which results in fuel mass-flow rates of 1.0 to 2.2 g/s, respectively. The fuel flow rate is measured with a Max Machinery positive-displacement flowmeter with $\pm 0.5\%$ full-scale accuracy. The air-flow system consists of three Sierra 5600-standard-liters-per-minute mass-flow controllers with $\pm 1\%$ full-scale accuracy. The inlet air is heated to 450 K with a constant flow rate of 0.028 kg/s. The air pressure drop across the combustor dome is ~ 4.8 –5.2% of the main supply. Most of the airflow enters the combustor through the swirl-cup injector, but a small

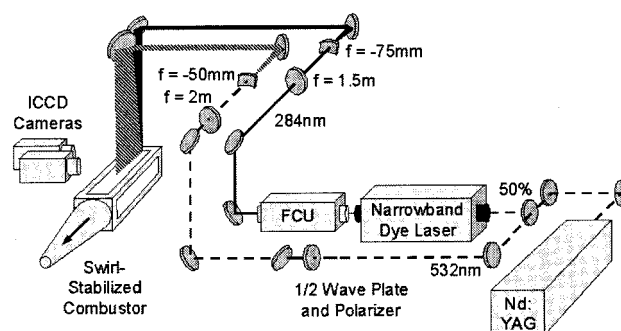


Fig. 2. Experimental setup for simultaneous planar LII, OH PLIF, and droplet Mie scattering in an atmospheric pressure, swirl-stabilized, liquid-fueled, model gas-turbine combustor. FCU, frequency-conversion unit.

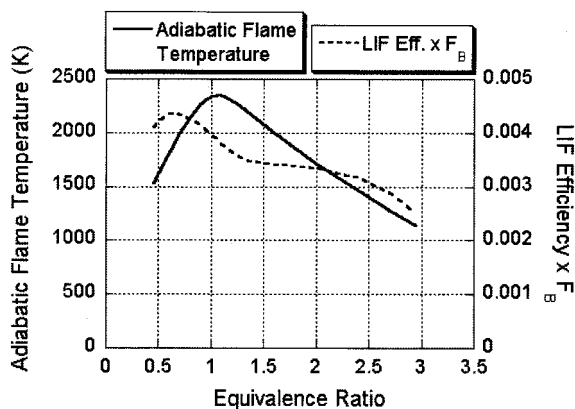


Fig. 3. Adiabatic flame temperature calculations in which equilibrium combustion products are assumed along with OH LIF efficiency multiplied by the Boltzmann fraction for JP-8 fuel at various equivalence ratios ϕ .

percentage enters through aspiration holes along the aft wall. No liner air jets are used in the secondary zone; therefore the fuel–air ratio depends almost entirely on the flow rates through the injector cup.

The combustor is optically accessible through 75-mm-wide quartz windows along the top and sides for *in situ*, laser-based diagnostics. In addition, a sampling probe used to measure particle number density (counts per cubic centimeter) with a condensation nuclei counter is located at the exit of the combustor.

B. Hydroxyl Radical Planar Laser-Induced Fluorescence System

A review of PLIF fundamentals can be found in Eckbreth.²⁶ As shown in the optical setup in Fig. 2, 50% of the laser energy from a frequency-doubled, Q-switched Nd:YAG laser (Spectra-Physics Pro290) is used to pump a dye laser (Sirah Precision Scan), the output of which is frequency doubled to obtain wavelengths in the (1,0) band of the OH A–X system. The dye laser is tuned to the $Q_1(9)$ transition at 283.922 nm (in air), which has less than $\pm 2.5\%$ variation in the ground-level Boltzmann fraction from 1600 to 2400 K. As shown in Fig. 3, this range of temperatures coincides with the equilibrium conditions expected for JP-8 fuel at equivalence ratios used in this study ($\phi = 0.5 - 1.15$).²⁷ Considering the full range of temperatures from 1100 to 2400 K, which are within typical lean and rich flammability limits,⁷ the Boltzmann fraction for this transition varies by up to $\pm 12.5\%$.

The maximum laser energy available for OH PLIF is 24 mJ. A 1.5-m focal-length spherical plano-convex lens and a -75 -mm focal-length plano-concave lens are used to form a laser sheet that enters the combustor through the top window. The laser-sheet thickness is 330 μm at a full thickness at half-maximum that we measured by translating a knife edge across the beam. We obtained a 7-cm, top-hat-like sheet-width profile that transitions to zero laser energy within approximately 1 mm by clipping the wings of the laser sheet at the last turning

mirror above the combustor. The sheet slowly expands with a 3° full-angle divergence.

We collected the fluorescence from approximately 306 to 320 nm through the (1,1) and (0,0) bands of OH using an intensified charge-coupled-device (ICCD) camera (Princeton Instruments PI-MAX SB) oriented slightly off normal to the sheet. Two 1-mm WG295 Schott Glass filters are used in front of the camera lens to reduce scattering from droplets at 283.922 nm. A UG11 filter nearly eliminates flame emission, scattering from the LII laser at 532 nm, and fluorescence from polycyclic aromatic hydrocarbons (PAHs). A 105-mm focal-length $f/4.5$ UV lens is used to collect the OH fluorescence. An intensifier gate width of 20 ns is used to capture the OH signal. Images are typically collected with 2×2 binning (512×512) to obtain adequate resolution and framing rate. The pixel viewing area in each 2×2 super-pixel is $200 \mu\text{m} \times 200 \mu\text{m}$.

On the basis of the dimensions of the OH PLIF laser sheet and total available laser energy of 24 mJ, it is estimated that the maximum laser irradiance of $1.36 \times 10^7 \text{ W/cm}^2$ is 2–3 orders of magnitude lower than that required to achieve 90–95% saturation.^{22,23} Therefore the OH PLIF signal is linearly related to laser energy variations. OH PLIF signal corrections (typically $\pm 15\%$) in the axial direction are performed in postprocessing, based on measurements of the laser-sheet profile after each run. Signal variation (typically $\pm 3\%$) due to the 3° laser-sheet expansion in the cross-stream direction is also corrected in postprocessing. Corrections are not made for laser energy attenuation due to OH absorption and droplet scattering as this leads to signal uncertainties of $\pm 10\%$ in the lower region of each image. The effect of this error is substantially reduced in the upper half of the combustor, where most of the data in this study are extracted. Shot-to-shot fluctuations in laser energy add an estimated $\pm 5\%$ uncertainty, as determined from data collected in a laminar diffusion flame with the same OH PLIF system.

For measurements with low laser irradiance, the effect of collisional quenching on fluorescence efficiency must also be considered. For a given imaging system and laser irradiance, the OH PLIF signal S_{OH} from each pixel volume is proportional to the OH number density N_{OH} and the fluorescence efficiency η ,²⁶ as shown in approximation (1):

$$S_{\text{OH}} \approx N_{\text{OH}} \eta = N_{\text{OH}} \frac{A_{\text{OH}}}{A_{\text{OH}} + Q_{\text{OH}}} \quad (1)$$

The fluorescence efficiency is proportional to the rate of spontaneous emission, A_{OH} , from molecules in the excited state and inversely proportional to the rate at which excited molecules are depleted by spontaneous emission and collisional quenching, Q_{OH} . Collisional quenching is a function of the temperature- and pressure-dependent quenching coefficient as well as the number densities of the quenching species.²⁸ As a result of offsetting effects in the equilibrium combus-

tion products of JP-8, the collisional quenching rate is found to be fairly constant for equivalence ratios less than unity, as shown in Fig. 3. Under rich conditions the conversion of CO to CO₂ decreases substantially, leading to an increase in collisional quenching and a decrease in fluorescence efficiency. In regions where equilibrium assumptions are valid, the LIF signal can be used along with approximation (1) and the Boltzmann distribution to determine the relative OH number density; this is discussed further in Section 3. In the liquid-spray region where lean and rich pockets coexist, qualitative signal interpretation is problematic since fluorescence efficiency can vary by more than $\pm 30\%$, according to Fig. 3.

C. Mie-Scattering System

Mie scattering is obtained with the same optical setup as that for the OH PLIF system. It is found that use of up to six optical filters can reduce but not altogether eliminate scattering from large droplets. Because of induced birefringence in the turning mirrors, the combustor windows, and the spray flame itself, use of parallel polarization in the detection scheme further reduces but does not altogether eliminate droplet scattering. It is found that two WG295 color glass filters (CVI Laser) and parallel-polarization detection provide optimal OH PLIF sensitivity and minimizes the likelihood of damaging the ICCD due to intense levels of droplet scattering. When the laser is tuned off the OH absorption line, as shown in Fig. 4, the intense, highly localized droplet scatter can be distinguished from the large, more uniformly distributed OH layers. Large droplet clusters appear primarily near the injector exit, and single droplets with trailing flames are often observed traveling into the recirculation region. The trailing flames of these droplets do not appear in the off-line images and therefore are not attributable to scattering from fuel vapor or fluorescence from broadband sources such as PAH compounds. The droplet-scattering signal intensity is approximately 1 order of magnitude higher than that of the OH PLIF, but the signal occurs primarily at isolated points. Therefore a false-color table is selected based on probability density functions of OH PLIF. The full range of OH PLIF signal levels is assigned colors from black to red whereas the Mie-scattering signals are above this range and appear in white.

D. Laser-Induced Incandescence System

Some of the first two-dimensional visualizations of soot volume fraction with LII were performed by Quay and co-workers¹⁵ and by Vander Wal and Weiland.¹⁶ The effects of various parameters such as laser fluence, laser-sheet profile, detection wavelength, camera gate width, and camera gate delay have been explored in a number of follow-up investigations.^{29–31} A list of reviews on the subject is provided by Urban and Faeth.³²

The LII optical layout employed in the current study is shown schematically in Fig. 2, where 50% of the energy from a frequency-doubled Nd:YAG is

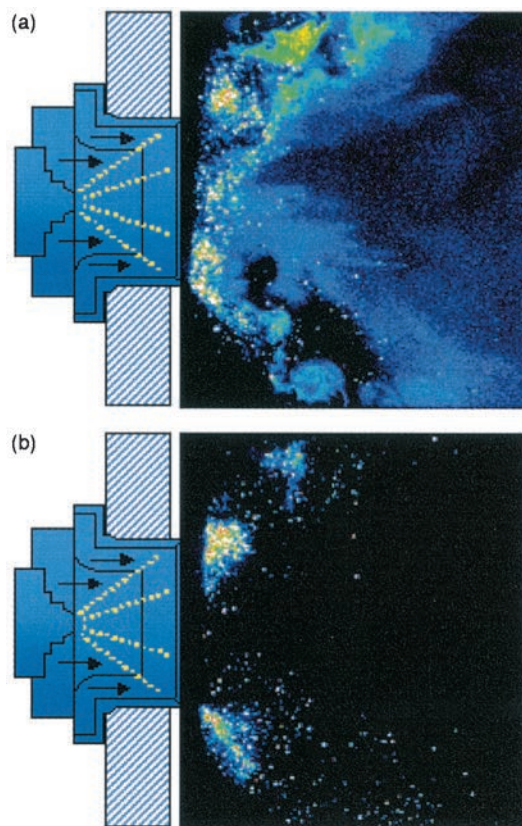


Fig. 4. Raw signal from (a) OH PLIF and droplet Mie scattering while on the $Q_1(9)$ line of the (1,0) band in the A-X system and (b) droplet Mie scattering while off the OH line. Overall, $\phi = 0.7$.

formed into a sheet by use of a 2-m plano-convex spherical lens and a -50-mm plano-concave cylindrical lens. The full thickness at half-maximum of the laser sheet is approximately 700 μm within the measurement volume, which we measured by traversing a knife edge across the sheet. As is the case for the OH PLIF laser sheet, the long 2-m focal-length lens is used to minimize variations in laser-sheet thickness within the measured region. The sheet width is ~ 14 cm, with wings that are clipped prior to the last turning mirror to generate a top-hat-like profile that transitions to zero laser energy within approximately 2 mm. The sheet has a full angle divergence of 6° within the test section. An overall tilt of 5° is used to overlap the LII and PLIF laser sheets. The laser fluence distribution varies by $\pm 15\%$ over the first 7 cm of the sheet, corresponding to the region where PLIF and Mie scattering are measured. Over the remaining 7 cm of the sheet, the laser fluence decreases more quickly from a peak of 460 mJ/cm^2 to a minimum of 180 mJ/cm^2 . To reduce systematic errors due to laser-sheet-width intensity variations in the downstream half of the laser sheet and due to laser extinction in the measurement volume, the LII system is operated in the saturated regime. A saturation fluence near 200 mJ/cm^2 , shown in Fig. 5, agrees with previous measurements in the literature.^{29,31} Figure 5 indicates that the uncertainty in the relative soot-

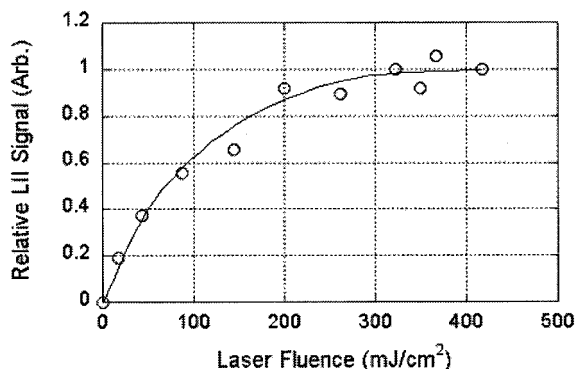


Fig. 5. LII saturation curve from averaged images in a swirl-stabilized combustor at an overall $\phi = 1.16$. The solid curve is for guidance only.

volume-fraction measurements is within $\pm 10\%$ over the full width of the laser sheet.

The LII signal is detected with a 1024×1024 ICCD camera (Princeton Instruments PI-MAX SB-MG) and an $f/1.2$, 58-mm focal-length glass lens. After 4×4 pixel binning, the measurement resolution is approximately $575 \times 575 \mu\text{m}$. A 500-nm short-pass filter (CVI Laser) is used for detection from 415 to 500 nm, which reduces contributions from nascent soot particles, OH fluorescence and chemiluminescence, redshifted fluorescence from PAH compounds, and C_2 Swan-band fluorescence and chemiluminescence. Chemiluminescent flame emission is further reduced by use of a 50- or 200-ns ICCD intensifier gate width; light leakage from flame luminosity while the ICCD intensifier is gated off is minimized by use of a 25-ms gate UNIBLITZ shutter. The relatively short-lived PAH and C_2 Swan-band fluorescence are also minimized by use of a time-delayed detection scheme. Scattering from the 532-nm laser source is eliminated by use of a 532-nm zero-degree reflective mirror with the 500-nm short-pass filter and delayed detection. During postprocessing the residual background signal from flame luminosity is subtracted from each image. A color scale is chosen with a minimum value of 5% above the background and a maximum value at a 100% signal.

To optimize the timing of LII detection, data are collected in the swirl-stabilized flame for a number of camera intensifier gate delays and widths. A camera delay of 20 ns after the laser pulse is found to reduce laser scatter to nearly the background level and maintain LII signal-to-noise ratios greater than 20:1. The LII signal decays quickly within the first 200 ns after the laser pulse, as shown in Fig. 6. The long decay in the signal after 200 ns is dominated by larger, slow-cooling particles. With an intensifier gate width of 50 ns, errors due to particle-size effects are estimated to be of the order of 5–10%.²⁹

E. Combined Laser-Induced Fluorescence and Laser-Induced Incandescence System

The OH PLIF and LII cameras are synchronized with an external delay generator (Stanford Research Sys-

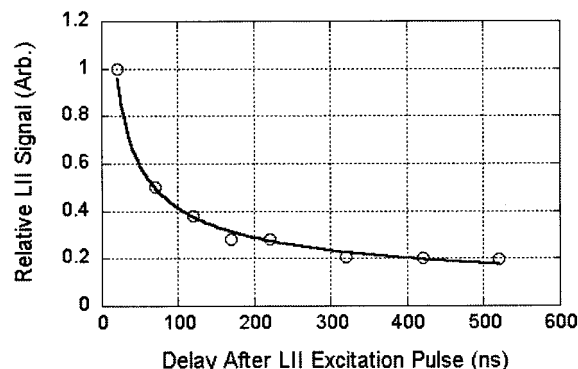


Fig. 6. Power-law temporal decay of the LII signal in a swirl-stabilized combustor at an overall $\phi = 1.1$.

tems DG535) driven by the advanced Q -switch TTL output of the Nd:YAG laser. The laser pulses are separated by a few nanoseconds to avoid fluid movement during LIF and LII detection. The precise camera delay required to capture each image is imposed with a timing generator in each ICCD controller. Because of spatial constraints within the test cell, both cameras are positioned on the same side of the combustor at slight 3.5° angles to overlap the two imaged regions. We minimized this angle by placing the LIF image to the far right of the camera viewing area and using a relatively large LII viewing area. Thus the PLIF image area overlaps the left half of the LII image nearest the injector cup. After camera alignment, registration images are collected prior to each run for use in postprocessing. At higher equivalence ratios (>0.7), thermal loading from flame radiation is significant, and heat shielding is employed to reduce misalignment of the LII-PLIF optics. During each run the OH PLIF and LII sheets are checked periodically with burn paper and adjusted to ensure that the laser intensity distributions and positions have not changed.

3. Results

A. Instantaneous Flame Structure

The average OH distribution at $\phi = 0.5$ is shown in Fig. 7(a). All images used for averaging are background subtracted and corrected for laser-sheet intensity variations and laser-sheet divergence. A slight asymmetry is apparent in the upper and lower halves, with the effects of laser attenuation being evident in the lower half of the image. For this reason, data are collected primarily in the upper (laser entrance) half of the combustor. As discussed in Subsection 3.C, the occurrence of soot is highly intermittent and is not expected to significantly alter the OH PLIF data.

The intermittency and spatial inhomogeneity of the instantaneous flame structure is shown by the OH PLIF images in Figs. 7(b) and 7(c). These images indicate that the fuel-preheat and reactant-mixing layers are highly turbulent. The instantaneous thickness of the OH layer varies significantly because of

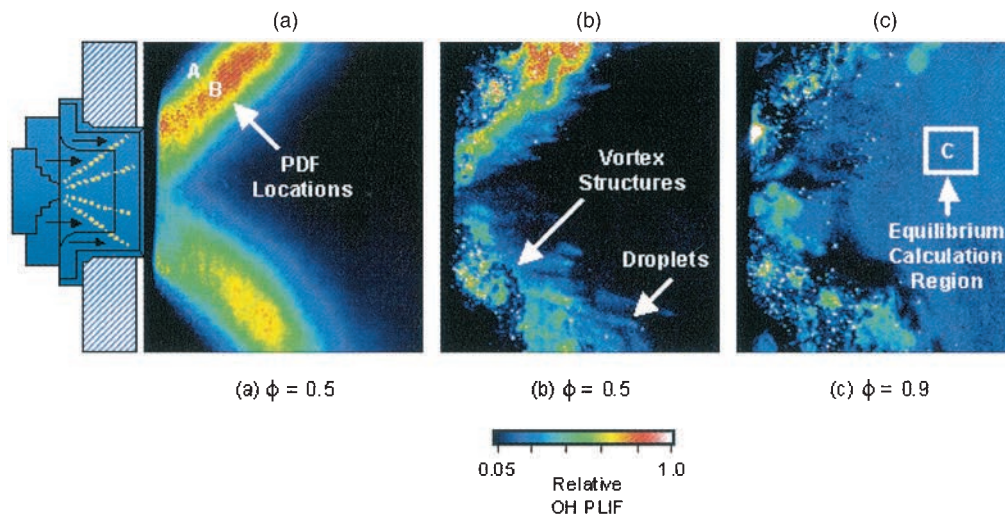


Fig. 7. Postprocessed OH PLIF images near the injector exit lip: (a) time-averaged image at an overall $\phi = 0.5$, (b) instantaneous image at an overall $\phi = 0.5$, (c) instantaneous image at an overall $\phi = 0.9$. The horizontal and vertical extent of the signal is 4–70 mm from the injector exit and –39–39 mm from the injector centerline. The false-color scale is 5% (black) to 100% (white) of peak signals. Regions greater than 100% represent droplet scattering.

fluid entrainment from large-scale vortex structures. These structures are shed from the shear layer that is anchored on the lip of the outer air swirler; they enhance the mixing process, bring fresh reactants into the outer conical flame, and can reach across the flame layer and be a source of local flame extinction and intermittency. The latter is more prominent in Fig. 7(c), which shows an instantaneous OH PLIF image at $\phi = 0.9$ with no contiguous flame in the viewing area. The size of the structures in Figs. 7(b) and 7(c) that are generated during the turbulent cascade from large to small scales ranges from approximately 0.5 mm to the entire width of the flame layer. Since the airflow rate is held constant, much of this intermittency can be attributed to the behavior of the liquid spray as it impinges on and sheds off the lip of the outer air swirler. This indicates that experiments and computations based on gaseous-fuel injection would not capture the significant changes in large-scale structure dynamics induced by increased liquid-fuel injection.

To quantify the intermittency of the primary flame layer, probability density functions (PDFs) of OH PLIF signals are computed and plotted in Fig. 8 for locations A and B shown in Fig. 7(a). Bin sizes of 200 counts are used along with 200 images. Normalization is performed only for data in the range of 0–6000 counts, which is below the range typically observed from droplet Mie scattering. Location A is within the mixing layer dominated by large-scale turbulent structures, whereas location B is within the central region of the outer conical flame. The PDFs at both locations show bimodal distributions but with opposite peaks. At location A high levels of intermittency lead to a primary peak with low signal counts and a secondary peak with 3000–3500 counts. At location B low signal counts have decreased in probability and high signal counts have increased in probability, in-

dicating that large-scale structures seldom bring fresh reactants to this point in the flame at $\phi = 0.5$.

B. Determination of Local Equivalence Ratio

Figures 7(b) and 7(c) also show the distribution of droplets marked by Mie scattering. This signal, which scales as the droplet diameter squared, is biased toward larger droplets and cannot be used to interpret the true size distribution. However, it can be used as a qualitative marker for those large droplets that escape the initial preheat zone. Interestingly, the droplets in Fig. 7(b) have trailing flames, which indicates that evaporation and mixing with available oxygen is occurring in their wakes. Figure 7(c), however, shows droplets entering the recirculation zone without trailing flames. Since the temperature, evaporation, and reaction rates are expected to be higher in this region for the higher equivalence

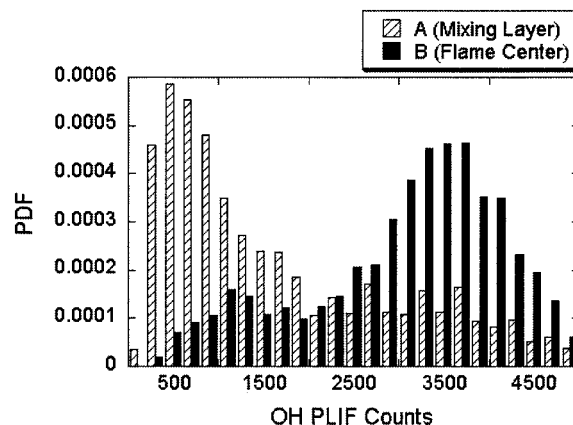


Fig. 8. PDFs of a corrected OH PLIF signal at location A (mixing layer) and location B (flame center) shown in the time-average image of Fig. 7(a).

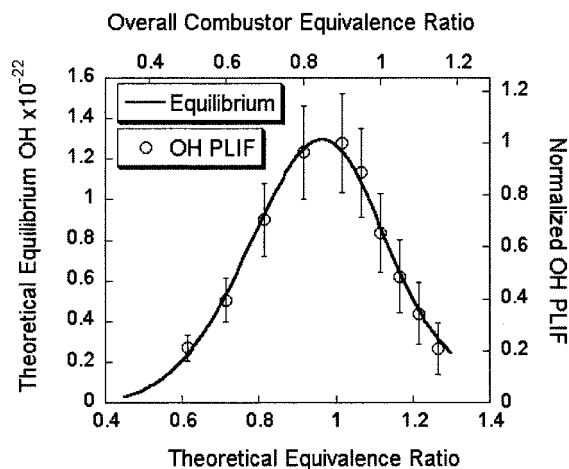


Fig. 9. Theoretical OH number density compared with OH PLIF data in a recirculation zone [region C in Fig. 7(c)]. OH PLIF data are corrected for variations in fluorescence efficiency and Boltzmann fraction with ϕ (see Fig. 3). Confidence intervals include PLIF uncertainty and flame fluctuation.

ratio of Fig. 7(c), the absence of trailing flames indicates a lack of sufficient oxygen for combustion.

In fact, it can be shown that the local equivalence ratio for the case of Fig. 7(c) is higher than the overall value of 0.9. Using a region in the recirculation zone that is free of droplet scatter [see Fig. 7(c)], we performed an equilibrium calculation²⁷ for JP-8 fuel at overall equivalence ratios varying from 0.5 to 1.15. The validity of equilibrium assumptions in this region is not known *a priori* but has been proposed in previous investigations of can-type gas-turbine combustors.^{3,4} The temperatures and species concentrations from this equilibrium calculation are then used to account for the effects of LIF efficiency and Boltzmann fraction on OH PLIF signals, as illustrated above in Fig. 3. The corrected and normalized OH PLIF data, shown in Fig. 9, display good agreement with the shape of the theoretical equilibrium curve. Nonequilibrium conditions may indeed exist in this region of the combustor, but it appears that they do not significantly alter the equivalence ratio profile. Note, however, that the OH PLIF data peak at an overall $\phi = 0.80\text{--}0.85$ whereas the equilibrium theory predicts that the peak occurs at $\phi = 0.95\text{--}1.0$. This indicates that the local equivalence ratio for combustion products feeding the recirculation zone may be higher than the overall equivalence ratio. Because the fuel spray is located in the center of the injector and air flows along an outer cone, the recirculation zone may contain a higher percentage of products from the inner, fuel-rich region of the spray flame. Correspondingly, images collected at an overall $\phi = 0.9$ show a transition from burning to non-burning wakes behind droplets [see Fig. 7(c)]; this indicates that the equivalence ratio may, in fact, be locally rich for this condition. The ability to track the local equivalence ratio is important for understanding soot formation in combustors with more complex secondary dilution configurations for which the over-

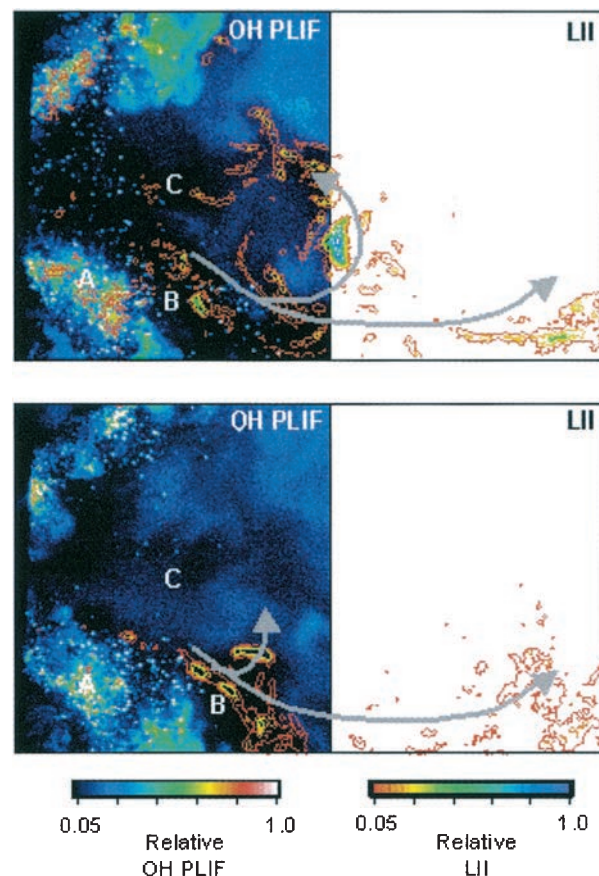


Fig. 10. Overlay of OH PLIF and LII images at an overall $\phi = 1.0$. The false-color scale for OH PLIF images are same as for Fig. 7. LII images shown with false-color contours from 5% (red) to 100% (blue) of peak signals.

all equivalence ratio is not representative of the primary flame zone. In the current study, the local equivalence ratio is important for understanding soot formation and oxidation induced along the interface between the spray flame and the recirculation zone.

C. Soot Formation Mechanisms

Figure 10 shows two instantaneous LII contour plots at $\phi = 1.0$ overlaid with OH PLIF images that are collected simultaneously. It should be noted that these LII images are typical for approximately 5% of the data set. More commonly, the spatial extent of the LII signal from highly concentrated soot pockets encompasses less than 1% of the primary flame zone. Images such as those in Fig. 10 therefore account for the turbulent flame brush noted in Fig. 1(b) that may be responsible for most of the soot production in liquid-spray flames. The flow patterns noted in Fig. 10 are derived by observations from high-speed digital images collected in the same combustor. Soot is generated along the inner cone of the flame in regions of low OH PLIF intensity. A portion of the soot is advected along the outer path of the recirculation zone, whereas a portion appears to enter immediately into the recirculation zone.

Most of the LII signal is detected in regions that are

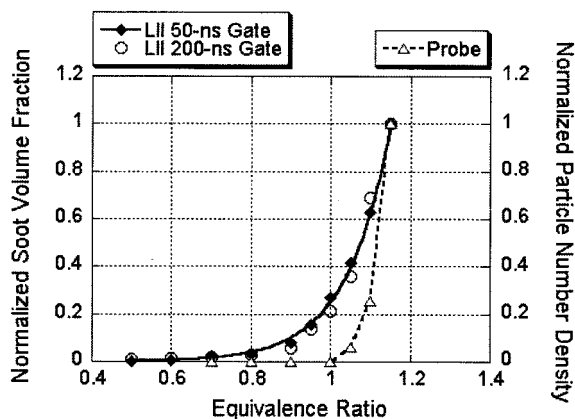


Fig. 11. Effect of overall ϕ on normalized soot volume fraction in primary flame zone and particulate number density from condensation nuclei counter data in exhaust. LII measurements with camera gate of 50 ns are fit with an exponential function. Data with a 200-ns camera gate are used to check for particle-size bias.

free of droplet Mie scattering (as verified with the OH PLIF camera) and is attributable to the presence of soot. Some of the signal from the LII camera does occur in regions of high Mie scattering (region A in Fig. 10), indicating that some, if not most, of the signal near the injector exit cannot be attributed to the presence of soot. The LII signal is not likely to come from PAH fluorescence, which would appear more consistently and have peak signals near the spray region. Background images collected without the laser sheet show that the contribution from nascent soot incandescence is less than 5%.

Thus it is likely that soot formation is, in fact, initiated along the inner-cone region (B) between the spray flame (A) and the recirculation zone (C). The absence of OH PLIF in region B is quite evident in the lower half of the spray flame (see Fig. 10), regardless of whether LII is detected. This region likely contains a rich mixture of fuel and air that escapes the main spray cone because of turbulent interactions. At low overall equivalence ratios [see Fig. 7], soot formed within this rich mixture may be oxidized by oxygen and the OH before entering the recirculation zone. At fuel-rich equivalence ratios soot formation is aided both by a drop in temperature and by the lack of an oxidizing partner. The soot formed in region B is advected either downstream or into the recirculation zone.

D. Averaged Soot-Volume-Fraction Measurements

The combined use of LII, OH PLIF, and Mie scattering has been shown above to provide physical insight into soot formation in the current flame environment. Data described in the discussion that follows demonstrate the utility of LII and OH PLIF for studying the effects of fuel-inlet conditions on soot production. This is illustrated in Fig. 11, where the temporally and spatially averaged relative soot volume fraction is plotted as a function of the overall equivalence ratio for the current spray flame. The LII data show an exponential increase in soot volume fraction with

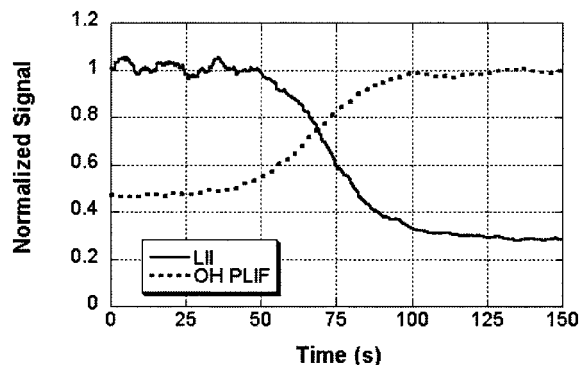


Fig. 12. Effect of methyl acetate ($C_3H_6O_2$) addition (20% by volume) to JP-8 fuel on LII and OH PLIF signals in the primary flame zone of a swirl-stabilized combustor. Signals are averaged for 100 shots.

equivalence ratio. The sampling probe condensation nuclei counter data display a threshold effect at approximately $\phi = 1.0$, below which soot in the exhaust is effectively oxidized due to long residence times and greater quantities of O_2 and OH. In the primary zone of the combustor, there is less time to oxidize the soot. In addition, the local ϕ is higher in the primary zone than in the exhaust.

The LII experiment is also performed at two camera gate widths to assess the sensitivity of the data to particle-size effects. A bias toward higher particle sizes for the longer gate duration of 200 ns would be expected. Because of normalization, this bias appears as a slight decrease in signal at lower equivalence ratios for which particle sizes are expected to be smaller. This effect appears to be minimal in Fig. 11 (to within experimental uncertainty), suggesting that detection with a 50-ns gate is also free of significant particle-size effects.

Since the dependence of soot volume fraction on ϕ is exponential, care must be exercised to differentiate the effect of soot-mitigating fuel additives on ϕ from potentially more complex chemical or physical mechanisms. An example is shown in Fig. 12 where methyl acetate, a high-oxygen-containing solvent, is added at 20% by volume to JP-8 fuel during a test at an overall $\phi = 1.05$. Note the large decrease in soot volume fraction during the methyl acetate addition, as measured by LII. This corresponds to a large decrease in particle counts at the sampling probe. A simultaneous increase in OH PLIF signal is also evident in Fig. 12 and, according to Fig. 9, corresponds to a decrease in overall ϕ . A certain ambiguity exists in the ϕ dependence of Fig. 9, however, because the final value could lie on either side of the peak OH signal. Noting that the OH signal increases continuously during methyl acetate addition, it is possible to conclude that the overall ϕ remains on the rich side of the peak value. Using Figs. 9 and 11 to determine the functional dependencies of the OH PLIF and LII signals, respectively, we found that a decrease from an overall ϕ of 1.05–0.93 took place during methyl acetate addition, with agreement between OH PLIF and

LII to within 1%. The value of 0.93 estimated from both techniques is close to the ϕ of 0.92 calculated from mass flow rates. This agreement suggests that a 20% methyl acetate addition to JP-8 in the current study affects soot production mainly through its effect on ϕ rather than on a fundamental change in the oxidation process. Therefore one can envision use of a combined LII PLIF system to track the performance of soot-mitigating additives without uncertainties in the equivalence ratio.

4. Conclusions

A simultaneous planar LII, OH PLIF, and Mie-scattering system is developed, tested, and demonstrated in a JP-8-fueled, liquid-spray, swirl-stabilized combustor. These combined diagnostics allow us to phenomenologically characterize soot formation mechanisms in this highly turbulent environment by mapping the soot volume fraction, instantaneous flame zone, and fuel droplet behavior. It is found that large-scale structures play a key role in flame intermittency and that soot formation is a strong function of spray-flame interactions as well as the local equivalence ratio. Experimental and numerical studies in gaseous-fueled combustors may not capture these dynamics properly. Soot formation in the inner conical flame region correlates with rich premixed regions with low OH PLIF and droplet Mie scattering. A qualitative study of equivalence ratio effects on the OH PLIF signals shows that equilibrium assumptions can be used for OH signal correction in the recirculation zone. LII data indicate an exponential dependence on the equivalence ratio and highlight the importance of the simultaneous tracking of the local equivalence ratio with OH PLIF, especially for the study of soot-mitigating additives.

The authors acknowledge the assistance of Sivaram Gogineni in the experimental setup and the editorial contributions of Marian Whitaker. We also thank Viswanath Katta, Matthew Dewitt, and Theodore Williams for their technical input, as well as Michael Arstingstall and Charles Frayne for assistance with the combustor facility. Funding for this research was provided by the U.S. Air Force Research Laboratory, Propulsion Directorate, Wright-Patterson Air Force Base under contracts F33615-00-C-2068, F33615-D-03-M2829, and F33615-00-C-3020, and by the U.S. Air Force Office of Scientific Research (Julian Tishkoff, program monitor).

References

1. W.-W. Kim, S. Menon, and H. Mongia, "Large-eddy simulation of a gas turbine combustor flow," *Combust. Sci. Technol.* **143**, 25–62 (1999).
2. S. Wang, S.-Y. Hsieh, and V. Yang, "Numerical simulation of gas turbine swirl-stabilized injector dynamics," paper AIAA-2001-0334 presented at the Thirty-Ninth Aerospace Sciences Meeting and Exhibit, Reno, Nev., 8–12 January 2001 (American Institute of Aeronautics and Astronautics, Reston, Va., 2001).
3. M. V. Heitor and J. H. Whitelaw, "Velocity, temperature, and species characteristics of the flow in a gas-turbine combustor," *Combust. Flame* **64**, 1–32 (1986).
4. A. F. Bicen, D. G. N. Tse, and J. H. Whitelaw, "Combustion characteristics of a model can-type combustor," *Combust. Flame* **80**, 111–125 (1990).
5. T. J. Held, M. A. Mueller, S.-C. Li, and H. Mongia, "Data-driven model for NO_x, CO and UHC emissions for a dry low emissions gas turbine combustor," paper AIAA-2001-3425 presented at the Thirty-Ninth Aerospace Sciences Meeting and Exhibit, Reno, Nev., 8–12 January 2001 (American Institute of Aeronautics and Astronautics, Reston, Va., 2001).
6. W. A. Eckerle, "Soot loading in a generic gas turbine combustor," paper AIAA-87-0297 presented at the Twenty-Fifth Aerospace Sciences Meeting, Reno, Nev., 12–15 January 1987 (American Institute of Aeronautics and Astronautics, New York, 1987).
7. T. C. Fang, C. M. Megaridis, W. A. Sowa, and G. S. Samuelsen, "Soot morphology in a liquid-fueled swirl-stabilized combustor," *Combust. Flame* **112**, 312–328 (1998).
8. A. H. Lefebvre, *Gas Turbine Combustion*, 2nd ed. (Taylor & Francis, Philadelphia, Pa., 1999).
9. J. D. Black, "Laser-induced incandescence measurements of particles in aero-engine exhausts," in *Conference on Environmental Sensing and Applications*, M. R. Carleer, M. Hilton, T. Lamp, R. Reuter, G. M. Russworm, K. Schaefer, K. Weber, K. C. H. Weitkamp, J.-P. Wolf, and L. Woppowa, eds., *Proc. SPIE* **3821**, 209–215 (1999).
10. T. P. Jenkins, J. L. Bartholomew, P. A. DeBarber, P. Yang, J. M. Seitzman, and R. P. Howard, "A laser-induced incandescence system for measuring soot flux in aircraft engine exhausts," paper AIAA-2002-3736 presented at the Fortieth Aerospace Sciences Meeting and Exhibit, Reno, Nev., 14–17 January 2002 (American Institute of Aeronautics and Astronautics, Reston, Va., 2002).
11. R. J. Santoro and C. R. Shaddix, "Laser-induced incandescence," in *Applied Combustion Diagnostics*, K. Kohse-Höinghaus and J. B. Jeffries, eds. (Taylor & Francis, New York, 2002), Chap. 9.
12. A. Leipertz, F. Ossler, and M. Aldén, "PAH and soot diagnostics by optical techniques," in *Applied Combustion Diagnostics*, K. Kohse-Höinghaus and J. B. Jeffries, eds. (Taylor & Francis, New York, 2002), Chap. 13.
13. Y.-H. Won, T. Kamimoto, H. Kobayashi, and H. Kosaka, "2-D soot visualization in unsteady spray flame by means of laser sheet scattering technique," SAE Tech. paper 910223 (Society of Automotive Engineers, Warrendale, Pa., 1991).
14. C. R. Shaddix, J. E. Harrington, and K. C. Smyth, "Quantitative measurements of enhanced soot production in a flickering methane/air diffusion flame," *Combust. Flame* **99**, 723–732 (1994).
15. B. Quay, T.-W. Lee, T. Ni, and R. J. Santoro, "Spatially resolved measurements of soot volume fraction using laser-induced incandescence," *Combust. Flame* **97**, 384–392 (1994).
16. R. L. Vander Wal and K. J. Weiland, "Laser-induced incandescence: development and characterization towards a measurement of soot-volume fraction," *Appl. Phys. B* **59**, 445–452 (1994).
17. M. S. Brown, T. R. Meyer, J. R. Gord, V. M. Belovich, and W. M. Roquemore, "Laser-induced incandescence measurements in the reaction zone of a model gas turbine combustor," paper AIAA-2002-0393 presented at the Fortieth Aerospace Sciences Meeting and Exhibit, Reno, Nev., 14–17 January 2002 (American Institute of Aeronautics and Astronautics, Reston, Va., 2002).
18. K. C. Smyth, J. H. Miller, R. C. Dorfman, W. G. Mallard, and R. J. Santoro, "Soot inception in a methane/air diffusion flame as characterized by detailed species profiles," *Combust. Flame* **62**, 157–181 (1985).
19. F. Cignoli, S. Benecchi, and Z. Giorgio, "Simultaneous one-dimensional visualization of OH polycyclic aromatic hydrocar-

- bons, and soot in a laminar diffusion flame," *Opt. Lett.* **17**, 229–231 (1992).
20. W.-P. Shih, J. G. Lee, and D. A. Santavicca, "Stability and emissions characteristics of a lean premixed gas turbine combustor," in the Twenty-Sixth Symposium (International) on Combustion (Combustion Institute, Pittsburgh, Pa., 1996), pp. 2771–2778.
 21. R. E. Foglesong, T. R. Frazier, L. M. Flamand, J. E. Peters, and R. P. Lucht, "Flame structure and emissions characteristics of a lean premixed gas turbine combustor," paper AIAA-99-2399 presented at the Thirty-Seventh Aerospace Sciences Meeting, Reno, Nev., 10–14 January 1999 (American Institute of Aeronautics and Astronautics, Reston, Va., 1999).
 22. R. P. Lucht, D. W. Sweeney, and N. M. Laurendeau, "Laser-saturated fluorescence measurements of OH concentration in flames," *Combust. Flame* **50**, 189–205 (1983).
 23. C. D. Carter, G. B. King, and N. M. Laurendeau, "Saturated fluorescence measurements of the hydroxyl radical in laminar high-pressure $C_2H_6/O_2/N_2$ flames," *Appl. Opt.* **31**, 1511–1522 (1992).
 24. K. Lee and B. Chehrودي, "Structure of a swirl-stabilized spray flame relevant to gas turbine and furnaces," *J. Propul. Power* **11**, 1110–1117 (1995).
 25. S. Roy, T. R. Meyer, R. P. Lucht, V. M. Belovich, E. Corporan, and J. R. Gord, "Temperature and CO_2 -concentration measurements in the exhaust stream of a liquid-fueled combustor using dual-pump coherent anti-Stokes Raman scattering (CARS) spectroscopy," *Combust. Flame* **138**, 273–284 (2004).
 26. A. C. Eckbreth, *Laser Diagnostics for Combustion Temperature and Species*, 2nd ed. (Gordon & Breach, Dordrecht, The Netherlands, 1996).
 27. S. R. Turns, *An Introduction to Combustion* (McGraw-Hill, New York, 1996).
 28. M. Tamura, P. A. Berg, J. E. Harrington, J. Luque, J. B. Jeffries, G. P. Smith, and D. R. Crosley, "Collisional quenching of CH(A), OH(A), and NO(A) in low pressure hydrocarbon flames," *Combust. Flame* **114**, 502–514 (1998).
 29. T. Ni, J. A. Pinson, S. Gupta, and R. J. Santoro, "Two-dimensional imaging of soot volume fraction by the use of laser-induced incandescence," *Appl. Opt.* **34**, 7083–7091 (1995).
 30. D. J. Bryce, N. Ladommatos, and H. Zhao, "Quantitative investigation of soot distribution by laser-induced incandescence," *Appl. Opt.* **39**, 5012–5022 (2000).
 31. H. A. Michelsen, "Understanding and predicting the temporal response of laser-induced incandescence from carbonaceous particles," *J. Chem. Phys.* **118**, 7012–7045 (2003).
 32. D. L. Urban and G. M. Faeth, "Soot research in combustion science: introduction and review of current work," paper AIAA-2001-0322 presented at the Thirty-Ninth Aerospace Sciences Meeting and Exhibit, Reno, Nev., 8–12 January 2001 (American Institute of Aeronautics and Astronautics, Reston, VA, 2001).

Dual-pump dual-broadband CARS for exhaust-gas temperature and $\text{CO}_2\text{--O}_2\text{--N}_2$ mole-fraction measurements in model gas-turbine combustors

T.R. Meyer^{a,*}, S. Roy^a, R.P. Lucht^b, J.R. Gord^c

^a Innovative Scientific Solutions, Inc., 2766 Indian Ripple Road, Dayton, OH 45440, USA

^b Department of Mechanical Engineering, Purdue University, West Lafayette, IN 47907, USA

^c Air Force Research Laboratory, Propulsion Directorate, Wright-Patterson Air Force Base, OH 45433, USA

Received 23 November 2004; received in revised form 11 February 2005; accepted 15 February 2005

Available online 24 March 2005

Abstract

Application of dual-pump, dual-broadband (DPDB) coherent anti-Stokes Raman scattering (CARS) for the measurement of temperature and multiple-species mole fractions is presented for the first time in a liquid-fueled combustor of practical interest. In this system pure rotational transitions of $\text{O}_2\text{--N}_2$ and the ro-vibrational transitions of $\text{CO}_2\text{--N}_2$ are probed using two narrowband pump beams, a broadband pump beam, and a broadband Stokes beam. This technique permits highly accurate temperature measurements at both low and high temperatures as well as mole-fraction measurements of two molecules with respect to N_2 from each laser shot. Single-shot measurements of temperature and mole-fraction ratios of CO_2/N_2 and O_2/N_2 in the exhaust stream of a swirl-stabilized, JP-8-fueled, model gas-turbine combustor are presented for equivalence ratios ranging from 0.45 to 1.0. Agreement between mean rotational and ro-vibrational temperatures is within $\sim 3\%$, and mean measurements of CO_2/N_2 and O_2/N_2 mole-fraction ratios are within $\sim 15\%$ of equilibrium theory. To illustrate the ability of the current measurement system to track multiple scalar statistics in turbulent reacting flows, histograms and scatter plots of temperature and species mole fractions are presented within the potential-core and turbulent-shear-layer regions of the exhaust stream.

© 2005 The Combustion Institute. Published by Elsevier Inc. All rights reserved.

Keywords: CARS; Temperature; Carbon dioxide; Oxygen; Nitrogen; Gas-turbine combustor

1. Introduction

Characterization of advanced propulsion systems requires the determination of performance and combustion efficiency through measurements of temperature and species mole fractions in the exhaust stream.

Typically these types of data are acquired using physical probes for thermometry or extractive sampling and involve the use of several independent techniques [1]. Diode-laser-based absorption is a nonintrusive alternative to extractive sampling, but it is a path-averaged approach and has limited spatial resolution [2]. For species such as O_2 , low sensitivity also limits the temporal resolution of diode-laser-based techniques. Ideally measurements of temperature and multiple species would be accomplished simultaneously with

* Corresponding author. Fax: +1 937 255 4110.

E-mail address: trmeyer@innssi.com (T.R. Meyer).

high spatial and temporal resolution while using a minimum number of diagnostics. Dual-pump, dual-broadband (DPDB) coherent anti-Stokes Raman scattering (CARS) offers the possibility of monitoring the local temperature and mole fractions of two target species with respect to a reference species (usually N_2) using a single hardware platform. The spatial resolution ranges from 50 μm normal to the beam propagation direction to 2 mm along the beam propagation direction. The temporal resolution is on the order of 10 ns.

We present here the first application of DPDB CARS for temperature and mole-fraction measurements in reacting flows of practical interest. This work extends previous DPDB CARS measurements in laboratory flames [3] and demonstrates the unique capability of using three laser wavelengths for acquisition of two pure rotational spectra (O_2 and N_2) and two ro-vibrational spectra (CO_2 and N_2). The ability to compare temperatures measured from both O_2 – N_2 and CO_2 – N_2 spectra provides a check on the accuracy and increases the dynamic range of the single-shot temperatures measurements. In the combustion zone or the exhaust stream of a real combustor, a wide spatial and temporal variation of temperature occurs because of the inherent turbulent nature of the flow field. In the current system the rotational spectra of O_2 – N_2 ensure high accuracy at lower temperatures, generally below 1500 K, because a higher percentage of the population resides at lower energy levels [4]. The ro-vibrational spectra of CO_2 – N_2 ensure high accuracy at elevated temperatures because a higher percentage of the population is transferred to higher energy levels.

The current approach is a variation of the triple-pump vibrational CARS technique, which provides two pairs of ro-vibrational spectra using single-longitudinal mode or very narrow-bandwidth pump beams [5]. The DPDB CARS system described here also employs three pump beams, but two are narrowband and one is broadband; this can be viewed, therefore, as a combination of the dual-pump and dual-broadband approaches. The dual-pump CARS technique, which was first demonstrated by Lucht [6], has been used for the simultaneous measurement of O_2 – N_2 [6,7], CO_2 – N_2 [8–10], H_2 – N_2 [11], CH_4 – N_2 [12], and O_2 – H_2 – N_2 [13]. In dual-pump CARS the wavelengths of the input beams are adjusted such that the CARS spectra for the two species under study are observed at nearly the same frequency. This arrangement largely eliminates the potential errors arising from wavelength-dependent variations in signal transmission or detector efficiency that complicate other multiple-species CARS techniques such as dual-Stokes and dual-broadband CARS [14]. Several other CARS techniques that have also been used for

temperature and multiple-species mole-fraction measurements are dual-broadband rotational CARS [15] and simultaneous vibrational and rotational CARS [16].

In the DPDB CARS technique implemented in the current work, three pump beams and a Stokes beam are used to generate four CARS signals near two distinct wavelengths. Both wavelength regions exhibit an N_2 –CARS signal along with the CARS signal from another target molecule. In much the same way as dual-pump CARS described above, each pair of CARS signals is generated over a relatively narrow wavelength region and can be captured with fixed-wavelength detection. This eliminates potential errors arising from wavelength-dependent variations in signal transmission or detector efficiency. Temperature and relative mole fractions of the target species (with respect to N_2) are extracted either by fitting the measured CARS spectrum with a theoretical spectrum or through a Boltzmann plot.

The objectives of this investigation were to perform single-laser-shot measurements of temperature and mole-fraction ratios of CO_2/N_2 and O_2/N_2 under realistic nonsooting and sooting gas-turbine conditions. Measurements were carried out in the exhaust stream of a liquid-fueled, swirl-stabilized CFM56 combustor for lean to rich overall equivalence ratios ranging from $\phi = 0.45$ to 1.0. A spatial traverse across the exhaust stream normal to the beam propagation direction was performed to illustrate statistical differences between the relatively steady centerline and the turbulent shear layer. Temperature and mole-fraction histograms and scatter plots are used to distinguish the relative effect of fluid-dynamic fluctuations from that of random error. The current work provides benchmark statistical distributions of temperature and mole-fraction ratios of CO_2/N_2 and O_2/N_2 in the exit plane of the combustor and is used to evaluate the effects of fuel composition and particulate-mitigating additives on flame chemistry. These measurements complement laser-induced incandescence (LII) and planar laser-induced fluorescence (PLIF) measurements of soot volume fraction and OH radical mole fraction, respectively, which are ongoing in the current combustor [17].

2. Experimental setup

2.1. DPDB-CARS system

The DPDB-CARS system schematic and the energy-level diagrams shown in Figs. 1a and 1b, respectively, are described in Ref. [3] and summarized here for reference. All CARS beams are generated from the frequency-doubled 532-nm output

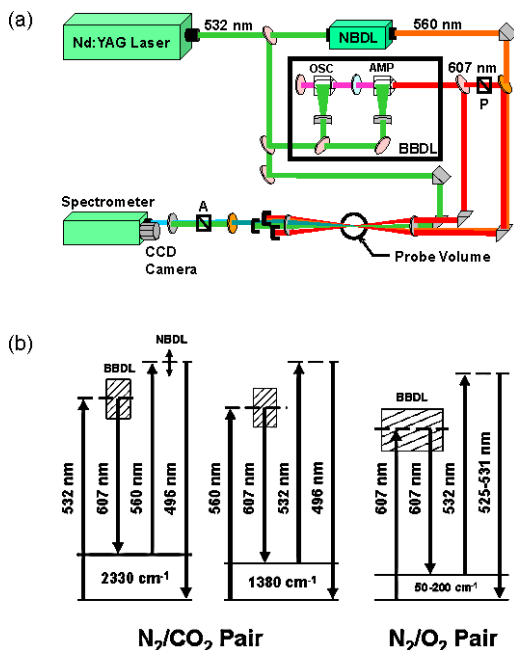


Fig. 1. (a) Schematic diagram of DPDB-CARS system for detecting temperature and mole-fraction ratios of O_2/N_2 and CO_2/N_2 . (b) Energy-level diagram of DPDB-CARS system [3].

of an injection-seeded Nd:YAG laser (Pro290, Spectra Physics), the 20-mJ, 560-nm output of a 532-nm-pumped narrowband dye laser (Precision Scan, Spectra Physics), and the 30-mJ, 607-nm output of a 532-nm-pumped custom-built broadband dye laser. For the $\text{CO}_2\text{--N}_2$ CARS system, spatial overlap of the 532-nm pump beam with the 607-nm Stokes beam produces a ro-vibrational N_2 Raman polarization that coherently scatters the 560-nm pump beam, yielding an N_2 CARS spectrum near 496 nm. At the same time, the 560-nm pump beam and the 607-nm Stokes beam produce a ro-vibrational CO_2 Raman polarization that scatters the 20-mJ, 532-nm pump beam, yielding a CO_2 CARS spectrum that also appears near 496 nm.

As shown in Fig. 1, approximately 15 mJ of the broadband 607-nm beam is redirected for use as a pump beam for the $\text{O}_2\text{--N}_2$ CARS System. The spectral width (FWHM) of the broadband dye laser is $\sim 200\text{ cm}^{-1}$, which is sufficiently large to excite the pure rotational transitions of O_2 and N_2 molecules at the ground and excited vibrational state up to rotational levels of $J \sim 30$. The broadband pump beam and the broadband Stokes beam produce rotational Raman polarizations for both O_2 and N_2 molecules, which then scatter the 532-nm pump beam. Both pure rotational CARS spectra appear at a wavelength of $\sim 525\text{--}531\text{ nm}$.

All incident beams are focused with a 600-mm focal-length lens and phase-matched using the folded BOXCARS geometry, with the 560- and 607-nm pump beams arranged colinearly. The frequency of the rotational CARS signal is very close to the pump beam at 532 nm. This poses the significant challenge of discriminating the scattered light at 532 nm from the CARS signal at 528 nm. To minimize the scattered light at 532 nm, the polarization of one of the broadband pump beams at 607 nm was oriented to be orthogonal to that of the 532-nm beam. The polarization of the broadband dye beam that serves as the Stokes beam for the $\text{CO}_2\text{--N}_2$ CARS was not rotated. With this configuration the polarization of the pure rotational CARS signal was orthogonal to that of the 532-nm pump beam. The CARS signal at 528 nm was isolated from the background 532-nm scattered light by placing a polarizer in the detection channel, with a transmission axis perpendicular to the 532-nm pump beam, as shown in Fig. 1.

Note that the ro-vibrational CO_2 and N_2 spectra near 496 nm can be detected on a single spectrometer, while a second spectrometer can be used to collect the pure rotational O_2 and N_2 spectra near 528 nm. Simultaneous detection of the ro-vibrational and rotational spectra was reported in a previous publication [5] but, in the current work, equipment availability necessitated the use of a single, 1.0-m spectrometer and a single back-illuminated CCD camera with an array of 2000×512 pixels (DH734, Andor Technologies). For each flame condition the spectrometer was first set for acquisition of the ro-vibrational spectra near 496 nm; the spectrometer grating was then moved to acquire the rotational spectra near 528 nm.

The CARS spectra are normalized using a nonresonant spectrum to account for the effects of pulse-to-pulse laser-power fluctuations, long-term power drift, and spectral variations in dye power [13]. The nonresonant spectrum is recorded by flowing pure argon into the beam-overlap region. Temperatures from the $\text{CO}_2\text{--N}_2$ and $\text{O}_2\text{--N}_2$ pairs were evaluated by fitting the CARS spectra with theoretical spectra. Since the N_2 mole fraction is typically known to within a few percent, the amplitude of the target-species signal relative to that of the paired N_2 signal can provide an absolute measure of the target-species mole fraction.

2.2. JP-8-fueled model combustor

The atmospheric-pressure combustor facility employed in the current study has been described in detail previously by Roy et al. [10] and Meyer et al. [17]. A brief overview is included here for reference. A single, JP-8-fueled pressure-swirl injector is center-mounted in a dual-radial air-swirling nozzle that feeds a 48-cm-long, $15.25 \times 15.25\text{-cm}$ square-cross-section

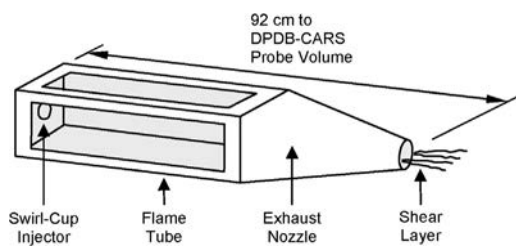


Fig. 2. Schematic diagram of JP-8-fueled, swirl-stabilized, model gas-turbine combustor. DPDB-CARS measurements performed along horizontal traverse 1.0 cm downstream of exhaust-nozzle exit plane.

flame tube, as shown in Fig. 2. Changes in equivalence ratio, ϕ , from 0.45 to 1.0 are achieved by varying the pressure drop across the fuel-spray nozzle to obtain fuel mass-flow rates of 0.9 to 1.9 g/s. The air-flow system consists of three Sierra 5600 SLPM mass-flow controllers with $\pm 1\%$ full-scale accuracy. In the present investigation air to the combustor was heated to 450 K, and the flow rate was held constant at ~ 0.0283 kg/s. The air-pressure drop across the combustor dome was $\sim 5\%$ of the main supply. The exhaust gases mix thoroughly and exit the combustor through a 43-cm long, tapered nozzle with an inner diameter of 4.8 cm at the exit plane. At high ϕ , unburned fuel forms a diffusion flame at the exit of the exhaust nozzle; while it does not contribute to the CARS signal in the center of the nozzle, it does contribute to background flame emission. The entire combustor test stand is on an x - y - z translation system.

3. Results and discussion

3.1. Single-shot spectra and statistics

Single-shot temperature and mole-fraction-ratio measurements of CO_2/N_2 and O_2/N_2 were performed in the exhaust stream of the JP-8-fueled, swirl-stabilized combustor over a wide range of equivalence ratios, ϕ , using the DPDB-CARS technique. Typical postprocessed single-shot spectra at $\phi = 0.5$ are presented in Fig. 3, which displays signal-to-noise ratios (SNRs) of 100:1 and 50:1 in the ro-vibrational and rotational CARS systems, respectively. The solid lines represent experimental CARS signals, and the dotted lines represent corresponding theoretical CARS spectra. The CO_2 - N_2 CARS spectra were fit using the Sandia CARSFT code [18], and the O_2 - N_2 rotational spectra were fit using the code described by Bood et al. [15]. The broad vibrational-signal contribution to the rotational spectrum was subtracted by fitting a smooth profile through the baseline [15]; the temperature and relative CO_2 and O_2 mole fractions were

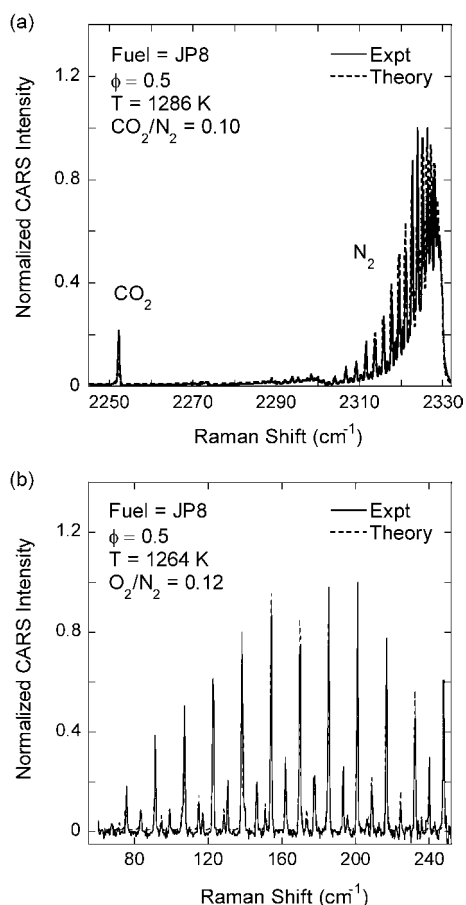


Fig. 3. Single-shot (a) ro-vibrational spectra of CO_2 - N_2 and (b) rotational spectra of O_2 - N_2 acquired in center of exhaust stream of JP-8-fueled combustor at $\phi = 0.5$.

evaluated by comparing the experimental and theoretical spectra. The CO_2 and N_2 signals in Fig. 3a are sufficiently close in wavelength to be detected with a single spectrometer, but are sufficiently far apart to be processed separately. This enabled determination of temperatures from the ro-vibrational spectra using only the N_2 spectral region, thereby reducing errors associated with baseline noise. The O_2 lines shown in the rotational spectra of Fig. 3b are interspersed with N_2 lines, and both are processed simultaneously.

Assuming that the center of the exhaust flow experiences minimal temporal variation of temperature and mole fraction, the histograms collected in this region display the best possible standard deviations of single-shot measurements in the current application. Histograms of temperature evaluated from the single-shot N_2 ro-vibrational spectrum and O_2 - N_2 rotational spectra are shown in Figs. 4a and 4b, respectively. Standard deviations of temperature for both techniques are less than 3.5% of the mean, indicating that the two different measurement systems, in-

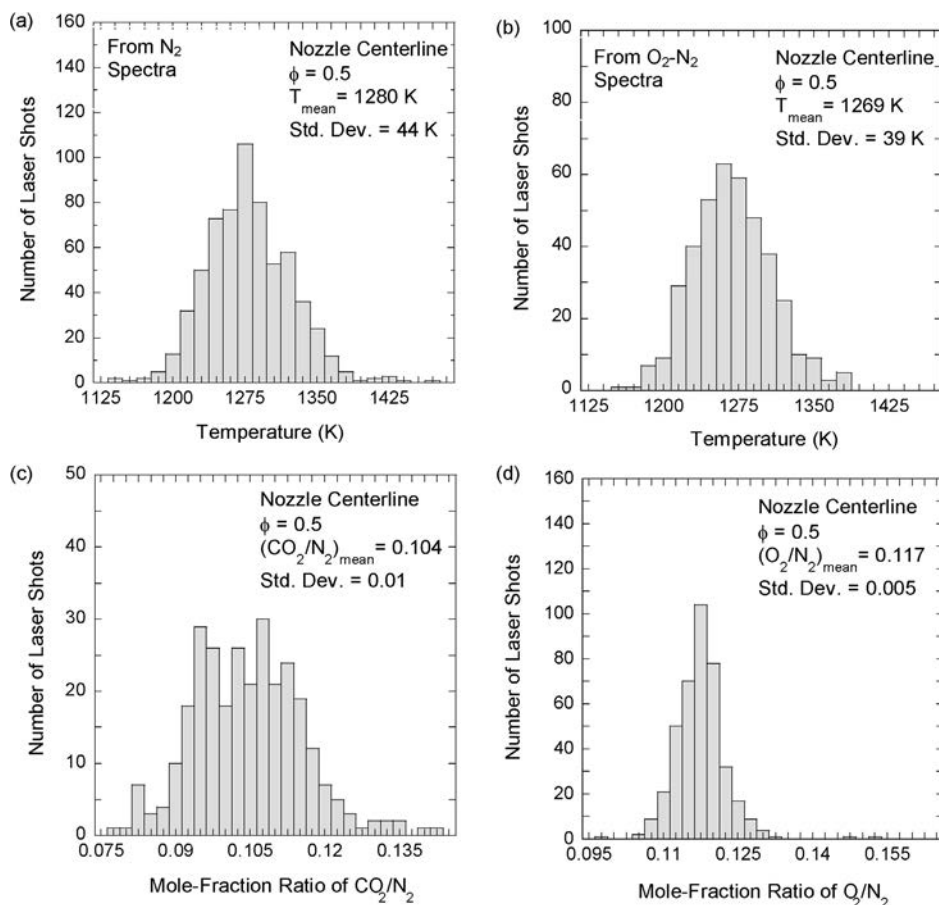


Fig. 4. Single-shot histograms in center of exhaust stream, showing statistical distributions of (a) temperature from ro-vibrational N_2 spectra, (b) temperature from O_2 - N_2 rotational spectra, (c) CO_2/N_2 mole-fraction ratio, and (d) O_2/N_2 mole-fraction ratio at $\phi = 0.5$.

cluding the theoretical codes used for fitting the ro-vibrational and rotational spectra, have similar precision. The Gaussian-like symmetry of the histograms and the similar standard deviations indicate that temporal variations result from unbiased experimental error or from random small-scale fluid-dynamic fluctuations.

Histograms of CO_2/N_2 and O_2/N_2 mole-fraction ratios are shown in Figs. 4c and 4d, with standard deviations of about 10 and 5%, respectively. The higher standard deviation in the CO_2/N_2 data reflects the opposite trend one might expect from the SNRs noted in Fig. 3. The primary reason for the increased variation in CO_2/N_2 mole-fraction-ratio measurements is that there are far fewer features in the CO_2 spectra than in the O_2 and N_2 spectra. This reduces the quality of least-square fitting and increases the standard deviation. The nearly identical standard deviations in temperature reported earlier in Figs. 4a and 4b make use of ro-vibrational N_2 features and rotational O_2 -

N_2 features and, therefore, do not exhibit reduced accuracy in least-square fitting.

Single-shot accuracy can also be degraded by reduced SNR. Histograms of single-shot temperature and CO_2/N_2 mole-fraction ratio at $\phi = 1.0$ are shown in Figs. 5a and 5b, respectively. The standard deviations are higher than in the case of $\phi = 0.5$ as a result of increased background flame emission as well as signal degradation caused by thermal displacement of various optics and mounts. Based on the data of Fig. 5, the standard deviation of the temperature data at $\phi = 1.0$ is 4.4% of the mean, and the standard deviation of CO_2/N_2 data is 20% of the mean, which are nearly $1.5\times$ and $2\times$ the respective standard deviations recorded at $\phi = 0.5$. In addition to reduced SNR, an increase in fluid-dynamic fluctuations may also accompany an increase in ϕ .

It was also very difficult to extract single-shot histograms of rotational-CARS temperature and O_2/N_2 mole-fraction ratios at $\phi = 1.0$ (not shown), not

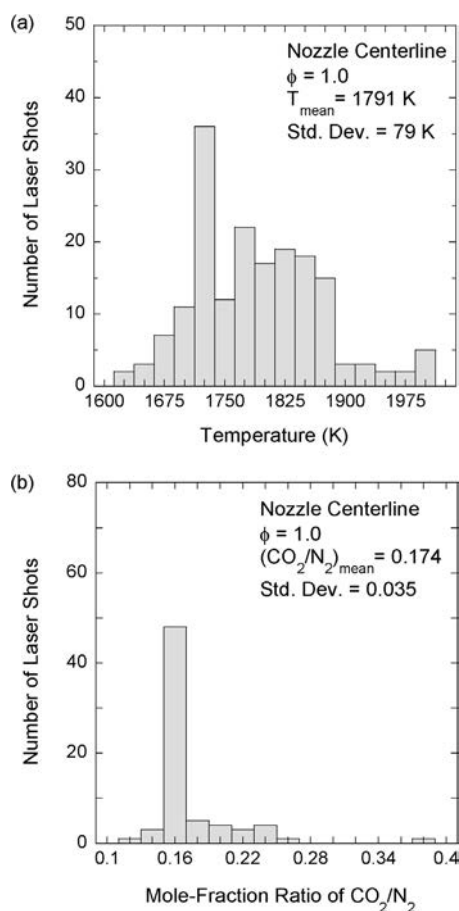


Fig. 5. Single-shot histograms of (a) temperature and (b) mole-fraction ratio of CO_2/N_2 determined from CO_2 – N_2 ro-vibrational spectra acquired in center of exhaust stream of JP-8-fueled combustor at $\phi = 1.0$ [10].

only because of thermal misalignment of optics and mounts but also because of decreased gas density. An increase in background signal from nonresonant susceptibility and mole fraction further degrades measurement accuracy at higher ϕ . In addition, the O_2 mole fraction decreases rapidly near $\phi = 1.0$ because of increased fuel consumption and approaches the CARS detectability limit for major species. Results from averaged spectra at higher ϕ are discussed below.

3.2. Equivalence-ratio study

The DPDB-CARS system used in the present study has been shown to exhibit high accuracy from $\phi = 0.15$ to 1.0 in a calibrated, laminar flame [3]. Temperature measurements were typically within 5% of equilibrium calculations, while mole-fraction ratios of CO_2/N_2 and O_2/N_2 were typically within 10% of theoretical values. In the current model gas-

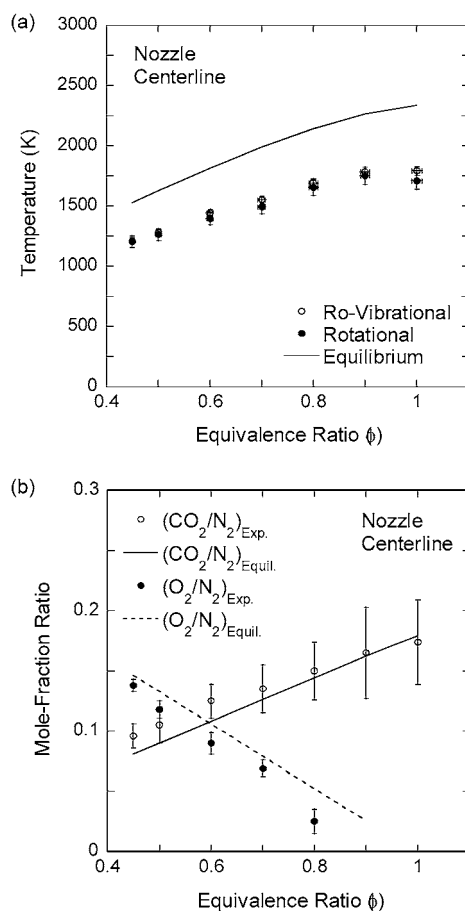


Fig. 6. Comparison of experimental data with equilibrium calculations of (a) temperature and (b) mole-fraction ratios of CO_2/N_2 and O_2/N_2 acquired in center of exhaust stream of JP-8-fueled combustor at various ϕ .

turbine combustor, measurements of temperature and CO_2/N_2 mole-fraction ratio were performed from $\phi = 0.45$ to 1.0, and measurements of O_2/N_2 mole-fraction-ratio were performed from $\phi = 0.45$ to 0.8. A comparison of experimental results with an equilibrium calculation using the theoretical code provided by Turns [19] is shown in Fig. 6. The molecular formula used for JP-8 fuel is $\text{C}_{10.9}\text{H}_{20.9}$, and the heat of formation is equal to $-2.48 \times 10^5 \text{ kJ/K}$ [9].

As evident in Fig. 6a, the measured temperatures (evaluated from the ro-vibrational N_2 spectra) are lower than the adiabatic flame temperatures by $\sim 20\%$ during lean combustor operation and by $\sim 25\%$ at the richest condition. The discrepancy between measured and calculated temperatures occurs primarily because data were collected $\sim 0.9 \text{ m}$ from the fuel nozzle and primary flame zone, leading to significant heat loss due to radiation and conduction. The increase in this discrepancy at higher ϕ is expected, therefore, because of increased heat transfer. Other pos-

sible reasons that are associated with operation in a test-cell environment include (1) degraded SNR from increased background flame emission and thermal displacement of optical components, (2) the means by which the broad vibrational-signal contribution to the rotational spectrum is subtracted [15], (3) flame unsteadiness and spatial averaging, (4) uncertainty in mass flow rates, and (5) $\pm 10\%$ uncertainty in the composition of JP-8 fuel and associated equilibrium calculations. Temperatures evaluated from the ro-vibrational and rotational spectra typically agree to within 40 K or 3%. This agreement indicates that decreased SNR and the method of vibrational-signal subtraction are not significant factors, even at $\phi = 1.0$ where the peak difference between the two techniques is still $< 5\%$.

The measured CO_2/N_2 mole-fraction ratios, shown in Fig. 6b, track equilibrium conditions to within 15% from $\phi = 0.45$ to 1.0, with better agreement near stoichiometric conditions where CO_2 mole fractions are higher. The O_2/N_2 mole-fraction ratios are also within 15% of equilibrium conditions up to $\phi = 0.7$ but are significantly below equilibrium at $\phi = 0.8$. It was not possible to extract the mole-fraction-ratio of O_2/N_2 beyond $\phi = 0.8$ because of decreased mole-fraction levels, thermal displacement of optical components, increased background interference, and increased coupling between nonresonant susceptibility and mole fraction.

3.3. Spatial profiles and statistics

The spatial distribution of temperature in the exhaust stream of gas-turbine combustors is an important performance consideration. In the current work a spatial traverse across the exit of the exhaust nozzle is performed to demonstrate the diagnostic capabilities of the current measurement system as well as to test its performance under unsteady, turbulent conditions. The spatial traverse was conducted in a vertical plane that is located 1 cm downstream of the nozzle exit and 92 cm downstream of the fuel injector, as shown previously in Fig. 2. The DPDB-CARS optics remained stationary, while the entire combustor test stand was translated until the probe volume reached ambient conditions on either side of the exhaust stream.

The spatial distribution of temperature at $\phi = 0.5$, shown in Fig. 7a, exhibits a fairly uniform, flat-top profile. The full-width-half-maximum (FWHM) is 48 mm wide, with shear layers that are 12.5 cm wide on either side. Note that the ro-vibrational and rotational spectra yield nearly identical results throughout the entire region, indicating that previous differences between the two techniques shown in Fig. 6a were probably due to the effects of flame emission on relative SNR rather than on spectroscopic variations

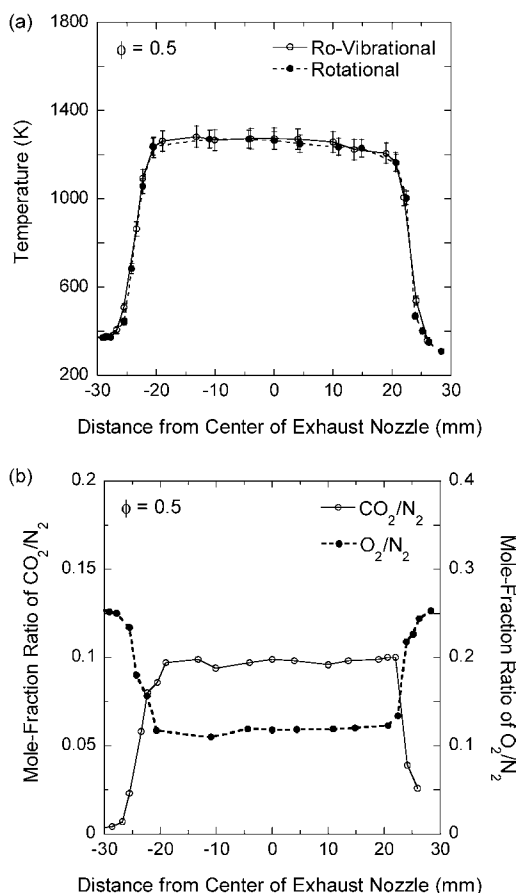


Fig. 7. Measurements of (a) temperature and (b) mole-fraction ratios of CO_2/N_2 and O_2/N_2 in spatial traverse across exhaust-nozzle exit plane at $\phi = 0.5$.

with temperature. The spatial distribution of CO_2/N_2 and O_2/N_2 mole-fraction ratios, shown in Fig. 7b, also displays uniform and flat-top profiles and illustrates the high precision of the ro-vibrational and rotational DPDB-CARS measurements. In addition, the FWHM locations and shear-layer widths are nearly identical for both mole-fraction ratios and agree with that of temperature, shown previously in Fig. 7a. The CO_2/N_2 mole-fraction ratio approaches zero outside the exhaust stream, as expected; and the O_2/N_2 mole-fraction ratio approaches 26%, as expected for ambient air.

As the probe volume approaches the turbulent shear-layer region of the exhaust stream, histograms of temperature and mole-fraction ratio are expected to broaden to reflect increased fluid-dynamic fluctuations. This phenomenon is captured in the shear-layer region 22 mm from the exhaust-nozzle centerline. Histograms of ro-vibrational and rotational temperature shown in Figs. 8a and 8b, respectively, exhibit both a decrease in temperature due to mixing with am-

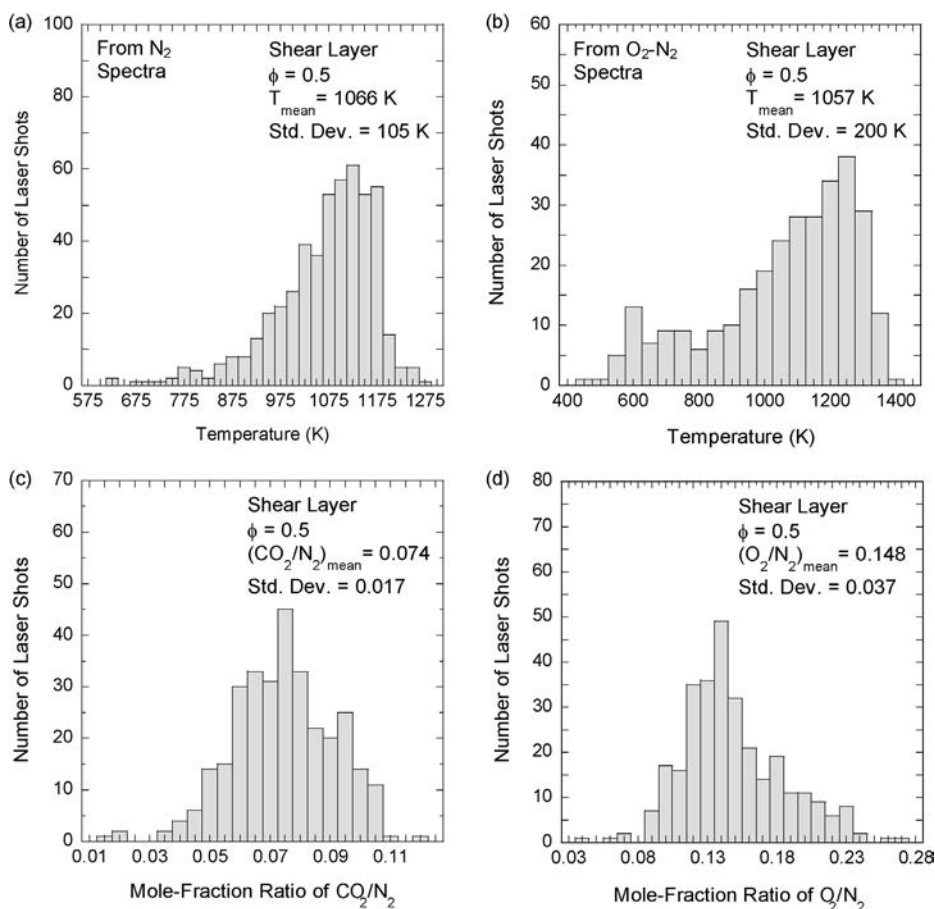


Fig. 8. Single-shot histograms within shear layer 22 mm from center of exhaust stream, showing statistical distributions of (a) temperature from ro-vibrational N_2 spectra, (b) temperature from O_2 - N_2 rotational spectra, (c) CO_2/N_2 mole-fraction ratio, and (d) O_2/N_2 mole-fraction ratio at $\phi = 0.5$.

bient air and an increased standard deviation due to turbulent fluctuations. The increase in standard deviation in the shear layer as compared with the exhaust centerline is about $2.5\times$ for the rotational temperature and $5\times$ for the ro-vibrational temperature. The difference between these two techniques is at least partially explained by the lower SNR of the O_2 - N_2 spectra. The apparent asymmetry in both the ro-vibrational and rotational temperature histograms is another feature of interest because it illustrates the effect of large-scale structures on the mixing process. Both temperature histograms show a significant number of laser shots for which the temperature is nearly 400 K below the mean temperature. These represent instances when large-scale fluid-dynamic structures carry ambient air deep into the shear layer. Because the measurement volume is only about the thickness of one shear layer downstream of the exit lip of the exhaust nozzle, one would expect that large-scale structures would not have broken down into smaller scales. Be-

cause the ro-vibrational and rotational temperatures are highly dependent on N_2 spectra, high CO_2 and O_2 mole-fraction gradients within the probe volume are not expected to result in significant differences in the temperatures measured by each technique.

Histograms of CO_2/N_2 and O_2/N_2 mole-fraction ratios in the shear layer also display the effects of broadening and increased asymmetry due to turbulent fluctuations, as shown in Fig. 8. The shear-layer CO_2/N_2 mole-fraction-ratio histogram of Fig. 8c has a lower mean value than the centerline histogram of Fig. 4c and has a longer tail toward lower values of CO_2/N_2 . Both effects signify incursions of ambient air into the probe volume. As expected these same incursions of ambient air have the opposite effect on the O_2/N_2 mole-fraction-ratio histogram—increasing the mean and extending the wing toward higher values of O_2/N_2 , as shown in Fig. 8d.

Another approach to evaluating the nature of single-shot CARS-signal fluctuations is the use of

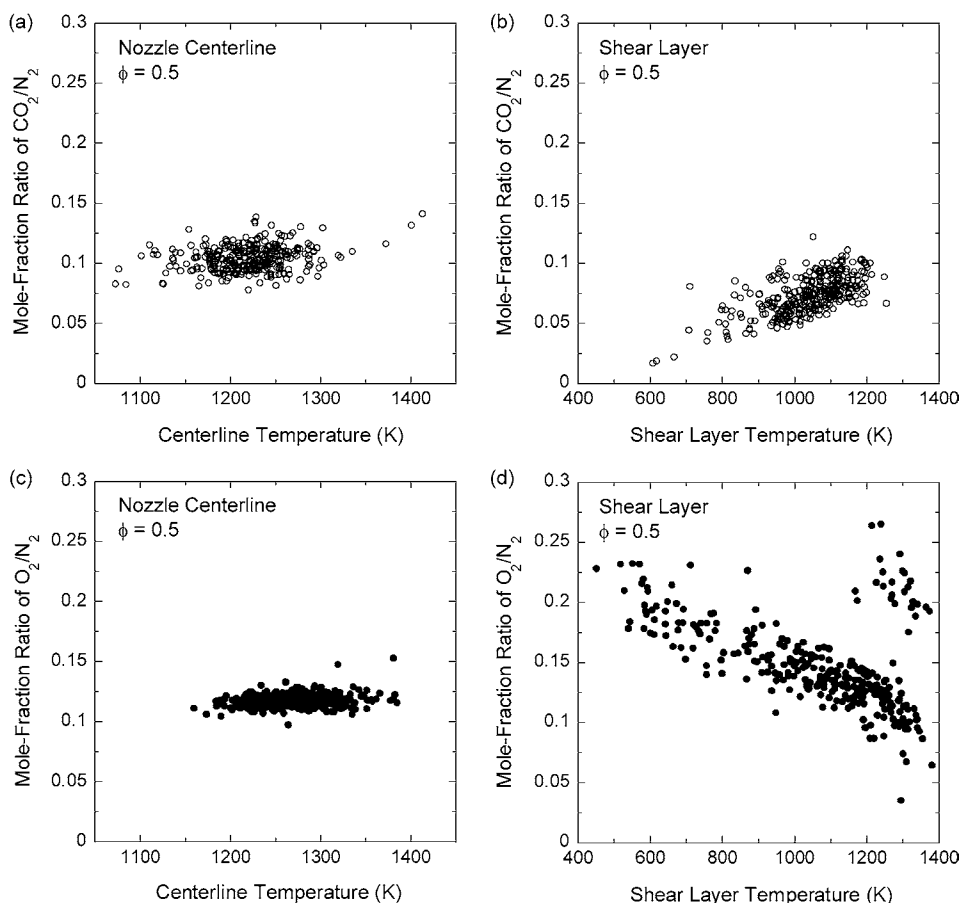


Fig. 9. Scatter plots of CO_2/N_2 mole-fraction ratio vs temperature in (a) exhaust centerline and (b) shear layer 22 mm from centerline at $\phi = 0.5$. Scatter plots of O_2/N_2 mole-fraction ratio vs temperature in (c) exhaust centerline and (d) shear layer 22 mm from centerline at $\phi = 0.5$.

scatter plots of mole-fraction ratio vs temperature. In Fig. 9a, for example, the scatter plot of CO_2/N_2 vs temperature shows a flat distribution at the center of the exhaust stream. In contrast, the scatter plot of Fig. 9b within the shear layer region 22 mm from the centerline shows that the CO_2/N_2 mole-fraction ratio is correlated with increasing temperature. Instances of high temperature correspond to cases in which the probe volume is within a fluid element that is composed primarily of exhaust gases and, therefore, correspond to higher levels of CO_2/N_2 mole-fraction ratios. This correlation between temperature and CO_2/N_2 mole-fraction ratio is further evidence that signal variations are related to large-scale fluid-dynamic fluctuations and are not random in nature.

A similar trend is apparent when comparing scatter plots of O_2/N_2 mole-fraction ratio vs temperature at the centerline and within the shear layer. The scatter plot of O_2/N_2 mole-fraction ratio vs temperature in the exhaust centerline, shown in Fig. 9c, is flat and fairly narrow, indicating that variations are

due primarily to random measurement error rather than fluid dynamic fluctuations. The scatter plot of Fig. 9d within the shear layer region 22 mm from the centerline, however, shows that the O_2/N_2 mole-fraction ratio is correlated with decreasing temperature. Instances of high temperature correspond to cases in which the probe volume is within a fluid element that is composed primarily of exhaust gases and, therefore, correspond to lower values of the O_2/N_2 mole-fraction ratio. These data illustrate the ability of the current DPDB-CARS system to evaluate both the mean and the dynamic features of reacting flows using single-shot measurements of temperature and multiple-species mole fractions.

4. Conclusions

The application of DPDB CARS to characterize the exit conditions in a swirl-stabilized, JP-8-fueled, model gas-turbine combustor has been demonstrated.

A variant of triple-pump CARS, DPDB-CARS employs three laser wavelengths for one broadband pump beam, two narrowband pump beams, and a broadband Stokes beam to generate ro-vibrational and rotational CARS spectra with the same hardware platform. This technique is capable of providing two separate measurements of temperature along with the mole fraction of two target species with respect to N_2 . Single-shot data acquisition using the combination of ro-vibrational and rotational CARS enhances the precision and accuracy of temperature measurements because of the correlation afforded by the common presence of N_2 in each of the two spectral windows.

Experiments were carried out to measure the temperature and mole-fraction ratios of CO_2/N_2 and O_2/N_2 in the exhaust stream of the JP-8-fueled combustor for equivalence ratios ranging from $\phi = 0.45$ to 1.0. Mean temperatures measured from ro-vibrational and rotational spectra typically agreed to within $\sim 3\%$. Standard deviations of temperature and CO_2/N_2 mole-fraction ratio as determined from single-laser-shot, ro-vibrational CARS spectra were ~ 3 –4 and ~ 10 –20% of mean values, respectively, for the full range of ϕ . Standard deviations of temperature and O_2/N_2 mole-fraction ratio as determined from single-laser-shot, rotational CARS spectra were ~ 5 –20% of the mean values for ϕ ranging from 0.45 to 0.8. The spatial variation of temperature and species-mole-fraction profiles across the exhaust stream was also studied to demonstrate the ability of the DPDB-CARS system to capture mean and dynamic features of reacting flows. Turbulent fluctuations were distinguished from random error by identifying asymmetries in temperature and mole-fraction histograms and by showing direct correlations between scatter-plot fluctuations of temperature and species mole fractions. This work represents the first application of triple-pump or DPDB-CARS in the exhaust of a liquid-fueled combustor of practical interest.

Acknowledgments

Funding was provided by the Air Force Research Laboratory, Propulsion Directorate, Wright-Patterson AFB, under Contracts F33615-D-03-M2829 and F33-615-00-C-3020, and by the Air Force Office of Scientific Research (Dr. Julian Tishkoff, Program Monitor). The authors gratefully acknowledge the assistance of Dr. Mikael Afzelius and Prof. Per-Erik Bengtsson of the Lund Institute of Technology, Sweden, for their assistance with the rotational CARS spectral simulation code. We also thank Dr. Vincent Belovich, Dr.

Edwin Corporan, and Dr. Matthew DeWitt for their assistance and technical input regarding the model gas-turbine combustor, and Ms. Marian Whitaker for editorial assistance.

References

- [1] A.H. Lefebvre, *Gas Turbine Combustion*, second ed., Taylor & Francis, Philadelphia, 1999.
- [2] M.G. Allen, E.R. Furlong, R.K. Hanson, in: K. Kohse-Hoinghaus, J.B. Jeffries (Eds.), *Applied Combustion Diagnostics*, Taylor & Francis, New York, 2002, p. 479.
- [3] S. Roy, T.R. Meyer, R.P. Lucht, M. Afzelius, P.-E. Bengtsson, J.R. Gord, *Opt. Lett.* 29 (16) (2004) 1843–1845.
- [4] M. Aldén, P.-E. Bengtsson, H. Edner, S. Kröll, D. Nilsson, *Appl. Opt.* 28 (1989) 3206–3219.
- [5] S. Roy, T.R. Meyer, M.S. Brown, V.N. Velur, R.P. Lucht, J.R. Gord, *Opt. Commun.* 224 (2003) 131–137.
- [6] R.P. Lucht, *Opt. Lett.* 12 (1987) 78–80.
- [7] R.D. Hancock, F.R. Schauer, R.P. Lucht, R.L. Farrow, *Appl. Opt.* 36 (1997) 3217–3226.
- [8] D. Brüggemann, B. Wies, X.X. Zhang, T. Heinze, K.F. Knoche, in: D.F.G. Durão, M.V. Heitor, J.H. Whitelaw, P.O. Witze (Eds.), *Combustion Flow Diagnostics*, Kluwer Academic, Dordrecht, 1992, pp. 495–511.
- [9] R.P. Lucht, V.N. Velur, G.J. Fiechtner, C.D. Carter, K.D. Grinstead Jr., J.R. Gord, P.M. Danehy, R.L. Farrow, *AIAA J.* 41 (2003) 679–686.
- [10] S. Roy, T.R. Meyer, R.P. Lucht, V.M. Belovich, E. Corporan, J.R. Gord, *Combust. Flame* 138 (2004) 273–284.
- [11] F.R. Schauer, Ph.D. thesis, University of Illinois at Urbana-Champaign, Urbana, IL (1998).
- [12] S.M. Green, P.J. Rubas, M.A. Paul, J.E. Peters, R.P. Lucht, *Appl. Opt.* 37 (1998) 1690–1701.
- [13] S. O'Byrne, P.M. Danehy, A.D. Cutler, *Dual-Pump CARS Thermometry and Species Concentration Measurements in a Supersonic Combustor*, in: 42nd AIAA Aerospace Sciences Meeting and Exhibit, Reno, NV, 5–8 January, 2004, AIAA paper No. 2004-0710.
- [14] A.C. Eckbreth, *Laser Diagnostics for Combustion Temperature and Species*, Gordon & Breach, Amsterdam, 1988.
- [15] J. Bood, P.-E. Bengtsson, M. Aldén, *Appl. Phys. B* 70 (2000) 607–620.
- [16] C. Brackmann, J. Bood, P.-E. Bengtsson, T. Seeger, M. Schenk, A. Leipertz, *Appl. Opt.* 41 (2002) 564–572.
- [17] T.R. Meyer, S. Roy, V.M. Belovich, E. Corporan, J.R. Gord, *Appl. Opt.* 44 (2005) 445–454.
- [18] R.E. Palmer, *The CARSFT Computer Code for Calculating Coherent Anti-Stokes Raman Spectra: User and Programmer Information*, Report No. SAND89-8206, Sandia National Laboratories, 1989.
- [19] S.R. Turns, *An Introduction to Combustion*, McGraw-Hill, New York, 1996.

Dynamics of an inverse diffusion flame and its role in polycyclic-aromatic-hydrocarbon and soot formation

Viswanath R. Katta^{a,*}, Linda G. Blevins^b, William M. Roquemore^c

^a Innovative Scientific Solutions, Inc., 2766 Indian Ripple Road, Dayton, OH 45440, USA

^b Combustion Research Facility, Sandia National Laboratories, Livermore, CA 94550-0969, USA

^c Air Force Research Laboratory, Propulsion Directorate, Wright-Patterson Air Force Base, OH 45433, USA

Received 26 June 2004; received in revised form 20 December 2004; accepted 15 February 2005

Available online 25 March 2005

Abstract

Residence time and thermo-chemical environment are important factors in the soot-formation process in flames. Recent studies have revealed that the soot generated in an inverse diffusion flame (IDF) is not fully carbonized as it is in a normal diffusion flame. For understanding the chemical and physical structure of the partially carbonized soot formed in inverse diffusion flames, knowledge of the flow dynamics of these flames is required. A time-dependent, detailed-chemistry computational-fluid-dynamics (CFD) model is developed for simulation of an ethylene–air inverse jet-diffusion flame that has been studied experimentally. Steady-state simulations show that all of the polycyclic-aromatic-hydrocarbon (PAH) species are produced outside the flame surface on the fuel side. Unsteady simulations reveal that buoyancy-induced vortices establish outside the flame because of the low fuel jet velocity (~40 cm/s) employed. These vortices in inverse diffusion flames, as opposed to those in normal diffusion flames, appear primarily in the exhaust jet. The advection of these vortices at 17.2 Hz increases mixing and causes PAH species to be more uniformly distributed in downstream locations. While the concentrations of rapidly formed radical and product species are not altered appreciably by the flame oscillation, concentrations of certain slowly formed PAH species are significantly changed. The dynamics of 20-nm tracer particles injected from the 1200 K fuel-side contour line suggest that soot particles are reheated and cooled alternately while being entrained into and advected by the buoyancy-induced vortices. This flow pattern could explain the experimentally observed large size and slight carbonization of IDF soot particles.

Published by Elsevier Inc. on behalf of The Combustion Institute.

Keywords: Inverse diffusion flame; Soot; PAH; Flicker; Soot inception; Benzene

1. Introduction

Soot is an undesirable combustion product, and its formation represents one of the most complex chemical systems in flames. Considerable progress

has been made in recent years in understanding the chemical and physical aspects of soot formation in hydrocarbon flames. Soot particles containing several thousands of carbon atoms are formed from simple fuel molecules within a few milliseconds of combustion initiation. After the first aromatic rings such as benzene and small polycyclic aromatic hydrocarbons (PAHs) are formed in the gas phase, acetylene and

* Corresponding author. Fax: +1 937 255 3139.

E-mail address: vrkatta@erinet.com (V.R. Katta).

other molecules react with these small PAHs to form larger PAHs [1]. The first soot particles are thought to be formed when two or more PAHs react to form a three-dimensional particle. This process is known as particle inception [2]. The formed soot particles interact with the gas-phase molecules by adding acetylene to their surface (surface growth) and by reacting with molecular oxygen and/or hydroxyl radicals (oxidation). Another process thought to increase soot mass is the collision of PAHs with a soot particle.

Several experimental and numerical investigations of soot formation have been performed using coflow and counterflow diffusion flames [3–6]. A few have focused on the importance of soot-particle pathways (i.e., residence time, temperature, and chemistry) [7,8]. Santoro et al. [7] used soot-volume-fraction, temperature, and velocity measurements in an ethylene–air jet-diffusion flame to examine the soot-growth process along individual particle paths. Based on the experimental data, they argued that the soot-formation rate increases in the annular region of the flame because of an increase in residence time. Lin and Faeth [8] found that the direction of soot-particle movement with respect to the flame sheet is important. They argued that if soot particles forming on the fuel-rich side of the flame remained entrained in the fuel-rich region for a long time before crossing the flame surface, then surface growth could be enhanced. In contrast, they argued that the amount of soot generated could be reduced if the soot particle were made to cross the flame surface quickly.

One method of altering the soot-particle pathway is to use inverse diffusion flames (IDFs) rather than normal diffusion flames. Wu and Essenhigh [9] studied inverse diffusion flames by exchanging the fuel and air jets of normal jet-diffusion flames. They found that in some cases, inverse diffusion flames are essentially nonluminous, with no apparent soot formation. However, in other cases, especially at higher air–jet velocities, a luminous region forms with an orange–yellow cap on top of the blue cone-shaped flame. Recently, Blevins et al. [10] further investigated IDFs under high-air-flow-rate conditions and found that the soot exiting an ethylene inverse flame is high in hydrogen and PAH content and chemically similar to precursor particles. They referred to these particles as “young soot.” They found that the soot particles in IDFs are large and partially carbonized relative to those collected from normal flames. A numerical study to aid the understanding of their experimental findings has also been performed by Blevins et al. [11]. Thermal and fluid-dynamics aspects of the flame were investigated in that study [11] by incorporating a global chemical-kinetics model. Particle tracking in the steady-state simulations showed that inverse-flame soot is expected to cool and quench

immediately after formation; it should not grow excessively or carbonize as the experiments indicated. It was speculated that the experimentally observed soot maturation is caused by flame unsteadiness that was not captured in the steady-state solutions. The purpose of the present study was to employ a time-dependent numerical model with detailed chemistry to examine such a possibility.

A numerical simulation of the IDF examined by Blevins et al. [10–12] was carried out using a well-tested CFD code and a detailed chemical-kinetics model for PAH formation in ethylene flames. Numerical results obtained for the steady-state and unsteady flames were compared. Calculations were also made by injecting nanometer-size particles in an attempt to determine the thermal and chemical environments encountered by soot particles in the dynamic inverse flame.

2. Experiment

A triaxial IDF burner having a 1-cm-diameter central air jet and a 3-cm-diameter coannular fuel jet was used in the present study. The burner is described in detail in Refs. [10–12]. The airflow was 32 mg/s (~ 35 cm/s), and the ethylene (C_2H_4) fuel flow was 49 mg/s (~ 7 cm/s). The visible flame height was 3.5 cm, and an orange cap constituted 90% of this flame height. A N_2 blanket flow, necessary to prevent flame formation between the fuel and the room air, was passed through the outer annulus of the burner. A nearly invisible soot stream exited the flame. The flame was photographed to permit comparison of experimental and computed results. Extensive experimental studies have been performed previously with this flame [10–12].

3. Mathematical model

A time-dependent, axisymmetric mathematical model known as UNICORN (UNsteady Ignition and COMbustion using ReactionNs) [13,14] was used to simulate the potentially unsteady jet-diffusion flames considered in this study. It solves for u - and v -momentum equations, continuity, and enthalpy- and species-conservation equations on a staggered-grid system. The body-force term due to the gravitational field is included in the axial-momentum equation for simulating vertically mounted flames. A clustered mesh system is employed to trace the large gradients in flow variables near the flame surface. A detailed chemical-kinetics model of Wang and Frenklach [15] was incorporated into UNICORN for the investigation of PAH formation in C_2H_4 flames. It consists

of 99 species and 1066 elementary-reaction steps. Thermo-physical properties such as enthalpy, viscosity, thermal conductivity, and binary molecular diffusion of all of the species are calculated from the polynomial curve fits developed for the temperature range 300–5000 K. Mixture viscosity and thermal conductivity are then estimated using the Wilke and Kee expressions, respectively. Molecular diffusion is assumed to be of the binary-diffusion type, and the diffusion velocity of a species is calculated using Fick's law and the effective diffusion coefficient of that species in the mixture. A simple radiation model based on the optically thin-media assumption [16] is incorporated into the energy equation. Only radiation from CH_4 , CO , CO_2 , and H_2O is considered in the present study. Due to lack of soot modeling in the present study, radiation from soot is not considered. This simplification could result in slightly higher flame temperatures but would not affect the dynamic behavior of the flame, which is the main focus of this study.

The finite-difference forms of the momentum equations are obtained using an implicit QUICKEST scheme [17], and those of the species and energy equations are obtained using a hybrid scheme of upwind and central differencing. At every time step, the pressure field is accurately calculated by solving all of the pressure Poisson equations simultaneously and using the LU (Lower and Upper diagonal) matrix-decomposition technique. The boundary conditions are treated in the manner reported in earlier papers [18].

The IDF [10–12] considered in the present study has a visible flame height of ~ 35 mm only. However, since the formation of PAHs is important not only in the flame zone but also in the exhaust products, axisymmetric calculations were made on a physical domain of 200×50 mm using a 401×121 non-uniform grid system. The computational domain is bounded by the axis of symmetry and an outflow boundary in the radial direction and by the inflow and another outflow boundary in the axial direction. The outer boundaries in the z and r directions are located sufficiently far from the burner exit (~ 20 inner-tube diameters) and the symmetry axis (~ 5 inner-tube diameters), respectively, that propagation of boundary-induced disturbances into the region of interest is minimized. Flat velocity profiles are imposed at the fuel and air inflow boundaries, while an extrapolation procedure with weighted zero- and first-order terms is used to estimate the flow variables at the outflow boundary. Additional details on the boundary conditions are given in Ref. [18].

The simulations presented here were performed on a Pentium III 1-GHz personal computer with 1.2 GB of memory. Typical execution time was ~ 120 s/time-

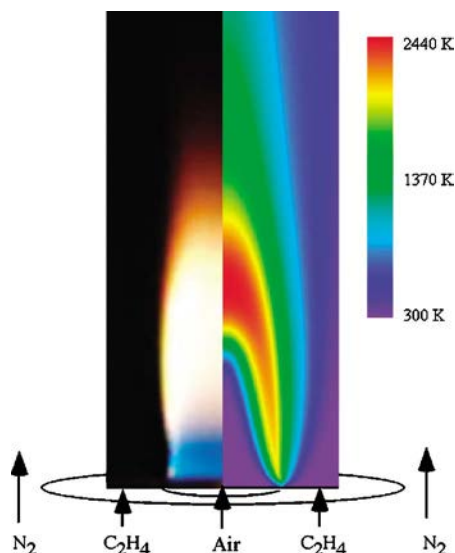


Fig. 1. IDF setup. Direct photograph of experimental flame (left) and steady-state solution obtained using UNICORN.

step. Steady-state flames were usually obtained in about 1000 time steps, starting from the solution obtained using the combustion part of the kinetics (i.e., not including PAH species). Unsteady simulations were performed for more than 20,000 time steps (~ 0.5 s real time or ~ 9 flicker cycles) to obtain a periodically oscillating flame structure.

4. Results and discussion

A direct photograph of the experimental flame is shown in Fig. 1, along with the computed temperature contours. This luminous flame is stably attached to the burner rim and has a luminous flame height of about 18 mm, based on the lower bright-yellow region of the computation. The blue emission in the base region of the photographed flame (where very little soot is generated) indicates that the flame becomes curved slightly inward as the air jet emerges from the burner. Unlike a normal diffusion flame, the IDF does not expand in the radial direction. This is due, in part, to the low stoichiometric equivalence ratio of 0.292 for C_2H_4 -air combustion, which establishes the flame surface on the air side. The inward curvature of the flame base may also be caused by the high air-to-fuel velocity ratio (5:1) used for this flame. Overall, the shape of the simulated flame matches that of the experimental flame very well. The yellow contour, which represents a temperature of 1800 K, matches the outer surface of the orange emission in the experiment. To further assess the accuracy of the IDF results predicted by UNICORN, the validation and grid-dependence studies described below were performed.

4.1. Model-validation studies

The CFD model UNICORN has been extensively validated in the past (for hydrogen and methane flames) by simulating various steady and unsteady counterflow [13,19] and coflow [13,20] jet-diffusion flames and comparing the results with experimental data. Thus, confidence has been gained in the ability of UNICORN to simulate the structure of dynamic flames accurately. However, the integration of C_2H_4 and PAH chemistry into UNICORN must be validated to establish the accuracy of the present predictions. Validation was achieved by simulating the burner-stabilized flame investigated extensively by Harris et al. [21] and Wang and Frenklach [15].

The flame chosen was a premixed $C_2H_4/O_2/Ar$ flame with an equivalence ratio of 2.76. The velocity of the cold reactants was 7.8 cm/s. The Ar: O_2

mole ratio was 79:21. Two-dimensional calculations for this burner-stabilized flame were made by enforcing periodic boundary conditions at the two boundaries in the radial (r) direction and using the measured temperature profile as input. These two-dimensional calculations eventually resulted in a one-dimensional flame, with all the variations in the radial direction diminishing.

Predicted variations in concentrations of several species with respect to flame height are compared with experimental data in Fig. 2. The temperature profile used in these calculations has a peak value of 1600 K (Fig. 2a). The calculations predict the proper trends in major-species concentrations such as the decrease in O_2 and C_2H_4 concentrations and the increase in CO and CO_2 concentrations. However, the computed H_2 concentrations are somewhat lower than the measured ones. Such a discrepancy was also

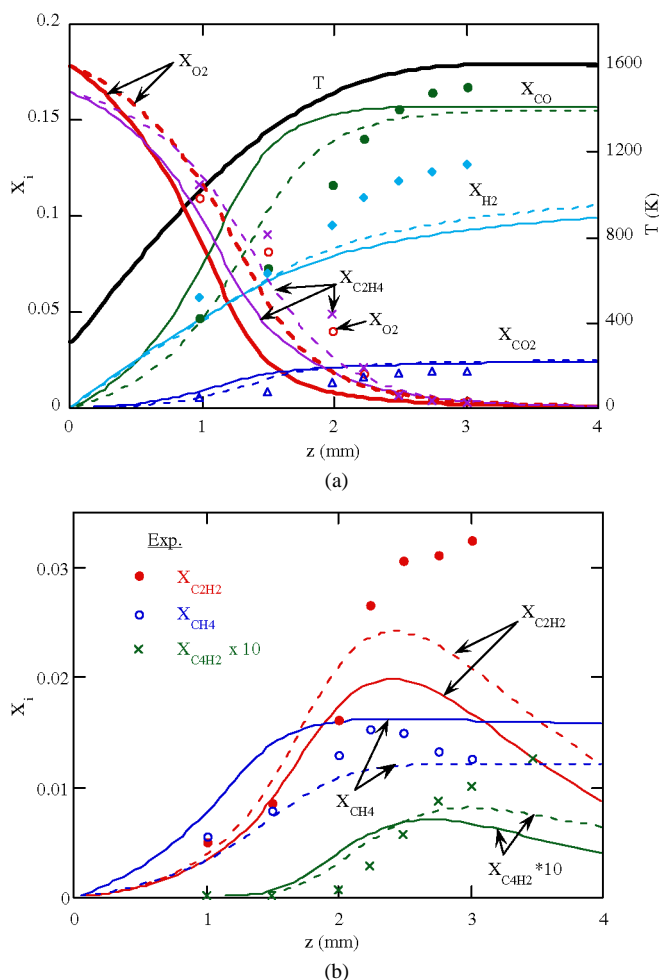


Fig. 2. Comparison of measured and computed species distributions for burner-stabilized premixed flame. Calculations for this one-dimensional flame were made using UNICORN and imposing the temperature profile shown in (a). Solid lines represent simulations made with the Wang/Frenklach mechanism; broken lines indicate simulations made with the NIST mechanism.

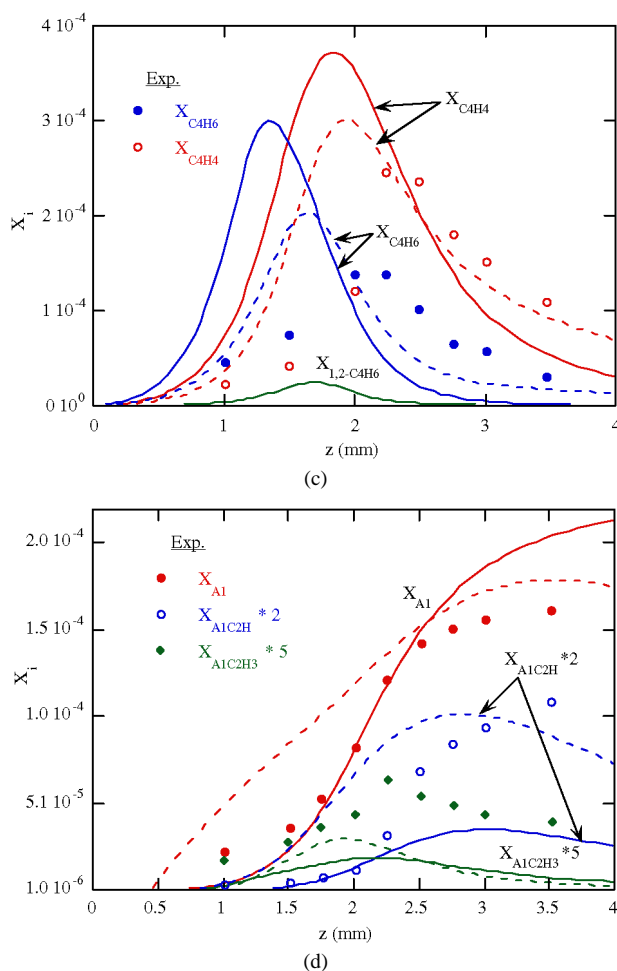


Fig. 2. (Continued.)

observed by Wang and Frenklach [15] while modeling this flame using the same chemistry model with the one-dimensional code CHEMKIN; the discrepancy was attributed to the higher concentrations of OH obtained with the present chemical mechanism.

It is important to recall that the main purpose of simulating this premixed $C_2H_4/O_2/Ar$ flame was to determine whether the detailed chemical-kinetics mechanism of Wang and Frenklach [15] was accurately incorporated into the multidimensional code UNICORN. Even though, the Wang/Frenklach chemical-kinetics mechanism is one of the most widely used [22,23] mechanisms for simulating ethylene/acetylene flames, the large discrepancies noted between the results of measurements and those predicted from simulations for certain important species such as the hydrogen molecule prompted further validation studies. Calculations for the premixed $C_2H_4/O_2/Ar$ flame were repeated using a recent and comprehensive mechanism of the National Institute of

Standards and Technology (NIST) [24]. This mechanism containing 197 species that are involved in 2757 reactions was incorporated into UNICORN. Results obtained with the NIST mechanism are also shown in Fig. 2 (broken lines).

The two chemical-kinetics models (Wang/Frenklach and NIST) predicted nearly identical concentrations for the major species C_2H_4 , O_2 , CO_2 , CO , and H_2 , especially at the downstream locations (Fig. 2a). Fuel pyrolysis seems slower in the NIST model than in the Wang/Frenklach model and the predictions from the former compared more favorably with the measured values for the major species in the upstream locations. However, the NIST model also did not predict the high concentrations of hydrogen molecules obtained in the experiments. Since the two models yielded nearly the same concentration distributions for H_2 with height, it is possible that some errors could have been involved in the measurements for hydrogen molecules.

The computed and measured mole fractions of CH_4 , C_2H_2 , and C_4H_2 at different heights are compared in Fig. 2b and those of C_4H_4 , and C_4H_6 are compared in Fig. 2c. In general, the two models yielded nearly the same distributions for these species. As evident from Figs. 2b and 2c, the key intermediate species are generally predicted well by both models. The computed peak concentrations of these species are within a factor of 2 of the measured values, which is probably within the experimental uncertainty [15]. Similarly, the predicted concentration profiles of one-ring aromatics (A1 , $\text{A1C}_2\text{H}$, and $\text{A1C}_2\text{H}_3$), as shown in Fig. 2d, compare reasonably well (allowing some degree of uncertainty in the experiments) with the measured ones. The steady increase of benzene (A1) is typical of C_2H_4 burner-stabilized flames and is well reproduced by both the Wang/Frenklach and NIST mechanisms. A closer look at the concentration profiles in Figs. 2a–2d suggests that the NIST model produces a better comparison with the measurement results; however, additional studies must be performed before a general conclusion can be reached on the relative accuracy of the models since the uncertainty in the measurements could mask the actual performance of these models. Nevertheless, based on the comparisons in Fig. 2, it can be concluded that both the Wang/Frenklach and the NIST mechanisms are accurately incorporated into the UNICORN code and that the modified code can simulate C_2H_4 flames reasonably well.

Calculations made for the steady-state IDF using the Wang/Frenklach mechanism are shown in Fig. 1, and the calculations performed using the NIST mechanism (not shown) yielded nearly the same flame shape and distributions for the temperature and major species. The focus of this study was to investigate the effect of unsteadiness on the production of PAH species and on soot formation in the IDF shown in Fig. 1. Since the accuracy of a chemical-kinetics mechanism remains the same in the simulation of steady-state and unsteady flames, the discrepancy noted in Fig. 2 between the calculations and the experiments is expected to play only a minor role in the present studies. Since the NIST mechanism has two times the number of species and nearly three times the number of reactions as compared to the Wang/Frenklach mechanism, unsteady calculations for the IDF were made using the latter mechanism for the sake of convenience.

4.2. Grid independence

To determine the grid sensitivity in simulating the IDF shown in Fig. 1, several calculations were performed using UNICORN and adopting different grid systems. The photograph of the flame in Fig. 1

suggests that the surface of the flame is smooth; its structure resembles that of a laminar steady-state flame. Calculations were initially performed on a 100×50 mm physical domain using a 251×91 grid system by omitting the unsteady terms in the model. The resulting laminar flame is shown in Fig. 1. The minimum spacing achieved with this grid system was 0.2 mm in both the r and z directions. In the simulations to minimize grid-stretching errors that might arise where flow variables change rapidly, this minimum spacing was enforced everywhere in the neighborhood of the high-temperature region. Even though the simulated flame matched that of the experiment (Fig. 1), calculations were also made using a 401×121 grid system to determine the grid sensitivity of the results. The physical domain was extended to 200 mm in the axial direction for this fine-grid system. Although the total number of grid points was increased only by a factor of 2, the grid spacing in the radial direction in the flame region was significantly reduced (by a factor of 4) in the fine-mesh calculations. The minimum spacings achieved with the 401×121 grid system were 0.05 and 0.2 mm in the r and the z direction, respectively.

Steady-state flames obtained with the coarse and fine mesh systems are compared in Fig. 3 using iso-temperature color contours. The two grid systems predicted the same flame-tip height (18 mm, based on the peak-temperature location along the centerline) and peak temperature (2440 K). On the other hand, the fine-grid system seems to yield slightly sharper temperature profiles on the fuel side and a shorter core length of the air jet for this IDF. The 2440 K peak flame temperature is ~ 60 K higher than the adiabatic flame temperature of the ethylene–air mixture at an equivalence ratio of one. The less-than-unity Lewis number associated with ethylene fuel, in conjunction with the concave curvature at the flame tip (with respect to the outer fuel jet), has increased the local flame temperature beyond the adiabatic value.

The temperature and species distributions along the centerline, obtained with the coarse and fine meshes, are compared in Fig. 4. While most of the species predicted by the two mesh systems are similar, the fine mesh predicts lower concentrations of heavier aromatics such as pyrene than the coarse mesh. Similar observations can be made by comparing the radial distributions (Fig. 5) of various species obtained with these two grid systems at 16 mm above the burner. The biphenyl concentration computed with the fine mesh is slightly lower than that computed with the coarse mesh. The comparisons shown in Figs. 3–5 suggest that the results obtained with the 251×91 grid system are nearly grid independent. However, to avoid any concerns that might arise in the predictions

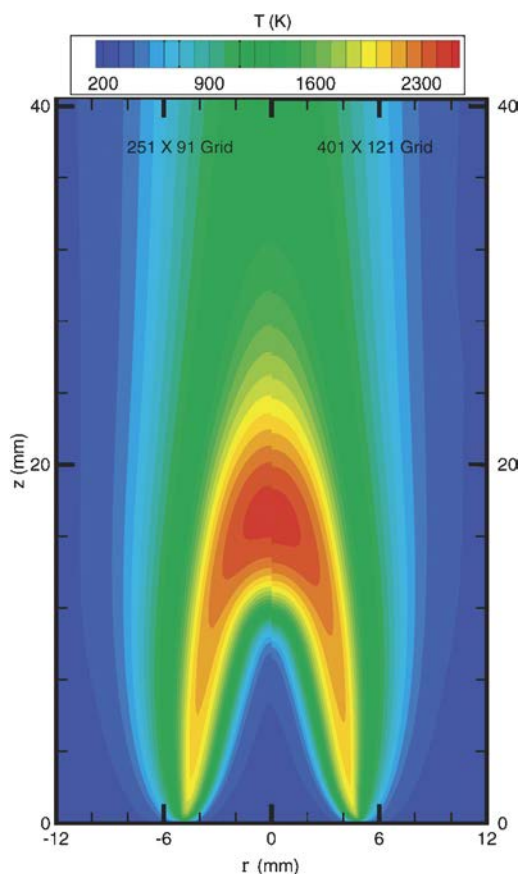


Fig. 3. Effect of grid resolution on temperature field computed for IDF. Coarse-mesh (left) and fine-mesh (right) calculations utilized grid spacings of 0.2 and 0.05 mm, respectively.

of PAH concentrations, the 401×121 grid system was used throughout the present study.

4.3. Dynamics of the inverse diffusion flame

Studies of normal jet-diffusion flames (i.e., with the fuel jet at the center) suggest that when the annular air flow is low (<40 cm/s), the flame tends to flicker with the development of buoyancy-induced vortices outside the flame surface. Generally, the flickering frequency for these flames is independent of or weakly dependent on fuel-jet diameter, fuel type, and air-flow velocity. The low annular fuel velocity of ~ 7 cm/s and the high-enthalpy C_2H_4 fuel (flame temperatures of about 2400 K) used for the IDF create an appropriate environment for flame flicker. The experimental image shown in Fig. 1 was obtained with a long shutter opening (~ 1 s); hence, the instantaneous structure of this flame that might be oscillating at a frequency of 10–20 Hz would not be captured.

To investigate the possibility that the IDF oscillates naturally, unsteady calculations were performed for the same flow conditions. Surprisingly, the unsteady simulations resulted in a flame with large vortices forming outside the flame surface. However, unlike in the case of normal diffusion flames, formation and advection of these vortices are observed only in locations downstream of the flame tip. Instantaneous images of the simulated unsteady IDF captured at two different phases (49 ms apart) are shown in Fig. 6. Here, iso-contours of temperature and benzene concentration are plotted in the left and right halves, respectively. The temperature field upstream of the flame tip ($0 < z < 18$ mm) is similar to that of the steady-state flame shown in Fig. 3. On the other hand, a large vortical structure ~ 30 mm in length is evident in the downstream locations. At this instant, exhaust gases with a temperature of less than 1000 K were entrained into the vortex. A significant amount of benzene is also entrained into the vortex. In contrast to the observations made for the steady-state flame, benzene concentration does not monotonically decrease (after reaching the peak value) with flame height in the unsteady flame (Fig. 6b).

The unsteady flame in Fig. 6 is oscillating at a low frequency, with large toroidal vortices naturally forming outside the flame surface. It is important to note that no artificial perturbation is introduced in the calculations for the development of these outer vortices. In the presence of gravitational force, the acceleration of hot gases along the flame surface generates the outer structures as part of the solution. However, since the flame-tip height is only 18 mm, much of the vortex (or instability) growth takes place downstream of the flame tip in the exhaust gases. Close examination of the flame images obtained at several instants suggests that the flame tip is also oscillating weakly. The computed frequency that corresponds to the passage of these outer vortices (also known as the flame-flickering frequency) is 17.2 Hz. Experimental images similar to the one shown in Fig. 1 cannot reveal the flame fluctuations at this frequency since the 1-s shutter opening used for capturing these images yields a flame structure that is averaged over ~ 58 cycles. However, recent experiments [11] using fast cameras for IDF under slightly modified boundaries (adapted for microgravity experiments) demonstrated the existence of such low-frequency fluctuations.

The effect of flame unsteadiness on PAH species is shown in Figs. 7a and 7b in plots of evolutions of the flame at 40 and 120 mm above the burner, respectively. The color content of these plots represents the changes in radial distributions of naphthalene (left) and benzene (right) concentrations with time as observed by one viewing the flame at a given height. The changes in temperature at these heights

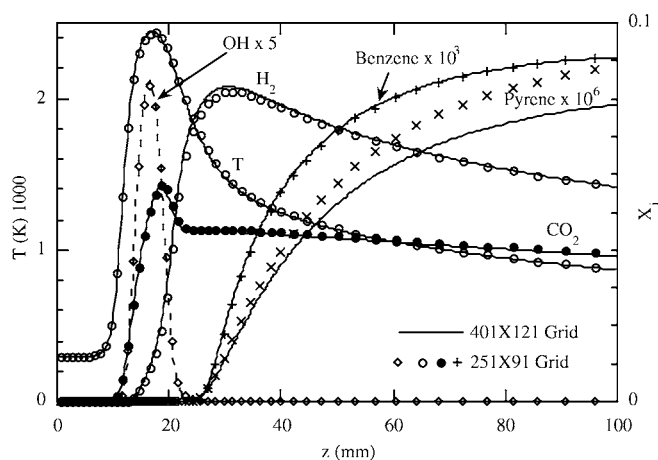


Fig. 4. Effect of grid resolution on temperature and species distributions along centerline.

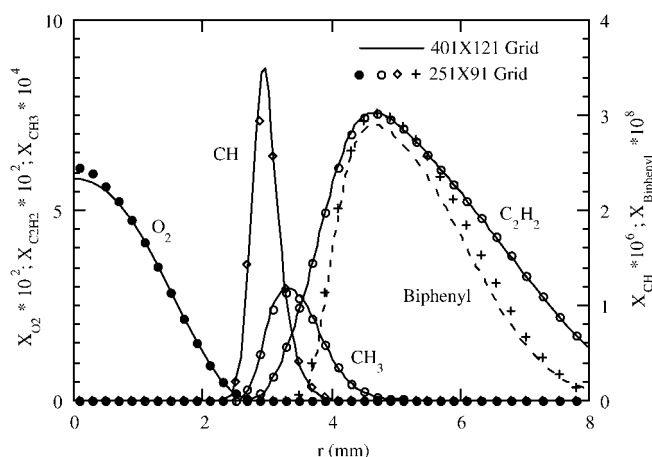


Fig. 5. Effect of grid resolution on species distributions in radial direction at $z = 16$ mm.

are also shown in Fig. 7 by a superimposition of iso-temperature contour lines. Strong fluctuations in PAH-species concentrations are evident at $z = 40$ mm. It is interesting to note that an island of high temperature (>1200 K) appears at the center, between 20 and 45 ms, when naphthalene and benzene concentrations are low. The strong outer vortex is pinching off the products from the jet and rolling them back into itself. This is also evident in the instantaneous plot in Fig. 6b. At this instant, hot products and benzene are cut off by the vortex at $z = 50$ mm. As seen in Fig. 7b, the vortex has dissipated significantly by the time it reaches a height of 120 mm above the burner. Only a weak roll-up of PAH species by the vortices is observed at this location. The remnant of the jet pinching that occurred at upstream locations caused the species concentrations to fluctuate at the center. In contrast to those observed at $z = 40$ mm, the concentrations of naphthalene and benzene at 120 mm

are high in the island of high temperature (>750 K) at the center between 27 and 42 ms.

4.4. Inadequacy of steady-state simulations

The experimental flame image in Fig. 1 represents a low-speed IDF in pseudo-steady state. The flow conditions and the presence of gravitational force naturally make these flames dynamic. One could model these low-speed IDFs using either a steady-state approach, assuming that the effects of flow unsteadiness are negligible, or a more cumbersome unsteady approach. Figs. 1 and 6 show the results obtained using these two approaches. Apparently, the structure of the dynamic flame in Fig. 6 is quite different from that captured using the steady-state approach. It is important to understand the differences one would obtain in species concentrations, especially those of PAH species, if a steady-state approach were used rather than an unsteady one. On the other hand, mea-

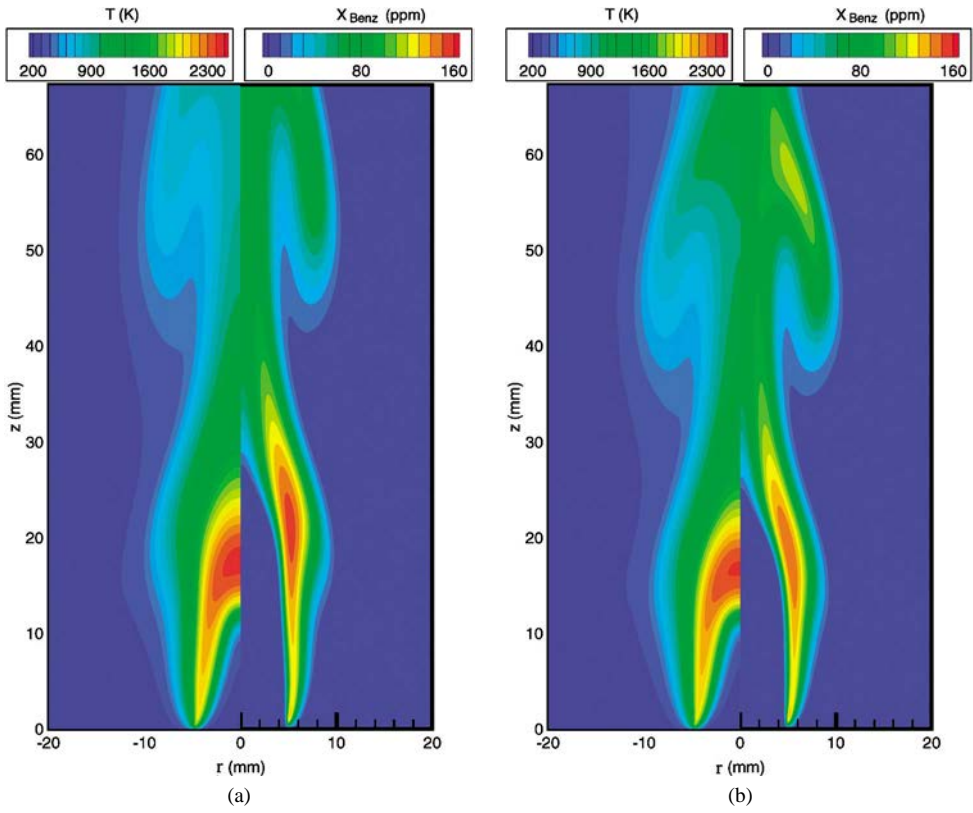


Fig. 6. Instantaneous temperature (left) and benzene concentration (right) obtained in unsteady simulations at (a) t_0 ms and (b) $t_0 + 49$ ms.

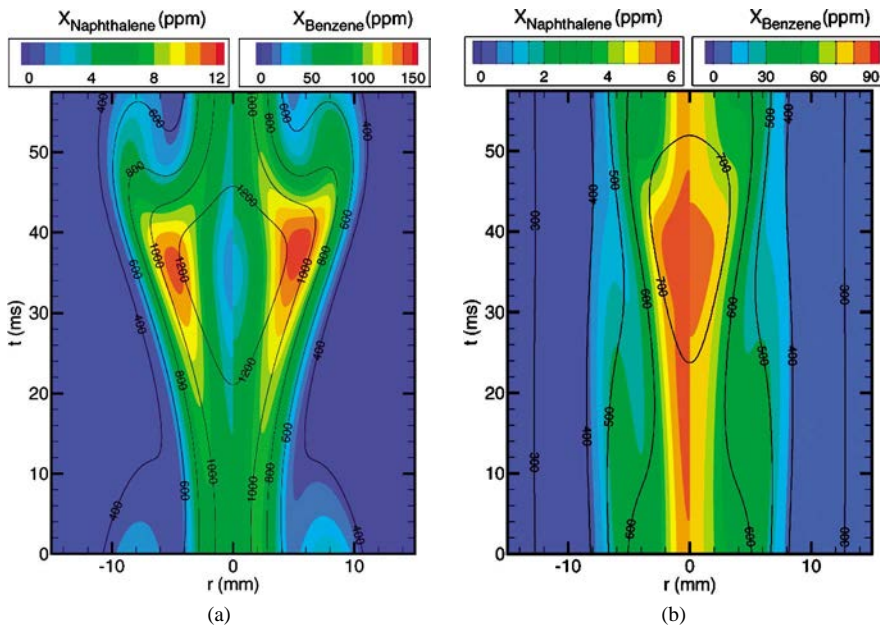


Fig. 7. Evolutions of benzene (right) and naphthalene (left) concentrations at axial distances of (a) 40 and (b) 120 mm from the burner exit.

measurements for PAH species are typically made using filters [10] and collection probes [21], which would yield only time-averaged data. From the point of view of these measurements, it is also necessary to estimate the differences between the averaged and the actual concentrations in IDFs.

The instantaneous temperature field of the unsteady flame (Fig. 6) downstream of the flame tip is different from that of the steady-state flame (Fig. 3). However, such a comparison between steady-state and unsteady flames is not appropriate since the solutions shown in Fig. 6 exist only during a fraction of a second. Solutions plotted at other instants look very different from those shown in Fig. 6. To determine the effect of flow unsteadiness on the generation of PAH species, a more reasonable comparison was made by constructing a time-averaged flame from several instantaneous solutions. For example, time-averaged temperature (T_{ave}) at each grid point is obtained using the formula

$$T_{\text{ave}} = \frac{1}{\tau} \int_{t_0}^{t_0 + \tau} T \, dt.$$

Here, τ is the period of oscillation, and t_0 is an arbitrary time in the simulation. Integration in the above equation is performed using 2325 instantaneous solutions.

The time-averaged temperature distribution of the unsteady flame and the temperature distribution of the steady flame are compared in Fig. 8a. The peak temperatures in these two images are the same and equal to 2440 K. As expected, these distributions are similar in the regions upstream of the flame tip where the flame oscillations are negligibly weak. The low-temperature region outside the flame surface and the exhaust-product region in the downstream locations are broader and more diffuse in the time-averaged result than in the steady result. The formation and advection of vortices outside the flame surface (i.e., on the fuel side) entrain cold fuel and globally enhance mixing between the high-temperature products and the cold fuel. Note that even though the local mixing between the cold fuel and the hot products takes place molecularly in this laminar flow, an increase in global mixing occurs through the increased interface surface area.

Short-lifetime radicals such as O, H, and OH and major combustion products such as H_2O and CO_2 are produced in the flame zone. As shown in Fig. 8b, their peak concentrations are not affected significantly by the advection of vortices. However, the product species that are present in the exhaust (such as H_2O and CO_2) are spread more evenly in the time-averaged flame, indicating that these species are affected more significantly by the outer vortices.

The influence of vortices on the distribution of a species becomes more pronounced as the production of that species is delayed in the flame. The benzene-concentration distribution of the time-averaged unsteady flame and the steady-state flame is compared in Fig. 8c. Since most of the benzene is produced in the low-temperature region (<1200 K) on the fuel side of the flame, its time-averaged concentration distribution is significantly affected by the vortex dynamics. The peak benzene concentration for the time-averaged flame is reduced by $\sim 20\%$ from its peak value of 150 ppm in the steady-state flame. On the other hand, the flame radius based on benzene concentration at a 40-mm height increased from 7.5 mm for the steady calculation to 10 mm for the time-averaged calculation. The presence of weak oscillations at locations far upstream of the flame tip (up to $z = 8$ mm) is evident in the benzene concentration (note the changes in peak concentration between the steady-state and the time-averaged flames in Fig. 8c).

For example, production of styrene, as compared to benzene, is delayed further in the flame. As a result, the distribution of styrene in the time-averaged flame became dramatically different from that observed in the steady-state flame (Fig. 8d). Both the location and the value for the peak styrene concentration are significantly modified in the time-averaged flame by the advecting vortices. The comparisons in Fig. 8 suggest that unsteady effects cannot be ignored, especially in the low-temperature regions of the IDF. They further suggest that a steady-state simulation is not adequate for predicting the time-averaged distributions of species—especially those formed in temperatures <1200 K; this implies that one must exercise caution in the use of steady-state simulations for comparing predicted values with time-averaged measured values when the flow is unsteady.

The interaction of vortices with various species and temperature has the following two important consequences in time-averaged studies: (1) As shown in Fig. 8, the interaction causes time-averaged species concentrations to be lower than those actually produced in the flame zone, which are pronounced in the locations upstream of the flame tip; and (2) the interaction enhances overall mixing through increased interface surface area, which will be pronounced in the locations downstream of the flame tip. The significance of the latter effect is discussed below.

As shown in Fig. 7b, flame oscillations are weakened in locations farther downstream of the flame tip, which is due, in part, to the reduced buoyancy forces acting upon cooler exhaust products and due, in part, to the dissipation of the vortices in the highly viscous exhaust flow. The dynamic IDF flame shown in Fig. 6 became nearly steady state at a height of 180 mm. The buoyancy-induced vortices have completely dis-

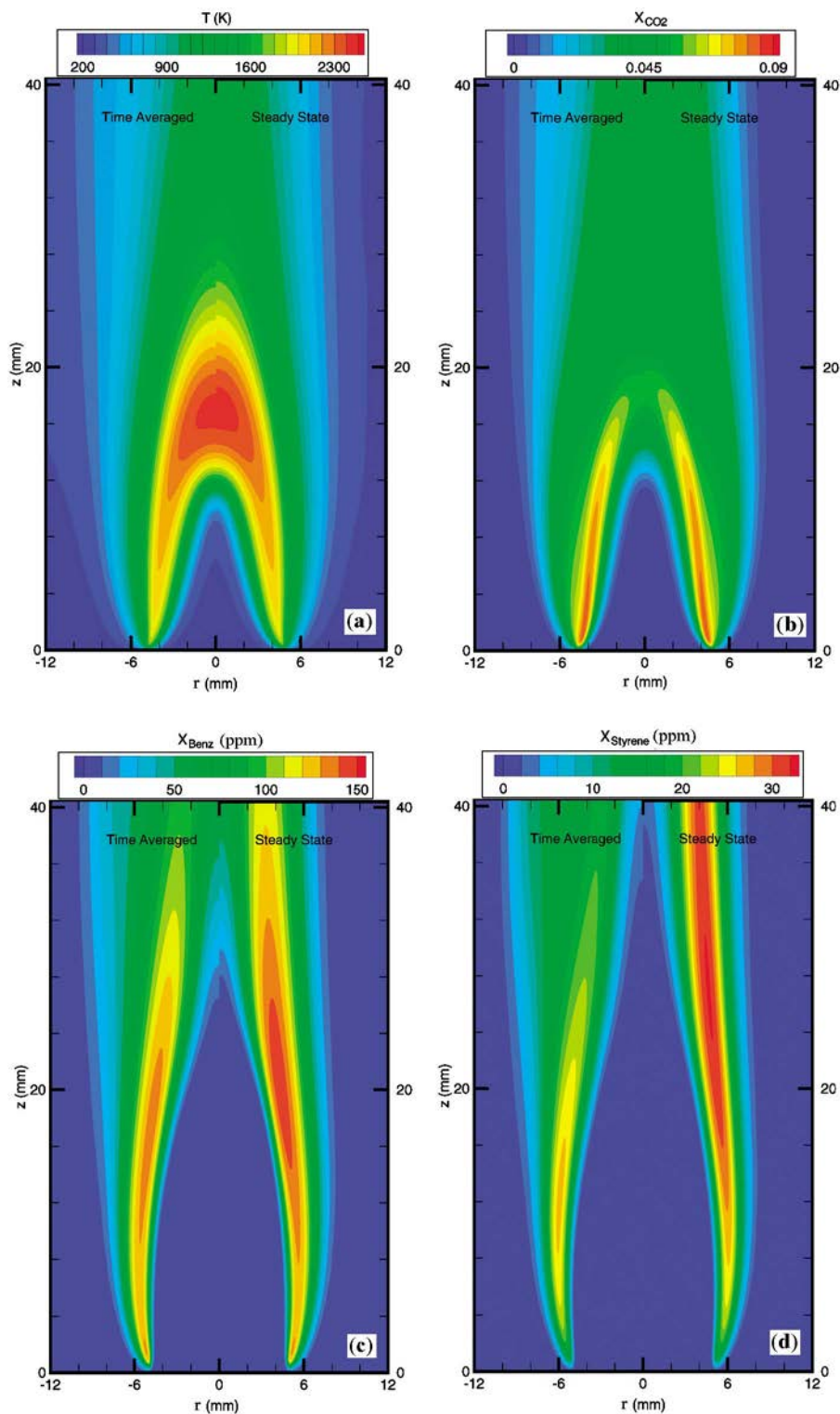


Fig. 8. Time-averaged (left) and steady-state (right) data for IDF. (a) Temperature, (b) CO_2 , (c) benzene, and (d) styrene concentrations.

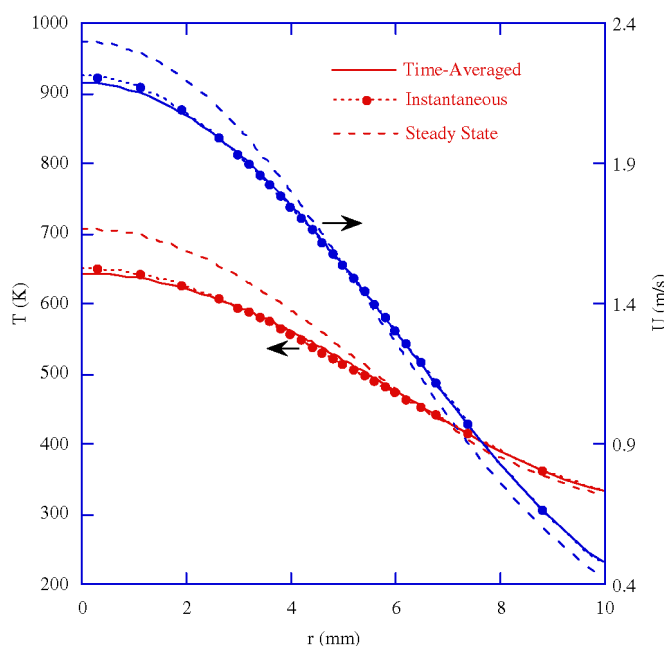


Fig. 9. Comparison of time-averaged, instantaneous, and steady-state data (axial velocity and temperature) at $z = 180$ mm. Time-averaged data were generated from several instantaneous solutions obtained during one flicker period of 58 ms. Instantaneous data represent the instantaneous solution that deviates maximum from time-averaged data.

sipated, and only faint oscillations in flow variables are observed at this height. Radial distributions of temperature and axial velocity obtained at a height of 180 mm from various simulations (steady state, instantaneous, and time-averaged) are shown in Fig. 9. The instantaneous solution was selected from several instants to ensure that the data would deviate most from the time-averaged data. As shown from Fig. 9, the instantaneous and time-averaged profiles are very similar, suggesting a nearly steady-state flow field at this height. However, the steady-state simulations resulted in significantly different profiles. Overall, the unsteady simulation yielded somewhat broadened profiles, which can occur only if the mixing upstream of this location is different in the steady-state and unsteady simulations. The buoyancy-induced vortices in unsteady simulations entrained low-speed fuel into the high-speed exhaust jet, thereby increasing the interface surface area between those two fluids. Over time, the cumulative molecular mixing that took place along the interface was also increased—causing the unsteady profiles to be more diffusive in Fig. 9, as compared to the steady-state ones.

In recent measurements of the IDF shown in Fig. 1, amounts of PAH species [10] were measured by collecting gas samples in the exhaust products at locations farther downstream of the high-temperature flame tip (~ 150 mm from the burner). To aid in the understanding of the differences one might expect by performing a steady-state simulation of this flame

rather than an unsteady one, time-averaged radial distributions of several species at a location 180 mm above the burner are compared with the steady-state solutions in Fig. 10. In general, the concentration of every species is overpredicted in the steady-state simulations. The products that were generated inside and within the high-temperature region, such as CO and CO₂, are overpredicted or remain nearly the same everywhere in the radial direction (at this height) in the steady-state simulations. On the other hand, PAH species, which were generated outside the flame surface in the lower temperature regions, appeared in higher concentrations in the steady-state flame at the center and in lower concentrations away from the center.

The combustion products CO and CO₂ are generated in large quantities in the IDF and remain closer to the central jet. As the vortices form outside the flame surface away from the central jet, they do not effectively distribute these abundant product species. On the other hand, PAH species are generated in smaller quantities and are formed away from the central jet; hence, they are mixed more effectively by the vortices. These differences in the distributions of major-product and PAH species are also evident in Fig. 8. At a flame height of 40 mm, the PAH species are located in a narrower region than the CO₂ in the steady-state simulation, while all of these species are equally distributed in the time-averaged data. A close examination of the results in Fig. 10 suggests that a 15 to 20%

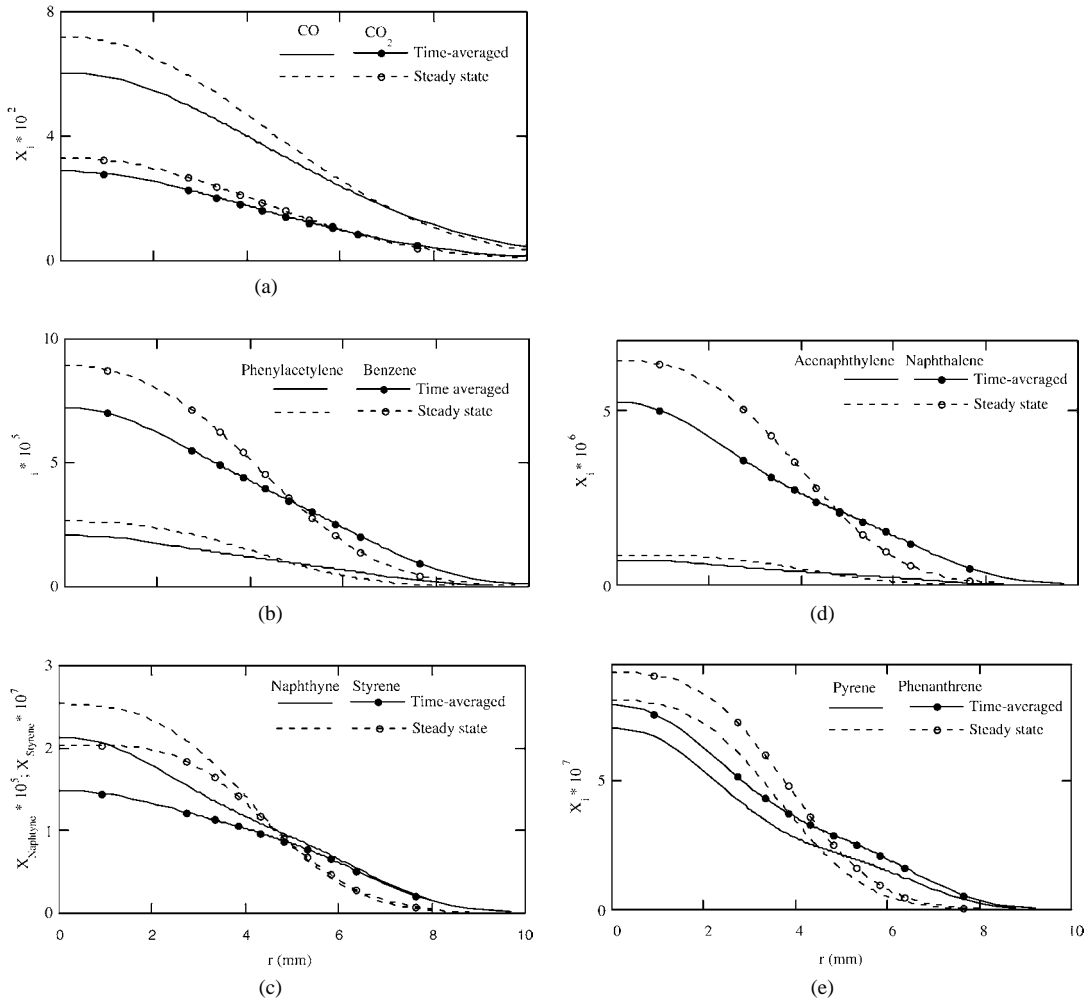


Fig. 10. Comparison of time-averaged and steady-state mole fractions for different species at $z = 180$ mm. Time-averaged data were generated from several instantaneous solutions obtained during one flicker period of 58 ms.

reduction in the peak PAH concentrations occurs in the IDF at a height of 180 mm because of the presence of vortices in the unsteady simulation.

4.5. Prediction of thermo-chemical environment for PAHs

The formation of benzene in flames initiates the generation of PAH species from fuel molecules. Some of the lower weight PAHs are likely to remain in the gaseous state, while some of the heavier PAHs may condense on particles. Small and large PAHs may also participate in surface growth. The use of a rigorous soot model developed based on particle dynamics and physical growth processes for understanding the effects of flow unsteadiness on soot formation in the IDF is beyond the scope of this work. However, one can assess the need for the accurate simulation of flow

dynamics in the prediction of soot formation by understanding the thermo-chemical environments that soot particles might encounter in the IDF.

Particle tracking is used in the present study to examine the time/temperature/PAH-chemistry pathways of incipient soot particles produced in the flow. Nanometer-size tracer particles are introduced into the flow from different locations, and their trajectories are calculated while the flow is evolving. Particles are assumed to be sparsely distributed and; hence, the particle–particle interaction is ignored. The trajectory of the individual particle is calculated based on a Lagrangian approach and by including inertial (momentum and drag), thermophoretic, and gravitational forces [25] acting on it. The particle transport model employed is based on the dynamics of small-size particles described by Fortiadis and Jensen [26,27]. Each particle is considered to be an isolated small sphere

whose Brownian diffusivity is negligible compared with the surrounding gas diffusivity. Since the soot particles, which are several orders larger in size than the incipient particles, do not diffuse through Brownian motion [28] and noting that the tracer particles are used only for the purpose of tracking soot, neglecting Brownian diffusivity for the particles is justified. The drag force is calculated assuming that both the particle Reynolds number (based on particle diameter, gas density and viscosity) and the Knudsen number ($Kn = 2\lambda/d_p$, where λ = gas molecule mean free path and d_p = particle diameter) are less than unity. The thermophoretic force is computed by means of an interpolating formula derived by Talbot et al. [29] to span a range of Knudsen numbers.

The trajectory of a particle depends strongly on the injection location; hence, care must be exercised in identifying the appropriate injection locations if the particles are to mimic soot. After conducting experiments on counterflow and coflow ethylene flames, Du and Axelbaum [6] postulated that soot suppression was possible in their experiments since the formation of soot was essentially bounded between two limits. They found that a temperature around 1300 K would set the limit on the fuel side, and the concentration of OH would set the limit on the air side. More recently, Sunderland et al. [30] found that soot formation in diffusion flames commences at 1250 K. Using chemical-kinetics calculations, Violi et al. [31] determined that the reaction rate of 1-acenaphthyl reaches values comparable to those of 5-acenaphthyl, starting from 1200 K. Based on these reaction rates, they predicted that molecular growth in combustion systems begins at 1200 K. For brevity, in the present study it was assumed that soot inception occurs at around 1200 K. Similarly, the size of the soot tracer particles was set as 20 nm in diameter. This size represents the smallest of the sizes observed by Dobbins et al. [32] (20–30 nm) and by Blevins et al. [12] (50–100 nm).

The unsteady IDF calculations were continued from the solution shown in Fig. 6b by introducing 20-nm particles into the flow field. Since soot inception is thought to occur around 1200 K on the fuel side, these nanometer-size tracer particles are introduced along the 1200 K contour line. The motion of the particles at every particle time step (which is set to be 1/10th of the flow time step) is calculated and thermophoretic, gravitational, drag, and viscous forces [25] acting on the particles are included. The instantaneous distribution of the particles after 120 ms of real-time calculations is shown in Fig. 11 along with the instantaneous temperature (left) and benzene-concentration (right) fields. Particle locations are shown in black, and the line (1200 K contour) along which these particles were released is shown in white. No particles were released from the air-side 1200 K line.

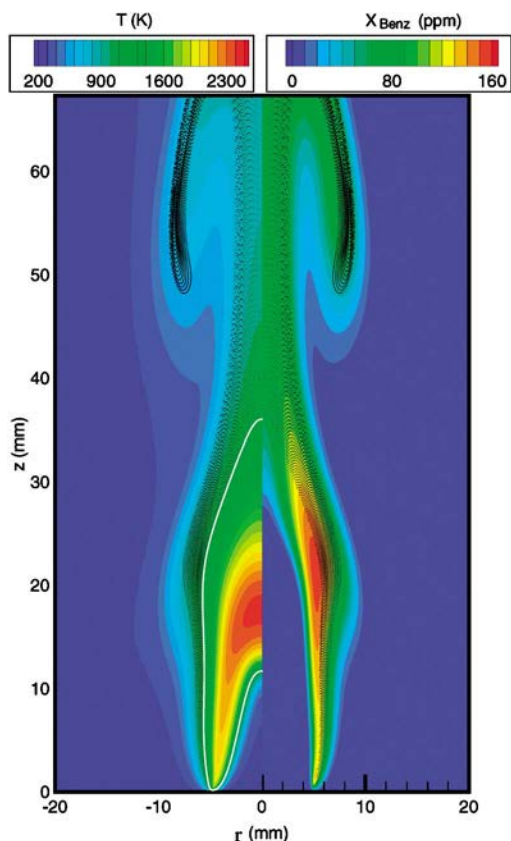


Fig. 11. Instantaneous locations of 20-nm-size particles superimposed on temperature (left) and benzene concentration (right). Nanometer-size tracer particles were injected from 1200 K iso-temperature line (white line) on fuel side.

Fig. 11 suggests that particles closely follow the gas flow. Particles enter the vortex along with the gaseous benzene. This is an important feature of the dynamic flame since the entrained particles have longer residence times in the vortex and are more susceptible to coagulation, surface condensation, and/or surface growth. This trend may explain the experimentally observed large-size soot particles emitted by the IDF. Close-up views of the trajectories of the particles originating from 3 and 30 mm above the burner are shown in Fig. 12. The residence times associated with these particles are also shown in this figure. Particles originating near the flame base, i.e., at a height (z_{p0}) of 3 mm and at a radial distance (r_{p0}) of ~ 5.2 mm, are traveling between radial locations of 2 and 9.2 mm. These particles also remain close to the core of the vortex as it convects downstream. On the other hand, the particles originating from a location downstream of the flame tip ($z_{p0} = 30$ mm and $r_{p0} = 1.9$ mm) remain in the periphery of the vortex while also traveling over a radial distance of 6.5 mm. Interestingly, particles originating near the flame base

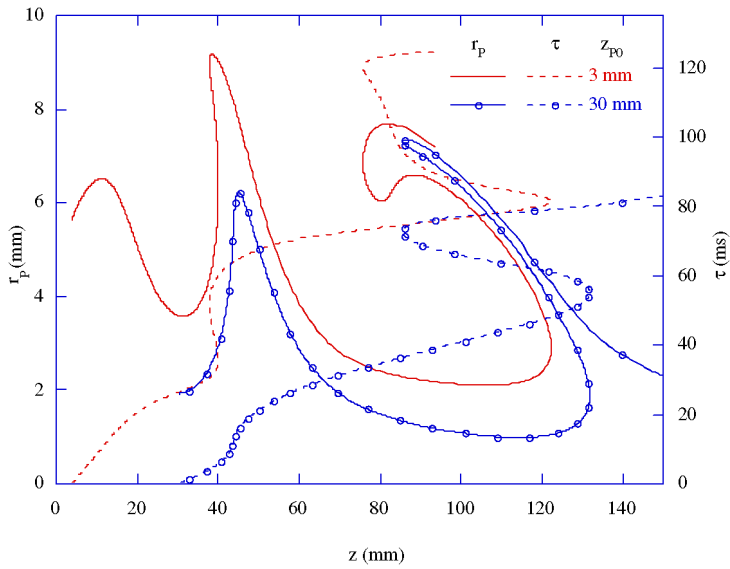


Fig. 12. Trajectories and corresponding residence times of particles originating from 1200 K fuel-side at locations 1 and 30 mm above the burner.

reside in the flame longer than those originating at downstream locations. For example, consider a flame region between 0 and 90 mm. The particles originating from a height of 3 mm reside in this flame zone for ~ 127 ms, while those originating from a 30-mm location reside only for 75 ms. Taking into account the 27-ms time required for the former particles to reach the flame height of 30 mm, it should be noted that the former particles spend 25 ms (or 33%) longer in the flame than the latter ones. This difference in residence time arises from the entrainment characteristics of the buoyancy-induced vortices.

To ensure that the particle entrainment and the resulting increase in particle residence time are not specific to the 1200 K temperature locations chosen in the flame for soot inception, calculations are also performed using 1000, 1100, and 1300 locations for particle injection. The trajectories of the particles injected at a height of 3 mm from various initial-temperature locations are shown in Fig. 13. Interestingly, particles injected from 1000, 1100, and 1200 K locations converged to nearly the same path as they traveled downstream, and those injected from the 1300 K location deviated significantly. This means that particles injected from the 1200 K location follow the dividing streamline of the IDF. The dividing streamline of a jet flame is defined as the streamline that encompasses the equivalent fluid mass that originated from the central jet [28]. This is an important boundary in soot studies since soot particles may not cross this line (diffusion of soot particles due to Brownian motion is negligibly small) [28].

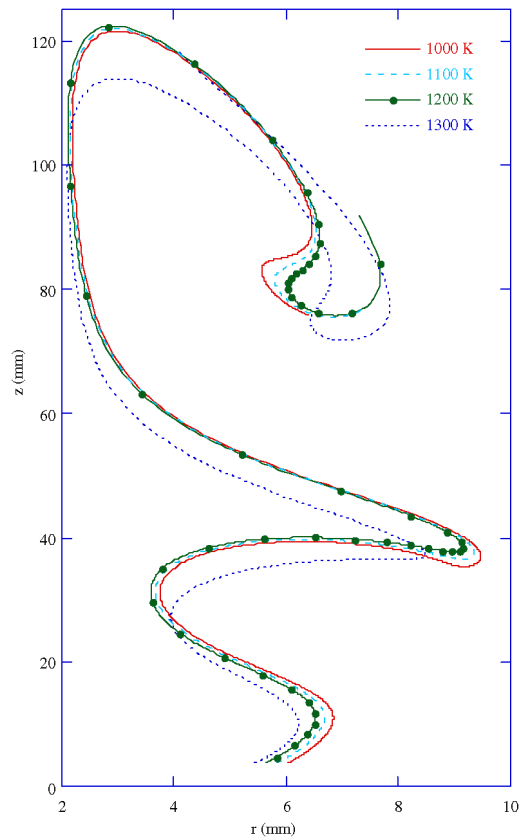


Fig. 13. Trajectories of particles originating at locations 3 mm above the burner and from several temperature locations on the fuel side.

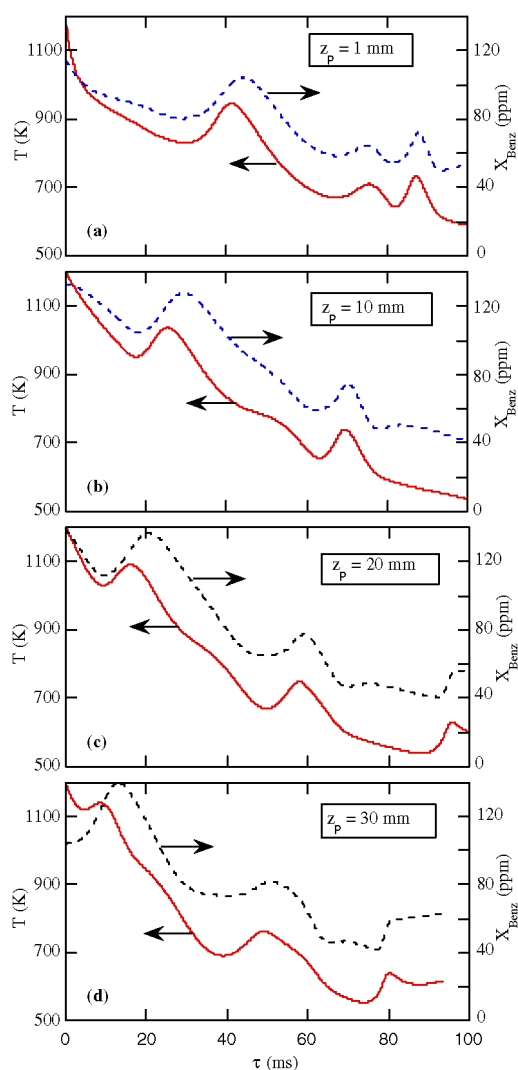


Fig. 14. Local-temperature and local-benzene histories of particles originating from 1200 K fuel-side location at different heights above burner exit.

The computed trajectories of the tracer particles are following the flow in the IDF as shown in Figs. 11 and 13, which suggests that the tracer particles are indeed mimicking soot in the flame. On the other hand, neglecting particle diffusion in the particle-dynamics model may have an effect during the very early stages of soot formation in which the size of the precursor particles is small enough. However, the effect of such Brownian diffusion of the incipient soot particles may be viewed as a shift in the soot inception location in the soot trajectory studies. Fig. 13 suggests that even though the particles injected from the 1300 K location follow a path that is different from the trajectories of the 1000, 1100, and 1200 K particles, all the particles are entrained by the buoyancy-induced vortices

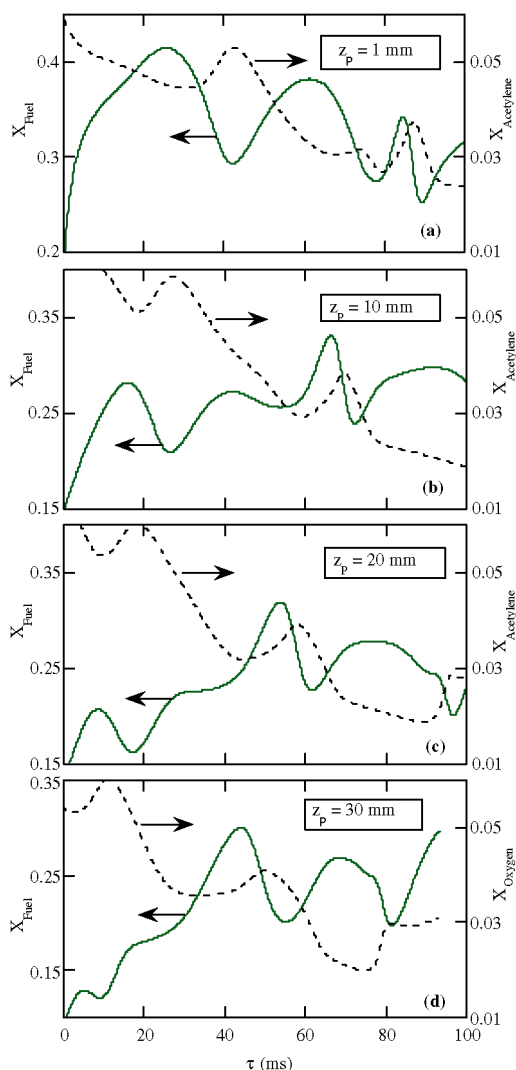


Fig. 15. Local-fuel and local-acetylene histories of particles originating from 1200 K fuel-side location at different heights above burner exit.

and consequently their residence times are increased. Therefore, irrespective of the chosen temperature (or location) for soot inception, the soot particles will be entrained by the buoyancy-induced vortices in the IDF.

The thermo-chemical environment that soot particles might encounter in the IDF is shown in Figs. 14 and 15. The local-temperature and local-benzene-concentration histories for 1200 K particles originating from different flame heights are plotted in Fig. 14. All of the particles start with a temperature of 1200 K; however, initially their temperatures decrease rapidly initially as they move away from the flame. As the particles are entrained into the vortex, they are drawn closer to the flame, and their temperatures increase

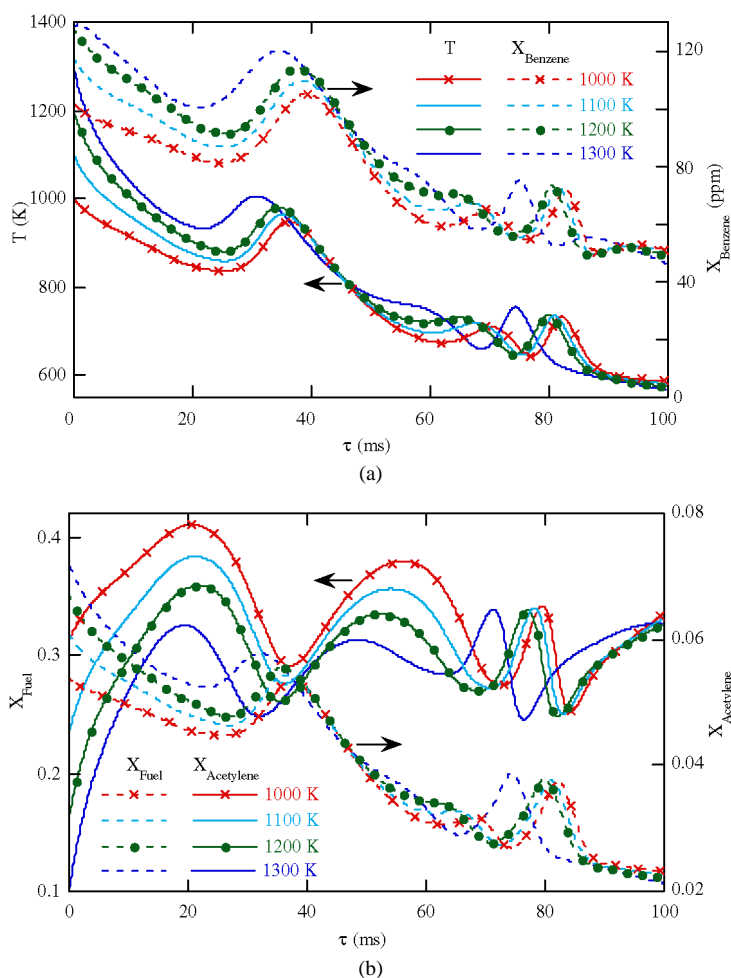


Fig. 16. Variations in thermo-chemical environments with residence time of particles injected at 3-mm height from different temperature locations. (a) Local-temperature and local-benzene histories and (b) local-fuel and local-acetylene histories.

by more than 100 K. This reheating of particles may lead to a slight degree of carbonization if there were actual soot particles, which is consistent with the experimental finding. Note that the particle trajectories in the steady-state flame did not reveal such reheating of particles [11].

The local benzene concentration encountered by a 1200 K particle as it is convected downstream in the IDF varies between 40 and 130 ppm (Fig. 14). In general, the changes in benzene-concentration environment follow those of temperature—suggesting that the so-called soot particles are periodically exposed to higher temperatures and benzene concentrations as they travel downstream in the flame. Interestingly, the peaks in temperature and higher benzene concentration associated with the first vortex are shifted by about 4 ms in time, with the former appearing ahead of the latter. Because of the longer reaction times associated with PAH formation, in a significant region

in the IDF, nonequilibrium chemistry is taking place and causing a delay in benzene production with respect to temperature.

The fuel and acetylene environments encountered by the 1200 K particles originating from different flame heights are shown in Fig. 15. The IDF shown in Fig. 1 is an underventilated (less oxygen) flame; hence, the particles originating at the 1200 K location encounter a significant amount of fuel throughout their journey. Moreover, the fluctuations in the fuel concentration encountered by these particles are more severe than those in temperature or any other major species. As the 1200 K particles advect downstream, they encounter less acetylene concentration. During the 100-ms time period that the particles are spending in the flame, they are encountering acetylene concentrations between 2 and 6%.

The presence of similar spikes in temperature (Fig. 14) for the particles originating from different

heights indicates that all of the particles formed along the 1200 K line are entrained into the vortices and are subjected to the reheating process. In fact, Fig. 14 further suggests that the particles entrained into the vortices roll inside the vortex and are reheated again and again as they advect downstream. This is consistent with the peaks appearing in the temperature and benzene-concentration distributions shown in Figs. 6 and 7. Therefore, the vortices appearing in the IDF not only increase the mixing among the species but also alter the thermal and chemical environment for the entrained species and particles. The latter process could lead to additional soot formation, enhanced surface growth, increased coagulation, and/or partial carbonization of the young soot.

The thermo-chemical environments for the soot particles originating at a height of 3 mm above the burner and from different temperature locations are shown in Fig. 16. As expected from the trajectories of the 1000, 1100, and 1200 K particles (Fig. 13), their thermo-chemical environments are also converging with time (or height). However, the typical behavior of cyclic exposure to higher and lower concentrations is the same for all of the particles, which suggests that the findings of the present study are not subject to the choice of soot-inception temperature.

5. Conclusions

A time-dependent, axisymmetric, detailed-chemistry CFD model was developed for the simulation of C_2H_4 -air inverse jet-diffusion flames. PAH formation was simulated using the 99-species, 1066-reactions mechanism of Wang and Frenklach [15]. The CFD model (UNICORN) was validated by simulating a burner-stabilized premixed flame and comparing the results with those from the measurements. Both steady-state and unsteady simulations for the IDF were performed. Steady-state simulations yielded a laminar flame and predicted that all PAH species are produced outside the flame surface on the fuel side. Unsteady simulations revealed that buoyancy-induced vortices establish outside the flame surface because of the low fuel jet velocity. No artificial perturbation was used in these unsteady simulations. Unlike the case of normal diffusion flames, vortices in the IDF appeared mainly in the exhaust gases.

The need for capturing the flow oscillations in the IDF simulations is assessed by comparing the flame obtained through steady-state simulation and that constructed from several instantaneous flames captured in the unsteady calculations. While the quickly formed radical and product species are not affected significantly by the flame oscillations, the generation of certain slowly formed PAH species is significantly

modified. It was found that the advection of these vortices at 17.2 Hz increased mixing of the species and caused PAH species to be distributed more uniformly in the downstream locations. Trajectories of 20-nm particles injected along the fuel-side 1200 K contour line indicated that soot particles could be cyclically heated and cooled while being entrained into and advected by the buoyancy-induced vortices. These particles also encounter a time-varying chemical environment as they travel downstream. The computed unsteady flow field may explain the slight maturation of young soot in the IDF that was observed experimentally.

Acknowledgments

Financial support for this work was provided by the Strategic Environmental Research and Development Program (SERDP, Dr. Charles Pellerin), the Air Force Office of Scientific Research (AFOSR, Dr. Julian Tishkoff), Air Force Contract No. F33615-00-C-2068 (Dr. Vincent Belovich), and the National Aeronautics and Space Administration (NASA). The authors thank Marian Whitaker for editorial help.

References

- [1] H. Richter, J.B. Howard, *Prog. Energy Combust. Sci.* 26 (2000) 565.
- [2] I.M. Kennedy, *Prog. Energy Combust. Sci.* 23 (1997) 95.
- [3] C.R. Kaplan, K. Kilasanath, *Combust. Flame* 124 (2001) 275.
- [4] M.D. Smooke, C.S. Mcenally, L.D. Pfefferle, R.J. Hall, M.B. Colket, *Combust. Flame* 117 (1991) 117.
- [5] G. Sugiyama, *Proc. Combust. Inst.* 25 (1994) 601–608.
- [6] J. Du, R.L. Axelbaum, *Combust. Flame* 100 (1995) 367.
- [7] R.J. Santoro, T.T. Yeh, J.J. Horvath, H.G. Semerjian, *Combust. Sci. Technol.* 53 (1987) 89.
- [8] K.-C. Lin, G.M. Faeth, *J. Propul. Power* 12 (1996) 10.
- [9] K.-T. Wu, R.H. Essenhigh, *Proc. Combust. Inst.* 20 (1984) 1932–1992.
- [10] L.G. Blevins, R.A. Fletcher, B.A. Benner, E.B. Steel, G.W. Mulholland, *Proc. Combust. Inst.* 29 (2002) 2325–2333.
- [11] L.G. Blevins, N.Y.C. Yang, M.A. Mikofski, G.W. Mulholland, R.W. Davis, in: *AIAA 41st Aerospace Sciences Meeting and Exhibit*, Reno, NV, January 2003, paper AIAA-2003-0985.
- [12] L.G. Blevins, N.Y.C. Yang, G.H. Mulholland, R.W. Davis, E.B. Steel, *Prepr. Symp.-Am. Chem. Soc. Div. Fuel Chem.* 47 (2) (2002) 740.
- [13] W.M. Roquemore, V.R. Katta, *J. Visual.* 2 (2000) 257.
- [14] V.R. Katta, W.M. Roquemore, *Combust. Flame* 100 (1995) 61.

- [15] H. Wang, M. Frenklach, *Combust. Flame* 110 (1997) 173.
- [16] Anonymous, Computational Submodels, International Workshop on Measurement and Computation of Turbulent Nonpremixed Flames, <http://www.ca.sandia.gov/TNF/radiation.html>, 2001.
- [17] V.R. Katta, L.P. Goss, W.M. Roquemore, *AIAA J.* 32 (1994) 84.
- [18] V.R. Katta, L.P. Goss, W.M. Roquemore, *Int. J. Numer. Methods Heat Fluid Flow* 4 (5) (1994) 413.
- [19] V.R. Katta, C.D. Carter, G.J. Fiechtner, W.M. Roquemore, J.R. Gord, J.C. Rolon, *Proc. Combust. Inst.* 27 (1998) 587–594.
- [20] V.R. Katta, W.M. Roquemore, *AIAA J.* 36 (11) (1998) 2044.
- [21] S. Harris, A.M. Weiner, R. Blint, *Combust. Flame* 72 (1988) 91.
- [22] M. Balthasar, M. Kraft, *Combust. Flame* 133 (2003) 289.
- [23] F. Tao, V.I. Golovitchev, J. Chomiak, *Combust. Flame* 136 (2004) 270.
- [24] V.I. Babushok, W. Tsang, J. Propul. Power 20 (3) (2004) 403.
- [25] L. Waldmann, K.H. Schmitt, in: C.N. Davies (Ed.), *Aerosol Science*, Academic Press, San Diego, 1966, pp. 137–162.
- [26] D.I. Fortiads, K.F. Jensen, *J. Crystal Growth* 102 (1990) 743.
- [27] J. Burns, R.W. Davis, E.F. Moore, *Aerosol Sci. Technol.* 26 (1997) 193.
- [28] G.M. Faeth, in: H.W. Ross (Ed.), *Microgravity Combustion*, Academic Press, San Diego, 2001, pp. 83–182.
- [29] L. Talbot, R.K. Chen, R.W. Schefer, D.R. Willis, *J. Fluid Mech.* 101 (1980) 737.
- [30] P.B. Sunderland, R.L. Axelbaum, D.L. Urban, in: *Proceedings of the 5th Microgravity Combustion Workshop*, Cleveland, OH, 1999.
- [31] A. Violi, A.F. Sorofim, T.N. Truong, *Combust. Flame* 126 (2001) 1506.
- [32] R.A. Dobbins, in: F.L. Dryer, R.F. Sawyer (Eds.), *Physical and Chemical Aspects of Combustion: A Tribute to Irvin Glassman*, Gordon & Breach, Newark, NJ, 1997, pp. 107–133.

Measurements of OH mole fraction and temperature up to 20 kHz by using a diode-laser-based UV absorption sensor

Terrence R. Meyer, Sukesh Roy, Thomas N. Anderson, Joseph D. Miller, Viswanath R. Katta, Robert P. Lucht, and James R. Gord

Diode-laser-based sum-frequency generation of ultraviolet (UV) radiation at 313.5 nm was utilized for high-speed absorption measurements of OH mole fraction and temperature at rates up to 20 kHz. Sensor performance was characterized over a wide range of operating conditions in a 25.4 mm path-length, steady, C₂H₄-air diffusion flame through comparisons with coherent anti-Stokes Raman spectroscopy (CARS), planar laser-induced fluorescence (PLIF), and a two-dimensional numerical simulation with detailed chemical kinetics. Experimental uncertainties of 5% and 11% were achieved for measured temperatures and OH mole fractions, respectively, with standard deviations of <3% at 20 kHz and an OH detection limit of <1 part per million in a 1 m path length. After validation in a steady flame, high-speed diode-laser-based measurements of OH mole fraction and temperature were demonstrated for the first time in the unsteady exhaust of a liquid-fueled, swirl-stabilized combustor. Typical agreement of ~5% was achieved with CARS temperature measurements at various fuel/air ratios, and sensor precision was sufficient to capture oscillations of temperature and OH mole fraction for potential use with multiparameter control strategies in combustors of practical interest. © 2005 Optical Society of America
OCIS codes: 120.1740, 280.2470, 300.1030, 300.6260, 300.6540.

1. Introduction

The hydroxyl radical (OH) is a key species in the chain-branching reactions for hydrocarbon flames. As such, knowledge of both OH mole fraction and temperature is important for understanding combustion chemistry and validating numerical models of combustors in a variety of applications. In addition, OH has been proven to be a good measure of heat release in unsteady strain-rate conditions¹ and a good marker of the reaction zone in highly strained diffusion flames.² Laser-induced fluorescence (LIF) and absorption spectroscopy are the most commonly used techniques for quantitative measurements of OH mole fraction in flames. Both methods have typically

focused on electronic transitions of OH in the ultraviolet (UV) region of the spectrum where the large absorption cross section and minimal spectral interference allow sensitive mole-fraction measurements. Until recently, frequency-doubled tunable dye-laser systems were used for these experiments.³ Advances in laser technology, however, have led to the use of compact, less-expensive diode-laser-based absorption systems⁴ that allow measurements in more practical and realistic combustion environments.

Although path averaged in nature, such absorption measurements can, in principle, capture combustor instabilities and large-scale transients such as ignition and global extinction provided that a high-speed tunable laser source is available. Until recently, such sources have only been demonstrated in the near-infrared wavelength region, allowing high-speed measurements of combustion species such as CO, CO₂ and H₂O.^{5,6} High-speed time-series measurements of species such as OH in the UV have only been demonstrated through the use of picosecond time-resolved laser-induced fluorescence⁷ (PITLIF). For operation in more demanding test-cell environments and to achieve higher detection rates, we have developed a high-speed UV absorption sensor for OH based on sum-frequency mixing (SFM) the output of a rap-

T. R. Meyer (trmeyer@innssi.com), S. Roy, J. D. Miller, and V. R. Katta are with Innovative Scientific Solutions, 2766 Indian Ripple Road, Dayton, Ohio 45440. T. N. Anderson (tanderson@purdue.edu) and R. P. Lucht are with the School of Mechanical Engineering, 585 Purdue Hall, West Lafayette, Indiana 47907. J. R. Gord is with the Propulsion Directorate, Air Force Research Laboratory, Wright-Patterson Air Force Base, Ohio 45433.

Received 18 February 2005; revised manuscript received 14 June 2005; accepted 28 June 2005.

0003-6935/05/316729-12\$15.00/0

© 2005 Optical Society of America

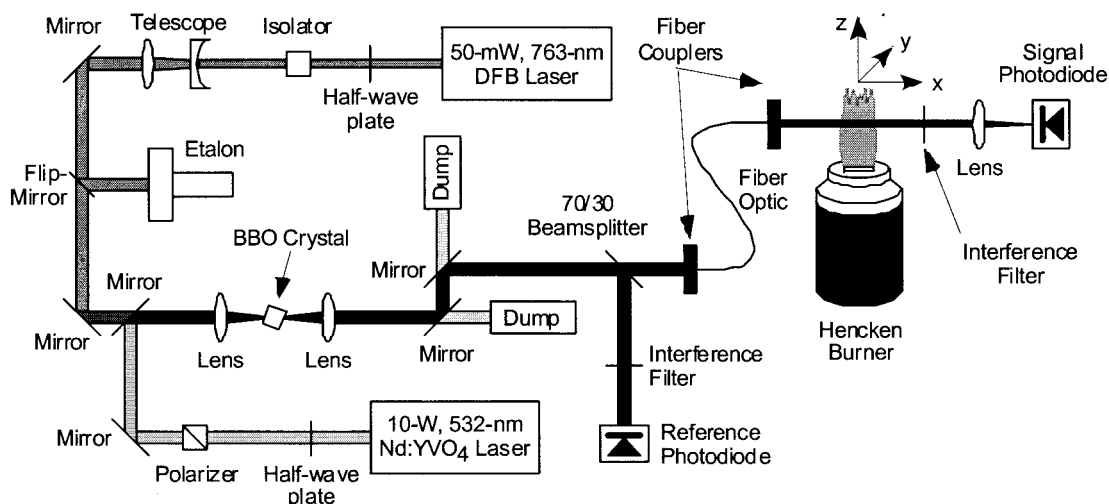


Fig. 1. Experimental layout of UV absorption sensor for measurements of OH mole fraction and temperature at rates up to 20 kHz.

idly tunable distributed-feedback (DFB) diode laser with the output of a high-power frequency-doubled Nd:YVO₄ laser. As reported in a preceding paper,⁸ we maintain the high sensitivity and selectivity in the UV spectral region with a compact, fiber-coupled, portable system. The resulting sensor provides quantitative, simultaneous measurements of OH mole fraction and temperature for tracking global instabilities in unsteady flames at rates up to 20 kHz.

In this paper, we first characterize the performance of the OH sensor in a steady C₂H₄-air diffusion flame stabilized over a Hencken burner for a wide range of temperatures and OH mole fractions, and we present comparisons with planar laser-induced fluorescence (PLIF), coherent anti-Stokes Raman spectroscopy (CARS), equilibrium calculations, and a two-dimensional computational fluid dynamics (CFD) code with detailed chemical kinetics. We discuss the accuracy of the sensor at moderate to high detection rates based on these comparisons, and we assess its precision and sensitivity. OH absorption data are then acquired for the first time in the unsteady exhaust of a liquid-fueled, swirl-stabilized combustor and compared with available CARS data under the same conditions, thus testing the accuracy of the sensor and its ability to track unsteady phenomena in combustors of practical interest. The measurement approach presented here brings diode-laser-based sensor technology one step closer to enabling combustor-control strategies based on simultaneous, high-speed detection of multiple parameters representing flame intermediates and overall heat release.

2. Diode-Laser-Based OH Absorption System

A. Lasers and Optics

Solid-state laser sources for high-speed OH absorption spectroscopy in the UV are not, to our knowledge, commercially available. In the current paper, therefore, narrow-linewidth radiation near 313.5 nm was

generated by sum-frequency mixing the output of a 763-nm distributed feedback (DFB) diode laser (Sacher Lasertechnik Group) with the output of a 532-nm diode-pumped, frequency-doubled Nd:YVO₄ laser (Coherent, Inc.) in a beta-barium borate (β -BBO) crystal.⁸ The optical layout, shown schematically in Fig. 1, is similar to a system first described by Hanna *et al.*⁹ for detection of nitric oxide in flames. The 763 nm beam was sent through a Faraday isolator (Electro-Optics Technology, Inc.), a half-wave plate, and a telescope ($f = -200$ mm and $f = 100$ mm) before being overlapped with the 532 nm beam. Both beams were focused into the crystal (Inrad, Inc.; 5 mm \times 7 mm \times 6 mm long; 37.4°) with a borosilicate lens ($f = 50$ mm). A fused-silica lens ($f = 50$ mm) was used to collimate the generated UV radiation, which was separated from the fundamental beams using two mirrors coated for 308 nm. The UV radiation was split into a reference beam (30%) that was sent directly to a detector and an absorption beam (70%) that was coupled into a 2 m long, 0.6 mm diameter core, fused-silica fiber. Before detection, the reference beam was directed through a 10 nm full-width-half-maximum (FWHM) interference filter centered at 313 nm to block residual fundamental radiation. The absorption beam was launched across the flame and through another narrowband interference filter before being focused onto a second detector. To allow measurements of OH along different paths through the flame, the fiber collimator, interference filter, lens, and absorption signal detector were mounted together on a two-axis translation stage. This provided controlled motion both vertically along the flame axis (z direction in Fig. 1) and horizontally across the flame width (y direction in Fig. 1) with 10 μ m resolution.

The absorption and reference signal detectors employed UV-enhanced silicon PIN photodiodes (Advanced Photonix), each with 20.3 mm² active area. To improve the bandwidth of the large-area detectors, each photodiode was installed in a transimpedance

amplifier circuit to maintain photovoltaic operation and to convert the photocurrent into voltage. The 3 dB bandwidth of the detectors was estimated to be 50 kHz. Output voltages from each detector were filtered and amplified with low-pass filter/preamplifiers (Stanford Research Systems) prior to digitization on a personal computer with a 10 MHz analog input/output card (National Instruments) and LabVIEW software.

After alignment of the sensor, we typically observed just under $1 \mu\text{W}$ of UV radiation on the detectors with pump-laser powers of 10 W and 35 mW for the 532 nm and 763 nm lasers, respectively. The UV power was calculated from the signal levels on each photodiode (without power to the operational amplifiers) and the quoted sensitivity of 0.15 A/W at 310 nm. Accounting for losses in the fiber (93%T), fiber coupling ($\sim 30\%$ T), and filter (12%T), an estimated $25 \mu\text{W}$ is generated during the SFM process in the BBO crystal. The maximum theoretical power for the mixing process is calculated to be roughly $130 \mu\text{W}$ for the input powers stated above and a spot size of $50 \mu\text{m}$ at the focus.¹⁰ The generated power was likely lower than expected because of differences in the spatial intensity profiles of the 763 nm and 532 nm beams, but this power was more than sufficient for making high-resolution, high-speed absorption measurements of OH.

For each experiment, the UV-radiation frequency was tuned back and forth across the transition by modulating the DFB laser current. The same computer and analog input/output card were used to generate a triangle-wave function to modulate the injection current of the DFB laser and tune across a single OH absorption line at rates of 2 to 20 kHz. During scanning, the frequency of the DFB laser was monitored with an etalon (Burleigh; 2 GHz free spectral range) that was simultaneously recorded along with the absorption and reference signals. Prior to each experiment, the center wavelength of the DFB laser was tuned to 762.96 nm (vacuum) to produce UV radiation at 313.526 nm (31895.31 cm^{-1}), which is in resonance with the $P_2(10)$ transition of the (0,0) band of the $A^2\Sigma^+ - X^2\Pi$ electronic transition of OH.

B. Data Collection and Processing

The theory behind absorption spectroscopy is described previously,¹¹ and relates the normalized transmission T_ν of radiation of frequency $\nu \text{ (cm}^{-1}\text{)}$ through an absorbing medium of length $L \text{ (cm)}$ to the gas state and the molecular properties through Beer's Law:

$$T_\nu = \frac{I}{I_0} = \exp \left[- \int_0^L k_\nu(x) dx \right], \quad (1)$$

where I_0 is the spectral intensity of the incident radiation at $x = 0$, I is the attenuated spectral intensity at $x = L$, and $k_\nu(x)$ is the spectral absorption coefficient (in cm^{-1}). Here we assume a homogeneous me-

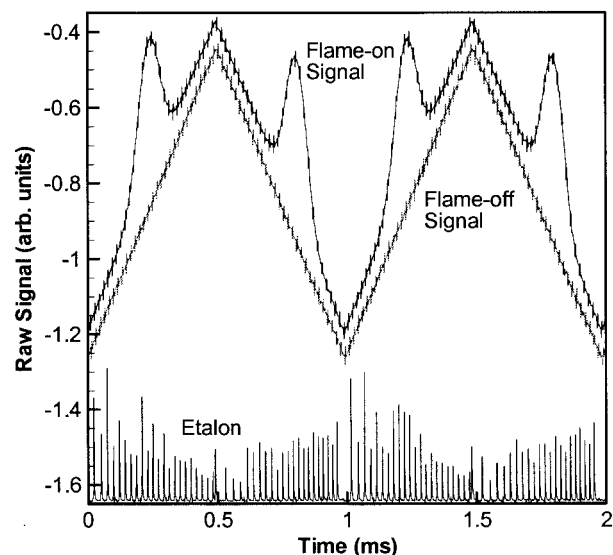


Fig. 2. Raw signals acquired over four laser sweeps in Hencken burner at $\Phi = 1.0$. Flame-off signal is shifted vertically for clarity. Free spectral range of etalon is 2 GHz.

dium with constant k_ν across the absorption path, such that

$$T_\nu = \frac{I}{I_0} = \exp(-k_\nu L). \quad (2)$$

The spectral absorption coefficient depends on both the line strength of the particular transition and the frequency separation between the laser and species transition through the lineshape function. The line strength is dependent upon the number density of the absorbing species as well as the ground-state population as determined from the Boltzmann distribution. For the molecular lineshape, we assume a Voigt profile to account for both collisional and Doppler broadening. In the current work, the laser spectral linewidths are typically over two orders of magnitude smaller than the width of a Doppler-broadened OH transition at flame temperatures. Thus, the laser linewidth can be assumed equal to a delta function, and the measured spectral intensities I_0 and I can be related directly to theory by Eqs. (1) and (2).

For the absorption measurements, a "scan" refers to 10–500 cycles of the triangle-wave current function applied to the DFB laser. The up-ramp or down-ramp of each cycle represents a laser sweep across the OH transition, during which the absorption (I) and reference (I_0) photodiode voltages and the etalon output voltage are recorded simultaneously, as shown in Fig. 2. The etalon trace was used to convert the normalized transmission from the time domain into the frequency domain because the frequency tuning of the DFB laser was not perfectly linear with time. Background flame emission was recorded with the UV beam blocked and used for subtraction from the absorption signal during postprocessing.

The least-squares fit to the experimental absorp-

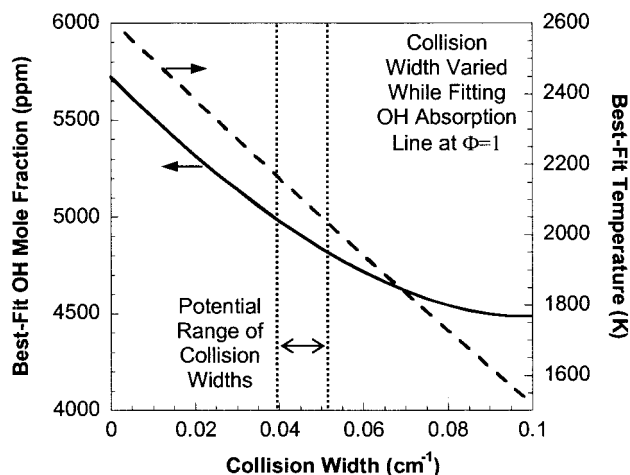


Fig. 3. Variation of best-fit OH mole fraction and temperature with collision width for averaged absorption spectrum acquired 15 mm above Hencken burner at $\Phi = 1.0$. Vertical lines show range of collision widths for $\Phi = 1.0 \pm 0.5$.

tion spectrum, performed using an evolutionary routine called differential evolution,¹² could vary seven parameters, including mole fraction, gas temperature, pressure, path length, collision width, frequency offset, and scale factor. The frequency offset allowed the entire experimental absorption spectrum to be shifted in frequency to match the theoretical spectrum. The scale factor accounted for slight broadband absorption or scattering in the flame by scaling the normalized transmission so that the off-resonant baseline matched the theoretical baseline.¹⁰ To determine the OH mole fraction and temperature in the flame, the pressure (~ 1 atm), path length, and collision width were held fixed while the remaining parameters were allowed to vary in the fitting routine. The path length was measured using an OH PLIF system and is discussed further in Subsection 4.B. For the flames in the current study, the major-species composition was estimated using an equilibrium code¹³ so that the collision width could be determined using known collision-broadening coefficients and temperature-broadening exponents for the major species. In this procedure, also used by Donovan *et al.*¹⁴ for measurements in a Hencken burner, one must make an initial estimate of the temperature in order to calculate the collision width and, in turn, measure the OH mole fraction and temperature. A sensitivity analysis performed for an equivalence ratio of $\Phi = 1.0$ indicated that one can vary the equilibrium composition and temperature by values corresponding to $\Phi = 0.5$ to 1.5 and induce maximum errors of only 4% in the best-fit OH mole fraction and 6% in the best-fit temperature (see Fig. 3). Successive iteration of the collision-width calculation was unnecessary, therefore, in the current study. Values of collision-broadening coefficients and temperature exponents were taken from Rea *et al.* for N_2 ,¹⁵ Rea *et al.* for H_2O and CO_2 ,¹⁶ and Kessler *et al.* for H_2 .¹⁷ Following Rea *et al.*,¹⁵ we assumed the remaining minor species and O_2 broadened to the same extent as ar-

Table 1. Equivalence-Ratio Settings and Flow Rates in Standard Liters per Minute (SLPM) in C_2H_4 -air Hencken-Burner Flame

ϕ	C_2H_4 SLPM	Air SLPM	N_2 Coflow SLPM
0.51	0.40	11.2	7.3
0.62	0.48	11.2	7.3
0.71	0.61	12.2	12.0
0.81	0.69	12.2	12.0
0.91	0.78	12.2	12.0
0.96	0.82	12.2	12.0
1.01	0.86	12.2	12.0
1.06	0.90	12.2	12.0
1.11	0.95	12.2	12.0
1.21	1.03	12.2	12.0
1.30	1.11	12.2	12.0
1.40	1.20	12.2	12.0
1.50	1.28	12.2	12.0

gon. Uncertainty in the calculated collision widths was approximately $\pm 10\%$, estimated from uncertainties given in each reference.

3. Combustor Test Articles

A. C_2H_4 -Air Hencken-Burner Diffusion Flame

A Hencken calibration burner was used to produce a flat, uniform, steady C_2H_4 -air flame for characterizing sensor performance in a hydrocarbon-fuel environment with similar major species equilibrium mole fractions as found in liquid-fueled combustors. The Hencken burner (Research Technologies, RD1 \times 1) has a 25.4 mm \times 25.4 mm square array of small-diameter fuel and oxidizer tubes that allow the reactants to rapidly mix above the burner surface. An inert gas coflow around the edges of the burner improves flame stability and helps to isolate the flame from room air. Details of the burner can be found in Woolridge *et al.*¹⁸ or, for a larger burner, in Kulatilaka *et al.*¹⁹ and Hancock *et al.*²⁰ With the proper flow conditions, the Hencken burner produces a nearly adiabatic flame with near-equilibrium species concentrations. The reactant flow rates used in this experiment are shown in Table 1. Tylan mass-flow controllers (Mykrolis Corporation) were used to regulate the gas flow rates, and calibration was performed with a DryCal DC-2 (Bios International Corporation) flowmeter. The accuracies of the flow controllers in standard liters per minute (SLPM) are ± 0.05 , ± 0.2 , and ± 0.12 for C_2H_4 , air, and N_2 , respectively, and the accuracy of the calibration is $\pm 1.4\%$.

B. Liquid-Fueled, Swirl-Stabilized Combustor

After validation in the Hencken burner, the OH sensor was tested in the exhaust of a preheated, atmospheric-pressure, JP-8-fueled, swirl-stabilized model gas-turbine combustor. This combustor is utilized for laser-based studies of flame structure and pollutant formation in the Atmospheric-Pressure Combustor Research Complex of the Air Force Research Laboratory's Combustion Branch. After exit-

ing the primary flame zone, the combustion products are allowed to mix thoroughly along a 48 cm long flame tube before entering a 32 cm long, 7.6 cm exit-diameter exhaust nozzle. For this reason, the combustion products have cooled several hundred degrees K due to radiative, conductive, and convective heat transfer, although the major species concentrations are expected to be frozen in a near-equilibrium condition. This is confirmed by previous measurements of O_2 and CO_2 for the same conditions.²¹ Further details on the design and operation of the burner are included in Ref. 22.

4. Validation Techniques

A. Numerical Model

A well-validated, time-dependent, axisymmetric CFD code with detailed chemical kinetics known as UNICORN (Unsteady Ignition and Combustion using Reactions)²³ is employed for simulation of the Hencken-burner flames. It solves for the u - and v -momentum equations, continuity, and the enthalpy- and species-conservation equations on a staggered-grid system. The body-force term due to the gravitational field is included in the axial-momentum equation for simulating vertically mounted flames. A clustered mesh system is employed to trace large gradients in flow variables within the flame zone. The detailed chemical-kinetics model of Wang and Frenklach²⁴ is incorporated into UNICORN for the investigation of temperature and species distributions in C_2H_4 flames. It consists of 99 species and 1066 elementary-reaction steps.

Thermo-physical properties such as enthalpy, viscosity, thermal conductivity, and binary molecular diffusion of all the species are calculated from polynomial-curve fits developed for the temperature range 300–5000 K. Mixture viscosity and thermal conductivity are then estimated using the Wilke and Kee expressions, respectively. Molecular diffusion is assumed to be of the binary-diffusion type, and diffusion velocities are calculated using Fick's law and effective-diffusion coefficients for various species in the mixture. A simple radiation model based on the optically thin-media assumption is incorporated into the energy equation. Only radiation from CH_4 , CO , CO_2 , and H_2O is considered in the present study.

The finite-difference forms of the momentum equations are obtained using an implicit QUICKEST (quadratic upstream interpolation for convective kinematics with estimated streaming terms) scheme,²⁵ and those of the species and energy equations are obtained using a hybrid scheme of upwind and central differencing. At every time step, the pressure field is accurately calculated by solving all the pressure Poisson equations simultaneously using the LU (lower and upper diagonal) matrix-decomposition technique. The boundary conditions are treated in the same way as that reported in earlier papers.²⁶

The square geometry of the Hencken burner consists of an inner layer of tubes for reactants and an outer layer of tubes for nitrogen flow. Within the

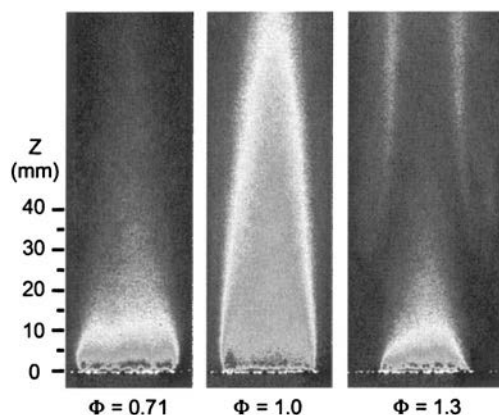


Fig. 4. Sample OH PLIF images acquired at $\Phi = 0.71, 1.0, 1.5$ for determining path length in Hencken burner.

inner layer, fuel and air are issued through separate tubes, which leads to the formation of 171 small diffusion flames. The highly regular pattern of these flames can be viewed as concentric layers of diffusion flames. The burner geometry is assumed to be formed with coannular rings of 0.7 mm fuel and 0.3 mm air jets arranged alternatively. A total of 9 fuel jets and 10 air jets are required to represent the 25.4 mm \times 25.4 mm wide Hencken burner. The physical domain of 70 mm high \times 50 mm radius is represented using a 371 \times 301 nonuniform grid system. The computational domain is bounded by the axis of symmetry and an outflow boundary in the radial direction and by the inflow and another outflow boundary in the axial direction. Flat velocity profiles are imposed at the fuel and air inflow boundaries, while an extrapolation procedure with weighted zero- and first-order terms is used to estimate the flow variables at the outflow boundary.²⁶

The simulations presented here are performed on an AMD Opteron 1.4-GHz personal computer with 2.0 GBytes of memory. Typical execution time was ~ 70 s per time step, and steady-state flames were usually obtained in about 10000 time steps.

B. OH PLIF

The array of small, lifted diffusion flames and subsequent flow structure above the Hencken burner are shown clearly in the OH PLIF images of Fig. 4, which were obtained with a different laser system than that used for OH absorption. The PLIF system utilized the pulsed output of a frequency-doubled, Nd:YAG-pumped dye laser for excitation of the $Q_1(9)$ transition in the (1,0) band of the OH $A^2\Sigma^+ - X^2\Pi$ system, followed by detection of the (1,1) and (0,0) bands.²² Relatively uniform conditions are achieved within 2 to 5 mm above the burner surface. As the distance from the burner surface increases, a mixing layer or thin diffusion flame can develop along the interface with the N_2 coflow and ambient air. These images and corresponding line plots (e.g., Fig. 5) are intended to enable direct measurements of the OH absorption path length, provide information on the ideal loca-

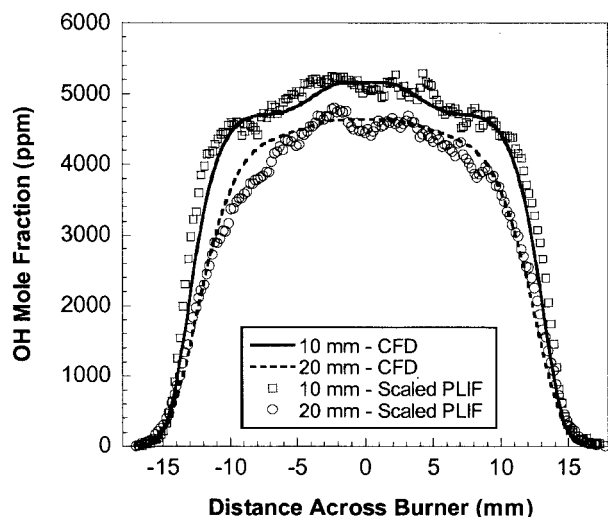


Fig. 5. Horizontal OH profiles at 10 mm and 20 mm above Hencken burner obtained from PLIF images and CFD code with detailed kinetics at $\Phi = 0.91$.

tions and conditions for validation studies, and help track qualitative trends in OH mole fraction for comparison with absorption measurements.

The OH PLIF system was used to determine the path lengths for all Hencken-burner conditions shown in Table 1 and for all burner locations in which absorption data were collected. In the linear LIF regime, the OH fluorescence signal is proportional to the number density of OH and the fluorescence quantum efficiency. Assuming the temperature and major-species mole fractions, and hence the fluorescence quantum efficiency, are relatively constant across the flame, then the OH PLIF signal gives the relative OH number-density profile. The effective path length was found from

$$L_{\text{eff}} = \frac{\int n_{\text{OH}}(x) dx}{n_{\text{OH,peak}}}, \quad (3)$$

where the number-density profile, $n_{\text{OH}}(x)$, and the peak relative OH number density, $n_{\text{OH,peak}}$, were obtained from 200-shot-average OH-PLIF signals. This effective path-length formulation was used to fit all theoretical and experimental absorption spectra in the current work, and the reported OH mole fractions represent the peak values in the central core region of the flame.

Due to the complex nature of the mixing layer, no corrections for spatial variations in OH PLIF quenching, fluorescence trapping, or laser-sheet attenuation were implemented for the path-length measurements. We stress, therefore, that these data are most accurate near the surface of the burner where the flame has a nearly top-hat profile and the path length is dominated by the relatively uniform core region of the flame. In this region, the sudden drop in temperature near the coflow fluid leads not only to a sudden

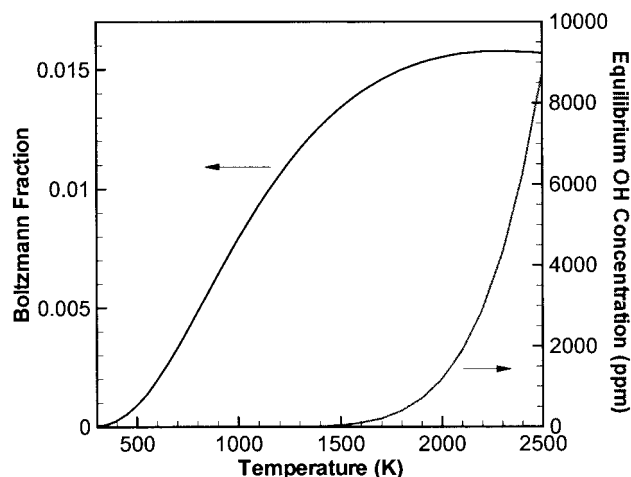


Fig. 6. Effect of temperature on Boltzmann fraction for $J = 9.5$ rotational level of OH and on equilibrium mole fraction of OH for C_2H_4 -air combustion at $\Phi = 0.91$.

drop in OH mole fraction, as illustrated in Fig. 6, but also to a sharp drop in the Boltzmann fraction for both the OH PLIF and absorption rotational transitions. Indeed, a comparison of OH PLIF line plots with data from the two-dimensional numerical simulation described in Subsection 4.A (see Fig. 5) indicates that this approach is accurate to within 5% near the burner surface and to within 10% further downstream.

Finally, OH PLIF measurements are useful not only for path-length measurements but also for direct comparison with absorption data. Data along the relatively uniform centerline region of the Hencken burner avoid a number of spectroscopic ambiguities in the mixing layer and allow relatively straightforward corrections assuming equilibrium conditions. These corrections include adjustments of up to 4% for laser-sheet attenuation in the (1,0) band and up to 9% for fluorescence trapping by the (0,0) and (1,1) detection bands as determined from Beer's Law and data collected at various flame locations. The PLIF signal was also corrected for spatial laser-sheet intensity variations up to 32%, Boltzmann fraction dependence up to 5%, and varying quenching rates up to 5%. The averaged PLIF data were scaled by a single factor for all equivalence ratios and measurement locations to enable direct, qualitative comparisons with OH absorption data, thereby adjusting for the fixed detection efficiency of the imaging system.

C. CARS Measurements

CARS has been widely used for absolute measurements of temperature and species concentrations in both laboratory flames and combustors of practical interest.^{27,28} CARS temperature data were collected in the Hencken burner as well as in the exhaust of the liquid-fueled combustor for the same conditions as the current study. The optical setup is described in Ref. 21 and allows for simultaneous detection of O_2 and CO_2 . The CARS system is utilized for valida-

tion of temperature measurements in the current work as well as for confirmation that a state of equilibrium exists for the major species in the exhaust of the liquid-fueled combustor. The latter is particularly important in the liquid-fueled combustor because it is highly nonadiabatic and, unlike the Hencken burner, the temperature is far from equilibrium. Knowledge of the major species concentrations also allows accurate determination of the collision width for OH absorption spectroscopy.

5. Experimental Results

A. Effect of Scan Rate

Representative absorption spectra of OH in the steady Hencken-burner flame acquired at 2 kHz and averaged over 38 laser sweeps are shown in Fig. 7(a) and compared with 20 kHz single-sweep data in Fig. 7(b). The experimental absorption lineshapes for high and low Φ in Fig. 7(a) are in close agreement with the theoretical lineshapes. A residual (experiment minus theory) of less than 0.5% of the peak signal is illustrated in the bottom panel of Fig. 7(a) for Φ of 1.1. The “gull-wing” shape of the residual is typical for fits of the Voigt profile to OH absorption spectra, since the Voigt profile does not account for slight collisional narrowing effects. To account for these motional-narrowing effects, a more complex lineshape such as the Galatry profile may be used.²⁹ However, this characteristic residual demonstrates that we have completely resolved the OH absorption lineshape with the sensor at these acquisition rates.

At the highest acquisition rate of 20 kHz in Fig. 7(b), we encountered some distortion of the experimental absorption lineshapes due to the 100 kHz cut-off frequency of the electronic low-pass filter. This filter, which was required to reduce noise from electromagnetic interference in the photodiode circuits, introduced artificial broadening into the absorption lineshape. A Gaussian instrument function with a 0.127 cm^{-1} FWHM was convolved with the theoretical spectrum and successfully accounted for this artificial broadening. The exact width of the instrument function was determined by comparing filtered spectra with averaged unfiltered spectra. Several consecutive 20-kHz, single-laser-sweep absorption spectra are shown in Fig. 7(b) along with a broadened Voigt fit to the data.

The noise seen in the residual in Fig. 7(b) is low, typically less than 1%, but the “gull-wing” shape is not present due to the distortion from the filter. However, the OH mole fractions and temperatures measured at $\sim 50\text{ Hz}$ (2 kHz averaged over 38 laser sweeps) agreed to within 28 parts per million (ppm) and 1 K, respectively, of the results from the measurements at 20 kHz.⁸ For the averaged 2 kHz measurements, the root-mean-square (RMS) standard deviation of the noise in the off-resonant baseline was $< 0.6\%$. Similar noise levels were observed in the single-laser-sweep measurements recorded at 20 kHz since the electronic filter provided roughly the same amount of noise reduction as the averaging.

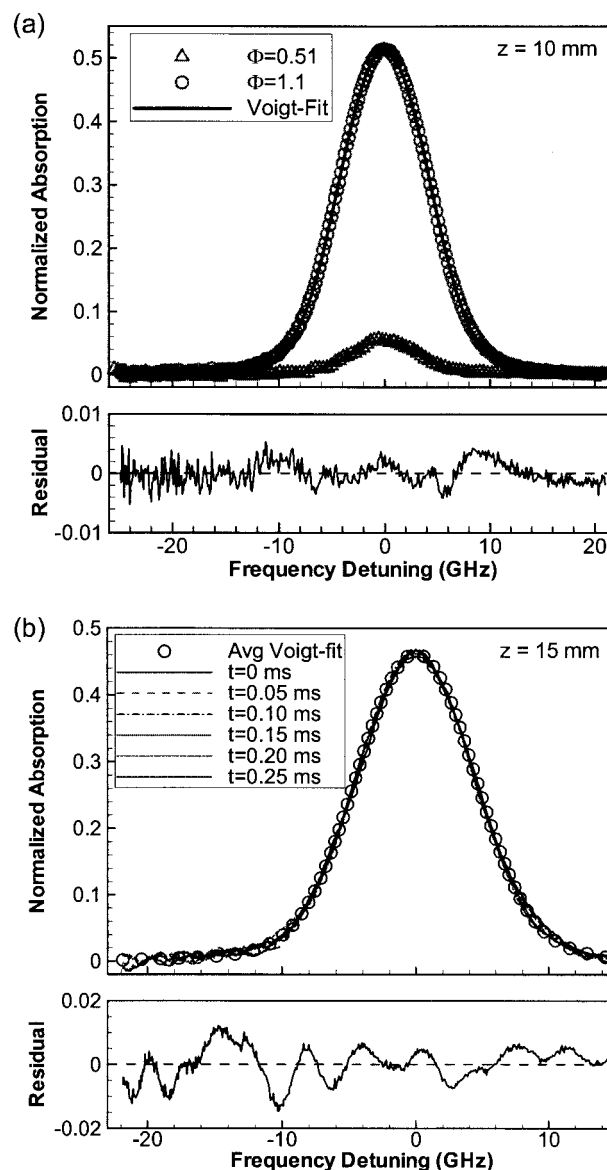


Fig. 7. (a) Voigt fit to 2 kHz 38-sweep-average OH absorption spectra acquired in Hencken burner at $\Phi = 0.51$ and 1.1; (b) artificially broadened Voigt fit (0.127 cm^{-1} Gaussian instrument function) to 20 kHz single-sweep OH absorption spectra acquired in Hencken burner at $\Phi = 1.0$. Residual in (a) is for $\Phi = 1.1$.

This corresponds to a detection limit of $< 1\text{ ppm}$ in a meter of path length for gas temperatures near 2400 K and assuming a signal-to-noise ratio of unity.

All data presented in this paper were collected in the acquisition range of 50 Hz to 20 kHz, which is two to five orders of magnitude higher than previous UV sensors^{4,9} and enables measurements in unsteady or high-speed flows. The time series data in Fig. 8, also acquired in the Hencken burner, were used to evaluate the repeatability and precision of the OH sensor at moderate to high scan rates. If one assumes that the flame is perfectly steady, then the data in Fig. 8 provide an upper limit on random noise in the measurement system. At 2 kHz (single sweep), the RMS values of the temperature and OH mole-

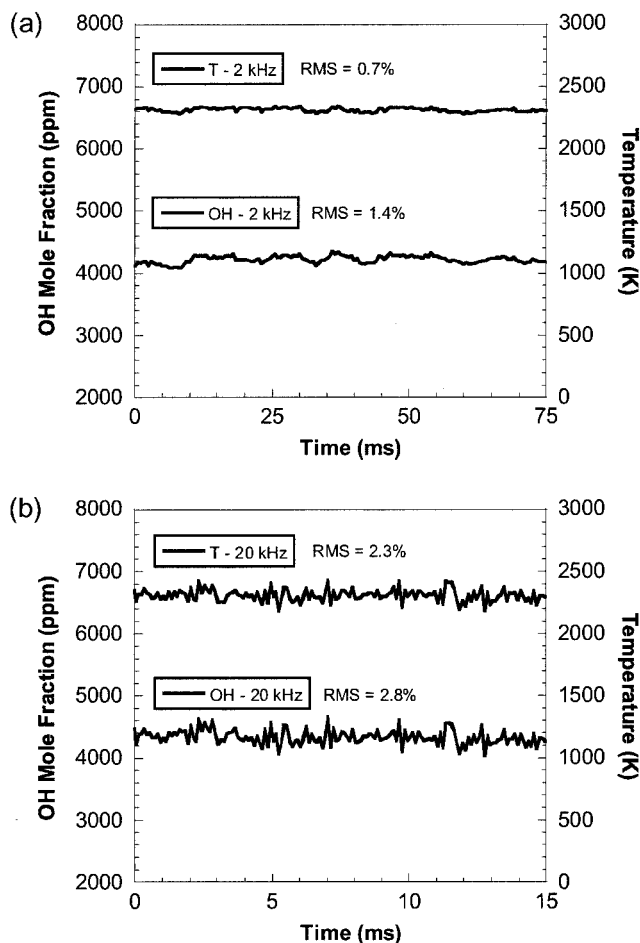


Fig. 8. Time series of OH mole fraction and temperature 15 mm above Hencken burner acquired for $\Phi = 1$ at (a) 2 kHz and (b) 20 kHz.

fraction measurements are 0.7% and 1.4%, respectively. At 20 kHz (single sweep), the RMS values are 2.3% and 2.8%, respectively. When combined with a sensitivity study assuming uncertainties of $\pm 10\%$, ± 5 Torr, and $\pm 10\%$ in the path length, pressure, and collision width, respectively, these values lead to combined uncertainties of approximately $\pm 5\%$ in temperature and $\pm 11\%$ in OH mole fraction for both low and high scan rates. In the following discussion, the absolute accuracy of the OH absorption system for a variety of conditions are explored further in a steady Hencken-burner flame and in the unsteady exhaust of a liquid-fueled combustor.

B. Steady C_2H_4 -Air Diffusion Flame

The steady C_2H_4 -air diffusion flame stabilized above the Hencken burner is used in the current work to validate measurements of OH mole fraction and temperature in regions of the flow that are relatively well characterized. Data are acquired at 2 kHz and averaged over 38 laser sweeps. As shown previously in Fig. 5, the assumption of a nearly top-hat profile is valid only several millimeters above the burner surface. The relatively slow flow rates required to stabilize the C_2H_4 -air flame lead to increased growth of

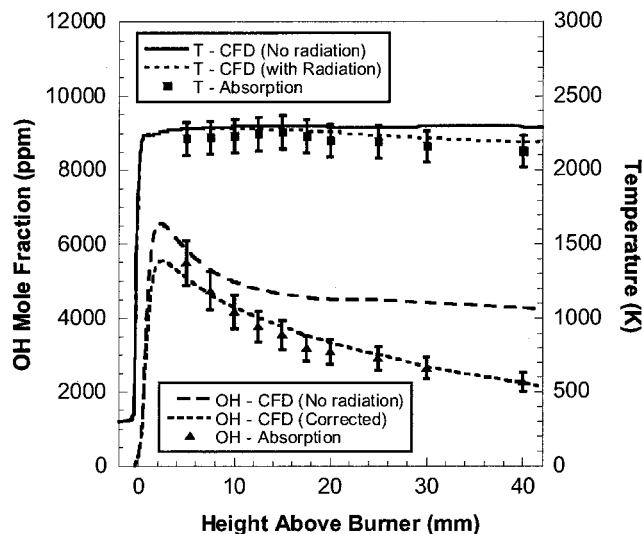


Fig. 9. Variation of centerline temperature and OH mole fraction with vertical height in Hencken burner at $\Phi = 0.91$ obtained from OH absorption sensor and CFD code with detailed kinetics. OH absorption data acquired at 2 kHz (38-sweep average).

the mixing layer between the flame and coflow fluid, and an outer diffusion flame develops for rich conditions higher in the flame. Thus, validation measurements are best performed within 5 to 10 mm of the burner surface. Absorption measurements across wider mixing layers higher in the flow may still be accurate, according to Ouyang and Varghese,³⁰ if the line strength decreases rapidly with temperature. For the $P_2(10)$ line studied here, the population of the $J = 9.5$ rotational level drops off relatively quickly with temperature, as shown previously in Fig. 6. In addition, the OH mole fraction is a strong function of temperature and may significantly reduce the contribution from the low-temperature mixing zone. Thus, data above the 10 mm location are presented to further evaluate the capabilities of the OH sensor, but these data must be interpreted carefully.

Measurements of temperature and OH mole fraction using the diode-laser-based sensor along the centerline of the Hencken burner are presented for $\Phi = 0.91$ in Fig. 9. Note that the two-dimensional CFD code with detailed chemical kinetics predicts that the flame reaches the equilibrium temperature of 2300 K in less than 2 mm. Beyond 10 mm, the numerical data indicate that the temperature begins to decline due to radiation heat losses from gaseous combustion products. The diode-laser-based measurements peak close to the burner surface and are consistently ~ 60 K below the numerical predictions after accounting for radiative heat losses from gaseous species. This consistent temperature deficit may be due to several factors, including additional radiative heat loss from heavy hydrocarbons or soot, conductive heat loss to the burner surface,³¹ mixing-layer effects, and uncertainties in spectroscopic parameters. Only the latter two factors are of concern for characterizing sensor performance, and they are clearly not very significant since the measured temperatures are

within 3% of the numerical predictions from 5 to 40 mm above the burner.

One may conclude from Fig. 9 that additional heat losses to the burner also do not significantly affect the measured temperature. These heat losses, however, do have a dramatic effect on radicals such as OH. The measured OH mole fractions in Fig. 9 are compared, therefore, with data from two numerical simulations: one that assumes there are no heat losses of any kind, and one that corrects the OH mole fraction by assuming that the measured temperatures are accurate. As shown in Fig. 9, the measured OH mole fractions closely track the numerical simulations only when corrected using the measured temperatures. Such a dramatic drop in OH mole fraction is unlikely to stem from large errors in spectroscopic parameters or from the growth of a mixing layer since the effective path length is measured directly with OH PLIF. It is reasonable to conclude, therefore, that the measured temperatures and OH mole fractions are affected by slight heat losses that are not accounted for in the numerical simulation. With regard to sensor validation, we note that measurements from 5 to 10 mm above the burner agree with both the adiabatic and corrected numerical predictions to within the experimental uncertainties of $\pm 5\%$ in temperature and $\pm 11\%$ in mole fraction.

To further evaluate the accuracy and limitations of the current OH sensor, data were collected in the Hencken burner at equivalence ratios ranging from 0.5 to 1.5 for heights of 5, 10 and 20 mm above the burner. Within this range, absorption data are acquired for mole fractions below the detection limit to a peak of over 6000 ppm. As shown in Fig. 10, the measured temperatures agree with equilibrium predictions to within $\pm 5\%$ for nearly the entire range of equivalence ratios and at all three burner locations. Previous CARS measurements in H_2 -air flames stabilized over a Hencken burner have also shown successful comparisons with equilibrium predictions.²⁰ The two least accurate temperature data points in Fig. 10 are recorded for lean conditions at the 20 mm location, where the OH absorption sensor predicts temperatures that are 300 K below equilibrium. To ensure that this deviation from equilibrium is not due to the entrainment of low-temperature coflow fluid, we performed targeted CARS temperature measurements specifically at these conditions, as shown in Figs. 10(b) and 10(c). The CARS temperatures are 60 to 70 K below equilibrium, as expected. This represents an apparent limitation to the accuracy of the OH sensor and can be attributed either to the growth of a mixing layer or, perhaps more likely, to the fact that the OH mole fractions for these conditions are near the detection limit of the sensor.

Comparisons between measured OH mole fractions and scaled OH PLIF data along the centerline, as shown in Fig. 10, show agreement to within experimental uncertainty for nearly all equivalence ratios at 5, 10, and 20 mm above the burner; both measurement techniques show deviations from equilibrium predictions at all three locations. At 5 mm, OH

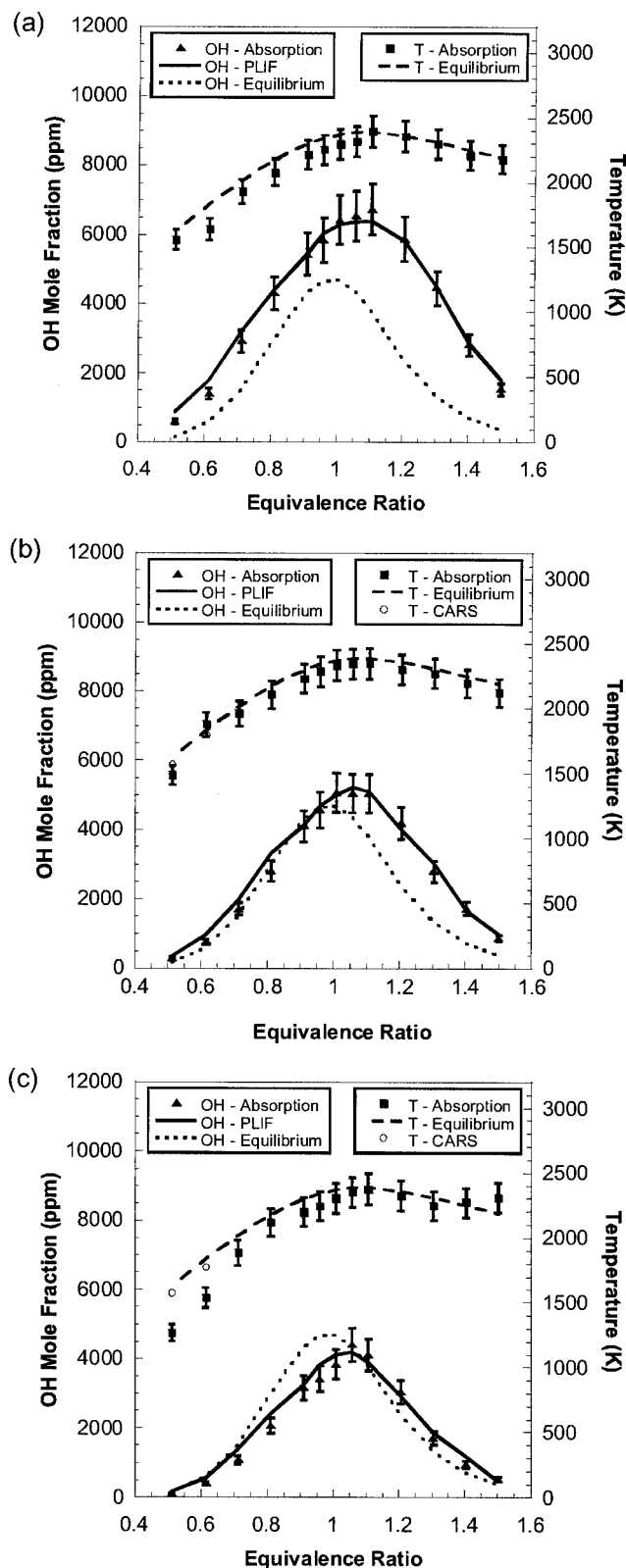


Fig. 10. Variation of temperature and OH mole fraction with equivalence ratio in Hencken burner for heights of (a) 5 mm, (b) 10 mm, and (c) 20 mm. OH absorption data acquired at 2 kHz (38-sweep average).

mole fractions are above equilibrium for all Φ due to the close proximity to the burner (see Fig. 9). At 10 mm, OH mole fractions approach equilibrium levels on the lean side but are still above equilibrium on the rich side. This phenomenon is expected because unburned fuel and radical generation persist for longer periods of time under rich conditions.

One should bear in mind that the two techniques used to measure OH mole fraction are artificially coupled for two reasons. First, all OH PLIF data were adjusted to match the OH absorption data using a single scaling factor. Thus, agreement between the techniques indicates qualitative trends with respect to flame location and equivalence ratio. Second, the path length for OH absorption was determined directly from OH PLIF data. To evaluate the significance of this second mechanism, we note that the path length at 5 mm is nearly constant for lean conditions (see Fig. 4), though the OH mole fraction changes dramatically (see Fig. 10). Thus, agreement with OH PLIF data collected at various Φ and heights along the centerline indicates that the accuracy of the OH absorption measurement is not severely affected by the growth of a mixing layer higher in the flame.

C. Exhaust of a Liquid-Fueled, Swirl-Stabilized Combustor

Data acquired in the steady C_2H_4 -air diffusion flame at rates up to 20 kHz indicate that the sensor can accurately measure the same temperatures and OH mole fractions as averaged data, and it can record temperatures and OH mole fractions with standard deviations of $<3\%$. Here, the sensor is tested in the exhaust stream of an unsteady, JP-8 fueled, swirl-stabilized combustor far enough downstream of the primary flame zone (~ 80 cm) that the main products of combustion can be assumed to exist in equilibrium. Previous time-averaged CARS measurements of O_2 and CO_2 mole fraction in this combustor verify this to be the case to within 5% from $\Phi = 0.5$ to 1.0.²¹ Thus, the collision widths used for fitting OH absorption spectra assume major-species mole fractions from equilibrium predictions of JP-8-air combustion.^{13,21} The temperature used in the collision-width calculation was obtained from previous CARS data,²¹ and the uncertainty due to the fluctuating component of temperature and major-species composition is expected to be minimal based on the sensitivity analysis of Fig. 3.

All measurements in the exhaust stream of the swirl-stabilized combustor were performed 10 mm downstream of the exhaust nozzle. The path length for OH absorption was estimated to be 7.6 cm based on the exit diameter of the nozzle. The 10% to 90% mixing-layer width along the outer region of the exhaust flow was determined to be of the order of 0.5 cm using previous CARS temperature, CO_2 , and O_2 data across the exhaust flow. In relative terms, this is less than the mixing-layer width in the 2.54 cm wide Hencken burner and should not significantly degrade the accuracy of the measurement. The collision widths calculated based on the equilibrium composi-

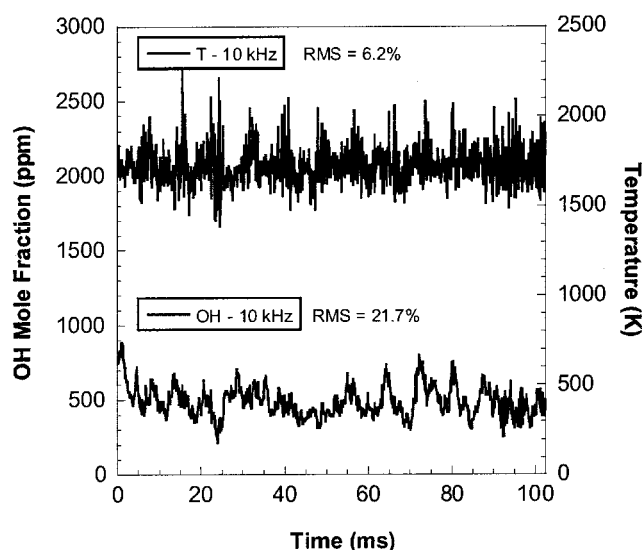


Fig. 11. Time series of temperature and OH mole fraction acquired at 10 kHz (single sweep) in exhaust stream of swirl-stabilized liquid-fueled combustor at $\Phi = 1.0$.

tion for C_2H_4 -air and JP-8-air combustion agree to within $\sim 1\%$ due to the similar H:C ratio of these fuels. Thus, the uncertainties of $\pm 5\%$ in temperature and $\pm 11\%$ in OH mole fraction reported in Subsection 5.A also apply in the exhaust flow of the liquid-fueled combustor.

Diode-laser-based absorption time series of temperature and OH mole fraction at 10 kHz were collected in the exhaust stream at $\Phi = 1.0$, as shown in Fig. 11. The time-averaged temperature from this measurement was computed to be 1730 K with an RMS of 6.2%. This mean temperature is within 3.4% of the mean CARS measurement of 1790 K for the same condition.²⁸ The time-averaged OH mole fraction was computed to be 500 ppm with an RMS of 21.7%. Strong periodicity in the time-series data appears as a source of increased RMS in both the temperature and OH mole fraction data shown in Fig. 11. The values of 6.2% and 21.7% are in stark contrast to the RMS values of $<3\%$ for the steady Hencken burner flame, and they indicate that the precision of the sensor is sufficient to capture combustion instabilities in the exhaust stream and, perhaps, in the primary flame zone of liquid-fueled combustors of practical interest.

Temperature measurements in the liquid-fueled combustor using the OH absorption sensor are compared with previous CARS temperature data in Fig. 12 for $\Phi = 0.5$ to 1.1.²¹ General agreement is achieved between the two measurement techniques, with both showing temperatures that are $\sim 20\%$ below equilibrium due to significant radiative, convective, and conductive heat losses. The OH mole fraction data, shown in Fig. 12, indicate that increased error in temperature measurements from the OH absorption sensor occurs for data points under lean conditions that are near the detection limit of the sensor. Data for absolute validation of the OH mole

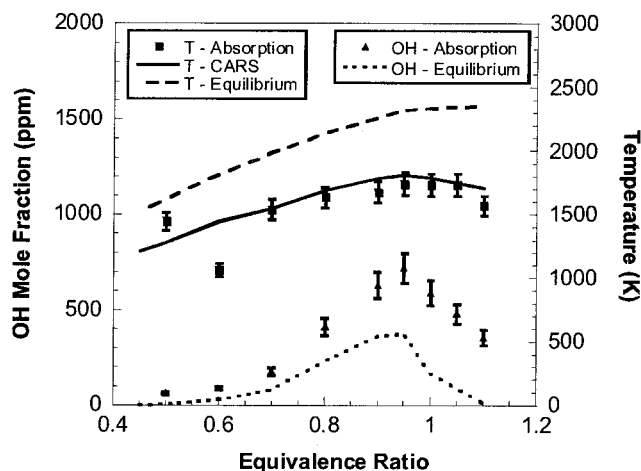


Fig. 12. Variation of temperature and OH mole fraction with equivalence ratio in exhaust stream of swirl-stabilized liquid-fueled combustor. Equilibrium prediction of OH mole fraction based on CARS temperature measurements. OH absorption data acquired at 2 kHz (38-sweep average).

fraction measurements in the exhaust stream of this combustor are not currently available. According to equilibrium theory, the OH mole fractions in the exhaust should drop by over an order of magnitude based on the measured CARS temperatures.¹³ This overpredicts the actual drop seen in the OH-absorption data, possibly because equilibrium theory does not capture the effect of ambient air reacting with unburned heavy hydrocarbons in the exhaust flow. Further study beyond the scope of this work is required to fully understand this phenomenon.

6. Conclusions

A compact, high-speed sensor has been developed for measurements of OH mole fraction and temperature in flames using UV absorption spectroscopy of the $P_2(10)$ line in the (0,0) band of the $A^2\Sigma^+ - X^2\Pi$ electronic transition of OH. Approximately 25 μW of rapidly tunable, narrow-linewidth radiation near 313.5 nm was generated by sum-frequency mixing the output of a 763 nm DFB diode laser with the output of a high-power 532 nm Nd:YVO₄ laser in a BBO crystal.

Time-series data acquired at 20 kHz in a steady Hencken burner flame were used to quantify repeatability in the measurements, with an RMS of 2.3% in temperature and 2.8% in OH mole fraction. The 20 kHz detection limit of < 1 ppm for a 1 m path length and 2400 K gas temperature, determined from residual noise in the line-fitting process, represents an improvement over previous slow-scan solid-state OH sensors used for combustion applications.³² Uncertainties in the temperature and OH mole-fraction measurements were estimated to be $\pm 5\%$ and $\pm 11\%$, respectively, with the latter occurring primarily due to path-length uncertainty.

A detailed investigation of OH in C₂H₄-air flames stabilized over a Hencken burner was performed to characterize sensor performance for a wide range of conditions, and comparisons were made with a two-

dimensional numerical simulation, equilibrium calculations, CARS measurements, and OH PLIF data. Temperature and OH mole fraction were measured along the centerline of the burner for heights of 5 to 40 mm and for equivalence ratios ranging from $\Phi = 0.5$ to 1.5. Measured temperatures and OH mole fractions were validated near the surface of the burner where the flame is most uniform. The OH absorption system was also shown to be a potentially robust sensor in the presence of mild mixing regions due to the rapid decrease of OH mole fraction and line strength with decreasing temperature.

Measurements were also performed in the exhaust of a liquid-fueled combustor and successfully compared with CARS temperature data. Time-series data in the exhaust illustrated that the precision of the measurement system is sufficient to capture high-frequency oscillations in temperature and OH mole fraction. These experiments represent the first demonstration of simultaneous, time-dependent, quantitative measurements of OH mole fraction and temperature to capture global instabilities in unsteady flames of practical interest at rates up to 20 kHz.

The authors gratefully acknowledge the late Ralph Swaine of Coherent, Inc., for providing the VerdiTM laser system and thank Vincent Belovich and Mark Laber for assistance with the liquid-fueled combustor. Funding for this work was provided by the Air Force Research Laboratory, Propulsion Directorate, under contracts F33615-00-C-2020 and F33615-03-D-2329, and by the Air Force Office of Scientific Research (Julian Tishkoff, Program Monitor). The participation of Thomas N. Anderson was supported by a National Science Foundation Graduate Research Fellowship.

References

1. H. N. Najm, P. H. Paul, C. J. Mueller, and P. S. Wyckoff, "On the adequacy of certain experimental observables as measurements of flame burning rate," *Combust. Flame* **113**, 312–332 (1998).
2. P. H. Renard, J. C. Rolon, D. Thevenin, and S. Candel, "Investigations of heat release, extinction, and time evolution of the flame surface, for a nonpremixed flame interacting with a vortex," *Combust. Flame* **117**, 189–205 (1999).
3. E. C. Rea, Jr., and R. K. Hanson, "Rapid laser-wavelength modulation spectroscopy used as a fast temperature measurement technique in hydrocarbon combustion," *Appl. Opt.* **27**, 4454–4464 (1988).
4. D. B. Oh, "Diode-laser-based sum-frequency generation of tunable wavelength-modulated UV light for OH radical detection," *Opt. Lett.* **20**, 100–102 (1995).
5. J. T. C. Liu, J. B. Jeffries, and R. K. Hanson, "Large-modulation-depth $2f$ spectroscopy with diode lasers for rapid temperature and species measurements in gases with blended and broadened spectra," *Appl. Opt.* **43**, 6500–6509 (2004).
6. X. Zhou, J. B. Jeffries, R. K. Hanson, G. Li, and E. J. Gutmark, "Rapid measurements of gas temperature in a swirl-stabilized flame," presented at the 2005 Joint Meeting of the U.S. Sections of the Combustion Institute, Philadelphia, PA, 20–23 March 2005.
7. M. W. Renfro, S. D. Pack, G. B. King, and N. M. Laurendeau,

- "Hydroxyl time-series measurements in laminar and moderately turbulent methane/air diffusion flames," *Combust. Flame* **115**, 443–455 (1998).
8. T. N. Anderson, R. P. Lucht, T. R. Meyer, S. Roy, and J. R. Gord, "Diode-laser based ultraviolet-absorption sensor for high-speed detection of the hydroxyl radical," *Opt. Lett.* **30**, 1321–1323 (2005).
 9. S. F. Hanna, R. Barron-Jimenez, T. N. Anderson, R. P. Lucht, J. A. Caton, and T. Walther, "Diode-laser-based ultraviolet absorption sensor for nitric oxide," *Appl. Phys. B* **75**, 113–117 (2002).
 10. SNLO nonlinear optics code available from A. V. Smith, Sandia National Laboratories, Albuquerque, NM 87185–1423, USA, through www.sandia.gov/imrl/XWEB1128/xxl.htm.
 11. T. N. Anderson, R. P. Lucht, R. Barron-Jimenez, S. F. Hanna, J. A. Caton, T. Walther, S. Roy, M. S. Brown, J. R. Gord, I. Critchley, and L. Flamand, "Combustion exhaust measurements of nitric oxide with an ultraviolet diode-laser-based absorption sensor," *Appl. Opt.* **44**, 1491–1502 (2005).
 12. R. Storn and K. Price, "Differential evolution: a simple and efficient heuristic for global optimization over continuous spaces," *J. Global Optim.* **11**, 341–359 (1997); source code available from www.icsi.berkeley.edu/~storn/code.html.
 13. S. R. Turns, *An Introduction to Combustion: Concepts and Applications*, 2nd ed. (McGraw-Hill, New York, 2000).
 14. M. T. Donovan, D. L. Hall, P. V. Torek, C. R. Schrock, and M. S. Wooldridge, "Demonstration of temperature and OH mole fraction diagnostic in $\text{SiH}_4/\text{H}_2/\text{O}_2/\text{Ar}$ flames using narrow-line UV OH absorption spectroscopy," *Proc. Combust. Instit.* **29**, 2635–2643 (2002).
 15. E. C. Rea, Jr., A. Y. Chang, and R. K. Hanson, "Shock-tube study of pressure broadening of the $A^2\Sigma^+ - X^2\Pi$ (0,0) band of OH by Ar and N_2 ," *J. Quant. Spectrosc. Radiat. Transfer* **37**, 117–127 (1987).
 16. E. C. Rea, Jr., A. Y. Chang, and R. K. Hanson, "Collisional broadening of the $A^2\Sigma^+ - X^2\Pi$ (0,0) band of OH by H_2O and CO_2 in atmospheric-pressure flames," *J. Quant. Spectrosc. Radiat. Transfer* **41**, 29–42 (1989).
 17. W. J. Kessler, M. G. Allen, and S. J. Davis, "Rotational level-dependent collisional broadening and line shift of the $A^2\Sigma^+ - X^2\Pi$ (1,0) band of OH in hydrogen–air combustion gases," *J. Quant. Spectrosc. Radiat. Transfer* **49**, 107–117 (1993).
 18. M. S. Wooldridge, P. V. Torek, M. T. Donovan, D. L. Hall, T. A. Miller, T. R. Palmer, and C. R. Schrock, "An experimental investigation of gas-phase combustion synthesis of SiO_2 nanoparticles using a multi-element diffusion flame burner," *Combust. Flame* **131**, 98–109 (2002).
 19. W. D. Kulatilaka, R. P. Lucht, S. F. Hanna, V. R. Katta, "Two-color, two-photon laser-induced polarization spectroscopy (LIPS) measurements of atomic hydrogen in near-adiabatic, atmospheric pressure hydrogen/air flames," *Combust. Flame* **137**, 523–537 (2004).
 20. R. D. Hancock, K. E. Bertagnolli, and R. P. Lucht, "Nitrogen and hydrogen CARS temperature measurements in a hydrogen/air flame using a near-adiabatic flat-flame burner," *Combust. Flame* **109**, 323–331 (1997).
 21. T. R. Meyer, S. Roy, R. P. Lucht, and J. R. Gord, "Dual-pump dual-broadband CARS for exhaust-gas temperature and CO_2 – O_2 – N_2 mole-fraction measurements in model gas-turbine combustors," *Combust. Flame* **142**, 52–61 (2005).
 22. T. R. Meyer, S. Roy, V. M. Belovich, E. Corporan, and J. R. Gord, "Simultaneous planar laser-induced incandescence, OH planar laser-induced fluorescence, and droplet Mie scattering in swirl-stabilized spray flames," *Appl. Opt.* **44**, 445–454 (2005).
 23. V. R. Katta and W. M. Roquemore, "On the structure of a stretched/compressed laminar flamelet: influence of preferential diffusion," *Combust. Flame* **100**, 61–70 (1995).
 24. H. Wang and M. Frenklach, "A detailed kinetic modeling study of aromatics formation in laminar premixed acetylene and ethylene flames," *Combust. Flame* **110**, 173–221 (1997).
 25. V. R. Katta, L. P. Goss, and W. M. Roquemore, "Numerical investigations of transitional H_2/N_2 jet diffusion flames," *AIAA J.* **32**, 84–94 (1994).
 26. V. R. Katta, L. P. Goss, and W. M. Roquemore, "Simulation of vertical structures in a jet diffusion flame," *Int. J. Num. Methods Heat Fluid Flow* **4**, 413–424 (1994).
 27. A. C. Eckbreth, *Laser Diagnostics for Combustion Temperature and Species*, 2nd ed. (Gordon & Breach, Dordrecht, The Netherlands, 1996).
 28. S. Roy, T. R. Meyer, R. P. Lucht, V. M. Belovich, E. Corporan, and J. R. Gord, "Temperature and CO_2 concentration measurements in the exhaust stream of a liquid-fueled combustor using dual-pump coherent anti-Stokes Raman scattering (CARS) spectroscopy," *Combust. Flame* **138**, 273–284 (2004).
 29. P. L. Varghese and R. K. Hanson, "Collisional narrowing effects on spectral line shapes measured at high resolution," *Appl. Opt.* **23**, 2376–2385 (1984).
 30. X. Ouyang and P. L. Varghese, "Line-of-sight absorption measurements of high temperature gases with thermal and concentration boundary layers," *Appl. Opt.* **28**, 3979–3984 (1989).
 31. S. Roy, T. R. Meyer, R. P. Lucht, M. Afzelius, P.-E. Bengtsson, and J. R. Gord, "Dual-pump dual-broadband coherent anti-Stokes Raman scattering in reacting flows," *Opt. Lett.* **29**, 1843–1845 (2004).
 32. G. J. Ray, T. N. Anderson, J. A. Caton, R. P. Lucht, and T. Walther, "OH sensor based on ultraviolet, continuous-wave absorption spectroscopy utilizing a frequency-quadrupled, fiber-amplified external-cavity diode laser," *Opt. Lett.* **26**, 1870–1872 (2001).

Planar Imaging of Soot, Droplets, and Fluorescence for Studies of Alternative Fuel Blends in Gas-Turbine Combustion

Amy C. Lynch and James R. Gord

Air Force Research Laboratory, Propulsion Directorate, Wright-Patterson Air Force Base, Ohio 45433-7103

Terrence R. Meyer and Sukesh Roy

*Innovative Scientific Solutions, Inc., Dayton, Ohio 45440-3638
trmeyer@innssi.com, Tel: (937) 904-4007, Fax: (937) 656-4110*

Abstract: Laser-induced incandescence (LII), OH planar laser-induced fluorescence (PLIF), and laser Mie scattering are used to track soot volume fraction, flame products, and droplet scattering for studies of alternative fuel blends in a swirl-stabilized gas-turbine combustor.

OCIS codes: (000.2170) Equipment and Techniques; (120.1740) Combustion Diagnostics

1. Introduction

A study to characterize the production of particulate-matter (PM) emissions is performed in a liquid-fueled model gas-turbine combustor while varying fuel blends and operating conditions. Laser-induced incandescence (LII), OH planar laser-induced fluorescence (PLIF), and laser Mie scattering are used to track soot volume fraction, measure flame products, and visualize droplet scattering in the reaction zone, respectively. Studies are performed on varying fuel blends comprised of kerosene-based jet fuel and synthetic fuel in varying concentrations over a range of equivalence ratios. Consistent with results of previous studies, fuels containing aromatics, which have been shown to promote PM production, produce higher quantities of soot than straight-chain hydrocarbons. Laser-based measurements show a significant correlation among physical flame structure, fuel type, and particle number density.

2. Experimental Setup

Experiments were conducted in an atmospheric pressure swirl-stabilized combustor located in the Atmospheric-Pressure Combustor-Research Complex of the Air Force Research Laboratory's Propulsion Directorate.¹ The combustor consists primarily of a fuel injector, a square cross-sectional flame tube (combustion section), and an exhaust nozzle (Fig.1). The injector configuration is a generic swirl-cup liquid-fuel injector consisting of a commercial pressure-swirl atomizer. The 4-cm exit diameter fuel injector is centrally located in the 15.25-cm × 15.25-cm cross-sectional dome. Most of the air to the combustor enters through the swirl-cup injector, while a small percentage enters through aspiration holes along the dome wall. The combustion products from the primary flame zone are allowed to mix thoroughly along the 48-cm-long flame tube before entering a 43-cm-long exhaust nozzle. The combustor is optically accessible for in-situ laser-based diagnostics via 75-mm-wide quartz windows along the top and sides.

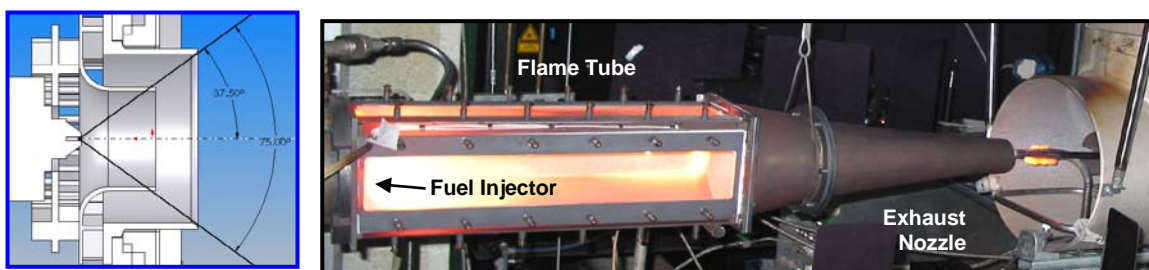


Fig. 1. Swirl-cup fuel injector (left) and atmospheric-pressure research combustor (right).

The combustor overall equivalence ratio was varied from $\Phi = 0.60$ to 1.10 by changing the pressure drop across the fuel injector from about 1.5 to 10 atm, resulting in fuel mass-flow rates of 1.0 to 2.2 g/s, respectively. The fuel flow rate was measured using a Max Machinery positive-displacement flow meter, and the air flow rate was measured with a sonic nozzle. The inlet air was heated to 450 K with a constant flow of approximately 0.028 kg/s throughout the study. The air pressure drop across the combustor dome was approximately 5.0% of the main supply.

Effects of alternative fuel blends on the concentration of hydroxyl radicals, fuel droplets, and soot particles in the combustor reaction zone were assessed using PLIF, Mie scattering, and LII, respectively. The PLIF/Mie scattering system consisted of a frequency-doubled, Q-switched Nd:YAG laser with 50% of the laser energy used to pump a dye laser tuned to the Q1(9) transition of the (1,0) band in the A-X system at 283.922 nm (in air). A 1.5-m-focal-length spherical plano-convex lens and a 75-mm-focal-length plano-concave lens were used to form a 330- μm full-thickness-half-max (FTHM) laser sheet that entered the combustor through the top window. Two 1-mm WG-295 (CVI Laser) filters were used to reduce scattering from droplets, and a UG11 (Schott Glass) color filter was used to eliminate flame emission, scattering from the LII laser, and fluorescence from polycyclic aromatic hydrocarbon (PAH) species. After eliminating these interferences, Mie scattering and OH PLIF were collected simultaneously using a 105-mm-focal length f/4.5 UV lens and an intensified CCD camera (Roper Scientific) with an intensifier gate width of 20 ns. The peak droplet-scattering signal intensity (after filtering) was over an order of magnitude higher than for LIF and could be distinguished using intensity scaling and by its spatial characteristics (see Fig. 2).

The 700- μm FTHM laser sheet for planar LII used 50% of the energy from the Nd:YAG laser and was formed using a 2-m plano-convex spherical lens and a 50-mm plano-concave cylindrical lens. The LII signal was detected using a second intensified CCD camera (Roper Scientific) and a f/1.2, 58-mm focal length glass lens. The PLIF and LII cameras were synchronized using an external delay generator driven by the advanced Q-switch TTL output of the Nd:YAG laser.

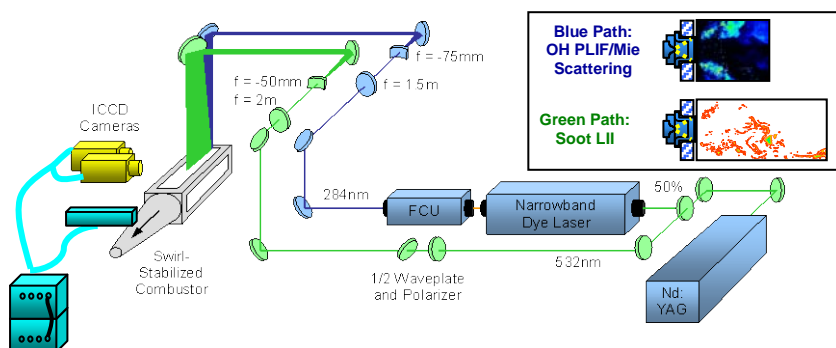


Fig. 2. Simultaneous imaging of OH PLIF, Mie scattering, and LII.

The alternative fuel blend consisted of JP-8 mixed with varying levels of a synthetic jet fuel. JP-8 is petroleum-based commercial Jet A-1 with a military additive package.² The synthetic jet fuel is a natural-gas-derived fuel produced by Syntroleum Corporation. In the natural-gas-to-jet-fuel conversion, the natural gas reacts with air in a proprietary auto-thermal reformer reactor to produce synthesis gas (syngas--carbon monoxide and hydrogen). The synthesis gas is then converted into synthetic crude via the Fischer-Tropsch process. Finally, the synthetic crude is processed to obtain the desired final product (e.g., jet or diesel fuel). The paraffinic feedstock used in this study provided physical properties consistent with those required to meet the specification of a JP-8. JP-8 is composed of numerous hydrocarbons with normal paraffins being the primary species. JP-8 also contains lower concentrations of cyclic paraffins, olefins, and aromatics. Similar to JP-8, the synjet fuel is also composed largely of paraffinic compounds, but it is mainly comprised of branched paraffins. Synjet fuel possesses a higher energy per mass content, thus offsetting its lower density.

3. Results and Discussion

In-situ PLIF, Mie-scattering, and LII images at $\Phi = 1.10$ for the combustor operating with JP-8 are compared with images for 100% synjet concentration in Fig. 3. For this equivalence ratio, the flame is located about one injector

diameter downstream where the fuel and air have had sufficient time to mix and fall within the combustible limit. Although these results are preliminary, the differences in combustion characteristics between JP-8 and the synjet fuel are evident in the flame zone just beyond the fuel injector. At this equivalence ratio for JP-8, the fuel scattering from liquid (unvaporized) droplets dominates the image and overwhelms the OH PLIF signal, clearly mapping the spray angle of the swirl injector. This is in contrast with the image for the synjet fuel, which shows little or no droplet scattering even though the signal in the image has been scaled up by a factor of ten. Due to the low amount of fuel scattering for the synjet fuel, it is possible to detect OH PLIF just downstream of the fuel-rich mixing zone. Based on these images, it is clear that JP-8 vaporizes much more slowly than the synthetic fuel. This is expected to contribute to higher soot production and unburned hydrocarbons for JP-8 than for the synjet fuel. The higher soot production with JP-8 is evident in the right-hand images of Fig. 3, which show soot volume fraction recorded using LII. For JP-8, localized regions of soot formation are clearly visible, while soot is nearly undetectable for the synjet fuel even though the signal has been scaled by a factor of ten. Therefore, it appears based on these images that the higher soot emissions with JP-8 relative to the synjet fuel may result not only from higher aromatics in JP-8 but may also be influenced to some degree by physical characteristics that affect fuel atomization and vaporization near the injector. The difference in vaporization characteristics between the two fuels was unanticipated considering that the physical properties (e.g., viscosity, density, surface tension, and vapor pressure) of both fuels are fairly similar. Lower vapor pressure of the higher molecular weight species in JP-8 may have contributed to the differences in fuel spray characteristics. Further investigations to explain these findings are warranted.

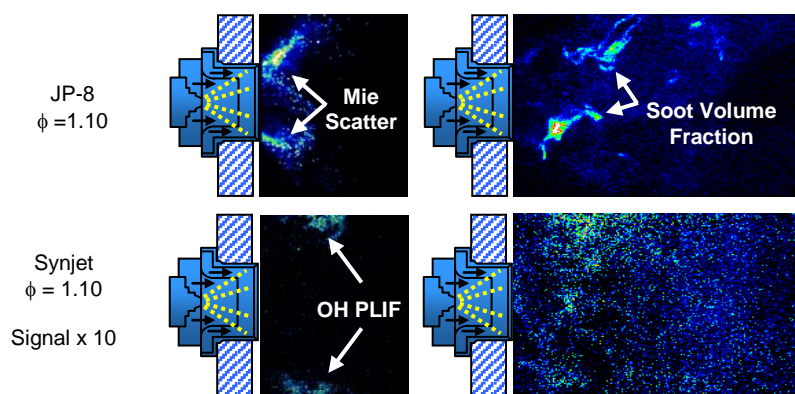


Fig. 3. Images of OH PLIF and Mie scattering (left) and soot volume fraction from LII (right) for JP-8 and synjet fuels at an equivalence ratio of 1.10. The signal levels in the images for the synjet fuel are scaled by a factor of ten (after background subtraction) as compared with that of JP-8.

4. Summary and Future Work

It is evident that these non-intrusive diagnostics provide insight into the two-phase combustion phenomena of swirl-stabilized flames, thus leading to increased understanding of the influence of alternative fuels on PM emissions. Significant reductions (18-99%) in combustor PM emissions were observed with the synjet and synjet/JP-8 blends relative to operation with JP-8. These reductions varied directly with the concentration of synjet in JP-8 and were more pronounced at higher equivalence ratios. Analysis to assess the correlation between the in-situ (laser-based) and extractive (probe) measurements for these blends will be reported in a future publication.

Acknowledgments

The authors thank Vincent Belovich, Edwin Corporan, and Robert Pawlik of the Air Force Research Laboratory, Propulsion Directorate for assistance with the CFM56 combustor rig and jet fuels. Funding for this research was provided by the Air Force Research Laboratory, Propulsion Directorate under contract No. F33615-03-D-2329.

References

1. Meyer, T.R., Roy, S., Gogineni, S.P., Belovich, V.M., Corporan, E., Gord, J.R., "Simultaneous Planar Laser-Induced Incandescence, OH Planar Laser-Induced Fluorescence, and Droplet Mie Scattering in Swirl-Stabilized Spray Flames," *Applied Optics* **44**(3):445-454, 2005.
2. Corporan, E., Belovich, V. M., DeWitt, M.J., Pawlik, R., Lynch, A.C., Gord, J. R., Meyer, T.R. "Impacts of Synthetic Jet Fuel on the Emissions of a Turbine Engine Combustor," 9th International Conference of the International Association for Stability, Handling, and Use of Liquid Fuels, Sitges, Spain, Sept. 18-22, 2005.

Coherent structures and turbulent molecular mixing in gaseous planar shear layers

By T. R. MEYER[†], J. C. DUTTON[‡] AND R. P. LUCHT[§]

Department of Mechanical and Industrial Engineering, University of Illinois
at Urbana-Champaign, Urbana, IL 61801, USA

(Received 29 October 2004 and in revised form 15 December 2005)

Quantitative planar visualization of molecular mixing dynamics in large- and intermediate-scale coherent structures is reported for the first time in the developing and far-field regions of gaseous planar shear layers. A dual-tracer (nitric oxide and acetone) planar laser-induced fluorescence (PLIF) technique is implemented as the gaseous analogue to acid/base chemical reactions that have previously been used to study molecular mixing in liquid shear layers. Data on low-speed, high-speed, and total molecularly mixed fluid fractions are collected for low- to high-speed velocity ratios from 0.25 to 0.44 and Reynolds numbers, Re_δ , from 18 600 to 103 000. Within this range of conditions, mixed-fluid probability density functions and ensemble-averaged statistics are highly influenced by the homogenizing effect of large-scale Kelvin–Helmholtz rollers and the competing action of intermediate-scale secondary instabilities. Small-scale turbulence leads to near-unity mixing efficiencies and mixed-fluid probabilities within the shear layer, with subresolution stirring being detected primarily along the interface with free-stream fluid. Current molecular-mixing data compare favourably with previous time-averaged probe-based measurements while providing new insight on the effects of coherent structures, velocity ratio, downstream distance, and differences between low- and high-speed fluid entrainment.

1. Introduction

Because of their simplicity, planar free shear layers are often used in numerical and experimental studies to represent the mixing process in fundamental flow fields found in many practical engineering applications. One of the most influential discoveries in this field involved the detection of a sudden increase in mixed-fluid quantities caused by the onset of small-scale turbulence within large-scale coherent motions (Konrad 1976). Subsequent experimental and numerical investigations have helped to decipher the complex nonlinear interactions that lead to this transition (Hussain & Zaman 1980; Huang & Ho 1990; Moser & Rogers 1991; Slessor, Bond & Dimotakis 1998; Dimotakis 2000; Meyer, Dutton & Lucht 2001). In the far-field self-similar region downstream of the mixing transition, the cascade to smaller turbulent length scales continues, and the concept of isotropic turbulence studied by Kolmogorov (1941) and Batchelor (1953) becomes relevant. This region is of fundamental interest to the turbulence modelling community and theoreticians because it sheds light

[†] Present address: Innovative Scientific Solutions, Inc., 2766 Indian Ripple Road, Dayton, OH 45440-3638, USA.

[‡] Present address: University of Texas at Arlington, Box 19018, Arlington, TX 76019-0018, USA.

[§] Present address: Purdue University, 585 Purdue Mall, West Lafayette, IN 47907-2088, USA.

on the elusive properties of fully developed turbulence. Studies at high Reynolds number ($Re_\delta > 30\,000$), for example, show evidence of mild to strong mixture-fraction inhomogeneities in the far-field region (Clemens & Mungal 1995; Karasso & Mungal 1996; King, Dutton & Lucht 1999). It is not clear how such mixing states are achieved, however, and the ambiguity is exacerbated by differences in experimental results.

The possible reasons for such disagreement are many, including Schmidt number differences between gases and liquids, planar versus axisymmetric shear-layer configurations, intrusive versus non-intrusive measurement techniques, time-averaged versus instantaneous experimental approaches, and differences in the spatial resolution of the measurements. Because of difficulties in resolving the smallest mixing scales, a number of investigations in gaseous and liquid flows have used chemical reactions to discern the true state of shear-layer molecular mixing. Numerous studies have used so-called acid/base visualizations to obtain comprehensive two-dimensional non-intrusive measurements of molecular mixing in turbulent liquid shear layers (Breidenthal 1981; Koochesfahani & Dimotakis 1986; Broadwell & Mungal 1988; Karasso & Mungal 1996). Owing to large differences in Schmidt number, Sc , results from these studies in liquids are not directly transferable to the case of gaseous shear-layer mixing. Previous studies in the latter regime are fewer in number and have relied on cold-wire measurements of low heat release reactions (Batt 1977; Mungal & Dimotakis 1984; Frieler 1992). The obvious disadvantages of this technique are the reliance on intrusive physical point probes and the inability to provide instantaneous planar images of molecular mixing. Previous investigations using the cold-wire approach have shown both marching (Batt 1977) and tilted (Frieler 1992) probability density functions (p.d.f.s) of mixed-fluid quantities, which indicate that different large and small-scale turbulent mixing dynamics may have been taking place in each of these experiments. An important motivation for the current investigation, therefore, is to provide planar images of molecular mixing and to enable deeper physical insight into the fundamental processes governing these statistics.

King, Lucht & Dutton (1997) developed a simultaneous dual-tracer nitric oxide (NO) and acetone planar laser-induced fluorescence (PLIF) technique that acts as the gaseous analogue of acid/base visualizations. With this technique, acetone PLIF is used as a passive-scalar marker of the mixture fraction within the shear layer, and NO PLIF is used as an optically reactive (i.e. cold-chemistry) marker of unmixed fluid. By subtracting the unmixed-fluid fraction from the passive-scalar (i.e. mixed plus unmixed) fluid fraction during post-processing, we can obtain instantaneous images of molecularly mixed fluid fraction across the entire width of the shear layer. King *et al.* (1999) successfully applied this technique to study near-field molecular mixing of turbulent jets with Reynolds numbers, Re_D , in the range of 1000 to 100 000. They noted two very distinct mixing regimes that were attributed to a mixing transition similar to that described by Konrad (1976). In a follow-up study, Meyer *et al.* (2001) investigated more closely the transitional regime between $Re_D = 16\,000$ and 30 000. They confirmed from mixed-jet-fluid statistics before, during, and after the cascade to small scales that, to first order, the location of this transition from the jet exit is inversely proportional to the initial instability wavelength of the jet shear layer.

The current investigation extends these studies of turbulent gaseous molecular mixing using the NO- and acetone-PLIF technique to planar shear layers. The planar case differs from axisymmetric jets in several respects: (i) planar shear layers have constant free-stream conditions and do not experience the effects of an increasing shear-layer thickness to diameter ratio; (ii) the enclosed planar shear-layer facility allows the seed species to be flipped for measurements of both low- and high-speed

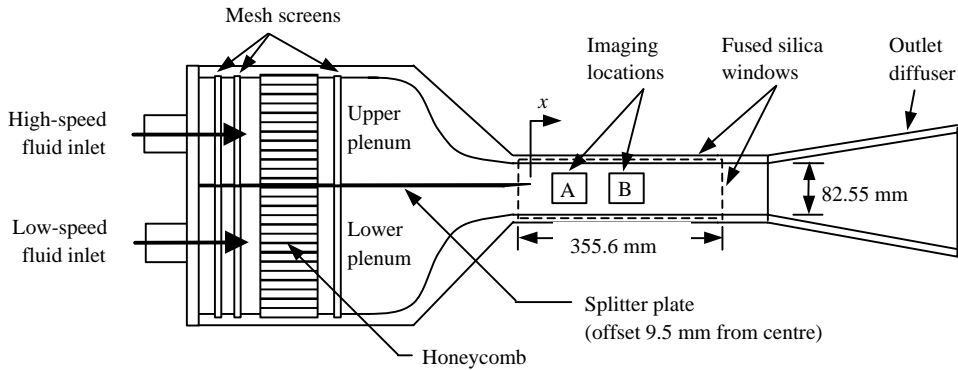


FIGURE 1. Schematic of the planar shear-layer facility. The cross-stream width is 101.6 mm.

fluid molecular mixing; (iii) the effect of velocity ratio can more readily be studied in the planar shear layer facility; and (iv) unlike jet measurements that are constrained to the region before the end of the jet potential core, measurements in planar shear layers can readily be performed in the far-field region.

The goal of this investigation is to provide a better understanding of the fundamental mechanisms that govern turbulent molecular mixing in incompressible gaseous planar shear layers, including the effects of coherent structures, Reynolds number, velocity ratio, initial instability wavelength and downstream distance. This is made possible by the use of simultaneous dual-tracer NO- and acetone-PLIF for the measurement of molecularly mixed fluid quantities along with instantaneous images across the entire width of the mixing layer. With this unique measurement capability, the interplay of large- and small-scale gaseous mixing phenomena can be studied directly, and the uncertainty due to subresolution stirring (pockets of pure fluid within the region imaged by a pixel element) is minimized. As with acid/base visualizations in liquid flows, this technique is also two-dimensional, non-invasive, time-resolved, and can be used to measure instantaneous mixed-fluid fractions in addition to time-averaged statistics.

After descriptions of the flow facility, measurement system, and flow conditions, we present and discuss the first two-dimensional measurements of low-speed, high-speed and total mixed-fluid statistics, time-averaged and instantaneous, in incompressible gaseous planar shear layers. Planar maps of molecular-mixing efficiency are used for the detection of small-scale subresolution stirring. The effect of coherent structures on the state of molecular mixing is further analysed through the use of probability density functions and time-averaged statistics. Comparisons are made with previous results from probe-based measurements of molecular mixing in gaseous planar shear layers, laser-based measurements of molecular mixing in gaseous axisymmetric shear layers, and laser-based measurements of molecular mixing in liquid planar shear layers.

2. Apparatus

2.1. Planar shear layer facility

The planar shear layer facility (figure 1) was initially built for compressible flow studies by Olsen (1999) and was subsequently modified for incompressible flow investigations by Meyer (2001). Compressed air from a PID-pressure-controlled

stagnation chamber passes through two mesh screens and a honeycomb block before entering the upper and lower plenum chambers via 76 mm diameter pipes. The plenum flow is further conditioned by passing through two mesh screens, a honeycomb block and a final mesh screen. The upper (high-speed) nozzle is 177.8 mm in height at the entrance and contracts to a height of 31.75 mm at the exit tip of the splitter plate, for a contraction ratio of 5.6:1. The lower (low-speed) nozzle is 227.1 mm in height at the entrance and contracts to a height of 50.8 mm at the exit tip of the splitter plate, for a contraction ratio of 4.5:1. The splitter plate is offset upward by 9.5 mm from the centre of the test section to compensate for the known deflection of the mixing layer toward the low-speed stream as a result of the continuity requirement. The spanwise dimension of the shear-layer test section is 101.6 mm, and the total height is 82.55 mm. All four walls of the test section have fused-silica windows for optical access in the ultraviolet. The total viewing length is 355.6 mm in the streamwise direction and begins slightly upstream of the splitter-plate tip. The flow exits the test section through a 610 mm long diffuser, enters the main exhaust line, and is vented to the exterior of the building.

The upper and lower plenum chambers are fed with either acetone-seeded air or NO-seeded nitrogen (N_2). The acetone seeding system consists of an atomizing nozzle located in the main air-supply pipe about 2 m upstream of the stagnation chamber to ensure complete vaporization and mixing. For the NO seeding system, nitrogen flow is supplied via an N_2 -cylinder manifold located about 5 m upstream of the 76 mm diameter supply pipe. Gas cylinders filled with 1000 p.p.m. NO-in- N_2 are diluted to 100–250 p.p.m. NO-in- N_2 , mixed in a swirl chamber, and conditioned with two mesh screens and a honeycomb block before entering the 76 mm supply pipe about 1 m upstream of the plenum chamber. The flow rate of the NO-in- N_2 gas was kept constant using a number of dual-stage regulators, as verified using hot-film measurements in the test section. Flip experiments are achieved by switching the seeded inlet flows to the 76 mm diameter pipes that feed the upper and lower plenum chambers.

2.2. NO/acetone PLIF measurement system

In a conventional passive-scalar (e.g. acetone) PLIF technique (Lozano, Yip & Hanson 1992), the detected LIF signal is linearly proportional to the tracer concentration, but the extent of molecular mixing is unknown since the smallest scales imaged are typically larger than the smallest diffusion scales. High-resolution measurements have been performed, but it is difficult to visualize molecular mixing at both the small and large scales simultaneously with this method (Dahm, Southerland & Buch 1991; Buch & Dahm 1996, 1998). In contrast to passive-scalar PLIF, cold-chemistry PLIF using NO seeding provides a measure of the extent of molecular unmixedness because its signal is highly quenched when it is molecularly mixed with oxygen (Paul & Clemens 1993). A 'flip' experiment can then be performed to obtain time-averaged total mixed-fluid-fraction statistics.

By using acetone PLIF as a passive-scalar measure of the fluid fraction from each fluid stream, and by using NO PLIF simultaneously as a measure of the unmixed fluid fraction from one fluid stream, instantaneous PLIF images of molecular mixing for the NO-seeded fluid can be obtained without resorting to a high-resolution imaging system (King *et al.* 1997). By performing the flip experiment, it is then possible to obtain instantaneous images of molecular mixing for both fluid streams. As this approach was initially being demonstrated, Island, Urban & Mungal (1996) proposed virtually the same idea but on a time-averaged basis. A similar approach that employs near-simultaneous passive-scalar acetone PLIF and cold-chemistry acetone

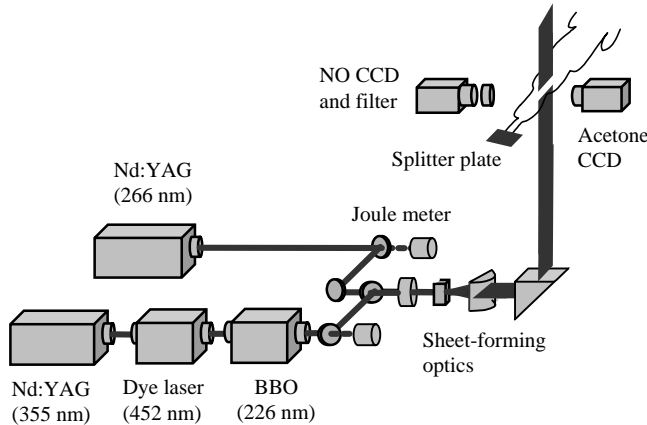


FIGURE 2. NO- and acetone-PLIF lasers and optics. BBO, beta barium borate crystal.

phosphorescence (Hu & Koochesfahani 2002) may also be considered as a gaseous analogue to acid/base reactions in that it can distinguish between fluid from each of the free streams. It is more easily implemented than the dual-tracer PLIF technique, but like other methods based on phosphorescence (Yip, Lozano & Hanson 1994), its limited temporal resolution can be a disadvantage for high-speed flows. The dual-tracer PLIF technique used here is to be distinguished from other multiple passive-scalar approaches (e.g. Seitzman *et al.* 1994) that fundamentally are neither intended for, nor are capable of, measuring the extent of molecular mixing. The theory and experimental set-up of the dual-tracer PLIF technique is fully described in the literature (King *et al.* 1997, 1999; Meyer *et al.* 1999, 2002); a brief summary is included below for reference.

As stated earlier, the shear flow consists of acetone-seeded air in one stream and NO-seeded N_2 in the other stream. Air is a convenient carrier for acetone because it quenches unwanted long-time-scale acetone phosphorescence and quenches NO PLIF upon molecular mixing within the shear layer. Nitrogen is a convenient carrier for NO because of its relatively small quenching cross-section. The technique requires coincident laser sheets at 226 nm and 266 nm for NO and acetone PLIF, respectively (figure 2). The NO PLIF signal from 226–300 nm is collected at 90° using a multi-element UV lens on an unintensified 512×512 CCD camera. The broadband acetone PLIF signal, centred at 450 nm, is collected simultaneously with the NO PLIF using a glass lens on a second CCD camera. For the current experiments, each camera images a $60 \text{ mm} \times 60 \text{ mm}$ physical region, which results in a probe area of $117 \mu\text{m} \times 117 \mu\text{m}$ per pixel. The probe depth is fixed by the NO and acetone laser-sheet thicknesses of $245 \pm 10 \mu\text{m}$, as measured by traversing a knife edge across the focal point. These values are well matched because differences in wavelength ($\sim 15\%$) and beam quality are offset by differences in beam diameter ($\sim 14\%$). Correspondingly, the focal depths differ by $\sim 3\%$.

Once acquired, the NO images are remapped to the same scale and orientation as the acetone images. This is accomplished to within pixel resolution using conformal mapping coefficients derived from a least squares fit to ~ 20 common points from images of aerosol scattering. After background subtraction to eliminate repeatable laser scatter, the NO and acetone PLIF signals from the mixing layer are normalized by reference signals from pure fluid regions. The latter normalization

is performed column-by-column and eliminates errors from shot-to-shot laser-sheet intensity variations as well as differences in camera sensitivity. As described above, the normalized and corrected acetone and NO PLIF signals represent the fraction of acetone-seeded fluid, f_{Ac} , and unmixed NO-seeded fluid, f_{uNO} , respectively. The mixed NO-seeded fluid fraction is then found from $f_{mNO} = f_{NO} - f_{uNO} = 1 - f_{Ac} - f_{uNO}$. By definition, the NO-seeded fluid molecular-mixing efficiency is the ratio of the molecularly mixed NO-seeded fluid to total NO-seeded fluid, or $\eta_{mNO} = f_{mNO}/f_{NO}$. Because NO is not fully quenched in the presence of small amounts of acetone and air, the final image-processing step is to perform a finite-quenching-rate correction for f_{uNO} based on an experimentally verified five-level model of NO fluorescence and the measured fluid fraction of acetone-seeded air (Meyer *et al.* 2002). At an acetone-seeded air fluid fraction of 5 %, for example, the current dual-tracer PLIF approach predicts that about 10 % of the NO signal remains unquenched. Accurate knowledge of the air fluid fraction and finite-quenching-rate effects, therefore, is one of the advantages of the current approach over previous measurements based on NO seeding alone (Clemens & Paul 1995; Island *et al.* 1996).

The signal-to-noise ratio (SNR) is typically 75:1 and 50:1 for the normalized acetone- and NO-PLIF images, respectively, in the corresponding free-stream regions. To estimate the uncertainty in f_{mNO} and η_{mNO} , one must account for both random errors associated with the SNR and bias errors due to image-matching (≤ 0.025), finite spatial resolution (≤ 0.01), sheet width (≤ 0.032), and differential diffusion of acetone and air in nitrogen (≤ 0.01). These errors are estimated based on the sensitivity in regions with high spatial gradients, and the error from differential diffusion is estimated from a direct numerical simulation of a jet mixing layer (Meyer *et al.* 2002). The final fractional uncertainties in f_{mNO} and η_{mNO} are highly dependent upon the local mixture fraction and can range from $\sim 6\%$ near the NO-seeded free stream to $\sim 19\%$ near the acetone-seeded freestream.

3. Flow conditions

Three velocity ratios (labelled 1, 2 and 3) and two downstream locations (labelled A and B) are studied in the current investigation, as shown in table 1. The high-speed fluid velocity is varied from about 30 to 50 ms^{-1} , while the low-speed fluid velocity is held nearly constant at about 13 to 14 ms^{-1} . Thus, flow conditions 1, 2 and 3 correspond to low- to high-speed velocity ratios, $r = U_{LS}/U_{HS}$, of 0.44, 0.34 and 0.25, respectively. Locations A and B at 80 mm and 178 mm downstream of the splitter-plate tip were selected to allow measurements early and late in shear-layer development while avoiding interaction with the channel walls. Dual-tracer PLIF images for flow conditions 1 and 3 were collected at both locations A and B, while data for flow condition 2 were collected at location B only. Based on these flow conditions and measurement locations, five pairing parameter values ranging from $Rx/\lambda = 6.6$ to 28.1 were investigated, as given in table 1. The pairing parameter is a non-dimensional downstream coordinate that accounts for the effects of velocity ratio and initial instability wavelength on the transition to small-scale turbulence (Karasso & Mungal 1996). The Reynolds number, which accounts for the effects of free-stream velocity difference and local shear-layer thickness, varies from $Re_\delta = 18\,600$ to 103 000, as given in table 1.

Characteristics of the boundary layers near the splitter-plate tip for both the low- and high-speed streams, as well as the downstream shear-layer velocity profiles, were measured using hot-film anemometry (Meyer 2001). The free-stream velocities

Parameter	Case		
	1 (Location A, B)	2 (Location B)	3 (Location A, B)
High-speed (HS) velocity, U_{HS} (m s ⁻¹)	29.5	42.0	50.5
Low-speed (LS) velocity, U_{LS} (m s ⁻¹)	12.8	14.1	12.8
Velocity ratio, $r = U_{LS}/U_{HS}$	0.44	0.34	0.25
Flip experiment performed	No, Yes	Yes	No, Yes
Velocity parameter, $R = (1 - r)/(1 + r)$	0.39	0.49	0.60
Initial instability wavelength, λ (mm)	4.7	4.1	3.8
Distance from splitter-plate tip, x (mm)	80, 178	178	80, 178
Pairing parameter, Rx/λ	6.6, 14.8	21.3	12.6, 28.1
2 % – 98 % mixing layer width, δ (mm)	16.7, 30.8	35.6	16.7, 41.4
Reynolds number, $Re_\delta = (U_{HS} - U_{LS})\delta/\nu$	18 600, 34 300	65 400	41 500, 103 000
Initial HS boundary-layer thickness, δ_{iHS} (mm)	1.4	1.2	1.1
Initial LS boundary-layer thickness, δ_{iLS} (mm)	2.6	2.6	2.6
Initial HS momentum thickness, θ_{iHS} (mm)	0.179	0.155	0.140
Initial LS momentum thickness, θ_{iLS} (mm)	0.32	0.32	0.32
Initial HS shape factor, $H_{iHS} = \delta_{iHS}^*/\theta_{iHS}^\dagger$	2.33	2.49	2.56
Initial LS shape factor, $H_{iLS} = \delta_{iLS}^*/\theta_{iLS}^\dagger$	2.58	2.58	2.58
Strouhal number, $St_\theta = \theta_{iHS}/\lambda$	0.038	0.038	0.038
Initial turbulence intensity, u'_i/U (%)	0.5–1.0	0.5–1.0	0.5–1.0
Pixel measurement area, L_{pix} (μm^2)	117×117	117×117	117×117
Laser sheet thickness, L_{las} (μm)	245 ± 10	245 ± 10	245 ± 10
Smallest diffusion length scale, L_D (μm)‡	140, 164	117	77, 96

$\dagger \delta_i^*$ is the initial boundary-layer displacement thickness.

$\ddagger L_D = 11.2\delta Re_\delta^{-3/4} Sc^{-1/2}$ (from Buch & Dahm 1998).

TABLE 1. Flow conditions.

remained uniform across the test section to within about 1 %. The shape factor of the low-speed boundary layer, $H = 2.58$, matches that of a laminar (i.e. Blasius) profile. The shape factor for the high-speed boundary layer deviates by as much as 10 % from a Blasius profile for flow condition 1, but is quite close to the Blasius profile for flow conditions 2 and 3. Table 1 gives these and other relevant boundary-layer and shear-layer parameters for comparison with other experimental investigations.

The initial instability wavelength, λ , varies with the high-speed fluid velocity, and is estimated from acetone PLIF visualizations of the initial vortex spacing, λ_{vis} , near the splitter-plate tip. Although it is difficult to obtain a ‘true’ measurement of λ for comparison with flow conditions from other facilities, a good estimate of λ was obtained by measuring the high-speed boundary layer momentum thickness, θ_{iHS} , near the splitter-plate tip. The results for flow conditions 1 to 3 are plotted in figure 3 and reliably fit the relation $\lambda_{vis} \approx 26\theta_{iHS}$. Many of the results in this work are compared with the acid/base liquid mixing-layer visualizations and measurements of Karasso & Mungal (1996), who used $\lambda_{vis} \approx 30\theta_{iHS}$. Mehta *et al.* (1987) used $\lambda_{vis} \approx 25\theta_{iHS}$ in a gaseous mixing layer, while a variety of other investigators have used other values near or within this range (Gutmark & Ho 1983). The expected linear dependence of λ on $U_{HS}^{-1/2}$ for laminar boundary layers is also shown in figure 3. Thus, the values of λ shown in table 1 should not only provide an appropriate instability length scale for the current investigation, but should also provide an approximate scaling for comparison with results from other facilities.

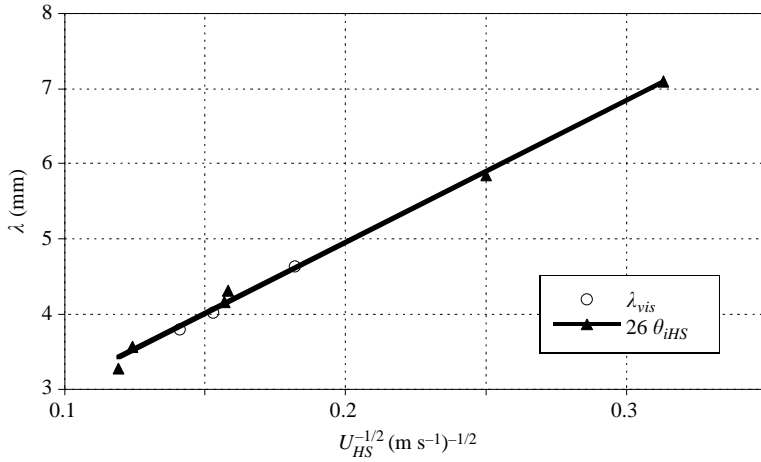


FIGURE 3. Variation of the initial instability wavelength, λ , with $U_{HS}^{-1/2}$. Initial vortex spacing, λ_{vis} , is compared with the relation $\lambda = 26\theta_{iHS}$.

The range of flow conditions given in table 1 was selected to allow measurements in the developing and fully developed turbulent regimes, the latter of which has been shown in past studies in gaseous and liquid mixing layers to require a minimum $Re_\delta \approx 10000$ (Slessor *et al.* 1998). All the flow conditions examined in this study are above this value. Other investigators have found, however, that hydrodynamic quantities become fully-developed at $Rx/\lambda \approx 8$ to 16 (Huang & Ho 1990; Karasso & Mungal 1996), while scalar quantities become fully developed by $Rx/\lambda \approx 22$ (Karasso & Mungal 1996). Thus, for Case 1A ($Rx/\lambda \approx 6.6$), fully developed hydrodynamic conditions may not be attained even though $Re_\delta > 10000$. Furthermore, Case 2B ($Rx/\lambda \approx 21.3$) is at the threshold for being fully developed in terms of scalar quantities, while only Case 3B ($Rx/\lambda \approx 28.1$) is beyond both the Re_δ and Rx/λ criteria for fully developed hydrodynamic and scalar quantities.

Another condition for self-similarity, proposed by Bradshaw (1966), states that the downstream distance from the splitter-plate tip must be greater than $1000\theta_{iHS}$. Subsequent studies have proposed criteria for self-similarity as high as $2000\theta_{iHS}$ or more (Dziomba & Fiedler 1985), although Bradshaw's original hypothesis has been found to hold true for laminar (Blasius-type) initial conditions. Thus, for the laminar conditions documented in the current study, Case 2B ($x \approx 1000\theta_{iHS}$) is again at the threshold for being fully developed, based on this criterion, while Case 3B ($x \approx 1300\theta_{iHS}$) is beyond this threshold. In fact, Bradshaw's criterion and that of the pairing parameter are identical insofar as the initial instability wavelength is directly proportional to θ_{iHS} , as shown in figure 3.

Another factor that has been shown to affect the development of mixing layers is the finite thickness of the splitter-plate tip. This thickness is more important for higher velocity ratios ($r > 0.6$), for which the splitter-plate wake has been found to have a lasting effect on the three-dimensional structure of the mixing layer (Wiecek & Mehta 1998). At $r = 0.44$, which is equivalent to the highest velocity ratio for the current study, Dziomba & Fiedler (1985) found that the trailing-edge thickness can affect shear-layer development if it exceeds 50 % of the total (low- and high-speed) boundary-layer displacement thickness. The splitter-plate thickness (0.35 mm) is less than 30 % of the total boundary-layer displacement thickness for all of the flow conditions in the current study and thus should not play a significant role in the far-field mixing dynamics.

Of final concern for the initial conditions is the initial free-stream turbulence intensity level, u'_i/U , which is shown in table 1 to vary between 0.5 and 1 %. Mehta (1991) has suggested that $u'_i/U < 0.2\%$ is required for the mixing-layer development to be independent of the velocity ratio. At the lower velocity ratios in the current study ($r < 0.5$), the local turbulence intensity in the mixing layer is much greater than the free-stream turbulence level and is more likely to develop independently of u'_i/U . Nonetheless, it is difficult to determine an exact threshold velocity ratio for which the effects of free-stream turbulence become significant, and this factor must be kept in mind when comparing the data at various velocity ratios from this and other investigations.

4. Instantaneous images

Representative instantaneous images from the dual-tracer PLIF technique for all of the conditions given in table 1 are shown in figures 4–7, with sample line plots in figure 8. The fractions of low- and high-speed fluid are represented by f_{LS} and f_{HS} , respectively, and sum to unity for the current binary fluid system. When acetone is seeded into the high-speed stream, f_{HS} is found directly from the normalized and corrected acetone-PLIF image and $f_{LS} = 1 - f_{HS}$. In this case, NO is seeded into the low-speed stream so that the fraction of unmixed low-speed fluid, f_{uLS} , is found from the normalized and corrected NO-PLIF image. From these two images, it is then possible to compute the fraction of molecularly mixed low-speed fluid from $f_{mLS} = f_{LS} - f_{uLS}$, as well as the low-speed fluid molecular-mixing efficiency, $\eta_{mLS} = f_{mLS}/f_{LS}$, which is also plotted in figures 4 to 8. By definition, η_{mLS} is unity when all of the NO-seeded fluid in a measurement volume is mixed at the molecular level (i.e. $f_{mLS} = f_{LS}$); non-unity values of η_{mLS} imply the existence of pure-fluid subresolution stirring. The flip experiment is accomplished simply by seeding acetone and NO in the opposite streams so that the PLIF images can be used to obtain f_{mHS} and η_{mHS} .

4.1. Primary and secondary entrainment

One of the more striking features in the passive-scalar images of Pickett & Ghandhi (2002) in moderate-speed gaseous planar shear layers is the existence of both primary and secondary structures associated with the original Kelvin–Helmholtz instability and localized shear layers, respectively. A similar observation can be made regarding the higher Re_δ conditions of the current study, as shown in figures 4 to 7. Superimposed on the large-scale roll-up of figure 5(a) are intermediate-scale structures with sizes of $\sim 0.1\delta$, some of which are identifiable as vortex roll-ups, but most of which are of random shape and orientation. These intermediate-scale structures, which may have their origin in the collapse of streamwise vortices (Moser & Rogers 1991), enhance mixing along the outer region of the shear layer such that large-scale roll-ups entrain mixed rather than unmixed fluid. This is illustrated further in figures 6(b) and 7(b), which show low-speed fluid being entrained intermittently. The result is a convoluted internal mixing layer with fluid structures that originate from the edge of the shear layer and that continue the transition to small-scale mixing through further interaction. The line plots of figure 8 are representative of this convoluted internal structure, with low-speed fluid being preferentially entrained on the low-speed side and high-speed fluid being preferentially entrained on the high-speed side. At various instances, the shear layer intermittently displays a predominant large-scale structure, as in figure 6(b), or a lack of large-scale organization, as in figure 6(a). In the absence of a large-scale Kelvin–Helmholtz roll-up, intermediate-scale structures enhance the

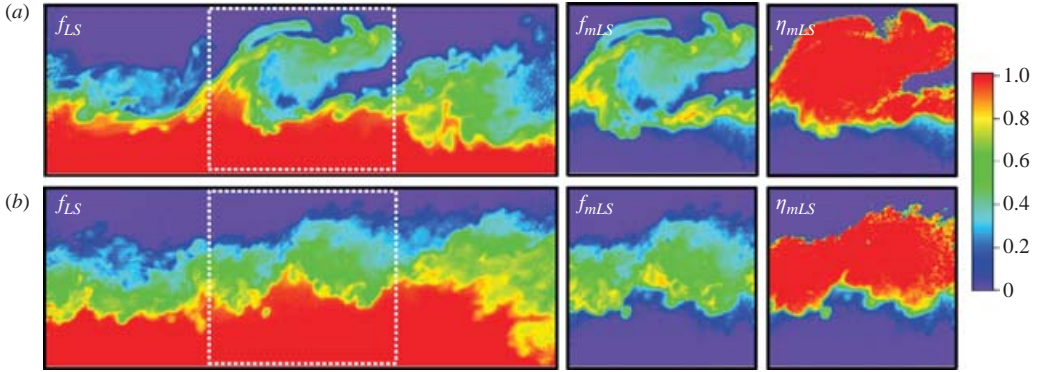


FIGURE 4. Instantaneous images of total low-speed fluid fraction, f_{LS} , mixed low-speed fluid fraction, f_{mLS} , and low-speed fluid molecular-mixing efficiency, η_{mLS} , for (a) Case 1A ($Re_\delta = 18\,600$, $Rx/\lambda = 6.6$) and (b) Case 3A ($Re_\delta = 41\,500$, $Rx/\lambda = 12.6$). Streamwise extent is $x = 50$ – 110 mm and cross-stream extent is $y/\delta = \pm 0.5$.

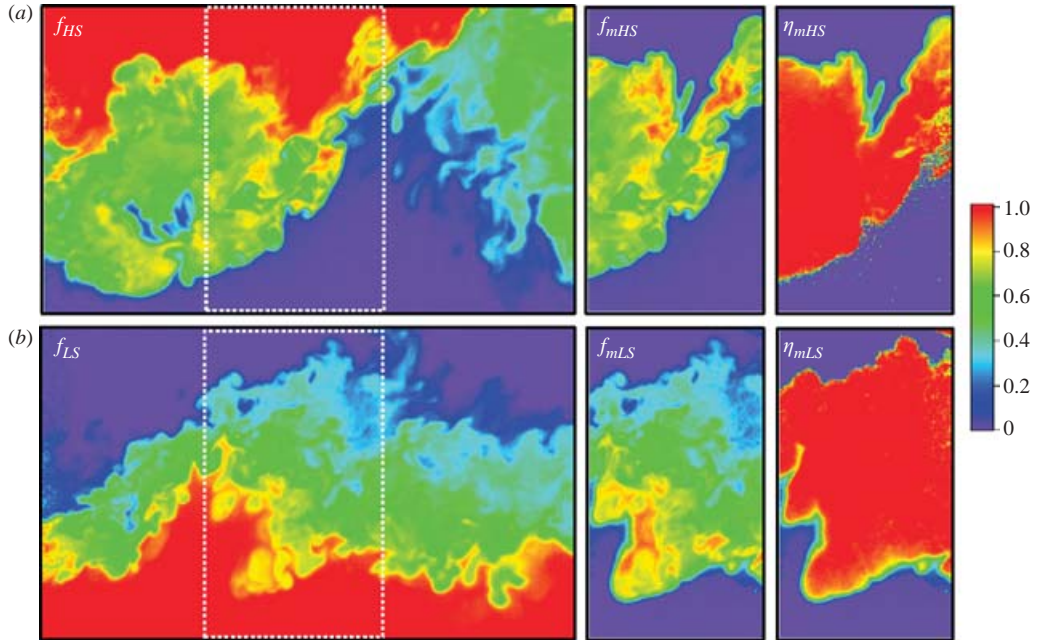


FIGURE 5. Instantaneous time-uncorrelated images of the flip experiment for Case 1B ($Re_\delta = 34\,300$, $Rx/\lambda = 14.8$) with NO seeded into (a) the high-speed stream and (b) the low-speed stream. Streamwise extent is $x = 148$ – 208 mm, and cross-stream extent is $y/\delta = \pm 0.5$.

entrainment of free-stream fluid into the outer regions of the shear layer and imply the existence of non-stationary mixed-fluid p.d.f.s.

These observations differ from the classical descriptions of Broadwell & Breidenthal (1982) and Masutani & Bowman (1986), whose data suggest that fluid in the mixing layer is composed of either pure fluid, homogeneously mixed fluid, or interfacial

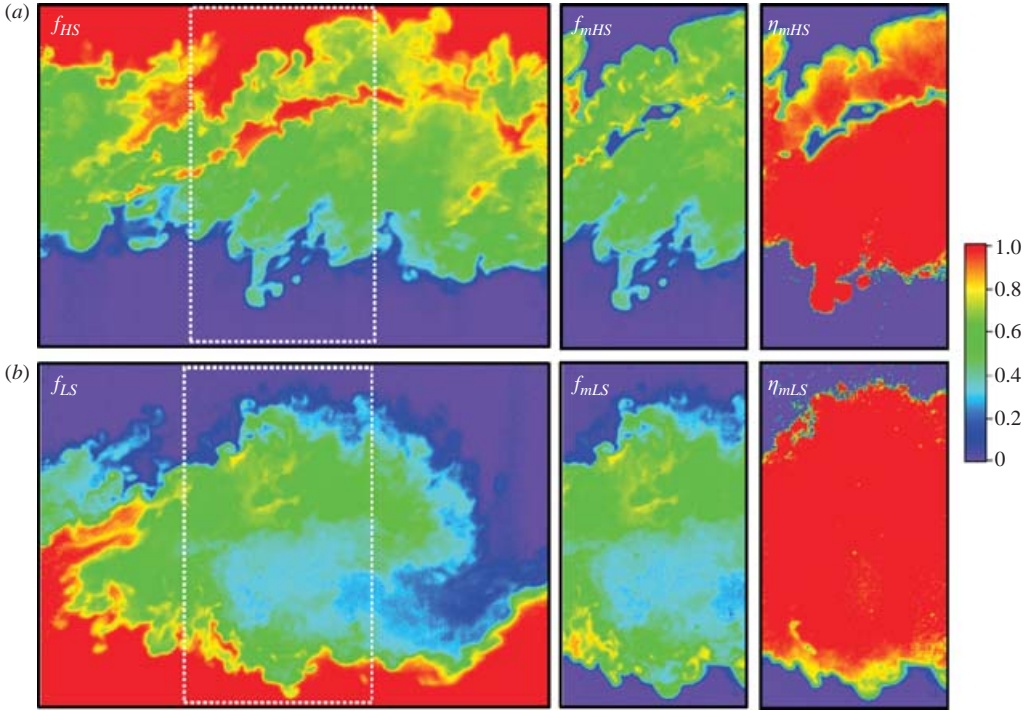


FIGURE 6. Instantaneous time-uncorrelated images of the flip experiment for Case 2B ($Re_\delta = 65\,400$, $Rx/\lambda = 21.3$) with NO seeded into (a) the high-speed stream and (b) the low-speed stream. Streamwise extent is $x = 148\text{--}208\text{ mm}$ and cross-stream extent is $y/\delta = \pm 0.5$.

diffusion layers between the pure and mixed fluids. The images shown in figures 4 to 7 indicate that the interfacial diffusion layers may be dominated by intermediate-scale secondary instabilities. The existence of intermediate-scale vortices leads to regions of inhomogeneously mixed fluid of widely varying concentration, as is shown in figure 8. A similar observation regarding the effects of primary and secondary structures was made by Meyer *et al.* (2001), who reported the frequent occurrence of two predominant mixed-fluid concentrations across axisymmetric gaseous mixing layers. In the current planar shear-layer data, instantaneous images show a wider variation in mixed-fluid concentrations associated with secondary instabilities as compared with the axisymmetric shear-layer results of Meyer *et al.* (2001). The size and frequency of primary and secondary structures have implications for the statistical character of the planar mixing layer, as discussed further in terms of probability density functions and ensemble-averaged statistics in § 5 and § 6, respectively.

4.2. Mixing efficiency and subresolution stirring

The dynamics of primary and secondary instabilities have important implications for the existence of subresolution stirring as large- and intermediate-scale structures entrain pure fluid at varying depths within the shear layer. Figure 4 shows typical instantaneous images of the low-speed fluid fraction, f_{LS} , mixed low-speed fluid fraction, f_{mLS} , and low-speed fluid molecular-mixing efficiency, η_{mLS} , for location A ($x = 80\text{ mm}$). The fluid fractions and molecular-mixing efficiency for the high-speed

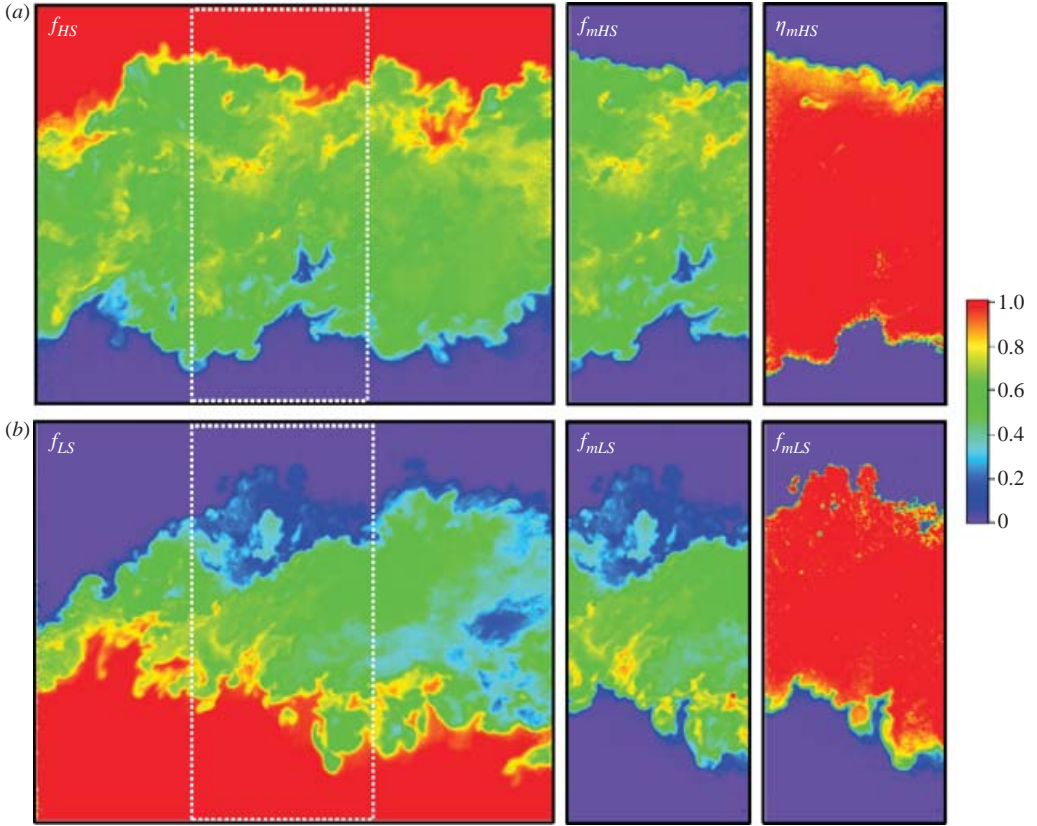


FIGURE 7. Instantaneous time-uncorrelated images of the flip experiment for Case 3B ($Re_\delta = 103\,000$, $Rx/\lambda = 28.1$) with NO seeded into (a) the high-speed stream and (b) the low-speed stream. Streamwise extent is $x = 148\text{--}208$ mm and cross-stream extent is $y/\delta = \pm 0.5$.

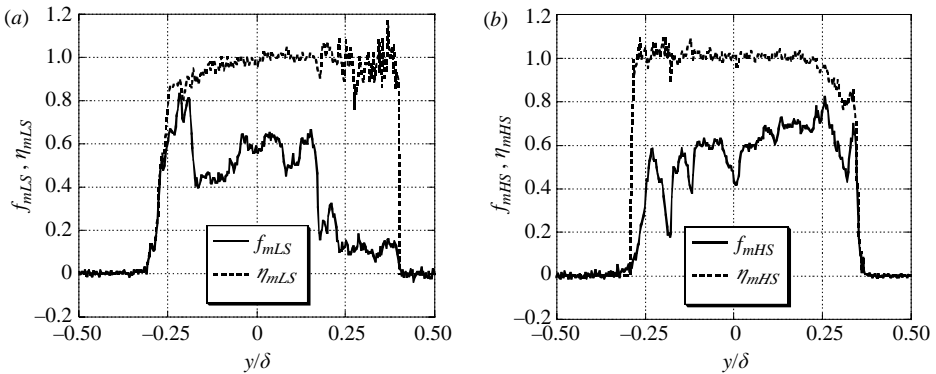


FIGURE 8. Sample cross-stream profiles of (a) f_{mLS} and η_{mLS} and (b) f_{mHS} and η_{mHS} for Case 3B ($Re_\delta = 103\,000$, $Rx/\lambda = 28.1$) collected at the central x location of figure 7. Negative y/δ toward the low-speed stream.

fluid are not presented because flip experiments were not performed for these conditions (see table 1). Note the increase in small-scale turbulence from Case 1A in figure 4(a) to Case 3A in figure 4(b). This increase corresponds to a change in pairing parameter from $Rx/\lambda = 6.6$ to 12.6 and a change in Reynolds number

from $Re_\delta = 18\,600$ to $41\,500$. Indeed, the smallest diffusion length scale is expected to decrease from $140\,\mu\text{m}$ to $77\,\mu\text{m}$ under these conditions, as shown in table 1. The limiting resolution of $245\,\mu\text{m}$, as defined by the laser sheet thickness, cannot fully resolve these scales. Nonetheless, images of f_{LS} (obtained from acetone PLIF) and f_{mLS} (obtained from NO and acetone PLIF) are nearly identical within the mixing layer. As a result, maps of low-speed-fluid molecular-mixing efficiency, $\eta_{mLS} = f_{mLS}/f_{LS}$, are nearly unity throughout most of the internal regions of the shear layer for Cases 1A and 3A. It is possible to conclude, therefore, that subresolution stirring of molecularly unmixed low-speed fluid is found primarily along the outer edges along the interface between the mixing layer and the low-speed (NO-seeded) fluid stream. This interface is also the region with the least uncertainty in both f_{mLS} and η_{mLS} ($\sim 6\%$). Subresolution stirring of low-speed fluid is not detected near the high-speed (acetone-seeded) fluid stream, presumably because all of the low-speed fluid in this region is molecularly mixed.

Instantaneous images with the same seeding configuration as for figure 4, as well as with the acetone- and NO-seeded flows flipped, are available at location B, which is 100 mm downstream of location A. This ‘flip’ experiment provides images of molecularly mixed high- and low-speed fluid, as well as time-averaged statistics of the total amount of molecularly mixed fluid. These images and associated statistics are the first to be obtained in a planar or axisymmetric gaseous shear layer and are used to resolve previous ambiguities regarding the relative molecular mixing behaviour of the high- and low-speed fluids. Figure 5 shows sample instantaneous time-uncorrelated flip images for Case 1B ($Re_\delta = 34\,300$, $Rx/\lambda = 14.8$). As shown in table 1, the shear-layer width has grown by nearly a factor of two from Case 1A in figure 4(a) to Case 1B in figure 5(b). Correspondingly, the fluid structures within the mixing layer and at the mixing-layer-to-free stream interfaces have also increased in size. This leads to an increase in diffusion length scale from Case 1A to 1B as given in table 1. Although the images are still underresolved, near-unity maps of low- and high-speed fluid molecular-mixing efficiency again indicate that subresolution stirring of pure fluid is confined to the outer regions of the mixing layer adjacent to the NO-seeded free stream.

The shear-layer width grows for Cases 2B ($Re_\delta = 65\,400$, $Rx/\lambda = 21.3$) and 3B ($Re_\delta = 103\,000$, $Rx/\lambda = 28.1$), as shown in figures 6 and 7, respectively. According to table 1, the smallest diffusion length scale should decrease by $\sim 30\%$ from Case 1B to 2B and by $\sim 40\%$ from Case 1B to 3B because of increasing Re_δ . Despite the presence of smaller diffusion length scales, no increase in subresolution stirring of pure low- or high-speed fluid is detected in the internal regions of the mixing layer. This is verified in the line plots of figure 8, in which only the outer low- and high-speed regions have sub-unity values of η_{mLS} and η_{mHS} , respectively. As will be discussed further in §6, this implies that the total mixed-fluid probability should be near unity for the internal regions of turbulent gaseous planar shear layers.

In previous studies of gaseous axisymmetric shear layers, King *et al.* (1999) and Meyer *et al.* (2001) also found near-unity mixing efficiency of high-speed fluid using the dual-tracer PLIF technique. Data collected with NO seeded into the high-speed jet showed unity values of η_{mHS} throughout most of the mixing layer, including the vortex roll-up, pairing, breakup, transitional and turbulent regions. As is the case in the current study, sub-unity values of η_{mHS} were detected primarily in a thin region along the interface between the mixing layer and the high-speed (NO-seeded) fluid stream. As stated in §1, the flip experiment was not performed by King *et al.* (1999) or Meyer *et al.* (2001), and so it is not possible to compare the low-speed fluid

molecular-mixing efficiency results for the planar and axisymmetric cases. Based on the data presented in figures 5 to 7, however, it is likely that near-unity low-speed mixing efficiencies are also typical throughout the internal regions of fully developed turbulent gaseous axisymmetric shear layers.

5. Probability density functions

Probability density functions of various fluid quantities are useful for detecting statistically relevant trends in the mixing process. Such trends can then be related to the instantaneous images of molecularly mixed fluid fraction and molecular-mixing efficiency discussed in §4. The probability density function of molecularly mixed NO-seeded fluid, f_{mNO} , is normalized to unity,

$$\int_0^1 P(f_{mNO}, x, y) df_{mNO} = 1, \quad (1)$$

where x and y for a digital image denote a pixel location in the mixing layer. When NO is seeded into the low- or high-speed stream, f_{mNO} is represented by f_{mLS} or f_{mHS} , respectively. Unlike ensemble-averaged quantities, which can mask large-scale structure intermittency, p.d.f. shapes show the likelihood of finding pure fluid (tagged as 0 or 1), indicate the range of f_{mNO} values found at a particular location (by a narrow or broad shape), and show the most likely or preferred f_{mNO} value at a particular location (from the peak in the profile). By analysing the changes in p.d.f. shape across a mixing layer, therefore, one can detect changes in the character of the intermittent mixing process and compare observations with other investigations. Differences in the processes of entrainment and mixing between the low- and high-speed fluids can also be obtained for the current experiments by flipping the NO-seeded fluid between the low- and high-speed streams.

Probability density functions for each condition given in table 1 were calculated from ensembles of about 100 images, concentration bin widths of 2.5 %, and spatial bin sizes of 350 μm (3 pixels) in the x and y directions. The concentration and spatial bin sizes are of the same order as the limiting SNR and imaging resolution, respectively, and allow for reasonably smooth p.d.f.s. All p.d.f.s presented herein were obtained at the centre- x location of the images. Each plot contains multiple p.d.f.s ranging from $y/\delta = \pm 0.5$ in the cross-stream direction (with negative values of y/δ toward the low-speed stream).

5.1. Effect of velocity ratio and downstream distance

Figure 9(a) shows p.d.f.s of the low-speed mixed-fluid fraction, $P(f_{mLS})$, for Case 1A ($r = 0.44$); the lower velocity-ratio condition of Case 3A ($r = 0.25$) is shown for comparison in figure 9(b). The decrease in velocity ratio means that the shear layer is more fully developed for Case 3A, with Re_δ increasing from 18 600 to 41 500 and the pairing parameter increasing from 6.6 to 12.6. The following is a detailed description of how p.d.f. trends in the cross-stream direction relate to shear-layer mixing dynamics and how these trends change with velocity ratio from Case 1A to 3A. On the high-speed side of figure 9(a) from $y/\delta = 0.1$ to 0.5, peaks in $P(f_{mLS})$ are found at f_{mLS} values of either 0 % or 35 %. These values represent times when the measurement volume is either within pure high-speed fluid entrainment regions, indicating the presence of large Kelvin–Helmholtz vortices, or within mixed-fluid structures, respectively. The peak near 35 % remains stationary as y/δ decreases, but at the centre of the mixing layer (near $y/\delta = 0$) the p.d.f. shape broadens and the

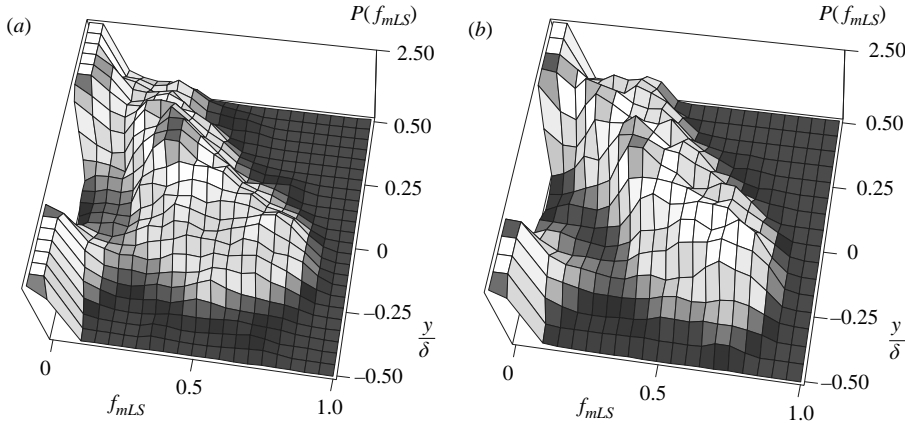


FIGURE 9. Cross-stream p.d.f.s of f_{mLS} for (a) Case 1A ($Re_\delta = 18\,600$, $R_x/\lambda = 6.6$) and (b) Case 3A ($Re_\delta = 41\,500$, $R_x/\lambda = 12.6$).

peak f_{mLS} shifts to about 40 %. The slight shift from 35 % to 40 % represents tilted p.d.f. behaviour, signifying a non-uniform mixed-fluid composition across the shear layer. Few, if any, f_{mLS} values of 0 % occur in this central region, which is indicative of reduced pure-fluid intermittency. On the low-speed side (toward $y/\delta = -0.5$), the peak at 40 % diminishes and a second peak appears at an f_{mLS} of 70 %, signifying increased entrainment of low-speed fluid within the shear layer. As discussed in §4.2, such preferential entrainment of low-speed fluid toward the low-speed free stream is indicative of intermediate- or small-scale mixing along the outer region of the mixing layer. The existence of intermediate scale-mixing in this region is apparent in the planar maps of figures 4 to 7, while the existence of small-scale mixing is confirmed by the presence of sub-unity molecular mixing efficiencies reported earlier in §4.2. The dual peaks at f_{mLS} of 40 % and 70 % toward the low-speed edge of the mixing layer represent the respective competition between large-scale Kelvin–Helmholtz vortices and intermediate- or small-scale structures induced by local turbulence.

For the lower velocity ratio of Case 3A in figure 9(b), the p.d.f.s of f_{mLS} take on a marching character from a peak at nearly 0 % on the high-speed side to 70 % on the low-speed side. This marching character results from a breakdown of large-scale Kelvin–Helmholtz vortices and the increased dominance of secondary entrainment, as shown in figure 4(b) and discussed in §4.2. Similar observations about the breakdown of large roller structures and the emergence of marching p.d.f.s are reported in the direct numerical simulation data of Rogers & Moser (1994).

The effect of velocity ratio can also be shown further downstream at location B, where flip experiments were performed for Cases 1B ($r = 0.44$) and 3B ($r = 0.25$); mixed-fluid p.d.f.s for these conditions are shown in figures 10(a) and 10(b), respectively. The effect of velocity ratio on the low-speed fluid p.d.f.s is very similar to that observed for Cases 1A and 3A, as described above in detail. The high-speed fluid p.d.f.s evolve from a stationary to a hybrid character in which the peak $P(f_{mHS})$ begins to march to lower values of f_{mHS} toward the low-speed stream. This marching behaviour signifies a slight decrease in the influence of large-scale structures and an increase in the influence of secondary entrainment for more fully developed turbulent conditions. The p.d.f.s for Case 3B are also narrower than for Case 1B, signifying reduced intermittency associated with a breakdown of large-scale vortices.

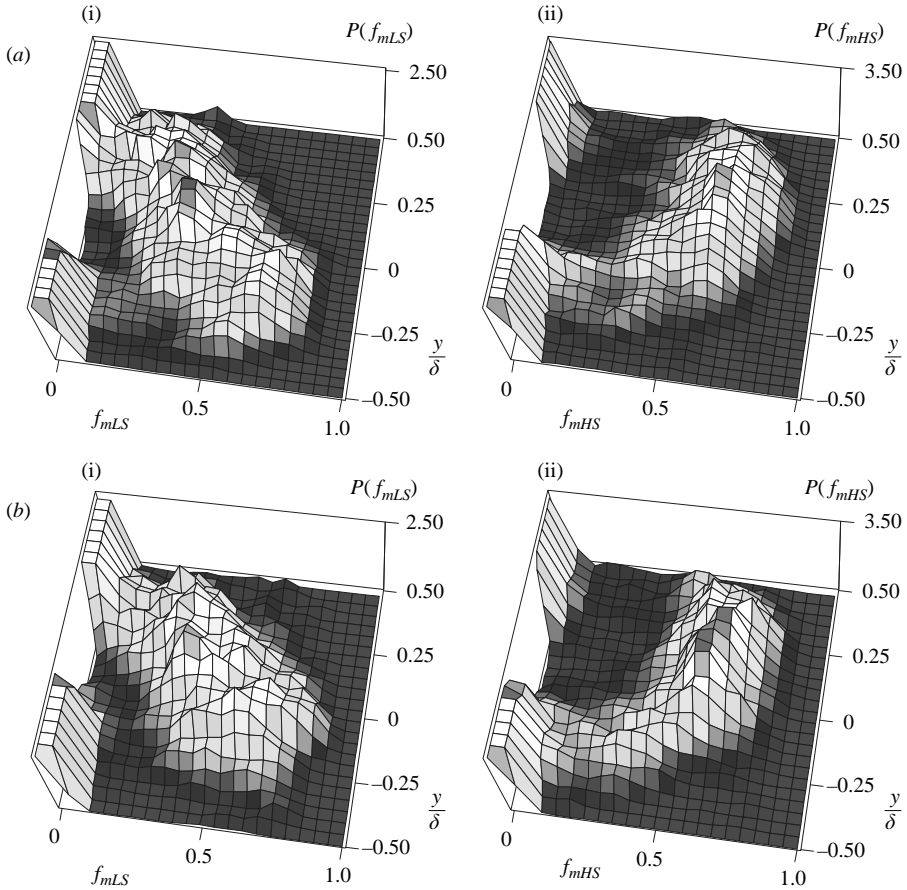


FIGURE 10. Cross-stream p.d.f.s of f_{mLS} and f_{mHS} for (a) Case 1B ($Re_\delta = 34\,300$, $Rx/\lambda = 14.8$) and (b) Case 3B ($Re_\delta = 103\,000$, $Rx/\lambda = 28.1$). (i) low-speed fluid; (ii) high-speed fluid.

The effect of downstream distance is not dramatic for Cases 1A and 1B, which have the same inflow conditions, but are separated by 100 mm in the streamwise direction. The low-speed fluid p.d.f.s of Case 1A in figure 9(a) are surprisingly similar to the p.d.f.s of Case 1B in figure 10(a). Indeed, the fluid structures in figures 4(a) and 5(b) show that the primary and secondary entrainment processes are quite similar despite a significant change in the shear-layer width with downstream distance. These observations are consistent with the concept of self-similarity for fully developed turbulence.

Comparison with the dual-tracer PLIF results of King *et al.* (1999) and Meyer *et al.* (2001) indicate that the effect of downstream distance is somewhat different in the case of gaseous axisymmetric shear layers. The character of the high-speed mixed-fluid p.d.f.s shown in figure 10 for the current investigation is predominantly stationary, with a slight increase in marching behaviour on the low-speed side at the more fully developed condition of figure 10(b). King *et al.* (1999) and Meyer *et al.* (2001) recorded similar molecularly mixed high-speed-fluid p.d.f. shapes in axisymmetric gaseous jets, but with stronger marching behaviour on the low-speed side. Instantaneous plots of molecularly mixed high-speed fluid fraction from these studies displayed homogeneous primary structures along the inner edge of the jet

that contained large amounts of mixed high-speed fluid and homogeneous secondary structures along the outer edge of the jet that contained small amounts of mixed high-speed fluid (Meyer *et al.* 2001). The resulting hybrid p.d.f. shape was stationary (constant peak f_{mHS}) on the high-speed side and marching (varying peak f_{mHS}) on the low-speed side. Unlike the planar mixing layer of the current study, the extent of the stationary p.d.f. region diminished as the axisymmetric mixing layer developed, while the extent of the marching p.d.f. region increased significantly. Since the Kelvin–Helmholtz instability mode diminishes toward the end of the potential core in axisymmetric jets, it is not surprising that the corresponding turbulent-jet p.d.f.s take on a more dominant marching character than in planar shear layers, which have a constant velocity ratio with downstream distance.

Previous probe-based measurements of mixed-fluid statistics in planar shear layers have recorded both stationary-tilted (Konrad 1976; Frieler 1992) and marching (Batt 1977) p.d.f.s. Pickett & Ghandhi (2002) recorded hybrid p.d.f.s at fairly low Re_δ (3300) with tripped or turbulent inlet boundary layers and stationary p.d.f.s with laminar inlet boundary layers. As expected, the large-scale rollers with uniform internal structures were more predominant in the latter case. Observations from the current investigation, as discussed above, indicate that stationary-tilted, marching and hybrid p.d.f.s may exist for various conditions in turbulent shear layers depending on the corresponding large- and intermediate-scale mixing dynamics. Unfortunately, two-dimensional maps of molecular mixing efficiency are not available from previous investigations in gaseous planar shear layers; direct comparisons are possible with respect to ensemble-averaged statistics as discussed further in §6.

5.2. Low-speed vs. high-speed fluid p.d.f.s

It is notable in figure 10 that the character of the high-speed fluid p.d.f.s is different from that of the low-speed fluid p.d.f.s. From the stationary peaks and higher vertical scale of $P(f_{mHS})$, it is clear that the mixed high-speed fluid is spatially more homogeneous and subject to a narrower range of mixed-fluid fractions, respectively, as compared with the mixed low-speed fluid. Significant regions of the mixing layer are at a preferred high-speed mixed-fluid fraction of about 60–65 %, with only slight marching behaviour toward the low-speed side. These differences between the low- and high-speed fluid mixing characteristics are consistent with observations regarding the mixed-fluid structure in the instantaneous images of figures 4 to 7. The line plot of figure 8(a), for example, shows low-speed fluid structures with widely varying values of f_{mLS} . The low-speed fluid structures undergo intermittent entrainment so that measurements of mixed-fluid fraction inside the shear layer are likely to yield a wider range of values, with an increasing probability of finding mixed low-speed fluid near the low-speed stream. This low-speed fluid mixing behaviour is in contrast to the more uniform internal structure for the high-speed fluid shown in figure 8(b). Entrainment of high-speed fluid that is more quasi-steady in nature would result in a shear-layer structure that is more uniform in mixed high-speed fluid composition. The inability of passive-scalar measurements to detect differences in low- and high-speed fluid mixing behaviour is discussed further in §5.3, where passive-scalar p.d.f.s of low- and high-speed fluid are presented for comparison with dual-tracer PLIF molecular mixing data.

5.3. Passive-scalar vs. molecularly mixed fluid quantities

Since the NO and acetone PLIF technique can provide molecularly mixed low- or high-speed fluid fractions, it is of interest to compare results from this method with those obtained using the passive-scalar approach with acetone PLIF alone. This can

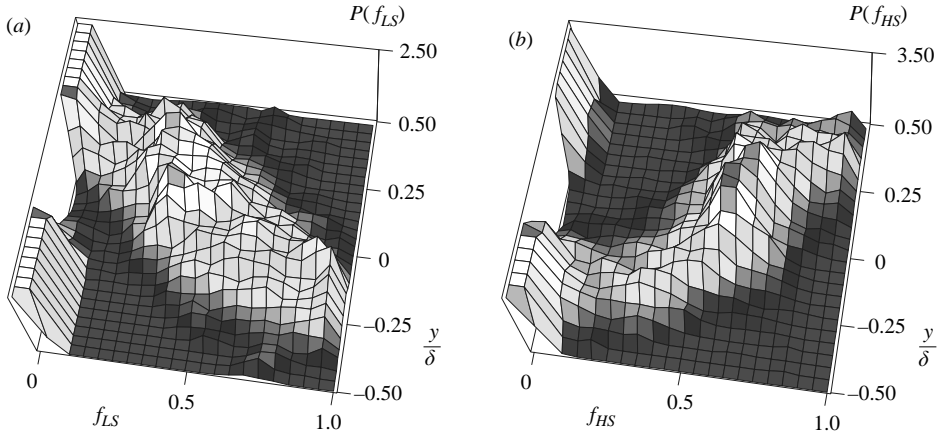


FIGURE 11. Passive-scalar cross-stream p.d.f.s of f_{LS} and f_{HS} for Case 3B ($Re_\delta = 103\,000$, $Rx/\lambda = 28.1$). (a) Low-speed fluid; (b) high-speed fluid.

shed light on the significance of measurement resolution and subresolution stirring when comparing turbulent shear-layer mixing results from previous investigations. For this purpose, p.d.f.s of f_{LS} and f_{HS} from acetone seeding alone are shown in figure 11 for Case 3B ($Re_\delta = 103\,000$, $Rx/\lambda = 28.1$). As noted earlier, passive-scalar methods cannot differentiate between pure and mixed fluid at subresolution scales. For this reason, they are fundamentally unable to define the extent of the molecularly mixed fluid; one must arbitrarily select a passive-scalar value (e.g. 10 % to 90 %) to do this, depending on the measurement uncertainty of the experiment. To define the extent of the mixing layer in the current work, values of f_{LS} greater than 97 % were considered pure (i.e. set to $f_{LS} = 0$), while low values of f_{LS} were allowed to drop to free-stream levels as they were in the dual-tracer PLIF technique. A cutoff margin of 97 % was possible because of the relatively high SNRs in the acetone PLIF images on the air side (typically 75:1). This represents an improvement over previous passive-scalar measurements with cutoff margins of 10 % and 90 % (Clemens & Paul 1995; Karasso & Mungal 1996), and more accurately captures the extent of the mixing layer as the fluid fractions asymptotically approach free-stream levels.

A notable feature in figure 11 is that the p.d.f.s of low- and high-speed fluid are quite similar in character. That is, both f_{mHS} and f_{mLS} display stationary behaviour on the high-speed side and marching behaviour on the low-speed side. In addition, it appears from the passive-scalar p.d.f.s of figure 11 that the fraction of low-speed fluid plus the fraction of high-speed fluid is nearly unity everywhere (as quantified in §6). These trends are in contrast to the data shown in figure 10(b), which display more dissimilar low- and high-speed mixed-fluid p.d.f.s. These observations underscore the importance of measuring molecularly mixed fluid quantities to detect differences in the mixing process between the low- and high-speed fluids, particularly along each interface with the adjacent free-stream fluid.

6. Ensemble-averaged statistics

Further evidence of differences in the mixing behaviour of low- and high-speed fluid can be found by studying ensemble-averaged statistics. To determine the effect of velocity ratio and downstream distance, the statistics of the total mixed-fluid fraction can be obtained by using ensemble-averaged values from the flip experiments.

In addition to analysing the effects of various operating conditions, comparisons are made with data from previous studies. To help in comparisons with previous investigations using acid/base reactions in liquid mixing layers (Koochesfahani & Dimotakis 1986; Karasso & Mungal 1996), low heat release cold-wire measurements in gaseous layers (Mungal & Dimotakis 1984; Frieler 1992), cold-chemistry flip experiments in compressible mixing layers (Clemens & Paul 1995; Island *et al.* 1996), and dual-tracer PLIF experiments in gaseous axisymmetric jets (Meyer *et al.* 2001), a number of definitions are introduced.

By integrating the ensemble average of the mixed-fluid fraction for the images, $\langle f_{mNO} \rangle$, across the mixing layer, it is possible to find the volume fraction of mixed NO-seeded fluid V_{mNO}/V , at various downstream locations:

$$\frac{V_{mNO}}{V} = \frac{\int_{y_1}^{y_2} \langle f_{mNO} \rangle dy}{\delta}, \quad (2)$$

where the subscript 'NO' is replaced with 'LS' or 'HS' if NO is seeded into the low- or high-speed streams, respectively. The ensemble average $\langle f_{mNO} \rangle$ is referred to as the probability of finding mixed NO-seeded fluid, P_{mNO} , at a particular location. The probability of finding mixed fluid of any composition, P_m , is simply the sum of $\langle f_{mNO} \rangle$ from the flip experiments. As shown in equation (3), the ensemble average can also be obtained by integrating the p.d.f.s, $P(f_{mNO})$, over all possible values of f_{mNO} .

$$P_{mLS} = \langle f_{mLS} \rangle = \int_0^1 f_{mLS} P(f_{mLS}) df_{mLS}, \quad (3a)$$

$$P_{mHS} = \langle f_{mHS} \rangle = \int_0^1 f_{mHS} P(f_{mHS}) df_{mHS}, \quad (3b)$$

$$P_m = P_{mLS} + P_{mHS} = \langle f_{mLS} \rangle + \langle f_{mHS} \rangle. \quad (3c)$$

In addition, the average concentration of mixed high-speed fluid, C_m , can be found from equation (4).

$$C_m = \frac{P_{mHS}}{P_m}. \quad (4)$$

Note that $\langle f_{mNO} \rangle$, P_{mNO} , P_m and C_m are functions of x and y . The total volume fraction of mixed fluid, P_M , is defined in equation (5) as the sum of the low- and high-speed fluid mixed volume fractions. The total average high-speed mixed-fluid concentration integrated across the shear layer (often called the mixing efficiency), C_M , is defined in equation (6). The entrainment ratio of high- to low-speed fluid, E , can then be found from equation (7):

$$P_M = \frac{V_{mLS}}{V} + \frac{V_{mHS}}{V}, \quad (5)$$

$$C_M = \frac{V_{mHS}/V}{P_M}, \quad (6)$$

$$E = \frac{C_M}{1 - C_M}, \quad (7)$$

where P_M , C_M and E represent quantities that are integrated across the shear layer, and are functions of x only (streamwise coordinate).

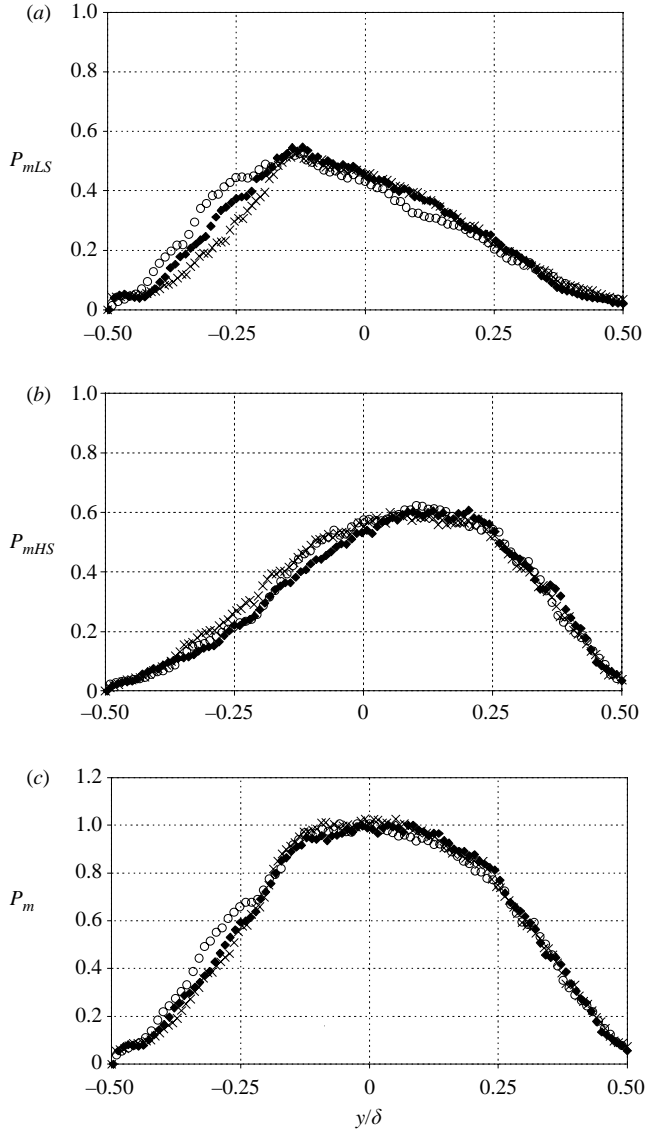


FIGURE 12. Effect of Rx/λ on the (a) low-speed (P_{mLS}) (b) high-speed (P_{mHS}), and (c) total (P_m) mixed-fluid probabilities. \circ , $Rx/\lambda = 14.8$; \blacklozenge , 21.3; \times 28.1.

6.1. Mixed-fluid probability

Mixed-fluid probabilities enable comparisons of the ensemble-averaged spatial distributions of low-speed, high-speed and total molecularly mixed fluid fractions, defined as P_{mLS} , P_{mHS} and P_m , respectively. Figure 12 shows distributions of P_{mLS} , P_{mHS} and P_m for Cases 1B ($Re_\delta = 34\,300$, $Rx/\lambda = 14.8$), 2B ($Re_\delta = 65\,400$, $Rx/\lambda = 21.3$) and 3B ($Re_\delta = 103\,000$, $Rx/\lambda = 28.1$). In terms of differences between the low- and high-speed fluids, P_{mLS} is typically lower than P_{mHS} and is indicative of the preferred entrainment of high-speed fluid into the shear layer. Both P_{mLS} and P_{mHS} peak closer to their respective free streams for all values of Rx/λ , as expected under fully developed conditions. This asymmetry from Rx/λ of 14.8 to 28.1 differs with the results of

Karasso & Mungal (1996) in liquid shear layers, in which they found that the P_{mLS} and P_{mHS} profiles were symmetrical about $y/\delta = 0$ at $Rx/\lambda = 18$, but asymmetric at $Rx/\lambda \geq 30$. The full-width-at-half-maximum (FWHM) of the P_{mHS} curve is also larger than that for P_{mLS} , showing that mixed high-speed fluid is likely to be found over a larger cross-stream extent of the mixing layer, while the molecularly mixed low-speed fluid is confined closer to the low-speed side.

The profiles of total mixed-fluid probability, P_m , as shown in figure 12(c) are nearly unity in the centre of the mixing layer for the three conditions, indicating that unmixed fluid is almost never found in this region. These ensemble-averaged statistics have significantly reduced random error (due to sample size) as compared with instantaneous images, and help corroborate values of η_{mNO} near unity in figures 4 to 7. The finding that very little subresolution stirring of NO-seeded fluid is found in the centre of the mixing layer differs slightly from previous results in gaseous shear layers, which show total mixed-fluid probabilities from cold-chemistry flip experiments to have peak values of 90–95 % (Clemens & Paul 1995; Island *et al.* 1996). Those authors did not correct for the finite quenching rate of NO PLIF in the presence of air, however, and state that their measurements underpredict the amount of mixed fluid. Thus, the true peak mixed-fluid probability can be expected to be higher than 90–95 % for gaseous flow, as is found in the current study. The results of Karasso & Mungal (1996) in liquid shear layers differ markedly with values of $P_m \approx 50$ –70 % in the centre of the mixing layer. In the context of the Broadwell–Breidenthal model, this result implies a decrease in molecular mixing in the interfacial regions between the two fluid streams at high Sc .

With regard to the effect of Re_δ or Rx/λ on the mixed-fluid probabilities, no clear trends are detected in P_{mHS} , with the data in figure 12(b) essentially collapsing for Cases 1B–3B. This is indicative of a self-similar-like character in the high-speed fluid entrainment and mixing processes. The axisymmetric jet results of Meyer *et al.* (2001) showed from axial p.d.f.s that the preferred high-speed fluid mixture fraction was also fully developed by about $Rx/\lambda \approx 12$ –15. In contrast with the high-speed mixed-fluid probabilities, a slight trend is observed in figure 12(a) in which P_{mLS} decreases on the low-speed sides of the profiles from Cases 1B to 3B and increases slightly on the high-speed sides (i.e. the profiles shift to the right). These trends also lead to slight irregularities in the profiles of P_m in figure 12(c). The agreement between Cases 1B to 3B for the mixed fluid probabilities across most of the shear layer, however, is more prominent than the slight trend noted for P_{mLS} .

6.2. Average mixed-fluid composition

The profile of the average mixed-fluid composition, C_m , across the shear layer provides a quantitative measure of the preferential entrainment of low- and high-speed fluids from the corresponding freestreams. The ‘S’-shaped profile in figure 13, with a higher mixed-fluid composition on the high-speed side, is common in both liquid and gaseous shear layers (Mungal & Dimotakis 1984; Karasso & Mungal 1996). Previous measurements in a gaseous shear flow at $Rx/\lambda = 40$ using low heat-release reactions (Mungal & Dimotakis 1984) show a similar mixed-fluid composition of about 0.4 on the low-speed side and 0.7 on the high-speed side. Also in agreement, Island *et al.* (1996) found values ranging from 0.3 to about 0.7 in compressible mixing layers. In contrast, Karasso & Mungal (1996) found much less variation in C_m across a liquid shear layer, with values ranging from 0.5 to 0.6. These variations, which are biased toward the corresponding free-stream fluid, imply that the total mixed-fluid p.d.f.s vary across the shear layer. Since the compositions toward the edges of the

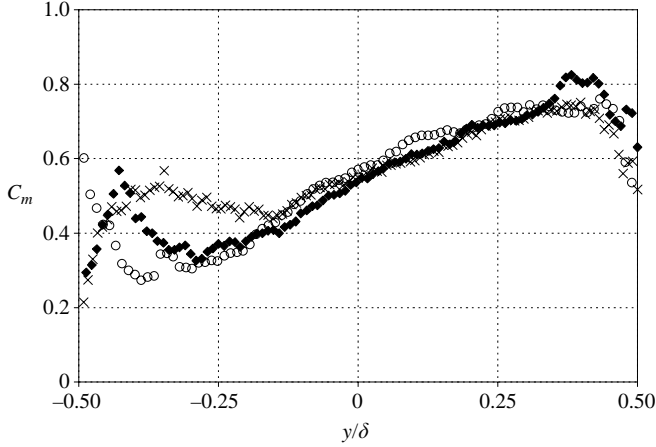


FIGURE 13. Effect of Rx/λ on the averaged high-speed mixed-fluid composition, C_m . Key as in figure 12.

mixing layer do not reach the corresponding free-stream values, Karasso & Mungal (1996) suggest that this implies a ‘tilted’ p.d.f. behaviour rather than a fully marching behaviour. A comparison of C_m profiles between Cases 1B to 3B shows that the shear layer may indeed be slowly evolving. In particular, the shear layer is becoming more homogeneous (less variation in mixed-fluid composition) at higher Re_δ or Rx/λ . This trend is indicative of the increased size and effect of intermediate-scale structures in the molecular mixing process rather than an increase in small-scale turbulent diffusion. The latter would have the opposite effect of increasing the variation of mixed-fluid composition across the shear layer.

Because of the relative lack of subresolution stirring within the mixing layer, it is of interest to determine whether an under-resolved passive-scalar measurement can accurately predict the mixed-fluid composition in gaseous mixing layers. As noted earlier, this issue can be examined in the current work simply by comparing data using acetone PLIF alone with data from simultaneous NO and acetone PLIF. Figure 14 shows that the magnitude of the C_m variation across the shear layer is overpredicted using the passive-scalar method, and is consistent with passive-scalar p.d.f.s exhibiting false marching behaviour, as illustrated in figure 11. In liquid ($Sc \sim 2000$) shear layers, however, Karasso & Mungal (1996) found much more dramatic errors when using the passive-scalar approach. The modest errors shown in figure 14 from the passive-scalar method are not surprising because of the high spatial resolution and high SNRs of the current measurement system, and since the gaseous shear layer is almost entirely molecularly mixed (Clemens & Paul 1995; Island *et al.* 1996). Nonetheless, the mixing rate along the outer region of the shear layer is more closely coupled to chemical reaction rates, and it is this region that displays the greatest potential for error when using the passive-scalar technique.

6.3. Mixed-fluid volume fraction and entrainment ratio

Further comparisons between current data and previous results in gaseous and liquid shear layers can be made regarding the low-speed, high-speed and total mixed-fluid volume fractions, V_{mLS}/V , V_{mHS}/V and P_M , respectively. These were computed using equations (2) and (5), and are shown as functions of Rx/λ in figure 15. Results from cold-wire low heat release studies in gaseous flows ($Sc \sim 1$) show $V_{mLS} \approx 0.25$ and

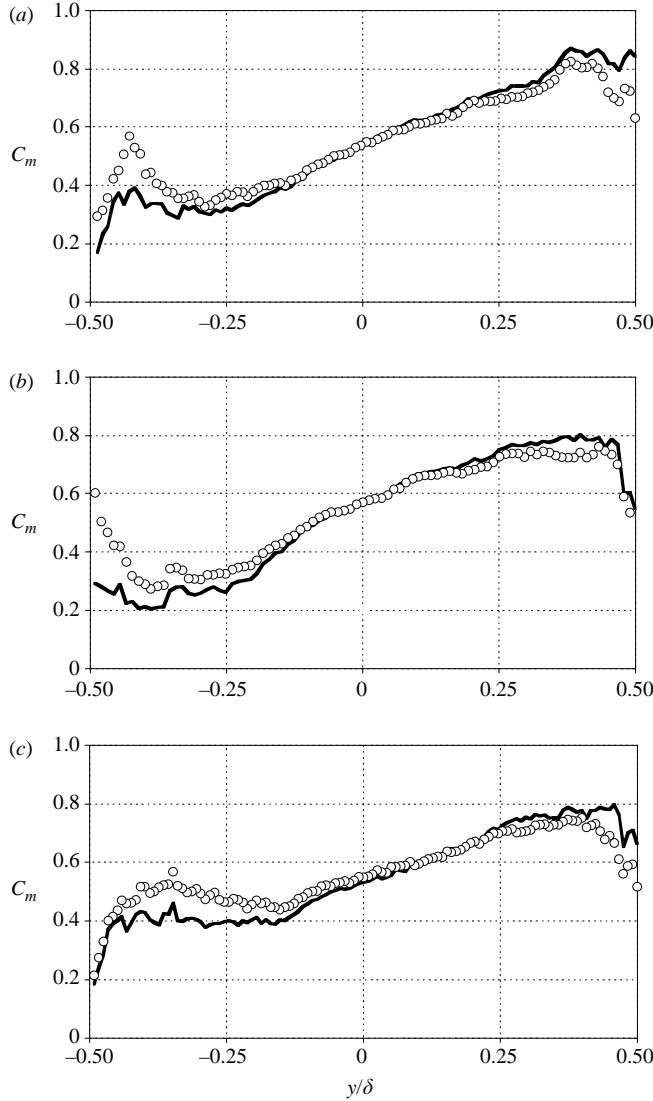


FIGURE 14. Averaged mixed-fluid composition, C_m , from the \circ , dual-tracer and —, passive-scalar methods for (a) Case 1B, (b) Case 2B and (c) Case 3B.

$V_{mHS} \approx 0.30$ in the range of Rx/λ from 16 to 56 (Frier 1992). These are in good agreement with the results shown in figure 15, which supports the accuracy of the probe-based measurements of Frier (1992). Similarly for gaseous axisymmetric jets, V_{mHS}/V has been found to vary from 0.25 to 0.28 in the range of Rx/λ from 15 to 30 (Meyer *et al.* 2001). In contrast, V_{mLS}/V and V_{mHS}/V in liquids ($Sc \sim 2000$) are about a factor of two smaller (Karasso & Mungal 1996). The slight drop in V_{mHS}/V , shown in figure 15, is nearly proportional to the drop in P_M as Rx/λ increases. Hence, the total averaged mixed-fluid concentration across the shear layer, C_M , from equation (6), stays nearly constant at 0.55 for Cases 1B to 3B. This corresponds to an entrainment ratio of $E = 1.24$ from equation (7). The model proposed by Dimotakis (1986) predicts values of C_M from 0.55 to 0.58 and values of E from 1.2 to 1.37

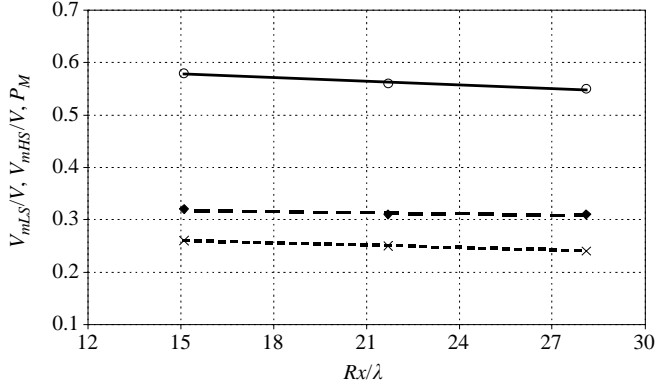


FIGURE 15. Low-speed, high-speed and total mixed fluid volume fractions (\times , V_{mLS}/V ; \blacklozenge , V_{mHS}/V ; \circ , P_M , respectively) as functions of Rx/λ .

for the current flow conditions (see table 1). By comparison, Frieler (1992) obtained values of $C_M \approx 0.5$ to 0.55 ($E \approx 1$ – 1.2) for nearly the same range of velocity ratios as for the current study. Island *et al.* (1996) reported values ranging from $C_M \approx 0.5$ to 0.59 ($E \approx 1$ – 1.44) in compressible mixing layers, while Karasso & Mungal (1996) reported values of $C_M \approx 0.58$ ($E \approx 1.37$) in liquid layers with $r = 0.25$. To first order, these results agree with the ensemble-averaged data from the current investigation. It is likely, therefore, that the molecular-mixing dynamics discussed in §§4 and 5 are applicable to previous studies of shear-layer mixing with similar Reynolds numbers and pairing parameters.

7. Conclusions

The dual-tracer (NO and acetone) PLIF technique employed in the current investigation is the gaseous analogue to acid/base visualizations in liquid flows and is used for the first time to study the role of large- and intermediate-scale structures in determining the state of molecular mixing in the developing and far-field regions of gaseous planar shear layers. Data are compared with acid/base measurements of molecular mixing in liquid planar shear layers, average probe-based measurements in gaseous planar shear layers, and dual-tracer PLIF studies in axisymmetric jets. The current work also reports the first ‘flip’ experiments using the dual-tracer PLIF technique, enabling measurements of gaseous low-speed, high-speed and total fluid molecular mixing. Data are obtained for low- to high-speed velocity ratios from $r = 0.25$ to 0.44 and Reynolds numbers from $Re_\delta = 18\,600$ to $103\,000$, corresponding to pairing parameter values of Rx/λ 6.6 to 28.1. Several key observations are made regarding instantaneous images, probability density functions, and ensemble-averaged statistics of molecularly mixed fluid within the planar shear layer, as enumerated below.

1. There is a very low probability of finding unmixed fluid or subresolution stirring in the centre of the shear layer. Sub-unity values of mixing efficiency, which indicate the presence of subresolution stirring or micro-scale mixing, are found most often in regions adjacent to the low- and high-speed fluid streams. Ensemble-averaged statistics, therefore, show that the total mixed-fluid probability, P_m , is nearly unity in the centre of the mixing layer. This differs most dramatically with previous

measurements in liquid shear layers (Karasso & Mungal 1996), and confirms the effect of Sc at high Re_δ . Slight differences with cold-chemistry flip experiments performed in gaseous shear layers (Clemens & Paul 1995; Island *et al.* 1996) are probably attributable to the inability of previous studies to correct for finite-quenching-rate effects.

2. Owing to the relative absence of subresolution stirring, passive-scalar data are found to compare well with measurements of molecularly-mixed fluid fraction in much of the central region of the mixing layer. The inherent ambiguity in defining the edges of the mixing layer, however, as well as subresolution stirring in the outer regions, still leads to an overprediction of mixed-fluid quantities using the passive-scalar approach.

3. The dynamics of large- and intermediate-scale structures are sensitive to the velocity ratio and have a significant impact on the molecularly mixed fluid distribution within the gaseous shear layer. Intermittent large-scale structures composed of intermediate and small-scale motions are the dominant mechanisms for pure fluid entrainment in both the developing and far-field regions. Intermediate structures generated by secondary instabilities augment fluid entrainment in the outer regions of the mixing layer and, when entrained into the shear layer, are a source of inhomogeneity in mixed-fluid statistics.

4. Both low-speed and high-speed mixed-fluid probability density functions (p.d.f.s) develop stronger marching characteristics with decreased velocity ratio, but are fairly independent of downstream distance, which is consistent with the concept of self-similarity. The transition to marching behaviour is not as prominent as previously found in axisymmetric gaseous shear layers (King *et al.* 1999; Meyer *et al.* 2001).

5. Differences in molecular-mixing behaviour between the low- and high-speed fluids are detected through analyses of p.d.f.s across the shear layer. These differences, as in the range of mixed-fluid fractions exhibited in the low- and high-speed fluid p.d.f.s, are not as apparent in passive-scalar data, which do not account for subresolution-scale molecular mixing.

6. The low- and high-speed mixed-fluid probabilities, P_{mLS} and P_{mHS} , are preferentially higher toward the low- and high-speed streams, respectively. Therefore, the averaged mixed-fluid composition, C_m , is also preferentially higher toward the corresponding free-stream fluid, as found in previous investigations (Mungal & Dimotakis 1984; Karasso & Mungal 1996). The value of P_{mHS} is higher than that of P_{mLS} , confirming that high-speed fluid is preferentially entrained into the shear layer.

7. The effects of Rx/λ on the mixed-fluid probabilities and the mixed-fluid composition are found to be slight from $Rx/\lambda = 14.8$ to 28.1, although a slow reduction in the aforementioned free-stream bias of the low- and high-speed mixed-fluid quantities is detected in C_m . The low-speed, high-speed and total mixed-fluid volume fractions are in agreement with previous measurements in the literature (Frieler 1992; Meyer *et al.* 2001) and remain nearly constant with Rx/λ . These results lend support to a quasi-self-similar state – one that evolves very slowly and is not universally independent of initial conditions.

This work was supported by the National Science Foundation, Division of Chemical and Transport Systems, Grant No. CTS 94-23280, with Dr R. E. A. Arndt and Dr J. F. Foss as Program Monitors. Additional funding was provided by a Ford Foundation Dissertation Fellowship and by Dr J. R. Gord of the Air Force Research Laboratory through a grant from the Air Force Office of Scientific Research (Dr J. M. Tishkoff, Program Manager).

REFERENCES

- BATCHELOR, G. K. 1953 *The Theory of Homogeneous Turbulence*. Cambridge University Press.
- BATT, R. G. 1977 Turbulent mixing of passive and chemically reacting species in a low-speed shear layer. *J. Fluid Mech.* **82**, 53–95.
- BRADSHAW, P. 1966 The effect of initial conditions on the development of a free shear layer. *J. Fluid Mech.* **26**, 225–236.
- BREIDENTHAL, R. 1981 Structure in turbulent mixing layers and wakes using a chemical reaction. *J. Fluid Mech.* **109**, 1–24.
- BROADWELL, J. E. & BREIDENTHAL, R. E. 1982 A simple model of mixing and chemical reaction in a turbulent shear layer. *J. Fluid Mech.* **125**, 397–410.
- BROADWELL, J. E. & MUNGAL, M. G. 1988 Molecular mixing and chemical reactions in turbulent shear layers. *Twenty-Second Symposium (International) on Combustion*, pp. 579–587. The Combustion Institute.
- BUCH, K. A. & DAHM, W. J. A. 1996 Experimental study of the fine-scale structure of conserved scalar mixing in turbulent shear flows. Part 1. $Sc \gg 1$. *J. Fluid Mech.* **317**, 21–71.
- BUCH, K. A. & DAHM, W. J. A. 1998 Experimental study of the fine-scale structure of conserved scalar mixing in turbulent shear flows. Part 2. $Sc \sim 1$. *J. Fluid Mech.* **364**, 1–29.
- CLEMENS, N. T. & MUNGAL, M. G. 1995 Large-scale structure and entrainment in the supersonic mixing layer. *J. Fluid Mech.* **284**, 171–216.
- CLEMENS, N. T. & PAUL, P. H. 1995 Scalar measurements in compressible axisymmetric mixing layers. *Phys. Fluids* **7**, 1071–1081.
- DAHM, W. J. A., SOUTHERLAND, K. B. & BUCH, K. A. 1991 Direct, high resolution, four-dimensional measurements of the fine scale structure of $Sc \gg 1$ molecular mixing in turbulent flows. *Phys. Fluids A* **3**, 1115–1127.
- DIMOTAKIS, P. E. 1986 Two-dimensional shear-layer entrainment. *AIAA J.* **24**, 1791–1796.
- DIMOTAKIS, P. E. 2000 The mixing transition in turbulent flows. *J. Fluid Mech.* **409**, 69–98.
- DZIOMBA, B. & FIEDLER, H. E. 1985 Effect of initial conditions on two-dimensional free shear layers. *J. Fluid Mech.* **152**, 419–442.
- FRIELER, C. E. 1992 Mixing and reaction in the subsonic 2-d turbulent free shear layer. PhD thesis, California Institute of Technology, Pasadena, California.
- GUTMARK, E. & HO, C. M. 1983 Preferred modes and the spreading rates of jets. *Phys. Fluids* **26**, 2932–2938.
- HU, H. & KOCHESFAHANI, M. M. 2002 A novel method for instantaneous, quantitative measurement of molecular mixing in gaseous flows. *Exps. Fluids* **33**, 202–209.
- HUANG, L. S. & HO, C. M. 1990 Small-scale transition in a plane mixing layer. *J. Fluid Mech.* **210**, 475–500.
- HUSSAIN, A. K. M. F. & ZAMAN, K. B. M. Q. 1980 Vortex pairing in a circular jet under controlled excitation. Part 2. Coherent structure dynamics. *J. Fluid Mech.* **101**, 493–544.
- ISLAND, T. C., URBAN, W. D. & MUNGAL, M. G. 1996 Quantitative scalar measurements in compressible mixing layers. *AIAA Paper* 96-0685.
- KARASSO, P. S. & MUNGAL, M. G. 1996 Scalar mixing and reaction in plane liquid shear layers. *J. Fluid Mech.* **323**, 23–63.
- KING, G. F., DUTTON, J. C. & LUCHT, R. P. 1999 Instantaneous, quantitative measurements of molecular mixing in the axisymmetric jet near field. *Phys. Fluids* **11**, 403–416.
- KING, G. F., LUCHT, R. P. & DUTTON, J. C. 1997 Quantitative dual-tracer planar laser-induced fluorescence measurements of molecular mixing. *Opt. Lett.* **22**, 633–635.
- KOLMOGOROV, A. N. 1941 On degeneration (decay) of isotropic turbulence in an incompressible viscous liquid. *Dokl. Akad. Nauk SSSR* **31**, 538–540.
- KONRAD, J. H. 1976 An experimental investigation of mixing in two-dimensional turbulent shear flows with applications to diffusion-limited chemical reactions. PhD thesis, California Institute of Technology, Pasadena, California.
- KOCHESFAHANI, M. M. & DIMOTAKIS, P. E. 1986 Mixing and chemical reactions in a turbulent liquid mixing layer. *J. Fluid Mech.* **170**, 83–112.
- LOZANO, A., YIP, B. & HANSON, R. K. 1992 Acetone: a tracer for concentration measurements in gaseous flows by planar laser-induced fluorescence. *Exps. Fluids* **13**, 369–376.

- MASUTANI, S. M. & BOWMAN, C. T. 1986 The structure of a chemically reacting plane mixing layer. *J. Fluid Mech.* **172**, 93–126.
- MEHTA, R. D. 1991 Effect of velocity ratio on plane mixing layer development: influence of the splitter plate wake. *Exps. Fluids* **10**, 194–204.
- MEHTA, R. D., INOUE, O., KING, L. S. & BELL, J. H. 1987 Comparison of experimental and computational techniques for plane mixing layers. *Phys. Fluids* **30**, 2054–2062.
- MEYER, T. R. 2001 Turbulent molecular mixing in gaseous free shear flows. PhD thesis, University of Illinois at Urbana-Champaign, Urbana, Illinois.
- MEYER, T. R., DUTTON, J. C. & LUCHT, R. P. 1999 Vortex interaction and mixing in a driven gaseous axisymmetric jet. *Phys. Fluids* **11**, 3401–3415.
- MEYER, T. R., DUTTON, J. C. & LUCHT, R. P. 2001 Experimental study of the mixing transition in a gaseous axisymmetric jet. *Phys. Fluids* **13**, 3411–3424.
- MEYER, T. R., KING, G. F., MARTIN, G. C., LUCHT, R. P., SCHAUER, F. R. & DUTTON, J. C. 2002 Accuracy and resolution issues in NO/Acetone PLIF measurements of gas-phase molecular mixing. *Exps. Fluids* **32**, 603–611.
- MOSER, R. D. & ROGERS, M. M. 1991 Mixing transition and the cascade to small scales in a plane mixing layer. *Phys. Fluids A* **3**, 1128–1134.
- MUNGAL, M. G. & DIMOTAKIS, P. E. 1984 Mixing and combustion with low heat release in a turbulent shear layer. *J. Fluid Mech.* **148**, 349–382.
- OLSEN, M. G. 1999 Planar velocity measurements in an incompressible and weakly compressible mixing layer. PhD thesis, University of Illinois at Urbana-Champaign, Urbana, Illinois.
- PAUL, P. H. & CLEMENS, N. T. 1993 Sub-resolution flowfield measurements of unmixedness using electronic quenching of NO $a^2\sigma^+$. *Opt. Lett.* **18**, 161–163.
- PICKETT, L. M. & GHANDHI, J. B. 2002 Passive scalar mixing in a planar shear layer with laminar and turbulent inlet conditions. *Phys. Fluids* **14**, 985–998.
- ROGERS, M. M. & MOSER, R. D. 1994 Direct simulation of a self-similar turbulent mixing layer. *Phys. Fluids* **6**, 903–923.
- SEITZMAN, J. M., MILLER, M. F., McMILLIN, B. K., HANSON, R. K., DEBARBER, P. A. & HESS, C. F. 1994 Multiple scalar planar fluorescence imaging for reacting flows. *AIAA Paper* 94-0228.
- SLESSOR, M. D., BOND, C. L. & DIMOTAKIS, P. E. 1998 Turbulent shear-layer mixing at high Reynolds numbers: effects of inflow conditions. *J. Fluid Mech.* **376**, 115–138.
- WIECEK, K. C. & MEHTA, R. D. 1998 Effects of velocity ratio on mixing layer three-dimensionality. *Expl. Therm. Fluid Sci.* **16**, 165–176.
- YIP, B., LOZANO, A. & HANSON, R. K. 1994 Sensitized phosphorescence: a gas phase molecular mixing diagnostic. *Exps. Fluids* **17**, 16–23.

Non-Reacting and Combusting Flow Investigation of Bluff Bodies in Cross Flow

Barry Kiel, Kyle Garwick, Amy Lynch, and James R. Gord, Ph.D.
Air Force Research Laboratory
Wright Patterson Air Force Base

Terrence Meyer, Ph.D.
Innovative Scientific Solutions, Inc.
Dayton, OH

ABSTRACT

This paper is the first in a series of papers studying the behavior of bluff body stabilized flames. In this research a combination of Laser Doppler Velocimetry (LDV), and High Speed Imaging are used to investigate these flames. LDV data taken over several non-combusting operating conditions detail the recirculation zone behind the bluff body as well as the effect of inlet conditions on the Karman Street vortex shedding that occurs. High speed images of combustion and equivalence ratio taken at blow out agree with assertions made by Ozawa (1971) and Zukoski (1957) on the transitional nature of the flame from "laminar" to "turbulent" at a Reynolds number of around 15,000. Lean blow out also correlate very well when using the correlation parameter set down by Dezubay (1950). Finally, high speed images also support assertions by Mehta and Soteriou (2003) Erickson et al. (2006) that under certain conditions Karman Street vortex shedding is not suppressed by momentum and baroclinic effects and are present in the flame near lean blowout.

1 INTRODUCTION

Flame stabilization by a bluff body is commonly used in propulsion systems including gas turbine and scram jet engines. Models are used to estimate the effectiveness of these stabilization methods. These modes vary in sophistication from simple empirical expressions to the solution of detailed partial differential equations. The accuracy of these models depends on extent the models are validated. Equally as important, these models are also only as accurate as the physical phenomenology the models capture.

For the past fifty years bluff body stabilized flames have been studied in detail. In the 1950s DeZubay (1950) and King (1957), studied

flames stabilized using bluff bodies. Both authors found that the fuel air ratio the flame blows out at correlates with the inlet pressure, temperature, and velocity, see Figure 1-1.

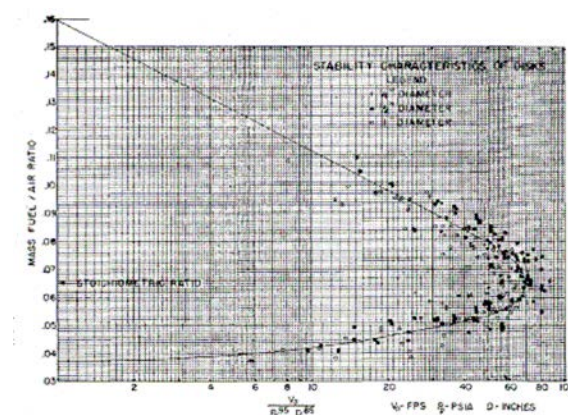


Figure 1-1 Dezubay's Blowout Correlation (Dezubay 1950)

In this work the authors studied blowout at relatively high Reynolds numbers. Dezubay studied a round disk shaped flame holders over a range of Reynolds numbers from 90,000 to 680,000. King on the other hand studied a v-shaped bluff body over a range of Reynolds Numbers from 60,000 to 130,000.

Due to the increasing inlet temperatures Reynolds numbers for modern systems are much lower than those of the 1960s and 1970s. Reynolds numbers vary typically in the range of 15,000 to 300,000. In his work Zukoski (1954, 1955) studied blowout. He found that the blow out characteristics behave quite differently at lower Reynolds numbers. Zukoski concludes that the flame transitions around a Reynolds numbers of 10,000. Later Ozawa (1971) also compiled data from several bluff body experiments. Ozawa also discusses this blowout transition at Reynolds Number of 10,000. Both authors conclude the flame surface transitions from "laminar" to "turbulent" near this Reynolds number. Further, they both

concluded that this transition greatly effects the velocity at which the flame will blow off at, or the characteristic of the blow-out curve.

More recently Mehta and Soteriou (2003), and Erickson et al. (2006) have commented on vortex shedding as it relates to bluff body flame blow-out. In their work they have conducted detailed modeling of bluff body stabilized flames. In their 2003 work they concluded that the baroclinic effect of the temperature rise across the flame suppresses the Karman Street type vortex shedding typically seen behind these bluff bodies under non-combusting conditions. In this paper they modeled a bluff body flame at 20,000 Reynolds number. They concluded that the flame was dominated not by large Karman Street vortices but much smaller vortices. They also concluded that the baroclinic torque generated by the temperature rise across the flame was responsible for suppressing the Karman Street vortex production.

Later in 2006, (Erickson et al. (2006)) they conducted another model study where the temperature rise across the flame was varied. In this study they concluded that at lower temperature ratios across the flame, the flame near blowout was dominated not by small turbulent vortices but by large Karman Street type vortices. These same structures were also captured by Porumbel and Menon (2006), and Fureby (2006) in their combustng Large Eddy Simulation (LES) investigations.

The objective of this research effort is two fold. First the objective is to provide detailed experimental data on bluff body stabilized flames for model validation. Second the objective is to enhance the phenomenological understanding of these bluff body flame stabilization. In this paper a detailed study of the velocity patterns, vortex shedding and blowout v-gutter bluff bodies is studied over a large range of Reynolds numbers, from 5,000 to 60,000. Detailed LDV data are collected of cold flow in the wake the v-gutters. From the LDV, mean, RMS, and turbulent spectra are collected. Combusting experiments are also conducted over the same range of Reynolds numbers. High Speed images of the flame just prior to blow out are recorded as are the equivalence ratio at blowout.

2 PROCEDURES

2.1 LDV Procedures

A two-component LASER Doppler Velocimetry (LDV) system was employed for measuring instantaneous velocity at various conditions in the wake region of the flame holder, Figure 2-1. The LDV system is driven by an argon-ion LASER with 514.5 nm and 488 nm output beams. When focused on a small control volume, the 514.5 nm and 488 nm beams generate orthogonal interference fringes from scattering off 1 micron aluminum oxide particles used to seed the flow. For a more detailed discussion of principles of LDV please reference Goldstein (1983).

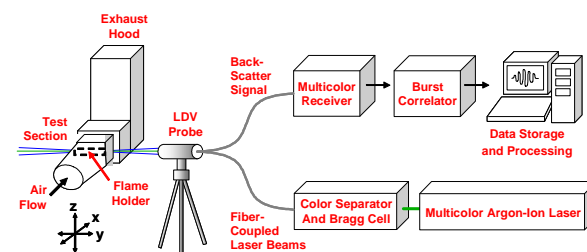


Figure 2-1. LASER Doppler Velocimetry Set-up.

2.2 Analysis of Randomly Time Sampled LDV Data

The quality of data from LDV depends on several factors, the most important of which is the seed density of the flow. In areas of recirculation seed density can vary so much as to produce periods of time where there are few velocity data. When the seed conditions are poor data can not be taken at a known interval of time, but must be collected at the time of arrival of the each particle. Figure 2-2 depicts a sample histogram of the various time intervals present in LDV data.

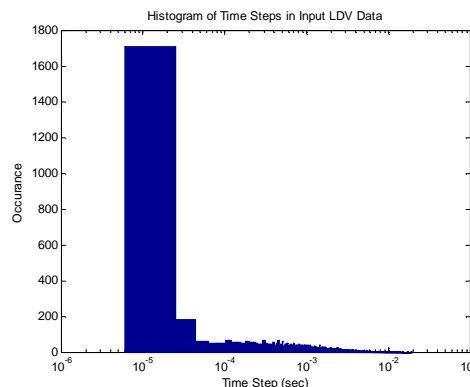


Figure 2-2. Histogram of Time Steps in LDV Data.

In this experimental campaign LDV is used to produce mean and RMS velocity data and the shedding frequency of the coherent vortex shed

behind the bluff body. For the mean and RMS velocities simple mathematical functions can be employed to obtain these parameters from the LDV data taken at each point. For the shedding frequency of the coherent vortex the data analysis is not as straight forward. Because the time interval produced by LDV is random, standard DFFT techniques can not be used to analyze LDV data. The spectral analysis of randomly spaced LDV data is traditionally conducted using the Lomb Algorithm for spectral analysis (Numerical Recipes in C, 1992).

In this experiment the entire spectrum of turbulence is not required to determine the shedding frequency of the coherent vortex. To obtain the shedding frequency, spectrum up to three times the shedding frequency is required to satisfy Nyquist. This results in maximum frequencies required on the order of 200-400 Hz. Because of this simpler techniques are used to analyze the data. A technique is used where the data are resample onto a uniformly spaced time interval through the use of cubic Hermite interpolation. The time step of the interpolation was chosen based the histogram of the time steps of the randomly spaced LDV data and the median of the time step data. An FFT of the interpolated velocity then performed in MATLAB. When compared to spectral data produced with the Lomb Algorithm, there was excellent agreement between the two, as will be discussed in a future paper.

3 EXPERIMENTAL SETUP

A 12MW experimental combustion facility located at the Propulsion Directorate of AFRL in Wright-Patterson Air Force Base, Dayton Ohio was used for the experiments, Figure 3-1. Flow

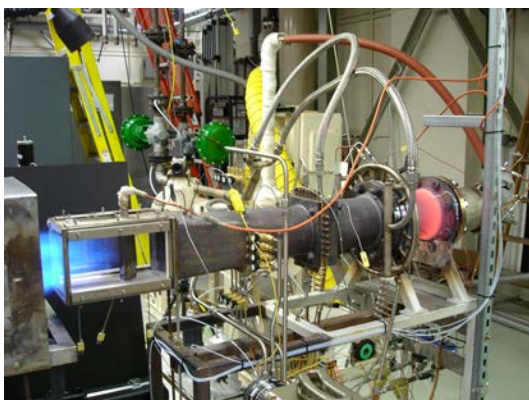


Figure 3-1 12 MW Experimental Test Facility

conditioning is employed in the facility which provides a uniform velocity and temperature profile ($\pm 3\%$), and 6-7% turbulence at the inlet of the test section. Tests were conducted on an "open and "closed" v-gutter bluff body mounted in the rig, see Figure 3-2. In these tests the

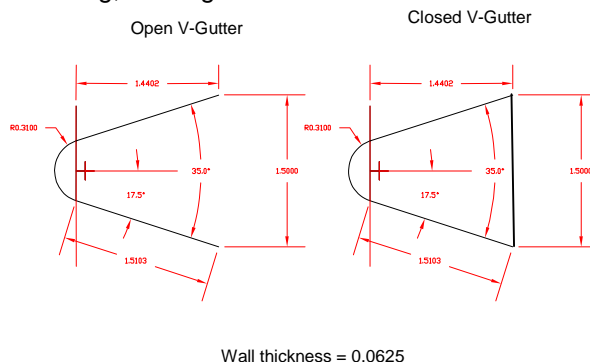


Figure 3-2. Open and Closed V-Gutter Flame Holders

flame holder traverses the length of the test section. In this configuration the flow is considered two-dimensional at the center of the test rig. Combustion tests were conducted with premixed propane and air.

4 DATA ANALYSIS

4.1 Mean and RMS Profiles

Detailed Velocity profiles were taken using LDV behind the non reacting wake of the v-gutters. Traverses were taken parallel and transverse to the centerline axes of the test section. Figure 4-1 depicts the location of these traverses. The orange traverses in Figure 4-1 are perpendicular to the centerline of the test section traversing across the wake of the bluff body. The green traverse in Figure 4-1 is parallel to the centerline of the test section.

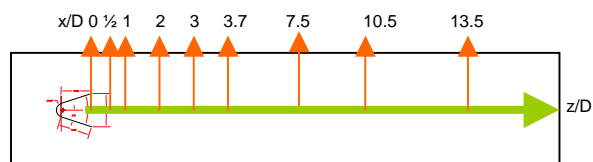


Figure 4-1 Locations of Velocity Traverses

Figures 4-2 and 4-3 are plots of mean and RMS axial velocity respectively along the "green" traverse in Figure 4-1. The gaps in both sets of data represent sections of the test

section where there was no optical access for the LDV LASER. Figure 4-2 depicts the mean velocity normalized by the inlet velocity. Figure 4-3 depicts the RMS normalized by the inlet velocity. The data presented are for 4 Reynolds numbers; 10,000, 25,000, 40,000, and 55,000. The mean axial velocity changes substantially from the near wake to the far wake region. From the trailing edge of the flame holder the mean velocity is increasingly negative, reaches

a maximum then increases to zero. The location where the velocity is zero represents the mean location of the trailing edge of the recirculation zone behind the bluff body. Note as the Reynolds number increases the length of the recirculation zone decreases. The location of the maximum negative velocity also moves closer to the trailing edge of the bluff body as the Reynolds number increases. In the far wake region the velocity increases asymptotically to

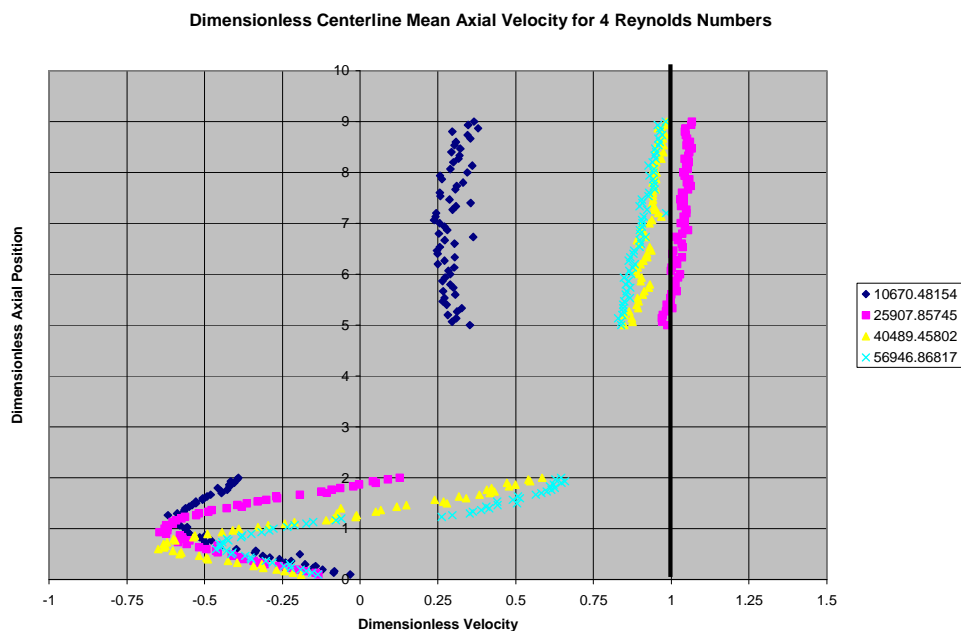


Figure 4-2 Travers of Axial Velocity Behind the Bluff Body

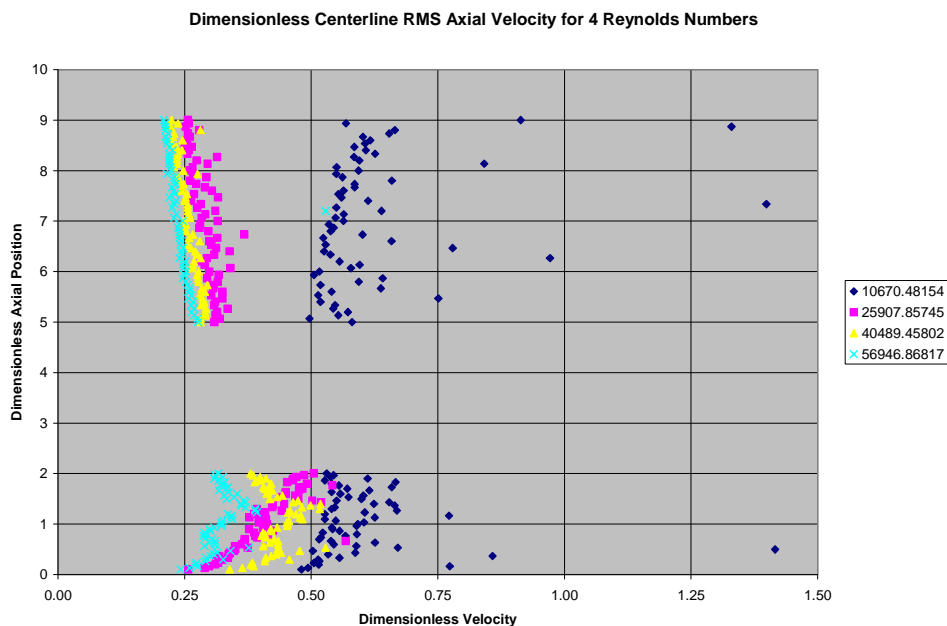


Figure 4-3 Traverse of RMS Velocity Behind the Bluff Body

the inlet velocity for all but the 10,000 Reynolds number case. In the case of Reynolds number 10,000 the low velocity wake persists the entire length of the test section behind the flame holder.

The RMS velocity also varies as the Reynolds number increases. For the lowest Reynolds number, 10,000, the wake is highly turbulent. For this Reynolds number the RMS velocity is routinely greater than 50% of the inlet velocity in the wake of the bluff body for the entire length of the test section. There is also a lot of scatter in the data due to the low data rate that occurred for many of these points. For the higher Reynolds numbers the RMS velocity is more similar.

For the higher Reynolds number cases the RMS velocity has two relative maximums in the

recirculation zone. Both maxima occur at the location where the derivative of the mean velocity is zero. The second maximum is higher than the first and represents the highest RMS value in the wake of the bluff body. In the far wake the RMS are still highly turbulent but turbulence is decaying. RMS values continue to decrease, below 25% of flame holder width's down stream of the bluff body.

Velocity profiles were also taken across the wake down stream of the bluff body, see the orange lines in Figure 4-1. Figures 4-4 to 4-6 depict the mean and RMS velocity profiles for 0.5L, 1.0L, and 2.0L down stream of the bluff body for a Reynolds number of 40,500. On the left of each figure are plots of mean and RMS velocity along the centerline axis while on the right are the mean and RMS of the transverse 0.

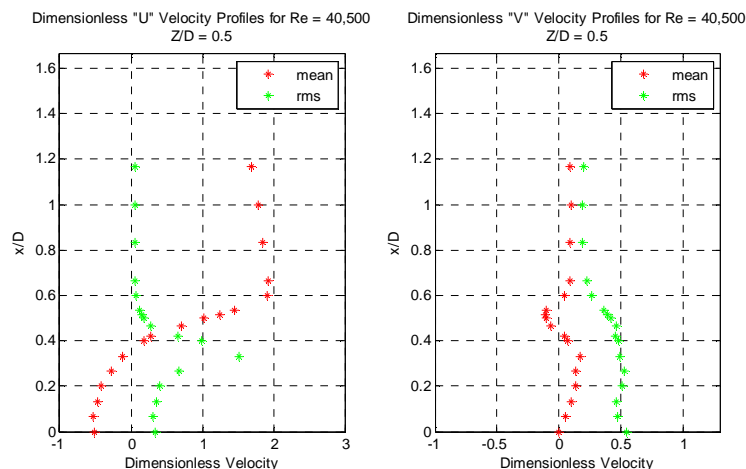


Figure 4-4 Velocity Profiles $Z/D = 0.5$ Down Stream of the Bluff Body for Reynolds Number = 40,500

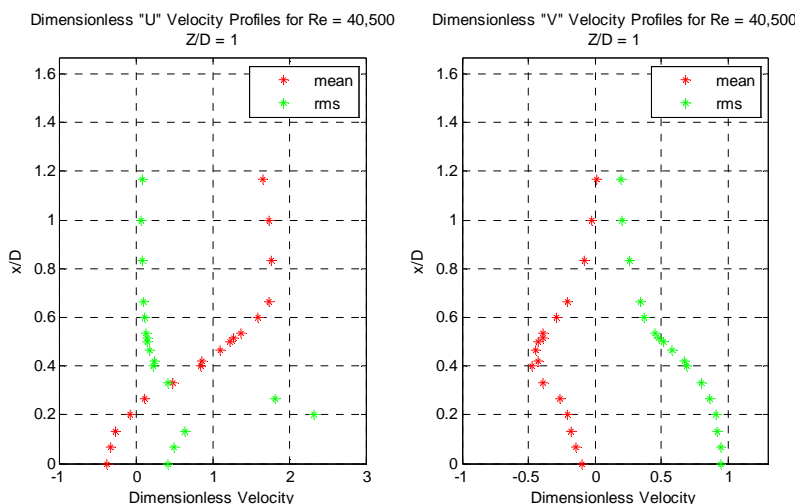


Figure 4-5 Velocity Profiles from $Z/D = 1$ Down Stream of the Bluff Body for Reynolds Number = 40,500

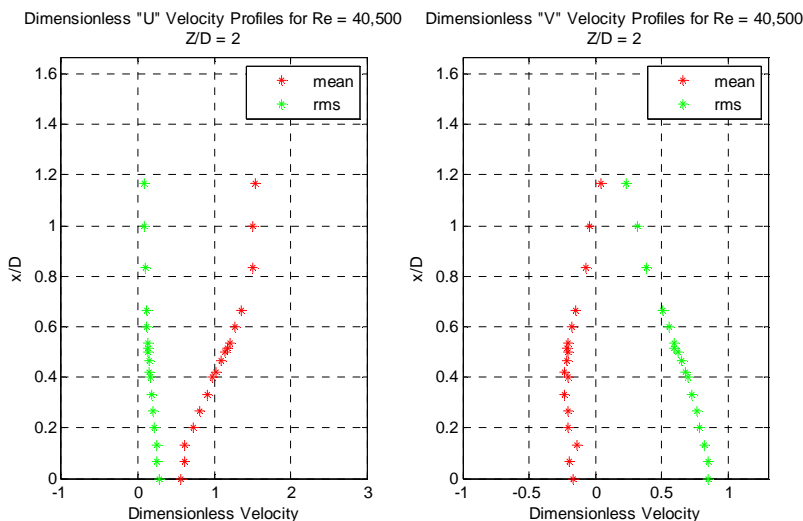


Figure 4-6 Velocity Profiles from $Z/D = 2$ Down Stream of the Bluff Body for Reynolds Number = 40,500

velocity. Data were also taken for Reynolds numbers of 10,000, 12,000, and 55,000

There are several points of interest in these figures. Figure 4-4, depicts the mean axial velocity $L/2$ down stream of the trailing edge of the bluff body. The edge of the bluff body is located at $X/D = 0.5$. At this point the velocity is approximately the same as the inlet velocity. Further away from the flame holder the velocity reaches a maximum of almost 2 times the inlet velocity. In this experiment the blockage ratio of the flame holder is approximately 1.43. Thus the "lip velocity" is higher than the velocity expected assuming an acceleration due to the blockage.

Also of note is the RMS velocity. In all three figures the RMS of the axial velocity reaches a maximum inside the wake of the flame holder. Close to the bluff body this maximum can be twice the inlet velocity, or 200%. The transverse RMS velocity also reaches a maximum in the wake region. Unlike the axial RMS the transverse RMS persists well outside the wake. A detailed analysis of the LDV supplemented with PIV data is the subject of a future paper.

4.2 LARGE COHERENT STRUCTURES

Another important aspect of the fluid dynamics of a bluff body in cross flow is the large Karman Street vortex seen shed in the wake of the bluff body. LDV was conducted over a wide range of Reynolds number for both

the open and closed v-gutter bluff bodies. The shedding frequency for a given Reynolds number was found by taking the DFFT of each set of interpolated data, as outlined in section 2. The frequency was then non-dimensionalized to Strouhal number using the effective or blockage velocity, not the inlet velocity, and the width of the v-gutter. Figure 4-7 is a plot of this data. Also plotted in Figure 4-7 are the data for a circular cylinder in cross flow for reference, Blevins (1985).

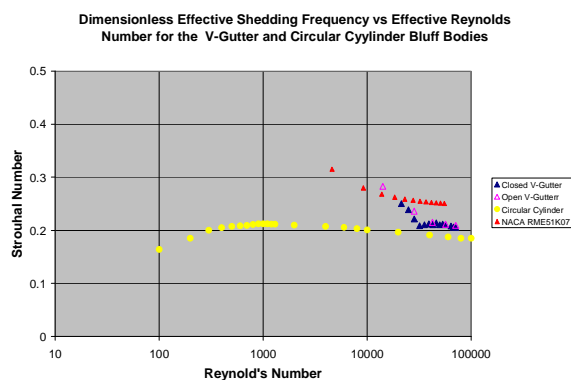


Figure 4-7. Dimensionless Shedding Frequency Several Reynolds Numbers.

4.3 LEAN BLOWOUT

Detailed lean blowout measurements were also taken for the combusting v-gutters. Figure 4-8 depict the equivalence ratio recorded at lean blow out (LBO) versus Reynolds Number for the

closed v-gutter flame holder at 4 different temperatures. In all cases the data plotted represent the average of at least 6 blow out points for the given Reynolds number. Due to facility limitations the highest Reynolds number for the 70F, 300F, and 460F inlet temperatures were 55,000, 34,000, and 29,000 respectively.

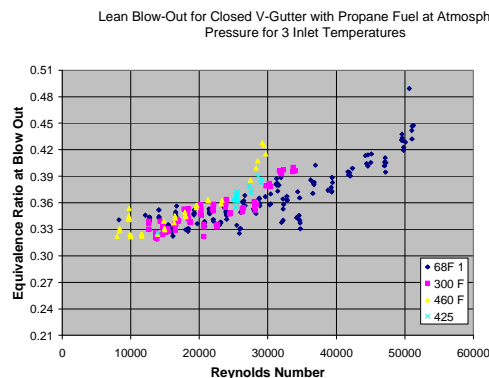


Figure 4-8 Lean Blow Out Equivalence Ratio vs. Reynolds Number for Several Inlet Temperatures

When studying Figure 4-8 two interesting results can be discerned. At lower Reynolds numbers, below 15,000 the lean blowout seems insensitive to Reynolds number. Above 20,000 Reynolds number, the LBO increases with increasing Reynolds number. Figure 4-9 depicts the LBO data plotted against the DeZubay correlation parameter instead of Reynolds number. When plotted this way the data correlate very well, similar to the shape of DeZubay's original data.

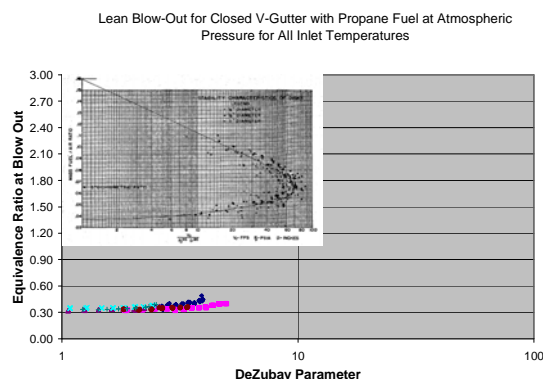


Figure 4-9 Lean Blow Out Equivalence Ratio vs. DeZubay Correlation Parameter

Another very interesting trend can be seen in Figure 4-8. As the inlet temperature increases for a given Reynolds number the equivalence ratio at LBO increases. Intuitively one would expect this value to decrease with temperature,

not increase. Ballal and Lefebvre (1979) studied the relationship between temperature and weak extinction for constant inlet velocity. They found the extinction limit decreases with inlet temperature. Figure 4-10 depicts the equivalence ratio at LBO for a constant inlet velocity of 25 m/s for several inlet temperatures. When plotted this way the equivalence ratio at LBO does show the expected decreasing trend.

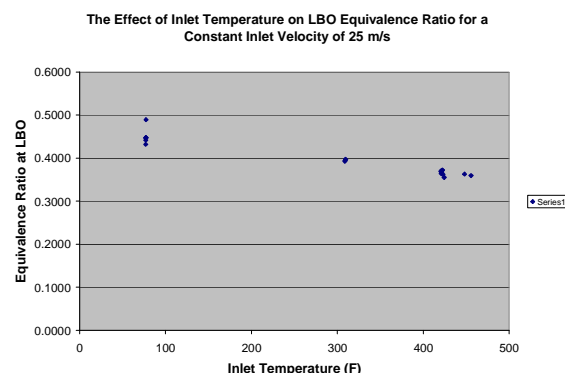


Figure 4-10 Lean Blow Out Equivalence Ratio vs. Inlet Temperature for Several Inlet Temperatures

4.4 HIGH SPEED IMAGES

Many high speed images were also taken of the flame behind the closed v-gutter flame holder with a Phantom 7.2 camera. Flame intensity images were captured at 5KHz. Figure 4-11 is a typical high speed image the flame behind a v-gutter bluff body with combustion. For this image the inlet temperature was, 70F, the Reynolds number is approximately 30,000 and the equivalence ratio 0.64. Note the flame is dominated by smaller vortices that seem to be generated by the boundary layer. This flame is absent of the large Karman Street vortices

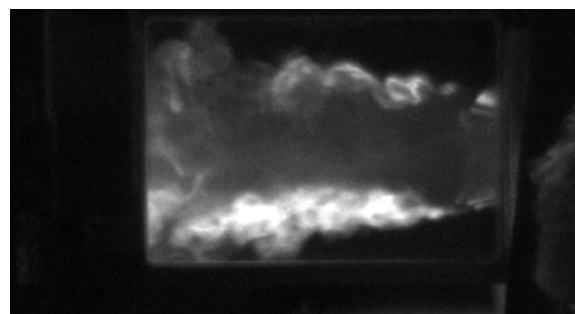


Figure 4-11 High Speed Image of Combusting V-Gutter at Higher Equivalence Ratio

typical of a non-combusting flow. This figure is representative of Reynolds numbers greater than 15,000 for equivalence ratios well above the lean limit. Figure 4-12 is a high speed image of the same conditions as Figure 4-10 near LBO, an equivalence ratio of 0.35. The flame structure of both images is very similar. In both images vortices are clearly seen in the shear layer and there is very little vortex motion in the wake region.

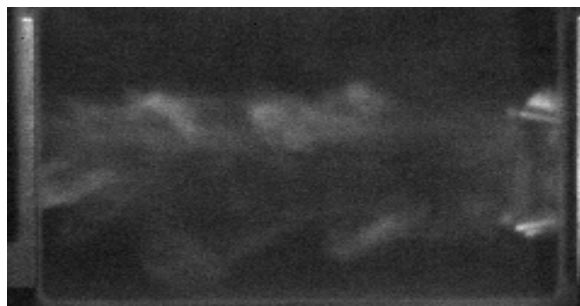


Figure 4-12 High Speed Image of Combusting V-gutter Near LBO

High speed images were also taken at elevated inlet temperatures. Figures 4-13 and 4-15 are images the flame near LBO for Reynolds number 26,000 and 32,000 respectively at an inlet temperature of 70F. In both of these images the largest vortices are those in the shear layer generated by the boundary layer of the flow. Figures 4-14 and 4-16 are images near LBO for Reynolds number is 25,000 and 35,000. In these images the inlet temperature was elevated to 460F with electric heaters. Note in these images one can easily see large vortices in the wake of the flame holder reminiscent of Karman Street vortices shed behind the bluff body without combustion.

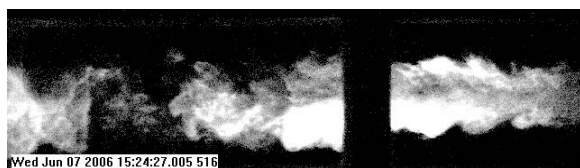


Figure 4-13 Combusting V-Gutter at 70F Inlet Temperature, Re = 26,000, Near LBO

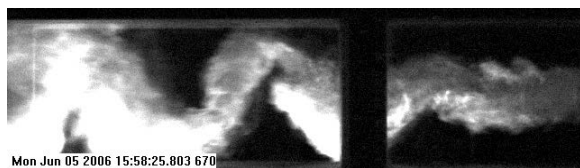


Figure 4-14 Combusting V-Gutter at 460F Inlet Temperature, Re = 25,000, Near LBO

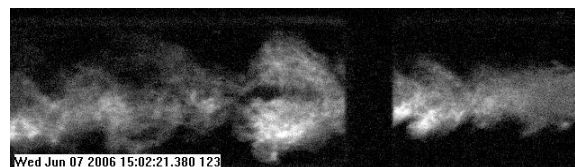


Figure 4-15 Combusting V-Gutter at 70F Inlet Temperature, Re = 32,000, Near LBO

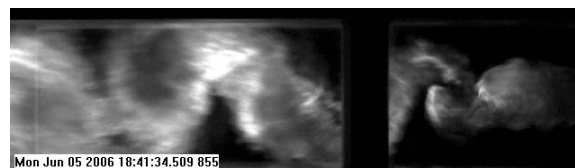


Figure 4-16 Combusting V-Gutter at 460F Inlet Temperature, Re = 35,000, Near LBO

This contrast is representative of the many high speed images taken above a Reynolds number of 15,000 for 70F and 460F inlet temperatures.

At lower Reynolds numbers the vortex shedding phenomena at LBO is different from those above Reynolds number of 15,000. Figures 4-17 and 4-18 are high speed images taken near the LBO limit. They depict Reynolds

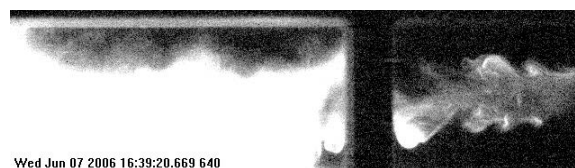


Figure 4-17 Combusting V-Gutter at 70F Inlet Temperature, Re = 8,300, Near LBO



Figure 4-18 Combusting V-Gutter at 460F Inlet Temperature, Re = 9,700, Near LBO

numbers of 8,300 and 9,600 and inlet temperatures of 70F and 460F respectively. Both of these images seem to be dominated by a combination of large and small vortices. It is difficult to discern a dominant vortex shedding mode.

5 CONCLUSIONS AND RECOMMENDATIONS

In this paper, several sets of data were presented for the closed flame holder. Experiments are ongoing to collect similar data for the open v-gutter configuration, a circular

cylinder and other bluff body configurations. In addition new instrumentation is also planned to collect point temperature and species measurements.

Currently analysis of this data and data from the open v-gutter flame holder are ongoing. From the data currently analyzed and presented conclusions can be drawn. Enough data are believed to exist to provide "necessary" conclusions. More data and analysis is required to provide conclusions that are supported by data that is both "necessary" and "sufficient". Given this, some interesting conclusions can be drawn from the data and analysis to date.

5.1 Turbulent Transition

Fluid dynamic transition of the v-gutter flame holders varies substantially from that of the circular cylinder. The slope of the curve at lower Reynolds numbers is discontinuous, unlike the circular cylinder. For a circular cylinder, the vortex shedding may be very different than that of a v-gutter. When comparing Panton's (1984) discussion of vortex shedding behind a circular cylinder with the data from Blevins (1985), the peak in Strouhal number for a circular cylinder occurs at a Reynolds number where there is still a very organized Karman Street vortex shed behind the cylinder. According to Panton (1984), as the Reynolds number increases the boundary layer of the cylinder separates. Also, as Reynolds number increases the point of separation moves forward. At the same time the separation moves forward on the cylinder the Strouhal number decreases. Panton concludes the flow behind the cylinder is not "turbulent" until the Reynolds number approaches 30,000.

The v-gutter data does not depict the same smooth decrease in Strouhal number as Reynolds number increases. Between Reynolds numbers of 20,000 and 25,000 there is a cusp in the shape of the curve denoting an abrupt change in the vortex shedding. This may be the transition from "laminar" to "turbulent" shedding in the wake for the v-gutter. These conclusions can be supported by better visualization around the range of Reynolds numbers where the cusp in the data occurs. This can be accomplished with highly spatially resolved Large Eddy Simulation (LES) or through the use of Particle Image Velocimetry (PIV) analysis of a v-gutter and a circular cylinder. Since this transition occurs at the lower range of Reynolds numbers

for current engines this is an area of further research.

As outlined in the Introduction, Zukoski (1954, 1955) and Ozawa (1971) concludes that the flame behind a bluff body transitions around a Reynolds numbers of 10,000. In the equivalence ratio data presented, the equivalence ratio at LBO below Reynolds number of 15,000 seem to be insensitive to Reynolds number supporting these conclusions. The high speed images in this Reynolds range also contain a mix of vortices being shed by the shear layer of the flame holder and larger wake vortices. When compared to high speed images at higher Reynolds numbers the images also seem to support the conclusions that the flame transitions in this Reynolds range.

Reynolds numbers below 10,000 are rarely achieved in modern engines, thus this conclusion may be academic. Regardless the ability to collect data at these conditions is relatively easy. Further data will be collected on different flame holder geometries and at different conditions in an attempt to further support this conclusion. Other instrumentation can be used to shed further light here. In addition to high speed imaging, Particle Image Velocimetry (PIV) of the combusting flow and highly temporally resolved temperature measurements may be applied at Reynolds numbers below "transition". The added data provided may shed more light as to the nature of the vortex shedding behind the bluff body.

5.2 Lean Blowout

From the lean blow out data two conclusions are drawn. The first is that the blow out data correlate well when DeZubay's correlation is used. The maximum correlation parameter value of 30 was achieved in the current testing. Research will continue at higher inlet temperatures and velocities to continue to populate this curve at correlation values greater than 30.

When plotted against Reynolds number the data seem counter intuitive. At higher temperatures, for the same Reynolds number the equivalence ratio at LBO are higher, not lower. When plotted against temperature, with constant inlet velocity, the equivalence ratio decreases with inlet temperature. This result would indicate that using the Reynolds number to correlate LBO does not properly account for

the competing effects of decreased density and increased viscosity as the temperature is increased.

5.3 Vortex Shedding in the High Speed Images

In their earlier paper Mehta and Soteriou (2003) concluded that the vortex shedding behind a bluff body changed substantially when combustion was present. They concluded that the baroclinic torque associated with the temperature rise across the flame dominated the flow. As a result their model showed a flame where flow behind the bluff body was dominated by vortices much smaller than the Karman Street vortices. At stoichiometry well above the LBO limit the high speed images seem to support this conclusion.

Later Mehta and Soteriou (Erickson et al. 2006) concluded from their modeling that certain conditions could exist where the flame could be dominated by the Karman Street vortices. They concluded that if the temperature ratio across the flame were reduced that these vortices eventually dominate the flow. This phenomenology is also supported by LES computations by Porumbel and Menon (2006), and Fureby (2006). High speed images qualitatively support these conclusion as well.

In the bluff body flow three forces seem to dominate depending on the operating conditions; momentum, viscous and baroclinic. For the high equivalence ratio combustng flow, above Reynolds number of 15,000, momentum and baroclinic forces seem to dominate. These forces suppress Karman Street vortex shedding and promote smaller vortices that stabilize the flame in the shear layer of the wake. As the inlet temperature is increased density falls and viscosity increases. Thus increased temperature decreases momentum and increases viscous effects. Further as inlet temperature increases the temperature ratio across the flame decreases for the same stoichiometry. The resultant effect is a reduction in the baroclinic effect of the flame. Combined the high speed images and modeling seem to support a situation where viscous forces and Karman Street vortex shedding dominate the combustng near LBO at Reynolds numbers as high as 35,000. Further testing using PIV in combustng flow as well as temporally resolved point temperature measurements are required to

provide more quantitative results to support these conclusions.

6 REFERENCES

- Adrian, R., 1983, "Laser Velocimetry," in Fluid Mechanics Measurements, ed. R. J. Goldstein, Hemisphere Publishing Corporation, New York, pp. 155-244.
- Ballal, D., and Lefebvre, A., 1979, "Weak Extinction Limits of Turbulent Heterogeneous Fuel/Air Mixtures", *Journal of Engineering and Power*, 101, 3, p 343-348.
- Blevins, 1985, "The Effect of Sound on Vortex Shedding from Cylinders", *J. Fluid Mech.*, Vol. 161, pp. 217-237.
- DeZubay, E. A., 1950, "Characteristics of Disk-Controlled Flame," *Aero Digest*, pp. 54-57.
- Erickson, R., Soteriou, M., and Prashant, M., 2006, "The Influence of Temperature Ratio on the Dynamics of Bluff Body Stabilized Flames", AIAA 2006-753.
- Fureby, C., 2006, "A Comparison of Flamelet LES Models for Premixed Turbulent Combustion", AIAA 2006-155.
- King, C. R., 1957, "A Semi Empirical Correlation of Afterburner Combustion Efficiency and Lean-Blowout Fuel-Air-Ratio with Several Afterburner Inlet Variables and Afterburner Lengths," NACA57RMF26.
- Mehta, P.G., and Soteriou, M.C., 2003, "Combustion Heat Release Effects on the Dynamics of Bluff Body Stabilized Premixed Reacting Flows", AIAA 2003-0835.
- Numerical Recipes in C: The Art of Scientific Computing, 1992, Cambridge University Press, pp. 575-584 .
- Ozawa, R. I., 1971, "Survey of Basic Data on Flame Stabilization and Propagation for High Speed Combustion Systems", AFAPL-TR-70-81
- Porumbel, I., and Menon, S. 2006, "Large Eddy Simulation of a Body Stabilized Premixed Bluff Flame:", AIAA 2006-0152

Roshko, A., 1954, "On the Drag and Shedding Frequency Two Dimensional Bluff Bodies", NACA TN 3169

Younger G., Gabriel, D., and Mickelsen, W., 1951, Experimental Study of Isothermal Wake-Flow Characteristics of Various Flame Holder Shapes", NACA RM E51K07.

Zukoski, E., 1954, "Experiments Concerning the Mechanism of Flame Blowoff From Bluff Bodies," Thesis, California Institute of Technology

Zukoski, E., and Marble, F., 1955, "The Role of Wake Transition in the Process of Flame Staboilization on Bluff Bodies", AGARD Combustion Research and Reviews, 167-180.

UNDERSTANDING OF TURBULENT FLAMES FROM VORTEX/FLAME-INTERACTION

STUDIES

V. R. Katta,^{*} S. Gogineni,^{*} T. R. Meyer⁺, J. R. Gord, W. M. Roquemore

Propulsion Directorate

Air Force Research Laboratory

Wright Patterson Air Force Base, OH

ABSTRACT

Various concepts for modeling turbulence-chemistry interaction in a nonpremixed combustion are examined by studying vortex/flame interactions in a hydrogen/air, opposed-jet nonpremixed flame. Unsteady flat flames are obtained by injecting vortices from fuel and air sides of the flame surface simultaneously. The conventional characteristic parameters such as stretch rate and scalar dissipation rate cannot be used for describing the quenching process in unsteady flames. The flow and chemical nonequilibrium states of the unsteady flames are responsible for the variations in extinction values of these traditional characteristic variables. It is proposed that a variable that is proportional to the air-side stretch rate and inversely proportional to the rate of change in the flame temperature can be used uniquely for characterizing the unsteady quenching process. Unsteady curved flames are obtained by injecting vortices from the air side. Vortex size is varied from centimeter to sub-millimeter. The dynamic changes occurred to the flame structure during these interaction processes are mapped on to scalar-dissipation-rate scale. The large centimeter-size vortices, irrespective of the propagation velocity, wrinkle and stretch the flame before causing local extinction—representing a typical laminar-flamelet behavior. On the other hand, the small sub-millimeter-size vortices replace the local fluid in the flame zone with fresh air and destroy the flame structure without causing any wrinkle or stretch on the reaction zone—representing a non-flamelet behavior. Depending on the vortex size, interactions between flame and millimeter-range vortices gradually deviate from the flamelet description.

INTRODUCTION

Studies on the structure of an unsteady flame are important for gaining an understanding of fundamental combustion processes. Such studies provide insight into turbulence-chemistry interaction and aid the development and evaluation of simplified models that can be used in design codes for practical combustion systems. Unsteady flames associated with turbulent combustion are subjected to stretching that varies with time; typically, the time scale for the changes in stretch rate is comparable to that of the chemical (e.g., reaction time) or physical (e.g., diffusion time) responses of the system. Because of the resulting nonequilibrium environment, the structure of a stretched unsteady flame differs from that of a stretched steady-state flame.

Numerous experimental and numerical investigations¹⁻³ have been performed to quantify the scalar structure of steady state, aerodynamically stretched, planar, opposed-jet nonpremixed flames. Such studies have not only provided benchmark experimental data but also yielded valuable insight into the steady-state behavior of the planar flame that is subjected to stretch (or strain) rates up to the extinction limits. In practical combustion devices, turbulent flames are subjected to severe unsteadiness that results from the random motion of the vortices.^{4,5} To retain the analytical and experimental simplicity offered by planar nonpremixed flames, however, the

^{*} Innovative Scientific Solutions, 2766 Indian Ripple Road, Dayton, OH

⁺ Iowa State University, Ames, IA

unsteady flame structure is also investigated in opposed-jet flames by fluctuating the fuel and air jets simultaneously and sinusoidally.⁶⁻⁸ Although the results have indicated that unsteady flames can be stretched beyond the steady-state extinction limit,⁹ these studies are mainly focused on understanding the behavior of the flame when subjected to moderate-amplitude fluctuations in stretch rate⁷, reactant composition,^{7,10} and partial premixing.¹¹ Since the extinction stretch rate, in general, is higher than the maximum stretch rate at which ignition can occur, temporal flame extinction that occurs at any time within the fluctuation cycle in a periodically oscillating opposed-jet flame could lead to complete flame extinction. Consequently, stretch rates near the extinction limit could not be used in the periodically oscillating flame experiments; as a result, the unsteady flame structure near the extinction limit has not been studied adequately.

Recent studies on vortex/flame interactions by Katta et al.¹² revealed that the extinction stretch rate of an unsteady flame is dependent on whether the flame is traveling or stationary. By issuing vortices from the fuel and air sides of an opposed-jet jet nonpremixed flame, they simulated traveling and stationary unsteady flames. In the traveling unsteady flame, not only the stretch rate on the flame but also its location changes with time; in the stationary unsteady flame, on the other hand, the stretch rate varies with time by locking the flame position spatially. The latter unsteady flames, established by issuing vortices simultaneously from the air and fuel sides, offer a pathway for understanding the unsteady flame structure near extinction.

During single-vortex/flame interactions, which are often considered to be the building blocks of statistical theories of turbulence, the flame surface is subjected not only to unsteadiness but also to deformation. To investigate the effects of curvature on unsteady flames, both theoretical and experimental studies have been initiated.¹³⁻¹⁶ In particular, experiments designed by Roberts et al.¹⁷ and by Rolon et al.¹⁸ have generated considerable interest, especially because of their unique ability to inject a well-characterized vortex toward the flame surface. Numerous investigations have been performed on wrinkled flames by varying the size and strength of the vortex in opposed-jet burners¹⁸ in attempts to understand global features such as scale^{19,20} and origin²¹ effects and localized features such as annular-quenching²² and nonadiabatic-equilibrium-temperature^{23,24} phenomena. In the present investigation, a well-tested CFDC model^{22,25,26} is used for understanding the effects of unsteady stretching on flat and wrinkled opposed-jet, nonpremixed flames. Large vortices issued from the fuel and air sides are used for establishing flat flames and centimeter-to-sub-millimeter-size vortices issued from air side are used for establishing wrinkled flames.

MATHEMATICAL MODEL

A time-dependent axisymmetric model known as UNICORN (UNsteady Ignition and COMbustion using ReactionNs)²⁶ is used for the simulations of unsteady flames associated with an opposed-jet burner. This model solves the Navier-Stokes and species- and energy-conservation equations written in the cylindrical-coordinate (z-r) system. A detailed-chemical-kinetics model is employed for describing the hydrogen-air combustion process. This model consists of 13 species--namely, H₂, O₂, H, O, OH, H₂O, HO₂, H₂O₂, N, NO, NO₂, N₂O, and N₂--and 74 elementary reactions among the constituent species. The rate constants for this H₂-O₂-N₂ reaction system are obtained from Ref. 27.

Temperature- and species-dependent property calculations are incorporated in the model. The governing equations are integrated on a nonuniform staggered-grid system. An orthogonal grid having rapidly expanding cell sizes in both the axial and the radial directions is employed. The finite-difference forms of the momentum equations are obtained using an implicit QUICKEST scheme,^{28,29} and those of the species and energy equations are obtained using a hybrid scheme of upwind and central differencing. At every time step, the pressure field is calculated by solving the pressure Poisson equations simultaneously and utilizing the LU (Lower and Upper diagonal) matrix-decomposition technique. UNICORN has been validated previously by simulating various steady and unsteady opposed^{21,22,24} and coflow^{25,30} jet nonpremixed flames.

BURNER CONFIGURATION:

The opposed-jet-flow burner used for the investigations of vortex/flame interactions was designed by Rolon, is shown in Fig. 1, and is described in detail in Ref. 18. A flat flame is formed between the fuel and air jets having velocities of 0.69 and 0.5 m/s, respectively. The hydrogen-to-nitrogen ratio used for the fuel jet is 0.38. While unsteady wrinkled flames are established by shooting vortices either from the fuel or air sides of the flame surface, unsteady flat flames are established by shooting vortices simultaneously from the fuel and air sides. The collision of the vortices at the flame surface in the latter case imposes unsteady stretch on the flame. Studies are performed to investigate various types of vortex/flame interactions by incorporating different sizes of fuel- and air-side injection tubes and varying the fluid injection durations. Air-side vortices are generated by injecting a specified amount of air through the syringe tube (Fig. 1) and then through an injection tube having a diameter of 0.2 - 5.0 mm. Similarly, fuel-side vortices are generated by injecting a specified amount of fuel through the respective syringe and injection tubes. The z - r coordinate system used for the simulation of flames associated with the Rolon burner is shown in Fig. 1. Calculations for these axisymmetric flames are made using a non-uniform 601×301 mesh system distributed over a physical domain of 40×40 mm, which yielded a mesh spacing of 0.05 mm in both the axial (z) and the radial (r) directions in the region between the two nozzles.

RESULTS AND DISCUSSION

UNSTEADY FLAT FLAMES:

Calculations for the unsteady stationary flat flames are made by issuing vortices simultaneously from the fuel and air sides via injecting respective fluids with a constant peak velocity. Variation in the strengths of the vortices and, thereby, the applied stretch rate on the flat flame is achieved by changing the rise time (acceleration) of the injection fluid in reaching the specified peak velocity. As the vortices interact with the flame surface the temperature of the

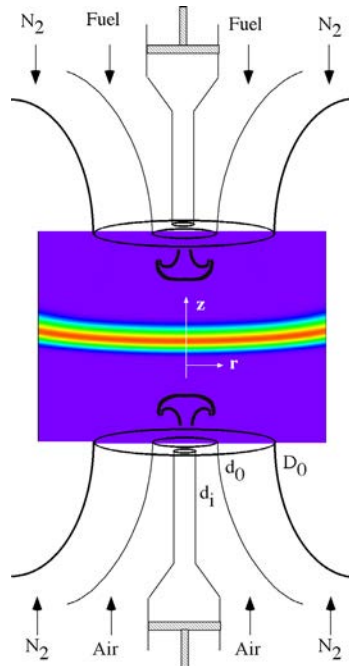


Fig. 1. Schematic diagram of opposed-jet-flow burner used for investigations of vortex/flame interactions. Nitrogen-diluted hydrogen fuel and air introduced from upper and lower nozzles, respectively. Structure of steady-state flame is also shown in form of iso-temperature distribution.

latter decreases. The extinction process for the flame is considered to begin when the temperature decreased to 1130 K. Further decrease in temperature during a vortex/flame interaction after the flame is locally extinguished results from the diffusion and conduction of products and heat, respectively, from the flame zone. As expected, the flame responded uniquely to the changes in the rate at which fluid is injected. The time at which extinction occurs is inversely proportional to the rate of increase in the injection velocity (a_0).

The changes in air-side stretch rate (k_a) during the vortex/flame-interaction process are shown in Fig. 2 for various a_0 cases. The strain rates at which extinction took place were obtained from the 1130-K-cutoff criterion and are indicated by filled circles in this figure. A linear decrease in extinction stretch rate with time can be observed. The extinction stretch rate increased from 2600 to 3200 s^{-1} when the injection-fluid accelerations are increased from 2450 to 4900 m/s^2 . The data in Fig. 2 indicate that using a unique value of air-side stretch rate one cannot predict the quenching condition of an unsteady flat flame. In other words, value of the air-side stretch rate at which extinction occurs in an unsteady flame depends on the rate at which the flame was stretched. The extinction values for k_a in unsteady flames range from 2610 to 3195 s^{-1} and are higher by 85 to 127% than the limit obtained in steady-state flames (1410 s^{-1}).

The stretch rate computed at a flame location represents the local flow structure and because of the flow nonequilibrium an accurate description of the quenching process using stretch rate alone is not possible as shown in Fig. 2. On the other hand, since the scalar dissipation rate (χ) represents the overall diffusion process, this rate calculated at a given flame location could be used for describing the flame quenching process. Variations in the scalar dissipation rate (calculated at the stoichiometric surface) with time are plotted for various vortex/flame-interaction cases in Fig. 3. The respective values at extinction for all of the unsteady flames, determined based on the 1130-K criterion, are represented by filled circles. From this figure, it is apparent that the scalar dissipation rate χ_{stoich} also failed to characterize the extinction process in unsteady flames uniquely, which means that extinction in unsteady flames cannot be

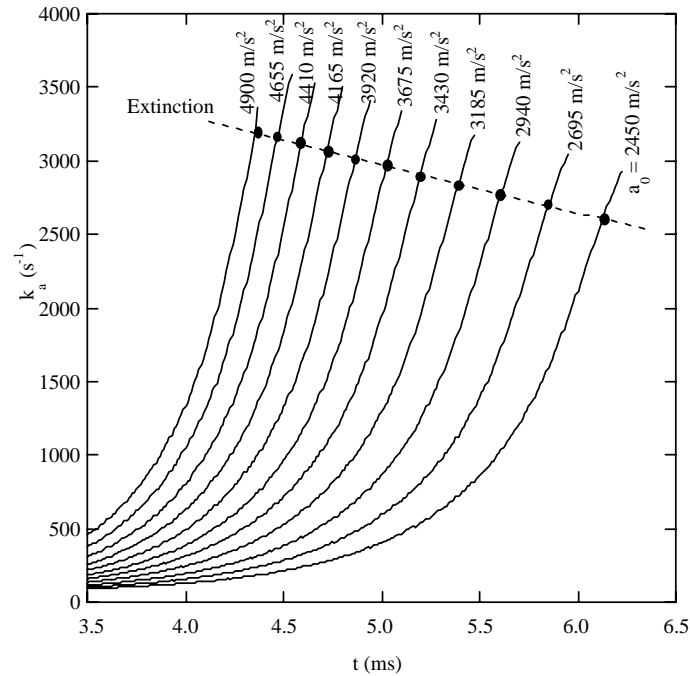


Fig. 2. Variations of air-side strain rate with time for different vortex/flame interactions. Vortices are injected from both sides of the flame. Extinction values based on 1130-K-temperature criterion indicated by solid circles.

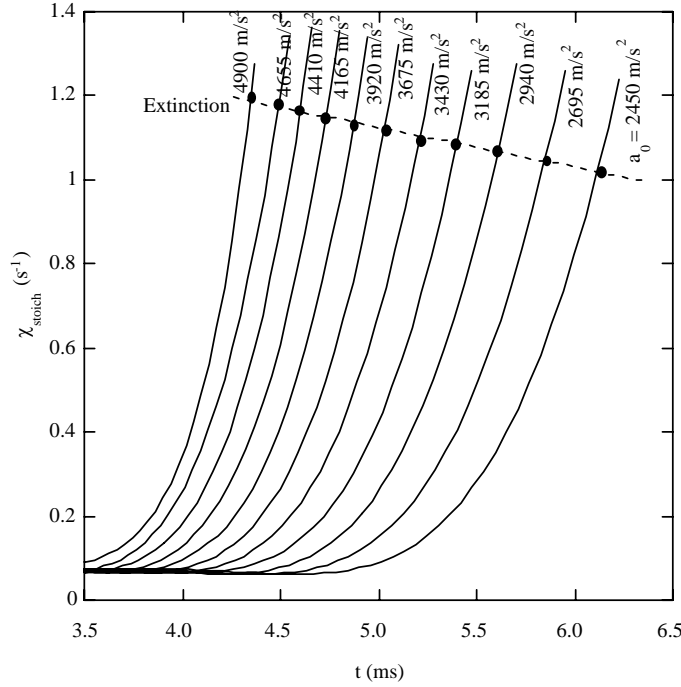


Fig. 3. Variations of scalar dissipation rate at stoichiometry with time for different vortex/flame interactions. Vortices are injected from both sides of the flame.

predicted using scalar dissipation rate. However, the variations in extinction values with respect to the changes in fluid-injection velocity seem to be smaller for scalar dissipation rates than for stretch rates. The extinction values for χ_{stoich} in unsteady flames range from 1.02 to 1.193 s⁻¹ and are higher only by 30 to 53% than the limit obtained in steady-state flames (0.78 s⁻¹).

The reason that the scalar dissipation rate describes unsteady flame extinction more closely than the stretch rate can be understood by considering the chemical and flow nonequilibrium processes that develop in these flames. As the stretch on the flame is increased, increasingly more reactants, through diffusion, are transported into the reaction zone. At lower stretch rates, the chemical kinetics can consume all of the entering reactants. However, at higher rates of stretch, chemistry cannot cope with the large reactant fluxes and, therefore, flame cooling occurs. As the stretch rate represents the reactant fluxes transported into the reaction zone only in the case of steady-state flames, when flow nonequilibrium occurs, the stretch rate does not take into account the time lag between the diffusion and convection processes and, hence, cannot represent the extinction process. Since the scalar dissipation rate describes the diffusion process, it is less sensitive to the flow nonequilibrium that develops in unsteady flames. However, scalar dissipation rate can represent the chemical kinetics in the flame zone only when the diffusion time scale is far greater than the chemical (reaction) time scale--which exists in unstretched flames where reactions are limited by the diffusion process. When chemical nonequilibrium occurs (chemistry-limited situation), the scalar dissipation rate does not take into account the time lag between the diffusion and chemical kinetics and, hence, fails to represent the extinction process. Nevertheless, since the scalar-dissipation rate reflects changes in diffusion more accurately than the stretch rate, it describes the unsteady extinction process more accurately.

To represent the unsteady-extinction process uniquely, one must consider a variable that takes into account both the flow- and the chemical-nonequilibrium processes. Since the stretch rate or scalar-dissipation rate can be used to estimate the former, a parameter that can be used for estimating the latter is required. If one assumes that no delay exists between chemical kinetics and heat-release rate, then dT_f/dt (rate of decrease in flame temperature) represents the rate of

change in chemical kinetics and, in other words, the rate of change in the chemical-nonequilibrium state. Vortices that move more rapidly result in higher dT_f/dt values at extinction, and those that move slowly result in lower dT_f/dt values. Therefore, by defining a variable that is proportional to the air-side stretch rate and inversely proportional to the temperature-decrease rate (dT_f/dt), one can obtain a universal value for identifying the quenching process in unsteady flames.

By considering both the chemical and flow nonequilibrium states of an unsteady flame, a new variable (σ) is defined as the ratio of the stretch rate to the rate of change in flame temperature as follows:

$$\sigma = T_\infty \frac{(k_a - k_{a0})}{\left(\frac{dT_f}{dt}\right)}$$

Here, T_f is the flame (peak) temperature and k_{a0} is the steady-state air-side extinction stretch rate. Values of σ computed at several instants during various vortex/flame interactions are plotted in Fig. 4. In each case as the vortices issued from the fuel and air sides approach the flame surface, σ decreases with interaction time, crosses zero when the instantaneous stretch rate reaches the steady-state extinction limit, reaches a minimum value, and then begins to increase. Interestingly, the minimum values of σ for all of the vortex/flame-interaction cases are the same--0.39. The striking feature of σ became evident when the extinction condition for each interaction case was plotted in Fig. 4 by filled circles. The extinction conditions coincided with the minima in σ .

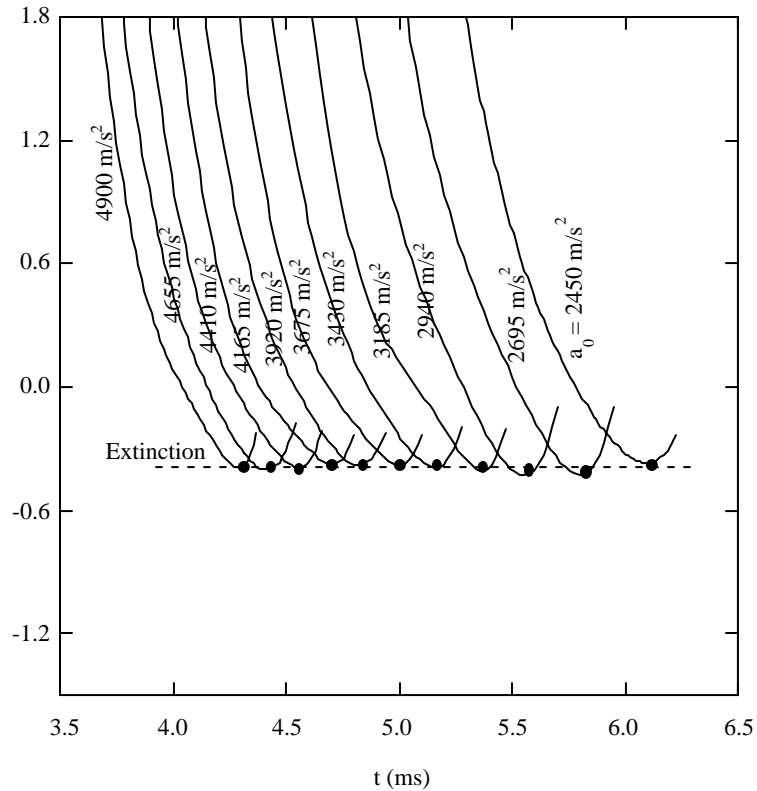


Fig. 4. Variations of new variable σ with time for different vortex/flame interactions. Vortices are injected from both sides of the flame.

UNSTEADY WRINKLED FLAMES:

Wrinkled flames are generated by issuing vortices either from the fuel or air side of the flame surface via injecting a specified amount of fluid through the respective syringe tube (Fig. 1) and then through an injection tube having a diameter in between 0.05 and 5.0 mm. Evolution of the injected vortex and its interaction with the flame surface depends on the injection time. In general, with the shorter injection times, the generated vortices travel faster toward the flame surface and then affect the flame structure as the local flow time scales approach the chemical time scales. As the injection time gets longer the resulting vortex/flame interaction tends to generate a perturbed flame rather than a wrinkled one. Also the interaction process strongly depends on the size of the vortex. A typical centimeter-size-vortex/flame interaction obtained with a 5.0-mm diameter injection tube is shown in Fig. 5. Here, computed instantaneous locations of the particles are superimposed on iso-temperature color contours in 5(a) and the measured OH-concentration distribution is shown in 5(b). Both the calculations and measurements show the unique annular quenching pattern. As the centimeter-size vortex interacts with the flame surface, the flame gets wrapped around the vortex and stretched. However, due to curvature effect extinction appeared first at a location away from the centerline.

Vortices generated on the air side of the flame surface by injecting air through the 5.0-mm diameter syringe tube grew to a size of ~1.0-cm diameter by the time they reached the reaction zone^{21,22}. The centimeter-size-vortex/flame interaction created a wrinkled stretched laminar flame, which extinguished after a certain interaction time. The amount of flame wrinkling and the time required for extinguishing the flame depend on the vortex propagation velocity. Results obtained for a wide range of vortex injection velocities are summarized in Fig. 6. Variations in flame (peak) temperature and peak H-radical production rate of the flamelet located along the centerline with respect to scalar dissipation rate at stoichiometry (χ_{st}) are shown for injection velocities ranging from 5 m/s through 160 m/s. Scalar dissipation rate (χ) is calculated from mixture-fraction formulation of Bilger³¹ and using 1 m²/s for diffusion coefficient²¹. Note that vortices injected at a propagation velocity less than 5 m/s could not cause flame extinction.

As the centimeter-size air-side vortex pushes the flame surface it increases oxygen flux into the flame zone and, by virtue of stoichiometric combustion, diffusion flame moves toward fuel nozzle for obtaining a balance between the oxygen and hydrogen fluxes. As shown in Fig. 6, increase in reactant fluxes increases scalar dissipation rate at stoichiometry (χ_{st}) and decreases flame temperature (T_f) due to thermal effect (heat conduction out of the reaction zone exceeds heat generation due to reaction)³². If combustion were to take place infinitely fast then all the curves in Fig. 6 would collapse on to a single curve. However, as the velocity of the vortex increases the diffusion time scales decrease and could become comparable or less than chemical time scales, which, in turn, brings in chemical-non-equilibrium effects (Damkohler-number effects) into vortex-flame interactions. When reaction rates cannot keep up with the reactant fluxes heat release rate decreases due to partial combustion and consequently for the given χ_{st} faster vortices are yielding lower flame temperatures.

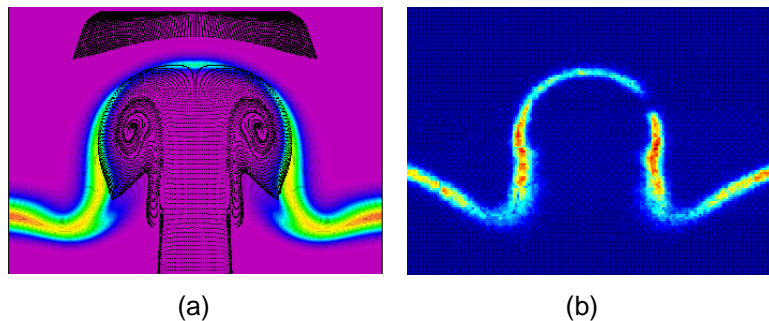


Fig. 5. Structure of the flame computed during its interaction with a centimeter-size-air-side vortex in (a). Instantaneous particle locations are superimposed on temperature ($T_{\max} = 1600$ K). OH-PLIF data obtained from experiments is shown in (b).

According to the flamelet concept for nonpremixed combustion³², which is treated as a non-equilibrium version of the classical Burke-Schumann limit, nonpremixed flames behave locally as a steady, one-dimensional, laminar, stretched flames. Considering the differences in diffusion and flow time scales flamelet concepts have been modified for unsteady effects³³. The main advantage of the flamelet concept is the fact that chemical time scales and length scales need not be resolved in calculating the turbulent flame. This means that flamelet structure can be uniquely resolved as a function of certain prescribed parameters. Most of the flamelet models use mixture fraction and scalar dissipation rate at stoichiometry as such prescribed parameters. Amazingly, the interactions of centimeter-size vortices with the flame over a wide range of velocities shown in Fig. 6 are following the unsteady flamelet concepts. The chemical activity, represented by peak ω_H , is in general following the flamelet concepts. Reaction rates increase initially with reactant fluxes (or χ_{st}) then decrease after reaching a peak value due to thermal effects and those of faster-vortex cases are decreasing even more rapidly due to chemical-non-equilibrium effects.

A typical experimental image of the millimeter-size-vortex/flame interaction obtained with a 0.2-mm-diameter injection tube is shown in Fig. 7. The left side of the image represents the OH-concentration field captured using PLIF measurement technique. Unlike in the centimeter-vortex/flame interaction, these millimeter-vortex/flame interactions show a significant increase in OH concentration in the head region of the vortex. Results obtained from the calculations made for this interaction are shown on the right-hand side of Fig. 7. Calculations also have predicted the significant increase in the concentration of OH in the head region. The computed OH distribution matches qualitatively with the uncorrected experimental OH-PLIF data. The somewhat broad and diffused distribution of OH in the vortex-head region of the experiment could be attributed to the alignment of laser sheet to the axis of the injection tube. The inner and outer radii of the protrusion of the OH layer that occurred due to the vortex motion are only ~ 0.3 and 0.7 mm, respectively; which are of the order of the laser-sheet thickness (~ 0.4 mm). Any small misalignment of the laser sheet to the centerline of the OH protrusion could capture the OH that is present circumferentially and make the fluorescence image blurry.

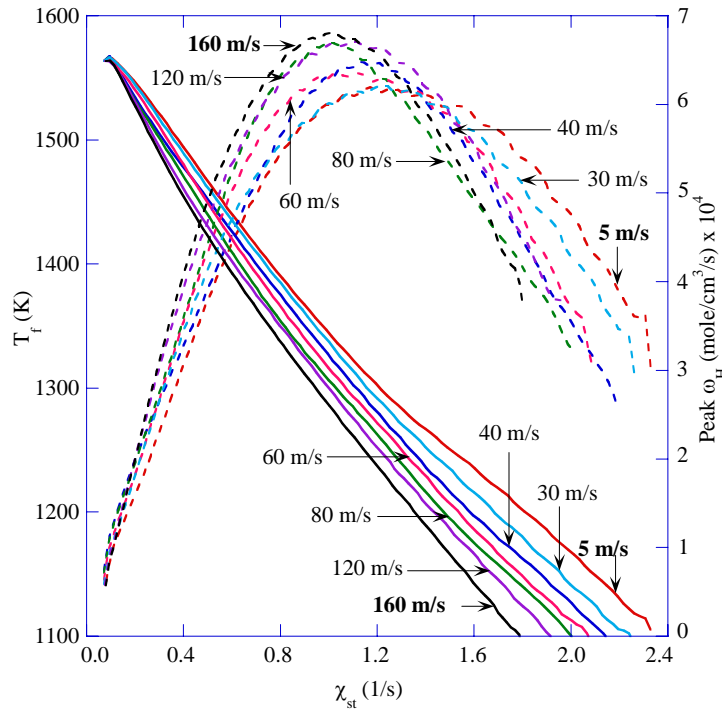


Fig. 6. Interactions of cm-size vortex with hydrogen-air diffusion flame for several vortex injection velocities. Variations in flame temperature (solid lines) and peak H-radical production rates (broken lines) are plotted with respect to scalar dissipation rate at stoichiometry.

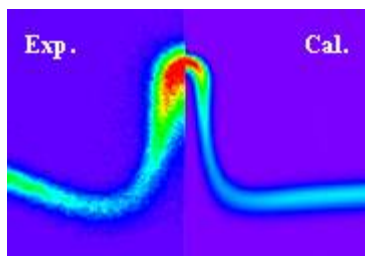


Fig. 7. Typical protruded flame obtained with a millimeter-size air-side vortex. Measured and computed flames in the form of OH-concentration distributions are shown on the left and right halves, respectively. Note the increase in concentration of OH at the tip.

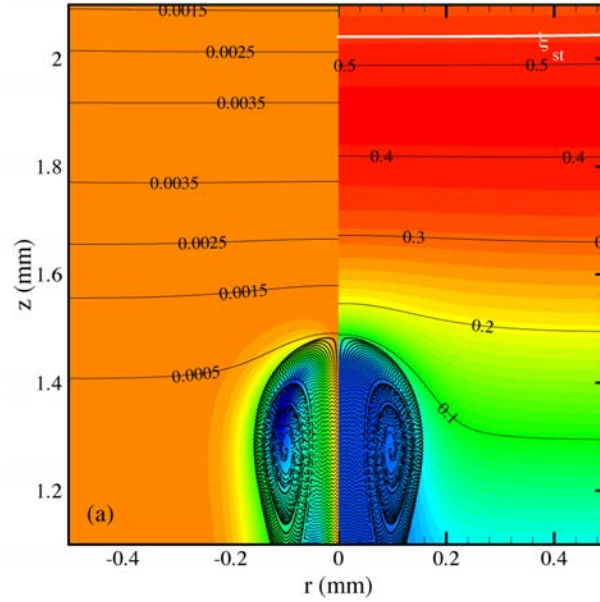
Both in the experiment and calculation, the interaction between millimeter-size vortex and flame resulted in local quenching of the latter along the stagnation line during the early stages and then the flame was reconnected within 1 ms. The temperature and OH concentration started increasing soon after the reconnection of the extinguished flame and their increase continued monotonically with time and with further propagation of the vortex. Calculations as well as experiments³⁴ made with different injection velocities resulted in very similar interaction sequences; namely, quenching, re-ignition, and increase in temperature above the adiabatic value in the head region of the vortex.

Turbulence consists of different length scales ranging from Kolmogorov scales (limited by kinematic viscosity) to geometrical scales (limited by the physical sizes of the combustion device). In order the flamelet concepts to be applied for the prediction of turbulent flows one must investigate how various size vortices behave during their interaction with flame. According to the regimes established by Peters for nonpremixed combustion³⁵ most of a turbulent flame can be described using flamelet concepts except near the nozzle exit and near the flame tip. Peters used the ratio between vortex turnover time (t_η) and chemical time (t_c) for separating the flamelet regime from distributed reaction zones. As the centimeter-size-vortex/flame interactions shown in Fig. 6 are truly following the flamelet concepts the ratio t_η/t_c associated with those interactions must be sufficiently large to place them in the flamelet regime of the turbulent combustion. Chemical time scales for the given fuel-oxidizer mixture do not change with vortex size, shape or velocity. Therefore, the smallest value of t_η/t_c occurs with the fastest vortex assuming that vortex size does not change much with the velocity, which is true for the cases shown in Fig. 6. In order to examine the applicability of flamelet concepts to different size vortices, one must keep values of t_η/t_c of different size vortices within the flamelet regime of turbulent combustion. Keeping the value of t_η/t_c of the fastest centimeter-size-vortex/flame interaction in Fig. 6 as the lower limit, the range for the vortex sizes is determined as 0.4 – 10 mm with a propagation velocity of 6.4 m/s. A 0.4 mm vortex traveling at 6.4 m/s gives the same value of t_η/t_c as that of a 1.0 cm vortex traveling at 160 m/s. The velocity of 6.4 m/s is chosen such that even the smallest vortex is able to cross the flame surface.

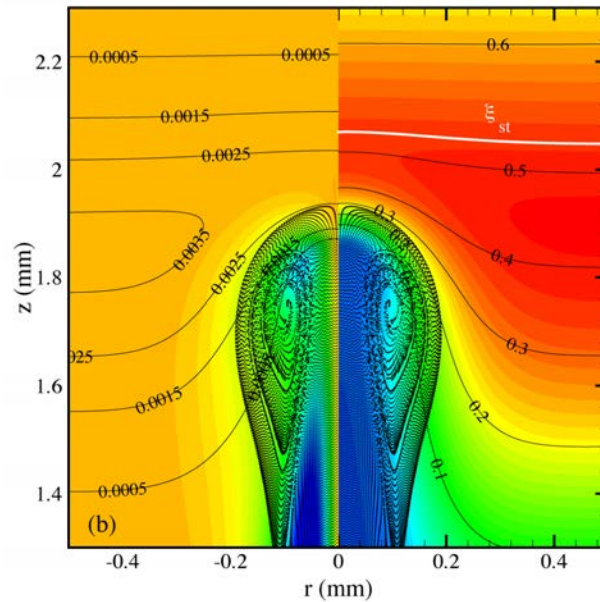
Calculations for the millimeter and sub-millimeter-vortex/flame interactions are performed using a micro version of the Rolon burner. Various size vortices on the air side of the flame surface are generated by injecting air at 6.4 m/s from injection tubes having different diameters. Interaction between a 0.4-mm-diameter vortex and flame is shown in Figs. 8(a) and 8(b) at two different phases. Instantaneous locations of the particles are super imposed on vorticity field on the left half and on temperature field on the right half. Iso contours of OH radicals and mixture fraction are also shown on the left and right halves, respectively.

The interaction process between a sub-millimeter-size vortex and the flame [Figs. 8(a) and 8(b)] is very different from that seen with larger vortices (Figs. 5 and 7). As the sub-millimeter vortex penetrates through the flame zone it hardly affects the remaining flame structure ahead of it. For example, the stoichiometric surface in Fig. 8(a) was not perturbed even though the vortex has penetrated to a distance that is only 0.5 mm away from it. Reaction zone surrounding the stoichiometric surface was also unperturbed. Even when the flame temperature and OH

concentrations decreased significantly due to the penetration of vortex [Fig. 8(b)] stoichiometric surface was shifted only by 0.1 mm. Over all, the flame is not getting stretched as the sub-millimeter-size vortex penetrates through it, which is contrary to the typical flamelet description of a vortex/flame interaction. Note that the ratio t_η/t_c , which determines whether a vortex/flame interaction belongs to flamelet regime or not, for the sub-millimeter case is same as that of the centimeter case.



(a)



(b)

Fig. 8. Sub-millimeter-size-vortex/Flame interactions captured at (a) 226 μ s and (b) 288 μ s after injecting the vortex. Contours of OH mole fraction (left) and mixture fraction (right) are superimposed on color fields of vorticity and temperature, respectively.

Evolution of the flame structure along the stagnation line during the sub-millimeter-size-vortex/flame interaction is shown in Fig. 9. The temperature and heat release rate distributions across the flame surface at different phases of interaction shown in 9(a) and 9(b), respectively illustrate the non-flamelet behavior associated with micro vortices. As the vortex penetrates through the flame it replaces the local products with fresh air through convection and the reaction zone upstream of the vortex is not affected. The temperature profiles at 232 μs and 256 μs suggest that the temperature of the flame (T_f) is decreasing due to convection, rather than due to stretching of the reaction zone. As the flame is not stretched, when oxygen is carried into the flame zone by a micro vortex, fuel flux does not increase to provide stoichiometric combustion. Consequently as shown in Fig. 9(b), heat release rate increases locally near the oxygen-rich-products region by more than an order of magnitude than that a stretched laminar flamelet would give. The high peak values are clipped in this plot for showing the unperturbed heat-release-rate profile of the steady state flame.

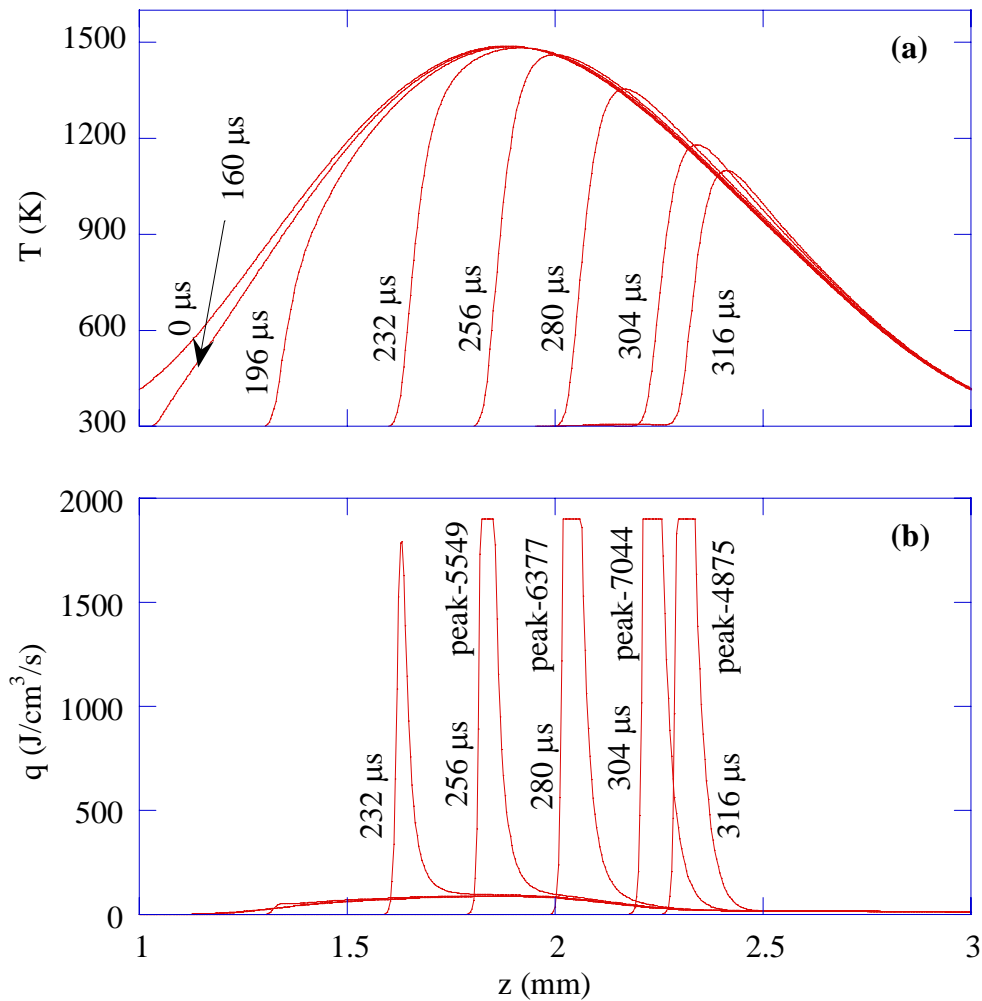


Fig. 9. Distributions of (a) temperature and (b) heat release rate across the flame surface at various phases of sub-mm-size-vortex/flame interaction. Heat release rates at certain phases are clipped and for those cases the respective peak values are indicated.

Results obtained from the interactions of different size vortices with flame are summarized in Fig. 10. Variations in flame temperature and peak H-radical production rates are plotted with respect to scalar dissipation rates obtained at stoichiometry for 15-mm, 2.2-mm, 1.1-mm, and 0.4-mm cases. This graph should be viewed in conjunction with Fig. 6 for realizing the non-flamelet behavior associated with micro vortices. The ratios t_η/t_c for 15-mm and 0.4-mm cases are the same and those of the 1.1-mm and 2.2-mm cases are larger than that of the 15-mm case. Fig. 6 demonstrates that 15-mm-vortex/flame-interactions follow flamelet description over a wide range of t_η/t_c ratios. Based on the regime diagram for turbulent combustion one would expect that all the interactions studied here and shown in Fig. 10 to follow the flamelet description. However, 0.4-mm case deviated the most from the flamelet description and 2.2-mm and 1.1-mm cases that are falling in between the 15-mm and 0.4-mm cases and are gradually deviating from the laminar flamelet behavior.

Velocities (6.4 m/s) used for the millimeter- and sub-millimeter-size-vortex/flame interactions are much lower than the highest velocity (160 m/s) used for the centimeter-size-vortex/flame interaction—suggesting that chemical non-equilibrium is of less concern in the former cases than in the latter. In fact, calculations for the sub-millimeter-vortex/flame interactions made with velocities lower than 6.4 m/s also deviated from the laminar flamelet behavior, even though, such interactions did not cause flame extinction. Apparently, the criterion for a vortex- or eddy/flame interaction in nonpremixed combustion to behave like a stretched laminar flamelet should depend on the vortex or eddy size rather than on the ratio t_η/t_c . The physical reasoning for using vortex size for determining flamelet regime is as follows:

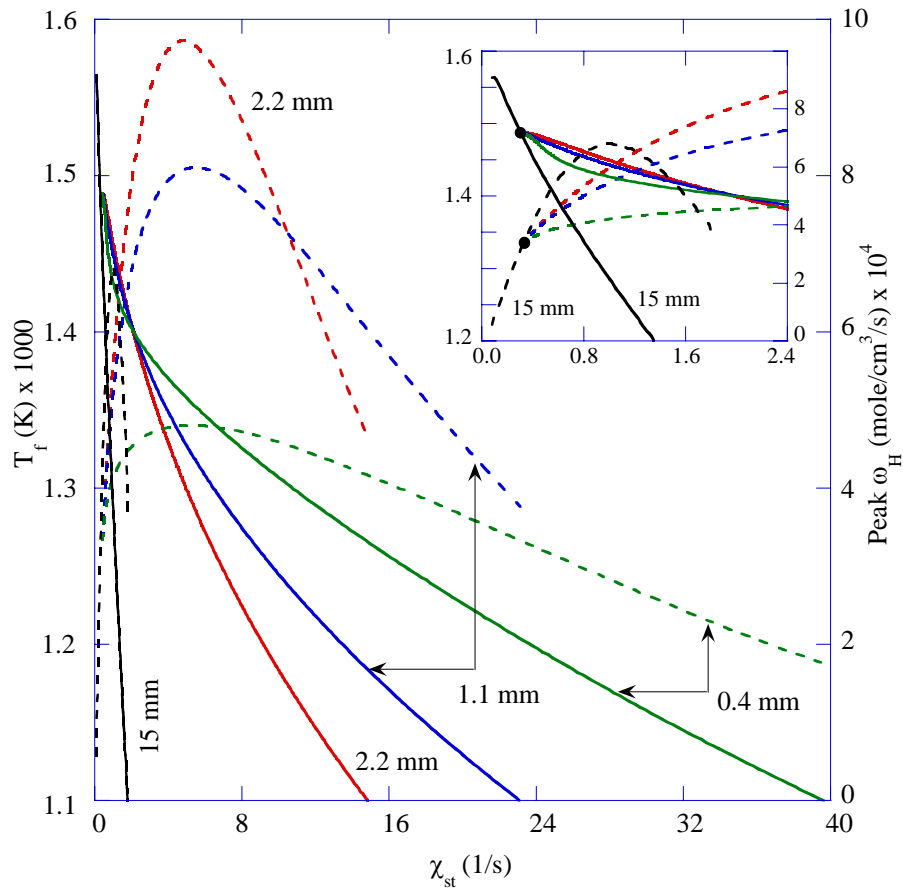


Fig. 10. Interactions of different size vortices with hydrogen-air diffusion flame. Variations in flame temperature (solid lines) and peak H-radical production rates (broken lines) are plotted with respect to scalar dissipation rate at stoichiometry. Inset shows the close-up view at lower scalar dissipation rates.

When a vortex propagates in an incompressible viscous media it not only displaces fluid occupied by it but also some fluid ahead of it. The upstream distance to which the influence of vortex is felt depends strongly on the vortex size and weakly on the vortex velocity. During a vortex/diffusion-flame interaction the fluid ahead of the vortex stretches the flame. As a result, an observer sitting on the flame in the reaction zone will feel stretching much earlier than the actual arrival of the vortex when the size of the incoming vortex is large. As the vortex size decreases the delay between flame stretching and arrival of the vortex decreases. If the reaction zone were to be infinitely thin then every vortex, independent of its size, stretches the reaction zone before it ever reaches the reaction zone. However, if the reaction zone has finite thickness then small vortices could displace the products in the reaction zone without stretching it. Reaction zone thickness (based on H-radical production rate) of a hydrogen-air nonpremixed flame could be anywhere between 1.6 mm and 4.8 mm depending on the applied stretch. Based on this, if a 5-mm-size vortex interacts with a 4.8-mm-thick flame, the interaction would not result flame stretching and would not follow flamelet description. Based on the lower limit for reaction zone thickness, interactions with any vortex smaller than ~ 2.0 mm would not belong to flamelet regime of turbulent combustion. Since turbulent eddies are two to three orders smaller than the 2.0-mm vortex limit one must exercise caution while using flamelet concepts for the prediction of turbulent flame structure.

SUMMARY AND CONCLUSIONS

Vortex/flame interactions are often studied to gain a better understanding of turbulent-flame structures; such studies facilitate the development of accurate turbulence-chemistry-interaction models. In an effort to identify the limitations of the current turbulence-chemistry-interaction models for nonpremixed turbulent flames, a numerical study has been performed through obtaining time-dependent flame structures established during interactions between vortices of different sizes and the flame surface. A time-dependent model, known as UNICORN, that incorporates 13 species and 74 reactions among the constituent species has been used for the simulation of vortex/flame interactions in opposed-jet hydrogen-air nonpremixed flames. In the past this model has been validated by direct simulation of several steady state and unsteady axisymmetric opposed-jet and coflow jet diffusion flames.

Differences between the steady state and dynamic extinction processes are studied by establishing stationary unsteady flames via forcing equal-size vortices from the fuel and air nozzles simultaneously. It was found that the air-side stretch rate and scalar dissipation rate at stoichiometry cannot be used for characterizing the quenching process associated with unsteady flames. In general, the extinction values of these variables in unsteady flames are higher than the respective ones in steady-state flames, and the differences increase with vortex speed. A new variable (σ) that is proportional to the air-side stretch rate and inversely proportional to the rate of change in the flame temperature is found to be uniquely characterizing the unsteady extinction process.

Simulations for single-vortex/flame interactions are made for studying the wrinkled unsteady flames. Centimeter-size-vortex-flame interactions obtained over a wide range of vortex injection velocities followed the stretched-laminar-flamelet description and resulted similar flame structures with respect to χ_{st} . Fast moving vortices tend to create chemical non-equilibrium in the reaction zone and cause a small shift along the χ_{st} scale toward lower values. Sub-millimeter-size vortices, in contrast to large-size vortices, do not possess the ability to push the fluid ahead of it into the reaction zone. Instead, they bring fluid into the reaction zone spontaneously and replace the local combustion products. Such transport mechanism increases χ_{st} dramatically without stretching the reaction zone. Temperature decreases as products are carried away through convection. Millimeter- and sub-millimeter-size-vortex/flame interactions did not completely follow the stretched-laminar-flamelet description. Interactions deviated more from the flamelet concepts as the size of the vortex decreased. On the other hand, velocity of the vortex did not cause such non-flamelet behavior.

ACKNOWLEDGMENTS

Financial support for this work was provided by the Air Force Office of Scientific Research (AFOSR, Julian Tishkoff) and the Air Force Contract #F33615-00-C-2068 (Vince Belovich).

REFERENCES

1. Kee, R. J., Miller, J. A., Evans, G. H., and Dixon-Lewis, G., *Proc. Combust. Inst.* 22: 1479-1486 (1988).
2. Dixon-Lewis, G., *Proc. Combust. Inst.* 23: 305-324 (1990).
3. Chelliah, H. K., Law, C. K., Ueda, T., Smooke, M. D., and Williams, F. A., *Proc. Combust. Inst.* 23:503-510 (1990).
4. Hottel, H. C., and Hawthorne, W. R. *Proc. Combust. Inst.* 3:254-266 (1949).
5. Roquemore, W. M., Chen, L.-D., Goss, L. P., and Lynn, W. F. in *Turbulent Reactive Flows*, Lecture Notes in Engineering (R. Borghi and S. N. B. Murthy, Eds.) (Springer-Verlag, Berlin, 1989), Vol. 40, p. 49.
6. Darabiha, N., *Comb. Sci. Technol.* 86:163 (1992).
7. Egolfopoulos, F. N., and C. S. Campbell, *J. Fluid Mech.* 318:1 (1996).
8. Im, H. G., Law, C. K., Kim, J. S., and Williams, F. A., *Combust. Flame* 100:21 (1995).
9. Brown, T. M., Pitz, R. W., and Sung C. J., *Proc. Combust. Inst.* 27:703-710 (1998).
10. Shamim, T., and Atreya, A., *Combust. Flame* 121:59-74 (2000).
11. Shamim, T., and Atreya, A., *Combust. Flame* 123:241-251 (2000).
12. Katta symp-double vortex
13. Paul, P. H., and Najm, H. N., *Proc. Combust. Inst.* 27:43-50 (1998).
14. Patnaik, G., and Kailasanath, K., *Proc. Combust. Inst.* 27:711-717 (1998).
15. Ashurst, W. T., *Combust. Sci. Technol.* 92:87 (1993).
16. Santoro, V. S., Kyritsis, D. C., Linan, A., and Gomez, A., *Proc. Combust. Inst.* 28:2109-2116 (2000).
17. Roberts, W. L., Driscoll, J. F., Drake, M. C., Ratcliffe, J. W., *Proc. Combust. Inst.* 24:169-176 (1992).
18. Rolon, J. C., Aguerre, F., and Candel, S., *Combust. Flame* 100:422 (1995).
19. Renard, P. H., Thevenin, D., Rolon, J. C., and Candel, S., *Prog. Energy Combust. Sci.* 26:225-282 (2000).
20. Tevenin, D., Renard, P. H., Fiechtner, G. J., Gord, J. R., and Rolon, J. C., *Proc. Combust. Inst.* 28:2101-2108 (2000).
21. V. R. Katta, T. R. Meyer, M. S. Brown, J. R. Gord, and W. M. Roquemore, *Combust. Flame* 137 (2004) 198-221.
22. Katta, V. R., Carter, C. D., Fiechtner, G. J., Roquemore, W. M., Gord, J. R., and Rolon, J. C., *Proc. Combust. Inst.* 27:587-594 (1998).
23. Yoshida, K., and Takagi, T., *Proc. Combust. Inst.* 27:685, (1998).
24. Katta, V. R., Meyer, T. R., Gord, J. R., and Roquemore, W. M., *Combust. Flame* 132:639 (2003).
25. Katta, V. R., and Roquemore, W. M., *AIAA J.* 36:2044 (1998).
26. Roquemore, W. M., and Katta, V. R., *J. Visualization*, 2:257 (2000).
27. Frenklach, M., Wang, H., Goldenberg, M., Smith, G. P., Golden, D. M., Bowman, C. T., Hanson, R. K., Gardiner, W. C., V. Lissianski, V., Gas Research Institute Technical Report No. GRI-95/0058 (Gas Research Institute, Chicago), November 1, 1995.
28. Katta, V. R., Goss, L. P., and Roquemore, W. M., *AIAA J.* 32:84 (1994).
29. Leonard, B. P., *Comput. Meth. Appl. Mech. Eng.* 19:59 (1979).
30. Grisch, F., Attal-Tretout, B., Bouchardy, P., Katta, V. R., and Roquemore, W. M., *J. Nonlin. Opt. Phys. Mater.* 5:505 (1996).
31. R. W. Bilger, *Proc. Combust. Inst.* 22 (1988) 475-488.
32. N. Peters, *Proc. Combust. Inst.* 21 (1986) 1231-1256.
33. B. Cuenot, F. N. Egolfopoulos, and T. Poinot, *Combust. Theory Modeling* 4 (2000) 77-97.
34. V. R. Katta, T. R. Meyer, J. R. Gord, and W. M. Roquemore, *Combust. Flame* 132 (2003) 639.
35. N. Peters, *Prog. Astronautics Aeronautics* 135 (1991) 155-182.

5th US Combustion Meeting
Organized by the Western States Section of the Combustion Institute
and Hosted by the University of California at San Diego
March 25-28, 2007.

Nitric oxide concentration profiles in atmospheric-pressure flames using electronic-resonance-enhanced coherent anti-Stokes Raman scattering (ERE-CARS)

N. Chai¹, S. V. Naik^{1}, W. D. Kulatilaka¹, R. P. Lucht¹, N. M. Laurendeau¹, S. Roy²,
V. R. Katta², J. P. Kuehner³, and J. R. Gord⁴*

¹*School of Mechanical Engineering, Purdue University,
West Lafayette, Indiana 47907, USA*

²*Innovative Scientific Solutions Inc.,
Dayton, Ohio 45440, USA*

³*Department of Physics and Engineering, Washington and Lee University,
Lexington, Virginia 24450, USA*

⁴*Air Force Research Laboratory, Wright-Patterson Air Force Base,
Dayton, Ohio 45433, USA*

We report measurements of nitric oxide (NO) in atmospheric-pressure flames using visible pump (532 nm) and Stokes (591 nm) beams with an ultraviolet probe beam (236 nm) near an electronic resonance, giving significantly enhanced CARS signal at 226 nm. For a hydrogen-air flame stabilized over a Hencken burner, good agreement is obtained between ERE-CARS measurements and flame computations using UNICORN, a two-dimensional flame code. Excellent agreement between measured and calculated NO spectra is obtained for heavily sooting acetylene-air flames on the same Hencken burner. The measured shapes of NO concentration profiles determined from ERE-CARS spectra without correcting for collisional effects is in excellent agreement with that predicted using the OPPDIF code in conjunction with GRI 3.0 kinetics for a laminar, counter-flow, non-premixed hydrogen-air flame. Effects of fuel-stream dilution (nitrogen and carbon dioxide) on measured NO concentrations are also studied in the counter-flow configuration. For diluted flames, comparisons between measured ERE-CARS signals and computed number densities show good spatial agreement and their relative magnitudes match well. Counter-flow flames with various hydrogen levels in the fuel stream (pure oxygen in the oxidizer stream) and various oxygen levels in the oxidizer stream (pure hydrogen in the fuel stream) are investigated to simulate fuel-rich and oxygen-rich flames and an optimum NO level is found. Pathway and sensitivity analyses are implemented to understand NO formation under these conditions. The current results establish the utility of ERE-CARS for detection of NO in flames with large temperature and concentration gradients as well as in sooting environments.

1. Introduction

Emissions of oxides of nitrogen (NO_x) are pollutants that have a direct impact on the formation of photochemical smog and upon the depletion of the ozone layer. Development of combustors for internal combustion and gas turbines engines that produce low NO levels is an important task facing the combustion community; moreover, such combustors benefit from advances in

fundamental knowledge regarding formation and destruction of NO in flame environments. Many previous researchers have developed laser-induced fluorescence (LIF) strategies for quantitative detection of nitric oxide in high-pressure flames [1-5]. However, the fluorescence signals from NO become difficult to interpret, especially with increasing pressure, owing to: (a) interferences from oxygen in fuel-lean regions and from hydrocarbons or soot in fuel-rich regions, (b) quenching of the LIF signal via collisions with O₂, CO₂ and H₂O, among other colliding partners, and (c) absorption of both the laser beam and the fluorescence signal by CO₂, H₂O and hydrocarbons at typical UV excitation wavelengths. To overcome these difficulties, researchers have considered other diagnostic techniques such as cavity ring-down spectroscopy, laser-induced polarization spectroscopy, and coherent anti-Stokes Raman scattering. While most practical combustion devices operate at high pressure, the robustness and utility of the above alternative techniques must first be tested in flames at atmospheric pressure.

Conventional coherent anti-Stokes Raman scattering (CARS) has previously been applied to NO measurements in the temperature range from 300 to 800 K at atmospheric pressure [6]. The detection limit for NO was found to be about 2500 ppm in N₂ buffer gas. A significant enhancement in the CARS detection limit can be obtained by tuning one or more of the pump, Stokes and probe beams into resonance with a suitable electronic transition. Previously, such electronic-resonance-enhanced (ERE) CARS has been applied successfully to measure radical species such as OH [7, 8] and CH [9]. For these explorations of resonance-enhanced CARS [7-9], the pump, Stokes and probe beams were all at ultraviolet frequencies. In contrast, an ERE-CARS technique has recently been reported for detection of NO using an ultraviolet probe beam in electronic resonance while using visible pump and Stokes beams far from electronic resonance [10-13]. The NO ERE-CARS signal was found to display little sensitivity to electronic quenching [11] which is significant for measurements related to practical gas-turbine combustors where the quenching environment can undergo rapid spatial and temporal variations. The NO ERE-CARS signal was found to increase from 0.1 to 2 bars and remained approximately constant at pressures from 2 to 8 bars [12]. By doping known quantities of NO into the flame, a detection limit of approximately 50 ppm was demonstrated in an atmospheric-pressure hydrogen-air flame stabilized on a Hencken burner [13].

In this paper, we present NO measurements via ERE-CARS for three different flame environments. First, a hydrogen-air flame was stabilized using a Hencken burner and ERE-CARS measurements of NO were obtained at various heights above the burner surface. The measured NO profile was compared with calculations using a detailed reactive flow code. In a second set of experiments, heavily sooting acetylene-air flames were stabilized using the same Hencken burner and spectral scans were recorded at various equivalence ratios. A third set of measurements was performed in a laminar, non-premixed, hydrogen-air flame at a global strain rate of 20 s⁻¹ stabilized using a counter-flow burner. NO concentration profiles were measured in this flame using three different Raman transitions. To understand the effect of diluents on NO formation, the fuel stream of the hydrogen-air counter-flow flame was doped with 10%, 25% and 35% N₂ and CO₂. Peak NO signals were also measured in a series of counter-flow flames by varying the fraction of H₂ in the fuel stream (remainder N₂) for pure O₂ in the oxidizer stream as well as by varying the fraction of O₂ in the oxidizer stream (remainder N₂) for pure H₂ in the fuel stream. For all counter-flow flame measurements, the measured NO profiles were compared with concentration profiles computed using an opposed-flow flame code. Pathway and sensitivity analyses were conducted so as to understand the chemical kinetics related to NO formation and destruction at various dilution levels for both fuel and oxidizer.

2. Experiment

A two-dimensional, non-premixed, near-adiabatic Hencken burner (Research Technologies Model RD15X15) was used to stabilize the atmospheric-pressure hydrogen-air and acetylene-air flames. An oxidizer mixture of 79% N₂ and 21% O₂ was employed instead of commercial air. Mass flow controllers (Models MKS 1559A and M100B) were used to regulate gas flow into the burner. A more detailed description of the Hencken burner is given elsewhere [14]. The burner is mounted on a translation stage that permits horizontal and lateral positioning so as to adjust the ERE-CARS probe volume within the flame. The counter-flow burner consists of two 1.9-cm diameter nozzles made of hastalloy C-276 designed to carry either the fuel or oxidizer mixture. The nozzles are water-cooled to prevent overheating and the water temperature is maintained around 30°C so as to avoid condensation on nozzle surfaces. The separation distance between the fuel and oxidizer nozzles was fixed at 2 cm and the velocity of the reactants at the nozzle exits was maintained at 20 cm/s, thus producing a global strain rate of 20 s⁻¹, where the global strain rate is defined as the sum reactant velocities at the nozzle exits divided by the nozzle separation distance. The counter-flow burner facility is described in more detail in a previous publication [15].

An energy-level diagram describing the ERE-CARS process for nitric oxide is shown in Fig. 1. The pump (ω_1) and Stokes (ω_2) lasers are visible beams with frequencies far detuned from the A²Σ⁺ - X²Π electronic system of the NO molecule. In contrast, the probe beam frequency (ω_3) is at or near electronic resonance. The CARS signal (ω_4) is generated using a three dimensional phase-matching geometry. Figure 2 shows a schematic diagram of the experimental system. The second harmonic output (~532 nm) of an injection-seeded, Q-switched Nd:YAG laser was used as the pump beam. This second harmonic output was also used to pump a narrowband dye laser to produce tunable radiation in the vicinity of 704 nm. The output of the dye laser was frequency-mixed with the third harmonic output (~355 nm) of the injection-seeded YAG laser to generate the probe beam ($\lambda_3 = 236$ nm). The second harmonic output of a separate unseeded, Q-switched Nd:YAG laser was used to pump another narrowband dye laser to produce tunable radiation in the vicinity of 591 nm, which acts as the Stokes beam. The full-width at half-maximum (FWHM) linewidth of the pump beam (532 nm) was 0.003 cm⁻¹ while the linewidth for the Stokes (591 nm) and the probe (236 nm) laser beam was 0.1 cm⁻¹. Using a translating razor blade, the diameters of the three beams at 20 mm away from the focus (CARS probe volume) were approximately 250 μm. A polarization-sensitive technique was employed to suppress the non-resonant background signal arising from four-wave mixing. The probe beam was vertically polarized while the polarizations of the pump and Stokes beams were set at an angle of 60° with respect to the vertical axis. A fine adjustment of the polarizer in the detection channel, orthogonal to the four-wave mixing signal, enables optimum suppression of non-resonant background [10].

For experiments performed using the Hencken burner, the ultraviolet probe wavelength was held fixed at 236.06 nm corresponding to the Q₁(13.5) transition in the (0,1) band of the A²Σ⁺ - X²Π electronic system of NO. Spectra were recorded at various heights above the burner by tuning the wavelength of the visible Stokes beam, so that UV fluorescence interferences and/or background scattering remained constant during the scan. Such scans, for which the Stokes wavelength was varied while the UV probe wavelength was fixed, are referred to as Stokes scans. The resulting baseline can be subtracted to obtain a background-corrected ERE-CARS

signal. This background-corrected signal is divided by the ultraviolet pulse energy to account for shot-to-shot variations in the energy of the pulsed probe beam.

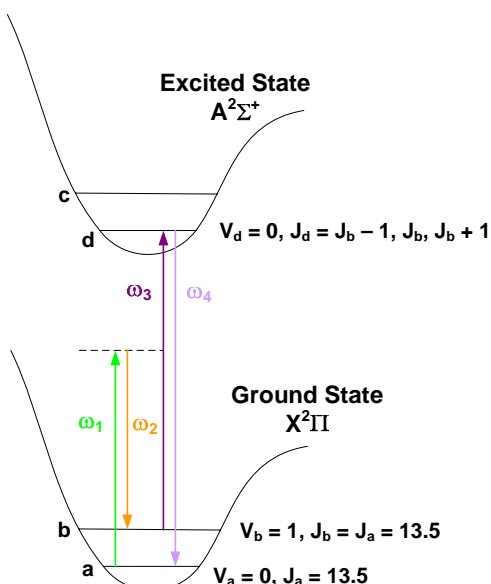


Figure 1: Energy level diagram showing the ERE-CARS process for NO. The transitions identify the pump beam (ω_1), Stokes beam (ω_2), probe beam (ω_3) and CARS signal beam (ω_4).

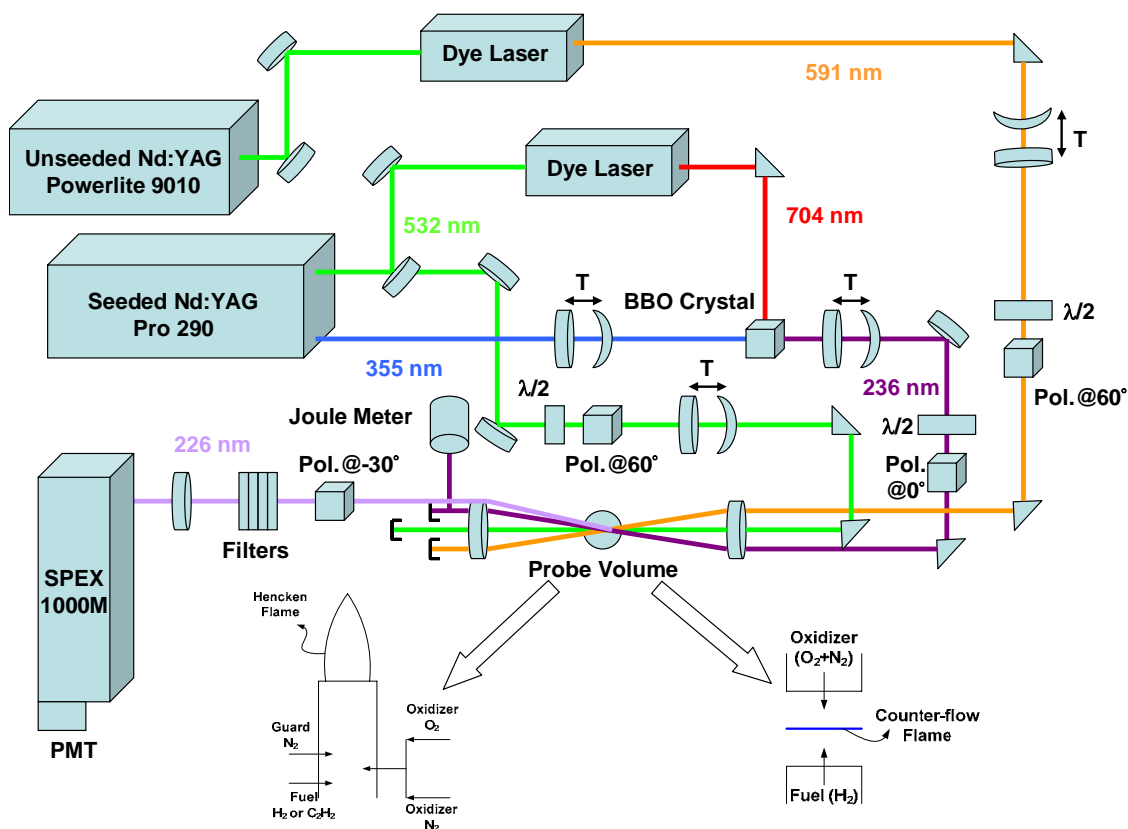


Figure 2: Schematic of the experimental setup for ERE-CARS of NO. T: telescope; $\lambda/2$: half-wave plate; PMT: photomultiplier tube. Polarizer angles are set with respect to the vertical axis. Filters are four 45°, 215-nm mirrors having 70% transmission at 226 nm and 1% transmission at 236 nm.

Three different Raman transitions were investigated for the counter-flow hydrogen-air flame. These Raman transitions, $Q_1(9.5)$, $Q_1(13.5)$, and $Q_1(17.5)$, were selected to assess the temperature sensitivity of the measured [NO] profile. For the three selected Raman transitions, the ultraviolet probe wavelength was held fixed at 236.19 nm, 236.06 nm and 235.87 nm, respectively, corresponding to the $Q_1(9.5)$, $Q_1(13.5)$ and $Q_1(17.5)$ transitions in the (1,0) band of the $A^2\Sigma^+ - X^2\Pi$ electronic system of NO. Stokes scans were recorded every 1 mm between the fuel and oxidizer nozzles for each of the three ERE-CARS transitions. For the remaining measurements in the counter-flow burner, the probe beam was fixed 236.06 nm corresponding to the $Q_1(13.5)$ transition in the (0,1) band of the $A^2\Sigma^+ - X^2\Pi$ electronic system of NO. Stokes scans were recorded and the baseline was subtracted to obtain a background-corrected signal. This signal was divided by the UV pulse energy and the normalized ERE-CARS signal was integrated over the width of the Raman transition and the square-root of the integrated signal was corrected to the ground-level population of NO via division by the Boltzmann fraction. The square-root of the Boltzmann fraction corrected NO ERE-CARS signal was compared directly with the computed NO number density. For the N_2 and CO_2 diluted flames, all reported measurements are relative to the peak NO concentration in the hydrogen-air flame.

3. Modeling

Numerical computations for the hydrogen-air flame stabilized using the Hencken burner was performed using the UNICORN (Unsteady Ignition and Combustion with Reactions) code [16-18]. The flame is modeled as a combination of several diffusion flamelets, where each flamelet is supported by fuel originating from each individual tube within the burner. The exact nature of the flamelet (premixed, partially premixed or non-premixed) can be varied, depending on experimental flow conditions. For the counter-flow flame, OPPDIF, a Sandia opposed-flow flame code [19], was used for calculations of temperature, velocity and species concentration profiles along the centerline between the two nozzles. The mathematical model for OPPDIF reduces the two-dimensional, axi-symmetric flow field to a one-dimensional formulation via a similarity transformation [20]. The GRI mechanism (version 3.0) [21] was used for the chemical kinetics and gas-phase radiation was considered by adding a radiation source term in OPPDIF. The effect of radiative heat loss was considered in the optically thin limit [22]. The radiation model utilizes Planck mean absorption coefficients for the major species CO_2 , H_2O , CO and CH_4 ; the temperature dependence of these coefficients was modeled using fourth-order polynomial fits to the results of narrow-band calculations. A time-dependent, axi-symmetric model in UNICORN was also employed for simulation of the weakly-stretched counter-flow hydrogen-air diffusion flame.

The ERE-CARS spectra obtained in the sooting acetylene-air flame were modeled using a perturbative analysis applicable at lower laser irradiances via modification of the Sandia CARSFT code [10, 23]. Spectral data for the NO molecule were obtained via LIFBASE [24] and from high-resolution CARS measurements [25, 26].

4. Results and Discussion

Stokes scans were recorded for various heights in a hydrogen-air flame stabilized on the Hencken burner at an equivalence ratio of 1.15. We previously added known quantities of NO to the oxidizer flow in a similar flame to determine the NO detection limit at atmospheric pressure

[12]. Figure 3 shows a typical spectrum at a height 55 mm above the burner surface. The spectrum exhibits a non-resonant background resulting from scattering of the UV probe beam and fluorescence induced by the UV probe beam. Because the UV probe wavelength is fixed during Stokes scans, this non-resonant background is nominally constant, independent of Stokes laser wavelength. Furthermore, the non-resonant background does not modulate the ERE-CARS signal and it can be subtracted in data processing. The value of non-resonant background signal was obtained via integration between Raman shifts of 1871 and 1871.5 cm^{-1} . After background subtraction and division by the UV probe energy, the ERE-CARS signal was integrated between Raman shifts of 1872 and 1874 cm^{-1} . Figure 4 shows a comparison between the measured concentration of NO, which is proportional to the square-root of the integrated ERE-CARS signal, and predicted NO concentrations computed using UNICORN at various heights above the burner surface. As fuel and oxidizer are rapidly mixed in the region above the burner surface, a sharp increase in temperature occurs owing to combustion reactions. In the post-flame regime, the temperature essentially remains constant; however, the NO concentration increases continuously because of the Zeldovich reactions. The data points are not corrected for variations in Boltzmann fraction owing to the nearly constant post-flame temperatures, as seen in Fig. 4.

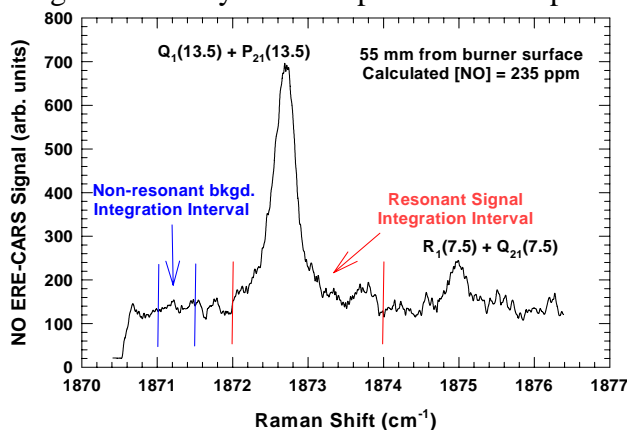


Figure 3: Stokes scan at 55 mm above the Hencken burner in an H_2 -air ($\phi = 1.15$) flame. The UV probe frequency was fixed at $42,361.46 \text{ cm}^{-1}$, corresponding to the $Q_1(13.5)$ transition. Pump, Stokes and probe energy levels were fixed at 14 mJ/pulse, 18 mJ/pulse and 0.6 mJ/pulse, respectively.

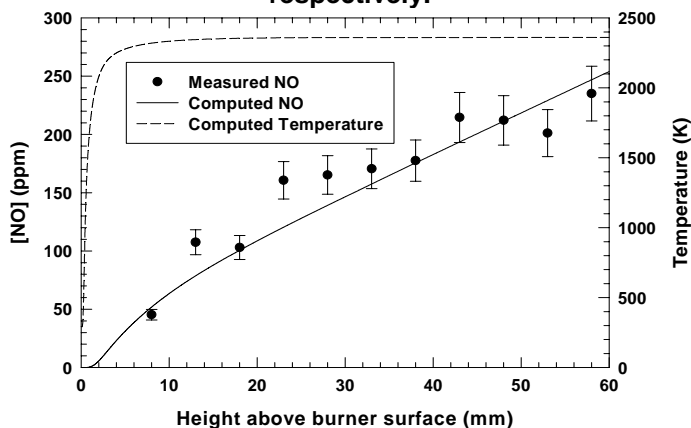


Figure 4: Comparison between measured and computed NO concentrations (using UNICORN) at various heights above the Hencken burner in an H_2 -air ($\phi = 1.15$) flame. The data was scaled so as to match measured and calculated [NO] at 48 mm above the burner surface.

Flames encountered in practical applications, such as gas turbine combustors, furnaces and internal combustion engines, are highly luminous and particle laden, especially when using liquid fuels. Hydrocarbon species, their fragments and soot particulates possess very broad absorption and emission signatures throughout the ultraviolet region [27]. Such broadband UV interferences complicate signal interpretation when detecting NO via LIF for excitation near 226 nm in the $\gamma(0,0)$ band [1-3]. Therefore, acetylene-air flames were studied from lean ($\phi = 0.8$) to rich ($\phi = 1.6$) conditions to assess the feasibility of ERE-CARS measurements under highly sooting conditions. Spectra recorded 55 mm above the burner surface are shown in Fig. 5 along with theoretical spectral fits obtained using the modified Sandia CARSFT code for the stoichiometric condition. Good agreement is observed between theory and experiment for these conditions. The excellent selectivity of the ERE-CARS technique arises from the fact that both Raman and electronic resonance conditions must be satisfied to generate the ERE-CARS signal.

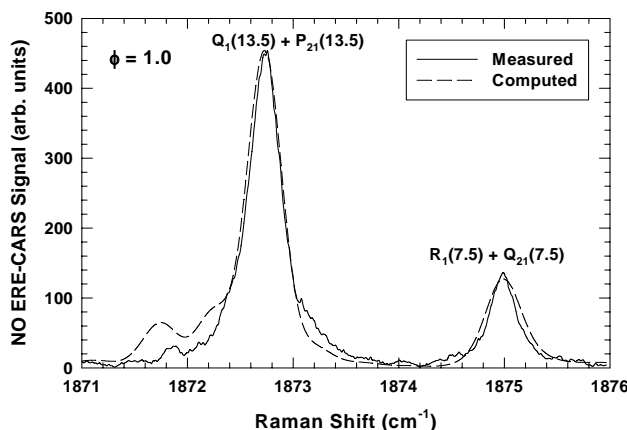


Figure 5: Comparisons between measured and computed ERE-CARS spectra at 55 mm above the Hencken burner for a highly sooting acetylene-air flame ($\phi = 1$). The UV probe frequency was fixed at 42,361.46 cm^{-1} , corresponding to the $Q_1(13.5)$ transition. Pump, Stokes and probe energy levels were fixed at 10 mJ/pulse, 16 mJ/pulse and 1.2 mJ/pulse, respectively.

Stokes spectra were recorded at various positions between the fuel and oxidizer nozzle for the non-premixed, hydrogen-air counter-flow flame at a global strain rate of 20 s^{-1} . A significant modulation in ERE-CARS signal was obtained between the fuel and oxidizer nozzles. Knowing the computed temperature at each position from OPPDIF, the Boltzmann fraction was calculated for the rotational-vibrational level. The square-root of the integrated ERE-CARS signal was then corrected for population differences using an appropriate Boltzmann fraction calculation. In Fig. 6, the square-root of the integrated signal, as divided by the Boltzmann fraction for the corresponding rotational level at the calculated temperature, is plotted versus the distance between the two nozzles for three different Raman transitions.

The three different profiles were scaled by setting the peak of the $Q_1(13.5)$ profile to unity. While the profile peaks for the $Q_1(9.5)$ and $Q_1(17.5)$ ERE-CARS signals were not scaled to match the $Q_1(13.5)$ case, the peaks for all three profiles agree to within 15%. This agreement was observed even though measurements for the three different transitions were acquired over several hours, thus indicating the stability of the experimental alignment. We observe that the shapes of the NO concentration profiles measured using three different Raman transitions are very similar, and that the peaks of the profiles, corrected for their respective Boltzmann

fractions, are in excellent agreement. We should note, however, that in regions of low NO concentration, the integrated ERE-CARS signal is sensitive to the background correction.

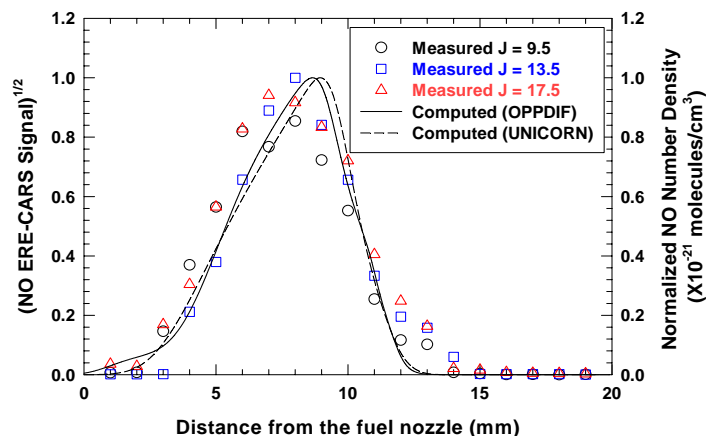


Figure 6: Comparison between measured NO signals and computed number density in an atmospheric pressure, laminar, counter-flow, non-premixed H₂-air flame at a global strain rate of 20 s⁻¹. Computed profiles using OPPDIF (one-dimensional calculation) and UNICORN (two-dimensional calculation) match well at the low strain rate of 20 s⁻¹.

The relative agreement, both in terms of spatial location and magnitude, between the experimental and computed [NO] profiles, either using OPPDIF (one-dimensional calculation) or UNICORN (two-dimensional calculation), is quite satisfactory. Indeed, considering potentially complicating factors such as variations in temperature, collisional width and quenching environment (the total electronic quenching rate varies by more than an order of magnitude in the region encompassing measurable NO concentrations for this flame), this excellent agreement between measured and calculated profiles is surely remarkable. Hence, we find that the proposed ERE-CARS technique should be applicable in complex collisional environments, while still giving a spatial resolution comparable to techniques such as LIF and conventional CARS. For our experimental conditions, we have demonstrated a detection limit of approximately 25 ppm for the hydrogen-air counter-flow flame using three different Raman transitions. This detection limit could potentially be improved by focusing the beams tightly and by employing strategies to reduce the UV scattering/fluorescence.

Figures 7 displays the comparisons between measured and predicted NO concentrations when diluting the fuel stream using various levels of N₂. The relative agreement in terms of spatial location and magnitude between the experimental and calculated profiles is quite good for different levels of N₂. As the concentration of inert gas in the fuel stream increases, the predicted peak NO position moves away from the fuel nozzle, which is also observed experimentally. Similar results were obtained when diluting the fuel stream using CO₂. The results also confirm that CO₂ is more effective than N₂ in reducing the flame temperature, thus leading to lower NO concentrations. In a previous study, similar observations were made using probe measurements [28].

To simulate high hydrogen-content fuels under oxygen-rich conditions, experiments were performed when varying either the H₂ to N₂ ratio in the fuel stream for pure O₂ in the oxidizer stream or the O₂ to N₂ ratio in the oxidizer stream for pure H₂ in the fuel stream. Figure 8 displays the variation in integrated NO signal at the location of peak [NO] as a function of

oxygen content in the oxidizer stream. The comparison between measurements and predictions at various H_2 and O_2 contents is excellent. Using a kinetic analysis, thermal NO was found to be the dominant pathway for NO formation in these flames; hence, good agreement should be expected as the kinetics for the Zeldovich reactions are relatively well-known. Similar results were observed when varying the hydrogen content in the fuel stream. In both cases, the NO concentration first rises with decreasing N_2 dilution, reaches a maximum around 40% N_2 dilution and then drops for increasing hydrogen or oxygen content. The lack of nitrogen clearly dominates the rise in temperature when dilution levels drops below about 40%, thus giving a maximum NO level. For co-flow, laminar, non-premixed methane-oxygen flames, the NO_x emission index was found to peak at 60% O_2 (40% N_2) in the oxidizer stream [29], which is consistent with our present measurements. In addition, for methane-air counter-flow flames, computations suggest a similar variation in peak NO concentration with N_2 dilution in the oxidizer stream [30]. The flame temperatures at a given oxygen content in the oxidizer stream are greater than the temperatures for the same hydrogen content in the fuel stream and we thus observe much higher NO levels for oxygen variation compared to hydrogen variation.

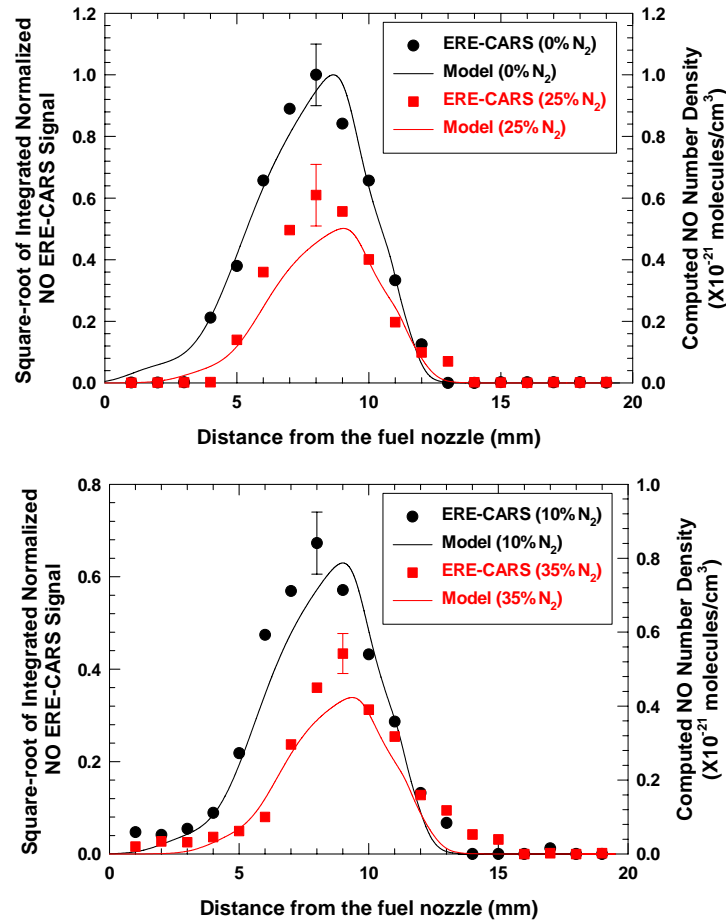


Figure 7: Comparison between measured NO signals and computed number densities in atmospheric pressure, laminar, counter-flow, non-premixed H_2 -air flames (diluted with different N_2 levels in the fuel stream) at a global strain rate of 20 s^{-1} .

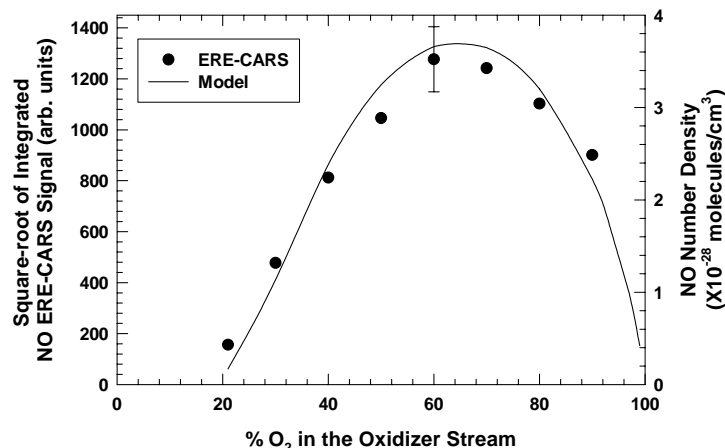


Figure 8: Comparisons between measured NO signals and computed number densities at peak locations in atmospheric-pressure, laminar, counter-flow, non-premixed H₂/O₂ flames (with various N₂ levels in the oxidizer stream and pure H₂ in the fuel stream) at a global strain rate of 20 s⁻¹. Pump, Stokes and probe energy levels are fixed at 10 mJ/pulse, 14 mJ/pulse and 0.5 mJ/pulse, respectively.

Fundamental knowledge regarding NO_x formation and destruction can be obtained by combining reliable experimental measurements with chemical kinetic analysis. Pathway analysis gives contributions from the four major NO formation mechanisms, viz., thermal, N₂O, NNH and prompt, to total NO production. Differences between total NO concentrations predicted with the full kinetic mechanism and those obtained by removing initiation reaction(s) for a particular route give the fractions contributed by each NO production pathway [5]. A sensitivity analysis within OPPDIF permits the computation of sensitivity coefficients for each species with respect to changes in the rate coefficient for each elementary reaction within the kinetic mechanism. Such an analysis identifies key reactions controlling peak NO concentrations. With decreasing dilution level of either N₂ or CO₂, the importance of the thermal pathway rises almost exponentially. Thermal NO is found to dominate the N₂O and NNH pathways and no contribution arises from the prompt route owing to lack of CH radicals. The sensitivity coefficients for initiation reactions of the thermal, N₂O and NNH mechanisms mirror the findings of the pathway analysis.

5. Conclusions

ERE-CARS was applied successfully to NO concentration measurements in different atmospheric pressure flames. Stokes scans were recorded at various heights in a slightly rich ($\phi = 1.15$) hydrogen-air flame stabilized on a Hencken burner. The axial profile of the background-corrected, square-root of the NO ERE-CARS signal proved to be in excellent agreement with calculated NO concentration profiles. Detection of NO was also demonstrated in acetylene-air flames under both fuel-lean and highly sooting fuel-rich conditions. Excellent agreement was obtained between measured and theoretical spectra when using a modified Sandia CARSFT code. An atmospheric-pressure, laminar, counter-flow non-premixed hydrogen-air flame was investigated at a global strain rate of 20 s⁻¹. Despite considerable variation in collisional and Doppler line widths, the measured and computed NO concentration profiles were found to be in excellent agreement.

NO concentration profiles for 10%, 25% and 35% dilution by N₂ and CO₂ in the fuel stream were compared with predictions using the GRI 3.0 kinetic mechanism. Spatial locations and relative magnitudes of [NO] measured using ERE-CARS were in good agreement with calculated NO number densities. Pathway and sensitivity analyses were implemented and the thermal mechanism was found to dominate as the dilution level decreased. For counter-flow flames, either with varying hydrogen content (30% to 90%) in the fuel stream (with pure oxygen in the oxidizer stream) or with varying oxygen content (30% to 90%) in the oxidizer stream (with pure hydrogen in the fuel stream), an optimum condition at 40% N₂ dilution was observed for peak NO production.

From a diagnostics viewpoint, the potential for ERE-CARS detection of NO with good spatial resolution has been demonstrated in challenging environments such as flames with large temperature and concentration gradients which exhibit substantial variations in collisional quenching as well as in heavily sooting flames. This demonstration in laboratory-scale flames paves the path for application of ERE-CARS diagnostics to pollutant measurements in practical combustion systems (gas turbine combustors and internal combustion engines) under high-pressure conditions.

Acknowledgments

Funding for this research was provided by the U.S. Department of Energy, Division of Chemical Sciences, Geosciences and Biosciences, under Grant No. DE-FG02-03ER15391, by the Air Force Research Laboratory, Propulsion Directorate, Wright-Patterson Air Force Base, under Contract No. F33615-03-D-2329, and by the Air Force Office of Scientific Research under Contract No. FA9550-05-C-0096 (Dr. Julian Tishkoff, Program Manager).

References

- [1] C. S. Cooper, N. M. Laurendeau, *Applied Physics B* 70 (2000) 903-910.
- [2] W. G. Bessler, C. Schulz, T. Lee, J. B. Jeffries, R. K. Hanson, *Applied Optics* 41 (2002) 3547-3557.
- [3] W. G. Bessler, C. Schulz, T. Lee, J. B. Jeffries, R. K. Hanson, *Applied Optics* 42 (2003) 2031-2043.
- [4] W. G. Bessler, C. Schulz, T. Lee, J. B. Jeffries, R. K. Hanson, *Applied Optics* 42 (2003) 4922-4936.
- [5] S. V. Naik, N. M. Laurendeau, *Combustion Science and Technology* 174 (2004) 1809-1853.
- [6] T. Doerk, J. Ehlbeck, R. Jedamzik, J. Uhlenbusch, J. Hoschele, J. Steinwandel, *Applied Spectroscopy* 51 (1997) 1360-1368.
- [7] B. Attal-Tretout, P. Berlemont, J. P. Taran, *Molecular Physics* 70 (1990) 1-51.
- [8] B. Attal-Tretout, S. C. Schmidt, E. Crete, P. Dumas, J. P. Taran, *Journal of Quantitative Spectroscopy and Radiative Transfer* 43 (1990) 351-364.
- [9] P. Doerk, M. Hertl, B. Pfelzer, S. Hadrich, P. Jauernik, J. Uhlenbusch, *Applied Physics B* 64 (1997) 111-118.
- [10] S. F. Hanna, W. D. Kulatilaka, Z. Arp, T. Opatrny, M. O. Scully, J. P. Kuehner, R. P. Lucht, *Applied Physics Letters* 83 (2003) 1887-1889.
- [11] S. Roy, W. D. Kulatilaka, S. V. Naik, N. M. Laurendeau, R. P. Lucht, J. R. Gord, *Applied Physics Letters* 89 (2006) 104105(1)-104105(3).
- [12] W. D. Kulatilaka, N. Chai, S. V. Naik, N. M. Laurendeau, R. P. Lucht, J. P. Kuehner, S. Roy, J. R. Gord, *Optics Letters* 31 (2006) 3357-3359.
- [13] W. D. Kulatilaka, N. Chai, S. V. Naik, S. Roy, N. M. Laurendeau, R. P. Lucht, J. P. Kuehner, J. R. Gord, *Optics Communications* (2007) in review.
- [14] W. D. Kulatilaka, R. P. Lucht, S. F. Hanna, V. R. Katta, *Combustion and Flame* 137 (2004) 523-537.
- [15] N. Vora, J. E. Siow, N. M. Laurendeau, *Combustion and Flame* 126 (2001) 1393-1401.
- [16] V. R. Katta, L. P. Goss, W. M. Roquemore, *Combustion and Flame* 96 (1994) 60-74.
- [17] V. R. Katta, L. P. Goss, W. M. Roquemore, *AIAA Journal* 32 (1994) 84-94.

- [18] L. P. Goss, V. R. Katta, W. M. Roquemore, *International Journal of Numerical Methods for Heat and Fluid Flow* 4 (1994) 413-424.
- [19] A. E. Lutz, R. J. Kee, J. F. Grcar, *Sandia National Laboratories Report No. SAND96-8243*, 1996.
- [20] R. J. Kee, J. A. Miller, G. H. Evans, G. Dixon-Lewis, *Proceedings of the Combustion Institute* 22 (1988) 1479-1494.
- [21] G. P. Smith, D. M. Golden, M. Frenklach, N. W. Moriarty, B. Eiteneer, M. Goldenberg, C. T. Bowman, R. K. Hanson, S. Song, W. C. Gardiner, Jr., V. Lissianski, Z. Qin, *GRI Mechanism (version 3.0)*, 1999. http://www.me.berkeley.edu/gri_mech.
- [22] J. P. Gore, J. Lim, T. Takeno, X. L. Zhu, *Proceedings of Fifth Joint ASME/JSME Joint Thermal Engineering Conference*, San Diego, CA, Paper AJTE99-6311 (1999).
- [23] R. E. Palmer, *Sandia National Laboratories Report No. SAND89-8206*, 1989.
- [24] J. Luque, D. R. Crosley, *SRI International Report No. MP99-009*, 1999.
- [25] J. Laane, W. Kiefer, *Journal of Raman Spectroscopy* 9 (1980) 353-360.
- [26] W. Lempert, G. J. Rosasco, W. S. Hurst, *Journal of Chemical Physics* 81 (1984) 4241-4245.
- [27] A. C. Eckbreth, *Laser Diagnostics for Combustion Temperature and Species*, Gordon and Breach, Amsterdam, The Netherlands, 1996.
- [28] G. J. Rortveit, J. E. Hustad, S. C. Li, F. A. Williams, *Combustion and Flame* 130 (2002) 48-61.
- [29] F. F. Kuligowski, N. M. Laurendeau, *Combustion Science and Technology* 130 (1997) 423-430.
- [30] C. J. Sung, C. K. Law, *Proceedings of the Combustion Institute* 27 (1998) 1411-1418.

N. CHAI¹
W.D. KULATILAKA¹
S.V. NAIK^{1,✉}
N.M. LAURENDEAU¹
R.P. LUCHT¹
J.P. KUEHNER²
S. ROY³
V.R. KATTA³
J.R. GORD⁴

Nitric oxide concentration measurements in atmospheric pressure flames using electronic-resonance-enhanced coherent anti-Stokes Raman scattering

¹ School of Mechanical Engineering, Purdue University, West Lafayette, IN 47907, USA

² Department of Physics and Engineering, Washington & Lee University, Lexington, VA 24450, USA

³ Innovative Scientific Solutions, Inc., 2766 Indian Ripple Road, Dayton, OH 45440, USA

⁴ Air Force Research Laboratory, Propulsion Directorate, Wright-Patterson AFB, OH 45433, USA

Received: 12 December 2006/

Revised version: 28 February 2007

Published online: 17 May 2007 • © Springer-Verlag 2007

ABSTRACT We report the application of electronic-resonance-enhanced coherent anti-Stokes Raman scattering (ERE-CARS) for measurements of nitric oxide concentration ([NO]) in three different atmospheric pressure flames. Visible pump (532 nm) and Stokes (591 nm) beams are used to probe the Q-branch of the Raman transition. A significant resonance enhancement is obtained by tuning an ultraviolet probe beam (236 nm) into resonance with specific rotational transitions in the ($v' = 0$, $v'' = 1$) vibrational band of the $A^2\Sigma^+ - X^2\Pi$ electronic system of NO. ERE-CARS spectra are recorded at various heights within a hydrogen-air flame producing relatively low concentrations of NO over a Hencken burner. Good agreement is obtained between NO ERE-CARS measurements and the results of flame computations using UNICORN, a two-dimensional flame code. Excellent agreement between measured and calculated NO spectra is also obtained when using a modified version of the Sandia CARSFT code for heavily sooting acetylene-air flames ($\phi = 0.8$ to $\phi = 1.6$) on the same Hencken burner. Finally, NO concentration profiles are measured using ERE-CARS in a laminar, counter-flow, non-premixed hydrogen-air flame. Spectral scans are recorded by probing the Q₁ (9.5), Q₁ (13.5) and Q₁ (17.5) Raman transitions. The measured shape of the [NO] profile is in good agreement with that predicted using the OPPDIF code, even without correcting for collisional effects. These comparisons between [NO] measurements and predictions establish the utility of ERE-CARS for detection of NO in flames with large temperature and concentration gradients as well as in sooting environments.

PACS 07.88.+y; 42.62.Fi; 42.65.Dr

1 Introduction

Emissions of oxides of nitrogen (NO_x) from internal combustion and gas turbine engines is a major environmental concern, owing to the direct impact of nitrogenous

species on the formation of photochemical smog and their role in global warming via depletion of the ozone layer. Combustion processes contribute about 95% of atmospheric NO_x and a majority of the NO_x from combustion sources is emitted in the form of nitric oxide (NO). Consequently, development of combustors producing low NO levels is an important task facing the combustion community; moreover, such combustors benefit from advances in fundamental knowledge regarding formation and destruction of NO in flame environments.

Laser-induced fluorescence (LIF) is frequently used for the measurement of minor species concentrations in flames, owing to its sensitivity, excellent spatial resolution and experimental simplicity. Many researchers have developed LIF strategies for quantitative detection of nitric oxide in high-pressure flames [1–5]. However, fluorescence signals from NO can become difficult to interpret, especially with increasing pressure, owing to: (a) interferences from oxygen in fuel-lean regions and from hydrocarbons or soot in fuel-rich regions, (b) quenching of the LIF signal via collisions with O₂, CO₂ and H₂O, among other colliding partners, and (c) absorption of both the laser beam and the fluorescence signal by CO₂, H₂O or hydrocarbons at typical UV excitation wavelengths.

Recently, quantification of NO LIF in a heavy-duty Diesel engine was demonstrated by correcting for attenuation of the laser beam and of the NO fluorescence signal arising from CO₂ and O₂ absorption [6, 7]. Additional corrections were made for nitrogen Raman scattering and for window fouling arising from soot. A combination of one-dimensional spectral line-imaging and spatially-resolved, two-dimensional NO-LIF in conjunction with a new multi-spectral detection strategy has also been utilized to quantify measurements in laminar, premixed methane-air flames at pressures up to 60 bar [8]. In addition, a two-photon LIF technique has been developed and applied to study in-cylinder Diesel combustion, eliminating many difficulties associated with the more common single-photon NO LIF [9].

While laser-induced fluorescence techniques are attractive, due to their simplicity and the substantial progress being made to overcome challenges in quantification of NO via LIF, other researchers have considered diagnostic techniques such as cavity ring-down spectroscopy, laser-induced polar-

✉ Fax: +1-765-494-0539, E-mail: naiks@ecn.purdue.edu

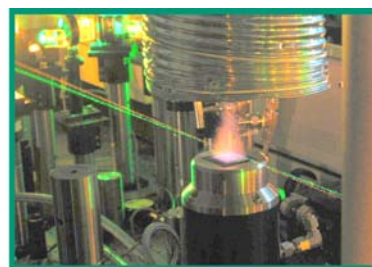
ization spectroscopy, and coherent anti-Stokes Raman scattering. While most practical combustion devices operate at high pressure, the robustness and utility of such alternative techniques must first be tested in atmospheric pressure flames.

Conventional coherent anti-Stokes Raman scattering (CARS) has previously been applied to NO measurements in the temperature range from 300 to 800 K at atmospheric pressure [10]. The detection limit for NO was found to be about 2500 ppm in N₂ buffer gas. In a subsequent effort, CARS was utilized to measure the reduction in NO resulting from a microwave generated nitrogen plasma at atmospheric pressure [11]. A polarization sensitive background suppression scheme was applied to detect NO concentrations down to a few hundred ppm.

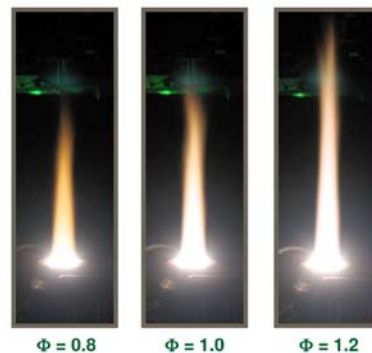
A significant enhancement in the CARS detection limit can be obtained by tuning one or more of the pump, Stokes and probe beams into resonance with a suitable electronic transition. Previously, such electronic-resonance-enhanced (ERE) CARS has been applied successfully to selected radical species. For example, hydroxyl (OH) concentrations were measured in a low-pressure microwave discharge as well as in atmospheric-pressure, premixed hydrogen-air and methane-air flames [12]. ERE-CARS detection of OH was also demonstrated in laminar, flat flames at pressures up to 9.6 bar [13]. In a later investigation, methylidyne (CH) concentrations were measured in a low-pressure H₂/CH₄/Ar microwave plasma using both LIF and ERE-CARS [14].

For these previous explorations of resonance-enhanced CARS [12–14], the pump, Stokes and probe beams were all at ultraviolet frequencies. In contrast, an ERE-CARS technique has recently been reported which implements an ultraviolet probe beam in electronic resonance while using visible pump and Stokes beams far from electronic resonance [15–18]. By employing a room-temperature jet of 1000 ppm NO in N₂, with substitution of N₂ buffer gas by up to 82% O₂ or CO₂, the NO ERE-CARS signal was shown to display little sensitivity to electronic quenching [16]. This finding is important for many practical combustors, for which the quenching environment can undergo rapid spatial and temporal variations. The pressure dependence of the ERE-CARS signal from 300 ppm NO in N₂ has also been studied within a gas cell at pressures up to 8 bar [17]. The NO ERE-CARS signal increased from 0.1 to 2 bar and remained approximately constant at pressures up to 8 bar. Finally, ERE-CARS has recently been applied to an atmospheric pressure hydrogen-air flame stabilized on a Hencken burner. By doping known quantities of NO into the flame, a detection limit of approximately 50 ppm was demonstrated [18].

In this paper, we present NO measurements via ERE-CARS for three different flame environments, as shown in Fig. 1. Our goal was to assess further the applicability of ERE-CARS for detection of NO in flames with low NO concentrations, with sooting interferences, and with steep temperature and concentration gradients. First, a hydrogen-air flame was stabilized using a Hencken burner and ERE-CARS measurements of NO were obtained at various heights above the burner surface. The measured NO profile was compared with calculations using a detailed reactive flow code. In a second set of experiments, heavily sooting acetylene-air flames were stabilized using the same Hencken burner and spectral scans



a Non-sooting hydrogen-air ($\phi = 1.15$) flame on a Hencken burner



b Sooting C₂H₂-air flames on a Hencken burner



c Non-premixed hydrogen-air flame within a counter-flow burner

FIGURE 1 Three different types of flames investigated in this study

were recorded at various equivalence ratios to demonstrate detection of NO, despite interferences typically precluding LIF measurements. A third set of measurements was performed in a counter-flow flame. The counter-flow configuration produces flat flames having a one-dimensional structure, which permits direct modeling of interactions between fluid mixing and chemical kinetics, thus promoting reliable calculations of flame structure and pollutant formation. Before applying ERE-CARS to NO measurements in high-pressure gas turbine combustors, we must unravel several diagnostic issues in atmospheric pressure, laboratory-scale counter-flow flames, which provide not only a challenging measurement environment but also a good diagnostic test from the perspective of chemical kinetics. Therefore, a laminar, non-premixed, hydrogen-air flame at a global strain rate of 20 s⁻¹ was stabilized using a counter-flow burner. In particular, this flame exhibits steep spatial gradients in both temperature and species concentrations. NO concentration profiles were measured in this flame using three different Raman transitions. Measured NO profiles were then compared with concentration profiles computed using an opposed-flow flame code.

2 Experiment

A two-dimensional, non-premixed, near-adiabatic Hencken burner (Research Technologies Model RD15X15) was used to stabilize the atmospheric-pressure hydrogen-air and acetylene-air flames. An oxidizer mixture of 79% N₂ and 21% O₂ was employed instead of commercial air. Mass flow controllers (Models MKS 1559A and M100B) were used to regulate gas flow into the burner. The burner surface is fabricated from a 36.5-mm square hastalloy honeycomb through which the oxidizer flows. The honeycomb structure supports stainless steel fuel tubes in every fourth honeycomb cell. Fuel and oxidizer remain separated before exiting at the burner surface. The burner is designed so as to ensure rapid mixing of fuel and oxidizer immediately above the burner. A co-flow of nitrogen gas was used in the region surrounding the 36.5-mm square honeycomb to shroud the flame. A more detailed description of the Hencken burner is given elsewhere [19]. The burner is mounted on a translation stage that permits horizontal and lateral positioning so as to adjust the ERE-CARS probe volume within the flame. A linear dial gauge was used to measure vertical movement of the burner so that spectra could be recorded at known heights above the burner surface.

The counter-flow burner consists of two 1.9-cm diameter nozzles made of hastalloy C-276 designed to carry either the fuel or oxidizer mixture. The nozzles are water-cooled to prevent overheating and the water temperature is maintained around 30 °C so as to avoid condensation on nozzle surfaces. An annular region surrounding the main reactant tube provides a nitrogen shroud which surrounds the nearly one-dimensional, non-premixed flame stabilized between the opposed nozzles. The separation distance between the fuel and oxidizer nozzles was fixed at 2 cm and the velocity of the reactants at the nozzle exits was maintained at 20 cm/s, thus producing a global strain rate of 20 s⁻¹, where the global strain rate is defined as the sum of reactant velocities at the nozzle exits divided by the nozzle separation distance. The counter-flow burner facility is described in more detail in a previous publication [20].

An energy-level diagram describing the ERE-CARS process for nitric oxide is shown in Fig. 2. The pump (ω_1) and Stokes (ω_2) lasers are visible beams with frequencies far detuned from the $A^2\Sigma^+ - X^2\Pi$ electronic system of the NO molecule. In contrast, the probe beam frequency (ω_3) is at or near electronic resonance. The CARS signal (ω_4) is generated using a three-dimensional phase-matching geometry. Figure 3 shows a schematic diagram of the experimental system. The second harmonic output (~ 532 nm) of an injection-seeded, Q-switched Nd:YAG laser was used as the pump beam. This second harmonic output was also used to pump a narrow-band dye laser to produce tunable radiation in the vicinity of 704 nm. The output of the dye laser was frequency-mixed with the third harmonic output (~ 355 nm) of the injection-seeded YAG laser to generate the probe beam (~ 236 nm). The second harmonic output of a separate unseeded, Q-switched Nd:YAG laser was used to pump another narrow-band dye laser to produce tunable radiation in the vicinity of 591 nm, which acts as the Stokes beam. The full-width at half-maximum (FWHM) linewidth of the pump beam

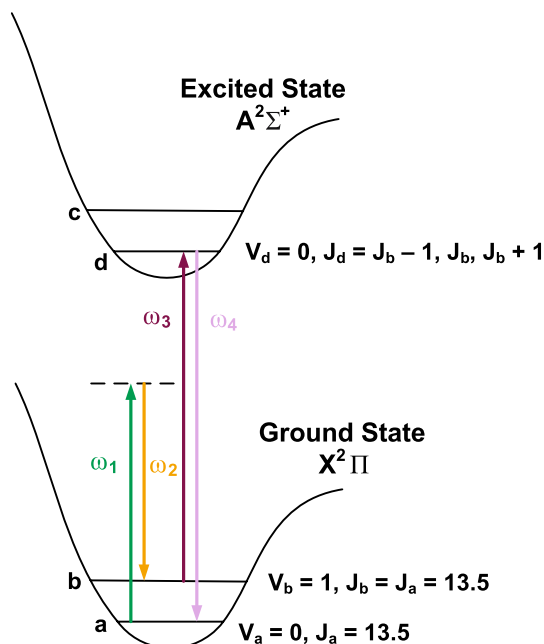


FIGURE 2 Energy level diagram showing the ERE-CARS process for NO. The transitions identify the pump beam ($\omega_1 = 18789.4$ cm⁻¹), Stokes beam ($\omega_2 = 16920.5$ cm⁻¹), probe beam ($\omega_3 = 42372.8$ cm⁻¹) and CARS signal beam ($\omega_4 = 44241.7$ cm⁻¹)

(532 nm) was 0.003 cm⁻¹ while the linewidths for the Stokes (591 nm) and the probe (236 nm) beams were 0.1 cm⁻¹. Using a translating razor blade, we measured the diameters of the three beams 20 mm away from the focus (CARS probe volume) to be approximately 250 μm.

A polarization-sensitive technique was employed to suppress the non-resonant background signal arising from four-wave mixing. The probe beam was vertically polarized while the polarizations of the pump and Stokes beams were set at an angle of 60° with respect to the vertical axis. Fine adjustment of the polarizer in the detection channel, orthogonal to the four-wave mixing signal, enables optimum suppression of any non-resonant background [14].

For experiments performed using the Hencken burner, the ultraviolet probe wavelength was held fixed at 236.06 nm corresponding to the Q₁ (13.5) transition in the (0,1) band of the $A^2\Sigma^+ - X^2\Pi$ electronic system of NO. Spectra were recorded at various heights above the burner by tuning the wavelength of the visible Stokes beam, so that UV fluorescence interferences and/or background scattering remained constant during the spectral scan. Such scans, for which the Stokes wavelength was varied while the UV probe wavelength was fixed, are referred to as Stokes scans. The resulting baseline can be subtracted to obtain a background-corrected ERE-CARS signal. This background-corrected signal is then divided by the measured UV pulse energy to account for shot-to-shot variations in the energy of the pulsed probe beam.

Three different Raman transitions were investigated for experiments performed using the counter-flow burner. A substantial temperature gradient exists between the fuel and oxidizer streams in the counter-flow configuration. In fact, NO is formed and destroyed over temperatures ranging from 700 K to 2500 K. For these experiments, the Q₁ (9.5), Q₁ (13.5) and Q₁ (17.5) Raman transitions were selected to assess the tem-

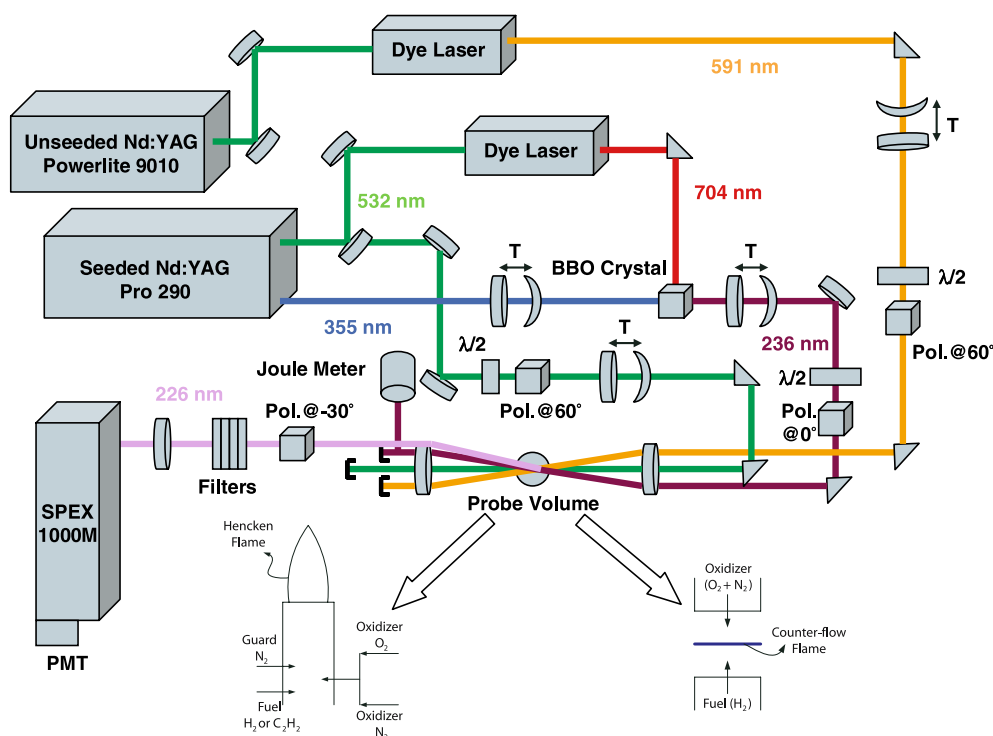


FIGURE 3 Schematic of the experimental setup for ERE-CARS of NO. T: telescope; $\lambda/2$: half-wave plate; PMT: photomultiplier tube. Polarizer angles are set with respect to the vertical axis. Filters are composed of four 45°, 215-nm mirrors having 70% transmission at 226 nm and 1% transmission at 236 nm

perature sensitivity of the measured [NO] profile. For the three selected Raman transitions, the ultraviolet probe wavelength was held fixed at 236.19 nm, 236.06 nm and 235.87 nm, respectively, corresponding to the Q_1 (9.5), Q_1 (13.5) and Q_1 (17.5) transitions in the (1,0) band of the $A^2\Sigma^+-X^2\Pi$ electronic system of NO. Stokes scans were recorded every one mm between the fuel and oxidizer nozzles for each of the three ERE-CARS transitions.

3 Modeling

Numerical computations for the hydrogen-air flame stabilized using the Hencken burner was performed using the UNICORN (UNsteady Ignition and COmbustion with ReactionNs) code [21–23]. The flame is modeled as a combination of several diffusion flamelets, where each flamelet is supported by fuel originating from each individual tube within the burner. The exact nature of the flamelet (premixed, partially premixed or non-premixed) can be varied, depending on experimental flow conditions. The flamelet established over the fuel tube is modeled as an axi-symmetric flow while the hexagonal opening around the fuel tube, through which the oxidizer mixture flows, is modeled as a co-annular tube. Adiabatic flow conditions are assumed at the fuel-tube wall. Symmetric boundary conditions are employed along the centerline of the flow as well as at the outer boundary in the radial direction of the burner; linear extrapolation of flow variables is implemented along the outflow boundary located at a height of several fuel-tube diameters above the burner surface. Fuel and air velocities are determined from the known mass flow rates of gases.

For the counter-flow flame, OPPDIF, a Sandia opposed-flow flame code [24], was used for calculations of temperature, velocity and species concentration profiles along the cen-

terline between the two nozzles. The mathematical model for OPPDIF reduces the two-dimensional, axi-symmetric flow field to a one-dimensional formulation via a similarity transformation [25]. The GRI mechanism (version 3.0) [26] was used for the chemical kinetics; gas-phase radiation was considered by adding a radiation source term in OPPDIF. The effect of radiative heat loss was considered in the optically thin limit [27]. The radiation model utilizes Planck mean absorption coefficients for the major species CO_2 , H_2O , CO and CH_4 ; the temperature dependence of these coefficients was modeled using fourth-order polynomial fits to the results of narrow-band calculations. A time-dependent, axi-symmetric model in UNICORN was also employed for simulation of a weakly-stretched counter-flow diffusion flame. The two-dimensional calculations were performed on a grid having 801 by 41 nodal points in the axial and radial directions, respectively.

The ERE-CARS spectra were modeled using a perturbative analysis applicable at lower laser irradiances via modification of the Sandia CARSFT code [15, 28]. Spectral data for the NO molecule were obtained via LIFBASE [29] and from high-resolution CARS measurements [30, 31].

4 Results and discussion

Figure 4 displays spectra recorded for various heights in a hydrogen-air flame stabilized on the Hencken burner at $\phi = 1.15$. We previously added known quantities of NO to the oxidizer flow in a similar flame to determine the NO detection limit at atmospheric pressure [18]. From Fig. 4, we find that the NO ERE-CARS signal along the centerline of the flame rises with height above the burner surface. The spectra in Fig. 4 exhibit a non-resonant background resulting from scattering of the UV probe beam and fluorescence induced

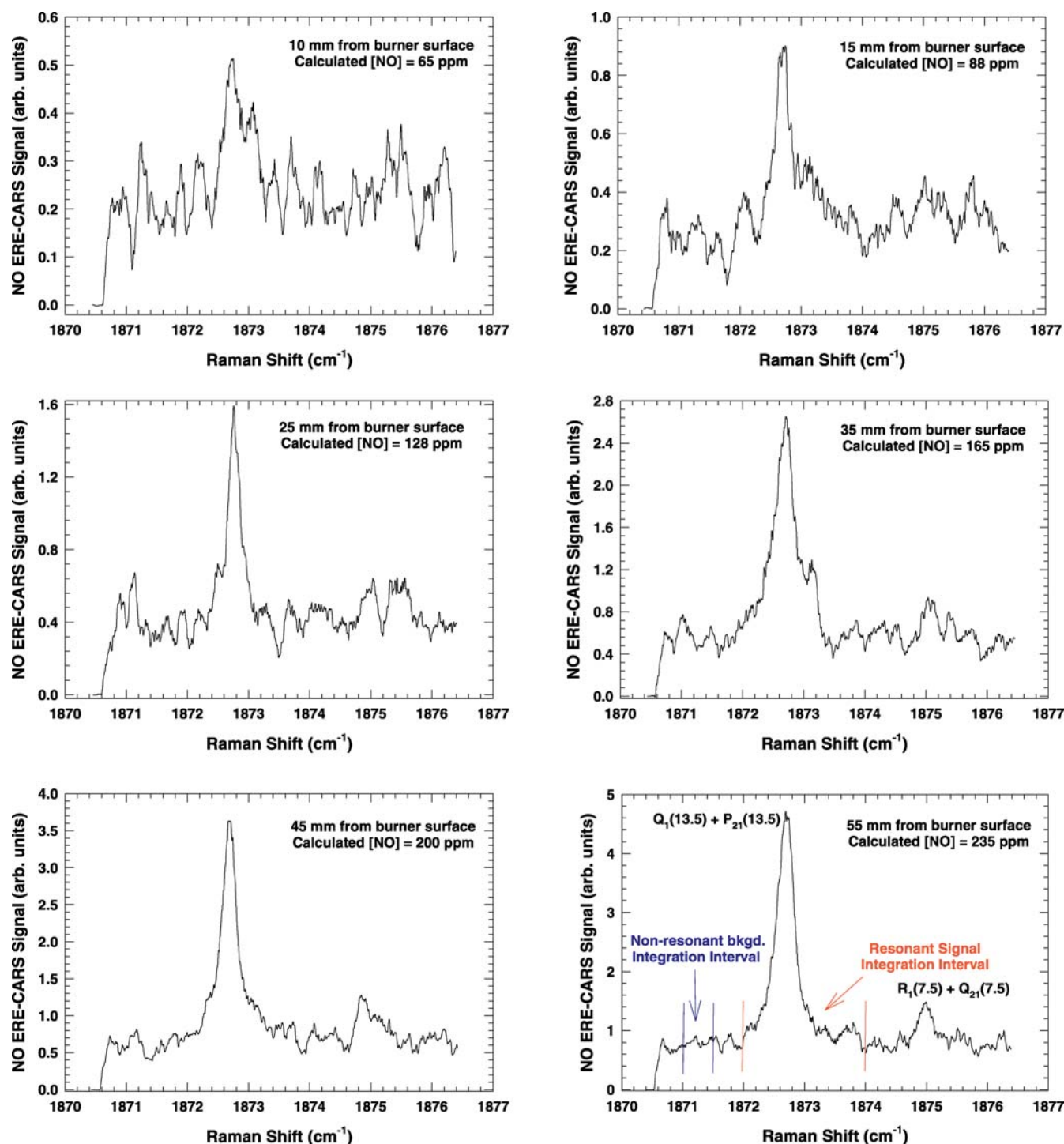


FIGURE 4 Spectral scans at various heights above the Hencken burner in an H_2 -air ($\phi = 1.15$) flame. The UV probe frequency was fixed at 42361.46 cm^{-1} , corresponding to the $Q_1(13.5)$ transition in the $A^2\Sigma^+ - X^2\Pi(1,0)$ band. Pump, Stokes and probe energy levels were fixed at 14 mJ/pulse, 18 mJ/pulse and 0.6 mJ/pulse, respectively

by the same UV beam. Because the UV probe wavelength is fixed during Stokes scans, this non-resonant background is nominally constant, independent of Stokes laser wavelength. Furthermore, the non-resonant background does not modulate the ERE-CARS signal, so that it can be subtracted in data processing. The overall non-resonant background signal was obtained via integration between Raman shifts of 1871.0 and 1871.5 cm^{-1} . After background subtraction and division by

the UV probe energy, the ERE-CARS signal was integrated between Raman shifts of 1872 and 1874 cm^{-1} .

Figure 5 shows a comparison between the measured concentration of NO, which is proportional to the square-root of the integrated ERE-CARS signal, and predicted NO concentrations computed using UNICORN at various heights above the burner surface. As fuel and oxidizer are rapidly mixed in the region above the burner surface, a sharp increase in tem-

perature occurs owing to combustion reactions. In the post-flame regime, the temperature remains essentially constant; however, the NO concentration increases continuously because of the Zeldovich reactions. We should note that the data points are not corrected for variations in Boltzmann fraction, owing to the nearly constant post-flame temperature, as shown in Fig. 5.

Flames encountered in practical applications, such as gas turbine combustors, furnaces and internal combustion engines, are highly luminous and particle laden, especially when using liquid fuels. Hydrocarbon species, their fragments and soot particulates possess very broad absorption and emission signatures throughout the ultraviolet region [32]. Such broadband UV interferences complicate signal interpretation when detecting NO via LIF for excitation near 226 nm in the γ (0,0) band [1–5]. Therefore, acetylene-air flames were studied from lean ($\phi = 0.8$) to rich ($\phi = 1.6$) conditions to assess the feasibility of ERE-CARS measurements under highly sooting conditions. Spectra recorded 55 mm above the burner surface are shown in Fig. 6 along with theoretical spectral fits obtained using the modified Sandia CARSFT code. Good agreement is observed between theory and experiment for these conditions. The excellent selectivity of

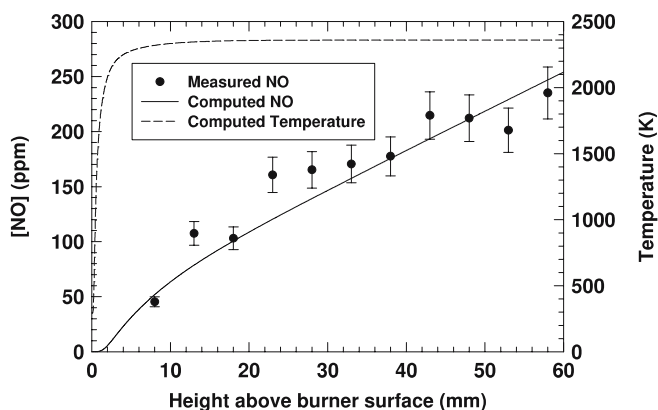


FIGURE 5 Comparison between measured and computed NO concentrations (using UNICORN) at various heights above the Hencken burner in an H_2 -air ($\phi = 1.15$) flame. The data were scaled so as to match measured and calculated [NO] at 48 mm above the burner surface. The temperature profile was also calculated using UNICORN

the ERE-CARS technique arises from the fact that both Raman and electronic resonance conditions must be satisfied to generate the ERE-CARS signal. Based on Fig. 6, ERE-CARS can be employed for detection of NO, even in heavily

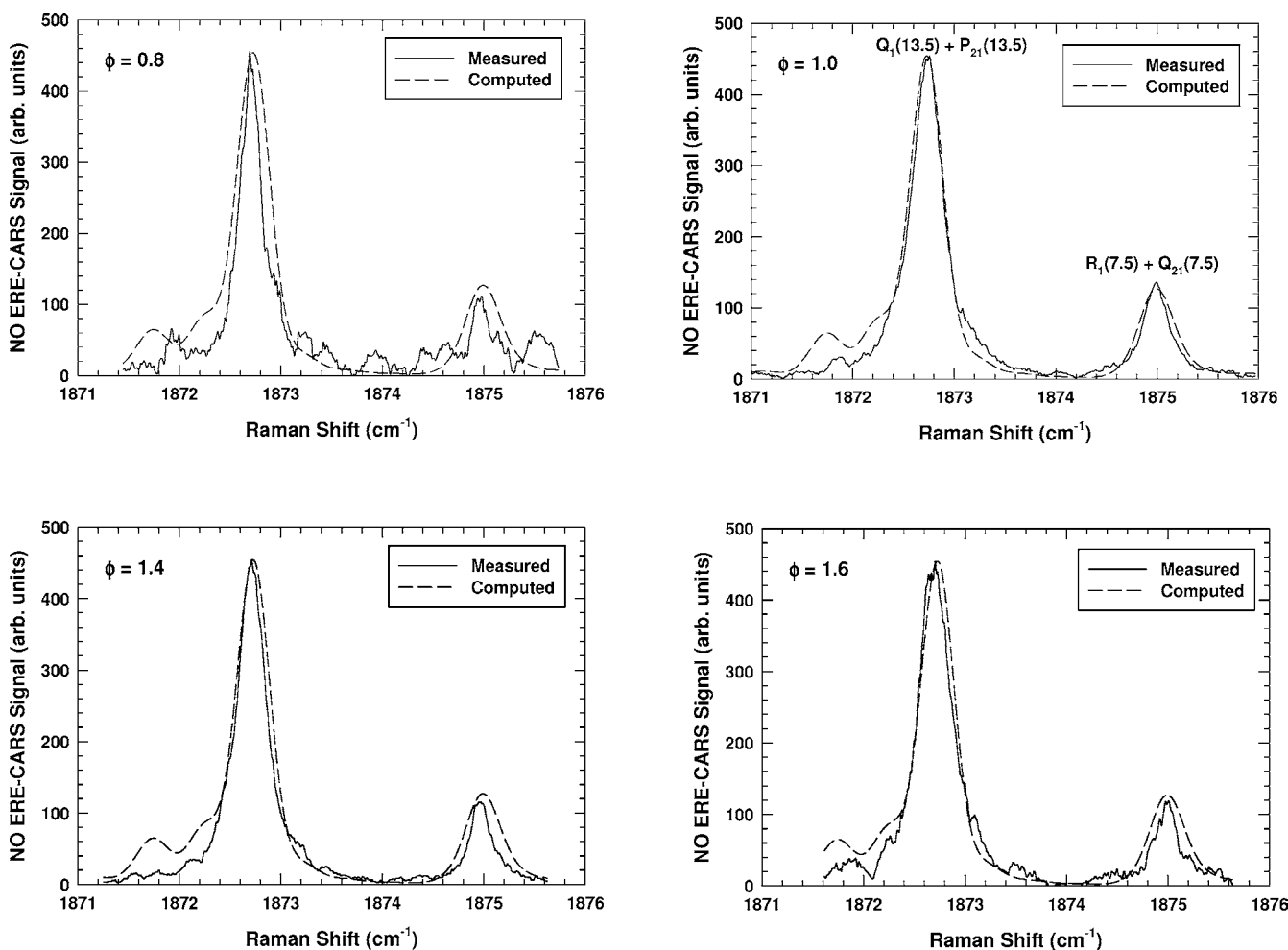


FIGURE 6 Comparisons between measured and computed ERE-CARS spectra at 55 mm above the Hencken burner for highly sooting C_2H_2 -air flames. The UV probe frequency was fixed at $42\,361.46\text{ cm}^{-1}$, corresponding to the $Q_1(13.5)$ transition in the $A^2\Sigma^+ - X^2\Pi(1,0)$ band. Pump, Stokes and probe energy levels were fixed at 10 mJ/pulse, 16 mJ/pulse and 1.2 mJ/pulse, respectively. For the theoretical calculations, linewidths of the Stokes and probe laser were selected to be 0.37 cm^{-1} and 3 cm^{-1} , respectively. The theoretical fits were obtained using a temperature of 2300 K and an NO concentration of 1000 ppm

sooting flames, thus overcoming one of the major drawbacks of LIF.

Figure 7 displays Stokes spectra recorded at various positions between the fuel and oxidizer nozzle for the non-premixed, hydrogen-air counter-flow flame at a global strain rate of 20 s^{-1} . A significant modulation in ERE-CARS signal is obtained between the fuel and oxidizer nozzles, as

shown in Fig. 7. The background-corrected and normalized ERE-CARS signals from these spectra were integrated between Raman shifts of 1871.2 and 1873.8 cm^{-1} . Knowing the computed temperature at each position from OPPDIF, we calculated the Boltzmann fraction for the $J'' = 13.5$, $N'' = 13$, $v'' = 0$ rotational-vibrational level. The square-root of the integrated ERE-CARS signal was then corrected for population

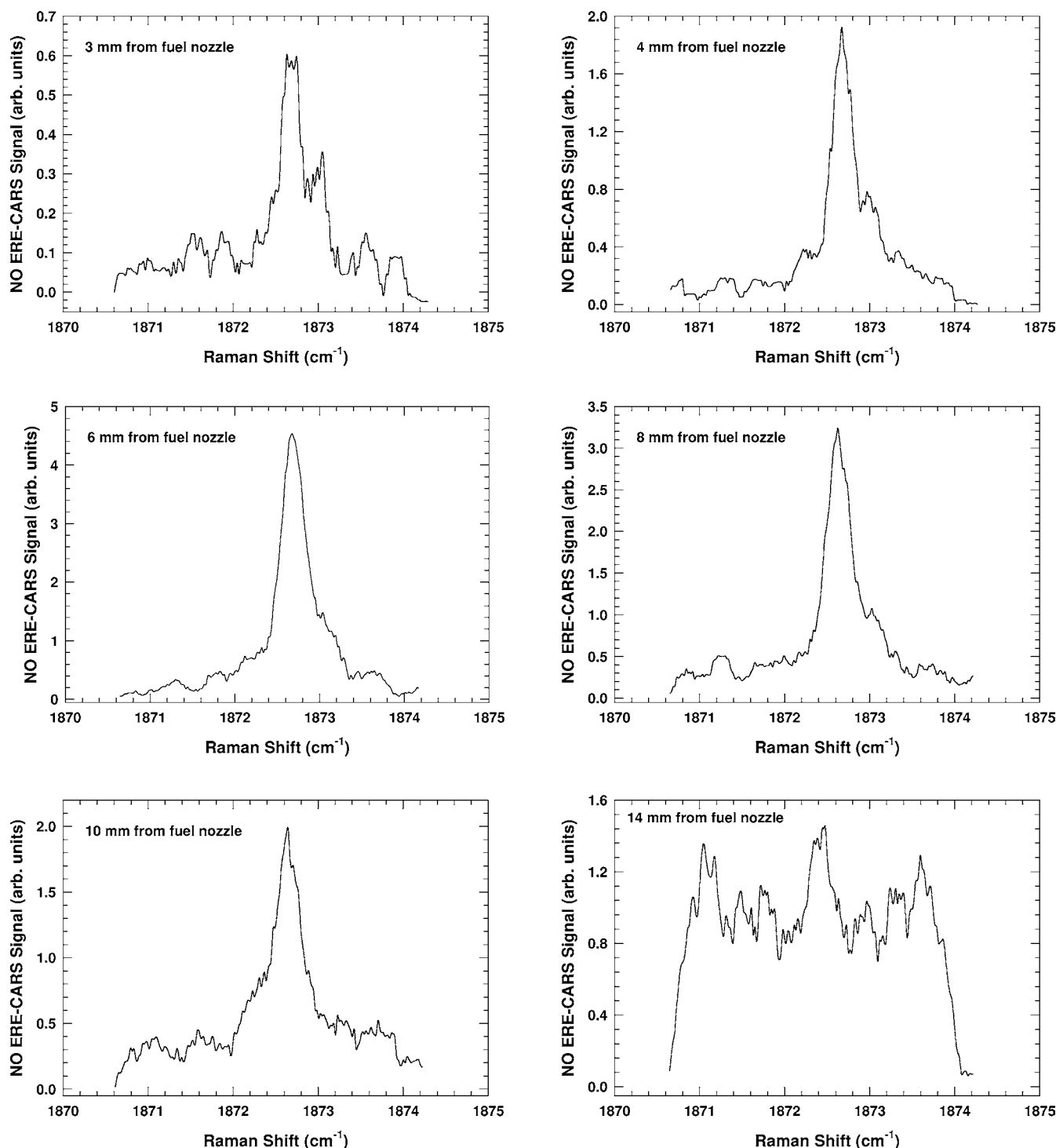


FIGURE 7 Spectral scans indicating NO ERE-CARS signals at various positions in an atmospheric pressure, laminar, counter-flow, non-premixed H_2 -air flame at a global strain rate of 20 s^{-1} . The UV probe frequency was fixed at 42361.46 cm^{-1} , corresponding to the Q_1 (13.5) transition in the $A^2\Sigma^+ - X^2\Pi$ (1,0) band. Pump, Stokes and probe energy levels were fixed at 14 mJ/pulse, 10 mJ/pulse and 0.5 mJ/pulse, respectively

differences using an appropriate calculation of Boltzmann fraction. The integration intervals for the two other Raman transitions, Q_1 (9.5) and Q_1 (17.5), were selected to be 1873 to 1875 cm^{-1} and 1869 to 1872 cm^{-1} , respectively. In Fig. 8, the square-root of the integrated signal, as divided by the Boltzmann fraction for the corresponding rotational level at the calculated temperature, is plotted versus distance between the two nozzles for three different Raman transitions.

The three different profiles were scaled by setting the peak of the Q_1 (13.5) profile to unity. While the profile peaks for the Q_1 (9.5) and Q_1 (17.5) ERE-CARS signals were not scaled to match the Q_1 (13.5) case, the peaks for all three profiles agree to within 15%. This agreement was observed even though measurements for the three different transitions were acquired over several hours, thus indicating the stability of the optical alignment. We observe that the shapes of the NO concentration profiles measured using three different Raman transitions are very similar, and that the peaks of the profiles, corrected for their respective Boltzmann fractions, are in excellent agreement. We should note, however, that in regions of low NO concentration, the integrated ERE-CARS signal is sensitive to any background correction.

The relative agreement, both in terms of spatial location and magnitude, between the experimental and computed [NO] profiles, either using OPPDIF (one-dimensional calculation) or UNICORN (two-dimensional calculation), is quite satisfactory. Indeed, considering potentially complicating factors such as variations in temperature, collisional width and quenching environment in the counter-flow configuration, the excellent agreement between measured and calculated profiles is surely remarkable. Hence, we conclude that the proposed ERE-CARS technique should be applicable in complex collisional environments, while still giving a spatial resolution comparable to techniques such as LIF and CARS.

Figure 9 shows a comparison between measured and predicted NO concentrations, including the variation in calculated temperature, for the counter-flow hydrogen-air

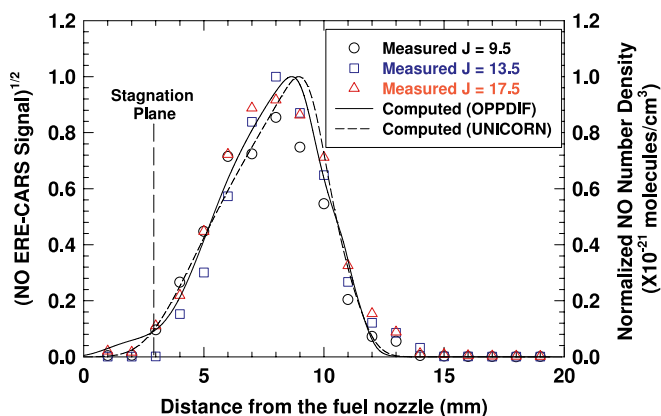


FIGURE 8 Comparison between measured NO signals and computed NO number density in an atmospheric pressure, laminar, counter-flow, non-premixed H_2 -air flame at a global strain rate of 20 s^{-1} . The integrated ERE-CARS signal has been corrected through background subtraction, division by the ultraviolet pulse energy, and division by the Boltzmann fraction using temperatures calculated from OPPDIF with GRI 3.0 chemical kinetics. Computed profiles using OPPDIF (one-dimensional calculation) and UNICORN (two-dimensional calculation) match well at the low strain rate of 20 s^{-1}

flame. Scaling the measured ERE-CARS signals via the predicted peak NO concentration, we estimate a detection limit of $\sim 25\text{ ppm}$ for the counter-flow flame measurements using three different Raman transitions. This detection limit could potentially be improved by focusing the beams more tightly and by employing strategies to reduce the UV scattering/fluorescence.

Collisions of the NO molecule with other atoms (e.g., O, H), diatomic radicals (e.g., OH, NO) and major species (e.g., H_2 , O_2 , H_2O , CO, CO_2 , CH_4 , N_2) depend on pressure and temperature. It is well-known that LIF signals decrease owing to such collisions, thus requiring corrections for quantification of NO LIF signals. We have previously shown that the ERE-CARS signal is nearly independent of electronic quenching when considering two important colliders, O_2 and CO_2 [16]. In a counter-flow non-premixed flame, temperature and species concentrations vary significantly in the flow field between the fuel and oxidizer nozzles. Figure 10 shows the computed variation in total quenching rate (Fig. 10a) as well as that for the collisional and Doppler linewidths (Fig. 10b) for a non-premixed H_2 -air flame. Quenching rate coefficients ($\text{cm}^3\text{ s}^{-1}$) for collisions of NO with H, H_2 , O, O_2 , OH, H_2O , N_2 , NH, NO, NO_2 and N_2O were obtained from the literature [33]. The number density of each collider and the temperature at different locations were obtained from OPPDIF, with the total quenching rate (s^{-1}) calculated from the sum of individual quenching rates.

As shown in Fig. 10a, the total electronic quenching rate varies considerably in the region encompassing measurable NO concentrations. In practical combustion systems, such variations in quenching rate, both in space and time, can cause substantial variations in signal levels when using LIF. The ERE-CARS spectra recorded using Stokes scans at different positions between the fuel and oxidizer nozzles were analyzed, without correction for variations in the collision rate. Hence, the good agreement between measured and calculated [NO] profiles, as shown in Fig. 8, demonstrates the effectiveness of the ERE-CARS technique despite large variations in collisional rate throughout the flame.

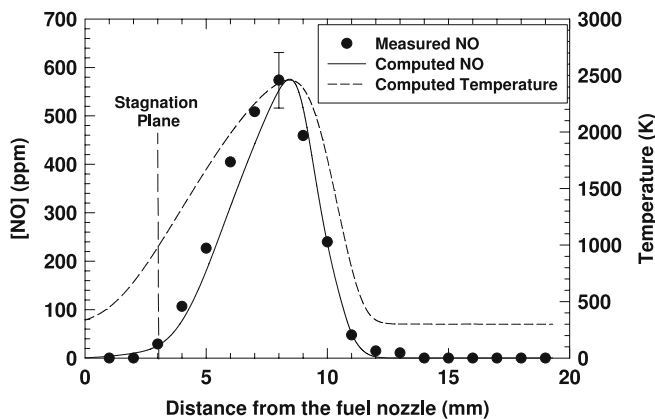


FIGURE 9 Comparison between measured and computed NO concentrations in an atmospheric pressure, laminar, counter-flow, non-premixed H_2 -air flame at a global strain rate of 20 s^{-1} . Data points were obtained by averaging the ERE-CARS measurements shown in Fig. 8 at each position, calibrating using the computed maximum NO number density, and converting from number density to ppm levels using temperatures calculated from OPPDIF with GRI 3.0 chemical kinetics

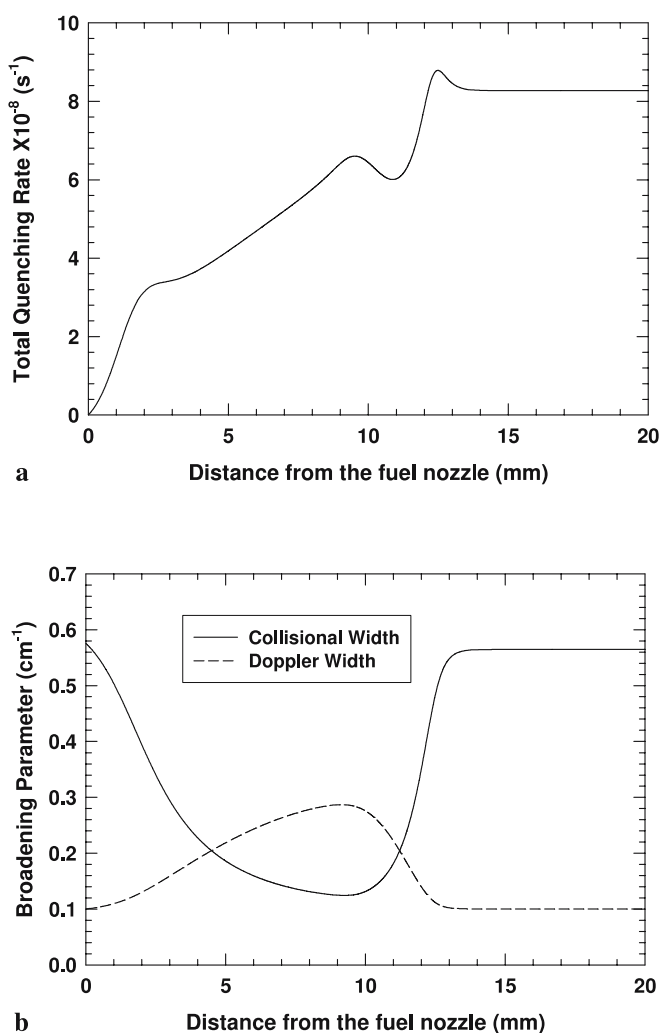


FIGURE 10 Variation of (a) total electronic quenching rate and (b) collisional and Doppler widths in an atmospheric pressure, laminar, counter-flow, non-premixed H_2 -air flame at a global strain rate of 20 s^{-1} . Temperature and species concentrations are obtained from OPPDIF using GRI 3.0 chemical kinetics

The CARS signal generated from the probe volume depends on the square of the third order non-linear susceptibility; the exact scaling is affected by the broadening mechanism for both the Raman transition and the UV probe transition, as well as on the transition spacing. Although much information is available on collisional broadening of ultraviolet transitions, little information is available on NO Raman linewidths at flame conditions. As the temperature increases from about 350 K in the wings of the NO profile to about 2500 K near the [NO] peak, the density decreases which produces a reduction in the collision-broadened linewidth. The Doppler width, on the other hand, increases somewhat in the high-temperature region, although at atmospheric pressure the Raman transition is predominantly collision-broadened even at flame temperatures. Figure 10b shows this variation in computed collisional and Doppler widths between the two nozzles. In the region between 4 to 12 mm from the fuel-side nozzle, the ratio of collisional to Doppler widths changes by over a factor of two. Such variations could cause substantial changes in laser interaction with the Raman and probe transitions, thus poten-

tially complicating the interpretation of ERE-CARS signals. However, based on Fig. 8, for which the experimental concentration profile was corrected only for changes in temperature, the measured NO profile still agrees very well with computations using rigorous transport and chemical kinetics. The factors which lead to such good agreement will be explored in future work. In particular, our intention is to investigate saturation effects on the Raman transition and/or the UV probe transition.

5 Conclusions

ERE-CARS was applied successfully to NO concentration measurements in three different atmospheric pressure flames. Stokes scans were recorded at various heights in a slightly rich ($\phi = 1.15$) hydrogen-air flame stabilized on a Hencken burner. The axial profile of the background-corrected, square-root of the NO ERE-CARS signal proved to be in excellent agreement with calculated NO concentration profiles. Background-corrected detection of NO was also demonstrated in acetylene-air flames under both fuel-lean and highly sooting fuel-rich conditions. Excellent agreement was obtained between measured and theoretical spectra when using a modified Sandia CARSFT code. Finally, an atmospheric-pressure, laminar, counter-flow non-premixed hydrogen-air flame was investigated at a global strain rate of 20 s^{-1} . Despite considerable variation in collisional and Doppler linewidths, the measured and computed NO concentration profiles were found to be in excellent agreement.

The above three experiments demonstrate that ERE-CARS is a robust diagnostic technique which can be used to detect flame-generated NO in challenging environments. The ERE-CARS signal appears to be much less dependent on collisional rates, especially electronic quenching rates, than is the case for NO LIF. Continuing efforts will focus on understanding the physics of the ERE-CARS process, on further development of the technique to enable single-shot measurements, and on applications of ERE-CARS to high-pressure laboratory flames as well as to gas-turbine combustors.

ACKNOWLEDGEMENTS Funding for this research was provided by the U.S. Department of Energy, Division of Chemical Sciences, Geosciences and Biosciences, under Grant No. DE-FG02-03ER15391, by the Air Force Office of Scientific Research under Contract No. FA9550-05-C-0096 (Dr. Julian Tishkoff, Program Manager), and by the Air Force Research Laboratory, Propulsion Directorate, Wright-Patterson Air Force Base, under Contract No. F33615-03-D-2329.

REFERENCES

- 1 C.S. Cooper, N.M. Laurendeau, *Appl. Phys. B* **70**, 903 (2000)
- 2 W.G. Bessler, C. Schulz, T. Lee, J.B. Jeffries, R.K. Hanson, *Appl. Opt.* **41**, 3547 (2002)
- 3 W.G. Bessler, C. Schulz, T. Lee, J.B. Jeffries, R.K. Hanson, *Appl. Opt.* **42**, 2031 (2003)
- 4 W.G. Bessler, C. Schulz, T. Lee, J.B. Jeffries, R.K. Hanson, *Appl. Opt.* **42**, 4922 (2003)
- 5 S.V. Naik, N.M. Laurendeau, *Combust. Sci. Technol.* **174**, 1809 (2004)
- 6 K. Verbeizen, R.J.H. Klein-Douwel, A.P. van Vliet, A.J. Donkerbroek, W.L. Meerts, N.J. Dam, J.J. ter Meulen, *Appl. Phys. B* **83**, 155 (2006)
- 7 K. Verbeizen, R.J.H. Klein-Douwel, A.P. van Vliet, A.J. Donkerbroek, W.L. Meerts, N.J. Dam, J.J. ter Meulen, *Proc. Combust. Inst.* **31**, 765 (2007)
- 8 T. Lee, J.B. Jeffries, R.K. Hanson, *Proc. Combust. Inst.* **31**, 757 (2007)
- 9 G.C. Martin, C.J. Mueller, C.F. Lee, *Appl. Opt.* **45**, 2089 (2006)

- 10 T. Doerk, J. Ehlbeck, R. Jedamzik, J. Uhlenbusch, J. Hoschele, J. Steinwandel, *Appl. Spectrosc.* **51**, 1360 (1997)
- 11 A. Pott, T. Doerk, J. Uhlenbusch, J. Ehlbeck, J. Hoschele, J. Steinwandel, *J. Phys. D Appl. Phys.* **31**, 2485 (1998)
- 12 B. Attal-Tretout, P. Berlemont, J.P. Taran, *Mol. Phys.* **70**, 1 (1990)
- 13 B. Attal-Tretout, S.C. Schmidt, E. Crete, P. Dumas, J.P. Taran, *J. Quantum Spectrosc. Radiat. Transf.* **43**, 351 (1990)
- 14 P. Doerk, M. Hertl, B. Pfler, S. Hadrich, P. Jauernik, J. Uhlenbusch, *Appl. Phys. B* **64**, 111 (1997)
- 15 S.F. Hanna, W.D. Kulatilaka, Z. Arp, T. Opatmy, M.O. Scully, J.P. Kuehner, R.P. Lucht, *Appl. Phys. Lett.* **83**, 1887 (2003)
- 16 S. Roy, W.D. Kulatilaka, S.V. Naik, N.M. Laurendeau, R.P. Lucht, J.R. Gord, *Appl. Phys. Lett.* **89**, 104105 (2006)
- 17 W.D. Kulatilaka, N. Chai, S.V. Naik, N.M. Laurendeau, R.P. Lucht, J.P. Kuehner, S. Roy, J.R. Gord, *Opt. Commun.* **274**, 441 (2007)
- 18 W.D. Kulatilaka, N. Chai, S.V. Naik, N.M. Laurendeau, R.P. Lucht, J.P. Kuehner, S. Roy, J.R. Gord, *Opt. Lett.* **31**, 3357 (2006)
- 19 W.D. Kulatilaka, R.P. Lucht, S.F. Hanna, V.R. Katta, *Combust. Flame* **137**, 523 (2004)
- 20 N. Vora, J.E. Siow, N.M. Laurendeau, *Combust. Flame* **126**, 1393 (2001)
- 21 V.R. Katta, L.P. Goss, W.M. Roquemore, *Combust. Flame* **96**, 60 (1994)
- 22 V.R. Katta, L.P. Goss, W.M. Roquemore, *AIAA J.* **32**, 84 (1994)
- 23 V.R. Katta, L.P. Goss, W.M. Roquemore, *Int. J. Numer. Methods Heat Fluids Flow* **4**, 413 (1994)
- 24 A.E. Lutz, R.J. Kee, J.F. Grcar, Sandia National Laboratories, Report No. SAND96-8243 (1996)
- 25 R.J. Kee, J.A. Miller, G.H. Evans, G. Dixon-Lewis, *Proc. Combust. Inst.* **22**, 1479 (1988)
- 26 G.P. Smith, D.M. Golden, M. Frenklach, N.W. Moriarty, B. Eiteneer, M. Goldenberg, C.T. Bowman, R.K. Hanson, S. Song, W.C. Gardiner Jr., V. Lissianski, Z. Qin, GRI Mechanism (version 3.0) http://www.me.berkeley.edu/gri_mech/ (1999)
- 27 J.P. Gore, J. Lim, T. Takeno, X.L. Zhu, *Proceedings of Fifth ASME/JSME Joint Thermal Engineering Conference*, San Diego, CA, Paper AJTE99-6311 (1999)
- 28 R.E. Palmer, Sandia National Laboratories, Report No. SAND89-8206 (1989)
- 29 J. Luque, D.R. Crosley, SRI International, Report. No. MP99-009 (1999)
- 30 J. Laane, W. Kiefer, *J. Raman Spectrosc.* **9**, 353 (1980)
- 31 W. Lempert, G.J. Rosasco, W.S. Hurst, *J. Chem. Phys.* **81**, 4241 (1984)
- 32 A.C. Eckbreth, *Laser Diagnostics for Combustion Temperature and Species* (Gordon and Breach, Amsterdam, 1996)
- 33 P.H. Paul, C.D. Carter, J.A. Gray, J.W. Thoman, M.R. Furlanetto, Sandia National Laboratories, Report No. SAND94-8237 (1995)

5th US Combustion Meeting
Organized by the Western States Section of the Combustion Institute
and Hosted by the University of California at San Diego
March 25-28, 2007.

The Effects of Oxygenated Compounds on PAH and Soot across a Suite of Laboratory Devices

*T.Litzinger¹, M Colket², M.Kahandawala⁶, V.Katta³, S.-Y.Lee¹, D.Liscinsky², K.
McNesby⁴, R.Pawlik⁵, M.Roquemore⁵, R Santoro¹, S. Sidhu⁶, S Stouffer⁷, J.Wu¹*

¹*Department of Mechanical and Nuclear Engineering, Penn State University,
University Park, PA, USA*

²*United Technologies Research Center
East Hartford, CT, USA*

³*Innovative Scientific Solutions, Inc.
Dayton, OH, USA*

⁴*Army Research Laboratory
Aberdeen, MD, USA*

⁵*Air Force Research Lab
Wright-Patterson Air Force Base, OH, USA*

⁶*Department of Mechanical Engineering, University of Dayton,
Dayton, OH, USA*

⁷*University of Dayton Research Institute,
Dayton, OH, USA*

The impact of oxygenated fuel additives on soot emissions has been investigated in a collaborative university, industry and government effort. The main objective of this program was to obtain fundamental understanding of how changes in fuel composition can reduce soot and PAH emissions from military aircraft combustors. The research team used a suite of laboratory devices that included a shock tube, a well-stirred reactor, a premixed flat flame, an opposed-flow diffusion flame, and a high pressure turbulent reactor. The two primary additives investigated were ethanol and cyclohexanone. Fuels included ethylene, heptane, a heptane/toluene blend and JP8. With one exception, an ethylene opposed-flow diffusion flame, the addition of an oxygenated compound led to substantial reductions in soot. Modeling of the premixed flame and opposed-jet diffusion flame was used to obtain insights into the mechanism behind the observed soot reductions.

1. Introduction

It is estimated that US military aircraft emit about 600,000 kg of particulate matter into the atmosphere each year. All of this particulate matter is in the form of particles with diameters less than 2.5 microns (PM_{2.5}), which a growing body of evidence indicates are the cause of significant health and environmental problems. Thus the military is seeking methods to reduce PM emissions.

There are two approaches to reducing PM_{2.5} emissions from gas turbine engines, modification or redesign of the combustion system and modification of the fuel either by reformulation or additives. For existing engines, hardware retrofits are normally prohibitively expensive. Thus, the preferred approach is fuel modifications.

The technical objective of this program was to develop fundamental understanding of the complex effects of changes in fuel composition on the processes that lead to PM emissions from military gas turbine engines. The overall project included investigations of organic compounds containing oxygen, nitrogen, and phosphorus. The work reported in this paper is a summary of experimental and modeling results on the effects of two oxygenated compounds, ethanol and cyclohexanone, on soot formation across a suite of laboratory devices; the fuels investigated were ethylene, heptane, heptane/toluene, and JP8.

2. Approach

Because of the inherent complexity of the combustion processes within gas turbine combustors and great difficulty in making measurements inside combustors, it was not possible to achieve the technical objective of this program by making measurements in gas turbine combustors. Furthermore, due to the complexity of the combustion process in a gas turbine combustor, no single laboratory flame or reactor is sufficient to serve as a model for a combustor. Therefore, multiple laboratory devices were applied to study the effects of additives on soot. These devices were a shock tube, a well-stirred reactor, a premixed flame, an opposed-jet diffusion flame, and a high pressure turbulent reactor.

The devices were chosen to cover the range of combustion regimes present in a gas turbine combustor. They were also chosen so that they covered a range of complexity in terms of the chemical and physical processes involved, from the shock tube, where chemical kinetics is the dominant process, to the high pressure turbulent reactor in which chemical kinetics, molecular diffusion, turbulent mixing, and spray processes are all involved. This set of devices was applied in an hierarchical manner to identify the key chemical and physical processes through which the additives affect soot.

Numerical simulation proved to be an invaluable tool for understanding the mechanisms by which oxygenated compounds reduce soot in these devices. Simulations were performed to the extent possible for each additive/fuel combination. CHEMKIN was used for modeling of the premixed flame and the opposed-jet diffusion flame. For modeling the effects of ethanol on ethylene chemistry, the research team combined several mechanism available in the literature [1, 2, 3].

The devices used in the study along with their associated diagnostics have all been described in detail elsewhere [4, 5, 6, 7, 8] so they will not be described here. Table 1 summarizes the range of fuel/oxygenate experiments that were conducted during the study. This paper will focus on the effects of ethanol and cyclohexanone on soot; cyclohexanone was studied because it was a component of a commercial additive that caused reductions in soot emissions. The fuels used included ethylene, pre-vaporized heptane and an 80/20 volume mixture of heptane and toluene, as well as liquid JP8. Details of the experimental methods can be found in the Final Report of the project; the data are available as well [9]. Because of the large volume of results only summary tables and plots will be presented along with key observations from the modeling studies.

Table 1: Experiments performed on oxygenated compounds

	Additive	Fuel	Effect on Soot	Comments
Shock tube	Ethanol	Ethylene	Decrease	
	Cyclohexanone	Heptane/ Toluene	Decrease	
Well-stirred reactor	Ethanol	Ethylene	Varies: decrease to slight increase	Effect is dependent on reactor temperature
	Cyclohexanone	Heptane/ Toluene	Decrease	
Premixed flame	Ethanol	Ethylene	Decrease	
	DME	Ethylene	Decrease	DME shows slightly greater effectiveness
Opposed-jet flame	Ethanol	Ethylene	Increase	
	Ethanol	Heptane	Decrease	
HP Turbulent reactor	Ethanol	JP8	Decrease	
	Cyclohexanone	JP8	Decrease	

3. Shock Tube

The test section for all ethylene experiments contained 5% fuel (v/v), 6.4% oxygen (v/v), and the balance argon; the equivalence ratio was 2.34. For ethylene + ethanol experiments, ethanol was added such that 5% (m/m) of ethylene-ethanol mix was oxygen. Since the diluent gas (Ar) is approximately 90%, the heat release from combustion will only cause a minor change in temperature. The results from ethylene and ethylene + ethanol experiments are shown in Table 2. The comparison of the sample means from ethylene and ethylene+ethanol experiments shows that addition of ethanol decreased the mean soot yield by 18 μg , a 20% decrease in mean soot production.

Table 2. Summary of Soot Yields From Premixed Ethylene Experiments

	Average Temperature, T_5 , ($^{\circ}\text{C}$)	Average Pressure, P_5 , (atm.)	Average Soot Yield (μg)
Ethylene	788	16.5	93.1
Ethylene + Ethanol	784	16.4	74.9

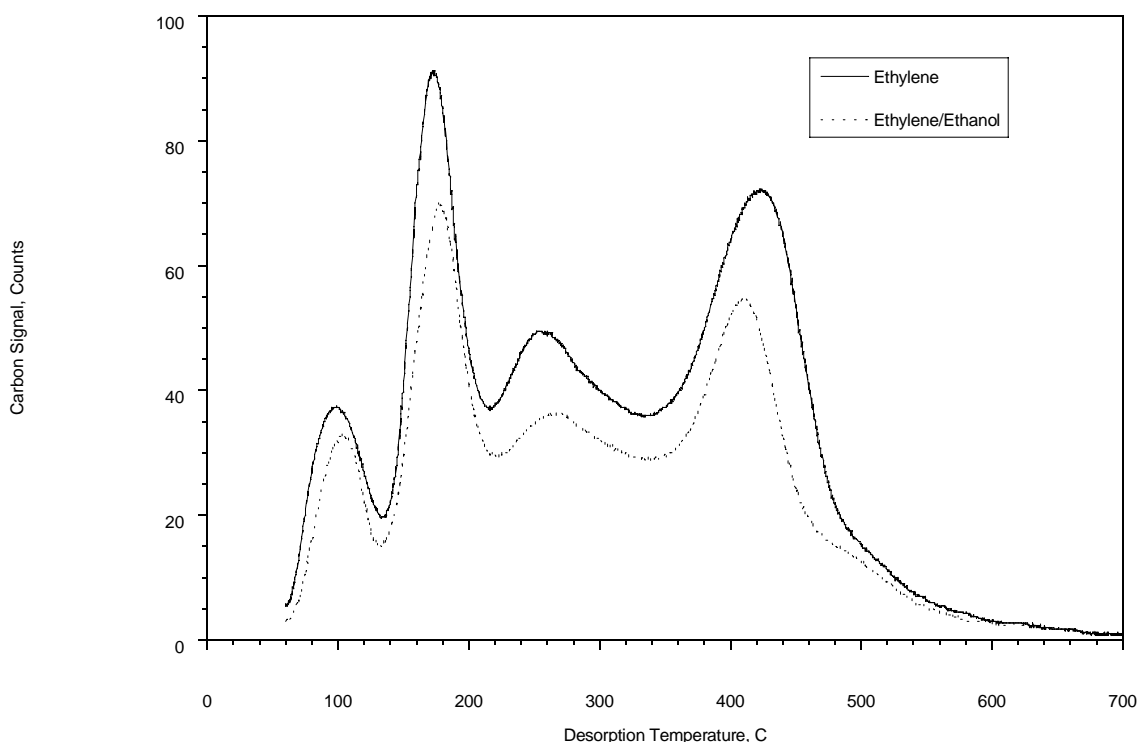


Figure 1. Averaged carbon signal obtained by desorbing soot samples collected from ethylene and ethylene+ethanol experiments in shock tube

Figure 1 compares averaged carbon signal obtained by desorbing soot samples collected from ethylene and ethylene+ethanol experiments. The results show that the soot produced in both sets of experiments has a high soluble organic fraction (carbon desorbed below 300°C) compared to diesel soot whose soluble organic fraction is usually in 5 to 25% range. This high soluble organic fraction is perhaps due to low post-shock temperature in these premixed experiments. Figure 1 also shows that addition of ethanol did not change the molecular weight distribution of soot; it just lowered the soot yield in all molecular weight divisions.

Figure 2 presents the effect of cyclohexanone on soot for pre-vaporized heptane /toluene. The overall equivalence ratio for these experiments was 3, and cyclohexanone was added to give 4 % oxygen in the fuel. The reaction temperature was varied by changing the initial pressure of the reaction mixture in the test section. The cyclohexanone caused substantial reductions in soot at all temperatures studied. The particle yield data for the base fuel forms a bell-shaped curve. The lower soot yields at the lower temperatures (~1150 K) are due to the slower rate of formation of soot precursors and the reduced combustion time due to the increased ignition delays. However, the lower soot yield at higher temperatures (~1500 K) is due to the rates of oxidation dominating the rate of particle formation. The maximum in soot yield curves thus occurs when temperatures are high enough for particle formation processes (e.g., precursor formation, nucleation and surface growth) but are still too low for particle oxidation to be

significant. Regardless of conditions, however, the cyclohexanone was effective in reducing soot.

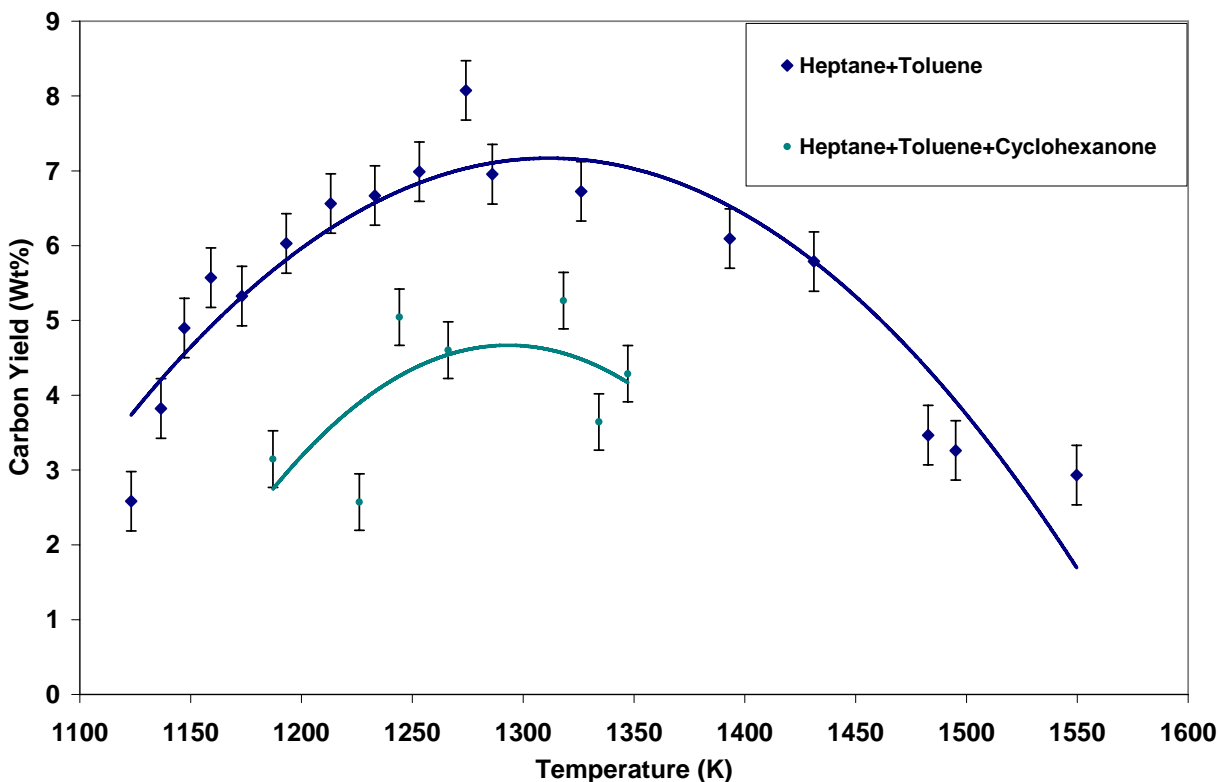


Figure 2: Carbon yield from shock tube experiments with heptane/toluene and cyclohexanone

4. Well-stirred Reactor

The effect of ethanol as an additive was studied by Reich et al. [10]. The air flow for the experiments was set at a constant 240 g/min with an inlet temperature set at 392 +/- 5K. The fuel/air equivalence ratio ranged from 1.9 to 2.6 for both neat and ethanol added to raise the oxygen mass fraction of the fuel to 5%. Soot samples for mass measurements were made in the plug flow region 16 cm downstream of the reactor and within the toroidal WSR. Figure 3 shows total carbon analysis of the quartz filter samples extracted from both the reactor and the plug flow sections of the WSR. The results show that the addition of ethanol decreases the carbon mass for all of the cases. In all cases an increase was shown in the total carbon mass between the reactor and the plug flow section. The particle size distributions sampled from the plug flow region of the reactor for both the neat ethylene and the ethylene-ethanol mixtures over a range of ϕ from 2.0 to 2.6; details are available in Reich et al. [10]. The ethylene-ethanol mixture was found to reduce particle concentration at all ϕ compared to the neat ethylene. The total particle number densities obtained by integrating the areas under the curves also showed a reduction for the ethanol additive cases as compared to the neat ethylene case.

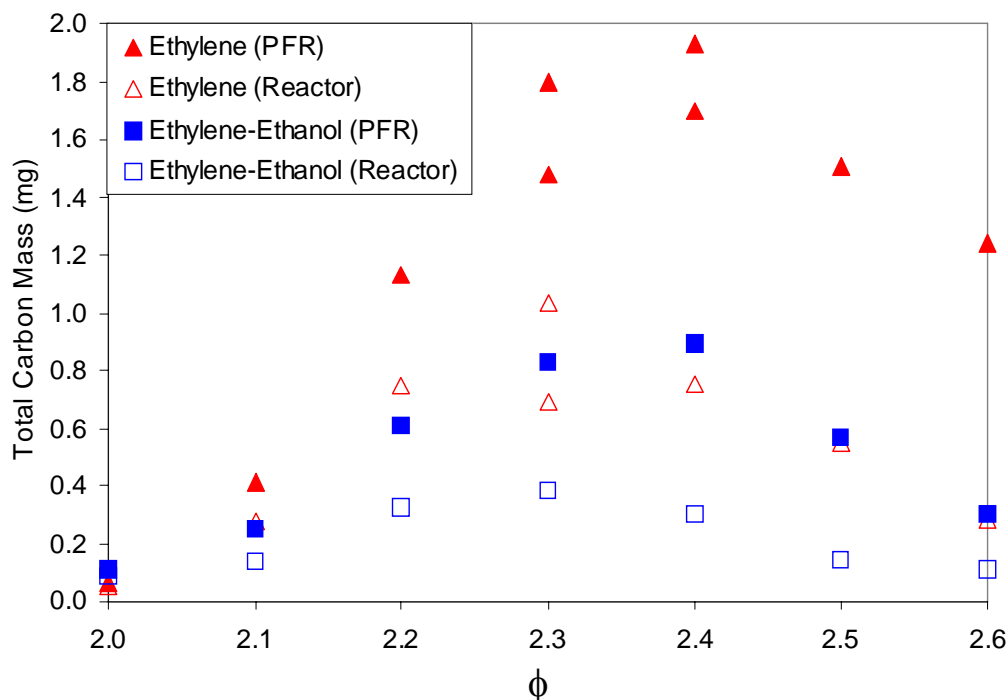


Figure 3: Total Carbon Measurements Results For Neat Ethylene and Ethanol Additives in well-stirred reactor

The effectiveness of cyclohexanone was studied in the Well-Stirred reactor (WSR) with the 80% heptane-20% toluene fuel. The results are summarized below and presented in more detail in Reference 5. Equivalence ratios between 1.90 and 2.10 were studied; cyclohexanone was added to the fuel at levels of such that either 2% or 4% of the fuel weight was from oxygen in the cyclohexanone. The experimental results shown will be predominately from the carbon mass determined from carbon burnoff from quartz filters. Particulate mass samples were drawn through an oil-cooled probe at a location 16 cm downstream of the WSR in the plug flow reactor region.

Figure 4 shows the total particulate carbon mass data for experiments with the cyclohexanone additive plotted vs. temperature measured in the WSR. The curve shows a peak at $\phi = 2$ and a familiar soot bell shape. The addition of cyclohexanone was shown to reduce soot at all equivalence ratios. At $\phi = 1.95$ the 4 % O additive case produced 36 % less carbon mass than the neat case. The effect of cyclohexanone on the temperature changed depending on the equivalence ratio. For the high temperature side of the soot bell the combustion temperature for the neat and the additive cases were nearly the same, implying that the effect of the additive in this region is chemical rather than thermal. On the low temperature side of the soot bell, the combustor temperature decreased for the additive case relative to the neat case as the equivalence ratio was further increased. For the highest equivalence ratio case studied ($\phi = 2.1$) the combustion temperature using the 4 % O additive was increased for one data point by increasing

the inlet conditions, and the soot mass increased to match that for the neat case, implying that for the low temperature side of the soot bell the effect of the additive is mainly due to a decrease in the combustor temperature.

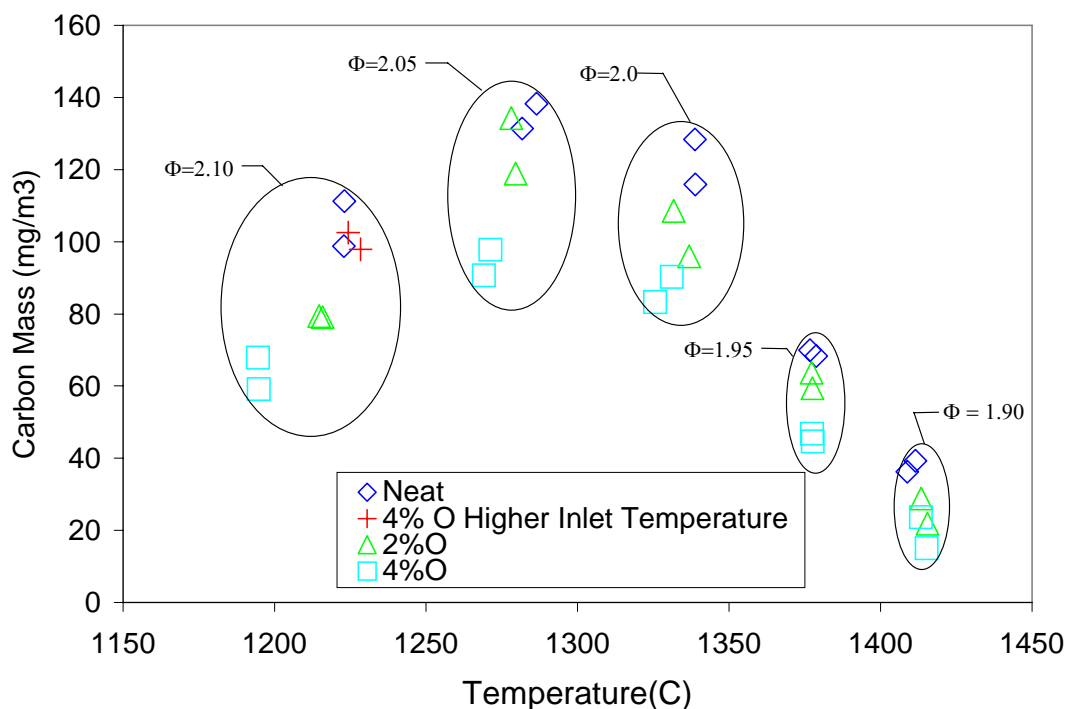


Figure 4: Effect of cyclohexanone on particulate mass with heptane/toluene fuel

5. Premixed Flame

Flames with equivalence ratios of 2.34, and 2.64 were studied to facilitate comparison to past work on ethylene flames. Two oxygen concentrations, 5 and 10 wt% in the ethylene/additive mixture, were studied. 5 wt% oxygen requires a 14.4 % mass fraction of ethanol in the fuel stream, and 10 wt% requires approximately twice this amount. When the ethanol was introduced into the fuel line, the ethylene flow rate was reduced in appropriate proportion in order to keep the total carbon flow rate constant. The equivalence ratio was not affected by the introduction of the ethanol so adjustment of the air flow rate was not required to keep the equivalence ratio constant. Detailed results on this flame are available in Wu et al. [6]

Figure 5 presents a comparison of the experimental and modeling results for the ethylene flames at the two equivalence ratios studied. In the simulations experimental temperature profiles were used. The model does reasonably well in capturing the trends in small and large PAH, but it underestimates the soot volume fraction and also the effect of equivalence ratio on soot. Similar comparisons of the model predictions and experimental data for the addition of ethanol shows that for small aromatic species and large PAH, the model results capture the general trend that

increasing the amount of oxygen leads to greater reductions in aromatic species. Also the magnitudes of the reductions relative to the baseline match the data reasonably well for the aromatic species. The soot predictions for $\Phi=2.34$ are reasonably consistent with the experimental data, although the volume fraction is under-predicted. For $\Phi=2.64$, the comparison of the model and experiment are not good. The model predicts no effect of 5% oxygen at this condition.

6. Opposed-jet Diffusion Flame

In experiments and calculations, addition of ethanol to the ethylene increases soot and soot precursors, while peak OH concentrations remain approximately constant. A graph of experimental measurements of peak light scattering and OH fluorescence and predictions of species maximum mole fraction based upon calculations, for fuel side addition of ethanol, is shown in Figure 6. The calculated data have been normalized to the experimental data to allow comparisons of the trends shown by each. Overall, the trend of the change (increasing), with increasing fuel side ethanol addition, of calculated peak mole fractions for the species A1 through A4 is in good agreement with peak experimental values (measured along the centerline between burner ducts) of light scattering, while the change, with increasing fuel side ethanol addition, of the calculated peak mole fraction of OH is in reasonable agreement with peak measured values of OH fluorescence. Calculation and experimental measurement show peak OH concentration to remain nearly constant with increasing ethanol addition.

Calculations predict that addition of 8 mole percent ethanol to the fuel stream increases the integrated mole fraction of aromatic species A1 (C_6H_6), A2 ($C_{10}H_8$), A3 ($C_{14}H_{10}$), and A4 ($C_{16}H_{10}$) by approximately 3%, 19%, 23%, and 22%, respectively. The peak increase in light scattering observed experimentally was approximately 19%. Temperature and OH concentration are predicted by calculation to remain approximately constant. Acetylene is predicted to remain approximately constant while propargyl concentration is predicted to decrease approximately 9% when 8% ethanol is added to the fuel stream.

Because the predicted change in propargyl mole fraction with ethanol addition was in the opposite direction of the change in A1 mole fraction for fuel side ethanol addition, an analysis of rate of formation of A1 by reaction was performed. The reactions contributing to A1 formation, and the change in A1 rate of formation per reaction, relative to the neat flame, when 8% ethanol was added to the fuel stream, are:

Calculated Change in Rate of A1 Formation - 8% Ethanol addition to Fuel	
$C_3H_3 + C_3H_3 \rightarrow A1$	-8%
$n-C_4H_5 + C_2H_2 \rightarrow A1 + H$	+23%
$l-C_6H_6 + H \rightarrow A1 + H$	+27%
$n-C_6H_7 \rightarrow A1 + H$	+34%

The increased production of A1 via these routes is predicted to be the consequence of methyl radical formation from the ethanol which leads to increased $C_3H_3 + CH_3 (+M) \rightarrow C_4H_6 (+M)$. This reaction shows a calculated increase in rate of production of C_4H_6 of 17% for the flame with 8% mole fraction ethanol compared to the neat ethylene/air flame. Mole fraction profiles (see

Figure 6) of propargyl show a slight decrease in concentration over this temperature range (1400K – 1700K). Approximately 85% of the C_4H_6 reacts with H to form C_4H_5 , which then reacts in the acetylene bath to form A1 and aromatic precursors. Details of the modeling and experiments can be found in McNesby et al. [7]

Figure 7 shows the results for the addition of ethanol to a heptane/air opposed-jet flame. In this case the addition of ethanol reduces soot. The postulated reason for the change in the trend compared to ethylene is the abundance of methyl radicals present with heptane as the fuel, so the added methyl production from the ethanol has a negligible effect on soot. Unfortunately the OPPDIF model would not converge for the heptane mechanism used.

7. High Pressure Turbulent Reactor

All tests with oxygenated additives in the high pressure turbulent reactor were run with JP8 as the fuel; a major consideration being its reasonable cost compared to the heptane/toluene blend. The air flow for the tests was 32 gm/s and the equivalence ratio was 1.3. The inlet air temperature was 550K and the chamber pressure was 0.5 MPa. Three oxygenated additives were investigated: ethanol, cyclohexanone, and methanol. Methanol was studied as a comparison to the ethanol since it had shown good potential to reduce soot in prior work with sooting diffusion flames. For cyclohexanone and ethanol a range of concentration was investigated up to 10% by volume. Methanol was only studied at the highest concentration. Figure 8 presents the results for these three compounds based on the mole fraction of oxygen introduced with the additive. It shows that the three oxygenates fall on essentially the same curve of soot reduction, which indicates that the soot reduction in each case is largely being driven by the same phenomena.

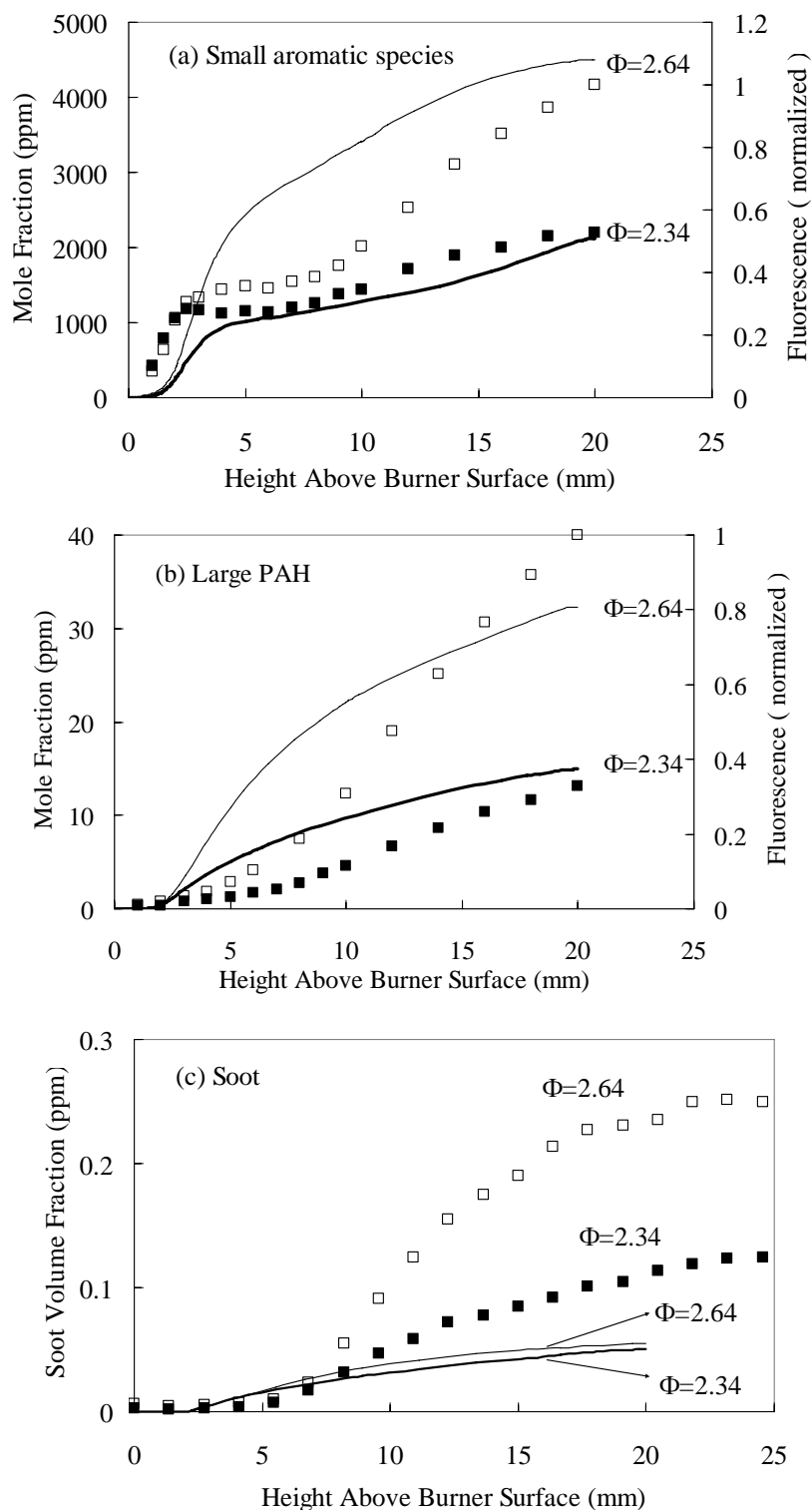


Figure 5. Comparison of experiments (square symbols) and model (solid lines) for (a) small aromatic species, (b) large PAH, (c) soot at base flames (LIF data normalized by the maximum signal observed at $\Phi=2.64$)

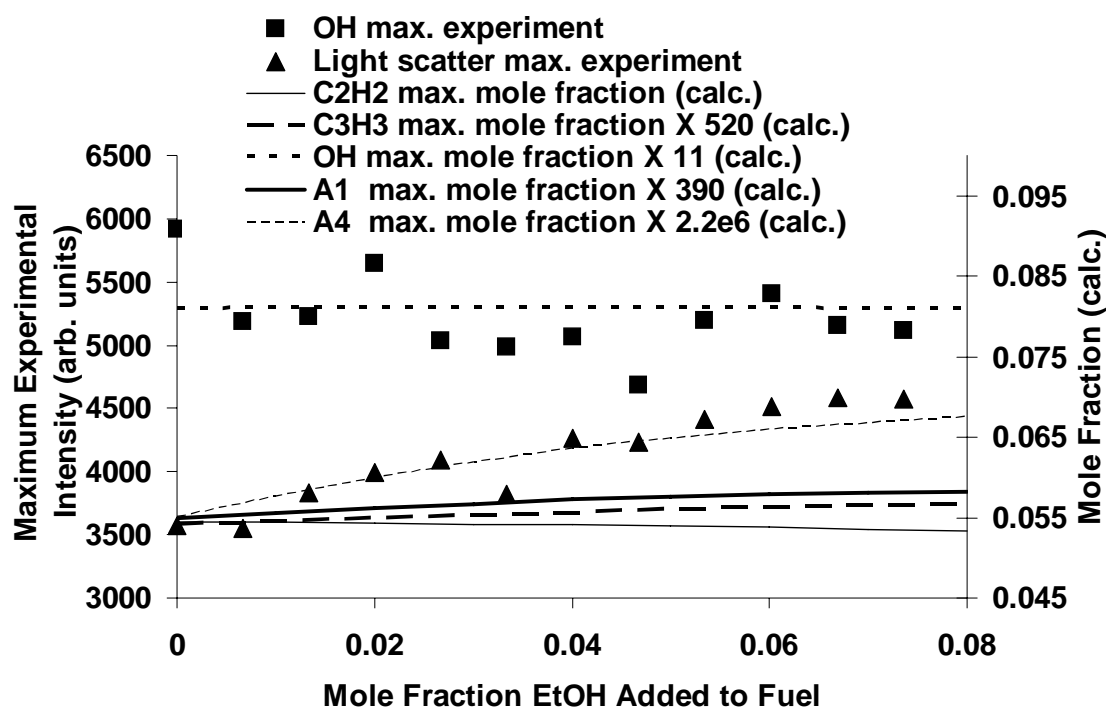


Figure 6: Comparison of measurements and predictions for OH, soot and soot precursors, for addition of ethanol to ethylene in an opposed-jet diffusion flame.

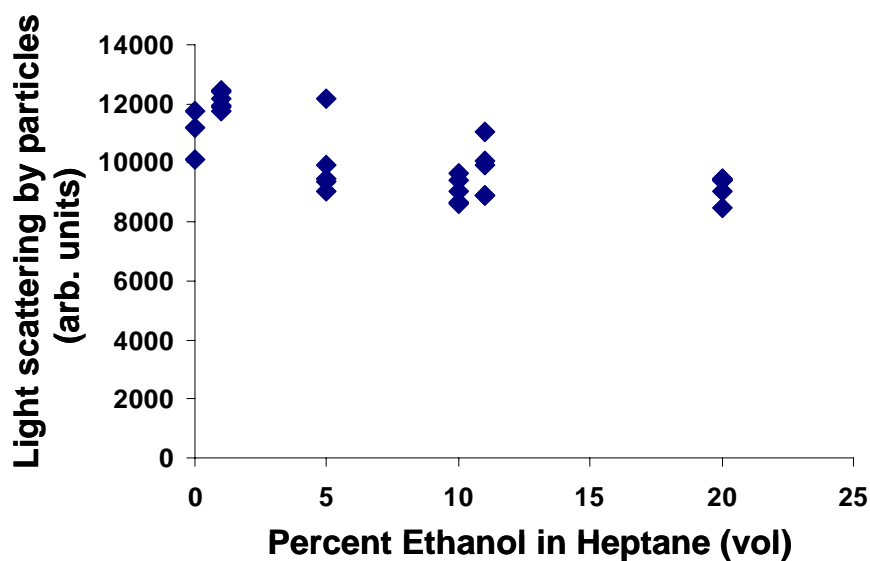


Figure 7: Light scattering by particles versus fuel side ethanol addition for heptane/air opposed-jet flames.

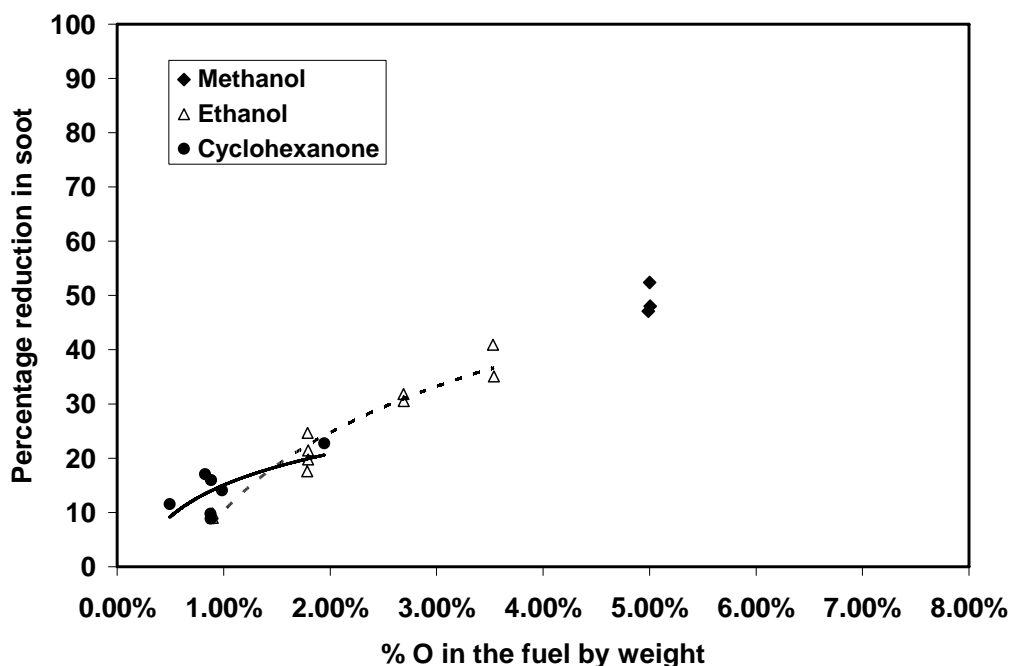


Figure 8: Effect of Oxygenated Additives on soot formation with JP-8

8. Conclusions

Reduction in soot was achieved by the addition of oxygenated compounds in all of the devices studied, with the single exception of the ethylene opposed-jet diffusion flame. Furthermore, reduction was achieved whether the fuel was introduced as a liquid or vapor and regardless of whether the conditions were laminar or turbulent. The ability to reduce soot across the suite of devices in which the key governing processes vary so significantly means that the process through which the soot reduction is effected must be common to all of the devices -- that common process is chemical kinetics. Therefore, these studies add to the evidence that kinetic processes are driving the reduction of soot by oxygenated additives.

Through detailed modeling studies, the mechanism by which soot is increased when ethanol was added to ethylene in the opposed-jet diffusion flame was determined to be kinetic in nature as well. Soot was increased due to the enhancement of the “even-carbon species” pathway to benzene as a result of the production of methyl radicals from ethanol, not via the enhancement of the “odd-carbon species,” as was originally expected. Detailed modeling of the results for addition of ethanol to the ethylene diffusion flames predict that the soot reduction in these flames is via effects on the propargyl radical pathway to the first aromatic ring. Comparison of the premixed flame results for ethanol and DME (not reported here, see reference 11) demonstrated that the chemical structure of the additive can play a role in the effectiveness of oxygenated additives in reducing soot. [12]

Together this set of results, from a wide range of experimental devices, serves as a challenging benchmark for modeling soot formation for ethylene and the effects of the addition of oxygenated compounds on soot.

Acknowledgments

The authors acknowledge the financial support for this work provided by the Strategic Environmental Research and Development Program (SERDP), Project PP1179, under the direction of Dr. Charles Pellerin.

References

1. J.B. Howard, et al., <http://web.mit.edu/anish/www/mitsootmodel1atmsymp2004.mec>; accessed October 2005.
2. N.M. Marinov, A Detailed Chemical Kinetic Model for High Temperature Ethanol Oxidation, *Int. J. Chem. Kinet.* 31 (1998) 183–220.
3. Frenklach, M. and Wang, H. (1990) Detailed mechanism and modeling of soot particle formation. *Springer Series in Chemical Physics*, 59, 165.
4. Kahandawala, M.S., Ph.D. Dissertation on “Fuel Composition Effects on Particle and PAH Emissions”, University of Dayton, Dayton, OH 2004.
5. Stouffer S.D., Mortimer B.M., Ostdiek, D.M., DeWitt, M.J., Pawlik, R., Reich, R.F., Frayne, C.W., and Mayfield, H.T., " Soot Reduction Research Using a Well-Stirred Reactor," AIAA 2005-1317, 43rd Aerospace Sciences Meeting, Reno, NV, January 13, 2005
6. Wu, J.; Song, K.H.; Litzinger, T.; Lee, S.-Y.; Santoro, R.; Linevsky, M.; Colket, M. Liscinsky, D., Reduction of PAH and soot in premixed ethylene-air flames by addition of ethanol; *Combust. Flame* 144:4, p 675-687 (2006); *Corrigendum* Litzinger, T., Wu, J.; Santoro, R. *Combustion and Flame*, v 146, n 4, p 698-699. (2006)
7. McNesby, K. L.; Miziolek, A. W.; Nguyen, T.; Delucia, F. C.; Skaggs, R. R.; Litzinger, T. A., Experimental and computational studies of oxidizer and fuel side addition of ethanol to opposed-jet air/ethylene flames, *Source: Combustion and Flame*, v 142, n 4, p 413-427 (2005)
8. Imschweiler, D., McKeand, M., Lee, S.-Y. , Saretto, S., Linevsky, M. ., Litzinger, T. A. and Santoro, R. J., Fuel additive studies of soot reduction in a high-pressure model gas turbine combustor, 39th AIAA/ASME/SAE/ASEE Joint Propulsion Conference, AIAA 2003-5088 (2003)
9. Roquemore, W.M. and Litzinger, T.A., Final Report of SERDP PP-1179, Reduced Particulate Matter Emissions for Military Gas Turbine Engines Using Fuel Additives. (Report # - AFRL/PR/WP/TR-2006-2211)
10. Reich, R. F., Stouffer, S.D. Katta, V.R., Mayfield, H.T., Frayne, C.W., Zelina, J., Particulate Matter and Polycyclic Aromatic Hydrocarbon Determination Using a Well-Stirred Reactor, AIAA 2003-0664, 2003.
11. Wu, J.; Song, K.H.; Litzinger, T.; Lee, S.-Y.; Santoro, R.; Linevsky, M., Reduction of PAH and soot in premixed ethylene-air flames by addition of dimethyl ether; *Combust Sci Technol*, 178:5 p 837-863 (2006)
12. Wu, Juntao, Soot Abatement Using Oxygenated Additives, Ph.D. Thesis, The Pennsylvania State University, 2004. (<http://etda.libraries.psu.edu/theses/approved/WorldWideIndex/ETD-671/index.html>)

5th US Combustion Meeting
Organized by the Western States Section of the Combustion Institute
and Hosted by the University of California at San Diego
March 25-28, 2006.

The Effects of Nitrogen-Containing Compounds on PAH and Soot across a Suite of Laboratory Devices

*M. Colket¹, T. Litzinger², M. Kahandawala⁶, V. Katta³, S.-L. Lee², D. Liscinsky¹,
K. McNesby⁴, A. Menon², M. Roquemore⁵, R. Santoro², S. Sidhu⁶, S. Stouffer⁷*

¹*United Technologies Research Center
East Hartford, CT, USA*

²*Department of Mechanical and Nuclear Engineering, Penn State University
University Park, PA, USA*

³*Innovative Scientific Solutions, Inc.
Dayton, OH, USA*

⁴*Army Research Laboratory
Aberdeen, MD, USA*

⁵*Air Force Research Lab
Wright-Patterson Air Force Base,
OH, USA*

⁶*Department of Mechanical Engineering, University of Dayton
Dayton, OH, USA*

⁷*University of Dayton Research Institute
Dayton, OH, USA*

The effect of nitrogen-bearing fuel additives on soot and PAH emissions formation has been investigated in a collaborative university, industrial and governmental effort. The overall objective of this program was to obtain fundamental understanding of how changes in fuel composition can effect soot and PAH emissions from military aircraft combustors. Six different laboratory burners, including a premixed flat flame, an opposed-flow diffusion flame, a well-stirred reactor, a turbulent spray flame, a shock tube, and a high pressure turbulent combustor were used to investigate the impact of additives covering a wide range of combustion conditions. The additives included various nitroalkanes (nitromethane, nitroethane, and nitropropane), i-propylnitrate, nitrogen dioxide, pyridine and quinoline. Fuels included ethylene, a heptane/toluene blend and JP8. The effects of many of the additives were examined in most experimental facilities and the results were contrasted and compared. The experimental results were also modeled using a variety of modeling packages and mechanisms. Reductions in soot were as large as 70%, although in some cases no change was detected; in others, increases were observed. Modeling failed to offer explanations for all of the experimental observations. This paper will summarize the key results, our interpretations, and suggest some needs for future research.

1. Introduction

US military aircraft emit about 600,000 kg of particulate matter into the atmosphere each year. This particulate matter is in the form of particles with diameters less than 2.5 microns (PM_{2.5}). Recent research indicates particulates are the cause of significant health and environmental problems. Thus, the military is seeking methods to reduce PM emissions. PM_{2.5} emissions from gas turbine engines can be reduced through modification or redesign of the combustion system or through modification of the fuel either by reformulation or additives. For existing engines, hardware retrofits are normally prohibitively expensive. Thus, the preferred approach is fuel modifications. The technical objective of this program was to develop fundamental understanding of the interactions of additives with the processes that lead to PM emissions from military gas turbine engines. The overall project included investigations of organic compounds containing oxygen, nitrogen, and phosphorus. The work reported in this paper is a summary of results on the effects of several nitrogen-bearing additives. Results of work on organic oxygenates and phosphorous-containing additives are reportedly separately [1,2].

The motivation for examining nitrogen-bearing compounds came from a series of screening tests on the effects of several commercial fuel additives. One of the commercial additives that reduced soot significantly was determined to be composed of nitroalkanes, cyclohexanone, toluene, and dichloroethane. The latter two compounds are known to increase soot so they were not investigated as possible additives. Cyclohexanone was not expected to have a significant impact, so the nitroalkanes, the primary constituents in the commercial additive, were identified as the likely constituents leading to soot reduction. Consequently, these compounds were investigated in detail with experiments and, to the extent possible, modeling; the three compounds selected for investigation were nitromethane, nitroethane, and nitropropane. It was recognized that such compounds could well increase total NO_x emissions and hence may not present a practical solution. Yet, this path was pursued with an expectation of learning more about the soot formation process and how it might be suppressed. As long as the nitroalkanes were under study, NO₂ and nitrogen-heterocyclics were included in the study; NO₂ is well-known to oxidize soot particles (for diesel engine emission control, for example) and pyridine had been shown to be an effective soot suppressing agent in premixed flames in at least one prior study [3].

In this manuscript, results for several nitro-alkanes will be presented. In addition, key results from the addition of NO₂, pyridine and quinoline will be summarized. The fuels investigated were a simple JP8 surrogate, heptane/toluene, and JP8. Complete documentation of this study can be found in [4].

2. Approach

Focusing only on measurements and interpretations of processes within a gas turbine combustor to achieve program goals seemed to be questionable, given the inherent complexity of combustion processes within gas turbine combustors and the difficulty in collecting a complete set of quantitative measurements inside combustors. Furthermore, no single laboratory flame or reactor is a model for a combustor. Therefore, multiple laboratory devices were applied to study the effects of additives on soot formation processes. These devices were a shock tube, a well-stirred reactor, a premixed flame, an opposed-jet diffusion flame, and a high pressure turbulent reactor.

Table 1. Summary of the Effects of Nitroalkanes on Soot.

	Additives	Fuel	Effect on Soot	Comments
Shock tube	Nitromethane	Heptane/ Toluene	Soot unchanged	
Well-stirred reactor	Nitromethane Nitroethane Nitropropane	Heptane/ Toluene	Decreased	Temperature plays a role but a chemical effect is present.
Premixed flame	Nitromethane Nitroethane	Heptane/ Toluene/ Ethylene	Decrease	The addition of ethylene was required to avoid instability on the flame.
	Nitropropane	Heptane/ Toluene/ Ethylene	Increase	2% oxygen level.
Opposed-jet flame	Nitromethane i-propyl nitrate	Heptane/ Toluene	Small increase	
Turbulent spray flame	Nitroethane Nitropropane	Heptane/ Toluene	Decrease	Nitromethane not run due to explosion hazard.
HP Turbulent reactor	Nitroethane Nitropropane	JP-8	Decrease	Nitromethane not run due to explosion hazard.

The devices were chosen to cover a range of combustion regimes present in a gas turbine combustor. They also cover a range of complexity in terms of the chemical and physical processes involved, from the shock tube, where chemical kinetics is the dominant process, to the high pressure turbulent reactor in which chemical kinetics, molecular diffusion, turbulent mixing, and spray processes are all coupled. The objective of these experiments was to identify the key chemical and physical processes through which the additives affect soot. In the related studies (on organic oxygenates, for example), numerical simulation proved invaluable for understanding the mechanisms by which added compounds reduce soot in these devices. For the nitrogen-bearing additives, this success cannot be claimed due to numerical convergence issues and because computational and experimental results were generally not in agreement. Simulations were performed to the extent possible for each additive/fuel combination.

For modeling the effects of nitromethane, the research team combined the reaction set of Zhang and Bauer [5,6] to the heptane mechanism of Babushok and Tsang [7] which also includes toluene reaction steps. The NIST mechanism also contains a compilation of the PAH formation steps from Appel, et al. [8] and Richter, et al. [9]. The devices used in the study along with their associated diagnostics have all been described in detail elsewhere [10-14] so they will not be described here. Table 1 and 2 summarizes the range of experiments that were conducted during the study for nitroalkanes and for several nitrogen-heterocyclics. These tables also have summary results for the different sets of additives. This paper will focus on the results of experiments with nitroalkanes added to fuels and interpretations. The fuels used included an 80%/20% volume mixture of heptane and toluene, as well as liquid JP8. Details of the experimental methods can be found in the Final Report of the project; the data are available as well [4]. Because of the large volume of results only summary tables and plots will be presented here along with key observations.

Table 2. Summary of the Effects of Pyridine on Soot.

	Additive	Fuel	Effect on Soot	Comments
Shock tube	Pyridine	Heptane/ Toluene	Varies: no change to increase	Variation occurs as reaction temperature increases.
Well-stirred reactor	Pyridine	Heptane/ Toluene	Varies: decrease to increase	Temperature of reactor appears to be key factor.
	Quinoline	Heptane/ Toluene	Increase	
Premixed flame	Pyridine	Heptane/ Toluene/ Ethylene	Decrease	
<i>Opposed-jet flame</i>	<i>Pyridine</i>	<i>Heptane/ Toluene</i>		<i>No data due to experimental difficulties.</i>
Turbulent spray flame	Pyridine	Heptane/ Toluene	Decrease	
HP Turbulent Reactor	Pyridine	JP-8	No Effect	
		Heptane/ Toluene	No effect	Run to determine if the lack of an effect was due to use of JP-8.

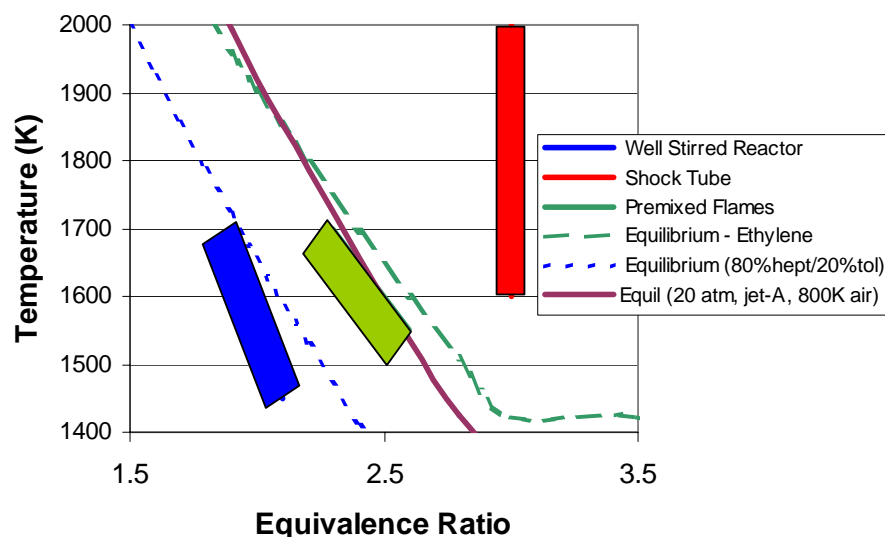


Figure 1. Comparison of the experimental ranges for several of the experiments with each other and against equilibrium curves. The turbulent flame and opposed jet experiments, presumably track close to the equilibrium curves.

As is apparent from Tables 1-2, there are differences in results amongst the experimental studies. Such contrary and confusing results are not inconsistent with prior studies on the effect of additives on soot formation. At least part of the differences may be due to the different set of experimental conditions present in each set of experiments. Figure 1 is a plot comparing the different conditions (temperature and equivalence ratio) for the well-stirred reactor, the shock tube and the premixed flame experiments. In addition to variations in temperature and equivalence ratio, there are of course difference in local turbulence, pressure (20 atm for the shock studies), diffusion, and back mixing of products amongst the different experiments.

3. Shock Tube

All nitroalkane additive experiments in the shock tube (7.6 cm ID x 2.74 m long driver section, a 5.08 cm ID x 2.75 m long driven section, and a 5.08 cm ID x 0.9 m long test section) were conducted at a pressure of ~ 21 atm over a post-shock, pre-combustion temperature range of 1100 K-1600 K (post-combustion temperature range of 1650 K-1950 K). The argon content in the test section was maintained at 93 vol% and the remainder comprised of oxygen and fuel. The experiments were conducted at an equivalence ratio of 3.0. The exothermic reactions of nitrocompounds cause an increase in post-combustion temperature [15]. To exclude thermal effects when interpreting the results, all product yields measured in this study were compared at post-combustion temperatures, defined here as the computed post-combustion temperature immediately after onset of ignition. Thus, any observation herein and associated conclusions are principally due to the chemical effect from the additive.

For the nitromethane experiments, 5 vol% of nitromethane was added to the base fuel mixture so that the oxygen content in the fuel mixture was 4 wt%. Both gaseous products and soot yields were measured and normalized with respect to the mass of carbon in the fuel to exclude any volumetric effect that may arise from normalization with respect to the mass of the fuel. Results from Leco carbon analysis of particle yields are shown in Fig. 2. The solid lines indicate polynomial trend lines fitted to the experimental soot yields. The trend lines show that addition of nitromethane had no discernable impact on soot yields.

The low carbon yields observed at the lower temperatures (Fig. 2) are due partially to the slower rate of particle formation, but also can be affected by finite ignition delay times that limits the total reaction time. (Total dwell times are ~ 7.5 msec; reaction times can be reduced by lengthy ignition delays, which generally are negligible under the higher temperatures of this work.) As the temperature is increased, particle formation dominates and the soot yield goes to a maximum. However, with further temperature increases, soot production decreases due to the decreased stability of the aromatic building blocks related to soot formation. Thus, particle yields decrease generating a classical bell-shaped curve for soot yield as a function of temperature. Closer to the maxima where the soot formation is high, small differences in reaction times can cause a significant change in soot formation, as it is formed late in the reaction process. This is the likely explanation for high experimental scatter close to the maxima.

The product yields were obtained by using a point calibration of the internal standards for a similar class of compounds. The yields from both product analysis and modeling were normalized with respect to the mass of carbon in the fuel. The product yields are given as yield % per unit mass of carbon in fuel. For clarity, only a few selected species are shown here; other data is provided in [15]. The experimental yields of various species have been fitted with

exponential trend lines and are shown as solid lines in Fig. 3. The broken lines represent model yields and have been plotted using point plots. While comparing experimental and model yields, the reader should be aware that axes showing experimental and model yields have different scales. As such, the difference observed from experimental yields with the additives may not be visible in product yields generated by the kinetic model.

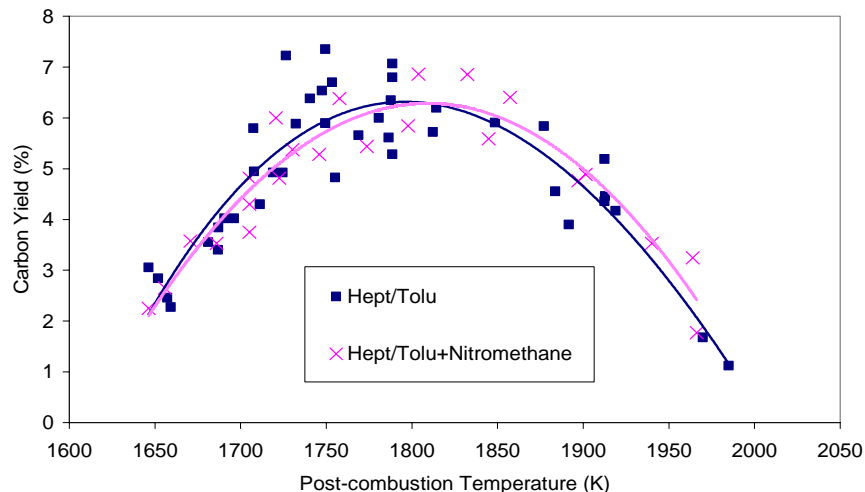


Figure 2. Carbon Yield from Combustion ($\Phi = 3$) of n-Heptane/Toluene and n-Heptane/Toluene + Nitromethane at 21 atm.

The measured lightweight species indicate that at the lower temperatures, the addition of nitromethane has a tendency to increase yield of every soot precursor yield except that of benzene (Fig. 3a), isomers of methyl naphthalene, and o-diethenylbenzene (latter two not shown). Alternatively, the modeling results indicate that at lower temperatures, the yield of all volatile and semivolatile species decreases with the addition of nitromethane; and for most modeled species the differences between the curves (with and without the additives) are significantly smaller than for the experimental data. Experimental scatter was higher at lower temperatures although the scatter was less than the base fuel for nitromethane.

Although no significant difference in soot yield was observed, PAH yields increase with the addition of nitromethane. In general, the predicted curves track the general shape of the experimental data remarkably well. However, the effect of the additive as predicted by the models did not match the observed experimental (relative) trends. For the base fuel, the model was able to qualitatively predict experimental trends in species profiles (except for benzo[ghi]perylene – not shown - and coronene), but the quantitative model over predicted from a factor of two for benzene to two orders of magnitude for most other species. The model does not include particle formation, which might scrub PAH species and, hence, is likely a large contributor to the errors. In addition, the model may have inaccuracies in the thermodynamic or kinetic data or perhaps key species are missing from the reaction mechanism. Dibenzo[ah]anthracene is an example of a species missing from the NIST mechanism.

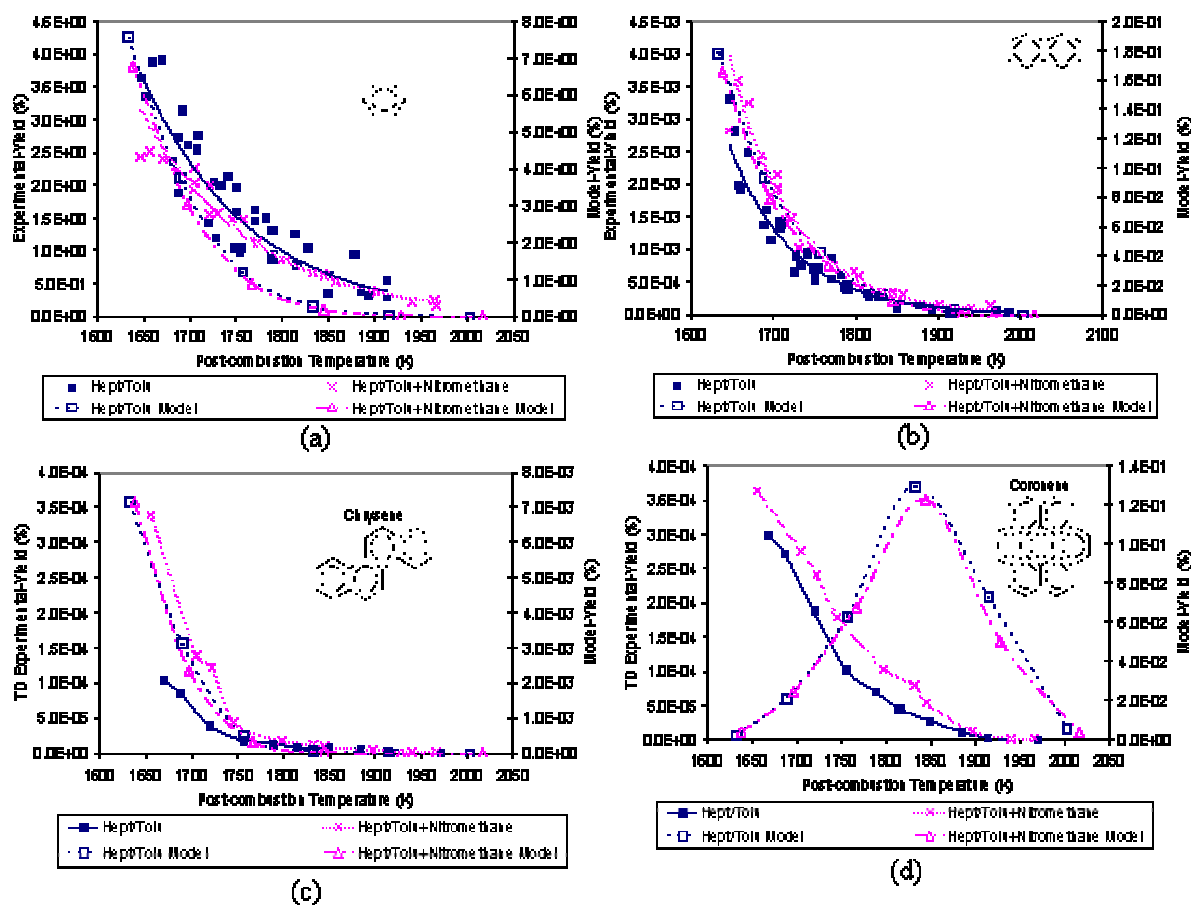


Figure 3. Yields of (a) Benzene, (b) Naphthalene, (c) Chrysene, and (d) Coronene from Combustion of n-Heptane/Toluene and n-Heptane/Toluene + Nitromethane at 21 atm.

An attempt was made to identify all species with significant yields, especially the nitrogenated compounds, in the hope that this information might help to better understand how nitromethane impacts the soot formation process. The following compounds were detected in this study when nitromethane was used as the additive: benzonitrile, 2-methyl-benzonitrile, 4-methyl-2-nitro-phenol, 5-methyl-2-nitro-phenol, and 2-nitro-phenol. The species with the largest concentration was benzonitrile, with data (concentration and shape) similar to that for the chrysene (with nitromethane present), as depicted in Fig. 3c.

4. Well-Stirred Reactor (WSR)

The effectiveness of three nitroalkanes (nitromethane, nitroethane and nitropropane) was studied in the WSR. The results are discussed below and in Stouffer, et al [16]. The neat fuel for the tests was 80% heptane/20% toluene by volume. The reactor material was amorphous fused silica which minimized both cracking and heat loss and could be used because the temperature in the reactor was less than the 1500°C melting point of the silica.

Equivalence ratios between 1.90 and 2.10 were studied. The WSR was limited to this equivalence ratio range on the low side by the melting point of the fused silica and on the high

side by the rich blowout limit. This range of equivalence ratios captures the peak along with the low temperature and high temperature sides of the so-called "soot bell". The airflow was held at a constant 240 g/s and the average residence time in the reactor was 10 +/- 0.4 ms. The reactor pressure was slightly (0.6-1.4 kPa) over the ambient atmospheric pressure for all of the tests.

The nitroalkane additives were added to the fuel in concentrations such that the oxygen mass fraction of the fuel was 0% (neat heptane/toluene mixture), 2% and 4%. The mass flows of the additive and the base fuel were adjusted to maintain the same equivalence ratio as the neat case. The additives concentrations used to achieve the desired oxygen levels are listed in Table 3.

Table 3. Additives and Concentration Levels (ppm by volume) Used in the Nitroalkane Experiments.

Additive	Formula	2% O in Fuel Additive Concentration	4% O in Fuel Additive Concentration
Nitromethane	CH ₃ NO ₂	24,660 ppm	50,020 ppm
Nitroethane	C ₂ H ₅ NO ₂	32,820 ppm	66,620 ppm
Nitropropane	C ₃ H ₇ NO ₂	40,820 ppm	82,950 ppm

For each of the nitroalkane additives, three test concentrations were considered with the same inlet fuel/air mixture temperature at each equivalence ratio: neat fuel, additive with 2% oxygen weight in the fuel, and additive with 4% oxygen weight. Highly energetic nitroalkane additive compounds, such as nitromethane, will increase the combustion temperature at the same inlet temperature and equivalence ratio. Temperature increases decrease soot produced on the high temperature side of the soot bell and increase soot produced on the low temperature side. To explore the effect of temperature on the soot formation, an additional test point was also considered where the combustion temperature of the neat case was adjusted to match that of one of the additive cases. The combustion temperature was increased by increasing the inlet temperature of the fuel/air mixture, and allowed differentiation between the thermal effect on the kinetic process and any chemical effect of the additive. At the highest equivalence ratios tested ($\phi = 2.1$), the increase in the inlet temperature also has an effect on the combustion temperature due to the increase in the combustion efficiency, as exhibited by a decreased measured oxygen levels in the exhaust emissions.

The experimental results shown are the carbon mass determined from carbon burn off from quartz filters and gaseous emissions from FTIR measurements. Particulate mass samples were drawn through an oil-cooled probe at a location 16 cm downstream of the WSR in the plug flow reactor region. Smoke number was also determined during the study and was found to track well with the soot mass.

Figure 4 shows the total particulate carbon mass data for experiments with the nitromethane additive plotted versus temperature measured in the WSR. The curve shows a peak and a familiar soot bell shape. Note however that the peak in soot occurs at a lower temperature (~1600K) than for the shock tube results (~1750-1800K). This shift may be due in part to the presence of high concentrations of O₂ and hence O-atoms under fuel-rich conditions in the WSR that act to oxidize soot particles and precursors (see Colket, et al. [17]). For the neat cases the peak is found for tests with $\phi = 2$. Above this equivalence ratio the carbon mass decreased as the

temperature increased (as ϕ was lowered or inlet temperature was increased) and is commonly referred to as the high temperature side of the soot bell. On the opposite (low temperature) side of the soot bell, the carbon mass production increased as the temperature increased. For ready comparison, data at the same equivalence ratios is outlined within the ovals on the plots. The data clearly show that nitromethane decreases the total carbon particulate mass for $\phi = 2.05$. As the concentration of nitromethane increased the carbon mass dropped further. The reduction in carbon mass at $\phi = 1.95$ was over 47% for the 4% O case. To explore the effect of temperature, the inlet temperature for the neat elevated inlet temperature case was increased until the WSR flame temperature was approximately the same for both the 2% O and the neat case. For the low temperature side of the soot bell, the increased combustion temperature associated with the inlet temperature increased the soot mass production. On the high temperature side of the soot bell, the soot produced for the neat case decreased as temperature was increased. However, the soot mass production for the nitromethane additive case at the same temperature was less than or equal to the neat case at the same combustion temperature. Therefore, it is apparent that the drop in soot production observed over most of the test points with the additive addition is not merely due to an increase in temperature caused by the additive, but rather by other features of the reaction mechanism associated with the additive. At the lowest equivalence ratio considered ($\phi = 1.90$), the additive case and the neat case had approximately the same total carbon mass.

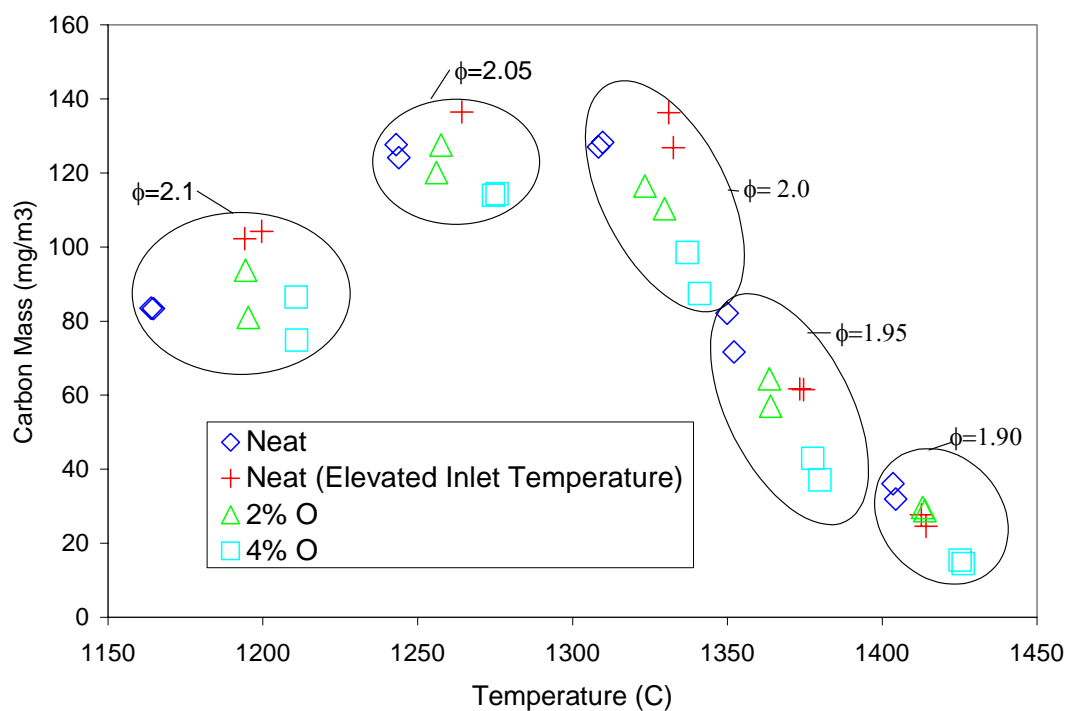


Figure 4. Total Carbon Mass for Nitromethane Additive Cases Studied in the WSR.

During the early work with the nitromethane additive, an MKS 2030 FTIR multigas analyzer was used to determine the concentrations of several hydrocarbon species at neat and 28,460 ppm additive concentrations. This additive level corresponds to 2.3 weight % O in the fuel. Both the acetylene and methane concentrations decrease (~10% and ~50% respectively) with the addition of nitromethane and increase with increasing equivalence ratio. Ethylene and formaldehyde also

are reduced by nitromethane (~50% each) and increase with an increase in equivalence ratio. Figure 5 shows the effect of the nitromethane on NO and HCN. The NO and HCN were both below the detection limits for the neat case and were increased dramatically with the addition of nitromethane. No measurable quantities of NO₂ were detected for either the neat or additive case. For the very fuel rich conditions of this study, this result is not surprising.

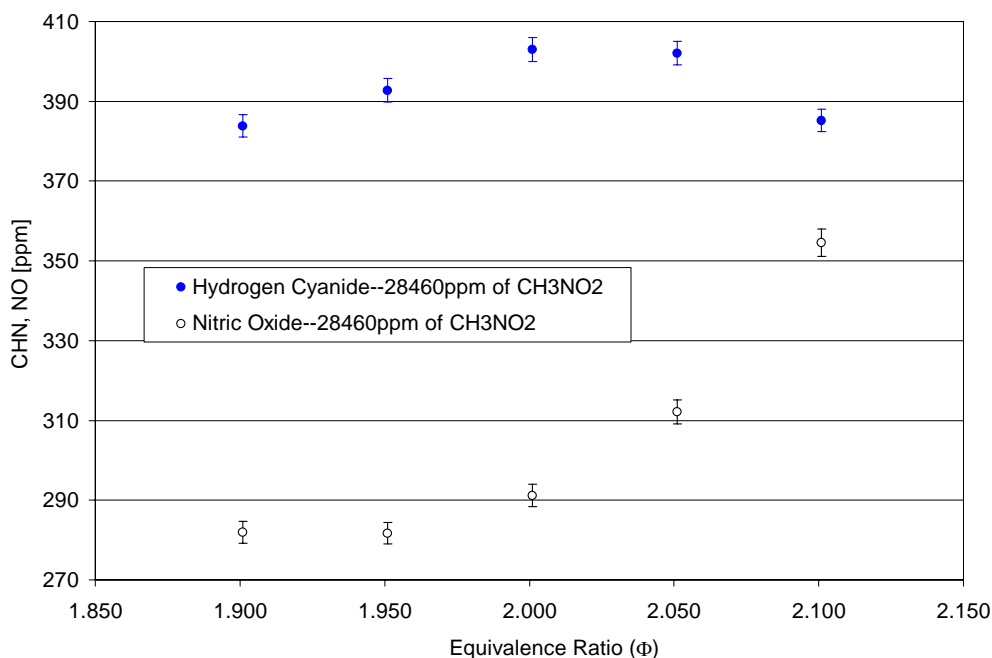


Figure 5. HCN and NO Emissions with Nitromethane Additive. (Neat case emissions were below detectable limits.)

Summary of all nitroalkanes

All three of the nitroalkane additives evaluated in the WSR showed a reduction in the amount of soot mass produced. While there is an effect of the additive on the flame temperature which will, in turn, affect the rates of reaction, temperature is not the only effect of these additives and altered chemistry plays a role.

The level of the reduction in carbon mass was similar for each of the additives as shown in Table 4 for three additives at oxygen levels of 4 % and an equivalence ratio of 1.95., at the same reaction temperature.

Analysis of the gaseous emissions showed that nitromethane reduced acetylene, ethylene and formaldehyde while increasing hydrogen cyanide and nitric oxide.

Table 4. Reduction in Carbon Mass with 4% O Addition

Additive	Reduction in Carbon Mass
Nitromethane	48%
Nitroethane	50%
Nitropropane	48%

5. Premixed Flame

Initial experiments with the 80% heptane/20% toluene mixture resulted in cellular flame structures using a perforated plate for stabilizing a premixed flames. The premix burner surface was changed to a porous plug due to concerns that jetting from discrete holes created localized non-uniformities in the flame. Repeat formation of the cellular structures in the porous burner and further investigations reminded us of the well-known structures in fuel-rich flames occurring with high molecular weight fuels [17]. Hence subsequent experiments were performed with 25% mass of the fuel as ethylene to mitigate this effect.

Control of reactant gas and coflow to the premixed burner was performed using Brooks 5800 series mass flow controllers. The additives were introduced (along with the liquid and gaseous reactants) into a 1 L vaporization/mixing chamber maintained at 200°C. The mixing chamber was connected to the base of the burner with 50 cm of 6.35mm OD heated stainless steel tubing.

Liquids were injected by use of high pressure syringe pumps. Two ISCO 500D precision syringe pump systems were installed which allowed on-demand control of fuel and additive(s) at any given flow rate from 0.001 to 200 ml/min. Delivery flow rates were verified to be better than 1% of setpoint by experiment. The additives and fuel were mixed with air and introduced into the heated vaporization chamber.

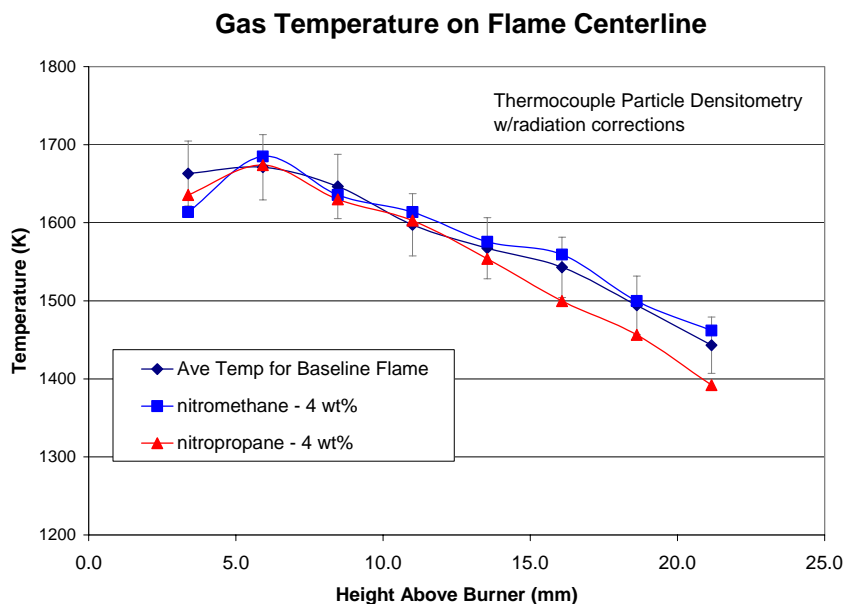


Figure 6. Flame temperatures as a function of height in the premixed flames.

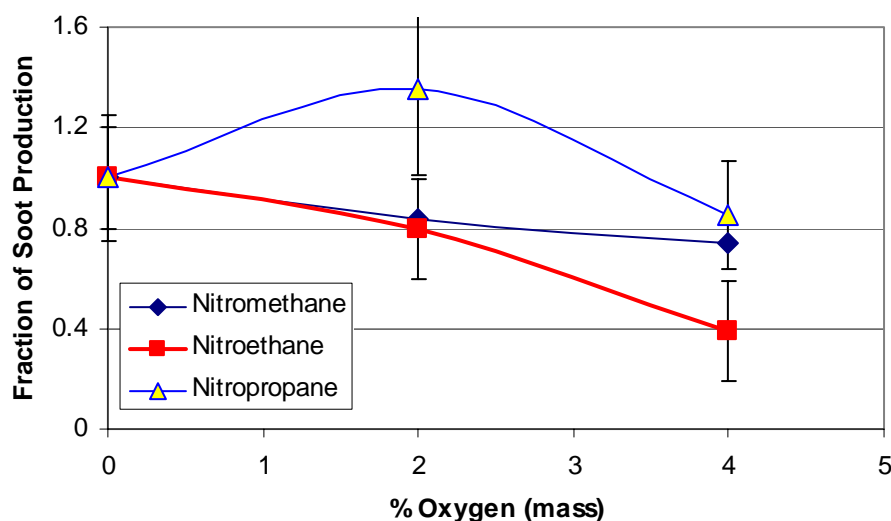
Additive studies have been performed using nitromethane, nitroethane, and nitropropane, the primary components in a commercial additive, which was found to have a relatively strong effect on soot formation. Flame temperatures (thermocouple particle densitometry - TPD) and soot volume fractions (laser extinction) have been measured as a function of height above the burner surface. Relatively small differences in flame temperatures were observed, as shown in Fig 6 for the baseline flame and for the additives nitropropane and nitromethane. Relative mass and flow conditions are reported in Table 5.

Table 5. Mass and mole fractions of fuels with various additives in premixed flame studies.

Additive	% (O)	Mole Fractions				Mass Fractions			
		C7H16	C7H8	C2H4	Additive	C7H16	C7H8	C2H4	Additive
none	0	0.344	0.118	0.538	0.000	0.570	0.180	0.250	0.000
nitromethane	2	0.331	0.114	0.518	0.037	0.549	0.173	0.241	0.037
nitromethane	4	0.318	0.109	0.498	0.075	0.527	0.167	0.231	0.076
nitroethane	2	0.331	0.114	0.518	0.038	0.543	0.172	0.238	0.046
nitroethane	4	0.317	0.109	0.497	0.076	0.517	0.163	0.227	0.093
nitropropane	2	0.330	0.114	0.517	0.039	0.538	0.170	0.236	0.056
nitropropane	4	0.316	0.109	0.496	0.079	0.506	0.160	0.222	0.112

At additive loadings of 4% by mass of oxygen, the most effective additives were nitromethane and nitroethane, with the former reducing the soot production by about 25% and the latter reducing soot production by more than 50%. For flames with $\phi = 2.4$, a comparison of the fractional reductions in soot as a function of additive levels is shown in Fig. 7.

The most unusual feature of the data in Fig. 7 is the contrary effects of different levels of the additive, nitropropane. All of the results (and trends) have been confirmed by using a time tracing method. In these tests, the flame height was kept constant and the make up of the inlet gases were altered in the following sequence: base flame, 4% oxygen (additive); base flame, 2% oxygen (additive). A typical time trace is shown in Fig. 8 for the nitropropane results which exhibited the unusual results of increasing soot at the lower concentration, but reducing soot at higher concentrations.

Figure 7. Relative Soot Production in Laminar Premixed Flame at $\Phi = 2.4$.

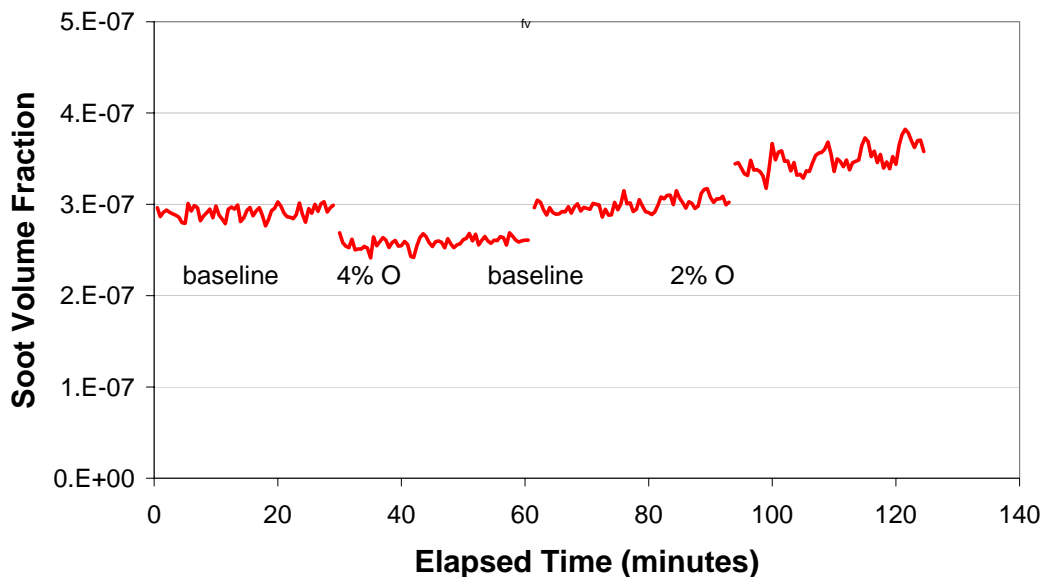


Figure 8. Time Trace Confirming Concentration Effect with Nitropropane.

Our interpretation of these results in the laminar, premixed flames is that a C_3 -hydrocarbon fragment (C_3H_5) from nitropropane enhances the propargyl radical (C_3H_3) concentration at low additive levels. Propargyl, in turn, is a known key intermediary to the formation of aromatic rings. We speculate that the formation of propargyl initially counterbalances any soot-reducing potential that the nitrate group provides. But at higher additive levels, the C_3 level is saturated, and the effect of the NO_2 component dominates, leading to reduced soot production. Nitromethane is a less active soot-reducing agent than is nitroethane since the former produces methyl radicals that add to C_2 hydrocarbons to form C_3 species. Nitroethane, on the other hand, is the most effective presumably because it barely perturbs the existing C_2 concentrations. Propargyl radicals are unaffected and there is no counterbalancing effect inhibiting the added NO_2 from reducing soot.

6. Opposed-Jet Diffusion Flame

The data reported here are for flames to which nitromethane was added to the fuel. The base fuel an 80% heptane/20% toluene mixture by liquid volume. This base flame was found to be much more soot producing than a neat heptane/air flame. Even with the heptane/toluene fuel mix, it was found that above an added oxygen component of approximately 2.4% by weight (about 3 ml of nitromethane added to 100 ml of heptane/toluene mix), some nitromethane would separate out if allowed to stand for a few minutes.

The experimental procedure was as follows. Fuel and air flows were initiated, and the flame was ignited by placing a small torch between the burner ducts. Once the flame was established, a heated nitrogen shroud was used to prevent outside air from being entrained in the fuel flow. Approximately half of the contents of the injection pump (50 ml capacity) were dispensed into the flame when collection of data began. Each data point represents the average of the Planar Laser Induced Incandescence (PLII) signal produced by 100 laser shots. After every few data

points the laser was blocked and an emission spectrum was recorded. The emission from the flame was typically 2.5 % of the PLII signal. Each charging of the injection pump yielded between 5 and 10 data points. An example PLII image of a heptane/air flame is provided in Figure 9.

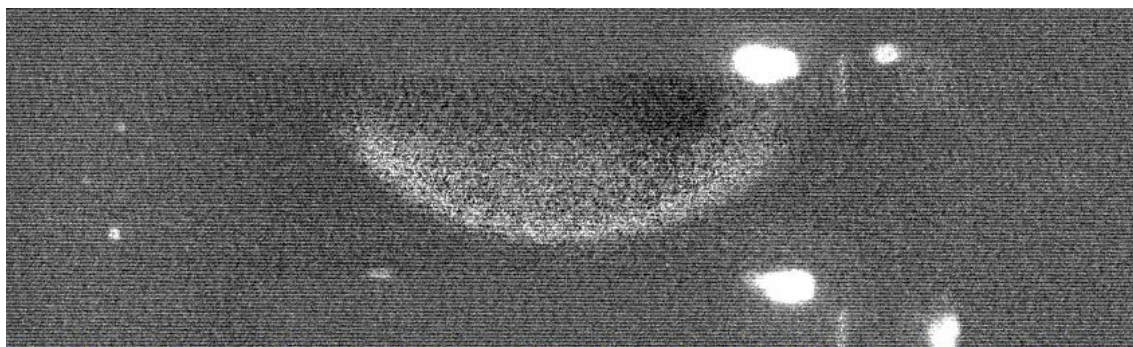


Figure 9. A PLII Image of a Heptane/Air Flame.

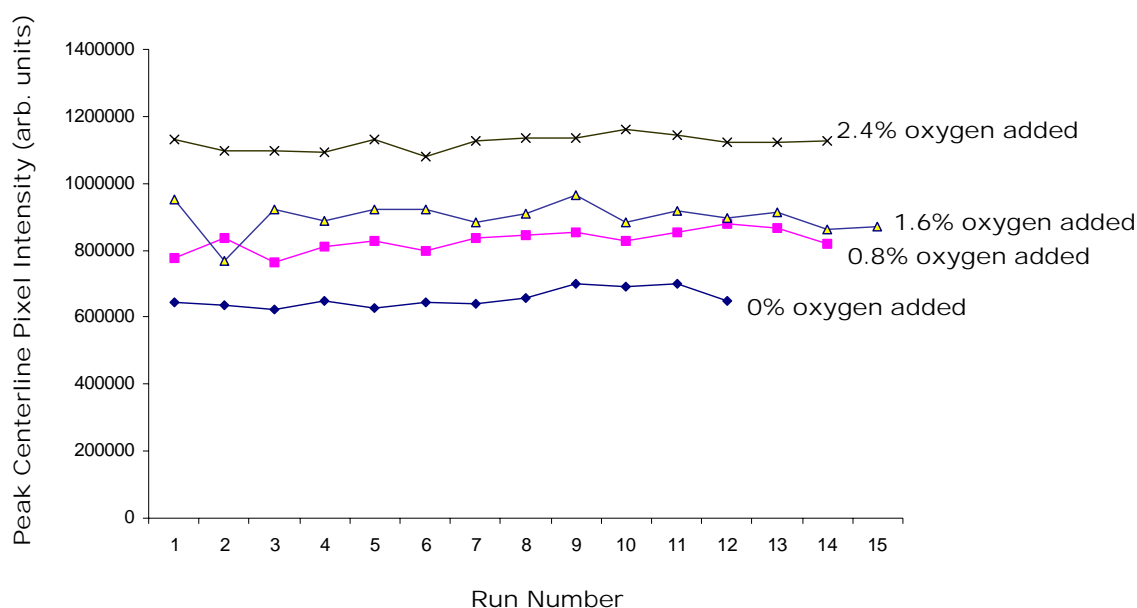


Figure 10. The Peak Pixel Value of the Raw PLII Signal Measured Along the Centerline of the Burner for Fuel Side Addition of Nitromethane to Heptane/Toluene/Air Flames. (Up to an oxygen addition from nitromethane corresponding to 2.4% oxygen by weight.)

Figure 10 shows the peak pixel value of the raw PLII signal measured along the centerline of the burner for fuel side addition of nitromethane to heptane/toluene/air flames, up to an oxygen addition from nitromethane corresponding to 2.4% oxygen by weight. The data shown in Figure 9 is not corrected for emission. For each addition of nitromethane to the fuel stream, an increase in particle formation was observed. The amount of soot formation was approximately proportional to the amount of nitromethane added to the fuel stream, and was independent of whether successive tests involved increases or decreases of the additive. The increase in soot

reported here for small nitromethane addition to the fuel stream was also seen for small additions of ethanol and isopropyl nitrate to the fuel stream of heptane/air opposed flow flames, and for ethanol addition to the fuel stream of ethylene/air opposed flow flames. Modeling results for ethanol addition suggest the increase in soot for the ethylene/air opposed flow flames upon addition of ethanol to the fuel stream may be attributed to introduction of hydrocarbon radicals in extremely fuel-rich areas near the stagnation plane. Modeling efforts (OPPDIF, Reaction Design) have been attempted to help understand the increase in soot formation observed for the heptane/toluene/air flames with fuel side nitromethane addition. However, to date we have been unsuccessful in achieving a convergent solution for this large reaction mechanism (1700 reactions).

The increase in soot with fuel side addition is also similar to the result observed by Hura and Glassman [19] who showed that soot increases when small amounts of oxidizers (e.g., oxygen) is added to the fuel side of a non-premixed flame.

7. Turbulent Spray Flame

A mixture of 20% toluene/80% heptane was used as the base fuel for these experiments to better approximate the composition of JP-8. The overall equivalence ratio for these experiments was 2.37. The airflow rate was the same as that for the heptane/ethanol experiments [1] so the cold flow Reynolds number was identical for the two sets of tests. The commercial additive was added at 5% by volume. At the time of the initial experiments with the commercial additive, its chemical constituents and properties were not available. Therefore, the fuel flow rates with and without the commercial additive were not corrected, but adopted the same value. The experimental conditions of the study are listed in Table 6.

Subsequent to the initial experiments with the commercial additive, its basic composition was determined and the main components with a potential to reduce soot were identified as cyclohexanone, nitromethane, nitroethane, and nitropropane. These components were run individually in the turbulent spray flame to determine their effectiveness in reducing soot under conditions similar to those listed in Table 6. Nitromethane was not run in these experiments because of the possibility that it could explode upon compression. The tests were done at two levels of oxygen addition, 2% and 4% of the fuel by mass.

The commercial additive showed very interesting time dependent behavior in these experiments. After it was first introduced, the amount of soot decreased slowly to a steady state level; when the additive was removed, the soot increased slowly toward the initial baseline level. This behavior is illustrated in Fig. 11. A number of experiments were run to determine the cause of this slow time response. Unfortunately, difficulty getting good repeatability in these experiments due to nozzle fouling made it impossible to determine the cause of the time dependent behavior. Variable level of nozzle fouling is in fact a leading contributing factor in the time-dependent behavior.

Data to determine the effect of the additive on soot were collected during the steady periods of behavior. Three hundred (300) shot averages were used and the results were background corrected and also corrected for pixel-to-pixel variation. Figure 12 presents a plot of the average LII intensity for the flame with and without the commercial additive. The results for the commercial additive show that it has a greater effectiveness than ethanol [1]. Soot yields

decreased by about 40%, even though its volume fraction is significantly less than that used for ethanol.

Following this work, experiments were performed to test the effective individual components in the commercial additive. Figure 13 presents summaries of the effect of the nitroethane and nitropropane on soot formation in the turbulent spray flame. The effectiveness of ethanol and cyclohexanone are also presented for comparison purposes. The nitroalkanes are both more effective than ethanol at equivalent oxygen levels, and the cyclohexanone leads to soot reductions on the order of those for ethanol.

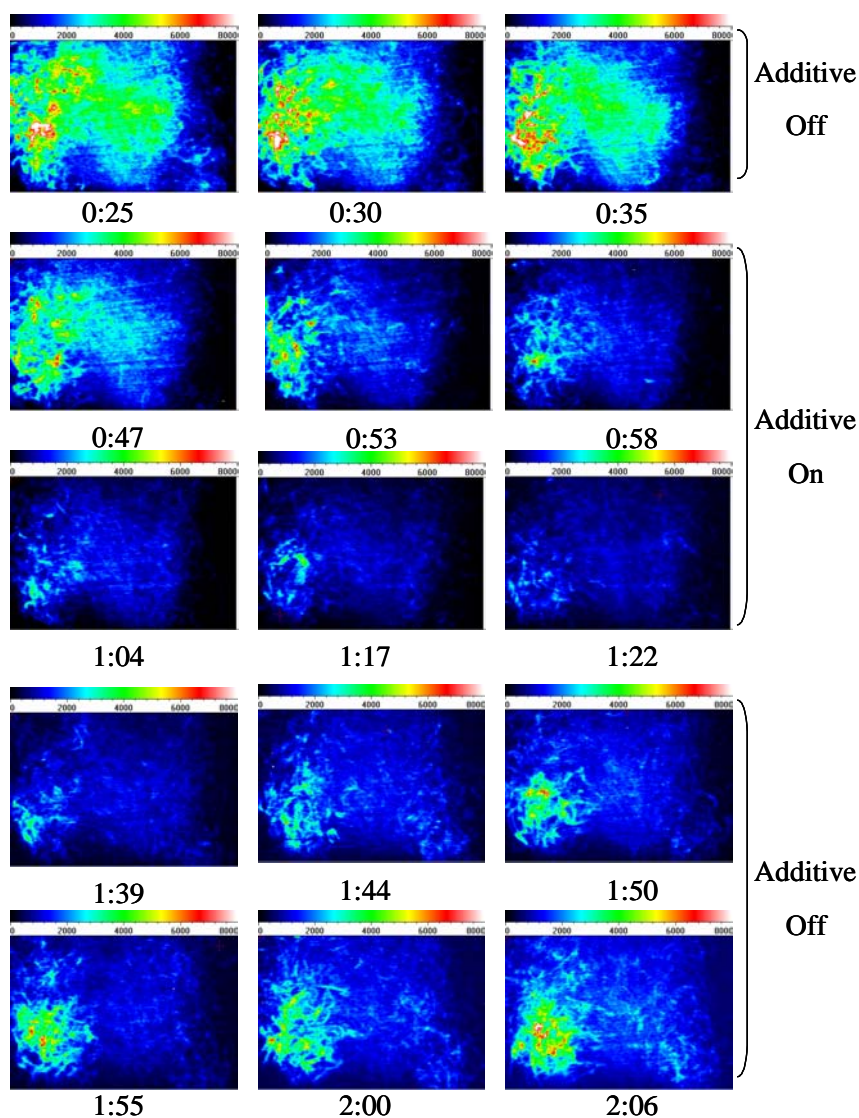


Figure 11. Series of LII Images Illustrating the Time Dependent Behavior of the Commercial Additive.

Table 6. Experimental Conditions for Heptane/Toluene Fuel and Commercial Additive

Base Fuel Formulation	80% Heptane, 20% Toluene by volume
Additive	Commercial Additive
Base Fuel Supply (g/s)	0.28
Fuel with Additive Supply (g/s)	0.28
Air Supply (g/s)	1.76
Equivalence Ratio for Baseline Test	2.37

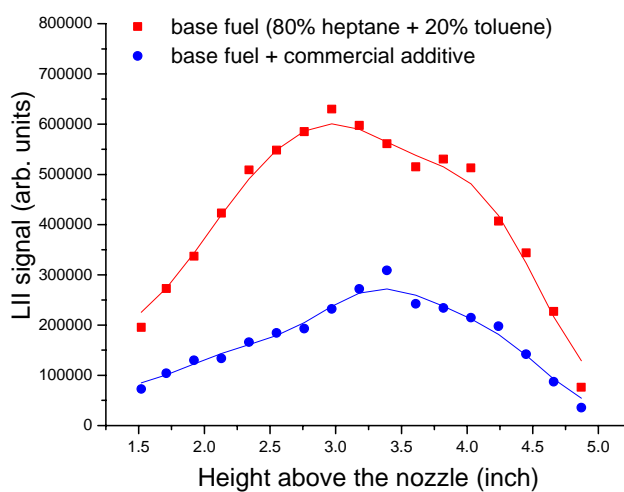


Figure 12. Effects of Commercial Additive on Soot.

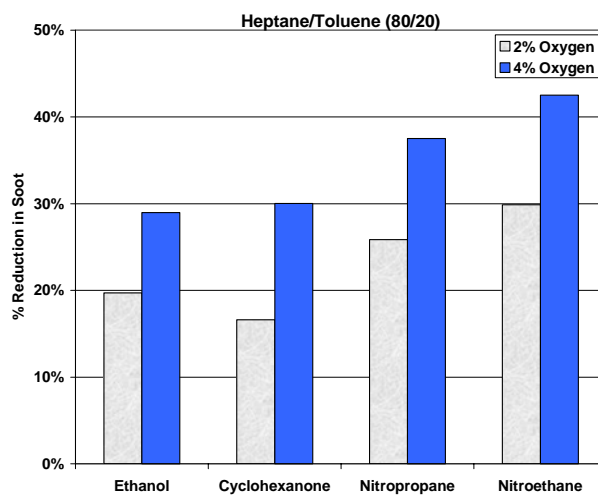


Figure 13. Effect of Individual Components of the Commercial Additive on Soot (ethanol included for comparison purposes).

8. High Pressure Turbulent Reactor

All tests with nitroalkane additives in the high pressure turbulent combustor were run with JP-8 as the fuel, a major consideration being its reasonable cost compared to the heptane/toluene blend. The airflow for the tests was 32 gm/s and the equivalence ratio was 1.3. The inlet air temperature was 550 K and the chamber pressure was 0.5 MPa. Only two of the three nitroalkanes from the commercial additive were studied, nitroethane and nitropropane. The third, nitromethane, can detonate due to compression so it was not run in these experiments.

Figure 14 presents a summary of the test results on soot volume fraction versus additive concentration. Nitroethane was added to JP-8 in concentrations ranging from approximately 2.5% to 10% by volume of the fuel. It was found that the nitroethane reduced soot at all concentrations. The soot suppression effect was found to increase with increases in the additive concentrations. At the lowest concentration of about 2.5%, the soot reduction was roughly 20%; at an additive concentration of 10% by volume in the fuel, the reduction was ~70%. Similar trends were observed with the addition of nitropropane. Although the reduction in soot was approximately the same as with nitropropane at the lowest additive concentrations, the reduction was slightly lower than nitroethane at higher additive concentrations. At an additive concentration of about 10% by volume of JP-8, nitropropane reduced soot by approximately 60%.

These levels of reduction were substantially greater than those obtained with ethanol. Modeling of the experiments could not be performed with standard tools in CHEMKIN due to the complexity of the problem, so the reasons for the greater effectiveness observed could not be identified through modeling.

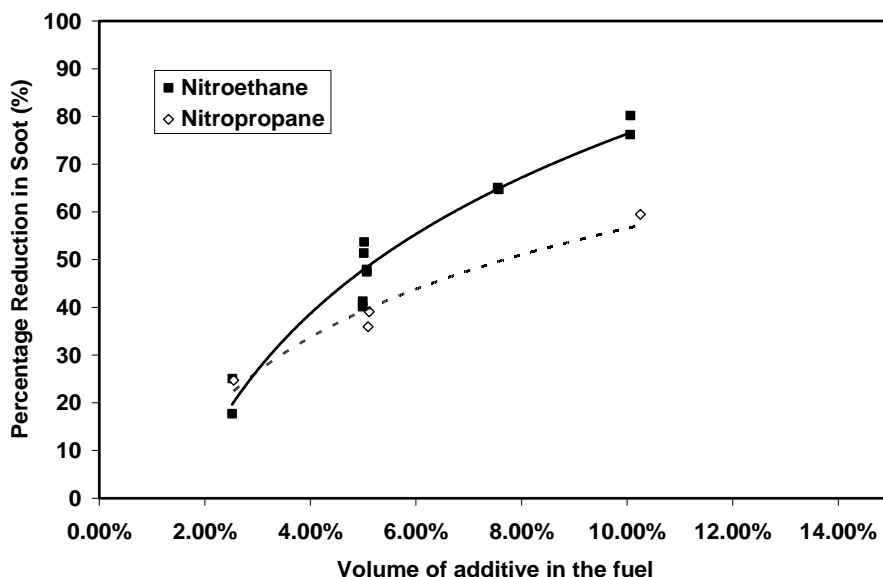


Figure 14. Effect of Nitroalkanes on Soot Formation in the Dump Combustor with JP-8.

9. Summary Effect of Other Additives

The study of NO₂ addition in the shock tube was directed at checking the hypothesis that the methyl radical formed when nitromethane decomposes could offset the tendency of the NO₂ to reduce soot, leading to the minimal benefits as observed with nitromethane in the shock tube experiments. The experimental results did not confirm this hypothesis; they showed a small decrease in soot at lower temperatures and a small increase at higher temperatures. Therefore, the results were not significantly different than those for nitromethane. Modeling was then undertaken to investigate the effect, but the study did not yield conclusive answers, potentially due to difficulties with the kinetic model.

A study of NO₂ addition to the ethylene flame was conducted in order to determine the relative contributions of temperature changes and direct kinetic effects on reducing soot. The study yielded the very unusual result that soot decreased, but the polycyclic aromatic hydrocarbons increased. Modeling of the flames with and without the addition of NO₂ was used to understand the reason for the increased PAH, which appears to be linked to higher yield of acetylene when NO₂ is added.

The study of nitroalkanes triggered a thought process that led the team to consider other species containing heteroatoms that might reduce soot, which eventually led to testing of pyridine. Pyridine, a six-membered ring containing five carbons and one nitrogen, is known to pyrolyze without forming much soot. Initial studies in a premixed flame showed substantial reductions in soot and led to the study in the full suite of devices.

The pyridine results show fairly complex behavior from variations on the effectiveness with temperature in the shock tube and the WSR to the complete lack of an effect in the HP Turbulent Reactor. Only the premixed flame and the turbulent spray flame showed decreases in soot. A possible explanation for the trends that were observed is that there are two competing effects: an inhibiting effect caused by the presence of the nitrogen in the ring that slows ring growth, and an accelerating effect resulting from the reaction of the ring producing products that contribute to soot formation. The inhibiting effect requires the ring to remain intact and would be more important at lower temperatures.

In order to check this hypothesis, a chemical kinetic mechanism was created based on available pyridine chemistry, which was added to the heptane/toluene mechanism. Modeling was undertaken for the shock tube and the premixed flame. The results showed that there were significant deficiencies in the model, so it was not possible to confirm or refute the hypothesis. So the data set stands as a challenge for future research after an improved mechanism can be formulated.

10. Summary

The study of nitroalkanes was motivated by testing of a commercial additive that showed promise in reducing soot. Analysis of the additive showed that its components that were most likely to be causing the soot reduction were nitroalkanes and cyclohexanone.

In the various test rigs, the nitroalkanes showed very complex effects on soot depending on experimental conditions and the structure of the additive. In the shock tube, negligible changes in the soot production were observed, although the concentration of nearly all aromatic soot

precursors increased with added nitromethane. Modeling indicated the opposite should occur. In the well-stirred reactor, all of the nitroalkanes showed reduced soot emissions, but their effectiveness varied with equivalence ratio. Measurement of product species demonstrates concerns about the viability of nitroalkane additives due to the HCN formation and added NO production. For the premixed flame, two of the additives (nitromethane and nitroethane) decreased soot monotonically with increases in additive concentrations. Alternatively, increasing the amount of nitropropane initially increased soot, but further increases in the amount of nitropropane decreased soot. This unusual result may be caused by added C₃-hydrocarbons with nitropropane causing increases in benzene formation. Under non-premixed opposed jet conditions, nitromethane increased soot production, consistent with prior studies on the effect of oxygen or oxygenated additives in the fuel-side of the flame. In the atmospheric pressure spray flame and the high pressure turbulent combustor the effectiveness was dependent on the structure of the alkyl group, although all additives provided a decrease in soot. Considering the opposing results obtained in the non-premixed jet flame configuration, it is rational to conclude that much of the fuel is burning in a partially premixed mode rather than purely, non-premixed.

Such a rich set of experimental results provide an excellent test for kinetic models of PAH and soot formation. In an effort to test a model for heptane/toluene combustion made available by the NIST SERDP team, kinetics related to nitromethane were added to the model. Unfortunately, it failed to model accurately even the shock tube data where kinetic processes must be dominant. The mechanism was too large to readily run when transport effects were included. Therefore, we were unable to establish whether the model supported conjectures on the mechanisms underlying the trends in the premixed flame data and the opposed-jet diffusion flame results.

Acknowledgments

The authors acknowledge the financial support for this work provided by the Strategic Environmental Research and Development Program (SERDP), Project PP1179, under the direction of Dr. Charles Pellerin.

References

- [1] T. Litzinger, M. Colket, M. Kahandawala, V. Katta, S.-Y. Lee, D. Liscinsky, K. McNesby, R. Pawlik, M. Roquemore, R. Santoro, S. Sidhu, S. Stouffer, J. Wu, "The Effects of Oxygenated Compounds on PAH and Soot across a Suite of Laboratory Devices," Paper F03, 5th US Combustion Meeting, March 25-28, 2006.
- [2] S. Sidhu, M. Colket, M. Kahandawala, V. Katta, D. Liscinsky, T. Litzinger, K. McNesby, R. Pawlik, M. Roquemore, R. Santoro, S. Stouffer, "The Effects of Phosphorus Compounds on PAH and Soot across a Suite of Laboratory Devices" Paper F03, 5th US Combustion Meeting, March 25-28, 2006.
- [3] M. Colket, D. Liscinsky, L. Chiappetta, M. Leong, R. Madabhushi, . Zeppieri, D. Hautman, "Mitigation of Particulate Emissions in Engines via Fuel Additives", Air Force Research Laboratories, AF Technology Investment Agreement F33615-00-2-2001, United Technologies Research Center, Report No. R03-6.100.0007-1, April, 2003.
- [4] W.M. Roquemore and T.A. Litzinger, "Reduced Particulate Matter Emissions for Military Gas Turbine Engines Using Fuel Additives," Final Report of SERDP PP-1179, (AFRL Report #), 2006.
- [5] Y. Zhang and S.H. Bauer, J. Phys. Chem. B101, (1997) 8717-8726.
- [6] Y. Zhang and S.H. Bauer, Int. J. Chem. Kinetics 31 (9), (1999) 656-673.
- [7] V.I. Babushok and W. Tsang, J. Propulsion and Power, 20 (3) (2004) 403-414.

- [8] J. Appel, H. Bockhorn, and M. Frenklach, *Combust. Flame*, 121:122, (2000); www.me.berkeley.edu-soot-codes.f.
- [9] H. Richter, W.J.Grieco and J.B. Howard, "Formation Mechanism of Polycyclic Aromatic Hydrocarbons and Fullerenes in Premixed Benzene Flames," *Combust.Flame*, 119 (1999) pp.1-22.
- [10] M.S Kahandawala, Ph.D. Dissertation on "Fuel Composition Effects on Particle and PAH Emissions", University of Dayton, Dayton, OH 2004.
- [11] S.D. Stouffer, B.M.Mortimer, D.M. Ostdiek,, M.J. DeWitt, R. Pawlik, R.F. Reich, C.W. Frayne and H.T. Mayfield, " Soot Reduction Research Using a Well-Stirred Reactor," AIAA 2005-1317, 43rd Aerospace Sciences Meeting, Reno, NV, January 13, 2005
- [12] J. Wu, K.H. Song, T. Litzinger, S.-Y. Lee, R. Santoro, M. Linevsky, M. Colket, D. Liscinsky, "Reduction of PAH and soot in premixed ethylene-air flames by addition of ethanol," *Combust. Flame* 144 (4) (2006) p 675-687; Corrigendum T. Litzinger, J. Wu, R. Santoro, *Combustion and Flame*, 146 (4) (2006) p 698-699.
- [13] K.L. McNesby, A.W. Miziolek, T.Nguyen, F.C. Delucia, R.R. Skaggs, T.A. Litzinger, "Experimental and computational studies of oxidizer and fuel side addition of ethanol to opposed flow air/ethylene flames," *Combust. and Flame*, 142 (4) (2005) p 413-427.
- [14] D. Imschweiler, M. McKeand, S.-Y. Lee, S. Saretto, M. Linevsky, T.A. Litzinger, and R.J. Santoro, "Fuel additive studies of soot reduction in a high-pressure model gas turbine combustor," 39th AIAA/ASME/SAE/ASEE Joint Propulsion Conference, AIAA 2003-5088 (2003)
- [15] M.S. Kahandawala, Ph.D. Dissertation on "Fuel Composition Effects on Particle and PAH Emissions", University of Dayton, Dayton, OH 2004.
- [16] S.D. Stouffer, B.M. Mortimer, D.M. Ostdiek, M.J. DeWitt, R. Pawlik, R.F. Reich, C.W. Frayne, and H.T. Mayfield, " Soot Reduction Research Using a Well-Stirred Reactor," AIAA 2005-1317, 43rd Aerospace Sciences Meeting, Reno, NV, January 13, 2005.
- [17] M.B. Colket, R.J. Hall and S.D. Stouffer, "Modeling Soot Formation in a Stirred Reactor", Proceedings of ASME Turbo Expo 2004, Paper No. GT2004-54001, Vienna, Austria, June 14-17, 2004.
- [18] R.A. Strehlow, *Fundamentals of Combustion*, International Textbook Company, Scranton, PA, pp. 221-227, 1968.
- [19] H.S. Hura and I. Glassman, *Proceedings of the Combustion Institute*, 22 (1988) 371-379.

5th US Combustion Meeting
Organized by the Western States Section of the Combustion Institute
and Hosted by the University of California at San Diego
March 25-28, 2007.

The Effects of Phosphorus Compounds on PAH and Soot across a Suite of Laboratory Devices

*S. Sidhu¹, V. Belovich², M Colket³, M.Kahandawala¹, V.Katta⁴, D.Liscinsky³,
T.Litzinger⁵ K.McNesby⁶, R.Pawlik², M.Roquemore², R Santoro⁵, S Stouffer¹,*

¹*Energy and Environment Division, University of Dayton Research Institute,
300 College Park, Dayton, OH 45469, USA*

²*Air Force Research Lab
Wright-Patterson Air Force Base, OH, USA*

³*United Technologies Research Center
East Hartford, CT, USA*

⁴*Innovative Scientific Solutions, Inc.
Dayton, OH, USA*

⁵*Department of Mechanical and Nuclear Engineering, Penn State University,
University Park, PA, USA*

⁶*Army Research Laboratory
Aberdeen, MD, USA*

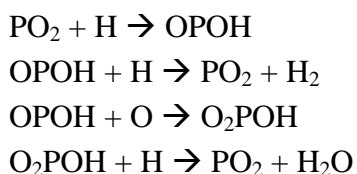
Recently researchers from universities, industry and governmental laboratories completed a collaborative study that investigated the impact of different types of organic fuel additives on soot and PAH emissions from military gas turbine engines. The main objective of this program was to obtain fundamental understanding of how even a small changes in fuel composition can affect soot and PAH emissions. Six different combustors namely, a premixed flame, a co-flow diffusion flame, an opposed-flow diffusion flame, a well-stirred reactor, a shock tube, and a swirl-stabilized combustor were used to investigate the impact of additives covering a wide range of combustion conditions. The experimental results from this study were then modeled using variety modeling packages and mechanisms. This paper will summarize the key results from studies of the effects of phosphorus additives, trimethyl phosphite, trimethyl phosphate, diethyl allyl phosphate, and dimethyl methyl phosphonate on soot and PAH for several gaseous fuels and a simple JP8 surrogate, heptane/toluene.

1. Introduction

The total amount of particulate matter (PM) emissions for aircraft in the United States is about 3 million kg per year. The US civil and military aviation uses about 20 and 25 billion gallons of aviation fuel per year. The fleet average emission index for soot has been estimated to be approximately 0.04 g/kg of fuel burned [International Civil Aviation Organization (ICAO) Data Base]. Although there is some uncertainty in these estimates, they are consistent with the magnitude being used to estimate global emissions from aircraft. There are two approaches to reducing PM_{2.5} emissions from gas turbine engines, modification or redesign of the combustion

system and modification of the fuel either by reformulation or additives. For existing engines, hardware retrofits are normally prohibitively expensive. Thus, the preferred approach is fuel modifications. The technical objective of this program was to develop fundamental understanding of the complex interactions of additives with the processes that lead to PM emissions from military gas turbine engines. The overall project included investigations of organic compounds containing oxygen, nitrogen, and phosphorus. The work reported in this paper is a summary of the key results from studies of the effects of phosphorus additives, trimethyl phosphite, trimethyl phosphate, diethyl allyl phosphate, and dimethyl methyl phosphonate on soot and PAH for several gaseous fuels and a simple JP8 surrogate, heptane/toluene.

The phosphorus compounds were chosen as additives because an earlier study by Hastie and Bonnell showed that the addition of 1000 ppm of trimethylphosphate (TMP) resulted in substantial reduction of soot in a propane-air diffusion flame. [1] The primary focus of the study was flame inhibition so only a small amount of information is available on the effects on soot including images of the flames with and without the additives. They also reported that 1000 ppm of TMP increased smoke in a propane-air premixed flame; however, the images in their report indicate that the amount of increase is small. Also, recently phosphorus has received significant attention again as a flame inhibitor and phosphorus compounds have been studied as surrogates for nerve agents that can be destroyed by incineration. [2, 3] As a result of these studies detailed kinetic mechanisms for phosphorus are appearing in the literature. The mechanism by which the phosphorus compounds inhibit premixed flames is postulated to be through a pseudo-catalytic mechanism, similar to the one identified for NO₂ in our work with nitro-alkanes. The key reactions are for fuel-rich premixed flames are:



These reactions lead to reductions in the radical concentration and lower the flame speed in premixed flames. The reduction in radicals will affect the soot formation, but precisely how is not clear.

The mechanism for the inhibition of diffusion flames by phosphorus has been studied in opposed-flow methane/O₂/N₂/Ar flames by MacDonald *et al.* [3] In this work the investigators made measurements of the OH concentration and discovered that peak OH concentration decreased by 23% with the addition of 572 ppm of dimethylmethylphosphate. The conditions of the experiments were such that these flames did not produce soot so no conclusions can be drawn about the effects on soot. However, it would be expected that decreasing the OH would lead to an increase in soot. For methane-air diffusion flames, this is precisely what Hastie and Bonnell report. [1]

No experimental or modeling work on the effect of phosphorus on soot appears in the literature after the work of Hastie and Bonnell. The enhanced understanding of the mechanism by which phosphorus affects premixed flames and diffusion flames has not been used to understand how it

reduces soot in diffusion flames or how it affects soot in premixed flames. Therefore we decided to investigate the effects of phosphorus additives on soot that would establish the mechanism by which it reduces soot and also its potential to reduce soot in gas turbine combustors.

2. Approach

Because of the inherent complexity of the combustion processes within gas turbine combustors and great difficulty in making measurements inside combustors, it was not possible to achieve the technical objective of this program by making measurements in gas turbine combustors. Furthermore, due to the complexity of the combustion process in a gas turbine combustor, no single laboratory flame or reactor is sufficient to serve as a model for a combustor. Therefore, multiple laboratory devices were applied to study the effects of additives on soot formation processes. These devices were a premixed flame, a co-flow diffusion flame, an opposed-flow diffusion flame, a well-stirred reactor, a shock tube, and a swirl-stabilized combustor. The devices were chosen to cover the range of combustion regimes present in a gas turbine combustor. They were also chosen so that they covered a range of complexity in terms of the chemical and physical processes involved, from the shock tube, where chemical kinetics is the dominant process, to the swirl-stabilized combustor in which chemical kinetics, molecular diffusion, turbulent mixing, and spray processes are all involved. This set of devices was applied in an hierarchical manner to identify the key chemical and physical processes through which the additives affect soot.

Numerical simulation proved to be an invaluable tool for understanding the mechanisms by which phosphorus compounds affected soot in these devices. Simulations were performed to the extent possible for each additive/fuel combination. CHEMKIN was used for modeling of the opposed-jet diffusion flame. The time dependent, axisymmetric mathematical model (UNICORN) was used to model co-flowing premixed and diffusion flames. The devices used in the study along with their associated diagnostics have all been described in detail elsewhere [4, 5, 6, 7, 8, 9] so they will not be described here.

Table 1 presents a summary of the effects of the phosphorus compounds tested. The use of different molecules to deliver the phosphorus resulted from a problem with MSDS data on the compound that was originally chosen. As a consequence, each lab took it upon itself to locate alternatives suitable for the device to be used. Past work in the literature indicates that the molecule used to deliver the phosphorus has little or no effect on the results for flame inhibition. The fire suppression works has shown that it's not the identity of parent organophosphorus compounds (OPC) but the small phosphor-bearing species such as HOPO_2 and HOPO produced from the parent OPC that alter the flame chemistry by catalytically recombining the key flame radicals, especially H, O, and OH.[2, 10] Table 1 shows that depending upon the device, and in some cases the experimental conditions, the phosphorus often had no effect; in the test of a device that is closest to an actual combustor, it increased soot emissions. The fuels used in this study included ethylene, propane, ethane and an 80/20 volume mixture of heptane and toluene. Details of the experimental methods can be found in the Final Report of the project; the data are available as well [9]. Because of the large volume of results only summary tables and plots will be presented along with key observations from the modeling studies.

Table 1. Summary of the Effects of OPCs on Soot.

	Additive	Fuel	Effect on Soot	Comments
Shock tube	Trimethyl phosphite	Heptane/ Toluene	Varies: decrease to increase	Variation with reaction temperature
Well-stirred reactor	Diethyl allyl phosphate	Heptane/ Toluene	Varies: no effect & reduction	Depends on temperature and treatment level. Experimental problems led to early termination of the test series.
Premixed flame	Trimethyl phosphate	Ethylene	No effect	
Coflow Diffusion Flame	Trimethyl phosphate	Ethylene	Decrease	
	Trimethyl phosphate	Propane	Decrease	
	Trimethyl phosphate	Ethane	No effect	
Opposed-jet flame	Demethyl methyl phosphonate	Ethylene	No effect	
CFM Combustor	Diethyl allyl phosphate	Heptane/ Toluene	Increases soot	Decreases particle size, but increases number density

3. Shock Tube

Premixed gas phase experiments were conducted using a single pulse shock tube. An OPC, trimethyl phosphite with an adequate vapor pressure (17 torr at 760 mmHg), was selected as the phosphorus additive for this study. For all phosphorus additive experiments 1.73 vol% (2.5wt%) of trimethyl phosphite was added to base fuel mixture (80 vol% heptane + 20 vol% toluene). Experiments were conducted over a temperature range of 1600 K – 1900 K at a pressure of ~21 atm, an equivalence ratio of 3.0, and dwell times (fuel exposure times) of ~7.5 ms.

Both gaseous products and soot yields were measured and normalized with respect to the mass of carbon in the fuel to exclude any volumetric effect that may arise from normalization with respect to the mass of the fuel. Results from Leco carbon analysis of particle yields are shown in Figure 1. The solid lines indicate polynomial trend lines that were used to fit the experimental soot yields. The trend lines show that addition of trimethyl phosphate decreased soot yields at lower temperatures and increased soot yields at higher temperatures. The experiments were done at close temperature intervals to cover the entire temperature range instead of repeating the same experiments at a fixed temperature. The measured ignition delay data shows (see Figure 2) addition of trimethyl phosphite reduced the ignition delay over the entire temperature range.

The lower ignition delay under fuel-rich conditions at the lower temperature region indicates a possible chemical effect in reducing the soot yields from reactions of the type $\text{HOPO}_2 + \text{H} = \text{PO}_2 + \text{H}_2\text{O}$ [2] that consume the H radicals. At the higher temperatures this effect is negated due to dissociation of HOPO_2 .

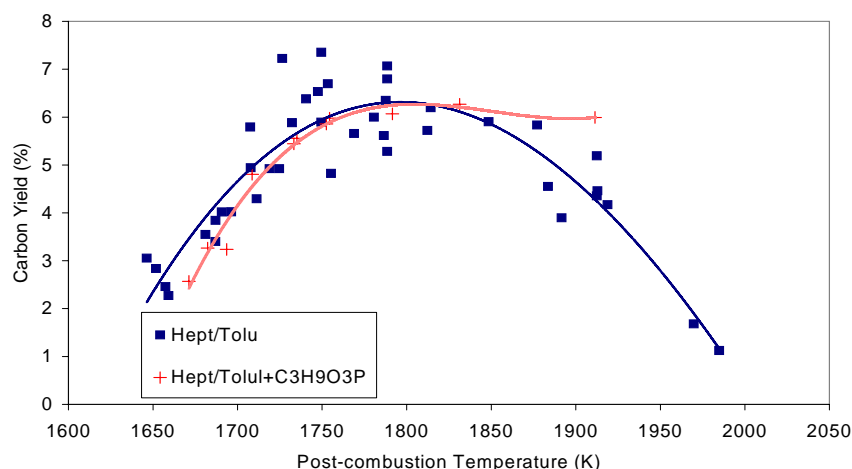


Figure 1. Carbon Yield from Combustion of Heptane/Toluene and Heptane/Toluene+(25K ppm) Trimethyl Phosphite.

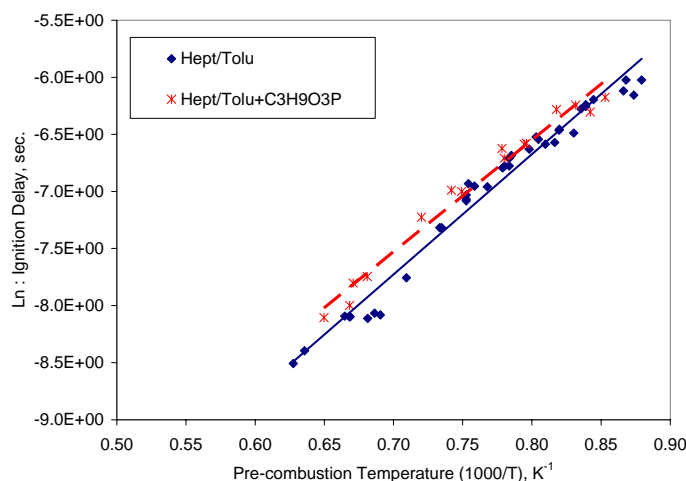


Figure 2. Ignition Delay from Combustion of Heptane/Toluene and Heptane/Toluene+(25K ppm) Trimethyl Phosphite.

4. Well-stirred Reactor

Diethyl allyl phosphate at concentrations of 2500 ppm and 1000 ppm was tested as a soot reduction additive in the WSR using a 80% heptane/20% toluene mixture as the neat fuel. The air mass flow rate for the WSR was 240 g/min, and the equivalence ratio, ϕ , was set to 1.92 or 2.0. The vapor pressure of this additive was much lower than had been advertised in the manufacturers literature, however, we estimate that at $\phi = 2.0$ and 2500 ppm, the additive needs to have a vapor pressure of only 0.125 Torr to remain in the vapor phase. To enhance

vaporization the fuel was heated to a temperature of 160°C, and the air to 200°C before entering the vaporizer, leading to a final inlet temperature 175°C. In contrast to studies of lean to slightly fuel-rich studies in the CFM56 combustor, no visual effect was observed on the exhaust plume when the additive was added. Soot mass samples were acquired from a probe located at a distance of 16 cm from the exit of the WSR in the plug flow region.

The results of carbon mass collected on quartz filters and determined by carbon burnoff in the LECO analyzer are shown in Figure 3. Most of the results obtained with the 1000 ppm additive concentration were compromised by a problem with the LECO apparatus. At the concentration levels studied, the additive was shown to reduce total measured carbon at $\phi = 2.0$ by approximately 20% and to have little effect on the total measured carbon mass at equivalence ratios of $\phi = 1.92$. The total carbon mass measured was divided into a volatile component, that was obtained by measuring the carbon burned off from the filter at temperatures below 330°C, and a carbonaceous component, obtained by the carbon mass burned off from the filter at temperatures above 330°C. The volatile carbon fraction results are shown in Figure 4. For $\phi = 2.0$ the greatest reduction in the carbon mass with the addition of the additive occurred in the volatile component, while the carbonaceous fraction of the carbon mass changed little for either cases with the additive.

Methane, acetylene, ethylene, formaldehyde and benzene were also monitored using the FTIR multigas analyzer. All of these gaseous species increased in concentration as the equivalence ratio changed from $\phi=1.92$ to $\phi=2.0$, but their concentrations increased further when the additive was used. These data suggest the concentrations of these soot precursors increase in association with the decrease in volatile carbon mass, associated with the use of the additive. The results of the gas analysis show no measurable increase or decrease in the already low NO_x values. Reactor temperature was measured for the $\phi = 2.0$ case and showed a slight difference (less than 5 °K) between the additive and nonadditive cases.

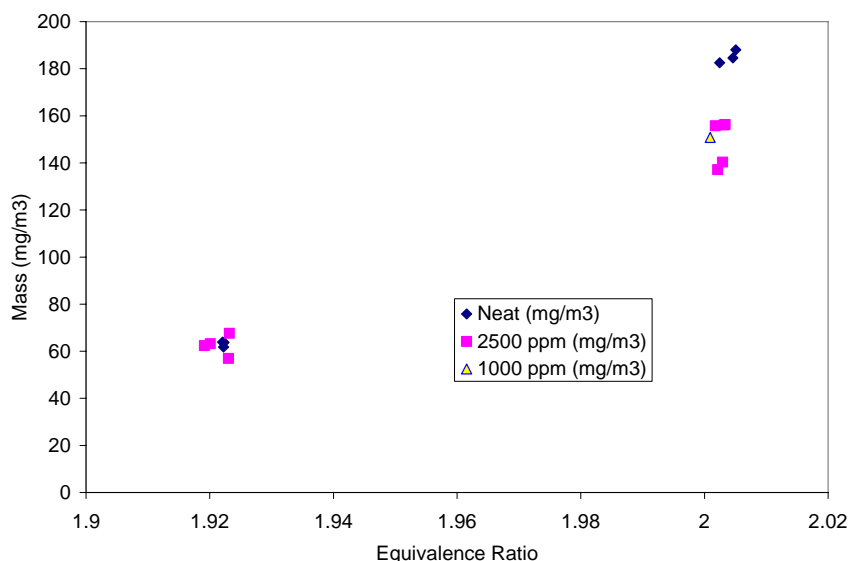


Figure 3. The Effect of Diethyl Allyl Phosphate on Measured Carbon Mass from Samples in the WSR.

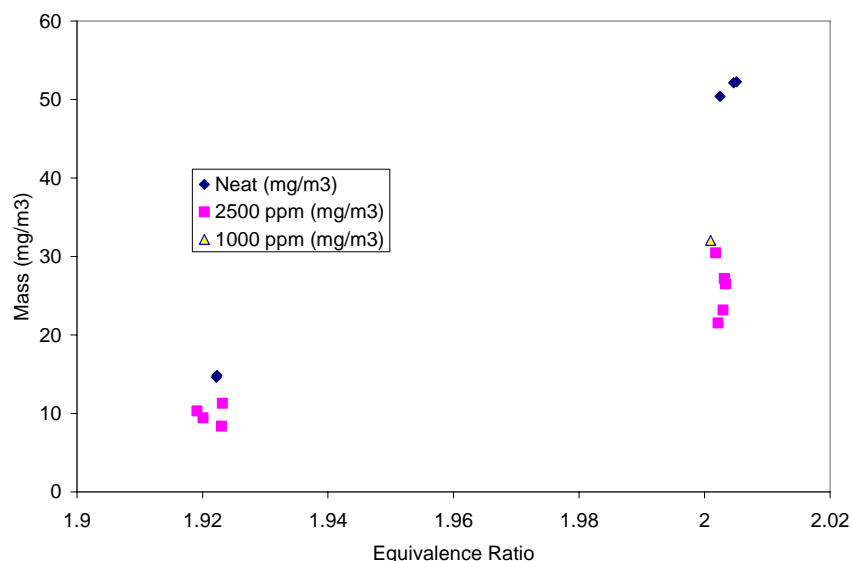


Figure 4. The Effect of Diethyl Allyl Phosphate on the Volatile Carbon Mass from Samples in the WSR.

5. Premixed Flame

The experiments were conducted on a laminar premixed flat flame burner using ethylene (C_2H_4) as the fuel and air as the oxidizer. The flame was shielded from the surrounding air using a shroud of nitrogen supplied through an annulus 11 mm thick, concentric to the burner, which was 60.3 mm in diameter. The soot volume fraction was measured using laser extinction, using the 514.5 nm line of an argon-ion laser (Coherent Innova 70). The total mass flow rate of the fuel/air mixture was approximately 225 mg/s. The additive was introduced into the reactant stream by passing the reactant's flow through a bed of glass beads ~4 mm in diameter and filled with trimethyl phosphate (TMP). Using the vapor pressure of TMP, it was estimated that the concentration of TMP in the reactant stream was approximately 0.1% by volume of the reactant stream or 0.7% by mass of the reactant stream. The experiment was conducted for equivalence ratios of 2.34 and 2.64, conditions used in all of the other premixed flame experiments conducted at Penn State. The flow conditions for the experiment are presented in Table 2.

Experiments were also attempted with propane in order to allow direct comparison to the work of Hastie and Bonnell [1]. However, the flame was just beginning to produce soot at the higher equivalence ratio of 2.64, and at those conditions it was beginning to become unstable. Consequently, no data could be collected for propane with and without TMP added. The difference between the present experiments and those of Hastie and Bonnell is the type of burner used. They used a small diameter premixed jet flame that could be stabilized at much richer conditions than the flat flame used in this study. The flat flame burner is necessary to allow optical diagnostics to be used.

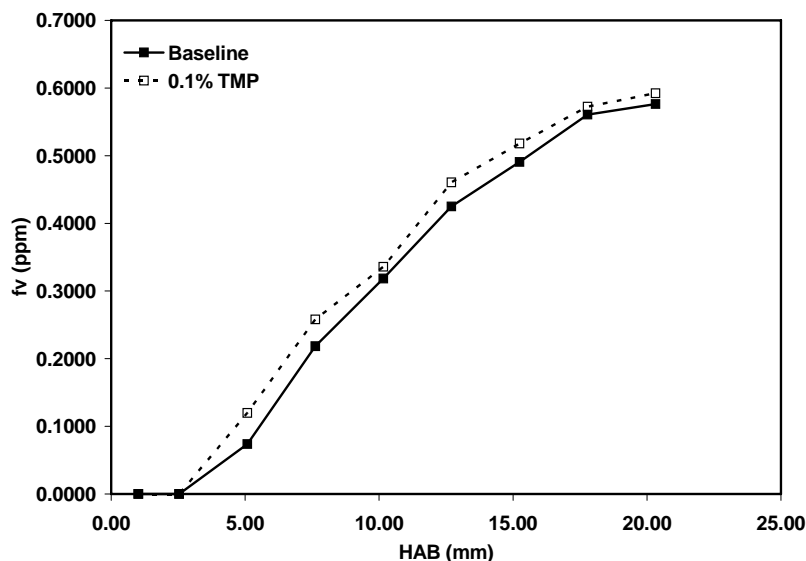
The soot volume fractions for the baseline and the flame with TMP added for an equivalence ratio of 2.34 is shown in Figure 5. It is seen that the soot volume fractions for the flame with

Table 2. Flow Conditions for Premixed Ethylene Flames with TMP.

Flame	Baseline	Additive	Baseline	Additive
Equivalence Ratio	2.34	2.34	2.64	2.64
C/O ratio	0.78	0.78	0.88	0.88
Fuel mass flow rate (C₂H₄), mg/s,(cc/s)^a	30.8 (26.45)	30.8 (26.45)	34.1 (29.28)	34.1 (29.28)
Air mass flow rate mg/s,(cc/s)^a	194.3 (161.93)	194.3 (161.93)	190.9 (159.09)	190.9 (159.09)
TMP mass flow rate mg/s,(cc/s)^b	0	1.19 (0.20)	0	1.19 (0.20)
Coflow N₂ mass flow rate mg/s,(cc/s)^a	557 (478.28)	557 (478.28)	557 (478.28)	557 (478.28)
Pressure (atm)	1	1	1	1
Temperature (K)	295	295	295	295
Fuel	Ethylene (99.5%)	Ethylene (99.5%)	Ethylene (99.5%)	Ethylene (99.5%)

a: volumetric flow rate calculated based on T=293K

b: TMP mass flow rate calculated based on T=293K and vapor pressure (110Pa at 293K)

Figure 5. Effect of TMP on Soot Volume Fractions for $\Phi = 2.34$ Premixed C₂H₄ Flame.

TMP added are slightly higher than the baseline flame, the increase in soot at the last measurement point being approximately 3%, which is within the uncertainty of error for the technique. The same trend is seen at an equivalence ratio of 2.64 but the increase in soot is slightly higher than the leaner flame, with an increase of approximately 6.5% at the final measurement point of 20 mm HAB. Within this program, an increase of soot was observed when

ethanol was added to ethylene/air opposed flow diffusion flames due to similar effects. Analysis of modeling results showed that the increase was due to the methyl radicals formed from the ethanol which increased the rate of formation of the first aromatic ring via a 4-carbon intermediate. The increase of soot with the addition of TMP may be a result of a similar effect.

6. Coflow Diffusion Flame

The fuels used in the study were ethylene (purity 99.5%), propane (purity 99.9%) and ethane (purity 99.5%). Coflow air was supplied from a laboratory compressor. The volumetric flow rates of ethylene, propane and ethane were 3.85, 2.5 and 4.13 cc/s, while air flow rate was fixed at 713.3 cc/s for each fuel. The TMP (purity $\geq 99\%$), supplied by Sigma-Aldrich Corp., and known as a chemically active flame inhibitor is liquid at room temperature with low vapor pressure (less than 1 torr at ambient temperature). Due to higher boiling point ($\sim 197^\circ\text{C}$) of TMP, it is impractical to make a vaporizer system. Instead, a glass aspirator was fabricated to convey the TMP vapor by the fuel volumetric flow. The volumetric percentage of TMP was approximately 0.1% of fuel volumetric flow rate based on vapor pressure of TMP.

The most obvious effect of additive was visible for ethylene and propane in which the TMP delayed the appearance of soot increasing the height above the burner at which soot is first observed. For ethane the soot concentration is so low that no difference was visible. Decreases in soot concentration do occur when TMP is added to the ethylene and propane flames, but they were difficult to see. The examination of radial soot concentration profiles at various heights in the flames showed that the decrease in soot was most discernable at the lowest flame heights. Finally, to give an overall sense of the effects on soot, volume fraction was integrated radially at each height according to the equation:

$$F_v(z) = \pi \left(\int_0^R f_v(z,r) r dr + \int_{-R}^0 f_v(z,r) r dr \right)$$

Figure 6 presents the overall trends showing that phosphorus leads to a decrease in soot for in the ethylene and propane flames. The reduction in soot with the addition of TMP to the propane flame is consistent with the original work of Hastie and Bonnell with this fuel.

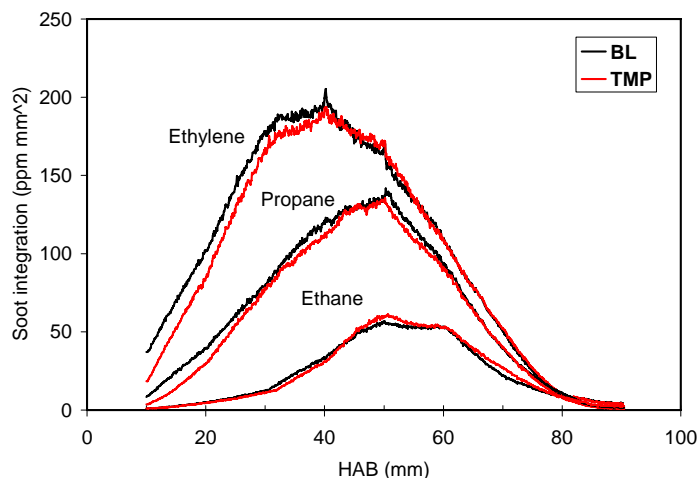


Figure 6. Integrated Soot Volume Fraction as a Height of the Flame

7. Opposed-flow Diffusion Flame

Because of the availability of a chemical mechanism (with transport files) in CHEMKIN format, dimethylmethylphosphonate (DMMP) was chosen for investigation as a soot suppressant at ARL. When the DMMP was added on the air side of the ethylene/air opposed-flow flame, at two different oxidizer global strain rates it caused the flame to appear more whitish than the neat flame and increased the apparent separation between combustion and sooting regions. At the time of these experiments, we were capable of supplying additives to only the upper gas stream in the opposed-flow burner. For this reason, it was necessary to move the fuel stream to the upper burner duct so we could add DMMP to the ethylene fuel.

Figure 7 shows a summary of experimental measurements of DMMP to fuel and oxidizer streams for the opposed-flow ethylene/air flames. As with ethanol addition to ethylene/air flames, addition of DMMP to the oxidizer stream was more effective at particle reduction than fuel side addition. However, it is worth mentioning that DMMP is a known flame suppressant.

A chemical kinetic mechanism for DMMP combustion in ethylene/air flames was compiled, in CHEMKIN format, with thermo and transport files. The low vapor pressure of DMMP limits the amount that can be introduced as vapor at room temperature, and the initial parameters of the calculations reflect this limitation. The calculations of DMMP addition to fuel and oxidizer sides of opposed-flow ethylene/air flames agree, qualitatively, with experiment. That is, addition of DMMP to the air side of the flame is predicted to be more effective at reducing soot precursors C_2H_2 and A_1 than for fuel side addition. However, as mentioned previously, DMMP is a known fire suppressant. The mechanism for suppression is believed to be radical scavenging of H and OH in a catalytic-like cycle.

A detailed analysis of flame chemistry such as was performed for ethanol addition to flames was not performed for the DMMP addition. However, we do not believe DMMP would be a suitable soot suppressant because of its flame inhibition characteristics. Additionally, we have a qualitative observation that for addition to ethylene/air and heptane/air opposed-flow flames, addition of DMMP produces a particulate (off white in color) in addition to soot.

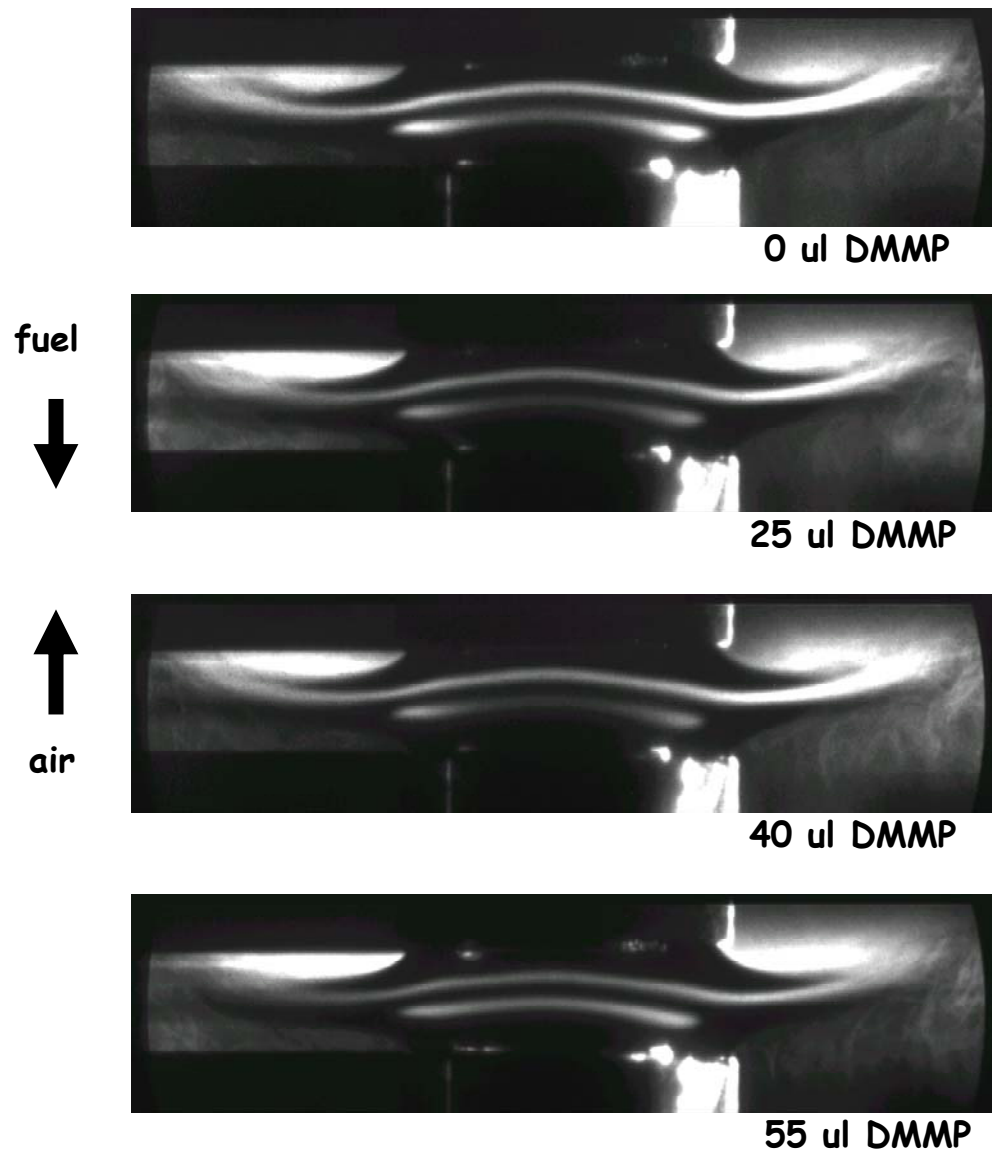
Fuel side addition of DMMP to C₂H₄/air flames

Figure 7. PLIF Images of Opposed Flow Ethylene/Air Flames to which DMMP has been Added to the Fuel (ethylene) Stream. Note the fuel stream enters the flame from above.

8. CFM Combustor

For this study, a fuel mixture of 80% heptane and 20% toluene was used as a fuel. The combustor overall equivalence ratio was varied from $\Phi=0.70$ to 1.10, which resulted in a fuel flow rate of 112-175 ml/min. The airflow rate was constant at 28 gm/sec. Additive concentrations of 1000 ppm, 2500 ppm and 5000 ppm were tested.

The particle emissions from heptane/toluene blend were compared with JP-8 particle emissions. And it was found that heptane/toluene generally produces much fewer particles than JP-8. Additive tests are generally run at a lean ($\Phi=0.7$) and a rich ($\Phi=1.1$) equivalence ratio. The procedure is to operate the TSI particle instrumentation in a continuous measurement mode while the additive is cycled on and off several times using syringe pumps. During the additive cycling, adequate time is given for the fuel system and combustor to come to equilibrium. This demonstrates repeatability and readily shows if there are any hysteresis affects. This additive required approximately 45-60 minutes for the particulate count to reach a steady state value, which is much longer than for most additives.

Figure 8 shows the results of adding 1000 ppm of diethyl allyl phosphate to the 80/20 heptane/toluene mixture. The additive substantially increases the particle count at 1000 ppm for both lean and rich conditions. The increase is several orders of magnitude for lean conditions and roughly an order of magnitude for rich conditions. At high PND, i.e., greater than 10000 counts, the particle counters operate in the photometric mode, which is less sensitive than the individual particle counting mode. This may explain why the increase in PND at rich conditions is not as dramatic as for lean conditions. When the additive was being injected at 1000 ppm, there was a visible color change to the exhaust gases, which filled the whole combustion chamber. These particles had an orange-yellow appearance, different from the mostly yellow color normally seen as soot. Additive concentration levels of 2500 ppm and 5000 ppm were also tested and were found to increase PND to a level such that our sampling system was not able to dilute the sample to a point at which we could get a measurement.

Particle size data was also taken in this study and it shows that JP-8 produces the largest mean particle size at an equivalence ratio of 1.1. The heptane/toluene mixture produces slightly smaller particles, while also producing less. The heptane/toluene mixture with 1000 ppm additive produced the smallest average particle size, but also produced many more particles. This is what one would expect when burning a metal-containing additive.

UNICORN results, to be discussed in the next section, predicted that phosphorus would reduce NO in premixed and diffusion flames; no prior discussion of such an effect was found in the literature. Based on this novel prediction, NO_x measurements were made in the CFM combustor. Even though no particulate data could be taken for additive levels above 1000 ppm, emissions data was still taken at higher additive levels. This data is shown in Figure 9. For the two equivalence ratios tested, NO_x emissions were reduced as the additive concentration increased, except for $\Phi=1.1$ at 5000 ppm. It is possible that this is an errant point, but further testing would be needed to verify this. This result is consistent with the UNICORN calculations that have shown NO_x emissions reduction using a phosphorus-containing additive.

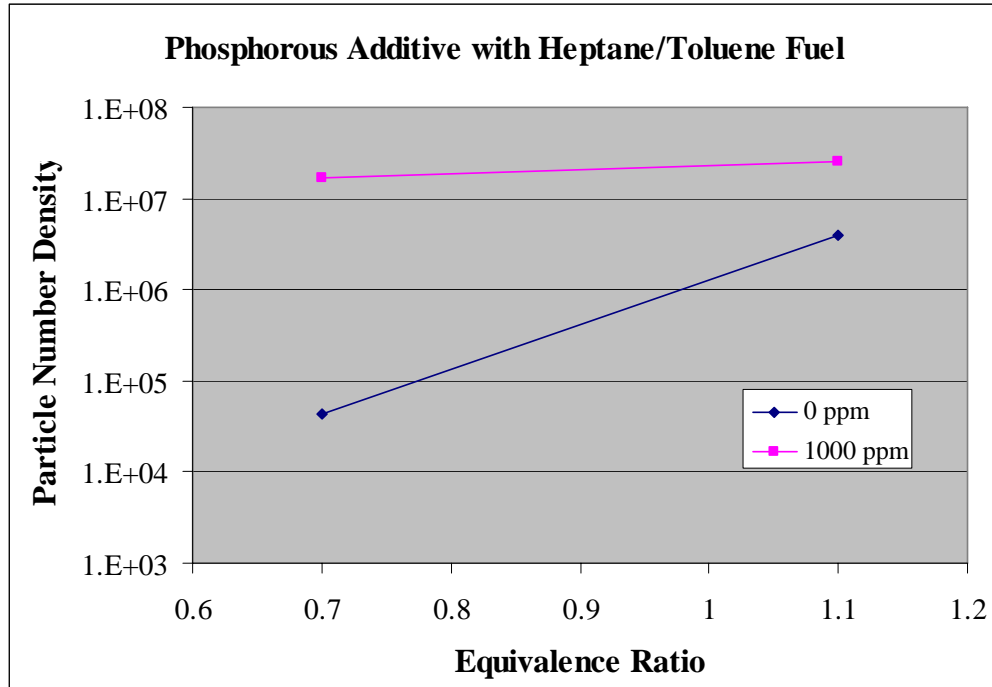


Figure 8. Particle Number Density Changes for Diethyl Allyl Phosphate Added to 80/20 Heptane/Toluene at 1000 ppm.

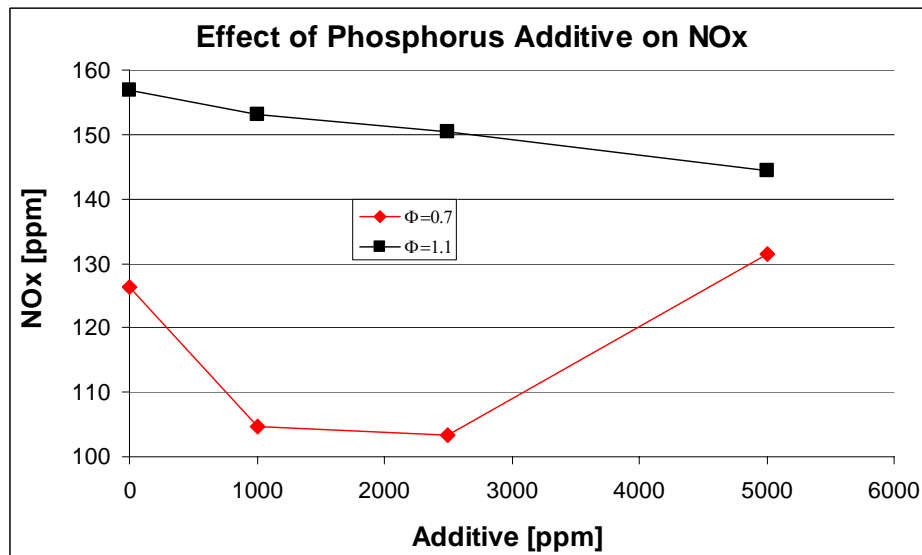


Figure 9. The Effect of the Phosphorus Additive on NOx Emissions.

9. Jet Flames, UNICORN Modeling

The time dependent, axisymmetric mathematical model (UNICORN) is used for the simulation of coflowing premixed and diffusion flames. The body force term due to the gravitational field is

included in the axial momentum equation for simulating vertically mounted flames. A clustered mesh system is employed to trace the large gradients in flow variables near the flame surface. A detailed chemical kinetics model developed by NIST is incorporated into UNICORN for the investigation of PAH formation in heptane flames. The combustion inhibition chemistry of TMP developed by LLNL [10] is also incorporated. The combined mechanism consists of 238 species and 3178 elementary reaction steps. A simple radiation model based on the optically thin media assumption is incorporated into the energy equation. Only radiation from CH₄, CO, CO₂, H₂O, and soot is considered. A two-equation model for soot with transport equations for particle number density and soot mass fraction is considered.

The code developed for the simulation of TMP effects on heptane flames could also be used for the simulation of methane, propane, or ethylene flames doped with TMP. Calculations are made for a propane flame with an equivalence ratio (ϕ) of 1.5. Fuel/air/TMP mixture is issued from a 6 mm-diameter tube at an average exit velocity of 0.5 m/s. Parabolic velocity profile which gives a peak value of 1.0 m/s is imposed at the exit of the tube. A low speed (0.01 m/s), coannular airflow is used in the region outside the flame. Distributions of temperature and soot volume fraction for the base flame (with no added TMP) are shown in Figures 10(a) and 10(b), respectively. Similarly, distributions for 0.1% added TMP are shown in Figures 10(c) and 10(d), and those for 1.0% TMP are shown in Figures 10(e) and 10(f). A common color scheme is used for each variable based on the peak value obtained from all the flames. As the peak soot concentration produced in the flame with 1% TMP (Figure 10(f)) is nearly two orders more than that of the base flame (Figure 10(b)), the linear color scale did not show the soot distribution in the latter flame. As seen from Figure 10, addition of TMP to the propane premixed flame is decreasing the burning velocity and increasing the soot formation. Based on the inner cone areas in Figures 10(c) and 10(e), the burning velocity has decreased by 45% and 56% when TMP was added by 0.1% and 1.0%, respectively. Decrease in burning velocity also resulted in an increase in flame standoff distance. This decrease compares favorably with that measured for stoichiometric flame.

Calculations were also performed for the propane jet diffusion flame with various amounts of TMP added to the fuel jet. Results obtained for a 0.01-m/s jet velocity case are shown in Figure 11. Interestingly, TMP has very little effect on the stability of the diffusion flame for concentrations up to 1%. However, soot has decreased by about 20%. This is in contrast with the premixed flame in which soot increased with the addition of TMP. Similar calculations were made for a higher fuel jet velocity (0.1 m/s) and found that TMP has negligible impact either on the stability or on the soot production even for concentrations up to 1%.

The predicted effects of TMP in propane premixed and diffusion flames matched qualitatively with those obtained in the experiments. Both calculations and experiment yielded increase in soot and flame inhibition for premixed flames and decrease in soot for diffusion flames. Calculations made with methane fuel also resulted in similar trends. Even though the methane flame stability is not affected with the addition of TMP, soot decreased more significantly than that noted in propane flames. However, quick experiments conducted for methane diffusion flame suggested an increase in soot production with TMP.

Calculations were also performed for heptane premixed and diffusion flames with various amounts of TMP added to the fuel. The diameter of the fuel tube was 12 mm and the fuel jet velocity was 0.005 m/s. Even with this low fuel velocity the diffusion flame formed was longer than those obtained for methane and propane fuels. This is inconsistent with the other diffusion flame calculations. Due to the length, the simulated heptane flame was insensitive to the added TMP. Flame structures were identical for 0% and 0.1% TMP cases. However, a trace amount of deviation was observed for the 1% case. Interestingly, NO decreased significantly with addition of 1% TMP. As expected from the other premixed calculations, burning velocity of heptane premixed flame also decreased with the addition of TMP, 5% when 0.1% TMP was added and 19% with 1% TMP. As expected, concentration of OH decreased and that of soot increased with the amount of TMP. The radical recombination promoted by the P-based species caused OH concentration to decrease. The increase in soot concentration correlates to that in benzene concentration. Significant reduction in NO is also noted. It seems TMP reduces NO production in both premixed and diffusion flames.

In general, soot is enhanced in premixed flames and suppressed in diffusion flames when TMP is added. Premixed flames are more sensitive to the presence of TMP compared to diffusion flames. Also, large flames are less sensitive to TMP compared to small ones. Among the fuels studied, methane is more sensitive than propane, which is more sensitive than heptane to the presence of TMP.

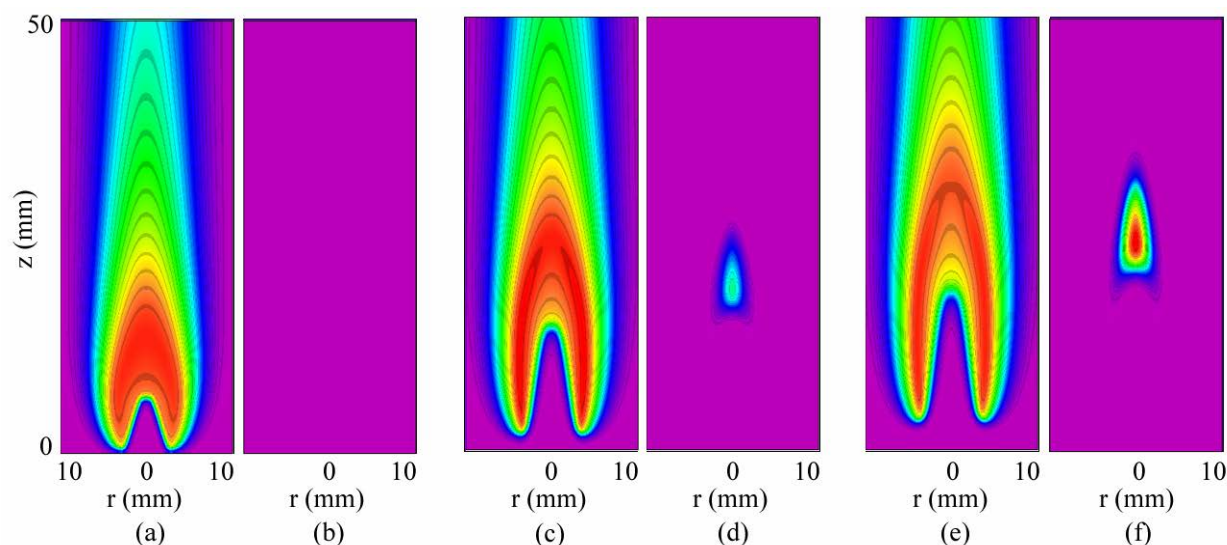


Figure 10. Effect of TMP on Premixed Propane Flame. Mixture of propane, air and TMP with $\phi = 1.5$ is issued from a 6 mm tube at 0.5 m/s. Distributions of (a) temperature and (b) soot volume fraction for base flame with 0% TMP, (c) and (d) for the flame with 0.1% TMP and (e) and (f) are for the flame with 1% TMP.

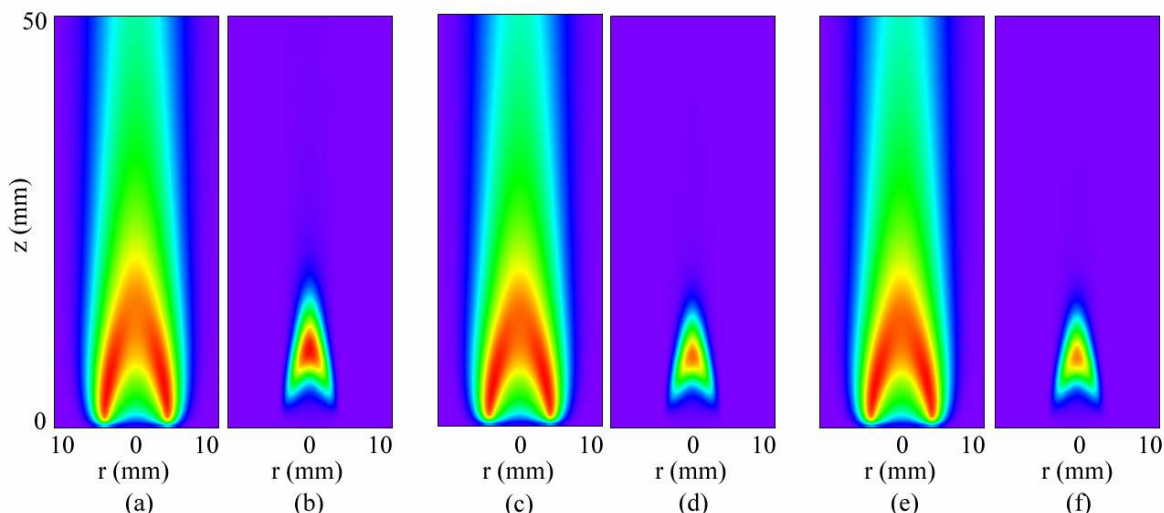


Figure 11. Effect of TMP on Propane Jet Diffusion Flame. Distributions of (a) temperature and (b) soot volume fraction for base flame with 0% TMP, (c) and (d) for the flame with 0.1% TMP, and (e) and (f) are for the flame with 1% TMP.

10. Conclusions

The impact of phosphorus additives on soot yield varied with combustor type and combustion conditions. In the shock tube study addition of phosphorus additive produced slight decrease in soot yields at lower temperatures but an increase in soot yields at higher temperatures. In WSR, impact of the phosphorus additive was minimal at Φ of 1.92 but caused a slight decrease in soot at Φ of 2. In flames, addition of phosphorus additives increased soot in premixed flames and decreased soot in diffusion flames. These flame observations were successfully modeled using UNICORN. However, in CFM combustor, the device closest to turbine engine, the soot yield increased with addition of phosphorus additive. From experimental and modeling results of this study, we can conclude that organophosphorus compounds are not suitable additives to decrease soot from turbine engines.

An important and unexpected result, however, came out of the modeling work that was part of this study. The modeling results indicated that the addition of phosphorus would lower NO_x emissions. As far as we can ascertain, this result has not been reported in the literature to date. This effect on NO_x emissions was predicted prior to the studies in the CFM combustor, so those studies were modified to include measurements of NO_x emissions. The measurements show that NO_x decreases with the addition of phosphorus under certain test conditions, so the predictions were partially verified by the experimental data.

Acknowledgments

The authors acknowledge the financial support for this work provided by the Strategic Environmental Research and Development Program (SERDP), Project PP1179, under the direction of Dr. Charles Pellerin.

References

- [1] F Hastie, J.W. and Bonnell, D. W., “Molecular Chemistry for Inhibited Combustion Systems,” NBSIR 80-2169 (1980).
- [2] T.M. Jayaweera, C.F. Melius a, W.J. Pitz, C.K. Westbrook, O.P. Korobeinichev b, V.M. Shvartsberg, A.G. Shmakov, I.V. Rybitskaya, H.J. Curran, “Flame inhibition by phosphorus-containing compounds over a range of equivalence ratios,” *Combustion and Flame*, Vol. 140, pp. 103-115 (2005)
- [3] M. A. Macdonald, F. C. Gouldin, and E. M. Fisher, “Temperature Dependence of Phosphorus-Based Flame Inhibition,” *Combustion and Flame*, 125:668–683 (2001).
- [4] Kahandawala, M.S., Ph.D. Dissertation on “Fuel Composition Effects on Particle and PAH Emissions”, University of Dayton, Dayton, OH 2004.
- [5] Stouffer S.D., Mortimer B.M., Ostdiek, D.M., DeWitt, M.J., Pawlik, R., Reich, R.F., Frayne, C.W., and Mayfield, H.T., " Soot Reduction Research Using a Well-Stirred Reactor," AIAA 2005-1317, 43rd Aerospace Sciences Meeting, Reno, NV, January 13, 2005
- [6] Wu, J.; Song, K.H.; Litzinger, T.; Lee, S.-Y.; Santoro, R.; Linevsky, M., Colket, M. Liscinsky, D., Reduction of PAH and soot in premixed ethylene-air flames by addition of ethanol; *Combust. Flame* 144:4, p 675-687 (2006); *Corrigendum* Litzinger, T., Wu, J.; Santoro, R. *Combustion and Flame*, v 146, n 4, p 698-699. (2006)
- [7] McNesby, K. L.; Miziolek, A. W.; Nguyen, T.; Delucia, F. C.; Skaggs, R. R.; Litzinger, T. A., Experimental and computational studies of oxidizer and fuel side addition of ethanol to opposed flow air/ethylene flames, Source: *Combustion and Flame*, v 142, n 4, p 413-427 (2005)
- [8] Imschweiler, D., McKeand, M., Lee, S.-Y. , Saretto, S., Linevsky, M. ., Litzinger, T. A. and Santoro, R. J., Fuel additive studies of soot reduction in a high-pressure model gas turbine combustor, 39th AIAA/ASME/SAE/ASEE Joint Propulsion Conference, AIAA 2003-5088 (2003)
- [9] Roquemore, W.M. and Litzinger, T.A., Final Report of SERDP PP-1179, Reduced Particulate Matter Emissions for Military Gas Turbine Engines Using Fuel Additives. (AFRL Report #)
- [10] Korobeinichev, O. P., Shvartsberg, V. M., Shmakov, A. G., Bolshova, T. A., Jayaweera, T. M., Melius, C. F., Pitz, W. J. and Westbrook, C. K., *Proceedings of the Combustion Institute*, Vol. 30, Issue 2, pp. 2350-2357, 2004; Lawrence Livermore National Laboratory, Livermore, CA, UCRL-CONF-201585.

Temperature measurements in reacting flows by time-resolved femtosecond coherent anti-Stokes Raman scattering (fs-CARS) spectroscopy

Sukesh Roy ^{a,*}, Paul J. Kinnius ^b, Robert P. Lucht ^b, James R. Gord ^c

^a *Innovative Scientific Solutions, Inc., 2766 Indian Ripple Road, Dayton, OH 45440, United States*

^b *School of Mechanical Engineering, Purdue University, 585 Purdue Mall, West Lafayette, IN 47907, United States*

^c *Air Force Research Laboratory, Propulsion Directorate, Wright-Patterson AFB, OH 45433, United States*

Received 8 August 2007; received in revised form 11 September 2007; accepted 14 September 2007

Abstract

Time-resolved femtosecond coherent anti-Stokes Raman scattering (fs-CARS) spectroscopy of the nitrogen molecule is used for the measurement of temperature in atmospheric-pressure, near-adiabatic, hydrogen-air diffusion flames. The initial frequency-spread dephasing rate of the Raman coherence induced by the ultrafast (~ 85 fs) Stokes and pump beams is used as a measure of gas-phase temperature. This initial frequency-spread dephasing rate of the Raman coherence is completely independent of collisions and depends only on the frequency spread of the Raman transitions at different temperatures. A simple theoretical model based on the assumption of impulsive excitation of Raman coherence is used to extract temperatures from time-resolved fs-CARS experimental signals. The extracted temperatures from fs-CARS signals are in excellent agreement with the theoretical temperatures calculated from an adiabatic equilibrium calculation. The estimated absolute accuracy and the precision of the measurement technique are found to be ± 40 K and ± 50 K, respectively, over the temperature range 1500–2500 K.

© 2007 Elsevier B.V. All rights reserved.

PACS: 78.47.p; 39.30.+w; 42.65.Dr; 82.53.Kp; 33.20.Fb

1. Introduction

Coherent anti-Stokes Raman scattering (CARS) spectroscopy of nitrogen and hydrogen using nanosecond (ns) lasers is widely employed for gas-phase temperature and species-concentration measurements [1,2]. The nonlinear interaction of the laser beams in ns-CARS generates a coherent nonresonant four-wave-mixing (FWM) signal along with the resonant CARS signal. Interpretation of the signal is complicated by the interference between the resonant and nonresonant signals. The nonresonant signal sometimes limits the accuracy and degrades the sensitivity of the technique [3]. Moreover, these measurements are

generally performed at low repetition rates (generally 10–20 Hz) because of the unavailability of high-repetition-rate, high-power ns lasers. This lack of temporal resolution hinders the study of unsteady phenomena in reacting flows.

The use of femtosecond (fs) laser systems for CARS spectroscopy has three significant potential advantages: (1) reduction or elimination of the nonresonant contribution to the CARS signal when the probe beam is delayed with respect to the pump beam, (2) reduction or elimination of the effects of collisions on the CARS signal, thereby reducing modeling uncertainty and increasing signal-to-noise ratio, and (3) the capability of generating signals at rates of 1 kHz or greater. The reduction or elimination of the nonresonant background and collisional effects will greatly simplify the modeling of CARS spectra and improve accuracy by eliminating the need for information

* Corresponding author. Tel.: +1 937 255 3115; fax: +1 937 656 4110.
E-mail address: sroy@woh.rr.com (S. Roy).

concerning Raman linewidths. The advent of high-fidelity picoseconds (ps) and fs lasers has revolutionized the field of optical spectroscopy and enabled the development of tabletop systems for laser machining, generation of X-rays, extreme ultraviolet light, and attosecond optical pulses [4–8].

Schematic diagrams of the CARS process and the Raman-excitation processes with ns- and fs-lasers are shown in Fig. 1. In CARS, the wavelengths of the pump and Stokes beams are chosen such that the pump-Stokes frequency difference matches a Raman resonance frequency of the molecule. For the nitrogen molecule, the Raman resonance frequency for the $v'' = 0$ to $v' = 1$ band is approximately 2330 cm^{-1} . This excitation process creates a Raman coherence in the medium, resulting in a shifted signal when the medium is probed by another laser beam. In multiplex CARS using ns lasers, a narrowband pump beam and a broadband Stokes beam are employed for simultaneous excitation of numerous transitions in the ro-vibrational Raman band of the molecule. As shown in Fig. 1, in ns-CARS each pair of pump and Stokes frequencies is resonant with only one transition. For fs-CARS, however, multiple pump-Stokes pairs contribute to the excitation of the same transition, thereby creating a significant Raman coherence in the medium [9,10] despite the large frequency bandwidths of the pump and Stokes beams. Numerous Raman transitions are excited with the same phase when the pump and Stokes beams are nearly Fourier transform-limited. This in-phase impulsive excitation creates a very large coherence in the medium, which then decays as a result of the slight frequency differences between the neighboring transitions. This decay rate can be used to determine the temperature [11].

Time-resolved fs-CARS has been used for the first time by Leonhardt et al. to study the molecular beat phenomena in liquid phase benzene, cyclohexane, and pyridine [12]. Hayden and Chandler [13] first used fs-CARS for investigating the molecular vibrational dynamics of ground-state gas-phase benzene and 1,3,5-hexatriene. Schmitt et al. [14] used fs-CARS to study the ground- and excited-electronic-state dynamics of iodine vapor. These studies demon-

strated the potential for applying broad-bandwidth fs-lasers for gas-phase spectroscopic studies. Previously, the application of these lasers was thought to be of little value because of the excitation of multiple transitions by the broad laser pulses and the relatively inefficient coupling of these broad pulses to an individual transition as compared to the narrowband pulses more closely matched to the linewidth of these transitions. Hayden and Chandler [13] examined the dephasing of the coherence established by the pump and Stokes beams during the first few ps after the initial excitation and observed markedly different decay rates for gas-phase benzene and 1,3,5-hexatriene. They observed that the decay rate of the initial coherence was much faster for 1,3,5-hexatriene than for benzene due to dephasing of the initial orientation created by the laser pulses. Unlike benzene, in 1,3,5-hexatriene the laser pulses create a superposition of spatially oriented, vibrationally excited, rotational states that starts to change from the initial orientation due to the variation of rotational speeds of different molecules in the ensemble. Recently our group recognized that this initial dephasing rate during the first few ps can be used as a measure of gas-phase temperature, independent of any collisional influence [10,11].

The use of fs lasers for investigating the ultrafast dynamics of isolated molecule was pioneered by Scherer et al. [15]. The work of Dantus et al. [16] for observing the molecular vibration and rotational dynamics was also ground breaking in this regard. The work of Zewail's group [15,16] was based on pump-probe techniques where they prepared an excited state with a pump beam and detected the laser-induced fluorescence signal when excited by a delayed probed beam; this is similar to the fs-CARS technique, where the molecular coherence is prepared by the overlapping pump and Stokes beam and is then probed by a delayed probe beam. The review paper by Dantus [17] provides a comprehensive discussion of the coherent nonlinear spectroscopy based on ultrafast lasers.

Lang et al. [18] used fs-CARS of the H_2 molecule for determining molecular parameters and gas-phase temperature from the time-resolved oscillatory pattern of the Raman coherence following pump-Stokes excitation.

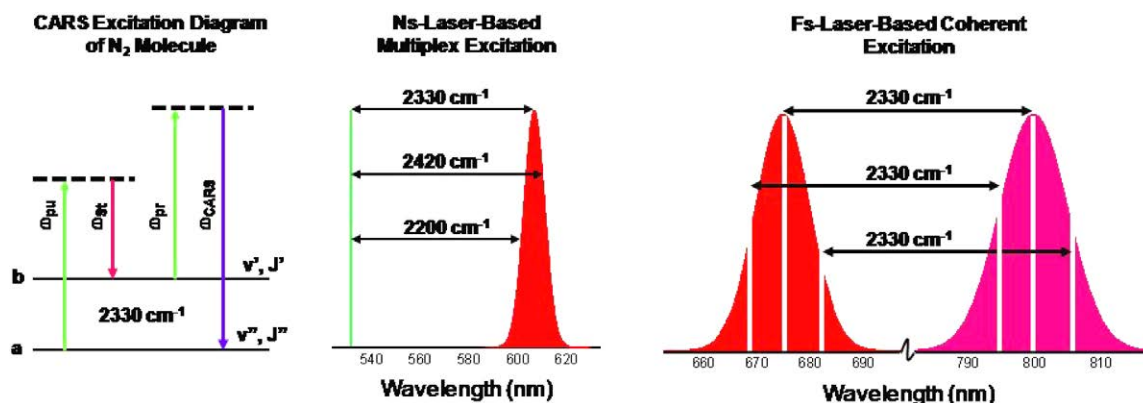


Fig. 1. Coherent excitation process in ns- and fs-laser-based CARS spectroscopy.

Those parameters were determined from the width and the relative heights of the recurrence peaks. Lang et al. [19] also used the time-resolved N_2 CARS signal for measuring temperature by focusing on recurrence peaks at ~ 320 ps or longer; on this time-scale, understanding of the collisional environment and the relaxation processes is essential for accurate temperature measurements. fs-CARS has also been used for measurements in a dense medium to investigate rotational energy-transfer processes [20], for determining the concentration of *ortho*- and *para*-deuterium [21], and for measuring single-shot temperature by probing the hydrogen molecule using a chirped probe pulse [22]. More recently, fs-CARS has been used for the detection of bacterial spores in the presence of other molecules [23], for the characterization of polymer thin films [24], and for background-free analysis of analytes trapped in aerogel pores [25].

The objective of the current study is to apply the time-resolved fs-CARS technique for temperature measurements in high-temperature flames, based on the frequency-spread dephasing rate after the initial impulsive excitation of the Raman coherence in the N_2 molecule by fs pump and Stokes beams. In this study, temperature from the time-resolved N_2 CARS signal is extracted by means of a simple theoretical model by concentrating on the signal decay during the first few ps after the pump-Stokes excitation. These decay results from the slight frequency mismatches between the neighboring Q-branch transitions and is completely insensitive to collisions [11]. The accuracy and precision of the measurement technique are also addressed.

2. Experimental system

A schematic diagram of the experimental system is shown in Fig. 2. The output of a 1-mJ, 1-kHz, 85-fs, Ti:Sapphire regenerative amplifier (Model: Libra, Coherent, Inc.) at 800 nm is used to pump an optical parametric amplifier (OPA). Approximately 15% of the energy of the regenerative amplifier is used as the Stokes beam, and the remainder is used to pump the OPA. The laser beam from the frequency-doubled OPA is centered at ~ 675 nm, with an approximate energy of 25 μ J/pulse. This beam is then split equally to yield the pump and probe beams for the CARS signal generation. The full-width-at-half-maxima (FWHM) of the frequency spectra of the pump (probe) and Stokes lasers were approximately 160 cm^{-1} and 220 cm^{-1} , respectively. The timing of the probe beam with respect to the pump and Stokes beams was varied for acquisition of the probe-delay scans using a motorized translation stage. A short-pass filter was used to block the scattered light from the pump and probe beams, and the CARS signal centered at 584 nm was detected with a low-noise, high-bandwidth photodetector (10-MHz Adjustable Photoreceiver, Model: 2051, New Focus). The signal was acquired using a lock-in amplifier, and each data point was averaged over 300 laser shots. Measurements were performed in an atmospheric-pressure, near-adiabatic hydrogen-air flame stabilized over a Hencken burner. Temperature was varied by changing the equivalence ratio (ϕ) of the flame (equivalence ratio is defined as the ratio of actual fuel-to-air over fuel-to-air for the stoichiometric condition [26]). The temperature of the flame stabilized

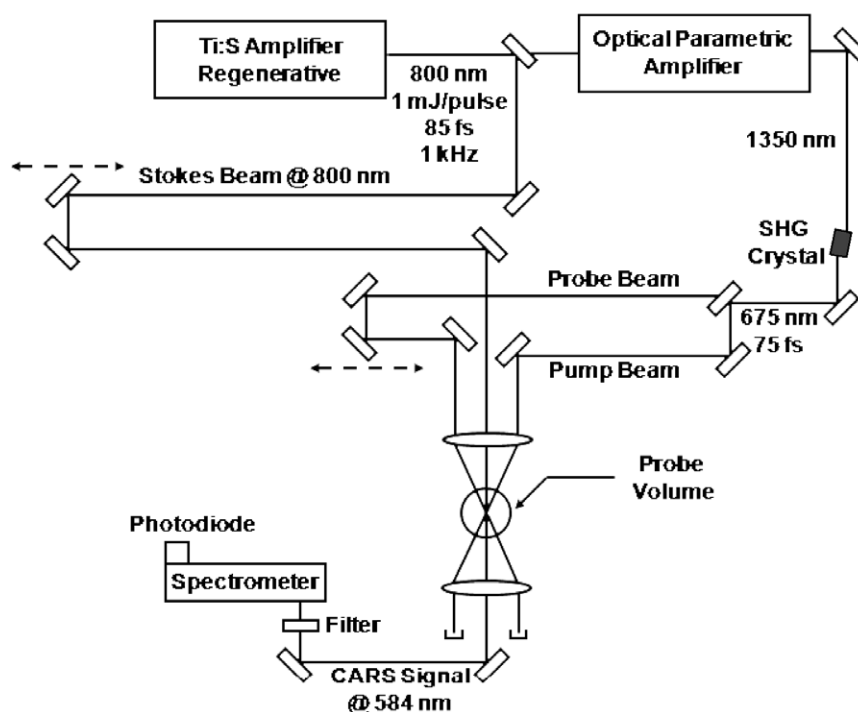


Fig. 2. Schematic diagram of fs-CARS system.

over the Hencken burner increases with equivalence ratio for $\phi \leq 1.0$, after which it decreases due to incomplete combustion of the fuel [27].

3. Results and discussion

Time-resolved fs-CARS signals of nitrogen as a function of probe pulse delay with respect to the pump beam at various equivalence ratios are shown in Fig. 3. The decay of the Raman coherence during the first few ps after the initial impulsive excitation by the nearly transform-limited pump and Stokes laser pulses is the focus of our experiments. The effects of collisions on this time scale are not important for pressures less than 10 bar. It is evident from the figure that the rate at which the signal decays increases with flame equivalence ratio and temperature. The signal decays faster with increasing temperature because of the contributions of more transitions over a wider frequency range to the initial Raman coherence. This results from redistribution of the population to higher energy levels with increasing temperature. The spectrally broad, nearly transform-limited pump and Stokes pulses simultaneously excite all the transitions accessible within the bandwidth, frequency pairs of the lasers. The resulting coherence decay thereafter as a result of the slight frequency mismatches between neighboring transitions. The signal reaches a maximum value at a probe delay of zero because of the contribution from both resonant and nonresonant signals. In Fig. 3 all signals were normalized to a peak intensity of 100 at time zero. The oscillatory behavior of the signal is qualitatively similar for temperatures in the range 1600–2400 K. The characteristic frequency of the oscillations observed in Fig. 3 is approximately 900 GHz, which corresponds to the beat frequency between the $v' = 1 \rightarrow v'' = 0$ and $v' = 2 \rightarrow v'' = 1$ vibrational bands and also between the $v' = 2 \rightarrow v'' = 1$ and $v' = 3 \rightarrow v'' = 2$ vibrational bands.

Theoretical spectra of N_2 CARS for three different temperatures are shown in Fig. 4. These spectra were calculated using the Sandia CARSFT code [28]. For

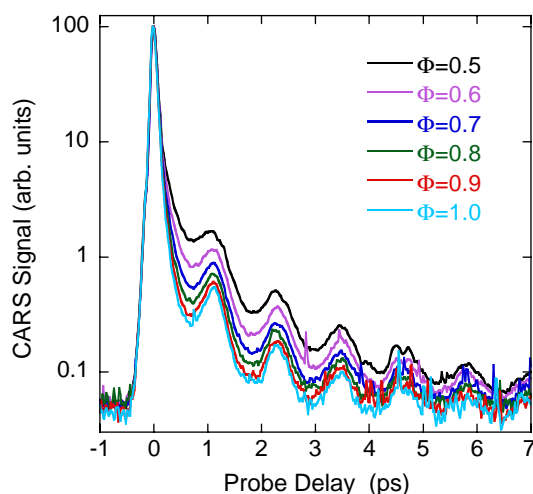


Fig. 3. Time-resolved fs-CARS signal for various equivalence ratios (ϕ).

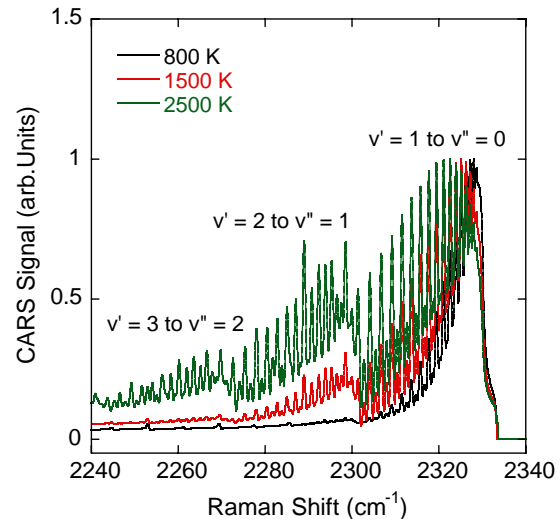


Fig. 4. Theoretical CARS spectra of nitrogen calculated using Sandia CARSFT code [26].

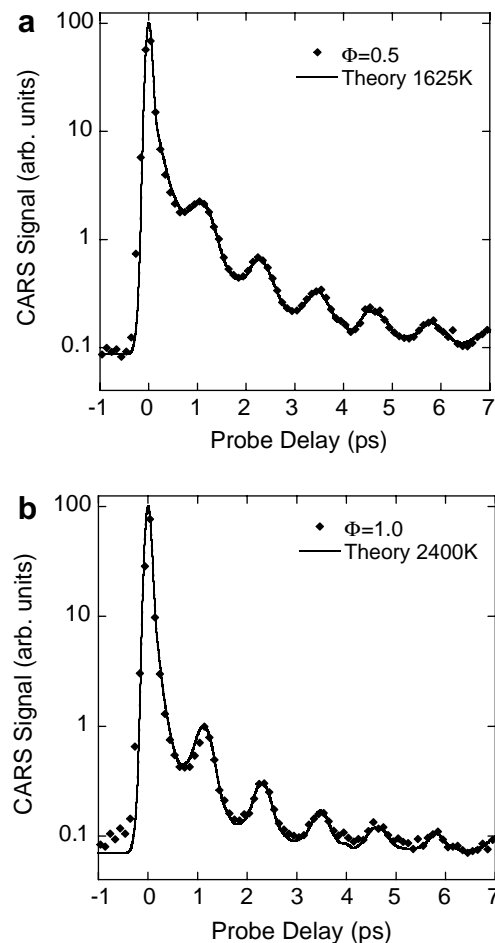


Fig. 5. Comparison of theoretical and experimental time-resolved fs-CARS signals for (a) $\phi = 0.5$ and (b) $\phi = 1.0$. Theoretical signals were calculated using Eq. (1). The solid lines represent the best-fit theoretical signal to the experimental data points and is determined by least-square fitting to the experimental data points.

temperatures less than 800 K, only the first vibrational band appears, which results in a time-resolved signal without oscillations during the first 10 ps after the initial excitation, as shown in our previous work [11]. The first hot-band ($v' = 2 \rightarrow v'' = 1$) begins to appear for temperatures greater than 1000 K, and the second hot-band ($v' = 3 \rightarrow v'' = 2$) appears at approximately 2000 K. The frequency difference between the band heads is approximately 30 cm^{-1} , as is evident in Fig. 4. This 30-cm^{-1} frequency difference corresponds to a 900 GHz in beat frequency.

Fig. 5 shows the fit between the theoretical and experimental probe-delay scans for $\phi = 0.5$ and $\phi = 1.0$. The best-fit theoretical probe-delay scans are used to extract temperatures from experimental scans. The theoretical modeling is discussed in detail by Lucht et al. [11]. The theoretical signal as a function of probe delay is calculated using the following equation.

$$S(\tau) = \int_{-\infty}^{+\infty} I_{\text{pr}}(t - \tau) [P_{\text{res}}(t) + P_{\text{nres}}(t)]^2 dt + \text{Background noise} \quad (1)$$

where the resonant signal (P_{res}) is calculated as

$$P_{\text{res}}(t) = \beta \left[\int_{-\infty}^t E_{\text{p}}(t') E_{\text{s}}(t') dt' \right] \times \sum_i \left\{ \Delta N_i \left(\frac{d\sigma}{d\Omega} \right)_i \cos(\omega_i t) \exp(-\Gamma_i t) \right\} \quad (2)$$

In Eq. (2), $E_{\text{p}}(t)$ and $E_{\text{s}}(t')$ are the time-dependent electric fields of the pump and Stokes laser fields, respectively, ΔN_i is the difference in population between the excited and ground levels of a transition, $\left(\frac{d\sigma}{d\Omega} \right)_i$ is the Raman cross section (for a particular transition i), ω_i is the frequency of the Raman transition, Γ_i is the coherence dephasing rate due to collisions, which will only be significant for longer time scales or higher pressures, and β is a scaling factor used to match the experimental signal with the theoretical spectrum. In Eq. (1), I_{pr} is the intensity of the probe beam, and P_{nres} is the nonresonant polarization calculated as

$$P_{\text{nres}}(t) = \alpha E_{\text{p}}(t) E_{\text{s}}(t) \quad (3)$$

where α is a nonresonant scaling factor. For each experimental scan, the ratio α/β is varied to match the theoretical

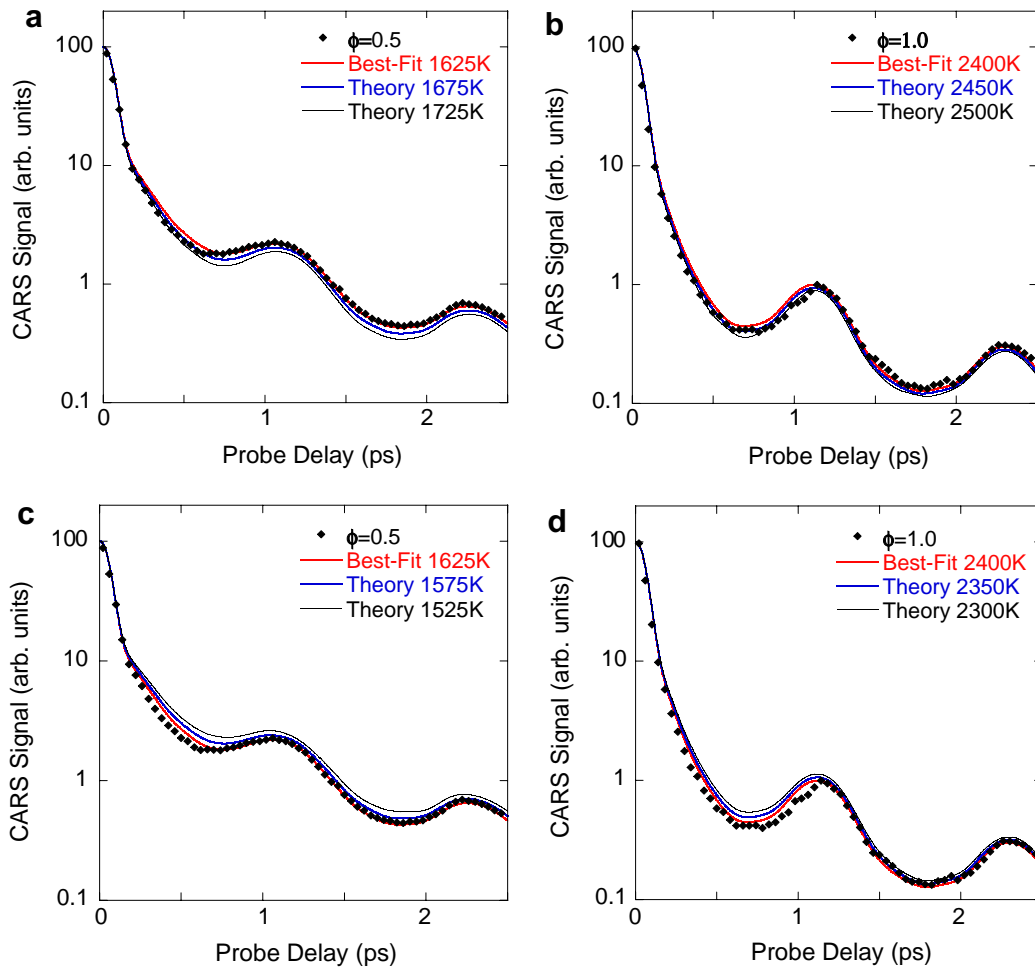


Fig. 6. Comparison of theoretical and experimental scans when the best-fit (based on least-square fit) temperature values were changed by $\pm 50 \text{ K}$ and $\pm 100 \text{ K}$ for $\phi = 0.5$ and $\phi = 1.0$. Scans are expanded versions of those shown in Fig. 5. Fig. 6a and b show probe-delay scans $\phi = 0.5$ and $\phi = 1.0$, respectively, when temperatures are varied by $+50 \text{ K}$ and $+100 \text{ K}$. Fig. 6(c) and (d) show probe-delays scans for $\phi = 0.5$ and $\phi = 1.0$, respectively, when temperatures are varied by -50 K and -100 K .

and experimental signal-decay rates. For the two equivalence ratios shown in Fig. 5, adiabatic flame temperatures are calculated to be 1642 K and 2382 K for $\phi = 0.5$ and $\phi = 1.0$, respectively, [26]. These measurements show very good agreement between the adiabatic flame temperatures and the temperatures extracted from the experimental scans by least-square fitting with the calculated theoretical time-resolved signal using Eq. (1). In Fig. 5, solid lines represent the theoretical best-fit signal and symbols represent the experimental data points.

To address the temperature sensitivity of the measurements, experimental scans shown in Fig. 5 were compared with theoretical scans by varying the best-fit temperature by ± 50 K and ± 100 K as shown in Fig. 6. Fig. 6a and b show the expanded versions of the time-resolved scans for $\phi = 0.5$ and $\phi = 1.0$ when the theoretical temperatures were varied by $+50$ K and $+100$ K from the best-fit values; Fig. 6c and d show the same scans when the theoretical temperatures were changed by -50 K and -100 K from the best-fit values. The clear mismatch between the experimental and theoretical signals for temperatures adjusted by 50 K and 100 K from the best-fit value shows the sensitivity of the current measurement technique is ± 50 K. Changing the temperature by ± 25 K did not yield any perceptible variation in the theoretical signal profiles.

To address the accuracy and precision of the proposed measurement technique, the temperature extracted from the experimental signals is compared with adiabatic flame temperatures, as shown in Fig. 7. The extracted temperatures are within 40 K of the adiabatic flame temperatures for equivalence ratios ranging from 0.5 to 1.0. The systematic error in the measurements cannot be evaluated quantitatively from these results, but appears to be much smaller than random errors of approximately ± 50 K. It might be expected that systematic errors in fs-CARS will be reduced compared to ns-CARS because collisions do not affect the

fs-CARS signal in the first few ps after impulsive pump-Stokes excitation. Consequently, no knowledge of Raman linewidths is required to model the fs-CARS signal behavior. For ns-CARS, on the other hand, accurate Raman linewidth data is required for temperature determination [29]. The three sets of data points shown in Fig. 7 were acquired on three different days spanning two weeks in time. The standard deviation of the extracted temperatures was approximately 50 K for an equivalence ratio of 1.0, but the standard deviation was approximately 11 K for $\phi = 0.5$ and $\phi = 0.8$. These measurements suggest the accuracy and precision of the measurement technique are within ± 40 K and ± 50 K, respectively.

4. Conclusions

Temperatures ranging from 1500 K to 2400 K is measured using the time-resolved fs-CARS technique in atmospheric-pressure, near-adiabatic, hydrogen-air diffusion flames. In this study, wavelengths of the pump and the Stokes beams are chosen to probe the vibrational transitions of the N_2 molecule. The initial decay of the Raman coherence results from the slight frequency mismatches among the transitions, excited by the broad pump and Stokes beams. The rate of decay of the initial Raman coherence was used as a measure of temperature. The fs-CARS signals within the first few ps after pump-Stokes excitation are free from collisional influence for pressures less than 10 bar and, therefore, do not require any knowledge of the collisional-relaxation processes for either temperature or concentration measurements from experimental signals. The temperatures extracted from the time-resolved signals agreed very well with the adiabatic flame temperatures for a range of equivalence ratios. The estimated accuracy and precision of the measurement technique are within ± 40 K and ± 50 K, respectively. The estimated systematic errors in the measurements are less than ± 50 K.

Acknowledgements

Funding for this research was provided by the Air Force Office of Scientific Research (Dr. Julian Tishkoff, Program Manager), by the Air Force Research Laboratory, Propulsion Directorate, Wright-Patterson Air Force Base under Contract No. F33615-03-D-2329; by the National Science Foundation, Combustion and Plasma Program under Award Number 0413623-CTS. The authors gratefully acknowledge the technical assistance of Mr. Kyle D. Frische.

References

- [1] S. Roy, W.D. Kulatilaka, R.P. Lucht, N.G. Glumac, T. Hu, *Combust. Flame* 130 (2002) 261.
- [2] A.C. Eckbreth, *Laser Diagnostics for Combustion Temperature and Species*, second ed., Gordon & Breach, St. Leonards, Australia, 1996.

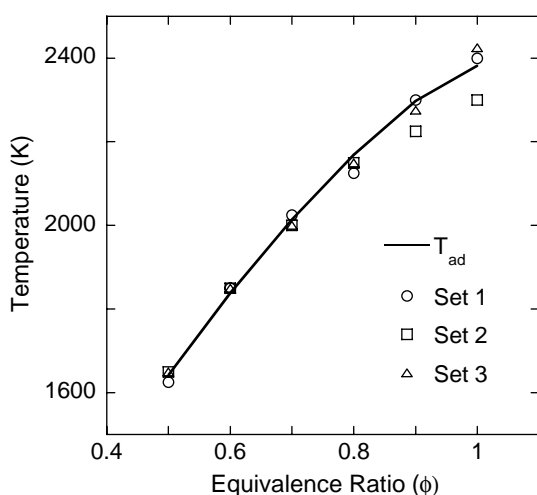


Fig. 7. Comparison of experimentally measured temperatures with adiabatic flame temperatures for atmospheric-pressure, near-adiabatic, hydrogen-air diffusion flame. Sets represent data acquired on three days over a two-week time period.

- [3] S. Roy, T.R. Meyer, J.R. Gord, *Appl. Phys. Lett.* 87 (2005) 264103.
- [4] M.D. Duncan, J. Reintjes, T.J. Manuccia, *Opt. Lett.* 7 (1982) 350.
- [5] W. Kiefer (Ed.), *J. Raman Spectrosc.* (special issue) 31, 2000.
- [6] A. Zumbusch, G.R. Holtom, X.S. Xie, *Phys. Rev. Lett.* 82 (1999) 4142.
- [7] X. Zhang, A.L. Lytle, T. Popmintchev, X. Zhou, H.C. Kapteyn, M.M. Murnane, O. Cohen, *Nature Phys.* 541 (2007) 1, doi:10.1038/nphys.
- [8] X. Liu, D. Du, G. Mourou, *IEEE J. Quant. Electron.* 33 (1997) 1706.
- [9] R.P. Lucht, *Science* 316 (2007) 207.
- [10] R.P. Lucht, P.J. Kinnius, S. Roy, J.R. Gord, *J. Chem. Phys.* 127 (2007) 044316.
- [11] R.P. Lucht, S. Roy, T.R. Meyer, J.R. Gord, *Appl. Phys. Lett.* 89 (2006) 251112.
- [12] R. Leonhardt, W. Holzapfel, W. Zinth, W. Kaiser, *Chem. Phys. Lett.* 133 (1987) 373.
- [13] C.C. Hayden, D.W. Chandler, *J. Chem. Phys.* 103 (1995) 10465.
- [14] M. Schmitt, G. Knopp, A. Materny, W. Keifer, *J. Phys. Chem. A* 102 (1998) 4059.
- [15] N.F. Scherer, J.L. Knee, D.D. Smith, A.H. Zewail, *J. Phys. Chem.* 89 (1985) 5141.
- [16] M. Dantus, R.M. Bowman, A.H. Zewail, *Nature* 343 (1990) 737.
- [17] M. Dantuus, *Ann. Rev. Phys. Chem.* 52 (2001) 639.
- [18] T. Lang, K.-L. Kompa, M. Motzkus, *Chem. Phys. Lett.* 310 (1999) 65.
- [19] T. Lang, M. Motzkus, H.M. Frey, P. Beaud, *J. Chem. Phys.* 115 (2001) 5418.
- [20] G. Knopp, P. Beaud, P. Radi, M. Tulej, B. Bougie, D. Cannavo, T. Gerber, *J. Raman Spectrosc.* 33 (2002) 861.
- [21] G. Knopp, K. Kirch, P. Beaud, K. Mishima, H. Spitzer, P. Radi, M. Tulej, T. Gerber, *J. Raman Spectrosc.* 34 (2003) 989.
- [22] T. Lang, M. Motzkus, *J. Opt. Soc. Am. B* 19 (2002) 340.
- [23] D. Pestov, R.K. Murawski, G.O. Ariunbold, X. Wang, M. Zhi, A.V. Sokolov, V.A. Sautenkov, Y.V. Rostovtsev, A. Dogariu, Y. Huang, M.O. Scully, *Science* 316 (2007) 265.
- [24] Z.D. Schultz, M.C. Gurau, L.J. Richter, *Appl. Spectrosc.* 60 (2006) 1097.
- [25] S.O. Konorov, R.F.B. Turner, M.W. Blades, *Appl. Spectrosc.* 61 (2007) 486.
- [26] S.R. Turns, *An Introduction to Combustion: Concepts and Applications*, McGraw-Hill, Inc., New York, 1996.
- [27] S. Roy, T.R. Meyer, R.P. Lucht, M. Afzelius, P.-E. Bengtsson, J.R. Gord, *Opt. Lett.* 29 (2004) 1843.
- [28] R.E. Palmer, *The CARSFT Computer Code for Calculating Coherent Anti-Stokes Raman Spectra: User and Programmer Information*, Report No. SAND89-8206 Sandia National Laboratories, Livermore, California, 1989.
- [29] R.L. Farrow, P.L. Mattern, L.A. Rahn, *Appl. Opt.* 21 (1982) 3119.

STATOR CASCADE FLOW VECTORING THROUGH COUNTER-FLOW BLOWING

Michael R. Harff* and J. Mitch Wolff†
Department of Mechanical and Materials Engineering
Wright State University
Dayton, Ohio

William W. Copenhaver‡ and David Car§
Air Force Research Laboratory
Dayton, Ohio

Jordi Esteveordal¶
Innovative Scientific Solutions, Inc.
Dayton, Ohio

ABSTRACT

Preliminary design computational results showed that a significant amount of increased flow turning (12 degrees) can be achieved in a high turning stator example with only 0.5% core flow counter-flow blowing (CFB). The loading is held nearly constant over the entire blade with counter flow blowing, thereby turning the flow over the entire chord. To explore this approach, an existing cascade section was modified to implement a “proof-of-concept” design. Experimental data from Particle Image Velocimetry (PIV) showed that an increase of 8 degrees in turning was achieved through counter-flow blowing of 1%. Furthermore, an optimum amount of blowing exists to minimize wake increase and maximize flow vectoring. For this investigation, the Advanced Ducted Propfan Analysis Code (ADPAC) 2-D model was calibrated by comparison to the experimental results for a range of 0.15% to 0.38% core flow counter-flow blowing. Based on this study, ADPAC has been shown to be a viable design tool for CFB applications.

NOMENCLATURE

C_m	mass blowing coefficient	
	$= m_{dot,j} / (3.03 m_{dot,inf})$	(1)
C_m^*	corrected mass blowing coefficient	
	$= m_{dot,j,c} / (3.03 m_{dot,inf})$	(2)
C_x	axial chord of blade	
m_{dot}	mass flow rate	
$m_{dot,c}$	corrected mass flow rate	
	$= m_{dot} \sqrt{\theta} / \delta$	(3)
M	Mach number	

M_e	cascade exit Mach number	
s	cascade blade spacing	
U	absolute velocity	
$\bar{U}_{k,m}$	mass-averaged, k th component of velocity	
	$= \sum_i U_{k,i} (\rho_i U_i A_i) / \sum \rho_i U_i A_i$	(4)

y^+	dimensionless wall coordinate	
	$= \frac{y}{\nu_{wall}} \sqrt{\frac{\tau_{wall}}{\rho_{wall}}} = y \sqrt{\frac{(du/dy)_{wall}}{\nu_{wall}}}$	(5)

α_e^*	design exit flow angle	
α_e	actual exit flow angle	
	$= \tan^{-1}(\bar{U}_y^m / \bar{U}_x^m)$	(6)

γ	deviation of flow	
	$= \alpha_e - \alpha_c$	(7)

δ	corrected total pressure	
	$= P_0 / P_{0,ref}$	(8)

δ_s^*	displacement thickness, as a fraction of s	
	$= \frac{1}{s} \int_{\xi=\xi_0}^{\xi=\xi_0+s} \left(1 - \frac{M}{M_{inf}} \right) d\xi$	(9)

θ	corrected total temperature	
	$= T_0 / T_{0,ref}$	(10)

Subscripts

j	blowing slot (jet)
x	x- component
y	y- component
inf	cascade inlet
$1.05 C_x$	105% axial chord

* Research Assistant, Student Member AIAA

† Associate Professor, Associate Fellow AIAA

‡ Principal Scientist, Turbine Engine Division, Propulsion Directorate, Associate Fellow AIAA

§ Engineer, Member AIAA

¶ Engineer, Senior Member AIAA

INTRODUCTION

Current fan designs in many cases require flapped IGV's (a segmented stator with only the back portion rotating like a flap on a wing of an aircraft) to assure correct inlet flow conditions during off-design operation. The ability to vector the flow without the need of the "flap" on the IGV would significantly reduce the mechanical complexity and weight of the fan system. In addition, flow vectoring within the fan and compressor could greatly reduce the need for variable stators, again reducing the cost and weight of the engine. This approach employs pressure surface counter-flow blowing to increase the circulation/loading and achieve considerable flow vectoring. The stator uses a carefully placed blowing jet to increase the circulation (i.e. loading) of the blade, thereby providing the necessary turning. The blowing jet is placed on the pressure surface of the blade near the trailing edge and is directed into the flow, i.e. in a counter-flow direction, as near to tangent to the surface of the blade as possible.

In this paper, a detailed experimental and computational investigation into the flow physics associated with CFB for an advanced design stator airfoil is reported. A transonic linear cascade wind tunnel is utilized to obtain detailed PIV measurements with and without CFB. In addition, a high fidelity computational fluid dynamics (CFD) model is used to model the experimental configuration. The CFD model, ADPAC, is compared with the experimental data with the intent that it could then be utilized to design a new circulation-controlled (CC) IGV, which would eliminate the need for the flap therefore reducing the weight and the required axial spacing of an engine using a flapped IGV.

EXPERIMENTAL SETUP

Modifications were made to an existing 2D cascade of the "Tescom" geometry, a counter-swirl stator, and called the "Tescom-CAR" geometry (see Figure 1). The trailing edge was rounded off to allow for installation of the blowing plenum and proper location of counter-flow blowing jets. These jet slots were added on the pressure surface near the trailing edge on the center three blades of the cascade, which contained a total of seven blades. The jets had a flow angle of 70° with respect to the normal to the blade surface, in the counter-flow direction, and a nominal width of 0.010". Particle Image Velocimetry (PIV) test data were acquired for nominal mass blowing coefficients of 0.0 (baseline), 0.005, and 0.01 of the core flow.¹⁻² For a mass blowing coefficient of 0.01, the injected flow passed through a slot spanning only 2.00" on a blade with a total span of 6.06", yielding a C_m value of

0.0303 per unit of span at the PIV test cross section. Test cases were conducted in a transonic blowdown wind tunnel at Virginia Tech University having a test section of 30.48 cm x 15.24 cm (12 in x 6 in) and with test durations of 10 seconds and a nominal inlet Mach number of 0.75.

A DPIV system was developed (see schematic, Figure 2) for transonic-cascade investigations.³ Two frequency-doubled Nd:YAG lasers are used for instantaneous marking of the seed particles in the flow field. The beams are combined and directed through sheet-forming optics and illuminate the test section with a 2D plane of thickness < 1 mm. The scattering from the seed particles is recorded on an ES1.0 Kodak CCD sensor (1008 x 1012 pixels). The camera maximum repetition rate is 15 double exposures per second and was set to 10 Hz for synchronization with the laser repetition rate. A 105-mm Nikon lens was used. The magnification for the present experiments was ~ 20 pixels/mm, which corresponds to a viewing width of ~ 50 mm. The time delay between the lasers was typically 2 μ sec. Once the PIV image has been captured and digitized, the velocity field is obtained using cross-correlation techniques. The correlation function is calculated over small segments (interrogation domains) of the PIV image. The peak of the correlation map corresponds to the average velocity displacement within the interrogation spot. An intensity-weighted peak-searching routine is used to determine the exact location of the peak to sub-pixel accuracy. To improve the signal-to-noise ratio in the correlation maps, a correlation-correction scheme is applied wherein each map is multiplied by its immediate four neighborhoods. An overlapping of 75% is used to include many of the same particles in the five maps that are multiplied to yield a single correlation map with lower noise. Zero padding is also employed for adding accuracy. For these experiments 100 image pairs were obtained during a 10 sec tunnel blowdown period. Of those images, 50 were chosen within the steady part of the run to be averaged with outlier rejection of two standard deviations. Averaging the instantaneous velocity fields has the effect of eliminating the fluctuations due to incoherent unsteadiness associated with turbulence and permitting a better comparison to the steady CFD predictions.⁴

A compact laser-sheet delivery system was utilized. This system consists of an optical probe designed with light-sheet-forming optics internal to the probe, which is similar to that reported by Copenhaver et al. (2002). The probe was placed downstream of the cascade in the flow path inside a glass rod that is transverse to the main flow direction. The cascade endwalls were

formed with 31.75-mm (1.25-in.) thick Plexiglas to allow optical access. The power required for laser-sheet illumination was very low (< 20 mJ/pulse) because of minimal optics losses. Seeding particles were injected into the flow approximately 10 blade-chord lengths upstream of the cascade section with an injection rake. Sub-micron particles of aluminum dioxide were used as the seeding material. Figure 2 is a schematic of the DPIV setup.

The uncertainty in the DPIV velocity measurements was determined as follows. The velocity was computed dividing the displacement (pixels) of each interrogation region, by the time interval between the two exposures, and by the magnification of the digital image relative to the object (pixels/mm). The time interval was adjusted to yield typical displacements of the free stream in the present experiments of > 10 pixels, with an uncertainty of $< 1\%$. Values in the wake region where the minimum velocity occurs, however, have higher uncertainties because of the lower displacements; for example, 1 pixel displacement could yield an uncertainty of $\sim 10\%$. The maximum uncertainty in the time interval was calculated from the time interval between the two laser pulses. It was found that this uncertainty increases with lower laser power and with lower time interval. A conservative number for the present experiments, which employed a time interval of $2 \mu\text{sec}$ and powers around 20 mJ, was found to be 1%. The magnification was measured from images of rulers located in the laser-sheet plane, and it is conservatively estimated that could be read to better than 1%. Combining these three conservative measurements of uncertainty yields a maximum error of $< \pm 2\%$ of the reported value for the free-stream velocity, which increases to $\sim \pm 10\%$ of the reported value at the wake-minimum-velocity location.

Inlet conditions during the test were set according to inlet total and static pressure measurements. Counter-flow blowing was measured with a calibrated orifice plate and supplied to the center three blades of the cascade. The estimated gauge pressures for C_m values of 0.0108 and 0.0047 were 40psi and 13psi, based on data from the test facility.

EXPERIMENTAL RESULTS

The exit flow fields obtained averaging 50 PIV frames are shown in Figure 4 for corrected mass blowing coefficients of 0.0, 0.0023, and 0.0027, as obtained from equations (2), (3), (8), and (10). Data were extracted directly from the contour plots for calculation of displacement thickness and deviation. Displacement thickness was calculated at 105% axial chord, numerically integrating the data across a full flow passage according to equation (9). This gives the

fraction of blockage in the flow passage due to the presence of the blade. Deviation was calculated along the same plane at 105% axial chord from mass-averaged x and y velocity components via equations (4), (6), and (7). Density, which varied by $< 10\%$ in the wake region for all CFD cases, was assumed constant in equation (4). All experimental results are presented in Table 1. To summarize, an increase of flow turning of 2° was achieved with C_m^* of 0.0023, while an increase of 7.5° was achieved with C_m^* of 0.0027.

A key assumption underlying the experimental C_m values is identical blowing slot widths on all three blades. This was not the case, as the average slot widths of the blades were 0.012", 0.011", and 0.013", the blade used for the PIV data being the smallest of the three. From continuity, and assuming steady flow with constant mass flux across each slot, the actual mass flow rates through the test blade would have been 0.93 of reported values. C_m^* values were adjusted from 0.0025 to 0.0023, and from 0.0029 to 0.0027. Experimentally, this implies that a greater increase of flow turning was achieved with a lesser percentage of the core mass flow.

2-D COMPUTATIONAL MODEL

In order to gauge the accuracy of computational tools in a CFB-type flow situation, a simulation of the Tescom-CAR case was run in ADPAC (Advanced Ducted Propfan Analysis Code).⁴ The solutions were run in 2D steady-state mode to save on computational time, and the Spalart-Allmaras (1-equation) turbulence model was used. The computational domain consisted of three blocks, with a capped O grid for the blade and two, 110%-axial-chord, extension H grids upstream and downstream of the blade. Figure 3 shows the capped O grid used in the coarse mesh. Each test case was run on coarse, medium, and fine meshes to demonstrate grid independence of the solution. Resolution was increased by a factor of 3.93 from the coarse to the medium mesh, and by a factor of 3.59 from the medium to the fine mesh. This corresponded to $\sim 1.98x$ and $\sim 1.89x$ increases along each dimension for the 2-D mesh.

Boundary conditions were set to model the experiment as follows: Inlet total pressure and temperature were set to standard values, and the exit static pressure was set to obtain inlet Mach ~ 0.75 for all cases. Periodic boundary conditions were set on the upper and lower edges of the mesh, and the flow solver was set to Cartesian coordinates, to model the linear cascade. The blade was defined as an adiabatic, viscous, solid, no-slip surface. Counter flow blowing was modeled with an inlet boundary condition at the appropriate location on the pressure surface of the blade. The code was restarted, adjusting the blowing jet total pressure and

flow angle to obtain the correct conditions. Mass flow rates, as well as mass-averaged velocity components, were measured with PROBE (boundary condition) at the inlet, at the blowing jet, and at 105% axial chord.

All solutions were run to iterative convergence, where the \log_{10} residual was -8.0 or lower. The initial \log_{10} residual values ranging from -2.0 to -3.0 , these results go well beyond the ADPAC manual's three orders of magnitude criterion for converged solutions.

COMPUTATIONAL RESULTS

The exit flow fields for $C_m^* = 0.0, 0.0022$, and 0.0030 are shown in Figure 5, corresponding to the three experimental test points in Figure 4. Displacement thickness was calculated as for the experiment. Deviation was calculated from the mass-averaged PROBE data. Details of the computational study are presented in Table 2 for C_m^* ranging from 0.0 to 0.0030 . Total pressure of the blowing jet was increased until the code became unstable for all three meshes, thereby determining the maximum blowing rate. The baseline mesh was the only one that was actually choked ($M \sim 1.0$) at its maximum blowing rate, whereas both the coarse and fine cases were not yet choked ($M \sim 0.95$). Slot geometries, as determined by inlet boundary conditions in ADPAC, were identical for all three meshes. Non-physical pressure gradients in the first two cells along the blowing slot are the likely cause of the instability.

The minimum, average, and maximum y^+ values, as given in the ADPAC output files for the first grid point off the blade, are also presented in Table 1. Generally, y^+ values less than 5 are needed to include the viscous sub-layer, while most research suggests that values less than 1 are required for good accuracy when the turbulence equations are integrated to the wall.⁵ This does not imply complete physical accuracy of the turbulence model, rather, that the full capability of the model—though limited—was being used. The y^+ values were independently calculated with equation (5) using second-order polynomial fits for the $(du/dy)_{\text{wall}}$ values and plotted in Figure 6. It is apparent from Figure 6(a) that a large part of the suction and pressure surfaces were at or above $y^+ = 1$. This, along with non-monotone convergence of the displacement thickness, indicated that there was significant error in the coarse-mesh boundary layer solution. Consequently, the coarse-mesh solution was out of the asymptotic range as described by Roache.⁶ The y^+ values were less than ~ 0.8 for the medium mesh and less than ~ 0.7 for the fine mesh everywhere along the blade, except for the leading edge and the immediate vicinity of the blowing slot. Therefore a two-grid analysis was used on the

medium and fine meshes with a factor of safety of 3 to determine the discretization error.

Table 3 presents the Grid Convergence Index data for the medium and fine mesh solutions. The grid convergence index for a fine mesh solution is calculated as follows:

$$[GCI]_{\text{fine}} = F_s \frac{|\varepsilon|}{r^p - 1} \quad (11a)$$

$$\text{where } \varepsilon = \frac{f_m - f_f}{f_m} \quad (11b)$$

for some characteristic function f (e.g., deviation) defined on the medium mesh, at level m , and the fine mesh, at level f . The recommended factor of safety for a two-grid convergence study is $F_s = 3$. The effective grid refinement ratio may be defined as

$$r = \left(\frac{N_2}{N_1} \right)^{1/D} \quad (11c)$$

where $D = 2$ is the dimensionality of the problem. For the medium-fine mesh comparison at hand, $r \sim 1.895$, and the order of convergence is assumed to be $p = 2$. According to the grid convergence index calculations, the discretization error of the fine mesh solution was $< 2.5\%$ for deviation and $< 3.9\%$ for displacement thickness.

EXPERIMENTAL/COMPUTATIONAL COMPARISON

Computational versus experimental results are presented in Figure 7 for deviation and displacement thickness, respectively. The code over-predicted the flow separation point for the baseline case, resulting in a difference of almost 9° in the predicted deviation of flow from experimental values. However, it also predicted the deviation to within $1-2^\circ$ of the experimental data, for corrected mass blowing ratios of 0.002 to 0.003 . The code over-predicted the flow blockage by $.02-.05$ for corrected mass blowing ratios up to 0.0023 , while it remained within ± 0.03 for values greater than 0.0023 .

The substantial error in the baseline case is probably due to some features of the blade geometry. First and foremost, the blowing slot was modeled with an inlet boundary condition at the surface, instead of using an actual "slot" within the computational mesh and inlet boundary condition within that slot. When the counter flow blowing was turned "off", that part of the blade became a smooth surface. It is reasonable that the existence of a physical blowing slot in the experiment, due to its counter-flow angle, created some blockage on the pressure surface near the trailing edge and,

consequently, increased turning of the flow. This lack of blockage in the computational model, in addition to the blunt trailing edge and high loading over the entire chord length, created a highly-separated flow for the baseline condition. The Spalart-Allmaras turbulence model and the ADPAC code itself have not been validated for flows of this nature. From an engineering standpoint though, it may still be possible to “calibrate” the results to experimental data for future design applications.

Some of the discrepancies over the full range of C_m^* values may also be attributed to the fact that a 2-D, instead of 3-D, analysis was performed. A full-blown, 3-D ADPAC solution would capture more real aspects of the flow physics, such as the 3-D relief effect and end wall boundary layer growth, and would therefore yield more realistic results. A 3-D analysis will not be used until later stages in the design process, if necessary.

SUMMARY

A transonic- linear cascade of advanced design stators has been utilized to perform a feasibility study of using CFB to achieve additional flow turning. The PIV data acquired in the cascade facility has been compared to a high fidelity CFD analysis, ADPAC. Considering limitations of the turbulence model and 2-D simulation taken into account, the code was shown to effectively predict values of deviation for CFB applications. Therefore, this study demonstrates the ability of ADPAC to effectively model the relevant flow physics. The CFD results did not compare favorably with the PIV data for no blowing, but modeling part of the slot configuration would provide a significant improvement. Based on this initial experimental and computational investigation, the potential of using CFB to replace a flapped IGV looks promising.

ACKNOWLEDGEMENTS

The authors would like to acknowledge Prof. Wing Ng for the help in the transonic linear cascade facility. Air Force Contract #F33615-98-C-2895, with technical monitor Dr. Charles J. Cross, and the Dayton Area Graduate Studies Institute (DAGSI) sponsored part this research. Their support is most gratefully acknowledged.

REFERENCES

¹ Copenhaver, W., Car, D., Koch, P., Estevadeordal, J., Guillot, S., Ng, W., Basic Research Studies in Compressor Flow Control, AIAA Dayton-Cincinnati Aerospace Science Symposium, March 2002.

² Copenhaver, W., Car, D., Koch, P., Estevadeordal, J., Guillot, Counter-Flow Blowing for Counterswirl

Designs/Vectoring, Flow Control Device Session and Video at AIAA 1st Flow Control Conference, St Louis, June 2002

³ Estevadeordal, J., Copenhaver, W., Car, D., Koch, P., Ng, W., Guillot, S., Carter, C., Macro- and milli-DPIV studies of a boundary-layer-based flow-control system for a transonic cascade. 11th Intl. Symp. On Appl. Of Laser Techniques to Fluid Mechanics, Lisbon (2002)

⁴ Copenhaver, W., Estevadeordal, J., Gogineni, S., Gorrell, S., Goss, L., DPIV study of near-stall wake-rotor interactions in a transonic compressor. Exp. In Fluids 2002, 33: 899-908

⁵ Hall, E.J., Heidegger, N.J., Delaney, R.A., ADPAC v1.0 – User’s Manual, NASA/CR – 1999-206600, February 1999.

⁶ Wilcox, D.C., *Turbulence Modeling for CFD*, DCW Industries, Inc., La Cañada, California, 1993.

⁷ Roache, P.J., *Verification and Validation in Computational Science and Engineering*, Hermosa Publishers, Albuquerque, NM, 1998.

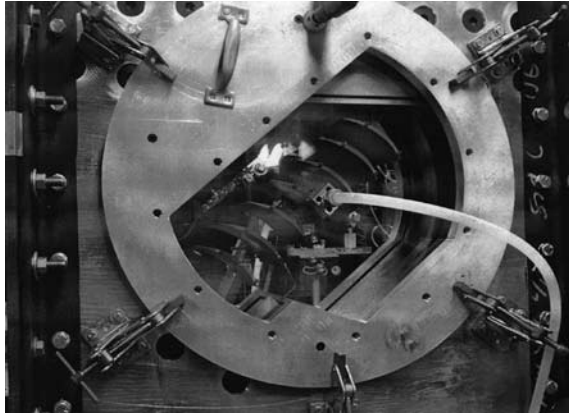


Figure 1a: 2D, scaled-up version of Tescom counter-swirl stator in cascade.

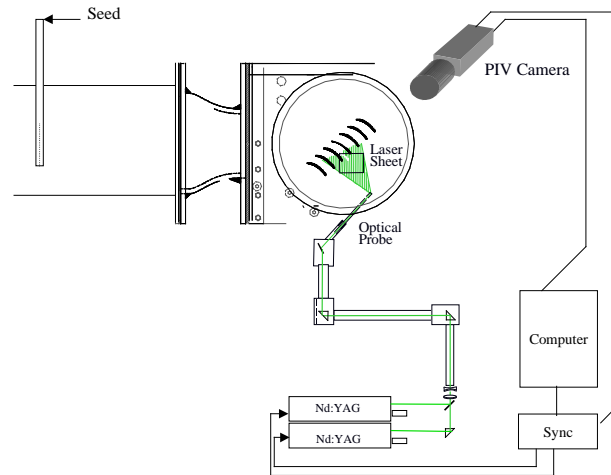


Figure 2: Schematic of DPIV setup for cascade measurements

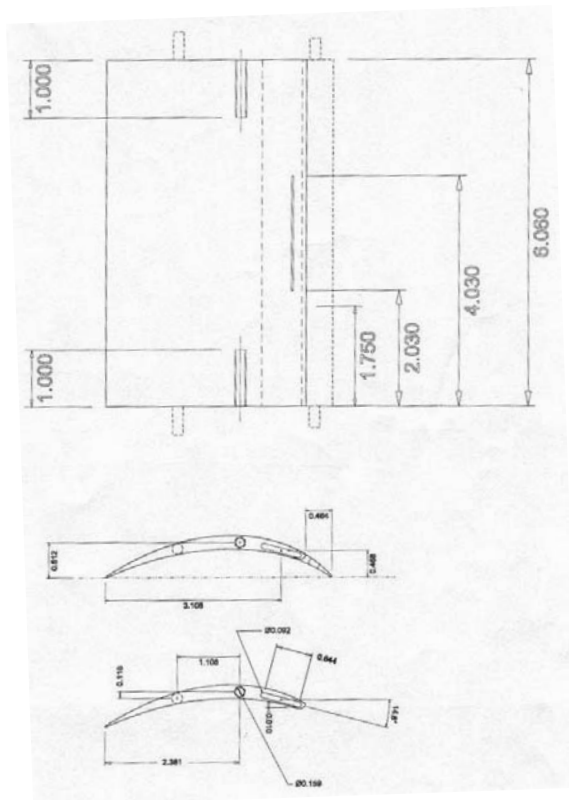


Figure 1b: Schematic of modifications made to create the Tescom-CAR geometry.

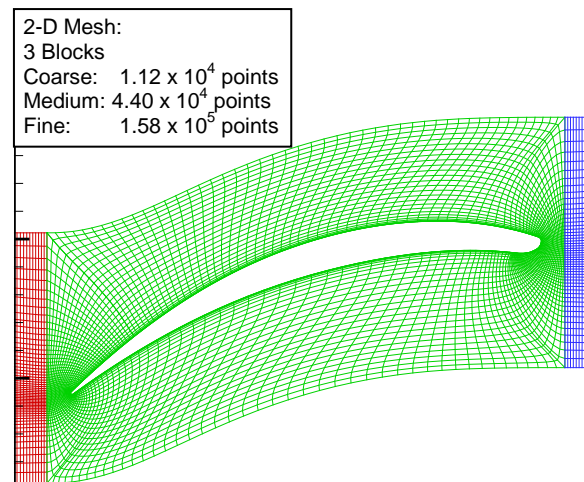


Figure 3: Capped O grid for Tescom-CAR geometry, coarse mesh.

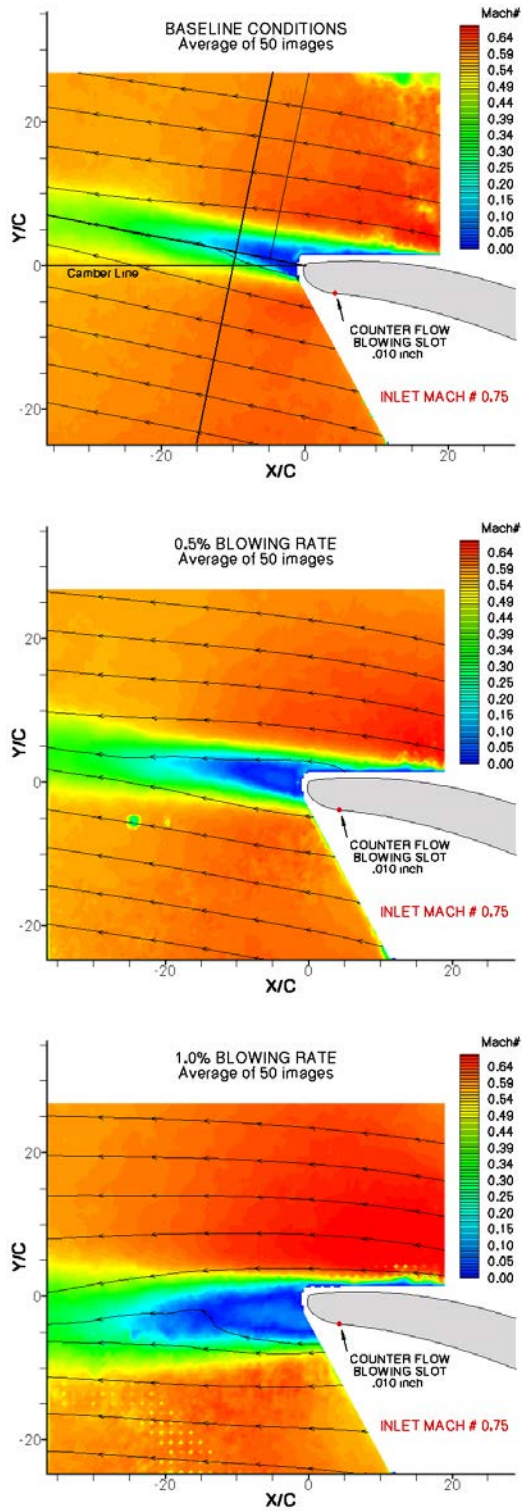


Figure 4: PIV data for Tescom-CAR geometry. From top to bottom, $C_m^* = 0.0, 0.0023$, and 0.0029 . Inlet Mach # = 0.75.

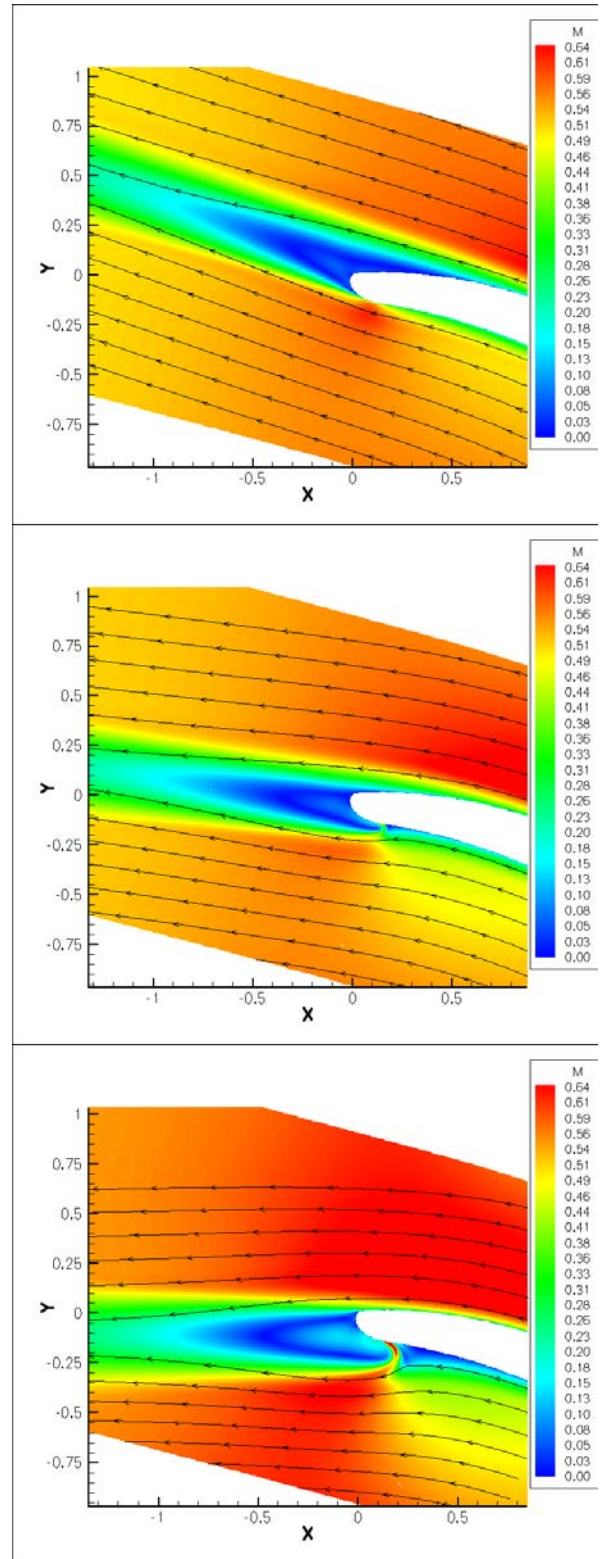


Figure 5: ADPAC solutions for Tescom-CAR. From top to bottom, $C_m^* = 0.0, 0.0022$, and 0.0030 . Inlet Mach # = 0.75.

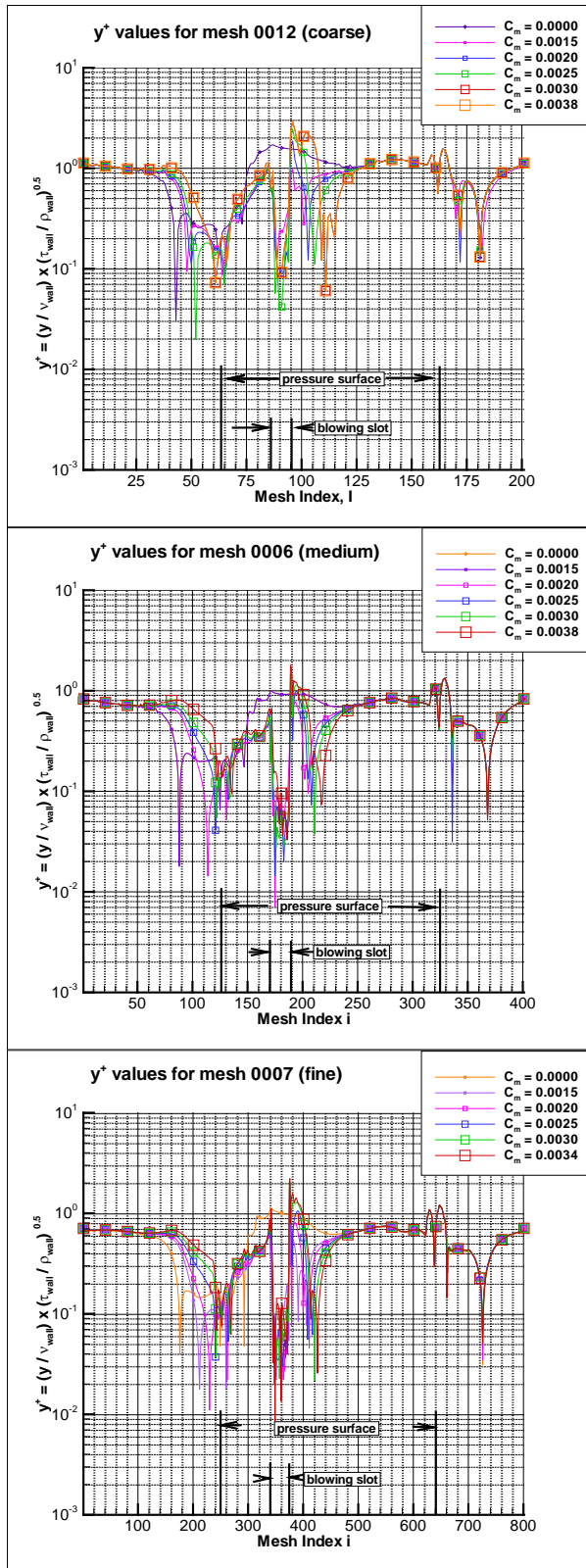


Figure 6: Calculated y^+ values around the blade for (a) coarse, (b) medium, and (c) fine meshes.

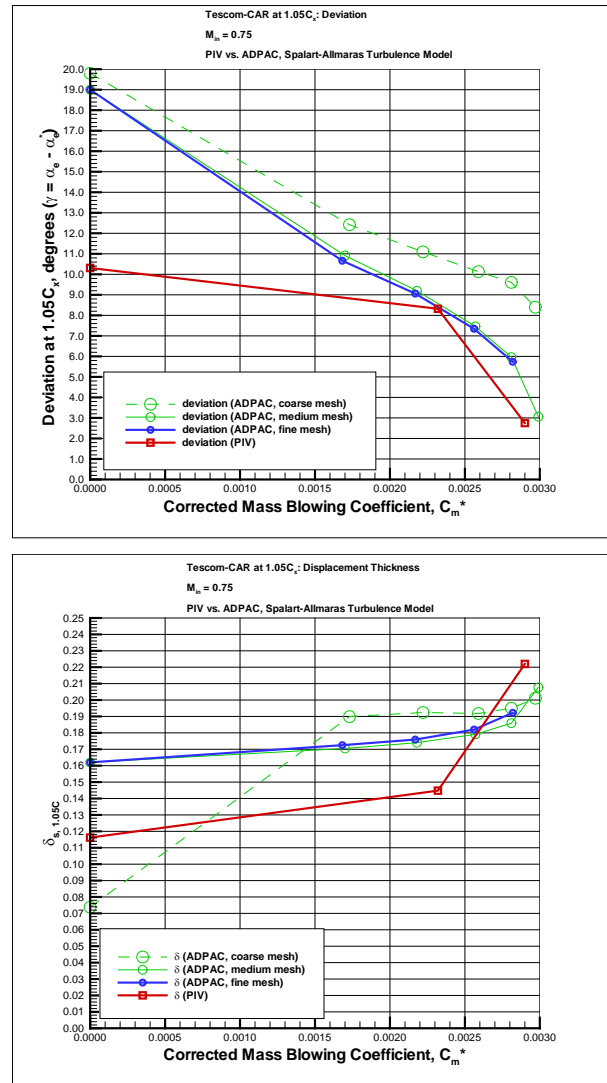


Figure 7: Experimental vs. Computational Values of Deviation (top) and Displacement Thickness (bottom), respectively. Inlet Mach # = 0.75.

Table 1: Experimental Details.

M_{inf}	$C_m (\times 10^{-3})$	P_j / P_{inf}	$C_m^* (\times 10^{-3})$	γ (degrees)	δ_s^*	M_e
0.75	0.00	N/A	0.00	10.45	0.116	0.62
0.75	0.44	1.88	2.32	8.43	0.145	0.63
0.75	1.00	3.72	2.70	2.61	0.222	0.67

Table 2: ADPAC Simulation Details.

case number	mesh level	M_{inf}	$m_{dot,j}$ (lbm/sec $\times 10^{-2}$)	$m_{dot,inf}$ (lbm/sec)	$C_m (\times 10^{-3})$	U_j / U_{inf}	P_j / P_{inf}	$C_m^* (\times 10^{-3})$	γ (degrees)	δ_s^*	M_e	\log_{10} (RMS error)	y^+ minimum	y^+ average	y^+ maximum
1	M	0.750	0.000	0.418	0.00	N/A	N/A	0.00	19.30	0.165	0.575	-7.4	0.039	0.58	1.14
2	M	0.748	0.192	0.418	1.51	0.54	0.89	1.69	10.91	0.171	0.575	-9.6	0.039	0.525	1.25
3	M	0.750	0.256	0.418	2.02	0.68	0.93	2.18	9.20	0.174	0.585	-9.6	0.018	0.537	1.25
4	M	0.752	0.321	0.418	2.53	0.85	0.99	2.57	7.46	0.179	0.599	-9.6	0.025	0.557	1.61
5	M	0.750	0.380	0.418	3.00	1.00	1.07	2.81	5.97	0.186	0.615	-8.4	0.043	0.577	1.85
6	M	0.745	0.480	0.417	3.80	1.30	1.27	2.99	3.06	0.208	0.668	-8.0	0.039	0.619	2.16
7	C	0.754	0.000	0.419	0.00	N/A	N/A	0.00	19.70	0.074	0.594	-8.2	0.06	0.861	1.57
8	C	0.748	0.193	0.418	1.53	0.54	0.88	1.74	12.42	0.190	0.598	-9.3	0.057	0.726	1.44
9	C	0.752	0.255	0.418	2.01	0.68	0.91	2.21	11.10	0.192	0.600	-9.3	0.063	0.737	2.03
10	C	0.751	0.321	0.418	2.53	0.86	0.98	2.59	10.13	0.192	0.604	-9.3	0.073	0.765	2.53
11	C	0.749	0.381	0.418	3.01	1.01	1.07	2.81	9.61	0.195	0.610	-9.3	0.052	0.79	2.74
12	C	0.753	0.480	0.419	3.78	1.23	1.28	2.96	8.40	0.201	0.633	-9.3	0.034	0.857	2.97
13	F	0.755	0.000	0.419	0.00	N/A	N/A	0.00	19.00	0.162	0.571	-8.0	0.02	0.51	1.11
14	F	0.744	0.190	0.418	1.50	0.54	0.89	1.68	10.66	0.173	0.570	-9.8	0.013	0.481	1.14
15	F	0.752	0.253	0.419	2.00	0.67	0.92	2.17	9.06	0.176	0.579	-9.0	0.019	0.494	1.76
16	F	0.750	0.318	0.419	2.50	0.84	0.98	2.56	7.35	0.182	0.592	-9.5	0.022	0.519	2.21
17	F	0.755	0.380	0.418	3.00	1.01	1.06	2.82	5.74	0.192	0.610	-9.8	0.008	0.543	2.39

Table 3: Grid Convergence Details.

mesh level	C_m ($\times 10^{-3}$)	C_m^* ($\times 10^{-3}$)	γ (degrees)	GCI_{fine}	δ_s^*	GCI_{fine}
M	0.00	0.00	19.300		0.1647	
F	0.00	0.00	19.000	1.80%	0.1620	1.90%
M	1.51	1.69	10.814		0.1705	
F	1.50	1.68	10.663	1.62%	0.1725	1.36%
M	2.02	2.18	9.101		0.1740	
F	2.00	2.17	9.061	0.51%	0.1759	1.26%
M	2.53	2.57	7.363		0.1791	
F	2.50	2.56	7.347	0.25%	0.1820	1.87%
M	3.00	2.81	5.865		0.1859	
F	3.00	2.82	5.738	2.50%	0.1922	3.90%

DPIV MEASUREMENTS OF THE FLOW FIELD BETWEEN A TRANSONIC ROTOR AND AN UPSTREAM STATOR

Steven E. Gorrell and William W. Copenhaver
U.S. Air Force Research Lab
Propulsion Directorate
Wright-Patterson AFB, Ohio

Jordi Estevadeordal
Innovative Scientific Solutions, Inc.
Beavercreek, Ohio

1. Introduction

The use of a planar non-intrusive measurement technique such as Digital Particle Image Velocimetry (DPIV) have made it possible to investigate many aspects of unsteady flows previously considered difficult due to the effect of a measurement probe on the flow field or too time consuming because of the pointwise nature of Laser Doppler Velocimetry or Laser Transit Anemometry. Furthermore, time-accurate CFD codes are being developed and are now commonly used to simulate compressors and investigate complex unsteady flow phenomenon.

In this paper DPIV measurements made in a transonic compressor stage are used to investigate interactions between an upstream stator and a downstream transonic rotor. In particular, the interaction between the rotor bow shock and the wake shed from the upstream stator are explored and offered as a test case for unsteady CFD comparison.

Blade-row interactions are known to have a significant impact on the aeromechanical and aerodynamic performance of compressors. For example, Sanders and Fleeter [1] have shown shock-induced rearward forcing to elicit significant upstream surface-pressure amplitudes and a complicated forcing environment that contributes to High Cycle Fatigue (HCF). Numerous low speed and high speed experimental and numerical investigations [2], [3], [4], [5], [6], [7] have

revealed how some blade row interactions improve stage pressure ratio and efficiency while others are detrimental to performance.

Previous experiments using pointwise velocimetry techniques have been used to better understand the three-dimensional geometry of rotor shocks [8], wake recovery [4], wake-shock interactions [9], [10], and for steady CFD code comparison [11].

2. Stage Matching Investigation Rig

The DPIV measurements were acquired on the U. S. Air Force's Stage Matching Investigation (SMI) rig. It is a high-speed, highly-loaded compressor consisting of three blade-rows: a wake generator, rotor, and stator as shown in Figure 1. The rig was designed so that the wake generator to rotor axial spacing and the wake generator blade count could be varied. The axial spacings were denoted as "close", "mid", and "far". The mid and far spacings represent typical axial gaps found in operational fans and compressors. However, the current generation of high performance fans and compressors are being designed with the goal of minimizing blade-row spacing in order to increase performance and reduce compressor length and thus weight. The wake generator blade count could be set to 12, 24, or 40, or the rig could be run without any wake generators (identified as the "clean inlet" configuration). Table 1 gives the wake generator to rotor axial spacings normalized by the wake generator chord.

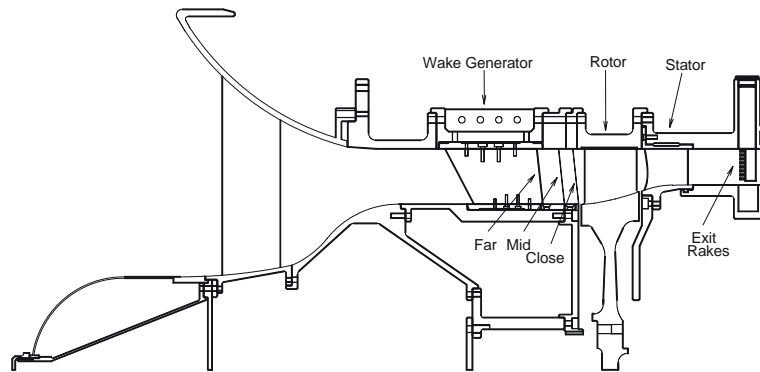


Figure 1. Stage Matching Investigation Rig Layout

2.1 Compressor Stage and Wake Generators

The rotor and stator were designed by Law and Wennerstrom [12]. A summary of the SMI stage aerodynamic design parameters is given in Table 2. The purpose of the wake generators was to create wakes typically found in modern-technology, highly-loaded, low-aspect-ratio fan and compressor front

Table 1. Wake Generator-Rotor Axial Spacing

Spacing	ax/c (mean)	ax/c (hub)	ax/c (tip)
Close	0.13	0.10	0.14
Mid	0.26	0.26	0.26
Far	0.55	0.60	0.52

ax = axial spacing

c = wake generator chord

Table 2. SMI Aerodynamic Design Parameters

PARAMETER	ROTOR	STATOR
Number of Airfoils	33	49
Aspect Ratio - Average	0.961	0.892
Inlet Hub/Tip Ratio	0.750	0.816
Flow/Annulus Area, kg/s/m ²	195.30	--
Tip Speed, Corrected m/s	341.37	--
M _{REL} LE Hub	0.963	0.820
M _{REL} LE Tip	1.191	0.690
Max D Factor	0.545	0.502
LE Tip Dia., m	0.4825	0.4825

stages. In general these wakes are turbulent and do not decay as rapidly as wakes from high-aspect-ratio stages with lower loading. The wake generators were designed with the intent of producing a two-dimensional representation of wakes measured at the exit of a high-pressure-ratio, low-aspect-ratio fan stage reported by Creason and Baghdadi [13]. A two-dimensional representation was desired in order to isolate the effect of different wake parameters during the experiment.

Details of the Wake Generator (WG) design were presented by Gorrell et al. [14]. In summary, the WG's are uncambered symmetric airfoils that do not turn the flow. They have a small leading edge and a blunt trailing edge. This shape creates a large base drag and no swirl. Solidity is held constant from hub to tip by varying the chord, the intent being to hold spanwise loss and wake width constant.

Calibration of the WG's showed this was the case except near the endwalls. The calibration procedure, instrumentation, and results are found in references [15] and [16]. From those results the widening of the wake from close to far spacing was clearly evident. Wake depth was deepest at close spacing and became shallower at mid and far spacing. The wake width was nearly constant from hub to case. This confirmed the intent of the wake generator design to produce a two-dimensional wake profile. The wake is constant in the circumferential and radial directions but not in the streamwise direction. Also evident from rake measurements near the endwalls was the boundary layer growth as the spacing increased from close to far.

From calculated velocity profiles it was observed that the wake depth was similar at the hub and case and deepest near mid span. Wake decay analyzed by Chriss et al. [16], showed that the SMI wake generator wakes demonstrated similar trends to that compared in the literature.

Due to the blunt trailing edge of the wake generator, its wakes may be wider than what would be produced from a normally cambered stator airfoil, but wake measurements for comparison are not found in the open literature. Regardless of the wake thickness, the loss produced was very near the design intent and well within the range typically found in highly loaded stators.

2.2 SMI Performance

Performance characteristics for the SMI rig are shown in Figure 2. There was a significant difference in performance between each of the three spacings tested. Both the pressure ratio and efficiency characteristics decreased significantly as the blade-row axial spacing was reduced from far to close. The choking mass flow rate decreased as the blade-row axial spacing was reduced. The difference in pressure ratio, efficiency, and mass flow rate between the far and close spacing configurations was greater than the repeatability documented in reference [14]. Therefore it was concluded that the observed change in performance with axial blade-row spacing was real and not due to experimental measurement uncertainty.

3. DPIV System

The DPIV system used to obtain the measurements presented in this paper has been described in detail by Estevadeordal et al. [17]. Figure 3 contains schematics of the optical system. Two frequency-doubled Nd:YAG lasers are employed for instantaneous marking of the seed particles in the flow field. Combined by a polarizing cube or a beam combiner, the beams are directed through sheet-forming optics and illuminate the test section with a 2D plane of thickness ~ 1 mm. The scattering from the seed particles is recorded on a cross-correlation CCD camera with 1008 x 1018 pixels (Redlake ES1.0). The camera

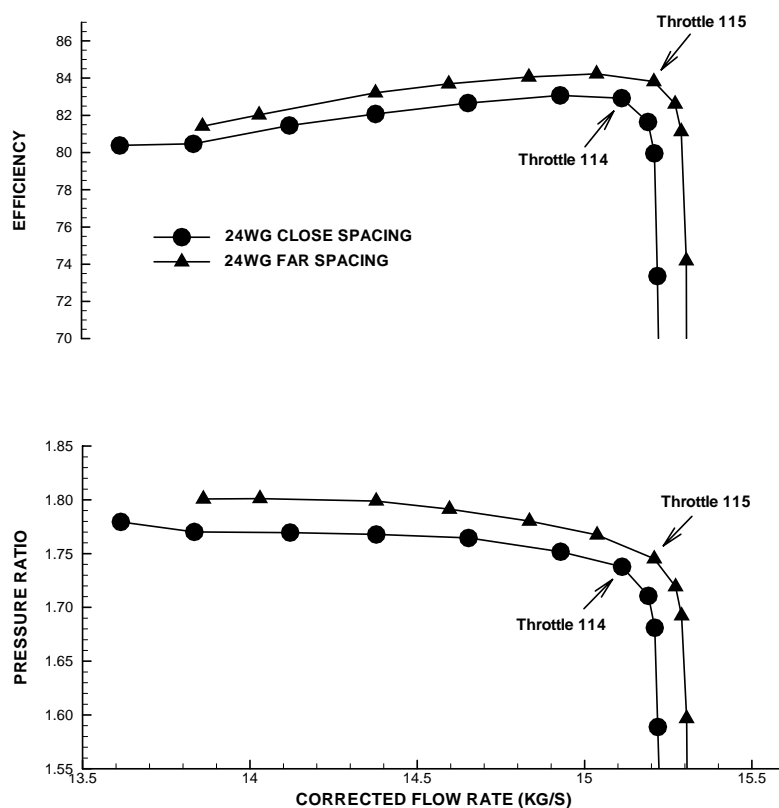


Figure 2. SMI Performance, 24WG's, 100% Corrected Speed

maximum repetition rate is 15 double exposures per second and was set to 10 Hz for synchronization with the laser repetition rate. The time delay between the lasers was typically $2 \mu\text{sec}$. For the present experiments where only a small area was to be captured, the camera offered sufficient resolution. A 105-mm Nikon lens was used. The magnification for the present experiments was 17 and 27 pixels/mm which corresponds to a viewing width of 59 mm (close spacing) and 37 mm (far spacing).

The laser-sheet delivery system consists of a probe inserted in an enlarged WG, light-sheet-forming optics, prisms, and probe holders for mounting the optics and for protecting them from contaminated seed materials. To minimize perturbations the modified WG was located two WGs below the WG that was centered at the receiving window. A receiving window made of chemically strengthened glass allowed optical access to the region of interest. Figure 3 shows schematic diagrams of the path for the laser system and the optical probe. Although the path was relatively long, the power required for laser-

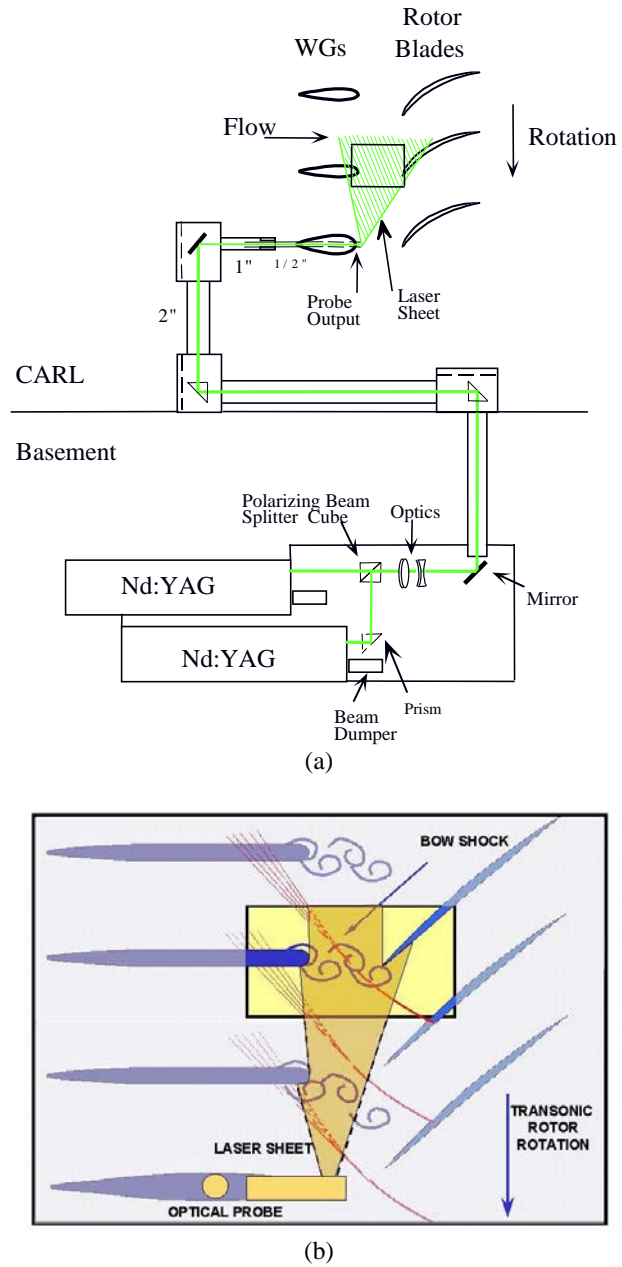


Figure 3. a) Schematic of optical path; b) schematic of flow features (drawn to scale) showing DPIV delivery and receiving optics

sheet illumination was very low (~ 10 mJ/pulse) because of the minimal amount of optics losses. The F stop of the 105 mm lenses was kept at 5.6 for these experiments; this allowed the laser power to be kept low which is important for the safety of the optical components in the optical probe as the beam starts focusing.

The shape of the laser sheet (thickness, width, focal distance) can be changed through various combinations of the spherical-lens focal length, the cylindrical-lens diameter, and the distance between them inside the WG as well as through external optics (a spherical lens) located in the laser path. The spanwise location of the laser sheet was changed by rotating the probe (Figure 4). As shown in this figure, the laser sheet is inclined and not at a constant radius.

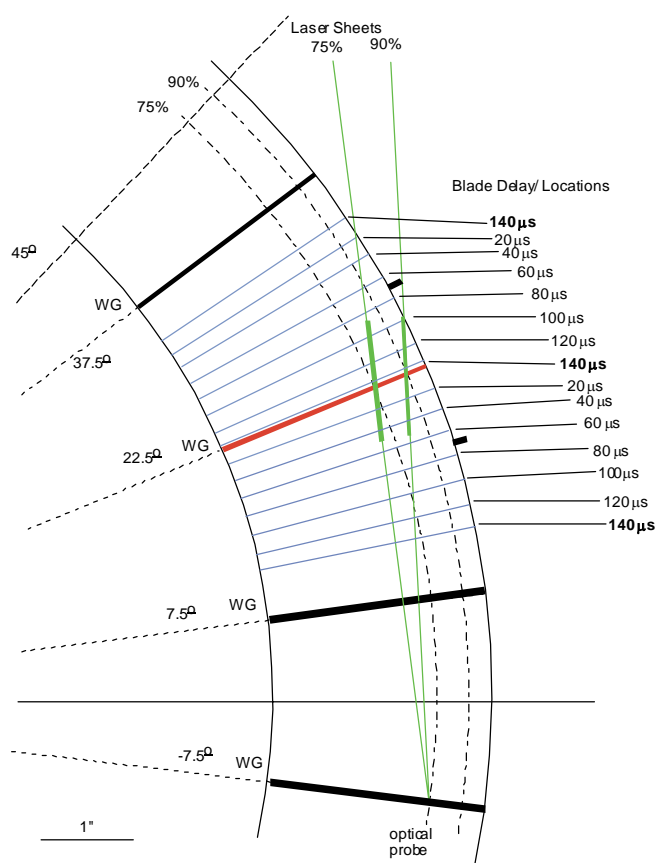


Figure 4. Laser sheet orientation. Blade LE locations are shown at $20 \mu\text{s}$ intervals with lighter lines. Thicker portions of laser sheets denote DPIV image locations.

The length of the probe that was outside the WG could also be changed to provide further flexibility in moving the laser-sheet in the streamwise direction. The probe was set manually before each experiment.

The camera was aligned and focused on the laser sheet prior to each run. It was mounted on a tripod to minimize the effect of rig vibrations. To account for possible motion of the camera with respect to the laser sheet that might occur, the camera was positioned by means of a translation stage that was remotely controlled to allow small corrections in the camera location. Large changes with respect to the laser sheet could produce magnification changes that must be taken into account. After every experiment the laser-sheet and camera locations were verified for possible misplacements. In the present experiments the only change required was slight refocusing, with negligible magnification effects.

The viewing window had the same curvature as the rotor housing (inner housing radius is 241.3 mm), was made of chemically strengthened glass and had a thickness of 2 mm. The effect of window curvature and thickness was investigated by Copenhaver et al. [18] and found to have a negligible effect for the present CARL setup.

Several options for seeding the high-flow (~ 16 kg/s) SMI rig in the CARL facility were evaluated [17], including the use of various seeding units and seed materials. Both local and global seeding was considered. The seed material used was sub-micron-size smoke particles generated from a glycerin and water mixture. During its use in the CARL facility, this system produced sufficient seed when the particles were introduced at the end of the settling chamber, before the contraction, and at the height of the receiving window. The machine can be remotely controlled. The seed material was introduced through a pipe of 50.4-mm diameter located under the contraction entrance.

The rotor one-per-revolution signal was used for triggering the synchronization system. A digital pulse generator (Stanford DG535) and a camera frame-grabber (National Instruments PCI-1424) were used.

Once the PIV images have been captured and digitized, the velocity field is obtained using cross-correlation techniques over interrogation domains of the images using DPIV software developed internally. The dimensions of each interrogation domain are dependent on particle density, estimated local velocity gradients, particle-image size, and desired spatial resolution. The peak of the correlation map corresponds to the average velocity displacement within the interrogation spot. An intensity-weighted peak-searching routine is used to determine the location of the peak to sub-pixel accuracy. To improve the signal-to-noise ratio in the correlation maps, a correlation-correction scheme [19] is applied wherein each map is multiplied by its immediate four neighborhoods. An overlapping of 75% is used to include much the same particles in the five maps that are multiplied to yield a single correlation map with lower noise. Zero

padding is also employed for adding accuracy. The software includes a grid feature that allows selection of areas of the image to be processed. This permits removal of solid regions such as blades and WGs and also shadows from the processing areas. It also provides a choice of various correlation engines and correlation peak locators and incorporates several improvements to standard (single-pass) PIV techniques such as recursive estimation of the velocity field through a multipass algorithm for increasing resolution. Two passes with interrogation cells overlapping 75% were performed. The interrogation domains are overlapped by three-quarters the domain size to yield more vectors. The overlapping includes new particles in every subregion. Average routines allow for removal of outliers beyond any number of standard deviations. Because of the strong phase-locked flow features, the median offers a valid, robust, and smooth statistical representation of the average velocity field [17].

Many factors are involved in the DPIV uncertainty-calculation process (laser, CCD, seeding, imaging, algorithms, oscilloscope, etc). The highest uncertainty was found to be associated with the velocity calculation which involves Δx (the displacement in pixels of each interrogation region), Δt (the time interval between the two exposures), and the magnification of the digital image relative to the object (pix/m). The displacement in pixels obtained by peak-locator algorithms can provide sub-pixel accuracy (< 0.1 pixels) after correction for various biases [20]. The Δt was adjusted to yield typical displacements of the main stream > 10 pixels, and the uncertainty is thus $< 1\%$. Values in the wake region, however, may have higher uncertainties due to the lower Δx . The maximum uncertainty in the Δt was calculated from the time interval between the two laser pulses with the aid of an oscilloscope (uncertainty 2%). It was found that this uncertainty increases with lower laser power and with lower Δt . A conservative number for the present experiments, which employed a Δt of about $2 \mu s$ and powers around 10 mJ, was found to be 1%. The magnification was measured using images of grids located in the laser-sheet plane to better than 1%. Combining these conservative measurements of uncertainty yields a maximum error of $< 2\%$ for the free-stream velocity and $\sim 10\%$ in the wake near the WG area.

4. Results

DPIV results are presented for close and far spacing configurations at 75% span, 100% corrected speed, peak efficiency. Of particular interest is the interaction between the wake generator wake and the rotor bow shock and the effect blade-row axial spacing has on the overall flow field. The median of 50 instantaneous images is plotted as it was found that it provided the clearest image of the flow field.

4.1 Close Spacing

Previous analysis of flow visualization and DPIV results from the SMI rig [17], [18], [21] have shown that at close spacing vortex shedding from the wake generator trailing edge is phase locked to the rotor blade pass frequency. The main source of the synchronization appears to be the strong pressure perturbation provided by the rotor bow shock to the wake generator trailing edge. At close spacing the instantaneous images of vortex shedding are similar for any given operating condition and blade delay. This is consistent with high response pressure measurements obtained on the wake generator surface, which showed a strong fluctuation in pressure at blade-passing frequency (7.7 kHz). Since the instantaneous DPIV data contains holes in velocity information where seeding was not sufficient to obtain a correlation, it is more informative to look at the average flow field where data intermittency can be minimized. Since the vortex shedding is phase locked to rotor passing, rotor phase locked averaging is possible without destroying the details of the velocity field in this interaction region.

At close spacing DPIV measurements were made at blade delay intervals of $5\ \mu\text{s}$ giving 30 different rotor blade locations for one blade-pass period. Seven of the blade delays are shown in Figure 5. The rotor bow shock is defined by the large velocity gradient and a change in flow angle toward the shock. Streamlines are drawn near the wake generator to highlight the wake motion at different rotor locations. The wavy motion of the wake is a result of a vortex being shed from the pressure or suction surface of the wake generator. This up and down motion continues as the wake convects downstream and interacts with the rotor bow shock and then is chopped by the rotor blade. Downstream of the rotor bow shock there is an expansion zone due to the flow accelerating around the rotor suction surface.

The DPIV images at blade delay $140\ \mu\text{s}$ and $20\ \mu\text{s}$ illustrates that the shock-wake interaction results in a wider and deeper wake downstream of the shock. At time $20\ \mu\text{s}$ the low velocity region downstream of the shock and within the wake moves up to 18% pitch suggesting that the shock-wake interaction has resulted in an increase in wake width.

From the plot at blade delay $140\ \mu\text{s}$ it is clear that the wake actually splits the shock into two distinct regions above and below the wake. It was also observed that the velocity magnitude at the wake generator trailing edge fluctuates significantly depending on the location of the rotor bow shock. As the shock approaches the wake generator the velocity increases first near the wake generator pressure surface, then on the suction surface. Once the shock is separated and propagates upstream the velocity magnitude decreases. Numerical analysis reported by Gorrell et al. [7] showed that the interaction of the wake generator trailing edge with the rotor bow shock causes the shock to turn more normal

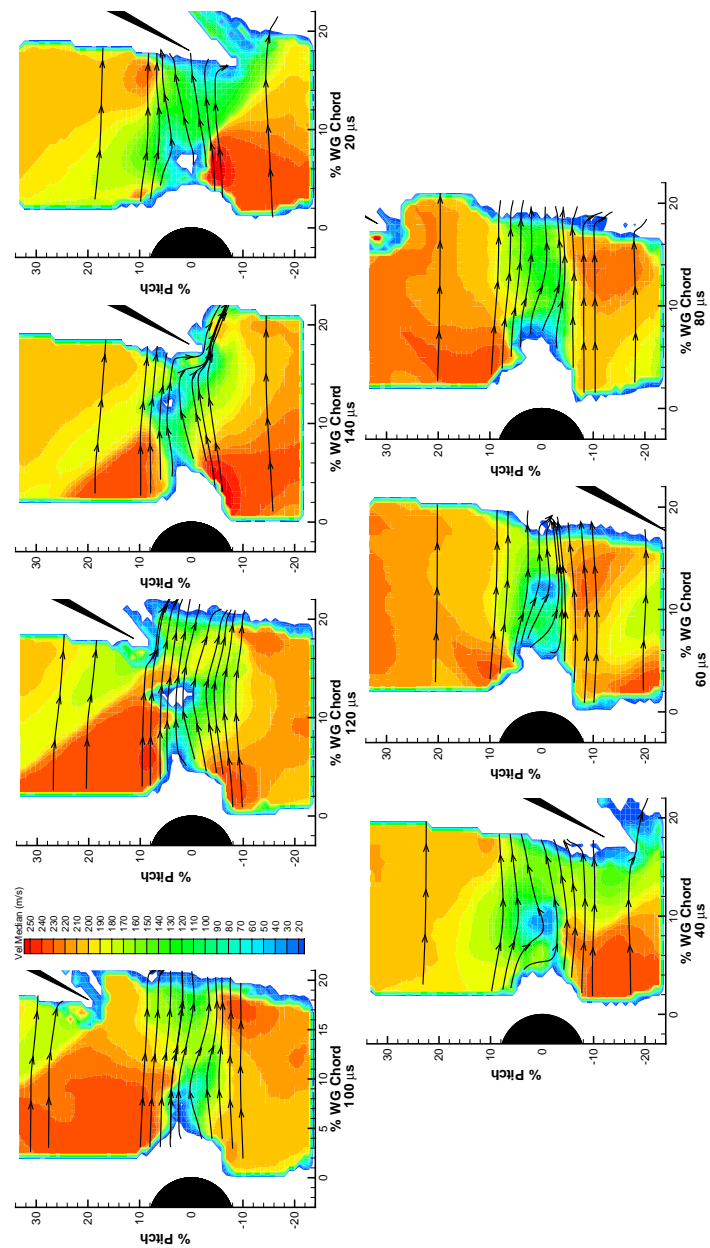


Figure 5. Close spacing, 75% span, median velocity

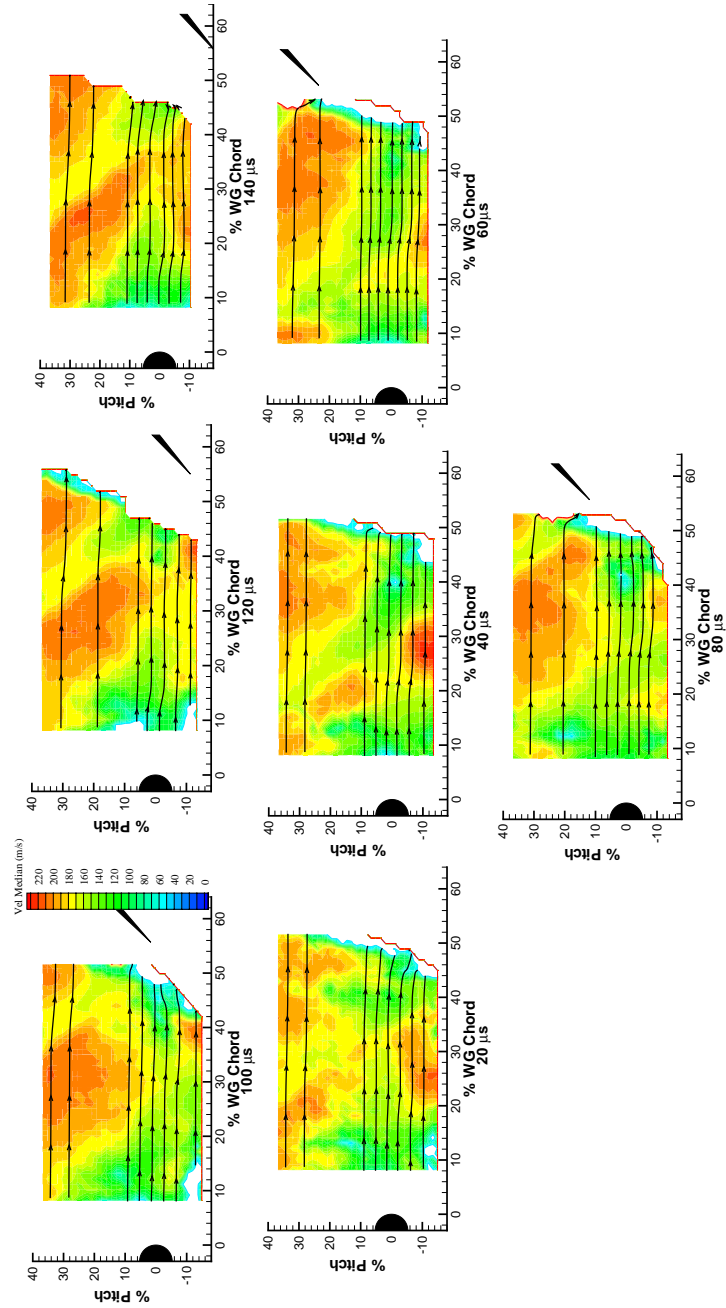


Figure 6. Far spacing, 75% span, median velocity

to the freestream flow. This phenomenon is also observed in the experimental data presented in Figure 5.

4.2 Far Spacing

DPIV plots of median velocity at the far spacing configuration are shown in Figure 6. Due to the limit in laser sheet width the flow field was not captured near the wake generator trailing edge. The wake shedding frequency is not easily determined as it was at close spacing. Hot wire measurements obtained downstream of the wake generator show the blade-pass frequency of 7.7 kHz and another frequency of 8.8 kHz are the most powerful peaks in the spectrum. Further analysis is required to determine the natural shedding frequency of the wake generator. An observation made from the instantaneous flow visualization images (not presented here) suggest a phase locking of the wake shedding to the bow wave perturbation but random motion of the vortices as they convect downstream. At far spacing two or three shed vortices are present at any given time in the gap between the wake generator and rotor. At close spacing there is only one vortex present. As a result the averaged instantaneous images at far spacing do not show as clear a view of the wake region as close spacing. Nevertheless, plots of median velocity still illustrate important details of the far spacing flowfield.

Analysis of Figure 6 shows bands of low and high velocity in the flow field that are a result of the rotor bow shock and expansion zone. At far spacing the rotor bow shock is not as well defined because it is weaker than at close spacing. This is evident from the peak velocity magnitude observed in the DPIV images. The peak velocity at far spacing is approximately 220 m/s while at close spacing it is 245 m/s. Due to the increased axial gap between the rotor leading edge and wake generator the rotor bow shock has dissipated into more of a bow wave at the location it interacts with the wake generator trailing edge.

The wake generator wake has mixed out more resulting in a wider and shallower wake. The interaction of a weaker wake with a weaker bow shock does not split the rotor bow shock into two clearly defined regions such as was observed at close spacing.

5. Summary

A DPIV system for use in transonic turbomachinery has been described. Results from an experiment conducted in the SMI rig are presented that show the complex flow field associated with the interaction of a downstream transonic rotor with an upstream stator. The effect of changing the axial gap between blade-rows is studied and the DPIV plots are presented as an experimental data set for time accurate CFD validation.

At close spacing the wake shedding is synchronized with the rotor blade-pass frequency. The interaction of the rotor bow shock and wake generator causes the wake to expand downstream of the shock. The shock is split into two regions above and below the wake. As the shock approaches the wake generator trailing edge the velocity increases and the shock to turn more normal to the freestream flow.

At far spacing the wake convects downstream in a chaotic fashion. Bands of high and low velocity are evident from the rotor bow shock and expansion waves downstream of the shock. The interaction between the rotor bow shock and wake generator is much weaker than the close spacing interaction. The wake has mixed out more at the location it interacts with the shock and does not split the shock in two nor turn the shock normal to the freestream flow..

Acknowledgments

The wake generators, rotor, and stator were built by Pratt & Whitney. From the CARL group at Wright-Patterson AFB the authors would like to recognize Dr. Herb Law, Robert Wirrig, Ron Berger, Terry Norris, Bill Ullman, and Chris Blackwell for their assistance in gathering the data. The assistance of Dr. Sivaram Gogineni and Dr. Larry Goss of ISSI in setting up the DPIV system is also recognized. Post processing of the results was assisted by Justen England and Nathan Woods. The authors thank the Propulsion Directorate management for supporting the research and allowing the presentation and publication of this paper.

References

- [1] Sanders, A. and Fleeter, S. Experimental Investigation of Rotor-Inlet Guide Vane Interactions in Transonic Axial-Flow Compressor. *AIAA Journal of Propulsion and Power*, 16(3):421–430, 2000.
- [2] Smith, L. H. Wake Dispersion in Turbomachines. *ASME Journal of Basic Engineering*, (3):668–690, 1966.
- [3] Smith, L. H. Wake Ingestion Propulsion Benefit. *AIAA Journal of Propulsion and Power*, 9(1):74–82, 1993.
- [4] Van Zante, D. E., Adamczyk, J. J., Strazisar, A. J., and Okiishi, T. H. Wake Recovery Performance Benefit in a High-Speed Axial Compressor. *ASME Journal of Turbomachinery*, 124:275–284, 2002.
- [5] Van de Wall, A. G., Kadambi, J. R., and Adamczyk, J. J. A Transport Model for the Deterministic Stresses Associated With Turbomachinery Blade Row Interactions. *ASME Journal of Turbomachinery*, 122:593–603, 2000.
- [6] Gorrell, S. E., Okiishi, T. H., and Copenhaver, W. W. Stator-Rotor Interactions in a Transonic Compressor, Part 1: Effect of Blade-Row Spacing on Performance. *ASME Journal of Turbomachinery*, 125:328–335, 2003.

- [7] Gorrell, S. E., Okiishi, T. H., and Copenhaver, W. W. Stator-Rotor Interactions in a Transonic Compressor, Part 2: Description of a Loss Producing Mechanism. *ASME Journal of Turbomachinery*, 125:336–345, 2003.
- [8] Strazisar, A. J. Investigation of Flow Phenomena in a Transonic Fan Rotor Using Laser Anemometry. *ASME Journal of Engineering for Gas Turbines and Power*, 107:427–435, 1985.
- [9] Ottavy, X., Trebinjac, I., and Vuillarmet, A. Analysis of the Interrow Flow Field Within a Transonic Axial Compressor: Part 1 - Experimental Investigation. *ASME Journal of Turbomachinery*, 123:49–56, 2001.
- [10] Ottavy, X., Trebinjac, I., and Vuillarmet, A. Analysis of the Interrow Flow Field Within a Transonic Axial Compressor: Part 2 - Unsteady Flow Analysis. *ASME Journal of Turbomachinery*, 123:57–63, 2001.
- [11] Calvert, W. J. Detailed Flow Measurement and Predictions for a Three-Stage Transonic Fan. *ASME Journal of Turbomachinery*, 116:298–305, 1994.
- [12] Law, C. H. and Wennerstrom, A. J. Two Axial Compressor Designs for a Stage Matching Investigation. Technical Report AFWAL-TR-89-2005, Air Force Wright Aeronautical Laboratory, WPAFB, OH, 1989.
- [13] Creason, T. and Baghdadi, S. Design and Test of a Low Aspect Ratio Fan Stage. AIAA Paper 88-2816, 1988.
- [14] Gorrell, S. E., Copenhaver, W. W., and Chriss, R. M. Upstream Wake Influences on the Measured Performance of a Transonic Compressor Stage. *AIAA Journal of Propulsion and Power*, 17(1):43–48, 2001.
- [15] Gorrell, S. E. *An Experimental and Numerical Investigation of Stator-Rotor Interactions in a Transonic Compressor*. PhD thesis, Iowa State State University, Ames, Iowa, 2001.
- [16] Chriss, R. M., Copenhaver, W. W., and Gorrell, S. E. The Effects of Blade-Row Spacing on the Flow Capacity of a Transonic Rotor. ASME Paper 99-GT-209, 1999.
- [17] Estevadeordal, J., Gogineni, S., Goss, L., Copenhaver, W., and Gorrell, S. Study of Wake-Blade Interactions in a Transonic Compressor Using Flow Visualization and DPIV. *ASME Journal of Fluids Engineering*, 124(1):166–175, 2002.
- [18] Copenhaver, W., Estevadeordal, J., Gogineni, S., Gorrell, S., and Goss, L. DPIV study of near-stall wake-rotor interactions in a transonic compressor. *Experiments in Fluids*, 33:899–908, 2002.
- [19] Hart, R. The Elimination of Correlation Errors in PIV Processing. In *9th International Symposium on Applications of Laser Techniques to Fluid Mechanics*, Lisbon, Portugal, 1998.
- [20] Westerweel, J. Fundamentals of Digital Particle Imaging Velocimetry. *Measurement Science and Technology*, 8:1379–1392, 1997.
- [21] J., Estevadeordal, Gogineni, S., Goss, L., Copenhaver, W., and Gorrell, S. DPIV Study of Wake-Rotor Synchronization in a Transonic Compressor. AIAA Paper 01-3095, 2001.

Investigation on Vortex Shedding of Jet in Crossflow

B. Kiel, A. Cox, J. Estevadeordal, and S. Gogineni

ABSTRACT

An experimental investigation of a circular jet issuing from a wall normal to a crossflow was conducted over a momentum-ratio range of 2.0 - 15 for various jet and crossflow Reynolds numbers. The flow field was interrogated using split-film and DPIV techniques to characterize the various regimes of the flow. The analyzed data revealed the three classic vortices that are present in a jet-in-cross-flow environment: the leading-edge horseshoe vortex, Karman-Street vortices, and the combined Kelvin-Helmholtz/Counter-Rotating Vortex Pair (K-H/CVP). It was observed that the penetration is a function not only of momentum ratio and axial location but also of both jet and crossflow Reynolds Numbers. The DPIV data qualitatively indicated an increase in the Kelvin Helmholtz vortex shedding frequency with crossflow Reynolds number.

NOMENCLATURE

CVP	Counter-Rotating Vortex Pair
DFFT	Discrete Fourier Transform
DPIV	Digital PIV
JICF	Jet in Crossflow
M	Momentum Ratio ($\rho_j U_j^2 / \rho_c U_c^2$)
k	Wave Number
Re	Reynolds Number
rms	Root Mean Square
St	Strouhal Number
U	Velocity

Subscripts

c	Crossflow
d	Dissipation Scale
j	Jet

INTRODUCTION

Jets in crossflow (JICF) are important design considerations for many components in gas turbine engines. For example, in the combustor, crossflow jets are introduced into the hot-gas path to promote primary-zone and dilution-zone mixing. The crossflow jets enhance mixing, which is required for high combustor efficiencies, are also used to create exit-temperature profiles for the turbine stages to allow high turbine efficiency and acceptable turbine durability. JICF are also used in the augmentor to cool hot parts. A greater understanding of the design parameters of a JICF can lead to performance improvements in the inlet, combustor, turbine, augmentor, and exhaust nozzle, (Lord, MacMartin, & Tillman 2000).

JICF have been studied for more than 70 years, (Sutton 1932 and Bosanquet & Pearson 1936). In the 1970s and 1980s a tremendous number of studies were conducted on JICF. These efforts have been summarized by Margason (1993). In this comprehensive paper, Margason reviewed many areas, including parametric studies associated with jet properties. One of Margason's conclusions was that only limited

B. V. Kiel, Cox, A. Air Force Research Laboratory, WPAFB, OH, 45433

J. Estevadeordal, S Gogineni, Innovative Scientific Solutions Incorporated, Dayton, OH, 45432

Correspondence to:

Barry Kiel, AFRL/PRTC, 1950 5th St, WPAFB, OH, 45433, E-mail: barry.kiel@wpafb.af.mil

efforts have been made to resolve the unsteady flow features of a JICF. More recent papers have addressed several aspects of JICF and the unsteady nature of the flow. Specifically, numerous authors have described a system of four vortices that emanate from the mixing process between the jet and the crossflow: horseshoe vortices, Karman-Street vortices, Kelvin-Helmholtz vortices, and the counter-rotating vortex pair (CVP). When the jet issues into the crossflow, it initially acts as a semi-rigid column of air. The formation of the horseshoe and Karman-Street vortices is similar to that of vortices formed by a solid cylinder in crossflow (Figures 1 and 2). The size and number of horseshoe vortices is dependent on the crossflow Re (Wei, Chen, & Du 2000 and Kelso & Smits 1995).

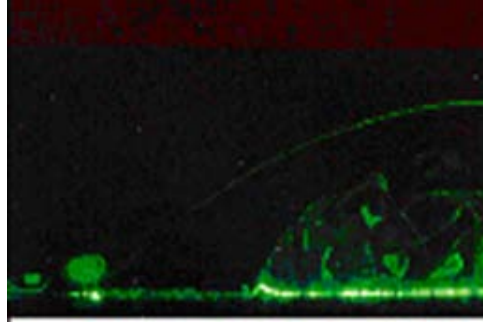


Fig. 1 Flow Visualization of Horseshoe Vortices on Leading Edge of Jet [Gogineni et al. (1995)]

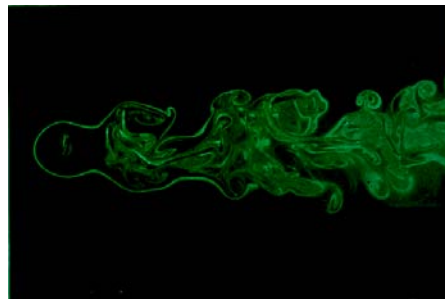


Fig. 2 Flow Visualization of Karman-Street Vortices [Gogineni et al. (1995)]

Regarding the Kelvin-Helmholtz vortices, Figure 3, shows a side view of three such vortices, with axes of rotation normal to the page. Figure 4 depicts the same type of vortices, with the laser sheet normal to the crossflow direction. The origins of the Kelvin-Helmholtz have been debated for more than 30 years. Several papers have supported the position that the origin of both the Kelvin-Helmholtz and the CVP is instabilities manifested from a vortex ring emanating from the jet. The mechanism for the formation of

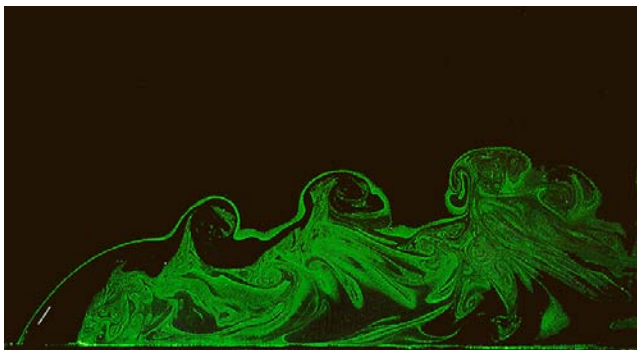


Fig. 3 Flow Visualization of Kelvin-Helmholtz Vortices [Gogineni et al. (1995)]

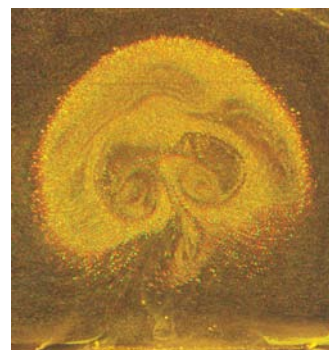


Fig. 4 PIV Image of CVP

these vortices is the Kelvin-Helmholtz instability at the jet exit. A vortex ring is formed as the jet issues into the crossflow. As the vortex ring convects in the wake, it is amplified by the velocity gradient between the jet and the recirculation zone. The vortex ring is also stretched and tilted by the strong velocity gradient

between the free stream and the jet wake. These assertions have also been recently verified by Kiel et. al. (2003).

SCOPE

Most recent studies on JICF have been concentrated in two areas. First, many studies have been focused on a specific vortex shedding in the flow. Here, the effect of Re or momentum ratio on the specific vortex-shedding phenomena was studied. Second, other studies have used computations, smoke, or lasers to visualize the flow. From the visualizations, conclusions were drawn on the nature of the vortices in the JICF interactions. These visualizations were typically at one momentum ratio and one Re . This paper reports the results of a split-film and DPIV experimental study that determined the frequency content of the vortices formed in the JICF over a wide range of conditions. Data were obtained on the horseshoe and Kelvin-Helmholtz vortices. Comparisons between split-film and DPIV data are made to shed further light on the nature of the vortices in this flow.

EXPERIMENTAL APPARATUS

The test article (Fig. 5) required two sources of air—one for the jet and one for the crossflow. The crossflow air was supplied by a 5.60-kW blower that delivered up to 0.567 kg/s of air (standard day). The mass flow from the blower was controlled by a variable-speed motor controller. Jet air was supplied by an 825-kPa air source. Air flow and pressure were controlled through the use of a pressure regulator and control valve. Subsequently, the air was metered by a rotameter with a flow range of 0.589 - 13 m³/s. Several factors were considered in the design of this test article. It was designed such that the Re based on jet velocity and jet diameter was in the range 13,000 - 34,000. This range was consistent with that of mixing jets, dilution jets, and film-cooling flows in combustors and augmentors. Consideration was also given to crossflow Re based on channel height. A range of 100,000 - 250,000 was achieved, which also is analogous to combustor and augmentor flows.

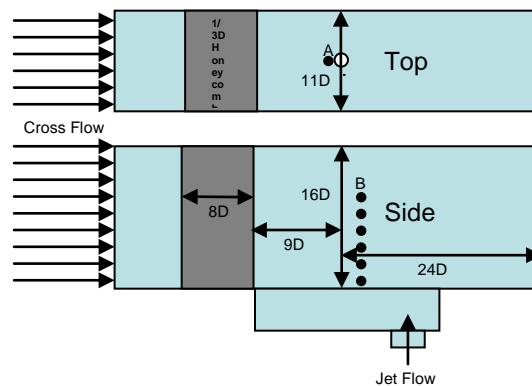


Fig. 5 Schematic of Test Article ($D = 0.001476\text{m}$)

DATA COLLECTION AND PROCESSING

Data were collected in a previous experiment (Kiel et. al., 2003) using a split-film probe; in the present experiment DPIV was employed. Horseshoe-vortex data were collected one-half diameter ahead of the upstream edge of the jet orifice. This point can be referred to as location "A" on Figure 5. The split-film probe was traversed in the flow to obtain Karman-Street and K-H/CVP data. Traverses were taken one diameter downstream of the trailing edge of the jet (location "B" in Fig. 5). Traverses proceeded normal to the bottom surface of the test article. The probe was traversed at increments of 0.0025 m until the measured velocity was parallel to the inlet crossflow. Rms velocity was also compared to the velocity of the inlet crossflow to assure matching. Traverses typically contained from 15 to 20 data points. Finally, frequency-domain information was calculated from raw velocity data obtained with the split film using a DFFT routine. The frequency-domain information was treated in two ways. First, the frequency-domain velocity data was studied, and data on dominant frequency and associated flow conditions were collected. Data were then non-dimensionalized and tabulated for vortex type.

Figure 6 is a schematic of the DPIV system used to collect instantaneous velocity and flow-visualization data. Two frequency-doubled Nd:YAG lasers are employed for instantaneous marking of the seed particles in the flow field. Combined by a beam combiner, the beams are directed through sheet-forming optics and illuminate the test section with a 2D plane ~ 1 mm thick. Scattering was created from seed particles introduced into the flow. The seed material used in the main flow was submicron-size smoke particles generated from a glycerin and water mixture and introduced directly into the system through the open blower. For seeding the jet, alumina-dioxide submicron particles were added in the line that feeds the jet using a cyclone-type seeder. The location of the seed particles is recorded on a cross-correlation CCD camera with 1008 x 1018 pixels (Redlake ES1.0). The camera repetition rate is set to 10 Hz for synchronization with the laser repetition rate. A 105-mm Nikon lens was used. Selection of the magnification and time delay between the lasers was dependent on the viewed area of the flow. The power required for laser-sheet illumination was very low (~ 10 mJ/pulse) because of the minimal amount of optics losses.

Once the PIV images have been captured and digitized, the velocity field is obtained using cross-correlation techniques over interrogation domains of the images using commercially available DPIV software. The dimensions of each interrogation domain are dependent on particle density, estimated local velocity gradients, particle-image size, and desired spatial resolution. The peak of the correlation map corresponds to the average velocity displacement within the interrogation spot. An intensity-weighted peak-searching routine is used to determine the location of the peak to sub-pixel accuracy. To improve the signal-to-noise ratio in the correlation maps, a correlation-correction scheme is applied wherein each map is multiplied by its immediate four neighborhoods. An overlapping of 75% is used to include about the same particles in the five maps that are multiplied to yield a single correlation map with lower noise. Zero padding is also employed for adding accuracy. The software includes a grid feature that allows selection of areas of the image to be processed. It also provides a choice of various correlation engines and correlation peak locators and incorporates several improvements to standard (single-pass) PIV techniques such as recursive estimation of the velocity field through a multipass algorithm for increasing resolution. The interrogation domains are overlapped by three-quarters the domain size to yield additional vectors. The overlapping includes new particles in every subregion. Average routines allow for removal of outliers beyond any number of standard deviations (Estevadeordal et al. 2002).

Many factors are involved in the DPIV uncertainty-calculation process (laser, CCD, seeding, imaging, algorithms, oscilloscope, etc). The highest uncertainty was found to be associated with the velocity calculation, which involves Δx (the displacement in pixels of each interrogation region), Δt (the time interval between the two exposures), and the magnification of the digital image relative to the object (pix/m). The displacement in pixels obtained by peak-locator algorithms can provide sub-pixel accuracy (< 0.1 pixels) after correction for various biases. The Δt was adjusted to yield typical displacements of ~ 10 pixels, and the uncertainty is, thus, $< 1\%$. Values in the wake region, however, may have higher uncertainties due to the lower Δx . The maximum uncertainty in the Δt was calculated from the time interval between the two laser pulses with the aid of an oscilloscope (uncertainty 2%). It was found that this uncertainty increases with lower laser power and with lower Δt . A conservative number for the present experiments, which employed a Δt of about 10-20 μ s and powers around 10 mJ, was found to be $< 1\%$. The

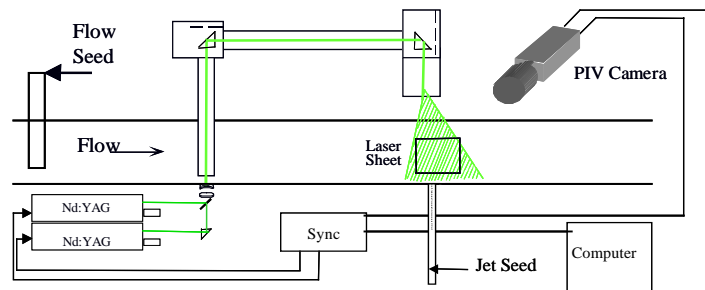


Fig. 6 Schematic of DPIV System

magnification was measured using images of grids located in the laser-sheet plane to better than 1%. Combining these conservative measurements of uncertainty yields a maximum error of < 2% for the free-stream velocity and ~10% in the lower speed areas of the jet.

RESULTS AND DISCUSSION

In this section results from split-film and DPIV measurements will be presented in two ways. Split-film data will be shown through the use of dimensionless energy spectra and dimensionless mean velocity profiles. Figure 7 is the dimensionless turbulent kinetic energy spectra for a momentum ratio of 10. It was taken one diameter behind the jet and at the point normal to the surface where maximum velocity occurred (~ 2.75 diameters above the surface). Figure 8 is representative of the dimensionless turbulent kinetic energy at all points in the flow. Plots differed only in the magnitude of dimensionless turbulent kinetic energy in the large-eddy region of the flow, in excellent agreement with the assertions made by Tennekes and Lumley (1990). Note that the split-film probe would resolve only dimensionless wave numbers less than $k/k_d \sim 0.08$. As a result, some of the dissipation range was not resolved.

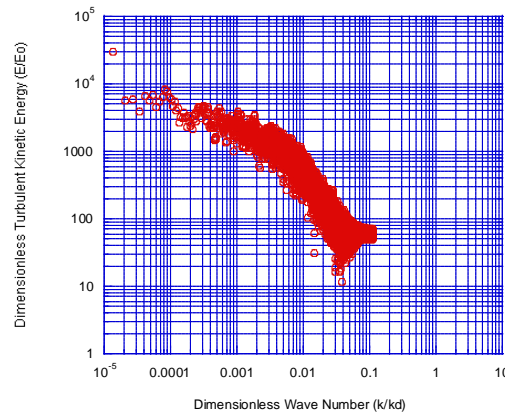


Fig. 7 Dimensionless Turbulent Kinetic Energy vs. Dimensionless Wave Number

Mean and rms velocity was also calculated for each point of data taken by the split-film probe. The mean of the time-varying data was then calculated. Figure 8 depicts mean-velocity profiles one diameter downstream of the probe for momentum ratios ranging from 2.5 to 15. It should be noted that generally the dimensionless mean-velocity peak increases with increasing momentum ratio. Furthermore, the maximum occurs higher and higher along the y-axis as the momentum ratio increases, as expected.

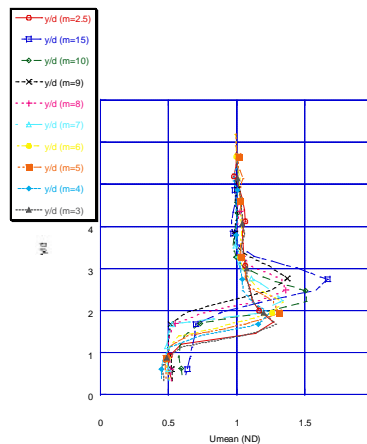


Fig. 8 Dimensionless Velocity Profiles at $x/D=1$

For the horseshoe vortex, instantaneous velocity data were collected over a momentum-ratio range of 3-25, and a range of Re , based on jet diameter and crossflow velocity, of 3,000 - 17,600. Re was varied independent of momentum ratio and visa versa. Four characteristic peaks were discerned in the data between 0 and 50 Hz. For frequencies greater than 50 Hz, a peak was rarely discernable. Figure 10 is a plot of St versus Re for all four peaks. Note in all cases that St decreased with increasing Re .

Kelso and Smits (1995) studied a laminar horseshoe vortex in front of the jet. Their data and flow visualization indicated that horseshoe vortices exist in three Re regions: steady, oscillating, and coalescing. For their conditions they indicated that for Re greater than 3,500 the vortices are a coalescing system. One could speculate that the vortices in this experiment are most likely in the oscillating or coalescing regions. In the oscillating case, the vortices oscillate as the Kelvin-Helmholtz vortex ring forms in the jet and sheds. In the coalescing case, vortices coalesce, and new vortices are constantly being formed. Both regions are characterized by three primary and several secondary vortices.

Figure 9 shows the St data for the four peaks noted in the frequency data for the horseshoe vortex. As indicated by Kelso & Smits (1995), three of the peaks in the data are associated with the three primary vortices. The fourth can be explained in two ways. Either it is due to the oscillatory nature of the flow (typically these oscillations are very low frequency, corresponding to the lowest St) or it corresponds to the formation and shedding of the Kelvin-Helmholtz ring in the jet boundary layer.

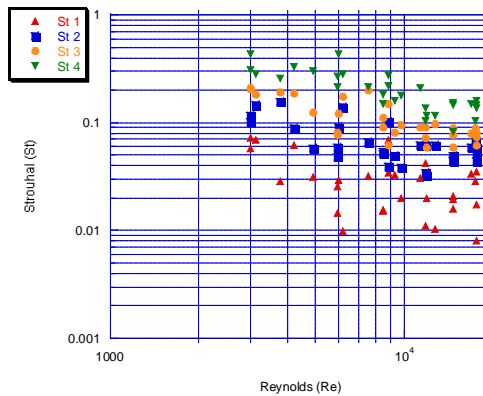


Fig. 9 St Versus Re for Horseshoe Vortex

Figure 10 depicts two typical results from the DPIV investigation of horseshoe vortices. At the top are flow visualization images, and at the bottom are average velocity vectors and streak lines. Areas of recirculation are noted on the leading edge of the jet. It is difficult to discern whether this area is created by horseshoe-vortex formation, Kelvin-Helmholtz vortex formation, or a combination of these two. Beyond this area it is difficult to discern other areas of possible recirculation because of the fine structures developing along the wall and on the wall of the jet as it issues into the crossflow. On the other hand, the raw and processed plots for the higher Reynolds number, lower momentum ratio flow depict more discernable areas of horseshoe vortex formation. In the color image, streak lines make it easy to recognize at least two horseshoe vortices.

Figure 11 depicts the DFFT of instantaneous velocity data from split film in the region of the Kelvin-Helmholtz vortices. These data were taken approximately one diameter downstream of the trailing edge of the jet and at a point above the surface where the velocity vector was maximum. This position depended on flow conditions. From Figure 11 it is noted that two bands of data were measured at the different conditions in the flow. Previously, Kiel et. al. (2003) proposed that the two sets of data correspond to the frequency of the K-H/CVP vortices and the frequency of the shedding of the vortex ring.

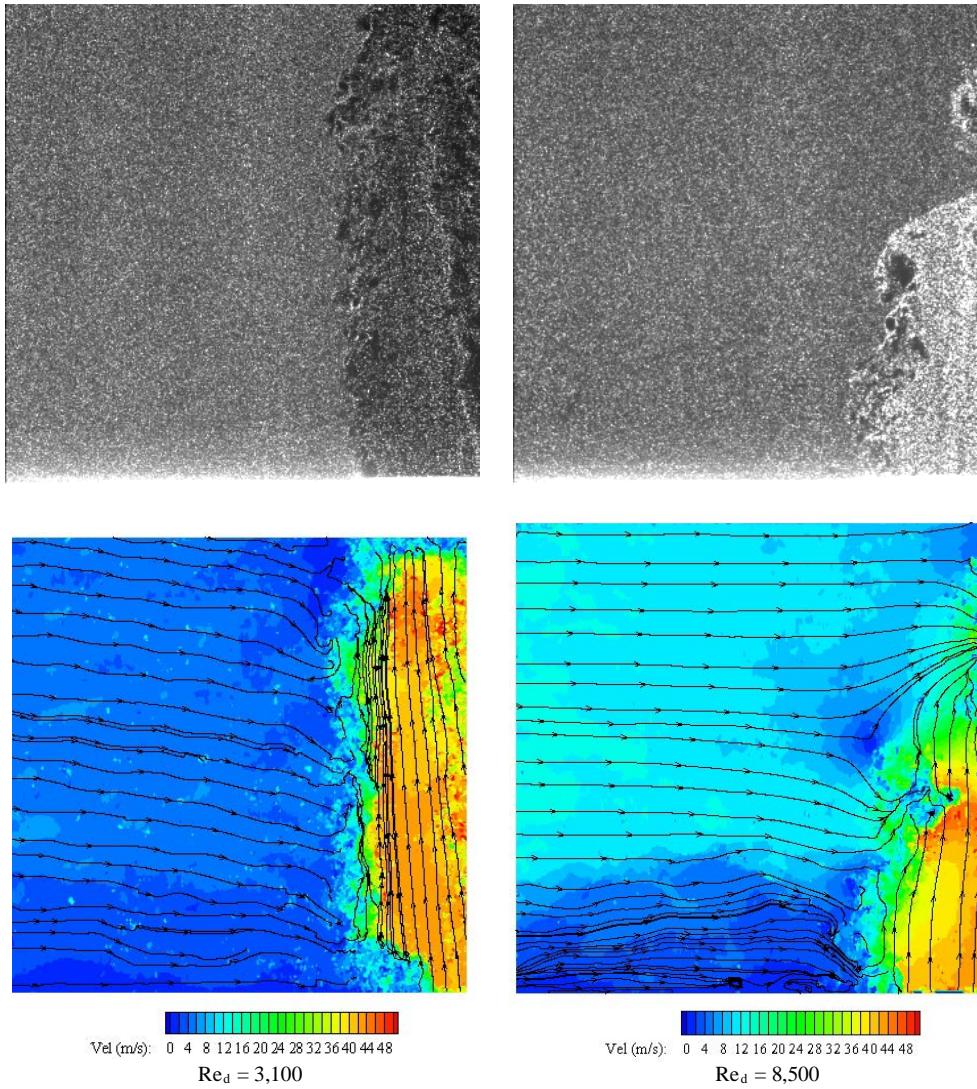


Fig. 10 Instantaneous DPIV Data Upstream of Jet Exit for Two Re Cases

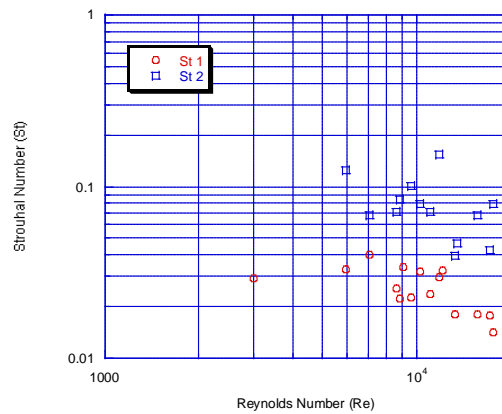


Figure 11 St Versus Momentum Ratio for KH-CVP

Figure 12 displays raw DPIV images corresponding to a jet Reynolds number of 36,000 with various momentum ratios. The effect of increasing the crossflow momentum in the jet can be qualitatively discerned. Figure 13 shows the average of 50 processed (median) DPIV images. Pictured are contours and vectors of velocity. The conditions for these data are the same as those depicted in Figure 12. The effect of increasing the crossflow momentum in the jet can be quantitatively discerned.

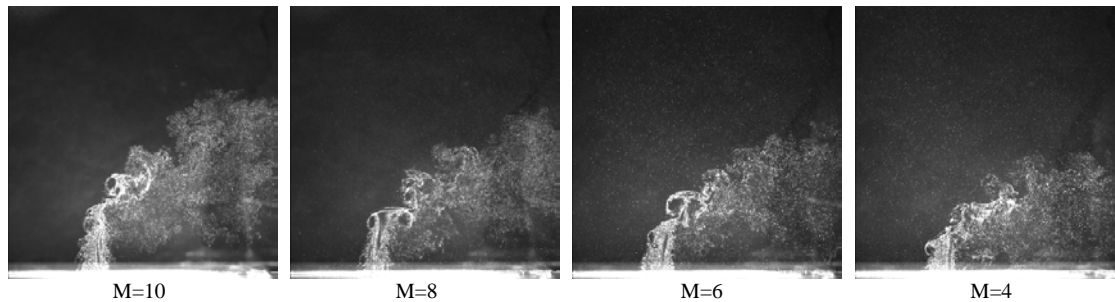


Fig. 12 Flow Visualizations for Various Momentum Ratios ($U_{jet}=59.6$ m/s)

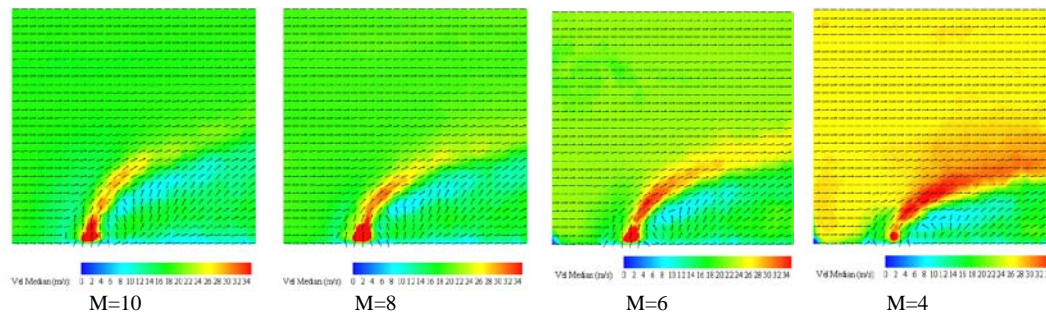


Fig. 13 Average Velocity Distribution for $Re_j=36,000$

In both Figures 12 and 13, it is evident that jet penetration is a function of the jet momentum ratio for a constant jet Reynolds number. In Figure 14 raw and processed data are displayed. The processed data are average (50 samples) vectors and velocity contours. The conditions for Figure 14 were such that the momentum ratio was held constant while jet and crossflow Reynolds numbers were varied. For a constant momentum ratio of 10 it is obvious that the jet penetration changes radically with Reynolds number. From this result we can assert that the jet penetration is a function not only of the momentum ratio and axial location but also of both jet and crossflow Re numbers.

Figure 11 (Kiel, et. al. 2003) depicts the St decreasing for the Kelvin-Helmholtz vortices. On further inspection, this result is counter-intuitive relative to shedding from circular cylinders and bluff bodies. Further assessment of the raw data in Figure 14 also sheds light on this issue. It is evident from the figure that the vortices are reduced in size as the Reynolds number of the crossflow is increased, which is analogous to the increase in frequency. This contradiction can be resolved when the frequency--not the Strouhal number--of the data is considered. Figure 15 depicts the frequency vs Reynolds number for the data in Figure 12. It should be noted that frequency is, in fact, increasing with Reynolds number, regardless of momentum ratio. When comparing Figures 11 and 15, the data indicate that the frequency is increasing. However, from the definition of the Strouhal number, the velocity (in the denominator) is apparently increasing more rapidly than the frequency (in the numerator). This would explain the negative trend in Strouhal number.

CONCLUSION AND RECOMMENDATIONS

DPIV was an invaluable tool in this study. It provided vital physical information concerning the flow that could not be obtained with a split-film probe alone and lent further insight into various JICF features and their apparent dependence on Reynolds number. It also revealed that for this range of Reynolds numbers, the jet penetration is a function of both jet and crossflow conditions in addition to momentum ratio and

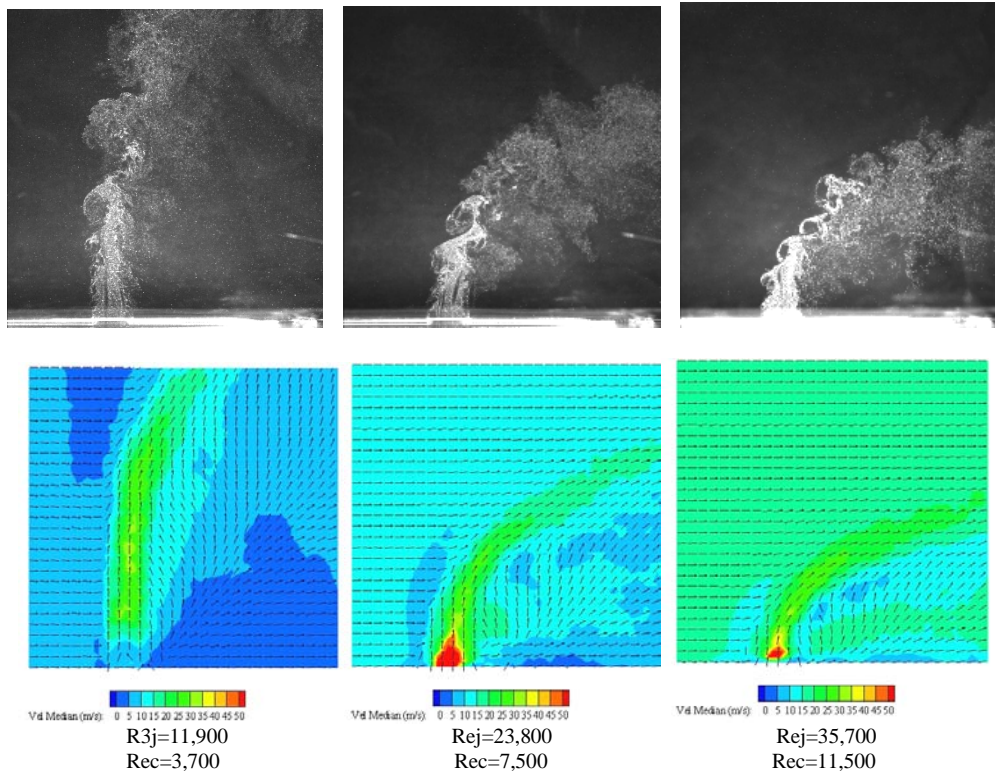


Fig. 14 Flow Visualizations and Average Velocity Distributions for Various Re Numbers at M=10

Fig. 15 Frequency vs Reynolds Number for the First Frequency Peak in Kelvin Helmholtz Data

axial location. Finally DPIV verified that while the frequency of the Kelvin-Helmholtz shedding was, in fact, increasing, the Strouhal number was decreasing. These findings are also valuable for flow-control efforts. In further efforts the physical understanding obtained in split-film and DPIV experiments will be used to develop and evaluate control-oriented modeling. In the future, studies on controllability and observability with different actuator and sensor configurations will be conducted using DPIV and split-film data-acquisition systems.

REFERENCES

- Blanchard, J., N., et al., 1999, "Influence of a Counter Rotating Vortex Pair on the Stability of a Jet in Cross Flow: an Experimental Study by Flow Visualization," *Experiments in Fluids*, Vol. 26, pp. 63-74.
- Brizzi, L., E., 1995, "Sur les structures tourbillonnaires generees a la frontiere d' un jet circulaire debouchant perpendiculairement dans une couche limite," *CRSA Paris*, 321, II.B, pp. 217-223.
- Bosanquet, C., & Pearson, J. L., 1936, "The Spread of Smoke and Gasses from Chimneys," *Transactions of the Farraday Society*, Vol. 32, p. 1249.
- Estevadeordal, J., Gogineni, S., Goss, L., Copenhaver, W., and Gorrell, S., 2002, "Study of Study of Wake-Blade Interactions in a Transonic Compressor Using Flow Visualization and DPIV," *Journal of Fluids Engineering*, Vol. 124, pp. 166-175.
- Gogineni, S., et al., 1995, "Investigation of a Jet in Cross Flow Using PIV," *AIAA-95-0790*.
- Incorporera, F., & De Witt, D., 1985, Fundamentals of Heat and Mass Transfer, John Wiley and Sons, New York.
- Kelso, R. M., & Smits, A. J., 1995, "Horseshoe Vortex Systems Resulting From the Interaction Between a Laminar Boundary Layer and a Transverse Jet," *Physics of Fluids*, Vol. 7, pp. 153-158.
- Kelso et al., 1992, "A Visual Study of a Round Jet in Cross Flow," *Symposium of Flow Visualization*, Yokohama Japan, pp. 173-177
- Kiel, et. Al., 2003, "Experimental Investigation of the Vortex Shedding of a Jet in Cross Flow," 2003, *AIAA 2003-0182*.
- Lim, T., et al. 2001, "On the Development of Large-scale Structures of a Jet Normal to a Cross Flow," *Physics of Fluids*, Vol. 13, No. 3, pp. 770-775.
- Lord, W.K., MacMartin, D. G., & Tillman, T. G., 2000, "Flow Control Opportunities in Gas Turbine Engines," *AIAA 2000-2234*.
- Margason, R., 1993, "Fifty Years of Jet in Cross Flow Research," *Proceedings of the 72nd AGARD Fluid Dynamics Panel Meeting*, pp. 1-12 to 1-17.
- Marzouk, Y.M., & Ghoniem, A. F., 2002, "Mechanism of Streamwise Vorticity Formation in a Transverse Jet," *AIAA 2002-1063*
- Moussa, Z. M., Trischka, J. W., & Eskinazi, S., 1977, "The Near Field in the Mixing of a Round Jet with a Cross-Stream," *Journal of Fluid Mechanics*, Vol. 89, Part 1, pp. 49-80.
- Sutton, O., G., 1932, *Proceedings of the Royal Society*, Vol. A135, p. 143.
- Tennekes, H., & Lumley, J., 1990, A First Course in Turbulence, MIT Press.
- Wei, Q-D., Chen, G., & Du, X-D., 2000, "An Experimental Study on the Structure of Juncture Flows," *The Visualization Society of Japan, Journal of Visualization*, Vol. 3, No. 4, pp. 341-348.

Stator Cascade Flow Vectoring Through Counter-Flow Blowing

Michael R. Harff and J. Mitch Wolff

Department of Mechanical and Materials Engineering, Wright State University, Dayton, Ohio

William W. Copenhaver and David Car

Air Force Research Laboratory, Wright-Patterson AFB, Ohio

Jordi Estevadeordal

Innovative Scientific Solutions, Inc., Dayton, Ohio

Abstract

Preliminary design computational results showed that a significant amount of increased flow turning (12 degrees) can be achieved in a high turning stator example with only 0.5% core flow counter-flow blowing (CFB). To explore this approach, an existing cascade section was modified to implement a "proof-of-concept" design. Experimental data from Particle Image Velocimetry (PIV) showed that an increase of 8 degrees in turning was achieved through counter-flow blowing of 0.28% of the core flow. For this investigation, a simplified 2-D model was run by the Advanced Ducted Propfan Analysis Code (ADPAC) and compared to the experimental results for a range of 0.0% to 0.30% core flow counter-flow blowing. Based on this study, ADPAC has been shown to be a viable design tool for CFB applications.

Nomenclature

$$C_m \quad \text{mass blowing coefficient} \\ = m_{dot,j} / (3.03 m_{dot,inf}) \quad (1)$$

$$C_m^* \quad \text{corrected mass blowing coefficient} \\ = m_{dot,j,c} / (3.03 m_{dot,inf}) \quad (2)$$

$$C_x \quad \text{axial chord of blade} \\ m_{dot} \quad \text{mass flow rate} \\ m_{dot,c} \quad \text{corrected mass flow rate} \\ = m_{dot} \sqrt{\theta} / \delta \quad (3)$$

$$M \quad \text{Mach number} \\ M_e \quad \text{cascade exit Mach number} \\ s \quad \text{cascade blade spacing} \\ U \quad \text{absolute velocity} \\ U_{k,m} \quad \text{mass-averaged, } k^{\text{th}} \text{ component of velocity} \\ = \sum_i U_{k,i} (\rho_i U_i A_i) / \sum_i \rho_i U_i A_i \quad (4)$$

$$y^+ \quad \text{dimensionless wall coordinate} \\ = \frac{y}{v_{wall}} \sqrt{\frac{\tau_{wall}}{\rho_{wall}}} = y \sqrt{\frac{(du/dy)_{wall}}{v_{wall}}} \quad (5)$$

$$\alpha_e^* \quad \text{design exit flow angle} \\ \alpha_e \quad \text{actual exit flow angle} \\ = \tan^{-1}(U_y^m / U_x^m) \quad (6)$$

$$\gamma \quad \text{deviation of flow} \\ = \alpha_e - \alpha_e^* \quad (7)$$

$$\delta \quad \text{corrected total pressure} \\ = P_0 / P_{0,ref} \quad (8)$$

$$\delta_s^* \quad \text{displacement thickness, as a fraction of } s \\ = \frac{1}{s} \int_{\xi=\xi_0}^{\xi=\xi_0+s} \left(1 - \frac{M}{M_{inf}} \right) d\xi \quad (9)$$

$$\theta \quad \text{corrected total temperature} \\ = T_0 / T_{0,ref} \quad (10)$$

Subscripts

j blowing slot (jet)
 x x- component
 y y- component
 inf cascade inlet
 $1.05C_x$ 105% axial chord

Introduction

Current fan designs in many cases require flapped IGV's (a segmented stator with only the back portion rotating like a flap on a wing of an

aircraft) to assure correct inlet flow conditions during off-design operation. The ability to vector the flow without the need of the “flap” on the IGV would significantly reduce the mechanical complexity and weight of the fan system. In addition, flow vectoring within the fan and compressor could greatly reduce the need for variable stators, again reducing the cost and weight of the engine. This approach employs pressure surface counter-flow blowing to increase the circulation/loading and achieve considerable flow vectoring. The stator uses a carefully placed blowing jet to increase the circulation (i.e. loading) of the blade, thereby providing the necessary turning. The blowing jet is placed on the pressure surface of the blade near the trailing edge and is directed into the flow, i.e. in a counter-flow direction, as near to tangent to the surface of the blade as possible.

In this paper, a detailed experimental and computational investigation into the flow physics associated with CFB for an advanced design stator airfoil is reported. A transonic linear cascade wind tunnel is utilized to obtain detailed PIV measurements with and without CFB. In addition, a high fidelity computational fluid dynamics (CFD)

model is used to model the experimental configuration. The CFD model, ADPAC, is compared with the experimental data with the intent that it could then be utilized to design a new circulation-controlled (CC) IGV, which would eliminate the need for the flap therefore reducing the weight and the required axial spacing of an engine using a flapped IGV.

Experimental Setup

Modifications were made to an existing 2D cascade of the “Tescom” geometry, a counter-swirl stator, and called the “Tescom-CAR” geometry (see Figure 1). The trailing edges were rounded off on the center three blades of the seven-blade cascade, to allow for installation of the blowing plenums and proper location of the counter-flow blowing jets. The jet slots were added at mid-span on the pressure surface near the trailing edge of the blades. The jets had a flow angle of 70° with respect to the normal to the blade surface, in the counter-flow direction, and a nominal width of 0.010". Particle Image Velocimetry (PIV) test data were acquired for

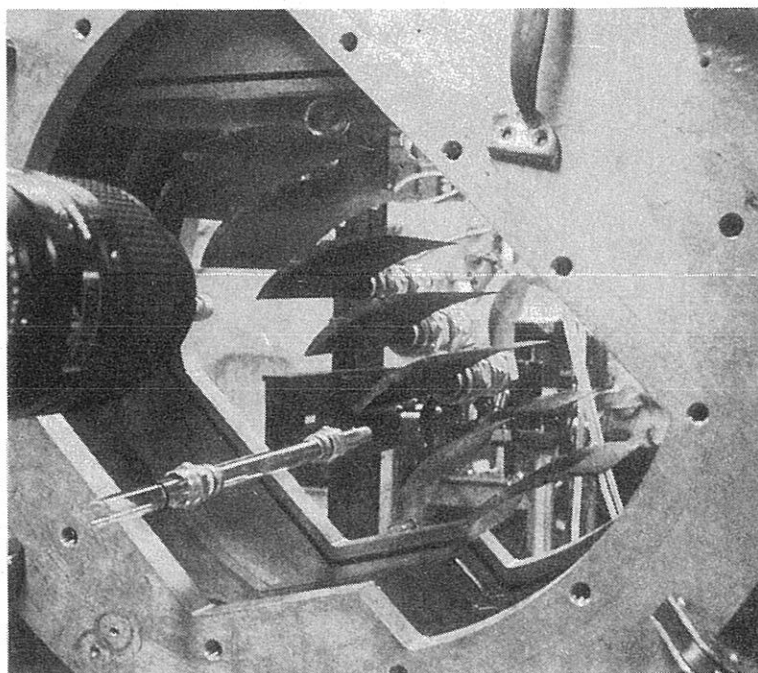


Fig. 1a: Tescom-CAR blades in Tescom counter-swirl cascade.

section with a 2D plane of thickness < 1 mm. The scattering from the seed particles is recorded on an ES1.0 Kodak CCD sensor (1008 x 1012 pixels). The camera maximum repetition rate is 15 double exposures per second and was set to 10 Hz for synchronization with the laser repetition rate. A 105-mm Nikon lens was used. The magnification for the present experiments was ~ 20 pixels/mm, which corresponds to a viewing width of ~ 50 mm. The time delay between the lasers was typically 2 μ sec. Once the PIV image has been captured and digitized, the velocity field is obtained using cross-correlation techniques. The correlation function is calculated over small segments (interrogation domains) of the PIV image. The peak of the correlation map corresponds to the average velocity displacement within the interrogation spot. An intensity-weighted peak-searching routine is used to determine the exact location of the peak to sub-pixel accuracy. To improve the signal-to-noise ratio in the correlation maps, a correlation-correction scheme is applied wherein each map is multiplied by its immediate four neighborhoods. An overlapping of 75% is used to include many of the same particles in the five maps that are multiplied to yield a single correlation map with lower noise. Zero padding is also employed for adding accuracy. For these experiments 100 image pairs were obtained during a 10 sec tunnel blowdown period. Of those images, 50 were chosen within the steady part of the run to be averaged with outlier rejection of two standard deviations. Averaging the instantaneous velocity fields has the effect of eliminating the fluctuations due to incoherent unsteadiness associated with turbulence and permitting a better comparison to the steady CFD prediction⁵ /4/.

A compact laser-sheet delivery system was utilized. This system consists of an optical probe designed with light-sheet-forming optics internal to the probe, which is similar to that reported by Copenhaver *et al.* (2002). The probe was placed downstream of the cascade in the flow path inside a glass rod that is transverse to the main flow direction. The cascade endwalls were formed with 31.75-mm (1.25-in.) thick Plexiglas to allow optical access. The power required for laser-sheet

illumination was very low (< 20 mJ/pulse) because of minimal optics losses. Seeding particles were injected into the flow approximately 10 blade-chord lengths upstream of the cascade section with an injection rake. Sub-micron particles of aluminum dioxide were used as the seeding material.

The uncertainty in the DPIV velocity measurements was determined as follows. The velocity was computed dividing the displacement (pixels) of each interrogation region, by the time interval between the two exposures, and by the magnification of the digital image relative to the object (pixels/mm). The time interval was adjusted to yield typical displacements of the free stream in the present experiments of > 10 pixels, with an uncertainty of $< 1\%$. Values in the wake region where the minimum velocity occurs, however, have higher uncertainties because of the lower displacements; for example, 1 pixel displacement could yield an uncertainty of $\sim 10\%$. The maximum uncertainty in the time interval was calculated from the time interval between the two laser pulses. It was found that this uncertainty increases with lower laser power and with lower time interval. A conservative number for the present experiments, which employed a time interval of 2 μ sec and powers around 20 mJ, was found to be 1%. The magnification was measured from images of rulers located in the laser-sheet plane, and it is conservatively estimated that it could be read to better than 1%. Combining these three conservative measurements of uncertainty yields a maximum error of $< \pm 2\%$ of the reported value for the free-stream velocity, which increases to $\sim \pm 10\%$ of the reported value at the wake-minimum-velocity location.

Experimental Results

The exit flow fields obtained averaging 50 PIV frames are shown in Figure 4 for corrected mass blowing coefficients of 0.0, 0.0023, and 0.0028, as obtained from equations (2), (3), (8), and (10). Data were extracted directly from the contour plots for calculation of displacement thickness and deviation.

Displacement thickness was calculated at 105% axial chord, numerically integrating the data across a full flow passage according to equation (9). This gives the fraction of blockage in the flow passage due to the presence of the blade. Deviation was calculated along the same plane at 105% axial chord from mass-averaged x and y velocity components via equations (4), (6), and (7). Density, which varied by <10% in the wake region for all CFD cases, was assumed constant in equation (4). All experimental results are presented in Table 1. To summarize, an increase of flow turning of 2° was achieved with C_m^* of 0.0023, while an increase of 7.8° was achieved with C_m^* of 0.0027.

Table 1
Tescom-CAR Experimental Results.

M_{inf}	$C_m (\times 10^2)$	P_j / P_{inf}	$C_m^* (\times 10^3)$	δ^* (degrees)	δ_s^*	Average exit Mach number
0.75	0.00	N/A	0.00	8.65	0.116	0.57
0.75	0.44	1.88	2.32	6.66	0.145	0.57
0.75	1.00	3.59	2.79	1.09	0.222	0.59

A key assumption underlying the experimental C_m values is identical blowing slot widths on all three blades. This was not the case, as the average slot widths of the blades were 0.012", 0.011", and 0.013", the blade used for the PIV data being the smallest of the three. From continuity, and assuming steady flow with constant mass flux across each slot, the actual mass flow rates through the test blade would have been 0.93 of reported values. C_m^* values were adjusted from 0.0025 and 0.0030 to 0.0023 and 0.0028, respectively. This did not change the basic trends for the proof-of-concept test; however, flow vectoring was achieved with a slightly lower CFB mass flow than what was originally believed.

2-D Computational Model

With the experimental data providing incentive for further computational investigation of counter-flow blowing, a simplified, two-dimensional "proof-of-concept" model was constructed to see if ADPAC (Advanced Ducted Propfan Analysis Code) /4/ could predict the basic trends. The solutions were run in 2D steady-state mode to save on computational time, and the Spalart-Allmaras (1-equation) turbulence model was used. The computational domain consisted of three blocks, with a capped O grid for the blade and two 110%-axial-chord, extension H grids upstream and downstream of the blade. Figure 3 shows the capped O grid used in the coarse mesh. Each test case was run on coarse, medium, and fine meshes to demonstrate grid independence of the solution. Resolution was increased by a factor of 3.93 from the coarse to the medium mesh, and by a factor of 3.59 from the medium to the fine mesh. This corresponded to $\sim 1.98x$ and $\sim 1.89x$ increases along each dimension for the 2-D mesh.

Boundary conditions were set to model the experiment as follows: Inlet total pressure and temperature were set to standard values, and the exit static pressure was set to obtain inlet Mach ~ 0.75 for all cases. Periodic boundary conditions were set on the upper and lower edges of the mesh, and the flow solver was set to Cartesian coordinates, to model the linear cascade. The blade was defined as an adiabatic, solid, no-slip surface. Counter flow blowing was modeled with an inlet boundary condition at the appropriate location on the pressure surface of the blade. The code was restarted, adjusting the blowing jet total pressure and flow angle to obtain the correct conditions. Mass flow rates, as well as mass-averaged velocity components, were measured with PROBE (boundary condition) at the inlet, at the blowing jet, and at 105% axial chord.

Converged solutions were obtained, where the \log_{10} residual was -7.4 or lower. The initial \log_{10} residual values ranged from -2.0 to -3.0 ; these results go well beyond the ADPAC manual's three orders of magnitude criterion for converged solutions.

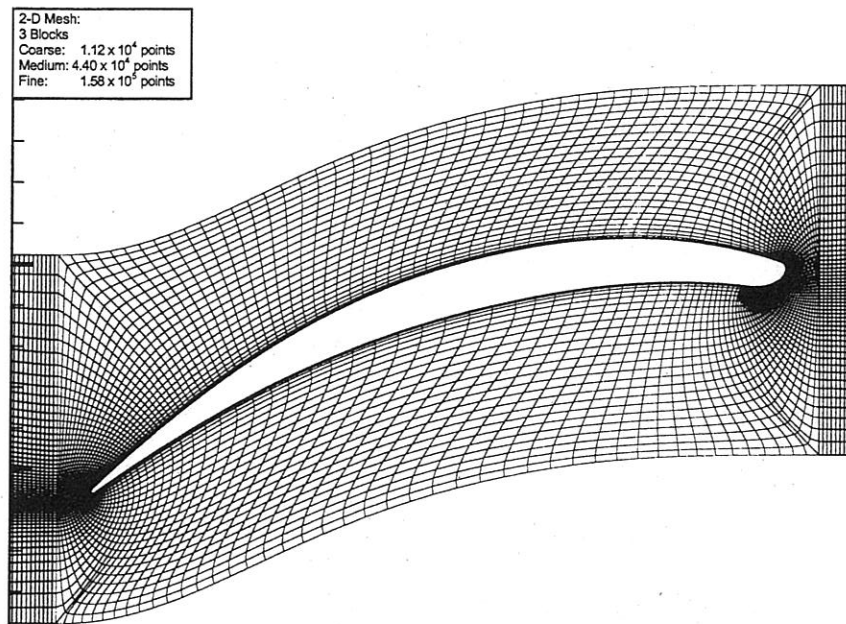


Fig. 3: Capped O grid for Tescom-CAR geometry, coarse mesh.

Computational Results

The exit flow fields for $C_m^* = 0.0$, 0.0022, and 0.00828 are shown in Figure 5, corresponding to the three experimental test points in Figure 4.

Displacement thickness was calculated as for the experiment. Deviation was calculated from the mass-averaged PROBE data. Details of the computational study are presented in Table 1 for C_m^* values ranging from 0.0 to 0.0030. Mesh levels

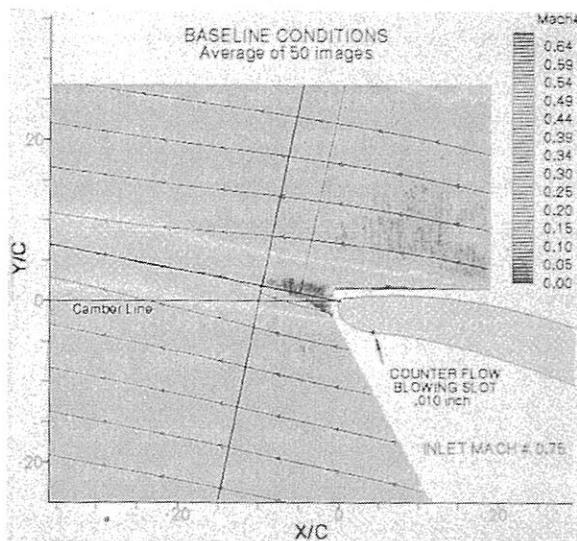


Fig. 4a: PIV data for Tescom-CAR geometry. $C_m^* = 0.0$. Inlet Mach # = 0.75.

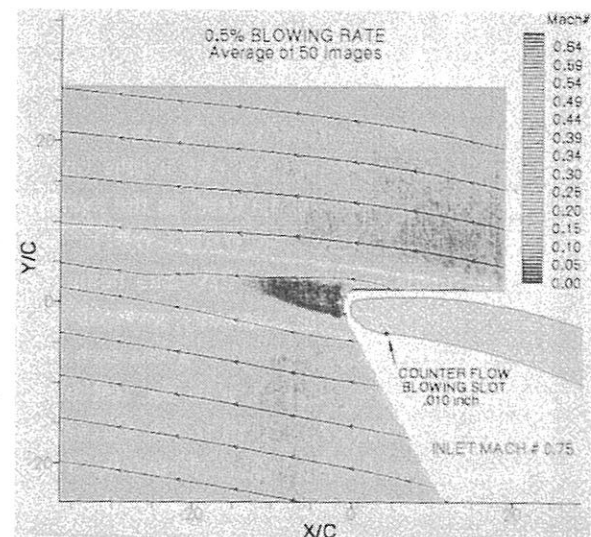


Fig. 4b: PIV data for Tescom-CAR geometry. $C_m^* = 0.0023$. Inlet Mach # = 0.75.

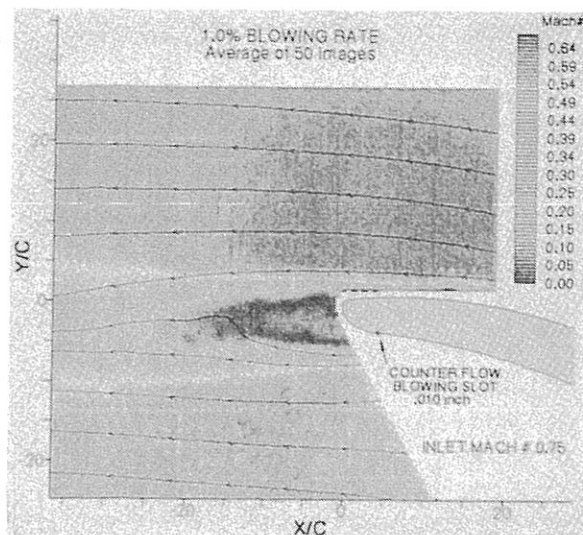


Fig. 4c: PIV data for Tescom-CAR geometry. $C_m^* = 0.0028$. Inlet Mach # = 0.75.

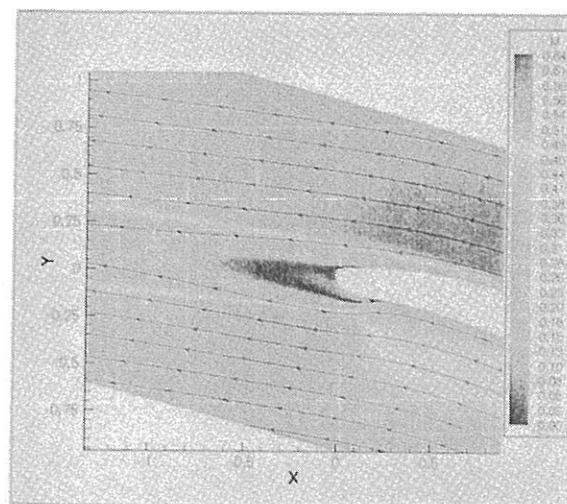


Fig. 5b: ADPAC solutions for Tescom-CAR. $C_m^* = 0.0022$. Inlet Mach # = 0.75.

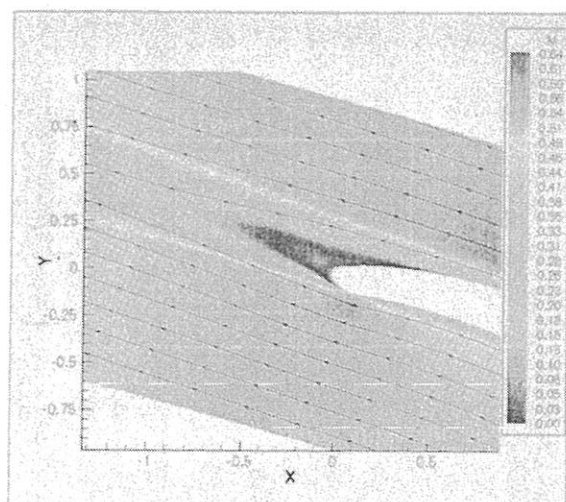


Fig. 5a: ADPAC solutions for Tescom-CAR. $C_m^* = 0.0$. Inlet Mach # = 0.75.

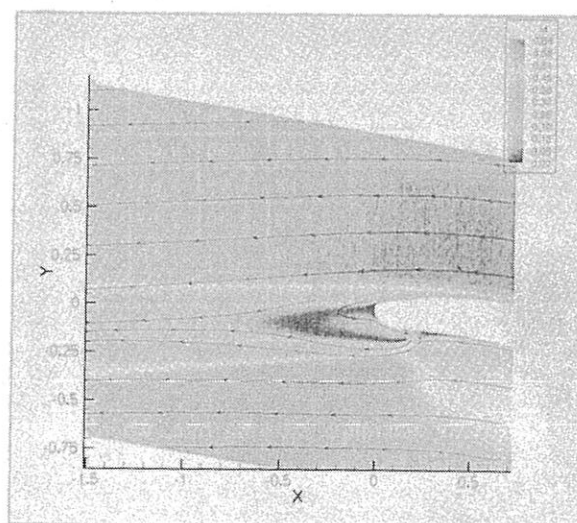


Fig. 5c: ADPAC solutions for Tescom-CAR. $C_m^* = 0.0028$. Inlet Mach # = 0.75.

(coarse, medium, or fine) are shown for each case, along with blowing and inlet mass flows as acquired from the PROBE output data, and the nominal mass blowing coefficient calculated from equation (1). The main parameters for Mach number, flow angle, deviation, and displacement thickness are also included in Table 2. Inlet quantities were measured at the model inlet plane, 115% chord length upstream from the leading edge of the blade. For improved consistency of the wake profiles obtained

on three mesh levels, exit quantities were measured at the 105%-chord exit plane, which was the common interface between the O-grid and downstream H-grid for all three meshes. Finally, CFB quantities were measured at the CFB inlet boundary on the surface of the blade. Total pressure of the blowing jet was increased until the code became unstable for all three meshes. The baseline mesh was the only one that was actually choked (M

Table 2
Tescom-CAR, ADPAC 2-D Simulation Details.

case number	mesh level	$m_{dot,j}$ (lbm/sec $\times 10^2$)	$m_{dot,inf}$ (lbm/sec)	C_m ($\times 10^3$)	C_m^* ($\times 10^3$)	Inlet Mach number	Exit Mach number	CFB Mach number	Inlet Flow Angle (degrees)	Exit Flow Angle (degrees)	Flow Turning Angle ($\alpha - \alpha_e$, degrees)	Deviation (degrees)	δ^+
7	C	0.000	0.419	0.00	0.00	0.754	0.570	0.000	44.000	4.045	39.955	13.545	0.074
8	C	0.193	0.418	1.53	1.74	0.748	0.563	0.388	44.000	-3.681	47.681	5.819	0.190
9	C	0.255	0.418	2.01	2.21	0.752	0.569	0.498	44.000	-5.004	49.004	4.496	0.192
10	C	0.321	0.418	2.53	2.59	0.751	0.574	0.638	44.000	-5.969	49.969	3.531	0.192
11	C	0.381	0.418	3.01	2.81	0.748	0.579	0.757	44.000	-6.492	50.492	3.008	0.195
12	C	0.480	0.419	3.78	2.96	0.753	0.602	0.953	44.000	-7.704	51.704	1.796	0.201
1	M	0.000	0.418	0.00	0.00	0.751	0.551	0.000	44.000	3.011	40.989	12.511	0.165
2	M	0.192	0.418	1.51	1.69	0.748	0.553	0.392	44.000	-5.186	49.186	4.314	0.171
3	M	0.256	0.418	2.02	2.18	0.750	0.561	0.492	44.000	-6.899	50.899	2.601	0.174
4	M	0.321	0.418	2.53	2.57	0.752	0.573	0.626	44.000	-8.637	52.637	0.863	0.179
5	M	0.380	0.418	3.00	2.81	0.750	0.587	0.753	44.000	-10.135	54.135	-0.635	0.186
6	M	0.480	0.417	3.80	2.99	0.745	0.630	1.004	44.000	-13.037	57.037	-3.537	0.208
13	F	0.000	0.419	0.00	0.00	0.755	0.571	0.000	44.000	2.154	41.846	11.654	0.162
14	F	0.190	0.418	1.50	1.68	0.750	0.551	0.387	44.000	-5.337	49.337	4.163	0.173
15	F	0.253	0.419	2.00	2.17	0.752	0.559	0.486	44.000	-6.939	50.939	2.561	0.176
16	F	0.318	0.419	2.50	2.56	0.753	0.570	0.624	44.000	-8.653	52.653	0.847	0.182
17	F	0.380	0.418	3.00	2.82	0.750	0.584	0.762	44.000	-10.262	54.262	-0.762	0.192
18	F	0.464	0.420	3.64	2.96	0.760	0.621	0.957	44.000	-12.495	56.495	-2.995	0.203

~ 1.0) at its maximum blowing rate, whereas both the coarse and fine cases were not yet choked ($M \sim 0.95$). Slot geometries, as determined by inlet boundary conditions in ADPAC, were identical for all three meshes. Instability may have been due to non-physical pressure gradients especially at the first two cells of the blowing slots, which were inadequately clustered near the edges for all three meshes.

The y^+ values for the first grid point off the blade were calculated with equation (5) using second-order polynomial fits for the $(du/dy)_{wall}$ values and plotted in Figure 6. Generally, y^+ values less than 5 are needed to include the viscous sub-layer, while most research suggests that values less than 1 are required for good accuracy when the turbulence equations are integrated to the wall [5].

This does not imply complete physical accuracy of the turbulence model, rather, that the full capability of the model—though limited—was being used. It is apparent from Figure 6(a) that a large part of the suction and pressure surfaces were at or above $y^+ = 1$. This, along with non-monotone convergence of the displacement thickness, indicated that there was significant error in the coarse-mesh boundary layer solution. Consequently, the coarse-mesh solution was out of the asymptotic range as described by Roache [6]. The y^+ values were less than ~ 0.8 for the medium mesh and less than ~ 0.7 for the fine mesh everywhere along the blade, except for the leading edge and the immediate vicinity of the blowing slot. Therefore a two-grid analysis was used on the medium and fine meshes with a factor of safety of 3 to determine the discretization error.

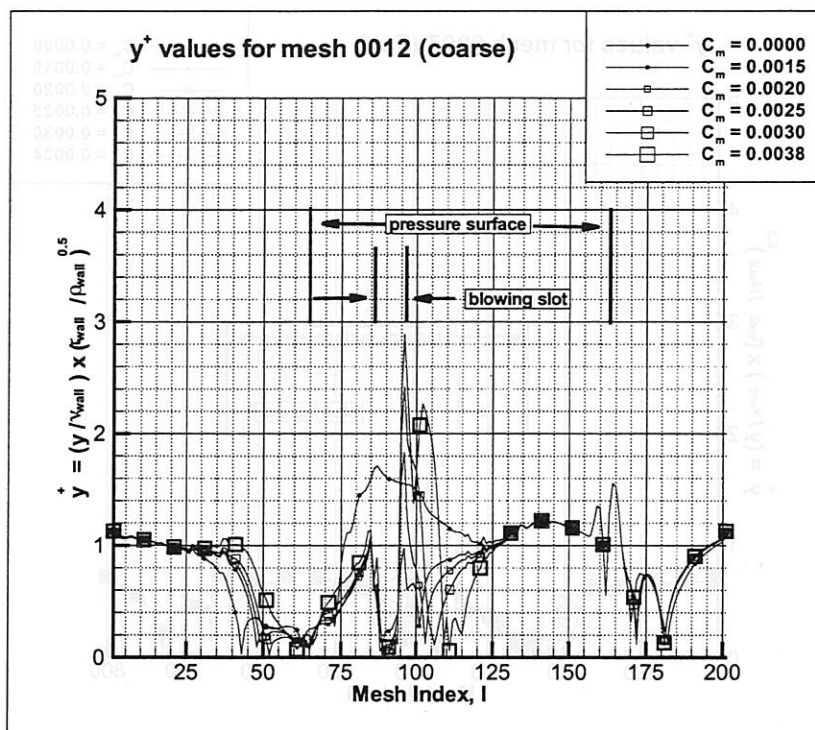


Fig. 6a: Calculated y^+ values around the blade for coarse mesh.

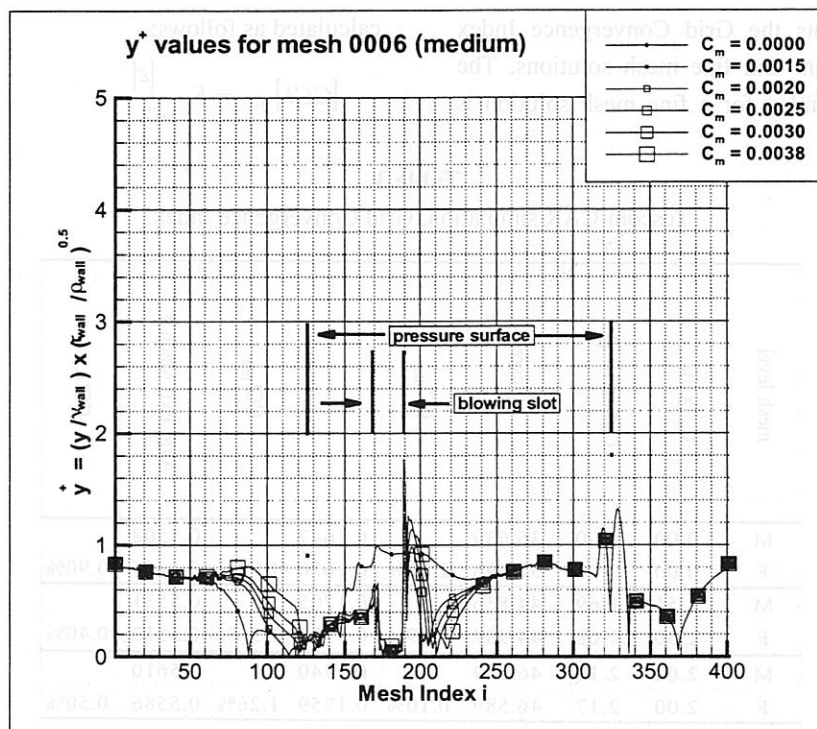


Fig. 6b: Calculated y^+ values around the blade for medium mesh.

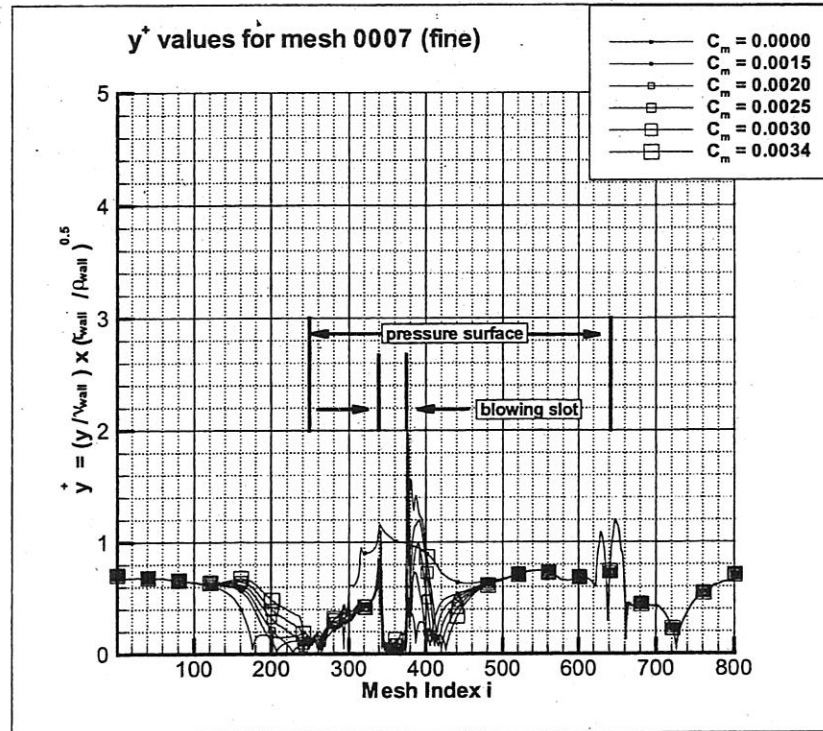


Fig. 6c: Calculated y^+ values around the blade for fine mesh.

Table 3 presents the Grid Convergence Index data for the medium and fine mesh solutions. The grid convergence index for a fine mesh solution is

calculated as follows:

$$[GCI]_{fine} = F_s \frac{|\epsilon|}{r^p - 1} \quad (11a)$$

Table 3

Tescom-CAR simulation, Grid Convergence Index.

mesh level	$C_m (\times 10^{-3})$	$C_m^* (\times 10^{-3})$	i (degrees)	GCI_{fine}	ϵ	GCI_{fine}	Avg. Exit Mach #	GCI_{fine}
M	0.00	0.00	36.639		0.1647		0.5508	
F	0.00	0.00	37.496	2.71%	0.1620	1.90%	0.5465	0.90%
M	1.51	1.69	44.836		0.1705		0.5531	
F	1.50	1.68	44.987	0.39%	0.1725	1.36%	0.5512	0.40%
M	2.02	2.18	46.549		0.1740		0.5610	
F	2.00	2.17	46.589	0.10%	0.1759	1.26%	0.5586	0.50%
M	2.53	2.57	48.287		0.1791		0.5730	
F	2.50	2.56	48.303	0.04%	0.1820	1.87%	0.5700	0.61%
M	3.00	2.81	49.785		0.1859		0.5868	
F	3.00	2.82	49.912	0.29%	0.1922	3.90%	0.5840	0.55%

$$\text{where } \varepsilon = \frac{f_m - f_f}{f_m} \quad (11b)$$

for some characteristic function f (e.g., deviation) defined on the medium mesh, at level m , and the fine mesh, at level f . The recommended factor of safety for a two-grid convergence study is $F_s = 3$. The effective grid refinement ratio may be defined as

$$r = \left(\frac{N_2}{N_1} \right)^{1/D} \quad (11c)$$

where $D = 2$ is the dimensionality of the problem. For the medium-fine mesh comparison at hand, $r \sim 1.895$, and the order of convergence is assumed to be $p = 2$. According to the grid convergence index calculations, the discretization error of the fine mesh solution was $\leq 2.7\%$ for deviation, $\leq 3.9\%$ for displacement thickness, and $\leq 0.9\%$ for free stream exit Mach number.

Experimental/Computational Comparison

Computational versus experimental results are presented in Figure 7 for deviation and displacement thickness, respectively. As noted above, the computational model was a simplified one; all the details of the experimental geometry and test conditions were not incorporated into the model, and therefore a direct, one-to-one comparison could not be made. However, according to Figure 7, the simplified, 2-D model predicted the trends reasonably well, on a scale similar to the experimental values: increasing the corrected mass flow of CFB was found to increase the amount of flow turning, increase the wake size, and increase the free stream exit Mach number.

Perhaps the most significant of the simplifying assumptions made for the model was the use of periodic boundary conditions. This assumption was not valid for the experimental cascade, which contained only three Tescom-CAR blades in a seven-blade array. The remaining four were Tescom

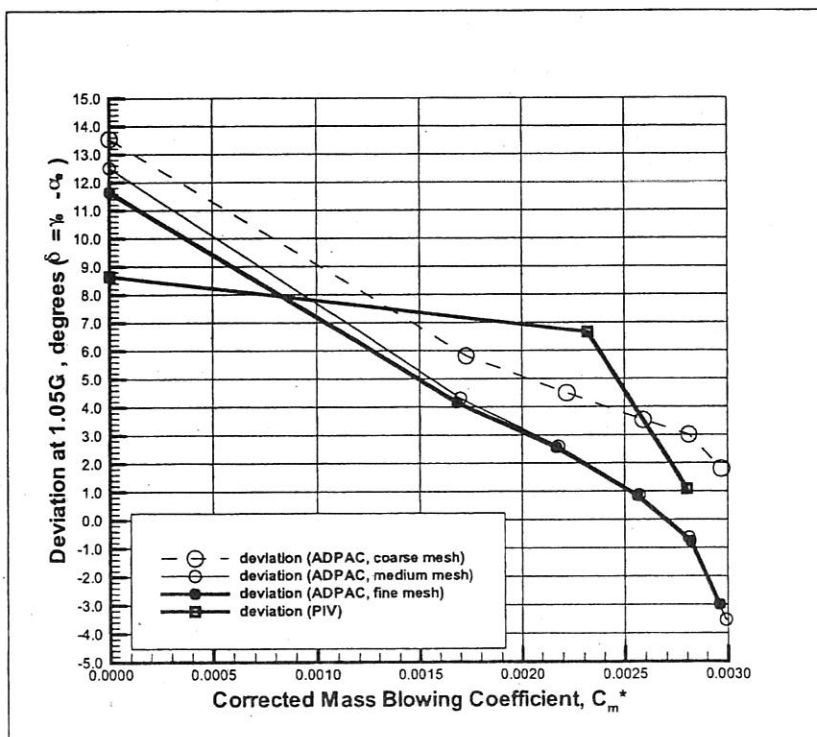


Fig. 7a: Experimental vs. Computational Values of Flow Deviation. Inlet Mach # = 0.75.

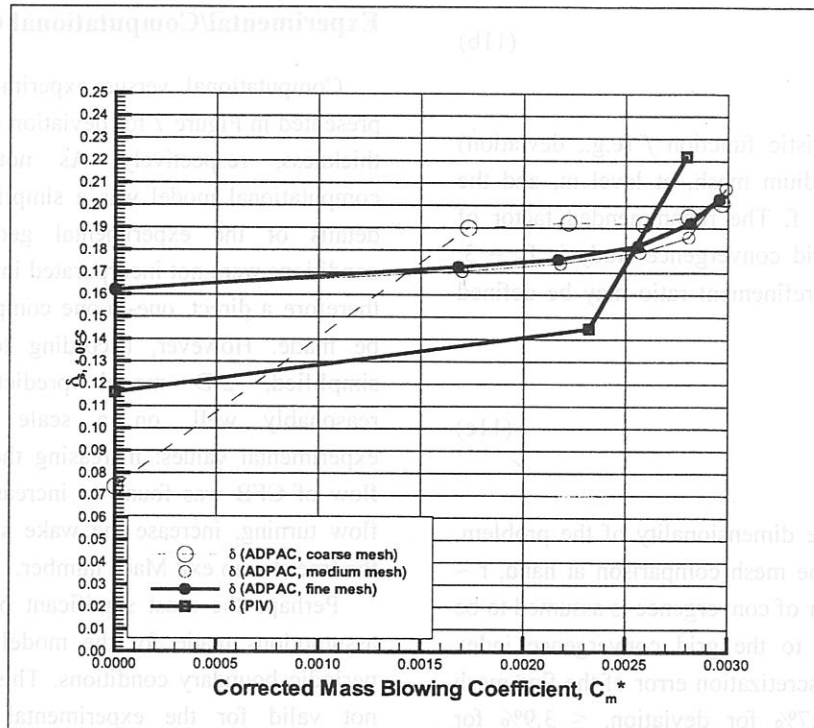


Fig. 7b: Experimental vs. Computational Values of Displacement Thickness. Inlet Mach # = 0.75.

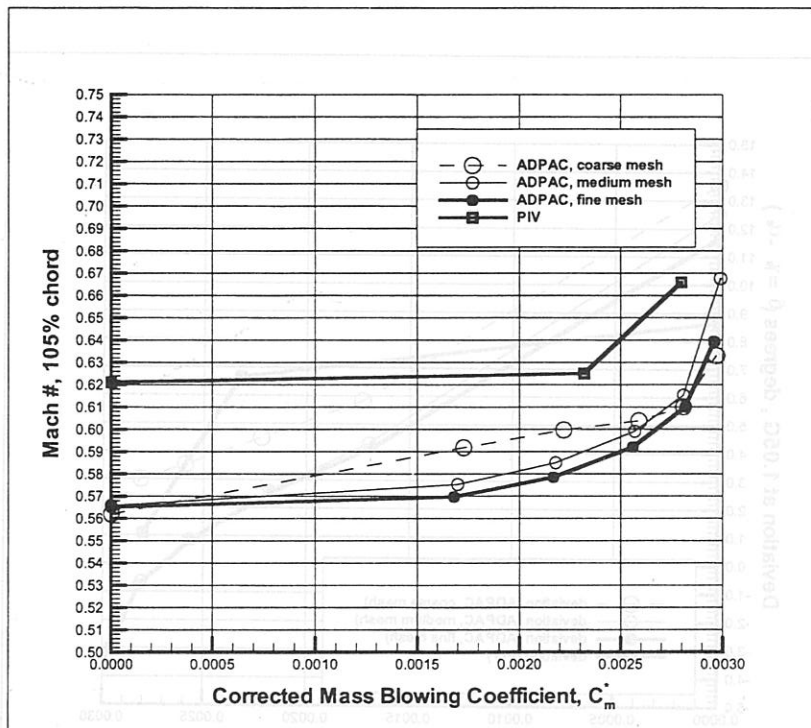


Fig. 7c: Experimental vs. Computational Values of Free Stream Exit Mach #. Inlet Mach # = 0.75.

blades, which have approximately 14% more chord length than the Tescom-CAR blades, and may therefore explain the increased baseline flow turning of the experiment compared to the ADPAC model. It is uncertain what impact, if any, this restraining effect would have on the cases where $C_m^* = 0.0023$ and $C_m^* = 0.0028$.

Second, the model assumed a 2-D, instead of 3-D, flow through the cascade. A full-blown, 3-D ADPAC solution would capture more real aspects of the flow physics, such as the 3-D relieving effect, which would contribute to diminished wake size, and end wall boundary layer growth, which contributes to an increased exit free stream Mach number. Typically, a 3-D analysis will not be used until later stages in the design process, if necessary.

Next, the 2-D model assumed a cascade angle of attack of $\sim 4.5^\circ$, which may or may not have been the case for the experiment. Sensitivity studies were performed for the baseline case over a range of α_i values from 38° to 44° , showing that a 6-degree decrement virtually eliminated the difference between computational and experimental free-stream exit Mach numbers. Additionally, the difference between experimental and computational wake size (i.e., displacement thickness) was reduced by 50%, and the free-stream deviation of flow was decreased by about 1° . This data was acquired near the outset of the investigation but was ignored due to confusion over the definition of the blade camber angle. To be more precise, the Tescom-CAR mesh was created to match the leading edge of the blade to an inlet angle of 44.0° ; however, the line was drawn to the suction surface instead of the true camber line passing through the center of the blade, resulting in an angle of attack ($\alpha_i - \gamma_i$) of about 4.5° .

Finally, the model assumed the blowing slot to be an inlet boundary condition at the blade surface, instead of using an actual "slot" within the computational mesh and inlet boundary condition within that slot. The counter-flow "slot" was not clustered near its edges, which may have limited the model's stability, as well as its ability to capture the viscous flow profile of the jet and its interactions with the primary flow.

Summary

A transonic linear cascade of advanced design stators has been utilized to perform a feasibility study of using CFB to achieve additional flow turning. The PIV data acquired in the cascade facility has been compared to a high fidelity CFD analysis, ADPAC. Considering limitations of the turbulence model and 2-D simulation taken into account, the code was shown to effectively predict values of deviation for CFB applications. Therefore, this study demonstrates the ability of ADPAC to effectively model the relevant flow physics. Based on this initial experimental and computational investigation, the potential of using CFB to replace a flapped IGV looks promising.

Acknowledgements

The authors would like to acknowledge the help of Prof. Wing Ng in the transonic linear cascade facility. Air Force Contract #F33615-98-C-2895, with technical monitor Dr. Charles J. Cross, and the Dayton Area Graduate Studies Institute (DAGSI) sponsored part of this research. Their support is most gratefully acknowledged.

References

1. Copenhaver, W., Car, D., Koch, P., Estevadeordal, J., Guillot, S., Ng, W., Basic Research Studies in Compressor Flow Control, *AIAA Dayton-Cincinnati Aerospace Science Symposium*, March 2002.
2. Copenhaver, W., Car, D., Koch, P., Estevadeordal, J., Guillot, S., Counter-Flow Blowing for Counterswirl Designs/Vectoring, Flow Control Device Session and Video at *AIAA 1st Flow Control Conference*, St Louis, June 2002
3. Estevadeordal, J., Copenhaver, W., Car, D., Koch, P., Ng, W., Guillot, S., Carter, C., Macro- and milli-DPIV studies of a boundary-layer-

- based flow-control system for a transonic cascade. *11th Intl. Symp. on Appl. of Laser Techniques to Fluid Mechanics*, Lisbon (2002)
4. Copenhaver, W., Esteveordal, J., Gogineni, S., Gorrell, S., Goss, L., DPIV study of near-stall wake-rotor interactions in a transonic compressor. *Exp. In Fluids* 2002, 33: 899-908
 5. Hall, E.J., Heidegger, N.J., Delaney, R.A., ADPAC v1.0 – User's Manual, NASA/CR – 1999-206600, February 1999.
 6. Wilcox, D.C., *Turbulence Modeling for CFD*, DCW Industries, Inc., La Cañada, California, 1993.
 7. Roache, P.J., *Verification and Validation in Computational Science and Engineering*, Hermosa Publishers, Albuquerque, NM, 1998.

PIV with LED: Particle Shadow Velocimetry (PSV)

Jordi Esteveordal* and Larry Goss**

Innovative Scientific Solutions, Inc.

2766 Indian Ripple Rd.,

Dayton, OH 45440, USA

A particle-shadow-velocimetry (PSV) technique that employs light sources with significantly lower power than lasers is introduced as a variant of particle-image velocimetry (PIV). The PSV technique uses a non-scattering approach that relies on direct in-line illumination by a pulsed source such as a light-emitting diode (LED) onto the camera imaging system. Narrow-depth-of-field optical setups are employed for imaging a two-dimensional plane within a flow volume, and images that resemble a “negative” or “inverse” of the standard PIV scattering mode are produced by casting particle shadows on a bright background. In this technique the amount of light reaching the image plane and the contrast of the seeding particles are significantly increased while requiring significantly lower power than scattering approaches. The limitations of the technique, its velocity ranges, and the setup parameters are discussed.

I. Introduction

PARTICLE-IMAGE VELOCIMETRY - (PIV) is a powerful diagnostic technique that is capable of providing accurate and resolved velocity fields in a variety of applications. High-speed PIV is becoming increasingly important with the emergence of high-speed laser sources and high-speed video cameras.¹ Most PIV techniques require laser light sources that are capable of high-power, short-duration pulses, allowing instantaneous marking of seed particles and capture of their scattered light by an imaging system. Presently lasers are the most expensive component in PIV systems, despite their relatively slow repetition rates in their commercial form. High-speed PIV is even more costly since it also requires expensive high-speed cameras.

In the present paper an alternative approach, particle-shadow velocimetry (PSV), is introduced, which allows low-power illumination sources such as LEDs to be used for PIV in many applications. LEDs are inexpensive and can be pulsed to nanosecond levels and at high-repetition rates;² their use is proposed here for applications to PIV measurements in various fields of view and over various velocity ranges. The PSV technique has further advantages with respect to laser-based PIV because it produces no glare or reflections from surfaces; since LEDs of many monochromatic wavelengths are available, two-color PIV and multicolor PIV is also feasible.

Applications of the technique for large areas through the use of LED clusters to increase short-pulses brightness and strategies for controlling the depth of field for imaging a two-dimensional (2D) plane will be also discussed.

One of the main aims of this research is to develop a technique for use in large-scale, high-speed wind-tunnel applications that can accommodate direct illumination. A schematic of the LED setup for one such application, a transonic-cascade experiment,³ is shown in Fig. 1. The small size of the LED light-source units and their relatively simple wiring also make them attractive and feasible for optical diagnostics inside turbomachines.

II. Particle-Shadow Velocimetry (PSV)

The PSV technique is a variant of PIV that utilizes direct in-line volume illumination and an imaging-optics setup that produces a narrow depth-of-field (DOF) for 2D plane imaging.

* Senior Research Engineer, ISSI, 2766 Indian Ripple Rd., Dayton, OH 45440, Associate Fellow.

** President, ISSI, 2766 Indian Ripple Rd., Dayton, OH 45440, Associate Fellow.

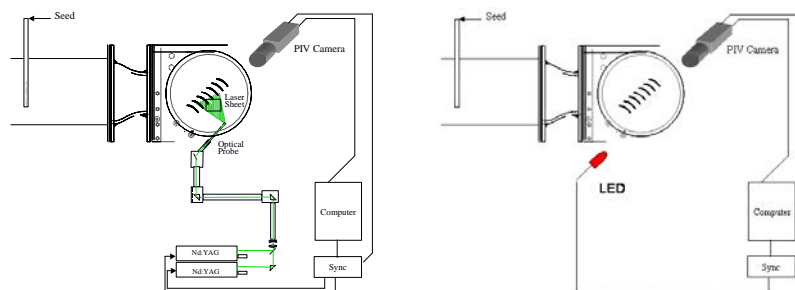


Fig. 1 LED substitutes the laser in transonic-cascade experiment. Narrow DOF imaging substitutes the laser-sheet thickness.

In PSV the setup permits the DOF, the field-of-view (FOV), and the working distance (WD) to be adjusted by introducing spacers or bellows between the camera body and various lenses (Fig. 2). In a simple setup that uses bellows (Fig. 2a), the required extension of the bellows attachment is the product of the reproduction ratio (magnification) and the focal length.

The DOF decreases with the spacing and large aperture and can produce a very thin, focused plane (e.g., sub-millimeter). The addition of more than one lens (Fig. 2b) increases flexibility in the combination of the key parameters (DOF, FOV, WD). Commercially available lenses were used in the present investigation, but custom designs could yield a smaller setup for achieving the desired parameters. For example, since the DOF is proportional to the diameter of the lenses, a larger diameter lens would produce a sharper DOF. In the present study the DOF was on the order of 1-3 mm, and the FOV and the WD could be varied from millimeters to several centimeters. Another mechanism that was considered for controlling key parameters such as the DOF is image post-processing. For example, image filtering allows removal of image data that fall beyond a certain intensity threshold, based on their location from the center of the focal plane. Most PIV techniques utilize such methods. For example, microscopic PIV^{4,5} approaches and miniature PIV with LED⁶ approaches utilize the principle of narrow DOF to image a 2D plane as well as imaging post-processing filtering techniques. Some approaches employ defocusing principles to measure the three-dimensional (3D) velocity field.^{5,7}

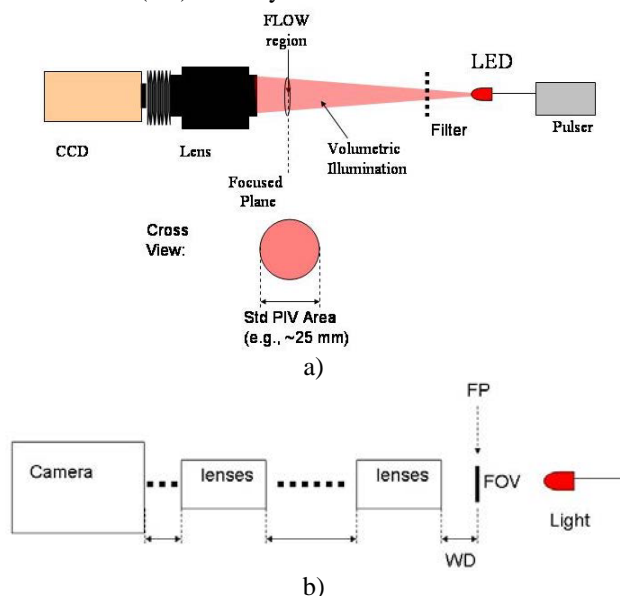


Fig. 2 Examples of PSV-setup schematics with narrow DOF and direct in-line LED volume illumination.

The micro-PIV approaches are often based on fluorescent tagging of particles⁴ or on light scattering through transmitted-light microscopy.⁵ In fluorescence approaches, particles suspended in the flow [e.g., polystyrene latex particles –(PSL)] are tagged with a dye to excite at a certain wavelength (typically chosen to be near the Nd:YAG-

laser wavelengths) and emit at another. In transmitted-light techniques, the light is transmitted from a source on the side of the specimen that is opposite the objective and passed through a condenser to focus it on the specimen for obtaining very high illumination. After the light passes through the specimen, the image of the specimen goes through the objective lens and to the oculars, where the enlarged image is viewed. The most widely used setup for proper specimen illumination and image generation is known as Köhler illumination, and there the micro-PIV applications rely on scattering.

The miniature approach of PIV with LED found in the literature⁶ discusses various setups and results from forward, backward, and side scattering. Because of weak scattering from the LED, the technique is applied only to small areas. In other approaches such as holography, scattering and its interaction with the background light is of major importance when using coherent laser light.⁸⁻¹²

PSV employs a fundamentally different approach that does not rely on principles such as fluorescence, scattering, coherence, Doppler, defocusing, or tagging but on the simpler particle shadow cast on a bright background. This is a consequence of the in-line, zero-degree-deviation direct-illumination setup. Figure 3 is a schematic of the differences between collection-of-scattering and collection-of-extinction (shadow-casting) alignment setups. In the PSV mode the angle between the components is zero. A particle lies between the source and the detector (a camera imaging system in this case) and casts a shadow of a certain area given by the light-extinction characteristics¹³ that can be considerably greater or smaller than the geometrical shadow of the particle. Contrast changes yield particle-shadow-diameter variations and permit the diameter to be adjusted by varying the intensity of the incident light. A brighter light produces a smaller particle shadow and, as a consequence, yields a sharper DOF.

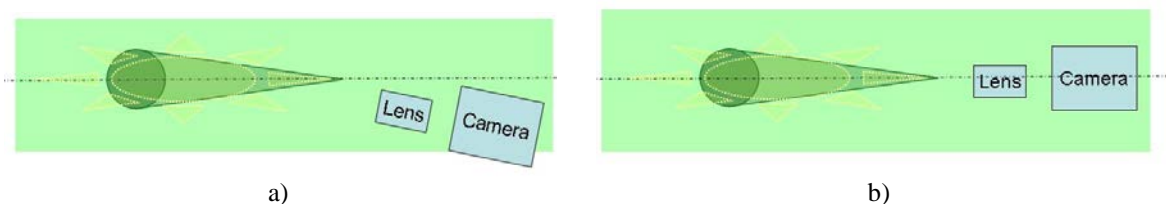


Fig. 3 Schematic of imaging alignment for scattering mode (a) and PSV mode (b), showing spherical particle, its scattering (dashed), and its shadow from background light directed from left to right.

Figure 4 shows image samples comparing the two setups in particle beads on a glass. Having the particles fixed in the glass allows the exposure time to be adjusted and reveals the differences in the images. Both have the same short DOF. The appearance of the images in the PSV approach is that of an “inverse” or “negative” image with respect to that from scattering. For given LED pulse characteristics, the efficiency of the scattering set-up (non-direct illumination) was observed to be very low compared to that of the PSV setup (zero-degree angle of illumination). As with the PIV-with-LED approaches found in the literature,⁶ the capture of scattering images could be accomplished only for very small distances and regions (WD and FOV). In the PSV mode, the LED light is directed straight onto the camera, and shadows of seeding in a bright background result, with a “inverse-PIV” or “negative-PIV” appearance.

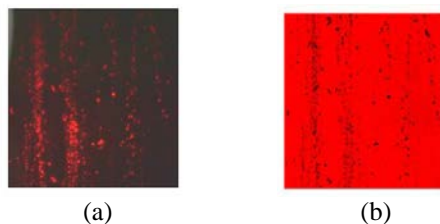


Fig. 4 Side-scattering image (a) and PSV image (b). Particle beads on glass were used.

Although a rigorous study has not yet been performed, some PSV features can be readily explained using particle absorption and scattering-of-light principles¹³ that predict the interaction between light and particles in the present PIV ranges. Of greatest interest here is the light-particle interaction and its effect behind the particle, the region associated with forward scattering or, using a term that shares some terminology with fluid mechanics, the “electromagnetic-wake region.” For example, the following argument clarifies why the region with the highest scattering efficiency--forward--has little to no effect. The particle image recorded on a camera is a result of the

extinction of the (in-line) light caused by absorption and scattering, as opposed to the forward scatter of any light by the particle. The extinction produces a shadow, while forward scatter brightens the particle image. In the basic setup, the only forward scatter that could contribute to the particle image is that of a very small angle, i.e., only the light that would be scattered directly into the recorded image of the particle. All other forward-scattered light would contribute only to an increased background over the entire image. This means that only a small angular fraction of the forward scatter affects the particle contrast. Therefore, the strong forward source light always has a much greater influence than the scattering.

The ratio of extinction to forward scatter depends on the particle size; but in most cases, extinction is ten times larger than forward scatter. This becomes further reduced since the only concern here is forward scatter in a very small angular region. Any scatter outside this region becomes extinction. This consideration likely reduces the ratio from 10 to 1 to more than 1000 to 1. Therefore, it is unlikely that any effects of the forward scatter are recorded.

From a diffraction perspective, it can also be explained that the contribution from diffraction in obscuring the region behind the particle would be negligible, unless the illumination was very strong. There the PSV setup can be thought of as just the inverse of the “slit experiment” for a sufficiently large particle. Therefore, the shadows result; diffraction would keep the light from being completely obscured, but blockage of the source light always dominates. In the Mie-scattering plots, the source intensity is not included; and in any event, it is indeed blocked by the particle (e.g., a geometrical, ideal single ray of light). In practice, all of the source rays that are not scattered by the particle can be detected.

The other crucial component in PSV is the use of short DOF to image (or cast) the focused shadows. The length of the shadow is a function of the intensity of the illumination, based on the previous arguments. Micro-PIV studies⁴ have shown that in a volumetric illumination, all particles in the volume contribute to scattering. Extension to the PSV technique, where scattering is “overshadowed,” yields a volumetric-particle shadow field that has similar results in the focal plane; that is, shadows are observed only when they are in focus with the maximum in the focal plane and become invisible (in the form of fainting background noise) when out of focus (Fig. 5). The rate of defocusing can also be assumed to be proportional to the diffraction pattern of the particles (assuming that they are point sources imaged through a circular aperture or lens), the pattern having a maximum intensity (corresponding to the Airy function for Fraunhofer diffraction) at the focal plane of the lens (Fig. 6) and decreasing very rapidly. Typically the DOF is arbitrarily defined as a specified fraction of that maximum. The overall signal-to-noise ratio can be improved through filtering, brightness, and seeding density. Therefore, for planar PSV measurements, the out-of-focus contribution can be minimized in the final contribution to the velocity correlation. Alignment is very critical also since aberrations (e.g., spherical) can occur if the components in the optical path are misaligned.

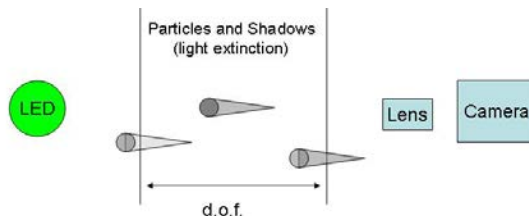


Fig. 5 Contribution of particle shadows to image is restricted to focal plane, with greater contribution from those at the center.

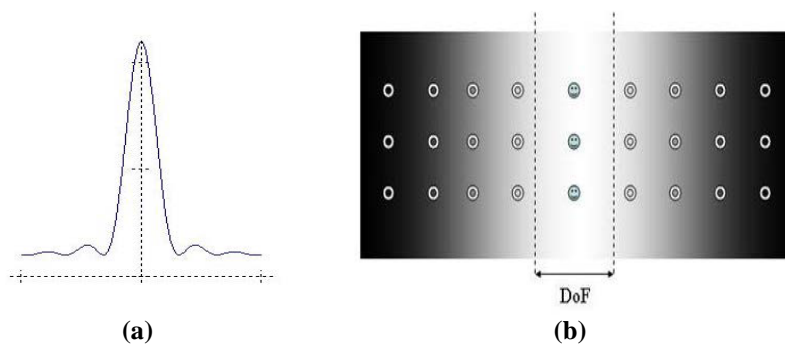


Fig. 6 With sharp DOF, all particles in illuminated volume scatter light and produce shadows, but diffraction pattern (a) has maximum intensity (Airy function) at focal plane of lenses. DOF is defined as specified fraction of that maximum. This effectively results in only 2D slice of illuminated volume being imaged (b).

In PIV, velocity is found by calculating the particle ensemble displacements between two instantaneous time snap-shots, which is generally accomplished through correlation techniques such as using FFT on the image signal. The signal information is generated from changes in intensities; therefore, the same technique can be used for PSV since it is based on information from particle ensembles, although the intensity information is inverted to that from PIV. A subtle difference is that in PIV the particles intensities have a shape such as Gaussian whereas in PSV this shape has not been determined yet and depends on the aforementioned light-particle interaction characteristics. Although this appears to have a negligible effect (e.g., in the correlation peak finding) the method has been calibrated for accuracy as will be explained in the following section. Moreover, since the interest is in the shift or displacement between two signals rather than the signal characteristics themselves, techniques such correlation are applicable to that effect. The PSV image with particles having the lowest intensity compared to the maximum intensity of the background can be readily inverted and generate a PIV-like signal if desired, as will be shown in the following section.

III. Results

In this section some results pertaining to the PSV technique are presented to proof the concept validity and feasibility. First, some samples of LED pulses are displayed, together with some applications showing their capabilities; next, images from a variety of particles and conditions are compared; then, some results from filtering techniques are presented; and finally, some results of flow tests with jets in water and air for several particle sizes and shapes are presented.

The fact that the LED can be pulsed at any rate made it very attractive for velocimetry. This capability is not shared by other sources like lasers or Nanopulsers² which generally have lower and fixed repetition rates (although shorter pulses at present). Pulses from LEDs that were used ranged from tenths of nanoseconds to microseconds. The choice of pulse depends on the velocity of the flow and the magnification, and the pulse must be sufficiently short to freeze the motion while providing sufficient illumination. The red LED is preferred since the CCD camera has its higher spectral sensitivity in the upper-red region. However, an available blue cluster (ISSI) was used to obtain most of the present results because it provided brighter shorter pulses. A red LED cluster will be tested in the future in attempts to gain more efficiency and shorter pulses that would be a requirement in many transonic and higher speed applications. A single LED can be also used if the velocity ranges and other parameters (WD, FOV) are appropriate.

Some sample pulses are shown in Fig. 7. It can be observed that short pulses can be obtained in the range of tenths of nanoseconds (a), even though they are shaper in the microsecond range (b). A train of pulses is also possible, as shown for the case of 100-nsec pulses (c, d). The vertical axis is in arbitrary units (A.U.) since it is the measured voltage from a photodiode. The actual optical energy was not measured. However, the amplitudes shown (except for “d”) can be compared since measurements were made under the same conditions. The photodiode has a rise time of tenths of nanoseconds, which should be taken into account when analyzing the pulses. Because of heat limitations, the LEDs have a limited duty cycle; therefore, unlimited pulses at very high repetition rates would require special designs.

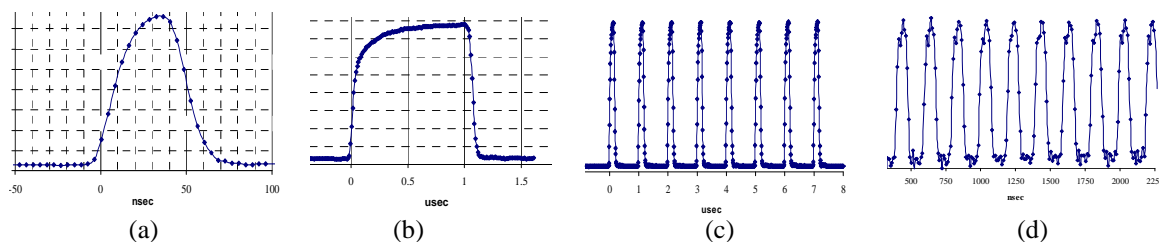


Fig. 7 LED pulse-shape samples: 40 nsec (a), 1 μsec (b), and train of pulses 100 nsec wide at repetition rate of 1 μsec (c) and 200 nsec (d). Y-axis is A.U. (voltage from photodiode).

The camera used in the present experiments was a standard cross-correlation PIV camera (ES1) with 1k x 1k pixels at a 15-Hz repetition rate. Other cameras with higher sensitivity and higher repetition rate were not tested but could be used to achieve better results. On the other hand, relatively inexpensive commercial cameras with detachable lenses have high resolution (although slow repetition rate) and could also be used in the auto-correlation or the two-color-PIV mode.^{14,15} If these cameras were coupled with a single LED, a very inexpensive PIV system could be achieved that would still useful for many experiments and yield high-resolution, accurate results.

The effect of exposure time is readily demonstrated in an air flow seeded with 10 micron ($10\text{-}\mu$) cornstarch particles (Fig. 8). With short pulses the particle shadows appear to be instantaneously frozen (a), but with longer exposures their traces appear (b). In a region of the flow with gradients, both particles and traces are observed (c). Traces could be used to generate velocity vectors, as in particle-streaking velocimetry, although the possibility of out-of-plane motion can produce uncertainties. For the auto-correlation and multiple-exposure mode, a train of pulses can be used; here they are shown in the double-exposure (auto-correlation) mode and multiple-exposure mode in a single frame (Fig. 9) for a slow flow with bubbles. The frames are also shown with image inversion to allow comparison with the standard PIV view (c, d). It can be noted how larger bubbles cast a bright spot in their center because of their lens effect, which focuses the light into a spot.

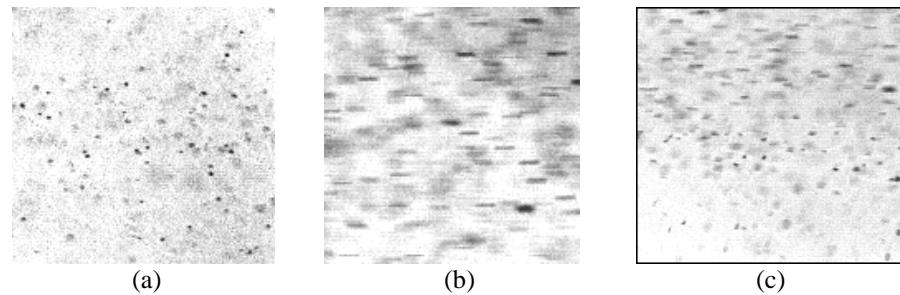


Fig. 8 Exposure time effect. Air jet seeded with cornstarch ($10\text{-}\mu$ diam) particles; details showing point (a), traces (b), and gradient (c) when LED pulse is $1\text{ }\mu\text{sec}$ exposure (a) and $5\text{-}\mu\text{sec}$ (b, c). Images show detailed regions with FOV of few millimeters from a larger image.

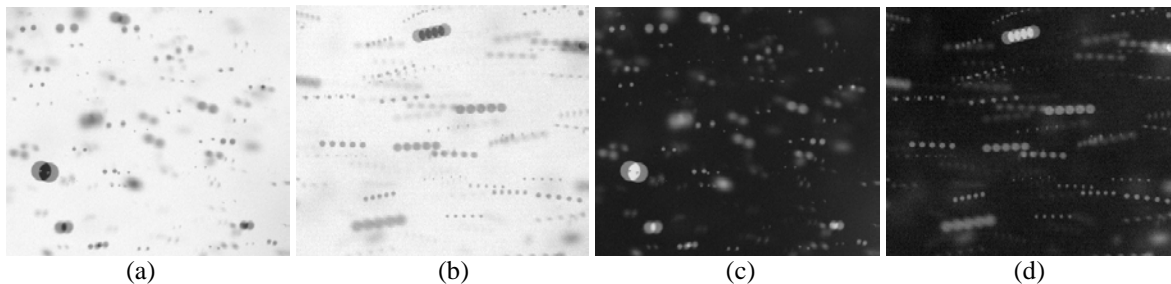


Fig. 9 Auto-correlation or single-frame double-exposed mode (a, c) and multiple-exposure mode (b, d). Particles are bubbles from jet in water. Exposure time was $4\text{ }\mu\text{sec}$ and DT 1 msec . Their inverted images are also shown (c, d) for comparison with standard PIV images. Images are detailed regions with FOV of various millimeters from a larger image.

The effect of coherence was also explored. Figure 10 compares a detail of bubble shadows from LED and laser light. The LED was tested initially with diverging, focused, and collimated illumination and yielded similar results. Laser light was collimated in a larger diameter beam and attenuated prior to directing it to the camera, in a similar manner as when performing digital in-line holography.^{9,10} Both cast particle shadows. LED images could be obtained with pulses on the order of hundreds of nanoseconds.

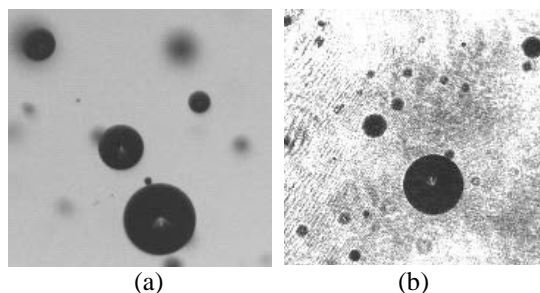


Fig. 10 Comparison of LED light versus coherent laser light in PSV mode. Bubble shadows from LED (a) vs laser coherent light (b); LED $4\text{ }\mu\text{sec}$.

It is obvious that PSV images contain a variety of background-noise textures due mostly to out-of-focus data. Their contribution to the correlation function can be reduced significantly by the optical characteristics of the technique; since these textures contribute to noise, they should be removed. During the experiment this can be done by increasing the illumination; but it can also be accomplished during post-processing by applying filtering techniques that effectively reduce that noise level and produce a sharper image, effectively reducing the 2D plane thickness. One example is shown in Fig. 11 where a threshold intensity filter was applied. Other filters available are based on analysis of the spectral content of the image and removal of the frequencies associated with noise. The image is orange due to the combination of the two greyscale frames in a two color mode (first frame colored red and second colored green) for presentation purposes. The inverted image is also added [Fig. 11(c)] for comparison with the laser-sheet image [Fig. 11(d)] obtained from the same flow. In an effort to perform further calibration of the technique, the flows were used to calculate velocity fields from LED and from laser sheets, and paired-statistical analyses showed negligible differences.

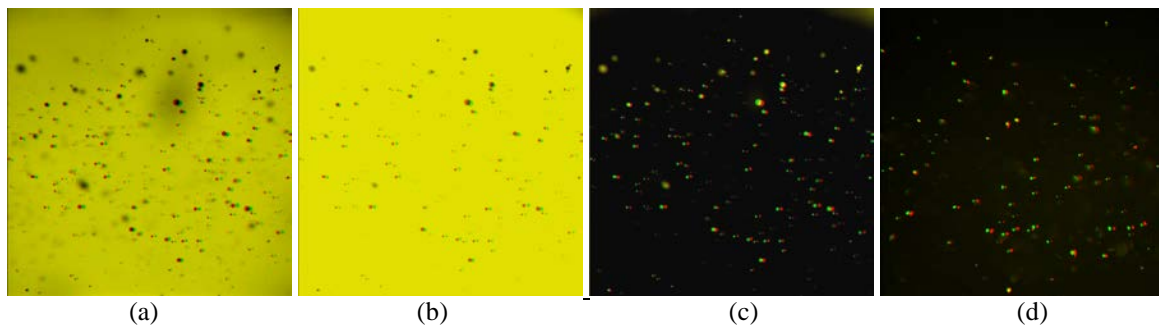


Fig. 11 Image post-processing to reduce out-of-focus and other background noise. Bubbly-jet images are shown for PSV original (a) vs filtered (b). Filtered image is also shown inverted (c) and compared with laser-sheet PIV image (d) of the same flow.

The particle size, its image-shadow size, and their relation to the illumination intensity were explored experimentally to assess the feasibility of the technique in various flow media. Figure 12 shows samples of bubbles imaged with 500-nsec pulses (a), submicron-sized PSL particles in water (b), and cornstarch (10- μ diam) in air with two exposure times (c, d).

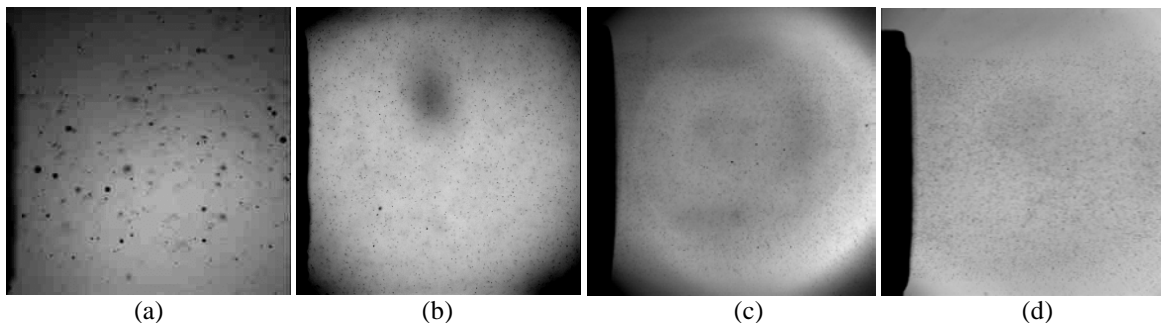


Fig. 12 Media, particle size and shape, and exposure-time effect: a) water jet (bubbles), 500-nsec exposure; b) water jet (PSL, 1- μ diam), 4 μ sec exposure; c) air jet (Cornstarch 10- μ diam) 1 μ sec exposure; d) same as (c) with 5 μ sec exposure FOV~10 mm.

Experiments were also conducted to assess experimentally the effect of the seeding density, and it was found that high-density seeding was also feasible since it did not have significant effect on the sharp DOF plane and velocity field. The cloud of seed remains invisible outside the DOF plane, and correlation could be readily obtained. Figure 13 shows two images (each two-color combined) for comparing medium seeding and heavy seeding. Both provided excellent correlation maps [sample shown in Fig. 13 (c)].

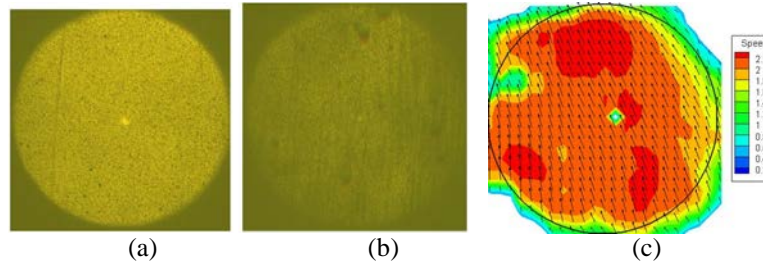


Fig. 13 Effect of seeding density: Medium (a) and heavy (b) and a velocity field (c). Exposures=200 μ sec, DT=5 μ sec, FOV ~25 mm.

Finally, some examples of velocity fields obtained with the PSV technique are presented. Figure 14 shows an example of double exposure from free flow using sub-micron smoke particles (mixture of glycerin and ionized water). A single LED (blue) in PSV “in-line” mode with two exposures of 100 μ sec and 5 μ sec apart was used (FOV is 3 mm). Figure 15 shows the PSV image and its derived velocity field from a jet in water using PSL seed (FOV is 10 mm), and Fig. 16 shows an air jet seeded with 10- μ cornstarch particles (FOV is 10 mm).

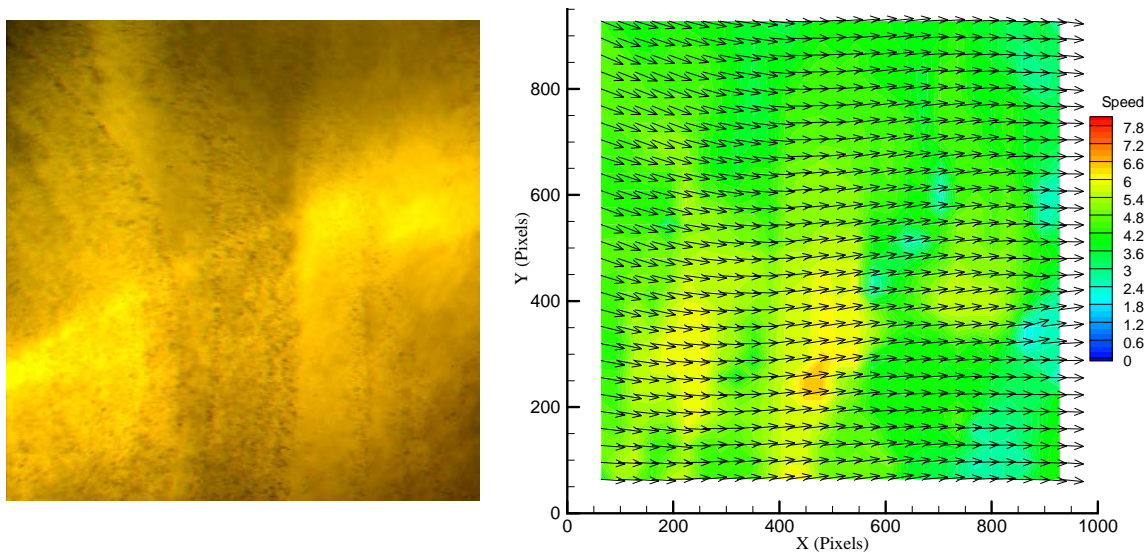


Fig. 14 PSV with LED. Example of air flow with smoke particles (0.5- μ diam); FOV = 3 mm.

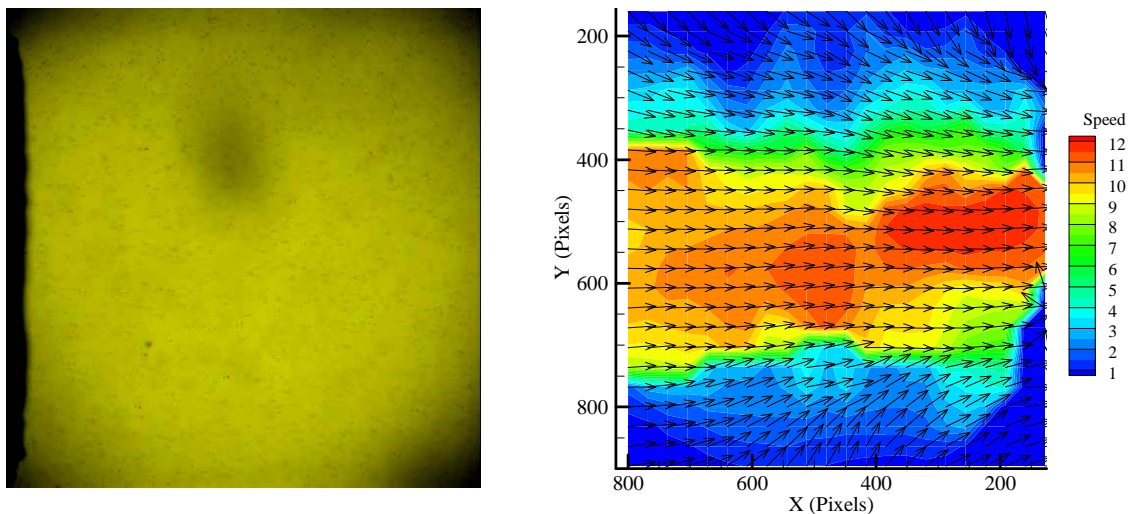


Fig. 15 PSV with LED. Example of water-jet flow with PSL particles; FOV=10mm.

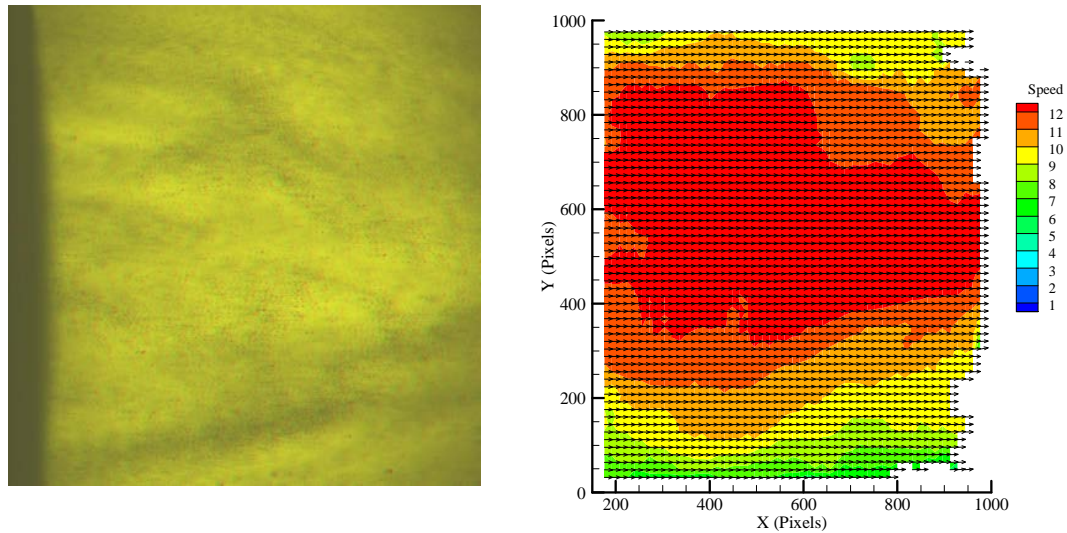


Fig. 16 PSV with LED. Example of air jet flow with cornstarch particles (10-micron); FOV=10mm.

The technique can also be used for flow visualization. Figure 17 is an example of flow visualization using PSV with LED in PSV mode, showing three instants of a drop of water heavily seeded with PSL particles into water.

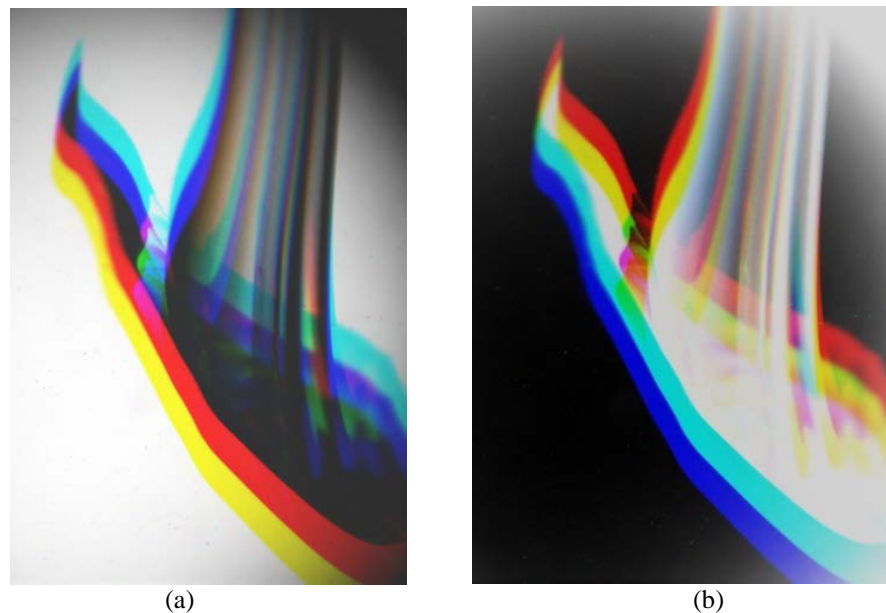


Fig. 17 PSL drop into water; three instants (colored). PSV original (a) and inverted (b).

Another attractive result of the technique is that, in addition to the significant reduction in cost by using LEDs rather than lasers, the camera need not be a costly PIV cross-correlation camera; a commercial less expensive camera in auto-correlation mode or in the two-color mode can be used.^{14,15} In the color-camera approach, the chip has red, green, and blue filters on the pixels (RGB). Each color plane RGB reacts only to that color, in principle. The exception is cross-talk between channels. This is solved in a manner similar to that used in a normal multiple-color PIV case, namely, by subtracting a small portion of the offending color plane from the color plane of interest. For example, if the red bleeds into the green by 10%, then this would be handled by subtracting 10% of the red image from the green. This is effective because the amplitude of the correlation peak is weighted by the number of pairs in the interrogation area, the size of the particle pairs, and the intensity of the pairs. By subtracting a bled component (red), the normal component (green) is effectively enhanced. This was tested with a commercial color camera, and a small bled between the blue and green components based on a RGB LED lamp (ISSI), was cleaned by

subtracting a small portion of the green from the blue. Two-color PSV-with-LED results and other applications such as particle sizing will be presented in a future paper.

IV. Conclusions

A PSV technique was introduced as a variant of PIV. This technique allows light sources with significantly lower power than lasers to be used. The technique employs a non-scattering approach that relies on direct in-line illumination by a pulsed source such as a LED onto the camera imaging system. The technique then uses narrow depth-of-field optical setups for imaging a two-dimensional plane within a flow volume and produces images that resemble a “negative” or “inverse” of the PIV mode by casting particle shadows on a bright background. In this technique the amount of light reaching the image plane and the contrast of the seeding particles are significantly increased while requiring significantly lower power than scattering approaches. Limitations and advantages of the technique, the velocity ranges covered, and other parameter ranges were discussed.

Acknowledgments

The help of B. Sarka and D. Trump of Innovative Scientific Solutions Inc. in the design and fabrication of the LED clusters is acknowledged. Helpful discussions with Dr. C. D. Carter of AFRL and D. Car and Dr. S. Puterbaugh and Dr. S. Gorrell of CARL group at AFRL are also acknowledged.

References

- ¹Boxx, I. G., Idicheria, C. A., and Clemens, N. T., “Kilohertz PIV/PLMS of Low-Gravity Turbulent Flames in a Drop Tower,” 12th International Symposium on Application of Laser Techniques to Fluid Mechanics, Lisbon, Portugal, 2004.
- ²Estevadeordal, J., Gogineni, S., Kimmel, R., and Hayes, J., “Schlieren Imaging for Hypersonic Plasmas,” AIAA Reno, NV, Jan 5-8, 2004
- ³Estevadeordal, J., Car, D., Gorrell, S., and Puterbaugh, S., “DPIV with LED Illumination: Application to Turbomachinery and Flow Control,” Presented at the 29th Annual AIAA Dayton-Cincinnati Aerospace Science Symposium, 9 March 2004, Dayton, OH; also in *Application of Advanced Laser Diagnostics to High Impact Technologies*, Quarterly Report 2829-3 on Contract F33615-03-D-2329 (Innovative Scientific Solutions, Inc., Dayton, OH, 2004).
- ⁴Meinhart, C. D., Wereley, S. T., and Gray, M. H. B., “Volume Illumination for Two-Dimensional Particle Image Velocimetry,” *Meas. Sci. tech.* **11**, 809, 2000.
- ⁵Ovryn, B., “Three-Dimensional Forward Scattering Particle Image Velocimetry Applied to a Microscopic Field-of-View,” *Exp. Fluids [Suppl.]* **S175-S184**, 2000.
- ⁶Chetelat, O. and Kim, K. C., “Miniature Particle Image Velocimetry System with LED In-Line illumination,” *Meas. Sci. tech.* **13**, 1006, 2002.
- ⁷Pereira, F., Gharib, M., Dabiri, D., and Modarress, D., “Defocusing Digital Particle Image Velocimetry: a 3-Component 3-Dimensional DPIV Measurement Technique. Application to Bubbly Flows,” *Exp. Fluids [Suppl.]* **S78-S84**, 2000.
- ⁸Barnhart, D. H., Adrian, R. J. and Pappen, G. C. 1994 “Phase conjugate holographic system for high resolution particle image velocimetry” *Appl. Opt.* **33** 7159–70, 1994.
- ⁹Estevadeordal, J., Copenhaver, W., Car, D., Koch, P., Ng, W., Guillot, S., and Carter, C., “Macro- and Milli-DPIV Studies of a Boundary-Layer-Based Flow-Control System for a Transonic Cascade,” 11th International Symposium on Application of Laser Techniques to Fluid Mechanics, Lisbon, Portugal, 2002.
- ¹⁰Xu, W., Jericho, M. H., Meinertzhagen, I. A., and Kreuzer, H. J., “Digital In-Line Holography of Microspheres,” *Appl. Opt.* **41**(s5), 5367-5375, 2002.
- ¹¹Meng, H., and Hussain, F., “In-line Recording and Off-Axis Viewing technique for Holographic Particle Velocimetry,” *Appl. Opt.*, **34**, 1827-40, 1995.
- ¹²Sheng, J., Malkiel, E., and Katz, J., “One Beam Two View Holographic Particle Image Velocimetry System,” Proc. 4th Int. Symp. on Particle Image Velocimetry, Gottingen, Germany, Paper 1022, 2001.
- ¹³Bohren, C. F., and Huffman, D. R., Absorption and Scattering of Light by Small Particles, John Wiley and Sons. 1983.
- ¹⁴Post, M. E., Trump, D. D., Goss, L. P., and Hancock, R. D., “Two-Color Particle Image Velocimetry Using a Single Argon-Ion Laser,” *Exp. Fluids* **16**, s. 263-272, 1994.
- ¹⁵Gogineni, S., Goss, L., Rivir, R., and Pestian, D., “Two-Color Digital PIV Employing a Single CCD Camera,” *Exp. Fluids*, **25**(4), 320-328, 1998.

Development of a Fiber-Optic PIV System for Turbomachinery Applications

Jordi Esteveordal,^{*} Terrence R. Meyer,[†] and Sivaram P. Gogineni,[‡]
Innovative Scientific Solutions, Inc., Dayton, OH 45440

and

Marc D. Polanka,[§] and James R. Gord^{**}
Air Force Research Laboratory, Propulsion Directorate, Wright-Patterson AFB, OH 45433

A fiber-optic particle-image velocimetry (FOPIV) system capable of delivering short, high-power laser pulses and of acquiring double-exposure images in flows without direct optical access is presented. The system is capable of delivering Nd:YAG laser pulses of 5-ns duration and up to 50 mJ/pulse at 15 Hz rates through a single multimode silica fiber of 1000- to 1500-micron diameter. The tip of the laser fiber is terminated into a housing block that contains the laser-sheet forming optics. Image transmission to the PIV camera is accomplished through a high-density 1.4-mm-diameter flexible fiber bundle composed of 100,000 quartz microfibers. A lens system is attached to the end of the imaging fiber and is designed for optimal flatness of the object plane with minimal distortion; for the current turbomachinery application it produces a flat image of a 25-mm diameter viewing area 50 mm from the object plane. This distance to the object plane is selected to maximize both viewing area and light-scattering intensity from the micron-sized seeding particles. The capabilities and limitations of the system are described, and results from various studies are presented, including preliminary data from a short-test-duration turbine-engine facility without direct optical access. This application required that the PIV hardware be mounted through an interior instrumentation ring that rotates during the experiment.

I. Introduction

OPTICAL-DIAGNOSTIC techniques for turbomachinery often demand special designs and strategies to allow measurements within interior regions. In some cases it is possible to allow optical access for imaging through windows on the machine housing and ports for probes to deliver the laser sheet.¹⁻³ In addition, optical guides can be designed for laser delivery, and micro cameras, tethered camera heads, or fibers can be used for imaging. These approaches minimize the modifications that may otherwise be imposed on existing test sections and enable the use of more realistic test geometries.

Although the advantages of using fibers for imaging and laser delivery are obvious, this approach is more limited in resolution and accuracy when compared to non-fiber-based methods and should be used selectively. The present work introduces a fiber-optic-based approach to allow PIV measurements in test facilities that do not have direct optical access, have limited space, or require the optical train to be mounted on moving interior components. The current design can be extended to applications with high temperature and pressure conditions, such as combustion chambers, provided that the probes are properly shielded.

The paper outlines the design characteristics of the imaging fiberscope and laser-sheet delivery fiber and characterizes the resolution and performance of the system through various laboratory tests in water and air flows. The seeding system used to acquire data in the turbomachinery application is also described, and preliminary results are presented from tests performed in a short-duration turbine-engine facility.

^{*} Senior Research Engineer, ISSI, 2766 Indian Ripple Rd., Dayton, OH 45440, Associate Fellow.

[†] Research Engineer, ISSI, 2766 Indian Ripple Rd., Dayton, OH 45440, Senior Member.

[‡] Senior Research Engineer, ISSI, 2766 Indian Ripple Rd., Dayton, OH 45440, Associate Fellow.

[§] Research Engineer, AFRL Propulsion Directorate, Wright-Patterson AFB, OH 45433, Senior Member.

^{**} Principal Research Chemist, AFRL Propulsion Directorate, Wright-Patterson AFB, OH 45433, Associate Fellow.

II. Experimental Set-Up

A. High-Density Imaging Fiber

Imaging in facilities without direct optical access typically requires insertion of probes such as rigid boroscopes. If the use of rigid probes is not possible, such as in turbine facilities with internal moving parts and small gaps, flexible boroscopes or fiberscopes can be used to transmit images.^{4,6} Fiberscopes are presently made with tens to hundreds of thousands of microfibers or ‘fiber pixels’. Whereas rigid boroscopes use optical lenses and are limited only by the camera CCD-chip resolution, fiberscope resolution is limited by the amount of fibers that compose it. Due to the microfiber array, they also produce a background pattern noise referred to as ‘honeycomb’ or ‘chicken wire’ pattern.

A high-density imaging fiber bundle composed of 100,000 microfibers, each of 4.5-micron diameter, was selected for the present fiberscope application. The outer diameter of the bundle was 1.7 mm, but the active image area was 1.4 mm in diameter. A 1000 × 1000 array CCD camera with pixel sizes of 9.4-microns and a magnification of 6.7 (9.4 mm / 1.4mm) occurs assuming full CCD area is usable; thus, each microfiber gets magnified to 30 microns (4.5 micron × 6.7) resulting in about three (30 / 9.4) CCD pixels per microfiber.

Figure 1 shows a schematic end view of the fiberscope tip along with the miniature lenses assembly within the imaging block. The lens arrangement was designed to accommodate the limited space available within the test section housing while yielding optimal brightness and flatness in the image of the particle field. The simplest approach would have utilized a pinhole camera, but this would have resulted in low signal levels. Since Mie-scattering from submicron particles must be collected in a small aperture, the most important criterion to achieve optimal brightness in the design of the lens system was low f-stop. As a result, the distance from the imaging lenses to the object plane was minimized. To reduce the spherical aberration incurred by the miniature lenses and near-field viewing, an achromat doublet for focusing and image flatness was utilized. Given the desired field of view of 25-mm to maintain sufficient resolution, a final f-stop of 1.9 was achieved with an object distance of 50 mm. Figure 2 shows pictures displaying the flatness and sharpness obtained with the fiberscope design. Since the fiber is circular, the useful image is a circular area inscribed within the square CCD chip. The outer region of this 25-mm diameter circular image experienced increased distortion and noise and was disregarded in the PIV image analysis. This approach minimized the need for target calibrations and post-processing corrections that always induce more errors. The 3-mm lenses were barrel mounted for easy assembly to the fiber tip. An additional steel barrel with a 45-degree turning prism can be attached at the end of the lens probe whenever necessary. A potential source of noise within the PIV images results from the ‘honeycomb’ or ‘chicken-wire’ pattern that occurs at the tip of the fiber bundle where the image is formed and transmitted, as shown in Figure 3. Techniques to remove or minimize this noise include image subtraction, out-of-focus filtering in post-processing,^{4,5} and lens defocusing. The latter approach, shown in Figure 3, produced good results in the calibration tests from laboratory PIV measurements.

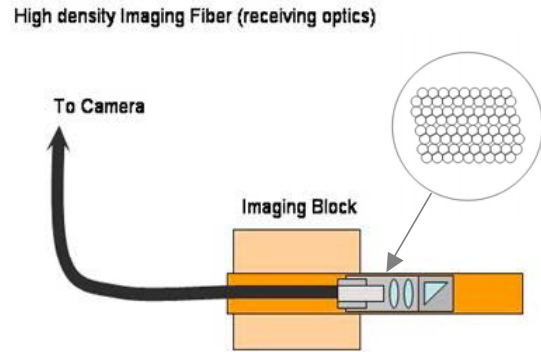


Figure 1. Schematic of the imaging-fiber tip design showing the lens housing (left) and the end face of the fiber bundle (right).

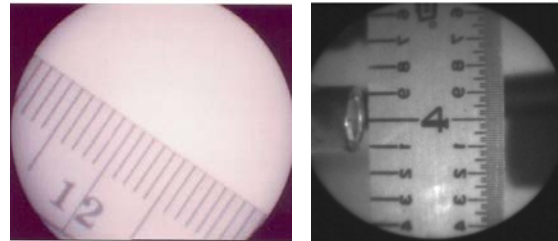


Figure 2. Imaging-fiber calibration targets showing image flatness and sharpness.

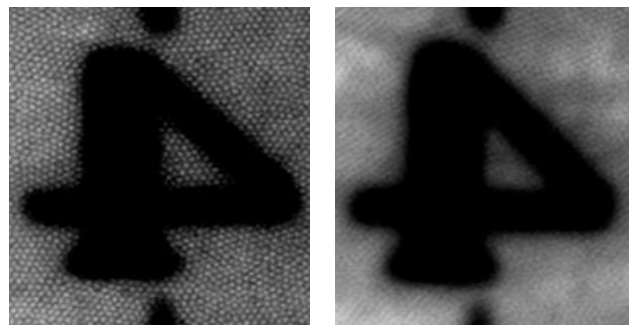


Figure 3. Fiber “chicken-wire” pattern (left) and effect of defocusing (right).

The present fiber is rated for temperatures up to 450°F and its maximum bending radius is 130 mm, due to the silicone resin limitations. Other than being more costly, there are no physical disadvantages in having long fibers since the fiber is made of quartz, which has less attenuation when compared with other materials such as borosilicate glass. The fiber was covered with a plastic outer sheath for protection. Applications in environments with higher temperatures and pressures, such as combustion chambers, would require further shielding of the fiber bundle and probe housings.

B. High-Power Fiber Optics for Nd:YAG Delivery

The criteria for choosing a fiber-based PIV laser-sheet delivery system include the capability to withstand short high-power pulses, low-noise output, small diameter, and flexibility. A multimode single fiber was selected because it eliminates the use of epoxy between microfibers and results in superior high-power performance along with cleaner output and reduced speckle when compared with fiber bundles. Single fibers also allow 100% of the fiber area to be utilized. This is in contrast to with fiber bundles, which have up to 35% transmission loss as well as increased noise because of gaps between the individual microfibers. As a result, the laser sheet quality from a single fiber is significantly superior to that achieved using from fiber bundles. In addition, no diffusers are necessary for PIV-image collection because noise and speckle are significantly reduced. A disadvantage of single fibers as compared with fiber bundles is reduced flexibility.

Relatively large fiber diameters (1000 to 1500 microns) were selected in the current work to allow for power transmission levels of up to 50 mJ/pulse while allowing bend radii of 100 mm or less. The In PIV applications that require a thin laser-sheet to be formed, smaller diameters are desirable to allow for smaller focusing and collimation capabilities at the output. Several designs for delivery of a variety of laser pulses for PIV applications can be found in the literature.⁷⁻¹⁰

The single fiber contained a fused silica core with a numerical aperture of 0.22. Various techniques were devised to allow control of the laser sheet characteristics, as shown in Figure 4. The connectors are modified to allow high power as these areas are more vulnerable to laser damage; The fiber ends are bored out to remove epoxy and other material from the fiber perimeter and the tip is held in a cantilevered manner. This significantly reduces the fiber breakdown that results when beam misalignment focuses laser energy outside the fiber core on portions of the connector that could easily burn. A heat sink can also be attached to the rear of the connector to conduct extraneous heat away from the fiber, further reducing the possibility of breakdown. This sink however is mostly intended for continuous-wave operation, however, and is not critical for pulsed applications like PIV. Short fiber cords 12 inches in length were used in most laboratory experiments reported here. The longer fibers employed in turbomachinery tests were armored with stainless-steel flexible cable for mechanical protection. A length of two meters was selected based to minimize transmission losses (0.1 dB/m or 2% per meter) while accommodating the test section geometry. Power losses of 4.5% occurred at the air-silica interfaces. The laser output had a solid-angle divergence of about 25.4 degrees.

The sheet formation optics were attached via a laser delivery probe and laser block attached to the tip of the fiber, as shown in Figure 4. Design of the optics was challenging due to the loss of coherence, high divergence, and high power of the output beam. While line-sheet generators for fiber optic laser systems are commercially available, they are not capable of handling high-power and large-diameter beams. Diverging light can be readily focused but not readily collimated for long distances. Speckle noise resulting from the interaction of the various modes within the fiber was observed to have negligible effect in the present PIV applications, alleviating the need for filters or diffusers in the laser delivery probe. In addition, there is no internal noise like those observed in bundles due to interfaces between individual fibers. A significant challenge in the turbomachinery application resulted from space requirements; the present module had to be capable of generating a laser sheet at less than 100 mm from the end of the laser-deliver probe. High-power coated cylindrical lenses in various combinations produced laser sheets at the various locations of interest with an evenly illuminated laser-sheet height of 25 mm and a thickness of sub-millimeter or higher depending on the required brightness. Larger areas can be covered with thicker sheets if uniform illumination is not important. For the present application, which requires the use of small imaging lenses, a 1.5- to 2-mm thick and 25-mm long laser sheet was formed. Figure 4 shows a picture of the laser sheet, a schematic of the probe-tip design, and a picture of the relatively homogeneous speckle pattern observed without sheet-forming optics. To avoid damaging the laser-delivery fiber, special adapters were used to prevent focusing inside the fiber. The relatively short two-meter length also avoided damage from nonlinear modes that can develop within lengthy fibers. Since the pressure inside the turbomachinery test section was above atmospheric conditions for these tests, a final requirement included sealed connections between the fiber and the laser-sheet deliver probe.

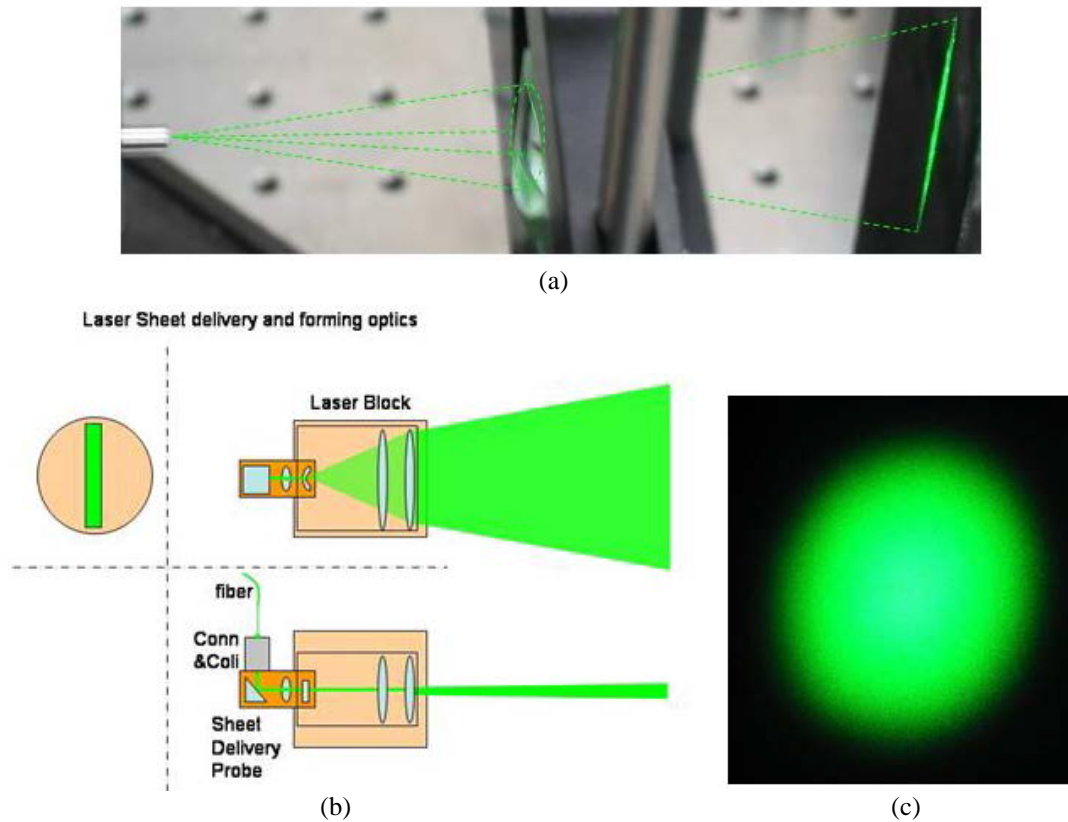


Figure 4. (a) Image of laser sheet from the fiber probe, (b) schematic of the laser-sheet delivery optics, and (c) image of the uncollimated laser output with low speckle.

The laser source for the current work was a New-Wave double-pulse laser at 15-Hz repetition rate, 4.5-mm beam diameter, 5-nsec pulse duration, 2-mrad divergence, and 120 mJ/pulse. This pulse duration and energy level produced enough scattered light to be captured by the fiberscope and PIV camera, which consisted of a MegaPlus ES1.0 with 9.4×9.4 -micron pixels and a fill factor 55%.

In all cases seed particles of 10 microns or larger were used to allow enough scattered light to be captured by the fiberscope system. This particle size was also optimal for PIV post processing given the limited resolution of the imaging fiber. A water jet flow with bubbles was chosen for seeding tests in liquids, and jet air flows seeded with cornstarch particles of 10 microns were chosen for seeding tests in air and for turbomachinery. The cornstarch particles faithfully follow the flow even beyond transonic speeds and they have the size to yield brighter particle images of around three pixels on the fiberscope image. The particle image size can be further adjusted through image defocusing to yield more accurate PIV results.

III. Results and Discussion

A. Fiber-Optic Particle Image Velocimetry (FOPIV)

The feasibility of the FOPIV approach was assessed in liquid and gaseous laboratory flows and demonstrated in a turbomachinery test facility. Initial calibrations were performed on the fiber-based light-delivery system to determine laser sheet thickness and span, image flatness, and resolution from various grids. Preliminary tests for PIV began with rotating wheel calibrations, and followed with channel and jet flows in water and air. Image brightness was tested using various particle shapes and sizes to determine an optimal seeding strategy. Results from the fiber-based system were compared with results from a standard PIV camera with a 105-mm macro lens to verify the

accuracy of the fiberscope and the adequacy of the laser sheet. Finally the fiber-based system was designed for installation in the Turbine Research Facility (TRF).

Figure 5 shows simultaneous images and PIV vectors collected using a 105-mm lens and the fiberscope system in a water flow perturbed by a bubbly jet moving upwards towards the free surface. The lens and fiberscope were mounted on two identical PIV cameras (ES 1.0) and were synchronized and aligned to obtain the same instantaneous picture for comparison. Paired-statistical analyses of the vector fields from the fiber- and non-fiber-based imaging systems were then performed to assess similarities or differences in performance. After matching the field of view of each image and disregarding obvious outliers from each vector field, the average difference in velocity magnitude was calculated to be 0.05 pixels per image pair, indicating that accurate velocities can be obtained by the fiberscope system even for sub-pixel displacements and despite the factor degradation in image resolution. Figure 6 shows a comparison between PIV data acquired using the 105-mm lens and data acquired using the fiberscope in an air jet seeded with cornstarch particles (10 microns). Again, both images were obtained simultaneously for direct comparison and were illuminated by the same non-fiber-based laser-sheet. The particle-scattering field clearly shows the expected degradation in resolution from the fiberscope, although the velocity fields are very similar. Figure 7 shows an image comparison for the air-jet flow but now comparing the full fiber-based imaging and laser delivery system with the standard PIV camera lens and sheet-forming optics. While the resolution is degraded by the fiberscope, accurate vector fields can still be acquired. When using the fiber-based sheet-forming optics with a 105-mm lens, as shown in Figure 8, the interrogation cells can be as small as standard PIV and the high-resolution vector field can be recovered through the use of multipass algorithms.² This produces details of the jet velocity field that are clearly discernible; vortical structures along the shear layer are highlighted in Figure 8 by subtracting the shear layer convective velocity.

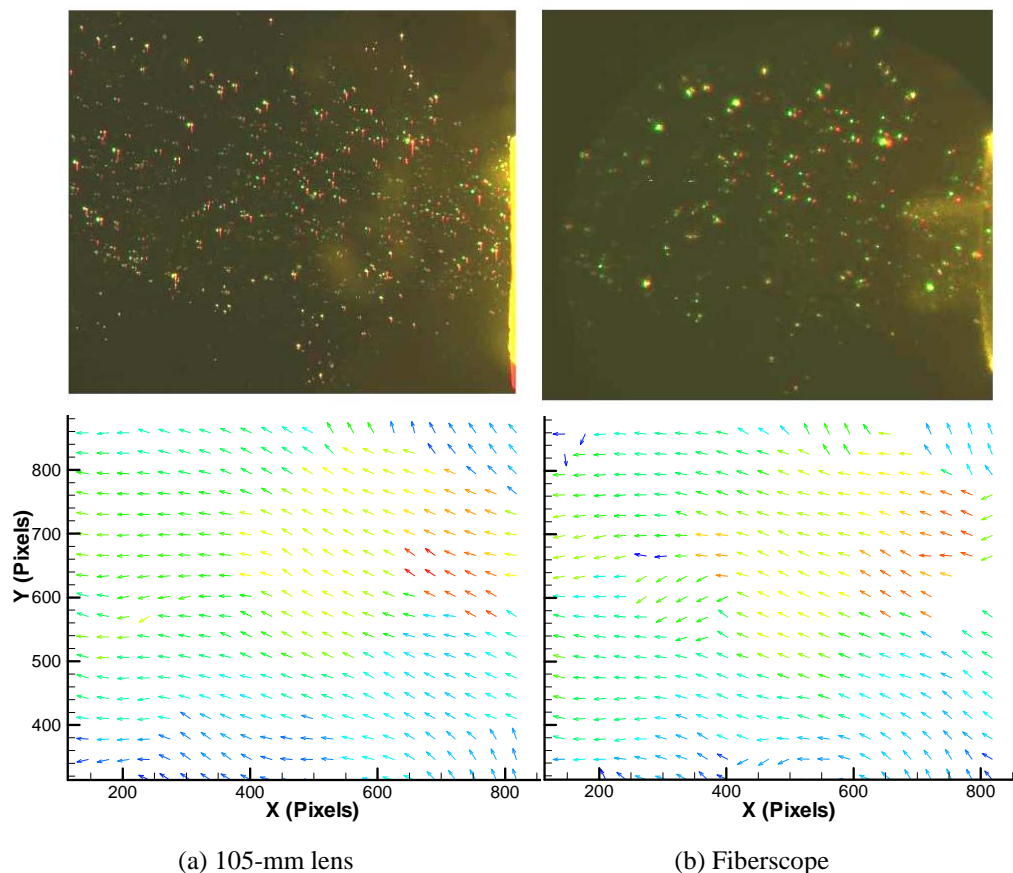


Figure 5. PIV images and vectors in a two-phase flow comparing the (a) 105-mm lens with the (b) fiberscope. Both images were aligned to same view and collected simultaneously with the same model camera.

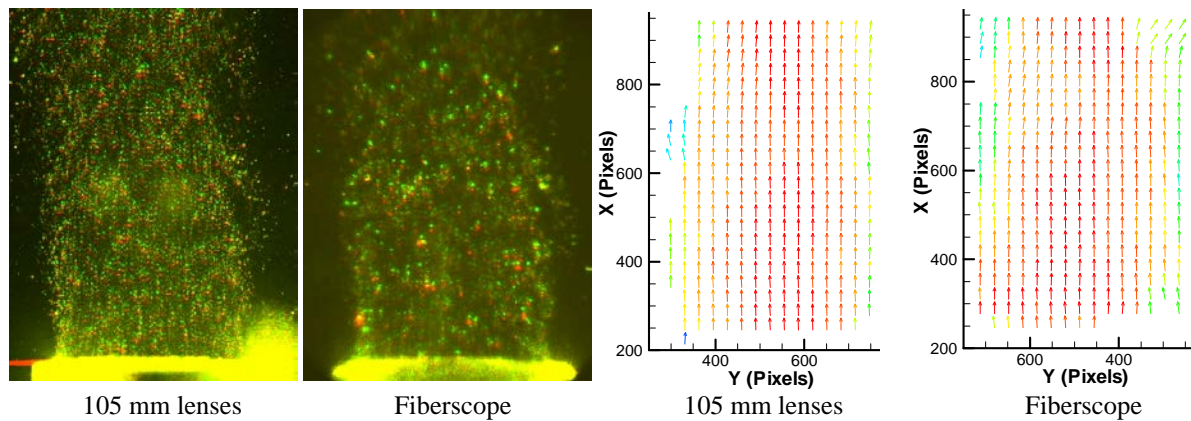


Figure 6. PIV images and vectors in an air jet seeded with 10-micron particles comparing the 105-mm lens with the fiberscope. Both images were illuminated with a non-fiber laser sheet, aligned to same view, and collected simultaneously with the same model camera.

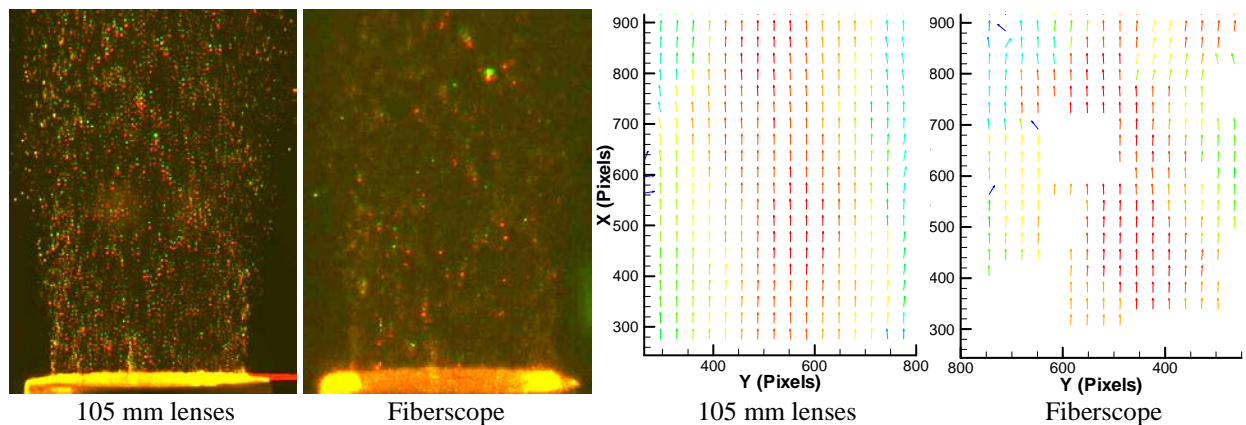


Figure 7. PIV images and vectors in an air jet seeded with 10-micron particles comparing the 105-mm lens with the fiberscope. Both images were illuminated with a fiber-based laser-sheet, aligned to same view, and collected simultaneously with the same model camera.

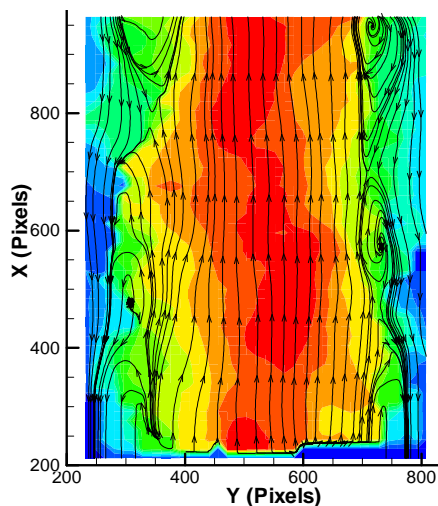


Figure 8. Data from Fig. 7 can produce high-resolution PIV with the 105-mm lens.



Figure 9. TRF rig showing supply tank, turbine test section, and vacuum tanks.

B. Turbine Research Facility (TRF)

The TRF, shown in Figure 9, is a blow-down rig capable of testing full-scale turbine hardware. It matches all relevant aerodynamic and heat transfer parameters including Reynolds number, corrected speed, and pressure ratio. A typical test sequence consists of the following steps. The supply tank is filled with test gas and then heated and pressurized to desired conditions to match Re. The dump tanks are evacuated and the isolation valve is set to a desired open flow area and pressure ratio. The turbine is then spun with the air motor to slightly above the test speed, the motor is disengaged and the turbine is allowed to spin down until it reaches the test speed. The system then automatically triggers the main valve to start the flow and the eddy brake controls the turbine speed during the five second test.

The PIV experiments presented here were performed in a combustor simulator producing inlet temperatures, pressures, and turbulence profiles that are representative of the real turbine environment. The goal is to understand turbine inlet flow-fields. The preliminary PIV experiments presented herein were designed to demonstrate the feasibility of inserting PIV probes within the instrumentation ring, acquiring images, delivering a laser sheet, and testing the seeding. Probes were custom made for the PIV tests and were inserted into housings mounted within the instrumentation ring. Figure 10 shows pictures of the probe designs. The 1.27-meter rotation ring is designed to rotate up to 120 degree during each test to capture data at various circumferential locations. Fiber-bending limitations restricted the PIV tests to a rotation of 16 degrees through the use of stainless-steel bellows for compression and expansion (Fig. 10). The probes could be extended in the radial direction also to allow data to be captured at various radial positions. Test of the seeding system showed that it provided an adequate particle density in the region encompassed by the 16 degrees rotation. The seeding system was a pressure-driven cyclone type filled with solid particles (cornstarch, 10 micron) and connected to a 12.5-mm diameter stainless steel rod inserted radially 20 diameters upstream of the PIV test area. The seed was injected from the rod into the turbomachinery housing via 3.175-mm-diameter jets facing upstream to minimize intrusion on the flow and produce a larger seeded region. The seeding jets were located in the rod such that they seeded various internal chambers of the flow facility that delivered air to the PIV test section.

The amount of runs are limited in a facility of such complexity and although all the FOPIV hardware was mounted and tested prior to the runs with the rig open (except actual seeding) the fiber for the laser delivery broke. Therefore for the present PIV results, the ring was kept stationary during the tests and the laser-sheet was delivered through a specially made delivery rigid probe similar to those used in previous turbomachinery applications.^{1,2} A laser-fiber delivery has not been tested in the facility. Results from four preliminary PIV runs of 5 seconds duration each are presented. Figure 11 shows samples of PIV images and velocity fields with linearly interpolated velocity contours obtained at 1.16 and 3.36 seconds after the main valve was opened. The bright tilted line in the images occurs due to scattering from the laser deliver optics and represents the inner surface of the turbomachinery test section. Note that instantaneous velocity vectors are captured within about 4 mm from the wall and successfully track the decrease in velocity over time.

IV. Conclusions

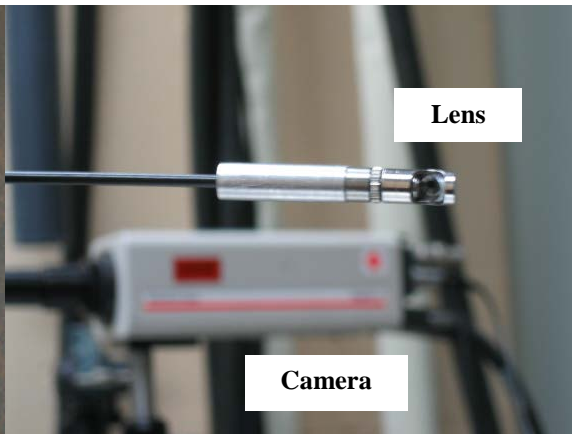
A fiber-optic particle-image velocimetry (FOPIV) system for laser-sheet delivery and double-exposure image acquisition in flows without direct optical access was presented. Results included laboratory tests for calibration and a fiberscope application to turbomachinery without direct optical access. Compared with standard PIV, the system limitations include lower resolution, smaller fields of view, increased noise, and the requirement of using larger seeding particles. For applications with internal regions of interest that are not directly accessible or that are housed within moving exterior housings, the current work demonstrates that the FOPIV approach is viable and can yield results with acceptable accuracy and resolution. Future work includes further characterization of system accuracy and further tests in turbomachinery applications. The next design phase will include the evaluation of more sensitive cameras with high-speed capabilities to enable the use of lower laser powers and longer pulses for increased data acquisition rates in the short-duration turbomachinery tests.

Acknowledgments

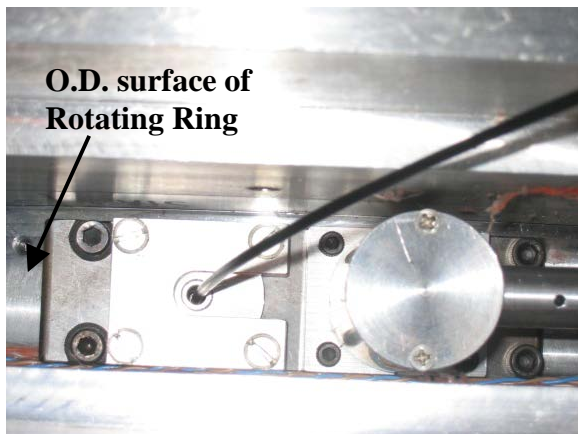
The help of Ben Sarka of Innovative Scientific Solutions, Inc. in the design and fabrication of the probes and fiber holders for the turbomachinery tests and the help of Turbine Research Facility staff in the experimental setup are acknowledged. This research was funded by the Air Force Research Laboratory under contract number F33615-03-D-2329.



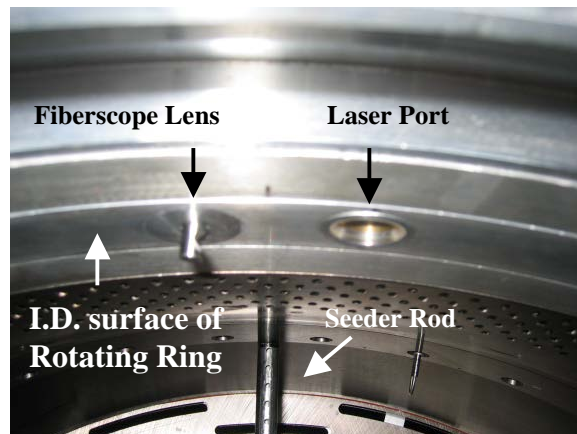
Holders for fiberscope lens and laser-sheet optics



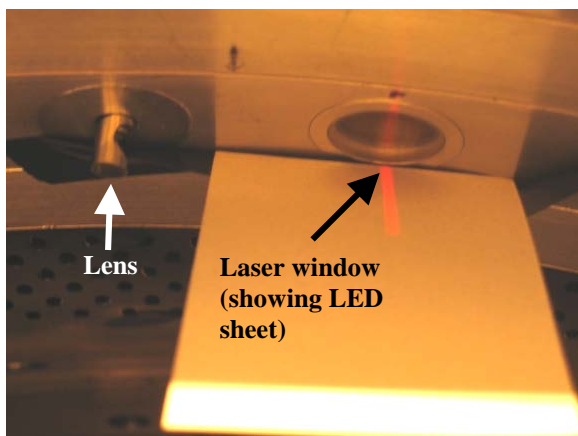
Fiberscope lens and Camera



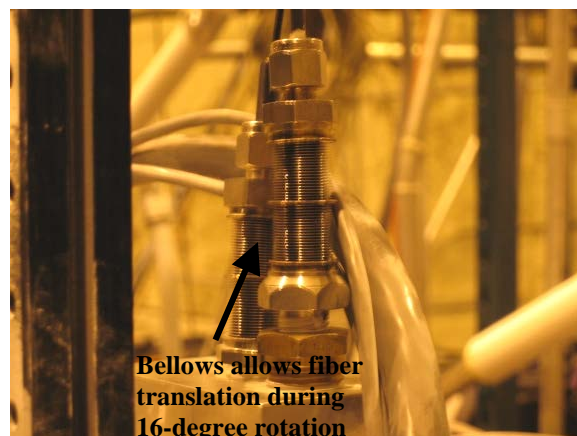
Exterior view of probes on rotating ring



Fiberscope, laser port, and seeder rod in rig



Lens and laser window



Bellows for fiber insertion into test section

Figure 10. TRF FOPIV Probe assembly on the rotating instrumentation ring.

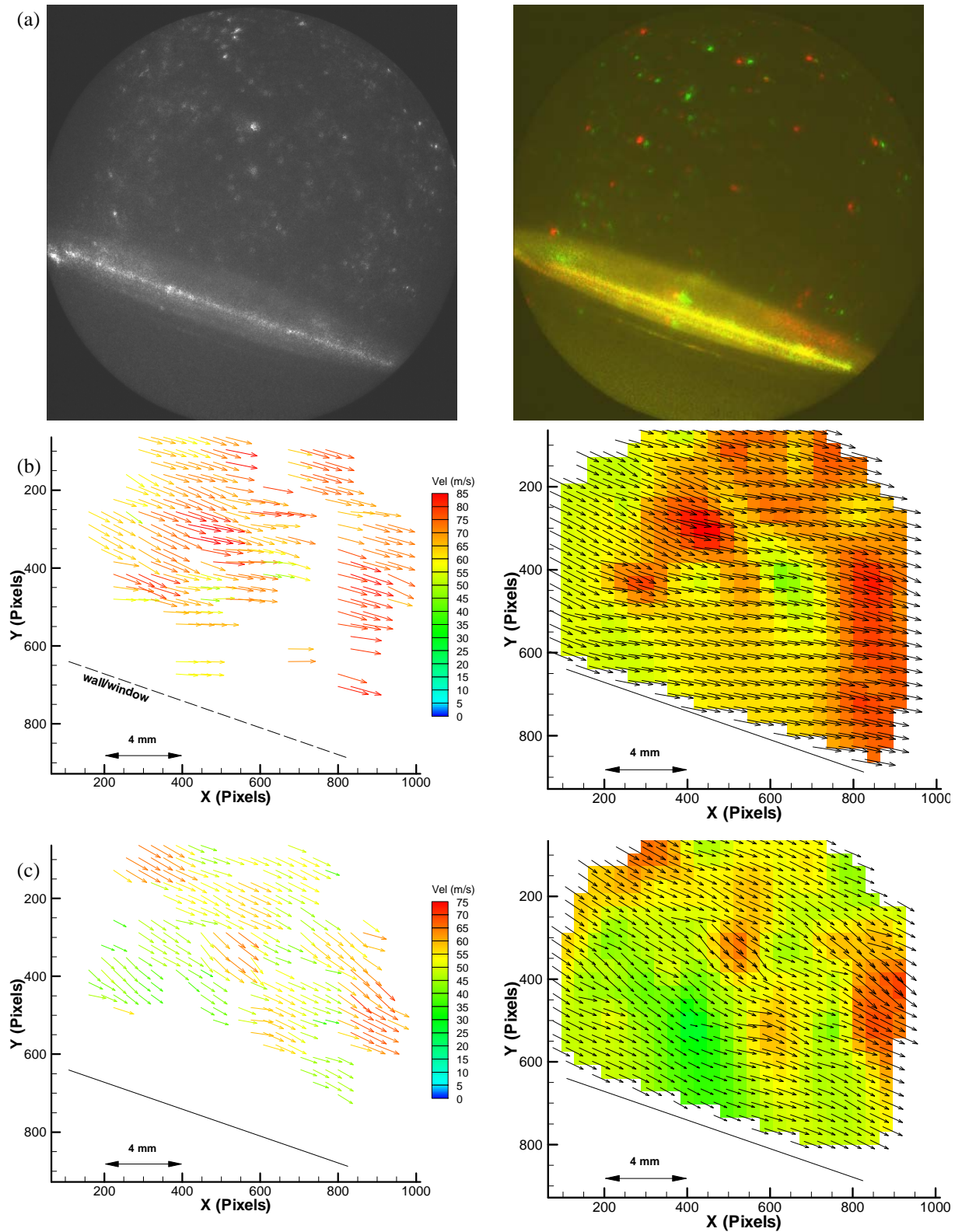


Figure 11. (a) Particle-scattering image (left) and double-exposure image (right) along with instantaneous velocities (left) and linearly interpolated contours (right) from tests in the TRF at (b) 1.16 seconds and (c) 3.36 seconds after the main valve is opened.

References

- ¹Estevadeordal, J., Gogineni, S., Goss, L., Copenhaver, W., and Gorrell, S., "Study of Wake-Blade Interactions in a Transonic Compressor Using Flow Visualization and DPIV," *Journal of Fluids Engineering*, Vol. 124, 2002, pp. 166-175.
- ²Copenhaver, W., Estevadeordal, J., Gogineni, S., Gorrell, S., and Goss, L., "DPIV Study of Near-Stall Wake-Rotor Interactions in a Transonic Compressor," *Experiments in Fluids*, Vol. 33, 2002, pp. 899-908.
- ³Wernet, M. P., "Development of Digital Particle Imaging Velocimetry for Use in Turbomachinery," *Experiments in Fluids*, Vol. 28, 2000, pp. 97-115.
- ⁴Tani, N., Mori, M., Hishida, K., Maeda, M., "Development of Fiber-Bundle-Image-Guided PIV," 10th International Symp. on Appl. of Laser tech. to Fluid mech., Lisbon, 10-13 July, 2000.
- ⁵Tani, N., Kondo, H., Mori, M., Hishida, K., and Maeda, M., "Development of fiberscope PIV system by controlling diode laser illumination," *Experiments in Fluids*, Vol. 33, 2002, pp. 752-758.
- ⁶Reeves, M. and Lawson, N. J., "Evaluation and Correction of perspective errors in endoscopic PIV," *Experiments in Fluids*, Vol. 36, No. 5, 2004, pp. 701-705.
- ⁷Anderson, D. J., Jones, J. D. C., Easson, W. J., and Greated, C. A., "Fiber-optic-bundle delivery system for high peak power laser particle image velocimetry illumination," *Review of Scientific Instruments*, Vol. 67, No. 8, August 1996.
- ⁸Hand, D. P., Entwistle, J. D., Wiles, D. P., Kuhn, A., Jones, J. D. C., and Greated, C. A., "Fibre Optic beam delivery system for high peak power laser PIV illumination," *Measurement Science and Technology*, Vol. 10, 1999, p. 239.
- ⁹Matsuura, Y., Hanamoto, K., Sato, S., and Miyagi, M., "Hollow-fiber delivery of light of high-power pulsed Nd:YAG laser light," *Optics Letters*, Vol. 23, No. 23, December 1998.
- ¹⁰Boxx, I. G., Idicheria, C. A., and Clemens, N. T., "Kilohertz PIV/PLMS of low-gravity turbulent flames in a drop tower," 12th International Symposium on Application of Laser Techniques to Fluid Mechanics, Lisbon, Portugal, 2004.

An Investigation Of Particle-Shadow Velocimetry (PSV) For Transonic-Flow Applications

Jordi Esteveordal* and Larry Goss**
Innovative Scientific Solutions, Inc.
2766 Indian Ripple Rd.,
Dayton, OH 45440, USA

The particle-shadow-velocimetry (PSV) technique that employs light sources with significantly lower power than lasers is investigated as a variant of particle-image velocimetry (PIV) for high-speed flow applications. The PSV technique uses a non-scattering approach that relies on direct in-line illumination by a pulsed source such as a light-emitting diode (LED) onto the camera imaging system. Narrow-depth-of-field optical setups are employed for imaging a two-dimensional plane within a flow volume, and images that resemble a “negative” or “inverse” of the standard PIV scattering mode are produced by casting particle shadows on a bright background. In this technique the amount of light reaching the image plane and the contrast of the seeding particles are significantly increased, while the power required is markedly lower than that demanded by scattering approaches. An investigation of the technique for transonic-flow applications is presented.

I. Introduction

PARTICLE-IMAGE VELOCIMETRY - (PIV) is a powerful diagnostic technique that is capable of providing accurate and resolved velocity fields in a variety of applications. High-speed PIV is becoming increasingly important with the emergence of high-speed laser sources and high-speed video cameras.¹ Most PIV techniques require laser light sources that are capable of high-power, short-duration pulses, allowing instantaneous marking of seed particles and capture of their scattered light by an imaging system. Presently lasers are one of the most expensive component in PIV systems, despite their relatively slow repetition rates in commercial form. High-speed PIV is even more costly since it also requires expensive high-speed cameras.

In the present paper an alternative approach, particle-shadow velocimetry (PSV),²⁻⁴ that allows low-power illumination sources such as LEDs to be used for PIV is investigated for high-speed flow applications. LEDs are inexpensive and can be pulsed to nanosecond levels and at high-repetition rates.²⁻⁵ The PSV technique has further advantages with respect to laser-based PIV because it produces no glare or reflections from surfaces; since LEDs of many monochromatic wavelengths are available, two-color PIV and multicolor PIV are also feasible.

Among the main challenges in applying the technique to high-speed flows are those related to the particle size and the light-pulse duration. The particles have to be small enough to faithfully follow the flow but their shadows have to be large enough to be recorded in the imaging sensor. At high speeds and large magnifications the light pulses used for PSV might not be short enough to instantaneously freeze the seeding particles motion and might produce traces or streaks. This investigation addresses these two challenges by studying various parameters that influence the particle-shadow image size and the capability of obtaining velocity information from their traces. A schematic of the PSV setup for a transonic-cascade experiment,^{2, 6, 7} is shown in Fig. 1. The LED light-source units are small and have relatively simple wiring, which makes them attractive for optical diagnostics inside turbomachines.

* Senior Research Engineer, ISSI, 2766 Indian Ripple Rd., Dayton, OH 45440, Associate Fellow.

** President, ISSI, 2766 Indian Ripple Rd., Dayton, OH 45440, Associate Fellow.

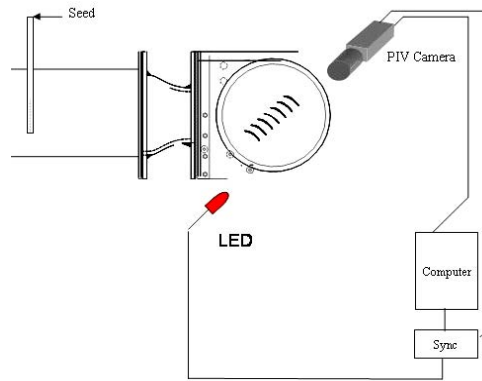


Fig. 1 Schematics of PSV setup in transonic cascade experiment. LED replaces laser and narrow DOF optics image a 2D plane.

II. Particle Shadow Velocimetry (PSV) Technique

The PSV technique is a variant of PIV that utilizes direct in-line volume illumination and an imaging-optics setup that produces a narrow depth-of-field (DOF) for 2D plane imaging. In PSV the setup permits the DOF, the field-of-view (FOV), and the working distance (WD) to be adjusted by introducing spacers or bellows between the camera body and various lenses (Fig. 2). In a simple setup where bellows are employed [Fig. 2(a)], the required extension of the bellows attachment is the product of the reproduction ratio (magnification) and the focal length. The DOF decreases with the spacing and large aperture and can produce a very thin, focused plane (e.g., sub-millimeter). The addition of more than one lens [Fig. 2(b)] increases flexibility in the combination of key parameters (DOF, FOV, WD). Commercially available lenses were used in the present investigation, but custom designs would yield a smaller setup for achieving the desired parameters. For example, since the DOF is proportional to the diameter of the lenses, a larger diameter lens would produce a sharper DOF.

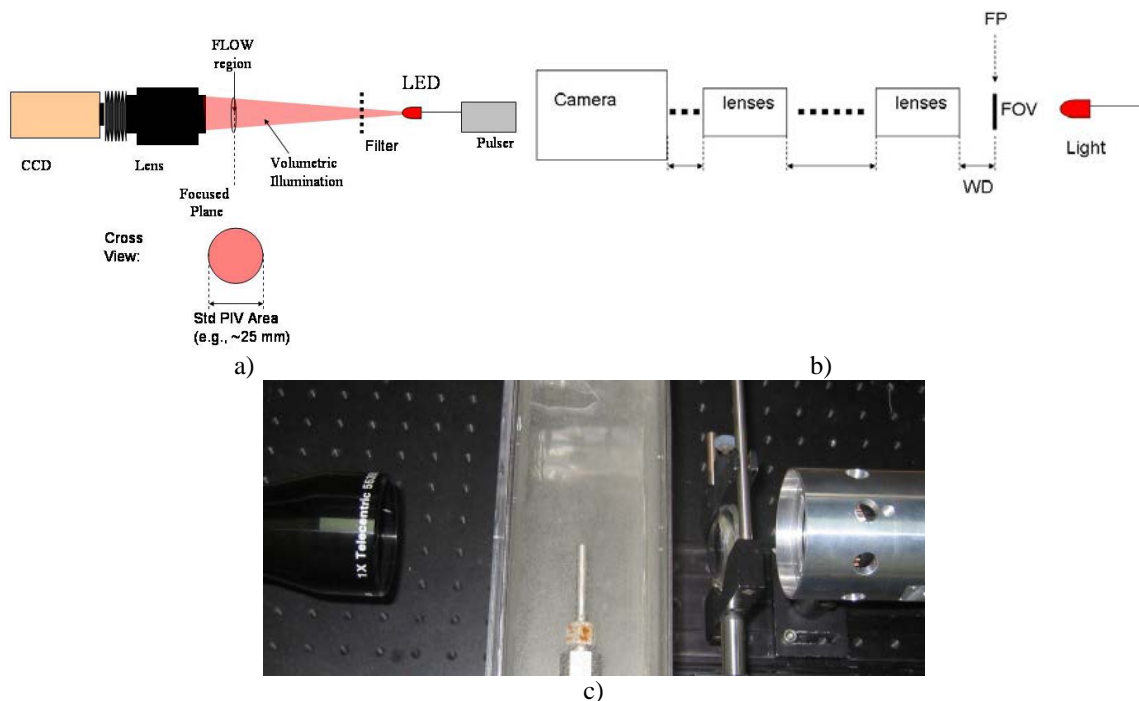


Fig. 2 Schematics (a, b) and picture (c) of PSV setup showing main parameters with narrow DOF and direct in-line LED volume illumination.

In the present study the DOF was on the order of 1-3 mm, and the FOV and WD could be varied from millimeters to tens of centimeters. Figure 3 shows an example of DOF estimate obtained with a telecentric lens that provides a constant magnification of 9 mm within the WD (here 100 mm); the ruler was tilted 53.13 degrees and DOF can be estimated within one mm from the focused center given the out-of-focus distance observed. Typically the DOF is arbitrarily defined as a specified fraction distance from the focused plane. The effect on real particles will be discussed later in the paper.

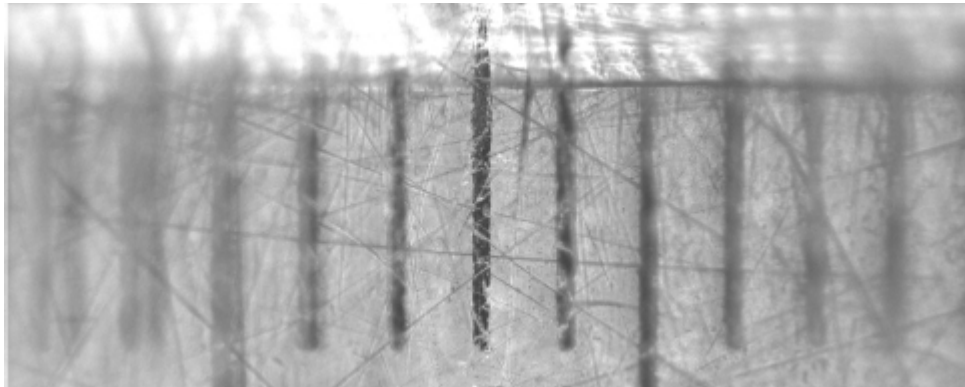


Fig. 3 Ruler tilted for DOF estimate (one mm) from a WD of 100 mm using telecentric lenses.

Image filtering allows removal of image data that fall beyond a certain intensity threshold, based on their location from the center of the focal plane and effectively shorten the DOF. Most PIV techniques utilize such methods. For example, microscopic PIV⁸ approaches and miniature PIV-with-LED⁹ approaches utilize the principle of narrow DOF to image a 2D plane as well as imaging post-processing filtering techniques. Some approaches employ defocusing principles to measure the three-dimensional (3D) velocity field.^{10,11} Shadow techniques can be found in two-phase flow applications for imaging and sizing large particles, bubbles and drops.¹²⁻¹⁵ Some of these shadowgraphy investigations use particle tracking techniques to measure bubbles/drops velocity coupled with a laser-sheet PIV technique to measure the full velocity field. The PSV technique, like PIV, aims to the full velocity field using correlation techniques on the shadow ensembles of seeding tracers in the full flow field, single- or multi-phase flows, low or high speed.

The micro-PIV approaches are often based on fluorescent tagging of particles⁸ or on light scattering through transmitted-light microscopy.¹⁰ In fluorescence approaches, particles suspended in the flow [e.g., polystyrene latex particles (PSL)] are tagged with a dye to excite at a certain wavelength (typically chosen to be near the Nd:YAG-laser wavelengths) and emit at another. In transmitted-light techniques, the light is transmitted from a source on the side of the specimen that is opposite the objective and passed through a condenser to focus it on the specimen for obtaining very high illumination. After the light passes through the specimen, the image of the specimen passes through the objective lens to the oculars, where the enlarged image is viewed. The most widely used setup for proper specimen illumination and image generation is known as Köhler illumination; here, the micro-PIV applications rely on scattering. A discussion of the miniature approach of PIV-with-LED in the literature⁹ includes various setups and results from forward, backward, and side scattering. Because of weak scattering from the LED, the technique is applied only to small areas. In other approaches such as holography, scattering and its interaction with the background light are of major importance when using coherent laser light.^{6, 16-20}

PSV employs a fundamentally different approach that relies not on principles such as fluorescence, scattering, coherence, Doppler, defocusing, or tagging but on the simpler particle-ensemble shadow cast from a bright background. The PSV principle is based on the in-line, zero-degree-deviation direct-illumination setup. Figure 4 shows schematically the differences between collection-of-scattering and collection-of-extinction (shadow-casting) alignment setups. In the PSV mode the angle between the components is zero. A particle lies between the source and the detector (a camera imaging system, in this case) and casts a shadow of an area determined by the light-extinction characteristics^{21,22} (Fig. 4) that can be considerably greater or smaller than the geometrical shadow of the particle.

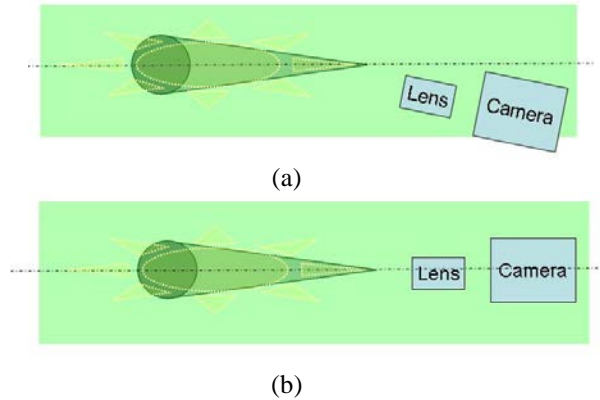


Fig. 4 Schematic of imaging alignment for (a) scattering mode and (b) PSV mode, showing spherical particle, its scattering (dashed), and its shadow from a background light directed from left to right.

Contrast changes yield particle-shadow-diameter variations and permit the diameter to be adjusted by varying the intensity of the incident light. The brightness of the light can be adjusted via pulse duration, light-source distance, light-source size, and attenuation techniques. A brighter light produces a smaller particle shadow and, as a consequence, yields a sharper DOF.

The shadow behind the sphere shown schematically in Fig. 5 shows several regions.²²

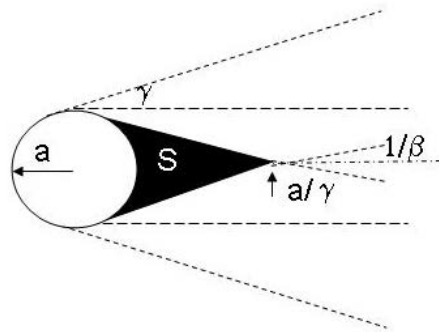


Fig. 5 Schematic of shadow from spherical particle and various geometrical parameters.²²

The ‘deep-shadow’ region (S) is of most use in PSV and is slightly smaller in diameter than the particle and the geometrical shadow (horizontal lines in Fig. 5). In order to study the possibility of imaging small shadows, for example, from micron-sized particles that could be used in high-speed PSV, reticle targets were used. These reticles have various circles of various micron sizes; a ‘Paterson’ gloves pattern with 10 discs of diameters 450, 360, 270, 225, 180, 145, 110, 74, 37, and 18 microns (± 3 microns) was used initially. Since the shadow thrown by a sphere is much darker than that of a circular disc,²² the shadows observed from the reticle circles are lighter than shadows from actual spherical particles. Figure 6 shows how illumination can be used to affect the shadow. The telecentric setup used in Fig. 2 allowing sub-mm DOF from a WD of 100 mm was used in these tests. A single red LED was used located at 85 mm from the reticle in the opposite side of the camera. For these conditions and without post-processing, the smallest circle (18 microns) shadow is captured with a short pulse (10 microsec) but when illumination is increased (e.g., here shown 50, 100, and 650 microsec pulses) the smallest circle shadows vanish.

Like in PIV, accurate PSV velocity demands the shadow be casted within several pixels. For example, if is only one pixel, velocity will have similar problem to the ‘pixel locking’ occurring in PIV. Higher resolution cameras are therefore desirable when smaller particles need to be used.

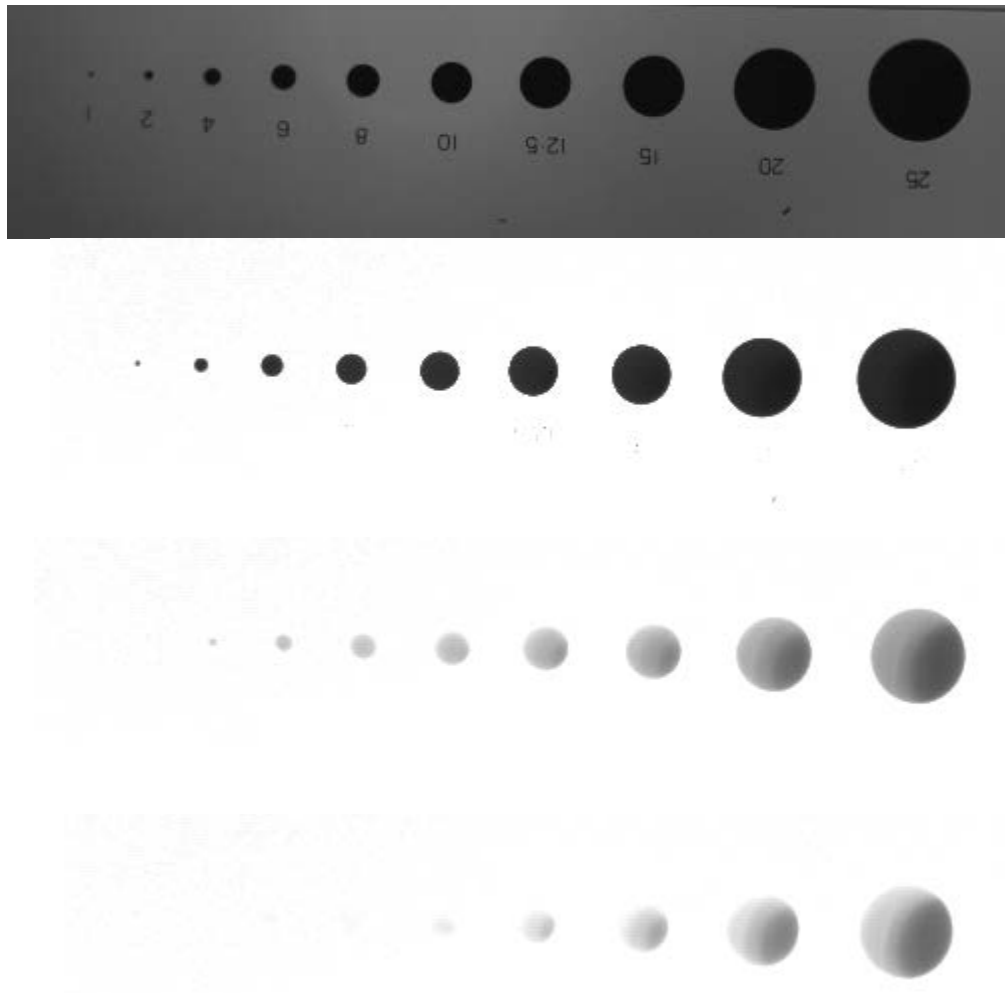


Fig. 6 Illumination effect on shadow characteristics of micron sizes discs.

Some PSV features can be explained using particle-absorption and scattering-of-light principles²¹ that predict the interaction between light and particles in the PIV ranges of the present study. Of greatest interest here is the light-particle interaction and its effect behind the particle--the region associated with forward scattering and deep shadow or, to use a term that shares some terminology with fluid mechanics, the “electromagnetic-wake region.” The following argument clarifies why the region with the highest scattering efficiency--forward--has little or no effect. The particle image recorded on a camera results from the extinction of the (in-line) light caused by absorption and scattering, as opposed to the forward scatter of light by the particle. The extinction produces a shadow, while forward scatter brightens the particle image. In the basic setup, the only forward scatter that could contribute to the particle image is that of a very small angle, i.e., only the light that would be scattered directly into the recorded image of the particle. All other forward-scattered light would contribute only to an increased background over the entire image. This means that only a small angular fraction of the forward scatter affects the particle contrast. Therefore, the strong forward source light has a much greater influence than the scattering.

The ratio of extinction to forward scatter depends on the particle size; however, in most cases extinction is ten times larger than forward scatter. This ratio becomes further increased since the only concern here is forward scatter in a very small angular region. Any scatter outside this region becomes extinction. This consideration probably increases the ratio from 10 to 1 to more than 1000 to 1. Therefore, it is unlikely that the effects of forward scatter are recorded in this mode.

The contribution from diffraction in the region behind the particle depends on the illumination. In this case the PSV setup is the inverse of the “slit experiment” for a sufficiently large particle. Diffraction prevents the light from being completely obscured, but blockage of the source light dominates. In the Mie-scattering plots, the source intensity is not included; and in any event, it is indeed blocked by the particle (e.g., a geometrical, ideal single ray of light). In practice, all of the source rays that are not scattered by the particle can be detected.

The other crucial component in PSV is the use of short DOF to image (or cast) the focused shadows. The length of the shadow is a function of the intensity of the illumination, based on the previous arguments. Micro-PIV studies⁸ have shown that in a volumetric illumination, all particles in the volume contribute to scattering. Extension to the PSV technique, where scattering is “overshadowed,” yields a volumetric-particle shadow field that yields similar results in the focal plane; that is, shadows are observed only when they are in focus with the maximum in the focal plane and become invisible (in the form of fainting background noise) when they are out of focus (Fig. 7). The rate of defocusing can also be assumed to be proportional to the diffraction pattern of the particles (assuming that they are point sources imaged through a circular aperture or lens), with the pattern having maximum intensity (corresponding to the Airy function for Fraunhofer diffraction) at the focal plane of the lens (Fig. 8) which decreases very rapidly. Typically the DOF is arbitrarily defined as a specified fraction of that maximum. The overall signal-to-noise ratio can be improved through filtering techniques, and brightness and seeding density variations. Therefore, for planar PSV measurements, the out-of-focus contribution can be minimized in the final contribution to the velocity correlation. Alignment is very critical also since aberrations (e.g., spherical) can occur if the components in the optical path are misaligned.

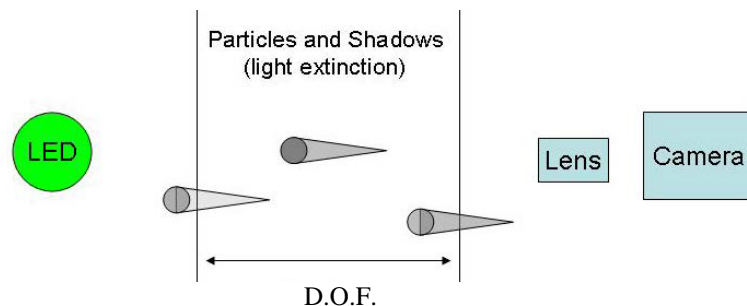


Fig. 7 Schematic of contribution of particle shadows to image, restricted to focal plane, with greater contribution from those at the center.

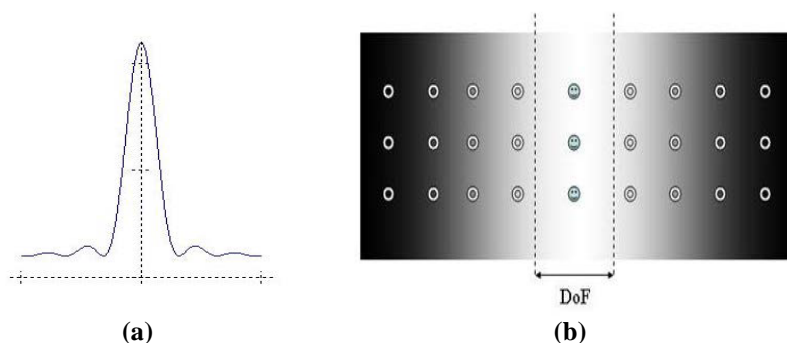


Fig. 8 Schematic of effective result of PSV; all particles are illuminated in the volume, scatter light, and produce shadows; but diffraction pattern (a) has maximum intensity (Airy function) at focal plane of lenses. Sharp DOF effectively results in only 2D slice of illuminated volume being imaged (b).

Following the illumination tests on the Patterson reticle it can be shown that illumination also has an effect on the DOF (Fig. 9). The shadows from large particles remain clearly in the image when the object plane is translated 1.27 mm forward while the small particles quickly become out of focus and invisible. Here post-processing has no effect once the shadow has vanished beyond the DOF region. It is noteworthy that large discs remain in focus for longer range.

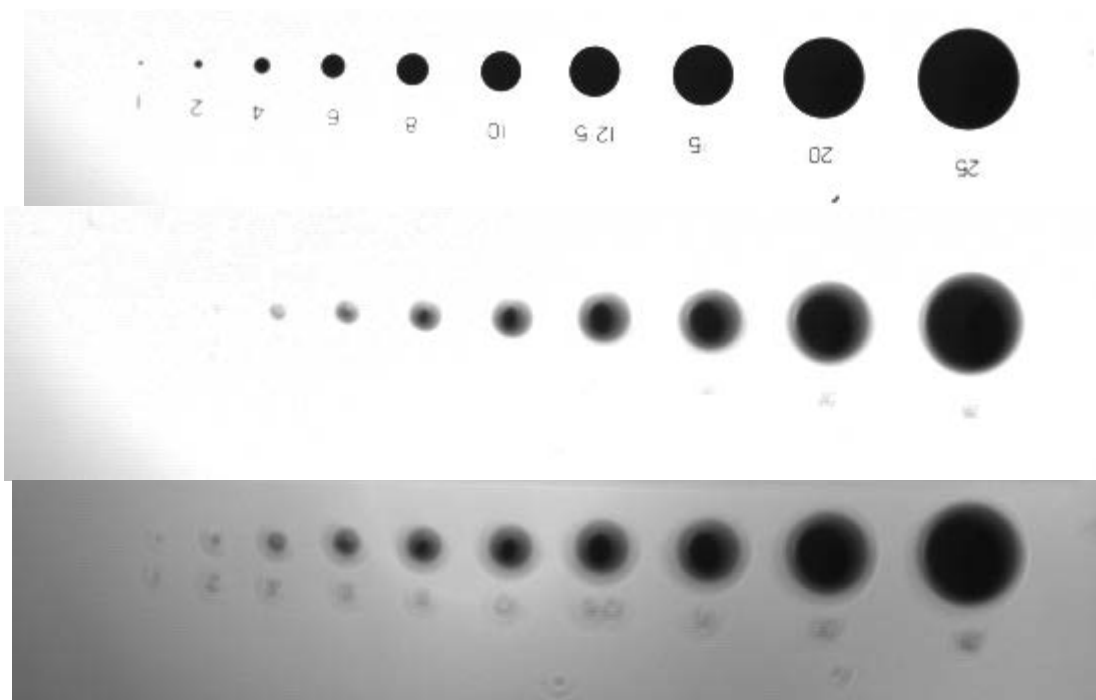
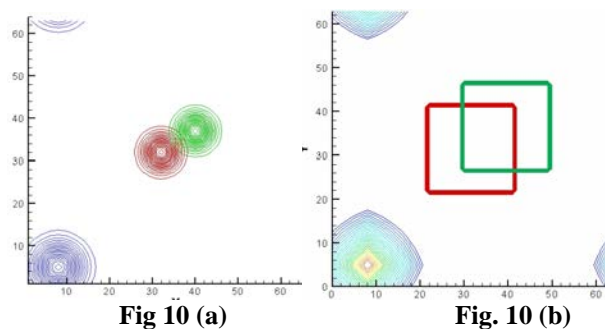


Fig. 9 Illumination and DOF variations on micron-sized discs. Target originally in the center of the focal plane (top, 40 microsec pulse) is translated towards the camera 1.27 mm and the small discs become invisible (center, 40 microsec pulse) or just out of focus (bottom, 20 microsec pulse).

In PIV, velocity is determined by calculating the particle-ensemble displacements between two instantaneous time snap-shots. This is generally accomplished through correlation techniques such as those that use FFT on the image signal. The signal information is generated from changes in intensity; therefore, the same technique can be used for PSV since it is based on information from particle ensembles, although the intensity information is inverted compared to that from PIV. Subtle differences exist; for example, in PIV the particle intensities have a shape, such as Gaussian, whereas in PSV this shape has not yet been determined and depends on the aforementioned light-particle interaction and extinction characteristics. To account for these differences that could affect the accuracy (e.g., in the correlation peak finding), the method has been tested for accuracy³.

Since the critical aspect is the shift between particle ensembles techniques such as correlation effective because the amplitude of the correlation peak is weighted by the number of pairs in the interrogation area, the size of the particle pairs, and the intensity of the pairs. On the other hand, the PSV image with particles having the lowest intensity compared to the maximum intensity of the background can be readily inverted and generate a PIV-like signal³. Examples of correlations are shown in Fig. 10 using various synthetic data.

When the pulse duration is too long to freeze the particle motion instantaneously then traces fields or streaks result. Figure 11 shows samples of correlation of traces on synthetic data. Correlation of traces is straightforward operation involving step signals (Fig. 12).



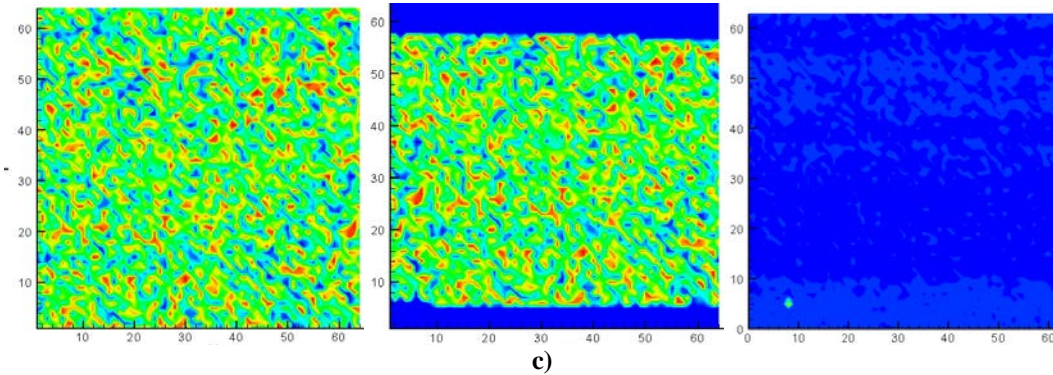


Fig. 10 Correlation examples for: a) Gaussian-image shaped particle of 10 pixels diameter, b) a square of 20 pixels side, c) a random field displaced (left and center). All yield a sharp correlation peak; time0= O(32,32); time1= O(40,37); correlation peak at (8, 5); all units pixels.

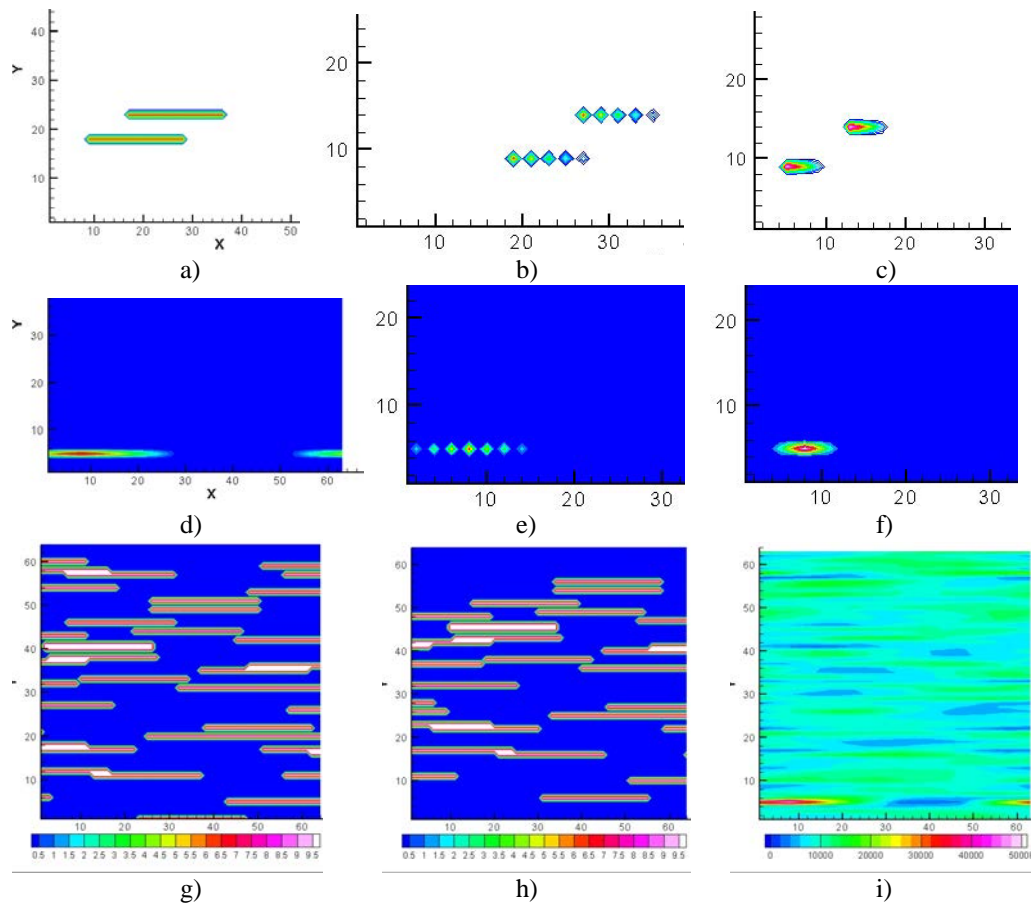


Fig. 11 Traces displacement fields (a-c, d-f, j): Single trace (a, d); fainting discrete trace (b, e); fainting continuous trace (c, f); Traces Field (30 traces, 20 pixels long) (h-j) ; all displacements from time0=O (32,32) to time1=O (40,37); correlation peak= (8, 5). All units pixels.

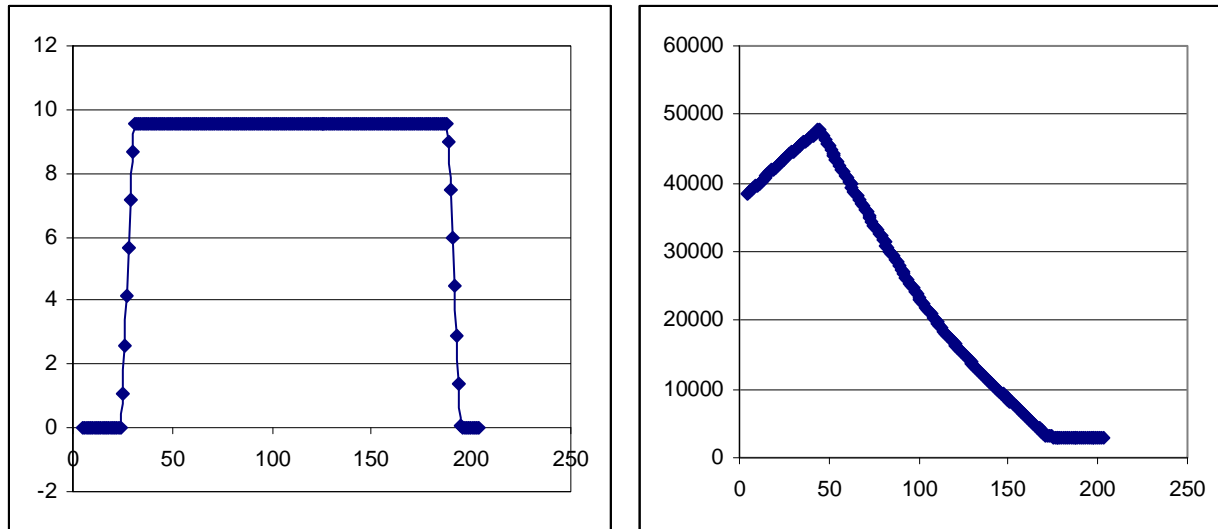


Fig. 12 Trace shape and Correlation peak trace shape for the Traces Field of Fig. 11 (g-i)

III. Results

Images and velocity fields from a variety of particles and conditions are compared and results of flow tests with jets in water and air for several particle sizes and shapes are presented. Results for low speed and are first presented and then some high-speed preliminary results are introduced.

The fact that the LED can be pulsed at any rate makes it very attractive for velocimetry. This capability is not shared by other sources such as lasers or Nanopulsers,⁵ which generally have lower and fixed repetition rates (although shorter pulses at present). Pulses from LEDs that were used ranged from tenths of nanoseconds to microseconds. The choice of pulse depends on the velocity of the flow and the magnification, and the pulse must be sufficiently short to freeze the motion while providing sufficient illumination. The red LED is preferred since the CCD camera has its higher spectral sensitivity in the upper-red region. A overdriven reed cluster (ISSI) was used to obtain most of the present results because it provided brighter, shorter pulses that would be a requirement in many transonic and higher speed applications. A single LED can be also used if the velocity ranges and other parameters (WD, FOV) are appropriate.

A sample pulse is shown in Fig. 13. The photodiode has a rise time of tenths of nanoseconds, which should be taken into account when analyzing the pulses. Because of heat limitations, the LEDs have a limited duty cycle; therefore, unlimited pulses at very high repetition rates would require special designs.

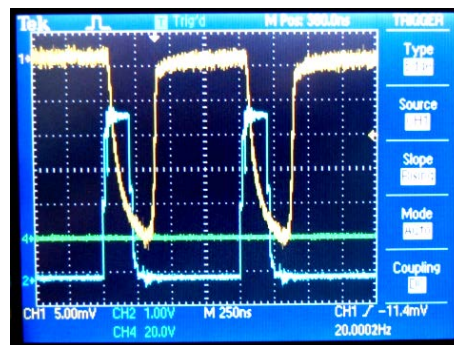


Fig. 13 LED pulse-shape sample 200 nsec. Drive pulse is rectangular (blue) and light pulse shows a raising time (yellow).

The camera used in the present experiments was a standard cross-correlation PIV camera (ES1) with 1k x 1k pixels at a 15-Hz repetition rate. Other cameras with higher sensitivity and resolution and higher repetition rate were not tested but could be used for the shorter pulses. On the other hand, relatively inexpensive commercial cameras with detachable lenses have high resolution (although slow repetition rates) and could also be used in the

auto-correlation or the two-color-PIV mode.^{23,24} If these cameras were coupled with a single LED, a very inexpensive PIV system could be achieved that would still be useful in many experiments and yield high-resolution, accurate results.

An example of velocity field obtained with the PSV technique in cross-correlation double-exposure mode is shown in Fig. 14 for two-phase bubbly flow using the red cluster with 200 nsec pulses. Velocity of the bubbles is readily calculated from cross-correlation techniques.

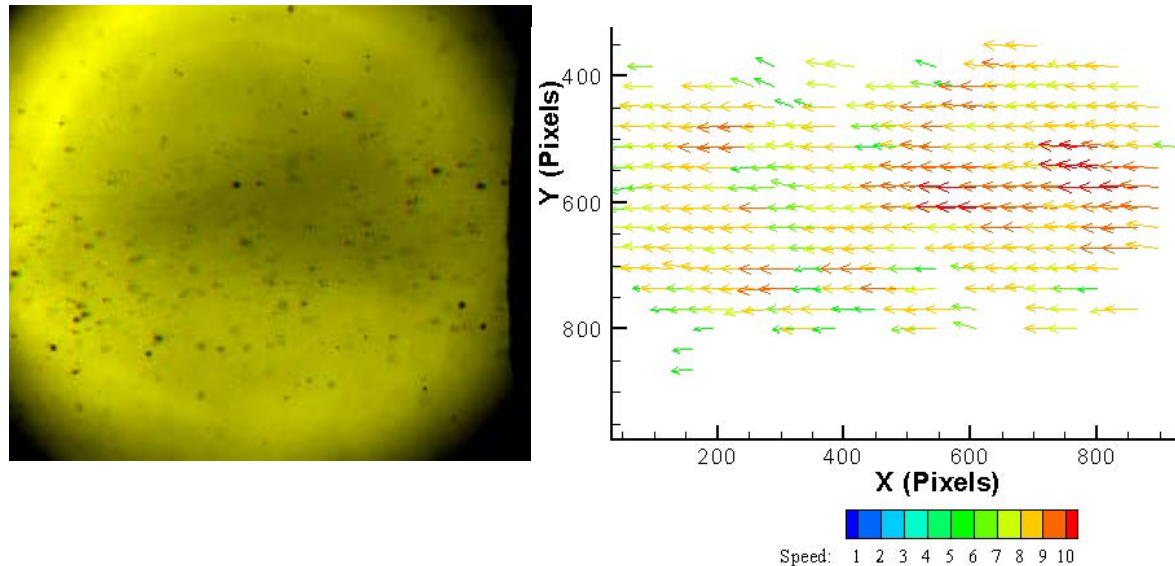


Fig. 14 Double-exposure modes in bubbly jet in water: Exposure time 200 nsec; time separation between frames (DT) 50 μ sec. FOV~9mm.

It is obvious that PSV images contain a variety of background-noise textures due mainly to out-of-focus data. Their contribution to the correlation function can be reduced significantly by the optical characteristics of the technique; since these textures contribute to noise, they should be removed. During the experiment this can be done by increasing the illumination, but it can also be accomplished during post-processing by applying filtering techniques that effectively reduce that noise level and produce a sharper image, effectively reducing the 2D plane thickness.³

While the technique appears straightforward for low speed flows with large particles in a ‘particle-tracking’ mode, such as bubbly two phase flows, its application to single phase flows in ‘PIV’ mode for full field velocimetry is not obvious, specially high speed. New challenges related to particle size and its image-shadow size are apparent.

To assess the feasibility of the technique in various flow media with typical PIV seeding density was studied with low speed flows. Figure 15 shows samples of micron-sized PSL particles in water and cornstarch (10- μ diam) in air for two exposure times.

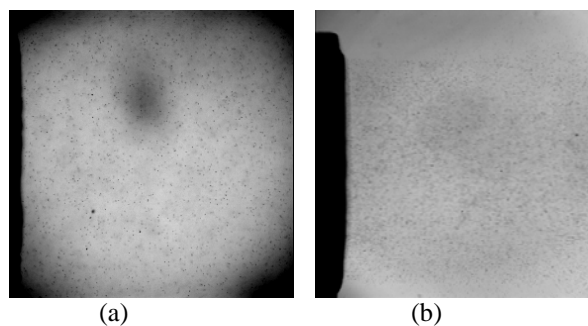
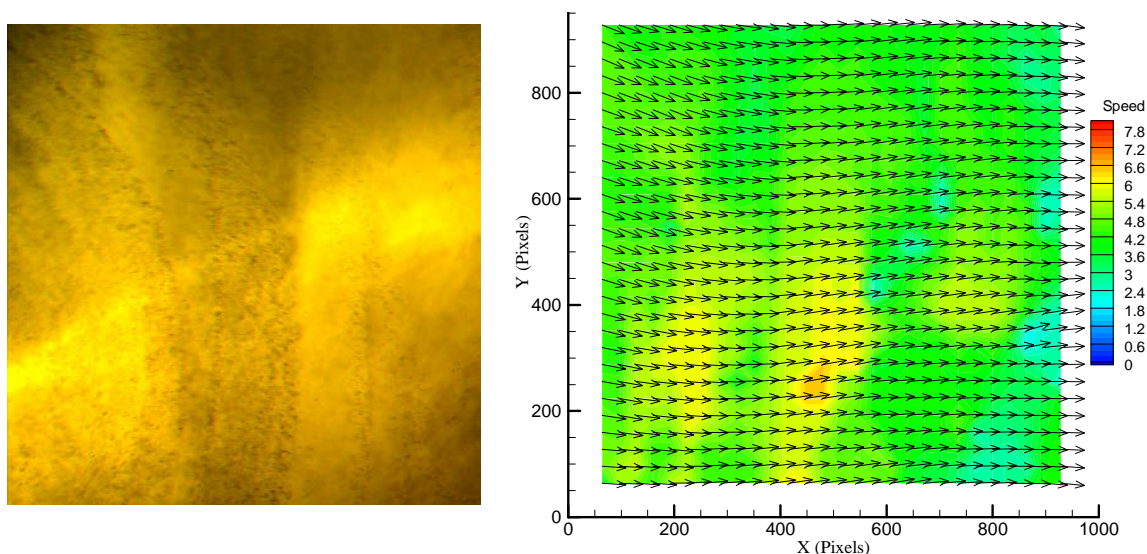
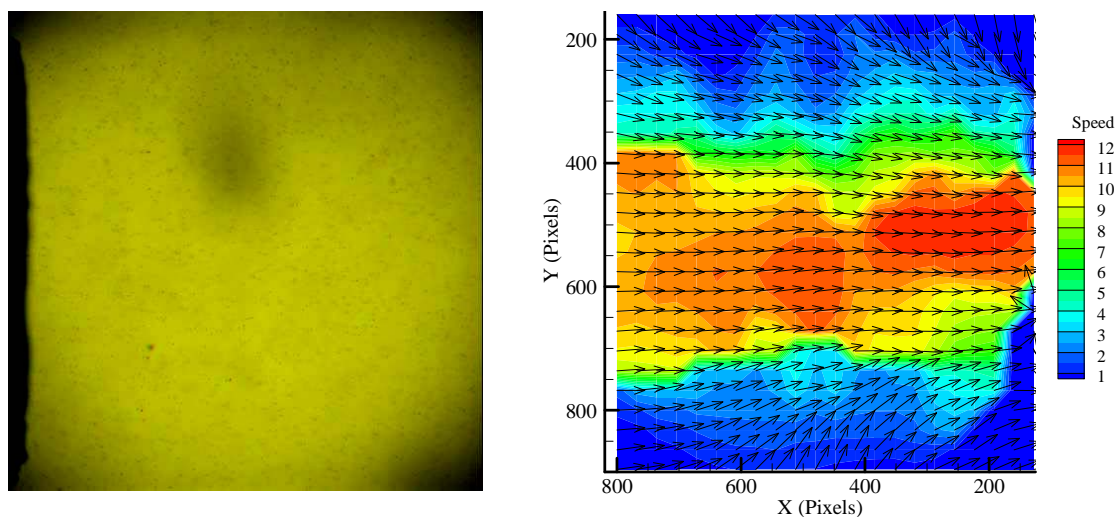


Fig. 15 Small particle-size shadow casting with PSV: a) water jet (PSL, 1- μ diam), 4- μ sec exposure; b) air jet (cornstarch 10- μ diam), 5- μ sec exposure. FOV ~ 10 mm.

Figure 16 contains an example of a double exposure and its derived velocity field from free flow where sub-micron smoke particles (mixture of glycerin and ionized water) were used. A single LED (blue) in the PSV mode with two exposures 100 μ sec and 5 μ sec apart was used (FOV is 3 mm). Figure 17 shows the PSV image and its derived velocity field of a jet in water using PSL seed (FOV is 10 mm), and Fig. 18 shows the PSV image and its derived velocity field of an air jet seeded with 10- μ cornstarch particles (FOV is 10 mm). Finally a medium speed flow ($M < 0.3$) was also tested (Fig. 19).



**Fig. 16 PSV with LED. Example of air flow with smoke particles (0.5- μ diam),
FOV = 3 mm. Speed in pixel units.**



**Fig. 17 PSV with LED. Example of water-jet flow with PSL particles,
FOV = 10mm. Speed in pixel units.**

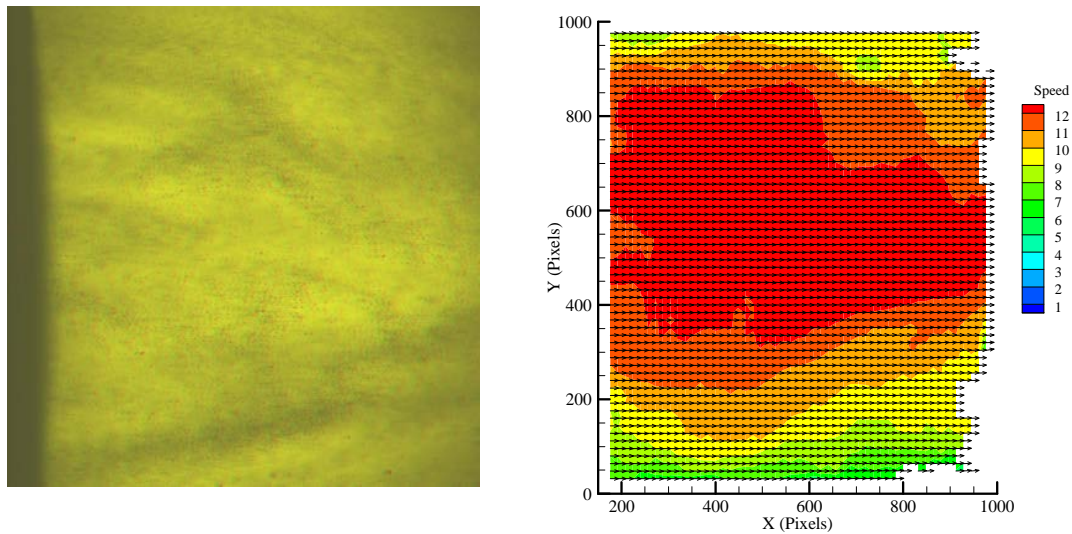


Fig. 18 PSV with LED. Example of air-jet flow with cornstarch particles (10- μ), FOV = 10mm. Speed in pixel units.

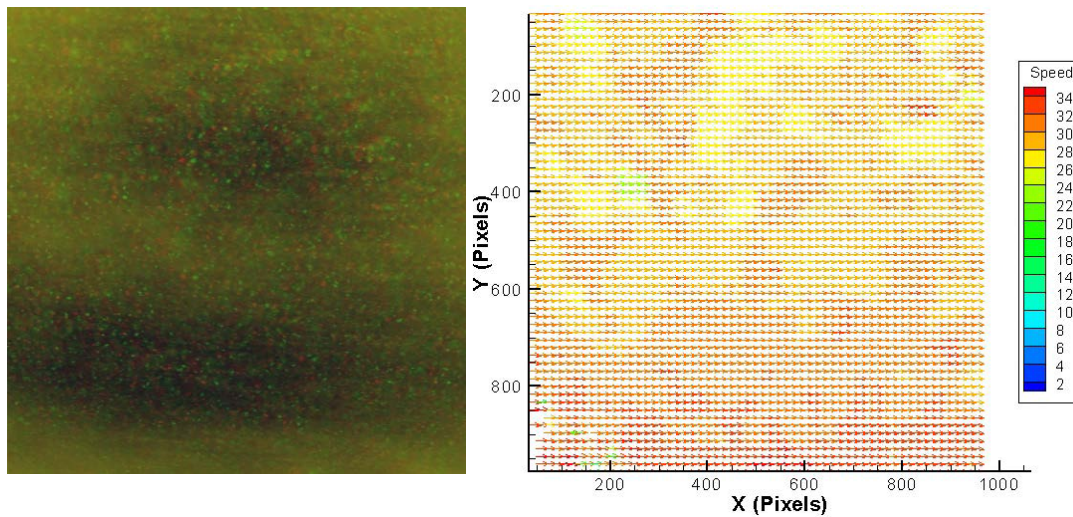


Fig. 19 PSV with LED. Example of higher speed flow (100 m/s) channel flow seeded with cornstarch particles (10- μ), FOV = 10mm. Speed in pixel units.

The technique was then tested in a transonic facility²⁵ and some preliminary results are presented. Fig. 20 shows samples of traces obtained at transonic flow conditions ($M \sim 0.7$) using large cornstarch (10 microns) particles. Fig. 21 shows details of regions of the same flow seeded with AlOx and TiOx particles and a velocity vector corroboration of the speed of the flow conditions ($M = 0.7$) through traces correlation.

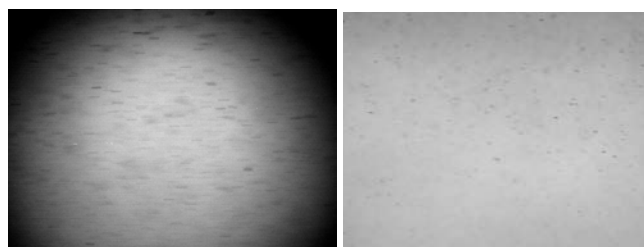


Fig. 20 Single exposure traces of Cornstach particles at $M \sim 0.7$

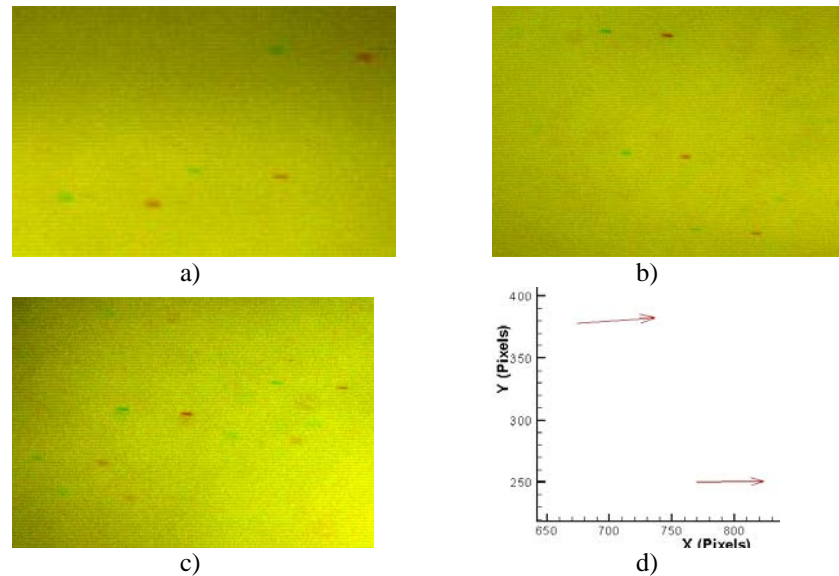


Fig. 21 Details of Traces Pairs 5-6 pix long in transonic flow ($M \sim 0.7$). a) Cornstarch; b) AlOx; c) TiOx; d) sample of vectors obtained through traces correlation with displacement red-green 45 pixels or 230 m/s.

IV. Conclusions

A PSV technique that allows light sources with significantly lower power than lasers to be used was investigated for high-speed flows. The technique employs a non-scattering approach that relies on direct in-line illumination by a pulsed source such as an LED onto the camera imaging system. Narrow depth-of-field optical setups are used for imaging a 2D plane within a flow volume, and images are produced that resemble a “negative” or “inverse” of the PIV mode by casting particle shadows on a bright background. In this technique the amount of light reaching the image plane and the contrast of the seeding particles are significantly increased, while the power required is markedly lower than that demanded by scattering approaches. Applications of the technique for various velocity ranges were presented including preliminary techniques and results for a transonic speed flow.

Acknowledgments

The help of B. Sarka and D. Trump of Innovative Scientific Solutions Inc. in the design and fabrication of the LED lamps is acknowledged.

References

- ¹Boxx, I. G., Idicheria, C. A., and Clemens, N. T., “Kilohertz PIV/PLMS of Low-Gravity Turbulent Flames in a Drop Tower,” 12th International Symposium on Application of Laser Techniques to Fluid Mechanics, Lisbon, Portugal, 2004.
- ²Estevadeordal, J., Car, D., Gorrell, S., and Puterbaugh, S., “DPIV with LED Illumination: Application to Turbomachinery and Flow Control,” Presented at the 29th Annual AIAA Dayton-Cincinnati Aerospace Science Symposium, 9 March 2004, Dayton, OH; also in *Application of Advanced Laser Diagnostics to High Impact Technologies*, Quarterly Report 2829-3 on Contract F33615-03-D-2329 (Innovative Scientific Solutions, Inc., Dayton, OH, 2004).
- ³Estevadeordal, J., and Goss, L. P., “PIV with LED: Particle Shadow Velocimetry,” AIAA Paper 2005-37, Reno, NV, Jan 10-13, 2005.
- ⁴Estevadeordal, J., and Goss, L. P., “Method and Means for Particle Shadow Velocimetry,” U.S. Patent Pending, 2005.
- ⁵Estevadeordal, J., Gogineni, S., Kimmel, R., and Hayes, J., “Schlieren Imaging for Hypersonic Plasmas,” AIAA Paper 2004-1139, Reno, NV, Jan 5-8, 2004.

- ⁶Estevadeordal, J., Copenhaver, W., Car, D., Koch, P., Ng, W., Guillot, S., and Carter, C., "Macro- and Milli-DPIV Studies of a Boundary-Layer-Based Flow-Control System for a Transonic Cascade," 11th International Symposium on Application of Laser Techniques to Fluid Mechanics, Lisbon, Portugal, 2002.
- ⁷Estevadeordal, J., Guillot, S., Ng, W., Koch, P., Car, D., Puterbaugh, S., "Benefits of suction-surface blowing in a transonic compressor stator vane," AIAA Paper 2004-2207; AIAA 2nd Flow Control Meeting, 'Gas Turbine Engine Flow Control', Portland OR, June 28-July 1, 2004.
- ⁸Meinhart, C. D., Wereley, S. T., and Gray, M. H. B.; "Volume Illumination for Two-Dimensional Particle Image Velocimetry," *Meas. Sci. Tech.* 11, 809, 2000.
- ⁹Chetelat, O. and Kim, K. C., "Miniature Particle Image Velocimetry System with LED In-Line Illumination," *Meas. Sci. Tech.* 13, 1006. 2002.
- ¹⁰Ovryn, B., "Three-Dimensional Forward Scattering Particle Image Velocimetry Applied to a Microscopic Field-of-View," *Exp. Fluids [Suppl.] S175-S184*, 2000.
- ¹¹Pereira, F., Gharib, M., Dabiri, D., and Modarress, D., "Defocusing Digital Particle Image Velocimetry: a 3-Component 3-Dimensional DPIV Measurement Technique. Application to Bubbly Flows," *Exp. Fluids [Suppl.] S78-S84*, 2000.
- ¹²Nishino, K., Kato, H., Torii, K., "Stereo imaging for simultaneous measurement of size and velocity of particles in dispersed two-phase flow," *Meas. Sci. technol.*, 11, 633-645, 2000.
- ¹³Tokuhiro, A., Maekawa, M., Iizuka, K., Hishida, K., Maeda, M., "Turbulent flow past a bubble and an ellipsoid using shadow-image and PIV techniques," *Int. J. of Multiphase Flow*, 24, 1383-1406, 1998.
- ¹⁴Ortiz-Villafuente, J., Schmidl, W. D., Hassan, Y. A., "Three-dimensional pvt study of the surrounding flow and wake of a bubble rising in a stagnant liquid," *Exp. Fluids [Suppl.] S202-S210*, 2000.
- ¹⁵Lindken, R., Merzkirch, W., "A novel PIV technique for measurements in multiphase flows and its application to two-phase bubbly flows," *4th Int. Symp. on Particle Image Velocimetry*, PIV'01 Paper P1078, Göttingen, Germany, September 17-19, 2001.
- ¹⁶Estevadeordal, J., Meng, H., Gogineni, S., Goss, L., and Roquemore, M., "3D Visualization of Vortex-Ring and Bag-Shaped Instabilities using Holography," *Phys. of Fluids (Gallery of Fluid Motion)*, 9, S5, 1997.
- ¹⁷Meng, H., Estevadeordal, J., Gogineni, S., Goss, L., and Roquemore, M., "Holographic Flow Visualization as a Tool for Studying Three-Dimensional Coherent Structures and Instabilities," *J. of Flow Visualization*, 1, (2), 1998.
- ¹⁸Xu, W., Jericho, M. H., Meinertzhagen, I. A., and Kreuzer, H. J., "Digital In-Line Holography of Microspheres," *Appl. Opt.* 41(5), 5367-5375, 2002.
- ¹⁹Barnhart, D. H., Adrian, R. J., and Pappen, G. C. 1994 "Phase Conjugate Holographic System for High Resolution Particle Image Velocimetry," *Appl. Opt.* 33, 7159-70, 1994.
- ²⁰Sheng, J., Malkiel, E., and Katz, J., "One Beam Two View Holographic Particle Image Velocimetry System," *Proc. 4th Int. Symp. on Particle Image Velocimetry*, Göttingen, Germany, Paper 1022, 2001.
- ²¹Bohren, C. F., and Huffman, D. R., *Absorption and Scattering of Light by Small Particles*, John Wiley and Sons. 1983.
- ²²Nussenzveig, H. M., *Diffraction Effects in Semiclassical Scattering*, Cambridge University Press. 1992.
- ²³Post, M. E., Trump, D. D., Goss, L. P., and Hancock, R. D., "Two-Color Particle Image Velocimetry Using a Single Argon-Ion Laser," *Exp. Fluids* 16, s. 263-272, 1994.
- ²⁴Gogineni, S., Goss, L., Rivir, R., and Pestian, D., "Two-Color Digital PIV Employing a Single CCD Camera," *Exp. Fluids*, 25(4), 320-328, 1998.
- ²⁵Bailie, S.T., Car, D., Baudendistel, C.M. Estevadeordal, J. "Fluidic Control Studies for Diffusion Enhancement in Axial Compression Systems," 44th AIAA Aerospace Sciences Meeting and Exhibit, Reno, NV, 9-12 January 2006.

Fluidic Control Studies for Diffusion Enhancement in Axial Compression Systems

David Car*, S. Todd Bailie*, Craig Baudendistel† and David Gebbie‡

Air Force Research Laboratory, WPAFB, OH, 45433, USA

Jordi Estevadeordal§

Innovative Scientific Solutions, Inc., Dayton, OH, 45440, USA

The design of an experimental research rig for evaluating candidate flow control concepts for diffusion enhancement in axial compression systems is presented. The research rig is modular in design and capable of continuous flow in a Mach 0.7 environment with both diffusion and curvature. Candidate concepts can be evaluated inexpensively in a realistic axial compression system flow environment. Baseline results will be presented along with three preliminary flow control modules; all are variations on a theme of blowing only flow control using a slot jet behind a backward facing step. Two of the variations are preliminary investigations into the effect of the lip thickness of the backward facing step and its impact on the flow control effectiveness. The other introduces streamwise vorticity as a means of enhancing the interaction between the blowing jet and the core stream in an effort to reduce the secondary flow control flow fraction requirements. Detailed PIV, PSP and exit total pressure traverse measurements are presented and observations discussed.

I. Introduction

Flow control particular to axial compression systems has become a very active research topic for the last few decades.¹⁻⁶ It has the potential to open the design envelope for axial compressors to higher loading levels for a given compressor stage, translating into higher overall pressure ratios for improved thrust specific fuel consumption (TSFC). Increased loading levels may also translate into higher thrust-to-weight (T/W) ratios by reducing turbine engine axial length for a given pressure ratio and as shown in 7 and repeated in Figure 1, engine thrust-to-weight ratios have practically leveled off since the 1970's.

Successful demonstrations have been carried out using aspiration to remove the boundary layer fluid along the suction surface of transonic rotors.^{1,2} As illustrated in Figure 2, these demonstrations have shown stage total pressure ratio on the order of 3 with marginal efficiency gains based on calculations using fairly conservative estimates to account for the aspirated boundary layer fluid. Also, aspiration in the transonic environment showed another benefit of shock 'holding', whereby the local aspiration behind the leading edge shock intersection with the suction surface resulted in maintained shock position as the rotor is throttled to higher loading levels. This effect may help to address stall margin reductions as loading levels are increased in transonic rotors. A limitation noted with increased rotor loading levels is the increased diffusion required of the downstream stator. This limitation, if not properly addressed, may overshadow any benefit in rotor performance using flow control.

Stator flow control through the use of ejector pumps has shown marginal gains in deviation reduction (i.e. the reduction in flow turning/diffusion caused by the increase in the suction surface boundary layer).⁶ The ejector pump strategy was a device by which a high momentum jet injected along the suction surface simultaneously provided aspiration upstream of the injection location through ports connected to the primary air stream. A series of experiments conducted in a transonic blow down wind tunnel with inlet Mach

*Aerospace Engineer, AFRL/PRTF, 1950 Fifth Street Bldg 18, WPAFB, OH 45433, AIAA Member.

†Student Co-op, AFRL/PRTF, 1950 Fifth Street Bldg 18, WPAFB, OH 45433

‡1st Lt USAF, AFRL/PRTF, 1950 Fifth Street Bldg 18, WPAFB, OH 45433, AIAA Member.

§Research Engineer, ISSI, 2766 Indian Ripple Rd., Dayton, OH 45440, AIAA Senior Member.

numbers of approximately 0.7-0.8 were carried out for these investigations. In a similar vein, flow-controlled stators using counter-flow blowing along the pressure surface near the trailing edge showed marginal gains in vectoring the stator exit flow.⁵ This method was more for enabling stator exit flow angle variability than for increasing diffusion.

Recently, successful demonstration of increased diffusion using blowing jets along the suction surface of a low speed axial compressor system stator has been carried out.⁴ The stator blade count was reduced by 30%, resulting in an increased diffusion requirement of the blade row through a solidity reduction. The blades were replaced with a blowing only variant which successfully matched the system performance levels of the original full blade count configuration. The system performance levels of the flow control configuration accounted for the air supplied for the flow control. It begs the question whether the increased complexity of the flow control is warranted considering the matching system performance between the original non-flow-controlled and the flow-controlled configurations. Blade count reduction in axial compression systems impacts maintenance cost of axial compression systems, but has a much lower influence on weight reduction. Weight reduction is more greatly affected through axial length reduction. This is better realized through a stage loading increase resulting in the required pressure ratio in a shorter axial length. This is a much more costly demonstration as building a new axial rotor can be as much as six times the cost of the stator.

The previous paragraphs are just a highlight of some recent research involving flow control for axial compression systems with an emphasis on increasing stage performance. What is clear among these efforts is the relative financial cost that can be accrued while investigating various approaches. The design and test of a single transonic compression stage can easily exceed one million dollars. Even transonic cascade experiments easily run into the tens of thousands of dollars. That is not to say that many initial flow control experiments do not occur in less costly environments. Many of the ideas tested are investigated in wind tunnel environments with Reynolds numbers and diffusion comparable to a transonic axial compression system, but these often lack wall curvature and compressibility effects. Most recently, tests examining the benefits of streamwise vorticity in boundary layer attachment in a diffusing environment with some wall curvature have been carried out, but again in an incompressible environment.³ Also, the integration of many flow control strategies is an afterthought, i.e. it occurs too late in the initial evaluation and must be considered early on as a metric of effectiveness. This leads to a key emphasis of this paper: the development of an experimental rig that can effectively evaluate candidate flow control strategies for axial compression systems, with emphasis on diffusion enhancement in a realistic environment at a low cost.

This paper will outline the design of the experimental flow control research rig and its capabilities. Current measurement locations and techniques will be discussed and initial baseline evaluations presented. Following will be the initial investigation and comparison of three flow control modules; all are variations on a theme of blowing only flow control using a slot jet behind a backward facing step. Two of the variations evaluate the effect of the lip thickness of the backward facing step on the flow control effectiveness. The other variation introduces streamwise vorticity as a means of enhancing the interaction between the blowing jet and the core stream in an effort to reduce the secondary flow control flow fraction requirements.

II. Experimental Approach

The eventual goal of the present work is enhanced performance of diffusers for axial compression systems. Most previous research efforts in this direction have relied primarily on wind tunnel testing of linear cascades of stator vanes, either based on passive designs or with some manner of flow control. However, such experiments are relatively expensive to conduct on a per-test-case basis. Moreover, due to typical measurement expense and access limitations, it is often difficult to discern why a given stator design does or does not perform well, or what limitations need to be addressed. Thus testing tends to take on a trial-and-error nature, and with it a great deal of uncertainty, which is clearly not ideal in the present climate of tight research budgets and schedules.

The authors have deemed it desirable, even necessary, to have a lower-cost facility with a higher degree of experimental flexibility than the available cascade wind tunnels. Thus a new wind tunnel, based on a simple diffuser passage with curvature, has been designed, fabricated and extensively tested. The tunnel was designed with flow and geometric parameters relevant for a notional highly-loaded, high-turning diffuser. Descriptions of the wind tunnel and the related measurements are provided in the following sections.

A. Facility

The Flow Control Augmented Diffusion (FCAD) wind tunnel facility is comprised of three major elements: the wind tunnel itself, the primary flow source, and a secondary flow source used for flow control implementation.

1. FCAD Tunnel

The FCAD wind tunnel is an atmospheric in-draft design. After passing through a bellmouth and flow straightener, the airflow accelerates through a converging inlet of roughly 12:1 area contraction to a rectangular throat, 1.5 x 10.2 cm (0.6 x 4.0 in). The throat, typically operated at Mach 0.7, is the beginning of the curved diffuser test section. The diffuser geometry is based on aggressive goals for an axial compression system. The diffuser passage has an exit-to-throat area ratio of 2.92, a flow turning angle of 70 degrees, with suction (convex) side radius of curvature nearly constant at 5.1 cm (2.0 in). Following the diffuser is a sudden expansion into a rectangular dump chamber. An adaptor piece guides the flow from the dump chamber into a flexible 7.6 cm (3 in) diameter duct connected to the primary flow source. Figure 3 illustrates the basic flowpath from the inlet (at right) to the dump chamber (left).

Because present research goals include identification of key physical mechanisms relating diffusion and flow control, emphasis has been placed on measurement techniques that can resolve details of the overall flow field. Optical techniques, especially particle image velocimetry (PIV), were chosen to fill this need. The tunnel was accordingly designed with optical access as a priority. The top and bottom walls are transparent acrylic sheets, and sandwiched in between are wall segments with height of 10.2 cm (4 in). Defining the convex (suction) side of the curved diffuser test section is a readily replaceable aluminum module for testing various flow control concepts. One such module is shown in Figure 4. The inlet contraction and pressure (or concave) side of the diffuser passage are machined from a single block of acrylic to maintain a smooth and dimensionally accurate profile, with all surfaces polished to restore high optical clarity.

2. Primary Flow System

To permit an atmospheric inlet, the FCAD wind tunnel is run in a suction configuration. An automotive centrifugal supercharger, with self-contained speed-increasing gearbox, provides the suction source. A 37 kW (50 hp) 3-phase AC induction motor drives the supercharger through a cogged belt system. A variable frequency drive (VFD) unit is used to precisely control the motor speed and match the desired tunnel flow conditions. Tunnel throat Mach number can typically be maintained and repeated within 0.3% of the intended value. Because of scale and related expense, cascade wind tunnels usually cannot be controlled this precisely. Flow is exhausted from the supercharger through a metal duct to the exterior of the building.

3. Flow Control System

Flow control supply air is available in the form of suction, blowing, or both. A 7.5 kW (10 hp) oil-less vane compressor is used to provide flow control air up to 6% of the primary stream massflow at the normal 0.7 Mach throat condition. A settling chamber is used to damp discharge pressure oscillations. After metering, the flow is routed to a plenum inside the flow control module. In testing to date, only blowing has been used for active flow control. However, the compressor can be readily plumbed for suction or a combination of both. As with the primary flow system, the vane compressor is precisely controlled by a VFD unit.

B. Measurements

The facility has been designed for a variety of measurement techniques. In addition to numerous steady pressure and temperature measurements, optical techniques are used to non-intrusively document the flow behavior. Particle image velocimetry (PIV) is used to obtain instantaneous flow visualization and vector fields, as well as the average flow field for planes of interest. The pressure sensitive paint (PSP) technique and rake probe traverses are used to map suction surface static and diffuser exit total pressures, respectively. An orifice meter is used to quantify the flow control massflow added or removed from the primary stream and a Venturi meter is used to measure the combined massflow downstream of the tunnel.

III. Slot Jet Study

The first set of modules tested were variations on a slot jet over a backward facing step as shown in Figure 4. The slot jet height for these studies was fixed at 0.508 mm and the jet surface was constructed as follows: 1) The baseline convex surface was a constant radius of 50.8 mm ; 2) This radius was reduced by 1.397 mm at the throat to accomodate the jet and lip thickness; 3) A linear function in the angular coordinate was used to fit this radius to the 50.8 mm radius at the exit of the passage. This surface was used for the parametric study that follows, with variations only being made to the removable throat plate.

A. Lip Thickness Variation

The edge thickness of the upper plate along the backward facing step was varied to examine the effect on the slot jet's diffusing capacity. This quick study was performed to determine a reasonable configuration that is manufacturable and will be used as a baseline for all subsequent studies. Two configurations were manufactured: 0.635 mm and 0.127 mm edge thicknesses. The two configurations in Figure 5 show the modification to the plate upper surface so that the slot jet would remain unaffected. The 0.635 mm edge was simply an extension of the tunnel throat, while the 0.127 mm was created by applying a 5 degree chamfer to the upper surface. The ratio of edge thickness to slot jet height was 1.25 and 0.25 for the 0.635 mm and 0.127 mm edges, respectively.

Figure 6 shows averaged PIV measurements at midspan for the two configurations. Details for the PIV technique can be found in Ref. 5. The left side of the figure shows the 1.25 edge-to-jet ratio upper plate with 2.25% secondary flow ratio. The right shows the 0.25 edge-to-jet ratio upper plate with 2.0% secondary flow ratio, i.e. the ratio of blowing mass flow to core mass flow. This clearly demonstrates the better diffusion performance, through significantly reduced separation, of the slot jet with the 0.25 edge-to-jet ratio. No exit traverse instrumentation was installed during these tests, but surface mounted static pressure measurements at approximately 20% and 80% chord along the convex (suction) surface and 80% chord along the convex (pressure) surface were used to estimate a static pressure rise coefficient for these two configurations. The 80% chord values were averaged and used as an exit static pressure value. Figure 7 shows the static pressure rise results for secondary flow ranges from 0 to 4% flow fraction. The 0.25 edge-to-jet ratio geometry achieved a similar static pressure rise with half the flow fraction of the 1.25 edge-to-jet ratio geometry. The 0.25 edge-to-jet ratio was then used for all subsequent testing and will be referred to simply as the "slot-jet configuration" for the remainder of this paper.

B. Counter-rotating Streamwise Vorticity Addition

The effect of adding pairs of counter-rotating streamwise vortices to the main flow ahead of the slot jet was investigated in an effort to determine if streamwise vorticity may be effective in reducing the amount of secondary flow required for a given level of diffusion. This was accomplished through the use of flat plate vortex generators placed on the upper surface of the flow control module plate as shown in Figure 8. Care must be taken when using counter-rotating vortices due to the induced motion the vortices have on one another and good references to that effect are given by Pearcey⁸ and Kuethe and Chow.⁹ Vortex pairs were designed with the intent that their induced motion was toward the surface and the slot jet. The induced velocity for a pair of vortices with circulation Γ and separated a distance, d , apart is:

$$V_i = \frac{\Gamma}{2\pi d} \quad (1)$$

A difficulty in using counter-rotating vortices for a flow control strategy is the migration of the vortices apart from each other along a solid surface once their 'images' begin to control their induced motion.⁸ If repeating pairs of counter-rotating vortices exist, spaced a distance D apart along the surface, the migration eventually causes vortices from neighboring pairs to match up. When this happens, their induced velocity on one another is away from the surface thereby reducing the vortices' effectiveness in promoting attached flow.

The desired circulation strength, Γ , and spacing, d , for the vortex pair was determined by considering a simplified flowfield. The flowfield was approximated as undergoing a transition from velocity V_1 at the throat to V_2 at the diffuser exit in a linear fashion. This of course assumes that the flowfield is diffusing ideally. The time at any point along the arc length of the surface, with $t=0$ being the throat reference time,

is given by:

$$\begin{aligned} t(s) &= \int_0^s \frac{ds}{V(s)} \\ &= -\left(\frac{C}{V_1}\right) \ln \left[\frac{(1 - \frac{DF}{C}s)}{DF} \right] \end{aligned} \quad (2)$$

where C is the surface arc length, V_1 is the throat velocity and DF is the diffusion factor, defined as:

$$DF = 1 - \frac{V_2}{V_1} \quad (3)$$

This can be solved for the fractional position, s/C , as a function of time, t , resulting in:

$$\frac{s}{C} = \left(\frac{1}{DF}\right) \left[1 - \exp\left(-DF \frac{V_1}{C} t\right) \right] \quad (4)$$

Now consider a counter-rotating vortex pair in isolation and assume that the vortex pair convects with the flowfield so that their position at any time, t , is given by the above equation. As mentioned earlier, the pair has a mutually induced velocity, V_i . This vortex pair will be generated by flat plate type vortex generators with a thickness to chord ratio of 0.12. An approximation of the circulation generated by a NACA 0012 vortex generator is given in Ref. 10 and is as follows:

$$\Gamma = \frac{k_1 \alpha v_\infty c}{1 + k_2/AR} \tanh[k_3(h/\delta)^{k_4}] \quad (5)$$

where

$$k_1 = 1.61; k_2 = 0.48; k_3 = 1.41; k_4 = 1.00$$

$$AR = \frac{8h}{\pi c}$$

and α is the angle of attack relative to the freestream; v_∞ is the freestream velocity; δ is the boundary layer thickness; c is the vortex generator chord; h is the vortex generator height. As a first approximation, the circulation strength will be assumed to be invariant with time. The time necessary for the vortex pair to travel the distance of the vortex generator height, h , due to their induced velocity, V_i , is:

$$t = h/V_i \quad (6)$$

Combining Equations (1), (5), (6) and simplifying yields:

$$t = \frac{\pi^2 (AR + k_2)}{4 k_1} \frac{d}{V_1 \alpha \tanh(k_3(h/\delta))} \quad (7)$$

This given time can be substituted into Equation (4), resulting in an expression for the fractional position along the flow path where the vortex pair will have traveled an induced distance relative to the bulk flow equal to the vortex generator height. The strength should be such that the $s/C \leq 1$ so that the pair reaches the surfaces prior to exiting the flow passage. This results in the following bounding expression:

$$\frac{F(AR, d/C)G(\alpha, h/\delta)}{H(DF)} \leq 1 \quad \text{for} \quad H(DF) > 0 \quad (8)$$

$$F(AR, d/C) = \left(\frac{AR + k_2}{k_1}\right) \left(\frac{d}{C}\right) \quad (9)$$

$$G(\alpha, h/\delta) = \left(\frac{1}{\alpha}\right) \left(\frac{1}{\tanh(k_3(h/\delta))}\right) \quad (10)$$

$$H(DF) = -\frac{4}{\pi^2} \frac{\ln(1 - DF)}{DF} \quad (11)$$

The function H is only dependent on the diffusion factor associated with passage. Functions F and G are dependent on the vortex generator geometric characteristics and their relation to the passage and boundary layer. A family of characteristic curves of FG/H were produced by fixing the function G through a choice of α and h/δ and using the diffusion factor of 0.724 for the passage under consideration. These curves are shown in Figure 9 for $(\alpha, h/\delta)$ equal to $(15^\circ, 0.8)$, $(25^\circ, 0.8)$, $(15^\circ, 1.5)$ and $(25^\circ, 1.5)$.

The figure shows that increasing both α and h/δ expands the family of curves up and to the right, although α has a much larger impact since the product of the functions are inversely proportional to it. Each constant FG/H curve represents a fractional distance along the passage surface at which the counter-rotating pair has traveled one vortex height due to the induced velocity V_i . This distance can be found by substituting the value for FG into Equation 4 along with DF to determine s/C .

Three other curves are superimposed on the plots in Figure 9. Two of the curves are geometric constraints (red and green lines) due to physical limitations of using the paired VG's which will be called CVG's (Counter-rotating Vortex Generators). The first (red line) is due to the constraint of generating two counter-rotating vortices a distance d apart using a pair of closely spaced VG's at an angle of attack α . Figure 10 shows a top-down view of the CVG's with relevant dimensions. It is approximated that the core of the vortices exist at the trailing edge of the VG's and that the distance d between the trailing edges is the distance between the vortex cores. The distance between the leading edges of the VG pair is labeled d_i . It can be shown geometrically that:

$$\frac{d}{C} = \frac{16}{\pi} \sin(\alpha) \frac{1}{AR} \frac{h}{C} \left(1 + \frac{(d_i/d)}{(1 - d_i/d)} \right)$$

and this can be shown to represent a lower bound for the CVG. Figure 9 shows this constraint with d_i/d set to 0.1. The other geometric constraint (green line) is derived from a heuristic argument that the distance, d , between the vortex pair should be less than the height of the CVG. This is considered so that the vortex images do not dominate initially and cause the true vortex pair to migrate apart. This upper bound is a conservative constraint, but will be used in this analysis. The blue line represents the non-dimensional circulation strength as a function of AR , since both h and α have been chosen.

A geometric configuration that maximizes the circulation and satisfies the two geometric constraints would be the intersection location of the two geometric constraint curves. For the present design, a point was chosen slightly to the right of this location at the location $(AR, d/C) = (2.45, 0.1215)$ on the $(25^\circ, 1.5)$ figure. The boundary layer thickness for the wind tunnel at the throat was approximated from a CFD calculation at 0.254 mm. Using the surface arc length, C , of 31 mm gives the following VG geometric parameters:

$$h = 3.81\text{mm}; d = 3.765\text{mm}; c = 3.962\text{mm}; \alpha = 25^\circ, d_i = 0.3765\text{mm}$$

Figure 8 shows the resulting flow control module upper plate using these geometric parameters at a spacing of $4.5d$ between CVG's. The spacing between pairs of vortices was chosen based on guidelines outlined in Ref. 8.

1. PIV Measurements

Figure 11 shows over 100 averaged PIV image pairs (vector fields) at midspan comparing the slot jet configuration with the CVG modified configuration. The baseline label in the figure refers to the condition with no secondary flow control active, i.e. 0% blowing for the CVG configuration only. This condition was not achievable with the slot-jet only configuration (non-CVG) due to a cavity resonance which did not allow us to run with the secondary flow system completely closed. Instead, the valve for the secondary flow system was opened until the resonance conditioned diminished and this was considered the baseline for this configuration. The actual secondary flow rate for the baseline of the non-CVG configuration was approximately 0.6% flow fraction. Three specific regions of interest are highlighted in the figure and are labeled A, B and C.

Region A brings attention to the significant separation reduction the CVGs provide, even with no active flow control present. No reversed flow is present in the CVG image although regions very close to the convex surface could not be processed due to sufficiently high noise in the data caused by seed agglomeration on the viewing window.

Region B compares the slot only and CVG modified case for 4% flow fraction as well as the baseline CVG with 0 and 4% blowing. First, the comparison between the slot only and CVG modified case shows the increase in passage velocity directly opposite the CVG due to the blockage generated by the CVG's. This

velocity increase appears to have an impact on the flow development along the concave (pressure) surface of the passage. It is believed that the increase in Mach number and subsequent reduction in boundary layer displacement thickness may result in a suppression of Görtler instabilities along this surface. This is evidenced by the larger low momentum region along the concave surface for the slot only configuration. Instantaneous PIV images also show a large chaotic swirling flow along this surface. Another interesting observation can be made when comparing the CVG case with and without blowing. Region B between these cases shows significant flow vectoring in the 4% blowing as evidenced by the migration of the streamlines towards the convex surface, which is not apparent in the baseline image. This influence is rapid and extends rather far from the slot jet (approximately 10 jet heights). It is conjectured that this effect is due to the interaction between the slot jet and the counter-rotating vortices generated by the CVG's. Because the slot jet flow has higher velocity than the primary stream in this case this interaction could result in the acceleration and subsequent streamwise stretching of the vortex core, causing an increase in vorticity with a local increase in momentum exchange. Note that the PIV image is taken at midspan down the centerline of the counter-rotating vortex pair.

This brings us to region C for the baseline CVG configuration. The diverging and coalescing streamlines in this region are indicative of a swirling pattern or out-of-plane flow. This is most likely an effect of the strong vortices generated by the CVG's. Future plans include stereo-PIV measurements to capture and quantify the strength and trajectory of the vortices. The vortex traces along the convex (suction) surface were captured fortuitously by deposits of residual PIV seed in subsequent tests. Figure 12 provides a picture, taken after a 4% flow fraction run, which clearly shows the vortex paths traced on the surface. The large endwall blockage is apparent, causing the vortex path migration toward the midspan.

2. Exit Total Pressure Traverse Measurements

Total pressure measurements were taken at the exit of the passage using a 5 probe rake oriented pitchwise (convex to concave surfaces) and traversed spanwise. The rake was indexed in 5% pitch increments to obtain 20 interlaced positions from 0.64% to 95.64% pitch and traversed through 3.125% spanwise increments for a total of 580 measurement locations. One data point consisted of one hundred samples take at 800 Hz and averaged at each location. A total of 10 such data points were taken at each location and used for statistical calculations. Effectively, this eliminated any high frequency unsteadiness and noise in the measurements, but still allowed us to look at low frequency fluctuations. A very conservative measurement error of 5066.24 N/m²(0.05 psi) is based on the full scale error of the transducer.

Figure 13 shows these measurements and requires a short explanation. The lower contour image in each subfigure surrounded by the grey box is the average exit gauge total pressure measurement divided by the inlet total pressure. The grey box signifies the actual flow domain, therefore the reader can see clearly where the measurements were taken in relation to the actual flow domain. The three dimensional domain projected above this plane is the same measurement with a topographical view of the standard deviation for the 10 samples data points, i.e. vertical is the standard deviation of the gauge total pressure measurements. The standard deviation was likewise non-dimensionalized by the inlet total pressure. The convex and concave surfaces are labeled to orient the viewer and the maximum non-dimensional standard deviation in the figure is given below the contour bar. Each subfigure is labeled with a caption showing the percent secondary flow fraction, and side-by-side comparisons are made for configurations with and without the CVG's. The CVG configuration appears on the right.

Figures 13[a,b] shows the baseline case (i.e. 0% flow control fraction) for each configuration. The slot-jet only configuration was run with a 0.6% flow fraction as compared to the 0% flow fraction for the CVG modified configuration. The 0.6% flow fraction for the slot-jet only configuration was due to a cavity resonance as explained in the PIV comparison section presented earlier. Bearing that in mind, there is a significant difference between the two conditions. In comparing both, the CVG configuration shows a reduction in total pressure loss accompanied by a significant increase in the total pressure standard deviation in the region close to the concave surface. The area-averaged non-dimensional gauge total pressure and the maximum standard deviation for each configuration is summarized in Table 1. With the CVG's, the total pressure loss was decreased by approximately 0.7% and had significant midspan flow attachment as previously shown in the PIV measurements of Figure 11. Also, the CVG configuration shows a more diffuse total pressure profile as evidenced by the more gradual contour banding. The measurement standard deviation, which will be referred to here as low frequency unsteadiness, is also remarkably different between the two cases. The CVG showed an approximate 2.1% increase in the maximum unsteadiness and the peaks were out-of-phase with the non-CVG configuration.

Moving on to the 2.2% flow fraction case, Figures 13[c,d] show a continuing trend in unsteadiness, but a reversal in the overall total pressure loss trend. The non-CVG configuration showed an approximate 3% improvement in total pressure loss and a 1.8% lower unsteadiness over the CVG variant. The unsteady pattern for the CVG remained the same, but the non-CVG showed some asymmetry over its baseline accompanied by a 1.4% increase. The non-CVG flowfield also appears more diffuse than the CVG flowfield, as evidenced by the contour band spread.

Finally, Figures 13[e,f] show the 4.1% flow fraction case for the two configurations. First, the level of unsteadiness is significantly reduced for both configurations, with the non-CVG geometry returning to its baseline value and the CVG geometry showing a 1.6% reduction over its baseline value. The non-CVG configuration was 0.6% lower in area averaged gauge total pressure compared to the CVG configuration. The total pressure distribution was concentrated in the mid 40% span over the entire pitch for the non-CVG configuration while the CVG configuration showed a concentration more toward the concave side covering a larger span. Note also the total pressure depression at midspan on the concave side of the non-CVG configuration, and that this correlates well with the PIV data taken at midspan and shown in Figure 11. The PIV data shows that this depression corresponds to a large low momentum region along the concave surface, likely due to a Görtler instability phenomenon. The CVG configuration does not exhibit this depression and shows a much better behaved flowfield along the concave surface in Figure 11. The three-dimensionality of the 4.1% cases, particularly the comparably poor endwall behavior, will be the subject of further investigation.

Table 1. Comparison of Exit Rake Measurements

Configuration	Flow Fraction	Area Average Non-dimensional Gauge Total Pressure	Max σ
CVG	0%	-16.15%	3.0%
	2.2%	-16.91%	4.1%
	4.1%	-12.61%	1.4%
No CVG	0.6%	-17.43%	0.9%
	2.2%	-13.97%	2.3%
	4.1%	-12.02%	0.9%

3. PSP Measurements

Pressure Sensitive Paint (PSP) data was taken on the convex surface at various flow conditions for this CVG configuration. Figure 14 shows the values at three different operating conditions: 0, 2.11 and 4.17% flow fraction. The figure clearly shows the endwall effects and the non-uniform conditions that develop spanwise as the slot jet blowing level increases. PIV measurements near the endwalls(not presented in this paper) showed ineffective control of the core flowfield, as is also evident in the exit traverse data shown in Figure 13 through significant total pressure loss at the endwalls. Combining the information from the PSP with the exit total pressure traverse data shows that the endwall regions contain much lower momentum flow than the midspan region simply by the total-to-static pressure ratio. The total-to-static pressure ratio in the endwall region at the exit plane is approximately 1.0625 while at midspan the value is 1.15. This is evidence of a significantly lower Mach number flow in the endwall region as compared to midspan.

Figure 15 shows the extracted PSP data along the chordwise lines shown in Figure 14 at approximately 17% and 50% span (midspan). Note that both of these extractions are also located down the centerline of the CVG's. A similar story to that of Figure 14 is seen in this data, with the 17% span location showing a more rapid increase to the exit static pressure level of approximately 0.8 as compared with the 50% span (midspan). The rapid increase in static pressure at approximately the $x=600$ location, combined with a leveling off in static pressure increase leads to the assumption flow separation. This is in contrast to the gradual increase in static pressure along the midspan, which is seen to be well-behaved by the PIV data in Figure 11. Another interesting feature shown in Figure 15 is the higher static pressure level for the 17% span compared to the 50% span location at the slot jet for the 4.17% flow fraction. The 17% span shows a

level of static pressure similar to the 0% baseline where the 50% span shows a 2-3% lower value than the baseline in this region. The 2% flow fraction case shows the opposite behavior with the 50% span location showing a higher static pressure closer to the baseline value as compared with the 17% span location.

This brings us to Figure 16 which shows the extracted PSP data along a spanwise cut along the slot jet exit. The figure shows that the difference in static pressure between the endwalls and midspan is greatly increased as the level of blowing is increased which appears to signify that the level of blockage is actually increases in the endwall region. It is hypothesized, and further testing is being conducted, to determine if this phenomenon is related to a breakdown of the slot jet shear layer due to its truncation at the endwalls. Other studies which conducted detailed investigations both numerically and experimentally showed a breakdown phenomenon in the endwall regions of planar jets with and without sidewalls.¹¹ The figure also shows the traces of the vortices generated by the CVG's, which are highlighted by the dashed circles in the figure. The vortex pairs are clearly not symmetrical except for the midspan location at $x=300$. This is also evident from the pressure asymmetry directly behind the CVG's in Figure 14.

IV. Conclusions

This paper has highlighted a new experimental facility for detailed investigation of flow control techniques for diffusion enhancement in flows relevant to axial compression systems. The experimental facility is a single curved diffusing passage wind tunnel configuration with a throat Mach number of 0.7 and exit to throat area ratio of 2.97. The tunnel has modular aspects which allow quick modification to test various flow control concepts. It also has generous optical access for PIV and PSP measurement techniques as well as high resolution exit total pressure measurements via a traversable exit rake.

A slot-jet configuration was tested and detailed measurements were presented to investigate the flow behavior. The configuration consisted of a continuous spanwise slot jet along the convex surface which was introduced at the tunnel throat via a backward facing step with a jet height of 0.508 mm. The slot jet was introduced on the convex surface of the flow passage. A crude parametric study was performed to set an effective separation distance between the slot jet and the core flow which is simply a limitation of manufacturing of the backward facing step and the requirement of finite metal thicknesses. Two configurations were evaluated: a 125% and 25% separation distance to slot jet height ratio. It was found that the 25% configuration resulted in a similar diffusion level as the 125% configuration with approximately half of the slot-jet blowing flow rate. This 25% configuration was then chosen as the baseline configuration for subsequent flow control schemes.

Streamwise vorticity was introduced to the baseline 25% separation distance configuration via pairs of flat plate vortex generators arranged to produce pairs of counter-rotating vortices upstream of the slot-jet. The findings of this studies are summarized as follows:

- 1) The introduction of pairs of counter-rotating vortices resulted in a significant diffusion enhancement over the baseline configuration even without the addition of slot jet flow. The diffusion enhancement or separation reduction due to the vortex generators is a well documented phenomenon, but the level of enhancement in this study was surprising. At midspan, PIV measurements show the flow completely attached although the flow along the convex surface had very low momentum. The total pressure exit traverse data showed that there was still a significant loss associated with the vortex generator induced mixing, but the quality of the flow was much improved over the baseline. Comparing this to the configuration with no vortex generators (non-CVG) showed a performance improvement of 1.3% in exit area averaged gauge total pressure loss. Also, the level of low frequency unsteadiness as determined by the standard deviation of the total pressure measurements was much higher for the CVG configuration than the non-CVG configuration.

- 2) A combination of slot-jet flow with counter-rotating vortex generators (CVG) showed a significant improvement in the midspan region depending on the blowing level. The CVG configuration produced a peak in total pressure loss between 0 and 4% blowing, i.e. the performance at first became worse before it improved. The non-CVG configuration did not exhibit this behavior, but showed a continual improvement in total pressure loss as the blowing level increased. The level of low frequency unsteadiness increased for both configurations initially and then subsided. The non-CVG configuration exhibited a lower total pressure loss as the slot-jet flow rate increased with an approximate 0.6% at a 4.1% blowing rate. Also, the addition of the slot-jet flow accentuated the variation in total pressure distribution at the exit of the passage for both configurations, i.e. more three-dimensionality was observed in the total pressure distribution with the slot jet active.

3) PSP measurements for the CVG configuration clearly showed three-dimensional behavior on the convex surface of the passage. Chordwise extraction of the PSP data showed a significant difference between the midspan and 17% span regions. The 17% span showed an abrupt change in static pressure accompanied by a plateau region, while the midspan showed a gradual increase to the exit of the passage. The abrupt change in static pressure accompanied by a plateau is indicative of separation at the endwalls.

4) The spanwise static pressure distribution at the exit of the slot-jet as determined from the PSP data showed a rapid increase in static pressure in the endwall region as the slot jet flow rate was increased. This level of static pressure in the endwall region surpassed lower flow rate pressure levels in this region while values of pressure at the midspan were lower for the higher flow rate conditions. It is conjectured that the level of blockage at the endwalls actually increased as the slot jet flow rate was increased, which is not intuitive. This increase could be due to the rapid breakdown of the slot jet shear layer as it abruptly ends at the endwalls. This phenomenon will be investigated in future experiments.

5) Flow traces of the vortices generated due to the vortex generators were clearly seen from residual PIV seed on the convex surface. The traces clearly showed the migration of the vortices away from the endwalls due to the significant blockage in these regions. Vortex lines advect with the fluid, so this showed strong evidence of the large flow blockage produced at the endwalls.

6) The increased concave surface velocity at the tunnel throat due to the blockage of the vortex generators helped to suppress what appeared to be Görtler vortices.

Future experiments using slot jet flow control will be performed to build on the observations presented in this paper. Particularly, the endwall flowfield breakdown will be investigated to determine if slot jet flow control can be rendered more effective in this region through judicious introduction of the slot-jet shear layer. Also note that the results for the counter-rotating vortex addition with slot-jet blowing are based solely on one vortex generator design and should not be construed in any general way. Vortex generator use to enhance diffusion levels in curved passages will be ongoing in this facility.

V. Acknowledgements

The authors would like to acknowledge Dr. Larry Goss and Jim Crafton of Innovative Scientific Solutions for their time and effort in obtaining the valuable PSP data. Also, we would like to thank the Air Force Office of Scientific Research for funding these investigations.

References

- ¹Schuler, B. J., Kerrebrock, J. L., and Merchant, A., "Experimental Investigation of a Transonic Aspirated Compressor," *ASME Journal of Turbomachinery*, Vol. 127, April 2005, pp. 340–348.
- ²Merchant, A., Kerrebrock, J. L., Adamczyk, J. J., and Braunscheidel, E., "Experimental Investigation of a High Pressure Ratio Aspirated Fan stage," *ASME Journal of Turbomachinery*, Vol. 127, January 2005, pp. 43–51.
- ³Luedke, J., Graziosi, P., Kirtley, K., and Cerretelli, C., "Characterization of Steady Blowing for Flow Control in a Hump Diffuser," *22nd Applied Aerodynamics Conference and Exhibit*, Providence, RI, 2004, AIAA Paper no. 2004-4963.
- ⁴Kirtley, K. R., Graziosi, P., Wood, P., Beacher, B., and Shin, H. W., "Design and Test of an Ultra-Low Solidity Flow-Controlled Stator," *ASME Turbo Expo 2004*, Vienna, AU, 2004, ASME Paper no. GT2004-53012.
- ⁵Harff, M. R., Wolff, J. M., Copenhaver, W. W., Car, D., and Esteveordal, J., "Stator Cascade Flow Vectoring through Counter-Flow Blowing," *International Journal of Turbo and Jet Engines*, Vol. 21, pp. 155–168.
- ⁶Carter, C. J., Guillot, S. A., Ng, W. F., and Copenhaver, W. W., "Aerodynamic Performance of a High-Turning Compressor Stator with Flow Control," *37th AIAA/ASME/SAE/ASEE Joint Propulsion Conference & Exhibit*, Salt Lake City, UT, 2001, AIAA Paper no. 2001-3973.
- ⁷Lord, W., MacMartin, D. G., and Tillman, T. G., "Flow Control Opportunities in Gas Turbine Engines," *Fluids 2000*, Denver, CO, 2000, AIAA Paper no. 2000-2234.
- ⁸Pearcey, H. H., "Shock Induced Separation and Its Prevention by Design and Boundary Layer Control," *Boundary Layer and Flow Control*, edited by G. V. Lachmann, Vol. 2, Pergamon Press Inc., New York, 1961, pp. 1170–1349.
- ⁹Kuethe, A. M. and Chow, C.-Y., *Foundations of Aerodynamics: Bases of Aerodynamic Design*, John Wiley & Sons, 4th ed., 1986.
- ¹⁰Wendt, B. J., "Parametric Study of Vortices Shed from Airfoil Vortex Generators," *AIAA Journal*, Vol. 42, No. 11, 2004, pp. 2185–2195.
- ¹¹Visbal, M. R., Gaitonde, D. V., and Gogineni, S. P., "Direct Numerical Simulation of a Forced Transitional Plane Wall Jet," *28th Fluid Dynamics Conference*, Snowmass Village, Co, 1998, AIAA Paper no. 1998-2643.

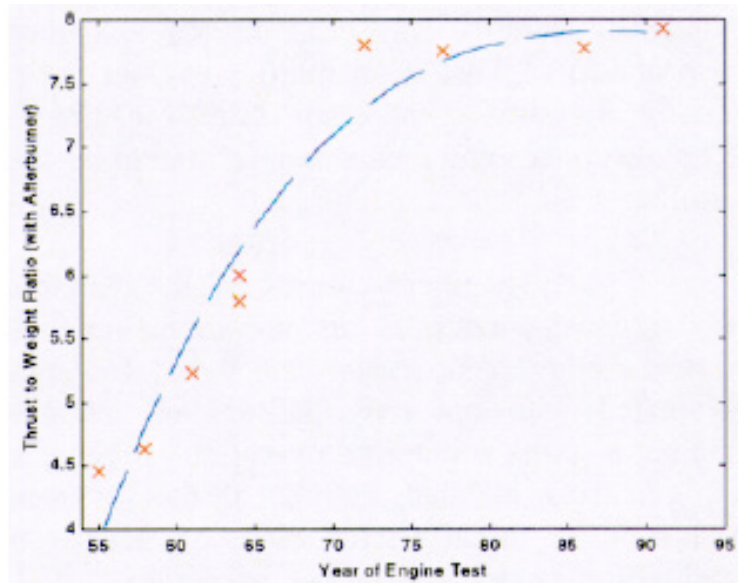


Figure 1. Engine Thrust-to-weight Ratio taken from Ref. 7

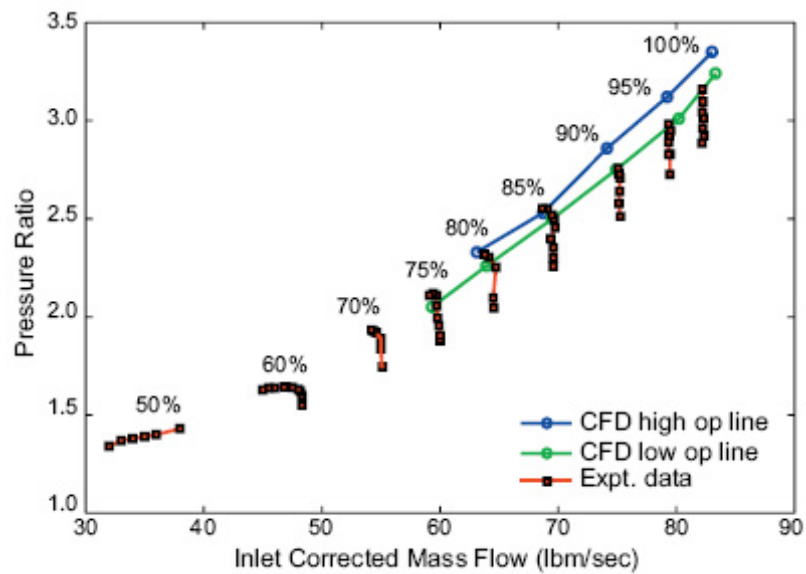


Figure 2. Aspirated Rotor Performance taken from Ref. 2

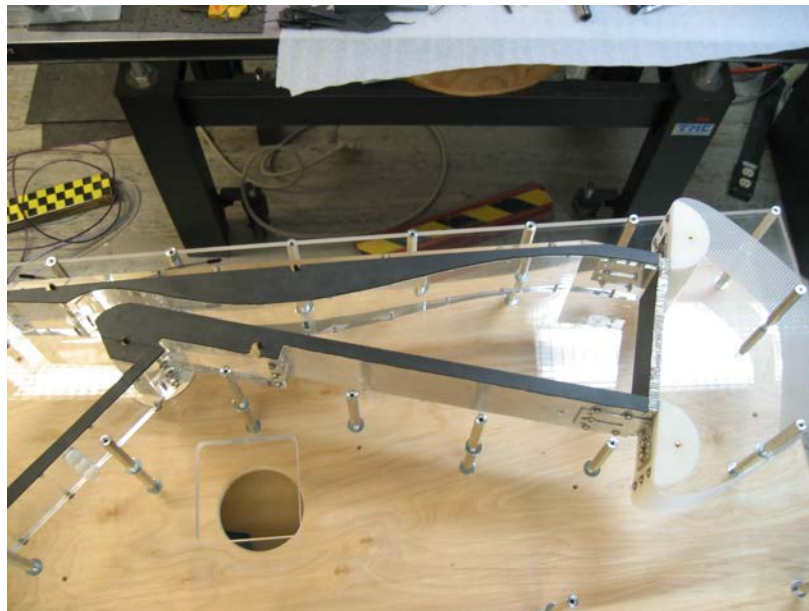


Figure 3. Top view of FCAD wind tunnel

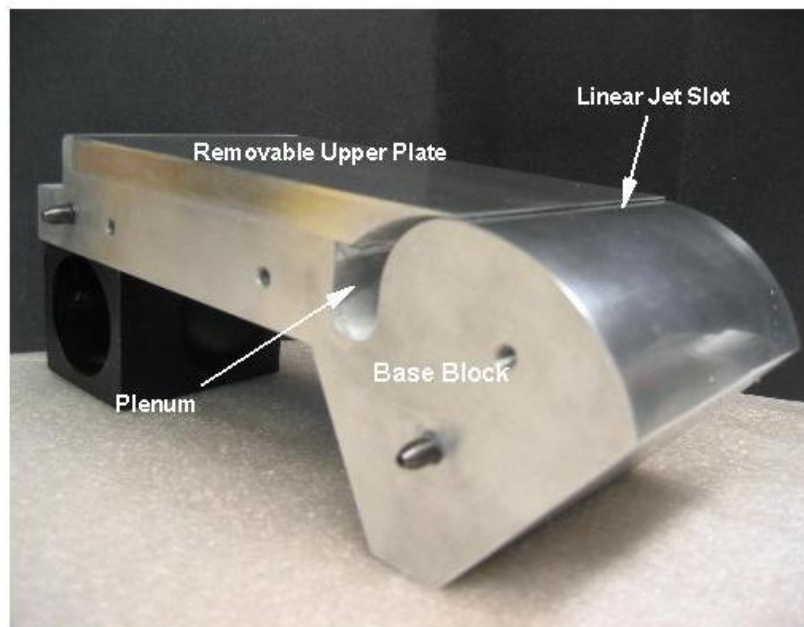


Figure 4. Flow control module with simple streamwise blowing slot

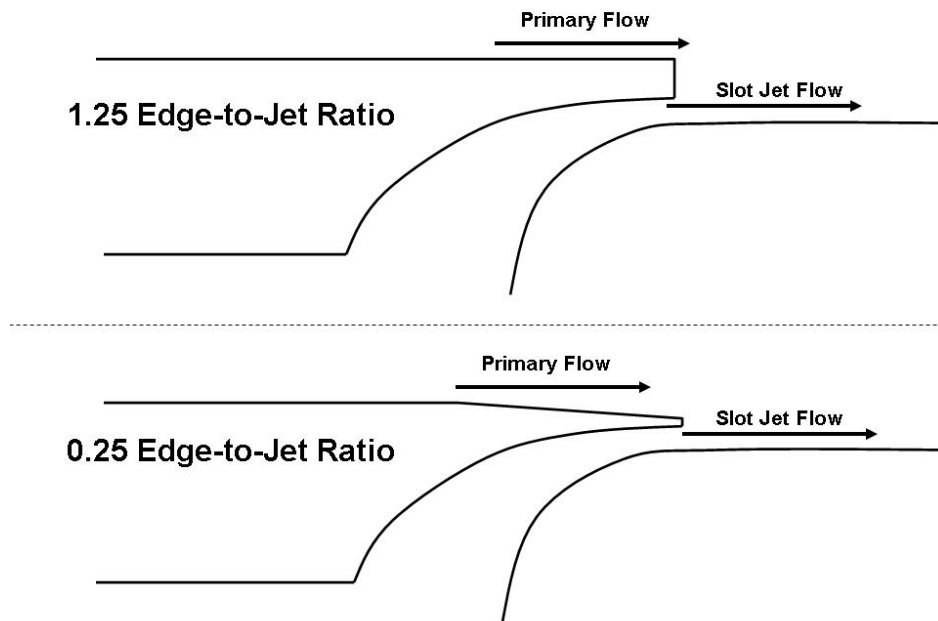


Figure 5. Upper Plate Edge Profiles

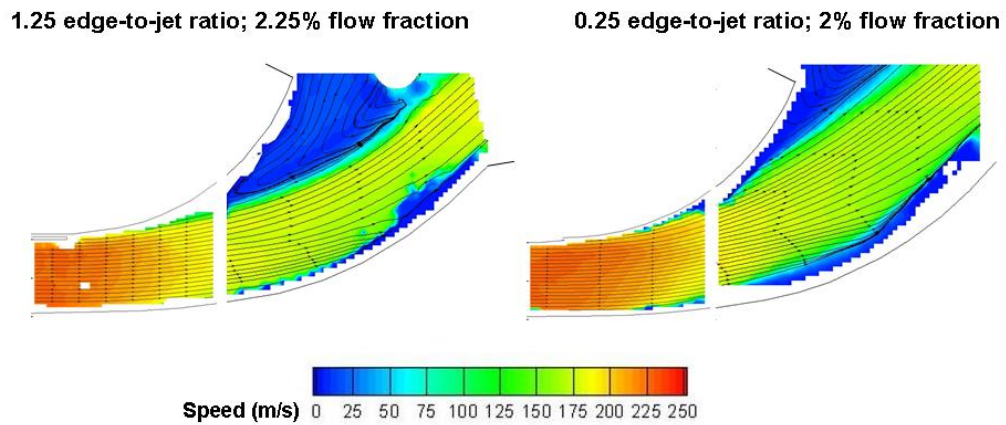


Figure 6. DPIV at Midspan Comparing Edge Thickness Variation on Effectiveness of Slot Jet Diffusion

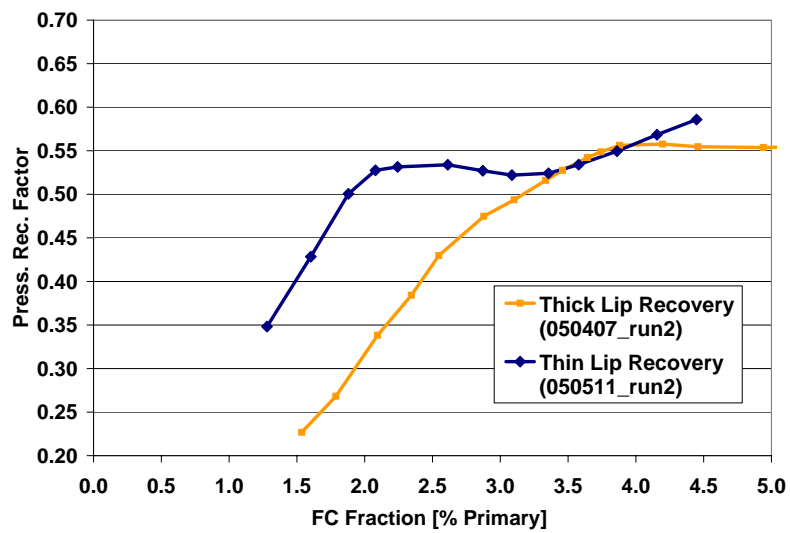


Figure 7. Static Pressure Rise Coefficient for 1.25 and 0.25 Edge-to-Jet Ratio Geometries

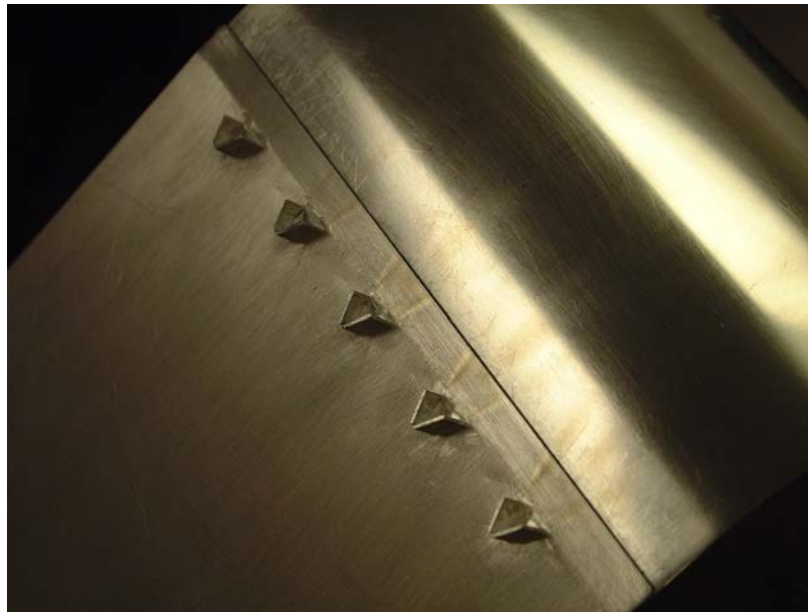
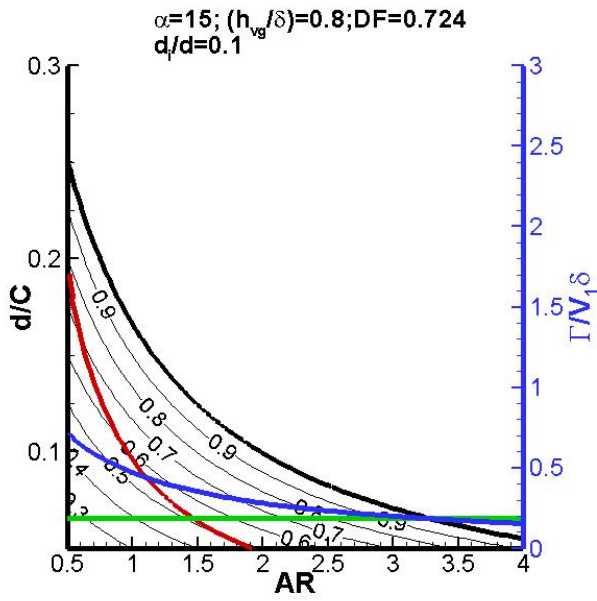
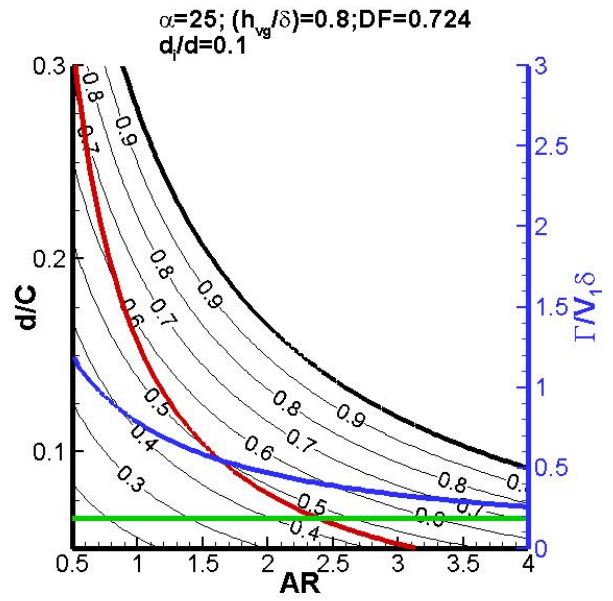


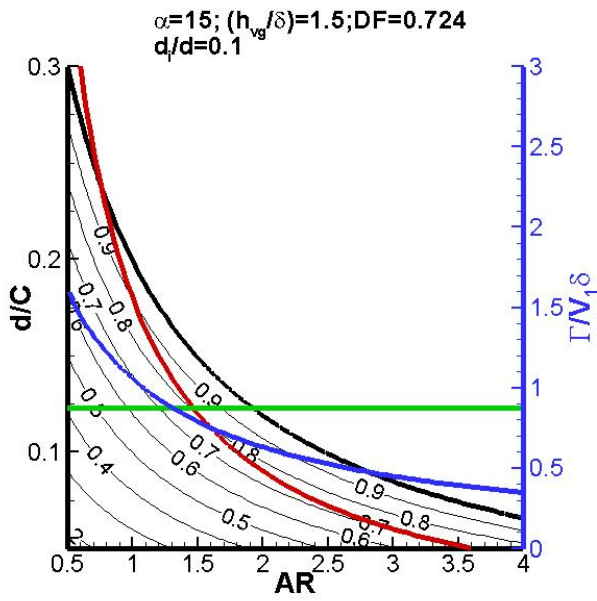
Figure 8. VG Flow Control Upper Plate



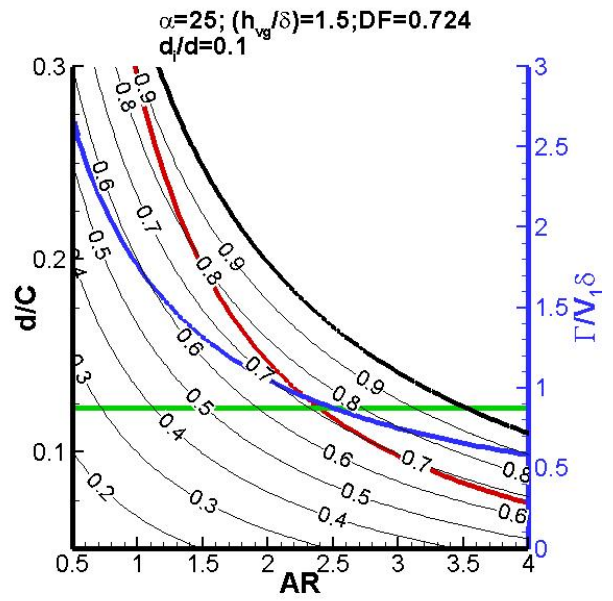
(a) (15,0.8)



(b) (25,0.8)



(c) (15,1.5)



(d) (25,1.5)

Figure 9. FG/H Curve Families

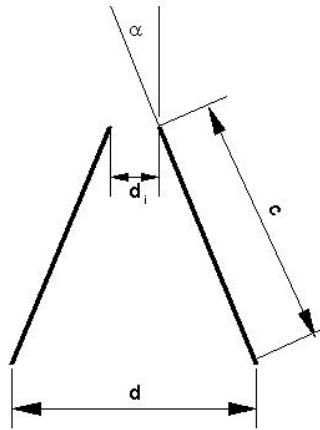


Figure 10. Counter-rotating Vortex Generator Geometry Definition

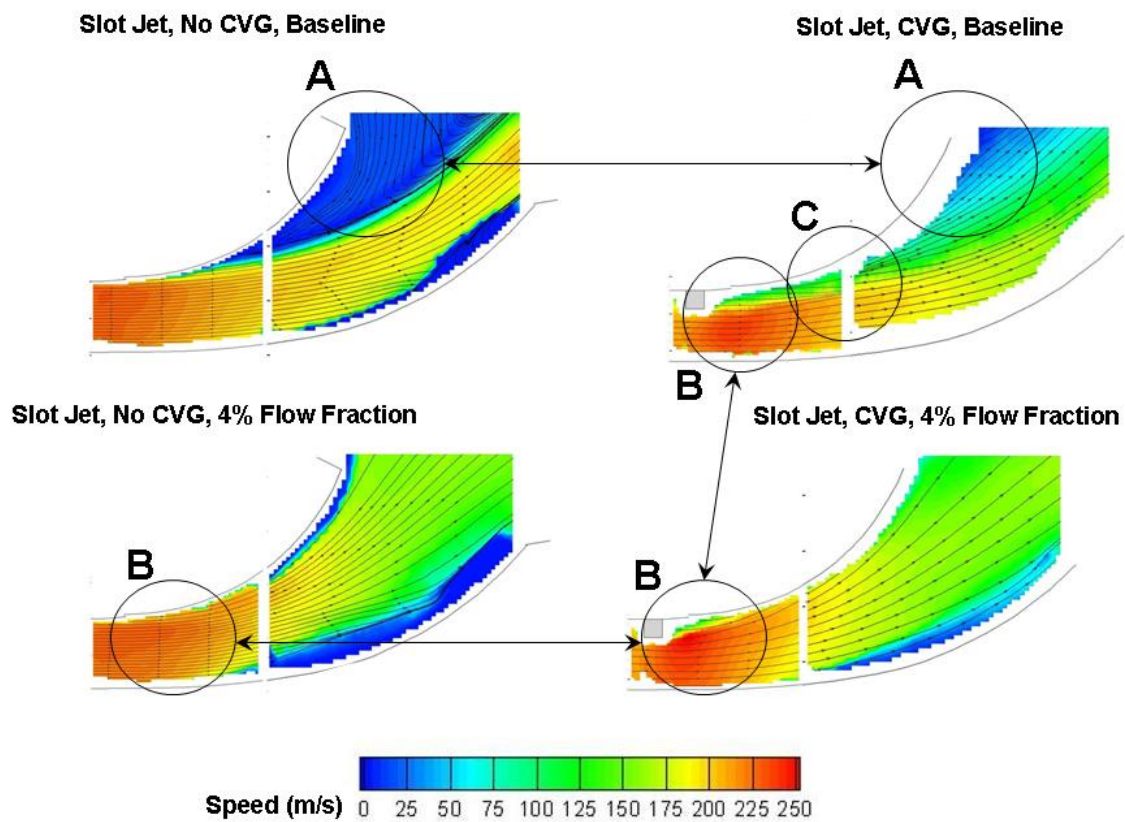


Figure 11. Averaged Midspan PIV Comparison of Slot Only and Slot with CVG Flow Control

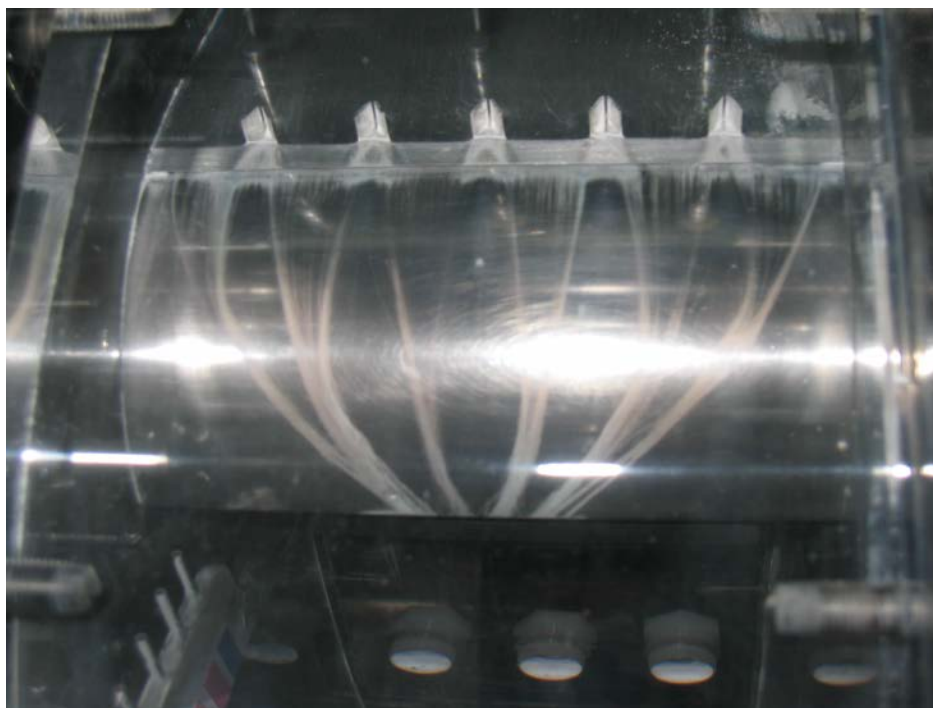
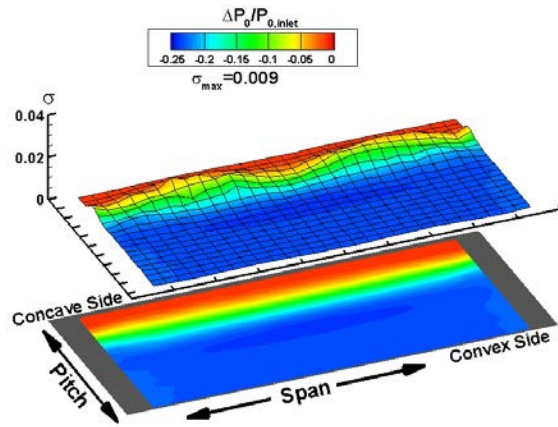
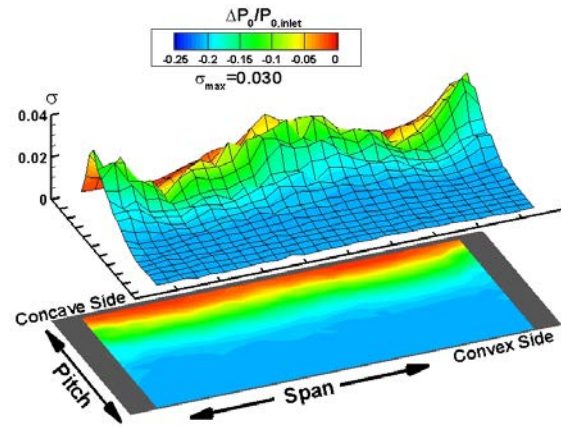


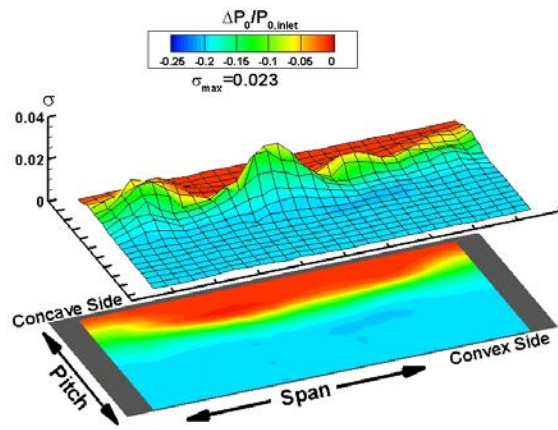
Figure 12. Vortex Traces Captured by Residue Seed



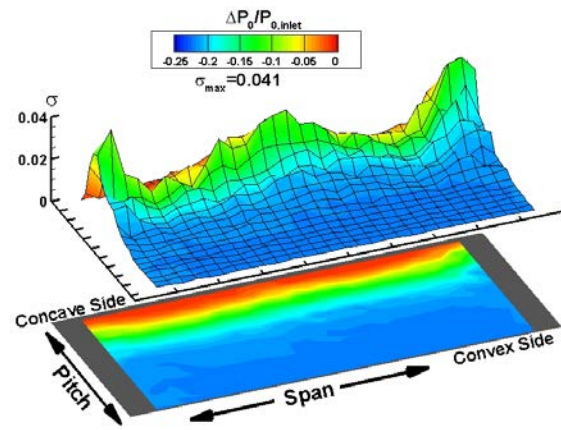
(a) 0.6%, Slot-jet Only



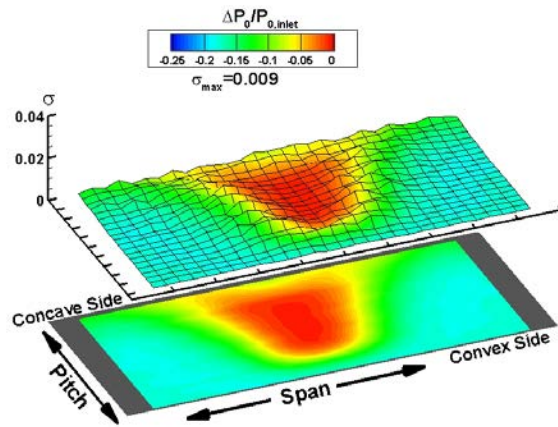
(b) 0%, CVG



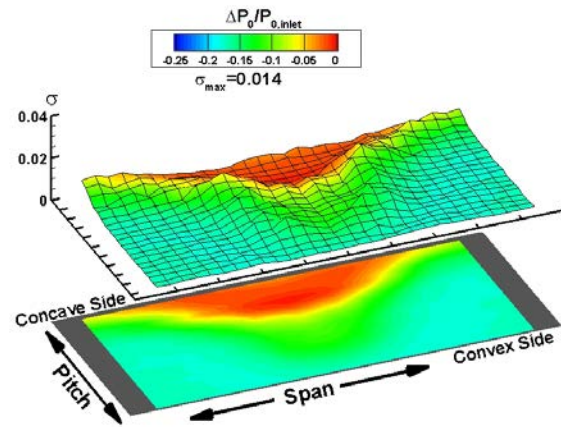
(c) 2.2%, Slot-jet Only



(d) 2.2%, CVG



(e) 4.1%, Slot-jet Only



(f) 4.1%, CVG

Figure 13. Exit Traverse Gauge Total Pressure Ratio

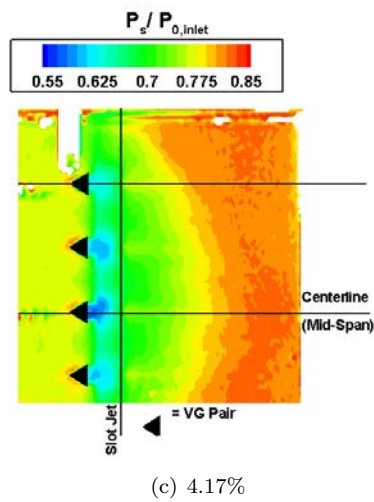
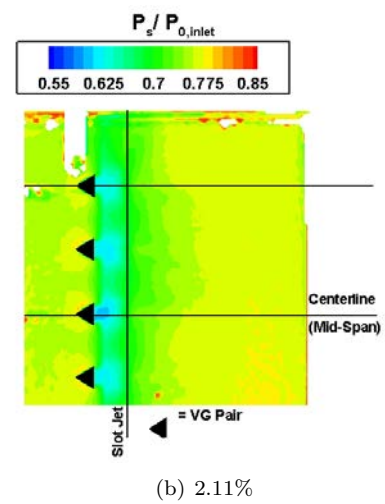
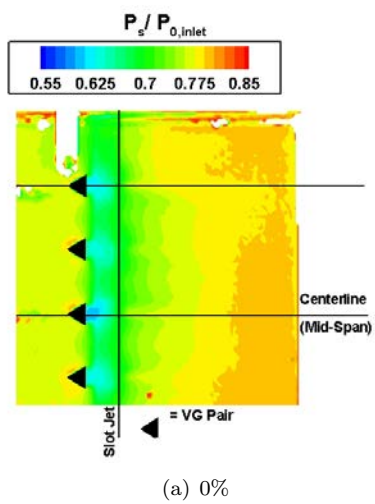


Figure 14. PSP for CVG Configuration

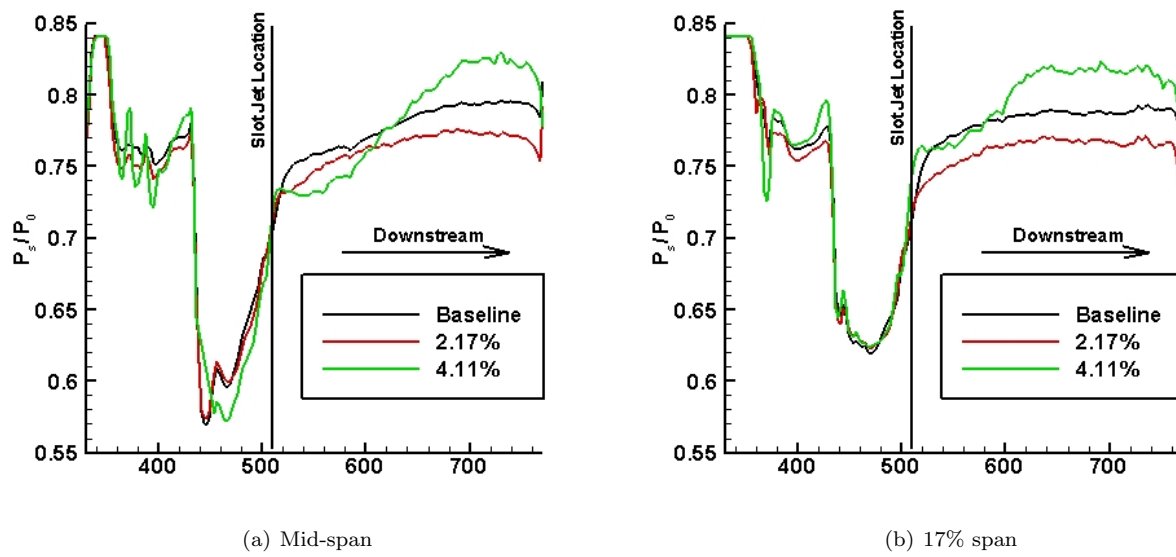


Figure 15. Chordwise Extracted PSP Data for CVG Configuration

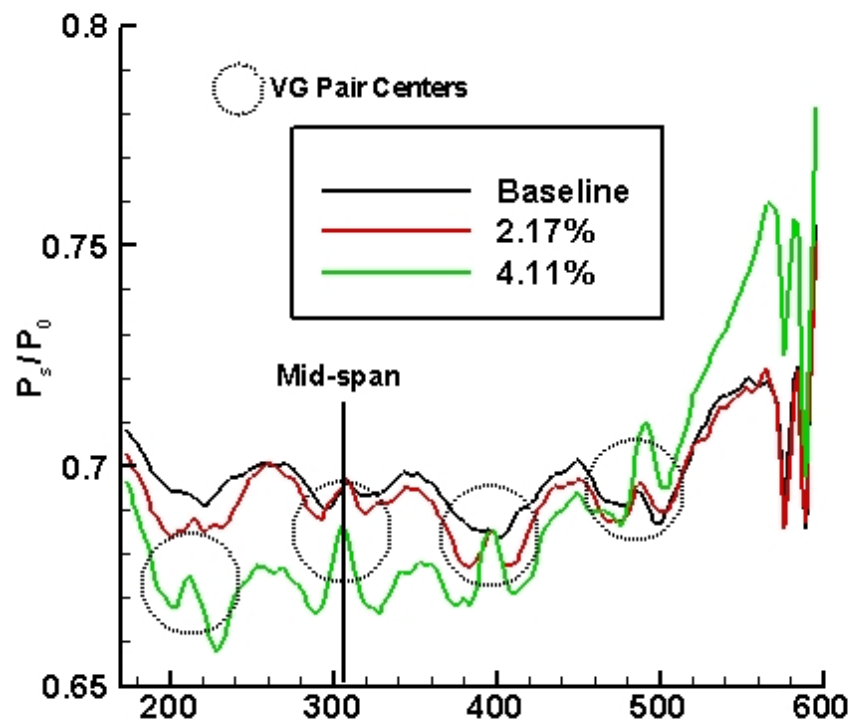


Figure 16. PSP for CVG at Slot Jet Exit

PIV Study of Wake–Rotor Interactions in a Transonic Compressor at Various Operating Conditions

Jordi Estevadeordal*

Innovative Scientific Solutions, Inc., Dayton, Ohio 45440

and

Steven E. Gorrell[†] and William W. Copenhaver[‡]

U.S. Air Force Research Laboratory, Wright–Patterson Air Force Base, Ohio 45433

DOI: 10.2514/1.17452

Details of the unsteady flowfield between an upstream wake generator and a downstream rotor that are closely spaced in a transonic compressor are studied at various operating conditions using particle-image velocimetry. Flow-visualization images and particle-image velocimetry data facilitate analysis of the details of shed vortices, wake motion, and wake–shock interaction phenomena. Such analysis not only aids the understanding of the effect of blade-row interactions on compressor performance but also allows verification of time-accurate CFD codes that are used to characterize transonic compressors. As the operating point changes from choke to stall and the rotor-bow shock moves upstream, distinct vortex-shedding patterns are observed that affect the wake deviation and rotor incidence. With close spacing between the wake generator and the rotor, vortex shedding from the wake generator and the passage of the rotor-bow shock are strongly synchronized and blade-passage “phase-locked” measurements are possible. The resulting multiple images of the flow corresponding to any blade position are averaged to yield vortex and rotor-bow-shock locations at various back pressures. Using various postprocessing methods, specific shed vortices and wake topological features are isolated and details of the wake–shock interaction are captured.

Introduction

BLADE-ROW–WAKE interactions are a significant source of unsteady flow in modern advanced high-performance turbomachines because their design incorporates closely spaced and heavily loaded blade rows to increase thrust/weight. Frequently observed unsteady phenomena such as the interactions of a shock with a vortex and a shock with a blade surface produce nonuniformities and irregular flow patterns that influence compressor performance and result in blade-row vibrations and high-cycle fatigue. A better understanding of these phenomena will aid the design of compressors with improved performance.

The majority of design tools currently in use do not explicitly account for unsteady flows. Multistage axisymmetric models assume that the incoming flow to a blade row is a mixed-out average of the flow exiting the preceding blade row and that potential effects between blade rows are negligible. These models employ empirical correlations based on engine-company design experience to account for the effects of unsteady flow. Another method is based on steady Navier–Stokes analysis, with unsteady interactions between blade rows being modeled as “deterministic stresses” [1]. Its accuracy is dependent on the models used to account for the effects of the unsteady-flow environment on the average-passage flowfield. Time-accurate CFD codes are now used to simulate compressor operation and to investigate complex unsteady-flow phenomena [2,3]. Experimental results that reveal unsteady-flow effects are crucial for validating these design tools and for providing additional understanding of the physical phenomena and interaction processes

involved in turbomachinery flows that are associated with closely spaced and heavily loaded compressor stages.

Use of the planar nonintrusive measurement technique particle-image velocimetry (PIV) [4] for complex geometries and unsteady applications has allowed researchers to make accurate measurements of instantaneous and averaged turbomachinery velocity fields [3,5–11]. In the present investigation a system that was developed for obtaining high-resolution velocity data from an axial-flow transonic compressor [12] (Fig. 1) was used to study blade-row interactions at various operation conditions.

The PIV system consists of two Nd:YAG lasers; transmitting and receiving optics; and seeding, synchronization, and camera hardware [6]. The remotely monitored and controlled system allows identification and investigation of the interaction and synchronization of the shed wake and rotor-blade bow shock.

The instantaneous nature of the PIV technique allows for the capture of the instantaneous unsteadiness that is typical of turbomachinery flows, and statistical characterization of the flow is possible through the use of averaging techniques.

Stage-Matching-Investigation Rig

The stage-matching-investigation (SMI) rig is a high-speed highly loaded compressor that consists of three blade rows: a wake generator (WG), a rotor, and a stator (Fig. 2). The rig was designed to permit the WG-to-rotor axial spacing to be set to three values, “close,” “mid,” and “far” [13], as shown in Fig. 2. The mean spacings that are normalized by the WG chord are given in Table 1.

The WGs were designed to produce a pressure loss typically found in modern-technology highly loaded low-aspect-ratio fan and compressor embedded front stages. To simplify the experiment the WGs were designed to be uncambered airfoils that do not turn the flow. Measurements of stator wakes from rig tests were used as the design target [14]. In general, these wakes are turbulent and do not decay so rapidly as wakes from high-aspect-ratio stages with lower loading. For simplicity and for isolating the effects of various wake parameters, a two-dimensional representation of the wake was desired.

The WG airfoils have a small leading-edge (LE) radius, with a relatively blunt trailing-edge (TE) radius. In the design process this produced the optimum combination of profile and base drag for

Received 29 April 2005; revision received 31 July 2006; accepted for publication 25 August 2006. This material is declared a work of the U.S. Government and is not subject to copyright protection in the United States. Copies of this paper may be made for personal or internal use, on condition that the copier pay the \$10.00 per-copy fee to the Copyright Clearance Center, Inc., 222 Rosewood Drive, Danvers, MA 01923; include the code \$10.00 in correspondence with the CCC.

*Research Engineer, Associate Fellow AIAA.

[†]Senior Aerospace Engineer, Compressor Aerodynamics Research Laboratory (CARL), Propulsion Directorate, Associate Fellow AIAA.

[‡]Principal Scientist, Turbine Engine Division, Propulsion Directorate, Associate Fellow AIAA.

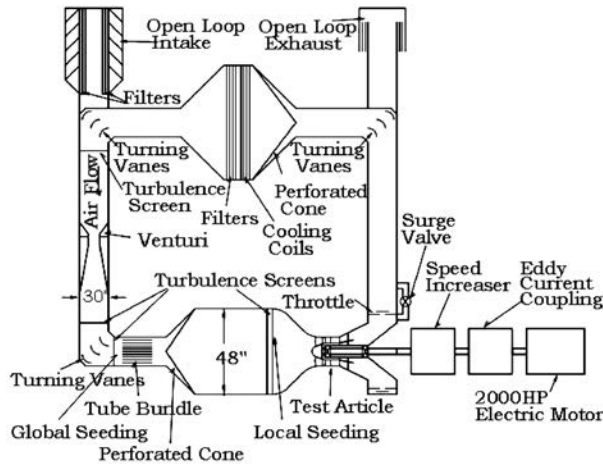


Fig. 1 Flowpath of the 2000-hp Compressor Aerodynamic Research Laboratory facility.

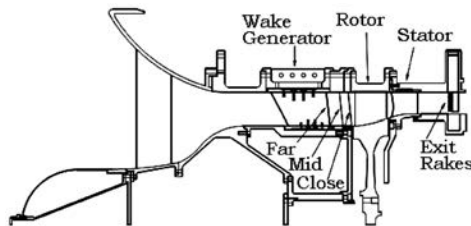


Fig. 2 SMI rig cross section in its general configuration.

matching the desired highly loaded stator wake. To help maintain a constant spanwise total-pressure-loss profile, the solidity of the WGs was held constant from hub to tip, which results in a tapered airfoil chord along the radius. The TE was swept to allow a constant nondimensional mixing length from hub to tip. The clearance was zero at the hub and at the tip.

A compressor map of the overall stage pressure ratio for the 24-WG configuration at close spacing is shown in Fig. 3 (throttle settings: 000, open throttle/choke; 114, peak efficiency; and 140, near stall). A summary of the aerodynamic design parameters is given in Table 2. The present PIV study contains data from measurements made from the 24-WG blade count at “close” spacing at various points on the map. The axial Mach number through the WGs at 75% span was determined to be 0.57; the Reynolds number based on WG TE thickness was 5.78×10^4 . The natural nondimensional vortex-shedding frequency (Strouhal number) [15] for an isolated WG airfoil based on the TE thickness is ~ 0.2 .

Particle-Image Velocimetry System

A PIV system that was developed for turbomachinery investigations was employed [6]. Figure 4 contains schematic diagrams of the optical system. Two lasers (Nd:YAG, 532 nm) are employed for double-instantaneous marking of the seed particles in the flowfield. The beams are combined and directed through sheet-forming optics and illuminate the test section with a two-dimensional plane of thickness that is ~ 1 mm. The scattering from the seed particles is recorded on a cross-correlation CCD camera with 1008×1018 pixels (model Megaplus ES1.0); this camera is capable of acquiring double exposures at 15 Hz. The camera repetition rate was

Table 1 Wake-generator axial spacing (normalized by the local WG chord)

Spacing	x/c , mean	x/c , hub	x/c , tip
Close	0.13	0.10	0.14
Mid	0.26	0.26	0.26
Far	0.55	0.60	0.52

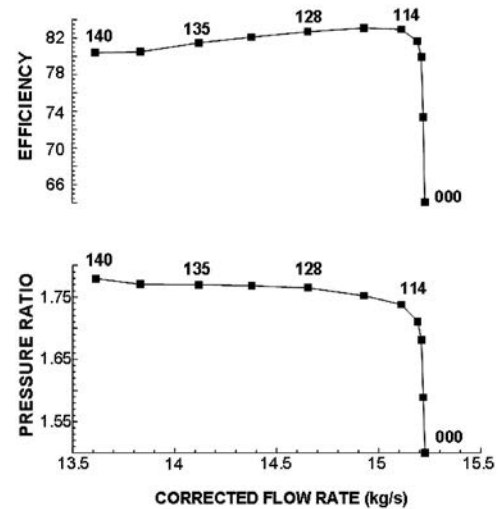


Fig. 3 Overall stage pressure ratio for 24-WG close-spacing configuration.

set at 10 Hz for synchronization with the laser repetition rate. The power for the laser-sheet illumination was ~ 20 mJ/pulse. A 105-mm Nikon lens set at an f-stop of 5.6 was used. For the present experiments the magnification was 27.4 pixels/mm, which corresponds to an object width of 36.8 mm. The time delay between the two frames of the double exposure was typically $1.25 \mu\text{s}$. These settings provided sufficient resolution and accuracy.

The laser-sheet delivery system consists of a probe inserted into an enlarged WG, light-sheet-forming optics, prisms, and probe holders. The outside diameter of the probe is 12.7 mm. To minimize perturbations the modified WG was located at the second WG below the WG that was centered at the receiving window. The optical path from the laser room to the compressor test rig was ~ 8 m and was covered and isolated from floor vibrations. Figure 4 also contains schematic diagrams of the path for the laser system and the optical probe.

The combined beam entered the SMI case perpendicularly through the center of the WG optical probe. The beam was then turned 90 deg inside the WG by a prism and directed to a spherical lens and a cylindrical lens to form a laser sheet. The laser sheet was turned 90 deg by a prism at the tip of the probe and exited the probe approximately normal to the spanwise (radial) direction. The spanwise location of the laser sheet (Fig. 5) at the window could be changed by rotating the probe. The figure shows two laser-sheet spanwise locations for the 24-WG configuration with respect to the blade clockings, WGs, and 75 and 90% circumferences; blade LE locations are shown at 20- μs intervals with lighter lines. The WG centered at the viewing window (marked by two small lines outward) is at 22.5 deg, and thicker portions of the laser sheets denote PIV

Table 2 SMI aerodynamic design parameters

Parameter	Rotor	Stator
Number of airfoils	33	49
Aspect ratio, average	0.961	0.892
Inlet hub/tip ratio	0.750	0.816
Flow (annulus area), $\text{kg}/(\text{s} \cdot \text{m}^2)$	195.04	—
Flow (frontal area), $\text{kg}/(\text{s} \cdot \text{m}^2)$	85.34	—
Flow rate, kg/s	15.63	—
Tip speed (corrected), m/s	341.6	—
M_{rel} LE hub	0.963	0.82
M_{rel} LE tip	1.191	0.69
Pressure ratio (rotor)	1.88	—
Pressure ratio (stage)	—	1.84
Diffusion factor (hub)	0.545	0.502
Diffusion factor (tip)	0.530	0.491
LE tip diameter, m	0.48260	0.48260
LE hub diameter, m	0.36195	0.39375
WG counts: 24, 40	—	1122

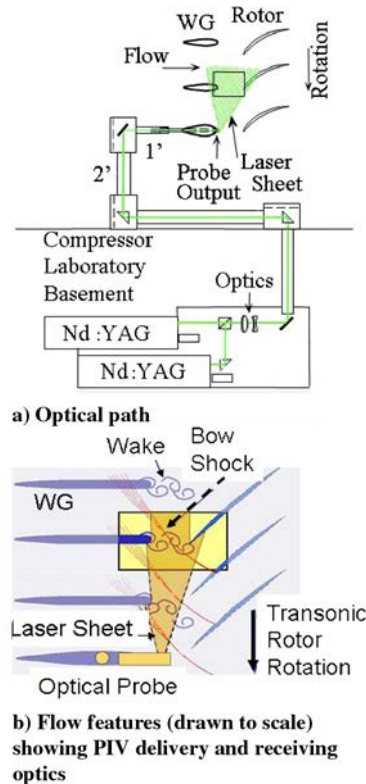


Fig. 4 Schematic diagrams of the PIV system.

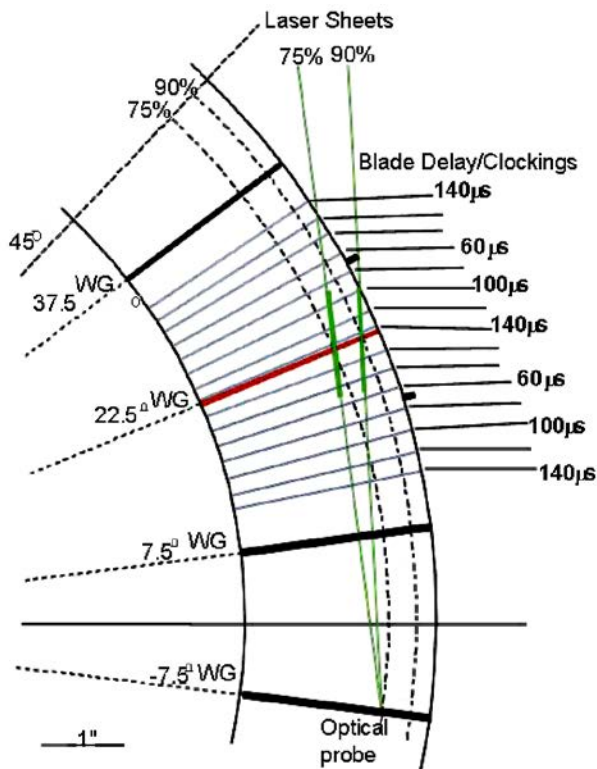


Fig. 5 Laser-sheet spanwise locations for the 24-WG configuration.

image locations. The shape of the laser sheet (thickness, width, and focal distance) could be altered through various combinations of the spherical-lens focal length, the cylindrical-lens diameter, and the distance between them inside the WG as well as through external optics (a spherical lens) located in the laser path. As shown in Fig. 5, the laser sheet was inclined and not at a constant radius. The

magnitude of inclination varies depending on the desired spanwise location at the WG TE. Comparison with three-dimensional CFD results can be accomplished in a straightforward manner, requiring interpolation of only the numerical solution to a grid that matches the inclination of the PIV laser sheet. Comparisons have shown that, with the grid densities required to obtain an accurate CFD simulation, an interpolation to a grid that matches the laser-sheet inclination is straightforward [3], and PIV data and unsteady CFD results can be readily compared.

Accurate positioning of the camera was accomplished using a remotely controlled translation stage. The viewing window had the same curvature as the rotor housing (inner housing radius of 241.3 mm), was made of chemically strengthened glass, and was 2 mm thick. Ray-tracing analysis was performed assuming monochromatic laser-sheet (green, 532 nm) glass with an index of refraction of 1.5 (at 20°C), a window with parallel sides, and small angles of incidence and refraction (paraxial approximation) [16]. Comparison of exposures with and without the window was also performed. The results revealed that a negligible magnification of $\sim 0.3\%$ occurs in the vertical direction (affecting the v component) for the present setup. If experiments were conducted with thicker and more curved windows, severe distortion would occur.

The rotor one-per-revolution signal was used for triggering the synchronization system. A digital pulse generator (Stanford DG535) and a camera interface were used. Programming and operation of the camera frame-grabber (National Instruments PCI-1424) and the delay generator were accomplished using drivers that were written especially for the National Instruments LabWindows/CVI development language; this facilitated integration with the PIV analysis software, which is also written in this environment [17].

The seed material employed in previous experiments [6] was sub-micron-size smoke particles that were generated from a smoke generator using a glycerin and water mixture. During its use in the compressor facility, the seeding system produced sufficient seed when the particles were introduced at the end of the settling chamber, before the contraction, and at the height of the receiving window (Fig. 1). These particles were also preferred for seeding transonic environments because small-size particles with specific gravity similar to that of the air minimize particle lag, including that which occurs when crossing a shock [4]. A pipe extending to the window height was typically inserted into the plenum. The end of the pipe is perforated with holes of increasing diameter toward its end, with a honeycomb and screen for optimal mixing, uniformity, and spreading of seed. Calculations based on flow speed at the beginning of the contraction (the area of maximum diameter and minimum speed), distance from the test area, pipe diameter, and mixing were performed to confirm that the seeding system exerted negligible perturbation on the flow.

Once the PIV images have been captured and digitized, the velocity field was obtained using cross-correlation techniques over interrogation domains of the images and PIV software [4,17]. The dimensions of the interrogation domains were dependent on particle density, estimated local velocity gradients, particle-image size, and desired spatial resolution. The peak of the correlation map corresponds to the average velocity displacement within the interrogation spot. An intensity-weighted peak-searching routine was used to determine the location of the peak to subpixel accuracy. Domain-shifting techniques for minimizing in-plane loss of pairs and correlation-multiplication techniques [18] are used to produce correlation maps with lower noise. Zero padding was also employed for added accuracy [4]. The software includes a grid feature that allows selection of the image areas to be processed, which permits removal of solid regions such as rotor blades and WGs as well as shadows from the processing areas. This feature also provides a choice of various correlation engines and correlation peak locators and incorporates recursive estimation of the velocity field through a multipass algorithm for increased resolution [18]. To maintain high accuracy, two and three passes were performed with interrogation cells overlapping 75%; this yielded a grid resolution of 16 and 8 pixels (corresponding to 0.58 and 0.29 mm), respectively. Overlapping of interrogation domains yields more vectors. The

overlapping is not merely interpolation because it includes new particles in every subregion.

In the present study analyses were performed using averages from the PIV velocity fields. PIV is instantaneous in nature but cannot provide temporal evolution of the flowfield because of the relatively slow repetition rate of the lasers that are suitable for this type of PIV application. The approach taken in this study was based on ensemble (or phase) averaging [19] because of the natural phase locking that is provided by the rotor-blade potential field. Then the temporal evolution could also be inferred from the phase information. The experiments provided a sufficient number of realizations [20,21] (>50) for each average velocity-field calculation. The calculation of turbulence characteristics would benefit from higher numbers, but this was not an objective of the present study. In this study the averaged data is presented using the median. The median is less affected by “outliers” than the mean (“robust statistic”) [22], does not require that data be normally distributed, and offers a smooth representation of the ensemble-average velocity fields. It is also an actual member of the data set (for an odd number of samples). The median has also been found to be advantageous when a lower number of realizations is available; the median is further enhanced in studies with low phase-randomness [19] such as the present study, which concentrates on a close-spacing configuration having strong phase locking on the large coherent structures. The ensemble-averaging mode on the instantaneous velocity fields eliminates the fluctuations due to incoherent unsteadiness that are associated with turbulence (resolving small scales was not an objective of this study) and still permits a comparison with CFD predictions. Statistical filtering was also performed employing routines that allow removal of outliers from the data using standard-deviation trimming and other techniques [6,20].

Many factors are involved in the instantaneous-PIV uncertainty-calculation process (e.g., laser, CCD, seeding, imaging, algorithms, photodiode, and oscilloscope). The highest uncertainty was found to be associated with the velocity calculation that involves Δx (the displacement in pixels of each interrogation region), Δt (the time interval between the two exposures), and the magnification of the digital image relative to the object (pixel/m). The displacement in pixels obtained by peak-locator algorithms can provide subpixel accuracy (<0.1 pixels) after correction for various biases [4]. The Δt was adjusted to yield typical displacements of the main stream of >10 pixels; the uncertainty is, thus, $<1\%$. Values in the wake region, however, may have higher uncertainties due to the lower Δx . The maximum uncertainty in Δt was calculated from the time interval between the two laser light pulses with the aid of a photodiode that was connected to an oscilloscope (uncertainty 2%). It was found that this uncertainty increases with lower laser power and with lower Δt . A conservative uncertainty for the present experiments, which employed a Δt of about $1\text{--}2\ \mu\text{s}$ and powers of around $10\text{--}20\ \text{mJ}$, was found to be 1% . The magnification was measured, using images of grids located in the laser-sheet plane, to better than 1% . Combining these conservative measurements of uncertainty yields a maximum error of $<2\%$ in the freestream velocity and $\sim 10\%$ in the wake velocity near the WG area.

The uncertainty that results from various PIV algorithms (e.g., single pass and multipass) and data-filtering techniques (e.g., standard-deviation trimming and median) was also calculated for the average velocity field. Mean, standard deviation, median, and median variability were calculated for the data sets and compared for each PIV algorithm and filtering technique. The average velocity field was interrogated at the various representative regions such as the freestreams above and below the WG and before and after the shock, the shock regions, and the wake regions. The median variability was calculated using the “median absolute deviation” (MAD), which is defined as the median of the absolute distances to the median and is computed as an alternative to the standard deviation when that is not available. That was the case in the present experiments with sample sizes of 50 elements, which effectively allowed the computing of only one median. Therefore, its uncertainty, variability, and standard deviation cannot be calculated from a large-series standpoint, which would require a large

population of medians. MAD is a robust measure of the median dispersion and does not have restrictions on the underlying distribution (such as normality). The mean uncertainty for Gaussian distributions is reduced by a factor of $1/\sqrt{N}$ (with N being the number of realizations) with respect to the uncertainty of the instantaneous values. If the sample size is low (<30), a t -distribution test is more adequate to measure confidence [20]. The results showed that, with proper multipass PIV algorithms and data-filtering techniques, the mean standard deviation and the median variability could be decreased to $<2\%$ and $<1\%$, respectively, with the median offering more uniform and consistently lower variability in all areas. In the wake region these values increased to $<12\%$ and $<10\%$, respectively, which could be attributed in part to actual phase-randomness [19].

Results

At 100% speed, consecutive rotor blades are separated in time by $140\ \mu\text{s}$ (~ 11 deg in angle, the blade-row pitch). Seven blade locations (“clockings”) separated by $20\ \mu\text{s}$ were chosen to characterize the flowfield in a blade-row pitch. Analyses were performed using both qualitative flow-visualization and quantitative velocity-field measurements. Data analysis includes inspection and selection of flow-visualization images (obtained by increasing the amount of seeding) and also reduction of data to velocity using PIV software [17].

Previous research on this test article [6] demonstrated the effect of changing the axial spacing on the synchronization between vortex shedding and the rotor LE; the influence and synchronization between the blade passage and the flow was shown to decrease with increasing axial spacing. It became evident that close spacing offers stronger phase-locked flow features. The present experiments were focused on the “close-spacing-and-75%-span” configuration for studying the effect of the compressor operating point on the vortex-shedding pattern. The various operating conditions were achieved by changing the throttle settings (000, open throttle; 114, peak efficiency; 128; 135; and 140, near stall; see Fig. 3). Figure 6 shows flow-visualization samples for four throttle settings and two blade clockings that capture the passage of the rotor blade behind the WG. The figure shows the effect of throttle variation (000, open throttle; 114, peak efficiency; 128; and 140, near stall) on vortex shedding at two instants of blade passage behind the WG ($140\ \mu\text{s}$, top, and $20\ \mu\text{s}$, bottom); dashed lines connecting the two vortex centers are shown to aid in visualizing their location. It can be readily inferred from these visualizations that vortex shedding from the WG displays a distinct pattern for each throttle condition. The vortices appear farther upstream as the throttle is closed to near stall (140), as opposed to when it is open (000). Increasing backpressure moves the bow-shock upstream, thus causing vortices to be shed sooner for the same rotor location. For the conditions of open throttle (000) and peak efficiency (114), a vortex appears to collide with the LE of the rotor blade, although at peak efficiency the vortex appears at a location of slightly higher pitch. When the throttle is closed to the

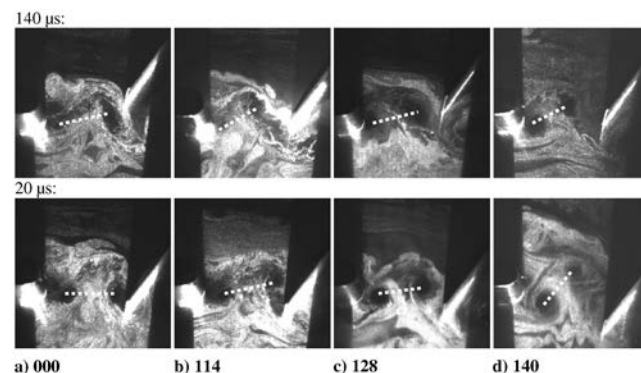


Fig. 6 Flow-visualization samples showing the effect of throttle variation on vortex shedding. 1124

near-stall operating condition (140), the rotor appears to chop the wake by the “braid” (the region of the wake between the coherent structures) [19]. The rotor-blade LE location at a given clocking does not coincide exactly with those for different throttle settings because the mechanical speed was varied during the experiments to maintain the same corrected speed.

As observed in previous studies [6], synchronization of the rotor-blade location and vortex shedding was apparent upon inspection of the many images captured under various blade-delay and throttle conditions. This study demonstrates that the synchronization is evident at all operating points between choke and stall. The images of vortex shedding were similar for any given operating condition and blade delay. These facts have suggested that the location of the vortices (and shedding) is phase locked to the rotor-blade pass frequency. Further studies of the relation among blade-row axial spacing, vortex shedding, and compressor–rotor performance can be found in the literature [3,6,23]. Other studies of the relation between the frequency of the vortex shedding and the blade-passing frequency in a multiblade row of a turbine stage can also be found in the literature [24,25].

In the present experiments the rotor-blade row appears to produce forcing of the vortex shedding that is sufficiently strong [19] to cause sharp synchronization between the rotor-blade position and the main flow features. Forced shedding is triggered by the rotor-blade potential field, which transmits a strong pressure perturbation to the WG. A pressure fluctuation translates to a velocity perturbation as it interacts with the solid surface of the WG. The location of the interaction determines the characteristics of the vortex shedding. Also, because the bow shock is a major cause of pressure change and because the shock location with respect to the rotor LE varies with throttle setting, the difference in the location of the vortices as a function of the throttle setting is related to the shock location. This is consistent with WG the results of surface-static-pressure measurements made using Kulite transducers, which showed a strong fluctuation in pressure at the blade-passing frequency [26]. Furthermore, a recent cascade experiment confirmed that large vortices can be induced by the passing of a shock wave [27].

An improved quantitative understanding of the many unsteady-flow features involved in complex blade-row interactions can be gained through analysis of the velocity field obtained with PIV. As pointed out earlier, because vortex shedding is phase locked to rotor passage, rotor phase-locked averaging is possible without destruction of the main details of the velocity field in this interaction region. Also, in the instantaneous-PIV data, gaps in the velocity information may be present where seeding was not sufficient to obtain a correlation; thus, more reliable information can be gained by considering the average flowfield where data intermittency can be minimized. In a phase-locked flow with strong statistical central tendencies of the events under study, the median is both an advantageous estimator of the central value and a robust statistic for removal of outliers, as explained in the PIV section.

The velocity field provides evidence of the relationship among vortex shedding, shock position, wake–shock interaction, and operating condition. Quantitative information on the actual location of the vortices and the shock with respect to the WG and rotor blade can be easily obtained.

Figure 7 shows the PIV velocity field (median of 50 files) overlaid with streamtraces for the choke (open throttle, 000) operating condition at three blade clockings that represent the rotor blade passage behind the WG. The rotor-bow shock, clearly discernible as an abrupt change in velocity, is at a constant distance from the rotor but is broken by the shed wake, which is clearly discernible as a low-velocity region. A significant pitchwise motion of the wake, defined by the shed vortices, was observed as it advected downstream (and also as a function of the rotor-blade location).

The velocity field for the blade clocking with the rotor LE aligned at the WG TE is presented in Fig. 8 (median of 50 files) for three throttle conditions. The rotor-bow shock can be easily identified for each operating condition. Between open throttle (000) and peak efficiency (114), the bow shock begins to move forward as the stage becomes unchoked and the backpressure increases. Furthermore,

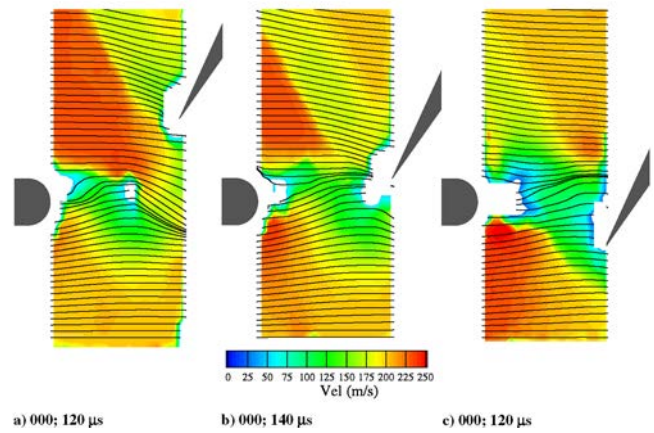


Fig. 7 Velocity field and streamtraces for open throttle condition at three blade clockings.

until the stage becomes completely unchoked, the mass flow rate is constant, as shown by the characteristic of Fig. 3. Thus, the velocity in the PIV image of Fig. 8a is similar to that of Fig. 7b. At near stall (where the shock is farther upstream for a given blade clocking), the vortex that is colliding with the rotor LE is actually shed from a previous rotor-blade-bow shock. As the throttle goes from open (000) to near stall (140), the rotor-bow shock becomes stronger and moves upstream, which causes the greatest changes in velocity magnitude and flow angle across the shock. The PIV image shows mainly the flow features upstream of the rotor blade and above the rotor suction side, but some figures (Figs. 7c and 8c) provide evidence of the pressure-side LE shock just below the rotor blade. At the peak-efficiency operating condition, the pressure-side shock is more normal to the rotor LE and, therefore, can be observed in the image view.

An approximation of the overall time-averaged velocity field can be obtained by averaging all seven blade delays of one blade passing behind the WG. Figure 9 shows the velocity field (median of the seven blade clockings with 50 files each) and the corresponding streamtraces for a blade-passage period behind the WG for three throttle conditions: a) peak efficiency, 114; b) 128; and c) near stall, 140. At peak efficiency, the magnitude of the velocity is high above and below the wake and rotor incidence is nearly zero. As the throttle is closed to near stall, the magnitude of the velocity is decreased significantly, and the flow enters the rotor at a negative angle. Further analyses of the velocity field yield details on the shock magnitude and location. The abrupt velocity change through the shock can be analyzed using line plots of velocity magnitude across the shock. Figure 10 shows three axial profiles of average speed (median) through the shock for the peak-efficiency case where the rotor LE is located at 10% WG pitch above the WG center (corresponding to a

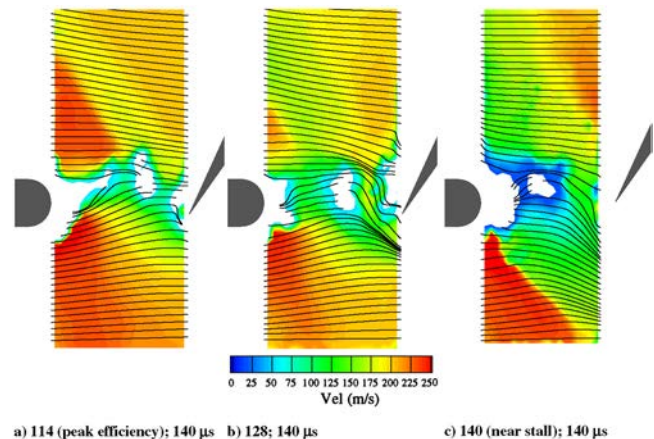


Fig. 8 Velocity field and streamtraces for a blade clocking at three throttle conditions.

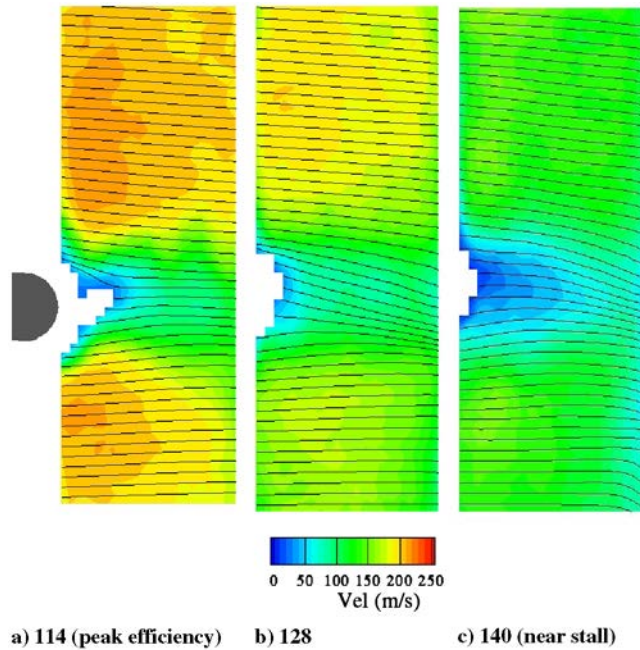


Fig. 9 Velocity field and streamtraces for a blade period at three throttle conditions.

clocking of $120 \mu\text{s}$). Here the resolution of the PIV was 32 pixel cells with 75% overlap that produce an 8 pixel (0.2925 mm) grid (shown in the figure). The shock is readily discernible far from the wake at 20 and 15% WG pitch above the WG center, but it widens and weakens close to the wake, such as at 10% pitch. The width of the bow shock is smeared by PIV resolution. Higher-resolution measurements or close-up approaches [28] would be required for more accurate determination of the actual shock location and velocity gradient, provided the seeding was appropriate [4]. However, the velocity jump across the shock can be readily estimated, for example, $235 - 181.5 = 53.5 \text{ m/s}$ for the case of 20% pitch above the WG. Also the shock location can be estimated from the curve where the speed changes rapidly. For example, here the center could be estimated to be at $\sim 12.5 \text{ mm}$ ($12.5 \pm 0.5 \text{ mm}$) or 22.5% chord upstream of the rotor LE. The shock width and sharpness are readily discernible far from the wake at 15 and 25% WG pitch above the WG center but become smeared near the wake region (e.g., 10% WG pitch above the WG center) because of the wake–shock interaction. Moreover, because the velocities across the shock wave can be calculated in the rotor frame of reference, the Mach number of the shock could be calculated and compared with the value from the known blade and flow velocities or shock angle.

The large vortices that appear in the wake flow can significantly influence the flow entering the rotor. These features are also

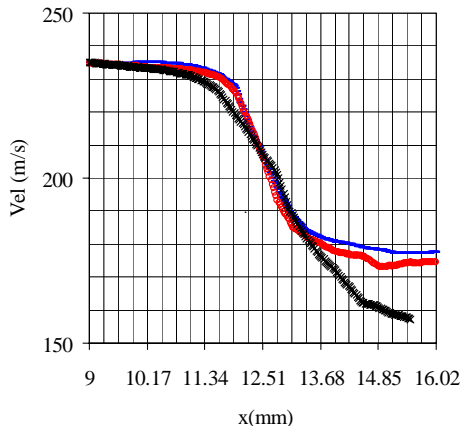


Fig. 10 Velocity axial profiles at 20% (—), 15% (○), and 10% (x) pitch.

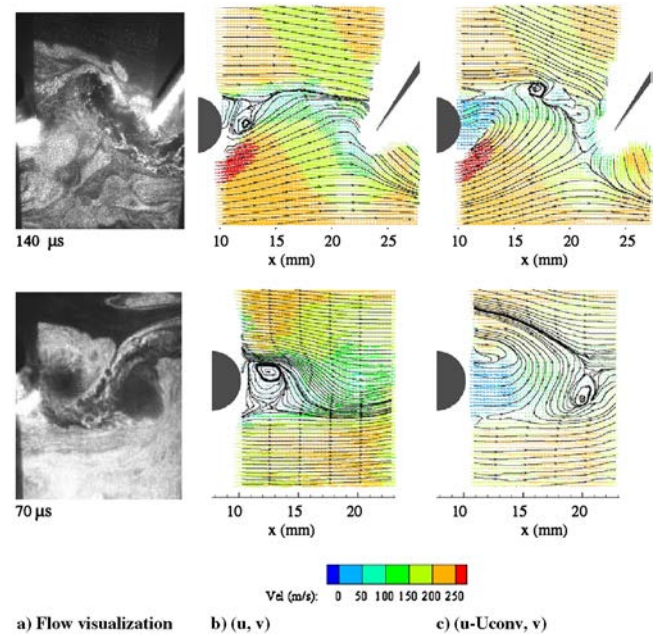


Fig. 11 Wake motion and wake–shock interaction characterizations at peak efficiency.

important for validating time-accurate CFD codes. The complex flowfield accompanying the shock, vortices, and wake can be investigated through additional processing of the PIV velocity data. Capturing higher levels of detail in these areas was accomplished using multipass high-resolution PIV with an increased grid resolution of 0.292 mm and various averaging filters that are explained in the PIV section. Figure 11 shows the manner in which these details can be obtained by subtracting a constant axial component (convective) of velocity to represent the motion from a frame of reference moving at that velocity [29]. Results at blade clockings of $70 \mu\text{s}$ (wake passing through the center of rotor passage) and $140 \mu\text{s}$ (rotor LE aligned with WG) for peak efficiency are shown to emphasize the wake motions. The wake vortices and the braid can be clearly seen in the instantaneous flow visualizations in Fig. 11a. Topological wake features can be identified from the streamline patterns; the first vortex shed (spiraling streamline pattern), the saddle points (outward-pointing streamline pattern from a center), and the strong downwash velocity between the vortices through the braid (in the $70\text{-}\mu\text{s}$ clocking) are clearly discernible from the mean velocity field and streamtraces (Fig. 11b). These motions occur close to the nearly quiescent region behind the WG, and convective velocity subtraction is not needed. Further insight regarding the interaction of the rotor–bow shock with the WG TE can be gained from PIV and flow-visualization data. In Fig. 11b, a shed vortex appears on the upper side (facing rotor revolution) of the WG, which suggests that the rotor–bow shock influences the WG boundary layer in a manner that drives the shedding of a vortex. The nature of the perturbation that drives vortex shedding has been described in the literature [3] through a comparison of the results of detailed experimental measurements with time-accurate CFD simulations. The second vortex and saddle point can also be readily identified when their convective velocity (obtained from the absolute velocity field, here $\sim 110 \text{ m/s}$) is subtracted from the mean (Fig. 11c). A shock–vortex interaction is captured for the second vortex at $140 \mu\text{s}$, as shown in Fig. 11c, which depicts the location of the vortex in the middle of the shock line.

Other details of the flow can be obtained by smoothing (weighted average of neighboring points) the velocity field. This technique emphasizes flow patterns that can be used for time-accurate CFD comparisons. Such a wake characterization is shown for the $70\text{-}\mu\text{s}$ clocking in Fig. 12. The first (Fig. 12a) and second (Fig. 12b) vortices and the saddle points from Fig. 11a are readily discernible with their characteristic patterns. The wake profiles and wake centerline (Fig. 13) also provide evidence of the wake motions, wake mass, and

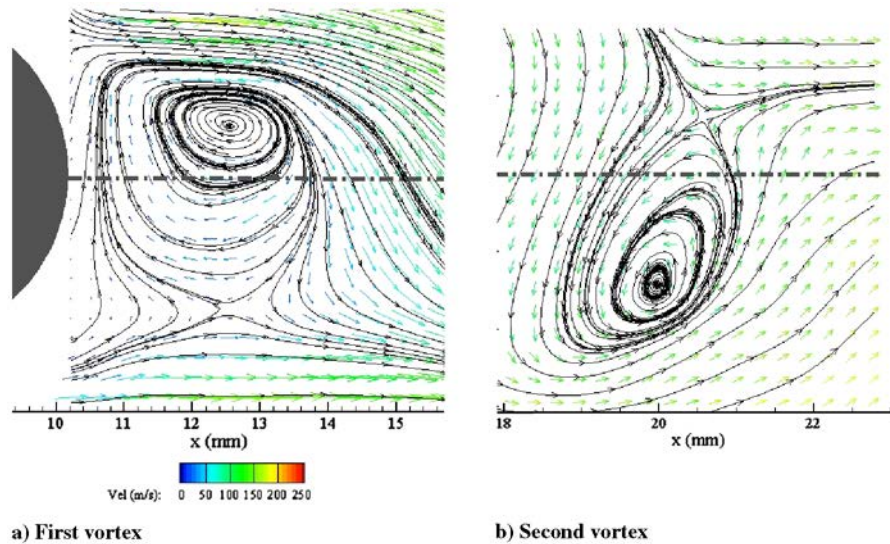


Fig. 12 Details of the wake displayed through smoothed vector field; WG axial centerline (dash-dotted lines).

reduction in incidence at the raw exit. The centerline was defined by joining the minima of the velocity profiles. Comparison of the averaged wakes over a period has proved to be very useful [30].

Conclusions

The flowfield between an upstream stator and a downstream rotor closely spaced in a high-speed highly loaded transonic compressor was investigated using flow-visualization and PIV measurements at various operating conditions. A distinct vortex-shedding and shock pattern was documented for several throttle positions from choke to stall. Because vortex shedding from the WG is strongly synchronized with the passage of the rotor-bow shock at close spacing, phase-locked measurements allow multiple images of any blade position to be averaged, producing a clear image of the flowfield. This study demonstrates that the vortex shedding is synchronized to the passage of the rotor-bow shock at all operating conditions from choke to stall. As the operating point changes from choke to stall and the rotor-bow shock moves upstream, the spatial relation between the rotor blade and shed vortex is modified. Thus the rotor LE may collide with a vortex or chop the wake by the braid, depending on the throttle position. The velocity fields exhibit the motion of the wake including

shed vortices as well as the changes in velocity magnitude and flow angle across the shock for each compressor operating condition. For each condition, PIV images present evidence of the shock location, velocity magnitude, and details of its interaction with the wake and vortex shedding. An average velocity field defined by seven positions in one rotor-blade period revealed that the incidence increased as the operating condition changed from peak efficiency to near stall.

Analysis of the PIV data has been used to provide insight into vortex shedding, rotor-bow-shock location, and wake-shock interaction. Through the use of data-processing techniques such as multipass high-resolution PIV with statistical data filtering and averaging, convective velocity subtraction, and smooth-weighted averaging, it has been demonstrated that the complex unsteady flowfield can be captured and visualized with great detail and clarity, allowing previously undetected unsteady-flow phenomena to be observed. These methods have proved useful for isolating specific shed vortices and the shock-vortex interaction in this advanced transonic compressor. Additionally, the data presented allows verification and validation of time-accurate CFD codes.

Acknowledgments

The authors acknowledge the technical assistance of personnel at Compressor Aerodynamics Research Laboratory (CARL), Wright-Patterson Air Force Base, OH, and at Innovative Scientific Solutions, Inc. (ISSI), during the experiments and the editorial assistance of Marian Whitaker of ISSI. The WG, rotor, and stator were built by Pratt & Whitney. The authors recognize Robert Wirrig, Ron Berger, and Terry Norris from the CARL group at Wright-Patterson Air Force Base, OH, for their assistance in gathering the data. Justin England and Nathan Woods assisted with postprocessing of the results. The authors acknowledge the Propulsion Directorate management for supporting the research and the presentation and publication of this paper. Very fruitful discussions with Josep Ginebra, Professor of Statistics at the Polytechnic University of Catalonia, are greatly appreciated.

References

- [1] Adamczyk, J. J., "Aerodynamic Analysis of Multistage Turbomachinery Flows in Support of Aerodynamic Design," *Journal of Turbomachinery*, Vol. 122, No. 2, 2000, pp. 189–217.
- [2] Gorrell, S. E., Okiishi, T. H., and Copenhaver, W. W., "Stator Rotor Interactions in a Transonic Compressor, Part 2: Description of a Loss Producing Mechanism," *Journal of Turbomachinery*, Vol. 125, No. 2, Apr. 2003, pp. 328–335.
- [3] Gorrell, S. E., Car, D., Puterbaugh, S. L., Estevadeordal, J., and Okiishi, T. H., "An Investigation of Wake-Shock Interactions in a Transonic

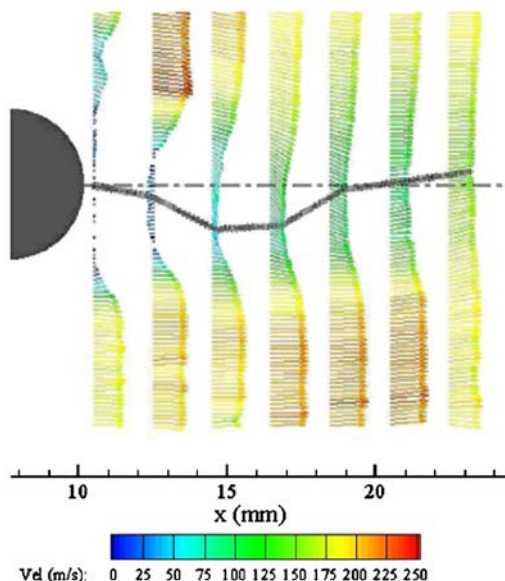


Fig. 13 Wake profiles and centerline waviness: wake characterization example at 70- μ s clocking.

- Compressor with DPIV and Time-Accurate CFD," *Journal of Turbomachinery*, Vol. 128, Oct. 2006, pp. 616–626; also *Proceedings of the ASME Turbo Expo*, American Society of Mechanical Engineers Paper GT-2005-69107, June 2005.
- [4] Raffel, M., Willert, C. E., and Kompenhans, J., *Particle Image Velocimetry: A Practical Guide*, Springer-Verlag, New York, 1998.
 - [5] Copenhaver, W., Esteveordal, J., Gogineni, S., Gorrell, S., and Goss, L., "DPIV Study of Near-Stall Wake-Rotor Interactions in a Transonic Compressor," *Experiments in Fluids*, Vol. 33, No. 6, 2002, pp. 899–908.
 - [6] Esteveordal, J., Gogineni, S., Goss, L., Copenhaver, W., and Gorrell, S., "Study of Wake-Blade Interactions in a Transonic Compressor Using Flow Visualization and DPIV," *Journal of Fluids Engineering*, Vol. 124, No. 1, 2002, pp. 166–175.
 - [7] Esteveordal, J., Gogineni, S., Goss, L., Copenhaver, W., and Gorrell, S., "DPIV Study of Wake-Rotor Synchronization in a Transonic Compressor," AIAA Paper 2001-3095, June 2001.
 - [8] Esteveordal, J., Gogineni, S., Copenhaver, W., Bloch, G., and Brendel, M., "Flow Field in a Low-Speed Axial Fan: A DPIV Investigation," *Experimental Thermal and Fluid Science*, Vol. 23, Nos. 1–2, 2000, pp. 11–21.
 - [9] Wernet, M. P., "Development of Digital Particle Imaging Velocimetry for Use in Turbomachinery," *Experiments in Fluids*, Vol. 28, No. 2, 2000, pp. 97–115.
 - [10] Balzani, N., Scarano, F., Riethmuller, M. L., and Breugelmans, F. A. E., "Experimental Investigation of the Blade-to-Blade Flow in a Compressor Rotor by Digital Particle Image Velocimetry," *Journal of Turbomachinery*, Vol. 122, No. 4, 2000, pp. 743–750.
 - [11] Sanders, A. J., Papalia, J., and Fleeter, S., "A PIV Investigation of Rotor-IGV Interactions in a Transonic Compressor," *Journal of Propulsion and Power*, Vol. 18, No. 5, Sept.–Oct. 2002, pp. 969–977.
 - [12] Law, C. H., and Wennerstrom, A. J., "Two Axial Compressor Designs for a Stage Matching Investigation," U.S. Air Force Wright Aeronautical Laboratories Rept. AFWAL-TR-89-2005, Wright-Patterson AFB, OH, 1989.
 - [13] Gorrell, S., Copenhaver, W., and Chriss, R., "Upstream Wake Influences on the Measured Performance of a Transonic Compressor Stage," *Journal of Propulsion and Power*, Vol. 17, No. 1, 2001, pp. 43–48.
 - [14] Creason, T., and Baghdadi, S., "Design and Test of a Low Aspect Ratio Fan Stage," AIAA Paper 88-2816, July 1988.
 - [15] Schlichting, H., *Boundary-Layer Theory*, McGraw-Hill, New York, 1979.
 - [16] Hecht, E., *Optics*, Addison Wesley Longman, Reading, MA, 1990.
 - [17] DPIV Software, Innovative Scientific Solutions, Inc., Dayton, OH, 2001.
 - [18] Hart, D. P., "Super-Resolution PIV by Recursive Local-Correlation," *Journal of Visualization*, Vol. 3, No. 2, Sept. 2000, pp. 187–194.
 - [19] Esteveordal, J., and Kleis, S., "High-Resolution Measurements of Two-Dimensional Instabilities and Turbulence Transition in Plane Mixing Layers," *Experiments in Fluids*, Vol. 27, No. 4, 1999, pp. 378–390.
 - [20] Coleman, H. W., and Steele, W. G., *Experimentation and Uncertainty Analysis for Engineers*, Wiley, New York, 1989.
 - [21] Inoue, L. Y. T., Berry, D. A., and Parmigiani, G., "Relationship Between Bayesian and Frequentist Sample Size Determination," *American Statistician*, Vol. 59, No. 9, Feb. 2005, p. 79.
 - [22] Press, W. H., Flannery, B. P., Teukolsky, S. A., and Vetterling, W. T., *Numerical Recipes in C: The Art of Scientific Computing*, Cambridge Univ. Press, New York, 1992.
 - [23] Zachcial, A., and Nummerger, D., "A Numerical Study on the Influence of Vane-Blade Spacing on a Compressor Stage at Sub- and Transonic-Operating Conditions," *ASME Turbo Expo: Power for Land, Sea, and Air*, American Society of Mechanical Engineers Paper GT-2003-38020, 2003.
 - [24] Sondak, D. L., and Dorney, D. J., "Simulation of Vortex Shedding in a Turbine Stage," *Journal of Turbomachinery*, Vol. 121, No. 3, 1999, pp. 428–435.
 - [25] Woisetschlager, J., Mayrhofer, N., Hampel, B., Lang, H., and Sanz, W., "Laser-Optical Investigation of Turbine Wake Flow," *Experiments in Fluids*, Vol. 34, No. 3, 2003, pp. 371–378.
 - [26] Koch, P., Probasco, D., Wolff, M., Copenhaver, W., and Chriss, R., "Transonic Compressor Influences on Upstream Surface Pressures with Axial Spacing," *International Gas and Aeroengine Congress and Exhibition*, American Society of Mechanical Engineers Paper 99-GT-384, June 1999.
 - [27] Langford, M., Guillot, S., Ng, W., Breeze-Stringfellow, A., Solomon, W., and Esteveordal, J., "Experimental Investigation of the Effects of a Moving Shock Wave on Compressor Stator Flow," *ASME Turbo Expo: Power for Land, Sea, and Air*, American Society of Mechanical Engineers Paper GT-2005-68722, 2005; also *Journal of Turbomachinery* (to be published).
 - [28] Esteveordal, J., Copenhaver, W., Car, D., Koch, P., Ng, W., Guillot, S., and Carter, C., "Macro- and Milli-DPIV Studies of a Boundary-Layer-Based Flow-Control System for a Transonic Cascade," *Proceedings of the 11th International Symposium on Application of Laser Techniques to Fluid Mechanics* [CD-ROM], 2002.
 - [29] Adrian, R. J., Christensen, K. T., and Liu, Z.-C., "Analysis and Interpretation of Instantaneous Turbulent Velocity Fields," *Experiments in Fluids*, Vol. 29, No. 3, 2000, pp. 275–290.
 - [30] Gorrell, S., Copenhaver, W., and Esteveordal, J., "DPIV Measurements of the Flow Field Between a Transonic Rotor and an Upstream Stator," *Proceedings of the International Symposium on Unsteady Aerodynamics, Aeroacoustics, Aeroelasticity of Turbomachines (ISUAAAT)*, Kluwer Academic, Norwell, MA, 2003, pp. 505–520.

L. Xu
Associate Editor

PIV Investigation of the Flow Field in a Transonic Compressor Cascade with a Moving Shock Wave

Jordi Esteveordal,¹ Matthew D. Langford,² Andrew Breeze-Stringfellow,³

Stephen A. Guillot,⁴ Wing F. Ng⁵

¹*Innovative Scientific Solutions Inc., Dayton, OH 45440;* ²*Techsburg, Inc., 265 Industrial Drive, Christiansburg, VA 24073;* ³*GE Aircraft Engines, 1 Neumann Way, Cincinnati, OH 45215;*

⁵*Mechanical Engineering Dept., 122 Randolph Hall, Virginia Tech., Blacksburg, VA 24061*

The unsteady flow field produced during the interaction of a shock wave with stator blades is investigated in a linear cascade using particle image velocimetry (PIV). The study investigates the interaction that occurs when shock waves traveling with the rotor blades in axial transonic compressors interact with upstream stator blades. This interaction produces unsteady phenomena such as vortices and separation that induce blockage and losses. Flow visualization and PIV data, synchronized with shock-wave-passage locations provide details of the flow field in various areas of the cascade passage. The experiments are conducted in a transonic blow-down wind tunnel with a nominal inlet Mach number of 0.65. A single moving normal shock is generated using a shock tube external to the wind tunnel, and this shock is introduced at the exit of the stator cascade to simulate the bow shock from a downstream rotor. PIV instantaneous measurements are made for three different shock strengths at various regions of interest and are synchronized with various instants of the shock passage. In each case, the passing shock induces a vortex of varying size and strength around the trailing edge of the stator. The flow pattern includes the disruption and recovery of the transonic free stream, shock waves, vortex flow, vortex blockage, suction-side separation, spiraling arms, secondary vortices, and endwall clearance flows.

I. Introduction

THE trend toward higher stage loadings in axial compressors is forcing designers to include embedded rotor stages with leading edge (LE) relative Mach numbers in excess of unity over most of the rotor span. Under these conditions the rotor will have either an oblique bow shock or possibly a detached normal shock upstream of the LE, depending on its design and operating condition. The relatively small stagnation pressure loss due to these shocks is generally acceptable in view of the increased mass flow rate and pressure ratio afforded by transonic rotor operation. At compressor operating points below the design rotational speed or when an elevated back-pressure is experienced, the shock structure detaches and is pushed entirely upstream of the rotor LE. Unlike the weak bow shock present at the design condition, the strong bow shock which occurs under off-design operation extends relatively far upstream from the rotor LE. If the axial spacing between the upstream stator and the embedded transonic rotor is consistent with normal compressor design practice, the rotor bow shocks will impact the stator trailing edge (TE) [1, 2].

The transonic rotor-stator interactions have been the topic of both experimental and analytical research. The general consensus among these researchers is that the losses in transonic compressors increase rapidly as the axial spacing between stages is reduced. Gorrell et al. (2003) [3, 4] conducted an experimental investigation of the effect of blade-row spacing on the performance of a transonic compressor using the Air Force Research Laboratory (AFRL) Stage Matching Investigation (SMI) rig. Mass flow rate, pressure ratio, and efficiency all decreased as the axial spacing between the upstream wake generator (WG) and the transonic rotor was reduced. At close spacing, an

¹ Senior Research Engineer, ISSI, AIAA Associate Fellow.

² Senior Research Engineer, Techsburg, Inc., AIAA Member.

³ Principal Engineer, GE Aircraft.

⁴ Vice-president of Engineering, Techsburg, Inc., AIAA Member.

⁵ Chris Kraft Endowed Professor, ME Dept. VT, AIAA Associate Fellow.

additional loss beyond that associated with mixing was present. Part 2 of this paper [4] presents CFD results for the same WG/transonic rotor system used in the experiment. At far axial spacing between the WG row and the rotor row, the rotor bow shock degenerates into a weaker pressure wave when it reaches the WG surface. At close axial spacing, however, the shock turns normal to the WG surface as it passes the TE and propagates upstream (Fig. 1) [1]. The WG flow is supersonic relative to this moving wave thus, Gorrell et al. (2003) [3, 4] concluded that this wave exhibits the same behavior as a normal shock, causing significant entropy generation and total pressure loss.

Estevadeordal et al. (2002, 2007) [5, 6] documented the flow field within a transonic compressor using Particle Image Velocimetry (PIV). These experimental studies were also conducted using the AFRL SMI rig. Data were gathered for two spanwise locations, two WG counts, two axial spacings between the WG and rotor, and various operating conditions. The WGs in these tests had blunt TE, which led to vortex shedding in the wake. These vortices were found to grow as they convected downstream. For the largest axial spacing tested, the vortices are estimated to be 30% larger than the WG thickness. The vortex-shedding frequency was largely dictated by the rotor-blade-passing frequency. Flow patterns such as the number and location of the vortices were always similar for a given rotor blade-passing frequency. The rotor bow shocks provided a strong periodic pressure fluctuation that forced the synchronization of the vortex shedding to the shock-passing frequency. Gorrell et al. (2006) [7] provided a detailed comparison of PIV data and CFD simulations for the SMI rig.

The current investigation represents a follow up to the study of Langford et al. (2007) [1]. In these experiments the stator flow environment within a close-stage-spacing embedded transonic compressor was simulated by a linear cascade of loaded stator blades. The steady performance of the stator cascade was measured to provide a baseline to which cases involving the moving shock could be compared. Pressure measurements indicated that the stator matched its design intent with regard to loading, turning, and loss under steady flow conditions. A moving shock wave was then introduced into the stator cascade to simulate the detached bow shock from a downstream transonic rotor operating at off-design conditions. The flow patterns due to the interaction of this passing shock and the stator flow field were explored qualitatively using flow visualization and quantitatively using PIV.

II. Experimental Setup

The experiments were conducted at the Transonic Cascade Wind Tunnel at Virginia Tech. This blow-down-type tunnel provides up to 20 sec of usable run time for the inlet Mach number of 0.65 that was used in these tests. A four-stage Ingersoll-Rand Type H reciprocating compressor provides the air supply for the tunnel. Before entering the tunnel, the air is filtered, cooled, dried, and stored in outdoor tanks. The tunnel is run by a computer-controlled main valve and simple feedback electronics, which maintain a specified stagnation pressure downstream of the control valve. A turbulence grid was mounted upstream of the test section, generating a turbulence intensity of about 1.6%, with a length scale of 1.7 cm. The cascade blades have a 0.76-mm endwall clearance from 50% chord to the TE. This clearance allows a small amount of leakage flow from the pressure surface to the suction surface, which aids in preventing corner separation that would otherwise spoil the two-dimensional (2D) nature of the experiment. Table 1 contains the main cascade parameters, and Fig. 2(a) contains a schematic of the cascade test section in the wind tunnel. Further details of the experimental set up and blade characteristics can be found in Langford et al. (2007) [1].

The moving shock was generated by rupturing a Mylar diaphragm within a pressurized shock tube and transferring the resulting shock into the test section. The shock tube consists of two sections of 3-in-nominal-diameter steel pipe separated by the diaphragm. The shock strength, measured as the static pressure ratio across the shock front, is directly proportional to the diaphragm thickness. To initiate the shock, the driver section was rapidly compressed with helium until the diaphragm ruptured. Helium was used as the driver gas because a greater shock static-pressure ratio can be achieved at a lower driver pressure when the ratio of fluid acoustic velocities between the driver and driven sections is increased. The acoustic velocity of helium is roughly three times greater than that of air. After the shock was fully developed within the driven section of the shock tube, it was transmitted through flexible reinforced tubing into the test section. Before being introduced into the cascade, the shock was passed through a shock-shaper apparatus to expand it and produce a purely cylindrical rather than spherical wave, as it passes the stator blades. Additional details on the shock tube can be found in Langford et al. (2007) [1].

Data on steady performance was gathered using various pressure probes to verify that the stator cascade was operating at design-intent loading [1]. The unsteady measurements involving the moving shock were conducted at an incidence angle of zero degrees for three shock strengths with static pressure rises of “1.42,” “1.76” (nominal), and “2.10,” respectively. The static-pressure rise across the shock (strength) was measured at the TE of the center blade in the cascade using wall-mounted Kulite high-bandwidth pressure transducers. The pressure data were sampled at 1 MHz using a 12-bit LeCroy 6810 A/D converter. The Kulite were also used for triggering the laser pulses for the

PIV measurements; the pressure transducer signal from the strong pressure fluctuation of the passing shock was sent to the external trigger of the electronics delay generator (Stanford DG535) that drives the PIV-system components (lasers and cameras). For every blow-down run a shock was generated; and because of the relatively slow repetition rate of the PIV system, only a single, instantaneous, double PIV image could be recorded. The shock location recorded by the PIV system was varied for every run by changing the triggering Kulite. The Kulites were spaced 0.5 in. apart and formed a line parallel to the stagger axis [Fig. 2(a)]. However, since the shock-propagation speed (and strength) decreased as the shock exited the shock-shaper tube, the actual time delay between triggering locations was not constant. The delay/location of each instant image shown in the Results Section is referred to by the corresponding triggering Kulite number, e.g. ‘K5’ indicates that Kulite No. 5 was used for triggering the PIV image-capture system.

The PIV experiment involved seeding the flow with small particles and then illuminating a two-dimensional slice of the particle flow path using two overlapped Nd:YAG (New-Wave Solo PIV 120) laser sheets in rapid succession (2 μ s apart in the present experiments) to calculate the flow velocity. Laser-sheet delivery was accomplished using a special optical probe [Fig. 2 (b)] that was inserted (and secured with a special nylon mount) in a glass rod mounted across the cascade and located sufficiently far downstream to have negligible effect on the flow in the area under study. The glass rod was sealed from leakage using o-rings and secured to the endwalls using compression fittings with nylon ferrules. The probe could be inserted at any span location by traversing it inside the glass rod, and it could be rotated; the distance of the embedded lenses from the prism could be changed to modify the focal distance and the spread of the laser sheet. This allowed illumination of any region of interest in the flow [Fig. 2(c)]. The majority of the data was gathered at mid-span but data was also gathered near the endwalls. Several ports were machined in the cascade windows to facilitate illumination of areas that could be in shade and to avoid seed deposition in front of the laser-sheet output. The beam was split prior to entering the optical probe, and one-half was sent to the top of the tunnel to generate a second laser sheet that illuminated the inlet flow (~ 1 in. view to the LE of the stators) through a window and allowed collection of inlet conditions for each run. The thickness of the laser sheets was ~ 1 mm.

The acrylic windows in which the cascade blades are mounted facilitate the setup of the receiving optics. Two cameras [ES1.0 Kodak CCD with 1k x 1k pixels (pix)] were used to provide inlet and passage views simultaneously with 105-mm Nikon lenses at F#4. Processing the image pair allowed calculation of the instantaneous 2D velocity vector field for the area of interest. The selection and implementation of the proper seeding strategy is of major importance in the successful performance of PIV measurements. The seeding particles must be extremely small and have specific gravity that is close to that of air to permit accurate tracking of the flow by avoiding the impact of viscous and inertia forces that can produce particle lag. The seeding particles must also scatter light efficiently to ensure that exposure of the recording media occurs. For minimizing particle agglomeration and ensuring uniform distribution, careful consideration must be given to the choice of particles and the mechanism for their introduction into the fluid flow. For the present experiments, high-purity submicron-sized ($\sim 0.5 \mu\text{m}$) alumina (Al_2O_3) particles were used; these particles were introduced sufficiently far upstream of the test section to avoid perturbations [Fig. 2(a)]. The seeding-system was based on seeders of the solid-powder cyclone type, and insertion of the particles into the tunnel was accomplished using a rod with a row of holes. Although the specific gravity of the particles is 3.06 and they are non-spherical (plates), numerous studies have shown that they can be used for seeding low-speed transonic and some higher Mach number flows. A more detailed discussion of the PIV system and associated uncertainties can be found in Langford et al. (2007) [1].

III Results

Extensive analysis of the velocity field near the TE that compares vortex strength and blockage for this cascade experiment can be found in Langford et al. (2007) [1] and detailed comparison and analysis with CFD simulations can be found in van de Wall et al. (2006) [2]. The present study focuses on identifying and describing the flow patterns in various regions as a function of the shock, vortex strength and location. For the three shock strengths, flow visualizations and PIV results are shown for the TE; downstream views capture details of the flow pattern of the wake, the vortex, the blockage region, and the separation region; passage views capture details of the shock location and the pressure and suction sides of the blade; finally near-the-endwall views capture some three-dimensional (3D) flow patterns that are typical of the influence of the clearance flow.

The flow-visualization images of Fig. 3 show the vortex location (unseeded core) that formed under the “1.42” strength shock in the TE area of the blade for various shock locations. The undisturbed wake [baseline image of Fig. 3(a)] is shown for comparison purposes, and the exit angle of the wake can be seen for reference. The flow-visualization sample of the wake was obtained by selecting a sample with more seeding in the wake region. The

wake seeding material can be seen emanating from the unseparated pressure side flow at the TE, mixing in the wake, and encountering the suction side (turbulent) boundary layer (with less amount of seeding). After the shock wave has interacted with the TE of the cascade blade, the vortex forms and grows as it travels downstream, as shown in the pictures of Fig. 3(b), 3(c), and 3(d), which display three instants of the vortex evolution corresponding to the Triggering Locations K6, K7 and K8, respectively. The vortices can be readily identified in each image that has a dark core (caused by the lack of seed). Upstream of the vortex and toward the suction side of the blade, an area with less amount of seeding is visible; it changes for each instant, following changes in the vortex size and location. The vortex travels downstream with an inclination which is different from that of the baseline wake because of the flow induced by the passing shock and the vortex-induced flow. The actual flow-field features can be better described using the PIV data. The PIV data for these images of Fig. 3 are shown in Figs. 4 and 5, including a broader area of the suction side. For the velocity plots in Fig. 4, a resolution of 64 pix grid cells was used with 75% overlap, yielding 0.44-mm grid spacing. This resolution was appropriate for purposes of displaying the general flow features. The first one [Fig. 4(a)] corresponds to the baseline flow and shows typical cascade suction and pressure-side flow including the low-speed region defining the wake; there is also evidence of a low-speed region corresponding to the turbulent boundary layer near the surface of the suction side of the blade (although the present resolution is not intended to resolve it), shown by blue contours and also evidence of back flow in the small area just behind the TE, which is typical of wakes behind blunt bodies. After the shock has passed through the TE and the vortex has formed, the flow pattern is considerably changed, as first depicted in Fig. 4(b). As explained by Langford et al. (2007) [1], the vortex flow rotates in opposite direction to the circulation around the stator and its interactions with the free stream yields a distinctive high-speed area in the lower side of the vortex (red contours) and a low-speed area on the upper side (blue contours). These two areas can be seen contacting each other around coordinates (288, 715) pix in Fig. 4(b), and they define a point of maximum gradients and a signature of the vortex core center. The exact location cannot be found from the data because of the lack of seeding in the vortex core and strong gradients in the region that lead to noise and inaccuracies. This also hampers determination of the exact shape of the vortex core [1]. In the frame of reference of the stator TE (which is the camera frame of reference also), the streamlines split to pass around the vortex. The streamlines from the low-speed area above the vortex appear to be deflecting downward and those lower than a splitting point go around and meet the high-speed region of the vortex. In the frame of reference traveling with the vortex, the spiraling streamline pattern results [Fig. 4(c)]. An approximate convective velocity of the region was subtracted for drawing these streamlines [8]. This pattern has been overlaid on the vorticity contours (invariant from the frame of reference) in Fig. 4(d) to show vortex location and compare it with the streamline pattern. A section of high vorticity is observed from the TE to the high-speed region of the vortex that is consistent with the flow visualization line emanating from the pressure side of the TE and is connected to the vortex [Fig. 3(b)]; this is an indication of the location of the vortex-sheet discontinuity that is produced in the interaction of the shock with the TE. As noted by Langford et al. (2007), traces of the shock can still be discerned in the upper right corner of this image as a distinctive velocity-magnitude discontinuity, and its shape is consistent with the shadowgraphs shown in Ref. [1]. The views over the passage will offer further details of the shape of shock as it propagates upstream. The evolution of the flow, showing the vortex growth, is depicted in Fig. 5 at four instants using a higher resolution grid (32 pix grid cells with 75% overlap, yielding 0.22-mm grid spacing). The core region and other areas without seeding or noise are blanked out. The streamlines, contours, and vectors show the motions around the core in greater detail. The initial vortex position nearest the TE (a and b) still exhibits the vortex-sheet characteristics from the TE to the vortex. In this stage two separate low-speed regions, one in the suction side of the blade and another downstream of the vortex, can be seen (blue contours). Subsequent to this stage, when the vortex initially grows and travels downstream (c and d), the flow pattern changes and includes a larger low-speed region (blue contours) that extends from the suction side to the far-downstream area of the vortex low-speed region. A recirculation region is obvious at this stage within the suction side of the TE area. The last location (e and f) shows a larger vortex, with the low-speed area having spread in the pitch direction while diminishing in magnitude; the area upstream of the vortex begins to recover from the shock passage, as signaled by the lack of strong low-speed regions (blue contours) upstream of the vortex and with streamlines oriented toward the free-stream pattern that existed before the shock interaction.

The characteristics of the velocity field when the shock strength is increased to the “1.76” (nominal) setting are displayed first in the flow visualizations of Fig. 6, for the same view of the TE as in the previous figures. With a shock of this strength, the vortex formation and the deviation of the wake region are even more apparent in the visualizations. The wake changes its overall inclination [Fig. 6(a, b)], as compared to the baseline [Fig. 3(a)] (also noted in the shadowgraph analyses in Ref. [1]); there is evidence of a strong bending of the wake at the TE from the pressure side [especially evident in Fig. 6(b)] induced by the passing shock. This sharply bent line that joins the TE and the wake is marked by the seeding that emanates from the pressure side and is the first indication of vortex roll-up.

After this, the vortex forms and appears to be clearly attached to the TE tip in Fig. 6(c) before moving downstream [Figs. 6(d-f)]. In its travel, the vortex grows in size and exhibits new features such as secondary motions and spiraling arms [9] in the periphery around the core. The quantitative PIV data (Fig. 7) offer further insight into the events taking place (using only the coarser grid resolution for general features). First, the shock passage can be followed in Fig. 7(a-d) as a strong velocity discontinuity. In the first location [Fig. 7(a)], a sharp discontinuity or change in flow direction has still not occurred, and only a change in velocity magnitude which is different from that of the baseline [Fig. 4(a)] is noticeable, indicating that the shock (the nature of which was shown also in shadowgraphs in Ref. [1]) is just entering the region. In the second location [Fig. 7(b)], it is clear that the shock has just passed the TE and that the flow pattern has been affected consequently with changes in the flow direction and generation of low-speed regions and a vortex region. The sequence of events is similar to that for the weaker shock but with stronger features and more distinct details. In this case, details of the formation and evolution of the low-speed region are clearer. As the flow evolves, the large low-speed band dominates a large region of the flow after the vortex has formed at the TE [Fig. 7(c)], with the wake deviating over the vortex. In the next instant [Fig. 7(d)] after the vortex has detached from the TE, the low-speed band begins to give way while the vortex flow gains strength and dominates the flow; the farther-downstream wake trace is rolled into the vortex downstream-spiraling arm [shown in blue contours for $x < 200$ pix and also very obvious in the flow visualization shown in Fig. 6(d)]. The suction side exhibits recirculations throughout the process [e.g. Fig. 7(e)], and its thickness decreases as the free stream re-enters the area [Fig. 7(f)]. Details with a higher resolution grid for this case were presented in Ref. [1], with analysis of the vortex shape, size, strength, and blockage. Details of streamlines overlaid on the velocity contours and vectors overlaid on the vorticity contours are shown in Fig. 8 with a higher resolution processing grid (32 pix cells ~ 0.89 mm \sim with 75% overlap, yielding a resolution grid of 0.22 mm) for the case of the nominal shock triggered on Kulite 8. The velocity contours show the typical high- and low-speed areas that accompany the vortex. At this stage these two regions appear to be connected to the upstream TE region in two different ways. The low-speed region no longer extends from the wake to the suction side separation region [which exhibits strong recirculations, e.g. at $\sim (450, 600)$ pix] but only exists as patches of low-speed areas upstream of the vortex (sparse light-blue contours), signaling that the free stream is entering the region as it recovers from the vortex event. The high-speed region, on the other hand, continues to be connected to the TE by the remains of the vortex sheet, which continues to roll up into smaller structures, as can be seen in the small vorticity traces all the way to the TE. The case with a stronger shock will next provide more details of the nature of this tail of the vortex as it leaves the TE, and an additional view will show the farther-downstream evolution of the vortex flow. Good comparisons of velocity field between unsteady CFD and the PIV experiment showing these details of the vortex roll-up process as the shock wave crosses the TE and of its growth and evolution can be found in Ref. [2].

As the shock strength is increased to the “2.10” setting, the events accompanying the vortex have sharper features. This can be readily seen in the flow-visualization pictures in Fig. 9. At the instant triggered on K5 [Fig. 9(a)], the vortex has formed, is attached to the TE, and is apparently blocking the passage from the TE to one vortex diameter. As it becomes detached, it begins to grow in size [Fig. 9(b-e)], and its periphery exhibits spiraling arms and secondary vortices. These observations indicate a laminar core (with a shape such as those analyzed in Refs. [1, 2]) with a turbulent periphery. The suction side of the blade also exhibits a growing separation region with backflow and recirculations (these can be inferred from the direction of individual particles in the PIV image). PIV quantifies these features, as shown in Fig. 10 with the use of the coarser grid. The initial vortex formation is shown in Fig. 10(a), which provides evidence that the vortex enters the area upstream of the TE as it rolls up sharply (dark-blue contours at TE, with streamlines deflecting downward); the shock has just passed, and it can be seen in the upper right corner. The suction side exhibits strong recirculation as a consequence of the blockage. A remarkable difference with respect to weaker shocks is that the flow in the pressure side and in the high-speed side of the vortex flow is turning much more sharply. This is shown, for example, by the streamline patterns in the figure, which exhibit noticeable bending, which is a consequence of the stronger and larger area of influence of the vortex in this case. The features are much more accentuated than in previous cases and allow sketching of the main flow patterns. A juncture ‘saddle’ point in the low-speed region (blue contours) where the streamlines are deflected downward can be seen clearly in each instant [e.g., centered at $(200, 400)$ pix in Fig. 10(d)]. It defines a center around which the pattern of the flow can be sketched: above it, the free-stream flow moves downstream with a slight bend; below it, the free-stream flow is blocked by the vortex. There are two other main areas—one below the vortex with high-speed region and another with the free-stream bending. Finally, there is the separation region on the suction surface with recirculations and backflows. Smaller details exist, such as the spiraling arms and secondary vortices. The evolution of these phenomena will be analyzed in greater detail in the next farther downstream view, obtained by triggering the PIV capture at later instants (farther Kulite locations).

In the new view that captures these farther-downstream events, following the passage of the stronger shock, the camera was tilted at an angle approximately perpendicular to the pitch. For reference, Fig. 11(a) shows a flow-visualization picture for the baseline with a wake. Then Figs. 11(b-e) display the instantaneous pictures obtained at four triggering locations beyond the initial vortex formation that capture the downstream evolution of the flow. It is clear that the main vortex has persisted downstream and moved pitchwise, dragging a series of smaller secondary vortices in its upstream spiraling arm. As noted in Langford et al. (2007) [1], this phenomenon bears a striking resemblance to the flow fields observed in impulsive or accelerating separation around sharp bodies, starting vortex separation occurring through acceleration and deceleration of a body, and in flows induced when shock waves encounter a corner asymmetrically [10-13]. The phenomenon can be clearly observed in the present investigation as first shown in the flow visualizations. The row of vortices can be clearly identified through their dark cores (resulting from lack of seeding). In the instants shown in Figs. 11(b and d), a new small secondary vortex is being generated as the vortex sheet rolls up from the pressure side to the suction side; and in the instants shown in Figs. 11(c and e), a newly rolled up secondary vortex has formed. The PIV will again serve to provide quantitative insight into the phenomenon. Figure 12 shows the coarser grid results for a baseline wake [Fig. 12(a)] for reference and for the four vortex-flow instants shown in Fig. 11. As in the flow visualizations, the four velocity plots corresponding to the shock cases are similar due to the fact that they were all triggered at a late stage of the shock passage through the TE. Again, it is obvious that several flow regions can be distinguished--the high- and low-speed areas of the vortex region, the blockage area defined by the vortex area, and the free stream (with tendency to recovery upstream of the vortex at this stage). The new details in this view involve the existence of the vortex sheet defined by the discontinuity in velocity between the flows from the suction and the pressure sides. This is defined by a line (separating green and blue contours) that can be followed from the TE to the vortex area, which has several traces of high- and low-speed spots defining the secondary vortices [e.g., at $\sim (650, 650)$ pix in Fig. 12(b), $\sim (600, 700)$ pix in Fig. 12(d and e)]. The blue area near the TE is indicative of the separation region and is disconnecting from the vortex low-speed area as the vortex travels downstream. The vorticity plots for the last two instants shown in Fig. 13 (baseline wake showing two vorticity signs is added for reference) using the finer grid further clearly reveal the existence of the secondary vortices. They have the same sign of vorticity (as in shear layers), confirming that the phenomenon is similar to that of impulsively starting vortex from sharp bodies [10-13], and their locations can be precisely tracked and traced back to the points connecting a high-speed with a low-speed velocity areas (Fig. 12) and also to the unseeded cores of the flow visualizations (Fig. 11). Even though these later stages of vortex evolution are of great fluid mechanics interest, they cannot be taken as representing realistically the flow in a transonic compressor because, for example, the effects of the subsequent passing blade, shock, and expansion wave are missing in the cascade experiment [1].

Finally, the passage and the near-wall views offered complementary interest. The passage views revealed the changes that the shock wave imparts inside the passage and its location and shape; it also shows a view with more than one blade simultaneously. The views near the endwall revealed the clearance flow pattern. Figure 14(a-c) displays flow visualizations for the normal shock in the passage views for three different instants. The most important feature in these figures is that the vortex formation is different at each of the TEs shown; this is because of the obvious delay of the shock wave in reaching each TE. Otherwise, the vortex in the lower blade TE is similar to previous visualizations for that instant. An instant for the stronger shock has been added [Fig. 14(d)] to aid realization that the large vortical region appears in all TEs and provides strong blockage in all passages. Another feature observed in all of these visualizations is the appearance of the spiraling arms in the periphery of the vortical region discussed in the previous sections. These arms are the connecting "braids" [9] between several vortices in vortex-sheet roll-up phenomena (such as those occurring in wakes and shear layers) and the onset of streamwise vorticity [14]--a 3D phenomenon beyond the scope of this investigation. Blurry areas observed in the pictures are caused by the seed deposition in the glass rod that blocked the laser-sheet light. The PIV data for the passage is shown in Fig. 15, which includes the baseline at two contour levels for reference (a, b). For the instant depicted in Fig. 15(c), which corresponds to the initial vortex formation at the TE, the shock can be discerned by a disruption of the velocity field in the lower left area of the figure. The flow direction has begun to be influenced by the shock, as shown by the turning of the streamlines in that area. In the next two instants [Fig. 15(d, f)], the shock has evolved to become normal to the blade surface, consistent with observations by Langford et al. (2007) [1] and Gorrell et al. (2003) [3]. Details of the pressure side at the TE area could be captured in these views, and a sample is displayed in Fig. 15(f) (obtained at higher resolution of 16 pix), showing the flow attachment and velocity magnitude and direction.

The near-endwall (0.25 in. from endwall) flow visualizations provide evidence of the strong turbulence and unsteadiness in the clearance (leakage) flow region; however, the vortex formation is similar to that of the mid-span, indicating a reasonable 2D spanwise vortex extending to the endwalls. In Fig. 16(a) the lack of seeding area shows some surface flow-visualization traces at the wall, indicative of the interaction of the clearance (leakage) flow and

the blockage by the vortex region. This is quantified in the samples of Fig. 17, which show the complex motions in the area. Three-dimensionality is evident from the various sink and source patterns shown in the higher resolution velocity field shown in Fig. 17 (b).

IV. Summary

The unsteady flow field produced during the interaction of shock waves with stator blades was investigated in a linear cascade using PIV. The study investigates the phenomena that occur when shock waves traveling with the rotor blades in axial transonic compressors interact with upstream stator blades. This interaction produces unsteady phenomena such as vortex and separation that induce blockage and losses. The present study focused on identifying and describing the flow patterns in various regions of the stator blade as a function of the shock and vortex strength and location. Flow-visualization and PIV data synchronized with shock-wave passage locations provided details of the flow field in various areas of the cascade passage. For three shock strengths, results were shown for the TE; downstream views captured details of the flow pattern of the wake, the vortex, the blockage region, and the separation region; passage views captured details of the shock location and the pressure and suction sides of the blade; finally near-the-endwall views captured some three-dimensional (3D) flow patterns that are typical of the influence of the clearance flow. In each case studied, the passing shock induced a vortex of varying size and strength around the TE of the stator. The flow pattern includes the disruption and recovery of the transonic free stream, shock waves, vortex flow, vortex blockage, suction-side separation, spiraling arms, secondary vortices, and endwall leakage flows.

Acknowledgments

The authors would like to thank GE Aircraft Engines for providing funding for this project and allowing the work to be published. Dr. Steve Gorrell of AFRL is acknowledged for many valuable discussions, and Ms. Marian Whitaker of ISSI is acknowledged for editorial assistance.

References

- ¹Langford, M. D., Guillot, S. A., Ng, W. F., Breeze-Stringfellow, A., Solomon, W., and Estevadeordal, J., "Experimental Investigation of the Effects of a Moving Shock Wave on Compressor Stator Flow," *ASME Journal of Turbomachinery*, Vol. 129, Issue 1, January 2007, p. 127.
- ²van de Wall, A., Breeze-Stringfellow, A., Dailey, L., "Computational Investigation of Unsteady Flow Mechanisms in Compressors with Embedded Supersonic Rotors," *Proceedings of GT2006 ASME Turbo Expo: Power for Land, Sea and Air*, May 8-11, 2006, Barcelona, Spain, GT2006-90633.
- ³Gorrell, S. E., Okiishi, T. H., and Copenhaver, W. W., "Stator-Rotor Interactions in a Transonic Compressor, Part 1: Effect of Blade-Row Spacing on Performance," *ASME Journal of Turbomachinery*, Vol. 125, 2003, pp. 328-335.
- ⁴Gorrell, S. E., Okiishi, T. H., and Copenhaver, W. W., 2003, "Stator-Rotor Interactions in a Transonic Compressor: Part 2 - Description of a Loss Producing Mechanism," *ASME Journal of Turbomachinery*, Vol. 125, 2003, pp. 336-345.
- ⁵Estevadeordal, J., Gogineni, S., Goss, L., Copenhaver, W., and Gorrell, S., "Study of Wake-Blade Interactions in a Transonic Compressor Using Flow Visualization and DPIV," *ASME Journal of Fluids Engineering*, Vol. 124, 2002, pp. 166-175.
- ⁶Estevadeordal, J., Gorrell, S., and Copenhaver, W., "PIV Study of Wake-Rotor Phenomena in a Transonic Compressor under Various Operating Conditions," *AIAA Journal of Propulsion and Power*, Vol. 23, No. 1, January-February 2007, pp. 235-242.
- ⁷Gorrell, S. E., Car, D., Puterbaugh, S. L., Estevadeordal, J., and Okiishi, T., "An Investigation of Wake-Shock Interactions in a Transonic Compressor with DPIV and Time-Accurate CFD," *ASME Journal of Turbomachinery*, Vol. 128, Issue 4, October 2006, p. 616.
- ⁸Adrian, R. J., Christensen, K. T., and Liu, Z.-C., "Analysis and Interpretation of Instantaneous Turbulent Velocity Fields," *Experiments in Fluids*, Vol. 29, 2000, pp. 275-290.
- ⁹Estevadeordal, J., and Kleis, S. J., "High-Resolution Measurements of Two-Dimensional Instabilities and Turbulence Transition in Plane Mixing Layers," *Experiments in Fluids*, Vol. 27, No. 4, 1999, pp. 378-390.
- ¹⁰Lugt, H. J., *Vortex Flow in Nature and Technology*, John Wiley and Sons, 1983.
- ¹¹Pullin, D.I., Perry, A.E., "Some Flow Visualization Experiments on the Starting Vortex," *Journal of Fluid Mechanics*, Vol. 97, Part 2, 1980, pp. 239-255.
- ¹²Auerbach, D., "Experiments on the Trajectory and Circulation of the Starting Vortex," *Journal of Fluid Mechanics*, Vol. 183, 1987, pp. 185-198.
- ¹³Lian, Q. X., Huang, Z., "Starting Flow and Structures of the Starting Vortex Behind Bluff Bodies with Sharp Edges," *Experiments in Fluids*, Vol. 8, 1989, pp. 95-103.
- ¹⁴Estevadeordal, J., and Kleis, S. J., "Influence of Vortex-Pairing Location on 3D Evolution of Plane-Mixing Layers," *Journal of Fluid Mechanics*, Vol. 462, 2002, pp. 43-77.

Table 1 Cascade parameters

Blade Chord	7.62 cm
Blade Span	15.24 cm
Blade Pitch	5.04 cm
Blade turning angle	35°
Solidity	1.512
Stagger angle	23.5°
Inlet flow angle	45°
Inlet Mach number	0.65
Blade count	7
Blade Trailing Edge Thickness	0.89 mm
Stator Reynolds number	1.05×10^6

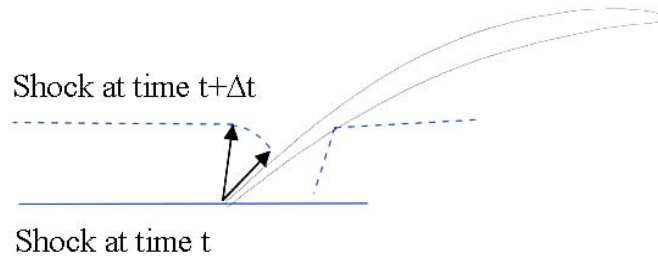


Figure 1. Schematic of the shock-turning phenomenon at the stator TE at two time (t) instants separated by a time delay (Δt).

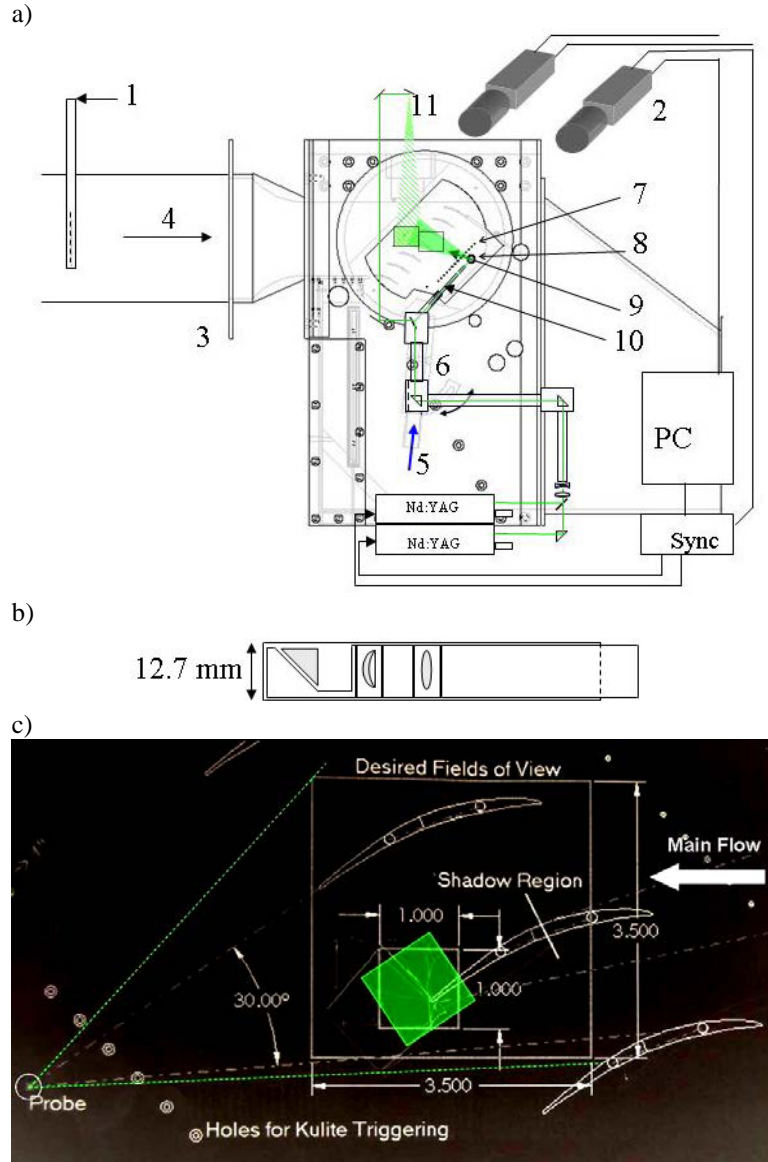


Figure 2. a) Drawing of the cascade test section in the Virginia Tech Transonic Cascade Wind Tunnel and PIV setup view schematics: (1) seed, (2) PIV camera, (3) turbulence grid, (4) main flow, (5) shock-tube exit, (6) shock shaper and angular adjustment, (7) transducer locations for shadowgraphy and PIV trigger, (8) optical probe glass port, (9) blade laser sheet and camera views, (10) optical probe, (11) inlet laser sheet; b) Optical probe schematic with prism, spherical and cylindrical lenses in separate tubing; c) PIV view schematics and orientation (with inlet main flow from right to left) with sample field-of-view (green).

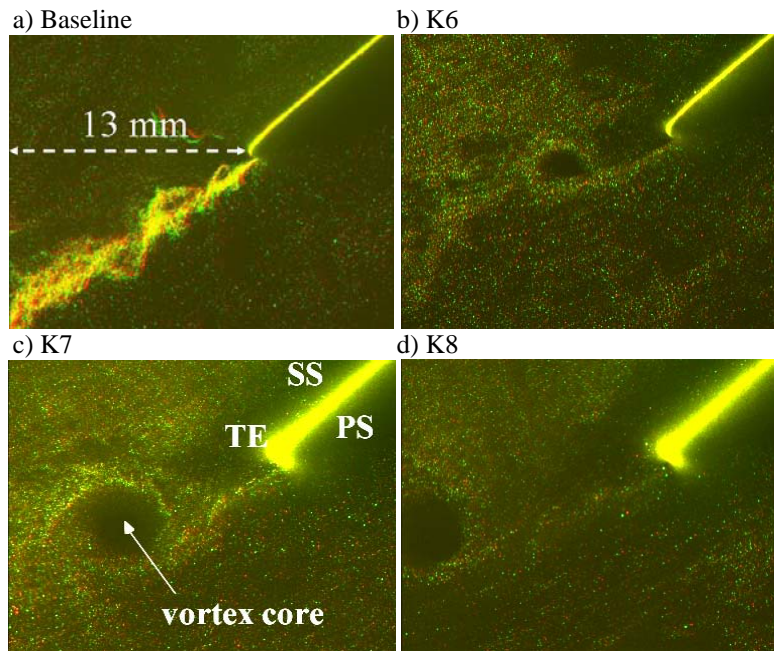


Figure 3. Flow visualization images of the wake and the trailing vortex for various locations of the “1.42” shock-strength passage: baseline (a), K6 (b), K7 (c), K8 (d). SS: Suction Side, PS: Pressure Side, TE: Trailing Edge.

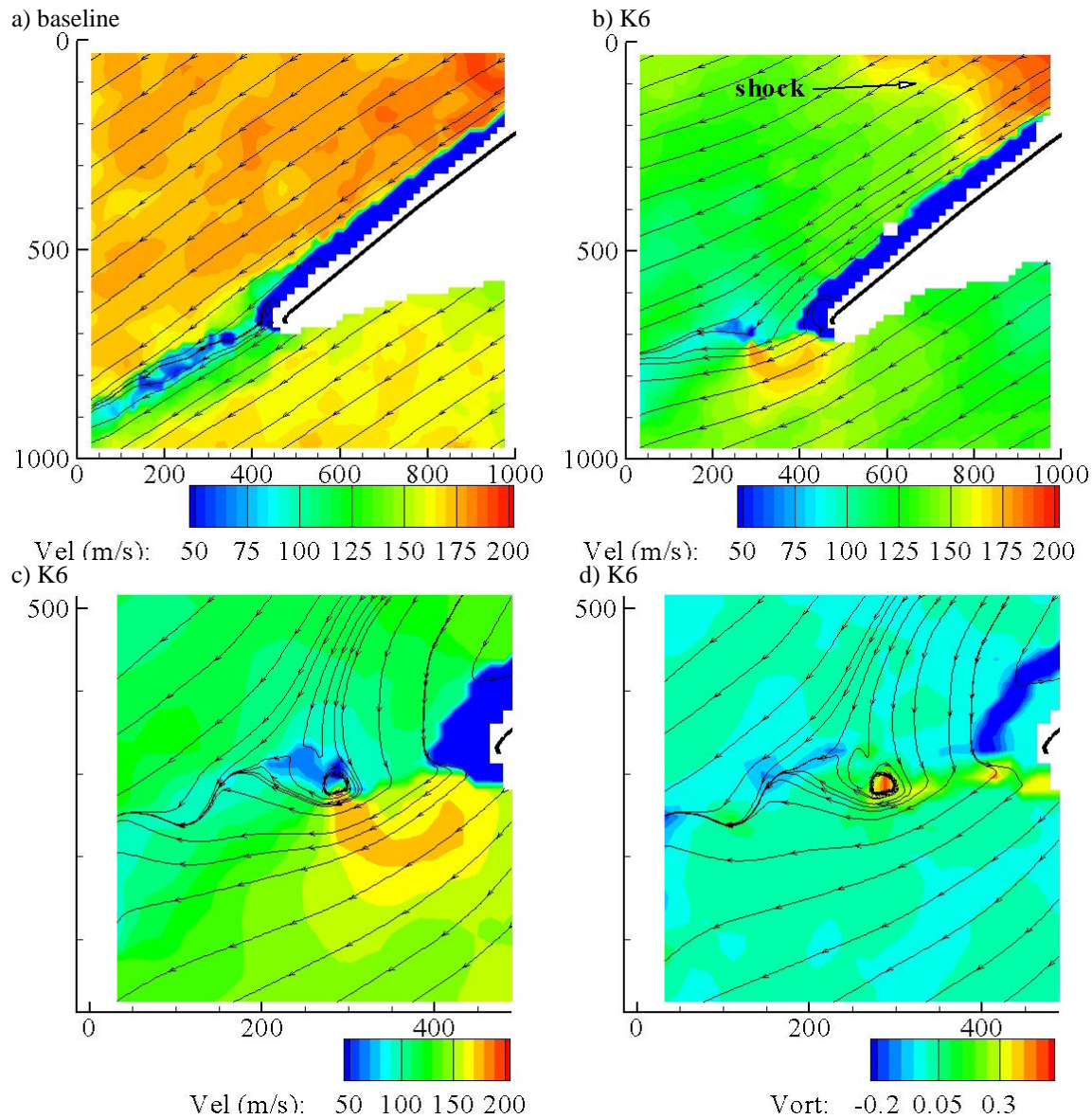


Figure 4. PIV of the wake and the trailing vortex for baseline and triggering location K6 of the “1.42” shock-strength passage : a) baseline, b-d) K6; c) and d) are details of velocity and vorticity contours at the TE, respectively, with streamlines with convective velocity subtracted; PIV cell sizes are 1.8 mm with 75% overlap yielding a resolution grid of 0.44 mm; axes units are pix (35.64 pix/mm).

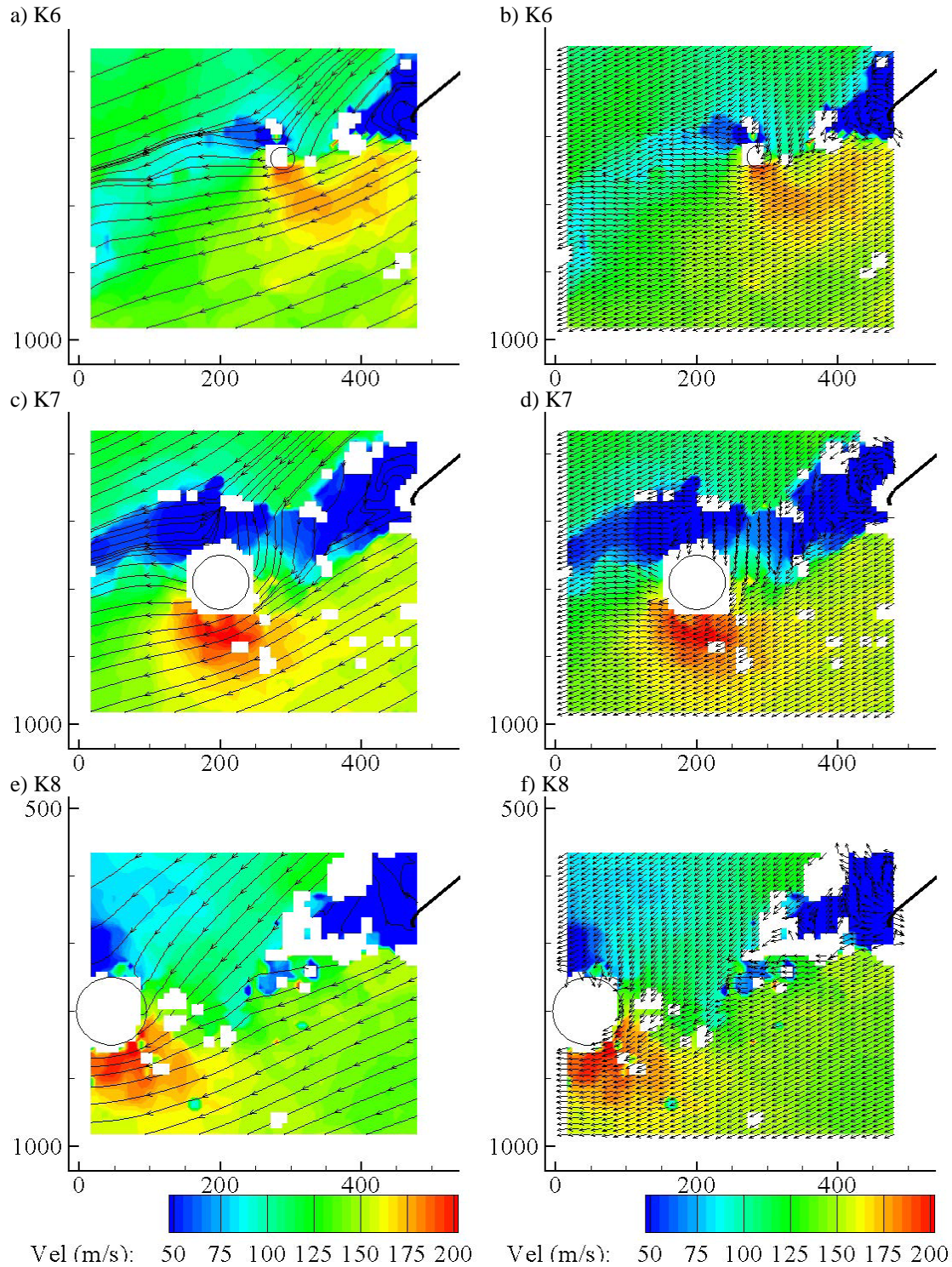


Figure 5. PIV details of the wake and the trailing vortex for various locations of the “1.42” shock-strength passage: a) and b) K6, c) and d) K7, e) and f) K8. Vortex core and other areas without data or noise are blanked out. PIV cell sizes are 0.9 mm with 75% overlap yielding a resolution grid of 0.22 mm; axes units are pix (35.64 pix/mm). Vectors are only shown for every other grid point for clarity.

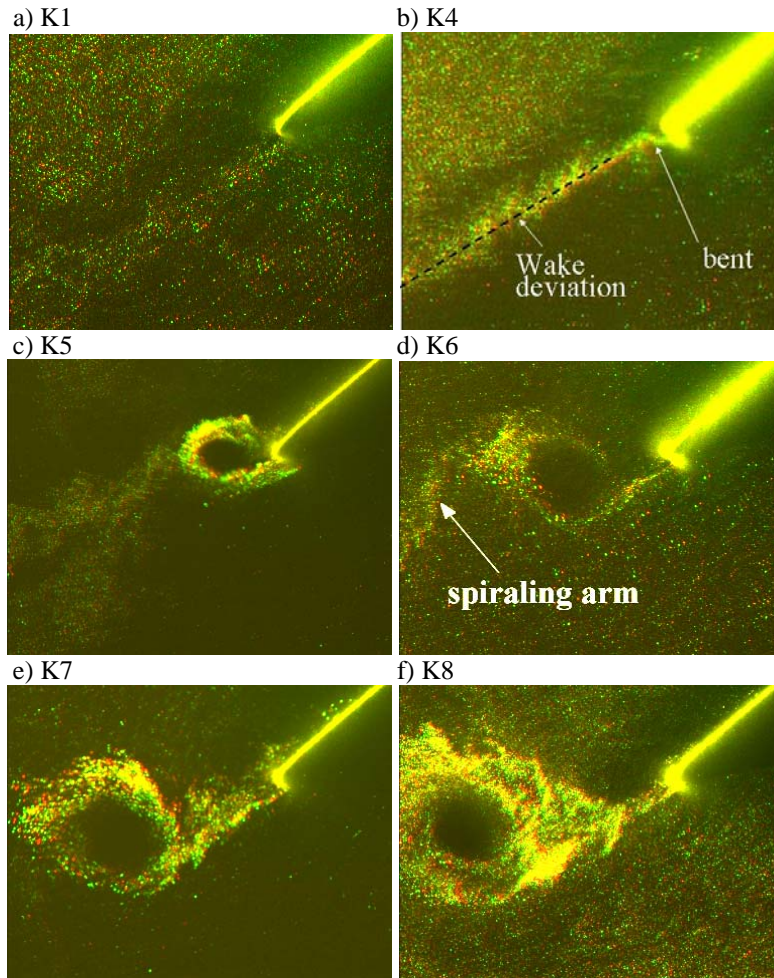


Figure 6. Flow visualization images of the trailing vortex for various phases of the “1.76” shock-strength passage: a) K1, b) K4, c) K5, d) K6, e) K7, f) K8.

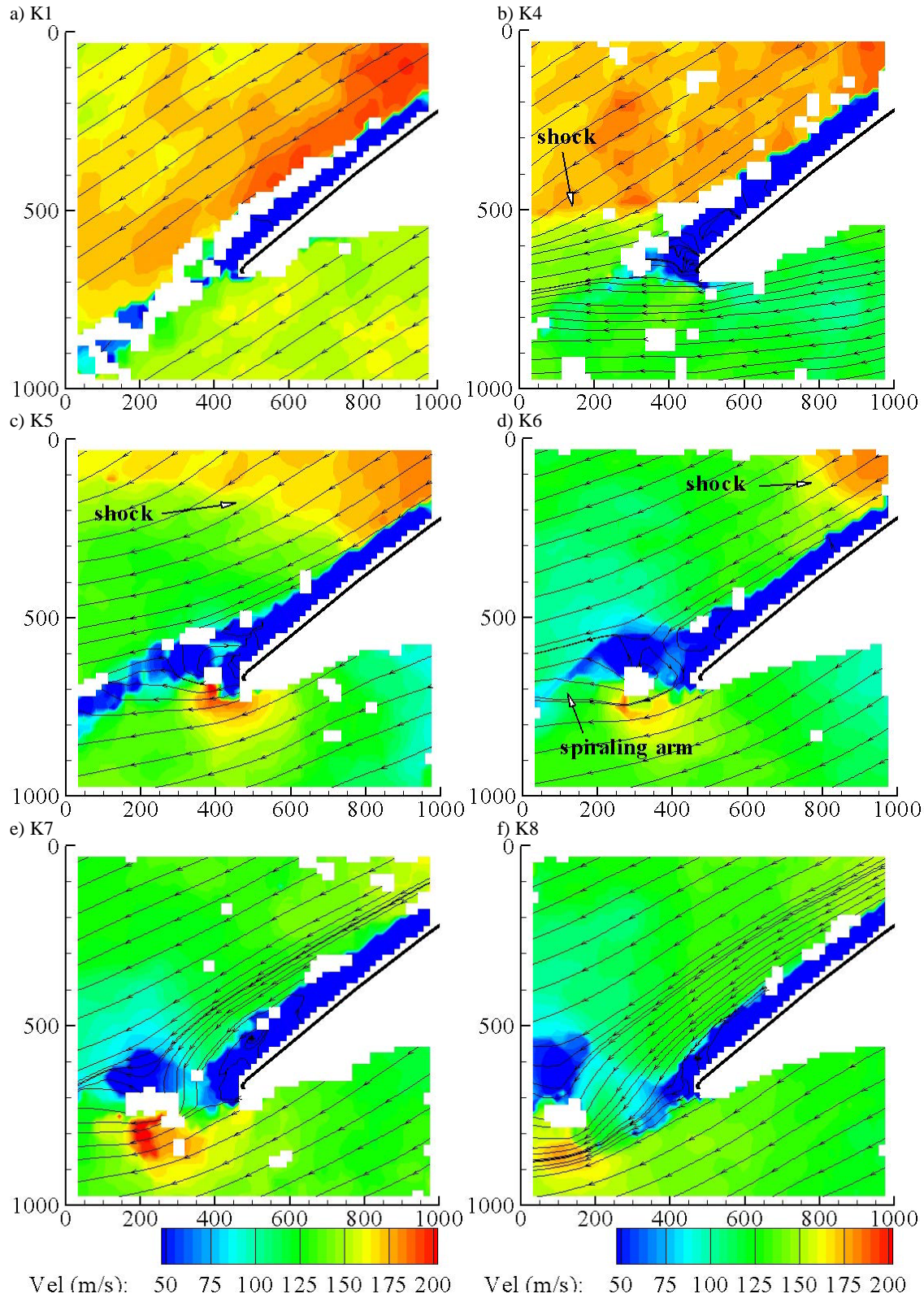


Figure 7. PIV of the trailing vortex for various phases of the "1.76" shock-strength passage: a) K1, b) K4, c) K5, d) K6, e) K7, f) K8); PIV cell sizes are 1.8 mm with 75% overlap yielding a resolution grid of 0.44 mm; axes units are pix (35.64 pix/mm).

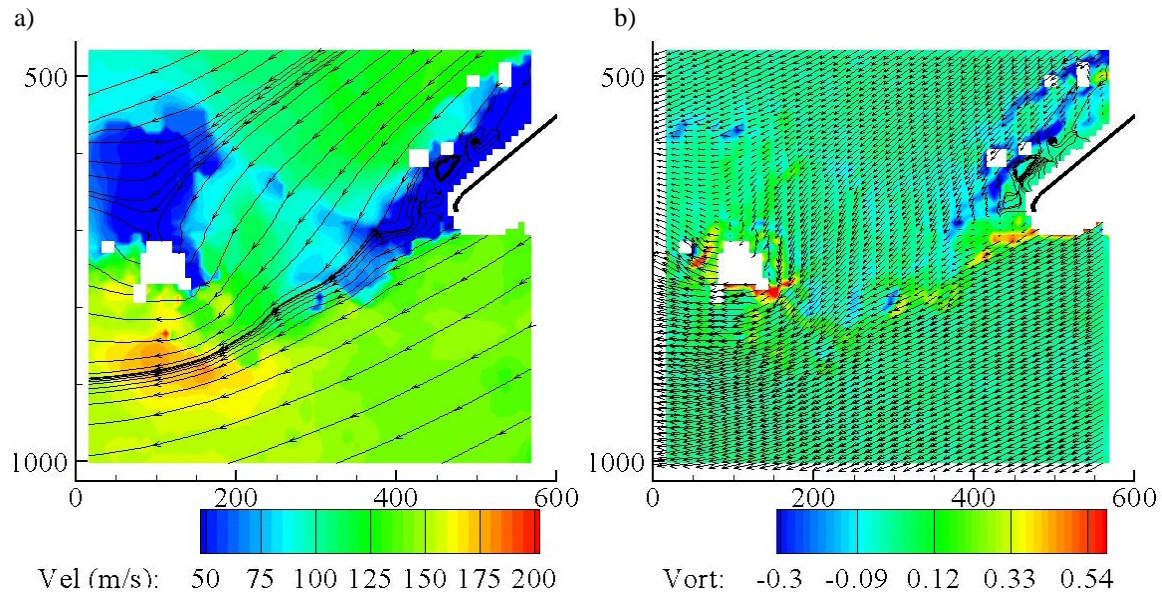


Figure 8. Details of streamlines overlaid on velocity contours (a) and vector field overlaid on vorticity contours (b) from the “1.76” shock-strength passage case (K8); PIV cell sizes are 0.9 mm with 75% overlap yielding a resolution grid of 0.22 mm; axes units are pix (35.64 pix/mm). Vectors are only shown for every other grid point for clarity.

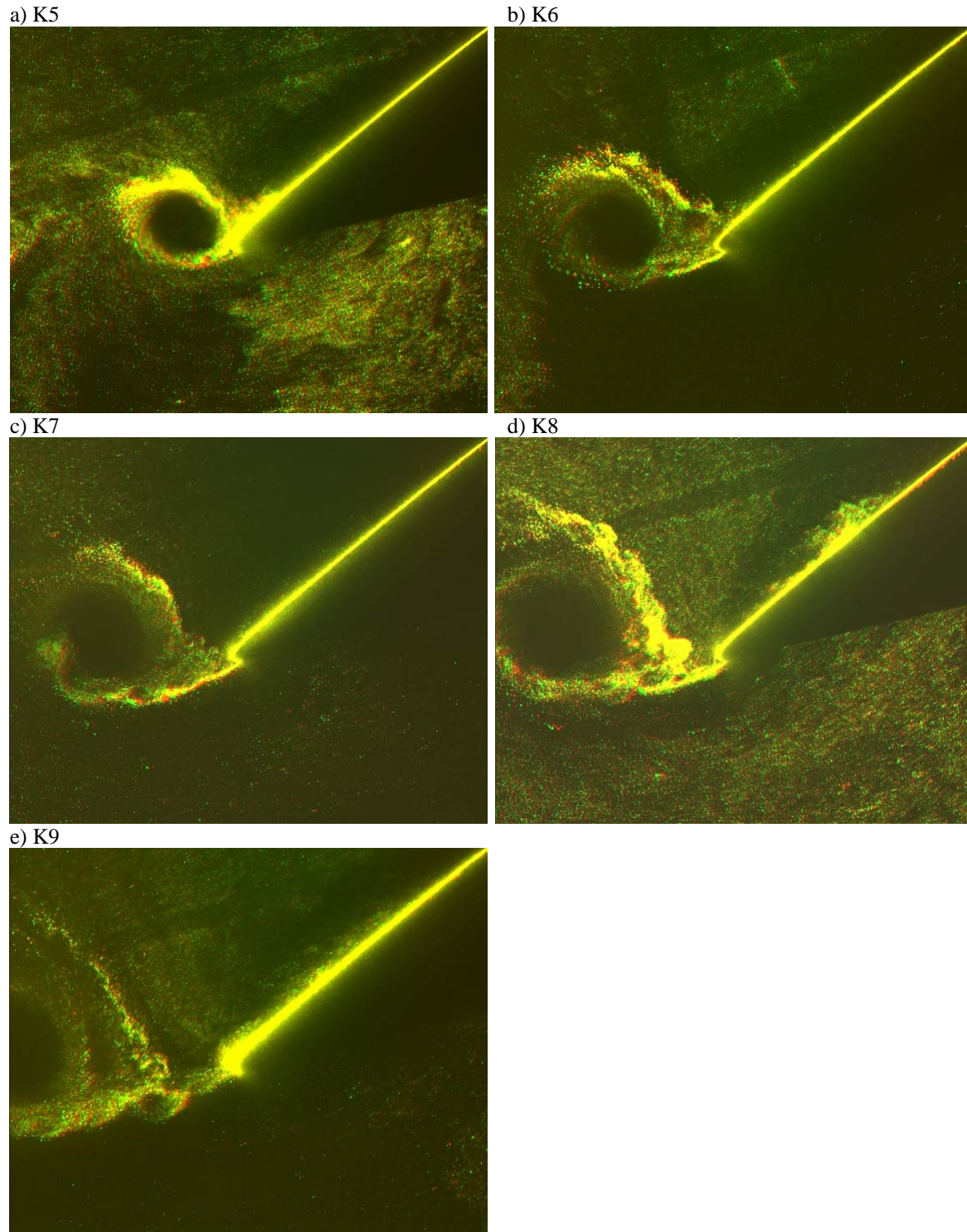


Figure 9. Flow visualization images of the trailing vortex for various phases of the “2.10” shock-strength passage: a) K5, b) K6, c) K7, d) K8, e) K9.

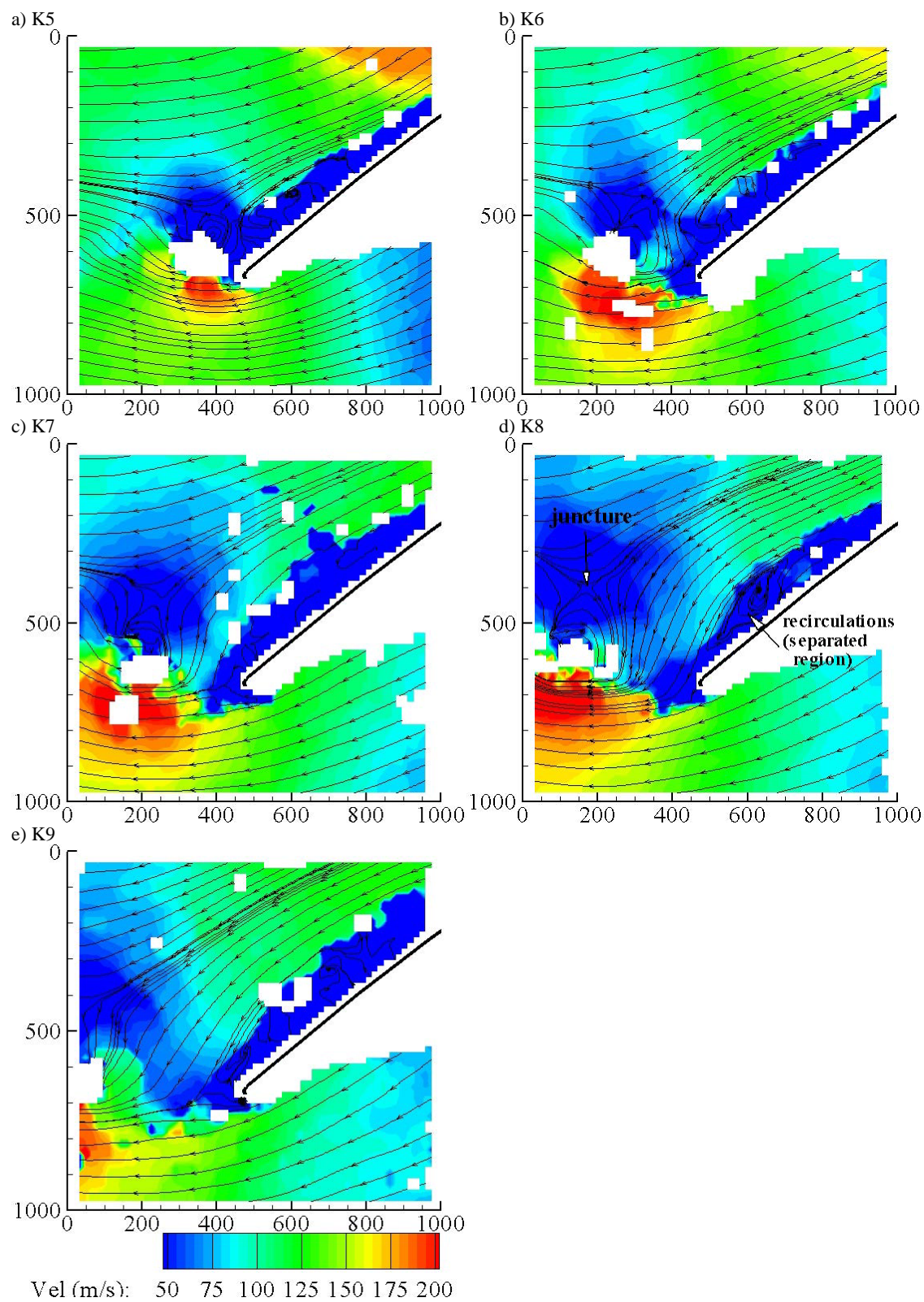
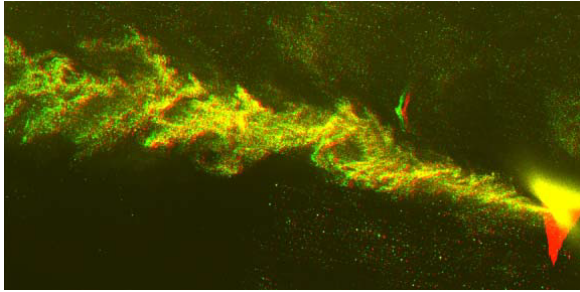
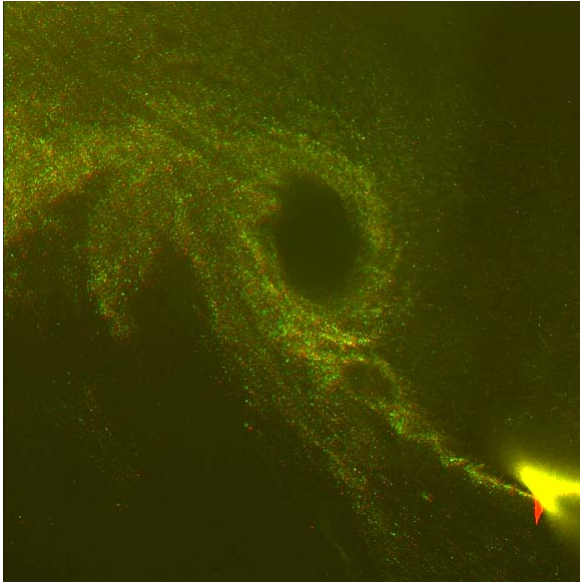


Figure 10. PIV of the trailing vortex for various phases of the “2.10” shock-strength passage: a) K5, b) K6, c) K7, d) K8, e) K9; PIV cell sizes are 1.8 mm with 75% overlap yielding a resolution grid of 0.44 mm; axes units are pix (35.64 pix/mm).

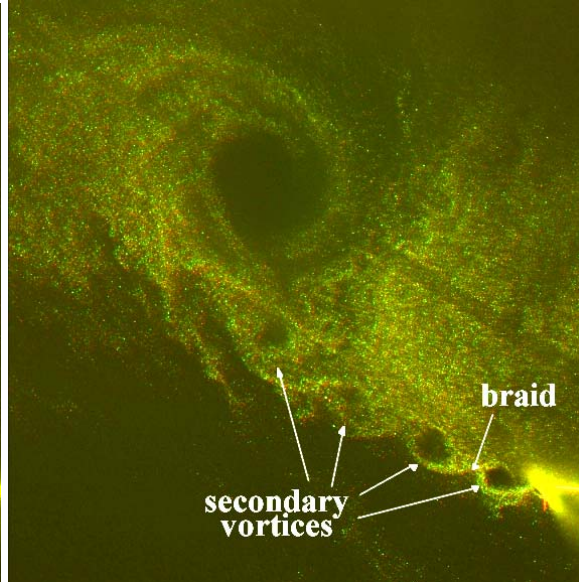
a) Baseline



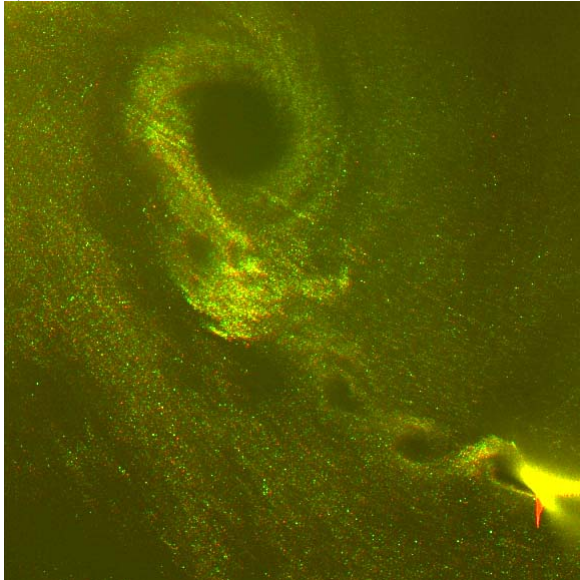
b) K11



c) K13



d) K14



e) K15

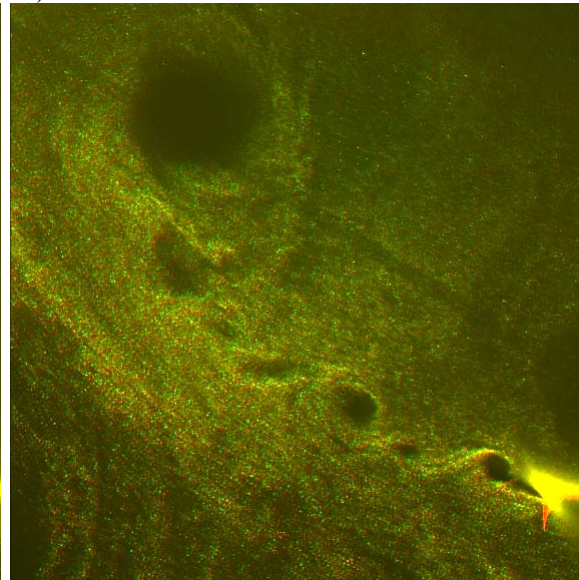


Figure 11. Flow visualization images of the trailing vortex for various phases of the “2.10” shock-strength passage: a) baseline, b) K11, c) K13, d) K14, e) K15.

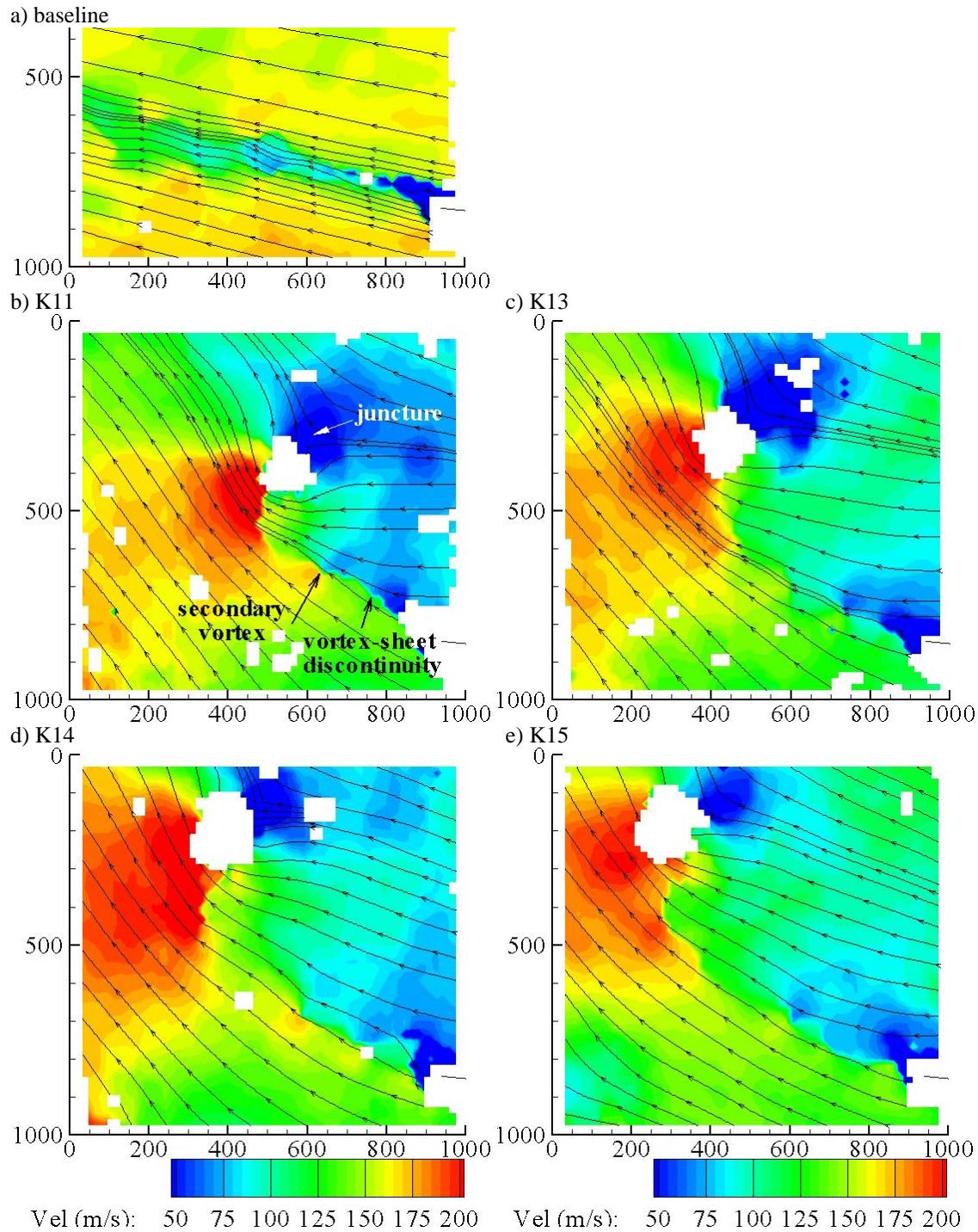


Figure 12. PIV of the trailing vortex for various phases of the “2.10” shock-strength passage in the downstream view: a) baseline, b) K11, c) K13, d) K14, e) K15. PIV cell sizes are 2.28 mm with 75% overlap yielding a resolution grid of 0.57 mm; axes units are pix (28.1 pix/mm).

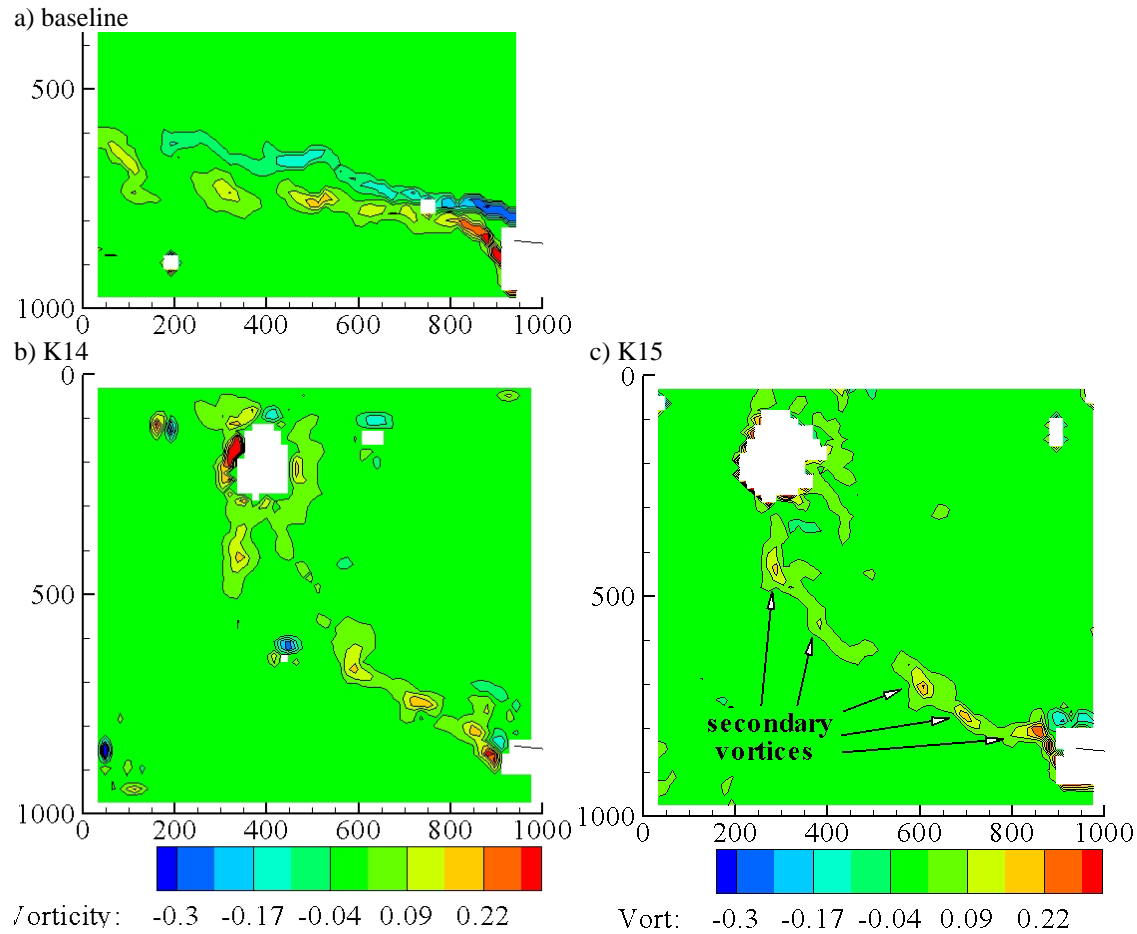


Figure 13. Vorticity plots of the trailing vortex for various phases of the “2.10” shock-strength passage in the downstream view: a) baseline, b) K14, c) K15. PIV cell sizes are 2.28 mm with 75% overlap yielding a resolution grid of 0.57 mm; axes units are pix (28.1 pix/mm).

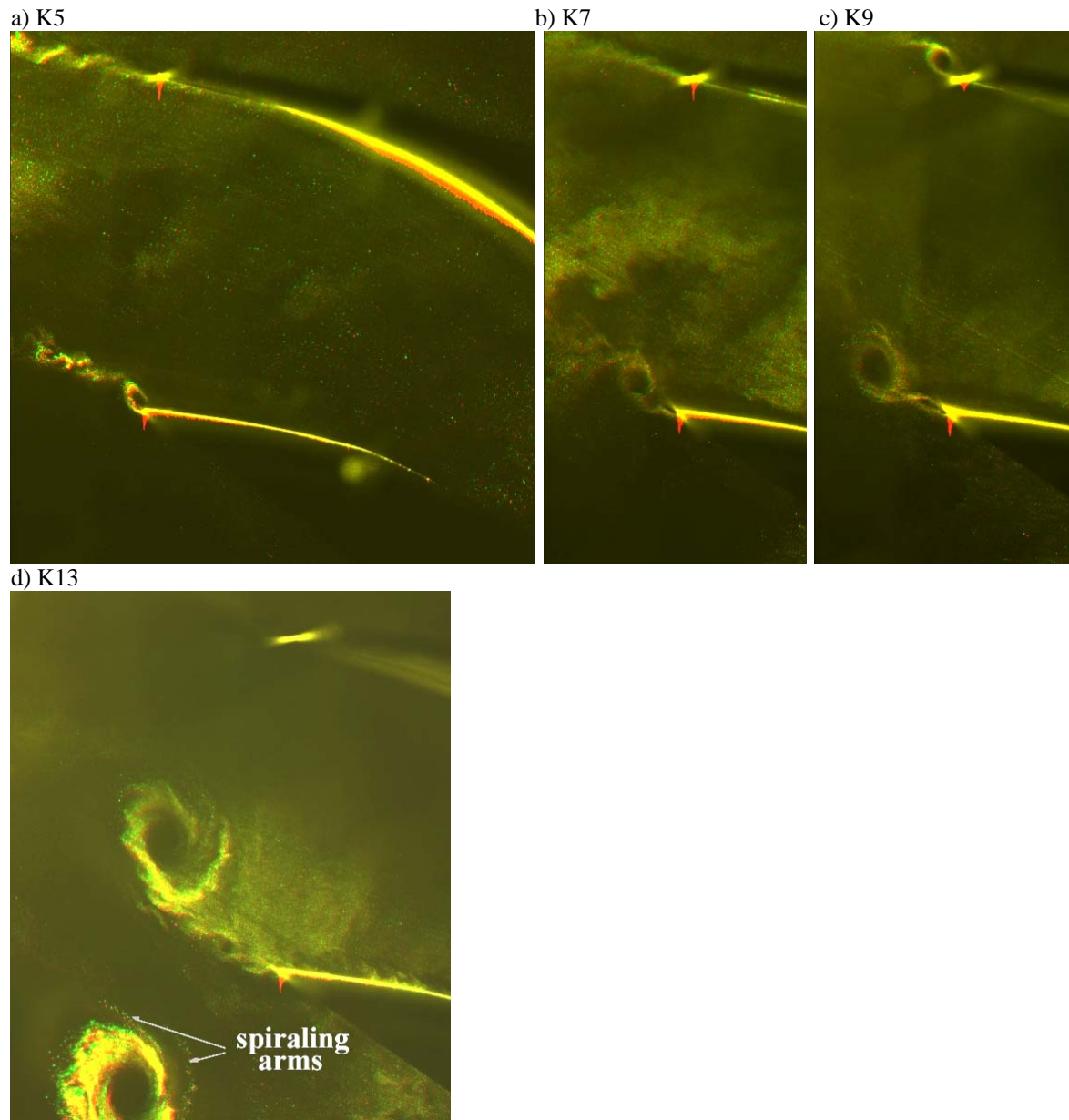


Figure 14. Flow visualization images of the trailing vortex for various phases of the “1.76” (a-c) and “2.10” (d) shock-strength passage: a) k5, b) K7, c) K9, d) K13.

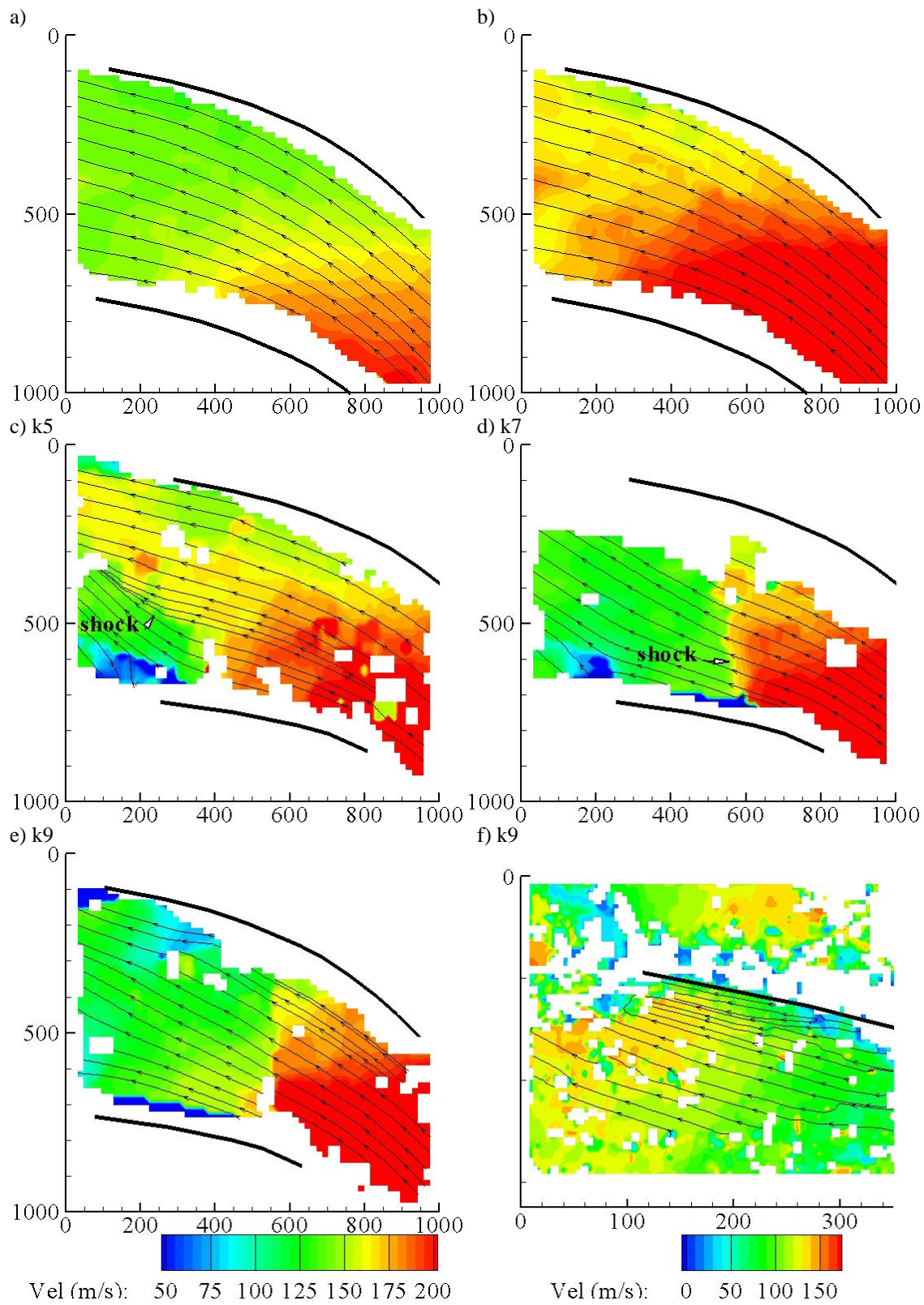


Figure 15. PIV of the passage for various phases of the "1.76" shock-strength passage: a) and b) baseline (two contour levels), c) K5, d) K7, e) K9 f) K9 TE-PS detail.

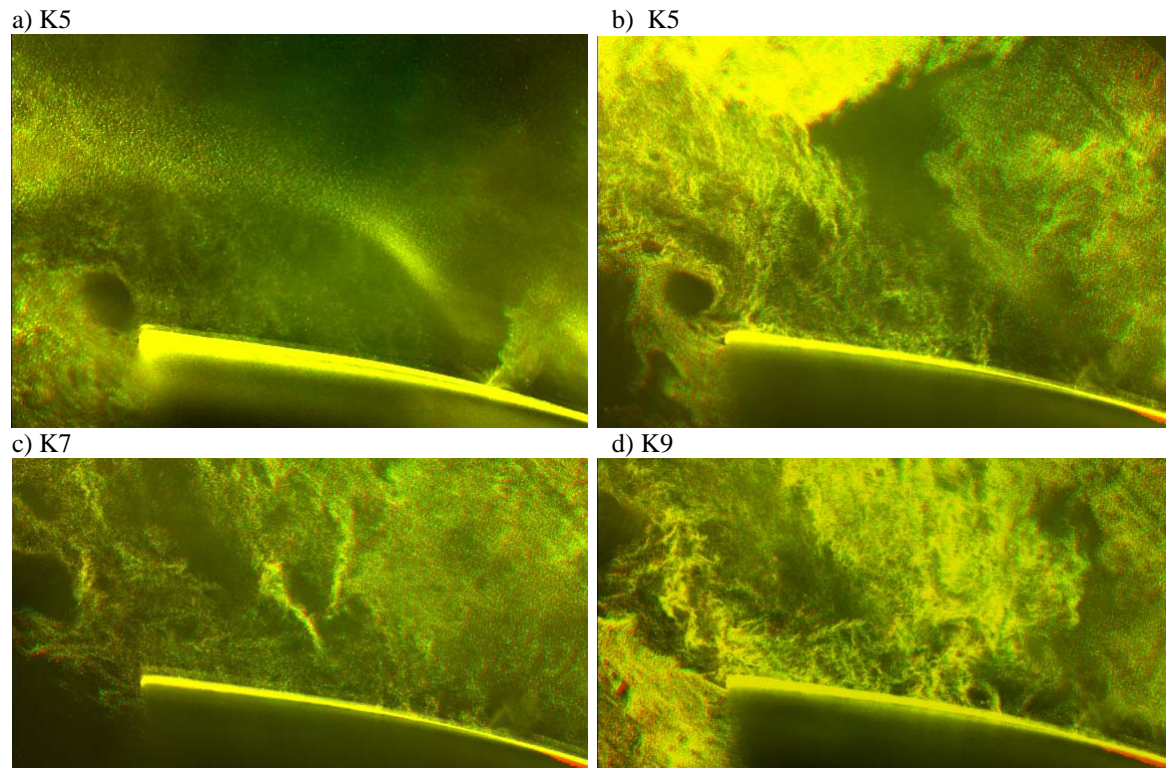


Figure 16. Flow visualization images near endwall span (0.25") for various phases of the "1.76" shock-strength passage: a) K5, b) K5, c) K7, d) K9.

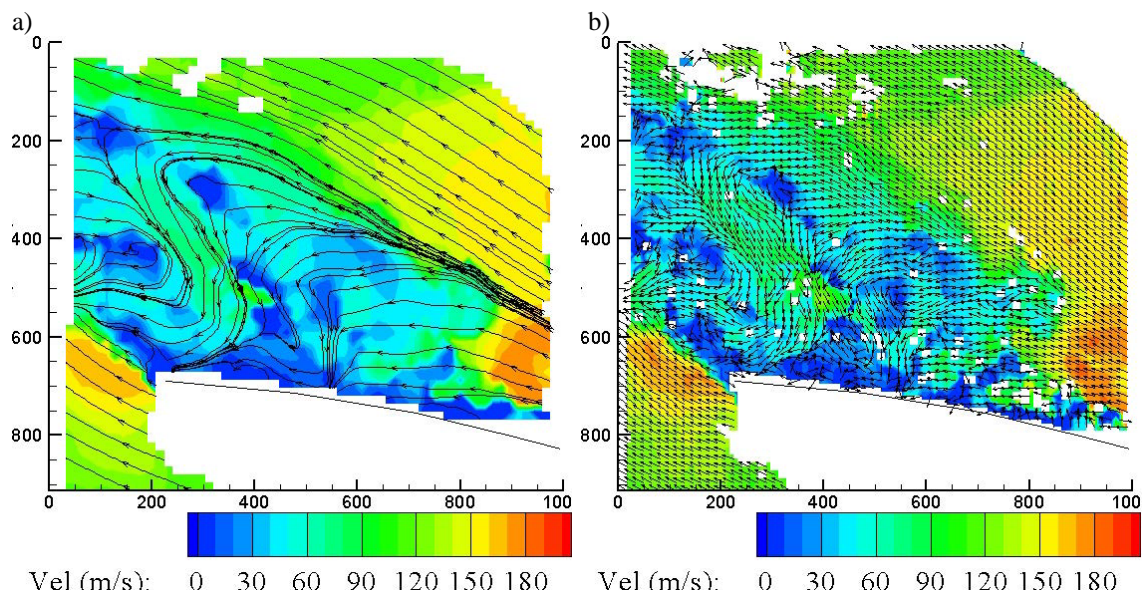


Figure 17. PIV near endwall span (0.25") for a phase of the "1.76" shock-strength passage (K9) with two resolutions: PIV cell sizes are 2.7 mm (a) and 1.35 mm (b) with 75% overlap yielding a resolution grid of 0.67 mm (a) and 0.34 mm (b) mm; axes units are pix (23.71 pix/mm). Vectors (b) are only shown for every other grid point for clarity.

PIV Study of Blade-Row Interactions in a Transonic Compressor

Jordi Esteveadeordal¹

Innovative Scientific Solutions Inc., Dayton, OH 45440

and

Steve Gorrell,² 1Lt Dave Gebbie,³ Steve Puterbaugh⁴

Air Force Research Laboratory, WPAFB, OH 45433

Details of the unsteady flow field between an upstream stator and a downstream rotor in a transonic compressor are obtained using Particle Image Velocimetry (PIV). Flow-visualization images and PIV data that facilitate analysis of vortex shedding, wake motion, wake deviation, rotor incidence, and wake-shock-interaction phenomena are presented. Such analysis not only aids the understanding of the effect of blade-row interactions on compressor performance but also allows verification of time-accurate CFD codes that are used to characterize transonic compressors. The present investigation introduces new methods for PIV implementation in complex turbomachinery environments. The PIV measurements are synchronized with various rotor-blade locations, and the instantaneous and averaged velocity fields of the flow are calculated. Stator wake and rotor-bow-shock flow interactions in the blade row are identified for various stator/rotor axial spacings and operating conditions. Using various post-processing methods, specific shed vortices and wake topological features are isolated and details of the shock-wake interaction captured. At far spacing, the vortices shed from the stator are phase-locked and shed as counter-rotating pairs in the wake. Rotor-bow-shock strength varied, depending on the axial gap between the stator and rotor and the operating condition. Results show that as the rotor-bow-shock is chopped by the stator TE, it turns more normal to the stator pressure surface and propagates upstream, validating a prior significant observation made with time-accurate CFD.

I. Introduction

BLADE-row interactions are a significant source of unsteady flow in advanced high-performance turbomachines because they incorporate closely spaced and heavily loaded blade rows to increase thrust/weight. Frequently observed unsteady phenomena such as the interaction of a shock with a shed vortex and of a shock with a blade surface produce non-uniformities and irregular flow patterns that influence compressor performance and result in blade-row vibrations and high-cycle fatigue. A better understanding of such phenomena is needed to identify the impact of unsteady aerodynamics on compressor performance, to develop and validate tools for measuring and modeling unsteady flows, and to develop design tools based on improved understanding of unsteady aerodynamics.

The Air Force Research Laboratory (AFRL) Compressor Aero Research Lab (CARL) has been conducting experimental and computational research on transonic-compressor blade-row interactions for several years [1-4]. Experience has shown that both high-fidelity experiments and simulations are essential for understanding the physics of blade-row interactions. As reported in Ref. [1], the Stage Matching Investigation (SMI) rig test confirmed that the axial spacing between an upstream stator and a downstream transonic rotor has a significant effect on stage performance. Mass flow rate, pressure ratio, and efficiency all decreased as the axial spacing

¹ Senior Research Engineer, ISSI, AIAA Associate Fellow.

² Senior Aerospace Engineer, Compressor Aero Research Lab, AIAA Associate Fellow.

³ Aerospace Engineer, Compressor Aero Research Lab, AIAA Member.

⁴ Group Leader, Compressor Aero Research Lab, AIAA Associate Fellow.

between the wake generator (WG) and the transonic rotor was reduced. This additional loss production occurs as a result of the interaction between the upstream WG and the downstream transonic rotor.

Time-accurate simulations using the 3D, unsteady, Navier-Stokes CFD solver known as TURBO combined with PIV data from the SMI experiment [2-3] revealed some important aspects of the production of this additional loss. At close spacing as compared to far spacing, the rotor bow shock is stronger at the location where it interacts with the WG trailing edge (TE). Two observations were made. The first was that the rotor bow shock formed a pressure wave on the upper surface of the WG that propagated upstream until it weakened. The magnitude of loss production was affected by the strength of the bow shock and to what degree it turned from oblique to normal as it interacted with the TE of the WG. The second observation was that at close spacing, vortices are shed from the TE of the upstream stationary blade row in response to the unsteady, discontinuous pressure field that is generated by the downstream rotor bow shock. These shed vortices increase in size and strength and generate loss as the spacing decreases--a consequence of the effective increase in rotor-bow-shock strength at the stationary blade-row TE. A relationship for the change in shed vorticity as a function of rotor-bow-shock strength was also presented that predicts the difference between close- and far-spacing TURBO simulations.

Time-accurate CFD codes are now used to simulate compressor operation and investigate complex unsteady-flow phenomena. Experimental results that reveal unsteady-flow effects are essential for validating these design tools and providing additional understanding of the physical phenomena and interaction processes involved in turbomachinery flows that are associated with closely spaced and heavily loaded compressor stages.

Use of the planar, non-intrusive measurement technique Particle Image Velocimetry (PIV) for complex geometries and unsteady applications has allowed researchers to make accurate measurements of instantaneous and averaged turbomachinery velocity fields [3, 4]. In the present investigation, a system was developed for obtaining high-resolution velocity data from a new swirler/deswirler stator configuration in an axial-flow transonic compressor at CARL (Figs. 1, 2), and the system was used to study blade-row interactions at various conditions. Most successful PIV approaches have relied on optical probes that are inserted in modified stator blades or in the flow field to deliver the laser sheet inside the various internal regions of the blade rows. These approaches have certain drawbacks, such as probe intrusiveness, shadows in areas of interest, and expensive glass windows. Presented here are various approaches that focus on minimum intrusiveness, effective laser delivery inside all regions of interest, and economical receiving windows. Introduced is a new design for PIV blades (that allows small optics to be embedded inside), with location, size, and shape determined through analysis of the flow path and CFD techniques. Also presented is an economical and fast technique based on the machining of transparent acrylic material for the receiving windows.

The present study introduces the new PIV design and implementation in a new compressor configuration and presents some illustrative PIV results. The PIV system allows the collection of data for studies of various parametric and operating-point conditions. It also aids the establishment of comparisons with other WG wakes such as those of the blade row of the SMI [5] and determination of the details of the shape of the shock as it travels through the pressure side of the vane and the angle of the flow entering the rotor passage for any condition.

II. Experimental Setup

A. Blade-Row-Interaction (BRI) Rig

The Blade-Row-Interaction (BRI) rig is a high-speed, highly loaded compressor that consists of an upstream swirler and deswirler (stator) combination, followed by a transonic fan stage (Fig. 2). The BRI rig is a variation of the AFRL SMI rig described by Gorrell et al. [5]. The blunt WG of the SMI rig was replaced with the swirler/deswirler combination. The objective of the new hardware was to simulate an embedded transonic fan stage while producing a wake through diffusion with realistic geometry (thin TE) rather than base drag. The rotors used in the SMI and BRI rigs were designed for axial inlet flow and, thus, required a swirler and deswirler to create a wake through diffusion while maintaining axial inlet flow to the rotor.

The rig was designed to permit the stator-to-rotor axial spacing to be set to three values--“close,” “mid,” and “far”--as shown in Fig. 2. The swirler/deswirler combination (Fig. 3) creates a wake through diffusion rather than base drag from the thick trailing-edge designs of previous WGs [1-5]. The BRI rig also incorporates variable stagger of the swirler vanes to alter the loading on the deswirler vanes and adjustable clocking between the swirler and deswirler blade rows to optimize the position of the swirler wake in the deswirler blade row and the amount of total pressure loss produced by the swirler and deswirler.

One of the objectives of the BRI investigation was to analyze the effect of changing the stagger angle, the stator/rotor axial spacing, and the operating condition (Fig. 4). The design parameters of the BRI rig stage are summarized in Table 1. The rotor and stator in the BRI rig are different from those used in the SMI rig. The SMI

simulated an embedded transonic core stage, while the BRI rig simulates an embedded-fan stage. The major differences between the fan and core stages are fewer rotor blades (28 in the fan versus 33 in the core) and higher tip speed (414.53 m/s in the fan versus 341.37 m/s in the core), resulting in the tip relative Mach number being increased (1.389 versus 1.191) and the hub relative Mach number being transonic (1.100 versus 0.963).

B. PIV System

The PIV system used in the SMI rig [3-4] was further developed for this investigation. The basic system includes two lasers (Spectra Physics Nd:YAG, 532 nm) for double-instantaneous marking of the sub-micron seed particles in the flow field. The combined beams are directed through sheet-forming optics using various approaches and illuminate the test section with a 2D plane of thickness of ~ 1 mm. The seeding-system design is based on seeders of the solid powder cyclone type and includes a valve system for seeding, stirring, and purging. The timing of these various valves can be controlled and synchronized to the rest of the PIV system through a series of BNC connectors. The seeding ports are located at the beginning of the contraction (the area of maximum diameter and minimum speed) to exert negligible perturbation on the flow; they are positioned in the flow path of the laser sheet. The seeder tube is located sufficiently far upstream of the PIV window area and injects negligible amounts of air and seed to avoid exerting any significant aerodynamics perturbation in the flow under study. The seeding uniformity was enhanced by adding a series of holes in the tube and a honeycomb in front of them. The light scattering from the seed particles (submicron high-purity alumina-- Al_2O_3) is recorded on a cross-correlation CCD camera with 1600 x 1200 pixels (Model PCO 1600); this camera is capable of acquiring double exposures with an interframe time of 150 nsec. Although the camera repetition rate can be set as high as 15 Hz, it is set at 10 Hz for synchronization with the laser repetition rate. A 105-mm Nikon lens is used at an F stop of 5.6. The rotor one-per-revolution signal is used for triggering the synchronization system. A customized interface and a digital pulse generator (Stanford DG535) are employed for synchronization and remote control of the system. The horizontal viewing area ranges from ~ 46 to 67 mm, and the time delay between the two frames of the double exposure is adjusted for each of the viewing areas and its flow speed to provide sufficient resolution and accuracy. In most experiments, this time was set at 1.5 μsec to yield free-stream displacements around 10 pixels. Once the PIV images have been captured and digitized, the velocity field is obtained using cross-correlation techniques over interrogation domains of the images and PIV software [4]. The uncertainty that results from various PIV algorithms (e.g., single pass, multi-pass) and data-filtering techniques (e.g., standard-deviation trimming, median) has been described in the literature [4].

Figure 5 contains schematics of the PIV swirler/deswirler assembly and the housing optical viewing area. The viewing windows used in SMI rig were made of chemically strengthened glass and, thus, could not be cut to the new dimensions of the BRI viewing areas; since manufacturing special curved-glass windows is an expensive and time-consuming process [e.g., Ref. 6], more economical and faster alternatives for manufacturing the viewing windows were investigated. Transparent acrylic material (commercial Plexiglas plastic) was considered since it can be machined and polished to optical-quality levels for curved wind-tunnel sections [7] and since the mechanical and thermal characteristics in the PIV window area can be maintained under the acrylic damage threshold for most of the present experiments.

For each spacing, a viewing window was machined on one side to have the same curvature as the rotor inner housing (radius of 241.3 mm) and on the other side to be flat (Fig. 6). This produced a small variable magnification across the field of view, which must be used for inferring the velocity field. The PIV windows were held in position with specially designed frames made of anodized aluminum (Fig. 6). Thermocouples were installed in the windows and monitored to ensure that temperatures did not reach the acrylic damage threshold in continuous operation ($\sim 200^\circ\text{F}$) during the experiments. The pressure differential across the window was negligible compared to the acrylic yield strength and would not produce acrylic deformation at the temperature of the experiments. The PIV surrounding viewing areas were painted flat black to minimize reflections.

From the computational and experimental results from the SMI rig, it was determined that taking PIV measurements on both the pressure and the suction surfaces of the deswirler over the last 30% chord would be very desirable. Several laser-sheet delivery systems were designed to accomplish this. One approach involves delivery of the laser from upstream in the settling chamber through the use of a mirror [Fig. 7(a)]. The laser sheet is formed outside the tunnel and is sent to the mirror through a port with a window in the settling chamber. Another involves the use of small (< 6 -mm-diam) cylindrical lenses mounted in an optical probe that is inserted and secured in the case just forward of the rotor [Fig. 7(b)]. Finally, two specially designed neighboring deswirler vanes are embedded with small optics (< 4 -mm-diam cylindrical lens and mirror) [Fig. 7(c)] and with a thin bent acrylic window to illuminate the pressure and suction sides of the central vane of interest (Figs. 5 and 8). Fiber-optics PIV [8] and

borescopes can also be implemented using these ports, if desired. The laser-sheet plane can be set perpendicular to the vane of interest at any span in all of these approaches.

III. Results

The PIV system allows acquisition of a significant amount of PIV data in the new BRI configuration. In this section, samples from the acquired data will be presented as well as illustrative flow analyses using flow visualization, instantaneous and averaged velocity fields, streamline patterns, and vorticity.

At 99% corrected speed, where most of the experiments were performed, consecutive rotor blades are separated in time by $\sim 140 \mu\text{sec}$ (~ 11 degrees in angle, the blade-row pitch). Seven blade locations (delays/clockings), separated by $20 \mu\text{sec}$, were typically chosen to characterize the flow field in a blade-row pitch. Analyses were performed using data from both qualitative flow-visualization and quantitative velocity-field measurements. Data analysis included inspection of selected flow-visualization images (obtained by increasing the amount of seeding) and analysis of instantaneous and averaged velocity-field data obtained using various PIV algorithms. Other property derivatives of the velocity field such as vorticity and streamlines were also used. The data reported in the present study were obtained using the upstream laser-sheet delivery method on the deswirl pressure side at 50% span.

Flow-visualization images displaying sample wakes from a far-spacing configuration (peak efficiency, 0° stagger) are shown in Fig. 9 (field of view is 66.67 mm). Figure 9(a) contains a picture combining the two cross-correlation PIV frames (separated in time by $1.5 \mu\text{sec}$), which are colored red and green. The rotor-blade position (or blade clocking or blade delay “BID”) was synchronized in these samples such that the deswirl TE was aligned at mid-pitch between two rotor leading-edge (LE) blades (“BID10”). Although shadows from the upstream stator blades prevent visualization of the lower section of the wakes, typical coherent structures of wake vortex shedding can be seen clearly; the approximate axial location of the centers of the structures (center of unseeded cores) are indicated by dashed lines, numbers and characters (a for top or pressure side, b for bottom or suction side) for reference. These labeling will be used throughout to identify the structure locations. Figure 9 (b) contains a sample picture that combines two independent frames (one colored red and the other, green) from the same relative rotor position, and it provides qualitative visualization of the wake motion or unsteadiness over time. Many other pairs compared similarly, with relative movement increasing with downstream distance and mainly in the pitchwise direction. As with free-wake phenomena, when the wake travels downstream, naturally more wake motion occurs due to the turbulent random nature of the wake vortices. At far spacing, the wake mixes out more as it travels farther downstream, and naturally more randomness occurs. Nevertheless, when studying the characteristics of a wake in a blade row of a transonic compressor, one must take into account a variety of complex interactions well beyond free-wake properties--interactions such as particular unsteadiness under the rotor passage and shocks, adverse pressure gradients, complex geometry, and three-dimensionality. While the above simple comparison provides qualitative insight into the unsteadiness of the location of the wake, quantitative information is essential for assessing the actual degree of variability between any two realizations and within the average flow. Statistical analysis can be used to determine the degree of similarity between flow events, and techniques such as phase-averaging have been successfully used in the past [4]. Quantitative analyses of the flow using instantaneous and averaged velocity fields will now be discussed for the same far-spacing-wake case of Fig. 9.

The corresponding PIV velocity field for the instantaneous wake of Fig. 9(a) is shown in Fig. 10. Lack of seeding in some areas precludes full velocity information. A low-speed region that defines the wake can be seen in the figure. The individual vortices observed in the flow visualization can be readily traced in the velocity field by subtracting their convective velocity; Figs. 10 and 11 employ subtraction of near-field and far-field convective velocities, respectively, to visualize vortices near and far from the deswirl TE. The mushroom structure of the wake and its topological features are obvious in these patterns, like those observed previously in the SMI PIV results [4]. These instantaneous velocity fields are, thus, very useful for analysis of individual realizations and instantaneous flow events and complement the averaged features of the flow field, which are of great interest in providing insight into the overall performance of the compressor at each condition. Average velocity-field characteristics for the far-spacing conditions of Figs. 9 to 11 are shown in Figs. 12 to 14 using the median (for robustness [4]) of 50 realizations. In Figure 12, the contour maps of the velocity are shown for two PIV grids, with two resolutions and interrogation cells overlapped by 75% [4]; this yields 64-pixel (2.67-mm) and 32-pixel (1.33-mm) grid sizes in Figs. 12(a) and 12(b), respectively. While both maps show the main features of the compressor flow (such as the low-velocity region of the wake, the abrupt changes in velocity across the shock, and the accelerating flow region into the rotor passage), the higher resolution displays more details and defines these features in greater detail. For example, the low-speed areas with blue contours at axial location $x \sim 500$ pix and the

high-speed areas with orange contours at axial location $x \sim 825$ pix (both indicative of vortex locations as in Figs. 10 and 11) appear in Fig. 12(b) but not in Fig. 12(a). The plots are shown both with velocity magnitude alone to emphasize the contours and with some vectors overlaid to emphasize the flow direction in the deswirler frame of reference. Flow direction can be also readily observed from the orientation of the streamlines (Fig. 13) in various frames of reference. It is noteworthy that the vortices do not become washed out in the averaged velocity field. This is an indication that for a fixed blade clocking, these vortices are “locked” at a spatial location, which is similar to the “phase-locked” phenomena observed in the SMI rig [3-4]. Analysis of the wake-location repeatability and variability in all directions can be performed using quantitative statistical information (such as standard deviation), and analysis of the vortices path and its synchronization with the blade location can be performed through examination of the various blade clockings; these will be studied in future efforts. The phenomenon is consistent with flow-visualization observations [e.g., Fig. 9(b)] that reveal certain repeatability in the axial location of the vortices and some meandering in the pitch direction. The averaged vorticity field [Fig. 14(a)], which is invariant with respect to frame of reference, further strengthens the identification of the vortices of the wake and reveals the typical counter-rotating vortex pairs; their underlying location relative to the averaged-velocity-field regions is revealed in Fig. 14(b). This underlying structure of the wake in the averaged quantities for a fixed blade clocking (phase-locking effect) was observed in the SMI rig [4] with different WGs. The effect (observed here at far spacing with the cambered stator geometry) will allow the use of “phase-averaging” analysis techniques [4]. In all of these instantaneous and averaged plots, the centers of the vortices can be precisely found and traced back to the centers of the flow-visualization vortices as well, except that the quantitative information yields their exact location; for example, the coordinates of the centers of the structures numbered from 2 to 6 [seen in the vorticity plot of Fig. 14(a)] match the axial location of the flow-visualization cores (numbered in Figs. 9) within 2 pixels. The quantitative information allows calculation of fundamental instantaneous and averaged properties such as size, strength, and blockage via properties such as circulation [9]. The information can also be used to gain insight into the relation between the passing shock and the impulsive vortex shedding. Data from the suction side would also be very valuable for identifying other mechanisms that can contribute to vortex shedding such as suction-side separation.

Analyzing specific flow features such as individual vortices and the rotor bow shock aids the investigation of any unsteady mechanisms that may produce additional loss as the spacing is reduced from close to far. An initial assessment of the flow for various axial spacings is presented by instantaneous velocity field plots. Since a phase-locking or synchronization effect was shown to occur, even at a far-spacing condition, it is considered that the instantaneous flow field, albeit with some limitations, can yield a good representation of the flow field. A more thorough analysis will be completed in the future as averaged data become available. Some preliminary observations and comparisons of axial spacings at -3° stagger will now be presented for some representative blade clockings. These clockings represent the flow during the collision of the wake with the rotor LE (“BID160”: deswirler-TE aligned to rotor-LE) and the route of the wake toward the rotor passage (“BID10”: deswirler-TE aligned with the mid-pitch between two consecutive rotor-LEs). The location of the deswirler vane and the TE of the rotor blade (for “BID160”) are schematically drawn in the plots for reference. A “BID100” was also selected in a close-spacing case to show some specific observations of the shock as it is captured on the pressure side of the deswirler. The magnifications are 24, 34, and 35 pix/mm for far, mid, and close spacings, respectively. Only results for the coarser grid (64 pix with 75% overlap) are presented. Some areas are blanked out due to lack of seeding which precludes full velocity information.

In Fig. 15 instantaneous velocity fields are presented for far spacing at peak efficiency. The lowest speed area (marked by green contour levels downstream of the deswirler TE), corresponding to the wake region and the abrupt change in velocity (contour colors change from red to green in very short distance) due to the shocks in each blade clocking position, can be readily observed in each plot. In addition to the bow shock accompanying the rotor blade, there is evidence of a second, weaker bow shock, corresponding to the previous rotor blade, interacting with the deswirler pressure side at “BID10”. When axial spacing is reduced to “mid” (Fig. 16), the magnitude of the velocity change across the shock and in the wake is greater as a consequence of the reduced spacing. The rotor bow-shock strength increases even more at the near-stall (Fig. 17) operating condition, and the bow shock is detached farther upstream of the rotor LE. The “BID10” clockings of Figs. 16 and 17 show the shock position and strength near the deswirler TE. An important observation is that the shock is clearly perpendicular to the deswirler pressure surface. This validates conclusions drawn from time-accurate CFD analysis of the SMI configuration [2-3] that the bow shock was oblique as it interacted with the WG TE but that the resulting pressure wave which formed was turned more normal to the WG blade surface. The resulting moving shock produced an entropy rise. The magnitude of loss production was affected by the strength of the bow shock and how much it turned as it interacted with the TE of the WG. The interaction is even stronger for close spacing (Fig. 18), where the bow shock collides with the stronger

part of the wake that exists close to the deswirler-TE. In this case a blade clocking has been added (“BID1100”) for visualizing the shape of the shock as it interacts with the pressure side of the deswirler vane, which is clearly stronger than in the mid-spacing peak-efficiency operating condition (Fig. 16). These observations were not observed experimentally in the SMI rig [4] because the PIV viewing window did not extend upstream enough of the WG TE. These results are the first experimental validation of the numerical observation.

Analysis continues, such as that shown in Figs. 9-14, for the purpose of establishing more comparisons between different parameters and conditions such as stagger angles, axial spacings, and operating point and drawing conclusions of their effects on compressor performance. Higher resolution data will also provide more details on the velocity field in various areas and will, for example, permit analysis of the interaction of the shock with the deswirler pressure side and its relation with vortex shedding and synchronization between events.

IV. Summary

Preliminary analysis of the AFRL BRI rig has been performed using PIV. New methods for adapting PIV techniques for complex turbomachinery environments, including the use of receiving windows made by economical and rapid prototyping techniques, were successfully implemented and evaluated. The effectiveness of these techniques has been demonstrated through full characterization of the interaction between a stator wake and rotor bow shock. Flow visualization--along with analysis of instantaneous and averaged velocity-field data, vorticity, and streamlines--was shown to permit identification of important details of the unsteady flow field.

Analysis was focused on wake shedding and rotor-bow-shock strength and position. At far spacing, the vortices shed from the deswirler (stator) are phase-locked and shed in counter-rotating pairs. Rotor-bow-shock strength varied, depending on the axial gap between the stator and rotor (close, mid, and far) and the operating condition (peak efficiency and near stall). The closer the spacing, the stronger the interaction between the rotor bow shock and the stator, a consequence of the higher shock strength. Through observation of various blade delays, it has been shown that as the rotor bow shock is chopped by the stator TE, it turns more normal to the stator pressure surface and propagates upstream. This validates with experimental data the suggestion that was made in Refs. [2-3], based on time-accurate CFD simulations. Extensive analysis using averages and other techniques was introduced and will be completed in future work for various parameters and conditions.

Acknowledgments

The authors acknowledge the technical assistance of the CARL group at Wright-Patterson AFB and ISSI personnel during the experiments and the editorial assistance of Ms. Marian Whitaker of ISSI. The authors recognize Dr. Todd Bailie of CARL for many valuable discussions and Robert Wrigg and Terry Norris of UTC for their assistance in preparing the experiments and gathering the data. The authors acknowledge the Propulsion-Directorate management for supporting the research and the presentation and publication of this paper. The fan stage was fabricated by Pratt & Whitney; the swirler and deswirler were built by Florida Turbine Technologies. Aerodyn is acknowledged for strain-gage assistance and Techsburg Inc. and Ketco for manufacturing the PIV frames and PIV windows, respectively. The authors acknowledge the Propulsion-Directorate management of Wright-Patterson AFB for supporting the research and the presentation and publication of this paper.

References

- ¹Gorrell, S. E., Okiishi, T. H., and Copenhaver, W. W., “Stator-Rotor Interactions in a Transonic Compressor, Part 1: Effect of Blade-Row Spacing on Performance,” *ASME Journal of Turbomachinery*, Vol. 125, No. 2, April 2003, pp. 328–335.
- ²Gorrell, S. E., Okiishi, T. H., and Copenhaver, W. W., “Stator Rotor Interactions in a Transonic Compressor: Part 2 - Description of a Loss Producing Mechanism,” *ASME Journal of Turbomachinery*, Vol. 125, No. 2, April 2003, pp.336-345.
- ³Gorrell, S. E., Car, D., Puterbaugh, S. L., Estevadeordal, J., and Okiishi, T. H., “An Investigation of Wake-Shock Interactions in a Transonic Compressor with DPIV and Time-accurate CFD,” *ASME Journal of Turbomachinery*, Vol. 128, October, 2006, pp. 616 - 626.
- ⁴Estevadeordal, J., Gorrell, S., Copenhaver, W., “PIV study of Wake-Rotor Phenomena in a Transonic Compressor under Various Operating Conditions,” *AIAA Journal of Propulsion and Power*, Vol. 23, No. 1, January-February 2007, pp. 235-242.
- ⁵Gorrell, S. E., Copenhaver, W. W., and Chriss, R. M., “Upstream Wake Influences on the Measured Performance of a Transonic Compressor Stage,” *AIAA Journal of Propulsion and Power*, Vol. 17, 2001, pp. 43-48.
- ⁶Verhoff, V. G., “Compound Curvature Laser Window Development,” *AIAA/SAE/ASME/ ASEE 29th Joint Propulsion Conference*, June 28-30, 1993, Monterey, CA.
- ⁷Bailie, T., Car, D., Estevadeordal, J., “Streamwise Vorticity Effects in a Curved Diffuser with Slot Jet Flow Control,” *AIAA Paper 2006-2808, 25th AIAA Aerodynamics Measurement Technology and Ground Testing Conference*, June 5-8, 2006, San Francisco, CA.

⁸Estevadeordal, J., Meyer, T.R., Gogineni, S.P., Polanka, M.D., Gord, J. R., “Development of a Fiber-Optic PIV System for Turbomachinery Applications,” *AIAA Paper 2005-38, 43rd AIAA Aerospace Sciences Meeting and Exhibit*, January 10-13, 2005, Reno, NV.

⁹Langford, M. D., Guillot, S. A., Ng, W. F., Breeze-Stringfellow, A., Solomon, W., Estevadeordal, J., “Experimental Investigation of the Effects of a Moving Shock Wave on Compressor Stator Flow,” *ASME Journal of Turbomachinery*, Vol. 129, No. 1, January 2007, p. 127.

Table 1. BRI Aerodynamic Design Parameters

PARAMETER	ROTOR	STATOR
Number of Airfoils	28	49
Aspect Ratio - Average	0.916	0.824
Inlet Hub/Tip Ratio	0.750	0.833
Flow/Annulus Area, kg/s/m ²	195.30	--
Tip Speed, Corrected m/s	414.53	--
M _{REL} LE Hub	1.100	0.830
M _{REL} LE Tip	1.389	0.700
Max D Factor	0.545	0.506
LE Tip Diam., m	0.4825	0.4825

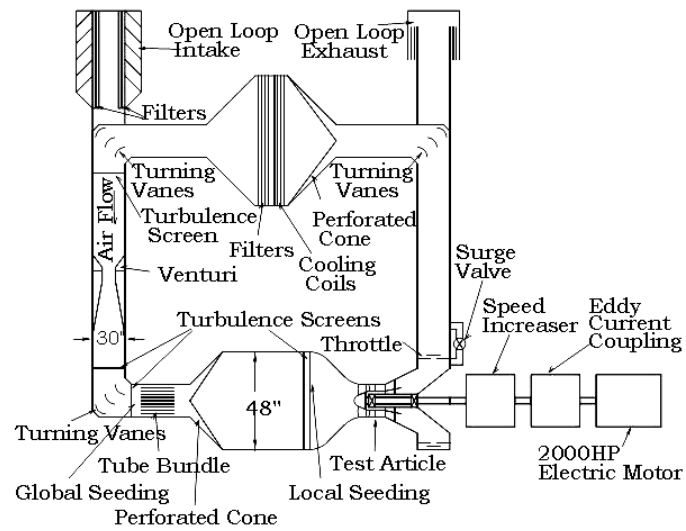


Figure 1. Flow path of 2000-hp Compressor Aerodynamic Research Laboratory facility.

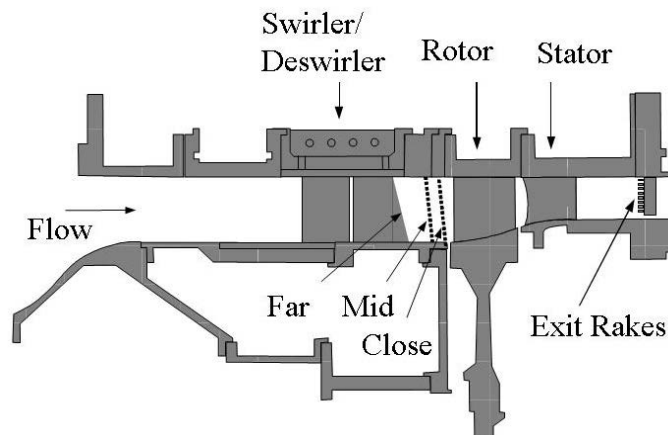


Figure 2. Blade-row-interaction (BRI) rig cross section in its general configuration.

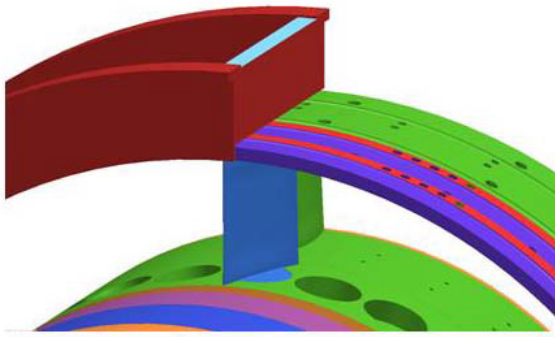


Figure 3. SMI swirler/deswirler stator-configuration schematic.

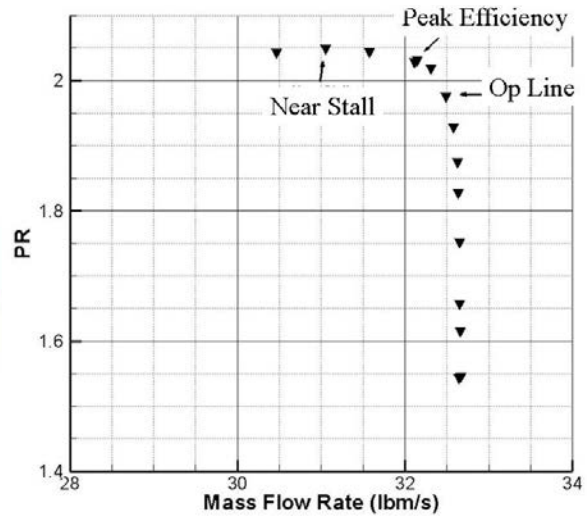


Figure 4. Overall stage pressure ratio (PR) for mid-spacing configuration (80% clocking, -30 stagger).

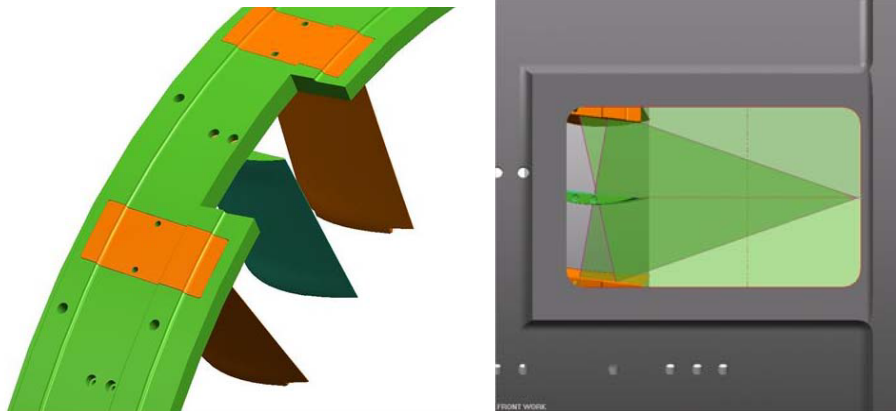


Figure 5. PIV deswirler-assembly schematic and typical PIV laser-sheet and window.

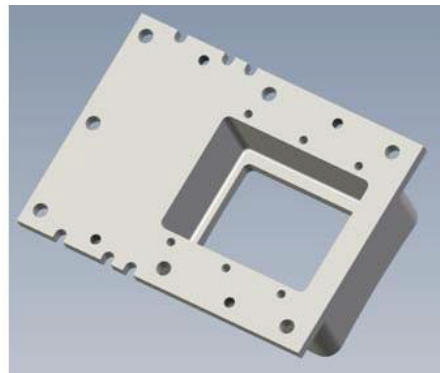


Figure 6. PIV acrylic machined optical window picture and aluminum-window-frame schematic.

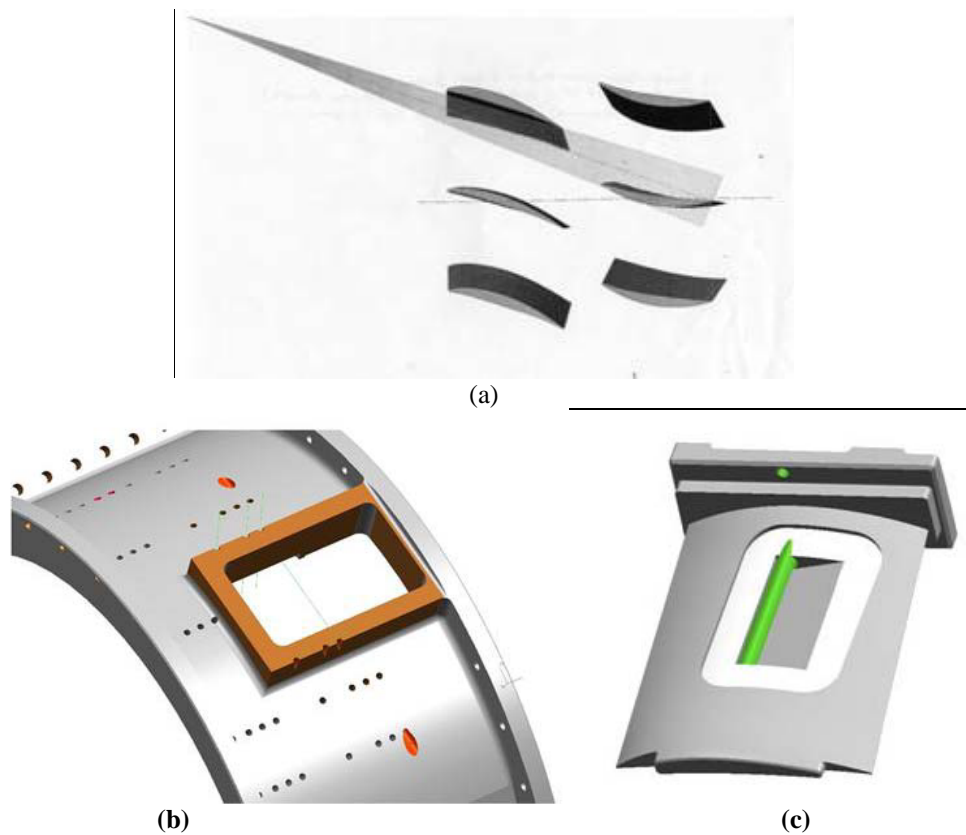


Figure 7. Laser-sheet delivery methods: upstream optics (a), optical-probe case insertion (b), and vane embedded (c).

Swirler | Deswirler | Rotor |

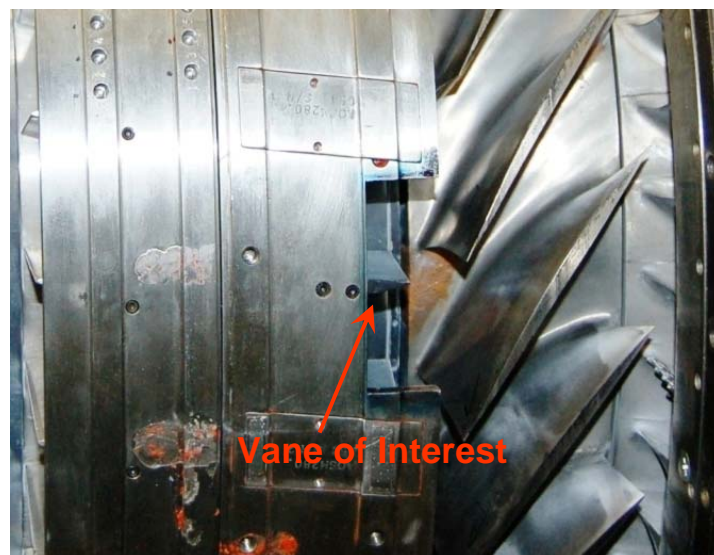


Figure 8. Photograph of vane of interest in BRI rig.

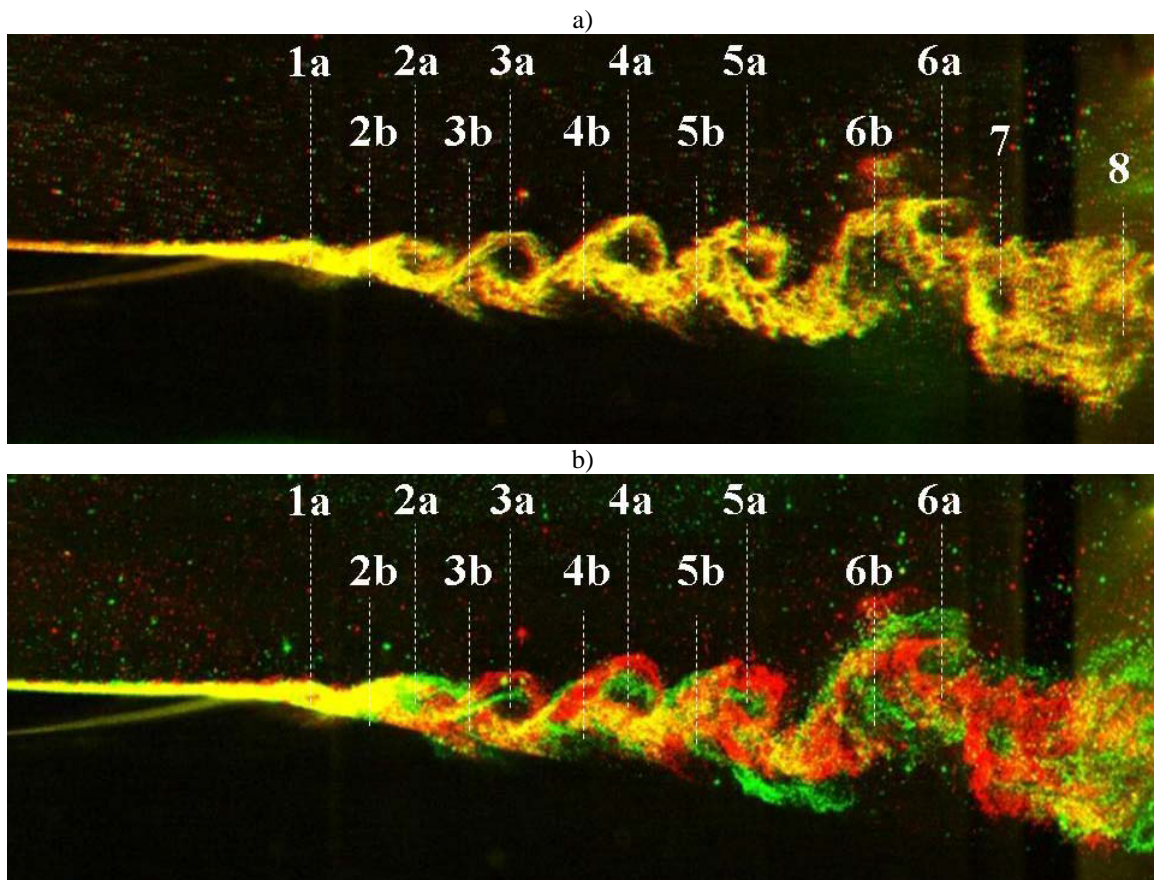


Figure 9. Deswirler-wake flow visualizations for far spacing, 0° stagger, “BID10”, at peak efficiency: PIV double exposure (red-green colored) (a) and independent frames (red and green colored) (b). View width is 66.67 mm. Dashed lines, numbers and characters (a for top or pressure side, b for bottom or suction side) indicate an approximate axial location of wake structures.

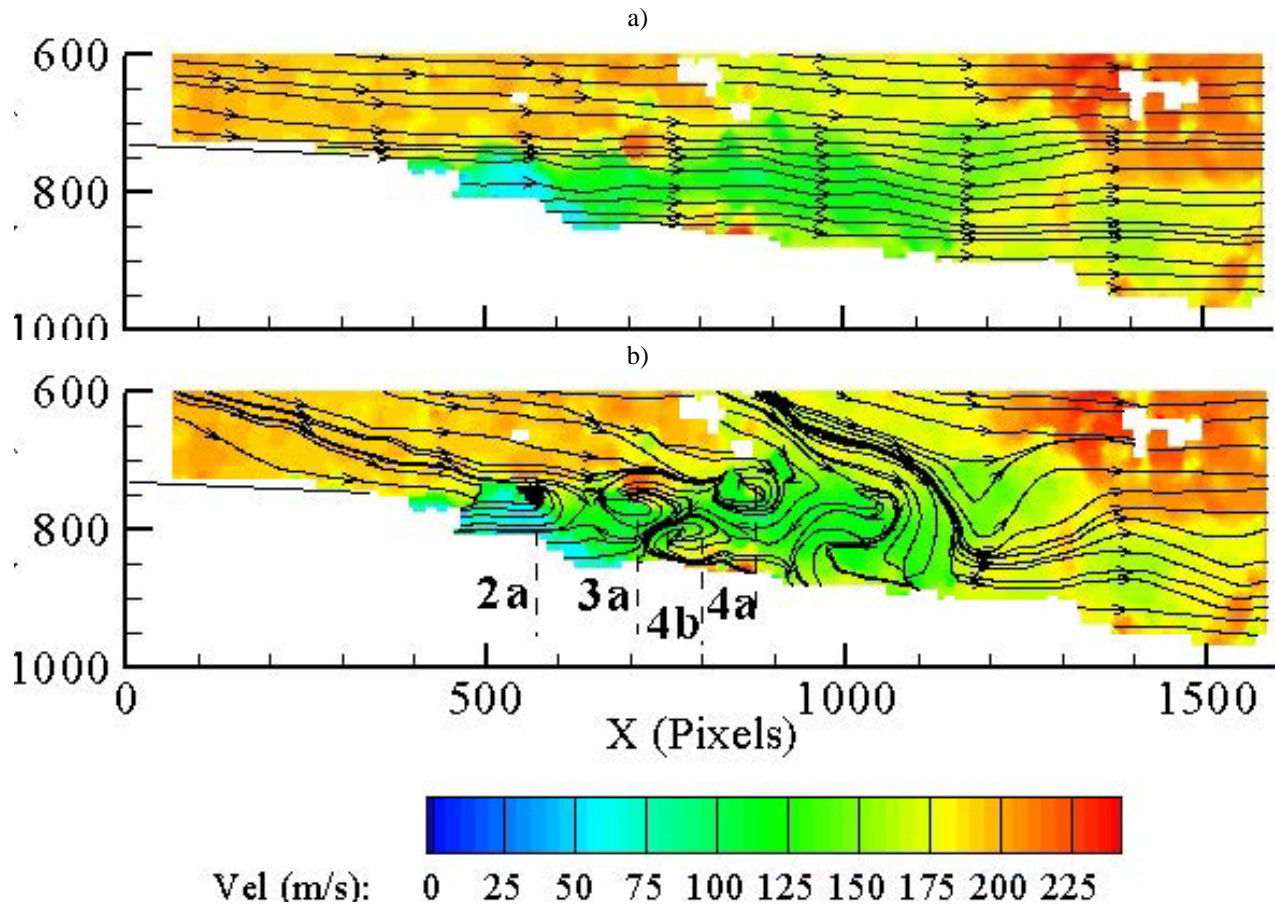


Figure 10. Deswirler-wake instantaneous velocity corresponding to Fig. 9(a): vector field (a) and streamlines with subtraction of convective velocity of vortices near field of deswirler TE (b). Dashed lines, numbers and characters (a for top or pressure side, b for bottom or suction side) indicate approximate axial location of wake structures.

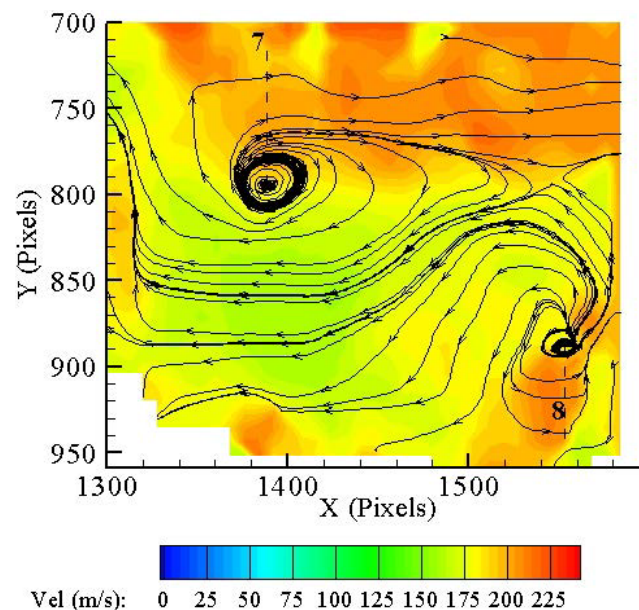


Figure 11. Deswirler-wake velocity detail of far-field wake from Fig. 10(b) close to rotor LE with subtraction of its convective velocity. Dashed lines and numbers indicate approximate axial location of wake structures.

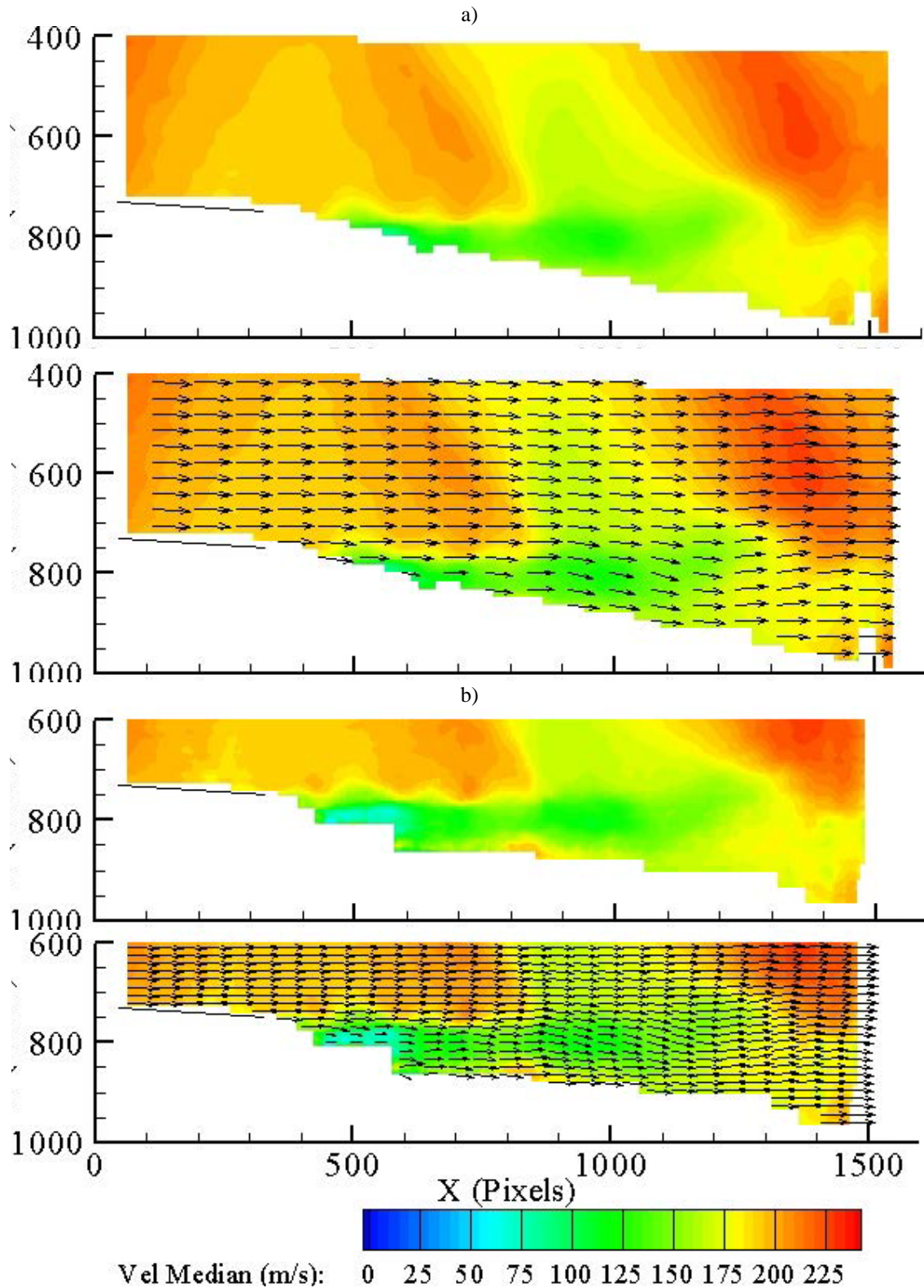


Figure 12. Average velocity contours and vectors for far spacing, 0° stagger, 80° clocking, "BID10", at peak efficiency: (a) 64/75% overlap pixel (2.67 mm) resolution grid, and (b) 32/75% overlap pixel (1.33 mm) resolution grid. Vectors in the x direction are shown only every other grid point for clarity.

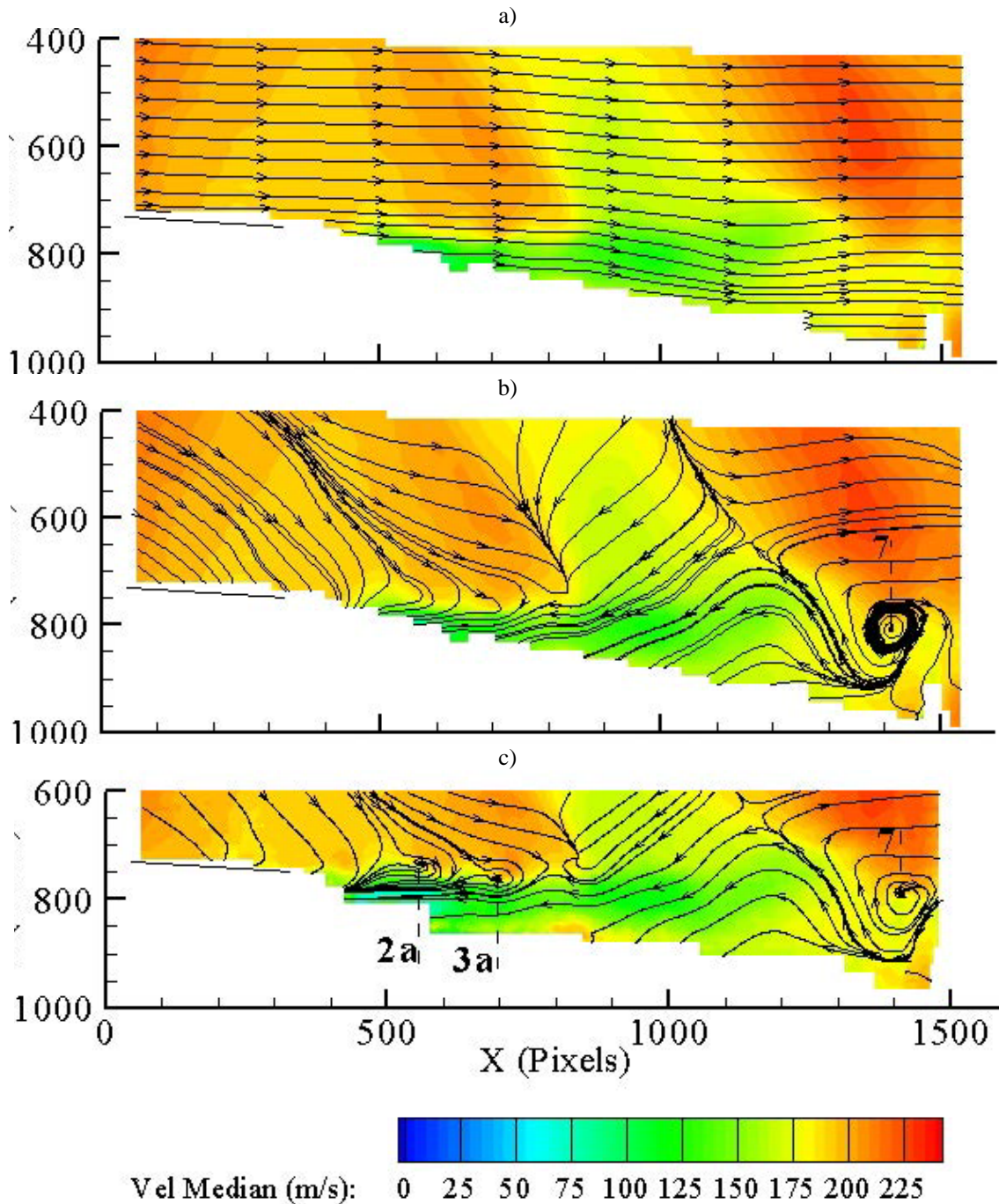


Figure 13. Streamline pattern of average velocity field of Fig. 12(a) (a, b) and Fig. 12(b) (c); convective velocity of far-field wake has been subtracted in (b) and (c). Dashed lines, numbers and characters (a for top or pressure side, b for bottom or suction side) indicate approximate axial location of wake structures.

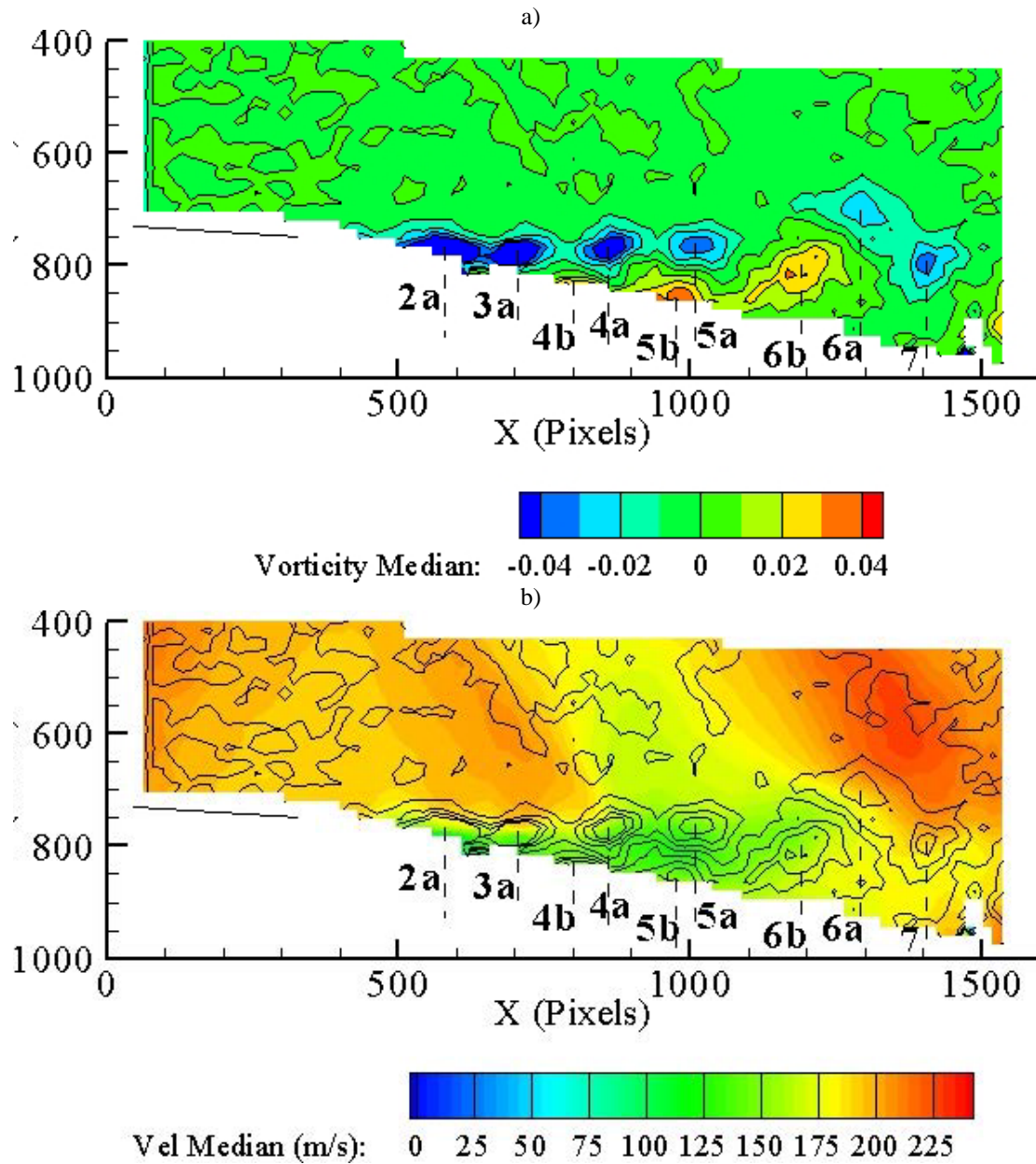


Figure 14. Vorticity contours from averaged velocity field of Fig.12(a) ($\times 1.5 \times 10^{-6} \text{ sec}^{-1}$) (a) and vorticity contours on velocity field (b). Dashed lines, numbers and characters (a for top or pressure side, b for bottom or suction side) indicate approximate axial location of wake structures.

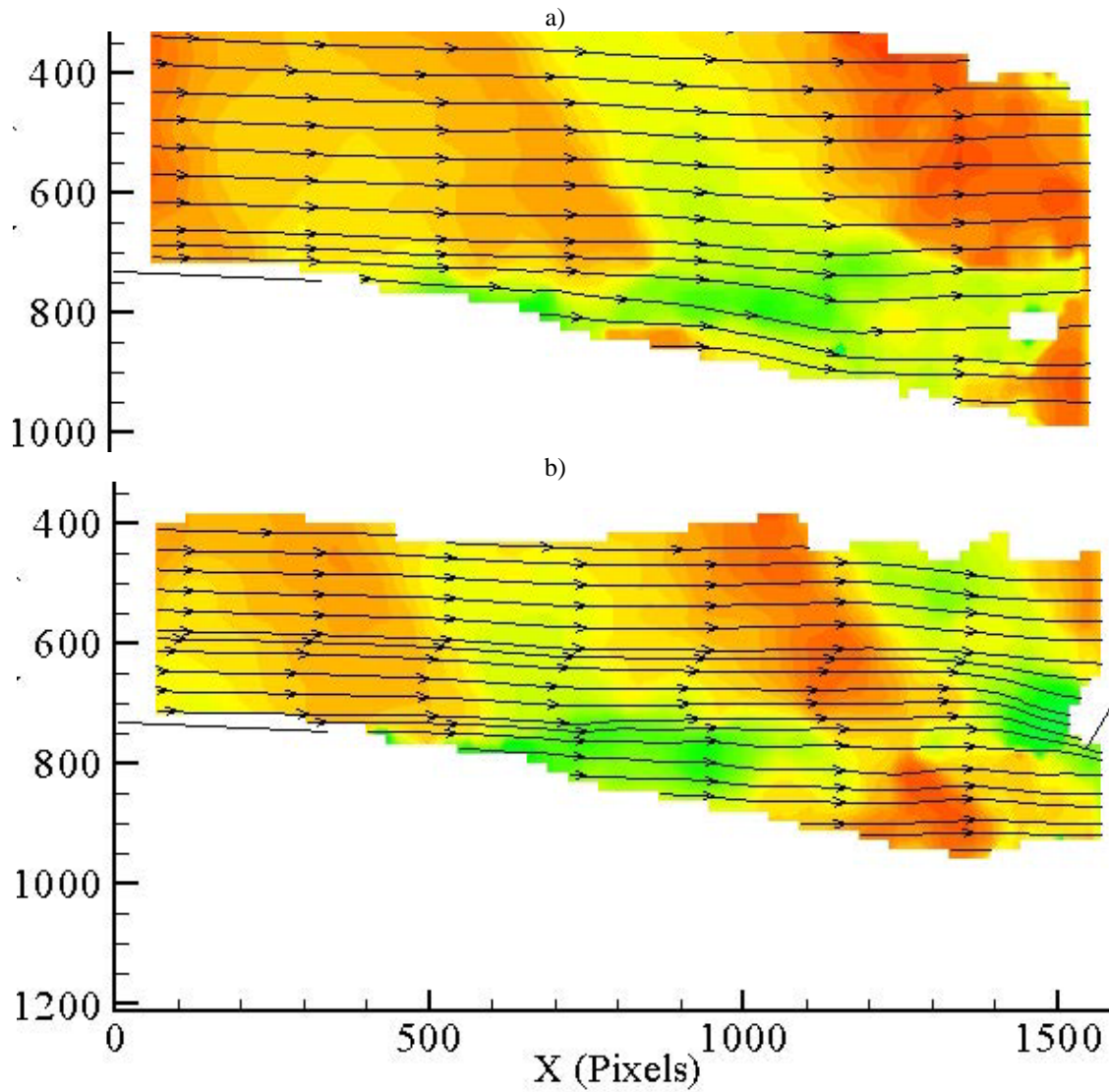


Figure 15. Instantaneous velocity for far spacing, -3° stagger, and peak efficiency for two blade clockings: “BID10” (a) and “BID160” (b).

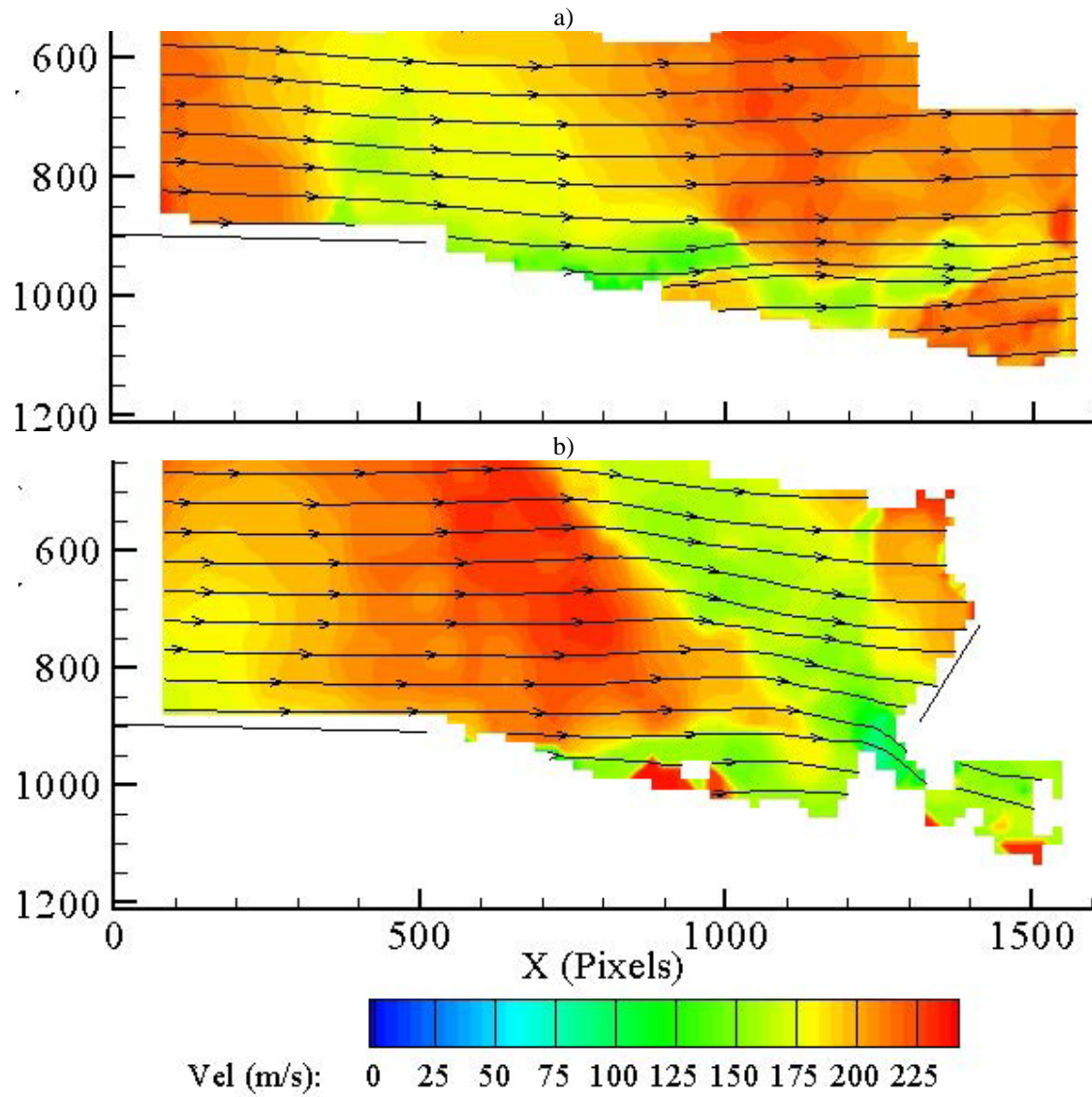


Figure 16. Instantaneous velocity for mid spacing, -3° stagger, and peak efficiency for two blade clockings: “BIDI0” (a) and “BIDI60” (b).

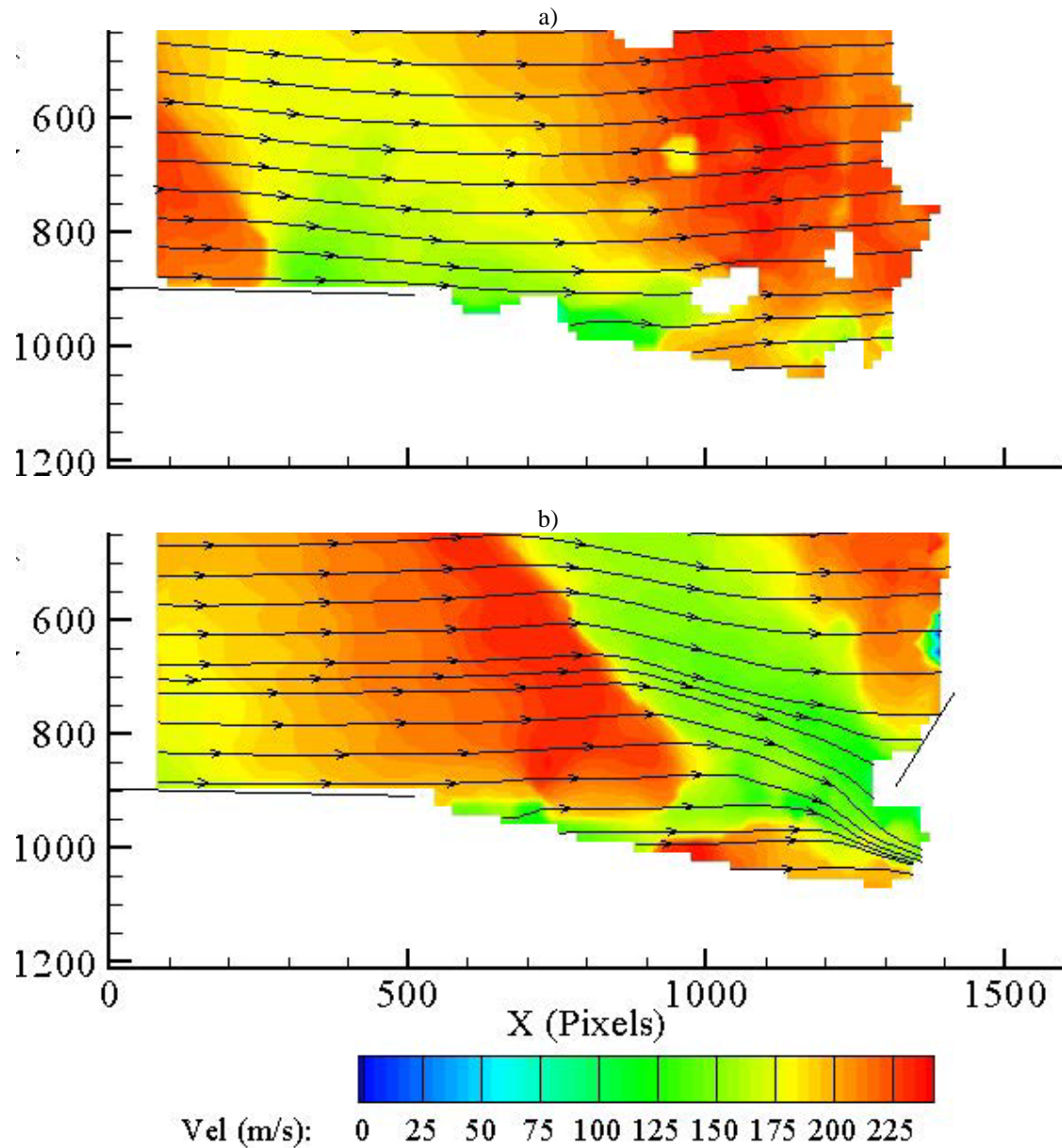


Figure 17. Instantaneous velocity for mid spacing, -3° stagger, and near stall for two blade clockings: "BID10" (a) and "BID160" (b).

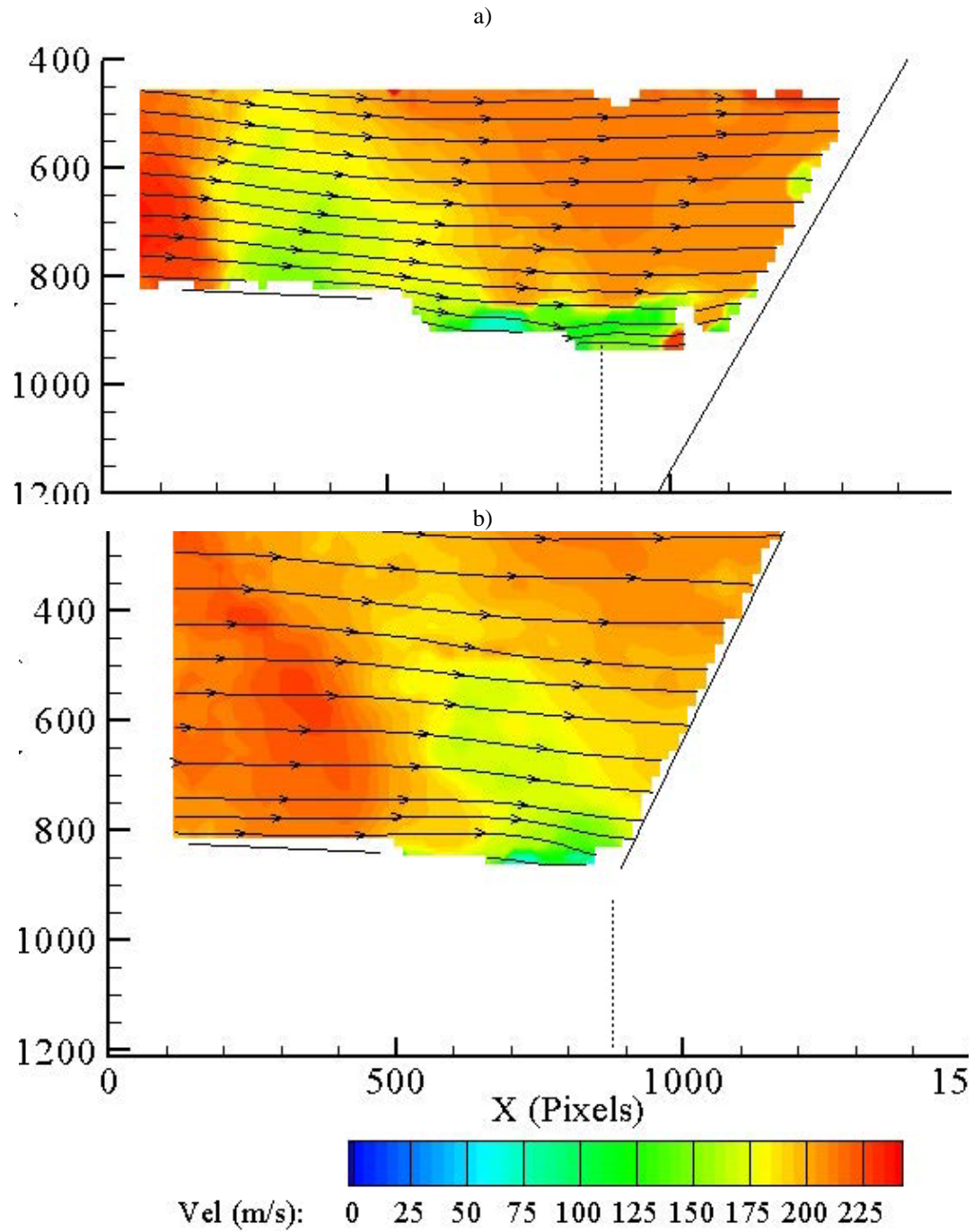


Figure 18. Instantaneous velocity for close spacing, 0° stagger, and peak efficiency for two blade clockings: “BID10” (a) and “BID160” (b). Dotted lines indicate rotor LE axial position.



Investigation of Blade-Row Interactions in a Transonic Compressor using PIV

Jordi Esteveadeordal, Steve Gorrell, and Steve Puterbaugh

*Innovative Scientific Solutions Inc., Dayton, OH 45440
Brigham Young University, Provo, UT 84602
Air Force Research Laboratory, WPAFB, OH 45433*

Acknowledgments:
ISSI, AFRL Propulsion Directorate

*AIAA Dayton-Cincinnati
March 4th, 2008*



OUTLINE

MOTIVATION
EXPERIMENTS
RESULTS
SUMMARY



MOTIVATION

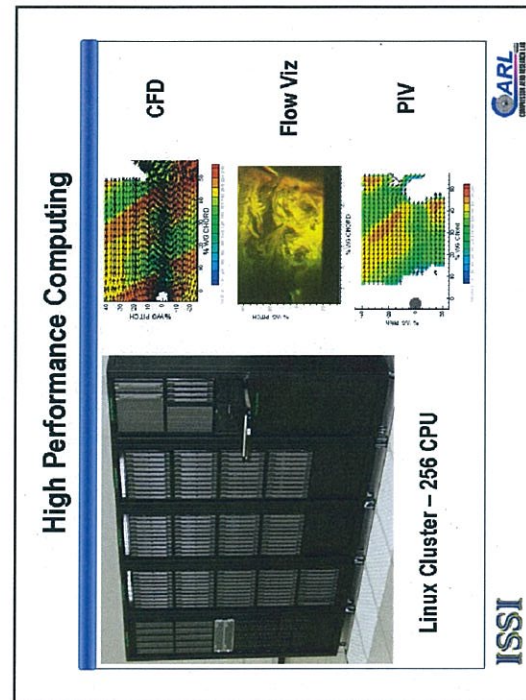
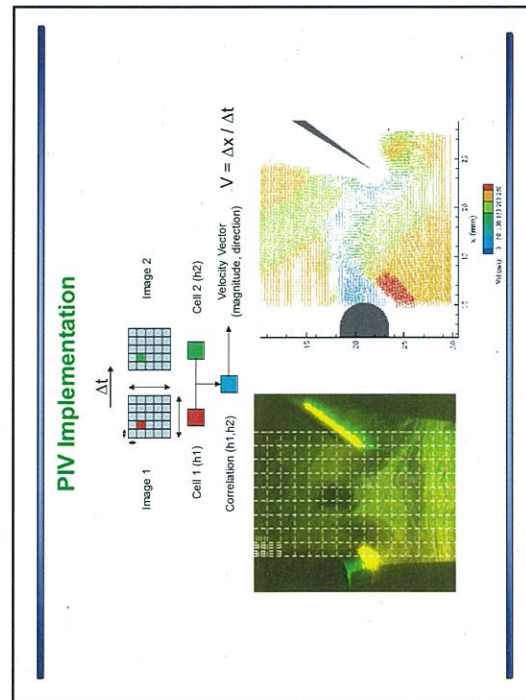
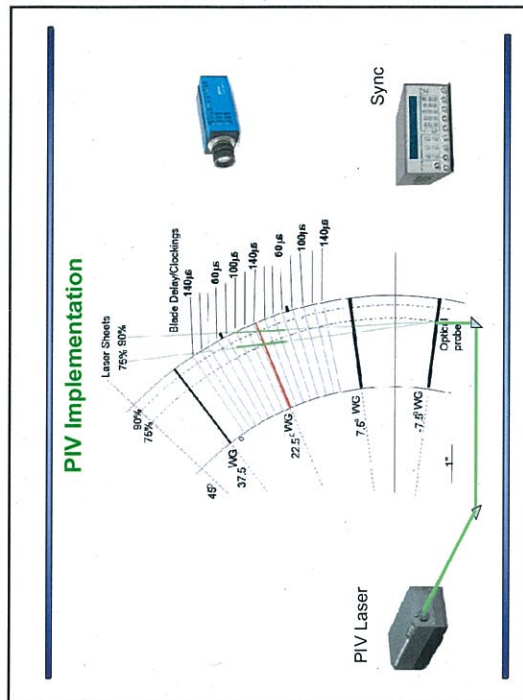
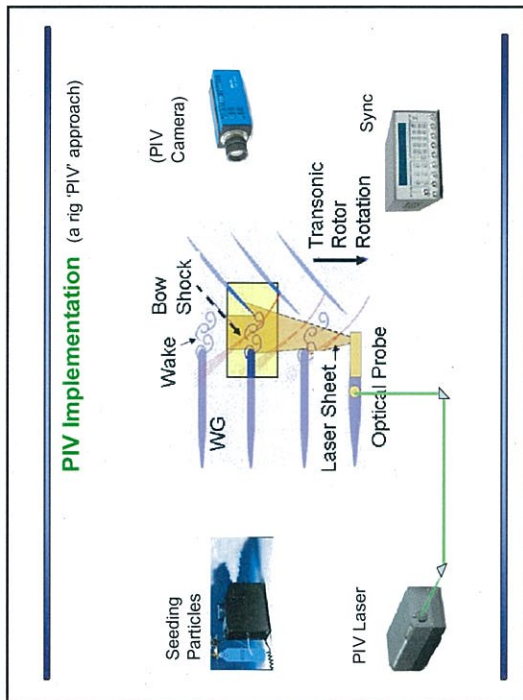


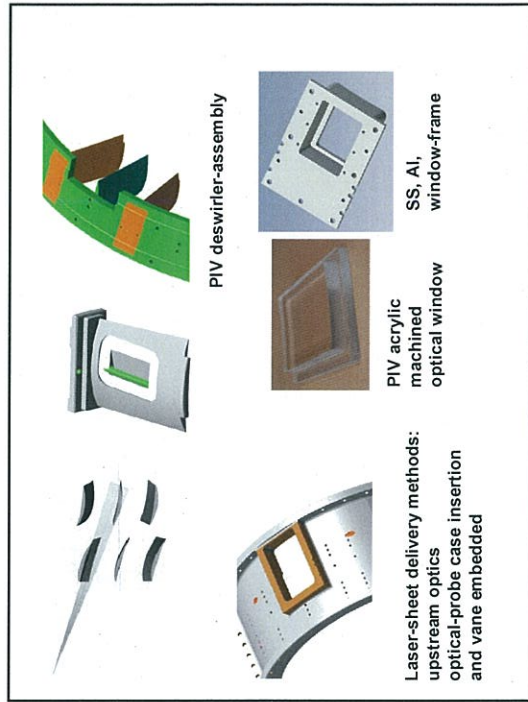
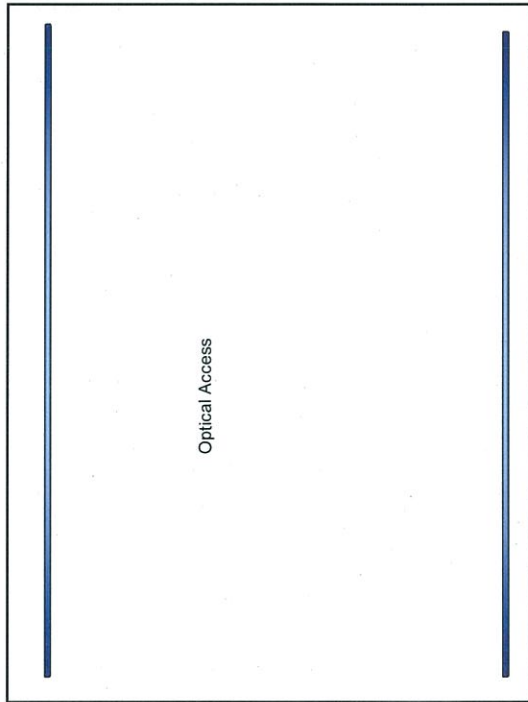
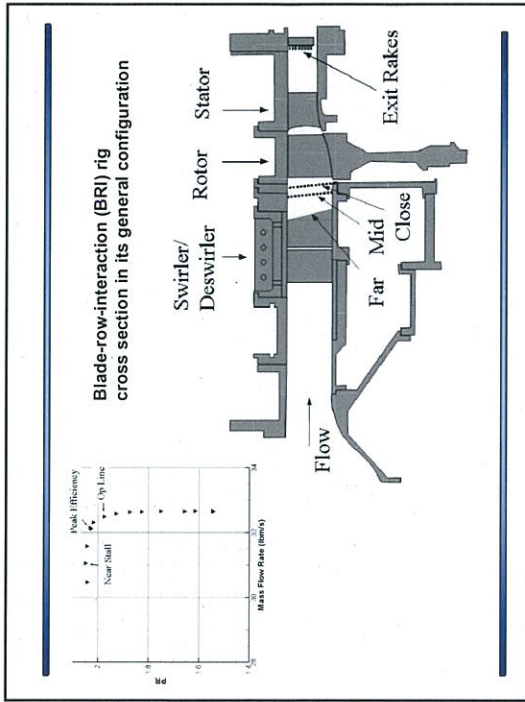
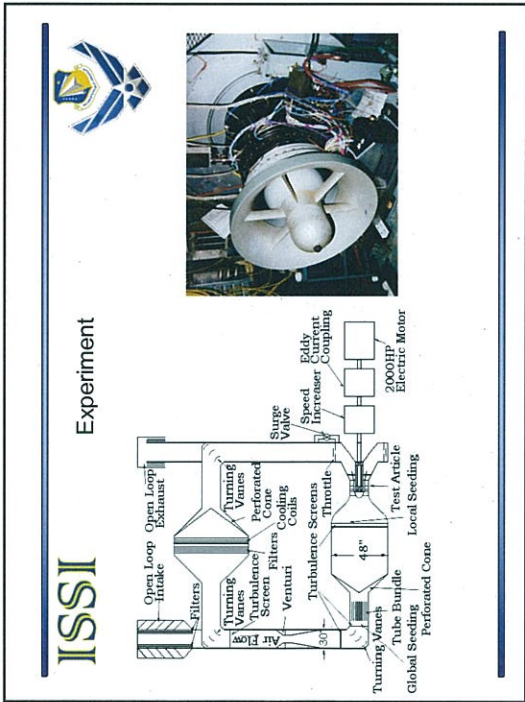
- Measuring velocity fields in rotating blade rows is extremely important to evaluate and improve design systems
- Turbomachinery flowfields are highly unsteady, 2D, 3D
- DPIV offers the potential to investigate the effect of unsteady flowfields on blade loading, blade structural response, wake transport, boundary-layer transition, and flow separation.

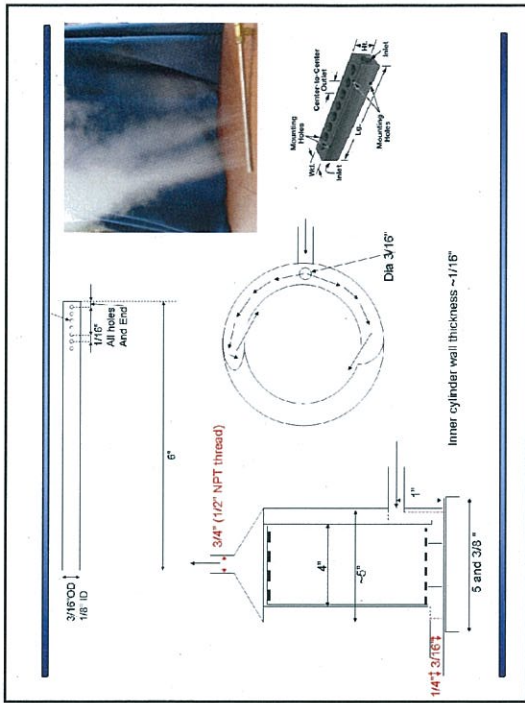
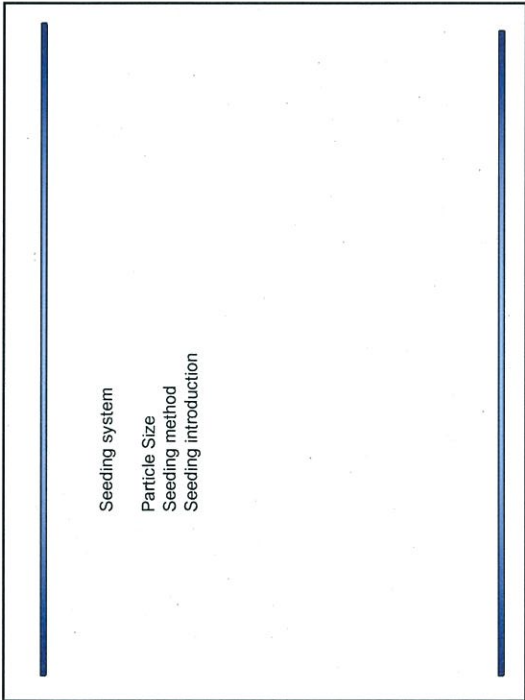
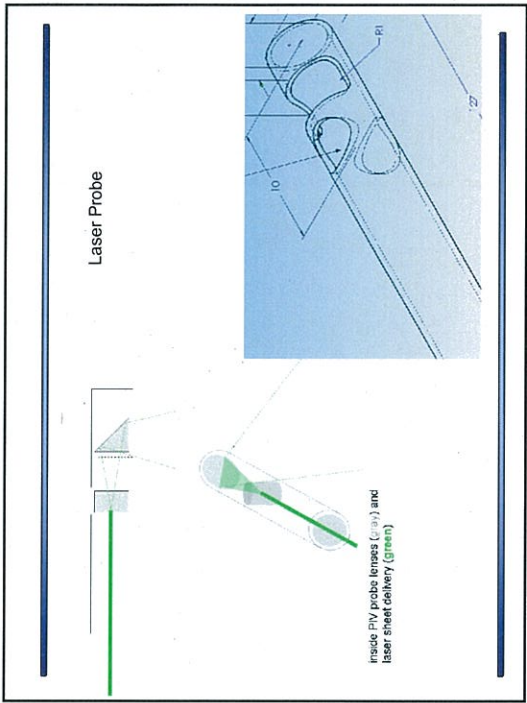
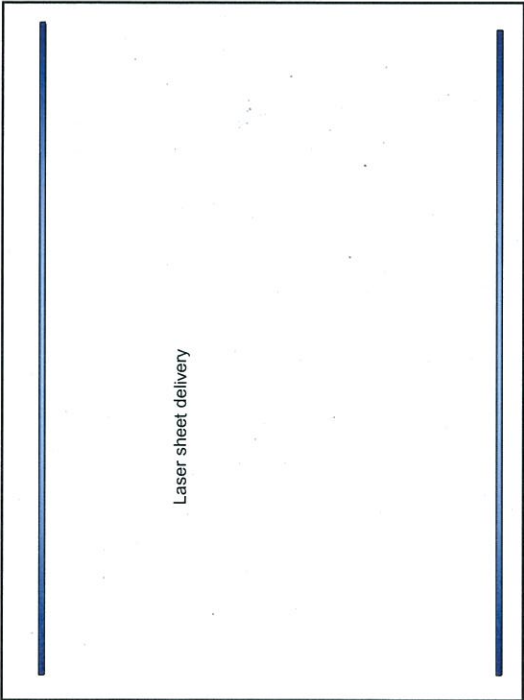


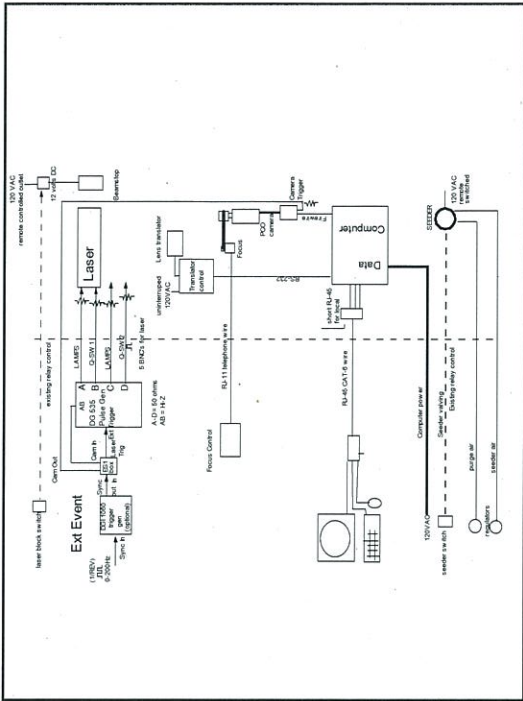
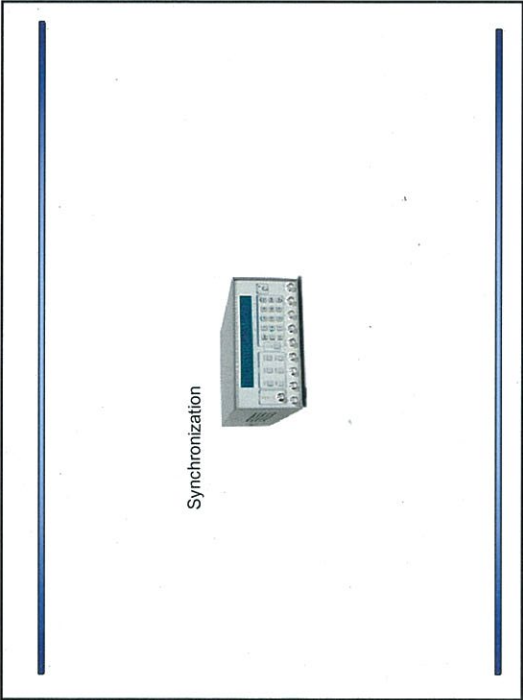
PIV FOR TURBOMACHINERY:

- OPTICAL ACCESS
- IMAGE QUALITY
- SEEDING STRATEGIES
- SURFACE GLARES
- SYNCHRONIZATION









FLOW VIZ

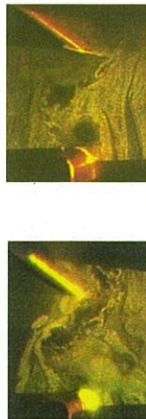
SPAN AND SPACING VARIATION

75% SPAN MID SPACING

90% SPAN CLOSE SPACING

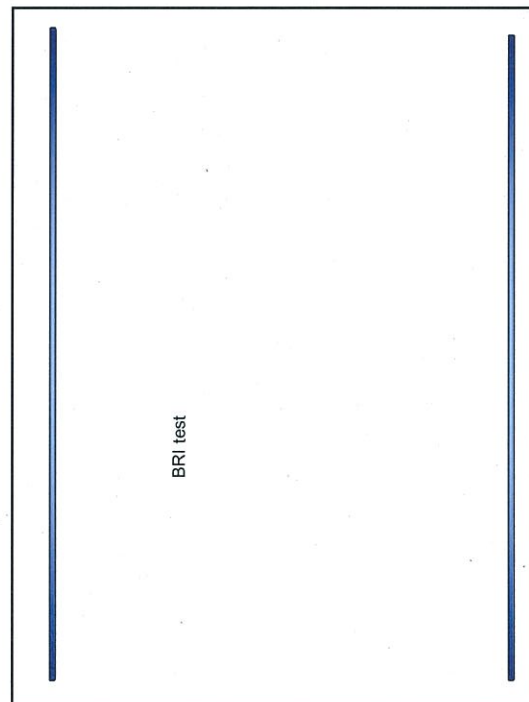
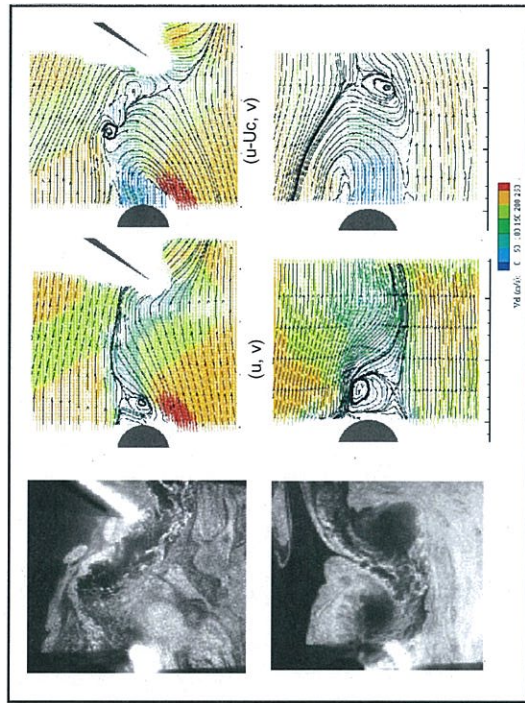
Sample Results

Synchronized Movies FLOW VIZ

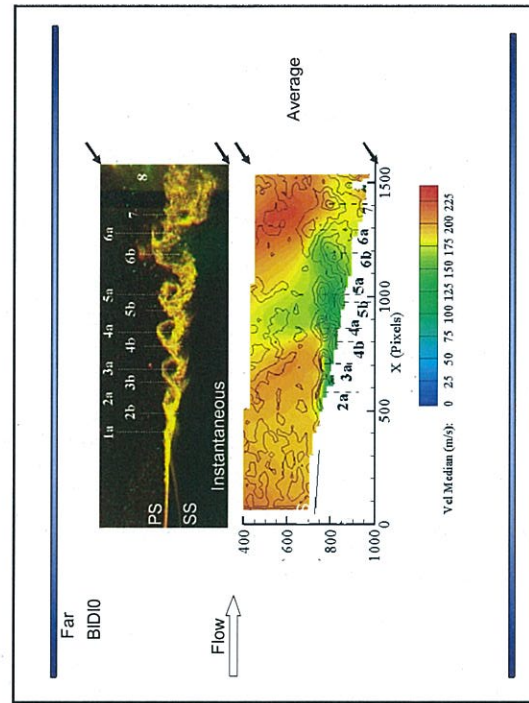


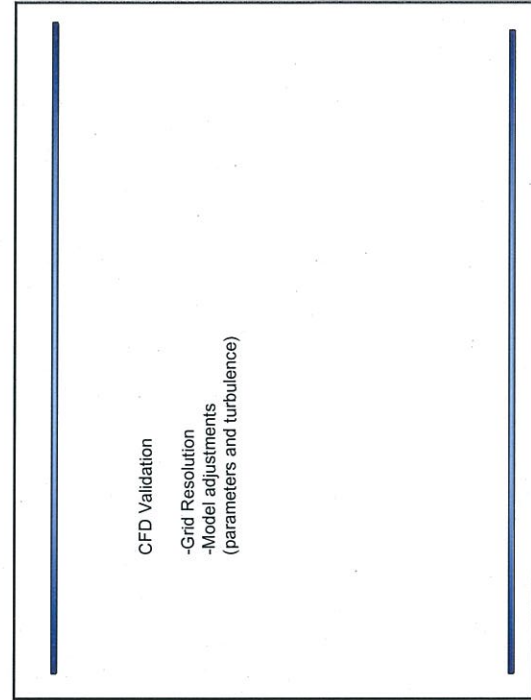
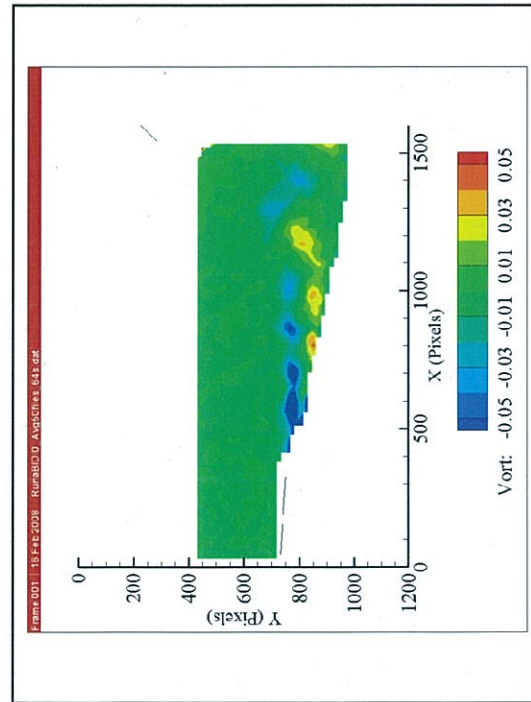
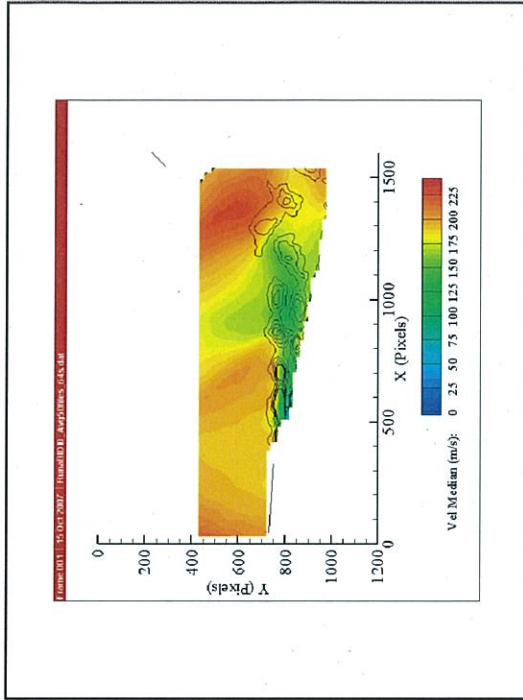
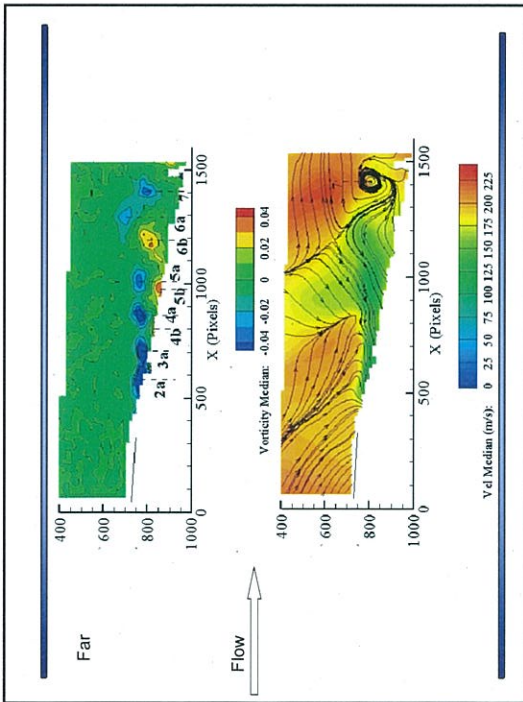
PE

NS

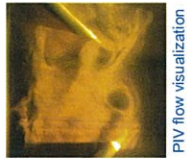
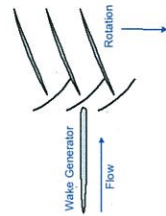


BRI test

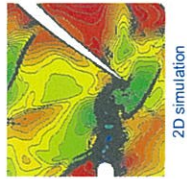




CFD VALIDATION



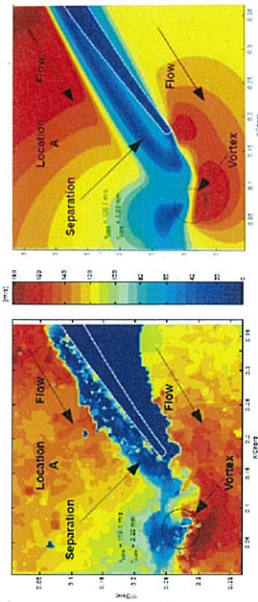
PIV flow visualization



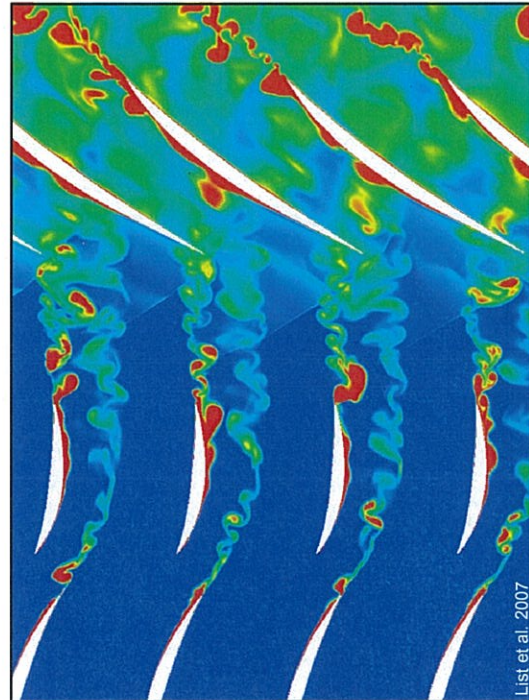
2D simulation

Vortex around the Trailing Edge induced by the passing shock

(absolute velocity as in PIV)



CFD (van de Wall et al. 2006)



List et al. 2007

ISSI

SUMMARY

- PIV FOR TURBOMACHINERY APPLICATIONS HAS BEEN DEVELOPED
- FLOW FIELD KINEMATICS ACCURATELY MEASURED
 - Vortex Shedding
 - Wake Properties
 - Wake-Shock Interaction
- IMPORTANT TEST CASES FOR UNSTEADY CFD VALIDATION
 - Vortex shedding synchronization
 - Shock Interaction
 - CFD grid resolution
 - CFD model validation

PIV Measurements of Blade-Row Interactions in a Transonic Compressor for Various Operating Conditions

Jordi Estevadeordal,¹ Steve Gorrell,² Steve Puterbaugh³

1, Innovative Scientific Solutions Inc., Dayton, OH 45440

2, Brigham Young University, Provo, UT 84602

3, Air Force Research Laboratory, WPAFB, OH 45433

Detailed PIV measurements of the unsteady flow field between an upstream swirler/deswirler stator configuration and a downstream rotor in a transonic compressor are presented. Flow-visualization images and PIV data provide details of vortex shedding, wake motion, and shock interaction phenomena for various operating conditions. The observations and analysis help understand the effects of blade-row interactions on compressor performance and allow verification of time-accurate CFD codes that are used to analyze transonic compressors. Synchronized measurements with various rotor-blade locations allow calculation of phase-averaged velocity fields of the flow and comparison with instantaneous realizations. Vortex shedding and wake topological features are isolated and details of the shock interactions captured. The results reveal details of the vortex shedding phenomena in the new configurations. Data obtained in the suction side of the deswirler using special optical probe approaches are also presented and comparisons with a previous SMI stator configuration are introduced. Different vortex shapes are produced due to different bow shock strength at near stall and peak efficiency. At close spacing, peak efficiency, it was observed that the wake is flatter than at far spacing. Reducing the loading on the BRI stator also produced thinner wakes.

I. Introduction

Blade-row interactions are a significant source of unsteady flow in advanced high-performance turbomachines due to closely spaced and heavily loaded blade rows. Frequently observed unsteady phenomena such as the interaction of a shock with a shed vortex and of a shock with a blade surface produce non-uniformities and irregular flow patterns that influence compressor performance and result in blade-row vibrations and high-cycle fatigue. A better understanding of such phenomena is needed to identify the impact of unsteady aerodynamics on compressor performance, to develop and validate tools for measuring and modeling unsteady flows, and to develop design tools based on improved understanding of unsteady aerodynamics.

The Air Force Research Laboratory (AFRL) Compressor Aero Research Lab (CARL) has been conducting experimental and computational research on transonic-compressor blade-row interactions for several years [1-5]. Experience has shown that both high-fidelity experiments and simulations are essential for understanding the physics of blade-row interactions. As reported in Ref. [1], the Stage Matching Investigation (SMI) rig test showed that the axial spacing between an upstream stator and a downstream transonic rotor has a significant effect on stage performance. Mass flow rate, pressure ratio, and efficiency all decreased as the axial spacing between the wake generator (WG) and the transonic rotor was reduced. Performance was affected by additional loss production that occurred as a result of the interaction between the upstream WG and the downstream transonic rotor.

¹ Senior Research Scientist, ISSI, AIAA Associate Fellow.

² Associate Professor, Dept. Mech. Eng. Brigham Young University, AIAA Associate Fellow.

³ Group Leader, Compressor Aero Research Lab, AIAA Associate Fellow.

Time-accurate simulations using the 3D, unsteady, Navier-Stokes CFD solver known as TURBO combined with PIV data from the SMI experiment [2-3] revealed some important aspects of the production of this additional loss. At close spacing as compared to far spacing, the rotor bow shock was stronger at the location where it interacted with the WG trailing edge (TE). It was observed that the rotor bow shock formed a pressure wave on the upper surface of the WG that propagated upstream until it weakened. The magnitude of loss production was affected by the strength of the bow shock and to what degree it turned from oblique to normal as it interacted with the TE of the WG. It was also observed that at close spacing, vortices were shed from the TE of the upstream stationary blade row in response to the unsteady, discontinuous pressure field that is generated by the downstream rotor bow shock. These shed vortices increased in size and strength and generated more loss as the spacing decreased--a consequence of the effective increase in rotor-bow-shock strength at the stationary blade-row TE. A relationship for the change in shed vorticity as a function of rotor-bow-shock strength was presented that captured the change in vorticity between close- and far-spacing TURBO simulations.

The Blade-Row Interaction (BRI) rig at CARL (Fig. 1) is a continuation of the SMI studies with the WG replaced by a swirler row to turn the flow and a deswirler row to create a wake by diffusion. Preliminary PIV results of the BRI experiments were presented in Ref. [5] and high-fidelity, time-accurate CFD simulations of the BRI rig have been presented in Ref. [6, 7].

Time-accurate CFD codes are now used to simulate compressor operation and investigate complex unsteady-flow phenomena. Experimental results that reveal unsteady-flow effects are essential for validating these design tools and providing additional understanding of the physical phenomena and interaction processes involved in turbomachinery flows that are associated with closely spaced and heavily loaded compressor stages.

Use of the planar, non-intrusive measurement technique Particle Image Velocimetry (PIV) for complex geometries and unsteady applications has allowed researchers to make accurate measurements of instantaneous and averaged turbomachinery velocity fields [3-5]. In the present investigation, a system developed for obtaining high-resolution velocity data from the BRI rig [5] was used to obtain data for various configurations and operating conditions. The PIV system focused on minimum intrusiveness, effective laser delivery inside all regions of interest, and economical receiving windows.

The system allows the collection of data for studies of various parametric and operating-point conditions and the present investigation introduces results comparing two stagger angles, two spacings, and two operating conditions. New data obtained in the suction side of the deswirler blade is also introduced. Data analyses reveal new insight in the vortex shedding characteristics and aid the establishment of comparisons with other WG wakes such as those of the blade row of the SMI [4].

A. Blade-Row-Interaction (BRI) Rig

The Blade-Row-Interaction (BRI) rig is a high-speed, highly loaded compressor that consists of an upstream swirler and deswirler (stator) combination, followed by a transonic fan stage (Fig. 1). The BRI rig is a variation of the AFRL SMI rig described in Ref. [8]. The blunt WG of the SMI rig was replaced with the swirler/deswirler combination. The objective of the new hardware was to simulate an embedded transonic fan stage while producing a wake through diffusion with realistic geometry (thin TE) rather than base drag. The rotors used in the SMI and BRI rigs were designed for axial inlet flow and, thus, required a swirler and deswirler to create a wake through diffusion while maintaining axial inlet flow to the rotor.

The rig was designed to permit the stator-to-rotor axial spacing to be set to three values--“close,” “mid,” and “far”--as shown in Fig. 1. The swirler/deswirler combination creates a wake through diffusion rather than base drag from the thick TE designs of previous WGs [1-3]. The BRI rig also incorporates variable stagger of the swirler vanes to alter the loading on the deswirler vanes and adjustable clocking between the swirler and deswirler blade rows to optimize the position of the swirler wake in the deswirler blade row and the amount of total pressure loss produced by the swirler and deswirler.

One of the objectives of the BRI investigation was to analyze the effect of changing the stagger angle, the stator/rotor axial spacing, and the operating condition. The design parameters of the BRI rig stage are summarized in Table 1 and a map of efficiency in Fig. 2. The rotor and stator in the BRI rig are different from those used in the SMI rig. The SMI simulated an embedded transonic core stage, while the BRI rig simulates an embedded-fan stage. The major differences between the fan and core stages are fewer rotor blades (28 in the fan versus 33 in the core) and higher tip speed (414.53 m/s in the fan versus 341.37 m/s in the core), resulting in the tip relative Mach number being increased (1.389 versus 1.191) and the hub relative Mach number being transonic (1.100 versus 0.963).

B. PIV System

The PIV system developed for the BRI rig [5] was used for this investigation. The basic system includes two lasers (Spectra Physics Nd:YAG, 532 nm) for double-instantaneous marking of the sub-micron seed particles in the flow field. The combined beams are directed through sheet-forming optics using various approaches and illuminate the test section with a 2D plane of thickness of ~ 1 mm. The seeding-system design is based on seeders of the solid powder cyclone type and includes a valve system for seeding, stirring, and purging. The timing of these various valves can be controlled and synchronized to the rest of the PIV system. The seeding ports are located at the beginning of the contraction (the area of maximum diameter and minimum speed) to exert negligible perturbation on the flow; they are positioned in the flow path of the laser sheet. The seeder tube is located sufficiently far upstream of the PIV window area and injects negligible amounts of air and seed to avoid exerting any significant aerodynamics perturbation in the flow under study. The seeding uniformity was enhanced by adding a series of holes in the tube and a honeycomb in front of them. The light scattering from the seed particles (submicron high-purity alumina-- Al_2O_3) is recorded on a cross-correlation CCD camera with 1600×1200 pixels (Model PCO 1600); this camera is capable of acquiring double exposures with an interframe time of 150 nsec. Although the camera repetition rate can be set as high as 15 Hz, it is set at 10 Hz for synchronization with the laser repetition rate. A 105-mm Nikon lens is used at an F stop of 5.6. The rotor one-per-revolution signal is used for triggering the synchronization system. A customized interface and a digital pulse generator (Stanford DG535) are employed for synchronization and remote control of the system. The horizontal viewing area ranges from ~ 46 to 67 mm, and the time delay between the two frames of the double exposure is adjusted for each of the viewing areas and its flow speed to provide sufficient resolution and accuracy. In most experiments, this time was set at 1.5 μsec to yield free-stream displacements around 10 pixels. Once the PIV images have been captured and digitized, the velocity field is obtained using cross-correlation techniques over interrogation domains of the images and PIV software. The uncertainty that results from various PIV algorithms (e.g., single pass, multi-pass) and data-filtering techniques (e.g., standard-deviation trimming, median) is between one and 10% as has been described in the literature [4].

Machined and polished to optical-quality curved acrylic windows were used for image receiving optics. For each spacing, a viewing window was machined on one side to have the same curvature as the rotor inner housing (radius of 241.3 mm) and on the other side to be flat. This produced a small variable magnification across the field of view, which must be used for inferring the velocity field. The PIV windows were held in position with specially designed frames made of anodized aluminum. Thermocouples were installed in the windows and monitored to ensure that temperatures did not reach the acrylic damage threshold in continuous operation ($\sim 200^\circ\text{F}$) during the experiments. The pressure differential across the window was negligible compared to the acrylic yield strength and would not produce acrylic deformation at the temperature of the experiments. The PIV surrounding viewing areas were painted flat black to minimize reflections.

From the computational and experimental results from the SMI rig, it was determined that taking PIV measurements on both the pressure and the suction surfaces of the deswirlers over the last 30% chord would be very desirable. Several laser-sheet delivery systems were designed to accomplish this [5]. Figure 3 contains schematics of the optical approaches used in the present investigation. One approach involves delivery of the laser from upstream in the settling chamber through the use of a mirror [Fig. 3(a)]. The laser sheet is formed outside the tunnel and is sent to the mirror through a port with a window in the settling chamber. Another involves the use of small (< 6 -mm-diam) cylindrical lenses mounted in an optical probe that is inserted and secured in the case just forward of the rotor [Fig. 3(b)]. The laser-sheet plane can be set perpendicular to the vane of interest [Fig. 4] at any span in both of these approaches. A new design that implements a curved laser-sheet that can follow any three-dimensional shape [9, 10] will allow obtain PIV data in circumferential planes.

II. Results

The PIV system allows acquisition of PIV data in the various BRI configurations. In a previous study [5], samples from the acquired data at far spacing for peak efficiency operating condition were presented as well as illustrative observations using flow visualization, instantaneous and averaged velocity fields, streamline patterns, and vorticity. This investigation continues that effort and includes new observations from data processed from far and close spacings, two stagger configurations (0 and -3 degrees) and peak efficiency and near stall operating conditions, all at 80% clocking. Another focus of this research is to compare the BRI flowfield with the previously tested SMI rig; this flow field comparison is introduced in the present study through preliminary analyses of vortex shedding characteristics. Most of the present data were obtained using the upstream laser-sheet delivery method on

the deswirler pressure side at 50% span. Data is also presented from the suction side acquired at 72% span using the optical probe approach.

At 99% corrected speed, where most of the BRI experiments were performed, consecutive rotor blades are separated in time by $\sim 140 \mu\text{sec}$ (blade period) corresponding to ~ 11 degrees in angle (blade-row pitch). Seven blade locations (delays/clockings), separated by $20 \mu\text{sec}$, were typically chosen to characterize the flow field in a blade-row pitch. Observations are made from both qualitative flow-visualization and quantitative velocity-field measurements. Data analysis included inspection of selected flow-visualization images (obtained by increasing the amount of seeding) and analysis of instantaneous and averaged velocity-field data obtained using various algorithms. Other property derivatives of the velocity field such as vorticity and streamlines were also used. Overlaying quantitative properties on flow visualization images is also used to highlight important features. Most averages consist of ~ 50 realizations, use the median, and the processing was performed using parallel computing in Linux clusters [11].

A. Vortex Shedding

One significant observation from the SMI and BRI experiments has been the synchronization between the wake vortex shedding and the rotor passing frequency [3-5]. This was attributed to the rotor bow shock impacting the TE of the upstream stator blade producing a change in circulation. On the SMI rig the influence and synchronization between the blade passage and the vortex shedding decreased with increasing axial spacing. This was attributed to a weakened rotor bow shock impacting the stator TE at larger axial spacing. It was also observed that the vortex location repeatability with respect to the rotor location (or 'phase') decreased with downstream distance (other names for the rotor locations or phases are blade clockings or delays and are denoted as 'BIDL'). This was attributed to natural downstream wake evolution. At closer spacing, both, the impacting shock was stronger and the downstream distance lower so most vortex shedding observed appeared 'strongly forced' and 'phase-locked' [12] by the rotor passage. Natural (or 'unforced') wakes (and shear layers) come about through small perturbations ('linear theory' regime) but can also be driven through artificial forcing such as acoustic waves from a loudspeaker [12]. The relation between the natural frequency and the forcing wave shape, frequency and amplitude determines the vortex dynamics [12]. In the compressor stator wakes the rotor potential field represents the hydrodynamic forcing with a frequency and amplitude that influences the vortex shedding.

In this section, new qualitative observations related to the strength of the synchronization and to the size and frequency of the vortex shedding is presented. One observation relates to the relative synchronization when the potential field accompanying the rotor does not include a shock and another relates to the different vortex shedding properties (vortex sizes and shedding frequencies) for the wakes of SMI and BRI. Quantitative analysis of the synchronization strength (through determination of phase-coherent and phase-random quantities [12]) and of the vortex shedding frequency and vortex strength will be performed in the future.

When the rotor speed was not transonic and did not produce a bow shock, for example, experiments at 85% speed at far spacing performed in the SMI rig, vortex shedding appeared only weakly 'locked' to the blade passage [Fig. 5 a,b]. This was first determined from examination of various instantaneous flow visualizations showing vortex shedding variations for a given BIDL. Lack of data near the TE of the stator however hindered determining the origin of the vortex shedding. Figure 5 (a, b) also shows the averaged vector field overlaid in a sample visualization image and the contours for two spans. In both cases the average field appears mostly washed out of special features like the obvious vortex seen in the visualizations; the low speed region (shown in green contours) corresponds to the wake area and appears approximately uniform, especially with downstream distance. As a consequence, the averaged vorticity appeared with constant positive and negative bands at the edges of the wake with the free stream. This is different from the transonic speed wakes where vortices are locked in a fixed position with respect to the blade delay and thus turn out in the averaged properties [5]. Close spacing samples are shown in Fig. 5 (c) to reveal that at 85% speed the close spacing potential field is sufficient to phase-lock the vortex in position. The averaged field shows that dependence in the vectors direction and in the contours, where low speed regions corresponding to the vortices are not washed out. Examination of various instantaneous flow visualizations indeed revealed that vortex locking for each blade delay at close spacing was consistent.

Flow-visualization images and PIV averages from a far-spacing configuration (peak efficiency, 0° stagger) already displayed the vortex shedding synchronization with the rotor for the BRI rig in Ref. [5]. In that investigation, although shadows from the upstream stator blades prevented visualization of the suction side of the deswirler TE, typical coherent structures of wake vortex shedding could be seen clearly; the approximate axial location of the centers of the structures (center of unseeded cores) were indicated by dashed lines, numbers and characters (a for top or pressure side, b for bottom or suction side) for reference. The vortex location consistency

persisted in the averaged velocity and vorticity for each rotor 'BIDI'. Again, as with free-wake phenomena, when the wake travels downstream, naturally more wake motion occurs due to the turbulent random nature of the wake vortices. At far spacing, the wake mixes out more as it travels farther downstream, and naturally more randomness occurs. Nevertheless, when studying the characteristics of a wake in a blade row of a transonic compressor, one must take into account a variety of complex interactions well beyond free-wake properties--interactions such as particular unsteadiness under the rotor passage and shocks, adverse pressure gradients, complex geometry, and three-dimensionality. Like in SMI, this 'phase-locking' was attributed to the synchronization between the rotor passage and the vortex shedding in which the transonic rotor blade passage produced a strong perturbation at the TE of the stator blade that forced the vortex shedding. It was found in SMI [3, 4] and BRI [5] that this effect is stronger as the spacing is reduced and also when the operating condition is changed toward near stall (due to the stronger potential field reaching the stator). The distinct features observed from data obtained in the SMI rig were the thicker wake with larger vortices (qualitatively about twice as large and scaled by the blunt TE) compared to those observed in BRI and that the number of vortices in SMI is about half that from BRI. This is consistent with both rigs having similar free stream and blade period conditions (~ 7 kHz, or 140 μsec) at 100% speed that yield a constant non-dimensional frequency (Strouhal number) ~ 0.2 in both cases based on measurements of vortex shedding wavelength, TE wake thickness and an appropriate free stream velocity. Quantitative studies are under way to determine the exact vortex size and frequency for each rig and the sequence of events at the TE that determine the wake characteristics for a given Reynolds number. The study in Ref. [13] reproduced a sequence of events (shock, vortex, blockage, and separation) that occur after the shock interacts with the TE and the study in Ref. [14] showed that the passage of the strong shock by the TE wake can produce strong separation that momentarily generates a shear layer (co-rotating vortices) prior to the wake (counter-rotating vortex pairs) recovery. These sequences provide insight in how strong forcing events (such as shock) can yield large vortices and with laminar cores even at high Reynolds numbers, consistent with present observations of large vortices in the transonic flow. In the case of far spacing the final shaping of the vortex shedding is more susceptible to an interaction of the rotor forcing with the natural wake evolution, a key of the blade-row interaction.

B. BRI Averaged Fields (Far and Close)

The BRI data for far spacing at 50% span presented in Ref. [5] was completed for one blade period in the present investigation for peak efficiency and near stall conditions. Figure 6 presents the velocity field for these two operating conditions using a coarse grid (two iterations, 64 pixel cell resolution, 75% cell overlap) to introduce the general flow field evolution in one blade period. Of interest is the distinct synchronization or phase-locking for each case. The near stall condition, having stronger shocks, shows different wake structure than the peak efficiency. Both cases display phase-locking but with distinct vortex configurations. These velocity maps show the main features of the compressor flow (such as the low-velocity region of the wake, the abrupt changes in velocity across the shock, and the accelerating flow region into the rotor passage) but higher resolution displays more details and defines these features in greater detail. The data was thus analyzed using higher resolution processing techniques [4] with a finer grid obtained from three iterations, 32 pixel cell resolution (1.33 mm) and 75% overlap that yielded grid points with separation of 8 pixels (0.33 mm). This produces noisier vorticity maps but provides kinematic details not possible at coarser resolutions. This was pointed out in Ref. [5] for example in the wake regions, where spots of lower velocity were captured. This finer grid also allowed tracking more vortices in the wake near the stator TE. In the velocity contour maps the vortex locations are in the regions with high velocity gradients which are readily seen by the areas of contact of a high and a low velocity in this absolute frame. An example of the averaged velocity field in the finer grid for one rotor blade period is shown in Fig. 7 with the seven blade delays corresponding to the peak efficiency, 0-deg, and 50% span configuration shown in Fig. 6 (a). The contours of velocity show more details of the flow field accompanying the rotor passage, more detailed structure of the wake, and more details of the vortices at each rotor blade delay. The averaged streamline patterns shown in Figure 8 (a, b) colored by averaged velocity for two blade delays used the subtraction of convective velocity for tracking the vortices; overlaying them on the flow visualization image reveals the consistency of their location. Figure 8 (c) adds a vorticity plot to further corroborate this fact. Further analyses will allow important properties and flow phenomena related to the performance be calculated [13, 14] and they are currently under study. It will also allow important verification of numerical simulations.

Some data has also been analyzed for close spacing, peak efficiency at 50% span and preliminary observations are presented in Fig. 9 for 0-degree stagger and three blade delays. A distinctive feature not observed before is the shape of the wake after the first vortex in the BIDI0. This flattening shape in that region was observed in all images and it is consistent with the averaged velocity field at this condition, which displays a high speed region upstream of the rotor that extends to the stator TE. This rotor potential field has thus a strong wake interaction at close spacing.

The other two BDI reveal the characteristics of the shock interaction with the stator blade and confirms the CFD prediction that the shock turns normal at the stator pressure side [3].

Preliminary results from -3 degree stagger experiments are presented for far spacing in Fig. 10 for two blade delays. The trend of the wake is to be thinner compared to the 0 degree stagger (Figs. 6-8). This is in agreement with the deswirl configuration having less separation (or boundary layer thickness) under lower loading and producing a thinner wake. Flow visualization for the -3 degree stagger at close spacing is shown in Fig. 11 and displays the interesting wake waviness in this case. Future analysis will concentrate in quantification of these wake characteristics for each configuration.

C. BRI Deswirl Suction Side

Using the current upstream laser-sheet delivery method the suction side is in a shadow. The view shows that the pressure side has a small thin (turbulent) boundary layer consistent with earlier studies [13, 14] and it can be inferred from that view that vortex shedding is emanating from the suction side in counter-rotating vortex pairs. These vortices can produce blockage and induce separation [13, 14]. The research continues with data being acquired in the suction side of the stator deswirl blade. In the present study some instantaneous results illuminating the suction side with the optical probe at 72% span about 25% chord upstream of the TE for the far spacing and -3 degree stagger at peak efficiency were obtained. They give some preliminary insight in the suction side flow. Figure 12 shows flow visualizations for two blade delays and display a clear region without seeding which can correspond to a thick boundary layer or a separation region. Lack of seeding in this area is most probably due to lack of mixing from the free stream into a separated region; this is similar to difficulties encountered when attempting to seed separated areas and inside of vortices. In the case of a vortex, for example, the center remains unseeded typically due to lack of mixing from the free stream [14]; the (laminar) viscous core of a vortex can often be modeled having similar properties to Rankine (solid body rotation core) vortex where the centrifugal forces are balanced by the pressure gradient. In this scenario, only particle lag can account for seeding being moved towards the center (negative lag) or outwards to the periphery (positive lag). In the present experiments it is clear that at higher spans (e.g. 90 %) and at increasing downstream distances, the mixing into the wake has occurred and seeding is present. The suction side unseeded area is of the same size of the wake emanating from the TE. Special design techniques would be required to allow seeding these areas. The data presented for the suction side view provide velocity maps using the finer grid as those shown in Fig. 13. The shock passage can be readily seen as well as the various counter-rotating vortices of the wake. Although this is evidence of the wake emanating from the suction side the lack of data in the surface prevents from finding the actual flow characteristics such as the finding in Ref. [6] simulations that have shown that a separation bubble periodically forms and collapses on the suction side of the deswirl aft of 50% chord. Designs to seed these areas are under investigation.

III. Summary

Further analysis of the AFRL SMI and BRI rigs has been performed using PIV. Flow visualizations, instantaneous and averaged PIV was presented for various configurations. Information from the data was used to gain insight into the relation between the passing shock and the impulsive vortex shedding. At 100% speed the BRI vortices were synchronized to the rotor passing at both close and far spacing. Analysis of SMI data at 85% speed showed that at close blade row axial spacing the rotor potential field may induce vortex shedding synchronization even when a rotor bow shock is not present. Comparing BRI far spacing data at different operating points showed that different vortex shapes are produced due to different bow shock strength at near stall and peak efficiency. At close spacing, peak efficiency, it was observed that the wake is flatter than at far spacing. Reducing the loading on the BRI stator also produced thinner wakes. Data from the suction side was introduced also and proved very valuable for identifying other mechanisms that can contribute to vortex shedding such as suction-side separation. Vortex shedding analyses and comparison with previous SMI rig was also introduced. It was observed that SMI had about twice as thick wake as the BRI and about half the vortex shedding frequency.

The methods for adapting PIV techniques for complex turbomachinery environments, including the use of receiving windows made by economical and rapid prototyping techniques and optical probes for illumination of areas with difficult optical access were successfully used. The effectiveness of these techniques has been demonstrated through full characterization of the interaction between a deswirl stator wake under various loadings and operating conditions and a rotor bow shock. Flow visualization--along with analysis of instantaneous and averaged velocity-field data, vorticity, and streamlines--was shown to permit identification of important details of the unsteady flow field.

Future work will include comparison of the aerodynamics effects on performance and analysis of other spacings.

Acknowledgments

The authors acknowledge the technical assistance of the CARL group at Wright-Patterson AFB and ISSI personnel during the experiments. The authors recognize Mr. Sean P. Nolan of CARL for many valuable discussions. The authors acknowledge the Propulsion-Directorate management for supporting the research and the presentation and publication of this paper. The authors acknowledge the Propulsion-Directorate management of Wright-Patterson AFB for supporting the research and the presentation and publication of this paper.

References

- ¹Gorrell, S. E., Okiishi, T. H., and Copenhaver, W. W., "Stator-Rotor Interactions in a Transonic Compressor, Part 1: Effect of Blade-Row Spacing on Performance," *ASME Journal of Turbomachinery*, Vol. 125, No. 2, April 2003, pp. 328-335.
- ²Gorrell, S. E., Okiishi, T. H., and Copenhaver, W. W., "Stator Rotor Interactions in a Transonic Compressor: Part 2 - Description of a Loss Producing Mechanism," *ASME Journal of Turbomachinery*, Vol. 125, No. 2, April 2003, pp. 336-345.
- ³Gorrell, S. E., Car, D., Puterbaugh, S. L., Estevadeordal, J., and Okiishi, T. H., "An Investigation of Wake-Shock Interactions in a Transonic Compressor with DPIV and Time-accurate CFD," *ASME Journal of Turbomachinery*, Vol. 128, October, 2006, pp. 616 - 626.
- ⁴Estevadeordal, J., Gorrell, S., Copenhaver, W., "PIV study of Wake-Rotor Phenomena in a Transonic Compressor under Various Operating Conditions," *AIAA Journal of Propulsion and Power*, Vol. 23, No. 1, January-February 2007, pp. 235-242.
- ⁵Estevadeordal, J., Gorrell, S., Gebbie, D., Puterbaugh, S., "PIV study of Blade-Row Interactions in a Transonic Compressor," AIAA Paper 2007-5017, *43th AIAA/ASME/SAE/ASEE Joint Propulsion Conference and Exhibit*, Cincinnati, OH, July 2007.
- ⁶List, M., Gorrell, S., Turner, M., "Investigation of Loss Generation in an Embedded Transonic Fan Stage at several Gaps Using High Fidelity, Time-Accurate CFD," Paper GT2008-51220, ASME Turbo Expo, Berlin, Germany, June 9-14, 2008.
- ⁷List, M. G., Gorrell, S. E., Turner, M. G., and Nimersheim, J. A., "High Fidelity Modeling of Blade Row Interactions in a Transonic Compressor," AIAA Paper 2007-5045, *43th AIAA/ASME/SAE/ASEE Joint Propulsion Conference and Exhibit*, Cincinnati, OH, July, 2007.
- ⁸Gorrell, S. E., Copenhaver, W. W., and Chriss, R. M., "Upstream Wake Influences on the Measured Performance of a Transonic Compressor Stage," *AIAA Journal of Propulsion and Power*, Vol. 17, 2001, pp. 43-48.
- ⁹Estevadeordal, J., "Curved Laser-Sheet for Conformal Surface Diagnostics, "Application of Advanced Laser Diagnostics to High Impact Technologies," Quarterly Status Report 2829-20 (Innovative Scientific Solutions, Inc., Dayton, OH, June 2008).
- ¹⁰Marks, C., Sondergaard, R., Estevadeordal, J., Wolff, M., "A Span-wise and Stream-wise PIV Investigation of Transitional Flow around a Highly Loaded LPT Blade Using a Curved Laser Sheet," *47th Aerospace Science Meeting, Orlando, FL, 5-8 January, 2009*.
- ¹¹McCrack, T.W., Estevadeordal, J. and Puterbaugh, S. L., "Parallel Computing for Linux Clusters—Application to Particle Image Velocimetry," AIAA Paper 2005-1385, Reno, NV, Jan 10-13, 2005.
- ¹²Estevadeordal, J., and Kleis, S., "High-Resolution Measurements of Two-Dimensional Instabilities and Turbulence Transition in Plane Mixing Layers," *Experiments in Fluids*, Vol. 27, No. 4, 1999, pp. 378-390.
- ¹³Langford, M. D., Guillot, S. A., Ng, W. F., Breeze-Stringfellow, A., Solomon, W., Estevadeordal, J., "Experimental Investigation of the Effects of a Moving Shock Wave on Compressor Stator Flow," *ASME Journal of Turbomachinery*, Vol. 129, No. 1, January 2007, p. 127.
- ¹⁴Estevadeordal, J., Langford, M., Breeze-Stringfellow, A., Guillot, S., Ng, W. "PIV Investigation of the flow field in a Transonic Compressor Cascade with a Moving Shock Wave," AIAA Paper 5064-509, *43th AIAA/ASME/SAE/ASEE Joint Propulsion Conference and Exhibit*, Cincinnati, OH, 8-11 July, 2007.

Table 1. BRI Aerodynamic Design Parameters

PARAMETER	ROTOR	STATOR
Number of Airfoils	28	49
Aspect Ratio - Average	0.916	0.824
Inlet Hub/Tip Ratio	0.750	0.833
Flow/Annulus Area, kg/s/m ²	195.30	--
Tip Speed, Corrected m/s	414.53	--
M _{REL} LE Hub	1.100	0.830
M _{REL} LE Tip	1.389	0.700
Max D Factor	0.545	0.506
LE Tip Diam., m	0.4825	0.4825

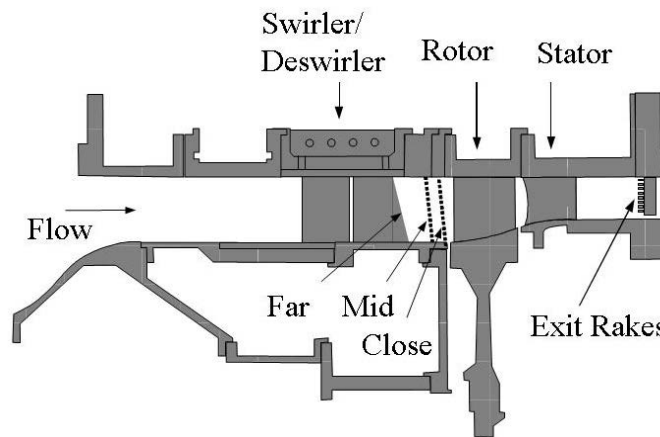


Figure 1. Blade-row-interaction (BRI) rig cross section in its general configuration.

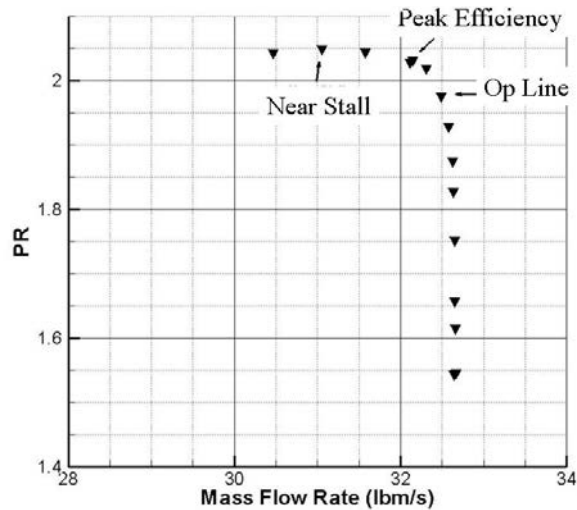


Figure 2. Overall stage pressure ratio (PR) for mid-spacing configuration (80% clocking, -3° stagger).

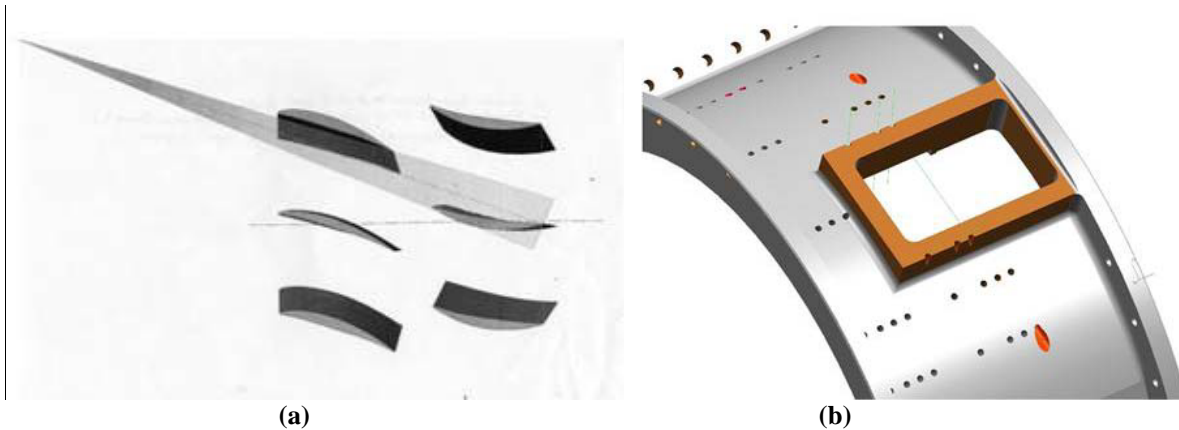


Figure 3. Laser-sheet delivery methods used: upstream optics (a), optical-probe case insertion (b)

Swirler | Deswirler | Rotor |

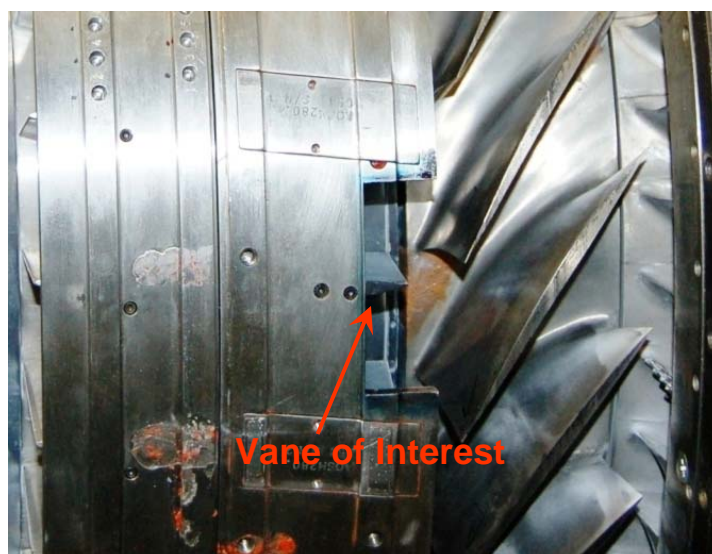


Figure 4. Photograph of vane of interest in BRI rig.

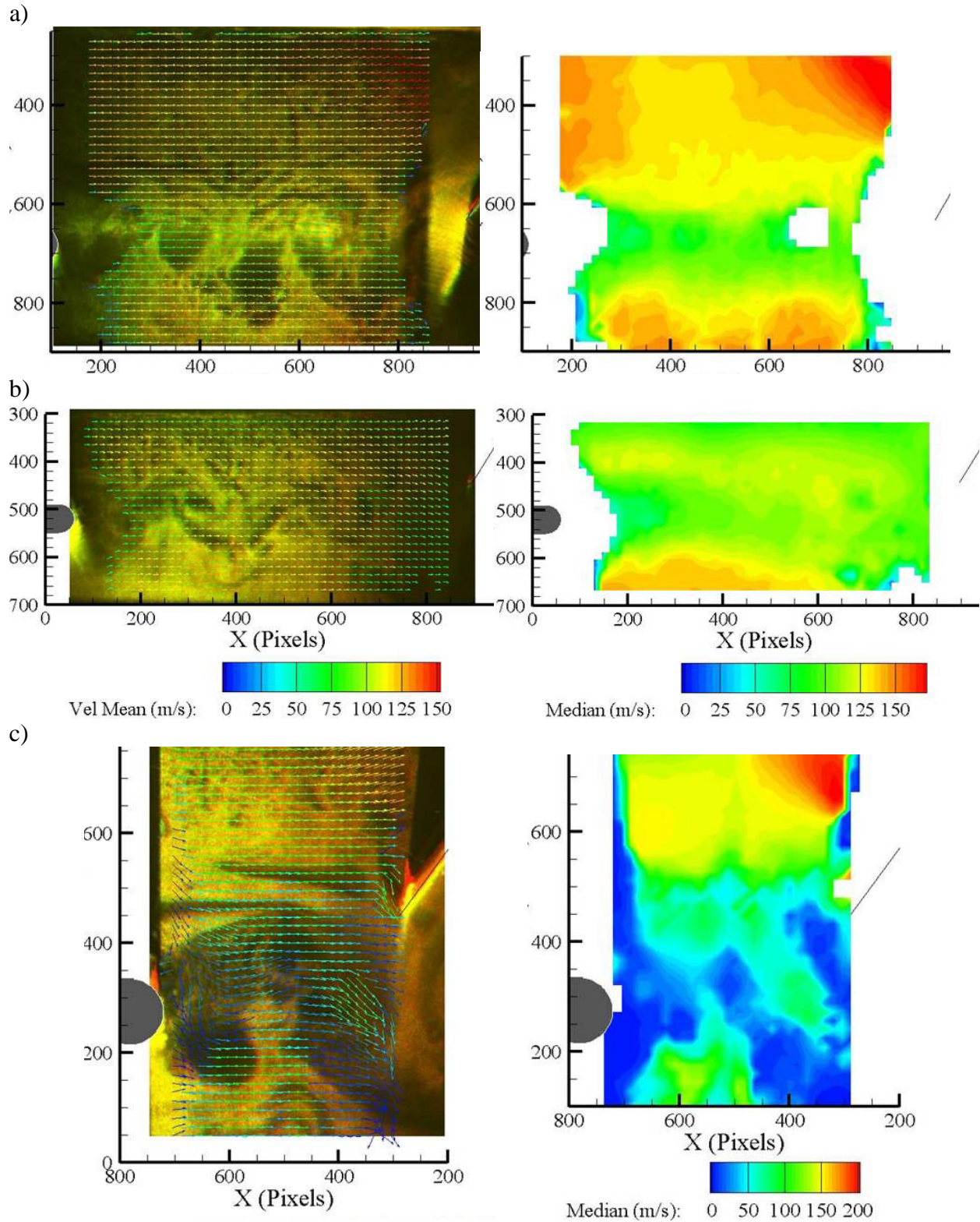


FIG 5 SMI samples visualizations and averaged velocity filed at 85% speed (BIDI 20): far spacing [a) 75% span, b) 90% span]; close spacing [c) 85% span].

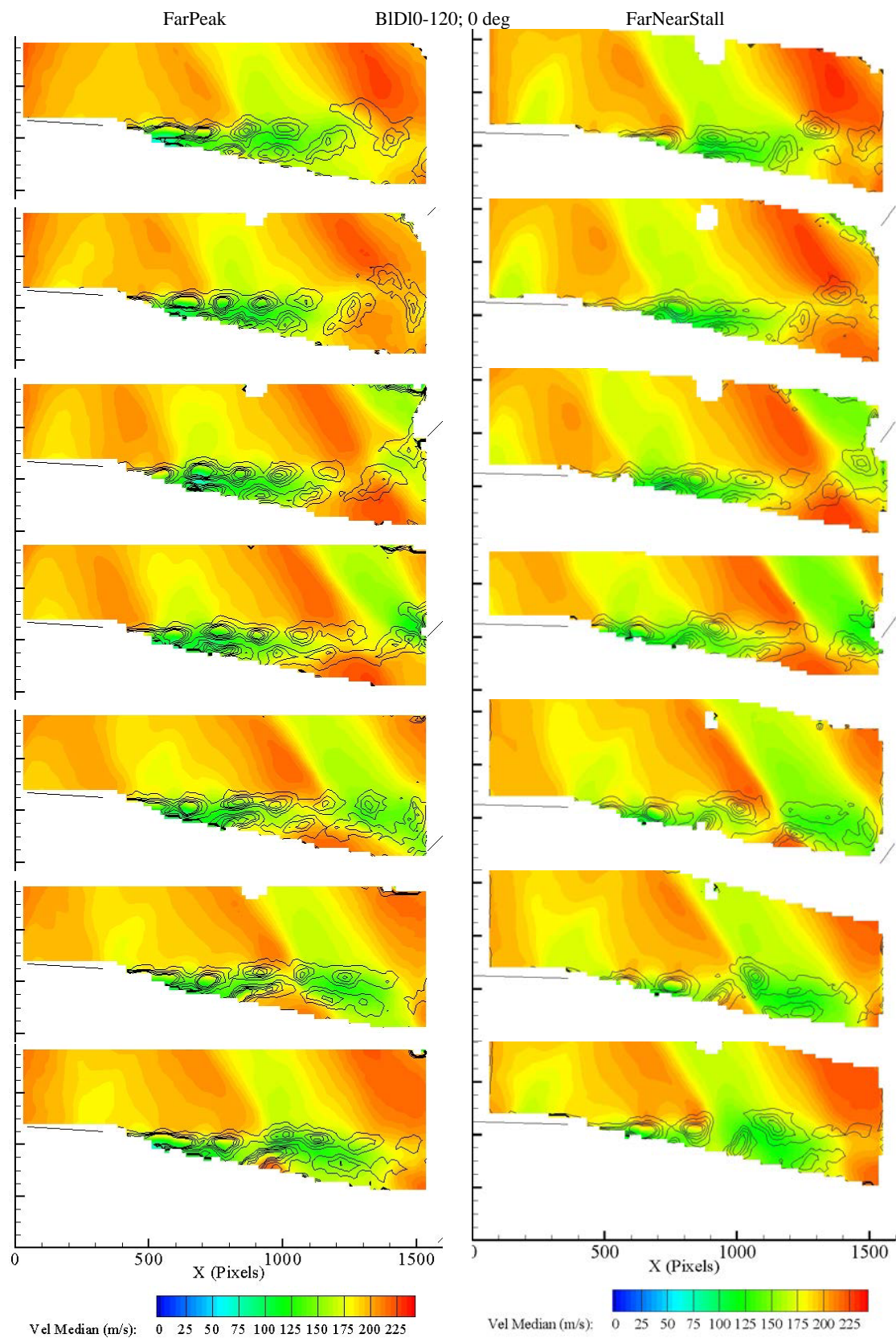


FIG 6 Far Spacing, 50% span, 0 deg, Peak Eff. and Near Stall): Averaged velocity with vorticity contours for one blade period (coarser grid).

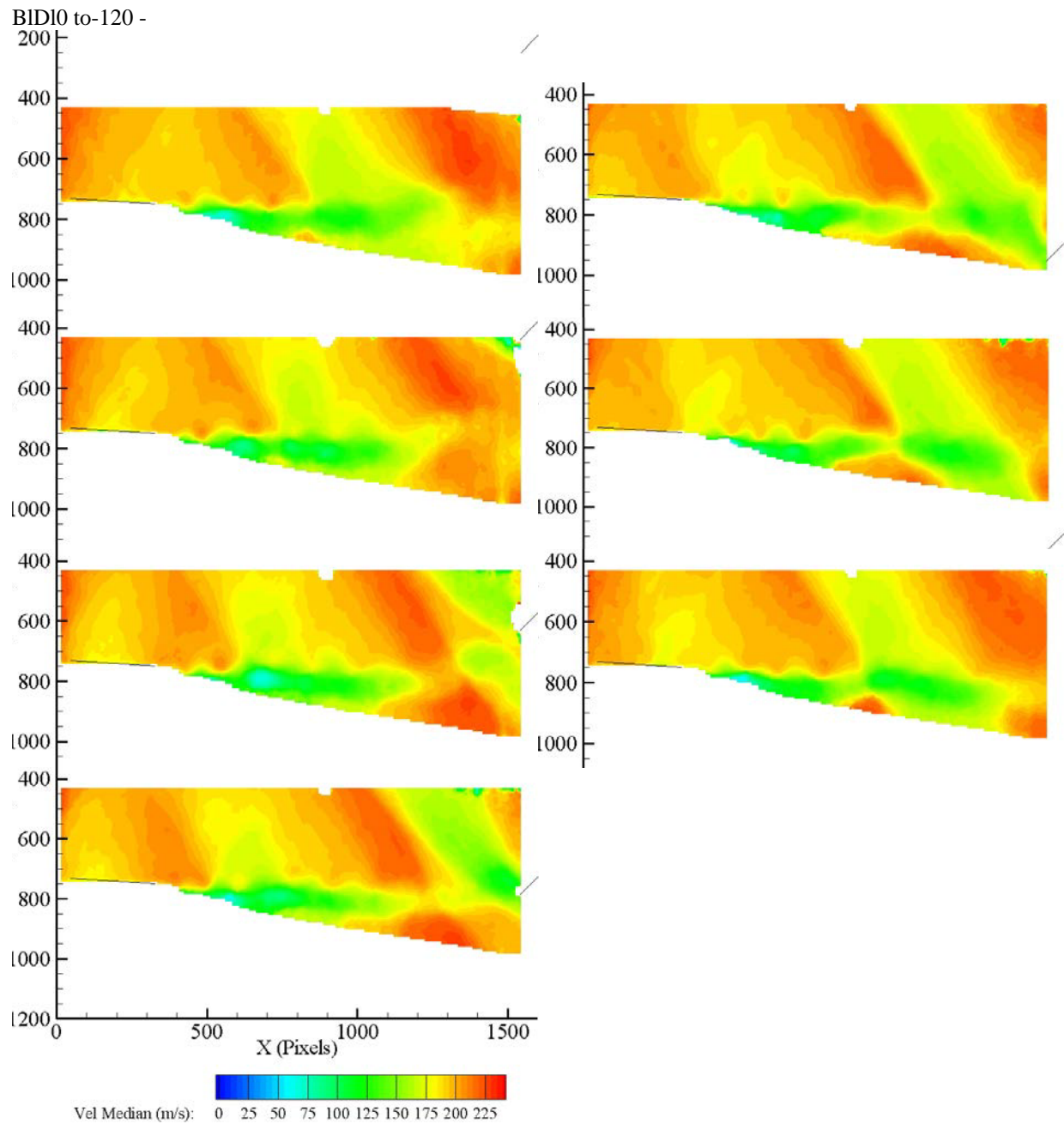
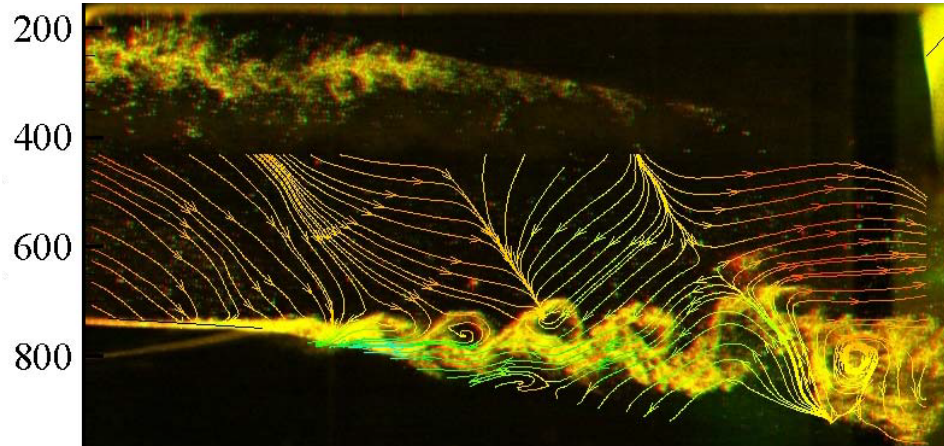
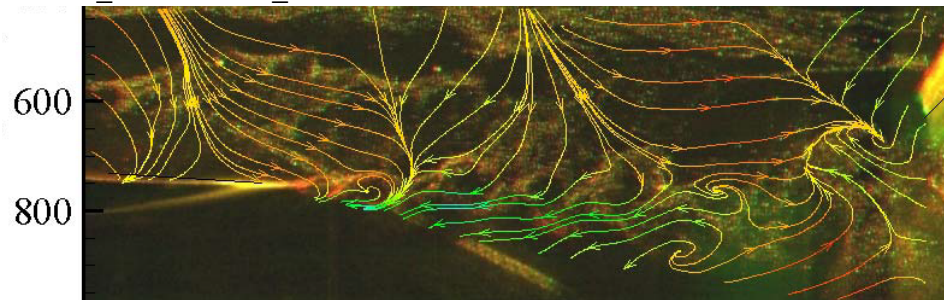


FIG 7 Far Spacing (Peak Eff., 0-deg, 50% span): details of the averaged velocity field for blade period (finer grid).

BID10_MedianStrm_

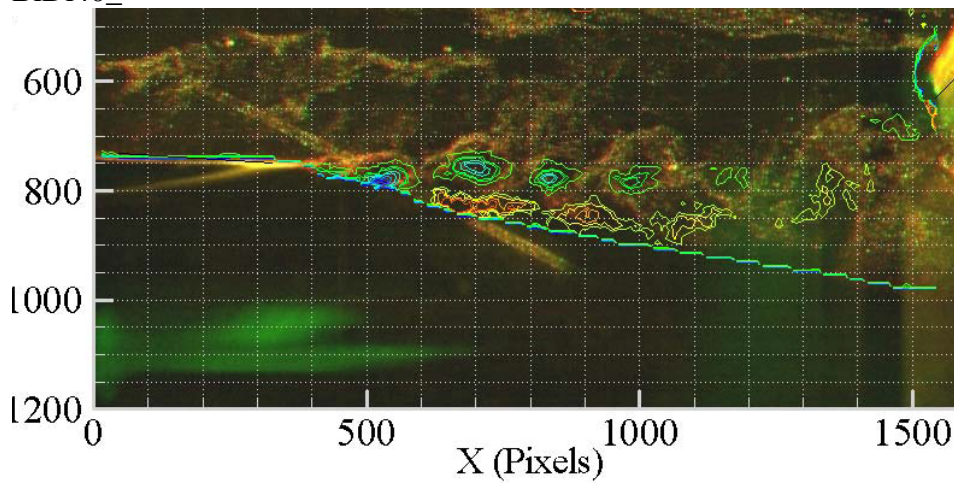


BID140_MedianStrm_



Vel Median (m/s): 0 25 50 75 100 125 150 175 200 225

BID140_



Vort: -0.2 0.025

FIG 8 Far Spacing (Peak Eff., 0-deg. 50% span): details of the averaged velocity and vorticity field for two blade period overlaid on instantaneous flow visualizations.

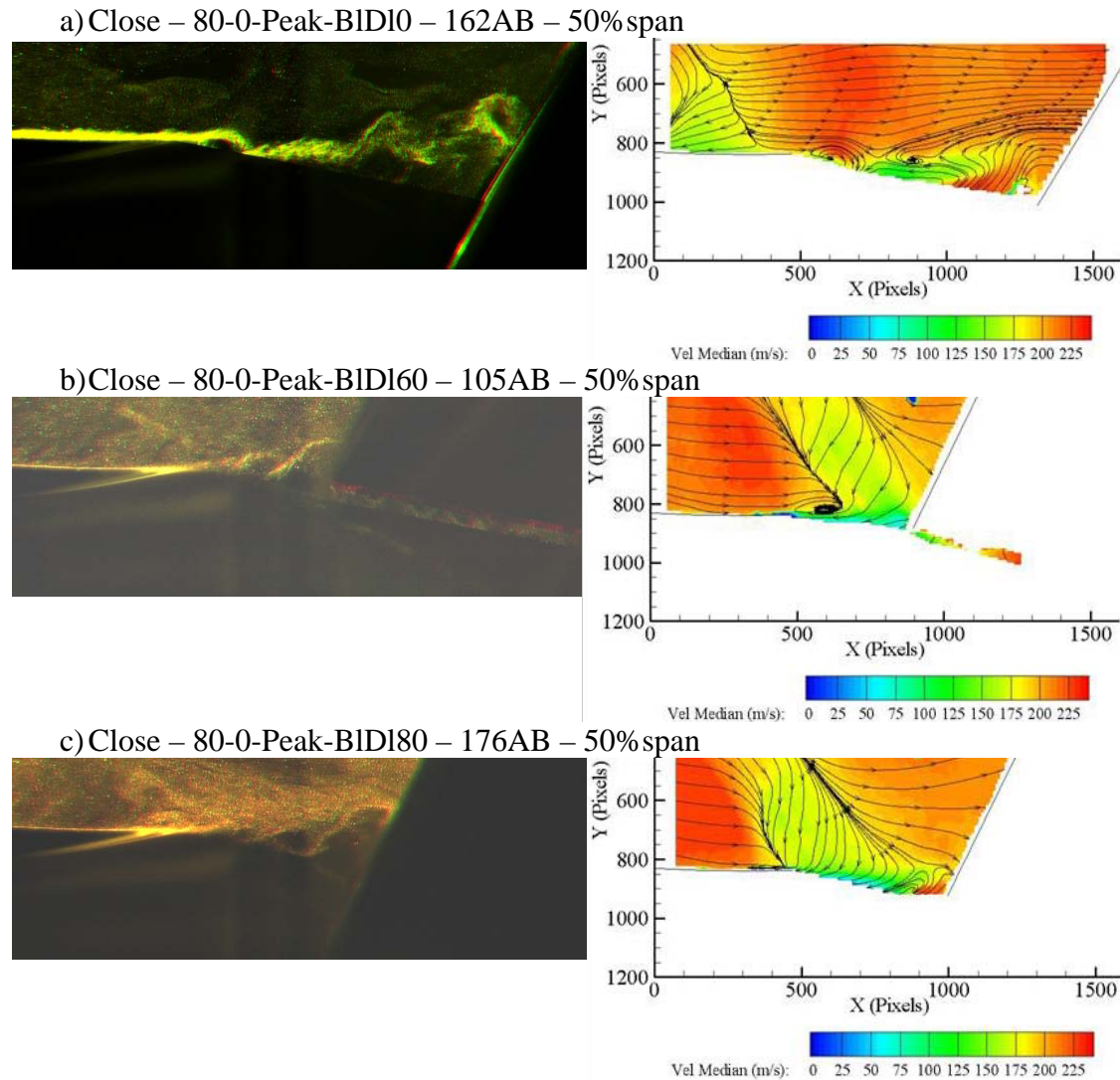


FIG 9 Close spacing (Peak Eff, 50% span, 0 deg) Flow visualizations and averaged velocity fields.

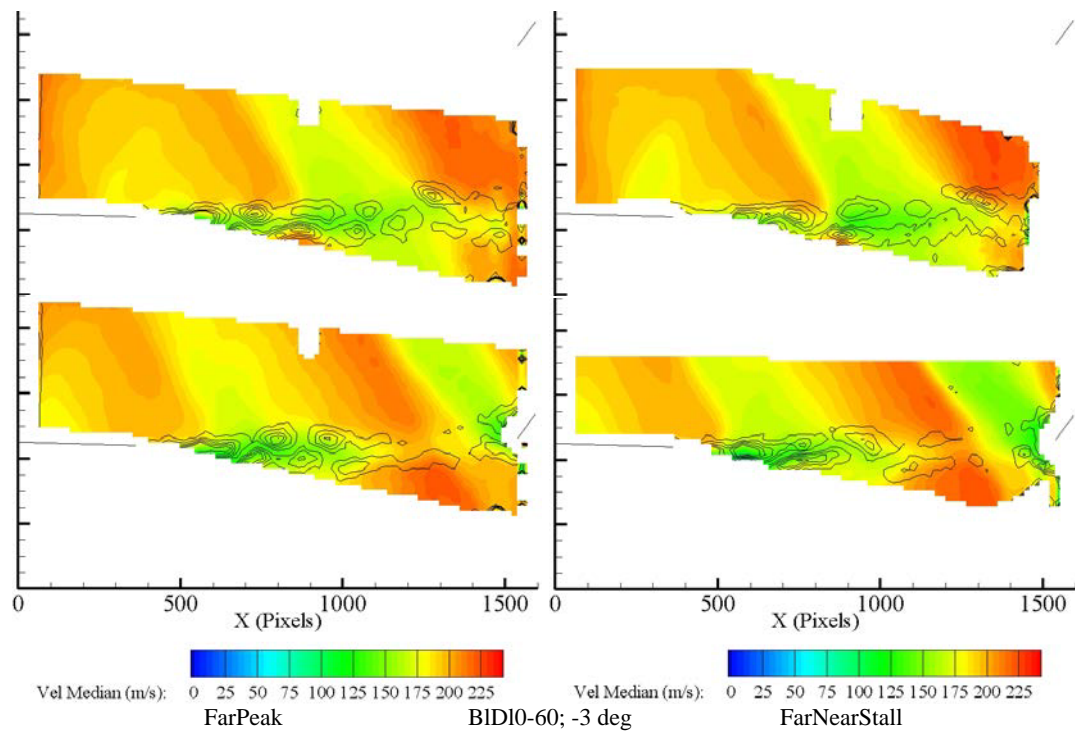


FIG 10 Far spacing, 50% span, stagger – 3 degrees and operating point comparison.

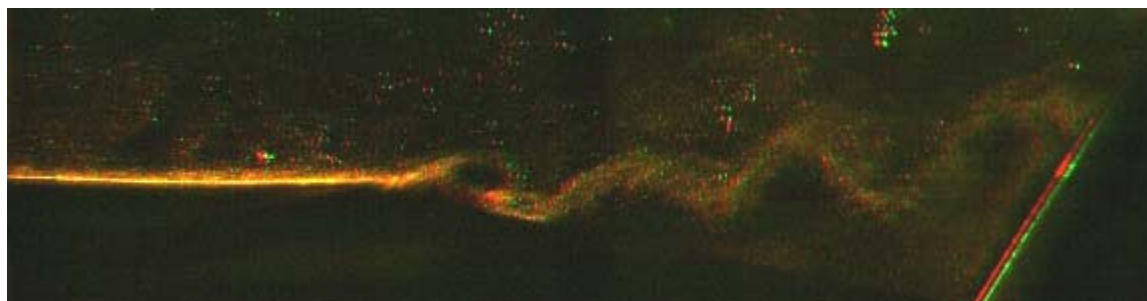


FIG 11 Close spacing (Peak Eff, 50% span, -3 deg) flow visualization (BID10)

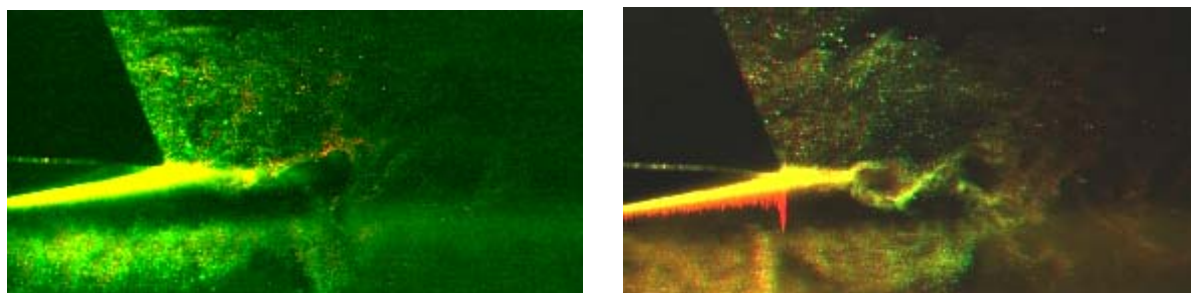


Fig 12 Far Spacing Flow Visualizations.

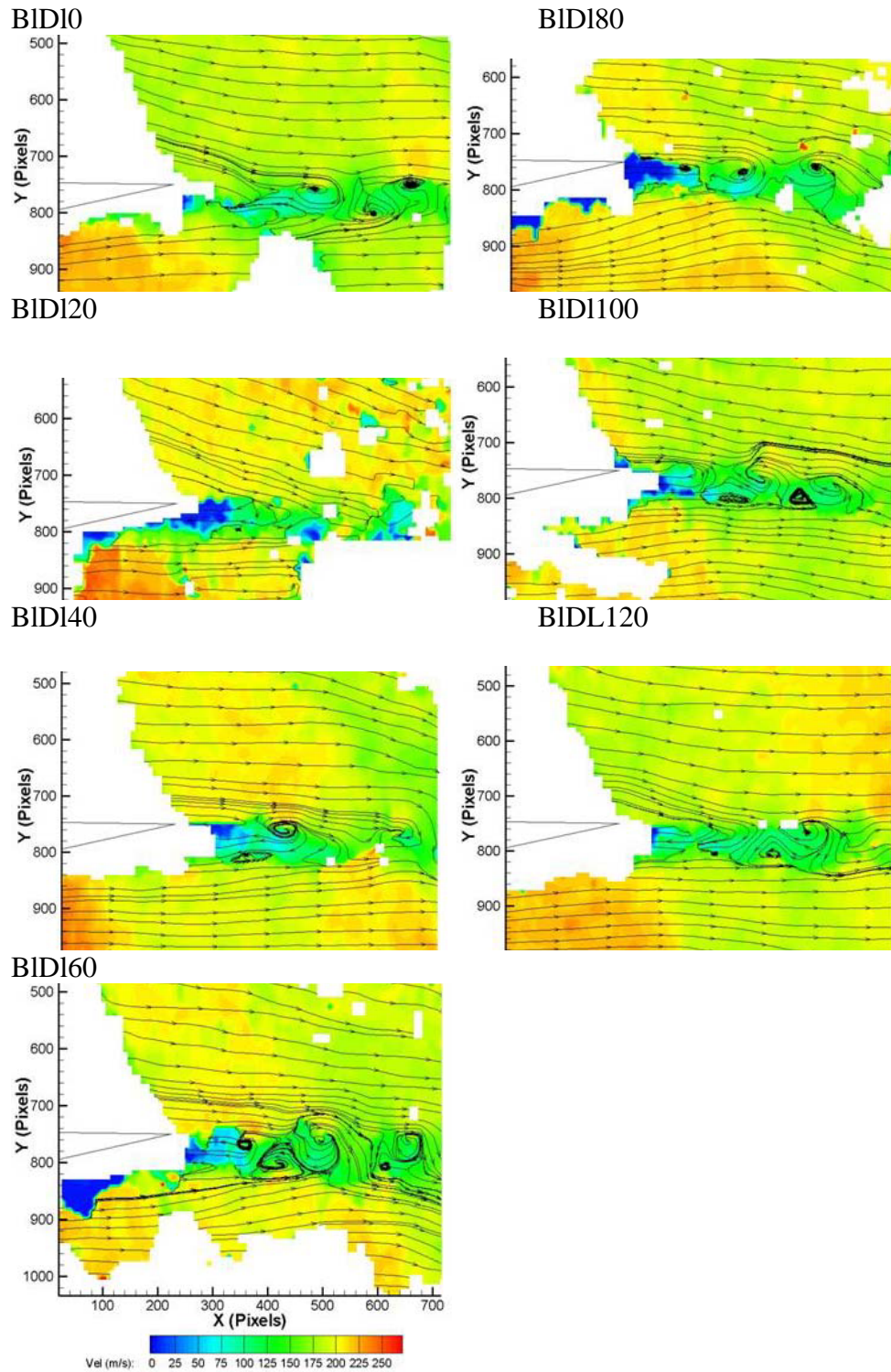


Fig. 13 Suction Side Instantaneous Velocity fields.

Initiation of Detonation in a Large Tube

Viswanath Katta*, Colin Tucker⁺, John Hoke* and Fredric Schauer

Propulsion Directorate
Air Force Research Laboratory
Wright Patterson Air Force Base, OHIO

*Innovative Scientific Solutions, Inc.

e-mail: vrkatta@erinet.com

⁺Air Force Institute of Technology

Abstract

One of the important design criteria in the development of Pulse Detonation Engines (PDEs) is to stabilize detonation in a large-diameter tube in the shortest possible distance. The initial shock train emanating from the ignition source plays an important role in transitioning the deflagration wave into a detonation. To sustain such transition in a large-diameter tube, innovative methods and strategies are required. An experimental-numerical investigation is conducted to understand the role of a contoured body suspended within the tube for enhancing detonation transition. A computational fluid dynamics (CFD) code based on flux corrected transport is used for the simulation of the fate of the two-dimensional detonation wave formed from the ignition source and expanded through the gap between the centerbody and the channel walls. It is found that the reflection of transverse waves at the walls and their collision near the leading shock front are critical in sustaining a detonation wave during expansion. The shock-wall and shock-shock interactions are enhanced by the centerbody. Simulations further suggested that the effectiveness of the inserted centerbody strongly depends on its length.

Introduction

Pulse Detonation Engines (PDEs) operate with a higher thermal efficiency than the conventional, constant-pressure combustion engines. PDEs also provide a very high specific impulse thrust at different operating frequencies. They can be designed without the use of any rotating machinery or valves in the flow path. However, the design and operation of the PDEs are complicated by the unsteady, high-speed, pulsed combustion. To reduce the deflagration-to-detonation transition (DDT) time several conceptual procedures have been proposed. The combustible mixture in the main chamber can be ignited using a detonation wave that was generated in a much-smaller, pre-detonation chamber. The primary concern in such approach is the success of the transmission of detonation wave from pre-detonation chamber to main chamber. Previous studies have indicated that the maximum expansion a detonation can successfully go through is of the order of 100%--placing a severe restriction on the detonation-tube diameter [1]. In

order to achieve detonation in large-size tubes, alternative techniques need to be developed either with or without using the pre-detonation tubes. This problem of initiating and sustaining detonation in large-diameter tubes is investigated in the present paper using experimental and numerical techniques.

The detailed cellular structures of gaseous detonations have been studied using experimental techniques since 1960's. However, only in the late 1970's Taki and Fujiwara [2] and later Oran et al. [3] were able to numerically simulate the cellular detonation structure for the two-dimensional case. Both the experiments and simulations have identified that the number of cells in a cellular detonation wave is a consequence of the chemistry of the problem, which is characterized by the reaction-zone length scale. The cell size was also found to be independent of the channel width.

An important concern in using cellular detonation wave as a source for burning the reactants comes from the stability of the cellular detonation wave. Experimentally it was found that the stability of the detonation wave increases with tube diameter. For example, a sudden increase in the tube diameter may not quench the detonation if the diameter is greater than thirteen cell widths. As shown by St-Cloud et al. [4] and Moen et al. [5], a finite perturbation may lead to complete destruction of one-cell-width detonations. Therefore, a small but sudden expansion of detonation (or ignition) hotspot may result in a deflagration wave. In the present paper, growth of the ignition spot is controlled via constraining it between the walls of a small tube. Subjecting the resulting localized detonation wave to a weak expansion over the centerbody, the growth of it is controlled.

Experimental Setup:

The photograph of the in-house research PDE used for testing the centerbody concepts is shown in Fig. 1. The engine was equipped with a 5.23-cm-diameter, 71-cm-long ignition tube and a 9.05-cm-diameter, 92.71-cm-long detonator tube. A contoured conical body was mounted inside the detonation tube in such away that its base faces the ignition tube. Hydrogen mixed with air at stoichiometric ratio is detonated at 10 Hz. The detonation tube was instrumented with high-frequency (2MHz) pressure transducers and ion sensors as shown in Fig. 2. The latter

sensors were used to detect the wave velocity when the detonation front is passing over. Details of the PDE assembly and the incorporated instrumentation are provided in Ref. 6.

Mathematical Model:

The conservation equations for mass, momentum, energy and the two progress variables are solved in Cartesian coordinate system. The gas mixture considered in the numerical investigations is a stoichiometric hydrogen-oxygen fuel diluted with Ar/He by 70%. This mixture is known to generate a well-behaving detonation. The hydrogen-oxygen reactions are represented by the two-step reaction mechanism of Korobeinikov [7]. This model has been successfully applied in the past for addressing various two-dimensional unsteady detonation problems [2,8]. The Chapman-Jouguet (C-J) Mach number of the premixed gas mixture considered is 4.8.

The present simulations used an explicit 2nd-order MacCormack predictor-corrector technique with 4th-order FCT (Flux Corrected Transport) scheme for capturing the shock waves accurately. A 1501x151 grid system is constructed with $\Delta x = \Delta y = L^*/9$. Here, L^* is the induction length—a characteristic distance related to the unburned gas mixture. All the calculations are started by filling the channel with combustible mixture and then by igniting it in a specified region. For the ignition purpose, a circular area of 9-grid-points radius is selected near the closed end of the channel and then replaced the fuel mixture within this region with the combustion products. In constant-width channels, a stably propagating multi-dimensional detonation wave establishes as the combustion products push the flame front.

Results and Discussion

Experiments were conducted by suspending a conical centerbody at 2.79 cm downstream of the reference point in the detonation tube (Fig. 2). Ignition was provided with spark plugs placed in the ignition tube. A weak deflagration combustion wave was established in the ignition tube and was expanded in the detonation tube. Typically, such expansion further weakens the combustion wave. In the absence of the centerbody, the responses from the pressure transducers 4 and 7 as the combustion wave passes over them are shown in Fig. 3. The relative pressure increased only to ~ 0.6 at the leading edge of the combustion wave. The measured wave speeds are ~ 650 m/s.

Placement of centerbody in the detonation tube helped the deflagration combustion wave to transition into a detonation wave. The pressure waves obtained from sensors 4 and 7 are shown in Fig. 4(a) and the voltages recorded by the ion sensors 8 and 10 are shown in Fig. 4(b). The measurement of wave speed varies from 1800 to 2200 m/s, depending on the sensor location. This wave speed compares favorably with the C-J velocity of 1966 m/s for the stoichiometric H_2 /Air mixture at 1 atm pressure.

To verify the DDT process assisted by the centerbody, simulations were made using the two-dimensional code described earlier. Calculations were made initially for a channel width of $9L^*$ without using a centerbody. A stably propagating detonation wave having two transverse waves was established after ~ 1000 time steps starting from a single ignition spot. The interaction between the transverse and detonation waves results in a triple-shock structure and thereby a cellular detonation front. As the detonation propagates, these transverse waves travel toward the walls and reflect back when they interact with the walls. The structure of the detonation front propagating in the $9L^*$ channel is shown in Fig. 5 at three instants. The iso-pressure plots shown in Figs. 5(a), 5(b), and 5(c) visualize the motion of the two triple shock structures between the lower and upper walls. The wave velocities obtained at upper and lower walls and at the mid section showed that the reflection of a triple shock from the wall and the interaction between two triple shocks result in enhanced combustion (increased propagation velocity) locally. However, the average non-dimensional propagation velocity was 4.96, which is close to the Chapman-Jouguet (C-J) velocity for the mixture considered.

Calculations were then repeated for a channel having a width of $18L^*$ and without placing a centerbody. A single ignition spot failed to yield a stably propagating detonation wave. Placing an additional ignition spot did not help much in detonating the gas all across the channel. The ignition spots are also partially enclosed in small chambers to enhance shock reflections off the walls. The failure of detonation initiation for this case is shown in Fig. 6(a). Here, the bottom image shows the deflagration wave that reached the channel exit $58 \mu s$ after the ignition and the top image shows the changes in pressure at the upper wall with time. However, detonations were successfully initiated when the ignition energy was doubled as shown in Fig. 6(b). This demonstrates that a stable detonation can be obtained, even though difficult, in the $18L^*$ -wide channel.

The possibility of achieving a stable detonation from the normal ignition energies is investigated by placing various centerbodies in the $18L^*$ -wide channel. Due to the orthogonal grid system used in the code, each centerbody is constructed with different-size blocks as shown in Figs. 7-9. Detonation could not be established with the $32L^*$ -long centerbody. A comparison of detonation developments shown in Figs. 6(a) and 7 suggests that the initial shock waves established from the ignition source have dissipated more rapidly in the presence of the centerbody. However, when the centerbody length was increased to $39L^*$, a stable detonation was established (Fig. 8). Interestingly, detonation could not be sustained when the centerbody length was further increased to $46L^*$. The three calculations with different centerbody lengths suggest that 1) placing a centerbody can help establishing detonation in a large-diameter tubes and 2) the effectiveness of the centerbody depends on its length, probably in relationship with the cell width. The variation in wall pressure at $100L^*$ downstream of the back plate are shown in Fig. 10 for different

centerbody cases. It clearly shows the establishment of detonation in the case of the medium-length ($39L^*$) centerbody and failure in the other cases.

References

- [1] V. R. Katta, L. P. Chin, F. Schauer, 17th International Colloquium on the Dynamics of Explosions and Reactive Systems, Heidelberg, Germany, July 25-30, 1999.
- [2] S. Taki, and T. Fujiwara, AIAA J. 16, 73 (1978).
- [3] E. S. Oran, T. R. Young, J. P. Boris, J. M. Picone, and D. H. Edwards, Nineteenth Symposium (International) on Combustion, P. 573, The Combustion Institute, PA, 1982.
- [4] J. P. Saint-Cloud, C. Gueraud, C. Brochet, and N. Manson, Astronautica Acta., 17, 487 (1972).
- [5] I. O. Moen, M. Donato, R. Knystautas, and J. H. Lee, Eighteenth Symposium (International) on Combustion, p. 1615, The Combustion Institute.
- [6] Schauer, F., Stutrud, J., and Bradley, R., AIAA Paper 2001-1129, Reno, NV, 2001.
- [7] Korobeinikov, V., Levin, V., Markov, V., and Chernyi, G., Astronautica Acta, Vol. 17, No. 4&5, p. 529, 1972.
- [8] K. V. Reddy, T. Fujiwara, and J. H. Lee, Memoirs of the Faculty of Engineering, Nagoya University, Vol. 40, No. 1, 1988.

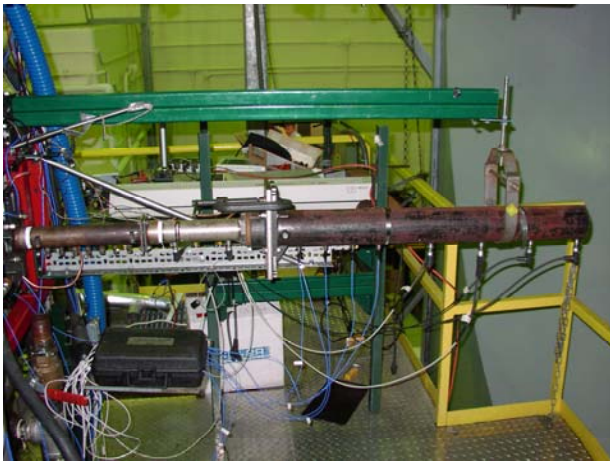


Fig. 1. Experimental facility used for the studies of fundamental concepts in detonation initiation and propagation.

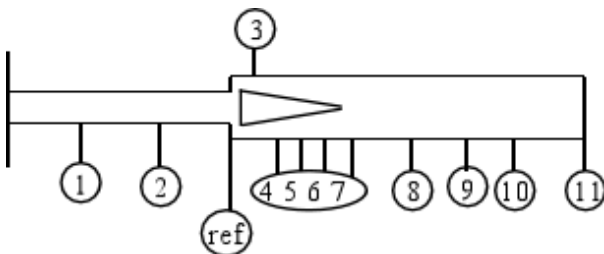


Fig. 2. Schematic diagram of the detonation tube assembly and locations of centerbody and sensors. 3-7 are pressure transducers and 1,2, 8-11 are ion detectors.

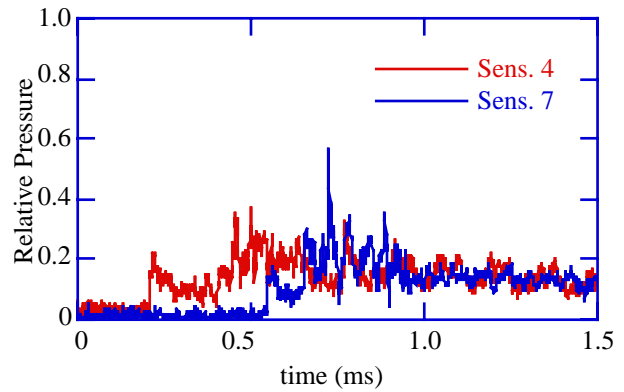


Fig. 3. Deflagration wave propagation detected by pressure transducers 4 and 5 in the absence of centerbody.

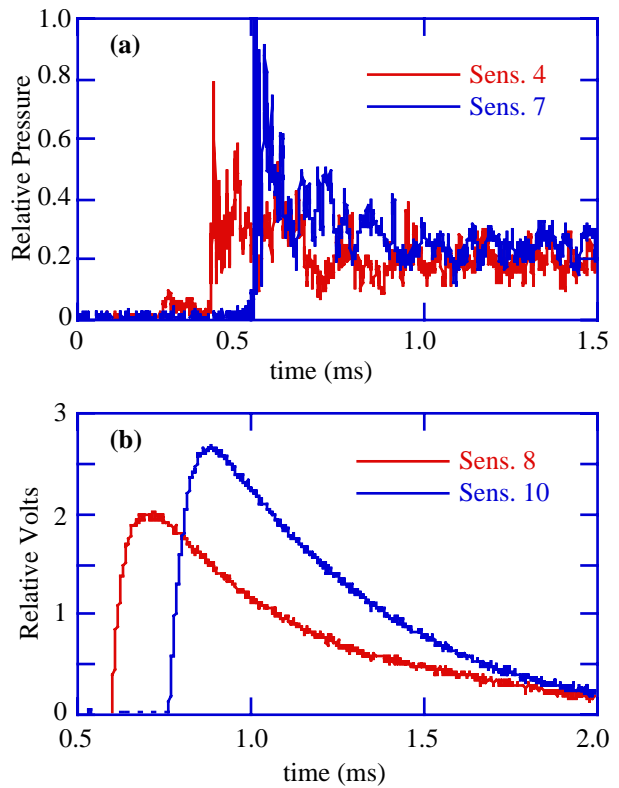


Fig. 4. Responses of (a) pressure transducers 4 and 7 and (b) ion detectors 8 and 10 during a successful detonation initiation achieved by placing centerbody.

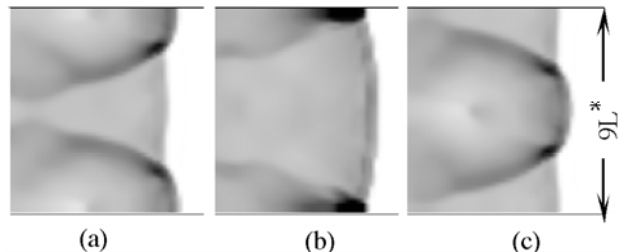
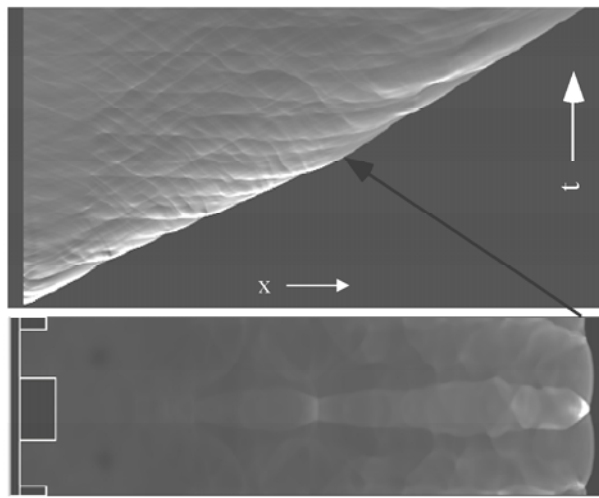
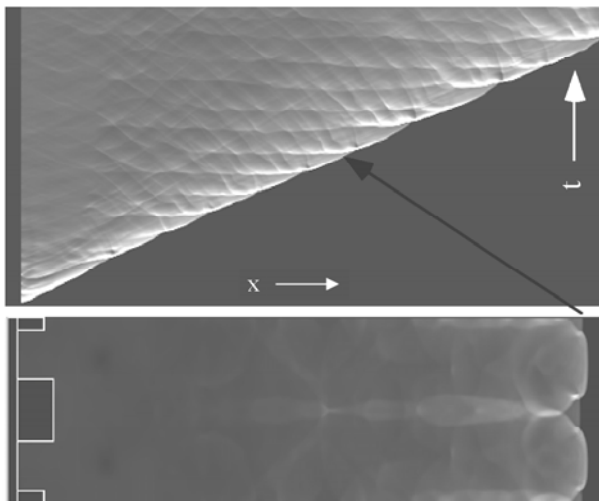


Fig. 5. Stably propagating detonation wave in a $9L^*$ channel at (a) t_0 μ s, (b) $t_0+1.6$ μ s, and (c) $t_0+3.2$ μ s.



(a)



(b)

Fig. 6. Detonation propagation in 18L* wide channel with (a) specified and (b) 100% more ignition energies.

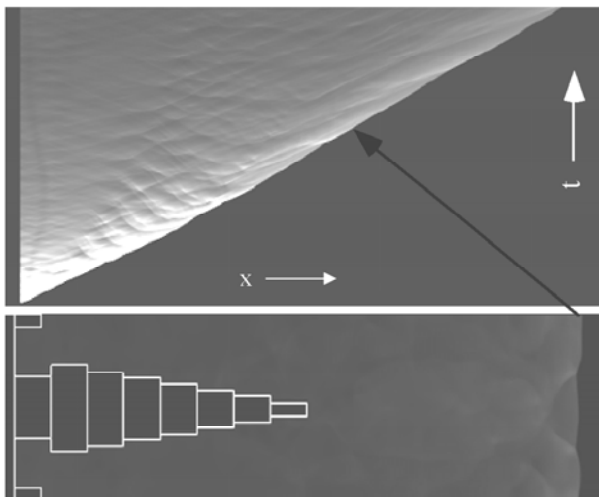


Fig. 7. Effect of placing 32L* long centerbody. Upper image shows wall pressure at different times.

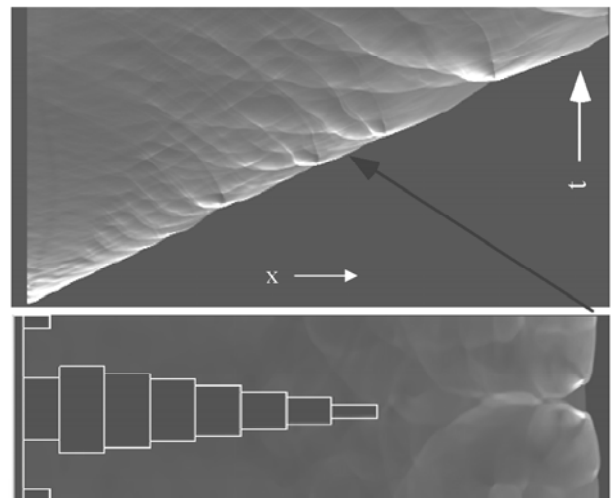


Fig. 8. Effect of placing 39L* long centerbody. Upper image shows wall pressure at different times.

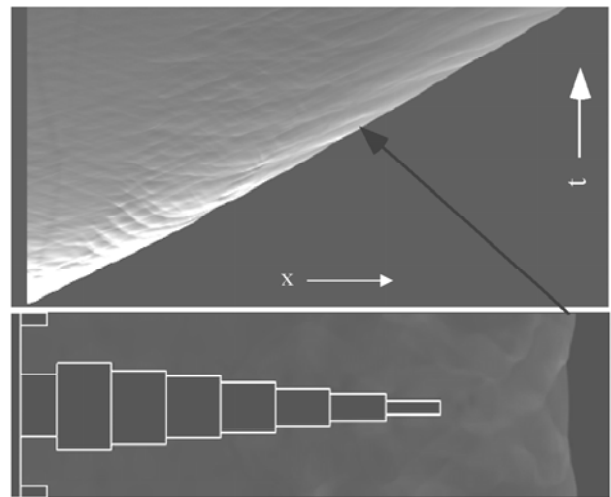


Fig. 9. Effect of placing 46L* long centerbody. Upper image shows wall pressure at different times.

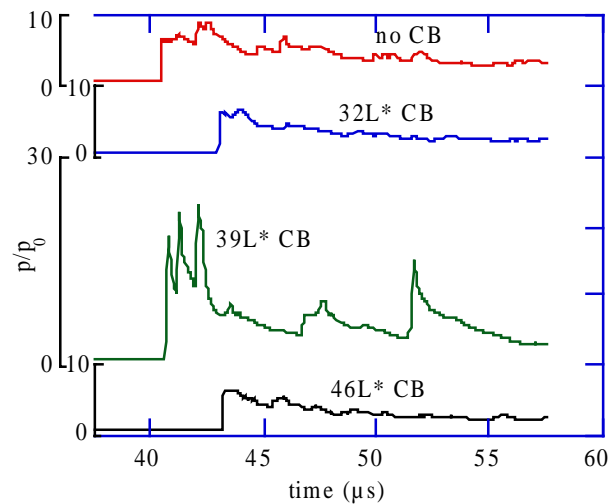


Fig. 10. Variation of wall pressure at a location 100L* downstream of back plate.

The Use of a Flash Vaporization System With Liquid Hydrocarbon Fuels in a Pulse Detonation Engine

K. Colin Tucker* and Paul I. King
Air Force Institute of Technology
Wright Patterson AFB OH 45433

Royce P. Bradley
Innovative Scientific Solutions, Inc.
Dayton OH 45440

Fredrick R. Schauer
Air Force Research Laboratory
Wright Patterson AFB OH 45433

Abstract

In recent research,^{1,2} liquid fuel droplets were found to hinder the detonation process in a pulse detonation engine (PDE). In the current work, multi-phase effects are eliminated with a flash vaporization system that vaporizes the liquid fuels prior to mixing with air. Hydrocarbon and air mixtures have been transitioned from deflagration to detonations previously,¹ but exhibited long ignition and deflagration to detonation transition (DDT) times. Here, two liquid hydrocarbon fuels, with different octane numbers (ON), are detonated with air in a PDE to determine the effect of octane number on the ignition time and the DDT time. The premixed, combustible mixture fills the PDE tubes via an automotive valve and cam system described in detail elsewhere.³ N-heptane (ON-0) and isooctane (ON-100) are evaluated individually to determine the effects of automotive octane number on pulse detonation engine combustion performance. The ON has been considered previously⁴ as an acceptable criterion in determining the detonability for PDEs, and it is derived based on the tendency to “knock” or detonate relative to isooctane in an automotive engine application.

*Correspondence can be addressed to: kelly.tucker@wpafb.af.mil. The views expressed in this paper are those of the authors and do not reflect the official policy or position of the United States Air Force, the Department of Defense or the US Government.

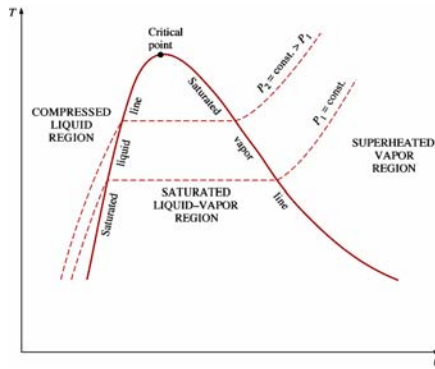
†This paper is declared a work of the U.S. Government and is not subject to copyright protection in the United States.

The goal of this research is to show that a flash vaporized liquid hydrocarbon fuel system can provide the fuel and air homogeneity required to achieve detonations. The octane number is studied to determine its influence on the ignition and DDT time for hydrocarbon fuels.

The flash vaporization system provided an outstanding method for achieving the desired mixing and vaporization, and the systems operating points matched well with the liquid vapor equilibrium model results. The ignition times showed little dependence on fuel injection temperatures or octane number and no droplet effects were noted. The DDT trends were octane number dependent and the isooctane was difficult to detonate with wave speeds below the stable Chapman-Jouget (CJ) wave speeds. The heptane readily detonated and produced wave speeds at or above CJ.

Background

Combustion performance of a liquid hydrocarbon fueled pulse detonation engine is hindered by the presence of fuel droplets and long ignition times^{5,6}. The presence of droplets indicates that locally fuel rich and fuel lean regions exist, and that the overall mixture lacks the required homogeneity for ideal combustion performance. The presence of droplets increases ignition time because the initial energy deposit (spark) must evaporate any surrounding fuel droplets to create an explosive mixture. A high-pressure fuel flash vaporization system was designed and built to eliminate the time required to evaporate liquid fuel droplets.

Figure 1. T-u diagram for simple substance⁷.

To remove the evaporation times, the fuel is injected into air at a temperature above the boiling temperature at the highest pressure the fuel air mixture will encounter before combustion. When the high pressure, high temperature fuel is injected into a lower pressure air stream via a pressure atomizing nozzle, the fuel will immediately vaporize and thereby remove the time required to evaporate the fuel. The phase change process is shown in Fig. 1 for a simple (single component) substance. As the pressure applied to the fuel goes higher, the saturation temperature also rises until both converge at the critical point. The pressure used during the tests is well above the critical pressure of each fuel and allows the fuel to be heated without boiling until reaching the supercritical temperature of the fuel. An added benefit is improved mixing of the fuel and air mixture. Since the flash vaporization system injects gaseous fuel, it will more readily achieve the desired fuel air homogeneity required to ignite and transition a detonation.

Octane number

In a spark initiated (SI) automobile engine, knock is noted by the noise emitted when the fuel air mixture inside the engine ignites prematurely relative to the desired burn rate initiated by the spark advance on the engine. However, compression heating of the unburned mixture from both the advancing piston and the evolving confined flame front can auto ignite the fuel air mixture (Fig. 2). The premature ignition event releases the stored chemical energy in the fuel at a rate between 5 and 25 times faster than the spark initiated rate⁸. A susceptibility to knock may represent a sensitivity to more quickly allow detonations to transition when a deflagration is channeled through an obstacle such as a Schelkin spiral.

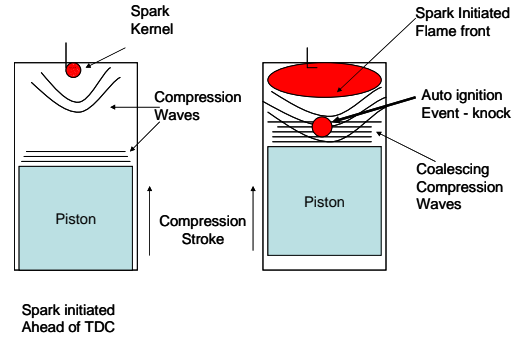


Figure 2. Automotive knock event.

The fuel's octane number relates the mixture's resistance to knock relative to a mixture of isooctane (ON=100) and n-heptane (ON=0). The higher the number, the more resistant the fuel is to exhibit the phenomena. Two methods are commonly used to determine the fuel octane number. The Research Method⁹ tests fuels at representative low speed city driving conditions, and the Motor Method¹⁰ tests fuels at representative high speed highway driving. The resulting research octane number (RON) and motor octane number (MON) are used to determine an antiknock index or AI. The historical standard ASTM Specification D 439 is used for determining the antiknock index by simply averaging the RON and MON¹¹.

Fuel	Formula	RON	MON	AI
n-heptane	C_7H_{16}	0	0	0
isooctane	C_8H_{18}	100	100	100

Table 1. Octane numbers¹¹.

Experimental Setup

This research was performed in the Air Force Research Laboratory (AFRL) Pulse Detonation Research Facility at Wright Patterson AFB, Ohio. The facility incorporates two electrically driven camshafts situated in a General Motors Quad 4 head. Four thrust tubes are attached where pistons would normally interact with the head and valves. A single thrust tube with a 5.2 cm diameter, 182.9 cm long steel pipe is fired at a frequency of 15 Hz. The rotating cams provide a three-part cycle with equal time (120 degrees) to fill, fire, and purge the tube. The manifold pressure behind the valves is adjusted to provide the correct fill volume at the desired operating frequency. The fill volume is defined as the volume of the thrust tube when the fuel air mixture expands to atmospheric pressure at the open end of the tube.

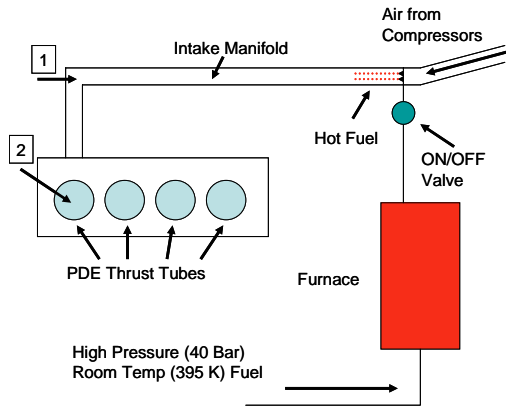


Figure 3. Flash vaporization system.

The flash vaporization system stores high pressure, high temperature fuel in the furnace and when a pneumatically operated ball valve opens, the fuel flows to three pressure atomizing fuel nozzles which are situated to inject the fuel tangentially into the main air flow (Fig. 3). The fuel air mixture has a mixing length of 1.52 meters before being fed into the thrust tube for combustion. The air is heated to 311K (± 1 K) prior to entering the manifold and mixing with fuel. In Fig. 4, pressure measurements during the filling process are recorded in the manifold (location 1 in Fig. 3) and at the closed end of the thrust tube (location 2 in Fig. 3). The ignition delay from the time the valve closes until the time the spark is deposited is 10 milliseconds. The delay enhances the ignition and DDT performance by utilizing the returning compression wave seen in the blue head pressure trace in Fig. 4. The zero time is denoted at the point the intake valves close.

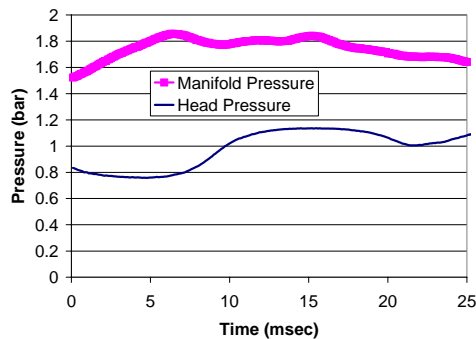


Figure 4. Premixed manifold and head pressure traces (absolute) for 15 Hz test conditions.

Fuel Air Premix Conditions

The fuel and air are premixed in the manifold (Fig. 3) prior to being feed into the PDE thrust tube. The pressure conditions in the

intake manifold are critical to understanding whether or not the fuel vapor will condense back into liquid due to any heat transfer or pressure effects.

The National Institutes of Standards and Technology (NIST) program SUPERTRAPP version 3.1 was used to determine how much liquid was in the premixed fuel air mixture in the manifold if left at the specified pressure and temperature until it reached equilibrium. The program uses the thermo physical properties of hydrocarbon mixtures database and computes the vapor-liquid equilibrium using the Peng-Robinson model¹².

The stoichiometric fuel air mixture was input into the program at a pressure of 2.0 bar which is slightly above the maximum pressure observed in Fig. 4. The mixture temperature was varied to determine the percentage of liquid fuel present at equilibrium.

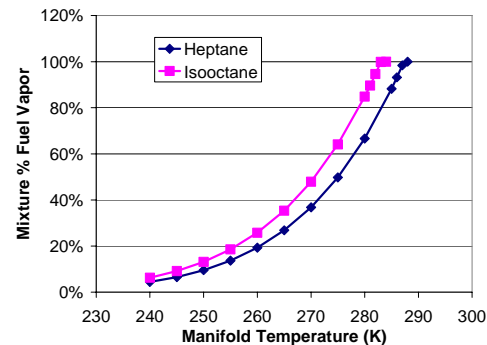


Figure 5. Equilibrium liquid vapor state for a stoichiometric fuel Air mixture at 2.0 bar.

Since both fuel and air are mixed as gases, they should reach equilibrium quickly and remain gaseous as long as the mixture temperatures do not drop below those shown in Fig. 5. If the temperatures in the manifold drops below 285 K, the fuel vapor may condense back into liquid.

Fuel Conditioning

Heating fuel above 450 K can cause particulate formation and carbon deposits on metal surfaces^{13,14}. To prevent the fuel from reacting with any dissolved oxygen, the dissolved oxygen was removed by sparging the fuel with nitrogen prior to pressurization and heating. In sparging, nitrogen is bubbled through the liquid fuel to agitate and replace any dissolved oxygen. In the ullage region above the liquid, the nitrogen leans out the oxygen and eventually replaces all the oxygen in the fuel tank.



Figure 6. Fuel tank sparge spiral.

The photo in Fig. 6 shows the sparging spiral with drilled holes that nitrogen was fed through to agitate the fuel. Tests were performed with air saturated fuel to determine the amount of nitrogen to fully deoxygenate the fuels. The fuels were sampled at different times with a gas chromatography machine until no oxygen could be measured. To prevent the reaction with metals, silicon based coatings were applied to all hot section components including the fuel nozzles. The coating provides a very thin non-reactive surface which prevents any contact between the fuel and the metals.

Constant Ignition Energy

A 12 volt DC automotive digital ignition system supplied power to the spark plug. The system provided a series of 105 – 115 milli-Joule sparks¹⁵ into the hydrocarbon fuel air mixture via a capacitance discharge. The number of sparks per cycle was verified using a 27,000 frame per second camera and noted a 250 μ s duration pulse every 1.1 milliseconds (\pm 37 μ s). A total of four sparks are deposited during each ignition event at the operating frequency of 15 Hz.

Results

Flash Vaporization System Validation

The flash vaporization system worked well in providing a gaseous fuel air mixture. This was verified from the manifold temperature changes as the fuel injection temperature was increased. For both heptane and isooctane, the required temperature to be fully flash vaporized was above 395 K (Fig. 7). Below the 395 K injection temperature, the air temperature in the manifold drops due to the enthalpy of evaporation from the evaporating liquid droplets. Above 395 K, no energy is required to evaporate

the droplet and excess fuel enthalpy is used to raise the manifold air temperature slightly.

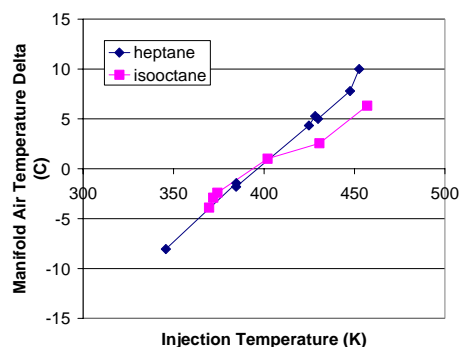


Figure 7. Manifold air temperature change after fuel injection.

The heptane and isooctane showed similar temperature changes after injection in the manifold. This is expected since the two fuels have nearly the same boiling point at the maximum pressure in the manifold of 1.85 bar listed in Tab. 2 below. The boiling point also denotes exactly the crossing point for which the fuel increases or decreases the mixture temperature in the manifold. Since the fuel air mixture was above 285 K (Fig.5), the mixture is assumed to be completely vaporized for all test points.

Fuel	Boiling Temperature (K) @ 1.85 bar	CJ Detonation Wave Speed (m/s)
n-heptane	393.4	1793.7
isooctane	395.0	1791.8

Table 2. Fuel boiling point and CJ detonation wave speeds¹⁹

Tests were performed to note any changes in the nozzle flow patterns at liquid injection temperatures below and above the boiling temperature. In Fig. 8, water is injected at room temperature, and the spray is very wide with individual droplets still discernible. In Fig. 9, the spray is more tightly confined and has features consistent with a supersonic jet, thus denoting a gaseous injection. The phase change occurs from the static pressure drop while accelerating to the throat of the constant area nozzle.



Figure 8. High pressure atomized water at 20C and 43 bar.



Figure 9. Flash vaporized water at 200C and 43 bar.

Ignition times

Two methods are used to determine the ignition time from when the initial spark energy is deposited. The first is a dynamic pressure transducer (Fig 10). The transducer records pressures in the PDE head and corresponds to the pressure rise due to the constrained heated gases in the closed end of the PDE tube. Opposite the pressure transducer is a photo multiplier tube (PMT) with a 307 nanometer filter. The sensor reacts to the radiative energy associated with OH production. The OH radical is in abundance during hydrocarbon combustion and gives a second method to determine the ignition time. The combination of these two techniques to determine ignition time has been used elsewhere¹⁶.

The combustion data from the pressure and OH sensors is shown in Fig. 11. The ignition event is said to have occurred at the initial point when the pressure rises sharply, which for this data occurs around 9 milliseconds after the spark energy has been deposited into the fuel air mixture in the head of the thrust tube.

Likewise, the OH trace drops sharply when the PMT senses light in the correct wavelength.

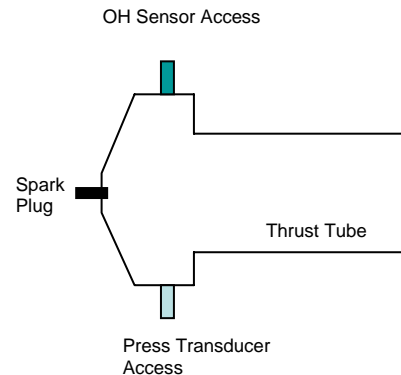


Figure 10. Sensor locations in PDE head.

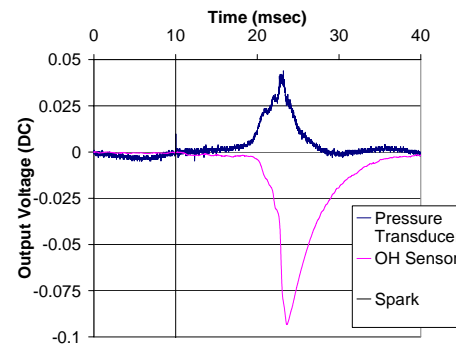


Figure 11. Ignition event after spark deposit at 10 milliseconds.

The ignition times for both sources are determined using an in-house program which filters the noise from the signal and looks for a slope change above or below a manually designated threshold.

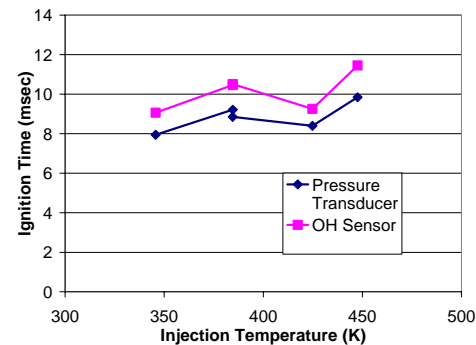


Figure 12. Measured ignition times for heptane.

The measured heptane ignition times from both the pressure trace and OH sensor were within 10 to 20 percent of one another with the OH sensor lagging. The ignition times did not show the expected dependency on injection

temperature. Lower fuel injection temperatures and a shorter mixing length in the manifold may allow a droplet effect on ignition time. Similar ignition times were seen for the isooctane data in Fig. 13. The octane number did not strongly influence the ignition times.

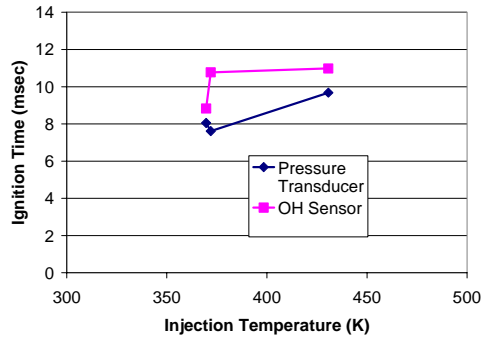


Figure 13. Measured ignition times for isooctane

The DDT time was determined as a time of flight through the DDT obstacle, a 1.22 meter Schelkin like spiral. The faster the DDT occurs, the shorter the time to travel through the spiral. The DDT time was computed from the time ignition was first observed to the time a detonation wave exited the spiral and was detected by an ion sensor. The results are shown in Fig. 14 below and show the influence of octane number.

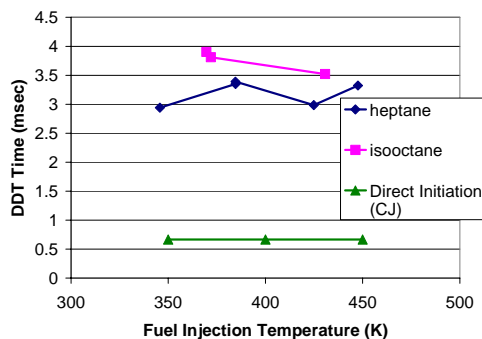


Figure 14. DDT Time for each Fuel

The isooctane took roughly 500 microseconds longer to traverse the spiral than the heptane. The wave speeds also reflect the difficulty in detonating the isooctane. Combustion performance of a PDE is primarily based on whether or not a detonation occurs within the thrust tube. The detonation is said to have occurred if the combustion wave speed is at the Chapman-Jouguet (CJ) point (Tab. 2). The CJ point is based on the Hugoniot curve, which relates continuity, energy, momentum, and the perfect gas law for a one dimensional, steady,

planar detonation wave. The CJ point denotes the conditions of maximum heat transfer rate from the energy stored in the fuel and converting it to a hypersonic detonation wave. This occurs at the point of minimum entropy for the process mathematically, and additionally, it is the equilibrium point for the process¹⁸.

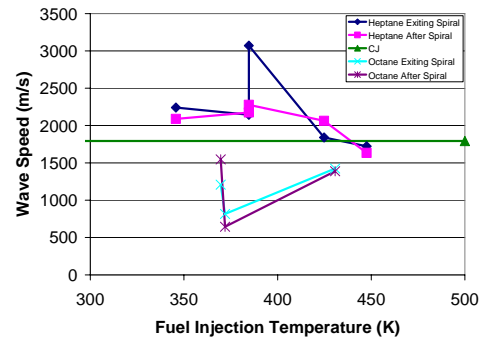


Figure 15. Detonation wave speeds observed for each fuel.

The detonation wave speeds are measured using ion probes downstream of the DDT spiral. No influence was seen in injecting the fuel at a higher temperature (Fig. 15). The heptane wave speeds were at or above the CJ wave speeds. Several super CJ speeds were observed at the 385 K injection temperature. These were transverse waves formed as the detonation transitioned through the spiral. The wave speeds after the spiral settled out to roughly 10 percent above CJ. The 450 K injection data were observed with a lower fill ratio and the mixture was more lean at the end of the tube, though a near CJ (- 9 percent) was still achieved. The isooctane was difficult to detonate and showed wave speeds below than the stable CJ wave speed.

Conclusions

The liquid hydrocarbon fueled flash vaporization system worked well to provide a fully vaporized, homogenous mixture that is required for a detonation wave. The fuel injection temperature raised or lowered the mixture temperature downstream of injection with the fuel's boiling temperature as the crossing point.

The correlation between octane number and ignition and DDT times was also studied. The ignition times did not show octane number dependence. The DDT trends and magnitudes did follow the expected octane number influence. The isooctane (ON=100) was more difficult to

detonate with wave speeds below the stable CJ wave speeds. The heptane (ON=0) readily detonated and saw wave speeds at or above CJ.

Future work will be performed at a wider range of injection temperatures and with lower vapor pressure fuels.

Acknowledgements

This work was funded by the Air Force Research Laboratory Propulsion Directorate and AFOSR. The authors wish to thank Kristin Panzenhagen, Curt Rice, Jason Parker, Dwight Fox, Jeff Stutrud, Ted Williams, Dr. Tim Edwards, and Dr. John Hoke who were all instrumental in helping make this project work.

References

1. Schauer, F., Stutrud, J., Bradley, R., Katta, V, and Hoke, J, "Detonation Studies and Performance Results for a Pulsed Detonation Engine," ICCD, 2002.
2. Brophy C., Sinibaldi, D., Netzer, D. and Johnson, R, "Operation of a JP-10/Air Pulse Detonation Engine," AIAA 00-3591 36th Joint Propulsion Conference, July 2000 Huntsville, AL.
3. Schauer, F. R., Stutrud, J.S. and Bradley, R.P., "Detonation Initiation Studies and Performance Results for Pulsed Detonation Engine Applications," 39th AIAA Aerospace Sciences Meeting and Exhibit, January 2001, Reno, Nevada.
4. Frolov, S.M., Basevich, V. Ya. and Belyaev, A.A., "The Use of Fuel Blends and Distributed Injections for Active Detonability Control in a PDE," ICDERS 99-252.
5. Brophy C., Netzer, D. and Forster, D, "Detonation Studies of JP-10 with Oxygen and Air for Pulse Detonation Engine Development," AIAA 98-4003 34th Joint Propulsion Conference, July 1998 Cleveland, OH.
6. Lu, P.L., Slagg, N., and Fishburn, B.O., "Relation of Chemical and Physical Processes in Two Phase Detonation" Sixth International Colloquium on Gas Dynamics of Explosion and Reactive Systems, Stockholm, Sweden, Aug 1977.
7. Moran, M.J., and Shapiro, H. *Fundamentals of Engineering Thermodynamics*, 4th edition Wiley & Sons, 1998.
8. Heywood, J. B., *Internal Combustion Engine Fundamentals*, McGraw-Hill, 1988.
9. ASTM D 2699-03a, "Standard Test Method for Research Octane Number of Spark-Ignition Engine Fuel," ASTM International.
10. ASTM D 2700-03a, "Standard Test Method for Motor Octane Number of Spark-Ignition Engine Fuel," ASTM International.
11. Wu, P. C., and Hottel, H. C., "Appendix: Data on Fuel and Combustion Properties," *Fossil Fuel Combustion, A Source Book*, John Wiley and Sons, NY, NY.
12. Peng, D. Y., and Robinson, D. B., "A New Two-Constant Equation of State," *Ind. Eng. Chem., Fundam.*, Vol. 15, No. 1, 1976.
13. Hazlett, R.N. "Thermal Oxidation Stability of Aviation Turbine Fuels," ASTM PCN 31-001092-12, Philadelphia, PA 1991.
14. Vranos, A. and Marteney, P.J., "Experimental Study of the Stability of Aircraft Fuels and Elevated Temperatures," NASA Report CR-165165, United Technologies Research Center on contract with NASA, Cleveland, OH December, 1980.
15. "MSD Installation Instructions," Autotronic Controls Corporation, El Paso, Texas.
16. Coket, M.B. and Spadaccini, L.J. "Scramjet Fuels Autoignition Study," *Journal of Propulsion and Power*, Vol. 17, No 2, March-April 2001.
17. *Knovel Solvents - A Properties Database*, ChemTec Publishing 2000.
18. Glassman, I., *Combustion*, San Diego: Academic Press, 1996.
19. Gordon, S and McBride B. "Computer Program for Calculation of Complex Chemical Equilibrium Compositions and Applications", NASA RP 1311 I&II, October 1994 and June 1996.

43rd AIAA Aerospace Sciences Meeting and Exhibit
January 10-13, 2005
Reno, Nevada

AIAA 2005-0228

Assessment of the Performance of a Pulsejet and Comparison with a Pulsed-Detonation Engine

Paul J. Litke and Frederick R. Schauer

Air Force Research Laboratory, Propulsion Directorate, Wright-Patterson AFB, OH 45433

Daniel E. Paxson*

NASA Glenn Research Center, 21000 Brookpark Road, Cleveland OH 44135

and

Royce P. Bradley and John L. Hoke

Innovative Scientific Solutions, Inc., Dayton, OH 45440

The performance of a Solar PJ32 pulsejet engine, which is a 1/5-scale model of the Argus V-1 pulsejet engine developed for the Navy in 1951, is evaluated under static conditions and compared with that of a pulsed-detonation engine (PDE) firing at similar inlet and operating conditions. The pulsejet has a fuel-flow operating range of 2.5-4.5 lbm/min, which corresponds to a thrust range of 40 lbf (at lean out) to 102 lbf (at flood out). Thrust is calculated from combustion-chamber pressure histories and agrees with measured thrust within 5-10%. Peak combustion-chamber head pressures range from 8 to 20 psig, while significantly higher pressures (80-120 psig) are attained in PDEs. Airflow at the inlet of the pulsejet is measured and used to calculate specific thrust and equivalence ratio. Specific thrust ranges from 40-100 lbf-s/lbm over the range of fuel flows from lean to rich conditions. A similarly operating PDE has a specific thrust around 120 lbf-s/lbm, making the PDE more efficient in terms of air flow. The pulsejet equivalence ratio ranges from 0.6-1.0, with rated/peak thrust occurring at rich conditions. Typical fuel-specific impulse (Isp) for the pulsejet is 1400-1500 s for rated thrust conditions, whereas PDE performance (with a fill fraction of 1) is around 1800 s. For the PDE operating in the same fill fraction range as the pulsejet (~0.1), PDE Isp is estimated to be 6000-8000 s making the PDE cycle far more efficient and desirable at comparable conditions.

I. Introduction

Pulse Detonation Engines (PDEs) and pulsejets both belong to a class of gas generators that is fundamentally unsteady in nature. Furthermore, they share the feature of being combustion-driven. That is, they operate on cycles in which an essential internal-combustion event occurs and from which useful work is extracted. It may also be argued that both have a combustion event which is confined or is an approximation of constant-volume heat release. Beyond these commonalities, however, the PDE and pulsejet have significant operational, theoretical, and practical differences. While PDEs closely approach the constant-volume combustion approximation (in fact, detonation produces less entropy), pulsejets do so only marginally. It can be shown that the fundamental PDE process of rapid detonation, followed by relaxation through a Taylor wave, results in a state close to that found in constant-volume combustion.¹ The pulsejet cycle, on the other hand, relies on relatively slow deflagration during the combustion event. Confinement is achieved fluidically which, when combined with the relatively slow mode of combustion, results in heat release occurring both before and after the combustible mixture has reached a minimum volume. This aspect of operation, combined with several other factors, tends to render pulsejets relatively inefficient as thrust-producing devices.

* Associate Fellow AIAA

This material is declared a work of the U.S. Government and is not subject to copyright protection in the United States.

Detailed descriptions of the pulsejet operational cycle can be found in the literature,^{2,3} and only a brief one will be presented here. Referring to Figure 1, the cycle may be divided into three phases:

1. Combustion - Reaction of an air and fuel mixture within the combustion chamber commences. The pressure begins to rise as a result of confinement of the flow. The pressure rise causes the inlet valves to close, preventing backflow. The reaction accelerates as the pressure and temperature rise; this, in turn, accelerates the pressure and temperature rise.
2. Expansion - The hot, high-pressure gases in the combustion chamber expand, forcing flow from the exhaust.
3. Ingestion - The momentum of the exhaust gases causes the combustion-chamber pressure to drop below the ambient value. This allows the inlet valves to open and a fresh charge of air to enter (mixed with fuel). Eventually, the exiting exhaust flow reverses and mixes with the fresh charge. This initiates a new reaction, and the cycle begins again.

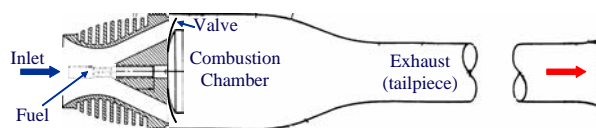


Figure 1. Pulsejet Schematic

For illustration purposes, Figure 2 shows contours of pressure, temperature, Mach Number, and reaction fraction for five cycles of a numerically simulated, valved pulsejet^{4,5} operating under static ambient conditions with stoichiometric combustion of a representative hydrocarbon fuel ($a/f=14.7$, $h_f=18,600$ BTU/lbm). The vertical direction represents time, while the horizontal dimension of each contour represents distance along the device. The colors represent levels of the variables, and all quantities have been normalized to reference conditions. The numbers next to each contour represent the high and low values of the plotted quantity observed in the x - t space. The geometry of the simulated device is shown as a scaled drawing in the bottom of Figure 2.

Two hundred numerical cells were used in this calorically perfect gas ($\gamma=1.3$), quasi-one-dimensional computation. The inlet valve was approximated by assuming a solid wall boundary condition during times when the pressure in the first interior cell was above the ambient value, and a partially open boundary condition⁶ when the pressure was below ambient (the inlet was assumed to have 15% of the combustion-chamber cross-sectional area). Extremely large diffusion coefficients were used in order to approximate the vigorous mixing that takes places during the filling process. The reaction rate term in the governing equations was modified from the original form by adding pressure dependence. This tended to slow the reaction during the filling process and accelerate it during times when the inlet valve was closed. The result was a self-sustaining cycle exhibiting pressure oscillations and operational frequency similar to those observed experimentally. The computed specific thrust of the cycle was 82 lbf-s/lbm, yielding a specific impulse of 1286 s. The latter value is consistent with reported values for pulsejets.⁷ Although the simulation is not quantitatively accurate, it demonstrates the key features of the pulsejet process. It is clear from the figure that the resonant cycle has both Helmholtz-like features and gas-dynamic features. It is clear that the geometry of the device is critical to its operation and performance. In the past, with no effective means of parametrically examining the effects of geometry, pulsejets were designed in a somewhat "hit-or-miss" fashion. Compounding this complexity is the fact that mixing of the fuel, air, and residual hot gases in the combustion chamber is extremely complex and does not lend itself to simple analysis. When a particular geometry was found that worked (i.e., ran), the design was frozen.

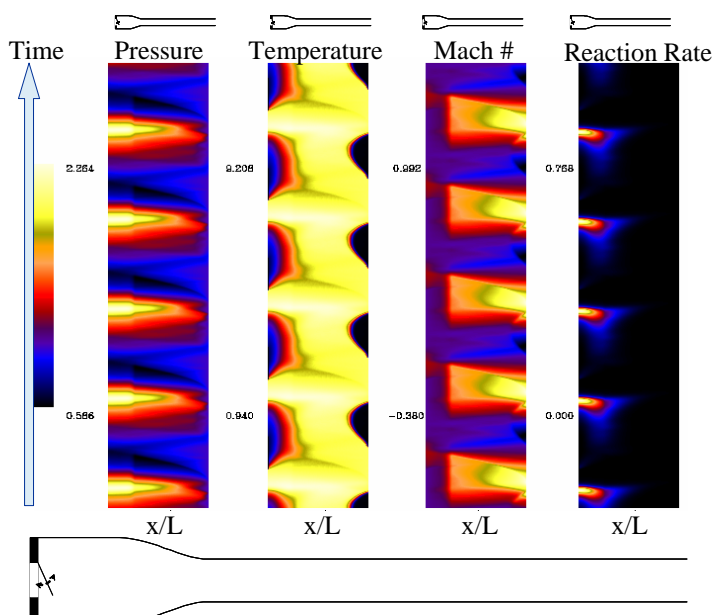


Figure 2. Contours of Pressure, Temperature, Mach Number, and Reaction Rate for Five Cycles of Numerically Simulated, Valved Pulsejet

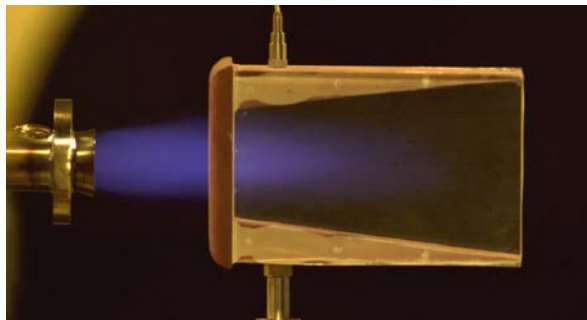


Figure 3. Tailpipe of a Small Pulsejet during Operation

Few attempts have been made to optimize pulsejet geometry. Most existing pulsejets were designed between 1940 and 1960.

In addition to the complexities of the unsteady flow field and the semi-constant volume nature of the cycle, pulsejets suffer from a need for rich combustion, as evidenced in the few previous experiments where pulsejet fuel and airflow were measured⁸ and by the common appearance of a blue “tail” flame observable during operation (see Figure 3). The rich combustion may be due to poor design; however, it is also possible that the time constants associated with a rich reaction are operationally critical.

All of these difficulties and losses have rendered the pulsejet non-competitive as a thrust-producing device with the conventional gas turbine on a performance basis. It would intuitively seem that the device would also yield relatively poor performance compared to a PDE, as will be shown. However, the static performance can be quite competitive.

In this paper an experiment is described with a pulsejet installed in the Pulsed Detonation Research Facility⁹ (PDRF) at Wright-Patterson Air Force Base. Performance results will be shown and compared to data from a statically operated PDE run at stoichiometric conditions with similar length scales.

II. Experimental Setup and Procedure

The pulsejet tested and discussed in this paper is a Solar PJ32, originally developed and manufactured by the Solar Aircraft Company for the Globe Corporation Aircraft Division in 1951. This engine, developed for use on a target drone (KD2G-2 Firefly) for the US Navy, is essentially a 1/5-scale version (in terms of thrust and inlet area) of the Argus pulsejet¹⁰ that powered the German V-1 “Buzz-Bomb” in World War II, with an overall engine length which is one-half that of the V-1.

One of the attractive features of pulsejets and PDEs is the relative simplicity of the design. Figure 4 contains a schematic of the engine and a photograph of the installation on the thrust stand⁹ in the PDRF. The engine has three major sections: 1) inlet and valve array that control combustion air, 2) fuel-injection ring, and 3) combustion chamber and tailpipe.

Combustion air enters the engine via the short diffuser at the inlet. Attached to the inlet, at the entrance to the combustion chamber, is the valve array shown in Figure 5A. The normally open valve array serves two purposes: it allows the inflow of a fresh charge of combustion air when open and, when shut acts as the thrust wall against which the higher pressure exhaust gasses push to produce thrust when shut. The valve array has an overall area of 26 in.² (5.4 in. x 4.8 in.) and is composed of reed valves and reed-valve shields that are separated by, and seal against, aluminum spacer blocks. The reed valves are fabricated from 0.010 in.-thick blue-tempered spring steel and bent approximately 15°. The actual air-passage area through the valves is only 42% of the available inlet area, which leads to rather significant losses across the valves. Because of the high temperatures and impact forces experienced by the valves during operation, the valves tended to only last 10-15 min before requiring replacement. Figure 5B shows a sample reed valve before and after operation.

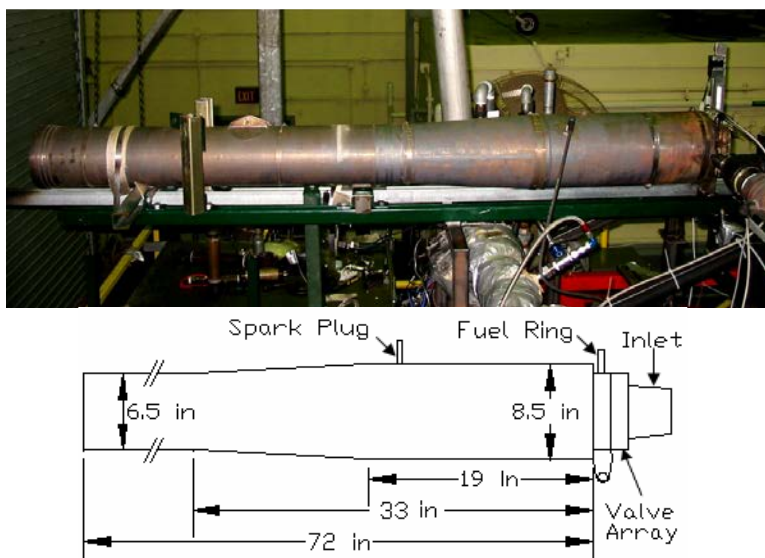


Figure 4. Pulsejet Installed on Thrust Stand

One major difference between this pulsejet and many carbureted pulsejets in use today (in addition to the obvious difference in size) is that it is operated on pressurized liquid-hydrocarbon fuel—in this case 100 Octane, low-lead Aviation Grade Gasoline (Avgas), injected at 4-15 psig directly into inlet air flow entering the combustion chamber. This injection is accomplished via the fuel-injection ring immediately following the valve array. A ¼-in.-diameter tube with a series of small holes drilled along each side surrounds the short passage between the valves and the main combustion chamber. A fuel line was connected from the top of the injection ring to a sealed 10-gallon fuel reservoir. Pressurized air, controlled with a pressure regulator, was connected to the fuel tank to pressurize the fuel. To test the fuel-delivery system and visualize the fuel-injection process, some preliminary injection tests were performed with water (see Figure 6). The fuel grid formed at the injection ring mixes with the combustion air as it passes through the valves and enters the combustion chamber.

The engine was instrumented, and operating parameters were recorded for fuel flows ranging from lean-out to flood-out. Five major parameters were recorded during testing: thrust, combustion chamber-pressure, external temperature along the length of the engine, fuel flow, and inlet-air flow. The engine was mounted on the previously described damped, pulsed thrust stand.⁹ Combustion-chamber pressure was measured through a ¼-in. NPT port that is 2 in. downstream of the fuel injection by means of an absolute pressure transducer. Type-J thermocouples were clamped to the exterior of the engine at intervals along the length to monitor tube temperature. Fuel flow was measured with an inline turbine flow meter located between the fuel tank and the injection ring. To ensure an accurate measurement of fuel flow, the fuel tank was weighed during operation, and a time-averaged fuel flow was derived to ensure that oscillations in fuel flow and fuel pressure due to the pulsed operation of the engine would not lead to errors in fuel-flow measurements. Because of the higher frequency response and resolution required for accurate quantification of the inlet air flow, air-flow measurements were made halfway along the length of the inlet duct with an IFA300 hot-wire anemometer. A hot-film probe was attached to a traverser to permit air flow in the duct to be measured at various locations within the duct.



Figure 6. Flow Visualization of Pulsejet Fuel Injection

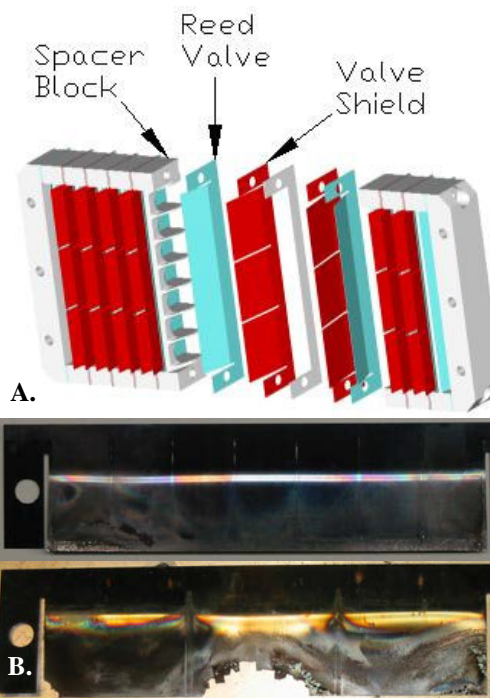


Figure 5. Pulsejet Valves

- A. Schematic of Valve Array*
- B. Two Damaged Reed Valves after Operation*

As with most pulsejets, this engine required a blast of air at the inlet to begin resonant operation. Given the lack of documentation on this particular pulsejet, a brief trial-and-error method was employed to develop a suitable startup procedure. In the end, a 2 in.-diameter nozzle was placed 18 in. upstream of the engine and directed at the inlet. Prior to ignition, facility air was fed into the engine from this nozzle at 50 lbm/min, which served two purposes. First, this arrangement provided the air necessary to begin resonant operation, and second, it acted as a safety device to ensure that the fuel, once ignited, was carried downstream. Once the air was on, the automotive spark plug that was installed 16 in. from the engine head was turned on, firing at 80 Hz. The fuel pressure was then set to a point above the desired set point, and the fuel solenoid valve was opened. The engine almost immediately began resonant operation, at which point the startup air and spark were turned off. The fuel pressure—and,

hence, the fuel flow rate--was then set at the desired set point, and the engine was allowed to operate for 30-60 s at the desired fuel flow rate. Once thrust leveled out, engine test data were logged, and air flow measurements at the inlet were made at various locations across the inlet. When the run was complete, the facility air was once again turned on to ensure that when fuel flow was shut off and the engine ceased resonant operation, any remaining fuel would be safely blown down the tailpipe.

III. Results and Discussion

Testing was carried out over the operating range of the pulsejet in an attempt to categorize performance fully. Initially, the pulsejet was run to determine the rich and lean fuel-flow limits and establish the control parameters. Because of the nature of the engine and fuel-delivery system, fuel pressure is the only variable that is controllable, once the engine is operating. The direct relation between fuel flow rate and the fuel-injection pressure can be seen in Figure 7. As discussed previously, fuel flow was measured with both a turbine flow meter upstream of the fuel injection and a load cell that weighed the fuel tank over time. The flow meter, of course, gave better time-resolved measurements, while the time-averaged load cell fuel-flow measurements were made to ensure that any oscillations in fuel flow and fuel pressure during operation would not adversely affect flow measurements with the turbine flow meter. Data from the steady flow measurements made with the two methods agreed to within 5%. The metered flow measurements were used in calculating the remaining derived engine-performance parameters.

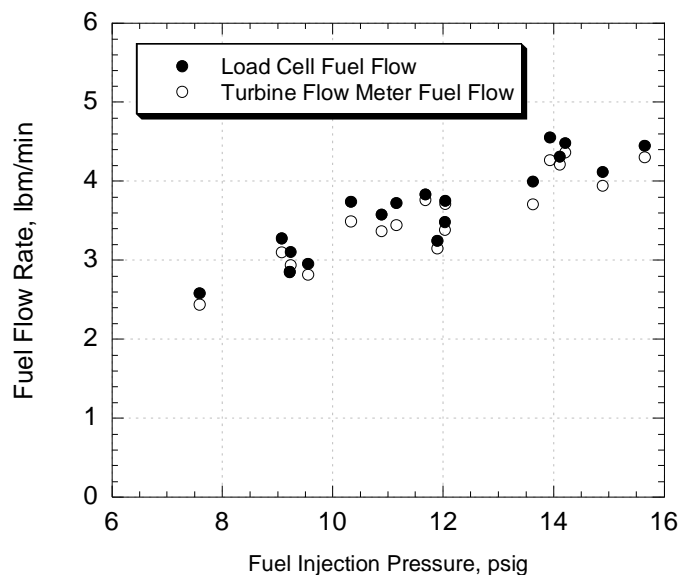


Figure 7. Plot of Fuel Flow Rate vs. Injection Pressure

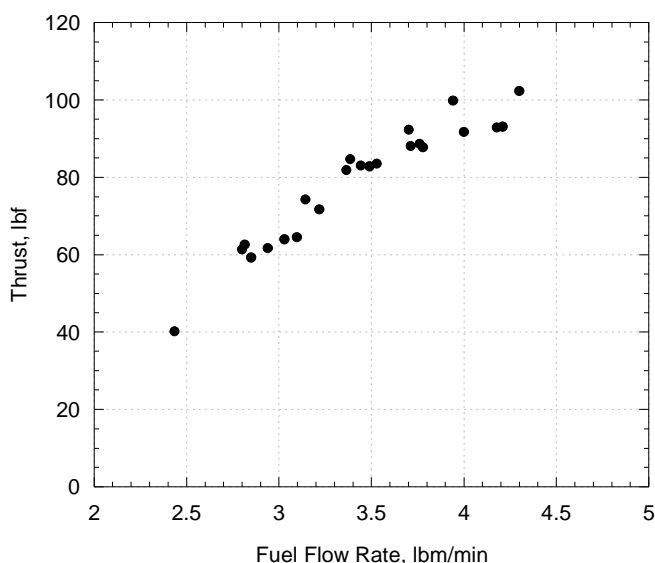


Figure 8. Plot of Thrust vs. Fuel Flow Rate

A. Pulsejet-Performance Summary

Once the pulsejet begins resonant operation, fuel flow is the only engine-control mechanism. As expected, thrust was found to increase with fuel flow rate, as shown in Figure 8. Lean out for the PJ32 is around 2.75 lbm/min fuel flow, which corresponds to around 60 lbf of thrust. As the fuel flow rate is increased, the thrust also increases, up to the flood-out limit of around 4.5 lbm/min fuel flow. At the upper fuel flow limit, the thrust topped out at 102 lbf. Because of the nature of the fuel-delivery system, throttling response of the engine was somewhat slow, but the thrust range was surprisingly large. Note that all of the pulsejet performance results presented here are for self-aspirated, static conditions and that pulsejet thrust will likely change as ram air at the inlet is increased.

Given that the amount of thrust produced is a result of the peak pressure within the combustion chamber during operation, it is not surprising to find that the peak head pressure also increases with fuel flow, as shown in Figure 9. Also shown here are the minimum head pressure and the engine operating frequency over the range of fuel flows. The minimum head pressure, i.e., the level of vacuum after cycle blow down that is available to suck in the next charge of combustion air, decreases with increasing fuel flow. This is to be expected, since the higher peak pressures will generate faster exhaust gases with increased momentum, leading to a stronger vacuum. Additionally, the cycle frequency was found to decrease from 80 Hz to around 75 Hz with increasing fuel flow.

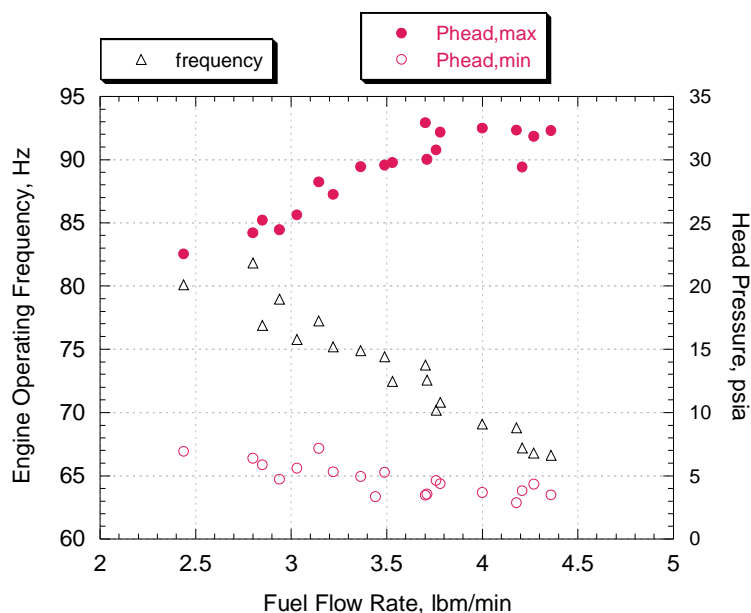


Figure 9. Plot of Engine Frequency and Peak/Minimum Head Pressures during Operation

At first glance at the fuel specific impulse (Isp) for this pulsejet (Figure 10), the operation appears to be relatively efficient. For a similarly operating PDE, one would expect an Isp of around 1800 s. Pulsejet Isp for extremely lean conditions was around 930 s; but under the higher fuel flow rates near the rated thrust levels (4.0-4.5 lbm/min) Isp is a more comparable 1400-1500 s. Thus, this engine appears to have quite good fuel economy, especially near the region of its rated thrust. However, bear in mind that all of the data reported here are for static operation, and Isp changes as flight speed increases.

In addition to fuel flow rate and thrust, head pressure and the inlet-air flow were measured. The inlet-air mass flow was calculated over time from the air-velocity measurements made in the inlet with the hot-wire anemometer. The anemometer traversed across the inlet halfway between the valves and the inlet opening; and inlet-air velocity had little to no dependence on location within the duct, with negligible fluctuations near the wall. Given the nature of engine operation, it is not surprising that air-flow fluctuations were dependent mainly on time. After verifying that inlet flow could be assumed to be independent of location at the measurement cross section, mass-flow measurements were derived from the time history of air-flow velocity measurements by simply multiplying the air velocity by the inlet cross-sectional area (at the axial location of the hot film probe) and atmospheric air density. This mass flow history was then integrated during the periods of time where there was inflow into the engine and

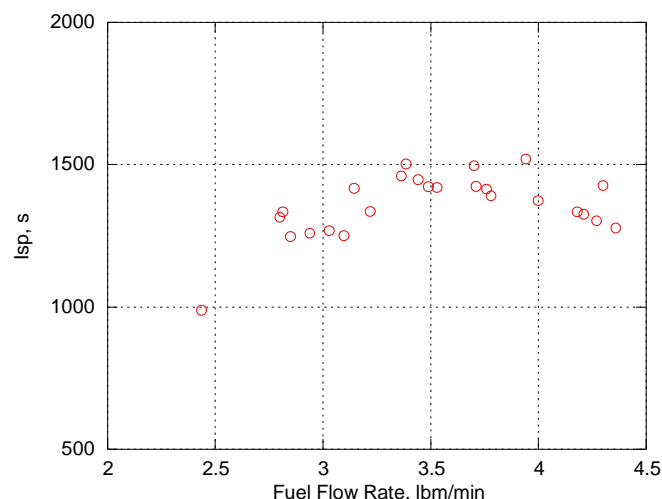


Figure 10. Plot of Statically Operating Pulsejet Fuel Specific Impulse (Isp) vs. Fuel Flow Rate

averaged over subsequent cycles to arrive at an average mass flow for the engine. Due to measurement difficulties and hardware issues, the centerline inlet velocity was measured, and the inlet velocity profile was assumed to be uniform. This is of course not the case. Given that this is a rather complex problem--unsteady, pulsed flow in the entrance length of a square diffuser--the velocity profile was assumed to be uniform and no correction factor was applied to reduce the calculated air flow.

To aid visualization of the important events during each cycle, the inlet-air flow and head pressure for one characteristic cycle are plotted and labeled in Figure 11. The cycle begins with the opening of the reed valves (Point A). This is followed by a rapid increase in inflow of air as the pressure in the chamber reaches its greatest vacuum (Point B), which is approximately the

same time that air flow reaches its peak flow rate (Point C). The incoming air mixes with the injected fuel as it is sucked into the combustion chamber. As the combustion-chamber pressure approaches atmospheric, the air flow at the inlet drops off drastically, until the ignition event occurs in the chamber (Point D). Immediately following ignition, a sharp rise in chamber pressure occurs as well as a sudden increase in inlet velocity (Point E). This apparent increase is not actual inflow. Because the single-channel hot-film probe used measures axial velocity regardless of direction, this rise in flow is, in actuality, exhaust gas being blown back through the valves. This blowback continues until the reed valves are forced shut (Point F). Once the valves are shut, the internal pressure continues to rise until it reaches its peak pressure (Point G), after which hot exhaust gases continue to be blown out of the tail pipe until the valves open (Point H) and the cycle begins again.

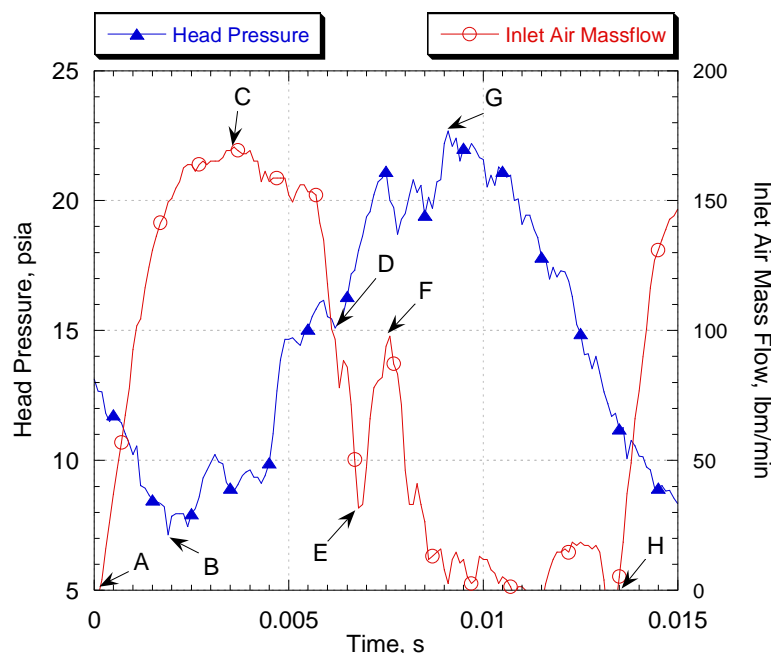


Figure 11. Plot of Head Pressure and Inlet-Air Mass-Flow History over One Cycle

The average mass flow rate of combustion air was calculated by integrating the inlet-air mass flow rate during those periods when the valves were open. This average air flow rate was then used to compute specific thrust and equivalence ratio, both of which are plotted versus fuel flow rate in Figure 12. As expected, specific thrust and equivalence ratio both increase as fuel flow is increased. Since pulsejets are noted for running with a richer fuel-air ratio, it is not surprising that the maximum thrust occurred in the operating region with higher equivalence ratios. As shown in the figure, specific thrust also increases as the operating mixture becomes richer. Again, it must be pointed out that the results are for static conditions. As in the case of Isp and thrust generated, specific thrust will change as ram air is increased.

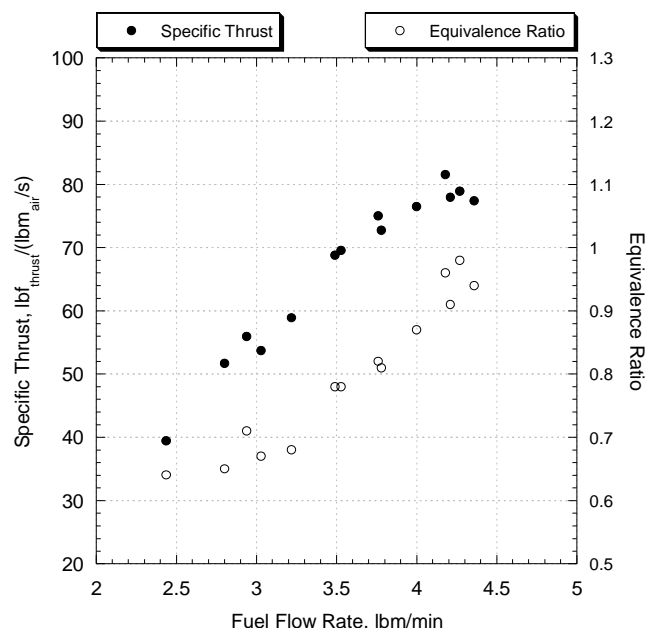


Figure 12. Plot of Specific Thrust and Equivalence Ratio vs. Fuel Flow Rate

Tube temperature is another characteristic that has an effect on engine performance. Figure 13A shows peak external tube temperatures as a function of location along the tube. Notice the "hot spot" 20-50 in. downstream from the head, which is indicative of where the significant portion of the combustion event is taking place. Elevated tube-wall temperatures aid in fuel vaporization and increase reaction rates. Unfortunately, if tube temperatures become too hot, the engine could fail; or in the case of PDEs, the engine could experience premature ignition and fail to operate properly. Figure 13B shows tube temperature over a 65-s run. For the results presented here, fuel flow was held constant at 3.7 lbm/min. Engine thrust required approximately 25-30 s to level off after the engine was ignited. Interestingly enough, this is the same point at which the slope of the tube temperatures initially begins to decrease.

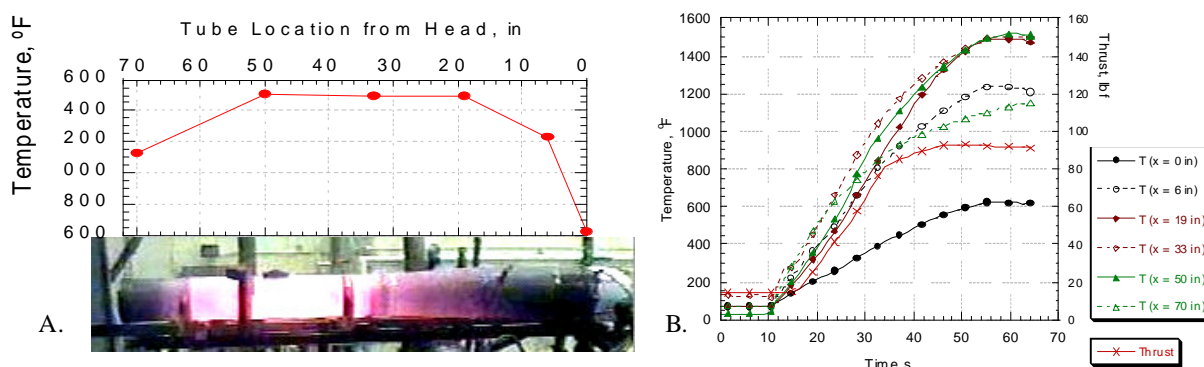


Figure 13. Tube Temperature

A. Maximum Tube Temperature as Function of Location

B. Thrust and External Tube Temperatures (T) at x-Location along Tailpipe Downstream of Engine Head for 3.7-lbm/min Average Fuel Flow Rate

B. PDE/Pulsejet Comparisons

The most fundamental difference between a PDE and a pulsejet is that during the PDE cycle, a detonation is established within the combustion tube, while combustion in a pulsejet is confined to deflagration. Because a detonation is established within a PDE, the combustion in a PDE more closely approximates constant-volume combustion. Considering its use as a single-stage propulsive device, the pulsejet is inherently limited to subsonic speeds; while theoretically the PDE cycle has the potential to attain speeds from 0 through Mach 4+.¹¹ If these engines are to be used for propulsion, it is desirable to view the pressure histories during their cycles, given that this is ultimately indicative of the thrust that could potentially be produced. Figure 14 shows the pressure history from experimental data for three different cycles: a PDE operating on Avgas with direct initiation,¹² a PDE operating on Avgas with DDT,¹² and the pulsejet tested here.

Since the thrust of a pulsejet or PDE is generated by pressure waves pushing on the thrust wall of the engine, it stands to reason that thrust can be easily derived from the pressure history. Figure 15 shows a comparison of the directly measured thrust of the pulsejet, with average thrust being calculated from the recorded head pressure. The

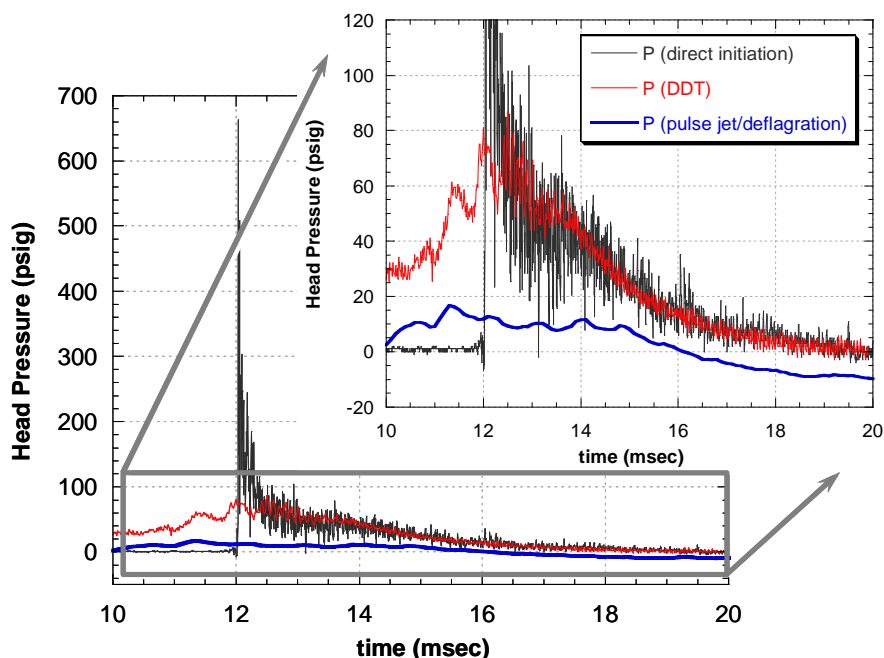


Figure 14. Cycle-Head-Pressure Comparison of PDE and Pulsejet

average calculated thrust was determined by integrating the pressure curve during the portion of the cycle in which the valves were closed and by assuming that this summed pressure acts over the area of the exit of the tail pipe. As can be seen in the plot, the results are within 5-10% of the measured thrust and would have been closer if losses and friction along the tube had been factored into the thrust calculation. This should be the case for PDEs as well. From Figure 14, the higher pressures of the PDE are quite desirable, and provide more high-speed potential. With the higher pressures of the PDE cycle, one would expect that higher thrust with more efficient expansion would be possible. The PDE with direct initiation is most desirable, but currently a number of major hurdles exist to incorporating this in a practical engine. PDEs using DDT would appear to be a viable solution; however, with DDT much of the potential thrust gain is sacrificed to the drag losses associated with DDT.¹³

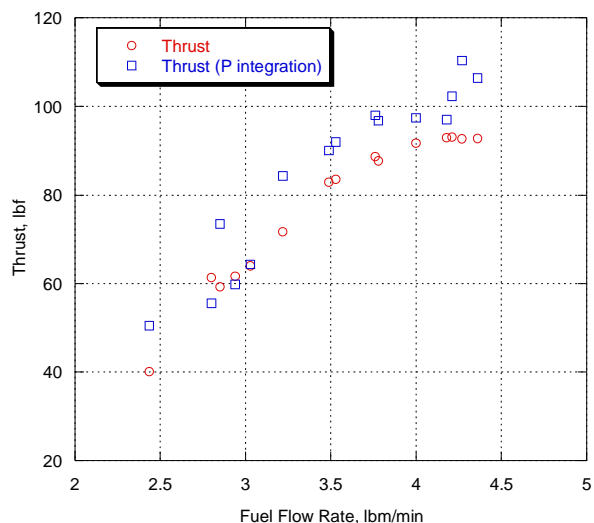


Figure 15. Measured and Calculated Thrust vs. Fuel Flow Rate

The static performance of a pulsejet has been shown to be comparable, in terms of Isp and specific thrust, to that of a PDE. One final comparison that should be made for the two devices is Isp versus fill fraction (i.e., the fraction of the tube that is filled during the cycle). Figure 16 shows the pulsejet Isp data alongside the validated model of Isp for partially filled PDE tubes.¹⁴ For purposes of comparison, pulsejet fill fraction was assumed to be the ratio of the volume occupied by the atmospheric air ingested by the engine through the inlet to the total engine volume. It has been shown that as fill fraction decreases, Isp increases significantly. Although the pulsejet at first appeared to have an Isp (1400-1500 s) comparable to that of a PDE (1800 s), when fill fraction is factored in, the pulsejet falls far from the mark. A PDE operating with a fill fraction comparable to that of the pulsejet would be expected to have an Isp between 6000 and 8000 s. Of course, a pulsejet is self-aspirated, and fill fraction cannot be controlled; however, if fill fraction were increased, the pulsejet Isp would be expected to decrease, following the same trend as that of the PDE.

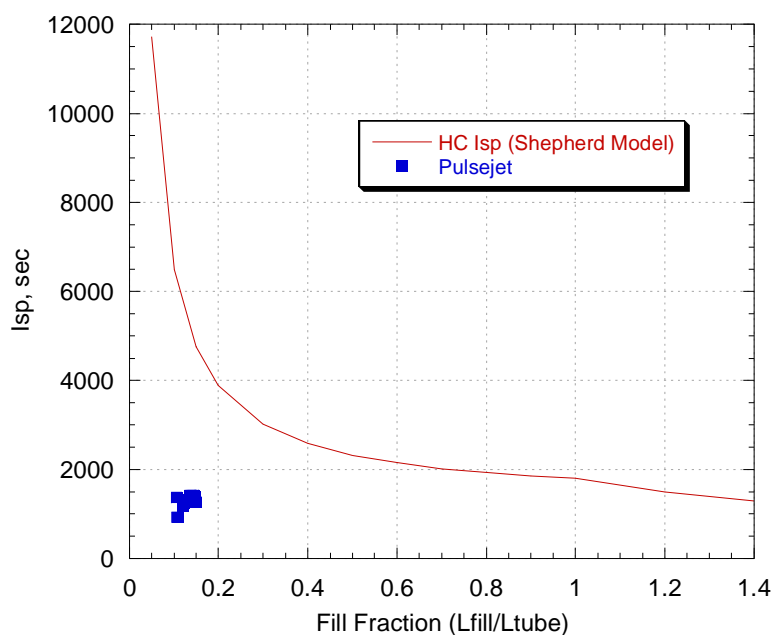


Figure 16. Plot Isp vs. Fill Fraction

IV. Summary and Conclusions

At first glance, the static performance of pulsejets appears to be comparable to that of PDEs. Upon further investigation, the significant differences in performance and potential become obvious. The pulsejet tested here was operated over a wide range of fuel flows (2.5-4.5 lbm/min), which corresponds to thrust levels ranging from 40 to 102 lbf. Thrust calculated from recorded head pressures agrees with measured thrust to within 5-10%. Specific thrust, calculated using air-flow measurements at the inlet, is in the range 40-100 lbf-s/lbm over the lean-out to flood-out fuel-flow conditions, which is somewhat lower than that of a PDE. Equivalence ratios for operating conditions range from 0.6 to 1.0. As expected, the pulsejet produced the highest thrust levels when operating with richer equivalence ratios. Static Isp for the pulsejet is 1400-1500 s, while that for a similarly operating PDE is 1800 s. The fill fraction of the pulsejet, however, is quite low; as the fill fraction of a PDE approaches that of the pulsejet, the PDE Isp is estimated to be 6000-8000 s, making the PDE cycle far more efficient and desirable at equal conditions. As stated previously, limited work has been done to optimize pulsejets. There is no debate that the PDE has far more potential than an optimized pulsejet; however, if an inexpensive, simple, low-thrust engine is desired, an optimized pulsejet would satisfy the requirements.

Acknowledgments

The authors are grateful to Curt Rice (ISSI) for his invaluable help on this project. The authors would also like to thank Jeff Stutrud (AFRL/PRTC) for his computer programs that were used to collect and analyze the data. The technical leadership of Dr. Mel Roquemore and Dr. Robert Hancock (AFRL/PRTC) continues to be invaluable. The funding required to complete this project was provided by the Propulsion Directorate, and the test article was generously provided by NASA Glenn.

References

- ¹ Heiser, W.H and Pratt, D.T., "Thermodynamic Cycle Analysis of Pulse Detonation Engines," *AIAA Journal of Propulsion and Power*, Vol. 18, No. 1, 2002, pp. 68-76.
- ² Kentfield, J.A.C., Nonsteady, One-Dimensional, Internal, Compressible Flows, Oxford University Press, 1993, pp. 191-235.
- ³ Putnam, A. A., Belles, F. E., and Kentfield, J.A.C., "Pulse Combustion," *Progress in Energy and Combustion Science*, Vol. 12, 1986, pp. 43-79.
- ⁴ Quinn, D. D., and Paxson, D. E., "A Simplified Model for Investigation of Acoustically Driven Combustion Instabilities," AIAA Paper 1998-3764, July 1998.
- ⁵ Nalim, R. M., and Paxson, D. E., "A Numerical Investigation of Premixed Combustion in Wave Rotors," *ASME Journal of Engineering for Gas Turbines and Power*, Vol. 119, no. 3, 1997, pp. 668-675.
- ⁶ Paxson, D. E., "An Improved Numerical Model for Wave Rotor Design and Analysis," AIAA Paper 1993-0482, January 1993.
- ⁷ CJB-5751 Dyna-jet Red Head Jet Engine Owner's Manual, 1975.
- ⁸ Paxson, D. E., Wilson, J., and Dougherty, K. T., "Unsteady Ejector Performance: An Experimental Investigation Using a Pulsejet Driver," AIAA Paper 2002-3915, July 2002.
- ⁹ Schauer, F.R., Stutrud, J., and Bradley, R.P., "Detonation Initiation Studies and Performance Results for Pulsed Detonation Engine Applications," AIAA Paper 2001-1129, January 2001.
- ¹⁰ Manganiello, E. J., Valerino, M. F., and Essig, R. H., "Sea-Level Performance Tests of a 22-Inch-Diameter Pulsejet Engine at Various Simulated Ram Pressures," NACA MR-E5J02, October 1945.
- ¹¹ Kailasanath, K., Patnaik, G. and Li, C., "Computational Studies of Pulse Detonation Engines: A Status Report," AIAA 99-2634, June 1999.
- ¹² Schauer, F.R., Miser, C., Tucker K.C., Bradley, R.P., and Hoke, J.L., "Detonation Initiation of Hydrocarbon-Air Mixtures in a Pulsed-Detonation Engine," AIAA Paper 2005-1343, January 2005.
- ¹³ Hoke, J.L., Bradley, R.P., and Schauer, F.R., "Impact of DDT Mechanism, Combustion Wave Speed, Temperature, and Charge Quality on Pulsed-Detonation-Engine Performance," AIAA Paper 2005-1342, January 2005.
- ¹⁴ M. Cooper, Shepherd, J.E., and Schauer, F., "Impulse Correlation for Partially-Filled Tubes," *Technical J. Propulsion Power*, Vol. 20, no. 5, 2004, pp. 947-950.

43rd AIAA Aerospace Sciences Meeting
January 10-13, 2005, Reno, NV

2005-1343

Detonation Initiation of Hydrocarbon-Air Mixtures in a Pulsed Detonation Engine

F.R. Schauer, C.L. Miser, K.C. Tucker,
Air Force Research Laboratory, WPAFB, OH 45433

R.P. Bradley, and J.L. Hoke
Innovative Scientific Solutions Inc., Dayton, OH 45440

Detonation initiation of hydrocarbon-air mixtures is critical to the development of the pulsed detonation engine (PDE). Conventionally, oxygen enrichment (such as a predetonator) or explosives are utilized to initiate detonations in hydrocarbon/air mixtures. While often effective, such approaches have performance and infrastructure issues associated with carrying and utilizing the reactive components. An alternative approach is to accelerate conventional deflagration-to-detonation speeds via deflagration-to-detonation transition (DDT). Analysis of hydrocarbon-air detonability indicates that mixing and stoichiometry are crucial to successful DDT. A conventional Schelkin-type spiral is used to obtain DDT in hydrocarbon-air mixtures with no excess oxidizer. The spiral is observed to increase deflagrative flame speeds (through increased turbulence and flame mixing) and produce 'hot-spots' that are thought to be compression-wave reflections. These hot spots result in micro-explosions that, in turn, then give rise to DDT. Time-of-flight analysis of high-frequency pressure-transducer traces indicate that the wavespeeds typically accelerate to over-driven detonation during DDT before stabilizing at Chapman-Jouget levels as the combustion front propagates down the detonation tube. Results obtained for a variety of fuels indicate that DDT of hydrocarbon-air mixtures is possible in a PDE. Successful DDT in air with no oxygen enrichment was achieved with propane, 100 octane low-lead aviation gasoline, kerosene based military jet fuel JP8, and the high energy-density military jet fuel JP10.

I. Introduction

Pulsed detonation engines (PDEs) have experienced renewed interest during the past several decades. To realize potential performance gains of the detonation process,^[1] a practical fuel-air mixture must be successfully detonated. Initiation of detonations remains a technology hurdle for development of practical PDE propulsion systems. As direct initiation of detonations in hydrocarbon-air mixtures requires large ignition energies,^[2] small tube predetonators with oxygen enrichment are often employed.^[3,4] Typically, a smaller volume of fuel-oxygen is utilized as a predetonator in order to initiate detonation of a larger volume of fuel-air. Although capable of reliably initiating detonations, systems of this type require either onboard oxygen tanks or generation systems and are, thus, undesirable for practical propulsion applications.

Alternatively, detonations may be indirectly initiated via acceleration of deflagration to detonation. This deflagration-to-detonation-transition (DDT) process is difficult to achieve in a small volume for complex hydrocarbon fuels in air. The key for performance is to achieve DDT before the deflagrative combustion expands the reactants from the detonation tube. Although direct initiation of detonation is possible, with air as the oxidizer, the magnitude of critical initiation energy for multi-cycle operation is impractical. As shown in **Figure 1**, which is a plot of critical initiation energy versus cell width (λ) for many fuel/oxidizers at stoichiometric and near standard temperature and pressure (STP) conditions, the critical initiation energy for practical hydrocarbon-air mixtures is on the order of 10^5 J,^[2] many orders of magnitude higher than the energy available from a typical spark plug (~100 mJ).

This material is declared a work of the U.S. Government and is not subject to copyright protection in the United States.

Consequently, a DDT process is probably required for practical detonation initiation of hydrocarbon-air mixtures without excess oxygen. Hydrocarbon-air DDT has been achieved by Santoro and co-workers who have had some success with ethylene-air mixtures^[5] and by Smirnov et al.^[6] who utilized confinement to promote DDT of gasoline-air.

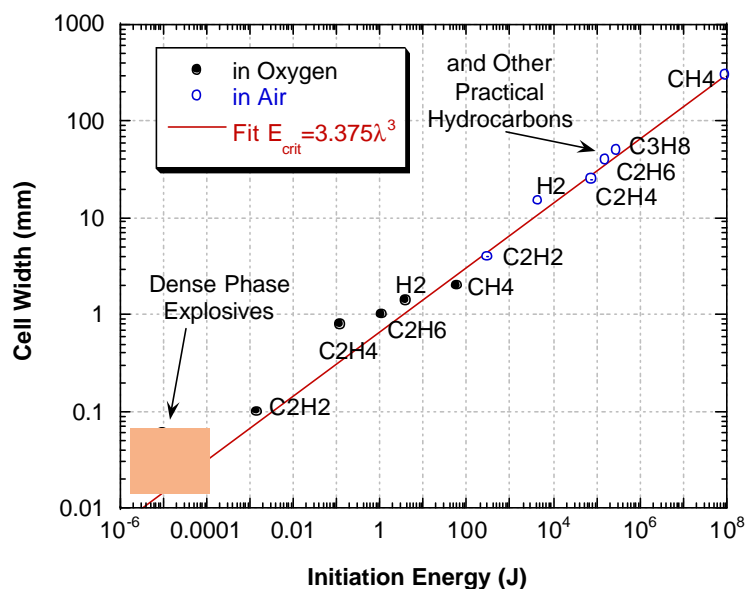


Figure 1. Detonation cell width versus critical initiation energy.^[2]

Researchers at the Pulsed Detonation Research Facility in the Air Force Research Laboratory at Wright-Patterson AFB have had some success in achieving DDT in hydrocarbon-air mixtures within research PDEs. The focus of this paper is detonation initiation of hydrocarbon-air mixtures using a Schelkin-type spiral in a PDE.

II. Theory and Background

Dorofeev et al.^[7] have shown that the minimum DDT distance scales by 7λ . For many practical stoichiometric hydrocarbon fuel-air mixtures near STP, including the fuels discussed herein, the cell width is on the order 50 mm,^[8] very similar to that of propane-air. In theory then, it should be possible to obtain DDT inside the length a typical 1 m long detonation tube with hydrocarbon-air mixtures.

Given that the detonation cell width scales by the total-heat-release induction time,^[9] it follows that any decoupling of heat release will result in increased cell width and a corresponding impact upon initiation requirements. Contributors to the total-heat-release induction time include: chemical-induction and heat-release time, droplet breakup, evaporation, and mixing. Consequently, large droplets and poor mixing will significantly increase cell width and dramatically impact initiation energy or DDT distance.

Figure 2 shows the impact of equivalence ratio upon cell size for several hydrocarbon-air mixtures that have cell sizes similar to those of fuels of interest.^[10] The resultant impact upon critical detonation initiation energy is dramatic as the equivalence ratio departs from stoichiometric, as indicated in **Fig. 2**.^[11] It is clear that there is a narrow minimum of cell width/initiation energy near stoichiometric. The critical detonation-initiation energy for equivalence ratios that are not near unity is measured in megajoules or kilograms of solid-explosives equivalent. Meyer and co-workers have shown via laser absorption measurements of fuel that significant variations in PDE equivalence ratio can occur in practice.^[12]

Though hydrocarbon-air mixtures should be readily detonable in theory, for the reasons cited above the proper nearly homogeneous mixture with an equivalence ratio near stoichiometric is required; otherwise the detonation initiation requirements can quickly become impractical. In PDE applications, it is extremely difficult to produce an unsteady flow with the proper equivalence ratio. Perhaps it is fortuitous that the difficulty in creating the proper mixture and conditions for detonation serves to reduce the explosive hazard of practical fuel-air mixtures.

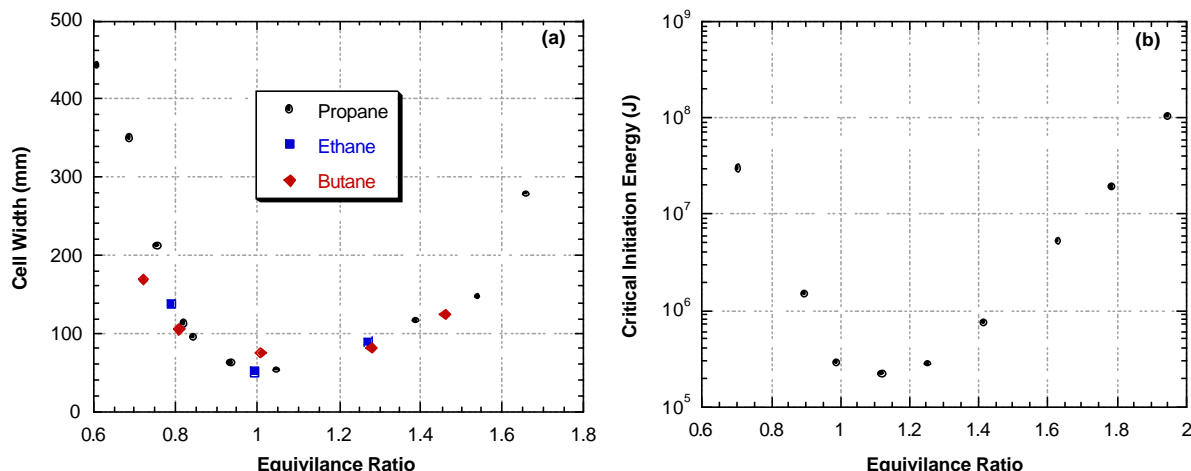


Figure 2. (a) hydrocarbon-air cell width^[10] and (b) propane-air critical detonation-initiation energy^[11] versus equivalence ratio.

III. Experimental Setup and Procedure

Experiments were conducted using the research PDE at the Air Force Research Laboratory's Pulsed Detonation Research Facility. This PDE controls the airflow and cycle timing for up to four detonation tubes using a four-valve-per-cylinder automotive cylinder head for valving. Further details of this engine can be found elsewhere.^[13]

The liquid-fuel injection system developed by Tucker and co-workers was utilized to premix fuel and air prior to the intake manifold.^[14,15] Fuel flow was controlled via selection of fuel-injector-nozzle(s) flow number and fuel pressure. Fuels included: propane, aviation gas (100 octane, low lead, henceforth referred to as 'avgas'), kerosene based USAF jet fuel JP8, and high energy density fuel JP10. Propane and avgas were obtained from local commercial suppliers, and military fuels were obtained from military stocks through the Air Force Research Laboratory's Fuels Branch (AFRL/PRTG).

Weak ignition was achieved in 50.1 mm internal diameter detonation tubes bolted to the cylinder head using an automotive-type spark plug in the stock location. The tubes were mounted to the valve system via an adapter plate which contained instrumentation ports for head pressure and optical sensors. Instrumentation ports were also located along the length of the 1.52 m long tubes. Schelkin-type spirals, 1.22m long, were located in each of the tubes. The experimental setup and instrumentation are shown schematically in Figure 3.

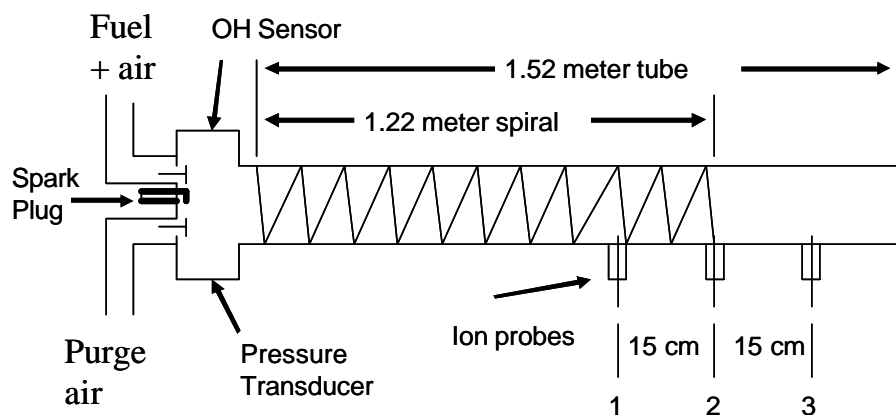


Figure 3. Experimental and instrumentation setup for hydrocarbon-air detonation experiments.

Although stainless-steel detonation tubes were utilized for the majority of experiments, DDT was observed with a polycarbonate detonation tube and fast imaging system, as described by Meyer et al.^[16] Figure 4 shows a typical result, with time evolving in subsequent images from top to bottom in Frames a through z. The spiral is

barely perceptible in these frames, and the visibly larger vertical bands are metal supports for instrumentation ports on the polycarbonate tube. Schelkin-type spirals accelerate flame speeds through turbulence and flame mixing.^[9] In addition to these mechanisms, the high-speed imaging reveals the interaction of compression-wave reflections off the spiral obstruction, that create ‘hot spots’ typified by those evident in Frames **f**, **k**, and **q**. The resultant compression waves from the intense heat release of these hot spots may coalesce and can produce ignition and a micro-explosion event or events such as those shown in Frame **x**. A sufficiently strong micro-explosion or the interaction of multiple explosions usually results in a DDT event (Frame **y**) with its subsequent left-running retonation wave and right-running detonation wave.

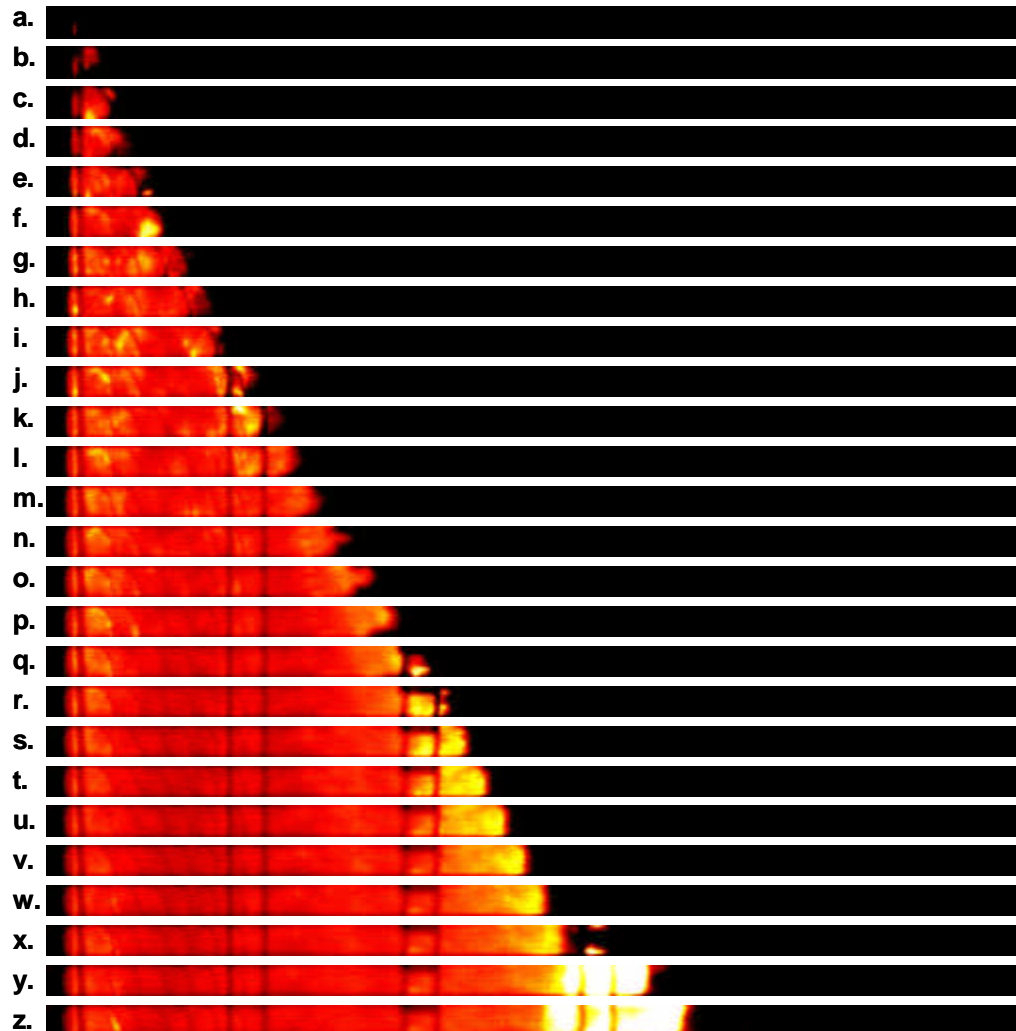


Figure 4. High speed imaging of deflagration-to-detonation-transition (DDT) using Schelkin spiral.
Subsequent Frames proceed from top to bottom.

Typical results for a successful hydrocarbon-air detonation initiation are plotted in **Figure 5**. Pressure traces from near the detonation tube head (P1 location) to the tail (P6) and offset from the bottom of the plot to the top by 30 atm for each location respectively, are shown in **Fig. 5a**. From time-of-flight analysis, the corresponding wavespeeds are shown in **Fig 5b**. Near the head, or P1 location, the pressure rise is gradual with ignition and subsequent flame acceleration. Flame speeds are ~1000 m/sec near this location, much lower than the theoretical Chapman-Jouget (CJ) detonation speed. Near the P2 location, DDT occurs, which is evident in the high overpressure of the von-Neuman spike and overdriven detonation wavespeed measurement near this location. The subsequent retonation wave is evident in P1, and the detonation wavespeed decays to the equilibrium value of ~1820 m/sec, which is very near the theoretical C-J wavespeed of ~1790 m/sec. The reduced pressure spike and

wavespeed near the very end of the tube, at location P6, are indicators of mixture dilution (due to mixing with air at the tube exit) near that location.

Because of the fragile nature, expense, and thermal drift of high-frequency pressure transducers, subsequent wavespeed results were obtained with ion probes^[17] located near the spiral end, as depicted in **Fig. 3**. It should be noted that ion probes of this type indicate the presence of ions from the combustion front--not the pressure variations detected via pressure transducers. Consequently, ion-probe measurements of wavespeed indicate the combustion wavespeed--not the shock-wavespeed. The combustion-wavespeed measurements are more accurate for evaluating detonation wavespeed since it is possible to have a shock-wavespeed without combustion.

A typical data set is shown in **Figure 6(a)** for two detonation tubes firing 180 degrees apart at approximately 15 Hz each (30 Hz aggregate). For each data set, results from two detonation tubes (Tubes 1 and 4) were recorded. For each tube, data included the ignition trigger (down transitions of **ign**), a head pressure trace (not shown in **Fig. 6(a)** for clarity) and three ion probes (Locations **a**, **b**, and **c** which were 15 cm upstream of the end of the spiral, at the end of the spiral, and 15 cm downstream of the spiral, respectively). As more clearly shown in the plot on the right of **Fig. 6**, the combustion wave front triggered the ion probes, facilitating wavespeed calculations from time-of-flight analysis. The data shown were from JP10-air at an equivalence ratio of 1.0 and a measured wavespeed of 2230 m/sec and 1823 m/sec, upstream and downstream of the spiral, respectively. The upstream wavespeed is probably overdriven beyond CJ because it is near the DDT location, but the downstream measurement indicates that the detonation is nearing equilibrium. Also shown is tube head pressure, which is significantly lower than the expected P_3 value because of thermal drift of the pressure transducer and possible loss mechanisms described in greater detail by Hoke et al.^[18]

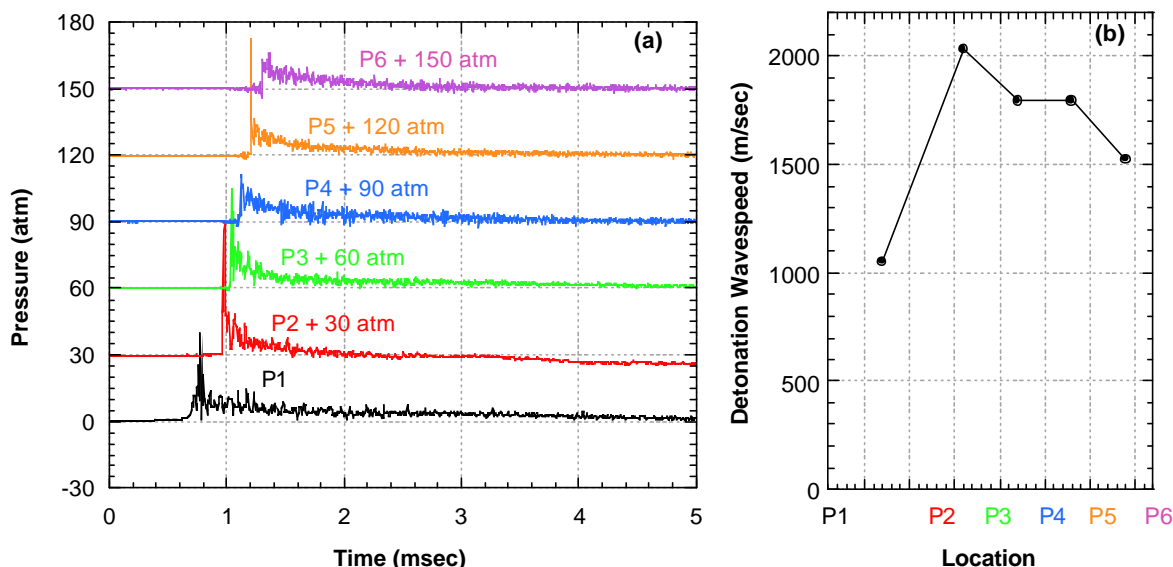


Figure 5. Typical pressure traces (a) for hydrocarbon-air mixtures from near head (P1) to exit (P6) on the tube and bottom to top on the plot, offset for clarity. Time-of-flight analysis provides wavespeed (b).

Due to the sheer volume of data collected (gigabytes), subsequent results contain only the downstream wavespeed measurements. This measurement location provided a convenient means of determining whether detonation occurred while avoiding charge-dilution problems near the end of the tube, as described above with regard to the P6 location measurement of **Fig. 5**.

Subsequent data were taken using two tubes to minimize equivalence-ratio variations caused by unsteady air flow across the injection system.^[15] Fuel flow, determined via a turbine flow meter and flow calculations across the fuel injectors, is described further elsewhere.^[14,15] Air flow was measured via critical flow nozzles upstream of the unsteady engine,^[13] and both air flow and operating frequency were varied in order to provide the desired equivalence ratio with a full tube fill. Operating frequency was between 10 and 20 Hz per tube. Spark ignition delay was between 6 and 8 msec after inlet valve closure. The inlet air was preheated to $\sim 90^\circ\text{C}$ to avoid puddling of liquid fuel in the intake manifold of this premixed injection system, but performance was found to be fairly insensitive to inlet-air temperature. The fuel heating capability developed by Tucker^[14,15] was not utilized except with JP10 and during a test series with JP8. In both cases the fuel was heated to $\sim 280^\circ\text{C}$. The PDE was run approximately 30-60 sec, allowing the flows to stabilize before data were collected for approximately 1 sec.

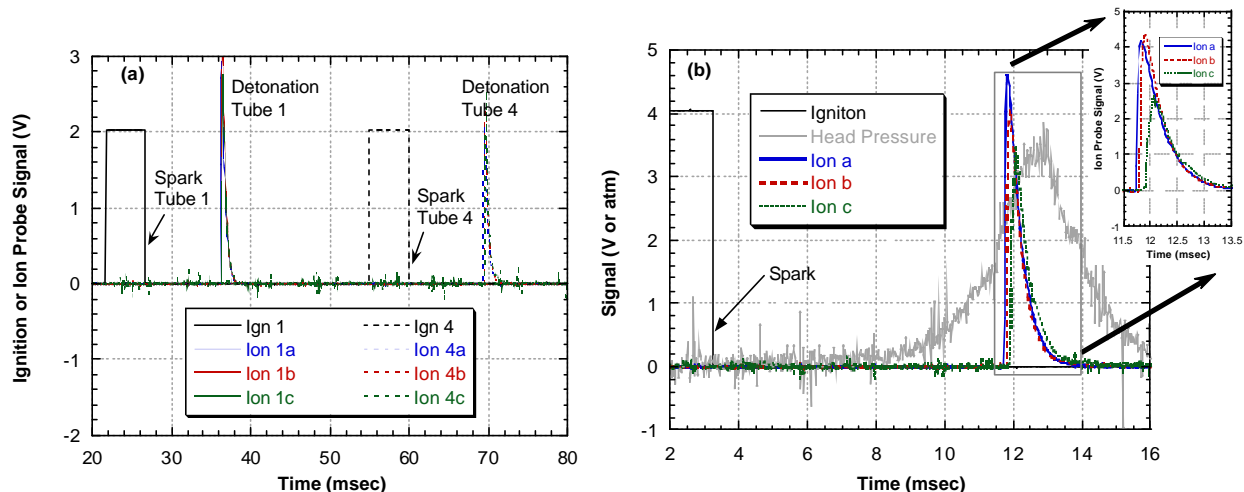


Figure 6. Typical data collected for hydrocarbon-air detonation analysis. Data was collected for multiple tubes (a.) and processed to calculate combustion wavespeeds from time-of-flight past ion-probe signals (b).

Data analysis consisted of post-processing using the routines developed by Parker,^[19] and the following results are the average of 8-20 detonation events for either 1 or 2 tubes. For each fuel, plots were made of the average measured wavespeeds downstream of the spiral versus measured equivalence ratio, along with the expected Chapman-Jouget (CJ) values, which were calculated using properties from Gordon and McBride,^[20] as implemented by Tucker.^[15] The measured equivalence ratio was found to vary no more than 2% and was confirmed using the hydrocarbon absorption diagnostic developed by Meyer and co-workers^[12] unless otherwise noted. Variations in the measured wavespeed are reflected in the calculated standard deviation, plotted as the vertical error bars for each data point.

In general, wavespeed results significantly above the CJ line are indicative of an overdriven detonation and probably indicate that DDT occurred near the measurement location and in this case, downstream wavespeeds are likely near CJ. Results within ~10% of the CJ value indicate that a steady detonation was achieved. If the results are significantly less than the CJ values, e.g. less than ~1500 m/sec, it is likely that detonation was probably not achieved or achieved only intermittently at that particular test condition. If the plotted wave speed error bars are small, results were fairly consistent. It follows that large error bars that widely vary across the theoretical CJ wavespeed either above or below indicate intermittent failure to DDT for the latter case and intermittently overdriven for the former.

IV. Results and Discussion

Detonation failed to occur if large droplets were present and/or the fuel-air mixture was not homogenous. In fact, it was extremely difficult to ignite a deflagration if these conditions were present. Ignition characteristics of the fuels tested are not particularly favorable near STP conditions. With the proper fuel injection scheme and mixing, DDT was observed for every fuel tested.

It should be noted, as shown in **Fig. 6(b)**, that the time required from spark to DDT was typically 10 msec and may hinder practical cycle rates. The majority of this time (~8 msec) was observed to be the time between spark and establishment of a deflagration flame kernel resulting from the long chemical induction times of hydrocarbon fuels in air at near-ambient conditions.

Measured propane-air wavespeeds versus equivalence ratio are plotted in **Figure 7** and compared to theoretical CJ wavespeeds. Results varied widely with propane-fuel. This is reflected in the data as many points are near 1000 m/sec (choked flame wavespeed). Still propane-air was observed to detonate consistently during some runs with an equivalence ratio of ~0.9. For the wavespeeds above 1500 m/sec near stoichiometric conditions, overdriven upstream wavespeeds (not shown) are indicative that DDT was achieved and the resulting slightly slower wavespeeds probably indicate poor mixing. In general, the ability to initiate a detonation in propane was poorer than with the other fuels reported herein. Factors which may have contributed to the difficulty in detonating include poor mixture control and fuel chemistry.

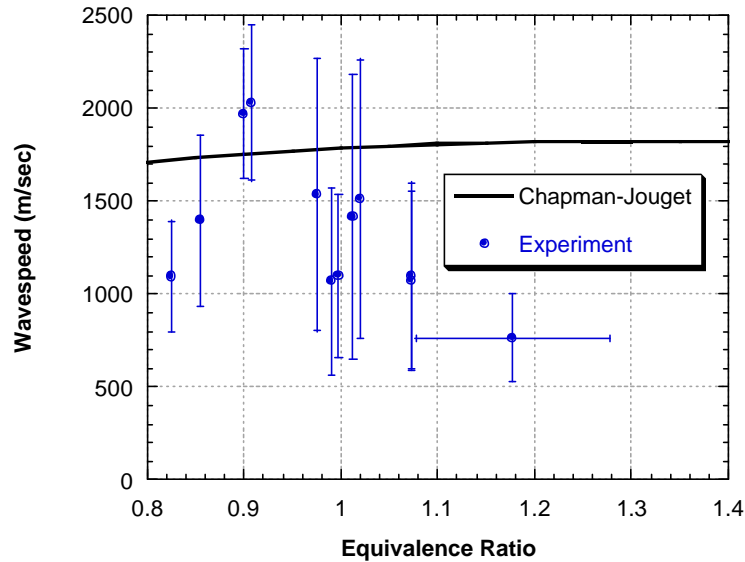


Figure 7. Wavespeed versus equivalence ratio for propane fuel-air.

Propane was the only fuel supplied from a multi-phase storage container. Although data were collected when flow measurements were as stable as possible, fluctuations in fuel flow measurements were indicative of some occurrences of multi-phase flow. Secondly, propane was supplied at lower feed pressures than the other fuels and was thus more susceptible to pressure oscillations in the fuel injection manifold caused by the unsteady inlet air flow. The impact of these effects was estimated and is reflected in the larger error bars shown for the equivalence ratio in **Fig. 7** relative to the other fuels in subsequent results.

Propane also has a higher octane number (108) than any other fuel tested in this engine. Tucker observed in the literature and in his own experiments that the octane number significantly impacted DDT events.^[15] Propane, a pure, single-component fuel, may detonate relatively inconsistently due to the lack of small amounts of more detonable species found in multi-component fuels that may contribute to phenomena critical to DDT.

Avgas, with results shown in Figure 8, was observed to detonate consistently for an equivalence ratio ranging from ~0.9 to ~1.3. In general the small error bars and results slightly above the theoretical values indicate that a detonation was consistently established upstream of the measurement location with this fuel. Both the fuel lean and rich results show moderately overdriven wavespeeds—indicative of late (near the measurement location) DDT events.

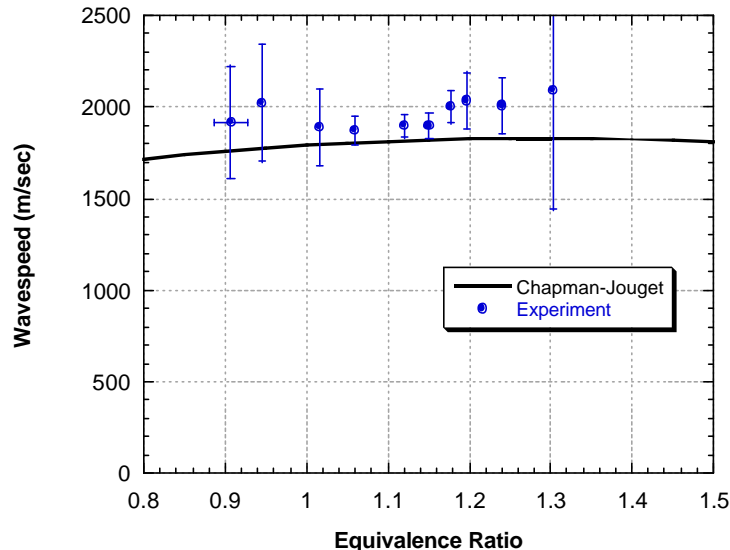


Figure 8 Wavespeed versus equivalence ratio for aviation gasoline fuel-air.

Unheated-JP8 injection results, plotted in **Figure 9**, show that the jet fuel did detonate, but only above an equivalence ratio of 1.05. Despite the low volatility of this military-grade jet fuel, which was specifically designed to minimize flammability and explosive hazards, DDT is achieved surprisingly consistently. This is reflected in the narrow error bars and consistent wavespeeds and is potentially a result of JP8 fuel's low octane rating relative to propane and avgas.

Upon heating JP8 to approximately 280°C prior to injection, the detonability range and repeatability were much better. **Figure 10** shows that detonation was achieved for equivalence ratios as low as 0.9 and in every test data point above an equivalence ratio of 0.95. For most of the results discussed above, data were not taken at higher equivalence ratio than shown because the engine began to run more intermittently as observed by the increasing deviation of the error bars in **Figs. 7-9** for the fuel-rich limit. That was not the case for the data shown in **Fig. 10**; here results were not obtained at higher equivalence ratio operating conditions with hot-JP8 injection because rich operation is of little interest for PDE performance.

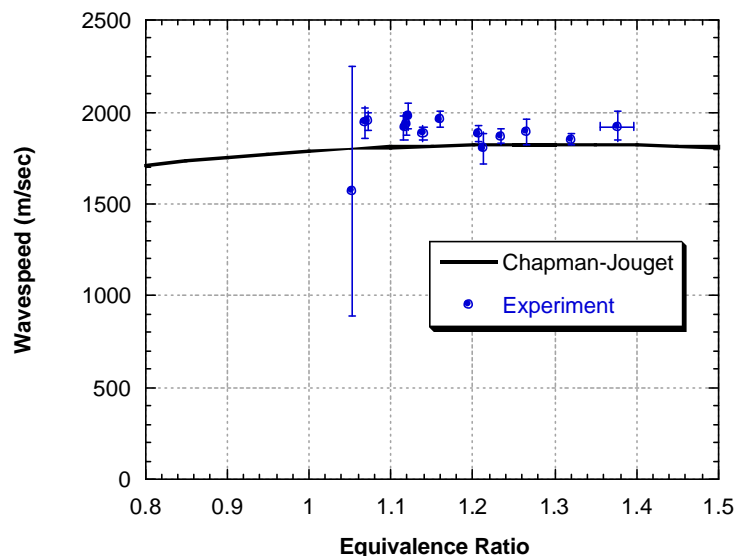


Figure 9. Wavespeed versus equivalence ratio for unheated JP8 fuel-air.

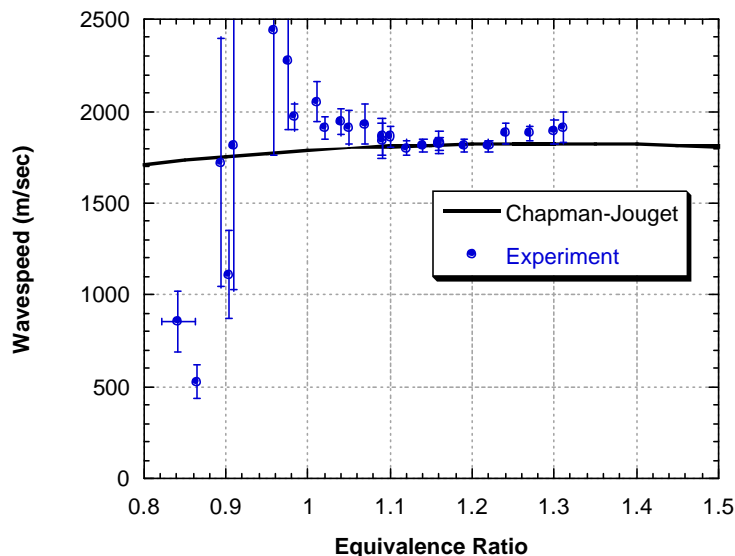


Figure 10. Wavespeed versus equivalence ratio for heated JP8 fuel-air.

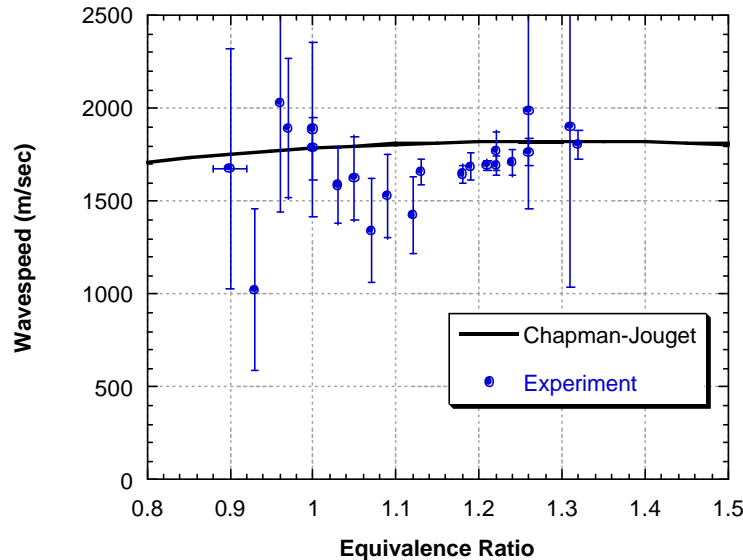


Figure 11. Wavespeed versus equivalence ratio for heated JP10 fuel-air.

Because JP10-air cell sizes are similar to JP8-air, little attention was dedicated to detonation of JP10-air. It was theorized that if JP8-air detonated in the research PDE, then JP10-air ought to detonate in a similar manner. The results in **Figure 11** were obtained to show that it is possible to DDT JP10 in air. Although many of the measured wavespeeds are lower than the theoretical CJ values, most of the results are above 1600 m/sec and well above the choked flame regime. Although these JP10 results represent a much smaller sample set than the other fuels, they indicate that it is possible to obtain DDT with JP10-air for a tested equivalence ratio range of 0.9-1.3. Like propane, JP10 is a signal component fuel, and this may have contributed to the variation in results.

V. Summary and Conclusions

Deflagration to detonation transition (DDT) was achieved within the first 1.22m in a research pulsed detonation engine for a variety of hydrocarbon fuels in air, including: propane, aviation gasoline, JP8, and JP10. The equivalence ratio for successful detonation initiation ranged from ~0.9 to 1.3, which corresponds to a cell width of less than ~100 mm. Thus, these results are consistent with Dorofeev's scaling rules for DDT.^[7] Mixture homogeneity was critical to successful detonation initiation. Failure to produce well mixed reactants with the proper equivalence ratio will likely result in increasing cell size and resultant difficulty in achieving DDT. Fuel heating was helpful when detonating low-volatility fuels. High octane number and single-component fuels had more variability in results.

VI. Acknowledgments

This work would not have been possible without the technicians who worked on this project; our thanks to Curtis Rice, Dave Baker, and Dwight Fox (ISSI). Dr. Tim Edwards (AFRL/PRTG) was extremely helpful in developing the fuel systems for this work. The authors would also like to thank Jeff Stutrud (AFRL/PRTC) for his controls and data acquisition expertise, and Dr. Terry Meyer, Dr. Mike Brown, and Dr. Jim Gord for help with laser and visualization diagnostics. The technical leadership of Dr. Mel Roquemore and Dr. Robert Hancock (AFRL/PRTC) was invaluable. Funding was provided by the Air Force Research Laboratory, Propulsion Directorate and AFOSR.

VII. References

1. P. Litke, F. Schauer, D. Paxson, R. Bradley, J. Hoke, "Assessment of the Performance of a Pulsejet and Comparison with a Pulsed-Detonation Engine," **AIAA 2005-0228**, 43rd AIAA Aerospace Sciences Meeting, Reno (2005).
2. M. Kaneshige and J.E. Shepherd, *Detonation Database*, **GALCIT Technical Report FM97-8** (1997).

3. C.M. Brophy, D.W. Netzer, and J. Sinibaldi, "Operation of a JP-10 / Air Pulse Detonation Engine," **AIAA 2000-3591**, 36th Joint Propulsion Conference, Huntsville, AL (2000).
4. C. Brophy, DNetzer, and D. Forster, "Detonation Studies of JP-10 with Oxygen And Air for Pulse Detonation Engine Development," **AIAA 98-4003**, 34th Joint Propulsion Conference, July 1998 Cleveland, OH (1998).
5. S.-Y. Lee, C. Conrad, J. Watts, R. Woodward, S. Pal, and R. J. Santoro, "Deflagration to Detonation Transition Study Using Simultaneous Schlieren and OH PLIF Images," **AIAA-2000-3217** 36th Joint Propulsion Conference, Huntsville, AL (2000).
6. N.N. Smirnov and M.V. Tyurnikov, "Deflagration to Detonation Transition in Gasoline-Air Mixtures," Physics of Combustion and Explosion, **22(2)**, pages 65-68 (1986).
7. S. B. Dorofeev, V. P. Sidorov, M. S. Kuznetsov, I. D. Matsukov, V. I. Alekseev, "Effect of Scale on the Onset of Detonations" 17th International Colloquium on the Dynamics of Explosions and Reactive Systems, Paper 141, Heidelberg, Germany (1999).
8. J. M. Austin and J. E. Shepherd. "Detonation in Hydrocarbon Fuel Blends." Combustion and Flame, **132(1-2)**, pages 79-90 (2003).
9. E. Schultz, E. Wintenberger, and J. Shepherd, "Investigation of Deflagration to Detonation Transition for Application to Pulse Detonation Engine Ignition Systems," 16th JANNAF Propulsion Meeting (1999).
10. R. Knystautas, C. Guirao, J.H. Lee, and A. Sulmistras. "Measurement of Cell Size in Hydrocarbon-Air Mixtures and Predictions of Critical Tube Diameter, Critical Initiation Energy, and Detonability Limits." Prog. Astronaut. Aeronaut., Vol 94, pages 23-37 (1984).
11. J.E. Elsworth, P.J. Shuff, and A. Ungut. "Galloping" Gas Detonations in the Spherical Mode," Prog. Astronaut. Aeronaut., Vol 94, pages 130-150 (1984).
12. T. R. Meyer, M. S. Brown, J. L. Hoke, J. T. Parker, J. R. Gord and F. R. Schauer, "Fiber-Coupled Laser Sensor for In-Situ Measurement of Hydrocarbon Fuels in Pulsed-Detonation Engines," 28th Annual Dayton-Cincinnati Aerospace Sciences Symposium, Dayton, OH, 4 March (2003).
13. F. R. Schauer, J.S. Stutrud, and R.P. Bradley, "Detonation Initiation Studies and Performance Results for Pulsed Detonation Engine Applications," **AIAA 2001-1129**, 39th AIAA Aerospace Sciences Meeting, Reno (2001).
14. K.C Tucker, P. I. King, R.P. Bradley, and F.R. Schauer, "The Use of a Flash Vaporization System With Liquid Hydrocarbon Fuels in a Pulse Detonation Engine," **AIAA 2004-0868**, 42nd AIAA Aerospace Sciences Meeting, Reno (2004).
15. K. Colin Tucker, "A Flash Vaporization System For Detonation Of Hydrocarbon Fuels In A Pulse Detonation Engine," Thesis **AFIT/DS/ENY/04-07** (2004).
16. T.R. Meyer, J.L. Hoke, M.S. Brown, J.R. Gord, and F.R. Schauer, "Experimental Study of Deflagration-To-Detonation Enhancement Techniques in a H₂/Air Pulsed Detonation Engine," **AIAA 2002-3270**, 38th Joint Propulsion Conference, Indianapolis, IN (2002).
17. J.S. Zdenek and R.A. Anthenien, "Ion Based High-Temperature Pressure Sensor," **AIAA 2004-0470**, 42nd AIAA Aerospace Sciences Meeting, Reno (2004).
18. J.L. Hoke, R.P. Bradley, F.R. Schauer, "Impact of DDT Mechanism, Combustion Wave Speed, Temperature and Charge Quality on Pulsed Detonation Engine Performance," **AIAA 2005-1342**, 43rd AIAA Aerospace Sciences Meeting, Reno (2005).
19. J. Parker and F. Schauer, "Data Analysis and Compression Techniques for Megabyte-Data PDE Experiments," **AIAA 2003-0892**, 41st AIAA Aerospace Sciences Meeting, Reno (2003).
20. S. Gordon and B. McBride, "Computer Program for Calculation of Complex Chemical Equilibrium Compositions and Applications," **NASA RP 1311 I&II**, October 1994 and June 1996.

43rd AIAA Aerospace Sciences Meeting
January 10-13, 2005, Reno, NV

2005-1342

Impact of DDT Mechanism, Combustion Wave Speed, Temperature, and Charge Quality on Pulsed-Detonation-Engine Performance

J. L. Hoke and R. P. Bradley

Innovative Scientific Solutions Inc., Dayton, OH 45440

F. R. Schauer

Air Force Research Laboratory, WPAFB, OH 45433

A number of factors can have an effect on the performance of a pulsed detonation engine (PDE), detonation initiation, combustion wave speed, detonator wall temperature and the homogeneity of the fuel-air charge. These factors are evaluated using a single-tube hydrogen-air PDE operating between 10 and 29 Hz. Geometries employed to transition the deflagration to detonation (DDT) degrade PDE performance during the exhausting process. This effect is insignificant for hydrogen-air mixtures because the DDT mechanism can be unobtrusive, but the effect can be significant for less reactive mixtures. Typical DDT geometries used for hydrocarbon-air mixtures result in a degradation of 35% for the hydrogen-air mixture. The drag on the DDT mechanism is also found to increase with distance from the thrust wall. In an effort to evaluate the effect of combustion wave speed on thrust, the ignition location is varied. For choked flames the performance difference from detonation is unmeasurable; but as the maximum flame velocity decreases from the choked-flame velocity, the performance decreases. At 800 m/s the thrust was 16% below that of a detonation and at 400 m/s the thrust degradation is between 17 and 34%. High tube-wall temperatures reduce the losses in heat during the blow-down process but increase the temperature and decrease the density of the fresh charge, resulting in lower peak pressures and charge spillage. As the tube temperature increases, the PDE performance decreases by 20% at 10 Hz and approximately 10% at 15 and 20 Hz. The axial homogeneity of the fuel-air charge is decreased by changing the location of the fuel injection. Decreases in performance of 14% are recorded at 10 Hz, even though detonation is achieved in both cases.

I. Introduction

Pulsed detonation engines (PDE's) are a topic of renewed interest during the past several decades. Recently, researchers have developed and demonstrated the technology of detonating practical hydrocarbon-fuel-air mixtures in a multi-cycle apparatus¹. As the technology develops toward a practical device, the subtle details become more significant. Several factors that have an adverse effect on PDE performance are examined. These factors are detonation initiation, combustion wave speed, tube-wall temperature, and charge homogeneity.

Several researchers have examined some of these factors. Cooper *et al.* found a reduction of 25% in impulse caused by the DDT mechanism for single-impulse experiments². At the extreme ends of combustion wave speed, constant pressure combustion verses constant volume, there is a significant difference in performance, but little work has been done in the unstable region between these conditions. Tube temperature has been examined with respect to loss of thrust due to heat transfer from the exhaust products to the tube wall and found to be insignificant in one study, 10 to 15% in another and up to 20% in a third study depending on tube aspect ratio³⁻⁵. Here the tube temperature was examined with respect to transferring heat to the fresh fuel-air charge. The quality of mixing of the fuel and air has been found to be a factor preventing the ability to detonate a fuel-air mixture and it is generally thought that for liquid fuel and air, the liquid droplet size must be below 10 μm . In this research, the effect of non-homogenous fuel-air mixture under two detonating conditions is evaluated.

This material is declared a work of the U.S. Government and is not subject to copyright protection in the United States.

II. Experimental Apparatus and Procedure

Experiments were conducted using the PDE at the Air Force Research Laboratory's Pulsed Detonation Research Facility. This PDE uses the "head" of a General Motors automotive engine to control the airflow into the detonation tube. The PDE cycle consisted of equal time allotted for: i) filling the detonation tube with pre-mixed hydrogen and air at an equivalence ratio of one, ii) ignition, detonation, and blow-down, and iii) purging of the detonation tube with air. For these experiments the pressure upstream of the automotive poppet valves was controlled such that during the fill cycle the mass flow of pre-mixed fuel and air was equivalent to the volume of the tube times the density of the fuel-air charge at the gas temperature upstream of the poppet valves and atmospheric pressure times the operating frequency. This was defined as a fill fraction (FF) of one and all tests during this research were conducted at a fill fraction of one. The purge fraction (PF) was defined in the same manner and was held constant at one-half for all experiments. The fuel-air mixture was ignited with a 115 mJ spark at the closed end for most experiments. Further details of this engine are given by Schauer et al.⁶

The PDE was operated at 10, 15, 20, 25, and 29 Hz. The ignition, detonation, and blow-down for the hydrogen-air mixture in a 72 in. (1.83 m) detonation tube requires approximately 8 ms to complete. There was unused time during the ignition, detonation and blow-down portion of the cycle for all frequencies tested. The ignition delay (ID) was either 0 or 6 ms (time between intake valve closure and spark).

The tube was instrumented with a dynamic pressure transducer at the closed end of the tube and ion probes at various intervals along the length of the detonation tube. Thrust was measured on a damped thrust stand where displacement was proportional to thrust. The thrust stand was oscillated, and the displacement averaged over several seconds to eliminate hysteresis and improve accuracy. The repeatability of the thrust measurement is shown in Fig. 1 and was within 2% of the average of three identical experiments conducted with 50 days elapsing between the first and last experiment.

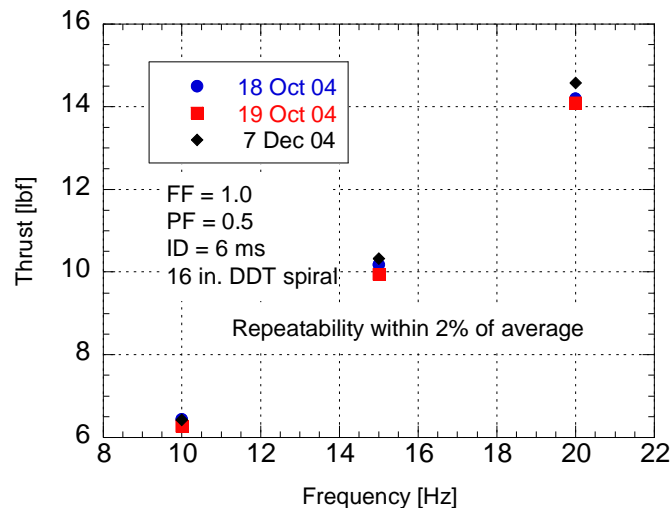


Figure 1. Thrust-Measurement Repeatability within 2% of Average.

The detonation tube consisted of 2 in. (51 mm)-diameter schedule-40 pipe nipples connected together with couplings to make a ~72 in. (1.83m) long detonation tube. A schematic of the various configurations tested is shown in Figure 2. The tube labeled "A" had no DDT mechanism, "B" had two 3/8 in. bolts inserted across the detonation tube at 4.25in. (0.108 m) and 10.25 in.(0.260 m) from the closed end of the tube. Tube "C" had the same two bolts inserted at 16.75 in. (0.425 m) and 22.75 in. (0.578 m) from the closed end. In experiments "D" thru "I" a 16 in. (0.406 m) Schelkin-like spiral was placed at various locations inside the detonation tube. The start of the spiral was located at the closed end of the detonation tube, 14, 26.5, 37.5, 49, and 60.25 in. (0.356, 0.673, 0.953, 1.245, and 1.578 m) from the closed end of the detonation tube. In experiment J, a 48 in. (1.219) spiral was inserted into the detonation tube, starting at the closed end. The volume and surface area of the DDT mechanism are given in Table 1. Note that configurations "H" and "I" did not detonate and that configuration "C" and "B" gave identical results.

During the experiments, the thrust and wave speeds were recorded at the maximum thrust which because of the averaging used in the thrust-measurement technique occurred approximately 35 sec. after the engine was started.

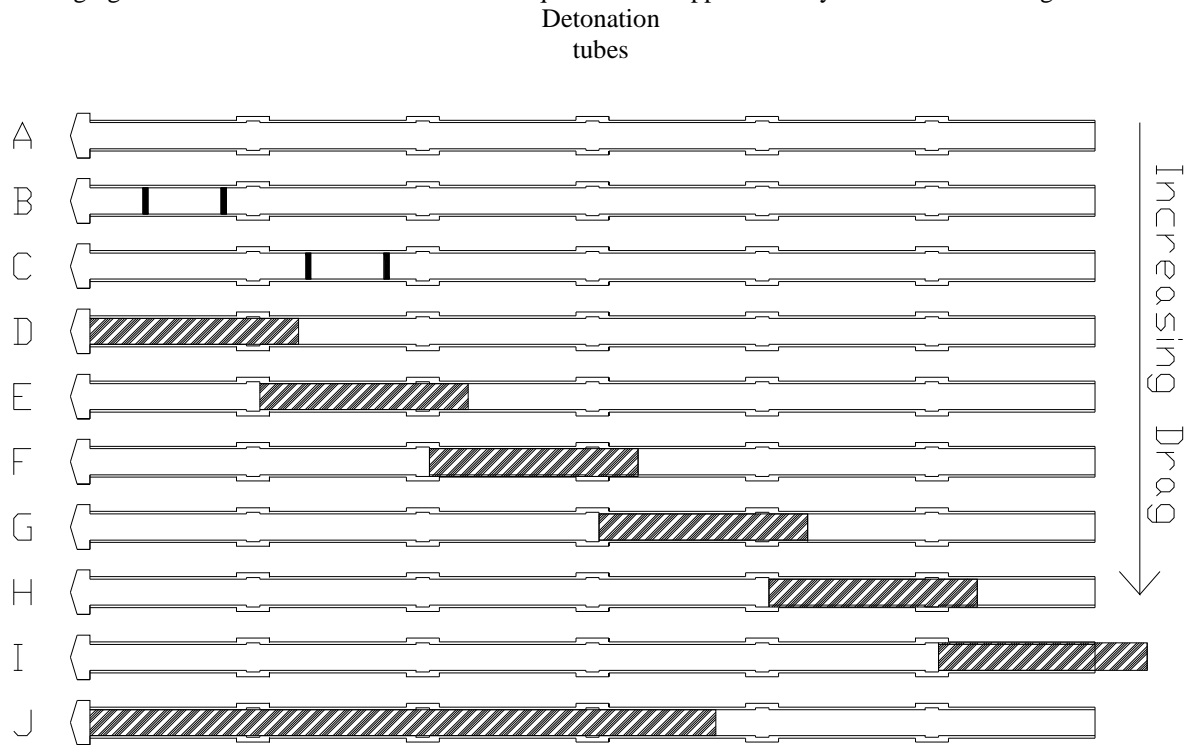


Figure 2. Schematic of Cross Section of Detonation Tubes Tested. Hatched area represents Schelkin-like DDT mechanism, and solid lines on B and C represent location of 3/8 in. bolts that were inserted into the detonation tube.

Table 1 Volume and Surface Area of DDT Internal Geometry in the Detonator Tube

Experiment	DDT Mechanism volume in ³ (m ³ x10 ⁶)	DDT Mechanism surface area in ² (m ² x 10 ³)
A	0	0
B	.46 (7.54)	4.9 (3.16)
C	.46 (7.54)	4.9 (3.16)
D	3.1 (50.7)	64.5 (41.6)
E	3.1 (50.7)	64.5 (41.6)
F	3.1 (50.7)	64.5 (41.6)
G	3.1 (50.7)	64.5 (41.6)
H	3.1 (50.7)	64.5 (41.6)
I	3.1 (50.7)	64.5 (41.6)
J	9.4 (154)	193 (124.5)

III. Experimental Results and Discussion

Pulsed detonation engines have potential for high performance; however, several aspects of the PDE design, if not given proper attention, can lead to degraded performance. The first factor is detonation initiation. Pre-detonators can lead to a large auxiliary oxygen tank, while a DDT mechanisms can reduce system performance due to drag. The second factor is combustion wave speed. This factor is difficult to evaluate, but several experiments

were conducted and analyzed. The third factor is low charge density due to heat transfer from the tube walls to the incoming charge. The fourth and final factor is the homogeneity of the fuel-air mixture.

A. Detonation Initiation and Thrust

The method used to achieve a detonation can influence the performance of the PDE. A pre-detonator should produce the maximum attainable thrust by a fuel-air mixture in the main detonation tube; however, it has been shown for single detonation events that the thrust produced was not dependent on the location of detonation initiation as long as a detonation was produced within the detonation tube⁷. With a pre-detonator a detonation propagates the entire length of the detonation tube with no retonation wave produced in the main detonator tube and no obstacles along the main detonator tube to restrict the exhausting of the detonation tube. The lack of obstacles is also beneficial from a pressure point of view during the filling process. In this research, a detonation was achieved in the pre-detonator but the combustion decoupled from the shock as the detonation transitioned into the main tube. The detonation reestablished approximately 20" (0.508) along the detonation tube. In the pre-detonator geometry tested, the pre-detonator was not ideal, and no thrust data was obtained with a properly designed pre-detonator.

Many experiments were conducted to determine the effect of the DDT mechanism on thrust. In Figure 3 the thrust produced by configurations "D" and "J" is plotted. In both cases, a detonation was produced within 20 in. (0.508 m) of the thrust wall however the thrust produced with the longer spiral is, on average, 35% lower than that produced using the shorter spiral. Of course the detonation wave speed was reduced through the 48 in. (1.219 m) spiral. The lower thrust was attributed to drag of the long spiral during the blow-down process. Additional tests were conducted with the 16 in. (0.406 m) spiral placed farther from the thrust wall in configuration "E, F, and G". As expected, the thrust decreases as a larger percentage of the combustion products flow over the DDT mechanism, see Fig 4. Interestingly, the sum of the thrust lost from configurations "D" to "E, F and G" is similar to the thrust loss from "D" to "J". If one adds the internal geometry of configurations "D, E, F and G", the resulting geometry is similar with some overlap to configuration "J". The thrust level computed when adding the drag of "E, F, and G" and subtracting that from "D" is within 14% of the thrust level of configuration "J".

As short as the spiral was in configuration "D" (16 in. or 0.406 m) the thrust was still significantly decreased by the drag over this spiral. In Figure 5 the thrust measured in configuration "B" and "D" is plotted. The thrust produced by the 16 in. (0.406m) spiral ("D") is on average, 6% lower than that produced using the two 3/8" bolts inserted across the detonator tube. In both experiments, detonation was achieved. Figure 6 shows the thrust comparison between configuration "D", a 16 in. (0.406 m) spiral and configuration "A", an unrestricted tube. At 10 and 15 Hz configuration "A" did not detonate and the thrust was approximately 20% lower. At 20 Hz, the thrust was identical and the mixture detonated some of the time. The lowest maximum wave speed recorded was 880 m/s. If the unrestricted tube was detonating all of the time, the thrust level should exceed that measured with the 16 in. (0.406 m) spiral. For multi-cycle PDE's detonation is easier to achieve at higher frequencies because the pressure oscillations induced during the fill cycle are stronger, interact with the developing combustion wave, and promote the transition to detonation.

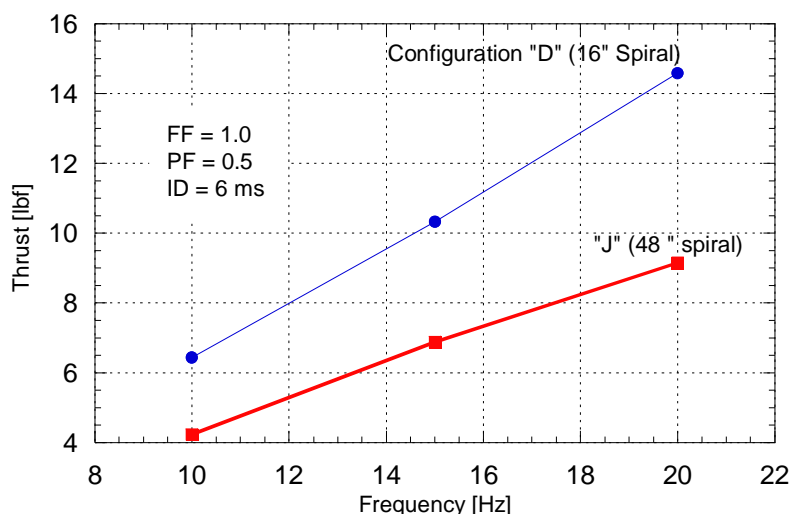


Figure 3 Effect of DDT Mechanism on Thrust for Configurations "D" and "J". In both cases a detonation was achieved within 20 in. (.508 m) of the thrust wall

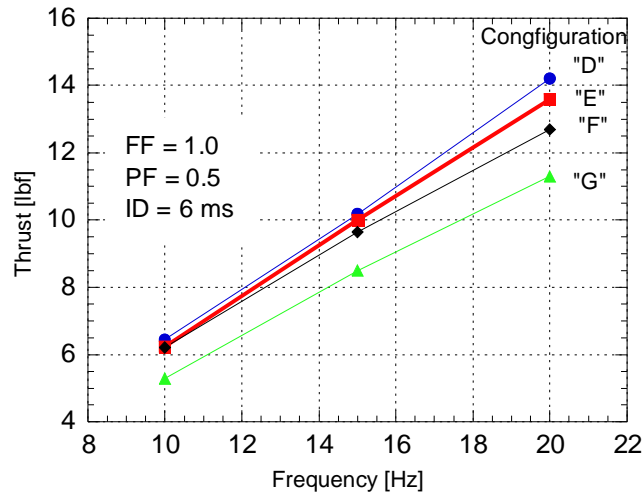


Figure 4 Thrust Measured for Different Locations of a 16 in. (0.406m) DDT mechanism along the detonator tube

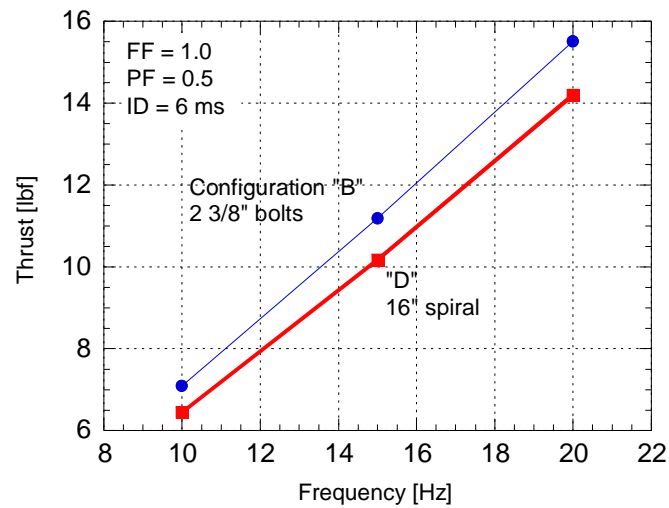


Figure 5 Comparison of the Thrust Produced Using a 16 in. (0.406 m) spiral and two 3/8 in. bolts.

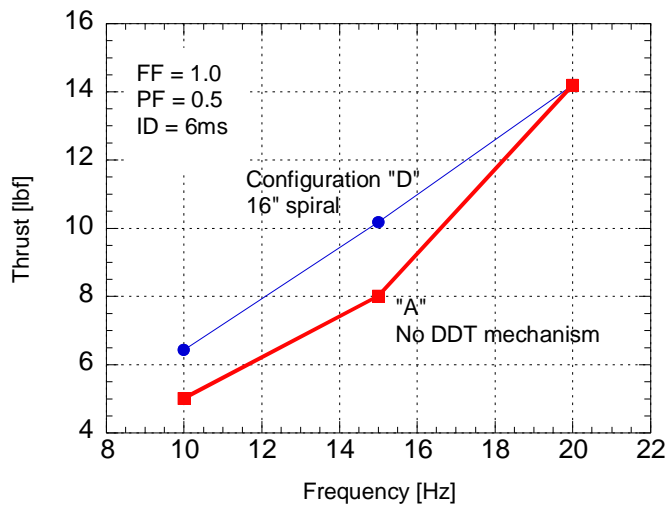


Figure 6 Comparison of Thrust for 16 in. (0.406 m) spiral and no DDT mechanism.

B. Combustion Wave Speed and Thrust

Controlling the combustion wave speed was difficult; however, by varying the ignition location along the detonation tube, the thrust was measured and plotted along with the maximum combustion wave speed achieved in the detonation tube. This was done to keep the internal drag and geometry identical from experiment to experiment in an attempt to isolate the effect of combustion wave speed on thrust. Figure 7 is a plot of the thrust versus frequency for four different spark locations and the maximum combustion wave speed is annotated adjacent to each point in the figure. With the ignition at the thrust wall, a detonation was achieved during every event at every frequency. When the ignition was moved to 17 in. (0.432 m) from the thrust wall, a detonation was only achieved at 20 Hz while the maximum combustion speed at 15 Hz was 1000 m/s and at 10 Hz was 800 m/s. Again, for multi-cycle PDE's, detonation is easier to achieve at higher frequencies because the pressure oscillations induced during the fill cycle are stronger, interact with the developing combustion wave, and promote the transition to detonation. The thrust at an ignition point of 17 in. (0.432 m) down the length of the tube was 16% lower than the thrust measured when the ignition was at the thrust wall at 10 Hz and almost indistinguishable at 15 Hz (4% lower) where a choked flame developed and at 20 Hz (3% lower) where a detonation was achieved.

When the ignition point was moved to 43 in. (1.092 m) from the thrust wall, the maximum combustion wave speed recorded was ~400 m/s for all frequencies, nearing the limit of sensitivity for the ion probes. The thrust recorded was considerably lower than a detonation being 34, 24, and 17% lower at 10, 15 and 20 Hz respectively. At an ignition point of 68 in. (1.727 m), the combustion wave speed could not be measured by the ion probes and was probably subsonic. The thrust levels recorded were 65, 47, and 35% lower than the detonation case at 10, 15, and 20 Hz, respectively.

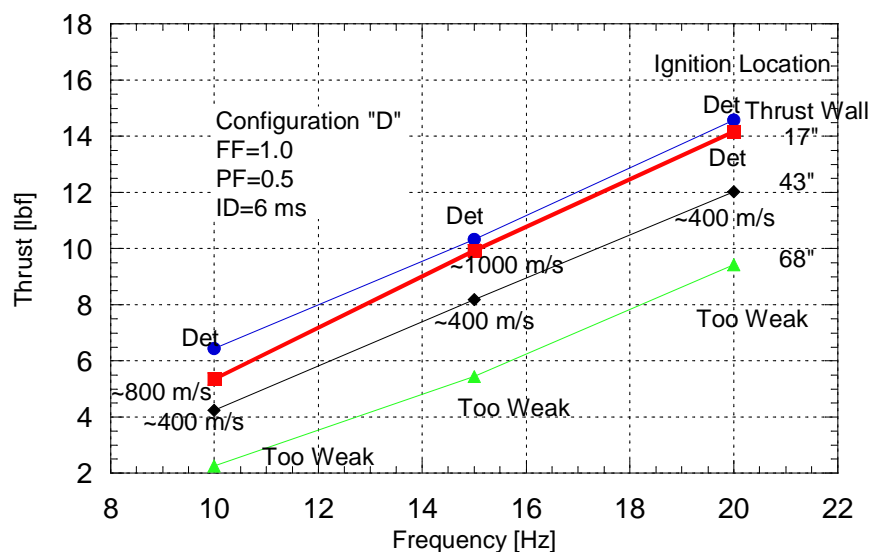


Figure 7 Combustion Wave Speed versus Thrust Produced. The ignition location was varied. “Det” refers to detonation.

C. Tube Wall Temperature and Thrust

A 72 in. (1.83 m) detonation tube in configuration “D” was run to thermal equilibrium. As shown in Fig. 8 the thrust initially reaches a maximum soon after the PDE was started; but as the detonator-tube temperature increased, the thrust decreased to a steady-state value approximately 300 seconds after the device was started. For this particular case of 10 Hz operation with a FF of 1, a PF of 0.5 and 6 ms ignition delay, the steady-state value of thrust was 80% of the maximum recorded. At 15 and 20 Hz, the steady state value of thrust was 90 and 88% of the maximum, respectively. The time constant to reach 63% of the steady state temperature was decreased with increasing frequency at 85, 75, and 65 seconds for 10, 15 and 20 Hz, respectively.

This decrease in performance was attributed to heat transfer from the detonator tube wall to the fuel-air charge during the filling process. The heat added to the fuel-air charge increases the temperature and decreases the density resulting in lower thrust pressure and a higher percentage of “spilled” fuel-air charge. The loss in thrust

decreased from 20% at 10 Hz to ~10% at 15 and 20 Hz. Thrust losses would be expected to decrease at higher frequencies because the heat-transfer coefficient is proportional to the Reynolds Number generally to a power of less than one, and the duration of heat transfer decreases proportionately with increasing frequency⁸. (The characteristic velocity of the filling process is proportional to frequency, but the associated heat-transfer coefficient increases with velocity to a power less than one.)

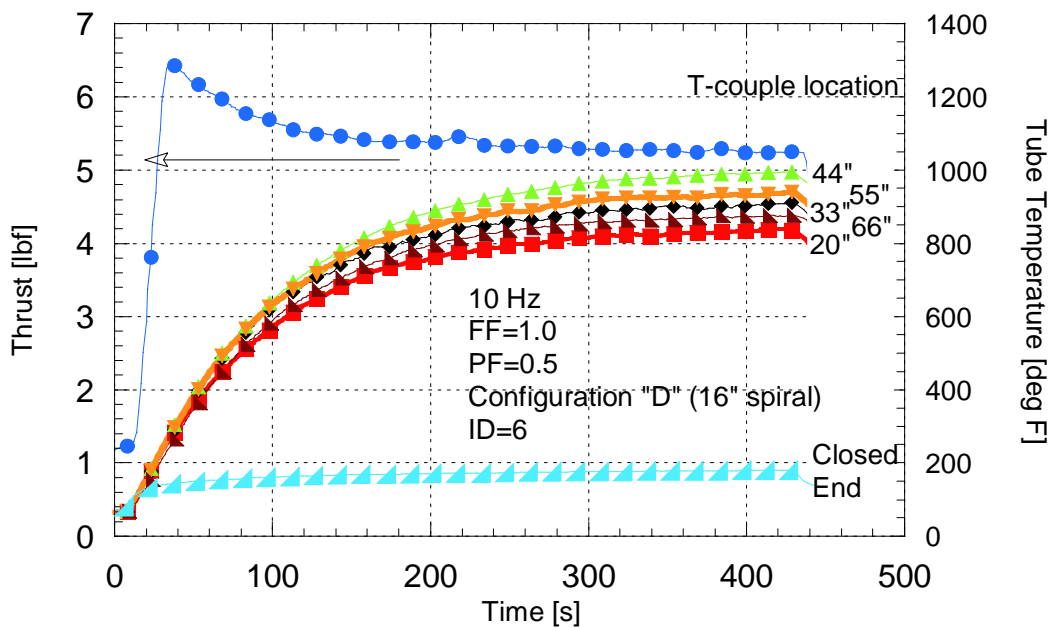


Figure 8 Thrust and Temperature versus Time Configuration "D"

D. Charge Homogeneity

Because of the speed of detonation, the fuel-air mixture must be homogeneous or near homogenous to achieve a detonation. For liquid fuels the droplet size required to achieve a detonation is thought to be below 10 μm . In this research hydrogen-air was used and mixing was fundamentally simpler with gas-gas mixtures than with liquid fuels; however, heterogeneous mixtures can be created. In the research PDE a single detonation tube was used for all of these experiments. The duty cycle of the combustion air flow was 33% so the combustion air is started and stopped at the inlet of the PDE; however, the hydrogen was injected into the combustion air-stream at a constant rate, being choked at the injection point. Typically the injection is performed at a location where the combustion air stream velocity is relatively constant and any variation in equivalence ratio is diminished by diffusion, and mixing since the pre-mixed charge traveled through several bends. The mixture quality was not evaluated but rather the hydrogen injection point was moved from 32 in. (0.813 m) upstream of the PDE valves to 99 in. (2.5 m) upstream of the valve. In both hydrogen injection configurations a detonation was achieved at all frequencies. The thrust measured for the 99 in. (2.5 m) upstream injection point was 14% higher at 10 Hz and decreased to 6% at 29Hz (see Fig. 9). This decrease in the difference in thrust with frequency was attributed to better mixing at the higher air velocities associated with the higher frequencies. In Fig. 10, the pressure at the thrust wall of the tube was compared for the two different injection points. There is a noticeable difference in the shape of the thrust wall pressure as well as the magnitude. These pressure traces shown are the average of four pressure traces acquired during each run and appear to be identical to the individual traces; thus the averaging reduces some of the noise associated with this dynamic pressure transducer.

We speculate that the fuel injection point at 32 in. (0.813 m) resulted in rich and lean regions along the detonator tube. Although the mixture was of sufficient quality to achieve a detonation, all of the fuel is not consumed in the rich regions and all of the oxygen is not used in the lean regions resulting in reduced performance.

This decrease in thrust due to fuel-air inhomogeneity could be responsible for some of the scatter reported in thrust measurements and will probably be responsible for scatter in emission data gathered when the technology reaches that level.

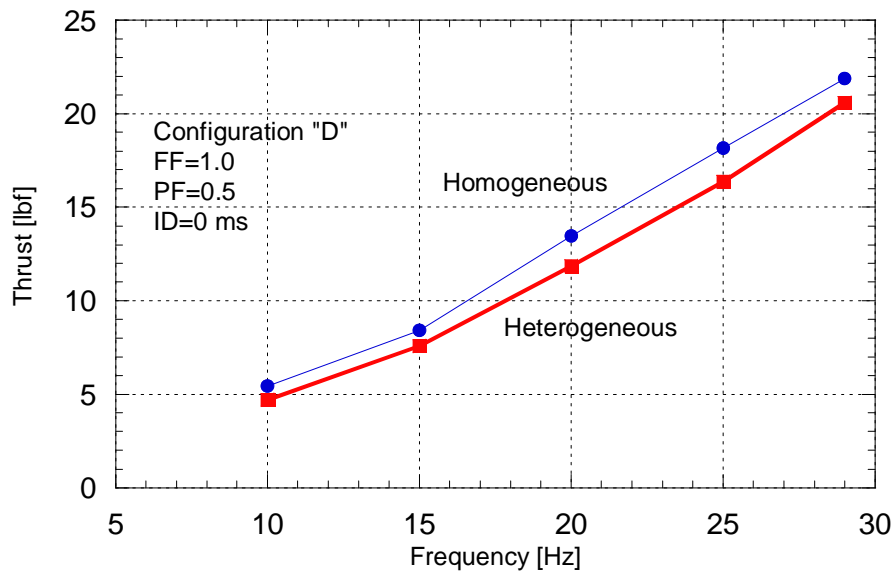


Figure 9 Effect of Hydrogen Injection Location on Thrust. A detonation was achieved in all experiments.

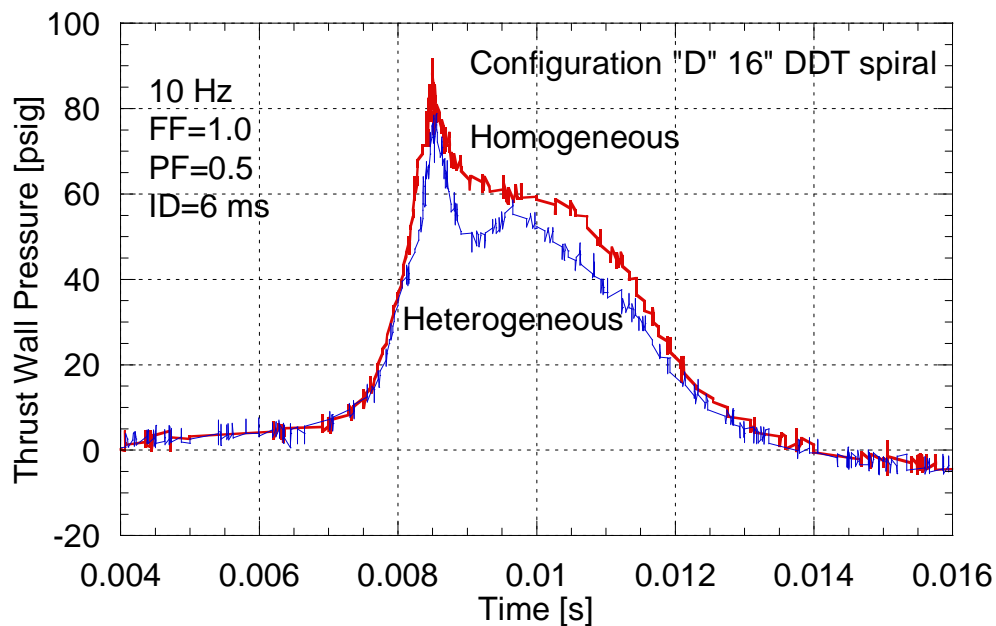


Figure 10 Effect of Hydrogen Injection Location on Thrust Wall Pressure History

IV. Summary and Conclusions

As the technology for creating practical pulsed detonation engines matures, more emphasis and research will be need on the subtle details. In this study it was reaffirmed that the DDT mechanism can have a significant impact on performance. For hydrogen and air the impact was small but for more non-reactive mixtures the impact could be up to 35%. Pre-detonators may not provide the answer because of the oxygen enrichment generally used; therefore, research into low drag DDT mechanisms is needed. The difference in performance between a detonation and choked flame was below the resolution of the thrust stand, but when the maximum combustion front velocity was below 800 m/s significant losses in performance were recorded. This information could be used to minimize the length of the DDT mechanism and increase performance. Although much effort has been expended to examine the heat lost from the combustion gasses, this study finds that heat transfer to the fresh fuel air charge decreases performance by up to 20%. A back-pressurization device is needed to minimize fresh charge expansion and losses caused by "spillage." Lastly, the homogeneity of the fuel-air mixture can cause performance losses even though the mixture is detonating. For hydrogen-air the performance decrease due to hydrogen-injection location was a maximum of 14%. For liquid fuels this could be a larger issue because of the difficulty of mixing liquid and gas and because the achievement of a detonation does not guarantee maximum performance.

V. Acknowledgments

Gratitude is expressed to the technicians who worked on this project: Curtis Rice, Dave Baker, and Dwight Fox (ISSI). The authors would also like to thank Jeff Stutrud (AFRL/PRTS) whose computer programs were used to collect and analyze the data. The technical leadership of Dr. Mel Roquemore and Dr. Robert Hancock (AFRL/PRTS) was invaluable. Funding was provided by the Propulsion Directorate.

VI. References

1. Schauer, F.R., R.P. Bradley, and J.L. Hoke. "Detonation Initiation of Hydrocarbon-Air in a Pulsed Detonation Engine." in *43rd AIAA Aerospace Sciences Meeting and Exhibit*. 2005. Reno, NV: AIAA.2005-1343
2. Cooper, M., S. Jackson, J. Austin, E. Wintenberger, and J. Shepherd, "Direct Experimental Impulse Measurements for Detonations and Deflagrations." *Journal of Propulsion and Power*, 2002. **18**(5): p. 1033-1041.
3. Eidelman, S., D. Sharov, and D. Book, "The Thermal Balance of PDE", in *Computational Methods and Experimental Measures*. 2001. p. 711-720.
4. Radulescu, M.I., C.I. Morris, and R.K. Hanson. "The Effect of Wall Heat Loss on the Flow Fields in a Pulsed-Detonation Wave Engine." in *42nd Aerospace Sciences Meeting and Exhibit*. 2004. Reno, NV: AIAA.2004-1124
5. Laviolette, J.P., C.B. Kiyanda, and A.J. Higgins. "The Effect of Friction and Heat Transfer on Impulse in a Detonation Tube." in *Canadian Section of the Combustion Institute Spring Technical Meeting*. 2002. Windsor, Ontario Canada
6. Schauer, F., J. Stutrud, and R. Bradley. "Detonation Initiation Studies and Performance Results for Pulsed Detonation Engine Applications." in *39th AIAA Aerospace Sciences Meeting and Exhibit*. 2001. Reno, NV.2001-1129
7. Harris, P.G., R. Farinaccio, R.A. Stowe, A.J. Higgins, P.A. Thibault, and J.P. Laviolette. "The Effect of DDT Distance on Impulse in a Detonation Tube." in *37th Joint Propulsion Conference & Exhibit*. 2001. Salt Lake City, Utah: AIAA.2001-3467
8. White, F.M., *Heat and Mass Transfer*. 1988, New York: Addison-Wesley Publishing Co.

Performance Measurements of Pulse Detonation Engine Ejectors

Daniel Allgood and Ephraim Gutmark*

*Department of Aerospace Engineering and Engineering Mechanics,
University of Cincinnati, Cincinnati, OH 45221-0070*

John Hoke and Royce Bradley

Innovative Scientific Solutions, Inc., Dayton, OH 45440

Fred Schauer

Air Force Research Laboratory, Propulsion Directorate, WPAFB, OH 45433

Abstract

An experimental study on the performance of pulse detonation engine (PDE) ejectors was performed. Time-averaged thrust augmentation produced by straight and diverging PDE ejectors was measured using a damped thrust stand. The ejector length-to-diameter ratio was varied from 1.25 to 5.62 by changing the length of the ejector and maintaining a nominal ejector diameter ratio of 2.75. In general, the level of thrust augmentation was found to increase with ejector length. Also, the ejector performance was observed to be strongly dependent on the operating fill-fraction. A new non-dimensional parameter incorporating the fill-fraction was proposed. When the PDE-ejector data was represented as a function of this new parameter, ejector data was reduced to one representative thrust augmentation curve for ejectors of similar internal geometry. Straight PDE-ejectors compared well with the available data on straight steady-flow ejectors. Diverging PDE-ejectors produced nearly twice the thrust augmentation as their straight ejector counterparts due to the additional thrust surface area the divergence provided. All PDE-ejectors tested were seen to be sensitive to the axial position of the ejector as well. The optimum ejector axial placement was found to be a function of fill-fraction due to a trade-off between the detonation-wave drag and increased mass entrainment. Downstream ejector placements performed the best at the low fill-fraction operating conditions.

Nomenclature

D_{PDE}	PDE detonation tube diameter
D_{EJECT}	ejector diameter
DE	diverging ejector
DR	ejector-to-PDE diameter ratio ($DR = D_{EJECT}/D_{PDE}$)
ff	fill-fraction
L_{EJECT}	ejector length
PDE	pulse detonation engine
SE	straight ejector
T_{PDE}	PDE thrust without an ejector
$T_{PDE-EJECTOR}$	PDE thrust with an ejector
Tref	reference thrust

Introduction

Pulse detonation engines (PDE) use controlled periodic detonations of a combustible mixture to generate thrust¹. One of the primary motivations for PDE development has been based on the potential gain in thermal efficiency that can be achieved with detonation combustion². Experimental and computational researchers have demonstrated some success in obtaining competitive specific impulse values with a simplistic PDE cycle^{3,4}. These promising results have lead to many PDE applications being proposed. For example, it has been suggested that PDEs can be used as cost effective replacements for small gas turbine engines, as potential replacements for combustors on existing large-scale gas turbines, or as thrust augmenters. However, even if PDE performance benefits ultimately reveal themselves to be insignificant in practical applications, the PDE cycle will still be an attractive propulsion system because of the reliability benefits of having very few moving

*Ephraim.Gutmark@uc.edu

parts, the scalability of the engine, and the flexibility in geometry it will provide.

A common approach to increasing the thrust of an engine is with an ejector. An ejector is a coaxial duct that is placed around the exhaust of an engine to direct the entrainment of the surrounding flow into the engine exhaust stream. The use of steady-flow ejectors and their associated design procedures is well established. The application of ejectors, however, to unsteady primary flows is less common. A large number of studies⁵⁻⁷ have examined unsteady ejectors driven by pulsejets or other devices where the primary airflow was unsteady. Lockwood⁵ showed that an unsteady primary flow is more efficient in producing mass entrainment than a comparable steady flow. His pulsejet studies showed thrust augmentation as high as 1.8, much greater than the theoretical isentropic steady-flow ejector. He attributed the unsteady ejector performance to a more efficient energy transfer process between the primary flow and the secondary (entrained) flow through inviscid processes, while the steady ejector relies primarily on viscous shear mixing. Due to the unsteady nature of a PDE, these results suggest that an ejector could be highly effective in increasing the PDE performance.

Computational studies of single shot PDE driven straight ejectors using an Euler code demonstrated the importance of the ejector-to-PDE tube diameter ratio in achieving thrust augmentation and its sensitivity to fill-fraction¹¹. Multiple cycle simulations of a specific converging-diverging ejector at approximately 120 Hz using an Euler code with finite rate chemistry showed thrust augmentation of almost 80%¹². Further non-detonation computational studies highlighted the importance of the starting vortices, pre-cursor shocks and direct pressure loads created by the gas dynamic (shock-tube) processes within the ejector to the overall thrust augmentation performance of the system¹³. These computations suggested that high thrust augmentation for PDE-Ejector applications is achievable and highlighted the need to understand the gas dynamics, resonance phenomena, and flow interactions of the PDE-ejector system for optimum performance.

Very few experimental studies of PDE-ejectors have been reported. One experimental

study by Rasheed et al⁹ using a 5 cm diameter H₂-Air PDE tube at 10 Hz with 7.62, 10.16, and 15.24 cm diameter ejectors showed thrust augmentation levels varying from +16% to -5% depending on the configuration. In all cases, the maximum thrust augmentation was found to occur with the ejector located fully downstream of the PDE tube. Similar experiments using C₂H₄-Air showed maximum thrust augmentation levels of 24% depending on the configuration, and additionally captured flow visualization shadowgraph images at the ejector inlet throughout one cycle¹⁰. In both of the above studies, the experimentally measured thrust augmentation was significantly lower than the factor of 1.8 achieved by Lockwood's pulsejet experiments.

One possible reason for the discrepancy in the referenced works on ejector thrust augmentation could be the lack of an appropriately designed ejector inlet. The shape of the ejector inlet is very important in determining the ejector performance since the inlet is an aerodynamic surface which guides the entrainment of the surrounding mass flow. Allgood et al¹⁴ performed high-speed shadowgraph visualizations of optically accessible PDE-ejectors. Their results showed significant losses in mass entrainment and strong flow separation when PDE-ejector inlets were *not* properly contoured. The importance of a rounded inlet has also been proposed by Lockwood⁵, Paxson et al⁶ and Wilson et al⁷ for steady and unsteady ejectors. However, out of the reviewed works in this paper, the only thrust measurements reported using contoured ejector inlets for PDE systems were those by Rasheed et al⁹.

In addition to ejector inlet geometry, the interior surfaces of the ejector can serve as thrust surfaces on which the pressure forces can act thereby generating additional thrust. Lockwood⁵ showed substantial thrust improvement when using a divergent type ejector versus a straight cylindrical ejector for pulsejet systems. The experimental work by Paxson et al⁶ and Wilson et al⁷ also used ejectors with a small diverging section at the end of the ejector for unsteady primary flow systems. To the authors' knowledge, no experimental results have been reported on thrust augmentation of diverging

ejectors for pulse detonation engine systems. Thus, the benefits of using a diverging ejector over a straight ejector are not known for PDE applications and should be quantified.

The relative size of the ejector to the primary flow driver is also known to have a significant influence on an ejector performance. An ejector diameter should be sized large enough to allow sufficient area for the primary flow to entrain the secondary flow. However, too large of an ejector diameter could reduce the effect of the accompanying pressure drop on the ejector inlet as well as the pressure rise on a diverging ejector interior surface. An optimum ejector-to-driver diameter ratio corresponding to a peak thrust augmentation level has been observed for a variety of ejector systems^{5,6,9}. Typical reported values of optimum diameter ratios range between 2.4 to 3.3.

In a similar manner, the axial placement of the ejector can also affect the ejector flow dynamics. Experimental results by Allgood et al¹⁴ have observed that the level and efficiency of the PDE-ejector entrainment can be restricted with an upstream axial placement of the ejector. On the other hand, a downstream ejector placement between one to two PDE diameters resulted in a cleaner flow path for the secondary flow to be entrained into the ejector. This observation is in agreement with the PDE-ejector thrust measurements reported by Rasheed et al⁹, and similar trends were found by Paxson et al⁶ for pulsejet-ejector systems.

In addition to ejector geometry and placement, there are many operating parameters that have been shown to drastically affect the performance of a PDE and thus will most likely affect the PDE-ejector performance as well. For example, PDE thrust has been observed to scale linearly with frequency of detonations since it is desirable to minimize the time of each filling event and maximize the frequency of the overall PDE cycle⁴. Thus, adjusting the PDE cycle frequency is one proposed method of throttling the engine. Another way of throttling the engine is to alter the amount of fuel-oxidizer mixture that fills the PDE tube prior to ignition. The ratio of the PDE tube filled with a detonable mixture relative to the total tube length is defined as the fill-fraction. While the PDE thrust has been shown to decrease with a

reduction in fill-fraction, the fuel-based specific impulse values increased at a faster rate⁴. This performance gain observed at lower fill-fractions was attributed to the detonation shock wave compressing the non-reactants occupying the remainder of the PDE tube⁴. Schauer et al.⁴ demonstrated experimentally the performance benefits of partially filling the detonation tube for a multi-cycle PDE operation. Their results showed the partial-fill effect being independent of PDE cycle frequency for a constant area detonation tube. Hoke et al⁸ performed a qualitative study suggesting the mass entrainment of the ejector deteriorates as the fill-fraction increased due to the strengthening of the exiting detonation wave.

The current work presents an experimental study on the performance benefits of axisymmetric ejectors for multi-cycle pulse detonation engines. The effect of fill-fraction on PDE-ejector performance has been quantified. The performance sensitivity of PDE-ejectors to ejector length, internal diverging geometry and relative axial placement has also been measured. A comparison between PDE-ejectors and other ejector systems was given, and a new normalization of PDE-ejector data has been proposed for comparing PDE-ejector data to other ejector systems. In addition to performance measurements, flow visualizations were performed on similar ejector geometries to further explain the trends observed in the performance data.

Experimental Setup

PDE Test Facility

Thrust augmentation measurements of pulse detonation engine (PDE) driven ejectors were performed. The pulse detonation engine test facility at the Air Force Research Laboratory at Wright-Patterson Air Force Base was used to obtain the thrust measurements. Premixed hydrogen and air were delivered to a single round detonation tube by way of a mechanical valve system constructed from a modified four-cylinder automotive head. The automotive valve system could be operated at frequencies up to 40Hz. Due to the nature of automotive valving, the PDE cycle was divided equally between

three main processes: (1) filling the PDE with fresh reactants, (2) ignition, detonation and blow-down of the high pressure products, and (3) purging the PDE with a buffer of cold-air. The hydrogen and air were metered through choked flow orifices. The deflagration-to-detonation transition of the hydrogen-air mixture was enhanced by the use of Shchelkin-type spirals of 0.3 m length for both diameter detonation tubes. The Shchelkin spiral occupied only 16% of the total PDE tube length. Two pressure transducers (PCB M102A) were mounted 6 inches apart to monitor detonation shock speeds and validate that Chapman-Jouget detonations were produced. The pressure data was collected via a remote 5MHz 16-channel ADC system. The measured wave speed for both detonation tubes was confirmed to be approximately the Chapman-Jouget wave speed of 1966 m/s at a fill-fraction of 1.0.

The PDE was mounted on a damped thrust stand rated for a maximum thrust load of 4,500 N. The thrust stand was designed to measure the time-averaged thrust of the dynamic PDE. The thrust stand consisted of linear bearings riding along a pair of low-friction rails. The PDE was allowed to freely move on the rails but its motion was weakly damped by springs to prevent any resonance effects. To remove the effects of static friction, the PDE was continuously actuated forward and backward by a linear actuator. Since this was a known force, it could be subtracted from the measurements to get the true average thrust of the engine. The thrust measurements were calibrated by placing static weights and measuring the displacement with a positional sensor. The maximum uncertainty (or repeatability) in the calibration was determined to be approximately ± 1 Newton for the entire range of PDE thrust loading anticipated during these tests. For a more detailed description of the PDE test facility the reader is referred to the recent paper by Schauer et al.⁴.

PDE-Ejector Test Conditions

The PDE detonation tube was constructed of a steel pipe of 5.08 cm diameter (D_{PDE}) and 1.83 m length. The main operating parameters that could be varied were the

following: (1) the fuel/air mixture, (2) the fill-fraction (ff), (3) the purge fraction (pf), (4) the ignition delay, and (5) the PDE cycle frequency. The fill-fraction and purge fractions are defined as the ratio of the detonation tube filled with a fuel/air or air mixtures respectively. The ignition delay was defined as the delay in time in which the spark was actuated after the valves closed. For all test conditions, the PDE was operated at a 30 Hz cycle frequency with a stoichiometric mixture of hydrogen and air, a purge fraction of 0.5 and an ignition delay of 0.5 ms. Only the operating fill-fraction was varied in the current tests.

Thrust augmentation levels of axisymmetric ejectors for pulse detonation engine applications were quantified. All ejectors were mounted coaxially to the PDE exhaust and had a rounded bell-mouth inlet. As depicted in Figure 1, two sets of ejectors were tested: straight cylindrical ejectors and straight cylindrical ejectors with a diverging exhaust end-piece. The length (L_{EJECT}) of the straight and diverging ejectors were varied by extending the length of the straight or straight-intermediate sections respectively. The diverging ejector end-piece had a 4-degree half-angle of divergence at a fixed length of 19.3 cm. A similar 4-degree half-angle of divergence was used by Lockwood⁵ in his pulsejet-ejector experiments. The diameter (D_{EJECT}) of the straight/straight-intermediate sections were set at a fixed value of 13.97 cm. Thus, the ejector-to-PDE diameter ratio was kept constant throughout the tests at a value of 2.75. This value was selected since it closely matched the optimum diameter ratios reported in other ejector experiments^{5,6,9}.

A range of ejector length-to-diameter ratios (L_{EJECT}/D_{EJECT}) were also tested and are listed in Table 1. The relative position between the PDE exhaust and the ejector inlet was varied as depicted in Figure 1. Both upstream ($x/D_{PDE} < 0$) and downstream ($x/D_{PDE} > 0$) ejector axial placements were tested. The range in axial placements tested for both straight and diverging ejectors are given in Table 1. To determine the PDE-ejector thrust augmentation dependence on fill-fraction, thrust measurements of both the baseline configuration with no ejector and the

integrated PDE-ejector system were obtained at

the same fill-fractions ranging from 0.4 to 1.1.

Table 1: PDE-Ejector Test Matrix ($D_{EJECT}/D_{PDE}=2.75$)

	Fill-Fraction (ff)	Ejector Length to Diameter Ratio (L_{EJECT}/D_{EJECT})	Ejector Axial Position (x/D_{PDE})
Straight Ejector	0.4 to 1.1	1.25 to 4.25	-1.5 to 2.0
Diverging Ejector	0.4 to 0.8	2.62 to 5.62	-2.0 to 4.0

Results and Discussion

Baseline Configuration

The selected baseline configuration for the nozzle tests was the 1.88 m length PDE detonation tube (5.08 cm diameter) without an exhaust nozzle. The fill-fraction for the baseline was varied from 0.4 to 1.1 while maintaining a near stoichiometric fuel-air ratio, an ignition delay of 0.5 ms, a purge-fraction of 0.5 and a cycle frequency of 30 Hz. The thrust values for the baseline PDE configuration are given in Figure 2 as function of experiment run time. The run time is represented in number of PDE cycles and the thrust is normalized according to a reference thrust value. The reference thrust used in normalizing this data was selected to be the thrust value (77 N) for the baseline configuration at a fill-fraction of 1.0. Since the PDE thrust was measured using a damped thrust stand, there was an associated time constant that delayed the average thrust from being recorded as shown by the slowly rising thrust curves in Figure 2. This transient delay between the first PDE cycle during each test and the time when a near steady-state thrust level was reached was approximately 33 seconds, or 1000 PDE cycles, for all fill-fractions tested. Although the wall temperature was not recorded, this extended run time required to obtain a steady-state average thrust also should have allowed time for the PDE to come close to thermal equilibrium. All thrust data presented in this paper corresponded to the average plateau in thrust recorded after the PDE had been operating continuously for approximately 1000 PDE cycles.

The variation in thrust and fuel-based specific impulse with fill-fraction is plotted in Figure 3. The trends observed were consistent with those found by other researchers. The

maximum thrust occurs at maximum fill-fraction and decreases non-linearly with fill-fraction. This nonlinear drop in thrust with reduced fill-fraction is attributed to the unfilled portion of the detonation tube acting as a straight nozzle. Two sets of expansion waves form during the detonation propagation for a straight nozzle configuration. The first set forms as the detonation shock wave crosses the interface between the filled and unfilled portion of the tube. The second set of expansion waves, which are much stronger than the first, forms as the detonation wave and exhaust gases exit the PDE tube. Essentially, the detonation shock wave serves to compress the gases occupying the unfilled portion of the detonation tube thereby maintaining the pressure inside the detonation tube at a higher pressure. This increased blow-down time with a straight nozzle results in higher thrust. For example, if this straight nozzle or “partial fill” effect were not present, the thrust at a fill-fraction of 0.5 would be approximately 50% of the thrust obtained with a fill-fraction of 1.0. The data in Figure 3 shows that the thrust at a fill-fraction of 0.5 was instead approximately 65%. Thus, a 15% thrust increase was generated by the partial-fill effect at a fill-fraction of 0.5. This effect continued to increase as the fill-fraction was reduced. Also, since the PDE thrust levels decreased at a slower rate than the reduction in fuel mass flow rate, the fuel-based specific impulse values increased as shown in Figure 3. Specific impulse values as high as 3700 seconds were obtained for the baseline configuration without an ejector.

Effects of Fill-Fraction

In the current work, the PDE-ejector performance has been reported as the percentage of the thrust the ejector produced relative to the

baseline PDE at the same fill-fraction. Thus, the ejector thrust augmentation is represented as

$$\left(\frac{T_{PDE-Ejector} - T_{PDE}}{T_{PDE}} \right) * 100\%. \quad (1)$$

The thrust of the PDE-ejectors was measured at fill-fractions ranging from 0.4 to 1.1. However, due to flow-rate restrictions and backfire problems into the delivery manifold, most tests were limited to a maximum fill-fraction of 0.8. Figure 4 is a plot of the percent thrust augmentation for a selected set of the straight and diverging ejectors tested as a function of fill-fraction. All ejectors showed that the best relative augmentation performance was obtained at the lowest operating fill-fraction, and the level of thrust augmentation was seen to have an inverse relation to fill-fraction. The maximum recorded thrust augmentation was with the longest diverging ejector ($L_{EJECT}/D_{EJECT}=5.62$) and was on the order of 65% of the baseline thrust at the fill-fraction of 0.4. Doubling the fill-fraction for this PDE-ejector system resulted in the relative thrust augmentation to decrease to roughly 51% of the baseline thrust. The straight ejectors did not perform as well as the diverging ejectors but had roughly the same dependency on fill-fraction. For the shortest straight ejector ($L_{EJECT}/D_{EJECT}=1.25$), negative thrust augmentation (or drag) was measured at the high fill-fraction conditions ($ff>0.8$).

To obtain a better understanding on why the increased fill-fraction resulted in reduced ejector performance, flow visualizations were performed on an optically accessible two-dimensional ejector of a similar geometry as those used in the current performance tests. Figures 5 and 6 are instantaneous snap-shots of high-speed flame luminosity imaging and particle flow visualizations of the PDE-ejector operating at a fill-fraction of 1.0. The time corresponding to each image has been specified relative to the exiting of the detonation wave. Both visualization techniques show the strong blast wave exiting the PDE and eventually impinging on the inlet surface of the ejector. The impingement of these high-pressure, high-temperature gases on the ejector inlet causes

significant drag (or negative thrust augmentation). As the fill-fraction of the PDE is increased, the strength of the blast wave and thus its drag contribution also is increased. In addition to the drag of the PDE blast wave, the exhaust gases were expelled out of the ejector inlet. The level of negative flow through the ejector inlet was observed to decrease in the high-speed movies as the fill-fraction was reduced. Thus, it is because of these two effects that that ejector performance is believed to vary inversely with fill-fraction. Later in the PDE-Ejector cycle, the flame and particle flow visualizations showed a positive direction of entrainment as depicted in Figures 5 and 6.

Effects of Ejector Length-to-Diameter Ratio

In addition to the operating condition of the PDE, the geometry of the ejector was seen to play an important role in the ejector performance. The lengths of the ejector were varied by changing the length of the straight or straight-intermediate sections as depicted in Figure 1, while maintaining a constant diameter of 13.97 cm. Conventionally, ejector augmentation data has been plotted as a function of the ejector length-to-diameter ratio (L_{EJECT}/D_{EJECT}). In Figure 7, the PDE-ejector thrust augmentation of the current work has been plotted as a function of L_{EJECT}/D_{EJECT} along with other available data from PDE-ejectors, pulsejet-ejectors and steady-ejectors. Figure 7 shows for the straight PDE-ejectors tested an increase in L_{EJECT}/D_{EJECT} ratio corresponded to an increase in the relative thrust augmentation. There existed a maximum at an L_{EJECT}/D_{EJECT} ratio between 3 and 4. The PDE straight-ejector ($DR=2.75$) thrust augmentation measured in the current study is in good agreement with those reported by Rasheed et al.⁹ ($DR=2.0$) for a fill-fraction of 1.0. The largest straight-ejector ($DR=2.9$) tested by Rasheed et al.⁹ had a better performance than the current work's straight-ejector ($DR=2.75$), while their smallest straight-ejector ($DR=1.5$) showed very poor performance. No data was reported by Rasheed et al.⁹ for other fill-fractions or ejector geometries.

The data plotted in Figure 7 also includes thrust augmentation values reported by Lockwood⁵ for straight walled steady-ejectors

and diverging pulsejet-ejectors. The straight steady-ejector augmentation levels agree very well with the current straight PDE-ejector data when the fill-fraction was close to 1.0. A straight PDE-ejector operating at a lower fill-fraction was observed to outperform the steady-ejector at a similar L_{EJECT}/D_{EJECT} ratio.

The diverging PDE-ejectors tested showed nearly twice as much thrust augmentation as the comparable straight PDE-ejectors. This improvement with a diverging ejector was also reported by Lockwood⁵. The pulsejet-ejectors tested by Lockwood were of a diverging type with the same 8-degree total angle used in the current work. However, the pulsejet ejectors appeared to outperform the PDE diverging-ejectors and have a much smaller optimum L_{EJECT}/D_{EJECT} ratio of about 1.5. The PDE diverging-ejectors showed an increase in performance with increased length. The diverging PDE-ejectors also showed a possible approach to leveling off of performance at an L_{EJECT}/D_{EJECT} ratio around a value of 6.0, a value much greater than the optimum L_{EJECT}/D_{EJECT} ratio of the straight PDE-ejectors.

Since the performance of the PDE-ejectors was observed to be inversely proportional to the operating fill-fraction for all ejector geometries, the authors have proposed a new non-dimensional parameter ($L_{EJECT}/D_{EJECT}/ff$) to be used in plotting PDE-ejector thrust augmentation. Figure 8 shows that when the data is plotted in this fashion all the thrust augmentation data collapses onto one curve. Thus, all the current PDE-ejector data of similar internal geometry can be represented by one function when plotted as a function of $L_{EJECT}/D_{EJECT}/ff$. Of course, the diverging and straight PDE-ejectors do not fall onto the same curve. This is attributed to the effect of the additional thrust surface area that the divergence provides. However, the correlation between straight steady-ejectors ($ff=1.0$) and straight PDE-ejectors was quite reasonable as shown in Figure 8. Furthermore, the PDE-ejector data provided by Rasheed et al.⁹ also agreed reasonable well when plotted in this fashion.

Effects of Ejector Axial Position

Another geometrical parameter varied in these tests was the relative position of the ejector inlet to the exhaust of the PDE. All previous results reported in this paper were for an axial position of $x/D_{PDE}=2.0$, meaning the ejector was placed a distance of two PDE diameters downstream of the PDE exit. However, many previous studies on ejectors showed that the augmentation is very sensitive to its axial location^{5-7,9,14}. For this reason, the straight ejector ($L_{EJECT}/D_{EJECT}=1.25$) and the diverging ejector ($L_{EJECT}/D_{EJECT}=5.62$) were moved upstream and downstream of the PDE exhaust. In addition, since the results shown previously also indicate a strong dependence on fill-fraction, the fill-fraction was varied at each ejector axial position.

Figure 9 shows results for the diverging ejector at three operating fill-fractions and for x/D_{PDE} locations extending from upstream of -2 diameters to 4 diameters downstream. The sensitivity to axial location was most pronounced with the lower fill-fraction of 0.4. For this operating condition, the optimum x/D_{PDE} was a downstream placement of +2 diameters. As the fill-fraction was increased, the performance of the downstream ejector placements decreased relative to the upstream placements. At a fill-fraction of 0.8, the optimum location was measured to be either inline or slightly upstream of the PDE exhaust. This effect can be attributed to the PDE wave drag discussed earlier in the report and shown in the visualizations of Figures 5 and 6. A downstream placement of the ejector at the lower fill-fractions was more optimal because it did not experience as high of a wave drag, and it allowed the secondary flow to be more readily entrained without restrictions. This effect was also observed by Allgood et al.¹⁴ in their PDE-ejector visualizations.

Figure 10 shows the relationship between the ejector thrust augmentation and the axial placement of the ejector and the PDE fill-fraction. The thrust augmentations are plotted as a function of fill-fraction for three representative ejector axial placements: upstream, inline and downstream. Both the straight and diverging ejector configurations showed that as the fill-fraction was increased, the downstream placement performance dropped and the

upstream placement performance increased. The inline placement performance stayed nearly constant. Since both the diverging and straight ejector geometries showed very similar trends, the effect of fill-fraction was most likely having a primary affect on the ejector bellmouth and not on the internal thrust surfaces.

Conclusions

An experimental study of the performance of pulse detonation engine (PDE) ejectors was performed. Time-averaged thrust augmentation produced by straight and diverging PDE ejectors was measured using a damped thrust stand. The ejector length-to-diameter ratio was varied from 1.25 to 5.62 by changing the length of the ejector while maintaining a nominal ejector-to-PDE diameter ratio of 2.75. The operating fill-fraction was varied from 0.4 to 1.1. The PDE-ejector thrust augmentation was found to be strongly dependent on the operating fill-fraction. A reduction in fill-fraction corresponded to higher levels of ejector thrust augmentation for all L_{EJECT}/D_{EJECT} ratios tested and for both the straight and diverging ejectors. This improvement in ejector performance by operating at low fill-fraction conditions was attributed to a reduction in wave drag on the ejector inlet produced by the detonation blast waves. The diverging ejector geometry showed the best performance due to increased thrust surface area. The diverging ejector produced a maximum of 65% thrust augmentation compared to a 28% thrust augmentation with the straight ejector at a fill-fraction of 0.4.

In general, longer ejectors outperformed short ejectors. Ejectors with L_{EJECT}/D_{EJECT} ratios greater than 3.0 showed the best performance. For the case of the straight ejectors, maximum augmentation was observed for L_{EJECT}/D_{EJECT} ratios between 3 and 4. The diverging ejectors however, did not show a maximum for the range of L_{EJECT}/D_{EJECT} ratios tested but began to level off at L_{EJECT}/D_{EJECT} ratios greater than 5.

The current results compared well with a limited set of PDE-ejector data. However, the behavior and thrust augmentation of all PDE ejectors were inconsistent with reported deflagration pulsejet ejector systems. This leads

to the conclusion that while there are some similarities between PDE and pulsejet driven ejectors, there can be a significant difference in the flow dynamics to warrant caution in grouping these two systems into the same classification. However, a new normalization parameter ($L_{EJECT}/D_{EJECT}/ff$) based on ejector length to diameter ratio and PDE fill-fraction was proposed. Using this normalization parameter, the PDE ejector performances for all fill-fractions compared well available steady ejector performances.

The axial placement of the ejector also greatly affected the performance of the PDE-ejector system. Unlike other ejector systems, a single optimum ejector placement for PDE applications was not found but rather a function of the operating fill-fraction. The sensitivity of ejector augmentation to the axial placement was believed to be a result of a trade-off between reduced detonation-wave drag with upstream placement and increased mass entrainment with downstream placement. For most test conditions, a *downstream* ejector placement provided the best performance. However, as the operating fill-fraction was increased (i.e. stronger blast waves), the relative performance of an upstream placement increased while the performance of a downstream placement decreased. In contrast, the inline ejector placement performance was nearly independent of fill-fraction.

Acknowledgements

The authors would like to thank the Propulsion Directorate at the Air Force Research Laboratory and Innovative Scientific Solutions Inc. for providing the financial support for this work. The technical support of Curtis Rice of Innovative Scientific Solutions Inc. was also appreciated. In addition, the authors are grateful for the financial support from NASA Glenn Research Center (NAG3-2669) for sponsoring the development of the University of Cincinnati pulse detonation engine research facility.

References

1. Bussing, T. and Pappas, G., "An Introduction to Pulse Detonation Engines", AIAA 94-0263.
2. Kuo, K., Principles of Combustion, John Wiley, New York, 1986.
3. Kailasanath, K. "Recent Developments in the Research on Pulse Detonation Engines", *AIAA Journal*, Vol. 41, No. 2, February 2003.
4. Schauer, F., Stutrud, J., and Bradley, R., "Detonation Initiation Studies and Performance Results for Pulse Detonation Engine Applications", AIAA 2001-1129, 39th AIAA Aerospace Sciences Meeting and Exhibit, Reno, NV, January 2001.
5. Lockwood, R., "Interim Summary Report on Investigation of the Process of Energy Transfer from an Intermittent Jet to Secondary Fluid in an Ejector-Type Thrust Augmenter", Hiller Aircraft Report No. ARD-286, March 1961.
6. Paxson, D.E., Wilson, J. and Dougherty, K.T., "Unsteady Ejector Performance: An Experimental Investigation Using a Pulsejet Driver", AIAA 2002-3915, 38th AIAA Joint Propulsion Conference, Indianapolis, IN, July 7-10, 2002.
7. Wilson, J. and Paxson, D.E., "Unsteady Ejector Performance: An Experimental Investigation Using a Resonance Tube Driver", AIAA 2002-3632, 38th AIAA Joint Propulsion Conference, Indianapolis, IN, July 7-10, 2002.
8. Hoke, J., Bradley, R., Stutrud, J. and Schauer, F., "Integration of a Pulsed Detonation Engine with an Ejector Pump and with a Turbo-Charger as Methods to Self-Aspirate", AIAA 2002-0615, 40th AIAA Aerospace Sciences Meeting and Exhibit, Reno, NV, January 14-17, 2002.
9. Rasheed, A., Tangirala, V., Pinard, P.F., Dean, A.J., "Experimental and Numerical Investigations of Ejectors for PDE Applications", AIAA 2003-4971, 39th AIAA Jet Propulsion Conference, Huntsville, AL, July 21-23, 2003.
10. Shehadeh, R., Saretto, S., Lee, S.-Y., Pal, S., Santoro, R.J., "Experimental Study of a Pulse Detonation Engine Driven Ejector", AIAA Paper 2003-4972, 39th AIAA Jet Propulsion Conference, Huntsville, AL, July 21-23, 2003.
11. Allgood, D., Gutmark, E. and Katta, V., "Effects of Exit Geometry on the Performance of a Pulse Detonation Engine", AIAA Paper 2002-0613, 40th AIAA Aerospace Sciences Meeting and Exhibit, Reno, NV, January 14-17, 2002.
12. Yungster, S. and Perkins, H.D., "Multiple Cycle Simulation of a Pulse Detonation Engine Ejector", AIAA Paper 2002-3630, 38th AIAA Joint Propulsion Meeting, Indianapolis, IN, July 7-10, 2002.
13. Groschel, E., Tsuei, H., Xia, G., Merkle, C., "Characterization of Thrust Augmentation by Unsteady Ejectors", AIAA 2003-4970, 39th AIAA Jet Propulsion Conference, Huntsville, AL, July 21-23, 2003.
14. Allgood, D., Gutmark, E., Rasheed, A., Dean, T., "Experimental Investigation of a Pulse Detonation Engine with a 2D Ejector", AIAA 2004-0864, 42nd Aerospace Sciences Meeting and Exhibit, January 2004.

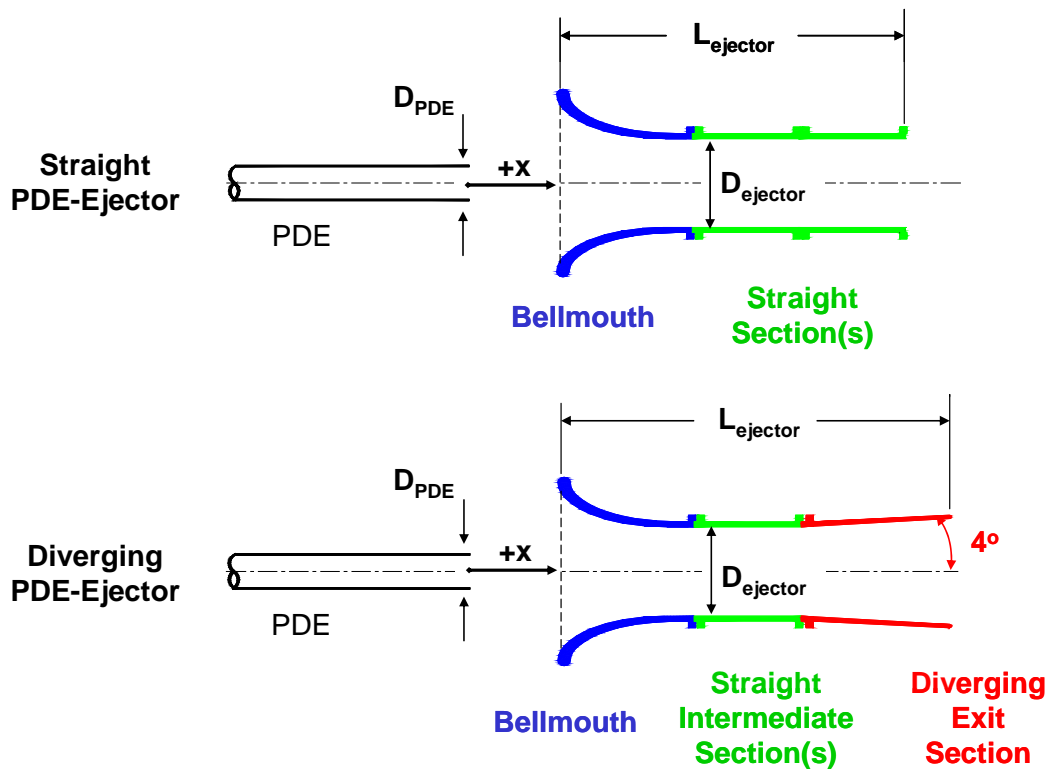


Figure 1: Schematics of the Straight and Diverging PDE-Ejectors

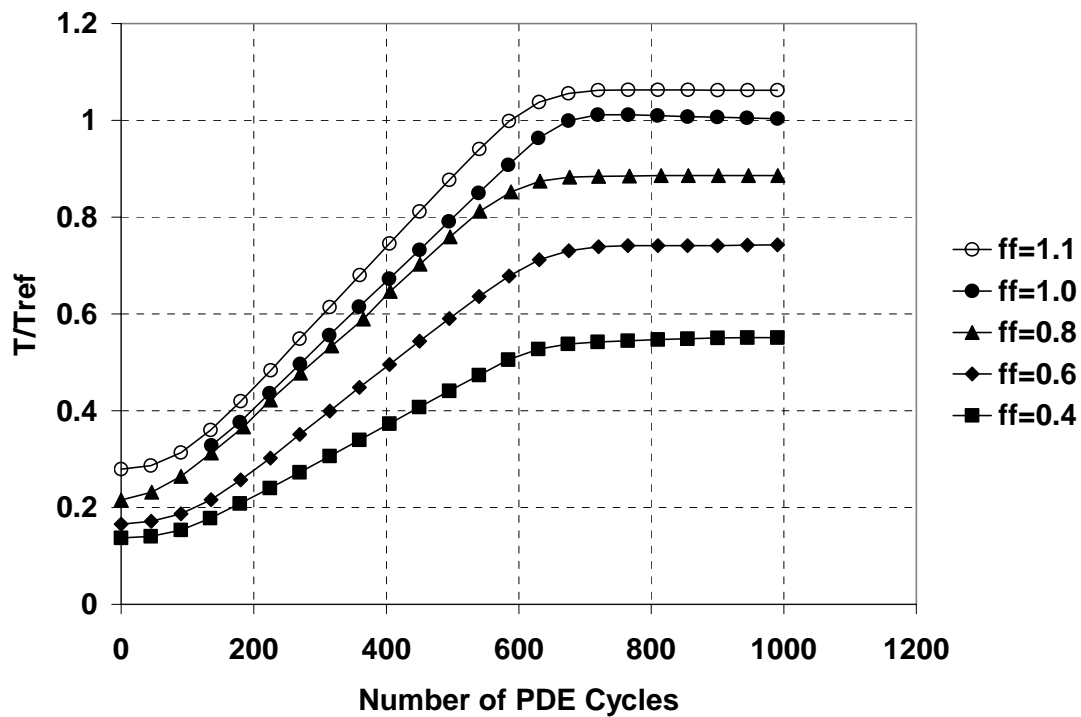


Figure 2: Baseline PDE Average-Thrust Measurements versus Number of PDE Cycles ($D_{PDE}=5.08$ cm, $T_{ref}=77$ N)

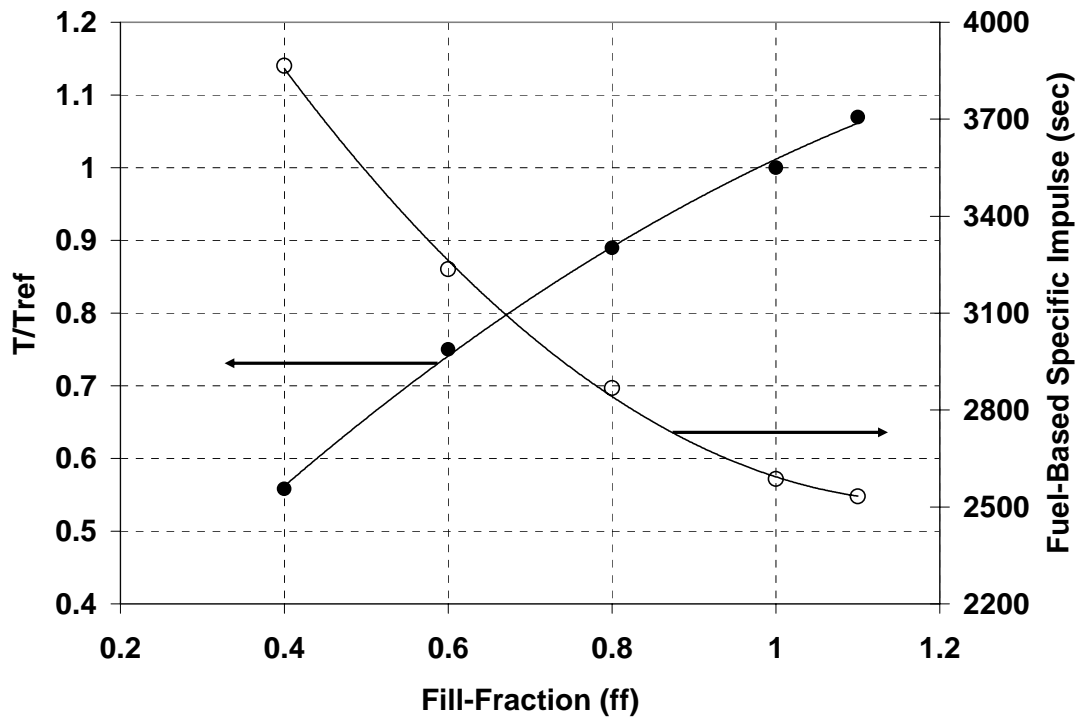


Figure 3: Baseline PDE Thrust and Fuel-Based Specific Impulse Variation with Fill-Fraction ($D_{PDE}=5.08$ cm, $T_{ref}=77$ N)

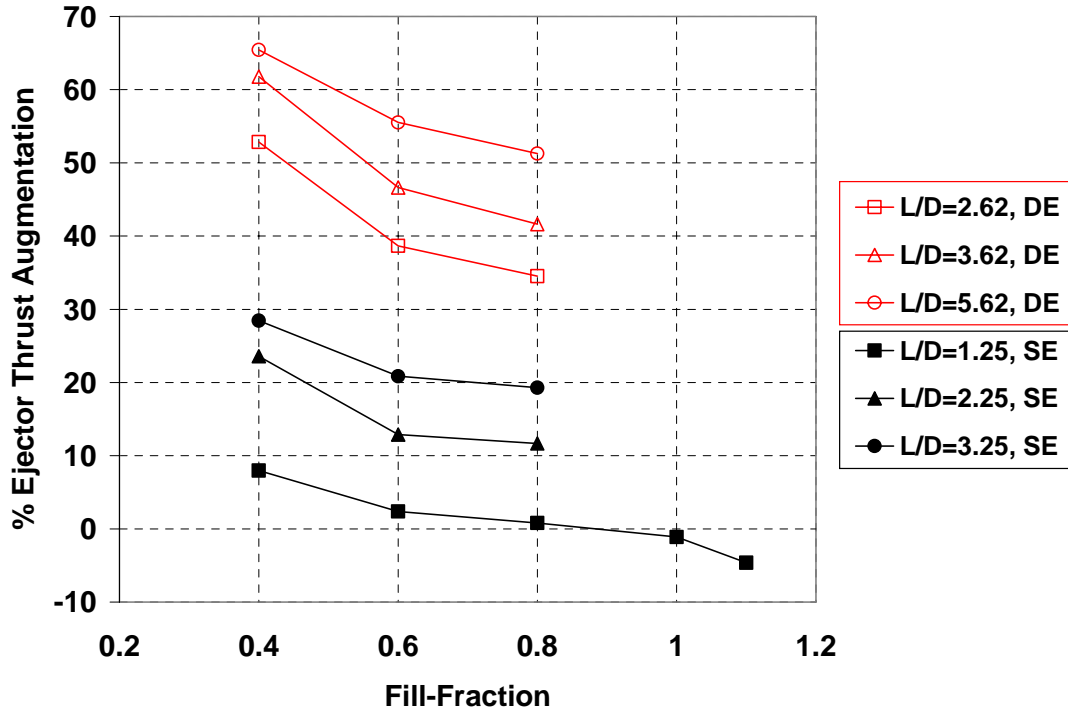


Figure 4: Straight (SE) and Diverging (DE) PDE-Ejector Thrust Augmentation Variation with Fill-Fraction for Three Ejector L/D Ratios ($DR=2.75$, $x/D_{PDE}=+2.0$)

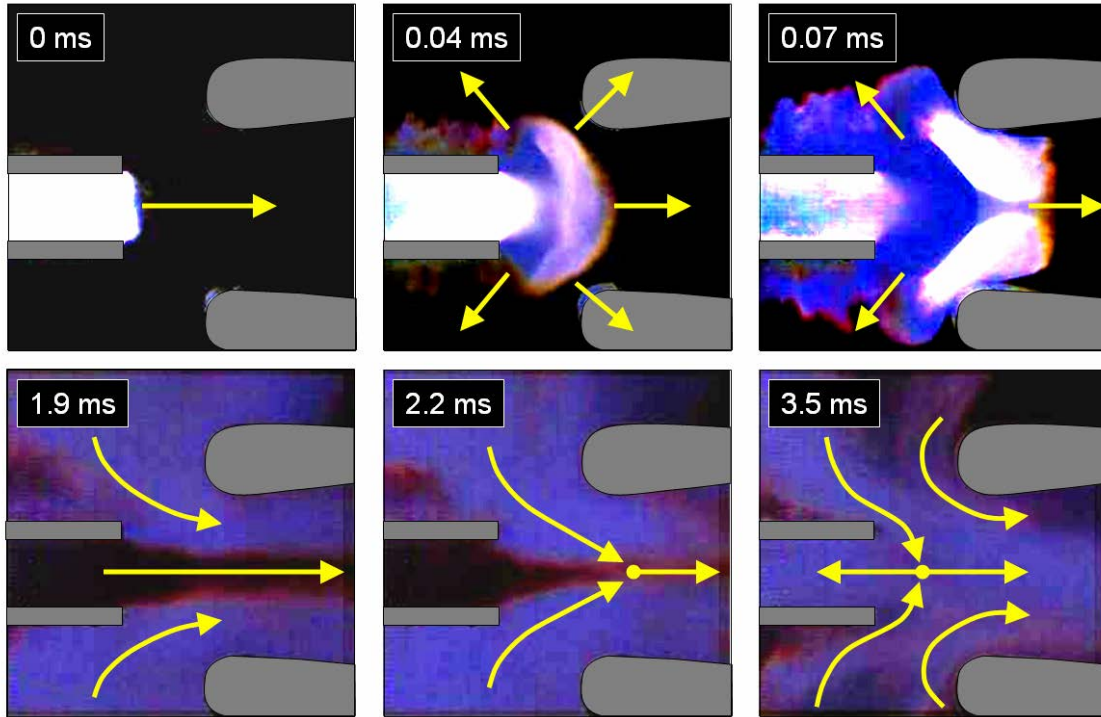


Figure 5: High-Speed Flame Luminosity Imaging of a Two-Dimensional Diverging PDE Ejector - The Vectors Indicate Direction of Visible Flame Propagation
 $(L_{EJECT}/D_{EJECT}=2.9, DR=2.2, x/D_{PDE}=+1.0, ff=1.0)$

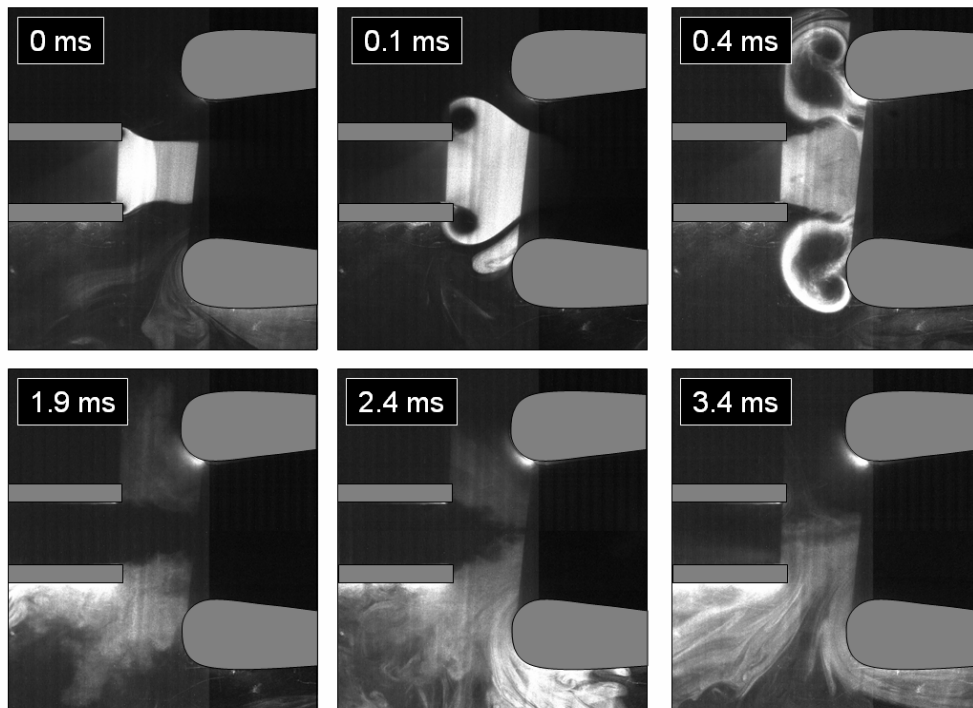


Figure 6: Particle Flow Visualizations of a Two-Dimensional Diverging PDE Ejector
 $(L_{EJECT}/D_{EJECT}=2.9, DR=2.2, x/D_{PDE}=+1.0, ff=1.0)$

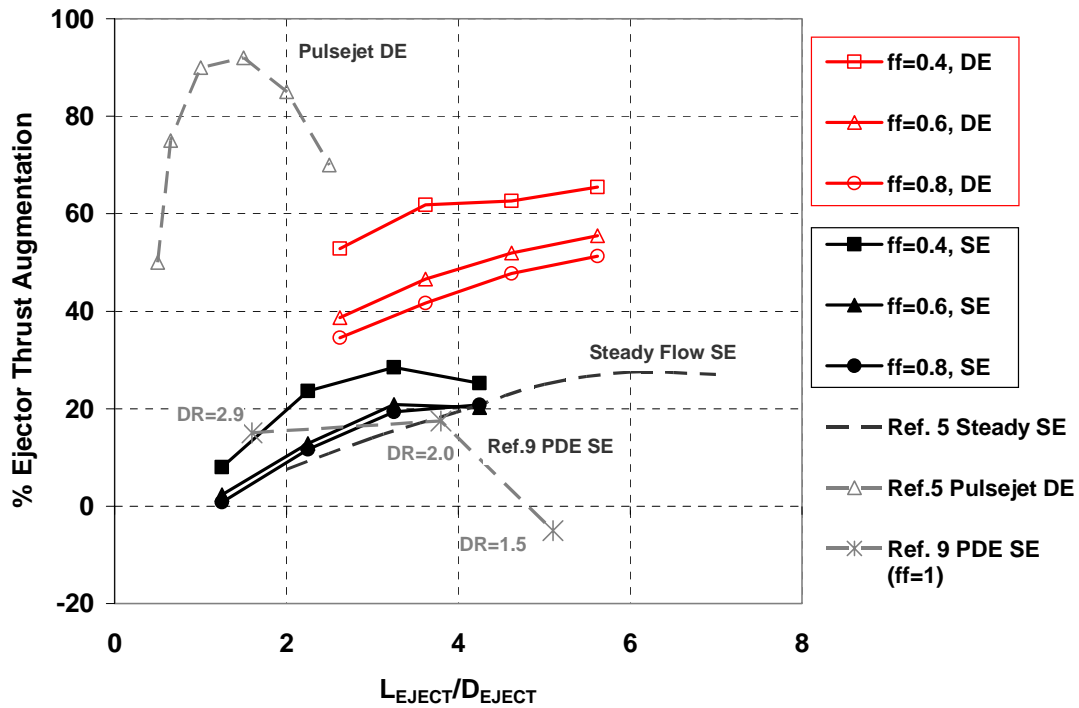


Figure 7: Normalization of Straight (SE) and Diverging (DE) Ejector Performances Using the Ejector L/D Ratio (DR=2.75, $x/D_{PDE}=+2.0$)

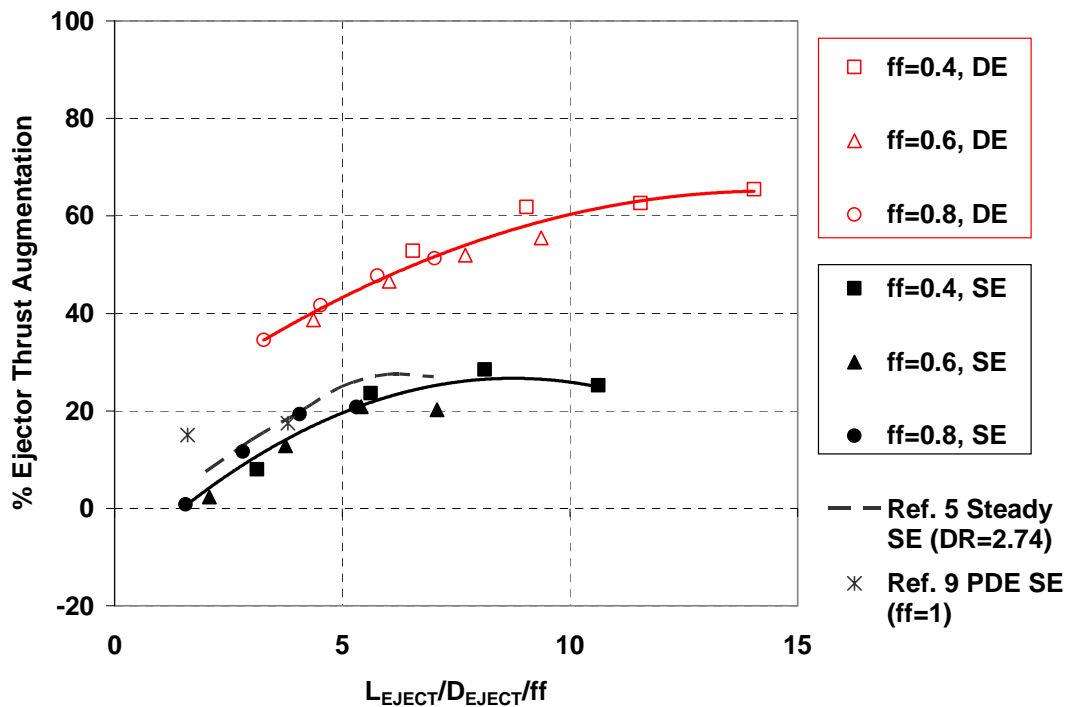


Figure 8: Proposed Normalization for PDE-Ejector Data Incorporating the PDE Fill-Fraction -- Note: For steady flow, ff=1.0 (DR=2.75, $x/D_{PDE}=+2.0$)

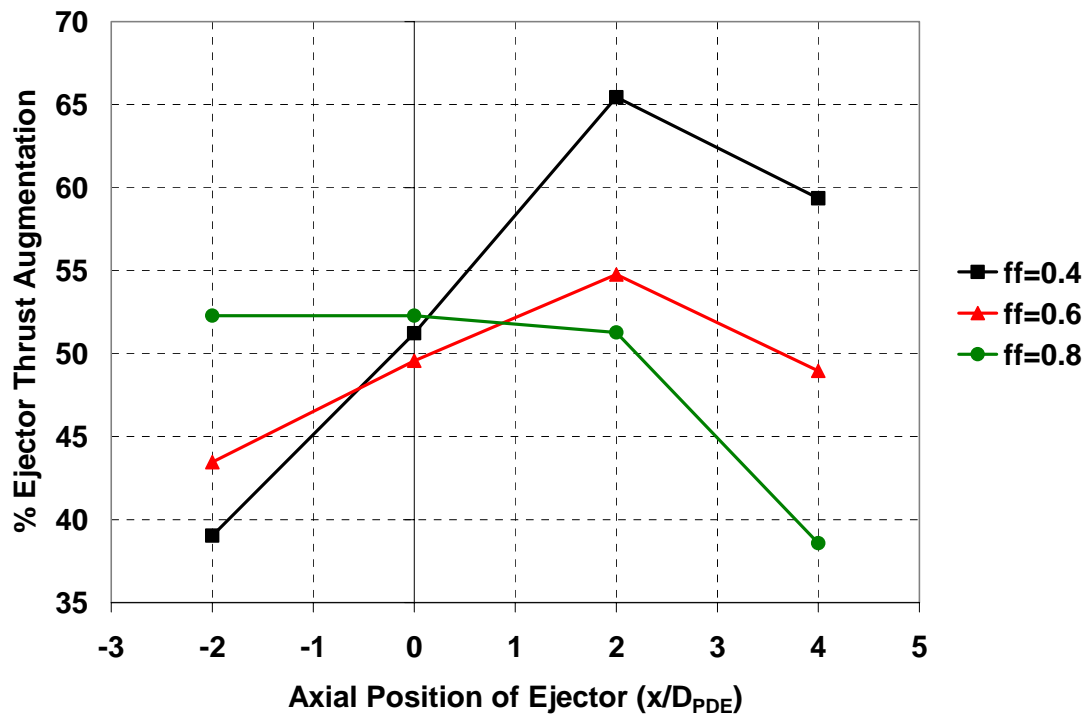


Figure 9: Effects of Axial Position on Diverging Ejector Performance for Three Operating Fill-Fractions ($L_{EJECT}/D_{EJECT}=5.62$, $DR=2.75$)

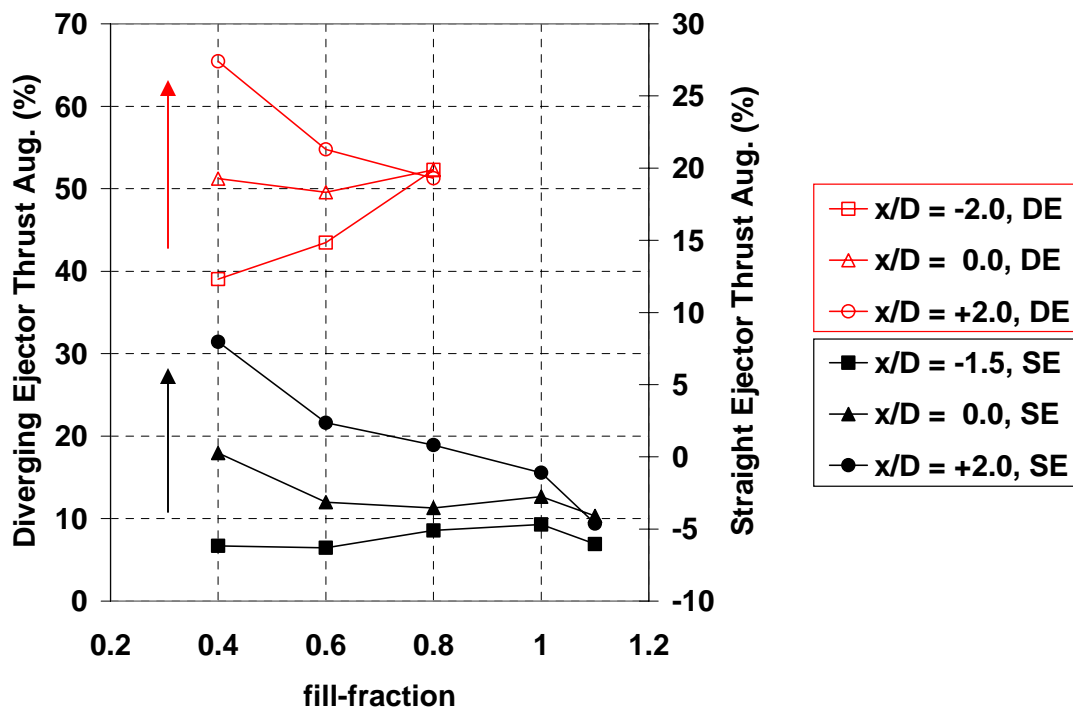


Figure 10: Performance Sensitivity of Straight ($L_{EJECT}/D_{EJECT}=1.25$) and Diverging ($L_{EJECT}/D_{EJECT}=5.62$) Ejectors to the Operating Fill-Fraction for Three Axial Ejector Positions (Arrows indicate a downstream change in position)

Performance Measurements of Multi-Cycle Pulse Detonation Engine Exhaust Nozzles

Daniel Allgood and Ephraim Gutmark*

*Department of Aerospace Engineering and Engineering Mechanics, University of Cincinnati,
Cincinnati, OH 45221-0070*

John Hoke and Royce Bradley

Innovative Scientific Solutions, Inc., Dayton, OH 45440

Fred Schauer

Air Force Research Laboratory, Propulsion Directorate, WPAFB, OH 45433

Abstract

Performance measurements of multi-cycle pulse detonation engine (PDE) exhaust nozzles were obtained using a damped thrust stand. A pulse detonation engine of 1.88 m length was operated on a cycle frequency of 30 Hz at stoichiometric conditions. Both converging and diverging bell-shaped exhaust nozzles were tested for fill-fractions ranging from 0.4 to 1.1. The area ratios of the nozzles were varied from 0.25 converging to 4.00 diverging. The nozzle length was negligible compared to the overall length of the PDE. Successful normalization of PDE nozzle thrust data was obtained based on nozzle area ratio for two PDE diameters tested (2.54 cm and 5.08 cm). The optimum nozzle area ratio was found to be a function of the PDE fill-fraction. For fill-fractions at or below 0.5, the optimum configuration was a PDE without an exhaust nozzle. However, as the operating fill-fraction was increased to values close to or above 1, thrust enhancement was obtained with a converging nozzle. The diverging nozzles also showed a relative increase in their performance with increased fill-fraction. However, unlike the converging nozzles, the diverging nozzles and baseline configuration were observed to be sensitive to the ignition delay.

Nomenclature

AR area ratio of nozzle ($D_{\text{nozz}}^2/D_{\text{PDE}}^2$)
 β nozzle length ratio ($L_{\text{nozz}}/L_{\text{PDE}}$)

D_{nozz} exhaust nozzle exit diameter
 D_{PDE} PDE detonation tube diameter
ff fill-fraction
 L_{nozz} length of nozzle
 L_{PDE} PDE detonation tube length
PDE pulse detonation engine
 T_{ref} reference thrust
 t_{cycle} PDE cycle time
 Φ percent nozzle thrust augmentation

Introduction

Pulse detonation engines (PDE) use controlled periodic detonations of a combustible mixture to generate thrust¹. One of the primary motivations for PDE development has been based on the potential gain in thermal efficiency that can be achieved with detonation combustion. Thermodynamic analysis of the fundamental combustion processes has shown that detonations produce less entropy than deflagrations^{1, 2}. Detonation combustion differs from the more common deflagration combustion in that the fuel/oxidizer mixtures are rapidly consumed due to the detonation flame front being closely coupled to a leading shock wave. The shock/flame front coupling is due to a feedback mechanism between the pressure rise of the shock wave and the heat release of the chemical reactions. Despite the theoretical benefits for using detonation combustion, one of the key technological challenges still facing researchers and engineers is to prove the feasibility of converting the higher thermal efficiency of pulse detonation combustors into practical PDE propulsive efficiency.

Experimental and computational researchers have demonstrated some success in

*Ephraim.Gutmark@uc.edu

obtaining competitive specific impulse values with a simplistic PDE cycle^{3,4}. These promising results have lead to many PDE applications being proposed. For example, it has been suggested that PDE's can be used as cost effective replacements for small gas turbine engines, as potential replacements for combustors on existing large-scale gas turbines, or as thrust augmenters. However, even if PDE performance benefits ultimately reveal themselves to be insignificant in practical applications, the PDE cycle will still be an attractive propulsion system because of the reliability benefits of having very few moving parts, the scalability of the engine, and the flexibility in geometry it will provide.

There are many operating parameters that have been shown to drastically affect the performance of a PDE. For example, PDE thrust has been observed to scale linearly with frequency of detonations since it is desirable to minimize the time of each filling event and maximize the frequency of the overall PDE cycle⁴. Thus, adjusting the PDE cycle frequency is one proposed method of throttling the engine. Another way of throttling the engine is to alter the amount of fuel-oxidizer mixture that fills the PDE tube prior to ignition. The ratio of the PDE tube filled with a detonable mixture relative to the total tube length is defined as the fill-fraction. While the PDE thrust has been shown to decrease with a reduction in fill-fraction, the fuel-based specific impulse values increased at a faster rate. This performance gain observed at lower fill-fractions was attributed to the detonation shock wave compressing the non-reactants occupying the remainder of the PDE tube^{4, 5}. Schauer et al.⁴ demonstrated experimentally the performance benefits of partially filling the detonation tube for a multi-cycle PDE operation. Their results showed the partial-fill effect being independent of PDE cycle frequency for a constant area detonation tube.

An alternative viewpoint of the partial-fill effect is that the thrust of a PDE can be increased by maintaining a constant amount of fuel-oxidizer mixture and simply adding additional length to the detonation tube. The additional tube length can be viewed as a constant-area straight nozzle that alters the

pressure relaxation process at the head wall of the PDE. The straight nozzle first generates a weak set of rarefaction waves that form at the entrance to the nozzle due to a mixture interface between the reactants of the detonation tube and the non-reactant gases occupying the nozzle. These weak rarefaction waves are then followed by a stronger set of rarefaction waves that form due to the sudden area change at the exit of the straight nozzle. Thus, by extending the length of the straight nozzle, the stronger exit-flow rarefaction waves can be delayed in time thereby allowing a slower rate of pressure relaxation at the head wall of the PDE. Li and Kailasanath⁵ have predicted that significant increases in peak impulse values can be obtained by increasing the length of a straight nozzle. However, while straight nozzles provide impressive performance benefits, they also limit the maximum cycle frequency of the PDE due to longer associated blow-down times.

More conventional nozzle geometries have also been shown to provide performance benefits for PDE applications. A very detailed review on the current level of PDE nozzle technology was given by Kailasanath³. The outcome of this review revealed some significant disagreements on the reported behavior of PDE nozzles. The source of the disagreements was attributed to the highly dynamic nature of the PDE and its sensitivity to the operating conditions. For example, most of the previous PDE nozzle research investigated the effects of nozzles that had relatively large lengths compared to the detonation tube ($\beta = L_{\text{nozz}}/L_{\text{PDE}} > 0.1$). Thus, for these nozzles of non-negligible length, partial-fill effects will have a significant impact on the PDE performance and should be taken into consideration when interpreting the results. Another common difference observed between the various PDE nozzle studies was that most studies modeled single-cycle detonations while very few looked at the behavior of a more practical multi-cycle operation³. These differences in PDE nozzle operating conditions lead to differing conclusions on an optimum nozzle geometry. Some highlights of these studies are discussed next.

Eidelman and Yang⁶ modeled a series of straight, converging and diverging nozzles for

a PDE operating in a single-shot detonation mode. The fill and purging processes and multi-cycle effects were not modeled. In their study, the nozzles represented a significant portion of the PDE ($\beta=0.167-0.4$). All nozzles showed an improvement over the baseline configuration without a nozzle, due to the partial-fill effect. While the converging and straight nozzles increased the peak thrust (impulse), the peak thrust did not occur until much later during the cycle due to the increase in blow-down time. The diverging nozzles on the other hand increased thrust due to increased thrust surface area but produced the higher peak thrust levels at a faster rate due to an increased rate of expansion. The one drawback observed with diverging nozzles was that due to overexpansion inside the PDE, the increased thrust surface area resulted in negative thrust later in the cycle. Despite this drawback, the bell-shaped diverging nozzle showed the best performance over all for this single-shot detonation operation.

Yungster⁷ confirmed the results by Eidelman and Yang⁶ in that a bell-shaped diverging nozzle performed the best and converging nozzles limit the operating frequency of the PDE. Yungster attributed the performance benefits of the bell-shaped nozzle over conical diverging nozzles to a slight minimization in over-expansion and therefore a reduction in negative thrust during the later stages of the blow-down process. The computations by Cambier and Tegner⁸ also are in agreement that a bell-shaped diverging nozzle, with its associated negative curvature in the change in internal surface area, performs better than a diverging nozzle with straight or positive surface area curvature. However, one distinct difference in the PDE operation modeled by Cambier and Tegner⁸ compared to the previously mentioned works was that the relatively large nozzles were filled with a detonable mixture. Thus, unlike the previous studies Cambier and Tegner⁸ predicted a decrease in specific impulse with diverging nozzles. This was due to the fact that the thrust gain provided by the diverging nozzle did not overcome the cost of providing additional fuel mass to fill the diverging nozzle. This negligible benefit of using a diverging conical nozzle with

a filled mixture was also predicted by Mohanraj and Merkle⁹ and by Cooper et al¹⁰.

These and other PDE nozzle simulations have primarily focused on predicting simplistic single-shot PDE operations where the subsonic fill and purge portions of a practical PDE cycle are not considered. In reality, the filling and purging processes of a multi-cycle operation are not insignificant portions of the cycle. Thus, although a diverging nozzle has been shown to expand the high pressure detonation gases and provide additional thrust surface on which this pressure may act, the diverging nozzle will act as a diffuser during the remainder and perhaps majority of the cycle. Yungster⁷ modeled the multi-cycle operation of PDE diverging nozzles and found that the first cycle showed nozzle thrust augmentation but no augmentation was observed during the following second and third PDE cycles. The loss in thrust augmentation was attributed to the cold-air that occupied the nozzle during the first cycle being replaced with low density combustion products. Wu et al.¹¹ have also modeled such multi-cycle operations and have shown that the performance enhancements of diverging nozzles during the detonation phase of the PDE cycle did not have a significant impact on the overall system. Rather, they found that a converging nozzle is helpful in maintaining significant backpressure at altitude conditions. From these and other studies, it can be concluded that the subsonic filling and purge portions of the cycle can significantly contribute to the thrust of the PDE during multi-cycle operations and thus should be considered in the nozzle design.

The current work is a unique experimental study of a multi-cycle PDE operation where the thrust augmentation levels provided by various converging and diverging bell-shaped exhaust nozzles were quantified. The nozzle area ratio was varied from 0.25 converging to 4.0 diverging. The nozzle length represented a negligible portion of the overall PDE length ($\beta=0.03$). The PDE operated on a stoichiometric mixture of hydrogen-air at a cycle frequency was 30 Hz. The PDE cycle time was divided evenly between three stages: a fill-stage, an ignition/detonation/blow-down stage, and a purge stage. For each nozzle configuration, the

operating fill-fraction was varied to quantify their corresponding partial-fill effects.

Experimental Setup

Thrust measurements of a pulse detonation engine (PDE) were performed to quantify the effects of exhaust nozzle geometry on PDE performance. The pulse detonation engine test facility at the Air Force Research Laboratory at Wright-Patterson Air Force Base was used to obtain the thrust measurements. Premixed hydrogen and air were delivered to a round detonation tube by way of a mechanical valve system constructed from a modified four-cylinder automotive head. In the standard automotive cycle, each cylinder has four ports, two for intake and two for exhaust. However for the PDE operation, two of the intake ports served to deliver the premixed hydrogen-air and the other two ports delivered purge air in order to “purge” the detonation tube of hot gases after each detonation and before injecting a fresh mixture of reactants. The combustion gases exited from the exhaust end of the detonation tube. The automotive valve system could be operated at frequencies up to 40 Hz. Due to the nature of automotive valving, the division of the cycle timing for various events such as fill-time and purge-time and detonation-time were fixed to be each 1/3 of the cycle. Only one of the four automotive valve sets was used to deliver mass flow to a single detonation tube. The hydrogen and air were metered through choked flow orifices and the flow rate and pressure data was collected via a remote 5 MHz 16-channel ADC system. For a more detailed description of the PDE test facility the reader is referred to the recent paper by Schauer et al.⁴.

For the current PDE nozzle performance tests, the pulse detonation engine was operated with a stoichiometric mixture of hydrogen and air. To determine the feasibility of normalizing PDE nozzle data based on the nozzle inlet-to-exit area ratio, two detonation tubes of 2.54 cm and 5.08 cm diameter (D_{PDE}) were tested. Both PDE detonation tubes had a length of 1.88 m, and the PDE cycle frequency was kept constant at 30 Hz. Bell-shaped exhaust nozzles of area ratios ($AR = D_{nozz}^2 / D_{PDE}^2$) ranging from 0.25 converging to 4.0 diverging were tested.

Representative schematic drawings are given in Figure 1. In all test cases, the nozzle length represented only 2-3% of the total length of the PDE. Nozzles of this length were chosen so as to limit the partial-fill effects introduced by adding the additional length to the PDE.

The two operating parameters varied during these tests were the fill-fraction (ff) and ignition delay. The fill-fraction was defined as the ratio of the detonation tube volume initially filled with a detonable mixture compared to the total tube volume. The fill-fraction was varied from 0.4 to 1.1 for all nozzle configurations. As mentioned previously, a purge-air cycle was added to cool the detonation tube and provide a buffer between the hot combustion products and the fresh reactants being injected for the next cycle. Due to the automotive valve system that was used, 1/3 of the cycle was allocated for purging. Similar to fill-fraction, the purge-fraction can be defined as the ratio of the tube volume filled with purge air relative to the PDE total volume. The purge-fraction was kept constant at 0.5 during all tests.

The ignition delay was defined as the time delay for the spark plug to ignite relative to the closing of the valves. Due to the response of the valve system, the ignition delay could not be set below a value of 0.5 ms without the risk of a backfire upstream into the injection manifold. The maximum delay time was set by the 30 Hz cycle frequency of the PDE. For the ignition delay studies, the delay time was varied from 0.5 to 7.5 ms for the baseline configuration of a PDE without an exhaust nozzle and for two representative converging ($AR=0.25$) and diverging ($AR=4.0$) nozzles. A maximum ignition delay of 7.5 ms allowed a sufficient amount of time (3.5 ms) for the DDT and blowdown to occur before the purge-air entered the detonation tube. All other nozzle tests were performed at a baseline ignition delay of 0.5 ms.

The deflagration-to-detonation transition of the hydrogen-air mixture was enhanced by the use of Shchelkin-type spirals of 0.3 m length for both the 2.54 cm and 5.08 cm diameter detonation tubes. The Shchelkin spiral occupied only 16% of the total PDE tube length. Two pressure transducers (PCB M102A) were mounted 0.152 m apart to monitor detonation shock speeds and validate that CJ detonations

were produced. The measured wave speed for both detonation tubes was confirmed to be approximately the Chapman-Jouget wave speed of 1966 m/s at a fill-fraction of 1.0.

The PDE was mounted on a damped thrust stand rated for a maximum thrust load of 4,500 N. The thrust stand was designed to measure the time-averaged thrust of the dynamic PDE. The thrust stand consisted of linear bearings riding along a pair of linear bearing rails. The PDE was allowed to freely move on the rails but its motion was weakly damped by springs to prevent any resonance effects. To remove the effects of static friction, the PDE was continuously actuated forward and backward by a linear actuator. Since this was a known force, it could be subtracted from the measurements to get the true average thrust of the engine. The thrust measurements were calibrated by placing static weights and measuring the displacement with a positional sensor. The maximum uncertainty (or repeatability) in the calibration was determined to be approximately ± 1 Newton for the entire range of PDE thrust loading anticipated during these tests.

Results and Discussion

Baseline Configuration

The selected baseline configuration for the nozzle tests was the 1.88 m length PDE detonation tube (5.08 cm diameter) without an exhaust nozzle. The fill-fraction for the baseline was varied from 0.4 to 1.1 while maintaining a near stoichiometric fuel-air ratio, an ignition delay of 0.5 ms, a purge-fraction of 0.5 and a cycle frequency of 30 Hz. The thrust values for the baseline PDE configuration are given in Figure 2 as function of experiment run time. The run time is represented in number of PDE cycles and the thrust is normalized according to a reference thrust value. The reference thrust used in normalizing this data was selected to be the thrust value (77 N) for the baseline configuration at a fill-fraction of 1.0. Since the PDE thrust was measured using a damped thrust stand, there was an associated time constant that delayed the average thrust from being recorded as shown by the slowly rising thrust curves in

Figure 2. This transient delay between the first PDE cycle during each test and the time when a near steady-state thrust level was reached was approximately 33 seconds, or 1000 PDE cycles, for all fill-fractions tested. Although the wall temperature was not recorded, this extended run time required to obtain a steady-state average thrust also should have allowed time for the PDE to come close to thermal equilibrium. All thrust data presented in this paper corresponded to the average plateau in thrust recorded after the PDE had been operating continuously for approximately 1000 PDE cycles.

The variation in thrust and fuel-based specific impulse with fill-fraction is plotted in Figure 3. The trends observed were consistent with those found by other researchers. The maximum thrust occurs at maximum fill-fraction and decreases non-linearly with fill-fraction. This nonlinear drop in thrust with reduced fill-fraction is attributed to the unfilled portion of the detonation tube acting as a straight nozzle. Two sets of expansion waves form during the detonation propagation for a straight nozzle configuration. The first set forms as the detonation shock wave crosses the interface between the filled and unfilled portion of the tube. The second set of expansion waves, which are much stronger than the first, forms as the detonation wave and exhaust gases exit the PDE tube. Essentially, the detonation shock wave serves to compress the gases occupying the unfilled portion of the detonation tube thereby maintaining the pressure inside the detonation tube at a higher pressure. This increased blow-down time with a straight nozzle results in higher thrust. For example, if this straight nozzle or “partial fill” effect were not present, the thrust at a fill-fraction of 0.5 would be approximately 50% of the thrust obtained with a fill-fraction of 1.0. The data in Figure 3 shows that the thrust at a fill-fraction of 0.5 was instead approximately 65%. Thus, a 15% thrust increase was generated by the partial-fill effect at a fill-fraction of 0.5. This effect continues to increase as the fill-fraction was reduced. Also, since the PDE thrust levels decreased at a slower rate than the reduction in fuel mass flow rate, the fuel-based specific impulse values increased as shown in Figure 3. Specific impulse values as

high as 3700 seconds were obtained for the baseline configuration.

Effects of Nozzle Area Ratio

The effects of converging and diverging bell-shaped exhaust nozzles on the PDE thrust were measured. The area ratios tested were 0.25, 0.39, 0.56, 1.0, 2.25, and 4.0, where ratios less than one are converging nozzles and greater than one are diverging nozzles. The nozzle lengths were approximately 5 cm in length, and therefore only extended the total length of the PDE by 2.6%. Thus, the partial-fill effect of adding these exhaust nozzles was negligible. The PDE was operated at the baseline operating conditions of a stoichiometric fuel-air mixture and cycle frequency of 30 Hz.

Since two-thirds of the PDE cycle involves filling the detonation tube with reactants and purge gases at subsonic speeds, initial cold-flow tests were performed to determine what effect the nozzles had on these portions of the cycle. The cold-flow thrust measurements were performed at the same operating conditions and configurations as in the detonation cases but without igniting the mixture. The cold-flow results are shown in Figure 4. At all fill-fractions, a decrease in area ratio resulted in an increase in thrust. The improvement in cold-flow thrust with a converging nozzle is a result of the fill-cycle and purge-cycle gases having subsonic velocities. Thus, nozzles with area ratios greater than 1.0 were acting as diffusers instead of nozzles. It should also be noted that the cold flow air thrust represented between 10 to 30 percent of the total thrust of the PDE further signifying the importance of the subsonic portions of the PDE cycle to the overall PDE performance and nozzle selection.

For incompressible flow, mass conservation ensures that a linear rate of increase in area ratio would result in a linear decay in velocity. Thus, since thrust scales linearly with exit velocity for a fully expanded steady flow, thrust should also decrease linearly with increased area ratio for these PDE cold-flow nozzle conditions. The cold-flow data given in Figure 4 however does not show this linear trend except for the intermediate area

ratios (0.56, 1.0, and 2.25) at the higher fill-fractions. For the extreme conditions of AR=0.25, 0.39 and AR=4.0, the variation was not linear. The thrust was observed to maintain a constant value for area ratios larger than 2.25. This was most likely due to increased flow separation from the walls of the larger bell-shaped nozzles. For the smallest area ratio converging nozzles, the thrust was also constant or slightly increasing. This deviation from a linear behavior was most likely a result of the increased PDE tube pressure and therefore increased profile drag of the small converging nozzles.

Once the cold-flow PDE thrust measurements were completed, the reacting-flow PDE thrust measurements were obtained and are plotted in Figure 5. For both the cold-flow and reacting-flow conditions, all nozzles tested exhibited an increase in thrust with a decrease in nozzle area ratio when the operating fill-fractions were above 0.8. The similarity between the cold flow (Figure 4) and the reacting flow (Figure 5) thrust profiles further suggest that the nozzle performances are being influenced substantially by the subsonic portions of the PDE.

To better show the relative thrust augmentation levels provided by the nozzles at each fill-fraction, a percent thrust augmentation was computed for each area ratio nozzle by referencing the thrust to the baseline thrust (AR=1.0) at the same corresponding fill-fraction using equation 1 given below.

$$\Phi = \frac{T_{AR} - T_{AR=1}}{T_{AR=1}} * 100\%. \quad (1)$$

The resulting percent thrust augmentation values are plotted in Figure 6. At a fill-fraction of 1.0, the smallest converging nozzle (AR=0.25) generated nearly a 15% thrust augmentation compared to the baseline configuration (AR=1.0). In addition to the previously mentioned benefits of the converging nozzle, this thrust augmentation was also believed to be a result of the increased detonation blow-down time generated by choking the exhaust flow for a longer time period. To support this claim, Figure 7 shows sample pressure time traces that

were recorded for the baseline and the $AR=0.56$ converging nozzle configurations. The data are plotted as a function of normalized time (time divided by the cycle time of 33.3 ms). A comparison between these two pressure traces shows that additional thrust provided by the converging nozzle was coming from the pressure rise inside the PDE tube and the associated increase in blow-down time. Also, Figure 7 shows that this additional compression inside the PDE tube was a result of the detonation shockwave reflecting from the converging walls of the nozzle back to the headwall of the PDE.

However, at fill-fractions below 0.8, the converging nozzles were observed to decrease the thrust of the PDE, eventually causing a 15% thrust deficit compared to the $ff=0.4$ baseline as shown in Figure 6. This shift in converging nozzle performance with reduced fill-fraction was believed to be due to the converging nozzle having less effect on the blow-down process due to the reduced pressures and the negative effect of its profile drag playing a dominant role in the overall nozzle performance.

The sensitivity of the diverging nozzles to area ratio did not appear to change with fill-fraction. All diverging nozzles at all fill-fractions were observed to have performance degradations with increased nozzle area ratio. The maximum diverging nozzle performance loss was approximately 20% and occurred at a fill-fraction 0.4.

The Scalability and Normalization of PDE Nozzle Thrust Data

It was desired to determine whether or not PDE exhaust nozzle thrust scales with the initial PDE detonation tube diameter, i.e. is nozzle area ratio the appropriate normalization for this data. Figure 8 is a plot of nozzle thrust measurements that were made on both the 5.08 cm diameter tube mentioned earlier and a 2.54 cm diameter tube. Both detonation tubes had lengths of 1.88 m. Both sets of converging and diverging nozzles were similar in shape and length. To compare the thrust profiles obtained for these two configurations, the data was normalized by a reference thrust value. The selected reference condition was the baseline

thrust value at $ff=1.0$ for the corresponding detonation tube. Therefore, each of the two data sets (2.54 cm and 5.08 cm diameter tubes) was normalized by one reference value of 16 N and 77 N, respectively. Theoretically, PDE thrust scales with the volume of the detonation tube. Thus, it would be expected that the ratio of the baseline reference thrusts would be close to a value of 4.0. The data obtained and referenced above showed a ratio of 4.8. The 0.8 deviation can be partially attributed to the larger relative uncertainty associated with the low thrust level measurements of the 2.54 cm diameter tube. Despite this uncertainty in the measurements, the normalized thrust data plotted in Figure 8 for these two detonation tube diameters does qualitatively show that the nozzle performance is independent of the initial PDE diameter. Therefore, the nozzle area ratio is believed to be an appropriate normalization for PDE nozzle data.

Effect of Ignition Delay

The ignition delay has been shown by researchers to play an important role in the performance of a pulse detonation engine when there are strong pressure oscillations occurring inside the detonation tube prior to ignition⁴. The sensitivity of thrust to the initial pressure is due to the pressure effects on the deflagration-to-detonation transition process. Igniting the mixture when the local gases are at a state of higher pressure can result in reduced DDT times and higher thrust. However, igniting when the local pressure is at a minimum can increase DDT times and reduce the thrust. Pressure oscillations can occur inside the PDE due to excitation of a fundamental acoustic mode or by forced excitation of the fuel-air valve system. Thus, the relative timing of ignition to the local pressure can have a significant impact on the PDE performance.

To determine the effects of ignition delay on the current PDE nozzle configurations, the ignition timing relative to the closing of the valves was varied from 0.5 ms to 7.5 ms for nozzles with area ratios of 0.25, 1.0 and 4.0. The fill-fraction was held constant at 1.0. These configurations and test conditions were selected to be representative of a typical converging,

baseline and diverging PDE nozzle system's response to changes ignition delay. The minimum ignition delay time was set by the response of the current valve system and could not be set below this value without resulting in a backfire upstream of the valves into the fuel-air premixed injection chamber. The maximum ignition delay time was chosen to be 7.5 ms so as to not allow the blow-down to extend into the PDE purge cycle.

The normalized thrust as a function of ignition delay is plotted in Figure 9. The baseline PDE thrust has a sinusoidal type behavior with changes in ignition delay resulting in a maximum of +8% deviation from the average thrust at the best delay and a -5% thrust deviation at the worst ignition delay. The large amplification in PDE thrust was presumably from igniting at a time in the cycle when there was a local compression wave near the ignition region, while the attenuation in thrust was a result of the ignition occurring while there was a local expansion wave present⁴. The sinusoidal type behavior is due to the acoustic properties of the closed/open ended detonation tube. The diverging nozzle configuration also had a sinusoidal type variation in thrust with ignition delay. The diverging nozzle (AR=4.0) thrust appeared to vary nearly in-phase and with similar amplitude of deviation from its mean thrust as that of the baseline configuration. The converging nozzle with AR=0.25 appeared to vary out-of-phase with respect to the baseline and diverging nozzle cases. Also, the level of deviations from its average thrust was much less (+/- 2%) presumably due to the constriction in the PDE exit area dampening the pressure oscillations inside the detonation tube thus making it less sensitive to ignition delay.

Conclusions

Performance measurements of pulse detonation engine (PDE) exhaust nozzles were obtained using a damped thrust stand. A pulse detonation engine of 1.88 m length was operated on a cycle frequency of 30 Hz at stoichiometric conditions. Both converging and diverging bell-shaped exhaust nozzles were tested for fill-fractions ranging from 0.4 to 1.1. The length of the nozzles represented only about 2-3% of the

total length of the PDE. The area ratio of the nozzle was varied from 0.25 converging to 4.00 diverging. Successful normalization of PDE nozzle thrust data was obtained based on the nozzle area ratio for the two PDE diameters (2.54 cm and 5.08 cm) tested. The optimum nozzle area ratio was found to be a function of the fill-fraction. For fill-fractions at or below 0.5, the optimum configuration was a PDE without an exhaust nozzle. However, as the operating fill-fraction was increased to values close to or above 1, thrust enhancement was obtained with a converging nozzle. The diverging nozzles showed a relative increase in their performance with increased fill-fraction as well. The baseline and diverging nozzle configurations tested were observed to be sensitive to the ignition delay, but the converging nozzle geometry was observed to dampen out any pressure wave dynamics that would alter the ignition/DDT process. The effect of the interior surface of the nozzle was found to play a minor role in the performance levels of the engine.

Acknowledgements

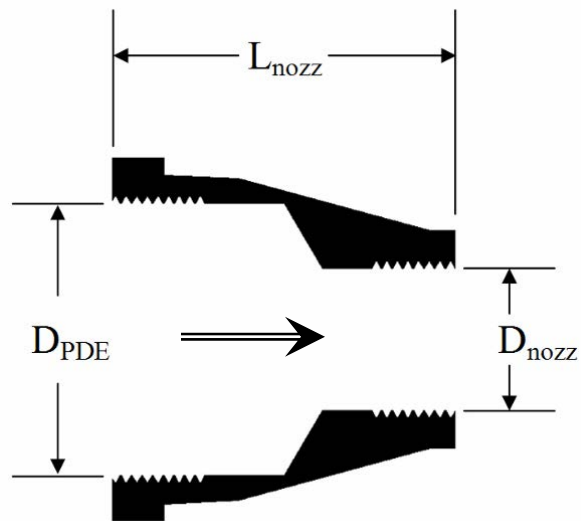
The authors would like to thank the Propulsion Directorate at the Air Force Research Laboratory and Innovative Scientific Solutions Inc. for providing the financial support for this work. The technical support of Curtis Rice of ISSI was also appreciated. In addition, the authors are grateful for the financial support from NASA Glenn Research Center (NAG3-2669) for sponsoring the development of the University of Cincinnati pulse detonation engine research facility.

References

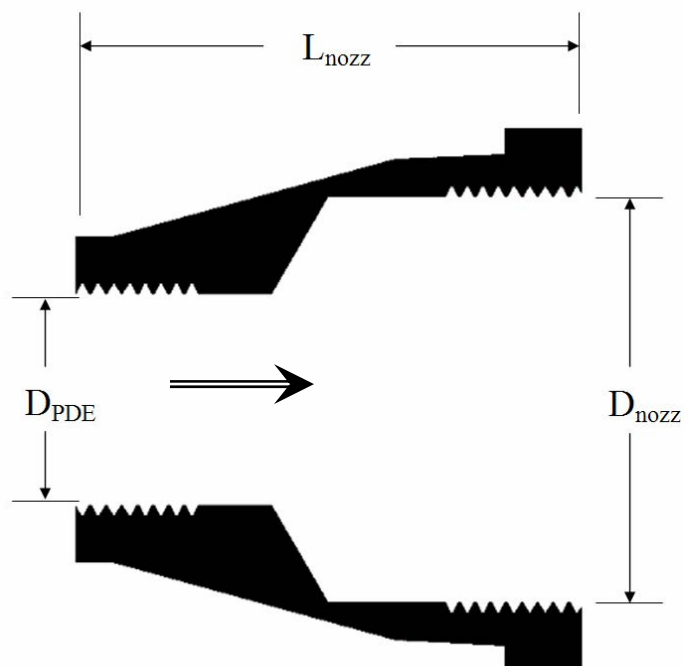
1. Bussing, T. and Pappas, G., "An Introduction to Pulse Detonation Engines", AIAA 94-0263.
2. Kuo, K., Principles of Combustion, John Wiley, New York, 1986.
3. Kailasanath, K. "Recent Developments in the Research on Pulse Detonation Engines",

AIAA Journal, Vol. 41, No. 2, February 2003.

4. Schauer, F., Stutrud, J., and Bradley, R., "Detonation Initiation Studies and Performance Results for Pulse Detonation Engine Applications", 39th AIAA Aerospace Sciences Meeting, AIAA 2001-1129.
5. Li, C. and Kailasanath, K., "Performance Analysis of Pulse Detonation Engines with Partial Fuel Filling", AIAA 2002-0610, 40th AIAA Aerospace Sciences Meeting, Jan. 14-17, 2002.
6. Eidemann, S. and Yang, X., "Analysis of the Pulse Detonation Engine Efficiency", AIAA 98-3877, 34th AIAA/ASME Joint Propulsion Conference, July 13-15, 1998.
7. Yungster, S., "Analysis of Nozzle Effects on Pulse Detonation Engine Performance", AIAA 2003-1316, 41st Aerospace Sciences Meeting, January 6-9, 2003.
8. Cambier, J. L. and Tegner, J. K., "Strategies for Pulsed Detonation Engine Performance Optimization", *Journal of Propulsion and Power*, Vol. 14, No. 4, July-August, 1998.
9. Mohanraj, R. and Merkle, C. L., "A Numerical Study of Pulse Detonation Engine Performance", AIAA 2000-0315, Jan. 2000.
10. Cooper, M., Jackson, S., Austin, J., Wintenberger, E. And Sheperd, J., "Direct Experimental Impulse Measurements for Detonations and Deflagrations", AIAA 2001-3812, July 2001.
11. Wu, Y., Ma, F. and Yang, V., "System Performance and Thermodynamic Cycle Analysis of Air-breathing Pulse Detonation Engines", *Journal of Propulsion and Power*, Vol. 19, No. 4, July-August 2003.



(a) Converging Nozzle



(b) Diverging Nozzle

**Figure 1: Representative Schematic Drawings of the PDE Exhaust Nozzles
(Flow Directions are Indicated by an Arrow)**

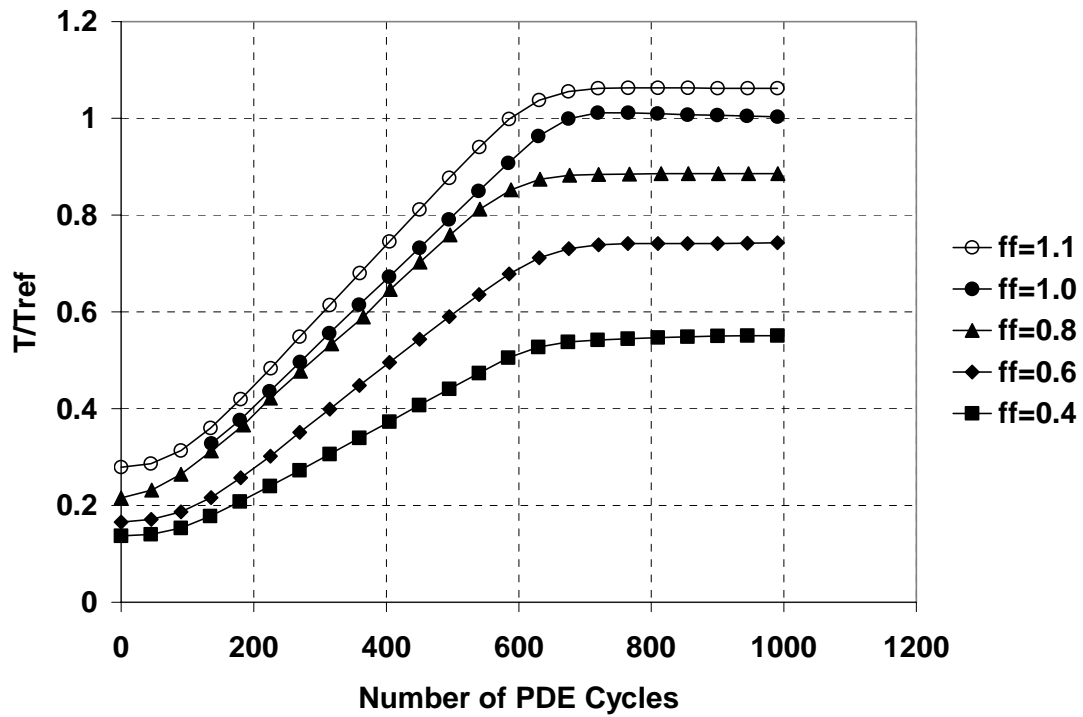


Figure 2: Baseline PDE Average-Thrust Measurements versus Number of PDE Cycles ($D_{PDE}=5.08$ cm, $T_{ref}=77$ N)

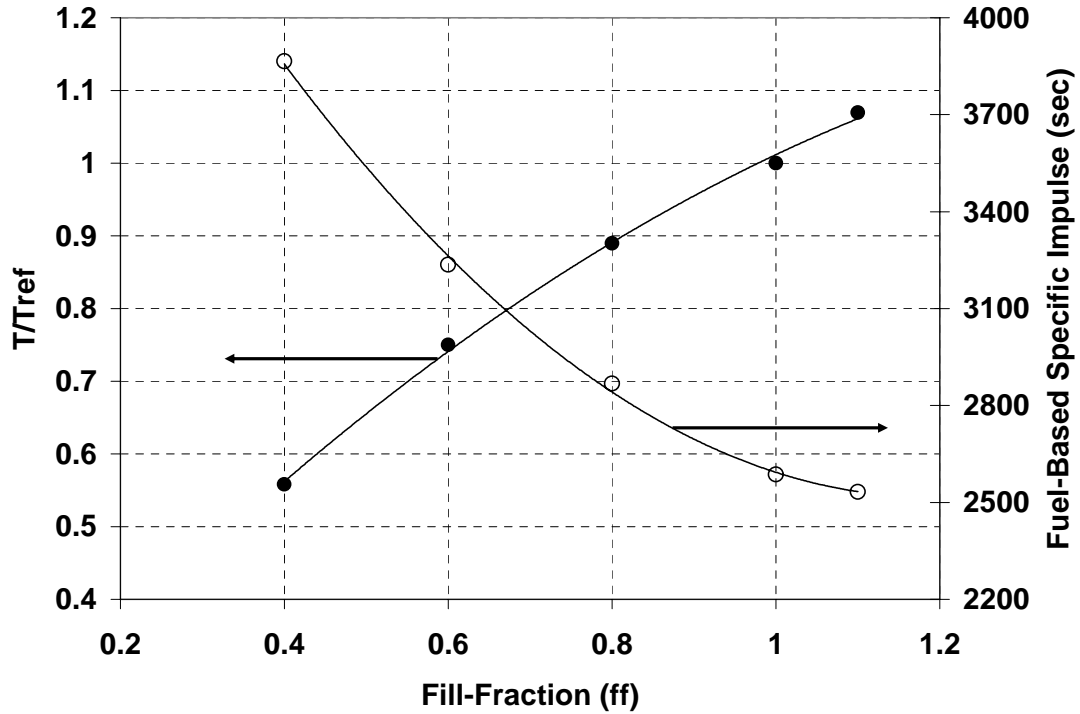


Figure 3: Baseline PDE Thrust and Fuel-Based Specific Impulse Variation with Fill-Fraction ($D_{PDE}=5.08$ cm, $T_{ref}=77$ N)

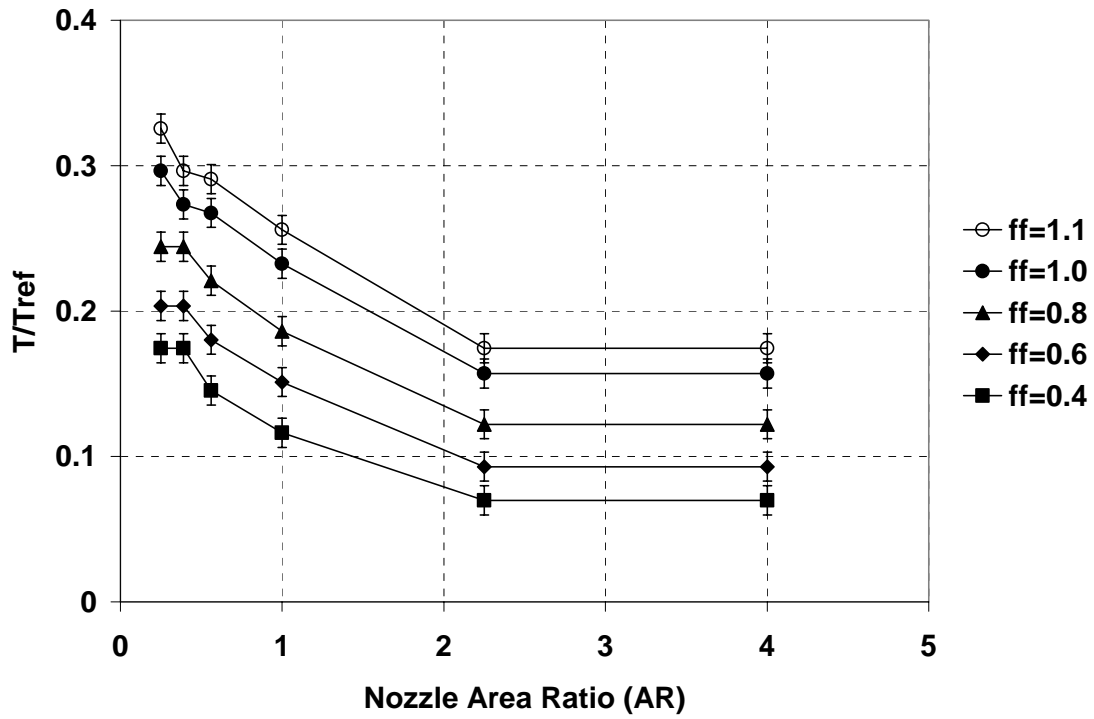


Figure 4: PDE Cold-Flow Thrust versus Exhaust Nozzle Area Ratio ($D_{PDE}=5.08$ cm, $T_{ref}=77$ N)

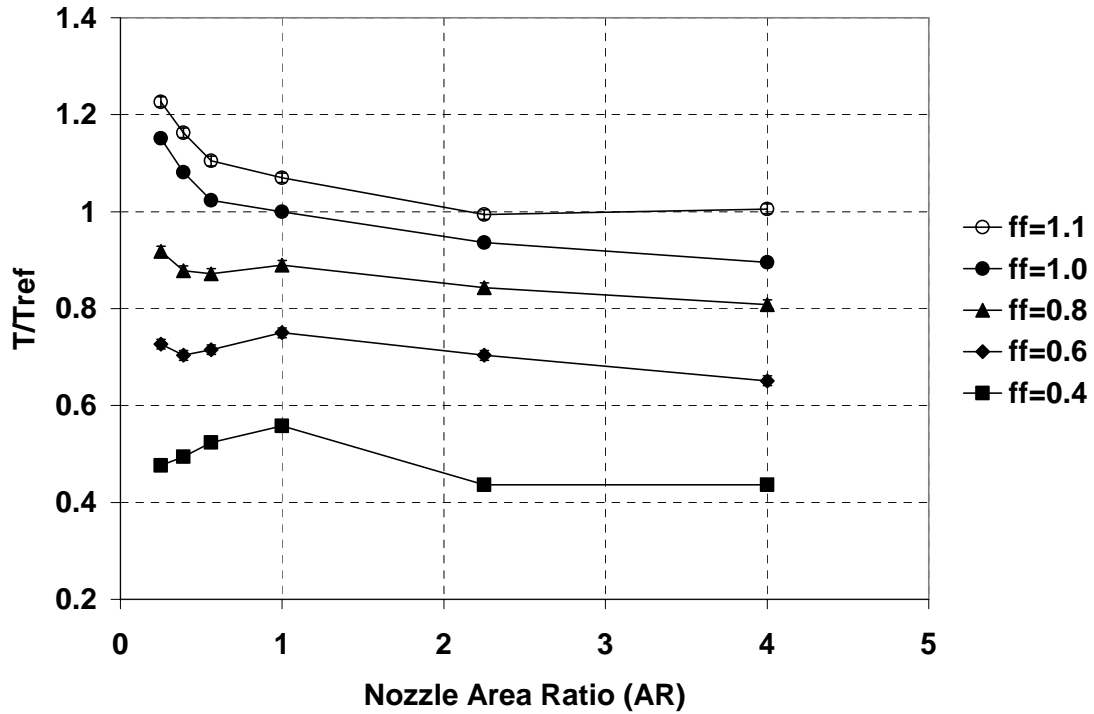


Figure 5: PDE Thrust versus Exhaust Nozzle Area Ratio ($D_{PDE}=5.08$ cm, $T_{ref}=77$ N)

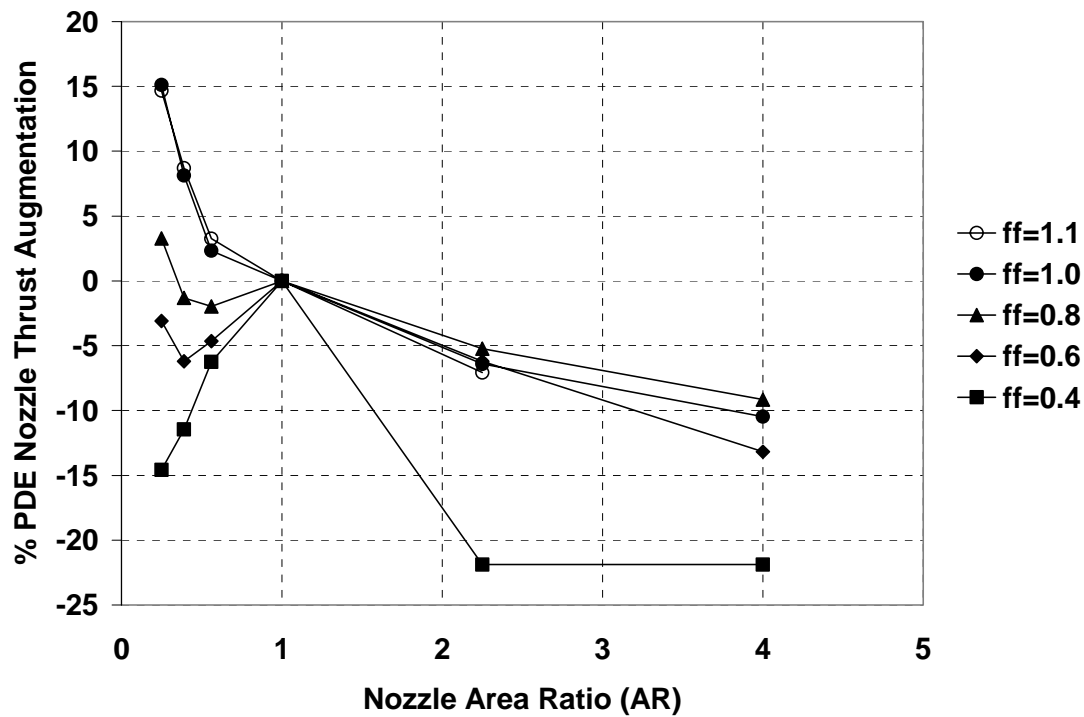


Figure 6: % PDE Nozzle Thrust Augmentation ($D_{PDE}=5.08$ cm)
(Values are Relative to the Baseline Thrust (AR=1.0) at the Corresponding Fill-Fraction)

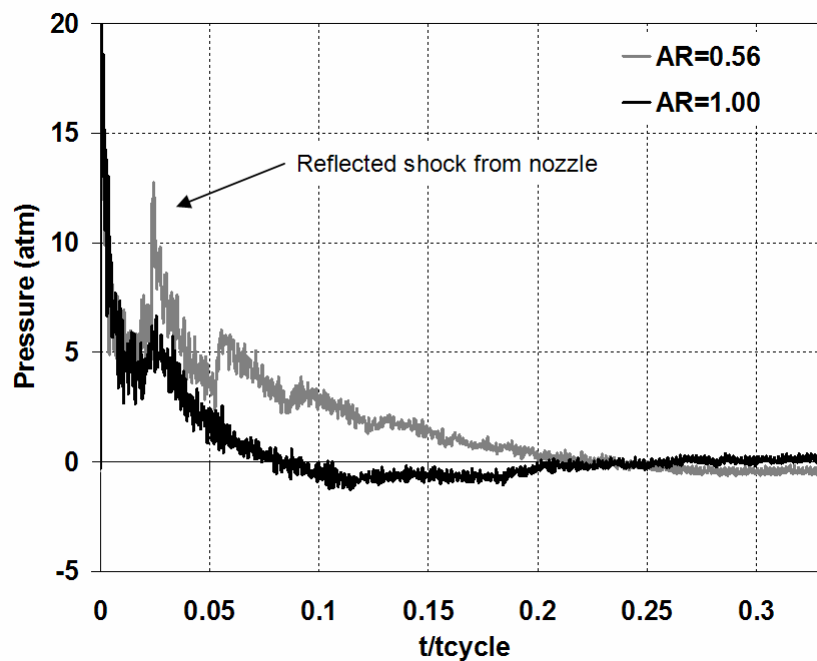


Figure 7: Pressure Time Traces for the Baseline and AR=0.56 Converging Nozzle
(ff=1.0, $t_{cycle}=0.033$ seconds)

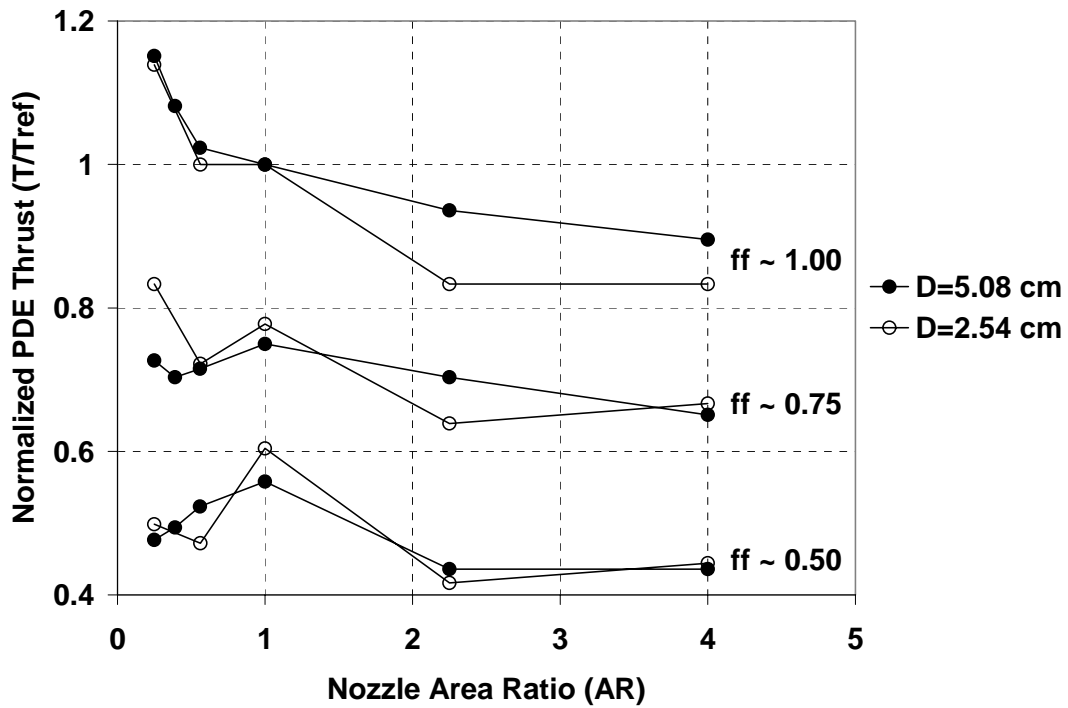


Figure 8: Normalization of PDE Thrust for Three Fill-Fractions ($D_{PDE}=2.54$ cm, $T_{ref}=16$ N & 5.08 cm, $T_{ref}=77$ N)

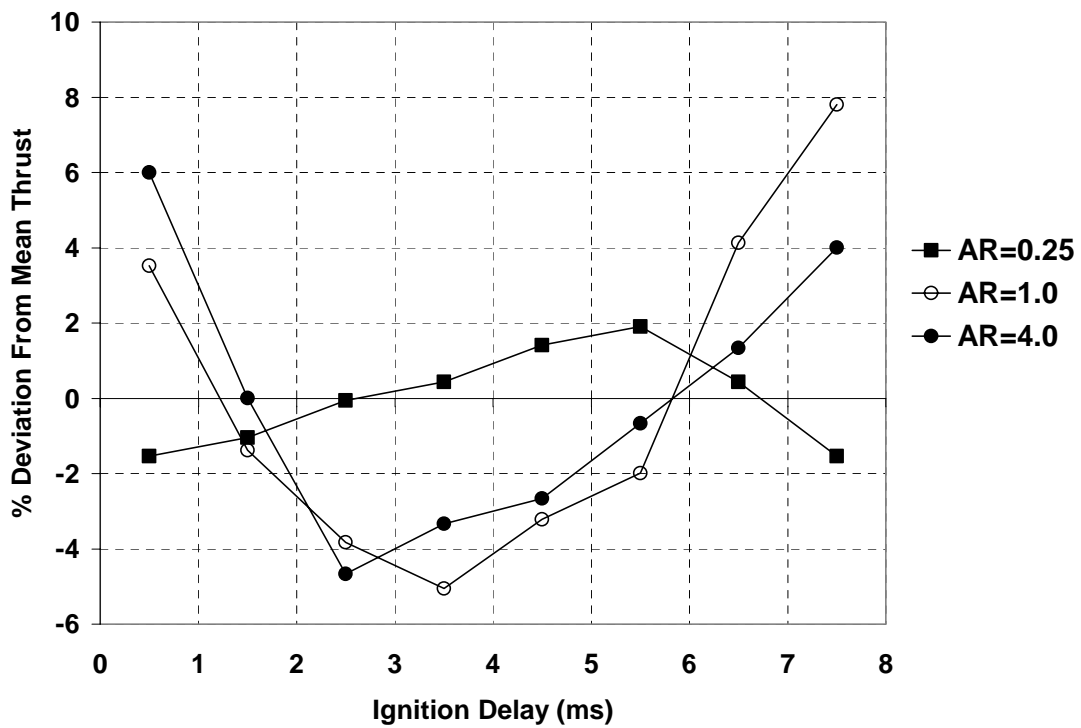


Figure 9: Variation in PDE Thrust with Ignition Delay ($D_{PDE}=5.08$ cm, $ff=1.0$)

Emissions Reduction Technologies for Military Gas Turbine Engines

G. J. Sturgess

Innovative Scientific Solutions, Inc., Dayton, Ohio 45440-3638

and

Joseph Zelina, Dale T. Shouse, and W. M. Roquemore

U.S. Air Force Research Laboratory, Wright–Patterson Air Force Base, Ohio 45433-7251



Geoffrey Sturgess is a founding member of Innovative Scientific Solutions, Inc. (ISSI), and has been in Dayton with ISSI for the last eight years. Before ISSI, he spent 23 years with Pratt and Whitney in East Hartford, Connecticut, and also worked at Parker-Hannifin in Cleveland, Ohio, and the Aircraft Engine Group of General Electric (GE) in Lynn, Massachusetts. He was recruited by GE in 1968 from England, where he was a research fellow on the faculty of Loughborough University after spending time with Rolls–Royce, plc., in both Bristol and Coventry, England, U.K. G. Sturgess was educated at Loughborough University, Loughborough, England, U.K., and Imperial College of Science and Technology, London. He currently lives in Maine, on beautiful Casco Bay. Sturgess is a Fellow of AIAA and has over 80 publications.



Joseph Zelina received his Ph.D. from the University of Dayton in 1995, where he conducted research at the U.S. Air Force Research Laboratory studying combustion processes and pollutant emission formation. He spent nearly six years at Honeywell Engines and Systems, formerly Allied Signal Engines, as principal engineer in the Combustion and Emissions Advanced Technology Group, where he was principal investigator for the NASA Advanced Subsonic Technology, NASA Ultra Efficient Engine Technology, and Department of Defense Joint Turbine Advanced Gas Generator combustor programs, and was principal investigator and program manager for several internally-funded research and development efforts including fuel injector coking, fuel spray laser diagnostics, and low-emissions combustor design programs. He has two patents and two patents pending on combustion system designs. Three years ago, he joined the U.S. Air Force Research Laboratory, Combustion Branch, as a senior combustion research engineer, where he leads the Ultra-Compact Combustor/Inter-Turbine Burner Research Program. J. Zelina is a Senior Member of AIAA.



Dale Shouse is a senior combustion research engineer in the Combustion Science Branch of the Turbine Engine Division. He is the director for in-house research and development activities for advanced military aircraft combustion systems. He participates on several integrated product teams and consults with various industry, university, and other government organizations on gas turbine combustion and augmentor programs. D. Shouse has 23 years experience in gas turbine engine research and development. He has a B.S. degree in mechanical engineering from the University of Dayton. He has published 29 technical papers including 5 journal articles and has received recognition for Best Applications Paper for Combustion and Fuels (1994 and 2001). D. Shouse has been the recipient of several U.S. Air Force Propulsion Directorate Awards for Engineer of the Year as well as the H. D. Heron Award. He holds several patents including one for the “Trapped Vortex Combustor.”



William M. (Mel) Roquemore serves as senior research scientist and independent researcher in the field of airbreathing combustion, diagnostics, and fuels technologies. He conceives, plans, and advocates major research and development activities; consults with the director of propulsion, division chiefs, and staff concerning the total reach program and results; monitors and guides the quality of scientific and technical resources; and provides expert technical consultation to other U.S. Air Force organizations, Department of Defense, and government agencies, universities, and industry. W. Roquemore entered federal service in 1963 and held a variety of technical leadership positions in airbreathing propulsion. He was appointed senior scientist, Combustion, in 2000. He is a Fellow of AIAA.

Future military gas turbine engines will have higher performance than current engines, resulting in increased compressor and combustor exit temperatures, combustor pressures, and fuel-air ratios with wider operating limits. These combustor characteristics suggest undesirable exhaust emission levels of nitrogen oxides and smoke at maximum power and higher carbon monoxide and unburned hydrocarbons at low power. To control emission levels while improving performance, durability and cost, requires major advances in combustor technology. Current emissions control approaches as applied to conventional swirl-stabilized combustors include rich- and lean-burn strategies, together with staged combustion. These approaches, even in fully developed form, may not be sufficient to satisfy the projected design requirements. Unconventional combustor configurations may become necessary. Different engine cycles other than the standard Brayton cycle may also be used for special applications in order to avoid the use of excessive combustion temperatures. The paper presents an overview of the currently utilized emissions control approaches, comparing their performances and likely potential for meeting future requirements. Experimental results are presented for two non-conventional combustor configurations that have shown promise for advanced engine applications. A brief discussion is offered on cycle changes that could result in lower peak temperatures while maintaining advanced performance.

Introduction

GLOBAL warming tends to excite the media and the public, via input from the various environmental groups. Global warming is, in fact, a major issue and is generally interpreted as extreme greenhouse warming of the atmosphere that leads eventually and progressively to catastrophic environmental consequences. Trace gases in the atmosphere play an important role in atmospheric equilibrium. They absorb infrared and ultraviolet radiation. The stored radiative energy increases the atmospheric temperature, which then influences the surface conditions. Because the trace gases are traces, their concentrations are easily changed by relatively small perturbations. Naturally occurring trace gases, which are also known as greenhouse gases because of their behavior, are carbon dioxide CO_2 , methane CH_4 , nitrous oxide N_2O , and water vapor H_2O . These gases are all increasing in the atmosphere. Industrial activity from fossil fuel burning is an undoubted contributor to these increases. Some of the introduced trace gases chemically affect the base-level trace gases through photo-chemical activity. The greenhouse effect, based on well-understood scientific principles, was predicted by Arrhenius (1859–1927) at the beginning of the 20th century. The role of industrial activity in global warming is highly controversial. Total human production of CO_2 is about 6 gigaton of carbon equivalent per year, and this is but a small fraction of the total exchanges of CO_2 occurring naturally each year between the oceans and the atmosphere, between vegetation and the atmosphere, and within the ocean itself and its biota. The observed rise in atmospheric CO_2 amounts to about one-half that of the estimated amount released due to total industrial activity. Nonetheless, CO_2 from industrial activity does contribute to the process. It is well-known that global temperatures are historically not constant. The Earth has been in a consistent warming trend since the end of the little ice age, 300 years ago, which predates the industrial revolution by 100 years. Northern hemisphere temperatures (a rolling 11-year average) since the little ice age correlate very well with the solar magnetic cycle length: The shorter the magnetic cycle, the more active and, hence, brighter the sun is.¹ The current length of the cycle is about 20–22 years. The radius of the sun also fluctuates sinusoidally with about an 80–100 year period. The solar variations observed are consistent and typical for stars similar in age and mass to the sun. The solar constant is in actuality, not a constant at all. The observed increases in atmospheric CO_2 during this period are entirely consistent with the oceans giving off dissolved gases as their temperatures increase. Therefore, although fossil fuel burning contributes to global warming, to an unknown but perhaps significant degree, it does not appear to be the root cause.

Each kilogram of jet fuel burned produces, on average, about 3.2 kg of CO_2 . Aviation is responsible for only 2 or 3% of the total due to human industrial activity. The best way to reduce CO_2 produced by aircraft is for aircraft to burn less fuel. Improvements in aircraft productivity and aerodynamic design, and in engine design, have reduced the fuel consumption per seat-kilometer for passenger aircraft by a factor of about 2.75 since the British Comet 1 introduced commercial jet transportation in the 1950s. Although the easy things have all been done, the downward trend in fuel consumption with

time is expected to continue, albeit at a reducing gradient. Therefore, CO_2 from aviation is not currently a prime concern given the natural levels in the Earth environment and its small contribution to the industrial activity total.

Transportation is responsible for most of the carbon monoxide CO, unburned hydrocarbons (UHCs), and oxides of nitrogen NOx introduced into the atmosphere through industrial activity. Although the aircraft contributions to the total transportation emissions of these pollutants are only very small (around 1%), unfortunately, they are concentrated at ground level around airfields and at altitude in well-defined flight corridors. The majority of the aircraft engine emissions are introduced into the 30–60° latitude band of the northern hemisphere, with the bulk of the emissions being introduced in the troposphere at 10–12 km altitude. Around airfields, these emissions contribute to smog formation; at altitude, there are a number of photochemical reactions taking place that have effects on the important trace gases. In addition, aviation fuels contain small quantities of sulphur (around 0.05% by mass) as impurities that are important contributors to fuel lubricity, which is very low. In the U.S. fuels the sulphur content has consistently increased over the last 20 years. At sea level, the sulphur appears in the engine exhaust as oxides of sulphur (SO_x that add to the smog issue); at altitude, based on airborne sampling by chase aircraft, the sulphur appears in the near-plume as sulphuric acid, H_2SO_4 (Refs. 2 and 3). There are clear indications that the resulting contrail formation, where the aerosols of H_2SO_4 /UHCs [or volatile organic compounds (VOCs)]/carbon particles found at high altitudes in persistent (3–18 h) aircraft exhaust plumes add substantially to the numbers of atmospheric microscopic particles. These serve as nucleation sites (10% increase in sites relative to out-of-plume) for water vapor and are affecting cirrus cloud formation along well-traveled flight corridors. The potential here is that increased cloud cover changes the Earth's albedo or reflectivity to solar radiation and, hence, affects atmospheric equilibrium.

The U.S. Environmental Protection Agency (EPA) has identified aircraft gas turbine engines as a significant emissions source and established regulations governing the emission of CO, UHCs, NOx, and smoke (47 Federal Register 58462). The EPA has amended the regulations by adopting the U.N. International Civil Aviation Organization (ICAO) regulations for CO and NOx (62 Federal Register 89). The amended regulations apply to commercial aircraft engines with rated thrust greater than 26.7 kN that are either newly certified or newly manufactured after 7 July 1997. The limits for gaseous emissions are expressed as integrated values around a defined landing and takeoff cycle for an engine operating at sea level on a standard day and, thus, govern emissions below 900-m altitude. The unit of measure is grams of pollutant per kilonewton of rated thrust, and the allowable maximum values are specific numbers for CO and UHCs, and for NOx they are expressed as a function of engine compression ratio. NOx is reported as nitrogen dioxide NO_2 corrected to 0.0063-lbm H_2O /lbm air specific humidity. UHCs are reported as methane CH_4 . Smoke limits are expressed in terms of an Aerospace Recommended Practices (ARP) smoke number, as a function of rated thrust. Because of the reduction

engines of the same type exhibit a degree of variability in performance, and because there is measurement uncertainty and repeatability to contend with as well as different atmospheric background levels and conditions, statistical compliance levels have been established. Over the years the limiting values for NO_x have been progressively lowered, and this continues, for example, committee on aviation environmental protection (CAEP)/4 rule (2004), with CAEP/6 and CAEP/8 to follow. For a summary of the status, see Ref. 4. Discussion is taking place concerning regulation for exhaust emissions at altitude.⁵ Although the regulations existing govern operations below 900 m in altitude, they also result in some inherent reduced emissions capabilities at altitude although they may not be optimized for those conditions. Furthermore, there are growing concerns over the particulates, which can be solid and liquid phase (VOCs), and their sizes that are associated with smoke. For these reasons, emissions control has become a major design requirement for combustors intended for commercial aircraft engines.

Although U.S. military aircraft are exempt from the EPA emissions standards governing commercial aircraft, there is a legal requirement currently applicable to military airbases that can impact military aircraft emissions. All Department of Defense bases must comply with the National Ambient Air Quality Standards (NAAQS) and State Implementation plans. Specifically, the military must comply with the general conformity requirement described in Section 176(c)(1) of the Clean Air Act, as implemented by the EPA in the General Conformity Rule (GCR). This requires that when a federal agency is proposing a new activity in nonattainment or maintenance areas, the agency must assure that the activity conforms to the State Implementation Plan, which documents the schedule and how the state will bring the region into conformity with the NAAQS.

Basing of future military aircraft systems may require emissions reductions to avoid deployment issues in areas of nonattainment. For a military airbase to comply with the GCR, the military must evaluate all emissions of the nonattainment pollutant from new stationary and mobile sources, including aircraft operating below 3000 ft and ships where appropriate. If the total amount of criteria pollutants [ozone, CO, or particulate matter (PM)] or precursors of ozone such as NO_x and VOCs exceeds the EPA established minimum levels, the military must demonstrate how they will conform to the State Implementation Plan for the area. Typically, the emissions from aircraft dominate the emissions from an active military airbase. In this situation, an airbase in a nonattainment region can have difficulties in deploying new aircraft systems and even transferring aircraft from one base to another. Commercial airports as communities must also comply with the NAAQS, although commercial aircraft movements themselves are exempt from the NAAQS.

Almost all of the emissions reductions technology extant has been developed specifically for the commercial engine market. Furthermore, it has been directed toward satisfying the ICAO landing/takeoff cycle emissions standards. Although lists of design requirements for aircraft gas turbine engine combustors for commercial and military applications would appear to be superficially similar, the emphasis, priorities, and parameter-values assigned to those lists would be quite different between the two applications. For these reasons, the suitability of various emissions reduction strategies for military applications is not equal in all cases. Nevertheless, although commercial and military aircraft can also have very different mission profiles, they can share general emissions reduction technologies in principle, provided appropriate balances are obtained between emissions reductions and operability issues. However, any commercially developed emissions strategy that is considered for military use has to be very carefully reviewed against the way that military aircraft are operated by the war-fighter. Under gun-to-gun combat conditions, aircraft maneuverability is paramount, with rapid high-gee, high-incidence turns taking place over wide ranges of altitude and subsonic speeds, with associated rapid and extreme throttle movements being normal. The combustion equipment must be robust enough to keep functioning perfectly at these conditions.

There follows a broad, yet necessarily brief, description concerning the development of current emissions reduction technology, its capabilities and limitations, and some advanced techniques that might offer further reductions in exhaust emissions. For the sake of brevity, the discussion is confined to the gaseous emissions of CO, UHCs, and NO_x only, except for where trades involving smoke are concerned. In addition to brevity, a reason for this decision is that visible smoke reduction technology is generally well understood. The recent concern over very small particulates (PM_{2.5s}) that visible smoke reduction technologies tend to produce and that exist as solids, liquids, and solids with liquid coatings, and that do not readily settle from the atmosphere is worthy of a separate study, as some passing remarks in the text suggest. Furthermore, the standard filter paper used in the ARP 1179 smoke test does pass dry particulates up to 117 nm in equivalent diameter. Because emissions reductions technology is largely considered to be company proprietary, the work presented is necessarily confined to material available in the open literature. Discussion is also limited to efforts of the two U.S. large engine manufacturers. This is not to imply that other sources have not contributed to the knowledge base. Small engine manufacturers, in particular, have a difficult time with respect to low-emissions combustor equipment because of obvious size limitations and the strong cost driver that they must live with.

Important Tradeoffs

Tradeoff in the area of emissions control can involve two types of trading: first, trades between the different emissions and second, trades between emissions and combustor performance. Both types of trading have been conducted at times to achieve overall emissions compliance. Ideally, any emissions control strategy should represent a true emissions reduction, that is, a simultaneous reduction for all gaseous and particulate emissions. Given the conflicting nature of emissions generation mechanisms at low and high engine power levels, it can be very difficult to reduce always simultaneously all emissions. Therefore, it is common to employ some form of limited trading between emissions. Extreme emissions trades, for example, reducing NO_x to very low levels at the expense of vastly increased CO, are not usually acceptable. Of course, the major trend of reducing fuel consumption, and hence CO₂ emissions, has been achieved by increasing engine overall pressure ratio and peak temperature ratio, along with increasing bypass ratio. These cycle changes make the NO_x problem more difficult. Therefore, there is an implicit trade that exists in modern engine design between CO₂ and NO_x emissions. Although NO_x is perceived as being more important than CO₂ in aircraft emissions, of course, economics also play the dominant role in the drive for reduced fuel burn.

Any component design changes incorporated for reasons of achieving low emissions must allow the combustion system to still satisfy the basic design requirements. However, once basic minimums have been satisfied, there are usually adequate margins for trading some combustor performance for improved emissions, provided that engine requirements are met. For example, it is not necessary to always achieve combustor lean blowout fuel/air ratios that are, for example, as low as 1/10th the minimum fuel/air ratio that the engine will ever experience.

Governing Philosophy

As already above successful emissions control usually involves two kinds of compromise and is, therefore, challenging. It encompasses considerations of initial control concepts, sensitivity determinations, and optimization of both emissions and performance behaviors. These necessary steps have to be considered together and not in isolation. Optimization requires sufficient understanding of the underlying chemistry and physics to allow formulation of some working hypotheses that frequently have to be bounded by engineering pragmatism. One constraint that has to be rigidly applied at all times is that safety should never be compromised.

Reacting flow behavior in combustors is governed by an elliptic set of simultaneous, nonlinear, second-order partial differential equations. The potential behavior of such an equation set implies that the fine details of the flow are important. Fortunately, there is always sufficient generality at an engineering working level such that, with care, useful guidance can be obtained to make low-emissions approaches both possible and portable from engine-to-engine designs.

Control Approaches

Approaches to control emissions can be divided into two broad types: 1) those approaches that may be applied to conventional-appearing combustors and 2) those approaches that result in nonconventional-appearing combustors. Under each type of reduced- or low-emissions combustor, control strategies can be grouped into general categories. For conventional-appearing combustors, the general categories have been separated into those affecting CO and UHCs and those affecting emissions of NO_x. For unconventional-appearing combustors, the general categories have been separated for convenience by geometric appearance. Regulatory compliance is requiring movement to emissions levels so low that conventional-appearing combustors are unlikely to be satisfactory for the long term.

Control Approaches for Conventional Combustors

Stoichiometry Adjustments for Reduced CO and UHC

Well-stirred reactor (WSR) studies with vaporized or gaseous hydrocarbon/air mixtures demonstrate the following for CO (Ref. 6): For short-residence times and/or low reactant temperatures, CO emissions will be high due to incomplete combustion. For very high temperatures, CO emissions will be high due to dissociation of carbon dioxide. Heavier fuels (high carbon numbers) will have higher CO emissions at given reactor temperature. For short-residence times and low reactor temperatures, UHC emissions will be high due to incomplete combustion. Heavier fuels will have higher UHC emissions at given reactor temperature.

This WSR behavior, which is reaction rate dominated, appears to be paralleled in engines. CO and UHC are predominantly generated at low engine power levels, when significant quantities of both can be evident at idle power settings. Oxidation of CO by the OH radical is an important but relatively slow reaction. It can go to completion if sufficient time is allowed for the conversion, or if the reaction is accelerated. It has been shown⁷ that for earlier engines high-idle power levels of CO in the exhaust were due to insufficient residence time. The design trend toward smaller length combustors⁸ obviates the increased residence time approach. The chemical reaction can be accelerated by raising the concentrations of the reactants, by increasing the temperature of the reactants, and by increasing the reaction pressure, according to the well-known Arrhenius reaction rate expression.

Modern gas turbines tend to idle at higher air pressures and, therefore, also higher air temperatures than did earlier engines. Hence, combustion conditions at low engine powers are slightly more favorable than they used to be. Note, however, that modern engines are unlikely to idle at the 7% power setting that forms a state-point in the ICAO emissions parameters; lower values of 3–5% are more typical. The most dramatic reductions in CO emissions have been achieved by increasing the idle-power bulk equivalence ratio in the primary zone of the combustor, where the flame is held. This is shown in Fig. 1 for an engine operating at idle power.⁹ In Fig. 1, two idle overall fuel/air ratio (OFAR) settings of 0.0126 and 0.0112 are shown, together with variation in the primary zone bulk equivalence ratio. The increase of primary zone bulk equivalence ratio increases the amount of fuel that is burned at and around the stoichiometric value due to fuel/air unmixedness effects.¹⁰ Therefore, the bulk flame temperatures are increased, resulting in the observed improvements in combustion efficiency, which implies reduced CO.

However, it is not immediately clear whether the observed effects in Fig. 1 are truly chemical in origin. Characteristic time studies have been conducted¹¹ for engine primary zones at idle-power conditions, which relate the characteristic time τ ratios for fuel vaporization to CO consumption, fuel/air mixing rates to CO consumption, and

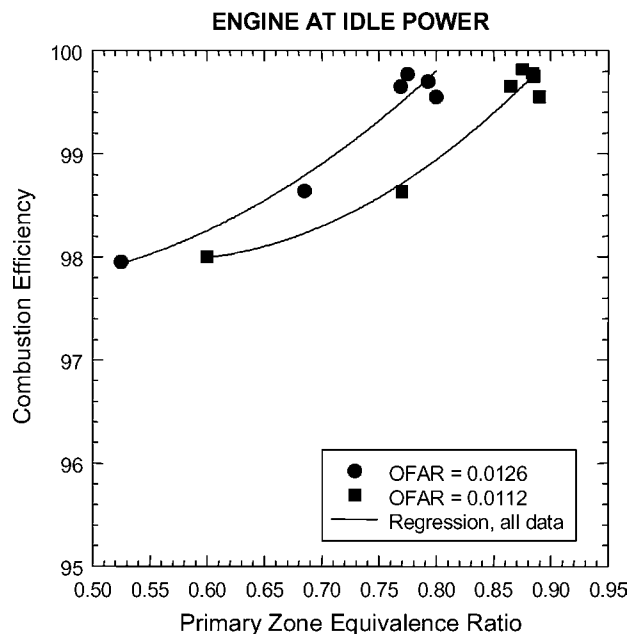


Fig. 1 Effect of primary zone equivalence ratio on combustion efficiency; engine at idle power.

fuel/air mixing rates to fuel evaporation rates. Individual characteristic times may be estimated by the methods of Washam and Mellor.¹² Comparison of the resulting ratios, $\tau_{\text{evap}}/\tau_{\text{CO}} = 1.75$, $\tau_{\text{mix}}/\tau_{\text{CO}} = 3.75$, and $\tau_{\text{mix}}/\tau_{\text{evap}} = 2.14$, shows that CO emissions are physically controlled, in order, by the degree of liquid fuel atomization (because evaporation rate depends on atomization and atomization itself is a very fast process, occurring in typically 10^{-5} s), fuel evaporation, and fuel vapor/air mixing. The behavior shown in Fig. 1 can, therefore, be explained primarily in terms of the increased temperatures resulting in improved evaporation rates of the liquid fuel spray.

The physical nature of CO emissions at low powers suggests that they might be reduced by improving liquid fuel spray evaporation rates through enhanced atomization and by intensifying fuel vapor/air mixing rates. In practice, such steps are difficult to accomplish in a viable fashion. Raising the air pressure drop across the combustor can increase air turbulence; however, high air pressure drop has an adverse impact on engine specific fuel consumption. Atomization from pressure atomizers can be improved by increasing the fuel pressure drop across them at given flow rate, that is, decreasing the injector flow number. However, fuel pump technology has not kept pace with the increased overall pressure ratios (OPRs) of modern engines sufficiently to permit this, even with dual-orifice injectors. Furthermore, the increase in combustor OFARs for improved engine thermal efficiency and higher specific thrust increases the ratio of maximum-to-minimum fuel flow rates (turn-down ratio), which increases the difficulty of pumping hot, low-lubricity fuel. Airblast atomizers can benefit from an increased air pressure drop across the combustor, but again, this adversely impacts engine performance. Atomization and fuel/air mixing can be enhanced by increasing the number of fuel injection points into the combustor. Unfortunately, this increases engine cost and must be done without reducing the individual fuel passage sizes to levels where internal coke formation arising from thermal degradation of the liquid fuel becomes a problem. For these reasons, adjustment of the primary zone bulk equivalence ratio at idle power conditions remains the most powerful tool for control of CO emissions in conventional combustors.

Recirculation Zone Changes for Reduced UHCs

Characteristic time studies relating the rates of CO consumption to hydrocarbon consumption times as a function of primary zone bulk equivalence ratio at idle power conditions show that, chemically, hydrocarbon consumption is tens of times faster than CO

consumption.¹¹ Therefore, for relatively high primary zone equivalence ratios at idle, there should be an insignificant emission of UHCs. WSR studies⁶ support this experimentally. This behavior was not at all the case in earlier engines, where the emission indices (EI) (grams pollutant per kilogram fuel burned) of CO and UHCs were comparable. Again, this suggests some physical control of UHC emissions.

Figure 2 shows the EI of UHC plotted against the EI of CO for several different engines along engine operating lines. The engines are both large and small and are by different manufacturers. Note that the different engines have similar characteristics where, as engine power level is increased from idle [upper right-hand side (RHS) of Fig. 2], the EI of CO and UHC decrease exponentially together at first as the combustion environments increase in pressure and temperature. However, at some point, CO continues to decrease but UHC emissions remain fixed at a plateau level. From a chemical standpoint, this behavior is counterintuitive because CO is derived from reaction of hydrocarbons and CO consumption is much slower than hydrocarbon consumption and, again, supports the idea of some physical control of UHC emissions.

For reasons associated with the recirculation flow patterns contained within the combustor primary zone, liquid fuel injection systems have traditionally been designed to provide a near-90-deg hollow-cone spray angle, as shown in Fig. 3. Liquid fuel droplets can be seen in the flame structures, which are illuminated with a green laser beam.¹³ The upper and lower edges Fig. 3 represent the

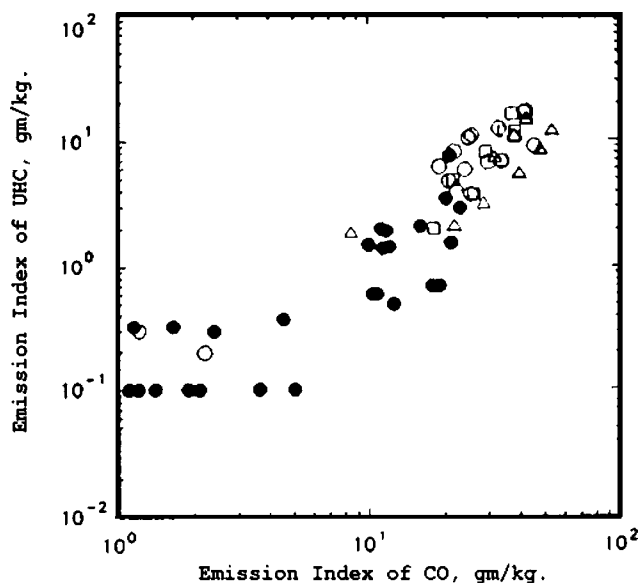


Fig. 2 Relationship between CO and UHC emissions for several engines down an engine operating line.

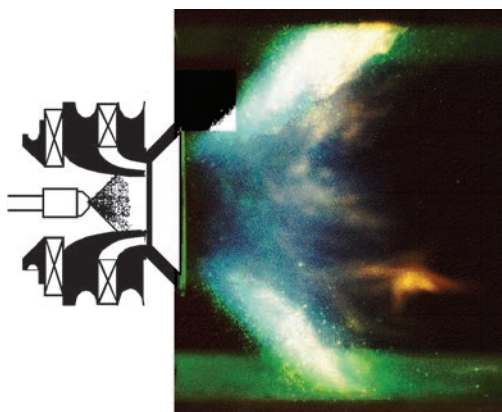


Fig. 3 Laser-illuminated photograph of 90-deg hollow-cone liquid fuel spray in model combustor primary zone.

edges of the optical access in the combustor and not the combustor liners, which are just out of view. However, it can be appreciated that liquid fuel droplets, fuel vapor, and partially reacted fuel vapor in the narrow shear layers of the 90-deg conical spray do reach the combustor liners at the low engine power conditions. On the surfaces of the combustor liners are relatively low-temperature cooling air films to protect the liners from thermal damage. The cooling films entrain and trap the liquid fuel, fuel vapor, and partially reacted fuel vapor. These entrained materials become chemically frozen in the relatively cool cooling air and are progressively diluted with each subsequent addition of cooling air along the liner surface. The chemically frozen constituents exit the combustor along with the cooling air without mixing in again with the hot mainstream. This is primarily the origin of UHC emissions at low engine power levels and is the reason for the behavior seen in Fig. 2.

Elimination of liner film cooling would largely solve the UHC problem at low engine power, and this technique is used in industrial gas turbines for power-generation burning gaseous fuels where high exterior convective air velocities and extended surfaces to enhance heat transfer are used. The combination of operating conditions with a high radiative heat load in aircraft gas turbines is such that reliance on combustor external cooling is not presently viable under most circumstances. Typical combustor liner cooling schemes used to use about 30–35% of the total combustor airflow, W_{AB} . Advanced cooling schemes, such as Pratt and Whitney's FloatwallTM, together with advanced materials, such as cast turbine alloys and single crystals, can reduce the cooling airflow down to 20–25% W_{AB} with excellent durability. Multihole cooling schemes bring manufacturing cost reductions and excellent durability for about 22% W_{AB} . The introduction of new molybdenum-based alloys together with the multihole approach could bring cooling down to 20% W_{AB} or less. Thermal barrier coatings (TBCs) can be used to advantage with all of these schemes. TBCs in aged condition, are worth about 100°F in liner temperature. Although these represent very useful reductions in cooling air, they are not sufficient of themselves to significantly reduce UHCs.

The root cause of the difficulty, which is one of fuel entrainment into the dome and liner cooling air films, is associated with the conventional recirculation zone traditionally used for flame stabilization in the primary zone.¹⁴ As can be seen from Figs. 3 and 4a, when used with a 90-deg spray angle fuel injector, this flow pattern directs raw fuel straight into the combustor liner wall region. These difficulties can be addressed by turning the conventional recirculation zone inside out in the manner of Fig. 4b.

The flow patterns of the inside-out recirculation were based on visualizations made in a water analogy rig. The inside-out recirculation can be achieved through a combination of two means: first, using an airblast atomizer fuel injector of modest air-swirl angle and with air passages that converge on the injector tip centerline and second, using a combustor dome within which the two-phase discharge from the fuel injectors experiences an immediate and significant sudden expansion on entering the combustor. The swirling discharge from the injectors maintains its coherence for a significant distance into the combustor. Eventually, the combination of swirl and entrainment demands cause large exterior recirculations to develop around and between individual injector discharges. Small recirculations internal to the swirling jet flow are developed under the combined influences of vortex bursting and the backpressure effects of the penetrating transverse combustion air jets from the liners. The position of the combustion air ports is a little farther downstream than is usual to facilitate the initial coherence of the fuel/air jet from the injector. As shown in Fig. 4b, there is a flow conflict between the large outer recirculation zones developed around the swirling jet and the dome and primary zone liner film cooling air. To optimize the flow patterns, the cooling air films in the dome and primary zone could be reversed in direction¹⁵ so that shear is reduced and recirculation strengthened.

Figure 5a shows the flame structure for an inside-out recirculation at lower power levels (injector equivalence ratios less than unity) by natural light, in the same model combustor as in Fig. 3. It can be seen that the flame is confined to the central portion of the

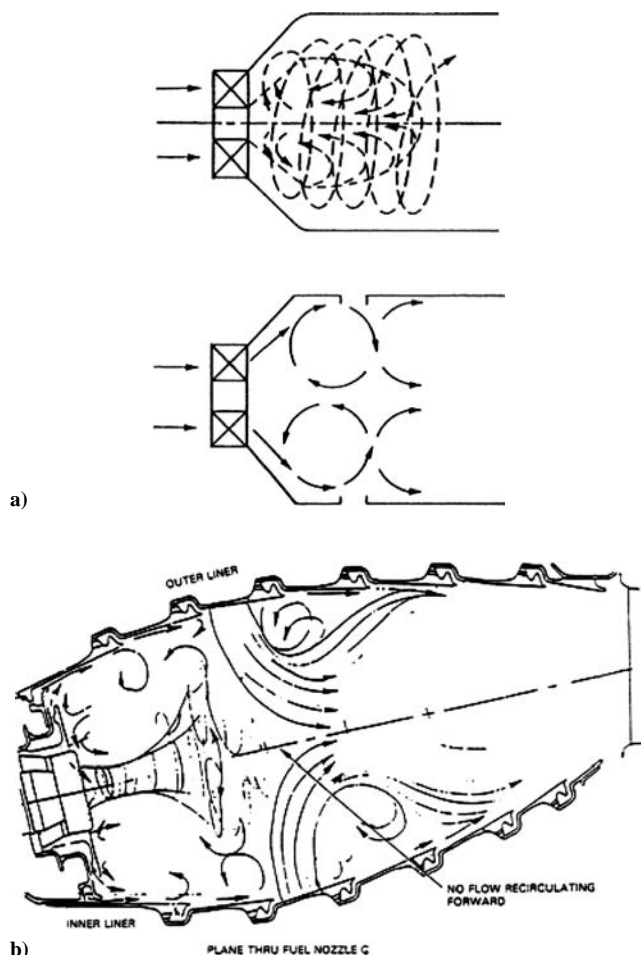


Fig. 4 Comparison of recirculation zones: a) conventional and b) inside out.

combustor. Flame holding is provided by means of a very small central recirculation zone [not visible here but shown by laser Doppler velocimetry (LDV) measurements] and large corner recirculation zones formed between the combustor dome, the liners, and the central flames and between the dome and adjacent fuel injectors.^{16,17} Composite planar laser-induced fluorescence (PLIF) images of OH (Fig. 5b) indicate regions of heat release and show that very little reaction takes place in flow that is recirculated to the liners and back into the dome for injector equivalence ratios that are less than unity, which is typical of idle power values. Separate laser doppler velocimetry LDV and coherent anti-stokes Raman spectroscopy (CARS) measurements revealed the recirculation patterns, which were similar to those shown in Fig. 4b.

The UHC engine emissions for a combustor having an inside-out recirculation zone and an advanced cooling scheme are compared in Fig. 6 with those for an engine having a conventional combustor design. The engine power level is represented by means of the compressor exit air temperatures, which essentially correspond to the temperature of the cooling air introduced onto the liner surfaces. It can be seen that, for the same operating conditions, the inside-out recirculation zone in the primary zone yields significantly lower UHCs. It can be shown that the major contribution of the UHC reduction is due to the recirculation zone changes.

A reasonable concern for the inside-out recirculation zone is that the concentration of fuel in the coherent swirling jet and the initial region of the bursting vortex might result in the generation of large amounts of CO from locally overrich mixtures. This possible tendency would be exacerbated by the selection of a relatively high (but less than unity) primary zone equivalence ratio at idle to speed liquid fuel droplet evaporation rates through high flame temperatures. Experience shows that this is not the case due to burn-up of CO in the intermediate zone of the combustor. CO levels were about half

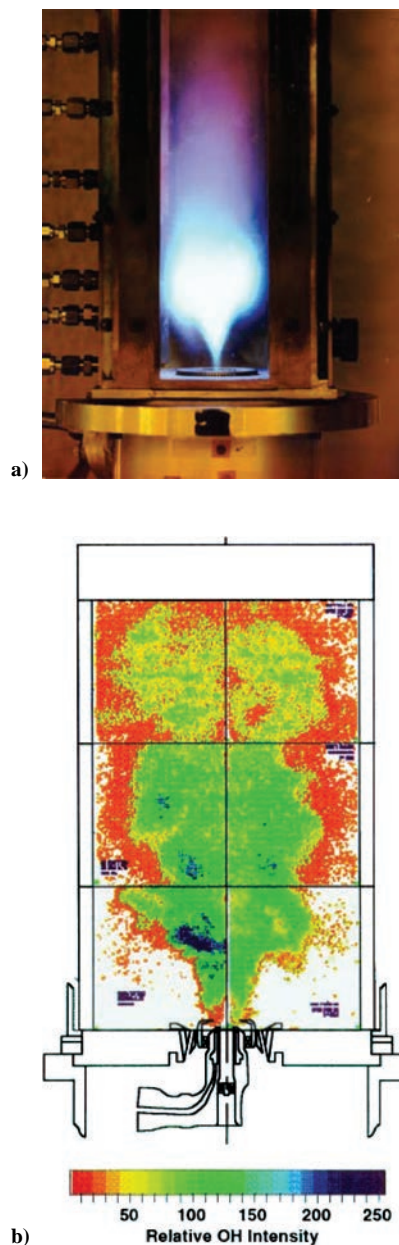


Fig. 5 Inside-out recirculation zone: a) natural light flame photograph and b) PLIF OH image.

those for a conventional recirculation zone. Of course, it is essential to ensure that the design of the intermediate zone is suitable to achieve the necessary CO burn-up. This involves appropriate selection of intermediate zone bulk temperature, mean residence time, and intermediate air jet patterns. For example, a suitable intermediate zone length of one-half a dome height and a mean equivalence ratio on 0.6 might represent appropriate values.

Similarly, the potential for locally overrich fuel/air mixtures due to the inside-out recirculation pattern, together with the use of high primary zone equivalence ratios at idle power, suggests a propensity for excess smoke generation at high-power levels. This is a genuine concern that is addressed by the introduction of very small quantities of smoke control air in close proximity to the fuel sources. However, UHC emissions may then rise at low power if significant quantities of relatively cool compressor air are introduced directly into the flame region. The chilling effects of such air can exert a powerful influence on local reaction rates that is reflected in a sharp increase in UHC emissions. This is shown in Fig. 7, which shows the UHC emissions at idle power for an inside-out recirculation zone as a function of the sum of injector and smoke control air. The UHC curve is essentially the reciprocal of the high-power smoke curve

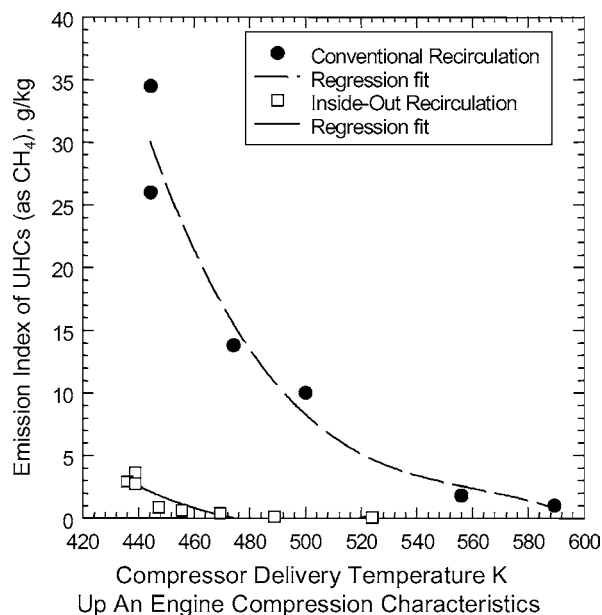


Fig. 6 Comparison of UHC emissions for conventional and inside-out recirculation zones.

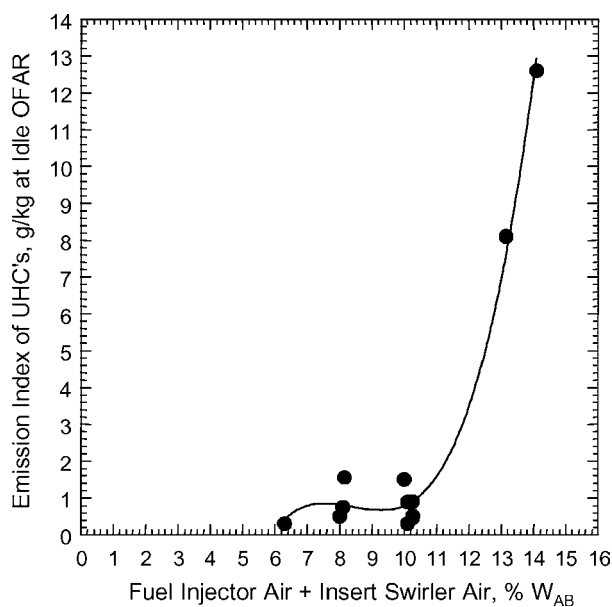


Fig. 7 Effect on UHC emissions of air injection into flame at idle power; PW experimental JT9D-70A engine.

for this engine. It arises because excess air introduced in this fashion results in a dome equivalence ratio that is too low; minimum UHC emissions were achieved when the dome equivalence ratio was unity. The UHC emission was relatively insensitive to the direction of the swirl of the smoke control air. With this type of arrangement, peak exhaust smoke is attained before maximum power. This is due to smoke particle burn-up immediately downstream of the inside-out recirculation zone when sufficiently high gas temperatures are reached.

By the means described, a favorable balance between low-power emission of CO and UHC and high-power smoke can be obtained. This forms an example of the interemission trading that was referred to earlier. The strategy proved portable engine-to-engine and was even more effective when used in conjunction with advanced liner cooling schemes.

Adjustments of Time/Temperature History for Reduced NO_x

Large amounts of NO_x are produced at high engine power levels, and at the engine exhaust, the NO_x consists mainly of nitric oxide, NO. Characteristic time studies¹¹ at engine conditions relating NO generation of hydrocarbon consumption illustrate clearly that NO is a postflame phenomenon for all ranges of likely equivalence ratio. These studies also show that NO generation is a slightly faster chemical process than is CO consumption, and hence, trade-offs between NO and CO will exist. WSR experiments⁶ confirm that NO emissions will be high for long-residence times and/or high reactor temperatures. Thermal NO, produced by the extended Zeldovich-Lavoie mechanism, which represents oxidation of atmospheric nitrogen, is a postflame phenomenon that is time-at-temperature driven. Therefore, early attempts at NO_x control aimed to cut both time and temperature by any means available.

Simply shortening the combustor can reduce the residence time. However, significant reductions in NO_x require significant reductions in residence time. Typically, a 60% reduction in primary zone residence time only results in about a 40% reduction in NO_x (Ref. 11). Unfortunately, at the greatest reductions in residence time, the combustion efficiency has also fallen dramatically to levels considerably less than 90%, and flame stability is seriously impaired.

NO is only sparingly soluble in water. Water, however, has a significant latent heat of vaporization and, therefore, offers an effective means of reducing flame temperatures, especially if it is introduced close to the fuel source.¹⁴ Injection of water equal to about 3% W_{AB} will reduce NO_x by 80% (Ref. 11). Figure 8 shows the NO_x reduction where the water is expressed in terms of the combustor airflow, and it can be seen that worthwhile NO_x reduction requires a water flow that is comparable to the fuel flow, as well as that CO emissions can be increased. However, this represents a considerable quantity of

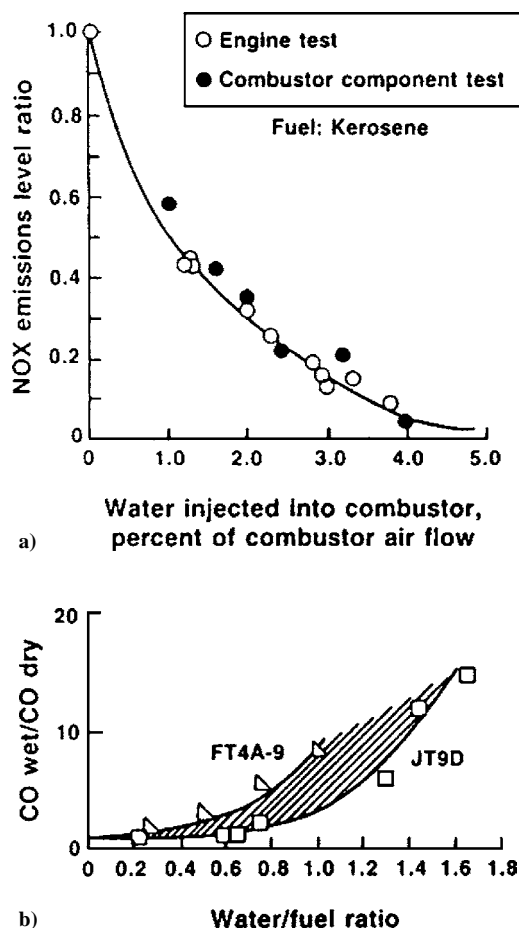


Fig. 8 Water injection into conventional combustor primary zones: a) NO_x reduction and b) CO increases.

water so that the technique would only be used on takeoff and initial climb-out. Therefore, there would be no NO_x control at altitude due to water injection. The water quality would have to be boiler-feed standard to avoid scale fouling of the turbine cooling system. The mass addition of the water can provide worthwhile engine thrust augmentation, which can be helpful for hot day, high-altitude take-offs. After the water has been injected the water tanks, distribution pipes and controls represent an increase in aircraft deadweight.

Quasi-Staged Rich–Quench–Lean Combustion for Reduced NO_x

Use of an elevated combustor primary zone equivalence ratio in the range of 0.8–0.9 at engine idle to minimize low-power CO emissions allows advantage to be taken of the reduced flame temperatures at high power that result from over-stoichiometric combustion. This over-stoichiometric primary zone behavior arises because of the fixed geometry of the conventional combustor,¹⁸ where there is a linear relationship between primary zone equivalence ratio and OFAR. A primary zone equivalence ratio set to around 0.8 at idle results in a value between 1.5 and 2.0 at takeoff with typical turndown ratios. Rich burning at takeoff suppresses the peak NO_x emissions attained. The efficacy of the approach is limited by fuel/air unmixedness effects, by the existence of stoichiometric interfaces, and by the onset of excess exhaust smoke. The first of these limitations is demonstrated in Fig. 9.⁷ Mixing studies¹⁰ indicate that there is little benefit of operating with initial burning zone (IBZ) equivalence ratios in excess of about 1.4.

The process was originally thought of simply as another time vs temperature control technique. However, general acceptance of the Fenimore prompt-NO process¹⁹ modified the view of the concept. Combustion at high temperatures in an oxygen-deficient atmosphere results in atmospheric nitrogen reacting preferentially with hydrocarbon fragments produced by fuel-cracking reactions. Subsequent reaction of these modified fragments that now contain chemically bound nitrogen, very efficiently and rapidly produces NO. This secondary reaction usually takes place in a fuel-lean atmosphere. For this reason the process is labeled as rich–quench–lean (RQL) burning and is given a separate category.

With fuel-rich burning in the primary zone, unburned fuel (as lower hydrocarbons containing bound nitrogen, soot, and CO) will enter the intermediate zone [or secondary burning zone (SBZ)] of the combustor, even with 100% oxygen consumption efficiency in the IBZ. The duty of the SBZ, therefore, undergoes a shift in emphasis. Its primary role shifts from CO burn-up at low powers and high-altitude cruise conditions²⁰ to CO, UHC, and soot consumption at high power. To complete this combustion process, the SBZ will operate fuel lean. To accomplish its expanded function, the combustion air jet array feeding the SBZ has to provide adequate

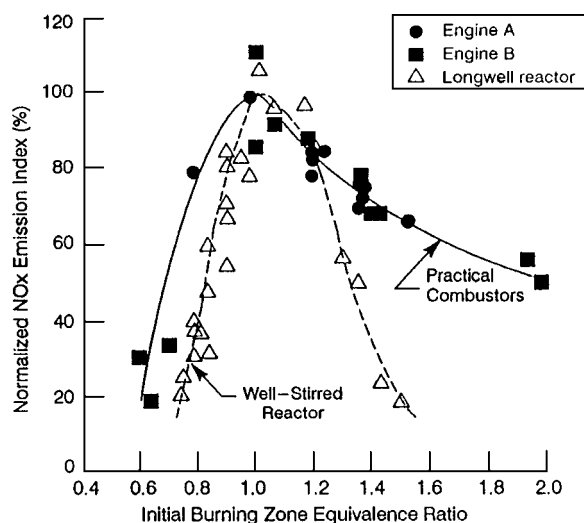


Fig. 9 Effects of primary zone (or IBZ) equivalence ratio on normalized NO_x emissions.

flame holding capability to confer satisfactory static stability on the combustor. The transverse air jet array then becomes the major source of NO_x generation due to the burn-up of the fuel fragments with their bound nitrogen, which produces in-flame NO and, subsequently, postflame NO through the Zeldovich–Lavoie mechanism. This is shown in Fig. 10 for a model combustor,²¹ where the pairs of air jets of equal and various diameters are opposed to each other and are positioned with a pair of jets placed inline with the fuel injector. Burning takes place around the jets and over the recirculation zone formed by their convergence, on the centerline of the combustor.

Design maps for this RQL approach as implemented in a conventional combustor geometry can be produced⁷ that link relative NO_x and IBZ and SBZ equivalence ratios. As an example, from such a map an engine operating with an IBZ equivalence ratio of 1.5 would have 50% of the NO_x of a conventional combustor of the same residence time if the SBZ had an equivalence ratio of 0.35. Figure 11 shows the measured NO_x reduction achieved in an engine with this simple type of RQL compared to the conventional combustor for the engine; engine power level is represented by combustor OFAR.

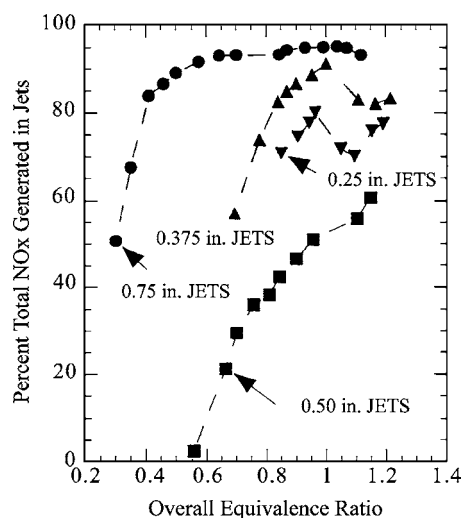


Fig. 10 Demonstration in model combustor of jet contribution to NO_x for lean SBZ with rich IBZ.

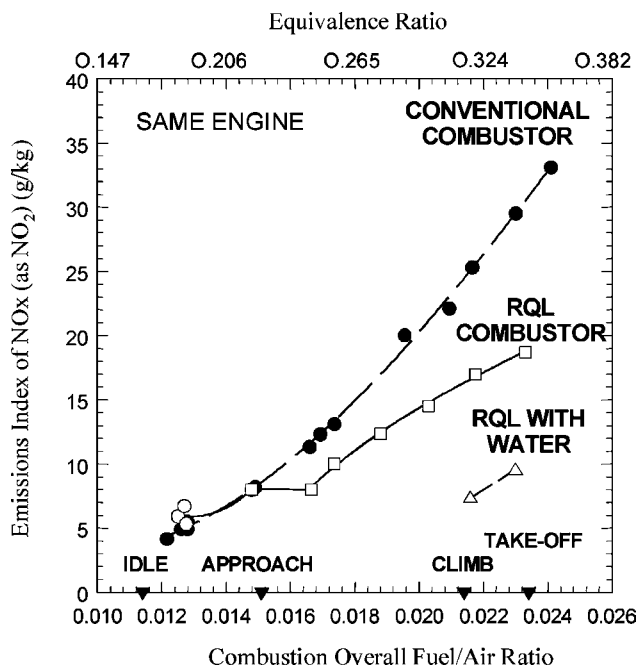


Fig. 11 Engine measured NO_x reductions with simple RQL combustor and with water injection.

It can be seen that with the RQL, NO_x at idle is increased slightly, and this reflects the elevated equivalence ratio for enhanced combustion efficiency. Noteworthy is the clear hesitation in NO_x around the approach power level, where NO_x remains fixed although engine power is increased. This hesitation is due to the IBZ reaching and then just exceeding unity equivalence ratio, where unmixedness suppresses NO_x and where the unburned fuel quantities entering the SBZ are low, giving very low equivalence ratios and, hence, a negligible SBZ NO_x contribution. This hesitation is in some respects similar to fuel staging, hence the use of the term quasi staging in the heading. It represents a form of axial staging and was dubbed quasi staging to distinguish it from mechanical axial staging, which is to be discussed later. At higher power levels, more and more unburned fuel leaves the increasingly richer IBZ. Mean equivalence ratios in the IBZ, therefore, increase, and IBZ NO_x starts to dominate total NO_x production. Further increases in power setting give an increase in NO_x. However, note that the NO_x curve for the conventional combustor is slightly but definitely concave upward whereas that for the RQL combustor is slightly but definitely concave downward. This behavior of the two curves results in a favorable divergence in NO_x for the RQL combustor as the engine power increases. This characteristic is due to fuel/air unmixedness effects in the IBZ as its equivalence ratio increases. Eventually, however, at higher power levels than those shown, the IBZ would in turn become stoichiometric, resulting in another NO_x hesitation until NO_x due to burning in the combustor dilution zone becomes dominant. Therefore, if smoke controllability limits the maximum IBZ equivalence ratio that can be used, then the RQL control approach is apparently limited in maximum OFAR capability.

As a matter of interest, this RQL realization was also evaluated with water injection (Fig. 11). The combination achieves a NO_x reduction at takeoff power (to the same OFAR) of 60%. The water in this instance was introduced in an expedient fashion and was not optimized in any way. NO_x along an operating line with water injection would follow the RQL curve until climb. At climb, water injection is turned on and NO_x drops instantaneously to the water curve, which is then followed through takeoff power.

Control Approaches for Unconventional Combustors

Optimized RQL

There are two major difficulties with the RQL as described for conventional combustors. These are 1) the necessary provision of liner cooling resulting in the formation of stoichiometric interfaces in the IBZ and 2) slow mixing rates resulting in the formation of stoichiometric interfaces around the transverse air jets in the SBZ. These two sets of stoichiometric interfaces are responsible for the generation of excess NO_x. Addressing these issues results in a combustor that is unconventional in appearance.

As part of NASA's now canceled high-speed civil transport (HSCT) program, Pratt and Whitney produced an optimized RQL combustor design²² that was functionally similar to that described earlier and embodied two burning zones in series while addressing the issues efficiently. The fuel-rich IBZ of the design was externally cooled via a closely fitting shroud to provide high convective cooling velocities. The convective cooling air for the IBZ, having completed its cooling task, then formed the quench air jets necessary to lower the bulk equivalence ratio to fuel lean for the SBZ. The quench air jets were introduced in a reduced cross-sectional area mixing section that was additional to the nonoptimized RQL configuration. The reduced flow area, together with the mass addition of the quench air, accelerated the internal gas flow to high velocities in an attempt to prevent burning from taking place in the mixing section. The SBZ was a short dump combustor immediately following the mixing section.

Several complications were encountered during development of this combustor. The best overall mixing for a quench section is provided with an optimum jet momentum flux for opposed jets that precludes direct jet impact. Therefore, it was extremely difficult to avoid a situation where, before mixing was complete, stoichiometric flames formed around the entering quench air jets. The high temperature of the spent cooling air forming the quench jets exacerbated this tendency.

In an attempt to address this issue, Pratt and Whitney introduced a can-annular configuration, where the IBZ was made up of 12 individual circular cross section cans, each with its own fuel injector, external cooling, and quench air jet system; the SBZ was annular. A later configuration was fully annular because these problems were eventually solved by working on the quench air patterns, although details of this have not been released. It also proved necessary to use nonmetallic ceramic composite liners for the IBZ. Finally, due to the high OFAR turndown ratio necessary for supersonic operation of the engine, the design ran into IBZ/SBZ equivalence ratio and smoke problems, as mentioned earlier. These were solved through use of variable-geometry fuel injectors that provided a limited degree of IBZ air modulation. The resulting combustor pressure loss changes were uncompensated without serious performance penalties.

Pratt and Whitney conducted parametric measurements of the emissions for this combustor in rigs and determined the pressure sensitivity of NO_x. With use of these scaling laws applied to the engine of Fig. 11 (without water injection), this optimized RQL design technology could have a takeoff NO_x falling slightly lower than halfway between the quasi-staged RQL dry and the quasi-staged RQL with water injection. This would represent an NO_x EI of about 12 g/kg. This signifies a creditable performance, that is, a 65% reduction in takeoff NO_x compared to the conventional combustor.

Staged Combustors

The consequences and limitations of a fixed-geometry combustion system have been mentioned already. If some form of staging is introduced, the combustor characteristic governing zone and overall equivalence ratios can be made much more flexible.¹⁸ Aeroderivative gas turbines for industrial power generation have been successfully produced (after great effort), with multiple-stage combustors.²³ However, whereas staging appears relatively simple, control of staging in an engine with a wide range of operating conditions is very complex. Part of the control complexity is that staging must not occur at any engine steady-state operating points to avoid hunting. Any staging system must also have a fast response in emergency conditions, and so a design requirement is that the combustor must always be fully staged when in the vicinity of critical flight conditions. Staging of course, must be completely transparent to the pilot. By this is meant that there should be no thrust bumps during the process. In addition, the pressure pulse propagated upstream as the main stage ignites must not adversely affect the engine compression system. Furthermore, there is the issue of liquid fuel coking in fuel injector passages due to heat soakback in stages that are shut down while the engine is operating at some power level. For these reasons, only two-stage combustors have been considered so far for aircraft applications. Either the airflow (as in the Pratt and Whitney optimized RQL combustor for the HSCT) or the fuel flow can be the quantity that is modulated. Generally, there are serious difficulties associated with air modulation, and so staging is usually applied to the fuel supply only.

Fuel staging normally implies that the combustor possess two separate burning zones, each fueled separately. The separate burning zones are commonly referred to as the pilot stage and the main stage. Functionally, the pilot stage fulfills most of the duties of a primary zone, whereas the main stage fulfills many of the duties of the intermediate zone of a conventional combustor. Engine starting and idling is accomplished on the pilot stage. At some point before an approach power condition is reached, the main stage is fueled and ignited. For all power levels above approach, both stages will be operated; however, the fuel split between stages can be adjusted by the fuel controller if so desired, to suit operating conditions and to minimize emissions.

The two burning zones can be arranged in one of three fundamental configurations: axially, radially, or circumferentially. The circumferential arrangement is extremely convenient because the combustor only differs from a conventional design in its fuel system. However, the circumferential arrangement is not favored because of the asymmetric temperature distribution for pilot-only operation

that can cause out-of-roundness problems for the turbine casings. Also, the chilling effects of the cold airflows at the edges of the unlit main stage bordering the operating pilot stage can result in an increase in low-power CO and UHCs. Figure 12 shows an example of a radially staged combustor by General Electric (GE). The main stage is placed inboard of the pilot stage, and the stage fuel injector tips are placed on a common support stem. The configuration results in a short and deep combustor that requires a complicated prediffuser design. The combustor, thus, has two separate flames arranged in parallel when both stages are fueled, and these flames are in communication with one another. Two separate flames that are in communication can "talk" to each other, and acoustic coupling can occur. This is a possible difficulty with the radial arrangement.

Axial staging, where a conventional upstream pilot feeds hot gases into the downstream main stage thereby assisting main stage lightoff and subsequent burning, does not necessarily result in an increase in combustion section length. Pratt and Whitney (PW) engine demonstrated an axially staged combustor (ASC)²⁴ that had 20 airblast-atomizing fuel injectors in each stage and had the same overall burning length of the quasi-staged RQL combustor it replaced. The pilot stage used inside-out recirculation technology. A similar combustor has been explored by Rolls-Royce Deutschland,^{25,26} where

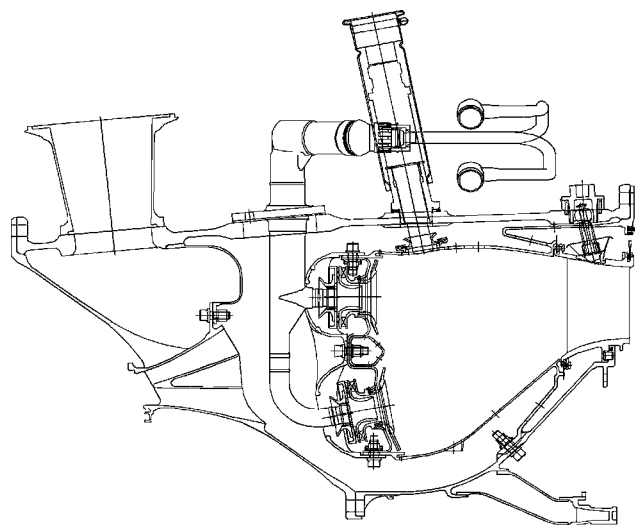


Fig. 12 Staged combustion, GE radially staged combustor (International Symposium on Air Breathing Engines) (ISABE Paper 2003-2657).³¹

it was found that careful optimization of the interactions between the two stages is necessary to achieve the best emissions. The PW ASC had an optimized pilot stage, where at engine idle the NO_x was acceptably low (around 5 g/kg) while maintaining good stage efficiency (greater than 99.9%) and lean blowout (LBO) overall fuel air ratio (OFAR) capability 40% or more below the most severe requirement. The integrated emissions values for the demonstrator engine were 46.6, 35, and 1.75% of the 1996 ICAO regulations for NO_x, CO, and UHCs, respectively, although note that the values for CO and UHCs were actually increased over those for the baseline engine. However, the baseline engine had very low values of CO and UHC emissions so that this was not a concern. Again, this is an example of emissions trading. Figure 13 shows a cross section of the ASC, where the main-stage fuel injectors for convenience are shown in the same plane as the pilot-stage injectors; actually, they were staggered relative to the pilot-stage injectors. The ASC was accommodated in the same pressure casings as the baseline combustor, with the only necessary modifications being the addition of pads to the outer casing to accept the main-stage fuel injectors. There was only a single ignitor plane (in the pilot stage).

The behavior of staged combustion is important and is best understood by considering the individual emissions characteristic variation with engine power.²⁷ The engine power level is here represented in terms of combustor inlet temperature, and Fig. 14 shows the CO, NO_x, and UHC characteristics, respectively, for the ASC. The staging point is clearly identifiable by fairly massive increases in CO and UHC emissions and by a modest decrease in NO_x. The NO_x characteristic should be compared to that shown in Fig. 11 for the quasi-staged combustor. The shift in the NO_x curve is ultimately the same, although it is achieved differently. Although the main stage of the ASC is assisted by the entering hot effluent from the pilot stage, initial combustion in the main stage when it is fueled is not easy, and the subsequent recovery of low CO and UHC emissions is slow. At the staging point, the overall combustion efficiency can be as low as about 90%. This behavior is typical for fuel-staged systems whatever their arrangement. In some instances, the loss in efficiency and slow recovery have been severe enough to result in unacceptable fuel-burn problems for the engine. The reason is the very lean main stage that results as the main fuel comes on immediately following staging. However, this problem can be worked on by means of fuel scheduling and optimized pilot/main-stage interaction. Care has to be taken however, not to introduce thrust bumps.

Staged combustors have been accepted as low-emissions combustors because staging takes place well away from any operating condition used for compliance evaluation. How they actually work as emissions control devices can best be illustrated by comparing

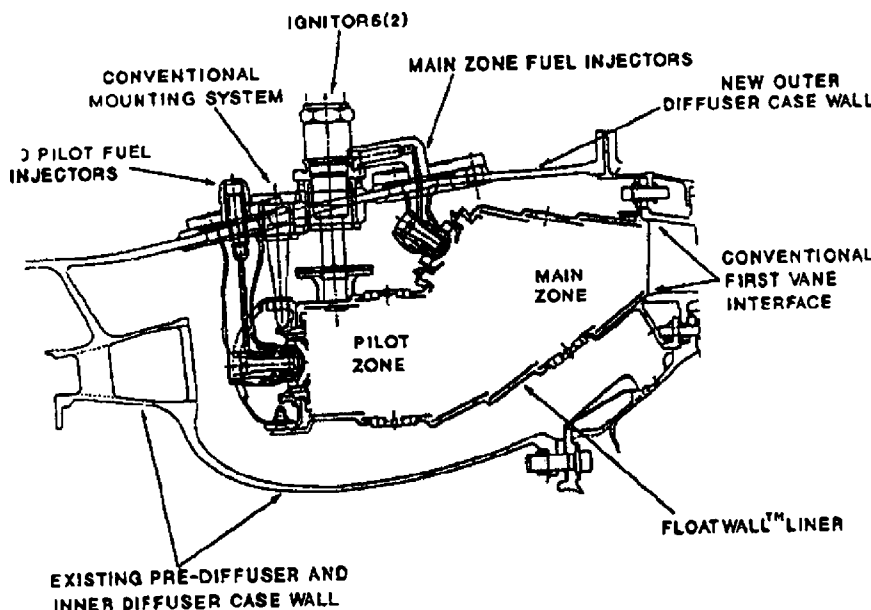
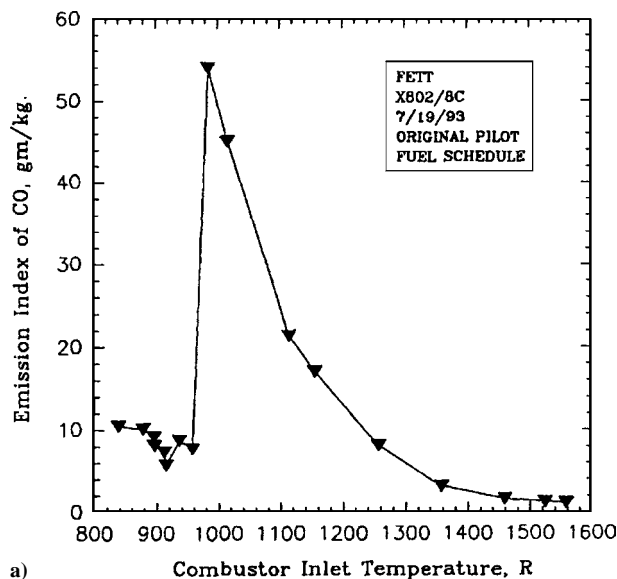
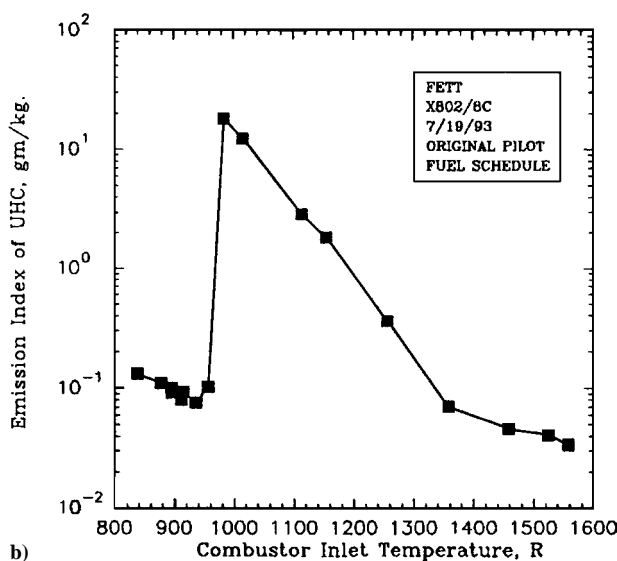


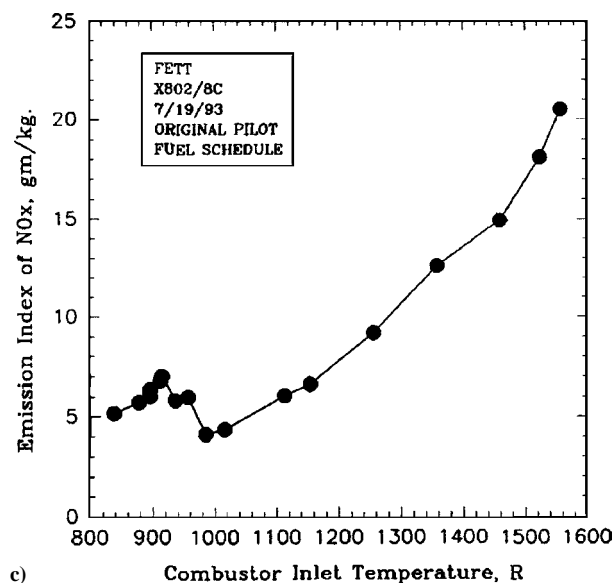
Fig. 13 PW's ASC as tested in IAE V2500 engine.



a)



b)



c)

Fig. 14 Effect of power level on emissions indices for staged combustor (PW ASC, first engine to test).

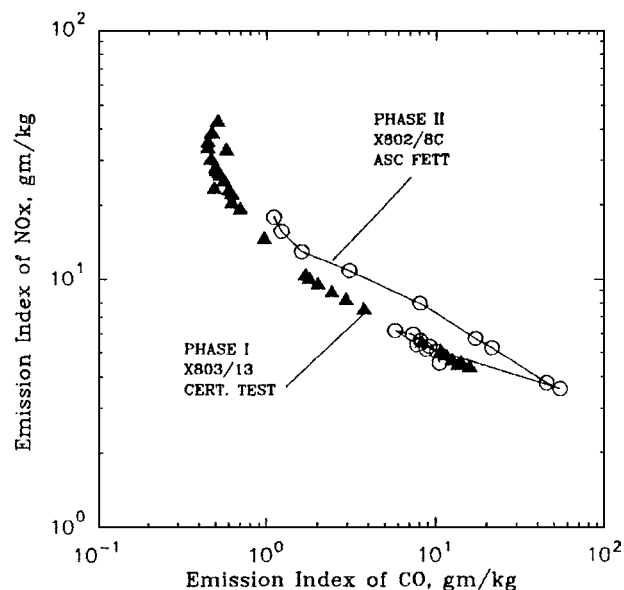


Fig. 15 Comparison of emissions tradeoffs for ASC and quasi-staged RQL combustors.

NOx vs CO for the ASC and quasi-staged RQL combustors, in Fig. 14.

For a CO vs NOx trade as shown in Fig. 15, movements of the curve toward the origin represent true overall emissions reductions, and movements along a curve represent a tradeoff between CO and NOx. In Fig. 15, the solid triangles represent the quasi-staged RQL combustor and the open circles represent the ASC combustor that replaced it; the engine model is the same in each case, and the engine numbers and builds are given. For the quasi-staged RQL combustor, the idle point is at the lower RHS of Fig. 15, and as engine power is increased, the plot is followed smoothly up the operating characteristic to the upper end of the curve, which represents takeoff power. For pilot-only operation, the ASC data points at the lower RHS follow identically those of the quasi-staged RQL combustor, which is as it should be because both use the inside-out recirculation and associated technology and have identical numbers of fuel injectors. When the ASC is staged, however, the curve is folded back on itself and moves far to the lower right of Fig. 15, which represents the maximum CO and minimum NOx condition; see Fig. 14 also. As power is further increased with both stages operating, the CO slowly is reduced and the NOx increases. The after-staging portion of the ASC curve is displaced to the right of the quasi-staged RQL curve. Because the ASC curve is to the right of the quasi-staged RQL curve, the ASC clearly represents an inferior overall low-emissions technology. It does so well in terms of the integrated emissions parameters because 1) the emissions are low at the very limited number of set points for which the ICAO integration is performed and 2) because the inside-out recirculation technology is so good that it permitted some NOx vs CO trading to be made. The ASC is, therefore, an example of trading emissions to advantage.

Improved Mixing, Lean-Burn Staged Combustors

For staged combustors, the pilot-stage contribution to the total NOx can be dominant unless the pilot fuel is modulated at high-power levels. When this is done, the pilot contribution to total NOx can become almost negligible. Regardless of the pilot equivalence ratio, the main-stage NOx for the ASC appears to be virtually independent of the main-stage equivalence ratio.²⁴ These points are shown in Fig. 16, which suggests, with reference to Fig. 9, that the main stage, which processes most of the fuel, is very poorly mixed. This is not unexpected because nothing serious has been done to address fuel/air mixing in these realizations.

Appreciation of the preceding points, together with the recognition of the infeasibility of premixing for aircraft applications, has led to some consideration of and a degree of concentration on, piloted

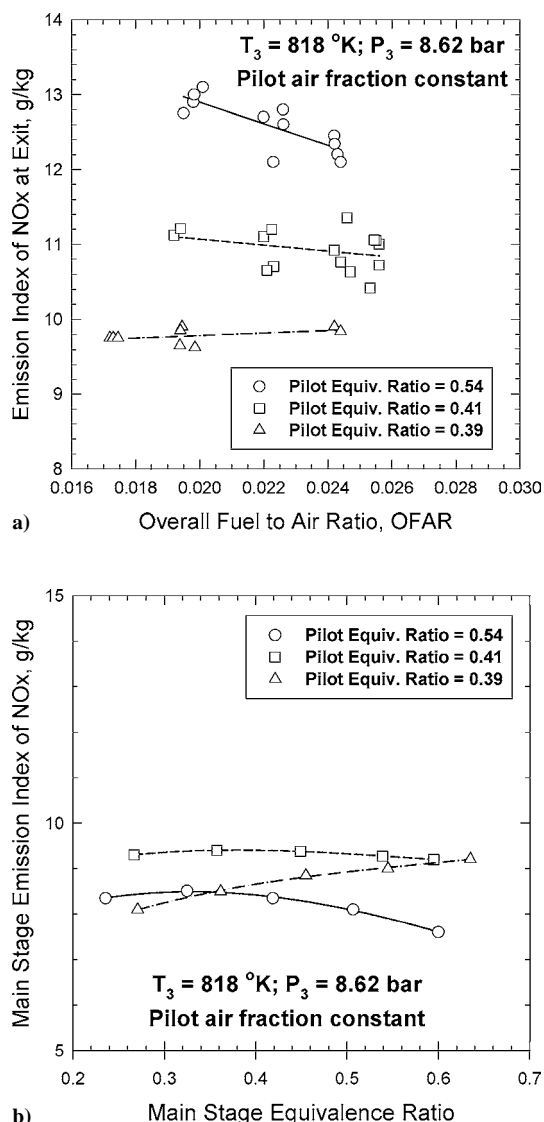


Fig. 16 Contributions to NOx in staged combustor: a) pilot stage and b) main stage.

lean direct injection (LDI) for advanced low-emissions concepts. A pilot of some form is still needed to satisfy engine operability requirements, but serious attempts are made for most of the fuel injected to improve fuel/air mixing such that combustion actually takes place close to the bulk equivalence ratio of the main stage.

LDI concepts can range from those having the pilot stage separated from the main stage (as in radial or axial staging as described earlier) with separate sets of fuel injectors, to those having the pilot stage central to a surrounding main stage in an integrated fuel injector. The pilot stage design can follow the design practices already described including fuel modulation at high power, whereas the essence of the LDI main stage is to improve the presentation of the stage fuel flow to the stage airflow to enhance mixing dramatically. This is accomplished by injecting the stage fuel (which makes up the majority of the total fuel flow) through a large number of atomizer tips. The intent is to approximate the probability distribution function for local equivalence ratio in the main stage to a delta function, that is, to a single-stage equivalence ratio, that is lean. Some designs incorporate main-stage swirl cups intended to allow some fuel spray evaporation and mixing of the resulting vapor with air before combustion. However, constraints of autoignition severely limit this potential. For those concepts that have a central pilot with a surrounding LDI main stage, the resulting flame zones cannot be allowed to merge because experience indicates that low NOx cannot then be achieved. Unfortunately, if the two flame zones, one within

the other, are distinctly separated, they will have a tendency to talk to each other, and acoustic coupling can occur.

How well mixed does the main-stage fuel and air need to be and at what equivalence ratio? Consideration of Fig. 9 suggests that the answers to these questions are respectively very well and quite low. There are many ways in which mixing can be represented but a mixing parameter S (Ref. 28) can be defined as

$$S = \sigma / \tilde{\varphi}$$

where σ is the standard deviation for a Gaussian distribution of equivalence ratio about the mean of $\tilde{\varphi}$ such that $S = 0$ represents perfect mixing. Figure 17 shows the influence of S on the formation rate of NO as a function of mean equivalence ratio. It can be seen that for enhanced mixing to be advantageous, $\tilde{\varphi}$ has to be less than 0.7 and S has to be less than 0.25 for lean combustion. Figure 18 gives estimates for S in practical combustors.¹⁰ Figure 19 shows the implications of Fig. 18 for a conventional pressure drop airblast injector fuel source combustor with a nominal lean-burn primary zone with mean equivalence ratio of 0.6. One, two, and three sigma bands

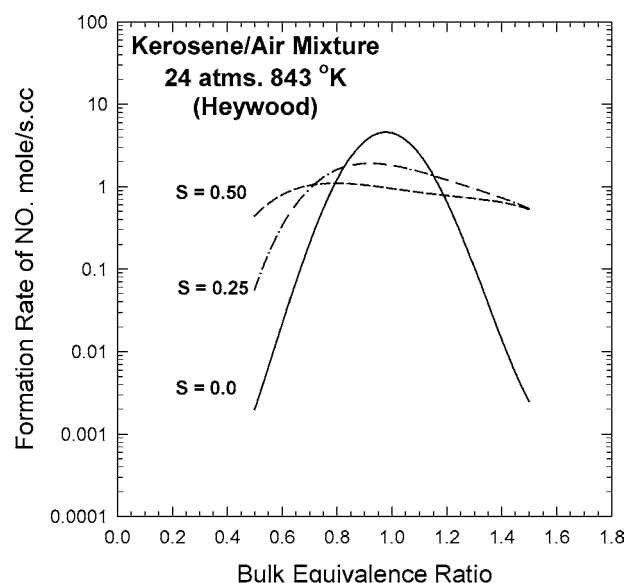


Fig. 17 Effect of mixing parameter on rate of formation of nitric oxide (Heywood and Mikus²⁸).

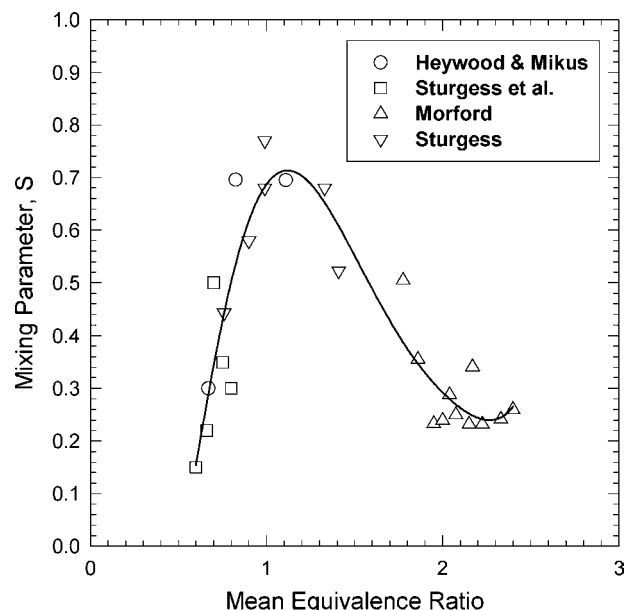


Fig. 18 Collected S experience for variety of practical combustors.¹²⁷⁵

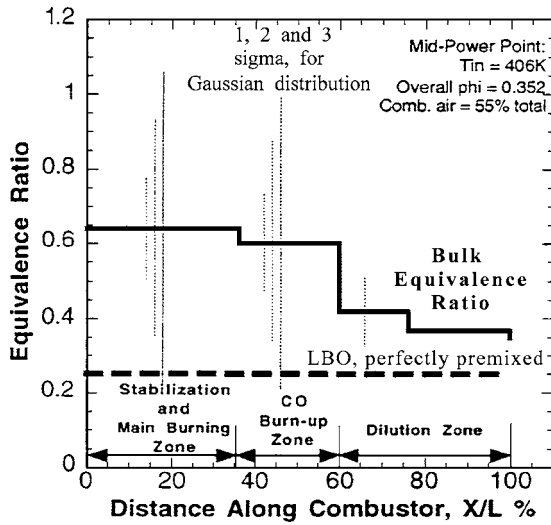


Fig. 19 Implications of fuel/air mixing in conventional lean-burn combustor.

of equivalence ratio for the Gaussian distribution are shown.^{10,11} It can be seen that the fuel really burns over a wide range of equivalence ratios and that some fuel components will actually leave the primary and intermediate zones of the combustor unburned.

For $\phi < 0.6$, Figs. 17 and 18 indicates an S value equal to about 0.10 would be necessary to yield formation rates $d[\text{NO}]/dt$ that are low. To then achieve low NOx emission indices, the mean residence time of products in the hot reaction zone has to be low also. These requirements together establish the design criteria for the LDI main stage.

The mixing parameter S will have two components, one that is associated with the total energy available for mixing in the combustor and one that is associated with the way the fuel is introduced. The total energy is mostly the air pressure drop across the combustor and generally cannot be increased because of the adverse effects on engine specific fuel consumption; the fuel introduction component includes the atomization level provided and the way the fuel sprays are presented to the air. It is mainly this latter component that LDI combustors seek to address by making large increases in the number of fuel sites. The main stage of the ASC, for example, had 20 injectors, whereas the main stage of an LDI combustor might have 100–200 fuel sources at a minimum. Typically, there might be 20 injector supports, each carrying 5–10 spray tips. One extreme example²⁹ had 864 injection sites, and another for the HSCT program had 1152 sites.

The large increases in the number of fuel injection sites tend to determine the type of fuel injection system that might be used. The injector tip flow number (FN_{tip}) is defined as

$$\text{FN}_{\text{tip}} = (m_f)_{\text{tot}} / n \sqrt{\Delta P_f}$$

where n is the number of tips, $(m_f)_{\text{tot}}$ is the engine fuel mass flow rate, and ΔP_f is the fuel pressure drop across the tip. Because $(m_f)_{\text{tot}}$ and ΔP_f are fixed by the engine cycle and the fuel pump, the individual injector FN_{tip} decreases dramatically as the number of tips increases, even allowing for the increase in fuel line pressure losses. Because the atomization performance in terms of Sauter mean diameter (SMD) of a simplex pressure atomizer can be expressed as³⁰

$$\text{SMD} \sim \frac{(\text{FN}_{\text{tip}})^{0.205}}{(\Delta P_f)^{0.251}}$$

fairly good atomization (around 40–60 μm typically) can be achieved without the use of excessive fuel pump pressures. This allows the use of macrolaminate technology for inexpensive manufacture of the tips. Conventional airblast atomization can usually achieve SMDs around 20 μm or less at high-power conditions, but

is probably a prohibitively expensive technology for this use. A practical limitation occurs when the FN_{tip} fall below unity. Even with macrolaminate technology, it is extremely difficult to manufacture to narrow tolerances in flow number without excessive production rejection rates. Significant local deviations in fuel flow rate that result produce severe local changes in S , causing high NOx generation. Care also has to be taken in introducing the injector air to not collapse the fuel spray cones, particularly if some form of carburetor tube is used.

The use of very large numbers of injection sites necessitates the use of multiple stages within the main stage itself to ameliorate the typical increase in CO and UHCs at staging, such as seen in Fig. 14. This is because the fuel flow rate per individual site at staging would be excessively small if all sites were fueled simultaneously, resulting in ultralean combustion.

Data on the performance of LDI systems are largely still proprietary. The HSCT program LDI configuration from GE, which had 1152 main-stage injection sites and 48 injection sites in the pilot stage, demonstrated in rigs single-digit NOx emission indices at 17 atm pressure and 811 K air inlet temperature (supersonic cruise conditions). There was a very strong sensitivity of NOx to mixer tube fuel/air ratio, as might be expected from Figs. 17 and 18. (This system is only functionally an LDI combustor. Fuel is introduced into arrays of air tubes mounted in the combustor dome. For this reason, it has been described as a premixed system. However, the degree of premixing actually achieved is negligible, and therefore, for convenience, the system has been described as being LDI here. Strictly, it could more correctly be referred to as a partially premixed system.) In addition to the pilot, the main stage had five fuel staging modes to bring it up to full-stage fuel flow. Data from a NASA concept²⁹ that is not really engine-worthy have results that are not especially encouraging, although this is almost certainly due to the particular implementation rather than to the LDI concept itself. All of the combustor air passed through the dome, which had a substantial annular height to accommodate all of the 864 swirl-cup injection sites. Although the flame length was very short, coupling the dome to the turbine inlet height resulted in the existence of an extensive thermal soak zone. It would be expected, therefore, that NOx would correlate strongly with combustor exit temperature. Figure 20 shows that this is, indeed, the case.

Comparison of the NOx vs CO trade curve for this NASA LDI with that of the quasi-staged RQL combustor given originally in Fig. 14 suggests that this realization does not actually represent an emissions technology improvement. This is shown in Fig. 21. There are indications that the LDI trade curve might cross the quasi-staged

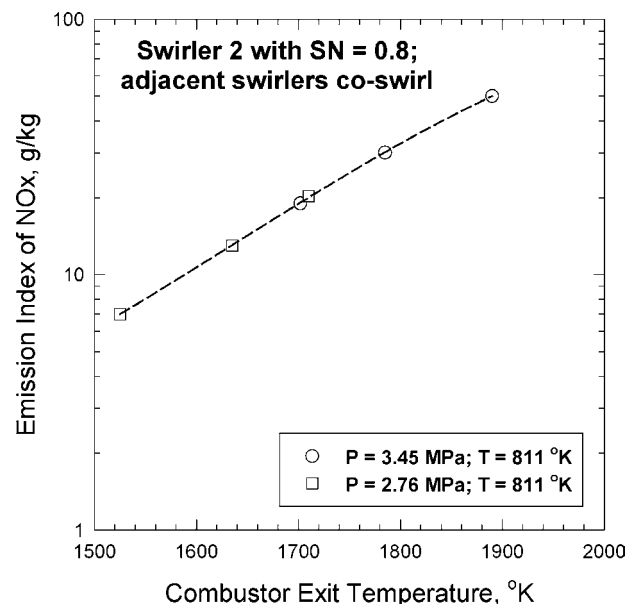


Fig. 20 NASA John H. Glenn Research Center LDI high-temperature NOx data related to combustor exit temperature.

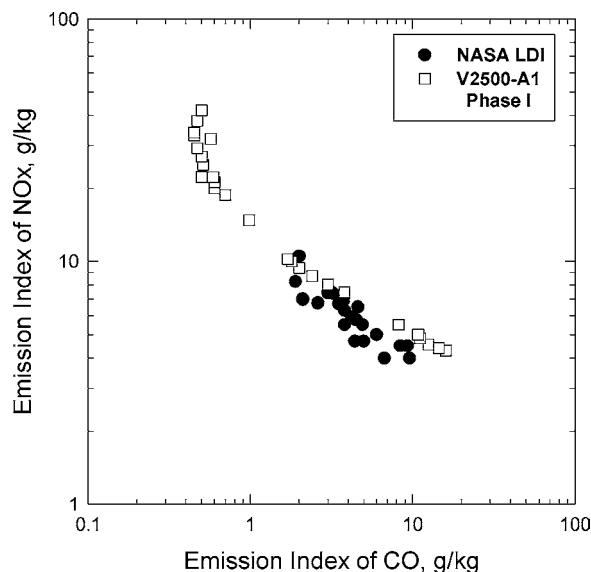


Fig. 21 Comparison of NASA John H. Glenn Research Center LDI emissions trade curve with a quasi-staged RQL trade curve.

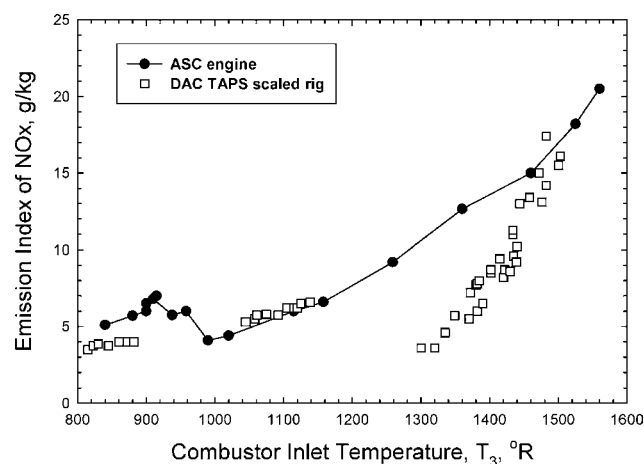


Fig. 22 NOx comparison up engine operating lines of GE DAC TAPS LDI concept with the ASC concept.

RQL trade curve. The major benefit appears to be lower NOx at low-power conditions. These LDI test data are sector-rig results.

Figure 22 shows a comparison of GE's twin annular premixing swirler (TAPS) LDI technology with the ASC engine NOx data. The TAPS LDI rig database was developed as functions of pressure, T_3 , and OFAR for each fuel staging mode, and the correlations were used to extend the data to an engine with an OPR of 30 (Ref. 31), which is appropriate also for the axially staged combustor (ASC) engine tests. The DAC TAPS combustor has a configuration like that of Fig. 12, with the substitution of the TAPS fuel injectors, which are of the type using a central pilot with staged secondary injection being arranged concentrically about each pilot to produce the flowfield shown in Fig. 23.³¹ The pilot/cyclone interaction zone is all important to this design. It is intended to allow the pilot flame to assist ignition and burning of the premixed flame. There are two design limits. One is when the pilot recirculation zone is fully merged with the premixing cyclone flame zone, that is, all interaction zone. The second is when the pilot recirculation zone is completely separated from the premixing cyclone flame zone, that is, zero interaction zone. For the first limit, experience teaches that the low NOx capability is lost or substantially reduced. For the second limit, two separate flame zones exist that can talk to one another, with potential acoustic problems. The secret to success is to get the interaction zone just right. All of the required airflow, with the exception of liner cooling air, can be passed through the dome with this approach to ensure lean operation of the cyclone stages, shown in Fig. 23. The

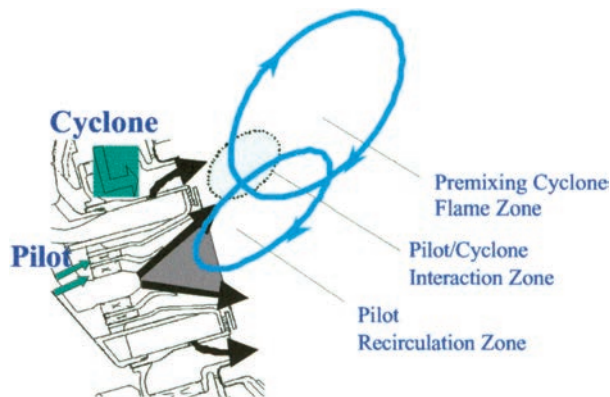


Fig. 23 GE TAPS LDI concept showing pilot, main and interaction burning zones.

TAPS data for simulated engine conditions are based on annular rig tests for OFARs to 0.037, combustor inlet temperatures T_3 to 1639°R, and pressures to 23.8 atm. No experimental uncertainties for the measurements were reported in the original GE paper.

The staging possibilities with the DAC TAPS design are somewhat flexible. It can be operated as a radially staged combustor, as in the existing DAC system, as a pilot/cyclone staging of all injectors of both banks, or as any combination of these. In addition, modulation as a function of engine power of the fuel split between pilot stages and cyclone stages provides further flexibility on NOx control. Actual staging mode and staging points for a given application would be determined by balancing emissions, operability, and fuel passage coking tendencies. Note that the DAC TAPS design has 30 fuel injector supports, each one mounting two tips. Within each tip there is a primary nozzle and a number of secondary nozzles, so that there are several hundred fuel sources altogether in the combustor. For the same air pressure drop as a conventional combustor, therefore, the DAC TAPS certainly achieves a lower value of the mixing parameter S than the standard DAC, although its values have not been assessed. Introducing all of the air through the dome reduces bulk equivalence ratio. Herein is the secret of the low NOx potential of the approach. Because the combustor was designed to be accommodated in the existing casing, there is no change in bulk residence times. This would not be the case though for a brand new design, however.

It can be seen from the Fig. 22 that the pilot stage of the DAC TAPS combustor has reduced NOx compared to that of the ASC. At T_3 around 800°R, 100% of the engine fuel flow is going to the TAPS pilots. Staging appears to take place at about 1160°R, which is much delayed in comparison with the ASC. However, the subsequent slope of the NOx curve is steeper than that for the ASC so that the two curves cross at about $T_3 = 1500^\circ\text{R}$. It is not immediately clear why the fully staged slopes are so different, but it is possibly associated with mixing differences. The potential benefits of multiple staging can be appreciated from Fig. 22.

Unfortunately, no CO data are available to allow construction of the NOx vs CO trade curve for the DAC TAPS combustor and to then allow comparison with the quasi-staged RQL trade curve as has been done for the other low-emissions concepts.

Situation Summary

Except for very high-temperature rise combustors, the nonequilibrium CO and UHC emissions result from incomplete combustion and are physically controlled. They can be addressed by attention to liquid fuel atomization, fuel placement, bulk stoichiometry adjustments in the combustor primary zone, and reduced dome and liner cooling air. Although CO and UHC can present serious problems for older engines, particularly where long ramp times are involved, they are much less of a problem with modern engines. NOx emissions constitute the major atmospheric concern and are much more difficult to deal with.

In terms of the international civil aviation organization (ICAO) landing and takeoff (LTO) integrated emissions parameter

D_p/F_{00} , NOx emissions are grouped by combustor design, specifically, by the emissions control technology incorporated in the combustor and its residence time. This is illustrated for some PW engines in Fig. 24 as a function of OPR using data obtained from the ICAO emissions databank. Engine data in the ICAO databank do not usually quote measurement uncertainties. However, the data reported are normally for three tests on a single engine, and the measurements are made with calibrated instrumentation and closely follow established EPA test protocols. The first group of JT9D data is for old combustors containing embryonic quasi-staged RQL reduced-emissions technology. The second group, involving the PW2000, PW4000 and IAE V2500 engines, are for modern design combustors (lower residence times, more effective aerodynamics reducing parasitic pressure losses) utilizing the quasi-staged RQL technology. The PW4000 Talon 2 combustor uses a refined version of the quasi-staged RQL technology and is conventional in appearance, as can be seen from Fig. 25. For all of these engines, the bypass ratio (BPR) ranges from 4.1 to 6.8 and is not a factor. Similarly, in Fig. 26 for GE's dual annular combustor (DAC) 1 and 2 technology in the CFM56 and GE-90 engines, where the BPRs range from 5.7 to 8.6, the NOx data group by combustor design.

If the engine data in Figs. 24 and 26 represent the current best standard of engine demonstrated reduced emissions technology, then these data in relation to the emissions regulations indicate the current low NOx status. The collected PW and GE data from Figs. 24 and 26 do group together, as is shown in Fig. 27, where they are compared with the ICAO Committee on Aircraft Environment Protection (CAEP)/4 standard (for OPRs greater than 30) adopted in 1999 for 2004 enforcement.

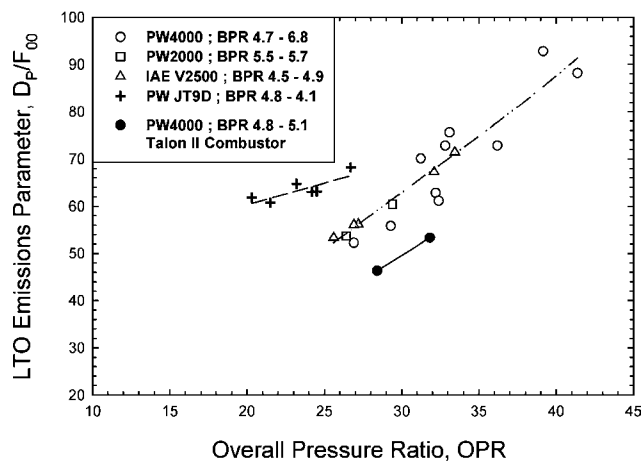


Fig. 24 PW's quasi-staged RQL NOx emissions technology.



Fig. 25 PW Talon 2 combustor showing simplicity and conventional appearance.

Note that the level of low-emissions technology has projected NOx emissions that equal and exceed the CAEP/4 line for OPRs just over 50. Because carbon dioxide is now becoming to be considered as important as NOx in terms of its effects on the environment, and because fuel burn is reduced by increasing OPR and BPR, the trend of increasing OPR will be continued at least into the 50 level. Therefore, for future engines with increased OPRs, further improvements in combustor low-emissions technology over the current best

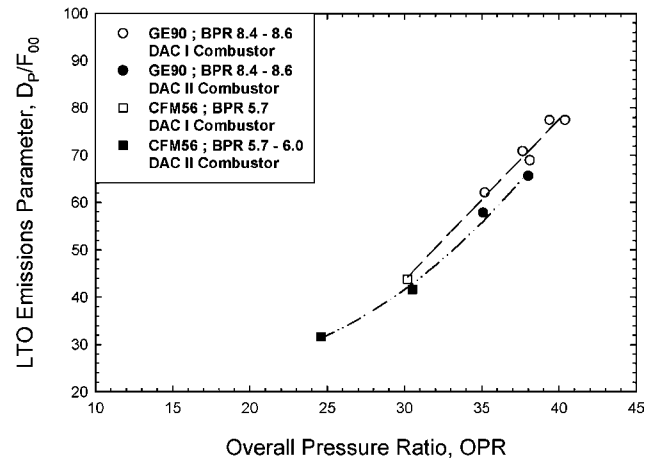


Fig. 26 GE's DAC 1 and 2 low NOx emissions technology.

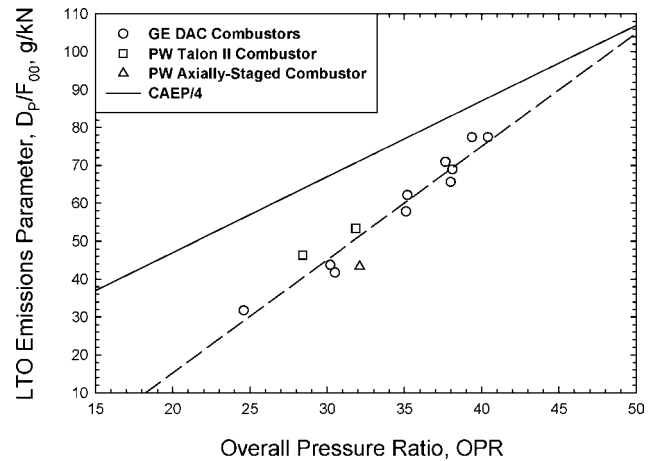
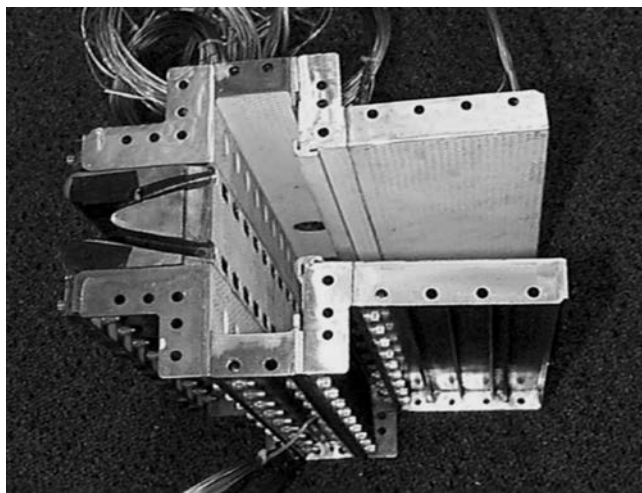
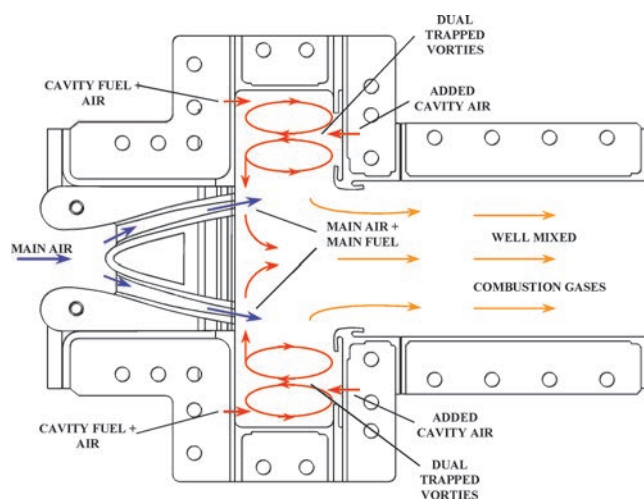


Fig. 27 Comparison of current engine low NOx technology with regulations.



a)



b)

Fig. 28 TVC: a) GE 12-in. planar-sector rig (two-passage diffuser) and b) schematic of TVC.

engine standard are going to be needed. TAPS-type technology, together with staging and reduced residence times, is a strong candidate. At the time of writing, recent verbal reports circulating in the industry suggest that PW's RQL technology in the form of the Talon-X combustor, which represents a further refinement of the Talon 2 combustor and has been explored under the NASA John H. Glenn Research Center Advanced Subsonic Technology/Ultra Efficient Engine Technology programs, has achieved additional and significant reductions in NO_x beyond the curve given in Fig. 28. It is apparently still a simple combustor, if less conventional in appearance than its predecessors. If this is so, then it is also a strong candidate.

The techniques for reducing CO and UHCs by recirculation zone changes have been introduced into service engines. GE's radially staged DAC combustion system is also in full commercial service. PW's ASC combustion system was engine demonstrated, but was not introduced into service. GE's DAC TAPS LDI combustor has been rig demonstrated. It requires some further work for CO and operability, and these issues are being actively worked. PW's Talon 2 and Talon-X combustors have been rig demonstrated and development continues.

Although it is really up to the original equipment manufacturers to assign appropriate technology readiness levels (TRLs) to their own low- or reduced-emissions approaches, some provisional assignments may be attempted based on the published information in the open literature. The NASA LDI has seen limited component testing and would be a TRL of 2 at best. The GE DAC 1 and 2 combustors have completed engine field service evaluations and are

in service and so would be TRL 8 or better. The TAPS LDI is in component testing and would be a TRL 5. PW ASC completed an engine demonstration and so would be a TRL 6; the Talon 1 and Talon 2 might be TRL 6 or higher, whereas Talon-X would still probably be a TRL 5.

U.S. Air Force Requirements and Considerations

The brief survey of the development of reduced-emissions combustors has revealed a story of steps forward, trades between emissions, and an ever-growing complexity in combustor hardware with consequent increases in cost and weight. The major difficulty is associated with NO_x reductions. Understanding of the details has grown tremendously, however. The issue of exhaust smoke has not been touched on here because it is worthy of separate treatment.

U.S. Air Force engine design requirements have traditionally stressed advanced performance in the form of increased thrust/weight ratio and specific thrust. Recently, affordability and life have also become issues of great importance. The combustor is expected to conform to previous design criteria, be fully affordable, and have long life with, now, the added concerns of exhaust emissions becoming important.

For engines to meet military design goals, combustors for fighter engines have always faced the issues of high-temperature rise and high combustor exit temperatures. Hand-in-hand with these have gone consequent reduced service intervals and high replacement costs. For future engines, if compression technology does not become limiting, high combustor exit temperatures are possible with only slight increases in temperature rise over current levels. Should compression technology become limiting, high combustor exit temperatures become essential, together with high-temperature rise. Clearly, these conditions imply turbine and combustor durability problems beyond those of today's engines. However, it is more complicated than this simple picture. High gas temperatures imply inherently high combustor exit NO_x levels, and as Fig. 17 demonstrates for high equivalence ratios, combustors that have good fuel/air mixing will have higher NO_x than combustors that have less perfect fuel/air mixing. Equilibrium chemistry allows dissociation of CO₂ to CO at such high temperatures, such that at an OPR of 35 the emission index of CO is 0.025-g/kg fuel burned for an exit equivalence ratio of 0.5 and is 15 g/kg for an exit equivalence ratio of unity. Treating the combustor as a perfectly stirred reactor with finite rate chemistry at a (cold) combustor residence time of 5 ms, the stoichiometric equivalence ratio of H₂/O₂ is reached for an exit equivalence ratio of 0.5, the stoichiometric equivalence ratio of C₂H₂/O₂ is reached at 0.9 exit equivalence ratio, and the stoichiometric equivalence ratio of CO/O₂ is reached at unity equivalence ratio. Because the high gravitational forces experienced by the gases exiting the combustor in flowing through the high-pressure turbine tend to concentrate cooler unburned gases and heavier molecules, significant combustion can take place in the turbine with the turbine and air-seal cooling air. Not only does this constitute a durability problem and increased pressure losses, it also implies further NO_x generation downstream of the combustor. These issues raise the question of whether or not future military combustors should have near-stoichiometric exit conditions. In other words, cycle performance might be traded for durability and reduced cost of ownership. The U.S. Air Force versatile affordable advanced turbine engine (VAATE) program is looking at the overall picture, which now involves not only performance, but also durability, emissions and affordability.

Clearly, the directions being pursued for low emissions in commercial engines are not completely consistent with U.S. Air Force design requirements, except for transport aircraft that use derivatives of commercial engines. Multiple injection sites and staging adds system weight and cost, whereas multiple-staging modes adds complexity and probably also has an adverse effect on reliability through fuel passage coking propensity. The thought of a low-emissions combustion system repeatedly staging and unstaging during combat maneuvers is disconcerting. Mechanically staged combustion systems, therefore, are most unlikely to be considered seriously for combat aircraft. It would seem prudent, therefore, that some alternative approaches for U.S. Air Force applications might be

advantageously considered in addition to pursuing TAPS/LDI technology. The Talon 2/Talon-X RQL technology is one approach that offers some possibilities here, provided smoke and particulates do not become serious issues from a stealth point of view.

Simpler Combustor Approaches for Military Applications

Trapped Vortex Combustor

A military combustor must have the best possible pilot to satisfy severe engine operability requirements. Most of the conditions for good pilot design have been described above. In all of the combustor designs discussed so far, the pilot recirculation zone that holds flame is exposed to the aerodynamically destabilizing influences of the main flow in one way or another. Therefore, it has to be substantial in size. The large size means long-residence times that contribute significantly to the total NO_x generated. Furthermore, smooth connection of the pilot with its large annular height to the turbine inlet results in the formation of thermal soak zones that also contribute to NO_x.

The trapped vortex combustor (TVC)³² was originally conceived as a high-performance (low-pressure drop, high-temperature rise) combustor specifically for advanced military applications. It also has the potential of reducing engine length, where in military engines 1 in. in axial length can be worth up to about 100 lbm in installed engine weight. A TVC mechanically anchors a pilot recirculation zone on a time-averaged basis by holding it within a specially designed cavity.³³ The cavity protects the recirculation zone from main-stage flows. The recirculation, therefore, can be smaller than a conventional recirculation zone, while having a superior operability performance.³⁴ The smaller recirculation region, through reduced residence time, offers the possibility of a less severe impact of the pilot on overall NO_x emissions. Furthermore, if the TVC is designed with its zones in parallel,³² that is, with the pilot being placed parallel to the main flow, the overall combustor length is further reduced. This saves weight and reduces the thermal soak zones for lower NO_x.

Figure 28a shows a GE-designed, TVC³⁵ planar-sector rig. The configuration shown is a staged combustor, where the main-stage fuel is introduced into the combustor two-passage diffuser section, which has been integrated to form the combustor dome to give another reduction in section length. The main stage forms an LDI. There are inner and outer cavities placed in parallel to the main stage that are separately fueled. In a generic sense, the hot combustion gases are recirculated within the cavity and are then extracted from it by the low-pressure wake regions formed by the mainstream flow from the diffuser passing through the combustor dome. An igniter plug is contained in the outer cavity; ignition of the inner cavity occurs by flame transport across the central bluff-body flameholder of the main stage. The downstream exit corners of the cavities are provided with film-cooling slots, and thermal barrier coating is applied to all surfaces. The main-stage flameholder and cavities have application of angled, multihole cooling passages for enhanced durability. The rig could be operated as a staged LDI combustor, or as a quasi-staged RQL combustor when only the cavities are fueled. Operating as a staged LDI, the overall flame length is extremely short. Emissions measurements indicate that the combustor shown in Fig. 28 could be shortened in exit length a further 40% without driving up CO. The section length of this concept in an engine is only a fraction of that of a conventional design.

Figure 28b shows the notional flow patterns described earlier. Note the double-vortex system formed in the cavities by means of mainstream flow over the cavity and the direct introduction of air jets into the cavity. Flow patterns in the cavity proved to be critical in determining performance. The vortex systems established proved to be remarkably stable in that flame movies shot at 12,000 frames/s still exhibited regular, vigorous, and tight recirculation zones fully contained within the cavities.

The performance of the TVC of Fig. 28 was extremely encouraging for a new concept when operated over a range of pressures from subatmospheric to 20 atm with a nonvitiated heated air supply on liquid JP-8+100 fuel. The static stability (LBO) was over twice

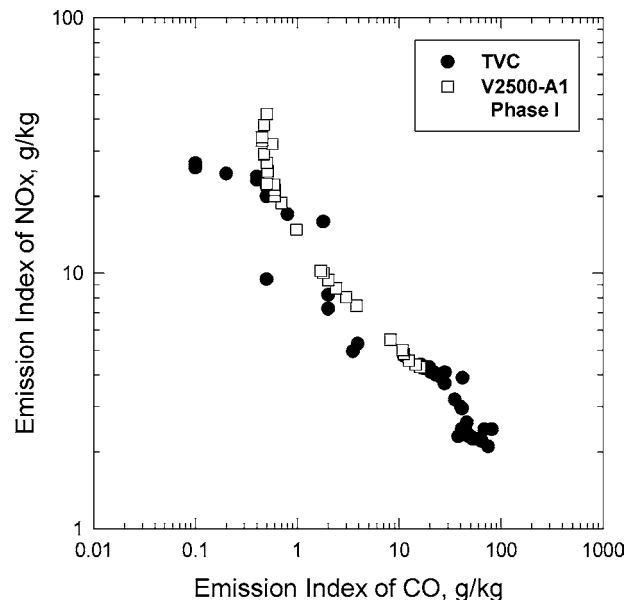


Fig. 29 NO_x vs CO trade comparison for TVC and quasi-staged RQL combustor.

as good as that of a conventional combustor at the same combustor loading over a wide range of loadings. Successful altitude relight was demonstrated up to engine conditions representative of over 20-km height, and stable combustion was maintained to conditions representative of greater than 40-km flight altitude. Propagation of flame from the outer cavity to inner cavity across the mainstream via the main-stage flameholder was satisfactory on starting. Without any dilution air jet assistance, combustor outlet temperature distributions (profile and pattern factors) were acceptable to a turbine, and operation at stoichiometric outlet conditions was successfully demonstrated. The combustion efficiency at idle conditions was in excess of 99%, and this was held over wide ranges of OFAR; the efficiency at the staging point was very high also, in excess of 99%.

When operating as a staged LDI device, the NO_x vs CO trade curve was moved closer to the origin compared to that for the GE-90 staged combustor shown in Fig. 14, thereby representing a truly reduced emissions device. Note that the initial main-stage injection system of this LDI was far from ideal, so further improvements in emissions could result from attention to the main-stage fuel system design. When operated as an RQL device (cavities only fueled), the NO_x vs CO trade curve moved even closer to the origin than that for the staged TVC, whereas NO_x levels were essentially the same as for the staged TVC. Figure 29 shows a comparison of the TVC NO_x vs CO trade curve to that for the quasi-staged RQL originally given in Fig. 15 and against which all subsequent concepts have been compared. It can be seen that the TVC emissions are either the same or slightly better than this standard. At very high OFARs, the TVC NO_x signature with engine power in the RQL mode became concave upward, and levels eventually exceeded those of the staged TVC. Although rig smoke numbers should always be viewed with care, the smoke decreased with increasing OFAR, indicating that the smoke originated in the fuel-rich cavities and was subsequently and progressively burned up in the main stage as this became hotter. Smoke levels at high-power conditions were less than 10.

It was surprising that the initial durability in the cavities where combustion is intense, and on the dome, was excellent, apart from the usual minor TBC loss on the dome. The multihole cooling used was industry standard and did not use excessive cooling air. Indeed, the cavity cooling air was also used to assist in driving the vortices. The double-headed film cooling slot on the downstream lips of the cavities suffered from the usual weaknesses of film-cooling slots and would need some redesign for engine application.

Although it has a novel configuration, the TVC appears to be a viable combustion device for aircraft applications. It certainly demonstrated its potential as a reduced length/weight savings

high-temperature rise combustor with enhanced operability for military applications. In addition and without any specific attempt to design for low emissions, it achieved the best low-emissions potential of all of the simpler combustor concepts reviewed. A full annular rig demonstration is planned for the future. At the present stage of its development, the TVC would be a TRL of 2.

Ultracompact Combustor

The primary zone, where flame is stabilized and most of the total heat release is achieved, forms the heart of a combustor. A poorly designed primary zone will always result in a poorly performing combustor, regardless of how much effort is put into the intermediate and dilution zones and flow around the combustor. It is not surprising, therefore, that significant gains in reducing emissions have come from major changes to the primary zone, as in the inside-out recirculation (Fig. 4) and the TVC (Fig. 28). More aggressive versions of the TVC offer the dual possibilities of further emissions reductions through reduced mainstream residence times and additional reductions in engine length and, hence, in engine weight. One version of a more aggressive TVC has been named the ultracompact combustor (UCC). It is presently a research project only and is intended for feasibility studies. However, it does represent a continuation of the line of thinking that combustors can be shortened very considerably over existing designs with the use of nonconventional approaches. With a short length, of course, goes a reduction in thermal NO generation.

One UCC concept that is being explored experimentally combines the combustor with the compressor exit guide vanes (CEGVs) and the turbine inlet guide vanes.^{36,37} This concept utilizes a swirl-based trapped vortex, where the major axis of the swirl is the engine centerline, in addition to the minor axis of swirl generated by flow over a cavity normal to the major flow direction. Thus, the motion of reacting flow within the cavity, which is nominally set normal to the flow through the engine, follows a spiral motion around the engine centerline. Swirling flow combustors have long held the interest of designers for high-intensity combustion systems with the elimination of the CEGVs, for example in Ref. 38. The large centrifugal force field generated by the major swirl enhances combustion through high levels of buoyancy-driven turbulence.^{39,40}

It can be shown that burning velocity S_b is proportional to a swirl parameter,

$$S_b \propto (T_b/T_u)\sqrt{g}$$

where

$$g = w^2/g_0 r_{\text{cav}}$$

T_b and T_u are the burned and unburned gas temperatures, respectively, w is the swirl velocity in the cavity, g_0 is Newton's constant (where the units used might necessitate its inclusion), and r_{cav} is the mean radius of the cavity. A typical value of gravitational force for conventional, swirl-stabilized combustors is about 90, whereas values experienced in the UCC rig are estimated to range from 350 to 3500.

Figure 30 shows the UCC concept. It can be seen that in addition to the main cavity, the wide-chord vanes also have radial cavities that transport partially burned mixture out of the main cavity to complete combustion and distribute the hot gases across the main flow. An optional circumferential flameholder is shown, whose purpose is to distribute hot gases circumferentially and to complete any remaining combustion under adverse burning conditions. All combustion takes place in low-velocity flow regions and is completed before the gauge point of the cascade to avoid high Rayleigh losses. Functionally, the circumferential cavity serves as primary zone, the radial cavities serve as the intermediate zone and the optional circumferential flameholder serves as a dilution zone. Computational fluid dynamics (CFD) studies of the concept show flow behavior as postulated, with field responses to geometrical changes as expected. To control weight of the combined vane pack/combustor, and for cavity durability, the use of composite materials is anticipated.

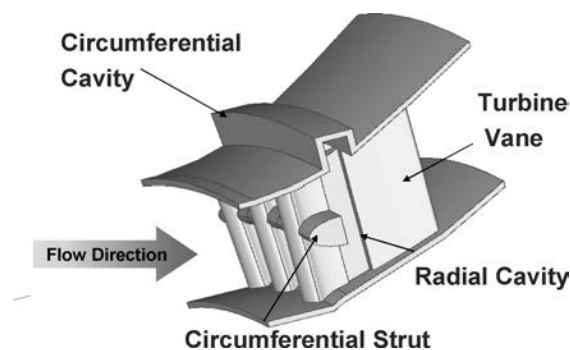


Fig. 30 UCC concept.

This UCC concept is too early in its development to permit any realistic comparisons of its emissions characteristics with the engine and developed rig combustor results presented earlier. Nonetheless, it is interesting to look provisionally at some of the emerging emissions behavior. A small rig is being used to study the main circumferential cavity at atmospheric pressure.³⁷

The initial rig consists of a small cavity mounted in the outer wall of a circular cross section duct that carries the main air. A number of air ports are positioned in the outer circumference of the cavity to provide separately metered combustion air with swirl around the cavity. All airflows are heated electrically to 500°F. The cavity contains six circumferentially disposed pressure atomizing fuel injectors, also mounted in the cavity outer circumference. The injector major axes can be changed from 0 deg (straight radial injection) to 37 deg off radial to give injection in the direction of the air swirl. The fuel is liquid JP-8+100. A centerbody is provided in the circular duct. This center-body is positioned by several thin support spiders upstream of the main cavity. Although not intended to function as simulations of the radial cavities of the concept, the low-pressure wakes from these spiders nevertheless do provide some mass transport from the main cavity. The major operating variables are mainstream velocity, air pressure drop across the cavity, and cavity equivalence ratio. The cavity equivalence ratios are in terms of the metered values. Because it is known that cavities such as this can entrain considerable quantities of mainstream flow, the actual cavity equivalence ratios will always be much less than the quoted values. The effects of buoyancy-driven turbulence on the combustion efficiency of the main cavity are discussed in Ref. 41, where many questions also remain to be answered.

Emissions results for two fuel injectors, C and D, are presented. Both injectors are pressure atomizers using Parker Hannifin's macrolaminate technology, with some integral supplemental injector air for an airblast contribution to the atomization. For the C injectors, the supplemental air was nonswirling with an effective area of 0.033 in². For the D injectors, the supplemental air was swirled clockwise relative to the tip face with a swirl number of 0.8 and an effective area of 0.0234 in². This swirling supplemental air generated a small tip recirculation zone. The injector flow numbers were in the range 0.7–0.9 pounds per hour (PPH)/(psi)^{1/2}. These small injector differences resulted in significant differences in performance.

To have an appreciation for the CO emissions of this UCC concept, it is necessary first to have a feel for the combustion efficiencies achieved. The circumferential cavity is capable of delivering very respectable combustion efficiencies. Combustion efficiency is normally expressed in terms of a primary zone loading parameter at various values of primary zone equivalence ratio. This form of presentation is used here, where combustion efficiencies from gas analysis are given in terms of a cavity loading parameter (LP), exponentially corrected to 400°K, at various metered cavity equivalence ratios, where

$$LP = m_{\text{tot}}/VP^{1.8}$$

and where

m_{Tot} = sum of fuel flow and cavity metered air, lbm/s

V = cavity volume, ft³

P = combustion pressure, atm

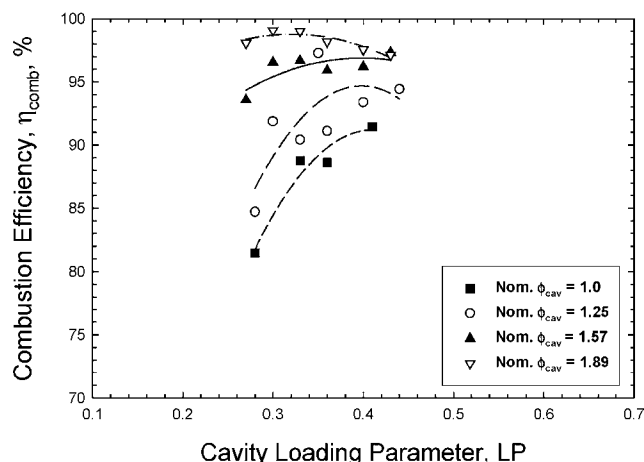


Fig. 31 Effect of cavity metered equivalence ratio on efficiency for D injectors at 20-deg injection angle.

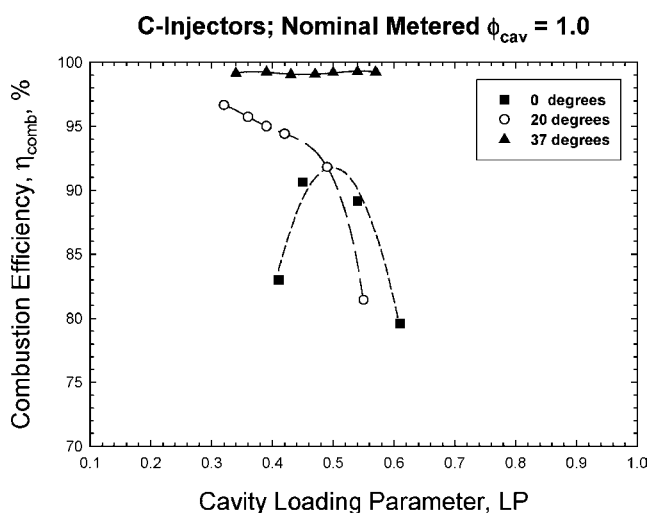


Fig. 32 Effect of injection angle on efficiency for C injectors at unity metered cavity equivalence ratio.

Figure 31 gives an example for the D injectors at 20-deg injection angle. Initially, efficiency grows as LP increases due to more effective swirl enhancing burning rates.⁴¹ After reaching a maximum value, it then falls due to increasingly inadequate residence time in the cavity as LP grows further. This falloff in efficiency begins at values of LP about 50–60% those for conventional combustors. The maximum levels of combustion efficiency increase with metered equivalence ratio ϕ_{cav} , and with increasing injection angle, as Fig. 32 shows for the C injectors. Under optimum conditions, the efficiencies are maintained at 99+% over acceptable ranges of LP.

NOx vs CO trades are presented in Fig. 33 at 0-deg injection angle for the C and D injectors over a range of ϕ_{cav} . The data for each injector group reasonably tightly and show no systematic dependence on ϕ_{cav} . Although each trade curve has the now familiar form, the differences for the two injectors are clearly apparent and result directly from the differences in combustion efficiency. (It would, of course, not be reasonable to compare this exploratory UCC rig data with the quasi-staged RQL engine trade data that has been made the standard of comparison in this paper.) The two injector trade curves cross, with the C injectors producing higher NOx at low CO than do the D injectors and, then, lower NOx at higher CO.

The effect of fuel injection angle on the trade curve for the D injectors is shown in Fig. 34, where going from purely radial injection to 37-deg angled injection shifts the curve to higher NOx levels. The effect of injection angle seen in Fig. 34 is again purely one of increased combustion efficiency, similar to that shown in Fig. 32 for the C injectors. However, the slope of the trade curve at the

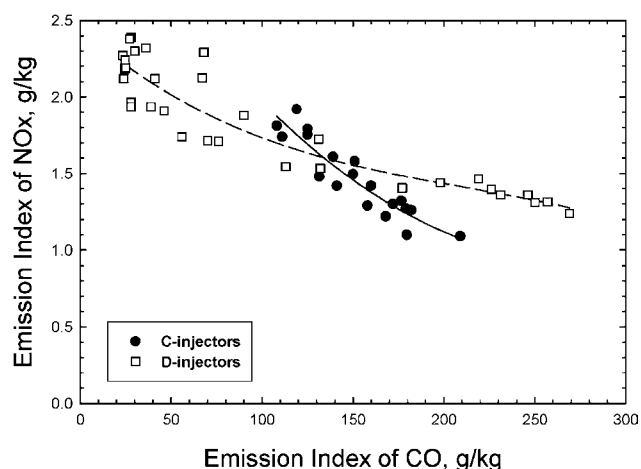


Fig. 33 NOx vs CO trade curves for C and D injectors at 0-deg injection angle: $1.0 < \phi_{cav} < 1.8$.

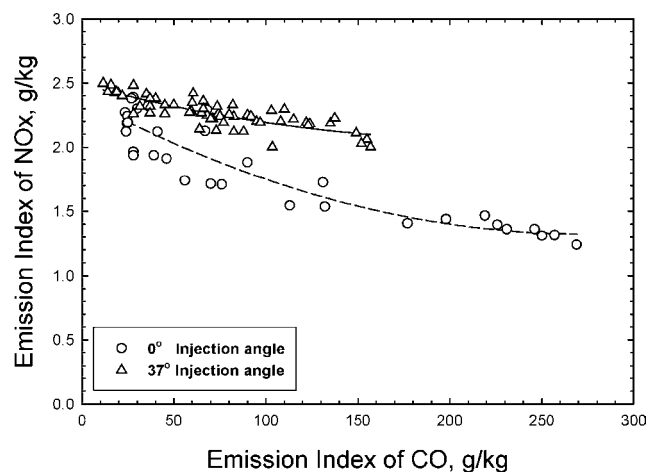


Fig. 34 Effects of injection angle on NOx vs CO trade curve for D injectors: all ϕ_{cav} .

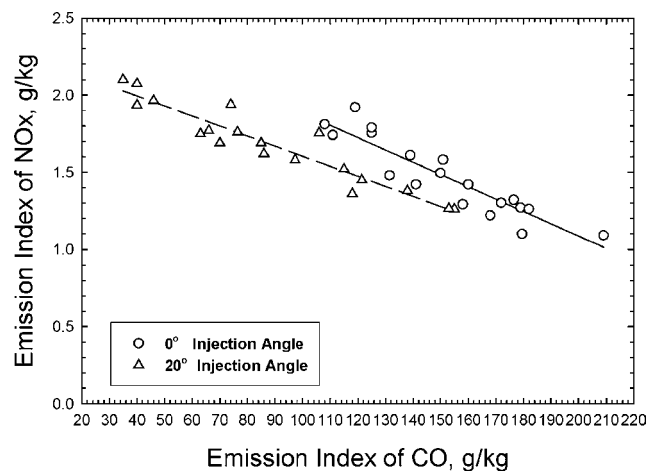


Fig. 35 Effects of injection angle in 0–20 deg range on NOx vs CO trade curve for C injectors: $1.1 < \phi_{cav} < 1.5$.

higher injection angle is less than that for radial injection. The data in Fig. 34 include all cavity equivalence ratios from unity to 1.8.

For the C injectors, the behavior of the NOx vs CO trade curves with injection angle is completely different than that for the D injectors. Figure 35 gives the trade curves for the C injectors at 0-deg injection angle for metered equivalence ratios in the range $1.1 < \phi_{cav} < 1.5$. At 20-deg injection angle when $\phi_{cav} > 1.5$, the correlation breaks down, and there is a systematic variation where individual curves exist for each equivalence ratio. This is believed to be

due to fuel burning outside of the cavity. Note that for the C injectors increasing the injection angle reduces the NOx.

For the C injectors at 37-deg injection angle, the relationship between NOx and CO breaks down into totally individual curves for each cavity equivalence ratio, as is shown in Fig. 36. For lean burning in the cavity (open symbols) the negative gradient of the curves increases with increasing metered cavity equivalence ratio until, for ϕ_{cav} equal to 1.16, NOx is virtually independent of CO. With allowance for entrainment of mainstream air into the cavity, this latter condition probably corresponds to stoichiometric burning within the cavity. The emission index of CO here is equal to about 15 g/kg. This considerably below the equilibrium value of CO for stoichiometric burning at 1 atm (137.9 g/kg); however, because the efficiency is not 100% and UHCs are present, and with the emissions measurement being taken downstream from the cavity in the mainstream, CO would be expected to be below this equilibrium level. As the lean-burning cavity equivalence ratios are increased, the individual curves move toward the ordinate of the graph, that is, a given NOx level is achieved at progressively lower levels of CO. The lower CO arises from the higher temperatures in the cavity. However, because the characteristic time for CO consumption is greater than the characteristic time for NO generation for lean burning, the gradients of the curves increase. At equivalence ratios slightly greater than unity, the characteristic times of CO consumption and NO generation become about equal.

For rich burning in the cavity (solid symbols in Fig. 36) the trade curves backtrack on themselves and become double valued. To understand this behavior, it is necessary to consider the constituent curves from which Fig. 36 is made up. Figure 37 shows the dependency of NOx on the cavity LP for metered cavity equivalence ratios

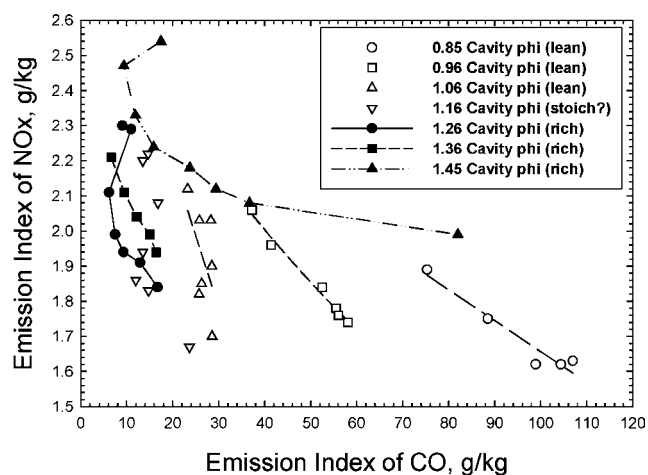


Fig. 36 NOx vs CO behavior for C injectors at 37-deg injection angle.

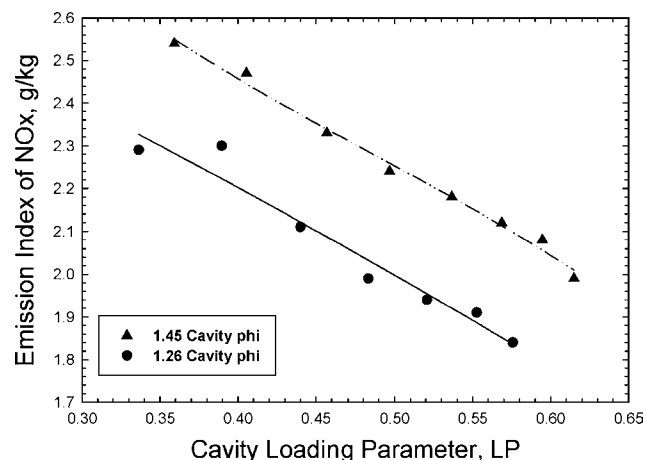


Fig. 37 Dependency of NOx on cavity loading for rich burning in cavity; C injectors at 37-deg injection angle.

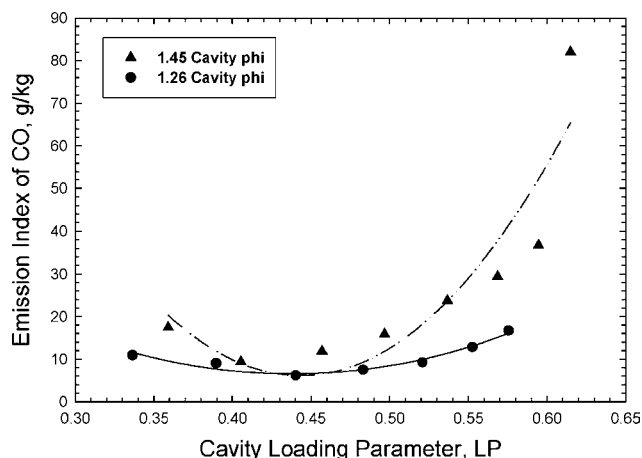


Fig. 38 Dependency of CO on cavity loading for rich burning in cavity; C injectors at 37-deg injection angle.

of 1.45 and 1.26; similarly, Fig. 38 shows the dependency of CO on LP at these equivalence ratios. LP is used here as the connector for consistency with the efficiency plots, Figs. 31 and 32.

Figures 37 and 38 show that NOx decreases essentially linearly with increasing cavity LP with increasing metered cavity equivalence ratio raising the levels of NOx and that CO varies in essentially parabolic fashion with increasing cavity LP with increasing metered cavity equivalence ratio raising the levels of CO, respectively. The minimum in CO is reached at about 0.44 cavity LP (units as given earlier) for both equivalence ratios, and the value of the minimum CO is around 10 g/kg. The characteristics of Figs. 37 and 38 explain the behavior seen in Fig. 33. Note that, for the lean-burning cases given in Fig. 36, NOx decreases for increasing LP with increasing metered cavity equivalence ratio raising the levels of NOx and that CO also increases for increasing cavity LP with increasing metered cavity equivalence ratio reducing the levels of CO.

The NOx behavior of Fig. 37 is explained by the decrease in cavity residence time associated with the increase in cavity LP and the NOx generated within the high-temperature cavity region. The initial decrease in CO of Fig. 38 is explained by an enhancement of burning rate in the cavity as the swirl is increased⁴¹ as cavity LP is increased. Eventually, however, the decrease in cavity residence time with further increases in LP overcomes the burning rate enhancement of increased swirl. There is then insufficient time at high temperatures to burn the CO, so that levels of it increase.

It can be appreciated that a detailed understanding of this combustor concept is still being worked on. More diagnostic evaluations of the behavior seen in Figs. 34–36, for example, are needed to comprehend fully the combustion behavior of the intensely swirling flow in the cavity. In the exploration of the behavior of the UCC, CFD is used as a tool in conjunction with experiment. An example of this use is given in Fig. 39, where the objective was to study mass extraction from the circumferential cavity by the radial strut wakes. In this instance, there are six fuel injectors equally disposed around the main cavity circumference and six non-turning struts, which are placed inline with the fuel injectors. The fuel injectors are angled at 38 deg off-radial and are positioned midway between pairs of angled air jets that generate circumferential swirl around the main cavity. The struts themselves have an angled cavity on the downwind side of the strut. The strut cavity is angled at 45 deg off the vertical from strut tip to hub; at the strut tip the strut cavity is aligned with the forward face of the circumferential cavity. Although the wire frame is a little difficult to interpret, the view is from the rear, and the strut with its cavity can be seen. Figure 39 shows a single fuel injector sector with its two pairs of air jets and the associated strut. It gives contours of gas temperature at two planes across the fore-and-aft cavity width. The first plane is taken through the centerline of the upstream of a pair of air jets, and the second plane is taken through the centerline of the fuel injector. It can be seen from Fig. 39 that

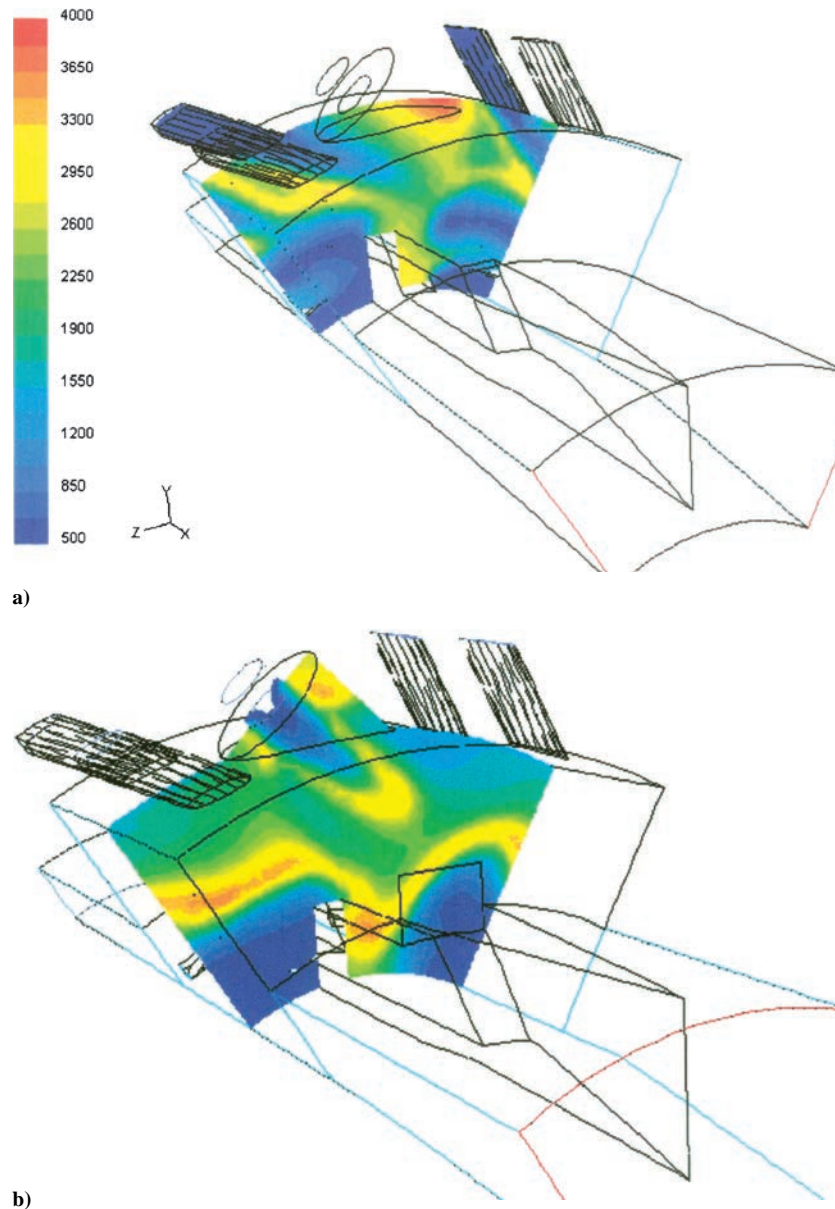


Fig. 39 CFD of UCC research rig; isotherms that reveal mass extraction from the circumferential cavity into radial strut cavities: a) inline with air jets and b) inline with fuel injectors.

hot gas is drawn from the circumferential cavity into the strut cavity, even in the upstream plane, and that this process is continued and strengthened in the injector plane, which is only a small distance downstream from the first plane. This mass extraction by the strut cavity, of course, is the design intent. The motion of mass from the circumferential cavity to the strut cavity is generated by the static pressure difference existing between the two cavities. It is the motion of the mainstream by the strut cavity that creates the necessary low wake pressures to drive the flow from the circumferential cavity. Note that the existence of a significant radial velocity component in the mainstream flow is sufficient to overcome the effects of the pressure difference between the circumferential cavity and the strut radial cavity and, thereby, inhibit mass transfer out of the circumferential cavity. Therefore, outward cant angles (away from the engine centerline in the downstream direction) to the ASC must be avoided.

Although the purpose of these particular CFD studies was to explore the strut cavity design, it can be appreciated that the regions of high temperature shown in Fig. 39 would also result in high rates of nitric oxide generation, $d[\text{NO}]/dt$, and that the CFD tool can also be used for the purpose of minimizing NO by reducing regions of high temperature and by reducing the residence times within such regions. Experimental investigation of the effect of the radial struts and their cavities is currently in progress.

Clearly, the UCC concept itself is at a very early stage of exploration (TRL 1), and much remains to be done to understand the behavior, to formulate design rules, and to develop a reliable combustor. If these tasks can be accomplished, the low-emissions potential appears to be promising. When it is considered that only the functional primary zone of the concept, that is, the circumferential cavity, has been run experimentally thus far, a promising start can be said to have been made; again, much more remains to be accomplished. If the effort is successful, the potential weight savings in a military engine are likely to be considerable so that the effort is well worthwhile.

Engine Thermodynamic Cycle

The formulation of the ICAO emissions regulations are such that engine fuel burn plays an important role in the integrated emissions. Thus, a rather mediocre low-emissions combustor concept, if placed in a really efficient engine, can, in fact, satisfy the regulations with adequate margins. Therefore, the engine cycle itself can be a powerful tool in the effort to reduce emissions. Reduction in fuel burn with the Brayton cycle translates into a requirement for higher OPRs, increased BPRs, and higher fuel/air ratio combustors. The aircraft gas turbine is mounted in a moving vehicle so that the

overall efficiency is a product of the propulsive and thermal efficiencies. The most practical way to increase overall efficiency is to increase propulsive efficiency by reducing the exhaust jet velocity. This may be done by increasing BPR. The use of higher peak temperatures in the core engine allows higher OPRs without a falloff in thermal efficiency, as well as increasing thermal efficiency directly. Combustion at high pressures with consequently high air inlet temperatures and high turbine inlet temperatures together with higher combustor exit temperatures makes control of NO_x much more difficult. The high temperatures also increase engine material maintenance costs substantially.

The difficulties described arise in part because all of the heat release takes place in a single stage. A gas turbine engine has been proposed that uses a constant temperature (CT) cycle and intraturbine combustion such that gases enter the low-pressure turbine at the same temperature as they enter the high-pressure turbine. This allows large amounts of power extraction to be made from the low-pressure turbine for a variety of purposes.^{42,43} A variant of the CT cycle is the near-CT (NCT) cycle, in which second-stage combustion is confined to the inter-turbine duct between the high- and low-pressure turbines⁴⁴ for two-shaft engines. The cycle is not really new and has been known since the 1950s, but there are many difficulties in the way to achieving such an engine, although one model has been built and sold for ground power generation.⁴⁵

Such a NCT engine has been dubbed the interturbine burner (ITB) engine. High levels of low-pressure turbine energy are achieved with only a modest temperature rise across the ITB, and with reduced maximum temperatures in the engine when compared to the equivalent power Brayton cycle engine. Clearly, reducing the maximum temperature in an engine lowers its thermal efficiency, and so the ITB engine is better for some applications than others. Some examples that have been identified are some supersonic cruise applications; those applications requiring modest thrust augmentation, where a conventional afterburner might be otherwise required; and military applications demanding generation of large amounts of electrical power, where a special purpose auxiliary engine might otherwise have to be carried. Note that many commercial applications are now facing similar difficulties where the growing electrical power-generation requirements can cause near-continual operation of the auxiliary power unit, which is also a source of exhaust emissions. An example of another military application where large amounts of power extraction are needed for short periods of time is to drive a lift fan for standard takeoff and vertical landing operations. For most subsonic commercial applications, the NCT cycle engine does not even approach competitiveness with the Brayton cycle engine until very high OPRs (greater than 40) and ultrahigh BPRs (greater than 10) are used. The use of ultrahigh BPRs improves the propulsive efficiency and tends to make up for the reduction in thermal efficiency.

For specific thrust to be maintained, no increases in an ITB engine length can be allowed. Therefore, the ITB itself must be exceedingly compact. The UCC discussed earlier is a possible combustor concept for an ITB engine, being considered for both the main and interturbine combustors. There are two benefits to the ITB engine. The lowered peak temperatures improve engine durability, and they offer the possibility of reduced NO_x.

One ongoing study⁴⁶ to assess the NCT cycle and to evaluate the combustion possibilities has been applied to a future, large (65,000-lbf class) long-range transport, geared-turbofan two-shaft engine of ultrahigh BPR and high OPR, where an ITB engine sized to thrust for a particular mission profile is being compared to the equivalent advanced Brayton cycle engine. The two engines were designed to thrust and matched in OPR and specific thrust at the aerodesign point (36,000 ft, 0.85 flight Mach number). This matching favors ITB engine durability and low exhaust emissions over fuel burn, and the two engines can have a common nacelle that favors fuel burn for the Brayton cycle engine. At sea level static conditions, the OPR was 45.8 and the BPR was 22. With reference to Fig. 28, it can be seen that at this OPR the current generation of low NO_x combustors could not meet the CAEP/4 regulation for NO_x with sufficient margin (industry practice of 20%) for single-engine certification.

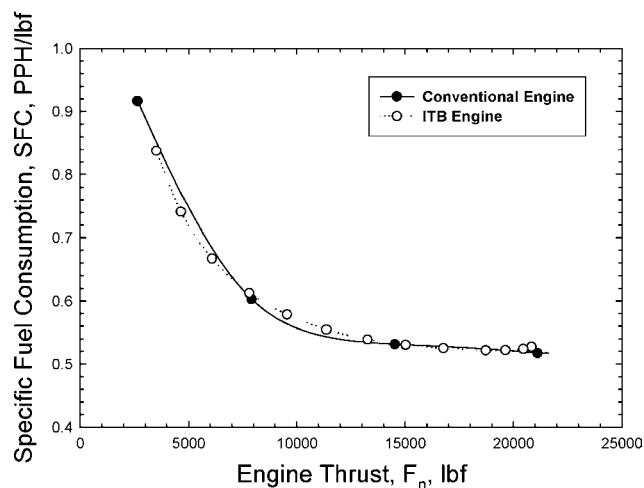


Fig. 40 Comparison of part-power specific fuel consumption for the Brayton and NCT cycle engines at initial cruise: initial cruise point 31,000 ft; and 0.85 M_0 .

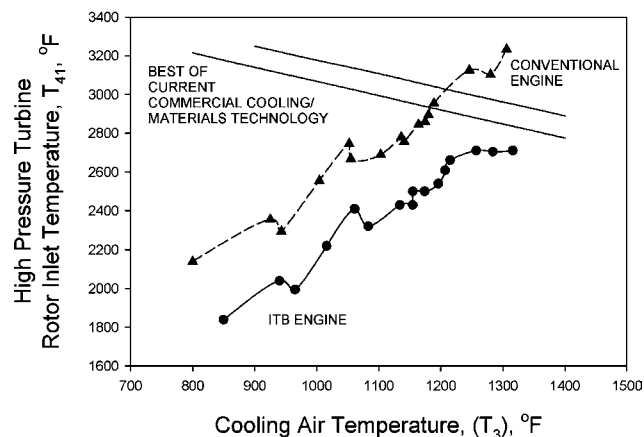


Fig. 41 Durability assessment for high-pressure turbine of the Brayton and NCT cycle engines around mission profile.

A comparison of the specific fuel consumption for the two engines at the initial cruise point is given in Fig. 40, where it can be seen that at this flight condition there is essentially no difference in part-power performance between the two engines. However, with the design choices imposed on the ITB engine for the comparison, the fuel burn for this very long-range mission of 7000 n miles unrefueled with complete crew of 21 plus their baggage, usual fuel reserves and 180,000 lbm of payload was +3.6% that of the baseline Brayton cycle engine. Relaxation of the common nacelle requirement would allow the ITB engine to utilize a higher BPR and, thus, reduce its fuel-burn penalty.

Figure 41 enables a durability assessment to be made for the expensive high-pressure turbines of the two engines from their installed performances. The temperatures given are around the entire mission profile. Note that the advanced Brayton cycle engine would severely challenge the best of current turbine blade cooling/materials technology, whereas the ITB engine would be more than satisfactory with 1990s technology.

The main combustor temperature rise requirements around the mission profile for the two engines, and for the ITB combustor, are given in Figs. 42 and 43, respectively. It can be seen that the main combustor of the ITB engine has a very easy task compared to that of the Brayton cycle engine, where the respective maximum temperature rises are 1500°F vs 2020°F. The ITB engine interturbine combustor has a maximum temperature rise of only 640°F at takeoff power; it is severely throttled back at cruise to only 185°F to minimize fuel-burn penalties. (Ideally, it should be shut down completely, but this would necessitate either a

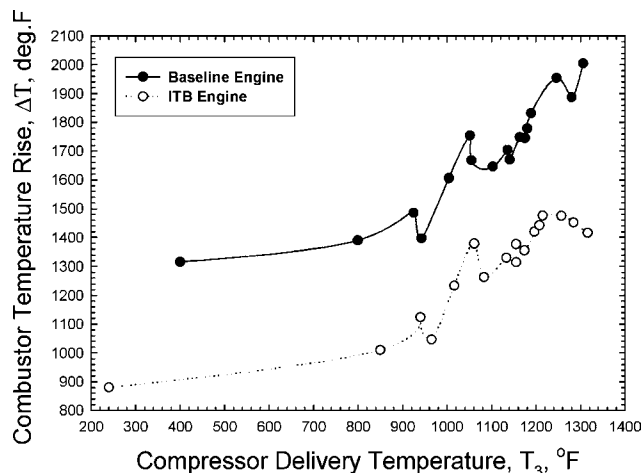


Fig. 42 Comparison of required temperature rise for main combustors of Brayton and NCT cycle engines around mission profile.

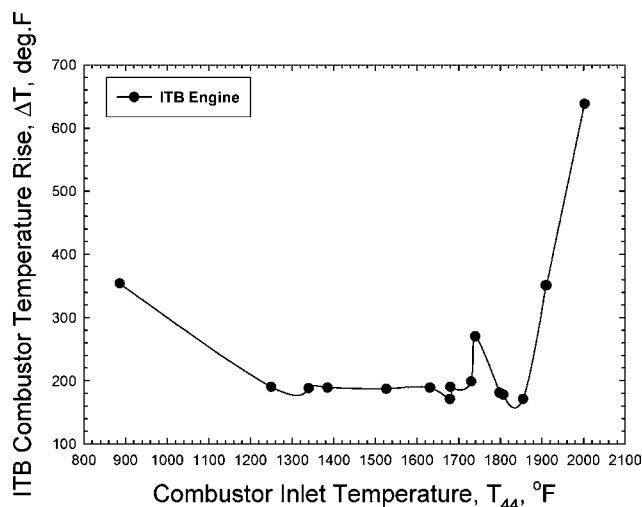


Fig. 43 Temperature rise requirements for interturbine combustor in NCT cycle engine around mission profile.

low-pressure turbine or a variable area propelling nozzle for the core engine.)

At takeoff (rotation), the maximum main combustor inlet temperature T_3 was 1316°F and the exit temperature T_4 was 2710°F; at the same conditions the inlet temperature to the ITB, T_{44} , was 2002°F and the exit temperature T_{45} was 2640°F. The combustion pressure for the main combustor, P_4 , was 853 psia, whereas the ITB combustion pressure P_{45} was 214 psia. With the modest temperature rise requirements given in Figs. 42 and 43, these are not especially severe conditions to design combustors for, and these combustors should not be severe NOx producers. For the baseline engine, the equivalent main combustor inlet and outlet temperatures were 1306 and 3310°F, respectively, and the combustion pressure was 825.5 psia. To get a general feel for the magnitude of the impact of these temperatures on possible NOx, consider Fig. 20 for the NASA John H. Glenn Research Center LDI combustor. The Brayton cycle baseline engine combustor exit temperature of 2094 K would indicate, with extrapolation, a NOx EI of around 100 g/kg, compared to a NOx EI of around 20 g/kg (interpolation only) for the ITB main combustor at its exit temperature of 1761 K.

Note that it was difficult to achieve a suitable engine flowpath for this two-shaft ITB engine. The rotational speed of the fan was so low that the booster compressor, which rotated at the same speed as the fan, had either very small annular passage heights in a conventional arrangement, or had too many stages if it was arranged inboard and parallel with the fan. A three-shaft engine would be a preferable layout. A three-shaft engine, with its three turbines, would also offer the possibility of using two ITB combustors. The use of two

ITB combustors is a thermally improved approximation to the ideal CT cycle engine.

The ITB engine and combustor concepts like the UCC that might help to make the ITB engine possible for some applications are both a long way from being made service-ready. They are included here to indicate some of the kinds of innovative thinking that are going to be necessary to continue the advancement of the combustion art in the face of ever-more demanding and restrictive design requirements.

Water injection also offers the possibility of Brayton cycle modifications to reduce takeoff NOx (Ref. 47). In this instance, rather than direct injection into the combustor as discussed earlier, water would be injected into the engine compression system. Through evaporation of the water spray, this gives a cooled compression process that reduces the amount of work that has to be extracted by the turbines to drive the compressors. For a constant thrust, therefore, the peak temperatures in the engine can be reduced. The mass of the injected water provides some thrust augmentation potential, so that again, for constant thrust, the peak temperatures can be lowered further. The combination of a cooled compression and reduced peak temperatures provides for a worthwhile NOx reduction. A system might be devised where this type of water injection could be used for NOx control during takeoff and where a low emissions combustor design without water injection is optimized for low NOx at altitude cruise conditions.

Again, the reduction in maximum temperatures for a constant thrust condition with cooled compression from water injection represents a reduction in engine thermal efficiency, and this could infer a specific fuel consumption issue. However, the time of water injection would only cover aircraft takeoff, climbout, and initial climb at most. Therefore, any fuel-burn penalties might not be severe. If combined with a low-emissions burner for low NOx at altitude, the injection of significant quantities of water into the compressor might exert some adverse effects on the combustion process, the magnitude of which would depend on the type of low-emissions combustor used. These could include local flame extinctions and increase in particulates. An additional concern where high stage loadings are used in the compression system, is the possible effect of water injection on movement of the operating line closer to the stall line for the compressor. Water injection requires careful consideration before implementation should be considered.

Summary

Control of engine exhaust emissions has become a leading design requirement of combustion equipment for aircraft gas turbine engines. It is an absolute requirement for commercial engines where compliance has to be demonstrated for certification. For military engines, it is becoming increasingly important even during peacetime, where aircraft operations and deployments can be affected through compliance with the NAAQS. The issue of direct emissions control in military engines will be addressed through the VAATE program. The story of reduced emissions combustors is one where progress has been made through coming to understand the root causes of pollutant generation. Emissions of CO and UHCs have proved relatively easy to control; NOx was harder, but progress has been made, albeit at the expense of an ever-growing complexity, cost, and weight of the combustion system. These developments are contrary to the desires of military engine designers, to whom thrust/weight ratio and specific thrust are vital issues. The complexity of these systems also adversely affects the cost and durability, and affordability is of growing importance to the military as well as to commercial operators. NOx generated by aircraft has emerged as being the really serious pollutant of the three gaseous emissions produced by aircraft gas turbine engines. The early successes in emissions reduction have resulted in a progressive lowering of the regulatory bar for this pollutant for commercial applications. However, the easy things in NOx reduction have all been done, and the way ahead requires more than incremental technology for continued successes. It appears as though more radical thinking beyond incremental technology may well be needed to meet the challenges presented in NOx reductions, especially for military applications. The regulations are now pressing low NOx technology to the point where changes to

the thermodynamic cycle are being thought about seriously for the future.

The issues of exhaust smoke and the particulates that make it up, together with the effects of contrails, have not been discussed here. However, they are growing in importance and are likely to receive increasing attention in the future, thereby exacerbating the difficulties of low-emissions combustor design.

The reduced emissions technology developed for commercial engines appears to be driven by NO_x considerations into systems that, by and large, are becoming ever more unsuitable for direct application to combat aircraft through their increased weight, cost, reliability, and operability penalties. Emissions reduction for such military applications can certainly borrow some of the commercial engine technology, but becomes very challenging for achieving low NO_x. Radical thinking in low-emissions design combustors will be needed, as well as some consideration of possible cycle trades, to satisfy the military application.

Acknowledgments

Part of this work is supported by Air Force Office of Scientific Research (AFOSR) with Julian Tishkoff serving as program manager, and we express our appreciation to J. Tishkoff for his courage, foresight, and enthusiasm. Another part of the work is supported by U.S. Air Force Contract F33615-01-C-2133 with J. Zelina as program manager. Hukam Mongia of General Electric was kind enough to make available to us a prepublication copy of his paper, AIAA Paper 2003-2657. Parts of this paper were extracted from Ref. 45, and the authors wish to thank C. Pellerin from the Strategic Environment Research and Development Program Office for his support. The authors wish to thank their colleagues in the U.S. Air Force and the industry for their many direct and indirect contributions over the years to this work.

References

- Robinson, A. B., Baliunas, S. L., Soon, W., and Robinson, Z. W., "Environmental Effects of Increased Carbon Dioxide," Oregon Inst. of Science and Medicine, Cave Junction, Oregon and George C. Marshall Inst., Washington, DC, Jan. 1998.
- "Ten Thousand Cloud Makers," editorial, *Science News*, Vol. 150, 6 July 1996, pp. 12, 13.
- Earth Science: "What Aircraft Leave Behind," editorial, *Science News*, Vol. 154, 18 July 1998, p. 47.
- Ballal, D. R., and Zelina, J., "Progress in Aero Engine Technology (1939–2003)," *Journal of Aircraft*, Vol. 41, No. 1, 2004, pp. 43–50.
- Lewis, J. S., and Niedzwiecki, R. W., "Aircraft Technology and Its Relation to Emissions," *Aviation and the Global Atmosphere*, Cambridge Univ. Press, London, 1999, Chap. 7.
- Blust, J. W., Ballal, D. R., and Sturgess, G. J., "Emissions Characteristics of Liquid Hydrocarbons in a Well-Stirred Reactor," *Journal of Propulsion and Power*, Vol. 15, No. 2, 1999, pp. 216–223.
- Sturgess, G. J., McKinney, R. G., and Morford, S. A., "Modifications of Combustor Stoichiometry for Reduced NO_x Emissions from Aircraft Engines," *Journal of Engineering for Gas Turbines and Power*, Vol. 115, No. 3, 1993, pp. 570–580.
- Sturgess, G. J., "Combustor Design Trends for Aircraft Gas Turbine Engines," American Society of Mechanical Engineers, ASME Paper 96-TA-29, June 1996.
- Sturgess, G. J., "Advanced Low-Emissions Catalytic Combustor Progress," Phase 1 Draft Final Rept. PWA-5587, Pratt and Whitney, East Hartford, CT, May 1979.
- Sturgess, G. J., "An Account of Fuel/Air Unmixedness Effects on NO_x Generation in Gas Turbine Combustors," *Intersociety Engineering Conference on Energy Conversion*, Paper IECEC-98-353, Aug. 1998.
- Sturgess, G. J., "Lecture Notes on Advanced Aircraft Engine Design, Vol. II—Engine Combustion and Emission Reduction," *Advanced Engine Design Workshop*, Inst. of Aeronautics and Astronautics, National Cheng Kung Univ., Tainan, Taiwan, Republic of China, 1994.
- Washam, R. M., and Mellor, A. M., "Emissions Correlations for Conventional Gas Turbines," EPA Grant No. R-804443-01—Final Report, Purdue Univ., Rept. PURDU-CL-77-06, Lafayette, IN, Dec. 1977.
- Takahashi, F., Switzer, G. L., and Shouse, D. T., "Structure of a Spray Flame on a Production Engine Combustor Swirl Cup," *Proceedings of the Twenty-Fifth International Symposium on Combustion*, Combustion Inst., Pittsburgh, PA, 1994, pp. 183–191.
- Lefebvre, A. H., *Gas Turbine Combustion*, McGraw-Hill, New York, 1983, Chap. 11.
- Tuthill, R. J., Madden, T. J., Craig, H., and Tuthill, R. S., "Combustor Bulkhead with Improved Cooling and Air Recirculation Zone," Patent 6,164,074 issued 26 Dec. 2000.
- Hedman, P. O., Sturgess, G. J., Warren, D. L., Goss, L. P., and Shouse, D., "Observations of Flame Behavior from a Practical Fuel Injector, Using Gaseous Fuel in a Technology Combustor," *Journal of Engineering for Gas Turbines and Power*, Vol. 117, July 1995, pp. 441–452.
- Switzer, G., Sturgess, G. J., Sloan, D., and Shouse, D., "Relation of CARS Temperature Fields to Lean Blowout Performance in an Aircraft Gas Turbine Generic Combustor," AIAA Paper 94-3271, July 1994.
- Bahr, D. W., "Technology for the Design of High Temperature Rise Combustors," *Journal of Propulsion and Power*, Vol. 3, No. 2, 1987, pp. 179–186.
- Fenimore, C. P., "Formation of Nitric Oxide in Premixed Hydrocarbon Flames," *Proceeding of the Thirteenth International Symposium on Combustion*, Combustion Inst., Pittsburgh, PA, 1971.
- Melconian, J. O., *The Design and Development of Gas Turbine Combustors*, Vols. 1 and 2, Northern Research and Engineering Corporation, Woburn, MA, 1980.
- Gogineni, S., Shouse, D., Frayne, C., Stutrud, J., and Sturgess, G. J., "Combustion Air Jet Influence on Primary Zone Characteristics for Gas Turbine Combustors," *Journal of Propulsion and Power*, Vol. 18, No. 2, 2002, pp. 407–416.
- Lohman, R., Pratt and Whitney, East Hartford, CT, 1996.
- Pandalai, R. P., and Mongia, H. C., "Combustion Instability Characteristics of Industrial Engine Dry Low Emission Combustion Systems," AIAA Paper 98-3379, July 1998.
- Segalman, I., McKinney, R. G., Sturgess, G. J., and Hung, L.-M., "Reduction of NO_x by Fuel-Staging in Gas Turbine Engines—A Commitment to the Future," *Fuels and Combustion Technology for Advanced Aircraft Engines*, CP-536, AGARD, 1993.
- Hassa, C., Carl, M., Frodermann, M., Behrendt, T., Heinz, J., Rohle, I., Boehm, N., Schilling, T., and Doer, T., "Experimental Investigation of an Axially Staged Combustor Sector with Optical Diagnostics at Realistic Operating Conditions," *Gas Turbine Engine Combustion, Emissions and Alternative Fuels*, RPT-MP-14, NATO Research and Technology Organization, June 1999.
- Brehm, N., Schilling, T., Mack, A., and Kappler, G., "NO_x Reduction in a Fuel Staged Combustor by Optimization of the Mixing Process and the Residence Time," *Gas Turbine Engine Combustion, Emissions and Alternative Fuels*, RPT-MP-14, NATO Research and Technology Organization, June 1999.
- Segalman, I., Smith, R., Sturgess, G. J., Morford, S., and Hoke, J., "Engine Demonstration of NO_x Reductions with a Fuel-Staged Gas Turbine Combustor," AIAA Paper 94-2712, July 1994.
- Heywood, J., and Mikus, T., "Parameters Controlling Nitric Oxide Emissions from Gas Turbine Combustors," *Atmospheric Pollution by Aircraft Engines*, CP-9-13, AGARD, April 1973.
- Tacina, R., Wey, C., Laing, P., and Mansour, A., "Sector Tests of a Low-NO_x, Lean-Direct-Injection, Multipoint, Integrated Module Combustor Concept," American Society of Mechanical Engineers, ASME GT-2002-30089, June 2002.
- Simmons, H. C., "Empirical Formulas (*sic*) for Prediction of Spray Drop Sizes," Parker-Hannifin Rept. 1966.
- Mongia, H. C., "TAPS—A 4th Generation Propulsion Combustor Technology for Low Emissions," AIAA Paper 2003-2657, July 2003.
- Roquemore, W. M., Vihinen, I., Hartrauft, J., and Mantis, P. M., "Trapped Vortex Combustor for Gas Turbine Engines," Annual Report to Strategic Environmental Research and Development Program, 1998.
- Hsu, K.-Y., Goss, L. P., and Roquemore, W. M., "Characteristics of a Trapped-Vortex Combustor," *Journal of Propulsion and Power*, Vol. 14, No. 1, 1998, p. 57.
- Sturgess, G. J., and Hsu, K.-Y., "Entrainment of Mainstream Flow in a Trapped-Vortex Combustor," AIAA Paper 97-0261, Jan. 1997.
- Roquemore, W. M., Shouse, D., Burrus, D., Johnson, A., Cooper, C., Duncan, B., Hsu, K.-Y., Katta, V. R., Sturgess, G. J., and Vihinen, I., "Trapped Vortex Combustor Concept for Gas Turbine Engines," AIAA Paper 2001-0483, Jan. 2001.
- Anthenian, R. A., Mantz, R. A., Roquemore, W. M., and Sturgess, G. J., "Experimental Results for a Novel, High Swirl, Ultra Compact Combustor for Gas Turbine Engines," *Western States Section Combustion Institute Meeting*, April 2001.
- Zelina, J., Ehret, J., Hancock, R. D., Shouse, D. T., Sturgess, G. J., and Roquemore, W. M., "Ultra-Compact Combustion Technology Using High Swirl to Enhance Burning Rate," AIAA Paper 2002-3725, June 2002.
- Mestre, A., and Benoit, A., "Combustion in Swirling Flow," *Proceedings of the Fourteenth International Symposium on Combustion*, Combustion Inst., Pittsburgh, PA, 1973, pp. 719–725.

³⁹Lewis, G. D., "Centrifugal-Force Effects on Combustion," *Proceedings of the Fourteenth International Symposium on Combustion*, Combustion Inst., Pittsburgh, PA, 1973, pp. 413–419.

⁴⁰Yonezawa, Y., Toh, H., Goto, S., and Obata, M., "Development of the Jet-Swirl High Loading Combustor," AIAA Paper 90-2451, July 1990.

⁴¹Zelina, J., Sturgess, G. J., Mansour, A., and Hancock, R. D., "Fuel Injection Design Optimization for an Ultra-Compact Combustor," International Society on Air Breathing Engines, Paper ISABE-2003-1089, Sept. 2003.

⁴²Sirignano, W. A., Delplanque, J. P., and Lui, F., "Selected Challenges in Jet and Rocket Engine Combustion Research," AIAA Paper 97-2701, July 1997.

⁴³Sirignano, W. A., and Liu, F., "Performance Increases for Gas-Turbine Engines Through Combustion Inside the Turbine," *Journal of Propulsion*

and Power, Vol. 15, No. 1, 1999, pp. 111–118.

⁴⁴Lui, F., and Sirignano, W. A., "Turbojet and Turbofan Engine Performance Increases Through Turbine Burners," AIAA Paper 2000-0741, Jan. 2000.

⁴⁵Eroglu, A., Dobbeling, K., Joos, F., and Brunner, P., "Vortex Generators in Lean-Premix Combustion," American Society of Mechanical Engineers, ASME 98-GT-487, June 1998.

⁴⁶Sturgess, G. J., "Turbine Burner for Near-Constant Temperature Cycle Gas Turbine Engine: Application to a Large Commercial Subsonic Transport Engine—A Progress Report," *Workshop on Inter-Turbine Burning Engines*, Air Force Research Lab. (AFRL), Cleveland, OH, Feb. 2003.

⁴⁷Daggett, D. L., "Water Misting and Injection of Commercial Aircraft Engines to Reduce Airport NOx," NASA CR-2004-212957, March 2004.

Acoustic Measurements for a Pulse Detonation Engine

Leonard Shaw, Kevin Harris, Fred Schauer
Air Force Research Laboratory
Wright Patterson AFB
Dayton, Ohio

John Hoke
Innovative Scientific Solutions, Inc
Dayton, Ohio

Abstract

The acoustic environment of a pulse detonation engine was measured. The engine consisted of one to four detonation tubes which were detonated at 20 or 40 Hertz. Fill fractions and equivalence ratios of 1 and 0.5 were tested. All of the testing was conducted in a test cell which was not acoustically treated. Measurements were made near the exit of the tubes and up to a distance 12 feet. Time histories and narrow band spectral analysis were generated. Comparisons of sampling frequencies of 200K and 20K were conducted. Numerous potential noise suppression approaches were evaluated. The results indicate that a very high level pulse is generated near the exit of the tubes but tends to decrease in amplitude fairly quickly with distance since the higher frequency energy dissipates in the atmosphere.

Introduction

The pulse detonation engine (PDE) consists of a single, or multiple tubes, which are utilized to detonate the fuel at very high pressures. Since the detonation is occurring at a very high pressure a shock wave is generated in the tube and exits at the end of the tube. The associated noise of the process is of great interest since shock waves can generate very intense noise levels. The purpose of this paper is to present some early developmental acoustic data acquired during the development of a revolutionary pulse detonation engine (PDE) at the Air Force Research Laboratory's Propulsion Directorate (AFRL/PR). The new PDE is being developed in-house with a fairly low level of funding by utilizing existing engine components such as the head off of a General Motor's Quad 4 engine. The engine test setup is shown in Figure 1. The revolutionary new PDE is a single cycle air breathing propulsion system capable of efficient Mach 0-4+ operation. The new engine will be substantially lighter than turbine engines and be at least an order of magnitude less expensive. The overall objectives of the program are to develop the new engine, integrate it into a subsonic manned airframe (LongEZ), and evaluate the flight performance of the system. One of the concerns of the integrated engine is the acoustic environment associated with the detonation process of the engine. The concerns are the noise levels the pilot will be exposed to and the potential structural damage from the high levels. The Air Vehicles Directorate (AFRL/VA) initiated an acoustic measurement and suppression program to define the acoustic levels generated by the engine and propose methods to mitigate the radiated noise. Preliminary acoustic measurements have been made while the engine was operated at several conditions. The different operating conditions included various fuel fill fractions (FF=percent of the detonation tube filled with fuel) and equivalence ratios (ER=ratio of fuel to air where an ER less than one is lean and greater than one is rich). Since the detonation process occurs at a very high speed, the acoustic data were acquired at a range of sampling rates up to and including 200,000 samples per second. The preliminary acoustic data shows that the detonation pulse is approximately 30 microseconds in duration with an average amplitude of almost 6 pounds per square inch (psi) at a distance of 12 inches from the tube exit. Figure 2 is a time history from one of the maximum conditions. Expressed in dB this would be greater than 185 dB. The broadband levels were of the order of 154 dB for the worst case measured. By changing the FF and ER the pulse amplitude could be reduced to 1.7 psi and the broadband levels to 143 dB. Additional acoustic measurements are planned to more fully define the levels of potential suppression concepts and directivity patterns. In addition to the test cell measurements, ground run-up and fly-over measurements will also be conducted. Background on the performance of the PDE is given in References 1 and 2 and will not be repeated here.

A large amount of research has been directed to the prediction and development of pulse detonation engines. Both computational and experimental efforts have addressed the problems associated with successful operation of the engine. However, very little effort has been directed to the noise generated by the engines. The most extensive paper addressing the acoustic environment of a pulse detonation engine is Reference 3. In it the authors present the results of an experimental test of a single detonation tube 2.54 cm diameter and

60.96 cm long operating in an anechoic test facility. The test matrix included various exhaust nozzle configurations, tube fuel fill fractions, and detonation frequency. Using an array of microphones located 2.89 meters from the exit of the nozzle, they recorded the acoustic environment of the detonations. They captured the very short duration pulses generated by the detonations and reported overall sound pressure levels from about 100 dB to 122 dB for the range of parameters tested. The high frequency energy in the spectra due to the very short pulses was captured. They concluded that sound pressure levels increase with increasing fill fraction and a converging nozzle reduces the sound pressure level. A diverging nozzle also reduced the sound pressure levels in the downstream direction but was not consistent for different nozzle lengths and fill fractions. No attempt to quantify the affect of the different configurations on thrust was undertaken but it was acknowledged that thrust must be a prime consideration in selecting an optimum noise suppression concept.

Results

The acoustic results presented in this paper were acquired from the same facility and pulse detonation engine described in References 1 and 2. A brief description will be repeated here for the convenience of the reader. The baseline configuration is shown in Figure 1. The photo shows four tubes but much of the testing was accomplished with only one tube operating. The time history shown in Figure 2 is representative of the pulse shape but the maximum level varies with engine operating parameters and the distance from the exit. It was shown in Reference 4 that the shock wave emanating from the tube exit rapidly forms a vortex ring which also generates sound. The shock wave rapidly decays resulting in less energy at the higher frequencies.

Most of the acoustic data were acquired with Gulton MVA 2400 ¼ inch microphones. To illustrate the lack of capability of some transducers to capture the high frequency energy that the shock wave generates, one of the Larson Davis microphones used to measure the acoustic environment of the Long EZ propeller aircraft was recorder for the PDE. The results for both microphones are shown in Figure 3. It is very evident that the peak level is not capture by the Larson Davis microphone since it does not have a fast enough response time and high enough frequency capability. Thus, all data presented in this paper will be from the Gulton microphones. The data were acquired with Labview software with a sampling frequency of 200 kilohertz. Five seconds of data were recorded from all four of the microphones shown in Figure 4. The microphone mounting rail was located 13 inches from the tube at a 45 degree angle. The microphones were spaced 15 inches apart on the mounting rail resulting in one being 15 inches behind the exit plane, one at the exit plane, one at 15 inches aft of the exit plane and the last one 30 inches aft of the exit plane. The data were reduced into narrowband spectra using custom written Labview software. A block size of 100,000 samples was used and 2.5 seconds of data were analyzed resulting in a frequency bandwidth of 2 Hertz.

The resulting spectra from each of the microphones are shown in Figures 5-8. The pulsed detonation engine was fired at 20 Hertz with hydrogen fuel. The fill fraction was 1 as well as the equivalence ratio. The firing frequency tone of 20 Hertz is clearly evident in each of the spectra except the most aft location. The tone is still there but hidden by the other noise being generated. It is observed that there is significant amount of energy at the higher frequencies, which is expected since the rise time of the pulse is very short. This high frequency energy contributes to the sharp pressure pulse but it is believed that it will not be a contributor to hearing concerns or structural vibration problems.

Besides defining the absolute noise levels of the PDE, methods to suppress the noise were investigated. Many different concepts were assessed as to their effectiveness in suppressing the generated noise. The range of designs included notches at the exit of the nozzle, small secondary air jets at the exit, elbow, tee, and a Helmholtz resonator. Five of the tested configurations are shown in figure 9 through 13. The results of these evaluations are summarized in Figure 14. The pressure pulse amplitude is shown in dB for convenience. The values shown in the figure are based on an average of the four microphones. As observed in the Figure, essentially only the fill fraction and equivalence ratio had any significant affect on the noise levels. Figure 15 shows in detail the effects of fill fraction (FF) and equivalence ratio (ER). Both were run at 1.0 and 0.5. Each alone reduced the levels, FF by 4 dB and ER by 2 dB. When both are tested simultaneously the reduction is the sum of the two individually, or 6dB. The affect on thrust of each of the concepts was measured but the results are not presented in this paper. Any noise suppression concept selected for application must have minimal impact on engine thrust.

The question arises as to how fast the sampling rate is required to be to capture the data. Since the pulses have a very short rise time, it is assumed that the sampling rate will have to high enough to capture high frequency data. Figure 16 shows a comparison of spectra for samplings rates of 200K and 20K. It appears that the data sampled at 20K is on top of the 200K data and there is only 1 dB difference in over all sound pressure level between the two curves. There is energy at the high frequencies but very little in

comparison to what is at the lower frequencies. Figure 17 shows the two spectra up 1000 Hertz. As seen in the figure they truly do lie on top of each other. Thus, it can be concluded that for structural response purposes, sampling at 20K will capture essentially all of the acoustic energy which will be exciting the local structure. Also, for environmental noise concerns, the high frequency energy will not propagate a long distance because of atmospheric attenuation. Thus, a 20K sampling rate would be sufficient if higher rates are not available.

To illustrate the amount of reduction in the sound pressure levels at further distances from the detonation tube, Figure 18 shows the time histories from a nominal 1 foot and 12 foot location. Clearly the change in the amplitude is quite large. Figure 19 shows the related spectra out to 50K. At the 12 foot location the higher frequency levels are lower than the noise floor of the data acquisition and thus appear flat. The decrease in the overall sound pressure level is 25 dB. For true spherical spreading one would expect approximately 23 dB. Since the measured level is lower than the expected level, one can conclude that the additional reduction is due to the atmospheric attenuation at the higher frequencies. The same spectra are shown in Figure 20 out to 10K. The same amount of reduction is observed only going out to 10K which seems to counter the high frequency argument. A possible explanation could be that the higher frequencies could include energy below 10K.

In conclusion, the noise generated by a pulse detonating engine was measured and the affect of several noise suppression concepts was evaluated. The overall sound pressure levels were shown to be in the range of 147dB to 159 dB at the microphone array located 13 inches from the exit of the detonation tube. There is a high amplitude pressure pulse generated as can be observed in the time history, but much of the energy contained in the pulse is at the very high frequencies above hearing and structural frequencies of interest. Numerous noise suppression concepts were evaluated but with very limited success.

References

1. Schauer, F., Stutrud, J., and Bradley, R., "Detonation Initiation Studies and Performance Results for Pulse Detonation engine Applications," 39th AIAA Aerospace Sciences Meeting, AIAA 2001-1129.
2. Hoke, J., Bradley, R., Stutrud, J., and Schaur, F., "Integration of a Pulsed Detonation Engine With an Ejector Pump and With a Turbo-charger as Methods to Self-Aspirate," 40TH AIAA Aerospace Sciences Meeting, AIAA 2002-0615.
3. Allgood, D., Glaser, A., Caldwell, N., and Gutmark, E., "Acoustic Measurements of a Pulse Detonation Engine," 12th AIAA/CEAS Aeroacoustics Conference, AIAA 2004-2879.
4. Das, D., Arakeri, J., Krothapalli, A., and Louenco, M., "Compressible Vortex Ring: A PIV Study," 7th AIAA/CEAS Aeroacoustic Conference, AIAA 2001-2214.

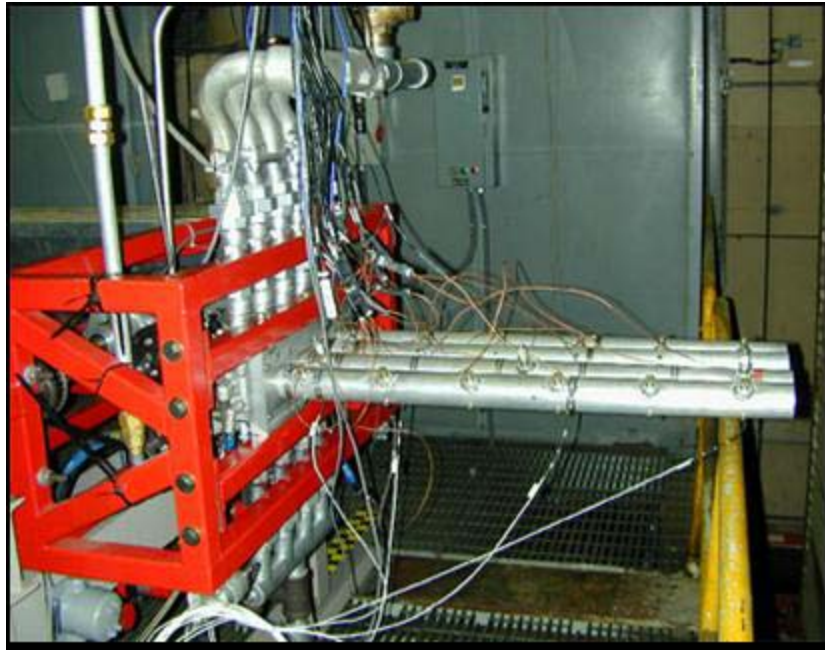


Figure 1. Baseline Configuration Showing Four Tubes

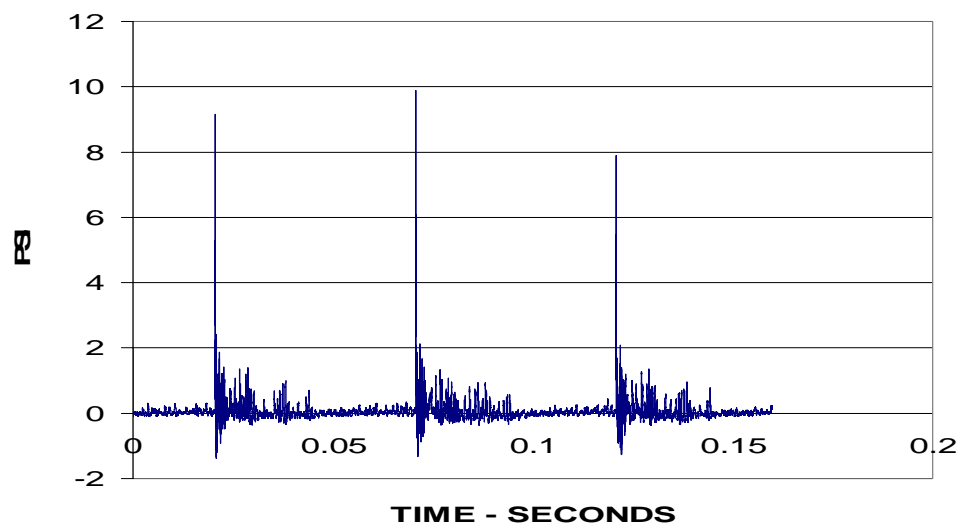


Figure 2 Typical Time History for 20 Hertz Firing Frequency, Fill Fraction and Equivalency Ratio of 1.0

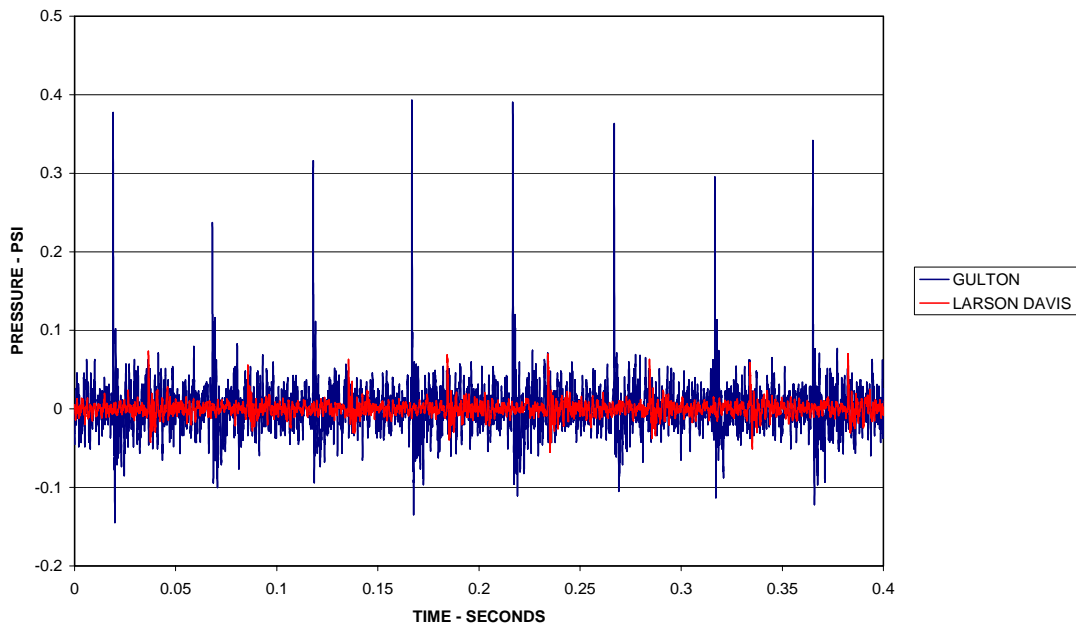


Figure 3 Comparison of Time Histories From Two Different Microphones

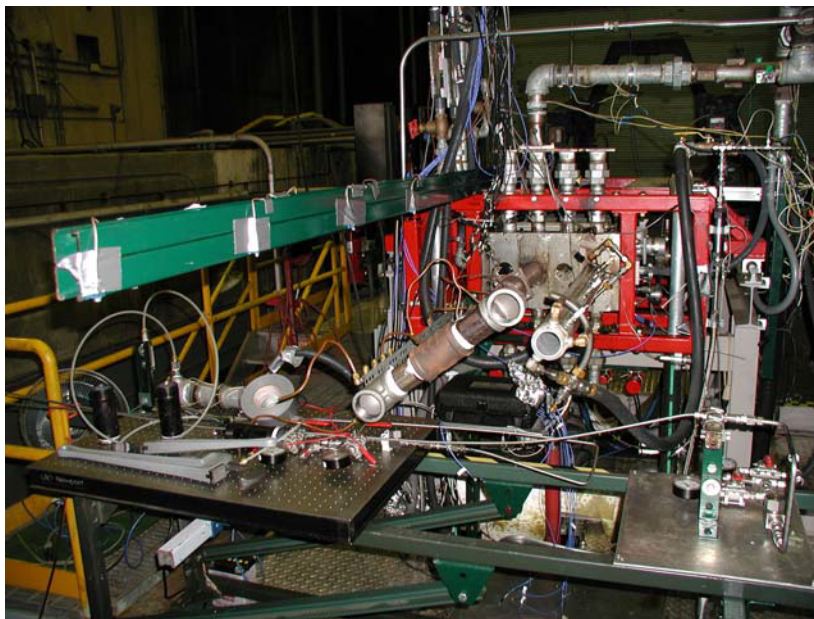


Figure 4 Picture of Microphones Relative to Detonation Tube

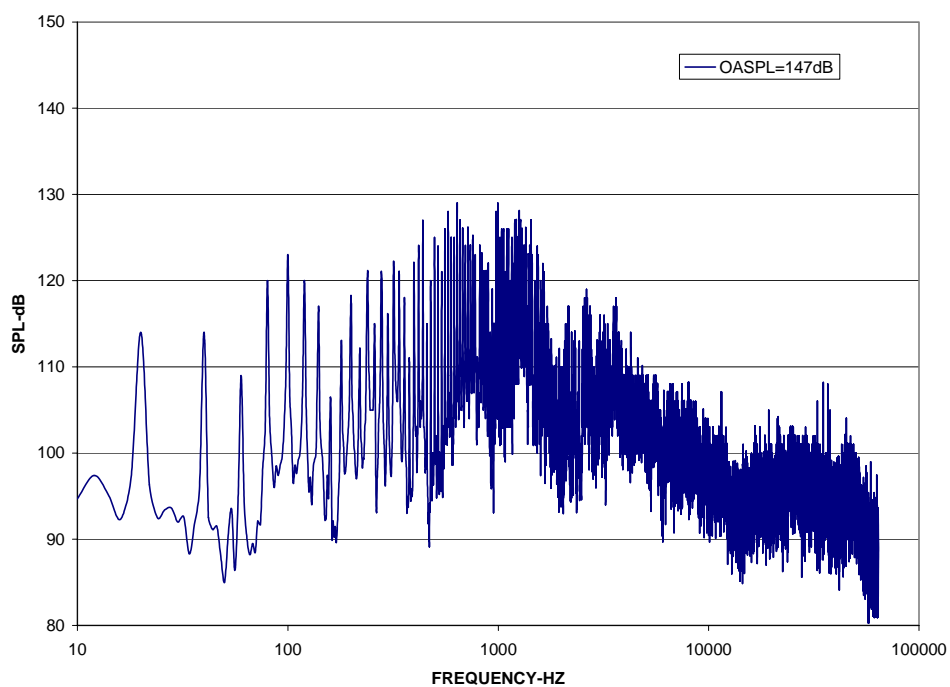


Figure 5 Spectrum From Microphone at 15 Inch Ahead of Tube Exit Plane

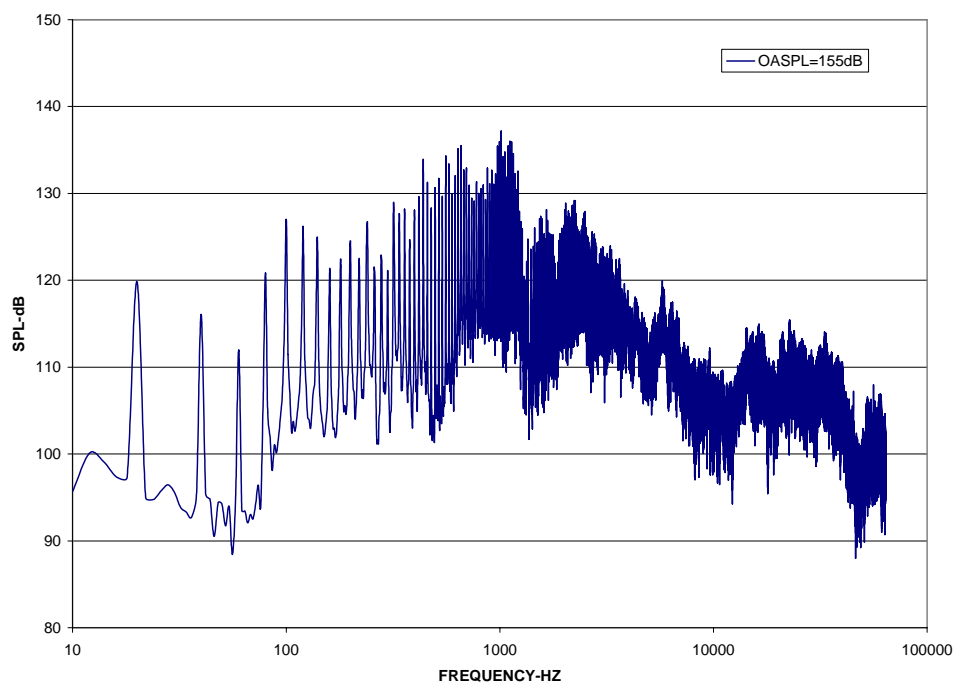


Figure 6 Spectrum From Microphone at Tube Exit Plane

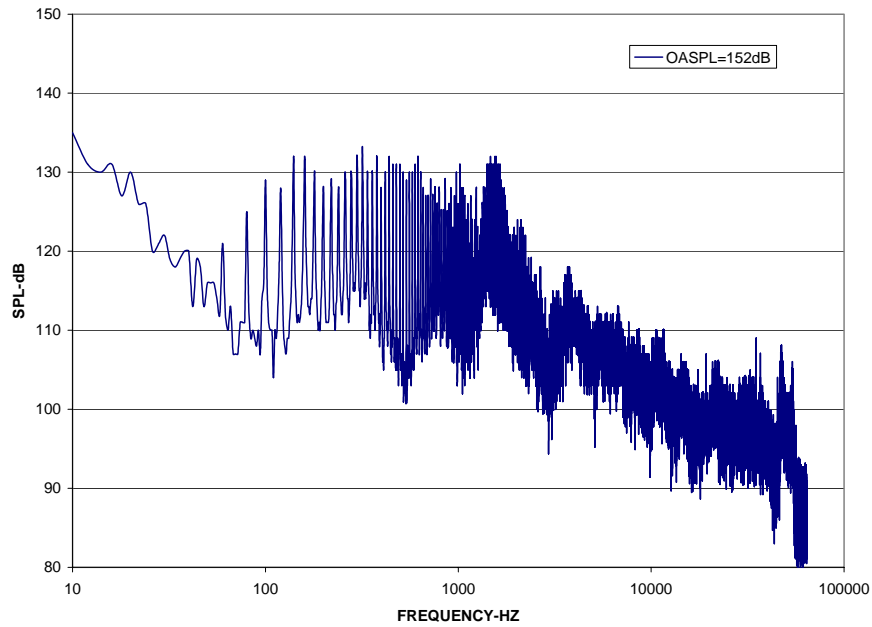


Figure 7 Spectrum From Microphone 15 Inches Aft of Tube Exit Plane

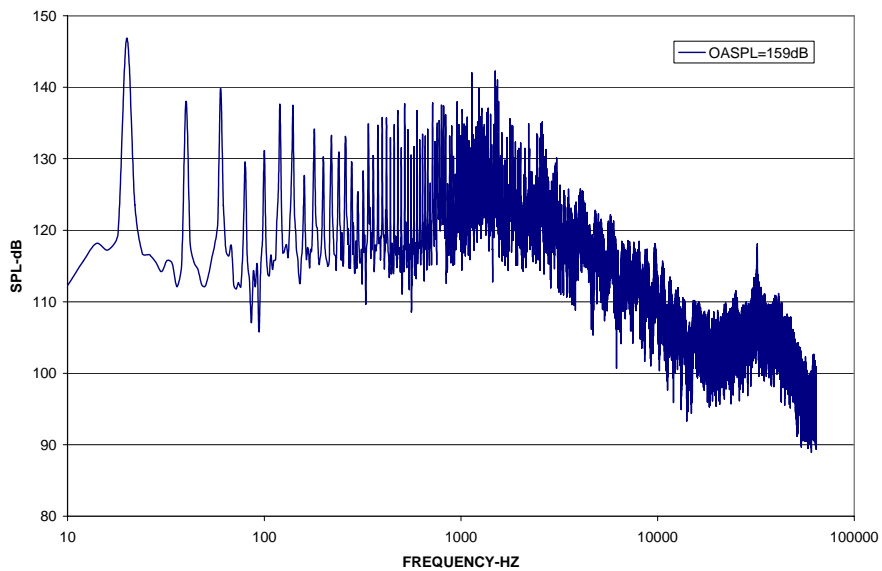


Figure 8 Spectrum From Microphone 30 Inches Aft of Tube Exit Plane



Figure 9 Converging Nozzle



Figure 10 Notched Nozzles



Figure 11 Secondary Air Jet

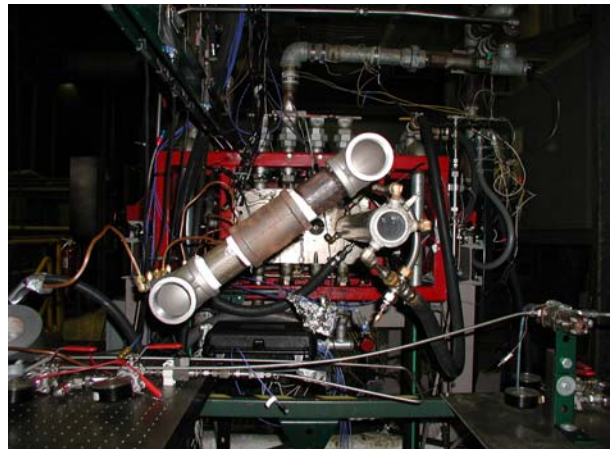


Figure 12 Split Exit

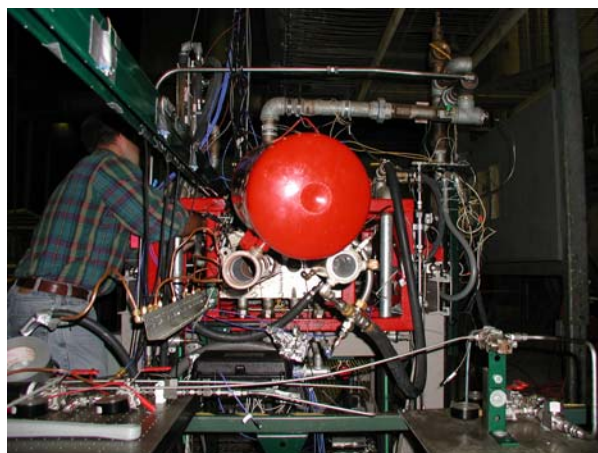


Figure 13 Helmholtz Resonator at Near Exit

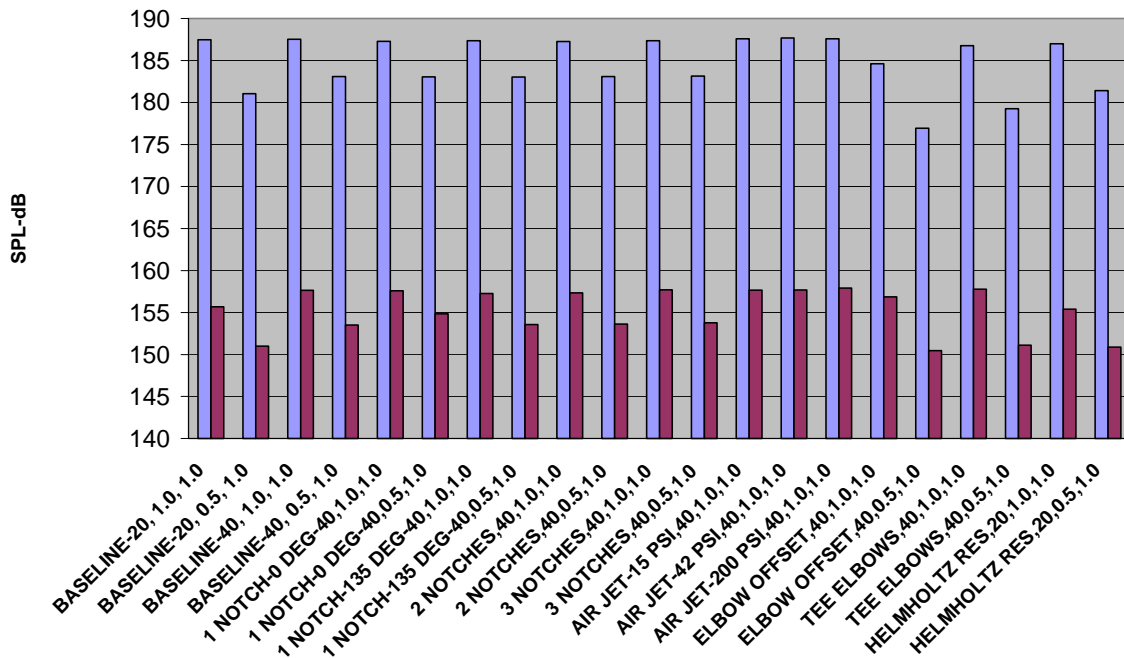


Figure 14 Comparison of Effectiveness of Noise Suppression Concepts

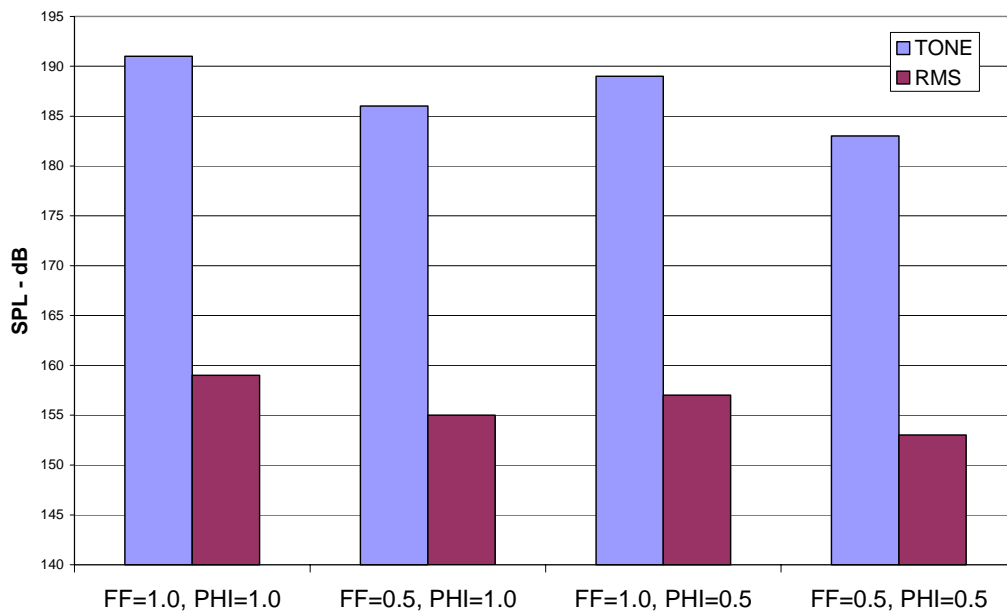


Figure 15 Effect of Fill Fraction and Fuel Ratio on Noise Levels

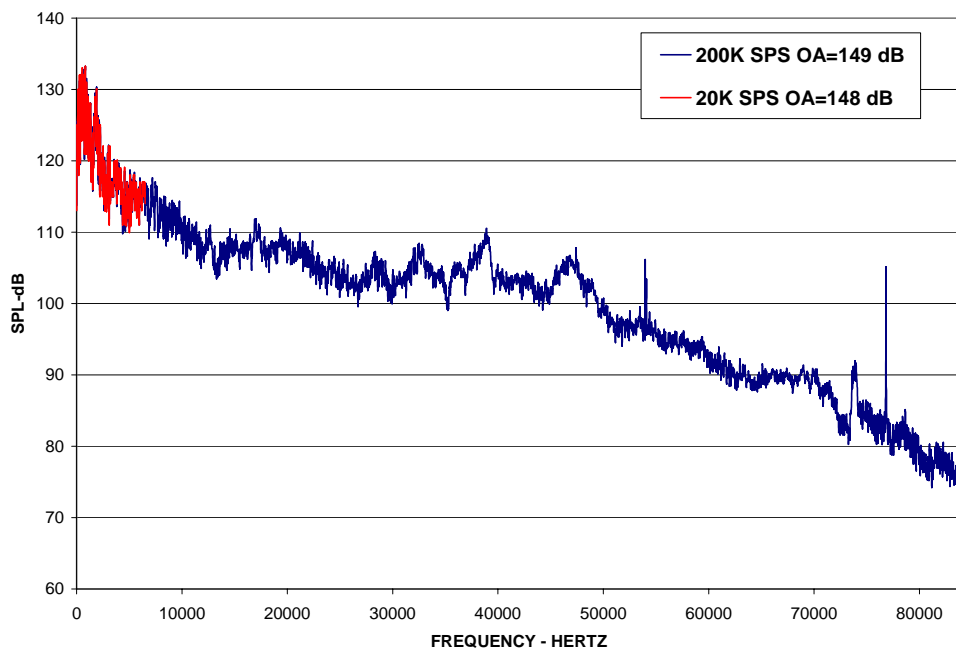


Figure 16 Comparison of 200K and 20K Sampling Rates for Single Tube

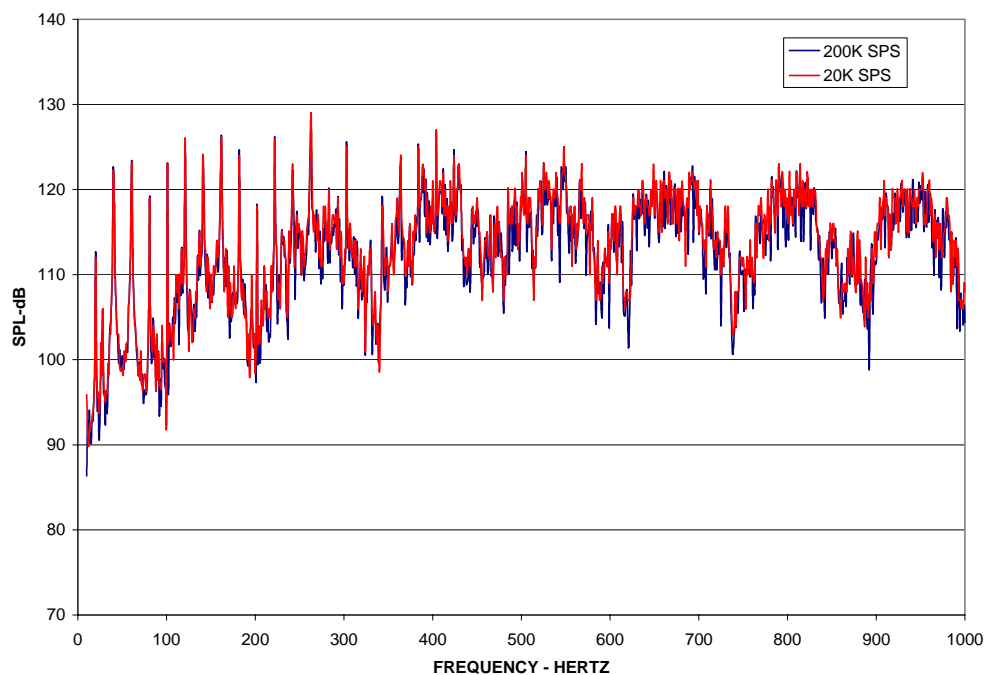


Figure 17 Comparison of 200K and 20K Sampling Rates for Single Tube up to 1000 Hertz

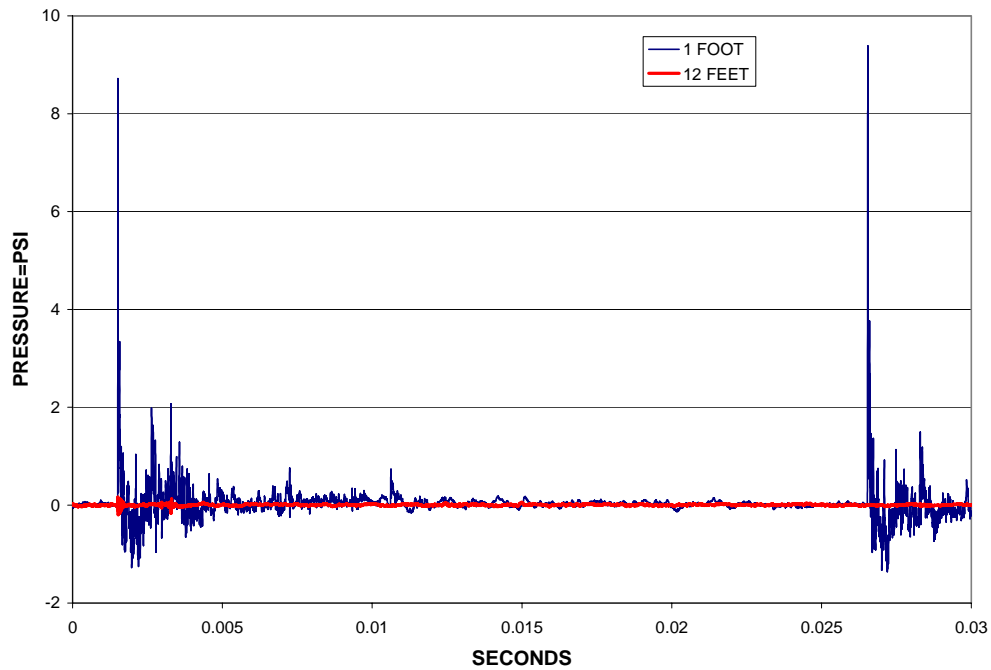


Figure 18 Time History Comparison for 1 Foot and 12 Foot Locations

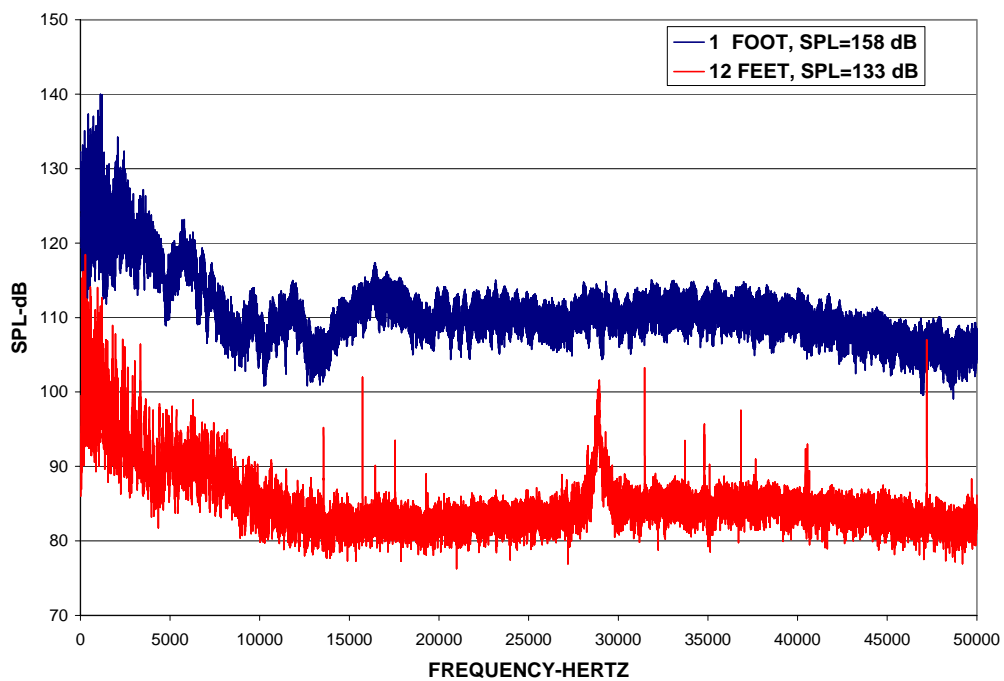


Figure 19 Spectral Comparison for 1 Foot and 12 Foot Locations

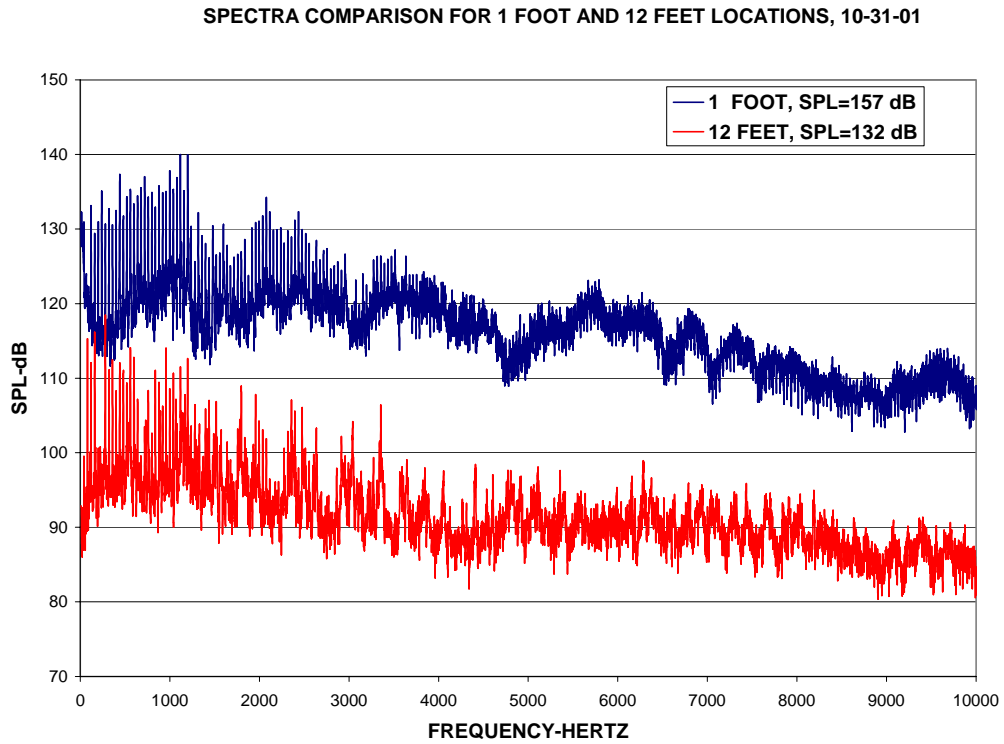


Figure 20 Spectral Comparison for 1 Foot and 12 Foot Locations up to 10K

Performance Assessment of a Large Scale Pulsejet-Driven Ejector System

Daniel E. Paxson*

NASA Glenn Research Center, 21000 Brookpark Road, Cleveland OH 44135

Paul J. Litke[†] and Frederick R. Schauer[§]

Air Force Research Laboratory, Propulsion Directorate, Wright-Patterson AFB, OH 45433

and

Royce P. Bradley and John L. Hoke[‡]

Innovative Scientific Solutions, Inc., Dayton, OH 45440

Unsteady thrust augmentation was measured on a large scale driver/ejector system. A 72 in. long, 6.5 in. diameter, 100 lb_f pulsejet was tested with a series of straight, cylindrical ejectors of varying length, and diameter. A tapered ejector configuration of varying length was also tested. The objectives of the testing were to determine the dimensions of the ejectors which maximize thrust augmentation, and to compare the dimensions and augmentation levels so obtained with those of other, similarly maximized, but smaller scale systems on which much of the recent unsteady ejector thrust augmentation studies have been performed. An augmentation level of 1.71 was achieved with the cylindrical ejector configuration and 1.81 with the tapered ejector configuration. These levels are consistent with, but slightly lower than the highest levels achieved with the smaller systems. The ejector diameter yielding maximum augmentation was 2.46 times the diameter of the pulsejet. This ratio closely matches those of the small scale experiments. For the straight ejector, the length yielding maximum augmentation was 10 times the diameter of the pulsejet. This was also nearly the same as the small scale experiments. Testing procedures are described, as are the parametric variations in ejector geometry. Results are discussed in terms of their implications for general scaling of pulsed thrust ejector systems.

I. Introduction

IN recent years there has been renewed interest in the concept of ejectors or thrust augmentors driven by unsteady propulsion devices. The reason for this stems primarily from the interest in Pulse Detonation Engine (PDE) based propulsion systems, which are decidedly unsteady, and which therefore seem natural candidates on which to use an ejector. It has been suggested in the past¹, and shown convincingly in numerous recent experiments²⁻⁹ that under the proper operating conditions, and with a well designed ejector, thrust augmentation levels approaching or even exceeding 2.0 can be achieved with unsteady thrust sources as drivers. Thrust augmentation, ϕ is defined as the total time-averaged thrust provided by the ejector and driver system, \bar{F}_{total} divided by the thrust of the driver alone, \bar{F}_{driver} .

$$\phi = \frac{\bar{F}_{total}}{\bar{F}_{driver}} \quad (1)$$

* Associate Fellow AIAA

^{†§‡} Members AIAA

It has further been shown that these high levels can be reached using remarkably small ejectors in comparison to their steady state counterparts. Several studies have been conducted using actual PDE's as drivers^{5, 7, 9}; however a number have used alternative unsteady thrust sources including simple pulsed valves^{2,8}, Hartmann-Sprenger resonance tubes⁴, synthetic jets⁶, and pulsejets³. The results from each of these varied experiments have helped identify the factors which contribute to the superiority of unsteady ejector systems in general (and therefore how they can be optimized), and which factors are unique to the particular driver. For example, it is now generally agreed that the frequency, unsteadiness level (the standard deviation of the exhaust velocity for example), and exhaust gas temperature of the thrust source play a significant role in the maximum thrust augmentation that can be achieved⁶. These and other parameters¹⁰ characterize the emitted vortex associated with each pulse of any unsteady thrust device. This vortex plays a critical role in determining thrust augmentation, though the physical mechanism is not understood. It has been shown through experimental measurements for example that vortex diameter is closely matched to the diameter of the ejector yielding maximum thrust augmentation^{5, 6, 10, 11}. On the other hand, it is believed that the strong emitted shock, uniquely associated with the PDE pulse, has a large, though currently not well understood, influence on the maximum attainable thrust augmentation.

Despite the many unsteady ejector experiments performed to date, and the growing body of understanding associated with them, generalization of some results is not yet possible because the experiments have shared a common scale, which is to say, small. The thrust levels have been low (less than 15 lbf), and the driver diameters have been between 1 and 2 inches. Rules have been suggested relating the optimal diameter of the ejector as a fixed ratio relative to that of the driver; however, they are not definitive because all the drivers tested are nearly the same size. The experiment described in this paper was developed to at least partially address this issue.

A large pulsejet, approximately an order of magnitude larger in exhaust cross-sectional area and thrust than most recent tests, was operated with a series of ejectors of varying diameter, length, and shape (cylindrical and tapered). The geometric ejector parameters, along with the spacing between the pulsejet tailpipe and ejector inlet were systematically varied in order to determine the configuration yielding the highest thrust augmentation, as measured by the thrust stand to which the system was mounted. The results were then compared to previous experiments both in terms of augmentation achieved, and in terms of optimized ejector dimensions. This paper will describe the experiment including the major components (pulsejet, ejector sets, and thrust stand), construction, testing procedures, and parametric variations of ejector dimensions. Results will then be presented, and a discussion of findings will follow.

II. Experimental Setup

The experimental setup is shown in Fig. 1 with the major components labeled. These are the ejector (1 of 4 tested), the pulsejet, and the thrust stand. Each will be described below.

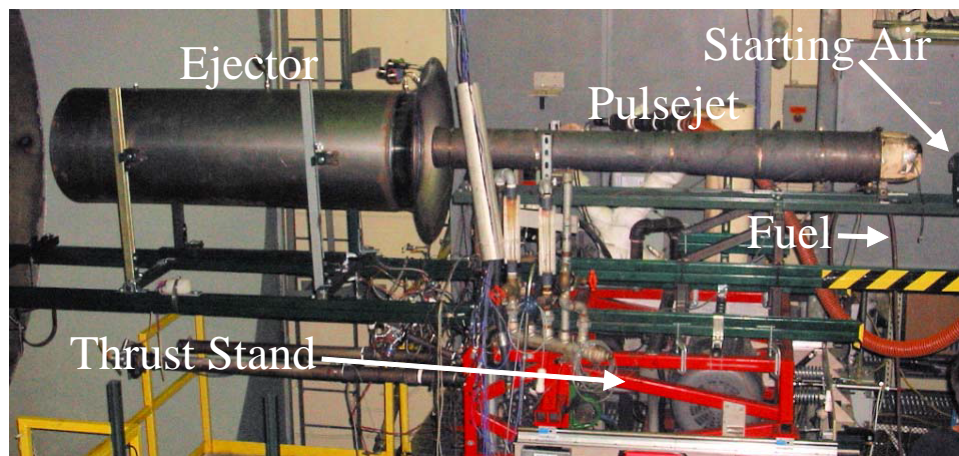


Figure 1. Experimental setup.

A. Pulsejet Driver

The pulsejet tested and discussed in this paper is a Solar PJ32, originally developed and manufactured by the Solar Aircraft Company for the Globe Corporation Aircraft Division in 1951. Details of the device and performance characteristics are described in Ref. 13. Relevant dimensions are shown in the schematic of Fig. 2.

In brief, it is a self-aspirating, valved, unit which operates on liquid fuel (Avgas in this experiment) that is fed directly into the combustion chamber via a pressurized fuel line. Like most pulsejets it requires forced air directed at the inlet and a high frequency sparking system in the combustion chamber in order to initiate operation. However, once operation has commenced, the resonant nature of the device does not require forced air or spark. The fact that that fuel supply is pressurized (as opposed to a venturi-based arrangement found in small scale units³) allows the

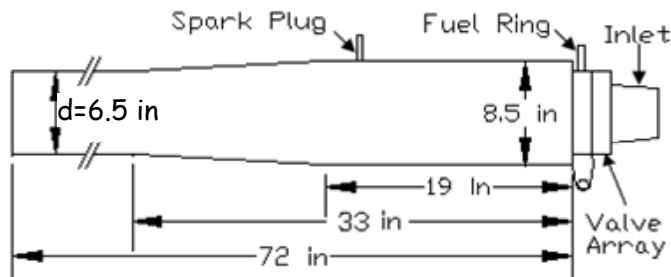


Figure 2. Pulsejet schematic.

pulsejet to be throttled in a reasonably predictable fashion. Figure 3 shows the relationship between measured thrust and fuel flow rate. Fuel flow rate is measured using an in-line turbine-type flow meter. Data is shown both from previous testing done to characterize the pulsejet¹³, and from baseline testing done in the present experiment without an ejector installed. Also shown are a cubic fit to the data, and the bounds representing two standard deviations above and below the fit. It can be seen that a certain amount of scatter is present, which appears to be typical for pulsejets. For the present experiment, the pulsejet was operated near the maximum thrust point during all testing. The scatter in this operating region results in a maximum uncertainty of $\pm 7\%$. For the present baseline data shown, the root-mean-square error between measured and curve-fit thrust was 3.7%. The maximum error was 6%

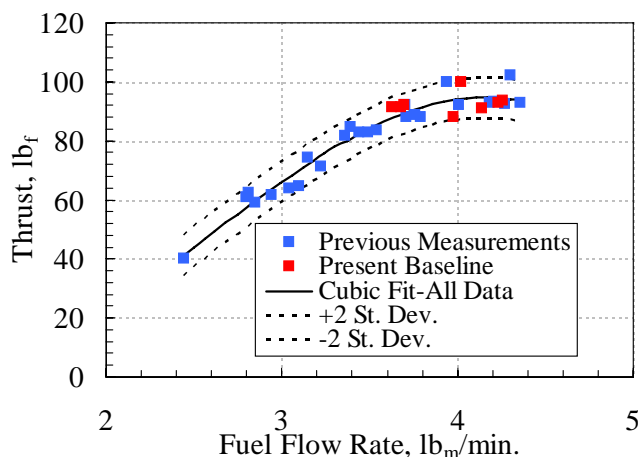


Figure 3. Pulsejet thrust as a function of fuel flow.

The thrust stand can only measure total system thrust (pulsejet and ejector combined); however, thrust augmentation can only be determined if the thrust of the jet alone is known. One way to determine this is to simply run the pulsejet on the thrust stand without an ejector and use that thrust value as the baseline for all subsequent ejector tests. However, it is prohibitively time consuming to do this for each of the many ejector configurations tested. Instead, this measurement was made on average of once every sixteen operational runs of the engine. This method of determining jet-alone thrust will be referred to as Method I in subsequent sections of the paper where results are presented. If the rate of fuel flow could be accurately controlled, this method would suffice, save for the run-to-run uncertainty already described. The fuel flow rate through the system varied over time however, possibly due to clogging at the injectors. As a result, the same pressure in the fuel system did not always yield precisely the same flow rate. To account for this, the jet-alone thrust was also determined using the curve-fit presented above and the measured fuel flow rate from each run. This estimation method, referred to later as Method II, could be made each run, with or without an ejector present.

The frequency of operation of this pulsejet was 69 hz, with a standard deviation of 2 hz for all of the testing performed. The operational frequency is weakly, and inversely related to the fuel flow rate. The observed frequency of the present tests was, like the thrust values, consistent with that observed in previous tests. It is interesting to note in passing that the product of operational frequency and length on this pulsejet is 15% higher than that for the small scale unit used in Ref. 3. Pulsejets are often thought of as gasdynamic devices with a frequency that is determined by the end-to-end transit time of a fixed set of dominant waves. All other things being equal, this conception implies that the product of frequency and length should be a constant. The observed difference therefore

either indicates that the average temperature of the combustion products is 30% higher in the large unit (which would probably melt the steel), or that there are other elements contributing to the resonance than simply wave reflections (e.g. Helmholtz-like behavior, heat release rate, etc.).

B. Ejectors

Four ejectors were constructed from mild-steel sheet ranging in gage from 18 to 20. Scaled drawings of each are shown in Fig. 4, which also shows symbolic nomenclature for the relevant dimensions. Those dimensions are listed in Table 1. The commercially available bellmouth inlets were seamless, and terminated with a 1.0 in. long straight section. The main body of each cylindrical ejector was composed of a single rolled piece with a welded seam along the length. It was joined to the bellmouth with a circumferential weld. The main body of the tapered ejector was composed of two symmetric halves. The conical shape was achieved through a process called “bumping” whereby a small bend is applied approximately every inch along the circumference. This actually creates a many-sided polygon rather than a pure circular cross-section. The two halves were welded together along the entire length. The finished body was then attached to the inlet with a circumferential weld.

Table 1 Ejector dimensions (as-built)

R (in.)	L (in.)	D (in.)
Straight, cylindrical		
3	64	13
4	65	16
4	65	20
Tapered, conical		
4	69	16

The dimensions of the ejectors were chosen by a geometrical scaling of the small scale ejectors tested in the pulsejet-based experiments of Ref. 3. The length and diameter of the Ref. 3 ejector yielding the highest thrust augmentation was normalized by the diameter of the pulsejet driver (1.25 in.). Those ratios were then multiplied by the pulsejet diameter in the present work (6.5 in.) to obtain the length and diameter of the central ejector. The other two diameters were then selected as 20% smaller and 25% larger than the central value with the supposition that this span would be sufficient to bound the value of the optimal diameter. The inlet radius, R was not variable because the bellmouth inlets were commercially available stock-items, and the radius was pre-determined based on the selected diameter, D . However, it has been shown that while inlet rounding is necessary (a sharp-edged inlet will produced almost no augmentation), rounding beyond values of $R/D=0.15$ shows little benefit. The ejectors used in this experiment had $R/D \geq 0.20$.

C. Thrust Stand

Details of the thrust stand have been presented elsewhere in the literature^{9, 14}. As such only a brief description will be given here. It consists of a cart with linear bearings which ride along a pair of fixed, low-friction rails. The test article (pulsejet or pulsejet and ejector combination) is rigidly attached to the cart. The cart pushes against a damped, calibrated spring, one end of which is fixed. Thrust is ultimately determined by measuring the cart displacement with a positional sensor which is low-pass filtered with a cut-off frequency of 0.5 hz. A time trace of measured thrust during a typical test run is shown in Fig. 5. The damping and filtering system is evidently quite

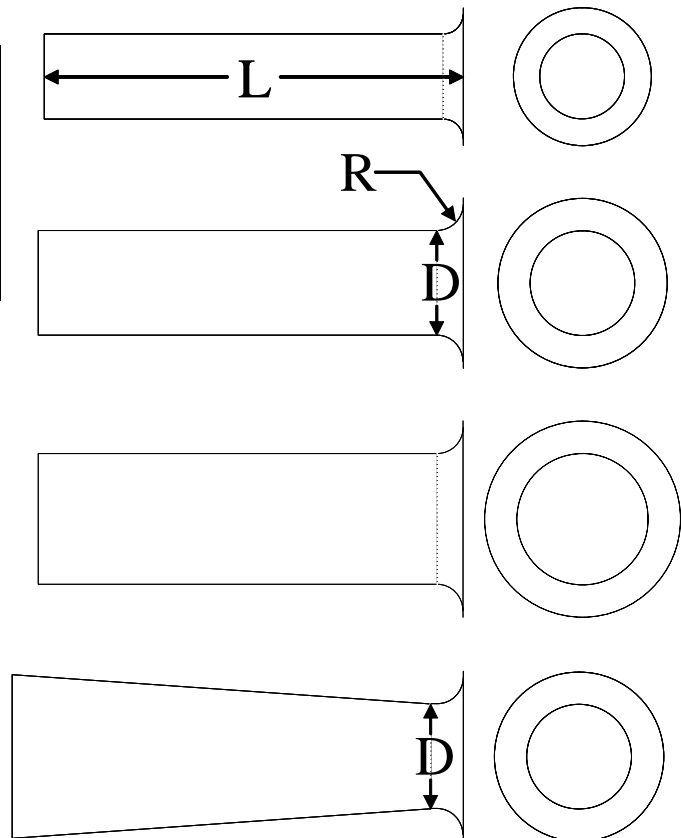


Figure 4. Ejector schematics and symbols for relevant dimensions.

effective, as there are no oscillations in the measured thrust. It is noted that there is a small positive thrust measured prior to engine ignition. This is the result of a preload applied to the spring at the zero point of the positional sensor.

D. Test Procedure

Each test run was approximately 30 seconds in duration and consisted of the following sequence. Fuel pressure was set. Starting air was then turned on as was the spark. Shortly thereafter the fuel flow valve was opened, and engine operation commenced. The starting air and spark were then shut off. After approximately 15 seconds, the thrust reading would level off and for the next 15 seconds thrust was measured at approximately 1.0 second intervals. After the thrust measurement was acquired the fuel valve was closed, and the starting air was re-activated in order to provide cooling. The thrust data to be presented represents a simple time-average over the 15 second sampling period. This basic sequence is illustrated in Fig. 5 which shows actual test data from a typical run.

For each ejector tested, the baseline thrust of the pulsejet was first measured without the ejector present. A straight-sided ejector was then mounted on the thrust stand, with its axis of symmetry aligned with that of the pulsejet. Thrust measurements were made with the ejector inlet placed at various axial positions relative to the exhaust plane, as shown in Fig. 6. For each ejector, an optimal spacing value was found which yielded the highest thrust augmentation. This procedure was followed for each of the three straight ejector diameters.

The diameter yielding the highest thrust augmentation was then selected for length variation testing. It was first lengthened by welding a 19.5 in. extension to the cylindrical section, at the exhaust end. This modified ejector was then tested according to the procedure just described. The length of the ejector was then reduced by simply cutting off a portion of the exhaust end. The length reduction was done in increments of one pulsejet diameter (6.5 in.).

Due to resource limitations, it was possible to test only one tapered ejector. The minimum diameter of this ejector was chosen to be the same as that of the cylindrical ejector yielding the highest thrust augmentation. A tapered ejector made the same way was tested on several small scale rigs and found to yield very high thrust augmentation levels^{1, 5, 15}. The spacing and length of this ejector were varied in the manner described above; however, no extension was made to the initial 70 in. length.

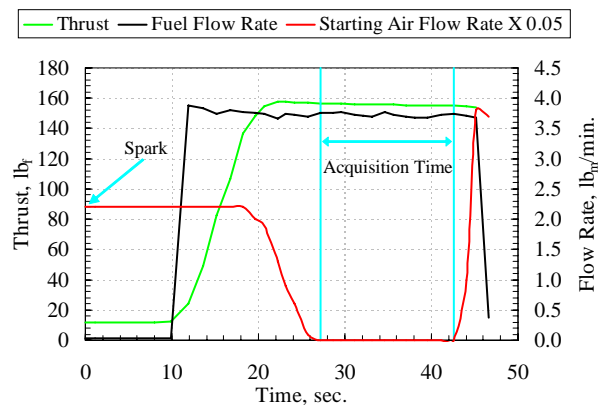


Figure 5. Measured thrust as a function of time for a typical pulsejet and ejector combination. Fuel and starting air flow rates are also shown.

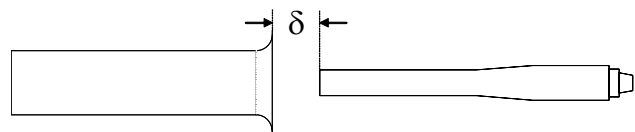


Figure 6. Schematic of ejector spacing variation. The schematic is to scale.

III. Results and Discussion

A. Straight, Cylindrical Ejectors

1. Driver-to-Ejector Spacing Variations

Although spacing variation testing was performed on every ejector configuration, the results tended to be similar in trend. As such, results from only one configuration will be shown. Figure 7 displays the thrust augmentation as a function of driver-to-ejector spacing for the 16 in. diameter ejector, of 65 in. length. The spacing has been normalized by the driver diameter, d . Results are presented using both Methods I (baseline measured pulsejet thrust) and II (pulsejet thrust estimated from the fuel flow rate curve-fit of Fig. 3) to compute thrust augmentation. Also shown are the results from the small scale pulsejet experiment of Ref. 3. Negative values of ejector spacing indicate that the exhaust plane of the pulsejet was actually inside the ejector. In the Ref. 3 experiment, such measurements were not possible as the pulsejet would cease to operate at low spacing values. The same phenomenon occurred in the present experiment, but at much smaller, even negative values. It is interesting to note that the augmentation reaches a peak as the ejector and driver are brought closer together. It then decreases to a minimum, and begins to rise again as the driver is brought into the ejector interior. It is not known whether a second peak exists because, as mentioned, the pulsejet stopped operating. Such 'twin peak' behavior was observed in the PDE driven experiment

of Ref. 5. The spacing yielding peak performance is approximately 2.0 pulsejet diameters. This value is similar to, but slightly larger than, the value found in the small scale experiment. Comparison with other experimental results^{4,5} indicates that the value varies between 1 and 2.5 driver diameters. It therefore appears to be a somewhat experiment specific parameter, perhaps depending on both the physical geometry of the driver and the characteristic of the unsteady pulse.

Optimal ejector spacing was found to be invariant with changing ejector length. However, it should be kept in mind that only one diameter ejector was varied in this manner.

For variations in diameter using a fixed length, the optimal spacing followed a nearly perfect linear relationship described by

$$\left(\frac{\delta}{d}\right)_{optimal} = 0.90\left(\frac{D}{d}\right) - 0.27 \quad (2)$$

The general increase in optimal spacing as ejector diameter increases is consistent with the results of Refs. 3-5.

2. EjectorDiameterVariations

Thrust augmentation levels obtained with optimally spaced, fixed length ejectors are shown as a function of ejector diameter in Fig. 8. The ejector diameter has been normalized by the driver diameter. Once again, results using both Methods I and II to obtain pulsejet thrust are shown. For comparison, results from the Ref. 3 small pulsejet experiment also appear. There is a clear optimal ejector diameter, and for both the large and small scale experimental results it appears to be very nearly 2.5 driver diameters. This result is remarkably consistent over a range of drivers. Table 2 lists the ejector to driver diameter ratios at which peak augmentation levels were found in a number of experiments using cylindrical or nearly cylindrical ejectors. The values all fall between 2.4 and 3.0, indicating that the optimal ejector diameter is a near constant multiple of the driver diameter, probably having a weaker secondary dependence on other, as yet unknown parameters. This result supports the notion that the vortex emitted with each pulse of the driver plays a key role in unsteady thrust augmentation since, as was pointed out in Refs. 5 and 6, its size (bounding diameter) appears to follow the same ratio when divided by the driver diameter.

It is noted that although the optimal value of D/d is nearly the same for all of these ejectors, the thrust augmentation obtained is not. Part of the reason for this may be that while all of the unsteady drivers emit a vortex, the amount of vorticity present, its velocity, the balance

Ref.	Driver Type	ϕ_{max}	Optimal D/d	d (in.)
Present	Large Pulsejet	1.71	2.4	6.50
2	Chopped Pulse	1.45	3.0	3.14
3	Small Pulsejet	1.83	2.5	1.25
4	Resonance Tube	1.38	2.7*	1.50
5	PDE	2.00	3.0	1.00
6	Synthetic Jet	1.67	2.4 ⁺	0.93
7	PDE	2.10	3.0	1.93

* Using the hydraulic diameter of the driver 275 hz. driver.
⁺ Using 'effective diameter' measured w/ PIV.

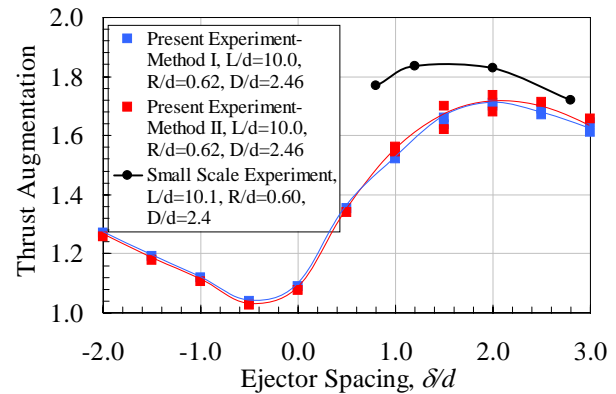


Figure 7. Thrust augmentation as a function of driver-to-ejector spacing for the $D/d=2.46$, $L/d=10.0$ ejector.

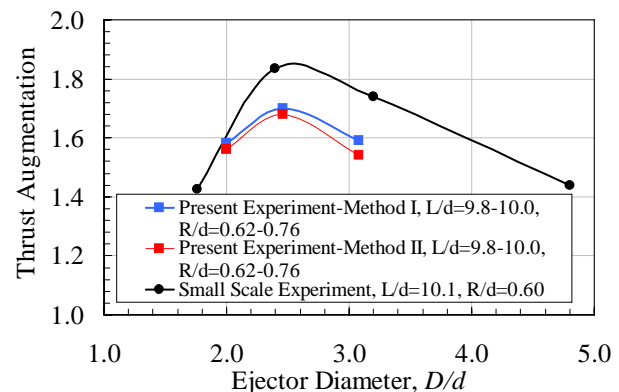


Figure 8. Thrust augmentation as a function of ejector diameter for the $L/d=10.0$ ejectors. The ejectors are optimally spaced for each point. Data from the Ref. 3 small scale experiment is also shown.

between fluid trapped in the vortex and that which follows behind, and the interaction between vortex bound fluid and trailing jet fluid may be vastly different. These features may play a key role in the entrainment of and momentum transfer to the secondary fluid in the ejector, although the mechanism isn't clear^{6,16}.

It was suggested in Ref. 6 (and based on the observations of Ref. 17) that a characterizing feature of the emitted pulse, essentially a type of inverted Strouhal Number, may be a correlating parameter to the peak thrust augmentation achievable with an ejector that has been optimized for length and diameter. In that paper, the parameter, heretofore referred to as the non-dimensional formation time, was defined as

$$\tau_f = \frac{\sqrt{u'^2}}{2fd} \quad (3)$$

where f is the frequency of operation, and $\sqrt{u'^2}$ is the root mean square of the periodic velocity fluctuations in the exit plane of the driver. This velocity can be estimate from measured thrust, mean flow rate and temperature of the driving jet. It was argued that peak thrust augmentation should rise with formation time up to some critical value, τ_f^{crit} . Beyond this value, peak thrust augmentation should slowly fall. Figure 9 shows the peak thrust augmentation

obtained as a function of formation time for the present experiment and several others for which sufficient data was available[‡]. A simple parabolic fit through the data is also shown. The data seems to follow the expected trend, indicating a value of τ_f^{crit} near 40; however, the data is admittedly sparse and much more is needed. Furthermore, it

was noted in Ref. 6 that other experimental results don't fall on this same curve. This implies that other factors such as the exhaust gas temperature (relative to the entrained secondary flow) may play a significant role in determining peak thrust augmentation. The experiments represented in Fig. 9 have vastly different exhaust temperatures for which no accounting has been made other than the effect on $\sqrt{u'^2}$. Beyond this, the use of formation time as is done here provides no insight into the physical mechanism of unsteady thrust augmentation. It only provides a potentially predictive correlating parameter, albeit one that is fairly compelling.

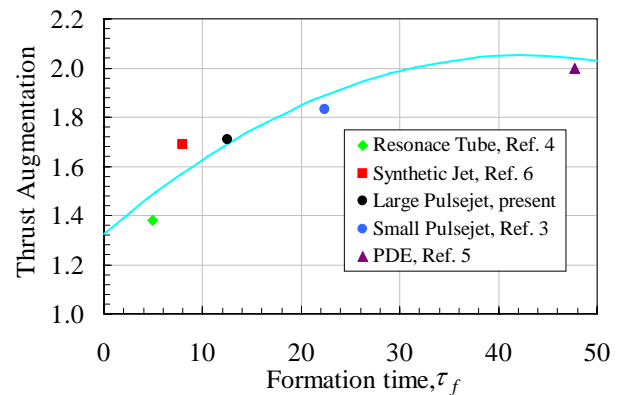


Figure 9. Peak thrust augmentation as a function of formation time for the present, and several other experiments.

3. Ejector Length Variation

As stated earlier, length variation tests were only performed on a single cylindrical ejector. The 16 in. diameter ejector was chosen ($D/d=2.46$) since it had yielded the highest performance at the as-built 65 in. length. The variation in thrust augmentation as a function of ejector length is shown in Fig. 10. The length has been normalized by the driver diameter. Results from the small pulsejet experiment of Ref. 3 are also shown. The trends of the two experiments are somewhat different; however, it is noted that the peak value of thrust augmentation occurs at the same value of $L/d=10$ for both. This turned out to be the as-built length in the present experiment.

This ratio does not hold for the other unsteady experiments; however, it is not clear that it should. There are several conceptual models for the mechanism by which fluid is entrained and energized in the ejector. One posits a sort of piston-like behavior of the driver flow which delivers momentum to the secondary flow via direct pressure exchange as the two flows collide within the ejector. A second notion suggests that the mechanism of entrainment and momentum exchange is the same as that for a steady ejector, namely shear flow and mixing (most likely driven by turbulence). Secondary fluid is literally dragged into the ejector and accelerated. In this concept, the emitted

[‡] For the Ref. 5 PDE experiment the rms velocity was obtained from a numerical simulation matching flow rate and thrust. Because the thrust producing period of a typical PDE is only a small fraction of the operating period, only the thrust producing period was used in the rms velocity calculation. The inverse of this period was used for f in Eqn. 3

vortex serves the function of vastly increasing the shearing surface area (compared to a steady jet) due both to its initial structure and to its observed disintegration[§].

If the latter mechanism is correct, it might be expected that the emitted vortex would decelerate (even as it broke apart) at a rate proportional to its surface area and to the square of the difference between its velocity and that of the secondary flow. That is

$$U_v \frac{dU_v}{dx} \approx -\alpha \left(\frac{\rho_s}{\rho_v} \right) \left(\frac{S}{V} \right) (U_v - U_s)^2 \quad (4)$$

where ρ_v is the density of the vortex, V is the vortex volume, S is the surface area, U_v is the velocity of the vortex, U_s is the average velocity of the secondary flow (assumed constant), α is a constant, and ρ_s is the density of the secondary flow. Assuming that the vortex volume and surface area are proportional to the cube and square of its diameter respectively, and assuming further that its diameter is proportional to the diameter of the driver, the ratio (S/V) in Eqn. 4 simply becomes proportional to $(1/d)$, i.e.

$$U_v \frac{d(U_v - U_s)}{d(x/d)} \approx -\kappa \left(\frac{\rho_s}{\rho_v} \right) (U_v - U_s)^2 \quad (5)$$

With κ a constant, Eqn. 5 can be solved numerically to yield x/d as a function of $(U_v - U_s)$, for any given ρ_s/ρ_v and $U_v^{initial}/U_s$, which is the initial vortex velocity as it enters the ejector divided by the average secondary flow velocity. If the optimal ejector length, L_{opt} is defined as that value of x for which $(U_v/U_s - 1)$ is less than some specified small value such as 0.1, and if estimates of $U_v^{initial}/U_s$ and ρ_s/ρ_v are available, then Eqn. 5 can be used to obtain L_{opt}/d . This is illustrated in Fig. 11 which shows the numerical solution to Eqn. 5 for different values of the parameters $U_v^{initial}/U_s$ and ρ_s/ρ_v .

Estimates for $U_v^{initial}$ and U_s were obtained for the Refs. 3, 4, and 5 experiments using PIV data from Refs. 11, 16, and 12^{**}. They are listed in Table 3. Values of ρ_s/ρ_v were not available. For the Ref. 4 resonance tube, this ratio should be near 1.0 since the driver gas was at near ambient temperature. For the Refs. 3 and 5 pulsejet and PDE driven experiments, the ratio was estimated at approximately 3.0. This estimate assumes that the very hot, low density gas from each driver entrains a certain amount of cooler air as it forms the emitted vortex.

Table 3 Vortex and secondary flow velocities, and optimal L/d values.

Ref.	Driver Type	U_v (ft/s)	U_s (ft/s)	$\frac{\rho_s}{\rho_v}$	L_{opt}/d
3	Small Pulsejet	460	303	3.0	10.1
4	Resonance Tube	275	245	1.0	6.5
5	PDE	800	115	3.0	14.6

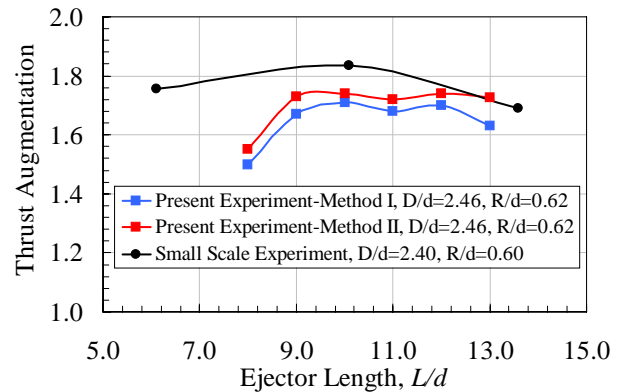


Figure 10. Thrust augmentation as a function of ejector length for the $D/d=2.46$ ejector. The ejectors are optimally spaced for each point. Data from the Ref. 3 small scale experiment is also shown.

[§] Observations of vorticity in the ejector exit region of the Refs. 11 and 12 indicate no coherent vortical flow structure at radial distances less than the ejector diameter.

^{**} For the Ref. 4 experiment, U_s was obtained from hotwire measurements taken in the exit plane of the ejector.

Table 4 Optimal ejector and actual driver operational frequencies.

Ref.	Driver Type	f_{opt} (hz)	f_{driver} (hz)
3	Small Pulsejet	350	220
4	Resonance Tube	335	275
5	PDE	135	20

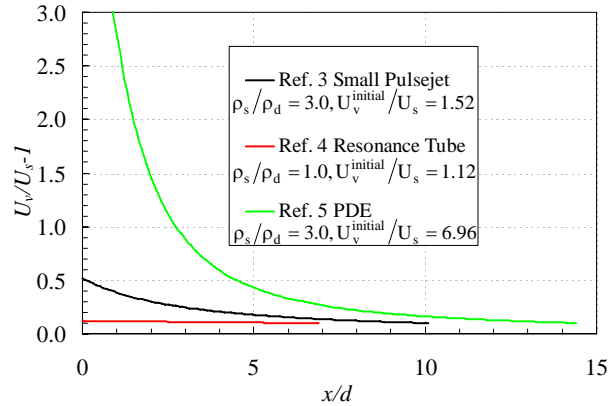


Figure 11. Numerical solution to Eqn. 5 for several relevant parameters of density ratio and vortex velocity ratio. The value of κ in Eq. 5 is 0.32

When these values of $U_v^{initial}$, U_s , and ρ_s/ρ_v were used in the numerical solution of Eqn. 5, together with an ending criterion $(U_v/U_s - 1) = 0.1$, it was found that for a single value of $\kappa = 0.32$, the values for L_{opt}/d calculated were almost exactly the values found experimentally, and listed in Table 3. This result is by no means proof of the shear mechanism for ejector entrainment and thrust augmentation, particularly given the scarcity of data and the density estimates used. It is nevertheless suggestive that this mechanism predominates.

Note that Eqn. 5 may be rewritten as an ordinary differential equation in time as

$$\frac{d(U_v - U_s)}{dt} \approx -\kappa \left(\frac{\rho_s}{\rho_v} \right) (U_v - U_s)^2 \quad (6)$$

Integrating this equation using the parameters listed above presumably gives the time required for the emitted vortex to travel down the ejector, decelerate, degenerate, and accelerate the secondary fluid. The inverse of this time provides an estimate for the optimal operational frequency from the perspective of shear-driven momentum transfer. For the Refs. 3, 4, and 5 experiments, these frequencies are listed in Table 4, along with the actual operational frequencies of the devices. All other things being equal, it would be intuitively expected that the closer together the optimal and operational frequencies, the higher the thrust augmentation. If this is true, it suggests that PDE's which for a given length ideally operate at a much higher frequency than that listed in Table 3, could obtain even higher augmentations levels than have been reported to date. It would also suggest that the present experiment, while generally exhibiting lower overall thrust augmentation values compared to those of the small scale pulsejet experiment of Ref. 3, is actually better matched in terms of this optimal frequency criterion. The reason for this is as follows. The value of L_{opt}/d found in the present experiment is identical to that of Ref. 3. It is expected that the values of ρ_s/ρ_v , $U_v^{initial}$, U_s are therefore quite similar. These can be used to integrate Eqn. 6 but with the larger diameter of the present experiment. The resulting optimal frequency is found to be 67 hz, which is very close, and therefore better matched, to the actual operating frequency of 69 hz.

B. Tapered, Conical Ejector

As mentioned earlier, only one diameter of tapered, conical ejector was tested. The length was varied using the same technique as that for the cylindrical ejector. Similarly, at each length the driver-to-ejector spacing was varied until the highest augmentation was achieved. As with the straight ejectors, this optimal spacing was very nearly 2 driver diameters for every length. The results of the length variation tests are shown in Fig. 12, along with those from the small scale pulsejet experiment of Ref. 3. Like the small scale experiment, the maximum augmentation achieved was higher with the tapered ejector than with the best of the straight type. Both experiments also show much more sensitivity at the shorter lengths than was seen with the straight ejectors. However, the small scale experiment has a clear length at which peak augmentation is observed, whereas the present experiment exhibits nearly flat region where the augmentation is high and insensitive to length. The start of this region and the peak

performance point of the small experiment both appear to occur between $8 < L_{opt}/d < 8.5$. The peak augmentation obtained in the present experiment was 1.83, while the small scale experiment yielded a value of 1.98. The same trend was seen with the straight ejectors. As mentioned earlier, part of the reason for this may be due to the somewhat different vortex parameters associated with the two drivers (despite their both being valved pulsejets).

Some of the difference may also be attributed to the slightly different nature of the ejectors used in the two experiments; however, these are fairly subtle. Figure 13 shows a profile of the best performing straight and tapered ejectors used in the Ref. 3 work. The straight ejector is seen to actually have a short diffusing section at the exhaust end, and both have a half circle inlet profile as opposed to the quarter round profile of the present work.

Another possible explanation for the comparatively lower peak augmentation in the large system may lie in the scale of the turbulence which is involved in the exchange of momentum between the driver and the secondary flow. There are numerous potential turbulence length scales in a pulsejet. Some are governed by the physical size of the unit, but others are not. It is possible that the scales from say, combustion, and the exhaust plane shear layer coincide in the small unit and thus, being encased in the emitted vortex, efficiently transfer the large scale vortex rotational energy to the secondary flow. In the large unit, this matching of scales may not hold. Of course, there is no proof yet for this (rather intuitive) explanation other than the observation that the measured turbulence levels in the emitted vortex of several unsteady thrust experiments are quite high^{6, 11, 12}. Clearly, much more investigation is needed into the issue of peak thrust augmentation in unsteady thrust systems in general, and in large versus small systems in particular.

IV. Conclusion

A large scale pulsejet-driven ejector system was tested with the objective of obtaining ejector dimensions which maximize thrust augmentation. Tests were conducted using ejectors of various length, diameter, and cross sectional profile. The spacing between the pulsejet exit and ejector inlet was also examined for its influence on performance. Comparisons with other unsteady ejector experiments were also made both in the level of augmentation achieved and in the dimensions of the optimized ejectors. A peak thrust augmentation value of 1.71 was obtained with straight ejectors. The optimized ejector diameter was found to be 2.46 times the pulsejet driver diameter of 6.5 in. This ratio was observed to be nearly constant over numerous experiments and may therefore be a sizing rule. The optimal length was found to be 10 times the driver diameter. This result was found to be the same as another, small scale pulsejet experiment, but somewhat different from those where another driving source was used. It was found that the tapered profile ejector yielded a higher thrust augmentation than the best of the straight profile series. The value obtained was 1.81. This result was consistent with numerous other unsteady thrust augmentation experiments. Additional research is needed to determine if there is an optimal ejector taper angle, and if that angle can be related to parameters of the driver.

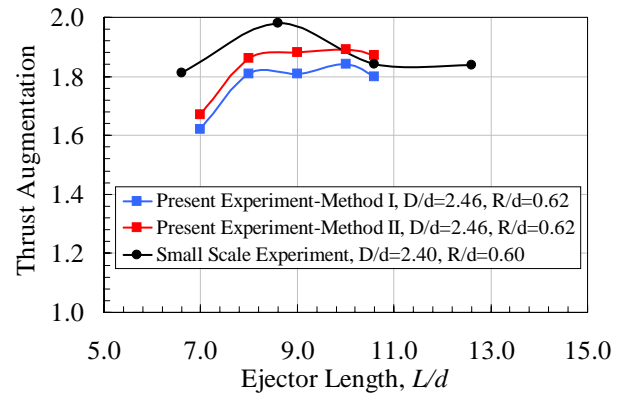


Figure 12. Thrust augmentation as a function of ejector length for the $D/d=2.46$ tapered ejectors. The ejectors are optimally spaced for each point. Data from the Ref. 3 small scale experiment is also shown.

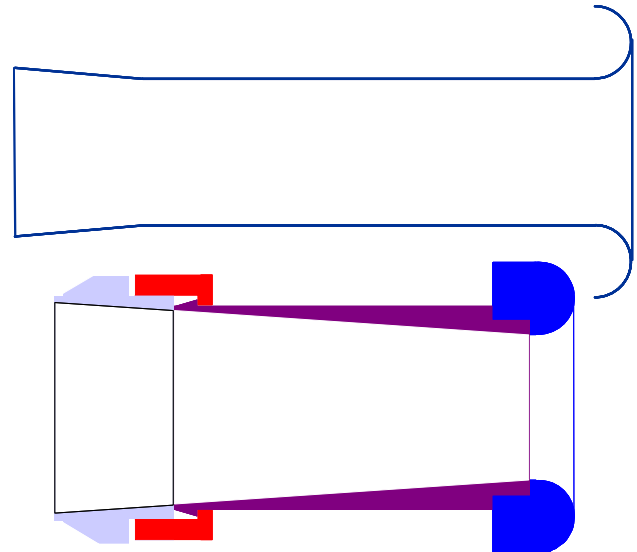


Figure 13. Straight and tapered ejector profiles used in the small scale pulsejet experiment of Ref. 3.

References

- ¹Lockwood, R. M. "Interim Summary Report on Investigation of the Process of Energy Transfer from an Intermittent Jet to Secondary Fluid in an Ejector-Type Thrust Augmenter," Hiller Aircraft Report No. ARD-286, March, 1961.
- ²Binder, G. and Didelle, H. "Improvement of Ejector Thrust Augmentation by pulsating or flapping Jets," Paper E3 of Proc. 2nd Symposium on Jet Pumps & Ejectors and Gas Lift Techniques, Cambridge, England, March 1975.
- ³Paxson, D. E., Wilson, J., and Dougherty, K. T., "Unsteady Ejector Performance: An Experimental Investigation Using a Pulsejet Driver," AIAA paper 2002-3915, July, 2002.
- ⁴Wilson, J., and Paxson, D. E., "Unsteady Ejector Performance: An Experimental Investigation Using a Resonance Tube Driver," AIAA paper 2002-3632, July, 2002.
- ⁵Wilson, J., Sgondea, A., Paxson, D. E., Rosenthal, R., "Parametric Investigation of Thrust Augmentation by Ejectors on a Pulsed Detonation Tube," AIAA paper 2005-4208, July, 2005.
- ⁶Paxson, D. E. Wernet, M. P., John, W. T., "An Experimental Investigation of Unsteady Thrust Augmentation Using a Speaker-Driven Jet," AIAA 2004-0092, January, 2004.
- ⁷Landry, K., Shehadeh, R., Bouvet, N., Lee, S.-Y, Pal, S., and Santoro, R. J., "Effect of Operating Frequency on PDE Driven Ejector Thrust Performance," AIAA paper 2005-3832, July, 2005.
- ⁸Choutapalli, I. M., Alkislal, M. B., Krothapalli, A. Lourenco, L. M., "An Experimental Study of Pulsed Jet Ejector," AIAA paper 2005-1208, January, 2005.
- ⁹Allgood, D. Gutmark, E. Hoke, J. Bradley, R., Schauer, F., "Performance Measurements of Pulse Detonation Engine Ejectors," AIAA paper 2005-223, January, 2005.
- ¹⁰Wilson, J. "Effect of Pulse Length and Ejector Radius on Unsteady Ejector Performance," AIAA paper 2005-3829, July, 2005.
- ¹¹John, W. T., Paxson, D. E., Wernet, M. P., "Conditionally Sampled Pulsejet Driven Ejector Flow Field Using DPIV," AIAA paper 2002-3231, June, 2002.
- ¹²Opalski, A. B., Paxson, D. E., Wernet, M. P., "Detonation Driven Ejector Exhaust Flow Characterization Using Planar DPIV," AIAA paper 2005-4379, July, 2005.
- ¹³Litke, P. J., Schauer, F. R., Paxson, D. E., Bradley, R. P., Hoke, J. L., "Assessment of the Performance of a Pulsejet and Comparison with a Pulsed-Detonation Engine," AIAA paper 2005-0228, January, 2005.
- ¹⁴Schauer, F. R., Stutrud, J., and Bradley, R. P., "Detonation Initiation Studies and Performance Results for Pulsed Detonation Engine Applications," AIAA Paper 2001-1129, January 2001.
- ¹⁵Paxson, D. E., "2003 Pulse Detonation Engine Project: University/Government Spring Ejector Meeting," unpublished presentation, 2003.
- ¹⁶Wilson, J. "Vortex Rings Generated by a Shrouded Hartmann-Sprenger Tube," AIAA paper 2005-5163, June 2005.
- ¹⁷Gharib, M., Rambod, E., Shariff, K., "A universal time scale for vortex ring formation," *Journal of Fluid Mechanics*, Vol. 360, pp. 121-140, 1998.

Performance Measurements of Straight and Diverging Ejectors Integrated with a Pulse Detonation Engine

Aaron J. Glaser^{*}, Nicholas Caldwell[†] and Ephraim Gutmark[‡]
University of Cincinnati, Cincinnati, OH, 45206

John Hoke[§] and Royce Bradley^{**}
Innovative Scientific Solutions Inc., Dayton, OH, 45440

and

Fred Schauer^{††}
Air Force Research Laboratory, WPAFB, Dayton, OH, 45433

Experimental studies were performed on a set of pulse detonation engine (PDE) driven straight and diverging ejectors to determine the system performance. Ejector performance was quantified by thrust measurements. The effects of PDE operating parameters and ejector geometric parameters on thrust augmentation were investigated. PDE operating parameters of fill-fraction and operating frequency were varied. Augmentation was observed to decrease with increasing PDE frequency. Axial placement of the ejector was varied over a broad range covering both upstream and downstream positions. It was found that for all cases tested the maximum thrust augmentation occurred at a downstream ejector placement. Ejector geometries tested covered five lengths, ranging from an L_{EJECT}/D_{EJECT} of 2.61 to 6.61. The exhaust sections tested had half-angles of 0, 4, 8, and 12 degrees. It was found that the exhaust section of half-angle 4 degrees performed better than the others. The optimum ejector geometry was determined to have an overall length of $L_{EJECT}/D_{EJECT}=5.61$. A maximum thrust augmentation of 85% was observed with the optimized ejector configuration at a fill-fraction of 0.6 and 30 Hz operating frequency.

Nomenclature

D_{PDE}	=	detonation tube diameter
D_{EJECT}	=	ejector diameter
DR	=	ejector-to-PDE diameter ratio
ff	=	fill-fraction
L_{EJECT}	=	ejector length
$L_{STRAIGHT}$	=	intermediate straight section length
L_{EXHST}	=	exhaust section length
x	=	ejector position

I. Introduction

THE pulse detonation engine (PDE) is an innovative propulsion technology that could potentially provide significant advantages over more traditional propulsion systems. Engine cycles based on detonation combustion offer a theoretical increase in thermal efficiency as compared to deflagration combustion based systems. For

^{*} Graduate Research Assistant, Department of Aerospace Engineering, ML0070, Student Member AIAA.

[†] Graduate Research Assistant, Department of Aerospace Engineering, ML0070, Student Member AIAA.

[‡] Professor and Ohio Eminent Scholar, Department of Aerospace Engineering, ML0070, Associate Fellow AIAA.

[§] Research Engineer, 2766 Indian Ripple Rd., Senior AIAA Member.

^{**} Senior Scientist, 2766 Indian Ripple Rd., No AIAA Affiliation.

^{††} Senior Engineer, Head PDRF, AFRL/PRTC, Bldg. 490, Senior AIAA Member.

practical PDE applications, one of the key challenges facing researchers is to make use of the increased efficiency of energy conversion due to detonative mode combustion, and most effectively convert that into a propulsive thrust force. A common measure of propulsion system performance is specific impulse (I_{sp}), which is defined as the ratio of thrust generated to the weight flow rate of fuel. Greater values of I_{sp} are desirable as this will decrease the specific fuel consumption. It has been suggested that the use of ejector augmenters on PDEs may be an effective way to increase the system thrust being generated, thus leading to an increased I_{sp} .

An ejector is a simple device used to augment the thrust of an engine. Essentially, an ejector consists of a coaxial duct placed around the exhaust of an engine performing as a fluidic pump. The surrounding ambient air is entrained by the primary exhaust flow and directed into the ejector. The entrained air causes an increase in momentum of the engine exhaust flow. This leads to the generation of a larger system thrust force. The theory and application of ejectors to a steady primary flow is well established. For steady-flow ejectors, the secondary flow is entrained primarily through viscous shear mixing¹. Ejectors being driven by an unsteady primary flow have not been as heavily studied. In particular, little work has been performed on PDE driven ejector systems. However, a number of ejector studies have been performed using various other means to generate an unsteady primary flow. These include cold flow studies employing fluctuating air streams², and unsteady combustion studies using pulsejets to drive the ejectors^{3,4}. This previous research has shown that unsteady ejectors are capable of producing more thrust augmentation than comparable steady-flow ejectors⁴. The increased performance of unsteady ejectors has been attributed to a more efficient energy transfer process between the primary and secondary flows due to dominant inviscid effects. Since PDEs are highly unsteady devices, it has been proposed that PDE driven ejectors have the potential to be highly effective at providing thrust augmentation.

Recent experimental work has shown promising results for ejectors in augmenting the thrust of PDEs. Studies have been performed on the effects of PDE operating parameters as well as on ejector geometric parameters. It has been observed that ejector performance is sensitive to the axial position of the ejector inlet relative to the PDE tube exit. There have been conflicting results reported in the literature as to the optimum ejector location for maximum thrust augmentation. Some research shows that a downstream ejector placement performs better than an upstream placement^{5,6}, while some have observed the opposite trend⁷. The internal surface geometry of the ejector is an important geometric parameter. An experimental study by Allgood et al⁶ was carried out using a contoured bell-mouth inlet with several ejector configurations. Results from those experiments showed maximum thrust augmentation levels of 28% for straight ejectors and 65% for diverging ejector geometries. It is apparent that the diverging ejectors tested were much more effective at producing thrust augmentation than were the straight ejectors. This performance increase with the diverging ejector is attributed to the additional thrust surface area of the diverging section. The study performed by Allgood et al, was limited to a diverging ejector with a half-angle divergence of 4 degrees, and with a fixed length diverging section. To the author's knowledge, no data has been published studying the effect that changing the diverging section half-angle has on thrust augmentation.

The current experimental work thoroughly investigated the effects of PDE operating parameters and ejector geometry on thrust augmentation. The operating parameters varied include fill-fraction, and operating frequency. The ejector geometric parameters studied were ejector axial position, ejector length, and ejector divergence angle. Ejector performance was quantified through thrust measurements of the PDE ejector system. Data from this work will serve to aid researchers in designing an optimized PDE ejector system, and provide performance trends over a range of engine operating conditions.

II. Experimental Setup

A. Description of PDE System

Experimental testing for the current work was carried out at the Air Force Research Laboratory PDE test facility at Wright-Patterson Air Force Base⁸. The detonation tube was constructed of type 316 stainless steel, and the geometry tested consisted of a 5.08 cm inner diameter with 154.94 cm length. The system was operated in a premixed manner, using hydrogen and air as the reactants. Injection of fuel and air into the detonation tube was accomplished using a mechanical valve system. This valve system was constructed from a modified four-cylinder automotive valve head with 4 valves-per-cylinder. The valve train was driven with a variable speed electric motor. The 2 intake ports are used to deliver premixed hydrogen and air, while the 2 exhaust ports deliver purge air. The purge air cycle is used to cool the detonation tube and provide a buffer between the hot combustion products and the fresh reactants being injected into the tube for the next cycle. Due to the nature of automotive valving, the division of the cycle timing for various events such as fill-time, purge-time, and detonation-time were fixed to be each 1/3 of the cycle. Spark ignition was accomplished using a capacitive discharge stock automotive spark system delivering approximately 40mJ of energy. In order to accelerate the deflagration-to-detonation transition process a Shchelkin-

type spiral was used. The spiral was mounted near the headwall and had an overall length of 40.64 cm, extending into approximately the first 26% of the detonation tube length.

The PDE system was mounted on a damped thrust stand designed to measure the time-averaged thrust generated by the PDE. The thrust stand consisted of linear pillow-block bearings riding along a pair of linear bearing rails. The PDE was allowed to move freely on the rails but its motion was resisted by springs to prevent any resonance effects. A novel approach was used to remove the effects of static friction. The PDE was continuously actuated forward and backward by a linear pneumatic actuator. Since the actuator produces a net zero average force, the average position of the thrust stand is a function of the PDE average thrust. The thrust stand was calibrated by placing static weights on a pulley/cable system to simulate a thrust force and measuring the average position of the thrust stand with a displacement sensor. The maximum uncertainty of the thrust stand, which was determined through repeated calibration tests, was found to be approximately ± 1.1 N for the range of PDE thrust loading observed during these tests.

Operation of the PDE system was computer controlled using a LabView interface program. The LabView interface provided the flexibility of specifying engine operating parameters such as PDE operating frequency, fill-fraction, and equivalence ratio. Unless otherwise stated all of the current tests were performed at an operating frequency of 30 Hz and an equivalence ratio of 1.0. Ionization probes were mounted along the detonation tube length to verify that Chapman-Jouguet (CJ) detonations were obtained. For a stoichiometric mixture of hydrogen and air the CJ wave speed is 1957 m/s. Data from these sensors was collected at 5 MHz using a 16 channel data acquisition system. This fast sampling rate was adequate to accurately resolve the detonation wave speed.

B. Ejector Hardware

The ejector hardware was mounted on the PDE system to determine its effect on the thrust generated by the PDE. All of the ejectors tested were mounted coaxially to the detonation tube. The ejectors were suspended from two parallel rails mounted above the detonation tube. The rails extended along the length of the tube allowing the axial position, x , of the ejector inlet to be varied from -12 to +6 tube diameters from the PDE tube exit plane. A negative axial position value corresponds to the ejector inlet placed upstream of the PDE exit with the ejector overlapping the detonation tube. For a positive value the ejector is mounted downstream of the detonation tube exit.

An ejector as used in these tests consisted of an inlet section, an intermediate straight section, and an exhaust section as shown in Fig. 1. The diameter of the ejector (D_{EJECT}) was defined as the diameter of the intermediate straight section, as this was the minimum diameter for any given ejector geometry. For the current work, D_{EJECT} was held at a fixed value of 13.97 cm. The ejector-to-PDE diameter ratio (DR) of 2.75 was therefore constant throughout the testing. This value closely matched the optimum diameter ratios reported in other ejector experiments^{5, 9}. Two inlet sections were used for this testing. The first inlet is a contoured bell-mouth inlet of elliptic cross-section⁶, and the other inlet used has a rounded inlet lip with a radius of 3.81 cm. The non-dimensional length of the intermediate straight section was varied from an $L_{\text{STRAIGHT}}/D_{\text{EJECT}}$ of 0 to 3, in increments of $L_{\text{STRAIGHT}}/D_{\text{EJECT}}=1$. For the limiting case where $L_{\text{STRAIGHT}}/D_{\text{EJECT}}$ of the intermediate straight section is zero, the ejector consisted of the inlet section with the exhaust section directly connected to it. The exhaust sections tested had a half-angle divergence of 0, 4, 8, and 12-degrees. For each divergence angle investigated, 2 separate length exhaust sections were tested. In all, 29 separate ejector geometric configurations were tested.

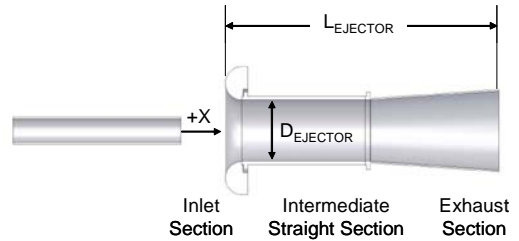


Figure 1. Diagram of the ejector geometry used for the current work.

III. Results and Discussion

A. Baseline Testing of PDE System

The baseline PDE system for these tests consisted of the detonation tube with no ejector installed. For the current tests, the amount of PDE thrust augmentation produced by use of an ejector is defined by the following

$$\alpha = \frac{(T_{\text{PDE-EJECT}} - T_{\text{PDE}})}{T_{\text{PDE}}} \cdot 100 \quad (1)$$

where $T_{\text{PDE-EJECT}}$ is the thrust generated by the PDE with an ejector installed, and T_{PDE} is the baseline thrust of the system with no ejector installed. As can be seen from the definition of thrust augmentation, initial testing of the baseline PDE system had to be performed in order to calculate ejector thrust augmentation. A suitable test duration time was determined which gave steady thrust measurements. Normalized thrust as a function of experiment run time is shown in Fig. 2. It can be seen that due to the thrust averaging process employed by the thrust stand, it takes approximately 20 seconds to reach a steady thrust value. All experiments reported in this work were run for a sufficient duration to achieve a steady thrust measurement. The PDE operating parameters that were varied during baseline testing were: 1) Operating frequency from 10 to 30 Hz, 2) Fill-fraction from 0.6 to 1.0, and 3) Equivalence ratio from 0.4 to 1.2. These operating parameters have been studied in previous work for a PDE with no ejector installed⁸. In these previous studies, thrust was seen to increase linearly with increasing operating frequency. The fill-fraction is defined as the ratio of the tube volume filled with a detonable mixture to the total tube volume. It has been shown that the fill-fraction is an effective way of throttling a PDE. It is interesting to note that as well as a simple scheme to control the thrust output, significant performance efficiency gains can be attained by decreasing the fill fraction due to partial fill effects. Varying the PDE equivalence ratio has the effect of changing the initial composition of the fuel-oxidizer mixture. Previous experimental work¹⁰ has shown that the CJ detonation parameters, such as wave speed and pressure ratio, are a function of the initial mixture composition, and can therefore be controlled by varying the equivalence ratio.

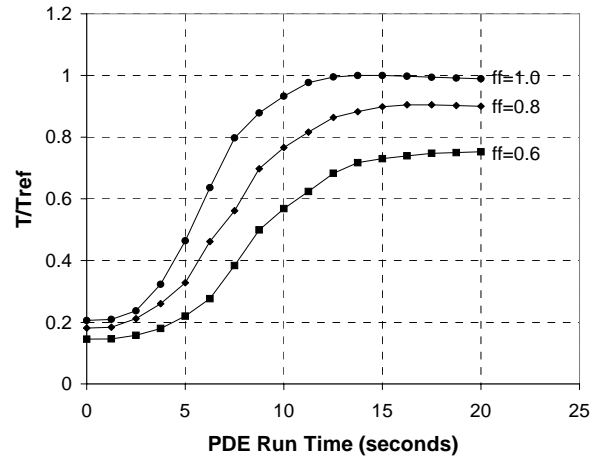


Figure 2. Determination of the PDE run time to achieve a steady thrust measurement.

B. Effect of PDE Operating Parameters

Testing was performed in order to determine the effects of several key PDE operating parameters on ejector thrust augmentation. The ejector hardware installed for all of the operating parameter tests performed had a total $L_{\text{EJECT}}/D_{\text{EJECT}}$ of 5.61. The diverging exhaust section used had an $L_{\text{EXHST}}/D_{\text{EJECT}}$ of 2.36, with a half angle divergence of 4 degrees. The ejector was mounted at a downstream axial position of $x/D_{\text{PDE}}=+2$.

The PDE operating frequency was varied from 10 Hz to 30 Hz, with 30 Hz being the highest achievable frequency of the current PDE setup. In the range of frequencies tested thrust augmentation was observed to decrease

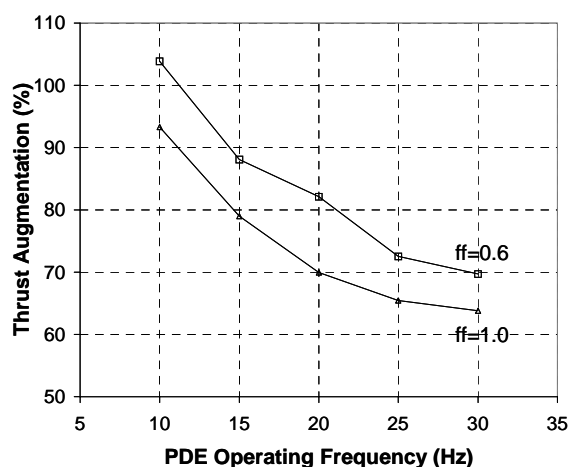


Figure 3. Thrust augmentation as a function of operating frequency, for two fill-fractions. Ejector geometry used had $L_{\text{EJECT}}/D_{\text{EJECT}}=5.61$, $L_{\text{EXHST}}/D_{\text{EJECT}}=2.36$ with 4 degree divergence. $x/D_{\text{PDE}}=+2$, $\Phi=1$.

with increasing frequency. This trend can be seen in Fig. 3, which includes data taken at two fill-fractions. It should be noted that as the frequency approaches 30 Hz, the change in thrust augmentation appears to be leveling off. The effect of PDE fill-fraction is also shown in this figure. Decreasing the fill-fraction increases the amount of thrust augmentation produced. To better understand why the augmentation decreases with increasing frequency, normalized thrust values as a function of PDE frequency are plotted in Fig. 4a. The baseline PDE thrust increases approximately linearly with operating frequency. Thrust levels with the ejector installed also increase with frequency. The difference between these two curves gives the thrust increase due to the ejector. Thrust augmentation was previously defined as the increase in thrust due to the ejector divided by the baseline PDE thrust. It can be seen from this figure that the amount of change in thrust due to the ejector is also increasing with frequency. This data is re-plotted in Fig. 4b, where both baseline PDE thrust and the amount of thrust increase due to the ejector are shown as a function of frequency. As both PDE thrust and thrust

increase are fairly linear, each data series is fitted with a linear trend-line as shown. From this figure it can be seen that the slope of the baseline thrust line is larger than that of the ejector thrust increase line. Hence, the baseline thrust is increasing at a greater rate than is change in thrust. This amounts to a decrease in thrust augmentation as the denominator in Eq. 1 is increasing faster than the numerator. If both lines had equal slopes, the augmentation would remain a constant with frequency. As thrust and change in thrust were seen to follow approximately linear trends within the frequency range tested, it is useful to speculate on the behavior of thrust augmentation at higher frequencies not achievable with the current PDE system. By dividing the equation of the straight line found for the change in thrust by the equation found for the baseline thrust, augmentation can be projected for any given frequency. Fig. 5 shows results from this simple analysis applied to frequencies up to 100 Hz. The current experimental data points are also plotted along with the projected augmentation data. Although the theoretical thrust augmentation continues to decrease with frequency, it is seen to be leveling off asymptotically.

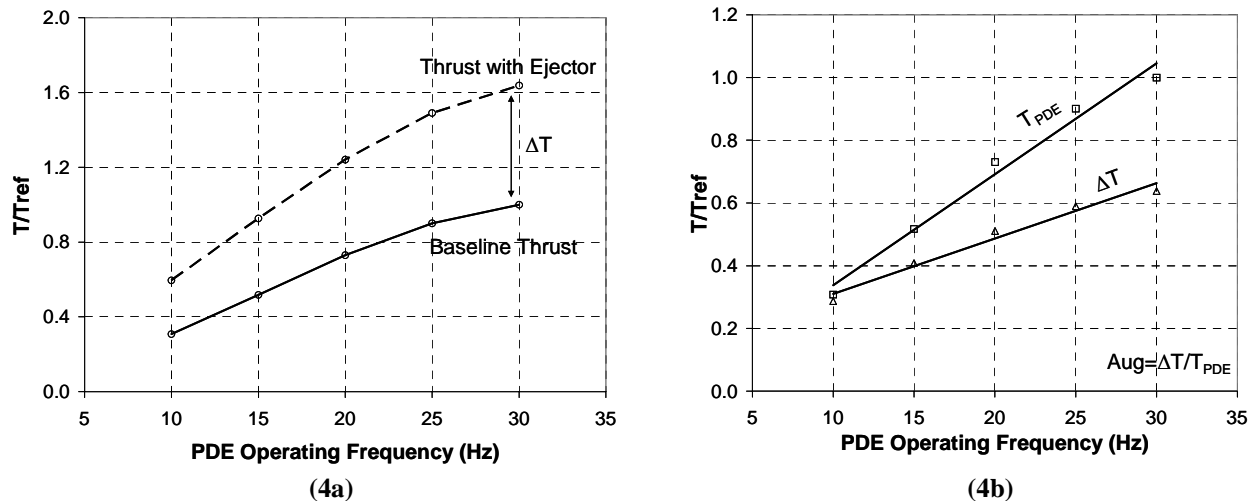


Figure 4. PDE-ejector system thrust levels: Baseline thrust and system thrust with ejector installed are shown in 4a. In 4b, the data has been re-plotted to show baseline thrust and amount of change in thrust due to the ejector. Ejector geometry used had $L_{EJECT}/D_{EJECT}=5.61$, $L_{EXHST}/D_{EJECT}=2.36$ with 4 degree divergence angle. $x/D_{PDE}=+2$, $\Phi=1$.

C. Effect of Ejector Axial Position

Previous work has shown that ejector performance is sensitive to the axial position of the ejector relative to the PDE tube exit. As previously discussed there have been conflicting results reported in the literature as to the optimum ejector position. In an effort to resolve these inconsistencies, a detailed mapping of ejector performance as a function of axial position was carried out. Results from this mapping are shown in Fig. 5, which includes data for two separate ejectors. Both of the ejectors shown are of length, $L_{EJECT}/D_{EJECT}=5.61$, with one being a straight ejector and the other being a diverging ejector. The diverging ejector has an exhaust section length of $L_{EXHST}/D_{EJECT}=2.36$, with a 4 degree divergence angle. It can be clearly seen that for both of the ejector configurations tested, a downstream ejector placement provided optimum performance. Maximum thrust augmentation occurred at $x/D_{PDE}=+1$ for the diverging ejector at all fill-fractions tested. For the straight ejector, the position for maximum augmentation was found to be at $x/D_{PDE}=+2$. At the downstream positions the inverse relationship between fill-fraction and thrust augmentation can

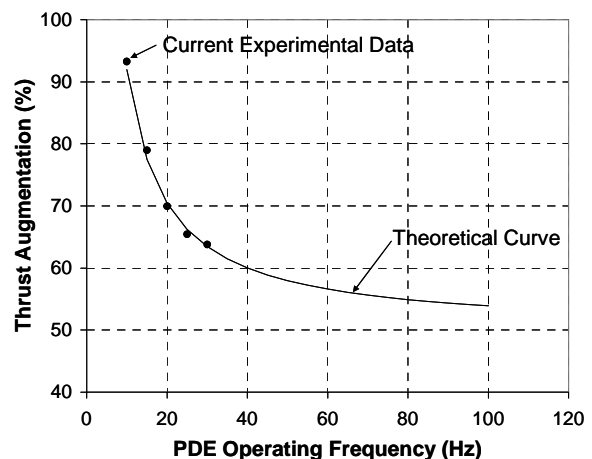


Figure 5. Projected thrust augmentation as a function of operating frequency.

be seen. As the ejectors were moved upstream, thrust augmentation was observed to continually drop off to levels approaching zero. At the upstream positions, fill-fraction was not seen to have a significant impact on thrust augmentation. The benefit of using a diverging ejector is apparent as the diverging ejector showed approximately 2.37 times the maximum thrust augmentation of the straight ejector.

A comparison was made between the two separate ejector inlets used in these studies. The first inlet is a contoured bell-mouth inlet and the second inlet has a rounded inlet lip. Results are shown in Fig. 7 for both inlets over a range of axial positions and PDE fill-fractions. The maximum thrust augmentations for both inlets occurred at a downstream position. Maximum augmentation levels for both inlets were within 1% of each other at all fill-fractions. Although the augmentation levels were approximately the same between the inlets, one noticeable effect was that the optimum axial position for the rounded inlet was shifted further downstream from the optimum axial position for the bellmouth inlet.

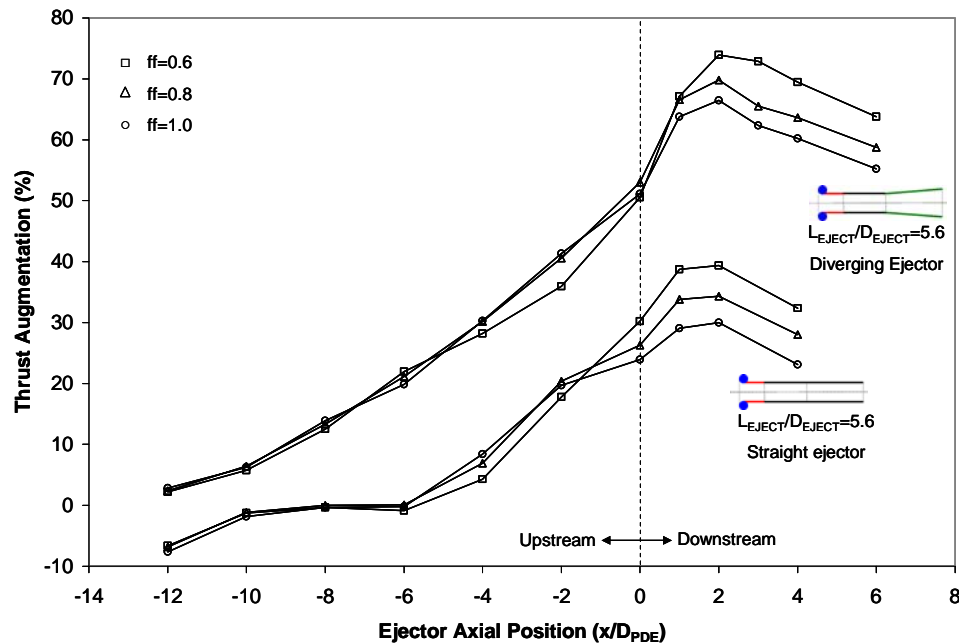


Figure 6. Effect of ejector axial position on thrust augmentation.

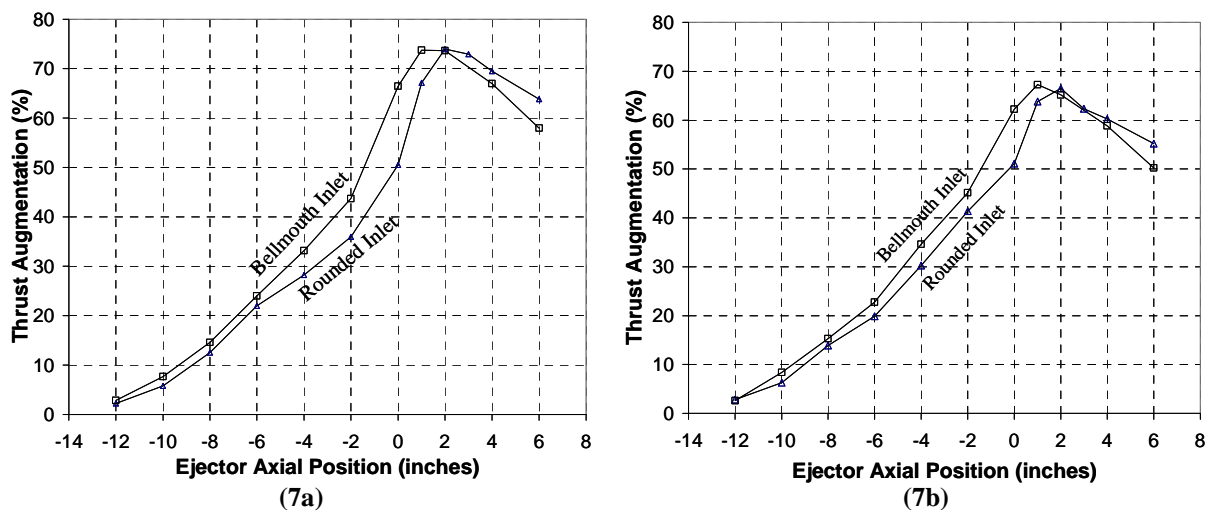


Figure 7. Comparison between bellmouth and rounded ejector inlets. 7a shows results for a fill-fraction of 0.6, and 7b is for a fill-fraction of 1.0. Ejector geometries used had $L_{EJECT}/D_{EJECT}=5.61$, $L_{EXHST}/D_{EJECT}=2.36$ with 4 degree divergence angle. $x/D_{PDE}=+2$, $\Phi=1$.

D. Effect of Ejector Length

The ejector length could be varied by changing the length of the intermediate straight section, changing the length of the exhaust section, or by a combination of the two. Due to the lengths of these sections it was possible to test ejectors with an equal overall L_{EJECT}/D_{EJECT} but made up of a different combination of straight and exhaust sections. The effect of the length of the intermediate straight section on augmentation was first studied. The ejector geometry consisted of the bellmouth inlet section, an intermediate straight section, and a diverging exhaust section of 4 degree half angle. The intermediate straight section length was varied from an $L_{STRAIGHT}/D_{EJECT}$ of 0 to 3, and data was taken for 3 PDE fill-fractions. Results from this study are plotted in Fig. 8. It can be seen that as the straight section length is increased, an optimum length is reached which gives maximum thrust augmentation. The optimum length for the straight section was found to be $L_{STRAIGHT}/D_{EJECT}=2$, which corresponds to an overall $L_{EJECT}/D_{EJECT}=5.61$. The optimum straight section length was not observed to vary with changing fill-fraction.

Another ejector geometric parameter of importance is the length of the diverging exhaust section. Two lengths of exhaust sections were tested, L_{EXHST}/D_{EJECT} of 1.36 and 2.36, both with a diverging half angle of 4 degrees. The data shown in Fig. 9 shows the combined effects of varying both the intermediate straight section and the exhaust section lengths. Each of the curves shown corresponds to a constant length of the exhaust section, with different values of L_{EJECT}/D_{EJECT} achieved by changing the intermediate straight section length. Comparing the 2 ejectors tested with an overall $L_{EJECT}/D_{EJECT}=5.61$ highlights the effect of the length of the diverging exhaust section. Although the total lengths of the ejectors are the same, they incorporate different length diverging sections, with the difference in ejector length made up by the length of the intermediate straight sections. The trend that can be seen is that by increasing the length of the diverging section, thrust augmentation is increased. At $L_{EJECT}/D_{EJECT}=5.61$, the ejector with the longer diverging section has a thrust augmentation approximately 15% greater than the short diverging section case.

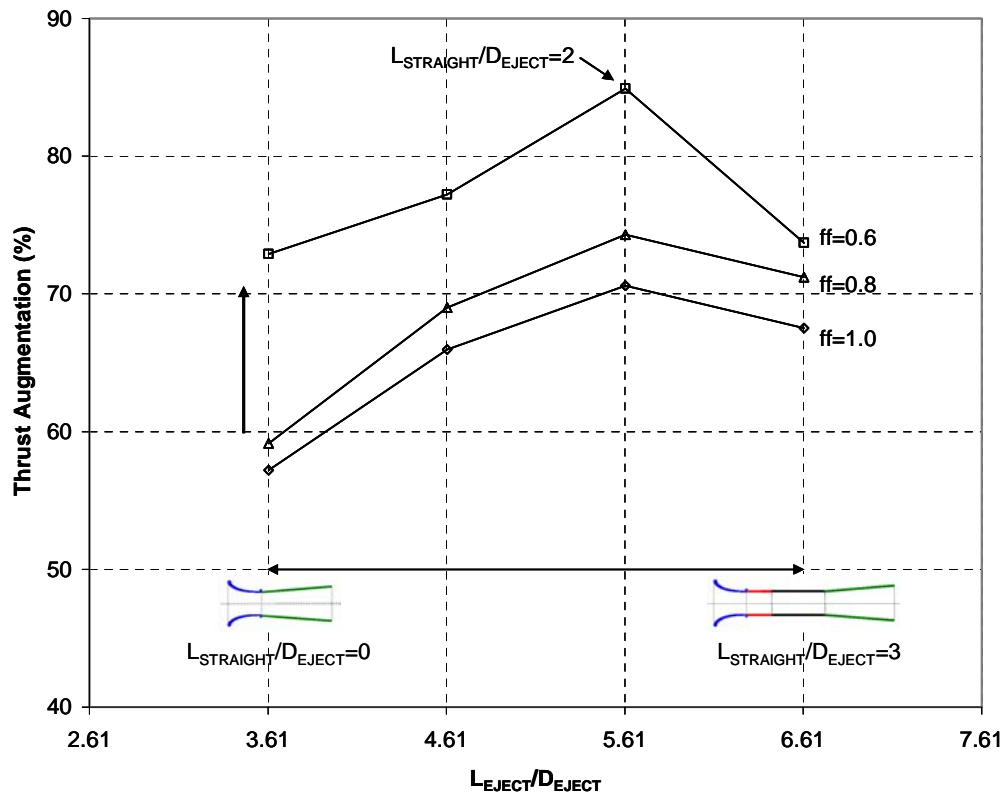


Figure 8. Effect of increasing the length of the intermediate straight section on thrust augmentation. Exhaust section had $L_{EXHST}/D_{EXHST}=2.36$, with 4 degree divergence angle. Ejector axial position of $x/D_{PDE}=+2$, $\Phi=1$.

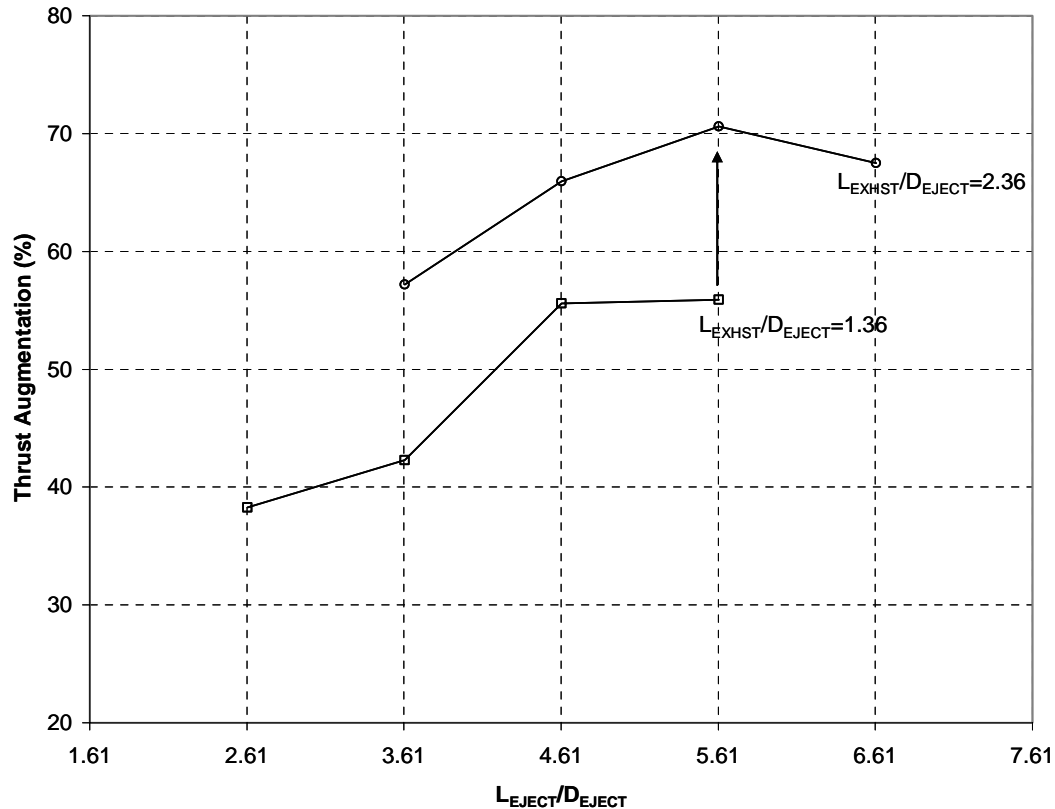


Figure 9. Effect of varying the intermediate straight section length, along with the length of the diverging exhaust section. Ejector axial position of $x/D_{PDE}=+2$. $ff=1.0$, $\Phi=1$.

E. Effect of Divergence Angle

For all of the data reported so far, the diverging section half-angle has been set to 4 degrees. This angle is an important geometric parameter of the ejector system, and no known data has been reported in the published literature on the effect that varying this angle has on thrust augmentation. Diverging angle data is shown in Fig. 10 for ejectors over a range of L_{EJECT}/D_{EJECT} ratios at a fill-fraction of 1.0. In Fig. 10a the exhaust section length is fixed at $L_{EXHST}/D_{EJECT}=2.36$. Different L_{EJECT}/D_{EJECT} ratios were obtained by changing the length of the intermediate straight section alone. The 4 degree diverging section shows the best performance at all lengths tested. The 12 degree diverging section performed much worse than the others; this can be explained by increased flow separation on the diverging section leading to a low pressure zone causing a drag force on the system. Optimum intermediate straight section length did not change with divergence angle, as the optimum L_{EJECT}/D_{EJECT} was always seen to be 5.61. It was observed that interactions exist between the geometric variables of diverging section length and divergence half-angle. In Figure 10b, the exhaust section length is fixed at $L_{EXHST}/D_{EJECT}=1.36$. The shorter diverging exhaust sections also showed the same optimum straight section length as the longer diverging sections. However due to shorter length of the exhaust section, the optimum total ejector length is decreased. For the short exhaust sections, the 8 degree outperformed both the 4 and 12 degree sections at all lengths tested. The interactions between geometric parameters are apparent in Fig. 11. Data is plotted as a function of diverging section half-angle for 2 different length exhaust sections. Straight ejector data is also shown in this figure with a diverging angle of 0 degrees. The long diverging section shows a peak augmentation at 4 degrees divergence. While the short diverging section shows a peak augmentation at a half-angle of 8 degrees. This data suggests that each divergence angle has an optimum length. The 4 degree half-angle showed the largest increase in augmentation with increasing diverging section length. It appears that the 4 degree section has not yet attained its optimum length and thus it would be beneficial to test a longer 4 degree diverging section.

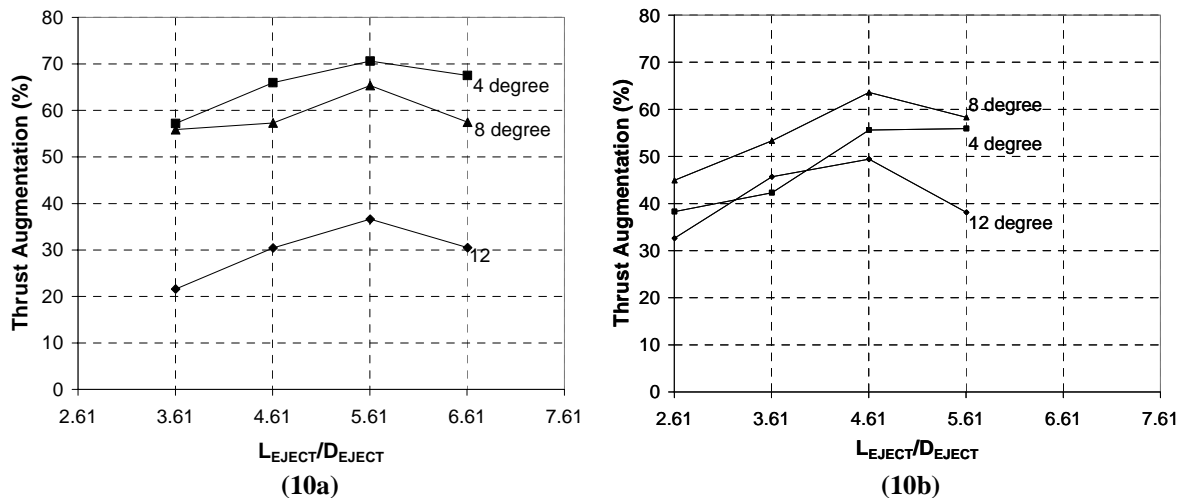


Figure 10. Thrust augmentation as a function of intermediate straight section length for 2 separate exhaust section lengths. Exhaust section in 10a has $L_{EXHST}/D_{EXHST} = 2.36$. Exhaust section in 10b has $L_{EXHST}/D_{EXHST} = 1.36$. Ejector axial position of $x/D_{PDE} = +2$.

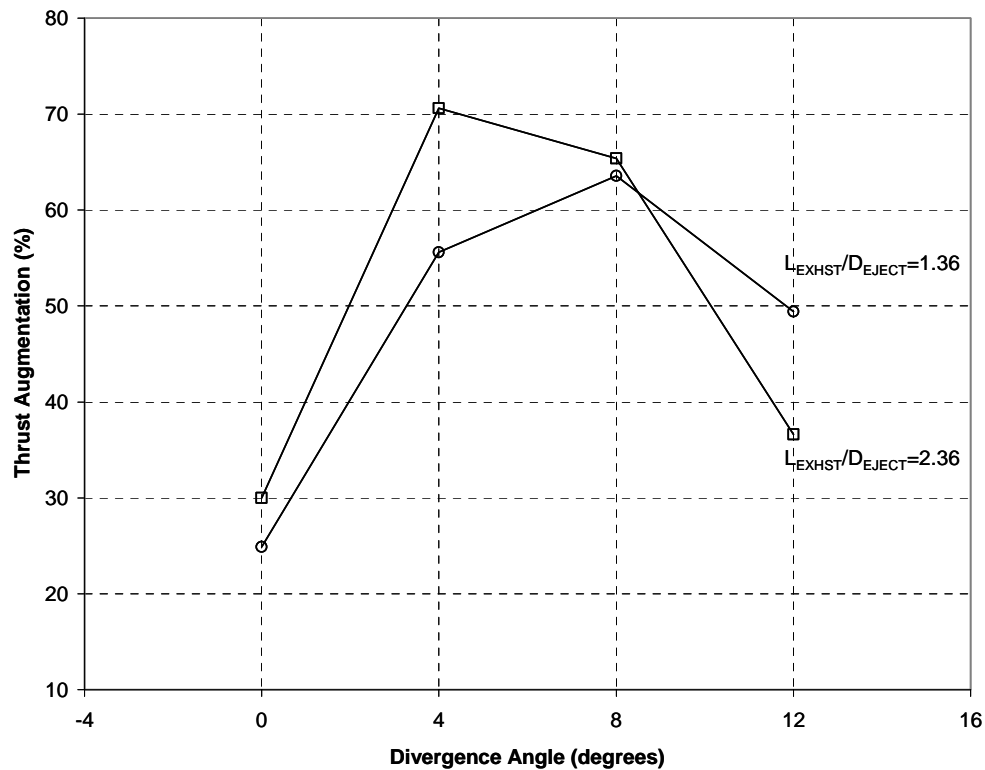


Figure 11. Thrust augmentation as a function of exhaust section divergence angle. Ejector axial position of $x/D_{PDE} = +2$. $ff = 1.0$, $\Phi = 1$.

IV. Conclusion

A parametric study was performed on a set of straight and diverging ejectors. Testing was performed to study the effects of the PDE operating parameters of fill-fraction and frequency on thrust augmentation. It was verified that at

a downstream ejector placement, fill-fraction has an inverse relationship with thrust augmentation. It was seen that over the range of 10 to 30 Hz, increasing the operating frequency of the PDE decreased thrust augmentation. Through a simple analysis it has been speculated that augmentation will continue to decrease with frequencies above 30 Hz. From this analysis thrust augmentation does appear to level off asymptotically as frequency is increased to higher levels. The axial placement of the ejectors was studied in detail. Axial position was varied from $x/D_{PDE} = -12$ to $+6$. For all ejectors tested, straight and diverging, a downstream placement gave maximum thrust augmentation. Thrust augmentation decreased towards zero as the ejectors were moved upstream, and at upstream placements fill-fraction had almost no effect on augmentation. The key ejector geometric parameters were varied and showed an optimum length of the intermediate straight section to be $L_{STRAIGHT}/D_{EJECT} = 2$. For the 4 degree diverging sections tested, increasing the length of the diverging section gave increased augmentation. This large increase in augmentation with diverging section length suggests that the 4 degree diverging section has not yet attained its optimum length. The divergence angle of the exhaust section was varied from 0 to 12 degrees. Interactions were observed between the variables of divergence angle and exhaust section length. The 4 degree diverging section performed the best overall of the divergence angles tested. Use of a diverging ejector was seen to provide approximately 2.37 times more thrust augmentation than a purely straight ejector of equal length. The optimum ejector configuration gave thrust augmentations of 71% at a fill-fraction of 1.0, and 85% at a fill-fraction of 0.6.

Acknowledgments

The authors would like to thank the Propulsion Directorate at the Air Force Research Laboratory and Innovative Scientific Solutions Inc. (ISSI) for providing the financial support for this work. The technical support of Curtis Rice of ISSI was also greatly appreciated.

References

- ¹Presz, W., Reynolds, G., Hunter, C., "Thrust Augmentation with Mixer/Ejector Systems", AIAA 2002-0230, 40th AIAA Aerospace Sciences Meeting and Exhibit, Reno, NV, January 14-17, 2002
- ²Wilson, J. and Paxson, D.E., "Unsteady Ejector Performance: An Experimental Investigation Using a Resonance Tube Driver", AIAA 2002-3632, 38th AIAA Joint Propulsion Conference, Indianapolis, IN, July 7-10, 2002
- ³Paxson, D.E., Wilson, J. and Dougherty, K.T., "Unsteady Ejector Performance: An Experimental Investigation Using a Pulsejet Driver", AIAA 2002-3915, 38th AIAA Joint Propulsion Conference, Indianapolis, IN, July 7-10, 2002.
- ⁴Lockwood, R., "Interim Summary Report on Investigation of the Process of Energy Transfer from an Intermittent Jet to Secondary Fluid in an Ejector-Type Thrust Augmenter", Hiller Aircraft Report No. ARD-286, March 1961.
- ⁵Rasheed, A., Tangirala, V., Pinard, P.F., Dean, A.J., "Experimental and Numerical Investigations of Ejectors for PDE Applications", AIAA 2003-4971, 39th AIAA Jet Propulsion Conference, Huntsville, AL, July 21-23, 2003.
- ⁶Allgood, D., Gutmark, E., "Performance Measurements of Pulse Detonation Engine Ejectors", AIAA 2005-0223, 43rd AIAA Aerospace Sciences Meeting and Exhibit, Reno, NV, January 10-13, 2005.
- ⁷Shehadeh, R., Saretto, S., Lee, S.-Y., Pal, S., Santoro, R.J., "Experimental Study of a Pulse Detonation Engine Driven Ejector", AIAA Paper 2003-4972, 39th AIAA Jet Propulsion Conference, Huntsville, AL, July 21-23, 2003.
- ⁸Schauer, F., Stutrud, J., and Bradley, R., "Detonation Initiation Studies and Performance results for Pulse Detonation Engine Applications," 39th AIAA Aerospace Sciences Meeting, AIAA 2001-1129
- ⁹Wilson, J., Sgondea, A., Paxson, D., Rosenthal, B., "Parametric Investigation of Thrust Augmentation by Ejectors on a Pulse Detonation Tube," 41st Joint AIAA/ASME/SAE/ASEE Propulsion Conference, Tucson, AZ, 2005, AIAA 2005-4208
- ¹⁰Glaser, A., Allgood, D., Gutmark, E., "Experimental Investigation into the Off-Design Performance of a Pulse Detonation Engine," AIAA 2004-1208, 42nd AIAA Aerospace Sciences Meeting and Exhibit, Reno, NV, January 5-8, 2004.

The Impact of Detonation Initiation Techniques on Thrust in a Pulsed Detonation Engine

John L. Hoke and Royce P. Bradley
Innovative Scientific Solutions, Inc., Dayton, Oh, 45440

Jason R. Gallia and Frederick R. Schauer
Air Force Research Laboratories, Wright-Patterson AFB, OH, 45433

Detonation initiation remains an impediment to pulsed detonation technology efficacy. Practical fuels can now be detonated regularly in the laboratory using conventional oxygen-rich predetonators or extended deflagration-to-detonation transition (DDT) geometries; however, these systems are not suited for field use due to the excess oxygen required for the predetonator and the reduced performance due to drag of DDT mechanisms. The performance of a hydrogen-air multi-cycle pulsed detonation engine is examined using two initiation schemes, a predetonator and a DDT device to determine a suitable initiation mechanism. DDT mechanisms typical for initiation of hydrogen and those typical of insensitive hydrocarbon fuels are examined. Because of the relative ease of detonation initiation, hydrogen is the fuel used in the main detonator tube, even with the longer DDT mechanisms used for insensitive fuels. The predetonator uses aviation gasoline and nitrous oxide in a small (1 to 3% of the volume of the main tube) chamber to initiate a detonation and generate an upper limit on the expected performance of DDT initiators. A fuel-specific impulse value of approximately 3900 sec is achieved with the predetonator at 10 Hz and an equivalence ratio and fill fraction of unity. For DDT initiation, a Schelkin-like spiral located in 10 to 70% of the main detonation tube volume is used. Below 10% of the main tube volume, DDT is found to generate identical impulse to the predetonator initiation, while for the longest DDT mechanism, located throughout 70% of the main tube volume, a reduction in fuel-specific impulse of 44% is measured. Head pressure measurements show a reduced thrust wall pressure for the DDT initiation, probably owing to the drag and dissipation of the detonation wave traveling upstream through the DDT mechanism.

I. Introduction

PULSED detonation engines (PDEs) require efficient detonation initiation for practical operation. Typically detonation initiation is obtained via the use of predetonators, which utilize a more readily detonable mixture in a small initiation tube that subsequently propagates a detonation into a main thrust detonation tube, and/or flame acceleration through successful deflagration-to-deflagration transition (DDT)¹. Depending on the sensitivity of the fuel, the amount of excess oxygen or DDT distance can become excessive. In recent years, kerosene-air mixtures have been detonated successfully in a variety of engine scale detonation tubes²⁻⁵; however, the practicality of the methods used to achieve hydrocarbon detonations continues to be an obstacle to PDE development.

Although predetonators can produce extremely short detonation initiation times and distances, they typically employ highly reactive components to overcome the difficulties associated with hydrocarbon-air detonation initiation. In addition to the logistic and hardware penalties associated with typical predetonator systems, minimizing the required size and obtaining efficient transition to a practical hydrocarbon-air mixture remain challenges. Typically oxygen is utilized due to its high reactivity and nominal detonation initiation requirements with hydrocarbon fuels. Oxygen is unpleasant to work with due to its proclivity for

exothermically oxidizing structural components. Additionally, even a 2% by-volume predetonator requires a significant oxygen supply.

DDT has been demonstrated successfully in hydrocarbon-air mixtures. Although high-energy ignition system or excess oxidizer may not be required, DDT typically requires both long distances and times for practical hydrocarbon-air mixtures. Significant cycle time penalties and inefficiencies have been identified as the negative consequences of hydrocarbon-air DDT used for the initiation process⁶. Most hydrocarbon-air mixtures can be readily detonated with a 48" Schelkin spiral if good mixing can be obtained⁵. However, the performance penalties for using long spirals can be quite significant. Kailasanath's review found that the generally recognized fuel based specific impulse for hydrogen air mixtures is around 4000-4500 seconds (with a fully detonating tube)⁷.

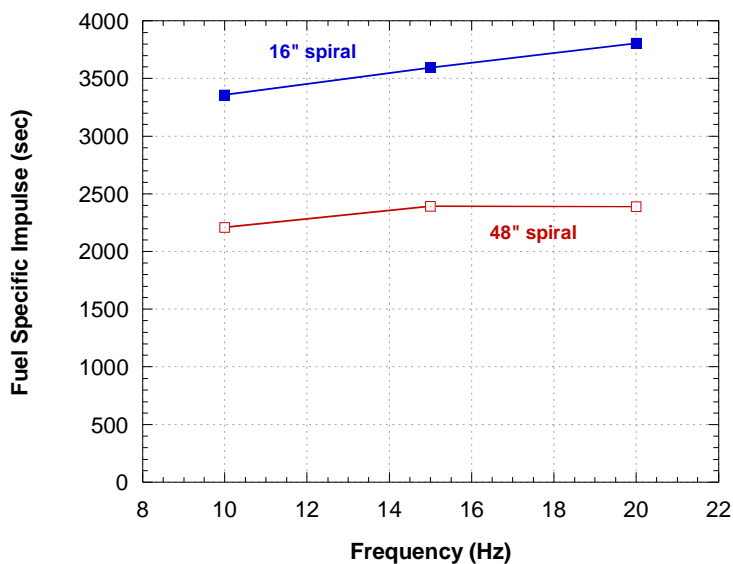


Figure 1. Specific impulse versus frequency for stoichiometric hydrogen-air with 16" and 48" spirals in a 72" long, 2" diameter tube.

Our past work⁶ demonstrated that even a 16" spiral in a 72" tube has an I_{sp} below 4000 seconds, and as shown in Fig. 1, the performance penalties associated with a long spiral are nearly 50%. These penalties were found to be caused by DDT obstacle drag in the blow-down processes and are in addition to pressure drop penalties which occur during the tube fill cycle. The authors found that turbulence and pressure effects can promote detonation initiation and enhance performance as shown by the I_{sp} increasing with frequency with a 16" spiral. However, losses offset gains when longer spirals are utilized, such as the 48" Schelkin spiral, (the performance of which is shown in Fig. 1.) which may be required for initiation of conventional hydrocarbon-air mixtures⁵.

Shepherd and co-workers found similar penalties associated with DDT processes in their detonation impulse measurements⁸. This paper will further quantify the performance of DDT initiation and transmission mechanisms in comparison to predetonators.

II. Experimental Setup & Procedures

Experiments were conducted using the research PDE at the Air Force Research Laboratory's Pulsed Detonation Research Facility. This PDE uses the "head" of a General Motors automotive engine to control the airflow into the detonation tube. The PDE cycle consisted of equal time allotted for: i) filling the detonation tube with pre-mixed hydrogen and air at an equivalence ratio of one, ii) ignition, detonation, and blow-down, and iii) purging of the detonation tube with air. For these experiments the pressure upstream of the automotive poppet valves was controlled such that during the fill cycle the mass flow of pre-mixed fuel and air was equivalent to the volume of the tube times the density of the fuel-air charge at the gas temperature upstream of the poppet valves and atmospheric pressure times the operating frequency. This was defined as a fill fraction (FF) of one, and all tests during this research were conducted at a fill fraction of one unless otherwise noted. The purge fraction (PF) was defined in the same manner and was held constant at one-half for all experiments.

The fuel-air mixture was ignited with a 115 mJ spark at the closed end of the main tube or predetonator. Further details of this engine are given by Schauer et al⁹.

The PDE was operated at 10Hz in order to minimize turbulent and dynamic pressure effects on the initiation processes and PDE performance. Unless otherwise noted, a stoichiometric mixture of hydrogen-air was used in the main detonation tube (equivalence ratio of unity). Detonation tubes were instrumented with a dynamic pressure transducer at the closed end of the tube and ion probes at various intervals along the length of the detonation tube. Thrust was measured on a damped thrust stand where displacement was proportional to thrust. The thrust stand was oscillated during each test, and the displacement averaged over several seconds to eliminate hysteresis and improve accuracy. The repeatability of the thrust measurement has been shown previously to be within $\pm 2\%$ ⁶.



Figure 2. 16" long x 2" diameter initiation section with Schelkin-type spiral connected to a 3.5" diameter detonation tube. Additional details of the 2" initiation section and ~17° half-angle transmission section are shown on the right.

For the purposes of assessing initiation on performance, two tube diameters were chosen and two initiation mechanisms were employed. A 2" diameter, 16" long Schelkin-type spiral was located in the head end of a 16" long 2" diameter pipe which was then connected to either more 2" diameter pipe (as described in previous work and in Fig 3a.), or through a ~17° half-angle coupling (2" to 4" pipe reducer fitting) to a 3.5" diameter pipe as shown in Fig. 2 and 3b. The initiation section was approximately 10 and 20% of the tube volume of the 3.5" and 2" main tubes respectively.

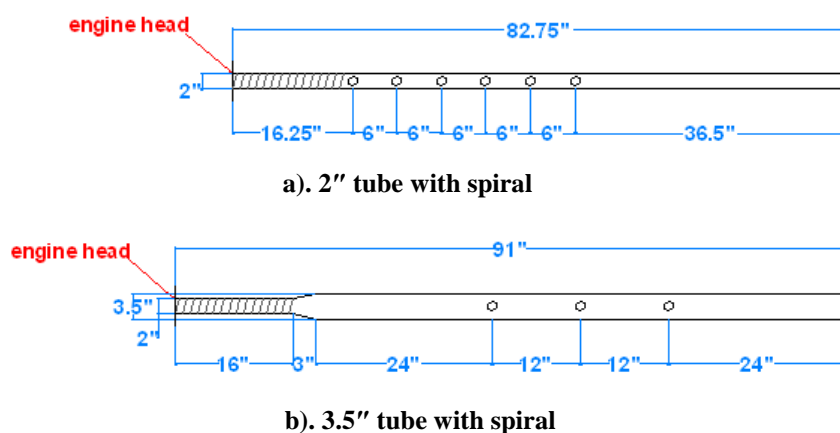


Figure 3. Geometry and instrumentation locations of 2" (a) and 3.5" (b) diameter detonation tubes, each initiated via a 2" diameter x 16" long Schelkin-type spiral section located adjacent to the closed ignition end.

An avgas-nitrous oxide predetonator was the second initiation scheme. The predetonator, pictured in Fig. 4, consisted of an outboard marine company's (OMC) two-stage injector originally developed for 2-stroke direct injection applications as well as an automotive company's high pressure direct injection injector. In this application, the fuel was injected at approximately 120 psig by the OMC injector and liquid nitrous oxide was injected by the high pressure direct injector at 600 to 800 psig, (dependant on the bottle supply temperature.) The second stage of the OMC injector was used to purge the predetonator at the end of a cycle with compressed air at 95 psig. The injectors were attached to a 1" pipe cap that screwed onto a 1" tube attached to an adapter. In this manner, the detonation was transferred from the predetonator to the main detonation tube.

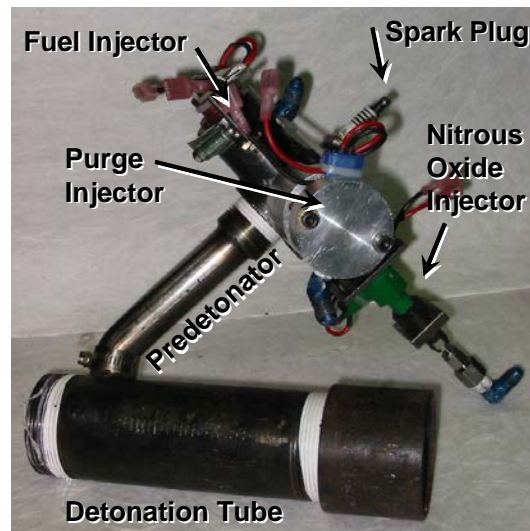


Figure 4. Avgas-nitrous oxide predetonator consisting of three fuel injectors, 1" tubing and a spark plug.

The predetonator transmitted the resultant detonation to either a 2" or 3.5" diameter main detonation tube containing a hydrogen-air mixture supplied by the research engine head. The transmission section was carefully designed to propagate the detonation from the predetonator to the main tube without quenching. Hardware configuration and instrumentation ports for the predetonator initiated hardware are shown in Fig. 5.

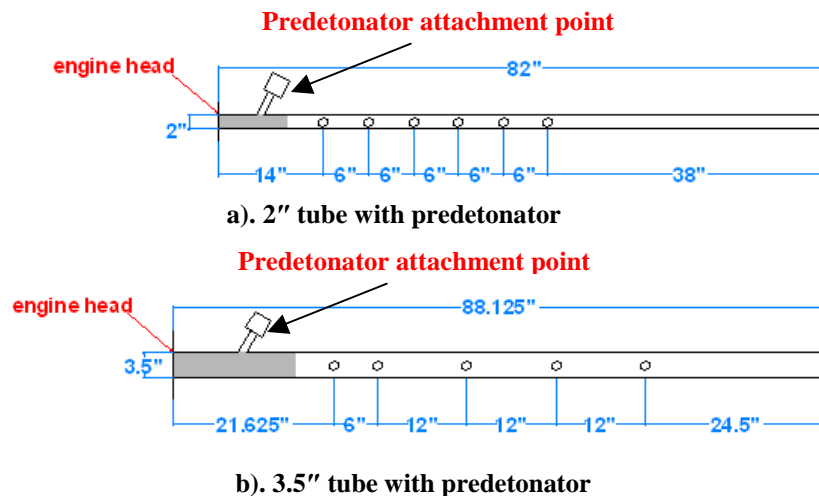


Figure 5. Geometry and instrumentation locations of 2" (a) and 3.5" (b) diameter detonation tubes, each initiated via a 1" diameter predetonator near the head end.

The predetonator was found to operate reliably with either vapor or liquid fuels, although liquid avgas was used here. Nitrous oxide was found to have the detonability of pure oxygen, but without the special handling and design requirements associated with pure oxygen. The use of liquid nitrous oxide was also beneficial because of the cooling from the heat of vaporization upon injection, which kept the injector assembly cool as shown in Fig. 6. The 1" diameter predetonator produced a detonation consistently within 6". Consequently a 7" long predetonator was employed, producing a predetonator volume ~1-3% of the main detonation tubes.

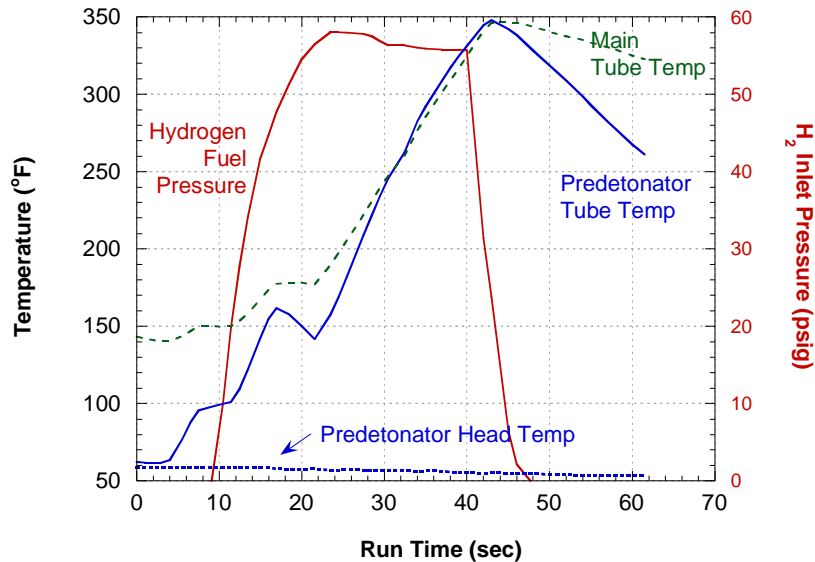


Figure 6. Temperature of predetonator head, predetonator combustion tube, and main thrust tube versus run time. H_2 pressure plotted for reference. Data acquired between 30 and 40 seconds.

In order to obtain consistent blow-down dynamics, all four geometries described were within 10% of the same length. Subsequently the four geometries will be referenced by main tube diameter and initiation method, e.g. “3.5” tube with spiral” refers to the geometry shown in Fig. 3b., “2” tube with predetonator” corresponds to the geometry shown in Fig. 5a., etc.

Operation consisted of setting frequency, main combustion air and purge air flow rates, followed by turning on the ignition system and/or predetonator. The main tube hydrogen fuel was then enabled and data collection commenced once the hydrogen fuel flow rate was stabilized. Consequently, the main detonation tube wall temperatures were ~300°F for all experiments. As typified in Fig. 6, data were collected between 30 and 40 seconds for the all experiments.

In some cases, the predetonator geometries were operated with a conventional spark in the main tube head with the predetonator off. As there was no geometry to aid DDT in these cases, no measurable detonation wavespeeds were observed. Consequently, these cases are subsequently referred to as “spark (no DDT)”.

III. Experimental Results

With both the spiral and predetonator initiations, DDT was obtained for both tube diameters, as shown in Fig. 7. The limited measurements presented here demonstrate that stable detonation wavespeeds were obtained for all four cases. Additional measurements indicated that detonation was achieved within the spiral or predetonator (as appropriate) and successfully transferred down the main detonation tube.

Although no wavespeeds were observable with ion probes for the spark only case, dynamic head pressure and average thrust measurements indicated significant pressure was achieved despite the failure to achieve detonation. This is clear in Fig. 8, in which the dynamic head pressures are compared for the varying tube sizes and initiation methods. Head pressures are off-set 200psi for each case in the interest of intelligibility for Fig. 8, but will be compared in further detail below. Previous measurements of ‘bare’ tubes’ with high speed pressure transducers indicated that the flame was nearly detonating at the end of the tube under similar conditions but did not transition according to the current instrumentation.

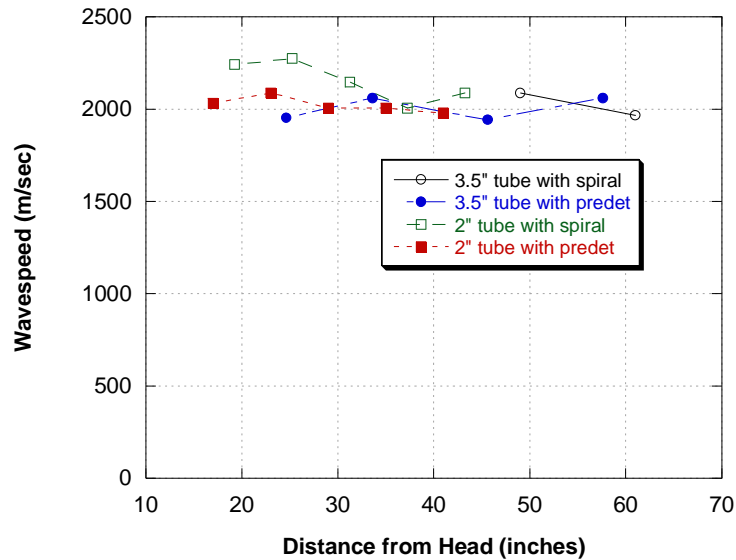


Figure 7. Ion probe wavespeed measurements confirming detonation initiation for the both tube diameters and initiation schemes. Note that the Chapman-Jouget wavespeed for stoichiometric hydrogen-air is 1970 m/sec¹¹.

For some cases, the head pressure could be integrated with time and area to provide a measure of pressure thrust⁸, as shown in Fig. 9 for the 2" tube with predetonator case. The average thrust was measured via the damped thrust stand. Before placing much significance on such thrust comparisons, it should be noted that the dynamic pressure transducers are noisy and sometimes experience significant thermal and DC drift. The integrated head pressure thrust measurement is highly sensitive to small DC offsets or changes in slope to the dynamic pressure signal.

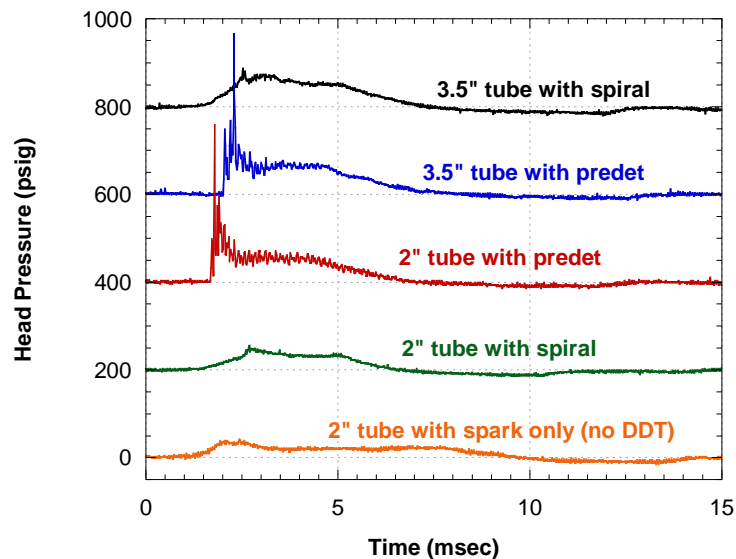


Figure 8. Head pressure traces versus time. Times are normalized to spark discharge and each pressure is offset 200psi for clarity.

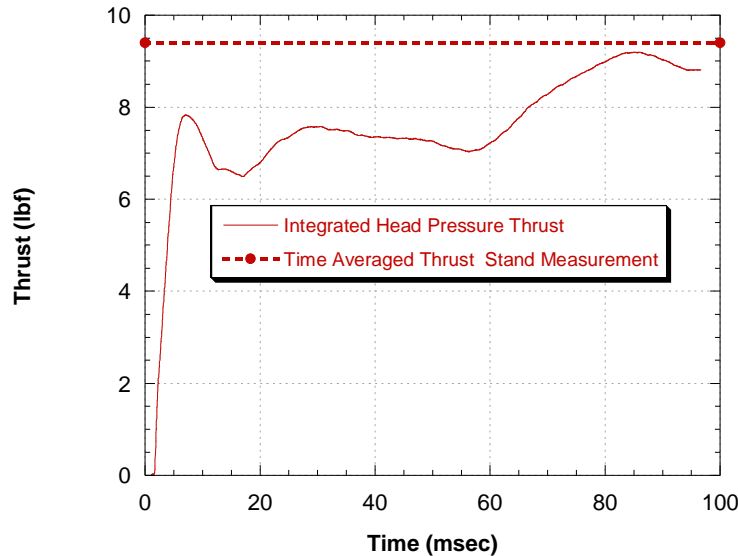


Figure 9. Integrated head pressure trace for one cycle in the 2" tube with predetonator. The average thrust is also plotted for comparison purposes and was obtained via the damped thrust stand.

Test data is summarized in Table 1, which indicates: the total tube length, the blow-down time as measured from beginning of pressure rise to the zero crossing of blow-down pressure (gauge), the ignition time from spark discharge to the beginning of head pressure rise, the DDT time from 'ignition' pressure rise to the first ion probe, the air thrust, the air thrust plus predetonator thrust, thrust (total) as measured by the damped thrust stand, and the integrated head pressure indicates the integrated head pressure thrust as demonstrated in Fig 9. In several instances, 'na' indicates the relevant parameter is not applicable. As defined above, the ignition time poorly reflects the actual predetonator performance as pressure rise begins well before the head pressure transducer indicates. Integrated pressure thrust is calculated based upon an assumed area and as noted by Shepherd et al.⁸, is not very accurate when obstructions such as spirals are present.

Table 1. Summary of test data.

Test Configuration and Data Summary	2" tube with 16" spiral	3.5" tube with 16"x 2" dia spiral	2" tube with 1" dia predet	2" tube, spark (No DDT)	3.5" tube with 1" dia predet	units
Total Length	83	91	82	82	88	in
Blow-down Time	3.9	5.0	5.1	7.7	4.9	msec
Ignition Time	1.2	0.8	1.7	1.2	2.0	msec
DDT Time	1.5	1.7	0.1	na	0.3	msec
Air Thrust	1	3.8	1	0.9	3.8	lbf
Air + Predet Thrust	na	na	1.6	na	4.8	lbf
Thrust	6.4	25.7	9.4	5.8	30.8	lbf
Integrated Head Pressure	4.4	25.5	9.2	5.8	30.2	lbf

Using damped thrust stand measurements, a fuel-based specific impulse was calculated for the subsequent plots. For these calculations, the predetonator mass flux was neglected. It is debatable whether this is a good assumption, but as noted previously, the predetonator volumes were small (~2%) and similar results have been demonstrated via cross tube ignition without the predetonator fuel and oxidizer penalties¹².

The specific impulse was plotted versus initiator section volume fraction as shown in Fig. 10, included are several previously obtained results⁶. The initiator volume fraction is defined as the initiator section tube volume (either the entire spiral or predetonator section) divided by the total tube volume.

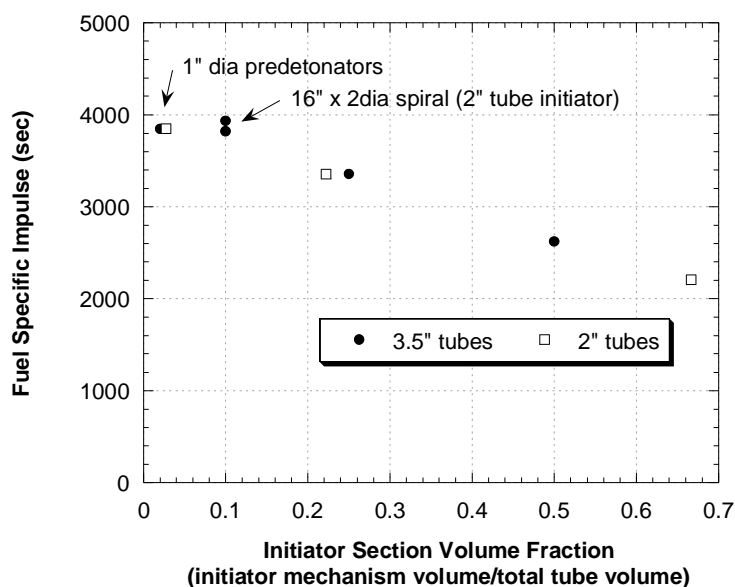


Figure 10. Specific impulse (fuel based and predetonator neglected) versus initiator volume fraction.

The above data enable an assessment of detonation initiation performance. Several additional parameters were varied in order to appraise performance sensitivity. Variations in equivalence ratio and fill fraction have dictated detonation performance results in the past; so these parameters were examined in the context of initiation performance.

Having varied equivalence ratio using spirals previously, the main tube stoichiometry was varied with the predetonator initiated schemes and compared to Shepherd's model^{9,13}. Figure 11 illustrates, as before, that good agreement (within 10%) was obtained with Shepherd's predicted value of 4335.4 seconds at stoichiometric conditions. Conventional spiral initiated tubes had lower DDT limits of 0.6-0.8 equivalence ratio for 2" tubes and 0.8-0.9 equivalence ratio for 3.5" tubes. The sudden decreases in specific impulse show that the predetonator initiator improved only modestly at best upon these limits, but surprisingly, Chapman-Jouget detonations were observed intermittently at even the lowest equivalence ratios as shown by the open symbols.

Similarly, varying fill fraction with both the most efficient of the initiation schemes (3.5 tube with spiral and predetonators) produced good agreement with Shepherd's model¹⁴ as shown in Fig. 12. The model was fit to an I_{sp} of 4000 sec at a fill fraction of one (fully detonating tube), which is about the best our group has been able to obtain experimentally with multi-cycle experiments. It should be noted that it is difficult to determine the exact fill fraction/local equivalence ratio during multi-cycle operation as previous experiments have shown that the fill process is far from slug-flow¹⁵. This is not to say that the fuel and air-flow rates through the engine were not precise, but rather that there was mixing between the purge air and the fuel-air charge of the next cycle as well as mixing of the fuel-air charge with ambient air at the end of the detonation tube. At the end of the detonation tube, the momentum of the in-flowing fuel-air charge carries it slightly past the exit of the detonation tube, creating a slight vacuum in the detonation tube (similar to the overexpansion that occurred after the blow-down process, but smaller in magnitude), which caused a mixture of fuel-air, purge air, ambient air and possibly exhaust to be pulled into the exit of the detonation tube in a spring-like action. The equivalence ratio in the last 12 to 18" of the detonation tube is at-best unknown and the wave speed in this region typically deteriorates.

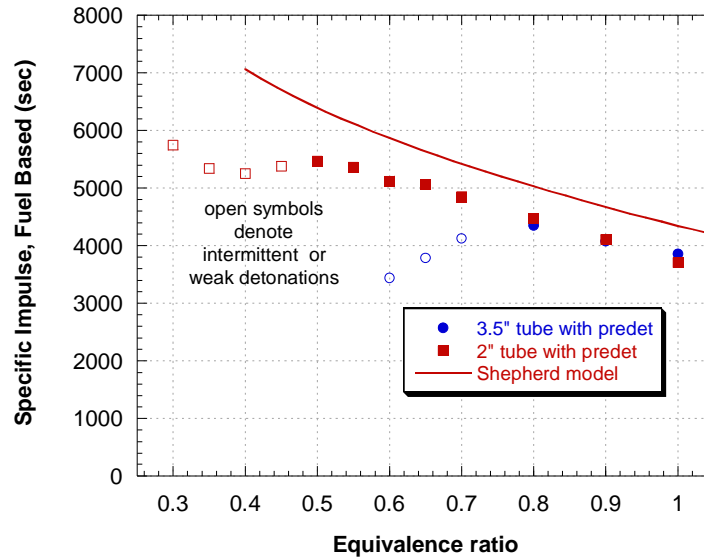


Figure 11. Specific impulse versus equivalence ratio for predetonator initiated tubes in comparison with Shepherd's model^{9,13}.

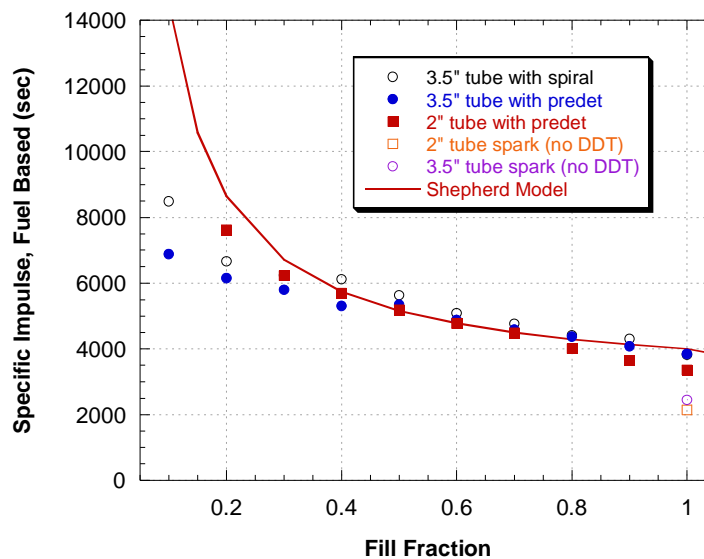


Figure 12. Specific impulse versus fill fraction (detonation reactant volume/total tube volume) in comparison with Shepherd's model¹⁵.

IV. Performance Analysis & Discussion

From the head pressure traces of Fig. 8, it is clear that predetonator initiated detonations produced near direct initiation of the main detonation tubes, as evidenced by the near von Neuman pressure peaks obtained. The spiral initiated cases universally produced sub Chapman-Jouget head pressures and it appears that spiral drag significantly weakens the retonation wave in addition to attenuating pressure thrust, as confirmed by Shepherd⁸. The obstruction-weakened retonation wave is more clearly visible in Fig. 13. below, where head

pressure has been normalized to the blow down time for the three 2" diameter tube cases. The spark with no DDT case clearly shows more thrust pressure than the spiral case in both Fig. 13 and Table 1. Yet the actual thrust measurement shows that it is better to have DDT even with the losses due to drag associated with the DDT mechanism (the spiral). Dynamic pressure transducer measurements in multi-cycle detonating environments are qualitative due to thermal and DC drift. Interestingly, the slow flame-speed results in a prolonged head pressure trace for the non-detonating case.

The integrated pressure method of calculating thrust is nearly meaningless for reasons cited above when spiral drag is significant, but is useful when there are no or minimal obstructions in the tube, such as the predetonator cases and the spark (no DDT) case shown in Table 1. By transitioning a 2" diameter spiral initiated tube section to a larger tube, spiral drag losses were minimized and produced virtually identical performance as the near-direct initiation via predetonator method, as seen in Fig. 10. It should be noted that although the expansion angle of the transition from 2" diameter to 3.5" diameter is larger than typically acceptable for detonation diffraction without quenching¹⁶, transverse wave reflections likely re-establish the detonation quickly for such a small area change¹⁷.

Figure 10, clearly indicates a strong correlation between initiator volume and PDE performance. A nearly 50% reduction in efficiency occurs with increasing initiator volume. This decrease in efficiency at high initiator volumes is especially significant for difficult to detonate mixtures such as kerosene-air, as larger DDT volumes are required.

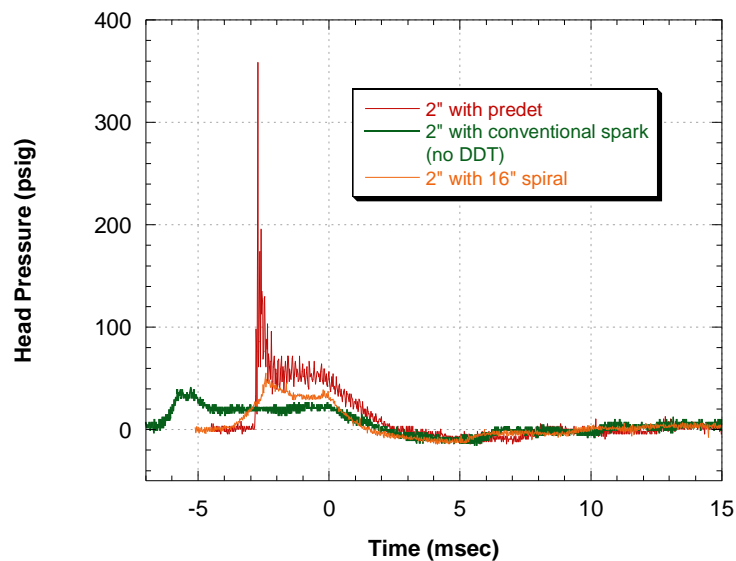


Figure 13. Head Pressure for 2" diameter tube cases normalized to blow down.

The impact of initiation upon throttling performance (via fill fraction), becomes even clearer when larger spirals were added to the 3.5" diameter detonation tube, producing the results shown in Fig. 14. Losses evident at full tube fill (the full throttle condition), continue to degrade efficiency when the fill fraction is reduced.

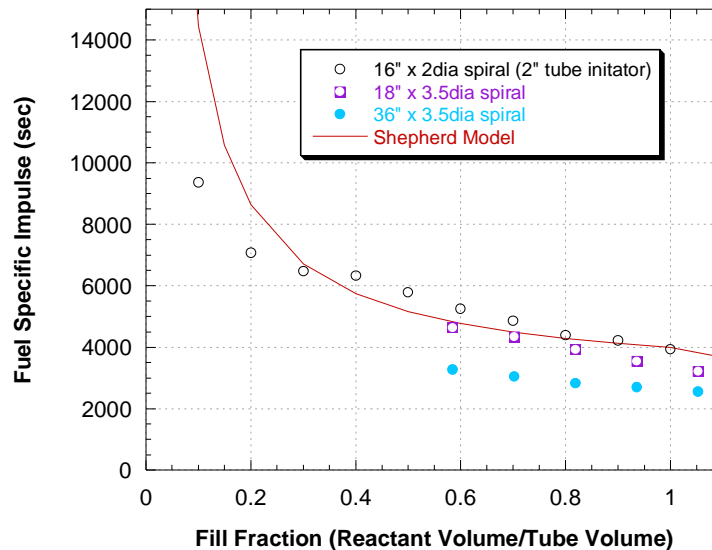


Figure 14. Specific impulse versus fill fraction (detonation reactant volume/total tube volume) in comparison with Shepherds model¹⁴ for 3.5" diameter tubes with varying 3.5" diameter Schelkin-type spiral initiators.

V. Conclusion

Pulsed detonation engine performance was shown to be sensitive to initiation strategy, varying over 40%, with the best initiation strategies approaching predicted performance. Predetonator initiation was used to provide an upper bound of 3900 sec for DDT initiation strategies, as well as to compare with current models. The predetonation initiation scheme was within 15% of predicted fuel-specific impulse for equivalence ratios from 0.5 to 1 and fill fractions from 0.3 to 1 when detonation was successful and consistent. An explanation for the consistently low impulse is the mixing and over-expansion of the main tube charge during the filling process in multi-cycle operation. Although a predetonator is effective, an oxygen-rich predetonator may not be practical outside of the laboratory because of the difficulty and bulk of storing or generating oxygen.

This sensitivity to initiation strategy also limits the methods of detonation initiation acceptable for an engine. The effect of the length and volume of DDT mechanism was shown through the performance as well as by the reduced head pressure (likely caused by the retonation wave passing through the DDT mechanism.) In general, the initiation volume for DDT should be less than 10% of the total tube volume. The implication is that detonation initiation, for all practical fuels and devices, must be accomplished somewhere other than the main detonation tube where effects of confinement can be maximized and obstacle drag can be minimized.

Detonation initiation for hydrocarbon or insensitive fuel continues to remain an area requiring innovations. Research is needed to develop low drag DDT mechanisms and air-fuel predetonators.

Acknowledgments

This work would not have been possible without the technicians who worked on this project; our thanks to Curtis Rice, Dave Baker, and Dwight Fox (ISSI). Dr. Tim Edwards (AFRL/PRTG) was extremely helpful in developing the fuel systems for this work. The authors would also like to thank Jeff Stutrud (AFRL/PRTC) for his controls and data acquisition expertise and Jacquelyn Kimmel for her help. The technical leadership of Dr. Mel Roquemore and Dr. Robert Hancock (AFRL/PRTC) was invaluable. Funding was provided by the Air Force Research Laboratory, Propulsion Directorate and AFOSR.

References

1. S. Jackson and J. Shepherd, "Initiation Systems for Pulse Detonation Engines," AIAA-2002-3627 38th AIAA/ASME/SAE/ASEE Joint Propulsion Conference and Exhibit, Indianapolis, IN, July 7-10, (2002).
2. J. Sinibaldi, J. Rodriguez, B. Channel, C. Brophy, F. Wang, C. Cathey, and M. Gundersen, "Investigation of Transient Plasma Ignition For Pulse Detonation Engines," Los Angeles, CA AIAA-2005-3774, 41st AIAA/ASME/SAE/ASEE Joint Propulsion Conference and Exhibit, Tucson, AZ, July 10-13, (2005).
3. C. M. Brophy, J. O. Sinibaldi, and P. Damphousse, "Initiator performance for liquid-fueled pulse detonation engines," AIAA-2002-472 AIAA Aerospace Sciences Meeting and Exhibit, 40th, Reno, NV, Jan. 14-17, (2002).
4. S. Jackson and J. Shepherd, "Detonation Initiation via Imploding Shock Waves," AIAA-2004-3919 40th AIAA/ASME/SAE/ASEE Joint Propulsion Conference and Exhibit, Fort Lauderdale, FL, July 11-14, (2004).
5. F. Schauer, C. Miser, C. Tucker, R. Bradley, and J. Hoke, "Detonation Initiation of Hydrocarbon-Air Mixtures in a Pulsed Detonation Engine," AIAA-2005-1343 43rd AIAA Aerospace Sciences Meeting and Exhibit, Reno, NV (2005).
6. J.L. Hoke, R.P. Bradley, F.R. Schauer, "Impact of DDT Mechanism, Combustion Wave Speed, Temperature and Charge Quality on Pulsed Detonation Engine Performance," AIAA 2005-1342, 43rd AIAA Aerospace Sciences Meeting, Reno, NV (2005).
7. K. Kailasanath, "On the Performance of Pulse Detonation Engines," presented at *The International Colloquium on Advances in Confined Detonations*, Moscow (2002).
8. Cooper, M., Jackson, S., Austin, J., Wintenberger, E., and Shepherd, J. E., "Direct Experimental Impulse Measurements for Detonations and Deflagrations," Journal of Propulsion and Power, Vol. 18, No. 5, pp. 1033–1041 (2002).
9. F. R. Schauer, J.S. Stutrud, and R.P. Bradley, "Detonation Initiation Studies and Performance Results for Pulsed Detonation Engine Applications," AIAA 2001-1129, 39th AIAA Aerospace Sciences Meeting, Reno, NV (2001).
10. E. Schultz, E. Wintenberger, and J. Shepherd, "Investigation of Deflagration to Detonation Transition for Application to Pulse Detonation Engine Ignition Systems," 16th JANNAF Propulsion Meeting (1999).
11. Soloukhin, R. I., Shock Waves and Detonations in Gases, Mono Book Corp, Baltimore (1963).
12. Kristin L. Panzenhagen, Paul I. King, Colin K. Tucker, and Fred R. Schauer, "Liquid Hydrocarbon Detonation Branching in a Pulse Detonation Engine," AIAA-2004-3401, Ft Lauderdale, FL (2004).
13. E. Wintenberger, J. M. Austin, M. Cooper, S. Jackson, and J. E. Shepherd, "An analytical model for the impulse of a single-cycle pulse detonation engine," AIAA-2001-3811 AIAA/ASME/SAE/ASEE Joint Propulsion Conference and Exhibit, 37th, Salt Lake City, UT, July 8-11, (2001)
14. Cooper, M., Shepherd, J., and Schauer, F., "Impulse correlation of partially filled detonation tubes," Journal of Propulsion and Power 0748-4658 vol.20 no.5, pp 947-950 (2004).
15. T. R. Meyer, M. S. Brown, J. L. Hoke, J. T. Parker, J. R. Gord and F. R. Schauer, "Fiber-Coupled Laser Sensor for In-Situ Measurement of Hydrocarbon Fuels in Pulsed-Detonation Engines," 28th Annual Dayton-Cincinnati Aerospace Sciences Symposium, Dayton, OH, 4 March (2003).
16. J. E. Shepherd, E. Schultz and R. Akbar, "Detonation Diffraction," *the 22nd International Symposium on Shock Waves*, Imperial College, London, UK, pp. 41-48, (2000).
17. Katta, V.R., Chin, L.P., and Schauer, F. "Numerical studies on cellular detonation wave subjected to sudden expansion," 17th International Colloquium on the Dynamics of Explosions and Reactive Systems, July 25-30, Heidelberg, Germany (1999).

Performance Measurements of Multicycle Pulse-Detonation-Engine Exhaust Nozzles

Daniel Allgood* and Ephraim Gutmark†

University of Cincinnati, Cincinnati, Ohio 45221-0070

John Hoke‡ and Royce Bradley§

Innovative Scientific Solutions, Inc., Dayton, Ohio 45440

and

Fred Schauer¶

U.S. Air Force Research Laboratory, Wright–Patterson Air Force Base, Ohio 45433

Performance measurements of multicycle pulse-detonation-engine (PDE) exhaust nozzles were obtained using a damped thrust stand. A pulse detonation engine of 1.88 m length was operated on a cycle frequency of 30 Hz at stoichiometric conditions. Both converging and diverging bell-shaped exhaust nozzles were tested for PDE fill-fractions ranging from 0.4 to 1.1. The area ratios of the nozzles were varied from 0.25 converging to 4.00 diverging. The nozzle length was negligible compared to the overall length of the PDE. The feasibility of normalizing the PDE nozzle thrust data was investigated by testing two different PDE combustion chamber diameters (2.54 and 5.08 cm) with the same nozzle area ratios. The optimum nozzle area ratio was found to be a function of the PDE fill-fraction. For fill-fractions at or below 0.5, the optimum configuration was a PDE without an exhaust nozzle. However, as the operating fill-fraction was increased to values close to or above one, thrust enhancement was obtained with a converging nozzle. The diverging nozzles also showed a relative increase in their performance with increased fill-fraction. Unlike the converging nozzles, the diverging nozzles and baseline configuration were observed to be sensitive to the ignition delay.

Nomenclature

AR	=	area ratio of nozzle (D_{nozz}^2/D_{comb}^2)
D_{comb}	=	PDE combustion chamber diameter
D_{nozz}	=	exhaust nozzle-exit diameter
ff	=	fill-fraction
Isp	=	fuel-based specific impulse
Isp_{ref}	=	reference fuel-based specific impulse
L_{comb}	=	PDE combustion chamber length
L_{nozz}	=	length of nozzle
M_{exit}	=	exit Mach number
T	=	thrust
T_{ref}	=	reference thrust
t	=	time
t_{cycle}	=	PDE cycle time
β	=	nozzle length ratio (L_{nozz}/L_{comb})

Introduction

PULSE detonation engines (PDE) use controlled periodic detonations of a combustible mixture to generate thrust.¹ Detonation combustion differs from the more commonly used deflagration combustion in that the fuel/oxidizer mixture is consumed much more

rapidly because of the detonation flame front being closely coupled to a leading shock wave. The shock/flame front coupling is caused by a feedback mechanism between the temperature rise caused by the shock wave and the chemical energy release and gas expansion caused by the reaction. Originally, one of the primary motivations for PDE development was the theory that higher thermal efficiency could be achieved using detonation combustion.^{1,2} However, the application of this theory assumes that a conventional steady-state thermodynamic analysis is appropriate for modeling a PDE.³ Although recent experimental studies have reported competitive performance values for laboratory-scale PDEs compared to constant-pressure combustion-cycle engines,⁴ the appropriateness of using a conventional thermodynamic analysis for the inherently unsteady PDE cycle is still in question.⁵ Thus, one of the key technological challenges still facing researchers and engineers is to quantify the range of propulsive efficiencies for a practical PDE system.

Experimental and computational researchers have demonstrated some success in obtaining competitive specific impulse values with a simplistic PDE cycle.^{4,6,7} These promising results have led to many PDE applications being proposed. For example, it has been suggested that PDEs can be used as cost-effective replacements for small gas-turbine engines, as potential replacements for combustors on existing large-scale gas turbines, or as thrust augmenters. However, even if PDE performance benefits ultimately reveal themselves to be insignificant in practical applications, the PDE cycle will still be an attractive propulsion system because of the reliability benefits of having very few moving parts, the scalability of the engine, and the flexibility in geometry it will provide.

Many operating parameters have been shown to drastically affect the performance of a PDE. For example, at a constant fill Mach number, PDE thrust has been observed to scale linearly with engine cycle frequency.⁷ The linear behavior in net thrust was a result of a linear increase in the percentage of time at which the combustion chamber was at the detonation-induced elevated pressure. Thus, adjusting the PDE cycle frequency is one proposed method of throttling the engine. Another way of throttling the engine is to alter the amount of fuel-oxidizer mixture that fills the PDE combustion chamber before ignition. The ratio of the PDE combustion chamber filled with a detonable mixture relative to the total combustion chamber

Received 12 June 2004; revision received 5 May 2005; accepted for publication 5 May 2005. Copyright © 2005 by the American Institute of Aeronautics and Astronautics, Inc. The U.S. Government has a royalty-free license to exercise all rights under the copyright claimed herein for Governmental purposes. All other rights are reserved by the copyright owner. Copies of this paper may be made for personal or internal use, on condition that the copier pay the \$10.00 per-copy fee to the Copyright Clearance Center, Inc., 222 Rosewood Drive, Danvers, MA 01923; include the code 0748-4658/06 \$10.00 in correspondence with the CCC.

*Graduate Student, Department of Aerospace Engineering and Engineering Mechanics; allgoodc@email.uc.edu. Student Member AIAA.

†Ohio Eminent Scholar, Department of Aerospace Engineering and Engineering Mechanics; Ephraim.Gutmark@uc.edu. Member AIAA.

‡Research Engineer; John.Hoke@wpafb.af.mil. Member AIAA.

§Research Technician.

¶Project Manager, Propulsion Directorate; frederick.schauer@wpafb.af.mil. Member AIAA.

length is defined as the fill-fraction. Although the PDE thrust has been shown to decrease with a reduction in fill-fraction, the fuel-based specific impulse values increased at a faster rate. This performance gain observed at lower fill-fractions was attributed to the leading shock wave of the detonation front compressing the nonreactants occupying the remainder of the PDE combustion chamber.^{7,8} Schauer et al.⁷ demonstrated experimentally the performance benefits of partially filling the combustion chamber for a multicycle PDE operation. Their results showed the partial-fill effect being independent of PDE cycle frequency for a constant-area combustion chamber.

An alternative viewpoint of the partial-fill effect is that the thrust of a PDE can be increased by maintaining a constant amount of fuel-oxidizer mixture and simply adding additional length to the combustion chamber. The additional combustion chamber length can be viewed as a constant-area straight nozzle that alters the pressure relaxation process at the head wall of the PDE. When the detonation wave interacts with the interface separating reactive and nonreactive gases, a shock wave is transmitted into the nonreactive gas while a reflected wave propagates back toward the thrust surface. In most cases of interest to PDE applications, the reflected wave is an expansion wave. A second expansion wave is generated at the end of the combustion chamber when the shock wave reaches the sudden area change. This expansion also propagates back toward the thrust wall. Thus, by extending the length of the straight nozzle, the stronger exit-flow rarefaction waves can be delayed in time, thereby allowing a slower rate of pressure relaxation at the head wall of the PDE. Li and Kailasanath⁸ have predicted that significant increases in peak impulse values can be obtained by increasing the length of a straight nozzle. However, although straight nozzles provide impressive performance benefits, they also limit the maximum cycle frequency of the PDE because of longer associated blowdown times.

More conventional nozzle geometries have also been shown to provide performance benefits for PDE applications. A very detailed review on the current level of PDE nozzle technology was given by Kailasanath.⁴ The outcome of this review revealed some significant disagreements on the reported behavior of PDE nozzles. The source of the disagreements was attributed to the highly dynamic nature of the PDE and its sensitivity to the operating conditions. For example, most of the previous PDE nozzle research investigated the effects of nozzles that had relatively large lengths compared to the combustion chamber ($\beta = L_{\text{nozz}}/L_{\text{comb}} > 0.1$). Thus, for these nozzles of nonnegligible length, partial-fill effects will have a significant impact on the PDE performance and should be taken into consideration when interpreting the results. Another common difference observed between the various PDE nozzle studies was that most studies modeled single-cycle detonations, whereas very few looked at the behavior of a more practical multicycle operation.⁴ These differences in PDE nozzle operating conditions lead to differing conclusions on an optimum nozzle geometry. Some highlights of these studies are discussed next.

Eidelman and Yang⁹ modeled a series of straight, converging, and diverging nozzles for a PDE operating in a single-shot detonation mode. The fill and purging processes and multicycle effects were not modeled. In their study, the nozzles represented a significant portion of the PDE ($\beta = 0.167\text{--}0.4$). All nozzles showed an improvement over the baseline configuration without a nozzle, as a result of the partial-fill effect. Although the converging and straight nozzles increased the peak thrust (impulse), the peak thrust did not occur until much later during the cycle because of the increase in blowdown time. The diverging nozzles, on the other hand, increased the thrust of the PDE by converting the thermal energy of the under-expanded gases into kinetic energy, but produced the higher peak thrust levels at a faster rate as a result of an increased rate of expansion. The one drawback observed with diverging nozzles was that because of overexpansion inside the PDE the increased thrust surface area resulted in negative thrust later in the cycle. Despite this drawback, the bell-shaped diverging nozzle showed the best performance overall for this single-shot detonation operation.

Yungster¹⁰ confirmed the results by Eidelman and Yang⁹ in that a bell-shaped diverging nozzle performed the best and converg-

ing nozzles limit the operating frequency of the PDE. Yungster attributed the performance benefits of the bell-shaped nozzle over conical diverging nozzles to a slight minimization in overexpansion and therefore a reduction in negative thrust during the later stages of the blowdown process. The computations by Cambier and Tegner¹¹ also are in agreement that a bell-shaped diverging nozzle, with its associated negative curvature in the change in internal surface-area, performs better than a diverging nozzle with straight or positive surface-area curvature. However, one distinct difference in the PDE operation modeled by Cambier and Tegner¹¹ compared to the works already mentioned was that the relatively large nozzles were filled with a detonable mixture. Thus, unlike the previous studies Cambier and Tegner¹¹ predicted a decrease in specific impulse with diverging nozzles. This was because the thrust gain provided by the diverging nozzle did not overcome the cost of providing additional fuel mass to fill the diverging nozzle. This negligible benefit of using a diverging conical nozzle with a filled mixture was also predicted by Mohanraj and Merkle¹² and by Cooper et al.¹³

These and other PDE nozzle simulations have focused primarily on predicting simplistic single-shot PDE operations in which the subsonic fill and purge portions of a practical PDE cycle were not considered. In reality, the filling and purging processes of a multicycle operation are not insignificant portions of the cycle. Thus, although a diverging nozzle has been shown to expand the high-pressure detonation gases and provide additional thrust surface on which this pressure can act, the diverging nozzle will act as a diffuser during the remainder and perhaps majority of the cycle. Yungster¹⁰ modeled the multicycle operation of PDE diverging nozzles and found that the first cycle showed nozzle thrust augmentation, but no augmentation was observed during the following second and third PDE cycles. The loss in thrust augmentation was attributed to the cold air that occupied the nozzle during the first cycle being replaced with low-density combustion products. Wu et al.¹⁴ have also modeled such multicycle operations and have shown that the performance enhancements of diverging nozzles during the detonation phase of the PDE cycle did not have a significant impact on the overall system. Rather, they found that a converging nozzle is helpful in maintaining significant backpressure at altitude conditions. From these and other studies, it can be concluded that the subsonic filling and purge portions of the cycle can significantly contribute to the thrust of the PDE during multicycle operations and thus should be considered in the nozzle design.

Other benefits of using exhaust nozzles for PDE applications have been recently proposed by Kaemming and Dyer.¹⁵ First, a converging exhaust nozzle for a PDE provided control over the pressurization inside the combustion chamber as in the case of a ramjet engine. By choking the exhaust flow, the Mach number and pressure inside the detonation chamber were independent of the flight speed and atmospheric conditions. If the pressure was not controlled, an increase in flight speed corresponded to an increase in the combustion chamber Mach number and a decrease in pressure inside the chamber. Kaemming and Dyer¹⁵ performed a thermodynamic analysis showing that the efficiency of a PDE diminished without the converging exhaust nozzle controlling the chamber pressure. In addition to the thermodynamic effects of backpressurization, the converging section of an exhaust nozzle provided a means of controlling the frequency of the engine. For example, Kaemming and Dyer¹⁵ have shown that a reduction in chamber pressure (increase in chamber Mach number) translated into an increase in the required operating frequency of the PDE engine. Because the PDE frequency has usually been controlled through valves, this lack of chamber pressure control might place an impossible requirement on the valve system. For these two reasons, an exhaust nozzle with a converging throat section appeared to be beneficial for PDE applications.

The current work is a unique experimental study of a multicycle PDE operation, in which gross thrust augmentation levels provided by various converging and diverging bell-shaped exhaust nozzles were quantified. The nozzle-area ratio was varied from 0.25 converging to 4.0 diverging. The nozzle length represented a negligible portion of the overall PDE length ($\beta < 0.042$). The PDE operated on a stoichiometric mixture of hydrogen air at a cycle frequency of 30 Hz.

The PDE cycle time was divided evenly between three stages: a fill stage, an ignition/detonation/blowdown stage, and a purge stage. For each nozzle configuration, the operating fill-fraction was varied to quantify their corresponding partial-fill effects. The PDE frequency and backpressure were held constant during testing, but because of their potential significant impact on an engine's performance should be investigated in future studies in order to fully understand the performance benefits of using exhaust nozzles for PDE applications.

Experimental Setup

Gross thrust measurements of a PDE were performed to quantify the effects of exhaust nozzle geometry on PDE performance. The pulse-detonation-engine test facility at the U.S. Air Force Research Laboratory at Wright-Patterson Air Force Base was used to obtain the thrust measurements. Premixed hydrogen and air were delivered to a cylindrical combustion chamber by way of a mechanical valve system constructed from a modified four-cylinder automotive head. In the standard automotive cycle, each cylinder has four ports, two for intake and two for exhaust. However, for the PDE operation, the two intake ports served to deliver the premixed hydrogen-air, while the two exhaust ports operated in reverse to deliver purge-air to purge the combustion chamber of hot gases after each detonation and before injecting a fresh mixture of reactants. The combustion gases exited from the exhaust end of the combustion chamber. The automotive valve system could be operated at frequencies up to 40 Hz. Because of the nature of automotive valving, the division of the cycle timing for various events such as fill time and purge time and detonation time were fixed to be each $\frac{1}{3}$ of the cycle. Only one of the four automotive valve sets was used to deliver mass flow to a single cylindrical combustion chamber. The hydrogen and air were metered through choked flow orifices, and the flow rate and pressure data were collected via a remote 5-MHz 16-channel analog-to-digital-converter system. For a more detailed description of the PDE test facility, the reader is referred to the recent paper by Schauer et al.⁷

For the current PDE nozzle performance tests, the pulse detonation engine was operated with a stoichiometric mixture of hydrogen and air. To determine the feasibility of normalizing PDE exhaust nozzle data based on the nozzle inlet-to-exit area ratio, two combustion chambers of 2.54 and 5.08 cm diameter (D_{comb}) were tested. Both PDE combustion chambers had a length of 1.88 m, and the PDE cycle frequency was kept constant at 30 Hz. Bell-shaped exhaust nozzles of area ratios ($AR = D_{\text{nozz}}^2 / D_{\text{comb}}^2$) ranging from 0.25 converging to 4.0 diverging were tested. In all test cases, the nozzle length represented only 2–4% of the total length of the PDE. Nozzles of this length were chosen so as to limit the partial-fill effects introduced by adding the additional length to the PDE.

The two operating parameters varied during these tests were the fill-fraction (ff) and ignition delay. The fill-fraction was defined as the ratio of the combustion chamber volume initially filled with a detonable mixture compared to the total combustion chamber volume. The fill-fraction was varied from 0.4 to 1.1 for all nozzle configurations. The fill-fraction was determined by measuring the volume flow rates of the reactants using upstream choked flow nozzles. Because the maximum error in volume flow rate measurements was found to be $\pm 3\%$, the relative error in fill-fraction measurement was also $\pm 3\%$.

A purge-air cycle was added to cool the combustion chamber and provide a buffer between the hot combustion products and the fresh reactants being injected for the next cycle. Because of the automotive valve system that was used, $\frac{1}{3}$ of the cycle was allocated for purging. Similar to fill-fraction, the purge-fraction can be defined as the ratio of the combustion chamber filled with purge-air relative to the total combustion chamber volume. The purge-fraction was kept constant at 0.5 during all tests.

The ignition delay was defined as the time delay for the spark plug to ignite relative to the closing of the valves. Because of the response of the valve system, the ignition delay could not be set below a value of 0.5 ms without the risk of a backfire upstream into the injection manifold. The maximum delay time was set by the 30-Hz cycle frequency of the PDE. For the ignition delay studies, the delay time

was varied from 0.5 to 7.5 ms for the baseline configuration of a PDE without an exhaust nozzle and for two representative converging ($AR = 0.25$) and diverging ($AR = 4.0$) nozzles. A maximum ignition delay of 7.5 ms allowed a sufficient amount of time (3.5 ms) for the deflagration-to-detonation transition (DDT) and blowdown to occur before the purge-air entered the combustion chamber. All other nozzle tests were performed at a baseline ignition delay of 0.5 ms.

The DDT of the hydrogen-air mixture was enhanced by the use of Shchelkin-type spirals of 0.3 m length for both the 2.54-cm- and 5.08-cm-diam combustion chambers. The Shchelkin spiral occupied only 16% of the total combustion chamber length. Two pressure transducers (PCB M102A) were mounted 0.15 m apart to monitor detonation wave speeds and validate that Chapman-Jouguet (CJ) detonations were produced. The transducer closest to the exit of the PDE was placed a distance of 0.36 m from the PDE exit. The detonation wave speed measured for both combustion chambers at a fill-fraction of 1.0 was on average 1988 m/s (± 13 m/s), which is less than 2% deviation from the theoretical CJ wave speed of 1966 m/s for a stoichiometric hydrogen-air mixture.

The PDE was mounted on a damped thrust stand rated for a maximum thrust load of 4500 N. The thrust stand was designed to measure the time-averaged thrust of the dynamic PDE. The thrust stand consisted of linear pillow-block bearings (Thompson Industries M/N SPB-16-0PN) riding along a pair of 25.4-mm-diam linear bearing rails (Thompson Industries P/N SR-16). The PDE was allowed to move freely on the rails, but its motion was weakly damped by springs to prevent any resonance effects. To remove the effects of static friction, the PDE was continuously actuated forward and backward by a linear pneumatic actuator (Bimba M/N 096-DXDEH) at an oscillation rate of 0.3 Hz. The linear actuator was a double acting balanced actuator that applied the same force in both directions for a set flow rate of air. The air pressure was generally set to deliver a ± 25.4 -mm travel distance. Because the actuator produced a net zero average force, the average position of the thrust stand was solely a function of the engine average thrust. A displacement sensor (Data Instruments P/N DCFS4) with a 101.6-mm stroke was used to measure the position of the thrust stand as a function of time. The frequency response of the displacement sensor was from dc to 10,000 Hz. The output of the displacement sensor was electrically filtered to remove spurious noise and isolate only the dc component of the signal that corresponded to the average position (or thrust) of the engine. Because of the time constant inherent in the filtering process and the time required to obtain an accurate measure of the average displacement of the 0.3 Hz oscillating thrust stand, a run time of at least 10 s would theoretically be needed. In practice however, run times on the order of 20 to 30 s were required to reach a steady-state average thrust measurement.

Calibration of the thrust stand position as function of applied load was obtained by placing static weights on a pulley/cable system and recording the time-averaged output of the displacement sensor. The procedure used in the calibration was to load the thrust stand from a zero applied load to a value above the maximum expected thrust level of the PDE. The applied loads were then removed sequentially to determine if any hysteresis effects were present. No hysteresis in the system was observed throughout the testing. Calibration curves were obtained before and after each set of tests to monitor changes in the system. A linear relationship between the applied load and measured thrust was observed for the entire range of PDE thrust loading with a maximum recorded standard deviation of approximately ± 1 N. The repeatability of the data was observed to be within this error band and thus indistinguishable from the measurement error.

Results and Discussion

Baseline Configuration

The selected baseline configuration for the nozzle tests was the 1.88-m-length combustion chamber (5.08 cm diam) without an exhaust nozzle. The fill-fraction for the baseline was varied from 0.4 to 1.1 while maintaining a near stoichiometric fuel-air ratio, an ignition delay of 0.5 ms, a purge-fraction of 0.5, and a cycle frequency of 30 Hz. The gross thrust values for the baseline PDE configuration

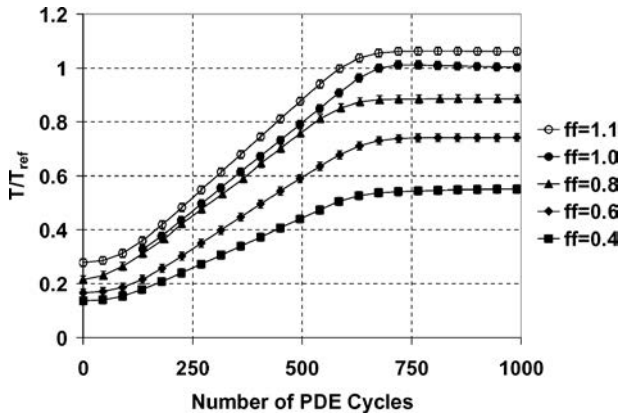


Fig. 1 Normalized PDE average-thrust measurements as a function of number of PDE cycles ($AR = 1.0$, $D_{\text{comb}} = 5.08$ cm, $T_{\text{ref}} = 77$ N).

are given in Fig. 1 as function of experiment run time. The run time is represented in number of PDE cycles, and the thrust is normalized according to a reference thrust value. The reference thrust used in normalizing this data was selected to be the thrust value (77 N) for the baseline configuration at a fill-fraction of 1.0. All reported thrust values in the current work correspond to the gross thrust of the engine, and no correction of the data for changes in the fill/purge stream thrust has been performed.

A transient delay between the first PDE cycle during each test and the time when a near steady-state thrust level was observed. Figure 1 shows this time delay to be approximately 30 s, or 1000 PDE cycles, for all fill-fractions tested. The transient delay was a direct result of the 0.3-Hz oscillating thrust stand, the signal filtering process, and the averaging used to obtain the thrust measurements. Although the wall temperature was not recorded, the extended run time required to obtain a steady-state average thrust also allowed time for the PDE to come to thermal equilibrium. All thrust data presented in this paper correspond to the average plateau in thrust recorded after the PDE had been operating continuously for approximately 1000 PDE cycles.

The variation in thrust with fill-fraction can be inferred from Fig. 1. An increase in fill-fraction resulted in higher average thrust values. The thrust increased nonlinearly with fill-fraction as a result of the shock compression of the nonreactant gases occupying the remainder of the PDE combustion chamber as has been reported previously in literature. However, the thrust continued to increase at fill-fractions above 1.0 because of the increase in mass flow rates and the fact that the reactants were not of a uniform stoichiometric mixture inside the PDE. Previous studies have suggested that the fuel-air mixture becomes leaner near the exit of the PDE because of a dynamic effect of entrainment of ambient air back into the PDE combustion chamber during the unsteady filling process.⁷ Overfilling the PDE can also have a dramatic impact on the performance when an excessively large exhaust nozzle ($\beta > 0.1$) is present as a result of the nozzle being occupied by reactant gases vs nonreactant or product gases.⁴

The current baseline data have been compared to previously reported PDE data by plotting the variation in fuel-based specific impulse with fill-fraction as shown in Fig. 2. The general trend of a nonlinear increase in fuel-based specific impulse with decreased fill-fraction was consistent with those found by other researchers. This behavior has been directly attributed to shock compression of the gases occupying the unfilled portion of the combustion chamber as discussed earlier in this paper. Essentially, the leading shock wave of the detonation served to compress the gases occupying the unfilled portion of the combustion chamber (straight nozzle) thereby maintaining the pressure inside the combustion chamber for a longer duration. This increased blowdown time with a straight nozzle resulted in higher thrust than would have been observed without the straight nozzle present. As a result of the PDE thrust levels decreasing at a slower rate than the reduction in fuel mass flow rate associated with reduced fill-fraction, the fuel-based specific impulse

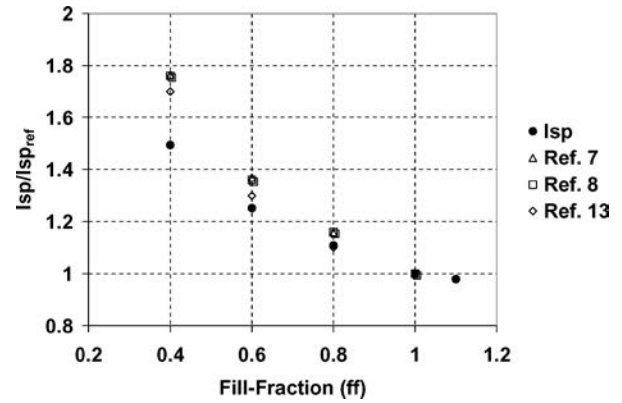


Fig. 2 Normalized fuel-based specific impulse as a function of fill-fraction for the baseline configuration ($AR = 1.0$, $D_{\text{comb}} = 5.08$ cm) ($I_{\text{sp,ref}}$ corresponds to I_{sp} @ $ff = 1.0$).

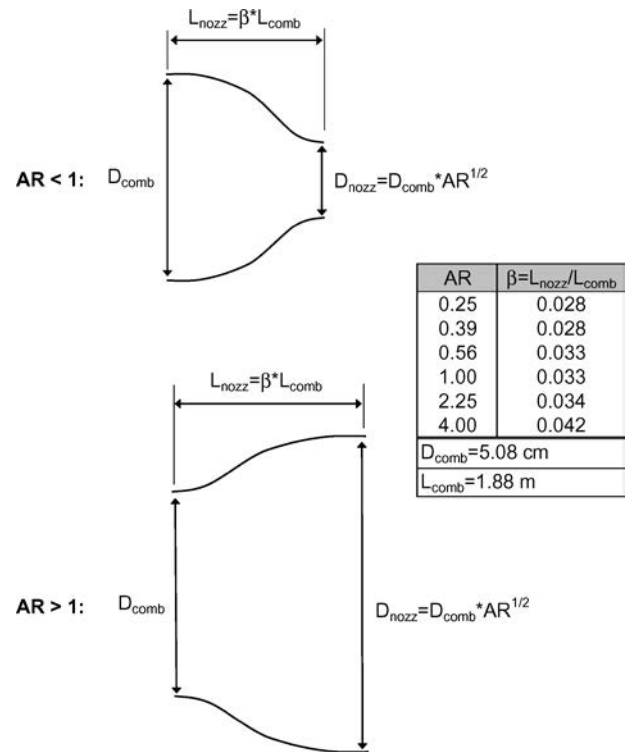


Fig. 3 Converging and diverging nozzle cross-sectional schematics and dimensions.

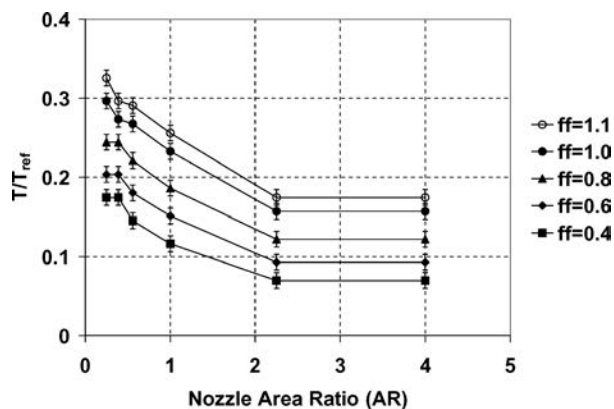
values increased as shown in Fig. 2. Although the current results ($I_{\text{sp,ref}} = 2600$ s) were lower than other reported relative specific impulse values, specifically at the lowest fill-fraction, the important performance variation with partial fill-fraction was captured in the current work.

Effects of Nozzle-Area Ratio

The effects of converging and diverging bell-shaped exhaust nozzles on PDE thrust were measured. Figure 3 shows representative schematic drawings for the exhaust nozzles and their respective dimensions. The area ratios of the nozzles tested were 0.25, 0.39, 0.56, 1.0, 2.25, and 4.0, where ratios less than one are converging nozzles and greater than one are diverging nozzles. The nozzle lengths ranged from 5.2 to 7.8 cm in length, and therefore only extended the total length of the PDE by a maximum of 4% (or $\beta = 0.04$). Because $\beta < 0.1$ and the uncertainty in fill-fractions has been reported to be $\pm 3\%$, the partial-fill effect of adding these exhaust nozzles was negligible. The PDE was operated at the baseline operating conditions of a stoichiometric fuel-air mixture and cycle frequency of 30 Hz.

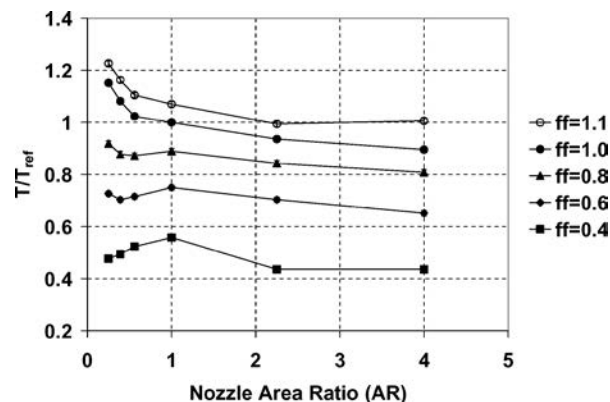
Table 1 Total reactant mass flow rates and Mach numbers during fill portion of cycle

Fill-fraction	Total reactant mass flow rate, kg/s	M_{exit}					
		$AR = 0.25$	$AR = 0.39$	$AR = 0.56$	$AR = 1.0$	$AR = 2.25$	$AR = 4.0$
0.4	0.042	0.201	0.129	0.090	0.050	0.022	0.013
0.6	0.064	0.307	0.197	0.137	0.077	0.034	0.019
0.8	0.085	0.411	0.263	0.183	0.103	0.046	0.026
1.0	0.107	0.513	0.329	0.229	0.128	0.057	0.032
1.1	0.116	0.560	0.359	0.250	0.140	0.062	0.035

**Fig. 4** Normalized PDE cold-flow thrust as a function of nozzle area ratio ($D_{\text{comb}} = 5.08$ cm, $T_{\text{ref}} = 77$ N).

Two-thirds (22 ms) of the PDE cycle involved filling the combustion chamber with reactants and purge gases at subsonic speeds. Initial cold-flow tests were performed to determine the effect of exhaust nozzles on these subsonic portions of the cycle. The cold-flow thrust measurements were performed at the same operating conditions and configurations as in the “hot” detonation cases but without igniting the mixture. The mass flow rates of the fill gases for each fill-fraction are given in Table 1 along with the exit Mach numbers for the baseline ($AR = 1.0$), most convergent nozzle ($AR = 0.25$), and most divergent nozzle ($AR = 4.0$). These data were provided to show the span from maximum ($AR = 0.25$) to minimum ($AR = 4.0$) exit Mach numbers during the filling process for the current test conditions. Table 1 shows that all exit Mach numbers associated with the fill portion of the cycle corresponded to subsonic Mach numbers. Although the majority of the Mach numbers were below a value of 0.3, the convergent nozzle did accelerate the fill gases to Mach numbers as high as 0.56. Thus, compressibility effects were present for these test conditions, but no exhaust nozzles produced choked conditions during the filling and purging portions of the cycle. In addition to the filling process, a constant purge fraction of 0.5 was used during purging producing a constant purge gas (air) mass flow rate of 0.073 kg/s for all test conditions.

The cold-flow thrust measurements are shown in Fig. 4. For all tested fill-fractions, a decrease in nozzle area ratio resulted in an increase in thrust. Because it has been established that the cold-flow exhaust was subsonic through the nozzles for all test conditions, convergent nozzles ($AR < 1.0$) were accelerating the exhaust flow during the filling and purging portions of the cycle while divergent nozzles ($AR > 1.0$) decelerated these gases. A linear rate of increase in thrust with contracting area ratio is shown in Fig. 4 for the intermediate nozzle-area ratios of 0.56, 1.0, and 2.25. However, this linear variation deviated for the smallest convergent nozzle of $AR = 0.25$ and the largest divergent nozzle of $AR = 4.0$. The large divergent nozzle most likely did not continue to cause a linear decrease in thrust because of increased flow separation from the walls, which is commonly observed from such a larger bell-shaped nozzle. Thus, interpretation of this large area-ratio nozzle data is questionable. Compressibility effects and increased profile drag were believed to cause the deviation from linear behavior for the smallest area ratio converging nozzle.

**Fig. 5** Normalized PDE thrust as a function of nozzle area ratio ($D_{\text{comb}} = 5.08$ cm, $T_{\text{ref}} = 77$ N).

In addition to the importance of documenting the variation of cold-flow thrust with nozzle-area ratio, it was also important to quantify the contribution of the filling and purging cycles to the overall thrust of the engine. Figure 4 shows that the cold-flow air thrust for the baseline configuration represented between 10 to 30% of the total hot thrust (reference thrust). This signifies that the subsonic gas flows occurring during the PDE cycle were substantially affecting the overall PDE performance. Thus, for PDE applications all portions of the cycle should be considered when selecting the appropriate nozzle design.

Once the cold-flow PDE thrust measurements were completed, the reacting-flow PDE thrust measurements were obtained for each nozzle/fill-fraction combination. The results of these tests are plotted in Fig. 5. For both the cold-flow and reacting-flow conditions, all nozzles tested exhibited an increase in thrust with a decrease in nozzle area ratio when the operating fill-fractions were above 0.8. This was the same trend observed in the cold-flow tests. However, at fill-fractions below 0.8, the converging nozzles were observed to decrease the thrust of the PDE. This shift in converging nozzle performance with reduced fill-fraction was believed to be caused by the converging nozzle having less effect on the blowdown process because of the reduced combustion chamber pressures and the negative effect of its profile drag playing a dominant role in the overall nozzle performance. On the other hand, the sensitivity of the diverging nozzles to area ratio did not appear to change with fill-fraction. All diverging nozzles at all fill-fractions were observed to have performance degradations with increased nozzle-area ratio. The maximum diverging nozzle performance loss was approximately 20% and occurred at a fill-fraction 0.4.

The fill-fraction condition of 1.1 generated more thrust than the $ff = 1.0$ despite the fact the PDE was overfilled. This was a result of two factors. First, an increase in the fill gas flow rates caused an increase in thrust as was shown in the cold-flow tests. Second, because the filling process involved a very dynamic process, the PDE had a tendency to have a lower equivalence ratio near the end of the PDE as a result of oscillating entrainment of ambient air into the PDE combustion chamber. By slightly overfilling the PDE, the mixture equivalence ratio near the open end of the PDE chamber was more likely to be close to the desired stoichiometric conditions.

The similarity between the cold flow (Fig. 4) and the reacting flow (Fig. 5) thrust profiles further suggests that the nozzle

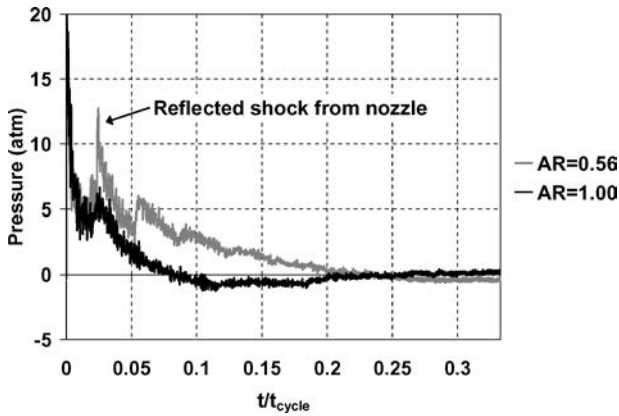


Fig. 6 Pressure-time traces for the baseline and $AR = 0.56$ converging nozzle ($ff = 1.0$, $t_{cycle} = 0.033$ s).

performances were being influenced substantially by the subsonic portions of the PDE. However, the filling and purge portions of the PDE cycle were not the only important factors that governed the PDE-nozzle performance. To demonstrate the effect of a nozzle on the entire PDE cycle, example combustion chamber pressure-time traces for two nozzle configurations ($AR = 1.0$ and 0.56) have been plotted in Fig. 6 for a fill-fraction of 1.0. These two configurations represent a comparison between the baseline configuration and a converging nozzle case that produced an increase in blowdown duration. The pressure data in Fig. 6 have been plotted as a function of normalized time (time divided by the cycle time of 33.3 ms). A comparison between the two pressure traces shows that additional thrust was provided by the converging nozzle because of the pressure rise inside the PDE combustion chamber and the associated increase in blowdown time. The additional compression inside the combustion chamber was a result of the leading shock wave of the detonation front reflecting from the converging walls of the nozzle back to the headwall of the PDE. Figure 6 shows that the pressure inside the PDE was near or below atmospheric pressure for more than 80% of the PDE cycle, or 26.4 ms. In comparison, it can be inferred from the baseline pressure trace that the exhaust flow was subsonic for more than 92% of the total PDE cycle, or 30.36 ms. In either case, the exhaust flow was only choked during a small portion of the entire cycle. This pressure data along with the hot- and cold-flow thrust measurements demonstrate that a convergent nozzle can outperform a diverging nozzle by increasing the headwall pressure during combustion and thereby increase the blowdown time during expansion. In addition to this thrust contribution of a convergent nozzle, the exhaust velocity during the purge and fill portions of the PDE cycle was also increased.

To demonstrate the performance effects of PDE exhaust nozzles for multicycle PDE operations, the current nozzle data were compared to data available in the literature by plotting the variation in fuel-based specific impulse as a function of nozzle area ratio for a fill-fraction of 1.0. Figure 7 shows that in the current study a significant enhancement in the PDE performance with a convergent nozzle was observed, whereas the divergent nozzles produced a loss in the overall engine performance for the range of tested nozzle-area ratios. This behavior was consistent with computational simulations performed by Cambier and Tegner.¹¹ Their studies showed that a loss in engine performance was associated with increasingly divergent nozzles for multicycle PDE operations. In addition to changes in the combustion chamber pressure-time behavior, this loss in thrust with the excessively large diverging nozzles could be a result of increased flow separation from the nozzle walls in both the current study and the referenced work. In addition, Cambier and Tegner¹¹ further demonstrated that a single-shot PDE operation can have different behavior because of the cycle-to-cycle variations of the gaseous mixtures inside the PDE combustion chamber and nozzles. This is also in agreement with the observations and conclusions reported in the current study.

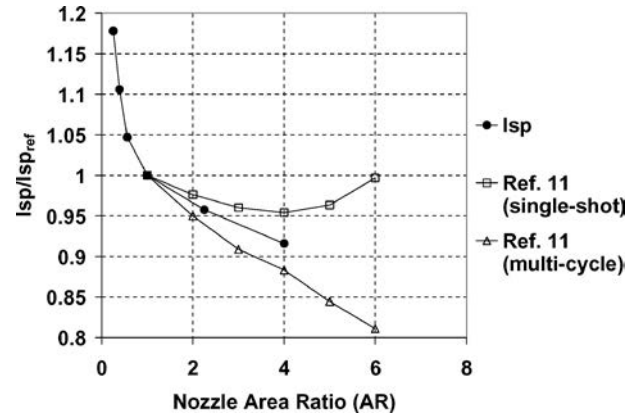


Fig. 7 Normalized fuel-based specific impulse as a function of nozzle area ratio ($ff = 1.0$, $D_{comb} = 5.08$ cm).

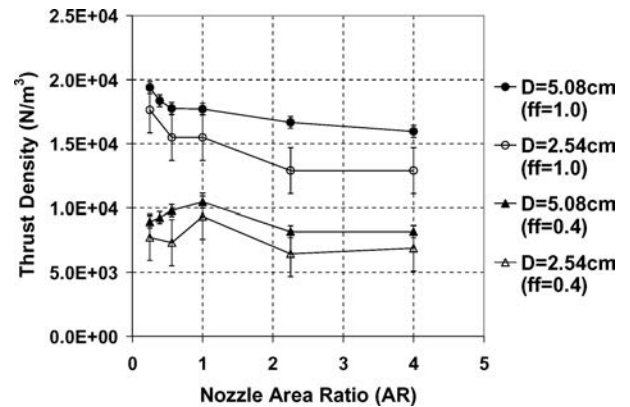


Fig. 8 PDE thrust density for two PDE combustion chambers ($D_{comb} = 2.54$ cm: $L_{comb} = 1.88$ m, $T_{ref} = 16$ N) and ($D_{comb} = 5.08$ cm: $L_{comb} = 1.88$ m, $T_{ref} = 77$ N).

Scalability and Normalization of PDE Nozzle Thrust Data

It was desired to determine whether the PDE exhaust nozzle thrust scales with the initial PDE combustion chamber diameter. To be more precise, the question to be answered was whether the nozzle area ratio was the appropriate normalization for the thrust data. Figure 8 is a plot of nozzle thrust measurements that were made on both a 2.54-cm-diam combustion chamber and a 5.08-cm-diam combustion chamber, which is associated with the data that have been discussed in the paper as of this point. Both combustion chambers had lengths of 1.88 m. Both sets of converging and diverging nozzles were similar in shape and length. To compare the thrust profiles obtained for these two configurations, the thrust values in Fig. 8 were converted to a thrust density, where thrust density has been defined as the ratio of the thrust to the volume of the combustion chamber. The error bars associated with each data point have been included in Fig. 8. Larger uncertainty was associated with the low thrust level measurements of the 2.54-cm-diam combustion chamber. Despite this uncertainty in the measurements, the comparison in thrust densities for these two combustion chamber diameters shows qualitatively that the nozzle performance was independent of the PDE combustion chamber diameter. Specifically, the relative variation in thrust density with nozzle area ratio was consistent for both combustion chamber diameters operating at a representative under-filled PDE condition ($ff = 0.4$) and a completely filled PDE. There was an absolute offset in thrust density between the two combustion chamber diameters demonstrating that the absolute variation in thrust density was not scalable in these tests. However, the relative variation in thrust density with nozzle area ratio was consistent and is therefore believed to be an appropriate normalization for comparing the relative changes in PDE nozzle data.

Effects of Ignition Delay

Ignition delay has been shown by researchers to play an important role in the performance of a pulse detonation engine when there are strong pressure oscillations occurring inside the combustion chamber prior to ignition.⁷ The sensitivity of thrust to the initial pressure has been contributed by Schauer et al.⁷ to the pressure effects on the DDT process. Igniting the mixture when the local gases are at a state of higher pressure can result in reduced DDT times^{16–22} and higher thrust. However, igniting when the local pressure is at a minimum can increase DDT times and reduce the thrust. Pressure oscillations can occur inside the PDE because of excitation of a fundamental acoustic mode or by forced excitation of the fuel-air valve system, which can commonly occur in multicycle PDE operations. Thus, the relative timing of ignition to the local pressure can have a significant impact on the PDE performance.

Another possible cause for the sensitivity of a PDE thrust to the acoustic pressure dynamics is that an increase in overall combustion chamber pressure corresponds to an increase in propellant density. Thus, because thrust scales with the propellant density, timing the ignition relative to the chamber pressure fluctuations can affect the PDE thrust in addition to the DDT effects. Furthermore, the convergent exhaust nozzles create a backpressurization (propellant density increase) that can significantly impact the thrust of the engine. The purpose of the current work was to quantify the overall effect of the ignition delay for various exhaust nozzles on the gross thrust of the engine. The specific relative contribution of the DDT effects, propellant density modifications, and backpressurization will be examined in future studies.

To determine the effects of ignition delay on the current PDE nozzle configurations, the ignition timing relative to the closing of the valves was varied from 0.5 to 7.5 ms for nozzles with area ratios of 0.25, 1.0, and 4.0. The fill-fraction was held constant at 1.0. These configurations and test conditions were selected to be representative of a typical converging, baseline, and diverging PDE nozzle system's response to changes in ignition delay. The minimum ignition delay time was set by the response of the current valve system and could not be set below this value without resulting in a backfire upstream of the valves into the fuel-air premixed injection chamber. The maximum ignition delay time was chosen to be 7.5 ms so as to not allow the blowdown to extend into the PDE purge cycle.

The normalized thrust as a function of ignition delay is plotted in Fig. 9. The baseline PDE thrust has a sinusoidal-type behavior with changes in ignition delay resulting in a maximum of +8% deviation from the average thrust at the best delay and a -5% thrust deviation at the worst ignition delay. The large amplification in PDE thrust was presumably from igniting at a time in the cycle when there was a local compression wave near the ignition region, whereas the attenuation in thrust was a result of the ignition occurring while there was a local expansion wave present.⁷ The sinusoidal-type behavior was caused by the acoustic properties of the closed/open-ended combustion chamber. The diverging nozzle configuration also had a

sinusoidal-type variation in thrust with ignition delay. The diverging nozzle ($AR = 4.0$) thrust appeared to vary nearly in phase and with similar amplitude of deviation from its mean thrust as that of the baseline configuration. On the other hand, the converging nozzle with $AR = 0.25$ appeared to vary out of phase with respect to the baseline and diverging nozzle cases.

The sensitivity of thrust to ignition delay was believed to be a direct result of the propagation of expansion/compression waves inside the PDE. Expansion waves reflect as compression waves near the open end of the PDE for the baseline configuration and the diverging nozzles. This explains the similarities between the baseline and diverging nozzle sensitivity to ignition delay. However, the convergent nozzles have an opposite boundary condition in which expansion waves reflect as expansion waves. Thus, the convergent nozzles were observed to be less sensitive to ignition delay and out of phase with respect to the baseline and divergent nozzles. Also, the level of deviations from its average thrust was much less (approximately $\pm 2\%$) for the convergent nozzles presumably because of the constriction in the PDE exit area dampening the pressure oscillations inside the combustion chamber.

Conclusions

Performance measurements of pulse-detonation-engine (PDE) exhaust nozzles were obtained using a damped thrust stand. A pulse detonation engine of 1.88 m length was operated on a cycle frequency of 30 Hz at stoichiometric conditions. Both converging and diverging bell-shaped exhaust nozzles were tested for fill-fractions ranging from 0.4 to 1.1. The length of the nozzles represented only about 2–3% of the total length of the PDE. The area ratio of the nozzle was varied from 0.25 converging to 4.00 diverging. Qualitatively, the variation in PDE thrust density with nozzle area ratio was consistent for the two PDE combustion chamber diameters (2.54 and 5.08 cm) tested. The optimum nozzle area ratio was found to be a function of the fill-fraction. For fill-fractions at or below 0.5, the optimum configuration was a PDE without an exhaust nozzle. However, as the operating fill-fraction was increased to values close to or above one, thrust enhancement was obtained with a converging nozzle. The diverging nozzles showed a relative increase in their performance with increased fill-fraction as well. The baseline and diverging nozzle configurations tested were observed to be sensitive to the ignition delay, but the converging nozzle geometry was observed to dampen out any pressure wave dynamics that would alter the ignition/DDT process.

Acknowledgments

The authors would like to thank the Propulsion Directorate at the U.S. Air Force Research Laboratory and Innovative Scientific Solutions, Inc., (ISSI) for providing the financial support for this work. The technical support of Curtis Rice of ISSI was also appreciated. In addition, the authors are grateful for the financial support from NASA Glenn Research Center (NAG3-2669) for sponsoring the development of the University of Cincinnati pulse-detonation-engine research facility.

References

- Bussing, T., and Pappas, G., "An Introduction to Pulse Detonation Engines," AIAA Paper 94-0263, Jan. 1994.
- Kuo, K., *Principles of Combustion*, Wiley, New York, 1986, Chap. 4.
- Heiser, W. H., and Pratt, D. T., "Thermodynamic Cycle Analysis of a Pulse Detonation Engine," *Journal of Propulsion and Power*, Vol. 18, No. 1, 2002, pp. 68–76.
- Kailasanath, K., "Recent Developments in the Research on Pulse Detonation Engines," *AIAA Journal*, Vol. 41, No. 2, 2003, pp. 145–159.
- Wintenberger, E., Austin, J. M., Cooper, M., Jackson, S., and Shepherd, J. E., "Analytical Model for the Impulse of Single-Cycle Pulse Detonation Tube," *Journal of Propulsion and Power*, Vol. 19, No. 1, 2003, pp. 22–38.
- Eidelman, S., Grossmann, W., and Lottati, I., "Review of Propulsion Applications and Numerical Simulations of the Pulsed Detonation Engine Concept," *Journal of Propulsion and Power*, Vol. 7, No. 6, 1991, pp. 857–865.
- Schauer, F., Stutrud, J., and Bradley, R., "Detonation Initiation Studies and Performance Results for Pulse Detonation Engine Applications," AIAA 2001-1129, Jan. 2001.

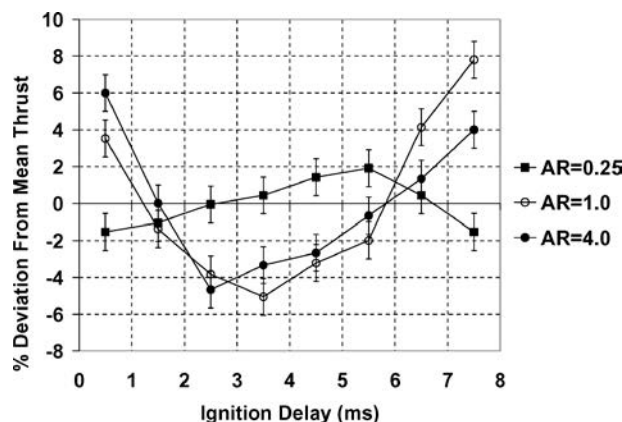


Fig. 9 Variation in PDE thrust with ignition delay ($D_{\text{comb}} = 5.08$ cm, $ff = 1.0$).

- ⁸Li, C., and Kailasanath, K., "Performance Analysis of Pulse Detonation Engines with Partial Fuel Filling," AIAA Paper 2002-0610, Jan. 2002.
- ⁹Eidelman, S., and Yang, X., "Analysis of the Pulse Detonation Engine Efficiency," AIAA Paper 98-3877, July 1998.
- ¹⁰Yungster, S., "Analysis of Nozzle Effects on Pulse Detonation Engine Performance," AIAA Paper 2003-1316, Jan. 2003.
- ¹¹Cambier, J. L., and Tegner, J. K., "Strategies for Pulsed Detonation Engine Performance Optimization," *Journal of Propulsion and Power*, Vol. 14, No. 4, 1998, pp. 489–498.
- ¹²Mohanraj, R., and Merkle, C. L., "A Numerical Study of Pulse Detonation Engine Performance," AIAA Paper 2000-0315, Jan. 2000.
- ¹³Cooper, M., Jackson, S., Austin, J., Wintenberger, E., and Sheperd, J., "Direct Experimental Impulse Measurements for Detonations and Deflagrations," *Journal of Propulsion and Power*, Vol. 18, No. 5, 2002, pp. 1033–1041.
- ¹⁴Wu, Y., Ma, F., and Yang, V., "System Performance and Thermodynamic Cycle Analysis of Air-Breathing Pulse Detonation Engines," *Journal of Propulsion and Power*, Vol. 19, No. 4, 2003, pp. 556–567.
- ¹⁵Kaemming, T. A., and Dyer, R. S., "The Thermodynamic and Fluid Dynamic Function of a Pulsed Detonation Engine Nozzle," AIAA Paper 2004-3916, July 2004.
- ¹⁶Lee, J. H. S., "Dynamic Parameters of Gaseous Detonations," *Annual Review of Fluid Mechanics*, Vol. 16, 1984, pp. 311–336.
- ¹⁷Lee, J. H. S., Knystautas, R., and Freiman, A., "High Speed Turbulent Deflagrations and Transition to Detonation in H₂-Air Mixtures," *Combustion and Flame*, Vol. 56, No. 2, 1984, pp. 227–239.
- ¹⁸Smirnov, N., and Tyurnikov, M., "Experimental Investigation of Deflagration to Detonation Transition in Hydrocarbon-Air Gaseous Mixtures," *Combustion and Flame*, Vol. 100, No. 4, 1995, pp. 661–668.
- ¹⁹Gelfand, B. E., Khomik, S. V., Bartenev, A. M., Medvedev, S. P., Gronig, H., and Olivier, H., "Detonation and Deflagration Initiation at the Focusing of Shock Waves in Combustible Gaseous Mixture," *Shock Waves*, Vol. 10, No. 3, 2000, pp. 197–204.
- ²⁰Knystautas, R., Lee, J. H. S., and Moen, I., "Direct Initiation of Spherical Detonation by a Hot Turbulent Gas Jet," *17th Symposium on International Combustion Proceedings*, Vol. 17, Combustion Inst., Pittsburgh, PA, 1978, pp. 1235–1245.
- ²¹Thomas, G. O., and Jones, A., "Some Observations of the Jet Initiation of Detonation," *Combustion and Flame*, Vol. 120, No. 3, 2000, pp. 392–398.
- ²²Gamezo, V., Desbordes, D., and Oran, E., "Formation and Evolution of Two-Dimensional Cellular Detonations," *Combustion and Flame*, Vol. 116, No. 1–2, 1999, pp. 154–165.

Effects of Tube and Ejector Geometry on the Performance of Pulse Detonation Engine Driven Ejectors

Aaron J. Glaser^{*}, Nicholas Caldwell[†] and Ephraim Gutmark[‡]
University of Cincinnati, Cincinnati, OH, 45221-0070

John Hoke[§] and Royce Bradley^{**}
Innovative Scientific Solutions Inc., Dayton, OH, 45440

and

Fred Schauer^{††}
Air Force Research Laboratory, WPAFB, Dayton, OH, 45433

Experimental studies are carried out to investigate the performance of various pulse detonation engine (PDE) driven ejector configurations. In particular the effects of detonation tube length and ejector-to-PDE diameter ratio (DR) are studied. This research employs a H₂-air PDE at 25 Hz operating frequency. Performance was quantified by thrust measurements. It was found that decreasing the detonation tube length increases the ejector thrust augmentation. An optimum ejector-to-PDE diameter ratio was found to exist in the range DR=3 to DR=3.67. The specific impulse of the PDE increases from the baseline no ejector value of 3400 s to approximately 6080 s with an ejector installed.

Nomenclature

D_{PDE}	=	detonation tube diameter
D_{EJECT}	=	ejector diameter
DR	=	ejector-to-PDE diameter ratio
ff	=	fill-fraction
I_{SP}	=	specific impulse
L_{EJECT}	=	ejector length
$L_{STRAIGHT}$	=	intermediate straight-section length
L_{EXHST}	=	exhaust-section length
x	=	ejector position

I. Introduction

THE pulse detonation engine (PDE) is currently being investigated as an alternative to more traditional aerospace propulsion systems. Engine cycles based on detonation combustion offer a theoretical increase in thermal efficiency as compared to deflagration combustion systems. For practical PDE applications, one of the key challenges facing researchers is to make use of the increased efficiency of energy conversion due to detonative-mode combustion and most effectively convert that into a propulsive thrust force. A common measure of propulsion system performance is specific impulse (I_{SP}), which is defined as the ratio of thrust generated to the weight flow rate of fuel. Greater values of I_{SP} are desirable since this will decrease the specific fuel consumption. It has been

^{*} Graduate Research Assistant, Department of Aerospace Engineering, ML0070, Student Member AIAA.

[†] Graduate Research Assistant, Department of Aerospace Engineering, ML0070, Student Member AIAA.

[‡] Professor and Ohio Eminent Scholar, Department of Aerospace Engineering, ML0070, Associate Fellow AIAA.

[§] Research Engineer, 2766 Indian Ripple Rd., Senior Member AIAA.

^{**} Senior Scientist, 2766 Indian Ripple Rd.

^{††} Senior Engineer, Head PDRF, AFRL/PRTC, Bldg. 490, Senior Member AIAA.

suggested that the use of ejector augmenters on PDEs may be an effective way to increase the system thrust being generated, thus leading to an increased I_{sp} .

An ejector is a simple device used to augment the thrust of an engine. Essentially, an ejector consists of a coaxial duct placed around the exhaust of an engine that performs as a fluidic pump. The surrounding ambient air is entrained by the primary exhaust flow and directed into the ejector. The entrained air causes an increase in momentum of the engine exhaust flow. This leads to the generation of a larger system thrust force. The theory and application of ejectors to a steady primary flow is well established. For steady-flow ejectors, the secondary flow is entrained primarily through viscous shear mixing.¹ Ejectors being driven by an unsteady primary flow have not been so extensively studied. In particular, only limited studies have been performed on PDE driven ejector systems. However, a number of ejector studies have been performed using various other means to generate an unsteady primary flow. These include cold flow studies employing fluctuating air streams² and unsteady combustion studies using pulsejets to drive the ejectors.^{3,4} This previous research has shown that unsteady ejectors are capable of producing more thrust augmentation than comparable steady-flow ejectors.⁴ The increased performance of unsteady ejectors has been attributed to a more efficient energy transfer process between the primary and secondary flows due to dominant inviscid effects. Since PDEs are highly unsteady devices, it has been proposed that PDE driven ejectors have the potential to be highly effective in providing thrust augmentation.

Recent experimental work has produced promising results for ejectors in augmenting the thrust of PDEs. Studies have been performed on the effects of PDE operating parameters as well as on ejector geometric parameters. It has been observed that ejector performance is sensitive to the axial position of the ejector inlet relative to the PDE tube exit. In most cases downstream ejector placement provides optimum levels of thrust augmentation.^{5,6} The importance of a properly contoured inlet has been investigated in various studies.⁷ The internal surface geometry of the ejector is also an important geometric parameter. An experimental study by Glaser et al⁸ was carried out using several ejector configurations. Results of those experiments showed maximum thrust augmentation levels of approximately 37% for straight ejectors and 85% for an optimized diverging ejector geometry. It is apparent that the diverging ejectors tested were much more effective at producing thrust augmentation than the straight ejectors. This increase in performance with the diverging ejector is attributed to the additional thrust surface area of the diverging section.

Another geometric parameter of importance is the ejector-to-PDE diameter ratio (DR). The diameter of the ejector should be sufficiently large to promote a favorable interaction with the exiting detonation wave and trailing vortex ring structure. Also sufficient area must be available for the secondary flow to enter the ejector duct efficiently. However, if the ejector is excessively large, then the pressure drop on the inlet caused by the entrained flow will be reduced, as will the pressure rise on the diverging section. The effect of this change in pressure loading will cause the thrust augmentation to decrease. A very large ejector will, in effect, begin to lose communication with the primary driver source. Previous work has been performed to investigate the effect of the relative size of the ejector to that of the primary flow driver. A wide variety of non-detonative unsteady sources have been used as the primary jet in ejector systems, and results from these efforts suggest that for unsteady ejectors, an optimum ejector-to-PDE diameter ratio is near $DR=3$.^{2,3} Very few experimental studies to investigate diameter ratio effects have been performed with PDE driven ejectors. One study by Rasheed et al⁵ used a 2 in. diameter H_2 -air PDE of 1 m length at 10 Hz. In the study three ejectors were investigated with ejector-to-PDE diameter ratios of $DR=1.5$, 2, and 3. Results showed that thrust augmentation increased with diameter ratio up to $DR=3$. However, an optimum diameter ratio could not be determined since diameter ratios above $DR=3$ were not tested. A study performed by Wilson et al⁷ investigated diameter ratios of 2.2, 3, and 4. These tests were performed using a H_2 -air PDE system operating at 20 Hz with a 1 in. diameter detonation tube of 36 in. length. Using statistical based Design-of-Experiment methods, the authors determined the optimum ejector-to-PDE diameter ratio to be $DR=3.2$. The current effort seeks to increase the amount of data available on diameter ratio effects for PDE driven ejector systems.

The length of the detonation tube being used to drive the ejector is a geometric parameter that can impact ejector performance. Alteration of this parameter changes the corresponding blowdown time of the exhaust cycle. The blowdown time is that required for the combustion products in the detonation tube to expand down to ambient pressure. This portion of the exhaust cycle is characterized by an underexpanded jet exiting the tube, with the jet eventually becoming subsonic near the end of the blowdown process. It is thought that a change in the blowdown time could affect the level of entrainment into the ejector. Specifically, an increase in the blowdown time may increase augmentation because more time is available for viscous shear mixing. No previous results have been reported on the effect of detonation tube length on PDE-ejector system performance.

The current study had two primary objectives. The first was to determine the effect of detonation tube length on thrust augmentation. The second was to investigate the effects of ejector-to-PDE diameter ratio and identify the optimum diameter ratio for ejector performance. To investigate tube length effects, a detonation tube was

constructed in which the length could be varied in increments down to 65% of the nominal length. Ejector performance was then evaluated at each tube length tested. Two approaches were used to study the ejector-to-PDE diameter ratio effects. In the first, a set of experiments was run while holding the ejector diameter constant and varying the diameter of the detonation tube. In the second, the detonation tube diameter was held constant while varying the ejector diameter.

II. Experimental Setup

A. Description of PDE Test Facility

Experimental testing for the current study was carried out at the Air Force Research Laboratory PDE test facility at Wright-Patterson Air Force Base.⁹ The system was operated in a premixed manner, using hydrogen and air as the reactants. Injection of fuel and air into the detonation tube was carried out using a mechanical valve system. This system was constructed from a modified four-cylinder automotive valve head with four valves-per-cylinder. The valve train was driven with a variable speed electric motor. The two intake ports were used to deliver premixed hydrogen and air, while the two exhaust ports delivered purge air. The purge air cycle is employed to cool the detonation tube between combustion cycles and provide a buffer between the hot combustion products and the fresh reactants being injected into the tube for the next cycle. Because of the nature of automotive valving, the cycle timing for various events such as fill time, purge time, and detonation time are fixed to be one-third of the cycle. Spark ignition was accomplished using a capacitive discharge stock automotive spark system that delivered approximately 40 mJ of energy. To accelerate the deflagration-to-detonation transition a Shchelkin-type spiral was used for all tests.

The PDE system was mounted on a damped thrust stand designed to measure the time-averaged thrust generated by the PDE. The thrust stand consisted of linear pillow-block bearings that rode along a pair of linear bearing rails. The PDE was allowed to move freely on the rails, but its motion was resisted by springs to prevent resonance effects. A novel approach was used to remove the effects of static friction. The PDE was continuously actuated forward and backward by a linear pneumatic actuator. Since the actuator produces a net zero average force, the average position of the thrust stand is a function of the PDE average thrust. The thrust stand was calibrated by placing static weights on a pulley/cable system to simulate a thrust force and measuring the average position of the thrust stand with a displacement sensor. The maximum uncertainty of the thrust stand, which was determined through repeated calibration tests, was found to be approximately ± 0.25 lb for the range of PDE thrust loading observed during these tests.

Operation of the PDE system was computer controlled using a LabView interface program. The LabView interface provided the flexibility to specify engine operating parameters such as PDE operating frequency, fill-fraction (ff), and equivalence ratio. Where fill-fraction is defined as the ratio of the tube volume filled with a detonable mixture to the total tube volume prior to combustion. Unless otherwise stated, all of the current tests were performed at an operating frequency of 25 Hz, fill-fraction of 1.0, and an equivalence ratio of 1.0. Ionization probes were mounted along the detonation tube length to verify that Chapman-Jouguet (CJ) detonations were obtained. For a stoichiometric mixture of hydrogen and air, the CJ wave speed is 1957 m/s. Data from these sensors were collected at 5 MHz using a 16 channel data acquisition system. This fast sampling rate was adequate to resolve accurately the detonation wave speed.

B. Detonation Tube and Ejector Hardware

The current study involved three separate but related investigations. All of the ejectors tested were mounted coaxially to the detonation tube. The ejectors were suspended from two parallel rails mounted above the detonation tube. The rails extended along the length of the tube, allowing the axial position, x , of the ejector inlet to be varied from -8 to +12 in. from the PDE tube exit plane. A negative axial position value corresponds to the ejector inlet being placed upstream of the PDE exit, with the ejector overlapping the detonation tube. For a positive value, the ejector is mounted downstream of the detonation tube exit.

The goal of the first set of experiments was to investigate the effect of detonation tube length on ejector performance. For these tests a variable length detonation tube was constructed. The tube was made from 2 in. diameter Schedule 40 pipe with a nominal baseline length of 61.25 in. Four separate detonation tube lengths could be obtained by removal of

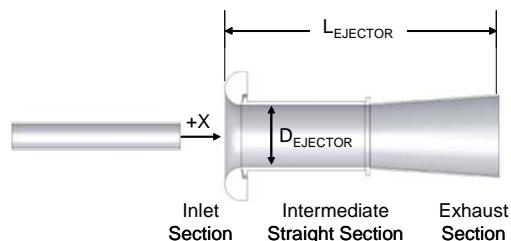


Figure 1. Diagram of the ejector geometry used for the current effort.

short tube sections that were connected using pipe couplers. The incremental lengths tested are given in Table 1. The single ejector used for these tests consisted of an inlet section, an intermediate straight section, and an exhaust section, as shown in Figure 1. The inlet had a rounded inlet lip with a radius of 1.5 in. The exhaust section had a half-angle divergence of 4° and a length of 13 in. The diameter of the ejector (D_{EJECT}) was defined as the diameter of the intermediate straight section, since this was the minimum diameter of the ejector geometry. For the current set of experiments, D_{EJECT} was held at a fixed value of 5.5 in. The ejector-to-PDE diameter ratio (DR) of 2.75 was, therefore, constant throughout this portion of the testing.

Range of Detonation Tubes Tested				
Tube Length	39.75"	47.25"	54.25"	61.25"
Normalized Tube Length	0.65	0.77	0.89	1.00
Tube Volume	142.6 in ³	167.8 in ³	191.3 in ³	214.8 in ³

Table 1. Detonation tube geometries tested to determine the effect of tube length on ejector performance. The ejector was held at a constant DR=2.75.

For the next portion of the study, the effects of varying the ejector-to-PDE diameter ratio were investigated by holding the ejector diameter constant and varying the detonation tube diameter. For this testing the same diverging ejector hardware as described above with a constant $D_{EJECT}=5.5$ in. was used. Different ejector-to-PDE diameter ratios were obtained by varying the detonation tube diameter. Five diameter ratios were tested, ranging from DR=1.83 to DR=5.5, as is given in Table 2.

Diameter Range of Detonation Tubes Tested					
Tube Diameter	1"	1.5"	2"	2.5"	3"
DR (D_{EJECT}/D_{PDE})	5.5	3.67	2.75	2.2	1.83
Tube Length	61.25"	61.25"	61.25"	40.88"	27.35"
Tube Volume	61.25 in ³	131.5 in ³	214.8 in ³	214.8 in ³	214.8 in ³

Table 2. Detonation tube geometries tested by varying the ejector-to-PDE diameter ratio. The ejector was held at a constant diameter of $D_{EJECT}=5.5$ ".

The goal of the final portion of the current study was to investigate the effect of ejector-to-PDE diameter ratio by holding the PDE tube diameter constant and varying the ejector diameter. A set of three ejectors designed and fabricated by General Electric Global Research was used. The detonation tube used for these tests was made from 2 in. diameter Schedule 40 pipe with a length of 61.25 in. The ejectors tested were all straight cylindrical ejectors with a length of 15 in. and a rounded inlet with a radius of 0.51 in. The ejector-to-PDE diameter ratio of the three ejectors varied from DR=1.5 to DR=3 as given in Table 3.

Ejector Geometries Tested			
DR (D_{EJECT}/D_{PDE})	1.5	2	3
Ejector Diameter	3"	4"	6"
Ejector Length	15"	15"	15"

Table 3. Ejector geometries tested by varying the ejector-to-PDE diameter ratio. The tube diameter was held constant at $D_{PDE}=2$ ".

III. Results and Discussion

A. Baseline Testing of PDE System

To determine the effect of the ejector augmenters on PDE performance, baseline testing of the PDE system without an ejector installed was performed. Performance measurements of the baseline configurations were made for the individual detonation tube lengths and diameters being considered in the study. A suitable test duration was determined, which yielded steady thrust measurements. Normalized thrust as a function of experiment run time is shown in Figure 2, where the reference thrust of 16.3 lb is the thrust generated at $ff=1$ and 25 Hz using a 2 in. diameter tube of 61.25 in. length. It can be observed that because of the thrust averaging process employed by the thrust stand, approximately 20 s is required to reach a steady thrust value. All experiments reported here were run for a sufficient duration to achieve a steady thrust measurement. A common performance metric used to assess ejector augmenters is the amount of PDE thrust augmentation produced by use of an ejector, as defined by the following

$$\alpha = \frac{(T_{PDE-EJECT} - T_{PDE})}{T_{PDE}} \cdot 100 \quad (1)$$

where $T_{PDE-EJECT}$ is the thrust generated by the PDE with an ejector installed, and T_{PDE} is the baseline thrust of the system with no ejector installed.

B. Effect of Detonation Tube Length

In this portion of the study, testing was performed to determine the effects of detonation tube length on ejector performance. It had been proposed that the length of the detonation tube for a given ejector-to-PDE diameter ratio may be an important geometric parameter to consider, mainly due to the effect of the tube length on the cycle blowdown time. The detonation process generates high pressure and temperature burned gasses within the detonation tube. The blowdown time is that required to expand these burned products out of the detonation tube and the tube pressure to relax to ambient conditions. Previous measurements of the blowdown time in a 2 in. diameter, H_2 -air PDE have shown that the blowdown time required increases by approximately 0.6 ms per foot of detonation tube.¹⁰ It was thought that the amount of time required for the exhaust jet to exit the end of the detonation tube during blowdown may affect thrust augmentation. Specifically, an increase in the blowdown time might increase augmentation because more time would be allowed for viscous shear mixing. No results have been reported previously on the effect of detonation tube length on PDE-ejector system performance.

For the current tests the diameter of the detonation tube was held constant while the length of the tube was decreased to 65% of its original length. The corresponding decrease in the blowdown time is approximately 1 ms. Results from the baseline PDE tests with no ejector installed are shown in Figure 3. An interesting comparison can be made by observing the effects of both tube length and fill-fraction on the thrust generated. These parameters have a similar effect on the PDE system in that when they are decreased, the amount of detonable mixture being consumed decreases and, thus, the thrust generated decreases. Fill-fraction can be thought of as the ratio of the length of tube filled with a detonable mixture to the total tube length. Tube length can be normalized by dividing by the initial tube length of 61.25 in. In this manner an equal value of fill-fraction and normalized tube length corresponds to a system with approximately equal fuel consumption. Normalized tube length is plotted along with fill-fraction in Figure 3 to show the effects of these parameters on baseline PDE performance. It can be observed that when both parameters are decreased, the thrust decreases at different rates. For example, at a fill-fraction and normalized tube length of 0.65, an approximately equal amount of fuel is being consumed; but the case where the

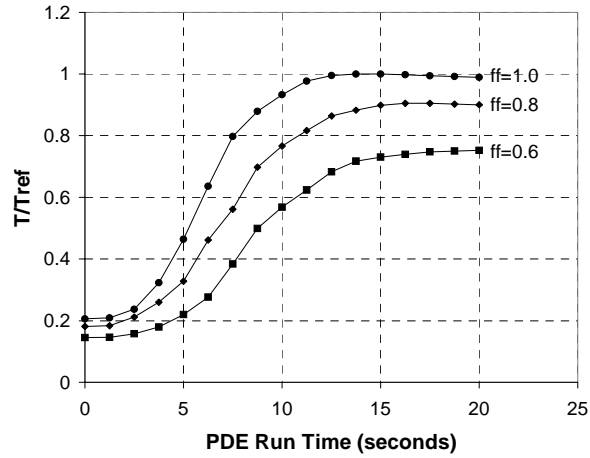


Figure 2. Determination of the PDE run time required to achieve a steady thrust measurement.

tube length is held constant with $ff=0.65$ produces more thrust than the shorter tube at fill-fraction, $ff=1$. The performance benefits of decreasing the fill-fraction can be illustrated by observing the variations in the specific impulse of the PDE, as shown in Figure 4. Decreasing the fill-fraction at a constant tube length has the effect of increasing I_{SP} . This trend has been observed by other researchers and is known as the partial fill effect. When the fill-fraction is decreased, the end portion of the tube is occupied by either burned exhaust gas or purge gas. As the detonation wave passes into the unfilled portion of the tube the gases in this region are compressed because of shock compression. In the case where $ff=0.65$ is used, compression of the remaining 35% of the tube increases the blowdown time and corresponding thrust over that in the case where the tube is 65% of its nominal length with $ff=1$. The unfilled portion of the tube can, thus, be thought of as a straight nozzle.

The effect of tube length on ejector thrust augmentation is shown in Figure 5. Results for decreasing fill-fraction are also shown for comparison. The inverse relationship between fill-fraction and thrust augmentation has been observed in previous work. In a similar manner, as tube length is decreased it can be seen that the level of thrust augmentation increases. To better understand the observed thrust augmentation trends, the thrust values obtained with the ejector installed were also analyzed. Thrust levels of the variable tube length case with and without an ejector are shown in Figure 6. It is clear that while the baseline thrust decreases with decreasing tube length, the change in thrust, ΔT , due to the ejector is relatively constant. Since thrust augmentation is defined as this change in thrust divided by the baseline thrust, it can be seen that as the baseline thrust decreases the thrust augmentation increases. The fact that the change in thrust at different tube lengths is nearly constant seems to suggest that the performance of a PDE driven ejector is controlled more by the inviscid effects than by viscous mixing effects. The inviscid effects are dictated by the strength of the exiting detonation wave and vortex ring. The strength of these structures exiting the detonation tube will not be a function of tube length, as long as there is sufficient tube length to form a CJ detonation wave.

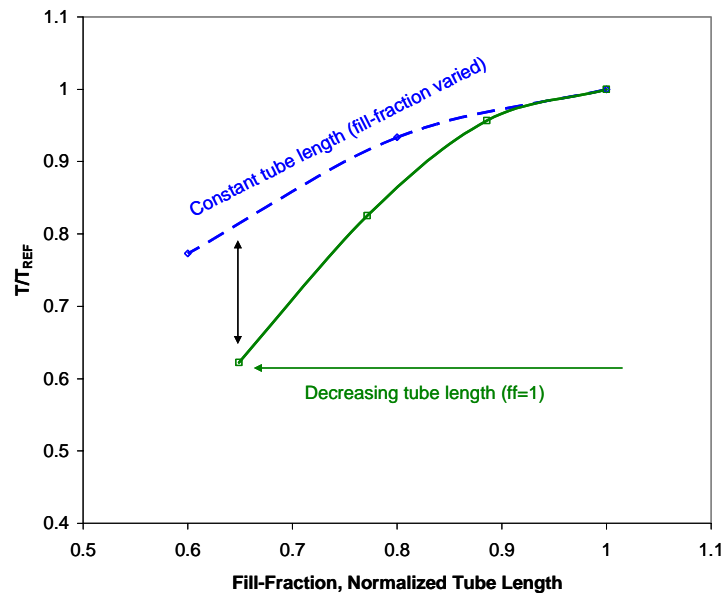


Figure 3. Effect of fill-fraction and normalized tube length on baseline PDE thrust.

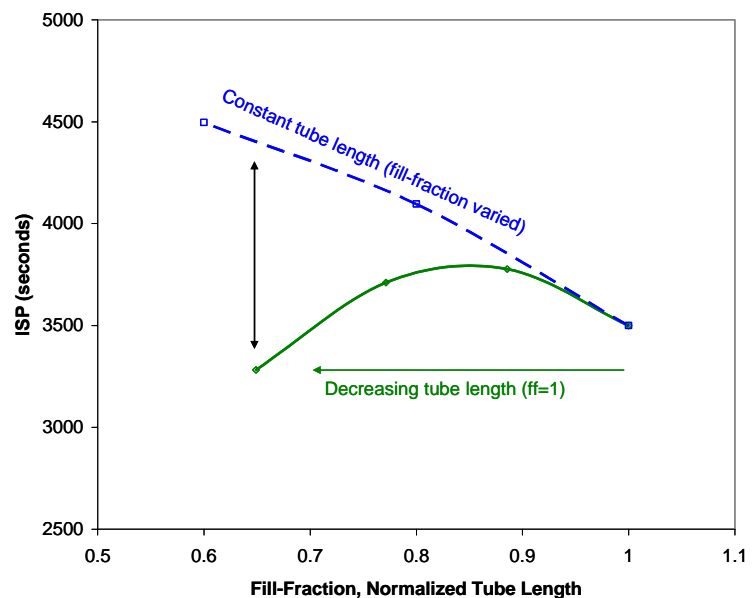


Figure 4. Effect of fill-fraction and normalized tube length on baseline PDE I_{SP} .

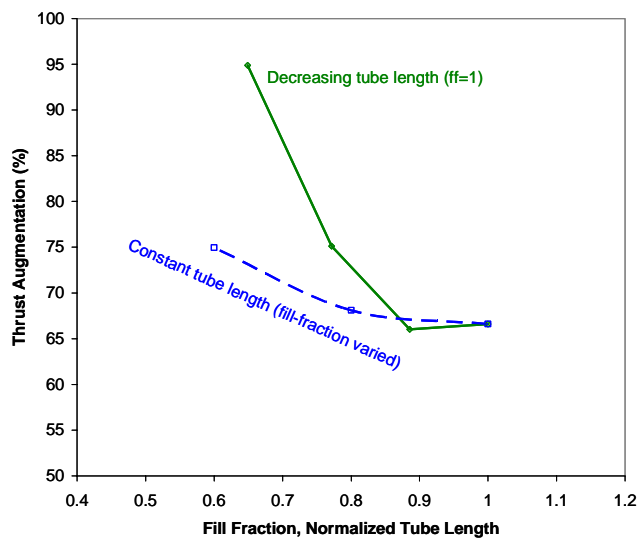


Figure 5. Effect of fill-fraction and normalized tube length on thrust augmentation.

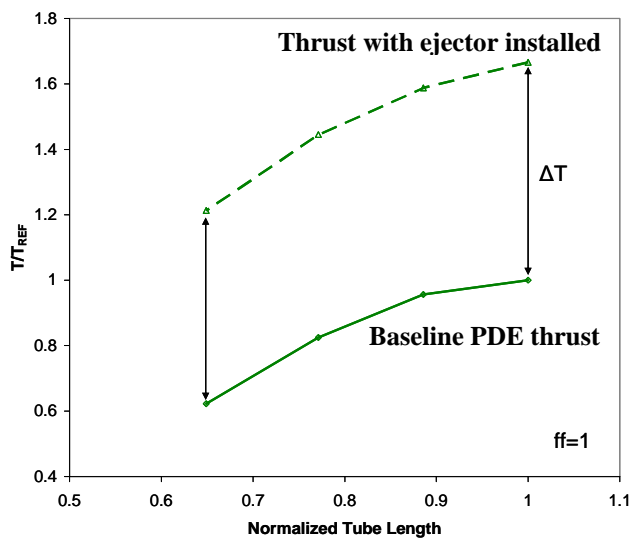


Figure 6. Baseline PDE and thrust augmented by an ejector as a function of normalized tube length.

C. Effect of Ejector-to-PDE Diameter ratio

Previous studies have been performed to investigate the effect of diameter ratio on ejector performance. A wide variety of unsteady sources have been used as the primary jet, and results suggest that for unsteady ejectors an optimum diameter ratio exists near $DR=3$. Limited tests to investigate diameter ratio effects have been performed with PDE-driven ejectors. Rasheed et al.⁵ studied three diameter ratios in the range $DR=1.5$ to $DR=3$. Results from that work showed that augmentation increased up to $DR=3$, but what happens at larger diameter ratios was not shown. Wilson et al.,⁷ investigated three diameter ratios in the range $DR=2.2$ to $DR=4$. Using statistical based Design-of-Experiment methods, the authors determined the optimum ejector-to-PDE diameter ratio to be $DR=3.2$. The current effort seeks to increase the amount of diameter ratio data. Two approaches were used to study the diameter ratio effects. In the first, a set of experiments was run holding the ejector diameter constant while varying the diameter of the detonation tube. The second approach was to hold the detonation tube constant while varying the ejector diameter.

1. Varying the Detonation Tube Diameter

As described in the experimental setup, five tube diameters were used for this portion of the testing. In this way the diameter ratio was varied from $DR=1.83$ to $DR=5.5$. For each of the five diameter ratios tested, the axial placement of the

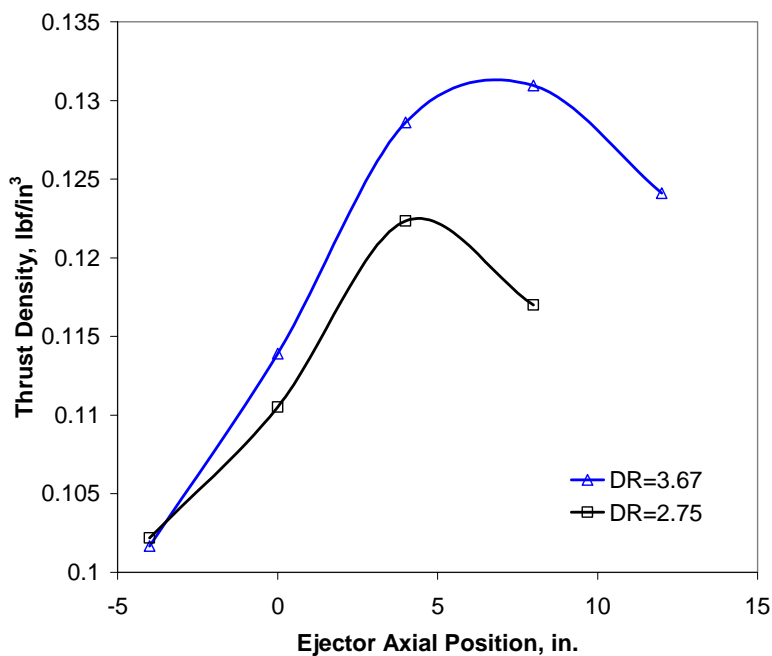


Figure 7. Effect of ejector axial position on PDE-ejector system thrust. $DR=2.75$ corresponds to a tube diameter of 2 in., and $DR=3.67$ corresponds to a 1.5 in. diameter tube.

ejector was varied from -4 in. to 12 in. In this manner, the optimum axial placement of each DR configuration could be found. Figure 7 shows the effect of ejector axial position on the DR=2.75 and DR=3.67 configurations. It can be observed that for both configurations the optimum axial placement is downstream of the detonation tube exit plane. Also, the optimum axial placement of the DR=3.67 is further downstream than for the DR=2.75 case. The optimum axial placements for all diameter ratios tested in this part of the study are shown in Figure 8. It can be observed that when the diameter ratio is increased, the optimum ejector placement shifts farther downstream from the PDE exit plane. The smallest diameter ratio tested, DR=1.8, had an optimum placement of $x=0$.

Changing the detonation tube diameter altered the value of the baseline thrust generated for the different tubes. Thrust augmentation, as previously defined, yields a percentage increase in thrust from the baseline value. According to this definition, thrust augmentation can indicate misleading trends when cases with differing baseline thrusts are compared. To better characterize the effects of diameter ratio on ejector system performance, other performance metrics were sought. In an attempt to normalize the baseline thrusts and make them more directly comparable, the thrust density of each of the tubes was computed. Thrust density is defined as the thrust produced divided by the detonation tube volume.¹¹ Thrust densities are shown for all diameter ratios tested both with and without ejectors installed in Figure 9. All data shown are at the

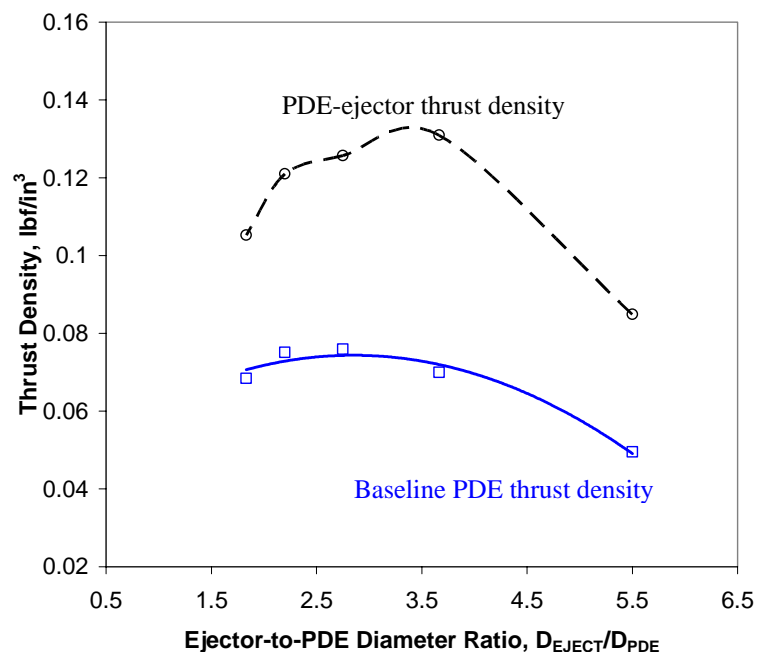


Figure 9. Thrust densities of baseline PDE tubes and PDE tubes with ejectors installed.

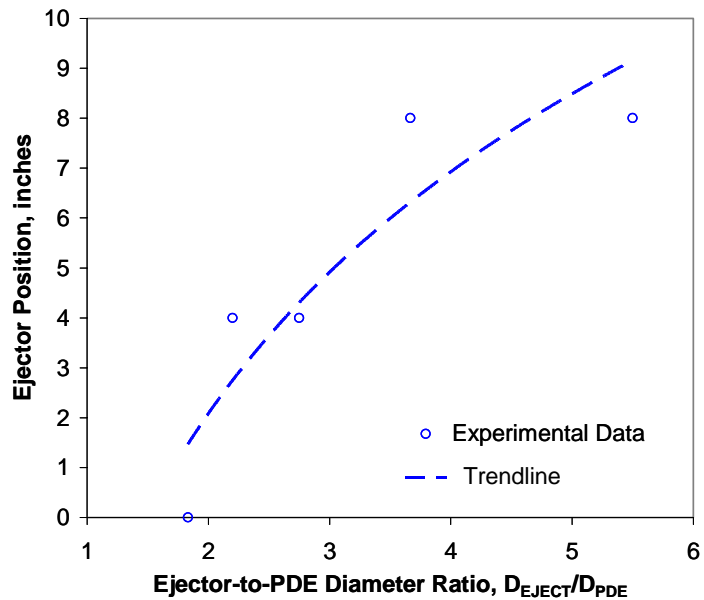


Figure 8. Effect of the ejector-to-PDE diameter ratio at the optimum axial ejector placement.

corresponding optimum axial position for each DR. The solid curve represents the baseline thrust data with no ejector installed. All tubes have a similar thrust density, except the 1 in. diameter tube (DR=5.5) which is much lower than the others. This reduction is most likely due to increased flow losses with the 1 in. diameter detonation tube. Although all tubes employ a Shchelkin-type spiral for deflagration-to-detonation transition, the spiral used in the 1 in. diameter tube occupies a larger fraction of the total tube volume than that used in the larger diameter tubes. Thus, the spiral in the 1 in. tube may incur a higher relative thrust loss than the other tubes. The dashed curve represents the measured thrust density with the ejector installed on the tubes. To correct for the offset in baseline thrust densities, ejector performance was evaluated against the relative change in thrust density for each tube diameter tested. The change in thrust density is defined as the difference between ejector installed and baseline thrust densities for each DR configuration. Therefore, the larger the change in thrust

density because of the ejector installed, the better that particular configuration is said to perform. Figure 10 is a plot of the change in thrust density as a function of the ejector-to-PDE diameter ratio. From the diameter ratios tested, it can be seen that the optimum diameter ratio lies in the range $DR=3$ to $DR=3.67$, and appears to be near $DR=3.5$. However, since no data are present within this range, additional tests would be necessary to determine the optimum diameter ratio. These values for diameter ratio are near the optimum of $DR=3.2$ determined by Wilson et al⁷ for a PDE driven ejector.

The diameter ratio data was also analyzed by considering the specific impulse of the PDE system. The specific impulse of the baseline detonation tubes is given in Figure 11. With exception of the 1 in. diameter tube, the different baseline tubes tested had an average specific impulse of $I_{SP}=3400$ s. As was observed in the thrust density data, the 1 in. diameter tube had a lower specific impulse of approximately 2300 s. The data are plotted to show the relative change in specific impulse as a result of installing the ejector in Figure 12. This data shows a similar trend to that observed when the thrust density data was considered. The optimum ejector-to-PDE diameter ratio is seen to be in the range $DR=3$ to $DR=3.67$, and appears to be near $DR=3.5$.

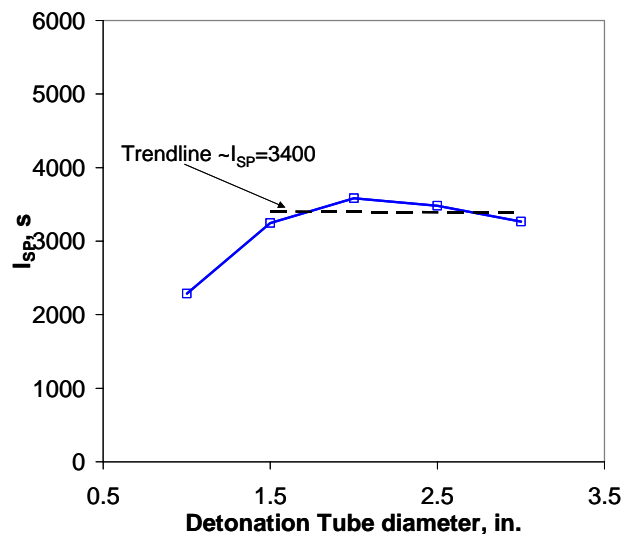


Figure 11. I_{SP} of the baseline PDE configurations. Tube diameters $D_{PDE}=1.5$ in. to $D_{PDE}=3$ in. give $\sim I_{SP}=3400$ s. $D_{PDE}=1$ in. gives $\sim I_{SP}=2290$ s.

2. Varying the Ejector Diameter

The second method used to evaluate the effect of ejector-to-PDE diameter ratio was holding the detonation tube diameter constant and varying the ejector diameter. For these tests a set of three straight cylindrical ejectors designed and fabricated by General Electric Global Research was used. These ejectors covered the diameter range

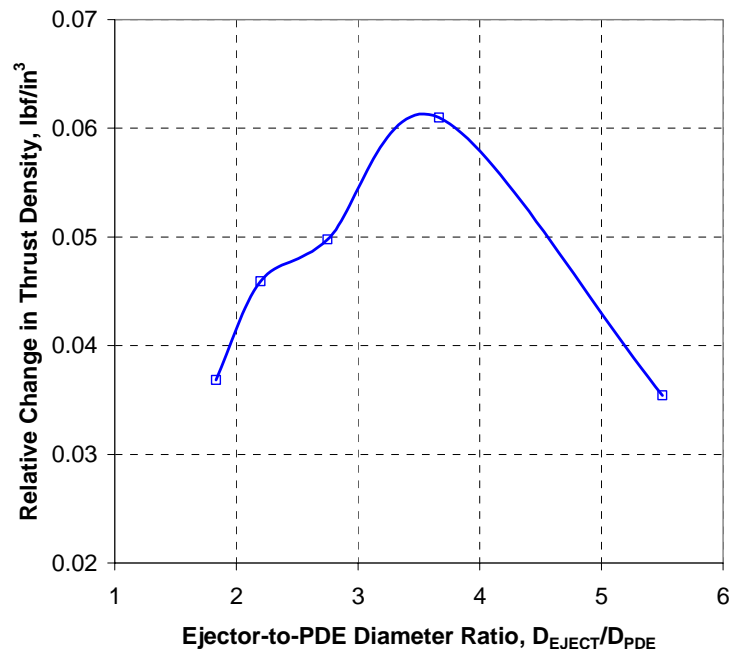


Figure 10. Relative changes in thrust density due to installation of the ejector.

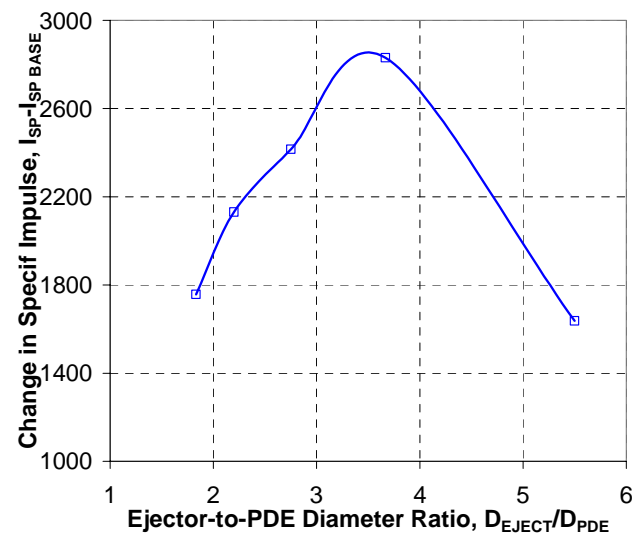


Figure 12. Relative changes in I_{SP} due to the installation of the ejector.

DR=1.5 to DR=3. The detonation tube used had a 2 in. diameter and a length of 61.25 in. After the baseline tube alone was run, the individual ejectors were installed; and each was tested over an axial placement range $x/D_{\text{EJECT}} = -4$ to $x/D_{\text{EJECT}} = +4$. The results are shown in Figure 13 for the three ejectors tested. One trend that can be observed clearly is that all of the ejectors produced their maximum thrust augmentation at downstream ejector placements. The ejector with diameter ratio DR=1.5 provides negative thrust augmentation until it is moved to a downstream placement. Secondly, in the diameter range investigated, thrust augmentation is observed to increase with diameter ratio. The observed trends are in good agreement with those reported by Rasheed et al⁵. That study used the same ejector hardware as in the current effort, with the exception being the length of the DR=3 ejector; the current study used a length of 15 in. while Rasheed et al⁵ used 9 in. It should also be noted that the previous study was performed using a different PDE system. The data from Rasheed et al⁵ shown in Figure 13

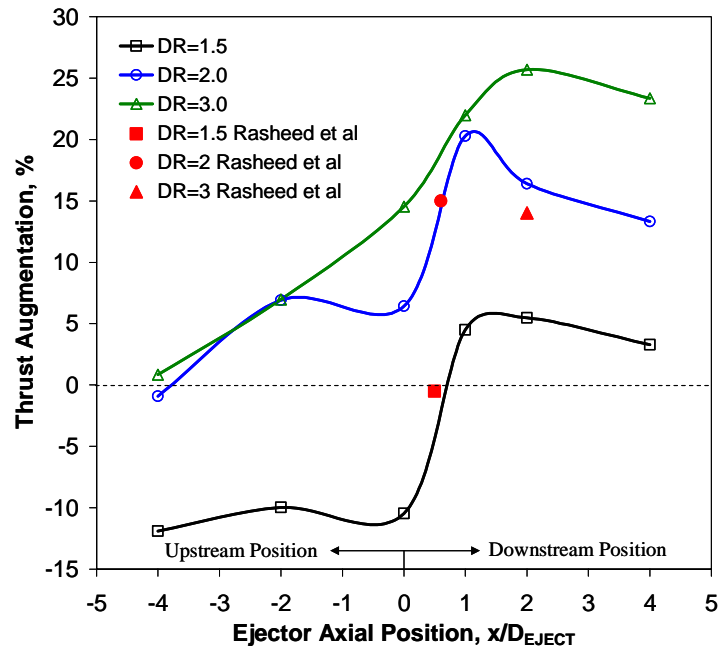


Figure 13. Effect of DR and axial position of ejector on thrust augmentation.

is the thrust augmentation reported at the optimum axial position for each DR. The largest discrepancy between the two studies is the augmentation of the DR=3 ejectors. At this DR the optimum axial positions are similar, however, the augmentation observed in the current study is ~ 11% greater. This difference is attributed to the extra length of

the DR=3 ejector used in the current study. The fact that the trends are comparable, despite all of the test facility differences serves to validate the data.

Figure 14 shows the combined results from both parts of the ejector-to-PDE diameter ratio study. It can be observed that the diverging ejector used in the portion of the study in which tube diameter was varied exhibited significantly better performance than the straight ejectors employed in the constant tube diameter tests. However, the trends for both sets of data are similar up to the diameter ratio, DR=3, cutoff of the straight ejector data. It appears that at DR=3, the straight ejector had not yet reached its optimum diameter ratio. This matches well with the results obtained from the tube diameter variation experiments, which show that the optimum diameter ratio lies in the range DR=3 to DR=3.67. The fact that similar trends were obtained when two different methods were used to investigate the diameter ratio lends confidence in the results. This figure also highlights the improved performance of a PDE that can be gained by use of a properly designed ejector.

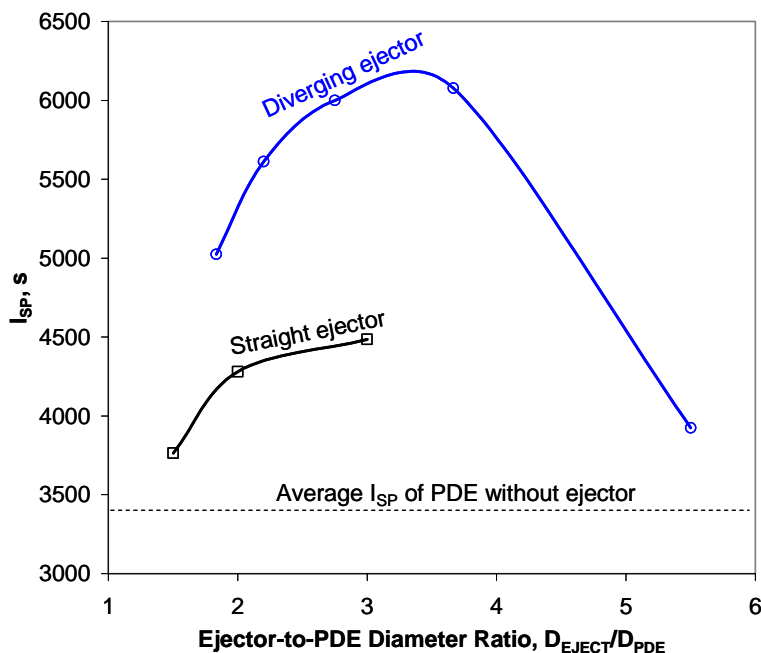


Figure 14. Effect of DR on PDE-ejector system I_{sp} . Results from both portions of the diameter ratio study are plotted.

The PDE specific impulse is increased from an approximate baseline $I_{sp}=3400$ s to $I_{sp}=6080$ s with an ejector installed.

IV. Conclusion

In this study the effects of detonation tube length and the ejector-to-PDE diameter ratio on ejector performance were investigated. It was shown that decreasing the tube length increases the level of thrust augmentation. This increase in augmentation was the result of a relatively constant change in thrust at all tube lengths caused by the ejector. This constant change in thrust divided by the decreasing baseline thrust yielded an increased augmentation percentage with decreasing tube length. The relatively constant change in thrust from the ejector at all tube lengths suggests that ejector performance is more heavily influenced by inviscid mechanisms than by viscous shear mixing. The effect of ejector-to-PDE diameter ratio was first investigated by varying the detonation tube diameter while holding the ejector size constant. In this manner the range of diameter ratios covered was $DR=1.83$ to $DR=5.5$. The optimum diameter ratio was found to lie between $DR=3$ and $DR=3.67$ and appeared to be approximately $DR=3.5$. However, to determine the optimum diameter ratio more accurately, more testing must be performed. The detonation tube diameter was then held constant, and the ejector diameter was varied. Although the thrust augmentation levels attained with these straight ejectors was much lower than those that can be achieved with diverging ejectors, the trend with diameter ratio remained the same. Increasing the diameter ratio from $DR=1.5$ to $DR=3$ increased the thrust augmentation. Use of a diverging PDE driven ejector with $DR=3.67$ was observed to increase the specific impulse of the PDE from the baseline no ejector value of $I_{sp}=3400$ s to $I_{sp}=6080$ s.

Acknowledgments

The authors would like to thank the Propulsion Directorate at the Air Force Research Laboratory and Innovative Scientific Solutions Inc. (ISSI) for providing financial support for this work. The technical support of Curtis Rice of ISSI is gratefully acknowledged. The support and technical guidance provided by General Electric Global Research is also greatly appreciated; specifically, thanks go to Adam Rasheed and Tony Dean for providing the straight ejector hardware used for portions of this testing.

References

- ¹Presz, W., Reynolds, G., Hunter, C., "Thrust Augmentation with Mixer/Ejector Systems", AIAA 2002-0230, 40th AIAA Aerospace Sciences Meeting and Exhibit, Reno, NV, January 14-17, 2002
- ²Wilson, J. and Paxson, D.E., "Unsteady Ejector Performance: An Experimental Investigation Using a Resonance Tube Driver", AIAA 2002-3632, 38th AIAA Joint Propulsion Conference, Indianapolis, IN, July 7-10, 2002
- ³Paxson, D.E., Wilson, J. and Dougherty, K.T., "Unsteady Ejector Performance: An Experimental Investigation Using a Pulsejet Driver", AIAA 2002-3915, 38th AIAA Joint Propulsion Conference, Indianapolis, IN, July 7-10, 2002.
- ⁴Lockwood, R., "Interim Summary Report on Investigation of the Process of Energy Transfer from an Intermittent Jet to Secondary Fluid in an Ejector-Type Thrust Augmenter", Hiller Aircraft Report No. ARD-286, March 1961.
- ⁵Rasheed, A., Tangirala, V., Pinard, P.F., Dean, A.J., "Experimental and Numerical Investigations of Ejectors for PDE Applications", AIAA 2003-4971, 39th AIAA Jet Propulsion Conference, Huntsville, AL, July 21-23, 2003.
- ⁶Allgood, D., Gutmark, E., "Performance Measurements of Pulse Detonation Engine Ejectors", AIAA 2005-0223, 43rd AIAA Aerospace Sciences Meeting and Exhibit, Reno, NV, January 10-13, 2005.
- ⁷Wilson, J., Sgondea, A., Paxson, D., Rosenthal, B., "Parametric Investigation of Thrust Augmentation by Ejectors on a Pulse Detonation Tube," 41st Joint AIAA/ASME/SAE/ASEE Propulsion Conference, Tucson, AZ, 2005, AIAA 2005-4208
- ⁸Glaser, A., Caldwell, N., Gutmark, E., Hoke, J., Bradley, R., and Schauer, F., "Performance Measurements of Straight and Diverging Ejectors Integrated with a Pulse Detonation Engine", AIAA 2006-1022, 44th AIAA Aerospace Sciences Meeting and Exhibit, Reno, NV, January, 2006.
- ⁹Schauer, F. Stutrud, J., and Bradley, R., "Detonation Initiation Studies and Performance results for Pulse Detonation Engine Applications," 39th AIAA Aerospace Sciences Meeting, AIAA 2001-1129
- ¹⁰Hoke, J., Personal Communication, Innovative Scientific Solutions Inc., Dayton, OH, June 14, 2006

¹¹Allgood, D., Gutmark, E., Hoke, J., Bradley, R., and Schauer, F., “Performance Measurements of Multi-Cycle Pulse-Detonation-Engine Exhaust Nozzles”, *Journal of Propulsion and Power*, 2006 0748-4658 vol.22 no.1 (70-779)

¹²Glaser, A., Allgood, D., Gutmark, E., “Experimental Investigation into the Off-Design Performance of a Pulse Detonation Engine,” AIAA 2004-1208, 42nd AIAA Aerospace Sciences Meeting and Exhibit, Reno, NV, January 5-8, 2004.

¹³Shehadeh, R., Saretto, S., Lee, S.-Y., Pal, S., Santoro, R.J., “Experimental Study of a Pulse Detonation Engine Driven Ejector”, AIAA Paper 2003-4972, 39th AIAA Jet Propulsion Conference, Huntsville, AL, July 21-23, 2003.

Effect of Supercritical Fuel Injection on the Cycle Performance of a Pulsed Detonation Engine

Timothy M. Helfrich* and Paul I. King†

Air Force Institute of Technology, Wright-Patterson AFB, OH, 45433

John L. Hoke‡

Innovative Scientific Solutions, Inc., Dayton, OH, 45440

and

Frederick R. Schauer§

Air Force Research Laboratory, Wright-Patterson AFB, OH, 45433

Pulsed detonation engines (PDEs) rely on rapid ignition and formation of detonation waves. Significant reduction in the time that elapses during the formation of detonation waves with low vapor pressure liquid hydrocarbons is still required to transition the PDE from experimentation to operational use. This study focuses on PDE operation enhancements using dual detonation tube, concentric-counter-flow heat exchangers to elevate the fuel temperature up to supercritical levels. Variation of several operating parameters included fuel type (JP-8, JP-7, JP-10, RP-1, JP-900, and S-8), spark delay, and firing frequency. To quantify the performance, four key parameters are examined: Ignition time, deflagration to detonation transition (DDT) time, detonation distance, and the percent of ignitions resulting in a detonation (detonation percentage). In general, for all fuels except JP-10, increasing the fuel injection temperature decreases DDT time by 15% and detonation distance by up to 30%, increases the detonation percentage by up to 180%, and has minimal impact on ignition time. JP-10 is difficult to detonate, resulting in poor performance. For all fuels an increase in firing frequency results in a 5% decrease in DDT time at high fuel injection temperatures, but has little effect on ignition time and detonation distance. Analysis of spark delay shows that 4 msec is the best spark delay at supercritical fuel injection temperatures, based on total time to detonation and detonation percentage.

Nomenclature

A	=	Arrhenius Constant
E_a	=	Activation Energy
E_{crit}	=	Critical Initiation Energy
$[fuel]$	=	Concentration of Fuel
$[oxidizer]$	=	Concentration of Oxidizer
P	=	Detonation Tube – Closed End Pressure
RR	=	Reaction Rate
R_u	=	Universal Gas Constant
T_{mix}	=	Fuel/Air Mixture Temperature
λ	=	Cell Size

* Graduate Student, Department of Aeronautics and Astronautics, 2950 Hobson Way, AIAA Member.

† Professor, Department of Aeronautics and Astronautics, 2950 Hobson Way, Senior AIAA Member.

‡ Research Engineer, 2766 Indian Ripple Road, Senior AIAA Member.

§ Senior Engineer, Head PDRF, AFRL/PRTC, 1950 5th Street, Senior AIAA Member.

I. Introduction

WHILE the pulsed detonation engine has the potential to provide significant advantages over current aircraft propulsion systems, it is still in the early stages of development. Several technological barriers need to be overcome before the PDE can be considered a practical means of providing propulsion to operational aircraft^{1,2}. A large hurdle is the efficient use of low vapor pressure hydrocarbon fuels, such as JP-8, JP-7, JP-10, JP-900^{**}, RP-1, and S-8^{††}. The vast majority of research into pulsed detonation engines has been performed with gaseous fuels, such as hydrogen and simple hydrocarbons³. The lack of liquid hydrocarbon fuel research has left a large gap between research and the operational use of pulsed detonation engines. While gaseous fuels are readily available for research, nearly all United States Air Force (USAF) aircraft and air-breathing missiles utilize liquid fuels, primarily JP-8 and JP-10. Therefore, the ability to utilize liquid hydrocarbon fuels efficiently in the PDE is necessary to bring pulsed detonation engine technology out of the research phase and into operation.

Four key cycle parameters are adversely affected by using liquid hydrocarbon fuels in lieu of gaseous fuels. The parameters are the time from spark deposition to the creation of a deflagration wave within the fuel/air mixture (ignition time), the time to transition the deflagration wave into a detonation wave (DDT time), the length of detonation tube required for the mixture to transition to a detonation (detonation distance), and the consistency of the detonations (detonation percentage)⁴. Both the ignition time and the DDT time are nearly an order of magnitude larger for complex liquid hydrocarbon fuels than for hydrogen. For example, ignition time for a hydrogen/air mixture is on the order of one millisecond, whereas the ignition time of a JP-8/air mixture is approximately seven milliseconds.

Until now, the cycle performance of a liquid hydrocarbon fueled PDE with fuel injection temperatures above the flash vaporization point was unknown. Previous research⁵ demonstrated that flash vaporization of liquid hydrocarbon fuels significantly decreased the ignition and DDT times, but no research has been conducted to determine the effect of operating with fuel injection temperatures beyond the point of flash vaporization. The focus of this research was to use a dual concentric counter-flow heat exchanger system to determine the effect of fuel injection temperature on the ignition time, DDT time, detonation distance, and detonation percentage with varying operating parameters. The operating parameters examined include; fuel type (JP-8, JP-7, JP-10, JP-900, RP-1, and S-8), spark delay and firing frequency.

II. Background and Theory

A. Global Reaction Theory

Global reaction theory assumes that the reaction of a fuel/oxidizer mixture can be modeled as a single global reaction. Low vapor pressure fuel/air mixture combustion is not governed by a single global reaction; however, global reaction theory can be used to predict ignition time trends. The ignition time is inversely related to the reaction rate, where the reaction rate is determined by the Arrhenius expression (Eq. 1)

$$IgnitionTime \propto \frac{1}{RR} = \frac{1}{A} P^{-n} [fuel]^{-m} [oxydizer]^{-j} e^{\left(\frac{E_a}{R_u T_{mix}}\right)} \quad (1)$$

where n, m, and j are experimentally determined constants⁶. Based on Eq. 1, the reaction rate of a fuel/oxidizer mixture will increase with increasing mixture temperature and pressure. The ignition time is inversely related to the reaction rate; hence, as the mixture temperature or pressure in the closed end of the detonation tube increases the ignition time will decrease. However, even with elevated fuel injection temperatures, only a small rise in the fuel/air mixture temperature occurred in this work; therefore, as shown later, there is no significant decrease in ignition time.

^{**} The fuel referred to as JP-900 in this paper is a coal-derived liquid hydrocarbon fuel developed at The Penn State University. It is denoted as JP-900 due to its thermal stability up to 900 °F.

^{††} S-8 is a synthetic fuel derived from natural gas via the Fischer-Tropsch process. S-8 is also referred to as Fischer-Tropsch JP-8 or simply Fischer-Tropsch.

B. Cell Size and Critical Initiation Energy

Previous experimental research⁷ has shown that a typical stoichiometric low vapor pressure liquid hydrocarbon/air mixture requires on the order of 10^5 J of energy to directly initiate detonation (critical initiation energy), six orders of magnitude greater than the energy available from a typical spark plug (~ 100 mJ). A mixture with a low critical initiation energy is more susceptible to DDT. Figure 1 is a plot of detonation cell size versus critical initiation energy for several stoichiometric fuel/oxidizer mixtures⁷. The detonation cell size is a physical characteristic of a detonation wave as it propagates. From a best-fit curve through the data, a simple relationship between the cell size and critical initiation energy is shown on Figure 1. The important item to notice is the critical initiation energy varies with the cube of the cell size, meaning that a decrease in cell size is an indication of an increase in detonability. Implications of this result are shown in part II-D.

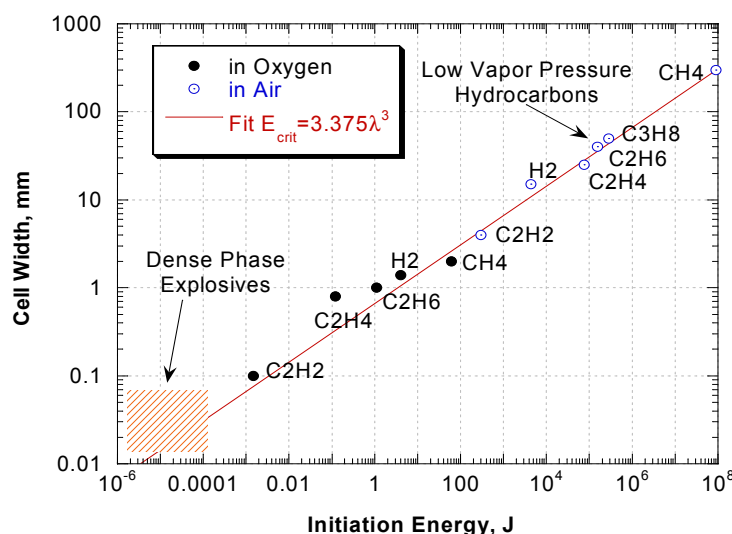


Figure 1. Experimentally determined relationships between cell size and critical initiation energy for various stoichiometric fuel/oxidizer mixtures (data taken from ref. 7).

C. Spark Delay and Initial Pressure

The pressure in the closed end of the PDE detonation tube fluctuates due to the presence of compression and expansion waves in the detonation tube. These waves are created as the fill and purge valves open and close, forcing air into the detonation tubes. By selection of a spark delay, it is possible to deposit the spark during a compression wave, when the detonation tube-closed end pressure is above ambient. Figure 2 is the pressure time history during the PDE fire phase without combustion at 15 Hz with a mixture temperature of 394 K. Spark delays of 2, 4, 6, 8, and 10 msec are denoted as vertical lines in Fig. 2.

Figure 2 demonstrates the benefit of selecting a high spark delay. Selection of a 6, 8, or 10 msec spark delay allows combustion to occur during a compression wave, while a 0 msec spark delay forces combustion to initiate during an expansion wave. The higher initial pressure of the 10 msec spark delay suggests that a high spark delay should be used, but the ignition time is not only affected by the initial pressure in the closed end of the detonation tube. The ignition time is also affected by the entire pressure history during the formation of a deflagration wave. As will be shown later, the initial pressure had a minimal effect on the ignition time, but did affect the DDT time. It will also be shown that the DDT time decreases with increased spark delay, but the overall time to detonation is a minimum at 4 msec; therefore, a spark delay of 4 msec was selected for all tests unless otherwise noted.

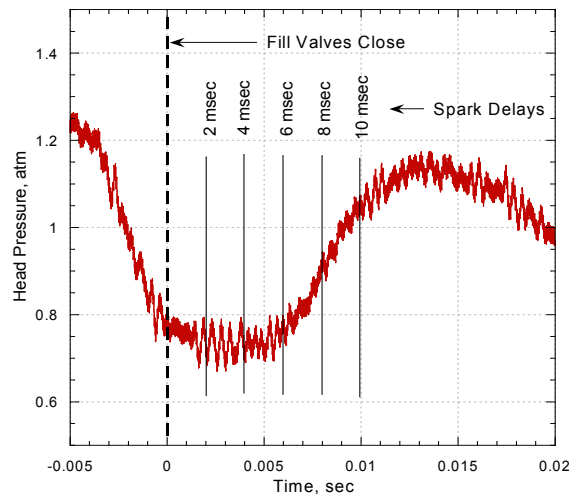


Figure 2. Pressure in the closed end of the detonation tube during fire phase without combustion (vertical lines denote various spark delays).

D. Effect of Initial Pressure and Temperature on Detonability

Little research has been performed to determine the relationship between initial mixture properties (temperature and pressure) and the detonability of a low vapor pressure fuel/air mixture. Literature is available for hydrocarbon/oxidizer mixtures that are lighter than those used in the current experiment⁷. The cell size of three light hydrocarbons as a function of initial mixture temperature is shown in Fig. 3(a). Figure 3(b) is a plot of cell size vs. initial pressure for three light hydrocarbon/oxidizer mixtures and one H_2/O_2 mixture.

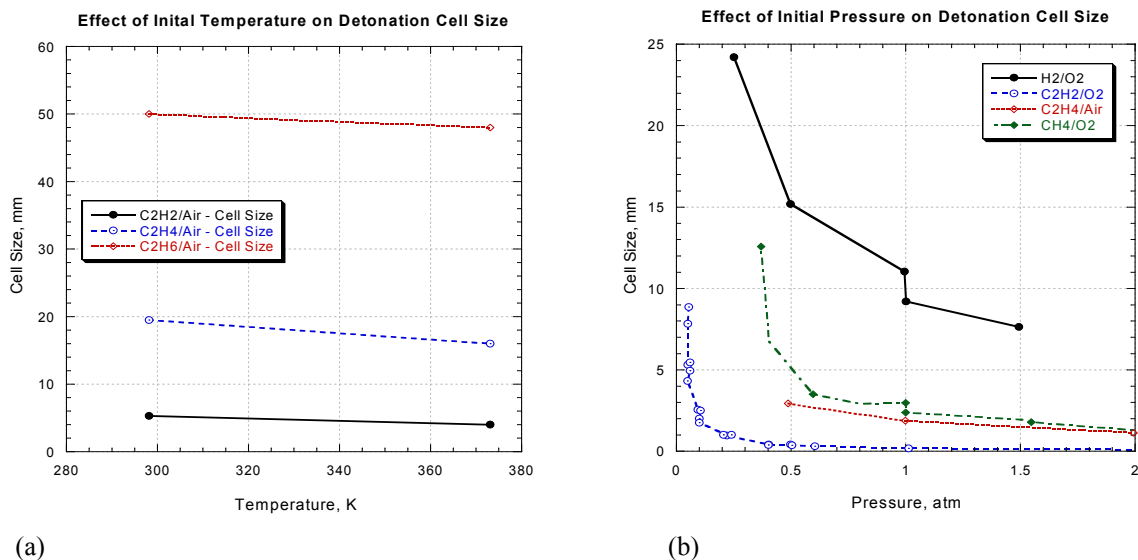


Figure 3. Effect of initial temperature (a) and initial pressure (b) on detonation cell size (data taken from ref. 7).

The trend of the light hydrocarbons is for the cell size to decrease with increased mixture temperature and pressure. The three hydrocarbons examined in Fig. 3(a) are all very light (with two carbon atoms apiece) compared to low vapor pressure liquid hydrocarbons. While the trends of lighter hydrocarbons do not dictate the trends of much heavier hydrocarbon, they do suggest that increasing initial mixture temperature and/or detonation tube-closed end pressure will decrease the cell size. According to the curve fit equation inset in Fig. 1, the critical initiation energy decreases by the cube of the cell size. As mentioned earlier, while the critical initiation energy decreases, the detonability of the mixture increases. As will be shown later, increases in both pressure at the closed end of the detonation tube and mixture temperature will result in decreased DDT time and detonation distance, as well as increased detonation percentage.

III. Experimental Setup and Instrumentation

A. Facilities and PDE Specifics

This research was conducted at the Pulsed Detonation Research Facility (PDRF) located in Building 71A, D Bay, Wright-Patterson AFB, Ohio (D-Bay). This facility was described in detail in other literature³, and only the details relevant to this effort are provided. The PDE for this research consisted of a GM quad four head with two 1.83 meter long schedule 40 stainless steel detonation tubes (50.8 mm diameter), each with a 0.91 meter long Schelkin-like spiral, with one end adjacent to the closed end of the detonation tube, to promote DDT⁸. The PDE was set up with two detonation tubes, each with a stainless steel heat exchanger (described later).

The PDE cycle consisted of three equally timed phases. The three phases, in order, are the fill, fire, and purge phases. During the fill phase the intake valves were opened filling the PDE detonation tube with a volume of premixed fuel and air equal to the volume of the detonation tube (fill fraction of one). For all tests the fill air was initially heated to 394 K prior to mixing with the fuel. For the fire phase an automotive ignition system provided spark pulses through modified spark plugs providing ignition energies of 115 mJ apiece. The spark delay after the intake valves closed was 4 msec, unless otherwise noted. The fire phase consists of time for the spark delay, ignition, DDT, and blowdown; the later three of which last approximately 11 msec for the configuration tested. The presence of a detonation wave was confirmed using ion probes to gather wave speed data. Combustion waves propagating at speeds within ten percent of the upper Chapman-Jouguet point (assumed to be 1800 m/s) were considered detonation waves. During the purge phase the exhaust valves were opened filling the detonation tube with a volume of air (unheated) equal to half the volume of the detonation tube (purge fraction of 0.5). The purge air cooled the detonation tube and removed a portion of the exhaust gases from the detonation tube preventing auto-ignition. Depending on the firing frequency, the time to complete the required phase events may not equal the time allotted for the phase. The PDE firing frequency was parametrically varied throughout the test, but remained between 10 and 20 Hz.

B. Supercritical Fuel Heating System

The liquid fuel required for this testing was supplied by two hydraulic bladder accumulators, pressurized by nitrogen bottles. The nitrogen bottles pressurized the fuel above the critical pressure for the duration of the test to prevent boiling. The fuel was pressure fed to the inlet of the supercritical fuel heating system (SFHS). The SFHS consisted of a nitrogen purge system (described later), two stainless steel heat exchangers, fuel filter assembly, fuel injection nozzles, instrumentation, and associated tubing and fittings necessary to connect the critical components [Ref. 2 has details on fuel injection nozzles]. The flow path and instrumentation are shown in schematic and photograph form in Fig. 4(a) and Fig. 4(b), respectively. The fuel entered the test stand through a ball valve where the flow was split into two fuel lines. One fuel line led to the inlet of the heat exchanger on tube four, while the other fuel line led to the inlet of the heat exchanger on tube one. After the two fuel paths exited their respective heat exchanger, they were teed back together. The fuel was then led through the filter to the fill air manifold, where it was injected into the air stream via the fuel injection nozzles. The fuel filter was necessary to remove the small amounts of coking that was formed due to endothermic cracking of the fuel⁹. The fuel lines that carried heated fuel (fuel that has traversed through a heat exchanger) were insulated with fiberglass insulation to prevent heat loss.

Fuel mass flow rate of the nozzles is proportional to the square root of the pressure drop across the fuel nozzles and fuel density^{10,11}. To compensate for the decrease in fuel density during heating of the fuel in the supercritical regime, the charge pressure of the accumulators was increased to maintain a constant fuel mass flow rate. To allow for variations in accumulator charge pressure during testing, a pneumatic dome loader was installed for nitrogen pressure regulation [For details, see Ref. 4].

To minimize carbon deposition in the SFHS, the JP-8 was de-oxygenated through a nitrogen sparging process. The sparging process involved bubbling a volume of nitrogen through the JP-8 which displaced the oxygen from the fuel. JP-8 was de-oxygenated prior to testing. The volume of nitrogen necessary to reduce the oxygen concentration to acceptable levels was determined experimentally in previous work^{2,12}, and to ensure acceptable levels a factor of safety of two was applied to all nitrogen volume calculations.

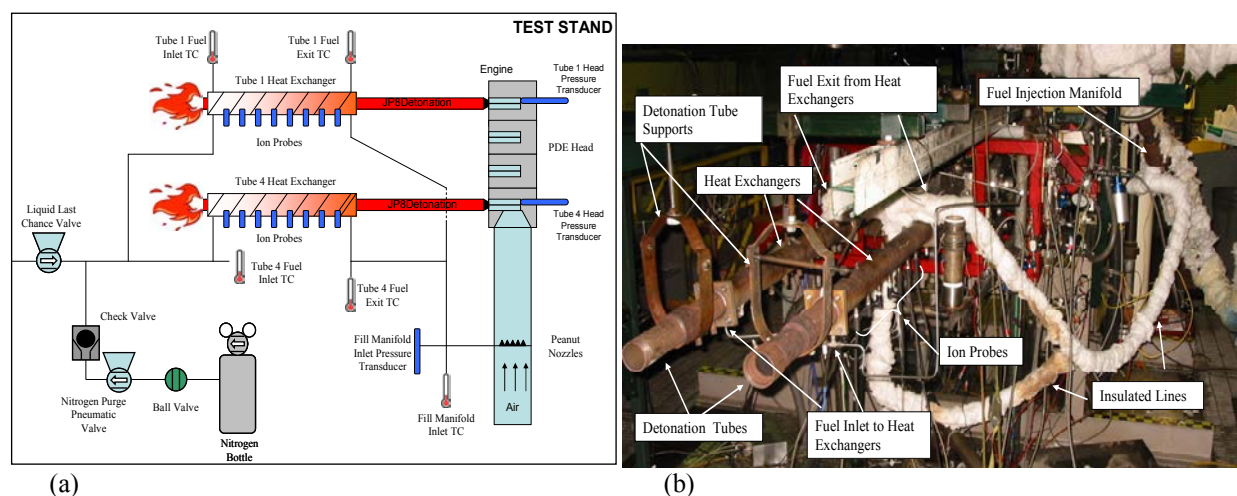


Figure 4. (a) Diagram and (b) photograph of the PDE with the supercritical fuel heating system and instrumentation.

C. Heat Exchangers

Two identical concentric tube heat exchangers were fabricated for this work. A 0.91 meter heat exchanger was fabricated with 50.8 mm dia, type 316 stainless steel, schedule 40 inner tube and 63.5 mm dia, type 316 stainless steel, schedule 40 outer tube allowing for a 1.22 mm annular thickness. A photograph of one heat exchanger with the associated instrumentation ports is shown in Figure 5.

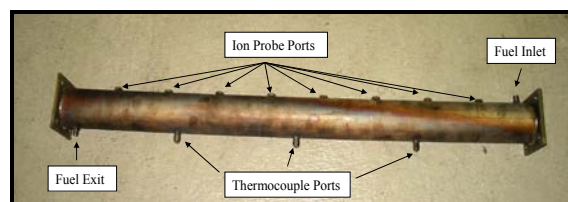


Figure 5. Photograph of one heat exchanger.

D. Nitrogen Purge System

A nitrogen purge system was designed to prevent supercritical fuel from remaining in the heat exchangers at the end of a test¹³. The nitrogen purge system consists of a high-pressure nitrogen bottle, manual pressure regulator, pneumatic valve, check valve, and ball valve (see Fig. 4). Before each test, the ball valve was opened to allow for operation of the nitrogen purge system. The manual pressure regulator was set above the critical pressure of the fuel. The pneumatic valve was placed in the nitrogen purge line to commence and terminate the nitrogen flow. Once a test ended, the pneumatic valve was opened remotely allowing the nitrogen to purge the heat exchangers of supercritical fuel. A check valve was located directly after the pneumatic valve to prevent fuel from entering the nitrogen line.

E. Instrumentation

Thermocouples were placed in the center of the flow path to gather temperature data at the inlet and outlet of each heat exchanger (J-type), and at the inlet to the fill air manifold (T-type). External heat exchanger wall temperatures were measured with J-type thermocouples mounted externally by compression clamps to the PDE detonation tube. A pressure transducer was situated at the closed end of the detonation tubes to measure the pressure used to determine the ignition time. Ion probes were placed in the ion probe ports (see Fig. 5) in both the tube one and four heat exchangers to gather wave speed data [c.f., Ref. 14].

F. Uncertainty Analysis

The total experimental uncertainty is determined by combining the bias and precision uncertainties using the root sum square method¹⁵. The bias uncertainties are constant for all data points of the same variable, while the precision uncertainties vary by data point. Therefore, the total experimental uncertainty varies by data point, and is included with the data. A comprehensive bias uncertainty analysis was performed, and the results are displayed in Table 1⁴.

Table 1. Summary of bias uncertainties for experimental results.

Experimental Result	Bias Uncertainty
Wavespeed	± 55.12 m/s
Ignition Time	± 0.292 msec
DDT Time	± 0.0568 msec
Detonation Distance	± 0.0568 m
Fuel Injection Temperature	± 3.6 K
Fuel/Air Mixture Temperature	± 2.5 K
Equivalence Ratio	± 0.0147

IV. Results and Discussion

The analysis of various operating parameters for increasing fuel injection temperature is presented. The results include ignition time, deflagration to detonation transition time, detonation distance, and detonation percentage, with all parameters plotted versus fuel injection temperature. Each data point represents the mean value of 40 to 60 ignitions, using data from two tubes. The total experimental uncertainty is presented whenever possible. The effect of fuel injection temperature on the performance of the PDE is shown with variation of the following operating parameters: Fuel selection, spark delay, and firing frequency. All testing was performed with an equivalence ratio of 1.1, which has been shown to produce the minimum ignition and DDT times for JP-8 in previous research².

A. Fuel Study

Figure 6(a) is a plot of ignition time as a function fuel injection temperature for all six fuels. Little differentiation among the fuels exists, though in Fig. 6(a) JP-8 has a slightly higher ignition time in the range of 586 to 755 K. The probable cause of this trend was adverse effects of thermal degradation (coking) of the JP-8. In addition, S-8 produced the lowest ignitions for almost the entire temperature range. JP-7, JP-900, and RP-1 demonstrate almost no difference in trend or magnitude, which was expected due the similarity of the fuels. With the exception of JP-8, ignition times for all fuels are independent of fuel injection temperature in the temperature range examined, as expected based on the earlier discussion of global reaction theory.

It was found that detonation of a JP-10/air mixture was very difficult with the current setup. Due to the lack of detonations, the DDT time and detonation distance data for JP-10 were scattered, rendering the results unusable; therefore, the DDT time and detonation distance results for JP-10 have been omitted. The DDT times for the other five fuels are displayed in Fig. 6(b) as a function of fuel injection temperature.

In Fig. 6(b), little variation was seen among the fuels with regards to the DDT time. The difference between any two fuels is within the experimental error for the entire temperature range. DDT times for all five fuels decrease with increasing fuel injection temperature, as expected due to the reduction in cell size associated with increased temperature. A nearly linear trend is shown for each fuel with approximately a 15% decrease in DDT time over the temperature range.

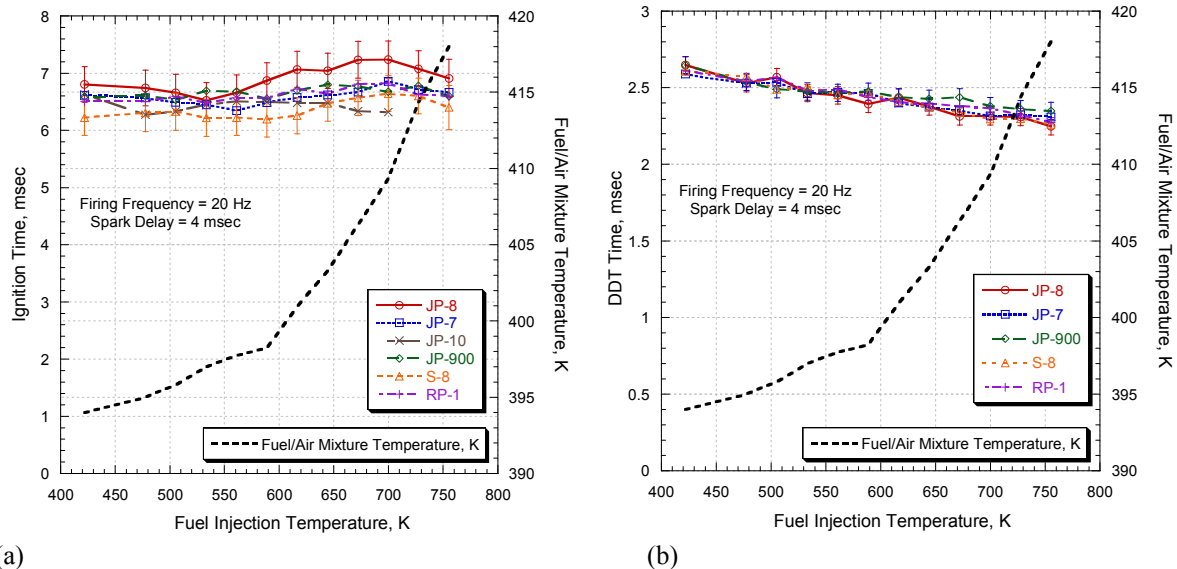


Figure 6. (a) Comparison of the ignition time as a function of fuel injection and (b) comparison of the DDT time as a function of fuel injection temperature for several fuels.

The next parameter analyzed was the detonation distance. The variation of detonation distance with fuel injection temperature for all fuels other than JP-10 is shown in Fig. 7(a). As expected, the detonation distance of all five fuels decreases with increasing fuel injection temperature. In Fig. 7(a), below approximately 650 K the detonation distance of the five fuels differs in both magnitude and slope, but above approximately 650 K the fuels produce roughly equal detonation distances. Below approximately 650 K, JP-8 has the smallest detonation distances, followed closely by JP-900, while JP-7 performs the poorest with a maximum value of 1.14 m. RP-1 and S-8 perform very similarly, both with detonation distance between JP-7 and JP-900. It was also noted that above roughly 675 K, detonations occur near the downstream end of the spiral for all five fuels shown.

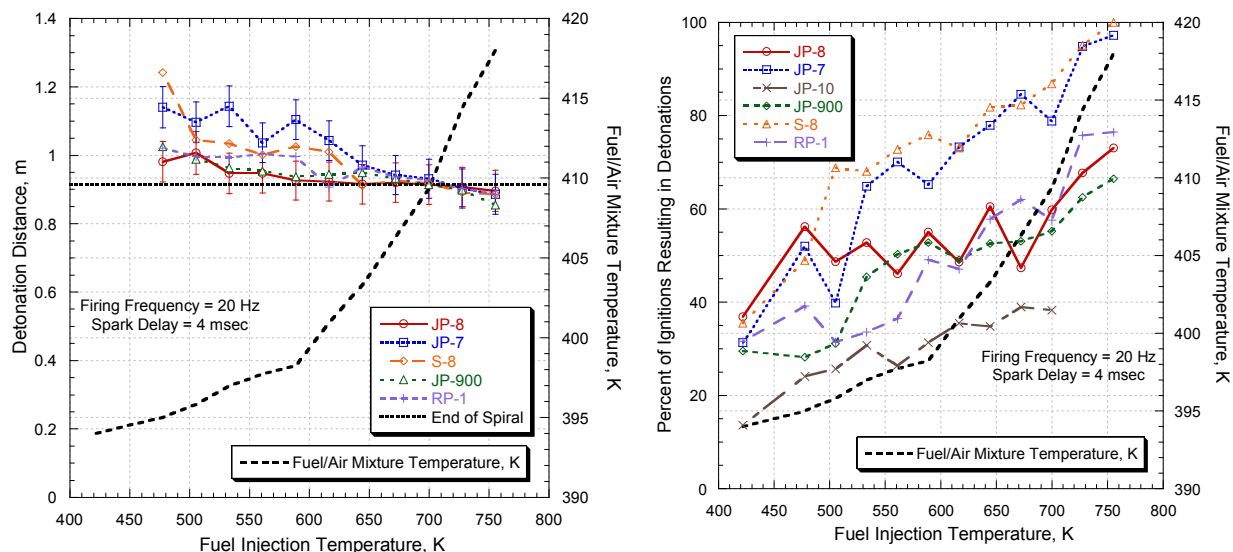


Figure 7. (a) Comparison of the detonation distance for five fuels as a function of fuel injection and (b) comparison of the detonation percentage for six fuels as a function of fuel injection.

The detonation percentage is shown in Fig. 7(b) as a function of fuel injection temperature. The detonation percentage is the percentage of ignitions that result in a combustion wavespeed of 1800 m/s or greater. In Fig. 7(b), all fuels demonstrate a strong trend of increasing detonation percentage for an increase in fuel injection temperature. JP-7 and S-8 stand out as the fuels that produce the largest percentage of detonations. The fuels can be lumped into three categories, based on Fig. 7(b). The first group, JP-7 and S-8, demonstrate the largest increases in detonations as fuel injection temperature increases. Both JP-7 and S-8 provide nearly 100% detonations at 755 K. JP-8, JP-900, and RP-1 make up the second category, producing detonation percentages between 65% and 75% at a fuel injection temperature of 755 K. The final category includes only JP-10. While JP-10 demonstrates an increase in detonation percentage as fuel injection temperature is increased, the magnitude of the detonation percentage remains low. The detonation percentage of JP-10 increases from 14% to 38%, leading to the large uncertainty in DDT time and detonation distance.

Table 2 is a summary of the important values determined during the fuels study. While these values are taken from Fig. 6 and Fig. 7, the table was added for quick reference. Since the ignition time was shown to be nearly constant for all fuel other than JP-8, an average value is presented in Table 2. DDT time, detonation distance, and detonation percentage all demonstrated nearly linear relationships with fuel injection temperature; therefore, the maximum and minimum values are presented in Table 2.

Table 2. Summary of important performance parameter values determined during fuels study.

Fuel	Average Ignition Time [msec]	DDT Time [msec]	Detonation Distance [m]	Detonation Percentage
JP-8	6.90	2.25 - 2.65	0.90 - 1.00	36.9 - 73.1
JP-7	6.59	2.31 - 2.59	0.89 - 1.14	31.3 - 97.2
JP-10	6.43	N/A	N/A	13.6 - 38.3
JP-900	6.63	2.35 - 2.65	0.85 - 1.03	29.5 - 66.5
RP-1	6.62	2.27 - 2.61	0.89 - 1.02	31.6 - 76.5
S-8	6.37	2.26 - 2.61	0.89 - 1.02	35.5 - 100.0

B. Spark Delay

All spark delay testing was performed with JP-8. As mentioned earlier, the sum of the ignition time, DDT time, and blowdown time is approximately 11 msec. In order to perform tests with spark delays up to 10 msec, a fire phase of at least 21 msec was required. Therefore, a firing frequency of 15 Hz, which provides a fire phase time of 22.22 msec, was used for all spark delay testing. Spark delays of 2, 4, 6, 8 and 10 msec were examined. The zero msec spark delay case resulted in auto-ignition in the detonation tube that propagated back into the fill manifold; therefore, no data was taken.

Figure 8 is a plot of the ignition time as a function of fuel injection temperature for a JP-8/air mixture with spark delays ranging from 2 to 10 msec. With the exception of the 2 msec spark delay case, there is no significant stratification among the spark delays. The 2 msec spark delay results demonstrate significantly higher ignition times for all temperatures as compared to the other spark delays. The 4 msec case produces slightly higher ignition times at low temperatures, but lower ignition times at higher temperature. The spark delays between 6 and 10 msec do not show significant stratification among each other. It should be noted that the difference between the 4 msec case and the higher spark delay cases was within the experimental error at temperatures below 589 K.

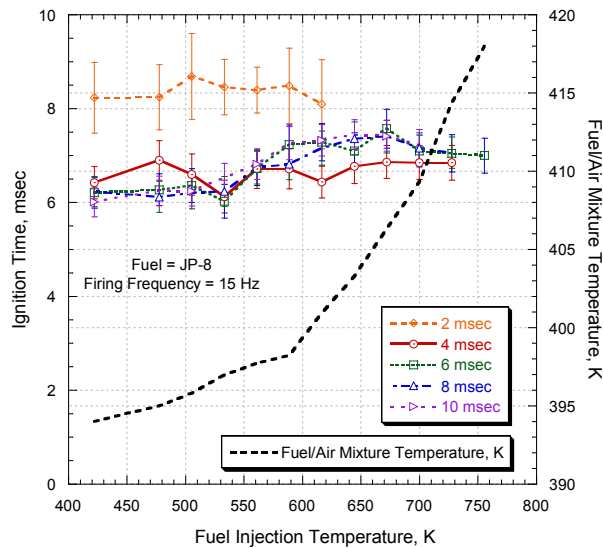
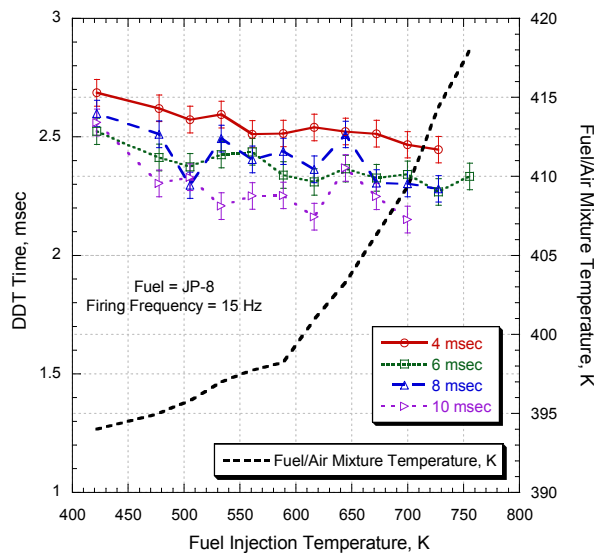
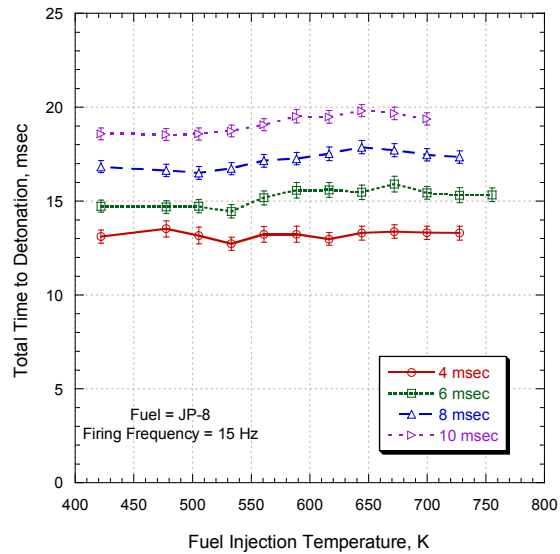


Figure 8. Ignition for varying spark delays as a function of fuel injection temperature for a JP-8/air mixture–firing frequency = 15 Hz.

Figure 9(a) shows the DDT time for a JP-8/air mixture as a function of fuel injection temperature for various spark delays. The 2 msec spark delay trials resulted in sporadic detonations, leading to extremely poor confidence in results, and thus are not presented. All other spark delays demonstrate the same trend - increasing fuel injection temperature leads to decreasing DDT time. It is also apparent that increasing the spark delay (which increases the initial pressure in the closed end of the detonation tube) reduced the DDT time, as expected based on the light hydrocarbon/air detonation data in Fig. 3(b).



(a)



(b)

Figure 9. (a) DDT time for a JP-8/air mixture as a function of fuel injection temperature for varying spark delays and (b) total time to detonation for a JP-8/air mixture as a function of fuel injection temperature for various spark delays – firing frequency = 15 Hz.

To compare the overall effect of varying spark delays in a PDE, the total time to detonation is plotted as a function of fuel injection temperature for various spark delays in Figure 9(b). The total time to detonation is the sum

of the spark delay, ignition time, and DDT time. The reduction in ignition time and DDT time as spark delay is increased is outweighed by the increase in spark delay. Therefore, a spark delay of 4 msec produces the lowest total time to detonation, and a spark delay of 10 msec produces the highest total time to detonation.

Figure 10(a) is a plot of the detonation distance of a JP-8/air mixture as a function of fuel injection temperature for various spark delays. No significant difference was noticed among the four spark delays. All detonations occurred near the downstream end of the spiral

Figure 10(b) is a plot of the detonation percentage of a JP-8/air mixture as a function of fuel injection temperature for various spark delays. The detonation percentage is significantly influenced by the spark delay. The detonation percentage increases steadily as the spark delay decreases. The 10 msec spark delay produces detonation percentages ranging from 13.3 to 37.7%, while the detonation percentage for the 4 msec spark delay case increases from 33.3 to 95.0%. In fact, the detonation percentage for the 4 msec spark delay is near 90% for all fuel injection temperatures above 505 K.

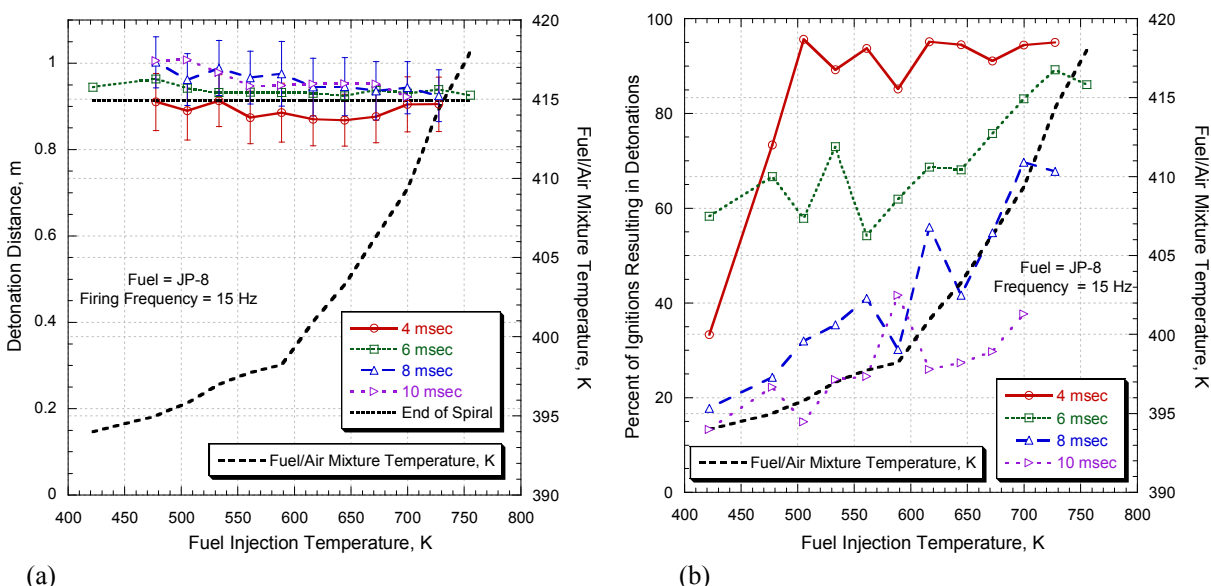


Figure 10. (a) Detonation distance for a JP-8/air mixture as a function of fuel injection temperature for varying spark delays and (b) detonation percentage as a function of fuel injection temperature for various spark delays using a JP-8/air mixture – firing frequency = 15 Hz.

C. Firing Frequency

The motivation to decrease ignition time and DDT time is to decrease the fire phase time, thus decreasing the PDE cycle time. If the cycle time is decreased, the PDE firing frequency can be increased, thereby increasing thrust. This rationale hinges on the assumption that increasing the firing frequency will not produce any adverse effects on PDE cycle time. To examine the effect of the firing frequency on PDE performance parameters, a study was conducted with two frequencies, 15 and 20 Hz. Frequencies above 20 Hz are not possible at this time due to limitations of the duration of the fire phase. For example, a system operating at 25 Hz allows only 13.3 msec to be spent on the fire phase; this time limit is too short for 15 msec required for the detonation of a JP-8/air mixture. The 10 Hz firing frequency did not provide enough energy to the heat transfer system to afford fuel injections temperatures above 644 K.

Figure 11(a) is a plot of ignition time and DDT time as a function of fuel injection temperature for a PDE operating at 15 Hz and 20 Hz. The frequencies show nearly identical ignition times for the entire temperature range. The difference between the results using the two frequencies is within the experimental error. The DDT time for the 20 Hz case is slightly less than the that for the 15 Hz case for the entire temperature range. The decrease in DDT time is a result of higher pressures within the detonation tube that occur at higher frequencies. The total time to detonation (sum of spark delay, ignition time and DDT time) for the 20 Hz case is slightly less than for the 15 Hz case.

Figure 11(b) is a plot of the detonation distance as a function of fuel injection temperature with varying firing frequency. The difference between the detonation distance results of the 15 and 20 Hz tests are within the measurement uncertainty for the entire temperature range. In addition, both frequencies result in detonations at the downstream end of the internal spiral. Again, no degradation in performance is noticed when operating at 20 Hz as compared to at 15 Hz. Therefore, in summary, increasing the firing frequency was found to have little effect on cycle performance.

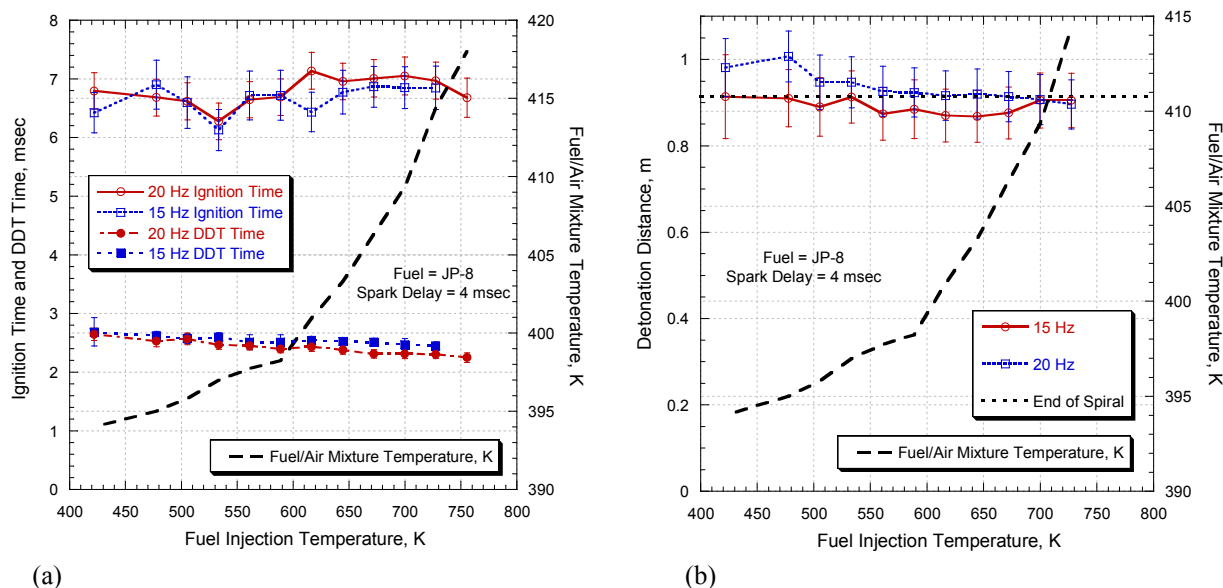


Figure 11. (a) Comparison of ignition time and DDT time for two frequencies as a function of fuel injection temperature for a JP-8/air mixture and (b) comparison of detonation distance for two frequencies as a function of fuel injection temperature for a JP-8/air mixture – spark delay = 4 msec.

V. Conclusions

This research marked the first analysis of the effect increasing fuel injection temperature, up to 755 K, had on key pulsed detonation engine performance parameters, including ignition time, DDT time, detonation distance, and detonation percentage. This effort has also provided an understanding of how the pressure-temperature profile affects the initial combustion event of the cycle.

The effects of increasing fuel injection temperature on ignition time, DDT time, detonation distance, and detonation percentage for JP-8, JP-7, JP-10, JP-900, RP-1, and S-8 were determined. Ignition time was found to be virtually independent of fuel injection temperature for all fuels, except JP-8. JP-10 was found to produce undesirably low levels of detonations, compared to the other fuels. The DDT time of the other five fuels demonstrated a nearly identical decrease with increasing fuel injection temperature; DDT time decreased linearly by approximately 15% for the temperature range tested. The detonation distance for all fuels, other than JP-10, linearly decreased with increasing fuel injection temperature. Above approximately 650 K, the detonation distance for all fuels other than JP-10 is roughly equal. The detonation percentage for all fuels increased considerably with increasing fuel injection temperature, with JP-7 and S-8 producing the most consistent detonations. Based on this performance criteria; JP-8, JP-7, JP-900, RP-1, and S-8 can all be used to fuel a PDE with elevated fuel injection temperatures and a 36" internal spiral.

The spark delay was found to have a small effect on all performance parameters other than detonation percentage for JP-8, although it was determined that operating the PDE with a spark delay below 4 msec yields very poor performance with the current experimental setup. A spark delay of 4 msec was found to be superior to the other spark delays studied for JP-8, based on total time to detonation and detonation percentage. Increasing firing frequency from 15 Hz to 20 Hz was found to have a slightly positive effect on the total time to detonation for a PDE. DDT time decreases as firing frequency increases due to the higher pressure in the detonation tube, while ignition time and detonation distance are relatively independent of firing frequency.

Acknowledgments

This work would not have been possible without the technicians who worked on this project; our thanks to Curtis Rice, Dave Baker, and Dwight Fox (ISSI). Dr. Tim Edwards (AFRL/PRTG) was extremely helpful in developing the fuel systems for this work. The authors would also like to thank Jeff Stutrud (AFRL/PRTC) for his controls and data acquisition expertise and Capt. Wesley for his help. The technical leadership of Dr. Robert Hancock (AFRL/PRTC) was invaluable. Funding was provided by the Air Force Research Laboratory, Propulsion Directorate and AFOSR.

References

- ¹Miser, C. L., King, P. I., and Schauer, F. R., "PDE Flash Vaporization System for Hydrocarbon Fuel Using Thrust Tube Waste Heat," AIAA 2005-3511, *41st AIAA/ASME/SAE/ASEE Joint Propulsion Conference and Exhibit*, Tucson AZ: 10-13 July 2005.
- ²Tucker, K. C., "A Flash Vaporization System for Detonation of Hydrocarbon Fuels in a Pulse Detonation Engine," Ph.D. Dissertation, Department of Aeronautics and Astronautics, Air Force Institute of Technology, Wright-Patterson AFB, OH, 2005.
- ³Schauer, F. R., Stutrud, J. S., and Bradley, R. P., "Detonation Initiation Studies and Performance Results for Pulse Detonation Engine Applications," AIAA 2001-129, *39th AIAA Aerospace Sciences Meeting and Exhibit*. Reno NV: 8 - 11 January 2001.
- ⁴Helfrich, T. M., "Cycle Performance of a Pulse Detonation Engine with Supercritical Fuel Injection," M.S. Thesis, Department of Aeronautics and Astronautics, Air Force Institute of Technology, Wright-Patterson AFB, OH, 2006.
- ⁵Tucker, K. C., King, P. I., Bradley, R. P., and Schauer, F. R., "The Use of a Flash Vaporization System with Liquid Hydrocarbon Fuels in a Pulse Detonation Engine," AIAA 2004-0868, *42nd AIAA Aerospace Sciences Meeting and Exhibit*. Reno NV: 5 - 8 January 2004.
- ⁶Lefebvre, A., Freeman, W., and Cowell, L., "Spontaneous Ignition Delay Characteristics of Hydrocarbon Fuel/Air Mixtures," NASA CR-175064, 1986.
- ⁷Kaneshige, M. and Shepherd, J. E., *Detonation Database*. Technical Report FM97-8, GALCIT, July 1997.
- ⁸Schelkin, K.L., "Soviet Journal of Technical Physics," Vol. 10, pg. 823-827, 1940.
- ⁹Spadaccini, L. J., Sobel, D. R., Haung, H., Dardas, Z., "Coke Deposition/Mitigation in Endothermic Fuels – Advanced Fuel Development and Fuel Combustion," AFRL-PR-WP-TR-1998-2098, June 1998.
- ¹⁰Bartok, W. and Sarofim, A. F., *Fossil Fuel Combustion – A Source Book*. New York City NY: John Wiley and Sons Incorporated, 1991.
- ¹¹Miser, C. L., Helfrich, T. M., Schauer, F. R., and Phelps D. K., "Supercritical Fuel Density from Experimental Pulse Detonation Engine," AIAA 2006-1025, *44th AIAA Aerospace Sciences Meeting*. Reno NV: 9-12 January 2006.
- ¹²Panzenhagen, K. L., "Detonation Branching in a PDE with Liquid Hydrocarbon Fuel." M.S. Thesis, Department of Aeronautics and Astronautics, Air Force Institute of Technology, Wright-Patterson AFB OH, 2004.
- ¹³Miser, C. L., "Pulse Detonation Engine Thrust Tube Heat Exchanger for Flash Vaporization and Supercritical Heating of JP-8," M.S. Thesis, Department of Aeronautics and Astronautics, Air Force Institute of Technology, Wright-Patterson AFB OH, 2005.
- ¹⁴Tucker, K.C., King, P.I. and Schauer, F.R., "Detonation Wave Speed Measurement with Ion Sensors," *28th Annual Dayton-Cincinnati Aerospace Sciences Symposium*, Dayton OH: 4 March 2003.
- ¹⁵Coleman, Hugh W. and Steele, W. Glenn, Jr., *Experimentation and Uncertainty Analysis for Engineers*. New York NY: John Wiley and Sons Incorporated, 1989.

Experimental Study of Ejectors Driven by a Pulse Detonation Engine

Aaron J. Glaser¹, Nicholas Caldwell², and Ephraim Gutmark³
University of Cincinnati, Cincinnati, OH, 45221-0070

John Hoke⁴ and Royce Bradley⁵
Innovative Scientific Solutions Inc., Dayton, OH, 45440

and

Fred Schauer⁶
Air Force Research Laboratory, WPAFB, Dayton, OH, 45433

Experimental studies were performed in order to better understand the operation of ejector augmenters driven by a pulse detonation engine (PDE). This research employed a H₂-air PDE at 30 Hz operating frequency. Static pressure was measured along the interior surface of the ejector including the inlet and exhaust sections. Thrust augmentation provided by the ejector was calculated by integration of the static pressure measured along the ejector geometry. The calculated thrust augmentation was in good agreement with the augmentation found from direct thrust measurements. Both straight and diverging ejectors were investigated. It can be seen from the diverging ejector pressure distribution that the role of the diverging section is to act as a subsonic diffuser. Ejector axial position was also studied. The ejector pressure data follows the same trend as that of the direct thrust measurements. The optimum axial placement was found to be downstream of the PDE near $x/D_{PDE}=+2$, while upstream placements tended towards a decreasing thrust augmentation. In order to better explain the observed performance trends, shadowgraph images of the detonation wave and trailing vortex interacting with the ejector inlet were obtained.

Nomenclature

D_{PDE}	=	detonation tube diameter
D_{EJECT}	=	ejector diameter
DR	=	ejector-to-PDE diameter ratio
ff	=	fill-fraction
L_{EJECT}	=	ejector length
L_{STRT}	=	intermediate straight section length
L_{EXHST}	=	exhaust section length
x	=	ejector axial position

I. Introduction

FOR practical PDE applications, one of the key challenges facing researchers is to make use of the increased efficiency of energy conversion due to detonative mode combustion, and most effectively convert that into a propulsive thrust force. A common measure of propulsion system performance is specific impulse (I_{sp}), which is

¹ Graduate Research Assistant, Department of Aerospace Engineering, ML0070, Student Member AIAA.

² Graduate Research Assistant, Department of Aerospace Engineering, ML0070, Student Member AIAA.

³ Professor and Ohio Eminent Scholar, Department of Aerospace Engineering, ML0070, Associate Fellow AIAA.

⁴ Research Engineer, 2766 Indian Ripple Road, Senior Member AIAA.

⁵ Senior Scientist, 2766 Indian Ripple Road.

⁶ Senior Engineer, Head PDRF, AFRL/PRTC, Bldg. 490, Senior Member AIAA.

defined as the ratio of thrust generated to the weight flow rate of fuel. Greater values of I_{sp} are desirable as this will decrease the specific fuel consumption. It has been suggested that the use of ejector augmenters on PDEs may be an effective way to increase the system thrust being generated, thus leading to an increased I_{sp} .

An ejector is a simple device used to augment the thrust of an engine. Essentially, an ejector consists of a coaxial duct placed around the exhaust of an engine performing as a fluidic pump. The surrounding ambient air is entrained by the primary exhaust flow and directed into the ejector. The entrained air causes an increase in momentum of the engine exhaust flow. This leads to the generation of a larger system thrust force. The theory and application of ejectors to a steady primary flow is well established. For steady-flow ejectors, the secondary flow is entrained primarily through viscous shear mixing¹. Previous research has shown that unsteady ejectors are capable of producing more thrust augmentation than comparable steady-flow ejectors^{2,3,4}. The increased performance of unsteady ejectors has been attributed to a more efficient energy transfer process between the primary and secondary flows due to dominant effects of the starting vortex. PDEs are highly unsteady devices generating a shock wave and vortex ring, thus it has been proposed that PDE driven ejectors have the potential to be highly effective at providing thrust augmentation.

Previous experimental work has shown PDE driven ejectors to be very effective in producing thrust augmentation. These past studies have quantified the effects of PDE operating parameters as well as ejector geometric parameters. The internal surface geometry of the ejector is an important geometric parameter. A study by Glaser et al⁵ was carried out using several ejector configurations. Results of those experiments showed maximum thrust augmentation levels of approximately $\alpha=30\%$ for straight ejectors and $\alpha=66.5\%$ for an optimized diverging ejector geometry at $ff=1.0$. It is apparent that the diverging ejectors tested were much more effective at producing thrust augmentation than the straight ejectors, but the mechanism responsible for this performance increase is not clear. The increased augmentation from diverging ejectors has commonly been attributed to the additional thrust surface area of the diverging section. Inherent in that explanation is the assumption that there is a positive net pressure on the diverging section, thus causing a thrust force. It has been observed that ejector performance is sensitive to the axial position of the ejector inlet relative to the PDE tube exit. In most cases downstream ejector placement provides optimum levels of thrust augmentation^{5,6,7,8}. For the straight and diverging ejector configurations previously tested by Glaser et al⁵ the optimum axial position was found to be downstream at $x/D_{PDE}=+2$.

The current effort seeks to increase the overall understanding of PDE driven ejector systems. Static pressure was measured along the interior surface of the ejector including the inlet and exhaust sections. High-speed shadowgraph flow visualizations were also obtained to better explain the observed performance trends. Comparisons are also made between this data and ejector performance data obtained through direct thrust measurements. Results from this study will provide insight into the governing flow dynamics and mechanisms responsible for thrust augmentation with PDE driven ejector systems.

II. Experimental Setup

A. Description of PDE System

Experimental testing for the current study was carried out at the Air Force Research Laboratory PDE test facility at Wright-Patterson Air Force Base⁹. The detonation tube was constructed of type 316 stainless steel, and the geometry tested consisted of a 5.08 cm inner diameter with 154.94 cm length. The system was operated in a premixed manner, using hydrogen and air as the reactants. Injection of fuel and air into the detonation tube was carried out using a mechanical valve system. This system was constructed from a modified four-cylinder automotive valve head with four valves per-cylinder. The valve train was driven with a variable speed electric motor. The two intake ports were used to deliver premixed hydrogen and air, while the two exhaust ports delivered purge air. The purge air cycle is employed to cool the detonation tube between combustion cycles and provide a buffer between the hot combustion products and the fresh reactants being injected into the tube for the next cycle. Because of the nature of automotive valving, the cycle timing for various events such as fill time, purge time, and detonation time are fixed to be one-third of the cycle. Spark ignition was accomplished using a capacitive discharge stock automotive spark system that delivered approximately 40 mJ of energy. To accelerate the deflagration-to-detonation transition (DDT) a Shchelkin-type spiral was used for all tests.

Operation of the PDE system was computer controlled using a LabView interface program. The LabView interface provided the flexibility to specify engine operating parameters such as PDE operating frequency, fill-fraction (ff), and equivalence ratio, where fill-fraction is defined as the ratio of the tube volume filled with a detonable mixture to the total tube volume prior to combustion. Unless otherwise stated, all of the current tests were performed at an operating frequency of 30 Hz, fill-fraction of 1.0, and an equivalence ratio of 1.0. Ionization probes were mounted along the detonation tube length to verify that Chapman-Jouguet (CJ) detonations were obtained. For

a stoichiometric mixture of hydrogen and air, the CJ wave speed is 1957 m/s. Data from these sensors were collected at 5 MHz using a 16 channel data acquisition system. This fast sampling rate was adequate to accurately resolve the detonation wave speed.

B. Ejector Hardware and Instrumentation

The ejector hardware was mounted on the PDE system to determine its effect on the thrust generated by the PDE. All of the ejectors tested were mounted coaxially to the detonation tube. The ejectors were suspended from two parallel rails mounted above the detonation tube. The rails extended along the length of the tube allowing the axial position, x , of the ejector inlet to be varied from -12 to +6 tube diameters from the PDE tube exit plane. A negative axial position value corresponds to the ejector inlet placed upstream of the PDE exit with the ejector overlapping the detonation tube. For a positive value the ejector is mounted downstream of the detonation tube exit.

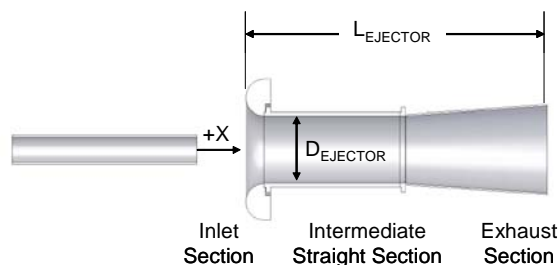


Figure 1. Picture of the installed ejector and diagram of the ejector geometry used for the current

Two ejector geometries were used during this testing. Each ejector consisted of an inlet section, an intermediate straight section, and an exhaust section as shown in Figure 1. The two ejectors were identical with the exception of the exhaust section: one section was straight while the other was diverging. The diameter of the ejector (D_{EJECT}) was defined as the diameter of the intermediate straight section, as this was the minimum diameter for any given ejector geometry. For the current work, D_{EJECT} was held at a fixed value of 13.97 cm. The ejector-to-PDE diameter ratio (DR) of 2.75 was therefore constant throughout the testing. This value is near the optimum diameter ratios reported in other ejector experiments^{6,8,10}. The inlet used had a rounded inlet lip with a radius of 3.81 cm. The overall non-dimensional length of the ejectors was $L_{EJECT}/D_{EJECT}=5.6$. The intermediate straight section had a length of $L_{STRAIGHT}/D_{EJECT}=3$, and the exhaust section had a length of $L_{EXHST}/D_{EJECT}=2.36$. The two exhaust sections tested had half-angle divergences of 0° and 4° .

To facilitate the static pressure measurements, each ejector was instrumented with 20 pressure ports along the ejector surface. Each pressure port consisted of a 0.04 inch diameter thru hole on the ejector surface, which then transitioned to a 1/16 inch diameter tube. Seven of the pressure taps were located on the ejector inlet at the angular locations given in Table 1. The other 13 pressure taps were distributed along the ejector body as shown in Figure 2, with seven placed on the intermediate straight section and six on the exhaust section. Although this figure depicts an ejector with a straight exhaust section, the diverging exhaust section had surface pressure taps in the same locations. Pressure was measured using a NetScanner Model 9116 Pressure Scanner. This system incorporated 16 silicon piezoresistive pressure sensors each sampling at a frequency of 1 Hz. Since the pressure measurement system had the ability to sample 16 pressure signals, only 16 of the 20 available ejector pressure taps could be used at a give time. The pressure ports used for the current study are given in Figure 2. Each pressure port on the ejector was connected to its corresponding pressure sensor by a 1/16 inch diameter flexible tube of approximately 2.5 m length. It should be noted that due to the setup of current system, the dynamic nature of the pressure field was not captured.

Inlet Pressure Tap Locations	
Tap Number	Tap Location
1	0°
2	30°
3	60°
4	90°
5	120°
6	150°
7	165°

Table 1. Locations of the pressure ports on the ejector inlet.

The length of tubing used between the sensors and surface pressure taps had the effect of damping out the high frequency pressure oscillations normally associated with PDE operation providing an averaging effect on the pressure history. The pressure measurement system used provided a measure of the average static pressure at the specified locations over a period of time.

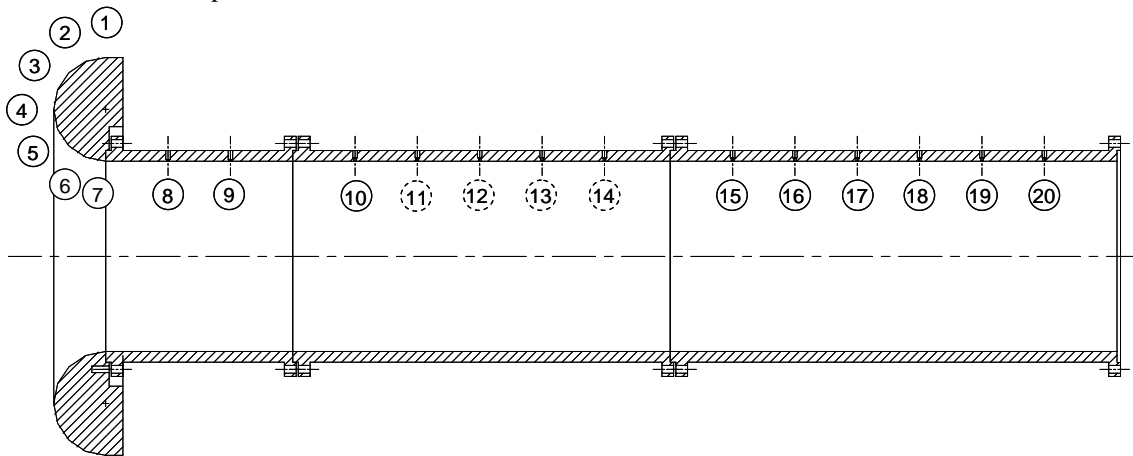


Figure 2. Placement of the pressure sampling ports on the ejector surface. Solid circles denote ports used during the current study.

III. Results and Discussion

A. Straight Ejector Surface Pressure Distribution

For each data point collected, the PDE was operated for a duration of approximately 45 seconds. In order to assess the variability of the experimental results, three test runs were performed for each configuration studied. A typical static pressure time history measured on the ejector surface is shown in Figure 3. Prior to detonation, cold air is pulsed through the PDE injection valves in order to allow sufficient time for the desired flow rate to stabilize. This initial unsteady cold flow causes flow entrainment into the ejector and thus a decreased pressure on the ejector inlet which is shown by the initial gauge pressure of approximately -0.15 psi in Figure 3. After the PDE starts detonating, the pressure drops down to a lower plateau indicating an increase in flow entrainment. It can be seen that although the measured pressure signal is reasonably steady the signal does have a small fluctuating component. For all results shown in the current study, the fluctuating pressure measured during PDE operation was time averaged to give a single value for the static pressure at that sample location. For the case shown, the time averaged PDE fired static pressure measured on the ejector inlet was -0.38 psi.

The surface pressure distribution measured on a straight ejector is shown in Figure 4. Results are shown comparing two primary unsteady driver sources. The first source is a PDE and the second is an unsteady cold jet, both operating at a frequency of 30 Hz. Both driver sources cause similar trends in the ejector pressure

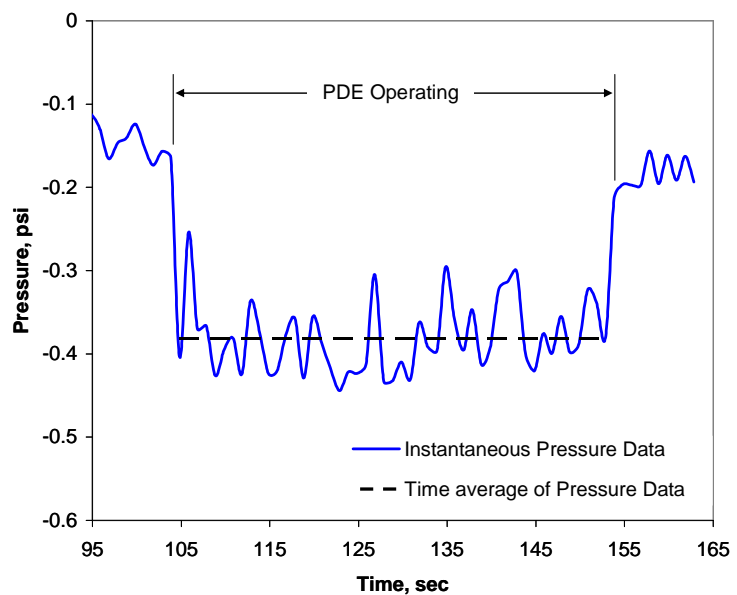


Figure 3. Pressure history measured on the ejector inlet at pressure tap 7. The configuration tested was a straight ejector with $x/D_{PDE}=+2$ and $ff=1.0$.

distribution. It can be seen that the entrained flow being directed into the ejector causes a significant vacuum

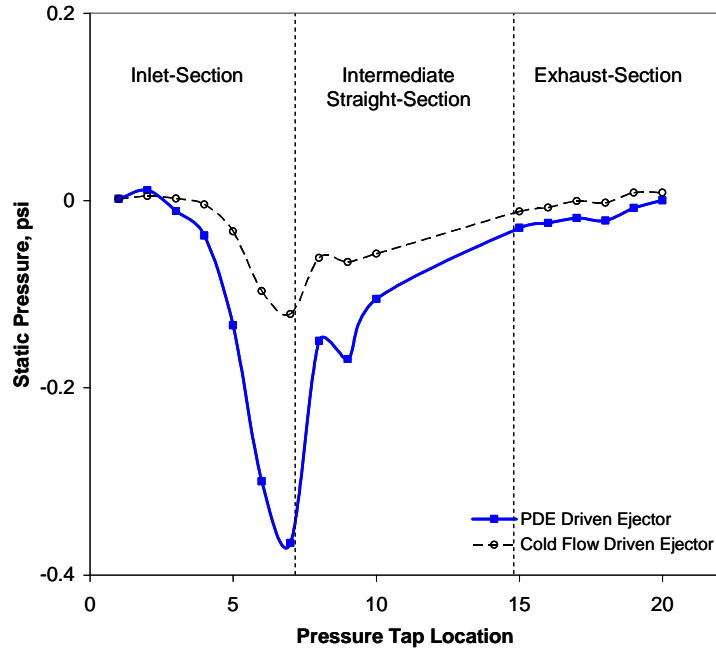


Figure 4. Ejector surface pressure distribution. The configuration tested was a straight ejector with $x/D_{PDE}=+2$, and $ff=1.0$.

found to gradually rise until reaching ambient pressure at the ejector exit. The flow area is constant through the straight ejector. The rising static pressure is attributed to mixing as the flow travels through the ejector. The amount

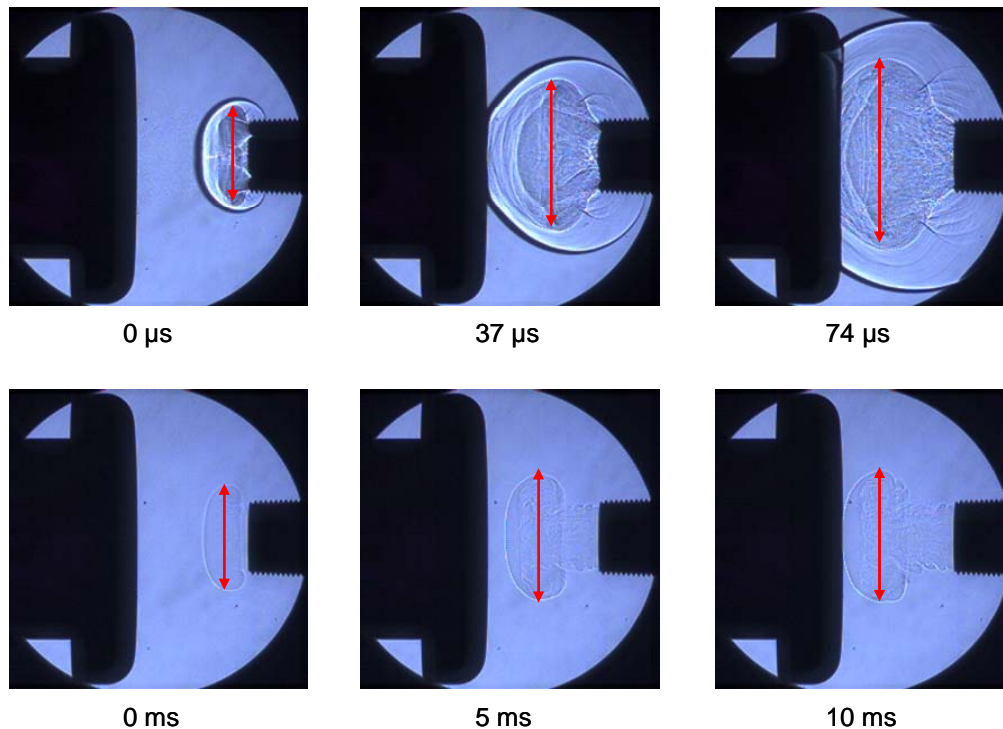


Figure 5. Shadowgraph images comparing PDE driven vortex ring (upper images) to cold flow starting vortex (lower images).

pressure on the inlet. The minimum inlet pressure occurred at pressure tap 7 which is at an angle of 165° as previously defined. It can also be seen that the outer area of the inlet, pressure taps one and two, did not see a pressure decrease and thus did not contribute to providing thrust augmentation. This finding implies that the entire rounded portion of the inlet may not be necessary. Comparable performance might be possible with a simplified inlet design. With a straight ejector, the only surface able to cause a thrust force is the ejector inlet. A larger negative inlet pressure would lead to an increase in thrust augmentation. Just downstream of the inlet section the pressure is seen to rise quickly and a region consistent with separated flow is observed at pressure tap 8. Since the flow separation was observed to occur in both the PDE and subsonic cold flow case, it is unlikely that the separation is caused by the presence of a stationary shockwave located in the ejector. The flow separation is most likely due to the strong adverse pressure gradient and large inlet turning angle experienced. Through the rest of the straight ejector, static pressure was

of thrust augmentation provided by the straight ejector configuration with $ff=1.0$ was calculated by integration of the measured static pressure around the ejector geometry. The calculated augmentation was found to be 26.1% which is slightly lower than the augmentation of 30.0% measured through direct thrust measurements.⁵

Figure 5 is a shadowgraph flow visualization showing the differences

between a detonation and cold flow primary driver. The visualizations were performed using a 1 inch diameter PDE operating at 20 Hz with a straight ejector. The diffracting detonation wave with trailing vortex structure can be clearly seen. The time scales are clearly different between the two cases as the velocity of the cold flow starting vortex is much lower than the detonation wave speed. The cold flow vortex was observed to increase in diameter at locations near the tube exit attaining a near constant diameter as it continues to travel forward. In contrast, the detonation-driven vortex structure shows rapid growth until reaching the ejector inlet. It can also be seen that upon reaching the ejector inlet, the diameter of detonation-driven vortex is noticeably larger than the cold flow vortex. These results are consistent with experimental ejector performance measurements which have shown that the optimum ejector-to-driver diameter ratio is larger for PDE driven ejectors as compared to cold flow driven systems.

Portions of a complete PDE driven ejector cycle are shown in Figure 6. At a time of 111 μ s the shock wave is observed to reflect and travel backwards from the ejector inlet. The mach disk structure present during the blowdown portion of the PDE cycle is visible near the ejector entrance at 148 μ s. An interaction can be seen between the exhaust plume and ejector inlet at 222 μ s in the form of a vortical structure attached to the inlet lip. The image at 9,065 μ s was taken much later in the PDE cycle. It can be seen that the shock and vortex structure are no longer present and that the ejector is entraining flow into the inlet. The pattern of the entrained flow at this time during the cycle appears to show a clustering of the flow streamlines near the inner radius of the inlet. This is indicative of a higher velocity at this location. Also there does not appear to be significant amounts of entrained flow passing over the outer radius of the inlet. These observed trends are consistent with the straight ejector pressure distribution discussed above.

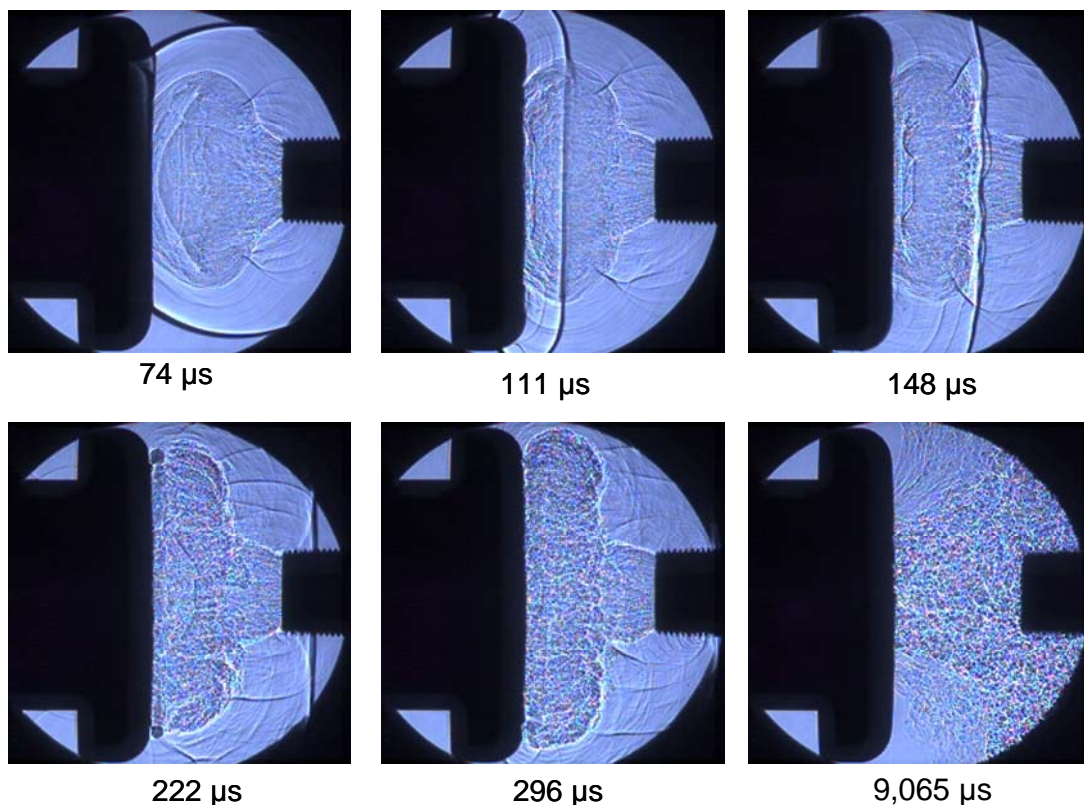


Figure 6. Sequence of shadowgraph images taken during the PDE driven ejector operating cycle. $ff=0.6$, $DR=3$, $x/D_{PDE}=+2$.

B. Effect of Diverging Section on Ejector Performance

Previous PDE driven ejector studies have found that there are significant performance advantages when incorporating a diverging exhaust section into the ejector. Direct thrust measurements showed that the thrust augmentation of the diverging ejector was approximately two times that of the straight ejector.

Figure 7 compares the pressure distribution of a straight and diverging ejector. It can be seen that the addition of the diverging exhaust section had a significant impact on the ejector inlet flow field. The diverging ejector showed a vacuum pressure at tap 7 which was two times lower than that of the straight ejector. This increase in inlet suction represents more flow entrainment which leads to an increase in thrust augmentation. What is also apparent is that the static pressure along the diverging section is negative, rising to equal ambient conditions at the ejector exit. This finding is significant in that it shows the performance enhancement afforded by diverging ejectors is not due to a positive thrust force acting on the diverging section area. In fact, the diverging section creates a slight drag force due to the negative pressure acting on it. The role of the diverging section appears to be that of a subsonic diffuser, decreasing the flow velocity and increasing static pressure in the exhaust section. The ejector exit plane boundary condition is that ambient static pressure is achieved in the exhaust jet. The added pressure recovery through the diverging section makes it possible for a decreased inlet pressure to exist while still maintaining the ejector exit boundary condition. In prior experimental testing, the current intermediate straight section length of $L_{\text{STRAIGHT}}/D_{\text{EJECT}}=3$ was found to be near the optimum length. Either decreasing or increasing the straight section length caused a decrease in thrust augmentation. It is speculated that the flow mixing which takes place within the intermediate straight section is beneficial for conditioning the flow prior to entering the diffuser. Without a sufficient amount of mixing, the velocity profile entering the diverging section may be more prone to separation causing increased diffuser pressure recovery losses. After the flow is fairly well mixed, further increasing of the straight section length leads to increased frictional drag forces, thus decreasing thrust augmentation.

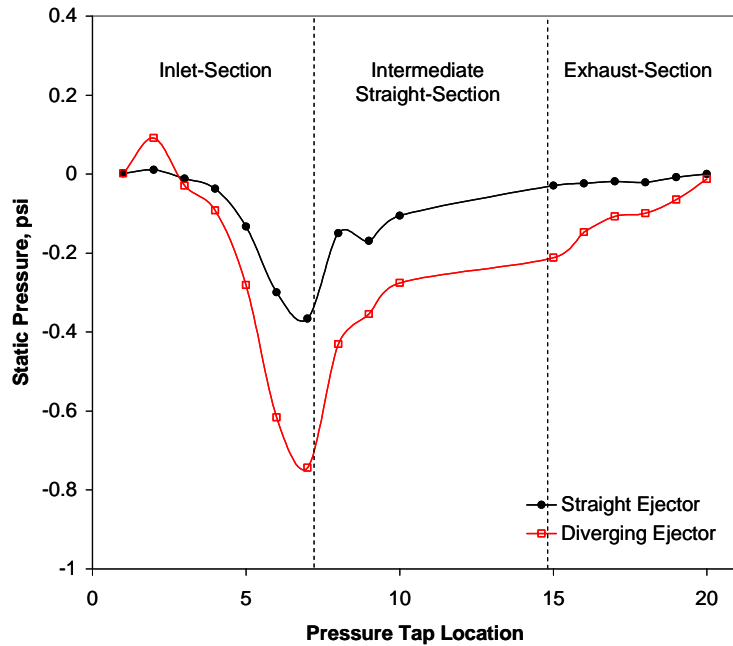


Figure 7. Static pressure distribution in a straight and diverging ejector. $ff=1.0$, $x/D_{\text{PDE}}=+2$.

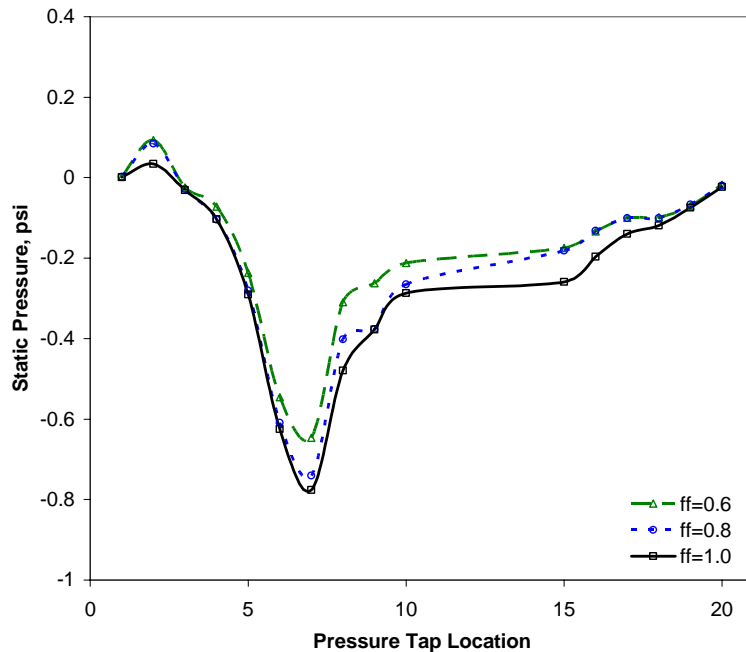


Figure 8. Effect of fill-fraction on ejector pressure distribution. Ejector geometry is a diverging ejector with $x/D_{\text{PDE}}=+2$.

The ejector exit plane boundary condition is that ambient static pressure is achieved in the exhaust jet. The added pressure recovery through the diverging section makes it possible for a decreased inlet pressure to exist while still maintaining the ejector exit boundary condition. In prior experimental testing, the current intermediate straight section length of $L_{\text{STRAIGHT}}/D_{\text{EJECT}}=3$ was found to be near the optimum length. Either decreasing or increasing the straight section length caused a decrease in thrust augmentation. It is speculated that the flow mixing which takes place within the intermediate straight section is beneficial for conditioning the flow prior to entering the diffuser. Without a sufficient amount of mixing, the velocity profile entering the diverging section may be more prone to separation causing increased diffuser pressure recovery losses. After the flow is fairly well mixed, further increasing of the straight section length leads to increased frictional drag forces, thus decreasing thrust augmentation.

Integrating the pressure distribution around the diverging ejector geometry

gives a calculated thrust augmentation $\alpha=50\%$. This is comparable to the thrust augmentation $\alpha=66\%$ obtained from direct thrust measurements.

C. Effect of Fill-Fraction on Ejector Performance

Previous studies have measured an inverse relationship between thrust augmentation and PDE fill-fraction at downstream ejector placements⁵. For the diverging ejector geometry being considered, thrust augmentation was increased from $\alpha=66\%$ to $\alpha=74\%$ by decreasing the fill-fraction from $ff=1.0$ to $ff=0.6$. Figure 8 shows that decreasing the fill fraction does not significantly alter the pressure distribution on the ejector. Thrust augmentation is defined as the change in thrust due to the ejector divided by the baseline PDE thrust with no ejector installed. When fill fraction is decreased the baseline PDE thrust decreases at a faster rate than the thrust produced by the ejector leading to an increased thrust augmentation.

D. Effect of Axial Position on Ejector Performance

It has been observed that ejector performance is sensitive to the axial position of the ejector inlet relative to the PDE tube exit. In most cases downstream ejector placement provides optimum levels of thrust augmentation^{5,6,7,8}. For the straight and diverging ejector configurations previously tested by Glaser et al⁵ the optimum axial position was found to be $x/D_{PDE}=+2$. Figure 9 shows the effect of axial position on diverging ejector pressure distribution. It can be seen

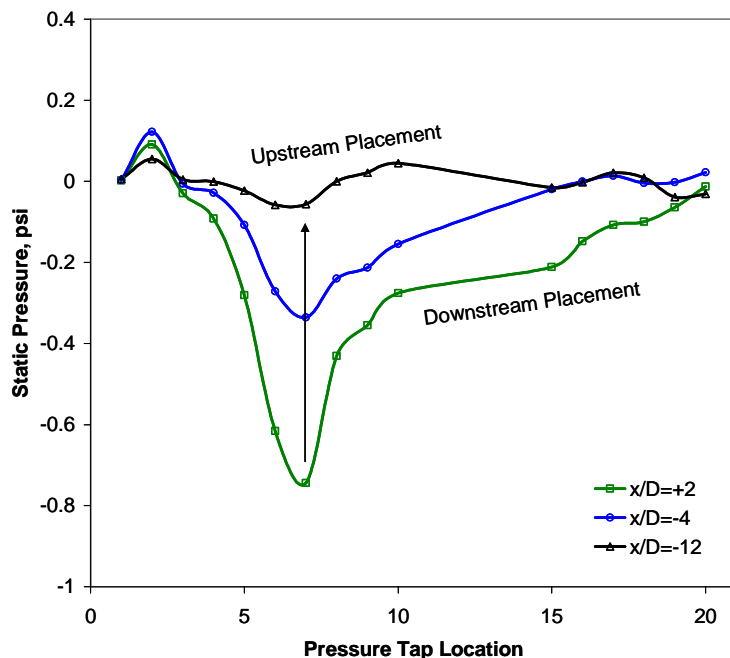


Figure 9. Effect of axial position on static pressure distribution. Ejector geometry is a diverging ejector with $ff=1.0$.

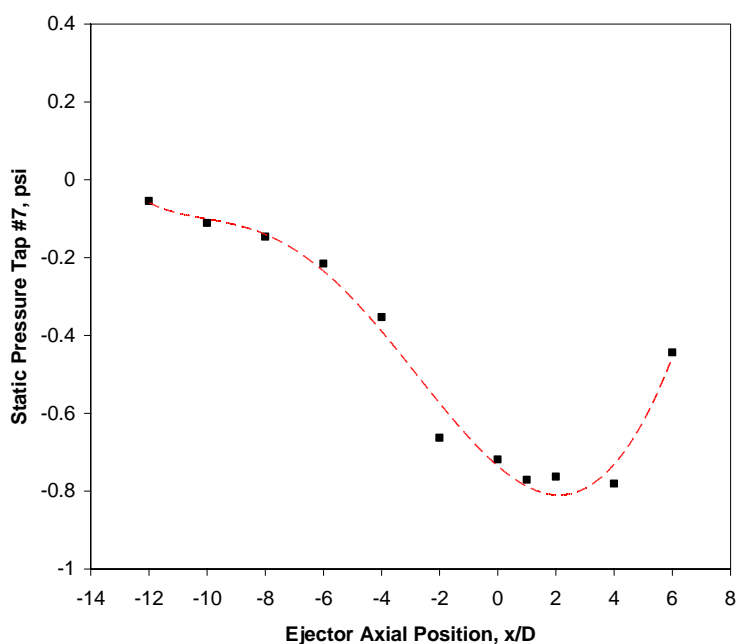


Figure 10. Effect of axial position on ejector inlet suction.

that as the ejector is moved upstream from $x/D_{PDE}=+2$ that the inlet suction is decreased. At the axial location of $x/D_{PDE}=-12$ it can be seen from the pressure distribution that almost no flow is being entrained through the ejector, implying an augmentation near 0%. At this overlap position, a region of slightly positive pressure was also observed in the straight section at pressure tap 10. This overpressure is due to the presence of the detonation tube exit located within the ejector. The axial position trend is more clearly seen in Figure 10. Static pressure data at tap seven is plotted for all axial positions tested. The pressure at this location represented the minimum pressure on the inlet for nearly all cases studied and therefore was a good indicator of the amount of flow entrainment into the ejector for a given configuration. The tap seven pressure data shows a minimum pressure near $x/D_{PDE}=+2$ which is the optimum location determined through direct thrust measurements. Placements of the ejector at positions away

from the optimum increase the minimum inlet pressure. Movement of the ejector in the upstream direction continually increases the inlet pressure, which implies continually decreasing flow entrainment. Figure 11 shows the thrust augmentation calculated by integration of the ejector pressure distribution. A maximum augmentation of $\alpha=50\%$ was found to occur at $x/D_{PDE}=+2$. This is the same position at which the minimum inlet pressure was measured. It can also be seen that placing the ejector upstream of the PDE exit decreases thrust augmentation. The observed trends are consistent with the experimental findings obtained through direct thrust measurements indicating that the optimum ejector placement is downstream of the PDE tube exit.

IV. Conclusion

An experimental study was performed to investigate the operation of PDE driven ejectors. A straight and a diverging ejector were both instrumented for static pressure measurements. Analysis of the straight ejector pressure distribution and shadowgraph images showed that a majority of the flow acceleration on the rounded inlet occurs at the inner inlet radius. This implies that the outer surface of the inlet is not significant in flow entrainment and thus does not have to be as well contoured as the inner section of the inlet. It was found that the role of the diverging exhaust section is to act as a subsonic diffuser. The pressure recovery that takes place in the diffuser has a large impact on the inlet pressure distribution, decreasing the inlet pressure by a factor of 2. The reason for the inverse relationship between fill-fraction and thrust augmentation was studied. It was found that the ejector pressure distribution was not very sensitive to fill-fraction. The axial placement of the ejectors was studied in detail. Axial position was varied from $x/D_{PDE}=-12$ to $+6$. The axial location of maximum inlet suction was found to be near $x/D_{PDE}=+2$. Inlet suction was found to continually decrease towards zero as the ejector was moved upstream. The calculated thrust augmentation showed a maximum at a position of $x/D_{PDE}=+2$. This also corresponds to the optimum axial location for thrust augmentation as determined through direct thrust measurements. The observed trends are consistent with the optimum ejector placement being at a downstream location.

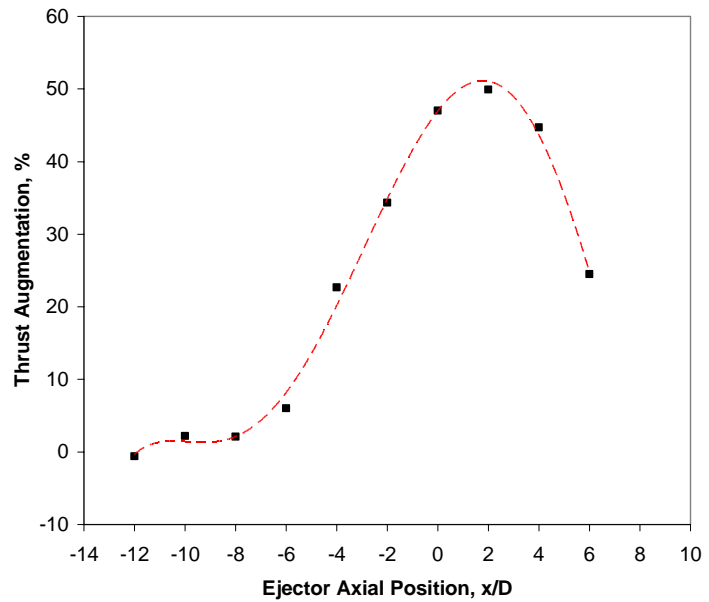


Figure 11. Effect of ejector position on the calculated thrust augmentation. Ejector configuration is a diverging ejector with $ff=1.0$.

Acknowledgments

The authors would like to thank the Propulsion Directorate at the Air Force Research Laboratory and Innovative Scientific Solutions Inc. (ISSI) for providing the financial support for this work. The technical support of Curtis Rice of ISSI was also greatly appreciated.

References

- ¹Presz, W., Reynolds, G., Hunter, C., "Thrust Augmentation with Mixer/Ejector Systems", AIAA 2002-0230, 40th AIAA Aerospace Sciences Meeting and Exhibit, Reno, NV, January 14-17, 2002
- ²Wilson, J. and Paxson, D.E., "Unsteady Ejector Performance: An Experimental Investigation Using a Resonance Tube Driver", AIAA 2002-3632, 38th AIAA Joint Propulsion Conference, Indianapolis, IN, July 7-10, 2002
- ³Paxson, D.E., Wilson, J. and Dougherty, K.T., "Unsteady Ejector Performance: An Experimental Investigation Using a Pulsejet Driver", AIAA 2002-3915, 38th AIAA Joint Propulsion Conference, Indianapolis, IN, July 7-10, 2002.
- ⁴Lockwood, R., "Interim Summary Report on Investigation of the Process of Energy Transfer from an Intermittent Jet to Secondary Fluid in an Ejector-Type Thrust Augmenter", Hiller Aircraft Report No. ARD-286, March 1961.

⁵Glaser, A., Caldwell, N., Gutmark, E., Hoke, J., Bradley, R., and Schauer, F., "Performance Measurements of Straight and Diverging Ejectors Integrated with a Pulse Detonation Engine", AIAA 2006-1022, 44th AIAA Aerospace Sciences Meeting and Exhibit, Reno, NV, January, 2006.

⁶Rasheed, A., Tangirala, V., Pinard, P.F., Dean, A.J., "Experimental and Numerical Investigations of Ejectors for PDE Applications", AIAA 2003-4971, 39th AIAA Jet Propulsion Conference, Huntsville, AL, July 21-23, 2003.

⁷Allgood, D., Gutmark, E., "Performance Measurements of Pulse Detonation Engine Ejectors", AIAA 2005-0223, 43rd AIAA Aerospace Sciences Meeting and Exhibit, Reno, NV, January 10-13, 2005.

⁸Glaser, A., Caldwell, N., Gutmark, E., Hoke, J., Bradley, R., and Schauer, F., "Effects of Tube and Ejector Geometry on the Performance of Pulse Detonation Engine Driven Ejectors", AIAA-2006-4790, 42nd AIAA/ASME/SAE/ASEE Joint Propulsion Conference and Exhibit, Sacramento, California.

⁹Schauer, F., Stutrud, J., and Bradley, R., "Detonation Initiation Studies and Performance Results for Pulse Detonation Engine Applications", AIAA 2001-1129, 39th AIAA Aerospace Sciences Meeting and Exhibit, Reno, NV, January 2001

¹⁰Wilson, J., Sgondea, A., Paxson, D., and Rosenthal, B., "Parametric Investigation of Thrust Augmentation by Ejectors on a Pulse Detonation Tube", AIAA 2005-4208, 41st AIAA/ASME/SAE/ASEE Joint Propulsion Conference, Tucson, Arizona, July 10-13, 2005

Ignition and Detonation-Initiation Characteristics of Hydrogen and Hydrocarbon Fuels in a PDE

Timothy M. Helfrich* and Frederick R. Schauer†
Air Force Research Laboratory, Wright-Patterson AFB, OH, 45433

and

Royce P. Bradley‡ and John L. Hoke§
Innovative Scientific Solutions, Inc., Dayton, OH, 45440

Over the past two decades, several fuels have been tested throughout the world in pulsed detonation engines (PDEs). The present research focuses on developing a baseline set of ignition and detonation-initiation performance measures for six fuels in air: Hydrogen, ethylene, propane, aviation gasoline (avgas), JP-8, and Fischer-Tropsch JP-8 (S-8). To quantify the ignition and detonation-initiation performance, four parameters are examined: Ignition time, deflagration-to-detonation transition (DDT) time, DDT distance, and the upper Chapman-Jouguet (CJ) wavespeed. These four parameters are presented as a function of equivalence ratio from lean-to-rich ignition limits for the six fuels of interest. Hydrogen was found to have the best ignition and detonation-initiation characteristics, followed by ethylene. Propane, avgas, JP-8, and S-8 exhibited similar ignition and detonation-initiation characteristics, as expected based on cell size. Minimum ignition times for all fuels occurred near an equivalence ratio of 1.3, whereas the minimum DDT times and distances occurred between equivalence ratios of 1.1 and 1.2. All experimental CJ wavespeeds were within 5% of the theoretical value, with the exception of hydrogen, with an experimental CJ wavespeed that is systematically between 6% and 8% lower than the theoretical value.

Nomenclature

E_{crit} = Critical Initiation Energy
 λ = Detonation Cell Size

I. Introduction

PULSED-detonation-engine (PDE) research over the last two decades has been driven by factors, such as potential for higher thermal efficiency, high thrust, low weight, low cost, scalability, and a large operational envelope.¹⁻³ The potential for higher thermal efficiency is based on the understanding that the constant-volume process that occurs in a PDE creates less entropy than the constant-pressure process which occurs in most modern gas turbine engines.⁴ Because of the attractive qualities of the PDE, it has received attention in many areas of the aeronautical-engineering community; spawning interest in several applications for the PDE including aircraft, spacecraft, cruise missiles, and hybrid functions with a gas turbine engine, ramjet, or scramjet.

To quantify the ignition and detonation-initiation characteristics of the fuel/air mixtures, four key performance parameters were examined: 1) time from spark deposition to the creation of a deflagration wave within the fuel/air

* Capt, USAF, Research Engineer, Deputy PDRF, AFRL/PRTC, 1950 5th Street, AIAA Member.

† Senior Engineer, Head PDRF, AFRL/PRTC, 1950 5th Street, AIAA Senior Member.

‡ Research Engineer, 2766 Indian Ripple Road.

§ Research Engineer, 2766 Indian Ripple Road, AIAA Senior Member.

mixture (ignition time), 2) time to transition the deflagration wave into a detonation wave (DDT time), 3) length of detonation tube required for the mixture to transition to a detonation (DDT distance), and 4) experimentally determined upper Chapman-Jouguet (CJ) wavespeeds.

This research was conducted to establish a baseline of ignition and detonation-initiation characteristics for a PDE fueled with a wide spectrum of conventional fuels in air--specifically, hydrogen, ethylene, propane, aviation gasoline (avgas), JP-8, and S-8.** These fuels were selected because they represent potential PDE fuels. Prior to the present research, substantial data on ignition time, DDT time, DDT distance, and CJ wavespeed were published,⁶⁻¹² in several papers. The previous data were gathered using different experimental setups, making comparison of the data sets difficult. Schauer et al.⁶ experimentally measured the CJ wavespeeds for mixtures of propane, avgas, JP-8, and JP-10 in air as a function of equivalence ratio using a setup similar to that in the present research. They were only marginally successful in detonating propane, because of the uncontrolled phase change in the fuel-supply system. Tucker et al.^{7,8} measured the ignition time, DDT time, and CJ wavespeed as a function of equivalence ratio for mixtures of avgas, JP-8, iso-octane, and heptane in air using a fuel flash-vaporization system to heat the fuel prior to injection into air. Card et al.⁹ determined the DDT distance for mixtures of hydrogen, ethylene, acetylene, and JP-10 in air as a function of equivalence ratio in a 100-mm-diameter tube. They defined the DDT distance as the length where the wavespeed jumps from the isobaric speed of sound of the products to the CJ wavespeed. Ciccarelli and Card¹⁰ examined the wavespeed of JP-10/air mixtures at elevated temperatures and pressures. Akbar et al.¹¹ measured the wavespeeds of unsensitized and sensitized mixtures of JP-10 and Jet-A, and Austin and Shepard¹² measured the wavespeed of JP-10/air mixtures as a function of equivalence ratio in a 280-mm-diameter tube.

II. Background and Theory

Previous experimental research⁶ has shown that a typical stoichiometric low-vapor-pressure liquid-hydrocarbon/air mixture requires energy on the order of 10^5 J for direct initiation of detonation (critical initiation energy), which is six orders of magnitude greater than the energy available from a typical spark plug (~100 mJ). Thus, a mixture with low critical initiation energy is more susceptible to DDT. Knystautas et al.¹³ and Schauer et al.⁶ independently developed correlations between the detonation cell size (λ) and the critical initiation energy (E_{crit}) of a mixture, where the critical initiation energy varies with the cube of the detonation cell size, as shown in Eq. 1:

$$E_{crit} \propto \lambda^3 \quad (1)$$

Therefore, a decrease in detonation cell size is an indication of greatly improved detonability. Schauer et al.⁵ developed the correlation based on data compiled by Kaneshige and Shepherd.¹⁴

The detonation cell size is a physical characteristic of a detonation wave, as shown in Fig 1. A more detailed discussion of detonation cell structure can be found in Fickett and Davis.¹⁵ Figure 2 is a plot of detonation cell size as a function of equivalence ratio for hydrogen, ethylene, propane, JP-4, and JP-10. JP-4 and JP-10 are liquid-hydrocarbon fuels that are on the same order of density as avgas, JP-8, and S-8. The hydrogen data exhibit the smallest detonation cell size of the five fuels presented. As will be shown, the smaller cell size translates directly to better ignition and detonation-initiation performance. Ethylene demonstrates the next larger cell sizes, which will be shown later to translate to the second best ignition and detonation-initiation performance. Propane, JP-4, and JP-10 exhibit similar detonation cell sizes, indicating that avgas, JP-8, and S-8 exhibit ignition and detonation-initiation characteristics similar to those of propane. The data from Fig. 2 were compiled by Kaneshige and Shepherd,¹⁴ but were experimentally obtained elsewhere.^{12,13,16,17}

**S-8 is a synthetic fuel derived from natural gas via the Fischer-Tropsch process.⁵ S-8 is also referred to as Fischer-Tropsch JP-8 or simply Fischer-Tropsch.

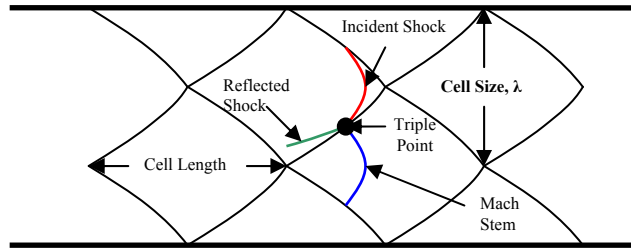


Figure 1. Representation of two-dimensional detonation cell structure.

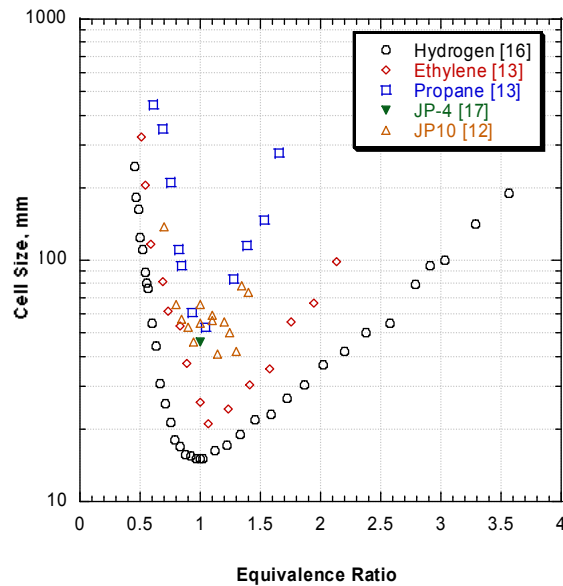


Figure 2. Plot of detonation cell size as function of equivalence ratio for five different fuels.

Figure 3 is a plot of detonation cell size as a function of carbon number for mixtures of several straight-chain hydrocarbons, JP-10, and hydrogen in air. As this figure demonstrates, once the carbon number reaches two (ethane) the difference in detonation cell size is negligible. All of the hydrocarbons, including JP-10, shown here with two or more carbon atoms have a cell between 40 and 50 mm at stoichiometric conditions. With the well known exception of methane, all of the alkanes (straight chain hydrocarbons) have nearly identical detonation cell sizes. From Figs. 2 and 3, it can be inferred that the heavy liquid hydrocarbons (avgas, JP-8, and S-8) will demonstrate performance similar to that of propane and also that the larger straight-chain hydrocarbons (butane through decane) will also demonstrate performance similar to that of propane. The data from Fig. 3 were compiled by Kaneshige and Shepherd,¹⁴ but were experimentally obtained elsewhere.^{12-14,16-18}

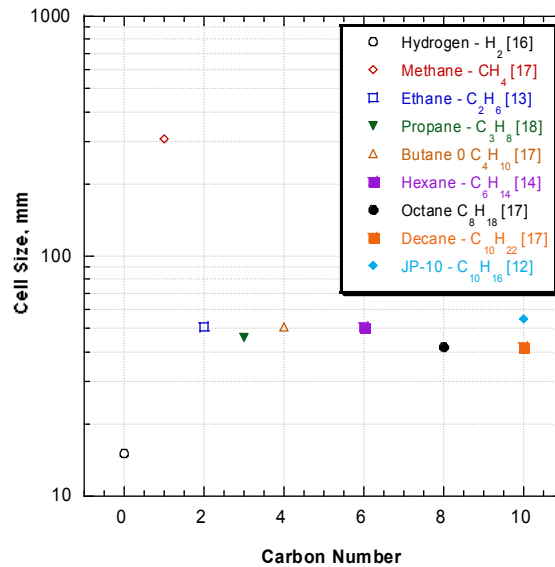


Figure 3. Plot of detonation cell size as function of carbon number for nine fuels.

III. Experimental Setup and Instrumentation

A. Facilities and PDE Details

This research was conducted in the Pulsed Detonation Research Facility (PDRF), which is located at Wright-Patterson AFB in Ohio. This facility was described in detail elsewhere,²⁰ and only these details that are relevant to the current research are provided here. The PDE for this study consisted of the valve train from a GM quad-four-engine head with two 2.44-m-long, Schedule-40 stainless-steel detonation tubes (50.8-mm diameter); each tube had a 1.22-m-long Schelkin-like spiral, with one end adjacent to the closed end of the detonation tube, to promote DDT.²¹ During testing of JP-8 and S-8, the fuel was preheated to temperatures above 561 K (the threshold for complete fuel flash vaporization²²) using a 38.1-cm-long concentric-counter-flow heat-exchanger that was developed by Miser et al.²³

The PDE cycle consisted of three equally timed phases--fill, fire, and purge, as shown in Fig. 4. During the fill phase, the intake valves were opened to fill the PDE detonation tube with a volume of premixed fuel and air that was equal to the volume of the detonation tube (fill fraction of one). For all tests the fill air was initially heated to 394 K prior to mixing with the fuel. During the fire phase, spark energy was released, causing the formation of a deflagration wave that transitioned to a detonation wave. The ignition system provided spark pulses through modified spark plugs, with each spark plug supplying an ignition energy of 115 mJ. The spark delay after the intake valves were closed was 4 ms. During the purge phase, the exhaust valves were opened to fill the detonation tube with a volume of air (unheated) that was equal to one-half the volume of the detonation tube (purge fraction of 0.5). The purge air cooled the detonation tube and removed a portion of the exhaust gases, preventing auto-ignition. The PDE firing frequency was held constant at 10 Hz for all testing.

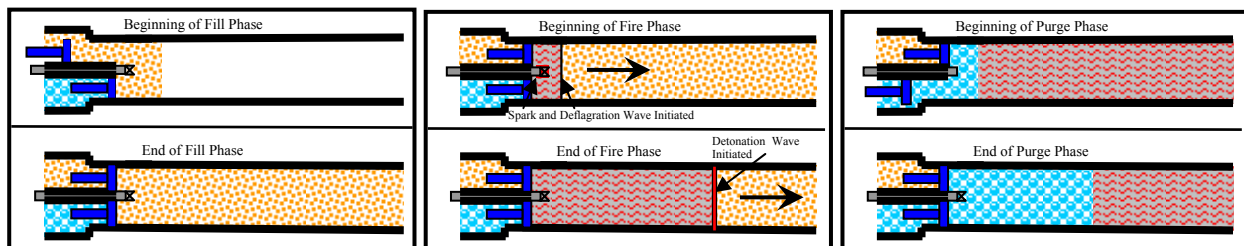


Figure 4. Diagrams of fill, fire, and purge phases of pulsed-detonation-engine cycle.

B. Fuel Delivery Systems

The hydrogen fuel was provided by a hydrogen tuber trailer that was located outside of the research facility, whereas ethylene was supplied via commercial tanks inside the test cell. The gaseous fuels were routed into the facility and through a dome-loaded pressure regulator to control the inlet pressure to a critical flow nozzle. A surge tank was located downstream of the critical flow nozzle to prevent pressure waves that are generated in the valve system from unchoking the critical flow nozzle. After traversing through the surge tank, the gaseous fuel was injected into the air stream.

The liquid fuel was supplied by two hydraulic bladder-type accumulators that were pressurized by nitrogen. The nitrogen pressurized the fuel above the critical pressure for the duration of the test to prevent phase change. The propane was supplied in commercial tanks but was fed into the hydraulic bladder accumulators to maintain sufficient fuel pressure to prevent boiling. Once in the accumulators, propane was supplied to the PDE in the same manner as was the other liquid fuels. For JP-8 and S-8, the fuel was pressure fed to the inlet of the heat exchanger. After traversing through the heat exchanger, the fuel was injected into the air stream. Avgas and propane were pressure fed directly into the air stream, bypassing the heat exchanger. A turbine flow meter, downstream of the accumulators, was used to measure the liquid-fuel mass flow rate. The mass flow rate of the fuel-injection nozzles is proportional to the square root of the pressure drop across the fuel nozzles and the fuel density.^{24,25} To compensate for the decrease in fuel density during heating of the fuel in the supercritical regime, the charge pressure of the accumulators was increased to maintain a constant fuel mass flow rate. The accumulator charge pressure was varied during the test using a pneumatic dome-loaded pressure regulator [for details, see Ref. 26].

To minimize oxidative carbon deposition in the heat exchanger, the JP-8 was de-oxygenated using a nitrogen sparging process, which reduced the oxygen concentration to <1 ppm. The sparging process involved bubbling a volume of nitrogen through the JP-8 to displace the trapped oxygen in the fuel. The volume of nitrogen necessary to reduce the oxygen concentration to acceptable levels was determined experimentally in previous work;²⁷ to ensure acceptable levels, a factor of safety of two was applied to all nitrogen volume calculations.

C. Instrumentation

For measuring the velocity of the combustion wave (wavespeed), ion probes were placed in ports, spaced 15.3 cm apart, along the length of the detonation tube. Thermocouples were placed in the center of the flow path for gathering fuel-temperature data at the inlet and outlet of the heat exchanger (J-type) to ensure proper flash vaporization. External-heat-exchanger wall temperatures were measured with J-type thermocouples that were mounted externally by compression clamps on the PDE detonation tube. A pressure transducer was situated at the closed end of the detonation tubes for measuring the pressure used to determine the ignition time.

D. Data Reduction

All combustion data were gathered on a dedicated computer that employs *LabVIEW*. 12 channels of raw data (a spark trace, a head-pressure trace, and 10 ion-probe traces) were collected in 0.5-sec intervals. The scan rate was set at 1,000,000 scans/sec; therefore, 500,000 data points were obtained for each channel in 0.5 sec. A C++ program segmented the data into separate firing cycles using the trigger trace. Each spark trace denoted a new firing cycle.

Each firing cycle was then analyzed for ignition-time information. The head-pressure trace data were passed through a fourth-order, 401-point, Savitzky-Golay, digital, finite-impulse response filter to reduce the high-frequency noise.²⁸ Linear regression was then used to determine the slope of the pressure curve. A 1000-point window, beginning with the first 1000 points of the pressure trace, moved forward along the pressure trace until an average pressure rise of 5000 psi/sec was detected. The time in the center of the window was taken to be the ignition time. Figure 5 is a plot of head-pressure traces, after passing through the Savitzky-Golay filter, for the six fuels. The pressure traces for all fuels, except that of hydrogen are shown with pressure offset (100 psi) for clarity. The pressure rise of hydrogen is steeper than that of the other fuels, although ethylene exhibits a pressure rise that is nearly as steep as that of hydrogen. Avgas, JP-8, and S-8 exhibit similar pressure traces; however, propane exhibits the poorest pressure rise.

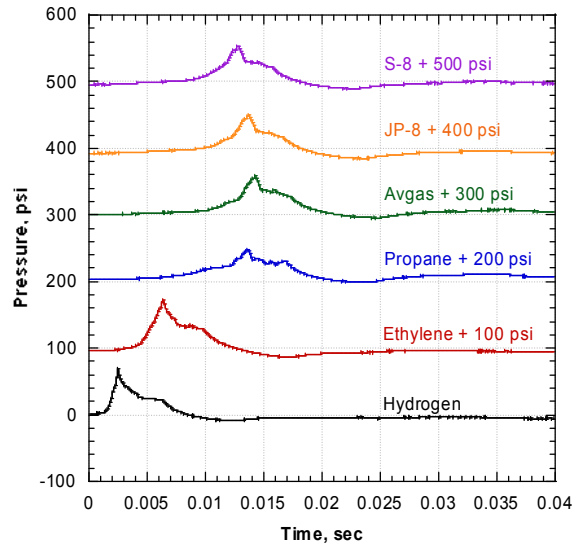


Figure 5. Head-pressure traces for hydrogen, ethylene, propane, avgas, JP-8, and S-8, with 100-psi offsets.

After the ignition time was determined, the probe times were calculated. The probe time is the time when the combustion wave crosses the ion probe. To determine the probe times, the C++ program took an average of the first 1000 points of the ion-probe traces to find a baseline value for that trace. The program then determined when the trace dropped below the baseline value for at least 500 consecutive data points. The probe time was the first point in the series of 500 points below the baseline value. This method essentially found the corners of the ion-probe trace and determined the time when they are found. Figure 6 is a plot of a sample pressure trace, along with a spark trace and 10 ion-probe traces.

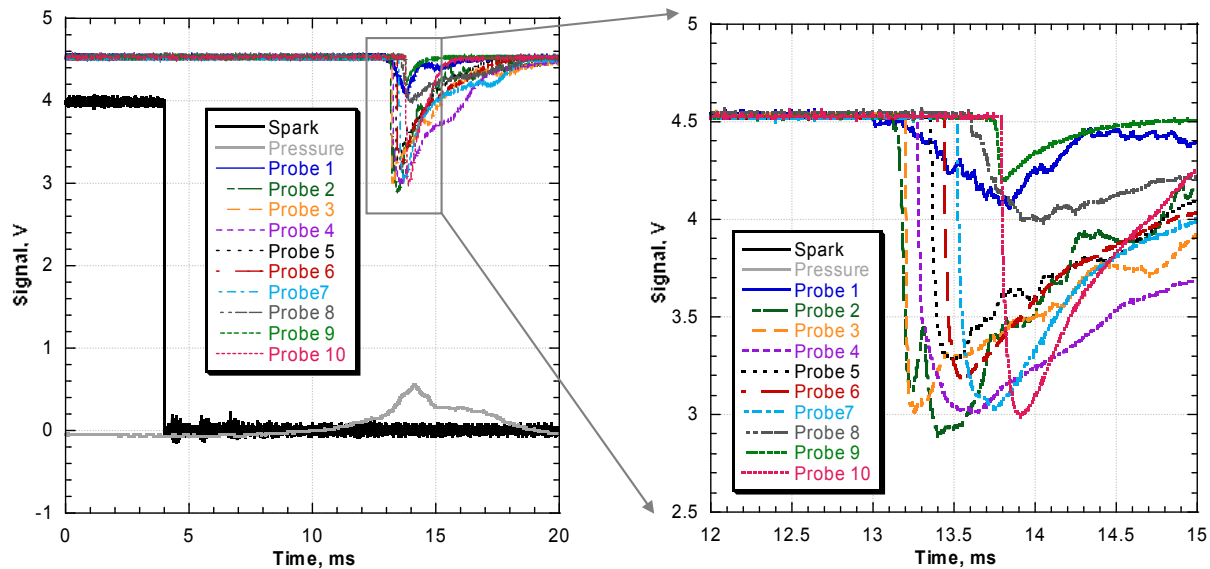


Figure 6. Representative output traces used to determine critical performance parameters.

Once both the ignition times and probe times were determined, they were inserted into an Excel spreadsheet. The spreadsheet first calculated the wavespeeds by dividing the difference in distance between two ion probes (15.3 cm for this effort) by the difference in the corresponding probe times. The wavespeed at 1.98 m downstream of the engine was recorded as the experimental CJ wavespeed. The spreadsheet then searched for wavespeeds above the theoretical CJ velocity. Once a wavespeed above the theoretical CJ limit was found, the program linearly interpolated between the wavespeed above the CJ wavespeed and the wavespeed at the location before it (below the

CJ wavespeed) to determine the time and location of a wavespeed matching the theoretical CJ wavespeed. The time and location determined were the DDT time and the DDT distance, respectively.

IV. Results and Discussion

Plots of the experimentally determined ignition time, DDT time, DDT distance, and CJ wavespeed as a function of equivalence ratio for mixtures of hydrogen, ethylene, propane, avgas, JP-8, and S-8 in air are presented. Each data point represents the mean value of 30 - 40 ignitions. The total experimental uncertainty is presented whenever possible. Schultz and Shepherd¹⁹ used STANJAN to calculate theoretical CJ wavespeeds of hydrogen, ethylene, and propane (shown later). The experimental CJ-wavespeed data from the present research were compared to the theoretical CJ wavespeeds of Schultz and Shepherd¹⁹. The experimental results are presented in tabular form in the appendix for reference.

A. Ignition Time

Figure 7(a) is a plot of ignition time as a function of equivalence ratio for mixtures of hydrogen, ethylene, propane, avgas, JP-8, and S-8 in air. These six fuels reached a minimum ignition time near an equivalence ratio of 1.3. Of all the fuels hydrogen produced the largest ignition limits as well as the lowest ignition times for the entire range of equivalence ratios. The rich limit of hydrogen was not reached because it was thought that no benefit would be derived from increasing the equivalence ratio further. Ethylene produced the second largest ignition limits and the second shortest ignition times. The propane, avgas, JP-8, and S-8 ignition trends were so similar that the plot had to be magnified to permit comparison Fig. 7(b). However, it can be observed in Fig. 7(a) that S-8 has larger ignition limits than JP-8 and avgas, most likely because S-8 typically contains fewer large hydrocarbons. Additionally, Fig. 7(b) shows that S-8 exhibits lower ignition times than JP-8 or avgas. Propane exhibits the lowest ignition times of all of the fuels that were fed in the liquid phase since it is a gas at ambient conditions, allowing for better mixing with the air. The longest ignition times and smallest ignition limits are observed in avgas.

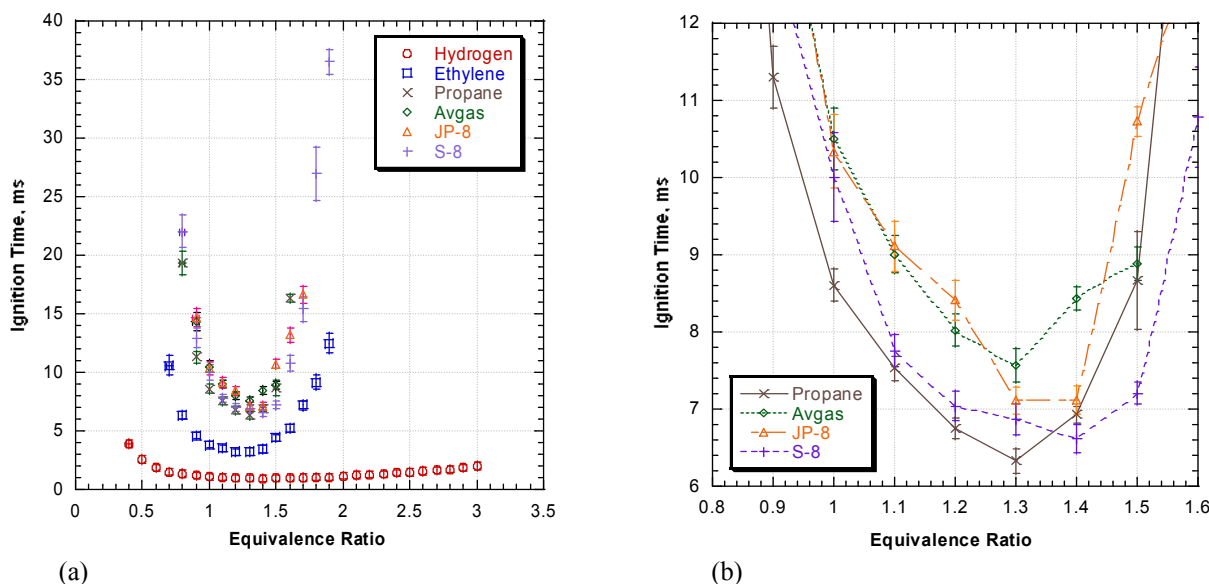


Figure 7. Plots of ignition time as function of equivalence ratio for mixtures of (a) hydrogen, ethylene, propane, avgas, JP-8, and S-8 in air and (b) propane, avgas, JP-8, and S-8 in air (magnified).

C. DDT Time

Figure 8(a) is a plot of DDT time as a function of equivalence ratio for mixtures of hydrogen, ethylene, propane, avgas, JP-8, and S-8 in air. Except avgas, all of the fuels reach a minimum DDT time between equivalence ratios of 1.1 and 1.2, which is lower than the equivalence ratio for minimum ignition time. The point of minimum DDT time for avgas is at the lean limit, 0.9. Hydrogen produces the largest detonatability limits of all of the fuels as well as the shortest DDT times for the entire range of equivalence ratios. Again, the rich limit of hydrogen was not reached during this research. Ethylene produced the second largest detonatability limits and the second shortest DDT times. Propane, avgas, JP-8, and S-8 detonation-initiation trends were so similar that the plot had to be magnified to permit comparison, Fig. 8(b). JP-8 and S-8 produce the shortest DDT times, except at the rich limits where S-8 has a lower

DDT time than JP-8. JP-8 and S-8 (octane no. ~40) outperform avgas and propane (octane no. ~100), possibly because of their lower octane number. Tucker et al.⁷ showed that the higher the octane number, the poorer the detonability for a given cell size.

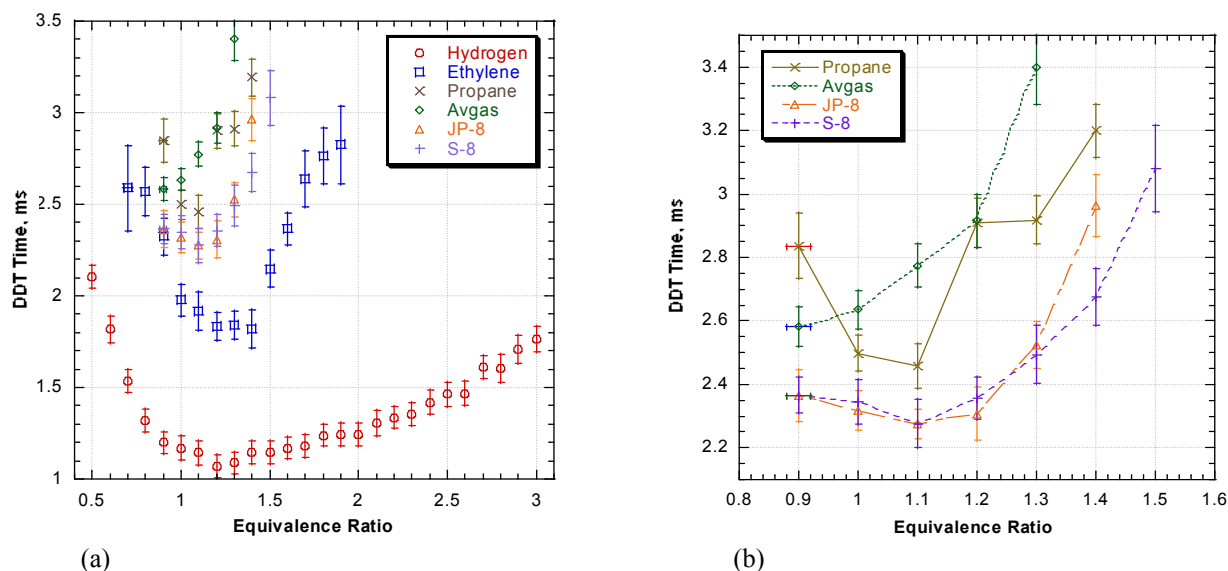


Figure 8. Plots of DDT time as function of equivalence ratio for mixtures of (a) hydrogen, ethylene, propane, avgas, JP-8, and S-8 in air and (b) propane, avgas, JP-8, and S-8 in air (magnified).

C. DDT Distance

Figure 9(a) is a plot of DDT distance as a function of equivalence ratio for mixtures of hydrogen, ethylene, propane, avgas, JP-8, and S-8 in air. The trends observed with DDT time are found in the DDT-distance results. Detonability is ranked as follows: Hydrogen > ethylene > S-8 ~ JP-8 > propane > avgas. Hydrogen detonates near 35 cm at a minimum, and ethylene detonates near 75 cm at a minimum. Again, the propane, avgas, JP-8, and S-8 detonation-initiation trends were so similar that the plot had to be magnified to permit comparison, Fig. 9(b). JP-8 and S-8 detonate in approximately the same distance, just < 1 m at a minimum. Propane detonates near 1.05 m at a minimum, and avgas detonates near 1.1 m at a minimum. Note: The trends in Figs. 7(a), 8(a), and 9(a) are the same as the trends of detonation cell size as a function of equivalence ratio shown in Fig. 2.

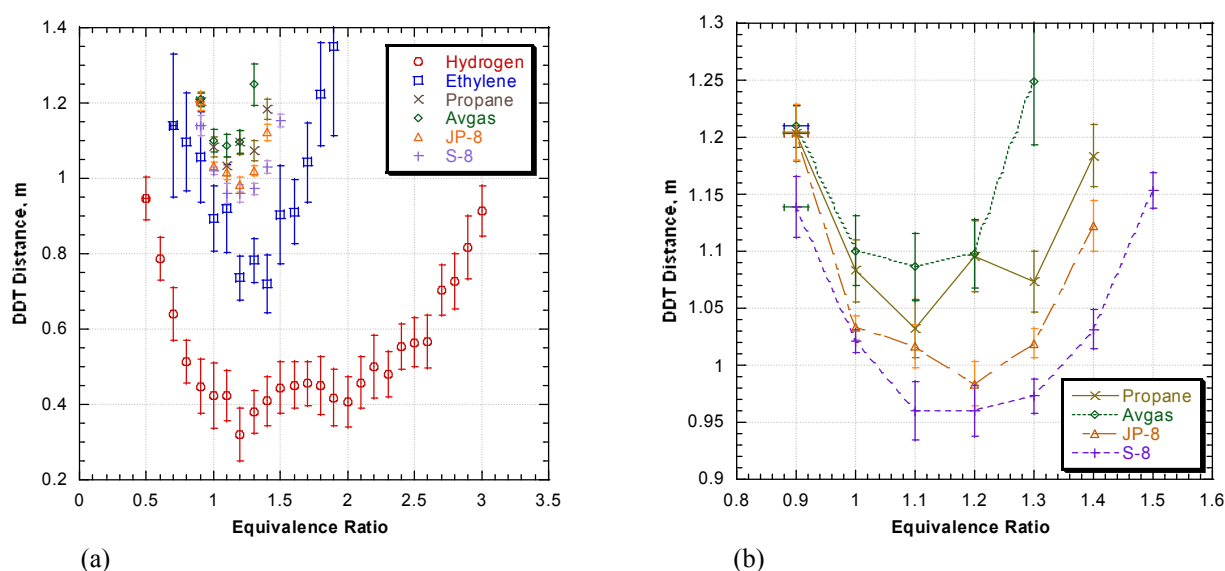


Figure 9. Plots of DDT time as function of equivalence ratio for mixtures of (a) hydrogen, ethylene, propane, avgas, JP-8, and S-8 in air and (b) propane, avgas, JP-8, and S-8 in air (magnified).

D. Wavespeed

Figure 10 contains plots of wavespeed for mixtures of (a) hydrogen and (b) ethylene in air as a function of equivalence ratio. The experimental CJ wavespeeds of hydrogen are systematically between 6 and 8% lower than the theoretical CJ wavespeed. The wavespeed was measured ~33 cm from the open end of the detonation tube. The measured wavespeeds were lower than the theoretical CJ velocities, presumably due to either diffusion of the hydrogen producing a lean mixture or the increased temperature of the fuel/air mixture. Wavespeed measurements of the hydrogen/air mixture taken farther upstream would have most likely fallen within 5% of the theoretical CJ wavespeeds. The experimental CJ wavespeed of the ethylene/air mixture is within 5% of the theoretical values, except at the rich limit. At the rich limit, the cell size for ethylene is near 100 mm, which is twice the diameter of the tube. Because of the large cell size the detonation was most likely overdriven.

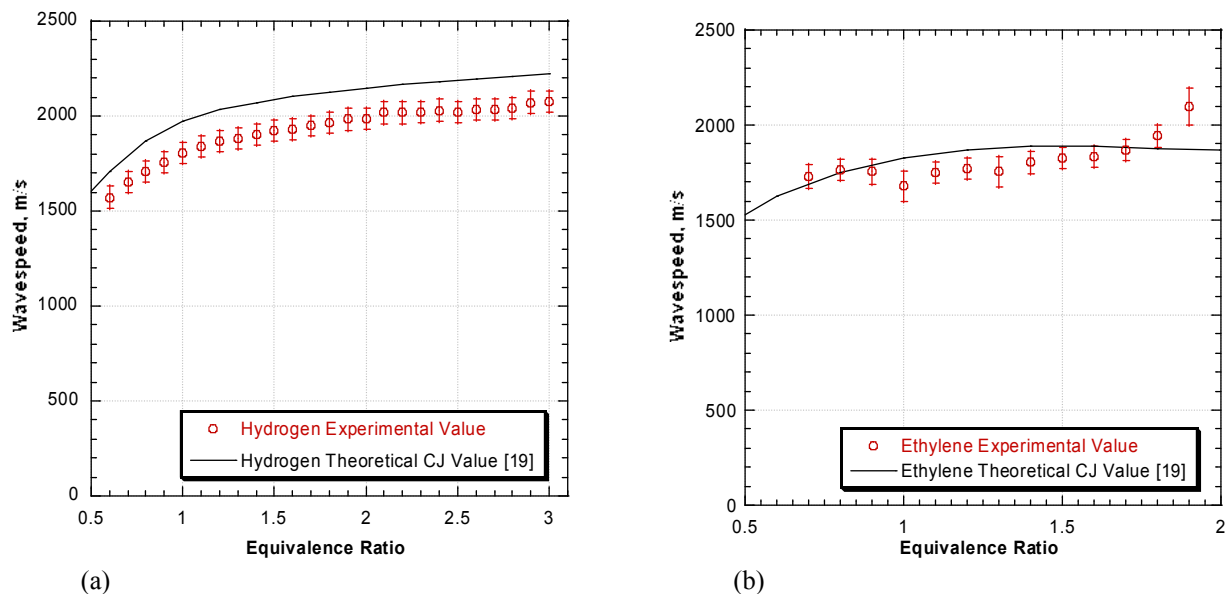


Figure 10. Plots of wavespeed as function of equivalence ratio for mixtures of (a) hydrogen in air and (b) ethylene in air (compared to theoretical CJ wavespeeds).

Figure 11 contains plots of wavespeed for mixtures of (a) propane and (b) avgas, JP-8, and S-8 in air as a function of equivalence ratio. With the exception of the rich limit, all experimental CJ wavespeeds for the propane/air mixtures fell within 5% of the theoretical CJ wavespeeds. The cell size of propane at the rich limit is slightly more than 100 mm, which probably led to an overdriven wavespeed. Since the cell sizes of avgas, JP-8, and S-8 are assumed to be similar to propane, the experimental CJ wavespeeds for these three mixtures are compared to the theoretical CJ wavespeeds for propane in Fig. 11(b). All of the experimental wavespeeds of avgas, JP-8, and S-8 fall within 5% of the theoretical CJ wavespeed for propane, further confirming the similarity in the detonation-initiation characteristics of propane and these liquid hydrocarbons.

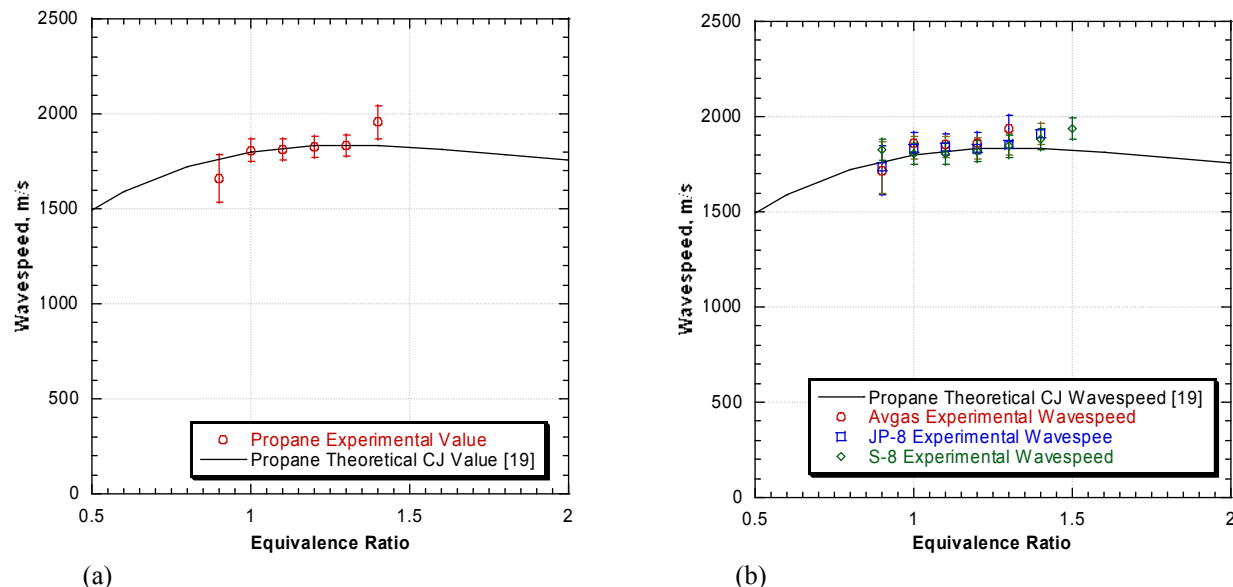


Figure 11. Plots of wavespeed as function of equivalence ratio for mixtures of (a) propane in air and (b) avgas, JP-8, and S-8 in air (compared to theoretical CJ wavespeeds for propane).

V. Conclusions

The ignition and detonation-initiation characteristics (ignition time, DDT time, DDT distance, and CJ wavespeed) have been determined for mixtures of hydrogen, ethylene, propane, avgas, JP-8, and S-8 in air. Hydrogen was found to have the best ignition and detonation initiation characteristics, followed by ethylene. Propane, avgas, JP-8, and S-8 exhibited similar ignition and detonation-initiation characteristics, although JP-8 and S-8 demonstrated slightly lower DDT times and distances than avgas and propane. All ignition and detonation-initiation trends closely matched the cell-size trends, further confirming the link between cell size and performance in a PDE. Minimum ignition times for all fuels occurred near an equivalence ratio of 1.3, whereas minimum DDT times and distances occurred between equivalence ratios of 1.1 and 1.2. Experimental CJ wavespeeds were found to be within 5% of the theoretical CJ wavespeeds for the majority of equivalence ratios; with the exception of hydrogen, which systematically exhibited experimental wavespeeds that were between 6% and 8% lower than the theoretical value.

Acknowledgments

This study would not have been possible without the technicians who worked on this project; our thanks to Curtis Rice and Dave Baker (ISSI). Dr. Tim Edwards (AFRL/PRTG) was extremely helpful in developing the fuel systems for this project. The authors would also like to thank Jeff Stutrud (AFRL/PRTC) for his controls and data-acquisition expertise. The technical leadership of Dr. Robert Hancock (AFRL/PRTC) was invaluable. Funding was provided by the Air Force Research Laboratory, Propulsion Directorate, and AFOSR.

References

- ¹Kailasanath, K., Patnaik, G., and Li, C., "On Factors Controlling the Performance of Pulsed Detonation Engines," *High-Speed Deflagration and Detonation: Fundamentals and Control*, edited by G. D. Roy, S. M. Frolov, D. W. Netzer, and A. A. Borisov, ELEX-KM Publishers, Moscow, 2001, pp. 193–206.
- ²Chuanjun, Y., Jun, L., Wei, F., Liming, H., and Hengren, L., "Principle and Cycle Analysis of Pulsed Detonation Engine," *Journal of Propulsion Technology*, Vol. 17, No. 3, June 1996, pp. 56–63.
- ³Kailasanath, K., "Review of Propulsion Applications of Detonation Waves," *AIAA Journal*, Vol. 38, No. 9, 2000, pp. 1704–1706.
- ⁴Eidelman, S., Grossman, W., and Lottati I., "Review of Propulsion Applications and Numerical Simulations of the Pulse Detonation Engine Concept," *Journal of Propulsion and Power*, Vol. 7, No. 6, November-December 1991.
- ⁵Edwards, T., "Liquid Fuels and Propellants for Aerospace Propulsion: 1903-2003," *Journal of Propulsion and Power*, Vol. 19, No. 6, 2003, pp. 1089–1107.

- ⁶Schauer, F. R., Miser, C. L., Tucker, K. C., Bradley, R. P., and Hoke, J. L., "Detonation Initiation Hydrocarbon-Air Mixtures in a Pulsed Detonation Engine," AIAA 2005-1343, 43rd AIAA Aerospace Sciences Meeting and Exhibit, Reno, NV, 10-13 January 2005.
- ⁷Tucker, K. C., King, P. I., Bradley, R. P., and Schauer, F. R., "The Use of a Flash Vaporization System with Liquid Hydrocarbon Fuels in a Pulse Detonation Engine," AIAA 2004-0868, 42nd AIAA Aerospace Sciences Meeting and Exhibit, Reno, NV, 5-8 January 2004.
- ⁸Tucker, K. C., "A Flash Vaporization System for Detonation of Hydrocarbon Fuels in a Pulse Detonation Engine," Ph.D. Dissertation, Department of Aeronautics and Astronautics, Air Force Institute of Technology, Wright-Patterson, AFB OH, 2005.
- ⁹Card, J., Rival, D., and Ciccarelli, G., "DDT in Fuel-Air Mixtures at Elevated Temperatures and Pressures," *Shock Waves*, Vol. 13, 2005, pp. 167-173.
- ¹⁰Ciccarelli, C. and Card, J., "Detonation in Mixtures of JP-10 Vapor and Air," *AIAA Journal*, Vol. 44, No. 2, 2006, pp. 362-367.
- ¹¹Akbar, R., Thibault, P. A., Harris, P. G., Lussier L.-S., Zhang, F., Murray, S. B., and Gerrard, K., "Detonation Properties of Unsensitized and Sensitized JP-10 and Jet-A in Air for Pulsed Detonation Engines," AIAA 2000-3592, 39th AIAA/ASME/SAE/ASEE Joint Propulsion Conference and Exhibit, Huntsville, AL, 20-23 July 2003.
- ¹²Austin, J. M. and Shepherd, J. E., "Detonation in Hydrocarbon Fuel Blends," *Combustion and Flame*, Vol. 132, No. 1-2, 2002, pp. 73-90.
- ¹³Knystautas, R., Guirao, C., Lee, J. H., and Sulmistras, A., "Measurement of Cell Size in Hydrocarbon-Air Mixtures and Predictions of Critical Tube Diameter, Critical Initiation Energy, and Detonability Limits," *Progress in Aeronautics and Astronautics*, AIAA, Vol. 94, pp. 23-37, 1984.
- ¹⁴Kaneshige, M. and Shepherd, J. E., *Detonation Database*, GALCIT Report FM97-8, GALCIT, Graduate Aeronautical Laboratories, California Institute of Technology, Pasadena, CA, July 1997.
- ¹⁵Fickett, W. and Davis, W. C., *Detonation: Theory and Experiment*, Dover Publications Incorporated, New York, NY, 1979.
- ¹⁶Guirao, C. M., Knystautas, R., Lee, J., Benedick, W., and Berman, M., "Hydrogen-Air Detonations," In 19th Symposium (International) Combustion Proceedings, Combustion Institute, Pittsburgh, PA, 1982, Vol. 19, pp. 583-590.
- ¹⁷Tieszen, S. R., Stamps, D. W., Westbrook, C. K., and Pitz, W. J., "Gaseous Hydrocarbon-Air Detonations," *Combustion and Flame*, Vol. 84, No. 3, 1991, pp. 376-390.
- ¹⁸Bull, D. C., Elsworth, J. E., Shuff, P. J., and Metcalfe E., "Detonation Cell Structures in Fuel/Air Mixtures," *Combustion and Flame*, Vol. 45, No. 1, 1982, pp. 7-22.
- ¹⁹Schultz, E. and Shepherd, J., "Validation of Detailed Reaction Mechanisms for Detonation Simulations," GALCIT Report FM99-5, Graduate Aeronautical Laboratories, California Institute of Technology, Pasadena, CA, 8 February 2000.
- ²⁰Schauer, F. R., Stutrud, J. S., and Bradley, R. P., "Detonation Initiation Studies and Performance Results for Pulse Detonation Engine Applications," AIAA 2001-129, 39th AIAA Aerospace Sciences Meeting and Exhibit, Reno, NV, 8-11 January 2001.
- ²¹Schelkin, K.L., *Soviet Journal of Technical Physics*, Vol. 10, pp. 823-827, 1940.
- ²²Tucker, K. C., King, P. I., Bradley, R. P., and Schauer, F. R., "The Use of a Flash Vaporization System with Liquid Hydrocarbon Fuels in a Pulse Detonation Engine," AIAA 2004-0868, 42nd AIAA Aerospace Sciences Meeting and Exhibit, Reno, NV, 5-8 January 2004.
- ²³Miser, C. L., King, P. I., and Schauer, F. R., "PDE Flash Vaporization System for Hydrocarbon Fuel Using Thrust Tube Waste Heat," AIAA 2005-3511, 41st AIAA/ASME/SAE/ASEE Joint Propulsion Conference and Exhibit, Tucson, AZ, 10-13 July 2005.
- ²⁴Bartok, W. and Sarofim, A. F., *Fossil Fuel Combustion – A Source Book*, John Wiley and Sons Incorporated, New York, NY, 1991.
- ²⁵Miser, C. L., Helfrich, T. M., Schauer, F. R., and Phelps D. K., "Supercritical Fuel Density from Experimental Pulse Detonation Engine," AIAA 2006-1025, 44th AIAA Aerospace Sciences Meeting, Reno, NV, 9-12 January 2006.
- ²⁶Helfrich, T. M., "Cycle Performance of a Pulse Detonation Engine with Supercritical Fuel Injection," M.S. Thesis, Department of Aeronautics and Astronautics, Air Force Institute of Technology, Wright-Patterson AFB, OH, 2006.
- ²⁷Panzenhagen, K. L., "Detonation Branching in a PDE with Liquid Hydrocarbon Fuel," M.S. Thesis, Department of Aeronautics and Astronautics, Air Force Institute of Technology, Wright-Patterson AFB, OH, 2004.
- ²⁸Parker, J. and Schauer, F. R., "Data Analysis and Compression Techniques for Megabyte-Data PDE Experiments," AIAA 2003-0892, 41st AIAA Aerospace Sciences Meeting, Reno, NV, January 2003.

Appendix: Results in Tabular Form

Table 1. Ignition time, DDT time, DDT distance, and experimental CJ wavespeed for hydrogen/air mixture

Equivalence Ratio	Ignition Time [ms]	DDT Time [ms]	DDT Distance [m]	CJ Wavespeed [m/s]
0.4	3.892	N/A	N/A	N/A
0.5	2.549	2.106	0.946	N/A
0.6	1.857	1.816	0.786	1573
0.7	1.503	1.534	0.641	1650
0.8	1.333	1.317	0.512	1710
0.9	1.202	1.198	0.448	1760
1	1.070	1.167	0.423	1806
1.1	1.048	1.143	0.424	1838
1.2	0.957	1.070	0.319	1868
1.3	0.952	1.087	0.379	1885
1.4	0.914	1.145	0.409	1904
1.5	0.965	1.146	0.444	1923
1.6	0.970	1.168	0.451	1933
1.7	1.012	1.179	0.456	1948
1.8	1.023	1.239	0.451	1968
1.9	1.059	1.242	0.418	1983
2	1.145	1.244	0.407	1986
2.1	1.225	1.305	0.457	2018
2.2	1.270	1.336	0.500	2020
2.3	1.316	1.355	0.481	2019
2.4	1.416	1.420	0.553	2031
2.5	1.461	1.464	0.565	2024
2.6	1.563	1.469	0.566	2036
2.7	1.625	1.611	0.705	2036
2.8	1.701	1.604	0.727	2043
2.9	1.849	1.712	0.817	2073
3	1.988	1.765	0.914	2075

Table 2. Ignition time, DDT time, DDT distance, and experimental CJ wavespeed for ethylene/air mixture

Equivalence Ratio	Ignition Time [ms]	DDT Time [ms]	DDT Distance [m]	CJ Wavespeed [m/s]
0.7	10.608	2.588	1.139	1728
0.8	6.355	2.568	1.097	1766
0.9	4.614	2.324	1.056	1754
1	3.831	1.977	0.894	1680
1.1	3.527	1.918	0.921	1751
1.2	3.200	1.836	0.735	1768
1.3	3.223	1.839	0.782	1754
1.4	3.446	1.817	0.720	1804
1.5	4.402	2.149	0.904	1825
1.6	5.244	2.366	0.912	1836
1.7	7.209	2.640	1.042	1871
1.8	9.152	2.765	1.225	1942
1.9	12.495	2.823	1.350	2097

Table 3. Ignition time, DDT time, DDT istance, and experimental CJ wavespeed for propane/air mixture

Equivalence Ratio	Ignition Time [ms]	DDT Time [ms]	DDT Distance [m]	CJ Wavespeed [m/s]
0.8	19.330	N/A	N/A	N/A
0.9	11.301	2.836	1.203	1659
1.0	8.608	2.499	1.083	1808
1.1	7.528	2.458	1.032	1811
1.2	6.750	2.908	1.095	1828
1.3	6.326	2.917	1.073	1831
1.4	6.926	3.199	1.184	1955
1.5	8.672	N/A	N/A	N/A
1.6	16.368	N/A	N/A	N/A

Table 4. Ignition time, DDT time, DDT istance, and experimental CJ wavespeed for avgas/air mixture

Equivalence Ratio	Ignition Time [ms]	DDT Time [ms]	DDT Distance [m]	CJ Wavespeed [m/s]
0.9	14.300	2.583	1.210	1717
1.0	10.502	2.636	1.101	1863
1.1	9.004	2.773	1.086	1854
1.2	8.024	2.916	1.098	1860
1.3	7.563	3.400	1.249	1936
1.4	8.430	N/A	N/A	N/A
1.5	8.884	N/A	N/A	N/A

Table 5. Ignition time, DDT time, DDT distance, and experimental CJ wavespeed for JP-8/air mixture

Equivalence Ratio	Ignition Time [ms]	DDT Time [ms]	DDT Distance [m]	CJ Wavespeed [m/s]
0.9	14.646	2.364	1.204	1734
1.0	10.337	2.318	1.033	1836
1.1	9.111	2.276	1.017	1837
1.2	8.411	2.307	0.984	1831
1.3	7.111	2.525	1.019	1854
1.4	7.118	2.964	1.122	1909
1.5	10.727	N/A	N/A	N/A
1.6	13.184	N/A	N/A	N/A
1.7	16.625	N/A	N/A	N/A

Table 6. Ignition time, DDT time, DDT distance, and experimental CJ wavespeed for S-8/air mixture

Equivalence Ratio	Ignition Time [ms]	DDT Time [ms]	DDT Distance [m]	CJ Wavespeed [m/s]
0.8	22.032	N/A	N/A	N/A
0.9	12.937	2.366	1.139	1826
1.0	10.006	2.346	1.021	1806
1.1	7.759	2.277	0.960	1805
1.2	7.038	2.357	0.960	1821
1.3	6.864	2.494	0.973	1844
1.4	6.614	2.676	1.031	1881
1.5	7.206	3.080	1.153	1939
1.6	10.783	N/A	N/A	N/A
1.7	15.431	N/A	N/A	N/A
1.8	26.975	N/A	N/A	N/A
1.9	36.534	N/A	N/A	N/A

Transient Plasma Ignition for Delay Reduction in Pulse Detonation Engines

Charles Cathey,¹ Fei Wang,² Tao Tang,³ Andras Kuthi,⁴ and Martin A. Gundersen⁵
University of Southern California, Los Angeles, Ca 90089

Jose O. Sinibaldi,⁶ and Chris Brophy⁷
Rocket Propulsion Laboratory, Naval Postgraduate School, Monterey, CA 93943

Ethan Barbour,⁸ and Ronald K. Hanson⁹
Stanford University, Stanford, CA 94305

John Hoke¹⁰ and Fred Schauer¹¹
Air Force Research Laboratory, Propulsion Directorate, Wright-Patterson AFB, OH 45433

Jennifer Corrigan¹² and John Yu¹³
Ohio State University, Columbus, OH 43210

This paper reviews the testing and evaluation of transient plasma for pulse detonation engine (PDE) ignition conducted at five laboratories. It also presents data showing significant reductions in times required for detonation. Critical to achieving functional levels of thrust are increased repetition rates, thus minimal delay to detonation times are an important parameter. Experiments have been conducted at the University of Southern California and in collaboration with researchers at the Naval Postgraduate School, Wright Patterson Air Force Research Laboratory, Stanford University, Ohio State University and the University of Cincinnati. In these studies it was observed that TPI significantly reduces delay times (factor of 2 to 9) in both static and flowing systems.

I. Introduction

THIS paper reviews testing and evaluation of transient plasma for pulse detonation engine (PDE) ignition under various conditions. The aerospace community has ongoing interests in the development of propulsion technologies based on pulse detonating engines (PDEs), and work is underway to determine whether this is a feasible technology. The PDE provides impulse through fuel detonation, and its potential advantages include efficient operation at both subsonic and supersonic speeds. In theory, a PDE can efficiently operate from Mach 0 to more than Mach 4.^{1, 2} In order to achieve almost continuous thrust, firing rates of 100 Hz or more are needed. Critical to achieving high repetition rates are minimal delay to detonation times. In work supported by the Office of Naval Research and the Air Force Office of Scientific Research, transient plasma ignition (TPI) has consistently

¹ PhD. Student, Department of Electrical Engineering - Electrophysics, AIAA Student Member.

² Scientist, Alpha & Omega Semiconductor, AIAA Member.

³ Scientist, Stanford Linear Accelerator.

⁴ Research Scientist, Department of Electrical Engineering - Electrophysics, AIAA Member.

⁵ Professor, Department of Electrical Engineering - Electrophysics, AIAA Member.

⁶ Research Associate Professor, Mechanical and Astronautical Engineering, AIAA Senior Member.

⁷ Research Associate Professor, Mechanical and Astronautical Engineering, AIAA Member.

⁸ PhD. Student, Department of Electrical Mechanical Engineering, AIAA Student Member.

⁹ Clarence J. and Patricia R. Woodard Professor, Department of Mechanical Engineering, AIAA Fellow.

¹⁰ Research Scientist, Propulsion Directorate, AIAA Member.

¹¹ Research Scientist, Propulsion Directorate, AIAA Member.

¹² Graduate Student, Department of Mechanical Engineering, AIAA Student Member.

¹³ Associate Professor, Mechanical Engineering, AIAA Senior Member.

shown substantial reductions in ignition delay time for various fuels.^{3,4,5} Experiments have been conducted at the University of Southern California and in collaboration with researchers at the Naval Postgraduate School, Wright Patterson Air Force Research Laboratory, Stanford University, Ohio State University, the University of Cincinnati, and California Institute of Technology.⁶ In these studies it was observed that TPI significantly reduces delay times in both static and flowing systems. Transient plasma ignition is attractive as an ignition source for PDEs because it produces reductions in ignition delay times, can reduce Deflagration to Detonation Transition (DDT) times, and has been shown to provide the capability to ignite under leaner conditions. This allows for high repetition rates, high altitude operation, and the potential for reduced NO_x emissions.^{7,8} The geometry of the discharge area is such that ignition is achieved with a high degree of spatial uniformity over a large volume relative to traditional spark ignition.

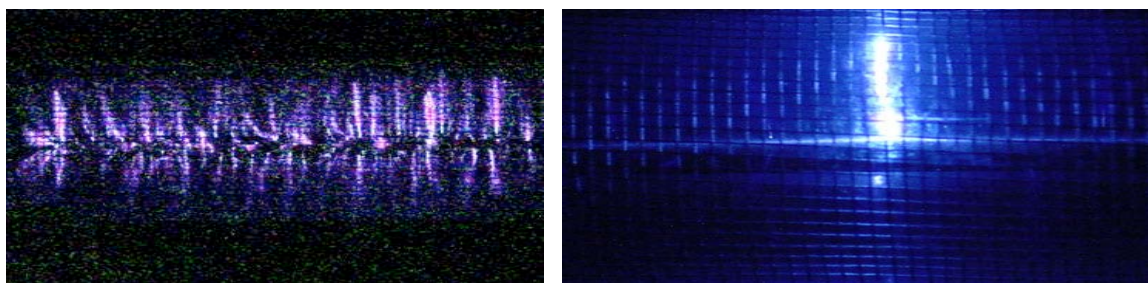


Figure 1: Transient plasma discharge (left), and spark discharge (right) to a metal mesh from a central anode. Observe the coaxial geometry allows for a voluminous array of streamers over the anode length.

The short timescale of the pulse (< 100 ns) prevents formation of an arc, and a voluminous array of streamers is used for ignition. It is possible that energetic electrons in the highly non-equilibrated electron energy distribution of the streamers cause dissociation of hydrocarbon chain molecules, producing active radicals throughout the ignition volume.⁹ The generation of a large number of radicals over the discharge volume seeds chain branching and propagation reactions such that multipoint ignition rapidly occurs.

In a PDE thrust scales linearly with repetition rate (and tube volume), thus if ignition delay is reduced by a factor of two, repetition rates can be potentially doubled, and thus thrust is potentially doubled (assuming there are no other limiting factors that occur). The two major limiting factors for high repetition rate operation in a PDE are ignition delay and the gas exchange time. Through the use of transient plasma as an ignition methodology, ignition delay has been substantially reduced (factor of 2 to 9) relative to a traditional spark, making it potentially an enabling technology for multi-cycle PDE operation. The duration of the PDE's operating cycle is generally on the order of 10s of milliseconds. It is important to note that for a PDE to achieve enough thrust to be a viable technology repetition rates of 60 Hz are needed, and 100 Hz or more are desired.

II. Experimental Setup

A. TPI Generation

For the work discussed in this paper the transient plasma is generated by a line type pseudospark switched pulse generator. The pulse generator is capable of creating a 50-75 ns pulse up to 90 kV, which creates a discharge as seen in Figure 1.¹⁰ The key element in the pulse generator is the pseudospark switch, which is a gas based cold, hollow cathode switch that is capable of switching 30 kA, with a rise time of 8 kA/ns. The pulse generator is based on the Blumlein architecture. However, instead of using transmission line, capacitors are used to make the pulse forming network. This results in a minimum pulse that is a critically dampened pulse, which will give voltage amplitudes of 64% of the charging voltage across the load. This differs from a traditional Blumlein pulse in which one obtains 100% of the charging voltage across the load. The pulse generator can be used in conjunction with a high voltage DC supply or a rapid charger for high repetition rate operation, typically for ignition application operation around 100 Hz. Figure 2 depicts the pseudospark pulse generator.

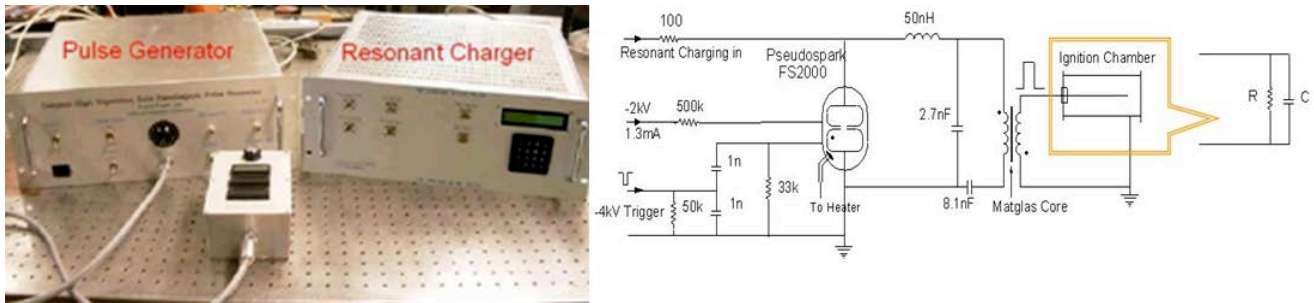


Figure 2: Pseudospark based pulse generator schematic.

The voltage and current traces for the transient plasma and a spark discharge are markedly different. In the transient plasma case, the voltage and current overlap, which implies that real power is being generated. However, in the spark discharge case the voltage will generally increase with no current, and then drop suddenly to zero with an increase in current as an arc is generated. This lack of overlap implies that in the spark discharge most of the energy is passing through the reactor and will be dissipated in the circuit, and not dropped across the load (typically less than 5% of the energy is deposited in the medium).

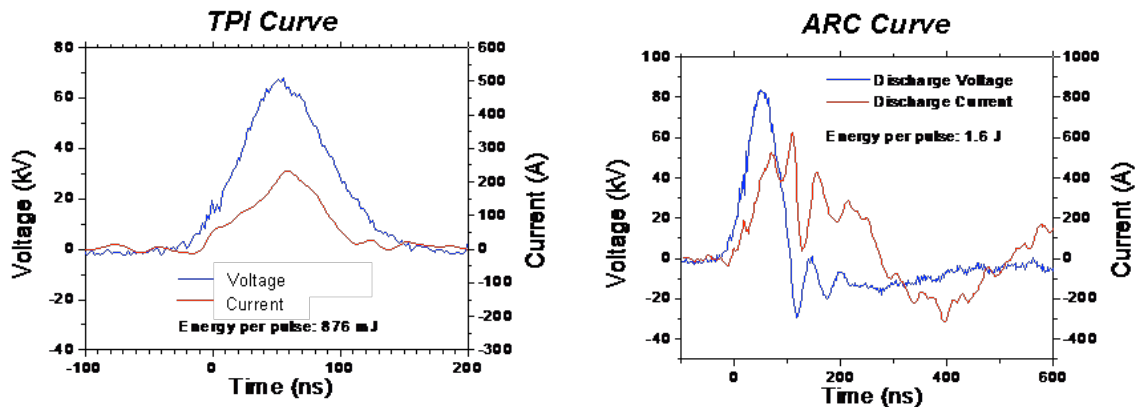


Figure 3: Transient Plasma (left) and transient plasma that coverts to an arc (right).

B. Experimental Setup

The interface between the TPI system and the PDE is largely the same for the various experiments (Figure 4). In general a HV charging source, in the form of a HV DC supply or a resonant charger, is used to charge the pseudospark switched pulse generator. Generally the pressure is measured with high speed pressure transducers, and wave speed is measured with multiple ion probes running the length of the tube.

A typical electrode is an 8-32" threaded rod, which is threaded for field enhancement to assist in streamer development. It is about 5" in length and acts as the anode running coaxially in the center of the tube at the engine head. The electrode seen in Figure 5 was developed for the Wright Patterson tests that follow, and is typical in structure of the electrodes used. The ceramic is MACOR, which is rated at about 1000 Volts/mil, and has a CTE relatively close to steel. The outer ground cylinder is steel, and acts as the return path for the discharge current. The electrode can be installed or removed from the system without the removal of the PDE tube (improvement over previous TPI electrode designs). Additionally the threaded rod's length can be adjusted to control the volume of the discharge. In previous designs the electrode had to be installed prior to mounting the tube, and thus any changes to its configuration or needed repair were difficult to achieve. It is also important to observe that it is a purely coaxial design. This was done largely to keep the noise down to a manageable level. EMI becomes a very large problem for nearby devices if unshielded connections are used.

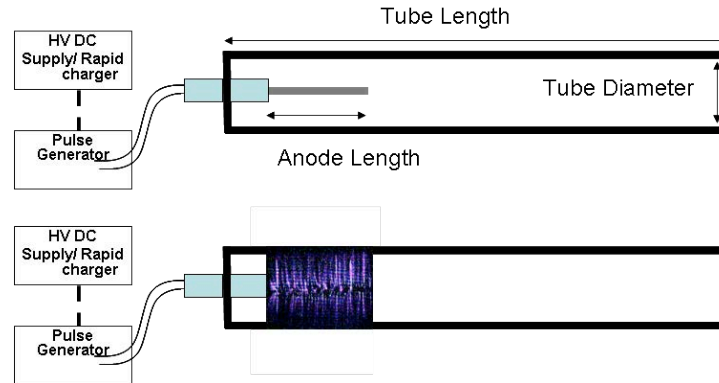


Figure 4: Top image is general configuration of TPI interface. Bottom illustrates streamer formation.



Figure 5: HV TPI electrode developed to feed through the 14mm interface used in the WP PDE.

The NPS experiment called for a 3" ID tube, with an electrode length of ~ 3 to 6 inches. The PDE is a valve less system that does not modulate the airflow through the engine. Its diameter is such that it allows for a minimum of 2 detonation cells sizes for a variety of fuels. The overall length of the engine was 1.13 m, with a Schelkhin spiral length of 0.914m. Repetition rates up to 40 Hz were tested under varying mass flow rates. For a detailed examination of the setup outlining the NPS experimental setup see the paper presented in reference 12.

The Wright Patterson experiment used a PDE consisting of a quad engine head and four detonation tubes.¹¹ The tubes were 2.067 inches in inner diameter, and were 73 inches long. Only two of the four detonation tubes were used for the Aviation gasoline (AVGAS) testing, and the one tube was used for the Hydrogen testing. In the multiple tube case, one tube was run with a sparkplug, and the other tube held the transient plasma electrode and was fired 180 degrees out of phase. This was done to maintain balance and reduce excess vibration in the system. The AVGAS was heated to 200° F upstream of the inlet to vaporize the fuel. A pressure transducer was located at the head of the tube, and there were seven ion probes spaced along the tube. Shchelkin-like spirals were used in both the AVGAS-air and the Hydrogen-air mixtures to ensure detonation. The transient plasma was tested at 10 Hz, and was charged with a 30 kV Glassman HV DC supply.

The Stanford experiment used a 1.5" ID tube with an electrode length of ~ 6 inches. Five pressure probes and seven ion probes were used. Additionally, a PDA 55 Silicon photodetector used in conjunction with a 308nm bandpass filter was used to monitor OH* emission.

III. Results and Discussion

A. Naval Postgraduate School

In work performed in collaboration with NPS we demonstrated at high flow rates where spark-initiated flames are normally extinguished, the transient plasma is able to ignite and effectively create a detonation wave.¹² Significant reduction (factor of 4) in ignition delay was shown for C₂H₄ – air mixtures. Additionally the TPI ignition

delay seemed relatively invariant to temperature and was at comparable energy levels with the conventional sparkplug baseline (Figure 6). Tests at NPS prior to the introduction of transient plasma as an ignition source were limited to low frequency operation, unless extra oxygen was introduced into the system. While extra oxygen in the lab may be okay, on an airborne platform the extra oxygen adds complexity, cost, weight, and increases the hazard levels to the overall system. Additionally, this experiment acted as a preliminary study showing that the mass flow rate has little effect on the ignition delay. However, as the mass flow rate increases, a decrease in the detonation wave speed is observed. The ignition delay varied from 3.95 ms to 4.25 ms as the mass flow rate varied from 0.1 to 0.4 kg/sec. As the ignition delay and mass flow rate increased, the detonation wave speed decreased from 1.5 km/sec to just over 1 km/sec. The latter case at 1 km/sec does not achieve a detonation wave. Moreover, this experiment tested possible multiple electrode configurations to facilitate pulsing the mixture several times as it transitioned down the tube. It was found that multiple pulses did in fact further reduce ignition delay, however, the drag losses introduced by the secondary electrode made this approach practically unfeasible. More recently, work has been performed at NPS using the TPI igniter in search of optimal spiral length for DDT reduction.¹³ This is a preface to work that is currently being done at NPS to test a new staged PDE engine design where TPI is the ignition source.

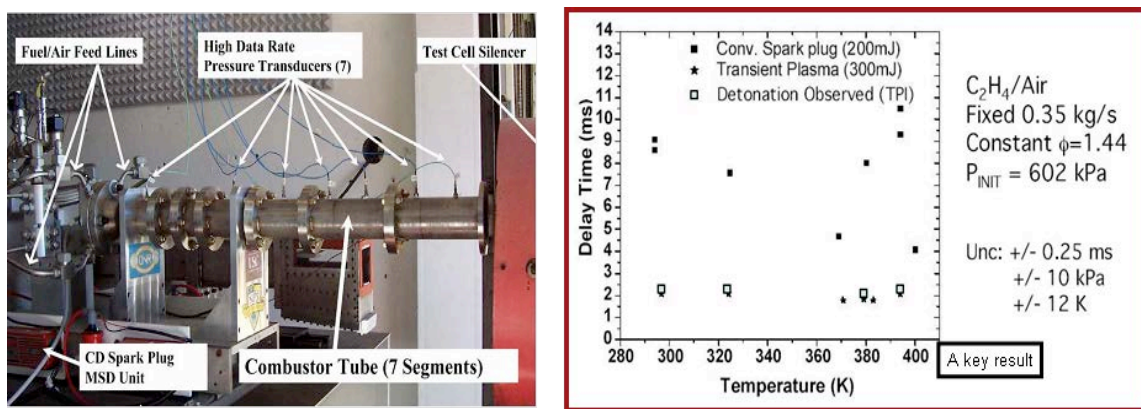


Figure 6: The left figure shows a valve less PDE setup at the Naval Postgraduate School. This type of architecture requires a booster, and its anticipated applications are missiles or rockets. The right figure shows a factor of 4 reduction in ignition delay for ethylene-air.

B. Wright Patterson Test

Tests conducted at Wright Patterson Air Force Base were performed, where TPI was first used on a valved PDE. For these first tests, H₂-air and aviation gasoline (AVGAS)-air mixtures were used. Shchelkin-like spirals were used for the H₂ as well as for the AVGAS mixtures in order to promote the DDT process. In hydrocarbon-air mixtures the reduction in ignition delay is of primary importance due to the low residence times experienced in vehicles traveling at high speeds (low hypersonic speeds) where ignition delay times can be orders of magnitude larger than the flow residence time. The ignition delay results for AVGAS are depicted in Figure 7. A reduction in the ignition delay by a factor of 2 was obtained here. The lean burn capabilities of the transient plasma ignition were also demonstrated. The transient plasma was able to reliably ignite AVGAS – air mixtures at equivalence ratios of nearly 0.65, whereas the baseline's lower limit was 0.71. The widening of the range of operation into the lean side of the curve is advantageous for high altitude engine operation. Also the lean operation allows for a more economical use of fuel when cruising, as well as reduces NO_x emissions. The reduced performance of the 66 kV pulse relative to the 59 kV pulse is likely resultant to small energy losses due to inadequate insulation between the electrode and the engine head. This is as compared to higher pulse voltages in which small parasitic arcing may have occurred from the HV cable/electrode interface to the engine head.

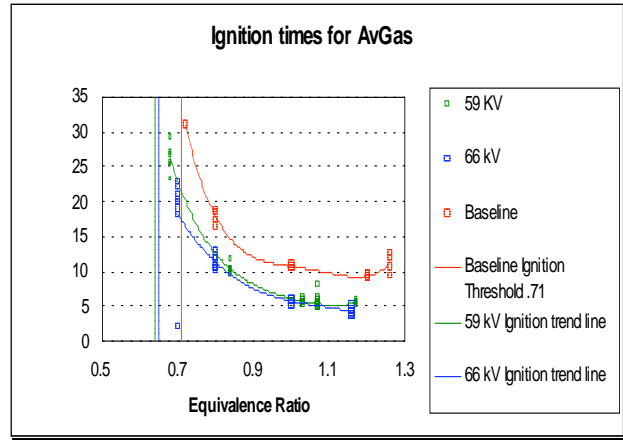


Figure 7: The left figure shows a valved PDE at Wright Patterson Air Force Base. The valved architecture would be used for an aircraft and would need no booster. The right figure shows a factor of 2 reduction in ignition delay for aviation gasoline.

For Hydrogen-air mixtures the reduction in ignition delay is important, primarily at high hypersonic cruising speeds where the flow residence time is very short. Hydrogen – air mixtures were also tested during these first experiments, primarily because they are relatively easy to detonate. Figure 8 depicts this ignition delay and the DDT times under these conditions. Observe that TPI was able to reduce the ignition delay time for H_2 – air mixtures almost by a factor of 2. The figure also depicts the DDT times for H_2 – air mixtures, which seemed to be on the order of the baseline with little or no improvement. The DDT times for AVGAS were similar in that TPI seemed to have little effect. That having been said, it should be noted that the error spread for the DDT times for H_2 and AVGAS – air mixtures were quite large, and efforts are currently underway to try to further process the data and reduce the error. To date there has not been a lot of work done on TPI's effects on DDT. Looking at the data taken at WP over the past two years, it suggests that besides ignition delay times, DDT is primarily controlled by fluid dynamics, and may be independent of ignition methodology.

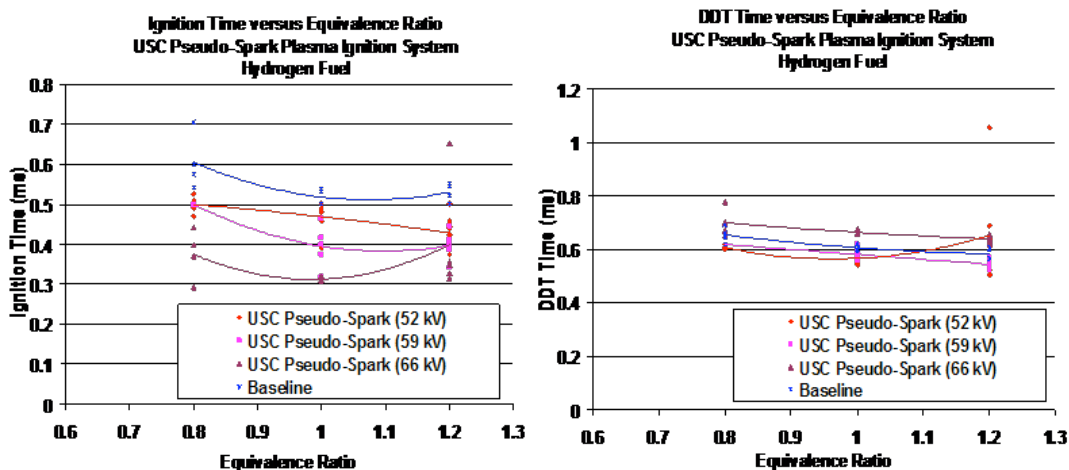


Figure 8: Ignition delay and DDT time for H_2 -air mixtures.

C. Stanford University

An example of TPI integration with a PDE is shown in Figure 9. TPI ignition of $C_2H_4 - O_2$ mixtures resulted in ignition delay reductions by nearly one order of magnitude (factor of 9). Of further interest are the OH emission measurements. There is a large difference in the amount and form of the emission signal shown in figure 10. This is a preliminary result and needs to be confirmed, however, it does possibly suggest that TPI is a new ignition process.

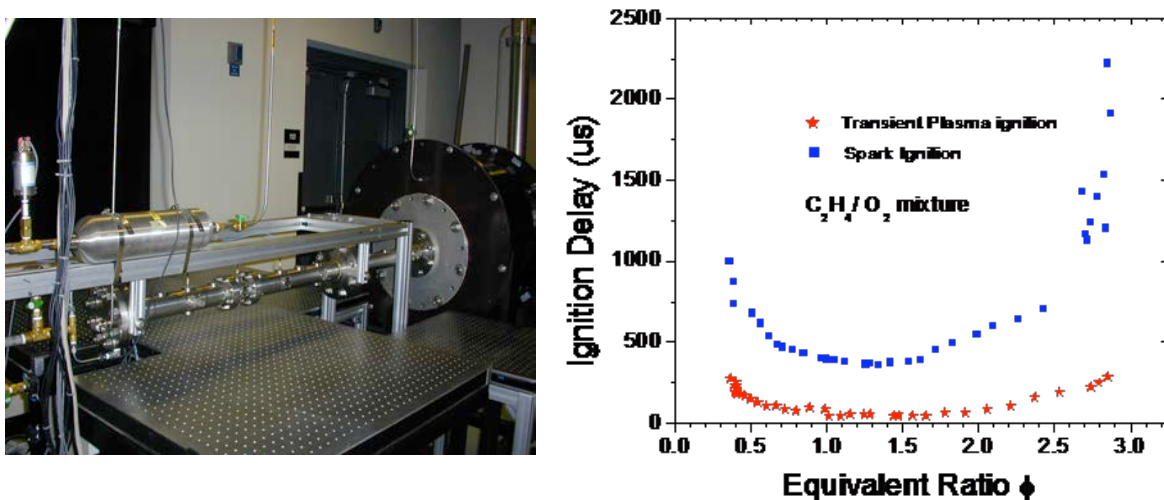


Figure 9: The left figure shows a PDE setup at Stanford University. The right figure shows a factor of 9 reduction in ignition delay for Hydrogen-Oxygen mixtures.

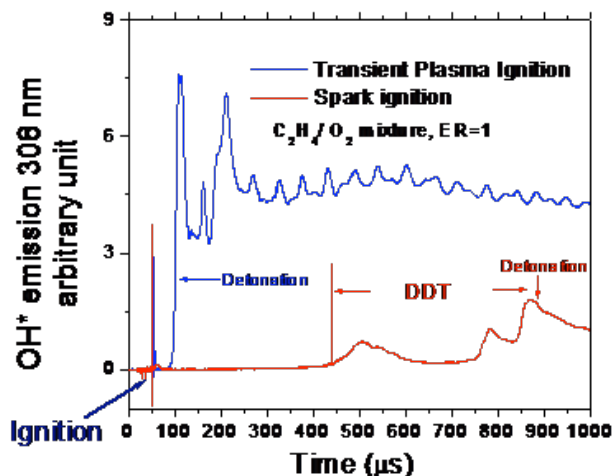


Figure 10: OH emission on Stanford PDE.

D. Summary

Table 1 depicts some of the ignition delay data taken at Stanford University, the Naval Postgraduate School, and Wright Patterson Air Force Base. Thrust scales linearly with repetition rate, and it is apparent from the results, tested under a variety of conditions, that transient plasma is potentially an enabling technology for high repetition

rate operations. Under varying test conditions delay to detonation reductions ranging from factors of 2 to 9 were found. Generally hydrocarbon-air mixtures were tested, however, hydrogen-air and hydrogen-oxygen mixtures were also tested. This table indicates the delivered energy per pulse. While in general TPI delivers more energy than a conventional sparkplug, it can deliver pulses of comparable energy and still provide significant reductions in ignition delay.¹⁴

Table 1: Transient plasma ignition of PDE results¹⁵

	Lab	Fuel	Oxidizer	Ignition Delay (msec)	DDT (ms)	Energy Delivered (J)
TPI	Stanford	C ₂ H ₄	O ₂	0.05	0.05	1.16
Spark	Stanford	C ₂ H ₄	O ₂	0.5	0.45	.075
TPI	NPS	C ₂ H ₄	Air	2		0.3
Spark	NPS	C ₂ H ₄	Air	8		0.2
TPI	WPAFB	AVGAS	Air	6	2.25	0.67
Spark	WPAFB	AVGAS	Air	10	1.7	.115
TPI	WPAFB	AVGAS	Air	5	2.5	0.87
Spark	WPAFB	AVGAS	Air	10	1.7	.115
TPI	WPAFB	H ₂	Air	0.4	0.57	0.67
Spark	WPAFB	H ₂	Air	0.51	0.61	.115
TPI	WPAFB	H ₂	Air	0.3	0.67	0.87
Spark	WPAFB	H ₂	Air	0.51	0.61	.115

Transient plasma ignition is definitely a viable technology and potentially an enabling technology for PDEs. This is still a relatively new area of research, and there is still a lot that needs to be explained, such as the physical processes behind transient plasma ignition. Transient plasma as an ignition source has a significant impact on the ignition delay times of the system, allowing for higher frequencies of operation. This increase in frequency directly correlates with thrust, and thus solves one of the biggest obstacles in producing a practical PDE to date at potentially comparable energy cost to the traditional spark.

IV. Conclusions

Transient plasma ignition is on the cutting edge of ignition methodologies for combustion engines. The PDE community in particular is interested in this technology for several reasons: 1) the capability to ignite in a manner that achieves detonation in hydrocarbon-air mixtures (without a previously required oxygen supplement); 2) the extension of the lower flammability limit of mixture and 3) the capability to reduce ignition delay times by factors of 2 – 9 offers comparable potential for increases in repetition rates. For these reasons transient plasma has the potential to overcome the traditional capacitive and inductive spark discharge, and laser discharge ignition techniques.

Acknowledgments

The authors would like to acknowledge the support of the ONR monitored by Dr. Gabriel Roy and that of the AFOSR monitored by Dr. Julian Tishkoff. We would also like to acknowledge all the technical staff and graduate students at the various institutions who directly and indirectly contributed to the success of these research campaigns over the past couple of years – our sincere gratitude is extended to all of you.

References

- ¹ P. G. Harris, R. A. Stowe, R. C. Ripley, and S. M. Guzik, "Pulse Detonations Engine as a Ramjet Replacement," AIAA-2006-462, Vol. 22, No. 2, March–April 2006.
- ² T. R. A. Bussing, T. E. Bratkovich, and J. B. Hinkey Jr., "Practical Implementations of Pulse Detonation Engines," AIAA-1997-2748 AIAA/ASME/SAE/ASEE Joint Propulsion Conference and Exhibit, 33rd, Seattle, WA, July 6-9, 1997.

- ³F. Wang, J. B. Liu, J. Sinibaldi, C. Brophy, A. Kuthi, C. Jiang, P. Ronney, and M. A. Gundersen, "Transient plasma ignition of quiescent and flowing air/fuel mixtures," IEEE Transactions on Plasmas, Volume: 33, Issue: 2, Part 2 April 2005, Pg 844-849.
- ⁴S. M. Starikovskaia, I. N. Kosarev, A. V. Krasnochub, E. I. Mintoussov, and A. Yu. Starikovskii, "Control of Combustion and Ignition of Hydrocarbon-Containing Mixtures by Nanosecond Pulsed Discharges," AIAA, AIAA-2005-1195, 43rd AIAA Aerospace Sciences Meeting and Exhibit, Reno, Nevada, Jan. 10-13, 2005.
- ⁵J. O. Sinibaldi, J. Rodriguez, B. Channel, C. Brophy, F. Wang, C. Cathey, and M. A. Gundersen, "Investigation of transient Plasma Ignition of Pulsed Detonation Engines," AIAA, AIAA-2005-3774, 41st Joint Propulsion Conference and Exhibit, Tucson, Arizona, July 10-13 2005.
- ⁶D. Lieberman, J. Shepherd, F. Wang and M. Gundersen, "Characterization of a Corona Discharge Initiator Using Detonation Tube Impulse Measurements," 43rd AIAA Aerospace Sciences Meeting and Exhibit, Reno, NV, Jan. 10-13, 2005. AIAA Paper 2005-1344.
- ⁷S. A. Bozhenkov, S. M. Starikovskaya, and A. Yu. Starikovskii, Combustion and Flame, 133(2003) 133-146.
- ⁸S. M. Starikovskia, E. N., Kukaev, and A. Yu. Kuksin, Combustion and Flame 139 (2004) 177-187.
- ⁹B. N. Ganguly, and J. W. Parish, "Absolute H atom density measurement in pure methane pulsed discharge," Applied Physics Letters, Vol. 84, No. 24, June 2004.
- ¹⁰F. Wang, A. Kuthi, M. A. Gundersen, "Compact High Repetition Rate Pseudospark Pulse Generator," IEEE Trans. on Plasma Science, 33, Issue: 4, Part 1, 1177 – 1181, Aug. 2005.
- ¹¹J. Corrigan, Masters Thesis 2006.
- ¹²J. Sinibaldi, J. Rodriguez, B. Chanel, C. Brophy, F. Wang, C. Cathey, and M. A. Gundersen, "Investigation for Transient Plasma for Pulse Detonating Engines," AIAA 2005-3774.
- ¹³P. Hutcheson, C. Brophy, J. Sinibaldi, C. Cathey, and M. A. Gundersen, "Investigation of Flow Field Properties on Detonation Initiation," 42nd AIAA/ASME/SAE/ASEE Joint Propulsion Conference 2006, Sacramento, California, 9 -12 July 2006.
- ¹⁴J. B. Liu, N. Theiss, P. D. Ronney, and M. A. Gundersen, "Minimum ignition energies and burning rates of flames ignited by transient plasma discharges," 2003 meeting of Western States Section/Combustion Institute, UCLA, Oct 20-21, 2003, Paper 03F-88. 2002.
- ¹⁵C. Cathey, F. Wang, T. Tang, A. Kuthi, M. A. Gundersen, J. Sinibaldi, C. Brophy, J. Hoke, F. Schauer, J. Corrigan, J. Yu, E. Barbour, and R. Hanson, "Transient Plasma Ignition for Delay Reduction in Pulse Detonation Engines," 45th AIAA Aerospace Sciences Meeting and Exhibit, Reno, Nevada, 2007, TBP.

Effects of Corona, Spark and Surface Discharges on Ignition Delay and Deflagration-to-Detonation Times in Pulsed Detonation Engines

Kenneth Busby¹

National Research Council, Wright-Patterson AFB, OH 45433

Jennifer Corrigan² and Sheng-Tao Yu³

Ohio State University, Columbus, OH 43210

Skip Williams,⁴ Campbell Carter,⁵ and Frederick Schauer⁶

Propulsion Directorate, Wright-Patterson AFB, OH 45433

John Hoke⁷

Innovative Scientific Solutions, Inc., Dayton, OH 45440

and

Charles Cathey⁸ and Martin Gundersen⁹

University of Southern California, Los Angeles, CA 90089

The purpose of the research described herein is to compare the ignition delays in an experimental pulsed detonation engine produced by thermal and non-thermal ignitions. The commercial thermal ignition has a pulse duration of about 1 μ s, whereas the non-thermal ignitions have pulse durations of 100 ns. Ignition delay is an important factor, along with fill and purge times, that limit the maximum repetition rate and thrust of pulsed detonation engines. For stoichiometric fuel-air mixtures with aviation gasoline at 1 atmosphere and 360-480 K, an ignition delay of 6 ms was observed with a non-thermal ignition, whereas the ignition delay was 11 ms with an aftermarket automotive ignition. By replacing the resistive cable and resistor of the aftermarket ignition with a non-resistive cable and surface discharge igniter, its ignition delay was reduced to 7 ms, which is comparable to that produced by the non-thermal ignitions.

Nomenclature

AFRL	=	Air Force Research Laboratory, located at the Wright-Patterson Air Force Base
CJ	=	Chapmann-Jouget
DDT	=	deflagration-to-detonation time; equal to detonation time minus ignition delay
Detonation Time	=	time from the ignition spark to initiation of a detonation wave
Exciter	=	high voltage ignition circuit consisting of capacitors, diodes, resistors, and switches
FWHM	=	full width at half the maximum height
Igniter	=	a spark-plug or device that produces electrical discharges; can also be an ignition system

¹ Senior Research Associate, AFRL/PRAS, AIAA Member

² Presently an Aerospace Engineer at GE Aviation, Evendale, OH, AIAA Member

³ Professor, Mechanical Engineering, AIAA Member

⁴ Senior Research Physicist, AFRL/PRAS, AIAA Senior Member

⁵ Senior Aerospace Engineer, AFRL/PRAS, AIAA Member

⁶ Aerospace Engineer, AFRL/PRTC, AIAA Member

⁷ Aerospace Engineer, AFRL/PRTC, AIAA Member

⁸ Graduate Student, Electrical Engineering Department, AIAA Student Member

⁹ Professor, Electrical Engineering Department, AIAA Member

<i>Ignition Delay</i>	=	time from the ignition pulse to a pressure rise due to heat release
<i>J</i>	=	Joule
<i>MSD</i>	=	Multiple Spark Discharge Ignition, an aftermarket automotive ignition
<i>nF</i>	=	nano-farad
<i>PDE</i>	=	pulsed detonation engine
<i>pF</i>	=	pico-farad
<i>pps</i>	=	pulses per second
<i>TE</i>	=	Transverse Exciter, a 100-ns ignition built at the Air Force Research Laboratory
<i>TPI</i>	=	Transient Plasma Ignition, a 100-ns ignition built at The University of Southern California
<i>WPAFB</i>	=	Wright-Patterson Air Force Base, located in Dayton, OH
Φ	=	fuel-air equivalence ratio

I. Introduction

Pulse detonation engines are being developed because of their mechanical simplicity and potential to operate efficiently at high speed. The basic constraint on PDE engine operating frequency is the time to fill, ignite, detonate, and purge each thrust tube. In the PDE engine under test, the ignition delays are much larger than the deflagration-to-detonation (DDT) times. Thus, an ignition system that can minimize the ignition delay over fuel-air equivalence ratios of 0.8 to 1 is highly desirable to increase PDE operating frequency and thrust, while reducing engine size.

Ignition systems that produce 100-ns electrical discharges have been shown to reduce the ignition delay below that obtainable with standard spark ignitions.¹ These ignitions are often referred to as pulsed corona, fast transient, transient plasma, non-equilibrium or non-thermal ignitions in the literature. A 100-ns electrical discharge is the initial breakdown phase of an arc, but here the discharge is terminated before its impedance collapses. Fast transient discharges produce streamers of highly reactive radicals and excited molecules which accelerate the ignition process.

Fast transient ignition has been shown to reduce the ignition time on other PDE engines.² Ignition with non-equilibrium electrical ignitions is under investigation by other research groups on a variety of propulsion systems, including PDE engines.^{3,4,5,6,7,8} For example, Starikovskii et al⁹ have proposed an array of fast-ionization discharges to reduce ignition delays in PDE engines.

The tests described below are a subset of an initial survey to compare the capabilities of thermal and non-thermal ignitions in a PDE engine over a variety of operating conditions. The engine is fueled with aviation gasoline. A more complete description of the tests is given elsewhere.¹⁰

II. Experimental Setup

A. Pulsed Detonation Engine

A schematic of the AFRL pulsed detonation engine located at Wright-Patterson AFB, OH is shown in Fig. 1. Compressed air and aviation gasoline were premixed and preheated to 370-480 K, then injected through a General Motors Quad 4 engine head and into two 5.2 cm internal diameter, 1.85 m long thrust tubes where it was ignited and then detonated. The fill volume of the fuel-air mixture within the thrust tubes was regulated by the fuel-air manifold pressure, the camshaft/valve timing in the engine head and the repetition rate. The fuel-air mixture filled approximately 100% of the thrust tubes before ignition. The valve timing was 120° each for the fill, fire, and purge cycles. The repetition rate was 10 pps. With aviation gasoline as the fuel, two thrust tubes were operated 180° out of phase to provide consistent fills. A Shchelkin spiral was installed inside one thrust tube to aid in detonation, whereas the second tube has no spiral. Only the tube with the spiral was ignited with a spark plug, corona igniter or surface discharge igniter; the detonated fuel was directed out the open end of the tube to the atmosphere, generating thrust. The fuel-air mixture in the second thrust tube (without the spiral) was not ignited with a spark plug, but flowed out the open end where it was ignited by the exhaust from the first tube. To monitor the progression of detonation waves, a series of the ionization probes were installed along the first thrust tube, as shown in Fig.2. The ionization probes were spark plugs with the center electrode charged to low voltage. An electrical discharge through the spark plug is an indication of plasma. Detonation wave fronts are weakly ionized and, thus, can be recorded by ionization probes as they propagate down the thrust tube.

Two important measurements are reduced from data recorded by a digital acquisition system: the ignition delay, which is the time from when the ignition system fires to when a pressure increase due to heat release is observed in the thrust tube, and the detonation time, which is the time from when the ignition system fires to when a detonation wave is first observed. A detonation wave is said to occur when the wave speed becomes 90% of the theoretical CJ

velocity of ~ 1800 m/s. From these two measurements, the deflagration-to-detonation time (DDT), which is equal to the detonation time minus the ignition delay, is calculated.

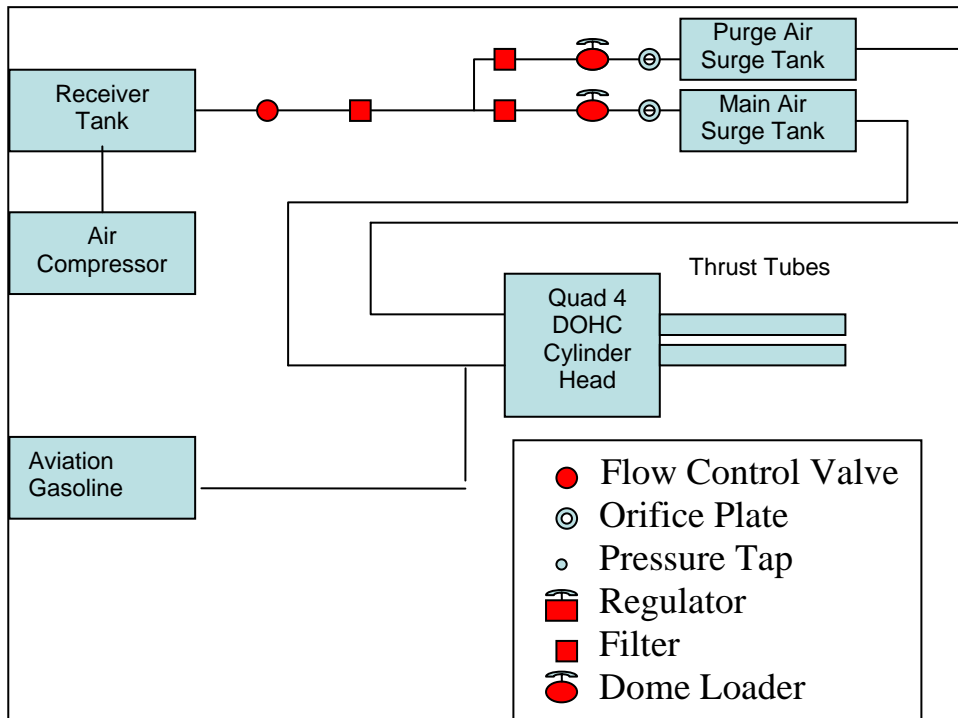


Figure 1. Pulsed Detonation Engine Configuration

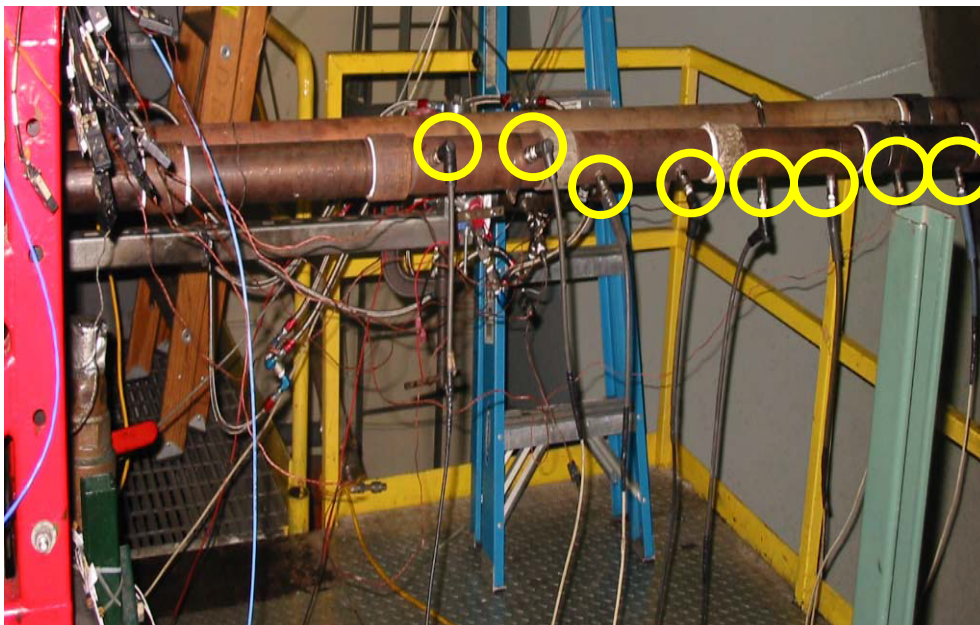


Figure 2. The location of ionization probes (highlighted by the yellow circles) along a thrust tube.

B. Exciters

Five different ignition systems were compared in these tests: the Transverse Exciter (TE), the Transient Plasma Ignition (TPI), the AFRL ignition, the Multi-Spark Discharge (MSD) ignition, and a modified MSD ignition. The TE, TPI and AFRL ignitions are non-thermal in nature, whereas the MSD and modified MSD ignitions are thermal ignitions. The ignitions allow comparisons based on the type of discharge (thermal and non-thermal), type of igniter (corona igniter, surface discharge igniter, or spark plug), polarity, and energy.

The TE ignition is a 100-ns, capacitive discharge ignition built at the AFRL. It is so named because its primary application is to inject electrical pulses transverse to high speed airflow in scramjet combustors. The TE ignition is a new system and was included here to test its reliability before progressing onto high speed air tunnel tests. Typical output pulse voltages are 25 to 40 kV. The TE ignition circuit can be arranged to produce either positive or negative pulses to test ignition capability of both polarities. TE ignition energy is adjusted by varying the exciter capacitance. The discharge generally begins with a corona like discharge and terminates in a spark. The efficiency of energy transfer from the exciter to the electrical discharge is 25 to 45% with surface discharge igniters, depending on discharge length, and about 45% with corona igniters. Circuit design and operation are described elsewhere.¹¹

The TPI ignition, built at the University of Southern California, is a capacitive discharge ignition consisting of a lumped element Blumlein and a 3:1 step-up transformer to produce high voltage output pulses, typically 52 to 66 kV peak with a full-width, half-maximum (FWHM) duration of 50 to 75 ns. The discharge is a corona discharge that fills a 2.5 to 5 cm long section of the thrust tube. Efficiency of energy transfer from the exciter to the electrical discharge is typically 50%. Exciter energy is varied by adjusting the charging voltage. In these tests, the TPI exciter was operated only in positive polarity with a corona igniter, although it can operate with negative polarity also. A description of the TPI ignition is provided in Ref. 2.

The AFRL ignition is a negative output pulse version of the TE igniter with the output switch removed. In this setup, the exciter capacitance and the high voltage electrode of the igniter are directly connected. The charging time is from 0.5 to 10 milliseconds (depending on capacitance) and, when the maximum hold-off voltage of the igniter is exceeded, a 100-ns discharge from the high voltage electrode of the igniter to ground occurs. Data from this ignition is not included in this paper, although the best results are comparable with those reported here.

The MSD ignition is an aftermarket automotive spark ignition, part number 6215. It is a multi-channel, programmable, capacitive-discharge ignition with a resistive cable and spark plug. The voltage rises to a peak of 6.5 kV (the spark gap breakdown voltage) in about 5 μ s, and, after breakdown, the ignition produces a peak current of 0.4 A. The FWHM of the power pulse is about 1 μ s, with the current pulse continuing for about 50 μ s thereafter. The current is limited by the resistance of the cable and the spark plug. The exciter energy is 0.105 to 0.115 J. The efficiency of energy transfer from the exciter to the electrical discharge is about 3%. All baseline measurements are done with this ignition. This ignition is also referred to as the unmodified MSD ignition.

The improved MSD ignition is the MSD exciter, with the resistive cable and spark plug replaced by a non-resistive cable and a surface discharge igniter, thus increasing the energy delivered to the electrical discharge.

C. Igniters

Three types of igniters are used in the tests: a corona igniter, a surface discharge igniter, and a spark plug. Schematics of the corona and surface discharge igniters are shown in Figs. 3 and 4. All igniters are mounted in the PDE engine head and centered in the cylindrical thrust tube. The gray areas are metallic flanges or pipes, the white areas enclosed by thin black lines are voltage-insulating ceramics, the thick black lines are wires or threaded rods, and the red areas are electrical discharges. All the figures have cylindrical geometry. The corona and surface igniters are made from the same device, consisting of a threaded 0.32 cm diameter metallic electrode, a 0.95 cm diameter ceramic tube surrounding the electrode, and a metallic fitting that screwed into the PDE engine head. With the corona igniter, the ceramic is pushed approximately 10 cm into the combustion chamber so that a radial electrical discharge forms between the high voltage electrode to the grounded thrust tube. The radial distance between the high voltage electrode and the grounded thrust tube is approximately 2.6 cm and, thus, a peak voltage of about 30-66 kV is required to form an electrical discharge. The TE and TPI ignitions were used with the corona igniter. With the surface igniter, the ceramic tube length is adjusted between 1 and 20 mm such that the electrical discharge forms along the surface of the ceramic, from the high voltage electrode to the grounded engine head. A peak voltage of 20 to 40 kV is required to form the electrical discharge. The TE and modified MSD ignitions were used with the surface discharge igniter. The spark plug is a modified AC Delco 41-629, or equivalent. The spark plug has a 1.1 cm outer diameter, 0.88 cm long metallic cylinder welded onto the end, with two vent holes located 180° from each other. This modified spark plug is used exclusively with the unmodified MSD exciter.

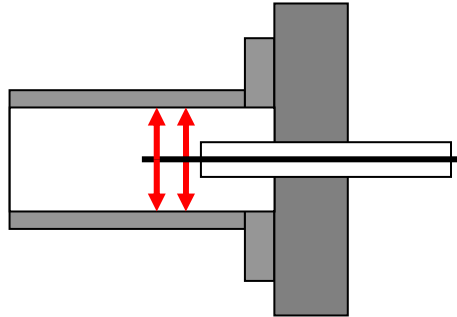


Figure 3. Placement and Operation of Corona Igniter in a PDE Thrust Tube

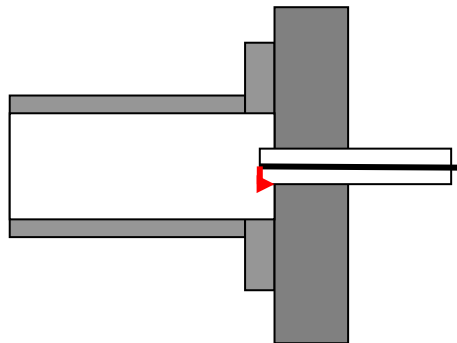


Figure 4. Placement and Operation of a Surface Discharge Igniter within a PDE Thrust Tube

III. Experimental Results

The baseline ignition delays and deflagration-to-detonation times as a function of fuel-air equivalence ratio (ϕ) are shown in Fig. 5. This data was taken with the unmodified MSD ignition with a modified spark plug operated in the PDE fueled by aviation gasoline. Data was recorded over a fuel-air equivalence range of 0.8 to 1.2. The ignition delay is 9.5 ms at $\phi = 1.2$, rising to 11 ms at $\phi = 1$ and 16.5 ms at $\phi = 0.8$. The DDT times remain approximately constant near 2 ms. The curves are second order polynomial fits to the data recorded at $\phi = 0.8, 1$, and 1.2. These curves are included in the following graphs for comparison.

Ignition delay and DDT data for a TE ignition that produces positive polarity pulses and the modified MSD ignition are shown in Fig. 6. A surface discharge igniter (shown in Fig. 4) is used with both ignitions. The PDE is fueled with aviation gasoline. Each data point (at each equivalence ratio) represents an average of 1 to 6 measurements. Data scatter is typically ± 2 ms. The curves are based on a second degree polynomial fit to the data

points. The energy levels quoted in the figures are estimated exciter energies. Neither the charging voltage nor the output voltage and current waveforms of the exciter were monitored during operation. All the TE ignition delay curves lie below the baseline MSD ignition delay curve. As the capacitance and energy increases, the ignition delay decreases, while the DDT times remain approximately constant. The shortest ignition delays are 6.5 ms at $\phi = 1$ and 1.2 and 11 ms at $\phi = 0.8$ when a 4 nF capacitor is installed in the TE exciter. The spread from the lowest capacitance (130 pF) to the highest capacitance (4nF) is 1.5 ms at $\phi = 1$ and 1.2 and 5 ms at $\phi = 0.8$.

A comparison between the TE ignition delays at two selected capacitances and the modified and unmodified MSD ignition delays are shown in Table 1. Note that the modified MSD ignition delays are comparable to those of the TE ignition, although the exciter energy of the modified MSD ignition is less. The data indicate that a thermal (modified MSD) ignition can produce ignition delays comparable to those of a non-thermal (TE) ignition, under the present PDE operating conditions of 1 atmosphere pressure and 360 to 480 K. By replacing a resistive cable and spark plug with a non-resistive cable and surface discharge igniter, the ignition delay produced by a MSD ignition system can be reduced by 4 ms at lean and stoichiometric fuel-air ratios.

Table 1. Comparison of TE, Improved MSD, and Unmodified MSD Ignition Delays

Fuel-Air Equivalence Ratio	0.8	1.0	1.2
TE Ignition, Surface Discharge Igniter, 650 pF, 0.25 J	12 ms	7 ms	7 ms
TE Ignition, Surface Discharge Igniter, 4 nF, 1.5 J	11 ms	6.5 ms	6.5 ms
Improved MSD Ignition, Surface Discharge Igniter, 0.115 J	12.5 ms	7 ms	8.5 ms
Unmodified MSD Ignition, Modified Resistor Spark Plug, 0.115 J	16.5 ms	11 ms	9.5 ms

A similar set of data for a TE ignition that produces negative polarity pulses is shown in Fig. 7. In this case, a corona igniter is used (shown in Fig. 3). The shortest ignition delays were produced with the largest capacitance, 1.3 nF, except at $\phi = 1.2$ where the 237.5 pF capacitance produced slightly better results. Comparisons of the ignition delays produced by positive and negative pulses at two selected capacitances are shown in Tables 2 and 3. For the case of a 237.5 pF capacitance, the ignition delays at $\phi = 1$ and 1.2 are about 7 ms for both polarities, whereas the ignition delay for the positive polarity is 3.5 ms longer. In the case of a 1.3 nF capacitance, the ignition delays were nearly the same at each of the fuel-air equivalence ratios (11 ms at $\phi = 0.8$ and 7 ms at $\phi = 1.0$ and 1.2). The data indicates that the negative polarity, corona igniter setup has an advantage over the positive polarity, surface discharge igniter at low energy and capacitance (237.5 pF). At the higher capacitance (1.3 nF), the difference in ignition delays between a positive pulse with a surface discharge igniter and a negative pulse with a corona igniter are small.

Table 2. Comparison of TE Ignition Delays with a 237.5 pF Capacitance

Fuel-Air Equivalence Ratio	0.8	1.0	1.2
Fig. 6 – Positive Polarity, Surface Discharge Igniter	14.5 ms	7 ms	7 ms
Fig. 7 – Negative Polarity, Corona Igniter	11 ms	7.5 ms	7 ms

Table 3. Comparison of TE Ignition Delays with a 1.3 nF Capacitance

Fuel-Air Equivalence Ratio	0.8	1.0	1.2
Fig. 6 - Positive Polarity, Surface Discharge Igniter	11 ms	7 ms	7 ms
Fig. 7 – Negative Polarity, Corona Igniter	10.5 ms	7 ms	7 ms

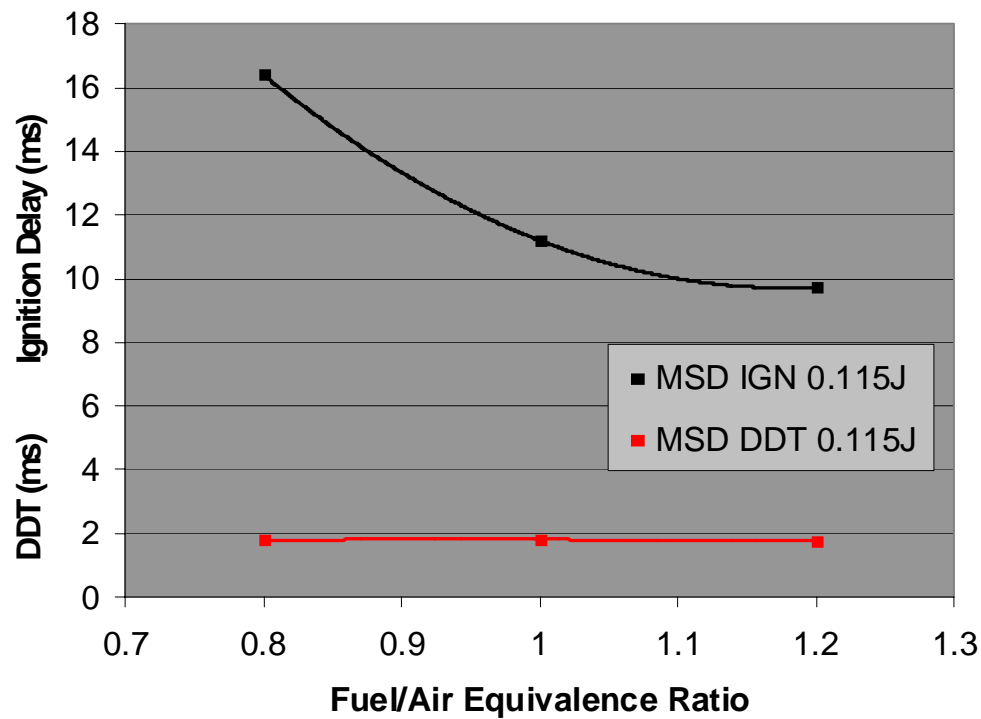


Figure 5. Baseline Ignition Delays and DDT Times with Aviation Gasoline

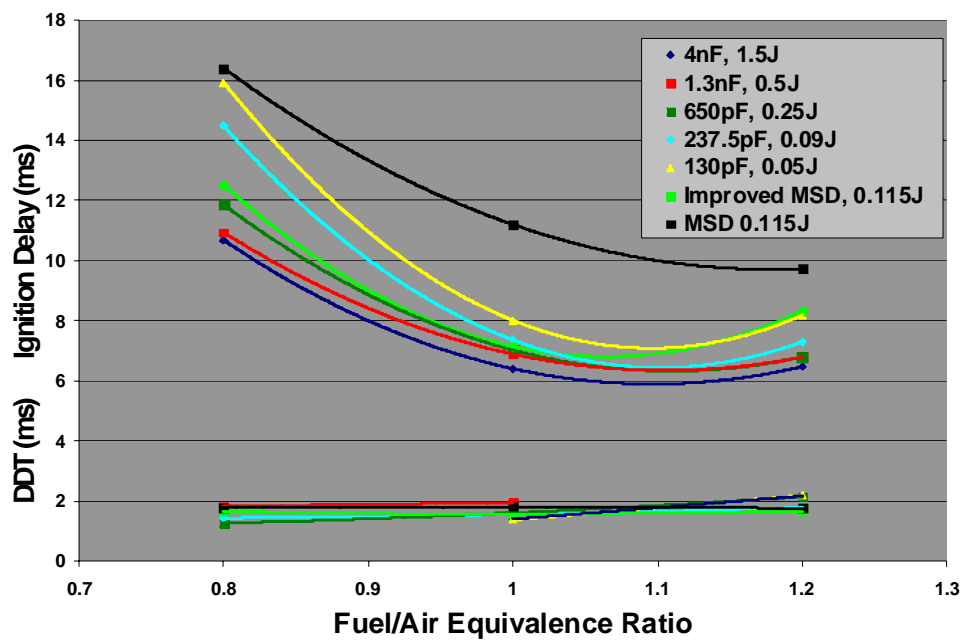


Figure 6. Ignition Delays and DDT Times for the Positive Polarity TE Ignition and the Modified MSD Ignition with a Surface Discharge Igniter

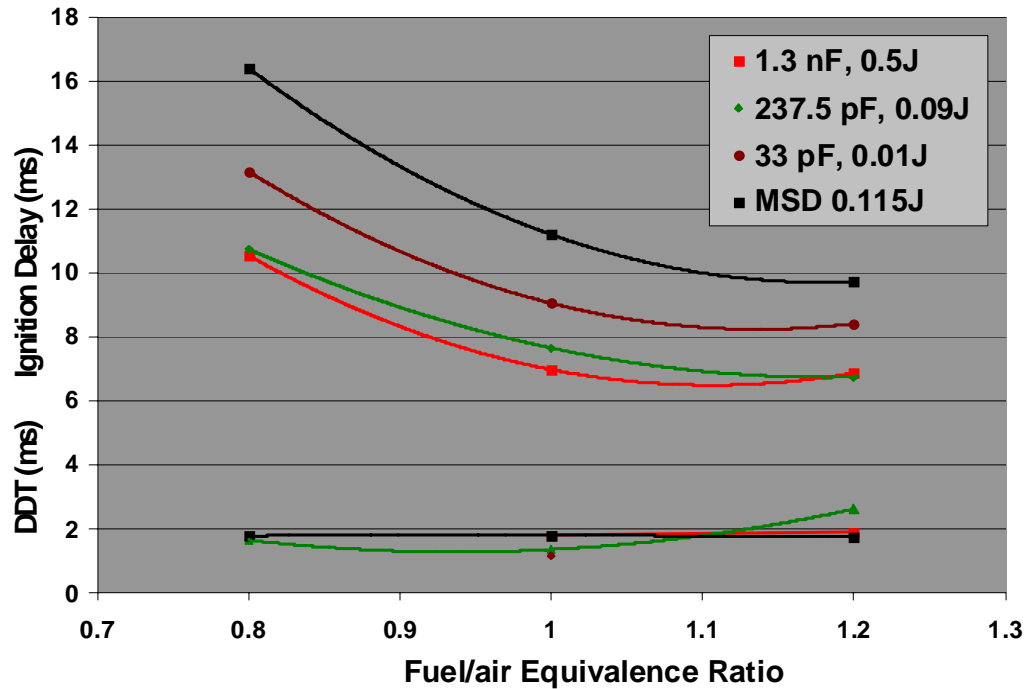


Figure 7. Ignition Delays and DDT Times for the Negative Polarity TE Ignition with a Corona Igniter

The ignition delays and DDT times produced by the TPI Ignition with a corona igniter are shown in Fig. 8. The ignition delays produced by the TPI ignition are less than those produced by the unmodified MSD ignition. The TPI ignition produces 52 to 66 KV pulses that over-stressed the ceramics of the corona igniter, producing undesired corona discharges that reduced the energy available for ignition. The length of the discharge volume was determined by the length of threaded rod exposed at the end of the igniter. The length was 2.5 to 5 cm. In Fig. 8, the lowest ignition delays are produced when the TPI exciter energy is 3.4 J, except at $\phi = 1.2$ where the 2.2 J setting produced slightly better results. The ignition delays for the 3.4 J setting are 11 ms at $\phi = 0.8$, 6 ms at $\phi = 1.0$, and 5.5 ms at $\phi = 1.2$. These ignition delays are equal to or slightly better than the ignition delays for the positive polarity 4 nF, 1.5 J TE igniter with a surface discharge igniter in Fig. 6 (11 ms at $\phi = 0.8$, 6.5 ms at $\phi = 1.0$, and 6.5 ms at $\phi = 1.2$). The ignition delays for ϕ between 0.8 and 1.0 are most important because it is desirable for the PDE to operate under lean conditions to conserve fuel. The DDT times appear to increase for the TPI when the exciter energy is 3.4 J. A similar trend was observed with hydrogen as the fuel (which is not presented in this paper).

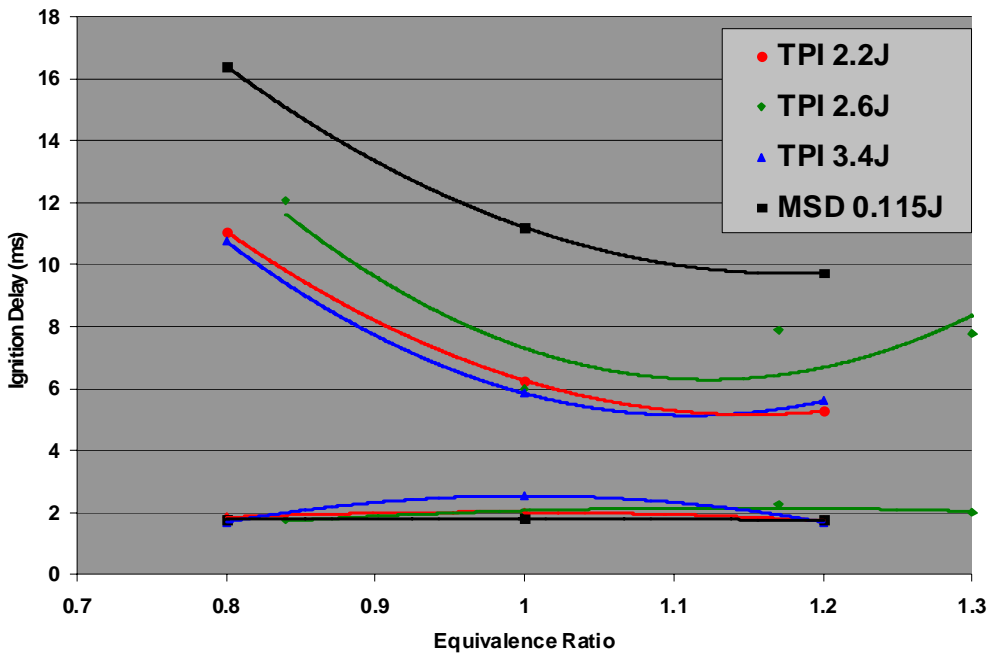


Figure 8. Ignition Delays and DDT Times for the Positive Polarity TPI Ignition with a Corona Igniter

IV. Conclusion

In a preliminary survey on an experimental pulsed detonation engine fueled with aviation gasoline, it has been demonstrated that non-thermal ignitions can reduce the ignition delay by 5-6 ms, or equivalently 30 to 45%, below that observed with an aftermarket automotive ignition at lean to stoichiometric fuel-air equivalence ratios. Non-thermal ignitions with 0.5 to 3 J energies produce the shortest ignition delays. Ignition delays are approximately the same for positive corona or negative spark discharges. It has also been demonstrated that by a simple modification of an aftermarket automotive thermal ignition, ignition delays can be reduced by 4 ms under the same PDE operating conditions, but with 0.115 J exciter energy. The shortest ignition delay at $\phi = 1$ was 6 ms, produced by the Transient Plasma Ignition. At $\phi = 0.8$, an ignition delay of 11 ms was observed with both the Transverse Exciter and the Transient Plasma Ignition. Ignition delays were substantially longer than the deflagration-to-detonation times, which were about 1 to 3 ms.

Acknowledgments

Distribution Statement A; Approved for public release; distribution is unlimited.

This effort was performed under contract number F49620-02-C-0015 with the AFOSR.

This research was performed while K.O. Busby held a National Research Associateship Award at Wright-Patterson AFB.

The authors gratefully acknowledge the technical assistance of Curt Rice, Royce Bradley and Kevin Kirkendall.

References

-
- ¹ J. Liu, P.D. Ronney, and M. Gundersen, "Premixed Flame Ignition By Pulsed Corona Discharges," Western States Section, The Combustion Institute, 2002 Spring Meeting, March 25-26, 2002.
- ² Fei Wang, J. B. Liu, J. Sinibaldi, C. Brophy, A. Kuthi, C. Jiang, P. Ronney, and Martin A. Gundersen, "Transient Plasma Ignition of Quiescent and Flowing Air/Fuel Mixtures," *IEEE Transactions on Plasma Science*, Vol. 33, No. 2, April, 2005, pp. 844-849.
- ³ W. Kim, H. Do, M.G. Mungal and M.A. Capelli, "Flame Stabilization Enhancement and NO_x Production using Ultra Short Repetitively Pulsed Plasma Discharges," *44th Aerospace Sciences Meeting and Exhibit*, January 9-12, 2006, Reno, Nevada, AIAA 2006-560.
- ⁴ V.P. Zhukov, A.E. Rakitin, A. Yu Starikovskii, "Initiation of Detonation by Nanosecond Gas Discharge," *44th Aerospace Sciences Meeting and Exhibit*, January 9-12, 2006, Reno, Nevada, AIAA 2006-952.
- ⁵ Kenichi Takita and Yiguang Ju, "Effect of Radical Addition on Extinction Limits of H₂ and CH₄ Flames," *44th Aerospace Sciences Meeting and Exhibit*, January 9-12, 2006, Reno, Nevada, AIAA 2006-1029.
- ⁶ Timothy Ombrello, Xian Qin, Yiguang Ju, Shailesh Gangoli, Alexander Gutsol and Alexander Fridman, "Non-Equilibrium Plasma Discharge: Characterization and Effect on Ignition," *44th Aerospace Sciences Meeting and Exhibit*, January 9-12, 2006, Reno, Nevada, AIAA 2006-1214.
- ⁷ Guofeng Lou, Ainan Bao, Menetake Nishihara, Saurabh Keshav, Yuri G. Utkin and Igor V. Adamovich, "Ignition of Premixed Hydrocarbon-Air Flows by Repetitively Pulsed, Nanosecond Pulse Duration Plasma," *44th Aerospace Sciences Meeting and Exhibit*, January 9-12, 2006, Reno, Nevada, AIAA 2006-1215.
- ⁸ P. Bletzinger, D.D. Trump, J. M. Williamson, B. N. Ganguly, M. A. Gundersen and A. Kuthi, "Large-Area Atmospheric Pressure Dielectric Discharge using a High-Power Plasma Switch," *44th Aerospace Sciences Meeting and Exhibit*, January 9-12, 2006, Reno, Nevada, AIAA 2006-1456.
- ⁹ Starikovskii et al, private communication, 2006.
- ¹⁰ Jennifer Corrigan, M.A. thesis, Ohio State University, 2006.
- ¹¹ K.O. Busby, C.D. Carter, K.A. Kirkendall, P.D. Barnes and D.R. Eklund, "Performance of Pulsed Scramjet Ignitions," Joint Army Navy NASA Air Force (JANNAF) Meeting, December 4-8, 2006.

Evaluation of Catalytic and Thermal Cracking in a JP-8 Fueled Pulsed Detonation Engine

Timothy M. Helfrich* and Frederick R. Schauer†
Air Force Research Laboratory, Wright-Patterson AFB, OH, 45433

and

Royce P. Bradley‡ and John L. Hoke§
Innovative Scientific Solutions, Inc., Dayton, OH, 45440

Pulsed detonation engines (PDEs) depend on rapid ignition and transition from deflagration to detonation. Converting the PDE from experimental to operational use will necessitate a considerable reduction in the time required to ignite and detonate a liquid hydrocarbon fuel, such as JP-8, in air. This research effort is focused on PDE operation enhancements using dual-detonation-tube, concentric-counter-flow heat exchangers to elevate the fuel temperature levels sufficiently to induce thermal cracking. Additionally, a zeolite catalytic coating is applied to the heat-exchanger surfaces to stimulate further cracking of the fuel and reduce coke deposition. To quantify the PDE performance, three parameters are examined, ignition time, deflagration-to-detonation transition (DDT) time, and DDT distance. As compared with flash-vaporized JP-8/air mixtures, the cracked JP-8/air mixture produces a shorter ignition time, DDT time, and DDT distance for the majority of equivalence ratios, with a reduction in ignition time of up to 60% at 908 K. Furthermore, both the ignition and detonability limits are expanded by cracking the fuel, with lean limits at an equivalence ratio of 0.75. Coke deposition found in the fuel filter consists of carbon as well as substantial concentrations of silicon and aluminum, resulting from deterioration of the silica-alumina zeolite structure. Additionally, the catalyst was coated in coke deposition after 5 hr of operation, although no degradation in performance is observed.

Nomenclature

E_{crit}	=	Critical Initiation Energy
M_{CJ}	=	Chapman-Jouguet Mach Number
P_o	=	Initial Fuel/Air-Mixture Pressure
γ_o	=	Initial Fuel/Air-Mixture Ratio of Specific Heats
λ	=	Cell Size

I. Introduction

THEORETICALLY, the pulsed-detonation-engine (PDE) cycle can provide nearly constant-volume combustion, with lower entropy gain and higher propulsive efficiency; but practical PDEs are still in the early stages of development.¹⁻³ Several technological barriers must be overcome before the PDE can be considered a realistic means of providing propulsion to operational aircraft.⁴ A large barrier is the efficient ignition and detonation

* Capt, USAF, Research Engineer, Deputy PDRF, AFRL/PRTC, 1950 5th Street, AIAA Member.

† Senior Engineer, Head PDRF, AFRL/PRTC, 1950 5th Street, AIAA Senior Member.

‡ Research Engineer, 2766 Indian Ripple Road.

§ Research Engineer, 2766 Indian Ripple Road, AIAA Senior Member.

initiation of low-vapor-pressure hydrocarbon fuels such as JP-8. While a substantial amount of research has been performed with gaseous fuels such as hydrogen and simple hydrocarbons,⁵ only recently have studies on liquid hydrocarbon fuels been conducted.⁶ This lack of research has resulted in a large gap between experimental and the operational use of PDEs. Nearly all United States Air Force (USAF) aircraft are operated with liquid hydrocarbon fuels primarily JP-8.⁷ Therefore, the ability to utilize those fuels efficiently in the PDE is necessary to transition PDE technology from the research phase to the operational-use phase.

The conversion from gaseous fuels to liquid hydrocarbon fuels has highlighted three key cycle-performance parameters that adversely affect efficient PDE operation: 1) time from spark deposition to the creation of a deflagration wave within the fuel/air mixture (ignition time), 2) the time required to transition the deflagration wave into a detonation wave (DDT time), and 3) the length of detonation tube required for the mixture to transition to a detonation (DDT distance). Both the ignition time and the DDT time are nearly an order of magnitude longer for complex liquid hydrocarbon fuels than for hydrogen. For example, the ignition time for a hydrogen/air mixture is on the order of 1 ms, whereas that for a JP-8/air mixture is ~7 ms.

This research marks the first evaluation of a PDE fueled with thermally and catalytically cracked JP-8 fuel. Previous research^{8,9} demonstrated the benefits of preheating JP-8 to flash vaporization and supercritical temperatures. Tucker et al.⁸ demonstrated that flash vaporization of JP-8 reduces both ignition time and DDT time, as well as increases the ignition and detonation limits. Helfrich et al.⁹ found that heating JP-8 to supercritical temperatures caused a decrease in DDT time and DDT distance and improved the consistency of detonations. The focus of the present research was to use a dual-detonation-tube, concentric-counter-flow heat-exchanger system to elevate the fuel temperatures sufficiently to crack the fuel thermally with the assistance of a zeolite catalytic coating.

II. Background and Theory

Previous experimental research⁵ has shown that a typical, stoichiometric, low-vapor-pressure liquid-hydrocarbon/air mixture requires on the order of 10^5 J of energy for direct initiation of detonation (critical initiation energy), which is six orders of magnitude greater than that available from a typical spark plug (~100 mJ). Thus, a mixture with low critical initiation energy is more susceptible to DDT. Knystautas et al.¹⁰ developed a correlation between the detonation cell size (λ) and the critical initiation energy of a mixture, shown in Eq (1):

$$E_{crit} = (2197/16)\pi\gamma_o P_o M_{CJ}^2 I \lambda^3 \quad (1)$$

where E_{crit} is the critical initiation energy of a fuel/air mixture, γ_o is the initial ratio of specific heats, P_o is the initial mixture pressure, M_{CJ} is the Chapman-Jouget Mach Number of the mixture, and I is a dimensionless constant. Additionally, Schauer et al.¹¹ developed a correlation for the detonation cell size and the critical initiation energy of a mixture based on data gathered by Kaneshige and Shepherd,⁵ Eq. (2):

$$E_{crit} = 3.375 \lambda^3 \quad (2)$$

Although the two equations appear to be different, the important point is that the critical initiation energy varies with the cube of the detonation cell size, which means that a decrease in cell size is an indication of improved detonability.

The detonation cell size is a physical characteristic of a detonation wave as it propagates, as shown in Fig 1. A more detailed discussion of detonation cell structure can be found in Fickett and Davis.¹² Figure 2 is a plot of detonation cell size as a function of equivalence ratio for acetylene, hydrogen, ethylene, and JP-10. JP-10 is a higher density liquid hydrocarbon with a density on the same order as that of JP-8. Acetylene, hydrogen, and ethylene are shown to have a smaller detonation cell size than JP-10 at corresponding equivalence ratios; therefore, it is inferred from Eqs. (1) and (2) that acetylene, hydrogen, and ethylene are more detonable than high-density liquid hydrocarbons. The data from Fig. 2 were compiled by Kaneshige and Shepherd⁵ but experimentally determined elsewhere.^{10,13,14}

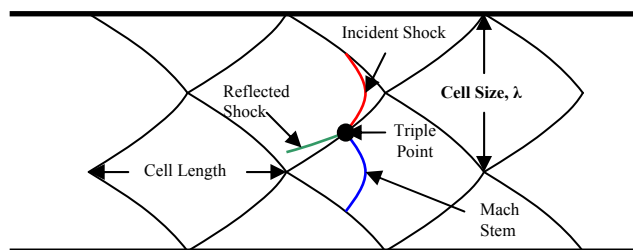


Figure 1. Representative two-dimensional detonation cell structure

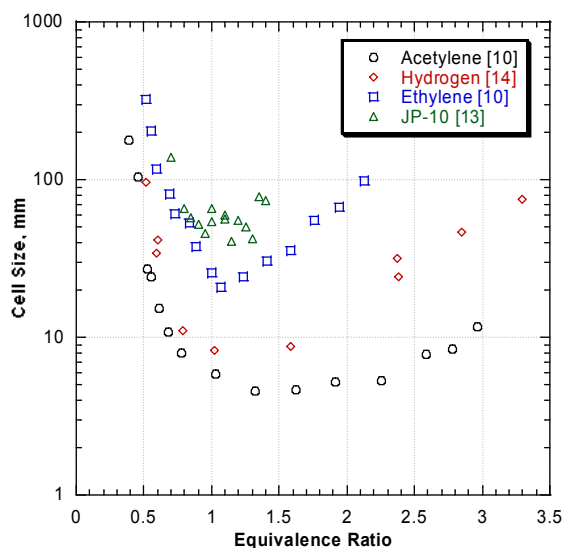


Figure 2. Plot of detonation cell size as function of equivalence ratio for four fuels in air.

If a liquid hydrocarbon fuel is heated to a sufficiently high temperature (~ 800 K), it will begin to undergo endothermic reactions known as thermal cracking.¹⁵ As a result of these endothermic reactions, the complex hydrocarbon bonds begin to break apart and form smaller, lighter hydrocarbons and hydrogen.^{16,17} Huang et al.¹⁵ have shown with Gas Chromatograph/Mass Spectrometer (GC/MS) analysis that when JP-8 was heated to ~ 960 K, a substantial shift in composition occurred. The concentrations of heavy liquid hydrocarbons (decane, undecane, dodecane, tridecane, tetradecane, and pentadecane) decreased, whereas that of lighter liquid hydrocarbons (butene, benzene, and toluene) increased.¹⁵ As these lighter hydrocarbons are formed (and heavier hydrocarbon concentration decreases) the ignition and DDT times are likely reduced. Using a gas chromatograph, Huang et al.¹⁵ showed that endothermic reactions also produced hydrogen and several gaseous hydrocarbons, such as ethylene. As shown in Fig. 2, hydrogen and ethylene have smaller cell sizes, leading to increased detonability. Austin and Shepherd¹³ have shown that adding hydrogen or ethylene to a liquid hydrocarbon decreases the cell size of the mixture, thereby increasing detonability.

Zeolite catalytic coatings have been used in several experiments¹⁵⁻¹⁹ to aid in fuel cracking and minimize coking. Huang et al.¹⁹ found that a wall-supported zeolite catalyst would permit an experiment to run five times longer. Galligan¹⁸ found that a zeolite catalyst could be used to obtain $>90\%$ conversion of JP-10 to other hydrocarbons. Shepherd et al.¹⁶ showed that the use of a zeolite catalyst could increase the percent of JP-10 conversion by an order of magnitude over that of thermal cracking alone.

III. Experimental Setup and Instrumentation

A. Facilities and PDE Details

This research was conducted in the Pulsed Detonation Research Facility (PDRF), which is located at Wright-Patterson AFB in Ohio. This facility was described in detail elsewhere,²⁰ and only the details that are relevant to the current research are provided here. The PDE for this study consisted of the valve train from a GM quad-four-engine head with two 1.83-m-long, Schedule-40 stainless-steel detonation tubes (50.8-mm diameter); each tube had a 1.22-m-long Schelkin-like spiral, with one end adjacent to the closed end of the detonation tube, to promote DDT.²¹ Each detonation tube had an inconel heat exchanger (described later).

The PDE cycle consisted of three equally timed phases--fill, fire, and purge, as shown in Fig. 3. During the fill phase, the intake valves were opened to fill the PDE detonation tube with a volume of premixed fuel and air that was equal to the volume of the detonation tube (fill fraction of one). For all tests the fill air was initially heated to 394 K prior to mixing with the fuel. During the fire phase, spark energy was released, causing the formation of a deflagration wave that transitioned to a detonation wave. The ignition system provided spark pulses through modified spark plugs, with each spark plug supplying an ignition energy of 115 mJ. The spark delay after the intake valves were closed was 6 ms. During the purge phase, the exhaust valves were opened to fill the detonation tube with a volume of air (unheated) that was equal to one-half the volume of the detonation tube (purge fraction of 0.5). The purge air cooled the detonation tube and removed a portion of the exhaust gases, preventing auto-ignition. The PDE firing frequency was kept constant at 15 Hz for all testing.

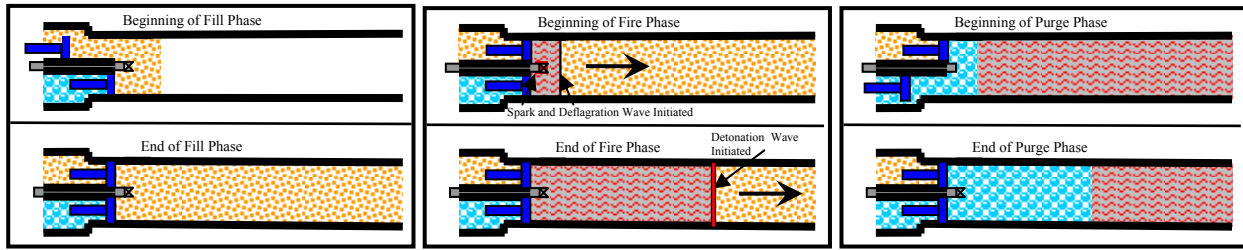


Figure 3. Diagrams of fill, fire, and purge phases of PDE cycle.

B. Fuel Heating System

The liquid fuel required for this testing was supplied by two hydraulic bladder accumulators that were pressurized by nitrogen. The nitrogen pressurized the fuel above the critical pressure for the duration of the test to prevent phase change. The fuel was pressure fed to the inlet of the fuel heating system (FHS). The FHS consisted of two inconel heat exchangers, a fuel filter assembly, fuel injection nozzles, instrumentation, and associated tubing and fittings necessary to connect the critical components. The flow path and instrumentation are shown in schematic and photographic form in Figs. 4(a) and 4(b), respectively. The fuel entered the test stand through a pneumatically-operated ball valve and then flowed through the heat-exchanger on tube three. The fuel was then routed through the heat-exchanger on tube two and through the filter to the fill-air manifold, where it was injected into the air stream via the fuel-injection nozzles. The fuel filter was used to remove the coking that was formed as a result of thermal cracking of the fuel.²² The fuel lines that carried heated fuel (fuel that had traversed through a heat-exchanger) were insulated with a ceramic-tape insulation to prevent heat loss [Note: Insulation is removed in Fig. 4(b) for visual clarity].

The fuel mass flow rate of the nozzles is proportional to the square root of the pressure drop across the fuel nozzles and the fuel density.^{23,24} To compensate for the decrease in fuel density during heating of the fuel in the supercritical regime, the charge pressure of the accumulators was increased to maintain a constant fuel mass flow rate. The accumulator charge pressure was varied during the test using a pneumatic dome-loaded regulator [for details, see Ref. 25].

To minimize oxidative carbon deposition in the FHS, the JP-8 was de-oxygenated through a nitrogen sparging process, reducing the oxygen concentration to <1 ppm. The sparging process involved bubbling a volume of nitrogen through the JP-8 to displace the dissolved oxygen in the fuel. The volume of nitrogen necessary to reduce the oxygen concentration to acceptable levels was determined experimentally in previous work;²⁶ and to ensure acceptable levels, a factor of safety of two was applied to all nitrogen volume calculations.

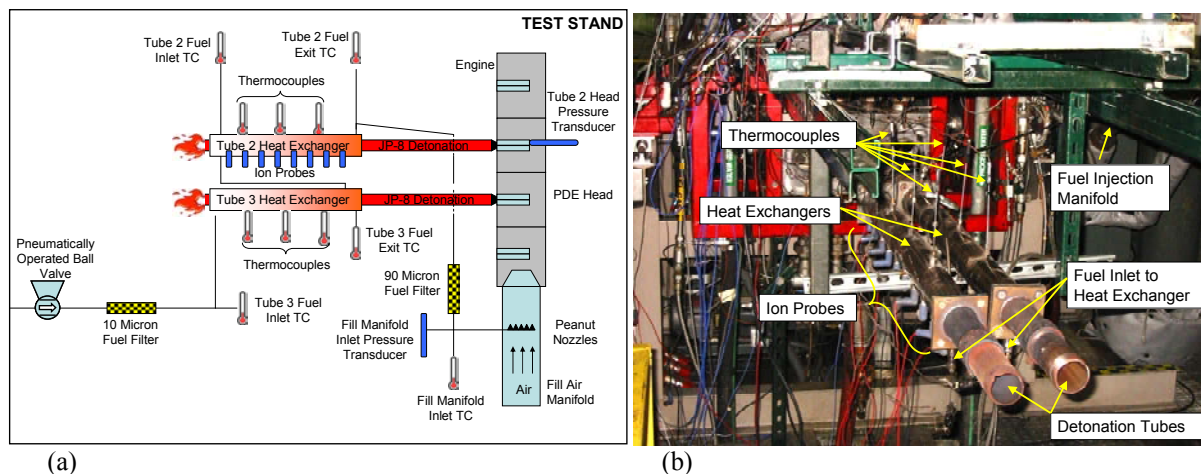


Figure 4. (a) Diagram and (b) photograph of the PDE with the fuel heating system and instrumentation.

C. Heat Exchangers

Two identical concentric-tube heat exchangers were fabricated for this research. Each 0.91-m-long heat exchanger was fabricated with a 50.8-mm-dia, inconel-625, Schedule-10 inner tube and a 63.5-mm-dia, inconel-600, Schedule-40 outer tube allowing a 1.22 mm annular gap. A photograph of one of the heat exchangers, with the associated instrumentation ports, is shown in Fig. 5.

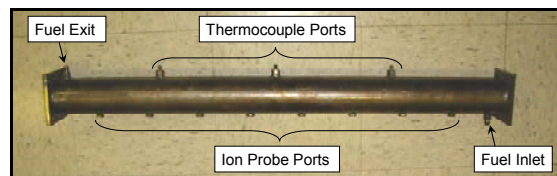


Figure 5. Photograph of heat exchanger.

D. Zeolite Catalytic Coating

The inner walls of the two heat exchangers and the tubing between them and the fuel injection nozzles were coated with an inexpensive zeolite catalyst in a ceramic-like binder. The catalyst was applied by a contractor using a proprietary method. The zeolite structure is known to be composed of a silica-alumina, but the catalytic agent is proprietary information. As mentioned earlier, the catalyst was applied to decrease coke deposition and increase fuel cracking.

E. Instrumentation

Ion probes were placed in ports, spaced 0.102 m apart, along the length of the detonation tube and heat exchanger (see Figs. 4 and 5), and were used to measure the velocity of the combustion wave (wavespeed). Combustion waves propagating at speeds within 10% of the upper Chapman-Jouguet point (assumed to be 1800 m/s) were considered to be detonation waves. Thermocouples were placed in the center of the flow path to gather temperature data at the inlet and outlet of each heat exchanger (J-type) and at the inlet to the fill-air manifold (T-type). Additional J-type thermocouples were placed in the thermocouple ports (see Fig. 5) in both heat exchangers to determine fuel temperature within the heat exchanger. External heat-exchanger wall temperatures were measured with J-type thermocouples that were mounted externally by compression clamps on the PDE detonation tube. A pressure transducer was situated at the closed end of the detonation tubes to measure the pressure that was used to determine the ignition time.

IV. Results and Discussion

The experimentally determined ignition time, DDT time, and DDT distance are plotted as a function of fuel-injection temperature (Figs. 6, 7, and 8, respectively) and equivalence ratio (Figs. 9, 10, and 11, respectively). Additionally, the results of a thorough examination of the coke deposition and catalyst condition are presented. Each data point represents the mean value of 30 - 40 ignitions. The total experimental uncertainty is presented whenever possible. Results presented as a function of equivalence ratio are shown with flash-vaporized JP-8 data determined by Helfrich et al.²⁷ Results presented as a function of fuel injection-temperature are shown with the supercritical fuel-injection results for JP-8 that were determined by Helfrich et al.⁹ Results presented as a function of fuel injection temperature were collected with a near-stoichiometric mixture of fuel and air. The measured equivalence ratio was found to vary no more than 2%.¹¹

A. Results as a Function of Fuel-Injection Temperature

Figure 6 is a plot of ignition time as a function of fuel-injection temperature for a near-stoichiometric JP-8/air mixture. The ignition time decreases rapidly at temperatures above 800 K, which is the threshold for significant cracking to occur.¹⁵ The ignition time is reduced by 19% when the fuel is heated from 800 K to 900 K. This appealing trend implies that further elevation of the fuel temperature will result in reductions in ignition time, although the temperature limit to the trend is unknown. The endothermic data matches well with the supercritical data of Helfrich et al.⁹ in the overlapping range.

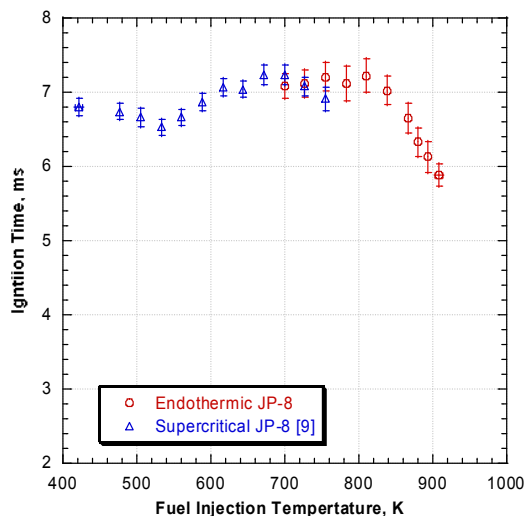


Figure 6. Plot of ignition time as function of fuel-injection temperature for JP-8/air mixture.

Figure 7 is a plot of DDT time as a function of fuel-injection temperature for a near-stoichiometric JP-8/air mixture. The DDT time appears to be independent of fuel-injection temperature, once the fuel has begun to crack, with a constant DDT time of 2.25 ms. The data of Helfrich et al.⁹ showed a nearly linear decrease in DDT time that does not appear in the present research, although the values of DDT time match quite well in the overlapping temperature range. The detonations become more consistent with increasing fuel-injection temperature, as shown by the decrease in uncertainty with increasing fuel-injection temperature.

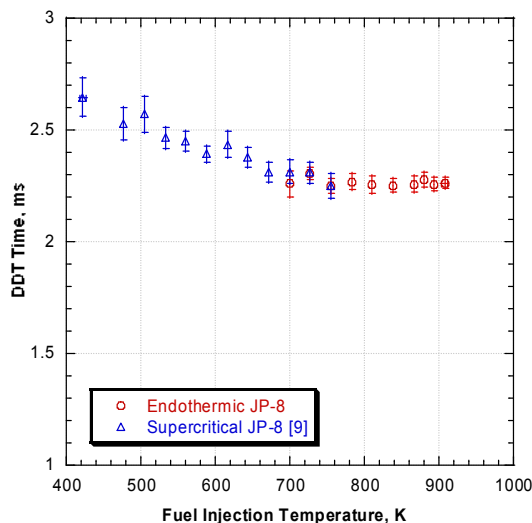


Figure 7. Plot of DDT time as function of fuel-injection temperature for JP-8/air mixture.

The DDT distance plotted as a function of fuel-injection temperature for a near-stoichiometric JP-8/air mixture is shown in Fig. 8. The DDT distance is independent of fuel-injection temperature, which is consistent with the data of Helfrich et al.⁹ However, the magnitude of the DDT distance was found to be slightly higher than in the data of Helfrich et al.⁹ because the earlier experiments incorporated a 0.914-m spiral and the current experiment was performed with a 1.22-m spiral. The longer spiral creates drag on the combustion wave, likely delaying detonation transition slightly.

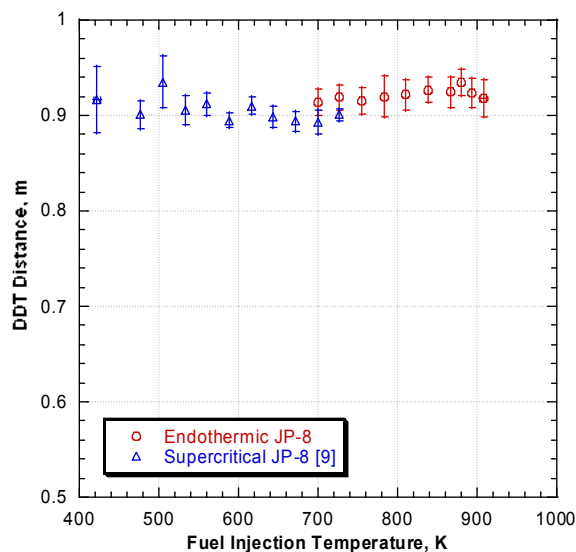


Figure 8. Plot of DDT distance as function of fuel-injection temperature for JP-8/air mixture.

B. Results as a Function of Equivalence Ratio

Figure 9 is a plot of ignition time as a function of equivalence ratio for a JP-8/air mixture at three temperatures. Because of fuel-system limitations, temperatures in excess of 866 K could not be reached for equivalence ratios greater than stoichiometric. As expected, a significant decrease in ignition time at all equivalence ratios is observed in JP-8 data at 866K, as compared to JP-8 data at 561K. For most equivalence ratios, at least a 30% reduction in ignition time occurs. The JP-8 data at 908 K show a further reduction in ignition time, with a 60% reduction at an equivalence ratio of 0.9. The JP-8 results at 866 K and 908 K are more consistent than those at 561 K, as demonstrated by a reduction in uncertainty. Additionally, the lean ignition limit of the JP-8 at 908 K is 0.75, which is significantly better than the 0.9 lean limit at 561 K.

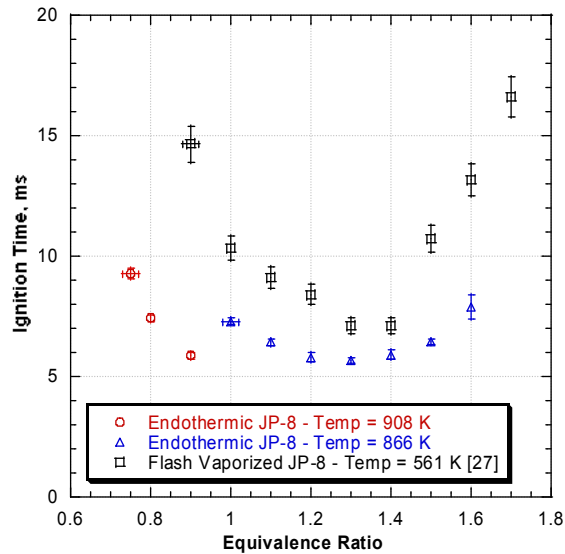


Figure 9. Plot of ignition time as function of equivalence ratio for JP-8/air mixture.

A plot of the DDT time as a function of equivalence ratio for a JP-8/air mixture at three temperatures is shown in Fig. 10. The minimum DDT time, occurring at an equivalence ratio of 1.1 for both the endothermic and flash-vaporized JP-8, is not affected by the fuel cracking. However, at equivalence ratios >1.2 and <1.0 , the endothermic JP-8 produces a shorter DDT time. The detonations occur more consistently with the endothermic JP-8 than the flash-vaporized JP-8, as shown by the smaller uncertainty. In addition, both the rich and lean detonability limits have been expanded. To the authors' knowledge, the lean limit of 0.75 is the leanest JP-8/air mixture to be detonated through spark initiation and DDT using a spiral in a PDE.

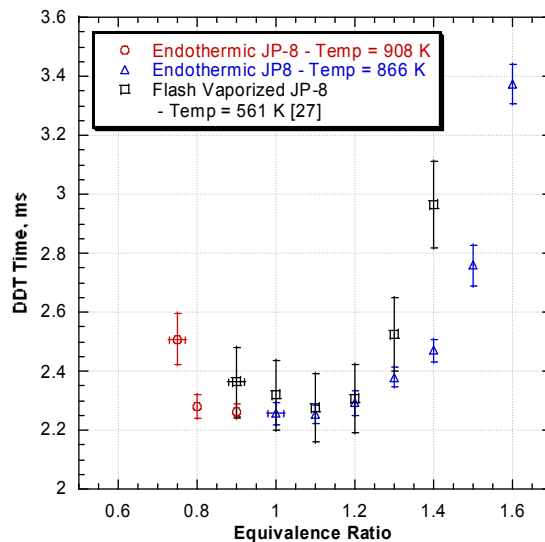


Figure 10. Plot of DDT time as function of equivalence ratio for JP-8/air mixture.

Figure 11 is a plot of DDT distance as a function of equivalence ratio for a JP-8/air mixture at three temperatures. The DDT distance of the endothermic JP-8 is shorter (greater than 10 cm for most equivalence ratios) than that required for the flash-vaporized JP-8 for all equivalence ratios. Both the flash-vaporized JP-8 experiment performed by Helfrich et al.²⁷ and the present experiment used a 1.22-m-long spiral, facilitating a good comparison of DDT distance.

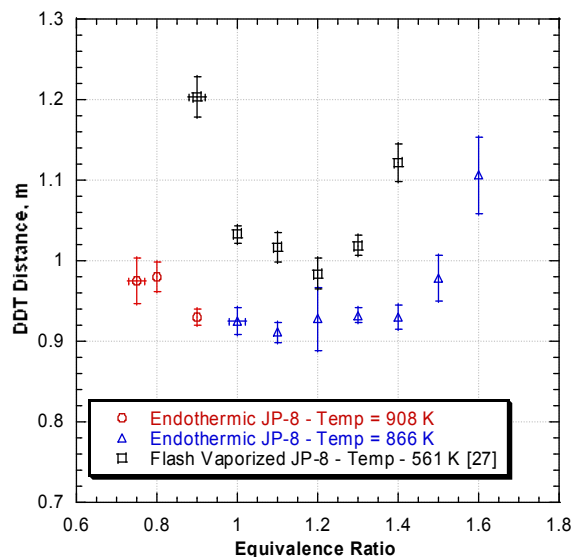


Figure 11. Plot of DDT time as function of equivalence ratio for JP-8/air mixture.

C. Analysis of Coke Deposit

After approximately 5 hr of accumulated run time, a significant increase in pressure drop across the fuel filter (see Fig. 4) was observed. The filter was subsequently removed and cleaned. An inspection of the filter housing resulted in the identification of a large quantity of loose black deposits, suspected to be coke. Additionally, the filter element was clogged with the same black deposits. Figure 12 is a photograph of the clogged filter element adjacent to a new one.

To confirm the content of the deposit, a sample was analyzed in a scanning electron microscope (SEM) that is equipped with an energy-dispersive x-ray detector (EDX). The SEM is capable of capturing photographs of a sample at the micron level (micrographs). The EDX is capable of identifying the elemental components of a sample, although it is not quantitatively accurate for determining the concentrations of carbon and oxygen. Figure 13(a) is a SEM micrograph of the carbon sample at 600x magnification. The large smooth structure in the lower-left corner of Fig. 13(a) is probably a carbon structure. Figure 13(b) is a plot of the relative concentrations of the elemental species as measured by the EDX. While the exact concentration of carbon cannot be determined with the EDX, it is apparent that significant carbon is present. In addition to carbon, two other elements are prominent, aluminum and silicon. The EDX data indicate that, excluding carbon and oxygen, 42.4% of the sample is aluminum and 41.5% of the sample is silicon. As mentioned earlier, the zeolite structure is made of silica-alumina. Thus, it is concluded that some of the zeolite catalyst has flaked off during testing, although no degradation in PDE performance was observed. The extremely porous structures apparent throughout Fig. 13(a) are probably the zeolite fragments.



Figure 12. Photograph of coke-filled filter element (left) and new filter element (right).

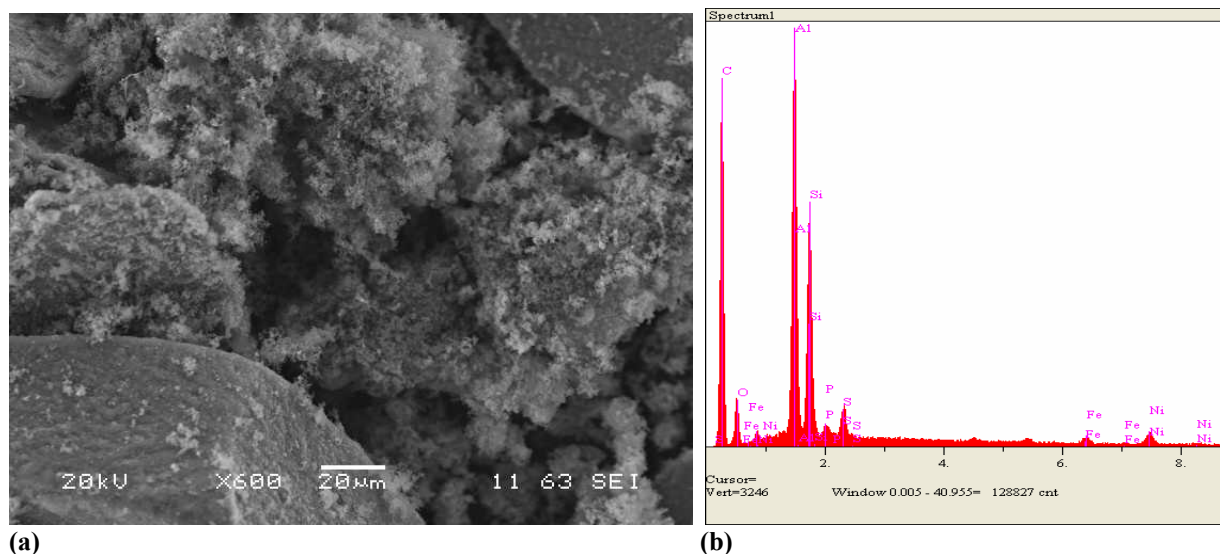


Figure 13. (a) SEM micrograph of black powder from filter housing, magnified to 600x, and (b) plot from EDX of relative concentrations of elements found in black deposit.

To determine the concentration of carbon, the sample was further analyzed using a Leco RC 412 surface carbon determinator (SCD). The SCD operates by heating the sample in a furnace with O_2 , thereby oxidizing the carbon in the sample to CO_2 .²⁸ The CO_2 is then measured using a calibrated IR detector to determine the concentration of carbon in the sample.²⁸ The SCD was set to heat the sample, starting at $150^\circ C$, increasing $20^\circ C/min$, ending at $750^\circ C$, and holding the sample at $750^\circ C$ for another 10 min. Figure 14(a) is a plot of the relative signal (amount of CO_2) and temperature (shown in $^\circ C$ on plot) as a function of time. The majority of the sample is oxidized between 650 K and 750 K, which is indicative of carbon rings. The SCD measurement showed that the sample contained 38% carbon. The portion of the sample that was left after the SCD test (49% by mass) is comprised of nonoxidizable elements, or ash. The ash was then analyzed with the SEM and the EDX. Figure 14(b) is a plot of relative concentrations of the ash. As expected, the only compounds remaining were aluminum and silicon. Therefore, approximately one-half of the deposit collected from the filter housing was composed of zeolite fragments.

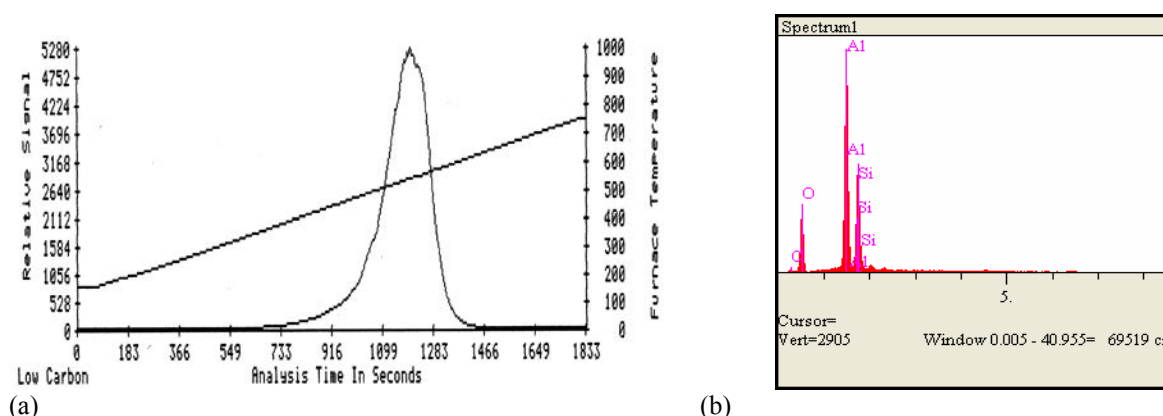


Figure 14. (a) Plot from SCD of relative signal intensity (oxidation level) and furnace temperature (in $^\circ C$) as function of time, and (b) plot from EDX of relative concentrations of nonoxidizable ash.

Because of the large amount of coking and zeolite fragments found in the filter housing, it was suspected that the zeolite catalyst was clogged with coke, although no reduction in performance was noted. When the zeolite structure in a catalyst becomes clogged, the fuel molecules cannot move through structure, rendering it useless. To determine the state of the zeolite structure, a section of the tubing directly upstream of the fuel filter was removed, and the surface with the catalyst was examined with the SEM and the EDX. Figure 15(a) is an SEM micrograph of the catalyst after use (5 hr of operation), and Fig. 15(b) is a plot from the EDX of the relative concentration of the

elements detected in the used catalyst. Additionally, a section of tube with fresh catalyst was examined with the SEM and EDX for comparison purposes. Figure 16(a) is an SEM micrograph of the fresh catalyst, and Fig. 16(b) is a plot from the EDX of the relative concentration of the elements detected in the fresh catalyst. Comparing Figs. 15(a) and 16(a), a distinct difference in the surface texture is apparent. The fresh catalyst is very smooth, with small cracks resulting from the application process, whereas the used surface is covered with micron-sized structures. The small structures on the surface of the used catalyst are probably coke deposits. This hypothesis is supported by the comparison of Figs. 15(b) and 16(b). The fresh catalyst contains no trace of carbon, whereas the used catalyst contains a large concentration of carbon. Therefore, although no noticeable reduction in performance, it is concluded that the catalyst was covered in coke deposits after 5 hr of operation.

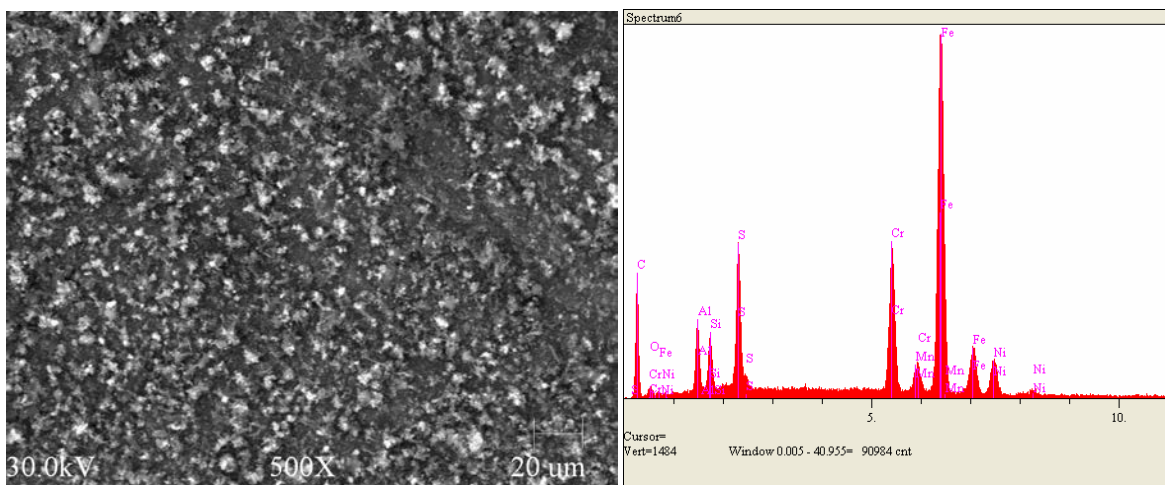


Figure 15. (a) SEM micrograph of used catalyst (5 hr of operation), and (b) plot from the EDX of relative concentration of elements detected in used catalyst.

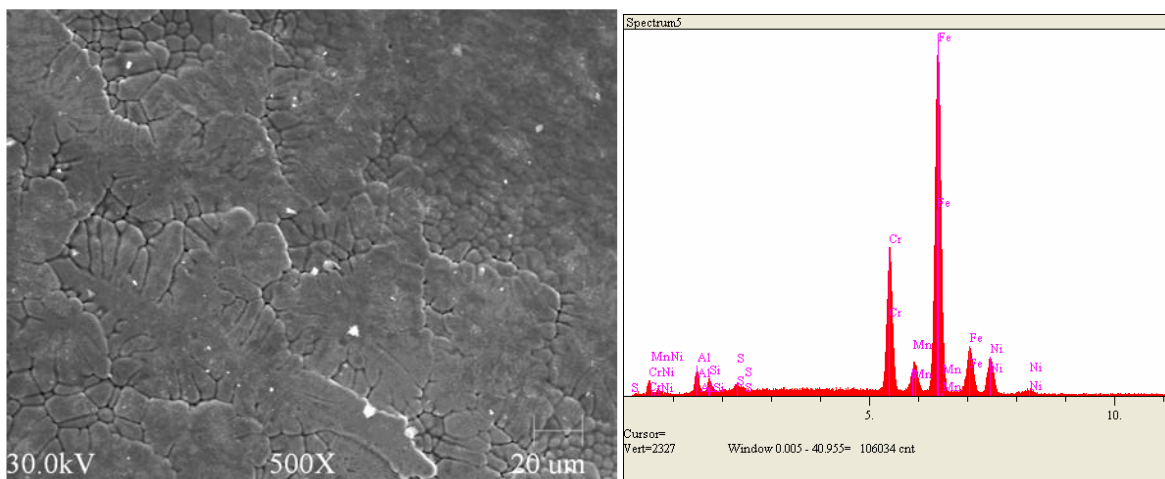


Figure 16. (a) SEM micrograph of fresh catalyst, and (b) plot from EDX of the relative concentration of elements detected in fresh catalyst.

V. Conclusions

This research marked the first analysis of the effect of thermal and catalytic cracking of JP-8 on key PDE performance parameters, including ignition time, DDT time, and DDT distance. Ignition time for a JP-8/air mixture was found to decrease rapidly when the fuel was heated above 800 K. DDT time and distance were found to be independent of temperature in the range tested at stoichiometric conditions, but the consistency of detonations increased. Endothermic JP-8 was found to require a shorter ignition time, DDT time, and DDT distance for the majority of equivalence ratios, as compared to flash-vaporized JP-8, with reductions in ignition time of up to 60%.

Furthermore, both the ignition and detonability limits were expanded by cracking the fuel, with lean limits at an equivalence ratio of 0.75.

Analysis of coke deposition resulting from thermal cracking of the JP-8 showed a large concentration of carbon molecules, probably large carbon rings. In addition to the carbon, a substantial quantity of silicon and aluminum was present in the filter, suggesting that the zeolite structure had deteriorated. The catalyst was also found to be completely covered by coke deposits after 5 hr of operation, although no degradation in performance was observed.

Acknowledgments

This work would not have been possible without the technicians who worked on this project; our thanks to Curtis Rice, Dave Baker, and Dwight Fox (ISSI). Dr. Tim Edwards (AFRL/PRTG) was extremely helpful in developing the fuel systems for this project. The authors would also like to thank Jeff Stutrud (AFRL/PRTC) for his controls and data-acquisition expertise and Maj. Dave Hopper for his assistance during experimentation. Assistance with analysis of coke formation was provided by Dr. Matt Dewitt and Dave Brooks (AFRL/PRTG), as well as Chris Klenke (AFRL/PRTM). The technical leadership of Dr. Robert Hancock (AFRL/PRTC) was invaluable. Funding was provided by the Air Force Research Laboratory, Propulsion Directorate, and AFOSR.

References

- ¹Kailasanath, K., Patnaik, G., and Li, C., "On Factors Controlling the Performance of Pulsed Detonation Engines," *High-Speed Deflagration and Detonation: Fundamentals and Control*, edited by G. D. Roy, S. M. Frolov, D. W. Netzer, and A. A. Borisov, ELEX-KM Publishers, Moscow, 2001, pp. 193–206.
- ²Chuanjun, Y., Jun, L., Wei, F., Liming, H., and Hengren, L., "Principle and Cycle Analysis of Pulsed Detonation Engine," *Journal of Propulsion Technology*, Vol. 17, No. 3, June 1996, pp. 56–63.
- ³Kailasanath, K., "Review of Propulsion Applications of Detonation Waves," *AIAA Journal*, Vol. 38, No. 9, 2000, pp. 1704–1706.
- ⁴Desbordes, D., Dauiau, E., and Zitoun, R., "Pulsed Detonation Propulsion: Key Issues," *High Speed Deflagration and Detonation: Fundamentals and Control*, edited by G. D. Roy, S. M. Frolov, D. W. Netzer, and A. A. Borisov, ELEX-KM Publishers, Moscow, 2001, pp. 177–192.
- ⁵Kaneshige, M. and Shepherd, J. E., *Detonation Database*, GALCIT Report FM97-8, GALCIT, Graduate Aeronautical Laboratories, California Institute of Technology, Pasadena, CA, July 1997.
- ⁶Fan, W., Yan, C., Huang, X., Zhang, Q., and Zheng, L., "Experimental Investigation of Two-Phase Pulse Detonation Engine," *Combustion and Flame*, Vol. 133, 2004, pp. 441–450.
- ⁷Edwards, T., "Liquid Fuels and Propellants for Aerospace Propulsion: 1903–2003," *Journal of Propulsion and Power*, Vol. 19, No. 6, 2003, pp. 1089–1107.
- ⁸Tucker, K. C., King, P. I., Bradley, R. P., and Schauer, F. R., "The Use of a Flash Vaporization System with Liquid Hydrocarbon Fuels in a Pulse Detonation Engine," AIAA 2004-0868, *42nd AIAA Aerospace Sciences Meeting and Exhibit*, Reno, NV, 5–8 January 2004.
- ⁹Helfrich, T. M., King, P. I., Hoke, J. L., and Schauer F. R., "Effect of Supercritical Fuel Injection on the Cycle Performance of a Pulsed Detonation Engine," AIAA-2006-5133, *42nd AIAA/ASME/SAE/ASEE Joint Propulsion Conference and Exhibit*, Sacramento, CA, 9–12 July 2006.
- ¹⁰Knystautas, R., Guirao, C., Lee, J. H., and Sulmistras, A., "Measurement of Cell Size in Hydrocarbon-Air Mixtures and Predictions of Critical Tube Diameter, Critical Initiation Energy, and Detonability Limits," *Progress in Aeronautics and Astronautics*, AIAA, Vol. 94, pp. 23–37, 1984.
- ¹¹Schauer, F. R., Miser, C. L., Tucker, K. C., Bradley, R. P., and Hoke, J. L., "Detonation Initiation Hydrocarbon-Air Mixtures in a Pulsed Detonation Engine," AIAA 2005-1343, *43rd AIAA Aerospace Sciences Meeting and Exhibit*, Reno, NV, 10–13 January 2005.
- ¹²Fickett, W. and Davis, W. C., *Detonation: Theory and Experiment*, New York, NY, Dover Publications Incorporated, 1979.
- ¹³Austin, J. M. and Shepherd, J. E., "Detonation in Hydrocarbon Fuel Blends," *Combustion and Flame*, Vol. 132, No. 1–2, 2002, pp. 73–90.
- ¹⁴Ciccarelli, G., Ginsberg, T., Boccio, J., Economos, C., Sato, K., and Kinoshita, M., "Detonation Cell Size Measurements and Predictions in Hydrogen-Air-Steam Mixtures at Elevated Temperatures," *Combustion and Flame*, Vol. 99, 2004, pp. 212–220.
- ¹⁵Huang, H., Sobel, D., and Spadaccini, L., "Endothermic Heat-Sink of Hydrocarbon Fuels for Scramjet Cooling," AIAA 2002-3871, *38th AIAA/AMSE/SAE/ASEE Joint Propulsion Conference and Exhibit*, Indianapolis, IN, 7–10 July 2002.
- ¹⁶Cooper, M. and Shepherd, J. E., "Thermal and Catalytic Cracking of JP-10 for Pulse Detonation Engine Applications," GALCIT Report FM2002.002, Graduate Aeronautical Laboratories, California Institute of Technology, Pasadena, CA, 2002.
- ¹⁷Cooper, M. and Shepherd, J. E., "Experiments Studying Thermal Cracking, Catalytic Cracking, and Pre-Mixed Partial Oxidation of JP-10," AIAA 2003-4687, *39th AIAA/ASME/SAE/ASEE Joint Propulsion Conference and Exhibit*, Huntsville, AL, 20–23 July 2003.

- ¹⁸Galligan, C., "Catalytic Cracking of Jet Propellant-10 for Pulsed Detonation Engine Applications," M.S. Thesis, Laval University, Quebec, Canada, March 2005.
- ¹⁹Huang, H., Sobel, D., and Wei, D., "Endothermic Fuel Characterization," AFRL-PR-WP-TR-2005-2032, Air Force Research Laboratories, Wright-Patterson AFB, OH, August 2004.
- ²⁰Schauer, F. R., Stutrud, J. S., and Bradley, R. P., "Detonation Initiation Studies and Performance Results for Pulse Detonation Engine Applications," AIAA 2001-129, *39th AIAA Aerospace Sciences Meeting and Exhibit*, Reno, NV, 8-11 January 2001.
- ²¹Schelkin, K.L., *Soviet Journal of Technical Physics*, Vol. 10, pp. 823-827, 1940.
- ²²Spadaccini, L. J., Sobel, D. R., Haung, H., and Dardas, Z., "Coke Deposition/Mitigation in Endothermic Fuels – Advanced Fuel Development and Fuel Combustion," AFRL-PR-WP-TR-1998-2098, Air Force Research Laboratories, Wright-Patterson AFB, OH, June 1998.
- ²³Bartok, W. and Sarofim, A. F., *Fossil Fuel Combustion – A Source Book*, New York, NY, John Wiley and Sons Incorporated, 1991.
- ²⁴Miser, C. L., Helfrich, T. M., Schauer, F. R., and Phelps D. K., "Supercritical Fuel Density from Experimental Pulse Detonation Engine," AIAA 2006-1025, *44th AIAA Aerospace Sciences Meeting*, Reno, NV, 9-12 January 2006.
- ²⁵Helfrich, T. M., "Cycle Performance of a Pulse Detonation Engine with Supercritical Fuel Injection," M.S. Thesis, Department of Aeronautics and Astronautics, Air Force Institute of Technology, Wright-Patterson AFB, OH, 2006.
- ²⁶Panzenhagen, K. L., "Detonation Branching in a PDE with Liquid Hydrocarbon Fuel," M.S. Thesis, Department of Aeronautics and Astronautics, Air Force Institute of Technology, Wright-Patterson AFB, OH, 2004.
- ²⁷Helfrich, T. M., Schauer, F. R., Bradley, R. P., and Hoke, J. L., "Ignition and Detonation-Initiation Characteristics of Hydrogen and Hydrocarbon Fuels in a PDE," AIAA 2007-0234, *45th AIAA Aerospace Sciences Meeting*, Reno, NV, 7-10 January 2007.
- ²⁸Altin, O. and Eser, S., "Analysis of Solid Deposits from Thermal Stressing JP-8 Fuel on Different Tube Surfaces in a Flow Reactor," *Industrial and Engineering Chemistry Research*, Vol. 40, 2001, pp. 596-603.

Detonation Propagation across an Asymmetric Step Expansion

David R. Hopper^{*} and Paul I. King[†]

Air Force Institute of Technology, Wright-Patterson AFB, OH 45433

Frederick R. Schauer[‡]

Air Force Research Laboratories, Wright-Patterson AFB, OH, 45433

Viswanath R. Katta[§] and John L. Hoke[§]

Innovative Scientific Solutions, Inc., Dayton OH, 45440

A study of confined detonation transmission across a step expansion was conducted using experimental and computational techniques. Transmission success of ethylene/air detonations at various equivalence ratios was compared to the transmission of hydrogen/air detonations. The highest rate of transmission success in the experimental results for ethylene was noted at equivalence ratios richer than the conditions of minimum cell size, indicating the presence of effects other than cell size and expansion ratio. Hydrogen proved to have better transmission success than ethylene, even when normalized to the cell size upstream of the expansion. The difference is theorized to result from the disparity in critical initiation energy of the two fuels. Computational results show the presence of a relationship between the number of transverse waves upstream of the expansion and the degree of expansion that correlates to success or failure of a confined detonation transmission. Detonation transmissions are also observed to fail when a single transverse wave in the upstream channel is partially reflected at the step expansion.

Nomenclature

CJ	= Chapman-Jouguet
CFD	= computational fluid dynamics
d_2/d_1	= expansion ratio, or degree of expansion
DDT	= deflagration to detonation transition
f	= engine cycle frequency
n	= number of cells
n_c	= critical number of cells
PDE	= pulsed detonation engine
$R1-R9$	= regions of detonation tube
ϕ	= equivalence ratio
λ	= detonation cell size

I. Introduction

Pulsed detonation engines (PDE) ignited by low-energy spark systems typically employ spiral or other obstacle devices in the detonation tube to encourage deflagration to detonation transition (DDT). Obstacles decrease the thrust produced by the PDE, and DDT significantly increases the required cycle time as well as the length of the PDE when compared to a directly initiated detonation. Direct initiation, however, requires a tremendous amount of energy in a tube large enough to be of practical use in a pulsed detonation engine¹. High energy ignition pulses may be achieved using a pre-detonator or some other method to establish a detonation in a small tube and then propagate

^{*} Major, USAF, Graduate Student, Department of Aeronautics, 2950 Hobson Way, AIAA Member.

[†] Professor, Department of Aeronautics, 2950 Hobson Way, AIAA Senior Member.

[‡] Senior Engineer, Head PDRF, AFRL/PRTC, 2950 5th Street, AIAA Senior Member.

[§] Research Engineer, 2766 Indian Ripple Road, AIAA Senior Member

the detonation into a larger tube. It is well known that a detonation emerging from a tube will propagate spherically into an unconfined space if the tube has a diameter of at least 13 times the detonation cell size λ .² This would require a pre-detonator diameter of nearly 200 mm (7.8 in) for detonations of hydrogen in air³ and larger diameters for detonations of hydrocarbon fuels, an impractically large size for a pre-detonator. Detonations emerging from diameters smaller than 13λ will fail when they diffract into an unconfined space, meaning that the leading shock of the detonation wave will decouple from the combustion wave front. However, a detonation propagating from a small tube into a larger tube will persist through the expansion for diameter ratios below some limit.⁴ The limits governing the success or failure of a confined detonation diffraction, however, have not been clearly defined.

References 5 and 6 describe three modes of unconfined detonation transmission at an expansion: 1) multi-front ignition, where the detonation transitions smoothly across the expansion, 2) critical transition, where the shock wave and combustion wave front initially separate, then the detonation is re-initiated by a localized explosion, and 3) failure, a deflagration wave behind an entirely separated shock front. References 7 and 8 define these modes as supercritical, near-critical, and sub-critical, respectively. The number of cell widths in the upstream tube determine the mode of transmission, with 13λ being the accepted minimum tube diameter for a successful transition (supercritical or near-critical).

The confined diffraction problem is somewhat more complex than unconfined diffraction, because the detonation interacts with the downstream tube walls as it diffracts. Experiments on detonation diffraction in hydrogen and air mixtures showed wavespeed phenomena consistent with detonation re-initiation resulting from wall reflection downstream of a step expansion.⁹ The authors of reference 10 found that the influence of the walls downstream vanished above expansion ratios of 5, and the detonation diffracted as if unconfined. The purpose of the current experiments is to determine the existence of a relationship between number of cells in the upstream tube, the degree of confinement, and the ultimate success or failure of a detonation transmission across a step expansion.

II. Background

A. Experimental

An experimental study was conducted to investigate detonation transmission across a confined step expansion in non-coaxial circular tubes. In particular, it was desired to determine the limits of successful transmission as a function of tube geometry and detonation cell size, λ . The experiments were carried out in the AFRL pulsed detonation research facility at Wright-Patterson AFB, Ohio. This facility has previously been described in detail,¹¹ and only the pertinent modifications for the current experiment are described.

Air and fuel were delivered to the detonation tubes through the valving of a General Motors quad-4 automotive cylinder head. The engine cycle was divided into three equal partitions; fill, fire, and purge. During the fill phase, the intake valves were opened, allowing a gaseous fuel and air mixture to enter the tubes. The volume of fuel/air that flowed into the tubes was a function of the fill manifold pressure and the length of time the intake valves remained open, or the engine cycle frequency (f). This volume, divided by the total volume of the tubes, is known as fill fraction, and was set to 1.0 for this experiment. The fire phase began when the intake valve closed and ended when the purge valves opened. When the intake valves closed, combustion was spark-initiated after a brief delay, known as spark delay.

The test section consisted of a 1.2 m (4 ft) section of 26 mm (1 in) diameter detonation tube, followed by a non-coaxial step expansion to a larger diameter detonation tube as shown in Fig. 1. The 26 mm detonation tube contained a Shchelkin-type spiral obstruction along the first two feet of its length to ensure successful deflagration-to-detonation transition (DDT) prior to reaching the step expansion. The diameter of the downstream (larger) detonation tube was varied to determine the effect of confinement on successful transmission of a detonation. Runs

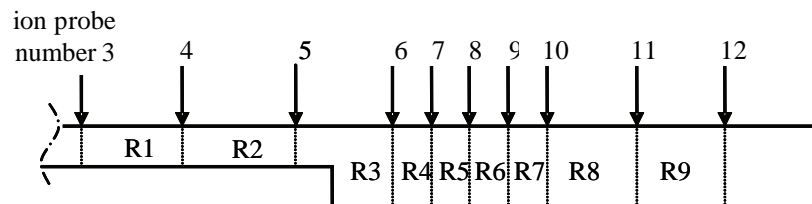


Fig. 1. Cutaway sketch of experimental apparatus, showing approximate ion probe locations relative to step expansion, and indicating regions of average wavespeed calculation (R1-R9).

were conducted with downstream tube diameters of 35 mm (1.4 in), 41 mm (1.6 in), 53 mm (2.1 in) and 63 mm (2.5 in), with $f = 10$ Hz. Table 1 shows a matrix of the conditions for each test run.

Ion probes were placed at intervals along the length of the detonation tubes to determine the combustion wavespeed. Wavespeeds in each region (labeled R1, R2, etc. in Fig. 1) were computed from the distance and the time of travel between probes. Due to manufacturing inconsistencies, the locations of the ion probes varied on the different downstream tubes. For this reason, Fig. 1 does not show measurements of the ion probe locations.

Table 1. Matrix of conditions for each test run

Run Number	Downstream Tube Diameter (mm)	Equivalence Ratio (ϕ) Range	Fuel/Oxidizer	Fill Fraction	Spark Delay (msec)
1	35	0.83 - 1.58	Ethylene/air	1.0	4
2	41	0.83 - 1.58	Ethylene/air	1.0	4
3	53	0.83 - 1.58	Ethylene/air	1.0	4
4	63	0.83 - 1.58	Ethylene/air	1.0	4
5	53	0.45 - 2.4	Hydrogen/air	1.0	4

The Chapman-Jouguet (CJ) wavespeed for ethylene and air at near-stoichiometric mixtures is approximately 1824 m/s.¹² Likewise, the CJ wavespeed for stoichiometric hydrogen and air is 1971 m/s.¹³ A combustion wave traveling within approximately 20 percent of the CJ value through consecutive regions was considered to be a detonation.

B. Computational

The computations were performed only for hydrogen in air using Euler type equations with exothermic chemical reactions in a 2-D channel. The equations can be expressed in the form:

$$\frac{\partial q}{\partial \tau} + \frac{\partial E}{\partial x} + \frac{\partial F}{\partial y} + H = 0 \quad (1)$$

Equation 1 represents a vector set of 6 equations, namely, mass, momentum (x and y), energy, and two progress variables. The reaction was stoichiometric hydrogen and air, and was represented by the two-step model of Korobeinikov.¹⁴ The two steps consist of a non-exothermic irreversible induction reaction followed by an exothermic reversible recombination reaction.

The simulation used an explicit 2nd-order MacCormack predictor-corrector technique with 4th-order flux-corrected transport for accurate resolution of properties across shock waves. All calculations were initiated with a planar Zeldovich, von-Neumann and Doering (ZND) detonation wave. Cellular character was generated by perturbing the ZND wave by artificially elevating the temperature in a few discrete locations near the wave, and allowing transverse waves to naturally develop. This technique has previously been used successfully and is discussed in greater detail elsewhere.¹⁵

The computations were performed for a channel of overall length approximately 0.98 m. The first 0.33 m of tube length was a narrower passage, followed by a wider passage 0.65 m in length. This was considered to be adequate length to allow the cellular structure upstream of the expansion to fully develop, and to allow for determination of transmission success downstream of the expansion. The widths of both the upstream and downstream channels were varied to obtain the desired number of cells upstream of the expansion and the desired expansion ratio.

III. Results

A. Character of the experimental data

Numerous studies have been conducted to measure the cell size of detonations in various fuel and oxidizer combinations.^{3, 12} The relationship between cell size (λ) and equivalence ratio (ϕ) has been shown to have an

approximately parabolic character, with the minimum cell size usually occurring in slightly rich mixtures, as shown in Fig. 2a. There is considerable spread to the available cell size data, particularly for ethylene/air, sometimes even within data taken by a single investigator. No cell size measurements were made as part of the current study, but rather the cell size estimations offered herein are based on correlations to the measured ϕ . Figure 2b presents critical initiation energy as a function of ϕ .

The minimum cell size for an ethylene/air mixture was shown in reference 12 to be 20.89 mm at $\phi = 1.07$. The inner diameter of the upstream tube used in the current experiment was 26 mm, slightly larger than the minimum cell size. The implication of this particular combination of geometry and cell size is that the upstream tube contains at most slightly more than one full detonation cell width, and in many cases, contains less than a complete detonation cell width. This small upstream tube diameter is believed to be a major factor in the low overall transmission success for ethylene/air detonations in the current experiment.

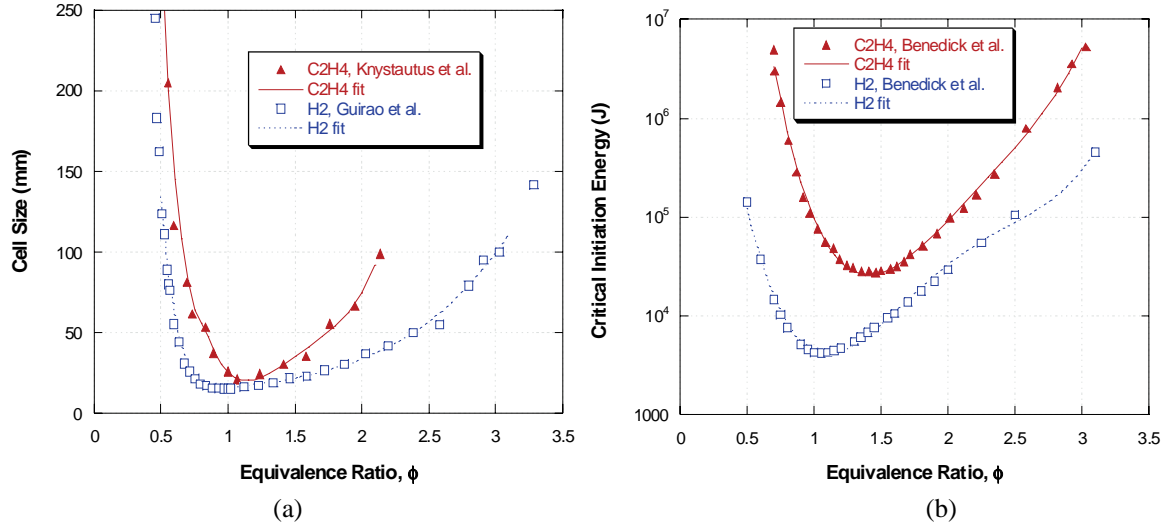


Fig. 2. (a) Cell size plotted as a function of equivalence ratio, from references 3 and 12. (b) Critical initiation energy plotted as a function of equivalence ratio, from reference 1.

Curves were fit to the data of cell size and critical initiation in Fig. 2a and Fig. 2b. The curve fit to the log of critical initiation energy was a straightforward 4th-order polynomial. A good fit for cell size, however, required two separate curves, a 4th-order polynomial for ϕ greater than 0.8 and a two parameter power function for ϕ less than 0.8

B. Experimental Results

Figure 3 shows the success rate of ethylene/air detonation transmissions at various equivalence ratios for four different expansion ratios and for hydrogen/air in a single expansion ratio, as shown in Table 1. The experimental data for ethylene/air showed unexpectedly high transmission success at high ϕ (1.41 and 1.58) and low ϕ (0.83 and 0.89). Upon further examination, overdriven wavespeeds were noted in the vicinity of the step expansion, indicating possible DDT in this region. Since the overdriven conditions of a DDT can reduce the cell size (and hence increase the number of transverse waves) by as much as an order of magnitude,¹⁶ data showing evidence of DDT near the step were eliminated from consideration. Only runs that showed consistent near-CJ wavespeeds in consecutive regions upstream of the expansion are shown in Fig. 3.

As might be expected, detonation transmissions for both fuels are more successful near stoichiometric ϕ where cell sizes are smaller, and success decreases in rich or lean mixtures as the cell size (presumably) grows. However, for ethylene, the peak transmission rates occur between $\phi = 1.24$ and 1.41, to the rich side of the anticipated minimum cell size ($\phi = 1.07$).

The critical initiation energy plot of Fig. 2b offers an explanation for the shifting of the transmission success data. Successful re-initiation of a detonation following a step expansion is thought to occur as a result of transverse wave interactions and wall reflections, which combine to produce a transverse detonation or local explosion of sufficient strength to re-ignite a detonation.⁹ This phenomenon is akin to direct initiation of a detonation using a high-energy ignition source. It follows that re-initiation behavior following a step expansion is similar to direct initiation behavior. In Fig. 2b, the minimum critical initiation energy for hydrogen is very near stoichiometric

equivalence. Ethylene, however, has a minimum at approximately $\phi = 1.45$. This means that for equivalence ratios between $\phi = 1.24$ and $\phi = 1.41$, the energy required to re-initiate a detonation will be far less than the energy required near stoichiometric conditions. As the mixture becomes too rich (above $\phi = 1.41$) the number of upstream transverse waves is presumably reduced to the point that detonations no longer survive the expansion, despite the fact that critical initiation energy is near minimum. It appears, then, successful transmission is influenced by critical initiation energy and the number of transverse waves upstream of the expansion.

Hydrogen/air detonations have a smaller cell size, and so transmit more easily across a step expansion than ethylene/air detonations. Additionally, hydrogen has lower critical initiation energy than ethylene at all equivalence ratios (Fig. 2b). As a result, hydrogen detonations are more consistently transmitted across a wider range of equivalence ratios (100% successful from $\phi = 0.65$ to 2.1).

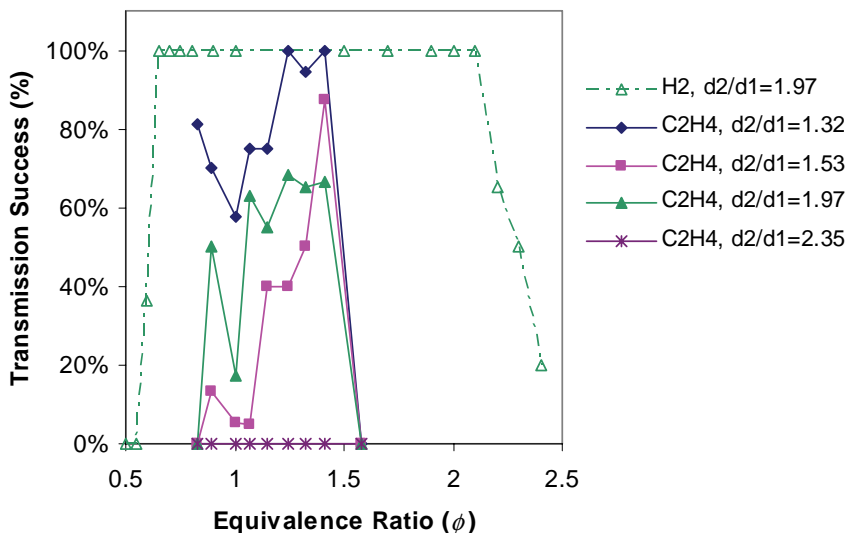


Fig. 3. Transmission success of hydrogen/ air and ethylene/air detonations across a step expansion

Increased step size is seen in Fig. 3 to have an effect on transmission success, but the results raise some questions. The smallest expansion ($d_2/d_1=1.32$) clearly has the best transmission rate, and the largest expansion ($d_2/d_1=2.35$) shows zero transmission success. The two intermediate expansions are almost cleanly reversed, with the $d_2/d_1=1.97$ expansion performing better than the smaller $d_2/d_1=1.53$ expansion. One could speculate that the larger geometry produces reflections that are more prone to release sufficient energy for re-initiation than the smaller expansion, but this seems unlikely. At $\phi = 1.41$, very near the minimum critical initiation energy, the $d_2/d_1=1.53$ expansion shows greater success than $d_2/d_1=1.97$, which is the expected result.

The transmission success for ethylene in the smallest expansion at $\phi = 0.83$ appears to be something of an outlier. While the other step sizes dropped to zero transmission success at this ϕ , the smallest expansion appears to improve over $\phi = 0.89$. Whatever the reason for this increase, it is unlikely that the trend will continue as ϕ is reduced.

Figure 4 further explores the relationship between critical initiation energy and cell size by correlating the curve fits of Fig. 2. Lean data are separated from rich data in Fig. 4 by plotting the lean cell sizes as negative numbers. Improved detonation transmission should be achieved by reducing both required initiation energy and the cell size, or in other words, by approaching the origin of the plot.

While the cell size and critical initiation energy of hydrogen both strictly approach the origin near stoichiometric equivalence, there is a “hook” in the ethylene data on the right hand (rich) side of Fig. 4. This hook clearly illustrates that the minimum critical initiation energy for ethylene, unlike other fuels, occurs well away from the equivalence ratio for minimum cell size. This hooked shape also means that the effects of cell size and critical initiation energy, in terms of successful detonation transmission across a step expansion, compete with one another for ethylene between $\phi = 1$ and 1.5. Another point clearly illustrated in Fig. 4 is that the minimum critical initiation energy of ethylene is equal to the critical initiation energy of hydrogen at approximately $\phi = 2.0$, meaning that hydrogen detonation transmissions will always be more successful than ethylene detonation transmissions, at any ϕ of interest.

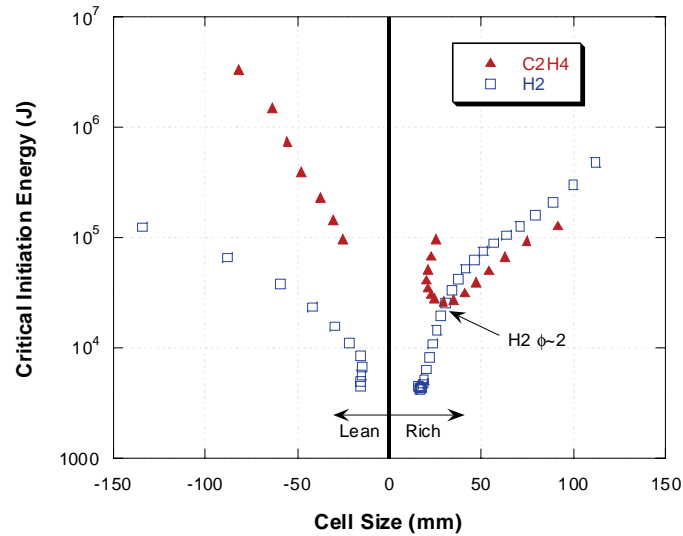


Fig. 4. Cell size vs. critical initiation energy for hydrogen/air and ethylene/air, correlated from the curve fits of Fig. 2. Lean cell sizes are shown as negative numbers.

Since hydrogen and ethylene detonations at a given equivalence ratio have different cell sizes, it would be useful to isolate the effects of cell size in relation to the success or failure of the detonation transmission. Unfortunately, there is an asymmetric character to the data that resists plotting as a simple function of cell size. An alternative method of display is to plot rich and lean data on separate halves of the figure, by allowing cell sizes below the minimum cell size (at $\phi = 1.07$) to take negative values, in much the same manner as Fig. 4

The transmission success of ethylene and hydrogen can be said to have the same basic character, with maximum transmission success near minimum cell size for hydrogen and near $\phi = 1.4$ for ethylene, most likely due to the effect of critical initiation energy. Again, hydrogen is seen to produce superior results for the current experimental setup. Transmission success rates for both hydrogen and ethylene fall off as ϕ becomes rich or lean, but the falloff points are at different cell sizes, reinforcing the idea that cell size alone does not determine transmission success.

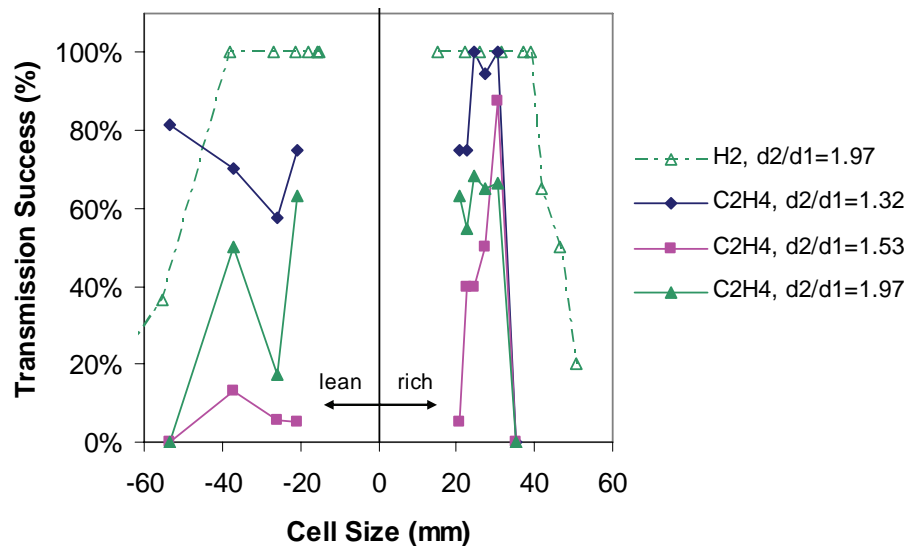


Fig. 5. Transmission success of ethylene/air and hydrogen air plotted as a function of cell size. Cell sizes for mixtures leaner than $\phi = 1.07$ are shown as negative numbers.

C. Computational Results

A number of computational runs were conducted for hydrogen/air using the 2-D computational fluid dynamics (CFD) code previously described, varying the channel width both upstream and downstream of a non-symmetric two-dimensional step expansion. The intent of this study was to search for the boundary of successful transmission of a detonation, and relate it to the degree of expansion and the cell size.

Successful transmission of a detonation was judged qualitatively by whether the characteristic detonation structure of incident shocks, Mach stems and transverse waves was preserved as the detonation negotiated the step. A successful detonation was marked by strong reflections off the downstream tube walls, interactions of these reflections with other transverse waves, and downstream re-establishment of regular cellular structure behind a strong wavefront. On the other hand, a failed detonation generally exhibited a weaker reflection off the tube walls, a lack of interaction with transverse waves, and a continued weakening and slowing of the combustion wave. Examples of successful and failed detonation transmissions are shown in Figs. 6 and 7, respectively.

In Fig. 6, the detonation is seen to be re-initiated as a result of a strong transverse wave reflection from the lower wall of the channel, possibly interacting with another transmitted transverse wave. At the larger step of Fig. 7, however, the transverse wave has been weakened by diffraction to the extent that the reflection is of insufficient strength to re-initiate the detonation.

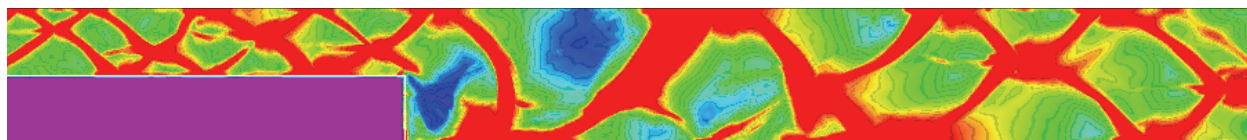


Fig. 6. CFD plot of peak pressure history in a sudden expansion, showing successful transmission of a detonation. Channel widths are 32.5 mm upstream, 65 mm downstream.

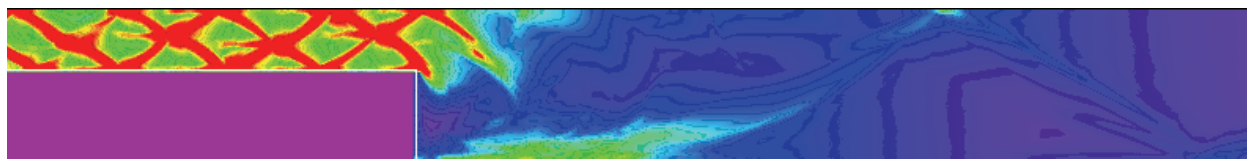


Fig. 7. CFD plot of peak pressure history in a sudden expansion, showing unsuccessful transmission of a detonation. Channel widths are 26 mm upstream, 65 mm downstream.

Because the downstream re-initiation was generally the result of a single reflection in the current CFD, the downstream wave structure usually contained a single transverse wave initially. Then, if the downstream channel width was sufficiently large, as in Fig. 6, other transverse waves were formed, eventually resulting in the normal detonation cellular structure.

The results of transmission success across a wide range of upstream and downstream channel widths are summarized in Fig. 8, expressed in a method similar to that suggested in reference 10. This method plots the degree of expansion (d_2/d_1) on the horizontal axis and a cell size parameter on the vertical axis. The cell size parameter is the ratio of critical number of cells (n_c) to the actual number of cells (n) in the upstream tube. As will be seen later, the cell size λ varies with geometry, so the cell size parameter is expressed as $n_c\lambda/d_1$, with $\lambda = 15$ mm and $n_c = 13$, both assumed constant for plotting purposes. As can be seen in Figs. 6, 7 and 9, λ in the current simulation is on the order of twice the assumed value. By fixing n_c and λ , the vertical axis of Fig. 8 becomes simply the inverse of upstream diameter multiplied by a constant. Different values of n_c and λ would scale the axis, but will not fundamentally affect the information presented.

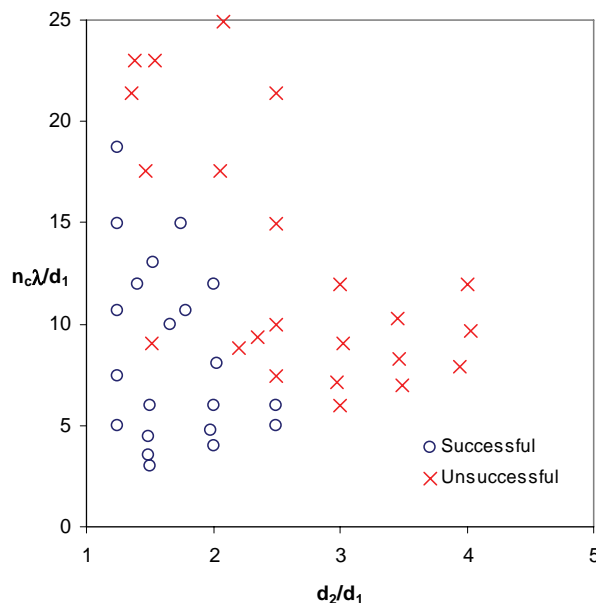


Fig. 8. Relationship between cell size parameter (critical number of cells (n_c), cell size (λ), upstream channel width (d_1)) and the expansion ratio (d_2/d_1), indicating points of successful and failed detonation transmission, as determined by CFD calculations.

The results in Fig. 8 indicate that there are distinct regions of failed transmissions and successful transmissions. The majority of failed transmissions can be separated from the successful transmissions by a curve extending from the upper left to the lower right of the plot. At the boundary of such a curve, however, there would be a number of exceptions—failed transmissions in the region of successful transmissions, or vice versa. These exceptions are thought to be related to the number of transverse waves in the upstream channel, which are discrete in nature, and cause an almost stepwise character to the data at the boundary. For the majority of runs above $n_c \lambda / d_1 = 5$ on the vertical axis of Fig. 8, only one transverse wave was present in the upstream channel. The successful transmissions at $d_2/d_1 = 2.5$, however, had two transverse waves. As the number of transverse waves increases further, the results will likely hold more to a continuous curve, but the difference between one and two waves is quite significant, likely disrupting the otherwise smooth character of the data.

Interestingly, λ is not found to be completely independent of channel width in the current simulation. When the channel width is less than λ , only one transverse wave exists in the channel. The normal failure/re-initiation that occurs in a planar detonation wave as a result of transverse wave interactions is not present when only one transverse wave exists, but rather the existence of the detonation is wholly dependent on re-initiation via wall reflections of the single transverse wave. As a result, the channel width (d_1) becomes half the cell width when only a single transverse wave is present in the 2-D channel, as seen in Figs. 9. A similar outcome is seen when only two transverse waves exist; that is, $d_1 \sim \lambda$, seen in Fig. 6.

There is a single failure point contained inside the region of successful transitions in Fig. 8. This failure occurs in a regime where only a single transverse wave is present upstream and, by coincidence, that transverse wave encounters the edge of the step in such a manner that part of the energy is reflected upward while the remaining energy continues downward (Fig. 9a). After the expansion, neither the reflected nor the non-reflected portions of the transverse wave possess sufficient energy to re-initiate detonation. To verify that this failure mode was simply a coincidental occurrence, additional runs were made using the same initial conditions and the same channel widths, but adjusting the position of the step relative to the transverse wave of the detonation. As can be seen in Fig. 9b, reducing the length of the step so that the downward-traveling transverse wave misses the corner of the step entirely results in a successful transmission. In Fig. 9c, a similar successful outcome is achieved by lengthening the step so that the entire transverse wave is reflected.

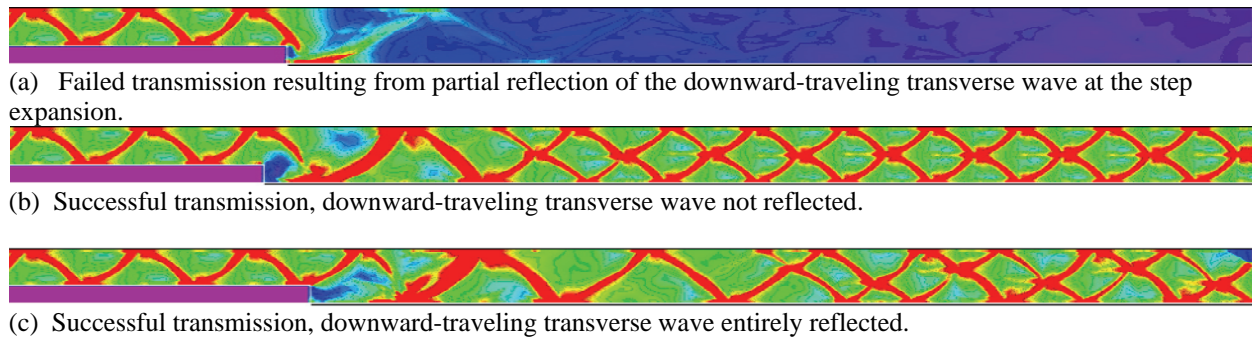


Fig. 9. CFD plots of peak pressure history in a sudden expansion. Channel width is 21.5 mm upstream, 32.5 mm downstream.

The data presented in Fig. 9 provide a possible explanation of some of the behavior of the experimental data of Figs. 3-5. In the CFD, a small change in upstream channel length can have a significant effect on the success or failure of detonation transmissions, depending on the location of the step relative to a transverse wave. In exploring the sensitivity of detonation success to position of the step expansion, the length of the upstream channel was varied in steps of approximately 6.5 mm from the original failed case at a length of 327 mm (Fig. 9a). Failed transmissions were observed in a zone of upstream lengths from 333 mm to 314 mm (not shown). Above 340 mm (Fig. 9c), detonation transmissions were observed to succeed to at least 372 mm, as well as from 307 mm (Fig. 9b) to 281 mm.

Recall that ethylene/air detonations in the $d_2/d_1 = 1.53$ expansion did not succeed as well at most equivalence ratios as did the detonations in the $d_2/d_1 = 1.97$ expansion. One possibility is that the upstream length was changed between the two tube geometries such that the smaller expansion was nearer to a “failure zone” than the larger expansion. This is quite possible, as variations existed between the different pieces of experimental hardware, and assembly of the pieces was a matter of threading pipes together. The fire phase of a PDE, including ignition, DDT and propagation of a 3-D detonation, is an inherently stochastic process. If a relatively minor change in a “clean” CFD environment makes the difference between success and failure, then operation of a PDE near the same conditions will likely produce a high number of failed transmissions.

IV. Conclusions

Successful transmission of a detonation across a step expansion appears to be dependent on the degree of expansion, the number of transverse waves in the upstream channel and the sensitivity of the fuel/air mixture to detonation. The computational results presented here also show that position of the step expansion relative to a transverse wave of a detonation can be a significant factor in determination of transmission success, particularly when only one transverse wave is present in the upstream channel. When a cell size parameter is plotted against expansion ratio, general regions of successful detonation transmission emerge, but as yet, no absolute guideline for predicting success or failure of a confined detonation expansion is apparent. To establish such a guideline, the cell size parameter will likely need to be modified to include information about the discrete number of transverse waves. Additionally, to generalize to different fuel/air mixtures, sensitivity to detonation initiation must also be considered.

Acknowledgments

The authors gratefully acknowledge the contributions of Paul Litke, Royce Bradley, Curt Rice, Dave Baker and Jeff Stutrud for their help in enabling this research. For their leadership and guidance, we also thank Dr Robert Hancock and Dr Mel Roquemore.

The views expressed in this article are those of the authors and do not reflect the official policy or position of the United States Air Force, Department of Defense, or the US Government.

References

- ¹ Benedick, W.B., Guirao, C.M., Knystautas, R., and Lee, J.H., "Critical Charge for the Direct Initiation of Detonation in Gaseous Fuel-Air Mixtures," *Progress in Astronautics and Aeronautics*, vol. 106, pp.181-202, 1986.
- ² Glassman, I., *Combustion*, 3rd Edition, 1996, p.259
- ³ Guirao, C.M., Knystautas, R., Lee, J., Benedick, W., and Berman, M., "Hydrogen-Air Detonations," *19th Symposium (Int.) on Combustion*, pages 583-590, 1982.
- ⁴ Katta, V.R., Tucker, K.C., Hoke, J., Schauer, F., "Initiation of Detonation in a Large Tube," *19th International Colloquium on the Dynamics of Explosions and Reactive Systems*, Hakone, Japan, July 2 – August 1, 2003.
- ⁵ Edwards, D.H., Thomas, G.O., Nettleton, M.A., "The Diffraction of a Planar Detonation Wave at an Abrupt Area Change," *Journal of Fluid Mechanics*, Vol. 95 part 1, pp. 79-96, 1979.
- ⁶ Edwards, D.H., Thomas, G.O., Nettleton, M.A., "Diffraction of a Planar Detonation in Various Fuel-Oxygen Mixtures at an Area Change," *Progress in Astronautics and Aeronautics*, Vol. 75, pp. 341-357, 1981.
- ⁷ Schultz, E., "Detonation Diffraction Through an Abrupt Area Expansion," PhD Dissertation, California Inst. of Tech., Pasadena, CA.
- ⁸ Arienti, M., "A Numerical and Analytical Study of Detonation," PhD Dissertation, California Inst. of Tech., Pasadena, CA.
- ⁹ Hopper, D.R., King, P.I., and Schauer, "Propagation of Detonations across a Step Area Change in a Pulsed Detonation Engine," AIAA Paper 2007-0446, 45th AIAA Aerospace Sciences Meeting and Exhibit, 8-11 January 2007, Reno NV.
- ¹⁰ Pantow, E.G., Fischer, M., and Kratzel, Th., "Decoupling and Recoupling of Detonation Waves Associated with Sudden Expansion," *Shock Waves*, Vol. 6, pp. 131-137, 1996.
- ¹¹ Schauer, F., Stutrud, J., and Bradley, R. "Detonation Initiation Studies and Performance Results for Pulsed Detonation Engine Applications." AIAA Paper No. 2001-129, *39th AIAA Aerospace Sciences Meeting & Exhibit*, 8-11 January 2001, Reno, NV.
- ¹² Knystautas, R., Guirao, C., Lee, J.H., and Sulmistras, A., "Measurements of Cell Size in Hydrocarbon-Air Mixtures and Predictions of Critical Tube Diameter, Critical Initiation Energy, and Detonability Limits," *Progress in Astronautics and Aeronautics*, vol. 94, pp.23-37, 1984.
- ¹³ Schultz, E., and Shepherd, J., "Validation of Detailed Reaction Mechanisms for Detonation Simulation," *Explosion Dynamics Laboratory Report FM99-5*, 2000
- ¹⁴ Korobeinikov, V., Levin, V., Markov, V., and Chernyi, G., *Astronautica Acta*, Vol. 17, No. 4 and 5, p. 529, 1972.
- ¹⁵ Katta, V.R., Chin, L.P., Schauer, F., *17th International Colloquium on the Dynamics of Explosions and Reactive Systems*, Heidelberg, Germany, July 25-30 1999.
- ¹⁶ Gamezo, V.N., Ogawa, T., and Oran, E.S., "Numerical Simulations of Flame Propagation and DDT in Obstructed Channels Filled with Hydrogen-Air Mixture," *Proceedings of the Combustion Institute* 30, pp. 2462-2471, 2007.

Effect of Supercritical Fuel Injection on Cycle Performance of Pulsed Detonation Engine

Timothy M. Helfrich* and Paul I. King†

Air Force Institute of Technology, Wright–Patterson AFB, Ohio 45433

John L. Hoke‡

Innovative Scientific Solutions, Inc., Dayton, Ohio 45440

and

Frederick R. Schauer§

U.S. Air Force Research Laboratory, Wright–Patterson AFB, Ohio 45433

DOI: 10.2514/1.26551

Pulsed detonation engines produce impulsive thrust through rapid ignition and formation of detonation waves. An operational goal is a reduction in time for the formation of detonation waves in conjunction with low-vapor-pressure liquid hydrocarbons. This study focuses on pulsed detonation engine operation enhancements using dual-detonation-tube, concentric-counterflow heat exchangers to elevate liquid hydrocarbon fuel temperatures up to supercritical levels. Variation of operating parameters includes fuel type (JP-8, JP-7, JP-10, RP-1, JP-900, and S-8) and firing frequency. Of interest is the effect on ignition time, deflagration to detonation transition time, detonation distance, and the percent of ignitions resulting in a detonation (detonation percentage). Except for JP-10, results for all fuels with increasing fuel injection temperatures indicate decreases in deflagration to detonation transition time by up to 15%, decreases in detonation distance by up to 30%, increases in the detonation percentage by up to 180%, and minimal impact on ignition time. JP-10 is difficult to detonate and results are inconsistent. An increase in firing frequency results in a 5% decrease in deflagration to detonation transition time at high fuel injection temperatures, but has little effect on ignition time and detonation distance.

Nomenclature

A	=	Arrhenius constant
E_a	=	activation energy
E_{crit}	=	critical initiation energy
[fuel]	=	concentration of fuel
[oxidizer]	=	concentration of oxidizer
P	=	detonation tube—closed-end pressure
RR	=	reaction rate
R_u	=	universal gas constant
T_{mix}	=	fuel/air mixture temperature
λ	=	cell size

I. Introduction

ALTHOUGH the pulsed detonation engine (PDE) has the potential to provide significant advantages over current aircraft propulsion systems, it is still in the early stages of development [1]. Several technological barriers need to be overcome before the PDE can be considered a practical means of providing propulsion to operational aircraft [2–4]. One is the efficient use of low-vapor-pressure hydrocarbon fuels, such as JP-8, JP-7, JP-10, JP-900,† RP-1, and S-8.** The majority of research with pulsed detonation engines

has employed gaseous fuels, such as hydrogen and simple hydrocarbons [6,7], resulting in a dearth of liquid hydrocarbon data and a large gap between research and the operational use of pulsed detonation engines. Also, nearly all U. S. Air Force aircraft and air-breathing missiles use liquid hydrocarbon fuels, primarily JP-8 and JP-10 [5]; therefore it is pertinent to develop a method to efficiently use these fuels.

Four key cycle parameters are adversely affected by using liquid hydrocarbon fuels in lieu of gaseous fuels. The parameters are 1) ignition time, the time from spark deposition to the creation of a deflagration wave within the fuel/air mixture, 2) deflagration to detonation transition (DDT) time, the time to transition the deflagration wave into a detonation wave, 3) detonation distance, the length of the detonation tube required for the mixture to transition to a detonation, and 4) detonation percentage [7], the percentage of ignitions that result in a detonation wave. Both the ignition time and the DDT time are nearly an order of magnitude larger for complex liquid hydrocarbon fuels than for hydrogen. For example, ignition time of a hydrogen/air mixture is on the order of 1 ms, whereas that of a JP-8/air mixture is approximately 7 ms. A reduction in DDT or ignition time would shorten the PDE cycle time, allowing for higher frequency operation and higher average thrust. Reduction in detonation distance allows for a decrease in detonation tube length, resulting in a decreased engine weight. An increase in detonation percentage directly improves the efficiency of the PDE, leading to an increase in specific impulse.

Until this work, the performance of a liquid-hydrocarbon-fueled PDE with fuel injection temperatures above the flash vaporization point was unknown. Previous research [8] demonstrated that flash vaporization of liquid hydrocarbon fuels significantly decreased the ignition and DDT times, but no work has been reported on the effect

Presented as Paper 5133 at the 42nd AIAA/ASME/SAE/ASEE Joint Propulsion Conference & Exhibit, Sacramento, California, 9–12 July 2006; received 30 August 2006; revision received 5 February 2007; accepted for publication 6 February 2007. This material is declared a work of the U.S. Government and is not subject to copyright protection in the United States. Copies of this paper may be made for personal or internal use, on condition that the copier pay the \$10.00 per-copy fee to the Copyright Clearance Center, Inc., 222 Rosewood Drive, Danvers, MA 01923; include the code 0748-4658/07 \$10.00 in correspondence with the CCC.

*Capt., USAF, AFIT, Department of Aeronautics and Astronautics, 2950 Hobson Way, Member AIAA.

†Professor, AFIT, Department of Aeronautics and Astronautics, 2950 Hobson Way, Senior Member AIAA.

‡Research Engineer, 2766 Indian Ripple Road, Senior Member AIAA.

§Senior Engineer, Head PDRF, AFRL/PRTC, 1950 5th Street, Senior Member AIAA.

†The fuel referred to as JP-900 in this paper is a coal-derived liquid hydrocarbon fuel developed at Penn State University. It is denoted as JP-900 due to its thermal stability up to 900°F.

**S-8 is a synthetic fuel derived from natural gas via the Fischer-Tropsch process [5]. S-8 is also referred to as Fischer-Tropsch JP-8 or simply Fischer-Tropsch.

of operation with fuel injection temperatures beyond the point of flash vaporization. Additionally, Cheatham and Kailasanath [9] have shown, using numerical simulations, that the vaporization of liquid JP-10 droplets is necessary for optimum performance. Card et al. [10] studied the effect of elevating initial mixture temperature (up to 573 K) on the DDT distance (called flame run-up distance in [10]) for gaseous hydrocarbon/air mixtures in a 10-cm diam tube. They found that there was no strong dependency of DDT distance on the initial mixture temperature in the range tested. The objective of this work was to examine the effect of heated fuel produced by a dual-concentric counterflow heat-exchanger system on the ignition time, DDT time, detonation distance, and detonation percentage. The variables included fuel type (JP-8, JP-7, JP-10, JP-900, RP-1, and S-8) and firing frequency.

II. Background and Theory

A. Ignition Time for a Hydrocarbon Fuel/Oxidizer Mixture

For single species chemical reactions, reaction rate is given by the Arrhenius expression (global reaction theory):

$$\text{Ignition Time} \propto \frac{1}{RR} = \frac{1}{A} P^{-n} [\text{fuel}]^{-m} [\text{oxydizer}]^{-j} e^{\left(\frac{E_{\text{fit}}}{R_{\text{u}} T_{\text{mix}}}\right)} \quad (1)$$

where n , m , and j are experimentally determined constants [11]. Low-vapor-pressure hydrocarbon fuel/air mixtures are not single species, but, as shown later, the trend of the ignition time can be inferred. The reaction rate of a fuel/oxydizer mixture will increase with increasing mixture temperature and pressure, thus decreasing the ignition time. For the moderate elevation of fuel temperatures in this work, only a small rise in the fuel/air mixture temperature occurred, and, as shown later, ignition time remained relatively constant.

B. Detonability of a Hydrocarbon Fuel/Oxidizer Mixture

The ability to initiate a detonation in a hydrocarbon fuel is related to its critical initiation energy, which for a low-vapor-pressure hydrocarbon/air mixture is around 10^5 J (a typical spark plug generates about 0.1 J). The critical initiation energy is related to the detonation cell size of a propagating detonation wave, shown in Fig. 1 for several stoichiometric fuel/oxydizer mixtures [12]. A curve fit shows a cubic relationship between the two (inset of Fig. 1). Knystautas et al. [13] also found the relationship between detonation cell size and critical initiation energy to be cubic.

Cell size, and thus critical initiation energy, is affected by the initial temperature and pressure. As shown in Figs. 2a and 2b for

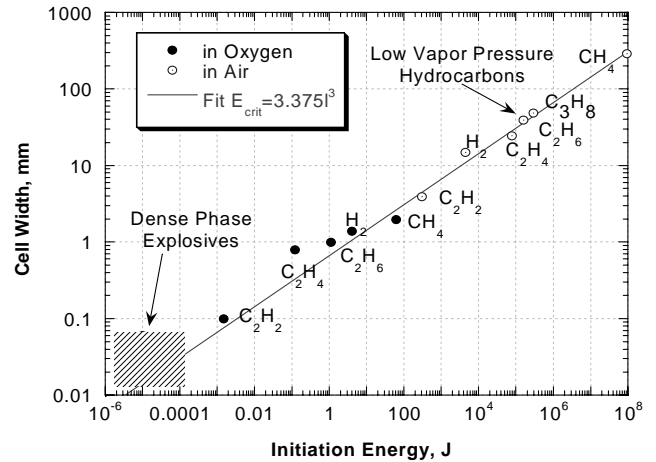


Fig. 1 Critical initiation energy for various stoichiometric fuel/oxydizer mixtures (data taken from [12]).

three light hydrocarbons and one H_2/O_2 mixture, cell size decreases with increased mixture temperature and pressure [14–17]. To improve detonability, therefore, pressure and temperature should be increased. Such data do not exist for heavy hydrocarbons, but the suggestion is that increasing initial mixture temperature and/or detonation tube closed-end pressure will decrease the cell size and improve detonability for those fuels also. As will be shown later, such increases in temperature did result in decreased DDT time and detonation distance, as well as increased detonation percentage.

III. Experimental Setup and Instrumentation

A. Facilities and PDE Specifics

This research was conducted at the detonation research facility located in Building 71A, D Bay, Wright–Patterson AFB, Ohio. This facility was described in detail in other literature [18], and only the details relevant to this effort are provided. The PDE for this research consisted of the valve train from a General Motors (GM) automobile quad four head with two schedule-40 stainless-steel detonation tubes. Each tube was 52.5 mm in diameter, 1.83 m in length, and equipped with a Schelkin-like spiral, 0.91 m in length, adjacent to the closed end of the detonation tube to promote DDT [19]. Each tube was outfitted with a stainless-steel heat exchanger (described later). Each spiral was constructed of 3/16 in. stainless-steel rod with a

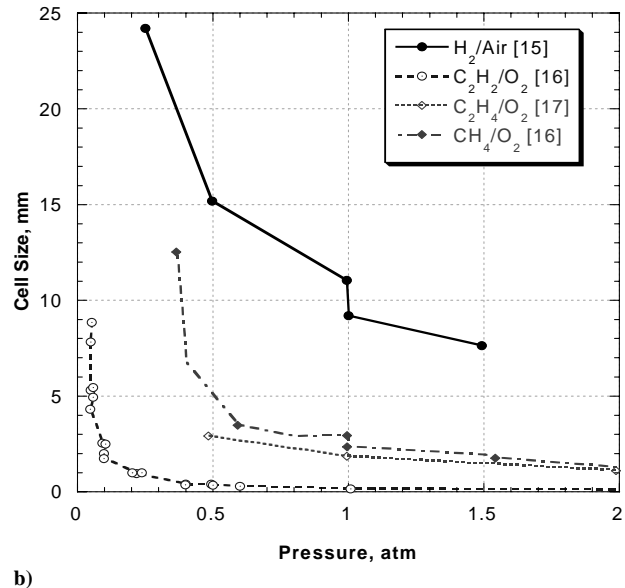
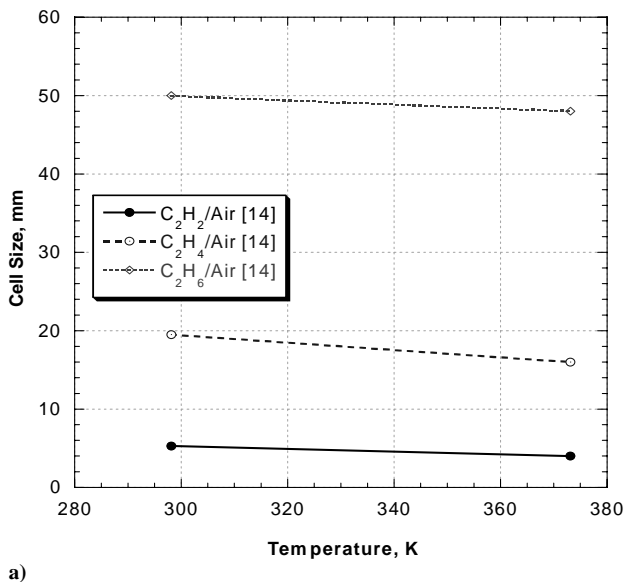


Fig. 2 Effect of a) initial temperature and b) initial pressure on detonation cell size (data taken from [12]).

spiral pitch of 38.1 mm. A schematic of one head cavity with valving and spark plug is shown in Fig. 3.

Because an automotive cam was used to drive the valve system, the three phases of the PDE cycle (fill, fire, and purge) were necessarily equal. The allotted time for each phase varied based on firing frequency: 33.33 ms for 10 Hz and 16.67 ms for 20 Hz. Firing frequency was a test parameter, which varied between 10 and 20 Hz. Depending on the firing frequency, the time required to complete any one phase could be less than the time allotted for the phase, where the time required for a phase is defined as the time necessary to complete all functions of that phase, for example, the necessary function of the fill phase is to introduce the fuel/air mixture to the detonation tubes. During the fill phase the intake valves introduce premixed fuel and air equal to the volume of the detonation tube (fill fraction of one at ambient pressure and fuel/air mixture temperature). For all tests the fill air was initially heated to 394 K before mixing with the fuel. For the fire phase an automotive ignition system provided 115 mJ spark pulses through modified spark plugs. The fire phase consists of spark delay, ignition, DDT, and blow down; the latter three totaling approximately 11 ms for the configuration tested. Figure 4 is a schematic of a typical fire phase, broken down into the critical segments. Detonation occurrence was confirmed using ion probes to measure wave speed, similar to the methods used by Card et al. [10] and Ciccarelli et al. [20]. Any combustion waves propagating at speeds within 10% of the upper Chapman–Jouguet point (assumed to be 1800 m/s) [21] were considered detonation waves. During the purge phase the exhaust valves introduced unheated air equal to half the volume of the detonation tube (purge fraction of 0.5 at ambient pressure and fuel/air mixture temperature). The purge air cooled the detonation tube and removed a portion of the exhaust gases from the detonation tube to prevent autoignition during the following fill phase.

B. Supercritical Fuel Heating System

The flow path and instrumentation are shown in schematic form in Fig. 5. The liquid fuel required for this testing was contained in two hydraulic bladder accumulators, pressurized by nitrogen bottles. The fuel pressure was maintained above critical pressure for the duration of the test to prevent phase change. The supercritical fuel heating system (SFHS) consisted of a nitrogen purge system (described

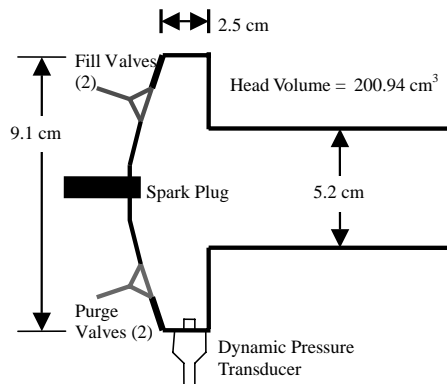


Fig. 3 Schematic of one head cavity with valving, spark plug, and dynamic pressure transducer.

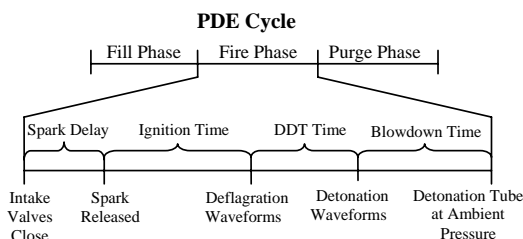


Fig. 4 Typical pulse detonation engine fire cycle divided into critical segments.

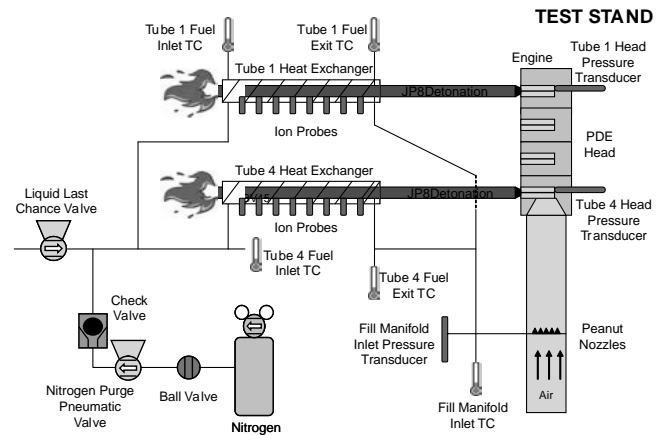


Fig. 5 Diagram of the PDE with the supercritical fuel heating system.

later), two stainless-steel heat exchangers, fuel filter assembly (not shown in Fig. 5), fuel injection nozzles, instrumentation, and associated tubing and fittings necessary to connect the critical components [22] contains details on fuel injection nozzles). The fuel entered the test stand through a pneumatically operated ball valve and split into two fuel lines, one for each heat exchanger. At the exit of the heat exchangers, the lines were tied together and run through a fuel filter. After the filter, fuel was fed to the fill air manifold and injected into the airstream via the fuel injection nozzles. The fuel filter removed small amounts of coking formed due to endothermic cracking of the fuel [23]. Lines carrying heated fuel were insulated with fiberglass to prevent heat loss. A nitrogen purge system cleared supercritical fuel from the heat exchangers at the end of a test [7] (Fig. 5) via a remotely activated pneumatic valve.

To compensate for the decrease in fuel density during heating in the supercritical regime [24,25], the charge pressure of the accumulators was increased to maintain a constant fuel mass flow rate. To allow for variations in accumulator charge pressure during testing, a pneumatic dome loader was installed for nitrogen pressure regulation (for details, see [5]). Pressures at the exit of the heat exchangers varied from 37 to 68 atm, with lower pressures at lower fuel injection temperatures and higher pressures at higher fuel injection temperatures to compensate for the density variation.

To minimize carbon deposition in the SFHS, the JP-8 was deoxygenated through a nitrogen sparging process. The sparging process involved bubbling a volume of nitrogen through the JP-8 to displace oxygen from the fuel. The volume of nitrogen necessary to reduce the oxygen concentration to acceptable levels was determined experimentally in previous work [22].

C. Spark Delay

Pressure fluctuations are created as fill and purge valves open and close. With compression and expansion waves in the head end of the tube, a spark delay can cause spark deposition during a beneficial pressure peak. Figure 6 shows the pressure-time history during an unsparked fire phase (no combustion) at 15 Hz with a mixture temperature of 394 K and spark delays from 2 to 10 ms. It can be seen that 6, 8, or 10 ms spark delays would initiate combustion during a compression wave, while a zero ms spark delay would do so during an expansion wave. However, because ignition time is also affected by the pressure history during the formation of a deflagration wave, selection of a 10 ms spark delay is not necessarily optimal. A 4 ms spark delay was chosen to minimize the overall time to detonation. Other spark delays (6, 8, and 10) showed inconsequential improvement in DDT time and ignition time; additionally, the 0 and 2 ms spark delays failed to produce detonations [26].

It was also beneficial to compare global reaction theory estimates with the ignition times for a series of spark delays (2, 4, 6, 8, and 10 ms) with fuel injected at 422 K. The global reaction theory approximation, shown in Eq. (1), for normalized ignition time as a function of average head pressure is shown in Fig. 7. Also,

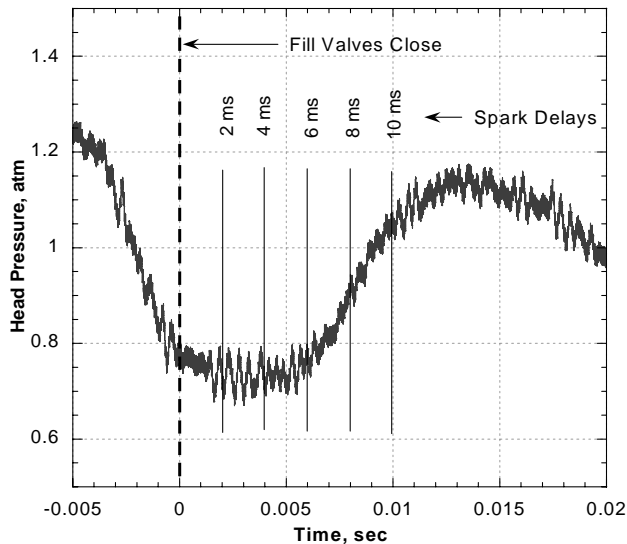


Fig. 6 Pressure in the closed end of the detonation tube during fire phase without combustion (vertical lines denote spark delays).

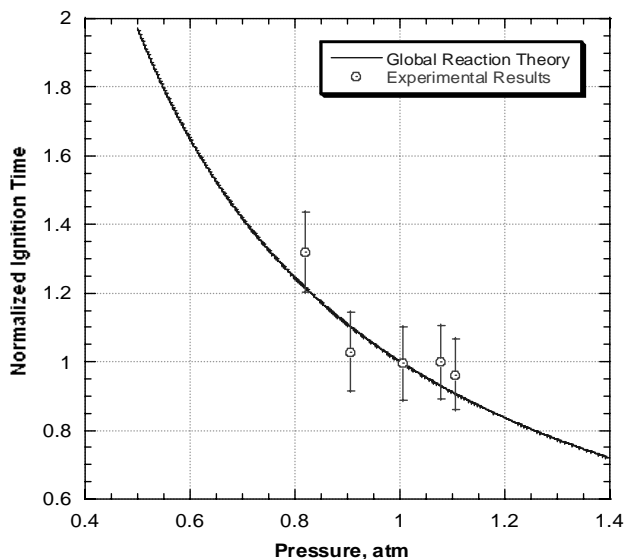


Fig. 7 Normalized ignition time as a function of initial head pressure.

experimentally determined normalized ignition times as a function head pressure for a JP-8/air mixture are displayed in Fig. 7. The ignition times for the global reaction theory were normalized by the ignition time corresponding to ambient pressure of the fuel/air mixture. Ignition times for the experiment were normalized by the 6 ms case for which the average pressure was nearly ambient (within 0.5%). The low temperature experimental results compare well with global reaction theory, falling within the experimental uncertainty.

D. Heat Exchangers

Two identical concentric-tube heat exchangers were fabricated from 316-stainless-steel schedule-40 tubes, with a length of 0.91 m, tube inner diameters of 52.5 and 63.5 mm, respectively, allowing for a 1.22-mm annular space. A photograph of one heat exchanger with the associated instrumentation ports is shown in Fig. 8.

E. Instrumentation

To gather temperature data, J-type thermocouples were placed in the center of the flowpath at the inlet and outlet of each heat exchanger, and a T-type thermocouple was placed at the inlet to the fill air manifold. Heat-exchanger external wall temperatures were measured with J-type thermocouples mounted externally with

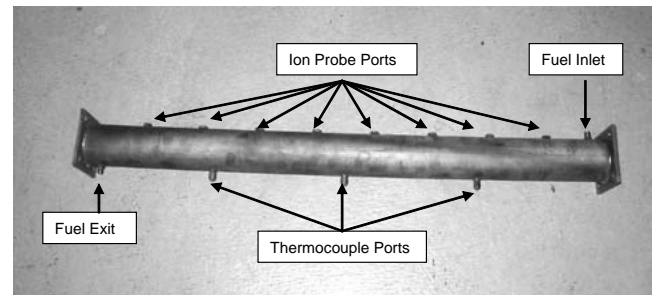


Fig. 8 Photograph of one heat exchanger.

compression clamps. A pressure transducer situated at the closed end of the detonation tubes measured the pressure used to determine the ignition time.

F. Data Reduction

All combustion data were gathered on a dedicated computer employing a *LabVIEW* program, and analyzed using a C++ program. The program segmented the data into separate firing cycles using the spark trace. Each spark trace denoted a new firing cycle. Each firing cycle was then analyzed for ignition time information. The head-pressure trace data were passed through a fourth-order, 401-point, Savitzky–Golay, digital, finite-impulse, response filter to reduce the high-frequency noise. The head-pressure trace is shown before and after the filter was applied, Fig. 9. Linear regression was then used to determine the slope of the pressure curve. The ignition time was taken as the time where an average pressure rise of 5000 psi/s was detected.

After the ignition time was determined, the probe times were calculated. The probe times were the time that the combustion wave crosses each of the ion probes. Wavespeeds were calculated by dividing the difference in distance between two ion probes by the difference in the corresponding probe times. Once a wavespeed above the Chapman–Jouguet (CJ) limit was found, linear interpolation between the wavespeed above the CJ wavespeed and the wavespeed at the location before it (below the CJ wavespeed) was performed to determine the time and location where a wavespeed matched that of the CJ wavespeed. The time and location found were the DDT time and the detonation distance, respectively.

G. Experimental Uncertainties

The total experimental uncertainty was determined by combining the bias and precision uncertainties using the root sum square method

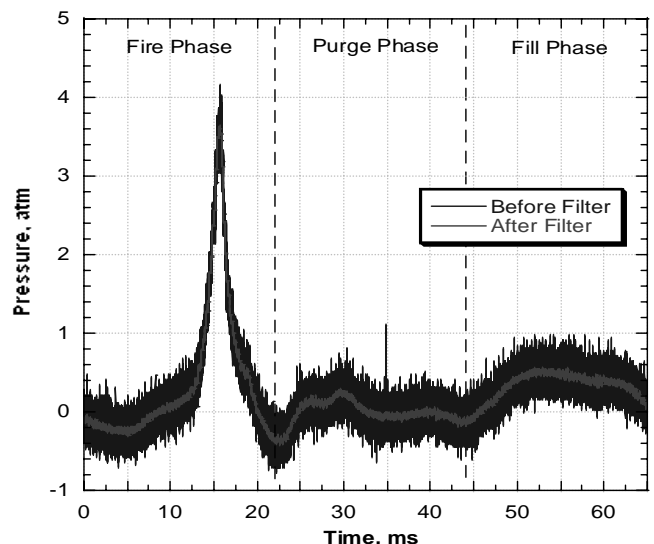


Fig. 9 Head-end pressure history during a single PDE cycle at a firing frequency of 15 Hz.

Table 1 Summary of bias uncertainties for experimental results

Experimental result	Bias uncertainty
Wavespeed	± 55.12 m/s
Ignition time	± 0.292 ms
DDT time	± 0.0568 ms
Detonation distance	± 0.0568 m
Fuel injection temperature	± 3.6 K
Fuel/air mixture temperature	± 2.5 K
Equivalence ratio	± 0.0247

[27,28]. The bias uncertainties were constant for all data points of the same variable, while the precision uncertainties varied by data point. Therefore, the total experimental uncertainty varies by data point and is included with the data. Total bias uncertainties are displayed in Table 1 [7].

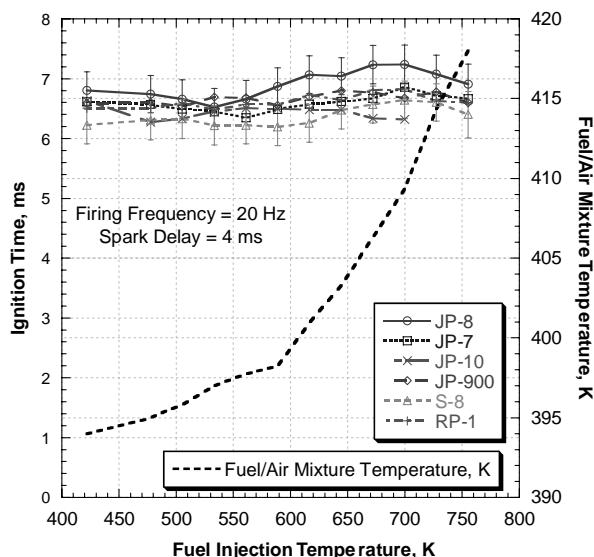
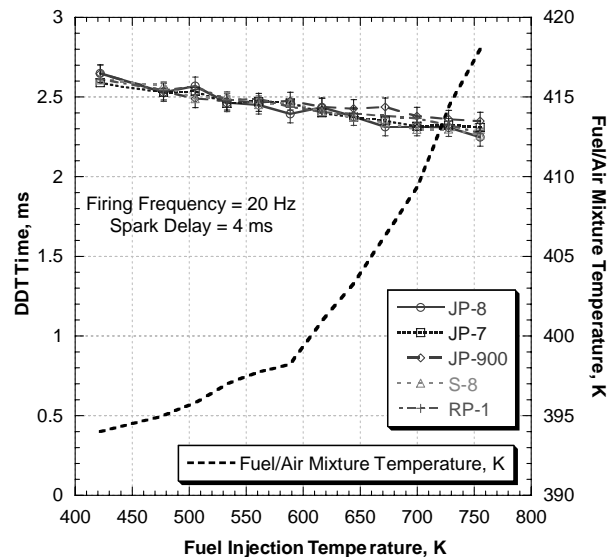
IV. Results and Discussion

For varying fuel injection temperatures, ignition time, deflagration to detonation transition time, detonation distance, and detonation percentage were measured. Each data point represents the mean value of 40 to 60 ignitions, using data averaged from two tubes. The effect of fuel injection temperature on the performance of the PDE is shown with variation of fuel type and firing frequency. All testing was performed with an equivalence ratio of 1.1, which has been shown by Tucker [22] to produce the minimum ignition and DDT times for JP-8.

A. Fuel Study

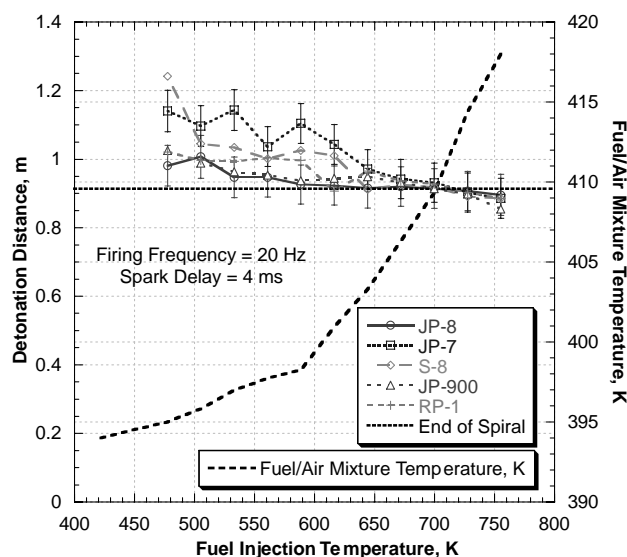
Figure 10 shows ignition time for all six fuels. Little variation occurred among the fuels, though JP-8 has a slightly higher ignition time in the range of 586 to 755 K. The probable cause of this higher time was adverse effects of thermal degradation (oxidative coking). S-8 produced the smallest ignition times for almost the entire temperature range. JP-7, JP-900, and RP-1 times displayed little difference in slope or magnitude, which was expected due to the similarity of the fuels. With the exception of JP-8, ignition times for all fuels were independent of fuel injection temperature in the temperature range examined, as mentioned in the earlier discussion of global reaction theory.

Attempts at detonation of a JP-10/air mixture were erratic and data were inconsistent, rendering the results unusable; therefore, the DDT time and detonation distance results for JP-10 have been omitted. The DDT times for the other five fuels are displayed in Fig. 11. In Fig. 11,

**Fig. 10** Ignition times for several fuels.**Fig. 11** DDT times for several fuels.

little variation in DDT time is seen among the fuels. The small differences between any two fuels are within the experimental uncertainty for the entire temperature range. DDT times for all five fuels decrease with increasing fuel injection temperature. The fuels display a nearly linear decrease in DDT time of approximately 15% over the temperature range. The DDT time decreases despite the two competing effects of increasing fuel/air mixture temperature and decreasing density that causes a decrease in pressure. The first effect tends to increase reaction rate and lower DDT time [cf., Eq. (1)], whereas the second reduces detonability (refer to Sec. II.B) and tends to increase DDT time. The net effect is a decrease in DDT time, but probably not as much as would occur without the reduced detonability effect.

The variation of detonation distance with fuel injection temperature for all fuels except JP-10 is shown in Fig. 12. As expected, the detonation distance of all five fuels decreases with increasing fuel injection temperature. The detonation distance decrease is probably less than would occur absent the competing effects of density decrease and reaction rate increase discussed above. In Fig. 12, only below approximately 650 K does the detonation distance of the five fuels differ in magnitude and slope. Below 650 K, JP-8 has the smallest detonation distances, followed closely by JP-900, while JP-7 is highest at 1.14 m. RP-1 and S-8 perform similarly, both with detonation distance between JP-7 and

**Fig. 12** Comparison of the detonation distance for five fuels.

JP-900. It was also noted that above roughly 675 K, detonations occur near the downstream end of the spiral for all five fuels shown. It was assumed that the difference in detonation distance of the five fuels would be negligible, similar to the DDT time trend. This stratification of detonation distances is possibly due to variation in laminar flame speeds between the fuels, although laminar flame speeds were not measured and data for all five fuels at these conditions are not available in literature. Card et al. [10] found that fuel/air mixtures with higher laminar flame speeds resulted in shorter detonation distances.

Detonation percentage is defined as the percentage of ignitions that result in a combustion wavespeed of 1800 m/s or greater. In Fig. 13, all fuels demonstrate a strong trend of increasing detonation percentage with increasing fuel injection temperature. The percentages displayed in Fig. 13 are dependent on the PDE configuration, but the trends demonstrate an increase in detonability with increasing fuel injection temperature. This increase is a result of a more homogenous mixture at higher fuel/air mixture temperatures but moderated by the same competing effects mentioned earlier (density decrease vs reaction rate increase). The effect of fuel injection temperature is more apparent in the detonation percentage as compared to the DDT time and detonation distance, most likely because detonation percentage is more dependent on the fuel/air mixing. Dounghip et al. [29] found that the injection of supercritical JP-8 resulted in greatly enhanced mixing compared to that of subcritical JP-8. The fuels can be divided into three categories based on Fig. 13. The first group, JP-7 and S-8, demonstrate the largest increases in detonations as fuel injection temperature increases, achieving nearly 100% detonations at 755 K. JP-8, JP-900, and RP-1 make up the second category, achieving detonation percentages between 65 and 75% at a fuel injection temperature of 755 K. The final category includes only JP-10. Although JP-10 slightly increases detonation percentage with increased fuel injection temperature, the magnitude of the detonation percentage remains low, 14–38%, leading to a large uncertainty in DDT time and detonation distance. The small detonability increase with increased JP-10/air mixture temperature is consistent with the findings of Ciccirelli and Card [20], which showed that the JP-10 detonation cell size was very insensitive to initial temperature.

B. Firing Frequency

The motivation to decrease ignition time and DDT time is to decrease the fire phase time, thus allowing a higher cycle frequency and higher average thrust. The relationship between firing frequency and thrust has been shown by Fan et al. [30]. To examine the effect of the firing frequency on PDE performance parameters, two frequencies, 15 and 20 Hz, were examined. Frequencies much

above 20 Hz, for example, 25 Hz, would allow only 13 ms for the fire phase, too short for 15 ms required for the detonation of a JP-8/air mixture. Also, at frequencies much below 15 Hz, for example, 10 Hz, insufficient waste heat was generated for the heat transfer system to elevate fuel injection temperatures above 644 K.

Figure 14 shows ignition and DDT times for a PDE operating at 15 and 20 Hz. Within experimental uncertainty, the ignition times are nearly equal for the entire temperature range. DDT time for the 20 Hz case is slightly less than the 15 Hz case for the entire temperature range. This 20 Hz decrease in DDT time is a result of higher pressures within the detonation tube that occur at higher frequencies, as shown by Tucker [22]. The total time to detonation, sum of spark delay (same for both), ignition time, and DDT time, is thus slightly less for the 20 Hz case.

Figure 15 shows detonation distance for two firing frequencies. The differences between the detonation distances are within the measurement uncertainty for the entire temperature range. From ion probe data (not shown) detonations occur at the downstream end of the internal spiral for both frequencies. DDT often occurs at the end of a tripping device, such as a spiral, due to the abrupt absence of such

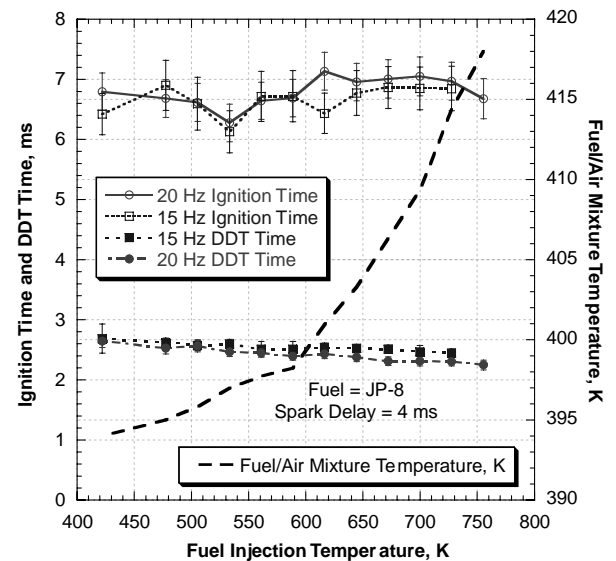


Fig. 14 Comparison of ignition time and DDT time for two frequencies for a JP-8/air mixture.

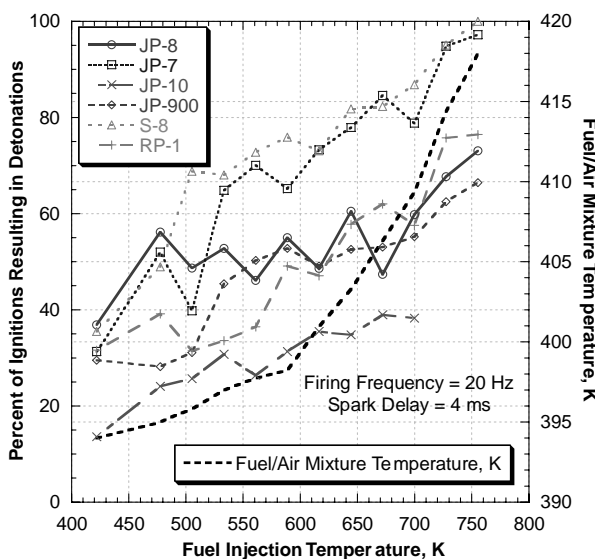


Fig. 13 Comparison of the detonation percentage for six fuels.

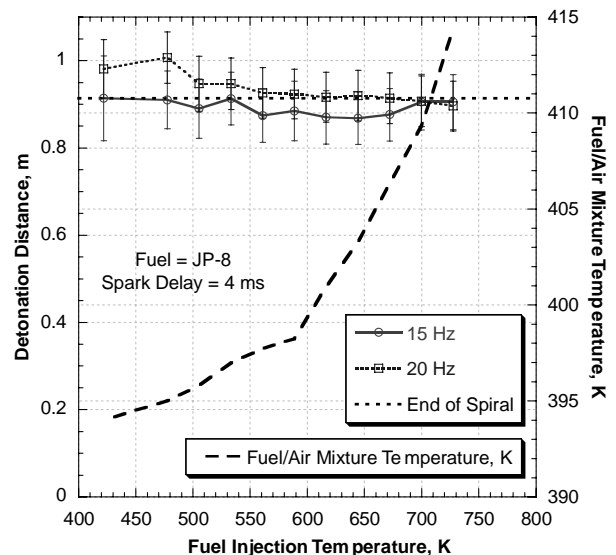


Fig. 15 Comparison of detonation distance for two frequencies for a JP-8/air mixture.

obstacle, as shown by Lee et al. [31]. In summary, increasing the firing frequency was found to have little effect on cycle performance.

C. Fuel Heating Value

Using the waste heat from PDE detonation tubes to preheat fuel to supercritical temperatures is important not only for detonation initiation. By regeneratively heating the fuel, the effective fuel heating value is increased, which corresponds directly to an improvement in specific fuel consumption (SFC). The significance of this effect is evaluated in Fig. 16, which is a plot of the percent of improvement in fuel heating value (over that of fuel at ambient temperatures) as a function of fuel injection temperature. Preheating the fuel to the supercritical temperatures results in a 2–3% improvement in fuel heating value, which directly corresponds to an SFC improvement of 2–3%. The percent of improvement in heating value was calculated using the heat of vaporization and heat capacity from the CRC Handbook of Aviation Fuel Properties [32]. The highly linear property data were extrapolated to the temperature limits shown in Fig. 15. This effective improvement in fuel heating value and thus fuel efficiency can be applied to conventional gas turbine engines using regenerative fuel cooling as well.

V. Conclusions

This research marked the first analysis of the effect of increasing fuel injection temperature, up to 755 K, on key pulsed-detonation-engine performance parameters, including ignition time, DDT time, detonation distance, and detonation percentage. Six fuels were examined, JP-8, JP-7, JP-10, JP-900, RP-1, and S-8. Ignition time was found to be virtually independent of fuel injection temperature for all fuels, except JP-8. JP-10 was found to detonate inconsistently, compared to the other fuels. The DDT time of the other five fuels demonstrated a nearly identical linear decrease of 15% over the temperature range tested. The detonation distance for all fuels, other than JP-10, linearly decreased down to a limit of spiral length with increasing fuel injection temperature. The detonation percentage for all fuels increased considerably with increasing fuel injection temperature, with JP-7 and S-8 producing the most consistent detonations. Based on this performance criterion, JP-8, JP-7, JP-900, RP-1, and S-8 can all be used to fuel a PDE with this configuration at elevated fuel injection temperatures; however, the configuration could be varied to aid in JP-10 detonation transition.

Increasing firing frequency from 15 to 20 Hz was found to slightly reduce the total time to detonation for a PDE. DDT time decreases with higher firing frequency, due to the higher pressure in the detonation tube, while ignition time and detonation distance are relatively independent of firing frequency.

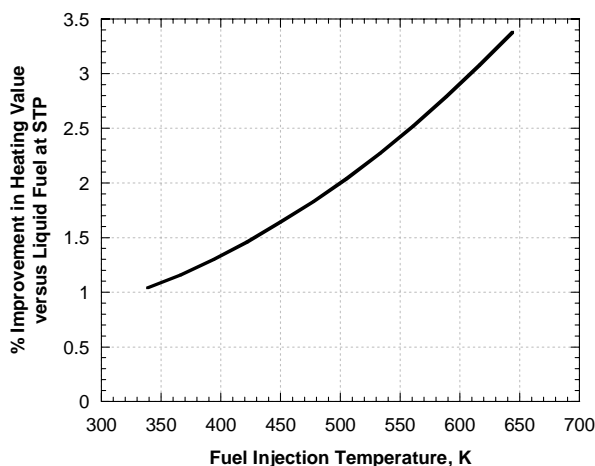


Fig. 16 Percent improvement in fuel heating value as a function of fuel injection temperature.

Acknowledgments

Funding was provided by the U.S. Air Force Research Laboratory Propulsion Directorate (AFRL/PR), and the U.S. Air Force Office of Scientific Research (AFOSR). This work would not have been possible without the technicians who worked on this project. Our thanks go to Curtis Rice, Dave Baker, and Dwight Fox of Innovative Scientific Solutions (ISSI). Tim Edwards (AFRL/PR) was extremely helpful in developing the fuel systems for this work. The authors would also like to thank Jeff Stutrud (AFRL/PR) for his controls and data acquisition expertise and Captain Wesley Knick (AFRL/PR) for his help. The technical leadership of Robert Hancock (AFRL/PR) was invaluable.

References

- [1] Desbordes, D., Dauiau, E., and Zitoun, R., "Pulsed Detonation Propulsion: Key Issues," *High Speed Deflagration and Detonation: Fundamentals and Control*, edited by G. D. Roy, S. M. Frolov, D. W. Netzer, and A. A. Borisov, ELEX-KM Publishers, Moscow, 2001, pp. 177–192.
- [2] Kailasanath, K., Patnaik, G., and Li, C., "On Factors Controlling the Performance of Pulsed Detonation Engines," *High-Speed Deflagration and Detonation: Fundamentals and Control*, edited by G. D. Roy, S. M. Frolov, D. W. Netzer, and A. A. Borisov, ELEX-KM Publishers, Moscow, 2001, pp. 193–206.
- [3] Chuanjun, Y., Jun, L., Wei, F., Liming, H., and Hengren, L., "Principle and Cycle Analysis of Pulsed Detonation Engine," *Journal of Propulsion Technology*, Vol. 17, No. 3, June 1996, pp. 56–63.
- [4] Kailasanath, K., "Review of Propulsion Applications of Detonation Waves," *AIAA Journal*, Vol. 38, No. 9, 2000, pp. 1704–1706.
- [5] Edwards, T., "Liquid Fuels and Propellants for Aerospace Propulsion: 1903–2003," *Journal of Propulsion and Power*, Vol. 19, No. 6, 2003, pp. 1089–1107.
- [6] Eidelman, S., Grossman, W., and Lottati, I., "Review of Propulsion Applications and Numerical Simulations of the Pulse Detonation Engine Concept," *Journal of Propulsion and Power*, Vol. 7, No. 6, 1991, pp. 857–865.
- [7] Helfrich, T. M., "Cycle Performance of a Pulse Detonation Engine with Supercritical Fuel Injection," M.S. Thesis, Department of Aeronautics and Astronautics, Air Force Institute of Technology, Wright–Patterson AFB, OH, 2006.
- [8] Tucker, K. C., King, P. I., Bradley, R. P., and Schauer, F. R., "The Use of a Flash Vaporization System with Liquid Hydrocarbon Fuels in a Pulse Detonation Engine," *AIAA Paper 2004-0868*, 5–8 Jan. 2004.
- [9] Cheatham, S., and Kailasanath, K., "Single-Cycle Performance of Idealized Liquid-Fueled Detonation Engines," *AIAA Journal*, Vol. 43, No. 6, 2005, pp. 1276–1283.
- [10] Card, J., Rival, D., and Ciccirelli, G., "DDT in Fuel-Air Mixtures at Elevated Temperatures and Pressures," *Shock Waves*, Vol. 13, No. 3, 2005, pp. 167–173.
- [11] Lefebvre, A., Freeman, W., and Cowell, L., "Spontaneous Ignition Delay Characteristics of Hydrocarbon Fuel/Air Mixtures," NASA CR-175064, Feb. 1986.
- [12] Kaneshige, M., and Shepherd, J. E., *Detonation Database*, GALCIT Rept. FM97-8, GALCIT, Graduate Aeronautical Laboratories, California Institute of Technology, Pasadena, CA, July 1997.
- [13] Knystautas, R., Guirao, C., Lee, J. H., and Sulmistras, A., "Measurement of Cell Size in Hydrocarbon-Air Mixtures and Predictions of Critical Tube Diameter, Critical Initiation Energy, and Detonability Limits," *Progress in Aeronautics and Astronautics*, Vol. 94, AIAA, New York, 1984, pp. 23–37.
- [14] Tieszen, S. R., Stamps, D. W., Westbrook, C. K., and Pitz, W. J., "Gaseous Hydrocarbon-Air Detonations," *Combustion and Flame*, Vol. 84, No. 3, 1991, pp. 376–390.
- [15] Stamps, D. W., and Tieszen, S. R., "The Influence of Initial Pressure and Temperature on Hydrogen-Air-Diluent Detonations," *Combustion and Flame*, Vol. 83, No. 3, 1991, pp. 353–364.
- [16] Manzhalei, V. I., Mitrofanov, V. V., and Subbotin, V. A., "Measurement of Inhomogeneities of a Detonation Front in Gas Mixtures at Elevated Pressures," *Combustion, Explosion, and Shock Waves*, USSR, Vol. 10, No. 1, 1974, pp. 89–95.
- [17] Bauer, P., Presles, H. N., Heuze, O., and Brochet, C., "Measurement of Cell Lengths in the Detonation Front of Hydrocarbon Oxygen and Nitrogen Mixtures at Elevated Initial Pressures," *Combustion and Flame*, Vol. 64, No. 1, 1986, pp. 113–123.
- [18] Schauer, F., Stutrud, J., Bradley, R., Katta, V., and Hoke, J., "Detonation Studies and Performance for a Research PDE," *Confined*

- Detonations and Pulse Detonation Engines*, edited by G. D. Roy, S. M. Frolov, R. J. Santoro, and S. A. Tsyganov, Torus Press, Moscow, 2003.
- [19] Schelkin, K. L., *Soviet Journal of Technical Physics*, Vol. 10, 1940, pp. 823–827.
- [20] Ciccarelli, C., and Card, J., “Detonation in Mixtures of JP-10 Vapor and Air,” *AIAA Journal*, Vol. 44, No. 2, 2006, pp. 362–367.
- [21] Austin, J. M., and Shepherd, J. E., “Detonation in Hydrocarbon Fuel Blends,” *Combustion and Flame*, Vol. 132, Nos. 1–2, 2002, pp. 73–90.
- [22] Tucker, K. C., “A Flash Vaporization System for Detonation of Hydrocarbon Fuels in a Pulse Detonation Engine,” Ph.D. Dissertation, Department of Aeronautics and Astronautics, Air Force Institute of Technology, Wright Patterson AFB, OH, 2005.
- [23] Altin, O., and Eser, S., “Analysis of Solid Deposits from Thermal Stressing JP-8 Fuel on Different Tube Surfaces in a Flow Reactor,” *Industrial and Engineering Chemistry Research*, Vol. 40, No. 2, 2001, pp. 596–603.
- [24] Bartok, W., and Sarofim, A. F., *Fossil Fuel Combustion—A Source Book*, Wiley, New York, 1991.
- [25] Miser, C. L., Helfrich, T. M., Schauer, F. R., and Phelps, D. K., “Supercritical Fuel Density from Experimental Pulse Detonation Engine,” AIAA Paper 2006-1025, 9–12 Jan. 2006.
- [26] Helfrich, T. M., King, P. I., Hoke, J. L., and Schauer, F. R., “Effect of Supercritical Fuel Injection on the Cycle Performance of a Pulsed Detonation Engine,” AIAA Paper 2006-5133, 9–12 July 2006.
- [27] Coleman, H. W., and Steele, W. G., Jr., *Experimentation and Uncertainty Analysis for Engineers*, Wiley, New York, 1989.
- [28] Dieck, R. H., *Measurement Uncertainty: Methods and Applications*, 3rd ed., Instrumentation, Systems, and Automation Society, Research Triangle Park, NC, 2002.
- [29] Dounghip, T., Ervin, J. S., Williams, T. F., and Bento, J., “Studies of Injections of Jet Fuels at Supercritical Conditions,” *Industrial and Engineering Chemistry Research*, Vol. 41, No. 23, 2002, pp. 5856–5866.
- [30] Fan, W., Yan, C., Huang, X., Zhang, Q., and Zheng, L., “Experimental Investigation of Two-Phase Pulse Detonation Engine,” *Combustion and Flame*, Vol. 133, No. 2, 2004, pp. 441–450.
- [31] Lee, S., Watts, J., Saretto, S., Pal, S., Conrad, C., Woodward, R., and Santoro, R., “Deflagration to Detonation Transition Processes by Turbulence-Generating Obstacles in Pulse Detonation Engines,” *Journal of Propulsion and Power*, Vol. 20, No. 6, 2004, pp. 1027–1036.
- [32] *Handbook of Aviation Fuel Properties*, 3rd ed., CRC Rept. No. 635, Coordinating Research Council Inc., Alpharetta, GA, 2004.

J. Powers
Associate Editor

Fuel Composition Analysis of Endothermically Heated JP-8 Fuel for Use in a Pulsed Detonation Engine

Eric A. Nagley¹ and Paul I. King²

Air Force Institute of Technology, Wright Patterson AFB, OH, 45433

Frederick R. Schauer³

Air Force Research Laboratory, Wright Patterson AFB, OH, 45433

Matthew J. DeWitt⁴

University of Dayton Research Institute, Dayton, OH, 45469

And

John L. Hoke⁵

Innovative Scientific Solutions, Inc., Dayton, OH, 45440

Waste heat from a pulsed detonation engine (PDE) was extracted via concentric tube-counter flow heat exchangers to produce supercritical pyrolytic conditions for JP-8 fuel. Offline analysis of liquid and vapor fuel samples obtained during steady state operation indicated fuel decomposition via typical pyrolytic reaction pathways. The liquid analysis showed conversion of parent fuel components with formation of unsaturates (aromatics and alkenes) and smaller alkanes. The gaseous products consisted of predominantly C₁-C₃ alkanes and alkenes (> 50% of total vapor yield) with moderate amounts of hydrogen and C₄-C₆ alkanes and alkenes. The components that were present in the stressed fuel samples were more detonable and could be linked to improved PDE performance; specifically shorter ignition time, shorter deflagration to detonation (DDT) time, and shorter DDT distance.

Nomenclature

E_{crit}	=	critical initiation energy
FN	=	flow number
\dot{m}_{fuel}	=	mass flow of fuel
p_{fuel}	=	pressure of fuel
λ	=	detonation cell size
ρ_{cal}	=	density of calibration fluid
ρ_{fuel}	=	density of fuel

¹ LT, USN, Graduate Student, Department of Aeronautics and Astronautics, 2950 Hobson Way, AIAA Member.

² Professor, Department of Aeronautics and Astronautics, 2950 Hobson Way, Senior AIAA Member.

³ Senior Engineer, Head PDRF, AFRL/RZTC, 1950 5th Street, Senior AIAA Member.

⁴ Senior Research Engineer, 300 College Park.

⁵ Research Engineer, 2766 Indian Ripple Road, Senior AIAA Member.

I. Introduction

JP-8 is the predominate kerosene fuel currently used in the United States Air Force (USAF) and is of particular interest concerning military operation of a pulsed detonation engine (PDE). A large challenge in using the PDE as a source of propulsion is the ignition and detonation of higher molecular weight straight-chain hydrocarbons. It is well known that if a hydrocarbon fuel can be decomposed outside of the combustion chamber combustion efficiency can be improved¹.

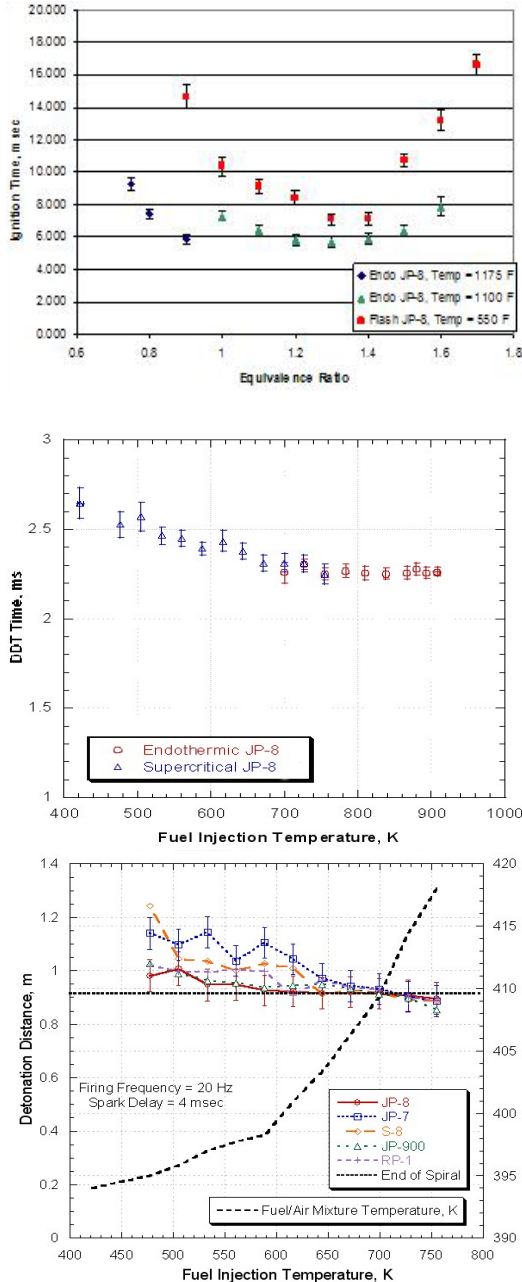


Figure 2. Plots of ignition time vs. equivalence ratio (a), DDT time (b), and DDT distance (c) versus fuel injection temperature^{2,12}.

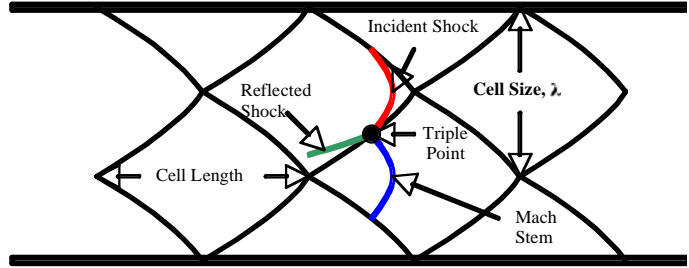


Figure 1. Characteristic two-dimensional detonation wave structure².

Previous work² conducted on a PDE with JP-8 preheated and cracked by detonation tube waste heat demonstrated performance benefits. There were other notable positive effects on cycle performance parameters that are specifically important to PDE operation.

The current research extended the investigation further into the oxygen-free thermal decomposition of JP-8 induced by PDE waste heat. An apparatus was developed that allowed in-line sampling of stressed fuel during steady state PDE operation. This investigation sought quantitative evidence of thermal cracking in the fuel after passing through thrust tube heat exchangers and the composition of both liquid and gaseous products present prior to combustion.

II. Background and Theory

As a detonation wave propagates downstream, an interaction of several shock fronts form the characteristic structure shown in Fig. 1^{2,3}. (For a detailed explanation of detonation wave structure the reader is referred to Fickett and Davis⁴.) The detonation cell size (λ), is a property inherent to each particular fuel. Previous research^{5,6} has shown a direct relationship between detonation cell size and critical initiation energy (E_{crit}).

$$E_{crit} = 3.375\lambda^3 \quad (1)$$

Equation 1 indicates that a decrease in cell size correlates to improved detonability. This relationship was validated by experimental research^{5,6,7,8,9} that showed strained hydrocarbons such as acetylene and ethylene were more detonable than high molecular weight hydrocarbons typically found in JP-8 and JP-10.

When JP-8 is heated to a sufficient temperature (>725 K), endothermic reactions known as thermal cracking occur^{2,10}. During this process, thermal decomposition of high molecular weight hydrocarbons results in lower molecular weight aromatics, alkenes and alkanes¹¹. As these lower molecular weight hydrocarbons are formed, initiation energy decreases and substantial benefits are seen in PDE performance.

Recent work² showed that waste heat from a PDE can elevate JP-8 to endothermic temperatures with a subsequent beneficial influence on ignition time, deflagration-to-detonation transition time, and detonation distance. Ignition time is defined as the time elapsed between ignition of the fuel at the closed end of a PDE tube and the commencement of

deflagration. DDT then occurs and a detonation wave speed of approximately 1800 m/s is achieved corresponding to the upper Chapman-Jouget (C-J) speed. DDT time is defined as the time duration for a deflagration wave to transition to a detonation wave. The detonation distance is measured from the closed end of the PDE tube to the first point at which C-J speed is achieved.

Previous work^{2,12} (Figures 2 a-c) shows the effect of endothermic fuel injection temperature on ignition time, DDT time, and DDT distance. As the injection temperature is increased from 800 to 900 K, the ignition time decreases by nearly 20 percent. While little impact was seen on DDT time in the endothermic temperature region, increased consistency of detonations occurred as evidenced by the decreased range of uncertainty shown in Fig. 2b. Figure 2c shows the decrease of DDT distance through the supercritical temperature regime.

III. Experimental Setup and Instrumentation

An experimental study was performed to investigate alteration of fuel composition at different pre-heat injection temperatures. The research was performed in the Pulsed Detonation Research Facility (PDRF) at Wright Patterson AFB in Dayton, OH. Detailed information about the facility has previously been published¹³. Only setup information that is uniquely important to this effort is provided. The major components of the PDE (schematic diagram shown in Fig. 4), will also be described.

A. PDE Description and Phases

The PDE cycle, shown in Fig. 3, is segmented into three phases: fill, fire, and purge. During fill, premixed fuel and air enters through intake valves to fill the tube volume to a pre-designated fraction (fill fraction). For these experiments, the tube volume was completely filled (unity fill fraction).

The head and valve train from a General Motors Quad Four engine provided the fuel and air delivery. Two detonation tubes of length 1.91 m were employed, each having a 1.22 m long Shchelkin-type spiral to facilitate DDT¹⁴. Mounted on each tube was a concentric-tube counter flow heat exchanger to pre-heat the fuel, (further fuel heating details discussed later). Air pre-heated to approximately 400 K was mixed with the heated fuel in a manifold upstream of the intake valves. As shown in Fig. 3 an ignition delay was employed, that being the time between the start of the fill phase and the release of spark. For this experimentation, an approximately 115 mJ spark was delivered to each of the thrust tubes with an ignition delay of 4-7 msec. At the completion of the fire phase, purge air entered through the open exhaust valves to cool the detonation tubes and clear out exhaust gases. During this purge phase, the air volume supplied was four-tenths of the total tube volume (purge fraction of 0.4).

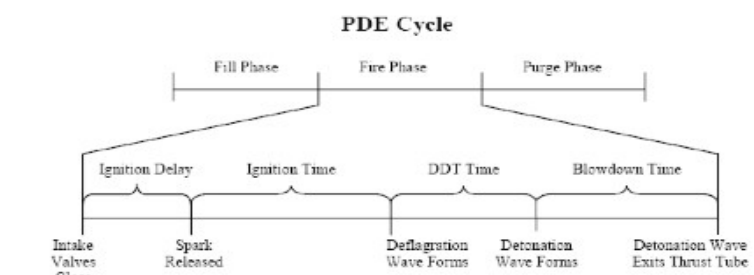


Figure 3. PDE cycle schematic with fire phase described in detail².

B. Fuel Preparation and Delivery

The objective of the heating process was to increase the fuel temperature to a level that initiated thermal cracking. Furthermore, the investigation was focused on changes in composition due to pyrolytic activity rather than changes from oxidation reactions caused by dissolved oxygen in the fuel¹. In order to reduce the amount of oxygen dissolved in the fuel to less than 1 ppm, oxygen-free nitrogen was sparged into the JP-8. The method for this is reported in previous work¹⁵. All of the fuel used for experimentation was sparged in this manner.

Before being delivered to the PDE, the sparged fuel was transferred to two bladder accumulators. Nitrogen pressure supplied to the accumulators enabled the metering of fuel flow to the PDE. Fuel pressure was maintained above the critical point (app. 340 psi) for the duration of testing to prevent boiling. After passing through a mass flow meter, the pressurized fuel was delivered to the fuel heating system described next.

C. Fuel Heating System

The fuel heating system (FHS), previously reported², consisted of two concentric tube heat exchangers fabricated from inconel, a single seven-micron particulate filter, instrumentation, and fuel injection peanut nozzles. As shown in Figs. 4 and 5, the fuel entered the heat exchanger attached to thrust tube number one, flowing counter to the direction of detonation flow. Fuel was subsequently transferred to the second heat exchanger attached to thrust tube number four maintaining a counter flow orientation. To prevent clogging of the fuel injection nozzles, a seven-

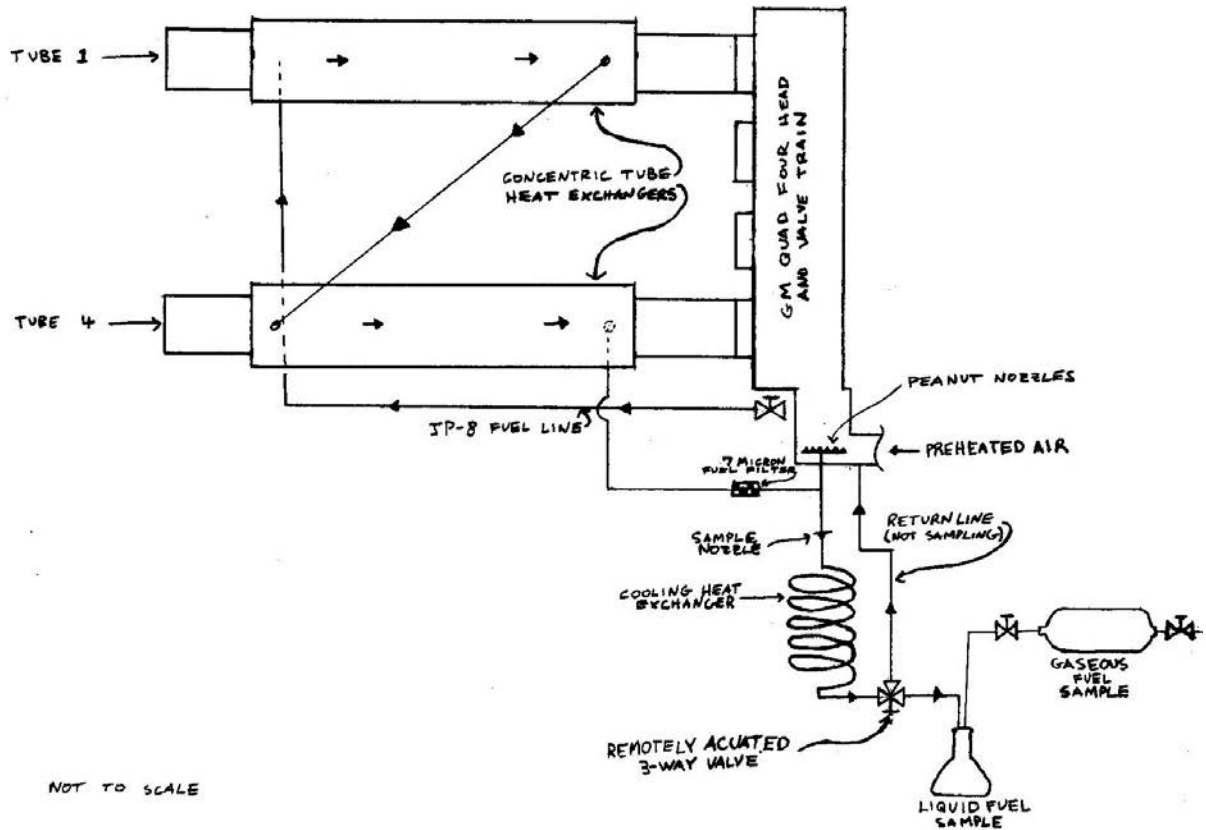


Figure 4. Schematic diagram of PDE showing fuel heating system and sample collection system.

micron filter was inserted in the flow path to collect carbonaceous deposits formed during fuel stressing. The heated and decomposed fuel was injected through the peanut nozzles into the manifold and mixed with the preheated air.

D. Sample Collection System

Samples of the stressed fuel were collected during steady state operation of the PDE. A sample fuel flow was extracted from engine feed fuel flow through a nozzle inserted downstream of the seven-micron filter. In this manner, the fuel flow rate was split and completely controlled by nozzle selection. The relationship for flow number (FN) is given by the following equation¹⁶

$$FN = \frac{\dot{m}_{fuel}}{\sqrt{\Delta p_{fuel}}} \sqrt{\frac{\rho_{cal}}{\rho_{fuel}}} \quad (2)$$

From this relationship, fuel mass flow (\dot{m}_{fuel}) is a function of nozzle flow number, square root of pressure drop (Δp_{fuel}) across nozzle, and square root of fuel density (ρ_{fuel}). Density of the fluid used to calibrate the nozzle (ρ_{cal}) must also be included. The density of the fuel was the same for both the peanut nozzles used for fuel injection and for the nozzle used for sample extraction. The pressure drop across the sample and fuel injection nozzles was

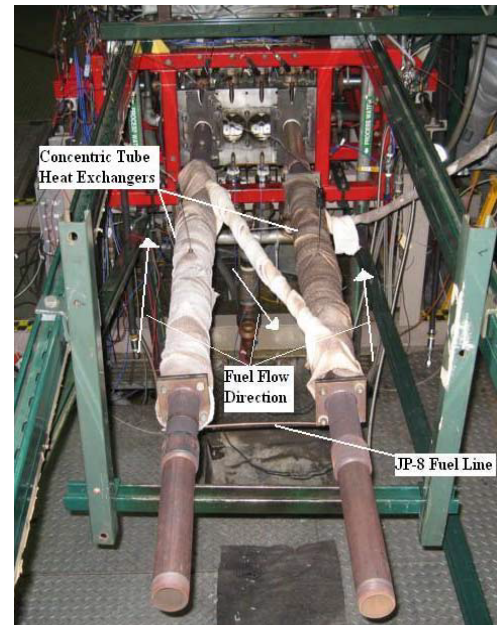


Figure 5. View of PDE showing thrust tubes, concentric tube-in-tube heat exchangers, and fuel flow direction.

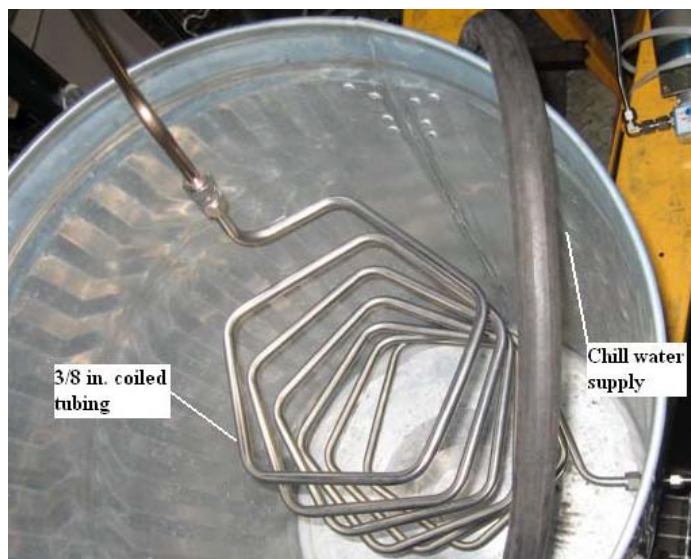


Figure 6. Coiled stainless steel tubing immersed in chilled water, used to cool fuel sample.

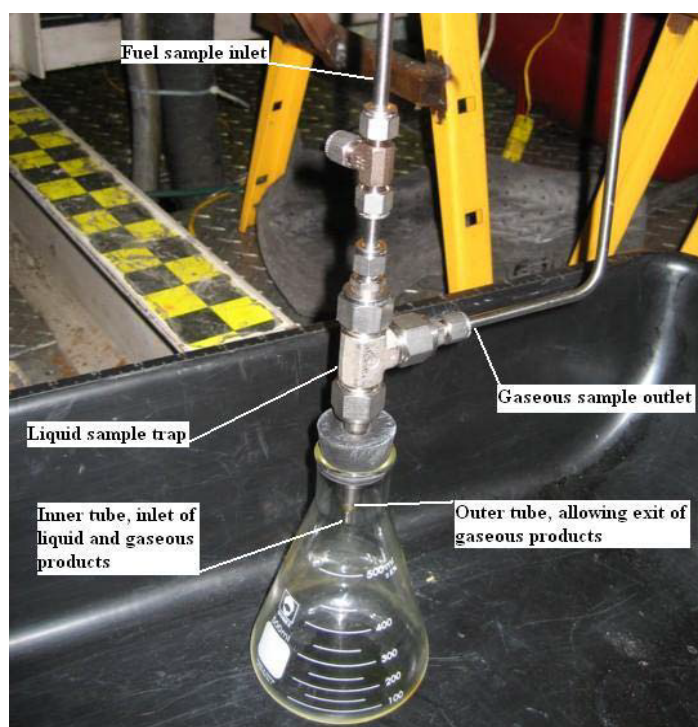


Figure 7. Liquid sample collection trap. *Erlenmeyer flask collects liquid products; gaseous products flow to a downstream stainless steel vessel through the outer tube.*

equal (verified by use of transducer measurement), and therefore selection of nozzle flow number determined the fraction of mass flow extracted for sampling (approximately 10 percent).

Upon expanding the sampled fuel through its nozzle, it was cooled to room temperature by flowing through a coiled 3/8 in. stainless steel tube immersed in chilled water as shown in Fig. 6. During normal operation (no sample storage) the cooled sample flow was redirected back into the main manifold through a remotely operated three-way valve. This occurred while the PDE was allowed to run up to a steady state operating temperature. When the system temperature stabilized (either 811 K or 867 K), the three-way valve was actuated to redirect the sample flow to the liquid and gas sample collection apparatus for a specified period of time.

Upon thermal cracking, the fuel will decompose into lower molecular weight products, including liquid and other components that are in gaseous phase at ambient conditions. The liquid portion was collected in a 500 ml Erlenmeyer flask while the gaseous portion was collected in a 1000 ml Swagelok stainless steel sample vessel. The trap shown in Fig. 7 directed both portions into the flask through an inner tube. The outer tube enabled the gaseous products to flow further downstream to be collected in the stainless steel sample vessel.

E. Analytical Measurements

Analyses of liquid and gas samples were performed post running (off-line). Liquid samples were volumetrically quantified using a 500 ml graduated cylinder. Sample analysis was performed at Air Force Research Laboratory, fuels branch (AFRL/RZTG). Liquid samples were analyzed using an Agilent gas chromatograph/mass spectrometer (GC/MS) model 6890/5973. Quantitative analysis of the gaseous samples was performed using an Agilent model 6890 gas chromatograph (GC) equipped with both flame ionization detector (GC/FID) and thermal conductivity detector (GC/TCD). Gaseous hydrocarbon products were quantified via GC/FID while the hydrogen was quantified using GC/TCD. Further details on the laboratory processes can be found in Ref.11.

IV. Results and Discussion

Stressed gaseous and liquid fuel products were consistent with those produced via free radical thermal decomposition. Figures 8a and b show composition of fuel as received and liquid products after heating, respectively. The time scale refers to the chromatography sample retention time, not to experimental time scales. A longer retention time corresponds to higher molecular weight components. Chromatograph abundance signals were normalized by the maximum signal outputted to form the normalized signals shown in Figs. 8a and b. Because of nozzle coking (discussed later) volumetric liquid-to-gas conversion was not determined and was not used as an indicator of pyrolytic stressing for this work. However, gas chromatography performed on the liquid products

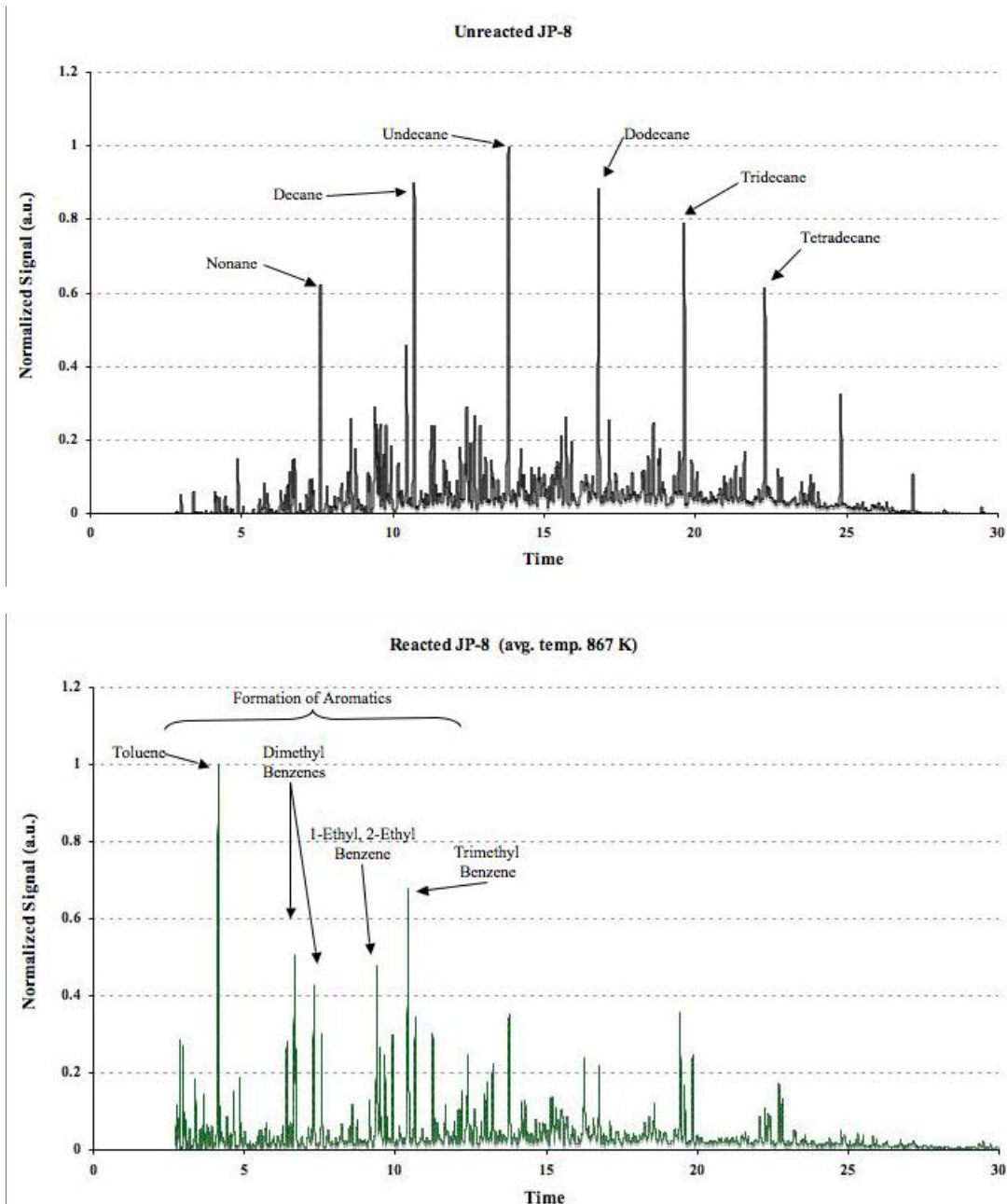


Figure 8. Comparison of the GC/MS spectra of (a) the unreacted JP-8 and (b) the cracked JP-8 liquid products. Notice the decrease of high molecular weight straight-chain alkanes and the increase in aromatics and lower molecular weight species. Average temperature of 867 K refers to the average maximum temperature measured heat exchanger exit.

showed that high molecular weight hydrocarbons were decomposed while shorter-chain alkanes, aromatics and alkenes were formed, confirming that the fuel was cracked in the heat exchangers. Overall, these results are consistent with free radical reaction chemistry observed during pyrolytic decomposition of long-chain hydrocarbons at intermediate temperature/high pressure for short reaction times¹¹. Analysis of the gaseous sample indicated that principal gaseous components were C₁-C₃ alkanes (> 50%) (Table 1).

Table 1. Primary Gaseous species obtained via GC/FID and GC/TCD analysis.

Products	Percent Volume in Gaseous Sample	
	Avg. Temp = 811 K	Avg. Temp = 867 K
Methane	23.7%	29.0%
Ethane	19.5%	18.9%
Ethylene	7.4%	5.1%
n-Propane	14.0%	13.6%
Propylene	13.6%	10.3%
iso-Butane	1.1%	1.7%
n-Butane	4.3%	4.5%
2-Butene (trans)	1.0%	1.3%
1-Butene	3.2%	2.9%
2-Butene (cis)	2.5%	2.5%
Hydrogen	3.4%	3.4%

Figure 8a shows that long straight-chain paraffins (C₉-C₁₅) are primary components in the JP-8 prior to heating with a molecular weight distribution spanning the C₇-C₁₈ hydrocarbons. Figure 8b shows that after the fuel was reacted (heated and cracked), the abundance of C₇-C₁₈ hydrocarbons was dramatically reduced. Additionally in Fig. 8b, there is a noticeably higher abundance of lower molecular weight alkanes, alkenes, and aromatics.

Table 1 shows the primary products found in the gaseous samples when the average maximum of the fuel heat exchanger outlet was either 811 K (1000 °F) or 867 K (1100 °F). The results show that the small temperature increase had minimal effect on hydrogen production (values on chart are an average of multiple samples). It is evident that C₁-C₃ alkanes and alkenes make up the majority relative yield of gaseous sample products.

Figure 9a shows the results of previous research^{5,6}.

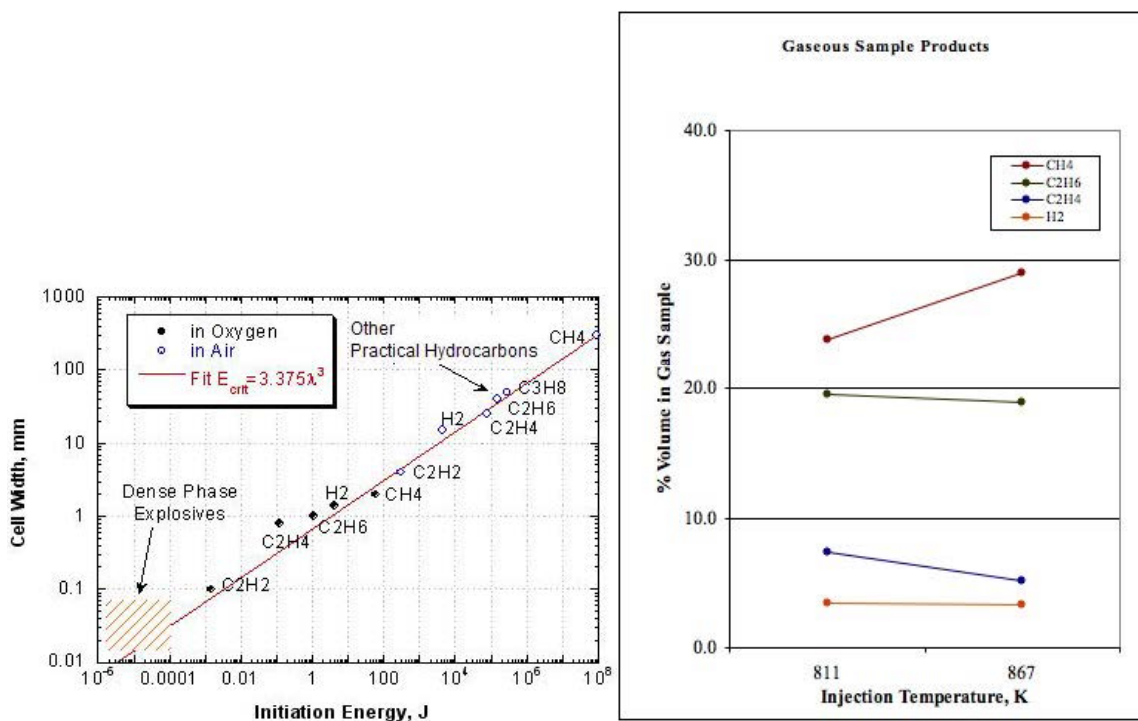


Figure 9. Critical initiation energy for various stoichiometric fuel/oxidizer mixtures (a) and those same fuels that have been produced as a result of thermal cracking (b). Notice the relationship of initiation energy to the decreasing cell width of the fuel (b)^{5,6}. The species that are desired to decrease initiation energy and cell size are present in the reacted fuel (b).

A comparison was made based on the initiation energy needed for selected stoichiometric fuel/oxidizer mixtures. Figure 9a shows that acetylene, hydrogen, and ethylene require a lesser initiation energy than that required for unstrained hydrocarbons. Therefore, it is more desirable for these three species to be present in the gaseous products. Figure 9b shows the amounts of these species that were present in the gaseous product samples. While the desired fuels were present in the sample, the fuels that required higher initiation energies (methane, ethane, and propane) were also present.

As mentioned earlier, volumetric liquid to gas conversion could not be quantified. The method used to determine conversion required knowledge of liquid fuel mass flow entering the sample stream. It was hypothesized that a ratio of nozzle flow numbers would allow determination of the volume of pre-heated liquid sample (see Eq. 2). It was later determined that carbonaceous deposits in the nozzles caused such a ratio based on flow number to be inaccurate. For this reason, volumetric liquid to gas conversion has been omitted from the results. Future work will investigate methods that enable determination of liquid to gas conversion.

V. Conclusion

Waste heat from a pulsed detonation engine (PDE) was extracted via concentric tube-counter flow heat exchangers to produce supercritical pyrolytic conditions for JP-8 fuel. Analysis of online liquid and vapor fuel samples during steady state operation indicated thermal decomposition. The liquid analysis showed conversion of high molecular weight fuel components and formation of aromatics, alkenes, and alkanes. The gaseous products found in the analyzed vapor consisted of predominantly C₁-C₃ alkanes and alkenes (> 50% of total vapor volume) with moderate amounts of hydrogen and C₄-C₆ alkanes and alkenes. The liquid and gas samples analyzed indicate that thermal cracking had occurred. These results are consistent with previous research² and lend insight to why ignition time, DDT time, and DDT distance all decrease when the cracked fuel is used for PDE operation. This work has not been entirely conclusive in that wider ranges in temperature require further analysis. Continued research in temperature effects as well as the volumetric liquid to gas conversion will bring more insight to help link PDE performance to pyrolytic reactivity. Further analysis will investigate maximization of desired products that improve PDE performance while minimizing undesired carbonaceous deposits and gaseous components that yield detrimental results.

Acknowledgments

This work would not have been possible without the team of researchers at PDRF. We express our deepest appreciation and thanks to Curtis Rice, Royce Bradley, and Adam Brown (ISSI). Linda Shafer and Rich Striebeck (UDRI) gave invaluable support and expertise in analyzing fuel samples. Dr. Tim Edwards (AFRL/RZTG) lent both research support and his scientific knowledge in fuels. Maj. Dave Hopper and 2nd Lt. Alex Hausman (AFIT) were crucial in running the PDE and exceptionally helpful in processing data. The technical leadership of Dr. Robert Hancock (AFRL/RZTC) and the funding of Air Force Research Laboratory/Propulsion Directorate and Air Force Office of Scientific Research (AFOSR) made this research possible.

References

- ¹Edwards, T., "Liquid Fuels and Propellants for Aerospace Propulsion: 1903-2003," *Journal of Propulsion and Power*, Vol. 19, No. 6, 2003, pp. 1098-1100.
- ²Helfrich, T. M., Schauer, F. R., Bradley, R. P., and Hoke, J. L., "Evaluation of Catalytic and Thermal Cracking in a JP-8 Fueled Pulsed Detonation Engine," AIAA2007-235, 45th AIAA Aerospace Sciences Meeting and Exhibit, Reno, NV, 8-11 January 2007.
- ³Turns, S. R., *An Introduction to Combustion: Concepts and Applications*, 2nd ed., McGraw Hill, Boston, 2000, pp. 613-617.
- ⁴Fickett, W. and Davis, W. C., *Detonation: Theory and Experiment*. New York NY, Dover Publications Incorporated, 1979.
- ⁵Kaneshige, M. and Shepherd, J. E., *Detonation Database*. Technical Report FM97-8, GALCIT, July 1997.
- ⁶Schauer, F. R., Miser, C. L., Tucker, K. C., Bradley, R. P., and Hoke, J. L., "Detonation Initiation Hydrocarbon-Air Mixtures in a Pulsed Detonation Engine," AIAA 2005-1343, 43rd AIAA Aerospace Sciences Meeting and Exhibit, Reno NV, 10-13 January 2005.
- ⁷Knystautas, R., Guirao, C., Lee, J. H., and Sulmistras, A., "Measurement of Cell Size in Hydrocarbon-Air Mixtures and Predictions of Critical Tube Diameter, Critical Initiation Energy, and Detonability Limits," *Progress in Aeronautics and Astronautics*, AIAA, Vol. 94, pp. 23-37, 1984.
- ⁸Austin, J. M. and Shepherd, J. E., "Detonation in Hydrocarbon Fuel Blends," *Combustion and Flame*, Vol. 132, No. 1-2, 2002, pp. 73-90.
- ⁹Ciccarelli, G., Ginsberg, T., Boccio, J., Economos, C., Sato, K., and Kinoshita, M., "Detonation Cell Size Measurements and Predictions in Hydrogen-Air-Steam Mixtures at Elevated Temperatures," *Combustion and Flame*, Vol. 99, 2004, pp. 212-220.

¹⁰Huang, H., Sobel, D., and Spadaccini, L., "Endothermic Heat-Sink of Hydrocarbon Fuels for Scramjet Cooling," AIAA 2002-3871, *38th AIAA/AMSE/SAE/ASEE Joint Propulsion Conference and Exhibit*, Indianapolis IN, 7-10 July 2002.

¹¹Edwards, T., DeWitt, M. J., Shafer, L., Brooks, D., Huang, H., Bagley, S. P., Ona, J. O., Wornat, M. J., "Fuel Composition Influence on Deposition in Endothermic Fuels," AIAA 2006-7973, *14th AIAA/AHI Space Planes and Technologies Conference*, Canberra, Australia, 6-9 November 2006.

¹²Helfrich, T. M., King, P. I., Hoke, J. L., and Schauer F. R., "Effect of Supercritical Fuel Injection on the Cycle Performance of a Pulsed Detonation Engine," AIAA-2006-5133, *42nd AIAA/ASME/SAE/ASEE Joint Propulsion Conference and Exhibit*, Sacramento CA, 9-12 July 2006.

¹³Schauer, F. R., Stutrud, J. S., and Bradley, R. P., "Detonation Initiation Studies and Performance Results for Pulse Detonation Engine Applications," AIAA 2001-129, *39th AIAA Aerospace Sciences Meeting and Exhibit*, Reno, NV, 8-11 January 2001.

¹⁴Shchelkin, K. L., "Soviet Journal of Technical Physics," Vol. 10, pg. 823-827, 1940.

¹⁵Panzenhagen, K. L., "Detonation Branching in a PDE with Liquid Hydrocarbon Fuel," M.S. Thesis, Department of Aeronautics and Astronautics, Air Force Institute of Technology, Wright-Patterson AFB, OH, 2004.

¹⁶Bartok, W., and Sarofim, A. F., *Fossil Fuel Combustion: A Source Book*, John Wiley & Sons, Inc., New York, 1991, pp. 552-553.

Direct Initiation by Detonation Branching in a Pulsed Detonation Engine

Alexander R. Hausman¹, Paul I. King², and David R. Hopper³
Air Force Institute of Technology, Wright-Patterson AFB, OH, 45433

John L. Hoke⁴
Innovative Scientific Solutions, Inc., Dayton, OH, 45440

Frederick R. Schauer⁵
Air Force Research Laboratories, Wright-Patterson AFB, OH, 45433

An experimental study is conducted to determine the requirements necessary to successfully branch a detonation initiated in a primary detonation tube, through a crossover tube and into a second detonation tube without the use of internal deflagration-to-detonation transition hardware. Tail-to-head branching is conducted and a hydrogen sourced detonation is seen to successfully sustain a diameter expansion ratio of 1:2. The head pressure trace of a successful detonation transfer resulting in Chapman-Jouguet wave speeds in the branch ignited tube is also reported.

Nomenclature

CJ	=	Chapman-Jouguet
f	=	engine cycle (cam shaft rotation) frequency
ϕ	=	equivalence ratio
λ	=	detonation cell size
DDT	=	deflagration to detonation transition
FF	=	fill fraction
PF	=	purge fraction
SD	=	spark delay

I. Introduction

A pulsed detonation engine (PDE) is an unsteady propulsion device that operates a series of open-ended detonation tubes on a continuous fill-fire-purge cycle. A design criteria vital to the eventual implementation of the PDE as a viable propulsion source is the fire phase time. The previously realized scalability of the PDE directly relates the engine frequency and resulting cycle time to the thrust produced¹. The fire phase duration is limited by both the time necessary for ignition and also that required for deflagration-to-detonation transition (DDT). The concept of detonation branching is the act of physically splitting a detonation wave into various detonations (two in this case), all of which maintain the defining qualities of the initial detonation. It has been shown that through branched detonation, ignition times have been nearly eliminated².

The PDE used in this research is housed at the Air Force Research Lab Pulsed Detonation Research Facility located at Wright-Patterson AFB, Dayton, OH. The specifics of the research facility used including valving, timing,

¹ 2Lt, USAF, Graduate Student, Department of Aeronautics, 2950 Hobson Way, AIAA Member.

² Professor, Department of Aeronautics, 2950 Hobson Way, AIAA Senior Member.

³ Major, USAF, Graduate Student, Department of Aeronautics, 2950 Hobson Way, AIAA Member.

⁴ Research Engineer, 2766 Indian Ripple Road, AIAA Senior Member.

⁵ Senior Engineer, Head PDRF AFRL/RZTC, 1950 5th Street, AIAA Senior Member.

control, instrumentation and diagnostics are discussed in detail by Schauer et al.¹. Only the differences present between the current setup and that described by Schauer et al. will be mentioned where necessary.

The focus of this research is to determine the necessary conditions required to successfully sustain a detonation from initiation in one detonation tube, through a tail-to-head crossover tube and into a secondary detonation tube. This is to be performed without the aid of any DDT hardware in the secondary tube as the detonation will be seen to successfully transition from its initiation in the primary thrust tube. This is a preliminary study and as such, gaseous hydrogen is the fuel used throughout.

It is well known that in order for a detonation wave to propagate from a circular tube into an unconfined space of similar mixture, that the tube must be sized such that its diameter is at least 13 times the detonation cell size (λ)³. This value is greatly reduced when the expansion occurs into a restricted tube similar in geometry but larger in size. Study has shown that detonations are capable of propagating across certain expansion diameter ratios below some limit.⁴ It is, in part, this capability of the shock to stay coupled with the reaction zone through a confined expansion that enables direct initiation by detonation branching.

II. Experimental Setup

Hardware for the project consisted principally of 2 in. (nominal) primary and secondary detonation tubes, a 1 in. crossover tube, and the mating hardware. The crossover tube was introduced to the secondary detonation tube approximately 2.5 in. downstream of the closed end (head) in a fashion that forced the flow to make two sharp 90 degree turns into the secondary tube. The schematic displayed in Fig. 1 illustrates the general layout as well as the various ion probe locations. It should be noted now that the wave speeds reported throughout are the average wave speeds of the midpoint between two ion probes and as such are reported at the midpoint location. The ion probes (and similarly the wave speeds reported later) are located based on their downstream distance from the head of the primary detonation tube and are recorded in Table 1.

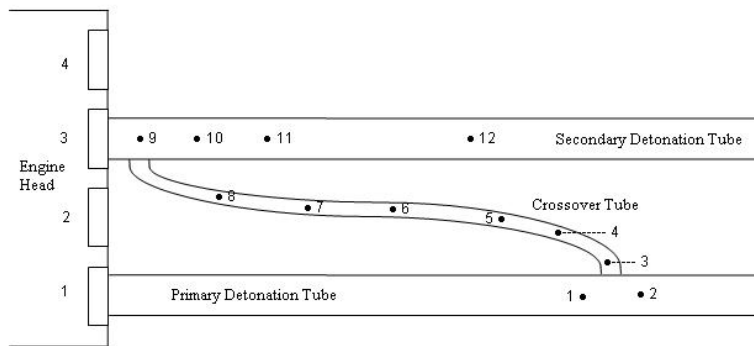


Figure 1. Schematic of test setup with approximate locations of ion probes.

Table 1. Distance of ion probes from the head of the primary detonation tube.

Ion Probe Location Number	Distance from Head 1 (inches)
1	35
2	42
3	42
4	51
5	57
6	67.25
7	72
8	78
9	92
10	95
11	98
12	105.25

Numerous parameters were held constant for the data presented in the results section below. Those varied, including ion probe locations used, are contained in the conditions matrix of Table 2. Unless otherwise noted, the following variables were held constant over the course of runs which the data presented represents. The equivalence ratio (ϕ) was held constant at the stoichiometric value in order to reduce the detonation cell size (λ) and to aid in the branched detonation pick-up success rate. The fill

Table 2. Conditions matrix for individual test runs.

Run Number	Equivalence Ratio (ϕ)	Ion Probe Location Number	Primary Tube Reducer	Secondary Tube Reducer
1	1	1 - 8	Y	N
2	1	1, 2, 7 - 12	Y	N
3	1	1, 2, 7 - 12	Y	Y
4	0.9	1, 2, 7 - 12	Y	Y

Table 3. Various spark delays shown vs. engine frequency; parameters used highlighted.

Frequency (Hz)	Time/Cycle (ms)	Time/Phase (ms)	Spark Delay (ms)
2	500.000	166.667	125.0
4	250.000	83.333	62.5
6	166.667	55.556	41.7
8	125.000	41.667	31.3
10	100.000	33.333	25.0
12	83.333	27.778	20.8
14	71.429	23.810	17.9
16	62.500	20.833	15.6
18	55.556	18.519	13.9
20	50.000	16.667	12.5
22	45.455	15.152	11.4
24	41.667	13.889	10.4
26	38.462	12.821	9.6
28	35.714	11.905	8.9
30	33.333	11.111	8.3
32	31.250	10.417	7.8
34	29.412	9.804	7.4
36	27.778	9.259	6.9
38	26.316	8.772	6.6
40	25.000	8.333	6.3

fraction (FF) and purge fraction (PF) were held constant at 1.5 and 0.7 respectively. These are ratios of either fill or purge air introduced during the time the respective valve is open, to the total volume of the tube. The over-fill ($FF > 1$) was used to ensure complete filling of the crossover tube. A similar relative increase in the PF over a non-crossover setup was also used. The engine frequency (f) was held at a constant 10 Hz for all runs.

The spark delay (SD) is the time allotted between the fill valve closure and the spark deposition in the primary detonation tube. In order to prevent backfiring into either the purge or fill manifolds, a SD was selected such that the spark was not deposited until the fill valve had also closed in the secondary tube. The two cylinders chosen are next to each other in the engine firing order, thereby allowing the detonation from the primary tube to act as the ignition source for the secondary tube. The firing order of the research PDE is 1-3-4-2; so, as illustrated in Fig. 1, tube 1 was the primary and tube 3 the secondary. The SD is directly related to the engine frequencies (f) of which various values are tabulated and displayed in Table 3.

Data were collected in runs with durations of one-half second. At the 10 Hz engine frequency and a data collection rate of one MHz, each run resulted in the capture of three to four complete detonation cycles. Each data point in the following wave speed plots is indicative of the happenings at a given tube location for a single cycle.

III. Results

A. Consistent CJ Wave Speeds through the Crossover Tube

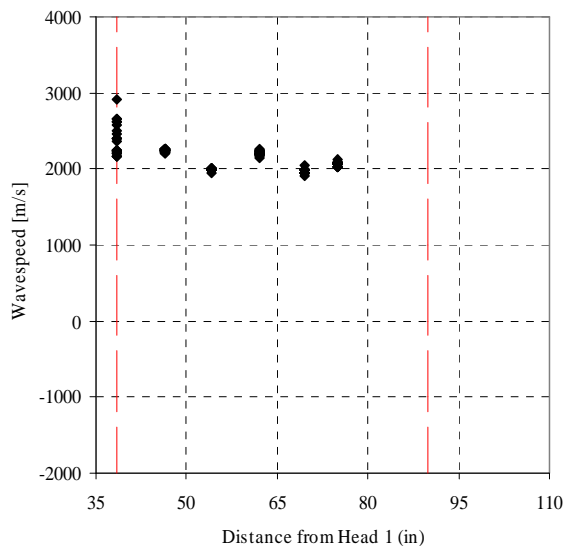


Figure 2. Run 1 wave speeds along the length of the crossover tube as a function of distance from the head of the primary detonation tube.

It has been shown that detonation branching is more successful when the branching occurs in the presence of an overdriven detonation², meaning that the wave speed is greater than the steady state CJ wave speed. At the conclusion of the DDT event, the detonation is commonly in an overdriven state. The CJ wave speed for the stoichiometric hydrogen-air mixture used throughout this research is known to be approximately 1971 m/s⁵. By varying the location of the Shchelkin-type spiral used to initiate the primary detonation, the DDT event was moved downstream such that the overdriven wave speed region spanned the crossover tube pickup location. This is indicated in Fig. 2 where the average pickup wave speed was 2394 m/s, approximately 21% greater than the CJ speed. The strategic placement of the DDT event along with an un-quantified tube pressure increase resulting from a 25% reduction in tail-end diameter through the use of a restrictor aided in this overdriven condition.

The present data acquisition system is capable of obtaining twelve channels of data simultaneously. Head pressures in both tubes and the spark (deposited in the primary detonation tube only) were recorded for every run. This limited the number of channels for ion probes

to a maximum of nine. Also for every run, the pickup wave speed was recorded to ensure that the overdriven case was obtained, leaving seven channels for additional ion probes. The pickup wave speed is that obtained from ion probe measurements at probe locations one and two, where the crossover tube and primary detonation tube meet. As such, the first portion of the experiment was limited to data acquisition from only the pickup location and along the crossover tube. These data were used to determine the nature of the detonations produced and also those captured in the cross-over tube by detonation branching. Note that the red dashed lines in Fig. 2 and subsequent plots indicate the span of the crossover tube.

The current engine parameters in conjunction with the primary tube restrictor produced consistently strong detonations both at the pickup location and also through the crossover tube. The wave speed throughout the crossover tube was slightly lower than the pickup speed averaging 2093 m/s. The lowest average wave speed recorded for a single location along the crossover tube was 1962 m/s; less than the one-half percent away from the CJ speed mentioned previously. Physical limitations of the test setup prohibited collecting wave speed measurements closer to the delivery end of the crossover. With the belief that strong detonations were present throughout the length of the tube, the focus of wave speed measurements was moved to the secondary detonation tube.

B. Focus of Wave Speed Measurements in the Secondary Thrust Tube

The data presented in Fig. 3 results from moving the ion probes at locations three through six in the crossover tube to locations nine through twelve in the secondary detonation tube. No other changes in the setup were made concerning the physical geometry or the engine parameters. Also as before, the primary detonation tube was equipped with a restrictor resulting in a 25% tail-end reduction in diameter. As mentioned, this caused an unquantified pressure rise in the primary detonation tube and further aided in successful detonation branching to the cross-over tube. Again consistently overdriven detonations are seen at the pickup location with average wave speeds of 2255 m/s. Conditions near the delivery end of the crossover tube were also similar to those observed in

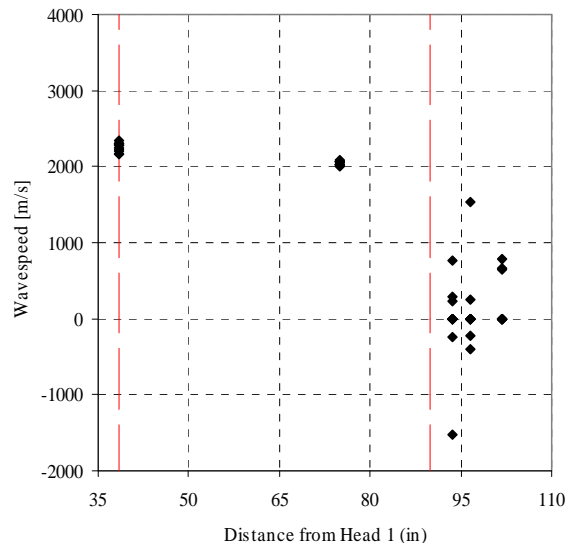


Figure 3. Run 2 pick-up, crossover, and second tube wave speeds shown as a function of distance from the head of the primary detonation tube.

Fig. 2 with wave speeds averaging 2042 m/s. The low and negative wave speeds observed in the secondary tube (to the right of the second red line) are caused by weak ion probe drops and indicate a possible decoupling of the shock and combustion front upon expansion into the secondary thrust tube. Three sets of data were collected with this setup, during which eleven detonation traces were recorded.

The wave speeds observed in the secondary detonation tube with no restrictors present (not shown) were poor, as were the results shown in Fig. 3 with only the primary tube tail-end diameter reduced. This led to the inspiration of placing restrictors on both the primary and secondary detonation tubes. The 25% reduction in tail-end diameter to the second tube was the only change from the previous setup of Run 2; all other variables were maintained. This

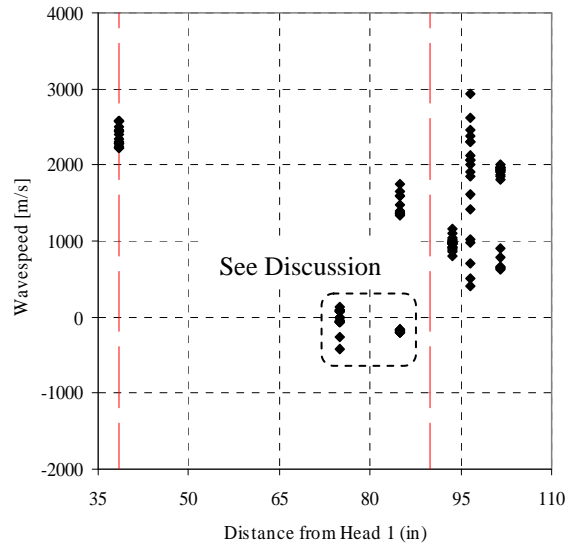


Figure 4. Run 3 CJ wave speeds seen in secondary detonation tube are indicative of successful detonation transitions.

resulted in the first successful detonations seen to travel from initiation, through the crossover tube and transition into the secondary thrust tube without the necessity of DDT hardware in the secondary tube. Fig. 4 displays the data recorded during run three consisting of nineteen traces; twelve traces in which the final measured wave speeds were 1800 m/s (91% of the CJ value) or greater.

Just downstream of the crossover at the 93.5 in. axial location, it appears that the detonation is initially slowing to ~1000 m/s which is consistent with a shock/combustion decoupling. The broad range of wave speeds at the next axial measurement location possibly indicates a re-initiation event for some percentage of the cycles. At the final wave speed measurement location of ~102 in., the individual traces appear to have separated into re-initiated detonations with wave speeds greater than 1800 m/s or failed detonations with speeds below 1000 m/s. The average wave speed at pick-up for the data present in Fig. 4 is 2382 m/s and the final most downstream wave speed including all values displayed averaged 1535 m/s.

There is concern pertaining to the wave speed measurements in the crossover tube circled in Fig. 4. While the pick-up wave speeds exhibit the same overdriven tendency presented in Fig. 2 and Fig. 3, all the wave speeds at the 75" location and approximately half of those at the 85" location are either negative or very near zero. There is no direct correlation between these low wave speed measurements and the ultimate success or failure of the detonation in the secondary tube (as will be evident in Fig. 5), indicating that the low wave speeds recorded do not signify a complete failure of the detonation in this case.

An examination of the individual detonation traces shows that near zero and negative wave speeds resulted from weak ion probe readings. The final wave speed measured in the crossover tube (shown at the 75" mark) is a product of two ion probe measurements: one at 72 in. from head one and the other at 78 in., locations 7 and 8 from Fig. 1 respectively. If the probe at the 72 in. location experiences a weak voltage drop, the program used to determine wave speeds will not be able to properly calculate the wave speed shown at the 75 in. location. If the ion probe at the 78 in. mark records a weak drop, then the wave speeds shown at both the 75 in. and 85 in. locations will be improperly calculated for the same reason. These weak ion probe readings are possibly due to a lower rate of ions being produced by the combustion process, as would be the case in a deflagration rather than detonation combustion.

Oran et al.⁶ have demonstrated the presence of un-reacted gas pockets in discrete locations behind a marginal detonation wave. In this case, the crossover tube diameter is small enough that the detonation wave can be classified as marginal, and it is theorized that the low/negative wave speeds resulted from relatively slow ion formations due to deflagration occurring within these un-reacted gas pockets.

A sort was conducted from the data presented in Fig. 4 to show only those runs with a final wave speed in the secondary tube (between locations eleven and twelve) greater than 1800 m/s; the result is Fig. 5. The successful unaided detonation transition occurred only when both thrust tubes had a tail-end diameter reduction of 25% due to the presence of the restrictors. This figure confirms the belief that the low and negative wave speeds recorded near

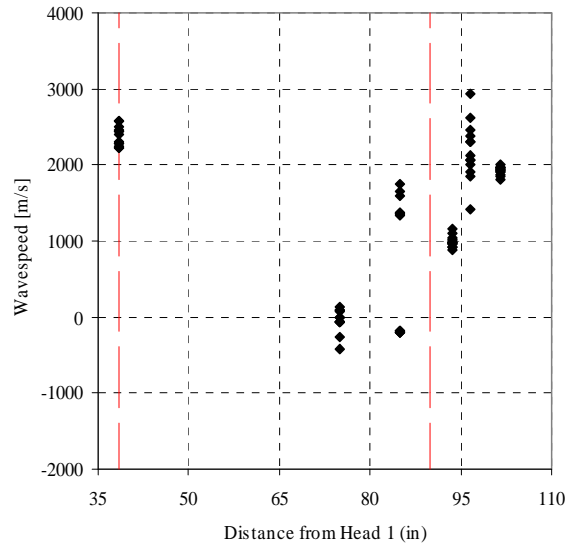


Figure 5. Traces from Run 3 with final wave speeds in the second tube greater than 1800 m/s.

the end of the crossover tube do not directly relate to the downstream wave speeds. The pickup detonations presented here are again overdriven to an average of 2382 m/s while the final wave speeds measured in the second tube are 1915 m/s, very nearly the recognized CJ speed.

C. Head Pressure Analysis of Branched Detonations

The head pressure traces of successful direct initiations due to branched detonations were next analyzed. Fig. 6 shows the secondary tube head pressure as a function of the nondimensional time; the Chapman-Jouguet time (t_{CJ}) is defined as the tube length divided by the CJ wave speed. A plot of the wave speeds corresponding to the head pressure trace of Fig. 6 (a) are included in Fig. 6 (b). The pickup wave speed recorded in Fig. 6 (b) is well overdriven at 2577 m/s.

The plateau magnitude displayed in Fig. 6 (a) is well below that of a typical detonation wave. This discrepancy is believed to be a calibration shift due to probe heating⁷. This effect was partially alleviated by the application of a layer of silicon-based sealant to protect the pressure transducers. It is believed that the relative pressures indicated

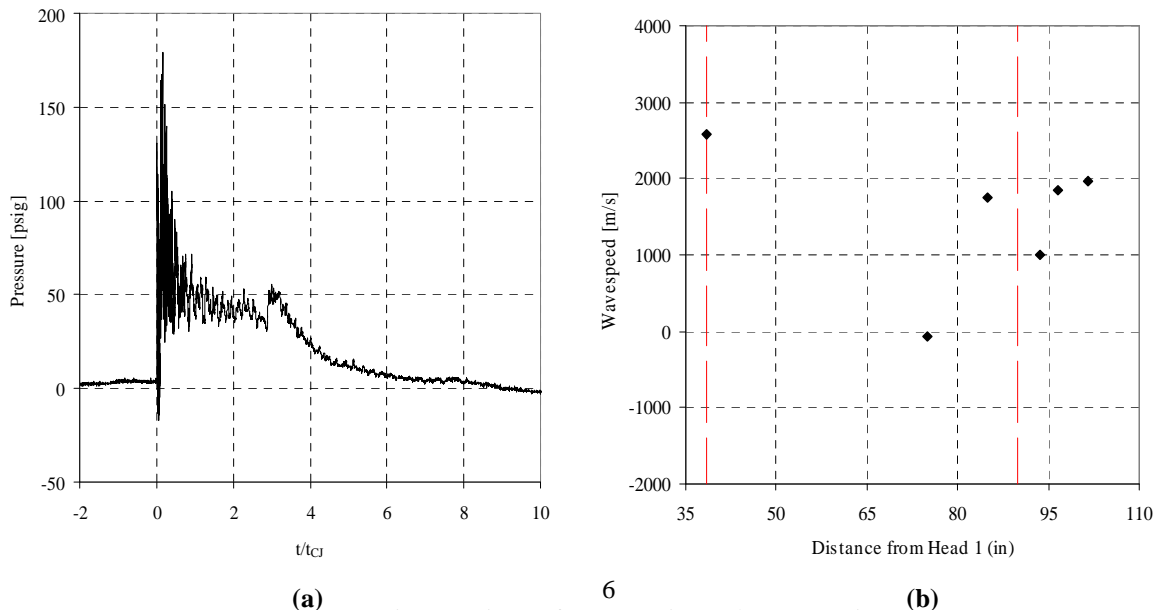


Figure 6. Run 3: (a) Secondary head pressure trace as a function of nondimensional time and (b) the responsible accompanying wave speed trace for a successful direct initiation through tail-to-head branch

in the head pressure traces are accurate but are not absolute pressures. Although quantitatively inaccurate, the pressure transducers are believed to produce a good quantitative indication of the pressure in the head during a detonation arrival.

The head pressure trace of Fig. 6 (a) exhibits most characteristics of a direct detonation initiation: a brief spike in pressure, an elevated pressure plateau while the detonation wave travels the length of the tube and reflects back as an expansion wave, and a blow down. There are a couple distinctive yet important differences that must be noted. First is the slight decrease in the plateau pressure at $t/t_{CJ} \sim 3$. This decrease is believed to be indicative of a partial blow down through the crossover tube, resulting from an expansion that follows the detonation wave through the crossover tube at approximately half of the CJ wave speed. The second feature of notable interest is the pressure spike immediately prior to the blow down. This is believed to be a result of the restrictor present on the tail-end of the secondary detonation tube. As the detonation wave reaches the end of the tube, it encounters a decrease in diameter and it is perceived that the wave is reflected back partially as a compression wave from the solid surface of the reducer and also as an expansion from the interface with the atmospheric air at the opening of the tube. Arriving back at the head of the secondary tube, the alleged compression wave followed closely by the expansion wave is seen through the pressure transducer as a brief pressure rise followed by blow down.

Fig. 7 is a head pressure trace and corresponding wave speed trace similar to Fig. 6 only in this case, the detonation wave appears to initially decouple upon emergence from the crossover tube as indicated by the low wave speeds measured at the 93.5 in. and 96.5 in. locations, then reinitiate downstream. This was the only run conducted at an equivalence ratio of 0.9. The pressure plateau is at a lower value than the direct initiation case of Fig. 6 and exhibits considerable variation. At $t/t_{CJ} \sim 2.5$ the pressure rapidly increases, likely indicating a retonation wave from the re-initiation event. This is followed by a pressure decrease believably corresponding to expansion through the crossover tube, as discussed in reference to Fig. 6. The similarly alleged compression/expansion waves traveling back towards the head are believed to result in a similar increase in pressure just prior to blow down. The delay in arrival (when compared to Fig. 6 (a)) is likely due to the additional time required for the re-initiation event.

The wave speed traces for the two figures may indicate the importance of the pickup detonation wave speed to the ultimate success of the detonation propagating into the secondary thrust tube. For the purpose of comparison with Fig. 6, the pickup wave speed recorded for the data in Fig. 7 is below that of the CJ value at 1833 m/s.

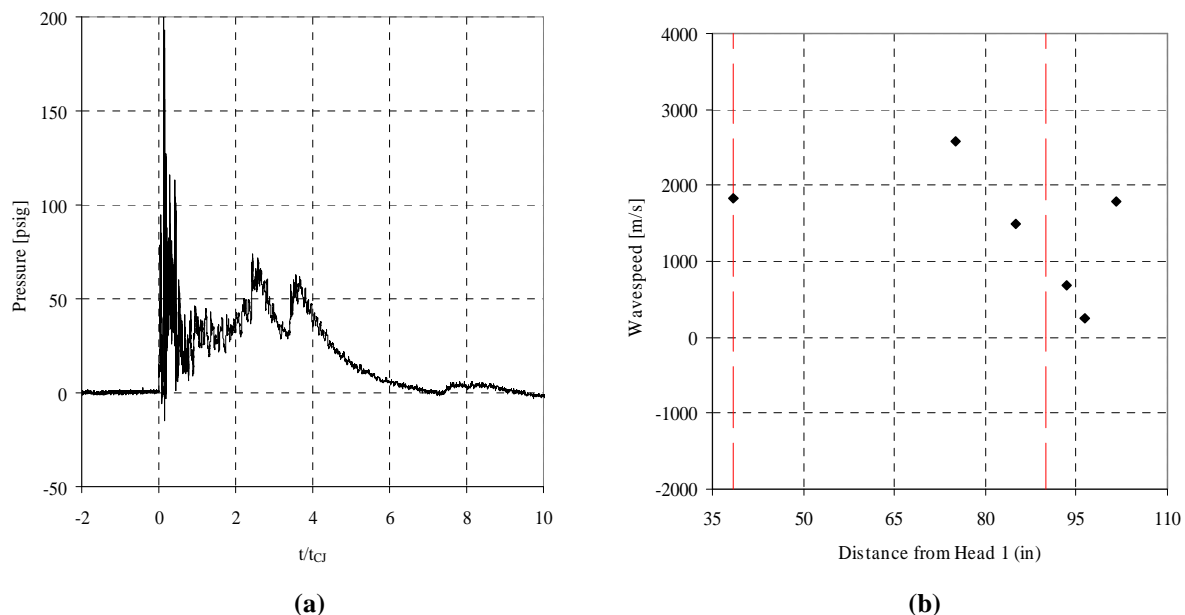


Figure 7. Run 4: (a) Secondary detonation tube head pressure trace as a function of nondimensional time and (b) the responsible accompanying wave speed trace for a tail-to-head branch detonation failure/re-initiation event.

IV. Conclusion

A. Conclusion

Ensuring successful detonation branching and sustaining the detonation throughout the entire crossover tube was the initial focus of this effort. This was necessary to ensure that strong detonations were presented to the junction of the crossover and the secondary tube where the detonation failure was most likely. Minor changes were made to the test setup (i.e. the 25% reduction in tail-end diameter) in order to obtain CJ or greater wave speeds in the secondary thrust tube. These wave speeds, indicate a successful detonation initiation in the secondary tube, and were obtained without the employment of internal DDT hardware (Shchelkin-like spirals).

Qualitative pressure traces were also presented, one which is indicative of a detonation hitting the head of the secondary detonation tube. A qualitative analysis of the pressure traces shows a characteristic direct detonation initiation in some cases and a decoupling/re-initiation in others; both exhibit some hardware-specific artifacts.

B. Recommendations for Future Work

In order to better understand the method in which the crossover tube is filled and purged, a pressure analysis is to be conducted. Focus will also be placed on success with more commercially accepted fuels (i.e. AV Gas, JP-8, etc.). Coupled with the alternate fuel work, the internal geometry at the point of union between the crossover and the secondary detonation tube will also be a focal point of future work. The concept of shock reflections has been seen to be advantageous in the formation of a detonation⁸ and as such could be employed at this connection to aid in either maintaining the coupling of the shock and combustion front or by reinitiating a new detonation altogether.

Acknowledgments

This work was sponsored by the Air Force Research Laboratory Propulsion Directorate, Turbine Engine Division, Combustion Sciences Branch at Wright-Patterson AFB, Ohio. The authors gratefully acknowledge the contributions of Curt Rice for his assistance in enabling the research conducted to collect the data presented here. The day to day operations of the Pulsed Detonation Research Facility could not happen without his unfailing dedication. Special thanks are also due to Mr. Jeff Stutrud who developed and wrote the data acquisition software heavily employed to produce this paper.

References

- ¹Schauer, F., Stutrud, J., and Bradley, R., "Detonation Initiation Studies and Performance Results for Pulsed Detonation Engine Applications," AIAA Paper No. 2001-1129, *39th AIAA Aerospace Sciences Meeting & Exhibit*, 8-11 January 2001, Reno, NV.
- ²Panzenhagen, K., King, P., Tucker K.C., Schauer, F., "Liquid Hydrocarbon Detonation Branching in a Pulse Detonation Engine," AIAA Paper No. 2004-3401, *40th AIAA/ASME/SAE/ASEE Joint Propulsion Conference and Exhibit*, 11-14 July 2004, Ft. Lauderdale, FL.
- ³Glassman, I., *Combustion*, 3rd Edition, 1996, p. 258
- ⁴Katta, V.R., Tucker, K.C., Hoke, J., Schauer, F., "Initiation of Detonation in a Large Tube," *19th International Colloquium of the Dynamics of Explosions and Reactive Systems*, Hakone, Japan, 2 July – 1 August, 2003.
- ⁵Schultz, E., and Shepherd, J., "Validation of Detailed Reaction Mechanisms for Detonation Simulation," *Explosion Dynamics Laboratory Report FM99-5*, 2000.
- ⁶Oran, E.S., Young, T.R., Boris, J.P., et al., "A Study of Detonation Structure: The Formation of Unreacted Gas Pockets," NRL Memorandum Report 4866, 26 July 1982, Naval Research Laboratory, Washington, DC 20375.
- ⁷Cooper, M., Jackson, S., Austin, J., Wintenberger, E. and Shepherd J.E., "Direct Experimental Impulse Measurements for Detonations and Deflagrations," *Journal of Propulsion and Power*, Vol. 18, No. 5, Pg. 1033-1041, Sep-Oct 2002.
- ⁸de Witt, B., Ciccarelli, G., Zhang, F., Murray, S., "Shock Reflection Detonation Initiation Studies for Pulse Detonation Engines," *Journal of Propulsion and Power*, Vol. 21, No. 6, Pg. 1117-1125, Nov-Dec 2005.

The views expressed in this article are those of the authors and do not reflect the official policy or position of the United States Air Force, Department of Defense, or the U.S. Government.

Development of a Continuous Branching Pulsed Detonation Engine

David R. Hopper* and Paul I. King†

Air Force Institute of Technology, Wright-Patterson AFB, OH 45433

John L. Hoke§

Innovative Scientific Solutions, Inc., Dayton OH, 45440

Frederick R. Schauer‡

Air Force Research Laboratories, Wright-Patterson AFB, OH, 45433

A one-dimensional analysis was developed for sizing of a continuous branching pulsed detonation engine (PDE). Length of the crossover tubes was found to depend on the number of thrust tubes in the engine and total engine cycle time for a given fuel/air mixture. The natural engine operating frequency was then inversely proportional to thrust tube length. Minimal crossover tube length was desirable, in order to reduce difficulties with detonation transmission and other inefficiencies associated with long crossover tubes. Proof of concept experimentation was performed on a pair of thrust tubes connected at the tail end by a perpendicular crossover tube. Transient variations in wavespeed were observed as the engine temperature increased, but under the right conditions, consistent detonation transmission was observed. A continuous branching PDE design is demonstrated, with short crossover tubes and alternating tail-tail and head-head detonation transmission.

Nomenclature

CJ	=	Chapman-Jouguet
DDT	=	deflagration to detonation transition
f	=	frequency
f_{branch_cycle}	=	the frequency of detonation travel through all tubes, arriving back at the first tube
f_{engine_cycle}	=	the frequency of the fill-fire-purge cycle
ff	=	fill fraction
L	=	length of the entire thrust tube
L_x	=	length of crossover tube
L_{1x}	=	length traveled in the thrust tube between detonation initiation and crossover tube pickup
L_{1-2}	=	path length of detonation in a single tube/crossover combination ($L_{1x} + L_x$)
ms	=	milliseconds
n	=	number of tubes
PDE	=	pulsed detonation engine
$PDRF$	=	Pulsed Detonation Research Facility, Air Force Research Laboratory, Wright-Patterson AFB, OH
pf	=	purge fraction
t	=	time
t_{CJ}	=	Chapman-Jouguet time, the time for a detonation wave to travel tube length at V_{CJ}
t_{engine_cycle}	=	time required for fill-fire-purge
t_{fill}	=	time for fill phase
t_{fire}	=	time for fire phase
t_{purge}	=	time for purge phase

* Major, USAF, Graduate Student, Department of Aeronautics, 2950 Hobson Way, AIAA Member.

† Professor, Department of Aeronautics, 2950 Hobson Way, AIAA Senior Member.

§ Research Engineer, 2766 Indian Ripple Road, AIAA Senior Member

‡ Senior Engineer, Head PDRF, AFRL/RZTC, 1950 5th Street, AIAA Senior Member.

t_{1-2}	=	time for detonation wave travel through tube 1 and arriving at tube 2 via crossover
V_{CJ}	=	Chapman-Jouguet velocity, the nominal detonation wave speed
V_{fill}	=	the average 1-D velocity of gases in the fill phase
τ	=	non-dimensional time

I. Introduction

Low-energy spark ignition of a pulsed detonation engine (PDE) incurs a time penalty for deflagration to detonation transition (DDT), decreasing the maximum cycle frequency and thus limiting thrust produced. At present, research PDEs typically use spiral or other obstacle devices to accelerate DDT,¹ but such obstacles further decrease thrust.¹⁻³ Direct initiation of detonation avoids the need for DDT obstacles and thus reduces drag in the PDE. Direct initiation also allows higher thrust levels by enabling faster engine operating frequencies, but the energy equivalent of a gram or more of high explosive is required to detonate the most sensitive hydrogen-air mixtures, and at least an order of magnitude more energy is required to directly initiate detonation in hydrocarbon fuels.⁴ One device used to achieve high energy for direct initiation is a pre-detonator. A pre-detonator uses a conventional spark to ignite a highly sensitive mixture in a small tube, transitions to detonation by means of obstacles, and the resulting detonation wave ignites the larger thrust tube. The major disadvantage of a pre-detonator is the need for oxygen enrichment, with associated cryogenic or high-pressure storage and delivery systems.⁵ Detonation branching is an alternative to a pre-detonator and has been shown to deliver sufficient energy to directly initiate detonation in a hydrogen-air mixture,⁶ while avoiding the need for a supply of pressurized oxygen.

This paper describes an analytical method for sizing a PDE that uses detonation branching as the ignition source for each of its thrust tubes. In such an engine, a detonation wave would continuously propagate from one tube to the next until arriving back at the first tube and repeating the process, and is thus termed a continuous branching PDE. In addition, a tail-tail detonation branching experiment was conducted as a stepping stone to a continuous branching PDE, and preliminary results are presented herein.

II. Modeling

Detonation branching is an ignition method that transmits the energy of an existing detonation through a crossover tube to a second thrust tube, providing a high-energy ignition pulse. Fig. 1 is a generalized representation of two PDE thrust tubes connected by a crossover tube for detonation branching. Various researchers at the PDRF have demonstrated detonation branching between two tubes in hydrogen/air^{6,7} and hydrocarbon/air^{8,9} mixtures. The crossover tube (L_c) in each of these experiments was sized arbitrarily and was aspirated as a part of the fill cycle of the engine, with fill fraction increased to compensate for the additional volume. In all cases, spark deposition in the first tube was delayed to allow the fill valves on the second tube to close before the arrival of the ignition pulse from the crossover tube.

In a continuous branching PDE the detonation branching concept is expanded to an array of tubes, each ignited by a detonation pulse from the previous tube in sequence. The last tube ignites the first tube, and the process repeats in a continuous fashion. Because ignition results from the branching process, the timing of a continuous branching PDE is dependent on detonation wave travel speeds and the lengths of the tubes in addition to the timing requirements of the fill-fire-purge PDE cycle. This means that the lengths of primary and crossover tubes, the number of tubes, the detonation properties of the fuel-air mixture, and the desired engine operating frequency are interrelated design elements and so a successful design approach requires consideration of these relationships.

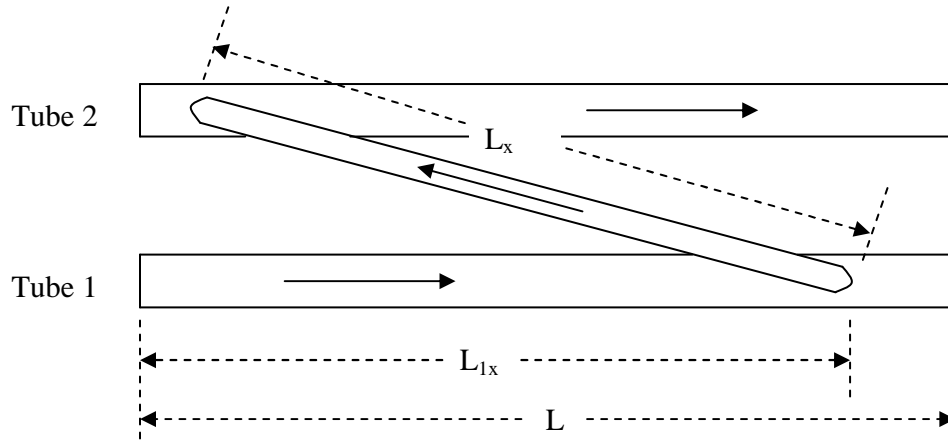


Fig. 1. Generalized sketch of two thrust tubes joined by a tail-head crossover tube. Arrows indicate the direction of travel of the detonation wave

Simplifying assumptions included one-dimensional detonations proceeding at the Chapman-Jouguet detonation velocity (V_{CJ}) for a stoichiometric fuel/air mixture through tubes at an initial pressure of 1 atm. Detonations were assumed to be directly initiated by the crossover tubes with no need for obstacles or other DDT devices. The first tube in sequence was also assumed to be directly initiated, which would require a pre-detonator or other high-energy ignition device to start the engine. Finally, all thrust tubes were assumed to be equal length, all crossover tubes were also assumed equal in length, and the crossover pickup location (L_{1x}) was assumed to be the same for all tubes. For the purposes of the model that follows, Fig. 1 is a generalized representation of two adjacent tubes in the larger array of a continuous branching PDE.

A. Analytical Model

In a continuous branching PDE, the fill-fire-purge engine cycle must be matched to the rate of detonation branching for the engine to operate. The fill-fire-purge engine cycle repeats at the engine cycle frequency, while simultaneously detonations are branched from the first tube to the next tube in sequence, cycling through all the detonation tubes in the engine and arriving back at the first tube at the same frequency as the engine cycle. That is:

$$f_{engine_cycle} = f_{branch_cycle} \quad (1)$$

Conversely, the period (time elapsed) of engine cycle and branch detonation cycle must match,

$$t_{engine_cycle} = nt_{1-2} \quad (2)$$

where, n is the number of tubes in the engine and t_{1-2} is the time elapsed from detonation initiation in one tube to initiation in the next tube. Engine cycle time is the sum of fill time, fire time and purge time for any one thrust tube. Wave travel time (t_{CJ}) is the time it takes a detonation to travel the length of the tube (L) at V_{CJ} . Fire time is non-dimensionalized using the t_{CJ} as the characteristic time,

$$\tau_{fire} = \frac{t_{fire}}{t_{CJ}} \quad (3)$$

Fill time can also be expressed in terms of t_{CJ} :

$$t_{fill} = \frac{L}{V_{fill}} ff = \frac{V_{CJ}}{V_{fill}} t_{CJ} ff \quad (4)$$

where ff is the fill fraction (filled volume/total volume) and V_{fill} is the 1-D average velocity across the tube while filling. For the purposes of this model, a fill fraction of 1.0 is considered nominal, and a lesser fill fraction indicates that the time for the fill phase has been decreased. Similarly, purge time is

$$t_{purge} = \frac{V_{CJ}}{V_{fill}} t_{CJ} pf \quad (5)$$

where pf is purge fraction. The total engine cycle time can then be expressed as

$$t_{engine_cycle} = \left(\tau_{fire} + \frac{V_{CJ}}{V_{fill}} (ff + pf) \right) t_{CJ} \quad (6)$$

The time for a detonation to travel from the location of detonation initiation in one tube to the location of detonation initiation in another via a crossover tube can be modeled as a simple function of the path length and V_{CJ} .

$$t_{1-2} = \frac{L_{1-2}}{V_{CJ}} = \frac{L_{1-2}}{L} t_{CJ} = \frac{L_{1x} + L_x}{L} t_{CJ} \quad (7)$$

The lengths L , L_{1x} and L_x are the thrust tube length, the crossover tube pickup, and the crossover tube length, respectively, as shown in Fig. 1. By the frequency match condition (Eq. 2),

$$\left(\tau_{fire} + \frac{V_{CJ}}{V_{fill}} (ff + pf) \right) t_{CJ} = n \left(\frac{L_{1x} + L_x}{L} \right) t_{CJ} \quad (8)$$

From Eq 8 the path length of the branched detonation can be calculated,

$$L_{1x} + L_x = \frac{L}{n} \left(\tau_{fire} + \frac{V_{CJ}}{V_{fill}} (ff + pf) \right) \quad (9)$$

The engine frequency is the inverse of the period (Eq. 8), given as

$$f_{cycle} = \frac{1}{t_{CJ} \left(\tau_{fire} + \frac{V_{CJ}}{V_{fill}} (ff + pf) \right)} = \frac{V_{CJ}}{n(L_{1x} + L_x)} \quad (10)$$

where f_{cycle} is either the engine cycle frequency or the branch cycle frequency, as the two are the same.

From the left hand side Eq. 10 it can be seen that for a given fuel/oxidizer combination (fixes V_{CJ}), the cycle frequency is determined solely as a function of L , the thrust tube length (recall that $t_{CJ} = L/V_{CJ}$). Another interesting result of Eq. 9 is that the branched detonation path length $L_{1x} + L_x$ increases linearly with the length of the thrust tubes and is inversely proportional to the number of thrust tubes.

Application of the above equations requires an estimate of the time required for each phase of the engine cycle. Table 1 lists some possible phase times and the resulting total engine cycle times. The first row of the table is

intended to represent a currently achievable engine cycle time. The last row is intended to represent a desired engine cycle time, although perhaps not achievable at present. The second and third rows of the table have the same engine cycle time but the duration of fire and purge phases are different, illustrating two different paths to the same overall cycle frequency.

Throughout Table 1 a fill phase of $10 t_{CJ}$ is used, corresponding to a 1-D filling velocity of approximately $M = 0.57$. This is perhaps an optimistic estimation of the minimum time requirement to fill the tube, but will suffice for the present discussion. The first row of Table 1 assumes equal phase times for fill, fire and purge. There is no requirement for equal phases, and a high-frequency PDE will probably not have equal phase times. Purge fraction (i.e. purge time) can be less than the fill fraction because the tube need not be filled completely to buffer between high temperature exhaust products and fresh reactants. In the final row, the purge phase time is reduced to zero, suggesting the optimal case.

Table 1. Engine Cycle Times Broken Down by Phase

Engine Phase Times (t/t_{CJ})			Total Engine Cycle Time (t/t_{CJ})
Fill	Fire	Purge	
10	10	10	30
10	8	5	23
10	10	3	23
10	6	0	16

Fire phase duration will also be shorter than the fill phase, as detonation time scales are much shorter than those of fill and purge. Research^{10,11} suggests that the maximum impulse for a single cycle of the engine will be obtained when the fire phase is between 8-10 t_{CJ} . Fig. 2 is the head pressure trace of a directly initiated detonation, normalized to t_{CJ} . Impulse is the area underneath the head pressure trace, and maximum impulse in Fig. 2 corresponds to the pressure dropping below atmospheric pressure at approximately 9 t_{CJ} . The majority of impulse is obtained during the pressure plateau, which typically lasts approximately 3.5 t_{CJ} .^{12, 13} While interrupting the blowdown process at slightly elevated pressure will to some extent decrease the thrust produced by a single firing, the resulting increase in engine frequency should more than offset the loss. For example, if a 10 t_{CJ} fire phase is decreased by 20 percent (2 t_{CJ}), the rate of detonations (and hence the thrust) will increase by 7.1 percent assuming initially equal phase times. The loss of impulse by truncating the fire phase 2 t_{CJ} will be insignificant by comparison, as the area under that portion of the head pressure trace (Fig. 2) is very small. Based on this justification, the fire phase is reduced to 8 t_{CJ} in the second row of Table 1, and further reduced to 6 t_{CJ} in the final row.

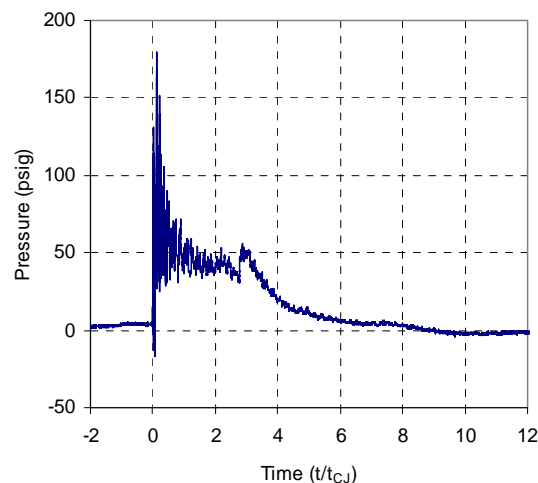


Fig. 2. Head pressure in a directly initiated detonation tube, from an experiment performed at the PDRF.¹⁴

B. Results of Modeling

The lines in Fig. 3 were found by solving Eq. 9 for L_x/L . Each line represents a family of continuous branching PDE designs that scale in size by tube length (L) and in operating frequency by t_{CJ} (itself a function of tube length and fuel properties). The dashed lines indicate the crossover tube pickup location is at the midpoint of the thrust tube ($L_{1x} = 0.5 L$ in Fig. 1) and the solid lines represent a pickup location at the end of the thrust tube ($L_{1x} = L$).

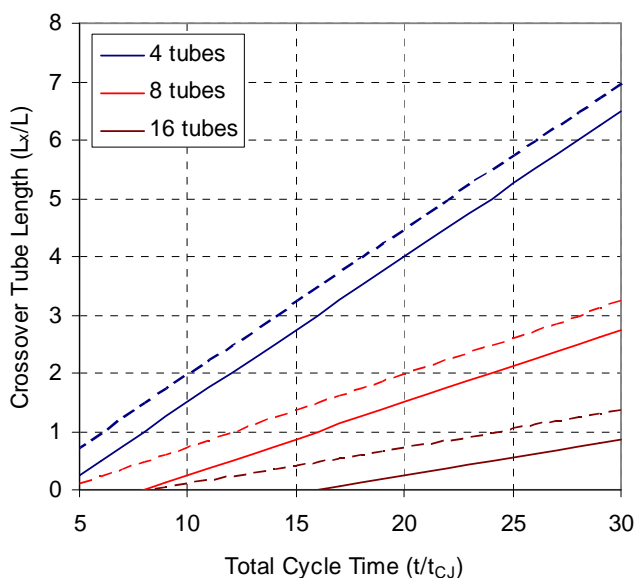


Fig. 3. Effect of number of thrust tubes and engine cycle time on crossover tube length. Solid lines indicate crossover tube pickup location at the tail and dashed lines indicate pickup at the midpoint of the thrust tube.

Generally speaking, shorter L_x is desirable in continuous branching PDE design, and the most likely designs have crossover tubes that are shorter than L . At high frequency, the time required to fill and purge the thrust tubes is likely to be a limiting factor, and filling crossover tubes that are longer than L will almost certainly prove problematic. Additionally a short crossover tube is more likely to successfully transmit a detonation from one tube to another. Finally, crossover tubes with high volume also increase specific fuel consumption since fuel burned in the crossover tube does not contribute to thrust produced by the engine.

Moving the crossover pickup location to the tail of the tube rather than the midpoint decreases L_x by precisely $0.5 L$, seen in the parallel dash-solid line pairs of Fig. 3. Because the detonation is required to travel $0.5 L$ farther in the thrust tube, that much less crossover length is required to comply with the frequency matching condition. The most likely reality is a pickup location somewhere between the midpoint and the end of the thrust tube, so each dash-solid line pair can be viewed as upper and lower bounds of crossover tube length.

The uppermost pair of lines represents engine designs with 4 thrust tubes. Assuming 3 equal cycle phases of $10 t_{CJ}$ each, the engine would have crossover tubes 7 times the length of the thrust tubes, which is clearly an unacceptable CDBE design. Two significant methods of reducing L_x are apparent by examination of Fig. 3; decreasing engine cycle time and increasing the number of thrust tubes. Engine cycle time can and should be reduced, but as shown in Table 1, cycle time can only be reduced to a lower limit of approximately $16 t_{CJ}$. Returning to Fig. 3, the only way to stay within a design space of $t/t_{CJ} > 16$ and $L_x/L < 1$ is increasing the number of thrust tubes to 16 or more. Interestingly, as the number of tubes is increased, the slope of the line decreases, meaning that L_x is less sensitive to overall cycle time.

A 16-tube engine with a $16 t_{CJ}$ cycle time and $L_{1x} = L$ is observed to have a design L_x of zero. This raises an interesting question, namely, how to physically construct a crossover of zero length. Further, any L_x less than L will not reach tail-head as shown in Fig. 1. L_x can be increased from zero by moving L_{1x} away from the tail of the tube,

resulting in enough length to at least bridge the perpendicular gap between adjacent tubes, but will not reach tail-head. Reducing L_x to lengths significantly less than L requires successive tail-head crossovers to be replaced with alternating tail-tail and head-head crossovers.

It has been shown (computationally) that igniting a detonation from the tail end of the tube does not significantly affect the impulse compared to a head-ignited tube.¹² Prior to the current work, however, tail-initiated detonations had not been demonstrated in a continuously operated PDE. An experiment was conducted to determine the feasibility of operating a short crossover between the tail ends of two tubes, and preliminary results of the experiment are given in the next section of this paper.

Table 2 takes selected engine cycles from Fig. 3 and, using Eq. 6, restores the physical dimensions to examine the effect of fuel choice, tube length and cycle times. Three engine cycles are considered: a 30 t_{CJ} engine cycle, a 23 t_{CJ} cycle, and a 16 t_{CJ} cycle.

Table 2. Selected Cycle Frequency Calculations

Tube Length (m)	Cycle Time (t/t_{CJ})	t_{CJ} (ms)	Cycle Frequency (Hz)
Stoichiometric H_2 /air		$V_{CJ} = 1971$ m/s	
1.0	30	0.51	65.7
	23		85.7
	16		123.2
0.5	30	0.25	131.4
	23		171.4
	16		246.4
Stoichiometric C_2H_4 /air		$V_{CJ} = 1824$ m/s	
1.0	30	0.55	60.8
	23		79.3
	16		114.0
0.5	30	0.27	121.6
	23		158.6
	16		228.0

Note that engine operation frequency changes with cycle time (which is obvious), and that, for a given fuel, halving the tube length corresponds to a doubling in the engine cycle frequency. Cycle frequency of a continuous branching PDE, then, is observed to be inversely proportional to tube length. From a design perspective, the cycle frequency will be limited by the time requirements of the phases of the engine cycle. The maximum achievable engine cycle rate can be matched in a continuous branching PDE simply by selecting the appropriate tube length.

III. Experiment

In the previous section, it was shown that short crossover tube lengths are achievable by increasing the number of thrust tubes and by decreasing the cycle time relative to detonation wave travel time. The implication of crossover tubes that are a small fraction of thrust tube length is that a crossover will no longer be able to reach from the tail end or even the midpoint of a thrust tube to the head end of a subsequent tube (as shown in Fig. 1), but will be just long enough for a perpendicular connection between adjacent tubes (see Fig. 4). Prior to the current work, it had not been shown experimentally that it is possible to ignite a detonation in the tail end of a tube using detonation branching, nor had tail-end detonation initiation been demonstrated on a continuously-operated PDE. An experiment was conducted using the hardware described earlier, to prove this concept as a milestone in the development of a continuous branching PDE. Preliminary results of this experiment are presented here.

A. Facility

The experiments were carried out in the AFRL pulsed detonation research facility (PDRF) at Wright-Patterson AFB, Ohio. This facility has previously been described in detail,¹⁵ and only elements important to the current experiments are presented herein.

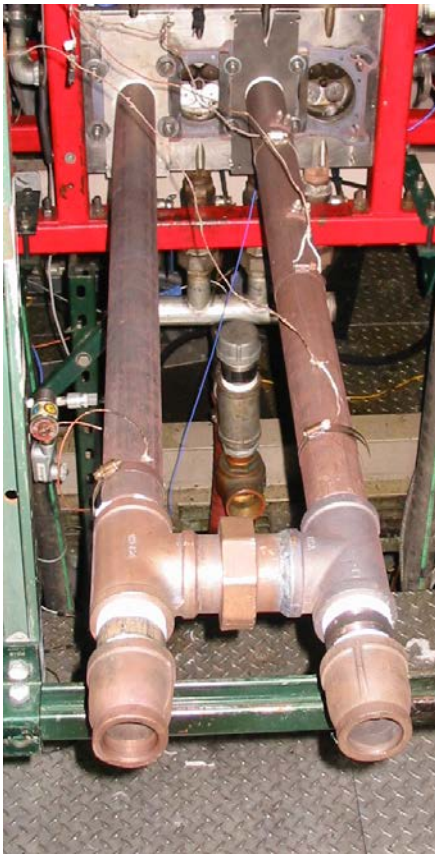


Fig. 4. Two-tube experimental configuration with crossover at the tail end

The research PDE at the PDRF utilizes a General Motors Quad-4 automotive engine head, visible at the top of Fig. 4. The engine cycle is divided into three equal phases, termed fill, fire and purge. During the fill phase, the engine intake valves open, allowing fuel and air mixture to enter the detonation tube. The fire phase begins when the fill valves close, allowing a confined combustion event isolated from the upstream manifold. The termination of the fire phase is indicated by the opening of the exhaust valves, purging the detonation tube with air.

The firing order of the engine is 1-3-4-2, with head ports numbered consecutively from left to right in Fig. 4. Ball valves in the intake and purge supply allow independent selection of only the desired tubes.

Two detonation tubes were used for the current experiment, mounted on head ports 1 and 3. Each detonation tube had an internal diameter of 53 mm (2.1 in) and a length of 1092 mm (43 in). The distance between the center lines of the two tubes was 200 mm (7.9 in.). The crossover tube was located 953 mm (37.5 in) from the head of the tubes.

Ion and pressure probes were placed at intervals along the length of tube 3 to measure the time of arrival of the detonation wave. Average detonation wavespeeds were calculated from the arrival times.

B. Tail-tail Crossover Experiment

The detonation tubes were filled with a stoichiometric hydrogen/air mixture at a cycle frequency of 10 Hz. Tube 1 was ignited by a spark, and DDT was achieved by means of a Shchelkin-type spiral obstruction. The spark in tube 1 was delayed by 25 ms from the beginning of the fire phase in tube 1, long enough for the fill valves in tube 3 to close. This was done to ensure that the detonation wave did not reach the head of tube 3 prior to closing of the fill valves, which would cause combustion in the fill manifold.

The tail-tail crossover experiment was successful, in that the observed wavespeeds indicated that detonations were consistently transmitted from tube 1 to tube 3 via the crossover tube without decoupling of the shock and combustion waves. Fig. 5a shows ion probe traces from a single detonation event in the branch-ignited tube 3, as well as the pressure in the head of tube 3. Drops in voltage on the ion probe signal passage of the combustion wave as it moves from the tail end of the tube toward the head. Fig. 5b shows the pressure traces from a single detonation event. The initial spike in pressure at each location is an indication of shock wave passage as the detonation wave moves from the tail end of the tube toward the head. Another pressure spike of smaller magnitude is also visible at approximately 4 msec on the trace of the transducer located 10.5 in from the head and further to the right on more distant transducers, indicating a shock reflected from the head.

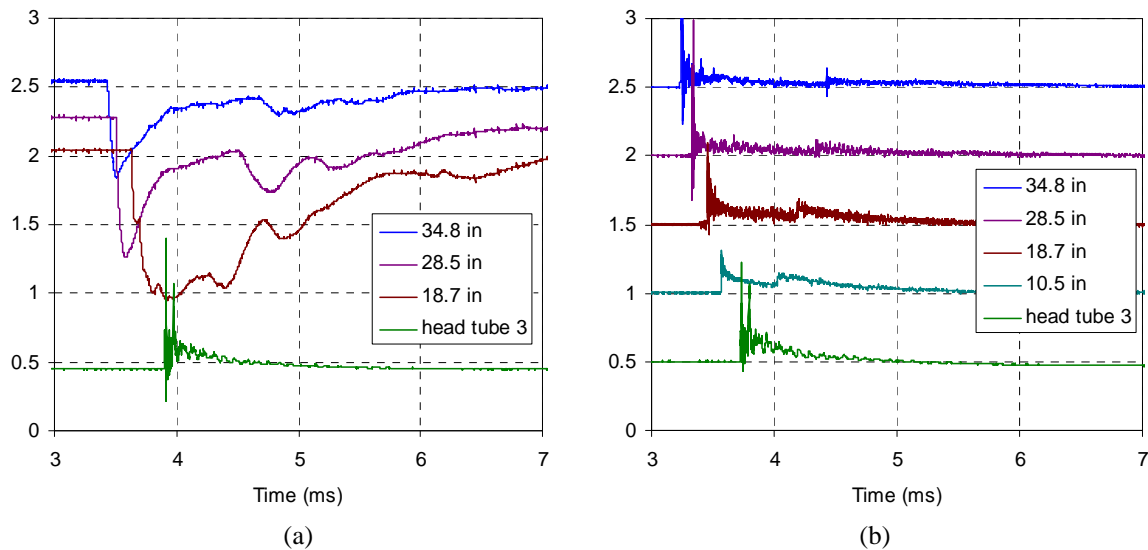


Fig. 5. Ion probe (a) and pressure (b) traces from probes on tube 3, showing tail-to-head passage of detonation wave. The pressure traces also show the head-to-tail passage of a reflected shock. Distances are measured from the head of tube 3 and arbitrary values are added to the mean of each signal to separate the traces on each plot.

Average wavespeeds measured by ion probes and pressure transducers for a number of runs showing successful detonation transmission via the crossover tube are shown in Fig. 6. One series of runs was performed while recording signals from ion probes. A similar series was run after replacing the ion probes with dynamic pressure transducers. Wavespeeds were found from the arrival times of the drops or spikes in voltage and the measured distances between adjacent transducers.

The pressure and ion probe wavespeeds show good agreement toward the head of the tube, but differ significantly near the tail. The ion probe wavespeed appears overdriven near the crossover tube, while the pressure wavespeeds are significantly less than V_{CJ} . Considerably more error is present at this location for both the ion and pressure measurements than at any other location in the tube, but 95 percent confidence intervals of the mean fail to overlap, indicating an effect beyond the variation in the data. A likely explanation of this behavior is temperature dependence of the data.

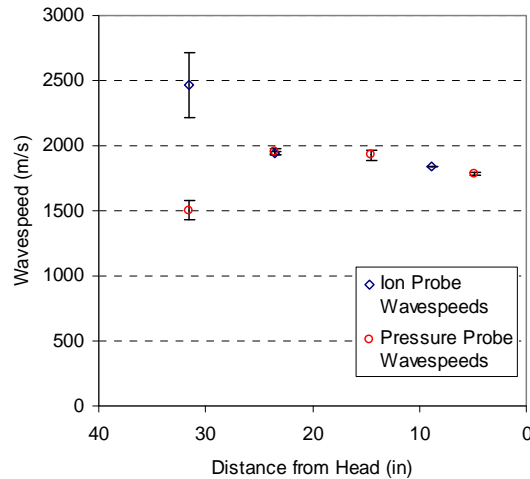


Fig. 6. Average wavespeeds measured by ion and pressure probes in a tube ignited by detonation branching. The plotted points are the mean values of 23 detonation events recorded by ion probes and 16 events recorded by pressure sensors, and 95 percent confidence intervals are indicated by error bars. Note that the ion and pressure measurements were taken at different tube temperatures.

A qualitative variation in engine operation with temperature was observed early in testing. Initially the engine would operate roughly, infrequently igniting tube 3 via the crossover tube. As the engine grew warmer, tube 3 would begin to ignite intermittently, then steadily. When ion probes measured wavespeed, the engine was run to temperatures above 500° F (260° C) before recording data. The dynamic pressure transducers, however, were much less tolerant to high temperature, so the engine temperatures were not allowed to exceed 350° F (177° C) at any time during these tests. The averaged wavespeeds of Fig. 7a show a clear time dependence of the data at the lower temperatures of the pressure test. Time dependence is still in evidence during the higher temperature ion probe testing (Fig. 7b), but appears to be limited to the location nearest the tail of the tube. Note that runs 14-16 in Fig. 7a never achieved V_{CJ} in tube 3 and were not considered in the plotted averages of Fig. 6.

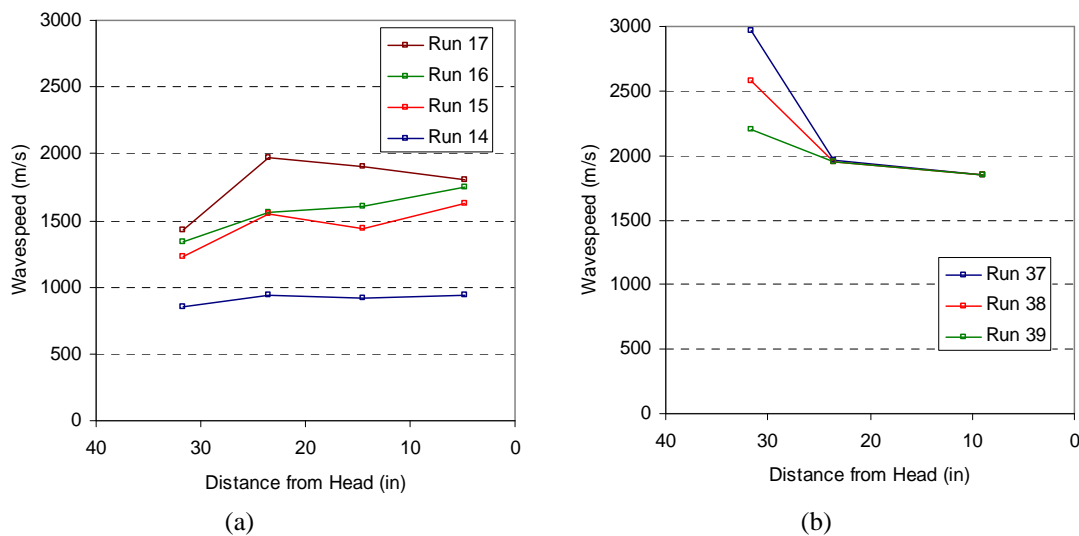


Fig. 7. Wavespeeds for low-temperature pressure runs (a) and higher temperature ion probe runs (b), showing time dependence of the data. Each run represents averaged values of 3 or 4 detonation events recorded in a single data sample.

Fig. 7 shows a reduction in wavespeed variation of the tail-ignited tube as the engine reaches a steady operating temperature, particularly away from the tail end of the tube. The extent of wavespeed variation at steady operating temperature is not fully known at this point. Quantification and reduction of transient (warmup) and constant temperature wavespeed variation are likely to be important in the development of a continuous branching PDE.

IV. Continuous Branching PDE Design

In a continuous branching PDE with the short crossover tubes previously described in the modeling results section of this paper, adjacent thrust tubes will not be identical because detonation initiation will necessarily alternate between the head end of the tube and the tail end of the tube. This idea is illustrated in Fig. 8, with tubes initiated at the head end labeled as “Tube A” and those initiated at the tail end labeled “Tube B.”

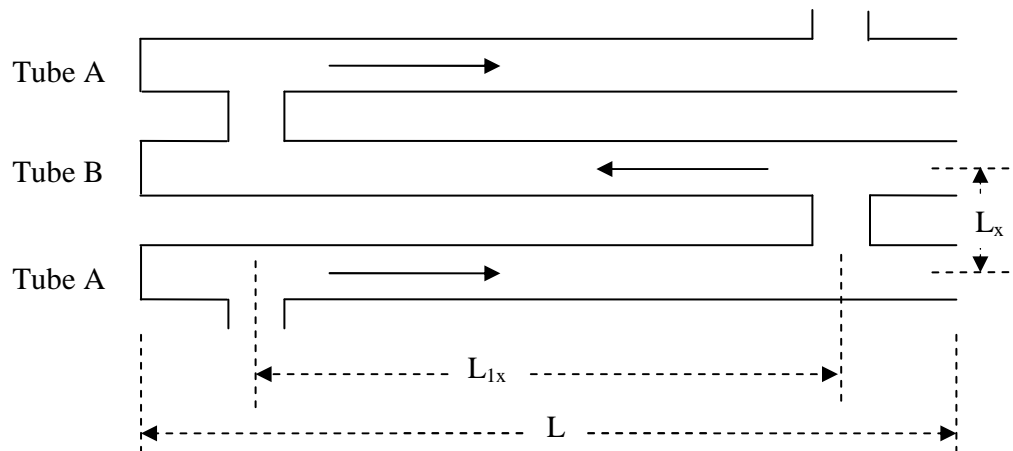


Fig. 8. Alternating tube arrangement for a continuous branching PDE with short crossover lengths. Arrows indicate direction of travel of the detonation wave.

The lengths L_x and L_{1x} are measured from centerline to centerline of the detonation tubes. This is consistent with the simplified, 1-dimensional analysis presented in Section II. In reality, detonations are complex, 3-dimensional structures containing forward- and transverse-traveling waves. The detonation wave will begin to enter the crossover tube as soon as the detonation front reaches the junction. The shortest time of flight ($t = \text{distance/velocity}$) for a detonation in the thrust tube should be $t = (L_{1x} - \text{diameter})/V_{CJ}$, and in the crossover tube, $t = (L_x - \text{diameter})/V_{CJ}$, assuming the wave travels no faster than V_{CJ} . Diffraction effects in the larger volumes at the tube junctions will likely delay the detonation wave by the amount of time required for the planar front to redevelop. For now, centerline to centerline measurement is thought to be a reasonable estimate for determining time of flight, and this presumption will be investigated by future testing and higher fidelity modeling.

Table 3 is a continuous branching PDE design based on the foregoing. It is presented to show how the model presented herein can be used as a design tool in the development of a continuous branching PDE.

Table 3. A Sample Continuous Branching PDE Design

Stoichiometric H ₂ /air with V _{CJ} = 1971 m/s		
Design Feature	Proposed Value	Source
frequency (f)	100 Hz	design target
cycle time	16 t _{CJ}	fill = 10 t _{CJ} , fire = 6 t _{CJ} , no purge
number of tubes (n)	16	select using Fig. 3
L _{1x} + L _x	1.23 m	Eq. 10
L	1.23 m	Eq. 9
L _x	0.1 m	fit to physical spacing between tubes
L _{1x}	1.13 m	(L _{1x} +L _x) - L _x

V. Conclusions

Increasing the number of thrust tubes and decreasing the cycle time of a continuous branching PDE allows the crossover tube to be shortened. For a given fuel/air mixture, the engine cycle frequency of a continuous branching PDE is determined by the thrust tube length. Tail-end detonation initiation via detonation branching has been demonstrated on a continuously operating PDE, paving the way for expanded continuous branching PDE experimentation. Future work should include examination of the transient and steady-state variation in detonation wave travel time.

Acknowledgments

The authors gratefully acknowledge the contributions of Lt Alexander Hausman, Curt Rice, Royce Bradley, Adam Brown, Dave Baker and Jeff Stutrud for their help in enabling this research. For their leadership and guidance, we also thank Dr Robert Hancock and Dr Mel Roquemore.

The views expressed in this article are those of the authors and do not reflect the official policy or position of the United States Air Force, Department of Defense, or the US Government.

References

- ¹ Cooper, M., Jackson, S., Austin, J., Wintenberger, E., and Shepherd, J.E., "Direct Experimental Impulse Measurements for Detonations and Deflagrations," *Journal of Propulsion and Power*, Vol. 18 (5), pp. 1033-1041, 2002.
- ² Hoke, J., Bradley, R., Schauer, F., "Impact of DDT Mechanism, Combustion Wave Speed, Temperature, and Charge Quality on Pulsed-Detonation-Engine Performance," AIAA-2005-1342, *43rd AIAA Aerospace Sciences Meeting and Exhibit*, Reno, NV, 2005.
- ³ Hoke, J., Bradley, R., Gallia J., and Schauer, F., "The Impact of Detonation Initiation Techniques on Thrust in a Pulsed Detonation Engine," AIAA-2006-1023, *44th AIAA Aerospace Sciences Meeting and Exhibit*, Reno, NV, 2006.
- ⁴ Benedick, W.B., Guirao, C.M., Knystautas, R., and Lee, J.H., "Critical Charge for the Direct Initiation of Detonation in Gaseous Fuel-Air Mixtures," *Progress in Astronautics and Aeronautics*, vol. 106, pp.181-202, 1986.
- ⁵ Werner, S.P., "Initiator Diffraction Limits for Pulse Detonation Engine Operation," MS Thesis, Naval Postgraduate School, Monterey, CA, 2002.

- ⁶ Tucker, K.C., King, P.I., Schauer, F.R., and Hoke, J.L., "Branched Detonation in a Multi-Tube PDE," ISABE Paper 2003-1218, *Sixteenth International Symposium on Air Breathing Engines*, 31 August – 5 September 2003, Cleveland OH.
- ⁷ Rolling, A.J., King, P.I., and Schauer, F.R., "Propagation of Detonation Waves in Tubes Split from a PDE Thrust Tube," AIAA Paper 2002-3714, *38th AIAA/ASME/SAE/ASEE Joint Propulsion Conference and Exhibit*, 7-10 July 2002, Indianapolis IN.
- ⁸ Panzenhagen, K.L., King, P.I., Tucker, K.C., and Schauer, F.R., "Liquid Hydrocarbon Detonation Branching in a Pulse Detonation Engine," AIAA Paper 2004-3401, *40th AIAA/ASME/SAE/ASEE Joint Propulsion Conference and Exhibit*, 11-14 July 2004, Fort Lauderdale FL.
- ⁹ Slack, J.D., "Branch Detonation of a Pulse Detonation Engine with Flash Vaporized JP-8," MS Thesis, Air Force Institute of Technology, WPAFB OH, 2007.
- ¹⁰ Wintenberger, E., and Shepherd, J.E., "A Model for the Performance of Air-Breathing Pulse Detonation Engines," AIAA Paper 2003-4511, *39th AIAA/ASME/SAE/ASEE Joint Propulsion Conference*, July 20-23 2003.
- ¹¹ Guzik, S.M., Harris, P.G., and De Champain, A., "An Investigation of Pulse Detonation Engine Configurations Using the Method of Characteristics," AIAA Paper 2002-4066, *38th AIAA/ASME/SAE/ASEE Joint Propulsion Conference*, 7-10 July 2002, Indianapolis, IN.
- ¹² Desbordes, D., Khasainov, B., Canteins, C., Franzetti, F., and Zitoun, R., "On the Performance of Pulse Detonation Engines," *19th International Conference on the Dynamics of Explosions and Reactive Systems*, 27 July – 1 August, 2003, Hakone, Japan.
- ¹³ Canteins, G., Franzetti, F., Zoctonska, E., Khasainov, B.A., Zitoun, R., and Desbordes, D., "Experimental and Numerical Investigations on PDE Performance Augmentation by Means of an Ejector," *Shock Waves*, Vol 15 (2), pp. 103-112, 2006.
- ¹⁴ Hausman, A., King, P., Hopper, D., Hoke, J., and Schauer, F., "Direct Initiation by Detonation Branching in a Pulsed Detonation Engine," AIAA-2008-0108, *46th AIAA Aerospace Sciences Meeting and Exhibit*, 7-10 January 2008, Reno, NV.
- ¹⁵ Schauer, F., Stutrud, J., and Bradley, R. "Detonation Initiation Studies and Performance Results for Pulsed Detonation Engine Applications." AIAA Paper No. 2001-129, *39th AIAA Aerospace Sciences Meeting & Exhibit*, 8-11 January 2001, Reno, NV.

Single-Ejector Augmentation of a Multi-Tube Pulsed Detonation Engine

John Hoke* and Royce Bradley†
Innovative Scientific Solutions Inc., Dayton, OH, 45440

Fred Schauer‡
Air Force Research Laboratory, Wright-Patterson AFB, OH, 45433

In this study, multiple detonation tubes are directed into a single ejector in an effort to reduce the added hardware required while maintaining the level of augmentation. By moving a single driver off axis it is found that the augmentation level can be maintained for x/d less than 4 and y/d up to at least 1.14, for a round ejector. The ejector augmentation, however, is found to decrease by about 25% during multi-tube operation, being approximately 1.3 ejector to baseline augmentation ratio. A linear arrangement of detonation tubes is constructed extrapolating typical unsteady ejector parameters. Four linear detonation tubes are directed at the linear ejector and the highest ejector augmentation ratio is 1.25 even with reduced fill fraction. With single tube operation, the performance of the linear ejector is at best 1.15, indicating multi-tube effects are significant.

Nomenclature

d	driver diameter
D_{ej}	ejector diameter
D_{ej}^*	ejector equivalent-area diameter (2-D ejector)
ϕ	equivalence ratio
ff	fill fraction
H_{ej}	ejector throat height (2-D ejector)
igd	ignition delay- time between valve closing and spark deposit
L_{ej}	ejector length
pf	purge fraction
R_{in}	ejector inlet radius
W	ejector width (2-D ejector)
x	ejector distance downstream from detonation tube exit
y	distance from detonation tube centerline

I. Introduction

With the use of an ejector the static thrust of a pulsed detonation engine (PDE) can be doubled¹⁻³. The optimum, unsteady, ejector diameter was found by other investigators to be between 2 and 3 diameters of the primary driver and the length was found to be 5 to 6 times the diameter of the ejector³. Additionally, a diffusion section was found to play a significant role. The augmentation created by the ejector is marred by the additional weight, structure and length. In this study, multiple detonation tubes are directed into a single ejector in an effort to reduce the added hardware required while maintaining thrust augmentation.

* Senior Engineer, 2766 Indian Ripple Rd, Dayton, OH 45440, AIAA Senior Member.

† Senior Engineer, 2766 Indian Ripple Rd, Dayton, OH 45440.

‡ Research engineer, 1790 Loop Rd, WPAFB, OH 45433, AIAA Senior Member.

Ejector performance is typically characterized by the thrust augmentation ratio (or augmentation ratio in subsequent figures) and is determined by dividing total thrust achieved with ejector (ejector thrust plus driver thrust) by the baseline thrust at equivalent conditions with no ejector (driver thrust alone). Ejector performance has been shown with a number of single tube unsteady drivers, including those at NASA Glenn Research Center, AFRL, Penn State, and UC. Despite large differences in driving pressure profiles, PDE's, chopped jets, and pulsejets show similar performance characteristics, as shown in numerous references and summarized in following figures²⁻⁶.

The data from Choutapalli and co-authors (Ref. 4) was of interest because it is relevant to linear ejector configurations. The unsteady driver reported in this reference consisted of a steady jet, with unsteadiness provided by a rotating chopper wheel. The chopped-jet drove a linear ejector. The Mach 0.8 jet results are shown here as they are most likely relevant to the predominately choked velocities expected from PDE drivers. Ejector performance as a function of ejector diameter and length (normalized by driver diameter) are shown in Figs. 1 and 2 respectively.

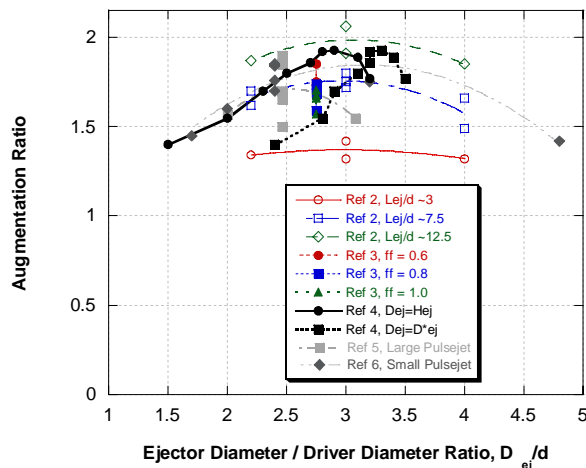


Figure 1. Ejector thrust augmentation ratio versus ejector over driver diameter ratio. $Lej/d \sim 10$ unless otherwise noted.

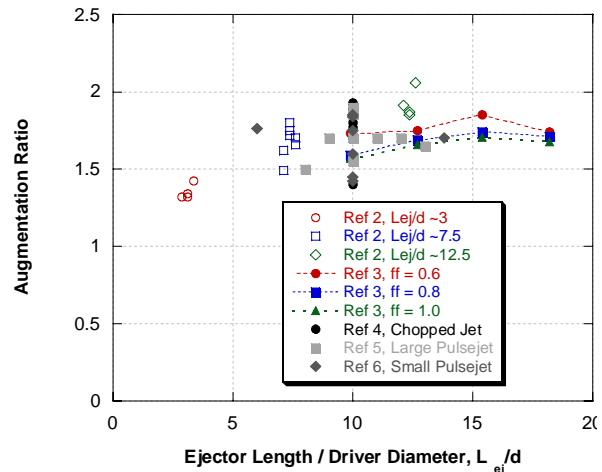


Figure 2. Ejector thrust augmentation ratio versus ejector length over driver diameter.

Despite disparities in driver ‘unsteadiness’ and experimental configurations, significant ejector augmentation occurs for a range of ejector parameters. For Figs. 1 and 3, the 2-D ejector ‘diameter’ for the linear ejector⁴, was calculated in two ways: by considering throat height, H_{ej} and secondly by calculating an equivalent area-based diameter, $D_{ej}^* \equiv \sqrt{\frac{4}{\pi} WH_{ej}}$. From Fig. 1, good ejector augmentation was achieved with ejector diameters 2-4

times greater than the driver diameter, with an optimum ejector/driver diameter ratio of ~ 3 . Thrust augmentation was only weakly proportional to ejector length, especially for ejector lengths greater than ~ 5 -7 times the driver diameter.

Figures 3 and 4 show the impact of ejector inlet radius upon thrust augmentation normalized by ejector and driver diameter respectively. Although an inlet radius is critical for efficient ejector thrust augmentation⁷, there appears to be no strong correlation between ejector inlet radius and ejector performance across a wide range of ejector inlet radii.

Other ejector results reported previously by AFRL, the University of Cincinnati, Penn-State University, and NASA Glenn Research Center had comparable performance with similar geometry scaling, despite significant differences in unsteady drivers and geometries.^{1, 6-10} The performance data cited above indicates that it is not unreasonable to expect 50% or more thrust augmentation with an unsteady ejector at static conditions. The impact of an off-axis driver was first examined with a round ejector. The same axisymmetric ejector was then used with multiple detonation tubes. Due to the linear configuration of the research pulsed detonation engine used, a linear array of three PDE tubes was aligned with the round ejector. A two-dimensional linear ejector was designed in order to take advantage of the four-tube, linear PDE configuration available.

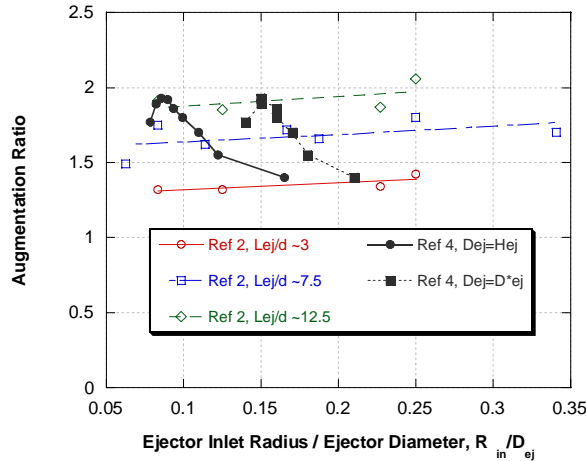


Figure 3. Effect of ejector inlet radius, normalized by ejector diameter

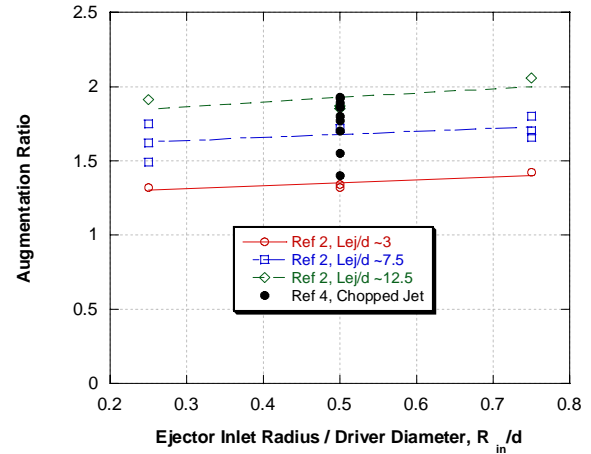


Figure 4. Effect of ejector inlet radius, normalized by driver diameter.

II. Experimental Setup

The thrust stand and research pulsed detonation engine located at the Pulsed Detonation Research Facility in the Air Force Research Laboratory was used for this study. The PDE utilizes automotive valving to feed up to four detonation tubes. The damped thrust stand was setup to measure PDE thrust alone for baseline tests or total thrust from ejector and PDE. This experimental setup has been described in detail previously¹¹. Unless otherwise noted, experiments were performed with stoichiometric hydrogen air, 10 Hz per detonation tube, 3.5" diameter detonation tubes, purge fraction of 0.5, 75" detonation tube length, with a 28" Schelkin-like spiral to promote deflagration-to-detonation transition. Detonation was found to occur for all test conditions. Static test conditions were used with the ejectors and ambient conditions were near STP (the lab is at ~800' altitude). Three ejector configurations were examined.

A. Off-Axis Ejector

Conventional single driver ejectors can run driver and ejector co-axially. In order to run multiple driver tubes into a single ejector, it is likely that some tubes will be off axis. In order to separate the effects of multi-tube effects from off-axis effects, a single detonation tube was mounted and a test series conducted while moving the ejector axially with co-axial alignment, and then moving the ejector off-axis (horizontally) at the optimum axial location. Axial displacement from the end of the detonation tube is noted in the following results as the x-axis and off-axis displacement is denoted as the y-axis, see Fig 5. The volume of the detonation tube was 744 in³ and the length 75" The ejector hardware available was a straight walled ejector with a rounded inlet. A tapered diffusion section was not available but was found previously to nearly double ejector augmentation³. The ejector to detonation tube diameter ratio, D_{ej}/d was 3.66, and x/d varied from 0 to 5. The ejector L_{ej}/D_{ej} was 5.7 and the inlet radius to ejector diameter was 0.66. The PDE operated at 10 Hz with an ignition delay of 0 ms, stoichiometric equivalence ratio, and a purge fraction of 0.5. The effect of fill fraction was determined at 0.5, 0.75, and 1.

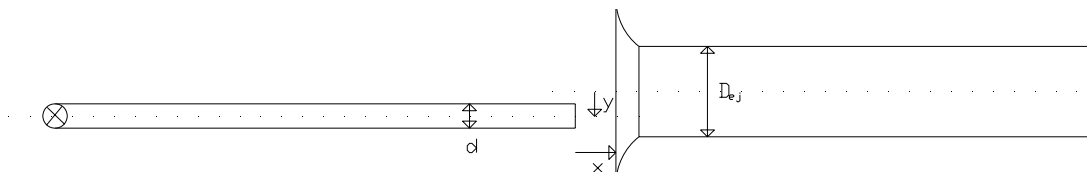


Figure 5. Schematic of PDE and ejector configuration, top view.

B. Round Ejector

In this experiment, three detonation tubes were directed into the inlet of a single, round, 13" diameter ejector, the same as used in the "Off-axis" study. The detonation tubes were 72" long with a volume of 651 in³, see Fig. 6. The diameter ratio of ejector to these detonation tubes was 3.86. The centerline spacing between the 3.5" diameter detonation tubes was 4", therefore tubes 1 and 3 were 4" or y/d of 1.14 off axis. The conditions were identical to those of the off-axis ejector experiment with each tube firing at a frequency of 10 Hz, ignition delay of 0 ms and an equivalence ratio of one. The purge fraction was 0.5 and the fill fraction was 0.75 or 1.0. The valves in this engine were operated by a cam shaft and therefore the relative timing between tube firing was fixed by the rotational speed of the cam shaft. This was a four tube engine and the firing order was 1, 3, 4, 2 (effectively: 2, 1, 3, with 4 skipped for this configuration). At 10 Hz, there was 25 ms between each tube firing. Since tube four was not used, there were 50 ms between the initiation of a detonation in tube 3 and that in tube 2.

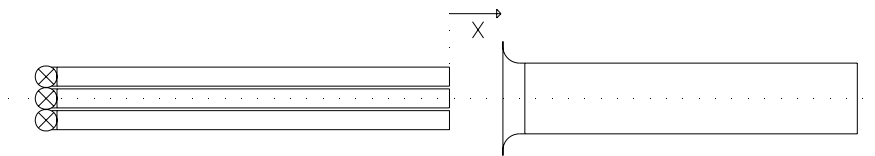


Figure 6. Schematic of multi-detonation tube single round ejector configuration

C. Linear Ejector

Although a round ejector has certain advantages, a linear arrangement of detonation tubes may be more desirable in application. In this experiment, four detonation tubes were directed into the inlet of a linear ejector. The ejector mouth was 22" wide and 7" high. The radius of the inlet lip was 1" giving an inlet radius to ejector height ratio of 0.133. The ejector was tapered by a half angle of four degrees from inlet to exit. The centerline spacing between the detonation tubes was 4" and two different sets of detonation tubes were used. The first set was identical to those used in the round ejector experiment, with the exception of the addition of a fourth tube. The second set of four detonation tubes was 2" in diameter and 72" long with a single-tube volume of 250 in³. The dimensionless ratios of ejector height to driver diameter tested were 2.1 and 3.8, and Lej/d was 6.3 and 11 for the 3.5" and 2" tubes respectively. A schematic of the ejector with the 3.5" detonation tubes is shown in Fig 7.

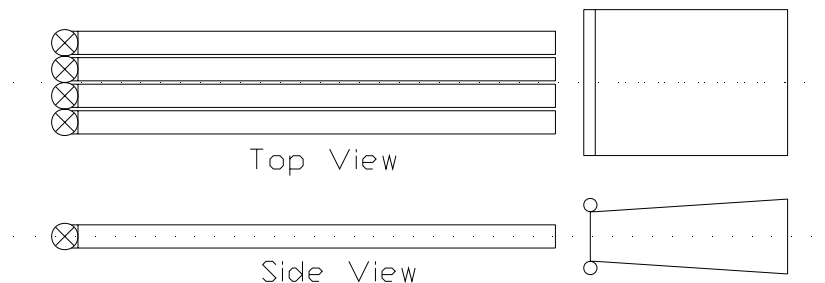


Figure 7. Schematic of PDE-linear ejector configuration with 3.5" detonation tubes.

III. Results and Discussion

Three different ejector-driver configurations were tested. The thrust measured with each ejector/driver combination was normalized by the thrust of the driver alone. An augmentation of one is no augmentation. Only at augmentations above one is the ejector providing a benefit.

A. Off-Axis Ejector Results

A picture of the single detonation tube and ejector used during the off-axis experiments is shown in Fig 8. With the ejector co-axial to the detonation tube, the augmentation was found to increase with decreasing fill fraction. A maximum augmentation appears to exist at positive x/d of about 4 or 5 depending on the fill fraction, see Fig 9a. At a fill fraction of 1.0 the augmentation was fairly constant at 50%. For a similar straight ejector with a smaller inlet radius, the augmentation was found to be approximately 30% by other authors³. The effect of horizontal-axial misalignment was tested by moving the ejector 0.5 and 1 diameter from centered on the detonation tube while maintaining the parallelism of the axis of the detonation tube and ejector at x/d of 2. Little if any difference in the augmentation was measured as the tube was moved relative to the ejector, see Fig 9b. The implication of this insensitivity to location is that multiple detonation tubes and a single ejector system may be effective.



Figure 8 Ejector and 3.5" detonation tube, as installed

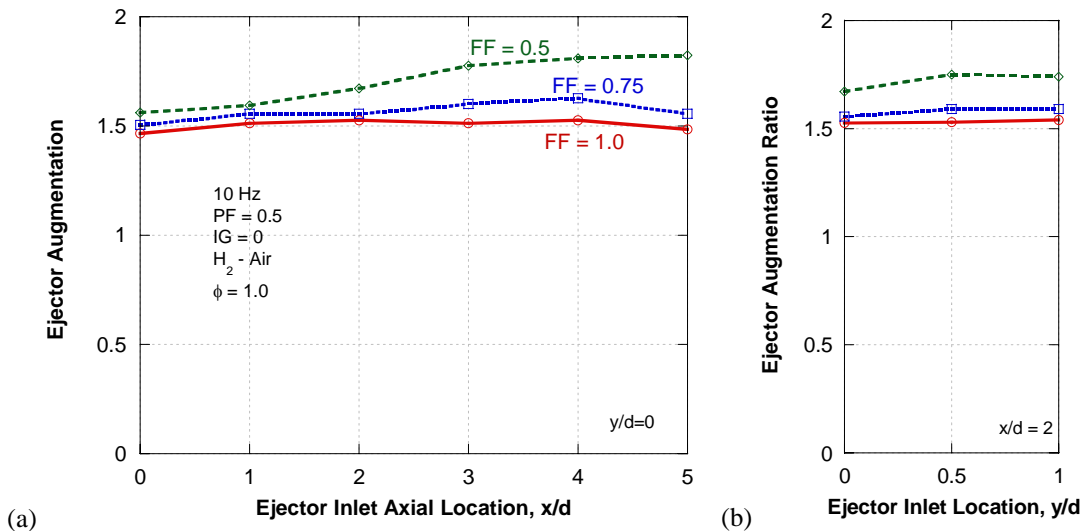


Figure 9. (a) Ejector augmentation versus axial location (normalized by driver diameter) and (b) horizontal misalignment (normalized by driver diameter) at an axial location of $x/d = 2$.

B. Round Ejector Results

The results of three detonation tubes directed into a single ejector are shown in Fig 10 and 11 for a fill fraction of 1.0 and 0.75 respectively. For a fill fraction of 1.0, single and double detonation tube firings resulted in an augmentation ratio of approximately 1.4 over most of the axial range tested. A negative interaction between the detonation tubes and the ejector was measured with all three tubes firing, as the augmentation decreased to approximately 1.3 for a fill fraction of 1.

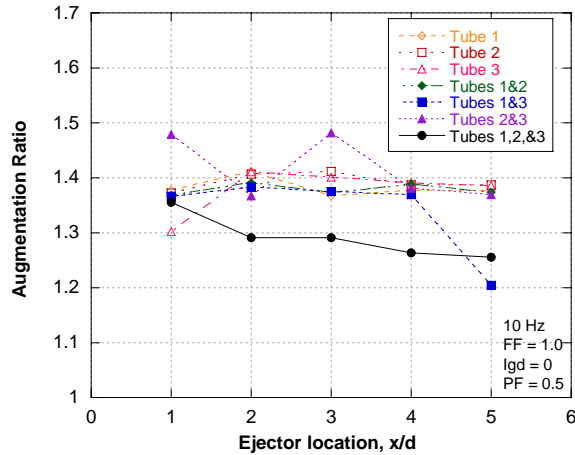


Figure 10. Ejector augmentation ratio versus axial location (normalized by driver diameter) for 1.0 fill fraction.

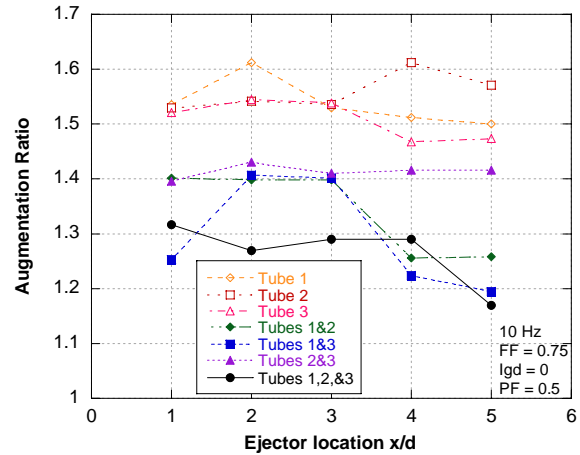


Figure 11. Ejector augmentation ratio versus axial location (normalized by driver diameter) for 0.75 fill fraction.

At a fill fraction of 0.75 this negative interaction was also observed as the augmentation ratio was again approximately 1.3. A single detonation tube, even at y/d of 1.14 produced an augmentation of over 1.5 for x/d less than 4. At x/d greater than 3, the co-axial detonation tube's (tube 2's) performance is greater than those located off axis, presumably because the vortex exhausted from the detonation tube expanded to a diameter greater than the ejector inlet at large x/d . With two detonation tubes firing, the augmentation ratio was adversely impacted as the augmentation ratio drops from over 1.5 for a single tube to around 1.4. Comparing the three combinations of two-tubes firing, it is again obvious that the expanding vortex makes the 1-3 tube combination the worst at large x/d . The tube-firing combination of 1-2 and 2-3 are spatially identical, however, because of the firing order of the PDE, (2,1,3,4), there is 50 ms between the ignition of tube 2 and tube 3 and only 25 ms between tube 2 and tube 1. Since there appears to be a negative interaction as more detonation tubes are added, the augmentation of the combination 2-3 should be greater than that of 1-2 because the temporal separation is greater. Experimentally, the performance between the 2-3 and 1-2 firing combinations is similar below x/d of 4 but for x/d of 4 and 5 there is a significant departure in augmentation.

C. Linear Ejector Results

Three detonation tubes firing into a single round ejector produced reduced augmentation over a single tube-ejector combination. With the linear ejector, four detonation tubes were directed at a single ejector as shown in Fig. 12. With the exception of low fill fraction (where $x/d \sim 3$ was optimum), as noted earlier, an optimum axial location of ~ 2 x/d was evident in the linear ejector performance. The augmentation of the linear ejector with four driver detonation tubes was lower than expected, being 1.14 at a fill fraction of 1 and x/d of 2, see Fig. 13. In comparison, at an x/d of 2 the round ejector with three detonation tubes achieved an augmentation of 1.3.



Figure 12. Picture of linear, 2-D ejector installed with four 3.5" diameter tubes.

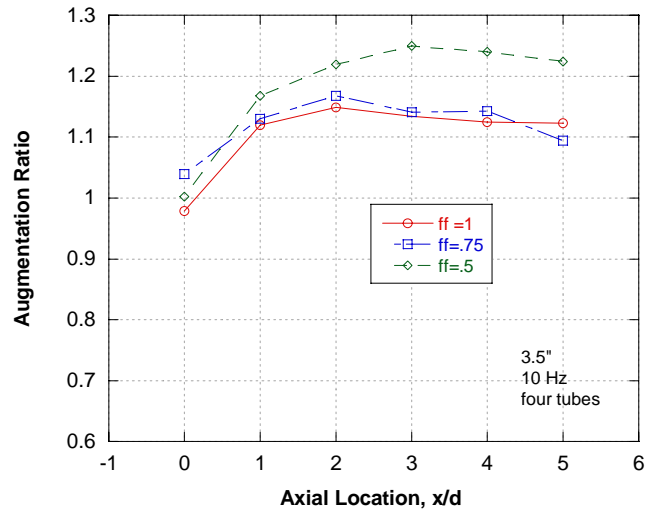


Figure 13. Linear ejector performance with varying axial location at 10Hz, $D_{ej}/d = 2.1$.

Several parameters were varied in an attempt to resolve the lack of performance, including: edge effects, driving frequency, and increasing D_{ej}/d . Also, it was anticipated that the structural ribs might impact entrainment, so large holes were cut in them, as evident in Fig 14.



Figure 14. Detail of modified ejector ribs, note large areas removed with plasma cutter .

Tubes 1 and 4 are on the ends of the linear ejector, and tubes 2 and 3 are in the middle. In Fig. 15, the effect of the edge of the ejector can be discerned based on the difference between the augmentation produced by the inboard tubes, 2 and 3 versus the tubes on the edges, 1 and 4. In the round tube investigation, it was determined that tube-to-tube interactions mitigated the performance of the ejector during multi-tube operation. With a single tube, the augmentation could be 1.4 or better. Of particular concern is the performance of the linear ejector with a single detonation tube, topping out at 1.15 for an inboard tube and unity for an outboard tube at a fill fraction of 1. There appears to be a positive interaction between the four detonation tubes and the ejector as the four tube augmentation is greater than the single or double tube augmentations. The linear ejector does follow the trend shown in Fig 1, that the ejector to driver diameter, D_{ej}/d , of 3.5 outperforms D_{ej}/d of 2.

The chopped jet which showed promising linear ejector performance previously was cycling at significantly higher frequencies⁴, so the frequency was increased to see if driver frequency had an impact upon ejector performance. In Fig 16, the driver frequency was doubled to 20 Hz. The augmentation generally decreased from that achieved at 10 Hz. Removing much of the material in the ribs of the ejector had no significant effect on the ejector augmentation.

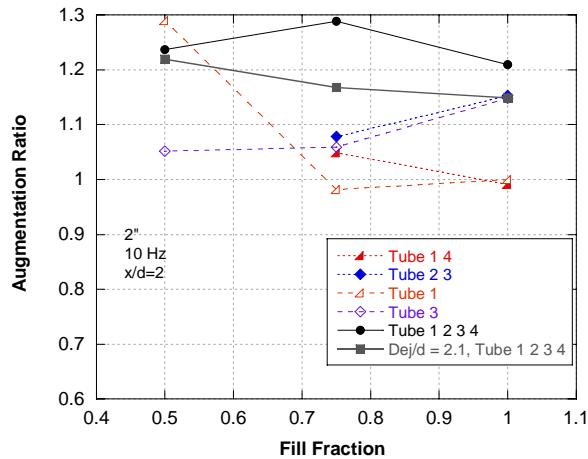


Figure 15. Linear ejector performance with varying fill fraction at 10Hz with axial location $x/d = 2$, $D_{ej}/d = 3.8$ unless noted.

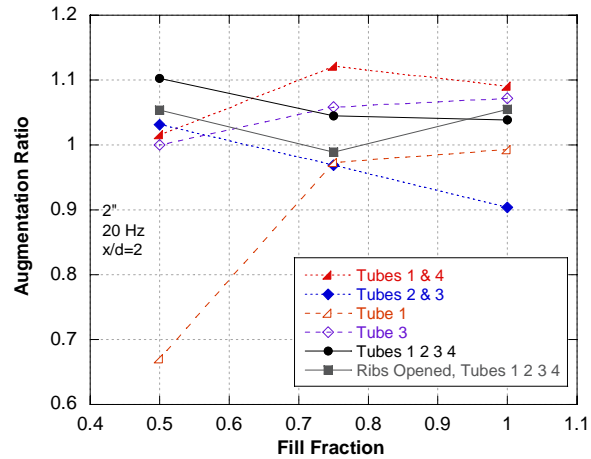


Figure 16. Linear ejector performance with varying fill fraction at 20Hz with axial location $x/d = 2$, $D_{ej}/d = 3.8$.

IV. Summary and Conclusions

The insensitivity to co-axial alignment of an ejector-driver system found in this work, implies that there is the potential to direct multiple drivers into a single ejector and maintain single-driver-ejector augmentation levels. The multi-tube single ejectors tested, however displayed a negative interaction during multi-tube operation, reducing the ejector thrust augmentation levels versus previously obtained conventional unsteady ejector results. For engine designers there is now a trade-off between multiple ejectors and the associated weight and bulk versus a single ejector with reduced performance. Further work is required to determine the interaction mechanism that mitigates the augmentation of a single ejector, multi-tube system.

Acknowledgments

The authors gratefully acknowledge the contributions of Curt Rice, Royce Bradley, Adam Brown, Dave Baker and Jeff Stutrud for their help in enabling this research. For their leadership and guidance, we also thank Dr Robert Hancock and Dr Mel Roquemore.

References

1. Landry, K., Shehadeh, R., Bouvet, S., Lee, S., Pal, S., and Santoro, R. "Effect of Operating Frequency on PDE Driven Ejector Thrust Performance". AIAA-2005-3832. in *41st AIAA/ASME/SAE/ASEE Joint Propulsion Conference and Exhibit*. Tucson, AZ: 2005.
2. Wilson, J., Sgondea, A., Paxson, D.E., and Rosenthal, B.N. "Parametric Investigation of Thrust Augmentation by Ejectors on a Pulsed Detonation Tube". AIAA-2005-4208. in *41st Joint Propulsion Conference*. Tucson, AZ: 2005.
3. Glaser, A., Caldwell, N., Gutmark, E., Hoke, J., and Schauer, F. "Performance Measurements of Straight and Diverging Ejectors Integrated with a Pulse Detonation Engine". AIAA-2006-1022. in *44th AIAA Aerospace Sciences Meeting and Exhibit*. Reno, NV: 2006.
4. Choutapalli, I.M., Alkislar, M.B., Krothapalli, A., and Lourenco, L.M. "An Experimental Study of Pulsed Jet Ejector". AIAA-2005-1208. in *43rd AIAA Aerospace Sciences Meeting and Exhibit*. Reno, NV: 2005.
5. Paxson, D.E., Litke, P.J., Schauer, F.R., Bradley, R.P., and Hoke, J.L. "Performance Assessment of a Large Scale Pulsejet-Driven Ejector System". AIAA-2006-1021. in *44th AIAA Aerospace Sciences Meeting and Exhibit*. 2006.
6. Paxson, D.E., Wilson, J., and Dougherty, K.T. "Unsteady Ejector Performance an Experimental Investigation Using a Pulsejet Driver". AIAA-2002-3915. in *38th AIAA/ASME/SAE/ASEE Joint Propulsion Conference & Exhibit*. Indianapolis, IN: 2002.

7. Shehadeh, R., Saretto, S., Lee, S.-Y., Pal, S., and Santoro, R.J. "Experimental Study of a Pulse Detonation Engine Driven Ejector". AIAA-2003-4972. in *39th AIAA/ASME/SAE/ASEE Joint Propulsion Conference and Exhibit*. Huntsville, AL: 2003.
8. Shehadeh, R., Saretto, S., Lee, S.-Y., and Santoro, R.J. "Thrust Augmentation Measurements for a Pulse Detonation Engine Driven Ejector". AIAA--2004-3398. in *40th AIAA/ASME/SAE/ASEE Joint Propulsion Conference and Exhibit*. Fort Lauderdale, FL: 2004.
9. Allgood, D., Gutmark, E., Hoke, J., Bradley, R., and Schauer, F. "Performance Measurements of Pulse Detonation Engine Ejectors". AIAA-2004-3398. in *40th AIAA/ASME/SAE/ASEE Joint Propulsion Conference*. Fort Lauderdale, FL: 2004.
10. Wilson, J. and Paxson, D.E. "Unsteady Ejector Performance: An Experimental Investigation Using a Resonance Tube Driver". AIAA-2002-3632. in *38th AIAA/ASME/SAE/ASEE Joint Propulsion Conference and Exhibit*. Indianapolis, IN: 2002.
11. Schauer, F., Stutrud, J., and Bradley, R. "Detonation Initiation Studies and Performance Results for Pulsed Detonation Engine Applications". AIAA-2001-1129. in *39th AIAA Aerospace Sciences Meeting and Exhibit*. Reno, NV: 2001.

Investigation of Fundamental Processes Leading to Pulse Detonation Engine / Ejector Thrust Augmentation

Nicholas Caldwell¹ and Dr. Ephraim Gutmark²
University of Cincinnati, Cincinnati, Ohio, 45221

John Hoke³ and Royce Bradley⁴
Innovative Scientific Solutions Inc., Dayton, Ohio, 45440

and
Fred Schauer⁵
Air Force Research Laboratory, WPAFB, Dayton, Ohio, 45433

This paper presents a series of shadowgraph flow visualizations in an effort to increase the understanding of the fundamental flow characteristics occurring inside an ejector driven by a pulse detonation engine (PDE). In an effort to supplement theories that have been developed through indirect thrust and static pressure measurements, these internal flow visualizations provide a uniquely direct insight into the fluid dynamics caused by the passage of the detached leading shock separated from the detonation wave and the subsequent blowdown cycle. Using a two-dimensional ejector model, flow visualizations are made of various ejector-PDE separation distances and ejector divergence angles. Additionally, the flow exhausting from the rear of an axisymmetric ejector is captured. To conclude, a new 2D ejector model design is presented which is being developed in order to visualize this type of flow while accessing more geometric parameters of interest. Furthermore, this new design allows for the measurement of dynamic and static pressure along the length of the internal surface of the ejector, and can simulate forward flight effects up to Mach 0.3.

Nomenclature

α	=	thrust augmentation, %
β	=	ejector divergence angle, deg
D_{EJECT}	=	ejector diameter, in
D_{PDE}	=	PDE tube diameter, in
PDE	=	pulse detonation engine
t	=	elapsed time since detonation wave passes PDE exit plane, msec
ff	=	fill fraction
x	=	distance between ejector inlet and PDE exit plane, in

I. Introduction

FOR practical pulse detonation engine (PDE) applications, one of the key challenges for researchers is to make use of the increased efficiency of energy conversion due to detonative-mode combustion by converting it most effectively into a propulsive thrust force. A common measure of propulsion system performance is specific impulse (I_{sp}), which is defined as the ratio of thrust generated to the weight flow rate of fuel. Higher values of I_{sp} are

¹ Graduate Research Assistant, Department of Aerospace Engineering, ML0070, Student Member AIAA.

² Professor and Ohio Eminent Scholar, Department of Aerospace Engineering, ML0070, Associate Fellow AIAA.

³ Research Engineer, 2766 Indian Ripple Road, Senior Member AIAA.

⁴ Senior Scientist, 2766 Indian Ripple Road.

⁵ Senior Engineer, Head PDRF, AFRL/PRTC, Bldg. 490, Senior Member AIAA.

desirable because of the attendant decrease in specific fuel consumption. It has been suggested that the use of ejector augmenters on PDEs may be an effective way to increase the system thrust and thus I_{sp} .

An ejector is a simple device used to augment the thrust of an engine. Essentially, an ejector is a coaxial duct placed around the exhaust of an engine that performs as a fluidic pump. The surrounding ambient air is entrained by the primary exhaust flow and directed into the ejector. The entrained air causes an increase in the momentum of the engine exhaust flow, which leads to the generation of a larger system thrust force. The theory and application of ejectors to a steady primary flow are well established. For steady-flow ejectors, the secondary flow is entrained primarily through viscous shear mixing¹. Previous research has shown that unsteady ejectors are capable of producing more thrust augmentation than steady-flow ejectors^{2,3,4}. The increased performance of unsteady ejectors has been attributed to a more efficient energy-transfer process between the primary and secondary flows that results from the dominant effects of the starting vortex. Since PDEs are highly unsteady devices that generate a shock wave and vortex ring, it has been suggested that PDE-driven ejectors may have the potential to be highly effective at providing thrust augmentation.

Experimental work confirmed that PDE-driven ejectors are extremely effective in producing thrust augmentation. Studies have quantified the effects of PDE operating parameters as well as ejector geometric parameters. The internal surface geometry of the ejector is an important geometric parameter. A study by Glaser et al⁵. was carried out using several ejector configurations. The results showed maximum thrust augmentation levels of $\sim \alpha=30\%$ for straight ejectors and $\alpha=66.5\%$ for an optimized diverging ejector geometry at $ff=1.0$. Although it is apparent that the diverging ejectors were much more effective at producing thrust augmentation than the straight ones, the mechanism responsible for this performance increase is not clear. The increased augmentation from diverging ejectors has commonly been attributed to the additional thrust surface area of the diverging section. Inherent in that explanation is the assumption of a positive net pressure on the diverging section, which causes a thrust force. It has been observed that ejector performance is sensitive to the axial position of the ejector inlet relative to the PDE tube exit. In most cases, downstream ejector placement provides optimum levels of thrust augmentation^{5,6,7,8}. For the straight and diverging ejector configurations previously tested by Glaser et al⁵, the optimum axial position was found to be downstream at $x/D_{PDE}=+2$.

The current effort seeks to increase the overall understanding of PDE-driven ejector systems. High-speed shadowgraph flow visualizations were obtained for the internal portion of a diverging ejector to provide a better explanation of previously determined performance trends. Results from this study will provide insight into the governing flow dynamics and mechanisms responsible for thrust augmentation in PDE-driven ejector systems.

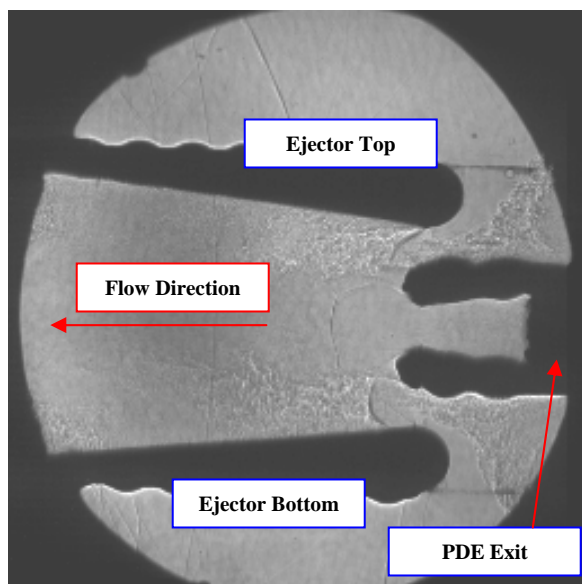


Figure 1. Ejector Shadowgraph Experimental Setup

II. Experimental Setup

This parametric visualization study of the flow field inside an ejector resulting from a propagating detonation wave was performed using the PDE test facility at the University of Cincinnati. The PDE tube had a total nominal length of 40". It consisted of two sections: the first section was a 25" long, 1" diameter pipe that contained a 0.625" diameter orifice plates to enhance the deflagration-to-detonation transition (DDT) process. This section was followed by a 15" long, 2x2 square-cross-section tube (3-mm wall thickness). The square section was mounted at the end of the round tube to convert the flow into a two-dimensional rectangular section. The ejector walls were constructed of 1" thick optical-grade cast acrylic sheets, allowing optical access to the internal flow as shown in Figure 1. The top and bottom walls of the ejector were interchanged to study various geometries. The ejector was 7.85" long for all tests, and the walls were spaced 1.75" apart to give an ejector-to-PDE area ratio of 3.0. Oxygen diluted with nitrogen was

used as the oxidizer, and these gases were mixed upstream prior to injection into the detonation tube. Ethylene fuel was pulsed via an electromagnetic valve to obtain nominally stoichiometric conditions. Fuel and oxidizer were mixed directly in the tube by impinging jets, and were ignited by a spark plug mounted 2.5 diameters downstream of

the detonation tube headwall. In order to preserve the acrylic sidewalls, the tube was fired at 20 Hz for only three detonations for each case. For all cases presented here, the equivalence ratio was maintained as stoichiometric, though the fill fraction was varied.

III. Shadowgraph Flow Visualizations

Using the 2D ejector model described above, a series of shadowgraph flow visualizations were made varying the geometric parameters allowed by the facility and the PDE operating parameters. While the images were captured with a high-speed camera at an extremely high frame rate, it is only possible to relay those that are most interesting and those which give a feel for the trends that have been observed through more indirect experimental measurements. It must be noted that while the obstruction presented by the ejector body takes on a solid black color in the shadowgraph images, the seemingly non-uniform shape of the ejector surfaces is caused by the head of the bolts that hold the ejector in place on the outside of the Plexiglas. Hence, the actual surfaces of the ejector are relatively smooth, as is the end of the detonation tube. Furthermore, due to imperfections in the Plexiglas, some regions of darkness will appear in the images and will remain stationary for the duration of the fluid flow phenomena. It must be kept in mind that these are not a result of these flow phenomena.

A. Fill Fraction

The first parameter that was investigated for flow through the interior of a diverging ejector was the fill fraction of the detonation tube. Fill fraction is defined as the ratio of the volume of the tube filled with a combustible mixture to the overall volume of the tube. For a constant area detonation tube, this simply translates into the length of tube that is filled with reactants divided by the length of the tube. Due to the extreme brightness that is generated by strong detonation waves, the images presented in this section are limited to fill fractions below 0.8.

Referring to Figure 2, the variation in the shock pattern inside the ejector varied significantly with fill fraction. Since lower fill fraction cases result in weaker detonation waves exiting the PDE, the speed of the propagating leading shock will likewise be lower. However, for each case it can be seen that the portion of the leading shock which does not reflect from the interior walls of the ejector develops into a normal shock before it reaches the exit of

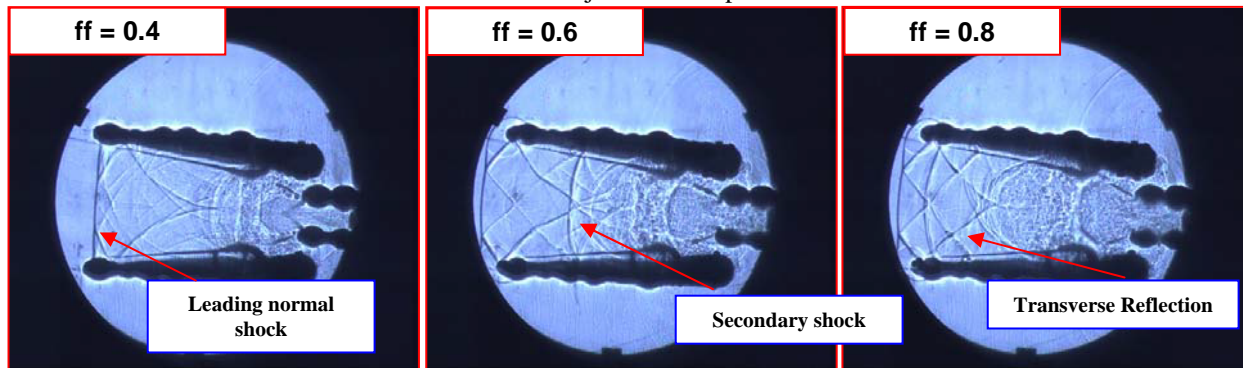


Figure 2. Comparison of Shock Pattern Formed in Ejector Interior for Various PDE Fill Fractions, $\beta = 4^\circ$, $x/D_{PDE} = -1$

the ejector. Another common trait between the three cases is that two rounded shock reflections extend nearly the entire length of the ejector and are symmetric about the ejector centerline. This flow characteristic results from the transverse portions of the leading shock wave that impinge on the walls of the ejector. Because of the time lag associated with the most axial portion of the leading shock hitting the ejector surface, the reflection of this shock near the inlet begins much sooner, and the resulting rounded shape occurs. It is also interesting to note the diamond shock patterns that form between the leading shock and the transverse reflections. For the low fill fraction case, the interior angle made by the shocks comprising these diamonds is much more obtuse than those corresponding to higher fill fraction cases. Additionally, the strength of these diamond patterns shows itself to be proportional to the fill fraction, presenting much steeper density gradients. It is interesting to note the resemblance between the diamond shock patterns formed in the ejector interior and the cellular pattern that characterizes detonation combustion. Although no combustion is occurring inside the ejector, the formation of these shock cells follows the same basic trend as detonation cells, created by the coalescence of transverse and axially propagating shock waves.

The final phenomenon of note from this basic study is the secondary shock that propagates through the ejector, much more notable in the cases corresponding to fill fractions of 0.6 and 0.8. Because of the higher fill fraction associated with the last case, it can be seen that this secondary shock has traversed a greater portion of the ejector length at the time step shown in the image. This secondary shock appears to serve an interesting purpose in the exhaust of the ejector, as will be shown later.

B. Ejector Diverging Angle

While no significant difference were noted in the leading shock pattern formed for various diverging angles, the blowdown cycles confirmed some interesting trends. It is expected that increasing the divergence angle would result in larger separation potential, but previous results have suggested that even for small divergences there is a degree of separation that forms off of the inlet. This is due to the large turning angle that the entrainment air encounters upon entering the system. Shadowgraph images confirm that even for shallow divergence angles separation does occur off of the inlet regardless of the contouring. In order to alleviate this separation, it may be that a more complex inlet design that extends deeper into the ejector is required. As can be seen in Figure 3, the larger divergence angle results in a significantly more pronounced separation region compared to the 4° ejector.

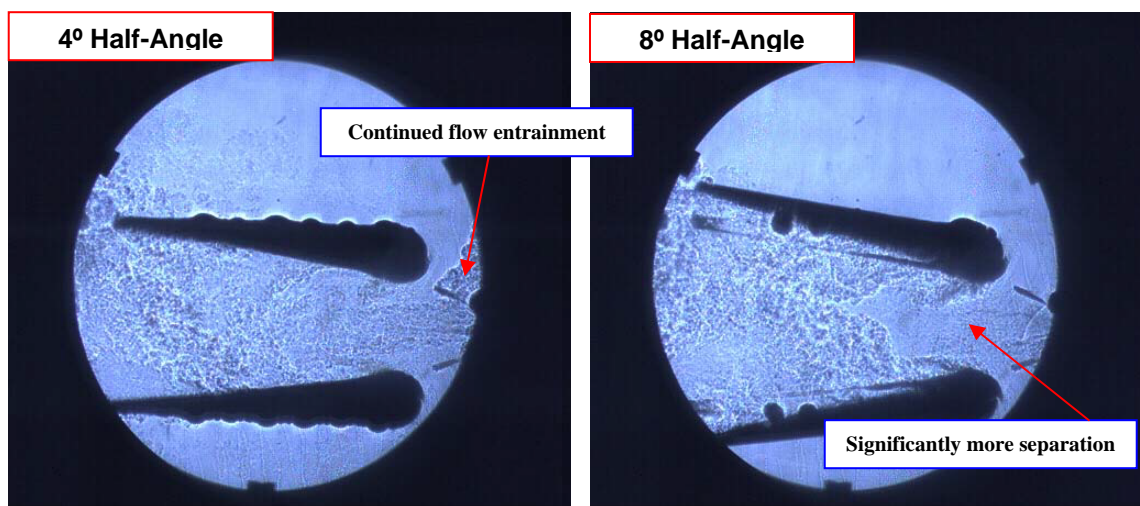


Figure 3. Comparison between Various Diverging Angles, Left – $\beta = 4^\circ$, Right – $\beta = 8^\circ$, $x/D_{PDE} = +1$, $ff = 0.80$, $t \approx 12.5$ msec

Because of the increased separation occurring in the larger divergence angle ejector, the ejector develops a back pressure that then hinders the entrainment of secondary air. This is shown by the visibly more significant flow entrainment occurring in the 4° divergence angle ejector as compared to its 8° counterpart. Again, while this is not surprising, this study highlights the fact that the divergence angle appears to be much steeper to the entrainment air that is entering the system than it does to the primary jet exhausting from the detonation tube. As a result the subsonic entrainment air will separate at nozzle half-angles which do not typically result in separation.

C. Ejector Axial Position

While there has been some dispute in the past over optimal ejector axial placement relative to the PDE exit plane, shadowgraph images further suggest support for the ejector producing the largest thrust augmentation at downstream placements in which the ejector does not overlap the detonation tube. Figure 4 shows one of the main differences resulting between the developments of the leading shock propagations. Since the downstream case allows for the escape of much of the transverse portion of the shock, a much less complex shock pattern exists inside the ejector. The diamond shock pattern resulting from the coalescence of the transverse and axially propagating shocks is not present to the degree that it is when the full extent of the detonation wave is forced into the ejector. When the ejector is placed slightly downstream of the PDE exit, a portion of the transverse shock escapes the ejector, suggesting that the structural loading on the ejector is much less severe.

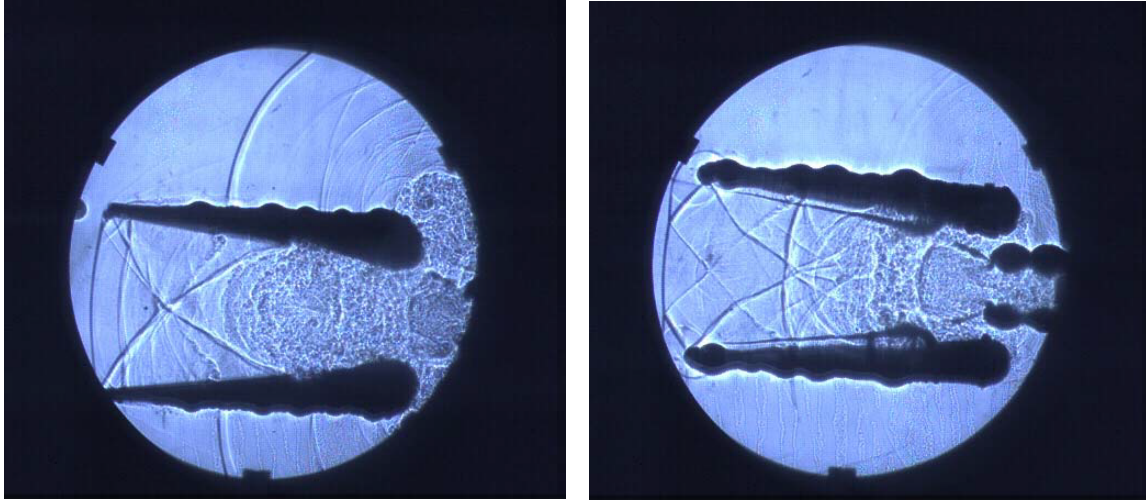


Figure 4. Comparison between Downstream (Left – $x/D_{PDE} = +1$) and Upstream (Right – $x/D_{PDE} = -1$) Ejector Placement, $\alpha = 4^\circ$, $ff = 0.80$, $t \approx 36 \mu\text{sec}$

One of the most important flow feature differences associated with changing the ejector axial position is the degree of secondary air entrainment that can occur. However, this does not take precedent until much later in the detonation cycle, during the blowdown process. Looking at Figure 5, it can be seen that during the blowdown phase, the downstream-placed ejector maintains a significant degree of secondary air entrainment much longer than the upstream ejector. At $t \approx 12.5 \text{ msec}$, entrainment can be seen to have stagnated in the upstream case. The advantage in the downstream ejector arises in the availability to the primary jet of a secondary air source. When the primary jet is overlapped by the ejector, the area through which secondary air may enter is greatly reduced, and the distance across which the viscous shearing forces must act is much greater. An additional flow feature that was noted is the supplementary flow entrainment that results from the overexpansion of the detonation tube. Not only is secondary air entrained as a result of the viscous shearing of the primary jet, but when the overexpansion occurs and the primary jet dies down secondary air continues to move into the PDE-ejector system due to the negative pressure inside the detonation tube. Once the tube begins to relax back to ambient pressure, this captured air is then pumped through the ejector and does not return into the ambient surroundings.

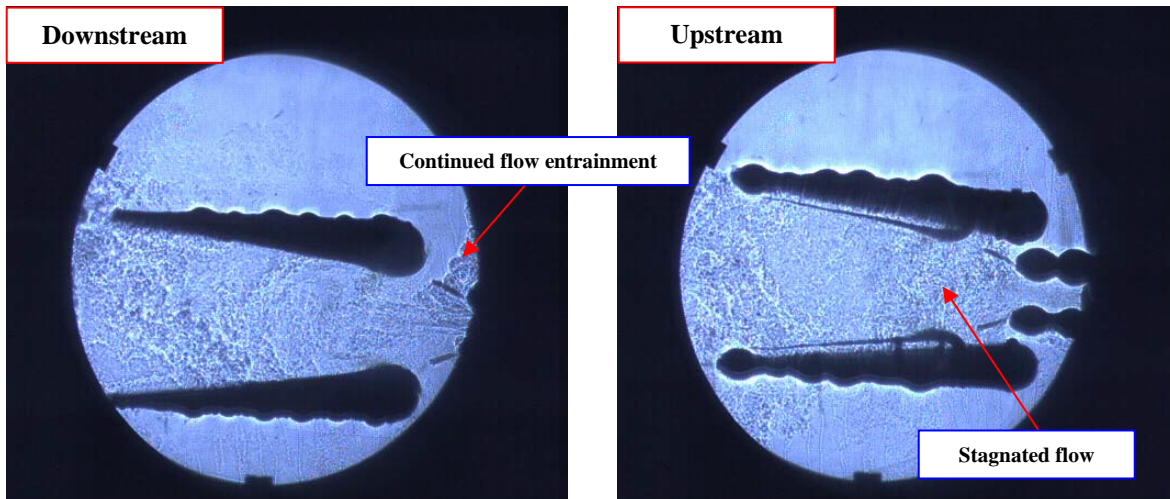


Figure 5. Comparison between Downstream (Left – $x/D_{PDE} = +1$) and Upstream (Right – $x/D_{PDE} = -1$) Ejector Placement, $\beta = 4^\circ$, $ff = 0.80$, $t \approx 12.5 \text{ msec}$

D. Ejector Exhaust Flow

A slightly different experimental setup was required to examine the flow exhausting from the rear of an ejector. Due to limitations of the current 2D ejector model, an axisymmetric ejector was used in conjunction with 6" parabolic mirrors to monitor the emanating flow. Referring to the time progression shown in Figure 6, it can be seen in the first image that the detached leading shock has just begun to emerge from the rear of the ejector. The diffraction of this shock into the open atmosphere results in a vortex ring trailing off of the ejector tail which begins

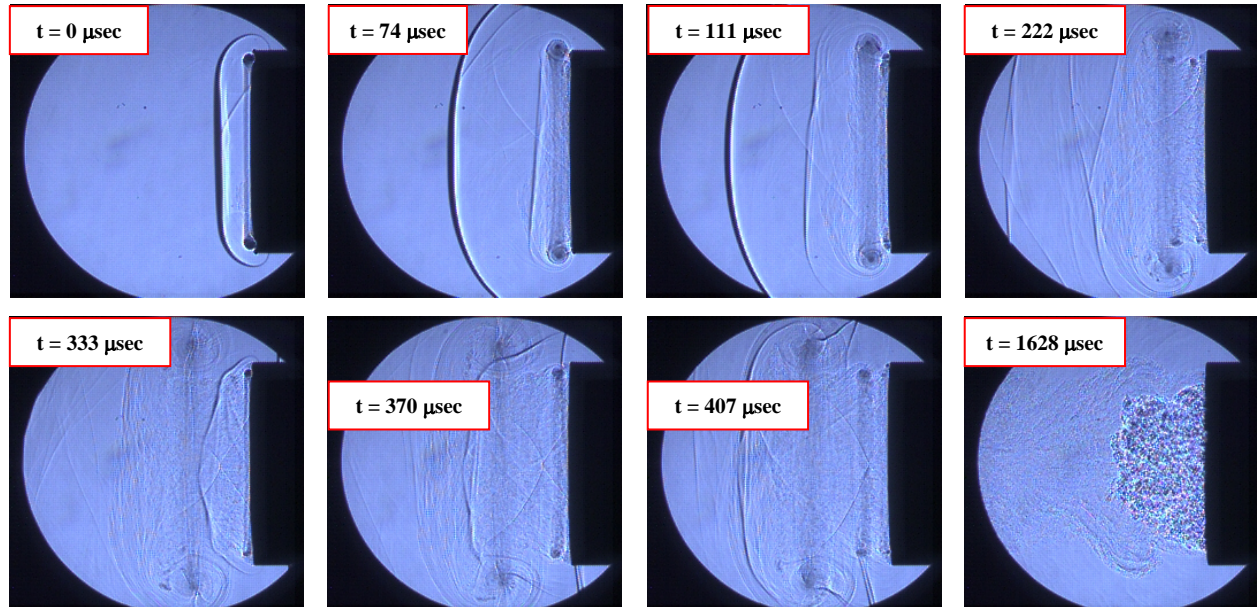


Figure 6. Time Progression of Ejector Exhaust Flow

slowly to propagate downstream. At $t = 222 \mu\text{sec}$, two smaller vortex rings can be seen trailing off the ejector exit while the primary vortex ring has begun to expand in size. These smaller vortex structures then appear to be captured by the primary vortex ring while a non-uniform shock begins to exhaust from the ejector. At $t = 407 \mu\text{sec}$, this shock catches up to the primary vortex ring and its transverse segments pass into the vortex ring. These portions of this shock are then seen to wrap into the vortex ring, while its axial segments have now taken on a more uniform normal shape. It has been found through previous research that noise escaping from an ejector driven by a PDE is reduced greatly in the sideline angles⁶. Though a significant contribution to this effect is undoubtedly the shielding presented by the ejector walls themselves, it is also likely that transverse shock noise is also reduced by the capturing of this shock by the primary vortex ring. The final image shows that it is much later before the combustion gases begin to emerge from the rear of the ejector.

IV. Development of New 2D Ejector Flow Visualization Model

In order to perform a more comprehensive flow visualization study of ejector fluid dynamics, a new facility has been designed with increased geometric variable adjustment and data acquisition capabilities. Furthermore, the facility will allow for the examination of more details of ejector performance that have not yet been experimentally studied. A diagram of the design is shown in Figure 7. While a similar Plexiglas design is employed, a more modular ejector model allow for the simple modification of the geometric and flow parameters. One of the most significant

features of this design is the inclusion of static and dynamic pressure ports along the length of the ejector. Separated by 1" these ports will allow for phase-locked flow visualization and static and dynamic pressure measurements on the internal surface of the ejector.

Referring to the figure, part (1) corresponds to an enclosed area which directs a high flow rate of

air parallel to both the PDE and the ejector to simulate the effect of forward flight. Previously this has only been capable of being studied numerically. While the results are expected to show performance degradation with increased flight speed due to drag on the ejector inlet, this model will provide the first experimental data in this

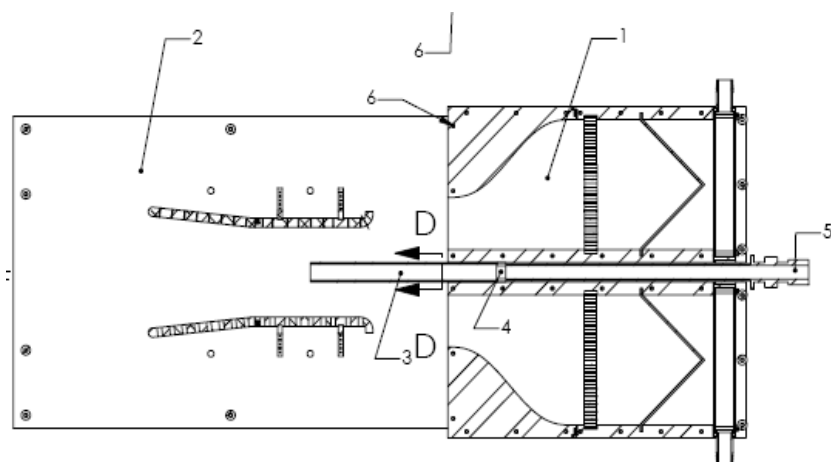


Figure 8. Section View of New 2D Ejector Flow Visualization Model

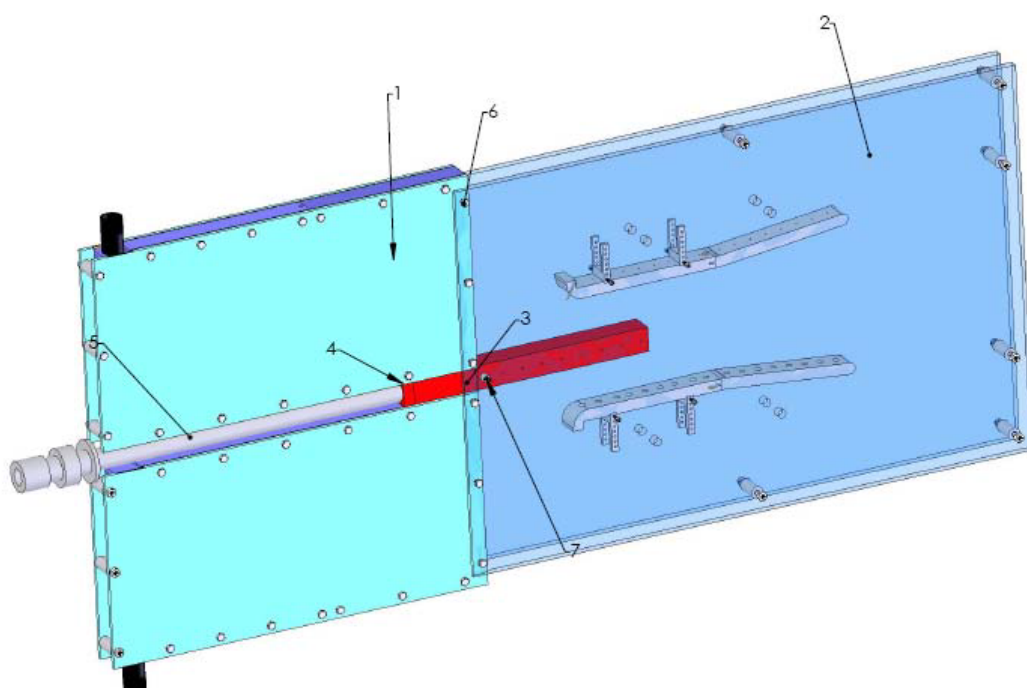


Figure 7. Diagram of New 2D Ejector Flow Visualization Model

regard. Using up to 1.6 lbm/sec of air, this system will be able to simulate forward flight at approximately Mach 0.3. This flow will enter the system perpendicular to the ejector centerline axis and enter separate manifolds on the upper and lower sides of the detonation tube. Afterwards, it will pass through a flow straightener and honeycomb for increased flow uniformity. A converging section will then increase the flow speed to attain the desired flight conditions. A cutaway section view of this part is shown in Figure 8 that may shed more light on the geometry

described above. Part (2) is the Plexiglas enclosure which supports the ejector model and maintains a two-dimensional combustion and bypass air flow. Compared to the existing model which is comprised of only an ejector inlet and diverging section, the new ejector model contains an inlet, intermediate straight section, and a diverging section. While the length of the straight section is not modifiable in this model, its length has been selected to correspond to the optimum ejector geometry found through thrust augmentation measurements. A column of closely spaced holes running perpendicular to the ejector centerline allows for the diameter of the ejector to be varied in the range $2.5 \leq D_{\text{EJECT}}/D_{\text{PDE}} \leq 5.5$ without exposing any holes to the internal detonation flow passing through the ejector. This range encompasses the optimum ejector-to-PDE diameter ratio for thrust augmentation that has been found by many research groups. Replaceable diverging section parts allow for the divergence angle to be varied in the range $0^\circ \leq \beta \leq 12^\circ$ in increments of 2° . Parts (3), (4), and (5) describe various aspects of the detonation tube itself, which is capable of being translated along the ejector centerline axis. By moving the detonation tube, the axial placement of the ejector may be varied in the range $-8 \leq x/D_{\text{PDE}} \leq 4$, where a positive placement refers to an overlapped ejector and detonation tube.

V. Conclusion

High-speed visualization of the internal flow of a PDE-driven ejector under various conditions has been performed using a much wider field of view than has been available in the past. Many flow features have been captured which support theories inferred from indirect measurements of surface pressure and thrust, including the degree of entrainment occurring for downstream ejector placement as compared to an overlapped PDE and ejector and the separation that arises off of the ejector inlet regardless of contouring. Complex shock patterns have been shown to form inside the ejector from the leading decoupled shock which bear a striking resemblance to the cellular structure characteristic of detonation waves. While secondary air entrainment through viscous shearing of the primary jet and ambient air has in the past been attributed to thrust augmentation, it was also found that the overexpansion of the detonation tube generates a significant source of flow entrainment as well by capturing secondary air from the same source. Once the overexpansion is complete, this captured air is then pumped into the ejector instead of back into the ambient surroundings. Images of the exhaust from the ejector show that the leading shock expands in the same manner as the detonation wave from the PDE. In the axial direction the expanding shock is much stronger and transverse portions are notably weaker. Furthermore, the primary vortex ring that emanates from the ejector may play a role in sideline shock noise reduction by capturing transverse portions of secondary shock waves. Finally, a design was presented for a new 2D ejector model which provides the capability of simulating an ejector in forward flight conditions as well as the ability to perform phase-locked flow visualizations and dynamic and static pressure measurements along the internal ejector surface. In addition, this model lends itself to the precise variation of an extensive range of ejector geometric parameters, including variables that are unable to be modified in the current facility.

Acknowledgments

The authors would like to acknowledge the Propulsion Directorate at the Air Force Research Laboratory and Innovative Scientific Solutions Inc. (ISSI) for providing financial support for this work. The technical support of Curtis Rice of ISSI in the previous collecting of thrust and static pressure measurements is also greatly appreciated. Furthermore, many thanks are due Russell Dimicco, the coordinator of the Gas Dynamics and Propulsion Laboratory (GDPL) at the University of Cincinnati.

References

- ¹Presz, W., Reynolds, G., and Hunter, C., "Thrust Augmentation with Mixer/Ejector Systems," *40th AIAA Aerospace Sciences Meeting and Exhibit*, AIAA 2002-0230, Reno, NV, January, 2002.
- ²Wilson, J. and Paxson, D., "Unsteady Ejector Performance: An Experimental Investigation Using a Resonance Tube Driver," *38th AIAA Joint Propulsion Conference*, AIAA 2002-3632, Indianapolis, IN, July, 2002.
- ³Paxson, D., Wilson, J., and Dougherty, K., "Unsteady Ejector Performance: An Experimental Investigation Using a Pulsejet Driver," *38th AIAA Joint Propulsion Conference*, AIAA 2002-3915, Indianapolis, IN, July, 2002.

⁴Lockwood, R., “Interim Summary Report on Investigation of the Process of Energy Transfer from an Intermittent Jet to Secondary Fluid in an Ejector-Type Thrust Augmenter,” Hiller Aircraft Report No. ARD-286, March 1961.

⁵Glaser, A., Caldwell, N., Gutmark, E., Hoke, J., Bradley, R., and Schauer, F., “Performance Measurements of Straight and Diverging Ejectors Integrated with a Pulse Detonation Engine,” *44th AIAA Aerospace Sciences Meeting and Exhibit*, AIAA 2006-1022, Reno, NV, January, 2006.

⁶Glaser, A., Caldwell, N., and Gutmark, E., “Experimental Investigation into the Acoustic Performance of a Pulse Detonation Engine with Ejector”, *43rd AIAA Aerospace Sciences Meeting & Exhibit*, Reno, NV, 2005, AIAA 2005-1345.

Performance Studies of Pulse Detonation Engine Ejectors

Daniel Allgood* and Ephraim Gutmark†

University of Cincinnati, Cincinnati, Ohio 45221-0070

John Hoke‡ and Royce Bradley§

Innovative Scientific Solutions, Inc., Dayton, Ohio 45440

and

Fred Schauer¶

U.S. Air Force Research Laboratory, Wright–Patterson Air Force Base, Ohio 45433

DOI: 10.2514/1.35001

An experimental study on the performance of pulse detonation engine ejectors was performed. Time-averaged thrust augmentation produced by straight and diverging pulse detonation engine ejectors was measured using a damped thrust stand. The ejector length-to-diameter ratio was varied from 1.25 to 5.62 by changing the length of the ejector and maintaining a nominal ejector diameter ratio of 2.75. In general, the level of thrust augmentation was found to increase with ejector length. Also, the ejector performance was observed to be strongly dependent on the operating fill fraction. A new nondimensional parameter incorporating the fill fraction was proposed. When the pulse detonation engine ejector data were represented as a function of this new parameter, the ejector data were reduced to one representative thrust augmentation curve for ejectors of similar internal geometry. Straight pulse detonation engine ejectors compared well with the available data on straight steady-flow ejectors. Diverging pulse detonation engine ejectors produced nearly twice the thrust augmentation as their straight-ejector counterparts due to the additional thrust surface area the divergence provided. All pulse detonation engine ejectors tested were seen to be sensitive to the axial position of the ejector as well. The optimum ejector axial placement was found to be a function of fill fraction due to a tradeoff between the detonation wave induced drag and increased mass entrainment. Downstream ejector placements performed the best at the low fill-fraction operating conditions.

Nomenclature

D_{EJECT}	= ejector diameter
D_{PDE}	= pulse detonation engine detonation tube diameter
DR	= ejector-to-pulse detonation engine diameter ratio ($DR = D_{\text{EJECT}}/D_{\text{PDE}}$)
L_{EJECT}	= ejector length
F_{PDE}	= pulse detonation engine thrust force without an ejector
$F_{\text{PDEEJECTOR}}$	= pulse detonation engine thrust force with an ejector
F_{ref}	= reference thrust force
u	= uncertainty
β	= pulse detonation engine ejector parameter ($\beta = L_{\text{EJECT}}/D_{\text{EJECT}}/\text{ff}$)
Φ	= ejector thrust augmentation ratio ($\Phi = F_{\text{PDEEJECTOR}}/F_{\text{PDE}}$)

I. Introduction

PULSE detonation engines (PDEs) use controlled periodic detonations of a combustible mixture to generate thrust [1]. One

of the primary motivations for PDE development has been based on the potential gain in thermal efficiency that can be achieved with detonation combustion [2]. Experimental and computational researchers have demonstrated some success in obtaining competitive specific impulse values with both simplistic [3] and practical [4,5] PDE cycles. These promising results have led to many PDE applications being proposed. For example, it has been suggested that PDEs can be used as cost-effective replacements for small gas turbine engines, as potential replacements for combustors on existing large-scale gas turbines, or as thrust augmenters. However, even if PDE performance benefits ultimately reveal themselves to be insignificant in practical applications, the PDE cycle will still be an attractive propulsion system because of the reliability benefits of having very few moving parts, the scalability of the engine, and the flexibility in geometry it will provide.

A common approach to increasing the thrust of an engine at subsonic flight conditions is with an ejector. An ejector is a coaxial duct that is placed around the exhaust of an engine to direct the entrainment of the surrounding flow into the engine exhaust stream. The use of steady-flow ejectors and their associated design procedures is well established. The application of ejectors, however, to unsteady primary flows is less common. Several studies [6–11] have examined unsteady ejectors driven by pulsejets or other nondetonation devices where the primary airflow was either unsteady or exhibited strong acoustic coupling with the ejector. Lockwood [6] showed that an unsteady primary flow is more efficient in producing mass entrainment than a comparable steady flow. His pulsejet studies showed ejector thrust augmentation ratios as high as 1.9, much greater than the theoretical isentropic steady-flow ejector. He attributed the unsteady ejector performance to a more efficient energy transfer process between the primary flow and the secondary (entrained) flow through inviscid processes, whereas the steady ejector relies primarily on viscous shear mixing. Because of the unsteady nature of a PDE, these results suggest that an ejector could be highly effective in increasing the PDE performance, specifically for subsonic applications.

Computational studies of single-shot PDE-driven straight ejectors using an Euler code demonstrated the importance of the

Presented as Paper 0223 at the Aerospace Sciences Meeting, Reno, NV, 10–13 January 2005; received 5 October 2007; revision received 11 August 2008; accepted for publication 12 August 2008. Copyright © 2008 by the American Institute of Aeronautics and Astronautics, Inc. The U.S. Government has a royalty-free license to exercise all rights under the copyright claimed herein for Governmental purposes. All other rights are reserved by the copyright owner. Copies of this paper may be made for personal or internal use, on condition that the copier pay the \$10.00 per-copy fee to the Copyright Clearance Center, Inc., 222 Rosewood Drive, Danvers, MA 01923; include the code 0748-4658/08 \$10.00 in correspondence with the CCC.

*Currently NASA Stennis Space Center, Mississippi 39529. AIAA Member.

†Professor and Ohio Eminent Scholar, Department of Aerospace Engineering. AIAA Associate Fellow.

‡Research Engineer, 2766 Indian Ripple Road. AIAA Senior Member.

§Senior Scientist, 2766 Indian Ripple Road.

¶Senior Engineer, Head Pulsed Detonation Research Facility, Propulsion Directorate, Building 490. AIAA Senior Member.

ejector-to-PDE tube diameter ratio in achieving thrust augmentation and its sensitivity to fill fraction [12]. An Euler code with finite-rate chemistry was used to simulate multiple cycles of a specific converging-diverging ejector driven by a PDE at approximately 120 Hz [13]. These simulations demonstrated the potential of thrust augmentation of almost 80%. Further nondetonation computational studies highlighted the importance of the starting vortices, precursor shocks, and direct pressure loads created by the gas dynamic (shock-tube) processes within the ejector to the overall thrust augmentation performance of the system [14]. These computations suggested that high thrust augmentation for PDE-ejector applications is achievable and highlighted the need to understand the gas dynamics, resonance phenomena, and flow interactions of the PDE-ejector system for optimum performance.

A few experimental studies of PDE ejectors have recently been reported. One experimental study by Rasheed et al. [15], using a 5-cm-diam H₂-air PDE tube at 10 Hz with 7.62, 10.16, and 15.24-cm-diam ejectors, showed thrust augmentation levels varying from +16 to -5%, depending on the configuration. In all cases, the maximum thrust augmentation was found to occur with the ejector located fully downstream of the PDE tube. Similar experiments using C₂H₄-air showed maximum thrust augmentation levels of 24%, depending on the configuration [16]. This study presented supporting flow visualizations in the form of shadowgraph images of the ejector inlet throughout one PDE cycle. In both of the preceding studies, the experimentally measured thrust augmentation ratio was significantly lower than the augmentation ratio of 1.9 achieved by Lockwood's pulsejet experiments [6].

One possible reason for the discrepancy in the referenced works on ejector thrust augmentation could be the lack of an appropriately designed ejector inlet. The shape of the ejector inlet is very important in determining the ejector performance because the inlet is an aerodynamic surface that guides the entrainment of the surrounding mass flow. Allgood et al. [17] performed high-speed shadowgraph visualizations of optically accessible PDE ejectors. Their results showed significant losses in mass entrainment and strong flow separation when PDE-ejector inlets were *not* properly rounded or contoured. The importance of an aerodynamic ejector inlet has also been proposed by Lockwood [6], Paxson et al. [7], and Wilson et al. [18].

In addition to ejector inlet geometry, the interior surfaces of the ejector can serve as thrust surfaces on which the pressure forces can act, thereby generating additional thrust. Lockwood [6] showed substantial thrust improvement when using a divergent-type ejector versus a straight cylindrical ejector for pulsejet systems. The experimental work by Paxson et al. [7] also used ejectors with a small diverging section at the end of the ejector for unsteady nondetonating primary flow systems. Wilson et al. [18] have demonstrated experimentally the augmentation benefits of using diverging ejectors for PDEs. However, the mechanisms by which a diverging ejector improves the thrust augmentation of a PDE still needs further investigation.

The relative size of the ejector to the primary flow driver is also known to have a significant influence on ejector performance. An ejector diameter should be sized large enough to allow sufficient area for the primary flow to entrain the secondary flow. However, too large of an ejector diameter could reduce the effect of the accompanying pressure drop on the ejector inlet as well as the pressure rise on a diverging ejector interior surface. An optimum ejector-to-driver diameter ratio corresponding to a peak thrust augmentation level has been observed for a variety of ejector systems [6,7,18]. Typical reported values of optimum diameter ratios range between 2.4 and 3.5.

In a similar manner, the axial placement of the ejector can also affect the ejector flow dynamics. Experimental results by Allgood et al. [17] have shown that the level and efficiency of the PDE-ejector entrainment can be restricted with an upstream axial placement of the ejector. On the other hand, a downstream ejector placement between one to two PDE diameters resulted in a cleaner flowpath for the secondary flow to be entrained into the ejector. This observation is in agreement with the PDE-ejector thrust measurements reported by

Rasheed et al. [15], and similar trends were found by Paxson et al. [7] for pulsejet-ejector systems. Recently, Glaser et al. [19] did an in-depth study on the effects of ejector axial placement and ejector geometry for PDE-ejector systems.

In addition to ejector geometry and placement, there are many operating parameters that have been shown to drastically affect the performance of a PDE, and thus will most likely affect the PDE-ejector performance as well. For example, PDE thrust has been observed to scale linearly with frequency of detonations because it is desirable to minimize the time of each filling event and maximize the frequency of the overall PDE cycle [3]. Thus, adjusting the PDE cycle frequency is one proposed method of throttling the engine. Another way of throttling the engine is to alter the amount of fuel-oxidizer mixture that fills the PDE tube before ignition. The fraction of the PDE tube filled with a detonable mixture relative to the total tube volume is defined as the fill fraction. Although the PDE thrust has been shown to decrease with a reduction in fill fraction, the fuel-based specific impulse values increased at a faster rate [4]. This performance gain observed at lower fill fractions was attributed to the detonation shock wave compressing the nonreactants occupying the remainder of the PDE tube. Allgood et al. [4] demonstrated experimentally the performance benefits of partially filling the detonation tube for a multicycle PDE operation. Their results showed the partial-fill effect being independent of PDE cycle frequency for a constant area detonation tube.

The current work presents an experimental study on the performance benefits of axisymmetric ejectors for multicycle pulse detonation engines. The effect of fill fraction on PDE-ejector performance has been quantified. The performance sensitivity of PDE ejectors to ejector length, internal diverging geometry, and relative axial placement has also been measured. A comparison between PDE ejectors and other ejector systems was given, and a new normalization of PDE-ejector data has been proposed for comparing PDE-ejector data to other ejector systems. In addition to performance measurements, flow visualizations were performed on similar ejector geometries to further explain the trends observed in the performance data.

II. Experimental Facility

A. Pulse Detonation Engine System Description

Thrust augmentation measurements of PDE-driven ejectors were performed. The pulse detonation engine test facility at the U.S. Air Force Research Laboratory at Wright-Patterson Air Force Base was used to obtain the thrust measurements. Premixed hydrogen and air were delivered to a single round detonation tube by way of a mechanical valve system constructed from a modified four-cylinder automotive head. The automotive valve system could be operated at frequencies up to 40 Hz. Because of the nature of automotive valving, the PDE cycle was divided equally between three main processes: 1) filling the PDE with fresh reactants, 2) ignition, detonation, and blowdown of the high-pressure products, and 3) purging the PDE with a buffer of cold air. The hydrogen and air were metered through choked flow orifices. The fill fraction (ff) was varied by controlling the upstream propellant delivery pressures via control valves. By measuring the fuel-air flow rates and controlling the valve timing and frequency, the fill fraction and purge fraction were known. The maximum error in volume flow rate measurements was found to be $\pm 3\%$. This translated directly into a relative error in fill-fraction measurements of also $\pm 3\%$. High-speed shadowgraph and chemiluminescence imaging of the exhaust flow, combined with exit pressure transducers, provided a secondary means of verifying the baseline reference condition of $ff = 1$.

The deflagration-to-detonation transition of the hydrogen-air mixture was enhanced by the use of Shchelkin-type spirals of 0.3 m length. The Shchelkin spiral occupied only 16% of the total PDE tube length. Two pressure transducers (PCB M102A) were mounted 0.1524 m apart to monitor detonation shock speeds and validate that Chapman-Jouguet detonations were produced. The transducer closest to the exit of the PDE was placed a distance of 0.36 m from the PDE exit. The pressure data were collected via a remote 5 MHz

16-channel A/D converter system. The measured wave speed at a fill fraction of 1.0 was on average 1988 m/s (± 13 m/s), which is less than 2% deviation from the theoretical Chapman–Jouguet wave speed of 1966 m/s for a stoichiometric–air mixture.

The PDE was mounted on a damped thrust stand rated for a maximum thrust load of 4500 N. The thrust stand was designed to measure the time-averaged thrust of the dynamic PDE. The thrust stand consisted of linear bearings riding along a pair of low-friction rails. The PDE was allowed to move freely on the rails but its motion was weakly damped by springs to prevent any resonance effects. To remove the effects of static friction, the PDE was continuously actuated forward and backward by a linear actuator. Because this was a known force, it could be subtracted from the measurements to get the true average thrust of the engine. The thrust measurements were calibrated by placing static weights and measuring the displacement with a positional sensor. No hysteresis in the system was observed throughout the testing. Calibration curves were obtained before and after each set of tests to monitor changes in the system. A linear relationship between the applied load and measured thrust was observed for the entire range of PDE thrust loading, with a maximum recorded standard deviation of approximately ± 1 N. The repeatability of the data was observed to be within this error band and thus indistinguishable from the measurement error. For a more detailed description of the PDE test facility and thrust measurement system, the reader is referred to the recent paper by Allgood et al. [4].

B. Pulse Detonation Engine Ejector Test Conditions

The PDE detonation tube was constructed of a steel pipe of 5.08 cm diameter D_{PDE} and 1.83 m length. The main operating parameters that could be varied were the following: 1) the fuel/air mixture, 2) the fill fraction, 3) the purge fraction (pf), 4) the ignition delay, and 5) the PDE cycle frequency. The fill fraction and purge fraction are defined as the ratio of the detonation tube filled with a fuel/air or air mixtures, respectively. The ignition delay was defined as the delay in time in which the spark was actuated after the valves closed. For all test conditions, the PDE was operated at a 30 Hz cycle frequency with a stoichiometric mixture of hydrogen and air, a purge fraction of 0.5, and an ignition delay of 0.5 ms. Only the operating fill fraction was varied in the current tests.

Thrust augmentation levels of axisymmetric ejectors for pulse detonation engine applications were quantified. All ejectors were mounted coaxially to the PDE exhaust and had a rounded or contoured bell-mouth inlet. As depicted in Fig. 1, two sets of ejectors were tested: straight cylindrical ejectors and straight cylindrical ejectors with a diverging exhaust end piece. The length L_{EJECT} of the straight and diverging ejectors were varied by extending the length of the straight or straight-intermediate sections, respectively. The diverging ejector end piece had a 4 deg half-angle of divergence at a fixed length of 19.3 cm. A similar 4 deg half-angle of divergence was used by Lockwood [6] in his pulsejet-ejector experiments. The diameter D_{EJECT} of the straight/straight-intermediate sections was set at a fixed value of 13.97 cm. Thus, the ejector-to-PDE diameter ratio was kept constant throughout the tests at a value of 2.75. This value was selected because it closely matched the optimum diameter ratios reported in other ejector experiments [6,7,17,18].

A range of ejector length-to-diameter ratios (L_{EJECT}/D_{EJECT}) were also tested and are listed in Table 1. The relative position between the PDE exhaust and the ejector inlet was varied as depicted in Fig. 1. Both upstream ($x/D_{PDE} < 0$) and downstream ($x/D_{PDE} > 0$) ejector axial placements were tested. The range in axial placements tested for both straight and diverging ejectors are given in Table 1. To determine the PDE-ejector thrust augmentation dependence on fill fraction, thrust measurements of both the baseline configuration with

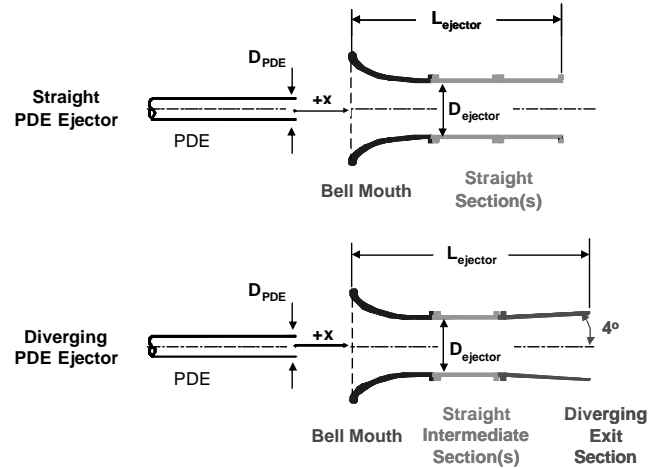


Fig. 1 Schematics of the straight and diverging PDE ejectors.

no ejector and the integrated PDE-ejector system were obtained at the same fill fractions ranging from 0.4 to 1.1. A PDE fill fraction greater than 1.0 means that the PDE combustion chamber was overfilled with a detonable mixture of fuel and oxidizer before ignition.

III. Results and Discussion

A. Baseline Testing of Pulse Detonation Engine

The selected baseline configuration for the ejector tests was the 1.83-m-length PDE detonation tube (5.08-cm-diam) without an exhaust nozzle. The fill fraction for the baseline was varied from 0.4 to 1.1 while maintaining a near stoichiometric fuel–air ratio, an ignition delay of 0.5 ms, a purge fraction of 0.5, and a cycle frequency of 30 Hz. The thrust values for the baseline PDE configuration are given in Fig. 2 as function of experiment run time. The run time is represented in number of PDE cycles, and the thrust is normalized according to a reference thrust value. The reference thrust used in normalizing this data was selected to be the thrust value (77 N) for the baseline configuration at a fill fraction of 1.0. Because the PDE thrust was measured using a damped thrust stand, there was an associated time constant that delayed the average thrust from being recorded, as shown by the slowly rising thrust curves in Fig. 2. This transient delay between the first PDE cycle during each test and the time when a near steady-state thrust level was reached was approximately 33 s, or 1000 PDE cycles, for all fill fractions tested. The observed 33 s time constant was a result of the characteristics of the highly damped thrust stand designed to measure an average thrust of a pulse detonation engine, and was also due to the transient time required for the PDE to reach thermal equilibrium. All thrust data presented in this paper corresponded to the average plateau in thrust recorded after the PDE had been operating continuously for approximately 1000 PDE cycles.

The variation in thrust and fuel-based specific impulse with fill fraction is plotted in Fig. 3. The trends observed were consistent with those found by other researchers. The maximum thrust occurs at maximum fill fraction and decreases nonlinearly with fill fraction. This nonlinear drop in thrust with reduced fill fraction is attributed to the unfilled portion of the detonation tube acting as a straight nozzle. Two sets of expansion waves form during the detonation propagation for a straight nozzle configuration. The first set forms as the detonation shock wave crosses the interface between the filled and unfilled portion of the tube. The second set of expansion waves, which are much stronger than the first, forms as the detonation wave

Table 1 Pulse detonation engine ejector test matrix ($D_{EJECT}/D_{PDE} = 2.75$)

	Fill fraction	Ejector length-to-diameter ratio (L_{EJECT}/D_{EJECT})	Ejector axial position (x/D_{PDE})
Straight ejector	0.4–1.1	1.25–4.25	–1.5–2.0
Diverging ejector	0.4–0.8	2.62–5.62	–2.0–4.0

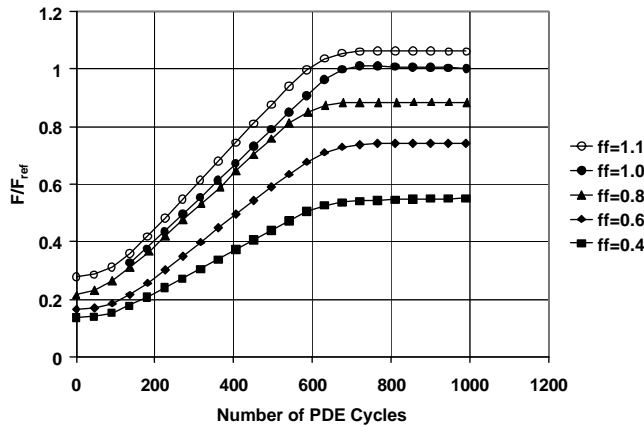


Fig. 2 Baseline PDE average-thrust measurements versus number of PDE cycles ($D_{\text{PDE}} = 5.08$ cm, $F_{\text{ref}} = 77$ N).

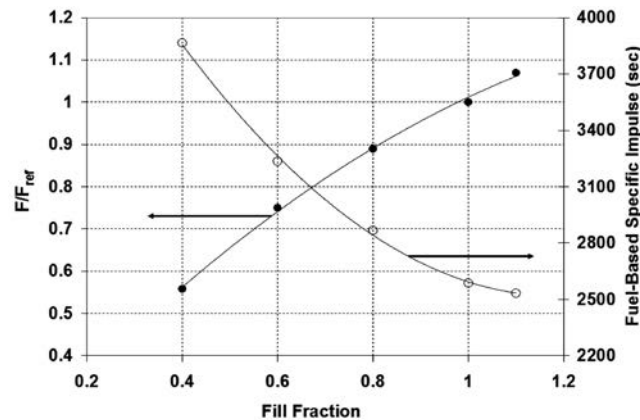


Fig. 3 Baseline PDE thrust and fuel-based specific impulse variation with fill fraction ($D_{\text{PDE}} = 5.08$ cm, $F_{\text{ref}} = 77$ N).

and exhaust gases exit the PDE tube. Essentially, the detonation shock wave serves to compress the gases occupying the unfilled portion of the detonation tube, thereby maintaining the pressure inside the detonation tube at a higher pressure. This increased blowdown time with a straight nozzle results in higher thrust. For example, if this straight nozzle or “partial-fill” effect were not present, the thrust at a fill fraction of 0.5 would be approximately 50% of the thrust obtained with a fill fraction of 1.0. The data in Fig. 3 show that the thrust at a fill fraction of 0.5 was instead approximately 65%. Thus, a 15% thrust increase was generated by the partial-fill effect at a fill fraction of 0.5. This effect continued to increase as the fill fraction was reduced. Also, because the PDE thrust levels decreased at a slower rate than the reduction in fuel mass flow rate, the fuel-based specific impulse values increased as shown in Fig. 3. Specific impulse values as high as 3700 s were obtained for the baseline configuration without an ejector.

B. Effects of Fill-Fraction

In current work, the thrust augmentation of the integrated PDE-ejector system has been represented by an augmentation ratio Φ , where Φ is the total thrust of the PDE-ejector system $F_{\text{PDE-EJECTOR}}$ normalized by the thrust of the PDE without an ejector F_{PDE} but operating at the same engine conditions. By normalizing the thrust data in this manner, the data will reflect solely the performance of the ejector at those engine conditions. This definition is consistent with the historical approach for representing ejector thrust augmentation. The authors would also like to point out that, although the contributions to thrust by the momentum of the “engine-cold” fuel/air and purge gases were known, as shown in Fig. 2, no correction to the thrust data by subtraction of these thrust values was performed.

The reasoning for this was that the true contribution to the total thrust by the fuel/air and purge gases during engine operation (i.e., ignition on) was unknown during the cycle, due to Rayleigh flow effects of heat addition to these gases by the PDE confining walls and its subsequent effects on the momentum of these gases. However, the selected normalization of the PDE-ejector thrust data attempts to correct for these effects by normalizing the PDE thrust data at the same engine operating condition.

As mentioned earlier, the total uncertainty in the thrust measurements was estimated to be ± 1 N. Using the standard propagation of uncertainty equation established by Kline and McClintock [20], the uncertainty in the thrust augmentation ratio Φ can be computed using the following relation:

$$u_{\Phi} = \sqrt{\left(\frac{\partial \Phi}{\partial T_{\text{PDE-EJECTOR}}} \cdot u_{\text{PDE-EJECTOR}}\right)^2 + \left(\frac{\partial \Phi}{\partial T_{\text{PDE}}} \cdot u_{\text{PDE}}\right)^2} \quad (1)$$

Substituting the equation for Φ given in the Nomenclature section of this paper gives the following reduced formula for the uncertainty in the thrust augmentation ratio as a function of the thrust of the PDE and the uncertainty in the thrust measurements:

$$u_{\Phi} = \sqrt{\left(\frac{u_{\text{PDE-EJECTOR}}}{T_{\text{PDE}}}\right)^2 + \Phi^2 \cdot \left(\frac{u_{\text{PDE}}}{T_{\text{PDE}}}\right)^2} \quad (2)$$

Equation (2) shows that the uncertainty in thrust augmentation measurements will be maximized when the thrust levels of the PDE are at a minimum and augmentation ratios are large. For the current tests, these occurred at the lowest PDE fill fraction tested ($ff = 0.4$). The maximum uncertainty of the current test data was found to be 0.048, whereas the average uncertainty was 0.033.

The thrust of the PDE ejectors was measured at fill fractions ranging from 0.4 to 1.1. However, due to flow rate restrictions and backfire problems into the delivery manifold, most tests were limited to a maximum fill fraction of 0.8. Figure 4 is a plot of the percent thrust augmentation for a selected set of the straight and diverging ejectors tested as a function of fill fraction. All ejectors showed that the best relative augmentation performance was obtained at the lowest operating fill fraction, and the level of thrust augmentation was seen to have an inverse relation to fill fraction. The maximum recorded thrust augmentation was with the longest diverging ejector ($L_{\text{EJECT}}/D_{\text{EJECT}} = 5.62$) and was on the order of 65% of the baseline thrust (or $\Phi = 1.65$) at the fill fraction of 0.4. Doubling the fill fraction for this PDE-ejector system resulted in a decrease of the relative thrust augmentation to roughly 51% of the baseline thrust (or $\Phi = 1.51$). The straight ejectors did not perform as well as the diverging ejectors but had roughly the same dependency on fill fraction. For the shortest straight ejector ($L_{\text{EJECT}}/D_{\text{EJECT}} = 1.25$), negative thrust augmentation (or drag) was measured at the high fill-fraction conditions ($ff > 0.8$).

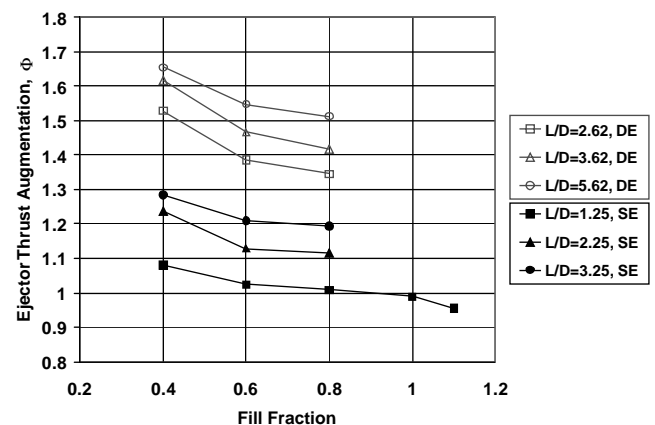


Fig. 4 Straight (SE) and diverging (DE) PDE-ejector thrust augmentation variation with fill fraction for three ejector L/D ratios ($DR = 2.75$, $x/D_{\text{PDE}} = +2.0$).

To obtain a better understanding of why the increased fill fraction resulted in reduced ejector performance, flow visualizations were performed on an optically accessible two-dimensional ejector of a similar geometry as those used in the current performance tests. Figures 5 and 6 are instantaneous snapshots of high-speed flame luminosity imaging and particle flow visualizations of the PDE ejector operating at a fill fraction of 1.0. The time corresponding to each image has been specified relative to the exiting of the detonation wave. Although these flow visualizations are qualitative, both visualization techniques clearly show a strong blast wave exiting the PDE and eventually impinging on the inlet surface of the ejector. The impingement of these high-pressure, high-temperature gases on the ejector inlet were believed to be a primary source of ejector drag (or negative thrust augmentation). As the fill fraction of the PDE was decreased, the strength of the blast wave and thus its induced drag contribution should also have decreased. In addition to the induced drag by the PDE blast wave, exhaust gases were observed to have been expelled out of the ejector inlet, with the level and duration of expelled flow decreasing as the fill fraction was reduced. This translated into negative entrainment during the early portion of the PDE cycle. Later in the PDE-ejector cycle, the flame and particle flow visualizations showed a positive direction of entrainment as depicted in Figs. 5 and 6. These observations were similar to those reported by Allgood et al. in a separate study [17].

C. Effects of Ejector Length-to-Diameter Ratio

In addition to the operating condition of the PDE, the geometry of the ejector was seen to play an important role in the ejector performance. The lengths of the ejector were varied by changing the

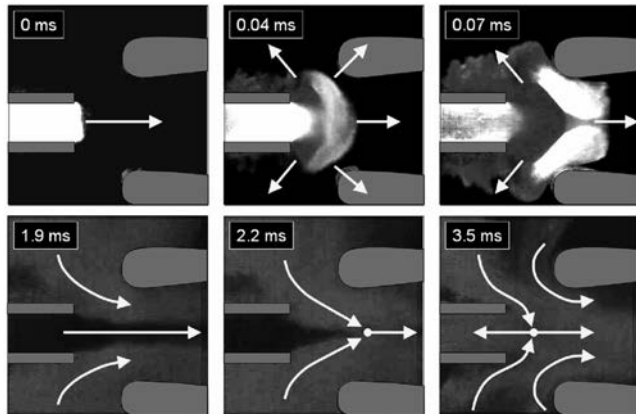


Fig. 5 High-speed flame luminosity imaging of a two-dimensional diverging PDE ejector; vectors indicate direction of visible flame propagation ($L_{\text{EJECT}}/D_{\text{EJECT}} = 2.9$, $DR = 2.2$, $x/D_{\text{PDE}} = +1.0$, $ff = 1.0$).

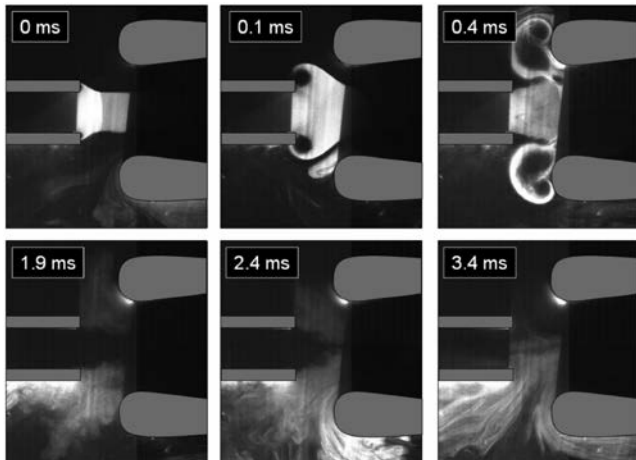


Fig. 6 Particle flow visualizations of a two-dimensional diverging PDE ejector ($L_{\text{EJECT}}/D_{\text{EJECT}} = 2.9$, $DR = 2.2$, $x/D_{\text{PDE}} = +1.0$, $ff = 1.0$).

length of the straight or straight-intermediate sections, as depicted in Fig. 1, while maintaining a constant diameter of 13.97 cm. Conventionally, ejector augmentation data have been plotted as a function of the ejector length-to-diameter ratio ($L_{\text{EJECT}}/D_{\text{EJECT}}$). In Fig. 7, the PDE-ejector thrust augmentation of the current work has been plotted as a function of $L_{\text{EJECT}}/D_{\text{EJECT}}$ along with other available data from PDE ejectors, pulsejet ejectors, and steady ejectors. Figure 7 shows that, for the straight PDE ejectors, an increase in $L_{\text{EJECT}}/D_{\text{EJECT}}$ ratio corresponded to an increase in the relative thrust augmentation. There existed a maximum at an $L_{\text{EJECT}}/D_{\text{EJECT}}$ ratio between 3 and 4. The PDE straight-ejector ($DR = 2.75$) thrust augmentation measured in the current study is in good agreement with those reported by Rasheed et al. [15] ($DR = 2.0$) for a fill fraction of 1.0. The largest straight ejector ($DR = 2.9$) tested by Rasheed et al. had a better performance than the current work's straight ejector ($DR = 2.75$), whereas their smallest straight ejector ($DR = 1.5$) showed very poor performance. No data were reported by Rasheed et al. for other fill fractions or ejector geometries.

The data plotted in Fig. 7 also include thrust augmentation values performed by Morrison [21] for straight-walled steady ejectors and diverging pulsejet ejectors. The straight steady-ejector augmentation levels agree very well with the current straight PDE-ejector data when the fill fraction was close to 1.0. A straight PDE ejector operating at a lower fill fraction was observed to outperform the steady ejector at a similar $L_{\text{EJECT}}/D_{\text{EJECT}}$ ratio.

The diverging PDE ejectors showed nearly twice as much thrust augmentation as the comparable straight PDE ejectors. This improvement with a diverging ejector was also reported by Lockwood [6]. The pulsejet ejectors tested by Lockwood were of a diverging type with the same 8 deg total angle used in the current work. However, the pulsejet ejectors appeared to outperform the PDE diverging ejectors and have a much smaller optimum $L_{\text{EJECT}}/D_{\text{EJECT}}$ ratio of about 1.5. The PDE diverging ejectors showed an increase in performance with increased length. The diverging PDE-ejector performance leveled off at an $L_{\text{EJECT}}/D_{\text{EJECT}}$ ratio around a value of 6.0, a value much greater than the optimum $L_{\text{EJECT}}/D_{\text{EJECT}}$ ratio of the straight PDE ejectors.

It has been demonstrated both numerically [3] and experimentally [4,22,23] that the fuel-based specific impulse of an air-breathing PDE varies inversely with the PDE fill fraction due to advantageous shock compression of the unfilled volume of the combustor by the detonation waves. This was also shown in Fig. 3 of the current paper. In theory, the partial-fill effect on PDE engine performance should be similar for a PDE-ejector system as well, because similar gas dynamics are occurring. To better understand and isolate the performance gains provided by the ejector, the authors have proposed a new nondimensional parameter ($\beta = L_{\text{EJECT}}/D_{\text{EJECT}}/ff$) to be used in plotting PDE-ejector thrust augmentation. Figure 8 shows that, when the current thrust augmentation data are plotted as a function of the PDE-ejector parameter β , the thrust augmentation collapses onto one performance curve for similar ejector types.

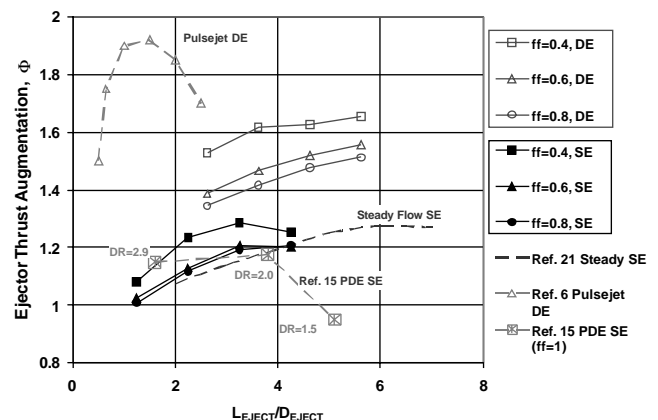


Fig. 7 Normalization of straight (SE) and diverging (DE) ejector performances using the ejector L/D ratio ($DR = 2.75$, $x/D_{\text{PDE}} = +2.0$).

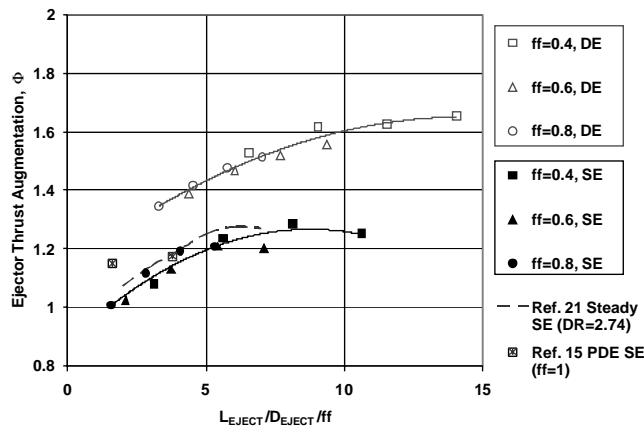


Fig. 8 Proposed normalization of PDE-ejector data for incorporating the PDE fill fraction ($DR = 2.75$, $x/D_{PDE} = +2.0$).

However, different thrust augmentation performance curves exist for different ejector geometry types, such as straight or diverging ejectors. For example, Fig. 8 indicates that a better thrust augmentation curve was obtained for a 4 deg diverging PDE ejector than that of a straight PDE ejector. This was attributed to the additional thrust surface area that the divergence of the internal surface of the ejector provided (see Fig. 1). Each ejector performance curve also indicated there was a single optimum β value. This means that PDE-ejector performance is not only highly dependent on its length-to-diameter ratio as typical ejector systems, but also on the operating conditions of the PDE. Other engine operating conditions, such as equivalence ratio and frequency, will obviously affect PDE-ejector performance as well and should be investigated further. However, the preliminary data shown in Fig. 8 indicate that the correlation between straight steady ejectors ($ff = 1.0$) and straight PDE ejectors was quite reasonable. In addition, the PDE-ejector data provided by Rasheed et al. [15] also agreed reasonably well when plotted in this fashion.

D. Effects of Ejector Axial Position

Another geometrical parameter varied in these tests was the relative position of the ejector inlet to the exhaust of the PDE. All previous results reported in this paper were for an axial position of $x/D_{PDE} = 2.0$, meaning the ejector was placed a distance of two PDE diameters downstream of the PDE exit. However, many previous studies on ejectors showed that the augmentation is very sensitive to its axial location [6–8,16–19]. For this reason, the straight ejector ($L_{EJECT}/D_{EJECT} = 1.25$) and the diverging ejector ($L_{EJECT}/D_{EJECT} = 5.62$) were moved upstream and downstream of the PDE exhaust. In addition, because the results shown previously also indicated a strong dependence on fill fraction, the fill fraction was varied at each ejector axial position.

Figure 9 shows results for the diverging ejector at three operating fill fractions and for x/D_{PDE} locations extending from upstream of -2 to 4 diameters downstream. The sensitivity to axial location was most pronounced with the lower fill fraction of 0.4 . For this operating condition, the optimum x/D_{PDE} was a downstream placement of $+2$ diameters. As the fill fraction was increased, the performance of the downstream ejector placements decreased relative to the upstream placements. At a fill fraction of 0.8 , the optimum location was measured to be either inline or slightly upstream of the PDE exhaust. This effect can be attributed to the induced drag generated by the PDE wave, which was discussed earlier in the paper and is shown in Figs. 5 and 6. A downstream placement of the ejector at the lower fill fractions was more optimal because it did not experience as high of an induced wave drag, and it allowed the secondary flow to be more readily entrained without restrictions. This effect was also observed by Allgood et al. [17] in their PDE-ejector visualizations.

Figure 10 shows the relationship between the ejector thrust augmentation and the axial placement of the ejector and the PDE

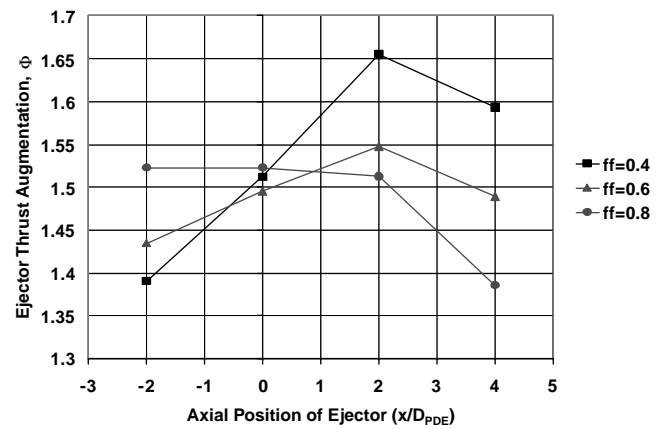


Fig. 9 Effects of axial position on diverging ejector performance for three operating fill fractions ($L_{EJECT}/D_{EJECT} = 5.62$, $DR = 2.75$).

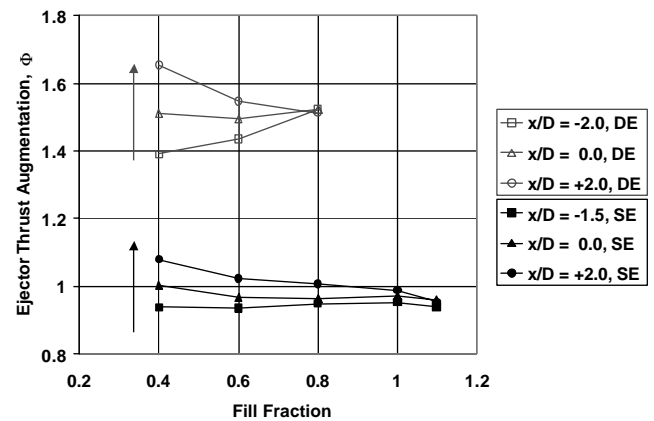


Fig. 10 Performance sensitivity of straight ($L_{EJECT}/D_{EJECT} = 1.25$) and diverging ($L_{EJECT}/D_{EJECT} = 5.62$) ejectors to the operating fill fraction (arrows indicate a positive downstream change in ejector axial position).

fill fraction. The thrust augmentation ratios are plotted as a function of fill fraction for three representative ejector axial placements: upstream, inline, and downstream. Both the straight and diverging ejector configurations showed that, as the fill fraction was increased, the downstream placement performance dropped and the upstream placement performance increased. This indicates again that the optimum axial placement of a PDE ejector is dependent on fill fraction. Furthermore, because both the diverging and straight ejector geometries showed very similar trends, the effect of fill fraction was most likely having a primary impact on the ejector bell mouth and not on the internal thrust surfaces. This conclusion is supported by the visualizations presented in Figs. 5 and 6.

IV. Conclusions

An experimental study of the performance of pulse detonation engine ejectors was performed. Time-averaged thrust augmentation produced by straight and diverging PDE ejectors was measured using a damped thrust stand. The ejector length-to-diameter ratio was varied from 1.25 to 5.62 by changing the length of the ejector while maintaining a nominal ejector-to-PDE diameter ratio of 2.75 . The operating fill fraction was varied from 0.4 to 1.1 . The PDE-ejector thrust augmentation was found to be strongly dependent on the operating fill fraction. A reduction in fill fraction corresponded to higher levels of ejector thrust augmentation for all L_{EJECT}/D_{EJECT} ratios tested and for both the straight and diverging ejectors. This improvement in ejector performance by operating at low fill-fraction conditions was attributed to a reduction in induced wave drag on the ejector inlet produced by the detonation blast waves. The diverging ejector geometry showed the best

performance due to increased thrust surface area. The diverging ejector produced a maximum of 65% thrust augmentation ($\Phi = 1.65$) compared to a 28% ($\Phi = 1.28$) thrust augmentation with the straight ejector at a fill fraction of 0.4.

In general, longer ejectors outperformed short ejectors. Ejectors with $L_{\text{EJECT}}/D_{\text{EJECT}}$ ratios greater than 3.0 showed the best performance. For the case of the straight ejectors, maximum augmentation was observed for $L_{\text{EJECT}}/D_{\text{EJECT}}$ ratios between 3 and 4. The diverging ejectors, however, did not show a maximum for the range of $L_{\text{EJECT}}/D_{\text{EJECT}}$ ratios tested but began to level off at $L_{\text{EJECT}}/D_{\text{EJECT}}$ ratios greater than 5.

The current results compared well with a limited set of PDE-ejector data [15,19]. However, the behavior and thrust augmentation of all PDE ejectors were inconsistent with reported deflagration pulsejet-ejector systems. This leads to the conclusion that, although there are some similarities between PDE and pulsejet driven ejectors, there can be a significant difference in the flow dynamics to warrant caution in grouping these two systems into the same classification. However, a new normalization parameter ($\beta = L_{\text{EJECT}}/D_{\text{EJECT}}/\text{ff}$) based on ejector length-to-diameter ratio and PDE fill fraction was proposed. Using this normalization parameter, the PDE-ejector performances for all fill fractions compared well with available steady ejector performances for the specific ejector geometries evaluated.

The axial placement of the ejector also greatly affected the performance of the PDE-ejector system. Unlike other ejector systems, a single optimum ejector placement for PDE applications was not found but rather a function of the operating fill fraction. The sensitivity of ejector augmentation to the axial placement was believed to be a result of a tradeoff between reduced detonation wave induced drag with upstream placement and increased mass entrainment with downstream placement. For most test conditions, a downstream ejector placement provided the best performance. However, as the operating fill fraction was increased (i.e., stronger blast waves), the relative performance of an upstream placement increased, whereas the performance of a downstream placement decreased. In contrast, the inline ejector placement performance was nearly independent of fill fraction.

Although these observations on the sensitivity of the ejector performance to axial placement are in qualitative agreement with the behavior reported by Glaser et al. [19], the optimum PDE-ejector placement has not been consistent in the reported literature, as was commented on in the recent work by Wilson et al. [18]. Despite this fact, what is consistent in all the reported studies performed on this subject, including the current paper, is that the optimum ejector axial placement is a strong function of the engine configuration and operating conditions (fill fraction [19], detonation frequency [18], etc.) and the ejector inlet and diffuser geometry [15,16,19]. This is a result of the augmentation being a strong function of the dynamics of the engine exhaust flow and its complex interactions with the ejector geometry.

Acknowledgments

The authors would like to thank the Propulsion Directorate at the U.S. Air Force Research Laboratory and Innovative Scientific Solutions, Inc., for providing the financial support for this work. In addition, the authors are grateful for the financial support from NASA Glenn Research Center (NAG3-2669) for sponsoring the development of the University of Cincinnati pulse detonation engine research facility. The technical support of Curtis Rice of Innovative Scientific Solutions, Inc., is also appreciated.

References

- [1] Bussing, T., and Pappas, G., "Pulse Detonation Engine Theory and Concepts," *Developments in High-Speed Vehicle Propulsion Systems*, edited by S. N. B. Murthy, and E. T. Curran, Vol. 165, Progress in Astronautics and Aeronautics, AIAA, Reston, VA, 1996, pp. 421–472.
- [2] Kuo, K., *Principles of Combustion*, Wiley, New York, 1986.
- [3] Kailasanath, K., "Recent Developments in the Research on Pulse Detonation Engines," *AIAA Journal*, Vol. 41, No. 2, 2003, pp. 145–159.
- [4] Allgood, D., Gutmark, E., Hoke, J., Bradley, R., and Schauer, F., "Performance Measurements of Multicycle Pulse Detonation Engine Exhaust Nozzles," *Journal of Propulsion and Power*, Vol. 22, No. 1, 2006, pp. 70–77.
doi:10.2514/1.11499
- [5] Helfrich, T., King, P., Hoke, J., and Schauer, F., "Effect of Supercritical Fuel Injection on Cycle Performance of Pulse Detonation Engine," *Journal of Propulsion and Power*, Vol. 23, No. 4, 2007, pp. 748–755.
doi:10.2514/1.26551
- [6] Lockwood, R., "Interim Summary Report on Investigation of the Process of Energy Transfer from an Intermittent Jet to Secondary Fluid in an Ejector-Type Thrust Augmenter," Hiller Aircraft Rept. No. ARD-286, March 1961.
- [7] Paxson, D. E., Wilson, J., and Dougherty, K. T., "Unsteady Ejector Performance: An Experimental Investigation Using a Pulsejet Driver," *38th AIAA Joint Propulsion Conference*, AIAA Paper 2002-3915, 2002.
- [8] Wilson, J., "Effect of Pulse Length and Ejector Radius on Unsteady Ejector Performance," *Journal of Propulsion and Power*, Vol. 23, No. 2, 2007, pp. 345–352.
doi:10.2514/1.19665
- [9] Wilson, J., Wemet, M., and Paxson, D., "Vortex Rings Generated by a Shrouded Hartmann–Sprenger Tube," *AIAA Journal*, Vol. 44, No. 11, 2006, pp. 2706–2718.
doi:10.2514/1.17560
- [10] Bogdanov, V., "Interaction of Masses in the Operating Process of Pulse Jet Engines as a Means of Increasing Their Thrust Efficiency," *Journal of Engineering Physics and Thermophysics*, Vol. 79, No. 3, 2006, pp. 506–511.
doi:10.1007/s10891-006-0128-8
- [11] Quinn, B., "Interactions Between Screech Tones and Ejector Performance," *Journal of Aircraft*, Vol. 14, No. 5, 1977, pp. 467–473.
doi:10.2514/3.58804
- [12] Allgood, D., Gutmark, E., and Katta, V., "Effects of Exit Geometry on the Performance of a Pulse Detonation Engine," *40th AIAA Aerospace Sciences Meeting and Exhibit*, AIAA Paper 2002-0613, 2002.
- [13] Yungster, S., and Perkins, H. D., "Multiple Cycle Simulation of a Pulse Detonation Engine Ejector," NASA TM 2002-211888, Oct. 2002.
- [14] Groschel, E., Tsuei, H., Xia, G., and Merkle, C., "Characterization of Thrust Augmentation by Unsteady Ejectors," *39th AIAA Jet Propulsion Conference*, AIAA Paper 2003-4970, 2003.
- [15] Rasheed, A., Tangirala, V., Pinard, P. F., and Dean, A. J., "Experimental and Numerical Investigations of Ejectors for PDE Applications," *39th AIAA Jet Propulsion Conference*, AIAA Paper 2003-4971, 2003.
- [16] Shehadeh, R., Saretto, S., Lee, S.-Y., Pal, S., and Santoro, R. J., "Experimental Study of a Pulse Detonation Engine Driven Ejector," *39th AIAA Jet Propulsion Conference*, AIAA Paper 2003-4972, 2003.
- [17] Allgood, D., Gutmark, E., Rasheed, A., and Dean, T., "Experimental Investigation of a Pulse Detonation Engine with a 2D Ejector," *AIAA Journal*, Vol. 43, No. 2, 2005, pp. 390–398.
doi:10.2514/1.8125
- [18] Wilson, J., Sgondea, A., Paxson, D., and Rosenthal, B., "Parametric Investigation of Thrust Augmentation by Ejectors on a Pulse Detonation Tube," *Journal of Propulsion and Power*, Vol. 23, No. 1, 2007, pp. 108–115.
doi:10.2514/1.19670
- [19] Glaser, A., Caldwell, N., Gutmark, E., Hoke, J., Bradley, R., and Schauer, F., "Performance Measurements of Straight and Diverging Ejectors Integrated with a Pulse Detonation Engine," *44th AIAA Aerospace Sciences Meeting and Exhibit*, AIAA Paper 2006-1022, 2006.
- [20] Kline, S. J., and McClintock, F. A., "Describing Uncertainties in Single-Sample Experiments," *Mechanical Engineering*, Vol. 75, Jan. 1953, pp. 3–8.
- [21] Morrison, R., "Jet Ejectors and Augmentation," NACA ACR-37, Sept. 1942.
- [22] Roya, G., Frolov, S., Borisov, A., and Netzerc, D., "Pulse Detonation Propulsion: Challenges, Current Status, and Future Perspective," *Progress in Energy and Combustion Science*, Vol. 30, No. 6, 2004, pp. 545–672.
doi:10.1016/j.pecs.2004.05.001
- [23] Cooper, M., Shepherd, J., and Schauer, F., "Impulse Correlation for Partially-Filled Tubes," *Journal of Propulsion and Power*, Vol. 20, No. 5, 2004, pp. 947–950.
doi:10.2514/1.4997

Study on the Operation of Pulse-Detonation Engine-Driven Ejectors

Aaron J. Glaser,* Nicholas Caldwell,* and Ephraim Gutmark†

University of Cincinnati, Cincinnati, Ohio 45221

John Hoke‡ and Royce Bradley§

Innovative Scientific Solutions, Inc., Dayton, Ohio 45440

and

Frederick Schauer¶

U.S. Air Force Research Laboratory,

Wright–Patterson Air Force Base, Ohio 45433

DOI: 10.2514/1.37869

Experimental studies were performed to improve the understanding of the operation of ejector augmenters driven by a pulse-detonation engine. The research employs an H_2 -air pulse-detonation engine at an operating frequency of 30 Hz. Static pressure was measured along the interior surface of the ejector, including the inlet and exhaust sections. Thrust augmentation provided by the ejector was calculated by integration of the static pressure measured along the ejector geometry. The computed thrust augmentation was in good agreement with that obtained from direct thrust measurements. Both straight and diverging ejectors were investigated. The diverging ejector pressure distribution shows that the diverging section acts as a subsonic diffuser and has a tremendous impact on the behavior of the inlet entrainment flow. Static pressure data were also collected for various ejector axial positions. These data supported the thrust augmentation trends found through direct thrust measurements. Specifically, the optimum axial placement was found to be downstream of the pulse-detonation engine near $x/D_{PDE} = +2$, whereas upstream placements tend to result in decreasing thrust augmentation. To provide a better explanation of the observed performance trends, shadowgraph images of the detonation wave and trailing vortex interacting with the ejector inlet were obtained.

Nomenclature

D_{EJECT}	=	ejector diameter, cm
D_{PDE}	=	detonation tube diameter, cm
DR	=	ejector-to-PDE diameter ratio
ff	=	fill fraction
L_{EJECT}	=	ejector length, cm
L_{EXHST}	=	exhaust-section length, cm
L_{STRT}	=	intermediate straight-section length, cm
T_{PDE}	=	PDE-system thrust with no ejector installed, N
$T_{PDE EJECT}$	=	PDE-system thrust with ejector installed, N
x	=	ejector axial position, cm
α	=	thrust augmentation, %

I. Introduction

ALTHOUGH pulse detonation engine (PDE) technology continues to make progress in gaining acceptance in the aerospace community, many hurdles remain in achieving a practical engine system. One of the key challenges for researchers is to make

use of the increased efficiency of energy conversion due to detonative-mode combustion by converting it most effectively into a propulsive thrust force. Many approaches have been undertaken in this effort to harness the transient power created by a train of propagating detonation waves [1]. Much initial work was expended on baseline performance characterization, and as a result a wide array of data has been presented in the literature [2–4]. These data have shown the performance trends in terms of thrust and impulse for both single-cycle and multicycle detonation tube operation. As a result of this work, many analytical models have been produced in an attempt to better predict PDE performance [5–7]. It can generally be shown that the specific impulse generated by a detonation wave depends heavily on the Chapman–Jouguet properties of the reactive mixture. This work has been supported by a large number of computational investigations, ranging from single-cycle predictions to limit-cycle studies [8–11]. Because of the inherent experimental difficulty in capturing unsteady flow phenomena in such a high-pressure, high-temperature environment, these studies have been vital to the understanding of the transient detonation process. This foundation of previous experimental and computational work has suggested that the use of ejector augmenters using a PDE as the primary driver may be an effective way to increase system thrust and specific impulse.

In the simplest terms, an ejector is a coaxial duct placed around the exhaust of an engine that performs as a fluidic pump. By entraining the surrounding ambient air with the primary exhaust flow and directing it into the ejector, the momentum of the engine exhaust flow is increased, leading to the generation of a larger system thrust force [12]. The theory and application of ejectors with regard to a steady primary flow are well established [13,14]. In this type of situation, the secondary flow is entrained primarily through viscous shear mixing [15,16]. Previous research has shown that unsteady ejectors tend to produce more thrust augmentation than steady-flow ejectors [17–19]. According to Wilson et al., the increased performance of unsteady ejectors can be attributed to a more efficient energy-transfer process between the primary and secondary flows that results from the dominant effects of the starting vortex [20]. Because PDEs are

Presented as Paper 0447 at the 45th AIAA Aerospace Sciences Meeting and Exhibit, Reno, NV, 8–11 January 2007; received 3 April 2008; revision received 28 July 2008; accepted for publication 28 July 2008. Copyright © 2008 by Aaron Glaser and Nicholas Caldwell. Published by the American Institute of Aeronautics and Astronautics, Inc., with permission. Copies of this paper may be made for personal or internal use, on condition that the copier pay the \$10.00 per-copy fee to the Copyright Clearance Center, Inc., 222 Rosewood Drive, Danvers, MA 01923; include the code 0748-4658/08 \$10.00 in correspondence with the CCC.

*Graduate Research Assistant, Department of Aerospace Engineering, ML0070. Student Member AIAA.

†Professor and Ohio Eminent Scholar, Department of Aerospace Engineering, ML0070. Fellow AIAA.

‡Research Engineer, 2766 Indian Ripple Road. Senior Member AIAA.

§Senior Scientist, 2766 Indian Ripple Road.

¶Mechanical Engineer, AFRL/PRTC, Building 490. Senior Member AIAA.

highly unsteady devices that generate shock waves and strong vortex rings, PDE-driven ejectors have the potential to be highly effective at providing thrust augmentation.

Experimental work has confirmed that PDE-driven ejectors are extremely effective in thrust augmentation. These studies have quantified both the effects of PDE operating parameters and important ejector geometric parameters such as the internal surface geometry. A study by Glaser et al. [21] carried out using several ejector configurations showed maximum thrust augmentation levels of $\alpha = 30\%$ for straight ejectors and $\alpha = 66.5\%$ for an optimized diverging ejector geometry driven by a completely filled detonation tube. Here the thrust augmentation α is defined as the percent increase in thrust compared to the baseline detonation tube without an ejector. Based on a large body of experimental work, it is apparent that diverging ejectors are much more effective at producing thrust augmentation than straight ones. The increased augmentation by diverging ejectors has commonly been attributed to the additional thrust surface area of the diverging section; however, inherent in that explanation is the possibly false assumption that a positive net pressure acts on the diverging section to create a thrust force. It has also been observed that ejector performance is extremely sensitive to the axial position of the ejector inlet relative to the PDE tube exit. In most cases downstream ejector placement provides optimum levels of thrust augmentation [21–24]; however, some researchers have found evidence to the contrary [25,26]. For the straight and diverging ejector configurations previously tested by Glaser et al. [21], the optimum axial position was found to be downstream at $x/D_{\text{PDE}} = +2$.

By measuring the static pressure along the interior surface of various ejector geometries, the current effort seeks to increase the overall understanding of PDE-driven ejector systems. To supplement these data, high-speed shadowgraph flow visualizations were also obtained to provide a better explanation of the observed performance trends. Comparisons were also made between these data and ejector performance data obtained through direct thrust measurements. Results from this study provide insight into the governing flow dynamics and mechanisms responsible for thrust augmentation in PDE-driven ejector systems and better explain the role of the diverging exhaust section in augmenting thrust.

II. Experimental Setup

A. Description of PDE System

Experimental testing for the current study was carried out at the U.S. Air Force Research Laboratory PDE Test Facility at Wright–Patterson Air Force Base [3]. The detonation tube was constructed of type-316 stainless steel, and the geometry tested had an inner diameter of 5.08 cm and a length of 154.94 cm. The system was operated in a premixed manner, using nonpreheated hydrogen and air as the reactants injected at approximately 21°C. Injection of fuel and air into the detonation tube was accomplished using a mechanical valve system that was constructed from a modified four-cylinder automotive valve head with four valves per cylinder driven with a variable-speed electric motor. While the two intake ports were used to deliver premixed hydrogen and air, the two exhaust ports delivered purge air. The purge air cycle was used to cool the detonation tube and provide a buffer between the hot combustion products and the fresh reactants being injected into the tube for the next cycle. Because of the nature of automotive valving, the division of the cycle timing for various events such as fill time, purge time, and detonation time was fixed at one-third of the total cycle. Spark ignition was accomplished using a capacitive-discharge, stock automotive spark system that delivered 105 mJ of energy per pulse. To accelerate the deflagration-to-detonation transition process, a Shchelkin-type spiral with an overall length of 40.64 cm was mounted near the headwall, extending nearly 26% of the detonation tube length.

The PDE system was mounted on a damped thrust stand that was designed to measure the time-averaged thrust generated by the PDE. The thrust stand consisted of linear pillow-block bearings riding along a pair of linear bearing rails. The PDE was allowed to move freely on the rails, but its motion was resisted by springs to prevent

resonance effects. To remove the effects of static friction, a novel approach was used by which the PDE was continuously moved forward and backward by a linear pneumatic actuator. Because the actuator produces a net-zero average force, the average position of the thrust stand is a function of the PDE average thrust. The thrust stand was calibrated by placing static weights on a pulley/cable system to simulate a thrust force and measuring the average position of the thrust stand with a displacement sensor. The maximum uncertainty of the thrust stand, which was determined through repeated calibration tests, was found to be ± 1.1 N for the range of PDE thrust loading observed during these tests.

Operation of the PDE system was computer controlled by means of a LabView interface program. This LabView interface provided the flexibility to specify engine operating parameters such as PDE operating frequency, fill fraction, and equivalence ratio. Unless otherwise stated, all of the current tests were performed at an operating frequency of 30 Hz and an equivalence ratio of 1.0. Ionization probes were mounted along the detonation tube length to verify that Chapman–Jouguet (CJ) detonations were obtained. Detonation wave speeds measured throughout experimentation all fell within ± 100 m/s of the theoretical CJ wave speed of 1957 m/s. Data from these sensors were collected at 5 MHz using a 16-channel data acquisition system. This fast sampling rate was adequate for accurate resolution of the detonation wave speed.

B. Ejector Hardware and Instrumentation

To determine the effect of the ejector hardware on the thrust generated by the PDE, the ejectors tested were mounted coaxially to the detonation tube at various positions relative to the PDE exit plane. Two parallel rails were mounted above the PDE which extended beyond the length of the detonation tube. By suspending the ejectors from these rails at different locations, the axial position x of the ejector inlet was able to be varied from -12 to $+6$ tube diameters from the PDE tube exit plane. A negative axial position value corresponds to the ejector inlet placed upstream of the PDE exit, with the ejector overlapping the detonation tube. Similarly, a positive value of axial position corresponds to a situation in which the ejector is mounted downstream of the detonation tube exit.

Two ejector geometries were used during these tests, each consisting of an inlet section, an intermediate straight section, and an exhaust section as shown in Fig. 1b. With the exception of the exhaust section, the two ejectors were identical: one exhaust section was straight whereas the other was diverging. The geometric parameters of the current ejectors were chosen based on results from previous optimization studies [21]. The diameter of the ejector D_{EJECT} was defined as the diameter of the intermediate straight section because this was the minimum diameter for any given ejector geometry. For the current work, D_{EJECT} was held at a fixed value of 13.97 cm. The ejector-to-PDE diameter ratio DR of 2.75 was therefore constant throughout the testing. Based on previous ejector experiments, this value is near the optimum diameter ratio for thrust augmentation [20,22,24]. The inlet used for this testing had a rounded inlet lip with a radius of 3.81 cm. This has been found through previous research to be an important geometric parameter affecting both the internal flowfield and the performance of an ejector [27,28]. The overall nondimensional length of the ejectors was $L_{\text{EJECT}}/D_{\text{EJECT}} = 5.6$, the length of the intermediate straight section was $L_{\text{STRAIGHT}}/D_{\text{EJECT}} = 3$, and the exhaust section had a length of $L_{\text{EXHST}}/D_{\text{EJECT}} = 2.36$. The two exhaust sections tested had half-angle divergences of 0 and 4 deg.

To facilitate the static pressure measurements, each ejector was instrumented with 20 pressure ports along the ejector surface. Each pressure port consisted of a 0.0157-cm-diam thru hole on the ejector surface, which transitioned to a 0.0246-cm-diam tube. Seven of the pressure taps were located on the ejector inlet at the angular locations given in Table 1. As shown in Fig. 2, the remaining 13 pressure taps were distributed along the ejector body: seven were placed on the intermediate straight section and six on the exhaust section. Although this figure depicts an ejector with a straight exhaust section, the diverging exhaust section also had surface pressure taps at the

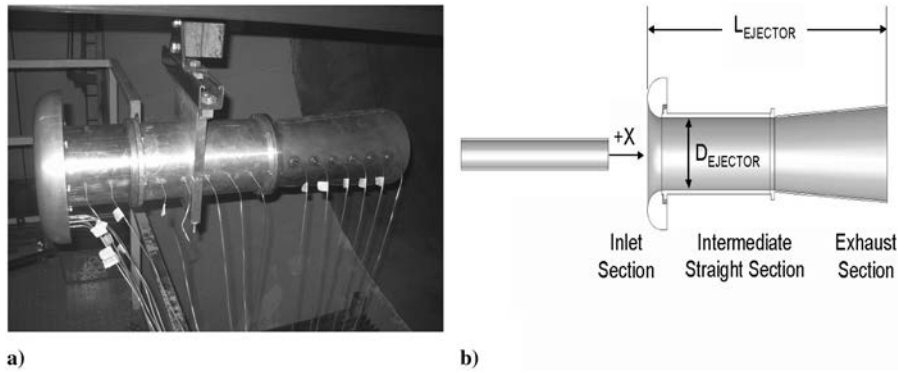


Fig. 1 a) Photograph of the installed ejector and b) diagram of ejector geometry used for current work.

same locations. Pressure was measured using a NetScanner Model 9116 Pressure Scanner incorporating 16 silicon piezoresistive pressure sensors, each sampling at a frequency of 1 Hz. Because the pressure measurement system had the ability to sample 16 pressure signals, only 16 of the 20 available ejector pressure taps could be used at a given time. The pressure ports used for the current study are shown schematically in Fig. 2. Each pressure port on the ejector was connected to its corresponding pressure sensor by a 0.0246-cm-diam flexible tube of ~ 2.5 m length. Because of the setup of the current system, the dynamic nature of the pressure field was not captured. The length of tubing used between the sensors and the surface pressure taps had the effect of damping out the high-frequency pressure oscillations that are normally associated with PDE operation and had an averaging effect on the pressure history. As a result, the 1-Hz pressure measurement system provided a measure of the time-averaged static pressure at the specified locations. However, high-frequency changes in the pressure field were incapable of being measured and individual detonation events were unable to be discerned in the measurements.

For each data point collected, the PDE was operated for a duration of ~ 45 s. To assess the variability of the experimental results, three test runs were performed for each configuration studied. A typical static pressure time history measured on the ejector surface is shown in Fig. 3. Before detonation, cold air is pulsed through the PDE injection valves to allow sufficient time for the desired flow rate to stabilize. This initial unsteady cold flow causes flow entrainment into the ejector and hence a decreased pressure on the ejector inlet, shown by the initial gauge pressure of -1.03 kPa in Fig. 3. After the PDE begins to detonate, the pressure drops to a lower plateau, indicating an increase in flow entrainment. It can be observed that although the measured pressure signal is reasonably steady due to the damping nature of the measurement setup as discussed above, the signal does have a fluctuating component. For all results reported in the current study, the sample mean of the fluctuating pressure was calculated to yield a single value for the static pressure at that sample location. For the case shown, the mean PDE-fired static pressure measured on the ejector inlet at pressure tap 7 was -2.62 kPa. The uncertainty of the static pressure was evaluated statistically by determining the standard deviation of the mean pressure averaged over a representative sample of data sets. By this method, the mean pressure data reported in the current study have an average associated uncertainty of ± 0.3 kPa as shown by the error bars in Fig. 3.

Table 1 Locations of pressure taps on ejector inlet section

Tap no.	Tap position, deg
1	0
2	30
3	60
4	90
5	120
6	150
7	165

III. Results and Discussion

A. Straight Ejector Surface Pressure Distribution

The surface pressure distribution measured on a straight ejector is shown in Fig. 4. Results are compared for two primary unsteady driver sources. The first source is a PDE, and the second is an unsteady cold jet, both operating at a frequency of 30 Hz. Both driver sources exhibit similar trends in ejector pressure distribution. For example, it can be observed that the entrained flow being directed into the ejector causes a significant pressure drop on the inlet, thus producing positive thrust on the ejector. The minimum inlet pressure occurred at pressure tap 7, which is at an angle of 165 deg as previously defined. It can also be observed that the outer area of the inlet, pressure taps 1 and 2, did not experience a pressure decrease and thus did not contribute to providing thrust augmentation. This finding implies that the entire rounded portion of the inlet may not be necessary, as comparable performance might be achieved with a simplified inlet design. With a straight ejector, the only surface capable of causing a thrust force is the ejector inlet, and hence a larger negative inlet pressure would always lead to an increase in thrust augmentation. Just downstream of the inlet section, the pressure is observed to rise quickly and a region consistent with separated flow is observed at pressure tap 8. Because the pressure rise is observed to occur in both the PDE and the subsonic cold flow case, it is unlikely that it is due to the presence of a stationary shock wave located in the ejector, but rather flow separation following the flow turning around the ejector inlet. The flow separation is probably due to the strong adverse pressure gradient and large inlet turning angle experienced by the entrainment air. Through the remainder of the straight ejector, static pressure is found to rise gradually until ambient pressure at the ejector exit is reached. The flow area is constant throughout the straight ejector. The rising static pressure is attributed to the primary jet mixing with the slower entrained flow throughout the extent of the ejector. By integrating the measured static pressure over the ejector surface geometry, the amount of thrust augmentation provided by the straight ejector configuration with $ff = 1.0$ was calculated. Defining thrust augmentation as the percent increase in thrust compared to the baseline detonation tube without an ejector,

$$\alpha = \frac{T_{PDE\ EJECT} - T_{PDE}}{T_{PDE}} \quad (1)$$

the computed augmentation was found to be 26.1%, which is slightly lower than the augmentation of 30.0% obtained by direct thrust measurements [21]. This previous study reported the absolute uncertainty of the thrust stand measured augmentation to be $\pm 2.5\%$. An uncertainty analysis was performed to determine the uncertainty associated with the pressure derived thrust augmentation of the current study. As previously shown, the pressure measurements have an average uncertainty of ± 0.3 kPa. Through a standard propagation of error analysis, it was determined that the reported pressure uncertainty translates into an absolute thrust augmentation uncertainty of $\pm 7.7\%$.

Figure 5 presents shadowgraph flow visualizations showing the differences between a detonation and cold flow primary driver. The

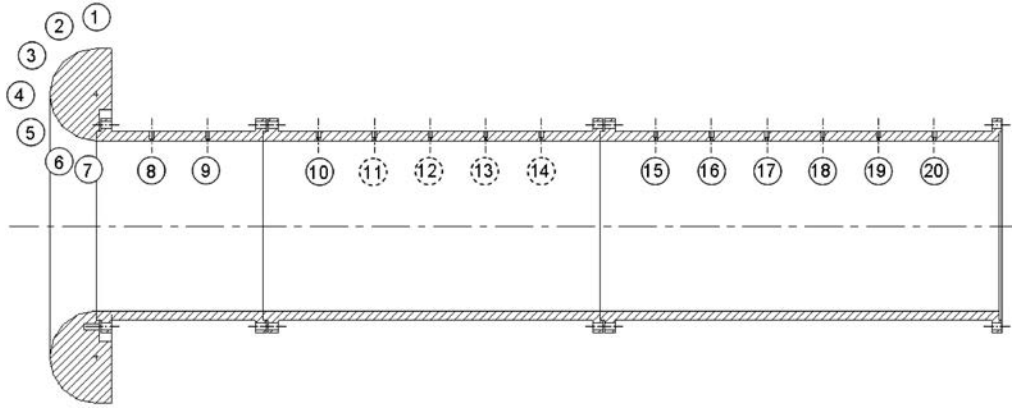


Fig. 2 Placement of pressure sampling ports on ejector interior surface. Solid circles denote ports used during the current study.

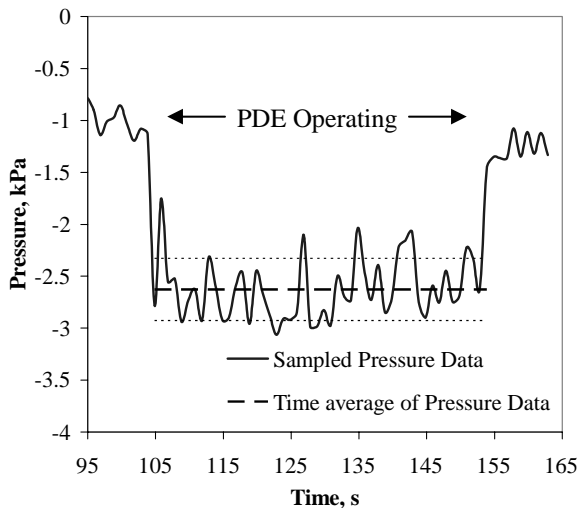


Fig. 3 Pressure history measured at pressure tap 7. The configuration tested was a straight ejector with $x/D_{PDE} = +2$ and $ff = 1.0$.

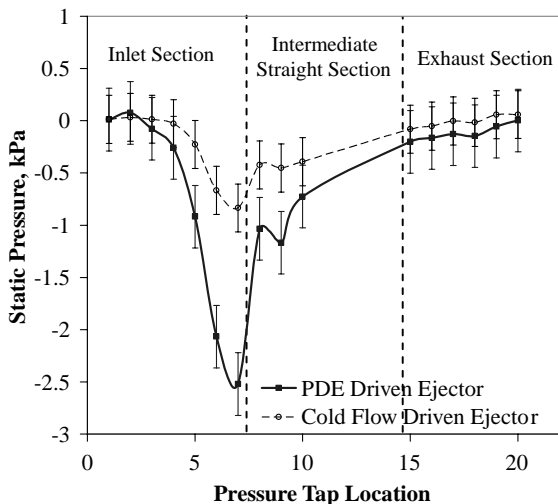


Fig. 4 Ejector surface pressure distribution. The configuration tested was a straight ejector with $x/D_{PDE} = +2$, and $ff = 1.0$.

visualizations were performed using a 2.54-cm-diam PDE operating at 20 Hz with a straight ejector. In the top row of images, the diffracting detonation wave with trailing vortex structure can be seen. In the bottom row, the vortex structure of the cold flow pulsation can be seen propagating toward the ejector. The time scales are clearly different for the two cases because the velocity of the cold

flow starting vortex is much lower than the detonation wave speed. The cold flow vortex is observed to increase in diameter at locations near the tube exit, but then attains a nearly constant diameter as it continues to travel forward. In contrast, the detonation-driven vortex structure exhibits rapid growth until it reaches the ejector inlet. It can also be observed that when the detonation-driven vortex reaches the ejector inlet, its diameter is noticeably larger than that of the cold flow vortex. These results are consistent with experimental unsteady ejector performance measurements which have shown that the optimum ejector-to-driver diameter ratio is larger for PDE-driven ejectors than for cold flow driven systems.

Portions of a complete PDE-driven ejector cycle are shown in Fig. 6. At a time of $111 \mu\text{s}$, the shock wave is observed to reflect and travel backward from the ejector inlet. The Mach disk structure present during the blowdown portion of the PDE cycle is visible near the ejector entrance at $148 \mu\text{s}$. In the image corresponding to $222 \mu\text{s}$, an interaction can be observed between the exhaust plume and the ejector inlet in the form of a vortical structure attached to the inlet lip. The image at $9065 \mu\text{s}$ was taken much later in the PDE cycle, when the shock and vortex structure are no longer present and the ejector is entraining flow into the inlet. The pattern of the entrained flow at this time during the cycle appears to show a clustering of the flow streamlines near the inner radius of the inlet, indicative of a higher velocity at this location. Furthermore, it appears that no significant amount of entrained flow is passing over the outer radius of the inlet. These observed trends are consistent with the straight ejector pressure distribution discussed above.

B. Diverging Ejector Surface Pressure Distribution

Previous PDE-driven ejector studies have found significant performance enhancement with the use of a diverging exhaust section. In some cases, thrust measurements indicated that the thrust augmentation of the diverging ejector was approximately 2 times that of the straight ejector.

Figure 7 compares the pressure distribution of a straight and a diverging ejector. Again, it must be emphasized that the measurement system employed does not capture the dynamic nature of the pressure field, but simply describes the time-averaged static pressure at each sensor location. It can be seen that the addition of the diverging exhaust section has a significant impact on the ejector inlet flowfield. The diverging ejector shows a vacuum pressure at tap 7 that is doubled in magnitude over that of the straight ejector. This increase in inlet suction represents additional flow entrainment which leads to an increase in thrust augmentation. Also of importance is the fact that the static pressure along the length of the diverging section is negative, rising to ambient conditions at the ejector exit. This suggests that the performance enhancement afforded by diverging ejectors is not due to a positive thrust force acting on the diverging section area. In fact, the diverging section actually creates a slight drag force due to the negative pressure acting on it. The role of the diverging section appears to be that of a subsonic diffuser, decreasing the flow velocity and increasing the static

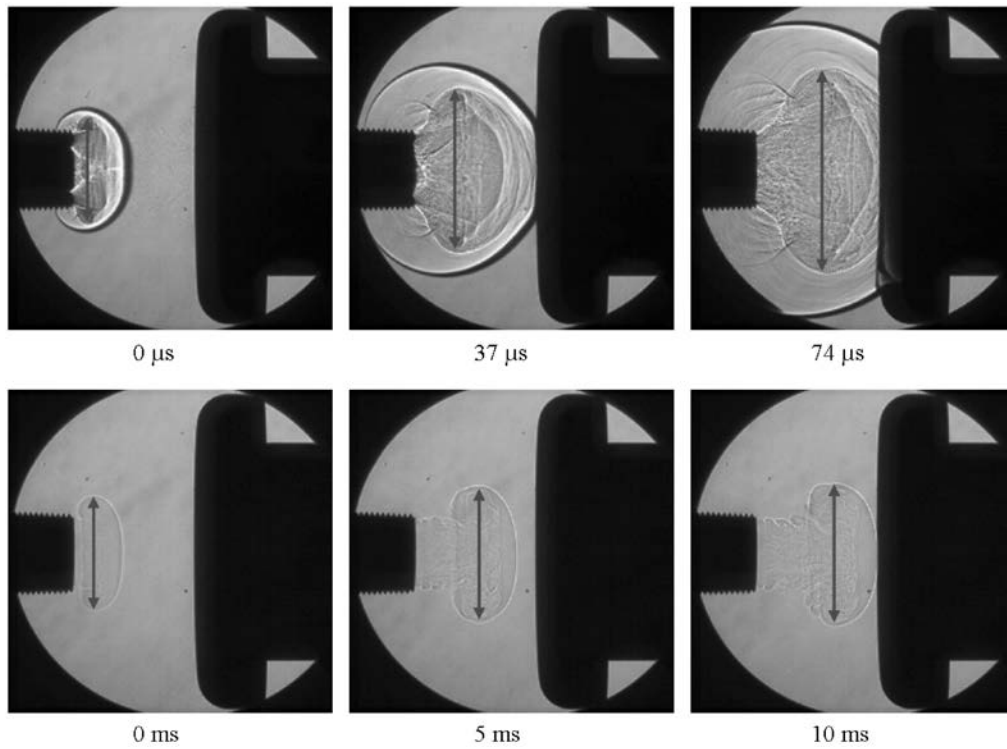


Fig. 5 Shadowgraph images comparing PDE-driven vortex ring (upper images) and cold flow starting vortex (lower images). $ff = 0.6$, $DR = 3$, and $x/D_{PDE} = +2$.

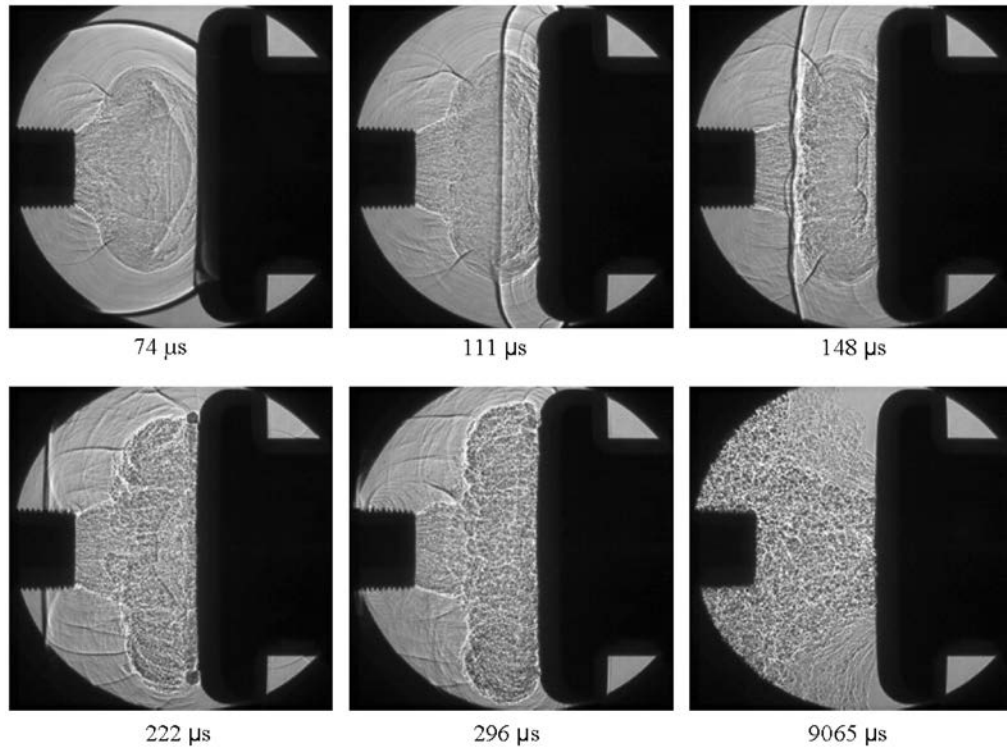


Fig. 6 Sequence of shadowgraph images taken during PDE-driven ejector operating cycle. $ff = 0.6$, $DR = 3$, and $x/D_{PDE} = +2$.

pressure in the exhaust section. Because the ejector exit-plane boundary condition is that ambient static pressure is achieved in the exhaust jet, the added pressure recovery through the diverging section makes it possible for a decreased inlet pressure to exist while the ejector exit boundary condition is still maintained. In prior experimental testing, the current intermediate straight-section length of $L_{STRAIGHT}/D_{EJECT} = 3$ was found to be near the optimum length. Either decreasing or increasing the straight-section length caused a

decrease in thrust augmentation. It is speculated that the flow mixing that takes place within the intermediate straight section is beneficial for conditioning the flow before it enters the diffuser. Without a sufficient amount of mixing, the velocity profile entering the diverging section may be prone to separation, causing increased diffuser pressure recovery losses. After the flow is sufficiently mixed, further increase of the straight-section length leads to increased frictional drag forces, and, in turn, decreased thrust augmentation.

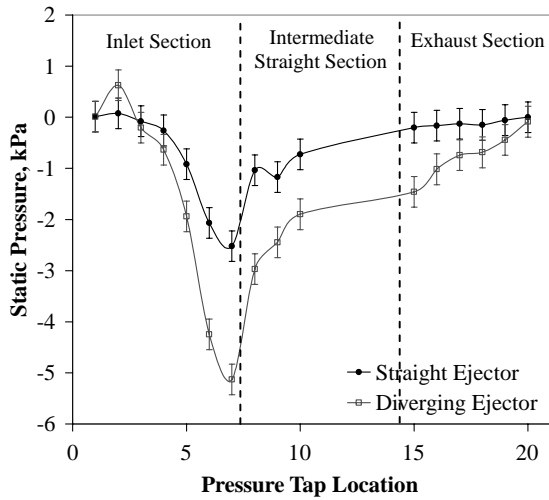


Fig. 7 Static pressure distribution in a straight and diverging ejector. $ff = 1.0$, and $x/D_{PDE} = +2$.

Integrating the pressure distribution over the diverging ejector surface geometry yields a calculated thrust augmentation of $\alpha = 50\%$, which is comparable to the thrust augmentation of $\alpha = 66\%$ obtained from direct thrust measurements.

C. Effect of Fill Fraction on Surface Pressure Distribution

Previous studies have shown an inverse relationship between thrust augmentation and the PDE fill fraction at downstream ejector placements [21,23]. For the diverging ejector geometry being considered, thrust augmentation was increased from $\alpha = 66\%$ to $\alpha = 74\%$ by decreasing the fill fraction from $ff = 1.0$ to $ff = 0.6$. Figure 8 shows that decreasing the fill fraction does not significantly alter the pressure distribution over the ejector surface. However, when the fill fraction is decreased, the baseline PDE thrust with no ejector installed decreases at a faster rate than the thrust produced by the ejector. Because thrust augmentation is defined as the change in thrust due to the ejector divided by the baseline PDE thrust, reducing the fill fraction leads to an increased thrust augmentation.

D. Effect of Ejector Axial Position on Surface Pressure Distribution

Ejector performance and internal flowfields have been observed to be sensitive to the axial position of the ejector inlet relative to the PDE tube exit [27]. In most cases, downstream ejector placement provides optimum levels of thrust augmentation [21–24]. For the straight and diverging ejector configurations previously tested by

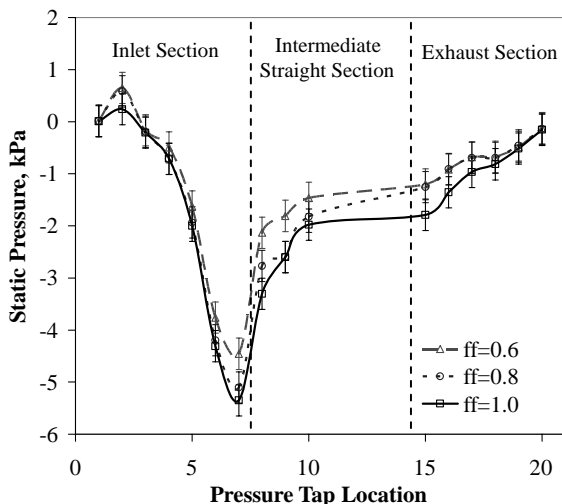


Fig. 8 Effect of the fill fraction on ejector pressure distribution. Ejector geometry is a diverging ejector with $x/D_{PDE} = +2$.

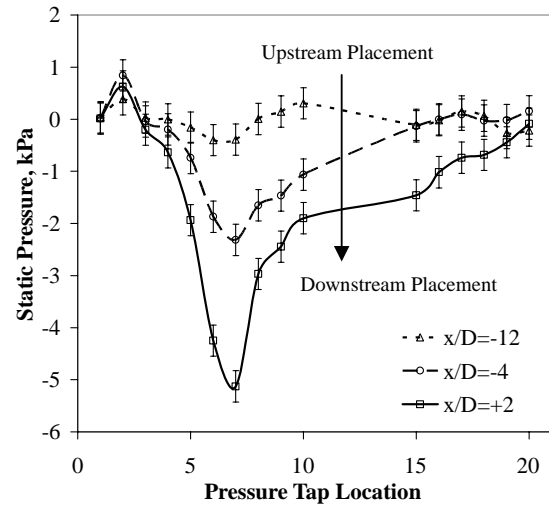


Fig. 9 Effect of axial position on static pressure distribution. Ejector geometry is a diverging ejector with $ff = 1.0$.

Glaser et al. [21], the optimum axial position was found to be $x/D_{PDE} = +2$. Figure 9 shows the effect of the axial position on the diverging ejector pressure distribution. It can be seen that as the ejector is moved upstream from $x/D_{PDE} = +2$, the magnitude of the inlet suction is increased. At the axial location of $x/D_{PDE} = -12$, it is observed from the pressure distribution that almost no flow is being entrained through the ejector, implying an augmentation near 0%. At this overlap position, a region of slightly positive pressure was also observed in the straight section at pressure tap 10. This overpressure is due to the presence of the detonation tube exit that is located within the ejector.

The axial position trend is more clearly evident in Fig. 10. In this figure static pressure data at tap 7 are plotted for all axial positions tested. The pressure at this location represented the minimum pressure on the inlet for nearly all cases studied and therefore was a good indicator of the amount of flow entrainment into the ejector for a given configuration. The tap 7 pressure data show a minimum pressure near $x/D_{PDE} = +2$, which is the optimum location for thrust augmentation determined through direct thrust measurements. Placements of the ejector at positions away from the optimum decrease the magnitude of the inlet vacuum pressure, which implies decreasing flow entrainment. Figure 11 shows the thrust augmentation calculated by integration of the ejector pressure distribution compared to that measured through direct thrust measurements. Using both techniques it can be seen that a maximum augmentation is found to occur at $x/D_{PDE} = +2$, the same position at which the minimum inlet pressure was measured. Although a

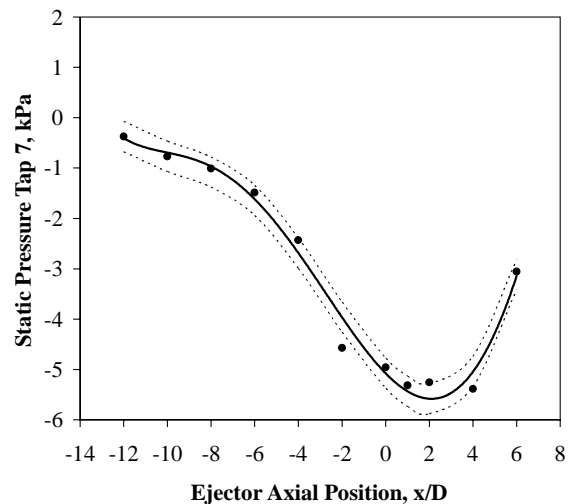


Fig. 10 Effect of axial position on ejector inlet suction.

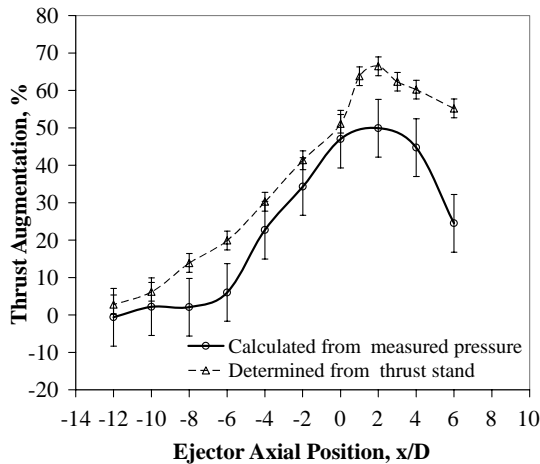


Fig. 11 Effect of ejector position on calculated thrust augmentation. Diverging ejector with $ff = 1.0$.

discrepancy is apparent in the relative magnitudes of thrust augmentation, the overall trend is unmistakable. It is believed that the inability of the integrated pressure distribution to capture the effect that the presence of the ejector has on the detonation tube flowfield is the source of this disparity. The increased blowdown cycle due to the downstream obstruction maintains a higher pressure on the thrust surface of the detonation tube compared to a system with no ejector present. As a result the calculated thrust augmentation based on ejector pressure measurements falls short of the measured thrust augmentation. However, the trend is apparent that placing the ejector upstream of the PDE exit decreases thrust augmentation, while the optimum ejector placement is downstream of the PDE tube exit. Beyond this optimum downstream placement thrust augmentation drops off at a rate similar to the rate of decrease with upstream placement.

IV. Conclusions

An experimental study was performed to investigate the operation of PDE-driven ejectors. To complete this work, both a straight and a diverging ejector were instrumented for static pressure measurements. Analysis of the straight ejector pressure distribution and shadowgraph images showed that a majority of the entrainment flow acceleration near the rounded inlet occurs at the inner inlet radius. This implies that the outer surface of the inlet is not significant in flow entrainment and thus does not need to be as carefully contoured as the inner section of the inlet. In addition it was found that the role of the diverging exhaust section is to act as a subsonic diffuser. The pressure recovery that takes place in this diffuser has a significant impact on the inlet pressure distribution, increasing the magnitude of the inlet vacuum pressure by a factor of 2. Furthermore, the reason for the inverse relationship between fill fraction and thrust augmentation was studied. It was found that the ejector pressure distribution is not very sensitive to the fill fraction. Finally, the axial placement of the ejector inlet relative to the PDE tube exit plane was studied in detail. By varying the axial position from $x/D_{PDE} = -12$ to $+6$, the axial location of the maximum inlet suction was found to be near $x/D_{PDE} = +2$. Moving the ejector farther upstream or downstream resulted in the inlet suction decreasing toward zero. Calculating the thrust augmentation based on integration of the pressure distribution showed a maximum at a position of $x/D_{PDE} = +2$, matching the optimum axial location for thrust augmentation as determined through direct thrust measurements. The observed trends are consistent with the optimum ejector placement being at a downstream location.

Acknowledgments

The authors would like to acknowledge the Propulsion Directorate at the U.S. Air Force Research Laboratory and Innovative Scientific

Solutions, Inc., (ISSI) for providing financial support for this work. The technical support of Curtis Rice of ISSI is also greatly appreciated, as is the assistance of Russell Dimicco of the Gas Dynamics and Propulsion Laboratory at the University of Cincinnati.

References

- [1] Kailasanath, K., "Review of Propulsion Applications of Detonation Waves," *AIAA Journal*, Vol. 38, No. 9, 2000, pp. 1698–1708. doi:10.2514/2.1156
- [2] Ma, F., Choi, J.-Y., and Yang, V., "Propulsive Performance of Airbreathing Pulse Detonation Engines," *Journal of Propulsion and Power*, Vol. 22, No. 6, 2006, pp. 1188–1203. doi:10.2514/1.21755
- [3] Schauer, F., Stutrud, J., Bradley, R., Katta, V., and Hoke, J., "Detonation Studies and Performance Results for a Research Pulse Detonation Engine," *Confined Detonation and Pulse Detonation Engines*, edited by G. Roy, S. Frolov, R. Santoro, and S. Tsyganov, Torus Press, Moscow, 2003, pp. 287–302.
- [4] Cooper, M., Jackson, S., Austin, J., Wintenberger, E., and Shepherd, J., "Direct Experimental Impulse Measurements for Detonations and Deflagrations," *Journal of Propulsion and Power*, Vol. 18, No. 5, 2002, pp. 1033–1041. doi:10.2514/2.6052
- [5] Zitoun, R., and Desbordes, D., "Propulsive Performance of Pulsed Detonations," *Combustion Science and Technology*, Vol. 144, No. 1, 1999, pp. 93–114. doi:10.1080/00102209908924199
- [6] Wintenberger, E., Austin, J., Cooper, M., Jackson, S., and Shepherd, J., "Analytical Model for the Impulse of Single-Cycle Pulse Detonation Tube," *Journal of Propulsion and Power*, Vol. 19, No. 1, 2003, pp. 22–38. doi:10.2514/2.6099
- [7] Wintenberger, E., and Shepherd, J., "Model for the Performance of Airbreathing Pulse-Detonation Engines," *Journal of Propulsion and Power*, Vol. 22, No. 3, 2006, pp. 593–602. doi:10.2514/1.5792
- [8] Ebrahimi, H., and Merkle, C., "Numerical Simulation of a Pulse Detonation Engine with Hydrogen Fuels," *Journal of Propulsion and Power*, Vol. 18, No. 5, 2002, pp. 1042–1048. doi:10.2514/2.6053
- [9] Li, C., and Kailasanath, K., "Partial Fuel Filling in Pulse Detonation Engines," *Journal of Propulsion and Power*, Vol. 19, No. 5, 2003, pp. 908–916. doi:10.2514/2.6183
- [10] Wu, Y., Ma, F., and Yang, V., "System Performance and Thermodynamic Cycle Analysis of Airbreathing Pulse Detonation Engines," *Journal of Propulsion and Power*, Vol. 19, No. 4, 2003, pp. 556–567. doi:10.2514/2.6166
- [11] Tangirala, V., Dean, A., Chapin, D., Pinard, P., and Varatharajan, B., "Pulsed Detonation Engine Processes: Experiments and Simulations," *Combustion Science and Technology*, Vol. 176, No. 10, 2004, pp. 1779–1808. doi:10.1080/00102200490487689
- [12] Viets, H., "Thrust Augmenting Ejector Analogy," *Journal of Aircraft*, Vol. 14, No. 4, 1977, pp. 409–411. doi:10.2514/3.44603
- [13] Keenan, J. H., Neumann, E. P., and Lustwerk, F., "An Investigation of Ejector Design by Analysis and Experiment," *Journal of Applied Mechanics*, Vol. 17, No. 3, 1950, pp. 299–309.
- [14] Quinn, B., "Ejector Performance at High Temperature and Pressures," *Journal of Aircraft*, Vol. 13, No. 12, 1976, pp. 948–954. doi:10.2514/3.44561
- [15] Quinn, B., "Compact Ejector Thrust Augmentation," *Journal of Aircraft*, Vol. 10, No. 8, 1973, pp. 481–486. doi:10.2514/3.60251
- [16] Arbel, A., Shklyar, A., Hershgal, D., Barak, M., and Sokolov, M., "Ejector Irreversibility Characteristics," *Journal of Fluids Engineering*, Vol. 125, No. 1, 2003, pp. 121–129. doi:10.1115/1.1523067
- [17] Kentfield, J., "Fundamentals of Idealized Airbreathing Pulse-Detonation Engines," *Journal of Propulsion and Power*, Vol. 18, No. 1, 2002, pp. 77–83. doi:10.2514/2.5900
- [18] Paxson, D., Wernet, M., and Wentworth, J., "Experimental Investigation of Unsteady Thrust Augmentation Using a Speaker-Driven Jet," *AIAA Journal*, Vol. 45, No. 3, 2007, pp. 607–614. doi:10.2514/1.18449

- [19] Lockwood, R., "Interim Summary Report on Investigation of the Process of Energy Transfer from an Intermittent Jet to Secondary Fluid in an Ejector-Type Thrust Augmenter," Hiller Aircraft Rept. No. ARD-286, March 1961.
- [20] Wilson, J., Sgondea, A., Paxson, D., and Rosenthal, B., "Parametric Investigation of Thrust Augmentation by Ejectors on a Pulse Detonation Tube," *Journal of Propulsion and Power*, Vol. 23, No. 1, 2007, pp. 108–115.
doi:10.2514/1.19670
- [21] Glaser, A., Caldwell, N., Gutmark, E., Hoke, J., Bradley, R., and Schauer, F., "Performance Measurements of Straight and Diverging Ejectors Integrated with a Pulse Detonation Engine," AIAA Paper 2006-1022, 2006 [*Combustion Science and Technology* (submitted for publication)].
- [22] Rasheed, A., Tangirala, V., Pinard, P., and Dean, A., "Experimental and Numerical Investigations of Ejectors for PDE Applications," AIAA Paper 2003-4971, 2003.
- [23] Allgood, D., and Gutmark, E., "Performance Measurements of Pulse Detonation Engine Ejectors," AIAA Paper 2005-0223, 2005.
- [24] Glaser, A., Caldwell, N., Gutmark, E., Hoke, J., Bradley, R., and Schauer, F., "Effects of Tube and Ejector Geometry on the Performance of Pulse Detonation Engine Driven Ejectors," AIAA Paper 2006-4790, 2006.
- [25] Canteins, G., Franzetti, F., Zocloniska, E., Khasainov, B., Zitoun, R., and Desbordes, D., "Experimental and Numerical Investigations on PDE Performance Augmentation by Means of an Ejector," *Shock Waves*, Vol. 15, No. 2, 2006, pp. 103–112.
doi:10.1007/s00193-006-0006-5
- [26] Shehadeh, R., Saretto, S., Lee, S., Pal, S., and Santoro, R., "Experimental Study of a Pulse Detonation Engine Driven Ejector," AIAA Paper 2003-4972, 2003.
- [27] Allgood, D., Gutmark, E., Rasheed, A., and Dean, A., "Experimental Investigation of a Pulse Detonation Engine with a Two-Dimensional Ejector," *AIAA Journal*, Vol. 43, No. 2, 2005, pp. 390–398.
doi:10.2514/1.8125
- [28] Wilson, J., "Effect of Pulse Length and Ejector Radius on Unsteady Ejector Performance," *Journal of Propulsion and Power*, Vol. 23, No. 2, 2007, pp. 345–352.
doi:10.2514/1.19665

J. Powers
Associate Editor




A Flight Ready Pulsed Detonation Engine

9 March 2004




2dLt Paul J. Litke, AFRL/PRTC
Royce P. Bradley, ISSI
Dr. John L. Hoke, ISSI
Dr. Fred Schauer, AFRL/PRTC



Program Mechanism

In-house PR technology with VA's flight research experience




AFRL/PR
Dr. Fred Schauer
2dLt Paul J. Litke
Jeff Stutrud

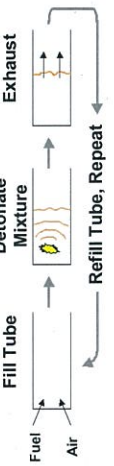
AFRL/VA
Leonard Shaw
Tom Presdorf
Ed Pendleton P.E
Michael Camden
Dr. Larry Byrd P.E

ISSI
Dr. John L. Hoke
Royce P. Bradley

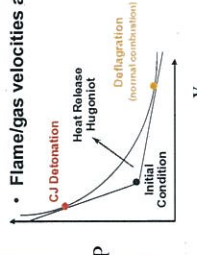
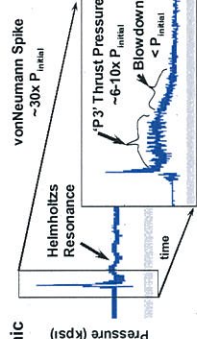
Additional Support
AFOSR, HE, ML




What is a PDE / Detonation?




- Detonation is one of two stable solutions to the combustion equations
- Temperatures typically 40% hotter than deflagration ('normal combustion')
- Most violent thing you can do with a given fuel-oxidizer mixture (worse than explosion)
- Flame/gas velocities are supersonic








P51D with Pulsejets

Experimental Aircraft at WPAFB post-WWII







- Ford copy of German Argus AS014 pulsejet
- 1,800 lb thrust
- Cost \$1,600



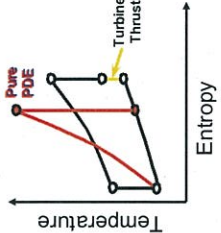
- Rolls-Royce V1650
- 1,695 hp
- Cost \$25,000




Why PDE's




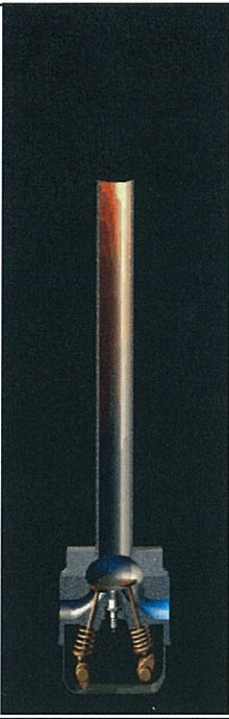
- Increased Efficiency
- High Impulse, Thrust
- Simple, Lightweight
- Very Low Cost
- Highly Scalable
 - multiple tubes
 - tube size
 - operating frequency
- Durability/manufacturability
- Single-cycle covers Mach 0-4+
- Good supersonic performance





Research Pulsed Detonation Engine Cycle







- Automotive cylinder head used for valving
- Low cost
- Flexible and durable

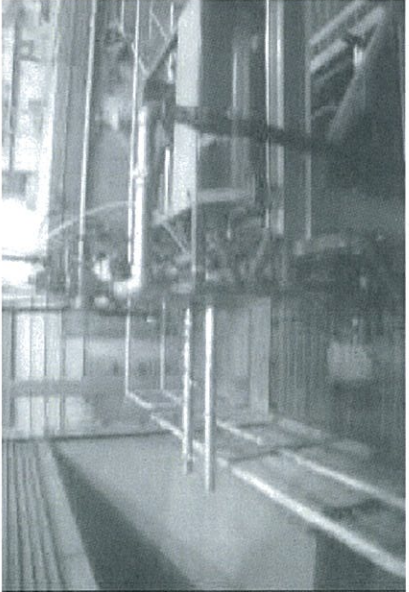
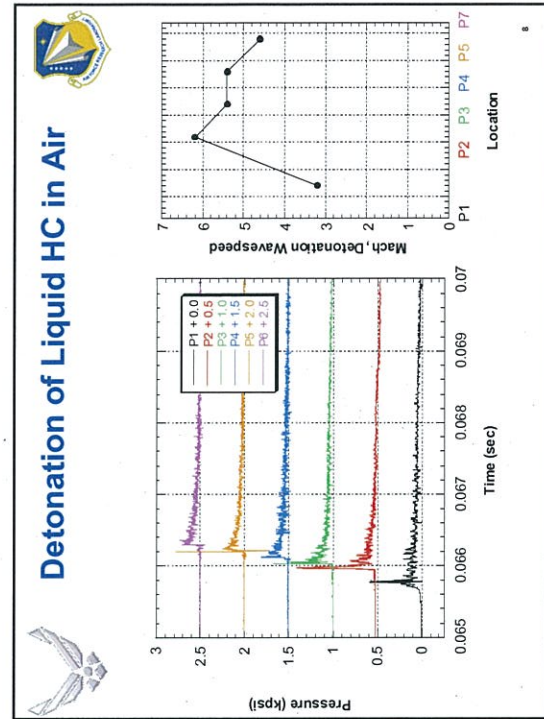
Cycle


- Intake valve - premixed fuel & air (green)
- Detonation and blow down (red/orange)
- Exhaust valve – purge cycle (blue)



Research PDE







Why Fly


9

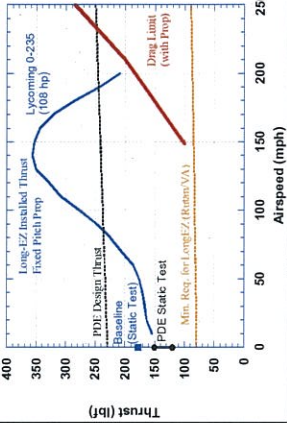


+




=






- Prove system is viable
- Long run times
- Unsteady Inlet
- Practical fuel
- No Oxygen Enrichment
- Static and subsonic operation
- Acoustic and Structural Issues
- Flight weight tubes
- Thermal Issues




Pulsed Detonation Powered Experimental Aircraft Selection


10

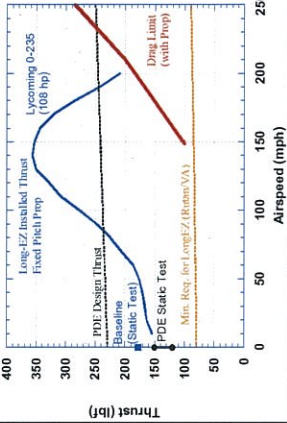


+



=





- PDE needed a pusher-configuration airframe
- Need approval to operate with an experimental propulsion system
- Need test pilots familiar with the selected airframe



PDE Flight Program Test Pilots

11



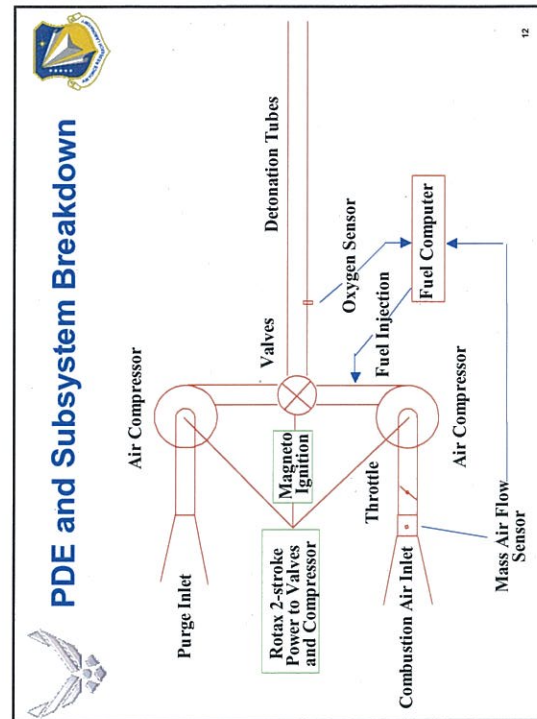
Burt Rutan





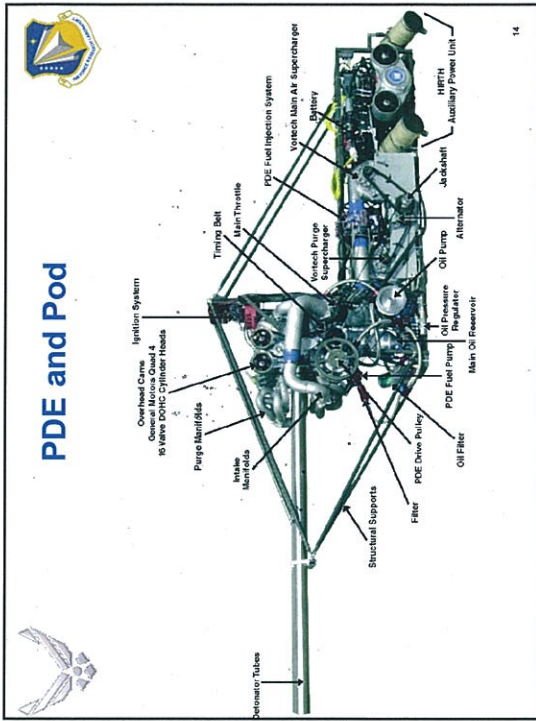
Mike Melvill

- ~5000 flight hours experience among Scaled test pilots with this platform
- 6 Flight test programs of different natures using this platform
 - Piston, Turbofan, now PDE propulsion systems
 - Technology testbed programs
 - Gross weights qualified to 3g/1800 lb/180kt; takeoff weights to 2200 lb+
 - No accidents or incidents
- Contractor-Run Commercial Flight Test Environment
- FAA Experimental R&D Airworthiness Certificate
- Standard for All Scaled Flight Test Programs Since 1982 (More than 30 test programs – no accidents)

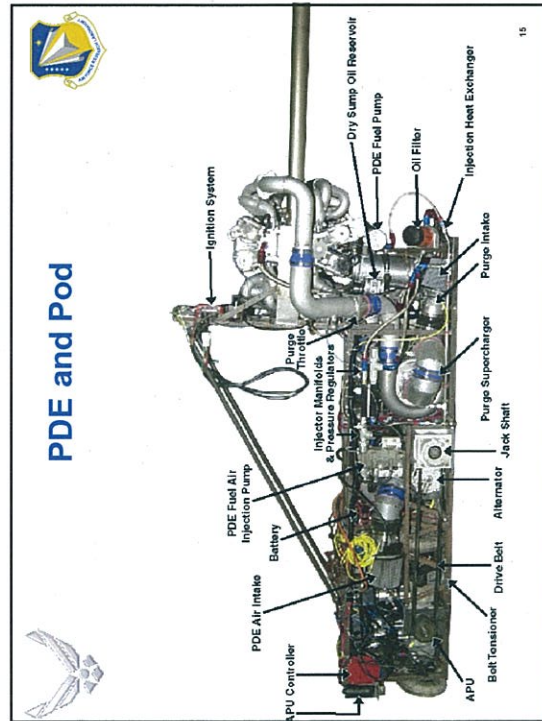




Flight Engine Development on Test Stand



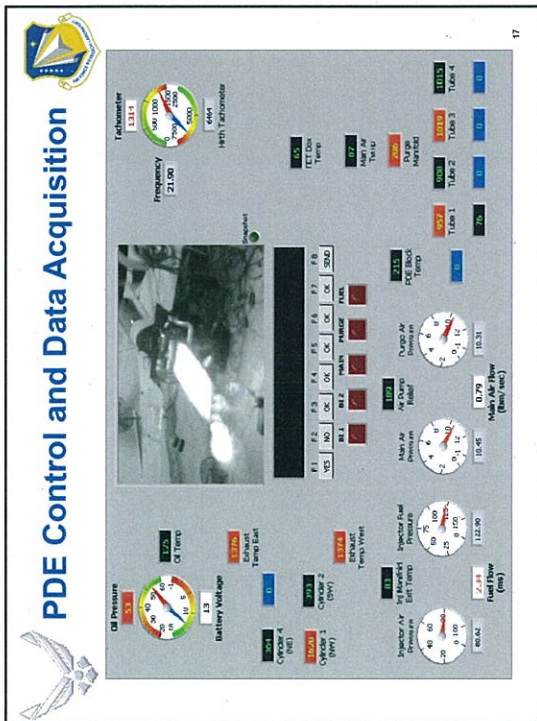
PDE and Pod



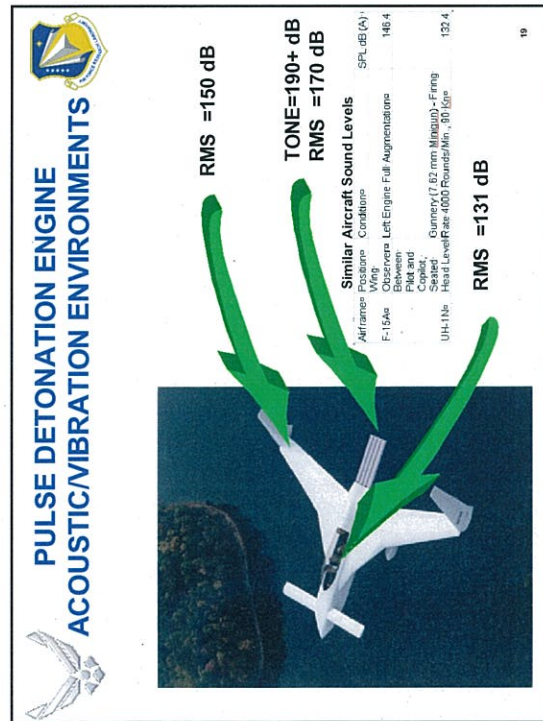
PDE and Pod



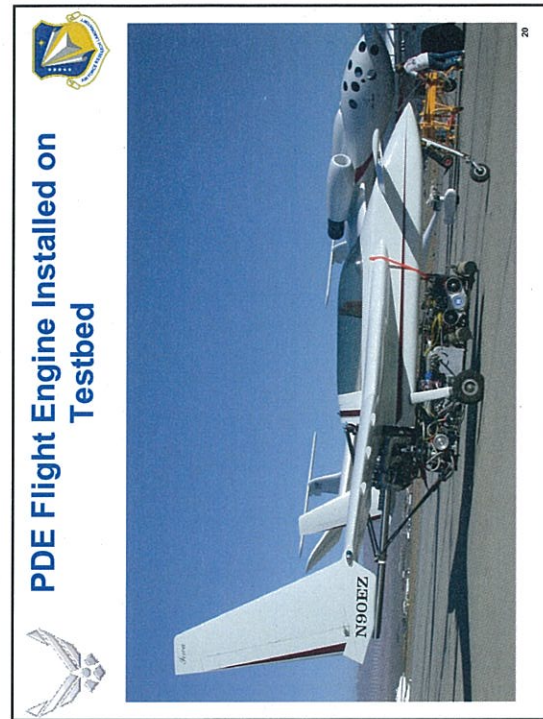
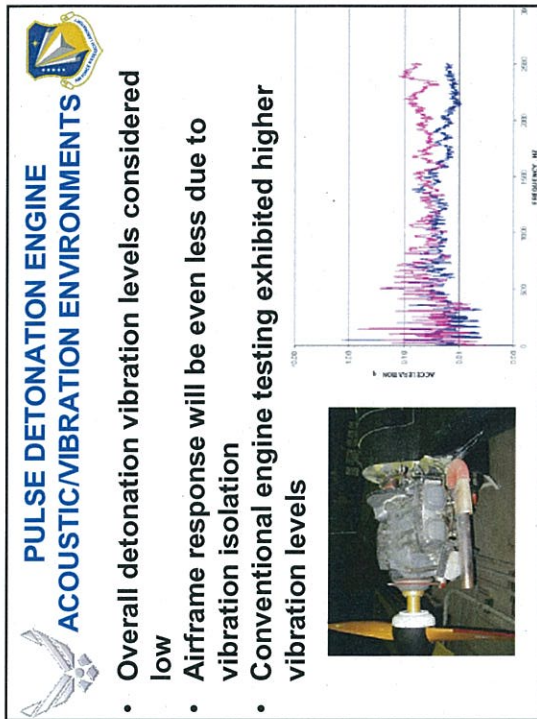
Flight Engine - Ground Test
Vibration, Acoustics, Structure Endurance Testing




17




19





20



PDE Flight Program Milestones



- ✓ PDE Engine Endurance Testing
- ✓ Structural/Acoustic Trials
- ✓ FAA Certification
- ✓ AF Safety Review Board
- ✓ Final PDE Engine Installation

Ground Testing (begins this week in Mojave)

Taxi Tests (upon completion of the ground tests)

First Ever PDE Powered Flight



Questions and Comments





Pulse Power

Pulse detonation engine-powered flight demonstration marks milestone in Mojave

GUY NORRIS/LOS ANGELES

U.S. Air Force researchers will push for more development funding for pulse detonation engines (PDEs) following the successful first-ever manned demonstration flight of an aircraft powered by the exotic propulsion system.

The milestone flight was accomplished at Mojave, Calif., on Jan. 31 when Scaled Composites test pilot Pete Siebold flew a heavily modified Long-EZ above the main runway in straight-and-level flight at altitudes up to 100

sources for commercial and military gas turbines. In its simplest form, the PDE is an air-breathing engine with few or no moving parts. Combustion takes place in an open-ended tube in which fuel is mixed with air and detonated. The detonation wave travels down the tube at supersonic speed, generating thrust and, at the same time, reducing inlet pressure to allow fresh air and fuel to be drawn in. Each pulse lasts milliseconds.

The AFRL's prototype "off-the-shelf"


at around 75 kt. during his one-way run down Mojave's 12,500-ft.-long Runway 12. Getting to grips with the unusual aircraft and its handling characteristics, Siebold encountered a "bit of Dutch roll, but corrected it by yawing," says Hoke, who adds that "we were planning on flying at around 25 ft., but as a result he ended up between 60 and 100 ft. above the runway." Siebold then "cruised for about 10 sec. using PDE power alone, and he thought he could have climbed using the engine."

Engine noise levels were substantial but very directional and safe from the cockpit, says Hoke, who adds that at ground level close by the aircraft, "you could feel your chest pound a bit—but it wasn't bad at all." Despite the acoustic levels at the tube exit being in the 195-200-dB. range, "there were no issues at all" with structural response. Hoke says "people wouldn't want to be directly behind it, but then what jet engine would anyone want to be standing behind?"

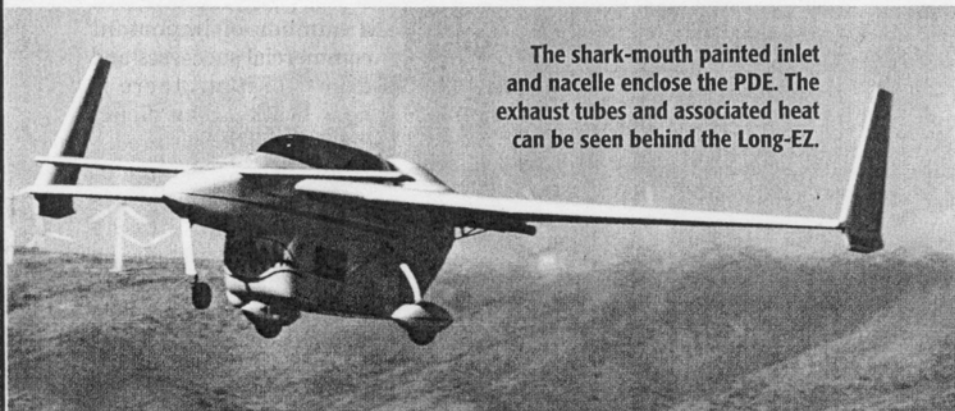
The flight also marked the success of several design changes and modifications made to overcome problems that prevented a flight test as far back as 2003 and early 2004. These included a change in fuel to improve the fuel-air mix detonation characteristics at the relatively lower atmospheric pressures found at Mojave's 2,800-ft. altitude.

"We switched from avgas [aviation gasoline, a high-octane fuel] to propane, which is easier to detonate," says Hoke. His recent work in hydrogen and hydrocarbon ignition at AFRL with PDE pioneer Fred Schauer compared the ignition and detonation performance of hydrogen, ethylene, propane, avgas, JP-8 and Fischer-Tropsch JP-8 (S-8). Hydrogen was found to have the best characteristics, followed by ethylene, propane, avgas, JP-8 and S-8.

Other changes included the addition of a fairing over the PDE to reduce vehicle drag, the fairing having originally been omitted owing to concerns over fuel leaks in earlier attempts, and changes in configuration to prevent exhaust from the Hirth motor being sucked into the PDE inlet.

Although there are no immediate plans for more flight tests, Hoke says fundamental research will continue. The demonstration will "hopefully be a springboard for more interest and funding," he adds. "As little as 10-20 years ago no one could even detonate these hydrocarbon-air mixtures, and hopefully developments like this will lead to a revolution of technology where it will be used, perhaps as a combustor." 

The shark-mouth painted inlet and nacelle enclose the PDE. The exhaust tubes and associated heat can be seen behind the Long-EZ.



MIKE HILL/SCALED COMPOSITES

ft. powered solely by the PDE. The engine was developed at the Air Force Research Laboratory (AFRL) by the on-site contractor, Innovative Scientific Solutions. At peak thrust at the start of the run, the PDE was producing more than 200 lb. thrust, says ISS research engineer John Hoke.

The prime objectives of the AFRL/ISS demonstration were to show that the PDE could be used to power an aircraft, the aircraft structure could survive the acoustic pressure of the Mach 5 shock waves exiting the detonation tubes, and that the noise level was not prohibitive for a manned flight. The test also sought to assess the durability of the detonation engine, which had already undergone more than 100 hr. of ground testing, plus a further 30 hr. on the integrated system.

The demonstration comes amid growing interest in the potential of PDEs for a range of simple, cost-effective missile propulsion systems, as well as in the possible development of combustion

PDE has been installed in a Scaled Composites-owned Long-EZ for the flight tests, and replaces a 100-hp. Textron Lycoming O-235 piston engine driving a pusher propeller. The PDE system, integrated into the Long-EZ by Scaled Composites crew chief Rick Aldrich, includes a JATO rocket-assist pack that provides a few seconds of additional thrust to shorten the takeoff run.

The propulsion system consists of a Hirth-built two-stroke auxiliary power unit that controls the valves and compressors in the PDE, which is based on a heavily modified General Motors Pontiac Grand Am Quad 4, 16-valve dual overhead camshaft automotive engine. The detonation takes place in four tubes projecting from the back of the aircraft, and is designed to generate a mass flow of up to 1.6 lb./sec. to produce a combined force of roughly 150-200 lb. thrust for flight speeds of up to 130 kt. In the AFRL engine, the PDE fires at a frequency of around 80 Hz.

Assisted by the JATO, Siebold took off

First flight for PDE = pretty darned extraordinary

Graham Warwick (Flight International, February 29, 2008)

It's not every day a new form of propulsion makes its first flight: the turbojet in August 1939 (Heinkel He178), the ramjet in April 1949 (Leduc 010), the scramjet in July 2002 (University of Queensland HyShot). Now it's the turn of the [pulsed detonation engine \(PDE\)](#) - a simple, lightweight powerplant that promises efficient operation over a wide range of speeds from 0 to Mach 4.

In a PDE, combustion is supersonic (detonation) rather than subsonic (deflagration), resulting in the more efficient conversion of fuel into thrust. PDEs have few moving parts. A fuel/air mixture is injected into a tube and ignited, creating a supersonic detonation wave that travels down the tube and is expelled, producing a pulse of thrust. Grouping several tubes together and firing each many times a second produces constant thrust.



It's taken a few years longer than planned, but the [US Air Force Research Laboratory](#) and partners [ISSI](#) and [Scaled Composites](#) finally accomplished the first PDE-powered flight in late January. The modified Long-EZ was powered by a four-tube PDE, each tube firing 20 times a second, producing 200lb peak thrust. The flight was short, just a few tens of seconds, taking place within the length of the Mojave runway, but it was a first.



(Pictures by Alan Radecki)

Aircraft



DATE:05/03/08

US AFRL proves pulse-detonation engine can power aircraft

By Graham Warwick

[Click here](#)

Researchers hope the first flight of an aircraft powered by a [pulse detonation engine \(PDE\)](#) will accelerate development of a propulsion concept that promises greater simplicity, lighter weight and a wider operating range than turbomachinery.

In late January, an experimental engine developed at the [US Air Force Research Laboratory \(AFRL\)](#) powered a modified [Scaled Composites](#) Long-EZ on a brief flight along the runway at Mojave, California, marking the first flight of a PDE-powered aircraft.

AFRL principal investigator Fred Schauer says the single flight, lasting "tens of seconds", proved the aircraft and its pilot could survive the noise and vibration of the PDE - concerns raised by an engine that delivers its thrust in pulses produced by the supersonic detonation of fuel and air in a tube.



Small JATO gas turbine helped Long-EZ get moving

© Alan Radecki

The experimental PDE, built by AFRL contractor [ISSI](#), had four tubes, each firing at 20Hz. Producing a peak thrust of about 200lb (0.9kN), the engine powered the Long-EZ to just over 100kt (190km/h) at 60-100ft (20-30m) above the Mojave runway.

Schauer says the flight proved the structure could survive the Mach 5 pulses and that noise was "reasonable" in the cockpit. With the PDE running at 80Hz, noise was low frequency, sounding like an "engine brake on steroids", he says.

Scaled test pilot Pete Siebold wore specially developed earplugs. Vibration was mitigated by tuning the engine mounts to the operating frequency, Schauer says.



PDE-powered cruise lasted about 10 seconds

January's flight followed aircraft and engine modifications after an unsuccessful attempt to fly in 2004. In particular, Scaled designed a fairing for the engine to reduce drag, while the fuel was switched from gasoline to propane to broaden the PDE's operating limits and increase its thrust.

Built using off-the-shelf parts, the experimental PDE "was just a proof of concept", says Schauer. The cylinder head from an automotive engine provided valves to admit first purge air then the fuel/air mixture into each tube, dual superchargers overcoming the pressure drop across the valves. A spark plug ignited subsonic combustion in the tube, which accelerated into the supersonic detonation wave.



"The engine is old technology. Now we have better initiation techniques, better valving, better injection schemes," says Schauer. Research continues within AFRL, but he expects the engine manufacturers to be next to fly a PDE. "We have shown the technical hurdles can be overcome," he says.